

Cover Picture

Woo Lee,* Roland Scholz, Kornelius Nielsch, and Ulrich Gösele

Uniform arrays of metallic nanotubes can be prepared with a newly developed electrochemical method. In their Communication on page 6050 ff., W. Lee et al. report the preparation of multisegmented metallic nanotubes with a bimetallic stacking configuration along the nanotube axis. The approach is based on the preferential electrodeposition of metal along the pore walls of anodic alumina membranes in the presence of metallic nanoparticles on the nanochannel surfaces.



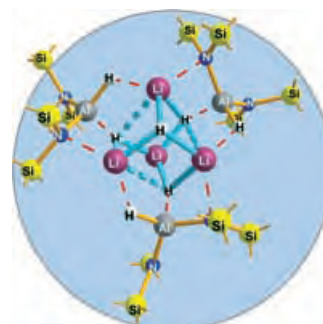
Nobel Lectures

Ubiquitin-mediated protein degradation is the focus of this year's Nobel Lectures by Irwin Rose, Avram Herskho, and Aaron Ciechanover. The prizewinners report first-hand in three Reviews on page 5926 ff.



Lithium Hydride

A Li_4H_4 cube coordinated by three bis(amino)alane units is reported by M. Veith et al. in their Communication on page 5968 ff. The compound was isolated and characterized by X-ray crystallographic analysis.



Triple Bonds with Ge

The first compounds with the structural unit $\{\text{M}\equiv\text{Ge}-\text{Ge}\equiv\text{M}\}$, in which a Ge_2 unit is bound between two transition-metal centers through triple bonds, is described by A. C. Filippou et al. on page 5979 ff. The $\text{M}\equiv\text{Ge}$ bonds are weakly conjugated within the linear chain.





The following Communications have been judged by at least two referees to be “very important papers” and will be published online at www.angewandte.org soon:

Sheereen Majid, Michael Mayer*

Hydrogel-Stamping of Arrays of Supported Lipid Bilayers with Various Lipid Compositions for Screening of Drug–Membrane and Protein–Membrane Interactions

Yoshitaka Ishibashi, Yuhki Bessho, Masahiro Yoshimura, Masaki Tsukamoto, Masato Kitamura*

Origin of the Minor Enantiomeric Product in a Noyori Asymmetric Hydrogenation

Holger Braunschweig,* Thomas Herbst, Daniela Rais, Fabian Seeler
Synthesis of Borirenes by Photochemical Borylene Transfer from $[(OC)_5M=BN(SiMe_3)_2]$ ($M = Cr, Mo$) to Alkynes

Y. Andrew Yang, Huimeng Wu, K. R. Williams, Y. Charles Cao*
Synthesis of CdSe and CdTe Nanocrystals without Precursor Injection

Masayuki Nihei, Mayumi Ui, Mizuho Yokota, Lingqin Han, Atsushi Maeda, Hideo Kishida, Hiroshi Okamoto, Hiroki Oshio*
Two-Step Spin Conversion in a Cyanide-Bridged Ferrous Square

Sean F. Brady,* Jon Clardy
Cloning and Heterologous Expression of Isonitrile Biosynthetic Genes from Environmental DNA

Meeting Review

EUCHEM: Nanoscale Surface Self-Assembly

H. Möhwald _____ 5920

Books

Applied Surfactants

Tharwat F. Tadros

reviewed by J. B. F. N. Engberts _____ 5922

Magnetism: Molecules to Materials V

Joel S. Miller, Marc Drillon

reviewed by W. Plass _____ 5922

Reviews

Protein Breakdown

I. Rose* _____ 5927 – 5931

Ubiquitin at Fox Chase (Nobel Lecture)

Protein breakdown is an exact, controlled process in which the protein molecule ubiquitin plays a decisive role by binding to a protein and labeling it for breakdown. The cellular mechanisms of this process

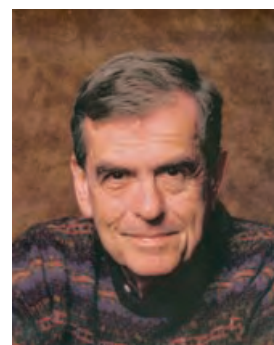
are widely known today thanks to the work of the 2004 Nobel Laureates Irwin Rose, Avram Hershko, and Aaron Ciechanover. The Laureates report at first hand in their Nobel Lectures.

A. Hershko* _____ 5932 – 5943

The Ubiquitin System for Protein Degradation and Some of Its Roles in the Control of the Cell-Division Cycle (Nobel Lecture)

A. Ciechanover* _____ 5944 – 5967

Intracellular Protein Degradation: From a Vague Idea, through the Lysosome and the Ubiquitin–Proteasome System, and onto Human Diseases and Drug Targeting (Nobel Lecture)



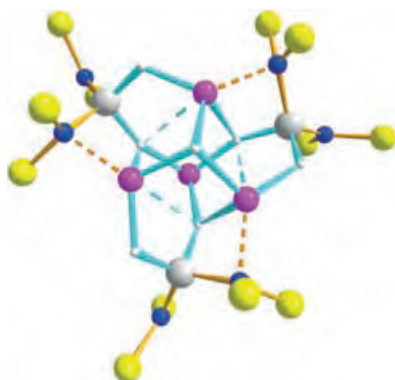
Communications

Lithium Hydride



M. Veith,* P. König, A. Rammo,
V. Huch _____ 5968 – 5971

Cubane-Like Li_4H_4 and $\text{Li}_3\text{H}_3\text{Li}(\text{OH})$:
Stabilized in Molecular Adducts with
Alanes

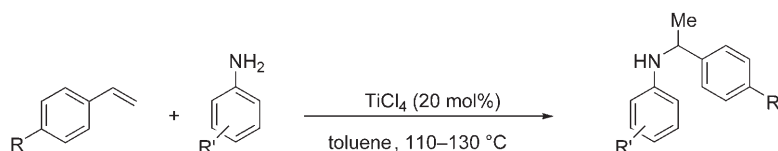


One in seven: A Li_4H_4 unit that is coordinated with three bis(amino)alane units takes the form of a cube; the compound was isolated in molecular form and characterized by X-ray analysis (see molecular structure; pink Li, blue N, gray Al, white H, yellow Si). During the reaction of this molecule with an equimolar amount of water only one of the seven H atoms reacts to give the hydrolysis product $\text{Li}_4\text{H}_3(\text{OH})[\text{HA}(\text{N}(\text{SiMe}_3))_2]_3$.

Hydroamination

L. T. Kaspar, B. Fingerhut,
L. Ackermann* _____ 5972 – 5974

Titanium-Catalyzed Intermolecular
Hydroamination of Vinylarenes



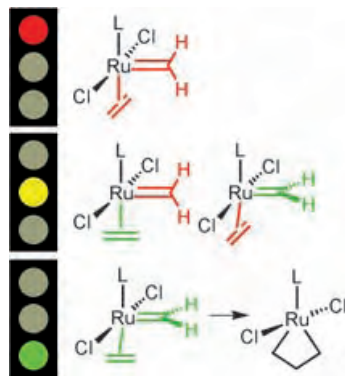
The Lewis acid TiCl_4 allows the intermolecular hydroamination of vinylarenes (see scheme). Some of the hydroamination products undergo rearrangements to give *ortho*-alkylated compounds. The catalyst

tolerates a range of functional groups ($\text{R}' = \text{CF}_3$, Cl, CN, F, Br) and provides the products in good yields. This method was also applied to the synthesis of a tetrahydroisoquinoline derivative.

Homogeneous Catalysis

B. F. Straub* _____ 5974 – 5978

Origin of the High Activity of Second-
Generation Grubbs Catalysts



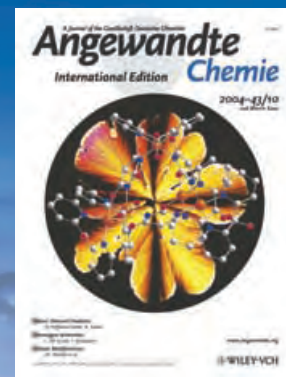
Green light for alkene metathesis: A strong σ -donor ligand L favors the active conformation (green in the scheme) of the carbene ligand in the ruthenium complex and thus leads to high catalytic activity of the second-generation Grubbs catalysts.

For the USA and Canada:
ANGEWANDTE CHEMIE International
Edition (ISSN 1433-7851) is published weekly
by Wiley-VCH PO Box 191161, D 69451 Wein-
heim, Germany. Air freight and mailing in the
USA by Publications Expediting Inc. 200
Meacham Ave., Elmont, NY 11003. Periodicals

postage paid at Jamaica NY 11431. US POST-
MASTER: send address changes to *Angewandte
Chemie*, Wiley-VCH, 111 River Street, Hoboken,
NJ 07030. Annual subscription price for insti-
tutions: US\$ 4948.00/4498.00 (valid for print
and electronic / print or electronic delivery); for
individuals who are personal members of a

national chemical society, or whose institution
already subscribes, or who are retired or self-
employed consultants, print only: US\$ 394.00.
Postage and handling charges included. All
Wiley-VCH prices are exclusive VAT.

The best in chemistry – for more than a hundred years



A Journal of the Gesellschaft Deutscher Chemiker
Angewandte
International Edition **Chemie**

www.angewandte.org

1888: The beginning
of a success story

Constant Innovations

- 1962:** First issue of the International Edition
- 1976:** Graphical abstracts
- 1979:** Cover pictures
- 1988:** Centenary of Angewandte
- 1989:** Routine use of color
- 1991:** New section: Highlights
- 1992:** Computerized editorial tracking system
- 1995:** Internet service for readers
- 1998:** Regular press service; full-text online
- 2000:** New section: Essays; EarlyView: Communications available online ahead of the printed version
- 2001:** New section: Minireviews
- 2002:** Online submission of manuscripts
- 2003:** Weekly publication; new section: News; new layout
- 2004:** Backfiles (1962-1997); ManuscriptXpress: Online system for authors and referees



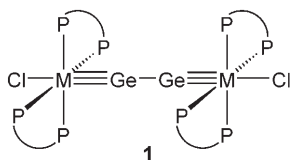
Angewandte's advisors...

Jean-Marie Lehn
Université Strasbourg
Collège de France

» **Angewandte Chemie** provides timely reviews of great depth and wide interest together with short reports of top quality frontier research. Creative work remains creative wherever it is published! However, **Angewandte Chemie** brings high visibility while keeping restraint and rigor. Finally, it is also supranational, as science is. «

Angewandte Chemie International Edition is
a journal of the German Chemical Society (GDCh)





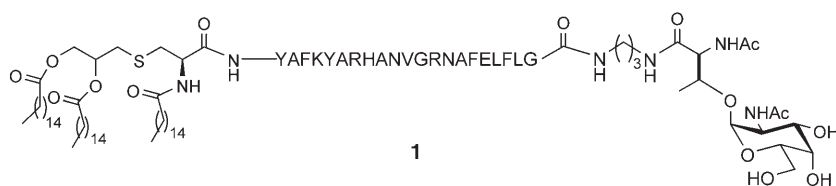
Going straight: Thermolysis of the germylidyne complexes $trans-[Cl(depe)_2M\equiv Ge(\eta^1-Cp^*)]$ ($M = Mo, W$; $depe = Et_2PCH_2CH_2PEt_2$, $Cp^* = C_5Me_5$) leads upon cleavage of the $Ge-Cp^*$ bond to **1**, the first compounds in which a Ge_2 unit is trapped between two transition-metal centers by triple bonds. Quantum chemical analyses suggest a weak conjugation of the $M-Ge$ triple bonds in the linear chain $M\equiv Ge-Ge\equiv M$.

Germanium Complexes



A. C. Filippou,* G. Schnakenburg,
A. I. Philippopoulos,
N. Weidemann ————— **5979 – 5985**

Ge_2 Trapped by Triple Bonds between Two Metal Centers: The Germylidyne Complexes $trans,trans-[Cl(depe)_2M\equiv Ge-Ge\equiv M(depe)_2Cl]$ ($M = Mo, W$) and Bonding Analyses of the $M\equiv Ge-Ge\equiv M$ Chain



A spoonful of sugar ... A carbohydrate-based fully synthetic vaccine **1**, composed of a tumor-associated Tn antigen, a peptide T epitope, and a lipopeptide (see structure), shows potential as a candidate

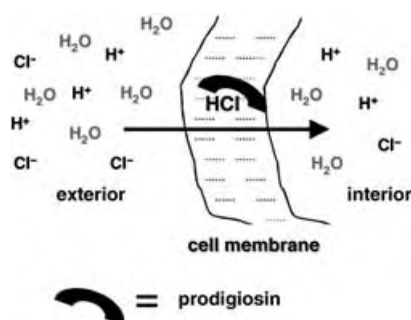
against cancer. Incorporation of the glycolipopeptide into liposomes gave a formulation that was able to elicit a T cell dependent antibody response in mice.

Biochemistry



T. Buskas, S. Ingale,
G.-J. Boons* ————— **5985 – 5988**

Towards a Fully Synthetic Carbohydrate-Based Anticancer Vaccine: Synthesis and Immunological Evaluation of a Lipidated Glycopeptide Containing the Tumor-Associated Tn Antigen



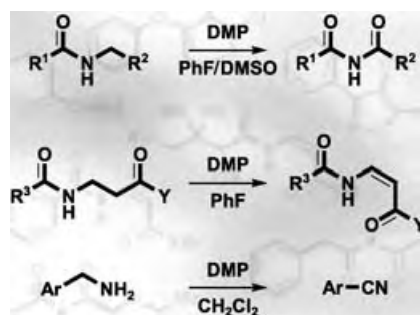
Pro and anti: Recognition of chloride ion and through-membrane H^+/Cl^- ion transport ("symport") could account for the biological effects (anticancer activity) of prodigiosin, as inferred from model studies involving pyrrole-based anion receptors designed to mimic the key features of this naturally occurring pigment (see picture).

Ion Transport

J. L. Sessler,* L. R. Eller, W.-S. Cho,
S. Nicolaou, A. Aguilar, J. T. Lee,
V. M. Lynch, D. J. Magda* — **5989 – 5992**

Synthesis, Anion-Binding Properties, and In Vitro Anticancer Activity of Prodigiosin Analogues

Expanding our synthetic tool repertoire: The DMP-mediated oxidation of a range of amide substrates has been demonstrated, affording the corresponding imides and *N*-acyl vinylogous carbamates and ureas. Likewise, an array of benzylic and related amines have also been successfully converted into their nitrile counterparts (see scheme; DMP = Dess–Martin periodinane).



Oxidations

K. C. Nicolaou,*
C. J. N. Mathison ————— **5992 – 5997**

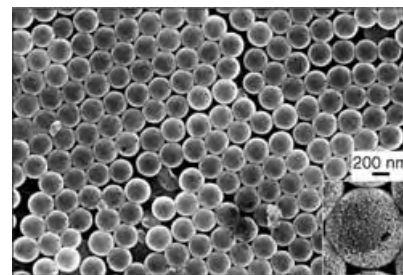
Synthesis of Imides, *N*-Acyl Vinylogous Carbamates and Ureas, and Nitriles by Oxidation of Amides and Amines with Dess–Martin Periodinane

Porous Materials

L. Lu, R. Capek, A. Kornowski, N. Gaponik, A. Eychmüller* — 5997 – 6001

Selective Fabrication of Ordered Bimetallic Nanostructures with Hierarchical Porosity

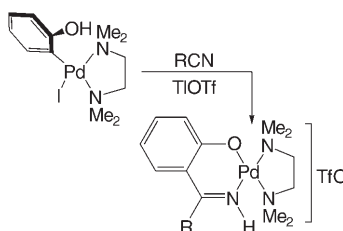
Space program: A general template technique has been developed that enables various Au/Pt nanostructures, such as macroporous 3D films and nanostructures constructed from hollow spheres, to be prepared on silicon wafers and glass substrates (see SEM image). These ordered metallic nanostructures with hierarchical porosity could be useful in industrial applications, including catalytic nanoreactors, sensors, porous electrodes, and fuel cells.



Insertion Reactions

J. Vicente,* J. A. Abad, M.-J. López-Sáez, P. G. Jones — 6001 – 6004

Reactivity of *ortho*-Palladated Phenol Derivatives with Unsaturated Molecules: Insertion of Nitriles into a Late-Transition-Metal–Carbon Bond



Helpful neighbors: $[\text{Pd}\{2-(\text{OH})\text{C}_6\text{H}_4\}\text{I}-(\text{tmeda})]$ reacts at room temperature with excess RCN ($\text{R} = \text{Me}, \text{C}_6\text{F}_5, \text{CH}_2=\text{CH}$) and TfOTf (1 equiv) to give $[\text{Pd}\{1\text{-O-2-[C(R)=NH]C}_6\text{H}_4\text{-}\kappa^2\text{-O,N}\}(\text{tmeda})]\text{OTf}$ (see scheme). The proximal OH group plays a crucial role in this first example of the insertion of a nitrile into a late-transition-metal–carbon bond. Tf = trifluoromethanesulfonyl, tmeda = *N,N,N',N'*-tetramethylethylenediamine.

Polymorphism

N. Nassif,* N. Gehrke, N. Pinna, N. Shirshova, K. Tauer, M. Antonietti, H. Cölfen* — 6004 – 6009

Synthesis of Stable Aragonite Superstructures by a Biomimetic Crystallization Pathway

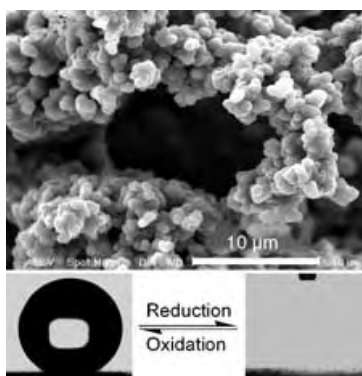
Selective nucleation of aragonite can be achieved at ambient conditions in water by using block copolymer microgels at a very low concentration (0.1 ppm). One polymer template particle is sufficient to control the nucleation of a ring of aragonite single crystals, which propagate into a sheaf structure (see SEM image). Each aragonite crystal is protected by an outer amorphous layer that results in prolonged stability of the aragonite.



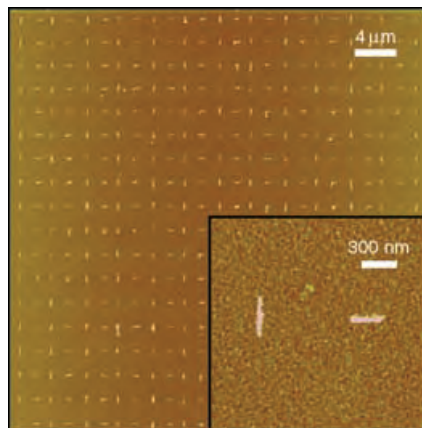
Polymer Films

L. Xu, W. Chen, A. Mulchandani, Y. Yan* — 6009 – 6012

Reversible Conversion of Conducting Polymer Films from Superhydrophobic to Superhydrophilic



On-again, off-again personality: Superhydrophobic conducting polypyrrole (PPy) films are synthesized through a facile electrochemical process. The PPy films exhibit an extended porous structure with both coarse- and fine-scale roughness (see image). By controlling the electrical potential, PPy films can be switched between the oxidized state and the neutral state, resulting in reversibly switchable superhydrophobic and superhydrophilic properties.



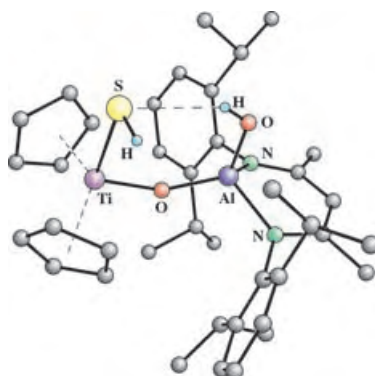
A mosaic pattern: Single virus particle nanoarrays can be made through the positioning and orientation of viral particles on nanotemplate surfaces generated by dip-pen nanolithography. Viral immobilization was characterized with antibody–virus recognition and infrared spectroscopy (an example array of particles is shown in the AFM image).

Nanolithography

R. A. Vega, D. Maspoch, K. Salaita, C. A. Mirkin* — 6013 – 6015

Nanoarrays of Single Virus Particles

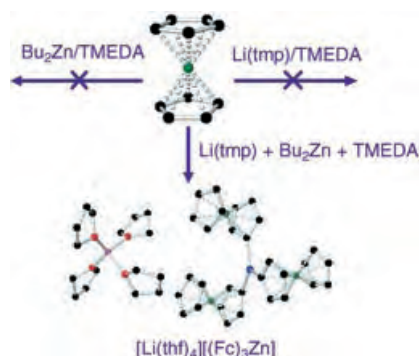
Heterobimetallic sulfides of composition $[La(\mu-S)_2MCP_2]$ ($M = Ti, Zr$) react smoothly with two equivalents of water by ring opening and chalcogen exchange to form the heterobimetallic oxide–hydroxide–hydrogensulfides $[La(OH)(\mu-O)MCP_2(SH)]$ (Ti derivative shown). The presence of the hydrolysis intermediate $[La(SH)(\mu-O)MCP_2(SH)]$ in the reaction mixture confirms the proposed pathway.



Mixed-Metal Complexes

V. Jancik, H. W. Roesky* — 6016 – 6018

Preparation of Heterobimetallic Oxide–Hydroxide–Hydrogensulfides $[La(OH)(\mu-O)MCP_2(SH)]$ ($M = Ti, Zr$)

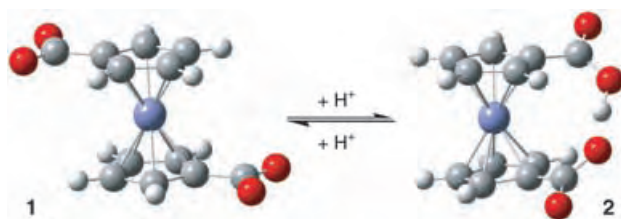


Deprotonative metalation of ferrocene by a lithium zincate reagent was carried out to form the neutral zinc complex $[(Fc)_2Zn(tmeda)]$ and the anionic zincate $[Li(thf)_4][(Fc)_3Zn]$ (see scheme; tmp = 2,2,6,6-tetramethylpiperidine, TMEDA = *N,N,N',N'*-tetramethylethylenediamine). A 1:1:1 mixture of TMEDA, Li(tmp), and *n*Bu₂Zn is used to readily prepare the lithium zincate reagent $[Li(nBu_2Zn(tmp)(tmeda))]$ in situ.

Zincation

H. R. L. Barley, W. Clegg, S. H. Dale, E. Hevia,* G. W. Honeyman, A. R. Kennedy, R. E. Mulvey* — 6018 – 6021

Alkali-Metal-Mediated Zincation of Ferrocene: Synthesis, Structure, and Reactivity of a Lithium Tmp/Zincate Reagent



Screw top: Photoelectron spectroscopy of doubly charged $[FeCp'_2]$ (**1**) and singly charged $[Cp'FeCp'H]$ (**2**; $Cp' = \eta^5-C_5H_4CO_2^-$) shows that strong intramolecular coulomb repulsion keeps **1** in the

trans form, with the two CO_2^- groups on the Cp' ligands oriented opposite to each other, whereas **2** assumes the *cis* form owing to formation of a strong intramolecular H bond. Fe blue, O red, C gray.

Ferrocenes

X.-B. Wang, B. Dai, H.-K. Woo, L.-S. Wang* — 6022 – 6024

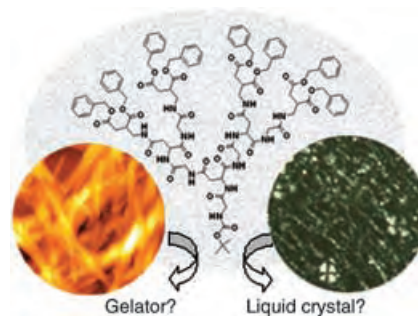
Intramolecular Rotation through Proton Transfer: $[Fe(\eta^5-C_5H_4CO_2^-)_2]$ versus $[(\eta^5-C_5H_4CO_2^-)Fe(\eta^5-C_5H_4CO_2H)]$

Amino Acid Dendrons

Y. Ji, Y.-F. Luo, X.-R. Jia,* E.-Q. Chen,
Y. Huang, C. Ye, B.-B. Wang, Q.-F. Zhou,
Y. Wei* 6025 – 6029

A Dendron Based on Natural Amino Acids: Synthesis and Behavior as an Organogelator and Lyotropic Liquid Crystal

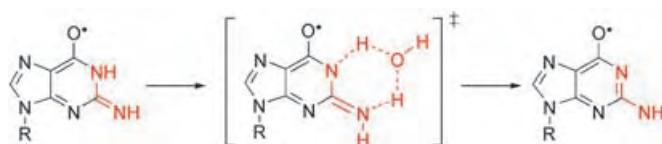
From linear to dendritic: Glycine is part of the predominant sequence in collagen proteins, and aspartate is similar to the repeating unit of poly(benzyl glutamate)s (PBG)s. Collagen and PBGs are linear peptides that self-organize into fibers and form liquid-crystalline phases and gel solvents. How would a molecule self-assemble if it was built by arranging Gly-Asp units in a dendritic way (see picture)? A dendron as both gelator and liquid crystal?



Guanosine Tautomers

C. Chatgililoglu,* C. Caminal, M. Guerra,
Q. G. Mulazzani 6030 – 6032

Tautomers of One-Electron-Oxidized Guanosine



Aminic or iminic: Two tautomeric forms of oxidized guanosine have been produced by chemical radiation methods—by direct oxidation of guanosine or from the protonation of the 8-bromoguanosine elec-

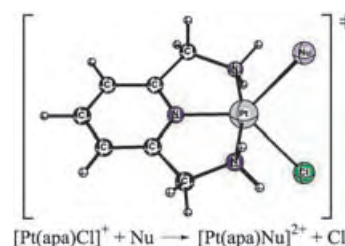
tron adduct—and identified. The tautomerization from the iminic to the aminic arrangement has an activation energy of 23.0 kJ mol^{-1} and occurs through a complex transition state (see scheme).

Ionic Liquids

C. F. Weber, R. Puchta,
N. J. R. van Eikema Hommes,
P. Wasserscheid,
R. van Eldik* 6033 – 6038

Transition-State Effects of Ionic Liquids in Substitution Reactions of Pt^{II} Complexes

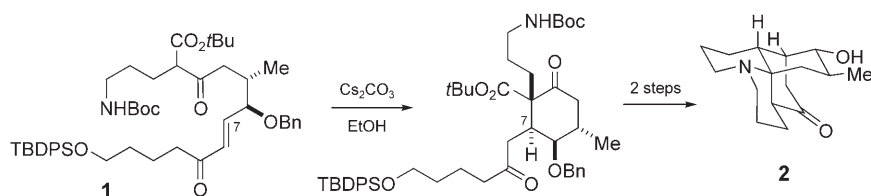
When normal is a surprise: Studies of a ligand-substitution reaction of a Pt^{II} complex (see picture; apa: 2,6-bis(aminomethyl)pyridine) in water, methanol, and the ionic liquid 1-butyl-3-methylimidazolium bis(trifluoromethylsulfonyl)amide reveal that the ionic liquid behaves “normally”, that is, as any other solvent. In the ionic liquid, changes in the polarity of the transition state only play a minor role.



Natural Products Synthesis

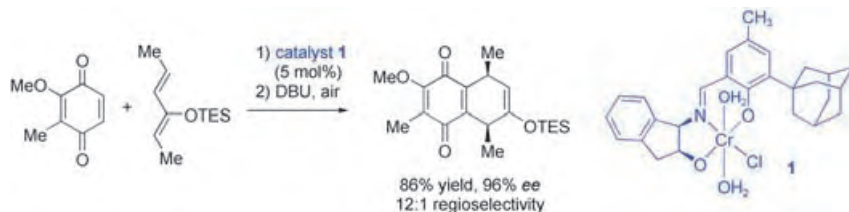
D. A. Evans,* J. R. Scheerer 6038 – 6042

Polycyclic Molecules from Linear Precursors: Stereoselective Synthesis of Clavolonine and Related Complex Structures



A clever way to clavolonine: The total synthesis of the lycopodium alkaloid clavolonine (2) from a linear precursor 1 that contains the complete 16-carbon-atom chain is reported (see scheme). Intramo-

lecular and transannular cascade reaction sequences are explored from both linear and macrocyclic precursors. A variety of polycyclic structures are rapidly constructed from simple acyclic precursors.



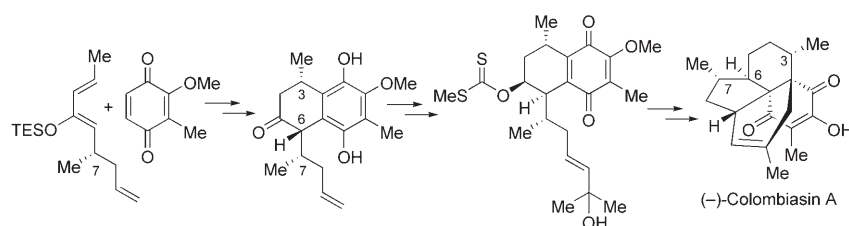
Natural product inspired asymmetric catalysis resulted from an effort directed toward colombiasin A and related complex targets. The discovery of highly selective quinone Diels–Alder reactions

catalyzed by the new, monomeric [(Schiff base)Cr^{III}] complex **1** was a requisite step in the synthetic endeavor (see scheme; TES = triethylsilyl, DBU = 1,8-diazabicyclo[5.4.0]undec-7-ene).

Asymmetric Catalysis

E. R. Jarvo, B. M. Lawrence,
E. N. Jacobsen* ————— **6043 – 6046**

Highly Enantio- and Regioselective Quinone Diels–Alder Reactions Catalyzed by a Tridentate [(Schiff Base)Cr^{III}] Complex



A made-to-order asymmetric catalytic reaction was applied in the key quinone Diels–Alder step of the total syntheses of

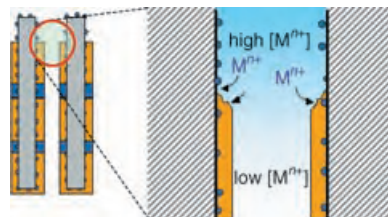
the title compounds (see scheme for the synthesis of colombiasin A). The reaction was highly regio- and diastereoselective.

Asymmetric catalysis

A. A. Boezio, E. R. Jarvo, B. M. Lawrence,
E. N. Jacobsen* ————— **6046 – 6050**

Efficient Total Syntheses of (–)-Colombiasin A and (–)-Elisapterosin B: Application of the Cr-Catalyzed Asymmetric Quinone Diels–Alder Reaction

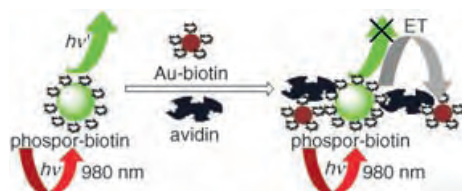
Bimetallic nanotubes: Uniform arrays of metal nanotubes were prepared by the electrodeposition of a thin metallic film on the pore walls of anodic aluminum oxide membranes decorated with metallic nanoparticles. Multisegmented nanotubes with a bimetallic stacking configuration along the nanotube axis can be fabricated (see picture). The technique is applicable to a wide variety of conducting and semiconducting materials.



Nanotubes

W. Lee,* R. Scholz, K. Nielsch,
U. Gösele ————— **6050 – 6054**

A Template-Based Electrochemical Method for the Synthesis of Multisegmented Metallic Nanotubes



A pair to fret about: Biotinylated phosphor nanoparticles that emit upconversion luminescence have been taken with biotinylated Au nanoparticles, which act as energy acceptors, and the pair has been

applied to the determination of trace amounts of avidin based on fluorescence resonant energy transfer (FRET; see picture).

Biosensors

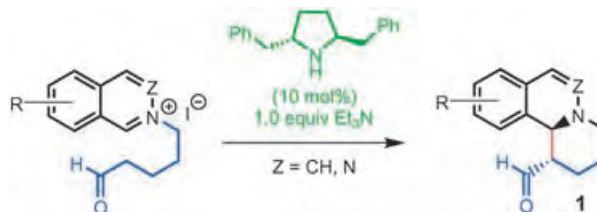
L. Y. Wang, R. X. Yan, Z. Y. Huo, L. Wang,
J. H. Zeng, J. Bao, X. Wang, Q. Peng,
Y. D. Li* ————— **6054 – 6057**

Fluorescence Resonant Energy Transfer Biosensor Based on Upconversion-Luminescent Nanoparticles

Organocatalysis

K. Frisch, A. Landa, S. Saaby,
K. A. Jørgensen* ————— 6058 – 6063

Organocatalytic Diastereo- and
Enantioselective Annulation Reactions—
Construction of Optically Active
1,2-Dihydroisoquinoline and
1,2-Dihydrophthalazine Derivatives



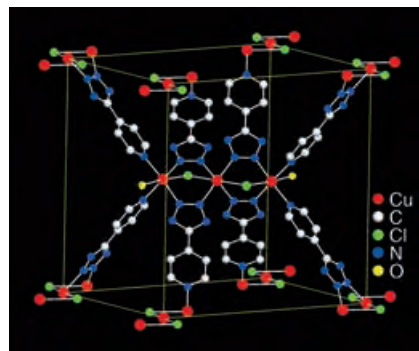
Good to high conversions (70–100%) into
optically active tri- or tetracyclic nitrogen-
containing compounds **1** based on 1,2-
dihydroisoquinolines and 1,2-dihydro-

phthalazines proceed with high dia-
stereoselectivity (d.r. $\geq 15:1$) and good to
excellent enantioselectivity (85–96% *ee*)
in the presence of a chiral amine.

Metal–Organic Frameworks

T.-T. Luo, H.-L. Tsai, S.-L. Yang, Y.-H. Liu,
R. D. Yadav, C.-C. Su, C.-H. Ueng, L.-G. Lin,
K.-L. Lu* ————— 6063 – 6067

Crystal Engineering: Toward Intersecting
Channels from a Neutral Network with a
bcu-Type Topology

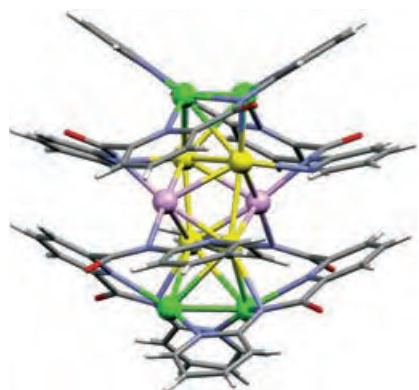


In rare form: Although the structure of the
body-centered cubic (bcu) net is com-
monly found in textbooks, its eight-con-
nected topology is extremely rare in
metal–organic frameworks owing to
severe geometric requirements. The first
example of a highly porous, neutral bcu-
type framework (see picture) assembled
from a unique eight-connected tricopper
cluster and a 5-(4-pyridyl)tetrazolate
ligand as linker is reported.

Cluster Compounds

H. W. Hou,* Y. L. Wei, Y. L. Song, L. W. Mi,
M. S. Tang, L. K. Li, Y. T. Fan — 6067 – 6074

Metal Ions Play Different Roles in the
Third-Order Nonlinear Optical Properties
of d^{10} Metal–Organic Clusters

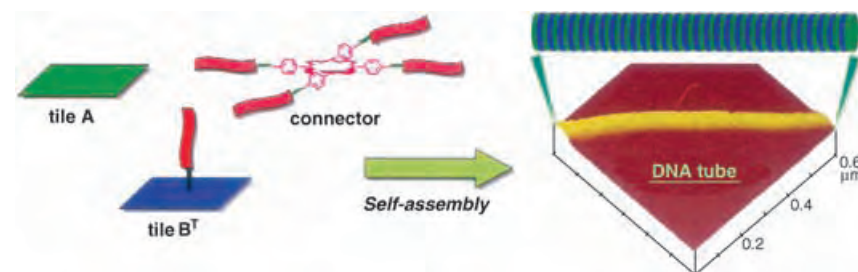


The heavy-atom effect cannot explain the
difference in the third-order nonlinear
optical properties of the clusters
[Ag₁₀(dcapp)₄](OH)₂·12 H₂O (**1**, see
structure), [Zn₄O(dcapp)₃](H₂O)₆ (**2**), and
[Hg₂(dcapp)₂] (**3**) (H₂dcapp = 2,6-dicar-
boxamido-2-pyridylpyridine). Quantum
chemical calculations show that the NLO
properties of **1** are controlled both by the
metal and the ligand, while those of **2** and
3 are controlled by the ligand only.

DNA Nanotubes

M. Endo,* N. C. Seeman,
T. Majima* ————— 6074 – 6077

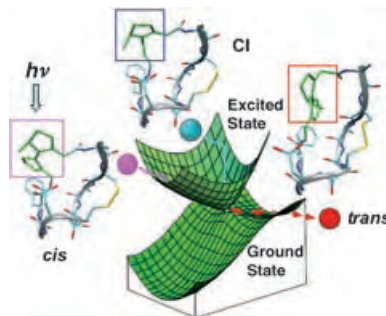
DNA Tube Structures Controlled by a
Four-Way-Branched DNA Connector



Tiles go down the tube: A novel method
for the preparation of DNA tubes by using
the DNA tile system with the assistance of
a four-way-branched DNA–porphyrin

connector is described (see schematic
representation). The detailed DNA tube
structures were characterized by atomic
force microscopy.

A light switch: The mechanism of transmission of the photoinduced torsional strain along a cyclic peptide, incorporating a biomimetic photochemical switch, is resolved by quantum mechanics/molecular mechanics and molecular dynamics simulations. The excited-state *cis*→*trans* motion of the switch does not affect the conformation of the peptide which only begins to change after decay to the ground state at a conical intersection (CI; see scheme).



Peptides

T. Andruniów, S. Fantacci,* F. De Angelis, N. Ferré, M. Olivucci* — 6077 – 6081

Mechanism of the Initial Conformational Transition of a Photomodulable Peptide



Communications labeled with this symbol have been judged by two referees as being “very important papers”.

The issues for September 2005 appeared online on the following dates:

Issue 33: August 15 · Issue 34: August 22 · Issue 35: September 1 · Issue 36: September 8

Sources

Product and Company Directory

You can start the entry for your company in “Sources” in any issue of *Angewandte Chemie*.

If you would like more information, please do not hesitate to contact us.

Wiley-VCH Verlag – Advertising Department

Tel.: ☎ 62 01 - 60 65 65

Fax: ☎ 62 01 - 60 65 50

E-Mail: MSchulz@wiley-vch.de

Service

Keywords _____ 6082

Authors _____ 6083

Angewandte's Sister Journals _____ 6084

Preview _____ 6085





EUCHEM: Nanoscale Surface Self-Assembly**

Helmuth Möhwald*

The last two decades have seen tremendous progress in the controlled self-assembly of molecular organized thin films at the nanometer level. These assemblies offer promise for many applications in optics, electronics, sensors, or biotechnology, and therefore it is important to review the progress in this field, highlight current developments, and discuss future directions. This was the aim of the EUCHEM Conference "Nanoscale Surface Self-Assembly", which was held on June 19–23 at Sigtuna (Sweden). The meeting brought together 100 scientists, of whom many have helped to shape the field over some years, and their younger colleagues, who presented their results through short oral contributions and 60 posters.

Films with probably the best-defined structure control are those formed by chemisorption of silanes or thiols on inorganic surfaces. Through suitable modification of the surface, these can be extended towards multilayers. They can also be laterally structured by various techniques, as presented in original contributions, through locally selective electrochemistry by means of an STM tip (J. Sagiv, Rehovot); through electron-beam-induced polymerization and desorption (M. Grunze, Heidelberg; Figure 1); and through the stamping of

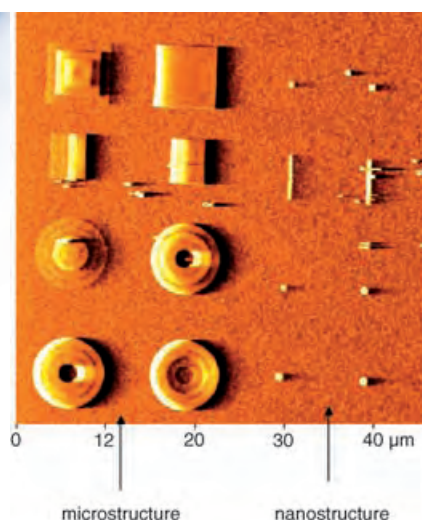


Figure 1. Three-dimensional poly(*N*-isopropylacrylamide) micro- and nanostructures can be grown onto various substrates by grafting the polymer brush from an initiator-coated surface. The dependence of the brush height on the density of the initiator (controlled by the electron-beam dose in the chemical lithography process) allows spatially defined polymer patterns with varying heights and unique surface topographies to be created in a single step. Image courtesy of Qiang He, Junbai Li, Alex Küller, and Michael Grunze (University of Heidelberg)

thiols on surfaces (G. Whitesides, Boston; R. Nuzzo, Urbana). This opens up potential applications towards electronics (Nuzzo), microfluidics (Whitesides), and the manipulation of the interactions of biological matter with surfaces. The latter holds for the passivating of surfaces to avoid inflammatory reactions (Grunze) as well as for stimulating cell growth (Montelius, Lund). It was also shown that by varying the composition of surface deposits, gradient films could be prepared which are suitable for lubrication studies at the nanoscopic level (T. Kraus and N. Spencer, Zürich). An interesting new approach to fabricate multifunctional films was introduced by D. Reinhoudt (Twente), who reported the synthesis of molecules with many supramolecular interactions that are able to assemble in well-defined films with a structure that can be manipulated by environmental conditions.

Owing to their ease of fabrication and versatility with regards to selection of the material, polyelectrolyte multilayers have received widespread interest. These films, which are predominantly based on electrostatic interactions, are

structurally controlled only at the nanometer level, but their robustness and high tolerance to imperfections makes them appealing for a variety of applications, including controlled-release surfaces or defined wettability. G. Decher (Strasbourg) presented spray-coating as a simple and efficient way to prepare multilayer films, and A. Rogach (Munich) demonstrated that different components, in this case semiconductor quantum dots, can be introduced with varying composition along the normal to allow an energy-transfer cascade through the film. H. Möhwald (Potsdam, Germany) presented an extension of the polyelectrolyte multilayer assembly technique in which sacrificial colloidal templates have been coated to yield micro- and nanocapsules with well-defined walls and surfaces, and controlled, switchable permeability.

Polyelectrolyte/surfactant assemblies are frequent in nature and are also used in many technical systems. To study them at interfaces, on the one hand, enables one to learn more about their interactions, and on the other hand, enables specific interfacial modifications, for example, in foams (Langevin, Orsay; Thomas, Oxford). Many of these complexes form 3D structures that may be of importance, for example, for gene therapy or conditioners. During the presentations it became clear that not only the rules of the assembly of the multicomponent systems have to be learnt but that also, especially for polymers as components, non-equilibrium states are relevant (Tilton, Pittsburgh).

Inorganic nanoparticles can be inserted into films as stable functional components, and it was shown by E. Hutter and J. Fendler (Potsdam, USA) that the scattering power of gold nanoparticles can be used for the very sensitive detection of interactions including DNA recognition. A new and versatile way of (grafting from) polymerization on nanoparticles that makes them functional building blocks of defined coatings was presented by D. Wang (Potsdam, Germany; Figure 2).

Nature provides us with membranes as multifunctional surfaces and films, and it is intriguing to arrange these on inorganic supports. Whereas the contribution of L. Evans (Leeds) mainly concentrated on solving problems related

[*] Prof. H. Möhwald
Max Planck Institute of Colloids and Interfaces
14424 Potsdam (Germany)
Fax: (+49) 331-567-9202
E-mail: moehwald@mpikg-golm.mpg.de

[**] EUCHEM Conference "Nanoscale Surface Self-Assembly", June 19–23 at Sigtuna, Sweden.

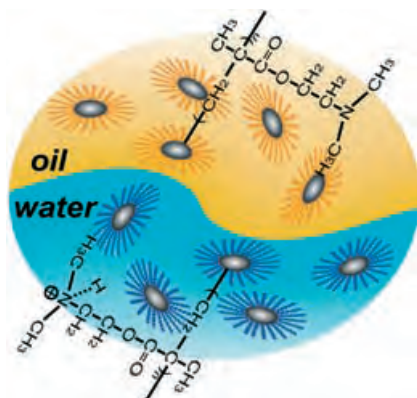


Figure 2. The pH-dependent chemical structure of a polymer brush on a nanoparticle surface. With the protonated brush, the nanoparticle is soluble in water; unprotonated, the nanoparticle is soluble in organic solvents. Image courtesy of Dayang Wang and Hongwei Duan (Max Planck Institute of Colloids and Interfaces).

to the coupling of the membrane on a solid support, the contribution of D. Stamou (Copenhagen) demonstrated the fabrication of reaction vessels on micropatterned surfaces.

Progress in the past has been also due to the development of new techniques, and this is expected to continue. T. McMaster (Bristol) demonstrated the applicability of new refinements of scanning force microscopy to probe soft interfaces, and M. Lefenfeld (New York) showed the applicability of high-energy X-ray reflectivity to probe buried interfaces. The latter is also applicable for sum-frequency genera-

tion and is especially suited to probe defects and symmetry breaks, as presented by S. Ye (Hokkaido). These techniques first emerged about 10 years ago, but it wasn't until recently that one could extract the quantitative information necessary for a controlled assembly. This is also true for neutron reflectometry, as presented by R. Thomas (Oxford), wherein systematic studies have now revealed a layered arrangement of some polyelectrolytes near interfaces. In a most impressive talk by W. Kern (Stuttgart) based largely on low-temperature scanning tunneling microscopy, the participants realized how much one still has to learn on going from an atom to a supramolecular assembly on a surface. With high-resolution techniques, chiral recognition in assemblies of linear aggregates could be realized, leading to periodic non-close-packed arrays on surfaces.

The program included some free time for informal discussions as well as a "round table" to discuss future perspectives. This developed into a very lively discussion hour, however, without any conclusions. The most evident problems identified from the discussion were as follows:

- 1) The field is highly multidisciplinary, and as no individual can cover all disciplines in depth, the integration of many specialists is mandatory but highly demanding.

- 2) Funding agencies and politicians have received many promises of nanotechnological applications. However, one still has to learn the rules of molecular assembly, and therefore long-term research is required and many promises will not be met in the near future.
- 3) Most scientists have their personal view on the areas of most promising applications. However, no consensus has been reached, as there have been many examples of unexpected breakthroughs.

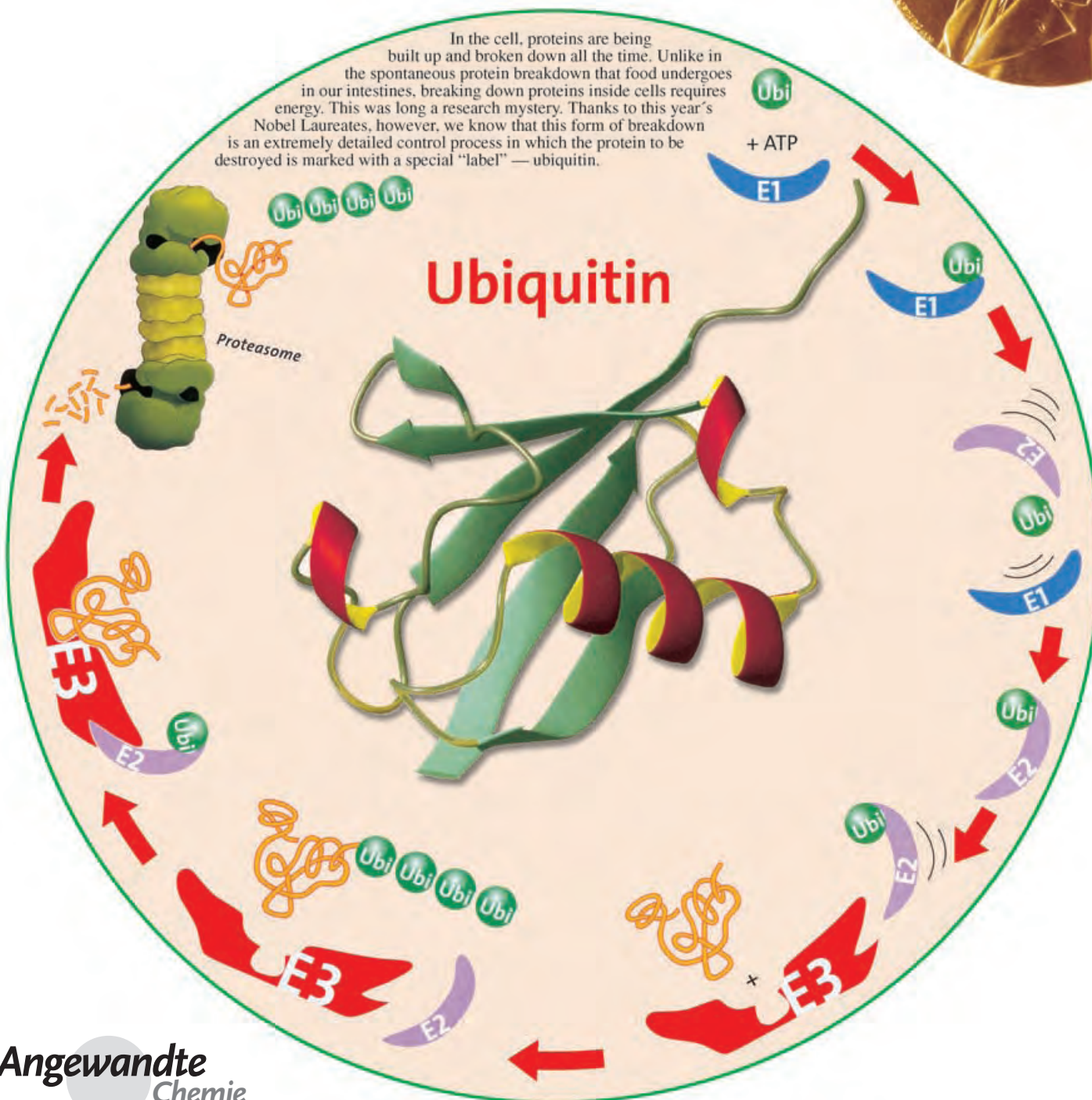
These lively, partly chaotic discussions, however, did not affect the extremely friendly spirit of the conference. One could profit from all contributions and discuss with all speakers at length. Much of this is due to the excellent selection and organization by M. Rutland and his team from the Royal Institute of Technology Stockholm and the Swedish Chemical Society. The success of the meeting is probably most clearly expressed in the result of a secret poll of the participants, with 95% rating the conference as very good or excellent. They also expressed a strong wish for a continuation, and hopefully this will be the case on a more regular basis.

DOI: 10.1002/anie.200502935

THE NOBEL PRIZE IN CHEMISTRY 2004



In the cell, proteins are being built up and broken down all the time. Unlike in the spontaneous protein breakdown that food undergoes in our intestines, breaking down proteins inside cells requires energy. This was long a research mystery. Thanks to this year's Nobel Laureates, however, we know that this form of breakdown is an extremely detailed control process in which the protein to be destroyed is marked with a special "label" — ubiquitin.



Angewandte
Chemie

Protein Breakdown

Ubiquitin at Fox Chase (Nobel Lecture)**

Irwin Rose*

Keywords:

enzymes · Nobel lecture · protein breakdown · ubiquitin

From the Contents

1. How it All Came Together	5927
2. The Ubiquitin Activating Enzyme	5928
3. Ubiquitin-Carboxy-Terminal Hydrolase: Discovery and Mechanism	5929
4. Unresolved Issues	5930

My interest in protein breakdown as a research problem began in 1955 at about the time I joined the Biochemistry Department of Yale University. It was known that proteins break down intracellularly in the mature animal.^[1,2] In 1955 I learned from Melvin Simpson about experiments he had published two years earlier^[3] showing that a variety of conditions that should lower the ATP level of liver slices (anaerobiosis, cyanide, 2,4-dinitrophenol) decreased the rate of liberation of labeled methionine from the protein of rat liver slices. Simpson and I had just joined the Biochemistry Department and we had labs down the hall from each other. Simpson's research goal at Yale was to look for an *in vitro* system that performed protein synthesis rather than protein breakdown. During my Yale years I concentrated on enzyme-mechanism questions relating to the keto-aldose isomerases by using tritium to establish the occurrence of proton transfer,^[4] but I kept an eye out for reports in the literature on progress in the field of protein breakdown.

Nothing new was being reported by 1963 when we relocated to the Institute for Cancer Research of Fox Chase, Philadelphia. At that time I began looking for a cell-free system that would show an ATP dependence using the Ehrlich ascites cells that were available from our animal colony. My usual procedure was to label cells in a suspension with an essential amino acid, wash the cells, lyse them by homogenization, and look for acid-soluble counts by adding either ATP or 2-deoxyglucose plus hexokinase to deplete the endogenous ATP.

During 1972, on a half-year sabbatical divided between Oxford (J. Knowles) and Jerusalem (Y. Stein), I was able to do further experiments with tissues supplied by Hans Krebs and by Jacob Mager (Avram Hershko's PhD research director at the Hadassah Medical School). Both men were highly supportive, but I was not able to find a cell-free system. At the same time I was often talking to Jacob Bar Tana of the

Biochemistry Department and we came up with a "pulse/chase" method that could be used to determine the functionality, binding constant, and rate of dissociation of potential enzyme-substrate complexes.^[5]

1. How it All Came Together

Hershko had been with Gordon Tompkins in San Francisco on a post-doctoral fellowship, where he essentially confirmed Simpson's findings but with the tyrosine aminotransferase of cells in cultures. When he returned to Israel to set up his own lab in Haifa he also looked for a cell-free system. I did not meet Avram Hershko until 1975, at a Fogerty Conference on Regulation in Bethesda, where we learned of each others interest in protein breakdown. Meanwhile, Tompkins died tragically during a brain tumor operation, and Hershko was looking for a US lab in which to expand his work further during sabbatical years and summers. It is not clear to me why he chose our lab in suburban Philadelphia for this purpose. We had no reputation in protein breakdown, having never published in the field. Our limited expertise was expected to be in mechanistic enzymology. The three American postdocs, Haas, Pickart, and Wilkinson, who

[*] Prof. Dr. I. Rose
Department of Physiology & Biophysics
College of Medicine
University of California
D340 Medical Science I, Irvine, CA 92697-4560 (USA)
Fax: (+1) 949-824-8540
E-mail: irwin@lworld.net

[**] Copyright© The Nobel Foundation 2004. We thank the Nobel Foundation, Stockholm, for permission to print this lecture.

came on board for that reason, could not have anticipated the diversion their research careers were about to take.

In 1977, when we joined forces at Fox Chase, Etlinger and Goldberg^[6] had done the first successful experiment using a cell-free system with lysates of rabbit reticulocytes. Hershko and his student Aaron Ciechanover^[7] had already started fractionating the reticulocyte extract and identified the heat-stable factor (APF-1) before they came to Fox Chase that summer. Their subsequent work, much of which was reported in collaboration with members of my group, is to be found in the following Nobel Lecture by Hershko. The key observation that the 8-kDa APF-1 formed units of a chain linked to the protein targeted for breakdown was the most unexpected and unique aspect of the process.^[8]

The identification of APF-1 with ubiquitin was made by three post-docs at Fox Chase: Keith Wilkinson and Arthur Haas from the Rose/Hershko lab and Mike Urban from the neighboring lab. Urban was working with chromatin and knew especially about their interesting components—the histones.^[9] The pivotal question asked of Urban was: Do you know any examples of two proteins that are linked covalently. This recalled the small protein of unknown function, ubiquitin, a covalent ligand of histone H2A. The size and amino acid composition of APF-1 reported by Hershko and known for ubiquitin were in agreement.

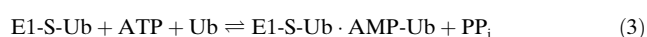
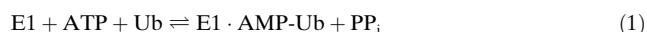
The failure of many cell extracts to give ATP-dependent protein breakdown is probably a consequence of a lysosomal trypsin-like protease that destroys the ubiquitin of the preparation. This was discovered by Haas et al.,^[10] who observed the loss of enzyme binding capacity of a ubiquitin affinity column when liver extracts were put through it. Haas was able to show ATP/ubiquitin-dependent protein breakdown with liver extracts that were preincubated to inactivate the trypsin-like activity. Ubiquitin was already known to be trypsin-sensitive at the Arg74–Gly75 bond.

2. The Ubiquitin Activating Enzyme

Enzymologists usually study the initial rates of reactions by measuring product formation as a function of substrate concentration or another variable. Cell biologists are more

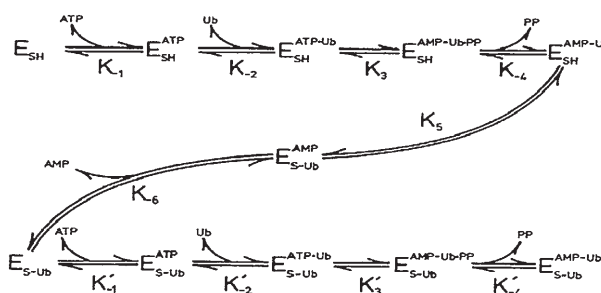
likely to want to know the effect of a change on the steady-state behavior of a complex system. When the ubiquitin activating enzyme E1 was discovered by Hershko, it could not be studied by the rate of product formation because the enzyme produced a covalently linked end product. In 1982 Art Haas used isotope exchange at equilibrium to establish the reaction sequence and a number of equilibrium and rate constants of E1—the only enzyme of the cell that uses ubiquitin, per se, as a substrate.

The ubiquitin (Ub) activation process is defined by the formation of two equivalents of pyrophosphate (PP_i), one equivalent of bound AMP-Ub, and two exchange reactions: ATP with PP_i and ATP with AMP, as shown in Equations (1)–(3).



AMP-Ub, which is prepared from E1, ATP, and Ub and eluted by denaturing the enzyme, is sensitive to both dithiothreitol (DTT) and hydroxylamine, thus indicating an acyl-P–anhydride linkage. The AMP-Ub could be converted back into ATP upon addition of PP_i and Mg²⁺ ions or to E-S-Ub, which did not require PP_i or Mg²⁺ ions.^[11–13] Only the formation of enzyme-bound Ub was inhibited by iodoacetamide, thus indicating transfer to the cysteine of the enzyme (Ub being cysteine-free). The linkage to Ub had already been established to involve the C-terminal glycine of Ub.^[14]

ATP was shown to precede Ub in combining with E1 and with E1-S-Ub (Scheme 1) since inhibition of ATP/PP_i exchange was seen at Ub above 10 μM and inhibition was complete at 400 μM. Addition was not random.^[12] Equilibrium constants of the expanded Scheme 1 could be estimated from the influence of varying AMP and PP_i on the concentrations of E1-AMP-Ub and E1-S-Ub, which were determined with tritium-labeled ATP by acid precipitation and labeled Ub by electrophoresis. The affinity for ATP (ca. 40 μM) is higher than the level of ATP in the cell, which ensures that the E1 in the cell will be in the E1-ATP or E1-S-Ub-(ATP) form ready to pick up any free Ub ($K_m = 0.58 \mu\text{M}$). The sensitivity to AMP as an inhibitor ($K_6 = 0.027 \mu\text{M}$) is much higher than ATP as a substrate, which suggests that AMP may be acting as a feedback inhibitor at an allosteric site as well as with E-S-Ub.



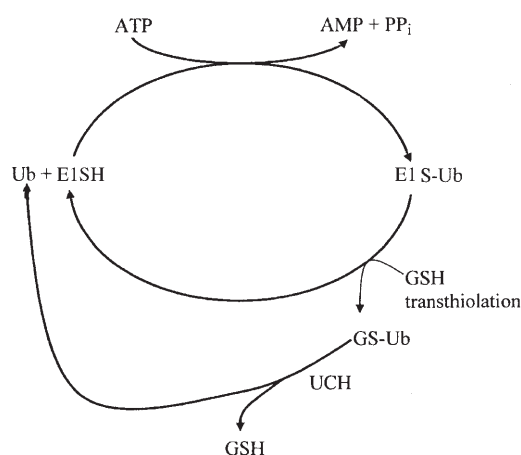
Scheme 1. Sequence and distribution of enzyme intermediates in the activation by ubiquitin.



Irwin Rose received his PhD in 1952 from the University of Chicago in Biochemistry for his work on the conversion of U-¹⁴C-cytidine into U-¹⁴C-deoxycytidine in the DNA of mouse tissues. In 1955 he joined the Biochemistry Institute at Yale Medical School. Here, he learned from Melvin Simpson that protein breakdown was inhibited, not stimulated, under energy-deficient conditions. At Fox Chase (1963–1997), after contributing to enzyme-mechanism research, he was joined by the Hershko/Ciechanover team in 1977 who were making progress fractionating reticulocyte extracts. He and his students contributed to studies of the ubiquitin activating enzyme, ubiquitin carrying protein, and ubiquitin C-terminal hydrolase leading to the isolation of ubiquitin aldehyde and an understanding of the hydrolase mechanism.

3. Ubiquitin-Carboxy-Terminal Hydrolase: Discovery and Mechanism

It was observed that the usual one-turnover assay of E1 used ATP well beyond expectation when glutathione was included in the assay. The explanation: The ubiquitin of E1-S-Ub is readily transferred nonenzymatically to mild nucleophiles such as glutathione, DTT, and hydroxylamine. By itself, this would increase the consumption of ATP to the amount of Ub present in the assay. However, much more was taken up. Were the Ub derivatives unstable? None of the expected Ub-S-DTT from an incubation of AMP-Ub and DTT could be isolated on a covalently bound Hg^+ column unless great care was taken in the conversion. Most revealingly, the yield was increased if urea was added immediately after the reaction. This result indicated that an enzyme carried over with the AMP-Ub from the E1 preparation was regenerating the Ub. These two observations—the transfer of Ub from E1-S-Ub to mild nucleophiles and an enzyme contaminating E1 that would restore free Ub—were needed to explain why much more ATP was consumed than could have been expected in the E1 assay.^[15] The combined action of E1, glutathione, and the hydrolase results in a futile cycle converting ATP into AMP + PP_i (Scheme 2). AMP-Ub is normally too tightly bound to E1 to lead to a futile cycle of its own in the presence of an active nucleophile.



Scheme 2.

Amides of ubiquitin were not available to test as substrates of the new ubiquitin thioesterase until their synthesis was made possible by Cecile Pickart through the action of E1 + E2 on primary amines.^[16] This research was of great interest because the enzymes required for recovery of Ub from conjugation in the newly emerging Ub system were believed to be isopeptidases. An E1·E2-S-Ub complex normally transfers Ub to the $\epsilon\text{-NH}_2$ group of lysine in proteins. To determine the substrate specificity of this system, Dr. Pickart found that a variety of small primary amines at much higher concentration are also very good Ub acceptors. The Ub amides were good substrates for the previously purified Ub thioesterase which henceforth has been known as ubiquitin-carboxy-terminal hydrolase (UCH).

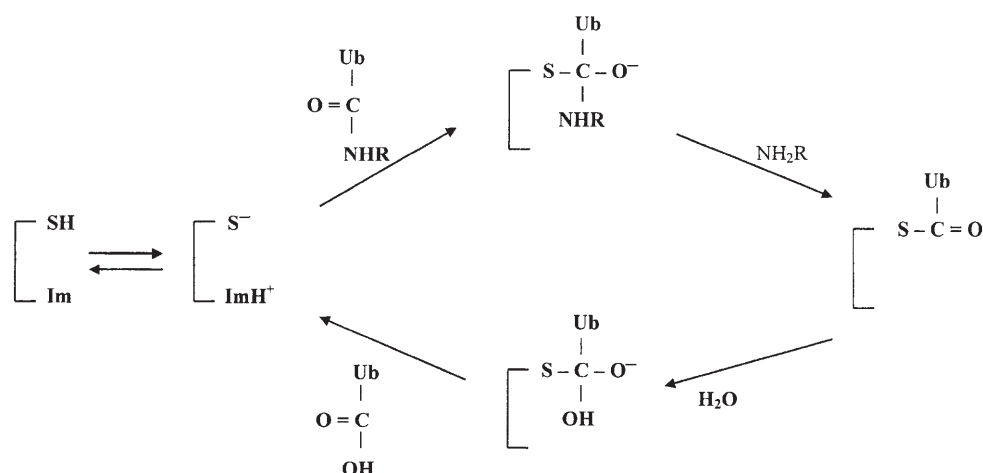
The pure enzyme ($M_w = 29$ kDa) was readily prepared from mature human red cells (ca. 0.1 units per mL of packed cells). Its turnover rate is quite high, almost diffusion limited, and its V_{max} value is approximately 10 s^{-1} . Ubiquitin conjugated to glutathione or to a polyamine in cells with such activity should be negligible.

The rate of the E1·E2/UCH/amine system can be determined by measuring ATP consumption in a futile cycle similar to that of Scheme 2, where the rate can be used to test the activity or the specificity of the component present in a rate-determining amount. UCH enzymes are limited in the size of the substrate they will act upon. Any role in the deubiquitination of polyubiquitin chains is doubtful. This activity is given over to much larger deubiquitinating enzymes (DUBs).

Considerations of the mechanism of UCH start with the observation that these enzymes are inactivated by iodoacetamide, protected by Ub, and therefore should have an active-site thiol group and possibly a ubiquitin thiolester intermediate. We found that inactivation of UCH was brought about by borohydride if ubiquitin was also present.^[17] Both the tritium from the borohydride and the label from Ub were tightly fixed to the inactive enzyme. Both isotopes were released upon mild acid denaturation, whereby tritium traveled with the Ub. The released product was about 1000 times more inhibitory than Ub in an assay using $[^3\text{H}]$ -butanol-4- NH_2 -Ub as a substrate. This effect was lost with borohydride addition to the inhibitor, which was protected from reduction if enzyme was added first. We concluded that the acid-liberated inhibitor must be the C-terminal aldehyde form of Ub (Ubal). This was shown with $[^3\text{H}]$ - NaBH_4 , and by isolation of $[^3\text{H}]$ -ethanolamine among the acid-hydrolysis products. The basis for the protection of the Ubal by the enzyme must be the formation of a strong complex that shields the aldehyde group. A combination of chemical and physical forces would result from the addition of the active-site SH to the carbonyl group, a thiohemiacetal on the one hand and multiple protein–protein interactions between the active site and the remainder of the Ubal. Additional stabilization may come from the resemblance of the thiohemiacetal to the tetrahedral intermediates and transition states in the amidase reaction, as would be drawn for papain and cathepsin B (Scheme 3).

This interpretation of the mechanism of action of Ubal has been confirmed and extended by X-ray crystallographic studies of Ubal complexed with the UCH of yeast Yuh 1 by Johnston et al.^[18] and with the 352-residue UCH domain that was cut out of the 1102-residue-long HAUSP (herpes virus preassociated ubiquitin-specific protease) deubiquitinating enzyme by Hu et al.^[19] In both cases, Ubal caused significant distance and angle rearrangements in the catalytic triad regions compared with structures obtained without Ubal,^[19,20] respectively, as well as placement of H-bonding residues to accommodate the expected oxyanion hole of a thiohemiacetal–Ub adduct.

The large DUBs, about 80 of which have been identified, serve to reverse the lengthening of the polyubiquitin chains that leads to the destruction of the targeted protein at the proteasome. HUASP is also known as a tumor-suppressor co-protein because deubiquitinating p53 (the tumor suppressor



Scheme 3.

transcription factor of tissues) should raise its steady-state level. The large size of DUBs is consistent with high specificity and signal control. The roles of the UCHs are not yet clear. The size of the Ub extension that can be removed by these smaller enzymes is smaller than a Ub molecule so that Ub–Ub cleavage intermediates, if they arise in the deubiquitination process, will not be further degraded by a UCH.

4. Unresolved Issues

- Current discussions of the E1–E2–E3 system often ignore the potential of E1–AMP–Ub to transport Ub units between the solvent and E1–SH to E2 without dissociation of the E1–E2 complex. This possibility should be easily evaluated by pulse/chase experiments using heavy-isotope-labeled Ub in the pulse, unlabeled Ub in the chase, and analyzing the product by mass spectrometric sequencing.
- This approach may fail if the E2–E3–protein interactions are weak. In addition, the experiment should give information about the processivity of the system, namely, how many Ub molecule can be added in succession.
- This approach should also answer the question of whether when Ubs are added to the growing chain they are added to the distally located end of the chain as is often stated, but which seems unreasonable as the chain-length increases.
- An interesting problem stems from the observation by Cecile Pickart^[16,17] that hydroxylamine at $K_m \approx 1$ mM inactivates the C-terminal hydrolase of erythrocytes, and possibly all UCHs, in the presence of Ub. Using the hydroxamate of Ub as a substrate, complete inactivation requires about 2000 turnovers of the enzyme. Labeled Ub is not found on the re-isolated enzyme, nor is activity recovered. Unless hydroxylamine has some unexplored way of reacting with the S- of the Ub-thioester-enzyme intermediate, the classical reaction products should be Ub-hydroxamate and active enzyme. In view of the important role of the deubiquitinating enzymes and a

practical interest in their inactivation, it will be useful to know how hydroxylamine works.

It is a pleasure to pay tribute to Dr. Avram Hershko whose analytic intuition was always productive and whose generous spirit made our interactions always harmonious. His graduate student Aaron Ciechanover played an important role in communicating the progress made in Israel to those at Fox Chase. He has continued adding many fundamental observations to the field. The post-docs: Aaron Ciechanover, Art Haas, Cecile Pickart, and Keith Wilkinson were all major contributors, who have continued their careers in the Ub field with notable success. Thanks are also due to Hannah Heller and Jesse Warms for their contributions in the lab.

Received: March 18, 2005

- [1] R. Schoenheimer, *The Dynamic State of Body Constituents*, Harvard University Press, Cambridge, **1942**.
- [2] R. T. Schimke, D. Doyle, *Annu. Rev. Biochem.* **1970**, 39, 929–976.
- [3] M. V. Simpson, *J. Biol. Chem.* **1953**, 200, 143–154.
- [4] See the note in the autobiography.
- [5] I. A. Rose, E. L. O'Connell, S. Litwin, J. Bar Tana, *J. Biol. Chem.* **1974**, 249, 5163–5168.
- [6] J. D. Etlinger, A. L. Goldberg, *Proc. Natl. Acad. Sci. USA* **1977**, 86, 7751–7755.
- [7] A. Ciechanover, Y. Hod, A. Hershko, *Biochem. Biophys. Res. Commun.* **1978**, 81, 1100–1105.
- [8] A. Hershko, A. Ciechanover, H. Heller, A. L. Haas, I. A. Rose, *Proc. Natl. Acad. Sci. USA* **1980**, 77, 1783–1786.
- [9] K. D. Wilkinson, M. K. Urban, A. L. Haas, *J. Biol. Chem.* **1980**, 255, 7529–7532.
- [10] A. L. Haas, K. E. Murphy, P. M. Bright, *J. Biol. Chem.* **1985**, 260, 4694–4703.
- [11] A. L. Haas, J. V. B. Warms, A. Hershko, I. A. Rose, *J. Biol. Chem.* **1982**, 257, 2543–2548.
- [12] A. L. Haas, I. A. Rose, *J. Biol. Chem.* **1982**, 257, 10329–10337.
- [13] A. L. Haas, J. V. B. Warms, I. A. Rose, *Biochemistry* **1983**, 22, 4388–4394.
- [14] A. Hershko, A. Ciechanover, I. A. Rose, *J. Biol. Chem.* **1981**, 256, 1525–1528.

- [15] I. A. Rose, J. V. B. Warms, *Biochemistry* **1983**, 22, 4288–4294.
[16] C. M. Pickart, I. A. Rose, *J. Biol. Chem.* **1985**, 260, 7903–7910.
[17] C. M. Pickart, I. A. Rose, *J. Biol. Chem.* **1986**, 261, 10210–10217.
[18] S. C. Johnston, S. M. Riddle, R. E. Cohen, C. P. Hill, *EMBO J.* **1999**, 18, 3877–3887.
[19] M. Hu, P. Li, M. Li, W. Li, T. Yao, J.-W. Wu, W. Gu, R. E. Cohen, Y. Shi, *Cell* **2002**, 111, 1041–1054.
[20] S. C. Johnston, C. N. Larsen, W. J. Cook, K. D. Wilkinson, C. P. Hill, *EMBO J.* **2000**, 19, 3787–3796.
-

Quality counts...

The best of chemistry every week



Wiley-VCH

P.O. Box 10 11 61
69451 Weinheim
Germany
Phone +49 (0) 6201–606-400
Fax +49 (0) 6201–606-184
e-mail: angewandte@wiley-vch.de

www.angewandte.org

Angewandte Chemie International
Edition is a journal of the GDCh,
the German Chemical Society

GDCh

 WILEY-VCH

The Ubiquitin System for Protein Degradation and Some of Its Roles in the Control of the Cell-Division Cycle (Nobel Lecture)**

Avram Hershko*

Keywords:

biochemistry · cell division · Nobel Lecture · protein breakdown · ubiquitin

From the Contents

1. Biographical Notes	5932
2. Introduction	5937
3. My First Encounter with Protein Degradation	5938
4. Discovery of the Role of Ubiquitin in Protein Degradation	5938
5. Identification of Enzymes of the Ubiquitin-Mediated Proteolytic System	5939
6. Mechanisms of the Degradation of Cyclin B: Discovery of the Cyclosome/Anaphase-Promoting Complex	5940
7. Role of Scf ^{SKP2} Ubiquitin Ligase in the Degradation of the Cdk Inhibitor P27 ^{Kip1}	5941
8. Concluding Remarks	5941

1. Biographical Notes

I was born on December 31, 1937, in Karcag, Hungary. Karcag is a small town of around 25000 inhabitants, about 150 kilometers east of Budapest. It had a Jewish community of nearly one thousand people. My father, Moshe Hershko, was a schoolteacher in the Jewish elementary school in Karcag; most of the Jewish children in that town were his students. His former students from Hungary, and later from Israel, described him with admiration as an inspiring teacher and a role-model educator. My mother Shoshana/Margit ("Manci") was an educated and musically gifted woman. She



gave some English and piano lessons to children in Karcag. My older brother Chaim was born in 1936, less than two years before me. My mother wanted very much to also have a baby girl, but the times were the eve of World War II, Hitler's screams could be frequently heard on the radio, my parents became apprehensive of the future and thus did not try to have more children. Still, my recollections of my early childhood

are of very happy times, with loving and supporting parents, growing up in a nice house with a beautiful garden, created by my father who was also an amateur (but avid) gardener. A family picture from these times, with my parents, my brother, and I as an infant, shows well the warmth of my family (Figure 1).

This early paradise was lost rapidly and brutally. World War II broke out, and soon Hungary joined in as an ally of Nazi Germany. In 1942, my father was taken by the Hungarian Army to serve as a forced laborer, with companies of other Jewish men. They were sent to the Russian front, where most of them perished. Luckily for my father, the Soviet Army advanced so rapidly after Stalingrad that he was captured by the Soviets before the Nazis could kill him. Then, he was used by the Soviets as a forced laborer. He was

[*] A. Hershko

Unit of Biochemistry
the B. Rappaport Faculty of Medicine
and
the Rappaport Institute for Research in the Medical Sciences
Technion-Israel Institute for Technology
Haifa 31096 (Israel)
Fax: (+972) 4-855-2296
E-mail: hershko@tx.technion.ac.il

[**] Copyright© The Nobel Foundation 2004. We thank the Nobel Foundation, Stockholm, for permission to print this lecture.



Figure 1. My parents, my brother (middle, top), and I (middle, bottom) at around the end of 1938.

released only in 1946, so we did not know for four years whether or not he was alive.

In the spring of 1944, Hungary's dictator Horthy understood that Germany was losing the war, and planned to desert. The Germans sensed this and quickly occupied Hungary. This was followed by the rapid extermination of much of the Jewish population of Hungary. In May/June 1944, most Jewish people were concentrated in ghettos and then transported to death camps in Poland. I was six years old at that time. We were in a ghetto on the outskirts of Karcag for a couple of weeks and then were transferred to a terribly crowded ghetto in Szolnok, which is a larger city in the same district. From there, Jews from the entire district were transported further on freight trains. They were told that they were being sent to work, but after the war we learned that most of the trains were headed for Auschwitz. By some random event, my family and I were put on one of the few trains that headed for Austria, where Jews were actually used for labor. This group included my mother with us two children, my paternal grandparents, and my three aunts. In Austria we were in a small village near Vienna, where adults worked in the fields and in a factory. We were liberated by the Soviet Army in the spring of 1945. My maternal grandparents perished in the Holocaust, along with 360 000 Hungarian Jews and almost two-thirds of the Jewish people of Karcag. Following our reunion with my father in 1946, the family lived for three years in Budapest, where my father found a job as a schoolteacher. The family emigrated to Israel in 1950.

In Israel we settled in Jerusalem and I started a new and very different life. Of course, there were initial difficulties in being new immigrants. We had to learn a new language, Hebrew. This was not too difficult for children (I was less than 13 at that time), but it was more difficult for my parents. Still, my father studied Hebrew and soon started to work, again as a schoolteacher. (Later he taught at a teachers' seminary and authored mathematics textbooks, which were very popular in Israel.) As always, education of their children was my parents' highest priority. Although we were quite poor immigrants at that time, my brother and I were sent to an expensive private school in Jerusalem. I suspect that most of the salary of my father was spent on our tuition fees.

At school I was received well by the other children. These were times of massive immigration to Israel, so a new immigrant child with a Hungarian accent did not stand out too much (I am told that I still have some Hungarian accent, especially in English, though my Hungarian language is quite poor now). I was a good student, and learned easily different subjects, such as mathematics, physics, literature, history, and even Talmud! That became a problem when I finished high school; I was interested in too many subjects, so it was difficult for me to decide how to continue. I chose to study medicine, probably by default, because my brother Chaim was already a medical student, so I could inherit his books for free! Chaim always wanted to be a physician, and he is now a very well-known hematologist and an authority on iron metabolism.

In 1956, I started to study at the Hebrew University–Hadassah Medical School in Jerusalem, which was the only medical school in Israel at that time (there are now four). In the basic science part of my medical studies, I fell in love with biochemistry. I studied biochemistry in three different courses: organic chemistry, basic biochemistry, and a course called “physiological chemistry”, which was medically oriented biochemistry. I was very fortunate to have outstanding teachers in all three courses. Organic chemistry was taught by Yeshayahu Leibowitz, a legendary person in Israel, a highly original thinker whose knowledge encompassed philosophy, political science, Bible, Talmud, medicine, chemistry, and more. He was probably my best teacher, it was an intellectual feast to listen to him. Leibowitz loved biochemistry, and he sneaked biochemistry into his lectures on organic chemistry whenever he could, which was often. Basic biochemistry was taught by Shlomo Hestrin, also an inspiring teacher who had a special talent to transfer his enthusiasm of science to the students. Physiological chemistry was taught by Ernst Wertheimer, a professor of German Jewish origin whom we had some difficulty to understand because of his heavy German accent, but who had an excellent perspective of integrating metabolism at the level of the total body and of physiological contexts of biochemistry. Another part of the same course was taught by Jacob Mager. Mager was an outstanding biochemist and a man of encyclopedic knowledge. However, he was very shy and quite a bad classroom teacher (although an excellent teacher in the laboratory, as I learned later). Most of his lectures were delivered while he was writing whole metabolic pathways on the blackboard, without any notes, with his face to the blackboard and his back directed to the class. Still, I was so much impressed by the depth and breadth of his knowledge of biochemistry that I decided to ask Mager if I could do some research in his laboratory (Figure 2).

I started to work in Mager's laboratory in 1960. At that time, there was no formal MD/PhD program at the Hebrew University, but it was possible to do a year of research between the preclinical and the clinical years of medical studies. I did that, and although I completed medical studies later on, I already knew by the end of that year that I was going to do research, rather than clinical practice. I was very fortunate to have had Jacob Mager as my mentor and tutor of biochemical research. He was a scientist of incredible scope of interests and knowledge. He was interested in every subject in



Figure 2. Jacob Mager.

biomedicine, he knew almost everything about every subject and he worked simultaneously on three to four completely different research projects. This undoubtedly caused fragmentation of his contributions to science, but provided his students with a broad experience in different areas of biochemistry in a single, relatively small laboratory. In a period of a few years I worked with Mager on subjects as different as the effects of polyamines on protein synthesis *in vitro*, glucose-6-phosphate dehydrogenase deficiency, and a variety of aspects of purine nucleotide metabolism, including enzymology and regulation. During this time, I also finished my medical studies, did my military service as a physician (1965–1967), and then returned for two more years to Mager's laboratory to finish my PhD thesis (1967–1969). I received not just a broad view of biochemistry from Mager, but also a very solid basis. He was a very rigorous experimentalist, every experiment had to be done with all possible positive and negative controls, all experiments were carried out in duplicate, and every significant new finding had to be repeated several times to make it sufficiently credible. I owe a lot to Jacob Mager for a strong background in rigorous biochemistry.

I met Judith (née Leibowitz) in 1963, and we married at the end of the same year. Judy was born and raised in Switzerland. After her studies in biology, she decided to spend a year in Israel. During this year, she worked in the hematology laboratory of the Hadassah hospital in Jerusalem. One day, I walked over to the hematology laboratory to get a blood sample that I needed for my research, and we literally bumped into each other. This collision caused her to stay in Israel for more than one year, and now we have been married for over 41 years. We have three sons: Dan (1964), Yair (1968), and Oded (1975). Dan is a surgeon, Yair is a computer engineer, and Oded is a medical student. We have now six grandchildren: Maya (1994), Lee, (1997), Roni (1998), Ela (2000), Ori (2002), and Shahar (2004). Needless to say, both

Judy and I are crazy about all our grandchildren. During all our years together, I got tremendous support from Judy. Although she came from one of world's most peaceful countries to one of the least, and from a very comfortable and pampering environment to quite primitive surroundings, she stood ground with a lot of energy, courage, and cheerful optimism. She always took care of all my possible needs, as well as the needs of our children and grandchildren. Judy is not only a very beautiful woman, but she also radiates a lot of caring, love, and compassion. In addition to providing so much support at home, she also helped me a lot in the laboratory, over a period of more than 15 years. The ubiquitin system was helped by Judy in more than one way (Figures 3 and 4).

In 1969 to 1971 I was a postdoctoral fellow with Gordon Tomkins at the Department of Biochemistry and Biophysics of the University of California in San Francisco. I met Gordon the previous year, when he gave some lectures in Israel. He was very different from Mager: outgoing, vivacious, bursting with original ideas (Figure 5). Unlike Mager, Gordon did not



Figure 3. Judy and Avram Hershko in 1977.



Figure 4. Judy, Avram, and family in 2003 (Judy's 60th birthday party). Left to right; standing: Vardit, Yair, Avram, Judy; middle row: Dan, Ori, Sharon, Oded; sitting: Lee, Maya, Roni, Ela.



Figure 5. Gordon Tomkins.

care much about controls or experimental detail, but he was a volcano of a man, constantly erupting with great ideas and he was a wonderful stimulator of many other researchers' work as well. Many distinguished scientists who knew Gordon Tomkins at that time (unfortunately, he died at an early age) still speak of him with great admiration. He exuded a great personal charm and I liked him instantly. I thought that Gordon may add some new dimensions to my development in science and this indeed was the case. I got a lot of stimulation and biological perspective from Gordon, while I continued to use what I learned from Mager about rigorous controls. As described in the main text, I learned about protein degradation and got fascinated with this process while I was working with Gordon Tomkins.

I returned from San Francisco to Israel in 1971. Originally, I planned to return to the Hebrew University in Jerusalem, but a new medical school opened in Haifa and I was offered the opportunity of being its Chairman of Biochemistry. This sounded very challenging and I agreed, but later it turned out to be a very minute unit of Biochemistry in a very small Faculty of Medicine of the Technion, so at the beginning I chaired mainly myself. One initial reason for its being so small was that there was not enough space to house much faculty. The whole Faculty of Medicine was housed, on a temporary basis, in an old two-floor monastery (Figure 6). This "temporary" situation lasted for more than 15 years, until the new building of the Faculty of Medicine was completed in 1987. However, I had great times in that old monastery, and much of the discovery of the ubiquitin system was done right there. Isolation may at times lead to creativity, since one is not bothered by what others are doing and does not feel compelled to work on currently popular, "fashionable" subjects. I was very fortunate to assemble there a highly devoted research team, which included at the beginning Hanna Heller and Dvora Ganoth, and later, at different times, Ety Eytan, my wife Judy, Sarah Elias, and Clara Segal. Dvora and Ety still work with me. My first graduate students were

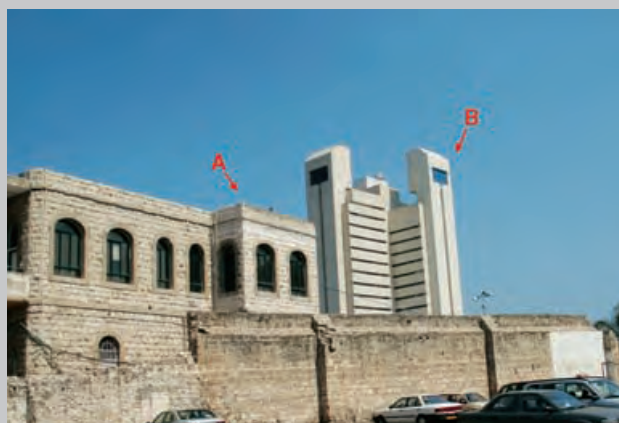


Figure 6. Old and new buildings of the Faculty of Medicine, Technion, Haifa. A) Old building. My laboratory was at the right corner of the upper floor. B) New building.

David Epstein, Yaacov Hod, and Michael Aviram. For a number of years, we tried to establish a cell-free system that reproduces energy-dependent protein degradation in the test tube, essential for the biochemical analysis of this system. For this purpose, we tried different sources, such as liver homogenates and extracts from cultured cells, and even from bacteria. We did not have any success in any of these attempts. I remember that a biochemist friend from Jerusalem visited my laboratory and at the end of the visit she told me that I should not have most of my laboratory working on a hopeless subject. However, I was very obstinate and was obsessed with the idea that it would be possible to find out how proteins are degraded only with a biochemically analyzable cell-free system. Maybe I was lucky to work in such a remote and small place; in a larger institution, my graduate students and research assistants may have deserted me for some less frustrating research. Finally we used the reticulocyte cell-free system established in the Goldberg laboratory for the biochemical fractionation (see Lecture). At that time, Aaron Ciechanover joined my laboratory for a DSc thesis, after completing his medical studies and Army service. Aaron was the most incredibly hard-working graduate student that I ever had. With his huge energies, he contributed a lot to the discovery of the ubiquitin system. He was also a natural manager, already as a graduate student. I recall that at the end of my sabbatical year in Philadelphia in 1978 (see below), after telling Ernie Rose how small Israeli research grants were, Ernie suggested that I should apply for a foreign research grant from the NIH to support my work in Israel. I was inclined to do a couple more experiments instead of writing a grant application, but Aaron pushed me into a chair and commanded: "now write the NIH grant application!". I wrote it and got the grant, the first of five consecutive grant periods supported by the NIH. It saved the situation in the Haifa lab at a very critical time. I am very grateful to the NIH for supporting my work and also to Aaron for forcing me to write the initial grant application.

The story of the discovery of the ubiquitin system is described in my lecture, and here I add only some anecdotal

episodes from these times. The fractionation of reticulocyte lysates into fractions 1 and 2 was based on a trick that I learned from Mager in the purification of enzymes of purine nucleotide metabolism from erythrocytes. Hemoglobin constitutes about 80–90 % of the total protein of erythrocytes and reticulocytes, and therefore the first task in the purification of any enzyme from these cells is to get rid of the great mass of hemoglobin. This is most conveniently done by using the anion-exchange resin DEAE-cellulose, which binds most nonhemoglobin proteins, but not hemoglobin. In our case this procedure resulted in loss of activity, which could be recovered by adding back fraction 1 that contained not only hemoglobin but also ubiquitin. In fact, in our laboratory jargon we called ubiquitin for some time “Red”, because of the red color of hemoglobin in this fraction. After we found that the factor in this fraction (that is, ubiquitin) remains active after boiling for 30 minutes, we consulted a protein expert at the Technion who told us that our factor cannot be a protein. We found, however, that it is a protein, based on its sensitivity to the action of proteinases. Maybe the lesson from this story is that it is dangerous to consult experts.

After working for six years at the Technion, I had a sabbatical year due in 1977/1978. I had a problem in choosing a person with whom I would spend my sabbatical year. I knew the people in the (then) small protein-degradation field, and I was not very enthusiastic. Many people in the field had their pet theories about the cause for the high selectivity of intracellular protein degradation, without much (or any) experimental evidence. Once again, I was lucky. In 1976, I attended a Fogarty meeting on a quite general subject at the National Institutes of Health. Irwin Rose also attended this meeting, and one morning I joined him at the breakfast table. Ernie was well known for his work on enzyme mechanisms. In the course of our conversation I asked Ernie in what else he was interested, and his reply was: “protein degradation”. I was a bit taken aback and told him that I never saw anything published by him on protein degradation. His reply was: “there is nothing worth publishing on protein degradation”! I liked his critical attitude and Ernie being such a character, and therefore I asked him if I could spend my sabbatical year in his laboratory (Figure 7). It turned out that Ernie Rose was really interested in protein degradation. When he had been a young faculty member in the fifties at the Department of Biochemistry of Yale University, he talked to Melvin Simpson, another young faculty member there, and Simpson told him about his experiments on the energy-dependence of the liberation of amino acids from proteins in liver slices (see Lecture). This aroused Ernie’s interest, and from time to time he did experiments trying to understand the energy-dependence of protein degradation. He did not make any significant progress in these experiments, and therefore he did not publish anything on protein degradation.

Ernie Rose is the third person, in addition to Mager and Tomkins, who had a great influence on my scientific life. He is very different from both Mager and from Tomkins. He likes problem solving, and his attitude to science is highly analytical. I am more intuitive, so we complemented each other very well. He is so brilliant that people do not always



Figure 7. Irwin Rose at Fox Chase Cancer Center in 1992.

understand his ideas and are a little afraid of him. People are also often apprehensive of him because he can be very critical, and does not hesitate to voice his criticisms. We got along very well over a period of 20 years, which included several sabbaticals and many summer visits in his laboratory at Fox Chase Cancer Center in Philadelphia. Our only disputes were when he refused to be co-author of work to which he actually made significant contributions. In the case of the few papers on which he is co-author, I had to force him to agree. He was most unselfish in our joint work, a rare phenomenon in today’s science. I asked him once why does he keep inviting me back to his laboratory, and his answer was: “I like the excitement”. Ernie always downplayed his contributions to the ubiquitin field. He wrote an autobiographical article for *Protein Science* in 1995, and the word “ubiquitin” is not mentioned in this recollections paper. In our conversations he always described his role in the ubiquitin story as being merely supportive, but this is certainly not true. Although on occasions when I worked in his laboratory, he was adsorbed with some problem in enzyme mechanisms, he would forget about my existence for a week or two, but then suddenly he would come up with a bright suggestion about my current work. I can state that Ernie’s input of ideas, inspiration, and helpful criticism were essential for the discovery of the ubiquitin system and for the delineation of some of the main enzymatic reactions in this pathway.

The rest of my story is a lot of more work, but also a lot of more scientific excitement and fun. I continued to be obstinate, and continued to do what many considered to be old-fashioned biochemistry in the eighties, when the powerful technologies of molecular biology became available. This biochemical work resulted in the discovery of the three types of enzymes involved in ubiquitin–protein ligation (E1, E2, and E3), and of some further enzymes of this system. Subsequently, I became interested in the roles of ubiquitin-mediated protein degradation in the cell division cycle. This led me to the Marine Biological Laboratory (MBL) at Woods Hole, due to the availability of a clam oocyte cell-free

system, which faithfully reproduces cell-cycle-related events in the test tube. This system was important for the discovery of the cyclosome/anaphase-promoting complex, as described in the Lecture. In the past decade, I have spent my summers at the MBL for the same reason that I spent my summers previously at Fox Chase Cancer Center—to be able to devote almost all my time to doing experiments in a tranquil environment. Benchwork is my great hobby; I also do benchwork in Haifa, but on a more part-time basis. I have always loved to do experiments with my own hands, both for peace of mind and for excitement. Also, my own experiments were important for almost every significant progress made in my laboratory. One cannot have a more beautiful place than

the MBL for doing experiments: the great natural beauty of the surroundings, the tranquility and outstanding scientific environment all combine to make the MBL a great place for doing summer research.

When I look back at my life until now, I am amazed how fortunate I have been in both my personal and my scientific life. After escaping the Holocaust, both my parents lived in Israel to a good old age. I am very happy with my wife, children, and grandchildren. I was very fortunate to have outstanding mentors in science, and then to be able to use the knowledge gained for a significant contribution. If only there were some peace in the world, including between Israel and its neighbors—I would be completely satisfied.

2. Introduction

All living cells contain many thousands of different proteins, each of which carries out a specific chemical or physical process. Due to the importance of proteins in basic cellular functions, there has been a great interest in the problem of how proteins are synthesized. In the fifties and sixties of the 20th century, the discovery of the double-helical structure of DNA and the cracking of the genetic code focused attention on the mechanisms by which the order of bases in DNA determines the sequence of amino acids in proteins, and on further molecular mechanisms that regulate the expression of specific genes. Because of the intensive research activity on protein synthesis, little attention was paid at that time to the fact that many proteins are rapidly degraded to amino acids. This dynamic turnover of cellular proteins had been previously known by the pioneering work of Schoenheimer et al., who were among the first to introduce the use of isotopically labeled compounds to biological studies. They administered ^{15}N -labeled L-leucine to adult rats, and the distribution of the isotope in body tissues and in excreta was examined. It was observed that less than one-third of the isotope was excreted in the urine, and most of it was incorporated into tissue proteins.^[1] Since the weight of the animals did not change during the experiment, it could be assumed that the mass and composition of body proteins also did not change. It was concluded that newly incorporated amino acids must have replaced those in tissue proteins in a process of dynamic protein turnover.^[1] Schoenheimer's studies on the dynamic state of proteins and of some other body constituents were published in a small booklet in 1942, soon after his untimely death (ref. [2], see Figure 8).

In the subsequent decades, research on protein degradation was neglected, mainly because of the great interest in the mechanisms of protein synthesis, as described above. However, experimental evidence gradually accumulated which indicated that intracellular protein degradation is extensive, selective, and has basically important cellular functions. It was observed that abnormal proteins produced by the incorporation of some amino acid analogues are selectively recognized and are rapidly degraded in cells.^[3] However, intracellular protein degradation was not thought to be merely a

“garbage disposal” system for the elimination of abnormal or damaged proteins. By the late sixties, it became apparent that normal proteins are also degraded in a highly selective fashion. The half-life times of different proteins ranged from several minutes to many days, and rapidly degraded proteins usually had important regulatory functions. These properties of intracellular protein degradation and the role of this process in the regulation of the levels of specific proteins were summarized in an excellent review by Schimke and Doyle in 1970.^[4] Thus, it was known at that time that protein degradation has important functions, but it was not known

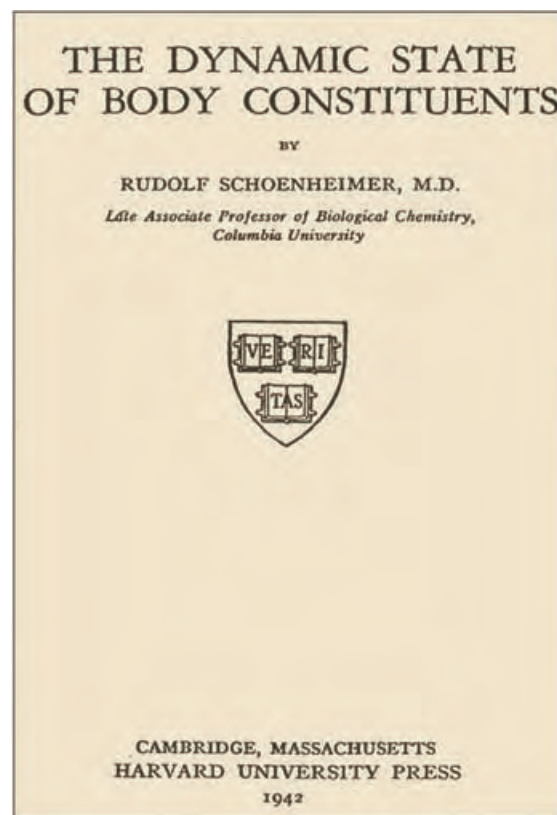


Figure 8. Front page of Schoenheimer's collected lectures, edited by his colleagues soon after his death.

what is the biochemical system that carries out this process at such a high degree of selectivity and sophistication.

3. My First Encounter with Protein Degradation

I became interested in the problem of how proteins are degraded in cells when I was a postdoctoral fellow in the laboratory of Gordon Tomkins in 1969–1971 at the University of California, San Francisco. At that time, Gordon was mainly interested in the mechanisms by which steroid hormones induce the synthesis of specific proteins. His model system for this purpose was the synthesis of the enzyme tyrosine aminotransferase (TAT) in cultured hepatoma cells. When I arrived there I saw that it was a large laboratory, with many postdoctoral fellows working on different aspects of the synthesis of TAT. I thought that this was a bit too crowded and I asked Gordon for a different project. He suggested that I should study the degradation of TAT, a process that also regulates the level of this enzyme. This was how I became involved in protein degradation, a problem on which I have been working ever since.

Figure 9 shows one of the first experiments that I did as a postdoctoral fellow in the Tomkins lab. It was quite easy to follow the degradation of TAT: first hepatoma cells were

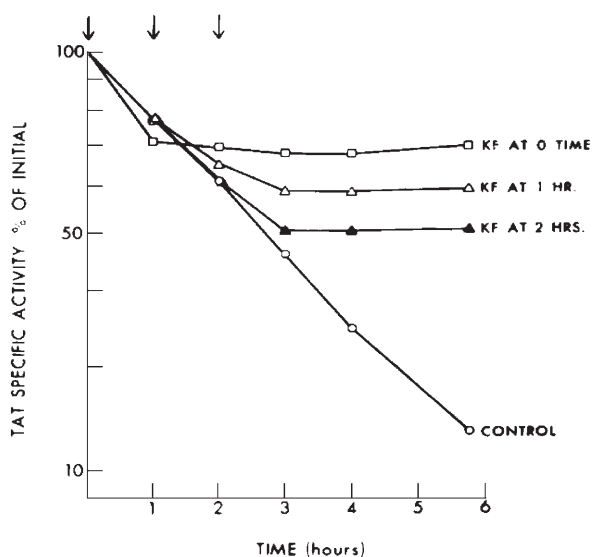


Figure 9. Energy-dependence of the degradation of tyrosine aminotransferase; from ref. [5].

incubated with a steroid hormone, which caused a great increase in the level of this protein. Then the hormone was removed by changing the culture medium, and a rapid decline in the level of this protein, due to its degradation, could be observed. As with other regulatory proteins, this protein also had a relatively rapid rate of degradation, with a half-life time of about 2–3 h. I found then that the degradation of TAT was completely arrested by potassium fluoride, an inhibitor of cellular energy production (ref. [5] and Figure 9). The effect was not specific to fluoride, because I got similar results with

other inhibitors of cellular energy production. These results confirmed and extended earlier findings of Simpson^[6] on the energy-dependence of the liberation of amino acids from proteins in liver slices. This observation was later dismissed as being indirect, and that energy is needed to keep the acidic pH value inside the lysosomes (described in ref. [7]). However, in the case of TAT, energy was needed for the selective degradation of a specific enzyme, and it did not seem reasonable to assume that engulfment into lysosomes could be responsible for the highly selective degradation of specific cellular proteins. Since ATP depletion also prevented the inactivation of the enzymatic activity of TAT, it was concluded that energy is required at an early step in the process of protein degradation.^[5]

I was very much intrigued by the energy-dependence of intracellular protein degradation. Energy is usually needed to synthesize a chemical bond, and not to break a chemical bond. Thus, the action of extracellular proteinases of the digestive system is an exergonic process, that is, it actually releases energy. This suggested that within cells a novel, as yet unknown proteolytic system exists, that presumably uses energy to attain the high selectivity of the degradation of cellular proteins.

4. Discovery of the Role of Ubiquitin in Protein Degradation

Parts of the story of the discovery of the ubiquitin system have been described previously.^[7–9] Following my return to Israel and setting up my own laboratory at the Technion in Haifa, I continued to pursue this problem of how proteins are degraded in cells, and why energy is required for this process. It was clear to me that the only way to find out how a completely novel system works is that of classical biochemistry. This consists of using a cell-free system that faithfully reproduces the process in the test tube, fractionation to separate its different components, purification and characterization of each component, and reconstitution of the system from isolated and purified components. A cell-free ATP-dependent proteolytic system from reticulocyte lysates was first established by Etlinger and Goldberg.^[10] Subsequently, my laboratory subjected this system to biochemical fractionation, with the aim of the isolation of its components and the characterization of their mode of action. A great part of this work was done by Aaron Ciechanover, who was my graduate student at that time (1976–1981). This work has also received a lot of support, great advice, and helpful criticism from Irwin Rose, in whose laboratory at Fox Chase Cancer Center I worked in a sabbatical year in 1977/1978 and in many summers afterwards.

In the initial experiments, we resolved reticulocyte lysates on DEAE-cellulose into two crude fractions: fraction 1, which contained proteins not adsorbed to the resin, and fraction 2, which contained all proteins adsorbed on the resin and eluted with concentrated salt solution. The original aim of this fractionation was to get rid of hemoglobin, which was known to be in fraction 1, while most nonhemoglobin proteins of reticulocytes were known to be in fraction 2. We found that

neither fraction was active by itself, but ATP-dependent protein degradation could be reconstituted by the combination of the two fractions.^[11] The active component in fraction 1 was a small, heat-stable protein; we have exploited its stability to heat treatment for its purification to near homogeneity. We termed this protein at that time APF-1, for ATP-dependent proteolysis factor 1. The identity of APF-1 with ubiquitin was established later by Wilkinson et al.,^[12] subsequent to our discovery of its covalent ligation to protein substrates, as described below. Ubiquitin was originally isolated by Goldstein et al. in a search for hormones of the thymus, but was subsequently found to be present in all tissues and eukaryotic organisms, hence its name.^[13] The functions of ubiquitin were not known, though it was discovered by Goldknopf and Busch that ubiquitin was conjugated to histone 2A by an isopeptide linkage.^[14]

The purification of APF-1/ubiquitin from fraction 1 was the key to the elucidation of the mode of its action in the proteolytic system. It looked smaller than most enzymes, so at first we thought that it might be a regulatory subunit of some enzyme (such as a protein kinase or an ATP-dependent protease) present in fraction 2. To test this notion, we looked for the association of APF-1/ubiquitin with some protein in fraction 2. For this purpose, purified radiolabeled APF-1/ubiquitin was incubated with fraction 2 in the presence or absence of ATP, and was subjected to gel-filtration chromatography. A marked ATP-dependent association of APF-1/ubiquitin with high-molecular-weight material was observed.^[15] It was very surprising to find, however, that ubiquitin was bound by a covalent amide linkage, as indicated by the resistance of high-molecular-weight derivative to alkali, hydroxylamine, and boiling with SDS (sodium dodecylsulfate) in the presence of mercaptoethanol.^[15] The analysis of reaction products by SDS-polyacrylamide gel electrophoresis showed that ubiquitin was ligated to a great number of endogenous proteins. Since crude fraction 2 from reticulocytes contained not only enzymes, but also endogenous substrates of the proteolytic system, we began to suspect that ubiquitin may be linked to protein substrates, rather than to an enzyme. We indeed found that proteins that are good (though artificial) substrates of the ATP-dependent proteolytic system, such as lysozyme, are conjugated to ubiquitin.^[16] The original experiment is shown in Figure 10. We found that similar high-molecular-weight derivatives were formed when ¹²⁵I-labeled ubiquitin was incubated with unlabeled lysozyme (Figure 10, lanes 3–5), or when ¹²⁵I-labeled lysozyme was incubated with unlabeled ubiquitin in the presence of ATP (Figure 10, lane 7). Based on these observations, we proposed that proteins are targeted for degradation by covalent ligation to APF-1/ubiquitin.^[16] The original hypothesis from 1980, formulated jointly with Irwin Rose, is shown in Figure 11a. We proposed that a putative enzyme, which we called “APF-1-protein amide synthetase”, ligates multiple molecules of ubiquitin to the protein substrate (step 1) and then some other enzyme degrades proteins which are linked to several molecules of ubiquitin (step 3), and finally free and reutilizable ubiquitin is released (step 4). According to this proposal, ubiquitin is essentially a tag, which when attached to a protein, dooms this protein to be degraded.

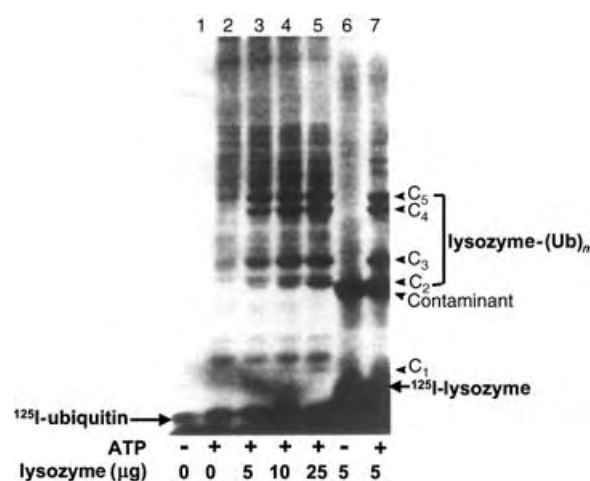


Figure 10. Discovery of covalent ligation of ubiquitin to substrate protein. See the text for more information; from ref. [16].

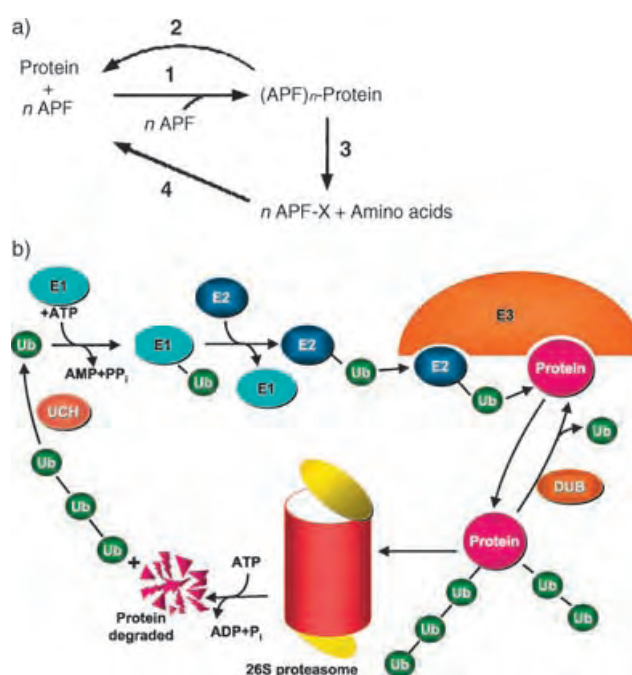


Figure 11. The ubiquitin system then and now. a) Original proposal of the sequence of events in protein degradation. See the text for more information; from ref. [16]. b) Our current view of the main enzymatic reactions in ubiquitin-mediated protein degradation. See the text for more information. Ub, ubiquitin; DUB, deubiquitylating enzyme; UCH, ubiquitin carboxyl-terminal hydrolase.

5. Identification of Enzymes of the Ubiquitin-Mediated Proteolytic System

In subsequent work, we tried to isolate and characterize enzymes of the ubiquitin pathway, by using the same biochemical fractionation/reconstitution approach. The original proposal of the mechanism (Figure 11a) was found to be essentially correct, but much important detail was added. Our present knowledge of the main enzymatic steps in the

ubiquitin-mediated proteolytic pathway is shown in Figure 11b (reviewed in ref. [17]). This scheme summarizes about 10 years of our work (1980–1990), as well as that of some other researchers. Thus, we found that ubiquitin is ligated to proteins not by one enzyme, but by the sequential action of three enzymes. These are the ubiquitin activating enzyme E1,^[18] a ubiquitin carrier protein E2,^[19] and a ubiquitin protein ligase E3.^[19] E1 carries out the ATP-dependent activation of the carboxy-terminal glycine residue of ubiquitin^[20] by the formation of ubiquitin adenylate, followed by the transfer of activated ubiquitin to a thiol site of E1 with the formation of a thioester linkage.^[18,21] Activated ubiquitin is transferred to a thiol site of E2 by transacylation, and is then further transferred to an amino group of the protein substrate in a reaction that requires E3.^[19] We found that the role of E3 is to bind specific protein substrates.^[22] Based on this observation, it was proposed that the selectivity of ubiquitin-mediated protein degradation is mainly determined by the substrate specificity of different E3 enzymes.^[23] This notion was verified by subsequent work in many laboratories on the selective action of a large number of different E3 enzymes on their specific protein substrates. Proteins ligated to polyubiquitin chains are degraded by a large 26S proteasome complex (discovered by other investigators) and free ubiquitin is released by the action of ubiquitin-C-terminal hydrolases or isopeptidases (reviewed in ref. [17]).

6. Mechanisms of the Degradation of Cyclin B: Discovery of the Cyclosome/Anaphase-Promoting Complex

All our studies on the basic biochemistry of the ubiquitin pathway were carried out with the reticulocyte system, using artificial model protein substrates. Though many gaps remained in our understanding of the basic biochemical processes of the ubiquitin system, at around 1990 I thought that it was important to turn to the question of how the degradation of specific cellular proteins is carried out by the ubiquitin system in a selective and regulated fashion. This is how I became interested in the roles of the ubiquitin system in the cell-division cycle, because the levels of many cell-cycle regulatory proteins oscillate in the cell cycle. I first worked on the biochemical mechanisms of the degradation of cyclin B in the early embryonic cell cycle. Cyclin B was discovered by Hunt and co-workers to be a protein that is degraded at the end of each mitosis.^[24] It was subsequently found that it is a positive regulatory subunit of protein kinase Cdc2/Cdk1 (cyclin-dependent kinase 1; reviewed in ref. [25]). In the early embryonic cell cycles, cyclin B is synthesized during the interphase and then is rapidly degraded in the metaphase–anaphase transition. The active protein kinase Cdk1–cyclin B (also called MPF or M phase-promoting factor) is formed at the beginning of mitosis and promotes entry of cells into mitosis. The inactivation of MPF, caused by the degradation of cyclin B, is required for exit from mitosis. Our question was: what is the system that degrades cyclin B and why does it act only at the end of mitosis?

I approached this problem again by biochemistry, and here the quest for a cell-free system led me to marine biology and to the surf clam *Spisula solidissima* (Figure 12). This is a large clam that produces large numbers of oocytes. Luca and

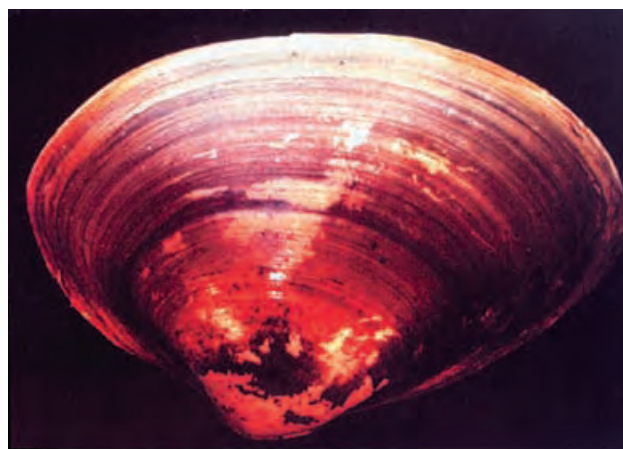


Figure 12. The North Atlantic surf clam *Spisula solidissima*.

Ruderman^[26] established a cell-free system from fertilized clam oocytes that faithfully reproduced cell-cycle stage-specific degradation of mitotic cyclins. In this work, I was greatly helped first by Robert Palazzo and Leonard Cohen, and then by collaboration with Joan Ruderman. Initial fractionation of the system^[27] showed that in addition to E1, two novel components were required for the ligation of cyclin B to ubiquitin: these were a specific E2 called E2-C and an E3-like activity, which in clam extracts was associated with particulate material. We solubilized the E3-like activity and found it to be a large (ca. 1500 kDa) complex that has ubiquitin ligase activity on mitotic cyclins. The activity of this enzyme is regulated in the cell cycle: it is inactive in the interphase and becomes active at the end of mitosis, an event that requires the action of Cdk1/cyclin B.^[28] We called this ubiquitin ligase complex the cyclosome, to denote its large size and important roles in cell-cycle regulation.^[28] A similar complex was isolated at about the same time from extracts of *Xenopus* eggs by the Kirschner laboratory and was called the anaphase-promoting complex.^[29] Parallel genetic work in yeast by the Nasmyth group identified several subunits of the anaphase-promoting complex/cyclosome (or APC/C, as it is now called) as products of genes required for exit from mitosis.^[30] Thus, the discovery of APC/C was due to the convergence of biochemical and genetic work. Subsequent work by other investigators showed that the APC/C is also involved in the degradation of several other important cell-cycle regulators, such as securin, an inhibitor of anaphase onset (reviewed in refs. [31,32]). In addition, APC/C is the target of the spindle assembly checkpoint system, an important surveillance mechanism that allows the separation of sister chromatids only after they are all properly attached to the mitotic spindle (reviewed in ref. [33]).

7. Role of Skp^{SKP2} Ubiquitin Ligase in the Degradation of the Cdk Inhibitor P27^{Kip1}

Another problem on which I have been working recently, in collaboration with Michele Pagano, is the mode of the degradation of the mammalian Cdk inhibitor p27^{Kip1} . This inhibitor is present at high levels in G0/G1, preventing the action of Cdk2/cyclin E and Cdk2/cyclin A to drive cells into the S-phase. Following growth stimulation by mitogenic agents, p27 is rapidly degraded, allowing the action of these kinases to promote entry into the S-phase (reviewed in ref. [34]). It has been shown that p27 is degraded by the ubiquitin system.^[35] We have tried to identify the ubiquitin ligase system that targets p27 for degradation. It was first found that the process of p27–ubiquitin ligation can be faithfully reproduced in vitro in extracts of HeLa cells. Thus, the rate of ligation of p27 to ubiquitin was much greater in extracts from growing cells than in extracts from G1-arrested cells. It was also found that the phosphorylation of p27 on T187 by Cdk2/cyclin E is required for p27–ubiquitin ligation in vitro,^[36] as is the case in vivo.^[37] Having established that the cell-free system accurately reflects the characteristics of p27 ubiquitylation in cells, we then proceeded to utilize this cell-free system to identify the ubiquitin ligase (E3 enzyme) involved in this process. Because of the requirement for the phosphorylation of the p27 substrate, we suspected that an SCF-type (Skp1-cullin1-F-box protein) ubiquitin ligase might be involved. SCF complexes comprise a large family of ubiquitin–protein ligases, whose variable F-box protein subunits recognize a variety of phosphorylated protein substrates (reviewed in ref. [38]). We have identified Skp2 (S-phase kinase-associated protein 2) as the specific F-box protein component of an SCF complex that ubiquitylates p27, based on the following biochemical evidence: 1) Immunodepletion of extracts from proliferating cells with an antibody directed against Skp2 abolished p27–ubiquitin ligation activity; 2) addition of recombinant, purified Skp2 to such immunodepleted extracts completely restored p27–ubiquitin ligation; 3) specific binding of p27 to Skp2, dependent upon phosphorylation of p27 on T187, could be demonstrated in vitro. Combined with further in vivo evidence from the Pagano group, Skp2 was identified as the specific and rate-limiting component of an SCF complex that targets p27 for degradation.^[39] It is notable that levels of Skp2 also oscillate in the cell cycle, being very low in G1, increasing upon entry of cells into the S-phase, and declining again later on.^[40] These fluctuations in Skp2 levels provide an important mechanism for cell-cycle, stage-specific regulation of p27 degradation.

We next tried to reconstitute the SCF^{Skp2} system that ligates p27 to ubiquitin from purified components. We found that in addition to the known components (cullin 1, Skp1, Skp2, Roc1, Cdk2/cyclin E, E1, and the E2 enzyme Cdc34), an additional protein factor is required for this reaction. We have purified the missing factor from extracts of HeLa cells and have identified it as Cks1 (cyclin kinase subunit 1), both by mass spectrometry sequencing and by functional reconstitution with recombinant Cks1 protein.^[41] Cks1 belongs to the highly conserved Suc1/Cks family of proteins, which bind to some cyclin-dependent kinases and to phosphorylated pro-

teins, and are essential for several cell-cycle transitions.^[42] Human Cks1, but not other members of this protein family, reconstituted p27–ubiquitin ligation in a completely purified system. While all members of the Suc1/Cks protein family have Cdk-binding and anion-binding sites, only mammalian Cks1 binds to Skp2 and promotes the association of Skp2 with p27 phosphorylated on T187.^[41] Similar results were independently obtained by another research group.^[43] More recently, we have mapped the Skp2 binding site of Cks1 by site-directed mutagenesis and found that it is located on a region that includes the $\alpha 2$ and $\alpha 1$ helices, well separated from the other two binding sites of Cks1. All three binding sites of Cks1 are required for its action to promote p27–ubiquitin ligation and for the association of Skp2 with T187-phosphorylated p27.^[44] Based on these and on further observations a model was proposed, according to which Cks1 serves as an adaptor necessary for enzyme–substrate interaction: the Skp2–Cks1 complex binds to phosphorylated p27, a process which requires the anion-binding site of Cks1. The affinity of Skp2 to the substrate is then further strengthened by the association of the Cdk binding site of Cks1 with Cdk2/cyclin E, to which phosphorylated p27 is tightly bound.^[44] It is notable that the expression of Cks1 also oscillates in the cell cycle,^[45,46] providing an additional mechanism for the regulation of p27 degradation.

8. Concluding Remarks

The ubiquitin system has come a long way since its humble beginnings described here. Ubiquitin-mediated degradation of positively or negatively acting regulatory proteins is involved in a variety of cellular processes such as the control of cell division, signal transduction, transcriptional regulation, immune and inflammatory responses, embryonic development, apoptosis, and circadian clocks, to mention but a few. The involvement of malfunction of ubiquitin-mediated processes in diseases such as certain cancers, and the therapeutic implications of this knowledge, are also beginning to emerge. I am quite certain that we are still seeing only the tip of the iceberg of the multitude of functions of the ubiquitin system in health and disease. The main lesson from the story of the discovery of the ubiquitin system that I would like to convey, mainly to young researchers, is the continued importance of biochemistry in modern biomedical research. In his book *For the Love of Enzymes*, Arthur Kornberg divided the history of biomedical research into four main periods. First were the “microbe hunters”, the great microbiologists of the 19th century. They were followed by the “vitamin hunters”, the discoverers of the vitamins. Next were the “enzyme hunters”—the biochemists, followed by the “gene hunters”—the molecular geneticists. However, the times of enzyme (or protein) hunting are far from being over. With the completion of the human genome project, all genes have been “hunted”, but we know the functions of only about one-third of our genes. If we want to know what the roles of the rest of our genes in health and in disease are, we shall have to continue to use biochemistry, in combination with functional genetics, well into the future. Our story shows that the ubiquitin system

could not have been discovered without biochemical approaches. We would not have a clue to the ubiquitin-tagging mechanisms by genetics alone, or by the sequence of the genes in the ubiquitin system. On the other hand, once the basic biochemistry was known, molecular genetic approaches were essential for the discovery of the multitude of functions of the ubiquitin proteolytic pathway. So my advice to young investigators in biomedical sciences is: if you have a problem that cannot be solved by molecular genetics alone, do not be afraid to use biochemistry, do not hesitate to enter the cold room, and do not be wary of approaching the FPLC machine!

In experimental sciences, including biochemistry, discoveries are not made by a single person, but require the assistance of dedicated research teams and the help of friends, colleagues, and collaborators. In my laboratory at the Technion, Haifa, I was very fortunate to receive devoted help, at different times over a period of more than 30 years, from Dvora Ganoth, Hanna Heller, Esther Eytan, Sarah Elias, Clara Segal, and from my wife, Judith Hershko. Among my former graduate students, Aaron Ciechanover did tremendous work in the exciting times of the discovery of ubiquitin–protein ligation 25 years ago. Subsequently, many other graduate students (too many to list here) did very important work on the basic biochemistry of the ubiquitin system and more recently, on some roles of this system in cell-cycle control. Out of my several friends/collaborators, mentioned here, Irwin Rose had a very special role. My association with Ernie started with a sabbatical year in his laboratory in Fox Chase Cancer Center, Philadelphia, in 1977–1978 (see also the biography at the beginning of this Review). During this year, I continued to work on the initial fractionation of the reticulocyte system and the purification of ubiquitin, which we started in Haifa. In the following summer of 1979, Ernie invited me back to his laboratory, together with my graduate student Aaron Ciechanover and research assistant Hanna Heller. When we got there we already knew, from work done in the Haifa lab, that ubiquitin becomes bound to proteins in an ATP-dependent process. However, the discovery that a covalent amide bond is

formed between ubiquitin and the substrate protein was made together with Ernie Rose in that summer in Philadelphia. A group picture, taken at the end of this memorable summer of 1979 at Fox Chase Center, included the people involved (Figure 13). The results of this summer's work are reported in ref. [16].

Received: May 19, 2005



Figure 13. At the end of summer of 1979 in Fox Chase Cancer Center, Philadelphia. Seated left to right: Avram Hershko, Sandy Goldman, Jessie Warms, Hanna Heller. Standing left to right: Zelda Rose, Arthur Haas, Aaron Ciechanover, Mary Williamson, Irwin Rose, Keith Wilkinson, and Leonard Cohen (last three people standing on the right side not identified).

- [1] R. Schoenheimer, S. Ratner, D. Rittenberg, *J. Biol. Chem.* **1939**, 130, 703–732.
- [2] R. Schoenheimer, *The Dynamic State of Body Constituents*, Harvard University Press, Cambridge, **1942**.
- [3] M. Rabinowitz, J. M. Fisher, *Biochim. Biophys. Acta* **1964**, 91, 313–322.
- [4] R. T. Schimke, D. Doyle, *Annu. Rev. Biochem.* **1970**, 39, 929–976.
- [5] A. Hershko, G. M. Tomkins, *J. Biol. Chem.* **1971**, 246, 710–714.
- [6] M. V. Simpson, *J. Biol. Chem.* **1953**, 201, 143–154.
- [7] A. Hershko, A. Ciechanover, A. Varshavsky, *Nat. Med.* **2000**, 6, 1073–1081.
- [8] A. Hershko, *Trends Biochem. Sci.* **1996**, 21, 445–449.
- [9] K. D. Wilkinson, *Cell* **2004**, 119, 741–745.
- [10] J. D. Etlinger, A. L. Goldberg, *Proc. Natl. Acad. Sci. USA* **1977**, 74, 54–58.
- [11] A. Ciechanover, Y. Hod, A. Hershko, *Biochem. Biophys. Res. Commun.* **1978**, 81, 1100–1105.
- [12] K. D. Wilkinson, M. K. Urban, A. L. Haas, *J. Biol. Chem.* **1980**, 255, 7529–7532.
- [13] G. Goldstein, M. Scheid, U. Hammerling, E. A. Boyse, D. H. Schlesinger, H. D. Niall, *Proc. Natl. Acad. Sci. USA* **1975**, 72, 11–15.
- [14] I. L. Goldknopf, H. Busch, *Proc. Natl. Acad. Sci. USA* **1977**, 74, 864–868.
- [15] A. Ciechanover, H. Heller, S. Elias, A. L. Haas, A. Hershko, *Proc. Natl. Acad. Sci. USA* **1980**, 77, 1365–1368.
- [16] A. Hershko, A. Ciechanover, H. Heller, A. L. Haas, I. A. Rose, *Proc. Natl. Acad. Sci. USA* **1980**, 77, 1783–1786.
- [17] A. Hershko, A. Ciechanover, *Annu. Rev. Biochem.* **1998**, 67, 425–479.
- [18] A. Ciechanover, H. Heller, R. Katz-Etzion, A. Hershko, *Proc. Natl. Acad. Sci. USA* **1981**, 78, 761–765.
- [19] A. Hershko, H. Heller, S. Elias, A. Ciechanover, *J. Biol. Chem.* **1983**, 258, 8206–8214.
- [20] A. Hershko, A. Ciechanover, I. A. Rose, *J. Biol. Chem.* **1981**, 256, 1525–1528.
- [21] A. L. Haas, J. V. Warms, A. Hershko, I. A. Rose, *J. Biol. Chem.* **1982**, 257, 2543–2548.
- [22] A. Hershko, H. Heller, E. Eytan, Y. Reiss, *J. Biol. Chem.* **1986**, 261, 11992–11999.
- [23] A. Hershko, *J. Biol. Chem.* **1988**, 263, 15237–15240.
- [24] T. Evans, E. T. Rosenthal, J. Youngbloom, D. Distel, T. Hunt, *Cell* **1983**, 33, 289–396.
- [25] M. Dorée, T. Hunt, *J. Cell Sci.* **2002**, 115, 2461–2464.
- [26] F. C. Luca, J. V. Ruderman, *J. Cell Biol.* **1989**, 109, 1895–1909.
- [27] A. Hershko, D. Ganoth, V. Sudakin, A. Dahan, L. H. Cohen, F. C. Luca, J. Ruderman, E. Eytan, *J. Biol. Chem.* **1994**, 269, 4940–4946.
- [28] V. Sudakin, D. Ganoth, A. Dahan, H. Heller, J. Hershko, F. C. Luca, J. V. Ruderman, A. Hershko, *Mol. Biol. Cell* **1995**, 6, 185–198.
- [29] R. W. King, J. M. Peters, S. Tugendreich, M. Rolfe, P. Hieter, M. W. Kirschner, *Cell* **1995**, 81, 279–288.
- [30] S. Irmiger, S. Piatti, C. Michaelis, K. Nasmyth, *Cell* **1995**, 81, 269–277.

- [31] W. Zachariae, K. Nasmyth, *Genes Dev.* **1999**, *13*, 2039–2058.
- [32] J. M. Peters, *Mol. Cell* **2002**, *9*, 931–943.
- [33] R. Bharadwaj, H. Yu, *Oncogene* **2004**, *23*, 2016–2027.
- [34] J. Slingerland, M. Pagano, *J. Cell. Physiol.* **2000**, *183*, 10–17.
- [35] M. Pagano, S. W. Tam, A. M. Theodoras, P. Beer-Romano, G. Del Sal, V. Chau, P. R. Yew, G. F. Draetta, M. Rolfe, *Science* **1995**, *269*, 682–685.
- [36] A. Montagnoli, F. Fiore, E. Eytan, A. C. Carrano, G. F. Draetta, A. Hershko, M. Pagano, *Genes Dev.* **1999**, *13*, 1181–1189.
- [37] J. Vlach, S. Hennecke, B. Amati, *EMBO J.* **1997**, *6*, 5334–5344.
- [38] R. J. Deshaies, *Annu. Rev. Cell Dev. Biol.* **1999**, *15*, 435–467.
- [39] A. Carrano, E. Eytan, A. Hershko, M. Pagano, *Nature Cell Biol.* **1999**, *1*, 193–199.
- [40] J. Lisztwan, A. Marti, H. Sutterluti, M. Gstaiger, C. Wirbelauer, W. Krek, *EMBO J.* **1998**, *17*, 368–383.
- [41] D. Ganoth, G. Bornstein, T. K. Ko, B. Larsen, M. Tyers, M. Pagano, A. Hershko, *Nat. Cell Biol.* **2001**, *3*, 321–324.
- [42] J. W. Harper, *Curr. Biol.* **2001**, *11*, R431–R435.
- [43] C. Spruck, H. Strohmaier, M. Watson, A. P. L. Smith, A. Ryan, W. Krek, S. I. Reed, *Mol. Cell* **2001**, *7*, 639–650.
- [44] D. Sitry, M. A. Seeliger, T. K. Ko, D. Ganoth, S. E. Breward, L. S. Itzhaki, M. Pagano, A. Hershko, *J. Biol. Chem.* **2002**, *277*, 42233–42240.
- [45] H. E. Richardson, C. S. Stueland, J. Thomas, P. Russel, S. I. Reed, *Genes Dev.* **1990**, *4*, 1332–1344.
- [46] T. Bashir, N. V. Dorrello, V. Amador, D. Guardavaccaro, M. Pagano, *Nature* **2004**, *428*, 190–193.
-

Intracellular Protein Degradation: From a Vague Idea, through the Lysosome and the Ubiquitin–Proteasome System, and onto Human Diseases and Drug Targeting (Nobel Lecture)**

Aaron Ciechanover*

Between the 1950s and 1980s, scientists were focusing mostly on how the genetic code is transcribed to RNA and translated to proteins, but how proteins are degraded has remained a neglected research area. With the discovery of the lysosome by Christian de Duve it was assumed that cellular proteins are degraded within this organelle. Yet, several independent lines of experimental evidence strongly suggested that intracellular proteolysis is largely non-lysosomal, but the mechanisms involved remained obscure. The discovery of the ubiquitin–proteasome system resolved the enigma. We now recognize that degradation of intracellular proteins is involved in regulation of a broad array of cellular processes, such as the cell cycle and division, regulation of transcription factors, and assurance of the cellular quality control. Not surprisingly, aberrations in the system have been implicated in the pathogenesis of human disease, such as malignancies and neurodegenerative disorders, which led subsequently to an increasing effort to develop mechanism-based drugs.

Keywords:

lysosomes · Nobel Lecture · proteasomes · protein breakdown · ubiquitin

From the Contents

1. Biographical Notes	5944
2. Introduction	5956
3. The Lysosome and Intracellular Protein Degradation	5957
4. The Lysosome Hypothesis Is Challenged	5959
5. The Ubiquitin–Proteasome System	5961
6. Concluding Remarks	5964

1. Biographical Notes

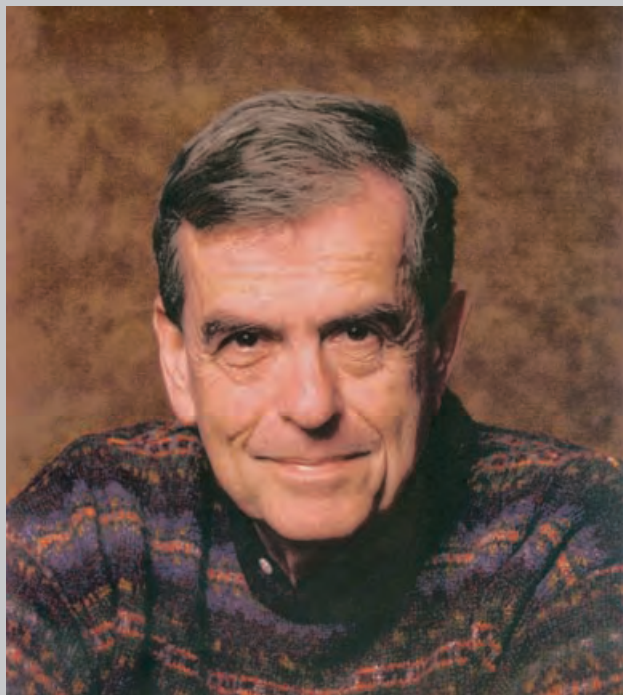
The Formative Years—Childhood in the Newly Born State of Israel

I was born in Haifa, a port city in the northern part of Israel, in October 1947, one month before Israel was recognized by the United Nations as an independent state. It took several additional months to establish the necessary institutions and for the British to leave, and on May 15th 1948, David Ben-Gurion, the founding father of the modern Jewish state and its first Prime Minister made Israel a fact and declared its establishment as a democratic state and a home for every Jew in the world. The neighboring, but even more distant Arab countries, along with powerful Arab parties from within did not accept the UN resolution and deliberately decided to alter it by force. A bloody and costly war erupted. It lasted a year, and more than 1 % of the population of the

newly born and defenseless state sacrificed their lives on its defense. I assume that the first two years of my life (1947–1949) were extremely difficult for my parents, Bluma (née Lubashevsky) and Yitzhak, who immigrated from Poland with their families as adolescents in the mid-1920s. Why did their families leave Poland—their “homeland”—their homes, working places, property, relatives, and friends, and decide to make their new home in a place with a vague, if any, clear

[*] Dr. A. Ciechanover
Faculty of Medicine
Technion-Israel Institute of Technology
Efron Street, Bat Galim
P.O.Box 9649, Haifa 31096 (Israel)
Fax: (+972) 4-852-3947, (+972) 4-851-3922
E-mail: c_tzachy@netvision.net.il

[**] Copyright© The Nobel Foundation 2004. We thank the Nobel Foundation, Stockholm, for permission to print this lecture.



future that was part of the British Empire? They were idealists who enthusiastically followed the call of the Zionist movement that was established at the turn of the century by Benjamin Ze'ev Herzl (the seer of the Jewish State) to settle the land and make it—after two thousand years in the Diaspora, since the destruction of the second temple in Jerusalem—a home for the Jews. Following the Jewish Congress in Basel (Switzerland) in 1896, Herzl declared: “*In Basel I founded the Jewish State*”. At that time Israel was part of the Ottoman Empire and became in 1917 part of the British Empire. My parents came from religious families, and the move, I believe, also had religious roots: Jews, throughout their lives in the Diaspora, have not stopped dreaming of having their own country, a dream that was driven by a biblical decree and prophecy:

“*Thus saith the Lord GOD: Behold, I will take the children of Israel from among the nations, whither they are gone, and will gather them on every side, and bring them into their own land*” (Ezekiel 37:21); “*And they shall dwell in the land that I have given unto Jacob my servant, wherein your fathers dwelt; and they shall dwell therein, they, and their children, and their children’s children, for ever*” (Ezekiel 37:25); “*And I will rejoice in Jerusalem, and joy in my people; and the voice of weeping shall be no more heard in her, nor the voice of crying*” (Isaiah 65:19); “*And they shall build houses, and inhabit them; and they shall plant vineyards, and eat the fruit of them*” (Isaiah 65:21).

The question of timing was an important one, as despite centuries of continuous persecution and discrimination in Europe, the initial idea to establish a Jewish State had been the dream of a few. Only small groups of Jews settled in Israel during the 18th, 19th, and the beginning of the 20th century. It was only towards the end of the 19th century, with the ideas of

Herzl and the moves that led to the Balfour declaration (the British Minister of Foreign Affairs who declared in 1917 the recognition of the need for a Jewish homeland) that an active Zionist movement and Institutions were established, resulting in the translation of the dream into reality. Yet, it took an enormous amount of courage and daring by these European Jews to materialize this dream and try to establish, with almost no resources or support, a homeland in a place they had dreamt of for two thousand years, but that was not theirs at the time. The process was clearly accelerated by the heavy clouds that then covered the skies of Europe and that ended with the Holocaust. Many members of my parents’ families immigrated to Israel before the Holocaust, but those who remained in Poland perished at the hands of the murderous Germans and their loyal Polish collaborators. The conversion of this movement into a State at that particular time (1947–1948) was no doubt the direct historical result of the holocaust, and symbolized the rise of the Jewish Nation from ash.

My father was a clerk in a law firm (later, in parallel with my brother, he studied law and became a lawyer), and my mother was a housewife and English teacher. My brother, Joseph (Yossi), who is 14 years older than me, was already on his national military compulsory service when I was 4 years old, the age from which I remember myself. I grew up in Haifa and enjoyed the wonderful beaches and Mount Carmel that rolls into the Mediterranean Sea. From my early days at home I remember a strong encouragement to study. My father worked hard to make sure we obtained the best possible education, and at the same time he was a member in the “Haganah” (defense), one of the prestate military organizations that fought the British for an independent Jewish State. Working in a law firm in the Arab section of the city, he risked his life daily going to work during the prewar hostilities and then the war time. My brother Joseph told me that the family waited daily on the balcony to see him return home peacefully. At home he used every free minute to delve into classic literature, Jewish religious law (Mishnah and Talmud), and modern law books. An important part of the education at home involved Judaism and Zionism. On the Jewish side, we obtained a liberal modern orthodox education. We attended services in the synagogue every Saturday and during holidays, and celebrated all Jewish holidays. Needless to say that my mother kept a Kosher kitchen.

It was extremely important for my parents to educate us as a new breed of proud Israeli Jews in their own independent country. I inherited from my father his love of Jewish studies and cultural life. To this very day, along with several physicians and scientist colleagues, I take regular periodical lessons taught by a Rabbinical scholar on how the Jewish law views moral and ethical problems related to modern medicine and science. Jewish cantorial music reflecting the prayers of Jews along many centuries has become my favorite music, and I avidly search for it in flea markets, used records stores, and auctions all over. Different Judaica artifacts also decorate my study.

In parallel, my parents made sure we should also receive an excellent general education. My father spoke several

languages fluently, Hebrew, Polish, Arabic, French, English, German, and Yiddish, and wanted me to acquire his strong love for books: while our home was not a rich one, we had a huge library. My parents also loved classical music, so we had a great collection of 78 rpm, and later 33 rpm records. I remember that Bizet's *Carmen* occupied more than 20 RCA (His Master Voice) 78 rpm bakelite records.

The apparently peaceful life of our family in Israel (although under the British Crown) during the years of the Holocaust in Europe was overshadowed by the murder of family members and of many families of friends and relatives that did not escape Europe in time. For my parents, the establishment of the State of Israel as an independent and sovereign Jewish State was a direct historical result of the Holocaust in Europe and a clear statement of "*Never Massadah shall fall again!*" (Massadah was one of the last strongholds of Jews during the Roman Empire. It fell into Roman hands after all its defenders committed suicide.) They left us with the idea that the Jewish State will not only protect us as free people, but will allow us to develop our own unique culture in a more general national context rather than as minorities scattered in different countries in the Diaspora.

Falling in Love with Biology

From early days I remember my strong inclination towards biology, though it has taken different directions at different times. I remember collecting flowers on Mount Carmel and drying them in the heavy Babylonian Talmud of my brother. I will never forget his rage on discovering my love of nature hidden among the pages of the old Jewish tracts. Then came the turtles and the lizards, extracting chlorophyll from leaves with alcohol, and the first microscope my brother bought me from his trip to England when I was 11 years old. With this microscope I discovered cells (in the thin onion epithelium) and did my first experiment in osmosis, when I followed the alteration in the volume of the cells after immersing the epithelium in salt solutions of different strengths. With friends we tried to launch a self-propelled rocket. The flower collection kept growing, now in special dedicated albums, and with it, a small collection of skeletons of different animals: fish, frog, toad, snake, turtle, and even some human bones I received from an older friend who was a medical student.

After several years of amateurish flirting with biology, I decided to formalize my knowledge and love of biology, and to major in Biology in high-school. While my years in elementary (1953–1959) and junior-high (1959–1962) school were mostly uneventful and passed without any thoughts on my future, the last two years in "Hugim" (Circles) high-school in Haifa (1963–1965) were not. I had wonderful and inspiring teachers in biology (Naomi Nof), chemistry (Na'ama Greenspon), and physics and mathematics (Harry Amitay). Biology at that time was largely a descriptive discipline: while we studied the mechanism of conversion of glucose into H_2O and CO_2 and production of energy in yeast and mammals (and the opposite process of photosynthesis in plants), and became

acquainted with simple graphic descriptions of mitotic and meiotic cell divisions, most of our studies were devoted to detailed descriptions of the flora and fauna in our region, to comparative zoology (I remember well the efforts invested in memorizing the twelve differences between the frog and the toad, or between the circulatory systems and skeletal structure of the cat and dog), and to basic descriptive human anatomy and physiology (for example, how the human skeleton enables posture to be maintained). Pathogenic mechanisms of diseases had not been mentioned, and the structure of DNA and the genetic code had entered our textbooks only towards the end of our high-school studies, in 1964/65. On the other hand, chemistry and physics appeared to me, maybe naively, to be strong mechanistic disciplines built on solid mathematical foundations. As a result, I had a deep feeling that the future somehow resided in biology, in deciphering basic mechanisms, as so little was then known. Yet, the complexity of biological and pathological processes looked to me enormous, almost beyond our ability to grasp, and I was intimidated: while I was clearly attracted to the secrets of biology, I was afraid to get lost. Importantly, I had nobody around, close enough, to consult, to clarify my thoughts. While deliberating between the largely unknown of biology and what I naively thought were the already well-founded physics and chemistry, medicine emerged as a compromise.

While it suffered from an even higher level of complexity compared to biology, it enjoyed some other advantages, such as the fascinating ability to cure or at least to provide some temporary solution to diseases. For me, this choice offered also a practical solution as in these years I lost both of my parents: my mother died in 1958 and my father in 1964. Their death meant that I needed to become independent as soon as I could. After the death of my mother, I was left with my father who took wonderful care of me. When my father died several years later, my late aunt Miriam (Wishniak; my mother's sister), with the support of my brother, took me to her home in Haifa, enabling me to seamlessly complete my high-school studies, in the same class and along with my friends, without interruption. The other option was to move to Tel Aviv, to my brother's home, but this would have been much more complicated. Their help was a true miracle, as thinking of it retrospectively, being left alone, without parents, at the age of sixteen, the distance to youth delinquency was shorter than the one to the high-school class. Yet, with the help of these wonderful family members, I managed to continue.

How My Love of Biology Evolved To Become a Career

Towards graduation from high-school I had to make a decision: The regular track would have taken me, like most Israelis, to national compulsory service in the Israeli Defense Forces (IDF), a duty we were all eager to fulfill. In addition to the regular service, the army encourages certain high-school graduates to postpone their service and first obtain a university education, particularly in areas that are relevant

to the military, such as medicine and different disciplines in engineering and sciences. Lacking any economic support, I thought it would be better to acquire a practical profession as soon as I could. As I mentioned, it was also a compromise between the complexity and mysteries of biological mechanisms to what I thought were the already exhausted physics and chemistry. What also attracted me to medicine was my impression that diseases could be cured: as children, we may have been influenced by short, self-limiting diseases that affected us, like influenza and measles, and were not directly aware of the major killers that left physicians and scientists alike helpless (much like these days), such as malignancies, vascular diseases, and neurodegenerative disorders. I had not appreciated at the time how far more descriptive medicine is, much more than biology. Practically, and no less important (which helped me solve my dilemma), was the fact that biology was not an option in the military-supported service postponement program.

So, after a fierce competition I was accepted at the only medical school in Israel at that time, that of the Hebrew University and “Hadassah” in Jerusalem (1965). The first four years (1965–1969) were exciting. We studied basic and clinical sciences, and I began to seriously entertain the idea of broadening my knowledge base in biochemistry or pharmacology. Towards the end of the fourth year, once we started to see patients, I started to have serious doubts whether I had made the right choice and truly wanted to become a practicing physician. The imbalance between phenomenology and pathogenetic mechanisms on one hand, and the lack of mechanism-based treatment for most of the major killers on the other hand, made me seriously think that I was on the wrong trail. I felt restless and started to realize how little we knew, how descriptive is our understanding of disease mechanisms and pathology, and as a consequence how most treatments are symptomatic in nature rather than causative. The statement “with God’s help” I heard so frequently from patients that were praying for a cure and health received a real meaning. I had a feeling clinical medicine was going to bore me, and decided to take one year off in order to “taste” true and “wet” basic research.

The Faculty of Medicine had a special, one-year program for the few who elected to broaden their knowledge in basic research, and I decided to major in biochemistry. I had to convince my brother that this was the right thing to do, as I needed his help to further postpone my military service by one year. This was not easy, as he too had a “dream”—to see me independent with a profession from which I could make my living, and which in the traditional Jewish spirit was nothing else but practical medicine. Following our parents’ death, he felt he was responsible for my future and well-being, and wanted to see me independent as soon as he could. I nevertheless managed to convince him, and during that year (1969–1970), under the guidance of first-rate biochemists, Jacob Bar-Tana and Benjamin Shapira, I investigated mechanisms of CCl_4 -induced fatty liver in a rat model, and discovered that it may be caused, at least partially, by an increased activity of phosphatidic acid phosphatase, a key enzyme involved in di- and triglyceride biosynthesis. Com-

pleting this research year (and obtaining an MSc degree), I knew I had found a new love—biochemistry. Jacob and Benjamin walked me through the exciting maze of biochemical pathways, and I was mystified. Yet, the consummation was still far away. Being loyal to the promise I made to my brother, and also to my commitment to the Israeli army, I completed the clinical years (1970–1972) and graduated Medical School.

To obtain my medical license, I still had to complete one additional year of rotating internship. At that time colleagues told me that a young talented biochemist, Dr. Avram Hershko, had just finished his postdoctoral training with Gordon Tomkins at the University of California in San Francisco (UCSF) and was recruited by the Dean and founder of the newly established Faculty of Medicine at the Technion in Haifa, the late Professor David Ehrlich, to establish a unit of Biochemistry. I wrote to Avram, with the intention to relocate to Haifa, to carry out my rotating internship there, and to use this year to carry out my MD thesis research project under his supervision. This was a small thesis I had to submit to the Medical School in partial fulfillment of the requirements for graduation. Typically for this thesis, most medical students evaluate statistically on-going treatments/procedures, but I decided to return to the laboratory and touch on yet another research project. He agreed to accept me as an MD student, and in October 1972 we started our more than three decades voyage.

Avram was still not certain about his own main research direction, and we discussed two possibilities for my MD thesis. One was obviously to further dissect the tyrosine aminotransferase (TAT) ATP-dependent proteolytic pathway. Avram started his own trip into the world of intracellular proteolysis with Gordon and discovered that the degradation of the gluconeogenic enzymes in cells requires energy. This was a corroboration of an earlier finding of Simpson who demonstrated in the early 1950s that the degradation of the entire population of cellular proteins in liver slices requires energy, but the mechanism(s) of this thermodynamically paradoxical requirement had remained elusive.

The other possibility was to study the mechanisms involved in the cell’s “pleiotropic response”—the immediate response of serum-starved, G0-synchronized cells to the addition of serum. During his postdoctoral studies with Gordon, Avram found that among the many stimulated processes are rapid uptake of nucleotides, amino acids, and phosphate. As during my studies on fatty liver I acquired experience working with lipids, and since Avram felt the elucidation of the TAT proteolytic mechanism may be a too difficult undertaking for a short MD thesis research project, we decided to add one additional layer to the study on the “pleiotropic response” and to analyze the effect of serum on the synthesis of phospholipids.

We assumed that following serum addition, cell membranes undergo major changes that will be reflected in phospholipid metabolism. Indeed, a few minutes after serum addition we were able to detect a dramatic increase in the turnover of the phosphoinositol moiety on the diglycerol skeleton. A review of the literature revealed a similar effect of

different target cells in response to a broad array of stimuli, including parasympathetic secretory cells responding to acetylcholine and thyroid gland cells to their cognate hormones, thyrotropin (TSH). The year (1972/73) I spent in the laboratory (it was not a real year but rather moonlighting, as a significant part of the time I was busy in the hospital rotating among the different clinical departments completing my duties as an intern towards graduation; I worked in the laboratory in my free evenings, nights, weekends, and holidays) finally convinced me to pursue a career in Biochemistry. But I still had three years of military service ahead of me (1973–1976).

Military Service and Professional Career—Have They Collided with One Another?

Following graduation, it was time to repay my national debt and serve in the IDF. I served for three years (1973–1976) and did it gladly. Serving in the army has always been regarded as an integral and important part of Israeli life and an entry card to its society, giving one the feeling of sharing—every one takes part in protecting this land and its inhabitants. In addition, the service itself was extremely interesting, technically, but also socially and historically. Technically, since I served in interesting units and socially, since the military service is a wonderful humane experience, the best melting pot one can go through, generating true friendships during hard times, friendships that are therefore deep, true, and lasting.

Historically, it spanned an interesting period. Initially I served in the navy, as a physician in the missile boats fleet. The year was 1973, immediately after the October Day of Atonement (Yom Kippur) war, and Israel faced a problem of protecting its southern gates, the Red Sea and the narrow Tiran (Sharm-a-Sheikh) strait that led to the port of Eilat. These were threatened by the Arab countries that neighbored the Red Sea, mostly Saudi Arabia and Egypt but also Yemen and Somalia, and Israel had to stretch its marine arm. To do so, it was necessary to transfer missile boats from the main naval bases in the Mediterranean to the Red Sea. At that time Israel did not have diplomatic relationship with Egypt, and the Suez Canal was closed by ships sunk by the Egyptians during the June 1967 Six Day War, so the decision was made to bring the boats from Haifa to Eilat, sailing through the Mediterranean Sea, and around the West and then East coasts of Africa. I was the physician on the “Reshef”, one of the two boats (modern Israeli missile boats that were built in the Haifa naval shipyard) selected for the mission. One can imagine that for small missile boats, such a long (several weeks) voyage, a large part of it in the open oceans, is rather complicated, and for many reasons also risky. Beyond fueling and provision of supplies and spare parts to the crews and boats, one has to think of sailing in waterways surrounded by hostile countries, many miles away from home and a long flight distance for the Israeli Air Force. Another problem was obviously medical, how one treats emergencies, from possible gunshot wounds through “simple” daily problems like appen-

dicitis, in a small ship, far from any medical facility and with limited diagnostic and treatment capabilities. I was particularly concerned, as I was a young physician with almost no clinical experience. I assume this would have been a challenge for more experienced physicians as well. Luckily, the voyage was smooth.

The remaining part of my three years service was also interesting. I spent that time in the Research and Development unit of the Medical Corps, developing a broad array of sophisticated devices for the soldier in the battlefield. Because of the broad range of experiences, the military service has been my ever best school for real “life sciences”. During all these years (1973–1976) I maintained tight connections with Avram and fulfilled my duties as an “external” department member: during vacations from the military and along with other members of the department, which grew meanwhile, I taught continuously the course in Clinical Biochemistry to third year medical students. I should mention in particular Michael (Mickey) Fry, with whom I have remained a good friend to the present day, and my good friend and colleague Erela Gorin, who died untimely in the early 1990s.

In 1975, during the military service, I married Menucha, a physician and a graduate of Tel Aviv University School of Medicine. Menucha was a resident in internal medicine in Tel Aviv Municipal Hospital, and we built our first home in this city. Marrying Manucha brought my wanderings to an end and I felt I had again a family and a home. During all the years since the death of my father (1963–1975) I did not have a really stable home, and I wandered between the homes of my brother and my aunt in Haifa. They were truly wonderful, but I needed a base, and Menucha, with her quiet approach and warm acceptance, along with our beautiful apartment, provided me with this so much needed shelter.

Discovery of the Ubiquitin System—Graduate Studies

Towards the end of the military service, I had to make what I assume has been the most important decision in my career: to start a residency in clinical medicine, in surgery, which was my favorite choice, or to enroll into graduate school and start a career in scientific research. It was clear to me that I was heading to graduate school. My disillusionment with clinical medicine that diseases can be cured based on the understanding of their pathogenetic mechanisms, along with a magical and enchanting attraction to biochemistry, made the decision easier. I received strong support and encouragement from my wife Menucha, who started to realize she was married to a graduate student with no clear future rather than to a physician with a bright career and broad financial horizons that she thought she had married.

So in November of 1976, after my discharge from the national service and a two months driving trip across the USA, I started my graduate studies with Avram Hershko. Since I had worked with him and known him for several years now, I thought he would be an excellent mentor. At that time his group focused mostly on studying intracellular proteolysis,

and I learnt from him that he had given up on trying to identify the mediator(s) and mechanism(s) involved in the serum-induced “pleiotropic response”. The choice of Avram was to work on the degradation of abnormal hemoglobin in reticulocytes, a terminally differentiating red blood cell. The reason for the selection of the reticulocyte as a model system was that we were looking for a non-lysosomal (and energy-requiring) proteolytic system, as from many studies it had become clear that regulated proteolysis of intracellular proteins is non-lysosomal, and the reticulocyte no longer contains lysosomes which are removed during the final stages of its maturation before its release into the circulation. From the work of others, it was clear that the reticulocyte contained such a proteolytic system.

Interestingly, in the summer of 1978, during a Gordon Conference on Lysosomes, I met Dr. Alex Novikoff from Yeshiva University School of Medicine in New York. Alex, along with Dr. Christian de Duve, was one of the pioneers of the lysosome research field. When I told him we were working on the reticulocyte because this cell does not have lysosomes, he angrily dismissed this argument, telling me that he characterized, though morphologically, acid-phosphatase-positive organelles in reticulocytes. He even gave me the relevant paper he published on the subject, though it was not clear that these are proteolytically functional organelles.

Another reason for the choice of the reticulocyte as a model for studying intracellular proteolysis was that in its final stages of maturation in the bone marrow and prior to entering the peripheral circulation, a massive proteolytic burst destroys most of its machineries, making it clear that the cell is equipped with an efficient proteolytic system. Earlier studies by Rabinovitz and Fisher demonstrated that the reticulocyte degrades abnormal, amino acid analogue containing hemoglobin, yet the mechanisms had remained elusive. We assumed that it was probably the same mechanism that was also involved in the natural maturation process and also in the removal of “naturally occurring” mutant abnormal hemoglobins that are synthesized in different hemoglobinopathies, such as thalassemias and sickle-cell anemia. Thus, this important piece of information—the existence of a non-lysosomal proteolytic system—made the choice of the reticulocyte an obvious one.

It was still necessary to demonstrate that the process required energy, and indeed, following an initial characterization of energy-requiring degradation of abnormal hemoglobin in the intact cell (which was published in 1978 in the proceedings of a proteolysis meeting held in Buffalo, NY), we felt the time was ripe to break the cell open and isolate and characterize the non-lysosomal and ATP-dependent proteolytic enzyme(s). Shortly before, in 1977, Dr. Alfred Goldberg and his postdoctoral fellow Dr. Joseph Etlinger at Harvard Medical School characterized, for the first time, a cell-free proteolytic system from reticulocyte, which was exactly the point where we wanted to start our own march, so we basically adopted their system.

I will not describe here the detailed history of the discovery of the ubiquitin system, but rather highlight two important points along the five years of my exciting graduate

studies (1976–1981) with Avram and Irwin A. (Ernie) Rose that led to the discovery of the system. The more detailed history can be found in several review articles written on the system at that time (see, for example, A. Herskho, A. Ciechanover, *Annu. Rev. Biochem.* **1982**, *51*, 335–364) and later, and in the accompanying Nobel Lecture.

The first point relates to the multiplicity of enzymatic components in the system: our first aim along the purification process of the ATP-dependent “protease” was to remove hemoglobin, the major protein in the crude extract. Towards that end, we resolved the extract on an anion-exchange resin, where we encountered the first exciting finding. The proteolytic activity could not be found neither in the non-adsorbed material, which we denoted fraction I, nor in the material eluted with a high salt concentration, denoted fraction II. Rather, we recovered the activity following reconstitution of the two fractions. We learnt two important lessons from this experiment which was published in 1978 in *Biochem. Biophys. Res Commun.* (in my opinion the first paper in the long historical trail of the ubiquitin proteolytic system) and which I regard as one of two or three key publications in the field. We learnt two lessons from this experiment: 1) The first lesson was that the protease we were after was not a “classical” single enzyme that degrades its substrate, but had at least two components. This was already a digression from the paradigm in the field at that time that proteolytic substrates, almost without exception, could be cleaved at least partially by single proteases with limited, yet defined specificities. Here we needed two components for proteolysis to occur. Now we know that the number of components of the ubiquitin system exceeds one thousand, but the first hint was already there; once one is left without a paradigm, all possibilities are open. 2) The second lesson was a methodological one. Each time we lost an activity during purification of any of the components we were characterizing, we returned to the chromatographic column fractions and tried to reconstitute it by complementation: “classical” biochemistry at its best was on our side.

Standing at a crossroads, we (luckily but thoughtfully) decided to start first with purification and characterization of the active component in fraction I. We decided so, because fraction I was the hemoglobin-containing fraction that did not adsorb onto the resin, and therefore we thought that it should not contain too many additional proteins. In the summer of 1977, ten months after I started my studies, Avram departed to a sabbatical with Ernie at the Fox Chase Cancer Center in Philadelphia, USA, and left me with the task of purifying the active component from fraction I. After many unsuccessful trials (along with another graduate student of Avram, Yaacov Hod), my colleague Mickey Fry, who was appointed as my substitute thesis advisor for this year (1977/78), came up with the “crazy” idea to heat fraction I and see if the active component was heat-stable, and indeed it was. He did so as all our attempts to resolve the activity from hemoglobin—despite the large difference in the molecular mass between the active protein (ca. 10 kDa) and hemoglobin (65 kDa)—failed. Following 5–10 min at 90°C, the hemoglobin in crude fraction I was “cooked” and precipitated like mud, and the activity remained soluble in the supernatant. It was hard to

believe it was a protein, but Mickey remembered several other heat-stable proteins. Immediately after, we showed directly that the activity in fraction I was also a protein: it was sensitive to trypsin and precipitable with ammonium sulfate. Further characterization revealed that the protein had a molecular mass of about 8500 Da, and we called it ATP-dependent proteolysis factor-1 (APF-1). All along the way I corresponded with Avram, sent him the data, and during his sabbatical we wrote the paper for *Biochemical and Biophysical Research Communications*.

The second key finding was also discovered in Haifa during the winter of 1978/79. We purified APF-1 to homogeneity and labeled it with radioactive iodine. When the radiolabeled protein was incubated in crude reticulocyte fraction II in the presence of ATP, we observed a dramatic increase in its molecular weight: it now migrated as a sharp peak in the void volume of the gel-filtration chromatographic column. For several months we tried to elucidate the mechanism that underlies this change, hypothesizing, for example, that APF-1 could be an activator of a protease that must generate a binary complex with the enzyme in order to stimulate it, but to no avail. An important breakthrough occurred during our 1979 summer stay of several months in the laboratory of Ernie. Through a series of extremely elegant, yet simple, experiments, in which we used the broad knowledge of Ernie in protein chemistry and enzymology, we found that APF-1 is covalently attached to the substrate through a bond that had all the characteristics of a peptide bond. Furthermore, we found that multiple moieties of APF-1 are attached to each substrate molecule, and that the reaction is reversible: APF-1 can dissociate from the substrate, though not by reversal of the conjugation reaction. Accordingly, we hypothesized that covalent attachment of multiple moieties of APF-1 to the target substrate is necessary to render it susceptible to degradation by a downstream protease that recognizes only tagged proteins, followed by the release of free and reusable APF-1.

The APF-1 cycle demonstrated unequivocally the existence of three, entirely novel activities: 1) APF-1-conjugating enzyme(s), 2) a protease that recognizes specifically the tagged substrates and degrades them, and 3) APF-1-recycling enzymes. All the enzymes involved were identified later by us (the three conjugating enzymes, E1, E2, and E3) or by others (the conjugates degrading protease known as the 26S proteasome complex, and the ubiquitin-recycling enzymes, the isopeptidases). The findings describing the covalent tagging of the target substrate by APF-1 as a degradation signal as well as its release, along with the first model of the newly discovered proteolytic system, were published in 1980 in two papers that appeared in the *Proceedings of the National Academy of Sciences*.

Another important development also occurred during our stay in Ernie's laboratory, and I am not sure whether it was sheer luck or serendipity, probably both. We were not aware of any other precedent of a modification of a protein by another protein. The neighboring laboratories of Martin Nemer, Alfred Zweidler, and Leonard Cohen studied dynamics of variants of different histones during sea urchin

development. They drew our attention to a protein called A24 (uH2A) which was discovered earlier by Ira Goldknopf and Harris Busch, and that was a covalent conjugate between two proteins: a small, approximately 8.5 kDa protein called ubiquitin and histone 2A (H2A). Goldknopf and Busch, and in parallel Margaret Dayhoff, identified the nature of the bond between the two protein moieties in the conjugate. They found that the ubiquitin–histone bond was an isopeptide/bifurcated bond between the C-terminal Gly⁷⁶ residue in the ubiquitin moiety, and the ϵ -NH₂ group of Lys¹¹⁹ in the histone moiety of the conjugate. The role of this conjugate was not clear at the time, though its level was found to be dynamic and change during differentiation, when the histone moiety is subjected to ubiquitination and deubiquitination.

This information on the ubiquitin–histone adduct and the similarity we found between APF-1 and ubiquitin in general characteristics, molecular mass, and amino acid composition, led Keith Wilkinson and his colleagues Arthur (Art) Hass from the laboratory of Ernie, along with Michael Urban from Zweidler's laboratory, to carry out a series of direct experiments, which showed unequivocally that APF-1 is indeed ubiquitin. Our study on the characterization of APF-1 and its possible similarity to ubiquitin, and Wilkinson's study (along with Urban and Haas) on the identification of APF-1 as ubiquitin, led to the convergence of two fields, that of histone research and of proteolysis. More importantly, they suggested that the bond between ubiquitin and the target proteolytic substrate maybe identical to that between ubiquitin and histone, which we demonstrated later to be true. The elucidation of the nature and structure of the bond clearly paved the road to the later identification of the conjugating enzymes and their mode of action. The two studies on APF-1, ours and that of Wilkinson and co-workers, were published in tandem in the *Journal of Biological Chemistry*.

As for ubiquitin, the protein was identified in the 1970s by Gideon Goldstein (in the Memorial Sloan–Kettering Cancer Center in New York City) as a small, 76-residue thymic polypeptide hormone that stimulates T-cell differentiation by activation of adenylate cyclase. Additional studies by Gideon Goldstein had suggested that it was universally distributed in both prokaryotes and eukaryotes, thus giving rise to its name (coined by Gideon Goldstein). Later studies by Allan Goldstein showed that the thymopoietic activity was due to an endotoxin contamination in the protein preparation, and not to ubiquitin. By using functional assays, it was found in my laboratory (and I believe in others as well) that ubiquitin was limited to eukaryotes, and its apparent presence in bacteria was due to contamination of the bacterial extract with the yeast extract in which the bacteria were grown: growing the bacteria in a synthetic medium resulted in the “disappearance” of ubiquitin from the preparation. The later unraveling of the bacterial genome demonstrated unequivocally that the ubiquitin tagging system does not exist in prokaryotes, though there is some similarity between the proteasome and certain bacterial proteolytic complexes. Thus, in a relatively short period of time, ubiquitin was converted from a ubiquitous thymopoietic hormone to a eukaryotic proteolytic marker. While the term ubiquitin is not justified anymore, as it is

clearly not ubiquitous, we stopped using the term APF-1 and adopted the term ubiquitin as the modifying protein in the newly discovered proteolytic system. At times habits and tradition are stronger from the scientific validity and/or from logic in nomenclature. Accordingly, we adopted a general policy to use in our terminology the name that was first coined by the discoverer of any novel protein.

From that point on, the road was relatively short to the identification and characterization of the conjugation mechanism and the three enzymes involved in this process. En route to the unraveling of the conjugation mechanism, we followed partially the footsteps of Dr. Fritz Lipmann, the great biochemist from Rockefeller University (who was awarded the 1953 Nobel Prize in Physiology or Medicine for the discovery of coenzyme A). Lipmann continued to contribute to our understanding of basic biochemical processes. Among his many discoveries was the mechanism of non-ribosomal (and hence nongenetically encoded) peptide-bond formation that occurs during the biosynthesis of bacterial oligopeptides such as gramicidin S. We learnt that the principles of basic biochemical reactions, such as generation of high-energy intermediates involved in peptide-bond formation, were preserved along evolution regardless of whether the bond is encoded genetically or not, or whether it links two amino acids or two proteins. Initially, we identified the general mechanism of activation of ubiquitin in a crude extract. Later, using “covalent” affinity chromatography over immobilized ubiquitin and a stepwise elution (that was based on the general activation mechanism we deciphered earlier), we purified the three conjugating enzymes that act successively in a cascadelike mechanism, and catalyze this unique process: 1) the ubiquitin-activating enzyme E1, the first enzyme in the ubiquitin system cascade, 2) the ubiquitin carrier protein E2, to which the activated ubiquitin is transferred from E1, and 3) the ubiquitin protein ligase E3, the last and critical component in the three-step conjugation mechanism that specifically recognizes the target substrate and conjugates it with ubiquitin. The binding of E1 and E2 was mediated by the activation mechanism. The E3 was also adsorbed onto the resin, although by a mechanism distinct from that of E1 and E2.

Later studies by Avram in the late 1980s revealed that the E3 adsorbed by the column was E3 α that recognizes substrates through their N-terminal residue. At this point, however, we were extremely lucky, when unknowingly we used as model substrates commercial proteins such as BSA, lysozyme, and RNase A that were all recognized by this ligase and through a similar targeting motif: their N-terminal residue. Had we used other substrates, such as globin, the model substrate we used in our initial experiments, the E3 α adsorbed to the column would have escaped our attention, as E3 enzymes do not typically adsorb to ubiquitin. In parallel and independently, I also used this enzyme in the late 1980s in order to characterize a distinct subset of proteins recognized by this signal (see below). Last, and most importantly, using antibodies that we raised against ubiquitin with the help of Arthur Haas, we found that the ubiquitin system is involved in degradation of abnormal, short-lived proteins in hepatoma

cells, thus demonstrating that the system was not limited to the terminally differentiating reticulocyte, but was probably distributed more “universally” in nucleated mammalian cells, playing a role in maintaining the cell’s quality control.

During my graduate studies at Avram’s laboratory, I collaborated with Hannah Heller, an extremely talented and knowledgeable research associate (who also joined us for some of our summer stays in the laboratory of Ernie in Philadelphia) and with Yaacov Hod who was also a graduate student with Avram at that time. Other colleagues in the laboratory provided me with a lot of help during this period, including Dvora Ganuth, Sarah Elias, and Esther Eythan who were research associates with Avram, and Clara Segal and Bruria Rosenberg, two dedicated technicians.

The Interaction with Irwin Rose

As noted, I spent an important part of my graduate studies in Ernie’s laboratory. Avram spent a sabbatical in his laboratory in 1977/78, and I joined him for the first time for several months in the summer of 1978, after I completed the initial characterization of APF-1 in Haifa. I returned to Ernie’s laboratory during the summers of 1979, 1980, and 1981. As noted, during our summer stay in 1979, we resolved the problem of the nature of the high-molecular-mass “compound” generated when APF-1 was incubated with fraction II in the presence of ATP. The change in the molecular mass of APF-1 was discovered several months earlier in Haifa, however, we were not able to unravel the nature of the “compound”; this had to await the knowledge and wisdom of Ernie. In a breakthrough discovery, we found that the target substrate is covalently modified by multiple moieties of APF-1, a modification that renders it susceptible to degradation. This was a novel type of posttranslational modification and clearly a new biological paradigm, that required—as I feel today in retrospect—a different type of knowledge and experimental approach. This would not have been possible without Ernie’s advice that was based on his immense knowledge in enzymology and protein chemistry, accompanied by his unbiased way of original thinking and approach to problem resolving. This discovery, along with the discovery that APF-1 is ubiquitin in 1980, made Ernie, his fellows (in particular Keith Wilkinson and Arthur Haas), and laboratory crucial players in the historical trail of the discovery of the ubiquitin system. Interestingly, Ernie also studied proteolysis before Avram joined him first, but had never published in the field before.

Postgraduate Training at MIT and How I Continued My Studies on the Ubiquitin System Independently

The five years in graduate school had a significant impact on my future career, not only because I played an active part in such an important discovery, but maybe more importantly, because I learnt several basic and important principles of how to approach a scientific problem. From my mentors, first and

foremost Avram, but also Ernie, I learnt two important principles: first, to select an important biological problem (but in order to avoid fierce competition and to be original to ascertain it is not in the mainstream), and second, to make sure there are appropriate research tools to approach it experimentally.

From Avram I also learnt to become a book rather than a short stories writer: I learnt not to be opportunistic but rather to adhere to a project, to dig deeply into a problem, to resolve it mechanistically, to untangle complex mazes—peeling them like an onion, and not to be tempted to be dragged after fashions. I learnt to pay attention to small details, to carefully examine hints, as the important findings were not always obvious from the beginning. I learnt to be stubborn, to fight difficulties uphill, and most importantly to be critical: I believe I developed good senses that enable me to distinguish false from truth, and artifacts from meaningful findings.

Interestingly, I learnt all these principles not in frontal lessons or formal presentations, but as an apprentice, following my mentors own attitude and way of thinking. But I also learnt to question, to doubt, to ask, and to discuss, to follow my own gut feeling when it was necessary, not to always take advice and direction for granted, and to trust myself too. It did help in many occasions along the way, although at times I found myself swimming against the stream in my own school. Altogether these principles generated an important philosophy and shaped my approach to science, something I try to instill to my own students, as I strongly believe it is the only way one can make an impact and leave an imprint behind.

Toward graduation I had to think of the next step: postdoctoral training and planning of my future career as an independent scientist. I was in a dilemma. On the one hand I knew it was important to obtain training somewhere else, under different mentorship, in a different environment, being exposed to a different culture of science. On the other hand I knew for certain that the ubiquitin system was extremely important and that we were seeing only the tip of its iceberg. I therefore wanted to continue my studies in a related field, learning more on regulated proteolysis, but also to continue my own studies on ubiquitin.

I had several ideas in mind of where to go. The choice was quite narrow and also risky, as I did not have any idea of how much independence I could have as a postdoctoral fellow. Searching for a mentor, and with the advice of my colleague Mickey Fry, I looked for scientists whose work was related to regulated proteolysis. I wrote to Günter Blobel in the Rockefeller University, who worked at that time on translocation of proteins to the endoplasmic reticulum (ER), a process which involves cleavage of the leader peptide by signal peptidase, to Jeffrey Roberts in Cornell, who worked on *E. coli* RecA protein directed cleavage of phage λ repressor and its requirement for polynucleotide, and to Harvey Lodish at the MIT, who worked, among other subjects, on the processing of viral polyproteins. I am not sure Harvey was that impressed with the ubiquitin system at that time, but he was the only one to respond positively. Typical of his etiquette (as I learnt later), his response was prompt and direct, and he invited me for an interview, after which he accepted me.

Günter was kind enough to let me know he did not have space in his laboratory at that time, and Jeffrey never responded.

With two fellowships, one from the Leukemia Society of America and one from the Israel Cancer Research Fund (ICRF), I started a period of three wonderful years (1981–1984) in Harvey's laboratory in the Department of Biology at MIT. Harvey gave me complete freedom to choose my research subjects. What I had in mind was to take advantage of the exceptional strength of the laboratory and Harvey's unique expertise in cell biology, but in parallel, to continue my own studies on the ubiquitin system.

I realized that Harvey was no longer interested in viral protein processing, and along with Alan Schwartz who was a visiting scientist (from Harvard Medical School) in the laboratory, we started to characterize the transferrin receptor on a human hepatoma cell line with the aim of later studying the mechanism of transferrin and transferrin receptor mediated iron delivery to cells. This collaboration led us, along with another fellow in the laboratory, Alice Dautry-Varsat (from the Pasteur Institute) who joined us later, to the discovery of a fascinating mechanism of how iron is delivered into cells: in the neutral pH of the growth medium, the iron-loaded holotransferrin binds to its receptor with a high affinity and is endocytosed into the cell. At the low endosomal pH, the affinity between the iron and transferrin is weakened dramatically. As a result, the iron cation is released, but the apotransferrin, which has high affinity for the receptor at acidic pH, remains bound. Along with the receptor, the apotransferrin recycles to the cell surface. At the neutral pH of the growth medium, the apotransferrin loses its high affinity to the receptor and is released into the extracellular fluid where it can load additional iron ions and then rebind to its receptor with high affinity.

The transferrin/transferrin receptor pH-dependent and iron loading-dependent cycle has become a “classic” in the field of receptor-mediated endocytosis. Based on this, other phenomena related to receptor and ligand recycling to the cell surface or targeting to the lysosome could be explained, which are also due to the pH difference between the external environment and the interior of the endocytic pathway vesicles.

However, throughout this time I lived under the strong feeling that the ubiquitin system had barely started to emerge, with only the basic principles unraveled. I felt compelled to get back and work on it. So gradually I started to “crawl” and return to my “alma mater” research subject.

On one fascinating subject I worked on my own—continuing to explore a mysterious finding I discovered during my graduate training and which I did not pursue at the time: when we purified APF-1/ubiquitin in Haifa, we noticed a large discrepancy between its dry weight and the Lowry assay quantitative protein measurement. Avram hypothesized that the protein could be a ribonucleoprotein (RNP), and the remaining mass is that of the nucleic acid component. To test this hypothesis, we added DNase to the crude extract (ATP- and ubiquitin-containing) assay in which we monitored degradation of bovine serum albumin (BSA) that was used as one of our model substrates. The enzyme had no effect. We

then added RNase A, and to our surprise proteolysis was completely inhibited, even with an extremely small amount—a mere few nanograms—of the enzyme added: it looked as though the enzyme exerted its effect by catalysis—RNA degradation.

Avram suggested testing the RNase effect on lysozyme as well—our second model substrate. Here we got no effect, which was kind of a surprise, as proteolysis of the two substrates, BSA and lysozyme, behaved in an identical manner all along the way. ATP as well as all the different factors resolved from the crude extract were all required for the degradation of both proteins. Avram suspected that the RNase effect could be an artifact. Meanwhile, APF-1 was identified by Keith Wilkinson and his colleagues as ubiquitin, and the amino acid sequence/composition of ubiquitin disclosed the “secret” of the dry weight/protein measurement discrepancy—the molecule has a single tyrosine residue, thus explaining the low readings at 280 nm and in the Lowry assays. So we decided not to pursue this subject, and the selective inhibitory effect of RNase A on BSA degradation remained an unsolved mystery—for the time.

I had not stopped suspecting however that the findings must represent some true biological phenomenon, and used the opportunity of my independence at Harvey's laboratory to pull out the late 1970s data from my notebook and to start dissecting the RNase effect in a systematic manner. With some advice from Alexander (Alex) Varshavsky (MIT), and a lot of help from Joan Steitz (Yale), Harvey Lodish, and Uttam RajBhandary (MIT), I managed to make some progress. I discovered that the degradation of BSA was completely dependent on specific tRNAs (for Arg and His), and that the destruction of the tRNA led to inhibition of the reaction. The nature of the mechanism of action of the tRNAs and the problem of why the degradation of lysozyme was insensitive to RNase had remained a mystery at that time, which I resolved only when I returned to Israel and established my own laboratory.

The other ubiquitin subject I was studying involved a collaboration with Alex Varshavsky and his then graduate student, Daniel (Dan) Finley. At that time Alex was studying the role of monoubiquitination of histones (see above for the histone H2A/ubiquitin adduct, also known as protein A24 or uH2A). He noted a series of publications on a temperature-sensitive cell-cycle-arrest mouse mutant cell ts85 that was generated and described by the group of M. Yamada. At the nonpermissive temperature, the cell lost the histone H2A/ubiquitin adduct. This loss could be due to one of two defects, either loss of ubiquitination, or activated deubiquitination. Alex asked me to collaborate with him and Dan to identify the mutation in this cell. We surmised that the defect in these cells was more likely due to loss rather than to gain of function, and set out to dissect the defect. The idea was that the same defect may also affect protein degradation, although it was clear that the single modification of the histone molecule by ubiquitin does not lead to its targeting to proteolysis.

Identification of the defect in the cells was not too difficult, as we used the isolation technique of the conjugation

enzymes developed in Haifa, and demonstrated that the defect results from a temperature-sensitive ubiquitin-activating enzyme E1, the first enzyme in the ubiquitin system cascade. Importantly, inactivation of the enzyme led to inhibition of ubiquitin conjugation to the general population of cellular proteins, and was not confined to inhibition of conjugation of histone H2A. Consequently, degradation of short-lived proteins was also inhibited, demonstrating that the same enzyme that is involved in ubiquitin activation for histone modification is also involved in activation of ubiquitin for modification of substrates destined for degradation. Identification and characterization of the cell defect further corroborated our earlier general hypothesis that ubiquitination signals proteins for degradation, and that it also occurs in nucleated cells, a finding we had already demonstrated, although indirectly, in Haifa, using the anti-ubiquitin antibody. Since the ts85 cell was also a cell-cycle-arrest mutant, we hypothesized, but did not prove experimentally at the time, that the system might be involved in regulating the cell cycle, a hypothesis that later turned out to be correct.

The Return to Israel—Independent Research Career

After three years at MIT (1981–1984), it was time to seek an independent academic position. After many deliberations and despite attractive offers and a big temptation to stay in the US, I decided to return home, to Israel. With the help of Avram, I obtained an independent academic position in the Department of Biochemistry at the Faculty of Medicine of the Technion (where I graduated), and returned home towards the end of 1984, after a productive postdoctoral period. Importantly, I already had a research subject I wanted to pursue, the effect of RNase on ubiquitin-mediated proteolysis.

The years that followed the postdoctoral fellowship (1984–present) have been extremely rewarding. I was happy to return to Israel to my family and friends, to a place I felt I belong. I established my own independent research group and laboratory, obtained extramural competitive funding, and continued my research on the ubiquitin system. I have been lucky to have, through the years, a group of extremely talented graduate students and postdoctoral fellows.

In our first series of studies we elucidated the role of tRNA in the proteolytic process, a subject I discovered as a graduate student and continued to study independently at MIT. Along with one of my first graduate students, Sarah Ferber, we demonstrated that proteins with acidic N-termini, such as Asp or Glu, undergo arginylation at the N-terminus, converting the acidic, negatively charged residue at this site into a positively charged residue. The reaction is catalyzed by arginine tRNA-protein transferase, a known protein with a hitherto unknown function. The enzyme uses charged tRNA^{Arg} as a source of activated Arg. Therefore, digestion of the cell extract RNA with RNase A inhibits this reaction. This finding explained the selectivity of the RNase effect to BSA and not to lysozyme: BSA has an Asp residue at the N-terminus, while lysozyme has lysine in this position. Interest-

ingly, the ligase involved is E3 α , which we discovered during my graduate studies. The ligase recognizes only proteins with basic termini, but not with acidic N-termini. Thus, what appeared initially as an artifact turned out to be part of the first specific recognition signal in a target substrate.

Parallel to our work on the RNase effect, Avram and his graduate student Yuval Reiss characterized the E3 α ligase and identified on it three distinct substrate binding sites for: 1) basic N-termini (the one involved in recognition of basic and Arg-modified acidic N-termini), 2) bulky-hydrophobic N-termini, and 3) "body" sites that reside downstream of the N-terminal residue. In parallel and by using a systematic genetic approach in the yeast *S. cerevisiae*, Alex Varshavsky and his colleagues formulated a general rule ("N-end rule") for recognition of all 20 different amino acid residues at the N-terminal site.

Research in the laboratory has also evolved in other directions. We have shown that N- α -acetylated proteins are also targeted by the ubiquitin system. This important finding demonstrated that the N-terminally modified proteins, a group that constitutes the vast majority of cellular proteins, must be targeted by signals that are distinct from the N-terminal residue and reside downstream to it: they do not have free N-termini and therefore cannot be recognized by the N-terminal amino acid residue. Along with the discovery of the "body" site in E3 α , we felt that N-terminal recognition is of minor physiological significance, an exception rather than a rule, and the mode of recognition of the numerous substrates of the system must be broad and diverse: they are recognized by multiple and distinct targeting motifs.

At that point, towards the end of the 1980s, we felt it was time to move from studying model substrates to investigating the fate of specific native cellular substrates. We have shown that an important group of cell regulators—tumor suppressors (e.g. p53) and growth promoters (c-Myc)—are targeted by the ubiquitin cell-free system. We believed that this was true also for the targeting of these substrates in vivo, which later turned out to be correct. We continued and demonstrated that, unlike the thinking in the field until that time, that degradation of proteins in the lysosome proceeds independently from the ubiquitin system, the two proteolytic pathways are actually linked to one another, and ubiquitination is required for stress-induced lysosomal degradation of cellular proteins. This area later evolved in a dramatic manner, and engulfed involvement of the ubiquitin system in receptor-mediated endocytosis and autophagy. Other studies involved elucidation of some of the mechanisms involved in the two-step ubiquitin-mediated proteolytic activation of the transcriptional regulator NF- κ B, demonstration of a role for heat-shock proteins in targeting certain protein substrates, and identification of a novel mode of ubiquitination at the N-terminal residue of the protein substrate. This modification is clearly different and distinct from recognition of the substrate by E3 α at the N-terminal residue. In the latter case, the ligase binds to the N-terminal residue while ubiquitination occurs on an internal lysine. In N-terminal ubiquitination, modification occurs at the N-terminal residue, while the ligase binds, most probably, to an

internal sequence in the protein target molecule. This subject has evolved in a surprising manner and changed another paradigm in the field that ubiquitination is limited to internal lysine(s) of the target substrate. We, and later others, have shown that the phenomenon is not limited to the one protein we identified initially (the muscle-specific transcriptional regulator MyoD), and identified a large group of proteins that undergo N-terminal ubiquitination. This group of proteins contain many that have internal lysine(s), but for some reason these residues cannot be targeted, and interestingly also a large group of proteins (such as p16^{INK4a} that plays an important role in cell-cycle regulation) that are devoid of any lysine residue. To be degraded by the ubiquitin system they must undergo N-terminal ubiquitination.

These years have not been simple, however. The Technion has traditionally been a school of engineering, and life sciences and biomedicine have been foreign to many of its senior faculty members and policy planners: we were treated in many ways like step-children, and thoughts of closing the school have been aired at times. This deeply rooted philosophy, which only now starts to change slowly, has severely hampered development in these fields and had left the body of researchers and infrastructure in these areas small and battling for survival. Through a network of wonderful colleagues all over the world (important among them is my friend Alan Schwartz from Harvard Medical School and then from Washington University in St. Louis) and fruitful collaborations, it was possible to establish an active research group and carry out what I believe was a good and original research program, even under less than optimal, and at times impossible conditions. This was important in balancing my desire to live in Israel, but at the same time to remain at the forefront of the ubiquitin research field that has grown in importance to become an extremely exciting, yet a highly competitive area.

Unpaid Debts

Last but not least, I owe a huge debt which I doubt I shall ever be able to repay to several people who helped me cross critical stormy waterways along my life. My aunt Miriam, who took me to her house after the death of my father and made her home a new home for me, thus enabling me to complete seamlessly my high-school studies without any interruption. My brother Yossi and my sister-in-law Atara, who opened their home for me during the fragile times of my high-school and medical studies, and made sure I would not collapse along the way, emotionally, but also economically. And last, my wonderful wife Menucha and my son Tzachi (Yitzhak, Isaac; named after my late father); they have flooded me with love, care, and deep understanding of my needs, and were always there for me, when I was flying high on the wings of my dreams, not always seeing them or listening to them or being with them, physically and emotionally. Without all these wonderful life partners, I could not have achieved anything.

I also owe special thanks to all my mentors, who each contributed in their own way to my upbringing as a scientist. I

have to thank Jacob Bar-Tana and Benjamin Shapira for taking me, hand in hand, through the complex maze of metabolic pathways, thus enabling me to fall in love with Biochemistry. Their enthusiasm and deep thinking convinced me, at a critical stage of my development, to pursue a career in biological sciences. I owe a big debt to my mentor, Avram Hershko, with whom I have come a long way in discovering the ubiquitin system, and from whom I learnt the very basic principles of how to approach a scientific problem. I owe special thanks to Ernie Rose for showing me that ordered thinking is not always necessary in science, and is even interfering at times, and that being erratic and disordered, absent minded at times, collecting sparks from all over the place, can yield wonderful ideas and results. Last, I owe a

huge debt to Harvey Lodish, who is not only a great cell biologist, but a wonderful spiritual mentor in a different way to how we tend to think of mentors. He gave me complete freedom to choose my own way, but did not let me fall. He always listened carefully and helped me to analyze data, and with his deep insight was able to find in the ocean of my numbers and graphic analyses new routes and pathways that I could have never seen or thought of. He used to gently comment on my approach when he felt I derailed, and helped redirecting me. Yet, he was never imposing: Harvey's active passive educational approach is truly unique. I owe many thanks to all my colleagues, in particular Alan Schwartz, Iasha Sznajder, and Kazuhiro Iwai, who helped me in many ways along this long voyage. I must also mention my laboratory

Table 1: Tabulated biography of Aaron Ciechanover.

Date and place of birth	October 1, 1947	Haifa, Israel
Education		
Elementary School	1953–1956	"Hashiloach" Elementary School, Haifa
High School	1959–1965	"Hugim" High School, Haifa
University (undergraduate studies)	1965–1972	"Hadassah" and the Hebrew University School of Medicine, Jerusalem (MSc, MD)
Clinical internship	1972–1973	"Rambam" Medical Center, Haifa
Military Service	1973–1976	Medical Corps, Israel Defense Forces (military physician)
University (graduate studies)	1976–1981	Faculty of Medicine, Technion, Haifa (DSc). Thesis advisor: Dr. Avram Hershko
Postdoctoral Training	1981–1984	Department of Biology and the Whitehead Institute, Massachusetts Institute of Technology, Cambridge, USA (with Dr. Harvey F. Lodish)
Faculty Position	1984–present	Faculty of Medicine, Technion, Haifa
Degrees		
MSc	1970	Medical Sciences. Faculty of Natural Sciences and the Department of Biochemistry, "Hadassah" and the Hebrew University School of Medicine, Jerusalem
MD	1974	"Hadassah" and the Hebrew University School of Medicine, Jerusalem
DSc	1981	Faculty of Medicine, Technion, Haifa
Academic Appointments		
1977–1979	Research Fellow	Department of Biochemistry, Faculty of Medicine, Technion, Haifa
1979–1981	Lecturer	
1984–1987	Senior Lecturer	
1987–1992	Associate Professor	
1992–	Full Professor	
2002–	Distinguished Research Professor	
Administrative Appointments		
1993–2000	Director	The Rappaport Family Institute for Research in the Medical Sciences, Technion, Haifa
Military Service		
1974–1977		Military Physician in the Israeli Navy and the Unit for Research and Development, Surgeon General Headquarters; discharged at the rank of Major
Visiting Appointments		
1978, 1979	Visiting Scientist	The Institute for Cancer Research, The Fox Chase Cancer Center, Philadelphia (with Dr. Irwin A. Rose)
1980–1981		
1985–present	Visiting Professor	The Dana Farber Cancer Institute and Harvard Medical School, Boston; Washington University School of Medicine, St. Louis; University of Kyoto School of Medicine; Northwestern University School of Medicine, Chicago; STINT Fellow. Microbiology and Tumor Biology Center (MTC), The Karolinska Institute, Stockholm, Sweden; City University of Osaka School of Medicine, Osaka, Japan; Rockefeller University, New York

research associates, initially Sarah Elias and then Hedva Gonen and Beatrice Bercovich, who have become my eyes and hands since I established my own laboratory. Last but not least, my wonderful graduate students, fellows, and visiting scientists, with whom I discovered new and exciting paths in the rapidly evolving and exciting ubiquitin field.

2. Introduction

The concept of protein turnover is barely 60 years old. Beforehand, body proteins were viewed as essentially stable constituents that were subject to only minor “wear and tear”. Dietary proteins were believed to function primarily as energy-providing fuel, which were independent from the structural and functional proteins of the body. The problem was hard to approach experimentally, as research tools were not available. An important research tool that was lacking at that time were stable isotopes. While radioactive isotopes were developed earlier by George de Hevesy (*Nobel Lectures in Chemistry 1942–1962*, World Scientific, 1999, pp. 5–41), they were mostly unstable and could not be used to follow metabolic pathways.

The concept that body structural proteins are static and the dietary proteins are used only as a fuel was challenged by Rudolf Schoenheimer at Columbia University in New York city. Schoenheimer, like many other Jewish scientists (for example, Albert Einstein), escaped from Germany after the rise of the Nazis, and joined the Department of Biochemistry in Columbia University, founded by Hans T. Clarke.^[1–3] There he met Harold Urey who was working in the Department of Chemistry and who discovered deuterium, the heavy isotope of hydrogen, a discovery that enabled him to prepare heavy water, D₂O. David Rittenberg, who had recently received his PhD in Urey's laboratory, joined Schoenheimer, and together they entertained the idea of “*employing a stable isotope as a label in organic compounds, destined for experiments in intermediary metabolism, which should be biochemically indistinguishable from their natural analog*”.^[1]

Urey later succeeded in enriching nitrogen with ¹⁵N, which provided Schoenheimer and Rittenberg with a “tag” for amino acids and thus for their study on protein dynamics. They discovered that following administration of ¹⁵N-labeled tyrosine to rats, only about 50 % was recovered in the urine, “*while most of the remainder is deposited in tissue proteins. An equivalent of protein nitrogen is excreted*”.^[4] They further discovered that from the half that was incorporated into body proteins “*only a fraction was attached to the original carbon chain, namely to tyrosine, while the bulk was distributed over other nitrogenous groups of the proteins*”,^[4] mostly as an NH₂ group in other amino acids. These experiments demonstrated unequivocally that the body structural proteins are in a dynamic state of synthesis and degradation, and that even individual amino acids are in a state of dynamic interconversion. Similar results were obtained using ¹⁵N-labeled leucine.^[5]

This series of findings shattered the paradigm in the field at that time that: 1) ingested proteins are completely metabolized and the products are excreted, and 2) that body

structural proteins are stable and static. Schoenheimer was invited to deliver the prestigious Edward K. Dunham lecture at Harvard University where he presented his revolutionary findings. After his untimely tragic death in 1941, his lecture notes were edited by Hans Clarke, David Rittenberg, and Sarah Ratner, and were published in a small book by Harvard University Press. The editors called the book *The Dynamic State of Body Constituents*,^[6] adopting the title of Schoenheimer's presentation. In the book, the new hypothesis is clearly presented: “*The simile of the combustion engine pictured the steady state flow of fuel into a fixed system, and the conversion of this fuel into waste products. The new results imply that not only the fuel, but the structural materials are in a steady state of flux. The classical picture must thus be replaced by one which takes account of the dynamic state of body structure*”. However, the idea that proteins are turning over was not accepted easily and was challenged as late as the mid-1950s. For example, Hogness and colleagues studied the kinetics of β -galactosidase in *E. coli* and summarized their findings:^[7] “*To sum up: there seems to be no conclusive evidence that the protein molecules within the cells of mammalian tissues are in a dynamic state. Moreover, our experiments have shown that the proteins of growing E. coli are static. Therefore it seems necessary to conclude that the synthesis and maintenance of proteins within growing cells is not necessarily or inherently associated with a 'dynamic state'*”. While the experimental study involved the bacterial β -galactosidase, the conclusions were broader, and included also the authors' hypothesis on mammalian proteins. The use of the term “dynamic state” was not incidental, as they challenged directly Schoenheimer's studies.

Now, after more than six decades of research in the field and with the discovery of the lysosome and later the complex ubiquitin–proteasome system with its numerous tributaries, it is clear that the area has been revolutionized. We now realize that intracellular proteins are turning over extensively, that this process is specific in most cases, and that the stability of many proteins is regulated individually and can vary under different conditions. From a scavenger, unregulated and nonspecific end process, it has become clear that proteolysis of cellular proteins is a highly complex, temporally controlled and tightly regulated process that plays major roles in a broad array of basic pathways. Among these processes are the cell cycle, development, differentiation, regulation of transcription, antigen presentation, signal transduction, receptor-mediated endocytosis, quality control, and modulation of diverse metabolic pathways. As a result, this development has changed the paradigm that regulation of cellular processes occurs mostly at the transcriptional and translational levels, and has placed regulated protein degradation in an equally important position. With the multitude of substrates targeted and processes involved, it is not surprising that aberrations in the pathway have been implicated in the pathogenesis of many diseases, among them certain malignancies, neurodegeneration, and disorders of the immune and inflammatory system. As a result, the ubiquitin system has become a platform for drug targeting, and mechanism-based drugs are currently developed, one of them is already on the market.

3. The Lysosome and Intracellular Protein Degradation

In the mid-1950s, Christian de Duve discovered the lysosome (see, for example, Refs. [8,9] and Figure 1). The lysosome was first recognized biochemically in rat liver as a vacuolar structure that contains various hydrolytic enzymes which function optimally at an acidic pH. It is surrounded by a membrane that endows the contained enzymes with latency that is required to protect the cellular contents from their action (see below). The definition of the lysosome has been broadened over the years. This is because it has been recognized that the digestive process is dynamic and involves numerous stages of lysosomal maturation together with the digestion of both exogenous proteins (which are targeted to the lysosome through receptor-mediated endocytosis and pinocytosis) and exogenous particles (which are targeted through phagocytosis; the two processes are known as heterophagy), as well as digestion of endogenous proteins and cellular organelles (which are targeted by micro- and macro-autophagy; see Figure 2).

The lysosomal/vacuolar system as we currently recognize it is a discontinuous and heterogeneous digestive system that also includes structures that are devoid of hydrolases, for example, early endosomes which contain endocytosed receptor–ligand complexes and pinocytosed/phagocytosed extracellular contents. At the other extreme it includes the residual bodies—the end products of the completed digestive processes of heterophagy and autophagy. In between these extremes one can observe: primary/nascent lysosomes that have not yet been engaged in any proteolytic process; early

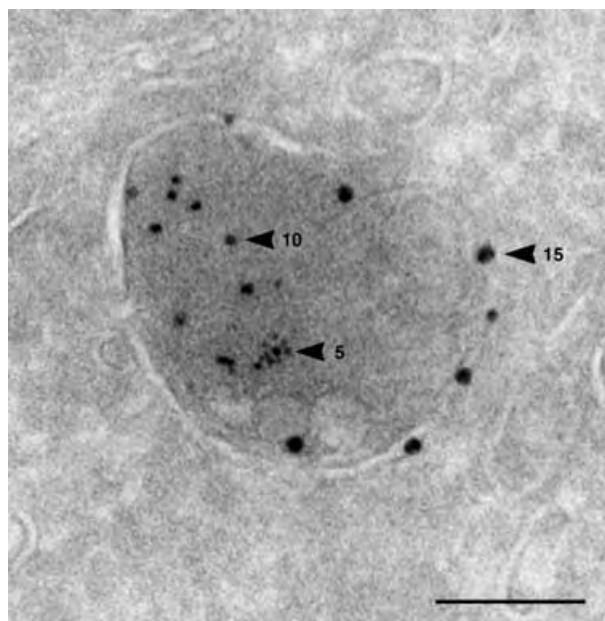


Figure 1. The lysosome: Ultrathin cryosection of a rat PC12 cell that had been loaded for 1 h with bovine serum albumin (BSA)·gold (5-nm particles) and immunolabeled for the lysosomal enzyme cathepsin B (10-nm particles) and the lysosomal membrane protein LAMP1 (15-nm particles). Lysosomes are recognized also by their typical dense content and multiple internal membranes. Scale bar, 100 nm. Printed with permission from Viola Oorschot and Judith Klumperman, Department of Cell Biology, University Medical Centre, Utrecht, The Netherlands.

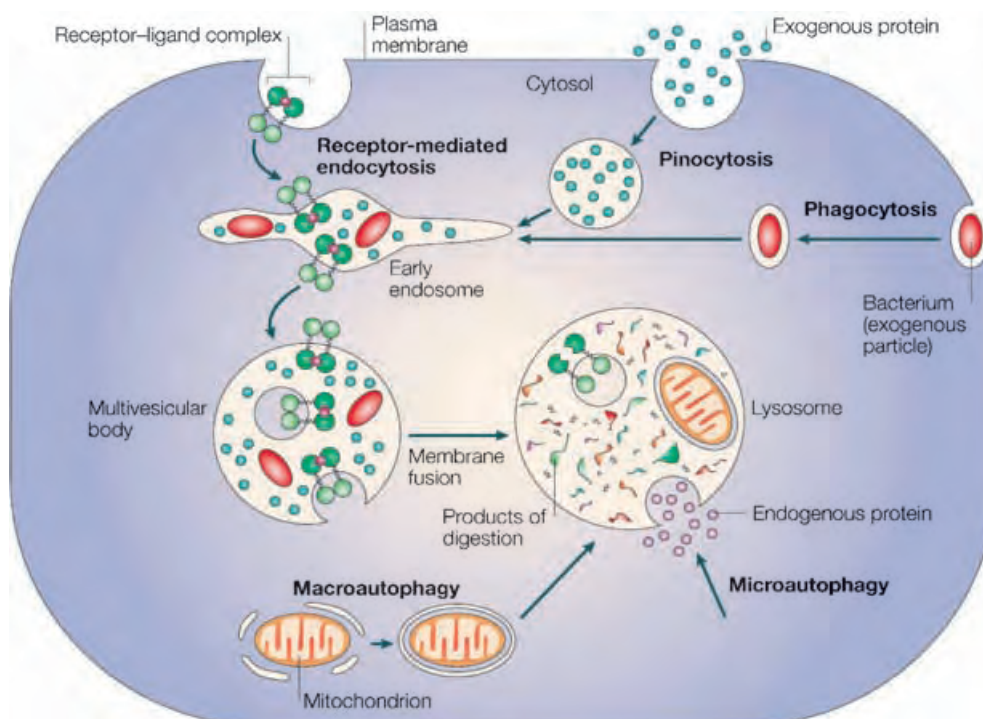


Figure 2. The four digestive processes mediated by the lysosome: 1) specific receptor-mediated endocytosis; 2) pinocytosis (nonspecific engulfment of cytosolic droplets containing extracellular fluid); 3) phagocytosis (of extracellular particles), and 4) autophagy (micro- and macro-autophagy of intracellular proteins and organelles). Printed from Ref. [83] with permission from Nature Publishing Group.

autophagic vacuoles that might contain intracellular organelles; intermediate/late endosomes and phagocytic vacuoles (heterophagic vacuoles) that contain extracellular contents/particles; and multivesicular bodies (MVBs) which are the transition vacuoles between endosomes/phagocytic vacuoles and the digestive lysosomes (Figure 2).

The discovery of the lysosome along with independent experiments that were carried out at the same time and that have further strengthened the notion that cellular proteins are indeed in a constant state of synthesis and degradation (see, for example, Ref. [10]), led scientists to feel, for the first time, that they had at hand an organelle that could potentially mediate degradation of intracellular proteins. The separation of the proteases from their substrates by a membrane provided an explanation for controlled degradation, and the only problem left to be explained was how the substrates are translocated into the lysosomal lumen, where they are degraded by the lysosomal proteases.

An important discovery in this respect was the unraveling of the basic mechanism of action of the lysosome, namely autophagy (reviewed in Ref. [11]). Under basal metabolic conditions, portions of the cytoplasm which contain the entire cohort of cellular proteins, are segregated within a membrane-bound compartment, and are then fused to a primary nascent lysosome and their contents digested. This process was denoted micro-autophagy. Under more extreme conditions (for example, starvation) mitochondria, endoplasmic reticulum membranes, glycogen bodies, and other cytoplasmic entities can also be engulfed by a process called macro-autophagy (see, for example, Ref. [12]). The different modes of action of the lysosome in digesting extra- and intracellular proteins are shown in Figure 2.

However, over a period of more than two decades (between the mid-1950s and the late-1970s) it became gradually more and more difficult to explain several aspects of intracellular protein degradation based on the known mechanisms of lysosomal activity. Accumulating lines of independent experimental evidence indicated that the degradation of at least certain classes of cellular proteins must be non-lysosomal. Yet, in the absence of any "alternative", researchers found different explanations, some more substantiated and others less, to defend the "lysosomal" hypothesis.

First was the gradually emerging notion, coming from different laboratories, that different proteins vary in their stability, and their half-life times ($t_{1/2}$) can span three orders of magnitude—from a few minutes to many days. Thus, the $t_{1/2}$ of ornithine decarboxylase (ODC) is about 10 min, while that of glucose-6-phosphate dehydrogenase (G6PD) is 15 h (for review articles, see, for example, Refs. [13,14]). Also, the rates of degradation of many proteins were shown to change with changing physiological conditions, such as availability of nutrients or hormones. It was conceptually difficult to reconcile the findings of distinct half-lives of different proteins with the mechanism of action of the lysosome, where the micro-autophagic vesicle contains the entire cohort of cellular (cytosolic) proteins that are therefore expected to degrade at the same rate. Likewise, if micro- and macro-autophagy had been the mechanisms that mediate intra-

cellular proteolysis, changing pathophysiological conditions, such as starvation or resupplementation of nutrients, would have been expected to affect the stability of all cellular proteins to the same extent. Clearly, this was not the case.

A second source of concern about the lysosome as the organelle in which intracellular proteins are degraded were the findings that specific and general inhibitors of lysosomal proteases have different effects on different populations of proteins, making it clear that distinct classes of proteins are targeted by different proteolytic machineries. Thus, the degradation of endocytosed/pinocytosed extracellular proteins was significantly inhibited, a partial effect was observed on the degradation of long-lived cellular proteins, and almost no effect could be detected on the degradation of short-lived and abnormal/mutated proteins.

Finally, the thermodynamically paradoxical observation that the degradation of cellular proteins requires metabolic energy, and more importantly, the emerging evidence that the proteolytic machinery uses the energy directly, were in contrast with the known mode of action of lysosomal proteases that under the appropriate acidic conditions, and similar to all known proteases, degrade proteins in an exergonic manner.

The assumption that the degradation of intracellular proteins is mediated by the lysosome was nevertheless logical. Proteolysis results from direct interaction between the target substrates and proteases, and therefore it was clear that active proteases cannot be free in the cytosol, which would have resulted in destruction of the cell. Thus, it was recognized that any suggested proteolytic machinery that mediates degradation of intracellular protein degradation must also be equipped with a mechanism that separates—physically or virtually—between the proteases and their substrates, and enables them to associate only when needed. The lysosomal membrane provided a physical fencing mechanism.

Of course, nobody could have predicted that a new mode of posttranslational modification—ubiquitination—could function as a proteolytic signal, and that untagged proteins would remain protected. Thus, while the structure of the lysosome could explain the separation necessary between the proteases and their substrates, and autophagy could explain the mechanism of entry of cytosolic proteins into the lysosomal lumen, major problems have remained unsolved. Important among them were: 1) the varying half-lives, 2) the energy requirement, and 3) the distinct response of different populations of proteins to lysosomal inhibitors.

Nevertheless, scientists tried to "defend" the lysosomal model. According to one model, it was proposed that different proteins have different sensitivities to lysosomal proteases, and their half lives in vivo correlate with their sensitivity to the action of lysosomal proteases in vitro.^[15] To explain an extremely long half-life for a protein that is nevertheless sensitive to lysosomal proteases, or alterations in the stability of a single protein under various physiological states, it was suggested that although all cellular proteins are engulfed into the lysosome, only the short-lived proteins are degraded, whereas the long-lived proteins exit back into the cytosol: *"To account for differences in half-life among cell components or of a single component in various physiological*

states, it was necessary to include in the model the possibility of an exit of native components back to the extralysosomal compartment".^[16]

According to a different model, selectivity is determined by the binding affinity of the different proteins for the lysosomal membrane which controls their entry rates into the lysosome, and subsequently their degradation rates.^[17] For a selected group of proteins, such as the gluconeogenic enzymes phosphoenolpyruvate carboxykinase (PEPCK), and fructose-1,6-bisphosphatase, it was suggested, though not firmly substantiated, that their degradation in the yeast vacuole is regulated by glucose through a mechanism called "catabolite inactivation" that possibly involves their phosphorylation. However, this regulated mechanism for vacuolar degradation was limited only to a small and specific group of proteins (see, for example, Refs. [18], [19]).

More recent studies have shown that at least for stress-induced macro-autophagy, KFERQ, a general sequence of amino acids that in its general structure was identified in many proteins, directs, by binding to a specific "receptor" and in cooperation with cytosolic and lysosomal chaperones, the regulated entry of many cytosolic proteins into the lysosomal lumen. While further corroboration of this hypothesis is still required, it explains the mass entry of a large population of proteins that contain a homologous sequence, but not the targeting for degradation of a specific protein under defined conditions (reviewed in Refs. [20,21]). The energy requirement for protein degradation was described as indirect, and necessary, for example, for protein transport across the lysosomal membrane^[22] and/or for the activity of the H⁺ pump and the maintenance of the low acidic intralysosomal pH that is necessary for optimal activity of the lysosomal proteases.^[23] We now know that both mechanisms require energy. In the absence of any alternative, and with lysosomal degradation as the most logical explanation for targeting all known classes of proteins at the time, Christian de Duve summarized his view on the subject in a review article published in the mid-1960s, saying: "*Just as extracellular digestion is successfully carried out by the concerted action of enzymes with limited individual capacities, so, we believe, is intracellular digestion*".^[24] The problem of different sensitivities of distinct protein groups to lysosomal inhibitors has remained unsolved, and may have served as an important trigger in the future quest for a non-lysosomal proteolytic system.

Progress in identifying the elusive, non-lysosomal proteolytic system(s) was hampered by the lack of a cell-free preparation that could faithfully replicate the cellular proteolytic events, degrading proteins in a specific and energy-requiring mode. An important breakthrough was made by Rabinovitz and Fisher who found that rabbit reticulocytes degrade abnormal, amino acid analogue containing hemoglobin.^[25] Their experiments modeled known disease states—the hemoglobinopathies. In these diseases abnormal mutated hemoglobin chains (such as sickle cell hemoglobin) or excess of unassembled normal hemoglobin chains (which are synthesized normally, but accumulate and found in excess in thalassemias, diseases in which the pairing chain is not synthesized at all or is mutated and rapidly degraded, and

consequently the hemoglobin complex is not assembled) are rapidly degraded in the reticulocyte.^[26,27] Reticulocytes are terminally differentiating red blood cells that do not contain lysosomes. Therefore, it was postulated that the degradation of hemoglobin in these cells is mediated by a non-lysosomal machinery.

Etlinger and Goldberg^[28] were the first to isolate and characterize a cell-free proteolytic preparation from reticulocytes. The crude extract selectively degraded abnormal haemoglobin, required ATP hydrolysis, and acted optimally at a neutral pH, which further strengthened the assumption that the proteolytic activity was of a non-lysosomal origin. A similar system was isolated and characterized later by our research group.^[29] Additional studies by our group led subsequently to resolution, characterization, and purification of the major enzymatic components from these extracts, and to the discovery of the ubiquitin tagging system (see below).

4. The Lysosome Hypothesis Is Challenged

As mentioned above, the unraveled mechanism(s) of action of the lysosome could explain only partially, and at times not satisfactorily, several key emerging characteristics of intracellular protein degradation. Among them were the heterogeneous stability of individual proteins, the effect of nutrients and hormones on their degradation, and the dependence of intracellular proteolysis on metabolic energy. The differential effect of selective inhibitors on the degradation of different classes of cellular proteins could not be explained at all.

The evolution of methods to monitor protein kinetics in cells, together with the development of specific and general lysosomal inhibitors, has resulted in the identification of different classes of cellular proteins, long- and short-lived, and the discovery of the differential effects of the inhibitors on these groups (see, for example, Refs. [30,31]). An elegant experiment in this respect was carried out by Brian Poole and his colleagues at the Rockefeller University. Poole was studying the effects on proteolysis of lysosomotropic agents—weak bases such as ammonium chloride and chloroquine—that accumulate in the lysosome and dissipate its low acidic pH. It was assumed that this mechanism also underlies the antimalarial activity of chloroquine and similar drugs, where they inhibit the activity of the parasite's lysosome, "paralyzing" its ability to digest the host's hemoglobin during the intraerythrocytic stage of its life cycle. Poole and his colleagues metabolically labeled endogenous proteins in living macrophages with ³H-leucine and "fed" them with dead macrophages that had been previously labeled with ¹⁴C-leucine. They assumed, apparently correctly, that the dead macrophages debris and proteins will be phagocytosed by the live macrophages and targeted to the lysosome for degradation. They monitored the effect of lysosomotropic agents on the degradation of these two protein populations. In particular, they studied the effect of the weak bases chloroquine and ammonium chloride (which enter the lysosome and neutralize the H⁺ ions), and the acid ionophore X537A which dissipates the H⁺ gradient across the lysosomal membrane.

They found that these drugs specifically inhibited the degradation of extracellular proteins, but not that of intracellular proteins.^[32]

Poole summarized these elegant experiments and explicitly predicted the existence of a non-lysosomal proteolytic system that degrades intracellular proteins: *“Some of the macrophages labeled with tritium were permitted to endocytose the dead macrophages labeled with ^{14}C . The cells were then washed and replaced in fresh medium. In this way we were able to measure in the same cells the digestion of macrophage proteins from two sources. The exogenous proteins will be broken down in the lysosomes, while the endogenous proteins will be broken down wherever it is that endogenous proteins are broken down during protein turnover”*.^[33]

The requirement for metabolic energy for the degradation of both prokaryotic^[34] and eukaryotic^[10,35] proteins was difficult to understand. Proteolysis is an exergonic process and the thermodynamically paradoxical energy requirement for intracellular proteolysis made researchers believe that energy cannot be consumed directly by proteases or the proteolytic process per se, and is used indirectly. As Simpson summarized his findings:^[10] *“The data can also be interpreted by postulating that the release of amino acids from protein is itself directly dependent on energy supply. A somewhat similar hypothesis, based on studies on autolysis in tissue minces, has recently been advanced, but the supporting data are very difficult to interpret. However, the fact that protein hydrolysis as catalyzed by the familiar proteases and peptidases occurs exergonically, together with the consideration that autolysis in excised organs or tissue minces continues for weeks, long after phosphorylation or oxidation ceased, renders improbable the hypothesis of the direct energy dependence of the reactions leading to protein breakdown”*. Being cautious, however, and probably unsure about this unequivocal conclusion, Simpson still left a narrow orifice opened for a proteolytic process that requires energy in a direct manner: *“However, the results do not exclude the existence of two (or more) mechanisms of protein breakdown, one hydrolytic, the other energy-requiring.”*

Since any proteolytic process must be at one point or another hydrolytic, the statement that makes a distinction between a hydrolytic process and an energy-requiring, yet nonhydrolytic one, is not clear. Judging the statement from a historical point of view and knowing the mechanism of action of the ubiquitin system, where energy is required also in the prehydrolytic step (ubiquitin conjugation), Simpson may have thought of a two-step mechanism, but did not give it a clear description: in retrospect, one can view ubiquitination as a nonhydrolytic, yet energy-requiring process. At the end of this clearly understandable and apparently difficult deliberation, he left us with a vague explanation linking protein degradation to protein synthesis, a process that was known at that time to require metabolic energy: *“The fact that a supply of energy seems to be necessary for both the incorporation and the release of amino acids from protein might well mean that the two processes are interrelated. Additional data suggestive of such a view are available from other types of experiments. Early investigations on nitrogen balance by Benedict, Folin, Gamble, Smith, and others point to the fact that the rate of protein catabolism varies with the dietary protein level. Since*

the protein level of the diet would be expected to exert a direct influence on synthesis rather than breakdown, the altered catabolic rate could well be caused by a change in the rate of synthesis.”^[10]

With the discovery of lysosomes in eukaryotic cells it could be argued that energy is required for the transport of substrates into the lysosome or for maintenance of the low intralysosomal pH, for example. The observation by Hershko and Tomkins that the activity of tyrosine aminotransferase (TAT) was stabilized following depletion of ATP^[36] indicated that energy may be required at an early stage of the proteolytic process, most probably before proteolysis occurs. Yet, it did not provide a clue for the mechanism involved: energy could be used, for example, for specific modification of TAT, for example, phosphorylation, that would sensitize it to degradation by the lysosome or by a yet unknown proteolytic mechanism, or for a modification that activates its putative protease. It could also be used for a more general lysosomal mechanism, one that involves transport of TAT into the lysosome or maintenance of the low intralysosomal pH, as it is clear that ATP depletion also inhibited completely lysosomal degradation. The energy inhibitors inhibited almost completely degradation of the entire population of cell proteins, confirming previous studies (see, for example, Ref. [10]) and suggesting a general role for energy in protein catabolism. An interesting finding was that energy inhibitors had an effect that was distinct from that of protein synthesis inhibitors, which affected only enhanced degradation (induced by steroid hormone depletion), but not basal degradation. This finding ruled out, at least partially, a tight linkage between protein synthesis and all classes of protein degradation.

In bacteria, which lack lysosomes, an argument involving energy requirement for lysosomal degradation could not have been proposed, but other indirect effects of ATP hydrolysis could have affected proteolysis in *E. coli*, such as phosphorylation of substrates and/or proteolytic enzymes, or maintenance of the “energized membrane state”. According to this model, proteins could become susceptible to proteolysis by changing their conformation, for example, following association with the cell membrane that maintains a local, energy-dependent gradient of a certain ion. While such an effect was ruled out,^[37] and since there was no evidence for a phosphorylation mechanism (although the proteolytic machinery in prokaryotes had not been identified at that time), it seemed that at least in bacteria, energy is required directly for the proteolytic process (which later turned out to be correct).

In any event, the requirement for metabolic energy for protein degradation in both prokaryotes and eukaryotes, a process that is exergonic thermodynamically, strongly indicated that in cells proteolysis is highly regulated, and that a similar principle/mechanism has been preserved in the evolution of the two kingdoms. From the possible direct requirement for ATP in the degradation of proteins in bacteria, it was not too unlikely to assume a similar direct mechanism involved in the degradation of cellular proteins in eukaryotes. Supporting this notion was the description of the cell-free proteolytic system in reticulocytes,^[28,29] a cell that lacks lysosomes, which indicated that energy is probably required directly for the proteolytic process, although here

too, the underlying mechanisms had remained enigmatic at the time. Yet, the description of the cell-free system paved the road for detailed dissection of the underlying mechanisms involved.

5. The Ubiquitin–Proteasome System

The cell-free proteolytic system from reticulocytes^[28,29] turned out to be an important and rich source for the purification and characterization of the enzymes that are involved in the ubiquitin–proteasome system. Initial fractionation of the crude reticulocyte cell extract on the anion-exchange resin diethylaminoethylcellulose (DEAE) yielded two fractions which were both required to reconstitute the energy-dependent proteolytic activity that was identified in the crude extract: The unadsorbed, flow-through material was denoted fraction I, and the adsorbed proteins which were eluted with a high concentration of salt was denoted fraction II (Table 2).^[38]

Table 2: Resolution of the ATP-dependent proteolytic activity from crude reticulocyte extract into two essentially required complementing activities (adapted from Ref. [38] with permission from Elsevier).

Fraction	Degradation of [³ H]globin [%]	
	–ATP	+ATP
lysate	1.5	10.0
fraction I	0.0	0.0
fraction II	1.5	2.7
fraction I + fraction II	1.6	10.6

This was an important observation and a lesson for the future dissection of the system. For one, it suggested that the system is not composed of a single “classical” protease that has evolved evolutionarily to acquire energy dependence (although such energy-dependent proteases such as the mammalian 26S proteasome and the prokaryotic *Lon* gene product, for example, were described later), but that it is made of at least two components. This finding of a two-component, energy-dependent protease left us with no paradigm to follow, and in attempts to explain the finding, we suggested, for example, that the two fractions could represent an inhibited protease and its activator.

Second, learning from this reconstitution experiment and the essential dependence of the two active components, we continued to reconstitute activity from resolved fractions whenever we encountered a loss of activity in further purification steps. This biochemical “complementation” approach resulted in the discovery of additional enzymes in the system, which are all required to be present in the reaction mixture in order to catalyze the multistep proteolysis of the target substrate. We chose first to purify the active component from fraction I. It was found to be a small, about 8.5 kDa heat-stable protein that was designated ATP-dependent proteolysis factor 1 (APF-1). APF-1 was later identified as ubiquitin (see below; I am using the term APF-1 to the point at which it was identified as ubiquitin, and then change terminology accordingly). In retrospect, the decision to start

the purification efforts with fraction I turned out to be important, as fraction I contained only one single protein, APF-1, that was necessary to stimulate proteolysis of the model substrates we used at the time, BSA and lysozyme, while fraction II turned out to contain many additional active factors. Later studies showed that fraction I contains other components necessary for the degradation of other substrates, but these were not necessary for the reconstitution of the system at that time. This enabled us not only to purify APF-1, but also to quickly decipher its mode of action. If we had started our purification efforts with fraction II, we would have encountered a significantly bumpier road. A critically important finding that paved the road for future developments in the field was that multiple moieties of APF-1 are covalently conjugated to the target substrate when incubated in the presence of fraction II, and the modification requires ATP (Figures 3 and 4).^[39,40] It was also found that the modification is reversible, and APF-1 can be removed from the substrate or its degradation products.^[40]

The discovery that APF-1 is covalently conjugated to protein substrates and stimulates their proteolysis in the presence of ATP and crude fraction II, led in 1980 to the proposal of a model, according to which protein–substrate modification by multiple moieties of APF-1 targets it for degradation by a downstream, at that time as yet unidentified, protease that cannot recognize the unmodified substrate; following degradation, reusable APF-1 is released.^[40] Amino

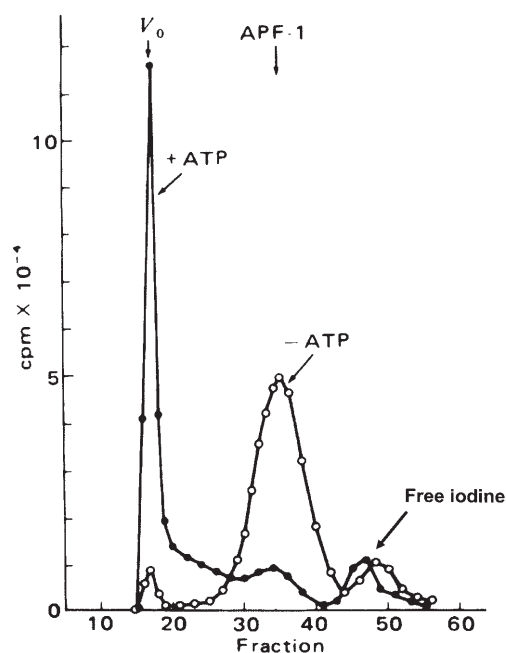


Figure 3. APF-1/ubiquitin is shifted to high-molecular-mass compound(s) following incubation in an ATP-containing crude cell extract. ¹²⁵I-labeled APF-1/ubiquitin was incubated with reticulocyte crude fraction II in the absence (○) or presence (●) of ATP, and the reaction mixtures were resolved by gel-filtration chromatography. The radioactivity measured in each fraction is shown. As can be seen, following addition of ATP, APF-1/ubiquitin becomes associated with some component(s) (another enzyme of the system or its substrate(s)) in fraction II. Printed from Ref. [39] with permission from the National Academy of Sciences.

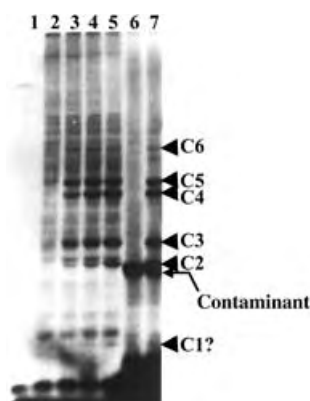


Figure 4. Multiple molecules of APF-1/ubiquitin are conjugated to the proteolytic substrate, probably signaling it for degradation. To analyze the data described in the experiment depicted in Figure 3 mechanistically and to test the hypothesis that APF-1 is conjugated to the target proteolytic substrate, ^{125}I -APF-1/ubiquitin was incubated along with crude fraction II in the absence (lane 1) or presence (lanes 2–5) of ATP and in the absence (lanes 1, 2) or presence (lanes 3–5) of increasing concentrations of unlabeled lysozyme. Reaction mixtures resolved in lanes 6 and 7 were incubated in the absence (lane 6) or presence (lane 7) of ATP, and included unlabeled APF-1/ubiquitin and ^{125}I -labeled lysozyme. C1–C6 denote specific APF-1/ubiquitin–lysozyme adducts in which the number of APF-1/ubiquitin moieties bound to the lysozyme moiety of the adduct increases, probably from 1 to 6. Reaction mixtures were resolved by SDS-polyacrylamide gel electrophoresis (SDS-PAGE) and visualized following exposure of the gel to an X-ray film (autoradiography). Printed from Ref. [40] with permission from the National Academy of Sciences.

acid analysis of APF-1, along with its known molecular mass and other general characteristics, raised the suspicion that APF-1 was ubiquitin,^[41] a known protein of previously unknown function. Indeed, Wilkinson and colleagues confirmed unequivocally that APF-1 was indeed ubiquitin.^[42]

Ubiquitin is a small, heat-stable, and highly evolutionarily conserved protein of 76 residues. It was first purified during the isolation of thymopoietin^[43] and was subsequently found to be ubiquitously expressed in all kingdoms of living cells, including prokaryotes.^[44] Interestingly, it was initially found to have lymphocyte-differentiating properties, a characteristic that was attributed to the stimulation of adenylate cyclase.^[44,45] Accordingly, it was named UBIP for ubiquitous immunopoietic polypeptide.^[44] However, later studies showed that ubiquitin is not involved in the immune response,^[46] and that it was a contaminating endotoxin in the preparation that generated the adenylate cyclase and the T-cell-differentiating activities. Furthermore, the sequence of several eubacteria and archaeobacteria genomes as well as biochemical analyses of cell extracts from these organisms (unpublished results) showed that ubiquitin is restricted only to eukaryotes. The finding of ubiquitin in bacteria^[44] was probably due to contamination of the bacterial extract with yeast ubiquitin derived from the yeast extract in which the bacteria were grown. While, in retrospect, the name ubiquitin is a misnomer, as it is restricted to eukaryotes and is not ubiquitous as was previously thought, for historical reasons it has still maintained its name. Accordingly, and in order to avoid confusion, I suggest that the names of other novel enzymes and

components of the ubiquitin system, as well as of other systems, should remain as they were first coined by their discoverers.

An important development in the ubiquitin research field was the discovery that a single ubiquitin moiety can be covalently conjugated to histones, particularly to histone-H2A and H2B. While the function of these adducts had remained elusive until recently, their structure was unraveled in the mid-1970s. The structure of the ubiquitin conjugate of H2A (uH2A; also designated protein A24) was deciphered by Goldknopf and Busch^[47,48] and by Hunt and Dayhoff,^[49] who found that the two proteins are linked through a forklike, branched isopeptide bond between the carboxy-terminal glycine of ubiquitin (Gly^{76}) and the $\epsilon\text{-NH}_2$ group of an internal lysine (Lys^{119}) of the histone molecule. The isopeptide bond found in the histone–ubiquitin adduct was suggested to be identical to the bond that was found between ubiquitin and the target proteolytic substrate^[50] and between the ubiquitin moieties in the polyubiquitin chain^[51,52] that is synthesized on the substrate and that functions as a proteolysis recognition signal for the downstream 26S proteasome. In this particular polyubiquitin chain the linkage is between Gly^{76} of one ubiquitin moiety and internal Lys^{48} of the previously conjugated moiety. Only Lys^{48} -based ubiquitin chains are recognized by the 26S proteasome and serve as proteolytic signals.

In recent years it has been shown that the first ubiquitin moiety can also be attached in a linear mode to the N-terminal residue of the proteolytic target substrate.^[53] However, the subsequent ubiquitin moieties generate Lys^{48} -based polyubiquitin chains on the first, linearly fused moiety. N-terminal ubiquitination is clearly required for targeting naturally occurring lysine-free proteins for degradation. Yet, several lysine-containing proteins have also been described that traverse this pathway, the muscle-specific transcription factor MyoD, for example. In these proteins the internal lysine residues are probably not accessible to the cognate ligases.

Other types of polyubiquitin chains have also been described that are not involved in targeting the conjugated substrates for proteolysis. Thus, a Lys^{63} -based polyubiquitin chain has been described that is probably necessary for the activation of transcription factors (see Ref. [54]). Interestingly, the role of monoubiquitination of histones has also been identified recently, and this modification is also involved in regulation of transcription, probably by modulation of the structure of the nucleosomes (see, for example, Refs. [55,56]).

The identification of APF-1 as ubiquitin, and the discovery that a high-energy isopeptide bond, similar to the one that links ubiquitin to histone H2A, links it also to the target proteolytic substrate, resolved at that time the enigma of the energy requirement for intracellular proteolysis and paved the road to the untangling of the complex mechanism of isopeptide-bond formation. This process turned out to be similar to that of peptide-bond formation that is catalyzed by tRNA synthetase following amino acid activation during protein synthesis or during the nonribosomal synthesis of short peptides.^[57] With the unravelled mechanism of ubiquitin activation and using immobilized ubiquitin as a “covalent” affinity bait, the three enzymes that are involved in the

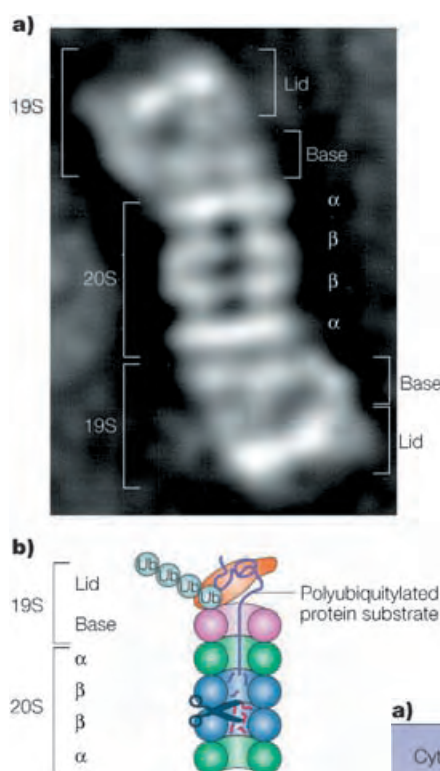


Figure 6. Structure of the proteasome. Printed from Ref. [83] with permission from Nature Publishing Group. a) Electron microscopy image of the 26S proteasome from the yeast *Saccharomyces cerevisiae*; b) schematic representation of the structure and function of the 26S proteasome.

channel opening function and the unfolding of the substrate require metabolic energy, and indeed, the 19S RP “base” contains six different ATPase subunits. Following degradation of the substrate, short peptides derived from the substrate are released, as well as reusable ubiquitin.

6. Concluding Remarks

The evolution of proteolysis as a centrally important regulatory mechanism is a remarkable example of the evolution of a novel biological concept and the accompanying battles to change paradigms. The five-decade journey between the early 1940s and early 1990s began with fierce discussions on whether cellular proteins are static, as had been thought for a long time, or are turning over. The discovery of the

dynamic state of proteins was followed by the discovery of the lysosome, that was believed between the mid-1950s and mid-1970s to be the organelle within which intracellular proteins are destroyed. Independent lines of experimental evidence gradually eroded the lysosomal hypothesis and resulted in a new idea that the bulk of intracellular proteins are degraded—under basal metabolic conditions—by a non-lysosomal machinery. This resulted in the discovery of the ubiquitin system in the late 1970s and early 1980s.

With the identification of the reactions and enzymes that are involved in the ubiquitin–proteasome cascade, a new era in the protein-degradation field began in the late 1980s and early 1990s. Studies that showed that the system is involved in the targeting of specific key regulatory proteins, such as light-regulated proteins in plants, and transcriptional factors, cell-cycle regulators, and tumor suppressors and promoters in mammalian cells, started to emerge (see, for example Refs. [74–78]). They were followed by numerous studies on the underlying mechanisms involved in the degradation of these specific proteins, each with its own unique mode of recognition and regulation. The unraveling of the human

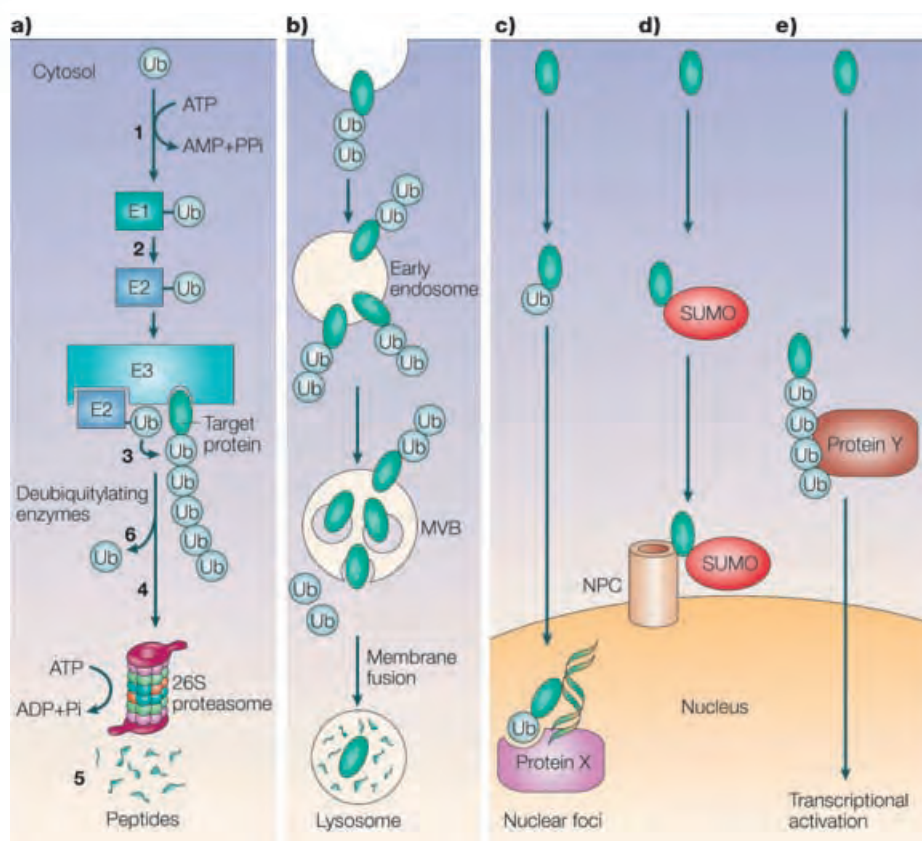


Figure 7. Some of the different functions of modification by ubiquitin and ubiquitin-like proteins: a) Proteasomal-dependent degradation of cellular proteins (see Figures 5 and 6). b) Mono- or oligoubiquitination targets membrane proteins to degradation in the lysosome/vacuole. c) Monoubiquitination, or d) a single modification by a ubiquitin-like (UBL) protein, for example, SUMO, can target proteins to different subcellular destinations such as nuclear foci or the nuclear pore complex (NPC). Modification by UBLs can serve other nonproteolytic functions, such as protecting proteins from ubiquitination or activation of E3 complexes. e) Generation of a Lys⁶³-based polyubiquitin chain can activate transcriptional regulators, directly or indirectly (through recruitment of other proteins, such as the shown protein Y, or activation of upstream components such as kinases). Ub = ubiquitin. Printed from Ref. [83] with permission from the Nature Publishing Group.

genome revealed the existence of hundreds of distinct E3s, attesting to the complexity and the high specificity and selectivity of the system.

Two important advances in the field were the discovery of the nonproteolytic functions of ubiquitin, among which are activation of transcription and routing of proteins to the vacuole, and the discovery of modification by ubiquitin-like proteins (UBLs) that are also involved in numerous nonproteolytic functions such as directing proteins to their subcellular destination, protecting proteins from ubiquitination, or controlling entire processes such as autophagy (see, for example, Ref. [79]). Some of the different roles of modifications by ubiquitin and UBLs are shown in Figure 7. All these studies have led to the emerging realization that this novel and general mode of covalent conjugation plays a key role in regulating a broad array of cellular processes—among them cell cycle and division, growth and differentiation, activation and silencing of transcription, apoptosis, the immune and inflammatory response, signal transduction, receptor-mediated endocytosis, various metabolic pathways, and cell-quality control—through proteolytic and nonproteolytic mechanisms. The discovery that ubiquitin modification plays a role in routing proteins to the lysosome/vacuole and that modification by specific and unique ubiquitin-like proteins and the conjugation mechanism controls autophagy, closed an exciting historical cycle, since it demonstrated that the two apparently distinct proteolytic systems communicate with one another.

With the many processes and substrates targeted by the ubiquitin pathway, it was not surprising to find that aberrations in the system underlie, directly or indirectly, the pathogenesis of many diseases. While inactivation of a major enzyme such as E1 is obviously lethal, mutations in enzymes or in recognition motifs in substrates that do not affect vital pathways, or that affect the involved process only partially, may result in a broad array of phenotypes. Likewise, acquired changes in the activity of the system can also evolve into certain pathologies. The pathological states associated with the ubiquitin system can be classified into two groups: 1) those that result from loss of function—mutation in a ubiquitin system enzyme or in the recognition motif in the target substrate that results in stabilization of certain proteins, and 2) those that result from gain of function—abnormal or accelerated degradation of the protein target.

Aberrations in the ubiquitin system that result in disease states are shown in Figure 8. Studies that employ targeted inactivation of genes coding for specific ubiquitin system enzymes and substrates in animals can provide a more systematic view into the broad spectrum of pathologies that may result from aberrations in ubiquitin-mediated proteolysis. A better understanding of the processes and identification of the components involved in the degradation of key regulatory proteins will lead to the development of mechanism-based drugs that will target specifically only the involved proteins. While the first drug, a specific proteasome inhibitor

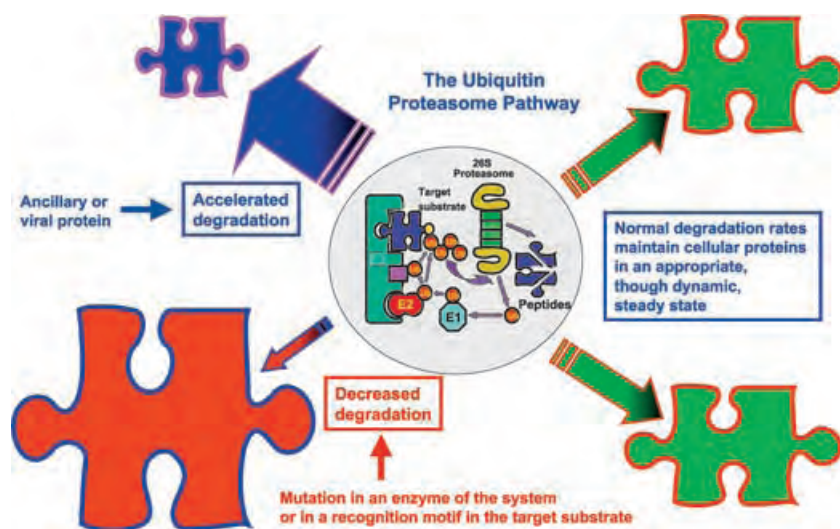


Figure 8. Aberrations in the ubiquitin–proteasome system and pathogenesis of human diseases: Normal degradation of cellular proteins maintains them at a steady-state level, although this level may change under various pathophysiological conditions (right side, top and bottom). When degradation is accelerated because of an increase in the level of an E3 (Skp2 in the case of p27, for example), or overexpression of an ancillary protein that generates a complex with the protein substrate and targets it for degradation (for example, the human papillomavirus E6 oncoprotein that associates with p53 and targets it for degradation by the E6-AP ligase, or the cytomegalovirus-encoded ER proteins US2 and US11 that target MHC class I molecules for endoplasmic reticulum-associated degradation, ERAD), the steady-state level of the protein decreases (top left). A mutation in a ubiquitin ligase (such as occurs in adenomatous polyposis coli, or EG-AP in Angelmans' syndrome), or in the substrate's recognition motif (such as occurs in β -catenin or in ENaC), will result in decreased degradation and accumulation of the target substrate (bottom left).

is already on the market,^[80] it appears that one important hallmark of the new era we are entering now will be the discovery of novel drugs based on the targeting of specific processes such as inhibiting aberrant Mdm2- or E6-AP-mediated accelerated targeting of the tumor suppressor p53 which will lead to regeneration of its lost function.

Many reviews have been published on different aspects of the ubiquitin system. The purpose of this article was to bring to the reader several milestones on the historical pathway along which the ubiquitin system has evolved. For additional reading on the ubiquitin system the reader is referred to the many reviews written on the system, such as Refs. [81,82]. Some parts of this Review, including several figures, are based on another recently published review article (Ref. [83]).

Research in my laboratory has been supported along the years by grants from the US-Israel Binational Science Foundation (BSF), the Israel Science Foundation (ISF) founded by the Israeli National Academy of Humanities, Arts and Sciences, the German-Israeli Foundation (GIF) for Scientific Research and Development, the Israel Cancer Research Fund (ICRF) USA, the Deutsche-Israeli Cooperation Program (DIP), the European Union (EU), the Israel Cancer Society (ICS), the Prostate Cancer Foundation (PCF) Israel, the Foundation for Promotion of Research in the Technion, and various research grants administered by the Vice President of the Technion for Research. Infrastructural equipment for the laboratory and for the Cancer and Vascular Biology Research Center has been

purchased with the support of the Wolfson Charitable Fund—Center of Excellence for Studies on Turnover of Cellular Proteins and its Implications to Human Diseases.

Received: April 26, 2005

- [1] H. T. Clarke, *Annu. Rev. Biochem.* **1958**, 27, 1–14.
- [2] E. P. Kennedy, *J. Biol. Chem.* **2001**, 276, 42619–42631.
- [3] R. D. Simoni, R. L. Hill, M. Vaughan, *J. Biol. Chem.* **2002**, 277, e1–e3; see also: R. Schoenheimer, D. Rittenberg *J. Biol. Chem.* **1935**, 111, 163–168; D. Rittenberg, R. Schoenheimer, *J. Biol. Chem.* **1937**, 121, 235–253
- [4] R. Schoenheimer, S. Ratner, D. Rittenberg, *J. Biol. Chem.* **1939**, 127, 333–344.
- [5] S. Ratner, D. Rittenberg, A. S. Keston, R. Schoenheimer, *J. Biol. Chem.* **1940**, 134, 665–676.
- [6] R. Schoenheimer, *The Dynamic State of Body Constituents*, Harvard University Press, Cambridge, **1942**.
- [7] D. S. Hogness, M. Cohn, J. Monod, *Biochim. Biophys. Acta* **1955**, 16, 99–116.
- [8] C. de Duve, R. Gianetto, F. Appelmans, R. Wattiaux, *Nature* **1953**, 172, 1143–1144.
- [9] R. Gianetto, C. de Duve, *Biochem. J.* **1955**, 59, 433–438.
- [10] M. V. Simpson, *J. Biol. Chem.* **1953**, 201, 143–154.
- [11] G. E. Mortimore, A. R. Poso, *Annu. Rev. Nutr.* **1987**, 7, 539–564.
- [12] T. P. Ashford, K. R. Porter, *J. Cell Biol.* **1962**, 12, 198–202.
- [13] R. T. Schimke, D. Doyle, *Annu. Rev. Biochem.* **1970**, 39, 929–976.
- [14] A. L. Goldberg, A. C. St. John, *Annu. Rev. Biochem.* **1976**, 45, 747–803.
- [15] H. L. Segal, J. R. Winkler, M. P. Miyagi, *J. Biol. Chem.* **1974**, 249, 6364–6365.
- [16] M. Haider, H. L. Segal, *Arch. Biochem. Biophys.* **1972**, 148, 228–237.
- [17] R. T. Dean, *Acta Biol. Med. Ger.* **1977**, 36, 1815–1820.
- [18] M. Müller, H. Müller, H. Holzer, *J. Biol. Chem.* **1981**, 256, 723–727.
- [19] H. Holzer, *Revis. Biol. Celular.* **1989**, 21, 305–319.
- [20] A. E. Majeski, J. F. Dice, *Int. J. Biochem. Cell Biol.* **2004**, 36, 2435–2444.
- [21] A. M. Cuervo, J. F. Dice, *J. Mol. Med.* **1998**, 76, 6–12.
- [22] M. Hayashi, Y. Hiroi, Y. Natori, *Nature New Biol.* **1973**, 242, 163–166.
- [23] D. L. Schneider, *J. Biol. Chem.* **1981**, 256, 3858–3864.
- [24] C. de Duve, R. Wattiaux, *Annu. Rev. Physiol.* **1966**, 28, 435–492.
- [25] M. Rabinovitz, J. M. Fisher, *Biochim. Biophys. Acta* **1964**, 91, 313–322.
- [26] R. W. Carrell, H. Lehmann, *Semin. Hematol.* **1969**, 6, 116–132.
- [27] E. R. Huehns, A. J. Bellingham, *Br. J. Haematol.* **1969**, 17, 1–10.
- [28] J. D. Etlinger, A. L. Goldberg, *Proc. Natl. Acad. Sci. USA* **1977**, 74, 54–58.
- [29] A. Hershko, H. Heller, D. Ganoth, A. Ciechanover in *Protein Turnover and Lysosome Function* (Eds.: H. L. Segal, D. J. Doyle), Academic Press, New York, **1978**, pp. 149–169.
- [30] S. E. Knowles, F. J. Ballard, *Biochem. J.* **1976**, 156, 609–617.
- [31] N. T. Neff, G. N. DeMartino, A. L. Goldberg, *J. Cell. Physiol.* **1979**, 101, 439–457.
- [32] B. Poole, S. Ohkuma, M. J. Warburton, *Acta Biol. Med. Ger.* **1977**, 36, 1777–1788.
- [33] B. Poole, S. Ohkuma, M. J. Warburton in *Protein Turnover and Lysosome Function* (Eds.: H. L. Segal, D. J. Doyle), Academic Press, New York, **1978**, pp. 43–58.
- [34] J. Mandelstam, *Biochem. J.* **1958**, 69, 110–119.
- [35] D. Steinberg, M. Vaughan, *Arch. Biochem. Biophys.* **1956**, 65, 93–105.
- [36] A. Hershko, G. M. Tomkins, *J. Biol. Chem.* **1971**, 246, 710–714.
- [37] A. L. Goldberg, J. D. Kowit, J. D. Etlinger in *Proteolysis and Physiological Regulation* (Eds.: D. W. Ribbons, K. Brew), Academic Press, New York, **1976**, pp. 313–337.
- [38] A. Ciechanover, Y. Hod, A. Hershko, *Biochem. Biophys. Res. Commun.* **1978**, 81, 1100–1105.
- [39] A. Ciechanover, H. Heller, S. Elias, A. L. Haas, A. Hershko, *Proc. Natl. Acad. Sci. USA* **1980**, 77, 1365–1368.
- [40] A. Hershko, A. Ciechanover, H. Heller, A. L. Haas, I. A. Rose, *Proc. Natl. Acad. Sci. USA* **1980**, 77, 1783–1786.
- [41] A. Ciechanover, S. Elias, H. Heller, S. Ferber, A. Hershko, *J. Biol. Chem.* **1980**, 255, 7525–7528.
- [42] K. D. Wilkinson, M. K. Urban, A. L. Haas, *J. Biol. Chem.* **1980**, 255, 7529–7532.
- [43] G. Goldstein, *Nature* **1974**, 247, 11–14.
- [44] G. Goldstein, M. Scheid, U. Hammerling, D. H. Schlesinger, H. D. Niall, E. A. Boyse, *Proc. Natl. Acad. Sci. USA* **1975**, 72, 11–15.
- [45] D. H. Schlesinger, G. Goldstein, H. D. Niall, *Biochemistry* **1975**, 14, 2214–2218.
- [46] T. L. K. Low, A. L. Goldstein, *J. Biol. Chem.* **1979**, 254, 987–995.
- [47] I. L. Goldknopf, H. Busch, *Biochem. Biophys. Res. Commun.* **1975**, 65, 951–955.
- [48] I. L. Goldknopf, H. Busch, *Proc. Natl. Acad. Sci. USA* **1977**, 74, 864–868.
- [49] L. T. Hunt, M. O. Dayhoff, *Biochem. Biophys. Res. Commun.* **1977**, 74, 650–655.
- [50] A. Hershko, A. Ciechanover, I. A. Rose, *J. Biol. Chem.* **1981**, 256, 1525–1528.
- [51] A. Hershko, H. Heller, *Biochem. Biophys. Res. Commun.* **1985**, 128, 1079–1086.
- [52] V. Chau, J. W. Tobias, A. Bachmair, D. Mariott, D. Ecker, D. K. Gonda, A. Varshavsky, *Science* **1989**, 243, 1576–1583.
- [53] A. Ciechanover, R. Ben-Saadon, *Trends Cell Biol.* **2004**, 14, 103–106.
- [54] M. Muratani, W. P. Tansey, *Nat. Rev. Mol. Cell Biol.* **2003**, 4, 192–201.
- [55] Y. Zhang, *Genes Dev.* **2003**, 17, 2733–2740.
- [56] M. A. Osley, *Biochim. Biophys. Acta* **2004**, 1677, 74–78.
- [57] F. Lipman, *Science* **1971**, 173, 875–884.
- [58] A. Ciechanover, S. Elias, H. Heller, A. Hershko, *J. Biol. Chem.* **1982**, 257, 2537–2542.
- [59] A. Hershko, H. Heller, S. Elias, A. Ciechanover, *J. Biol. Chem.* **1983**, 258, 8206–8214.
- [60] D. T. Chin, L. Kuehl, M. Rechsteiner, *Proc. Natl. Acad. Sci. USA* **1982**, 79, 5857–5861.
- [61] A. Hershko, E. Eytan, A. Ciechanover, A. L. Haas, *J. Biol. Chem.* **1982**, 257, 13964–13970.
- [62] Y. Matsumoto, H. Yasuda, T. Marunouchi, M. Yamada, *FEBS Lett.* **1983**, 151, 139–142.
- [63] D. Finley, A. Ciechanover, A. Varshavsky, *Cell* **1984**, 37, 43–55.
- [64] A. Ciechanover, D. Finley, A. Varshavsky, *Cell* **1984**, 37, 57–66.
- [65] K. Tanaka, L. Waxman, A. L. Goldberg, *J. Cell Biol.* **1983**, 96, 1580–1585.
- [66] A. Hershko, E. Leshinsky, D. Ganoth, H. Heller, *Proc. Natl. Acad. Sci. USA* **1984**, 81, 1619–1623.
- [67] R. Hough, G. Pratt, M. Rechsteiner, *J. Biol. Chem.* **1986**, 261, 2400–2408.
- [68] L. Waxman, J. Fagan, A. L. Goldberg, *J. Biol. Chem.* **1987**, 262, 2451–2457.
- [69] R. Hough, G. Pratt, M. Rechsteiner, *J. Biol. Chem.* **1987**, 262, 8303–8313.
- [70] S. Wilk, M. Orlowski, *J. Neurochem.* **1980**, 35, 1172–1182.
- [71] E. Eytan, D. Ganoth, T. Armon, A. Hershko, *Proc. Natl. Acad. Sci. USA* **1989**, 86, 7751–7755.
- [72] J. Driscoll, A. L. Goldberg, *J. Biol. Chem.* **1990**, 265, 4789–4792.
- [73] L. Hoffman, G. Pratt, M. Rechsteiner, *J. Biol. Chem.* **1992**, 267, 22362–22368.

- [74] J. Shanklin, M. Jaben, R. D. Vierstra, *Proc. Natl. Acad. Sci. USA* **1987**, *84*, 359–363.
- [75] M. Hochstrasser, A. Varshavsky, *Cell* **1990**, *61*, 697–708.
- [76] M. Scheffner, B. A. Werness, J. M. Huibregtse, A. J. Levine, P. M. Howley, *Cell* **1990**, *63*, 1129–1136.
- [77] M. Glotzer, A. W. Murray, M. W. Kirschner, *Nature* **1991**, *349*, 132–138.
- [78] A. Ciechanover, J. A. DiGiuseppe, B. Bercovich, A. Orian, J. D. Richter, A. L. Schwartz, G. M. Brodeur, *Proc. Natl. Acad. Sci. USA* **1991**, *88*, 139–143.
- [79] N. Mizushima, T. Noda, T. Yoshimori, Y. Tanaka, T. Ishii, M. D. George, D. J. Klionsky, M. Ohsumi, Y. Ohsumi, *Nature* **1998**, *395*, 395–398.
- [80] J. Adams, *Drug Discovery Today* **2003**, *8*, 307–315.
- [81] M. H. Glickman, A. Ciechanover, *Physiol. Rev.* **2002**, *82*, 373–428.
- [82] C. M. Pickart, R. E. Cohen, *Nat. Rev. Mol. Cell Biol.* **2004**, *5*, 177–187.
- [83] A. Ciechanover, *Nat. Rev. Mol. Cell Biol.* **2005**, *6*, 79–86.



Saved Search Alerts – Quick and Easy

Simply register. Registration is fast and free to all internet users.

Saved Search Alerts:

You are notified by e-mail whenever content is published online that matches one of your saved searches—complete with direct links to the new material.

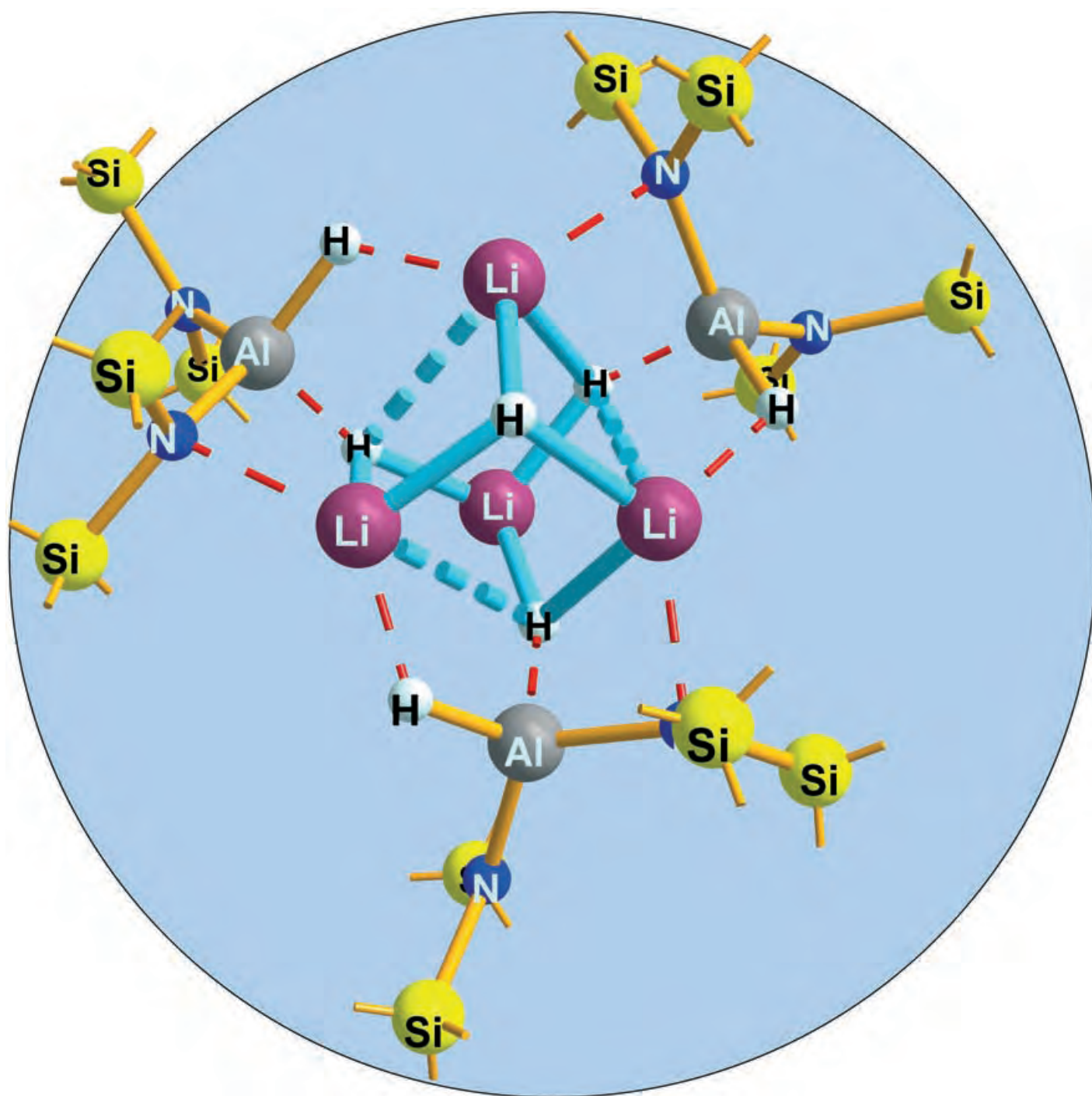
To set a Saved Search alert: Run a search on Wiley InterScience, then click

- **Save Search** on the results page



Once you have saved the query, login to "My Profile" and go to **SAVED SEARCHES**. Click **+ Activate Alert** to start getting e-mail results for that query.

Communications



A cubic Li_4H_4 species can be isolated in molecular form through the coordination of three $\text{HAl}\{\text{N}(\text{SiMe}_3)_2\}_2$ ligands. Steric factors prevent the coordination of a fourth ligand and result in the formation of an aggregate with nearly perfect C_3 symmetry. For more information see the Communication by M. Veith et al. on the following pages.

distances (see Figure 1). Owing to the insertion of the Al–H units into the three edges of the Li_4H_4 cube the Li1–H6, Li3–H4, and Li4–H5 distances are greatly elongated, which is reinforced by the concomitant N coordination to these atoms (Figure 1). The different coordination behavior of the two hexamethyldisilylazyl groups on each Al atom is also evident from the angle-sum around the nitrogen atoms, almost trigonal planar environment are found for N1, N4 and N5, whereas N2, N3, and N6 are slightly pyramidalized. The lithium atoms Li1, Li3, and Li4 are approximately tetrahedrally coordinated by three hydride ligands and a nitrogen base, whereas Li2 is surrounded by a trigonal-pyramidal arrangement of hydrides. The hydrides can be divided into three categories: H1–H3 form angular bridges (mean value: 117°) between lithium and aluminum atoms, H4–H6 are coordinated by the metal atoms in an almost trigonal-planar arrangement, whereas H7 is surrounded only by lithium atoms (mean angle: $100.6(3)^\circ$) in a trigonal-pyramidal arrangement. Thus hydrogen atom H7 is the most accessible, at least in the kinetic sense (see below).

The other two main products of the reaction form coordination polymers in their crystal structures (Figure 2 and Figure 3). In the case of $[\{\text{Li}\{\text{H}(\text{OrBu})_2\text{Al}[\text{N}(\text{SiMe}_3)_2]\}_n]$ (2) one-dimensional helical structures are formed from two crystallographically different units through almost linear Li–H–Al hydrogen bonds. They consist formally of aluminate units $\{\text{H}(\text{OrBu})_2\text{Al}[\text{N}(\text{SiMe}_3)_2]\}$ that chelate the formal lithium cation through the oxygen atom of the alcohol residue (Figure 2).^[20] The lithium atoms are coordinated by oxygen

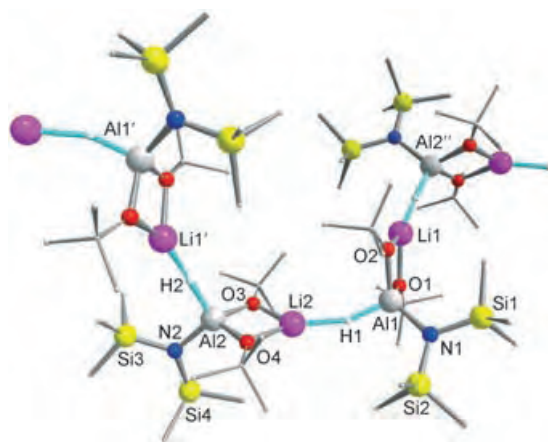


Figure 2. Molecular structure of **2**. Selected bond lengths [Å] and angles $^\circ$: Al1–H1 1.61(1), Al2–H2 1.61(1), Li1'–H2 1.95(2), Li2–H1 1.86(2), Al1–N1 1.843(5), Al1–O1 1.769(4), Al1–O2 1.788(4), Li1–O1 1.910(7), Li1–O2 1.924(7), Al2–N2 1.848(5), Al2–O3 1.780(4), Al2–O4 1.771(4), Li2–O3 1.883(7), Li2–O4 1.890(7); O1–Li1–O2 82.2(1), O1–Al1–O2 90.27(8), Al1–H1–Li2 159.3(2), O3–Li2–O4 83.7(1), O3–Al2–O4 90.32(8), Al2–H2–Li1' 164.7(2).

and hydrogen atoms in a distorted trigonal-planar arrangement, and the hexamethyldisilylazyl substituents form simple terminal ligands to the aluminum atoms. An example of an isolated lithium alinate that is chemically very similar to **2** is $[\text{Li}(\text{OEt})_2(\mu\text{OCMe}t\text{Bu})_2\text{Al}(\text{H})(\text{OCMe}t\text{Bu})]$ in which polymerization is impeded by the bonding of the Et_2O base to the lithium atom.

The crystal structure of **3** is remarkable (Figure 3).^[20] Two crystallographically independent strands of $[\{\text{Li}(\text{H}_2\text{Al}[\text{N}(\text{SiMe}_3)_2]_2)\}_n]$ run through the crystal as Al–H–Li–H–Al zigzag chains, which surprisingly (in spite of the weak Lewis basicity of the nitrogen atom in $\{\text{N}(\text{SiMe}_3)_2\}$) are reinforced by Al–N–

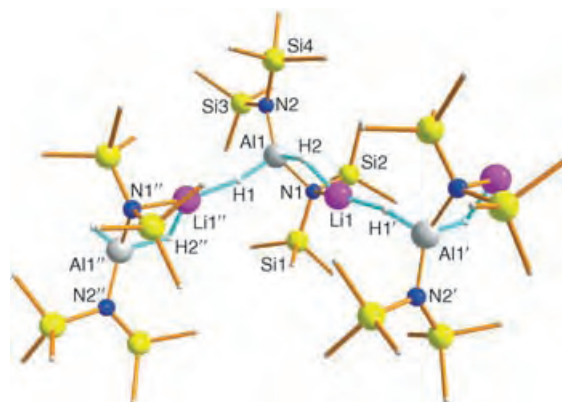
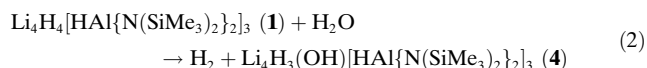


Figure 3. Molecular structure of **3**. (only one of the two crystallographically independent but structurally very similar polymers is shown). Selected (averaged) bond lengths [Å] and angles $^\circ$: Al1–H1 1.52(1), Al1–H2 1.79(1), Al1–N1 1.932(5), Al1–N2 1.846(5), Li1–H2 1.62(2), Li1–H1' 1.81(2), Li1–N1 2.135(8), N1–Si(1,2) 1.752(9), N2–Si(3,4) 1.745(1); H2–Al1–N1, Al1–N1–Li1, N1–Li1–H2, Li1–H2–Al1 101.6(2), Li1–H1'–Al1' 166.8(2).

Li bridges so that four-membered Al–N–Li–H rings are formed. An alternative description is that the lithium atom is coordinated by two hydrogen atoms and a nitrogen atom, this is in contrast to the isolated molecular diethyl ether adduct $[\text{Li}(\text{OEt})_2(\mu\text{H})_2\text{Al}[\text{N}(\text{SiMe}_3)_2]_2]$ in which the lithium atom is chelated by only two hydride hydrogen atoms.^[16] Clearly the loss of base requires the lithium atoms to expand their coordination sphere from 2 to 3 with the silylazyl ligands.

If $\text{Li}_4\text{H}_4[\text{HAl}[\text{N}(\text{SiMe}_3)_2]_2]_3$ (**1**) is treated with a small amount of water only H7 of the seven hydride atoms (Figure 1) reacts, in the hydrolysis product $\text{Li}_4\text{H}_3(\text{OH})[\text{HAl}[\text{N}(\text{SiMe}_3)_2]_2]_3$ (**4**; Figure 4 and the reaction in Equation (2)) it is substituted by an OH group.



In many respects the structure of **4** resembles that of **1** since the whole basket-shaped $\text{Li}_4\text{H}_3[\text{HAl}[\text{N}(\text{SiMe}_3)_2]_2]_3$ part is essentially identical in both molecules (Figure 1 and Figure 4).^[20] **1** and **4** crystallize in different crystal lattices and are therefore not isotopic. The Li–O1 bond in **4** is about 0.15 Å longer than the Li–H7 bond in **1**, thus, the $\text{Li}_4\text{H}_3\text{--}[\text{HAl}[\text{N}(\text{SiMe}_3)_2]_2]_3$ basket part of **4** is somewhat extended (the nonbonding Li⋯Li distances in **4** are about 0.08 Å longer than in **1**) and consequently the angles at the oxygen atom O1 are also more acute than at H7. As can be seen from the hydrolysis of **1**, the three $\text{HAl}[\text{N}(\text{SiMe}_3)_2]_2$ loops not only stabilize the Li_4H_4 units coordinatively but also protect them in the kinetic sense. It is only at the unprotected, free position (H7 in **1**) that substitution occurs (in careful hydrolysis).

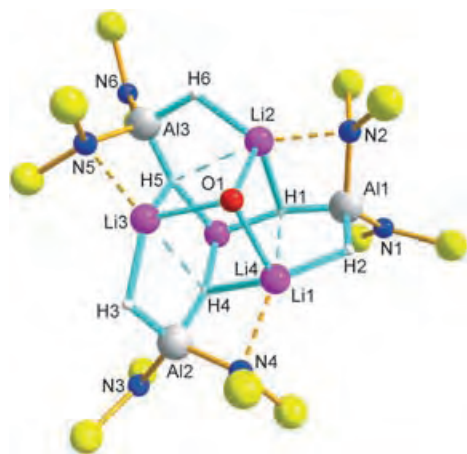


Figure 4. Molecular structure of **4**. The methyl groups of the trimethylsilyl units (yellow Si) have been omitted for clarity. Selected (averaged) bond lengths [Å] and angles [°]: O1–Li(1,2,3) 2.183(9), Al(1,2,3)–N(2,4,6) 1.896(5), Al(1,2,3)–N(1,3,6) 1.841(5), Li4–H(1,4,5) 1.85(1), Li(1,2,3)–H(2,6,3) 1.90(1), Al(1,2,3)–H(2,3,6) 1.57(1), Al(1,2,3)–H(1,4,5) 1.62(2); Li1–O1–Li2 94.5(1), Li2–O1–Li3 94.4(1), Li1–O1–Li3 94.6(1).

Experimental section

A stirred solution of $(\text{H}_2\text{AlO}t\text{Bu})_2$ (0.79 g, 3.84 mmol) in toluene (5.0 mL) at room temperature was slowly treated dropwise with a solution of $\text{LiN}(\text{SiMe}_3)_2$ (2.58 g; 13.4 mmol) in toluene (15.0 mL). After 18 h stirring the reaction mixture was heated for 7 h at about 95 °C. After cooling overnight in the oil bath the partly crystalline precipitate (amount: 0.6 g) is collected by filtration. Colorless crystals of **1** (0.05 g, 1.8 %) and **2** (0.40 g, 15.3 %) separate from the filtrate at room temperature. The crystals differ in their crystalline habit. After further concentration, further crystals separate, which after recrystallization from toluene yields 0.20 g (7.3 %) of colorless crystals of **3**. If a solution of **1** is treated with wet toluene, crystals of **4** form after a few hours. Solvent in each case $[\text{D}_8]\text{toluene}$: **1**: ^1H NMR (200.13 MHz): δ = 0.38 ppm, ^{13}C NMR (50.3 MHz): δ = 5.96 ppm, ^{29}Si NMR (39.7 MHz): δ = 0.01 ppm; IR: (Al–H): $\tilde{\nu}$ = 1732, 1700 cm^{-1} ; **2**: ^1H NMR: δ = 0.45 (SiCH), 1.31 ppm (CCH), ^{13}C NMR: δ = 6.04 (SiC), 33.7 (CH), 68.9 ppm (CC), ^{29}Si NMR: δ = –2.96 ppm; **3**: ^1H NMR: 0.37 ppm, ^{13}C NMR: δ = 5.90 ppm, ^{29}Si NMR: δ = 0.25 ppm. **4** was only characterized by X-ray diffraction.

Received: May 30, 2005

Published online: August 31, 2005

Keywords: alanes · hydrides · lithium · structure determination

- [8] H. H. Giese, T. Haberer, J. Knizek, H. Nöth, M. Warchold, *Eur. J. Inorg. Chem.* **2001**, 1195.
- [9] T. Haberer, H. Nöth, *Z. Anorg. Allg. Chem.* **2001**, 627, 1003.
- [10] G. Linti, W. Kostler, A. Rodig, *Z. Anorg. Allg. Chem.* **2002**, 628, 1319.
- [11] W. Uhl, *Z. Anorg. Allg. Chem.* **1989**, 570, 37.
- [12] C. Eaborn, I. B. Gorrell, P. B. Hitchcock, J. D. Smith, K. Tavakkoli, *Organometallics* **1994**, 13, 4143.
- [13] R. J. Wehmschulte, J. J. Ellison, K. Ruhlandt-Senge, P. P. Power, *Inorg. Chem.* **1994**, 33, 6300.
- [14] M. M. Andrianarison, A. G. Avent, M. C. Ellerby, I. B. Gorrell, P. B. Hitchcock, J. D. Smith, D. R. Stanley, *J. Chem. Soc., Dalton Trans.* **1998**, 249.
- [15] H. Nöth, A. Schlegel, J. Knizek, I. Krossing, W. Ponikwar, T. Seifert, *Chem. Eur. J.* **1998**, 4, 2191.
- [16] A. Heine, D. Stalke, *Angew. Chem.* **1992**, 104, 941; *Angew. Chem. Int. Ed. Engl.* **1992**, 31, 854.
- [17] D. Hoffmann, T. Kottke, R. J. Lagow, R. D. Thomas, *Angew. Chem.* **1998**, 110, 1630; *Angew. Chem. Int. Ed.* **1998**, 37, 1537.
- [18] M. Veith, S. Faber, H. Wolfanger, V. Huch, *Chem. Ber.* **1996**, 129, 381.
- [19] U. Wannagat, H. Niederprüm, *Chem. Ber.* **1961**, 94, 1540.
- [20] Crystal data: **1**: $\text{C}_{36}\text{H}_{115}\text{Al}_3\text{Li}_4\text{N}_6\text{Si}_{12}$, M_r = 1078.12 g mol^{-1} , orthorhombic, space group $Pbca$, a = 1547.9(3), b = 1960.8(4), c = 4791.7(10) pm, V = 14543(5) $\times 10^6$ pm³, Z = 8, ρ_{calc} = 0.985 Mg m^{-3} , $F(000)$ = 4736, Stoe-IPDS-Image-Plate-System, T = 293 K, $1.57 \leq \theta \leq 18.29^\circ$, 40984 reflections, of which 5219 were symmetry independent (SHELXS-86,97), refinement (SHELXL-93,97) with anisotropic temperature factors for all non-hydrogen atoms; the hydrogen atoms on the aluminum atoms were freely refined, whereas those on the carbon atoms were treated as rigid groups; R_1 = 0.0386 ($I > 2\sigma_1$), wR_2 = 0.0899. **2**: $\text{C}_{28}\text{H}_{74}\text{Al}_2\text{Li}_2\text{N}_2\text{O}_2\text{Si}_4$, M_r = 683.09 g mol^{-1} , monoclinic, space group $P2_1/c$, a = 1065.3(2), b = 2588.1(5), c = 1701.0(3) pm, β = 106.54(3)°, V = 4495.8(14) $\times 10^6$ pm³, Z = 4, ρ_{calc} = 1.009 Mg m^{-3} , $F(000)$ = 1504, Stoe-IPDS, T = 293 K, $2.01 \leq \theta \leq 24.06^\circ$, 27817 reflections, of which 7004 were symmetry independent, (R_{int} = 0.0450), 7004 data, no restraints, 387 parameters, solution and refinement as for **1**, R_1 = 0.0369 ($I > 2\sigma_1$), wR_2 = 0.0908. **3**: $\text{C}_{24}\text{H}_{75}\text{Al}_2\text{Li}_2\text{N}_4\text{Si}_8$, M_r = 712.44 g mol^{-1} , monoclinic, space group $P2_1$, a = 1345.4(3), b = 952.2(2), c = 1898.7(4) pm, β = 100.60(3)°, V = 2390.9(9) $\times 10^6$ pm³, Z = 2, ρ_{calc} = 0.990 Mg m^{-3} , $F(000)$ = 782, Stoe-IPDS, T = 293 K, $2.04 \leq \theta \leq 23.97^\circ$, 14969 reflections, of which 6965 were symmetry independent, (R_{int} = 0.0701), 6965 data, 1 restraint, 373 parameters, solution and refinement as for **1**, R_1 = 0.0800 ($I > 2\sigma_1$), wR_2 = 0.2521. **4**: $\text{C}_{36}\text{H}_{115}\text{Al}_3\text{Li}_4\text{N}_6\text{OSi}_{12}$, monoclinic, space group $I2/a$, a = 2495.5(5), b = 2107.0(4), c = 2974.0(6) pm, β = 96.05(3)°, V = 15550(5) $\times 10^6$ pm³, Z = 8, ρ_{calc} = 0.977 Mg m^{-3} , $F(000)$ = 4996, Stoe-IPDS, T = 293 K, $1.81 \leq \theta \leq 24.13^\circ$, 48651 reflections, of which 11659 were symmetry independent, (R_{int} = 0.0970), 11659 data, no restraints, 605 parameters, solution and refinement as in **1**, R_1 = 0.0545 ($I > 2\sigma_1$), wR_2 = 0.1446. CCDC-275399 (**1**), CCDC-275400 (**2**), CCDC-275401 (**3**), and CCDC-275402 (**4**) contain the detailed crystallographic data of this publication. The data may be obtained free of charge under www.ccdc.cam.ac.uk/conts/retrieving.html erhältlich (or may be requested from: Cambridge Crystallographic Data Centre, 12 Union Road, Cambridge CB2 1EZ; Fax: (+44) 1223-336-033; oder deposit@ccdc.cam.ac.uk).

- [1] D. R. Armstrong, W. Clegg, H. M. Colquhoun, J. A. Danils, R. E. Mulvey, I. R. Stephenson, K. Wade, *J. Chem. Soc., Chem. Commun.* **1987**, 630.
- [2] A. Heine, D. Stalke, *J. Organomet. Chem.* **1997**, 542, 25.
- [3] D. L. Reger, J. E. Collins, M. A. Matthews, A. I. Rheingold, L. M. Liable-Sands, I. A. Guzei, *Inorg. Chem.* **1997**, 36, 6266.
- [4] H.-H. Giese, H. Nöth, H. Schwenk, S. Thomas, *Eur. J. Inorg. Chem.* **1998**, 941.
- [5] H.-H. Giese, T. Haberer, H. Nöth, W. Ponikwar, S. Thomas, M. Warchold, *Inorg. Chem.* **1999**, 38, 4188.
- [6] J. Knizek, H. Nöth, *J. Organomet. Chem.* **2000**, 614, 168.
- [7] C. Eaborn, S. M. El-Hamruni, M. S. Hill, P. B. Hitchcock, M. Hopman, A. Le Gouic, J. D. Smith, *J. Organomet. Chem.* **2000**, 597, 3.

Titanium-Catalyzed Intermolecular Hydroamination of Vinylarenes**

Ludwig T. Kaspar, Benjamin Fingerhut, and Lutz Ackermann*

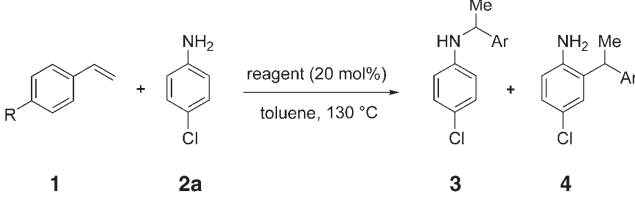
Most substituted amines are made today by multistep syntheses. Therefore, addition reactions of simple amines onto unsaturated carbon–carbon multiple bonds, hydroamination reactions,^[1–6] are of considerable importance for industry and academia. Transformations of alkynes and allenes can be catalyzed by a variety of reagents.^[7] However, protocols for intermolecular hydroamination reactions of more readily available olefins have thus far proven limited. Various lanthanide complexes catalyze hydroamination reactions of alkenes, but they lack compatibility with a number of important functional groups.^[8,9] Significant research activity has focused on the use of late-transition-metal complexes for intermolecular hydroamination reactions of olefins, featuring iridium,^[10–12] rhodium,^[13–18] nickel,^[19,20] palladium,^[21–24] platinum,^[25,26] and ruthenium.^[27,28] The high cost of these complexes, their stabilizing ligands, or the additives constitute a limitation of these protocols. Recently, we reported a Group 4 metal catalyzed^[29] intermolecular^[30] hydroamination of norbornene.^[31] Herein we present titanium-catalyzed^[32] hydroamination reactions of vinylarenes as well as an application of this procedure to the synthesis of a tetrahydroisoquinoline.

Initial experiments showed that catalytic amounts of the Lewis acid TiCl₄ converted styrene (**1a**) in the presence of four equivalents of 4-chloroaniline (**2a**) efficiently at 130 °C (Table 1, entry 1). Control experiments indicated that a

simple Brønsted acid mediated reaction is not operative (entries 3 and 4). These results are in agreement with observations made by Hartwig et al., who found that even the *intramolecular* addition of amines, not bearing an electron-withdrawing group, does not occur in the presence of concentrated sulfuric acid.^[33,34]

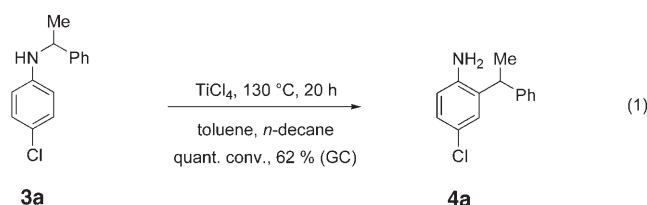
Under the above reaction conditions, mixtures of hydroamination and *ortho*-hydroarylation products were obtained. While the reaction time for quantitative conversion could be reduced significantly with microwave irradiation, the amount

Table 1: Hydroamination of vinylarenes **1** with 4-chloroaniline (**2a**).^[a]

						
Entry	Reagent	R	t [h]	3/4 ^[b]	Yield 3 [%] ^[c]	Yield 4 [%] ^[c]
1	TiCl ₄	H (1a)	22	61:39	30 (3a)	32 (4a)
2	–	H (1a)	22	–	–	–
3	H ₂ SO ₄	H (1a)	22	–	–	–
4	4-ClC ₆ H ₄ NH ₃ Cl	H (1a)	22	–	–	–
5	Cp ₂ TiCl ₂	H (1a)	22	–	–	–
6	TiCl ₄	H (1a)	4 ^[d]	13:87	–	61 (4a)
7	TiCl ₄	H (1a)	22 ^[e]	16:84	–	52 (4a)
8	TiCl ₄	Me (1b)	22	41:59	40 (3b)	40 (4b)
9	TiCl ₄	Me (1b)	2 ^[d]	7:93	–	68 (4b)
10	TiCl ₄	F (1c)	6 ^[d]	42:68	29 (3c)	37 (4c)

[a] Reaction conditions: **1** (1 mmol), **2a** (4 mmol), toluene (2 mL), 130 °C. [b] By GC analysis. [c] Yields of isolated product. [d] With microwave irradiation. [e] 1.0 equiv TiCl₄.

of hydroarylation product increased (entries 6, 9, and 10). As the *ortho*-alkylated product was also predominantly formed when stoichiometric amounts of the Lewis acid TiCl₄ were employed (entry 7), we wondered if a rearrangement of the hydroamination product occurs. Accordingly, we synthesized secondary amine **3a** independently through a palladium-catalyzed amination reaction^[35] and subjected it to the hydroamination reaction conditions [Eq. (1)]. Indeed, the secondary amine **3a** was quantitatively converted, while the primary amine **4a** remained unchanged under the reaction conditions [Eq. (2)].



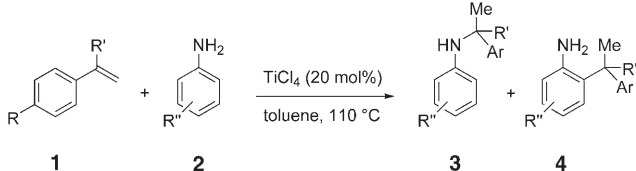
Subsequently, we studied the scope of the catalytic intermolecular hydroamination of styrene derivatives (Table 2). A number of vinylarenes **1** and aniline derivatives **2** were efficiently converted with catalytic amounts of TiCl₄, leading to the functionalized products in high yields. Electron-poor amines underwent more efficient reactions

[*] Dipl.-Chem. L. T. Kaspar, B. Fingerhut, Dr. L. Ackermann
Ludwig-Maximilians-Universität München
Department of Chemistry and Biochemistry
Butenandtstrasse 5–13, Haus F, 81377 München (Germany)
Fax: (+49) 089-2180-77425
E-mail: Lutz.Ackermann@cup.uni-muenchen.de

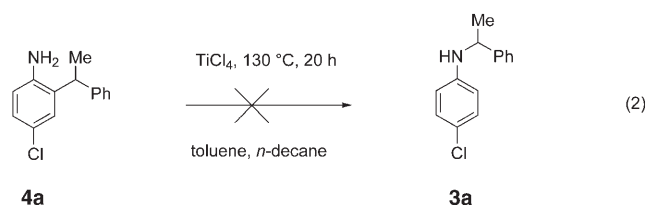
[**] We thank Professor Paul Knochel, the DFG (Emmy Noether-Programm), the Fonds der Chemischen Industrie, and the Ludwig-Maximilians-Universität for generous support.

Supporting information for this article is available on the WWW under <http://www.angewandte.org> or from the author.

Table 2: Titanium-catalyzed hydroamination of vinylarenes **1**.^[a]

								
Entry	R	R'	Amine	t [h]	3/4 ^[b]	Yield 3 [%] ^[c]	Yield 4 [%] ^[c]	Yield 3 + 4 [%] ^[c]
1	H	H (1a)	3,5-(CF ₃) ₂ C ₆ H ₃ NH ₂ (2b)	30	> 99:1	87 (3d)	–	87
2	Cl	H (1d)	3,5-(CF ₃) ₂ C ₆ H ₃ NH ₂ (2b)	30	99:1	68 (3e)	–	68
3	F	H (1c)	3,5-(CF ₃) ₂ C ₆ H ₃ NH ₂ (2b)	30	> 99:1	81 (3f)	–	81
4	H	H (1a)	2-CN C ₆ H ₄ NH ₂ (2c)	22 ^[d,e]	91:9	62 (3g)	–	62
5	H	H (1a)	2,4-Br ₂ C ₆ H ₃ NH ₂ (2d)	20 ^[d]	7:93	–	65 (4h)	65
6	H	H (1a)	4-FC ₆ H ₄ NH ₂ (2e)	3 ^[f,g]	32:68	21 (3i)	47 (4i)	68
7	H	H (1a)	3,5-(CH ₃) ₂ C ₆ H ₃ NH ₂ (2f)	20 ^[g,h]	8:92	–	50 (4j)	50
8	H	Me (1e)	2-ClC ₆ H ₄ NH ₂ (2g)	19 ^[d]	< 1:99	–	85 (4k)	85
9	H	H (1a)	2,4,6-Cl ₃ C ₆ H ₂ NH ₂ (2h)	16 ^[d]	–	–	–	–
10	OMe	H (1f)	2,4-Br ₂ C ₆ H ₃ NH ₂ (2d)	22	< 1:99	–	51 (4l)	51
11	H	H (1a)	3,5-(CF ₃) ₂ C ₆ H ₃ NH ₂ (2b)	22 ^[i]	> 99:1	85 (3d)	–	85

[a] Reaction conditions: **1** (1 mmol), **2** (4 mmol), TiCl₄ (20 mol%), toluene (2 mL). [b] By GC analysis. [c] Yields of isolated product. [d] 130 °C. [e] **1a** (4 mmol), **2c** (1 mmol). [f] With microwave irradiation. [g] 170 °C. [h] TiCl₄ (1 mmol). [i] HfCl₄ (20 mol%).



(entries 1–6). A variety of functional groups was tolerated by the catalyst, such as CF₃ (entries 1–3), Cl (entry 2), CN (entry 4), F (entries 3 and 6), and Br substituents (entries 5 and 10). Additionally, α -methylstyrene (**1e**) was quantitatively converted into product **4k**, which contains a quaternary carbon center (entry 8). Interestingly, di-*ortho*-substituted aniline **2h** was not converted (entry 9).^[31] In the reaction of aniline **2b** catalytic amounts of the Lewis acid HfCl₄ led to comparable results (entry 11).

Finally, we applied the titanium-catalyzed hydroamination reaction to a regioselective synthesis of a tetrahydroisoquinoline (Scheme 1).^[36] The highly regio- and chemoselective titanium-catalyzed hydroamination^[37,38] of enyne **5** and subsequent one-pot reduction gave aminoalkene **6** in good yield. Intramolecular hydroamination of the remaining

double bond yielded the desired tetrahydroisoquinoline **7** with excellent regioselectivity and a diastereoselectivity of 4:1.^[39]

In summary, we have described a protocol for titanium-catalyzed hydroamination reactions of styrene derivatives. A subsequent rearrangement gives rise to *ortho*-alkylated products. The catalytic system was applied to the synthesis of a tetrahydroisoquinoline derivative.

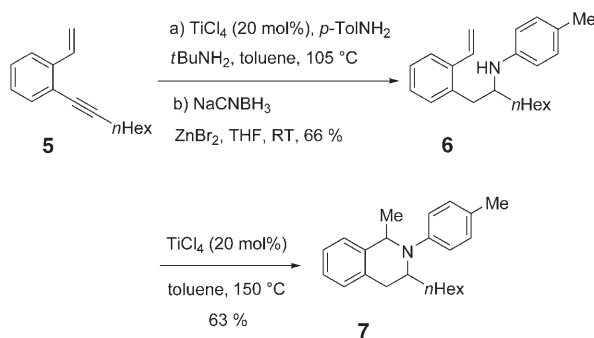
Experimental Section

Representative procedure for titanium-catalyzed hydroamination: A sealed tube was equipped with a septum and purged with N₂. The tube was charged with dry toluene (2 mL), 3,5-bis(trifluoromethyl)aniline (**2b**; 917 mg, 4.00 mmol), and styrene (**1a**; 104 mg, 1.00 mmol). TiCl₄ (0.022 mL, 0.20 mmol, 20 mol %) was added, the tube was sealed, and the resulting mixture was stirred for 30 h at 110 °C. CH₂Cl₂ (5 mL), Et₂O (60 mL), aq NH₄OH (1 N, 15 mL), and brine (50 mL) were added to the cold suspension. The separated aqueous phase was washed with Et₂O (2 × 60 mL). The combined organic phases were dried over MgSO₄ and concentrated in vacuo. Purification by column chromatography (silica gel, *n*-pentane/Et₂O 100:1) yielded *N*-1-phenylethyl-3,5-bis(trifluoromethyl)aniline (**3d**) as a yellow oil (290 mg, 87 %).

Received: April 25, 2005

Published online: August 12, 2005

Keywords: alkenes · catalysis · heterocycles · hydroamination · titanium


Scheme 1. Titanium-catalyzed synthesis of tetrahydroisoquinoline **7**.

- [1] T. E. Müller, M. Beller, *Chem. Rev.* **1998**, 98, 675–704.
- [2] J. J. Brunet, D. Neibecker in *Catalytic Heterofunctionalization* (Eds.: A. Togni, H. Grützmacher), Wiley-VCH, Weinheim, **2001**, pp. 91–132.
- [3] J. Seayad, A. Tillack, C. G. Hartung, M. Beller, *Adv. Synth. Catal.* **2002**, 344, 795–813.

- [4] P. W. Roesky, T. E. Müller, *Angew. Chem.* **2003**, *115*, 2812–2814; *Angew. Chem. Int. Ed.* **2003**, *42*, 2708–2710.
- [5] M. Beller, J. Seayad, A. Tillack, H. Jiao, *Angew. Chem.* **2004**, *116*, 3448–3479; *Angew. Chem. Int. Ed.* **2004**, *43*, 3368–3398.
- [6] K. C. Hultsch, *Adv. Synth. Catal.* **2005**, *347*, 367–391.
- [7] F. Pohlki, S. Doye, *Chem. Soc. Rev.* **2003**, *32*, 104–114.
- [8] Y. K. Kim, T. Livinghouse, Y. Horino, *J. Am. Chem. Soc.* **2003**, *125*, 9560–9561.
- [9] S. Hong, T. J. Marks, *Acc. Chem. Res.* **2004**, *37*, 673–686.
- [10] A. L. Casalnuovo, J. C. Calabrese, D. Milstein, *J. Am. Chem. Soc.* **1988**, *110*, 6738–6748.
- [11] R. Dorta, P. Egli, F. Zürcher, A. Togni, *J. Am. Chem. Soc.* **1997**, *119*, 10857–10858.
- [12] J. Zhao, A. S. Goldman, J. F. Hartwig, *Science* **2005**, *307*, 1080–1082.
- [13] D. R. Coulson, *Tetrahedron Lett.* **1971**, *12*, 429–430.
- [14] J.-J. Brunet, G. Commenges, D. Neibecker, L. Rosenberg, *J. Organomet. Chem.* **1994**, *469*, 221–228.
- [15] M. Beller, O. R. Thiel, H. Trauthwein, *Synlett* **1999**, 243–245.
- [16] M. Beller, O. R. Thiel, H. Trauthwein, C. G. Hartung, *Chem. Eur. J.* **2000**, *6*, 2513–2522.
- [17] M. Beller, C. Breindl, M. Eichberger, C. G. Hartung, J. Seayad, O. R. Thiel, A. Tillack, H. Trauthwein, *Synlett* **2002**, 1579–1594.
- [18] M. Utsunomiya, R. Kuwano, M. Kawatsura, J. F. Hartwig, *J. Am. Chem. Soc.* **2003**, *125*, 5608–5609.
- [19] J. Pawlas, Y. Nakao, M. Kawatsura, J. F. Hartwig, *J. Am. Chem. Soc.* **2002**, *124*, 3669–3679.
- [20] L. Fadini, A. Togni, *Chem. Commun.* **2003**, 30–31.
- [21] M. Kawatsura, J. F. Hartwig, *J. Am. Chem. Soc.* **2000**, *122*, 9546–9547.
- [22] T. Minami, H. Okamoto, S. Ikeda, R. Tanaka, F. Ozawa, M. Yoshifuji, *Angew. Chem.* **2001**, *113*, 4633–4635; *Angew. Chem. Int. Ed.* **2001**, *40*, 4501–4503.
- [23] U. Nettekoven, J. F. Hartwig, *J. Am. Chem. Soc.* **2002**, *124*, 1166–1167.
- [24] M. Utsunomiya, J. F. Hartwig, *J. Am. Chem. Soc.* **2003**, *125*, 14286–14287.
- [25] J.-J. Brunet, M. Cadena, N. C. Chu, O. Diallo, K. Jacob, E. Mothes, *Organometallics* **2004**, *23*, 1264–1268.
- [26] C. F. Bender, R. A. Widenhoefer, *J. Am. Chem. Soc.* **2005**, *127*, 1070–1071.
- [27] M. Utsunomiya, J. F. Hartwig, *J. Am. Chem. Soc.* **2004**, *126*, 2702–2703.
- [28] J. Takaya, J. F. Hartwig, *J. Am. Chem. Soc.* **2005**, *127*, 5756–5757.
- [29] A tantalum-catalyzed intermolecular hydroamination was reported: L. L. Anderson, J. Arnold, R. G. Bergman, *Org. Lett.* **2004**, *6*, 2519–2522.
- [30] For an elegant study on intramolecular hydroamination reactions using a cationic zirconium catalyst, see: a) P. D. Knight, I. Munslow, P. N. O'Shaughnessy, P. Scott, *Chem. Commun.* **2004**, 894–895. See also; b) K. C. Hultsch, D. V. Gribkov, *Angew. Chem.* **2004**, *116*, 5659–5663; *Angew. Chem. Int. Ed.* **2004**, *43*, 5542–5546.
- [31] L. Ackermann, L. T. Kaspar, C. J. Gschrei, *Org. Lett.* **2004**, *6*, 2515–2518.
- [32] I. Bytschkov, S. Doye, *Eur. J. Org. Chem.* **2003**, 935–946.
- [33] B. Schlummer, J. F. Hartwig, *Org. Lett.* **2002**, *4*, 1471–1474.
- [34] See also: S. K. Talluri, A. Sudalai, *Org. Lett.* **2005**, *7*, 855–857.
- [35] For studies from this laboratory on palladium-catalyzed amination reactions, see: L. Ackermann, R. Born, *Angew. Chem.* **2005**, *117*, 2497–2500; *Angew. Chem. Int. Ed.* **2005**, *44*, 2444–2447.
- [36] J. D. Scott, R. M. Williams, *Chem. Rev.* **2002**, *102*, 1669–1730.
- [37] L. Ackermann, *Organometallics* **2003**, *22*, 4367–4368.
- [38] L. Ackermann, L. T. Kaspar, C. J. Gschrei, *Chem. Commun.* **2004**, 2824–2825.
- [39] The relative stereochemistry of the diastereomers has not yet been elucidated.

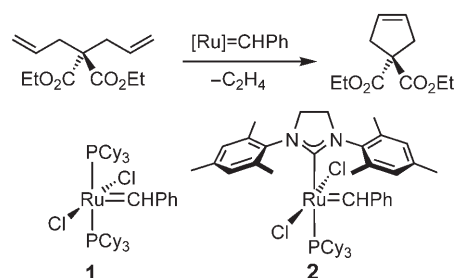
DOI: 10.1002/anie.200501114

Origin of the High Activity of Second-Generation Grubbs Catalysts**

Bernd F. Straub*

Dedicated to Professor Rolf Huisgen
on the occasion of his 85th birthday

Alkene metathesis has experienced a breathtaking success in the last decade. Organic synthetic applications were mainly facilitated by the development of highly active ruthenium carbene catalysts.^[1] The increase in activity from the catalysts of the first generation **1**^[2] to those of the second generation **2** further broadened their significance (Scheme 1).^[3] However,



Scheme 1. Alkene metathesis with first-generation and second-generation Grubbs catalysts.

“there is so far no unique explanation for the enhanced reactivity of the ‘second-generation’ Grubbs-type ruthenium complexes”.^[4]

The influence of the ligands is reflected in Grubbs’ conclusion: “Phosphines, which are larger and more electron donating, and likewise halogens, which are smaller and more electron withdrawing, lead to more active catalysts.”^[5] Since N-heterocyclic carbenes (NHC) behave as if they were extremely electron-donating phosphines, Grubbs’ rule was

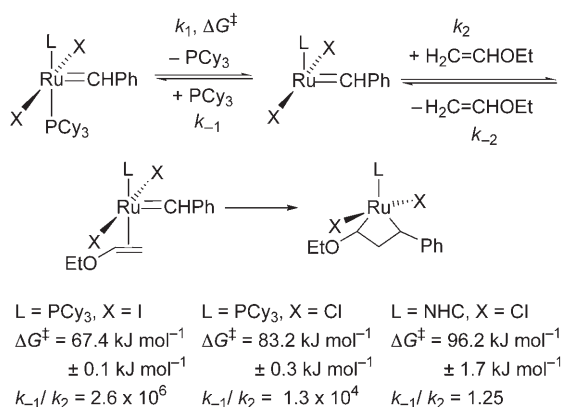
[*] Dr. B. F. Straub
Department of Chemie und Biochemie
Ludwig-Maximilians-Universität München
Butenandtstrasse 5–13 (Haus F)
81377 München (Germany)
Fax: (+49) 89-2180-77717
E-mail: Bernd.F.Straub@cup.uni-muenchen.de

[**] This research was supported by a Liebig-Fellowship of the Fonds der Chemischen Industrie. Generous support by the LMU Munich, Prof. Dr. Thomas Carell, and Prof. Dr. Herbert Mayr is gratefully acknowledged. Some of these results were presented in a lecture by B.F.S. at the Chemiedozententagung in Munich on March 9, 2005. The model structures **3b,c** to **11b,c** have been included in ref. [9] for a comparison of the overall activation energies of alkene metathesis and enyne metathesis.



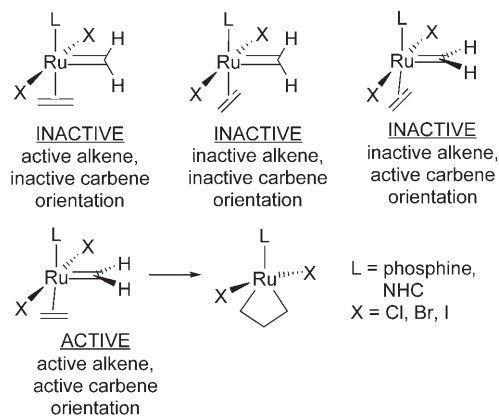
Supporting information for this article is available on the WWW under <http://www.angewandte.org> or from the author.

confirmed by the development of the second-generation catalysts. A first assumption concerning the origin of their high activity was based on the higher electronic *trans*-influence of NHC ligands compared to phosphines. An expected, more favored phosphine dissociation would result in higher concentrations of the active 14 valence-electron complexes. These complexes undergo [2+2] cycloaddition reactions with alkene substrates according to the Chauvin mechanism.^[6] However, NMR spectroscopy studies by Sanford and Grubbs demonstrated exactly the opposite behavior for the ease of phosphine dissociation.^[7] The least active first-generation iodide complex has the lowest barrier for phosphine dissociation, while the most active second-generation complex has the highest barrier (Scheme 2).



Scheme 2. Gibbs free activation energies for phosphine dissociation and the efficiency of alkene metathesis according to Grubbs et al.^[7]

A more efficient partitioning between the coordination of the phosphine ligand and the alkene substrate by the 14 valence-electron ruthenium carbene complexes has been proposed to account for the high activity of second-generation Grubbs catalysts.^[7,8] We encountered the challenging question concerning the origin of their outstanding catalytic activity in our recent quantum-chemical investigation on enyne metathesis.^[9] The key to the understanding of metathesis activities is the existence of active and inactive conformations in the alkene–carbene intermediates (Scheme 3). Three conformers are inactive, and only one



Scheme 3. Inactive and active alkene–carbene complexes.

conformer is active for an immediate rearrangement into a ruthena(IV)cyclobutane.^[10]

Based on this almost trivial consideration, two findings by Hansen and Hofmann are decisive for a deeper understanding of the electronic origin of catalyst activity:^[11] 1) “The orientation of the carbene moiety allows for optimal back-bonding from the metal fragments [of both Grubbs complexes and Hofmann *cis*-diphosphine ruthenium complexes] to the carbene acceptor orbital”. 2) The ruthenium–ligand unit (P–Ru–P, C–Ru–P, Cl–Ru–Cl, or Cl–Ru–P) “that interacts with the π -acceptor orbital of the methylene carbon is more strongly bent” than the unit which has an orthogonal orientation to the carbene π orbital.

The formally ideal angles at the ruthenium center can be derived from the classification of Grubbs carbene complexes as 16 valence-electron $d^6\text{-ML}_5$ species. As the Cl–Ru–Cl angle decreases from 180° , the nonbonding interaction between occupied chloride orbitals and an occupied ruthenium d orbital becomes increasingly antibonding (Figure 1, first

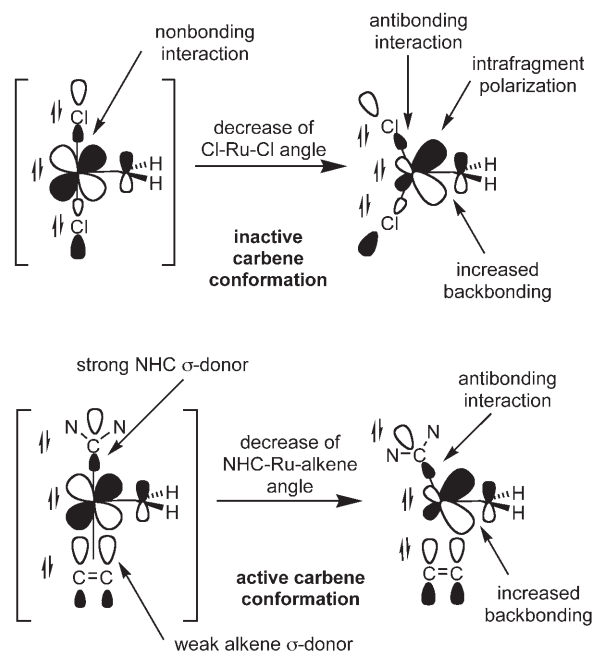


Figure 1. Stabilization of inactive and active carbene orientations: better backbonding by bending.

row). Intrafragment polarization (mixing of 5p and 4d orbitals) of the ruthenium fragment minimizes this antibonding orbital interaction and leads to increased backbonding to the empty p orbital of the carbene ligand. Overall, the bending of the chloride ligands results in a stronger ruthenium–carbene double bond and thus to a stabilization of the inactive carbene orientation. More electropositive iodide ligands are expected to further stabilize the inactive carbene conformation. An analogous line of argumentation can also be applied to the decrease of the NHC–Ru–alkene angle (Figure 1, second row). The alkene ligand is a worse σ donor than a chloride ligand, while the NHC ligand is a better σ donor and leads to a pronounced antibonding orbital interaction. With increasing antibonding interaction between

the NHC sp^2 orbital and a ruthenium d orbital, the back-bonding of the ruthenium fragment to the carbene acceptor orbital increases, and the active carbene conformation is stabilized.

This qualitative hypothesis can be tested by the quantum-chemical calculation of relative energies of catalytic intermediates, particularly of the four alkene-carbene conformers.^[12] To our knowledge, the relative stabilities of the four alkene carbene conformations have not yet been investigated at the same level of theory. The catalytic cycle of alkene metathesis has already been thoroughly studied theoretically.^[4,13] Thus, the predicted catalytic pathway in Scheme 4 comes as no surprise.

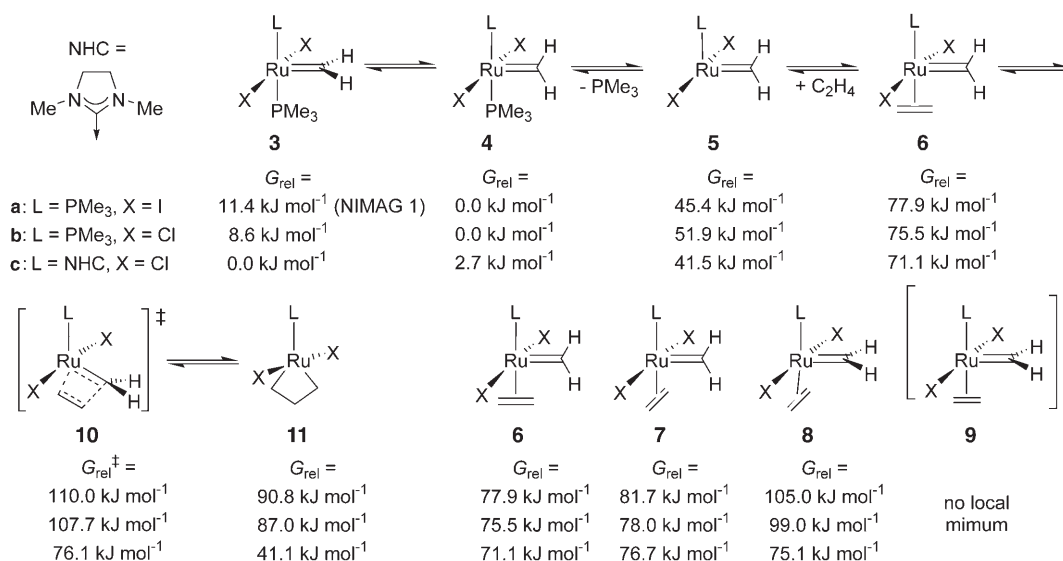
Even in the isomeric simplified Grubbs catalyst models **3a-c** and **4a-c**, the acceptor orbitals of the carbene fragments prefer a parallel orientation with the stronger σ -donor ligands ($2I^-$ or $NHC + PMe_3 > 2Cl^- > 2PMe_3$). Intrinsic electronic barriers for the rotation of the methylene unit between model structures **3** and **4** are small.^[14] Dissociation of PMe_3 from the models **4a-c** leads to the active carbene complexes **5a-c**. Then, alkene association yields the alkene-carbene complexes **6a-c**,^[15] or their conformers **7a-c**, **8a-c**, and **9a-c**. [2+2] Cycloaddition via the transition states **10a-c** results in the ruthenacycles **11a-c**.^[16] Interestingly, the low relative Gibbs free energy of the sterically simplified complex **5c** is in contrast to the high, experimentally observed dissociation barrier for PCy_3 from complex **2**. This result indicates that electronic factors are not responsible for the experimental anomaly. The overall Gibbs free activation energies in the transition state models **10a-c** fit nicely to the analogous experimental catalyst activities.

The computed Gibbs free energies of the alkene carbene ruthenium complexes show little preference for a particular alkene rotamer. The rotation of the alkene in the most stable conformers **6a-c** to give the rotamers **7a-c** is only slightly disfavored by 2.5 to 5.6 kJ mol^{-1} .^[17] The orientation of the carbene fragment, however, strongly depends on the choice of the spectator ligands. The rotation of the carbene ligand into

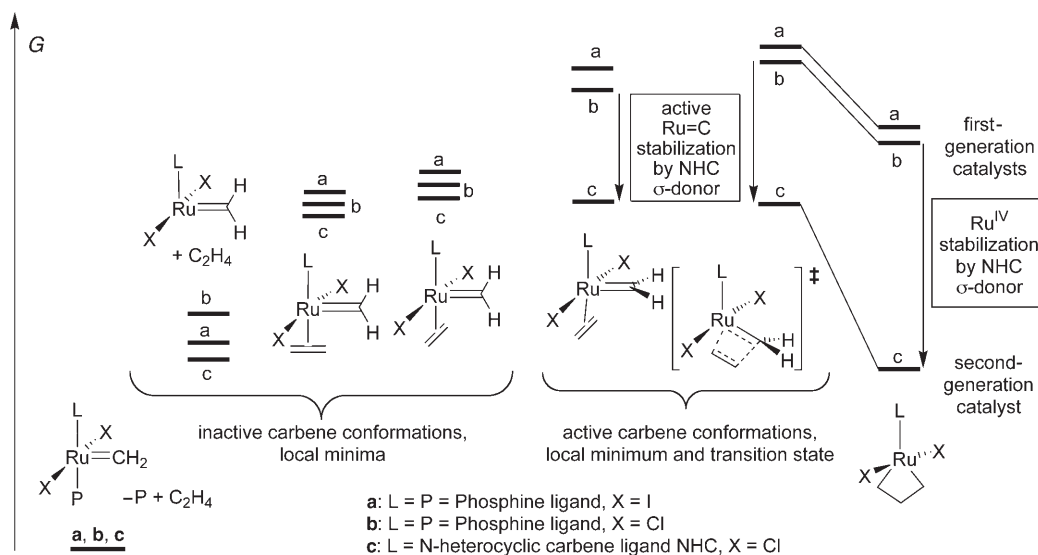
its active orientation in **8a-c** is highly disfavored for the first-generation iodide model complex (**7a** versus **8a**, $\Delta G = 23.3 \text{ kJ mol}^{-1}$), and it is also disfavored for the first-generation chloride complex (**7b** versus **8b**, $\Delta G = 21.0 \text{ kJ mol}^{-1}$). In contrast, carbene rotation is essentially degenerate for the second-generation chloride complex (**7c** versus **8c**, $\Delta G = -1.6 \text{ kJ mol}^{-1}$). We were unable to localize minimum structures **9a-c**, because either alkene-carbene structures **6a-c** or ruthenacycles **11a-c** were obtained after geometry optimization. The transition states **10a-c**, however, have the same alkene and carbene conformation as the hypothetical structures **9a-c**. Indeed, the transition states **10a-c** with their active carbene orientation have similar Gibbs free energies to the active carbene conformers **8a-c**.

Thus, the high reactivity of second-generation Grubbs catalysts mainly originates in the electronic stabilization of the active carbene conformation by the N-heterocyclic carbene ligands (Scheme 5). The computed total electronic energies for phosphine dissociation of the models **12a**, **12b**, and **14** to the model complexes **13a**, **13b**, and **15** correlate nicely with experimental Gibbs free activation energies for PCy_3 loss (Scheme 6 versus Scheme 2).^[18] The differences in phosphine dissociation barriers for first- and second-generation complexes are caused almost exclusively by specific steric congestion. In this case the repulsive interaction of α - and β -hydrogen atoms of the cyclohexyl substituents with the halogen ligands is of primary importance.

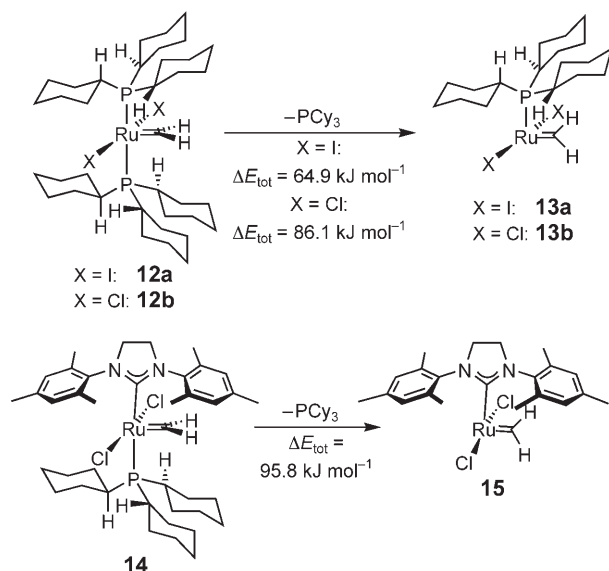
In addition to the electronic benefit of using the strong σ -donor NHC ligands, their mesityl substituents also contribute to a favored active carbene orientation (Scheme 7). The association of ethene to complex **15** and the subsequent carbene rotation proceed without enthalpic barrier to the intermediate **16**, which is formally a minimum structure (NIMAG0). The additional σ -donor ligand ethene as well as the steric repulsion between the hydrogen of an inactive carbene ligand and a mesityl substituent enforce an active carbene orientation. Finally, an essentially barrierless transformation leads to the cycloadduct **17**.



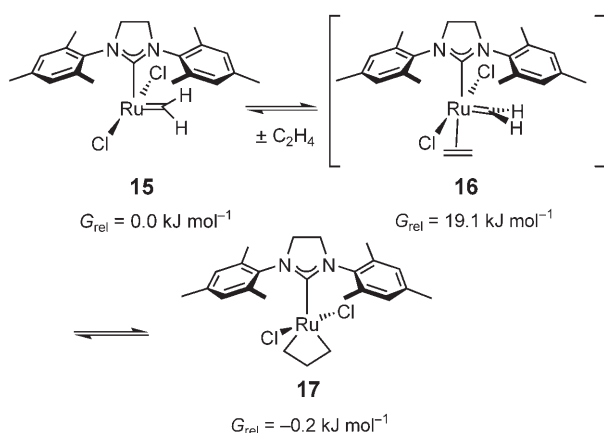
Scheme 4. Computed Gibbs free energies of simplified catalyst intermediate models.



Scheme 5. Qualitative energy diagram for ruthenium carbene conformers. Sterically demanding phosphine ligands result in a destabilization of the precatalyst.



Scheme 6. Computed total energy differences for phosphine dissociation.



Scheme 7. Computed Gibbs free energies of non-simplified catalyst intermediates.

In summary, second-generation alkene–carbene complexes are characterized by their high efficiency in partitioning between unproductive alkene dissociation and successful [2+2] cycloaddition. The electronic and steric stabilization of the active conformation of the carbene moiety in second-generation Grubbs catalysts is responsible for their exceptional alkene metathesis activity.

Received: March 29, 2005

Published online: August 11, 2005

Keywords: carbene ligands · cycloaddition · density functional calculations · metathesis · ruthenium

- [1] a) T. M. Trnka, R. H. Grubbs, *Acc. Chem. Res.* **2001**, *34*, 18; b) M. Schuster, S. Blechert, *Chem. unserer Zeit* **2001**, *35*, 24; c) R. Roy, S. K. Das, *Chem. Commun.* **2000**, 519; d) A. Fürstner, *Angew. Chem.* **2000**, *112*, 3140; *Angew. Chem. Int. Ed.* **2000**, *39*, 3012; e) R. H. Grubbs, S. Chang, *Tetrahedron* **1998**, *54*, 4413; f) M. Schuster, S. Blechert, *Angew. Chem.* **1997**, *109*, 2124; *Angew. Chem. Int. Ed. Engl.* **1997**, *36*, 2036; g) recently published: K. C. Nicolaou, P. G. Burger, D. Sarlah, *Angew. Chem.* **2005**, *117*, 4564; *Angew. Chem. Int. Ed.* **2005**, *44*, 4490.
- [2] P. Schwab, R. H. Grubbs, J. W. Ziller, *J. Am. Chem. Soc.* **1996**, *118*, 100.
- [3] T. Weskamp, W. C. Schattenmann, M. Spiegler, W. A. Herrmann, *Angew. Chem.* **1998**, *110*, 2631; *Angew. Chem. Int. Ed.* **1998**, *37*, 2490.
- [4] C. Adlhart, P. Chen, *J. Am. Chem. Soc.* **2004**, *126*, 3496.
- [5] E. L. Dias, S. T. Nguyen, R. H. Grubbs, *J. Am. Chem. Soc.* **1997**, *119*, 3887.
- [6] J.-L. Hérisson, Y. Chauvin, *Makromol. Chem.* **1971**, *141*, 161.
- [7] a) M. S. Sanford, M. Ulman, R. H. Grubbs, *J. Am. Chem. Soc.* **2001**, *123*, 749; b) S. Sanford, J. Love, R. H. Grubbs, *J. Am. Chem. Soc.* **2001**, *123*, 6543.
- [8] For near-degenerate metathesis reactions, the different local symmetry of the NHC and phosphine spectator ligands has been proposed to be relevant. C. Adlhart, P. Chen, *Angew. Chem.* **2002**, *114*, 4668; *Angew. Chem. Int. Ed.* **2002**, *41*, 4484.
- [9] J. J. Lippstreu, B. F. Straub, *J. Am. Chem. Soc.* **2005**, *127*, 7444.

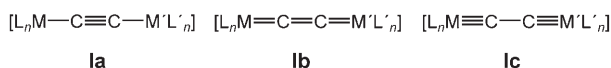
- [10] On the ^1H NMR spectroscopy time scale at room temperature, carbene rotation is rapid in a ruthenium complex. See T. Weskamp, F. J. Kohl, W. Hieringer, D. Gleich, W. A. Herrmann, *Angew. Chem.* **1999**, *111*, 2416; *Angew. Chem. Int. Ed.* **1999**, *38*, 2573. This feature indicates that the rotation barrier is below about 50 kJ mol^{-1} . The assumption of a “free” carbene rotation might have been a factor for considering the carbene rotation as irrelevant for the overall catalytic barrier.
- [11] a) S. M. Hansen, F. Rominger, M. Metz, P. Hofmann, *Chem. Eur. J.* **1999**, *5*, 557; b) S. M. Hansen, diploma thesis, Ruprecht-Karls-Universität Heidelberg, **1996**; See also c) J. N. Coalter III, J. C. Bollinger, J. C. Huffman, U. Werner-Zwanziger, K. G. Caulton, E. R. Davidson, H. Gerard, E. Clot, O. Eisenstein, *New J. Chem.* **2000**, *24*, 9.
- [12] The B3LYP/LACV3P** + //B3LYP/LACVP* level of theory as implemented in the Jaguar 4.1 program package was used. Gibbs free energies refer to ideal gas-phase conditions at 298.15 K and 1 atm. a) Jaguar 4.1, release 59, Schrödinger, Inc., Portland, OR, USA, **2001**; b) A. D. Becke, *J. Chem. Phys.* **1993**, *98*, 5648; c) S. H. Vosko, L. Wilk, M. Nusair, *Can. J. Phys.* **1980**, *58*, 1200; d) C. Lee, W. Yang, R. G. Parr, *Phys. Rev. B* **1988**, *37*, 785; e) W. J. Hehre, R. J. Ditchfield, A. Pople, *J. Chem. Phys.* **1972**, *56*, 2257; f) P. C. Hariharan, J. A. Pople, *Theor. Chim. Acta* **1973**, *28*, 213; g) M. J. Frisch, J. A. Pople, J. S. Binkley, *J. Chem. Phys.* **1984**, *80*, 3265; h) R. Krishnan, J. S. Binkley, R. Seeger, J. A. Pople, *J. Chem. Phys.* **1980**, *72*, 650; i) P. J. Hay, W. R. Wadt, *J. Chem. Phys.* **1985**, *82*, 299; j) G. Schaftenaar, J. H. Noordik, *J. Comput.-Aided Mol. Des.* **2000**, *14*, 123.
- [13] See, for example a) S. F. Vyboishikov, M. Bühl, W. Thiel, *Chem. Eur. J.* **2002**, *8*, 3962; b) L. Cavallo, *J. Am. Chem. Soc.* **2002**, *124*, 8965; c) C. Costabile, L. Cavallo, *J. Am. Chem. Soc.* **2004**, *126*, 9592.
- [14] The transition state for rotation of the methylene unit from model **3b** to model **4b** has a relative Gibbs free energy of $G_{\text{rel}} = 11.2\text{ kJ mol}^{-1}$. The transition state connecting structures **3c** and **4c** has a relative Gibbs free energy of $G_{\text{rel}} = 11.8\text{ kJ mol}^{-1}$; see ref. [9].
- [15] A derivative of model **6b** has been characterized crystallographically; see J. A. Tallarico, P. J. Bonitatebus, Jr., M. L. Snapper, *J. Am. Chem. Soc.* **1997**, *119*, 7157.
- [16] Recently, a derivative of model **11c** has been characterized by NMR spectroscopy; see P. E. Romero, W. E. Piers, *J. Am. Chem. Soc.* **2005**, *127*, 5032.
- [17] Owing to the low binding strength of the alkene ligand to ruthenium, alkene reorientation may proceed either by alkene dissociation and re-association or by intramolecular alkene ligand rotation. Since the active alkene conformation is more stable than the inactive conformation anyway, alkene rotation should be irrelevant in the catalytic cycle.
- [18] Zero-point energy corrections to E_0 values would result in a decrease of the energy differences of about 5 kJ mol^{-1} .

DOI: 10.1002/anie.200501968

Ge₂ Trapped by Triple Bonds between Two Metal Centers: The Gernylidyne Complexes *trans,trans*-[Cl(depe)₂M≡Ge–Ge≡M(depe)₂Cl] (M = Mo, W) and Bonding Analyses of the M≡Ge–Ge≡M Chain**

Alexander C. Filippou,* Gregor Schnakenburg,
Athanasios I. Philippopoulos, and Nils Weidemann

Complexes, in which sp-hybridized carbon chains span two transition-metal centers, [L_nMC_xM'L'_n]^{y+}, (L_n, L'_n = ligand sphere; x, y = integer) have attracted particular attention in recent years.^[1] These compounds form an important class of carbon-based molecular wires,^[2] which are appealing for studies of the electronic communication between redox-active metal termini,^[3] and are of potential practical importance in molecular electronics^[4] and in nonlinear optics.^[5] Moreover, these compounds can be viewed, at large carbon-chain lengths, as polymeric sp-hybridized carbon allotropes, revealing a conceptual relationship to the classical polymeric sp²- and sp³-hybridized carbon allotropes, graphite and diamond.^[6] For x = 2, three classes of metal complexes have been reported to date (**1a–1c**, Scheme 1). The ethynediyl

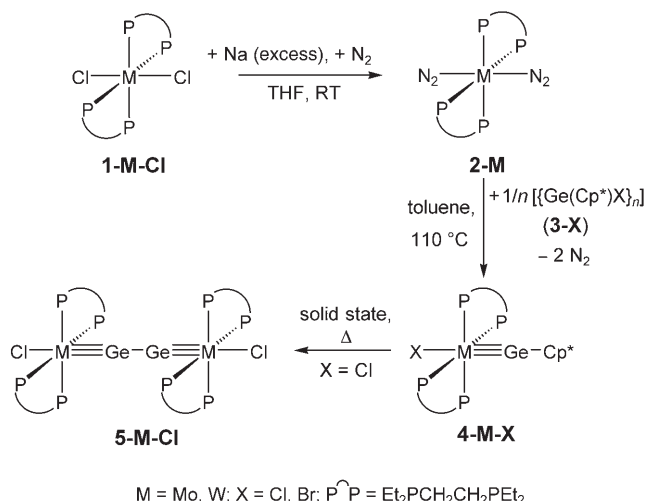


Scheme 1. Valence bond structures of C₂ bridged complexes.

complexes **1a** are by far the most prevalent.^[1a,b,d,f,7] In contrast, analogous compounds of the heavier Group 14 elements Si–Pb are not known to date.^[8] This situation is not surprising given the reluctance of these elements to form triple bonds.^[9,10] A rich elimination and substitution chemistry of main-group elements was elaborated in recent years using the

heterolytic or homolytic cleavage of Cp*–element bonds (Cp* = C₅Me₅).^[11] A successful implementation of this method in the synthesis of the first transition-metal complexes with triply bonded Ge₂ chains is presented herein.

For the synthesis, the dichloro complexes *trans*-[MCl₂(depe)₂] (depe = Et₂PCH₂CH₂PEt₂; M = Mo (**1-Mo-Cl**), M = W (**1-W-Cl**)) were employed. Complex **1-Mo-Cl** was obtained upon reduction of *mer*-[MoCl₃(thf)₃]^[12] with zinc in THF in the presence of 2.1 equivalents of depe, and **1-W-Cl** upon heating of *trans*-[WCl₂(PMe₃)₄]^[13] with 2.1 equivalents of depe in toluene at reflux. Both compounds were isolated as slightly air-sensitive, orange-yellow solids in 90 % yield and decompose upon melting at 211 and 205 °C, respectively.^[14] Reduction of **1-M-Cl** with sodium powder in THF under N₂ atmosphere afforded selectively the dinitrogen complexes *trans*-[M(depe)₂(N₂)₂] (M = Mo (**2-Mo**), M = W (**2-W**)), which were isolated as air-sensitive, orange (**2-Mo**) and bright red (**2-W**) solids in 98 and 72 % yields, respectively (Scheme 2).^[14,15]



Scheme 2. Stepwise synthesis of the gernylidyne complexes **4-M-X** and **5-M-Cl** starting from the dichlorides **1-M-Cl**.

Treatment of **2-Mo** with a stoichiometric amount of the germanium(II) halides [Ge(Cp*)X]_n (X = Cl, n = 1 (**3-Cl**); X = Br, n = 2 (**3-Br**))^[16] in toluene at reflux gave the brown-orange, air-sensitive molybdenum gernylidyne complexes **4-Mo-Cl** and **4-Mo-Br** in 32 % and 44 % yields, respectively (Scheme 2).^[14,17] Both compounds are very soluble in pentane and melt in sealed capillaries under vacuum at 152 and 155 °C, respectively. Simultaneous thermal analysis (thermogravimetry/differential thermal analysis/mass spectrometry (TG-DTA-MS)) of **4-Mo-Cl** revealed that the gernylidyne complex melts at the extrapolated onset temperature T_{on}^{ex} = 144 °C (peak temperature, T_p = 149 °C) and then decomposes at 181 °C releasing C₅Me₅H.^[14,18] These results prompted us to study the thermolysis of **4-Mo-Cl** on a preparative scale. Upon heating the gernylidyne complex **4-Mo-Cl** at 180–185 °C under static vacuum, the brown-orange sample of **4-Mo-Cl** melted and then turned progressively to a red-brown mass. Analysis of the molten mass by ¹H and ³¹P{¹H} NMR

[*] Prof. Dr. A. C. Filippou, Dipl.-Chem. G. Schnakenburg, Dipl.-Chem. N. Weidemann
Institut für Chemie
Humboldt-Universität zu Berlin
Brook-Taylor Strasse 2, 12489 Berlin (Germany)
Fax: (+49) 30-2093-6939
E-mail: filippou@chemie.hu-berlin.de
Dr. A. I. Philippopoulos
Institute of Physical Chemistry
NCSR Demokritos
Ag. Paraskevi Attikis, 15310 Athens (Greece)

[**] We are grateful to the Humboldt-Universität zu Berlin, the Deutsche Forschungsgemeinschaft (project FI 445/6-1), and the IKYDA program (D/03/40387) for the generous financial support of this work, Dipl. Ing. I. Hinz for assistance in the experimental work, Dr. U. Hartmann and U. Käfel for the elemental analyses and Dr. M. Feist for the STA analysis. N. Weidemann thanks the Fonds der Chemischen Industrie for a fellowship. depe = Et₂PCH₂CH₂PEt₂.

Supporting information for this article is available on the WWW under <http://www.angewandte.org> or from the author.

spectroscopy revealed a gradual conversion of **4-Mo-Cl** into the digermanium complex **5-Mo-Cl**, which after completion of the reaction and work-up was obtained as an air-sensitive, brown solid in 27 % yield (Scheme 2).^[14] During the thermolysis of **4-Mo-Cl**, a yellow volatile material deposited on the cold top part of the reaction tube and was identified by NMR spectroscopy to be a mixture of depe, Cp*H,^[19] 1,2,3,4-tetramethylpentafulvene,^[20] and some [GeCp*₂].^[21] These results suggest that homolysis of the Ge–Cp* bond occurs upon thermal activation of **4-Mo-Cl** to generate [MoCl(Ge)(depe)₂] and Cp* radicals. The [MoCl(Ge)(depe)₂] radicals dimerize to form **5-Mo-Cl**, whereas the Cp* radicals disproportionate under the reaction conditions to give Cp*H and 1,2,3,4-tetramethylpentafulvene.^[22] Heating of an equimolar mixture of complex **2-W** and **3-Cl** in toluene at reflux afforded a 7.7:1 mixture of the tungsten germylidyne complexes **4-W-Cl** and **5-W-Cl** (Scheme 2). Thermolysis of this mixture at 190 °C under static vacuum transformed **4-W-Cl** into the digermanium complex **5-W-Cl**, which was isolated as a very air-sensitive, green-brown solid in 30 % overall yield. Complex **5-W-Cl** decomposes upon melting at 240 °C.^[14] The molecular structures of **4-Mo-Br** and **5-W-Cl** were determined by single-crystal X-ray diffraction (Figures 1 and 2). The

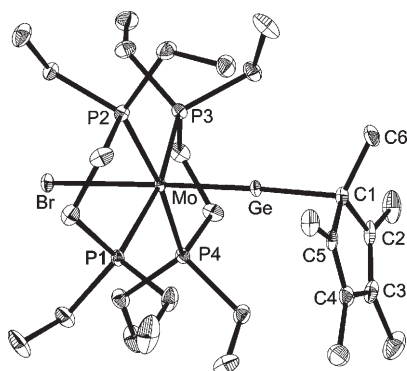


Figure 1. DIAMOND plot of the molecular structure of **4-Mo-Br**, thermal ellipsoids set at 30% probability. Hydrogen atoms are omitted for clarity. Selected bond lengths [Å] and bond angles [°]: Mo–Ge 2.2798(5), Ge–Cl 2.046(3), Mo–Br 2.6899(5), Mo–P1 2.479(1), Mo–P2 2.498(1), Mo–P3 2.465(1), Mo–P4 2.4812(9), C1–C2 1.504(4), C2–C3 1.356(5), C3–C4 1.466(5), C4–C5 1.353(4), C1–C5 1.485(4); Mo–Ge–Cl 177.46(8), Ge–Mo–Br 177.94(2), Ge–Mo–P1 95.38(2), Ge–Mo–P2 95.30(2), Ge–Mo–P3 96.86(2), Ge–Mo–P4 92.80(2), Ge–Cl–C2 99.8(2), Ge–Cl–C5 99.9(2), Ge–Cl–C6 114.0(2).

trans-configured octahedral complex **4-Mo-Br** has a very short Mo–Ge triple bond (2.2798(5) Å) and an almost linear coordinated germanium atom (Mo–Ge–Cp* 177.46(8)°) which has an η¹-bonded Cp* substituent as shown by the Ge–Cl/C5 distances, the alternating (C–C)_{ring} bond lengths, and the bond angles at the C1 atom (Figure 1).^[23] The Mo–Ge bond of **4-Mo-Br** is even shorter than those of the dppe complexes *trans*-[X(dppe)₂Mo≡Ge(η¹-Cp*)] (dppe = Ph₂PCH₂CH₂PPh₂, X = Cl, 2.3185(6) Å; X = Br, 2.3103(6) Å).^[9c] This situation suggests that sterically less-demanding phosphine ligands of higher σ-basicity strengthen the metal–germanium triple bonds. Complex **5-W-Cl** features a crystallographically

imposed center of symmetry at the midpoint of the Ge–Ge bond, an almost linear Ge₂ chain spanning the two *trans*-configured, octahedral tungsten centers (W–Ge–Ge# 175.13(3)°), and two W–Ge triple bonds (2.3087(5) Å) that are linked by a short Ge–Ge single bond (2.362(1) Å) (Figure 2). The W–Ge bonds of **5-W-Cl** compare well with

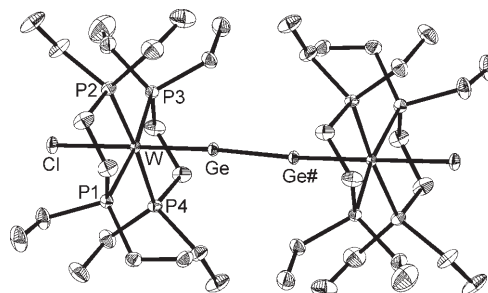


Figure 2. DIAMOND plot of the molecular structure of **5-W-Cl**, thermal ellipsoids set at 30% probability. Hydrogen atoms are omitted for clarity. Selected bond lengths [Å] and bond angles [°]: W–Ge 2.3087(5), Ge–Ge# 2.362(1), W–Cl 2.518(1), W–P1 2.455(1), W–P2 2.459(1), W–P3 2.470(1), W–P4 2.461(1); W–Ge–Ge# 175.13(3), Ge–W–Cl 176.66(3), Ge–W–P1 92.96(3), Ge–W–P2 94.47(3), Ge–W–P3 95.59(3), Ge–W–P4 90.28(3).

those of the germylidyne complexes *trans*-[X(dppe)₂W≡Ge(η¹-Cp*)] (X = H, Cl, Br, I, NCO, CN; W–Ge 2.293(1)–2.3184(6) Å).^[9c,gl] The Ge–Ge distance (2.362(1) Å) is the shortest known for a Ge–Ge single bond.^[24,25] This distance can be rationalized with the increased s character of the σ hybrid orbitals forming the Ge–Ge bond and the π conjugation of the W≡Ge bonds (see below). Note the Ge–Ge bond length of **5-W-Cl** lies close to the range of lengths calculated for Ge₂ (2.36–2.46 Å).^[26] The ¹H, ¹³C{¹H}, and ³¹P{¹H} NMR spectra corroborate the structures of complexes **4-M-X** and **5-M-Cl** (X = Cl, Br; M = Mo, W). Thus, the ¹H and ¹³C{¹H} NMR spectra display a double set of resonances for the diastereotopic ethyl groups and methylene protons of the depe ligands, as expected for diamagnetic complexes of the general formula *trans*-[M(depe)₂(L')(L')].^[14] In addition, the NMR spectra of **4-M-X** reveal a fast haptotropic shift of the Cp* substituent. This shift gives rise to one singlet signal for the methyl protons in the ¹H NMR spectra, and two singlet resonances in the ¹³C{¹H} NMR spectra, one for the methyl carbon and one for the ring carbon nuclei of the Cp* group.^[14] The ³¹P{¹H} NMR spectra display a singlet resonance confirming the *trans*-configuration of **4-M-X** and **5-M-Cl**. The ³¹P NMR signals of the Ge₂-bridged complexes (**5-Mo-Cl**, δ = 56.3 ppm; **5-W-Cl**, δ = 38.2 ppm) appear slightly upfield of those of the mononuclear complexes (**4-Mo-Cl**, δ = 57.2 ppm; **4-W-Cl**, δ = 39.2 ppm), and for the tungsten compounds are flanked by a pair of satellites arising from coupling with the ¹⁸³W nucleus (**4-W-Cl**, ¹J(W,P) = 259 Hz; **5-W-Cl**, ¹J(W,P) = 249 Hz).^[14]

Density functional theoretical (DFT) calculations of the model complex *trans,trans*-[Cl(PH₃)₄WGe₂W(PH₃)₄Cl] (**5-PH₃-W-Cl**) were performed without symmetry restraints using the exchange correlation functionals B3LYP and BP86 and various basis sets.^[14,27] Geometry optimization of the

model compound at the B3LYP/IIa level of theory led to six minimum structures on the ground-state singlet potential-energy surface, which can be classified into one pair of isomers featuring an end-on coordinated Ge_2 ligand (**A**), and two pairs of isomers displaying a side-on bonded Ge_2 ligand (**B**, **C**; Figure 3). Each pair consists further of an eclipsed (**e**)

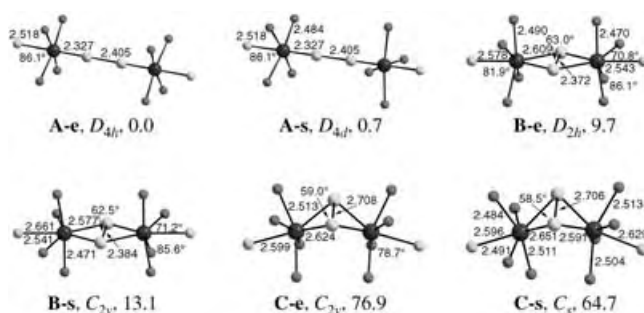


Figure 3. Selected bond lengths [Å] and bond angles [°], symmetries, and relative energies [kJ mol^{-1} , ZPVE corrected] of the minimum structures of **5-PH₃-W-Cl** (B3LYP/IIa). Hydrogen atoms are omitted for clarity.

and a staggered conformer (**s**) differing in the orientation of the $[\text{WCl}(\text{PH}_3)_4]$ fragments. The eclipsed isomer **A-e** of D_{4h} symmetry and the corresponding D_{4d} symmetric staggered isomer **A-s**, which feature a linear end-on bonded Ge_2 chain, are the most stable compounds and differ in energy by less than 1 kJ mol^{-1} . The isomers **B** displaying a planar W_2Ge_2 bicyclic ring lie at slightly higher energy than **A** (10 – 13 kJ mol^{-1}), whereas the species **C** with a W_2Ge_2 butterfly structure are considerably less stable than **A** (Figure 3). The calculated bond lengths and angles of the eclipsed isomer **A-e** compare well with the experimental values of **5-W-Cl** (Table 1).

Table 1: Comparison of selected bonding parameters of **5-PH₃-W-Cl** (**A-e** isomer) with those of **5-W-Cl**.

Method/basis set	W–Ge [Å]	Ge–Ge [Å]	W–Cl [Å]	P–W–Cl [°]	P–W–P _{eq} [°]
B3LYP/IIa	2.327	2.405	2.518	86.1	89.7
RI-BP86/I	2.357	2.453	2.541	86.9	89.8
BP86/IIb	2.328	2.389	2.456	86.2	89.7
X-ray (5-W-Cl)	2.3087(5)	2.362(1)	2.518(1)	86.7 ^[a]	89.8 ^[a]

[a] Mean value.

Table 2: Results of the W–Ge and Ge–Ge bonding analyses of the isomer **A-e** (B3LYP/IIa).

Bond	occ.	% (A)	NBO analysis ^[a]			q(A)	WBI	EDA ^[b] [kJ mol^{-1}]			
			hyb.	% (B)	hyb.			ΔE_{Pauli}	ΔE_{elstat}	ΔE_{orb}	ΔE_{int}
W–Ge	σ : 1.90	35.2	$\text{sd}^{2.1}$	64.8	$\text{sp}^{0.5}$	−1.25	1.71	507.4	−622.6	−751.8 (55%)	−866.5
	π_1 : 1.85	71.6	d	28.4	p					$\Delta E_{\sigma}(\text{a}_1)$: −144.1	
	π_2 : 1.85	71.6	d	28.4	p					$\Delta E_{\pi}(\text{e})$: −588.4	
Ge–Ge	1.96	50.0	$\text{sp}^{1.9}$	50.0	$\text{sp}^{1.9}$	+0.30	1.10	909.4	−398.4	−795.3 (67%)	−283.8
										$\Delta E_{\sigma}(\text{a}_1)$: −730.1	
										$\Delta E_{\pi}(\text{e})$: −65.0	

[a] NBO analysis of the W–Ge and Ge–Ge bonds: NBO occupancies, bond polarization in % (W) and % (Ge), orbital hybridization, NPA partial charges $q(\text{A})$ and Wiberg bond index (WBI). [b] Energy decomposition analysis of the W–Ge and Ge–Ge bonds (BP86/IIb): Pauli repulsion (ΔE_{Pauli}), electrostatic interaction (ΔE_{elstat}), orbital interaction ($\Delta E_{\text{orb}} = \Delta E_{\sigma}(\text{a}_1) + \Delta E_{\pi}(\text{e}) + \Delta E_{\text{rest}}(\text{b}_1 + \text{b}_2)$), and total interaction energy (ΔE_{int}) between the closed-shell C_{4v} -symmetric fragments $\text{trans-}[\text{WCl}(\eta^1\text{-Ge}_2)(\text{PH}_3)_4]^+$ and $[\text{WCl}(\text{PH}_3)_4]^-$ (W–Ge bond) and the C_{4v} -symmetric doublet fragments $\text{trans-}[\text{WCl}(\text{Ge})(\text{PH}_3)_4]$ (Ge–Ge bond) in the frozen geometry of **A-e**; the percentage of ΔE_{orb} in the total attractive interactions ($\Delta E_{\text{elstat}} + \Delta E_{\text{orb}}$) reflects the covalent character of the bonds and is given in parenthesis; $\Delta E_{\text{int}} = \Delta E_{\text{Pauli}} + \Delta E_{\text{elstat}} + \Delta E_{\text{orb}}$.

Analysis of the electronic charge distribution of **A-e** using the natural bond orbital (NBO) partitioning scheme^[28] gives an optimal Lewis structure with two W–Ge triple bonds connected by a Ge–Ge single bond. Both W–Ge triple bonds are composed of one σ component, which is polarized towards germanium (64.8%), and two degenerate π bonds, which result from the overlap of pure tungsten d orbitals and germanium p orbitals and are polarized towards tungsten (71.6%) (Table 2). The polarity of the W–Ge bonds is reflected in the partial charges of the W and Ge atoms (−1.25 and +0.30, respectively) and the Wiberg bond index of 1.71.^[29] Further evidence for the considerable ionic character of the W–Ge triple bonds of **A-e** was provided by the energy-partitioning analysis of the interaction between the closed-shell fragments $\text{trans-}[\text{WCl}(\eta^1\text{-Ge}_2)(\text{PH}_3)_4]^+$ and $[\text{WCl}(\text{PH}_3)_4]^-$ using the energy decomposition analysis (EDA) method,^[30] which revealed a considerable contribution of the electrostatic term ΔE_{elstat} ($−622.6 \text{ kJ mol}^{-1}$) to the total attractive interactions ($\Delta E_{\text{elstat}} + \Delta E_{\text{orb}} = −1374.4 \text{ kJ mol}^{-1}$), leading to a 55% covalent character of the W–Ge triple bonds (Table 2). The EDA analysis also showed that the degenerate W–Ge π bonds make the largest contribution (78%) to the orbital interaction energy ΔE_{orb} indicating the same high π -bonding character of the W–Ge bonds in **A-e** as in $\text{trans-}[\text{Cl}(\text{CO})_4\text{W}\equiv\text{GeH}]$.^[31] Taking into account the polarization of the W–Ge σ and π bonds, an extreme view of isomer **A-e** is that of a Ge_2^{2+} ion, which is embedded in an $\eta^1:\eta^1$ bonding mode between two d^6 $[\text{WCl}(\text{PH}_3)_4]^-$ fragments by two σ ($[\text{Ge}_2]^{2+} \rightarrow [\text{WCl}(\text{PH}_3)_4]^-$) and four π ($[\text{WCl}(\text{PH}_3)_4]^- \rightarrow [\text{Ge}_2]^{2+}$) donor–acceptor bonds. Ge_2^{2+} has a singlet ground state with a very weak and long Ge–Ge bond (3.099 Å) owing to Coulomb repulsion.^[32] Metal complexation is accompanied by a considerable electron drift from the metal fragments to Ge_2^{2+} , which decreases the partial charges on the germanium atoms from +1 to +0.3,

reduces thereby the Coulomb repulsion, and shortens the Ge–Ge bond by 0.694 Å (B3LYP/IIa, Table 1).

The π bonding and π^* anti-bonding orbitals of the W–Ge–Ge–W chain form four doubly degenerate levels (HOMO−3, HOMO,

LUMO, and LUMO + 3; Figure 4) resulting from the in-phase or out-of-phase combination of the tungsten $d_{xz}(d_{yz})$ orbitals and the germanium $p_x(p_y)$ orbitals (the z axis of the Cartesian coordinate system and the C_4 symmetry axis of **A-e** are collinear).^[33] Four electrons occupy the lowest energy e_{1u}

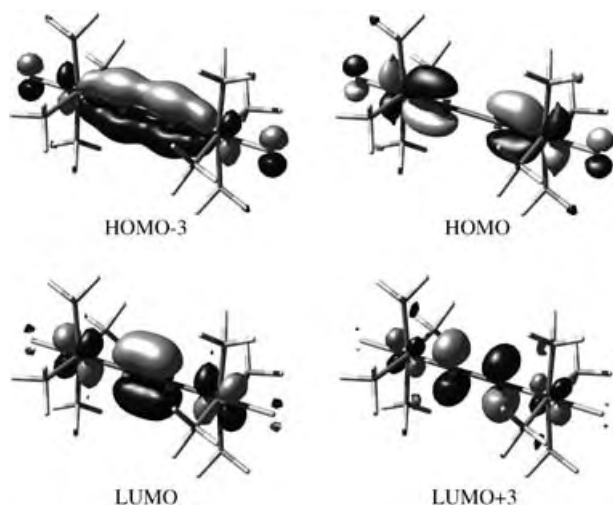


Figure 4. π and π^* Kohn–Sham orbitals of the W–Ge–Ge–W chain in **A-e**. Only one of the doubly degenerate π and π^* levels is depicted.

symmetric pair of molecular orbitals (HOMO–3), which are bonding with respect to the W–Ge and Ge–Ge linkages, and four electrons occupy the e_{1g} symmetric pair of orbitals (HOMO), which are bonding with respect to the W–Ge linkages but antibonding with respect to the Ge–Ge linkage (Figure 4).^[33,34] This molecular orbital picture corresponds in valence bond terms to the digermanehexayl formula $[L_nW \equiv Ge-Ge \equiv WL_n]$ and suggests some π conjugation of the W–Ge triple bonds.^[35] This proposal is supported by the NBO and EDA analyses, which indicate the presence of a Ge–Ge σ bond with low π -bonding character (WBI (Ge–Ge) = 1.10; ΔE_π is 8.2 % of ΔE_{orb} ; Table 2), and the natural resonance theoretical (NRT) analysis of **A-e**,^[36] which provides 21 different resonance structures with a resonance weight greater than 1 % leading to a natural bond order of 2.76 for the W–Ge bonds and 1.06 for the Ge–Ge bond.^[37]

Analysis of the wave function using the electron localization function (ELF)^[38] at the B3LYP/IIa level of theory shows, that the density of localized electrons between tungsten and germanium has a toroidal shape typical for triple bonds.^[9f,14,39] Volume integration of the electron density over the valence disynaptic basins connecting the W with the Ge nuclei and linking the two Ge nuclei, leads to a population of 5.7 electrons in the W–Ge bonding region and 2.6 electrons in the Ge–Ge bonding region, which supports the bonding picture of two conjugated W–Ge triple bonds in **A-e**.^[40] This result is further confirmed by the quantification of conjugation in **A-e** using the anisotropy of the induced current density (AICD) of the Ge–Ge bond.^[41] The AICD isosurface plot of **A-e** at an isosurface value of 0.015 displays strong delocalization over the atoms (Figure 5). The continuous boundary surface enclosing the conjugating Ge atoms breaks at an

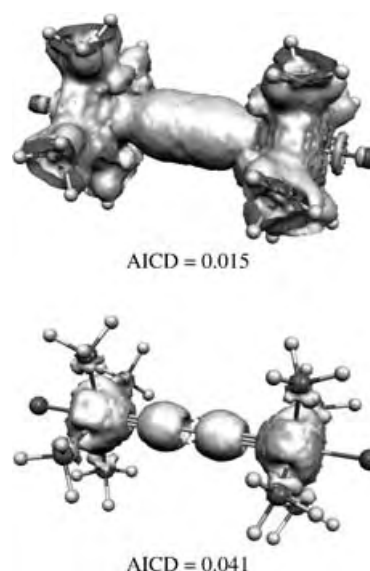


Figure 5. Isosurface plots of the AICD in **A-e** at 0.015 (top) and the critical value of 0.041 (bottom), at which the topology of the AICD boundary surface changes.

isosurface value of 0.041 (Figure 5), which suggests that the extent of conjugation in **A-e** is lower than in benzene (0.08) or butadiene (0.069), but higher than in 1,3-butadiyne (0.013) at the same level of theory.^[42] Conjugation in **A-e** might be caused by the small HOMO–LUMO gap of 2.7 eV which leads to an excitation energy of 2.67 eV ($\lambda = 464$ nm) for the allowed one-electron transition (TD-RIDFT/TZVPP).^[43]

The Ge–Ge bond fragmentation energy of **A-e** ($\Delta E_{frag} = 221.0$ kJ mol^{−1}) is lower than that of Ge₂H₆ (288.5 kJ mol^{−1}) calculated at the same level of theory (B3LYP/IIa, Table 3).^[44] Inclusion of relaxation and zero-point vibrational effects (ZPVE) leads to a theoretical value of 217.1 kJ mol^{−1} for the Ge–Ge bond dissociation energy of **A-e** (D^0), which is also lower than that of Ge₂H₆ ($D^0 = 270.4$ kJ mol^{−1}; Table 3),^[44] the latter value comparing well with the experimental value ($D^0 = 276$ kJ mol^{−1}).^[45] In comparison, the Ge–Ge bond length of **A-e** (2.405 Å) is shorter than that of Ge₂H₆ (2.439 Å, Table 3) leading to an opposite bond length/dissociation energy correlation to that usually observed. This result suggests that the radicals *trans*-[WCl(Ge)(PH₃)₄] formed upon Ge–Ge bond homolysis are stabilized by delocalization of the unpaired electron in the electronic ground state (²A₁).^[46] This electronic stabilization provides a rationale for the preferred formation of the radicals *trans*-[WCl(Ge)(depe)₂] during thermolysis of **4-W-Cl**. The energy (ZPVE corrected) required to cleave the W≡Ge bond of **A-e** into the fragments *trans*-[WCl(η^1 -Ge₂)(PH₃)₄]^[47] and [WCl(PH₃)₄] in the respective ²A₁ and ⁴A electronic ground states and minimum geometries, was calculated to be slightly lower (333.9 kJ mol^{−1}) than that of the germylidyne complex *trans*-[Cl(PH₃)₄W≡Ge-Me] (354.8 kJ mol^{−1}) (Table 3). The species *trans*-[WCl(η^1 -Ge₂)(PH₃)₄] is a local minimum on the energy potential surface and relaxes to a C_{2v} symmetric species featuring a side-on bonded Ge₂ ligand.^[47] The released relaxation energy of −52.2 kJ mol^{−1} reduces the W–Ge bond dissociation energy of **A-e** to 281.7 kJ mol^{−1} (Table 3).

Table 3: Fragmentation, bond dissociation, and Gibbs free dissociation energies [kJ mol⁻¹] of the Ge–Ge and W–Ge bonds of **5-PH₃-W-Cl (A-e isomer)**, Ge₂H₆, and *trans*-[Cl(PH₃)₄W=Ge-Me] (B3 LYP/IIa).

Compound	Bond	Length [Å]	$\Delta E_{\text{frag}}^{[a]}$	$\Delta E_{\text{relax}}^{[b]}$	$\Delta E_{\text{ZPVE}}^{[c]}$	$D_0^{[d]}$	$\Delta E_{\text{therm}}^{[e]}$	$\Delta G^\circ^{[f]}$
5-PH₃-W-Cl (A-e)	Ge–Ge	2.405	+221.0	–0.2	–3.7	+217.1	–55.4	+161.7
Ge ₂ H ₆	Ge–Ge	2.439	+288.5	–2.3	–15.8	+270.4	–45.8	+224.6
5-PH₃-W-Cl (A-e)	W–Ge	2.327	+476.6	–133.1	–9.6	+333.9	–74.3	+259.6
						+281.7 ^[g]	–69.6 ^[g]	+212.1 ^[g]
[Cl(PH ₃) ₄ W=Ge-Me]	W–Ge	2.304	+622.3	–251.9	–15.6	+354.8	–56.4	+298.4

[a] Homolytic fragmentation energy to the fragments in the geometry adopted by the molecule prior to fragmentation and in the electronic state, in which the number of unpaired electrons corresponds to the number of broken bonds. [b] Relaxation energy of both fragments to their minimum geometry and electronic ground state. [c] Zero point vibrational energy correction to the bond dissociation energy. [d] Bond dissociation energy at 0 K; $D_0 = \Delta E_{\text{frag}} + \Delta E_{\text{relax}} + \Delta E_{\text{ZPVE}}$. [e] Thermal and entropic corrections to the dissociation energy (298.15 K, 1 atm). [f] Gibbs free homolytic bond dissociation energy at standard conditions; $\Delta G^\circ = D_0 + \Delta E_{\text{therm}}$. [g] See text and ref. [47].

Several experimental and theoretical studies have been carried out on the diatomic molecule Ge₂.^[48] Ge₂ can be regarded as the lightest member in the family of germanium clusters Ge_n, which are of importance owing to their potential applications in nanoelectronics.^[48] Encapsulation of this very reactive species in the complexes **5-M-Cl** provides a new example for the ability of stereoelectronically well-defined transition-metal fragments to stabilize high temperature molecules in unprecedented bonding patterns.

Received: June 7, 2005

Published online: August 17, 2005

Keywords: density functional calculations · germanium · molybdenum · triple bonds · tungsten

- Reviews and accounts on metal-bonded sp-hybridized carbon chains: a) W. Beck, B. Niemer, M. Wieser, *Angew. Chem.* **1993**, 105, 969; *Angew. Chem. Int. Ed. Engl.* **1993**, 32, 923; b) H. Lang, *Angew. Chem.* **1994**, 106, 569; *Angew. Chem. Int. Ed. Engl.* **1994**, 33, 547; c) M. Akita, Y. Moro-oka, *Bull. Chem. Soc. Jpn.* **1995**, 68, 420; d) U. Bunz, *Angew. Chem.* **1996**, 108, 1047; *Angew. Chem. Int. Ed. Engl.* **1996**, 35, 969; e) M. I. Bruce, *Coord. Chem. Rev.* **1997**, 166, 91; f) F. Paul, C. Lapinte, *Coord. Chem. Rev.* **1998**, 178–180, 431; g) S. Szafert, J. A. Gladysz, *Chem. Rev.* **2003**, 103, 4175; h) M. Akita, A. Sakurai, M.-C. Chung, Y. Moro-oka, *J. Organomet. Chem.* **2003**, 670, 2; i) M. I. Bruce, P. J. Low, *Adv. Organomet. Chem.* **2004**, 50, 179.
- a) M. D. Ward, *Chem. Soc. Rev.* **1995**, 24, 121; b) A. Harriman, R. Ziessel, *Chem. Commun.* **1996**, 1707.
- Selected references on the electronic coupling between C_x-bridged metal centers: a) M. Brady, W. Weng, Y. Zhou, J. W. Seyler, A. J. Amoroso, A. M. Arif, M. Böhme, G. Frenking, J. A. Gladysz, *J. Am. Chem. Soc.* **1997**, 119, 775; b) F. Coat, M.-A. Guillevis, L. Toupet, F. Paul, C. Lapinte, *Organometallics* **1997**, 16, 5988; c) M. Guillevis, L. Toupet, C. Lapinte, *Organometallics* **1998**, 17, 1928; d) P. Belanzoni, N. Re, A. Sgamellotti, C. Floriani, *J. Chem. Soc. Dalton Trans.* **1998**, 1825; e) S. Kheradmandan, K. Heinze, H. W. Schmalle, H. Berke, *Angew. Chem.* **1999**, 111, 2412; *Angew. Chem. Int. Ed.* **1999**, 38, 2270; f) M. I. Bruce, P. J. Low, K. Costuas, J.-F. Halet, S. P. Best, G. A. Heath, *J. Am. Chem. Soc.* **2000**, 122, 1949; g) F. Paul, W. E. Meyer, L. Toupet, H. Jiao, J. A. Gladysz, C. Lapinte, *J. Am. Chem. Soc.* **2000**, 122, 9405; h) H. Jiao, J. A. Gladysz, *New J. Chem.* **2001**, 25, 551.
- a) *An Introduction to Molecular Electronics* (Eds.: M. C. Petty, M. R. Bryce, D. Bloor), Oxford University Press, New York, **1995**; b) D. Astruc, *Acc. Chem. Res.* **1997**, 30, 383; c) S. Creager, C. J. Yu, C. Bamdad, S. O'Connor, T. Maclean, E. Lam, Y. Chong, G. T. Olsen, J. Luo, M. Gozin, J. F. Kayyem, *J. Am. Chem. Soc.* **1999**, 121, 1059, and references therein.
- a) N. J. Long, *Angew. Chem.* **1995**, 107, 37; *Angew. Chem. Int. Ed. Engl.* **1995**, 34, 21; b) I. R. Whittall, A. McDonagh, M. G. Humphrey, M. Samoc, *Adv. Organomet. Chem.* **1998**, 43, 349.
- For sp carbon allotropes see: a) F. Diederich, Y. Rubin, *Angew. Chem.* **1992**, 104, 1123; *Angew. Chem. Int. Ed. Engl.* **1992**, 31, 1101; b) R. J. Lagow, J. J. Kampa, H.-C. Wei, S. L. Battle, J. W. Genge, D. A. Laude, C. J. Harper, R. Bau, R. C. Stevens, J. F. Haw, E. Munson, *Science* **1995**, 267, 362; c) T. Gibtner, F. Hampel, J.-P. Gisselbrecht, A. Hirsch, *Chem. Eur. J.* **2002**, 8, 408.
- C₂-bridged transition-metal complexes having the valence formulae **1b** and **1c** are very rare: a) M. L. Listemann, R. R. Schrock, *Organometallics* **1985**, 4, 74; b) D. R. Neithamer, R. E. LaPointe, R. A. Wheeler, D. S. Richeson, G. D. Van Duyne, P. T. Wolczanski, *J. Am. Chem. Soc.* **1989**, 111, 9056; c) K. G. Caulton, R. H. Cayton, M. H. Chisholm, J. C. Huffman, E. B. Lobkovsky, Z. Xue, *Organometallics* **1992**, 11, 321; d) B. E. Woodworth, P. S. White, J. L. Templeton, *J. Am. Chem. Soc.* **1998**, 120, 9028.
- The dimetallaheterocumulenes [Cp^R(CO)₂Mn=E= Mn(CO)₂Cp^R] (E = Ge, Sn, Pb; Cp^R = η⁵-C₅H₅, η⁵-C₅H₄Me, η⁵-C₅Me₃) are the only members of the complex series [L_nME_xM'L_n]^{y+} (E = Si–Pb) known. Their syntheses and reactions are described in: a) W. Gäde, E. Weiss, *J. Organomet. Chem.* **1981**, 213, 451; b) N. M. Kostic, R. F. Fenske, *J. Organomet. Chem.* **1982**, 233, 337; c) D. Melzer, E. Weiss, *J. Organomet. Chem.* **1984**, 263, 67; d) J. D. Korp, I. Bernal, R. Hörlein, R. Serrano, W. A. Herrmann, *Chem. Ber.* **1985**, 118, 340; e) W. A. Herrmann, H.-J. Kneuper, E. Herdtweck, *Angew. Chem.* **1985**, 97, 1060; *Angew. Chem. Int. Ed. Engl.* **1985**, 24, 1062; f) W. A. Herrmann, *Angew. Chem.* **1986**, 98, 57; *Angew. Chem. Int. Ed. Engl.* **1986**, 25, 56; g) H.-J. Kneuper, E. Herdtweck, W. A. Herrmann, *J. Am. Chem. Soc.* **1987**, 109, 2508; h) F. Ettel, G. Huttner, L. Zsolnai, *Angew. Chem.* **1989**, 101, 1525; *Angew. Chem. Int. Ed. Engl.* **1989**, 28, 1496; i) W. A. Herrmann, H.-J. Kneuper, E. Herdtweck, *Chem. Ber.* **1989**, 122, 437; j) F. Ettel, G. Huttner, W. Imhof, *J. Organomet. Chem.* **1990**, 397, 299; k) F. Ettel, G. Huttner, L. Zsolnai, C. Emmerich, *J. Organomet. Chem.* **1991**, 414, 71; l) B. Schiemenz, F. Ettel, G. Huttner, L. Zsolnai, *J. Organomet. Chem.* **1993**, 458, 159; m) F. Ettel, M. Schollenberger, B. Schiemenz, G. Huttner, L. Zsolnai, *J. Organomet. Chem.* **1994**, 476, 153.
- For transition-metal complexes featuring triple bonds to germanium, tin, or lead see: a) L. Pu, B. Twamley, S. T. Haubrich, M. M. Olmstead, B. V. Mork, R. S. Simons, P. P. Power, *J. Am. Chem. Soc.* **2000**, 122, 650; b) A. C. Filippou, A. I. Philippopoulos, P. Portius, D. U. Neumann, *Angew. Chem.* **2000**, 112, 2881; *Angew. Chem. Int. Ed.* **2000**, 39, 2778; c) A. C. Filippou, P. Portius, A. I. Philippopoulos, *Organometallics* **2002**, 21, 653; d) A. C. Filippou, P. Portius, A. I. Philippopoulos, H. Rohde,

- Angew. Chem.* **2003**, *115*, 461; *Angew. Chem. Int. Ed.* **2003**, *42*, 445; e) A. C. Filippou, A. I. Philippopoulos, G. Schnakenburg, *Organometallics* **2003**, *22*, 3339; f) A. C. Filippou, H. Rohde, G. Schnakenburg, *Angew. Chem.* **2004**, *116*, 2293; *Angew. Chem. Int. Ed.* **2004**, *43*, 2243; g) A. C. Filippou, A. I. Philippopoulos, P. Portius, G. Schnakenburg, *Organometallics* **2004**, *23*, 4503; h) A. C. Filippou, N. Weidemann, G. Schnakenburg, H. Rohde, A. I. Philippopoulos, *Angew. Chem.* **2004**, *116*, 6674; *Angew. Chem. Int. Ed.* **2004**, *43*, 6512.
- [10] For experimental studies on heavier Group 14 element analogues of alkynes see: a) A. Sekiguchi, S. S. Ziegler, R. West, J. Michl, *J. Am. Chem. Soc.* **1986**, *108*, 4241; b) M. Bogey, H. Bolvin, C. Demuynck, J.-L. Destombes, *Phys. Rev. Lett.* **1991**, *66*, 413; c) M. Cordonnier, M. Bogey, C. Demuynck, J.-L. Destombes, *J. Chem. Phys.* **1992**, *97*, 7984; d) N. Wiberg, C. M. M. Finger, K. Polborn, *Angew. Chem.* **1993**, *105*, 1140; *Angew. Chem. Int. Ed. Engl.* **1993**, *32*, 1054; e) L. Pu, B. Twamley, P. P. Power, *J. Am. Chem. Soc.* **2000**, *122*, 3524; f) R. Pietschnig, R. West, D. R. Powell, *Organometallics* **2000**, *19*, 2724; g) C. Bibal, S. Mazieres, H. Gornitzka, C. Couret, *Angew. Chem.* **2001**, *113*, 980; *Angew. Chem. Int. Ed.* **2001**, *40*, 952; h) A. D. Phillips, R. J. Wright, M. M. Olmstead, P. P. Power, *J. Am. Chem. Soc.* **2002**, *124*, 5930; i) M. Stender, A. D. Phillips, R. J. Wright, P. P. Power, *Angew. Chem.* **2002**, *114*, 1863; *Angew. Chem. Int. Ed.* **2002**, *41*, 1785; j) N. Wiberg, W. Niedermayer, G. Fischer, H. Nöth, M. Suter, *Eur. J. Inorg. Chem.* **2002**, 1066; k) P. P. Power, *Chem. Commun.* **2003**, 2091; l) L. Pu, A. D. Phillips, A. F. Richards, M. Stender, R. S. Simons, M. M. Olmstead, P. P. Power, *J. Am. Chem. Soc.* **2003**, *125*, 11626; m) A. Sekiguchi, R. Kinjo, M. Ichinohe, *Science* **2004**, *305*, 1755.
- [11] P. Jutzi, G. Reumann, *J. Chem. Soc. Dalton Trans.* **2000**, 2237.
- [12] a) R. Poli, H. D. Mui, *J. Am. Chem. Soc.* **1990**, *112*, 2446; b) F. Stoffelbach, D. Saurenz, R. Poli, *Eur. J. Inorg. Chem.* **2001**, 2699.
- [13] a) P. R. Sharp, *Organometallics* **1984**, *3*, 1217; b) P. R. Sharp, J. C. Bryan, J. M. Mayer, *Inorg. Synth.* **1990**, *28*, 326.
- [14] The Supporting Information contains the Experimental Section including the syntheses, analytical, and spectroscopic data of the complexes **1-M-Cl**, **2-M**, **4-Mo-X** and **5-M-Cl** (M = Mo, W; X = Cl, Br). It also contains the crystallographic data of the germylidyne complexes **4-Mo-Br** and **5-W-Cl** and details of the simultaneous thermal analysis of **4-Mo-Cl** and of the electronic structure calculations of **5-PH₃-W-Cl**. CCDC-259718 (**4-Mo-Br**) and CCDC-259719 (**5-W-Cl**) contain the supplementary crystallographic data for this paper. These data can be obtained free of charge from the Cambridge Crystallographic Data Centre via www.ccdc.cam.ac.uk/data_request/cif.
- [15] Alternative methods for the synthesis of **2-Mo** and **2-W** are described in: a) J. Chatt, G. A. Heath, R. L. Richards, *J. Chem. Soc. Dalton Trans.* **1974**, 2074; b) W. Hussain, G. J. Leigh, H. M. Ali, C. J. Pickett, D. A. Rankin, *J. Chem. Soc. Dalton Trans.* **1984**, 1703; c) T. A. George, M. E. Noble, *Inorg. Chem.* **1978**, *17*, 1678; d) G. J. Kubas, C. J. Burns, J. Eckert, S. W. Johnson, A. C. Larson, P. J. Vergamini, C. J. Unkefer, G. R. K. Khalsa, S. A. Jackson, O. Eisenstein, *J. Am. Chem. Soc.* **1993**, *115*, 569.
- [16] a) J. G. Winter, P. Portius, G. Kociok-Köhn, R. Steck, A. C. Filippou, *Organometallics* **1998**, *17*, 4176; b) ref. [9c].
- [17] ¹H and ³¹P{¹H} NMR spectra of the crude products isolated after completion of the reactions, revealed the concomitant formation of **1-Mo-X**, [GeCp*₂], and **5-Mo-X**. Several recrystallizations from pentane were necessary to separate the complexes **4-Mo-X** from the by-products decreasing the overall yields (see Supporting Information).
- [18] Signals for the ions [C₃Me₃H]⁺ (*m/z* 136) and [C₇H₇]⁺ (*m/z* 91) appeared in the EI mass spectra of the gases evolved with the beginning of decomposition. The intensity of these signals increased rapidly above 181 °C (see Supporting Information).
- [19] a) R. S. Threlkel, J. Bercaw, *J. Organomet. Chem.* **1977**, *136*, 1; b) J. M. Manriquez, P. J. Fagan, L. D. Schertz, T. J. Marks, *Inorg. Synth.* **1982**, *21*, 181; c) F. X. Kohl, P. Jutzi, *J. Organomet. Chem.* **1983**, *243*, 119.
- [20] a) J. C. Pando, E. A. Mintz, *Tetrahedron Lett.* **1989**, *30*, 4811; b) P. Jutzi, A. Mix, *Chem. Ber.* **1992**, *125*, 951; c) P. Jutzi, T. Heidemann, B. Neumann, H. G. Stammler, *Synthesis* **1992**, 1096; d) S. Döring, G. Erker, *Synthesis* **2001**, 43.
- [21] P. Jutzi, F. Kohl, P. Hofmann, C. Krüger, Y.-H. Tsay, *Chem. Ber.* **1980**, *113*, 757.
- [22] a) A. G. Davies, J. Lusztyk, *J. Chem. Soc. Chem. Commun.* **1980**, 554; b) A. G. Davies, J. Lusztyk, *J. Chem. Soc. Perkin Trans. 2* **1981**, 692; c) P. N. Culshaw, J. C. Walton, L. Hughes, K. U. Ingold, *J. Chem. Soc. Perkin Trans. 2* **1993**, 879; d) W. R. Roth, F. Hunold, *Liebigs Ann.* **1995**, 1119.
- [23] For a detailed discussion of the bonding parameters of η¹-bonded Cp* substituents in germylidyne complexes see ref [9c].
- [24] The Ge–Ge distance in elemental germanium is 2.44 Å: A. F. Wells, *Structural Inorganic Chemistry*, 5th ed., Clarendon, Oxford, **1984**, p. 1279.
- [25] For Ge–Ge single bonds connecting unsaturated germanium centers see: a) A. Sekiguchi, H. Yamazaki, C. Kabuto, H. Sakurai, S. Nagase, *J. Am. Chem. Soc.* **1995**, *117*, 8025; b) H. Schäfer, W. Saak, M. Weidenbruch, *Angew. Chem.* **2000**, *112*, 3847; *Angew. Chem. Int. Ed.* **2000**, *39*, 3703; c) A. Sekiguchi, Y. Ishida, N. Fukaya, M. Ichinohe, *J. Am. Chem. Soc.* **2002**, *124*, 1158; d) G. Ramaker, A. Schäfer, W. Saak, M. Weidenbruch, *Organometallics* **2003**, *22*, 1302; e) G. Ramaker, W. Saak, D. Haase, M. Weidenbruch, *Organometallics* **2003**, *22*, 5212.
- [26] W. Xu, Y. Zhao, Q. Li, Y. Xie, H. F. Schäfer III, *Mol. Phys.* **2004**, *102*, 579, and references therein.
- [27] Basis set I is of valence double-ζ quality (LANL2DZ) and includes the quasi-relativistic effective core potentials LANL2. The auxiliary basis sets for the density fitting were generated automatically. Basis set IIa is of valence triple-ζ quality (6-311G* for C, H, Cl, P; TZVPP for Ge and W [ECP(MEFIT, WB)]), and IIb is a triple-ζ Slater-type basis set with two sets of polarization functions. More details can be found in the Supporting Information.
- [28] A. Reed, L. A. Curtiss, F. Weinhold, *Chem. Rev.* **1988**, *88*, 899.
- [29] K. B. Wiberg, *Tetrahedron* **1968**, *24*, 1083.
- [30] a) K. Morokuma, *Acc. Chem. Res.* **1977**, *10*, 294; b) T. Ziegler, A. Rauk, *Theor. Chim. Acta* **1977**, *46*, 1.
- [31] M. Lein, A. Szabó, A. Kovács, G. Frenking, *Faraday Discuss.* **2003**, *124*, 365.
- [32] Ge₂²⁺ is suggested to be metastable with respect to dissociation to Ge⁺ ions: W. A. Saunders, *Phys. Rev. B* **1989**, *40*, 1400.
- [33] As in linear polyynes, the parity of the π-bonding orbitals of the W-Ge-Ge-W chain alternates with respect to the mirror plane bisecting the Ge–Ge bond of **A-e** (σ_h plane of the molecule). The lowest energy orbital (HOMO–3) has zero nodes, the number of nodes increases by one on going from one orbital to the one next highest in energy, and the nodes are symmetrically located with respect to the σ_h plane of **A-e**.
- [34] HOMO–2 and HOMO–1 are molecular orbitals of δ symmetry resulting, respectively, from the in-phase and out-of-phase combination of the tungsten d_{xy} orbitals (see Supporting Information).
- [35] The coefficients of the germanium p_x(p_y) atomic orbitals are larger in the HOMO–3 than in the HOMO suggesting some Ge–Ge π overlap. Since the W–Ge π bonds are polarized towards the tungsten, the occupancies of the corresponding natural atomic orbitals at germanium are quite low (occ. p_x and p_y = 0.64e[–]) depleting the π overlap of the germanium p_x(p_y) functions.
- [36] E. D. Glendening, F. Weinhold, *J. Comput. Chem.* **1998**, *19*, 593.

- [37] 13 of these resonances structures have W–Ge triple bonds and eight have W–Ge double bonds. The combined weight of resonance structures featuring W–Ge triple bonds is 76%.
- [38] a) B. Silvi, A. Savin, *Nature* **1994**, 371, 683; b) A. Savin, B. Silvi, F. Colonna, *Can. J. Chem.* **1996**, 74, 1088.
- [39] a) H. Grützmacher, T. F. Fässler, *Chem. Eur. J.* **2000**, 6, 2317; b) N. O. J. Malcolm, R. J. Gillespie, P. L. A. Popelier, *J. Chem. Soc. Dalton Trans.* **2002**, 3333.
- [40] The high population of the W–Ge disynaptic basins justifies the denotation of the W–Ge bonds as triple bonds, for which six electrons would be needed. The disynaptic basin of the Ge–Ge bond has a population of 2.6 electrons, which suggests the Ge–Ge bond to be slightly more than a classical single bond, reflecting the effect of π conjugation.
- [41] R. Herges, D. Geuenich, *J. Phys. Chem. A* **2001**, 105, 3214.
- [42] For the recent dispute on the conjugative stabilization of 1,3-butadiyne see: a) D. W. Rogers, N. Matsunaga, A. A. Zavitsas, F. J. McLafferty, J. F. Liebman, *Org. Lett.* **2003**, 5, 2373; b) P. D. Jarowski, M. D. Wodrich, C. S. Wannere, P. v. R. Schleyer, K. N. Houk, *J. Am. Chem. Soc.* **2004**, 126, 15036; c) D. Cappel, S. Tüllmann, A. Krapp, G. Frenking, *Angew. Chem.* **2005**, 117, 3683; *Angew. Chem. Int. Ed.* **2005**, 44, 3617.
- [43] This excitation gives the strongest absorption band in the calculated UV/Vis spectrum of **A-e** and may rationalize the green-brown color of complex **5-W-Cl** (see Supporting Information).
- [44] The calculated Ge–Ge fragmentation energy of Ge_2H_6 compares well with that reported by H.-J. Himmel, H. Schnöckel, *Chem. Eur. J.* **2003**, 9, 748. Our calculations show, however, that the GeH_3 radicals have a pyramidal C_{3v} symmetric minimum geometry (Ge–H 1.544 Å; H–Ge–H 110.8°) in the doublet ground state, which differs marginally from the geometry adopted by the GeH_3 fragments (Ge–H 1.540 Å; H–Ge–H 108.5°) in the D_{3d} symmetric minimum structure of Ge_2H_6 . Our results lead to a very low relaxation energy of the two GeH_3 fragments (-2.3 kJ mol^{-1}) and differ from those of H.-J. Himmel and Schnöckel, according to which the GeH_3 radicals have a trigonal-planar minimum geometry.
- [45] M. J. Almond, A. M. Doncaster, P. N. Noble, R. Walsh, *J. Am. Chem. Soc.* **1982**, 104, 4717.
- [46] Selected bond lengths [Å] and bond angles [°] of the radicals *trans*- $[\text{WCl}(\text{Ge})(\text{PH}_3)_4]$ in their C_{4v} symmetric minimum structure and doublet ground state: W–Ge 2.329, W–Cl 2.528, W–P 2.483; P–W–Cl 85.9, P–W–P_{cis} 89.7. Additional evidence for the delocalization of the unpaired electron in *trans*- $[\text{WCl}(\text{Ge})(\text{PH}_3)_4]$ was provided by NBO and ELF analyses.
- [47] Two minimum structures were found for the fragment *trans*- $[\text{WCl}(\text{Ge}_2)(\text{PH}_3)_4]$ on the potential energy surface, a C_{4v} symmetric structure featuring an end-on bonded Ge_2 ligand, and a C_{2v} symmetric isomer featuring a side-on bonded Ge_2 ligand, which is 52.5 kJ mol^{-1} lower in energy than the end-on bonded species (see Supporting Information). Preference of the side-on coordination mode was also found in $[\text{W}(\text{CO})_5(\text{Ge}_2)]^{2-}$ by calculations: C. Esterhuysen, G. Frenking, *Chem. Eur. J.* **2003**, 9, 3518.
- [48] a) A. Kant, B. H. Strauss, *J. Chem. Phys.* **1966**, 45, 822; b) J. Harris, R. O. Jones, *Phys. Rev. A* **1978**, 18, 2159; c) J. E. Kingcade, Jr., U. V. Choudary, K. A. Gingerich, *Inorg. Chem.* **1979**, 18, 3094; d) J. E. Northrup, M. L. Cohen, *Chem. Phys. Lett.* **1983**, 102, 440; e) G. Pacchioni, *Chem. Phys. Lett.* **1984**, 107, 70; f) J. E. Kingcade, H. M. Nagarathna-Naik, I. Shim, K. A. Gingerich, *J. Phys. Chem.* **1986**, 90, 2830; g) P. W. Deutsch, L. A. Curtiss, J. P. Blaudeau, *Chem. Phys. Lett.* **1997**, 270, 413; h) J. Wang, G. Wang, J. Zhao, *Phys. Rev. B* **2001**, 64, 205411.

DOI: 10.1002/anie.200501818

Towards a Fully Synthetic Carbohydrate-Based Anticancer Vaccine: Synthesis and Immunological Evaluation of a Lipidated Glycopeptide Containing the Tumor-Associated Tn Antigen***Therese Buskas, Sampat Ingale, and Geert-Jan Boons***Dedicated to Professor Steven V. Ley
on the occasion of his 60th birthday*

A common feature of oncogenic transformed cells is the overexpression of oligosaccharides, such as Globo-H, Lewis^Y, and Tn antigens.^[1–4] Numerous studies have shown that this abnormal glycosylation can promote metastasis,^[5] and hence its expression is strongly correlated with poor survival rates of cancer patients.

Several elegant studies have exploited the differential expression of tumor-associated carbohydrates for the development of cancer vaccines.^[6,7] The inability of carbohydrates to activate helper T lymphocytes has complicated, however, their use as vaccines.^[8] For most immunogens, including carbohydrates, the production of antibodies depends on the cooperative interaction of two types of lymphocytes, B cells and helper T cells.^[9] Saccharides alone cannot activate helper T cells and therefore have a limited immunogenicity. The formation of low-affinity IgM antibodies and the absence of IgG antibodies manifest this limited immunogenicity.

To overcome the T cell independent properties of carbohydrates, past research has focused on the conjugation of saccharides to a foreign carrier protein (e.g. Keyhole Limpet Hemocyanin (KLH) or detoxified tetanus toxoid).^[8,9] In this approach, the carrier protein enhances the presentation of the carbohydrate to the immune system and provides T epitopes (peptide fragments of 12–15 amino acids) that can activate helper T cells.

However, the conjugation of carbohydrates to a carrier protein poses several problems. In general, the conjugation chemistry is difficult to control, resulting in conjugates with ambiguities in composition and structure which may affect the reproducibility of an immune response.^[10] Additionally, the foreign carrier protein can elicit a strong B cell response, which may lead to the suppression of an antibody response against the carbohydrate epitope. The latter is a greater

[*] Dr. T. Buskas, S. Ingale, Dr. G.-J. Boons
Complex Carbohydrate Research Center
University of Georgia
315 Riverbend Road, Athens, GA 30602 (USA)
Fax: (+1) 706-542-4412
E-mail: gjboons@ccrc.uga.edu

[**] This research was supported by the National Cancer Institute of the National Institutes of Health (Grant No RO1 CA88986).



Supporting information for this article is available on the WWW under <http://www.angewandte.org> or from the author.

problem when self-antigens are employed, such as tumor-associated carbohydrates. Also linkers for the conjugation of carbohydrates to proteins can be immunogenic, leading to epitope suppression.^[11] Not surprisingly, several clinical trials with carbohydrate–protein conjugate cancer vaccines failed to induce sufficiently strong helper T cell responses in all patients.^[7,12] Therefore, alternative strategies need to be developed for the presentation of tumor-associated carbohydrate epitopes that will result in a more efficient class switch to IgG antibodies.^[13–18]

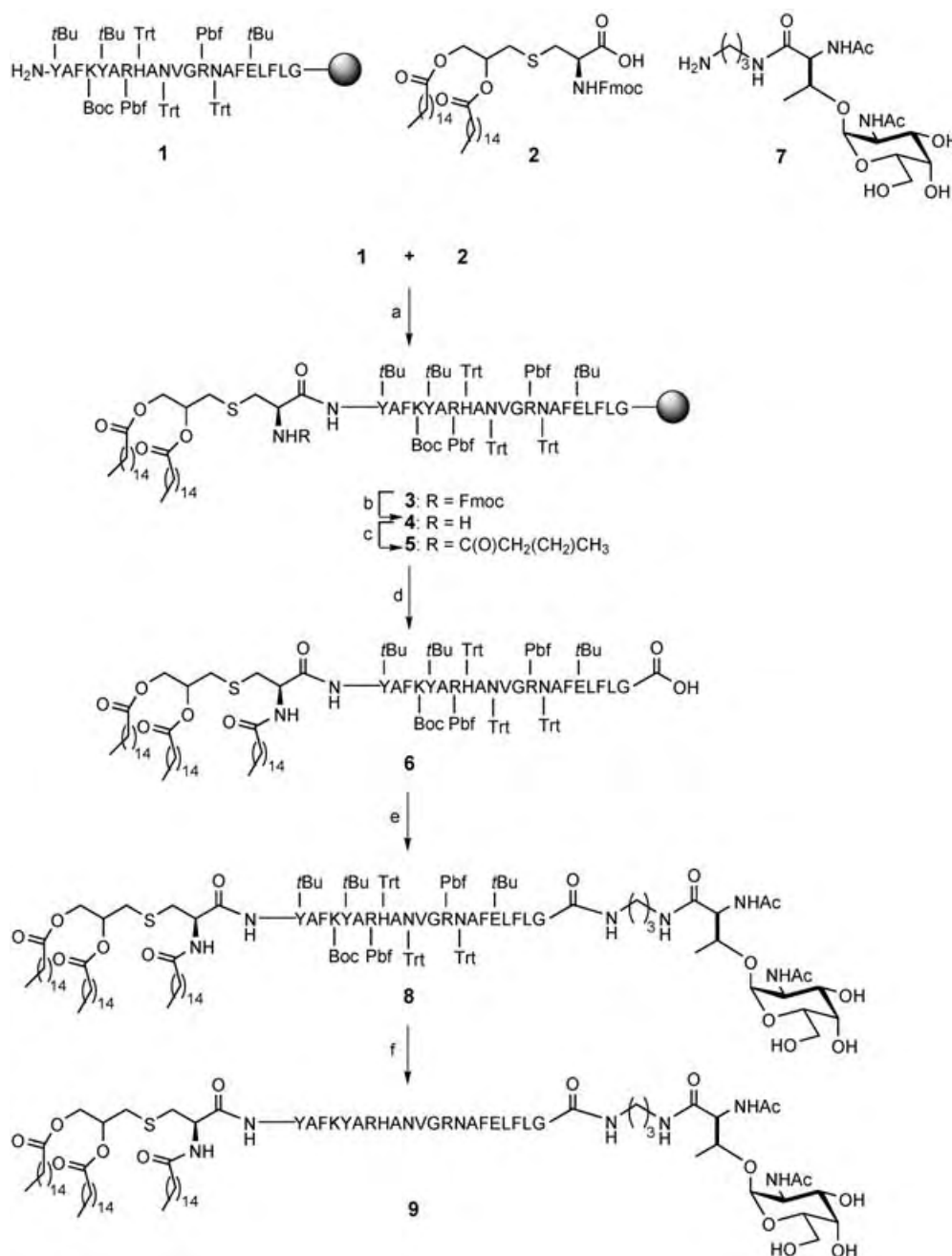
Herein, we report the synthesis and immunological evaluation of a structurally well-defined, fully synthetic anticancer vaccine candidate **9** that constitutes the minimal structural features required for a focused and effective T cell dependent immune response. The vaccine candidate is composed of the tumor-associated Tn antigen, the peptide T epitope YAFKYARHANVGRNAFELFL (YAF), and the lipopeptide *S*-[(*R*)-2,3-dipalmitoyloxy-propyl]-*N*-palmitoyl-(*R*)-cysteine (Pam₃Cys). The Tn antigen, which will serve as a B epitope, is overexpressed on the surface of human epithelial tumor cells of the breast, colon, and prostate.^[3] This antigen is not present on normal cells, which thus renders it an excellent target for immunotherapy.^[3,13,18] To overcome the T cell independent properties of the carbohydrate antigen, the YAF peptide was incorporated. This 20-amino acid peptide sequence is derived from an outer-membrane protein of *Neisseria meningitidis* and has been identified as an MHC class II restricted site for human T cells.^[19] It was envisaged that this helper T cell epitope would induce a T cell dependent immune response that results in the production of IgG antibodies against the Tn antigen. The combined B cell and helper T cell epitope lacks the ability to provide appropriate “danger signals”^[20] for dendritic cell maturation. Therefore, the lipopeptide Pam₃Cys, which is derived from the immunologically active N-terminal sequence of the principal lipoprotein of *Escherichia coli*,^[21] was incorporated. This lipopeptide has been recognized as a powerful immunoadjuvant,^[22] and recent studies have shown that it exerts its activity through the interaction with Toll-like receptor 2 (TLR-2).^[23] This interaction results in the production of pro-inflammatory cytokines and chemokines, which, in turn, stimulate antigen-presenting cells (APCs) and thus initiate development and activation of helper T cells.^[24] The lipopeptide also facilitates the incorporation of the antigen into liposomes. Liposomes have attracted interest as vectors in vaccine design^[25] owing to their low intrinsic immunogenicity, thus, avoiding undesirable carrier-induced immune responses.

The synthesis of target compound **9** requires a highly convergent synthetic strategy which employs chemical manipulations that are compatible with the presence of a carbohydrate, peptide, and lipid moieties. It was envisaged that **9** could be prepared from spacer-containing Tn antigen **7**, polymer-bound peptide **1**, and *S*-[2,3-bis(palmitoyloxy)-propyl]-*N*-Fmoc-Cys (Pam₂FmocCys, **2**).^[26] Fmoc = 9-fluorenylmethoxycarbonyl. The resin-bound peptide **1** was assembled by automated solid-phase peptide synthesis using Fmoc-protected amino acids in combination with the extremely acid-sensitive HMPB-MBHA (HMPB = 4-(4-hydroxymethyl-3-methoxyphenoxy)butyryl; MBHA = *p*-

methylbenzhydrylamine) resin and 2-(1*H*-benzotriazol-1-yl)-oxy-1,1,3,3-tetramethyluronium hexafluorophosphate/1-hydroxybenzotriazole (HBTU/HOBt)^[27] as activators (Scheme 1). The HMPB-MBHA resin was selected because it allows the cleavage of a compound from the resin without concomitant removal of side-chain protecting groups. This feature was important because side-chain functional groups of aspartic acid, glutamic acid, and lysine would otherwise interfere with the incorporation of the Tn antigen derivative **7**. Next, the Pam₂FmocCys derivative (**2**) was coupled to the N-terminal amine of peptide **1** using PyBOP^[28] and HOBt in the presence of DIPEA in a mixture of DMF and dichloromethane to give the resin-bound lipopeptide **3**. The Fmoc group of **3** was removed under standard conditions, and the free amine of the resulting compound **4** was coupled with palmitic acid in the presence of PyBOP and HOBt to give the fully protected and resin-bound lipopeptide **5**. The amine of the Pam₂Cys moiety was palmitoylated after coupling with **1** to avoid racemization of the cysteine moiety.^[26] Cleavage of compound **5** from the resin was achieved with 2% TFA in dichloromethane followed by the immediate neutralization with 5% pyridine in methanol. After purification by LH-20 size-exclusion chromatography, the C-terminal carboxylic acid of lipopeptide **6** was coupled with the amine of Tn derivative **7**, employing DIC/HOAt/DIPEA^[29] as coupling reagents, to give, after purification by Sephadex LH-20 size-exclusion chromatography, fully protected lipidated glycopeptide **8** in 79% yield. MALDI-TOF mass spectrometry revealed signals at $m/z = 5239.6$ and $m/z = 5263.0$, which correspond to $[M+H]^+$ and $[M+Na]^+$ ions, respectively. Finally, the side-chain protecting groups of **8** were removed by treatment with 95% TFA in water using EDT as a scavenger. The alternative use of triisopropylsilane resulted in the formation of unidentified byproducts. The target compound **9** was purified by size-exclusion chromatography followed by reverse-phase HPLC using a Synchropak C4 column. Analysis of **9** by MALDI-TOF mass spectrometry revealed a signal at $m/z = 3760.3$ corresponding to $[M+Na]^+$.

Next, compound **9** was incorporated into phospholipid-based liposomes. Thus, after hydration of a lipid film that contained **9**, cholesterol, phosphatidylcholine, and phosphatidylethanolamine, small unilamellar vesicles (SUVs) were prepared by extrusion through 100-nm Nuclepore polycarbonate membranes. Transmission electron microscopy (TEM) by negative stain confirmed that the liposomes were uniformly sized with an expected diameter of approximately 100 nm (Figure 1). The liposome preparations were analyzed for *N*-acetyl galactosamine (GalNAc) content by hydrolysis with TFA, followed by quantification with anion-exchange chromatography at high pH values. Concentrations of approximately 30 $\mu\text{g mL}^{-1}$ of GalNAc were determined which corresponded to an incorporation of **9** of approximately 10%.

Groups of five female BALB/c mice were immunized subcutaneously with freshly prepared liposomes containing 0.6 μg carbohydrate at weekly intervals. To explore the adjuvant properties of the built-in lipopeptide Pam₃Cys, the antigen-containing liposomes were administered with or without the potent saponin immunoadjuvant QS-21 (Anti-



Scheme 1. a) PyBOP, HOBt, DIPEA, DMF/CH₂Cl₂ (5:1); b) piperidine/DMF (1:5); c) CH₃(CH₂)₁₄COOH, PyBOP, HOBt, DMF/CH₂Cl₂ (1:5); d) 2% TFA in CH₂Cl₂; e) **7**, DIC, HOAt, DIPEA, DMF/CH₂Cl₂ (2:1), 79%; f) TFA/H₂O/EDT (95:2.5:2.5), 79%. Boc = *tert*-butoxycarbonyl; Trt = trityl; Pbf = 2,2,4,6,7-pentamethyldihydrobenzofuran-5-sulfonyl; PyBOP = (benzotriazol-1-yloxy)tripyrrolidinophosphonium hexafluorophosphate; DIPEA = diisopropylethylamine; DMF = *N,N*-dimethylformamide; TFA = trifluoroacetic acid; DIC = diisopropylcarbodiimide; HOAt = 1-hydroxy-7-azabenzotriazole; EDT = 1,2-ethanedithiol. Ratios for solvent mixtures are indicated as v/v.

genics Inc., Lexington, MA). Anti-Tn antibody titres were determined by coating microtitre plates with a BSA–Tn conjugate (BSA = bovine serum albumin) and detection was accomplished with anti-mouse IgM or IgG antibodies labeled with alkaline phosphatase. As can be seen in Table 1, the mice that were immunized with the liposome preparations elicited IgM and IgG antibodies against the Tn antigen (Table 1, entries 1 and 2). The presence of IgG antibodies indicated

that the helper T epitope peptide of **9** had activated helper T lymphocytes. Furthermore, the observation that IgG antibodies were raised by mice which were only immunized with liposomes (group 1) indicated that the built-in adjuvant Pam₃Cys had triggered appropriate signals for the maturation of dendritic cells and their subsequent activation of helper T cells. However, the mice which received the liposomes in combination with QS-21 (group 2), elicited higher titres of anti-Tn antibodies. This stronger immune response may be due to a shift from a mixed Th1/Th2 to a Th1 response.^[30]

The results presented herein provide, for the first time, a proof of principle for the use of lipidated glycopeptides as minimal subunit vaccines. Previous immunizations with a saccharide coupled to an immunoadjuvant such as Pam₃Cys resulted in no or very low titres of IgG antibodies^[15,31,32] demonstrating that the incorporation of a peptide T epitope^[16,17] is critical for a class switch to IgG antibodies.

It is to be expected that several improvements can be made to the tricomponent vaccine candidate presented here. For example, it has been found that a clustered presentation of the Tn antigen is a more appropriate mimetic of mucins, and hence antibodies raised against this structure recognize better Tn antigens

expressed on cancer cells.^[33–36] The Th epitope employed in this study is known to be a MHC class II restricted epitope for humans. Thus, a more efficient class switch to IgG antibodies may be expected when a murine Th epitope is employed. On the other hand, compound **9** is a more appropriate vaccine candidate for use in humans. A recent report indicated that Pam₂Cys is a more potent immunoadjuvant than Pam₃Cys.^[37] It has also been suggested that the Pam₂Cys adjuvant has

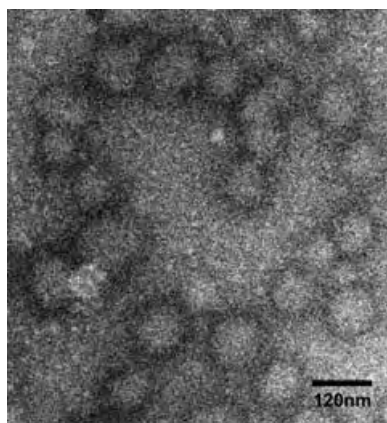


Figure 1. Negative-stain transmission electron micrograph of the liposome preparation.

Table 1: ELISA anti-Tn antibody titres^[a] after four immunizations with the glycolipopeptide/liposome formulation.

Entry	Group	IgM titres	IgG titres
1	1) Pam ₃ Cys-YAF-Tn	250	1410
2	2) Pam ₃ Cys-YAF-Tn + QS-21	170	2675

[a] ELISA plates were coated with a BSA-BrAc-Tn conjugate (BrAc = 3-(bromoacetamido)propionate). All titres are medians for a group of five mice. Titres were determined by regression analysis, plotting log₁₀ (dilution) versus the absorbance. The titres were calculated to be the highest dilution that gave 0.1 or higher than the absorbance of normal saline mouse sera diluted 1:100.

improved solubility properties,^[38] which is a problematic feature of compound **9**. Studies addressing these issues are ongoing.

Received: May 25, 2005

Published online: August 18, 2005

Keywords: antitumor agents · glycopeptides · liposomes · solid-phase synthesis

- [1] K. O. Lloyd, *Am. J. Clin. Pathol.* **1987**, *87*, 129–139.
- [2] T. Feizi, R. A. Childs, *Trends Biochem. Sci.* **1985**, *10*, 24–29.
- [3] G. F. Springer, *J. Mol. Med.* **1997**, *75*, 594–602.
- [4] S. Hakomori, *Acta Anat.* **1998**, *161*, 79–90.
- [5] D. S. A. Sanders, M. A. Kerr, *J. Clin. Pathol. Mol. Pathol.* **1999**, *52*, 174–178.
- [6] G. Ragupathi, *Cancer Immunol.* **1996**, *43*, 152–157.
- [7] C. Musselli, P. O. Livingston, G. Ragupathi, *J. Cancer Res. Clin. Oncol.* **2001**, *127*, R20–R26.
- [8] B. Kuberan, R. J. Linhardt, *Curr. Org. Chem.* **2000**, *4*, 653–677.
- [9] H. J. Jennings, R. K. Snood, *Neoglycoconjugates, Preparation and Application*, Academic, San Diego, **1994**.
- [10] P. W. Anderson, M. E. Pichichero, E. C. Stein, *J. Immunol.* **1989**, *142*, 2464–2468.
- [11] T. Buskas, Y. Li, G.-J. Boons, *Chem. Eur. J.* **2004**, *10*, 3517–3523.
- [12] P. J. Sabbatini, V. Kudryashov, G. Ragupathi, S. J. Danishefsky, P. O. Livingston, W. Bornmann, M. Spassova, A. Zatorski, D. Spriggs, C. Aghajani, S. Soignet, M. Peyton, C. O'Flaherty, J. Curtin, K. O. Lloyd, *Int. J. Cancer* **2000**, *87*, 79–85.

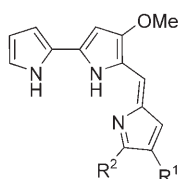
- [13] T. Toyokuni, S. Hakomori, A. K. Singhal, *Bioorg. Med. Chem.* **1994**, *2*, 1119–1132.
- [14] F. Reichel, P. R. Ashton, G.-J. Boons, *Chem. Commun.* **1997**, *21*, 2087–2088.
- [15] S. J. Danishefsky, J. R. Allen, *Angew. Chem.* **2000**, *112*, 882–912; *Angew. Chem. Int. Ed.* **2000**, *39*, 836–863.
- [16] S. Keil, C. Claus, W. Dippold, H. Kunz, *Angew. Chem.* **2001**, *113*, 379–382; *Angew. Chem. Int. Ed.* **2001**, *40*, 366–369.
- [17] R. Lo-Man, S. Vichier-Guerre, R. Perraut, E. Deriaud, V. Huteau, L. BenMohamed, O. M. Diop, P. O. Livingston, S. Bay, C. Leclerc, *Cancer Res.* **2004**, *64*, 4987–4994.
- [18] E. Kagan, G. Ragupathi, S. Yi, C. A. Reis, J. Gildersleeve, D. Kahne, H. Clausen, S. J. Danishefsky, P. O. Livingston, *Cancer Immunol. Immunother.* **2005**, *54*, 424–430.
- [19] E. J. H. J. Wiertz, J. A. M. van Gaans-van den Brink, H. Gausepohl, A. Prochnicka-Chalufour, P. Hoogerhout, J. T. Poolman, *J. Exp. Med.* **1992**, *176*, 79–88.
- [20] R. Medzhitov, C. A. Janeway, Jr., *Science* **2002**, *296*, 298–300.
- [21] V. Braun, *Biochim. Biophys. Acta* **1975**, *415*, 335–377.
- [22] K. H. Wiesmuller, W. G. Bessler, G. Jung, *Hoppe-Seyler's Z. Physiol. Chem.* **1983**, *364*, 593–606.
- [23] A. O. Aliprantis, R. B. Yang, M. R. Mark, S. Suggett, B. Devaux, J. D. Radolf, *Science* **1999**, *285*, 736–739.
- [24] D. Werling, T. W. Jungi, *Vet. Immunol. Immunopathol.* **2003**, *91*, 1–12.
- [25] G. F. A. Kersten, D. J. A. Crommelin, *Biochim. Biophys. Acta* **1995**, *1241*, 117–138.
- [26] J. W. Metzger, K.-H. Wiesmuller, G. Jung, *Int. J. Pept. Protein Res.* **1991**, *38*, 545–554.
- [27] R. Knorr, A. Trzeczal, W. Bannwarth, D. Gillessen, *Tetrahedron Lett.* **1989**, *30*, 1927–1930.
- [28] F. Martinez, J.-P. Bali, M. Rodriguez, B. Castro, J. Laur. M.-F. Lignon, *J. Med. Chem.* **1988**, *28*, 1874–1879.
- [29] L. A. Carpino, *J. Am. Chem. Soc.* **1993**, *115*, 4397–4398.
- [30] A. Moore, L. McCarthy, K. H. G. Mills, *Vaccine* **1999**, *17*, 2517–2527.
- [31] T. Toyokuni, B. Dean, S. Cai, D. Boivin, S. Hakomori, A. K. Singhal, *J. Am. Chem. Soc.* **1994**, *116*, 395–396.
- [32] S. F. Slovin, G. Ragupathi, C. Musselli, K. Olkiewicz, D. Verbel, S. D. Kuduk, J. B. Schwartz, D. Sames, S. J. Danishefsky, P. O. Livingston, H. I. Scher, *J. Clin. Oncol.* **2003**, *21*, 4292–4298.
- [33] H. Nakada, Y. Numata, M. Inoue, N. Tanaka, H. Kitagawa, I. Funakoshi, S. Fukui, I. Yamashima, *J. Biol. Chem.* **1991**, *266*, 12402–12405.
- [34] H. Nakada, M. Inoue, Y. Numata, N. Tanaka, I. Funakoshi, S. Fukui, A. Mellors, I. Yamashima, *Proc. Natl. Acad. Sci. USA* **1993**, *90*, 2495–2499.
- [35] M. A. Reddish, L. Jackson, R. R. Koganty, D. X. Qiu, W. Hong, B. M. Longenecker, *Glycoconjugate J.* **1997**, *14*, 549–560.
- [36] C. A. Reis, T. Sorensen, U. Mandel, L. David, E. Mirgorodskaya, P. Roepstorff, J. Kihlberg, J. E. Hansen, H. Clausen, *Glycoconjugate J.* **1998**, *15*, 51–62.
- [37] D. C. Jackson, Y. F. Lau, T. Le, A. Suhrbier, G. Deliyannis, C. Cheers, C. Smith, W. Zeng, L. E. Brown, *Proc. Natl. Acad. Sci. USA* **2004**, *101*, 15440–15445.
- [38] W. Zeng, S. Ghosh, Y. F. Lau, L. E. Brown, D. C. Jackson, *J. Immunol.* **2002**, *169*, 4905–4912.

DOI: 10.1002/anie.200501740

Synthesis, Anion-Binding Properties, and In Vitro Anticancer Activity of Prodigiosin Analogues**

Jonathan L. Sessler,* Leah R. Eller, Won-Seob Cho, Sergios Nicolaou, Apolonio Aguilar, Jeong Tae Lee, Vincent M. Lynch, and Darren J. Magda*

Prodigiosins, for example, **1** and **2**, are a family of naturally occurring tripyrrolic red pigments that were first isolated in



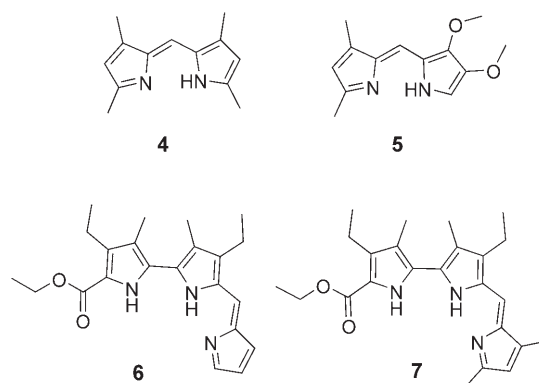
- 1:** R¹ = H, R² = *n*-undecyl (prodigiosin 25-C)
2: R¹ = *n*-pentyl, R² = Me (prodigiosin)
3: R¹ = H, R² = Et

the 1930s from microorganisms including *Serratia* and *Streptomyces* and are characterized by a common pyrrolylpyrromethene skeleton.^[1] These molecules, especially prodigiosin 25-C (**1**) but also synthetic analogues such as **3**,^[2,3] have been studied extensively for their promising immunosuppressive^[4] and anticancer activities.^[5,6]

To date, two very different modes of action have been put forward to explain their anticancer activity. One suggestion, proposed by Manderville, Melvin, and co-workers,^[7] and further supported by Fürstner and Grabowski,^[8] is that prodigiosin mediates its anticancer effect through copper-mediated cleavage of double-stranded DNA. The second

mechanistic suggestion, proposed by Ohkuma, Wasserman, and co-workers in 1998,^[9] is that the biological activity of prodigiosin derives from its ability to effect concurrent transmembrane transport (“symport”) of H⁺ and Cl[−] ions into cells.^[9] Support for this mechanism came partly from the finding that the activity of prodigiosin as well as prodigiosin-based lysosomal acidification were dependent on the concentration of extracellular chloride ion and that chloride ion channels were not responsible for these effects.^[9] However, to date, little in the way of direct chemical support for the mechanism has been provided.^[10,11] Accordingly, we have undertaken a detailed study of the anion-binding and through-membrane transport properties of several prodigiosin analogues and corresponding dipyrromethene constituents. Herein, we report that it is the rate of transport, rather than the anion-binding ability, that correlates most closely with anticancer activity in vitro, as judged from cell proliferation assays involving A549 human lung and PC3 human prostate cancer cells.

To investigate the presumed anion binding and transport ability of prodigiosins, model compounds **3–7** were pre-



pared.^[12] These systems contain either the basic prodigiosin skeleton or the key constituent dipyrromethene motif and were thus thought to provide a “basis set” sufficient to allow some limited structure–activity correlations to be made.

The first indication that the protonated forms of prodigiosins and dipyrromethenes can bind chloride ions came from X-ray crystal structure analyses of salts **4**·HCl and **7**·HCl.^[12] As seen in Figures 1 and 2, 1:1 complexes are formed in the solid state as the result of oriented hydrogen-bonding interactions and, presumably, electrostatic effects. In the case of salt **4**·HCl the complex is essentially flat, whereas

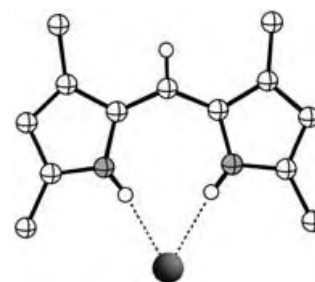


Figure 1. Crystal structure of **4**·HCl. This complex is essentially planar.

[*] Prof. J. L. Sessler, L. R. Eller, W.-S. Cho, S. Nicolaou, A. Aguilar, J. T. Lee, V. M. Lynch
Department of Chemistry and Biochemistry
Institute for Cellular and Molecular Biology
1 University Station–A5300
University of Texas at Austin
Austin, Texas 78712-1065 (USA)
Fax: (+1) 512-471-7550
E-mail: sessler@mail.utexas.edu

Dr. D. J. Magda
Pharmacyclics Inc.
995 E. Arques Ave
Sunnyvale, CA 94085 (USA)
Fax: (+1) 408-774-0340
E-mail: dmagda@pcyc.com

[**] This work was supported by the National Institutes of Health (GM 58907). Dr. Wyeth Callaway is thanked for providing samples of pyrrole **10**. We thank Ms. Beth McNally of Prof. Bradley Smith's group for her help in developing a working liposomal model membrane system.

Supporting information for this article is available on the WWW under <http://www.angewandte.org> or from the author.

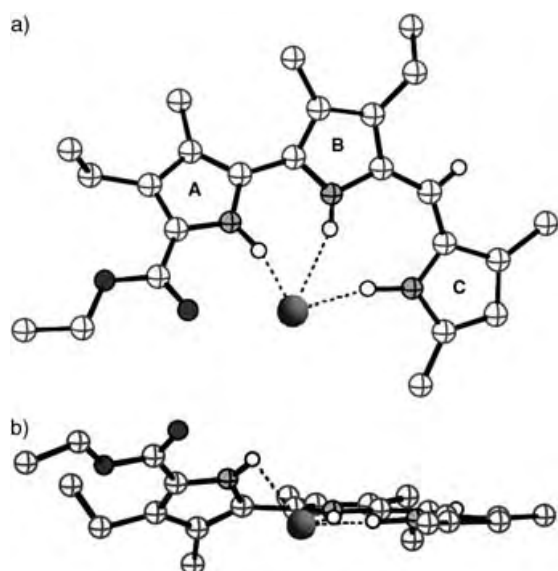


Figure 2. Two views of the crystal structure of the complex formed between monoprotonated prodigiosin **7** and chloride ion.

some deviation from planarity is seen in **7**·HCl. In **4**·HCl, the NH···Cl distances (2.25 Å) are roughly equal, while in the case of **7**·HCl they are found to be longer for ring A than rings B and C (NH···Cl = 2.72, 2.28, and 1.97 Å for rings A, B, and C, respectively).

Evidence in support of chloride ion binding in solution came from isothermal titration calorimetry (ITC) studies carried out in acetonitrile at 303 K using tetrabutylammonium chloride (TBACl) as the source of chloride ions. Whereas the free-base forms of prodigiosins **6** and **7** as well as various neutral bipyrroles were found to display affinities for chloride ion that were too low to be determined by ITC methods in CH₃CN, the corresponding monoprotonated HI salts of these prodigiosin species were found to exhibit rather substantial apparent affinities for chloride ion (see Table 1). The same

Table 1: Apparent association constants (K_a) for binding of chloride ion to the monoprotonated (HI) salts of dipyrromethenes and prodigiosin analogues **3–7** in CH₃CN, as determined by ITC analysis at 30°C using TBACl as the anion source. Errors are estimated to be 10%.

	3	4	5	6	7
ΔH [kcal mol ⁻¹]	-4.2	-3.35	-2.27	-1.59	-2.03
$T\Delta S$ [kcal mol ⁻¹]	3.8	4.88	5.33	5.35	4.93
ΔG [kcal mol ⁻¹]	-8.0	-8.23	-7.60	-6.94	-6.96
K_a [M ⁻¹]	5.9×10^5	8.8×10^5	3.0×10^5	1.1×10^5	1.1×10^5

proved true for the protonated dipyrromethene fragments **4** and **5**. As a rule, these latter compounds demonstrated slightly higher affinities for chloride ions than did the corresponding monoprotonated prodigiosins; a finding that reflects presumably the higher effective charge densities present in the smaller dipyrrolic species.

The efficiency of transport of chloride ions was determined by monitoring their efflux across a 200-nm POPC/POPS (POPC = 1-palmitoyl-2-oleoyl-*sn*-glycero-3-phosphocholine; POPS = 1-palmitoyl-2-oleoyl-*sn*-glycero-3-phospho-L-serine) liposome membrane as a function of time.^[13] The

vesicles were loaded with a solution of NaCl (500 mM) and then diluted to produce a 1 mM suspension in a solution of NaNO₃ (500 mM). The integrity of the liposome membranes was established according to reported procedures.^[14] The efflux of chloride ion was monitored as a function of time using an Accumet glass-bodied chloride-selective electrode in conjunction with a Jenco multimeter. The results of the transport studies are summarized in Figure 3. Note that

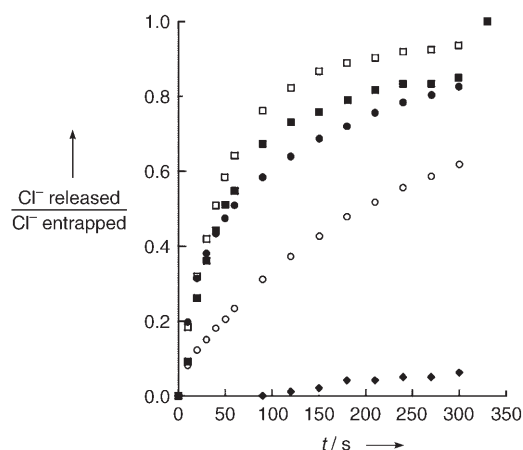


Figure 3. Time-dependent efflux of chloride ion from 200-nm vesicles loaded with a solution of NaCl (500 mM) and suspended in a solution of NaNO₃ (500 mM) and triethylsilane (5 mM), adjusted to pH 7.4. Prodigiosins are indicated by filled markers (**3** ●, **6** ■, **7** ◆); dipyrromethenes are indicated by open markers (**4** □, **5** ○).

tripyrrole **3**, the compound that bears the greatest structural similarity to the natural prodigiosins, demonstrated remarkably high transport efficiency. In fact, the rate of efflux of chloride ion was sufficiently rapid that studies were conducted using a 0.5 μM solution of the carrier. The remaining compounds were studied using 2 μM solutions. The order of transport efficiency, as inferred from initial rates, was found to

be **3** ≫ **6** ≈ **4** > **5** ≫ **7**. Additionally, compounds **3–6** were all seen to prompt ≥ 60% release of chloride ions from the interior of the vesicles within 300 seconds.

To determine the mechanism of transport, the experiments were repeated with the pH of the external solution initially set at pH 5.5. The efflux of chloride ions was less efficient than when the external

solutions were neutral or basic. This behavior is consistent with an H⁺/Cl⁻ ion mechanism of transport, as it is expected that the driving force for proton egress would be reduced with a lower external pH value.

Experiments were also carried out in which 8-hydroxypyrene trisulfonate (HPTS), a pH-sensitive fluorescent dye,^[15] was included within the liposomes and the external solution was basified using NaOH. The excitation maxima (λ_{max}) for HPTS are 450 (at pH 7–8) and 405 nm (pH < 6). Excitation ratio experiments were performed in which the sample was excited at both 405 and 450 nm while the emission

intensity was monitored at 511 nm. Following addition of the carrier, an increase in the peak at 450 nm and a corresponding decrease in the peak at 405 nm were observed. Upon lysis of the vesicles and subsequent contact with external hydroxide ion, these spectral changes became even more pronounced. In contrast, in the absence of chloride ion (but in the presence of carrier) no effects were seen. Such findings are also consistent with an H^+/Cl^- ion symport mechanism.

Finally, transport experiments were performed in which the external nitrate ion was replaced by sulfate ion. No significant changes in the transport rates or overall efficiency were observed under these conditions, as would be expected for anion efflux conducted through a H^+/Cl^- ion symport mechanism. However, if transport were to occur through an anion-exchange (antiport) mechanism, the transport rates would be expected to change as a function of the lipophilicity of the external anion.

Anticancer activity in vitro was assessed using a cell proliferation assay with A549 human lung cancer and PC3 human prostate cell lines.^[16] The order of activity in vitro in both cell lines was found to be similar, namely, $3 > 6 > 4 > 5 > 7$ (A549; see Figure 4) and $3 > 6 > 4 > 5 \approx 7$ (PC3; see

the low antiproliferative activity of **7** can be rationalized in terms of an anion affinity that is too low to make it a highly effective chloride ion carrier. The present findings thus provide support for a mechanism such as H^+/Cl^- ion symport that is dominated by kinetic rather than thermodynamic factors.

The present study does not address the issue of whether recruitment of copper and DNA modification plays a significant role in mediating the action of prodigiosin. However, the strong correlation between transport rates and anticancer activity in vitro, in conjunction with evidence for anion binding in the solid state and solution phase, lead us to suggest that the H^+/Cl^- ion symport mechanism proposed by Ohkuma, Wasserman, and co-workers^[9] is chemically reasonable. If such a conclusion is correct, it leads to the suggestion that other chloride ion transport systems, including those that may have no direct structural resemblance to prodigiosins, may show interesting anticancer activity.

Received: May 20, 2005

Published online: August 22, 2005

Keywords: ion transport · membranes · molecular recognition · nitrogen heterocycles · prodigiosin

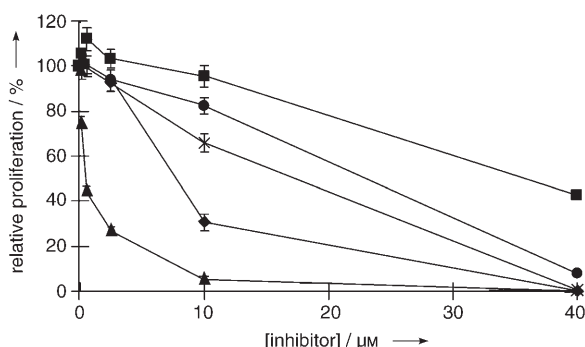


Figure 4. Antiproliferative activity of prodigiosin analogues and dipyrromethenes in A549 human lung cancer cells. Exponential phase cells were treated with compounds **3–7** at the indicated concentrations for 24 h (**3** ▲, **4** ×, **5** ●, **6** ◆, **7** ■). The number of viable cells was determined after 3 days using a standard tetrazolium salt reduction assay. Data are presented as the fraction of untreated cells (see Supporting Information for details).

Supporting Information). Compounds **3**, **4**, **5**, and **6** all exhibited significant cytotoxic activity, with 100% of cancer cells killed at a concentration of 40 μM in both cell lines. As observed earlier in the transport studies, compound **3** proved to be more efficient than the other compounds examined, displaying a notably greater antiproliferative effect.

Among the prodigiosin analogues examined in this study, the rates of through-liposome transport and in vitro activity were found to correlate well. A general sequence of efficiency of $3 > 6 \geq 4 > 5 \geq 7$ is seen in both cases. In contrast, the values of the effective association constant (K_a) in Table 1 do not correlate well with the observed activity in vitro. For instance, compound **4**- H^+ , which displays the highest overall K_a value, is far less active in cell culture than prodigiosin **3**. Such reduced activity could reflect an anion affinity that is too high to afford an optimal rate of release of chloride ion. Likewise,

- [1] A. Fürstner, *Angew. Chem.* **2003**, *115*, 3706–3728; *Angew. Chem. Int. Ed.* **2003**, *42*, 3582–3603.
- [2] R. D'Alessio, A. Bargiotti, O. Carlini, F. Colotta, M. Ferrari, P. Gnocchi, A. Isetta, N. Mongelli, P. Motta, A. Rossi, M. Rossi, M. Tibolla, E. Vanotti, *J. Med. Chem.* **2000**, *43*, 2557–2565.
- [3] M. S. Melvin, J. T. Tomlinson, G. Park, C. S. Day, G. R. Saluta, G. L. Kucera, R. A. Manderville, *Chem. Res. Toxicol.* **2002**, *15*, 734–741.
- [4] S. B. Han, H. M. Kim, Y. H. Kim, C. W. Lee, E.-S. Jang, K. H. Son, S. U. Kim, Y. K. Kim, *Int. J. Immunopharmacol.* **1998**, *20*, 1–13.
- [5] D. Yamamoto, Y. Kiyozuka, Y. Uemura, C. Yamamoto, H. Takemoto, H. Hirata, K. Tanaka, K. Hioki, A. Tsubura, *J. Cancer Res. Clin. Oncol.* **2000**, *126*, 191–197.
- [6] B. Montaner, R. Perez-Toma, *Life Sciences* **2001**, *68*, 2025–2036.
- [7] a) M. S. Melvin, M. W. Calcutt, R. E. Nofle, R. A. Manderville, *Chem. Res. Toxicol.* **2002**, *15*, 742–748; b) G. Park, J. T. Tomlinson, M. S. Melvin, M. W. Wright, C. S. Day, R. A. Manderville, *Org. Lett.* **2003**, *5*, 113–116.
- [8] A. Fürstner, E. J. Grabowski, *ChemBioChem* **2001**, *2*, 706–709.
- [9] a) T. Sato, H. Konno, Y. Tanaka, T. Kataoka, K. Nagai, H. H. Wasserman, S. Ohkuma, *J. Biol. Chem.* **1998**, *273*, 21455–21462; b) S. Ohkuma, T. Sato, M. Okamoto, H. Matsuya, K. Arai, T. Kataoka, K. Nagai, H. H. Wasserman, *Biochem. J.* **1998**, *334*, 731–741.
- [10] In previous work, the HCl complexes of extended “vinyllogous” prodigiosin analogues,^[17] a cyclic prodigiosin derivative,^[18] and a phenyl-substituted dipyrromethene derivative^[3] were reported. While single-point binding of chloride ion is seen in the case of the latter system, the first two structures revealed binding modes that are analogous to those seen in the case of **4**-HCl and **7**-HCl, respectively.
- [11] During the course of preparing this manuscript, we became aware of a parallel study of H^+/Cl^- ion symport using a different set of prodigiosin analogues, namely a set of wholly synthetic pyrrole amides. See: P. A. Gale, M. E. Light, B. McNally, K. Navakhun, K. E. Sliwinski, B. D. Smith, *Chem. Commun.* **2005**,

3773–3775. We thank the authors for making their manuscript available to us prior to publication.

- [12] Experimental details and characterization data are included in the Supporting Information. CCDC 271587 and 271586 (**4**·HCl and **7**·HCl, respectively) contain the supplementary crystallographic data for this paper. These data can be obtained free of charge from the Cambridge Crystallographic Data Centre via www.ccdc.cam.ac.uk/data_request/cif.
- [13] A. Koulov, T. N. Lambert, R. Shukla, M. Jain, M. Boon, B. D. Smith, H. Li, D. N. Sheppard, J.-B. Joos, J. P. Clare, A. P. Davis, *Angew. Chem.* **2003**, *115*, 5081–5083; *Angew. Chem. Int. Ed.* **2003**, *42*, 4931–4933; .
- [14] a) F. Nicol, S. Nir, F. C. Szoka, Jr., *Biophys. J.* **2000**, *78*, 818–829; b) J. P. Koniarek, J. L. Thomas, M. Vazquez, *Adv. Space Res.* **2004**, *34*, 1373–1377; c) M. Castaing, A. Loiseau, L. Djoudi, *Eur. J. Pharm. Sci.* **2003**, *18*, 81–88; d) A. G. Krishna, S. T. Menon, T. J. Terry, T. P. Sakmar, *Biochemistry* **2002**, *41*, 8298–8309.
- [15] K. Kano, J. H. Fendler, *Biochim. Biophys. Acta* **1978**, *509*, 289–299.
- [16] T. Mosmann, *J. Immunol. Methods* **1983**, *65*, 55–63.
- [17] A. Treibs, M. Strell, I. Strell, D. Grimn, *Justus Liebigs Ann. Chem.* **1978**, 289–305.
- [18] A. Fürstner, J. Grabowski, C. W. Lehmann, *J. Org. Chem.* **1999**, *64*, 8275–8280.

Oxidations

DOI: 10.1002/anie.200501853

Synthesis of Imides, *N*-Acyl Vinylogous Carbamates and Ureas, and Nitriles by Oxidation of Amides and Amines with Dess–Martin Periodinane***K. C. Nicolaou* and Casey J. N. Mathison*

The synthetic utility and pervasiveness of hypervalent iodine(v) reagents have become increasingly evident in recent decades, as underscored by a multitude of protocols that highlight the oxidative capabilities of λ^3 -iodanes and their

successful employment for the construction of diverse arrays of molecular targets.^[1–3] As part of our explorations into the realm of hypervalent iodine(v) chemistry, we recently reported a number of useful applications involving both Dess–Martin Periodinane (DMP) and *o*-iodoxybenzoic acid (IBX). Included in these discoveries are the IBX-induced conversion of amines into imines^[4] and the initiation of cascade reactions by DMP leading to a variety of imidoquinones and heterocycles from anilide precursors.^[5,6] The intelligence gathered in the course of these investigations led us to hypothesize about additional modes of reactivity that could perhaps be unveiled through further explorations of the chemistry of such hypervalent iodine(v) reagents toward other classes of heteroatom-containing substrates. These speculations proved fruitful, and herein we report the direct oxidation of amides into imides and *N*-acyl vinylogous carbamates and ureas, the dehydrogenation of benzylic and related amines to aromatic nitriles by DMP, and applications thereof.

Imides are well represented in the literature, often appearing as productive components in a variety of reactions, ranging from condensations to alkylations and from acylations to cycloadditions.^[7] This structural motif also appears in certain natural products such as fumaramidmycin,^[8] coniothyriomycin,^[9] and SB-253514.^[10] Despite several procedures being available for their preparation, new methods for the synthesis of imides are nevertheless of considerable importance, especially when their direct access from readily available substrates could be secured under mild conditions.

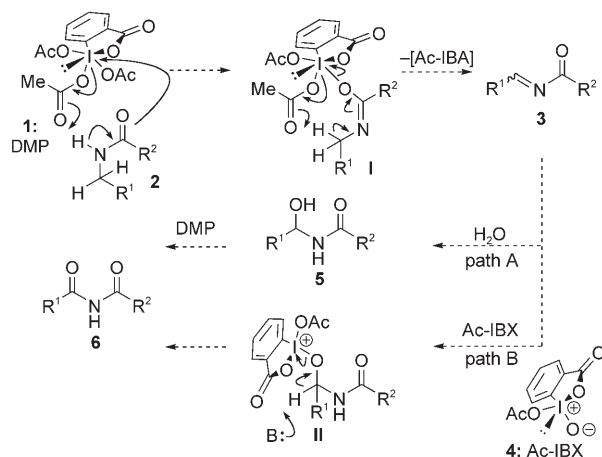
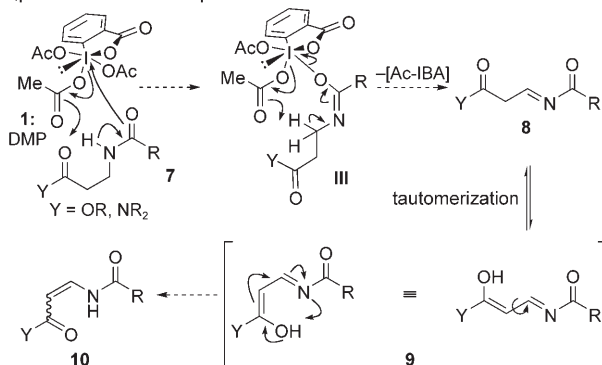
The mechanistic rationale for the oxidation of amides to imides with DMP is shown in Scheme 1 A. Thus, it was anticipated that nucleophilic attack onto the iodine core of the reagent by the amide oxygen atom with concomitant expulsion of an acetate group may lead to intermediate **I**, whose spontaneous intramolecular rearrangement was anticipated to result in its collapse to Ac-IBA, AcOH, and *N*-acyl imine intermediate **3**. The latter, highly reactive, species **3** may then be transformed into imide **6**, either by addition of H₂O, with subsequent oxidation of the putative hemiaminal with DMP (Scheme 1 A, path A), or by the incorporation of Ac-IBX (**4**), to generate an intermediate of type **II** (Scheme 1 A, path B).

This hypothesis proved correct as secondary amides were smoothly oxidized to imides by heating with DMP in a mixture of fluorobenzene and DMSO at 80–85°C. As seen by inspection of Table 1, an extensive range of functional groups is tolerated by this protocol, including aromatic halides, olefins, and acetates. Particularly significant are the results in Table 1, entries 3 and 5, which demonstrate the superiority of the present method over contemporary techniques employing RuO₄,^[11] a reagent whose tolerance of the olefinic and ethereal sites of substrates **15** and **19**, respectively, would be questionable, at best.^[12] Table 1, entries 7 and 8 are also noteworthy as they provide information regarding chemoselectivity preferences for the action of DMP on amide-containing substrates. Thus, carbamates are inert to these oxidation conditions (Table 1, entry 7), as are benzylic positions (Table 1, entry 8). The latter observation is expected as DMP is not, unlike IBX,^[13] a willing single-electron-

[*] Prof. Dr. K. C. Nicolaou, C. J. N. Mathison
Department of Chemistry
The Skaggs Institute for Chemical Biology
The Scripps Research Institute
10550 North Torrey Pines Road, La Jolla, California 92037 (USA)
and
Department of Chemistry and Biochemistry
University of California, San Diego
9500 Gilman Drive, La Jolla, California 92093 (USA)
Fax: (+1) 858-784-2469
E-mail: kcn@scripps.edu

[**] We thank Dr. D. H. Huang and Dr. G. Siuzdak for NMR spectroscopic and mass spectrometric assistance, respectively. Financial support for this work was provided by grants from the National Institutes of Health (USA) and the Skaggs Institute for Chemical Biology.

A) DMP-mediated oxidation of amides to imides


B) DMP-mediated oxidation of β -amido esters and amides to their α,β -unsaturated counterparts


Scheme 1. Mechanistic rationale for the DMP-mediated oxidation of amides (A) and β -amido esters and amides (B). Ac-IBA = 1-acetoxy-1,2-benziodoxol-3(1*H*)-one; Ac-IBX = 1-acetoxy-1-oxide-1,2-benziodoxol-3(1*H*)-one.

transfer reagent. The minimal amount of DMSO is recommended for this reaction as it was found that larger amounts of this solvent (needed to ensure dissolution of certain substrates) proved deleterious (see Table 1, entry 5).

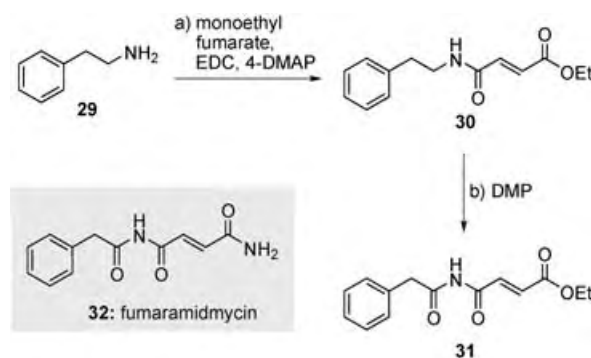
The relevance and potential utility of this novel route to imides is underscored by a facile synthesis of the ethyl ester analogue **31** of the antibiotic fumaramidmycin (**32**), as depicted in Scheme 2. Thus, coupling of monoethyl fumarate with amine **29** and subsequent oxidation of the resulting amide (**30**) with DMP led to the targeted fumaramidmycin analogue **31** (Table 4). This endeavor was instructive, as it not only resulted in the specific synthesis of **31** in a most expeditious manner but also hinted at the wealth of additional natural or designed structures that could be easily accessed through the developed technology.

Encouraged by these results, we further postulated that secondary amides equipped with *N*- β -carbonyl structural motifs could furnish vinylogous carbamates and ureas under suitable conditions. This speculation, which rested on the mechanistic rationale shown in Scheme 1B, proved well founded as demonstrated in Table 2. Thus, the reaction conditions have been demonstrated to favor the *cis*-configured product, likely due to the stabilization provided by the

Table 1: Synthesis of imides by oxidation of amides with DMP.^[a]

Entry	Substrate	Product	<i>t</i> [h]	Yield [%] ^[b]
1			1.0	98
2			0.5	86
3			3.0	61
4			0.5	98
5			5.0	96 ^[c]
6			1.0	86
7			3.5	86 ^[d]
8			2.0	98
9			1.0	92

[a] Reactions were conducted on a 0.2–0.5 mmol scale in PhF/DMSO (minimal amount of DMSO) at 85 °C with DMP (2.0 equiv), unless otherwise noted. [b] Yield of isolated product with no chromatography necessary. [c] Based on 42% recovery of **19**. [d] DMP: 6.0 equiv. DMSO = dimethyl sulfoxide.



Scheme 2. Synthesis of the ethyl ester analogue of fumaramidmycin. Reagents and conditions: a) monoethyl fumarate (0.5 equiv), EDC (0.6 equiv), 4-DMAP (0.05 equiv), CH₂Cl₂, 25 °C, 19 h, 73%; b) DMP (2.0 equiv), PhF/CH₂Cl₂/H₂O (40:20:1), 85 °C, 14 h, 96% (36% conversion). EDC = 1-ethyl-3-(3-dimethylaminopropyl)carbodiimide hydrochloride; 4-DMAP = 4-dimethylaminopyridine.

Table 2: Synthesis of *N*-acyl vinylogous carbamates and ureas by oxidation of β -amido esters and amides with DMP.^[a]

Entry	Substrate	Product	<i>cis/trans</i>	Yield [%] ^[b]
1			> 25:1	98
2			19:1	55 ^[b]
3			> 25:1	67
4			23:1	59 ^[c]
5			> 25:1	52
6			> 25:1	29
7			6:1	73

[a] Reactions were conducted on 0.1–0.3 mmol scale in PhF at 85 °C for 1 h with DMP (5.0 equiv). [b] Based on 45 % recovery of **35**. [c] Based on 41 % recovery of **39**. Bn = benzyl; Bz = benzoyl; THP = tetrahydropyranyl.

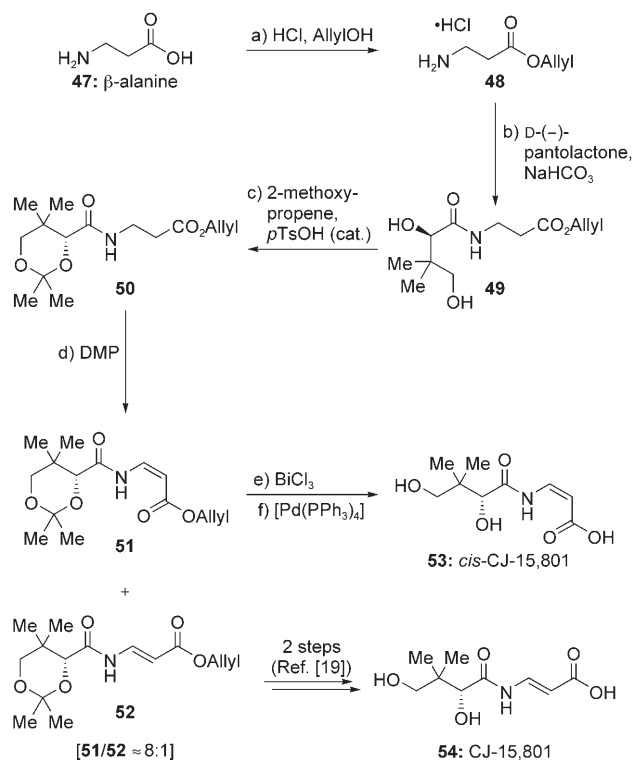
intramolecular hydrogen bond present within **9** and **10** (Scheme 1B) which is reinforced by the use of a nonpolar solvent (fluorobenzene);^[14] these conditions also tolerate the presence of phenolic acetates (Table 2, entry 3) and *N,N*-dibenzylamides (Table 2, entry 5). The latter example, in particular, along with that in Table 2, entry 6, underscores the oxidative potential of DMP, as it represents a direct dehydrogenation between two amide functionalities, a task very few reagents, if any, can smoothly achieve. Possible applications of this type of synthetic transformation include the construction of the *N*-acyl vinylogous urea and carbamic acid structural domains found in palytoxin,^[15] enamidonin,^[16] and CJ-15,801,^[17] as specifically highlighted in Table 2, entry 7, in which tetrahydropyranyl derivative **45** was oxidized with DMP to compound **46**, which could, in principle, be converted into a palytoxin-like side chain following, among other steps, *cis*–*trans* isomerization of the alkene.^[14]

To highlight the applicability of this reaction further, a formal total synthesis of the antibiotic CJ-15,801, along with the construction of its *cis* isomer, was also completed from commercially available starting materials (Scheme 3). Thus, allylation of β -alanine (**47**),^[18] followed by subsequent reaction of the resulting amino ester **48** with D-(–)-pantolactone in refluxing toluene, afforded diol **49**. Acetonide formation within **49** led to **50**, whose oxidation with DMP gave a mixture

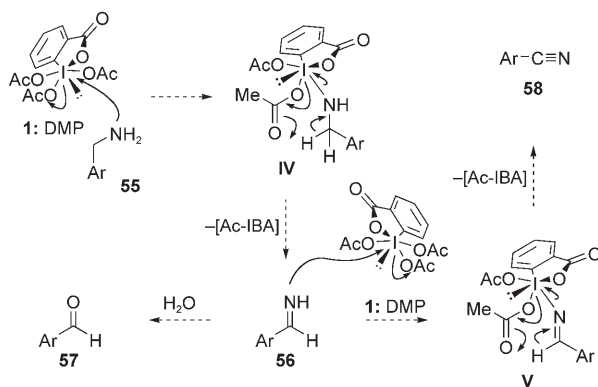
of the *N*-acyl vinylogous carbamates **51** (*cis* isomer) and **52** (*trans* isomer) in approximately 8:1 ratio in favor of the *cis* compound. While the arrival at **52** (Table 4) signals a formal total synthesis^[19] of antibiotic CJ-15,801, the major isomer **51** was converted into *cis*-CJ-15,801 (**53**) by sequential cleavage of the acetonide (BiCl₃) and allyl ester ([Pd(PPh₃)₄])^[20] protecting groups (Scheme 3).

As a result of the aforementioned successes, we sought to test the reactivity of DMP on additional nitrogen-containing substrates, namely benzylic primary amines. We were attracted by the prospect of directly accessing nitrile compounds, intermediates and products whose ubiquitous applications in synthesis are well appreciated and documented.^[21] Our reasoning for this expectation is encapsulated in Scheme 4. Thus, it was hypothesized that aromatic amine substrates such as **55** could associate with DMP to form complexes such as **IV** with concomitant loss of AcOH, followed by an intramolecular benzylic hydrogen abstraction by an acetate group. This would then result in a net dehydrogenation to afford aldimines of type **56**. These fleeting intermediates would then be expected to be either hydrolyzed by H₂O to aldehydes (e.g. **57**) or oxidized a second time by DMP to furnish nitriles (e.g. **58**).

Indeed, we were pleased to discover that an assortment of benzylic and related primary amines undergo the projected



Scheme 3. Formal total synthesis of the antibiotic CJ-15,801 (**54**) and its *cis* isomer **53**. Reagents and conditions: a) see reference [18]; b) D-(-)-pantolactone (1.5 equiv), NaHCO₃ (5.0 equiv), PhMe, reflux, 20 h, 59% (23% of **48** was also observed by ¹H NMR prior to purification of crude mixture); c) 2-methoxypropene (10 equiv), *p*TsOH (0.1 equiv), acetone, 0°C, 1 h, 78%; d) DMP (5.0 equiv), PhF, 85°C, 2 h, 93% (based on 39% recovered **50**, *cis* and *trans* isomers isolated in ≈8:1 ratio, respectively); e) BiCl₃ (0.2 equiv), H₂O, MeCN, 25°C, 14 h, 98%; f) [Pd(PPh₃)₄] (0.2 equiv), dioxane/H₂O (4:1), 25°C, 14 h, 87%. Ts = *p*-toluenesulfonyl.



Scheme 4. Mechanistic rationale for the oxidation of benzylic and related amines to aromatic nitriles with DMP.

transformation into nitriles upon reaction with DMP at 25°C in CH₂Cl₂. The generality and scope of this reaction is demonstrated in Table 3 with examples of substrates containing halide (Table 3, entries 3, 4, and 6), ether (entries 1 and 3), electron-donating (entry 1), and electron-withdrawing (entries 4 and 6) groups, as well as isoxazoles (entry 7) and

Table 3: Dehydrogenation of amines to nitriles.^[a]

Entry	Substrate	Product	<i>t</i> [min]	Yield [%]
1			10	95
2			10	71
3			15	94
4			10	77
5			15	90 ^[b]
6			15	77
7			15	84

[a] Reactions were conducted on a 0.2–0.5 mmol scale in CH₂Cl₂ at 25°C with DMP (2.0–3.0 equiv), unless otherwise noted. [b] DMP: 5.0 equiv.

bifunctional systems (entry 5). Aside from demonstrating considerable tolerance, this DMP dehydrogenation protocol has proven capable of affording nitriles through the implementation of brief reaction times, without excessive amounts of aldehyde by-products, unlike previously reported procedures employing iodosobenzene^[22] or IBX.^[4b]

The described chemistry expands the repertoire of reactions carried out by DMP, a versatile oxidant with ever-increasing utility in chemical synthesis. Among the reported examples of new reactivity for this hypervalent iodine reagent are the one-step oxidation of secondary amides to imides and *N*-acyl vinyllogous carbamates or ureas, and the direct oxidation of benzylic and related primary amines to their nitrile counterparts. The relevance of the present new synthetic technology to a rapid synthesis of analogues of fumaramidmycin and antibiotic CJ-15,801 demonstrates the mildness and applicability of some of these protocols to chemical synthesis, and bodes well for their future utilization in other situations.

Experimental Section

General procedure (amides): Generation of imides: In a sealed tube the amide (0.1–0.3 mmol) was dissolved in fluorobenzene (0.15 M) and several drops of wet DMSO were added (or enough to ensure dissolution of substrate). After addition of DMP (2.0 equiv), the mixture was heated behind a blast shield at 80–85°C until the starting material was consumed (monitored by TLC analysis). The resulting mixture was allowed to cool and was then quenched with saturated

Table 4: Selected physical properties for **31**, *cis*-**34**, **52**, **53**, and **64**.

31: R_f = 0.50 (silica gel, EtOAc/hexanes 1:2); IR (film): $\tilde{\nu}_{\max}$ = 3282, 2981, 1723, 1690, 1508, 1453, 1367, 1300, 1157, 1031 cm^{-1} ; ^1H NMR (400 MHz, CDCl_3): δ = 8.04 (br s, 1 H), 7.46 (d, J = 15.2 Hz, 1 H), 7.38–7.32 (m, 3 H), 7.28–7.26 (m, 2 H), 6.90 (d, J = 15.5 Hz, 1 H), 4.27 (q, J = 7.0 Hz, 2 H), 3.95 (s, 2 H), 1.32 ppm (t, J = 7.0 Hz, 3 H); ^{13}C NMR (125 MHz, CDCl_3): δ = 172.1, 165.0, 164.4, 134.8, 134.3, 133.0, 129.7, 129.1, 127.8, 61.7, 44.4, 14.2 ppm; HRMS (ESI TOF): calcd for $\text{C}_{14}\text{H}_{15}\text{NO}_4\text{Na}^+$ [$M+\text{Na}$] $^+$: 284.0893; found: 284.0898

cis-**34:** R_f = 0.78 (silica gel, EtOAc/hexanes 1:2); IR (film): $\tilde{\nu}_{\max}$ = 3311, 1673, 1616, 1480, 1395, 1378, 1220, 1030, 802, 695 cm^{-1} ; ^1H NMR (400 MHz, CDCl_3): δ = 11.53 (br s, 1 H), 7.97–7.95 (m, 2 H), 7.74 (dd, J = 8.9, 11.2 Hz, 1 H), 7.61–7.57 (m, 1 H), 7.52–7.49 (m, 2 H), 5.26 (d, J = 9.0 Hz, 1 H), 4.24 (q, J = 7.4 Hz, 2 H), 1.33 ppm (t, J = 7.4 Hz, 3 H); ^{13}C NMR (150 MHz, CDCl_3): δ = 169.8, 164.7, 138.9, 133.1, 132.3, 129.1, 127.9, 97.4, 60.5, 14.4 ppm; HRMS (ESI TOF): calcd for $\text{C}_{12}\text{H}_{13}\text{NO}_3\text{Na}^+$ [$M+\text{Na}$] $^+$: 242.0788; found: 242.0782

52: R_f = 0.78 (silica gel, EtOAc/hexanes 1:1); [α] $_D^{25}$ = +38 (CHCl_3 , c = 0.13); IR (film): $\tilde{\nu}_{\max}$ = 3331, 2947, 1715, 1635, 1495, 1378, 1298, 1256, 1195, 1134 cm^{-1} ; ^1H NMR (500 MHz, CDCl_3): δ = 8.41 (br d, J = 11.9 Hz, 1 H), 8.00 (dd, J = 13.8, 11.9 Hz, 1 H), 5.98–5.90 (m, 1 H), 5.62 (d, J = 13.8 Hz, 1 H), 5.33 (d, J = 16.5 Hz, 1 H), 5.23 (d, J = 10.1 Hz, 1 H), 4.65–4.64 (m, 2 H), 4.20 (s, 1 H), 3.71 (d, J = 11.9 Hz, 1 H), 3.32 (d, J = 11.9 Hz, 1 H), 1.52 (s, 3 H), 1.45 (s, 3 H), 1.05 (s, 3 H), 1.00 ppm (s, 3 H); ^{13}C NMR (125 MHz, CDCl_3): δ = 168.1, 166.9, 136.5, 132.5, 118.1, 102.8, 99.7, 77.3, 71.4, 65.0, 33.6, 29.6, 22.0, 19.0, 18.8 ppm; HRMS (ESI TOF): calcd for $\text{C}_{15}\text{H}_{23}\text{NO}_5\text{Na}^+$ [$M+\text{Na}$] $^+$: 320.1468; found: 320.1464

53: [α] $_D^{25}$ = +18 (MeOH, c = 0.08); IR (film): $\tilde{\nu}_{\max}$ = 3317, 2960, 2873, 1655, 1625, 1467, 1402, 1320, 1243, 1108, 1044 cm^{-1} ; ^1H NMR (500 MHz, CD_3OD): δ = 7.37 (d, J = 8.4 Hz, 1 H), 5.18 (br s, 1 H), 4.03 (s, 1 H), 3.48 (d, J = 11.0 Hz, 1 H), 3.39 (d, J = 11.0 Hz, 1 H), 0.93 (s, 3 H), 0.92 ppm (s, 3 H); ^{13}C NMR (125 MHz, CD_3OD): δ = 174.4 (2 C), 133.8, 129.9, 77.0, 70.0, 40.7, 21.4, 20.6 ppm; HRMS (ESI TOF): calcd for $\text{C}_9\text{H}_{14}\text{NO}_5^-$ [$M-\text{H}$] $^-$: 216.0877; found: 216.0875

64: R_f = 0.68 (silica gel, EtOAc/hexanes 1:2); IR (film): $\tilde{\nu}_{\max}$ = 3449, 1570, 1488, 1449, 1262, 1199, 929, 765 cm^{-1} ; ^1H NMR (500 MHz, CDCl_3): δ = 7.43 (dd, J = 8.5, 7.4 Hz, 2 H), 7.36 (t, J = 8.5 Hz, 1 H), 7.27–7.24 (m, 1 H), 7.17 (dd, J = 8.1, 0.8 Hz, 1 H), 7.11–7.09 (m, 2 H), 6.73 ppm (dd, J = 8.8, 0.8 Hz, 1 H); ^{13}C NMR (125 MHz, CDCl_3): δ = 161.5, 154.7, 138.3, 134.2, 130.4, 125.7, 123.5, 120.5, 114.6, 113.3 ppm; HRMS (ESI TOF): calcd for $\text{C}_{13}\text{H}_8\text{ClNOH}^+$ [$M+\text{H}$] $^+$: 230.0367; found: 230.0359

aqueous $\text{Na}_2\text{S}_2\text{O}_3$ (2 mL) and stirred vigorously until the solution became clear. The mixture was poured into Et_2O (15 mL) and the ethereal phase was washed twice with 10% aq. $\text{Na}_2\text{S}_2\text{O}_3$ /aq. NaHCO_3 (1:1 mixture, 15 mL) and brine (15 mL), and then dried (MgSO_4). Removal of the solvent in vacuo afforded the imide, often pure enough (by ^1H NMR spectroscopic analysis) to forgo chromatography. Generation of *N*-acyl vinylogous carbamates and ureas: In a sealed tube the amide (0.1–0.3 mmol) was dissolved in fluorobenzene (0.1 M) and DMP (5.0 equiv) was added. The mixture was heated at 80–85 °C until full consumption of starting material was noted (monitored by TLC analysis). The reaction mixture was then quenched and purified in the same manner as for the preparation of imides described above.

General procedure (amines): The amine (0.1–0.4 mmol) was dissolved in a small amount of CH_2Cl_2 and added dropwise over a period of 5–10 min to a homogeneous mixture of DMP (2.0 equiv) in CH_2Cl_2 to form a 0.15 M solution with respect to the amine. The reaction mixture was stirred at 25 °C until the starting material was consumed (as observed by TLC analysis), at which time the reaction

was quenched with saturated aqueous $\text{Na}_2\text{S}_2\text{O}_3$ (2 mL) and the resulting mixture was stirred vigorously until it became clear. The mixture was then poured into Et_2O (15 mL) and the ethereal phase was washed twice with 10% aq. $\text{Na}_2\text{S}_2\text{O}_3$ /aq. NaHCO_3 (1:1 mixture, 15 mL) and brine (15 mL) and then dried (MgSO_4). Removal of the solvent in vacuo afforded the nitrile, which was purified by silica-gel column chromatography.

Received: May 27, 2005

Published online: August 26, 2005

Keywords: carbamates · hypervalent iodine · imides · nitriles · oxidation

- [1] D. B. Dess, J. C. Martin, *J. Org. Chem.* **1983**, *48*, 4155.
- [2] D. B. Dess, J. C. Martin, *J. Am. Chem. Soc.* **1991**, *113*, 7277.
- [3] V. V. Zhdankin, P. J. Stang, *Chem. Rev.* **2002**, *102*, 2523, and references therein.
- [4] a) K. C. Nicolaou, C. J. N. Mathison, T. Montagnon, *Angew. Chem.* **2003**, *115*, 4211; *Angew. Chem. Int. Ed.* **2003**, *42*, 4077; b) K. C. Nicolaou, C. J. N. Mathison, T. Montagnon, *J. Am. Chem. Soc.* **2004**, *126*, 5192.
- [5] a) K. C. Nicolaou, P. S. Baran, R. Kranich, Y.-L. Zhong, K. Sugita, N. Zou, *Angew. Chem.* **2001**, *113*, 208; *Angew. Chem. Int. Ed.* **2001**, *40*, 202; b) K. C. Nicolaou, K. Sugita, P. S. Baran, Y.-L. Zhong, *Angew. Chem.* **2001**, *113*, 213; *Angew. Chem. Int. Ed.* **2001**, *40*, 207; c) K. C. Nicolaou, Y.-L. Zhong, P. S. Baran, K. Sugita, *Angew. Chem.* **2001**, *113*, 2203; *Angew. Chem. Int. Ed.* **2001**, *40*, 2145; d) K. C. Nicolaou, K. Sugita, P. S. Baran, Y.-L. Zhong, *J. Am. Chem. Soc.* **2002**, *124*, 2221.
- [6] a) K. C. Nicolaou, Y.-L. Zhong, P. S. Baran, *Angew. Chem.* **2000**, *112*, 636; *Angew. Chem. Int. Ed.* **2000**, *39*, 622; b) K. C. Nicolaou, P. S. Baran, Y.-L. Zhong, K. Sugita, *J. Am. Chem. Soc.* **2002**, *124*, 2212.
- [7] Representative procedures highlighting the utility of imides in synthesis include the reported construction of various 3-hydroxypyrroles, 1,3,4-triazines, and multifarious enantioenriched β -substituted imides and esters: a) for 3-hydroxypyrroles, see: W. Flitsch, K. Hampel, M. Hohenhorst, *Tetrahedron Lett.* **1987**, *28*, 4395; b) for 1,3,4-triazines, see, for example: N. Jagerovic, L. Hernandez-Folgado, I. Alkorta, P. Goya, M. Navarro, A. Serrano, F. Rodriguez de Fonseca, M. T. Dannert, A. Alsasua, M. Suardiaz, D. Pascual, M. I. Martin, *J. Med. Chem.* **2004**, *47*, 2939; c) for β -substituted imides and esters, see: C. D. Vanderwal, E. N. Jacobsen, *J. Am. Chem. Soc.* **2004**, *126*, 14724.
- [8] a) H. B. Maruyama, Y. Suhara, J. Suzuki-Watanabe, Y. Maeshima, N. Shimizu, M. Ogura-Hamada, H. Fujimoto, K. Takano, *J. Antibiot.* **1975**, *28*, 636; b) Y. Suhara, H. B. Maruyama, Y. Kotoh, Y. Miyasaka, K. Yokose, H. Shirai, K. Takano, P. Quitt, P. Lanz, *J. Antibiot.* **1975**, *28*, 648.
- [9] K. Krohn, C. Franke, P. G. Jones, H.-J. Aust, S. Draeger, B. Shultz, *Liebigs Ann. Chem.* **1992**, 789.
- [10] J. Thirkettle, E. Alvarez, H. Boyd, M. Brown, E. Diez, J. Hueso, S. Elson, M. Fulston, C. Gershater, M. L. Morata, P. Perez, S. Ready, J. M. Sanchez-Pulles, R. Sheridan, A. Stefanska, S. Warr, *J. Antibiot.* **2000**, *53*, 664.
- [11] a) For the first report of a RuO_4 -based oxidation of an acyclic amide, see: L. M. Berkowitz, P. N. Rylander, *J. Am. Chem. Soc.* **1958**, *80*, 6682; b) for the scope of the reaction with RuO_4 , see: K. Tanaka, S. Yoshifuji, Y. Nitta, *Chem. Pharm. Bull.* **1987**, *35*, 364.
- [12] V. S. Martin, J. M. Palazon, C. M. Rodriguez in *Encyclopedia of Reagents for Organic Synthesis* (Ed.: L. A. Paquette), Wiley, West Sussex, **1995**, p. 4415.
- [13] a) For the role of IBX as a single-electron-transfer oxidant in benzylic oxidations, see: K. C. Nicolaou, P. S. Baran, Y.-L.

- Zhong, *J. Am. Chem. Soc.* **2001**, *123*, 3183; b) See also: K. C. Nicolaou, T. Montagnon, P. S. Baran, Y.-L. Zhong, *J. Am. Chem. Soc.* **2002**, *124*, 2245.
- [14] For a discussion of the thermodynamic preference for the *cis*-isomer in nonpolar solvents and the possibility of *cis*–*trans* interconversion of specific *N*-acyl vinylogous ureas, see: E. M. Suh, Y. Kishi, *J. Am. Chem. Soc.* **1994**, *116*, 11205.
- [15] a) R. E. Moore, G. Bartolini, *J. Am. Chem. Soc.* **1981**, *103*, 2491; b) D. Uemura, K. Ueda, Y. Hirata, H. Naoki, T. Iwashita, *Tetrahedron Lett.* **1981**, *22*, 2781.
- [16] S. Koshino, H. Koshino, N. Matsuura, K. Kobinata, R. Onose, K. Isono, H. Osada, *J. Antibiot.* **1995**, *48*, 185.
- [17] Y. Sugie, K. A. Dekker, H. Hirai, T. Ichiba, M. Ishiguro, Y. Shiomi, A. Sugiura, L. Brennan, J. Duignan, L. H. Huang, J. Sutcliffe, Y. Kojima, *J. Antibiot.* **2001**, *54*, 1060.
- [18] J. Schroer, M. Sanner, J.-L. Reymond, R. A. Lerner, *J. Org. Chem.* **1997**, *62*, 3220.
- [19] C. Han, R. Shen, S. Su, J. A. Porco, Jr., *Org. Lett.* **2004**, *6*, 27.
- [20] S. S. Flack, J. D. Kilburn, *Tetrahedron Lett.* **1995**, *36*, 3409.
- [21] F. A. Carey, R. J. Sundberg, *Advanced Organic Chemistry, Part B*, 4th ed., Kluwer Academic/Plenum, New York, **2001**, p. 965.
- [22] R. M. Moriarty, R. K. Vaid, M. P. Duncan, M. Ochiai, M. Inenaga, Y. Nagao, *Tetrahedron Lett.* **1988**, *29*, 6913.

Porous Materials

DOI: 10.1002/anie.200501471

Selective Fabrication of Ordered Bimetallic Nanostructures with Hierarchical Porosity**

Lehui Lu, Richard Capek, Andreas Kornowski,
Nikolai Gaponik, and Alexander Eychmüller*

There has recently been intensive effort to develop porous metallic materials because of their promising applications in catalysis, separation technology, sensors, and fuel cells. The success of these applications strongly relies on the availability of porous metallic materials with specific pore sizes and structures. In the quest to fabricate porous metallic materials with desired pore sizes and structures, attempts have been

made to use templates in a replication process.^[1–6] For example, anodic alumina^[1] and lyotropic liquid crystals^[2] were used as templates to fabricate mesoporous (voids < 50 nm) metal films with cylindrical and parallel pores. It was also shown that techniques involving colloidal templates could be used to create ordered macroporous (voids > 50 nm) metal films.^[3–6] The latter method is attractive because of its pore-size tuneability and the ordered structure it produces. A critical issue in using this method is how to controllably fill the interstitial space of the colloidal templates with a desired composition. In previous work,^[3–6] the use of this method invariably led to a complete infiltration of the interstitial space with different materials, which, to some extent, limits the application of such a method to produce porous metal materials with novel structures.

Porous hollow metallic spheres often exhibit catalytic activities different from their solid counterparts and have the advantages of low density and the use of less material.^[7,8] For example, Hyeon and co-workers^[7] showed that hollow Pd spheres possess excellent catalytic activity in Suzuki reactions and can be recycled without loss of the catalytic activity. The extension of such a structure to bimetallic nanomaterials is of great importance since the properties of one metal are usually improved by the addition of another.^[9,10] Nevertheless, we are not aware of publications on the generation of such materials with ordered structures that may lead to the formation of hierarchical porosity.

Herein we describe how two different kinds of ordered bimetallic nanostructures with hierarchical porosity, namely a macroporous nanostructure and a nanostructure consisting of hollow spheres, can selectively and conveniently be fabricated by a general template technique on silicon wafers and glass substrates.

The starting material for the template is a colloidal suspension of highly monodisperse silica spheres in ethanol. The silica spheres were prepared by the improved Stöber growing procedure,^[11,12] and subsequently modified with 3-aminopropyltrimethoxysilane (APTMS). The closely packed colloidal template was assembled on silicon wafers or glass substrates that were placed vertically in a slowly evaporating dispersion of APTMS-modified silica spheres in ethanol, as described by Jiang et al.^[13] The colloidal template was then immersed in an aqueous solution of gold nanoparticles having an average diameter of 3 nm. Since the cross-sectional area of the smallest channel inside the colloidal template is much larger than the gold nanoparticles, the nanoparticles can flow freely throughout the colloidal template. Different kinds of nanostructures can be prepared by varying the immersion times and concentrations of the gold solution (see below and the Experimental Section). Finally, the dried colloidal template with the gold nanoparticles was dipped into a plating solution for coating with platinum. During the plating process, the small gold nanoparticles can serve as seeds to accelerate the reduction of the PtCl_6^{2-} ions by ascorbic acid. Removing the silica template with 4% HF solution gave black self-supporting flakes. Shrinkage of the pores was avoided since the silica template was removed at room temperature.

It is very important to generate high-quality templates for this template-directed method since the quality of any

[*] Dr. L. Lu, R. Capek, A. Kornowski, Dr. N. Gaponik,^[†]
Dr. A. Eychmüller^[†]
University of Hamburg
Institute of Physical Chemistry
Grindelallee 117, 20146 Hamburg (Germany)
Fax: (+49) 351-4633-7164
E-mail: alexander.eychmueller@chemie.tu-dresden.de

[†] Current address:
Institute of Physical Chemistry and Electrochemistry
Technical University of Dresden
Bergstrasse 66b, 01062 Dresden (Germany)

[**] We would like to thank Almut Barck for the XRD characterization. We also thank the Alexander von Humboldt Foundation (the DIP D-3.1. "Functional Nanoparticle Architectures") and the EU NoE "PHOREMOST" for financial support.

material formed by this method depends sensitively on the ordering and the properties of the starting template. Figure 1a shows a typical scanning electron microscopy (SEM) image of the top view of one of the silica colloidal templates. The SEM image reveals that the 267-nm silica spheres are

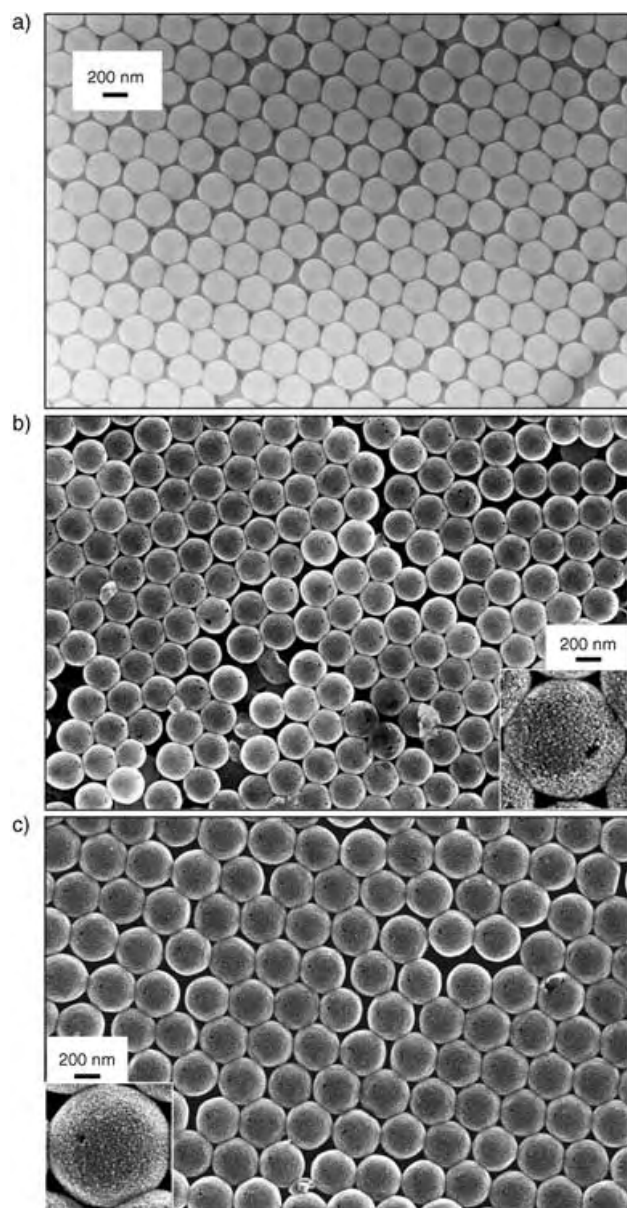


Figure 1. a) SEM image of a template consisting of 267-nm silica particles, and SEM images of typical ordered hollow nanostructures formed using b) 267-nm and c) 300-nm silica colloidal crystals as templates, respectively. The insets show the corresponding high-magnification images.

organized in a close-packed arrangement with long-range hexagonal order. These high-quality colloidal crystals can be used as templates for the fabrication of ordered structures constructed from hollow metallic spheres. The resulting materials exhibit a tunable hollow volume since the starting template can be formed from silica spheres with different sizes. Figure 1b,c show typical SEM images (top views) of

hollow metallic nanostructured materials made by using 267-nm and 300-nm silica colloidal crystals as templates, respectively. It is evident from Figure 1b,c that after removal of the template, the ordering feature—the original porous structure of the starting template—and the spherical shape of the silica spheres have clearly been retained. The hollow structure character of these materials is anticipated by inspection of the broken spheres seen in Figure 1b,c. A closer look at Figure 1b,c reveals another interesting feature, namely the existence of a hole with an average diameter of about 20 nm in almost every hollow sphere. These holes are arranged in order and the distances between neighboring holes are roughly equal to the center-to-center distances of the hollow metallic spheres. The detailed mechanism for the formation for this structural feature will be investigated further since it may open up a new route to the design of novel nanostructured materials. Higher magnification SEM images in Figure 1b,c (insets) show that these hollow spheres consist of small nanoparticles (average diameter below 10 nm), which are interconnected to form relatively uniform porous hollow metallic nanoshells. The average nanoshell thickness of the hollow metal spheres in Figure 1b and c is estimated to be about 20 nm and about 45 nm, respectively. The nanoparticle framework of the as-prepared materials provides yet another level of porosity which gives the structure a very high surface area: the size of the small pores and the overall surface area are determined by the size of the Au/Pt nanoparticles. Nanostructured materials with such controlled hierarchical porosity may be particularly suitable for catalytic applications.

Energy-dispersive X-ray analysis (EDX) is a technique that enables the elemental composition of a small selected area of the sample to be identified with a sensitivity of about 1 % for elements heavier than beryllium. Figure 2a shows an EDX analysis of the hollow nanostructures shown in Figure 1b before (left) and after removal (right) of the SiO_2 template as an example. The EDX analysis shows strong Au and Pt peaks from the hollow nanostructures. The reasonably strong O peak present before removal stems from the SiO_2 template. The Si peak in both Figures originates most probably from the silicon wafer. The appearance of the remaining very weak O peak after the removal of the template can be attributed to the reduction reagents (citrate ions or ascorbic acid); this proposal is further supported by the presence of the C peaks (not shown). On the basis of the above EDX analysis it is reasonable to conclude that the silica template is completely removed and, thus, ordered hollow Au/Pt nanostructures are formed. Figure 2b presents an X-ray diffraction (XRD) pattern of the sample shown in Figure 1b. Broad diffraction peaks corresponding to metallic Au and Pt are observed which are indicative of the presence of nanosized Au/Pt particles (see the bulk reflexes, bottom of Figure 2b).

Ordered macroporous metallic nanostructures are another kind of important porous material. We found that the current method is also applicable to the formation of such structures if the experimental conditions are suitably controlled (see Experimental Section, Method B). Figure 3 shows a typical SEM image (top view) of the macroporous structure

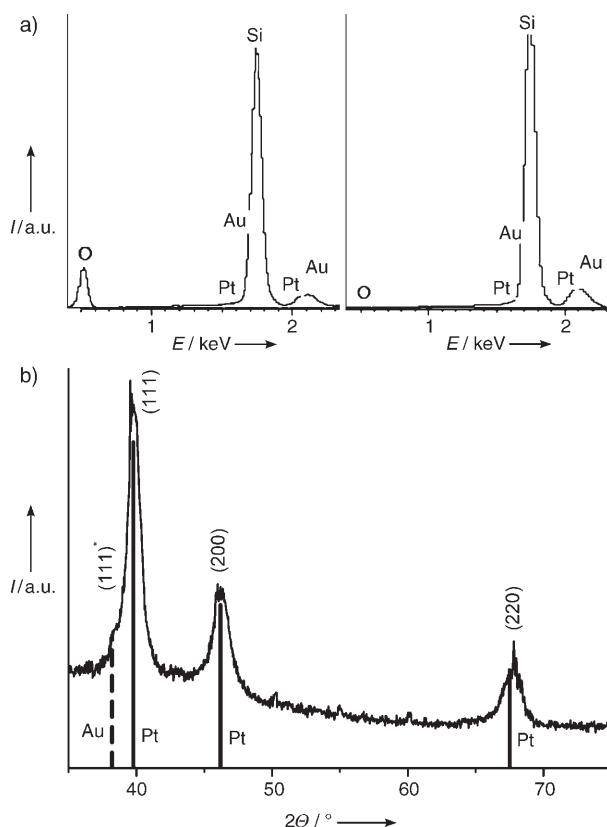


Figure 2. a) EDX analysis of the ordered Au/Pt nanostructures shown in Figure 1 b before (left) and after (right) HF treatment, and b) XRD pattern of the hollow nanostructure from Figure 1 b.

formed by this method. It is evident that the resulting material exhibits relatively uniform porosity with hexagonal close packing, while the pores match the size of the starting silica, thus indicating that negligible shrinkage of the metallic structure occurs.^[3a] The ordered regions can extend to several hundreds of micrometers. The small nanoparticles around the large pores in the original interstitial space can be clearly observed in the corresponding higher magnification images (Figure 3, inset). EDX and XRD analysis show that the as-prepared materials consist of nanosized metallic Pt and Au.

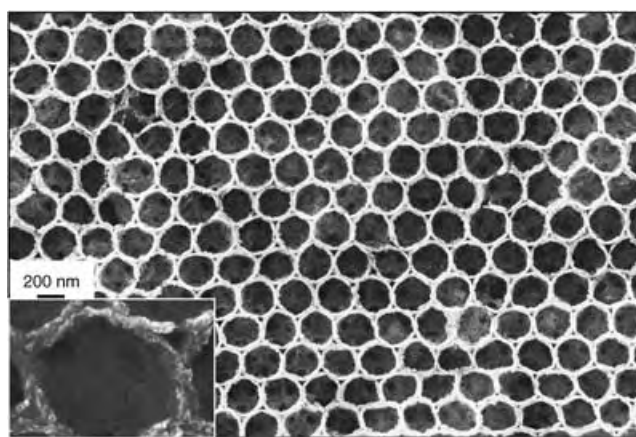


Figure 3. Typical SEM image of an ordered macroporous Au/Pt nanostructure. The inset shows a corresponding high-magnification image.

The success of the current method for selective fabrication of two different kinds of ordered bimetallic nanostructures with hierarchical porosity is rationalized as follows. According to previous reports,^[3] in which the colloidal template was immersed in an aqueous solution of gold nanoparticles, small gold nanoparticles were deposited in the interstices of the colloidal template by an infiltration process to form a mesoporous structure around the silica spheres. Since the porosity allowed the solvent to flow freely through the structure, the pores can be completely filled with gold nanoparticles. However, the situation is different in the present study. Modification of the silica spheres with APTMS results in the APTMS molecules bonding to the surface of the silica spheres with their NH_2 groups directed outwards. Immersion of this modified colloidal template leads to an intense coverage of gold nanoparticles on the surface of the silica spheres through the interaction between the negatively charged gold nanoparticles and the positively charged NH_2 groups (see also ref. [14]). If the concentration of the gold nanoparticles is relatively low ($[\text{Au}] = 0.06 \text{ mM}$) and the immersion time in the gold solution is comparatively short (8 h), the assembly of the gold nanoparticles on the surface of the silica spheres predominates. A small quantity of residual gold nanoparticles in the interstices of the colloidal template can be removed by rinsing with deionized water (and/or by deposition on the surface of the silica spheres during the drying process). This is followed by a 16-minute electroless deposition of Pt only on the surface of the silica spheres (Method A). As a result, the removal of the template leads to the formation of ordered porous Au/Pt nanostructures constructed from hollow spheres. In contrast, if the concentration of the gold nanoparticles is higher ($[\text{Au}] = 0.3 \text{ mM}$) and the immersion time in the gold solution is long (16 h), besides the assembly of gold nanoparticles on the surface of the silica spheres, the relatively large amount of small gold nanoparticles in the interstices of the colloidal template in combination with those on the surface of the silica spheres associate into a larger, mesoporous structure. The following 16-minute Pt deposition leads to almost complete infiltration of the pores of the colloidal template, and macroporous Au/Pt nanostructures are obtained after removal of the template (Method B).

In a second set of experiments, monodisperse but non-ordered APTMS-modified silica spheres were used as templates and the same experimental procedures were performed. We found that only hollow porous Au/Pt nanostructures were obtained by both Methods A and B (Figure 4a). As evidenced in higher magnification images, the shell of the hollow spheres is built-up by stringlike, structured aggregates consisting of small Au/Pt nanoparticles which results in many pores with an average diameter of 32 nm. Such nanostructured materials can be particularly desirable for application in catalytic nanoreactors. This result further strengthens our above explanation: Since the templates are non-ordered and the silica spheres within the template are loosely arranged, the assembly of the gold nanoparticles and the following Pt deposition only occurred on the surface of the silica spheres. As a result, only hollow nanostructures can be formed under Methods A or B. Interestingly, porous

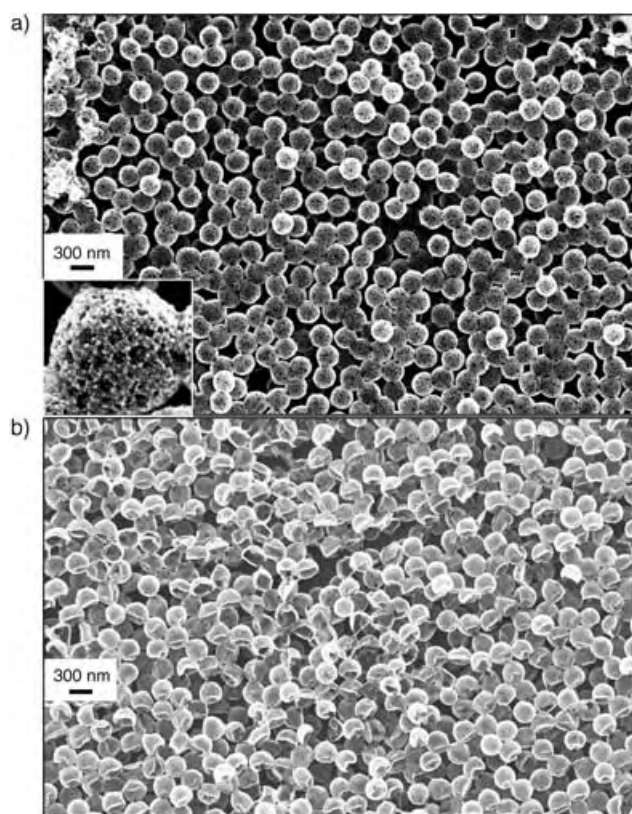


Figure 4. SEM images of a) hollow spheres prepared by Method B, and b) hollow hemispheres prepared by Method A with a concentration of gold of 0.06 mM, an immersion time in the gold solution of 10 h, and a Pt plating time of 12 min. Non-ordered APTMS-modified silica spheres on silicon wafers were used as templates.

hollow Au/Pt hemispheres can also be fabricated under appropriate experimental conditions (such as, for example, an increase in the Au concentration compared to Method A; Figure 4b), which may provide an alternative method for the synthesis of such materials.

In summary, ordered Au/Pt nanostructures with hierarchical porosity, such as macroporous nanostructures and nanostructures constructed from hollow spheres, can be selectively and conveniently prepared by a general template technique on silicon wafers and glass substrates. A possible explanation for the selective fabrication of the above-mentioned nanostructures is given. Furthermore, since protocols exist for the deposition of many other metals, such as Cu,^[15] Pd,^[16] and Ag,^[17] this method could be successfully extended to other bimetallic systems including Au/Cu, Au/Pd, and Au/Ag (see Supporting Information). These ordered metallic nanostructures with hierarchical porosity could be useful in industrial applications including catalytic nano-reactors (see Supporting Information), sensors, porous electrodes, and fuel cells.

Experimental Section

3-nm gold nanoparticles:^[18] A 1% solution of H₂AuCl₄ (1 mL) was added to water (90 mL) at room temperature. After stirring the mixture for 1 min, 1% sodium citrate solution (2 mL) was added. Freshly prepared 0.075% NaBH₄ (in 1% sodium citrate solution;

1 mL) was added 1 min later. The resulting solution was stirred for an additional 5 min and kept at about 4 °C until use.

Synthesis and modification of the silica spheres: Equal volumes of a solution containing absolute ethanol (50 mL) and 0.2 M tetraethyl orthosilicate (TEOS), and another containing absolute ethanol (50 mL), water (28 mL), and ammonia (28–30%; 4 mL) to give a total volume of about 100 mL were mixed rapidly. The reaction was allowed to continue for 6 h at room temperature. APTMS (100 µL) was then added and the mixed solution was stirred for an additional 12 h. The resultant APTMS-modified silica spheres were cleaned by consecutive centrifuging, decanting, and redispersing in ethanol by sonication (five times). Removal of aggregates and smaller spheres was performed by fractionation by removing the upper and the lower fractions (three times).

Assembly of the silica template and introduction of gold nanoparticles and deposition of platinum: The APTMS-modified silica spheres were assembled onto a silicon wafer that was placed vertically in a slowly evaporating dispersion of silica spheres in ethanol for 2 days. The dried colloidal template was then immersed in solutions of the gold nanoparticles at different concentrations for different times. The dried colloidal templates with the gold nanoparticles were dipped into a plating solution (50 mL) that contained 10% H₂PtCl₆ (1 mL) and 0.1 M ascorbic acid (3 mL) for different times (Method A: [Au] = 0.06 mM, immersion time in the gold solution = 8 h, Pt plating time = 16 min; Method B: [Au] = 0.3 mM, immersion time in gold solution = 16 h, Pt plating time = 16 min). All samples were placed into deionized water and were dried in air.

Removal of the colloidal template: All samples were dipped into 4% HF solution for 5 min. The metallic film could then be peeled off the silica wafer. This procedure was repeated to completely remove the silica spheres.

Characterization: SEM images were obtained with a Leo 1550 supra instrument equipped with an EDX Si-detector (Oxford Instruments). All structures were characterized by XRD (Philips; X'pert MPD).

Received: April 28, 2005

Published online: August 24, 2005

Keywords: gold · nanostructures · platinum · porous materials · template synthesis

- [1] H. Masuda, K. Fukuda, *Science* **1995**, 268, 1466–1468.
- [2] G. S. Attard, P. N. Bartlett, N. R. B. Coleman, J. M. Elliott, J. R. Owen, J. H. Wang, *Science* **1997**, 278, 838–848.
- [3] a) O. D. Velev, P. M. Tessier, A. M. Lenhoff, E. W. Kaler, *Nature* **1999**, 401, 548; b) P. M. Tessier, O. D. Velev, A. T. Kalambur, J. F. Rabolt, A. M. Lenhoff, E. W. Kaler, *J. Am. Chem. Soc.* **2000**, 122, 9554–9555; c) P. M. Tessier, O. D. Velev, A. T. Kalambur, A. M. Lenhoff, J. F. Rabolt, E. W. Kaler, *Adv. Mater.* **2001**, 13, 396–400.
- [4] a) P. Jiang, J. F. Bertone, V. L. Colvin, *Science* **2001**, 291, 453–457; b) P. Jiang, J. Cizeron, J. F. Bertone, V. L. Colvin, *J. Am. Chem. Soc.* **1999**, 121, 7957–7958; c) K. M. Kulinowski, P. Jiang, H. Harsha, V. L. Colvin, *Adv. Mater.* **2000**, 12, 833–838.
- [5] a) H. W. Yan, C. F. Blanford, B. T. Holland, M. Parent, W. H. Smyrl, A. Stein, *Adv. Mater.* **1999**, 11, 1003–1006; b) H. W. Yan, C. F. Blanford, J. C. Lytle, C. B. Carter, W. H. Smyrl, A. Stein, *Chem. Mater.* **2001**, 13, 4314–4321; c) H. W. Yan, C. F. Blanford, W. H. Smyrl, A. Stein, *Chem. Commun.* **2000**, 1477–1478.
- [6] a) J. E. G. J. Wijnhoven, S. J. M. Zevenhuizen, M. A. Hendriks, D. Vanmaekelbergh, J. J. Kelly, W. L. Vos, *Adv. Mater.* **2000**, 12, 888–890; b) Q. Luo, Z. Liu, L. Li, S. H. Xie, J. L. Kong, D. Y. Zhao, *Adv. Mater.* **2001**, 13, 286–289; c) Z. Liang, A. S. Susha, F. Caruso, *Adv. Mater.* **2002**, 14, 1160–1164; d) Z. Liang, A. S. Susha, F. Caruso, *Chem. Mater.* **2003**, 15, 3176–3183.

- [7] S. W. Kim, M. Kim, W. Y. Lee, T. Hyeon, *J. Am. Chem. Soc.* **2002**, *124*, 7642–7643.
- [8] H. P. Liang, H. M. Zhang, J. S. Hu, Y. G. Guo, L. J. Wan, C. L. Bai, *Angew. Chem.* **2004**, *116*, 1566–1569; *Angew. Chem. Int. Ed.* **2004**, *43*, 1540–1543.
- [9] S. U. Son, Y. Jiang, J. Park, H. B. Na, H. M. Park, H. J. Yun, J. Lee, T. Hyeon, *J. Am. Chem. Soc.* **2004**, *126*, 5026–5027.
- [10] R. W. Scott, A. K. Datye, R. M. Crooks, *J. Am. Chem. Soc.* **2003**, *125*, 3708–3709.
- [11] W. Wang, B. H. Gu, L. Y. Liang, W. Hamilton, *J. Phys. Chem. B* **2003**, *107*, 3400–3404.
- [12] W. Stöber, A. Fink, E. Bohn, *J. Colloid Interface Sci.* **1968**, *26*, 62–69.
- [13] P. Jiang, J. F. Bertone, K. S. Kwang, V. L. Colvin, *Chem. Mater.* **1999**, *11*, 2132–2140.
- [14] S. L. Westcott, S. J. Oldenburg, T. R. Lee, N. J. Halas, *Langmuir* **1998**, *14*, 5396–5401.
- [15] E. Kim, Y. N. Xia, G. M. Whitesides, *J. Am. Chem. Soc.* **1996**, *118*, 5722–5731.
- [16] L. H. Lu, H. S. Wang, S. Q. Xi, H. J. Zhang, *J. Mater. Chem.* **2002**, *12*, 156–158.
- [17] Z. Chen, P. Zhan, Z. L. Wang, J. H. Zhang, W. Y. Zhang, N. B. Ming, C. T. Chan, P. Shen, *Adv. Mater.* **2004**, *16*, 417–422.
- [18] K. R. Brown, D. G. Walter, M. J. Natan, *Chem. Mater.* **2000**, *12*, 306–313.

catalytic metal-mediated conversions of organonitriles into important organic compounds are currently being developed.^[1,3] In contrast to other unsaturated molecules, such as alkynes, alkenes, CO, or RNC, nitriles insert less easily into metal–carbon bonds. Most of the known examples involve nitriles RCN and early-transition or actinide metal organo-complexes [M]–R' to give azaalkenylidene complexes [M]–N=CRR' upon insertion.^[4,5] In a few cases, the azaalkenylidene ligand in [M]–N=C(R)CH₂R' rearranges by a 1,3-H shift to the corresponding enamide [M]–NHC(R)=CHR'.^[5] Some special cases involve low-valent transition-metal organocomplexes [M]–CH₂C(O)R' that react at high temperature with a nitrile RCN and PPh₃ to give a κ^2 -C,O-cyclometalated imino complex [M]–NHC(R)CHC(O)R'.^[6] Another unusual case is the reaction between the extremely reactive Fe₂Mes₄ (Mes = 2,4,6-Me₃C₆H₂) and PhCN to give the dimer [(PhCN)–(Mes)Fe]₂(μ -N=CPhMes)₂.^[7] Herein, we report a new type of nitrile insertion that also represents the first example of the insertion of a nitrile into a C–M bond (in which M is a late-transition element).

[Pd{2-(OH)C₆H₄}I](tmeda)] (tmeda = *N,N,N',N'*-tetramethylethylenediamine) reacts at room temperature with excess RCN and 1 equivalent of TlOTf (OTf = CF₃SO₃) to give [Pd{1-O-2-[C(R)=NH]C₆H₄– κ^2 -O,N}(tmeda)]OTf [R = Me (**1**), C₆F₅ (**2**), CH₂=CH (**3**)] (Scheme 1). As many known

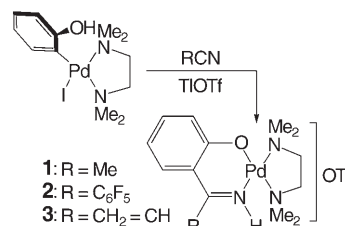
Insertion Reactions

DOI: 10.1002/anie.200501202

Reactivity of *ortho*-Palladated Phenol Derivatives with Unsaturated Molecules: Insertion of Nitriles into a Late-Transition-Metal–Carbon Bond**

José Vicente,* José Antonio Abad,
María-José López-Sáez, and Peter G. Jones

Nitriles have a very rich coordination chemistry because they are activated by some metals towards nucleophilic or electrophilic attack.^[1,2] Based on this reactivity, stoichiometric and



Scheme 1. Reaction of [Pd{2-(OH)C₆H₄}I](tmeda)], excess nitrile, and TlOTf (1 equiv).

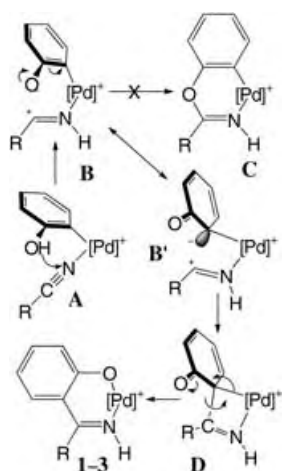
stable alkyl- and aryl-palladium complexes contain a *cis*-coordinated nitrile ligand,^[8] we can assume that the *ortho*-hydroxy group plays a crucial role in the process and that after substitution of the iodo ligand by RCN (**A** in Scheme 2), the following step **B** is the protonation of the nitrogen atom of the nitrile. Unexpectedly, however, the usual nucleophilic attack at the nitrile carbon atom by the oxygen function^[1,2] to give the addition product **C** does not occur. In our opinion, the resonance form **B'** contributes significantly to the electronic structure of the protonated intermediate because of the electron-withdrawing character of the positively charged metal center and the electron-releasing nature of the negatively charged oxygen substituent. Both favor the location of a partial negative charge on the *ipso* carbon atom of the aryl ligand. Therefore, our results can be explained through the nucleophilic attack at the nitrile carbon by the *ipso* carbon atom, probably via the four-membered metallacycle **D**. Consequently, this insertion process differs from those reported previously with other unsaturated molecules in the role played by the *ortho*-hydroxy group, first in the proto-

[*] Prof. Dr. J. Vicente, Dr. J. A. Abad, M.-J. López-Sáez
Grupo de Química Organometálica
Departamento de Química Inorgánica
Facultad de Química, Universidad de Murcia
Apto. 4021, 30071 Murcia (Spain)
Fax: (+34) 968-364-143
E-mail: jvs1@um.es

Prof. Dr. P. G. Jones
Institut für Anorganische und Analytische Chemie
Technische Universität Braunschweig
Postfach 3329, 38023 Braunschweig (Germany)

[**] This work was supported by the Ministerio de Educación y Ciencia (MEC, Spain) and the FEDER (EU) by contract CTQ2004-05396. M.-J.L.S. is grateful to the MEC for a grant.

Supporting information for this article is available on the WWW under <http://www.angewandte.org> or from the author.



Scheme 2. Proposed mechanism for the reaction of $[\text{Pd}\{2\text{-(OH)C}_6\text{H}_4\}\text{I}(\text{tmeda})]$ with nitriles.

nation of the nitrile ligand and then in the generation of a partial negative charge on the *ipso* carbon atom of the aryl ligand.

Recently, the reaction of acrylonitrile with $[\text{PdMe}(\text{NMe}_2\text{Ph})\text{L}_2]^+$, $[\text{PdMe}(\text{L}_2)]_2(\mu\text{-Cl})^+$ (L_2 = various bidentate N-donor ligands),^[9] and $[\text{Pd}(\text{O,N})\text{Me}(\text{NCMe})]$ (O,N = Grubbs salicylaldiminato and related diazene ligands)^[10] were reported to give α -cyanopropyl derivatives, that is, the insertion products of the olefinic part of the nitrile into the Pd–Me bond. In all cases, the first step was, as we propose in our case, the N-coordination of the nitrile but the difference from our result (complex **3**) proves to be the crucial role played by the hydroxy group in our reactions. We have reported that CO and olefins insert into the C–Pd bond of $[\text{Pd}\{2\text{-(OH)C}_6\text{H}_4\}\text{I}(\text{tmeda})]$ without intervention of the hydroxy group.^[11]

The insertion of a nitrile group into an aryl–Pd bond has been postulated as a step in the mechanism of the synthesis of aryl ketones by the Pd-catalyzed reaction of arenes with nitriles at 75–100 °C.^[12] The proposed subsequent step is the protonation of the resulting imido complex to give an imine. Our results suggest that these two steps could occur in the reverse order.

Complexes similar to **1–3** were prepared by the reaction of 1) $[\text{Ru}(\text{L}_2)_2(\text{CO}_3)]$ (L_2 = bpy (2,2'-bipyridyl), phen (1,10-phenanthroline)) with $p\text{-}\{\text{CH}_2\text{N}=\text{C}(\text{Me})(2\text{-OHCH}_2\text{C}_6\text{H}_4)\}_2\text{C}_6\text{H}_4$,^[13] 2) $[\text{Ru}(\text{PPh}_3)_3\text{Cl}_2]$ with oximes of salicylaldehyde, 2-hydroxyacetophenone, or 2-hydroxynaphthylaldehyde,^[14] and 3) aqueous ammonia, 2-hydroxy-4-methoxyacetophenone, and copper(II) salts.^[15] Therefore, in the known complexes the main skeleton of the ligand is preformed in the organic reagent. Complexes **1–3** contain ligands of the same family as that present in Grubbs nickel catalysts.^[16]

The crystal structures of the three complexes were solved by X-ray diffraction studies (Figures 1–3).^[17] They show a distorted square-planar geometry at the palladium center, with normal bond lengths and angles. The chelate ring involving N1 and O1 is essentially planar in **1** but becomes less planar for **2** and **3** (mean deviations 0.03, 0.08, 0.11 Å).

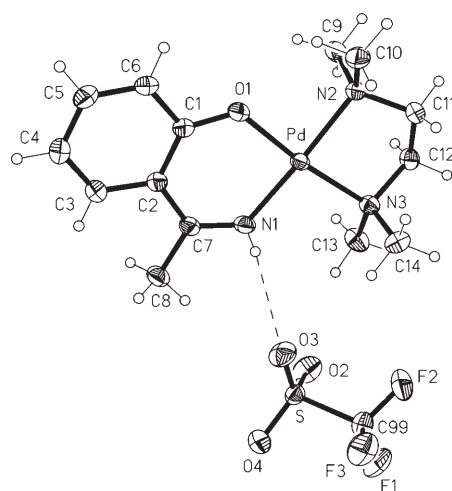


Figure 1. Thermal ellipsoid plot (50% probability) of **1**. Selected bond lengths [Å] and angles [°]: Pd–O1 1.9655(14), Pd–N1 1.9800(16), Pd–N2 2.0685(16), Pd–N3 2.0710(16), N1–C7 1.297(3), O1–C1 1.313(2); O1–Pd–N1 91.58(6), O1–Pd–N2 87.55(6), N1–Pd–N3 95.55(7), N2–Pd–N3 85.62(6), C7–N1–Pd 128.74(14), C1–O1–Pd 126.31(12), N1–C7–C2 123.24(17), N1–C7–C8 117.75(18), C2–C7–C8 118.95(17).

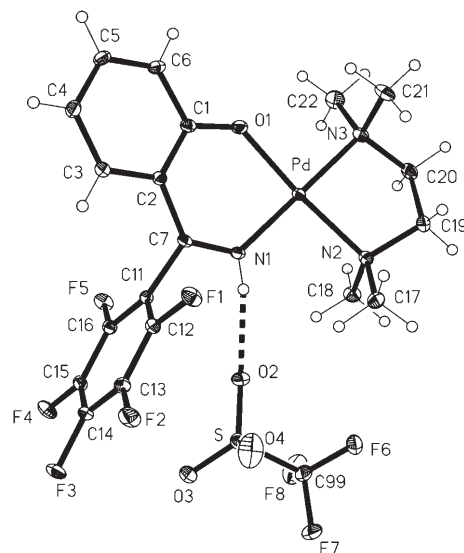


Figure 2. Thermal ellipsoid plot (30% probability) of **2**. Selected bond lengths [Å] and angles [°]: Pd–N1 1.9769(13), Pd–O1 1.9804(12), Pd–N2 2.0636(15), Pd–N3 2.0698(14), O1–C1 1.308(2), N1–C7 1.288(2); N1–Pd–O1 90.91(5), N1–Pd–N2 94.21(6), O1–Pd–N3 89.00(5), N2–Pd–N3 85.88(6), C1–O1–Pd 125.59(10), C7–N1–Pd 127.26(11), N1–C7–C2 125.08(15), N1–C7–C11 115.63(14), C2–C7–C11 119.29(14).

Cation/anion $\text{N-H}\cdots\text{O}(\text{O}_2)\text{SCF}_3$ hydrogen bonds are observed.

In conclusion, we have reported the first examples of the insertion of nitriles into a late-transition-metal–carbon bond. The process involves the insertion of an alkyl (Me), aryl (C_6F_5), or vinyl nitrile into an aryl–palladium bond. The insertion is assisted by the protonation of the nitrile nitrogen atom by the *ortho*-hydroxy group present in the aryl ligand and thus represents a new type of insertion reaction.

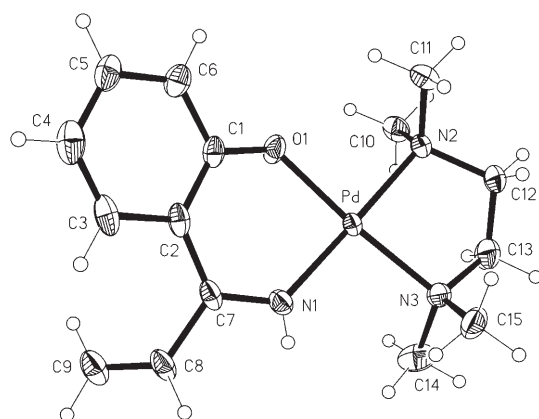


Figure 3. Thermal ellipsoid plot (30% probability) of **3**. The anion has been omitted. Selected bond lengths [Å] and angles [°]: Pd–O1 1.966(2), Pd–N1 1.983(2), Pd–N3 2.054(2), Pd–N2 2.060(2), O1–C1 1.319(3), N1–C7 1.287(4), C8–C9 1.310(4); O1–Pd–N1 90.11(11), N1–Pd–N3 95.10(11), O1–Pd–N2 88.65(9), N3–Pd–N2 86.12(10), C1–O1–Pd 123.44(18), C7–N1–Pd 128.7(2), N1–C7–C2 121.4(3), N1–C7–C8 116.8(3), C2–C7–C8 121.8(3).

Preliminary results allow us to state that the process also occurs with other alkyl and aryl nitriles.

Experimental Section

General procedure: The nitrile (1.15 mmol) and TiOTf (81 mg, 0.23 mmol) was added to a solution of [Pd{2-(OH)C₆H₄}I(tmeda)]^[11] (100 mg, 0.23 mmol) in CH₂Cl₂ (15 mL). The resulting mixture was stirred for 4 h at room temperature, the suspension was filtered over celite, the yellow solution was concentrated (3 mL), and Et₂O (10 mL) was added, which resulted in the precipitation of a solid. The precipitate was filtered, washed with Et₂O (3 × 5 mL), and dried to give the corresponding complex as a yellow solid.

1: Yield: 90 mg, 78%; m.p. 164 °C; $\Lambda_M = 143 \Omega^{-1} \text{cm}^2 \text{mol}^{-1}$. IR: $\tilde{\nu} = 3275 \nu(\text{NH})$, $1605 \text{ cm}^{-1} \nu(\text{C}=\text{N})$; ¹H NMR (300 MHz, CDCl₃): $\delta = 8.71$ (s, 1H; NH), 7.47 (dd, 1H, ³J_{HH} = 8.3 Hz, ⁴J_{HH} = 1.5 Hz; C₆H₄), 7.27 (ddd, 1H, ³J_{HH} = 6.9 Hz, ³J_{HH} = 8.4 Hz, ⁴J_{HH} = 1.6 Hz; C₆H₄), 6.91 (dd, 1H, ³J_{HH} = 8.4 Hz, ⁴J_{HH} = 1 Hz; C₆H₄), 6.64 (ddd, 1H, ³J_{HH} = 6.9 Hz, ³J_{HH} = 8.1 Hz, ⁴J_{HH} = 1.6 Hz; C₆H₄), 2.92 (s, 6H; Me (tmeda)), 2.85 (s, 4H; CH₂), 2.74 (s, 6H; Me (tmeda)), 2.68 ppm (s, 3H; Me (MeCN)); ¹³C{¹H} NMR (100 MHz, CDCl₃): $\delta = 172.11$ (C), 163.24 (C), 134.30 (CH), 130.93 (CH), 121.04 (CH), 120.92 (C), 115.93 (CH), 63.30 (CH₂), 60.39 (CH₂), 50.92 (Me (tmeda)), 48.99 (Me (tmeda)), 24.53 ppm (Me (MeCN)); elemental analysis: calcd for C₁₅H₂₄N₃O₄SPd: C 35.62, H 4.78, N 8.31, S 6.34; found: C 35.31, H 4.67, N 8.21, S 6.09; single crystals were grown by slow diffusion of *n*-hexane into a solution of **1** in CH₂Cl₂.

2: Yield: 125 mg, 83%; m.p. 218 °C (decomp.); $\Lambda_M = 125 \Omega^{-1} \text{cm}^2 \text{mol}^{-1}$; IR: $\tilde{\nu} = 3193 \nu(\text{NH})$, $1601 \text{ cm}^{-1} \nu(\text{C}=\text{N})$; ¹H NMR (400 MHz, [D₆]acetone): $\delta = 9.75$ (s, 1H; NH), 7.39 (ddd, 1H, ³J_{HH} = 6.9 Hz, ³J_{HH} = 8.6 Hz, ⁴J_{HH} = 1.7 Hz; C₆H₄), 7.11 (dd, 1H, ³J_{HH} = 8.3 Hz, ⁴J_{HH} = 1 Hz; C₆H₄), 7.04 (dd, 1H, ³J_{HH} = 8.6 Hz, ⁴J_{HH} = 1 Hz; C₆H₄), 6.58 (ddd, 1H, ³J_{HH} = 7 Hz, ³J_{HH} = 8.30 Hz, ⁴J_{HH} = 1.1 Hz; C₆H₄), 3.14 (s, 4H; CH₂), 2.96 (s, 6H; Me), 2.91 ppm (s, 6H; Me); ¹³C{¹H} NMR (100 MHz, [D₆]acetone): $\delta = 166.65$ (C), 161.16 (C), 136.80 (CH), 133.27 (CH), 122.64 (CH), 120.70 (C), 117.15 (CH), 64.15 (CH₂), 61.45 (CH₂), 51.31 (Me), 49.67 ppm (Me); elemental analysis: calcd for C₂₀H₂₁N₃O₄SPd: C 36.52, H 3.22, N 6.39, S 4.87; found: C 36.41, H 3.20, N 6.43, S 4.80; single crystals were grown by slow diffusion of *n*-hexane into a solution of **2** in acetone.

3: Yield: 100 mg, 84%; m.p. 169 °C (decomp.); $\Lambda_M = 100 \Omega^{-1} \text{cm}^2 \text{mol}^{-1}$; IR: $\tilde{\nu} = 3293 \nu(\text{NH})$, $1603 \text{ cm}^{-1} \nu(\text{C}=\text{N})$;

¹H NMR (400 MHz, CDCl₃): $\delta = 8.38$ (s, 1H; NH), 7.46 (dd, 1H, ³J_{HH} = 8.2 Hz, ⁴J_{HH} = 1.6 Hz; C₆H₄), 7.29 (ddd, 1H, ³J_{HH} = 8.5 Hz, ⁴J_{HH} = 1.7 Hz; C₆H₄), 6.96–6.89 (m, 2H; C₆H₄, CH₂=CH), 6.64 (ddd, 1H, ³J_{HH} = 7.0 Hz, ³J_{HH} = 8.1 Hz, ⁴J_{HH} = 1.1 Hz; C₆H₄), 5.83 (m, 2H; CH₂=CH, CH₂=CH), 2.91 (s, 6H; Me), 2.89 (s, 4H; CH₂ (tmeda)), 2.75 ppm (s, 6H; Me); ¹³C{¹H} NMR (400 MHz, CDCl₃): $\delta = 171.05$ (C), 164.64 (C), 134.77 (CH (C₆H₄)), 133.32 (CH₂=CH), 132.34 (CH (C₆H₄)), 126.73 (CH₂=CH), 121.10 (CH (C₆H₄)), 115.85 (CH (C₆H₄)), 120.58 (C), 115.85 (CH (C₆H₄)), 63.30 (CH₂ (tmeda)), 60.46 (CH₂ (tmeda)), 50.91 (Me), 49.36 ppm (Me); elemental analysis: calcd for C₁₆H₂₄N₃O₄F₃SPd: C 37.11, H 4.67, N 8.11, S 6.19; found: C 36.86, H 4.78, N 8.11, S 6.03; single crystals were grown by slow diffusion of Et₂O into a solution of **3** in CH₂Cl₂.

Received: April 5, 2005

Published online: August 22, 2005

Keywords: insertion · N ligands · neighboring-group effects · nitriles · palladium

- [1] V. Y. Kukushkin, A. J. L. Pombeiro, *Chem. Rev.* **2002**, *102*, 1771; V. Y. Kukushkin, A. J. L. Pombeiro, *Inorg. Chim. Acta* **2005**, *358*, 1.
- [2] R. A. Michelin, M. Mozzon, R. Bertani, *Coord. Chem. Rev.* **1996**, *147*, 299.
- [3] M. N. Kopylovich, V. Y. Kukushkin, M. Haukka, K. V. Luznyanin, A. J. L. Pombeiro, *J. Am. Chem. Soc.* **2004**, *126*, 15040.
- [4] M. Bochmann, L. M. Wilson, M. B. Hursthouse, M. Motevalli, *Organometallics* **1988**, *7*, 1148; G. Erker, W. Ahlers, R. Fröhlich, *J. Am. Chem. Soc.* **1995**, *117*, 5853; G. Erker, R. Pfaff, D. Kowalski, E.-U. Würthwein, C. Krüger, R. Goddard, *J. Org. Chem.* **1993**, *58*, 6771; Y. W. Alelyunas, R. F. Jordan, S. F. Echols, S. L. Borkowsky, P. K. Bradley, *Organometallics* **1991**, *10*, 1406; Y. W. Alelyunas, Z. Y. Guo, R. E. Lapointe, R. F. Jordan, *Organometallics* **1993**, *12*, 544; E. Boring, M. Sabat, M. G. Finn, R. N. Grimes, *Organometallics* **1997**, *16*, 3993; K. C. Jantunen, C. J. Burns, I. Castro-Rodriguez, R. E. D. Re, J. T. Golden, D. E. Morris, B. L. Scott, T. F. L., J. L. Kiplinger, *Organometallics* **2004**, *23*, 4682; A. Dormond, A. Elbouadili, C. Moise, *J. Org. Chem.* **1989**, *54*, 3747; J. E. Bercaw, D. L. Davies, P. T. Wolczanski, *Organometallics* **1986**, *5*, 443; K. H. de Haan, G. A. Luinstra, A. Meetsma, J. H. Teuben, *Organometallics* **1987**, *6*, 1509; D. S. Richeson, J. F. Mitchell, K. H. Theopold, *Organometallics* **1989**, *8*, 2570.
- [5] R. Duchateau, E. A. C. Brussee, A. Meetsma, J. H. Teuben, *Organometallics* **1997**, *16*, 5506.
- [6] J. G. Stack, J. J. Doney, R. G. Bergman, C. H. Heathcock, *Organometallics* **1990**, *9*, 453.
- [7] A. Klose, E. Solari, R. Ferguson, C. Floriani, A. Chiesivilla, C. Rizzoli, *Organometallics* **1993**, *12*, 2414.
- [8] See, for example: S. Das, S. Pal, *J. Organomet. Chem.* **2004**, *689*, 352; K. Y. Ghebreyessus, N. Gul, J. H. Nelson, *Organometallics* **2003**, *22*, 2977; J.-M. Valk, R. van Belzen, J. Boersma, A. L. Spek, G. van Koten, *J. Chem. Soc. Dalton Trans.* **1994**, 2293; P.-H. Leung, K.-H. Ng, Y. Li, A. J. P. White, D. J. Williams, *Chem. Commun.* **1999**, 2435; T. Murahashi, T. Otani, T. Okuno, H. Kurosawa, *Angew. Chem.* **2000**, *112*, 547; *Angew. Chem. Int. Ed.* **2000**, *39*, 537; J. Vicente, J.-A. Abad, E. Martínez-Viviente, P. G. Jones, *Organometallics* **2002**, *21*, 4454; A. Bacchi, M. Carcelli, M. Costa, P. Pelagatti, C. Pelizzi, J. Chem. Soc. Dalton Trans. **1996**, 4239; L. P. Wu, Y. Suenaga, T. Kuroda-Sowa, M. Maekawa, K. Furuichi, M. Munakata, *Inorg. Chim. Acta* **1996**, *248*, 147; M. Tsoureas, A. A. Danopoulos, A. A. D. Tulloch, M. E. Light, *Organometallics* **2003**, *22*, 4750; L. R. Falvello, S. Fernandez, R. Navarro, A. Rueda, E. P. Urriolabeitia, *Organometallics* **1998**, *17*, 5887; M. A. Zuideveld, B. H. G. Swennenhuis,

- M. D. K. Boele, Y. Guari, G. P. F. van Strijdonck, J. N. H. Reek, P. C. J. Kamer, K. Goubitz, J. Fraanje, M. Lutz, A. L. Spek, P. W. N. M. van Leeuwen, *J. Chem. Soc. Dalton Trans.* **2002**, 2308; H.-R. Wu, Y.-H. Liu, S.-M. Peng, S.-T. Liu, *Eur. J. Inorg. Chem.* **2003**, 3152; H.-P. Chen, Y.-H. Liu, S.-M. Peng, S.-T. Liu, *Organometallics* **2003**, 22, 4893; H.-P. Chen, Y.-H. Liu, S.-M. Peng, S.-T. Liu, *Dalton Trans.* **2003**, 1419; J. Feldman, S. J. McLain, A. Parthasarathy, W. J. Marshall, J. C. Calabrese, S. D. Arthur, *Organometallics* **1997**, 16, 1514; S. P. Meneghetti, P. J. Lutz, J. Kress, *Organometallics* **1999**, 18, 2734; O. Daugulis, M. Brookhart, P. S. White, *Organometallics* **2002**, 21, 5935; S. P. Meneghetti, P. J. Lutz, J. Kress, *Organometallics* **2001**, 20, 5050.
- [9] F. Wu, S. R. Foley, C. T. Burns, R. F. Jordan, *J. Am. Chem. Soc.* **2005**, 127, 1841.
- [10] L. F. Groux, T. Weiss, D. N. Reddy, P. A. Chase, W. E. Piers, T. Ziegler, M. Parvez, J. Benet-Buchholz, *J. Am. Chem. Soc.* **2005**, 127, 1854.
- [11] J. Vicente, J. A. Abad, M. J. López-Sáez, W. Förtsch, P. G. Jones, *Organometallics* **2004**, 23, 4414.
- [12] C. X. Zhou, R. C. Larock, *J. Am. Chem. Soc.* **2004**, 126, 2302.
- [13] S. Chakraborty, M. G. Walawalkar, G. K. Lahiri, *Polyhedron* **2001**, 20, 1851.
- [14] A. K. Das, S.-M. Peng, S. Bhattacharya, *J. Chem. Soc. Dalton Trans.* **2000**, 181.
- [15] E. R. J. Sillanpää, A. Al-Dhahir, R. D. Gillard, *Polyhedron* **1991**, 10, 2051.
- [16] C. Wang, S. Friedrich, T. R. Younkin, R. T. Li, R. H. Grubbs, D. A. Bansleben, M. W. Day, *Organometallics* **1998**, 17, 3149; E. F. Connor, T. R. Younkin, J. I. Henderson, A. W. Waltman, R. H. Grubbs, *Chem. Commun.* **2003**, 2572; T. R. Younkin, E. F. Connor, J. I. Henderson, S. K. Friedrich, R. H. Grubbs, D. A. Bansleben, *Science* **2000**, 287, 460; S. J. Diamanti, P. Ghosh, F. Shimizu, G. C. Bazan, *Macromolecules* **2003**, 36, 9731.
- [17] CCDC-267823 (**1**), -267824 (**2**), and -267825 (**3**) contain the supplementary crystallographic data for this paper. These data can be obtained free of charge from the Cambridge Crystallographic Data Centre via www.ccdc.cam.ac.uk/data_request/cif. Data were recorded at -140°C on a Bruker SMART 1000 CCD diffractometer in ω and ϕ scan modes to $2\theta_{\text{max}} 60^{\circ}$ with monochromated $\text{MoK}\alpha$ radiation ($\lambda = 0.71073 \text{ \AA}$). Absorption corrections were based on multiple scans. Structures were refined on F^2 by using the program SHELXL-97 (G. M. Sheldrick, University of Göttingen). Hydrogen atoms were refined using rigid methyl groups or a riding model, except for NH hydrogen atoms, which were refined freely. The triflate group of **3** is disordered over two positions in the ratio 4:1. Crystal data for **1**: $\text{C}_{15}\text{H}_{24}\text{F}_3\text{N}_3\text{O}_4\text{PdS}$, monoclinic, $a = 8.4900(6)$, $b = 12.0785(8)$, $c = 19.4179(14) \text{ \AA}$, $\beta = 95.648(4)^{\circ}$, $U = 1981.6 \text{ \AA}^3$, space group $P2_1/n$, $Z = 4$, $\mu(\text{MoK}\alpha) = 1.10 \text{ mm}^{-1}$, 36424 reflections measured, 5789 unique ($R_{\text{int}} = 0.026$); refinement proceeded to $wR(F^2)$ 0.073 (all data), $R(F)$ 0.027 for 253 parameters; max. $\Delta\rho 1.3 \text{ e \AA}^{-3}$. Crystal data for **2**: $\text{C}_{20}\text{H}_{21}\text{F}_8\text{N}_3\text{O}_4\text{PdS}$, orthorhombic, $a = 8.9198(6)$, $b = 11.4033(8)$, $c = 23.1269(14) \text{ \AA}$, $U = 2352.4 \text{ \AA}^3$, space group $P2_12_12_1$, $Z = 4$, $\mu(\text{MoK}\alpha) = 0.98 \text{ mm}^{-1}$, 49530 reflections measured, 6890 unique ($R_{\text{int}} = 0.027$); refinement proceeded to $wR(F^2)$ 0.047 (all data), $R(F)$ 0.019, Flack parameter $-0.009(11)$ for 342 parameters; max. $\Delta\rho 0.7 \text{ e \AA}^{-3}$. Crystal data for **3**: $\text{C}_{16}\text{H}_{24}\text{F}_3\text{N}_3\text{O}_4\text{PdS}$, orthorhombic, $a = 8.0816(11)$, $b = 13.332(2)$, $c = 19.339(3) \text{ \AA}$, $U = 2083.6 \text{ \AA}^3$, space group $P2_12_12_1$, $Z = 4$, $\mu(\text{MoK}\alpha) = 1.04 \text{ mm}^{-1}$, 44074 reflections measured, 6095 unique ($R_{\text{int}} = 0.047$); refinement proceeded to $wR(F^2)$ 0.063 (all data), $R(F)$ 0.029, Flack parameter $-0.01(2)$ for 334 parameters and 307 restraints; max. $\Delta\rho 1.0 \text{ e \AA}^{-3}$. The Supporting Information for this article contains a listing of all refined and calculated atomic coordinates, anisotropic thermal parameters, and bond lengths and angles for complexes **1–3**.

DOI: 10.1002/anie.200500081

Synthesis of Stable Aragonite Superstructures by a Biomimetic Crystallization Pathway**

Nadine Nassif,* Nicole Gehrke, Nicola Pinna,
Natasha Shirshova, Klaus Tauer, Markus Antonietti,
and Helmut Cölfen*

Many organisms make use of calcium carbonate as a construction material, and for this purpose are able to selectively control the formation of the different polymorphs of this material. This is not the case for technical processes. Calcite is thermodynamically more stable at ambient pressure and temperature^[1] than the other anhydrous CaCO_3 polymorphs (vaterite and aragonite), and thus is most easily obtained with long reaction times. There are some technical procedures which generate vaterite (usually the first polymorph formed as a result of the Ostwald rule of stages) by performing the precipitation along the kinetic pathway and yielding the kinetic metastable vaterite product or by trapping and stabilizing the very early crystals^[2] with appropriate stabilizers. However, the mechanically very interesting aragonite (usually a high-pressure modification) is virtually inaccessible by chemical means, except by adding extreme amounts of Mg^{2+} ions to the mother liquor.^[3,4] It should be recalled that nacre, with its extraordinary mechanical performance, is based on pure aragonite platelets^[5] and shows clear long-time stability even in the presence of water. In contrast, aragonite usually starts to transform to calcite within a day or faster depending on the pH value and temperature.^[6,7] Thus, one of the main challenges in the crystallization of calcium carbonate remains the synthesis of pure aragonite of uniform size and morphology under ambient conditions.

It has previously been described that aragonite is formed in a biomimetic pathway in the presence of several extracted

[*] Dr. N. Nassif, N. Gehrke, Dr. N. Shirshova, Dr. K. Tauer,
Dr. M. Antonietti, Dr. H. Cölfen
Max-Planck Institute of Colloids and Interfaces
Colloid Chemistry
Research Campus Golm, 14424 Potsdam (Germany)
Fax: (+49) 331-567-9502
E-mail: nadine.nassif@mpikg-golm.mpg.de
coelfen@mpikg-golm.mpg.de

Dr. N. Pinna
Martin-Luther-Universität Halle-Wittenberg
Institut für Anorganische Chemie
Kurt-Mothes-Strasse 2, 06120 Halle (Saale) (Germany)

[**] We thank Dr. Cornelia Sinn, Dr. Reinhard Sigel, and Dr. Miles Page for their kind scientific assistance and the Deutsche Forschungsgemeinschaft for financial support within the priority program 1117: "Principles of Biomineralization". We also thank the Fritz Haber Institute and Prof. R. Schlögl for use of the electron microscope and Klaus Weiss for his technical assistance.



Supporting information for this article is available on the WWW under <http://www.angewandte.org> or from the author.

macromolecules from different shells in the presence^[8] or absence^[9] of an organic matrix, under compressed monolayers^[10,11] or at the liquid–liquid interface in a radial Hele–Shaw cell.^[12] More recently, aragonite was obtained as a metastable intermediate at the air–water interface by the use of a basic polymer.^[13] Other reported ways to obtain aragonite include, for example, the transformation of amorphous calcium carbonate nanoparticles in reverse surfactant microemulsions,^[14] by heat-induced precipitation onto self-assembled monolayers of anthracene-terminated thiol chains,^[15] or by high-power ultrasonic irradiation at certain sound amplitudes.^[16]

Herein we report the simple synthesis of homogeneous aragonite crystals with structural complexity by applying the standard vapor diffusion method to particles of a hydrophilic block copolymer.^[17] These particles are composed of a triblock copolymer, poly(diethylaminoethyl methacrylate)-*b*-poly(*N*-isopropylacrylamide)-*b*-poly(methacrylic acid) (PDEAEMA-*b*-PNIPAM-*b*-PMAA), in which the poly(methacrylic acid) core is cross-linked by 1,3-diisopropylenebenzene.^[18,19] The current process, contrary to previously reported syntheses, does not rely on an excess of inorganic metal ions nor the presence of a whole assembly of macromolecules or surfactants; only cheap and commonly accessible chemicals are required for the polymer preparation as well as a small amount of polymer template particles under bio-inspired crystallization conditions, that is, water at ambient pressure and temperature. Furthermore, the experiment is particularly easy to set up.

The beneficial and useful application of block copolymers with more than one hydrophilic block in crystallization has been known for several years.^[20,21] So-called “double hydrophilic block copolymers” are currently used to mimic the processes occurring in natural biological materials. They consist of two hydrophilic blocks: one is a polyelectrolyte, and thus strongly interacts with crystal surfaces, and the other one is a non-ionic block, which provides the water solubility without interacting with the crystal.

The current system is such that it contains both an outer positive and an inner negative polymer block, the poly(diethylaminoethyl methacrylate) and poly(methacrylic acid) PDEAEMA and PMAA blocks, respectively, which can interact with both ions and different crystal moieties and faces. In this way, its role is expected to act as an ion sponge and to nucleate and stabilize nanocrystals which will constitute the building units of a crystalline superstructure. The PNIPAM part is expected to mediate sufficient steric stability to the particles throughout all steps of the process at room temperature where PNIPAM is hydrophilic. PDEAEMA-PNIPAM-*b*-PtBMA/MAA (cross-linked) also exhibits some hydrophilic microgel properties, which are provided mostly by the third block (PMAA). The hydrodynamic diameter of the microgel particles dispersed in water is about 1 μm , but after drying, TEM images show an average particle size of about 200 nm with a narrow size distribution between 170 and 220 nm.^[19] Thus, the size of these spherical microgels can vary by swelling according to the medium (dried or in water) in which they are placed.

Precipitation experiments were performed using the so-called vapor diffusion method, with calcium carbonate

synthesized by the diffusion of carbon dioxide vapor (obtained from the thermal decomposition of ammonium carbonate) into a calcium chloride solution (0.01 M) mixed with very small amounts of PDEAEMA-PNIPAM-*b*-PtMA/MAA ($10^{-4} \text{ mg mL}^{-1}$, 0.1 ppm). It is emphasized that the relative ratio of these compounds is so high that the polymer practically does not contribute by weight to the final crystals (ratio $\text{CaCO}_3/\text{block copolymer} \leq 10^4:1$), that is, it is essentially its influence on nucleation which is relevant.

Scanning electron microscopy (SEM) studies of a sample collected after 12 days from the bottom of the reaction flasks shows “sheaf bundle” crystals^[10–12] as the predominant morphology, slightly contaminated with a few calcite rhombohedra from the free growth of CaCO_3 (Figure 1 a). A higher

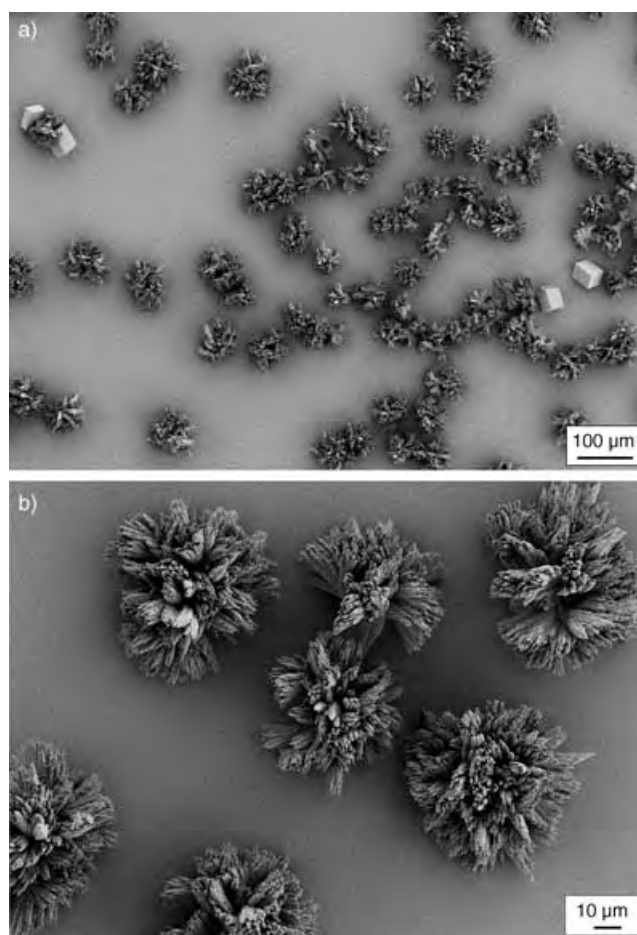


Figure 1. Lower (a) and higher (b) magnification SEM images showing a rather narrow distribution of “sheaf bundle” crystals at the bottom of the precipitation flask.

magnification (Figure 1 b) reveals the high uniformity of this superstructure morphology and the quite narrow size distribution with a diameter of about 60 μm . It will be shown below that all the superstructures have been heterogeneously nucleated at interfaces. We therefore assume that the calcite contamination arises from the co-occurrence of free calcite nucleation in homogeneous solution, which cannot be completely suppressed by the very low concentrations of polymer modifier employed (0.1 ppm).

The identification of the phase of the synthesized CaCO_3 was carried out by X-ray powder diffraction (XRD) analysis. The XRD pattern of the sample displays the following diffraction peaks (2θ [°]): 26.12, 27.10, 32.74, 33.06, 36.12, 37.29, 37.89, 38.48, 39.42, 41.27, 43.01, 45.96, 48.44, 50.25, 52.44, and 52.92, which can be correlated to the (hkl) indices (111), (021), (121), (012), (200), (031), (112), (130), (211), (220), (221), (202), (132), (113), (321), respectively, of pure aragonite. For the sample collected from the bottom of the flask, peaks of rhombohedral calcite are also observed (diffraction peaks 2θ [°] (hkl): 29.27 (104), 39.42 (202), 47.36 (018)). These results are in agreement with the SEM observations. The identification of the phase of these crystals was also confirmed by Fourier transform infrared (FTIR) spectroscopy, which showed characteristic vibrational bands at 699, 711, 852, and 1082 cm^{-1} . The characteristic vibrational band corresponding to the asymmetric C–O stretch is 1469 cm^{-1} for aragonite and 1422 cm^{-1} for calcite. However, the broadness in this wavenumber region means that it is not possible to assign the band at 1445 cm^{-1} .

Nucleation at interfaces is also proven by analyzing finer details of the “sheaf bundles”. Analysis of the trunk attachment on the glass surface (Figure 2a) and the fine structure of fallen-off crystal trunks (Figure 2b) leads us to suggest that nucleation of these crystals indeed occurs from the two-

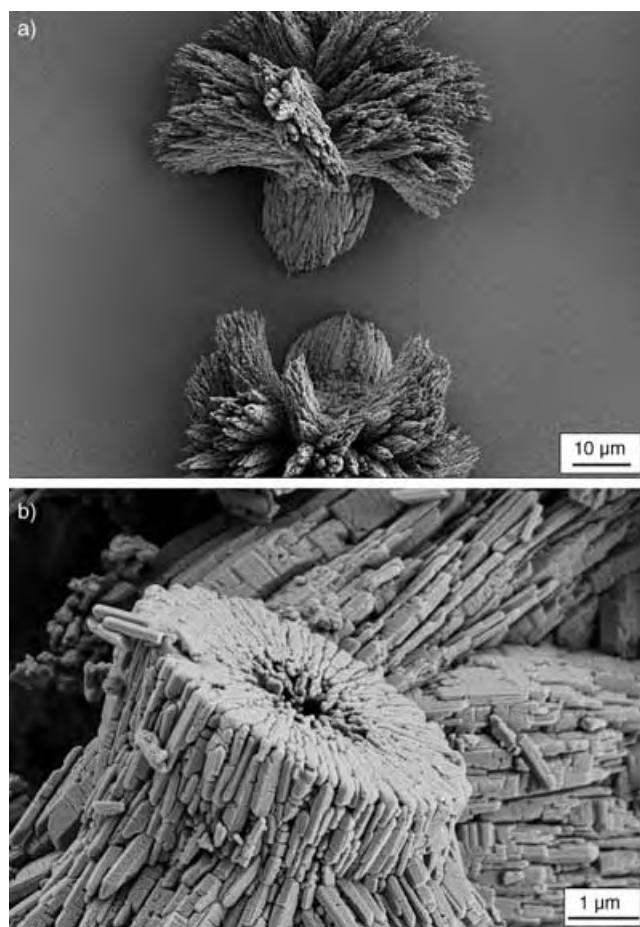


Figure 2. SEM images showing the trunk attachment to the glass wall (a) and the root (b) of a fallen-off “sheaf bundle” crystal.

dimensional structure already present at the flat end of the trunk. The central hole in the trunk even has the correct size (of about 1 μm) to formerly have hosted one of the microgel particles of the polymer, that is, one polymer particle promotes the heterogeneous nucleation of one crystal superstructure. This view is supported by attachment of the externally positively charged particles (outer PDEAEMA layer) to the negatively charged glass surface at the starting pH value of 5.8 for crystallization, as shown by the adsorption of positive dyes or positively charged latexes onto the glass slide (see also the Supporting Information for the adsorption of the triblock copolymer particle).

Other experiments were performed to understand how such stable aragonite crystallization can occur under ambient conditions. Figure 3 presents TEM measurements performed

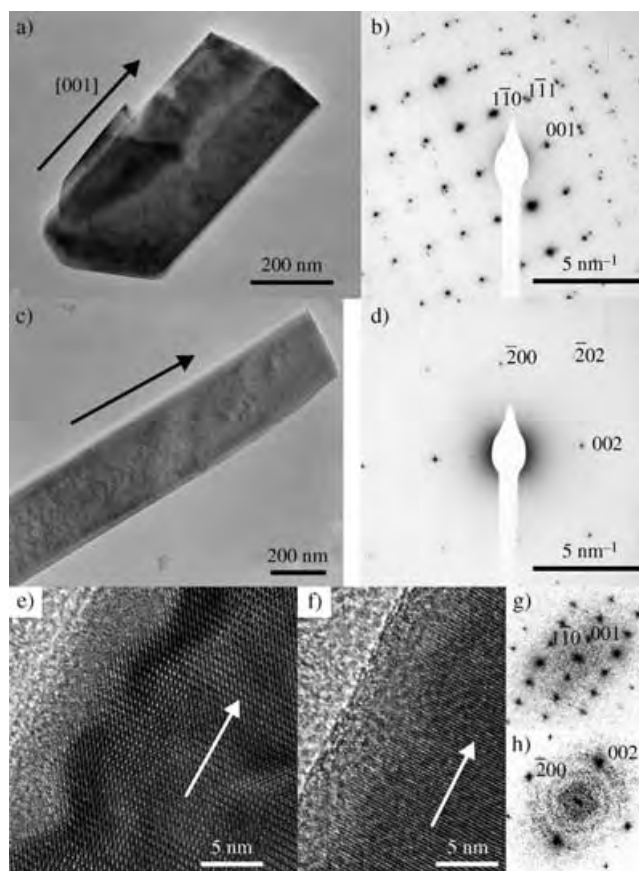


Figure 3. TEM overview images of two building blocks (a, c) and their respective electron diffractions (b, d). HRTEM image of parts of different building blocks (e, f) and their respective power spectra (g, h). The arrows indicate the [001] direction.

on the primary building blocks seen clearly in Figure 2b. These subunits are quite homogeneous and have a rodlike shape with lengths ranging from 500 nm to a few micrometers (Figure 3a and 3c). Their diffraction patterns are in some cases typical of mesocrystals such as the particle presented in Figure 3a (Figure 3b; in this case the crystal is oriented along the [110] direction) or typical of a single crystal such as the one presented in Figure 3d which is characteristic of the [010] zone axis. In both cases the long axis of the crystal is [001].

High-resolution TEM (HRTEM) was used to study the crystallinity and the surface of the particles (Figure 3 e and f). The particles show a well-defined crystalline core as demonstrated by their power spectra (PS, Figure 3 g and 3 h), which are characteristic of single crystals viewed along the [110] and [010] directions, respectively. Surprisingly, they also show a clearly developed amorphous layer of around 5-nm thickness on their surface. This layer can not be formed by organic compounds such as the 1- μm polymer template used to induce the nucleation, and in fact this thin layer starts to crystallize slowly under the intense electron beam of the microscope. This observation suggests that this layer is composed of amorphous calcium carbonate (ACC), as was found recently on the aragonite platelets of nacre.^[22] Thus, the above observations show the possibility to retrosynthesize the amorphous-layer-coated aragonite platelets in nacre by using the current synthetic polymers and crystallization conditions. The exact reason for the stabilization of the aragonite polymorph by a protective ACC layer is as yet unknown and the subject of ongoing work. Nevertheless, this amorphous “coating” could protect the aragonite against recrystallization when in contact for longer times with water.

Finally, experiments were also performed with higher polymer concentrations (10^{-3} to 1 mg mL^{-1}), while keeping the CaCl_2 concentration (0.01M) constant. The increase leads first to a higher heterogeneity of the crystals until the specific crystal shape disappears. Only the mineralization of the microgel particles towards amorphous composite structures could be observed at the highest polymer concentrations (Figure 4), because of the lower available mineral concen-

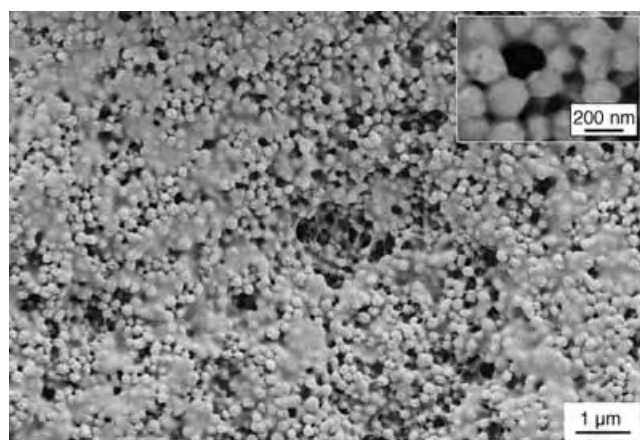


Figure 4. SEM images at lower and higher (inset) magnification of the mineralized polymer microgels (1 mg mL^{-1}).

tration for each polymer particle. Dynamic light scattering (DLS) investigations confirmed the interactions between the core of the particle, which is mainly composed of acidic groups (PMAA), and the calcium ions of the solution. Indeed, DLS studies have shown that an increase in the ionic strength of the solution leads to a decrease in the average particle diameter of the stabilizing microgel particles (the average diameter of the triblock particles is ca. 1000 nm in water^[19] whereas it decreases to ca. 800 nm in 0.01M CaCl_2 solution).

The increase in the pH value in the experimentally important range from the starting value of 5.8 to the end value of 9.5 slightly increases the size of the particles to 1200 nm as a consequence of PMAA charge repulsion in the core.

Presumably the higher polymer concentrations model the very early stages of the formation of the “sheaf bundles”. The amphoteric microgels are strong enough to bind all counterions and amorphous intermediates up to a critical concentration. When the binding concentration is exhausted (which is the case for concentration/weight ratios of CaCl_2 /polymer greater than 1:1), this highly concentrated salt phase can specifically nucleate the aragonite phase, presumably as a result of the stabilization effects specific for the precursor-loaded polymer. The hydrogen exchange between the amine and the acid blocks could be expected to contribute to this effect. Indeed, such an interaction has been observed in the diblock copolymer poly(diethylaminoethyl methacrylate)-*b*-poly(methacrylic acid) and led to insolubility in water even at high pH values.^[23] However, in the case of the triblock microgel particles here, their solubility and their size in water (ca. 1000 nm) prove that the interaction between the outer poly(diethylaminoethyl methacrylate) block and the inner poly(methacrylic acid) block is only of minor importance. Apparently, both the reduced mobility of the poly(methacrylic acid) acid groups, because of cross-linking, and a shielding action of the poly(*N*-isopropylacrylamide) middle block efficiently prevent this interaction. On the basis of Figure 4 it can be suggested that the amphoteric polymer microgel increases the salt concentration in its interior/proximity as a consequence of some zwitterionic moieties (this proposal is supported by the decrease in the particle size upon the addition of salt, as evident from DLS studies), whereas the excess of the outer PDEAEMA block nucleates a ring of radially aligned primary aragonite nanocrystals (see Supporting Information). Other molecules containing tertiary amine functions also induced aragonite formation.^[24] This observation is in line with a recent finding that many molluscan shell proteins found in nacre could be less acidic than previously thought.^[25] However, the controlled crystallization experiment with the PDEAEMA homopolymer additive indicated the beginning of the formation of elongated aragonite particles as well as the typical calcite rhombohedra found in the experiment with polymer concentrations greater than 1 mg mL^{-1} . At lower concentrations, the morphology of the formed calcite was still modified and resulted in roughly spherical particle superstructures up to polymer concentrations of 0.01 mg mL^{-1} , when the default calcite rhombohedra are almost exclusively obtained. This observation indicates that a high local polycation concentration should be present for the aragonite nucleation (see Supporting Information). Regardless, this ring of nanocrystals, once nucleated, propagates by growth to a distance of about $20\text{ }\mu\text{m}$ from the glass wall until the single components lose vectorial alignment and fold up to the head of the aragonite superstructure.

The lower the polymer concentration, the fewer the nucleation sites, so that the most developed and diversified structures are indeed formed at the extremely low concentration of 0.1 mg L^{-1} (0.1 ppm), a reactant concentration well

below usual values chosen to modify a physicochemical process. The fact that the aragonite superstructures nucleate on the glass walls indicates that the amphoteric microgels with a cationic outer layer indeed interact with the negatively charged glass wall. This interaction was confirmed by SEM investigations (see Supporting Information). Indeed, the triblock particles were still found to be attached to the glass surface after immersion of the glass slide in the 0.01M CaCl_2 solution and extensive washing.

In conclusion, it has been shown that it is possible to generate aragonite crystals by the gas-diffusion technique under ambient pressure and temperature. As the employed amphoteric polymer microgels only act as a highly selective nucleation and polymorph control agent, and are already active at the lowest concentrations (0.1 mg L^{-1} , 0.1 ppm), the resulting aragonite particles are practically free from organic contaminants and can potentially be used as they are.

Furthermore, all the structures are found to adopt a structurally well-defined, highly reproducible, "sheaf bundle" morphology. This shows that propagation of a structurally confined nucleation on the micrometer scale (a ring of radially aligned aragonite nanocrystals) can lead to control of crystals with high structural complexity, even without the action of geometric confinements, templates, and outer force fields. The formed superstructures are stable against recrystallization for at least two weeks even in contact with water, thus indicating the stability of the formed aragonite in this special morphology, which is in contrast to literature reports on aragonite stability in water.^[6,7] This stability could arise from the observed outer ACC layer (Figure 3) preventing the aragonite–water contact. The unexpected stability of the ACC layer in water is the subject of ongoing investigations. However, this ACC layer does not seem to perfectly protect the aragonite crystals as deduced from the observation that a single microgel particle is able to nucleate a whole trunk of apparently unconnected aragonite crystals (Figure 2). As calcite is observed as the default solution-nucleated product (Figure 1a) and there is no additional polymer available beside the microgel templates, the exclusive formation of aragonite in the complex superstructures (Figure 2) could not be explained unless a crystallographic bridge is present between the individual particles. Such a bridge extending throughout the ACC layer could then act as a nucleation site for the formation of another aragonite particle by mesoscopic transformation of ACC precursors.^[26] This result means that the whole particle superstructure is crystallographically connected, thus giving a possible explanation for the finding in biomineralization that very minute amounts of additive can influence a much larger amount of inorganic crystals. The present synthetic block copolymer microgels are indeed able to selectively nucleate aragonite at 0.1 ppm at ambient conditions in water. In summary, our study reveals three important and novel points: an easy biomimetic set-up to obtain aragonite with only a negligible concentration of polymer, the presence of an ACC layer never observed before around each single crystal block of the bundle, and the probable influence of the tertiary amine in this example as opposed to acidic molecules which are normally discussed as effective crystallization additives.

Experimental Section

CaCO_3 synthesis: Calcium carbonate polycrystals were grown by diffusion of carbon dioxide into calcium chloride solutions according to the gas diffusion method by thermal decomposition of ammonium carbonate. Experiments were performed at room temperature ($22 \pm 1^\circ\text{C}$). Two flasks containing 0.01M calcium chloride solutions (20 mL) mixed with different concentrations of DHBC particles (10^{-4} , 10^{-3} , 10^{-2} , 0.1, and 1 mg mL^{-1}) and fresh ammonium carbonate (2 g) were placed into a closed chamber (1000 cm^3). The aqueous solutions of CaCl_2 were prepared in doubly distilled water and bubbled with N_2 overnight before use. The decomposition of ammonium carbonate produced ammonia and carbon dioxide diffusing through 5 needle-holes pierced into the parafilm cover of the flasks. The initial solution was slightly acidic (pH 5.8) but the pH value rose to 9.5 because of the dissolved NH_3 . After completion of mineral deposition (12 days), the sample was removed from solution, rinsed with filtered water and ethanol, then air-dried.

Polymer synthesis: After preparation by aqueous heterophase polymerization, cleaning by ultrafiltration, and isolating by freeze drying, the solid could easily be dispersed into water.^[19]

Crystal characterizations: The crystals were washed with distilled water then ethanol and dried in air for further characterization. Powder X-ray diffraction (XRD) patterns were recorded on a PDS 120 diffractometer (Nonius GmbH, Solingen) with $\text{Cu K}\alpha$ radiation. The SEM measurements were performed on a LEO 1550-GEMINI with gold-coated samples. FT-IR spectra were recorded either on a Nicolet Impact 400 or a BioRad FTS6000 spectrometer. For TEM studies one or more drops of the solution of the nanoparticles dispersed in ethanol were deposited on an amorphous carbon film. A Phillips CM200 FEG microscope, 200 kV, equipped with a field emission gun was used. The coefficient of spherical aberration was $C_s = 1.35 \text{ nm}$. The average particle diameter was determined by dynamic light scattering methods with a NICOMP particle sizer (model 370, NICOMP particle sizing systems, Santa Barbara, California, USA) as well as with a commercial goniometer with a digital correlator (both ALV, Langen, Germany) and a helium–neon laser (Polytec, Waldbronn, Germany) with wavelength $\lambda = 633 \text{ nm}$. The data evaluation of the correlation functions was based on the computer program CONTIN (Provencher, 1982), which performs an inverse Laplace transformation.

Received: January 10, 2005

Revised: June 24, 2005

Published online: August 17, 2005

Keywords: block copolymers · calcium carbonate · microgels · nucleation · polymorphism

- [1] Reviews in Mineralogy: *Carbonates: Mineralogy and Chemistry, Vol. 11* (Ed.: R. J. Reeder), Mineralogical Society of America, Washington, DC, **1983**.
- [2] H. Cölfen, M. Antonietti, *Langmuir* **1998**, *14*, 582.
- [3] Y. Kitano, *Bull. Chem. Soc. Jpn.* **1962**, *35*, 1973.
- [4] K. M. Wilbur, A. M. Bernhardt, *Biol. Bull.* **1984**, *166*, 251.
- [5] H. Nakahara, *Calcification of Gastropod Nacre Biomineralization and Biological Metal Accumulation* (Ed.: P. Westbroeck, E. W. De Jong), D. Reidel Publishing, Dordrecht, **1983**, pp. 225–230.
- [6] A. Richter, D. Petzold, H. Hofmann, B. Ullrich, *Chem. Tech.* **1996**, *48*, 271.
- [7] G. T. Zhou, Y. F. Zheng, *Neues Jahrb. Mineral. Abh.* **2001**, *176*, 323.
- [8] G. Falini, S. Albeck, S. Weiner, L. Addadi, *Science* **1996**, *271*, 67.
- [9] A. M. Belcher, X. H. Wu, R. J. Christensen, P. K. Hansma, G. D. Stucky, D. E. Morse, *Nature* **1996**, *381*, 56.

- [10] A. L. Litvin, S. Valiyaveetil, D. L. Kaplan, S. Mann, *Adv. Mater.* **1997**, *9*, 124.
- [11] B. R. Heywood, S. Mann, *Chem. Mater.* **1994**, *6*, 311.
- [12] D. Rautaray, A. Banpurkar, S. R. Sainkar, A. V. Limaye, N. R. Pavaskar, S. B. Ogale, M. Sastry, *Adv. Mater.* **2003**, *15*, 1273.
- [13] H. K. Park, I. Lee, K. Kim, *Chem. Commun.* **2004**, *1*, 24.
- [14] L. Mei, B. Lebeau, S. Mann, *Adv. Mater.* **2003**, *15*, 2032.
- [15] J. Küther, G. Nelles, R. Seshadri, M. Schaub, H.-J. Butt, W. Tremel, *Chem. Eur. J.* **1998**, *4*, 1834.
- [16] G.-T. Zhou, J. C. Yu, X.-C. Wang, L.-Z. Zhang, *New J. Chem.* **2004**, *28*, 1027.
- [17] L. Addadi, J. Moradian, E. Shay, N. G. Maroudas, S. Weiner, *Proc. Natl. Acad. Sci. USA* **1987**, *84*, 2732.
- [18] K. Tauer, V. Khrenov, *Macromol. Symp.* **2002**, *179*, 27.
- [19] K. Tauer, V. Khrenov, N. Shirshova, N. Nassif, *Macromol. Symp.* **2005**, in press.
- [20] H. Cölfen, *Macromol. Rapid Commun.* **2001**, *22*, 219.
- [21] S. H. Yu, H. Cölfen, *J. Mater. Chem.* **2004**, *14*, 2124.
- [22] N. Nassif, N. Pinna, N. Gehrke, M. Antonietti, C. Jäger, H. Cölfen, **2005**, *Proc. Natl. Acad. Sci. USA*, submitted.
- [23] K. Tauer, M. Mukhamedjanova, unpublished results.
- [24] N. Nassif, J. Polleux, unpublished results.
- [25] F. Marin, G. Luquet, *C. R. Palevol* **2004**, *3*, 469.
- [26] H. Cölfen, S. Mann, *Angew. Chem.* **2003**, *115*, 2452; *Angew. Chem. Int. Ed.* **2003**, *42*, 2350.

Polymer Films

DOI: 10.1002/anie.200500868

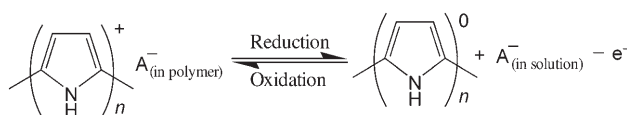
Reversible Conversion of Conducting Polymer Films from Superhydrophobic to Superhydrophilic**

Lianbin Xu, Wilfred Chen, Ashok Mulchandani, and Yushan Yan*

Controlling the wettability of a solid surface is important for myriad applications, ranging from self-cleaning surfaces to microfluidics to biomedicine.^[1–3] Recently, a variety of smart surfaces with reversibly switchable wettability have been developed. The reversible switching is realized through the adjustment of electrical potential,^[4–6] temperature,^[7,8] and light illumination,^[9–13] adsorption of biopolymer,^[14] and treatment of selective solvents.^[15,16] Among these approaches, the

switch of the electrical potential receives special attention because it is simple and conveniently controlled by electricity. Moreover, the switching is readily individually addressable when an array of small surfaces is involved. Lahann et al.^[4] constructed a reversibly switching surface by depositing a low-density carboxylate-terminated self-assembled monolayer on a gold surface. Electrical potential was used to trigger the conformational transition of the monolayer, resulting in switching of the surface wettability. However, the change in surface wettability is small (20 to 30° water contact angle), which is likely to limit its practical applications. It is reported that ZnO films^[11,12] and poly(*N*-isopropylacrylamide)-modified patterned surfaces^[7] can undergo reversible wettability switching between two extremes, superhydrophobicity (water contact angle > 150°) and superhydrophilicity (water contact angle < 5°) through the use of ultraviolet light and a temperature change, respectively. The photoswitching requires several days to achieve the hydrophilic-to-hydrophobic conversion, and both the photoswitching and thermal switching are difficult to implement to individually address an array of small surfaces. Herein we report a simple electrochemical process to fabricate superhydrophobic conducting polypyrrole (PPy) films and demonstrate that their properties can be switched conveniently from superhydrophobic to superhydrophilic by changing the electrical potential.

Conducting polymers (also called conjugated polymers or synthetic metals) such as polypyrrole (PPy) have been studied in great detail because their unique optical, electrical, and mechanical properties offer many new possibilities for device fabrication.^[17,18] Interest has recently developed in their surface properties such as wettability because of potential applications in corrosion protection,^[19] conductive textiles,^[20] and antistatic coatings,^[21] and in the immobilization of biopolymers^[22] and growth control of living cells.^[23] Usually the conducting polymers contain a positively charged conjugated backbone and negatively charged counterions (dopants). The wettability of conducting polymers depends greatly on the types of dopants used.^[22] For example, a PPy film containing a perfluorinated dopant exhibited hydrophobicity (water contact angle > 90°), while ClO₄[–]-doped PPy was hydrophilic.^[21] Furthermore, the doping level can be controlled by changing the electrical potential, resulting in reversibly switchable surface wettability.^[23,24] Scheme 1



Scheme 1. A[–] = anion.

shows the reversible switching process between the doped (oxidized) state and dedoped (neutral) state of PPy. To achieve a large variation in wettability (water contact angle difference ≥ 80°) between the doped and neutral states of conjugated polymers, researchers have focused on fabricating hydrophilic conducting polythiophene and then converting it into hydrophobic neutral polythiophene.^[25,26] This study

[*] Dr. L. Xu, Prof. W. Chen, Prof. A. Mulchandani, Prof. Y. Yan
Department of Chemical and Environmental Engineering
University of California, Riverside, CA 92521 (USA)
Fax: (+1) 951-827-5696
E-mail: yushan.yan@ucr.edu

[**] This work was supported by a US NSF grant (CCF0330451) and a US DoD/DARPA/DMEA grant. We thank A. Yu for help on the conductivity measurement of the samples.



Supporting information for this article is available on the WWW under <http://www.angewandte.org> or from the author.

describes the first synthesis of superhydrophobic conducting polymers and the reversible control of the wettability of conducting polymer films between superhydrophobicity and superhydrophilicity.

Superhydrophobic PPy films were synthesized on a conducting surface such as Au-coated glass by electrochemical polymerization. The electroplating solution contained 0.1 M pyrrole, 0.05 M tetraethylammonium perfluorooctanesulfonate (TEAPFOS, $\text{Et}_4\text{N}^+\text{CF}_3(\text{CF}_2)_7\text{SO}_3^-$), and 2.0×10^{-4} M FeCl_3 in acetonitrile. The electropolymerization was carried out galvanostatically. Figure 1 a) is a typical top view obtained

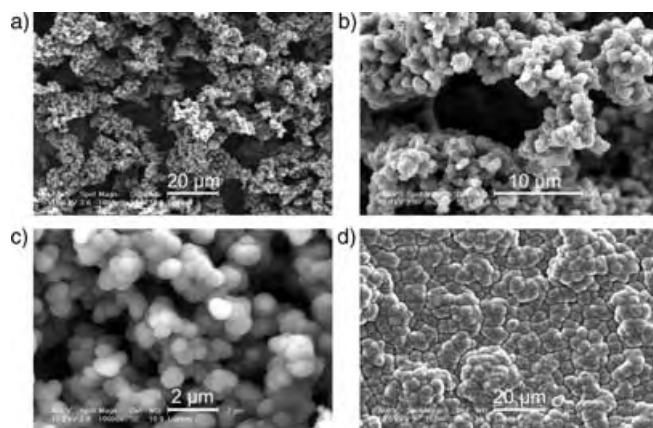


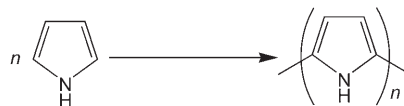
Figure 1. SEM images of PPy films. a) Top view of a large area of the porous film. The pore size ranges from 10–50 μm . b) Top view of a single pore and the surrounding PPy particle assemblies. c) Structure of the pore wall of the porous PPy. The small pores are on the order of 1–4 μm ; the diameters of the PPy particles range from 0.5–1 μm . d) Top view of the compact PPy film.

by scanning electron microscopy (SEM) of the as-deposited perfluorooctanesulfonate (PFOS)-doped PPy film. The image reveals an extended porous structure of the PPy film. The pore size ranges from 10 to 50 μm . A magnified image of a single pore shows that the pore wall is also highly porous (Figure 1 b). Figure 1 c reveals the structure of the pore wall. The smaller pores (compared with the pores in Figure 1 a) are on the order of 1–4 μm . The particle assemblies surrounding the smaller pores are composed of submicron PPy particles with diameters of 0.5–1 μm . As will be discussed later, this porous structure with roughness on both coarse and fine scales is most effective in achieving superhydrophobicity and superhydrophilicity.

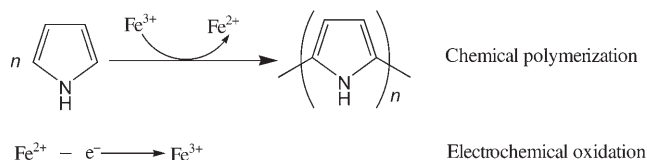
The tiny amount of Fe in the plating solution plays a key role in the formation of this highly porous structure. When no Fe was in the solution, a compact structure (Figure 1 d) was obtained. Fe^{3+} and Fe^{2+} salts have been used as catalysts for the chemical polymerization of conducting polymers such as PPy and polyaniline (PAni), while oxygen, ozone, or H_2O_2 were used as the oxidizing reagent.^[27–29] In our system, the formation of the porous PPy film may be attributed to the coexistence of electropolymerization and chemical polymerization processes. Without Fe in the plating solution, the PPy was produced by only electropolymerization and had a compact structure. When Fe^{3+} was included in the solution,

besides the electropolymerization, Fe^{3+} -catalyzed bulk chemical polymerization may also occur (Scheme 2). For the Fe^{3+} -catalyzed polymerization, the tiny amount of Fe^{3+} first oxidizes the pyrrole monomer to give PPy and the Fe^{3+} ions are reduced to Fe^{2+} ions. Then the Fe^{2+} ions are oxidized into

1) Electropolymerization:



2) Catalytic chemical polymerization:



Scheme 2.

Fe^{3+} by the positive potential and used again to chemically synthesize PPy. Thus, Fe^{3+} acts as a catalyst in the synthesis of PPy. The need to regenerate Fe^{3+} by the electrode is believed to confine the chemical polymerization to the vicinity of the electrode surface, leading to closely coupled electropolymerization and chemical polymerization. And this combined polymerization process promotes the growth of porous and rough PPy film.

Other types of iron salts, such as FeCl_2 , $\text{Fe}(\text{ClO}_4)_3$, $\text{Fe}(\text{ClO}_4)_2$, and FeSO_4 , can also be used to produce similar PPy structures. To control the rate of chemical polymerization and the import of excess amounts of codopants such as Cl^- , ClO_4^- , and SO_4^{2-} , the concentration of the iron salts is usually kept very low ($< 10^{-3}$ M).

As-prepared highly porous PPy films have interesting surface properties. As can be seen from the SEM images (Figure 1 a–c), the porous PPy films exhibit both coarse-scale and fine-scale roughness (so-called double-roughness structure), which is a favorable structure for mimicking the lotus-leaf effect for repelling water.^[30] When low-surface-energy perfluorooctanesulfonate (PFOS) was used as a dopant in the polymerization, the PPy films showed superhydrophobicity with a static water contact angle as high as $152 \pm 2^\circ$ (Figure 2 a left), while the water contact angle of the compact smooth PPy film was about $105 \pm 2^\circ$ (Figure 2 b left). It is well-known that surface roughness amplifies hydrophobicity.^[31–33] The common way to obtain superhydrophobicity is to modify a rough surface with low-surface-energy materials such as perfluorinated materials, or to produce a rough structure on a hydrophobic surface. The advancing (θ_A) and receding (θ_R) contact angles of the superhydrophobic surface were measured to be $155 \pm 2^\circ$ and $147 \pm 2^\circ$, respectively. The low contact angle hysteresis ($\sim 8^\circ$) of water on the PPy surface confirms the lotus effect which results from the double-roughness structure of the porous PPy films. Our method offers a simple, one-step process to fabricate conducting

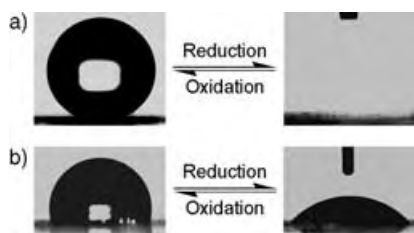


Figure 2. Electrical-potential-induced wettability conversion between PFOS-doped (oxidized) PPy films and dedoped (neutral) PPy films. Under negative potential (-0.6 V vs. Ag/AgCl), the oxidized PPy films were reduced to neutral PPy films, and under positive potential (1.0 V vs. Ag/AgCl), the neutral PPy films were again oxidized to oxidized PPy films. The conversion is reversible. a) The profile of a water drop on a highly porous PPy film. Oxidized PPy film shows superhydrophobicity with a water contact angle of $152 \pm 2^\circ$ (left); neutral PPy film shows superhydrophilicity with a water contact angle of $\approx 0^\circ$ (right). b) The profile of a water drop on a compact PPy film. Oxidized PPy film is hydrophobic with a water contact angle of $105 \pm 2^\circ$ (left); neutral PPy film is hydrophilic with a water contact angle of $48 \pm 2^\circ$ (right).

polymers with superhydrophobicity. The superhydrophobic PPy films can be deposited on common conducting substrates such as metals and indium tin oxide (ITO)-coated glasses. Our experiments revealed that the superhydrophobic PPy films adhered well to the Au-coated glass surface, and they can be easily peeled off for convenient transfer to other substrates.

Conducting polymers like PPy can be reduced and oxidized reversibly by controlling the electrochemical potential. It is expected that the oxidized (doped) PPy and neutral (dedoped) PPy show different wettability. Neutral PPy, which contains pyrrole moieties, is usually slightly hydrophilic. Surface roughness enhances both the hydrophilicity of hydrophilic surfaces and the hydrophobicity of hydrophobic ones. When we held the PFOS-doped PPy in a 0.05 M solution of TEAPFOS in acetonitrile at a negative potential (-0.6 V vs. Ag/AgCl reference electrode) for 20 minutes, the superhydrophobic PPy film was converted to neutral PPy film, which exhibits a water contact angle of about 0° , indicating that a superhydrophilic PPy surface was achieved (Figure 2a). The superhydrophilicity results from the imbibition of water into the texture of neutral PPy films with high roughness and a hydrophilic nature (see Supporting Information). Under similar switching conditions, the compact PPy film changed to a neutral one having a contact angle of $48 \pm 2^\circ$ (Figure 2b). When we held the superhydrophilic (neutral PPy) film in a 0.05 M solution of TEAPFOS in acetonitrile at a positive potential (1.0 V vs. Ag/AgCl reference electrode) for 20 minutes, the superhydrophobic (oxidized PPy) surface was regenerated. Through controlling the electrochemical potential, PPy films were changed between the oxidized state and neutral state repeatedly, resulting in a reversibly switchable superhydrophobic and superhydrophilic surface (Figure 3).

The neutral and oxidized PPy films are different not only in their surface properties but also in their chemical composition, electronic structure, color, conductivity, and volume. Energy dispersive X-ray (EDX) spectra reveal that little PFOS dopant exists in the neutral PPy films but significant amounts are found in the oxidized ones. Neutral PPy films are

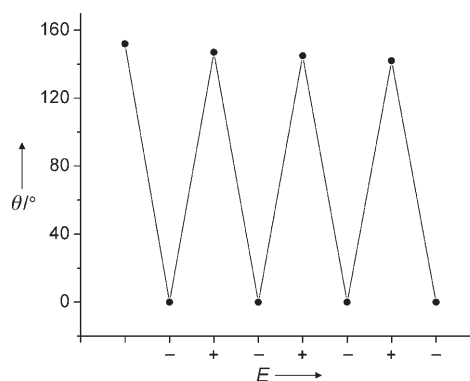


Figure 3. Reversible superhydrophobic-to-superhydrophilic conversion of the porous PPy films through applying alternative negative potential (-0.6 V vs. Ag/AgCl) and positive potential (1.0 V vs. Ag/AgCl). θ = contact angle.

brown, while the PFOS-doped PPy films are black. The major UV/Vis absorption band of the PPy film is blue-shifted from 460 nm (2.7 eV in energy) for the PFOS-doped PPy film to 395 nm (3.1 eV in energy) for the neutral one. The conductivities of the PFOS-doped PPy film and the neutral film are around 50 S cm^{-1} and 0.02 S cm^{-1} , respectively. (A trace amount of the PFOS dopant still exists in the neutral film.) The volume (the pores and submicron PPy particles) of the PPy film retracted after the oxidized PPy was reduced to neutral PPy.

In summary, we have demonstrated a simple facile electropolymerization of superhydrophobic PPy films and the reversible switching of the PPy films between superhydrophobicity and superhydrophilicity. The PPy films exhibit an extended porous structure. These highly porous conducting polymers may have unique surface properties. Though we used pyrrole monomer and PFOS dopant in our synthesis, it is expected that our method can be extended to prepare other types of conducting polymers such as polythiophene, polyaniline, and poly(*N*-methyl pyrrole), and polypyrrole with other types of dopants. The reversible superhydrophobic-to-superhydrophilic switching of the PPy films is achieved by simply adjusting the electrical potential. These smart films may find numerous applications, for example, in drug delivery, biochips, microfluidics (e.g., switches and pumps), and biosensors. In addition to the wettability switching, the volume, conductivity, and color of the PPy films also undergo reversible conversion, making it possible to construct multifunctional conducting polymer devices combining special mechanical, electrical, optical, and interfacial properties.

Experimental Section

Synthesis of superhydrophobic polypyrrole films: The electrochemical cell, which consisted of a glass tube 3 cm in diameter that terminated in a 1.6-cm^2 "O" ring seal, was placed on top of the conducting substrate (such as Au-coated glass slides, steel foils, and ITO-coated glass slides) and held in place with a clamp. The electroplating solution, which contained 0.1 M pyrrole, 0.05 M tetraethylammonium perfluorooctanesulfonate (TEAPFOS), and 2.0×10^{-4} M FeCl_3 in acetonitrile, was then added to the cell, and conducting polypyrrole (PPy) was plated at a constant current of ≈ 0.25 mA cm^{-2}

in an argon atmosphere using a Solartron 1287 A potentiostat/galvanostat. Pt wire and Ag/AgCl electrode (sat. KCl) were used as the counter electrode and reference electrode, respectively. The time for the polymerization was usually 1 h. After polymerization, the PPy films were washed in acetonitrile and then dried under a flow of argon.

Switching experiments: The device for the switching experiments was the same as that used for the synthesis of the PPy films. The solution for switching contained 0.05 M TEAPFOS in acetonitrile. By holding the PFOS-doped (oxidized) PPy films in the solution at a negative potential (−0.6 V vs. Ag/AgCl reference electrode) for 20 min, the oxidized PPy was converted to neutral PPy. Neutral PPy films were then washed in acetonitrile and dried under a flow of argon. By holding the neutral PPy films in the solution at a positive potential (1.0 V vs. Ag/AgCl reference electrode) for 20 min, the neutral PPy was converted to oxidized (PFOS-doped) PPy. Oxidized PPy films were then washed in acetonitrile and dried under a flow of argon. The switching experiments can be conducted repeatedly on the same sample.

Characterization: SEM images and EDX spectra were obtained on an XL30 FEG scanning electron microscope. Contact angle measurements were performed using a VCA Optima contact angle instrument at ambient temperature (AST Products, Inc.). The water droplets used for measurements had a volume of 3.0 μ L. Dynamic advancing (θ_A) and receding (θ_R) contact angles were recorded as water was added to and withdrawn from the water droplet, respectively. The conductivity of the samples in the plane direction was determined by a standard four-probe method. UV/Vis absorption spectra of PPy films were recorded on Varian Cary 50 UV/Vis spectrophotometers (190–1000 nm).

Received: March 9, 2005

Revised: May 10, 2005

Published online: August 17, 2005

Keywords: electrochemistry · hydrophobic effect · polymers · porous films · surface chemistry

- [14] J. Deval, T. A. Umali, E. H. Lan, B. Dunn, C. M. Ho, *J. Micromech. Microeng.* **2004**, *14*, 91–95.
- [15] S. Minko, M. Muller, M. Motornov, M. Nitschke, K. Grundke, M. Stamm, *J. Am. Chem. Soc.* **2003**, *125*, 3896–3900.
- [16] D. Julthongpipit, Y. H. Lin, J. Teng, E. R. Zubarev, V. V. Tsukruk, *Langmuir* **2003**, *19*, 7832–7836.
- [17] P. Chandrasekhar, *Conducting Polymers, Fundamentals and Applications: A Practical Approach*, Kluwer Academic Publishers, New York, **1999**.
- [18] E. Smela, *J. Micromech. Microeng.* **1999**, *9*, 1–18.
- [19] G. Kousik, S. Pitchumani, N. G. Renganathan, *Prog. Org. Coat.* **2001**, *43*, 286–291.
- [20] H. H. Kuhn, A. D. Child, W. C. Kimbrell, *Synth. Met.* **1995**, *71*, 2139–2142.
- [21] D. Mecerreyes, V. Alvaro, I. Cantero, M. Bengoetxea, P. A. Calvo, H. Grande, J. Rodriguez, J. A. Pomposo, *Adv. Mater.* **2002**, *14*, 749–752.
- [22] A. Azioune, M. M. Chehimi, B. Miksa, T. Basinska, S. Slomkowski, *Langmuir* **2002**, *18*, 1150–1156.
- [23] J. Y. Wong, R. Langer, D. E. Ingber, *Proc. Natl. Acad. Sci. USA* **1994**, *91*, 3201–3204.
- [24] J. Isaksson, C. Tengstedt, M. Fahlman, N. Robinson, M. Berggren, *Adv. Mater.* **2004**, *16*, 316–320.
- [25] W. Torres, J. C. Donini, A. A. Vlcek, A. B. P. Lever, *Langmuir* **1995**, *11*, 2920–2925.
- [26] G. Kossmehl, M. Niemitz, *Synth. Met.* **1991**, *41*, 1065–1071.
- [27] N. Toshima, O. Ihata, *Synth. Met.* **1996**, *79*, 165–172.
- [28] H. Yan, M. Kajita, N. Toshima, *Macromol. Mater. Eng.* **2002**, *287*, 503–508.
- [29] Z. C. Sun, Y. H. Geng, J. Li, X. H. Wang, X. B. Jing, F. S. Wang, *J. Appl. Polym. Sci.* **1999**, *72*, 1077–1084.
- [30] N. A. Patankar, *Langmuir* **2004**, *20*, 8209–8213.
- [31] A. Nakajima, K. Hashimoto, T. Watanabe, *Monatsh. Chem.* **2001**, *132*, 31–41.
- [32] A. Lafuma, D. Quéré, *Nat. Mater.* **2003**, *2*, 457–460.
- [33] L. Feng, S. H. Li, Y. S. Li, H. J. Li, L. J. Zhang, J. Zhai, Y. L. Song, B. Q. Liu, L. Jiang, D. B. Zhu, *Adv. Mater.* **2002**, *14*, 1857–1860.

- [1] T. P. Russell, *Science* **2002**, *297*, 964–967.
- [2] R. Langer, D. A. Tirrell, *Nature* **2004**, *428*, 487–492.
- [3] I. Luzinov, S. Minko, V. V. Tsukruk, *Prog. Polym. Sci.* **2004**, *29*, 635–698.
- [4] J. Lahann, S. Mitragotri, T. N. Tran, H. Kaido, J. Sundaram, I. S. Choi, S. Hoffer, G. A. Somorjai, R. Langer, *Science* **2003**, *299*, 371–374.
- [5] X. M. Wang, A. B. Kharitonov, E. Katz, I. Willner, *Chem. Commun.* **2003**, 1542–1543.
- [6] B. S. Gallardo, V. K. Gupta, F. D. Egerton, L. I. Jong, V. S. Craig, R. R. Shah, N. L. Abbott, *Science* **1999**, *283*, 57–60.
- [7] T. L. Sun, G. J. Wang, L. Feng, B. Q. Liu, Y. M. Ma, L. Jiang, D. B. Zhu, *Angew. Chem.* **2004**, *116*, 361–364; *Angew. Chem. Int. Ed.* **2004**, *43*, 357–360.
- [8] G. de Crevoisier, P. Fabre, J. M. Corpart, L. Leibler, *Science* **1999**, *285*, 1246–1249.
- [9] S. Abbott, J. Ralston, G. Reynolds, R. Hayes, *Langmuir* **1999**, *15*, 8923–8928.
- [10] K. Ichimura, S. K. Oh, M. Nakagawa, *Science* **2000**, *288*, 1624–1626.
- [11] X. J. Feng, L. Feng, M. H. Jin, J. Zhai, L. Jiang, D. B. Zhu, *J. Am. Chem. Soc.* **2004**, *126*, 62–63.
- [12] H. Liu, L. Feng, J. Zhai, L. Jiang, D. B. Zhu, *Langmuir* **2004**, *20*, 5659–5661.
- [13] R. Rosario, D. Gust, A. A. Garcia, M. Hayes, J. L. Taraci, T. Clement, J. W. Dailey, S. T. Picraux, *J. Phys. Chem. B* **2004**, *108*, 12640–12642.

Nanoarrays of Single Virus Particles**

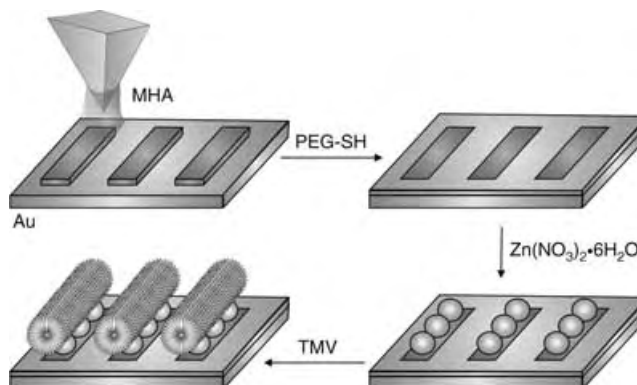
Rafael A. Vega, Daniel Maspoch, Khalid Salaita, and
Chad A. Mirkin*

Microarray technology has led to significant advances in many areas of medical and biological research,^[1] opening up avenues for the combinatorial screening and identification of single-nucleotide polymorphisms (SNPs),^[2] high-sensitivity expression profiling of proteins,^[3,4] and high-throughput analysis of protein function.^[5] With the advent of high-resolution direct-write lithographic methods such as dip-pen nanolithography (DPN),^[6] it is possible to conceive of methods for miniaturizing such structures to the nanometer-length scale.^[7–9] Such massive miniaturization provides the clear potential advantages of larger, denser libraries for screening complex chemical and biological systems. However, miniaturization on this size scale also provides the potential to site-isolate nano- and microscale biological entities (proteins, viruses, and cells) at the single-particle level. Once this can be done routinely for many different systems, new opportunities will be available to the biochemical and biomedical research communities to study such entities individually rather than collectively. Herein, we describe a novel strategy that uses DPN in combination with coordination chemistry to precisely immobilize and position many individual virus particles in the context of large arrays. Tobacco mosaic virus (TMV) was chosen as the test case scenario because of its anisotropic tubular structure (length ≈ 300 nm, diameter = 18 nm), size, stability, and well-characterized carboxylate-rich surface.^[10] It serves as an excellent model system to evaluate how DPN can be used to control the positioning and orientation of nano-scale virus particles within an extended array.

Prior to this study, advances were made in immobilizing virus particles on templates created by DPN and μ -contact printing.^[11,12] Thus far, there has been no demonstration of the ability to chemically control the position of the immobilized virus structures at the single-particle level. This is partially the result of limited resolution, the size of the particles interrogated, and the chemistry used to immobilize them. Indeed, previous efforts focused on the genetic modification of a virus particle to present unnatural surface binding functionality to

the patterned interface.^[11,12] This strategy has allowed researchers to prepare arrays of collections of virus particles at individual feature sites, but not to site-isolate individual particles. The approach used herein relies on the ability of metal ions (Zn^{2+}) to bridge a surface patterned with features made of 16-thiohexadecanoic acid (MHA) and the TMV with its carboxylate-rich surface.

Virus nanoarrays were fabricated by initially generating chemical templates of MHA on a gold thin film by using DPN (Scheme 1). The regions surrounding these features were



Scheme 1. Selective immobilization of single virus particles on DPN-generated MHA nanotemplates treated with $\text{Zn}(\text{NO}_3)_2 \cdot 6\text{H}_2\text{O}$.

passivated with a monolayer of 11-thioundecyl-penta(ethylene glycol) (PEG-SH) by immersing the substrate in an alkanethiol solution (5 mM in ethanol) for 30 min followed by copious rinsing with ethanol. The passivation layer minimizes nonspecific binding of the virus particles to the unpatterned areas. The carboxylic acid groups of MHA were coordinated to Zn^{2+} ions (represented as spheres) by exposing the substrate to a solution of $\text{Zn}(\text{NO}_3)_2 \cdot 6\text{H}_2\text{O}$ (5 mM in ethanol) for one hour followed by rinsing with ethanol to remove any unbound metal ions from the surface. The metallated substrate was then exposed to TMV ($100 \mu\text{g mL}^{-1}$, American Type Culture Collections) in phosphate-buffered saline (PBS, 10 mM with NaCl (0.15 M), pH 7) for 24 h at room temperature in an air-tight humidity chamber. Excess virus particles were removed by washing the substrates with highly purified (NANOpure) water. The cleaned substrates were then dried under a stream of N_2 . All virus arrays were characterized by tapping mode AFM (TMAFM), and the chemical identity of the surface-immobilized virus particles was confirmed by treatment with a highly specific antiserum (American Type Culture Collections) against TMV, which upon binding increases the height of each virus particle (see below).

A series of DPN-patterned linear nanostructures of MHA with varied dimensions (length \times width: $600 \times 200 \text{ nm}^2$, $500 \times 180 \text{ nm}^2$, $400 \times 50 \text{ nm}^2$, and $350 \times 110 \text{ nm}^2$) were systematically studied to determine the optimal feature size for single virus particle attachment. Under the conditions studied, MHA templates with feature dimensions of $350 \times 110 \text{ nm}^2$ spaced one micrometer apart were ideal for individual particle assembly. The tendency of each virus to occupy the largest number of coordination sites results in near-perfect alignment

[*] R. A. Vega, Dr. D. Maspoch, K. Salaita, Prof. C. A. Mirkin
Department of Chemistry and Institute for Nanotechnology
Northwestern University
2145 Sheridan Road, Evanston, IL 60208-3113 (USA)
Fax: (+1) 847-467-5123
E-mail: chadnano@northwestern.edu

[**] C.A.M. acknowledges the AFOSR, ARO, DARPA, NIH, and NSF for support of this work. R.A.V. thanks the NIH for predoctoral support, and D.M. is grateful to the Generalitat de Catalunya for a postdoctoral grant.

Supporting information for this article is available on the WWW under <http://www.angewandte.org> or from the author.

of all the virus particles along the long axis of each rectangular template (Figure 1 a,b). The average height of each feature on the template is 16 ± 1 nm. Furthermore, each virus particle on the lines is 45 ± 2 nm wide and 320 ± 40 nm long (measured at the base, disregarding tip convolution), parameters consistent

particle was tested by immobilization along two different directions within one array. Indeed, the use of an MHA template consisting of 350×110 nm² features perpendicular to each other produced an array of site-isolated single TMV virus particles perpendicular to each other (Figure 1 b).

Polarization modulation infrared reflection absorption spectroscopy (PM-IRRAS) was used to characterize bulk gold thin-film substrates modified with TMV by using the same coordination chemistry approach used to generate the TMV arrays (Figure 2 a). The MHA monolayer exhibits two main bands in the high-frequency CH₂ stretch region at 2856 and 2930 cm⁻¹ and two in the C=O stretch region at 1741 and 1718 cm⁻¹, which are attributed to the presence of free and hydrogen-bonded carboxylic groups,^[15] respectively. After the substrate was immersed in an ethanolic solution of Zn(NO₃)₂·6H₂O (5 mM) for 1 h, the coordination of MHA carboxylic groups to Zn²⁺ metal ions was confirmed by Δ_{CO} band shifts to lower energy ($\tilde{\nu} = 1602/1556$ and 1453 cm⁻¹). The C=O stretch region changes again after exposing the MHA–Zn²⁺ surface to the TMV solution. Three main bands are detected in this spectral region that can be identified as the amide I band centered at 1661 cm⁻¹ (which is characteristic of proteins in TMV^[16]), the amide II and asymmetric COO⁻ bands centered at 1546 cm⁻¹, and a symmetric COO⁻ band at 1458 cm⁻¹. Also, the presence of CH₃ features,

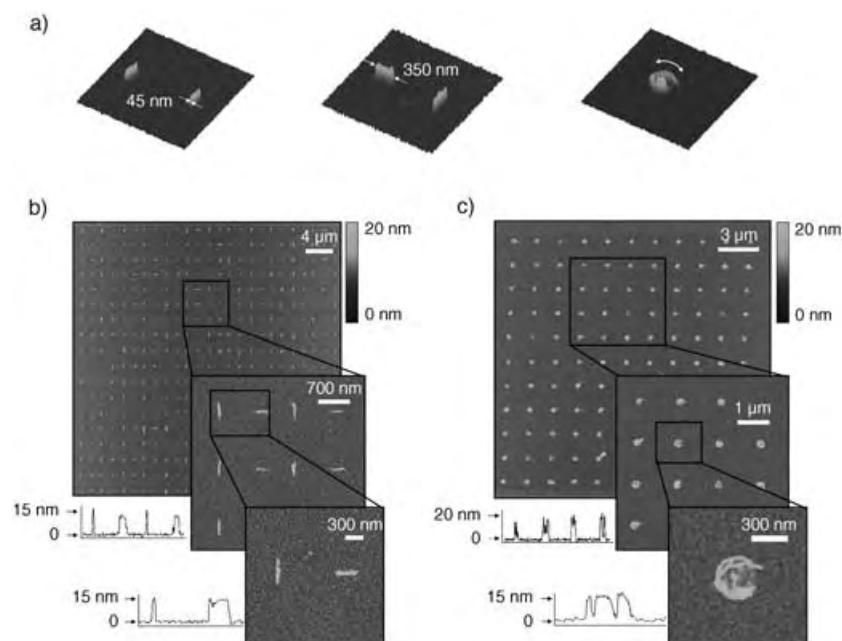


Figure 1. AFM tapping mode (silicon cantilever, spring constant ≈ 40 N m⁻¹) images and height profiles of TMV nanoarrays: a) 3D topographical images of pairs of virus particles within larger arrays: a parallel array (left), a perpendicular array (middle), and dot arrays (right); b) topography images and height profiles of a perpendicular array of single virus particles (40×40 μm²); c) topography image and height profiles of a TMV nanoarray (20×20 μm²) formed on an array of MHA dot features ($\varnothing = 350$ nm) pretreated with Zn(NO₃)₂·6H₂O. All images were collected at a scan rate of 0.5 Hz.

with the presence of only one TMV particle on each MHA feature.^[13] The dimensions of the features within the array are critical for virus particle site-isolation. For example, rectangular templates greater than 500 nm long or 200 nm wide yield multiple yet oriented viruses at each site, thus preventing the formation of a single virus particle array (see Supporting Information). Features significantly smaller (less than 300×100 nm²) do not result in uniform assembly of the virus particles; numerous sites remain unoccupied.

The chemical templates can also be used to control the assembly of the flexible virus into unnatural conformations such as circles and other curved architectures. For example, dot templates 350 nm in diameter can capture multiple virus particles, many of which adhere to the rim of the dot and adopt a curved shape (Figure 1 c). Curved TMV structures have been made previously, but through mechanical manipulation of the virus.^[14] This approach to virus bending is different from the templated chemical approach described herein.

To demonstrate that the virus orientation is not the result of external variables such as washing, drying with N₂, or capillary effects, the independent organization of each virus

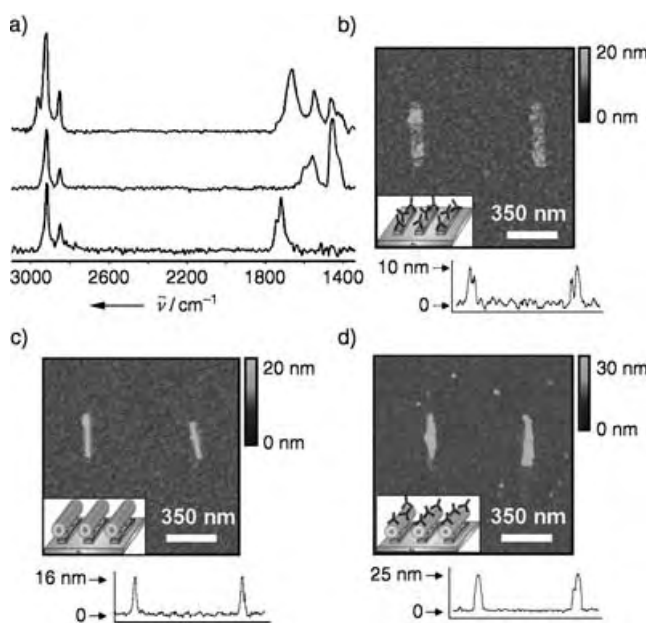


Figure 2. a) PM-IRRAS spectra of a monolayer of MHA on Au (bottom spectrum), after treatment with Zn(NO₃)₂·6H₂O (middle spectrum), and subsequent incubation with TMV (top spectrum). b) Topography image and height profile of an MHA array treated with the antiserum against TMV. The antibodies are electrostatically attached to the MHA features. Topography images and height profiles of a pair of parallel single virus particles c) before and d) after treatment with a PBS solution containing the antiserum against TMV. All AFM images were taken at a scan rate of 0.5 Hz in tapping mode.

attributed to proteins with methyl groups, is confirmed by the emergence of a new band at 2967 cm^{-1} after incubation with TMV.

The coordination chemistry of Zn^{2+} is essential for the virus particle assembly process. The results of control experiments support this conclusion, as TMV does not assemble on MHA coated or patterned substrates (dot diameter = $1\text{ }\mu\text{m}$), even after exposure of the template to the virus in a PBS solution for 48 h.

To provide further evidence for the chemical identity of the tubular virus structures imaged by AFM, the single virus arrays were treated with a PBS solution containing an antiserum against TMV ($200\text{ }\mu\text{g mL}^{-1}$, pH 7) at 37°C for 30 minutes. The substrates were rinsed with PBS and then dried under a stream of N_2 . A comparison of the AFM images of the substrate before and after incubation with antibody shows a height increase of approximately 9 nm (Figure 2c,d). This increase is consistent with the height of the antibody (Figure 2b) and therefore, the presence of TMV particles on the arrays.^[17] Note that the expected height increase upon antibody binding was independently modeled and measured by using direct adsorption of the antibody onto an MHA array (Figure 2b). This approach has been used to study protein binding events in the context of other protein immobilization experiments.^[8]

In conclusion, we report a versatile coordination-chemistry-based approach for the immobilization of TMV virus particles on surfaces and show that through the use of DPN and small features, it is possible to isolate and control the orientation of these virus particles. Many virus particles have metal-binding groups for Zn^{2+} and other ions in their protein coats.^[18] Therefore, it is likely that this approach can be generalized for manipulating many virus structure classes at the single-particle level. Such capabilities will expand the scope of application for virus structures in fields ranging from biology to molecular electronics,^[19] in which such control opens new opportunities for research that cannot be addressed with microarrays or bulk systems.

Experimental Section

All DPN patterning was done with a CP AFM (ThermoMicroscopes) interfaced with commercialized lithographic software (DPNwrite, NanoInk Inc., Chicago, IL) and conventional Si_3N_4 cantilevers (ThermoMicroscopes-sharpened Microcantilever A, force constant = 0.05 N m^{-1}). Tapping mode images were taken with a Nanoscope IIIa and MultiMode microscope (Digital Instruments). Unless noted otherwise, all DPN patterning experiments were conducted at 35 % relative humidity and 24°C with a tip–substrate contact force of 0.5 nN. DPN was used to pattern MHA on gold substrate (50 nm Au and 10 nm Cr on a silicon wafer, Silicon Sense, Inc.). PM-IRRAS spectra of 2048 scans at a resolution of 4 cm^{-1} were obtained with a Thermo Nicolet Nexus 870 with tabletop optics module (TOM) (courtesy of the Keck II Center at Northwestern University). The PM-IRRAS differential reflectance ($\%\Delta R/R$) values were converted into absorbance units for comparison with conventional IRRAS data.

Received: June 7, 2005

Published online: August 22, 2005

Keywords: coordination modes · nanotechnology · scanning probe microscopy · surface chemistry · viruses

- [1] U. R. Miller, D. V. Nicolau, *Microarray Technology and Its Applications*, Springer, New York, **2005**.
- [2] K. Lindroos, S. Sigurdsson, K. Johansson, L. Ronnblom, A. C. Syvanen, *Nucleic Acid Res.* **2002**, *30*, e70–e78.
- [3] M. Schena, D. Shalon, R. W. Davis, P. O. Brown, *Science* **1995**, *270*, 467–470.
- [4] R. A. Heller, M. Schena, A. Chai, D. Shalon, T. Bedilion, J. Gilmore, D. E. Woolley, R. W. Davis, *Proc. Natl. Acad. Sci. USA* **1997**, *94*, 2150–2155.
- [5] G. MacBeath, S. L. Schreiber, *Science* **2000**, *289*, 1760–1763.
- [6] a) D. S. Ginger, H. Zhang, C. A. Mirkin, *Angew. Chem.* **2004**, *116*, 30–46; *Angew. Chem. Int. Ed.* **2004**, *43*, 30–45; b) R. D. Piner, J. Zhu, F. Xu, S. Hong, C. A. Mirkin, *Science* **1999**, *283*, 661–663.
- [7] For an example of DNA nanoarrays, see: L. M. Demers, D. S. Ginger, S.-J. Park, Z. Li, S.-W. Chung, C. A. Mirkin, *Science* **2002**, *296*, 1836–1838.
- [8] For an example of protein nanoarrays, see: a) K.-B. Lee, S.-J. Park, C. A. Mirkin, J. C. Smith, M. Mrksich, *Science* **2002**, *295*, 1702–1705; b) K.-B. Lee, J.-H. Lim, C. A. Mirkin, *J. Am. Chem. Soc.* **2003**, *125*, 5588–5589; c) J.-H. Lim, D. Ginger, K.-B. Lee, J. Heo, J.-M. Nam, C. A. Mirkin, *Angew. Chem.* **2003**, *115*, 2411–2414; *Angew. Chem. Int. Ed.* **2003**, *42*, 2309–2312.
- [9] For an example of peptide nanoarrays, see: J. Hyun, W. K. Lee, N. Nath, A. Chilkoti, S. Zauscher, *J. Am. Chem. Soc.* **2004**, *126*, 7330–7335.
- [10] a) T. M. A. Wilson, R. N. Perham, *Virology* **1985**, *140*, 21–27; b) L. King, R. Leberman, *Biochim. Biophys. Acta* **1973**, *322*, 279–293.
- [11] C. L. Cheung, J. A. Carnarero, B. W. Woods, T. Lin, J. E. Johnson, J. J. Yoreo, *J. Am. Chem. Soc.* **2003**, *125*, 6848–6849.
- [12] J. C. Smith, K.-B. Lee, Q. Wang, M. G. Finn, J. E. Johnson, M. Mrksich, C. A. Mirkin, *Nano Lett.* **2003**, *3*, 883–886.
- [13] a) M. Knez, M. P. Sumser, A. M. Bittner, C. Wege, H. Jeske, D. M. P. Hoffmann, D. M. P. Kuhnke, K. Kern, *Langmuir* **2004**, *20*, 441–447; b) H. Maeda, *Langmuir* **1997**, *13*, 4150–4161, and references therein.
- [14] M. Guthold, M. Falvo, W. G. Matthews, S. Paulson, J. Mullin, S. Lord, D. Erie, S. Washburn, R. Superfine, F. P. Brooks Jr., R. M. Taylor II, *J. Mol. Graphics Modell.* **1999**, *17*, 187–197.
- [15] B. L. Frey, R. M. Corn, *Anal. Chem.* **1996**, *68*, 3187–3193.
- [16] R. D. B. Fraser, *Nature* **1952**, *170*, 491.
- [17] Antibody arrays were generated by first using DPN to pattern rectangular lines of MHA with feature dimensions of $350 \times 110\text{ nm}^2$. The area around these features was passivated with PEG-SH for 30 min, followed by copious rinsing with ethanol to inhibit nonspecific binding. Finally, the antiserum against TMV was incubated with the MHA-passivated substrate at 4°C for 24 h. For more details, see reference [8].
- [18] a) A. Nedoluzhko, T. Douglas, *J. Inorg. Biochem.* **2001**, *84*, 233–240; b) G. Basu, M. Allen, D. Willits, M. Young, T. Douglas, *J. Biol. Inorg. Chem.* **2003**, *8*, 721–725.
- [19] a) W. Shenton, T. Douglas, M. Young, G. Stubbs, S. Mann, *Adv. Mater.* **1999**, *11*, 253–256; b) E. Dujardin, C. Peet, G. Stubbs, J. M. Culver, S. Mann, *Nano Lett.* **2003**, *3*, 413–417; c) M. Knez, A. M. Bittner, F. Boes, C. Wege, H. Jeske, E. Mai, K. Kern, *Nano Lett.* **2003**, *3*, 1079–1082.

**Preparation of Heterobimetallic
Oxide–Hydroxide–Hydrosulfides
[LAl(OH)(μ-O)MCp₂(SH)] (M = Ti, Zr)****

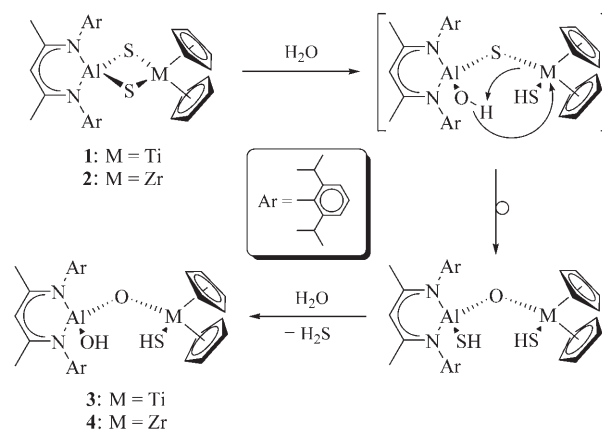
Vojtech Jancik and Herbert W. Roesky*

Dedicated to Professor Thomas B. Rauchfuss

Recently we reported the preparation of heterobimetallic sulfides that contained aluminum atoms [LAl(μ-S)₂MCp₂] (M = Ti, **1**; M = Zr, **2**; L = HC[C(Me)N(2,6-*i*Pr₂C₆H₃)₂; Cp = C₅H₅).^[1] The X-ray crystal structural analysis of the titanium compound **1** confirmed the presence of a highly strained {Al(μ-S)₂Ti} four-membered ring (S–Al–S 102.5(1), Al–S–Ti 84.7(1) and 83.6(1), S–Ti–S 89.3(1)°). The ring strain and the short Al···Ti separation (3.118 Å) prompted us to examine the reactivity of **1** and **2** with water in expectation of a nucleophilic attack that would lead to the opening of the ring and to the isolation of compounds containing the {LAl(EH)(μ-E)M(EH)Cp₂} framework (E = O or S depending on the degree of hydrolysis). Such species could serve as unique precursors for the preparation of trimetallic systems comparable with the alumoxane [(μ-O)[LAl(μ-O)]₂AlMe], which is prepared from [(μ-O)[LAl(OH)]₂] and AlMe₂H.^[2] Although a few dinuclear systems that contain the {M'(EH)(μ-E)M(EH)} arrangement have been described (M' = Al,^[2] Fe,^[3a] Ge,^[3b,c] In,^[3d] Re,^[3e] Ru,^[3f] Sn,^[3g] V,^[3h] Zr^[3i]) none has been structurally characterized that contains two different metal atoms stabilized by organic ligands.

The addition of two equivalents of water to a solution of **1** or **2** in THF at room temperature led, after overnight stirring, to the precipitation of a crystalline material. H₂S was identified as a by-product. The solid product was filtered off, dried in vacuo, and isolated as pale brown (Ti) or pale yellow (Zr) microcrystals. The ¹H NMR spectroscopic, EI mass spectrometric, and X-ray crystal structural analysis of these products confirmed that the ring-opening reaction had occurred, but revealed the presence of two derivatives in the samples. The major component (about 85 %) was identified as [LAl(OH)(μ-O)MCp₂(SH)] (M = Ti, **3**; M = Zr, **4**) whereas the minor component (about 15 %) was the intermediate of the hydrolysis, [LAl(SH)(μ-O)MCp₂(SH)]. One of the first steps of the hydrolytic ring opening is the formation of an unobserved intermediate [LAl(OH)(μ-S)MCp₂(SH)], which subsequently rearranges into [LAl(SH)(μ-O)MCp₂(SH)].

The driving force for this intramolecular rearrangement is the high oxophilicity of the metal centers and the higher stability of the {Al–O–Ti} frame compared to {Al–S–Ti}.^[4] Compound [LAl(SH)(μ-O)MCp₂(SH)] reacts with a second equivalent of water with elimination of H₂S to form **3** or **4** (Scheme 1).



Scheme 1. Preparation of compounds **3** and **4**.

After elucidating the course of the hydrolysis, we focused on the optimization of the hydrolysis conditions. The presence of the intermediates in the final product can be explained by the low solubility of the bridged species in THF and their crystallization from the mother liquor before the reaction was complete. Thus, the use of THF/CH₂Cl₂ (1:1) in the reaction mixture led to the formation of pure **3** or **4**. It is surprising that in these reactions, the Al–S bond is more reactive than the M–S bond. [LAl(SH)₂] reacts smoothly with two equivalents of water to give [LAl(OH)₂] with elimination of H₂S,^[5] but the reaction is relatively slow and needs at least 20 minutes to reach completion at room temperature. It was reported that even traces of moisture in systems that contain Ti–S or Zr–S bonds lead to fast hydrolysis of these bonds.^[6] As reported earlier, the alumoxane [(LAl(OH))₂O]^[2] is stable, whereas [LAl(OH)₂] decomposes even under an inert atmosphere.^[7] It seems that the presence of at least one bridging oxygen atom is necessary for the stabilization of the species containing the {AlO₂} unit.

The isomorphous compounds **3** and **4** crystallize in the monoclinic space group *P*2₁/*n*, with one molecule in the asymmetric unit (Figure 1).^[8] We were not able to crystallize pure **4**, thus data for **4** contaminated with about 15 % of the intermediate [LAl(SH)(μ-O)Zr(SH)Cp₂] were used. The OH moiety on the Al atom and the SH groups on the Ti (**3**) and Zr (**4**) atoms adopt a *cis* conformation and are involved in an intramolecular hydrogen bond O–H···S (**3** 2.66 Å; **4** 2.80 Å). The Al–O(H) (**3** 1.726 Å; **4** 1.720 Å) and Al–O(M) (**3** 1.717 Å; **4** 1.713 Å) bond lengths are similar to those in [LAl(OH)₂] (1.711 and 1.695 Å),^[9] [(LAl(OH))₂O] (1.694–1.741 Å),^[2] and in the trimeric alumoxane [(μ-O)[LAl(μ-O)]₂(MeAl)] (1.726–1.708 Å),^[2] but considerably shorter than those in the μ-OH derivatives (1.787–1.928 Å).^[10] The O–Al–O angles (**3** 114.0°; **4** 114.7°) are similar to those of

[*] Dr. V. Jancik, Prof. Dr. H. W. Roesky
Institut für Anorganische Chemie der Universität
Tammannstrasse 4, 37077 Göttingen (Germany)
Fax: (+49) 551-39-3373
E-mail: hroesky@gwdg.de

[**] L = HC[C(Me)N(Ar)]₂, Ar = 2,6-*i*Pr₂C₆H₃. This work was supported by the Deutsche Forschungsgemeinschaft and the Fonds der Chemischen Industrie.

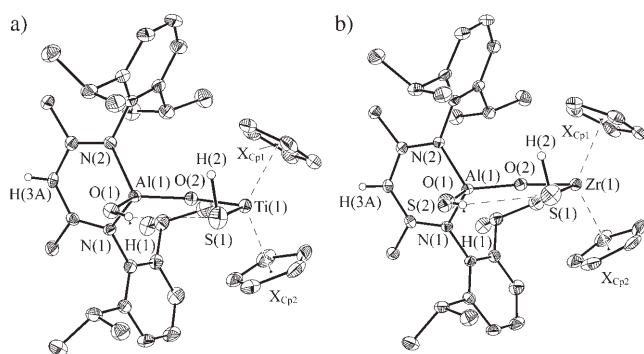


Figure 1. XP plots at the 50% probability level of **3** (a) and **4** (b); the presence of the reaction intermediate that contains an SH group on the aluminum atom, the proton of which could not be localized, is obvious). Hydrogen atoms except those of the SH and OH groups and the H(3A) protons are omitted for clarity. Selected bond lengths [Å] and angles [°]: **3**: Al(1)–N(1) 1.897(2), Al(1)–N(2) 1.901(2), Al(1)–O(1) 1.726(2), Al(1)–O(2) 1.719(2), O(1)–H(1) 0.85(2), Ti(1)–O(2) 1.820(2), Ti(1)–S(1) 2.482(1), S(1)–H(2) 1.25(3), Ti(1)–X_{Cp1} 2.107(3), Ti(1)–X_{Cp2} 2.098(3); N(1)–Al(1)–N(2) 95.7(1), O(1)–Al(1)–O(2) 114.0(1), Al(1)–O(1)–H(1) 119(3), Al(1)–O(2)–Ti(1) 148.9(1), O(2)–Ti(1)–S(1) 97.3(1), Ti(1)–S(1)–H(2) 100(2), X_{Cp1}–Ti(1)–X_{Cp2} 128.6(2). **4**: Al(1)–N(1) 1.895(2), Al(1)–N(2) 1.898(2), Al(1)–O(1) 1.720(6), Al(1)–S(2) 2.08(1), Al(1)–O(2) 1.713(2), O(1)–H(1) 0.85(2), Zr(1)–O(1) 1.939(2), Zr(1)–S(1) 2.573(1), S(1)–H(2) 1.19(3), Zr(1)–X_{Cp1} 2.237(3), Zr(1)–X_{Cp2} 2.240(3); N(1)–Al(1)–N(2) 96.1(1), O(1)–Al(1)–O(2) 114.7(2), O(2)–Al(1)–S(2) 112.2(4), Al(1)–O(1)–H(1) 122(3), Zr(1)–S(1)–H(1) 100(2), Al(1)–O(2)–Zr(1) 147.2(1), O(2)–Zr(1)–S(1) 98.7(1), X_{Cp1}–Zr(1)–X_{Cp2} 128.0(2).

[LAl(OH)₂], [[LAl(OH)₂]₂O], and [(μ-O)[LAl(μ-O)]₂–(MeAl)] (108.3–115.3°);^[2,9] the Al–O–M angles are 148.9° for **3** and 147.2° for **4**. The Ti–O (1.820 Å) and Ti–S (2.482 Å) bond lengths and the O–Ti–S angle (97.3°) are similar to those reported for other [Cp₂TiOS] fragments: Ti–O 1.845–1.872 Å; Ti–S 2.314–2.467 Å; O–Ti–S 87.7–97.9°.^[11] Furthermore, in the zirconium derivative the Zr–O (1.939 Å) and Zr–S (2.573 Å) bond lengths and the O–Zr–S angle (98.7°) are similar to those reported previously for species that contain the {Cp₂ZrOS} moiety: Zr–S 2.459–2.554 Å; Zr–O 1.941–2.199 Å; O–Zr–S 92.6–103.3°.^[6b,12]

In summary, the heterobimetallic sulfides [LAl(μ-S)₂–MCp₂] are ideal precursors for the preparation of the heterobimetallic oxide–hydroxide–hydrogensulfides **3** and **4** by hydrolysis. The presence of two free reactive functionalities in a *cis* arrangement makes them potential starting materials for the heterotrimetallic oxide–sulfides. Such reactions are the subject of our ongoing research.

Experimental Section

All manipulations were performed under a dry and oxygen-free atmosphere (N₂ or Ar) by using Schlenk-line and glovebox techniques.

3: H₂O (26 μL, 1.46 mmol) was added quickly to a solution of **1** (0.50 g, 0.73 mmol) in THF/CH₂Cl₂ (45 mL, 1:1) at room temperature. The suspension was stirred for 10 h and filtered. All the volatile species were removed under vacuum to leave a brown solid residue, which was treated twice with cold toluene (5 mL). After filtration and drying in vacuo, **3** was obtained as a light brown powder. Yield 0.31 g (60%); m.p.: 227°C (decomp); ¹H NMR (500.13 MHz, CDCl₃, 25°C, TMS): δ = 1.07 (s, 1H, OH), 1.10 (d, ³J_{H-H} = 6.9 Hz, 6H, CH(CH₃)₂),

1.20 (d, ³J_{H-H} = 6.7 Hz, 6H, CH(CH₃)₂), 1.37 (d, ³J_{H-H} = 6.9 Hz, 6H, CH(CH₃)₂), 1.44 (d, ³J_{H-H} = 6.7 Hz, 6H, CH(CH₃)₂), 1.77 (s, 6H, CH₃), 2.08 (s, 1H, SH), 3.03 (sept, ³J_{H-H} = 6.9 Hz, 2H, CH(CH₃)₂), 3.49 (sept, ³J_{H-H} = 6.7 Hz, 2H, CH(CH₃)₂), 5.20 (s, 1H, γ-CH), 5.36 (s, 10H, Cp–H), 7.04–7.20 ppm (m, 6H, *m*-, *p*-Ar–H); ¹³C NMR (125.77 MHz, CDCl₃, 25°C, TMS): δ = 23.6, 24.2, 24.4, 24.7 (CH(CH₃)₂), 26.1, 27.5 (CH(CH₃)₂), 28.7 (CH₃), 97.5 (γ-CH), 113.9 (C of Cp) 124.0, 125.2, 127.3, 140.9, 142.9, 145.6 (*i*-, *o*-, *m*-, *p*-C of Ar), 170.6 ppm (C=N); IR (KBr pellet): ν̄ = 3551 br (OH), 2574 vw (SH) cm^{–1}; EI MS (70 eV): *m/z* (%): 623 (10, [M–Cp]⁺), 605 (50, [M–Cp–H₂O]⁺); elemental analysis calcd for C₃₉H₅₃AlN₂O₂Sti (688.78 g mol^{–1}): C 68.0, H 7.8, N 4.1; found: C 67.5, H 8.0, N 4.2%.

4: The synthesis of **4** was similar to that of **3**. Compound **4** was obtained from the reaction of H₂O (25 μL, 1.37 mmol) with **2** (0.50 g, 0.69 mmol) as a pale yellow powder. Yield 0.31 g (62%); m.p.: 235°C (decomp); ¹H NMR (500.13 MHz, CDCl₃, 25°C, TMS): δ = 0.36 (s, 1H, OH), 1.11 (d, ³J_{H-H} = 6.8 Hz, 6H, CH(CH₃)₂), 1.21 (d, ³J_{H-H} = 6.8 Hz, 6H, CH(CH₃)₂), 1.38 (d, ³J_{H-H} = 6.8 Hz, 6H, CH(CH₃)₂), 1.39 (d, ³J_{H-H} = 6.8 Hz, 6H, CH(CH₃)₂), 1.65 (s, 1H, SH), 1.77 (s, 6H, CH₃), 3.04 (sept, ³J_{H-H} = 6.8 Hz, 2H, CH(CH₃)₂), 3.50 (sept, ³J_{H-H} = 6.8 Hz, 2H, CH(CH₃)₂), 5.20 (s, 1H, γ-CH), 5.46 (s, 10H, Cp–H), 7.04–7.20 ppm (m, 6H, *m*-, *p*-Ar–H); ¹³C NMR (125.77 MHz, CDCl₃, 25°C, TMS): δ = 23.5, 24.4, 24.5, 24.6 (CH(CH₃)₂), 27.5, 28.6 (CH(CH₃)₂), 28.7 (CH₃), 97.4 (γ-CH), 111.8 (C of Cp) 124.0, 125.1, 127.3, 140.6, 143.2, 145.5 (*i*-, *o*-, *m*-, *p*-C of Ar), 170.6 ppm (C=N); IR (KBr pellet): ν̄ = 3560 br (OH), 2562 vw (SH) cm^{–1}; EI-MS (70 eV): *m/z* (%): 665 (5, [M–Cp]⁺), 647 (50, [M–Cp–H₂O]⁺); elemental analysis calcd for C₃₉H₅₃AlN₂O₂SZr (732.12 g mol^{–1}): C 64.0, H 7.3, N 3.8; found: C 63.5, H 7.4, N 3.9%.

Received: May 2, 2005

Published online: August 17, 2005

Keywords: aluminum · hydroxides · sulfides · titanium · zirconium

- [1] V. Jancik, H. W. Roesky, D. Neculai, A. M. Neculai, R. Herbst-Irmer, *Angew. Chem.* **2004**, *116*, 6318–6322; *Angew. Chem. Int. Ed.* **2004**, *43*, 6192–6196.
- [2] G. Bai, H. W. Roesky, J. Li, M. Noltemeyer, H.-G. Schmidt, *Angew. Chem.* **2003**, *115*, 5660–5664; *Angew. Chem. Int. Ed.* **2003**, *42*, 5502–5506.
- [3] a) C. Duboc-Toia, S. Ménage, J.-M. Vincent, M. T. Averbuch-Pouchot, M. Fontecave, *Inorg. Chem.* **1997**, *36*, 6148–6149; b) J. Beckmann, K. Jurkschat, M. Schurmann, *Eur. J. Inorg. Chem.* **2000**, 939–941; c) Y. Zhang, F. Cervantes-Lee, K. H. Pannell, *Organometallics* **2003**, *22*, 510–515; d) S. Abram, C. Maichle-Mossner, U. Abram, *Polyhedron* **1998**, *17*, 131–143; e) F. A. Cotton, E. V. Dikarev, M. A. Petrukhina, *Inorg. Chim. Acta* **2002**, *334*, 67–70; f) H. Masuda, T. Taga, K. Osaki, H. Sugimoto, M. Mori, H. Ogoshi, *J. Am. Chem. Soc.* **1981**, *103*, 2199–2203; g) M. A. Edelman, P. B. Hitchcock, M. F. Lappert, *J. Chem. Soc. Chem. Commun.* **1990**, 1116–1118; h) P. Knopp, K. Wiegardt, B. Nuber, J. Weiss, W. S. Sheldrick, *Inorg. Chem.* **1990**, *29*, 363–371; i) G. Jany, R. Fawzi, M. Steimann, B. Rieger, *Organometallics* **1997**, *16*, 544–550.
- [4] One can argue that the unobserved intermediate could be [LAl(SH)(μ-S)MCp₂(OH)], rather than [LAl(OH)(μ-S)MCp₂(SH)]. However, the higher stability of the Ti–SH bond towards hydrolysis, the shielding of the Ti center by two Cp rings, and the easy replacement of the Al–SH group by an Al–OH moiety in the next reaction step support our conclusion.
- [5] V. Jancik, H. W. Roesky, unpublished results.
- [6] a) G. A. Zank, C. A. Jones, T. B. Rauchfuss, A. L. Rheingold, *Inorg. Chem.* **1986**, *25*, 1886–1891; b) D. Coucouvanis, A. Hadjikyriacou, R. Lester, M. G. Kanatzidis, *Inorg. Chem.* **1994**,

- 33, 3645–3655; c) F. Bottomley, D. F. Drummond, G. O. Eggar, P. S. White, *Organometallics* **1986**, 5, 1620–1625; d) M. A. F. Hernandez-Gruel, J. J. Pérez-Torrente, M. A. Ciriano, J. A. López, F. J. Lahoz, L. A. Oro, *Eur. J. Inorg. Chem.* **1999**, 2047–2050.
- [7] V. Jancik, L. W. Pineda, J. Pinkas, H. W. Roesky, D. Neculai, A. M. Neculai, R. Herbst-Irmer, *Angew. Chem.* **2004**, 116, 2194–2107; *Angew. Chem. Int. Ed.* **2004**, 43, 2142–2145.
- [8] a) Crystal data for **3**: $C_{39}H_{53}AlN_2O_2STi$ (688.77), monoclinic, space group $P2_1/n$, $a = 10.903(2)$, $b = 20.543(4)$, $c = 16.222(3)$ Å, $\beta = 99.02(3)^\circ$, $V = 3589(1)$ Å³, $Z = 4$, $\rho_{\text{calcd}} = 1.275$ Mg m⁻³, $F(000) = 1472$, $\lambda = 1.54178$ Å, $T = 100(2)$ K, $\mu(\text{Cu}_{K\alpha}) = 3.075$ mm⁻¹. Of the 22938 measured reflections, 5087 were independent ($R_{\text{int}} = 0.0495$). The final refinements converged at $R1 = 0.0397$ for $I > 2\sigma(I)$, $wR2 = 0.1125$ for all data. The final difference Fourier synthesis gave a min/max residual electron density of $-0.260/+0.477$ e Å⁻³; b) crystal data for **4**: $C_{39}H_{53}AlN_2O_{1.87}S_{1.13}Zr$ (734.14), monoclinic, space group $P2_1/n$, $a = 11.064(2)$, $b = 20.627(3)$, $c = 16.242(3)$ Å, $\beta = 97.76(3)^\circ$, $V = 3673(1)$ Å³, $Z = 4$, $\rho_{\text{calcd}} = 1.328$ Mg m⁻³, $F(000) = 1548$, $\lambda = 1.54178$ Å, $T = 100(2)$ K, $\mu(\text{Cu}_{K\alpha}) = 3.548$ mm⁻¹. Of the 15708 measured reflections, 5150 were independent ($R_{\text{int}} = 0.0351$). The final refinements converged at $R1 = 0.0291$ for $I > 2\sigma(I)$, $wR2 = 0.0764$ for all data. The final difference Fourier synthesis gave a min/max residual electron density of $-0.447/+0.399$ e Å⁻³; c) data for the structures were collected on a Bruker three-circle diffractometer equipped with a SMART 6000 CCD detector. Intensity measurements were performed on a rapidly cooled crystal ($0.40 \times 0.30 \times 0.30$ mm³) in the range $7.00 \leq 2\theta \leq 117.92^\circ$ (**3**) and in the range $6.96 \leq 2\theta \leq 117.94^\circ$ (**4**; $0.10 \times 0.05 \times 0.05$ mm³). The structures were solved by direct methods (SHELXS-97)^[13] and refined against all data by full-matrix least-squares on F^2 .^[14] All the C–H hydrogen atoms except H(3A) were included in geometrically idealized positions and refined with the riding model. Localization of the H(3A) hydrogen from the electron-density map in both structures proved to be more accurate than its fixing in the idealized position and led to a lowering of the $R1$ and $wR2$ values. The hydrogen atoms of the OH and SH moieties in **3** and **4** were localized from the difference electron-density map and refined isotropically with U_{ij} tied to the parent atom. The Al–SH proton belonging to the $[LAl(SH)(\mu-O)ZrCp_2(SH)]$ in the crystal of **4** could not be localized due to its low content (about 15%). CCDC-270756 (**3**) and CCDC-270757 (**4**) contain the supplementary crystallographic data for this paper. These data can be obtained free of charge from the Cambridge Crystallographic Data Centre via www.ccdc.cam.ac.uk/data_request/cif.
- [9] G. Bai, Y. Peng, H. W. Roesky, J. Li, H.-G. Schmidt, M. Noltemeyer, *Angew. Chem.* **2003**, 115, 1164–1167; *Angew. Chem. Int. Ed.* **2003**, 42, 1132–1135.
- [10] a) M. Veith, M. Jarczyk, V. Huch, *Angew. Chem.* **1997**, 109, 140–142; *Angew. Chem. Int. Ed. Engl.* **1997**, 36, 117–119; b) J. Storre, A. Klemp, H. W. Roesky, H.-G. Schmidt, M. Noltemeyer, R. Fleischer, D. Stalke, *J. Am. Chem. Soc.* **1996**, 118, 1380–1386; c) C. Schnitter, H. W. Roesky, T. Albers, H.-G. Schmidt, C. Röpkén, E. Parisini, G. M. Sheldrick, *Chem. Eur. J.* **1997**, 3, 1783–1792; d) Y. Koide, A. R. Barron, *Organometallics* **1995**, 14, 4026–4029.
- [11] a) F. Bottomley, R. W. Day, *Can. J. Chem.* **1992**, 70, 1250–1259; b) G. A. Zank, T. B. Rauchfuss, S. R. Wilson, A. L. Rheingold, *J. Am. Chem. Soc.* **1984**, 106, 7621–7623; c) Z. K. Sweeney, J. L. Polse, R. A. Anderson, R. G. Bergman, *J. Am. Chem. Soc.* **1998**, 120, 7825–7834; d) R. Steudel, A. Prenzel, J. Pickardt, *Angew. Chem.* **1991**, 103, 586–588; *Angew. Chem. Int. Ed. Engl.* **1991**, 30, 550–552.
- [12] a) W. E. Piers, L. Koch, D. S. Ridge, L. R. MacGillivray, M. Zaworotko, *Organometallics* **1992**, 11, 3148–3152; b) J. L. Petersen, *J. Organomet. Chem.* **1979**, 166, 179–192; c) V. W. Yam, G.-Z. Qi, K.-K. Cheung, *J. Organomet. Chem.* **1997**, 548, 289–294; d) H.-M. Gau, C.-A. Chen, S.-J. Chang, W.-E. Shih, T.-K. Yang, T.-T. Jong, M.-Y. Chien, *Organometallics* **1993**, 12, 1314–1318.
- [13] SHELXS-97, Program for Structure Solution: G. M. Sheldrick, *Acta Crystallogr. Sect. A* **1990**, 46, 467.
- [14] G. M. Sheldrick, *SHELXL-97, Program for Crystal Structure Refinement*, Universität Göttingen, Göttingen, **1997**.

Zincation

DOI: 10.1002/anie.200501560

Alkali-Metal-Mediated Zincation of Ferrocene: Synthesis, Structure, and Reactivity of a Lithium Tmp/Zincate Reagent**

Helen R. L. Barley, William Clegg, Sophie H. Dale, Eva Hevia, Gordon W. Honeyman, Alan R. Kennedy, and Robert E. Mulvey**

Lithium dialkyl tetramethylpiperidino zincates of the general formula “[LiR₂Zn(tmp)]” (tmp = 2,2,6,6-tetramethylpiperidine) represent an important subfamily of organozincate reagent. Established only in 1999 through the pioneering work on “[LiBu₂Zn(tmp)]” by Kondo et al.,^[1] “tmp zincates” have found application as highly chemo- and/or regioselective bases for the metalation of alkyl benzoates and related aza aromatic compounds, bromopyridines, and various halobenzenes.^[2,3] Recent reports^[4] have highlighted the poverty of structural information available on lithium zincates in general. Tmp zincates are no exception in this regard, with a ¹³C NMR spectroscopic study of “[LiBu₂Zn(tmp)]” in solution^[1] providing the only morsel of structural evidence

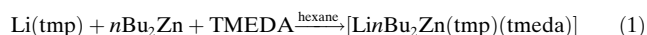
[*] H. R. L. Barley, Dr. E. Hevia, G. W. Honeyman, Dr. A. R. Kennedy, Prof. R. E. Mulvey
Department of Pure and Applied Chemistry
University of Strathclyde
Glasgow, G1 1XL (UK)
Fax: (+44) 141-552-0876
E-mail: eva.hevia@strath.ac.uk
r.e.mulvey@strath.ac.uk

Prof. W. Clegg, Dr. S. H. Dale
School of Natural Sciences (Chemistry)
University of Newcastle
Newcastle upon Tyne, NE1 7RU (UK)

[**] This work was supported by the UK Engineering and Physical Science Research Council through grant award no. GR/R81183/01 and use of the National Crystallography Service Synchrotron Component; the UK Council for the Central Laboratories of the Research Councils through a Synchrotron beamtime allocation; and the EU through a Marie Curie Fellowship to E.H. We also thank Dr. D. R. Armstrong and Dr. P. C. Andrews for many helpful discussions. tmp = 2,2,6,6-tetramethylpiperidine.

gathered hitherto. Elucidation of the structures of zincate reagents and the intermediates formed in deprotonative zincation processes would enhance our understanding of zincate chemistry; not least in the case of tmp zincates, which because of their heteroleptic formulation can act as alkyl, amido, or dual alkyl/amido bases. Previously, we reported a series of mixed alkali-metal/magnesium amides, a number of which are tmp magnesiate.^[5] This magnesium-based research uncovered several remarkable mixed-metal-induced synergic effects, which most notably lead to “inverse-crown” ring compounds.^[6] The likelihood that mixed alkali-metal/zinc amides would exhibit similar synergic behavior provided a further incentive to extend our studies to the tmp zincates. Thus, we introduce herein the lithium tmp/zincate reagent [(tmeda)Li(μ-*n*Bu)(μ-tmp)Zn(*n*Bu)] (**1**; tmeda = *N,N,N',N'*-tetramethylethylenediamine) and break new ground with a report of its structure and the structure of two zincated intermediates generated when **1** is used to selectively (mono)deprotonate ferrocene (Fc) in the first example of direct zincation of a metallocene.

It is surprising that prior to this investigation *n*Bu₂Zn had not been subjected to a transformation to prepare a tmp zincate system given that both the parent organozinc reagent^[7] and its homoleptic zincate derivative “[Li*n*Bu₃Zn]”^[8] have reasonably well developed chemistries. In the event, the transformation proved straightforward by applying the same method of addition as that used previously to prepare “[Li*n*Bu₂Zn(tmp)]”;^[1] however, the bulk solvent was changed from polar THF to nonpolar hexane and then the reaction was completed with the introduction of a stoichiometric amount of the donor solvent, TMEDA, in a deliberate attempt to afford a crystalline zincate [Eq. (1)].^[9]



The new zincate **1** was produced as colorless crystals (65 % yield of the isolated product). NMR (¹H, ⁷Li, and ¹³C) spectroscopic characterization of these crystals in a solution of deuterated benzene established the co-complexed nature of **1**, as revealed most diagnostically in the chemical shift of the M–CH₂ resonance of the M–*n*Bu linkage. This signal appears at δ = 0.24 ppm in **1** relative to δ = 0.27, –0.23, and –0.83 ppm in *n*Bu₂Zn, “[Li*n*Bu₃Zn]”, and *n*BuLi, respectively, thus suggesting that the *n*Bu group in the new mixed-metal co-complex retains much of its original “zinc character”.

This last point was confirmed when the complete molecular structure of **1** was revealed through an X-ray crystallographic study (Figure 1).^[10] Both *n*Bu ligands remain attached to the Zn center, one at a modestly shorter distance than the other (namely, C(5)–Zn: 2.011(2) Å; compare with C(1)–Zn: 2.041(2) Å). The *n*Bu attachment is terminal for the shorter bond; however, the other *n*Bu ligand bridges to the Li center, which explains the slight bond elongation. The Li–C(1) connection is relatively long (2.551(5) Å) relative to corresponding bonds in, for example, [(Li*n*Bu)₄(tmeda)]_∞ (2.131(8)–2.326(8) Å)^[11] but markedly shorter than the Li⋯C separation (2.736 Å) in the hexamethyldisilazido zincate [Li{μ-N(SiMe₃)₂}Zn(CH₂SiMe₃)₂(tmta)] (tmta = trimethylenediamine-*N,N,N',N'*-tetraacetic acid),^[12] which is

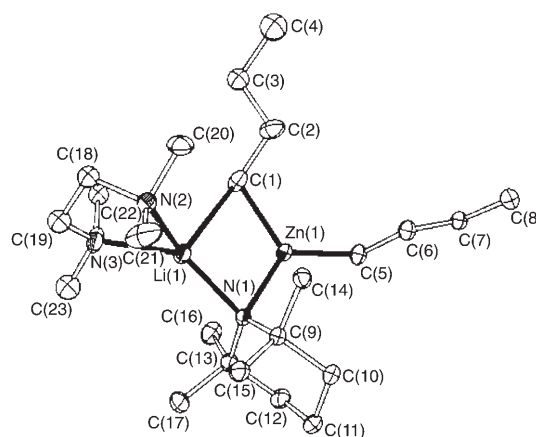
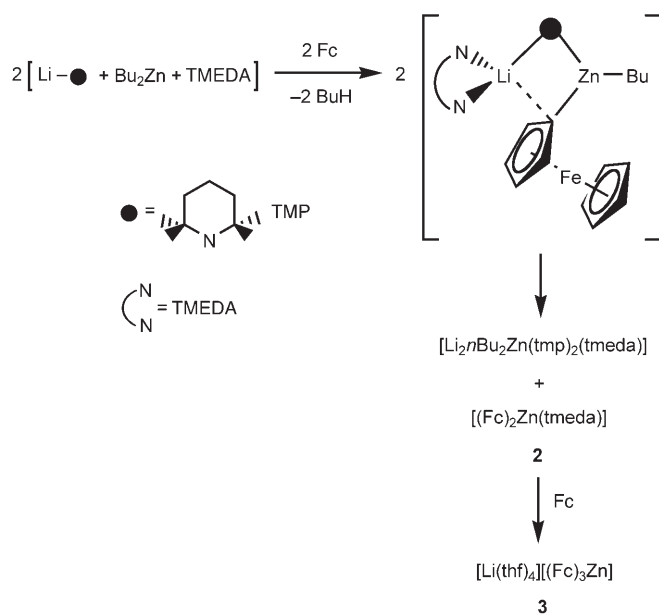


Figure 1. Molecular structure of **1**. The hydrogen atoms are omitted for clarity. Only one component is shown for each disordered group. Displacement ellipsoids are shown at the 30 % probability level.

considered to have an open rather than a closed cyclic arrangement, such as the {Li*n*Bu₃Zn} unit. This weak, but significant, attraction of the Li center to the C(1) center results in a slight pyramidalization of the {LiNNN} coordination sphere (sum of the N–Li–N bond angles: 350.98°) that is made up of μ-tmp and bidentate tmeda ligands. In contrast, the {Zn–N(1)–C(1)–C(5)} coordination is nearly perfectly planar (sum of the bond angles around Zn: 359.98°). Completing the four-membered {Li*n*Bu₂Zn} ring, the tmp nitrogen bridge, unlike its *n*Bu carbon bridge counterpart, is much more symmetrical (span lengths: 2.047(4) and 2.0612(18) Å to the Li and Zn centers, respectively).

We explored the reactivity of **1** toward ferrocene under a range of conditions to probe its deprotonative metalation ability in solution. This investigation revealed a complicated sequence of stoichiometry- and time-dependent reactions (Scheme 1). The first detectable (and isolable) metalated product was the lithium-free neutral bis(ferrocenyl) zinc complex [(Fc)₂Zn(tmeda)] (**2**). This orange solid, which precipitated from the reaction mixture within minutes, was characterized by NMR spectroscopy and X-ray crystallography (see below). Its formation is both surprising and significant, as it establishes for the first time that intermediate metallo products from the deprotonative metalation of a substrate by a lithium zincate (prior to any electrophilic workup) are not necessarily zincates themselves (in contrast to what appears to be the case with “[Li*n*Bu₂Zn(tmp)]” and related reagents)^[1–3] but could possibly be, depending on the conditions, distinct Li and Zn compounds. No lithium-containing products could be isolated from solution at this stage, though investigation of the filtrate following removal of **2** suggested the presence of [Li₂*n*Bu₂Zn(tmp)₂(tmeda)], which exists as an oil when prepared independently from a Li(tmp)/*n*Bu₂Zn/tmeda (2:1:1) mixture. When the reaction is repeated over a longer time (24 h), a small amount of tris(ferrocenyl) zincate separated from the solvent. This product was characterized as the THF adduct [Li(thf)₄][(Fc)₃Zn] (**3**) and is formed in addition to **2**. On repeating the reaction with two equivalents of ferrocene, precipitation of **2** still occurred but the yield of **3** was significantly increased. In support of the



Scheme 1. Reaction of **1** (formed in situ) with ferrocene in hexane to yield both neutral zinc and anionic zincate products.

reaction pathway shown in Scheme 1, it was found that pure “[Li₂*n*Bu₂Zn(tmp)₂(tmeda)]” also metalates ferrocene to yield **3**. The first step in the pathway remains an open question as no intermediate could be detected/isolated at this juncture, though logically it is likely to be the hypothetical “[Li*n*Bu(Fc)Zn(tmp)]”, which must undergo a fast disproportionation reaction to the neutral zinc and the zincate species [(Fc)₂Zn(tmeda)] and “[Li₂*n*Bu₂Zn(tmp)₂(tmeda)]”, respectively.

Two polymorphs of **2** crystallize from hexane/toluene and hexane/THF solutions to form monoclinic and orthorhombic systems, respectively. Because of the general similarity of these systems, only the former is discussed herein. A simple mononuclear arrangement is revealed,^[13] with Zn at the center of a distorted (2 × C; 2 × N) tetrahedron, which is made up of two monodeprotonated ferrocene units and one bidentate tmeda ligand (Figure 2). The Zn center, on a twofold rotation axis, is almost coplanar (0.064 Å deviation) with each of the C₅H₄ rings to which it is bonded. This structure bears some similarity to [Zn{2-(CH₂NMe₂)₂C₅H₃FeC₅H₅}₂],^[14] though the ligating nitrogen atoms belong to *N,N*-dimethylaminomethyl side arms on the ferrocenyl framework. However, there is a major synthetic distinction, as the latter compound is not prepared through direct zincation but by a common metathetical approach from ZnCl₂ and the analogous ferrocenyllithium. Three crystallographically independent ion pairs that have essentially the same structure make up the asymmetric unit of **3**, together with three uncoordinated THF molecules.^[15] The anion is unprecedented, with the Zn center in a distorted trigonal planar (3 × C) arrangement comprising three monodeprotonated ferrocenyl ligands (Figure 3). The counteranion, pseudotetrahedral [Li(thf)₄]⁺ ion, is known. The crystal structure shows extensive disorder, thus requiring the use of

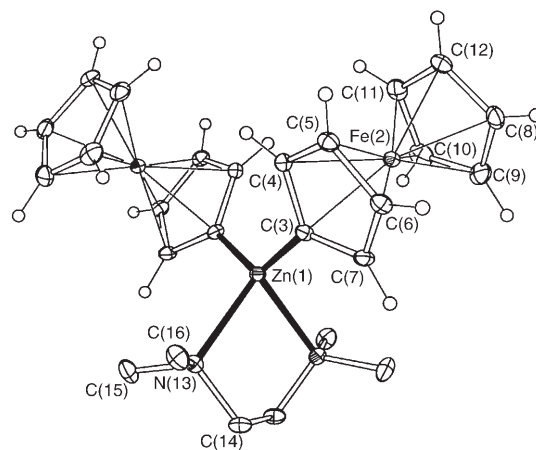


Figure 2. Molecular structure of **2**. The hydrogen atoms, except those belonging to the ferrocene rings, are omitted for clarity. Displacement ellipsoids are shown at the 30% probability level.

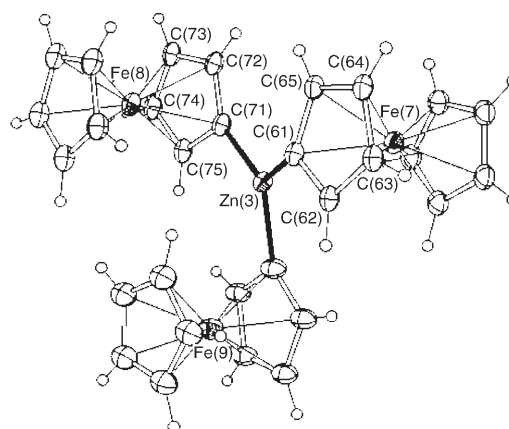


Figure 3. Molecular structure of one anion of **3**. Displacement ellipsoids are shown at the 10% probability level. Only one component of the disorder is shown.

synchrotron radiation for data collection and a combination of constraints and restraints in the refinement.

Control reactions have established that the monometallic reagents Li(tmp) and *n*Bu₂Zn are both inert towards ferrocene, even in the presence of TMEDA. Therefore the success of the solution of **1** formed in situ in the production of **2** and **3** can be attributed to a mixed-metal synergic effect or, more specifically, to alkali-metal-mediated zincation. Future work will now be directed towards pinpointing the active base species in solution that produce such an alkali-metal-mediated zincation of organic substrates.^[16,17]

Experimental Section

All reactions were carried out in a protective argon atmosphere.

1: Bu₂Zn (5 mL, 1 M solution in hexane, 5 mmol) was added to a suspension of Li(tmp) in hexane (prepared in situ by reaction of BuLi (3.1 mL, 1.6 M solution in hexane, 5 mmol) with TMP(H) (0.85 mL, 5 mmol)). The reaction mixture was stirred for 30 min, thus affording a pale yellow solution. At this stage, TMEDA (0.75 mL, 5 mmol) was introduced. After the solution was stirred for 15 min, it was

concentrated by removal of some solvent in vacuo. Placed in the refrigerator at 0°C, the resulting pale yellow solution deposited a crop of colorless crystals (1.42 g, 64%). ¹H NMR (400 MHz, 25°C, C₆D₆): δ = 2.08 (m, 4H; CH₂ Bu), 1.84 (m, 14H; CH₃ tmeda and H_γ tmp), 1.79 (s, 4H; CH₂ tmeda), 1.69 (m, 4H; CH₂ Bu), 1.51 (m, 4H; H_β tmp), 1.21 (m, 18H; 12H of CH₃ tmp and 6H of CH₃ Bu), 0.28 ppm (m, 4H; Zn-CH₂ Bu); ¹³C{¹H} NMR (100.63 MHz, 25°C, C₆D₆): δ = 57.70 (CH₂ tmeda), 53.47 (C_α tmp), 47.30 (CH₃ tmeda), 39.04 (C_β tmp), 36.24, 34.28 (CH₃ tmp), 33.53 (CH₂ Bu), 31.44 (CH₂ Bu), 20.41 (C_γ tmp), 16.42 (Zn-CH₂ Bu), 15.15 ppm (CH₃ Bu); ⁷Li NMR (155.50 MHz, 25°C, C₆D₆, reference LiCl in D₂O at 0.00 ppm): δ = 0.561 ppm.

2: Bu₂Zn (1 mL, 1M solution in hexane, 1 mmol) was added to a solution of Li(tmp) in hexane (prepared in situ by reaction of BuLi (0.62 mL, 1.6M solution in hexane, 1 mmol) with TMP(H) (0.17 mL, 1 mmol)), and TMEDA (0.15 mL, 1 mmol) was introduced, thus affording a pale yellow solution. Ferrocene was added (0.18 g, 1 mmol), and the reaction mixture was stirred for 12 h. An orange solid started to precipitate after 0.5 h. THF (2 mL) was added to this suspension to afford an orange solution that was placed in the freezer at -20°C. A crop of orange crystals was obtained after 24 h (0.20 g, 35%; note: maximum yield possible is only 50%). ¹H NMR (400 MHz, 25°C, C₆D₆): δ = 4.55 (m, 4H; CH_β C₅H₄ Fe), 4.30 (s, 10H; C₅H₅ Fe), 4.17 (m, 4H; CH_γ C₅H₄ Fe), 1.97 (s, 12H; CH₃ tmeda), 1.60 ppm (s, 4H; CH₂ tmeda); ¹³C{¹H} NMR (100.63 MHz, 25°C, C₆D₆): δ = 79.39 (Zn-C_α Fe), 77.94 (C_β Fe), 70.60 (C_γ Fe), 68.04 (C₅H₅ Fe), 57.45 (CH₂ tmeda), 48.10 ppm (CH₃ tmeda).

3: A solution of **1** in hexane was prepared in situ as described above for **2** by reaction of Bu₂Zn (1 mmol), Li(tmp) (1 mmol), and TMEDA (1 mmol). Two equivalents of ferrocene (0.37 g, 2 mmol) were then introduced, and the reaction mixture was stirred for 24 h, thus producing an orange solid. THF (2 mL) was added to the reaction mixture to afford an orange solution. Placed in the refrigerator at 0°C, this solution deposited a crop of orange crystals (0.34 g, 34%). ¹H NMR (400 MHz, 25°C, C₆D₆): δ = 4.57 (m, 6H; CH_β C₅H₄ Fe), 4.49 (m, broad, 21H; 6H of CH_γ C₅H₄ and 15H of C₅H₅ Fe), 3.41 (m, 16H; CH₂O thf), 1.36 ppm (m, 16H; CH₂ thf); ¹³C{¹H} NMR (100.63 MHz, 25°C, C₆D₆): δ = 86.70 (Zn-C_α Fe), 79.38 (C_β Fe), 70.33 (C_γ Fe), 68.37 (CH₂O thf), 67.67 (C₅H₅ Fe), 26.11 ppm (CH₂ thf); ⁷Li NMR (155.50 MHz, 25°C, C₆D₆, reference LiCl in D₂O at 0.00 ppm): δ = -1.05 ppm.

Received: May 7, 2005

Published online: August 26, 2005

Keywords: amides · ferrocene · metalation · synergy · zinc

- [1] Y. Kondo, M. Shilai, M. Uchiyama, T. Sakamoto, *J. Am. Chem. Soc.* **1999**, *121*, 3539.
- [2] T. Imahori, M. Uchiyama, T. Sakamoto, Y. Kondo, *Chem. Commun.* **2001**, 2450.
- [3] M. Uchiyama, T. Miyoshi, Y. Kajihara, T. Sakamoto, Y. Otani, T. Ohwada, Y. Kondo, *J. Am. Chem. Soc.* **2002**, *124*, 8514.
- [4] M. Uchiyama, S. Nakamura, T. Ohwada, M. Nakamura, E. Nakamura, *J. Am. Chem. Soc.* **2004**, *126*, 10897; A. E. H. Wheatley, *New J. Chem.* **2004**, *28*, 435; D. J. Linton, P. Schooler, A. E. H. Wheatley, *Coord. Chem. Rev.* **2001**, *223*, 53.
- [5] For recent examples, see: E. Hevia, G. W. Honeyman, A. R. Kennedy, R. E. Mulvey, D. C. Sherrington, *Angew. Chem.* **2005**, *117*, 70; *Angew. Chem. Int. Ed.* **2005**, *44*, 69; E. Hevia, D. J. Gallagher, A. R. Kennedy, R. E. Mulvey, C. T. O'Hara, C. Talmard, *Chem. Commun.* **2004**, 2422; K. W. Henderson, A. R. Kennedy, R. E. Mulvey, C. T. O'Hara, R. B. Rowlings, *Chem. Commun.* **2001**, 1678.
- [6] R. E. Mulvey, *Chem. Commun.* **2001**, 1049.

- [7] P. Knochel, P. Jones, *Organozinc Reagents*, Oxford University Press, Oxford, **1999**.
- [8] For examples, see: T. Harada, D. Hara, K. Hattori, A. Oku, *Tetrahedron Lett.* **1988**, *29*, 3821; T. Harada, T. Katsuhira, K. Hattori, A. Oku, *Tetrahedron Lett.* **1989**, *30*, 6035; T. Harada, K. Hattori, T. Katsuhira, A. Oku, *Tetrahedron Lett.* **1989**, *30*, 6039; T. Harada, Y. Kotani, T. Katsuhira, A. Oku, *Tetrahedron Lett.* **1991**, *32*, 1573; T. Harada, T. Katsuhira, A. Osada, K. Iwazaki, K. Maejima, A. Oku, *J. Am. Chem. Soc.* **1996**, *118*, 11377.
- [9] For a similar strategy used to prepare a sodium tmp/zincate system, see: P. C. Andrikopoulos, D. R. Armstrong, H. R. L. Barley, W. Clegg, S. H. Dale, E. Hevia, G. W. Honeyman, A. R. Kennedy, R. E. Mulvey, *J. Am. Chem. Soc.* **2005**, *127*, 6184.
- [10] Crystal data for **1**: C₂₃H₅₂LiN₃Zn, *M_r* = 443.0, triclinic, space group *P* $\bar{1}$, *a* = 10.5066(3), *b* = 11.2545(3), *c* = 12.4831(4) Å, *a* = 92.151(2), *β* = 108.109(2), *γ* = 106.064(2)°, *V* = 1335.80(7) Å³, *Z* = 2, *ρ*_{calcd} = 1.101 g cm⁻³, *μ* = 0.93 mm⁻¹, *T* = 123 K, *R*(*F*; *F*² > 2σ) = 0.0427, *R_w*(*F*², all data) = 0.1049, *S* = 1.025 for 6050 unique data (*θ* < 27.5°; nonius kappaCCD diffractometer, MoK_α radiation, *λ* = 0.71073 Å) and 279 refined parameters; final difference synthesis within ± 0.95 e Å⁻³.
- [11] N. D. R. Barnett, R. E. Mulvey, W. Clegg, P. A. O'Neil, *J. Am. Chem. Soc.* **1993**, *115*, 1573.
- [12] M. Westerhausen, B. Rademacher, W. Schwarz, *Z. Naturforsch. B* **1994**, *49*, 199.
- [13] Crystal data for **2**: C₂₆H₃₄Fe₂N₂Zn, *M_r* = 551.6, monoclinic, space group *I*2/a, *a* = 11.5061(8), *b* = 15.0879(11), *c* = 14.0876(10) Å, *β* = 101.967(1)°, *V* = 2392.5(3) Å³, *Z* = 4, *ρ*_{calcd} = 1.531 g cm⁻³, *μ* = 2.21 mm⁻¹, *T* = 150 K, *R*(*F*; *F*² > 2σ) = 0.0185, *R_w*(*F*², all data) = 0.0481, *S* = 1.032 for 2889 unique data (*θ* < 28.3°; Bruker SMART 1 K diffractometer, MoK_α radiation, *λ* = 0.71073 Å) and 144 refined parameters; final difference synthesis within ± 0.34 e Å⁻³.
- [14] N. Seidel, K. Jacob, P. Zanello, M. Fontani, *J. Organomet. Chem.* **2001**, *620*, 243.
- [15] Crystal data for **3**: C₄₆H₅₉O₄Fe₃LiZn·C₄H₈O, *M_r* = 987.9, triclinic, space group *P* $\bar{1}$, *a* = 10.0396(4), *b* = 10.3045(4), *c* = 38.1464(16) Å, *a* = 86.678(1), *β* = 89.840(1), *γ* = 61.239(1)°, *V* = 3452.7(2) Å³, *Z* = 3, *ρ*_{calcd} = 1.425 g cm⁻³, *μ* = 1.49 mm⁻¹, *T* = 120 K, *R*(*F*; *F*² > 2σ) = 0.0848, *R_w*(*F*², all data) = 0.2429, *S* = 0.980 for 27691 unique data (*θ* < 26.0°; Bruker APEX2 diffractometer, synchrotron radiation, *λ* = 0.6768 Å) and 2118 refined parameters; final difference synthesis within ± 1.63 e Å⁻³. CCDC-267370–267372 (**1–3**, respectively) contain the supplementary crystallographic data for this paper. These data can be obtained free of charge from the Cambridge Crystallographic Data Center via www.ccdc.cam.ac.uk/data_request/cif.
- [16] Though rarely stated, heteroaggregation (same metal, but different ligand) can sometimes also lead to enhanced reactivity; for an example in organolithium chemistry, see: W. Peascoe, D. E. Applequist, *J. Org. Chem.* **1973**, *38*, 1510.
- [17] For a recent review of heteroaggregation in aryl and alkyl lithium reagents, see: R. A. Gossage, J. T. B. H. Jastrzebski, G. van Koten, *Angew. Chem.* **2005**, *117*, 1472; *Angew. Chem. Int. Ed.* **2005**, *44*, 1448.

DOI: 10.1002/anie.200501564

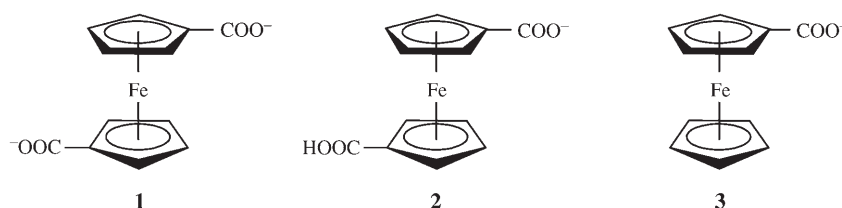
Intramolecular Rotation through Proton Transfer: $[\text{Fe}(\eta^5\text{-C}_5\text{H}_4\text{CO}_2^-)_2]$ versus $[(\eta^5\text{-C}_5\text{H}_4\text{CO}_2^-)\text{Fe}(\eta^5\text{-C}_5\text{H}_4\text{CO}_2\text{H})]**$

Xue-Bin Wang, Bing Dai, Hin-Koon Woo, and Lai-Sheng Wang*

Intramolecular rotation is important in molecular dynamics; it is a fundamental molecular property and can be used to understand the concept of molecular motors. Inspired by elegant biological and macroscopic analogues,^[1–3] the fabrication of molecular machines has been very actively pursued recently,^[4] resulting in a variety of molecular devices, such as rotors,^[5–8] shuttles,^[9–11] and ratchets.^[12] The central theme of molecular devices is to control molecular motions and bindings upon external stimuli. The smallest molecular machine can downscale to a single molecule, and such a single molecular rotor has been observed.^[13] Herein, we report the observation of intramolecular rotations of a single ferrocene derivative through proton transfer.

Ferrocene is a prototypical sandwich complex with an iron atom symmetrically situated between two C_5H_5 (cyclopentadienyl, Cp) rings and has been the subject of many experimental and theoretical studies since its discovery.^[14–19] It has many applications in both fundamental research and materials science. In the solid phase the two Cp rings are in a staggered confirmation (D_{5d}),^[14] whereas in the gas phase they are eclipsed (D_{5h}).^[20] The rotational barrier of the two rings along the C_5 axis is very small in the gas phase ($E \approx 1.1 \text{ kcal mol}^{-1}$).^[20] Therefore, ferrocene would be an ideal candidate

for a molecular rotor if the rotational freedom can be controlled. Proton transfer, that is, acid–base chemical reaction, is one of the most commonly used external stimuli along with photoinduced processes and electrochemical reactions in realizing molecular devices.^[4,21] Proton transfer is also ubiquitous and plays a vital role in biological motors.^[22] It changes the charge state of a molecule to result in alternation of electrostatic interactions. Such effects may influence molecular binding, particularly in the gas phase or hydrophobic environments. Here, we study the energetics and conformations of two ferrocene derivatives, the doubly charged $[\text{Fe}(\eta^5\text{-C}_5\text{H}_4\text{CO}_2^-)_2]$ ($[\text{FeCp}'_2]$, **1**) and the singly charged $[(\eta^5\text{-C}_5\text{H}_4\text{CO}_2^-)\text{Fe}(\eta^5\text{-C}_5\text{H}_4\text{CO}_2\text{H})]$ (**2**; see Scheme 1), and demonstrate that they can be viewed to form a model molecular rotor system controlled by proton transfer.



Scheme 1. Structures of the ferrocene derivatives 1–3.

Complexes **1** and **2** were produced using electrospray ionization, and their geometric and electronic structures were probed by photoelectron spectroscopy (PES) and theoretical calculations. The experiments were carried out on a newly developed low-temperature PES apparatus coupled with an electrospray source.^[23] We detected abundant **1** and **2** by electrospray of a 1 mM solution of 1,1'-ferrocenedicarboxylic acid in a water/methanol mixed solvent system. The 193-nm (6.424 eV) PES spectrum of **1** (Figure 1a) reveals two broad spectral bands, which likely contain many overlapping detachment transitions. No transitions were observed beyond binding energies of 3 eV owing to the cut-off by the repulsive coulomb barrier, unique to photodetachment of multiply charged anions.^[24–26] We also measured the photoelectron spectrum of **1** at 266 nm (4.661 eV) with slightly better resolution. Molecular orbital analysis based on the optimized structure (see below) indicates that the lower-binding-energy features (0.2–1 eV) are due to detachments from primarily lone-pair electrons of the carboxylate groups, whereas the higher-binding-energy features (1.5–2.5 eV) are due to detachments from the ferrocene framework, which contains closely spaced molecular orbitals from both the Fe 3d orbitals and the Cp' rings. The surprising observation is the extremely low electron-binding energy for **1**. We measured an adiabatic detachment energy (ADE) of $0.25 \pm 0.05 \text{ eV}$ for **1** (Figure 1a). This low electron-binding energy is a result of the strong intramolecular coulomb repulsion due to the two negative charges in **1**. To assess the influence of the coulomb repulsion, we performed a control experiment on a monocarboxylated ferrocene anion, $[(\eta^5\text{-C}_5\text{H}_5)\text{Fe}(\eta^5\text{-C}_5\text{H}_4\text{CO}_2^-)]$ (**3**, Scheme 1), as shown in Figure 1c. Three spectral bands were observed, all with very high electron-binding energies, in

[*] Dr. X.-B. Wang, Dr. B. Dai, Dr. H.-K. Woo, Prof. Dr. L.-S. Wang
Department of Physics
Washington State University
2710 University Drive
Richland, WA 99352 (USA)

and

W. R. Wiley Environmental Molecular Sciences Laboratory and
Chemical Sciences Division
Pacific Northwest National Laboratory
P.O. Box 999, Richland, WA 99352 (USA)
Fax: (+1) 509-376-6066
E-mail: ls.wang@pnl.gov

[**] We thank Dr. Jun Li for valuable discussions and help with the theoretical calculations. This work was supported by the U.S. National Science Foundation (CHE-0349426) and performed at the W. R. Wiley Environmental Molecular Sciences Laboratory, a national scientific user facility sponsored by the DOE's Office of Biological and Environmental Research and located at Pacific Northwest National Laboratory, which is operated for DOE by Battelle. All the calculations were performed using supercomputers at the Molecular Sciences Computing Facility of EMSL.

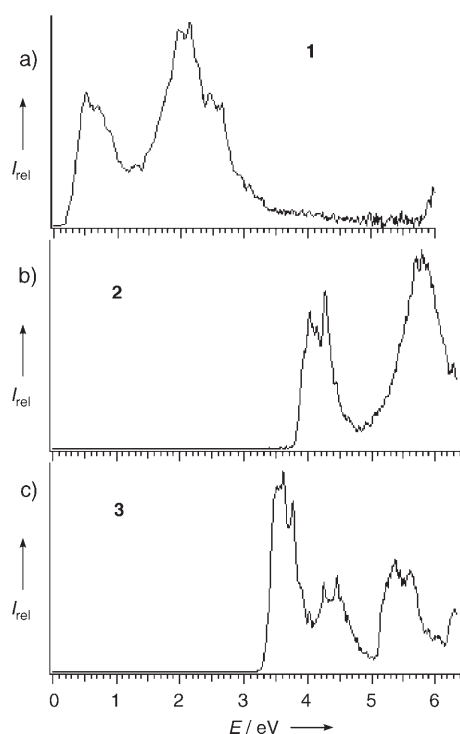


Figure 1. Photoelectron spectra at 193 nm (6.426 eV) of a) the $[\text{Fe}(\eta^5\text{-C}_5\text{H}_4\text{CO}_2^-)_2]$ dianion (**1**), b) its protonated singly charged anion **2**, and c) the monocarboxylated ferrocene anion, $[(\eta^5\text{-C}_5\text{H}_5)\text{Fe}(\eta^5\text{-C}_5\text{H}_4\text{CO}_2^-)]$ (**3**).

contrast to **1**. The ADE of **3** was measured to be 3.31 ± 0.03 eV, which is almost identical to that of acetate and other long-chain aliphatic carboxylate groups.^[27] Thus, the extremely low ADE of **1** is purely due to the intramolecular coulomb repulsion, which can be approximately estimated as the difference in ADE between **3** and **1**; a very large value of approximately 3 eV is obtained.

Figure 1b displays the 193-nm spectrum of **2**, which reveals spectral patterns that are similar to those for **1** but at much higher binding energies. We expected that **2** would have binding energies similar to **3** because the first electron detachment in both systems should be from the CO_2^- group. However, the ADE of **2** was measured to be 3.80 ± 0.03 eV, about 0.5 eV higher than that of **3**. This observation suggests that the CO_2^- group in **2** is stabilized relative to that in **3**. The only mechanism for this stabilization is through an intramolecular hydrogen-bonding interaction between the CO_2^- group and the COOH group on the second Cp' ligand. This is possible if the two Cp' ligands in **2** would adopt a staggered conformation, that is, if the two Cp' ligands would be rotated 180° relative to each other, as shown in Scheme 1.

To obtain more definitive information about the structures and energetics, we performed theoretical calculations on the three species.^[28] The optimized structure of **1** indeed shows C_{2h} symmetry (Figure 2), in which the two CO_2^- groups are opposite each other in a *trans* conformation. For **2**, an intramolecular hydrogen bond is observed between the $-\text{COOH}$ and $-\text{COO}^-$ groups, as expected, that lock the two Cp' ligands in a *cis* conformation. The two Cp' ligands are not

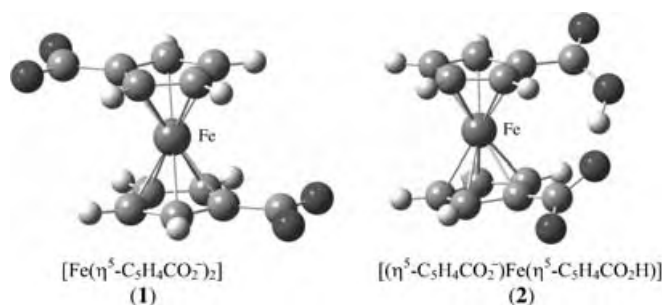


Figure 2. Optimized structures of the $[\text{Fe}(\eta^5\text{-C}_5\text{H}_4\text{CO}_2^-)_2]$ dianion (**1**) and its protonated singly charged anion **2** (O dark gray, C pale gray, H white). Note that the two Cp' ligands in **2** are staggered by 68° .

precisely staggered. Instead, there is a 68° angle between them to optimize the intramolecular hydrogen-bond formation. The *trans* conformation of **2** lies 0.62 eV higher in energy relative to the *cis* form (also see Figure 3a). The calculated

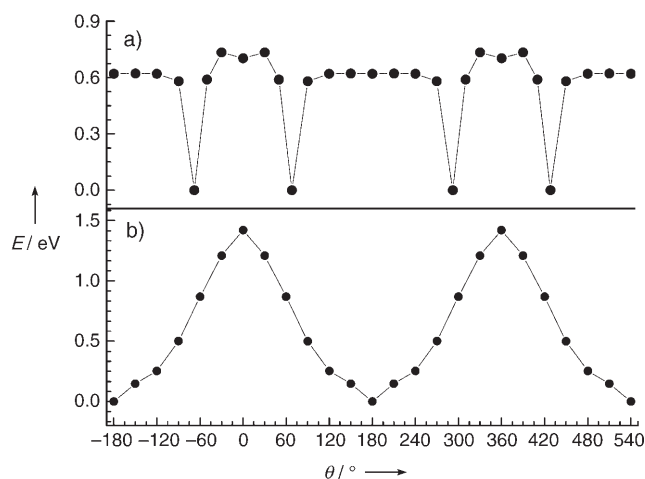


Figure 3. Calculated energies as a function of rotational angle defined by the two carboxylate groups for a) **2** and b) **1**. The two minima located at 68° and -68° for **2** are identical. At these angles, the intramolecular hydrogen bond is optimized. Deviation from these angles disrupts the hydrogen bond to result in a non-hydrogen-bonded form of **2**. The sharp minima in (a) reflect the narrow angles for the hydrogen bonding, outside which the rotational potential is relatively flat. The potential for **1** is primarily coulombic and is simpler: the minimum at 180° corresponds to the *trans* structure, whereas the maxima at 0° and 360° correspond to the *cis* form.

ADEs for **1**, **2**, and **3** are compared with the experimental values in Table 1. Although the theoretical values are consistently lower than the experimental values by approximately 0.2 eV, they reproduce the experimental trend very well. In particular, a significantly smaller ADE is predicted for the *trans* confirmation of **2**. In fact, the predicted ADE for the *trans* form of **2** is in remarkable agreement with the ADE of **3**, and confirms unequivocally that the hydrogen-bonded *cis* form is more stable and is the structure that was observed experimentally.

Therefore, we see that the different electrostatic interactions lock **1** and **2** in two different conformations. The

Table 1: Experimental adiabatic detachment energies (ADEs [eV]) of **1**, **2**, and **3**, compared to calculated values.

Species	Experimental	Calculated
1	0.25 ± 0.05	−0.03
2 (<i>cis</i>)	3.80 ± 0.03	3.64
2 (<i>trans</i>)		3.32
3	3.31 ± 0.03	3.18

intramolecular coulomb repulsion dictates that the two negative charges in **1** lie as far apart as possible, locking it in the *trans* conformation, whereas intramolecular hydrogen bonding locks **2** in the *cis* conformation. Deviation from the optimal angle of 68° disrupts the hydrogen bond and results in non-hydrogen-bonded forms of **2**. The rotational barriers for **1** and **2** are 1.4 and 0.6 eV, respectively (see Figure 3), in the gas phase, which are much higher than thermal energies at ambient temperatures. As shown in the Figure 2, structures **1** and **2** are controlled by a proton-transfer process. Protonation of **1** induces a 112° rotation that leads to **2**, while deprotonation of **2** results in **1** by also involving a 112° intramolecular rotation.

Received: May 8, 2005

Revised: June 21, 2005

Published online: August 12, 2005

Keywords: anions · cyclopentadienyl ligands · iron · photoelectron spectroscopy · protonation

- [1] R. D. Vale, R. A. Milligan, *Science* **2000**, 288, 88.
- [2] H. Noji, R. Yasuda, M. Yoshida, K. Kinoshita, *Nature* **1997**, 386, 299.
- [3] I. Rayment, H. M. Holden, M. Whittaker, C. B. Yohn, M. Lorenz, K. C. Holmes, R. A. Milligan, *Science* **1993**, 261, 58.
- [4] V. Balzani, A. Credi, F. M. Raymo, J. F. Stoddart, *Angew. Chem.* **2000**, 112, 3484–3530; *Angew. Chem. Int. Ed.* **2000**, 39, 3348–3391.
- [5] T. R. Kelly, H. De Silva, R. A. Silva, *Nature* **1999**, 401, 150.
- [6] N. Koumura, R. W. J. Zijlstra, R. A. van Delden, N. Harada, B. L. Feringa, *Nature* **1999**, 401, 152.
- [7] V. Bermudez, N. Capron, T. Gase, F. G. Gatti, F. Kajzar, D. A. Leigh, F. Zerbetto, S. Zhang, *Nature* **2000**, 406, 608.
- [8] D. A. Leigh, J. K. Y. Wong, F. Dehez, F. Zerbetto, *Nature* **2003**, 424, 174.
- [9] R. A. Bissell, E. Cordova, A. E. Kaifer, J. F. Stoddart, *Nature* **1994**, 369, 133.
- [10] A. S. Lane, D. A. Leigh, A. Murphy, *J. Am. Chem. Soc.* **1997**, 119, 11092.
- [11] H. Murakami, A. Kawabuchi, K. Kotoo, M. Kunitake, N. Nakashima, *J. Am. Chem. Soc.* **1997**, 119, 7605.
- [12] T. R. Kelly, I. Tellitu, J. P. Sestelo, *Angew. Chem.* **1997**, 109, 1969–1972; *Angew. Chem. Int. Ed. Engl.* **1997**, 36, 1866–1868.
- [13] M. F. Hawthorne, J. I. Zink, J. M. Skelton, M. J. Bayer, C. Liu, E. Livshits, R. Baer, D. Neuhauser, *Science* **2004**, 303, 1849.
- [14] M. Rosenblum, *Chemistry of the Iron Group Metallocenes*, Interscience, New York, **1965**.
- [15] J. W. Rabalais, L. O. Werme, T. Bergmark, L. Karlsson, M. Hussain, K. Siegbahn, *J. Chem. Phys.* **1972**, 57, 1185.
- [16] S. Evans, M. L. H. Green, B. Jewitt, A. F. Orchard, C. F. Pygall, *J. Chem. Soc. Faraday Trans. 2* **1972**, 68, 1847.
- [17] M. D. Rowe, A. J. McCaffery, *J. Chem. Phys.* **1973**, 59, 3786.
- [18] O. Plashkevych, H. Ågren, L. Karlsson, L. G. M. Pettersson, *J. Electron Spectrosc. Relat. Phenom.* **2000**, 106, 51.
- [19] G. Wilkinson, F. A. Cotton, *Prog. Inorg. Chem.* **1959**, 1, 86.
- [20] R. K. Böhn, A. Haaland, *J. Organomet. Chem.* **1966**, 5, 470.
- [21] R. Ballardini, V. Balzani, A. Credi, M. T. Gandolfi, M. Venturi, *Acc. Chem. Res.* **2001**, 34, 445.
- [22] C. A. Schalley, K. Beizai, F. Vögtle, *Acc. Chem. Res.* **2001**, 34, 465.
- [23] The experiments were carried out on a new homebuilt instrument, which couples electrospray ionization with a magnetic-bottle time-of-flight photoelectron spectrometer and the capability of controlling ion temperatures. The electrospray source and the magnetic-bottle photoelectron spectrometer are similar to that described previously (L. S. Wang, C. F. Ding, X. B. Wang, S. E. Barlow, *Rev. Sci. Instrum.* **1999**, 70, 1957). Briefly, the anions of interest were produced from a solution of the corresponding acids under slightly basic conditions in a mixed solvent system of methanol/water (3:1 v/v). After their desolvation from the electrospray source, anions were guided by a RF-only (RF = radiofrequency) octapole device and transported through a quadrupole mass filter (operated at RF-only mode), before they entered a 3D Paul trap. The trap was attached to a cryostat, which consists of a closed-cycle helium refrigerator and a feedback heater. Temperatures of the trap can be controlled from 18–400 K. Ions were trapped for a period of 20–100 ms and collisionally cooled by using a 10^{−4} Torr He background gas containing about 10% H₂. The cold anions were then unloaded from the trap and were analyzed using a time-of-flight mass spectrometer. The ions of interest were selected and decelerated before they were intercepted with a laser beam in the interaction zone: 266 nm from a Nd:YAG laser and 193 nm from an ArF excimer laser. The lasers were operated at 20 Hz repetition rate, with the ion beam off at alternate laser shots for background subtraction. The photodetached electrons were collected with nearly 100% efficiency by a magnetic bottle and analyzed in a 5-m long electron-flight tube. The electron-energy resolution of the apparatus is $\Delta E/E \approx 2\%$, that is, 20 meV for 1 eV electrons. Photoelectron time-of-flight spectra were collected and then converted to kinetic-energy spectra, calibrated by the known spectra of ClO₂[−] and I[−]. The electron-binding-energy spectra presented were obtained by subtracting the kinetic-energy spectra from the detachment photon energies.
- [24] M. K. Scheller, R. N. Compton, L. S. Cederbaum, *Science* **1995**, 270, 1160.
- [25] L. S. Wang, X. B. Wang, *J. Phys. Chem. A* **2000**, 104, 1978.
- [26] X. B. Wang, X. Yang, L. S. Wang, *Int. Rev. Phys. Chem.* **2002**, 21, 473.
- [27] L. S. Wang, C. F. Ding, X. B. Wang, J. B. Nicholas, *Phys. Rev. Lett.* **1998**, 81, 2667.
- [28] We optimized the structures of **1** and **2** at the density functional theory level using the B3LYP hybrid functional (A. D. Becke, *J. Chem. Phys.* **1993**, 98, 1372; A. D. Becke, *J. Chem. Phys.* **1993**, 98, 5648) and the standard Ahlrichs VTZ basis set (A. Schafer, H. Horn, R. Ahlrichs, *J. Chem. Phys.* **1992**, 97, 2571). Vibrational frequencies were calculated by numerical differentiation methods to confirm the ground states. All the calculations were performed using the NWChem 4.6 program (High Performance Computational Chemistry Group, NWChem, A Computational Chemistry Package for Parallel Computers, Version 4.6, Pacific Northwest National Laboratory, Richland, Washington 99352, USA, **2003**) and the Molecular Science Computing Facility (MSCF) located at the Environmental Molecular Sciences Laboratory.
- [29] E. R. Lippincott, R. D. Nelson, *Spectrochimica Acta* **1958**, 10, 307–329.

A Dendron Based on Natural Amino Acids: Synthesis and Behavior as an Organogelator and Lyotropic Liquid Crystal**

Yan Ji, Yu-Fei Luo, Xin-Ru Jia,* Er-Qiang Chen, Yun Huang, Chun Ye, Bing-Bing Wang, Qi-Feng Zhou, and Yen Wei*

Biomolecules are prone to self-assemble in vivo and in vitro.^[1] For example, collagen proteins can self-organize initially into triple helices and then into ordered fibers, gels, and liquid-crystalline (LC) phases through noncovalent forces.^[2a,b] Elucidation of the underlying mechanisms is important but tremendously challenging. An alternative is to decipher nature's bewildering tricks with the help of synthetic systems made from natural starting materials.^[2] In this context, the natural amino acid based dendrons or dendrimers (NAADs) are of great significance because of their similarity to proteins in composition and topology,^[3] as well as their architectural difference from currently prevalent linear model peptides. In addition, potentially chiral and biocompatible NAADs provide exciting possibilities in the creation of new materials for nano- and biotechnology.^[4]

However, little attention has been paid to the self-assembly of NAADs,^[5] and especially to their gelation and LC properties. Only polylysine dendrimers have been studied as gelators by Smith et al.^[6] and gelation is mentioned for dendrimers built from glutamates by Ranganathan et al.^[3c,7] Research on NAADs as liquid crystals is even scarcer. Moreover, to the best of our knowledge, there is no report on amino acid based dendrimers that function as gelators and form liquid crystals. We have been interested in the synthesis and self-assembly of dendrimers for many years.^[8] Herein, we

present the synthesis of a dendron composed of two natural amino acids, glycine and aspartic acid, and its self-assembly which leads not only to organogels but also to lyotropic liquid crystals. Recently, a type of amphiphilic dendritic dipeptide was described by Percec et al.^[9] as self-assembling in helical pores. In contrast to their design of an aromatic dendron and a peptide core, our NAADs have peptidic dendrons with a benzyl periphery.

The poly(Gly-Asp) dendrons were convergently synthesized as depicted in Scheme 1. It is well-known that glycine appears at every third position in the predominant sequences of collagen,^[2] and aspartic acid is similar to the building unit of a well-investigated linear model peptide, poly(benzyl L-glutamate) (PBLG), which behaves as a gelator and liquid crystal.^[10] The dendrons, which resemble the repetitive patterns always found in the sequences of natural fibrous proteins,^[2d] were branched iteratively with Gly-Asp dipeptides, instead of with one amino acid as in other NAADs,^[11] and without any help from a nonnatural amino acid linkage.

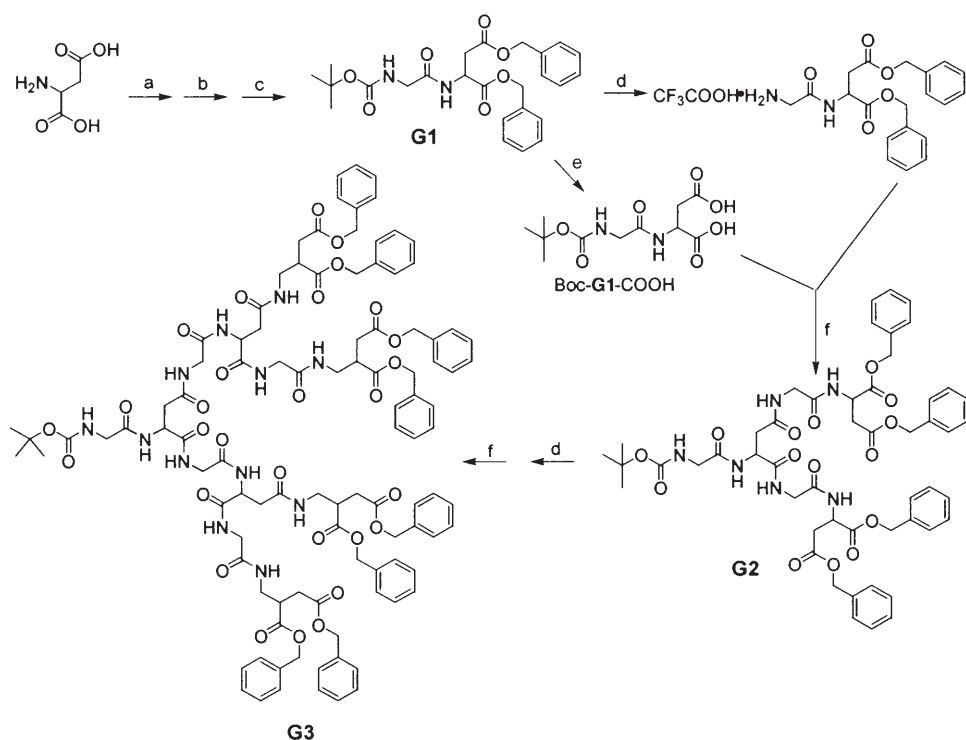
Standard DCC coupling of Boc-glycine and benzyl-protected aspartic acid, which was readily prepared by the benzyl esterification of aspartic acid, gave the branching unit in 60% yield. This is the first generation (**G1**) of the dendron. The second (**G2**) and third generations (**G3**) were synthesized convergently in 35 and 17% yields, respectively, by repeating a two-reaction cycle, that is, by removing the Boc group of the lower-generation dendron with TFA, and then coupling the resultant *N*-deprotected intermediate to the *C*-deprotected **G1** (Boc-**G1**-COOH), prepared by hydrogenative debenzylation of the dipeptide. Currently, one of the major obstacles that hindered the research and applications of NAADs is the tedious process for the purification of the dendritic products.^[10] Notably, **G3** is relatively easy to obtain by simple precipitation in water and MeOH consecutively (see Supporting Information). ¹H, ¹³C, two-dimensional, and DEPT NMR techniques, MALDI-TOF mass spectrometry, and elemental analyses were used to verify the structure and purity of the **G3** dendron (see Supporting Information).

We found that **G3** could act as an efficient low-molecular-mass organogelator (LMOG). LMOGs^[12c] are a family of low-molecular-mass organic molecules ($M_w \leq 3000$) that can gel organic solvents at very low concentrations through noncovalent forces. LMOGs have attracted considerable renewed interest in recent years, not only because of their interesting roles in materials science and supramolecular chemistry but also because gelation remains poorly understood. Most organogels are achieved through the ordered arrangement of gelators during the cooling of the mixture of LMOGs and organic solvents after heating to form a homogeneous solution.^[12] However, a solvent-solvent gel preparation procedure distinguishes **G3** from other LMOGs, including the previously reported dendritic ones.^[13] In a typical example, **G3** (0.04 g) was first dissolved in CHCl₃/CH₃OH (9:1 v/v; 6 mL) by sonication. Then, with the addition of ethyl acetate (4 mL), the solution immediately became viscous and gelled within 5 seconds. Meanwhile, a 10-mL gel as dilute as 0.2 wt % (0.98 mM, one **G3** molecule entraps about 9000 solvent molecules) in a 1-cm-diameter test tube could be turned upside down without downward flow of the gel. A thin

[*] Y. Ji, Y.-F. Luo, Prof. X.-R. Jia, Prof. E.-Q. Chen, Y. Huang, C. Ye, B.-B. Wang, Prof. Q.-F. Zhou
Department of Polymer Science & Engineering and
The Key Laboratory of Polymer Chemistry and Physics of the
Ministry of Education
College of Chemistry & Molecular Engineering
Peking University, Beijing 100871 (China)
Fax: (+86) 10-62751708
E-mail: xrlia@pku.edu.cn
Prof. Y. Wei
Department of Chemistry, Drexel University
Philadelphia, PA 19104 (USA)
Fax: (+1) 215-895-1265
E-mail: weiyen@drexel.edu

[**] This work was supported by the National Natural Science Foundation of China (NSFC Grant Nos. 20374002 and 20340420002) and by the National Institutes of Health (NIH Grant No. DE09848). We are most grateful to Prof. Dr. Kenji Hanabusa of Shinshu University in Japan for discussions on gelators and to all four reviewers of this article for their comments and suggestions.

Supporting information for this article is available on the WWW under <http://www.angewandte.org> or from the author.



Scheme 1. Convergent synthesis of the first three generations of poly(Gly-Asp) dendrons **G_n** ($n=1-3$). Reagents and conditions: a) *p*-toluenesulfonic acid, benzene, benzyl alcohol, reflux; b) CH₃OH, KOH; c) Boc-glycine, DCC, -10 °C; d) TFA, CH₂Cl₂; e) Pd-C, H₂, ethanol; and f) DCC, Boc-**G1**-COOH, *N*-methylmorpholine, NHS, -10 °C. Boc = *tert*-butoxycarbonyl, DCC = dicyclohexylcarbodiimide, TFA = trifluoroacetic acid, NHS = *N*-hydroxysuccinimide.

layer of liquid exuded as time went by, but the main part kept its gel state for more than half a year. The transmission electron microscopy (TEM) image of the **G3** gel showed that the **G3** dendrons self-assembled into a ramified network of intertwined fibers. The width of the fibers ranged from several dozen to more than a hundred nanometers (Figure 1 a). The

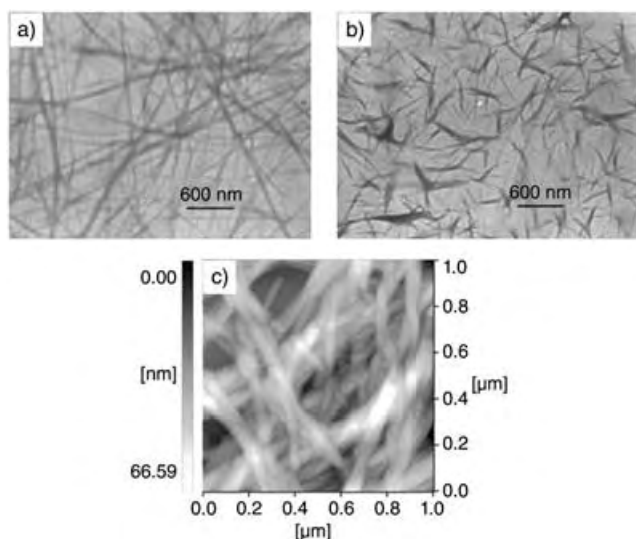


Figure 1. Morphology of **G3**: a) TEM image of a **G3**/CH₃Cl/CH₃OH/ethyl acetate gel; b) TEM image of a **G3**/CH₃Cl/CH₃OH/ethyl acetate suspension; c) AFM image of the **G3**/CH₃Cl/CH₃OH/ethyl acetate gel ([**G3**] = 0.02 wt %).

atomic force microscopy (AFM) image recorded in the tapping mode (Figure 1 c) revealed that the smaller fibers were about 30–70 nm in width, many micrometers in length, but less than 20 nm in height. Considering the convolution effect arising from the finite size of the AFM tips, the real width of the fibers should be even less.

The gel preparation details have a great effect on gelation. If ethyl acetate was added before **G3** was totally dissolved in CH₃OH/CHCl₃, an opaque suspension was formed instead of a gel. TEM shows a rather different morphology of the aggregates in such a suspension (Figure 1 b). In addition to the above case, **G3** dissolved in and gelled a mixture of CH₃OH and THF in several hours. However, the resultant gels were less stable than the CH₃Cl/CH₃OH/ethyl acetate gels at the same concentrations. Neither **G1** nor **G2** formed a gel in the above-mentioned mixed solvents under similar experimental conditions. CH₃OH, CHCl₃, CH₂Cl₂, THF, acetone, ethyl acetate, diethyl ether, ethanol, petroleum ether, hexane, cyclohexane, dioxane, acetonitrile, *N,N*-dimethylformamide,

dimethyl sulfoxide, styrene, water, and benzyl alcohol were tested for the preparation of **G3** gels by the conventional heating and cooling method. Except for benzyl alcohol, none of the single solvents could be gelled by **G3**.

Noncovalent forces, mainly hydrogen-bonding and aromatic-stacking interactions, were proposed to be the driving force for the self-assembly of **G3** dendron. The role of hydrogen bonding in gelation is supported by the fact that the gels changed into clear solutions after the addition of LiCl, which is known to interact strongly with amides and break hydrogen bonds (see Supporting Information). The FT-IR spectrum of the dry gel also revealed characteristic stretching vibrations as a result of hydrogen-bonding interactions in the N–H (3309 cm⁻¹) and C=O (amide I: 1660 cm⁻¹) moieties. However, further proof is needed to verify the presence of hydrogen bonds in the gel state. Other weak interactions may also play an important role in the self-assembly. Fluorescence spectroscopy^[14] with pyrene as a probe was employed to examine the effect of benzyl rings. The intensity ratio I_1/I_3 of pyrene emissions is an established index for the polarity of the environment. This ratio decreased as the concentration of **G3** was increased in THF/CH₃OH (9:1; see Supporting Information), which suggests that nonpolar domains were formed as a consequence of the aromatic stacking of peripheral benzyl rings.

What is the relationship between the structure of a native gel and the organization of gelators in the solid state? This is an important question that has puzzled researchers for many years. To address this question in the case of **G3**, as well as to

obtain some hints on its packing pattern in native gels, X-ray diffraction (XRD) was carried out on the native gel, xerogel, and dendrite. No reflection could be detected in the CH₃OH/CHCl₃/ethyl acetate gel, presumably as a consequence of strong scattering from the electron-rich CHCl₃ solvent. The one-dimensional (1D) XRD pattern of the xerogel is shown in Figure 2. The large scattering halo with a maximum in 2θ at

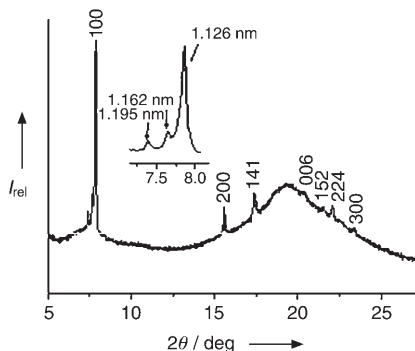


Figure 2. 1D XRD pattern of the **G3**/CH₃OH/CHCl₃/ethyl acetate xerogel. The inset shows reflections around $2\theta = 7.86^\circ$.

around 20° (corresponding to a d spacing of ≈ 0.45 nm) indicates that the major portion of **G3** in the xerogel was amorphous. However, the existence of a series of sharp diffractions reveals that the **G3** of the xerogel could partially crystallize. Efforts were made to grow single crystals, but failed. However, **G3** dendrites up to centimeter dimensions were obtained in DMF through evaporation at room temperature for a month. Figure 3 shows a two-dimensional (2D)

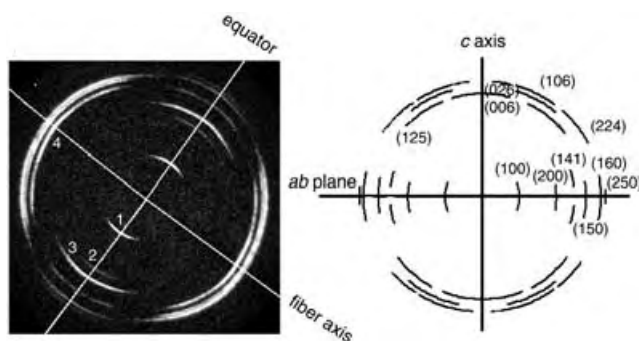


Figure 3. 2D WAXD pattern (left) and its schematic drawing (right) for one fiber-like branch in a **G3** dendrite.

wide-angle XRD (WAXD) pattern obtained from one fiber-like branch of a dendrite, which was collected in the transmission mode with the X-ray incident beam perpendicular to the long axis of the fiber. The sample was rotated through 360° around the long axis during exposure. It was difficult to deduce the precise crystal structure of **G3** because of the scarcity of diffraction lines. However, by assuming that the crystallographic c axis is parallel to the fiber long

axis, and that the diffraction lines that correspond to a d spacing of 1.162, 0.581, 0.522, and 0.451 nm are the (100), (200), (141), and (006) planes, respectively (Figure 2), we might tentatively propose an orthorhombic lattice with $a = 1.162$, $b = 2.395$, and $c = 2.706$ nm. As shown in the right-hand side of Figure 3, all the diffraction lines observed can be indexed. The calculated d spacings fitted the measured ones quite well (see Supporting Information). Meanwhile, we noted that the (100) diffraction with a d spacing of 1.162 nm in the dendrite could also be identified in the xerogel (see the inset of Figure 2). Although the intensity is relatively weaker, it indicates that the crystal in the xerogel could have the same structure as the dendrite. However, the coexistence of three peaks with very close d spacings proves that the **G3** crystals are in fact polymorphic. Still assuming an orthorhombic lattice, we found that the strongest diffraction with a d spacing of 1.126 nm and following peaks in the higher 2θ region in Figure 2 could be indexed with $a = 1.126$, $b = 2.331$, and $c = 2.582$ nm, values that deviate only slightly from those proposed for the dendrite. Reexamination of the dendrite testified that polymorphism also occurred. Occasionally, two sets of diffractions could be detected (see Supporting Information) in one fiber. This polymorphism may arise from the rich intra- and intermolecular hydrogen-bonding interactions, which lead to a **G3** molecular packing trapped in different local Gibbs energy minima during crystallization by solvent evaporation.

The gel became a turbid solution and would not regel after it was destroyed by mechanical agitation. Therefore, the morph responsible for gelation is probably not of the most thermodynamically stable phase. Recently, it was proposed^[15] that one prerequisite of gel formation is the 1D alignment of gelator molecules. If so, the morph in the gel state should be different from that in the 3D orthorhombic crystals. A structure change, such as crystallization, is quite possible during the formation of a xerogel from a gel by the evaporation of solvents.

G3 can self-organize into lyotropic LC phases in benzyl alcohol. When the concentration of **G3** exceeds a certain limit (about 6 wt %), spherulites and oily streaks (Figure 4a) appeared, as viewed by polarizing optical microscopy (POM). With an increase of the concentration, more spherulites formed and eventually the whole field of view became dominated by a polygonal texture (Figure 4b). The textures can be deformed with pressure and are self-healing. No evidence of microcrystallites was observed. The lyotropic LC

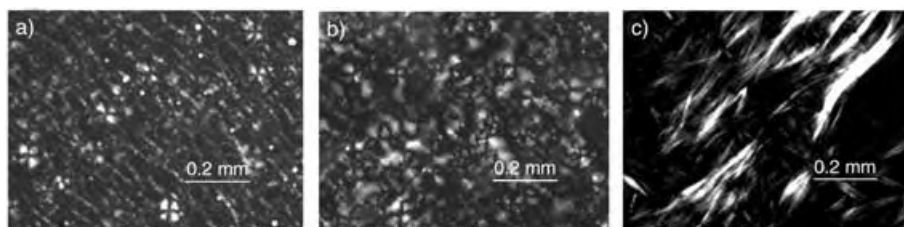


Figure 4. Representative microphotographic textures of **G3** in benzyl alcohol under crossed polarizers. a) Spherulites and oily streaks in 14-wt% samples at room temperature (RT); b) polygonal texture (or focal-conic-like texture) in 30-wt% samples at RT; c) filament texture of 40-wt% samples heated at 10 K min^{-1} and held for 5 min at 100°C .

behavior of the **G3**/benzyl alcohol phase at several representative concentrations was also examined by differential scanning calorimetry (DSC; see Supporting Information). A single endothermic peak was observed on heating 8-, 14-, and 20-wt % samples. The peak temperature increased monotonously from 60 °C for 8-wt % samples to 80 °C for 20-wt % samples, which was in accordance with the trend of transition of birefringence from anisotropic to isotropic observed by POM.

In the cases of 25-, 30-, 40-, and 50-wt % samples, the DSC heating traces showed a broad endothermic process with two peaks, which indicates two possible transitions. For example, the 40-wt % sample exhibited a lower peak at 88 °C and a higher peak at 95 °C before it completely entered the isotropic state after 105 °C. A new POM texture different to that in Figure 4b developed above the lower transition temperature (Figure 4c). This was also the case for the other samples in the range of 25–50 wt %. The combination of the POM and DSC results suggests that the **G3**/benzyl alcohol mixture may have one lyotropic LC phase below the isotropic temperature at a concentration of 5–20 wt %. As the concentration ranged from 25 to 50 wt %, the samples may have one low- and one high-temperature LC phase prior to the LC-to-isotropic transition.

In contrast to most other LC dendrimers,^[16] **G3** is lyotropic and intrinsically mesogenic with relatively flexible chains. It may serve as a good testing bench for the study of the structure–mesophase relationship. The lyotropic LC phase structure of the **G3**/benzyl alcohol mixture at low temperature (below the isotropic temperature for 5- to 20-wt % samples and below the lower transition temperature for 25- to 50-wt % samples) was identified by XRD. In the low 2θ region (Figure 5), a series of scatterings up to the fourth order could be observed for all the concentrations investigated, and the corresponding scattering vector ratios exactly followed 1:2:3:4 which clearly indicated a lamellar structure. This finding agrees well with the spherulites, oily streaks, and polygonal textures observed with POM, which were believed to be the characteristic features of the lyotropic lamellar phase.^[17]

Despite varying the concentration, the long period of the lamellae was measured as 4.59 nm. This result indicated that,

at low temperature, the samples shared the same lyotropic LC phase where the lamellae coexisted with the solvent. We expected that the lamellae should be a bilayer structure. According to our preliminary computer modeling of the **G3** molecule, the distance from the focal point to the periphery was estimated to be about 2.8 nm if the **G3** molecules were fully extended. Hence, each lamella might consist of two layers of **G3** molecules that are partially interdigitated. In the inner part of the lamellae, the **G3** molecules might associate with their neighbors through hydrogen bonds, while the benzyl rings of the **G3** molecules are packed on the lamellar top and bottom surfaces. More systematic structural and thermodynamic transition property analyses, as well as more morphological studies, are necessary to finally identify the textures and the corresponding phases.

In summary, we have successfully synthesized a novel dipeptide-branched poly(Gly-Asp) dendron (**G3**) capable of self-organizing into organogels and lyotropic LC phases. With a solvent–solvent gel preparation process, the **G3** dendrons self-assembled into a network of intertwined fibers. Both hydrogen-bonding and aromatic-stacking interactions might be responsible for the aggregation. The ordered structure in the xerogel has a close relationship with the orthorhombic packing of **G3** in dendritic crystals. **G3** exhibits lyotropic LC behavior in benzyl alcohol, and a low-temperature lamellar phase with a long period of 4.59 nm can be identified. Fibrous proteins are ubiquitous in nature. Silk fibroin, amyloid, and collagens are but a few remarkable examples.^[18] The systems described herein may give us more chance to understand the basic principles governing their supramolecular organization from a new angle different to that offered by linear model peptides. Further investigation is in progress to gain deeper insight into the mechanisms of gelation and mesophase formation, and to unravel the precise molecular-packing patterns of **G3** in the gels, crystals, and liquid crystals. In addition, the applications of such nanostructured materials could be explored as potentially biocompatible systems for drug delivery, molecular recognition, and other diagnostic or therapeutic functions.

Received: January 31, 2005

Revised: June 17, 2005

Published online: August 17, 2005

Keywords: amino acids · dendrimers · gelators · liquid crystals · self-assembly

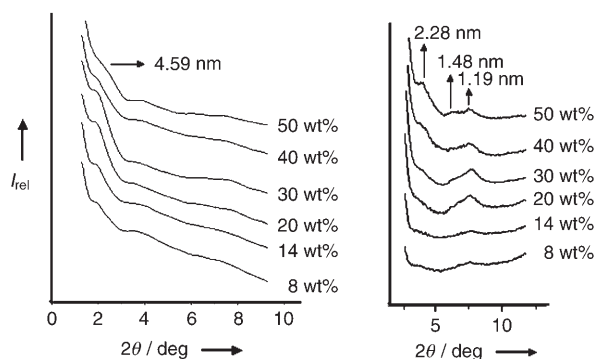


Figure 5. 1D XRD patterns of **G3** in benzyl alcohol. Left: diffraction patterns from $2\theta = 2.5^\circ$ to $2\theta = 12^\circ$ with a prolonged exposure time. Right: overview diffraction patterns at different concentrations.

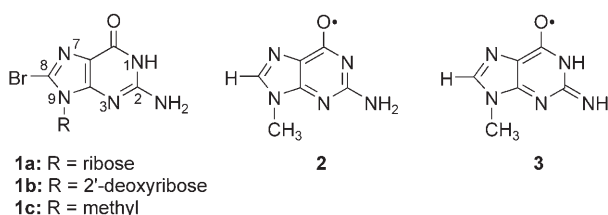
- [1] a) I. S. Choi, N. Bowden, G. M. Whitesides, *Angew. Chem.* **1999**, *111*, 3265–3268; *Angew. Chem. Int. Ed.* **1999**, *38*, 3078–3081; b) A. M. Smith, S. F. A. Acquah, N. Bone, H. W. Kroto, M. G. Ryadnov, M. S. P. Stevens, D. R. M. Walton, D. N. Woolfson, *Angew. Chem.* **2005**, *117*, 329–332; *Angew. Chem. Int. Ed.* **2005**, *44*, 325–328.
- [2] a) R. Martin, L. Waldmann, D. L. Kaplan, *Biopolymers* **2003**, *70*, 435–444; b) D. G. Lynn, S. C. Meredith, *J. Struct. Biol.* **2000**, *130*, 153–173; c) H. A. Lashuel, S. R. LaBrenz, L. Woo, L. C. Serpell, J. W. Kelly, *J. Am. Chem. Soc.* **2000**, *122*, 5262–5277; d) D. M. Marini, W. Hwang, D. A. Lauffenburger, S. G. Zhang, R. D. Kamm, *Nano Lett.* **2002**, *2*, 295–299.

- [3] a) D. A. Tomalia, B. Huang, D. R. Swanson, H. M. Brothers, J. W. Klimash, *Tetrahedron* **2003**, *59*, 3799–3813; b) P. J. Dandliker, F. Diederich, J. P. Gisselbrecht, A. Louati, M. Gross, *Angew. Chem.* **1995**, *107*, 2906–2909; *Angew. Chem. Int. Ed. Engl.* **1995**, *34*, 2725–2728; c) D. Ranganathan, S. Kurur, R. Gilardi, I. L. Karle, *Biopolymers* **2000**, *54*, 289–295.
- [4] a) U. Boas, P. M. H. Heegaard, *Chem. Soc. Rev.* **2004**, *33*, 43–63; b) F. Aulenta, W. Hayes, S. Rannard, *Eur. Polym. J.* **2003**, *39*, 1741–1771.
- [5] J. S. Choi, D. K. Joo, C. H. Kim, K. Kim, J. S. Park, *J. Am. Chem. Soc.* **2000**, *122*, 474–480.
- [6] For articles on polylysine dendritic gelators, see: a) A. R. Hirst, D. K. Smith, M. C. Feiters, H. P. M. Geurts, *Langmuir* **2004**, *20*, 7070–7077; b) C. S. Love, A. R. Hirst, V. Chechik, D. K. Smith, I. Ashworth, C. Brennan, *Langmuir* **2004**, *20*, 6580–6585; c) K. S. Partridge, D. K. Smith, G. M. Dykes, P. T. McGrail, *Chem. Commun.* **2001**, 319–320; d) A. R. Hirst, D. K. Smith, M. C. Feiters, H. P. M. Geurts, A. C. Wright, *J. Am. Chem. Soc.* **2003**, *125*, 9010–9011; e) A. R. Hirst, D. K. Smith, M. C. Feiters, H. P. M. Geurts *Chem. Eur. J.* **2004**, *10*, 5901–5910.
- [7] D. Ranganathan, S. Kurur, K. P. Madhusudan, R. Roy, I. L. Karle, *J. Pept. Res.* **1998**, *50*, 297–302.
- [8] a) B. B. Wang, X. Zhang, X. R. Jia, Z. C. Li, Y. Ji, L. Yang, Y. Wei, *J. Am. Chem. Soc.* **2004**, *126*, 15180–15194; b) L. Yang, Y. F. Luo, X. R. Jia, Y. Ji, L. P. You, Q. F. Zhou, Y. Wei, *J. Phys. Chem. B* **2004**, *108*, 1176–1178; c) J. F. Wang, X. R. Jia, H. Zhong, H. Z. Wu, Y. Y. Li, X. J. Xu, M. Q. Li, Y. Wei, *J. Polym. Sci. A* **2000**, *38*, 4147–4153; d) J. F. Wang, X. R. Jia, H. Zhong, Y. Qin, J. Y. Chen, X. S. Zhao, W. X. Cao, M. Q. Li, Y. Wei, *Chem. Mater.* **2002**, *14*, 2854–2858.
- [9] V. Percec, A. E. Dulcey, V. S. K. Balagurusamy, Y. Miura, J. Smidrkal, M. Petercal, S. Nummelin, U. Edlund, S. D. Hudson, P. A. Heiney, H. Duan, S. N. Magonov, S. A. Vinogradov, *Nature* **2004**, *430*, 764–768.
- [10] Y. Cohen, A. Dagan, *Macromolecules* **1995**, *28*, 7638–7644.
- [11] For selected publications on the synthesis of natural amino acid based dendrimers, see: a) L. Crespo, G. Sanclimens, B. Montaner, R. Perez-Tomas, M. Royo, M. Pons, F. Albericio, E. Giralt, *J. Am. Chem. Soc.* **2002**, *124*, 8876–8883; b) M. Driffield, D. M. Goodall, A. S. Klute, D. K. Smith, K. Wilson, *Langmuir* **2002**, *18*, 8660–8665, and references therein; c) L. Twyman, A. E. Beezer, J. C. Mitchell, *Tetrahedron Lett.* **1994**, *35*, 4423–4424; d) D. Ranganathan, S. Kurur, *Tetrahedron Lett.* **1997**, *38*, 1265–1268; e) I. B. Rietveld, E. Kim, S. A. Vinogradov, *Tetrahedron* **2003**, *59*, 3821–3831, and references therein; f) J. Kress, A. Rosner, A. Hirsch, *Chem. Eur. J.* **2000**, *6*, 247–257; g) B. Buschhaus, W. Bauer, A. Hirsch, *Tetrahedron* **2003**, *59*, 3899–3915; h) Y. Kim, F. W. Zeng, S. C. Zimmerman, *Chem. Eur. J.* **1999**, *5*, 2133–2138; i) L. J. Twyman, A. E. Beezer, R. Esfand, B. T. Mathews, J. C. Mitchell, *J. Chem. Res. Synop.* **1998**, *12*, 758–759.
- [12] a) P. Terech, R. G. Weiss, *Chem. Rev.* **1997**, *97*, 3133–3159; b) O. Gronwald, E. Snip, S. Shinkai, *Curr. Opin. Colloid Interface Sci.* **2002**, *7*, 148–156; c) D. J. Abdallah, R. G. Weiss, *Adv. Mater.* **2000**, *12*, 1237–1246.
- [13] For publications on dendritic gelators other than polylysine dendrimers, see: a) G. R. Newkome, G. R. Baker, M. J. Saunders, P. S. Russo, V. K. Gupta, Z. Q. Yao, J. E. Miller, K. Bouillion, *J. Chem. Soc. Chem. Commun.* **1986**, *10*, 752–753; b) G. R. Newkome, G. R. Baker, S. Arai, M. J. Saunders, P. S. Russo, K. J. Theriot, C. N. Moorefield, L. E. Rogers, J. E. Miller, T. R. Lieux, M. E. Murray, B. Phillips, L. Pascal, *J. Am. Chem. Soc.* **1990**, *112*, 8459–8465; c) G. R. Newkome, C. N. Moorefield, G. R. Baker, R. K. Behera, G. H. Escamilla, M. J. Saunders, *Angew. Chem.* **1992**, *104*, 901–903; *Angew. Chem. Int. Ed. Engl.* **1992**, *31*, 917–919; d) G. R. Newkome, X. F. Lin, C. Yaxiong, G. H. Escamilla, *J. Org. Chem.* **1993**, *58*, 3123–3129; e) K. H. Yu, P. S. Russo, L. Younger, W. G. Henk, D. W. Hua, G. R. Newkome, G. Baker, *J. Polym. Sci. B* **1997**, *35*, 2787–2793; f) M. Jorgensen, K. Bechgaard, T. Bjornholm, P. Sommer-Larse, L. G. Hansen, K. Schaunberg, *J. Org. Chem.* **1994**, *59*, 5877–5882; g) W. D. Jang, D. L. Jiang, T. Aida, *J. Am. Chem. Soc.* **2000**, *122*, 3232–3233; h) C. Kim, K. T. Kim, Y. Chang, H. H. Song, T. Y. Cho, H. J. Jeon, *J. Am. Chem. Soc.* **2001**, *123*, 5586–5587; i) W. D. Jang, T. Aida, *Macromolecules* **2003**, *36*, 8461–8469; j) W. Zhang, S. O. Gonzalez, E. E. Simanek, *Macromolecules* **2002**, *35*, 9015–9021.
- [14] M. Yumoto, M. Kimura, H. Shirai, K. Hanabusa, *Chem. Eur. J.* **2003**, *9*, 348–354.
- [15] a) O. Gronwald, S. Shinkai, *Chem. Eur. J.* **2001**, *7*, 4329–4334; b) K. Sugiyasu, N. Fujita, S. Shinkai, *Angew. Chem.* **2004**, *116*, 1249–1253; *Angew. Chem. Int. Ed.* **2004**, *43*, 1229–1233, and references therein.
- [16] For selected publications on LC dendrimers, see: a) V. Percec, M. Kawasumi, *Macromolecules* **1992**, *25*, 3843–3850; b) V. Percec, M. Glodde, G. Johansson, V. S. K. Balagurusamy, P. A. Heiney, *Angew. Chem.* **2003**, *115*, 4474–4478; *Angew. Chem. Int. Ed.* **2003**, *42*, 4338–4342; c) M. Lehmann, I. Fischbach, H. W. Spiess, H. Meier, *J. Am. Chem. Soc.* **2004**, *126*, 772–784; d) Y. Li, S. T. Lin, W. A. Goddard, *J. Am. Chem. Soc.* **2004**, *126*, 1872–1885; e) G. Ungar, Y. S. Liu, X. B. Zeng, V. Percec, W. D. Cho, *Science* **2003**, *299*, 1208–1211; f) R. Elsässer, G. H. Mehl, J. W. Goodby, M. Veith, *Angew. Chem.* **2001**, *113*, 2760–2762; *Angew. Chem. Int. Ed.* **2001**, *40*, 2688–2690; g) P. Busson, H. Ihre, A. Hult, *J. Am. Chem. Soc.* **1998**, *120*, 9070–9071; h) D. J. Pesak, J. S. Moore, *Angew. Chem.* **1997**, *109*, 1709–1712; *Angew. Chem. Int. Ed. Engl.* **1997**, *36*, 1636–1639, and references therein; i) M. Nishii, T. Matsuoka, Y. Kamikawa, T. Kato, *Org. Biomol. Chem.* **2005**, *3*, 875.
- [17] a) G. Wang, A. D. Hamilton, *Chem. Eur. J.* **2002**, *8*, 1954–1961; b) Y. Rangon, J. Charvolin, *J. Phys. Chem.* **1988**, *92*, 6339–6344; c) J. Yang, G. Wegner, *Macromolecules* **1992**, *25*, 1786–1790.
- [18] a) N. L. Goeden-Wood, J. D. Keasling, S. J. Muller, *Macromolecules* **2003**, *36*, 2932–2938; b) K. Lu, J. Jacob, P. Thiagarajan, V. P. Conticello, D. G. Lynn, *J. Am. Chem. Soc.* **2003**, *125*, 6391–6393; c) A. Aggeli, M. Bell, N. Boden, J. N. Keen, P. F. Knowles, T. C. B. McLeish, M. Pitkeathly, S. E. Radford, *Nature* **1997**, *386*, 259–262.

Tautomers of One-Electron-Oxidized Guanosine**

Chrysostomos Chatgililoglu,* Clara Caminal, Maurizio Guerra, and Quinto G. Mulazzani

8-Bromoguanine derivatives, such as **1a** and **1b**, capture electrons (e_{aq}^-) with quantitative formation of the corresponding debrominated nucleosides^[1,2] and, therefore, they are efficient detectors of excess electron-transfer processes.^[3] Indeed, in two recent papers 8-bromo-2'-deoxyguanosine (**1b**) was incorporated in a variety of single- and double-



stranded oligonucleotides and G-quadruplexes, and the reaction with e_{aq}^- indicated that excess electron transfer is effective.^[2,4]

The reaction of e_{aq}^- with **1a** was previously studied by pulse-radiolysis techniques in some detail.^[1] These experiments revealed the formation of two short-lived intermediates at pH \approx 7. Figure 1 shows the absorption spectrum of the first observable species (solid line) obtained 2 μ s after the pulse. This species of uncertain structure decays by first-order kinetics ($k = 5.0 \times 10^4 \text{ s}^{-1}$) to produce the one-electron-oxidized guanosine (dashed line).^[1] In the present work we studied the kinetics in the temperature range of 5.8–50.3 °C and obtained the following Arrhenius parameters: $\log(A/\text{s}^{-1}) = 8.7 \pm 0.4$ and $E_a = 23.0 \pm 2.5 \text{ kJ mol}^{-1}$ (errors correspond to one standard deviation).

What is the structure of the first observable species, which has a characteristic absorbance around 600 nm? We found previously that time-dependent (TD) DFT calculations at the B3LYP/6-31G* level^[5,6] provide reliable optical transitions for nucleoside radicals.^[7,8] In neutral solution, the initial electron adduct of **1** should be rapidly protonated.^[9] Therefore, TD-B3LYP/6-31G* calculations were carried out on 8-

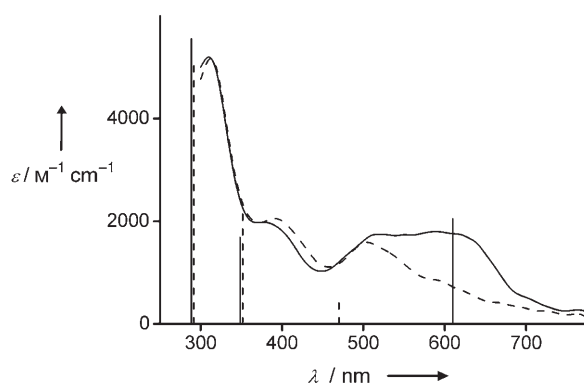
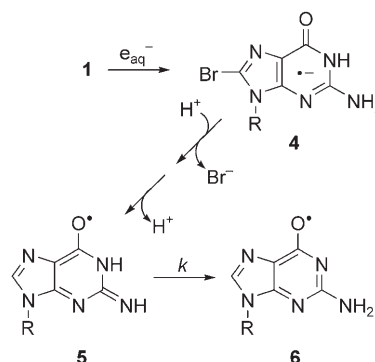


Figure 1. Absorption spectra obtained from the pulse radiolysis of Ar-purged solutions containing 1 mM **1a** at pH \approx 7 with 0.25 M *t*BuOH, recorded 2 μ s (solid line) and 45 μ s (dashed line) after the pulse (adapted from ref. [1]). The lines show the calculated vertical optical transitions for radical **2** (dashed lines, $\lambda(f)$: 290 (0.128), 350 (0.054), 470 nm (0.014)) and its tautomer **3** (solid lines, $\lambda(f)$: 290 (0.138), 350 (0.042), 610 nm (0.051)).

bromo-9-methylguanine (**1c**) radical anion, protonated at N7 (as suggested previously^[1]) and at any other possible sites; no optical transition was predicted to exist above 500 nm. Interestingly, protonation at C8 produces loss of Br^- , and it could be hypothesized that the first observable species in pulse radiolysis had already lost Br^- . Consequently, we computed the optical spectra (transition wavelengths λ and oscillator strengths f) of the deprotonated 9-methylguanine radical cation (i.e., oxidized 9-methylguanine **2**) and its tautomers bearing an iminic substituent at C2. The computed data for the radical **2** are reported in Figure 1 and are in good accord with values assigned with certainty to the oxidized guanosine.^[10] More interestingly, calculations showed that a band is computed at wavelengths longer than 500 nm only for the tautomer **3**. The computed optical transitions are also reported in Figure 1 and are in good agreement with the experimental spectrum recorded 2 μ s after the pulse; these data correspond to the transient of uncertain structure.

On the basis of these findings, we propose a revised mechanism for the reaction of e_{aq}^- with **1** (Scheme 1). The



Scheme 1. Proposed mechanism for the reaction of e_{aq}^- with 8-bromoguanosine (**1a**). The initial adduct **4** is rapidly protonated to give the first observable species **5**. The tautomer **6** is assigned to the second transient species observed in the pulse-radiolysis studies (see Figure 1).

[*] Dr. C. Chatgililoglu, Dr. C. Caminal, Dr. M. Guerra, Dr. Q. G. Mulazzani
ISOF, Consiglio Nazionale delle Ricerche
Via P. Gobetti 101, 40129 Bologna (Italy)
Fax: (+39) 051-639-8349
E-mail: chrys@isof.cnr.it

[**] This research was supported in part by the European Community's Marie Curie Research Training Network under contract MRTN-CT-2003-505086 (CLUSTOXDNA). We thank A. Monti and A. Martelli for technical assistance.

initial electron adduct **4** is rapidly protonated at the C8 position to release Br^- and the first observable transient species **5**,^[11] which should have a pK_a value similar to that of oxidized guanosine ($\text{pK}_a = 3.9$).^[10] The subsequent tautomerization **5**→**6** occurs with a $\log(A/\text{s}^{-1}) = 8.7$, which suggests a complex transition state, and an activation energy of 23.0 kJ mol^{-1} . Another point supporting a complex transition state is also the previously reported kinetic isotope effect $k(\text{H}_2\text{O})/k(\text{D}_2\text{O}) = 8.0$.^[1]

The reaction barrier (E_a) for the direct tautomerization **3**→**2** is computed to be $183.7 \text{ kJ mol}^{-1}$ at the B3LYP/6-31G* level. Such a large value is in evident contrast with the

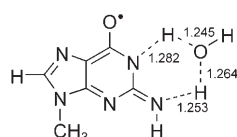
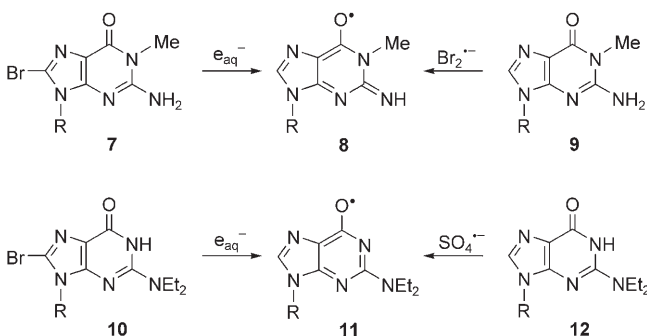


Figure 2. Structure of the transition state for the water-assisted tautomerization **3**→**2** computed at the B3LYP/6-31G* level. Distances are in Å.

activation energy measured for the tautomerization **5**→**6**. In analogy with the keto–enol tautomerization in guanine^[12] and 8-oxo-7,8-dihydroguanine,^[13] the water-assisted proton transfer is computed to occur with a much lower reaction barrier (the calculated transition-state structure is given in Figure 2). Indeed, the reaction barrier is computed to be as small as 18.8 kJ mol^{-1} , in good accord with experiment.^[14]

To gain insight into the different tautomeric forms, the 8-bromo derivatives **7** and **10** (Scheme 2) were prepared, since the analogous tautomeriza-



Scheme 2. Reactions of e_{aq}^- with 8-bromoguanosine derivatives **7** and **10**, of Br_2^- with **9**, and of SO_4^- with **12**. The radicals **8** and **11** are assigned to the transient species observed in the pulse-radiolysis studies (see Figures 3 and 4, respectively).

tion **5**→**6** could not occur as a result of alkylation at NH and NH_2 moieties. γ -Radiolysis of **7** and **10** in aqueous solutions at $\text{pH} \approx 7$ was followed by product studies, which showed the quantitative formation of debrominated derivatives **9** and **12**, respectively.^[15] Rate constants of 1.1×10^{10} and $8.0 \times 10^9 \text{ M}^{-1} \text{ s}^{-1}$ were determined at $\text{pH} \approx 7$ for the reactions of e_{aq}^- with **7** and **10**, respectively, by measuring the rate of the optical density decrease of e_{aq}^- as a function of the concentration of the added nucleoside.^[18] Figures 3 and 4 show the optical absorption spectra obtained from these reactions. The ϵ values were calculated using $G = 0.27 \mu\text{mol J}^{-1}$, since HO^\bullet species are scavenged by the added *t*BuOH, and the H^\bullet atoms follow another path and therefore do not contribute to the reaction.^[16] The decay of these transients follows second-

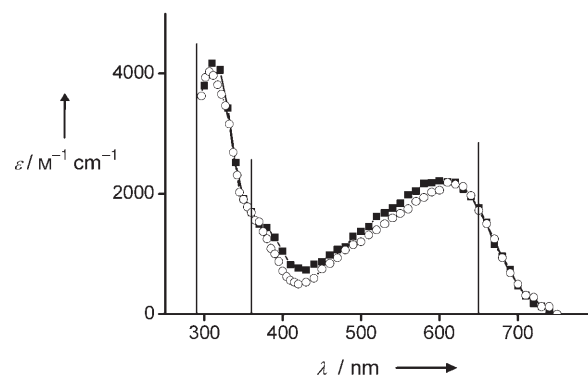


Figure 3. Absorption spectrum (■) obtained from the pulse radiolysis of Ar-purged solutions containing 0.5 mM **7** at $\text{pH} \approx 7$ and 0.25 M *t*BuOH, recorded 10 μs after the pulse. Absorption spectrum (○) is taken from reference [10] and refers to the reaction of Br_2^- with **9**. The lines show the calculated vertical optical transitions for radical **8** ($R = \text{Me}$) ($\lambda(f)$: 290 (0.063), 360 (0.036), 650 nm (0.040)).

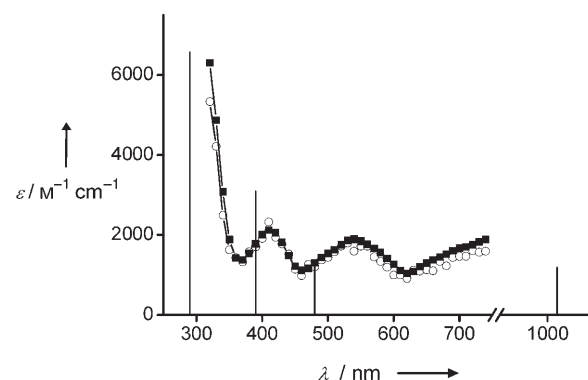


Figure 4. Absorption spectrum (■) obtained from the pulse radiolysis of Ar-purged solutions containing 0.5 mM **10** at $\text{pH} \approx 7$ and 0.25 M *t*BuOH, recorded 2 μs after the pulse. Absorption spectrum (○) obtained from the pulse radiolysis of Ar-purged solutions containing 0.1 mM **12** and 10 mM $\text{K}_2\text{S}_2\text{O}_8$ at $\text{pH} \approx 7$ with 0.1 M *t*BuOH, recorded 6 μs after the pulse. The lines show the calculated vertical optical transitions for radical **11** ($R = \text{Me}$) ($\lambda(f)$: 290 (0.149), 390 (0.070), 480 (0.029), 1030 nm (0.027)).

order kinetics and their disappearance does not lead to other transients. Furthermore, these spectra are identical to those obtained after the oxidation of **9** by Br_2^- ^[10] and of **12** by SO_4^- at $\text{pH} \approx 7$ (Figures 3 and 4).

Therefore, the spectra in Figures 3 and 4 are assigned to radicals **8** and **11**, respectively, which can be obtained either from the reduction of 8-bromoguanine derivatives or from the oxidation of the debrominated compounds as illustrated in Scheme 2. TD-B3LYP/6-31G* calculations carried out on the corresponding 9-methyl derivatives of radicals **8** and **11** fit very well with our assignment. Indeed, the computed optical spectra for the radical **8** and for the radical **11**^[19] are in good agreement with the spectra shown in Figures 3 and 4, respectively. Interestingly, both the spectrum of radical **8** and that of radical **5** have a band at 610–620 nm, which is consistent with an iminic substitution at the C2 position. Obviously, radical **5** can tautomerize to **6**, whereas radical **8** is blocked in one form.

In conclusion, our work here demonstrates the first directly observed differences of the two tautomeric forms of oxidized guanosine. The energetically most stable form **6** is the one that is obtained directly by oxidation of guanosine. The less stable form **5** is obtained from the protonation of the 8-bromoguanosine electron adduct, and its tautomerization to **6** has an activation energy of 23.0 kJ mol⁻¹.

Experimental Section

Pulse radiolysis with optical absorption detection was performed by using a 12-MeV linear accelerator, which delivered 20–200 ns electron pulses with doses between 5 and 50 Gy, by which HO•, H•, and e_{aq}⁻ were generated with concentrations of 1–20 μM. Continuous radiolyses were performed at room temperature using a ⁶⁰Co-Gammacell, with a dose rate of ca. 15 Gy min⁻¹. Compounds **7**, **10**, and **12** were prepared following known procedures.^[20]

Received: March 25, 2005

Revised: May 23, 2005

Published online: August 17, 2005

Keywords: density functional calculations · kinetics · nucleosides · pulse radiolysis · tautomerism

- [1] M. Ioele, R. Bazzanini, C. Chatgililoglu, Q. G. Mulazzani, *J. Am. Chem. Soc.* **2000**, *122*, 1900–1907.
- [2] M. De Champdoré, L. De Napoli, D. Montesarchio, G. Piccialli, C. Caminal, Q. G. Mulazzani, M. L. Navacchia, C. Chatgililoglu, *Chem. Commun.* **2004**, 1756–1757.
- [3] For selected recent papers on the excess electron transfer, see: H.-A. Wagenknecht, *Angew. Chem.* **2003**, *115*, 2558–2565; *Angew. Chem. Int. Ed.* **2003**, *42*, 2454–2460; T. Carell, C. Behrens, J. Gierlich, *Org. Biomol. Chem.* **2003**, *1*, 2221–2228; S. Breeger, U. Hennecke, T. Carell, *J. Am. Chem. Soc.* **2004**, *126*, 1302–1303; T. Iko and S. E. Rokita, *J. Am. Chem. Soc.* **2004**, *126*, 15552–15559; B. Giese, B. Carl, T. Carl, T. Carell, C. Behrens, U. Hennecke, O. Schiemann, E. Feresin, *Angew. Chem.* **2004**, *116*, 1848–1851; *Angew. Chem. Int. Ed.* **2004**, *43*, 1848–1851.
- [4] T. Kimura, K. Kawai, S. Tojo, T. Majima, *J. Org. Chem.* **2004**, *69*, 1169–1173.
- [5] Unrestricted DFT calculations were carried out with the Gaussian 98 system of programs employing the B3LYP functional and the valence double- ζ basis set supplemented with polarization d-functions on heavy atoms (B3LYP/6-31G*).
- [6] Optical transitions were computed by using the time-dependent density-functional response theory (TD-DFT), see: R. E. Stratmann, G. E. Scuseria, M. J. Frisch, *J. Chem. Phys.* **1998**, *109*, 8218–8224.
- [7] C. Chatgililoglu, C. Ferreri, R. Bazzanini, M. Guerra, S.-Y. Choi, C. J. Emanuel, J. H. Horner, M. Newcomb, *J. Am. Chem. Soc.* **2000**, *122*, 9525–9533.
- [8] C. Chatgililoglu, M. Guerra, Q. G. Mulazzani, *J. Am. Chem. Soc.* **2003**, *125*, 3839–3848.
- [9] L. P. Candeias, P. Wolf, P. O'Neill, S. Steenken, *J. Phys. Chem.* **1992**, *96*, 10302–10307.
- [10] L. P. Candeias, S. Steenken, *J. Am. Chem. Soc.* **1989**, *111*, 1094–1099.
- [11] For the protonation at the C8 position of electron adducts of adenine nucleosides, see: L. P. Candeias, S. Steenken, *J. Phys. Chem.* **1992**, *96*, 937–944.
- [12] L. Gorb, J. Leszczynski, *J. Am. Chem. Soc.* **1998**, *120*, 5024–5032.
- [13] J. Llano, L. A. Eriksson, *Phys. Chem. Chem. Phys.* **2004**, *6*, 4707–4713.
- [14] A detailed computational investigation of the water-assisted tautomerization including the effect of the basis set and of a polarizable continuum model for the aqueous solution will be presented in a full account; preliminary calculations indicate that E_a should increase by only 3–4 kJ mol⁻¹ at the higher level of theory.
- [15] Deaerated aqueous solutions containing ca. 1.5 mM **7** (or **10**) and 0.25 M *t*BuOH at pH ≈ 7 were irradiated under stationary-state conditions with a total dose of 2 kGy at a dose rate of ca. 15 Gy min⁻¹ followed by HPLC analysis.^[16] Compound **9** (or **12**) was the only detectable product, and the mass balances were close to 100%; analysis of the data, in terms of radiation chemical yield, gives $G(-7) = 0.36$, $G(9) = 0.33$, $G(-10) = 0.33$ and $G(12) = 0.30$ μmol J⁻¹. Taking into account that $G(e_{aq}^-) + G(H^+) = 0.33$ μmol J⁻¹, our results lead to the conclusion that solvated electrons and hydrogen atoms react with **7** and **10** to yield the observed product.
- [16] Radiolysis of neutral water leads to e_{aq}⁻ (0.27), HO• (0.28), and H• (0.062), the values in parentheses represent the radiation chemical yields in units of μmol J⁻¹; in the presence of 0.25 M *t*BuOH, HO• is scavenged efficiently ($k = 6.0 \times 10^8$ M⁻¹ s⁻¹), whereas H• reacts only slowly ($k = 1.7 \times 10^5$ M⁻¹ s⁻¹).^[17]
- [17] A. B. Ross, W. G. Mallard, W. P. Helman, G. V. Buxton, R. E. Huie, P. Neta, *NDRL-NIST Solution Kinetic Database - Ver. 3*, Notre Dame Radiation Laboratory, Notre Dame, IN and NIST Standard Reference Data, Gaithersburg, MD, **1998**, and references therein.
- [18] For e_{aq}⁻ at 720 nm, $\epsilon = 1.9 \times 10^4$ M⁻¹ cm⁻¹, see: G. L. Hug, *Natl. Stand. Ref. Data Ser. U. S. Natl. Bur. Stand.* **1981**, No. 69.
- [19] The corresponding optical transition (lone-pair NH₂ → π*-(SOMO) β transition) in radical **2** is computed to occur at 830 nm with a very weak intensity ($f = 0.005$). The optical-absorption band associated with π → π*-(SOMO) β spin transition is computed at 470 nm for **2** and 610 nm for **3**.
- [20] K. Yamauchi, T. Tanabe, M. Kinoshita, *J. Org. Chem.* **1979**, *44*, 638–639; M. Sako, H. Kawada, K. Hirota, *J. Org. Chem.* **1999**, *64*, 5719–5721.

Transition-State Effects of Ionic Liquids in Substitution Reactions of Pt^{II} Complexes**

Christian F. Weber, Ralph Puchta,
Nico J. R. van Eikema Hommes, Peter Wasserscheid,
and Rudi van Eldik*

Ligand-substitution reactions of square-planar complexes of d⁸ metal ions such as Pt^{II} and Pd^{II} play a fundamental role in many chemical processes, for instance, in the treatment of tumors and in homogeneous catalysis.^[1,2] Detailed mechanistic studies have demonstrated that such complexes usually undergo associative ligand-substitution reactions as a result of the 16-valence-electron structure of the square-planar complex.^[3] The transition state has either a semi-five-coordinate character in the case of an associative interchange (I_a) mechanism, or forms a short-lived, five-coordinate intermediate in the case of a limiting associative (A) mechanism. Exceptions are found in cases in which two neighboring spectator ligands form metal–carbon bonds with the metal center and induce a dissociative mechanism.^[4]

In terms of the biological or catalytic application of such metal complexes, the fundamental understanding of the ligand-substitution mechanisms enables a systematic tuning of the lability of the metal center, that is, the efficiency of the chemical process. A distinction between the three mechanisms can usually be made on the basis of activation parameters derived from the temperature and pressure dependence of the reaction, that is, ΔH^\ddagger , ΔS^\ddagger , and ΔV^\ddagger .^[3,5,6] In recent work performed in our laboratories, the lability of Pt^{II} complexes could be systematically tuned through the

introduction of σ -donor and π -acceptor spectator chelates.^[7,8] Rate and activation parameters clearly supported the associative nature of the underlying substitution mechanism.

In recent years, ionic liquids have become a popular research area that is expected to grow as a result of their potential industrial application.^[9] Not only are such liquids interesting in terms of applications in separation techniques but also they may be used to improve the solubility of weakly soluble gases and enhance the catalytic activity of metal complexes.^[10] The first industrial process based on the application of ionic liquids has been launched.^[11]

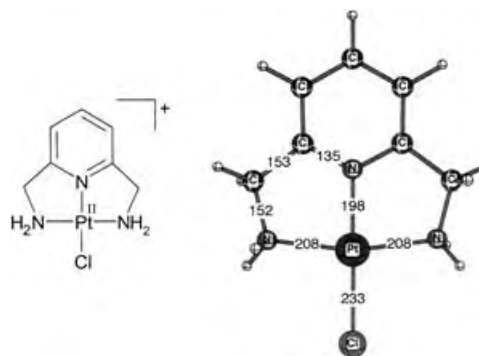
Mechanistic studies on chemical reactions in ionic liquids have only been performed to a limited degree. Skrzypczak and Neta determined the rate constants for the reaction of 1,2-dimethylimidazole with benzyl bromide (Menschutkin reaction) in a series of ionic liquids and organic solvents. The rate constants in the ionic liquids are comparable with those for polar aprotic solvents, but much larger than those for weakly polar organic solvents and alcohols.^[12] Chiappe and Pieraccini determined rate constants and activation parameters (ΔH^\ddagger and ΔS^\ddagger) for the reactions of Br₃[−] and ICl₂[−] ions with some alkenes and alkynes in a series of ionic liquids and in 1,2-dichloroethane.^[13] McLean and co-workers^[14] studied the effect of ionic liquids on bimolecular rate constants for the displacement of solvent from [(C₆H₆)Cr(CO)₂(sol)]⁺. Inhibition of the catalytic activity of a Ru^{II} catalyst in ionic liquids was recently reported by Daguene and Dyson for a reaction system in which chloride dissociation is a crucial step.^[15] More recently, work in our laboratory demonstrated that this inhibition could be related to the selected anionic component of the employed ionic liquids, since other anions in our hands clearly lead to a faster chloride dissociation step from a Pt^{II} complex in the catalytic process studied.^[16] Following the submission of this work, Shaughnessy and co-workers reported kinetic data for oxidative-addition and ligand-substitution reactions in ionic liquids.^[17,18]

A fundamental question, however, does remain: Do ionic liquids really behave as “normal” solvents, or are there unknown aspects that could affect the substitution behavior of square-planar Pt^{II} complexes? We report herein a detailed kinetic study of the substitution reactions of the [Pt^{II}(apa)Cl]⁺ complex **1** (apa = 2,6-bis(aminomethyl)pyridine; Scheme 1) with thiourea and iodide as nucleophiles, in water, methanol, and the ionic liquid 1-butyl-3-methylimidazolium bis(trifluor-

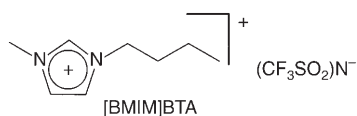
[*] Dr. C. F. Weber, Prof. Dr. R. van Eldik
Institut für Anorganische Chemie
Universität Erlangen-Nürnberg
Egerlandstrasse 1, 91058 Erlangen (Germany)
Fax: (+49) 9131-8527387
E-mail: vaneldik@chemie.uni-erlangen.de
Dr. R. Puchta, Dr. N. J. R. van Eikema Hommes
Computer Chemistry Center
Universität Erlangen-Nürnberg
Nägelsbachstrasse 25, 91052 Erlangen (Germany)
Prof. Dr. P. Wasserscheid
Lehrstuhl für Chemische Reaktionstechnik
Universität Erlangen-Nürnberg
Egerlandstrasse 3, 91058 Erlangen (Germany)

[**] The authors gratefully acknowledge financial support from the Deutsche Forschungsgemeinschaft, Fonds der Chemischen Industrie, Max-Buchner-Forschungstiftung and the European Commission within the framework of the RTN contract no. MRTN-CT-2003-503864. Prof. Tim Clark, Computer Chemistry Center, is kindly acknowledged for his support of this work. We thank the Regionales Rechenzentrum Erlangen (RRZE) for a generous allocation of computer time.

Supporting information for this article is available on the WWW under <http://www.angewandte.org> or from the author.

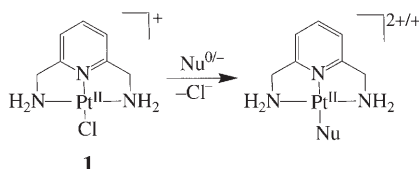


omethylsulfonyl)amide ([BMIM]BTA) as solvents. This ionic liquid has a melting point of -4°C ^[19] and a polarity close to that of ethanol.^[9d] We studied the reaction as a function of the concentration of the entering ligand, the temperature, and the pressure to determine all the rate and activation parameters



(ΔH^{\ddagger} , ΔS^{\ddagger} , and ΔV^{\ddagger}). This is, as far as we know, the first time that a systematic pressure-dependence study was undertaken for a chemical reaction in an ionic liquid. The reported rate and activation parameters show a rather “normal” behavior for the employed ionic liquid and demonstrate some unique properties of the ionic liquid as medium for the investigated substitution reactions.

The solvent dependence of the ligand-substitution reactions of **1** with thiourea (TU) and iodide (Scheme 2) were



Scheme 2. The investigated substitution reaction for thiourea (Nu^0) and iodide ion (Nu^-).

studied by dissolving the isolated complex **1-Cl** in the selected solvents followed by rapid mixing with a stock solution of the nucleophile. Typical examples of the observed spectral changes and kinetic traces are shown in Figure 1. The overall spectral changes were found to be rather similar for the studied solvents, with the exception of [BMIM]BTA due to the absorption of this liquid in the wavelength range $\lambda < 350\text{ nm}$ (see Figure 1c). All kinetic traces (Figure 1b,d) showed excellent fits to a single-exponential function, in line with pseudo-first-order behavior. The calculated pseudo-first-order rate constants, k_{obs} , were plotted against the concentration of the entering nucleophiles, TU and iodide, and are linear with a zero intercept under all conditions (see typical examples given in the Supporting Information). The rate constant k_{obs} can be expressed as a function of the concentration of the entering ligand, namely, $k_{\text{obs}} = k_2[\text{Nu}]$, in which k_2 is the second-order rate constant.

We also studied the effect of the water content of the ionic liquid on the second-order rate constant for the reaction of **1** with TU in [BMIM]BTA. The following k_2 values were obtained at 25°C (water content in ppm in brackets): 0.260 (23) , 0.245 (100) , and $0.259\text{ M}^{-1}\text{s}^{-1}\text{ (200)}$. It follows that the water content has no significant effect on the rate constant in the investigated concentration range.

The activation parameters were determined from the effect of temperature and pressure on k_2 . Spectral changes observed for the reaction in [BMIM]BTA at 100 MPa (see Supporting Information) are in excellent agreement with those observed at ambient pressure. The thermal activation parameters, ΔH^{\ddagger} and ΔS^{\ddagger} , were obtained from Eyring plots (see example in the Supporting Information), whereas ΔV^{\ddagger} was calculated from the gradient ($-\Delta V^{\ddagger}/RT$) of the plot of $\ln k$ versus pressure (see Supporting Information). Table 1 summarizes the values of the dielectric constants (ϵ), E_{T}^{N} , k_2 , ΔH^{\ddagger} , ΔS^{\ddagger} , and ΔV^{\ddagger} for the studied reactions in the three selected solvents. It should be noted that the reactions in the ionic liquid showed the same behavior as that found for other more conventional solvents as a function of the experimental variables.

The reaction of **1** with TU, a strong nucleophile, is considerably faster than the reaction with iodide in the same solvent. The k_2 values show that the substitution reactions depend significantly on the polarity of the solvent, namely, $k_2(\text{H}_2\text{O}) \gg k_2(\text{MeOH}) \approx k_2(\text{ionic liquid})$. A likely reason is an increase in the dipole moment during the course of the reaction due to partial lengthening of the Pt–Cl bond in the five-coordinate trigonal-bipyramidal transition state. In general, a decrease in solvent polarity results in a decrease in the rate of a reaction that involves an increase in dipole moment in going from the reactant to the transition state.^[22] The trend in the values of k_2 clearly indicates that the ionic liquid behaves like methanol and that no drastic acceleration or deceleration of the substitution of chloride, as reported for other Pt^{II} complexes in this and closely related ionic liquids, can be observed.^[15,16]

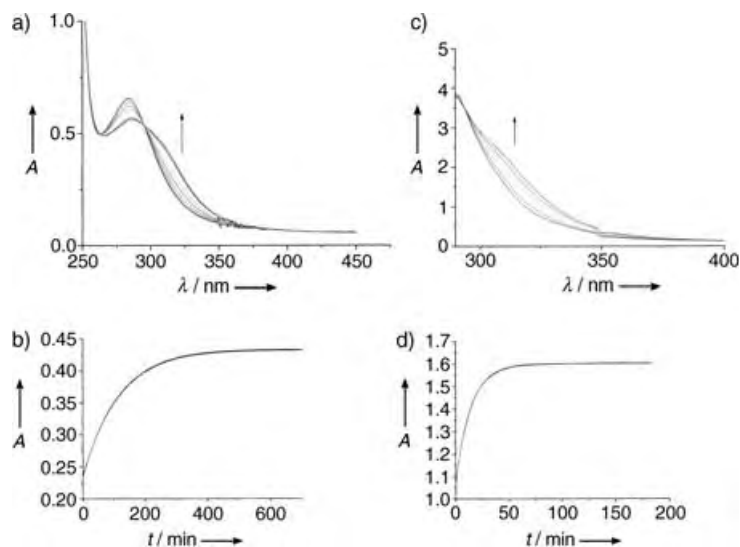


Figure 1. UV/Vis spectra (a,c) and typical kinetic traces at 320 nm (b,d) recorded for the reaction of **1** with iodide in methanol (a,b) and [BMIM]BTA (c,d). The experimental kinetic traces can be perfectly fitted with a single-exponential function. Experimental conditions: a) $[\text{Pt}^{\text{II}}] = 9.5 \times 10^{-5}\text{ M}$, LiCl (0.002 M), $[\text{I}^-] = 0.015\text{ M}$, ionic strength = 0.2 M (LiClO_4), pH 2 (0.01 M trifluoromethanesulfonic acid), $T = 25^{\circ}\text{C}$, optical path length = 10 mm. b) $[\text{Pt}^{\text{II}}] = 9.5 \times 10^{-5}\text{ M}$, LiCl (0.002 M), $[\text{I}^-] = 0.0090\text{ M}$, ionic strength = 0.2 M (LiClO_4), pH 2 (0.01 M trifluoromethanesulfonic acid), $T = 25^{\circ}\text{C}$. c,d) $[\text{Pt}^{\text{II}}] = 3.3 \times 10^{-4}\text{ M}$, $[\text{I}^-] = 0.0392\text{ M}$, $T = 25^{\circ}\text{C}$, optical path length = 5 mm.

Table 1: Summary of second-order rate constants and activation parameters^[a] for the displacement of chloride by iodide and thiourea in **1** in different solvents.

	Solvent	$\epsilon(298\text{ K}), E_T^{\text{N}}^{\text{[b]}}$	$10^3 k_2$ at 25 °C [M ⁻¹ s ⁻¹]	ΔH^\ddagger [kJ mol ⁻¹]	ΔS^\ddagger [J K ⁻¹ mol ⁻¹]	ΔV^\ddagger [cm ³ mol ⁻¹]
I ⁻	water	78.30, 1.000	253 ± 2	58 ± 1	-62 ± 3	-6.9 ± 0.3
I ⁻	methanol	32.66, 0.762	15.3 ± 0.2	69 ± 1	-51 ± 4	-10.0 ± 0.2
I ⁻	[BMIM]BTA	-, 0.642	32.1 ± 0.2	66 ± 1	-53 ± 5	-14.1 ± 0.4
TU	water	78.30, 1.000	1620 ± 10	49 ± 1	-77 ± 4	-10.4 ± 0.5
TU	methanol	32.66, 0.762	385 ± 2	63 ± 1	-42 ± 4	-6.6 ± 0.1
TU	[BMIM]BTA	-, 0.642	277 ± 3	49 ± 1	-92 ± 2	-13.9 ± 0.2

[a] Activation parameters were calculated from the temperature and pressure dependence of the second-order rate constant in the usual way. No corrections were made for changes in solvent density^[20] or viscosity^[21] as a function of temperature and pressure. [b] Dielectric constant (ϵ) of the solvent and its polarity (E_T^{N}).

The activation parameters summarized in Table 1 show some interesting trends. Throughout the series of reactions studied, the negative activation entropy and volume data clearly support the operation of a compact transition state in terms of an associative mechanism.^[3] For the reaction between complex **1** and TU, significantly more negative activation entropies and volumes are found for water and [BMIM]BTA as the solvent irrespective of their significant difference in polarity. This finding suggests that reorganization in the transition state is not controlled by solvent electrostriction. The less negative activation entropies and volumes for the reaction in methanol once again illustrate that solvent electrostriction does not contribute significantly to the transition state, otherwise the opposite effect would occur. In this case, TU is a neutral entering nucleophile and the mentioned activation parameters mainly correspond to intrinsic entropy and volume changes.

In the case of iodide as the entering nucleophile, the values of the activation entropy are almost the same for the different solvents, whereas the activation volumes are significantly more negative in the case of methanol and [BMIM]BTA as solvents. This result suggests that charge neutralization in the five-coordinate transition state leads to a decrease in electrostriction—that is, a less negative activation volume—in the more polar solvents (water and methanol). This trend, however, does not show up in the values of the activation entropy, which is probably related to the usually larger error limits of this parameter. Nevertheless, the trend in the activation volumes for the different solvents is quite convincing.

The activation volumes for the reactions with TU and iodide in [BMIM]BTA are indeed very similar, which suggests that volume changes in this ionic liquid do not respond to changes in the overall charge of the transition state. We suggest that this lack of response is due to strong hydrogen bonding and possibly also van der Waals forces in ionic liquids, which result in specific solvent structures that consist of well aligned cation–anion aggregates. The formation of such aggregates in ionic liquids has recently been investigated by using microcalorimetry.^[23] The stability of such aggregates will show a resistance towards solvent structural changes (electrostriction/solvation) as a result of charge neutralization or charge creation. The value of about $-14\text{ cm}^3\text{ mol}^{-1}$ for ΔV^\ddagger is close to that expected for an associative ligand-substitution

mechanism and represents the intrinsic volume collapse associated with the formation of a five-coordinate transition state.^[5,6]

To gain further insight into the details of the ligand-substitution mechanism, in particular, the question of associative interchange (I_a) versus associative (A), we calculated the pathways for the reactions of **1** with chloride (chloride exchange), iodide, and thiourea by using B3LYP hybrid density functional theory^[24] and the LANL2DZ ECP basis set augmented with

polarization functions.^[25,26] We have employed this theoretical level in previous work.^[16,27]

The first step in the reaction is the formation of a precursor complex between the platinum complex **1** and the incoming ligand. As **1** bears a positive charge, interaction energies in the gas phase are dominated by electrostatics and exaggerated interaction energies are calculated, particularly for the complexes with the anionic nucleophiles chloride and iodide. Nevertheless, the structures of the precursor complexes for all incoming ligands indicate rather weak bonding. The main contact consists of a hydrogen bond to one of the amine hydrogen atoms (202, 249, and 221 pm for Cl⁻, I⁻, and S, respectively). On the other hand, the platinum–halide distances, 386 (chloride) and 437 pm (iodide), and the platinum–sulfur separation (for the reaction with thiourea), 458 pm, are very long. The other bonds around platinum differ only to a minor extent from those in **1**.

Hydrogen bonds to an amine hydrogen atom are well known in the solid state,^[28] but may be unrealistic in the gas phase. Therefore, we also studied the reactions for the dimethylamino derivative, [Pt{2,6-bis(dimethylamino)methyl}pyridine]Cl⁺ ([Pt^{II}(mapa)Cl]⁺, **2**). As expected, the platinum–ligand bonds are shorter in the absence of the hydrogen bonds, but only modestly: Pt–Cl 346, Pt–I 409, Pt–S 378 pm.

All reactions proceed through a single transition-state structure. Despite extensive searches along the reaction coordinate, no stationary points other than the precursor and product complexes could be located. Thus, the reactions clearly proceed by an interchange-type mechanism. The calculated activation barriers range from 64 to 89 kJ mol⁻¹ and show that the nucleophile has a remarkably small influence (Table 2). Due to the presence of the hydrogen bond in the precursor complex, the barriers for the reactions of **1** are somewhat higher than for the reactions of **2**. The influence of *N*-methylation on the coordination sphere around the platinum center appears to be negligible.

The transition-state structures are compact, with relatively short bonds to the ligands that are being exchanged (Figure 2). This compactness is best seen in the reaction of **1** with Cl⁻: the Pt–Cl bonds of the transition state are 259 pm, only 26 pm longer than the Pt–Cl bond in **1** itself and 23 pm longer than the Pt–Cl bond in the precursor complex. The situation in the other transition-state structures is very similar.

Table 2: Computational results for the reactions **1**+X and **2**+X (X=Cl[−], I[−], TU).

Reaction	Relative energies [kJ mol ^{−1}] ^[a]			Distances [pm] (Pt–Cl/Pt–X)		
	<i>E</i> _{cpx}	<i>E</i> _{react}	<i>E</i> _{act}	precursor	transition state	product
1 +Cl [−]	451	0	89	236/386	259/259	386/236
1 +I [−]	364	3	77	235/437	259/287	385/266
1 +TU	86	13	72	235/458	259/268	298/238
2 +Cl [−]	415	0	66	237/346	260/260	346/237
2 +I [−]	334	21	75	237/409	262/291	345/269
2 +TU	59	13	64	237/378	265/268	318/239

[a] *E*_{cpx}: complexation energy released on the formation of the precursor complex; *E*_{react}: reaction energy for the formation of the product complex; *E*_{act}: activation energy for the formation of the transition state relative to the precursor complex.

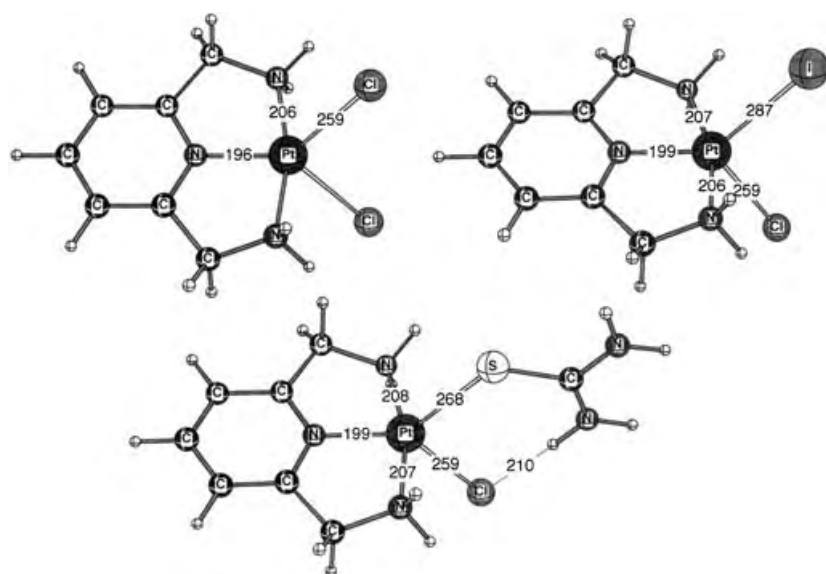


Figure 2. Calculated transition-state structures for the reaction of **1** with Cl[−], I[−], and thiourea. Distances are given in pm.

Hence, the reactions are best characterized as proceeding by an associative interchange, *I_a*, mechanism. In addition, in the reactions with thiourea, a hydrogen bond between chloride and one of the thiourea hydrogen atoms is preserved throughout the reaction.

The reactions of **1** with I[−] and TU are both calculated to be mildly endothermic (+3 and +13 kJ mol^{−1}, respectively) in the gas phase. This is due to the lack of stabilizing solvation of the leaving chloride ion. For the reaction of **1** with iodide, inclusion of the influence of the bulk solvent through the isodensity polarizable continuum model (IPCM) gives a reaction energy of −7 kJ mol^{−1}.^[29]

In conclusion, the studied substitution reaction was selected as a test system to investigate the behavior of ionic liquids as reaction medium for ligand-substitution reactions in comparison to conventional solvents. The observed spectral changes, kinetic traces, rate, and activation parameters clearly demonstrate the “normal” behavior and innocence of the selected ionic liquid in ligand-substitution reactions of Pt^{II} complexes. The kinetic data can be treated according to the transition-state theory as for any other solvent. No deviations

whatsoever were observed. For the first time it has been possible to determine the activation volume for a ligand-substitution reaction on a metal complex in an ionic liquid. An analysis of the thermal and pressure activation parameters indicates that the ionic liquid exhibits rather unique properties in terms of electrostriction/solvation of transition states that involve different degrees of polarity as reflected by similar activation parameters in conventional solvents. The apparent insensitivity of the ionic liquid

towards changes in polarity on going to the transition state can be ascribed to its tendency to form well-structured cation–anion aggregates. As a result of the apparent absence of solvent reorganization due to changes in electrostriction in this medium, the observed activation volume can be directly correlated with intrinsic volume changes that result from changes in bond lengths and bond angles on going to the transition state. This factor can, in principle, considerably simplify the accurate assignment of intimate mechanisms in cases in which changes in the polarity of the transition state cause large solvent effects in terms of electrostriction/solvation in conventional solvents and complicate the mechanistic assignment on the basis of activation parameters, especially activation entropy and volume data. This unique property of ionic liquids may come in very handy to resolve mechanistic discrepancies in conventional solvents.

Experimental Section

All chemicals used were of analytical reagent grade and of the highest purity commercially available. K₂[PtCl₄] was obtained from Strem Chemical Co.; [BMIM]Cl and lithium bis(trifluoromethylsulfonyl)amide were obtained from Solvent Innovation. Ultrapure water was used for the spectroscopic and kinetic measurements. The solvatochromic Reichardt's dye, (2,6-diphenyl-4-(2,4,6-triphenylpyridinium-1-yl)phenolate hydrate, was obtained from Aldrich.

The complex **1**·Cl·H₂O, was synthesized following a reported procedure.^[7] The ligand, 2,6-bis(aminomethyl)pyridine, was prepared according to a method used to synthesize 6-(aminomethyl)-2,2'-bipyridine^[30] by using 2,6-bis(bromomethyl)pyridine^[31] as the starting material. The corresponding platinum complex was prepared as described previously and was obtained in the same quality (see Supporting Information).^[7]

The ionic liquid [BMIM]BTA was synthesized by using a reported procedure.^[32,33] A solution of [BMIM]Cl (705 g, 4.04 mol) in H₂O (200 mL) was added to a solution of Li(bis(trifluoromethylsulfonyl)amide) (1.054 kg, 3.67 mol) in H₂O (200 mL; 1.1:1 molar ratio). The reaction media was mixed whereupon two phases formed: the bottom, slightly yellow phase was [BMIM]BTA; the

top phase was aqueous LiCl. The reaction mixture was stirred overnight at room temperature and the top phase was decanted off. CH₂Cl₂ (200 mL) was then added and the mixture was washed three times with H₂O (500 mL). The addition of CH₂Cl₂ led to an improved separation of the phases. After removal of CH₂Cl₂ and addition of activated carbon, the mixture was stirred for over 48 h at room temperature. Filtration of the mixture through a normal frit followed by Millipore filtration (pore size 0.22 µm) afforded a colorless liquid, which was washed with water once more, dried at 50–60 °C under vacuum for 48 h and filtered through a Millipore filter (pore size 0.22 µm). The product, [BMIM]BTA, was a clear colorless liquid; its NMR data are in close agreement with those reported for an acetone solution (see Supporting Information).^[33] The water content of [BMIM]BTA was determined by a Karl–Fischer titration by using a Metrohm 756 KF coulometer and found to be 23 ppm.

Instrumentation and measurements: [BMIM]BTA was dried and degassed before use. Its polarity was determined by using the solvatochromic Reichardt's dye (see the Supporting Information). The dimensionless normalized E_T^N values of the solvent were calculated according to reference [34].

Carlo Erba Elemental Analysers 1106 and 1108, and Bruker Avance DPX 300 and DRX 400 NMR spectrometers were used for chemical analysis and compound characterization, respectively. The UV/Vis spectra for the study of slow reactions were recorded on a Varian Cary 1G spectrophotometer equipped with a cell holder and thermostat. For the kinetic measurements on fast reactions an Applied Photophysics SX 18MV stopped-flow instrument was used. The wavelengths used are listed in the Supporting Information. Kinetic experiments at elevated pressure (1 to 130 MPa) were performed in a laboratory-made high-pressure stopped-flow instrument^[35] or a Shimadzu UV-2101-PC spectrophotometer equipped with a high-pressure cell designed for the study of slow reactions.^[36] The temperature of the instruments was controlled within an accuracy of ±0.1 K. TU and I[−] (as LiI) were used as entering nucleophiles. Their high nucleophilicity prevents the back reaction. The starting complex was dissolved in water and methanol that contained LiCl (0.002 M) to avoid its solvolysis. Trifluoromethanesulfonic acid (0.01 M) was added to avoid formation of hydroxo or alcoholate ions, which could compete in the chloride displacement. In the case of iodide as nucleophile and methanol and water as solvent, the ionic strength was kept at 0.2 M (LiClO₄). The reactions were studied under pseudo-first-order conditions by using at least a tenfold excess of the nucleophiles. All listed rate constants represent an average value of at least five kinetic runs for each experimental condition.

Calculations: Structures were fully optimized at B3LYP/LANL2DZp^[24–26] and characterized by calculation of vibrational frequencies. Relative energies include corrections for zero-point vibrational energy differences. Solvent effects were probed with IPCM single-point energy calculations by using the default parameters, that is, water as solvent.^[29] The Gaussian program was used.^[37]

Supporting Information available: Yields, elemental analyses, and ¹H NMR data for synthesized compounds; plots showing the concentration, temperature, and pressure dependence of the observed rate constants for the reactions between complex **1** and thiourea or iodide.

Received: April 16, 2005

Revised: June 19, 2005

Published online: August 22, 2005

Keywords: density functional calculations · ionic liquids · kinetics · platinum · reaction mechanisms

[1] B. Lippert, *Cisplatin. Chemistry and Biochemistry of a Leading Anticancer Drug*, Wiley-VCH, Weinheim, **1999**.

[2] U. Fekl, K. I. Goldberg, *Adv. Inorg. Chem.* **2003**, *54*, 260.

- [3] M. L. Tobe, J. Burgess, *Inorganic Reaction Mechanisms*, Longman, Essex, **1999**, p. 46.
- [4] R. Romeo, A. Grassi, L. M. Scolora, *Inorg. Chem.* **1992**, *31*, 4383.
- [5] R. van Eldik, C. Dücker-Benfer, F. Thaler, *Adv. Inorg. Chem.* **2000**, *49*, 1.
- [6] R. van Eldik, C. D. Hubbard in *High Pressure Chemistry: Synthetic, Mechanistic, and Supercritical Applications* (Eds.: R. van Eldik, F.-G. Klärner), Wiley-VCH, Weinheim, **2002**, chap. 1.
- [7] A. Hofmann, D. Jaganyi, O. Q. Munro, G. Liehr, R. van Eldik, *Inorg. Chem.* **2003**, *42*, 1688.
- [8] A. Hofmann, L. Dahlenburg, R. van Eldik, *Inorg. Chem.* **2003**, *42*, 6528.
- [9] a) T. Welton, *Coord. Chem. Rev.* **2004**, *248*, 21; T. Welton, *Coord. Chem. Rev.* **2004**, *248*, 2459; b) J. Dupont, R. F. de Souza, P. A. Z. Suarez, *Chem. Rev.* **2002**, *102*, 3667; c) M. Freemantle, *Chem. Eng. News* **2004**, *82*(45), 44; d) *Ionic Liquids in Synthesis* (Eds.: P. Wasserscheid, T. Welton), Wiley-VCH, Weinheim, **2003**.
- [10] E. T. Silveira, A. P. Umpierre, L. M. Rossi, G. Machado, J. Morias, G. V. Soares, I. J. R. Baumvol, S. R. Teixeira, P. F. P. Fichtner, J. Dupont, *Chem. Eur. J.* **2004**, *10*, 3734.
- [11] M. Volland, V. Seitz, M. Maase, M. Flores, R. Papp, K. Massonne, V. Stegmann, K. Halbritter, R. Noe, M. Bartsch, W. Siegel, M. Becker, O. Huttenloch (BASF AG), WO 062251,200, **2003**.
- [12] A. Skrzypczak, P. Neta, *Int. J. Chem. Kinet.* **2004**, *36*, 4.
- [13] C. Chiappe, D. J. Pieraccini, *Org. Chem.* **2004**, *69*, 6059.
- [14] K. Swiderski, A. McLean, C. M. Gordon, D. H. Vaughan, *Chem. Commun.* **2004**, 590.
- [15] C. Daguenet, P. J. Dyson, *Organometallics* **2004**, *23*, 6080.
- [16] P. Illner, A. Zahl, R. Puchta, N. J. R. van Eikema Hommes, P. Wasserscheid, R. van Eldik, *J. Organomet. Chem.* **2005**, *690*, 3567.
- [17] S. J. P'Pool, M. A. Klingshirn, R. D. Rogers, K. H. Shaughnessy, *J. Organomet. Chem.* **2005**, *690*, 3522.
- [18] M. D. Slinger, S. J. P'Pool, R. K. Traylor, J. McNeill III, S. H. Young, N. W. Hoffman, M. A. Klingshirn, R. D. Rogers, K. H. Shaughnessy, *J. Organomet. Chem.* **2005**, in press.
- [19] D. J. Adams, P. J. Dyson, S. J. Tavener, *Chemistry in Alternative Reaction Media*, Wiley, Chichester, **2004**, p. 81.
- [20] It has been pointed out that corrections made to second-order rate constants to compensate for changes in solvent density are incorrect as all kinetic parameters are defined in terms of concentration units under ambient conditions, that is, the conditions under which all solutions were prepared, see: S. D. Hamann, W. J. le Noble, *J. Chem. Educ.* **1984**, *61*, 658.
- [21] No corrections were made to compensate for the temperature and pressure dependence of the solvent viscosity as the investigated bimolecular reaction is slow and far away from a diffusion-controlled chemical process for which viscosity dependence is to be expected. It has been demonstrated elsewhere that slow bimolecular reactions in general do not exhibit meaningful viscosity dependence, see: C. F. Weber, R. van Eldik, *J. Phys. Chem. A* **2002**, *106*, 6904.
- [22] C. Reichardt, *Solvents and Solvent Effects in Organic Chemistry*, Wiley-VCH, Weinheim, **2003**, p. 163.
- [23] C. S. Consorti, P. A. Z. Suarez, R. F. de Souza, R. A. Burrow, D. H. Farrar, A. J. Lough, W. Loh, L. H. M. da Silva, J. Dupont, *J. Phys. Chem. B* **2005**, *109*, 4341.
- [24] a) P. J. Stevens, F. J. Devlin, C. F. Chabrowski, M. J. Frisch, *J. Phys. Chem.* **1994**, *98*, 11623; b) A. D. Becke, *J. Chem. Phys.* **1993**, *98*, 5648; c) C. Lee, W. Yang, R. G. Parr, *Phys. Rev. B* **1988**, *37*, 785.
- [25] P. J. Hay, W. R. Wadt, *J. Chem. Phys.* **1985**, *82*, 270, 284, 299.
- [26] S. Huzinaga, *Gaussian Basis Sets for Molecular Calculations*, Elsevier, Amsterdam, **1984**.

- [27] The performance of the computational level employed in this study is well documented, see for example: S. Klaus, H. Neumann, H. Jiao, A. Jacobi von Wangelin, D. Gördes, D. Strübing, S. Hübner, M. Hately, C. Weckbecker, K. Huthmacher, T. Riermeier, M. Beller, *J. Organomet. Chem.* **2004**, 689, 3685–3700; R. W. Saalfrank, C. Deutscher, H. Maid, A. M. Ako, S. Sperner, T. Nakajima, W. Bauer, F. Hampel, B. A. Heß, N. J. R. van Eikema Hommes, R. Puchta, F. W. Heinemann, *Chem. Eur. J.* **2004**, 10, 1899–1905.
- [28] S. W. A. Bligh, A. Bashall, C. Garrud, M. McPartlin, N. Wardle, K. White, S. Padhye, V. Barve, G. Kundu, *Dalton Trans.* **2003**, 184.
- [29] J. B. Foresman, T. A. Keith, K. B. Wiberg, J. Snoonian, M. J. Frisch, *J. Phys. Chem.* **1996**, 100, 16098–16104; the default $\epsilon = 78.39$ (H₂O) was used throughout.
- [30] R. Ziessel, J.-M. Lehn, *Helv. Chim. Acta* **1990**, 73, 1149.
- [31] W. Baker, K. M. Buggle, J. F. W. McOmie, D. A. M. Watkins, *J. Chem. Soc.* **1958**, 3594.
- [32] J. G. Huddleston, A. E. Visser, W. M. Reichert, H. D. Willauer, G. A. Broker, R. D. Rogers, *Green Chem.* **2001**, 3, 156.
- [33] P. Bonhôte, A.-P. Dias, N. Papageorgiou, K. Kalyanasundaram, M. Grätzel, *Inorg. Chem.* **1996**, 35, 1168.
- [34] Reference [22], p. 417.
- [35] R. van Eldik, W. Gaede, S. Wieland, J. Kraft, M. Spitzer, D. A. Palmer, *Rev. Sci. Instrum.* **1993**, 64, 1355.
- [36] M. Spitzer, F. Gärtig, R. van Eldik, *Rev. Sci. Instrum.* **1988**, 59, 2092.
- [37] Gaussian 98 (Revision A11.3), M. J. Frisch, G. W. Trucks, H. B. Schlegel, G. E. Scuseria, M. A. Robb, J. R. Cheeseman, V. G. Zakrzewski, J. A. Montgomery, Jr., R. E. Stratmann, J. C. Burant, S. Dapprich, J. M. Millam, A. D. Daniels, K. N. Kudin, M. C. Strain, O. Farkas, J. Tomasi, V. Barone, M. Cossi, R. Cammi, B. Mennucci, C. Pomelli, C. Adamo, S. Clifford, J. Ochterski, G. A. Petersson, P. Y. Ayala, Q. Cui, K. Morokuma, N. Rega, P. Salvador, J. J. Dannenberg, D. K. Malick, A. D. Rabuck, K. Raghavachari, J. B. Foresman, J. Cioslowski, J. V. Ortiz, A. G. Baboul, B. B. Stefanov, G. Liu, A. Liashenko, P. Piskorz, I. Komaromi, R. Gomperts, R. L. Martin, D. J. Fox, T. Keith, M. A. Al-Laham, C. Y. Peng, A. Nanayakkara, M. Challacombe, P. M. W. Gill, B. Johnson, W. Chen, M. W. Wong, J. L. Andres, C. Gonzalez, M. Head-Gordon, E. S. Replogle, J. A. Pople, Gaussian, Inc., Pittsburgh, PA, **1998**.

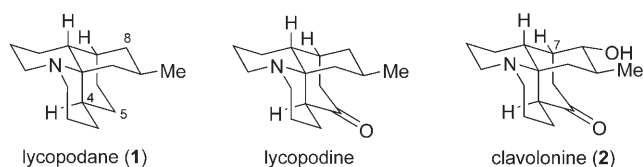
DOI: 10.1002/anie.200502296

Polycyclic Molecules from Linear Precursors: Stereoselective Synthesis of Clavonine and Related Complex Structures**

David A. Evans* and Jonathan R. Scheerer

At the time of this publication, over 100 lycopodium alkaloids have been isolated.^[1] The 16-carbon-atom-containing lycopodium alkaloid family features a variety of polycyclic ring sizes, stereochemistry, and oxidation patterns. The classic tetracyclic skeleton of the lycopodane family has a rich history in organic chemistry and has been a proving ground for new approaches to the synthesis of polycyclic alkaloid targets.^[2] Despite the number of research groups that have contributed to the synthesis of this family of alkaloids, all have proceeded in a linear fashion from cyclic starting materials.

The structure of lycopodine provides an instructive model to explore a strategy centered on 1) a convergent synthesis of a linear precursor that contains the complete carbon backbone and 2) the incorporation of a reaction cascade sequence to construct the remaining carbon–carbon bonds. In this study, we pursued the synthesis of clavonine (**2**), which was



first isolated in Jamaica in 1960^[3] from the club moss *Lycopodium clavatum* and was synthesized as a racemate by Wenkert and Broka.^[4a]

The disconnections required to transform the lycopodium skeleton **3** into its derived acyclic precursor may be accomplished with three principal constructions: 1) a Mannich reaction, 2) a Michael addition, and 3) a C–N alkylation (Figure 1). If the C–N alkylation is the last skeletal disconnection, then these reactions are implemented in a macrocyclic manifold (path A). Alternatively, if the C–N alkylation is the first skeletal disconnection, the same reactions are implemented in a linear environment (path B). Herein, we report the evaluation of both distinct approaches to the synthesis of the lycopodium skeleton.

[*] Prof. D. A. Evans, J. R. Scheerer
Department of Chemistry & Chemical Biology
Harvard University
Cambridge, MA 02138 (USA)
Fax: (+1) 617-495-1460
E-mail: evans@chemistry.harvard.edu

[**] Financial support was provided by the National Institutes of Health (GM 33328-20), Eli Lilly, Merck, and Amgen.



Supporting information for this article is available on the WWW under <http://www.angewandte.org> or from the author.

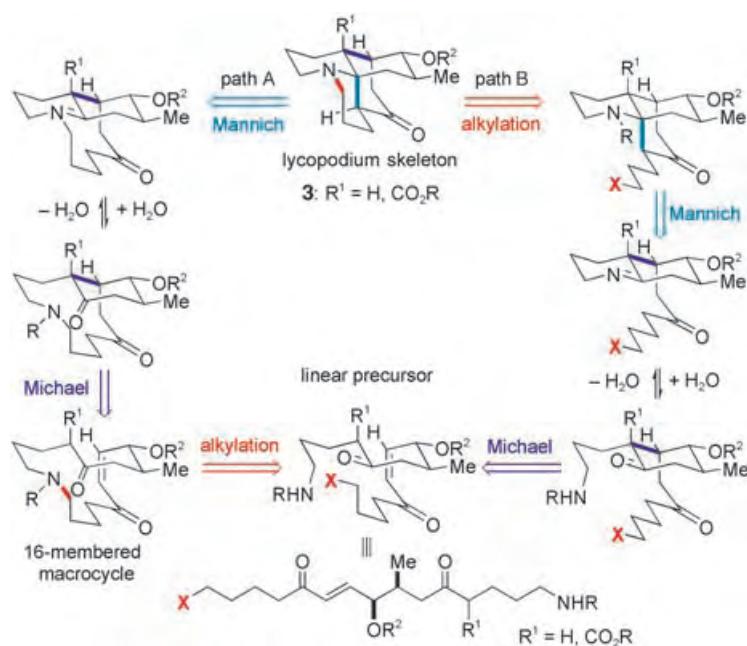
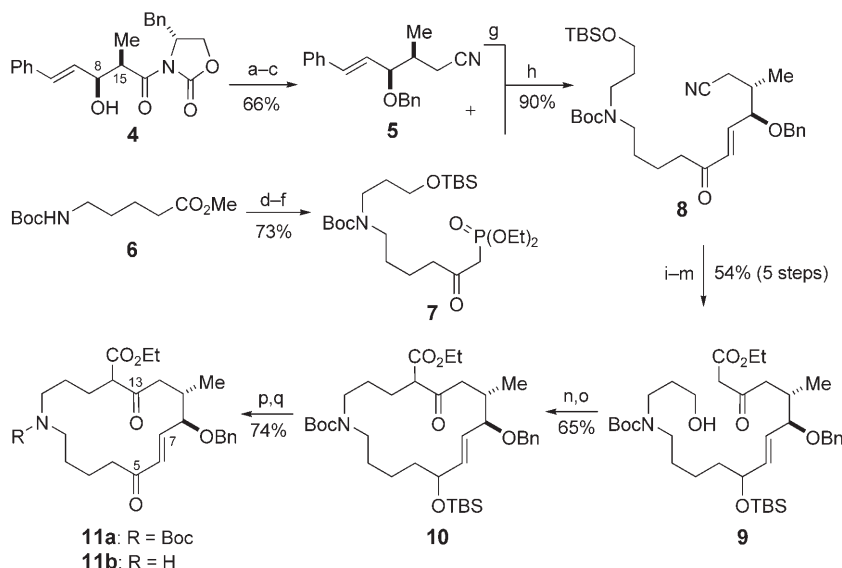


Figure 1. Synthesis plan: macrocyclic path A and linear path B.

First, let us consider path A. Macrocycles often adopt well-defined conformations that exhibit a pronounced influence on the stereochemical course of reactions.^[5] The investigation of this route required the synthesis of the 16-membered macrocycle **11a** (Scheme 1). The synthesis began by the boron-mediated aldol addition of (*R*)-3-propionyl-4-benzyloxazolidinone to cinnamaldehyde to provide crystal-



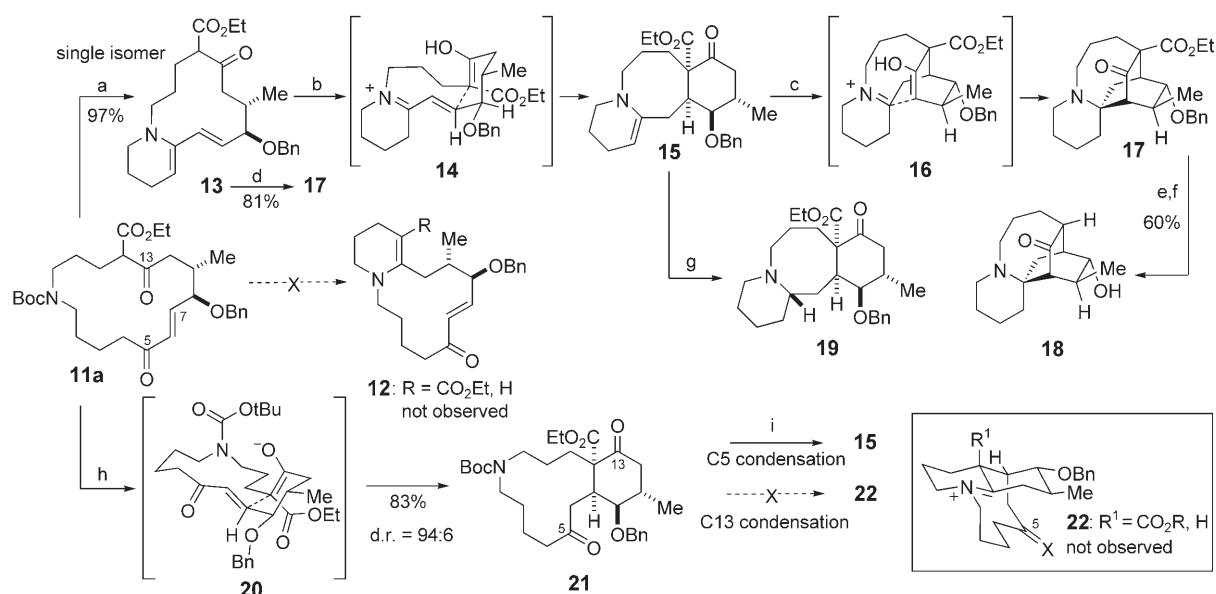
Scheme 1. Reagents and conditions (see reference [7] for explanation of abbreviations):

a) LiBH₄, Et₂O, H₂O, 0°C; b) PhCH(OMe)₂, TsOH, 93%; c) DibalH, CH₂Cl₂, -35°C, 76%; d) TsCl, NEt₃, DMAP; KCN, DMSO, 50°C, 94%; e) NaH, allyl bromide, DMF, -20 to 10°C, 55%, 90% based on recovered material; f) 9-BBN, H₂O₂; TBSCl, imid, DMF, 83%; g) *n*BuLi, MePO(OEt)₂, THF, -78°C, 98%; h) O₃, -78°C; DMS; i) NaH, THF, -78 to -20°C, 90%; j) L-selectride, THF, -78°C; k) TBSCl, imid, DMF, 81% (2 steps); l) DibalH, CH₂Cl₂, -50°C, 87%; m) ethyldiazoacetate, SnCl₂, 82%; n) HF-py, THF, 0°C, 72% (93% based on recovered material); o) I₂, PPh₃, imid, -5°C; p) Cs₂CO₃, THF (0.007 M), 37°C, 65% (2 steps); q) F-py, THF, 23°C; q) DMP, NaHCO₃, 74% (2 steps).

line **4** as a single diastereomer.^[6] This aldol adduct was successively reduced to the diol and trapped as the derived benzylidene acetal. Subsequent reductive cleavage revealed the primary alcohol (DibalH, CH₂Cl₂, -35°C) which was transformed into nitrile **5** via the intermediate tosylate.^[7] Following ozonolysis of the styrene moiety, the aldehyde derived from **5** was condensed with β-ketophosphonate **7** to afford α,β-unsaturated ketone **8** in 90% yield.^[8] After protection of the enone in **8**, the nitrile and protected hydroxyl termini were modified to the macrocyclization requisite precursor **9**.^[9] Macrocyclization was accomplished by activation of the primary alcohol as its iodide derivative, which was immediately subjected to ketoester alkylation conditions (Cs₂CO₃, THF, 37°C, 0.007 M).^[10] In this manner, macrocycle **10** was reproducibly obtained in good yield. Oxidation of the allylic alcohol afforded the desired enone **11a**, which was crystallized as a single diastereomer (m.p.: 127°C) and analyzed by X-ray diffraction.

The deprotected macrocyclic amine **11b** may react with either the C13 or the C5 carbonyl groups. We predicted that deprotection of the amine would result in condensation at the C13 ketone to provide the vinylogous urethane **12** (Scheme 2).^[11] In the event, carbamate cleavage of amine **11a** afforded none of the desired enaminone **12**; rather, exclusive formation of **13** (attack at C5) was observed (97% yield). Exposure of **13** to protic or Lewis acids promoted a stereoselective transannular Michael addition of the ketoester to the α,β-unsaturated iminium ion **14**. The derived tricyclic enamine **15** was unstable and underwent a spontaneous intramolecular Mannich cyclization to the tetracyclic ketoester **17** upon attempted purification by chromatography on silica gel or alumina. In practice, enamine **13** was transformed directly into **17** (81% yield) upon heating in ethanol with piperidinium acetate. The structural assignment of this compound was verified by X-ray diffraction analysis of derivative **18** (m.p.: 194°C). For the purpose of complete characterization, enamine **15** was selectively reduced to amine **19** and analyzed by X-ray diffraction as its hydrochloride salt (m.p.: 225°C). An examination of the solid-state conformation of macrocycle **11a** provides no clear rationale for the observed N-C5 condensation of amine **11b**. The protected amine is positioned at the same distance from both the ketones at C5 and C13 (5.38 and 5.41 Å, respectively). As a result of the undesired chemoselectivity of the transannular amine condensation,^[12] we turned our attention to an alternative sequence of events.

Macrocycle **11a** underwent a selective transannular Michael reaction upon exposure to base (Cs₂CO₃, EtOH, -78°C) to

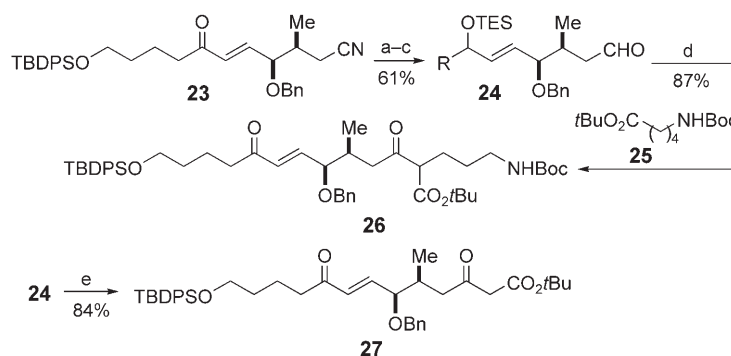


Scheme 2. Reagents and conditions: a) TFA, CH₂Cl₂, DMS, 0°C, 97%; b) ZnCl₂; c) SiO₂; d) piperidinium acetate, EtOH, 80°C, 48 h, 81%; e) *t*BuOK, DMSO; HCl, 40°C, 85%; f) H₂, Pd(OH)₂/C, EtOH, 70%; g) NaBH₃CN, MeOH, AcOH; h) Cs₂CO₃, EtOH, –78°C, 83%; i) TMSOTf, CH₂Cl₂, –20°C.

provide **21** as a mixture of diastereomers (94:6) in 83% yield (Scheme 2, m.p.: 136°C). The stereochemical outcome of this cyclization was established by X-ray crystallography. Both newly formed stereocenters are those desired for construction of the lycopodium core. The crystal structure of the Michael product **21** depicts a cyclohexane-ring conformer that minimizes non-bonding interactions. If we assume that the transition state resembles the solid-state conformer, then the transannular addition of the dipole minimized *E,E*-enolate **20** into a pseudo-axially disposed enone rationalizes the outcome and minimizes developing *syn*-pentane interactions. Removal of the carbamate protecting group in **21** results in condensation at C5 to yield the previously described tricyclic enamine **15**. It was apparent that protection of the ketone at C5, which is positioned in close proximity to the carbamate nitrogen center (4.7 Å by X-ray crystallography), would be necessary to divert the condensation to the carbonyl group at C13. A variety of protections at C5 were investigated, however, no reaction between the free amine and C13 ketone could be observed. In conclusion, it appears that the C13 condensation pathway to provide intermediate **22** is disfavored for both entropic and steric reasons. To effect reaction between the amine and C13, we reasoned that disconnection of the N–C1 bond would be necessary (Figure 1, path B).

With respect to path B, the linear precursors **26** and **27** were selected as targets and assembled in a manner analogous to the preparation of **8** (see above, Scheme 1). This synthesis employed a similar Horner–Wadsworth–Emmons coupling to afford **23**. After reduction of the ketone and protection of the alcohol as its silyl ether, the nitrile terminus was converted into aldehyde **24** (DibalH, CH₂Cl₂, –50°C). An aldol–

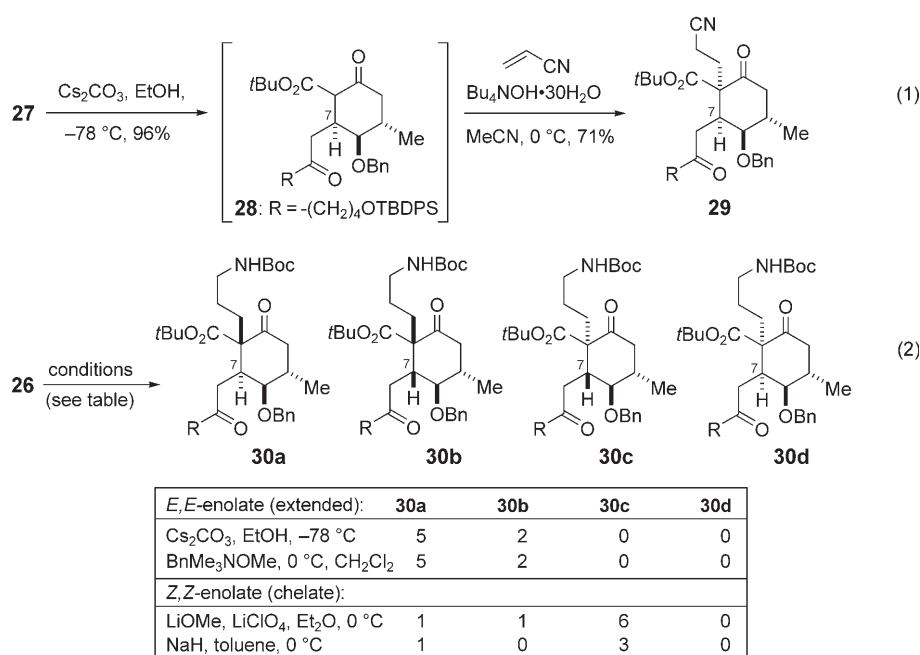
oxidation sequence provided flexibility in the synthesis of both substituted and unsubstituted β-ketoesters **26** and **27** (Scheme 3)



Scheme 3. Reagents and conditions: a) L-selectride, –78°C; b) TESCl, imid., DMF, 73%; c) DibalH, CH₂Cl₂, –50°C, 83%; d) LDA, **25**; PPTS, EtOH; DMP, NaHCO₃, 87% (3 steps); e) LDA, *t*BuOAc; PPTS, EtOH; DMP, NaHCO₃, 84% (3 steps).

A survey of conditions to effect a selective intramolecular Michael reaction was undertaken (Scheme 4). The unstable β-ketoester precursor **27** was immediately subjected to cyclization conditions (Cs₂CO₃, EtOH, –78°C) to provide **28** as a mixture (>10:1) of diastereomers (Scheme 4, equation (1)).^[13] The additional three carbon atoms and amino terminus were appended through an acrylonitrile Michael addition (Bu₄NOH·30H₂O, MeCN, 0°C, 71%) to provide **29** as a single diastereomer.

In general, Michael additions with the substituted β-ketoester **26** were less selective than with its unsubstituted counterpart **27** (Scheme 4, equation (2)). Products **30a** and



Scheme 4. Survey of conditions for selective intramolecular Michael reaction; the table shows the conditions for equation (2), and the relative proportions of product obtained.

30d contain the requisite stereochemistry at C7 for elaboration to the lycopodium skeleton. Generation of chelate-organized *Z,Z*-enolate complexes (NaH or $\text{LiOMe}/\text{LiClO}_4$) afforded predominately diastereomer **30c**.^[14] Conditions that favor extended or dipole-minimized *E,E*-ketoester enolates (Me_3NBnOMe or Cs_2CO_3) afforded a turnover in selectivity, providing a modest bias for the desired diastereomeric Michael reaction product **30a**.^[15,14c-f] Both Me_3NBnOMe or Cs_2CO_3 reaction conditions were equally convenient to execute and high yielding (55–60% **30a**, 22–24% **30b**). Product **30d** was not detected under any conditions.^[16]

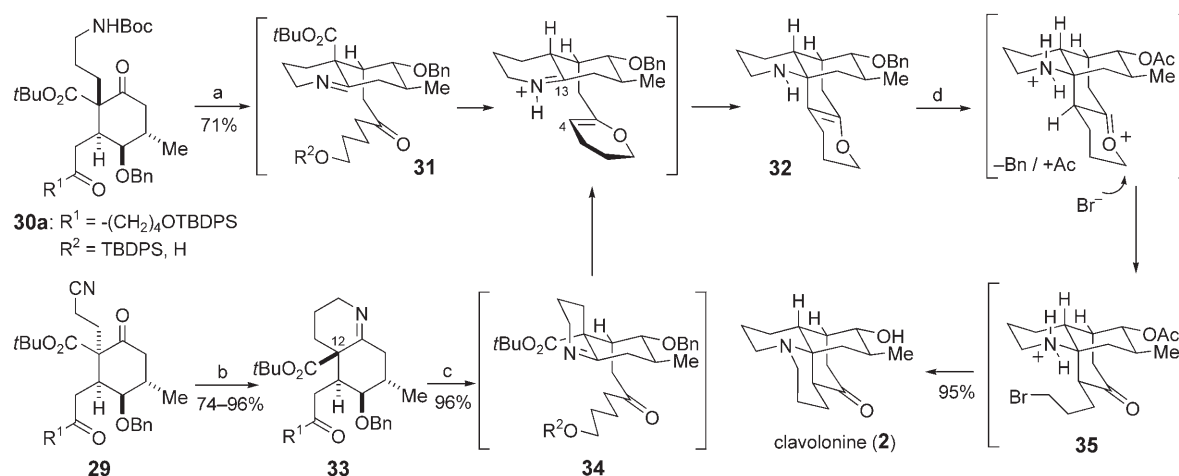
With the configuration at C7 established through a selective Michael reaction, the next objective toward the lycopodium skeleton was the Mannich addition between the

C4 enol and C13-derived iminium ion. This objective was realized on both Michael adducts **30a** and **29** which were independently carried forward to the common tetracyclic dihydropyran **32** (Scheme 5). Carbamate deprotection (TFA , CH_2Cl_2) of **30a** initiated condensation, leading to intermediate imine **31**. On exposure to methanolic HCl ,^[17] a series of reactions ensued, including decarboxylation, formation of a dihydropyran, and Mannich cyclization to provide **32** in 71% yield. To effect a similar sequence from **29**, it was necessary to reduce the nitrile (Raney Ni , H_2) to give imine **33**. The adjacent quaternary center sufficiently retards reduction of the imine moiety to prevent over-reduction.^[18] Methanolic HCl converted imine **33** into the aforementioned dihydropyran **32**. Inspection of intermediates **31** and **34** indicates an epimeric configuration at C12.

Owing to the stereoelectronic imperatives of the Mannich reaction, the latter will not undergo cyclization without prior decarboxylation and formal inversion.^[19]

Treatment of dihydropyran **32** with HBr/HOAc cleaved both the benzyl ether and the dihydropyran functions to provide intermediate ammonium bromide salt **35**. On exposure to methanolic base, intramolecular *N*-alkylation and saponification of the acetate was realized, leading to clavonine (**2**) in 95% yield. The structure of clavonine (**2**) was verified by single-crystal X-ray crystallography (m.p.: 227°C).^[20]

In conclusion, the synthesis of clavonine (**2**) has been an exercise in the conversion of functionalized linear carbon chains into polycyclic architectures. The end products include



Scheme 5. Reagents and conditions: a) TFA , DMS , CH_2Cl_2 , 23°C ; HCl , MeOH , 70°C , 24 h (71%); b) Raney Ni , H_2 , EtOH , 74–96%; c) HCl , MeOH , 70°C , 42 h, 96%; d) HBr , HOAc , CH_2Cl_2 ; MeOH , NaOH , 95%.

not only the target structure but also a diverse array of complex nitrogen-containing polycyclic structures that are accessible from simple Michael–Mannich reaction cascades. The illustrated strategy of cyclization-based multistep bond constructions is currently being applied to other complex natural products.

Received: June 30, 2005

Published online: August 24, 2005

Keywords: alkaloids · Michael addition · natural products · polycycles · synthetic methods

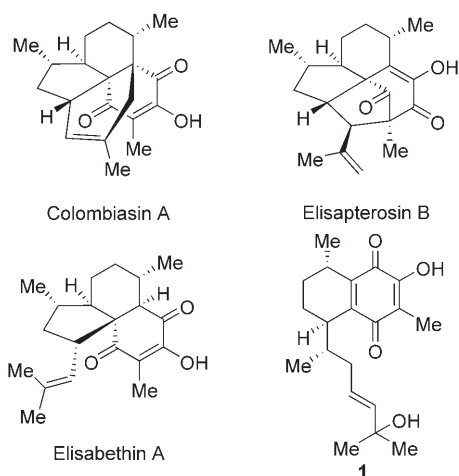
- [1] a) D. B. McLean, *The Alkaloids: Chemistry and Physiology*, Vol. 14 (Ed.: R. H. F. Manske), Academic Press, New York, **1973**, p. 347; b) D. B. McLean, *The Alkaloids: Chemistry and Physiology*, Vol. 10 (Ed.: R. H. F. Manske), Academic Press, New York, **1968**, p. 305; c) J. C. Braekman, L. Nyembo, P. Bourdoux, N. Kahindo, C. Hootele, *Phytochemistry* **1974**, *13*, 2519; d) W. A. Ayer, G. C. Kasitu, *Can. J. Chem.* **1989**, *67*, 1077; e) M. Castillo, L. A. Loyola, G. Morales, I. Singh, C. Calvo, H. L. Holland, D. B. MacLean, *Can. J. Chem.* **1976**, *54*, 2893.
- [2] a) C. H. Heathcock, E. F. Kleinman, E. S. Binkley, *J. Am. Chem. Soc.* **1982**, *104*, 1054; b) G. Stork, R. A. Kretschmer, R. H. Schlessinger, *J. Am. Chem. Soc.* **1968**, *90*, 1647; c) W. A. Ayer, W. R. Bowman, T. C. Joseph, P. Smith, *J. Am. Chem. Soc.* **1968**, *90*, 1648; d) G. A. Kraus, Y. S. Hon, *J. Am. Chem. Soc.* **1985**, *107*, 4341; e) A. Padwa, M. A. Brodney, J. P. Marino, S. M. Sheehan, *J. Org. Chem.* **1997**, *62*, 78; f) P. A. Grieco, Y. J. Dai, *J. Am. Chem. Soc.* **1998**, *120*, 5128; g) M. Mori, K. Hori, M. Akashi, M. Hori, Y. Sato, M. Nishida, *Angew. Chem.* **1998**, *110*, 659; *Angew. Chem. Int. Ed.* **1998**, *37*, 636. For reviews of lycopodium alkaloid chemistry, see also references [1a,b].
- [3] a) R. H. Burnell, D. R. Taylor, *Chem. Ind.* **1960**, 1239; b) R. H. Burnell, B. S. Mootoo, *Can. J. Chem.* **1961**, *39*, 1090.
- [4] a) E. Wenkert, C. A. Broka, *J. Chem. Soc. Chem. Commun.* **1984**, 714; b) E. Wenkert, B. Chauncy, K. G. Dave, A. R. Jeffcoat, F. M. Schell, H. P. Schenk, *J. Am. Chem. Soc.* **1973**, *95*, 8427.
- [5] W. C. Still, I. Galynker, *Tetrahedron* **1981**, *37*, 3981.
- [6] D. A. Evans, S. L. Bender, J. Morris, *J. Am. Chem. Soc.* **1988**, *110*, 2506.
- [7] Abbreviations: 9-BBN = 9-borabicyclo[3.3.1]nonane; Bn = benzyl; Boc = *tert*-butoxycarbonyl; DibalH = diisobutylaluminum hydride; DMAP = 4-dimethylaminopyridine; DMP = Dess–Martin periodinane; DMF = *N,N*-dimethylformamide; DMS = dimethyl sulfide; DMSO = dimethyl sulfoxide; imid = imidazole; LDA = lithium diisopropylamide; PPTS = pyridinium *p*-toluenesulfonate; py = pyridine; TBDPS = *tert*-butyldi-phenylsilyl; TBSCl = *tert*-butyldimethylsilyl chloride; TESCl = triethylsilyl chloride; TFA = trifluoroacetic acid; TMSOTf = trimethylsilyl trifluoromethanesulfonate; TsOH = *p*-toluenesulfonic acid.
- [8] β -Ketophosphonate **7** was prepared in four steps from the previously synthesized protected δ -amino valeric acid **6**: D. L. Flynn, R. E. Zelle, P. A. Grieco, *J. Org. Chem.* **1983**, *48*, 2425.
- [9] C. R. Holmquist, E. J. Roskamp, *J. Org. Chem.* **1989**, *54*, 3258.
- [10] a) P. Deslongchamps, *Pure Appl. Chem.* **1996**, *68*, 1831; b) D. A. Evans, J. T. Starr, *Angew. Chem.* **2002**, *114*, 1865; *Angew. Chem. Int. Ed.* **2002**, *41*, 1787; c) D. A. Evans, J. T. Starr, *J. Am. Chem. Soc.* **2003**, *125*, 13531.
- [11] If carbinolamine dehydration is rate-limiting, formation of the stabilized vinylogous urethane **12** is predicted to occur favorably. If carbinolamine formation is rate-determining, condensation at the more electrophilic (C13) ketone should be observed. These predictions are reinforcing for C13 condensation. Saturated ketones are more electrophilic than unsaturated ketones. This can be observed spectroscopically (e.g. IR shift approximately $\Delta\tilde{\nu} = 40\text{ cm}^{-1}$) and experimentally, for example, by competitive reductive amination. A saturated carbonyl group is preferentially reduced in the presence of NaB(OAc)₃H, as noted in the following reference: A. F. Abdel-Magid, K. G. Carson, B. D. Harris, C. A. Maryanoff, R. D. Shah, *J. Org. Chem.* **1996**, *61*, 3849. Macrocycle **11a** demonstrates no enol content by ¹H NMR or IR spectroscopy. For this reason, the ketone at C13 should be regarded as a saturated ketone.
- [12] Macrocycle **11a** was decarboxylated under Krapcho conditions. This material also exclusively favors condensation at C5.
- [13] Ketoester **28** exists as a mixture of keto and enol tautomers. For this reason, an accurate diastereomeric ratio of the preceding Michael addition could not be determined. A small amount of **28** was decarboxylated under Krapcho conditions. The derived ketone was isomerically pure (d.r. $\geq 10:1$), and the stereochemistry at C7 was proven by 2D ¹H NMR spectral analysis (NOESY).
- [14] a) G. Stork, J. D. Winkler, N. A. Saccomano, *Tetrahedron Lett.* **1983**, *24*, 465; b) G. Stork, C. S. Shiner, J. D. Winkler, *J. Am. Chem. Soc.* **1982**, *104*, 310; c) E. M. Arnett, S. G. Maroldo, S. L. Schilling, J. A. Harrelson, *J. Am. Chem. Soc.* **1984**, *106*, 6759; d) M. Raban, D. P. Haritos, *J. Am. Chem. Soc.* **1979**, *101*, 5178; e) M. Raban, E. A. Noe, G. Yamamoto, *J. Am. Chem. Soc.* **1977**, *99*, 6527; f) L. M. Jackman, B. C. Lange, *Tetrahedron* **1977**, *33*, 2737.
- [15] L. N. Mander, S. G. Pyne, *J. Am. Chem. Soc.* **1979**, *101*, 3373.
- [16] Product **30d** was prepared independently by alkylation of **28** with 1-iodo-3-amino-*tert*-butylcarbamate and *t*BuOK provided **30d** as a single isomer in less than 30% yield.
- [17] The use of methanolic HCl to effect a Mannich addition finds precedent in the Heathcock synthesis of lycopodine; see reference [2a].
- [18] C. H. Heathcock, M. H. Norman, D. A. Dickman, *J. Org. Chem.* **1990**, *55*, 798.
- [19] a) R. V. Stevens, A. W. M. Lee, *J. Am. Chem. Soc.* **1979**, *101*, 7032; b) R. V. Stevens, *Acc. Chem. Res.* **1984**, *17*, 289.
- [20] CCDC 280174–280177 contain the supplementary crystallographic data for this paper. These data can be obtained free of charge from The Cambridge Crystallographic Data Centre via www.ccdc.cam.ac.uk/data_request/cif. **19** (280174) C₂₆H₃₈ClNO₄: *a* = 33.325(6), *b* = 7.0106(12), *c* = 10.5283(17), space group P2₁2₁2₁; **18** (280175) C₁₆H₂₅NO₂: *a* = 7.0625(6), *b* = 9.9378(9), *c* = 20.3461(18), space group P2₁2₁2₁; **11a** (280176) C₃₁H₄₅NO₇: *a* = 9.3342(17), *b* = 10.0515(17), *c* = 16.339(3), β = 93.755(4), space group P2₁; **2** (280177) C₁₆H₂₅NO₂: *a* = 13.5174(12), *c* = 7.7656(10), space group P4₁.

DOI: 10.1002/anie.200502176

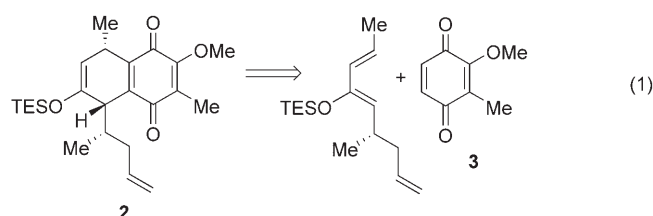
Highly Enantio- and Regioselective Quinone Diels–Alder Reactions Catalyzed by a Tridentate [(Schiff Base)Cr^{III}] Complex**

Elizabeth R. Jarvo, Brian M. Lawrence, and
Eric N. Jacobsen*

The octocoral *Pseudopterogorgia elisabethae* produces a variety of terpenoids, such as colombiasin A, elisapterosin B, and elisabethin A, that display diverse structural frameworks and bioactivities.^[1] These secondary metabolites are possibly



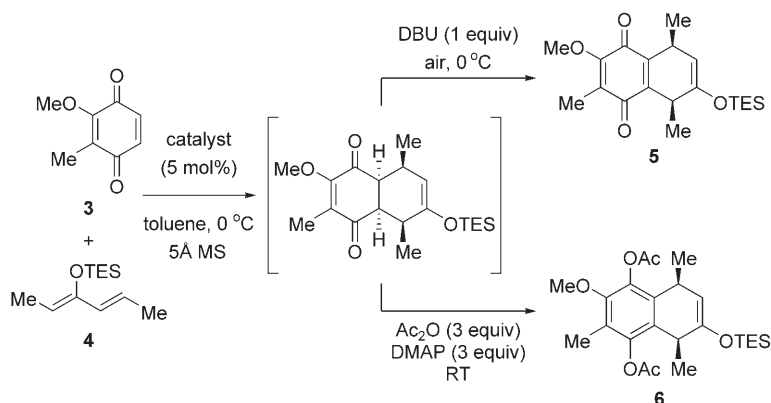
derived from a relatively simple common biosynthetic precursor; indeed, compounds such as **1**, which could undergo transformation to the more complex polycyclic natural products by divergent cyclization pathways, have been isolated from the same organism.^[2] We became interested in developing efficient quinone Diels–Alder (qDA) catalysts for the preparation of intermediates related to **1** [e.g. **2**, Eq. (1)] as part of a unified biomimetic strategy for the syntheses of this family of natural products. Herein, we report a new method for highly enantioselective qDA reactions of quinones with a variety of dienes catalyzed by a new, monomeric [(Schiff base)Cr^{III}] complex.^[3] In the following paper in this issue, we describe concise asymmetric catalytic syntheses of



(–)-colombiasin A and (–)-elisapterosin B employing this methodology in the pivotal step.^[4]

The reaction of quinones with dienes was the first class of cycloaddition pathways to be recognized by Diels and Alder,^[5] and it has enjoyed widespread use in organic synthesis ever since.^[6] However, until recently, effective catalysts for enantioselective qDA reactions have remained elusive. In seminal studies by Mikami and co-workers, Ti-binolate complexes were found to be effective for a limited range of substrates.^[7,8] Subsequently, Evans and co-workers reported bis(oxazoline)–lanthanide complexes as asymmetric catalysts for reactions of methyl-substituted dienes with ester-substituted quinones capable of two-point binding.^[9] Corey and co-workers described the use of cationic oxazaborolidines as enantioselective qDA catalysts that promote cycloaddition through single-point binding, with unsymmetrical quinones undergoing reaction by activation of the most Lewis basic carbonyl group.^[10] Despite these important advances, identification of new and highly active qDA catalysts with broad substrate scope remains an important goal, particularly for accessing the diversity of cycloadducts of interest in the synthesis of biologically active compounds.

Our own catalyst development studies focused initially on the reaction of quinone **3** and diene **4**, a model relevant to the colombiasin A effort and designed to gauge both catalyst enantioselectivity and regioselectivity (Scheme 1). As the



Scheme 1. Quinone Diels–Alder (qDA) reaction followed by in situ derivatization of the cycloadduct. TES = triethylsilyl; DBU = 1,8-diazabicyclo[5.4.0]undec-7-ene; DMAP = 4-dimethylaminopyridine.

qDA cycloadduct obtained is not stable to air or silica gel at room temperature, further functionalization of the cycloadduct was performed to facilitate isolation and analysis. In situ air oxidation to the quinone **5**, or tautomerization and

[*] Dr. E. R. Jarvo, B. M. Lawrence, Prof. Dr. E. N. Jacobsen
Department of Chemistry and Chemical Biology
Harvard University
Cambridge, MA 02138 (USA)
Fax: (+1) 617-496-1880
E-mail: jacobsen@chemistry.harvard.edu

[**] This work was supported by the NIH (GM-59316). We are grateful to Dr. R. Staples for carrying out the X-ray crystal structure analyses.

Supporting information for this article is available on the WWW under <http://www.angewandte.org> or from the author.

trapping with acetic anhydride to **6**, provided stable materials that could be handled easily using standard laboratory techniques.^[11,12]

Recognizing the demonstrated ability of chiral [(Schiff base)Cr^{III}] catalysts to activate simple carbonyl compounds to cycloaddition through one-point binding mechanisms,^[3,13] we explored their possible application to the qDA reaction. Preliminary studies with the broadly useful dimeric catalyst **8**^[14] led to an intriguing and unexpected observation: catalysts prepared by different extractive workup procedures led to dramatically different results in the model reaction (Table 1).

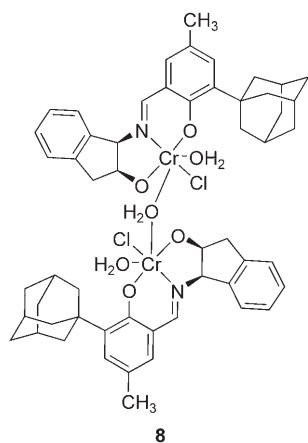


Table 1: Effect of catalyst preparation conditions on the asymmetric qDA reaction of quinone **3** with diene **4**.^[a]

Entry	Catalyst preparation		Quinone Diels–Alder			
	Extractive workup	Predominant species	Reaction time	Yield [%] ^[b]	<i>ee</i> [%]	Regioselectivity ^[c]
1	H ₂ O	8	26 h	82	39	3.3:1
2	1 N HCl	8 (+ 9)	35 min	70	96	12:1
3	3 N HCl	9	10 min	86	96	12:1

[a] Reactions were carried out with 5 mol% catalyst and 1.5 equiv diene **4** in the presence of crushed 5 Å molecular sieves in toluene (0.2 M). [b] Yield of isolated product after oxidation to quinone **5** and purification by silica gel chromatography. [c] Determined by HPLC analysis with commercial chiral stationary phases. See Supporting Information for full details.

We had found previously that synthesis of **8** accompanied by aqueous workup under either neutral or acidic (1 N HCl) conditions afforded catalysts that performed similarly in hetero-Diels–Alder (HDA) reactions, with the preferred method of catalyst preparation involving extraction with neutral H₂O.^[15] Catalyst prepared in this manner is dimeric in the solid state^[3b] and in solution.^[16] However, the qDA reaction catalyzed by dimer **8** was sluggish and afforded products with low enantio- and regioselectivity, whereas catalyst prepared by acidic workup procedures afforded markedly improved results (Table 1, entry 2, 96% *ee*, 12:1 regioselectivity). This suggested that another chromium–ligand complex was being generated as a minor component under the acidic workup conditions, and that this impurity

could be the active species in the quinone DA reaction. The conditions for catalyst preparation were therefore varied systematically to optimize the rate and enantioselectivity in the qDA reaction. Catalyst prepared by using 3 N HCl for the extractive workup proved most effective, affording product **5** with 96% *ee* and 12:1 regioselectivity after a reaction time of only 10 min. The major regioisomer was found to be that which would arise from Lewis acid coordination to the less Lewis basic carbonyl group, as would be required for our syntheses of colombiasin A and related natural products.^[17]

Catalyst prepared by using the 3 N HCl workup protocol was recrystallized to afford single crystals suitable for X-ray analysis. In the solid state, complex **9** has a monomeric, pseudooctahedral structure with two water molecules and a chloride ligand in the coordination sphere of the metal (Figure 1).^[18] This crystalline material was introduced in the

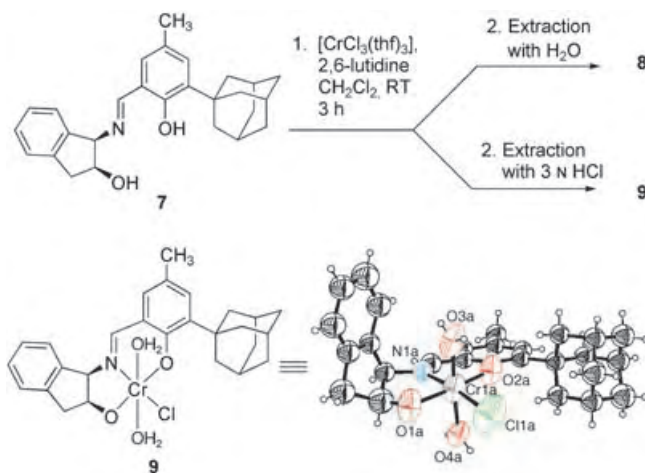


Figure 1. Preparation of catalysts **8** and **9**, and the X-ray crystal structure of **9**. Ellipsoids are drawn at the 30% probability level.

qDA reaction between **3** and **4**, and it exhibited nearly identical selectivity to the bulk catalyst (95% *ee* versus 96% *ee*, 12:1 regioselectivity). Thus, Cr^{III} complexes derived from the same tridentate Schiff base ligand **7** are generated in different aggregation states depending only on the workup conditions (Figure 1), with the dimeric complex **8** being optimal for HDA reactions, and the monomeric complex **9** optimal for qDA reactions.^[19] While the aggregation state of the active catalyst derived from **9** has not yet been elucidated, it is clear that it is distinct from the dimeric catalyst derived from **8**.^[20]

The scope of catalyst **9** in qDA reactions is illustrated by the examples in Tables 2 and 3. A variety of cycloadducts were prepared with greater than 90% *ee* in reactions carried out at 0 °C.^[21] Despite the fact that quinone **3** undergoes reaction by apparent activation of the less basic carbonyl group adjacent to the methoxy group, bidentate chelation to the catalyst by the quinone is not required. Thus, naphthoquinone (**10**) and 2,3-dimethylquinone both underwent reaction with diene **4** to yield products in 94% *ee* (Table 2, entries 2 and 3). The same sense of stereinduction was observed in reactions with **3** as in reactions with quinones incapable of two-point binding.^[22]

Table 2: Enantio- and regioselective qDA reactions of a variety of quinones with diene **4**.^[a]

Entry	Quinone	Temperature [°C]	Reaction time	Yield [%] ^[b]	ee [%], regioselectivity ^[c]
1		0	10 min	83 (q)	96, 12:1
2		0	10 min	85 (q)	94
3 ^[d]		0	30 min	75 (q)	94
4		−40	3 h	80 (hd)	86

[a] Unless noted otherwise, reactions were carried out using 5 mol% catalyst **9** with 1.1 equiv diene **4** in the presence of crushed 5 Å molecular sieves in toluene (0.2 M). [b] Yields of isolated quinone (q) or hydroquinone diacetate (hd, see Scheme 1), after purification by silica gel chromatography. [c] Determined by HPLC. [d] Reaction carried out at higher concentration (0.8 M in quinone). See Supporting Information for full details.

The reactions of a variety of dienes with naphthoquinone (**10**) and methoxy-substituted quinone **3** were also examined (Table 3). Electronic activation of the diene by silyloxy or alkoxy substituents is not required, as dienes such as 1,3-pentadiene and 2-methyl-1,3-pentadiene were found to

undergo reaction with acceptable rates to afford highly enantioenriched qDA products (Table 3, entries 1–3). Sterically demanding substituents at both the 1- and 3-positions of the diene are well tolerated: *i*Pr-substituted dienes **11** and **12** (Table 3, entries 6 and 8) required prolonged reaction times, but afforded products with high levels of enantioselectivity (90 and 96% ee, respectively). Reaction of diene **11** with quinone **3**, a model system for our synthetic efforts [see Eq. (1)], provided the required isomer with high regioselectivity (9:1).

In conclusion, a seemingly minor change in the conditions used for workup in the catalyst synthesis resulted in the identification of a new, monomeric [(Schiff base)Cr^{III}] complex with broad scope in the asymmetric qDA reaction. The utility of this catalyst in natural product synthesis is illustrated in the following communication, where we report the total syntheses of (−)-colombiasin A and (−)-elisapterosin B.^[4] Further studies related to the scope and mechanism of catalyst **9** are underway.

Received: June 22, 2005

Published online: August 31, 2005

Keywords: asymmetric catalysis · chromium · cycloaddition · quinones · Schiff bases

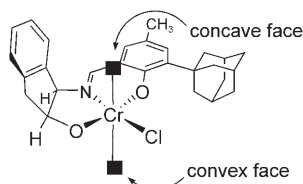
Table 3: Enantio- and regioselective qDA reactions of a variety of dienes with quinones **3** and **10**.^[a]

Entry	Quinone	Diene	Temperature [°C]	Reaction time	Yield [%] ^[b]	ee [%], regioselectivity ^[c]
1 ^[d]	10		0	14 h	90 (hd)	90
2	3		−40	15 h	86 (hd)	93, >30:1
3	10		0	1.5 h	75 (hd)	91
4	3		−40	1 h	62 (hd)	97, 25:1
5 ^[e]	10		0	25 min	91 (hd)	90
6 ^[f,g]	3		0	20 h	75 (q)	90, 9:1
7 ^[f,g]	10		−20	43 h	88 (q)	97
8 ^[d]	10		−40	19 h	83 (hd)	96
9 ^[d]	10		0	1 h	62 (hd)	91

[a] Unless noted otherwise, reactions were carried out with 5 mol% catalyst **9** and 1.5 equiv diene in the presence of crushed 5 Å molecular sieves in toluene (0.8 M). [b] Yields of isolated quinone (q) or hydroquinone diacetate (hd), after purification by silica gel chromatography. [c] Determined by HPLC. [d] 3 equiv diene. [e] 0.2 M [quinone]. [f] 10 mol% catalyst **9**. [g] 1.2 equiv diene. See Supporting Information for full details.

- [1] a) A. D. Rodriguez, C. Ramirez, *Org. Lett.* **2000**, 2, 507–510; b) A. D. Rodriguez, C. Ramirez, I. I. Rodriguez, C. L. Barnes, *J. Org. Chem.* **2000**, 65, 1390–1398; c) A. D. Rodriguez, E. Gonzalez, S. D. Huang, *J. Org. Chem.* **1998**, 63, 7083–7091.
- [2] a) A. D. Rodriguez, Y.-P. Shi, *Tetrahedron* **2000**, 56, 9015–9023; b) for a discussion, see reference [1b].
- [3] a) A. G. Dossetter, T. F. Jamison, E. N. Jacobsen, *Angew. Chem.* **1999**, 111, 2549–2552; *Angew. Chem. Int. Ed.* **1999**, 38, 2398–2400; b) K. Gademann, D. E. Chavez, E. N. Jacobsen, *Angew. Chem.* **2002**, 114, 3185–3187; *Angew. Chem. Int. Ed.* **2002**, 41, 3059–3061; c) R. T. Ruck, E. N. Jacobsen, *J. Am. Chem. Soc.* **2002**, 124, 2882–2883; d) R. T. Ruck, E. N. Jacobsen, *Angew. Chem.* **2003**, 115, 4919–4922; *Angew. Chem. Int. Ed.* **2003**, 42, 4771–4774.
- [4] See following paper in this issue: A. A. Boezio, E. R. Jarvo, B. M. Lawrence, E. N. Jacobsen, *Angew. Chem.* **2005**, 117, in press; *Angew. Chem. Int. Ed.* **2005**, 44, in press; DOI: 10.1002/anie.200502178.
- [5] O. Diels, K. Alder, *Justus Liebigs Ann. Chem.* **1928**, 460, 98–122.
- [6] a) K. C. Nicolaou, S. A. Snyder, T. Montagnon, G. Vassilikogiannakis, *Angew. Chem.* **2002**, 114, 1742–1773; *Angew. Chem. Int. Ed.* **2002**, 41, 1669–1698; b) Q.-Y. Hu, G. Zhou, E. J. Corey, *J. Am. Chem. Soc.* **2004**, 126, 13708–13713.
- [7] K. Mikami, Y. Motoyama, M. Terada, *J. Am. Chem. Soc.* **1994**, 116, 2812–2820.

- [8] The Mikami catalytic qDA was applied successfully in the Nicolaou synthesis of colombiasin A: K. C. Nicolaou, G. Vassilikogiannakis, W. Magerlein, R. Kranich, *Chem. Eur. J.* **2001**, *7*, 5359–5371.
- [9] D. A. Evans, J. Wu, *J. Am. Chem. Soc.* **2003**, *125*, 10162–10163.
- [10] D. H. Ryu, G. Zhou, E. J. Corey, *J. Am. Chem. Soc.* **2004**, *126*, 4800–4802, and references therein.
- [11] Y. Naruta, K. Maruyama in *The Chemistry of the Quinoid Compounds, Vol. II* (Eds.: S. Patai, Z. Rappoport), Wiley, Chichester, **1988**, pp. 242–336.
- [12] All yields therefore reflect a one-pot, two-step procedure. ¹H NMR analyses of the unpurified qDA reaction mixtures suggest that the cycloadditions are clean and that product loss occurs during workup.
- [13] Cr^{III}–salen complexes have also been shown to catalyze enantioselective Diels–Alder reactions of 1-amino-1,3-butadienes. See: Y. Huang, T. Iwama, V. H. Rawal, *Org. Lett.* **2002**, *4*, 1163–1166, and references therein.
- [14] For selected examples of the application of **8** in target-oriented synthesis, see: a) FR901464: C. F. Thompson, T. F. Jamison, E. N. Jacobsen, *J. Am. Chem. Soc.* **2000**, *122*, 10482–10483; C. F. Thompson, T. F. Jamison, E. N. Jacobsen, *J. Am. Chem. Soc.* **2001**, *123*, 9974–9983; b) fostriecin: D. E. Chavez, E. N. Jacobsen, *Angew. Chem.* **2001**, *113*, 3779–3782; *Angew. Chem. Int. Ed.* **2001**, *40*, 3667; ; c) ambruticin: P. Liu, E. N. Jacobsen, *J. Am. Chem. Soc.* **2001**, *123*, 10772; d) apicularen A: A. Bhattacharjee, J. K. De Brabander, *Tetrahedron Lett.* **2000**, *41*, 8069–8073; e) laulilamide: I. Paterson, C. De Savi, M. Tudge, *Org. Lett.* **2001**, *3*, 3149–3152; f) iridoid natural products: D. E. Chavez, E. N. Jacobsen, *Org. Lett.* **2003**, *5*, 2563–2565; g) thiomarinol antibiotic: X. Gao, D. G. Hall, *J. Am. Chem. Soc.* **2005**, *127*, 1628–1629.
- [15] D. E. Chavez, E. N. Jacobsen, *Org. Synth.*, in press.
- [16] Kinetic and mechanistic studies of HDA reactions promoted by **8** indicate a dimeric catalyst structure both in the ground state and in the rate-determining transition state. R. T. Ruck, E. N. Jacobsen, unpublished results.
- [17] See Supporting Information for details. Cationic oxazaborolidine catalysts afford products with opposite regioselectivity (see ref. [10]).
- [18] Details of the crystal structure analysis are provided as Supporting Information. CCDC-262884 (**9**) contains the supplementary crystallographic data for this paper. These data can be obtained free of charge from the Cambridge Crystallographic Data Centre via www.ccdc.cam.ac.uk/data_request/cif.
- [19] For example, the inverse electron demand hetero-Diels–Alder reaction employed in the first step of the colombiasin synthesis (see preparation of **6** in Scheme 3 in reference [4]) proceeded with 78 % *ee* with monomeric catalyst **9** and 93 % *ee* with dimeric catalyst **8**.
- [20] If a monomeric catalyst structure analogous to that of **9** is assumed in the *ee*-determining step with one of the water molecules replaced by the quinone substrate, then the intriguing question arises about which of the two stereochemically inequivalent binding sites is engaged. Qualitatively, it would appear that binding to the inner, concave face of the catalyst would be most consistent with the high enantioselectivities observed in the qDA.
- [21] Reactions carried out at –40 °C generally afforded higher enantioselectivity, albeit with slower rates; these conditions were employed for those substrates that were generated in < 90 % *ee* at 0 °C. For example, the reaction of benzoquinone with diene **4** afforded cycloadduct in 79 % *ee* at 0 °C, and 86 % *ee* at –40 °C (Table 2, entry 4).
- [22] See Supporting Information for details.



Asymmetric catalysis

DOI: 10.1002/anie.200502178

Efficient Total Syntheses of (–)-Colombiasin A and (–)-Elisapterosin B: Application of the Cr-Catalyzed Asymmetric Quinone Diels–Alder Reaction***Alessandro A. Boezio, Elizabeth R. Jarvo, Brian M. Lawrence, and Eric N. Jacobsen**

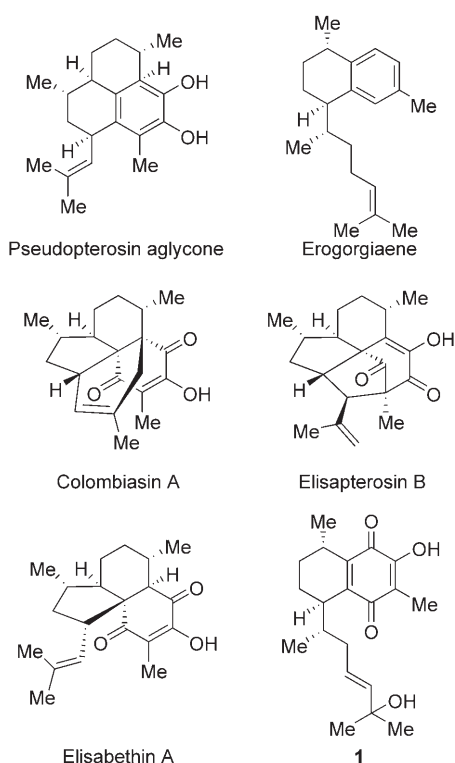
The gorgonian corals are notable as sources of many diverse pharmacological agents,^[1] and substantial effort has been directed toward isolation of natural products from these organisms. One species from this family, the soft coral *Pseudopterogorgia elisabethae*, has provided compounds with antiinflammatory, analgesic, cytotoxic, antiviral, antibacterial, antituberculosis and antimalarial activity.^[2] Members of the pseudopterogorgia family of diterpene glycosides (Scheme 1) were isolated from this organism and have subsequently been found to be potent antiinflammatory and analgesic agents.^[3] This class of natural products, which contains more than 15 variants, has been shown to be derived from a common biosynthetic precursor, erogorgiaene.^[4] More recently, other secondary metabolites that appear to originate from a related biosynthetic pathway have been recovered from extracts of this species.^[5] These compounds, such as colombiasin A, elisapterosin B, and elisabethin A, have attracted considerable interest from the synthetic community, due in significant part to the challenge presented by their interesting molecular architectures.^[6–8] It has been proposed that these natural products could be derived from a common intermediate such as **1** by different cyclization pathways.^[9]

[*] Dr. A. A. Boezio, Dr. E. R. Jarvo, B. M. Lawrence,
Prof. Dr. E. N. Jacobsen
Department of Chemistry and Chemical Biology
Harvard University
Cambridge, MA 02138 (USA)
Fax: (+1) 617-496-1880
E-mail: jacobsen@chemistry.harvard.edu

[**] This work was supported by the NIH (GM-59316). We are grateful to Dr. R. Staples for carrying out the X-ray crystal structure analyses.



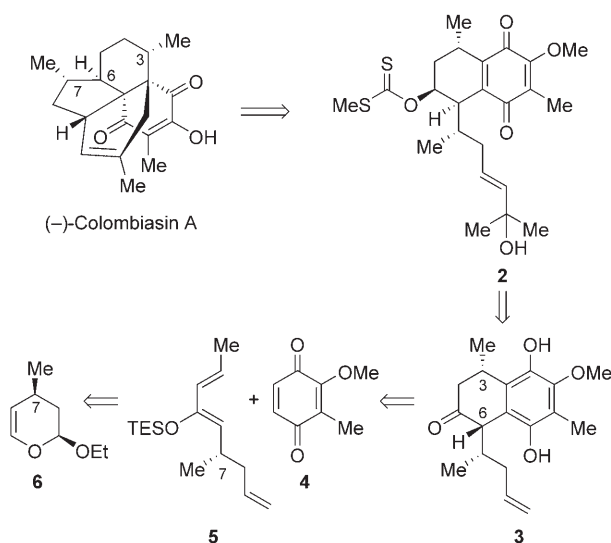
Supporting information for this article is available on the WWW under <http://www.angewandte.org> or from the author.



Scheme 1. Representative secondary metabolites isolated from *Pseudopterogorgia elisabethae*.

Such diversity-oriented synthesis practiced on a biosynthetic level would allow the organism to generate an array of compounds for chemical defence, and is supported by the observation of **1** in extracts from *P. elisabethae*.^[10]

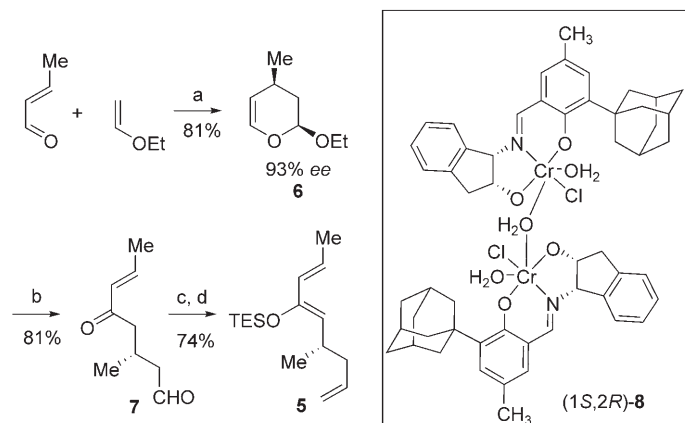
We were intrigued by the versatility of putative biosynthetic intermediate **1**, and became interested in developing a synthetic route to (–)-colombiasin A that would proceed through a similar advanced intermediate, such as alcohol **2** (Scheme 2). We envisioned preparation of **2** by a diastereo-



Scheme 2. Retrosynthetic analysis applied to colombiasin A.

and regioselective quinone Diels–Alder (qDA) reaction. This strategy would require a method to adjust the stereochemistry at C6 (colombiane numbering) in a subsequent step. Indeed, while several elegant syntheses of colombiasin A have been reported, control over all stereochemical elements of the molecule has proven to be a most significant challenge.^[6] To insure high selectivity in the qDA reaction, we undertook an effort to develop new catalysts for this reaction as an integral part of our synthetic plan. The details of those studies are presented in the preceding communication in this issue.^[11] To address the stereochemistry at C6, we chose to employ silyl enol ether **5** as the diene component, with the thought that the ketone **3** could undergo epimerization to afford the desired diastereomer. The silyl enol ether would also serve to differentiate the diene termini, and thus allow high regioselectivity in the qDA reaction.

Our synthesis of diene **5** began with an inverse electron demand hetero-Diels–Alder (HDA) reaction catalyzed by dimeric chromium complex **8**, a reaction that was developed in our group for the preparation of optically pure dihydropyrans.^[12,13] Reaction of ethyl vinyl ether with *trans*-crotonaldehyde afforded cycloadduct **6** in good yield (81%) and high enantioselectivity (93% *ee*) on multigram scale, thereby introducing the requisite stereochemistry of the methyl-bearing stereocenter at C7 (Scheme 3). Palladium-catalyzed



Scheme 3. Synthesis of diene **5**. a) (1S,2R)-**8** (5 mol %), MS 4 Å, 20 h; b) 1. *t*BuLi, THF, –78 to 0°C, 0.5 h; 2. ZnCl₂, THF, 0°C to RT, 0.5 h; 3. [Pd-(PPh₃)₄] (2.5 mol %), 1-bromopropene (2 equiv, *cis/trans* 1:1), THF, 2 h; 4. HCl (aq.) (0.5 M), 1 h; c) 1. BrCH₂PPh₃, KHMDS, PhMe, 0°C, 1 h; 2. **7**, –78 to 0°C, 82%; d) 1. KHMDS, THF, –78°C, 0.5 h; 2. TESCl, –78°C, 0.5 h, 90% (90% isomerically pure). HMDS = bis(trimethylsilyl)amide, TES = triethylsilyl.

Negishi coupling with 1-bromopropene (1:1 *E/Z* mixture) was performed after lithiation of **6** with *t*BuLi and transmetalation with ZnCl₂.^[14] The isomerically pure cross-coupled product was hydrolyzed directly to afford ketoaldehyde **7** in 81% yield. Selective olefination of the aldehyde in the presence of the enone was achieved by a standard Wittig olefination. The enone was then treated with KHMDS and the resultant enolate was quenched with TESCl to provide diene **5**.^[15]

With diene **5** in hand, catalysis of the key qDA reaction was investigated (Table 1). Reactions of simpler model dienes

suggested that monomeric chromium complex **12** might be a suitable catalyst (see previous paper for a detailed discussion).^[11,16] The inherent substrate-induced diastereoselectivity, as measured by catalysis with achiral catalyst **11**, was low (1.8:1 d.r., 3:1 regioselectivity; Table 1, entry 1), though the

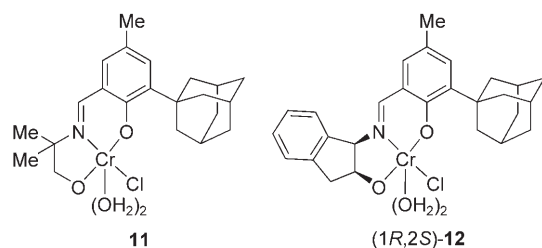


Table 1: Diels–Alder reaction of quinone **4** and diene **5**.

Entry	Catalyst	d.r. (9a : 9b)	Regioselectivity (9 : 10)
1	achiral 11	1.8:1	3:1
2	(1R,2S)- 12	17:1	10:1
3	(1S,2R)- 12	1:6.5	4.6:1

9a: X = OMe, Y = Me
10a: X = Me, Y = OMe
9b: X = OMe, Y = Me
10b: X = Me, Y = OMe

[a] Catalyst (10 mol %), MS 5 Å, PhMe, 0 °C; b) salcomine (10 mol %), DBU, O₂, 0 °C, 0.5 h.

diastereomer required for the synthesis was obtained as the major product.^[17] Gratifyingly, chiral catalyst **12** was found to exert high levels of stereocontrol over the reaction. In the matched case, catalyst (**1R,2S**)-**12** provided the desired product in high diastereoselectivity (17:1) and regioselectivity (10:1; Table 1, entry 2). The mismatched catalyst, (**1S,2R**)-**12**, though less selective overall, induced a reversal in diastereoselectivity (1:6.5 d.r., 4.6:1 regioselectivity; Table 1, entry 3).

Having demonstrated the highly stereo-selective qDA reaction, we next investigated the crucial epimerization of the C6 stereo-center (Figure 1). The qDA reaction of **4** and **5** afforded silyl enol ether **13**, along with an olefin isomer **13'**, in 86% yield.^[18] These isomers were not separated as both led to the desired ketone upon hydrolysis. Treatment with a 1:1 mixture of concentrated HCl and methanol effected deprotection of the silyl enol ether, tautomerization of the enedione to the hydroquinone, and epimerization to the desired diastereomer (>10:1 d.r. as measured by ¹H NMR spectroscopy).^[19] The relative stereochemistry of ketone **14** was confirmed

by X-ray crystallography (Figure 1).^[20] A highly diastereoselective reduction followed by in situ aerobic oxidation furnished quinone alcohol **15** in 75% yield (over two steps from **13** + **13'**).^[21]

We planned to install the tertiary allylic alcohol by a cross-metathesis reaction catalyzed by the Grubbs second-generation ruthenium catalyst **18** (Scheme 4).^[22] Preliminary studies suggested that the free secondary alcohol of **15** could interfere with the subsequent dehydration reaction to the requisite diene, so we chose to block this group first. As deoxygenation at C5 would ultimately be required, xanthate was chosen as a functional protecting group.^[23,24] The cross-metathesis reaction of quinone **16** with 2-methyl-3-buten-2-ol catalyzed by **18** (10 mol %) proceeded smoothly at room temperature (87% yield).^[25] Warming a solution of tertiary alcohol **2** in benzene to reflux in the presence of MgSO₄ resulted in a tandem dehydration-intramolecular qDA reaction to assemble the tetracyclic colombiane framework (77% yield). The ¹H and ¹³C NMR spectra of xanthate **17** matched those reported by Nicolaou and co-workers for this intermediate in their synthesis of colombiasin A.^[6a] Completion of the synthesis proceeded in a straightforward fashion. Deoxygenation and demethylation were performed by using modifications of the literature conditions,^[6a,c] affording the natural product, (–)-colombiasin A in 67% yield for the two-step sequence. Spectral data (NMR, HRMS, IR) of synthetic material and natural (–)-colombiasin A were in complete accord.^[26]

During the course of investigations into alternate deprotection conditions for methyl colombiasin A, we discovered that treatment of (–)-colombiasin A with superstoichiometric quantities of BF₃·Et₂O resulted in smooth conversion to (–)-elisapterosin B (Scheme 5). This reaction may proceed by a fragmentation reaction, affording an allylic cation that undergoes subsequent cyclization, or by a retro [4+2] cycloaddition followed by a [5+2] cycloaddition. While the mechanism of this reaction has yet to be determined, it is stereoselective and

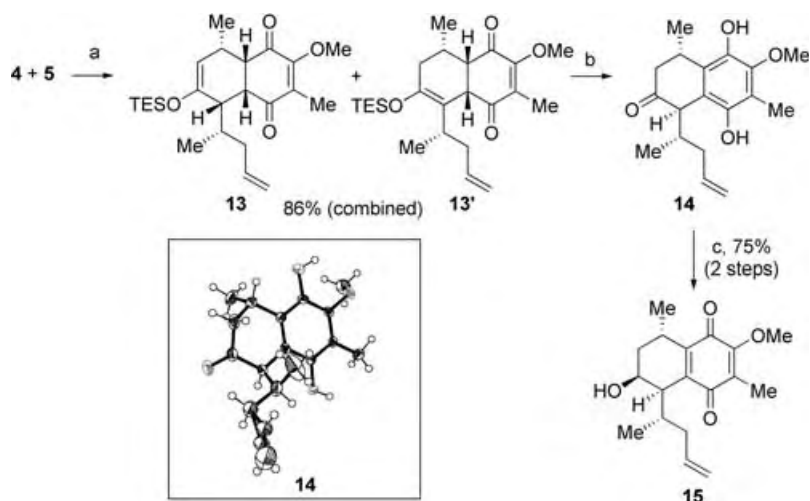
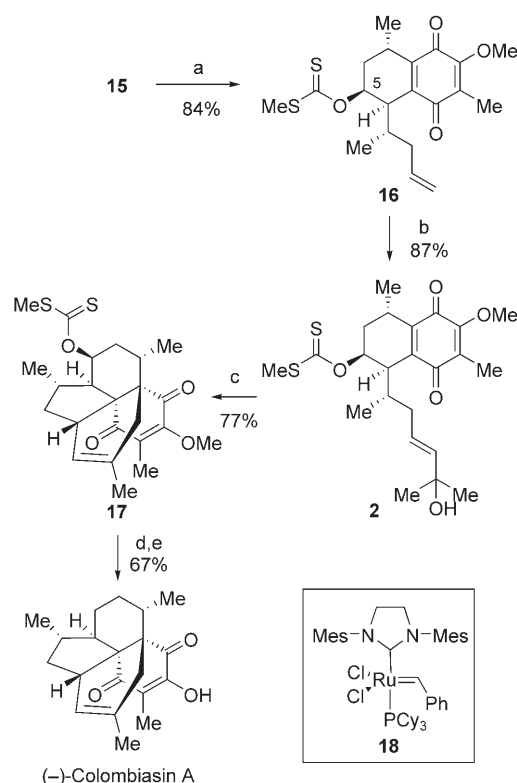
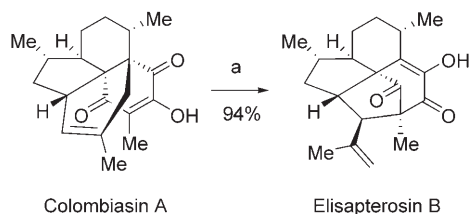


Figure 1. Synthesis of alcohol **15** and the X-ray crystal structure of **14**. Ellipsoids are drawn at the 50% probability level. a) (**1R,2S**)-**12** (10 mol %), 5 Å MS, PhMe, 0 °C, 24 h; b) HCl (conc.), MeOH, 0 °C to RT, 10 h; c) 1. NaBH₄, CeCl₃·7H₂O, MeOH, –78 °C, 1 h; 2. air, RT, 2 h.



Scheme 4. Completion of the synthesis. a) 1. NaH, THF, 0°C to RT, 0.5 h; 2. CS₂; 3. MeI, 9 h; b) 1. 2-methyl-3-buten-2-ol, catalyst **18** (10 mol%), CH₂Cl₂, 24 h; c) MgSO₄, PhH, reflux, 3 h; d) AIBN, *n*Bu₃SnH, PhMe, 110°C, 0.5 h; e) AlCl₃, PhNMe₂, CH₂Cl₂, 0°C to RT, 0.5 h. AIBN = 2,2'-azobisisobutyronitrile.



Scheme 5. Conversion of colombiasin A to elisapterosin B. a) BF₃·Et₂O, CH₂Cl₂, RT, 4 h

high-yielding (94%), and underlines the close structural relationship between these natural products.

The enantioselective synthesis of (–)-colombiasin A was accomplished in 12 steps and 11.5% overall yield from ethyl vinyl ether and *trans*-crotonaldehyde. A stereoselective qDA reaction catalyzed by a [(Schiff base)Cr^{III}] complex developed expressly for this purpose allowed control of diastereo- and regioselectivity in one of the key steps of the sequence. Other key steps included highly selective installation of the C6 stereocenter under thermodynamic control, and a tandem dehydration-qDA reaction to assemble the tetracyclic framework of the molecule. The use of protecting groups was minimized by careful synthetic design. (–)-Elisapterosin B was prepared by a remarkably facile Lewis acid-mediated rearrangement of colombiasin A. Current studies focus on

biomimetic syntheses of other natural products isolated from *Pseudopterogorgia elisabethae* by way of intermediates such as tertiary alcohol **2**.

Received: June 22, 2005

Published online: August 18, 2005

Keywords: asymmetric catalysis · cycloaddition · metathesis · natural products · quinones

- [1] A. D. Rodríguez, *Tetrahedron* **1995**, *51*, 4571–4618.
- [2] I. I. Rodríguez, Y.-P. Shi, O. J. Garcia, A. D. Rodríguez, A. M. S. Mayer, J. A. Sanchez, E. Ortega-Barria, J. Gonzalez, *J. Nat. Prod.* **2004**, *67*, 1672–1680.
- [3] a) S. A. Look, W. Fenical, G. K. Matsumoto, J. Clardy, *J. Org. Chem.* **1986**, *51*, 5140–5145; b) V. Roussis, Z. Wu, W. Fenical, S. A. Strobel, G. D. VanDuyne, J. Clardy, *J. Org. Chem.* **1990**, *55*, 4916–4922.
- [4] A. C. Kohl, R. G. Kerr, *Mar. Drugs* **2003**, *1*, 54–65.
- [5] a) A. D. Rodríguez, C. Ramirez, *Org. Lett.* **2000**, *2*, 507–510; b) A. D. Rodríguez, C. Ramirez, I. I. Rodríguez, C. L. Barnes, *J. Org. Chem.* **2000**, *65*, 1390–1398; c) A. D. Rodríguez, E. Gonzalez, S. D. Huang, *J. Org. Chem.* **1998**, *63*, 7083–7091.
- [6] Total syntheses of colombiasin A: a) K. C. Nicolaou, G. Vassilikogiannakis, W. Magerlein, R. Kranich, *Angew. Chem.* **2001**, *113*, 2543–2547; *Angew. Chem. Int. Ed.* **2001**, *40*, 2482–2486; b) K. C. Nicolaou, G. Vassilikogiannakis, W. Magerlein, R. Kranich, *Chem. Eur. J.* **2001**, *7*, 5359–5371; c) elisapterosin B: A. I. Kim, S. D. Rychnovsky, *Angew. Chem.* **2003**, *115*, 1305–1308; *Angew. Chem. Int. Ed.* **2003**, *42*, 1267–1270; d) elisapterosin B: D. C. Harrowven, D. D. Pascoe, D. Demurtas, H. O. Bourne, *Angew. Chem.* **2005**, *117*, 1247–1248; *Angew. Chem. Int. Ed.* **2005**, *44*, 1221–1222.
- [7] a) For a review of synthetic approaches toward elisabethin A, see: G. Zanoni, M. Franzini, *Angew. Chem.* **2004**, *116*, 4942–4946; *Angew. Chem. Int. Ed.* **2004**, *43*, 4837–4841; b) elisabethin A: T. J. Heckrodt, J. Mulzer, *J. Am. Chem. Soc.* **2003**, *125*, 4680–4681; c) elisapterosin B: N. Waizumi, A. R. Stankovic, V. H. Rawal, *J. Am. Chem. Soc.* **2003**, *125*, 13022–13023.
- [8] For approaches toward colombiasin A, see: a) D. C. Harrowven, M. J. Tyte, *Tetrahedron Lett.* **2001**, *42*, 8709–8711; b) J. H. Chaplin, A. J. Edwards, B. L. Flynn, *Org. Biomol. Chem.* **2003**, *1*, 1842–1844.
- [9] a) A. D. Rodríguez, Y.-P. Shi, *Tetrahedron* **2000**, *56*, 9015–9023; b) for a discussion, see reference [3b].
- [10] a) R. S. Thornton, R. G. Kerr, *J. Chem. Ecol.* **2002**, *28*, 2083–2090; b) W. O'Neal, J. R. Pawlik, *Mar. Ecol. Prog. Ser.* **2002**, *240*, 117–126.
- [11] See preceding paper in this issue: E. R. Jarvo, B. M. Lawrence, E. N. Jacobsen, *Angew. Chem.* **2005**, *117*, in press; *Angew. Chem. Int. Ed.* **2005**, *44*, in press; DOI: 10.1002/anie.200502176.
- [12] K. Gademann, D. E. Chavez, E. N. Jacobsen, *Angew. Chem.* **2002**, *114*, 3185–3187; *Angew. Chem. Int. Ed.* **2002**, *41*, 3059–3061.
- [13] For applications of the inverse electron demand HDA reaction in natural product synthesis, see: a) D. E. Chavez, E. N. Jacobsen, *Org. Lett.* **2003**, *5*, 2563–2565; b) H. Gao, D. G. Hall, *J. Am. Chem. Soc.* **2005**, *127*, 1628–1629.
- [14] a) V. Boucard, K. Larrieu, N. Lubin-Germain, J. Uziel, J. Augé, *Synlett* **2003**, 1834–1837; b) M. A. Tius, J. Gomez-Galeno, X.-Q. Gu, J. H. Zaidi, *J. Am. Chem. Soc.* **1991**, *113*, 5775–5783; c) F. Tellier, R. Sauvetre, J.-F. Normant, *J. Organomet. Chem.* **1989**, *364*, 17–28; d) P. Villiers, N. Vicart, Y. Ramondenc, G. Ple, *Tetrahedron Lett.* **1999**, *40*, 8781–8784.

- [15] M. Arisawa, Y. Torisawa, M. Nakagawa, *Synthesis* **1995**, 1371–1372.
- [16] Although not required for the synthetic sequence, in situ oxidation of the cycloadduct to quinones **9** and **10** was performed to facilitate determination of the diastereo- and regioselectivity of the reaction by HPLC.
- [17] This would be predicted by reaction of a ground state conformation of diene **5** wherein allylic strain is minimized.
- [18] Formation of isomer **13'**, wherein the olefin has isomerized to the tetrasubstituted silyl enol ether, presumably occurs during chromatographic purification. Analogous isomerizations are not observed with less hindered cycloadducts. See Supporting Information for details. For an example of isomerization of a silyl enol ether upon exposure to silica gel, see: P. Magnus, I. S. Mitchell, *Tetrahedron Lett.* **1998**, 39, 9131–9134.
- [19] While this intermediate is quite stable under acidic conditions, it undergoes decomposition under basic conditions and upon chromatography on silica gel, presumably due to oxidation to the corresponding quinone.
- [20] Details of the crystal structure analysis are provided as Supporting Information. CCDC-263118 (**14**) contains the supplementary crystallographic data for this paper. These data can be obtained free of charge from the Cambridge Crystallographic Data Centre via www.ccdc.cam.ac.uk/data_request/cif.
- [21] High diastereoselectivity in the reduction step was desirable to facilitate analysis of ¹H NMR spectra of subsequent intermediates.
- [22] A. K. Chatterjee, T.-L. Choi, D. P. Sanders, R. H. Grubbs, *J. Am. Chem. Soc.* **2003**, 125, 11360–11370.
- [23] Catalyst **18** has been shown to be more tolerant to sulfur-containing functionality than previous generations of ruthenium-based metathesis catalysts; a) F. D. Toste, A. K. Chatterjee, R. H. Grubbs, *Pure Appl. Chem.* **2002**, 74, 7–10; b) G. Spagnol, M.-P. Heck, S. P. Nolan, C. Mioskowski, *Org. Lett.* **2002**, 4, 1767–1770.
- [24] Attempts to effect deoxygenation of this intermediate led only to complex decomposition mixtures.
- [25] Access to tertiary alcohol **2** could prove interesting in synthetic routes toward other related natural products, such as elizabethin A. However, cross metathesis of quinone **16** with isoprene would serve as a shorter route to colombiasin A. Tandem cross-metathesis/qDA reactions did provide the desired product, but in consistently lower yields than the two-step cross-metathesis/dehydration/qDA sequence. For examples of cross-metathesis reactions of conjugated dienes, see: T. W. Funk, J. Efskind, R. H. Grubbs, *Org. Lett.* **2005**, 7, 187–190.
- [26] We are grateful to Professor A. D. Rodríguez of the University of Puerto Rico for kindly supplying a sample of natural colombiasin A.

DOI: 10.1002/anie.200501341

A Template-Based Electrochemical Method for the Synthesis of Multisegmented Metallic Nanotubes***Woo Lee,* Roland Scholz, Kornelius Nielsch, and Ulrich Gösele*

Tubular nanostructures have stimulated extensive research efforts in recent years because of their technological importance in advanced electronic or magnetic devices^[1] and prospective applications in catalysis,^[2] sensors,^[3] and biological separation and transport.^[4] To date, various methods^[5] including reductive sulfidization,^[6] thermal decomposition of precursors,^[7] atomic layer deposition (ALD),^[8] hydrothermal pyrolysis,^[9] galvanic replacement reactions,^[10] and surfactant- or template-based growth^[11] have been developed for the fabrication of such tubular nanostructures. Among them, template-based synthesis using anodic aluminum oxide (AAO) or track-etched polymer membranes has attracted much attention, because it provides several distinct advantages over other approaches. It offers a convenient way for producing structurally uniform nanostructures periodically aligned in template matrices. A wide range of materials including metals, semiconductors, and polymers have been prepared in the form of nanotubes.^[12] However, few examples have been reported on the fabrication of metal nanotubes despite their technological importance. The development of a generalized method for the fabrication of aligned metal-nanotube arrays remains a challenge. Precise control of the nanotube growth process and formation of well-aligned arrays will greatly assist investigations of their physical properties and their potential use in nanoscale fluidics, chemical and biological separations, sensors, and catalysts.

Herein, we report a novel approach for the preparation of metallic nanotubes based on the preferential electrodeposition of a metal along the pore walls of an AAO membrane in the presence of metallic nanoparticles on the wall surfaces (Figure 1). Several reports on the immobilization of metallic nanoparticles on the pore walls of AAO have been published previously. Schmid and co-workers showed that Au nanoparticles can be self-assembled on AAO channels modified with organosilane molecules, which function as molecular anchors binding the nanoparticles.^[13] More recently, Rubin-

[*] Dr. W. Lee, Dr. R. Scholz, Dr. K. Nielsch, Prof. Dr. U. Gösele
Max Planck Institute of Microstructure Physics
Weinberg 2, 06120 Halle (Germany)
Fax: (+49) 345-5511-223
E-mail: woolee@mpi-halle.de

[**] Financial support from the German Federal Ministry for Education and Research (BMBF, Project No. 03N8701) is gratefully acknowledged.



Supporting information for this article is available on the WWW under <http://www.angewandte.org> or from the author.

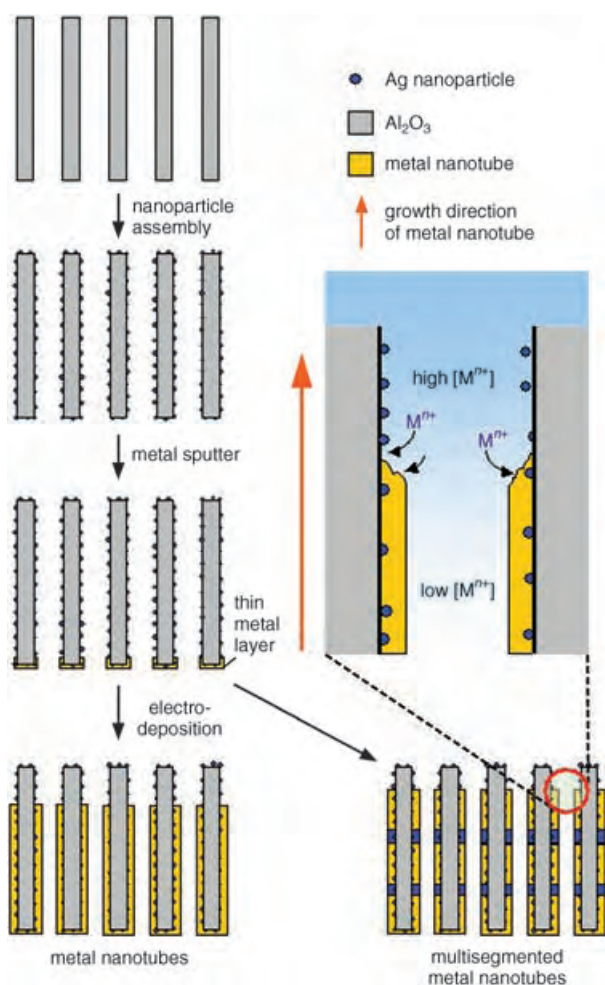
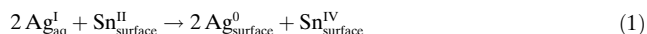


Figure 1. Procedure for the preparation of metal nanotubes and the proposed mechanism of metal nanotube growth (see text).

stein and co-workers demonstrated the preparation of Au nanoparticle nanotubes (NPNTs) by introducing a colloid solution of Au nanoparticles into the pores of an organosilane-modified AAO, followed by spontaneous coalescence of the surface-bound Au nanoparticles.^[14] In an alternative approach, Johansson et al. deposited Pd nanoparticles on the pore walls of AAO by using a sequential electroless deposition technique, in which a palladium complex ($[\text{Pd}(\text{NH}_3)_4]^{2+}$) was thermally reduced to metallic Pd.^[15] In the present study, metallic nanoparticles (for example, Ag) were immobilized on the pore walls of an AAO membrane by the spontaneous reduction of Ag^{I} by Sn^{II} , which is a modification of the previously established sensitization–preactivation process of AAO^[16] or polymer membranes^[17] prior to the electroless deposition of metals. To induce the selective reduction of metal cations on the surfaces of oxide membranes, Sn^{II} was first deposited on the pore walls by immersing the membranes in an aqueous solution of SnCl_2 . After a drying step, the resulting membranes were soaked in an aqueous solution of AgNO_3 . These two steps constitute one deposition cycle and were repeated several times (typically six cycles). The standard reduction potential of $\text{Sn}^{\text{IV}}/\text{Sn}^{\text{II}}$ (0.151 V versus standard hydrogen electrode, SHE) is lower than that of the

$\text{Ag}^{\text{I}}/\text{Ag}^0$ pair (0.80 V versus SHE). Therefore, the surface-bound $\text{Sn}^{\text{II}}_{\text{surface}}$ cations would be spontaneously oxidized into Sn^{IV} , thus producing discrete metallic Ag nanoparticles on the surface of the Sn^{II} -treated AAO membrane upon immersion in an aqueous solution of AgNO_3 [Eq. (1)].



This process results in homogeneous deposition of metal nanoparticles over the entire surface (pore walls and faces) of AAO membranes (Figure 2a). The size and the number of

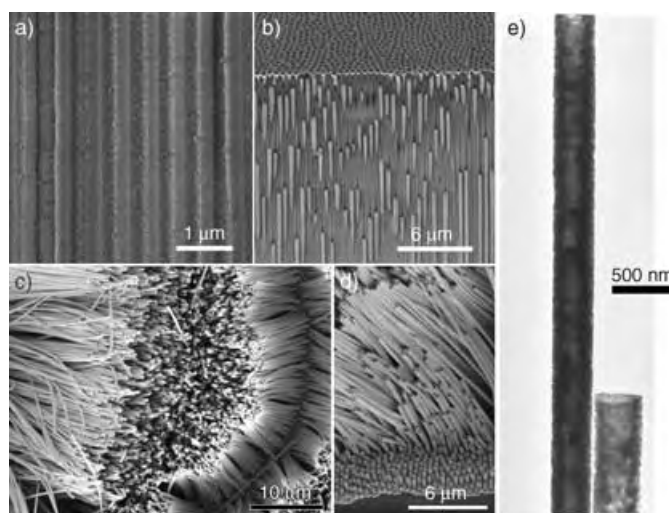


Figure 2. a) Cross-sectional SEM image of the Ag-nanoparticle-immobilized anodic aluminum oxide (AAO) membrane. b) Cross-sectional SEM image of the Au nanotube–AAO composite showing Au nanotubes embedded in the alumina matrix. c) and d) SEM images of Au nanotubes after removal of alumina matrix with NaOH (1.0 M); part c) illustrates the open-end tips of Au nanotubes at the levels of different length. e) Representative TEM image of Au nanotubes showing their tubular structure.

metal nanoparticles depend on the number of deposition cycles. The average particle size determined by TEM analyses was 11 ± 4 nm (Supporting Information). Unlike the Au NPNTs reported by Rubinstein and co-workers^[14] which showed good electrical conductivity with a specific resistivity of $6 \, \Omega \text{ cm}$, our Ag-nanoparticle-modified AAO membranes exhibited a typical insulating behavior even after 10 deposition cycles. This finding indicates that the Ag nanoparticles immobilized on the surfaces of AAO membranes are isolated from each other without the formation of a continuous conduction path for current transport. Electrodeposition of Au at current densities ranging from 2.2 to 2.5 mA cm^{-2} resulted in the formation of Au nanotubes embedded in the alumina matrix (Figure 2b). Subsequent removal of the oxide matrix with NaOH (1.0 M) led to the release of Au nanotubes with surfaces decorated with Ag nanoparticles (Figure 2c,d). The presence of Ag nanoparticles on the surface of the metal nanotubes is inevitable, and results in mixed-metal nanotubes. TEM investigations of Au nanotubes revealed that the average outer diameter of the nanotubes is 330 nm (Figure 2e). Further evidence for the tubular nanostructure was

obtained directly from water permeation experiments through the gold nanotube arrays embedded in the alumina matrix: a drop of water placed on one side of the membrane was transported to the other side.

In the process described herein, the growth of metal nanotubes starts at the base-metal electrode at the bottom of the pores (that is, a bottom-up deposition of metal) as a result of the nonconducting nature of the nanochannels. It is believed that Ag nanoparticles immobilized on the oxide nanochannel surfaces play a key role in the growth of the metallic nanotubes, and enable preferential electrodeposition of metal along the nanochannel surfaces. Nanotube formation in this electrodeposition process can be understood in terms of the relative rates of deposition and the diffusion of metal ions. It is believed that the deposition process takes place at the tube tips, and therefore the deposition interfaces and the diffusion layers of metal ions move dynamically with the growth process of the tubes (Figure 1). Once a small conducting path is created by electrodeposition between the tube tip and an isolated Ag nanoparticle, the deposition interface will move toward the recently created area, and a majority of the metal ions will be deposited on the newly connected nanoparticle until another isolated particle is electrically connected. This electrodeposition effect establishes a depletion layer of metal ions, and thus the ion concentration below the tube tips should be very low, and the metal deposition on the inner tube wall should be negligible. Our assumptions were proven by electrodeposition experiments with different deposition rates. The electrodeposition carried out at a low current density ($< 0.4 \text{ mA cm}^{-2}$), at which the focusing effect at the tube tip could be neglected as a result of the slow deposition rate, produced only arrays of solid metal nanorods. In contrast, the electrodeposition performed at a high current density ($> 3.0 \text{ mA cm}^{-2}$) resulted in mechanically unstable metal nanotubes with highly porous wall surfaces (Supporting Information).

For cases in which the whole surface of the membrane is electrically conductive, electrodeposition of metal should occur evenly over the entire membrane surface at the same time. In other words, radial growth of metal nanotubes occurs inside the nanochannels, gradually decreasing the channel diameter. The underpotential deposition (UPD) technique is required^[18] for the fabrication of pore walls of uniform thickness over the whole length of the membranes. The deposition rate must be sufficiently lower than that of the axial mass transfer of metal cations to guarantee a homogeneous ion concentration over the whole pore length.

By taking advantage of the preferential deposition of metal along the wall surfaces of oxide nanochannels, we were able to prepare multisegmented metallic nanotubes with a bimetallic stacking configuration along the nanotube axes. Figure 3 shows representative SEM images of multisegmented metallic nanotubes with a stacking configuration of Au-Ni-Au-Ni-Au, before (Figure 3a) and after (Figure 3b,c) removal of the alumina matrix with a solution of NaOH (1.0 M). The average outer diameter of the nanotubes was estimated to be 300 nm. Ni segments about 800 nm long with a dark image contrast can be clearly observed between adjacent Au nanotube sections (Figure 3c; see also the color-



Figure 3. SEM images of multisegmented metal nanotubes with a stacking configuration of Au-Ni-Au-Ni-Au along the nanotube axis. a) Cross-sectional SEM image of as-prepared metal nanotube-AAO composite, which shows metal nanotubes embedded in an alumina matrix. The signals from Au and Ni are shown in yellow and purple, respectively. b) and c) SEM images of multisegmented metal nanotubes after removal of alumina matrix with NaOH (1.0 M); part c) clearly shows the stacking configuration of multisegmented metal nanotubes in which the segments with bright and dark image contrasts correspond to Au and Ni, respectively.

enhanced view of Au-Ni segments in Figure 3a). This contrast in the SEM images results from differences in the intensity of backscattered electrons from the two metals. In this nanofabrication process, various metallic segments (Ag, Au, Pt, Pd, Fe, Co, Ni, etc.) can be incorporated into the nanotube structure, thus enabling the fabrication of barcode-type nanotubes.^[19] The length of each metal segment can be tuned by controlling the amount of total integrated charges involved in the electrochemical reaction. Such a unique capacity for tailoring the nanotube structure could provide an opportunity for engineering the physical properties of nanotube materials.

Arrays of continuous Ni nanotubes and of multisegmented nanotubes (Au-Ni-Au-Ni-Au stacking configuration, Figure 3) were examined by a superconducting quantum interference device (SQUID) magnetometer at 298 K for comparison of their magnetic properties. The corresponding hysteresis loops are presented in Figure 4. With the magnetic field applied along the nanotube axis (\parallel), both samples showed coercivities $H_{c\parallel}$ in the range of 85 to 90 A m^{-1} and relatively low remanence values (4 and 17%). As the saturation field $H_{s\parallel} \gg H_{c\parallel}$, both samples exhibited reversible magnetic behavior. The nanowire diameter was at least one order of magnitude larger than the magnetic exchange length for nickel $\lambda_{\text{Ni}} \approx 13 \text{ nm}$, and we therefore assume that the Ni nanotubes switched by a curling-like switching mode.^[20] The

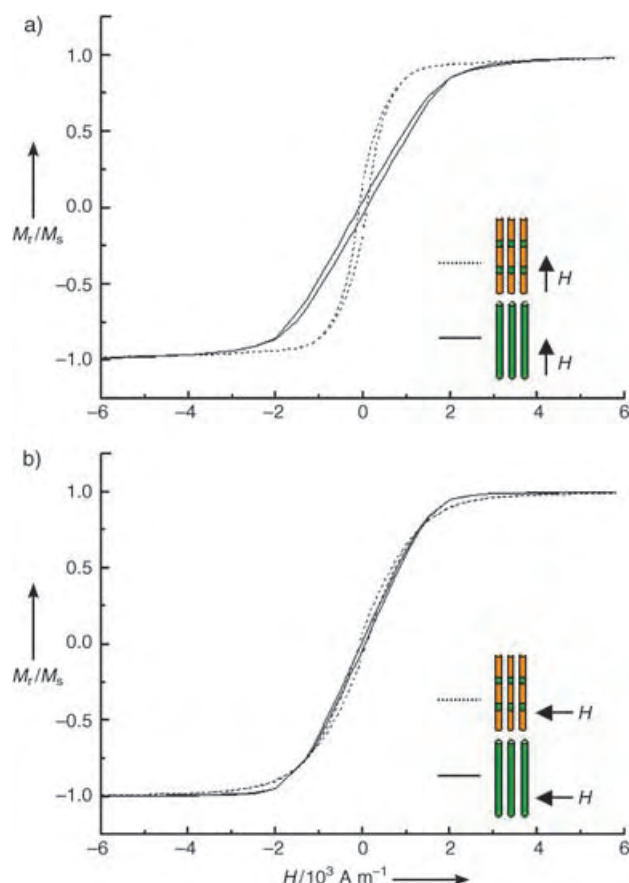


Figure 4. Magnetic hysteresis loops for arrays of Au-Ni-Au-Ni-Au nanotubes shown in Figure 3 (----) and ferromagnetic Ni nanotubes (—), measured with the applied magnetic field a) parallel and b) perpendicular to the nanotube axis.

multisegmented nanotube arrays could be completely magnetized at lower saturation fields ($H_{s\parallel} \approx 750 \text{ A m}^{-1}$) than the array of continuous Ni nanotubes ($H_{s\parallel} \approx 2300 \text{ A m}^{-1}$). The positions of the Ni segments along the pore axis showed large variations (Figure 3a). Although the tube diameter, spacing, and wall thickness for both samples were similar, we assume that the array of multisegmented nanotubes exhibited lower dipolar interactions. The average distance between the neighboring Ni segments was larger than the intertube distance of the continuous nanotube array. In the perpendicular field direction (\perp), both samples were completely magnetized around $H_{s\perp} \approx 2000 \text{ A m}^{-1}$ and show highly similar hysteresis loops with a reversible magnetic behavior ($H_{s\perp} \gg H_{c\perp}$). In comparison of the hysteresis loops for both magnetization directions the array of continuous nanotubes showed a nearly isotropic magnetic behavior, whereas the multisegmented sample exhibited a preferential magnetic orientation along the direction of the magnetic nanotubes as a consequence of the low dipolar interactions and the magnetic anisotropy resulting from the nanotube shape.

In summary, we have developed a simple electrochemical method for the preparation of metal nanotubes. The process is based on the preferential electrodeposition of a metal along the pore walls of an anodic alumina membrane in the

presence of Ag nanoparticles on the wall surfaces. We have demonstrated for the first time the preparation of multi-segmented metallic nanotubes with a bimetallic stacking configuration along the nanotube axes. This nanofabrication method can be readily extended to a wide range of metallic or semiconducting materials. Furthermore, the unique capacity for tailoring the nanotube structure, along with the functionalization of the inner wall surface of metal nanotubes with various molecules (for example, proteins and DNA), are expected to be particularly useful in the field of catalysis, advanced microfluidics, biological and magnetic sensors, and molecule separation.

Experimental Section

Membrane preparation: Self-ordered nanoporous Al_2O_3 membranes were prepared by the two-step anodization^[21] of surface-finished aluminum. In brief, Al sheets (typical diameter 4 cm) were anodized under a regulated cell voltage of 195 V with H_3PO_4 as electrolyte. The first anodization was started under relatively mild electrochemical conditions with H_3PO_4 (0.5 wt.%, 0.6°C) to prevent the Al from breakdown in the early stages of anodization. After 3 h, the concentration of the H_3PO_4 was increased to 1.0 wt.% by directly injecting 85 wt.% H_3PO_4 into the electrochemical cell, and the temperature of the electrolyte was adjusted to 1.4°C . The anodization proceeded for 15 h under these conditions. Afterward, the porous oxide layer was completely removed by immersion in an acid mixture (1.8 wt.% chromic acid and 6 wt.% H_3PO_4) at 43°C for 12 h to obtain a textured surface on the Al sheet. The second anodization was conducted in H_3PO_4 (1.0 wt.%, 1.4°C) for 16 h. Subsequently, free-standing alumina membranes were obtained by a stepwise voltage reduction technique. The membranes had nominal pore diameters of 300 nm and contained 4.6×10^8 pores per cm^2 of membrane surface area.

Immobilization of metal nanoparticles: The immobilization of metal nanoparticles on the surfaces (pore walls and faces) of an AAO membrane was carried out as follows. First, Sn^{II} was deposited on the surfaces by immersing an AAO membrane in an aqueous mixture of SnCl_2 (0.02 M) and HCl (0.01 M) for 2 min. The membrane was thoroughly rinsed in distilled water several times, subsequently in acetone, and finally dried at 70°C for 1 min. Second, the resulting membrane was dipped into an aqueous solution of AgNO_3 (0.02 M) for 2 min to deposit Ag nanoparticles on the pore walls of the AAO, followed by the same drying process used in the first step. These two steps constituted one cycle for metal nanoparticle deposition on the surfaces of a membrane. Typically, six deposition cycles were employed.

Electrodeposition: A thin Au layer was deposited by sputtering on the pore-mouth surface of a nanoparticle-modified AAO membrane to make the surface electrically conductive. This Au layer served as a working electrode in the subsequent electrodeposition of the desired metal. A commercially available plating solution (Auruna 5000) was used for Au nanotubes. Nickel was deposited from a solution of $\text{NiCl}_2 \cdot 6\text{H}_2\text{O}$ ($8.41 \times 10^{-2} \text{ M}$), $\text{Ni}(\text{H}_2\text{SO}_3)_2 \cdot 4\text{H}_2\text{O}$ (1.59 M), H_3BO_3 (0.33 M), and sodium acetate buffer (pH 3.4). The typical current density was about 2.4 mA cm^{-2} . The total membrane area in contact with the electrolyte was 2.7 cm^2 ; the total pore area (actual deposition area) was estimated to be 33% of this area.

Received: April 18, 2005

Published online: August 26, 2005

Keywords: electrochemistry · gold · nanotubes · nickel · template synthesis

- [1] a) J. Goldberger, R. He, Y. Zhang, S. Lee, H. Yan, H.-J. Choi, P. Yang, *Nature* **2003**, 422, 599–602; b) Z. Liu, D. Zhang, S. Han, C. Li, B. Lei, W. Lu, J. Fang, C. Zhou, *J. Am. Chem. Soc.* **2005**, 127, 6–7; c) Y. J. Xing, Z. H. Xi, Z. Q. Xue, X. D. Zhang, J. H. Song, R. M. Wang, J. Xu, Y. Song, S. L. Zhang, D. P. Yu, *Appl. Phys. Lett.* **2003**, 83, 1689–1691.
- [2] a) M. S. Sander, M. J. Côté, W. Gu, B. M. Kile, C. P. Tripp, *Adv. Mater.* **2004**, 16, 2052–2056; b) M. A. Sanchez-Castillo, C. Couto, W. B. Kim, J. A. Dumesic, *Angew. Chem.* **2004**, 116, 1160–1162; *Angew. Chem. Int. Ed.* **2004**, 43, 1140–1142.
- [3] a) P. Kohli, M. Wirtz, C. R. Martin, *Electroanalysis* **2004**, 15, 9–18; b) A. Kros, R. J. M. Nolte, N. A. J. M. Sommerdijk, *Adv. Mater.* **2002**, 14, 1779–1782.
- [4] a) K. B. Jirage, J. C. Hulthen, C. R. Martin, *Science* **1997**, 278, 655–658; b) S. B. Lee, D. T. Mitchell, L. Trofin, T. K. Nevanen, H. Soderlund, C. R. Martin, *Science* **2002**, 296, 2198–2220; c) S. Yu, S. B. Lee, C. R. Martin, *Anal. Chem.* **2003**, 75, 1239–1244; d) P. Kohli, C. C. Harrell, Z. Cao, R. Gasparac, W. Tan, C. R. Martin, *Science* **2004**, 305, 984–986.
- [5] For recent reviews on inorganic nanotubes, see: a) C. N. R. Rao, M. Nath, *Dalton Trans.* **2003**, 1, 1–24; b) M. Remskar, *Adv. Mater.* **2004**, 16, 1497–1504.
- [6] a) H. A. Therese, F. Rocker, A. Reiber, J. Li, M. Stepulat, G. Glasser, U. Kolb, W. Tremel, *Angew. Chem.* **2005**, 117, 267–270; *Angew. Chem. Int. Ed.* **2005**, 44, 262–265; b) Y. Feldman, E. Wasserman, D. J. Srolovitz, R. Tenne, *Science* **1995**, 267, 222–225.
- [7] a) M. Nath, C. N. R. Rao, *Angew. Chem.* **2002**, 114, 3601–3604; *Angew. Chem. Int. Ed.* **2002**, 41, 3451–3454; b) L. Qu, G. Shi, X. Wu, B. Fan, *Adv. Mater.* **2004**, 16, 1200–1203.
- [8] a) H. Shin, D.-K. Jeong, J. Lee, M. M. Sung, J. Kim, *Adv. Mater.* **2004**, 16, 1197–1200; b) Y.-S. Min, E. J. Bae, K. S. Jeong, Y. J. Cho, J.-H. Lee, W. B. Choi, G.-S. Park, *Adv. Mater.* **2003**, 15, 1019–1022.
- [9] Y. Li, J. Wang, Z. Deng, Y. Wu, X. Sun, D. Yu, P. Yang, *J. Am. Chem. Soc.* **2001**, 123, 9904–9905.
- [10] a) Y. Sun, Y. Xia, *Adv. Mater.* **2004**, 16, 264–268; b) B. Mayers, X. C. Jiang, D. Sunderland, B. Cattle, Y. Xia, *J. Am. Chem. Soc.* **2003**, 125, 13364–13365.
- [11] a) R. Fan, Y. Wu, D. Li, M. Yue, A. Majumdar, P. Yang, *J. Am. Chem. Soc.* **2003**, 125, 5254–5255; b) T. Kijima, T. Yoshimura, M. Uota, T. Ikeda, D. Fujikawa, S. Mouri, S. Uoyama, *Angew. Chem.* **2004**, 116, 230–234; *Angew. Chem. Int. Ed.* **2004**, 43, 228–232.
- [12] a) T. Yanagishita, M. Sasaki, K. Nishio, H. Masuda, *Adv. Mater.* **2004**, 16, 429–432; b) Z. Liang, A. S. Susha, A. Yu, F. Caruso, *Adv. Mater.* **2003**, 15, 1849–1853; c) M. Wirtz, M. Parker, Y. Kobayashi, C. R. Martin, *Chem. Eur. J.* **2002**, 8, 3573–3578; d) G. Wu, L. Zhang, B. Cheng, T. Xie, X. Yuan, *J. Am. Chem. Soc.* **2004**, 126, 5976–5977; e) F.-S. Cai, G.-Y. Zhang, J. Chen, X.-L. Gou, H.-K. Liu, S.-X. Dou, *Angew. Chem.* **2004**, 116, 4308–4312; *Angew. Chem. Int. Ed.* **2004**, 43, 4212–4216; f) P. Kohli, J. E. Wharton, O. Braide, C. R. Martin, *J. Nanosci. Nanotechnol.* **2004**, 4, 605–610; g) J. Bao, C. Tie, Z. Xu, Q. Zhou, D. Shen, Q. Ma, *Adv. Mater.* **2001**, 13, 1631–1633; h) C. Mu, Y. Yu, R. Wang, K. Wu, D. Xu, G. Guo, *Adv. Mater.* **2004**, 16, 1550–1553.
- [13] T.-A. Hanaoka, A. Heilmann, M. Kröll, H.-P. Kormann, T. Sawitowski, G. Schmid, P. Jutzi, A. Klipp, U. Kreibitz, R. Neuendorf, *Appl. Organomet. Chem.* **1998**, 12, 367–373.
- [14] M. Lahav, T. Sehayek, A. Vaskevich, I. Rubinstein, *Angew. Chem.* **2004**, 116, 5734–5737; *Angew. Chem. Int. Ed.* **2003**, 42, 5576–5579.
- [15] A. Johansson, J. Lu, J.-O. Carlsson, M. Boman, *J. Appl. Phys.* **2004**, 96, 5189–5194.
- [16] a) X. Y. Yuan, G. S. Wu, T. Xie, B. Y. Geng, Y. Lin, G. W. Meng, L. D. Zhang, *Solid State Sci.* **2004**, 6, 735–738; b) X. Y. Yuan, G. S. Wu, T. Xie, Y. Lin, L. D. Zhang, *Nanotechnology* **2004**, 15, 59–61.
- [17] a) C. R. Martin, *Science* **1994**, 266, 1961–1966; b) V. P. Menon, C. R. Martin, *Anal. Chem.* **1995**, 67, 1920–1928.
- [18] J.-R. Ku, R. Vidu, R. Talroze, P. Stroeve, *J. Am. Chem. Soc.* **2004**, 126, 15022–15023.
- [19] S. R. Nicewarner-Peña, R. G. Freeman, B. D. Reiss, L. He, D. J. Peña, I. D. Walton, R. Cromer, C. D. Keating, M. J. Natan, *Science* **2001**, 294, 137–141.
- [20] C.-R. Chang, C. M. Lee, J.-S. Yang, *Phys. Rev. B* **1994**, 50, 6461–6464.
- [21] a) H. Masuda, K. Yada, A. Osaka, *Jpn. J. Appl. Phys.* **1998**, 37, L1340–L1342; b) H. Masuda, M. Satoh, *Jpn. J. Appl. Phys.* **1996**, 35, L126–L129.

Biosensors

DOI: 10.1002/anie.200501907

**Fluorescence Resonant Energy Transfer
Biosensor Based on Upconversion-Luminescent
Nanoparticles****

*Leyu Wang, Ruoxue Yan, Ziyang Huo, Lun Wang,
Jinghui Zeng, Jie Bao, Xun Wang, Qing Peng, and
Yadong Li**

The rapid development of pharmacogenomic research and drug discovery, diagnostics of infectious and genetic diseases, and methodologies for forensic and genetic identification is now challenging chemists to find more efficient biological labels than traditional organic dyes which are resistant to photobleaching, nontoxic, biocompatible, monochromatic,

[*] L. Y. Wang, R. X. Yan, Z. Y. Huo, Dr. J. H. Zeng, J. Bao, Dr. X. Wang, Dr. Q. Peng, Prof. Dr. Y. D. Li
Department of Chemistry
Tsinghua University
Beijing, 100084 (P.R. China)
and
National Center for Nanoscience and Nanotechnology
Beijing, 100084 (P.R. China)
Fax: (+ 86) 10-6278-8765
E-mail: ydli@tsinghua.edu.cn
L. Y. Wang, Prof. L. Wang
Anhui Key Laboratory of Functional Molecular Solids
College of Chemistry and Materials Science
Anhui Normal University
Wuhu, 241000 (P.R. China)

[**] This work was supported by the NSFC (90406003, 50372030, 20131030, 20401010), the Specialized Research Fund for the Doctoral Program of Higher Education, the Foundation for the Authors of National Excellent Doctoral Dissertation of P.R. China, and the State Key Project of Fundamental Research for Nano-materials and Nanostructures (2003CB716901).



Supporting information for this article is available on the WWW under <http://www.angewandte.org> or from the author.

highly luminescent, and, more importantly, ultrasensitive in both *in vitro* and *in vivo* bioassays. To find fluorophores that can meet these requirements, various semiconductor quantum dots (QDs) with tunable size-dependent emission, high quantum yields of photoluminescence (PL), broad excitation spectra, and narrow emission bandwidths have been developed and successfully applied in biological analyses.^[1–5] However, they also have intrinsic limitations. On the one hand, their inherent toxicity and chemical instability limits their application in biological detection and medical diagnosis.^[6] On the other hand, although these QDs work well under laboratory conditions, an increase in their background signal may be noted in the presence of interfering biomolecules (such as green-fluorescent proteins) and other fluorescent organic molecules that are usually present in biological and environmental samples and which can also be excited by UV radiation. The sensitivity of detection would hence be lowered. To improve the sensitivity, fluorescence resonant energy transfer (FRET) has been introduced into QD-based bioanalysis of molecular structure and protein–protein, protein–nucleic acid, and other interactions.^[7,8] Owing to the specificity and the intrinsic sensitivity of FRET to small changes in donor–acceptor distances,^[9] these FRET-QD systems have been demonstrated to show higher sensitivity. However, the inherent limitations of the fluorescence of QDs, including high background noise, potential toxicity, and instability, as mentioned above, cannot be eliminated by incorporating FRET technology and still restrict their application in the analysis of biological samples.

Hence, to find a more appropriate luminescent label remains a challenging task and is crucial to the development of modern gene technology and medical sciences. Upconversion (UC) nanophosphors, which are excited in the infrared region instead of the UV region to give emission in the visible domain, may be such an alternative. These UC nanophosphors show a high chemical stability, high quantum yields, and low toxicity, and their optical properties can be tuned by variation of lanthanide dopants and the host matrix.^[10] In particular, the fluorescence from biological samples (background) upon excitation with IR radiation is extremely low as the interfering biomolecules in question absorb in the UV (not the IR) region. All these favorable properties have indicated the great potential of UC nanoparticles in the analysis of biological and environmental samples, and especially for fluorescence imaging *in vivo*.^[11] Furthermore, if FRET technology can be coupled with bioassays based on UC nanoparticles, a further enhancement in the selectivity and sensitivity of detection can be expected. However, to the best of our knowledge, no such system has yet been reported. Herein, we demonstrate a novel biosensor for the detection of trace amounts of avidin which is based on FRET between bioconjugated UC nanoparticles and gold nanoparticles.

The UC nanoparticles we chose are $\text{Na}(\text{Y}_{1.5}\text{Na}_{0.5})\text{F}_6\text{:Yb}^{3+},\text{Er}^{3+}$. As can be seen in the spectrum shown in Figure 1a, the nanoparticles show three emission bands at $\lambda = 525, 540,$ and 655 nm , which correspond to energy-transfer processes from the excited states $^2\text{H}_{11/2}, ^4\text{S}_{3/2},$ and $^4\text{F}_{9/2}$, respectively, to the ground state $^4\text{I}_{15/2}$.^[12] However, the peak at 540 nm is the main peak, while the other peaks are very

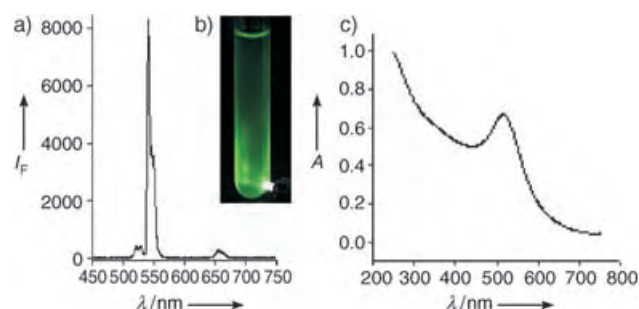


Figure 1. a) Upconversion luminescence spectrum of hexagonal-phase upconversion nanoparticles in solution upon excitation with a 980-nm laser; b) green luminescence observed from sample. c) UV/Vis absorption spectrum of 7-nm gold nanoparticles in aqueous solution.

weak in comparison, which makes it an excellent single-emission biological label. As typical organic fluorescent dyes display broad emission spectra with a long tail, an “impurity” in the form of the emission from the nanoparticles can introduce spectral cross-talk between different detection channels which thus makes them unsuitable for biological applications and creates difficulties in the quantification of the relative amounts of different probes. An ideal probe for multicolor experiments should emit at spectrally resolvable energies with a narrow, symmetric emission spectrum, and the complete set of probes should be excitable at a single wavelength.^[2] Here, the monodispersed nanoparticles emit strong and pure green fluorescence with a symmetric and narrow emission spectrum upon excitation at a single wavelength (980-nm laser), which makes them more suitable as a probe for multicolor biological detection. The strong green UC luminescence from suspensions of the nanoparticles in water upon excitation with a 980-nm laser is easily visible to the naked eye.

It is also well-known that gold nanoparticles have good absorption properties in the UV region.^[13] The 7-nm gold nanoparticles used in our experiments show a strong absorption at $\lambda \approx 520\text{ nm}$, which matches well with the UC emission of $\text{Na}(\text{Y}_{1.5}\text{Na}_{0.5})\text{F}_6\text{:Yb}^{3+},\text{Er}^{3+}$. According to the theory of FRET, when the absorption of the energy acceptor is close to the emission of the phosphor and when the donor and the acceptor are close enough, the emission of the energy donor (upconversion phosphor nanoparticles) will be quenched by the energy acceptor (gold nanoparticles). Thus it is intrinsically possible to couple the UC $\text{Na}(\text{Y}_{1.5}\text{Na}_{0.5})\text{F}_6\text{:Yb}^{3+},\text{Er}^{3+}$ nanoparticles (energy donors) with 7-nm gold nanoparticles (energy acceptors) to give a FRET biosensor.

To test the UC phosphor-based FRET biosensor, first, we functionalized the UC nanoparticles by the layer-by-layer (LbL) method^[14] to introduce an NH_2 group that can be attached to biotin. The LbL approach is based on the electrostatic attraction between the oppositely charged species deposited, and its major advantage is that it permits the preparation of coated colloids of different shapes and sizes, with uniform layers of diverse composition as well as controllable thickness.^[14] To enable the application of the green upconversion phosphors as fluorescent biological probes, the 50-nm upconversion hexagonal-phase nanoparticles were

functionalized by the LbL method (Figure 2; see also Supporting Information). Zeta potential experiments indicated that the UC nanoparticles were negatively charged under weakly basic conditions (Figure 3a), so the fabrication of the polyelectrolyte was performed at pH 8.5. The fabrica-

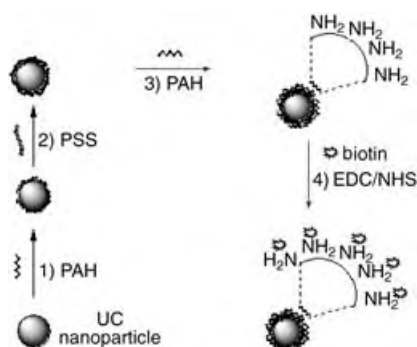


Figure 2. Schematic illustration of the functionalization of the upconversion nanoparticles. PAH = poly(allylamine hydrochloride); PSS = poly(styrene sulfonate), EDC = 1-ethyl-3-(3-dimethylaminopropyl)-carbodiimide; NHS = *N*-hydroxysuccinimide.

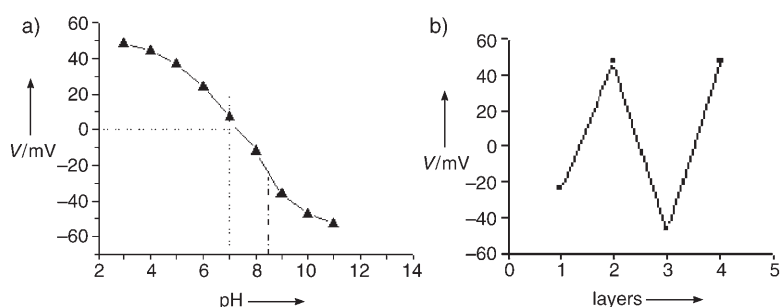


Figure 3. Zeta potentials a) of the upconversion-luminescent nanoparticles at different pH values and b) of negatively charged (under weakly basic conditions) phosphor nanoparticles as a function of the number of layers of the polyelectrolyte: 1) naked phosphor nanoparticle; 2) phosphor/PAH; 3) phosphor/PAH/PSS; 4) phosphor/PAH/PSS/PAH.

tion process slightly affected the luminescence of the phosphors. The functionalized upconversion-luminescent nanoparticles were then conjugated with biotin according to a reported procedure^[15] (see Supporting Information). The phosphor/PAH/PSS/PAH nanocomposites were characterized by analysis of the zeta potential (Figure 3b) and FTIR spectroscopy (Figure 4). The zeta potential of the nanocomposites alternated from negative to positive values with the alternating absorption of the polyelectrolyte, which indicated that PAH and PSS were absorbed alternately onto the surface of the phosphor nanoparticles. Figure 4 presents a series of peaks corresponding to the stretching vibrations of organic functional groups in the polyelectrolyte absorbed onto the phosphor nanoparticles. Strong bands at $\tilde{\nu} = 3433 \text{ cm}^{-1}$ indicate the N–H stretch for the amine group in PAH. The weak bands at $\tilde{\nu} = 1647$ and 1414 cm^{-1} result from the vibrations of the C–C skeleton of the benzene rings in PSS. The band at $\tilde{\nu} = 739 \text{ cm}^{-1}$ results from the bending

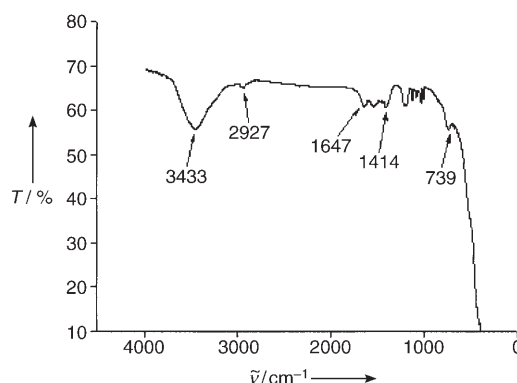


Figure 4. IR spectrum of the as-prepared phosphor/PAH/PSS/PAH nanocomposite.

vibration of the N–H bond in the primary amine in PAH which further indicates the existence of amine groups on the surface of the functionalized phosphor nanoparticles. Thus, the data from zeta potential and FTIR experiments indicated that the fabrication of phosphor/PAH/PSS/PAH nanocomposites was successful. Similarly, we prepared biotin-conjugated gold nanoparticles (Au-biotin; see Supporting Information). Thus, on the basis of Au-biotin nanoparticles and biotinylated UC phosphor nanoparticles, the FRET system was developed as shown in Figure 5.

To demonstrate the practicality of the UC nanoparticle-based FRET method, the probe was applied to the detection of trace amounts of avidin. Different concentrations of avidin were added to the mixture of the biotin-phosphor nanoparticles (80 nm) and Au-biotin nanoparticles (144 nm), and PL spectra were measured as a function of the concentration of avidin. When avidin was added, Au-biotin nanoparticles were conjugated to the surface of the UC phosphor-biotin nanoparticles through the sensitive and selective interaction between avidin and biotin. As shown in Figure 6a, the luminescence was gradually quenched with increasing amounts of avidin added to the system. Figure 6b shows the linear relationship between the relative intensity of PL (F_0/F) of the system and the concentration of avidin, wherein F_0 and F represent the intensity of luminescence in the absence and presence of different amounts of avidin, respectively. The

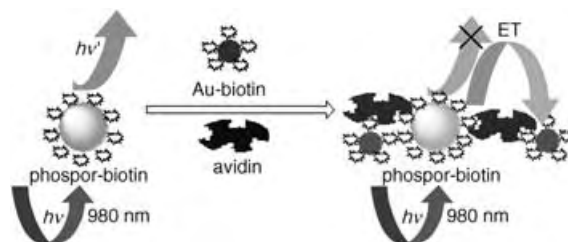


Figure 5. Scheme of the FRET system, with phosphor-biotin nanoparticles as energy donors and Au-biotin nanoparticles as energy acceptors, in the analysis of avidin. ET = energy transfer.

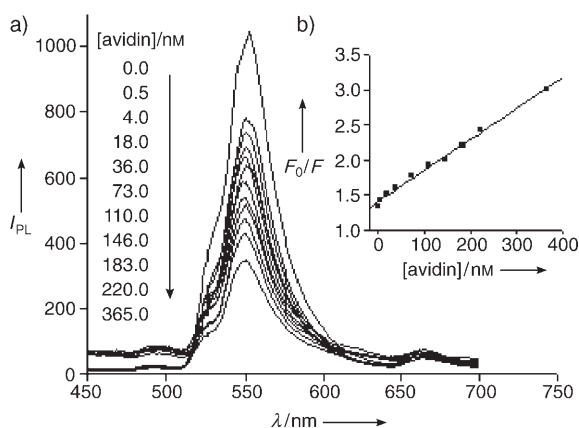


Figure 6. FRET-based assay of avidin: a) PL spectra of the FRET system at different concentrations of avidin as indicated (nM); b) linear relationship between the relative intensity of PL (F_0/F) and the concentration of avidin in the system.

intensity of upconversion luminescence varied linearly with the concentration of avidin in the solution from 0.5 nM to 370 nM. The results indicated that a FRET system based on upconversion-luminescent nanoparticles was reasonable and feasible.

To further test the FRET system based on the upconversion-luminescent nanoparticles, we also prepared $\text{Na}(\text{Y}_{1.5}\text{Na}_{0.5})\text{F}_6:\text{Yb}^{3+},\text{Tm}^{3+}$ nanoparticles using solvothermal technology. The as-prepared upconversion-luminescent $\text{Na}(\text{Y}_{1.5}\text{Na}_{0.5})\text{F}_6:\text{Yb}^{3+},\text{Tm}^{3+}$ nanoparticles emit violet fluorescence with single excitation at $\lambda = 980$ nm. These nanoparticles were also bioconjugated with biotin and applied to a FRET study using Au-biotin nanoparticles to quench the violet emission (see Supporting Information). The results showed that the FRET system based upon the single-emission upconversion nanoparticles was very efficient and versatile. Applications of the FRET system in fluorescence immunoassays, DNA detection, and fluorescence imaging are in progress.

In conclusion, hexagonal-phase $\text{Na}(\text{Y}_{1.5}\text{Na}_{0.5})\text{F}_6:\text{Yb}^{3+},\text{Er}^{3+}$ and $\text{Na}(\text{Y}_{1.5}\text{Na}_{0.5})\text{F}_6:\text{Yb}^{3+},\text{Tm}^{3+}$ nanoparticles with good crystallinity, strong single-emission upconversion fluorescence, good monodispersibility, and controllable size have been successfully prepared. The synthetic methodology also can be used to prepare other single-emission upconversion-luminescent nanoparticles. A FRET system with upconversion-luminescent nanoparticles as energy donors and gold nanoparticles as energy acceptors has been developed and applied to detect trace amounts of avidin. The results indicated that such a FRET system is sensitive and simple for use in biological analyses. Further studies may pave the way to wider applications of these upconversion phosphors in ultrasensitive multicolor detection of nucleic acids and proteins, fluorescence immunoassays, and fluorescence imaging performed in vitro and in vivo.

Experimental Section

Bioconjugation of nanoparticles: Biotin (0.1 mmol) was added to morpholine ethanesulfonic acid (MES) buffer solution (pH 6.0, 2.5 mL) containing functionalized luminescent nanoparticles

(20 mg; ≈ 50 nm), and the mixture was ultrasonicated for 10 min. Then, EDC (0.1 mmol) and NHS (0.2 mmol) were added, and the mixture was mixed slowly with a vortex stirrer for 3 h. Excess biotin, EDC, and NHS were removed by three repeated separation/wash/redispersion centrifugation cycles. The biotin-conjugated phosphors were dispersed in water (10 mL) and stored at 4°C.

Determination of avidin: Different concentrations of avidin were added to the mixture of the biotin-phosphor nanoparticles (concentration fixed at 80 nM) and biotin-Au nanoparticles (concentration fixed at 144 nM), and the mixtures were mixed thoroughly. After stirring the mixtures with a vortex stirrer at room temperature for 30 min and ultrasonication for a further 5 min, PL spectra were measured of the samples.

Received: June 2, 2005

Published online: August 24, 2005

Keywords: biosensors · FRET (fluorescence resonant energy transfer) · nanostructures · upconversion spectroscopy

- [1] W. C. W. Chan, S. Nie, *Science* **1998**, *281*, 2016–2018.
- [2] M. Bruchez, D. J. Moronne, P. Gin, S. Weiss, A. P. Alivisatos, *Science* **1998**, *281*, 2013–2016.
- [3] a) J. R. Taylor, M. M. Fang, S. Nie, *Anal. Chem.* **2000**, *72*, 1979–1986; b) R. C. Bailey, J. M. Nam, C. A. Mirkin, J. T. Hupp, *J. Am. Chem. Soc.* **2003**, *125*, 13541–13547.
- [4] E. R. Goldman, E. D. Balighian, H. Mattoussi, M. K. Kuno, J. M. Mauro, P. T. Tran, G. P. Anderson, *J. Am. Chem. Soc.* **2002**, *124*, 6378–6382.
- [5] a) S. J. Rosenthal, I. Tomlinson, E. M. Adkins, S. Schroeter, S. Adams, L. Swafford, J. McBride, Y. Wang, L. J. DeFelice, R. D. Blakely, *J. Am. Chem. Soc.* **2002**, *124*, 4586–4594; b) J. K. Jaiswal, H. Mattoussi, J. M. Mauro, S. M. Simon, *Nat. Biotechnol.* **2003**, *21*, 47–51.
- [6] a) Y. A. Wang, J. J. Li, H. Y. Chen, X. G. Peng, *J. Am. Chem. Soc.* **2002**, *124*, 2293–2298; b) M. Green, E. Howman, *Chem. Commun.* **2005**, *5*, 121–123.
- [7] a) I. L. Medintz, G. P. Anderson, M. E. Lassman, E. R. Goldman, L. A. Bettencourt, J. M. Mauro, *Anal. Chem.* **2004**, *76*, 5620–5629; b) I. L. Medintz, S. A. Trammell, H. Mattoussi, J. M. Moauro, *J. Am. Chem. Soc.* **2004**, *126*, 30–31.
- [8] D. J. Maxwell, J. R. Taylor, S. Nie, *J. Am. Chem. Soc.* **2002**, *124*, 9606–9612.
- [9] I. L. Medintz, G. P. Anderson, M. E. Lassman, E. R. Goldman, L. A. Bettencourt, J. M. Mauro, *Anal. Chem.* **2004**, *76*, 5620–5629.
- [10] S. Heer, O. Lehmann, M. Hasse, H. U. Güdel, *Angew. Chem.* **2003**, *115*, 3288–3291; *Angew. Chem. Int. Ed.* **2003**, *42*, 3179–3182.
- [11] G. S. Yi, H. C. Lu, S. Y. Zhao, Y. Ge, W. J. Yang, D. P. Chen, L. H. Guo, *Nano Lett.* **2004**, *4*, 2191–2196.
- [12] J. H. Zeng, J. Su, Z. H. Li, R. X. Yan, Y. D. Li, *Adv. Mater.*, in press.
- [13] a) T. A. Taton, C. A. Mirkin, R. L. Letsinger, *Science* **2000**, *289*, 1757–1760; b) J. J. Storhoff, R. Elghanian, R. C. Mucic, C. A. Mirkin, R. L. Letsinger, *J. Am. Chem. Soc.* **1998**, *120*, 1959–1964.
- [14] a) G. Decher, *Science* **1997**, *277*, 1232; b) D. Wang, A. L. Rogach, F. Caruso, *Nano Lett.* **2002**, *2*, 857.
- [15] a) M. A. Gilles, A. Q. Hudson, C. L. Borders, *Anal. Biochem.* **1990**, *184*, 244–248; b) J. V. Staros, R. W. Wright, D. M. Swingle, *Anal. Biochem.* **1986**, *156*, 220–222.

DOI: 10.1002/anie.200501900

Organocatalytic Diastereo- and Enantioselective Annulation Reactions—Construction of Optically Active 1,2-Dihydroisoquinoline and 1,2-Dihydrophthalazine Derivatives**

Kim Frisch, Aitor Landa, Steen Saaby, and Karl Anker Jørgensen*

The isoquinoline skeleton is found in a large number of naturally occurring and synthetic biologically active heterocyclic compounds.^[1] In particular, interesting characteristics of 1,2-dihydroisoquinolines and the closely related 1,2,3,4-tetrahydroisoquinolines have been reported. Such characteristics include the ability to act as delivery systems that transport drugs through the otherwise highly impermeable blood-brain barrier.^[2] These substances also exhibit sedative,^[3] antidepressant,^[4] antitumor, and antimicrobial activity.^[1d,5] Many of these compounds, natural or synthetic in origin, are chiral and owe their chirality to a stereogenic carbon atom located adjacent to the nitrogen atom (carbon 11b in Scheme 1).^[1,6] Herein, we present the construction of optically active 1,2-dihydroisoquinoline and -phthalazine derivatives based on the general structure shown in Scheme 1.

Scheme 1. Structural skeleton of the optically active synthesized compounds (R = CH₂OH, CHO; Z = CH, N).

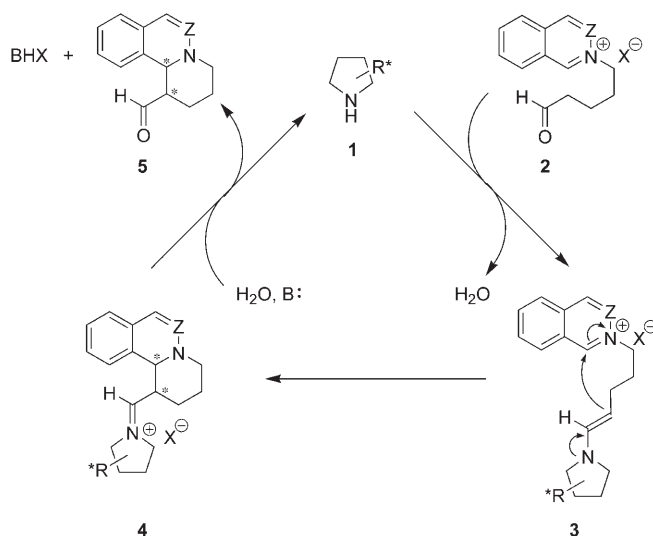
Synthetic methodologies for the formation of chiral isoquinoline derivatives either involve the use of chiral building blocks or rely on diastereoselective reactions with a stoichiometric amount of chiral sources.^[6,7a–d] To our knowledge, only few approaches are based on asymmetric catalysis.^[7e–g,8] Herein we present a novel approach based on organocatalysis employing chiral C₂-symmetric secondary amines for the diastereo- and enantioselective annulation reaction of 2-(5-oxopentyl)isoquinolinium and -phthalazinium derivatives.

Asymmetric amine catalysis has received much attention in recent years, and a large number of reactions catalyzed by chiral secondary amines have been reported.^[9,10] As 1,2-dihydroisoquinolines may be prepared by nucleophilic addition to isoquinolinium salts^[7,11] we envisioned that aldehydes

and/or ketones would be able to add to appropriate isoquinolinium salts under organocatalysis. Potentially, such a reaction would lead to the formation of optically active 1,2-dihydroisoquinoline derivatives that contain two adjacent stereocenters together with a carbonyl group suitable for further chemical transformations.

Initially, isoquinolines activated by ethyl chloroformate, were treated with, for example, 3-methylbutyraldehyde in the presence of different organocatalysts. However, all reactions studied proceeded with very low yield and stereoselectivity.

We next turned our attention to the intramolecular variant of the reaction.^[12] Scheme 2 outlines our proposal for the catalytic intramolecular annulation reaction cycle. The



Scheme 2. Mechanistic proposal for the organocatalytic asymmetric annulation reaction.

first is the reaction of the chiral amine **1** with the aldehyde of the 2-(5-oxopentyl)isoquinolinium derivative **2** which results in the formation of the corresponding enamine **3** and H₂O. Attack of the nucleophilic enamine carbon atom at the electrophilic carbon atom of the isoquinolinium moiety then results in ring closure and formation of iminium ion **4**. Finally, **4** is hydrolyzed to give the 1,2-dihydroisoquinoline derivative **5** and HX, which is scavenged by an external base to regenerate the organocatalyst.

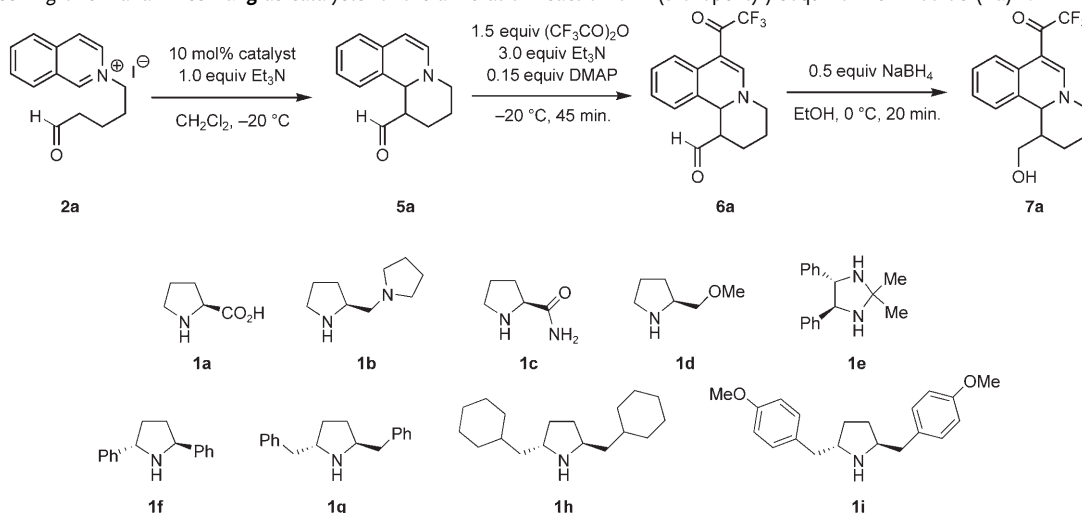
The synthetic route for model substrate 2-(5-oxopentyl)-isoquinolinium iodide (**2a**) (Scheme 2, Z = CH) used in the screening process is outlined in the Supporting Information. Table 1 presents the results for the screening of different chiral amines **1a–g** as catalysts for the annulation reaction of **2a**. It should be stressed that in all cases the reactions proceeded with good to high conversions without formation of by-products. However, the product **5a** was unstable and was protected to facilitate its isolation and full analysis.^[13] Protection of the enamine moiety of **5a** in situ using (CF₃CO)₂O gave the isolable compound **6a**, which was subsequently reduced with NaBH₄ to produce the fully analyzable alcohol **7a**.

(–)-(S)-Proline (**1a**) proved to be an effective catalyst for the annulation reaction of 2-(5-oxopentyl)isoquinolinium

[*] K. Frisch, Dr. A. Landa, Dr. S. Saaby, Prof. Dr. K. A. Jørgensen
The Danish National Research Foundation: Center for Catalysis
Department of Chemistry, Aarhus University
8000 Aarhus C (Denmark)
Fax: (+45) 8919-6199
E-mail: kaj@chem.au.dk

[**] This work was made possible by a grant from The Danish National Research Foundation. A.L. thanks Eusko Jaurilitza/Gobierno Vasco for financial support (postdoctoral fellowship). Thanks are expressed to Dr. Jacob Overgaard from the Department of Chemistry, University of Aarhus for performing the X-ray crystallographic analysis.

Supporting information for this article is available on the WWW under <http://www.angewandte.org> or from the author.

Table 1: Screening of chiral amines **1a–g** as catalysts for the annulation reaction of 2-(5-oxopentyl)isoquinolinium iodide (**2a**)^[a].


Entry	Catalyst	<i>t</i> [min]	Conversion [%] ^[b]	d.r. (<i>trans</i> : <i>cis</i>) ^[c]	<i>ee</i> [%] ^[d]
1 ^[e]	1a	20	95	2:1	rac
2	1b	5	88	2:1	rac
3	1c	90	40	2:1	7
4	1d	10	92	2:1	11
5	1e	180	40	3:1	rac
6	1f	90	47	8:1	8
7	1g	190	94	8:1	84

[a] All reactions were performed on a 0.20-mmol scale. [b] The conversion of **2a** into **5a** was estimated by ¹H NMR spectroscopy. [c] Determined by ¹H NMR spectroscopy. The *trans*/*cis* ratio refers to the relationship between 1-H and 11 b-H. [d] The *ee* value of the major diastereomer of compound **7a** was determined by chiral HPLC. [e] The reaction was performed at room temperature.

iodide **2a** with almost full conversion into the desired product **5a** after 20 min at room temperature (Table 1, entry 1). However, the diastereoselectivity of the reaction was low, and the two diastereomers were formed as racemates. For the catalysts **1b–e**, the annulation reaction also proceeded with low diastereo- and enantioselectivity (Table 1, entries 2–5). Improved diastereoselectivities were observed for the catalysts (2*S*,5*S*)-2,5-diphenylpyrrolidine (**1f**) and (2*S*,5*S*)-2,5-dibenzylpyrrolidine (**1g**). However, whereas **1f** gave very low enantioselectivity, catalyst **1g** produced the major diastereomer with 84 % *ee* (Table 1, entries 6 and 7). A number of solvents were also screened for the annulation reaction of **2a** catalyzed by **1g**. In all cases high conversions (> 75 %) were observed; however, the stereoselectivity of the annulation reaction performed in CH₂Cl₂ was superior.^[14]

Table 2 summarizes the results obtained from the screening of external bases in the annulation reaction of **2a**. In the absence of an external base, the reaction did not proceed (Table 2, entry 2). Furthermore, a 1:1 ratio of the amount of added base and the amount of formed product resulted (Table 2, entry 3 vs. 1). A possible explanation for these observations is protonation of the catalyst which renders it unreactive. Also, compound **5a** could revert back to **2a** owing to the presence of HI. The essential external base also promotes a racemic background reaction in the absence of the chiral amine catalyst (Table 2, entry 4), and dropwise addition of Et₃N over the course of 4 h resulted in a significant improvement only in the diastereoselectivity (Table 2, entry 5 vs. 1). Application of a stronger base, such as DBU, resulted in

Table 2: Screening of external bases for the organocatalytic annulation reaction of **2a** catalyzed by **1g**.^[a]

Entry	External base (equiv)	<i>t</i> [h]	Conv. [%] ^[b]	d.r. ^[c]	<i>ee</i> [%] ^[d]
1	Et ₃ N (1.0)	3	94	8:1	84
2	none	5	0	–	–
3	Et ₃ N (0.15)	5	15	n.d.	n.d.
4 ^[e]	Et ₃ N (1.0)	3	25	> 98:2	rac
5 ^[f]	Et ₃ N (1.0)	4	94	12:1	86
6	DBU (1.0)	0.5	94	10:1	7
7	DIPEA (1.0)	o.n. ^[g]	92	10:1	84
8	quinuclidine (1.0)	1	94	12:1	78
9	<i>N</i> -methylmorpholine (1.0)	96	37	8:1	44
10	2,6-di- <i>tert</i> -butylpyridine (1.0)	96	0	–	–

[a] All reactions were performed at –20 °C in the presence of **1g** (10 mol %) in CH₂Cl₂ on a 0.20 mmol scale. [b] The conversion of **2a** into **5a** was estimated by ¹H NMR spectroscopy. [c] Determined by ¹H NMR spectroscopy of **7a** (the *trans*/*cis* ratio refers to the relationship between 1-H and 11 b-H). [d] The *ee* value of the major diastereomer of compound **7a** was determined by chiral HPLC. [e] Reaction performed without a catalyst. [f] Slow addition of the external base. [g] Overnight reaction.

a conversion and diastereomeric ratio similar to those obtained with Et₃N. However, the reaction was almost racemic, therefore indicating that the background reaction caused by the achiral base superseded the chiral-amine-catalyzed reaction (Table 2, entry 6). The use of bases of similar strength to that of Et₃N, such as diisopropylethylamine (DIPEA) and quinuclidine, resulted in a higher diastereo-

meric ratio, whereas the conversion and enantioselectivity were either unaltered or lower (Table 2, entries 7, 8 vs. 1). A decrease in the strength of the added base had a significant effect on the conversion of the reaction. The use of *N*-methylmorpholine resulted in a slow reaction and the production of compound **5a** with low conversion and low enantiomeric excess, whereas 2,6-di-*tert*-butylpyridine gave no conversion at all (Table 2, entries 9 and 10, respectively). In conclusion, 1 equivalent of Et₃N as an external base proved to be optimal for the annulation reaction.

Table 3 summarizes the results of the annulation reaction of **2a** catalyzed by C₂-symmetric disubstituted pyrrolidines **1g**–

Table 3: Catalyst modifications and screening of catalyst loading and reaction temperature for the annulation reaction of 2-(5-oxopentyl)-isoquinolinium iodide **2a**^[a].

Entry	Cat.	<i>t</i> [h]	<i>T</i> [°C]	Loading [mol %]	Conv. [%] ^[b]	d.r. ^[c]	<i>ee</i> [%] ^[d]
1	1g	4.5	–20	2	95	9:1	41
2	1g	3	–20	5	94	9:1	71
3	1g	3	–20	10	94	8:1	84
4	1g	3	–20	20	94	8:1	87
5	1g	<i>o.n.</i> ^[e]	–40	10	94	15:1	92
6	1h	6	–20	10	90	7:1	36
7	1i	<i>o.n.</i> ^[e]	–40	10	96	15:1	88

[a] All reactions were performed in the presence of Et₃N (1 equiv) in CH₂Cl₂. Entry 1 was performed on a 0.40-mmol scale, entries 2–7 on a 0.20-mmol scale. [b] The conversion of **2a** into **5a** was estimated by ¹H NMR spectroscopy. [c] Determined by ¹H NMR spectroscopy of **7a** (the *trans/cis* ratio refers to the relationship between 1-H and 11 b-H). [d] The *ee* value of the major diastereomer of compound **7a** was determined by chiral HPLC. [e] Overnight reaction.

i under various reaction conditions. The conversion and diastereoselectivity of the annulation reaction were found to be independent of the catalyst loading (Table 3, entries 1–4). However, a significant drop in the enantiomeric excess (indicating considerable involvement of the racemic background reaction caused by the external base) was observed with low catalyst loadings. An increase in the catalyst loading from 10 to 20 mol% did not significantly improve the stereoselectivity (Table 3, entries 1–4). A decrease in the reaction temperature from –20 to –40 °C maintained a high conversion of the reaction, but resulted in a significant increase in both the diastereo- and enantioselectivity to 15:1 and 92 % *ee*, respectively (Table 3, entry 5 vs. 3).

The dependence of the structural and electronic properties of **1g** on the stereoselectivity of the reaction was also investigated. Replacement of the phenyl groups of **1g** by bulky non-aromatic groups, such as cyclohexyl groups (catalyst **1h**), did not change the diastereoselectivity of the reaction. However, catalyst **1h** was slightly less active than catalyst **1g**, and the enantioselectivity decreased significantly (Table 3, entry 6 vs. 3). The effect of the electron density of the aromatic substituents was tested by applying a catalyst with electron-donating substituents such as (2*S*,5*S*)-2,5-bis(4-methoxybenzyl)pyrrolidine (**1i**). The results in Table 3, entry 7 show that no significant changes in the outcome of the reaction were observed when **1i** was applied as catalyst.

With the optimized conditions for the catalytic diastereo- and enantioselective annulation reaction at hand, the scope and limitation of the system was investigated (Table 4). In general, the annulation reactions proceeded with good to high conversions (70–100 %), high diastereoselectivity (d.r. ≥ 15:1) and excellent enantioselectivity (85–96 % *ee*). Products with functional groups suitable for further manipulations were obtained (Table 4, entries 2 and 4), and the scope of the annulation reaction could be extended beyond isoquinolinium salts to substrates based on the phenanthridine and phthalazine skeleton (Table 4, entries 5 and 6). Limitations of the reaction were observed for substrates based on the electron-rich isoquinolines 5,7-dimethoxyisoquinoline (Table 4, entry 7) and 6,7-dimethoxyisoquinoline (the latter gave < 10 % conversion after several days).

The reported yields are for two (Table 4, entries 3, 5, and 6) or three (Table 4, entries 1, 2, 4, and 7) reaction steps that were performed to obtain compounds that could be isolated and fully analyzed.^[15] Additionally, although the final products **7a–g** were obtained in low yields, the conversions of **2a–g** into **5a–g** in the catalytic enantioselective annulation step were high. With the exception of substrate **2g** (Table 4, entry 7), the catalytic annulation reaction proceeded without the formation of by-products.

Compound **7b** was obtained as a white solid, which after a single recrystallization from CH₂Cl₂ and hexane gave crystals suitable for X-ray crystallographic analysis.^[16] The analysis revealed that the absolute configurations of the newly formed stereocenters at C1 and C11b could both be described as *S* (Figure 1).

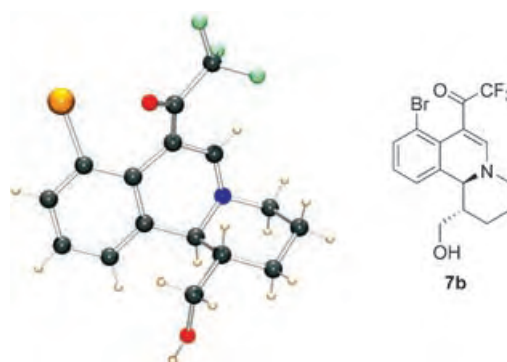


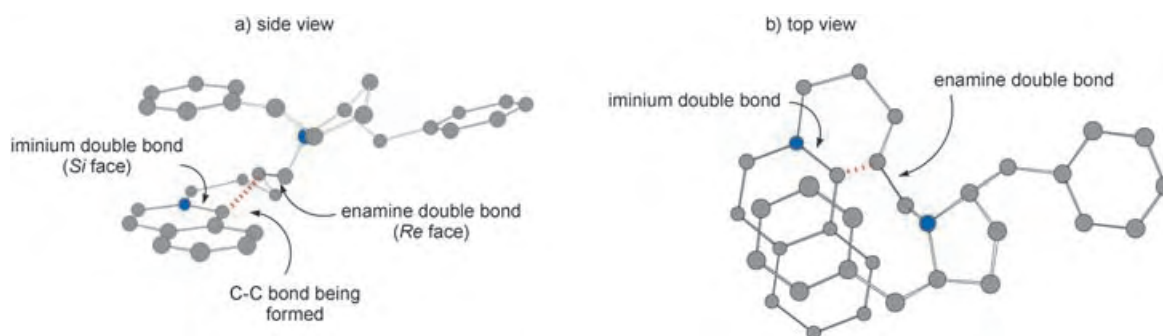
Figure 1. X-ray crystal structure of compound **7b**.

A proposal for the transition state involved in the stereoselective step of the annulation reaction is presented in Figure 2. In this transition state a favorable interaction between the isoquinolinium moiety and a phenyl ring of the catalyst—a cation– π interaction^[17]—was anticipated. The phenyl ring, positioned parallel to and above the cationic isoquinolinium moiety with a face-to-face interaction,^[17a–c] allows the *Re* face of the enamine double bond to approach the *Si* face of the iminium double bond without significant steric hindrance. With this approach, the annulation reaction results in the product with 1*S* and 11 *bS* configurations at the formed stereocenters in accordance with the experimental observation.

Table 4: Scope and limitation of the organocatalytic annulation reaction catalyzed by **1g**.^[a]

Entry	Substrate	Product	Conv. [%] ^[b]	Yield [%] ^[c]	d.r. ^[d]	ee [%] ^[e]
1			94	41	15:1	92
2			70	40	24:1	92
3			70	18	16:1	85
4			100	38	36:1	93
5			100	73	> 98:2	96
6			100	59	> 98:2	93
7			50	18	10:1	49

[a] All reactions were performed at -40°C in the presence of **1g** (10 mol%) and Et_3N (1.0 equiv) in CH_2Cl_2 on a 0.40 mmol scale. Reaction were carried out overnight (15–21 h) for entries 1–6. For entry 7 the reaction time was 10 days. [b] The conversion of **2a–g** into **5a–g** was estimated by ^1H NMR spectroscopy. [c] Yields of isolated compounds **7a–g** based on **2a–g**, respectively. [d] Determined by ^1H NMR spectroscopy of compounds **5a–g** or **6a–g** (the *trans/cis* ratio refers to the relationship between 1-H and 11 b-H). [e] The *ee* values of the major diastereomer of compounds **7a–g** were determined by chiral HPLC.


Figure 2. Proposed transition state in the annulation reaction catalyzed by **1g**.

In conclusion, we have developed the first organocatalytic diastereo- and enantioselective annulation reaction of 2-(5-oxopentyl)isoquinolinium derivatives. The reactions generally proceed with good to high conversions (70–100%), high diastereoselectivities (d.r. \geq 15:1), and good to excellent enantioselectivities (85–96% *ee*). The scope of the annulation reaction is demonstrated in the synthesis of a series of optically active 1,2-dihydroisoquinoline and -phthalazine derivatives. The stereochemical outcome of the organocatalytic asymmetric annulation reaction is explained on the basis of a favourable cation– π interaction between the isoquinolinium moiety and one of the phenyl rings of the catalyst.

Received: June 1, 2005

Published online: August 26, 2005

Keywords: annulation · isoquinolines · nitrogen heterocycles · organocatalysis · phthalazines

- [1] a) K. W. Bentley, *The Isoquinoline Alkaloids*, 1st ed., Pergamon, London, 1965; b) K. W. Bentley, *Nat. Prod. Rep.* **2001**, 18, 148; c) J. P. Michael, *Nat. Prod. Rep.* **2002**, 19, 742, and references therein; d) J. D. Scott, R. M. Williams, *Chem. Rev.* **2002**, 102, 1669; e) *Comprehensive Medicinal Chemistry*, Vol. 3, 1st ed. (Eds.: C. Hansch, P. G. Sammes, J. B. Taylor), Pergamon, Oxford, **1990**.
- [2] For example, see: a) E. Pop, W.-M. Wu, E. Shek, N. Bodor, *J. Med. Chem.* **1989**, 32, 1774; b) M. M. Sheha, N. A. El-Koussi, H. Farag, *Arch. Pharm. Pharm. Med. Chem.* **2003**, 1, 47; c) S. Mahmoud, T. Aboul-Fadl, H. Farag, A.-M. I. Mouhamed, *Arch. Pharm. Pharm. Med. Chem.* **2003**, 336, 573; d) L. Prokai, K. Prokai-Tatrai, N. Bodor, *Med. Res. Rev.* **2000**, 20, 367.
- [3] E. Lukevics, I. Segal, A. Zablotkaya, S. Germane, *Molecules* **1997**, 2, 180.
- [4] a) B. E. Maryanoff, D. F. McComsey, J. F. Gardocki, R. P. Shank, M. J. Costanzo, S. O. Nortey, C. R. Schneider, P. E. Setler, *J. Med. Chem.* **1987**, 30, 1433; b) K. L. Sorgi, C. A. Maryanoff, D. F. McComsey, D. W. Graden, B. E. Maryanoff, *J. Am. Chem. Soc.* **1990**, 112, 3567.
- [5] a) L. F. Tietze, N. Rackehmann, I. Müller, *Chem. Eur. J.* **2004**, 10, 2722, and references therein; b) H.-J. Knölker, S. Agarwal, *Tetrahedron Lett.* **2005**, 46, 1173, and references therein.
- [6] a) M. Chrzanowska, M. D. Rozwadowska, *Chem. Rev.* **2004**, 104, 3341; b) A. I. Meyers, D. A. Dickman, M. Boes, *Tetrahedron* **1987**, 43, 5095; c) J. Royer, M. Bonin, L. Micouin, *Chem. Rev.* **2004**, 104, 2311.
- [7] For example, see: a) N. Cabedo, I. Andreu, M. C. Ramirez-de Arellano, A. Chagraoui, A. Serrano, A. Bermejo, P. Protais, D. Cortes, *J. Med. Chem.* **2001**, 44, 1794; b) T. Itoh, K. Nagata, M. Miyazaki, K. Kameoka, A. Ohsawa, *Tetrahedron* **2001**, 57, 8827; c) J.-J. Youte, D. Barbier, A. Al-Mourabit, D. Gnecco, C. Marazano, *J. Org. Chem.* **2004**, 69, 2737; d) D. Barbier, C. Marazano, C. Riche, B. C. Das, P. Potier, *J. Org. Chem.* **1998**, 63, 1767; e) M. Takamura, K. Funabashi, M. Kanai, M. Shibasaki, *J. Am. Chem. Soc.* **2000**, 122, 6327; f) M. Takamura, K. Funabashi, M. Kanai, M. Shibasaki, *J. Am. Chem. Soc.* **2001**, 123, 6801; g) K. Funabashi, H. Ratni, M. Kanai, M. Shibasaki, *J. Am. Chem. Soc.* **2001**, 123, 10784; h) O. Sieck, M. Ehwald, J. Liebscher, *Eur. J. Org. Chem.* **2005**, 663.
- [8] a) Y. Sato, T. Nishimata, M. Mori, *J. Org. Chem.* **1994**, 59, 6133; b) T. Ooi, M. Takeuchi, K. Maruoka, *Synthesis* **2001**, 1716; c) K. Ito, S. Akashi, B. Saito, T. Katsuki, *Synlett* **2003**, 1809; d) M. S. Taylor, E. N. Jacobsen, *J. Am. Chem. Soc.* **2004**, 126, 10558.
- [9] For example, see: a) P. I. Dalko, L. Moisan, *Angew. Chem.* **2004**, 116, 5248; *Angew. Chem. Int. Ed.* **2004**, 43, 5138; b) A. Berkessel, H. Gröger, *Asymmetric Organocatalysis*, Wiley-VCH, Weinheim, 2004; c) J. Seayad, B. List, *Org. Biomol. Chem.* **2005**, 3, 719.
- [10] For example, see: Mannich reaction: a) B. List, *J. Am. Chem. Soc.* **2000**, 122, 9336; b) B. List, P. Pojarliev, W. T. Biller, H. J. Martin, *J. Am. Chem. Soc.* **2002**, 124, 827; c) A. Córdova, S. Watanabe, F. Tanaka, W. Notz, C. F. Barbas III, *J. Am. Chem. Soc.* **2002**, 124, 1866; d) A. Córdova, *Acc. Chem. Res.* **2004**, 37, 102; aldol: e) B. List, R. A. Lerner, C. F. Barbas III, *J. Am. Chem. Soc.* **2000**, 122, 2395; f) K. Sakthivel, W. Notz, T. Bui, C. F. Barbas III, *J. Am. Chem. Soc.* **2001**, 123, 5260; g) A. B. Northrup, D. W. C. MacMillan, *J. Am. Chem. Soc.* **2002**, 124, 6798, amination: h) B. List, *J. Am. Chem. Soc.* **2002**, 124, 5656; i) A. Bøgevig, K. Juhl, N. Kumaragurubaran, W. Zhuang, K. A. Jørgensen, *Angew. Chem.* **2002**, 114, 1868; *Angew. Chem. Int. Ed.* **2002**, 41, 1790; j) N. Kumaragurubaran, K. Juhl, W. Zhuang, A. Bøgevig, K. A. Jørgensen, *J. Am. Chem. Soc.* **2002**, 124, 6254; aminoxylation/hydroxylation: k) G. Zhong, *Angew. Chem.* **2003**, 115, 4379; *Angew. Chem. Int. Ed.* **2003**, 42, 4247; l) S. P. Brown, M. P. Brochu, C. J. Sinz, D. W. C. MacMillan, *J. Am. Chem. Soc.* **2003**, 125, 10808; m) H. Sundén, M. Engqvist, J. Casas, I. Ibrahim, A. Córdova, *Angew. Chem.* **2004**, 116, 6532; *Angew. Chem. Int. Ed.* **2004**, 43, 6694; chlorination: n) M. P. Brochu, S. P. Brown, D. W. C. MacMillan, *J. Am. Chem. Soc.* **2004**, 126, 4108; o) N. Halland, A. Brautun, S. Bachmann, M. Marigo, K. A. Jørgensen, *J. Am. Chem. Soc.* **2004**, 126, 4790; p) M. Marigo, S. Bachmann, N. Halland, A. Brautun, K. A. Jørgensen, *Angew. Chem.* **2004**, 116, 5623; *Angew. Chem. Int. Ed.* **2004**, 43, 5507; sulfenylation: q) M. Marigo, T. C. Wabnitz, D. Fielenbach, K. A. Jørgensen, *Angew. Chem.* **2005**, 117, 804; *Angew. Chem. Int. Ed.* **2005**, 44, 794; fluorination: r) M. Marigo, D. Fielenbach, A. Brautun, A. Kjærgaard, K. A. Jørgensen, *Angew. Chem.* **2005**, 117, 3769; *Angew. Chem. Int. Ed.* **2005**, 44, 3703; s) D. D. Steiner, N. Mase, C. F. Barbas III, *Angew. Chem. Int. Ed.* **2005**, 117, 3772; *Angew. Chem. Int. Ed.* **2005**, 44, 3706; t) T. D. Beeson, D. W. C. MacMillan, *J. Am. Chem. Soc.* **2005**, 127, 8826.
- [11] For example, see: a) A. Reissert, *Ber. Dtsch. Chem. Ges.* **1905**, 38, 1603; b) K.-Y. Akiba, K. Araki, M. Nakatani, M. Wada, *Tetrahedron Lett.* **1981**, 22, 49, 4961; c) K.-Y. Akiba, M. Nakatani, M. Wada, Y. Yamamoto, *J. Org. Chem.* **1985**, 50, 63; d) A. Dondoni, T. Dall'Occo, G. Galliani, A. Mastellari, F. Medici, *Tetrahedron Lett.* **1984**, 25, 3637; e) R. Yamaguchi, B. Hatano, T. Nakayasu, S. Kozima, *Tetrahedron Lett.* **1997**, 38, 403; f) L. N. Babichenko, A. A. Tolmachev, T. S. Chmilenko, A. K. Sheinkman, *Chem. Heterocycl. Compd. (Engl. Transl.)* **1988**, 582; g) R. Lavilla, T. Gotsens, M. Guerrero, C. Masdeu, M. C. Santano, C. Minguillón, J. Bosch, *Tetrahedron* **1997**, 53, 13959; h) J. L. Díaz, M. Miguel, R. Lavilla, *J. Org. Chem.* **2004**, 69, 3550; i) M. A. A. Meziane, J. P. Bazureau, *Molecules* **2002**, 7, 252. See also: j) W. Benson, E. Winterfeldt, *Chem. Ber.* **1979**, 112, 1913; k) A. I. Meyers, D. B. Miller, F. H. White, *J. Am. Chem. Soc.* **1988**, 110, 4778.
- [12] R. M. Wilson, F. DiNinno, Jr., *Tetrahedron Lett.* **1970**, 289.
- [13] Compound **5a** was stable enough in solution for characterization by ¹H NMR spectroscopy.
- [14] In THF results similar to those observed for CH₂Cl₂ were obtained (95% conversion, d.r. = 7:1 and 80% *ee* at 0°C); MeCN also led to reasonable results (94% conversion, d.r. = 6:1 and 77% *ee* at –20°C).
- [15] Compounds **7c** and **7g** were slightly unstable, which can account for the lower yield of isolation of these compounds.
- [16] The Cambridge Crystallographic Data Centre (CCDC) contains the supplementary crystallographic data for this paper. These data can be obtained free of charge from the CCDC via www.ccdc.cam.ac.uk/data_request/cif.

- [17] For cation- π interactions in related systems, see, for example: a) S. Yamada, C. Morita, *J. Am. Chem. Soc.* **2002**, *124*, 8184; b) T. Kawabata, M. Nagato, K. Takasu, K. Fujii, *J. Am. Chem. Soc.* **1997**, *119*, 3169; c) D. L. Comins, S. P. Joseph, R. R. Goehring, *J. Am. Chem. Soc.* **1994**, *116*, 4719; for reviews on cation- π or π - π interactions, see: d) J. C. Ma, D. A. Dougherty, *Chem. Rev.* **1997**, *97*, 1303; e) C. A. Hunter, K. R. Lawson, J. Perkins, C. J. Urch, *J. Chem. Soc. Perkin Trans. 2* **2001**, 651.

Metal–Organic Frameworks

DOI: 10.1002/anie.200462674

Crystal Engineering: Toward Intersecting Channels from a Neutral Network with a bcu-Type Topology**

Tzuoo-Tsair Luo, Hui-Lien Tsai, Shang-Li Yang,
Yen-Hsiang Liu, R. Dayal Yadav, Chan-Cheng Su,
Chuen-Her Ueng, Lee-Gin Lin, and Kuang-Lieh Lu*

A great deal of interest has developed in the synthesis of metal–organic coordination polymers as they offer opportunities for preparing materials with controllable functionalities.^[1] Although remarkable progress has been made in this new field of chemistry and materials science, largely due to efficient design strategies,^[2,3] it is still difficult to prepare metal–organic frameworks with predictable topologies, even structures composed of simple inorganic salts.^[4] The mimicking of topologies of natural minerals has rapidly become one of the most challenging issues in the design of metal–organic frameworks.^[3c] Many 3D structures with mineral topologies such as NbO, quartz, pyrite, rutile, sodalite, CdSO₄, and halite^[5] have been reported recently from attempts to obtain geometric characteristics with designable functionalities. From the reported characterization of the net topologies,^[6]

all of these networks are based on the use of three-, four-, or six-connected building blocks.^[5] Connectivities of five, seven, or eight are extremely rare as a result of limitations in the symmetry or steric hindrance associated with connected nodes.^[7,8] Although the body-centered cubic (bcu) net^[8a-c] and the fluorite (flu) net^[8d] are commonly seen in textbooks, such topologies with eight connecting nodes in a cubic geometry have only appeared in a few examples. To fulfill their geometric limitations, an eight-coordinated metal center or an eight-connecting polynuclear metal cluster block would be required; neither is easily achieved.^[8] The former has been obtained with eight-coordinated lanthanide ions or [M(CN)₈]^{4−} to form the bcu-type net,^[8a,b] and the latter by using an eight-connecting cluster containing a tetracadmium carboxylate moiety and a four-connecting ligand to form the flu-type net. However, the bcu-type topology with only an eight-connecting polynuclear metal cluster unit has not yet been realized.

As part of our ongoing efforts in the design and synthesis of functional crystalline materials,^[3e] we report herein the rare, porous bcu-type framework of {[Cu₃Cl₂(4-ptz)₄(H₂O)₂·3DMF·5H₂O]_n} (1), assembled from 5-(4-pyridyl)-tetrazolate (4-ptz) as a bridging ligand and an eight-connecting tricopper cluster (Cu₃Cl₂⁴⁺ = Cu₃ cluster) as a building block. To the best of our knowledge, this is the first bcu-type structure with an eight-connecting polynuclear metal cluster unit, and represents one of the highest connected topologies known for coordination polymers. The appropriate choice of an organic ligand with specific functional groups and geometry is also a major factor in achieving this target. The reasons for using the 4-ptz ligand are twofold: first, the tetrazole group is a widely known alternative to a carboxylate moiety, and second, the five-membered heterocyclic tetrazole group, which contains four N donors and a pyridine group, could serve both as a potential active coordination site and a hydrogen-bond acceptor, thus permitting the polymeric framework to be expanded through hydrogen-bonding interactions. Interestingly, until now, such coordination polymers based on tetrazole derivatives^[9,10] have not been extensively studied, in contrast to metal carboxylates.^[1e] Inspired by the work of Sharpless and co-workers,^[11] the preparation of 5-substituted 1*H*-tetrazoles is now a safe and convenient route. Nevertheless, the generation of tetrazole-based coordination polymers would be a new and potentially useful research theme, which is currently in its infancy.

Compound 1 was synthesized by the reaction of copper(II) chloride and 5-(4-pyridyl)tetrazole (4-H-ptz) in DMF at ambient temperature in high yield by a single-step self-organization process (Scheme 1). The asymmetric unit consists of two Cu^{II} centers, one bridging chloride ion, one 4-ptz ligand, one coordinated water molecule, and other disordered guest molecules (Figure 1a). An analysis of the local symmetry of the two nonequivalent Cu centers reveals that the Cu1 center resides on a special symmetry site (SOF = 0.25) containing three mutually perpendicular twofold axes of rotation, and the Cu2 center resides on the other special symmetry site (SOF = 0.5) containing a twofold axis of rotation. Cu1 is bound to four tetrazole nitrogen atoms and two bridging chlorine atoms, and Cu2 is bound to two

[*] Prof. Dr. Y.-H. Liu, Dr. R. D. Yadav, Prof. Dr. K.-L. Lu
Institute of Chemistry, Academia Sinica, Taipei 115 (Taiwan)
Fax: (+886) 2-27831237
E-mail: lu@chem.sinica.edu.tw

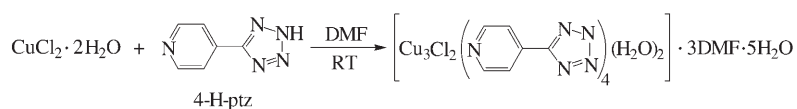
T.-T. Luo, Prof. Dr. C.-C. Su, Prof. Dr. C.-H. Ueng
Department of Chemistry, National Taiwan Normal University
Taipei 116 (Taiwan)

Prof. Dr. H.-L. Tsai
Department of Chemistry, National Cheng Kung University
Tainan 701 (Taiwan)

S.-L. Yang, Prof. Dr. L.-G. Lin
Department of Chemistry, Chinese Culture University
Taipei 111 (Taiwan)

[**] We are grateful to the Academia Sinica and the National Science Council, Taiwan, for financial support of this research. bcu = body-centered cubic.

Supporting information for this article is available on the WWW under <http://www.angewandte.org> or from the author.



Scheme 1. Synthesis of **1** by a one-step organization; DMF = *N,N*-dimethylformamide.

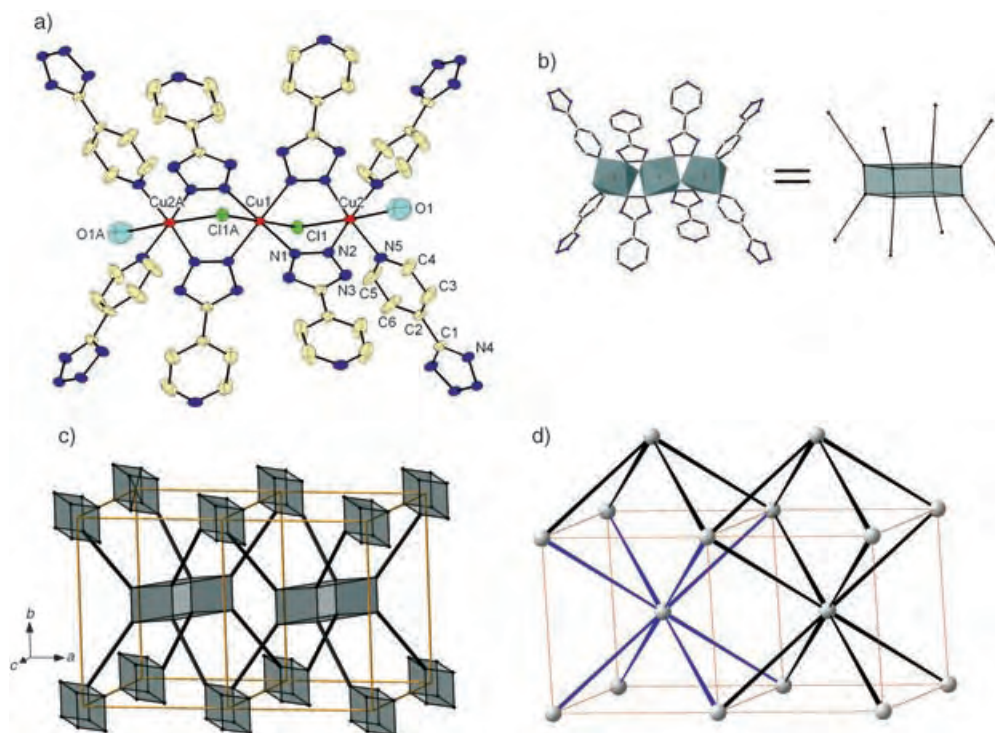


Figure 1. a) Local coordination environment of Cu^{II} in **1** (atoms are represented as 30% thermal ellipsoids); hydrogen atoms and disordered molecules have been omitted for clarity. b) Simplified view of an eight-connected Cu_3 -cluster subunit. c) Perspective view of the network of **1** simplified according from part (b). d) The body-centered cubic lattice net (bcu net).

tetrazole nitrogen atoms, two pyridyl nitrogen atoms, one bridging chlorine atom, and one coordinated water molecule. The two nonequivalent Cu atoms adopt a distorted octahedral ($\text{Cu1Cl}_2\text{N}_4$) and ($\text{Cu2ClN}_4\text{O}$) coordination geometry, respectively. The tetrazole ligands adopt a bridging mode with a coordinating pyridyl group and a μ_2, η^2 -tetrazolato bridge. The copper–copper separation, bridged by the chloride and tetrazole moiety of the 4-ptz ligands, is 3.545(1) Å. Each 4-ptz ligand coordinates through the 1,2-nitrogen atoms of the tetrazole group and the pyridyl nitrogen atom. Each Cu2 atom is weakly coordinated by a water molecule ($\text{Cu}–\text{O} = 2.890(3)$ Å) resulting from a strong Jahn–Teller effect. Except for the coordinated water molecules, all donor atoms form reasonably strong bonds with the copper atoms. All of the $\text{Cu}–\text{N}$ distances are in the range between 2.015(3) and 2.024(3) Å.

From further analysis of the structure of **1**, five unique features are apparent: 1) a three-dimensional neutral network with a bcu-type topology; 2) eight-connected Cu_3 -cluster-building subunits; 3) large octahedron-shaped chambers; 4) potential functionalization sites on the copper atoms; 5) nanoscale open windows and a 3D intersecting channel system with an extra-framework volume of 57%.

The bcu-type topology of **1** is as follows: the motif of the Cu_3 cluster connected to eight 4-ptz linkers is represented by a box connected with eight bars (Figure 1b). The positions of the eight connecting nodes correspond to the four pyridyl nitrogen atoms and the centers of the 2,3-nitrogen atoms of the tetrazole group, which results in an eight-connected net with the Schlafli symbol $\{4^{24}6^4\}$ that resembles the topology of a bcu net (Figure 1c, d). To fulfill a bcu-type topology, our design strategies were focused on the selection of clusters with eight connectivities as secondary building units (SBUs)^[12] as they provide a suitable geometry that permits the target structures to be constructed. The assembly of the eight-connected Cu_3 clusters and the tetrazolate ligand successfully forms the first example of a neutral body-centered-type metal–organic framework. Owing to limitations in geometry, the angle of the unit cell diagonals is distorted from 90° to 75.8° and the symmetry of the crystal system is lowered from cubic to orthorhombic (see Supporting Information).

As a result of the geometry of the bcu-type net, the combination of channels running parallel and perpendicular to each other gives rise to large pockets of extra-framework space. Considering the octahedron-shaped chamber (Figure 2a) in the

framework, the diagonal distances of the chamber are 15.507(0) Å ($\text{Cu1}–\text{Cu1}$) and 19.917(3) Å ($\text{Cu1}–\text{Cu1}$). Such a

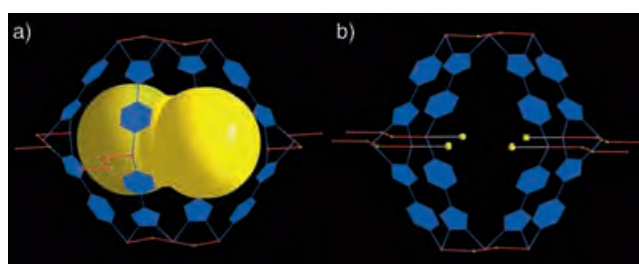


Figure 2. Views of the octahedron-shaped chamber: a) A few large van der Waals spheres with diameters of about 5.78–7.14 Å inside. b) Weakly coordinated water molecules on Cu_3 clusters act as removable shutters.

chamber, with an inner void space, can accommodate at least two van der Waals spheres with maximum diameters of up to 7.14 Å without coming into contact with the framework. The calculated density (in the absence of guests) of compound **1** is 0.99 g cm^{−3}. Analysis with the PLATON^[13] software tool

indicates that the extra-framework volume per unit cell is approximately 57%. The use of the “CAVITY” routine in PLATON indicates that the six largest voids are located at (0.3, 0, 0.625) and other symmetric sites with diameters of 7.14 Å, four other middle voids at (0, 0.5, 0) with diameters of 5.84 Å, and so on, with fourteen other cavities with diameters in the range of 5.78–5.04 Å (van der Waals surfaces considered). Furthermore, the overall shape of the void does not allow the packing of spheres larger than 7.14 Å, although several spheres with different diameters can be accommodated by the same large elongated void. The void is actually a large ellipsoid with a total volume of 1775 Å³. These large free spaces within the framework cause the structure to be highly porous. In addition, four weakly coordinated water molecules serve to gate the chamber (Figure 2b). The O1–O1 distance is 4.63(1) Å, and the naked Cu2–Cu2 distance is 10.338(1) Å. Therefore, the chamber is a potential candidate for a micro-reactor with metal-containing active sites. These sites in crystalline porous materials have functionalities that could permit molecular recognition, catalysis, or gas storage.^[3f]

An inspection of Figure 3 reveals that the overall array contains a 3D intersecting channel system and nanoscale open windows, with an approximate diameter of up to 10 Å. Notably, the 3D intersecting channels, which frequently occur in zeolites, are constructed by the interconnection of 1D channels from different directions. Coordination polymers with 3D intersecting channels are often unstable upon loss of solvent as a result of framework instability associated with high porosity.^[1d]

Compound **1** is non-interpenetrating, despite the large pores and channels within its framework, mainly because the bcu-type net is not self-dual.^[5a] The unique eight-connected Cu₃-cluster SBUs cause compound **1** to contain nbo-type intersecting channels, which is the dual net of body centered cubic (Figure 4). Thus, compound **1** is a perfect candidate for a highly porous network.

A thermogravimetric analysis of **1** shows that guest molecules are eliminated from the network (calcd. 71%; found 74%) when the temperature is increased from room temperature to about 220 °C, after which decomposition of the framework occurs. Powder X-ray diffraction spectra recorded after heating samples of **1** at 220 °C show some indication of stability upon the removal of guest molecules. However, the broadening and decrease of intensity of the

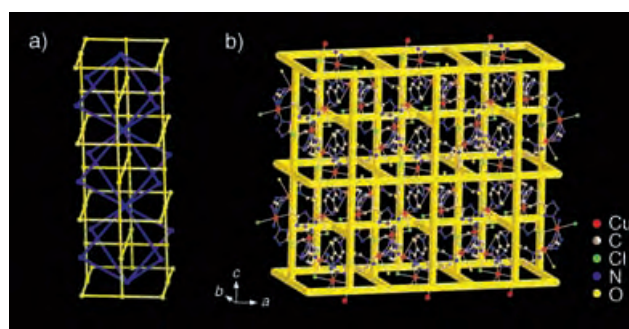


Figure 4. a) Dual relationship of the bcu net (blue) and the nbo net (yellow). b) The nbo-type intersecting channels (yellow) in the bcu-type framework of **1**.

peaks implies that the material appears to lose crystallinity gradually, thus producing an amorphous phase upon heating.

The magnetic exchange coupling between the copper centers for compound **1** was analyzed based on the Curie–Weiss expression and a trinuclear magnetic model. The negative values of the Weiss constant and the magnetic exchange coupling constant indicate the antiferromagnetic characteristics of the copper centers. At temperatures below 20 K, the Cu^{II} ions are weakly antiferromagnetically coupled, with $J = -2.84 \text{ cm}^{-1}$ (based on the Hamiltonian $\mathcal{H} = -2J[(S_{\text{Cu1}}S_{\text{Cu2}}) + (S_{\text{Cu1}}S_{\text{Cu2A}})]$ and using the expression for the molar magnetic susceptibility $S = 1/2$ of a linear trinuclear system). The observed antiferromagnetic interaction is resolved into contributions arising from each Cu–ligand–Cu linkage. The propagation of the antiferromagnetic exchange interaction in the linear Cu₃ unit is expected to depend predominantly on 4-ptz bridges. It may be processed through the $d_{x^2-y^2}$ orbitals on the Cu^{II} ions that interact with the σ orbitals of the nitrogen atoms of the tetrazolate ligands, which are all situated in the equatorial plane and contain Cu–N–N–Cu torsion angles of -3.41° . Crystal engineering of the substituent on the 4-pyridyl moiety could increase the Cu–N–N–Cu torsion angles in the tricopper center and thereby change the exchange coupling from antiferromagnetic to ferromagnetic.^[14]

In conclusion, compound **1** is the first porous, neutral, bcu-type structure that contains an eight-connected polynuclear cluster unit and a tetrazole-based ligand. The synthesis of bcu-type frameworks with expanded analogous ligands offers the

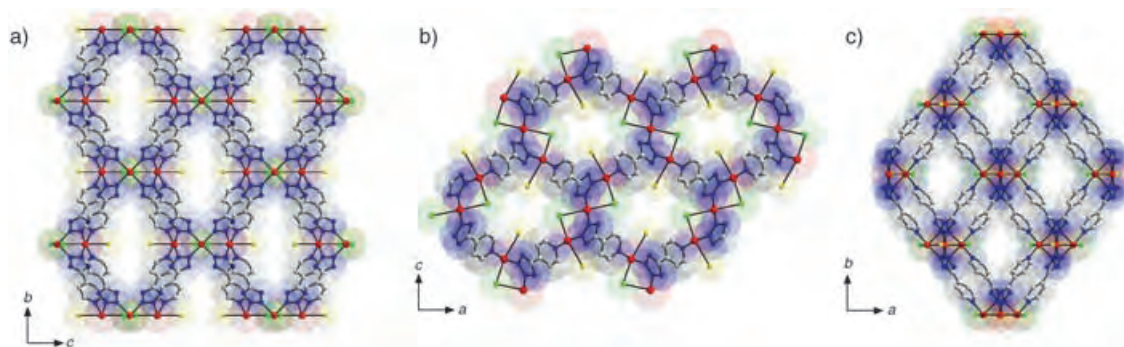


Figure 3. Superimposed space-filling representation of **1** showing channel openings along the *a*, *b*, and *c* axes. Hydrogen atoms have been omitted for clarity (red = Cu, blue = N, green = Cl, yellow = O).

potential for pore-size expansion in their nbo-type intersecting channel systems. The preparation of a rare framework from 4-ptz and Cu₃ clusters confirms the potential for synthesizing new structures of functional materials using tetrazole derivatives as ligands. Further research is currently in progress.

Experimental Section

1: A solution of CuCl₂·2H₂O (0.10 mmol) and 4-H-ptz (0.13 mmol) in DMF (8 mL) was stirred for 15 min. It was then allowed to stand at room temperature for several days, whereupon deep-blue, rhombus-like crystals were formed in 61 % yield (based on 4-H-ptz). The solid product was washed with deionized water and ethanol, and dried in air. Elemental analysis (%) calcd for C₃₃H₅₁Cl₂Cu₃N₂₃O₁₀: C 33.27, H 4.31, N 27.04; found: C 33.59, H 4.51, N 25.66. The formula [Cu₃Cl₂(4-ptz)₄(H₂O)₂]₃·3DMF·5H₂O was assigned by elemental microanalysis, thermogravimetric analysis, and single-crystal X-ray diffraction studies.^[15]

Received: November 19, 2004

Revised: May 12, 2005

Published online: August 17, 2005

Keywords: crystal engineering · microporous materials · organic–inorganic hybrid composites · self-assembly · topochemistry

- [1] a) G. R. Desiraju, *Nature* **2001**, 412, 397; b) M. J. Zaworotko, *Nature* **1999**, 402, 242; c) M. Ruben, J. Rojo, F. J. Romero-Salguero, L. H. Uppadine, J. M. Lehn, *Angew. Chem.* **2004**, 116, 3728; *Angew. Chem. Int. Ed.* **2004**, 43, 3644; d) S. Kitagawa, R. Kitaura, S. Noro, *Angew. Chem.* **2004**, 116, 2388; *Angew. Chem. Int. Ed.* **2004**, 43, 2334; e) C. N. R. Rao, S. Natarajan, R. Vaidhyanathan, *Angew. Chem.* **2004**, 116, 1490; *Angew. Chem. Int. Ed.* **2004**, 43, 1466; f) K. T. Holman, A. M. Pivovar, M. D. Ward, *Science* **2001**, 294, 1907; g) M. D. Ward, *Science* **2003**, 300, 1104.
- [2] a) G. Ferey, *Science* **2001**, 291, 994; b) G. Ferey, *Science* **1999**, 283, 1125; c) H. K. Chae, D. Y. Siberlo-Perez, J. Kim, Y. Go, M. Eddaoudi, A. J. Matzger, M. O'Keeffe, O. M. Yaghi, *Nature* **2004**, 427, 523; d) S. Kitagawa, M. Kondo, *Bull. Chem. Soc. Jpn.* **1998**, 71, 1739; e) B. Moulton, M. J. Zaworotko, *Chem. Rev.* **2001**, 101, 1629; f) F. A. Cotton, C. Lin, C. A. Murillo, *Acc. Chem. Res.* **2001**, 34, 759; g) C. Janiak, *Dalton Trans.* **2003**, 2781; h) M. O'Keeffe, M. Eddaoudi, H. Li, T. Reineke, O. M. Yaghi, *J. Solid State Chem.* **2000**, 152, 3.
- [3] a) O. M. Yaghi, M. O'Keeffe, N. W. Ockwig, H. K. Chae, M. Eddaoudi, J. Kim, *Nature* **2003**, 423, 705; b) J. S. Siegel, *Science* **2004**, 304, 1256; c) C. Mellot-Draznieks, J. Dutour, G. Ferey, *Angew. Chem.* **2004**, 116, 6450; *Angew. Chem. Int. Ed.* **2004**, 43, 6290; d) M. Eddaoudi, J. Kim, N. Rosi, D. Vodak, J. Wachter, M. O'Keeffe, O. M. Yaghi, *Science* **2002**, 295, 469; e) Y. H. Liu, H. C. Wu, H. M. Lin, W. H. Hou, K. L. Lu, *Chem. Commun.* **2003**, 60; f) B. Chen, M. Eddaoudi, T. M. Reineke, J. W. Kampf, M. O'Keeffe, O. M. Yaghi, *J. Am. Chem. Soc.* **2000**, 122, 11559.
- [4] J. D. Dunitz, *Chem. Commun.* **2003**, 545.
- [5] For a few representative examples, see: a) M. Eddaoudi, J. Kim, M. O'Keeffe, O. M. Yaghi, *J. Am. Chem. Soc.* **2002**, 124, 376; b) J. Sun, L. Weng, Y. Zhou, J. Chen, Z. Chen, Z. Liu, D. Zhao, *Angew. Chem.* **2002**, 114, 4651; *Angew. Chem. Int. Ed.* **2002**, 41, 4471; c) H. K. Chae, J. Kim, O. D. Friedrichs, M. O'Keeffe, O. M. Yaghi, *Angew. Chem.* **2003**, 115, 4037; *Angew. Chem. Int. Ed.* **2003**, 42, 3907; d) S. R. Batten, B. F. Hoskins, B. Moubaraki, K. S. Murray, R. Robson, *J. Chem. Soc. Dalton Trans.* **1999**, 2977; e) B. F. Abrahams, M. G. Haywood, R. Robson, D. A. Slizys, *Angew. Chem.* **2003**, 115, 1144; *Angew. Chem. Int. Ed.* **2003**, 42, 1111; f) V. Niel, A. L. Thompson, M. C. Munoz, A. Galet, A. E. Goeta, J. A. Real, *Angew. Chem.* **2003**, 115, 3890; *Angew. Chem. Int. Ed.* **2003**, 42, 3759; g) Z. Wang, B. Zhang, T. Otsuka, K. Inoue, H. Kobayashi, M. Kurmoo, *Dalton Trans.* **2004**, 2209.
- [6] a) A. F. Wells, *Three-Dimensional Nets and Polyhedra*, Wiley, New York, **1977**; b) O. D. Friedrichs, M. O'Keeffe, O. M. Yaghi, *Acta Crystallogr. Sect. A* **2003**, 59, 22; c) O. D. Friedrichs, M. O'Keeffe, O. M. Yaghi, *Acta Crystallogr. Sect. A* **2003**, 59, 515.
- [7] a) B. Moulton, J. Lu, M. J. Zaworotko, *J. Am. Chem. Soc.* **2001**, 123, 9224; b) D. L. Long, A. J. Blake, N. R. Champness, C. Wilson, M. Schröder, *J. Am. Chem. Soc.* **2001**, 123, 3401.
- [8] a) D. L. Long, A. J. Blake, N. R. Champness, C. Wilson, M. Schröder, *Angew. Chem.* **2001**, 113, 2509; *Angew. Chem. Int. Ed.* **2001**, 40, 2443; b) J. Lu, W. T. A. Harrison, A. J. Jacobson, *Angew. Chem.* **1995**, 107, 2759; *Angew. Chem. Int. Ed. Engl.* **1995**, 34, 2557; c) J. U. Schütze, R. Eckhardt, R. D. Fischer, D. C. Apperley, N. A. Davies, R. K. Harris, *J. Organomet. Chem.* **1997**, 534, 187; d) H. Chun, D. Kim, D. N. Dybtsev, K. Kim, *Angew. Chem.* **2004**, 116, 989; *Angew. Chem. Int. Ed.* **2004**, 43, 971; e) D. L. Long, R. J. Hill, A. J. Blake, N. R. Champness, P. Hubberstey, D. M. Proserpio, C. Wilson, M. Schröder, *Angew. Chem.* **2004**, 116, 1887; *Angew. Chem. Int. Ed.* **2004**, 43, 1851; f) L. Pan, H. Liu, X. Lei, X. Huang, D. H. Olson, N. J. Turro, J. Li, *Angew. Chem.* **2003**, 115, 560; *Angew. Chem. Int. Ed.* **2003**, 42, 542; g) Q. R. Fang, X. Shi, G. Wu, G. Tian, G. S. Zhu, Y. F. Li, L. F. Wang, C. L. Wang, Y. Chen, Z. D. Zhang, Z. Guo, T. C. Shang, X. H. Cai, S. L. Qiu, *Acta Chim. Sinica* **2002**, 60, 2087.
- [9] a) Z. R. Qu, H. Zhao, X. S. Wang, Y. H. Li, Y. M. Song, Y. J. Liu, Q. Ye, R. G. Xiong, B. F. Abrahams, Z. L. Xue, X. Z. You, *Inorg. Chem.* **2003**, 42, 7710; b) L. Z. Wang, Z. R. Qu, H. Zhao, X. S. Wang, R. G. Xiong, Z. L. Xue, *Inorg. Chem.* **2003**, 42, 3969; c) R. G. Xiong, X. Xue, H. Zhao, X. Z. You, B. F. Abrahams, Z. L. Xue, *Angew. Chem.* **2002**, 114, 3954; *Angew. Chem. Int. Ed.* **2002**, 41, 3800; d) X. Xue, X. S. Wang, L. Z. Wang, R. G. Xiong, B. F. Abrahams, X. Z. You, Z. L. Xue, C. M. Che, *Inorg. Chem.* **2002**, 41, 6544.
- [10] a) L. Carlucci, G. Ciani, D. M. Proserpio, *Angew. Chem.* **1999**, 111, 3700; *Angew. Chem. Int. Ed.* **1999**, 38, 3488; b) S. Bhandari, M. F. Mahon, K. C. Molloy, J. S. Palmer, S. F. Sayers, *J. Chem. Soc. Dalton Trans.* **2000**, 1053; c) P. J. van Koningsbruggen, Y. Garcia, H. Kooijman, A. L. Spek, J. G. Haasnoot, O. Kahn, J. Linares, E. Codjovi, F. Varret, *J. Chem. Soc. Dalton Trans.* **2001**, 466; d) A. F. Stassen, M. Grunert, A. M. Mills, A. L. Spek, J. G. Haasnoot, J. Reedijk, W. Linert, *Dalton Trans.* **2003**, 3628; e) C. Jiang, Z. Yu, S. Wang, C. Jiao, J. Li, Z. Wang, Y. Cui, *Eur. J. Inorg. Chem.* **2004**, 3662; f) A. Facchetti, A. Abbotto, L. Beverina, S. Bradamante, P. Mariani, C. L. Stern, T. J. Marks, A. Vacca, G. A. Pagani, *Chem. Commun.* **2004**, 1770; g) J. Tao, Z. J. Ma, R. B. Huang, L. S. Zheng, *Inorg. Chem.* **2004**, 43, 6133.
- [11] a) F. Himo, Z. P. Demko, L. Noodleman, K. B. Sharpless, *J. Am. Chem. Soc.* **2003**, 125, 9983; b) F. Himo, Z. P. Demko, L. Noodleman, K. B. Sharpless, *J. Am. Chem. Soc.* **2002**, 124, 12210; c) Z. P. Demko, K. B. Sharpless, *J. Org. Chem.* **2001**, 66, 7945; d) Z. P. Demko, K. B. Sharpless, *Angew. Chem.* **2002**, 114, 2217; *Angew. Chem. Int. Ed.* **2002**, 41, 2113; e) Z. P. Demko, K. B. Sharpless, *Angew. Chem.* **2002**, 114, 2214; *Angew. Chem. Int. Ed.* **2002**, 41, 2110; f) Z. P. Demko, K. B. Sharpless, *Org. Lett.* **2002**, 4, 2525; g) Z. P. Demko, K. B. Sharpless, *Org. Lett.* **2002**, 4, 4091.
- [12] R. Prins, M. Biagini-Cingi, M. Drillon, R. A. G. de Graaff, J. Haasnoot, A. M. Manotti-Lanfredi, P. Rabu, J. Reedijk, F. Uguzzoli, *Inorg. Chim. Acta* **1996**, 248, 35.
- [13] A. L. Spek, *J. Appl. Cryst.* **2003**, 36, 7–13.

- [14] Y. Garcia, P. J. van Koningsbruggen, G. Bravic, D. Chasseau, O. Kahn, *Eur. J. Inorg. Chem.* **2003**, 356.
- [15] A suitable single crystal of **1** with dimensions $0.12 \times 0.10 \times 0.08 \text{ mm}^3$ was mounted on the tip of a glass fiber and placed onto the goniometer head for indexing and intensity data collection using a Bruker Smart CCD diffractometer ($\text{MoK}\alpha = 0.71073 \text{ \AA}$). The raw frame data for **1** were integrated into SHELX-format reflection files and corrected for Lorentz and polarization effects with the Denzo program. An empirical absorption correction was applied by using the Multiscan method. The structure of **1** was solved by direct methods and refined against F^2 by the full-matrix least-squares technique, using the WINGX, PLATON, and SHELX software packages. Except for the guest molecules, non-hydrogen atoms were refined with anisotropic displacement parameters, and the hydrogen atoms of aromatic rings were calculated and refined as riding modes. The water and DMF guest molecules that show positional disorder could not be fixed in the structure model. During the final stages of refinement, several Q peaks were found, which probably correspond to highly disordered solvent molecules and were fixed as oxygen atoms and refined with isotropic displacement parameters. The hydrogen atoms associated with the coordinated water molecules and disordered guest molecules could not be located from difference Fourier maps, and no attempt was made to place them. However, they are included in the empirical formula. Further details of experimental and magnetic studies are given in the Supporting Information. Crystal data for **1**: $\text{C}_{33}\text{H}_{51}\text{Cl}_2\text{Cu}_3\text{N}_{23}\text{O}_{10}$ $\{[\text{Cu}_3\text{Cl}_2(4\text{-ptz})_4(\text{H}_2\text{O})_2] \cdot (3 \text{ DMF} \cdot 5 \text{ H}_2\text{O})\}$, $M_r = 1191.45$, orthorhombic, $Pnmm$, $a = 12.3305(2)$, $b = 15.5069(3)$, $c = 15.6412(3) \text{ \AA}$, $V = 2990.72(9) \text{ \AA}^3$, $Z = 2$, $\rho_{\text{calcd}} = 1.366 \text{ g cm}^{-3}$, $\mu = 1.180 \text{ mm}^{-1}$, $\lambda(\text{MoK}\alpha) = 0.71073 \text{ \AA}$, $F(000) = 1780$, $T = 293(2) \text{ K}$, A total of 19921 reflections were collected in the range $\theta = 4.12\text{--}27.49^\circ$, of which 3538 were unique ($R_{\text{int}} = 0.0512$). Final R indices: $R_1 = 0.0399$, $wR_2 = 0.1716$ for 2818 reflections [$I > 2\sigma(I)$]; $R_1 = 0.0725$, $wR_2 = 0.1830$ for 3538 independent reflections (all data) and 147 parameters, $\text{GOF} = 1.060$. CCDC-256347 (**1**) contains the supplementary crystallographic data for this paper. These data can be obtained free of charge from the Cambridge Crystallographic Data Center via www.ccdc.cam.ac.uk/data_request/cif.

DOI: 10.1002/anie.200463004

Metal Ions Play Different Roles in the Third-Order Nonlinear Optical Properties of d^{10} Metal–Organic Clusters***Hongwei Hou,* Yongli Wei, Yinglin Song, Liwei Mi, Mingsheng Tang, Linke Li, and Yaoting Fan*

Research into nonlinear optical (NLO) materials has become increasingly intensive because of their potential applications in optical fibers, data storage, optical computing, image processing, optical switching, and optical limiting.^[1] Thus, the design and synthesis of new materials with large NLO capability represents an active field in modern chemistry, physics, and materials science.^[2] Metal clusters are reported to be excellent candidates for NLO materials^[3] since they involve $d\pi$ – $p\pi$ delocalized systems and $d\pi$ – $d\pi$ conjugated systems.^[4] These compounds have a large variety of structures and diverse electronic properties that can be tuned by virtue of the coordinated metal;^[5] thus the opportunity exists to tune the NLO properties of metal complexes. Metal clusters can also extend the π -conjugated length, which is one of the many methods used to increase molecular NLO susceptibility $\chi^{(3)}$ values. Moreover, the NLO properties of metal clusters can be enhanced by the introduction of metal→ligand and ligand→metal charge-transfer states.^[6] Although many methods can be used to promote the NLO properties of metal clusters, the origination of the NLO properties is the delocalization of the π -electron cloud.^[7] This delocalization in metal clusters is mainly brought about by metal ions constructing the skeleton and organic ligands fixing the skeleton, thus both the metal ions and the organic ligands should be important for the nonlinear optical properties of the clusters. To the best of our knowledge, however, all studies confirm that heavy-metal ions play very important roles on the third-order NLO properties of metal clusters because their incorporation introduces more sublevels into the energy hierarchy, which permits more allowed electronic transitions to take place and hence a larger NLO effect to be produced.^[8]

[*] Prof. H. W. Hou, Dr. Y. L. Wei, L. W. Mi, Prof. M. S. Tang, L. K. Li, Prof. Y. T. Fan
Department of Chemistry
Zhengzhou University
Henan 450052 (P.R. China)
Fax: (+86) 371-67761744
E-mail: houghongw@zzu.edu.cn
Prof. Y. L. Song
Department of Applied Physics
Harbin Institute of Technology
Heilongjiang 150001 (P.R. China)

[**] This work was supported by the National Natural Science Foundation of China (Nos. 20001006 and 20371042) and the Outstanding Young Foundation of Henan Province.



Supporting information for this article is available on the WWW under <http://www.angewandte.org> or from the author.

However, we believe that both metal ions and ligands affect the NLO properties from their contribution to the delocalization of the π -electron cloud. If metal ions make a greater contribution than ligands, then the effect of the metal ions on the NLO properties will be greater; however, ligands can also make an important contribution to the NLO properties.

How do we investigate the contribution of metal ions and ligands to the delocalization of the π -electron cloud? The frontier molecular orbital corresponds to the delocalization of the π -electron cloud, so we can understand the contribution of metal ions and ligands to the delocalization of the π -electron cloud by calculating their component of the frontier molecular orbital. We can then deduce whether the metal ions or ligands play more important roles in the NLO properties. This approach has been utilized herein. We prepared 2,6-dicarboxamido-2-pyridylpyridine (H_2dcapp), the unique crownlike cluster $[Ag_{10}(dcapp)_4] \cdot 2(OH) \cdot 12H_2O$ (**1**), as well as clusters $[Zn_4O(dcapp)_3] \cdot 6H_2O$ (**2**) and $[Hg_2(dcapp)_2]$ (**3**), and studied their third-order NLO properties. We determined by quantum chemical calculations the contribution the metal ions and organic ligands make to the NLO properties and found them to be consistent with the experimental results. In addition, we found that the population of the triplet excited state for nanosecond laser radiation is responsible for the third-order nonlinear properties of these compounds.

The reaction of $AgNO_3$ with 0.5 equivalents of H_2dcapp in a mixture of THF, DMF (*N,N*-dimethylformamide), and H_2O leads to the formation of the light-yellow decanuclear cluster $[Ag_{10}(dcapp)_4] \cdot 2(OH) \cdot 12H_2O$ (Figure 1).^[9] The main unit is a decanuclear silver aggregate $[Ag_{10}(dcapp)_4]^{2+}$, which has a crownlike architecture. The ten silver atoms are arranged in two irregular tetrahedrons ($Ag1-Ag1A-Ag2-Ag2A$ and $Ag1B-Ag1C-Ag2B-Ag2C$) and a distorted octahedron ($Ag2-Ag2A-Ag2B-Ag2C-Ag3-Ag3A$). The two tetrahedrons and the octahedron are connected by the two edges $Ag2-Ag2A$ and $Ag2B-Ag2C$. The edge lengths of the tetrahedra are in the range 2.8329(16)–3.0259(9) Å, and in the octahedron the closest $Ag \cdots Ag$ contacts are found and range from 2.6521(9) to 2.9345(11) Å. The $Ag2 \cdots Ag3$ distance (2.6521(9) Å) is much shorter than that in elemental silver (2.88 Å). The distances of 2.8329(16)–3.0259(9) Å are comparable to 2.88 Å and twice the van der Waals radius for silver atoms (3.44 Å). We could calculate Wiberg bond orders^[10] by quantum chemical calculation and found that the $Ag2-Ag3$ bond order is 0.1354, thus indicating a strong metal–metal bond between the $Ag2$ and $Ag3$ atoms, while other $Ag-Ag$ bond orders are in the range from 0.0847 to 0.0371, thus suggesting the existence of further metal–metal bonds. In addition, Wiberg bond orders of $Ag-N$ range from 0.2329 to 0.3453 and the $C-C$ bond orders are about 1.4.

There are three crystallographically distinct silver ions in the decanuclear silver cluster $[Ag_{10}(dcapp)_4]^{2+}$. $Ag1$ ions are located on both sides of the crown and are coordinated to three nitrogen atoms and three Ag ions; $Ag3$ ions coordinate with two N atoms and further bond to four $Ag2$ ions; and $Ag2$ ions are surrounded by two N atoms and six Ag ions. Each ligand surrounds the silver ions in a helical conformation and functions as a pentadentate building block, in which

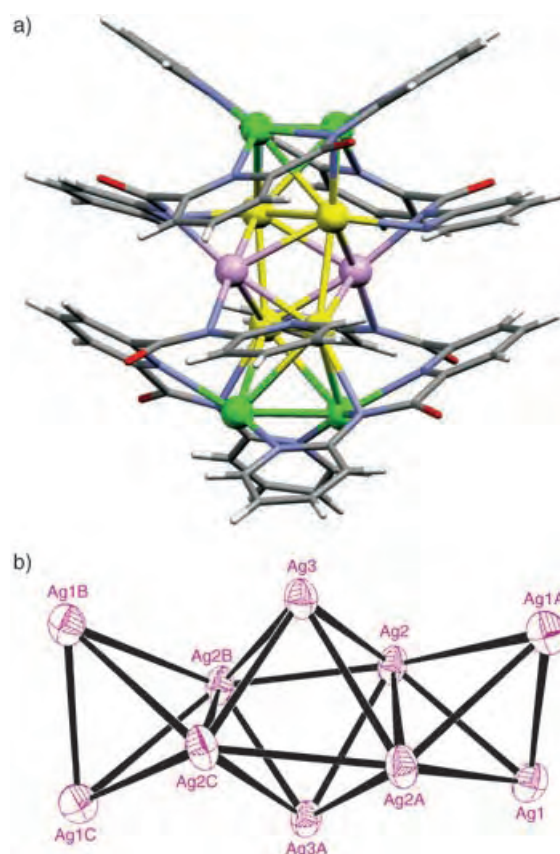


Figure 1. a) Crystal structure of the decanuclear cluster $[Ag_{10}(dcapp)_4] \cdot 2(OH) \cdot 12H_2O$ (**1**). Ag atoms are shown as green, yellow, and pink spheres; O red, N blue, C gray, H white. b) Arrangement of the 10 silver atoms.

$N1$, $N3$, $N4$, and $N5$ are monocoordinated to a silver center, while $N2$ acts as a μ_2 donor.

The colorless tetranuclear cluster **2** was prepared from H_2dcapp and $Zn(OAc)_2 \cdot 6H_2O$.^[9] The arrangement of the zinc ions and the bridging modes of the $dcapp^{2-}$ ligands are shown in Figure 2. The cluster consists of three $dcapp^{2-}$ and four zinc ions and a central oxygen atom. Five N atoms of each ligand coordinate to three Zn ions. The four $Zn-O_{central}$ bond lengths are almost equivalent, and the $Zn-O_{central}-Zn$ bond angle (α) is 109.4°. The Zn_4O^{6+} core is an almost perfect tetrahedron, with $Zn \cdots Zn$ separations ranging from 3.117 to 3.240 Å, which is consistent with tetrazinc carbamate complexes having a Zn_4O^{6+} core.^[11] Wiberg bond orders of $Zn-Zn$ are about 0.01, thus showing the presence of a weak $Zn-Zn$ metal bond. The corresponding Wiberg bond orders of $Zn-O$ and $Zn-N$ are about 0.38 and 0.26, respectively. The Zn_4O^{6+} cluster ion plays an important role in metal organic frameworks (MOFs), which are novel microporous materials that show potential applications in catalysis, gas storage, and molecular recognition.^[12]

The reaction of H_2dcapp with $Hg(OAc)_2 \cdot 2H_2O$ leads to colorless block crystals $[Hg_2(dcapp)_2]$ (**3**, Figure 3).^[9] The $Hg(1) \cdots Hg(2)$ distance is 3.157 Å, which is comparable to twice the van der Waals radius of Hg atoms (3.10 Å). The Wiberg bond order of $Hg(1)-Hg(2)$ is 0.0106, thus indicating

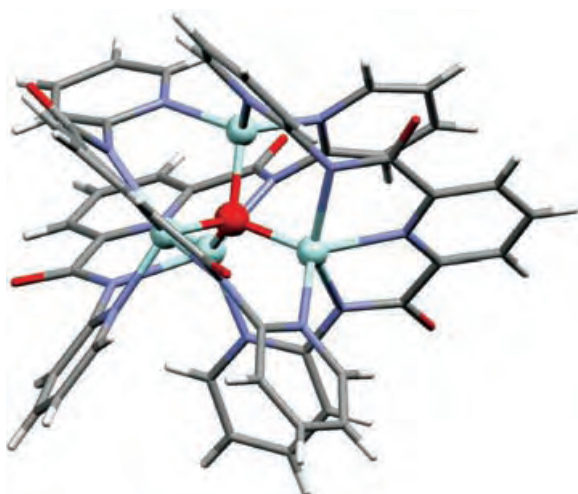


Figure 2. The structure of cluster $[\text{Zn}_4\text{O}(\text{dcapp})_3] \cdot 6\text{H}_2\text{O}$ (**2**). Zn pale blue spheres; O red, N blue, C gray, H white.

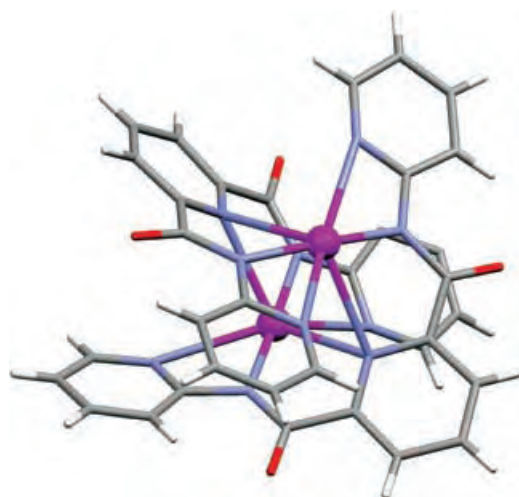


Figure 3. The molecular structure of $[\text{Hg}_2(\text{dcapp})_2]$ (**3**). Hg purple spheres; O red, N blue, C gray, H white.

a weak interaction between the two Hg ions. The corresponding Wiberg bond orders of Hg–N are about 0.52. There are few reports of polynuclear Hg complexes,^[13] apart from organomercury compounds.^[14] The two dcapp^{2-} ligands wrap helically around the two Hg centers, with the length of the double helix being 3.157 Å.

The third-order NLO properties of **1–3** and H_2dcapp were investigated with laser pulses of wavelength 532 nm and duration 8 ns by a Z-scan experiment in DMF solution. The results show that cluster **1** exhibits both very strong NLO absorptive and refractive effects, while H_2dcapp as well as clusters **2** and **3** show weaker NLO absorption and strong NLO refractive behavior. The linear absorption spectra of H_2dcapp and **1–3** in DMF are shown in Figure 4. The absorption of the ground state is low in the visible and near-infrared wavelength region (>380 nm); the maxima of the absorption bands for the ground state are 286 nm for H_2dcapp , 282 nm for **1**, 311 nm for **2**, and 296 nm for **3**. The

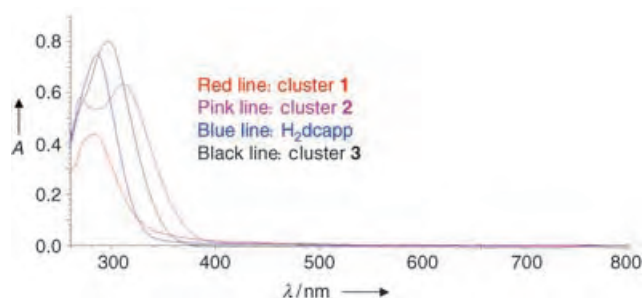


Figure 4. The linear absorption spectra of H_2dcapp , **1**, **2**, and **3**, at 6.2×10^{-4} , 2.0×10^{-5} , 3.7×10^{-5} , and 4.8×10^{-5} M, respectively, in DMF.

wavelength of the laser light (532 nm) is within the non-resonant absorption region.

The NLO absorption components were evaluated by a Z-scan experiment using an open-aperture configuration. Figure 5 depicts the NLO absorptive properties of **1** and

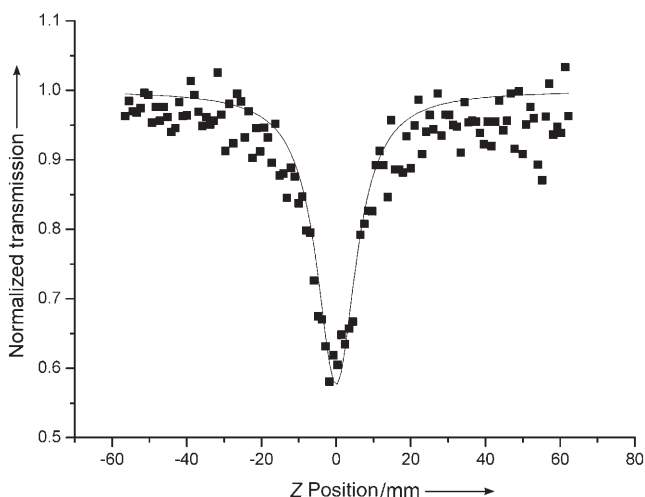


Figure 5. NLO absorptive properties of a 4.1×10^{-4} M solution of $[\text{Ag}_{10}(\text{dcapp})_4] \cdot 2(\text{OH}) \cdot 12\text{H}_2\text{O}$ (**1**) in DMF. The black squares are the experimental data, and the solid curve is the theoretical fit.^[15]

clearly illustrates that the absorption increases as the intensity of the incident light rises, with light transmittance (T) being a function of the Z position of the samples. A reasonably good fit between the experimental data and the theoretical curves was obtained. This result suggests that the experimentally detected NLO effects have an effective third-order characteristic. It is clear that the theoretical curves qualitatively reproduce the general pattern of the observed experimental data.^[16] The nonlinear absorptive index a_2 is calculated to be $1.4 \times 10^{-9} \text{ mW}^{-1}$ for a 4.1×10^{-4} M solution in DMF.

The nonlinear refractive components were assessed by dividing the normalized Z-scan data obtained under a closed-aperture configuration by the normalized Z-scan data obtained under the open-aperture configuration. Figure 6 depicts the nonlinear refractive effects of **1–3** and H_2dcapp . The valleys and peaks occur at equal distances from the focus. These results are consistent with the notion that the observed optical nonlinearity has an effective third-order dependence

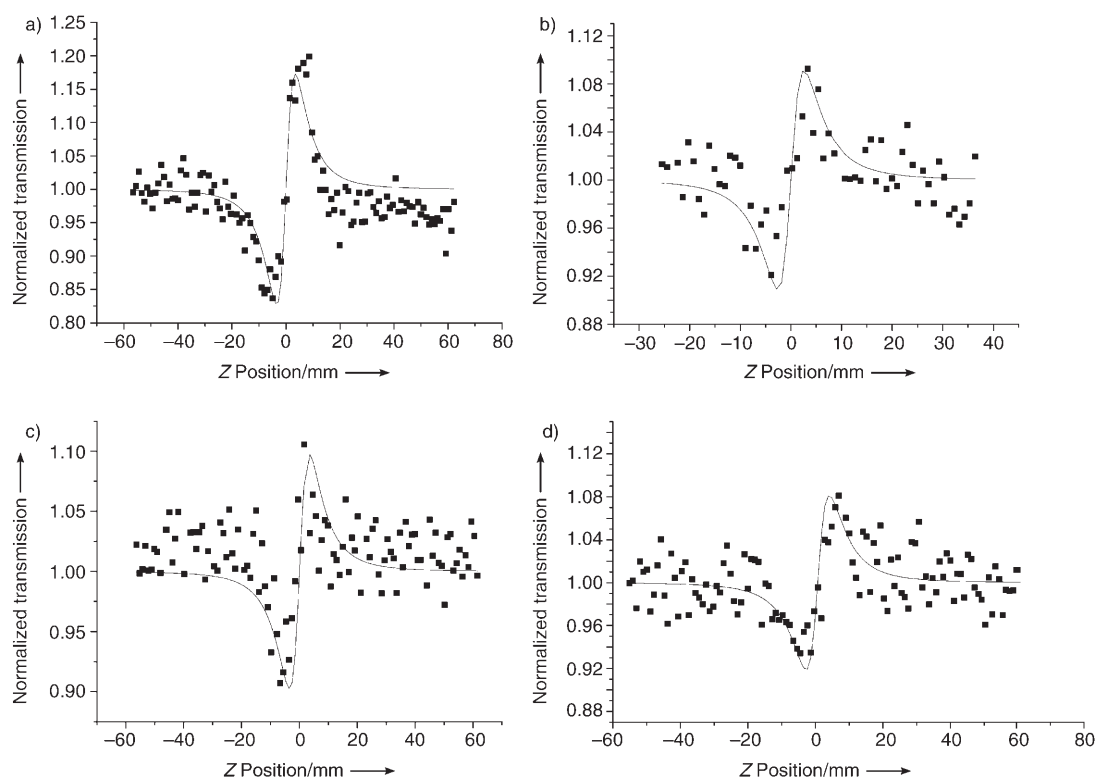


Figure 6. NLO refractive properties: a) $[\text{Ag}_{10}(\text{dcapp})_4] \cdot 2(\text{OH}) \cdot 12\text{H}_2\text{O}$ ($4.1 \times 10^{-4} \text{ M}$) in DMF; b) $[\text{Zn}_4\text{O}(\text{dcapp})_3] \cdot 6\text{H}_2\text{O}$ ($7.5 \times 10^{-4} \text{ M}$) in DMF; c) $[\text{Hg}_2(\text{dcapp})_2]$ ($9.7 \times 10^{-4} \text{ M}$) in DMF; d) H_2dcapp ($3.1 \times 10^{-3} \text{ M}$) in DMF. The black squares are the experimental data, and the solid curves are the theoretical fit.

on the incident electromagnetic field.^[16] A reasonably good fit between the experimental data (black squares) and the theoretical curves (solid curves) was obtained.^[15] The effective third-order refractive index n_2 of **1–3** and H_2dcapp are calculated to be 2.2×10^{-11} , 1.2×10^{-11} , 1.3×10^{-11} , and 1.1×10^{-11} esu, respectively.

It is very interesting that the NLO properties of **1** are completely different from those of **2**, **3**, and H_2dcapp . Cluster **1** shows strong NLO absorption and refractive effects, but **2**, **3**, and H_2dcapp only show NLO refractive behavior and give the same refractive index n_2 value. It can be seen from the results that the Ag ions play very important roles in the NLO behavior of **1**, while the influence of the Zn and Hg ions to the optical nonlinearity of **2** and **3** is very small, with the dcapp^{2-} ligands dominating the optical nonlinearity. The reason for this difference cannot be explained by the heavy-atom effect: the strength of the NLO properties can be altered by the π -back-donation capacity of the metal ions to the ligands, and the increased π -back-donation capacity of the metal ions to the ligands may enhance the extension of the electronic π system and improve the NLO properties.^[8]

It was reported that the NLO properties of π -conjugated complexes originate from the delocalization of the π -electron cloud.^[7] Since the delocalization corresponds to the frontier molecular orbital, we can determine the contribution of the Ag^+ , Zn^{2+} , Hg^{2+} , and dcapp^{2-} ions to the NLO properties of clusters **1–3** by molecular orbital theory. We have calculated the frontier molecular orbitals of cluster skeletons $[\text{Ag}_{10}(\text{dcapp})_4]^{2+}$, $[\text{Zn}_4\text{O}(\text{dcapp})_3]$, and $[\text{Hg}_2(\text{dcapp})_2]$ by density

functional theory (DFT) and Hartree–Fock (HF) calculations using the LanL2MB basis set.^[17] It can be seen from Figure 7 that the frontier molecular orbitals of $[\text{Ag}_{10}(\text{dcapp})_4]^{2+}$, namely HOMO–1, HOMO, LUMO, and LUMO + 1, are Ag^+ - and dcapp^{2-} -based orbitals (DFT/B3LYP 11.08, 5.01, 37.06, 80.84 %, respectively, and HF 6.13, 6.94, 63.96, 83.28 %, respectively, for Ag^+_{10}): HOMO–1 and HOMO are primarily dcapp^{2-} -based orbitals, while LUMO + 1 is primarily an Ag^+ -based orbital. The frontier molecular orbitals in $[\text{Zn}_4\text{O}(\text{dcapp})_3]$ (Figure 8) are primarily dcapp^{2-} -based orbitals (DFT/B3LYP 0.92, 0.94, 1.80, 2.03 %, respectively, and HF 1.48, 1.24, 2.01, 2.22 %, respectively, for Zn^{2+}_4), and the four orbitals have barely any Zn^{2+} character. In addition, the frontier molecular orbitals in $[\text{Hg}_2(\text{dcapp})_2]$ (Figure 9) are also primarily dcapp^{2-} -based orbitals (DFT/B3LYP 1.48, 1.58, 1.58, 1.61 %, respectively, and HF 1.88, 1.79, 1.32, 7.50 %, respectively, for Hg^{2+}_2). It is usually found that the electron in the highest occupied molecular orbital (HOMO) or the next highest occupied molecular orbital (HOMO–1) is excited to the lowest unoccupied molecular orbital (LUMO) or the next lowest unoccupied molecular orbital (LUMO + 1) to give the first excited singlet state S_1 or the first excited triplet state T_1 . In general, the photochemical and photophysical properties of compounds are governed by the first excited singlet state S_1 and the first excited triplet state T_1 , thus the most important frontier orbital is LUMO or LUMO + 1. Both the Ag^+ and dcapp^{2-} ions contribute to the LUMO and LUMO + 1 of $[\text{Ag}_{10}(\text{dcapp})_4]^{2+}$, while the LUMO and LUMO + 1 of $[\text{Zn}_4\text{O}(\text{dcapp})_3]$ and $[\text{Hg}_2(\text{dcapp})_2]$ primarily have dcapp^{2-} charac-

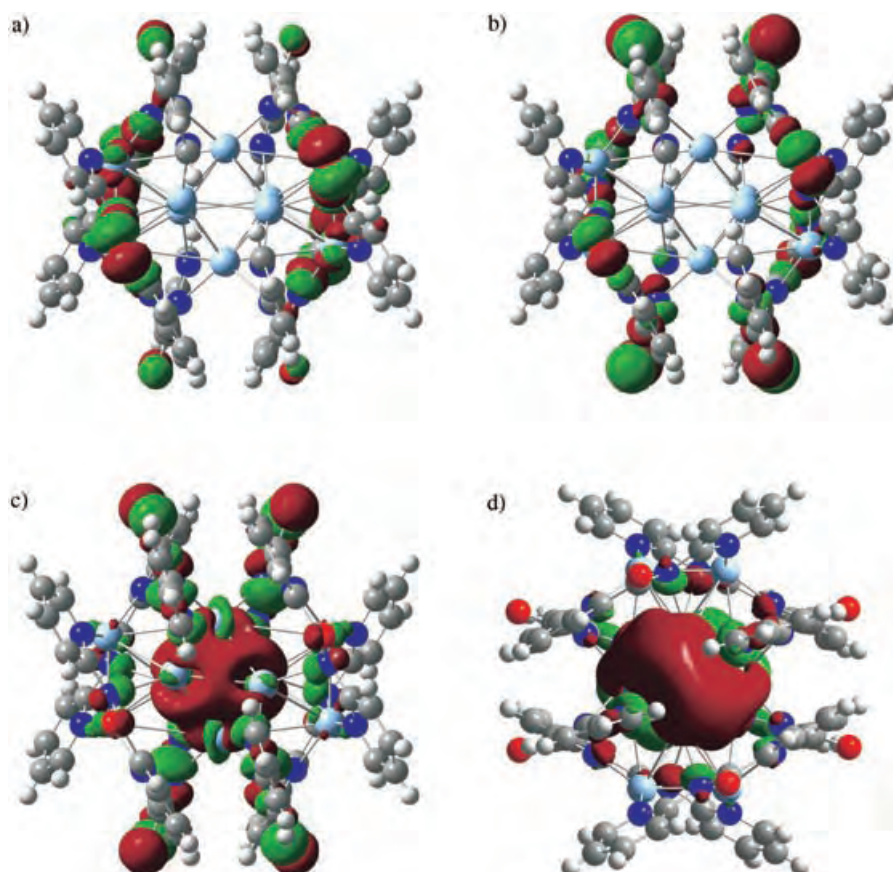


Figure 7. The frontier molecular orbital of $[\text{Ag}_{10}(\text{dcapp})_4]^{2+}$: a) HOMO–1, b) HOMO, c) LUMO, d) LUMO+1. Ag light blue, N dark blue, O red, C gray, H white.

ter. Therefore, we can deduce that the NLO properties of cluster **1** are controlled by the Ag^+ and dcapp^{2-} ions while in clusters **2** and **3** the Zn^{2+} and Hg^{2+} ions have no influence on the NLO properties, which are dominated by the dcapp^{2-} ligands. This finding is consistent with the experimental results: **2**, **3**, and H_2dcapp show the same NLO refractive behavior (self-focusing effect) and also have the same refractive index n_2 value, while **1** not only shows a strong NLO refractive effect (self-focusing) but also displays strong NLO absorptive properties. It should be pointed out that both the excited-state population (and absorption) and the two-photon absorption can be responsible for the measured NLO effect.^[16] In addition, it can be seen from Figure 7 that there are large $\text{d}\pi\text{--d}\pi$ conjugated systems in the LUMO and LUMO+1 of $[\text{Ag}_{10}(\text{dcapp})_4]^{2+}$ which can enhance the molecular NLO properties.

The strong nonlinear absorption makes cluster **1** an interesting case for an optical limiting (OL) study. An ideal OL material

should be able to respond quickly to the incident light and become increasingly opaque as the incident light increases in intensity. Cluster **1** displays such an OL ability, but **2**, **3**, and H_2dcapp do not; they give weaker OL effects. The optical limiting effect of **1** is depicted in Figure 10. The linear transmittance is 70 %. The light energy transmitted starts to deviate from Beer's law as the intensity of the input light reaches 0.03 J cm^{-2} , and the material becomes increasingly less transparent as the intensity rises. The optical limiting threshold, which is defined as the incident intensity at which the actual transmittance falls to 50 % of the corresponding linear transmittance, is 0.15 J cm^{-2} , with a saturation intensity transmitted of 0.23 J cm^{-2} . Lower limiting thresholds and saturation levels provide a greater safety margin for device protection. It is interesting to compare cluster **1** with other well-known optical limiting materials for nanosecond pulsed radiation of 532 nm wave-

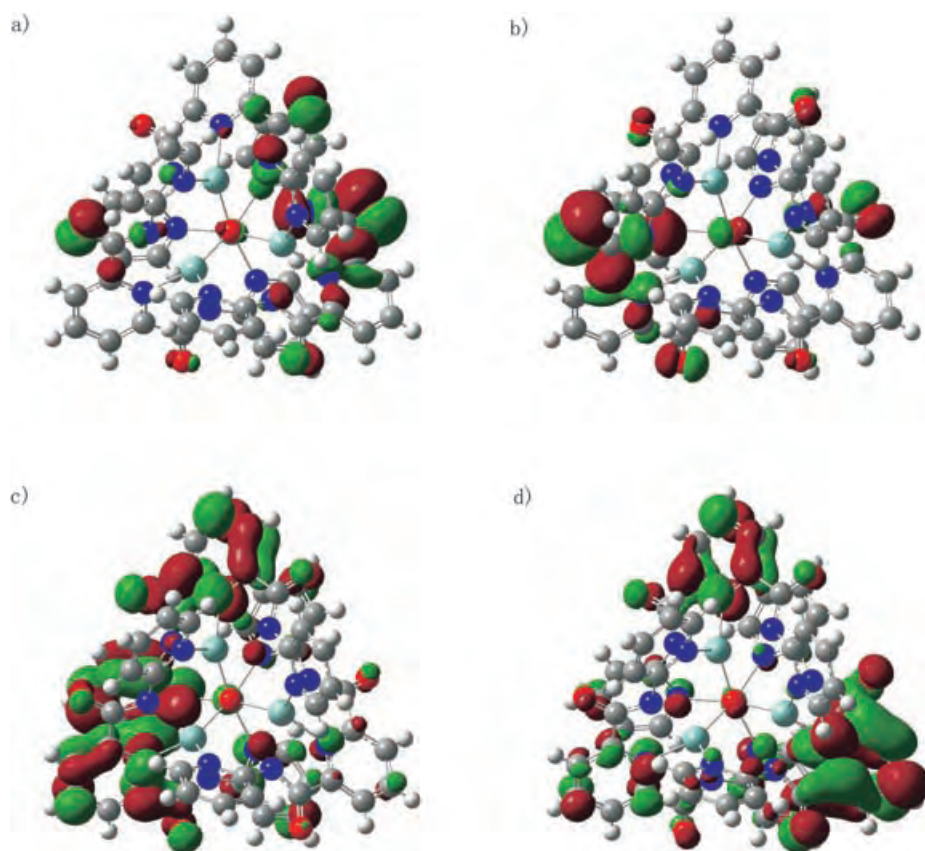


Figure 8. The frontier molecular orbital of $[\text{Zn}_4\text{O}(\text{dcapp})_3]$: a) HOMO–1, b) HOMO, c) LUMO, d) LUMO+1. Atoms colors as in Figure 2.

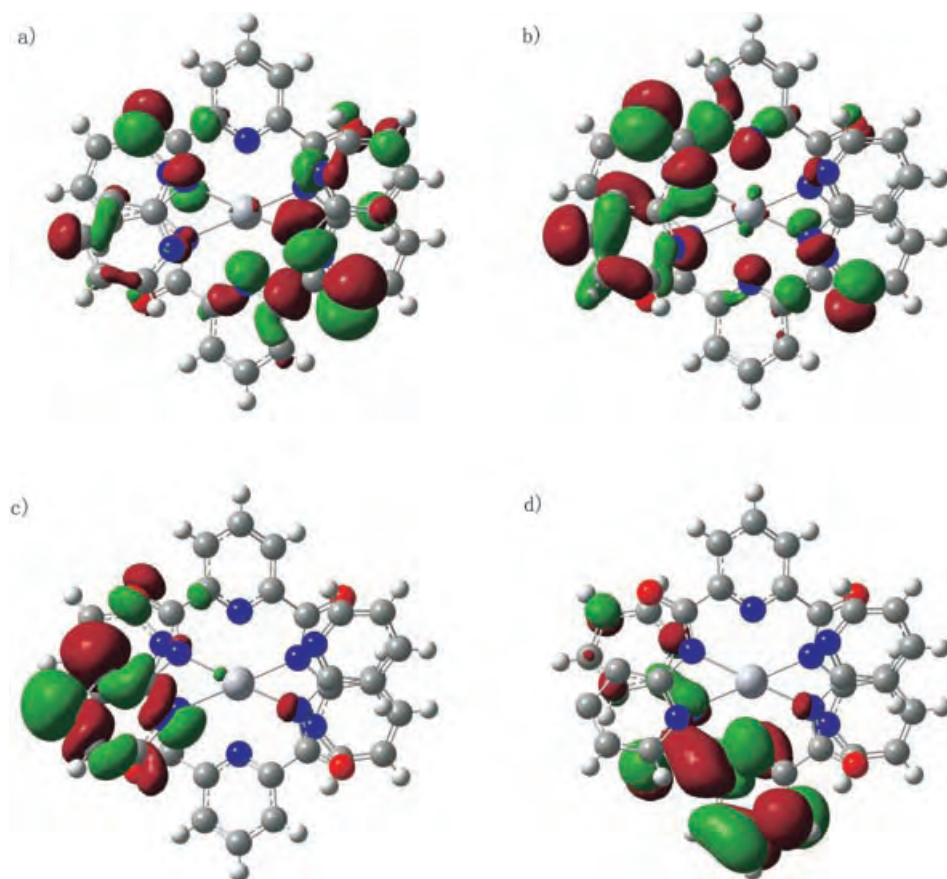


Figure 9. The frontier molecular orbital of $[\text{Hg}_2(\text{dcapp})_2]$: a) HOMO-1, b) HOMO, c) LUMO, d) LUMO+1. Hg silver, N blue, O red, C gray, H white.

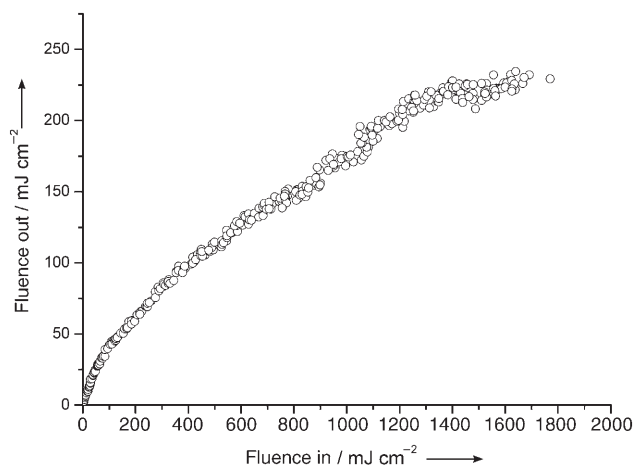


Figure 10. Optical limiting effect of $[\text{Ag}_{10}(\text{dcapp})_4] \cdot 2(\text{OH}) \cdot 12\text{H}_2\text{O}$ ($4.1 \times 10^{-4} \text{ M}$) in DMF.

length. The optical limiting threshold of **1** (0.15 J cm^{-2}) is lower than that observed in C_{60} and the octanuclear Ag cluster $[\text{Ag}_8(2,4,6\text{-iPr}_3\text{C}_6\text{H}_2\text{Se})_8]$.^[18] The lower limiting threshold makes cluster **1** a very promising candidate for broadband OL applications.

It should be pointed out that our measurement of the transmitted pulse energy was conducted with a full collection

of the transmitted pulse, and no aperture was used. Therefore, the observed OL originates from an NLO absorptive process.^[16] Most nanosecond OL performances, such as that of C_{60} , can be interpreted by the five-level (three singlet states and two triplet states) model, and a triplet-triplet transition has been identified as the main mechanism responsible for nanosecond OL effects.^[19] Ji et al. developed a five-level model for metal clusters: one ground state, one excited singlet state, one ionized state, one first excited triplet state, and one higher excited triplet state. The initial absorption promotes molecules from the ground to the excited singlet state, the ionized state, and to the first excited triplet state, and then further absorption excites the molecules in the first excited triplet state to the higher excited triplet state. If the absorption cross-section of the triplet state is greater than that of the ground state, then the absorption becomes stronger as the incident intensity increases, which results in an OL effect.^[16]

To further study the third-order optical nonlinearity performance of **1–3**, and H_2dcapp we investigated their NLO properties with laser pulses of wavelength 532 nm and duration 30 ps by the closed-aperture Z-scan experiment in

DMF solution (Figure 11). We find from the data that the closed-aperture Z-scan experimental curves of **1–3** and H_2dcapp in DMF solution are the same as that of the DMF solvent for laser radiation of picosecond duration. Moreover, the experimental curve (+) of H_2dcapp at a higher concen-

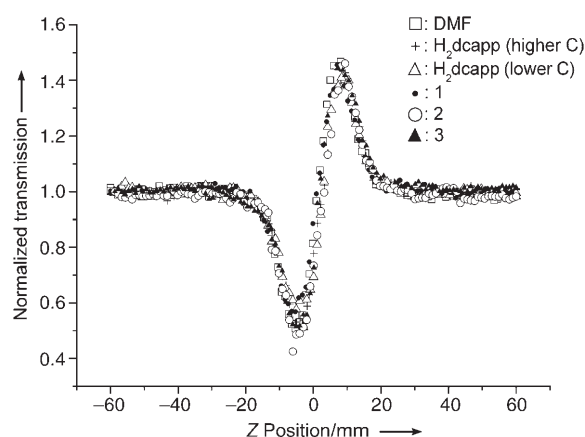


Figure 11. The NLO properties of clusters **1**, **2**, **3**, and H_2dcapp (3.4×10^{-4} , 2.3×10^{-4} , 3.4×10^{-4} , and $2.0 \times 10^{-3} \text{ M}$ (or $9.3 \times 10^{-3} \text{ M}$), respectively) in DMF solution, as well as DMF itself, with laser pulses of wavelength 532 nm and duration 30 ps by the closed-aperture Z-scan experiment.

tration (9.3×10^{-3} M) in DMF solution is the same as that (Δ) of H₂dcape at lower concentration (2.0×10^{-3} M). Hence, we believe that there exists no third-order optical nonlinearity for **1–3** and H₂dcape with laser radiation of picosecond duration. This result also shows that the population of the singlet excited state cannot contribute to the third-order optical nonlinearity performance of **1–3** and H₂dcape with laser radiation of nanosecond duration. The third-order nonlinearity performance results from the population of the triplet excited state in nanosecond laser radiation. For comparison, the closed-aperture Z-scan experiment of a solution of C₆₀ in toluene was also investigated with laser pulses of wavelength 532 nm and 30 ps duration (C₆₀ gives strong NLO properties; see Supporting Information). This result illustrates that the NLO performance of C₆₀ is brought about by the population of the singlet excited state and triplet excited state in laser radiation of nanosecond duration, and it is different from those of **1–3** and H₂dcape.

Experimental Section

H₂dcape: 2,6-Pyridyldicarboxylic acid (1.67 g, 10 mmol) was dissolved in SOCl₂ (20 mL). The resulting 2,6-pyridinedicarboxylic acid chloride was dissolved in anhydrous pyridine (10 mL), and a solution of 2-aminopyridine (1.90 g, 20 mmol) in pyridine was added dropwise with stirring in an ice bath. Yield: 4.21 g (70%). IR (KBr): $\tilde{\nu}$ = 1698, 1579, 1545, 1442, 1322, 999, 780 cm⁻¹. Elemental analysis (%) calcd for C₁₇H₁₃N₃O₂: C 63.95, H 4.08, N 21.94; found: C 63.14, H 4.51, N 21.81; ¹H NMR (400 MHz, DMSO, 25 °C, TMS): δ = 7.25 (quin, 2H; C₆H₄), 7.93 (hept, 2H; C₆H₄), 8.31 (hept, 3H; C₆H₃), 8.41 (d, 2H; C₆H₄), 8.50 ppm (d, 2H; C₆H₄); ESI-MS: m/z : 319.9 [H₂dcape + H]⁺.

1: The cluster was prepared by reaction of AgNO₃ (0.0169 g, 0.1 mmol) with H₂dcape (0.0161 g, 0.05 mmol) in a mixture of THF (1 mL), water (1 mL), and DMF (4 mL). The reaction mixture crystallized at room temperature on slow evaporation of the solvent to give the desired decanuclear silver cluster as a light-yellow crystalline solid. Yield: 63%. IR (KBr): $\tilde{\nu}$ = 1702, 1572, 1532, 1439, 1419, 1384, 1319, 1148, 774 cm⁻¹. Elemental analysis (%) calcd for C₃₄H₃₅Ag₅N₁₀O₁₁: C 32.15, H 2.75, N 11.03; found: C 33.01, H 2.12, N 11.03.

2: A solution of H₂dcape (0.0161 g, 0.05 mmol) in DMF (5 mL) was added to a solution of Zn(OAc)₂·2H₂O (0.1 mmol, 0.0219 g) in methanol (5 mL). The mixture solution was left to stand in the air at room temperature for a week, which resulted in colorless crystals suitable for X-ray diffraction analysis. Yield: 46%. IR (KBr): $\tilde{\nu}$ = 1616, 1578, 1556, 1477, 1434, 1381, 1312, 1160, 779 cm⁻¹. Elemental analysis (%) calcd for C₅₁H₄₅N₁₅O₁₅Zn₄: C 45.76, H 3.36, N 15.70; found: C 44.98, H 3.21, N 15.38.

3: Complex **3** was prepared in an analogous manner to that used to prepare **2**, except that Hg(OAc)₂·2H₂O was used instead of Zn(OAc)₂·2H₂O. Yield: 40%. IR (KBr): $\tilde{\nu}$ = 1630, 1581, 1460, 1433, 1385, 1355, 779 cm⁻¹. Elemental analysis (%) calcd for C₃₄H₂₂Hg₂N₁₀O₄: C 39.47, H 2.13, N 13.54; found: C 38.95, H 2.00, N 13.27.

Received: December 21, 2004

Revised: May 31, 2005

Published online: August 11, 2005

Keywords: cluster compounds · density functional calculations · ligand effects · nonlinear optics · silver

- [1] a) T. S. Wang, Z. L. Ahmadi, T. C. Green, A. Henglein, M. A. Elsayed, *Science* **1996**, 272, 1924–1926; b) J. W. Perry, K. Mandour, I. Y. S. Lee, X. L. Wu, P. V. Bedworth, C. T. Chen, D. Ng, S. R. Marder, P. Miles, T. Wada, M. Tian, H. Sasabe, *Science* **1996**, 273, 1533–1536.
- [2] a) J. G. Qin, D. Y. Liu, C. Y. Dai, *Coord. Chem. Rev.* **1999**, 188, 23–34; b) J. L. Bredas, C. Adant, Tackx, *Chem. Rev.* **1994**, 94, 243–278; c) R. Signorini, M. Zerbetto, M. Meneghetti, R. Bozio, M. Maggini, C. D. Faveri, M. Prato, G. Scorrano, *Chem. Commun.* **1996**, 1891–1892; d) M. Spassova, V. Enchev, *Chem. Phys.* **2004**, 298, 29–36.
- [3] a) S. Vagin, M. Barthel, D. Dini, M. Hanack, *Inorg. Chem.* **2003**, 42, 2683–2694; b) S. Shi, W. Ji, S. H. Tang, J. P. Lang, X. Q. Xin, *J. Am. Chem. Soc.* **1994**, 116, 3615–3616; c) W. F. Sun, M. M. Bader, T. Carvalho, *Opt. Commun.* **2003**, 215, 185–190.
- [4] K. Mashima, M. Tanaka, Y. Kaneda, A. Fukumoto, H. Mizomoto, K. Tani, H. Nakano, A. Nakamura, T. Sakaguchi, K. Kamada, K. Ohta, *Chem. Lett.* **1997**, 411–412.
- [5] a) V. Carcia, P. J. Van Koningsbruggen, H. Kooijman, A. L. Spek, J. G. Haasnoot, O. Kahn, *Eur. J. Inorg. Chem.* **2000**, 307–314; b) A. V. A. Gerard, C. G. Reinier, G. H. Jaap, L. Martin, L. S. Anthony, R. Jan, *Eur. J. Inorg. Chem.* **2000**, 121–126; c) Effendy, F. Marchetti, C. Pettinari, B. W. Skelton, A. H. White, *Inorg. Chem.* **2003**, 42, 112–117.
- [6] a) C. E. Powell, J. P. Morrall, S. A. Ward, M. P. Cifuentes, E. G. Notaras, A. M. Samoc, M. G. Humphrey, *J. Am. Chem. Soc.* **2004**, 126, 12234–12235; b) N. J. Long, *Angew. Chem.* **1995**, 107, 37–54; *Angew. Chem. Int. Ed. Engl.* **1995**, 34, 21–38.
- [7] a) T. Wada, L. Wang, H. Okawa, T. Masuda, M. Tabata, M. Wan, M. Kakimoto, Y. Lmai, H. Sasabe, *Mol. Cryst. Liq. Cryst. Sci. Technol. Sect. A* **1997**, 294, 245–250; b) C. Francis, K. White, G. Boyd, R. Moshrefzadeng, *Chem. Mater.* **1993**, 5, 506–510; c) S. Morina, T. Yamashita, K. Horie, T. Wada, H. Sadabe, *Rec. Func. Polymer* **2000**, 44, 183–188; d) H. S. Nalwa, *Adv. Mater.* **1993**, 5, 341–358.
- [8] a) W. B. Lin, Z. Y. Wang, L. Ma, *J. Am. Chem. Soc.* **1999**, 121, 11249–11250; b) H. W. Hou, X. R. Meng, Y. L. Song, Y. T. Fan, Y. Zhu, H. J. Lu, C. X. Du, W. H. Shao, *Inorg. Chem.* **2002**, 41, 4068–4075; c) H. Chao, R. H. Li, B. H. Ye, H. Li, X. L. Feng, J. W. Cai, J. Y. Zhou, L. N. Ji, *J. Chem. Soc. Dalton Trans.* **1999**, 3711–3717.
- [9] Crystal data for **1**: C₃₄H₃₅Ag₅N₁₀O₁₁, M_r = 1299.07, hexagonal, space group P6(2)22, a = 20.775(3), b = 20.775(3), c = 17.673(4) Å, γ = 120°, V = 6605.8(18) Å³, Z = 6, ρ_{calcd} = 1.959 Mg m⁻³, μ = 2.249 mm⁻¹, $F(000)$ = 3792, T = 291(2) K, λ = 0.71073 Å, R_1 = 0.0452, wR_2 = 0.0819. Crystal data for **2**: C₅₁H₄₅N₁₅O₁₅Zn₄, M_r = 1337.50, triclinic, space group $P\bar{1}$, a = 10.036(2), b = 19.327(4), c = 19.382(4) Å, α = 119.90(3)°, V = 3259.3(11) Å³, Z = 2, ρ_{calcd} = 1.363 mg m⁻³, μ = 1.520 mm⁻¹, $F(000)$ = 1360, T = 291(2) K, λ = 0.71073 Å, R_1 = 0.0772, wR_2 = 0.2033. Crystal data for **3**: C₃₄H₂₂Hg₂N₁₀O₄, M_r = 1033.78, monoclinic, space group $P2(1)/c$, a = 11.231(2), b = 20.994(4), c = 13.196(3) Å, β = 91.34(3)°, V = 3110.6(11) Å³, Z = 4, ρ_{calcd} = 2.207 mg m⁻³, μ = 9.918 mm⁻¹, $F(000)$ = 1944, T = 291(2) K, λ = 0.71073 Å, R_1 = 0.0677, wR_2 = 0.1659. CCDC 223369–223371 contain the supplementary crystallographic data for this paper. These data can be obtained free of charge from the Cambridge Crystallographic Data Centre via www.ccdc.cam.ac.uk/data_request/cif.
- [10] a) K. Wiberg, *Tetrahedron* **1968**, 24, 1083–1096; b) K. K. Pandey, *Inorg. Chem.* **2003**, 42, 6764–6767.
- [11] C. S. McCowan, T. L. Groy, M. T. Caudle, *Inorg. Chem.* **2002**, 41, 1120–1127.
- [12] a) M. Eddaoudi, J. Kim, N. Rosi, D. Vodak, J. Wachter, M. O’Keeffe, O. M. Yaghi, *Science* **2002**, 295, 469–472; b) H. L. Li, M. Eddaoudi, M. O’Keeffe, O. M. Yaghi, *Nature* **1999**, 402, 276–

- 279; c) O. M. Yaghi, M. O'Keeffe, N. W. Ockwig, H. K. Chae, M. Eddaoudi, J. Kim, *Nature* **2003**, 423, 705–714; d) H. K. Chae, D. Y. S. -Pérez, J. Kim, Y. B. Go, M. Eddaoudi, A. J. Matzger, M. O'Keeffe, O. M. Yaghi, *Nature* **2004**, 427, 523–525; e) M. J. Zaworotko, *Nature* **1999**, 402, 242–243.
- [13] C. Brückner, S. J. Retting, D. Dolphin, *Inorg. Chem.* **2000**, 39, 6100–6106.
- [14] a) M. Enders, G. Ludwig, H. Pritzkow, *Eur. J. Inorg. Chem.* **2002**, 539–542; b) K.-M. Lee, J. C. C. Chen, I. J. B. Lin, *J. Organomet. Chem.* **2001**, 617–618, 364–375.
- [15] M. Sheik-Bahae, A. A. Said, T. H. Wei, D. J. Hagan, E. W. Van Stryland, *IEEE J. Quantum Electron* **1990**, 26, 760–764.
- [16] W. Ji, H. J. Du, S. Shi, *J. Opt. Soc. Am. B* **1995**, 12, 876–881.
- [17] a) C. Lee, W. Yang, R. G. Parr, *Phys. Rev. B* **1988**, 37, 785–789; b) H. B. Schlegel, *J. Comput. Chem.* **1982**, 3, 214–219; c) P. J. Hay, W. R. Wadt, *J. Chem. Phys.* **1985**, 82, 299–310.
- [18] a) M. K. M. Low, H. W. Hou, H. G. Zheng, W. T. Wong, G. X. Jin, X. Q. Xin, W. Ji, *Chem. Commun.* **1998**, 505–506; b) H. W. Hou, Y. T. Fan, C. X. Du, Y. Zhu, W. L. Wang, X. Q. Xin, M. K. M. Low, W. Ji, H. G. Ang, *Chem. Commun.* **1999**, 647–648; c) C. Zhang, Y. L. Song, B. M. Hung, Z. L. Zue, X. Q. Xin, *Chem. Commun.* **2001**, 843–844; d) L. W. Tutt, A. Kost, *Nature* **1992**, 356, 224–227; e) C. L. Liu, X. Wang, Q. H. Gong, K. L. Tang, X. L. Jin, J. He, P. Cui, *Adv. Mater.* **2001**, 13, 1687–1690.
- [19] a) L. W. Tutt, T. F. Boggess, *Prog. Quantum Electron.* **1993**, 17, 299–338; b) F. Henari, J. Callaghan, H. Stiel, W. Blau, D. J. Cardin, *Chem. Phys. Lett.* **1992**, 199, 144–148; c) D. G. McLean, R. L. Sutherland, M. C. Brant, D. M. Brandelik, P. A. Fleitz, T. Pottenger, *Opt. Lett.* **1993**, 18, 858–860.
-

DOI: 10.1002/anie.200501034

DNA Tube Structures Controlled by a Four-Way-Branched DNA Connector***Masayuki Endo,* Nadrian C. Seeman, and Tetsuro Majima**

The programmed self-assembly of molecular building blocks into desired structures is one of the most fascinating challenges in the field of supramolecular chemistry, and the basic methodology is also applicable for the creation of nanoscale materials.^[1–3] Double-stranded DNA is a promising candidate for achieving the desired structural formation and arrangement, because of the reliable molecular assembly based on the base-pairing system and well-defined periodic structure of the double helix DNA. Structurally controlled crossover DNA motifs, called “DNA tiles”, have been used as building blocks for creating one- and multi-dimensional nanostructures.^[4–7] Recently, by utilizing these crossover DNA molecules, extended structures such as tube structures have been created.^[8–10] Further extension of the design of desired DNA structures could be achieved by employing various chemically modified oligonucleotides.

Here we report a novel method for preparation of structurally controlled DNA tubes by using a DNA tile system^[4–7] with the assistance of a four-way-branched DNA connector. Branched DNA can assemble multiple double helices by duplex formation.^[11] In this study, we designed and synthesized a DNA–porphyrin connector, Porph-(Tc)₄ **1**, in which 10-mer DNA strands are connected to four spacers of a tetraphenylporphyrin derivative (Figure 1a). We also employed the DNA tile system which can assemble two planar DNA tiles (tile A and tile B) into two-dimensional (2D) array structures by using the geometry of 2.5 helical turns between two DNA tiles (Figure 1b and the upper part of

[*] Dr. M. Endo, Prof. Dr. T. Majima
The Institute of Scientific and Industrial Research
Osaka University
8-1 Mihogaoka, Ibaraki, Osaka 567-0047 (Japan)
Fax: (+81) 6-6879-8499
E-mail: endo@sanken.osaka-u.ac.jp
majima@sanken.osaka-u.ac.jp

Prof. Dr. N. C. Seeman
Department of Chemistry, New York University
New York, NY 10003 (USA)

[**] We thank Dr. Ruojie Sha (New York University) for assistance with the experiments. This work has been partly supported by Grants-in-Aid for Scientific Research (Project no. 17105005, Priority Area (417), 21st Century COE Research, and others) from the Ministry of Education, Culture, Sports, Science, and Technology (MEXT) of the Japanese Government to M.E. and T.M., as well as by grants to N.C.S. from the National Institute of General Medical Sciences, National Science Foundation, Office of Naval Research, Army Research Office, and Nanoscience Technologies, Inc.



Supporting information for this article is available on the WWW under <http://www.angewandte.org> or from the author.

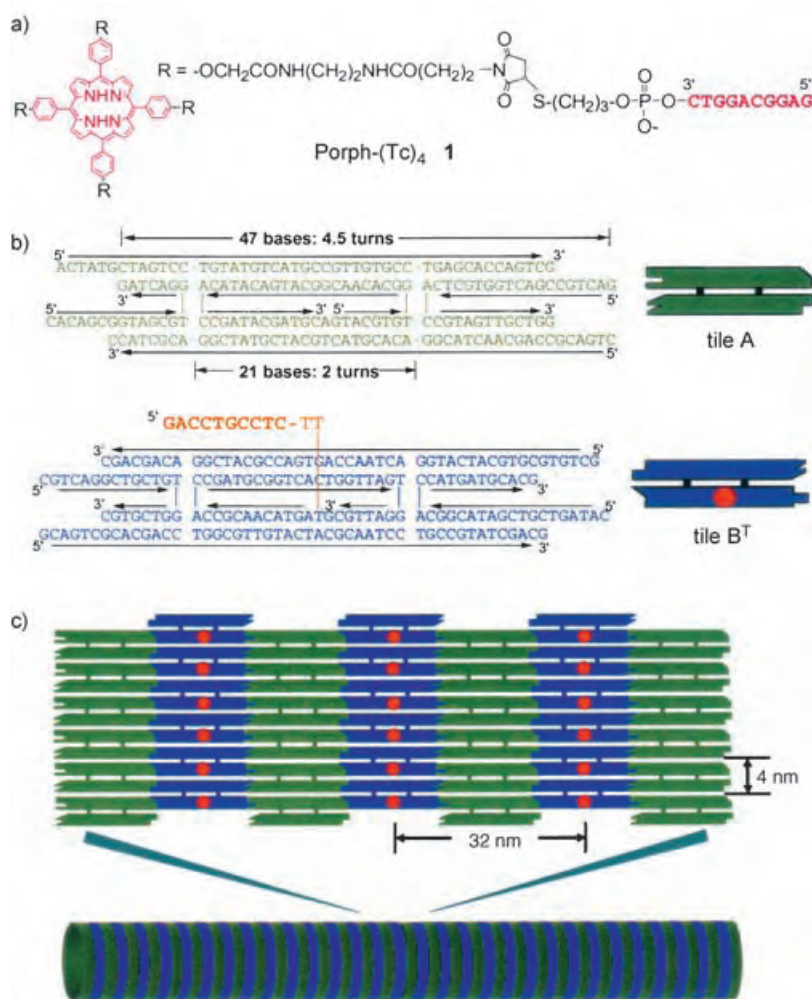


Figure 1. The DNA–porphyrin connector and the DNA tiles system employed in the experiment. a) Structure of the DNA–porphyrin conjugate, Porph-(Tc)₄ **1**. b) The sequences of DNA tile A (green) and DNA tile B^T (blue), which has an extra single strand (orange sequence). The orange dot on tile B represents the extra single strand. c) Two-dimensional DNA array prepared from the tiles A and B^T (top) and the three-dimensional DNA tube structure formed in the presence of Porph-(Tc)₄ **1** (bottom).

Figure 1 c).^[4–7] The center strand of tile B^T has an extra 12-mer single strand (T=tag strand) that has 10 bases as a recognition sequence for hybridization with a complementary DNA strand (Tc=complementary to the tag strand) and two additional thymidines as a linker. We planned to assemble the four B^T tiles by using the DNA–porphyrin connector, which captures and brings multiple B^T tiles together by hybridizing with the extra tag strands of the B^T tiles. The four neighboring tiles constrained by the DNA–porphyrin connector could then induce tube formation during assembly with the A tiles. The length between the center of the porphyrin and the 5'-end of the DNA strand in the DNA–porphyrin connector is 7–8 nm (Figure 1 a), which could allow the alignment of the four short axes of the B^T tiles side by side (total 16 nm) for A–B^T array formation.

DNA–porphyrin conjugate **1** was synthesized by coupling the tetramaleimide-linked tetraphenylporphyrin with a 3'-

thiol-modified 10-mer DNA strand (Tc) that is complementary to the tag strand of the tile B^T (see Supporting Information). Ten DNA strands and Porph-(Tc)₄ **1** were mixed together and annealed from 95°C to room temperature for 36 h in a buffer containing 2-[4-(2-hydroxyethyl)-1-piperazinyl]ethanesulfonic acid (HEPES; pH 7.5), ethylenediaminetetraacetate (EDTA), and Mg²⁺.^[12]

After complex formation, we observed the DNA nanoscale structures by using atomic force microscopy (AFM) in solution.^[12] In the case of annealing with tiles A and B^T only, 2D DNA arrays were obtained which were similar to those previously described with the A–B array system (Figure 2 a).^[6,7] By contrast, with addition of 1/4th of an equivalent of Porph-(Tc)₄ **1** connector and annealing with tiles A and B^T, the large 2D structures were not observed and fiber-like structures appeared (Figure 2 b), the lengths of which reaching over 20 μm. When 1/16th of an equivalent of **1** was annealed with tiles A and B^T, we obtained a mixture of fibers and the usual 2D arrays (see Supporting Information). Thus, the formation of fiber structures depended on the stoichiometry between the tiles and Porph-(Tc)₄ **1**.

To characterize the detailed nanoscale structures, we analyzed the surface of the DNA fibers. A cross-section analysis of the long axis of the DNA fiber structure reveals

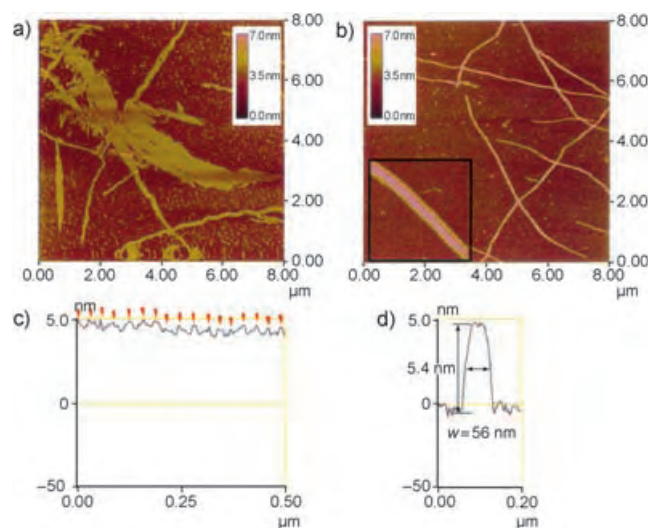


Figure 2. AFM images of the DNA structures. a) Annealing with tiles A and B^T. Image size: 8 × 8 μm². b) Annealing with tiles A and B^T in the presence of Porph-(Tc)₄ **1**. Image size: 8 × 8 μm². Inset: Expanded image of the DNA structure prepared from tiles A and B^T with **1**. Image size: 500 × 500 nm². c) Cross-section analysis of the long axis of the DNA structure shown in the inset of (b). Orange arrows represent peaks of the periodical stripes. d) Cross-section analysis of the short axis of the DNA structure shown in the inset of (b).

that periodic stripes are observed on the surface of the fiber (Figure 2c). The distance between two stripes was 29–34 nm, which corresponds to the total length of the long axis of the A and B tiles (32 nm; Figure 1c). Therefore, these stripes originated from the extra strand of tile B^T. In the case of the initial A–B^T 2D array without the addition of the connector **1**, stripes were not clearly observed, because the extra single strand (tag strand T) attached to the B^T tile was flexible (see Supporting Information). In contrast, the A–B* 2D array, which has hairpins on the 2D tile that work as topological markers, showed clear stripes, because the stable hairpins are oriented out of the plane of the 2D array as described previously (see Supporting Information).^[6,7] These suggest that the strong stripe formation on the DNA fiber is induced by duplex formation between the tag strand of the tile B^T and its complementary strand (Tc) of the connector **1**. The individual DNA fibers showed uniform width (approximately 55 nm) and height (5.2–5.6 nm; Figure 2d). The height of the stripes was 0.3–0.8 nm. The analysis indicates that the height of the DNA fiber structures is larger than the two layers of the double helices. According to the cross-section analysis of the DNA fiber (Figure 2b, inset), the center of the top surface is slightly squashed by 0.2–0.3 nm as compared to both edges (Figure 2d).^[13] From these observations, the DNA structures observed here exhibited the features of DNA tube structures, similar to those described in previous reports.^[8,12,13] We conclude that the DNA structures obtained here are tube structures. In the present study, the locations of the DNA–porphyrin connectors in the DNA tube structures remain unclear. Casual inspection of the AFM images gives the impression that the DNA–porphyrin connectors are on the outside of the tube structures. However, from thickness measurements, we cannot exclude the possibility that they are on the inside, the circumstance that is most likely to lead to tube formation.

We also obtained DNA structures with a height lower than the tubes, and these two structures were located on the same DNA fibers (Figure 3a). We noted that in the detailed images of these lower-height structures (Figure 3b), each stripe on the DNA surface has two or three blocks of dotlike structures, which were characterized by a cross-section analysis of the stripes (red arrows in Figure 3d). Cross-section analysis for the long axis revealed that the stripes were separated by 29–34 nm (Figure 3c), which corresponds to the total length of the long axis of the A–B^T tiles as described previously. The height of the surface of the lower-height structures was 2.7 nm (Figure 3d). The height of the stripes was 0.3–1.0 nm, which is comparable to the stripes of the tube structures shown in Figure 2. A high-resolution AFM image of the DNA surface in the lower-height structures in a different area is shown in Figure 3e. Each stripe is separated and the individual A tiles can be observed to be the same as those of the A–B* arrays. In this lower-height section, the visible part of the array contains seven A tiles and a similar number of less well resolved B^T tiles as repeating units.

To examine the difference between the tube and lower-height structures, we analyzed the boundaries of these structures on the same fiber (Figure 3a), and two interesting features were observed: 1) The stripes in the tube and lower-

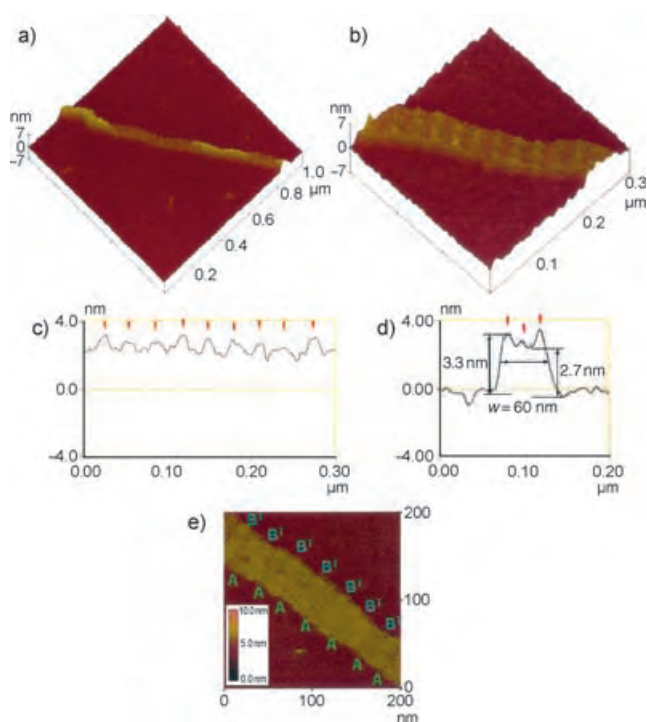


Figure 3. AFM images of the DNA structures. a) Mixed area of normal and lower-height DNA structures. Image size: $1 \times 1 \mu\text{m}^2$. b) Expanded image of the lower-height structures. Image size: $300 \times 300 \text{ nm}^2$. c) and d) Cross-section analysis of the lower-height area in Figure 3b for the long (c) and short (d) axes. Orange arrows in (c) represent peaks of the periodical stripes and red ones in (d) represent dotlike structures on the stripe of the lower-height area. e) High-resolution AFM image of the DNA nanostructure of the lower-height area. Image size: $200 \times 200 \text{ nm}^2$.

height areas are successive without any gap. 2) The height of the lower-height DNA structures is clearly changed to almost half the height of the tube ones, and the width of the short axis of the lower-height structures (ca. 65 nm) is always larger than that of the tubes (ca. 55 nm) on the successive DNA structures. From these observations, we conclude that the lower-height areas on the DNA fibers are incomplete tubes with the height of single-layer duplexes, as described previously.^[8,13]

We estimated the complex-formation process by using the UV absorption change at 260 nm versus temperature. The duplex formation of Porph-(Tc)₄ **1** with its complementary strand occurs at 46 °C, which is slightly higher than the initial temperature of the A–B array formation (40–45 °C). This indicates that the complex formation between **1** and four B^T tiles precedes assembly of the A–B tiles, and then the constrained B^T tiles with **1** and the A tiles form some constrained array leading to the tube formation.

We have demonstrated a novel method for the preparation of DNA tubes, by using the A–B tile system and the four-way-branched DNA connector which converts DNA arrays into DNA tube structures. The DNA–porphyrin connector clearly restricted the extension to the short axis of the tile, while the long axis did not change as compared to that of the usual A–B tile system. We expect that the DNA tubes

prepared by using this method can be employed as nanoscale scaffolds for the preparation of structurally defined materials and devices.^[13,14]

Received: March 22, 2005

Revised: May 24, 2005

Published online: August 26, 2005

Keywords: DNA · nanostructures · nanotubes · self-assembly · supramolecular chemistry

-
- [1] a) J.-M. Lehn, *Supramolecular Chemistry*, VCH, Weinheim, **1995**; b) J.-M. Lehn, *Chem. Eur. J.* **2000**, *6*, 2097–2102.
- [2] a) D. J. Hill, M. J. Mio, R. B. Prince, T. S. Hughes, J. S. Moore, *Chem. Rev.* **2001**, *101*, 3893–4011; b) L. Brunsveld, B. J. B. Folmer, E. W. Meijer, R. P. Sijbesma, *Chem. Rev.* **2001**, *101*, 4071–4097.
- [3] a) C. A. Mirkin, *Inorg. Chem.* **2000**, *39*, 2258–2272; b) C. M. Niemeyer, *Angew. Chem.* **2001**, *113*, 4254–4287; *Angew. Chem. Int. Ed.* **2001**, *40*, 4128–4158.
- [4] a) N. C. Seeman, *Angew. Chem.* **1998**, *110*, 3408–3428; *Angew. Chem. Int. Ed.* **1998**, *37*, 3220–3238; b) N. C. Seeman, *Biochemistry* **2003**, *42*, 7259–7269.
- [5] T. J. Fu, N. C. Seeman, *Biochemistry* **1993**, *32*, 3211–3220.
- [6] E. Winfree, F. Liu, L. A. Wenzler, N. C. Seeman, *Nature* **1998**, *394*, 539–544.
- [7] F. Liu, R. Sha, N. C. Seeman, *J. Am. Chem. Soc.* **1999**, *121*, 917–922.
- [8] D. Liu, S. H. Park, J. H. Reif, H. Yan, *Proc. Natl. Acad. Sci. USA* **2004**, *101*, 717–722.
- [9] J. C. Mitchell, J. R. Harris, J. Malo, J. Bath, A. J. Turberfield, *J. Am. Chem. Soc.* **2004**, *126*, 16342–16343.
- [10] P. W. K. Rothmund, A. Ekani-Nkodo, N. Papadakis, A. Kumar, D. K. Fygenson, E. Winfree, *J. Am. Chem. Soc.* **2004**, *126*, 16344–16352.
- [11] a) M. Scheffler, A. Dorenbeck, S. Jordan, M. Wüstefeld, G. von Kiedrowski, *Angew. Chem.* **1999**, *111*, 3514–3518; *Angew. Chem. Int. Ed.* **1999**, *38*, 3311–3315; b) L. H. Eckardt, K. Naumann, W. M. Pankau, M. Rein, M. Schweitzer, N. Windhab, G. von Kiedrowski, *Nature* **2002**, *420*, 286; c) K. M. Stewart, L. W. McLaughlin, *J. Am. Chem. Soc.* **2004**, *126*, 2050–2057; d) K. M. Stewart, J. Rojo, L. W. McLaughlin, *Angew. Chem.* **2004**, *116*, 5932–5935; *Angew. Chem. Int. Ed.* **2004**, *43*, 5808–5811.
- [12] Complex formation was carried out in a solution (100 μ L) containing 0.5 μ M oligonucleotides (total 10 strands), 0.125 μ M Porph-(Tc)₄ **1**, 10 mM HEPES (pH 7.5), 1 mM EDTA, and 5 mM Mg(OAc)₂. Samples were annealed from 95 °C to room temperature over 36 h in a 2-L water bath kept in a styrol box.^[7] A sample (4 μ L) was deposited on a freshly cleaved mica plate and left for 1 min to adsorb onto the surface. After addition of a solution (30 μ L) containing 10 mM HEPES (pH 7.5), 1 mM EDTA, and 5 mM Mg(OAc)₂ in a fluid cell and another 30 μ L of the same solution onto the AFM tip, images were acquired on a Digital Instruments NanoScope IV atomic force microscope by using the tapping mode.
- [13] H. Yan, S. H. Park, G. Finkelstein, J. H. Reif, T. H. LaBean, *Science* **2003**, *301*, 1882–1884.
- [14] J. D. Le, Y. Pinto, N. C. Seeman, K. Musier-Forsyth, T. A. Taton, R. A. Kiehl, *Nano Lett.* **2004**, *4*, 2343–2347.

DOI: 10.1002/anie.200501145

Mechanism of the Initial Conformational Transition of a Photomodulable Peptide**

Tadeusz Andruniów, Simona Fantacci,*
Filippo De Angelis, Nicolas Ferré, and
Massimo Olivucci*

The ability to control the specific conformation of peptides or proteins is highly desirable in the design of bioactive materials,^[1] optical data storage devices,^[2] or for triggering the folding/unfolding of oligopeptide chains.^[3,4] Conformational changes in macromolecules can be achieved by incorporating a photoresponsive “monomer” into the molecule backbone;^[5] such a monomer is capable of converting light energy into a permanent change in geometry. This approach is also seen in biological receptors^[6–9] where the photoisomerization of organic chromophores is used to switch between different conformations. One of the most prominent examples of such switches is the protonated Schiff base (PSB) of retinal found in rhodopsin proteins. This chromophore undergoes a *cis*→*all-trans* photoisomerization that triggers a conformational change of the native protein scaffold.^[10,11]

We recently concluded that synthetic PSBs may provide suitable frameworks for the design of molecular switches or motors.^[12] We demonstrated that 5-methyl-4-(5'-methyl-

[*] Dr. S. Fantacci, Dr. F. De Angelis
Istituto CNR di Scienze e Tecnologie Molecolari (ISTM)
c/o Dipartimento di Chimica
Università degli Studi di Perugia
via Elce di Sotto 8, 06123 Perugia (Italy)
Fax: (+39) 075-585-5606
E-mail: simona@thch.unipg.it

Dr. T. Andruniów, Prof. Dr. M. Olivucci
Dipartimento di Chimica
Università degli Studi di Siena
via Aldo Moro, 53100 Siena (Italy)
Fax: (+39) 0577-234-278
E-mail: olivucci@unisi.it

Dr. T. Andruniów
Institute of Physical and Theoretical Chemistry
Department of Chemistry, Wrocław University of Technology
Wyb. Wyspińskiego 27, 50-370 Wrocław (Poland)

Dr. N. Ferré
Laboratoire de Chimie Théorique et de Modélisation Moléculaire
UMR 6517-CNRS Universités Aix-Marseille
Case 521, Centre de Saint-Jérôme
13397 Marseille Cedex 20 (France)

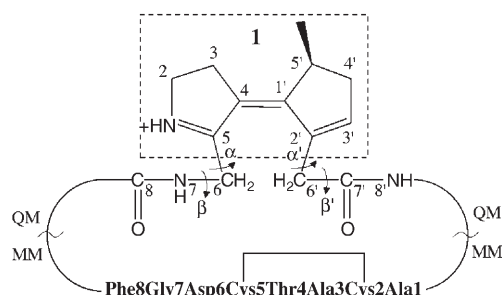
[**] The authors are grateful to Prof. Peter Hamm, Dr. Jan Helbing, and Prof. Gerhard Stock for useful comments. This work was supported by the Università di Siena (PAR02/04), FIRB (RBAU01EPMR), and COFIN2004. M.O. and T.A. are grateful for a Marie-Curie grant (HPMF-CT-2002-01769).



Supporting information for this article (computational details, coordinates of all QM/MM and full QM optimized structures, tables of the energies and properties) is available on the WWW under <http://www.angewandte.org> or from the author.

cyclopent-2'-enylidene)-3,4-dihydro-2*H*-pyrrolinium, **1** in Scheme 1, a PSB featuring a “locked” backbone, satisfies the criteria for an efficient switch.

Previous studies on the octapeptide (**OP**) H₂N-Ala1-Cys2-Ala3-Thr4-Cys5-Asp6-Gly7-Phe8-COOH, derived



Scheme 1. Subsystems of *cis*-**1-OP** treated by quantum mechanics (QM) and molecular mechanics (MM). Box (dotted lines) encloses **1**. Angles α , β , α' , and β' are discussed in the text.

from the thioredoxin reductase active site, revealed that this chain can be conveniently used to prepare a bicyclic peptide incorporating the azobenzene (Ab) photoisomerizable unit and a disulfide bridge.^[7–9] In such a system light irradiation may be used to permanently switch the conformation of the peptide.

Herein, our target is to investigate the photoisomerization mechanism of an analogue system, **1-OP** in Scheme 1, where Ab is replaced with the computationally tractable^[13] PSB unit **1**. While in previous studies,^[3] which focused on longer timescales, the photochemical step was treated empirically, herein we show that the photoisomerization of *cis*-**1-OP** can be characterized by the novel quantum mechanics/molecular mechanics (QM/MM)^[14,15] strategy recently applied to rhodopsin^[16] and featuring a CASPT2//CASSCF QM level (see Experimental Section). To determine the intrinsic factors driving the transmission of the photoinduced strain to the peptide backbone we focus on gas-phase **1-OP**. The results indicate that while the switch starts to change immediately after excited state (*S*₁) population, the change of the peptide moiety occurs only after decay to the ground state (*S*₀). The resolution of the structure of the conical intersection funnel (CI) driving the *S*₁→*S*₀ decay, allows the effect of the *S*₀ energy surface on the initial *S*₀ dynamics of **1-OP** to be explored. This effect is simulated at the QM level by running a 3 ps ground state Car–Parrinello^[17] molecular dynamics (CPMD) trajectory.

Photoexcitation of *cis*-**1-OP** initiates the relaxation along the *S*₁ energy surface (Figure 1), ultimately leading to a CI located approximately 30 kcal mol^{−1} lower in energy. The deformation driving the reactant out of the Franck–Condon (FC) region corresponds to a skeletal single-bond contraction and double-bond expansion (the reactive C4–C1' double bond is lengthened to 1.48 Å) coupled with an approximate 3° increase of the C5–C4–C1'–C2' torsion angle. Further evolution along the same coordinate, leads to a transition structure (TS_{ex}) located about 4 kcal mol^{−1} higher than *cis*-**1-OP**. Analysis of the TS_{ex} structure indicates that the corresponding

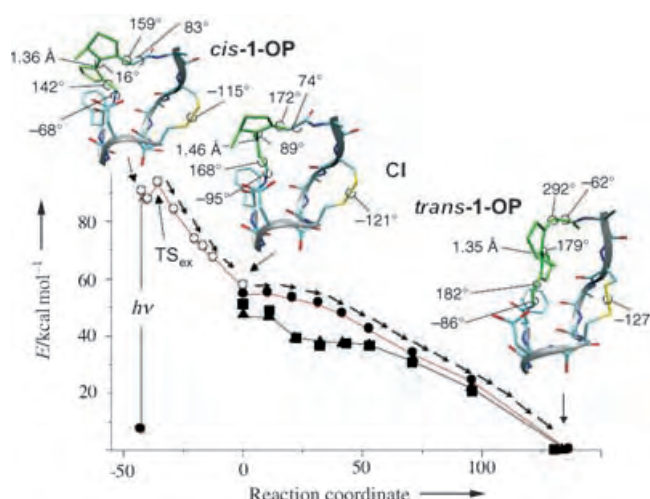


Figure 1. Energy profiles along the paths describing the *S*₁ and *S*₀ relaxation. The structures (geometrical parameters in [Å] and [°]) document the progression of the molecular structure of **1** and related link regions. The agreement between different computational methods is also shown (for computational details see Experimental Section and Supporting Information). ○ *S*₁ CASPT2//CASSCF/6-31G*/Amber, ● *S*₀ CASPT2//CASSCF/6-31G*/Amber, ■ PBE/6-31G*, ▲ CP plane-wave PBE.

barrier is due to the steric repulsion between the hydrogen at C3 and methyl group at C5'. The steric repulsion is decreased by further twisting about the C4–C1' bond that drives the system along a barrierless region of the *S*₁ path. Along this region the stretching deformation of **1** decreases, the C4–C1' bond length stabilizes at 1.46 Å, and the twisting about this bond becomes dominant. The CI structure, located at the bottom of the *S*₁ surface, features a central double bond twisted by 89°.

Inspection of superimposed peptide backbones of the *cis*-**1-OP** and CI structures (Figure 2) reveals that, despite the difference in twist of unit **1** of approximately 75° in these two structures, the peptide conformations are still remarkably similar with a root-mean-square (rms) deviation of less than 0.6 Å. Both conformations exhibit a right-handed helical shape at Ala3 and an inverse γ turn centered on Asp6.

To provide mechanistic insight into the ground-state decay we have calculated the *S*₀ path departing from CI and leading to the photoproduct (*trans*-**1-OP**; Figure 1). The *S*₀ energy profile displays an approximately 0.9 kcal mol^{−1} barrier at 102° twisting, suggesting the presence of a restrain force, attributed to initial peptide deformation. Further progression along the isomerization coordinate induces a limited change in energy up to 114° followed by a slope leading to the *trans*-**1-OP** energy minimum (characterized by a *trans* configuration of the switch).

Even though the superimposed peptide backbones of *cis*-**1-OP**, CI, and photoproduct structures share a common overall fold, *trans*-**1-OP** displays a more extended (stretched) conformation. Rms deviation between the CI and *trans*-**1-OP** peptide is about 1.5 Å. Analysis of the standard dihedral angles ϕ and ψ along the backbone reveals that the helical character of Ala3 in the product is less pronounced than in the

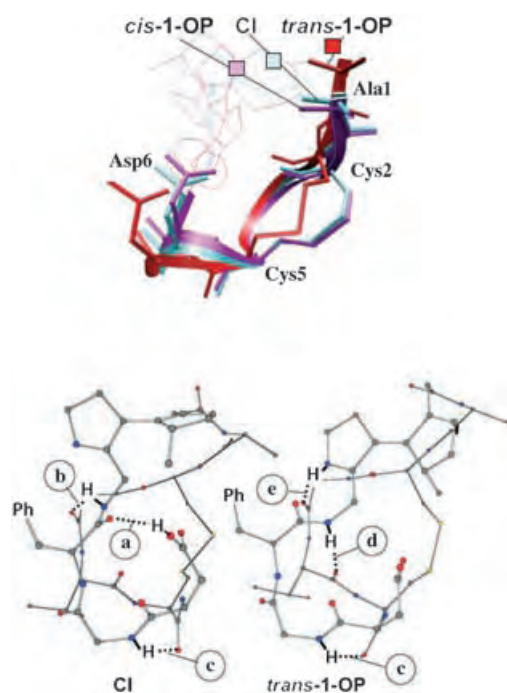


Figure 2. Top: superposition of the *cis*-1-OP (red), CI (blue), and *trans*-1-OP (magenta) structures. Bottom: hydrogen-bond patterns of CI and *trans*-1-OP. The hydrogen bonds a–e are discussed in the text.

reactant. However, *cis*- and *trans*-1-OP differ mainly in the orientation of the inner cycle formed by the disulfide bridge between Cys2 and Cys5. In fact, the limited twisting of the Cys2-S-S-Cys5 dihedral angle by about 25° is accompanied by the reorientation of residues Asp6, Gly7, and Phe8 of the C-terminal part of the peptide backbone.

The response of the peptide secondary structure to the isomerization of **1** is described in terms of the changes in the hydrogen-bond pattern (a–e, see Figure 2). The results suggest that on S_1 there is no change in the number or location of the hydrogen bonds (three hydrogen bonds, indicated as a, b, and c in Figure 2, could be detected). However, upon departure from the CI structure and relaxation on the S_0 energy surface, two new hydrogen bonds d and e that run between the Thr4 carbonyl group and the N7-H group of the link region and between the N⁺-H group of **1** and the Ala3 carbonyl group are formed. Similarly, the hydrogen bonds a and b between the Asp6 hydroxy and Phe8 carbonyl groups and between the N7-H of the link group and the Ala3 carbonyl, respectively, are broken. The only hydrogen bond that remains intact during both the S_0 and S_1 relaxations is c between the N-H group of Gly7 and the carbonyl group of Cys5. The treatment of the hydrogen bonds between atoms treated by QM and MM methods, has been validated by comparing the QM/MM and the full PBE-functional optimized structures of *cis*- and *trans*-1-OP. It is shown that by the QM/MM methods the hydrogen bonds a, b, and d are less than 0.04 Å longer at the PBE level. A larger difference is found for the bent hydrogen bond e that is 0.14 Å longer when computed at the PBE level.

The link regions between the switch **1** and the octapeptide are made up of the -CH₂-NH- and -CH₂-CO- groups

connected to carbon atoms C5 and C2', respectively (see Scheme 1). Accordingly, the evolution of these links is characterized in terms of the values of the angles α (C4-C5-C6-N7) and β (C5-C6-N7-C8), and α' (C1'-C2'-C6'-C7') and β' (C2'-C6'-C7'-N8'). It is apparent from Figure 1 that α and β undergo a limited overall change (+40° and -18°) with respect to α' and β' (+133° and -145°). Since, these changes provide information on the way the photoinduced torsional strain is transmitted from the switch to the octapeptide, we conclude that the strain is transmitted asymmetrically by the two link regions. This behavior is easily related to the fact that α and β are made stiffer by the involvement of the N7-H, C8=O, and N⁺-H groups in the hydrogen-bond network. Notice that the change of α' and β' along the S_1 path is very limited. Thus, similar to the octapeptide chain, the link region changes mainly during S_0 relaxation.

Information on the effect of the S_0 path on the early S_0 relaxation dynamics including the relative timescales of the leading molecular modes, are obtained through the analysis of a 3 ps CPMD trajectory. As shown in Figure 1, both CPMD (CP plane-wave PBE) and Gaussian98 PBE/6-31G* yield energy profiles qualitatively close to the QM/MM one. The largest discrepancies are found in the initial part of the path where the density functional theory (DFT) curves show an inflection. The consistency of DFT//CASSCF and CASPT2//CASSCF S_0 energy profiles for PSBs has been previously evaluated.^[18] The relaxation process of the chromophore is monitored by the time evolution of the torsional deformation and length of the C4-C1' bond. The relaxation of the peptide is monitored by studying four hydrogen-bond lengths. Finally, the evolution of the link region between the switch and the peptide is studied by monitoring the α' and β' angles.

As shown in Figure 3 the relaxation of the switch is characterized by coherent changes in torsional deformation

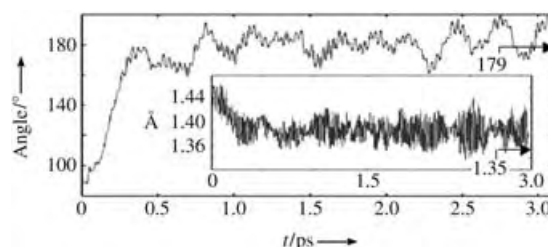


Figure 3. Time evolution of the C5-C4-C1'-C2' dihedral angle [°] and C4-C1' bond length [Å]. The arrows indicate the *trans*-1-OP values.

and bond lengths. In fact, both quantities approach the S_0 equilibrium values in less than 0.5 ps. No back oscillation towards the S_1 values is observed. On the other hand, the change in the peptide secondary structure reported in Figure 4 is consistent with a slower process (> 3 ps). In fact, although breaking of hydrogen bond a seems to occur on the picosecond timescale, a large oscillation is observed which continues up to 3 ps. An oscillatory behavior is also observed for the switching in the hydrogen bonds b and d. After 1 ps b is broken while d is formed. However, after 2 ps these hydrogen bonds are pushed back to their original positions, while at 2.5 ps a new inversion takes place. Remarkably, after 3.0 ps a,

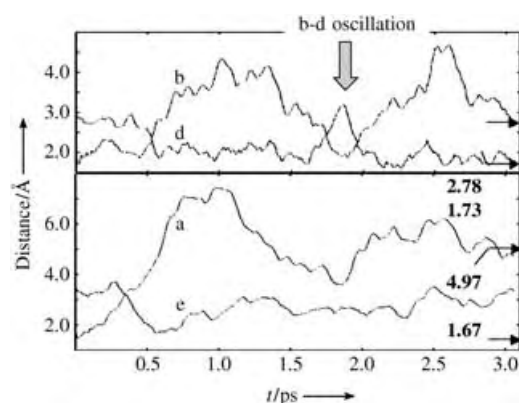


Figure 4. Evolution of the hydrogen bonds a, b, d, and e defined in Figure 2. The arrows indicate the *trans*-1-OP values.

b, and d seem to have reached the final values of the S_0 *trans*-1-OP energy minimum. The behavior of hydrogen bond e is different. Although initial relaxation promotes formation of this (looser and bent) hydrogen bond just after 0.6 ps, the bond breaks and remains substantially broken up to the end of the simulation. This bond will require a longer time to reach the predicted equilibrium value. A behavior that can be associated to the bent geometry of e that features a N–H...O angle of 132°.

The dynamics of the link region is displayed in Figure 5. There is a high correlation between angles α' and β' all along

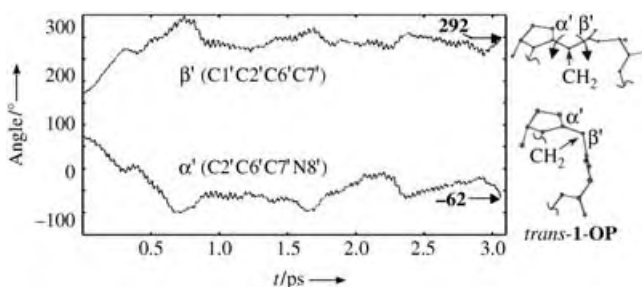


Figure 5. Time evolution of the link-region torsional angles α' and β' . The arrows indicate the *trans*-1-OP values.

the simulation. They move according to a hula-twist motion (a clockwise and counterclockwise twist about two adjacent bonds) of the $-\text{CH}_2-$ unit of the link. This movement provides a way to efficiently bend the linkage without introducing angular strain. The *trans*-1-OP product values are reached in less than 1 ps.

In conclusion, we describe the mechanism of photo-induced strain transmission in a naked macrocyclic cation. (Of course, owing to its effect on the hydrogen-bond stability and formation, a protic solvent may substantially change the mechanism and timescale of the relaxation. Solvent and counterion effects on 1-OP are currently under investigation). While the photoinduced conformational transition from *cis*-1-OP to *trans*-1-OP involves a total rms deviation of 2.0 Å, only a fraction of this change occurs during the S_1 evolution, which mainly features stretching relaxation and an approximately

90° twisting of the switch unit 1. The documented S_1 relaxation path indicates an ultrafast $S_1 \rightarrow S_0$ decay dynamic at room temperature. In fact, 1) there is only a small barrier restraining the S_1 evolution and 2) a S_1/S_0 conical intersection provides a fully efficient $S_1 \rightarrow S_0$ decay channel. These conclusions are consistent with the behavior observed for experimentally accessible Ab-peptide analogues^[3,9] where decay to S_0 occurs in under 1 ps. Our reaction path and trajectory analysis indicate that the peptide relaxation occurs entirely on S_0 on a much longer timescale. Indeed, while the relaxation of the switch is substantially completed within 0.5 ps, the hydrogen bonds b, d, and e oscillate even after 2 ps with e still broken after 3 ps. On the other hand, the asymmetric relaxation of the link regions is found to occur on an intermediate time scale (< 1 ps) indicating a sequential (switch \rightarrow link \rightarrow peptide) mechanism for the transmission of the strain generated by the switch. Loosely, these results are consistent with ultrafast IR spectroscopy measurements on an Ab-peptide analogue indicating that the photoinduced peptide stretching dynamics (that is associated with the redistribution of the strain) is completed in a time window between 6 and 20 ps.^[9] Finally, notice that within the first half-oscillation in Figure 4, the backbone changes described by the trajectory and S_0 relaxation path of Figure 1 (i.e. the static minimum energy path) are similar. Indeed, a transient geometry close to *trans*-1-OP is generated and lost after 0.7 ps indicating that the path accelerates the system directly towards the product structure.

Experimental Section

Computational Details: Our QM/MM implementation is based on a hydrogen link-atom scheme with the frontier placed at the $\text{CO}-\text{C}_\alpha\text{H}$ and $\text{NH}-\text{C}_\alpha\text{H}$ bonds of Ala1 and Phe8, respectively (see Scheme 1). The ab initio QM calculations are based on a CASSCF/6-31G* level. The active space comprises the full π system of 1 (six electrons in six π orbitals). For the MM part we use the Amber force field^[19] with standard or re-parameterized van der Waals potentials. CASSCF/6-31G*/Amber geometry optimizations are carried out with the GAUSSIAN98^[20] (G98) and TINKER^[21] programs. To account for dynamic electron correlation effects, re-evaluation of the energy of the optimized structures was carried out at the multiconfigurational second-order perturbation theory level using the CASPT2 implementation of MOLCAS-5^[22] and a two-root state-averaged CASSCF zeroth-order wavefunction (CASPT2//CASSCF/6-31G*/Amber level). The initial relaxation direction (IRD) method^[23] was used to locate the steepest-descent direction to be followed when computing the S_1 (starting at *cis*-1-OP) and S_0 (starting at CI) branches of the reaction path of Figure 1. To simulate the S_0 relaxation dynamics a single CPMD trajectory starting at CI with zero initial velocities (the sensitivity of the trajectory to a random distribution of velocities at CI has been tested. α' and β' are found to be the most sensitive variables) was calculated at the full QM level, using the PBE exchange-correlation functional^[24] with a plane-wave basis set and ultrasoft pseudopotentials.^[25,26] Additional single-point CPMD and G98 PBE/6-31G* calculations were performed on the QM/MM S_0 branch to check the consistency of DFT and QM/MM results. See Supporting Information for further computational details.

Received: March 31, 2005

Revised: May 6, 2005

Published online: August 18, 2005

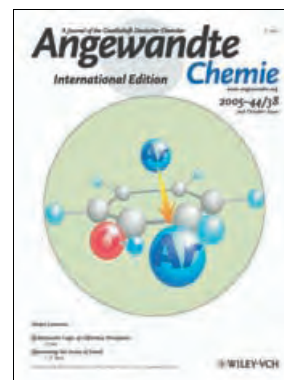
Keywords: ab initio calculations · molecular switches · peptides · photochemistry · reaction mechanisms

- [1] a) V. J. Hruby, J.-M. Ahn, S. Liao, *Curr. Opin. Chem. Biol.* **1997**, *1*, 114–119; b) A. S. Ripka, D. H. Rich, *Curr. Opin. Chem. Biol.* **1998**, *2*, 441–452.
- [2] a) B. L. Feringa, W. F. Jager, B. De Lange, *Tetrahedron* **1993**, *49*, 8267–8310; b) P.-O. Astrand, P. S. Ramanujam, S. Hvilsted, K. L. Bak, S. P. A. Sauer, *J. Am. Chem. Soc.* **2000**, *122*, 3482–3487.
- [3] S. Spörlein, H. Carstens, H. Satzger, C. Renner, R. Behrendt, L. Moroder, T. Tavan, W. Zinth, J. Wachtveitl, *Proc. Natl. Acad. Sci. USA* **2002**, *99*, 7998–8002.
- [4] V. Kräutler, A. Aemissegger, P. H. Hünenberger, D. Hilvert, T. Hansson, W. F. van Gunsteren, *J. Am. Chem. Soc.* **2005**, *127*, 4935–4942.
- [5] a) I. Willner, S. Rubin, *Angew. Chem.* **1996**, *108*, 419–439; *Angew. Chem. Int. Ed. Engl.* **1996**, *35*, 367–385; b) I. Willner, *Acc. Chem. Res.* **1997**, *30*, 347–356.
- [6] L. Ulysse, J. Cubillos, J. Chmielewski, *J. Am. Chem. Soc.* **1995**, *117*, 8466–8467.
- [7] R. Behrendt, C. Renner, M. Schenk, F. Wang, J. Wachtveitl, D. Oesterheld, L. Moroder, *Angew. Chem.* **1999**, *111*, 2941–2943; *Angew. Chem. Int. Ed.* **1999**, *38*, 2771–2774.
- [8] C. Renner, R. Behrendt, S. Spörlein, J. Wachtveitl, L. Moroder, *Biopolymers* **2000**, *54*, 489–500.
- [9] J. Bredenbeck, J. Helbing, A. Sieg, T. Schrader, W. Zinth, C. Renner, R. Behrendt, L. Moroder, J. Wachtveitl, P. Hamm, *Proc. Natl. Acad. Sci. USA* **2003**, *100*, 6452–6457.
- [10] R. A. Mathies, J. Lugtenburg In *Handbook of Biological Physics*, Vol. 3 (Eds.: D. G. Stavanga, W. J. de Grip, E. N. Pugh), Elsevier Science B.V., Dordrecht, **2000**, pp. 56–90.
- [11] H. Kandori, Y. Shichida, T. Yoshizawa, *Biochemistry (Moscow)* **2001**, *66*, 1583–1598.
- [12] D. Sampedro, A. Migani, A. Pepi, E. Busi, R. Basosi, L. Latterini, F. Elisei, S. Fusi, F. Ponticelli, V. Zanirato, M. Olivucci, *J. Am. Chem. Soc.* **2004**, *126*, 9349–9359.
- [13] The reactivity of the Ab chromophore is presently untractable at the CASSCF level used herein. This problem is mainly due to the large active space required (18 electrons in 16 orbitals).
- [14] A. Warshel, M. Levitt, *J. Mol. Biol.* **1976**, *103*, 227–249.
- [15] M. J. Field, P. A. Bash, M. Karplus, *J. Comput. Chem.* **1990**, *11*, 700–733.
- [16] T. Andruniów, N. Ferré, M. Olivucci, *Proc. Natl. Acad. Sci. USA* **2004**, *101*, 17908–17913.
- [17] R. Car, M. Parrinello, *Phys. Rev. Lett.* **1985**, *55*, 2471–2474.
- [18] S. Fantacci, A. Migani, M. Olivucci, *J. Phys. Chem. A* **2004**, *108*, 1208–1213.
- [19] P. A. Kollman, R. Dixon, W. Cornell, T. Fox, C. Chipot, A. Pohorille in *Computer Simulation of Biomolecular Systems*, Vol. 3 (Eds.: A. Wilkinson, P. Weiner, W. F. Gunsteren), Elsevier, Dordrecht, **1997**, pp. 83–96.
- [20] Gaussian 98 (Revision A.7), M. J. Frisch, G. W. Trucks, H. B. Schlegel, G. E. Scuseria, M. A. Robb, J. R. Cheeseman, V. G. Zakrzewski, J. A. Montgomery, R. E. Stratmann, J. C. Burant, S. Dapprich, J. M. Millam, A. D. Daniels, K. N. Kudin, M. C. Strain, O. Farkas, J. Tomasi, V. Barone, M. Cossi, R. Cammi, B. Mennucci, C. Pomelli, C. Adamo, S. Clifford, J. Ochterski, G. A. Petersson, P. Y. Ayala, Q. Cui, K. Morokuma, D. K. Malick, A. D. Rabuck, K. Raghavachari, J. B. Foresman, J. Cioslowski, J. V. Ortiz, B. B. Stefanov, G. Liu, A. Liashenko, P. Piskorz, I. Komaromi, R. Gomperts, R. L. Martin, D. J. Fox, T. Keith, M. A. Al-Laham, C. Y. Peng, A. Nanayakkara, C. Gonzalez, M. Challacombe, P. M. W. Gill, B. G. Johnson, W. Chen, M. W. Wong, J. L. Andres, M. Head-Gordon, E. S. Replogle, J. A. Pople, Gaussian, Inc., Pittsburgh, PA, **1998**.
- [21] J. W. Ponder, F. M. Richards, *J. Comput. Chem.* **1987**, *8*, 1016–1024.
- [22] K. Andersson, M. R. A. Blomberg, M. P. Fülscher, G. Karlström, R. Lundh, P.-A. Malmqvist, P. Neogrády, J. Olsen, B. O. Roos, A. J. Sadlej, M. Schütz, L. Seijo, L. Serrano-Andrés, P. E. M. Siegbahn, P.-O. Widmark, University of Lund, Lund, Sweden, **2002**.
- [23] O. Celani, M. A. Robb, M. Garavelli, F. Bernardi, M. Olivucci, *Chem. Phys. Lett.* **1995**, *243*, 1–8.
- [24] J. P. Perdew, K. Burke, M. Ernzerhof, *Phys. Rev. Lett.* **1996**, *77*, 3865–3868.
- [25] A. Pasquarello, K. Laasonen, R. Car, C. Lee, D. Vanderbilt, *Phys. Rev. Lett.* **1992**, *69*, 1982–1985.
- [26] P. Giannozzi, F. De Angelis, R. Car, *J. Chem. Phys.* **2004**, *120*, 5903–5915.

Cover Picture

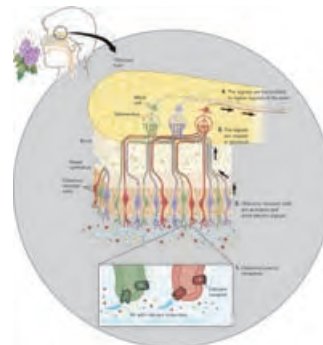
Shun-ichi Ishiuchi, Makoto Sakai, Yuji Tsuchida, Akihiro Takeda, Yasutake Kawashima, Masaaki Fujii,* Otto Dopfer,* and Klaus Müller-Dethlefs*

The intermolecular binding motif of the argon atom in a phenol...Ar dimer has been monitored on the picosecond timescale by time-resolved UV–UV(pump)–IR(probe) ionization depletion spectroscopy. The cover picture shows the dynamic process, which involves a shift of the initially π -bound Ar atom to a hydrophilic, hydrogen-bound site. For more details, see the Communication by M. Fujii, K. Müller-Dethlefs, and co-workers on page 6149 ff.



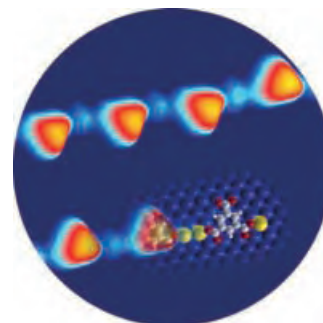
Odor Perception

Humans can distinguish more than 10000 odors. But how are these odors perceived and processed in the brain? R. Axel and L. Buck describe their research on page 6111 ff. and page 6128 ff., respectively, work for which they received the 2004 Nobel Prize for Medicine or Physiology.



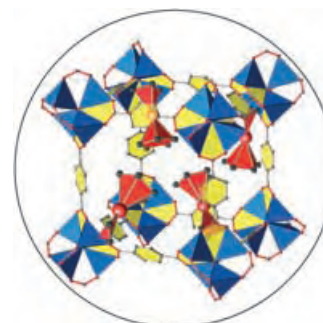
Coordination Chains

In their Communication on page 6142 ff., T. Classen, S. Fabris, K. Kern, and co-workers describe the templating effect of the Cu(110) surface on trimesitylic acid that results in the formation of one-dimensional metal–organic coordination chains.



Metal Nanoparticles

Porous coordination polymers such as MOF-5 readily accept MOCVD precursors, and the stored compounds are easily reduced to give the corresponding metal nanoparticles, as described by R. Fischer et al. in their Communication on page 6237 ff.





The following Communications have been judged by at least two referees to be “very important papers” and will be published online at www.angewandte.org soon:

Sheereen Majid, Michael Mayer*

Hydrogel-Stamping of Arrays of Supported Lipid Bilayers with Various Lipid Compositions for Screening of Drug–Membrane and Protein–Membrane Interactions

Yoshitaka Ishibashi, Yuhki Bessho, Masahiro Yoshimura, Masaki Tsukamoto, Masato Kitamura*

Origin of the Minor Enantiomeric Product in a Noyori Asymmetric Hydrogenation

Holger Braunschweig,* Thomas Herbst, Daniela Rais, Fabian Seeler
Synthesis of Borirenes by Photochemical Borylene Transfer from $[(OC)_5M=BN(SiMe_3)_2]$ ($M = Cr, Mo$) to Alkynes

Y. Andrew Yang, Huimeng Wu, K. R. Williams, Y. Charles Cao*
Synthesis of CdSe and CdTe Nanocrystals without Precursor Injection

Masayuki Nihei, Mayumi Ui, Mizuho Yokota, Lingqin Han, Atsushi Maeda, Hideo Kishida, Hiroshi Okamoto, Hiroki Oshio*
Two-Step Spin Conversion in a Cyanide-Bridged Ferrous Square

Sean F. Brady,* Jon Clardy
Cloning and Heterologous Expression of Isonitrile Biosynthetic Genes from Environmental DNA

Meeting Reviews

ADHOC 2005 in Cologne: The Latest in Dioxxygen Activation and Homogeneous Catalytic Oxidation

C. Limberg* _____ 6102

Books

Books for the (Chemical) Senses

reviewed by P. Kraft _____ 6105

Reviews

Odor Perception

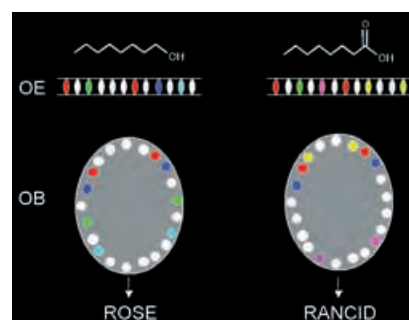
R. Axel* _____ 6111–6127

Scents and Sensibility: A Molecular Logic of Olfactory Perception (Nobel Lecture)

L. B. Buck* _____ 6128–6140

Unraveling the Sense of Smell (Nobel Lecture)

A sense of occasion: Around 20 years after the start of their pioneering studies on the function of the nose and brain in odor perception, R. Axel and L. Buck have received the 2004 Nobel Prize for Medicine or Physiology. The picture shows schematically the coding of different odors in the olfactory epithelium (OE) and olfactory bulb (OB).



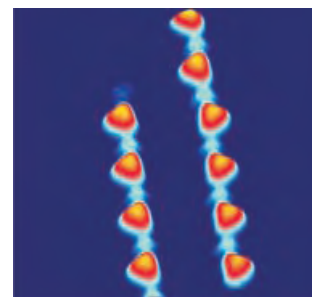
Communications

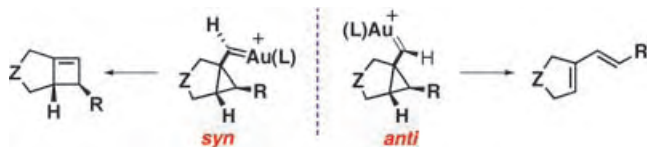
Coordination Chains

T. Classen,* G. Fratesi, G. Costantini, S. Fabris,* F. L. Stadler, C. Kim, S. de Gironcoli, S. Baroni, K. Kern* _____ 6142–6145

Templated Growth of Metal–Organic Coordination Chains at Surfaces

Line them up: Metal–organic chains (see scanning tunneling microscopy image) have been created in situ by self-organized growth at a metal surface under ultrahigh vacuum. These 1D arrangements of metal centers (Fe, Cu), regularly spaced by organic linkers such as trimesitylic acid, open new possibilities for the study of low-dimensional magnetism.





Support for the direct route: That cyclobutenes are not necessary intermediates in the skeletal rearrangement of enynes is supported by DFT calculations and kinetic

studies. Cyclobutenes may arise from the corresponding *syn*-cyclopropylgold(I) carbenes (see scheme).

Reaction Mechanisms

C. Nieto-Oberhuber, S. López,
M. P. Muñoz, D. J. Cárdenas, E. Buñuel,
C. Nevado,
A. M. Echavarren* ——— 6146–6148

Divergent Mechanisms for the Skeletal
Rearrangement and [2+2] Cycloaddition
of Enynes Catalyzed by Gold



That's quite a switch! The ionization-induced switch in the preferred intermolecular binding motif of the phenol...Ar interaction from π bonding to hydrogen bonding (see picture) has been monitored in real time by time-resolved picosecond UV-UV-IR pump-probe spectroscopy. The timescale for this prototypical intermolecular hydrophobic \rightarrow hydrophilic ($\pi \rightarrow$ H) isomerization process (10 ps) has been measured for the first time.

Molecular Dynamics

S. Ishiuchi, M. Sakai, Y. Tsuchida,
A. Takeda, Y. Kawashima, M. Fujii,*
O. Dopfer,*
K. Müller-Dethlefs* ——— 6149–6151

Real-Time Observation of Ionization-
Induced Hydrophobic \rightarrow Hydrophilic
Switching

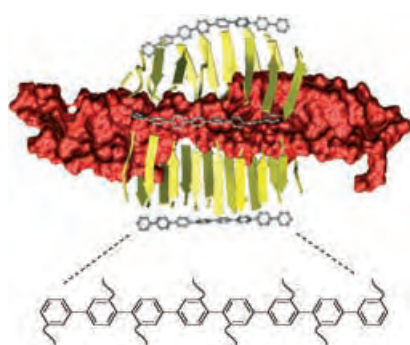


The liquid–solid transition: Automatic assignment of solid-state NMR data as well as fast and accurate calculation of the structure of immobilized proteins at atomic resolution can be achieved by using the program SOLARIA (a modification of the ARIA protocol). The picture shows the lowest energy structures of the α -spectrin SH3 domain calculated by SOLARIA (blue) overlaid with the X-ray crystal structure (red).

Structure Elucidation

M. Fossi, F. Castellani, M. Nilges,
H. Oschkinat,*
B.-J. van Rossum* ——— 6151–6154

SOLARIA: A Protocol for Automated
Cross-Peak Assignment and Structure
Calculation for Solid-State Magic-Angle
Spinning NMR Spectroscopy



Caught in a barrel: AFM studies indicate that the host–guest complexes formed between β -barrel pores and polymer blockers are pseudorotaxanes. The non-statistical location of the contracted supramolecular barrels on the polymers indicates that the sticky polymer templates insert quickly into the β barrels (see schematic representation) and then undergo slow motion through the barrels.

Molecular Recognition

J. Kumaki,* E. Yashima, G. Bollot,
J. Mareda, S. Litvinchuk,
S. Matile* ——— 6154–6157

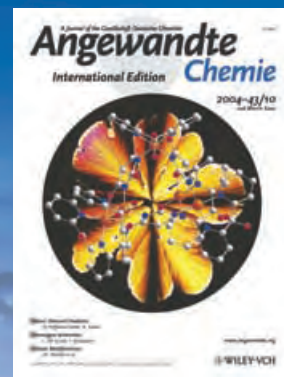
AFM Snapshots of Synthetic
Multifunctional Pores with Polyacetylene
Blockers: Pseudorotaxanes and Template
Effects

For the USA and Canada:
ANGEWANDTE CHEMIE International
Edition (ISSN 1433-7851) is published weekly
by Wiley-VCH PO Box 191161, D 69451 Wein-
heim, Germany. Air freight and mailing in the
USA by Publications Expediting Inc. 200
Meacham Ave., Elmont, NY 11003. Periodicals

postage paid at Jamaica NY 11431. US POST-
MASTER: send address changes to *Angewandte
Chemie*, Wiley-VCH, 111 River Street, Hoboken,
NJ 07030. Annual subscription price for insti-
tutions: US\$ 4948.00/4498.00 (valid for print
and electronic / print or electronic delivery); for
individuals who are personal members of a

national chemical society, or whose institution
already subscribes, or who are retired or self-
employed consultants, print only: US\$ 394.00.
Postage and handling charges included. All
Wiley-VCH prices are exclusive VAT.

The best in chemistry – for more than a hundred years



A Journal of the Gesellschaft Deutscher Chemiker
Angewandte Chemie
International Edition

www.angewandte.org

1888: The beginning
of a success story

Constant Innovations

- 1962:** First issue of the International Edition
- 1976:** Graphical abstracts
- 1979:** Cover pictures
- 1988:** Centenary of Angewandte
- 1989:** Routine use of color
- 1991:** New section: Highlights
- 1992:** Computerized editorial tracking system
- 1995:** Internet service for readers
- 1998:** Regular press service; full-text online
- 2000:** New section: Essays; EarlyView: Communications available online ahead of the printed version
- 2001:** New section: Minireviews
- 2002:** Online submission of manuscripts
- 2003:** Weekly publication; new section: News; new layout
- 2004:** Backfiles (1962-1997); ManuscriptXpress: Online system for authors and referees



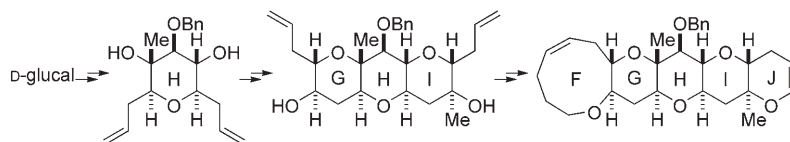
Angewandte's advisors...

Stefan Marcinowski
BASF AG
Ludwigshafen

» In our company **Angewandte Chemie** is seen as an outstanding journal that combines first class performance in publishing innovative chemistry with a high international visibility. With its global recognition **Angewandte Chemie** functions as a seed cell for innovative technologies to be applied on a commercial basis in the future. «

Angewandte Chemie International Edition is
a journal of the German Chemical Society (GDCh)





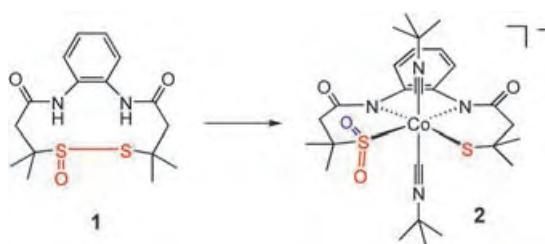
D-glucal is the starting point for the efficient synthesis of the F-J fragment of the gambieric acids (see scheme). The H-ring diol was subjected to double two-directional alkynyl ether formation, carbocupration ring-closing metathesis, and

hydroboration. The tricyclic G-I diol was then converted into the F-J fragment by a sequence that involves another double two-directional ring-closing metathesis reaction.

Synthetic Methods

J. S. Clark,* M. C. Kimber, J. Robertson, C. S. P. McErlean, C. Wilson **6157–6162**

Rapid Two-Directional Synthesis of the F-J Fragment of the Gambieric Acids by Iterative Double Ring-Closing Metathesis



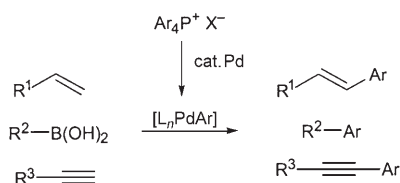
Cyclic pseudopeptidic thiosulfonates reveal a new type of reaction that may be important in biological systems. It involves hydrolytic cleavage of the S(O)–S bond on **1** followed by metalation to form

a dissymmetrical Co^{III} complex with a mixed diamidato-N, thiolato-S, sulfinato-S donor set in **2** that is related to the nitrile hydratase active site.

Enzyme Modeling

E. Bourles, R. Alves de Sousa, E. Galardon, M. Giorgi, I. Artaud* **6162–6165**

Direct Synthesis of a Thiolato-S and Sulfinato-S Co^{III} Complex Related to the Active Site of Nitrile Hydratase: A Pathway to the Post-Translational Oxidation of the Protein



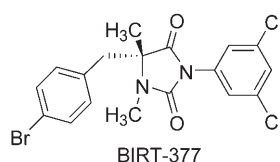
Highly efficient: Tetraarylphosphonium halides, $\text{Ar}_4\text{P}^+\text{X}^-$, as arylating reagents efficiently deliver an aryl group in Pd-catalyzed reactions with olefins, organoboron compounds, and terminal alkynes (see scheme).

Synthetic Methods

L. K. Hwang, Y. Na, J. Lee, Y. Do, S. Chang* **6166–6169**

Tetraarylphosphonium Halides as Arylating Reagents in Pd-Catalyzed Heck and Cross-Coupling Reactions

The benzhydryl group is the key: Efficient alkylation of 3-substituted aziridine-2-carboxylates is only possible with *N*-benzhydryl-protected aziridines and occurs with complete retention of the configuration at the 2-position. Sequential catalytic asymmetric aziridination and aziridine alkylation reactions have been applied to the synthesis of BIRT-377 (see structure).



Synthetic Methods

A. P. Patwardhan, V. R. Pulgam, Y. Zhang, W. D. Wulff* **6169–6172**

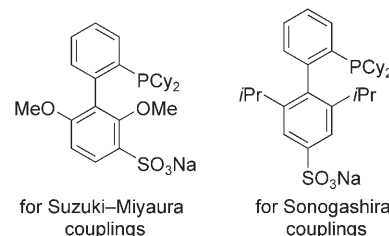
Highly Diastereoselective Alkylation of Aziridine-2-carboxylate Esters: Enantioselective Synthesis of LFA-1 Antagonist BIRT-377

C–C Coupling Reactions

K. W. Anderson,
S. L. Buchwald* ————— **6173–6177**

General Catalysts for the Suzuki–Miyaura and Sonogashira Coupling Reactions of Aryl Chlorides and for the Coupling of Challenging Substrate Combinations in Water

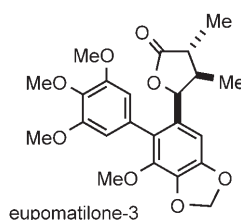
Amphiphilic phosphine ligands (see structures; Cy = cyclohexyl) were prepared and utilized in palladium-catalyzed Suzuki–Miyaura and Sonogashira coupling reactions in water or water/organic biphasic solvents, providing excellent yields of functionalized biaryls and aryl alkynes, respectively.



Stereoselective Butenolide Reduction

M. P. Rainka, J. E. Milne,
S. L. Buchwald* ————— **6177–6180**

Dynamic Kinetic Resolution of α,β -Unsaturated Lactones through Asymmetric Copper-Catalyzed Conjugate Reduction: Application to the Total Synthesis of Eupomatilone-3

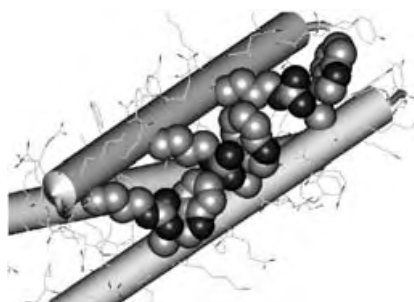


Only six steps were needed for the total synthesis of eupomatilone-3 in 48% overall yield thanks to the development of a dynamic kinetic resolution that allowed the reductive conversion of a racemic α,β -unsaturated butenolide in high yield and high enantiomeric and diastereomeric excess. This copper-catalyzed dynamic kinetic resolution was then applied to several γ -aryl-containing α,β -unsaturated butenolides.

Helical Structures

Y. Sakurai, T. Mizuno, H. Hiroaki,
K. Gohda, J.-i. Oku,
T. Tanaka* ————— **6180–6183**

High Thermal Stability Imparted by a Designed Tandem Arg–Trp Stretch in an α -Helical Coiled Coil

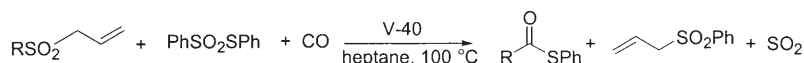


Let's twist again: A cation– π interaction between Trp and Arg is designed at the interface between two α helices of a coiled-coil structure and stabilizes the structure more than Glu and Lys ion-pair interactions. Two or three Trp–Arg sets form an extended array of interactions (see picture) and increase the melting temperature of the peptide.

Synthetic Methods

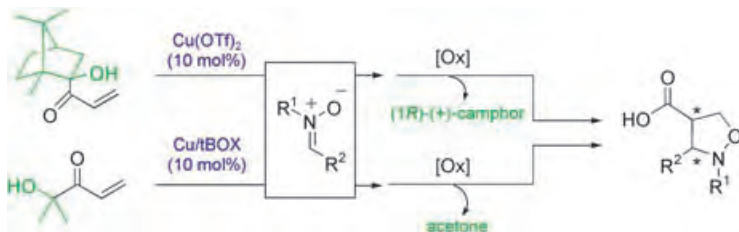
S. Kim, S. Kim,* N. Otsuka,
I. Ryu* ————— **6183–6186**

Tin-Free Radical Carbonylation: Thiol Ester Synthesis Using Alkyl Allyl Sulfone Precursors, Phenyl Benzenethiosulfonate, and CO



Remove contents from tin ... Thiol esters have been successfully synthesized through tin-free radical carbonylation (see scheme; V-40 = initiator). This approach

can be further extended to sequential radical reactions involving cyclization, carbonylation, and trapping of acyl radicals by phenyl benzenethiosulfonate.



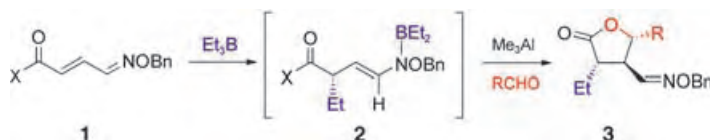
A fine pair: Excellent levels of regio-, *endo*/*exo*-, diastereo-, and/or enantioselectivity are attained in the Cu-catalyzed cycloaddition of nitrones with α' -hydroxy enones

(see scheme). The resulting adducts can be further elaborated to the corresponding isoxazolidines bearing aldehyde, ketone, and carboxylic acid functions.

Enantioselective Synthesis

C. Palomo,* M. Oiarbide, E. Arceo, J. M. García, R. López, A. González, A. Linden ————— **6187–6190**

Lewis Acid Catalyzed Asymmetric Cycloadditions of Nitrones: α' -Hydroxy Enones as Efficient Reaction Partners



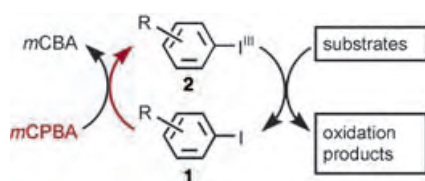
The direct generation of boryl enamine **2** by radical addition to the chiral α,β -unsaturated oxime ether **1** (X = (1*R*)-camphorsultam, Bn = benzyl) followed by reaction with aldehydes gave rise to a

tandem carbon–carbon bond-forming method, yielding lactones **3**. The result is a novel asymmetric synthesis of γ -butyrolactones and γ -amino acids by way of both a radical and an ionic process.

Tandem Reactions

M. Ueda, H. Miyabe, H. Sugino, O. Miyata, T. Naito* ————— **6190–6193**

Tandem Radical-Addition–Aldol-Type Reaction of an α,β -Unsaturated Oxime Ether

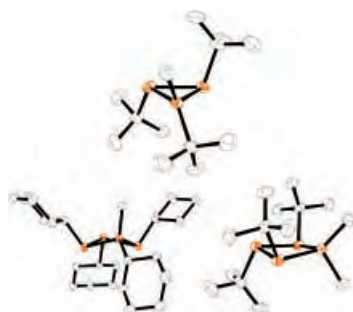


A new and effective use of hypervalent iodine(III) reagents as catalysts involves the transformation of iodoarenes **1** into hypervalent iodine(III) species **2** with *meta*-chloroperbenzoic acid (*m*CPBA) as the appropriate cooxidant. With observed turnover numbers greater than 70, this procedure paves the way for broader application of these useful oxidants in organic synthesis.

Catalytic Oxidation

T. Dohi, A. Maruyama, M. Yoshimura, K. Morimoto, H. Tohma, Y. Kita* ————— **6193–6196**

Versatile Hypervalent-Iodine(III)-Catalyzed Oxidations with *m*-Chloroperbenzoic Acid as a Cooxidant



Methylation or phosphonium insertion reactions with cyclopolyphosphines (PtBu)₃ or (PCy)₄ (Cy = cyclohexyl) are presented as stereospecific and high-yielding preparative approaches to cyclopolyphosphinophosphonium cations. The cations [(PtBu)₃PMe]⁺, [(PCy)₄PMe]⁺, and [(PtBu)₃PMe₂]⁺ (see picture; P orange, C gray) are prepared as trifluoromethanesulfonate salts and represent key frameworks in fundamental *catena*-phosphorus chemistry.

Phosphorus Cations

N. Burford,* C. A. Dyker, M. Lumsden, A. Decken ————— **6196–6199**

Small Cyclopolyphosphinophosphonium Cations: Systematic Development of Fundamental *catena*-Phosphorus Frameworks

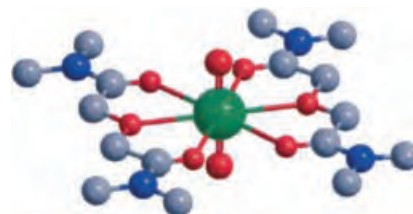
Actinide Chemistry

G. Tian, J. Xu, L. Rao* — 6200–6203

Optical Absorption and Structure of a Highly Symmetrical Neptunium(V) Diamide Complex

A reflection on neptunium absorption:

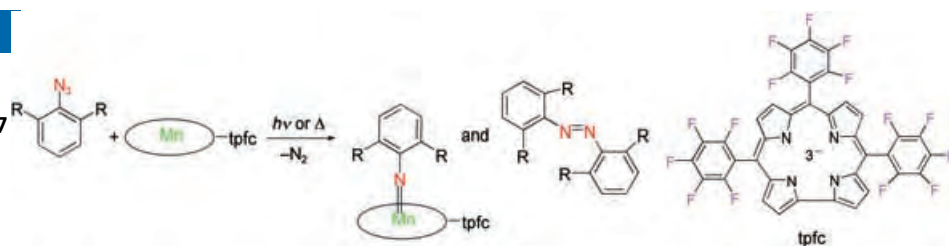
The absorption spectrum of Np^{V} around 980 nm originates from a $5f \rightarrow 5f$ electric-dipole transition, which is allowed if the Np^{V} ion lies in a coordination environment that lacks a center of inversion, such as in $[\text{NpO}_2(\text{H}_2\text{O})_5]^+$. However, the transition is completely forbidden by Laporte's rule in the highly symmetrical Np^{V} diamide complex $[\text{NpO}_2(\text{L})_2]^+$ (see structure; Np green, O red, N blue, C gray).



Imido Complexes

M. M. Abu-Omar,* C. E. Shields, N. Y. Edwards, R. A. Eikey — 6203–6207

On the Mechanism of the Reaction of Organic Azides with Transition Metals: Evidence for Triplet Nitrene Capture



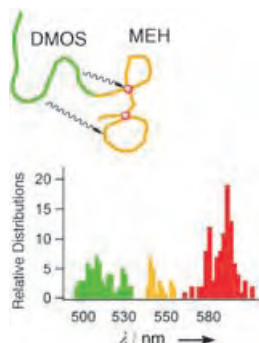
High-valent imido complexes are obtained by reaction of the manganese-(III) corrole $[\text{Mn}(\text{tpfc})]$ with aryl azides by a novel reaction mechanism in which singlet nitrene undergoes intersystem

crossing to the triplet state, which is trapped by the metal corrole, in competition with dimerization to the azo compound (see scheme).

Conjugated Polymers

J. K. Grey, D. Y. Kim, Y. J. Lee, J. J. Gutierrez, N. Luong, J. P. Ferraris, P. F. Barbara* — 6207–6210

Single-Molecule Studies of Electronic Energy Transfer in a Diblock Conjugated Polymer

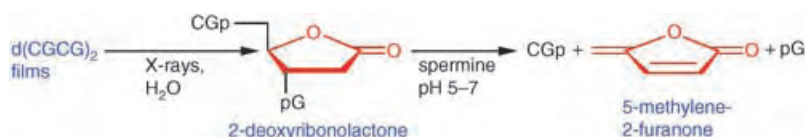


Energy transfer at the interface of two dissimilar conjugated polymer chains (see picture; DMOS = 2-dimethyloctylsilyl-*p*-phenylenevinylene; MEH = 2-methoxy-5-(2'-ethylhexyloxy)-*p*-phenylenevinylene) has been studied using single-molecule spectroscopy. Morphological features control energy-transfer processes between the blocks and lead to strongly heterogeneous efficiencies of energy transfer.

DNA Cleavage

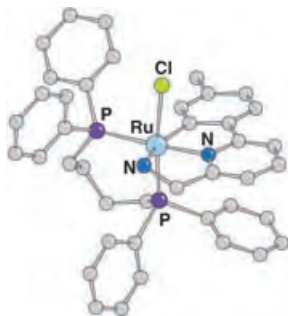
M. Roginskaya, Y. Razskazovskiy, W. A. Bernhard* — 6210–6213

2-Deoxyribonolactone Lesions in X-ray-Irradiated DNA: Quantitative Determination by Catalytic 5-Methylene-2-furanone Release



Torn genes: DNA tetramers containing the 2-deoxyribonolactone (dL) lesion have been isolated by HPLC from $d(\text{CGCG})$ and $d(p\text{CGCG})$ films irradiated with X-rays. Upon treatment with spermine as a

catalyst, the dL-containing tetramers decompose to 5-methylene-2-furanone (5-MF; see scheme), a characteristic product of dL decomposition. Hence, 5-MP can be used to quantify dL lesions in DNA.

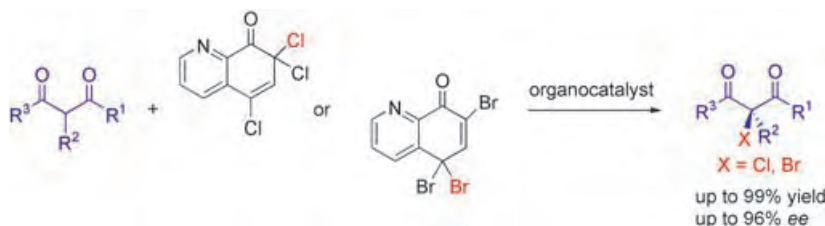


Very low loading and short reaction times are characteristic features of the quantitative reduction of different ketones using 2-propanol and terdentate $[\text{RuX}(\text{CNN})\text{-(dppb)}]$ ($\text{X} = \text{H}, \text{Cl}$ (see structure); $\text{dppb} = \text{Ph}_2\text{P}(\text{CH}_2)_4\text{PPh}_2$) complexes prepared from 6-(4'-methylphenyl)-2-pyridyl-methylamine. The reduction apparently takes place by reversible insertion of the substrate into the Ru-H bond, thus leading to a Ru^{II} alkoxide.

Homogeneous Catalysis

W. Baratta,* G. Chelucci, S. Gladiali, K. Siega, M. Toniutti, M. Zanette, E. Zangrando, P. Rigo — **6214–6219**

Ruthenium(II) Terdentate CNN Complexes: Superlative Catalysts for the Hydrogen-Transfer Reduction of Ketones by Reversible Insertion of a Carbonyl Group into the Ru-H Bond



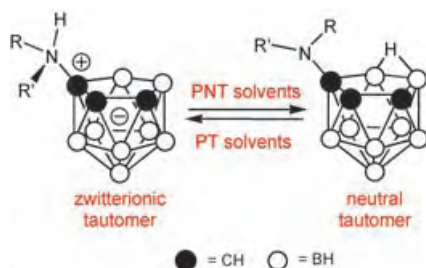
No metal required: A protocol for the enantioselective organocatalytic chlorination of cyclic and acyclic β -keto esters and cyclic β -diketones has been developed which is also effective for the asymmetric

bromination of β -keto esters. The methodology employs an inexpensive organocatalyst (e.g. benzoylquinidine) and poly-halogenated quinolinones as the source of the halogen (see scheme).

Synthetic Methods

G. Bartoli,* M. Bosco, A. Carlone, M. Locatelli, P. Melchiorre,* L. Sambri — **6219–6222**

Organocatalytic Asymmetric α -Halogenation of 1,3-Dicarbonyl Compounds

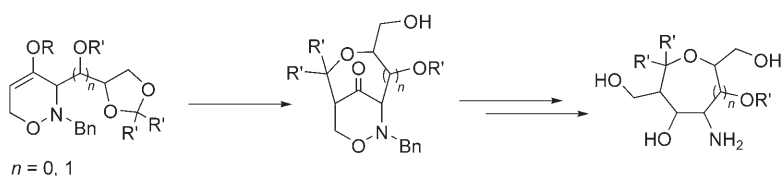


The dual in the crown: The same compound can adopt two different, non-equilibrium tautomeric structures. This unique structural dualism is demonstrated by the isolation of pure tautomeric pairs, 7- $\text{RR}'\text{NH}$ -7,8,9- $\text{C}_3\text{B}_8\text{H}_{10}$ (zwitterionic) and 7- $\text{RR}'\text{N}$ -7,8,9- $\text{C}_3\text{B}_8\text{H}_{11}$ (neutral) (where $\text{R}, \text{R}' = \text{H}$ or alkyls, see scheme, PNT = proton nontransferring, PT = proton transferring) in the tricarbolide series.

Carboranes

M. Bakardjiev, J. Holub, D. Hnyk, I. Císařová, M. G. S. Londesborough, D. S. Perekalin, B. Štíbr* — **6222–6226**

Structural Dualism in the Zwitterionic 7- $\text{RR}'\text{NH}$ -*nido*-7,8,9- $\text{C}_3\text{B}_8\text{H}_{10}$ Tricarbolide Series: An Example of Absolute Tautomerism



Under control: Lewis acids induce an unexpected rearrangement of 1,3-dioxolanyl-substituted 1,2-oxazines to provide bicyclic compounds in a stereocontrolled

manner. They are precursors for enantiopure carbohydrate mimetics containing 3-aminotetrahydropyran or 4-aminooxepane substructures (see scheme; $\text{Bn} = \text{benzyl}$).

Heterocycles

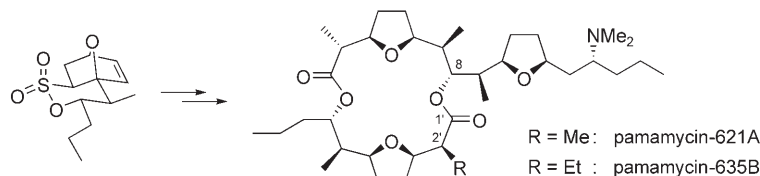
A. Al-Harrasi, H.-U. Reißig* — **6227–6231**

Synthesis of Enantiopure Carbohydrate Mimetics by Lewis Acid Catalyzed Rearrangement of 1,3-Dioxolanyl-Substituted 1,2-Oxazines

Natural Product Synthesis

P. Fischer, A. B. García Segovia,
M. Gruner, P. Metz* — 6231 – 6234

A General Sultone Route to the
Pamamycin Macrodiolides—Total
Synthesis of Pamamycin-621A and
Pamamycin-635B



Sultones swing again: The first total syntheses of the title antibiotics (see scheme) were achieved by application of sultone methodology. Since the final lactonizations with formation of the ester linkage between C1' and the oxygen sub-

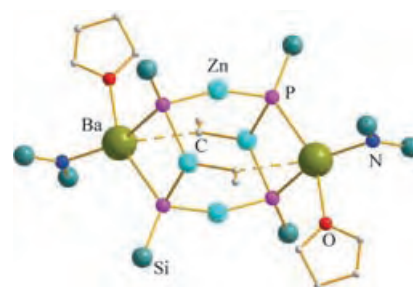
stituent on C8 proceeded with complete epimerization at C2', the more readily available C2' epimeric smaller fragments could be used for streamlining the synthetic sequence.

Alkyl Complexes

M. Westerhausen,* G. Sappelza,
P. Mayer — 6234 – 6237

Activation of a Zinc-Bound Ethyl Group by
Formation of a Zn-C_{Et}-Ba Moiety and
Crystal Structure of [(Me₃Si)₂N]Ba(thf)-
Zn₂(μ-Et)(μ₃-PSi₂Bu₃)₂ with Bridging
Ethyl Substituents

The phosphane unit is deprotonated in the reaction of dialkylzinc with H₂PSi₂Bu₃ and (thf)₂Ba[N(SiMe₃)₂]₂ to give the title compound (molecular structure shown), which has a coordinatively unsaturated barium center. In the absence of excess THF, the zinc-bound alkyl groups are activated by formation of Ba-C_{Et}-Zn three-center bonds.

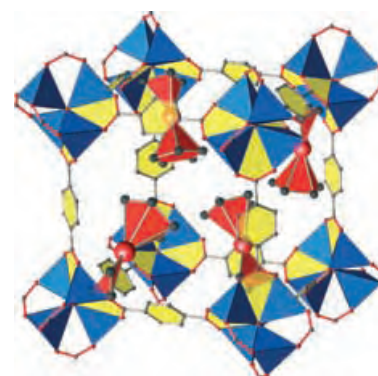


Metal Nanoparticles

S. Hermes, M.-K. Schröter, R. Schmid,
L. Khodeir, M. Muhler, A. Tissler,
R. W. Fischer, R. A. Fischer* — 6237 – 6241

Metal@MOF: Loading of Highly Porous
Coordination Polymers Host Lattices by
Metal Organic Chemical Vapor
Deposition

Precursors and particles captured in a net: Porous coordination polymers such as MOF-5 are efficient gas storage devices and are also able to absorb metal organic chemical vapor deposition (MOCVD) precursors (see picture, red: [(η⁵-C₅H₅)Pd(η³-C₃H₅)]). These incorporated compounds are easily reduced to give the corresponding metal nanoparticles. Applications in heterogeneous catalysis, for instance, methanol synthesis or hydrogenation, are described.

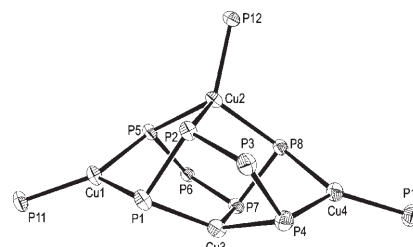


Copper Oligophosphanides

R. Wolf, E. Hey-Hawkins* — 6241 – 6244

Synthesis and Molecular Structure of
the Cu₄P₈ Cage Compound
[Cu₄(P₄Ph₄)₂(PCyp₃)₃]

Plenty of phosphorus: The first Cu^I oligophosphanido complex [Cu₄(P₄Ph₄)₂(PCyp₃)₃] (**1**; Cyp = *cyclo*-C₅H₉), synthesized from [CuCl(PCyp₃)₂] and [Na₂(thf)₄(P₄Ph₄)], displays a remarkable cage structure in the solid state. The central Cu₄P₈ core of **1** (with appendant phosphane P atoms) is shown in the picture.



Sources

Product and Company Directory

You can start the entry for your company in "Sources" in any issue of *Angewandte Chemie*.

If you would like more information, please do not hesitate to contact us.

Wiley-VCH Verlag – Advertising Department

Tel.: ☎ 62 01 - 60 65 65

Fax: ☎ 62 01 - 60 65 50

E-Mail: MSchulz@wiley-vch.de

Service

Keywords 6246

Authors 6247

Angewandte's
Sister Journals 6248 – 6249

Preview 6251

Corrigendum

New results have revealed that some values given in this original contribution are incorrect. The determined cloud point of polymer **5** does not lie over 95 °C as originally reported, but is actually 17 °C. The previously observed high optical transparency of a dispersion of polymer **5** was a result of the very small particle size that resulted from ultrasonic treatment. In light of this new result, the data for cyclodextrin-free polymer **5** presented in Table 1 and Figures 1, 2, and 3 are incorrect. In Table 1, the LCST value of polymer **5** of > 95 °C should be replaced by 17 °C,

while the monomer ratio (n/m) for polymers **5** and **6** should now read as 20:1 instead of 1:20. In Figures 1 and 3, the plotted data for polymer **5** in the absence of cyclodextrin should be replaced by a function which shows a turbidity point at 17 °C. In Figure 2, the LCST value of > 95 °C should be corrected to 17 °C. In the text, all passages that refer to the cloud point of cyclodextrin-free polymer **5** are incorrect. However, all the other presented data as well as the conclusion remain valid.

Influence of Cyclodextrin Molecules on the Synthesis and the Thermoresponsive Solution Behavior of *N*-Isopropylacrylamide Copolymers with Adamantyl Groups in the Side Chains

H. Ritter,* O. Sadowski,
E. Tepper 3171–3173

Angew. Chem. Int. Ed. **2003**, 42

DOI 10.1002/anie.200250814



ADHOC 2005 in Cologne: The Latest in Dioxygen Activation and Homogeneous Catalytic Oxidation**

Christian Limberg*

The selective functionalization of hydrocarbons is one of the most important challenges of chemistry and is of great interest for the purposes of basic research and technology. Homogeneous, heterogeneous, and enzymatic processes are being pursued worldwide as potential solutions to this problem. The mechanisms of oxidation reactions remain among the most puzzling issues in chemistry. To gain better insight, model systems with well-defined active sites are being developed, while with the aid of kinetic measurements, sophisticated isotope-labeling experiments, molecular probes, and especially computational chemistry, structure–activity relationships can be discussed and current proposed mechanisms can be either supported or rejected. Naturally, there is an intense interest in new oxidation reactions and catalysts as well as in novel applications of oxidation chemistry. All of this was the subject of the 9th International Symposium of Activation of Dioxygen and Homogeneous Catalytic Oxidation (ADHOC) in Cologne, Germany, which was organized for over 200 participants from

industry and academia by Albrecht Berkessel (University of Cologne) and Henrique Teles (BASF, Germany).

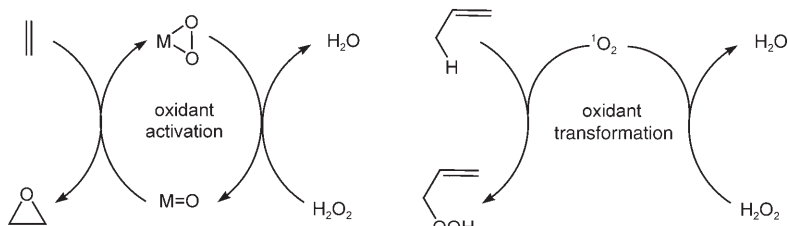
The opening lecture was given by R. Diercks (BASF, Germany) in which he introduced industrially relevant oxidation processes for the production of base chemicals, explained some problems therein, and addressed the importance of catalyst and reactor design. It was clearly pointed out that the use of HNO_3 as an oxidizing agent is frowned upon, as the nitrogen oxide byproducts are frequently cited in the literature as environmental hazards. However, the coupling of industrial oxidations to other processes (NO_x recovery, N_2O decomposition) can effectively turn HNO_3 into a “green” reagent. Remaining N_2O can also be an attractive source of oxygen, as outlined in the talk given by G. I. Panov (Boreskov Institute, Novosibirsk, Russia). With this reagent it is possible to oxidize benzene to phenol and its derivatives, as well as various olefins to carbonyl compounds, and to carry out the chemical modification of polymers such as polybutadiene.

New perspectives in the use of singlet oxygen were also highlighted. It has been known for some time that Na_2MoO_4 at appropriate pH values can catalyze the disproportionation of H_2O_2 to give $^1\text{O}_2$. J.-M. Aubry (ENSCL, Lille, France) reported that $[\text{Mo}(\text{O}_2)_3\text{O}]^{2-}$ represents the catalytically active species. He introduced a method with which the $^1\text{O}_2$ produced can be used for “dark” oxygenations of hydrocarbons. A problem with this is the short lifetime of $^1\text{O}_2$ in aqueous medium, which opposes the oxidation of hydrophobic compounds. It is possible, however, to carry out peroxidations as a continuous process by using specially designed multiphase microemulsions. P. Alsters (DSM, The Netherlands) discussed the applications of this procedure

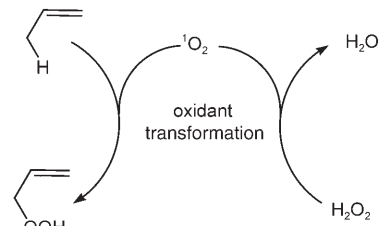
and simultaneously presented a way to solve the problem of parallel concurrent activation of H_2O_2 for epoxidations (Scheme 1): the use of pure inorganic compounds in heterogeneous phases. Elsewhere, A. Griesbeck (University of Cologne, Germany) described how $^1\text{O}_2$, with the aid of tetraarylporphyrin-loaded polystyrene, can be used for ene reactions, [4+2] cycloadditions, and can make ordinary organocatalytic reactions “chiral”.

Many contributions this year also focused on natural approaches toward oxygen activation. These include direct investigations of metalloenzymes and studies concerning for the use of biocatalysts, as well as the development of biomimetic and bioinspired systems. J. D. Lipscomb (University of Minnesota, USA) was able to show that in soluble methane monooxygenase, the formation of a complex between the regulatory protein MMOB and the active component MMOH creates a very narrow pore, through which only methane has access to the active site (Scheme 2). This was proposed as one reason for this enzyme’s high substrate selectivity for methane. This understanding should facilitate mutagenesis experiments designed to expand the oxidation capacity of this enzyme. Furthermore, this represents the first time that the dioxygenase mechanism could be followed spectroscopically through systematic substrate variation.

Such non-heme-containing enzymes were also the basis for the talk given by L. Que, Jr. (University of Minnesota, USA). He reported molecular models that catalyze the H_2O_2 -mediated oxidation of olefins through a nonradical mechanism. The results of isotope-labeling experiments with these systems have led him to conclude that the active species bears an $\text{O}=\text{Fe}^{\text{V}}\text{-OH}$ unit (Scheme 3).

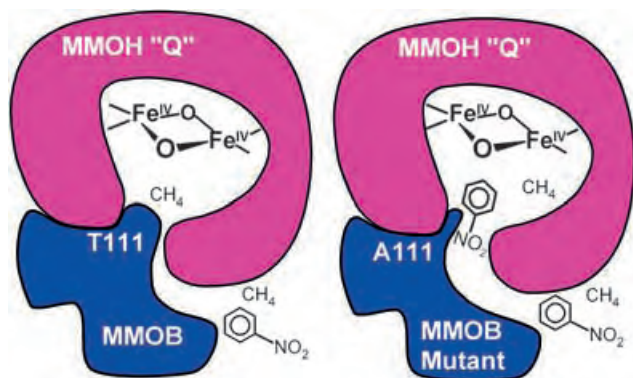


Scheme 1.



[*] Prof. Dr. C. Limberg
Humboldt-Universität zu Berlin
Institut für Chemie
Brook-Taylor-Straße 2
12489 Berlin (Germany)
E-mail: Christian.limberg@chemie.
hu-berlin.de

[**] 9th International Symposium of Activation of Dioxygen and Homogeneous Catalytic Oxidation (ADHOC), July 25–29, 2005, in Cologne, Germany.



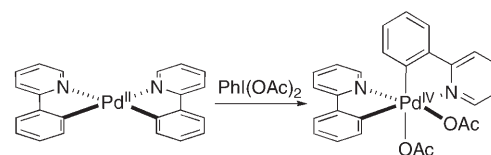
Scheme 2.

A dioxygenase reaction intermediate inspired T. D. P. Stack (Stanford University, USA) to employ single-core Fe and Mn complexes to catalyze the epoxidation of terminal olefins with peracids. A group of Mn complexes has proven itself especially active and selective, and its heterogenization by binding to silica gel adds to its list of advantages. W. Kroutil (University of Graz, Austria) was able to show that a dehydrogenase from *Rhodococcus ruber*, which is stable in organic solvents, can carry out highly stereoselective alcohol oxidations. It differentiates between not only *R* and *S* stereocenters, but also primary and secondary alcohols (intramolecular as well).

Many newly developed systems use Pd catalysts in combination with O_2 . The prime example for such systems, namely the Wacker process, occasionally served as a source of ideas. S. S. Stahl (University of Wisconsin, Madison, USA) discussed an aza-Wacker process, which gives rise to enamines, and M. S. Sigman (University of Utah, USA) reported the dialkoxylation of olefins. Alcohol oxidations can also be carried out in aqueous media with water-soluble catalysts, as described by I. W. C. E. Arends (TU Delft, The Netherlands). D. De Vos (University of

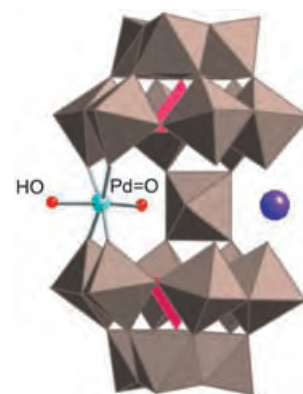
Leuven, Belgium) introduced a new procedure for the alkenylation of aromatic compounds, the mechanism of which was also studied in detail. Furthermore, he discussed the application of immobilized tungstate catalysts with haloperoxidase activity: these effect the oxidation of bromide to bromonium ions, which in turn, can be reactive under nonacidic conditions with olefins and aromatic compounds. M. S. Sanford (University of Michigan, USA) dealt with ligand-directed oxidations of C–H bonds, and in the process of investigations with the oxidizing agent $PhI(OAc)_2$ she successfully isolated and characterized a Pd^{IV} intermediate. The relevance of the +4 oxidation state in Pd-catalyzed reactions has been the subject of controversy for some time, and here could be some initial evidence that such compounds actually do exist (Scheme 4).

The “slow-burners” of oxidation catalysis are the polyoxometallates (POMs), for instance, as ligands for other transition-metal oxo units, which then become active as the oxidant. M. Bonchio (University of Padova, Italy) reported the synthesis of POM–Ru and POM–Fe complexes, which catalyze reactions with O_2 upon microwave irradiation. POMs can also exhibit interest-

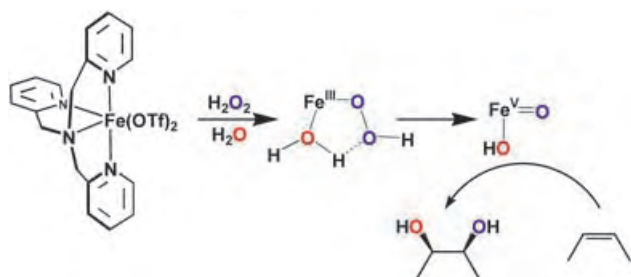


Scheme 4.

ing chemistry in combination with noble metals. Not long ago, $M=O$ compounds of late transition metals were unknown, as their d electrons occupy the π^* orbitals of the $M=O$ bond. The latter, however, are clearly stabilized by POM ligands; their use, as described by C. L. Hill (Emory University, Atlanta, USA), had recently allowed the isolation and characterization of the first $Pd=O$ complex, and now he reported $K_9Na_4[(O=Pd^{IV}-OH)WO(OH_2)L_2]$ ($L = [PW_9O_{34}]^{9-}$). Furthermore, there is evidence for the first $O=Au$ complexes, which can be produced by oxidation in air (Scheme 5).


Scheme 5. Blue circle right: K^+

The talk given by R. Neumann (Weizmann Institute, Israel) made it clear just how broad the range of POM–transition-metal-catalyzed oxidation reactions really is. Interestingly, with substrate-immobilized dipyrimidyl-platinum–POM hybrid compounds, even the catalytic oxidation of methane with O_2 in water was achieved, whereby methanol and acetaldehyde are formed, the mechanism of the surprising formation of $CH_3C(O)H$ is currently investigated. Altogether, there is still great interest in the oxidation of methane, the simplest natural yet most resistant source of C_1 hydrocarbons. After a mechanistic discussion of proton-coupled electron transfer, J. M. Mayer (Uni-



Scheme 3. Tf = trifluoromethylsulfonyl.

versity of Washington, Seattle, USA) first introduced results of his investigation of the reaction of OsO_4 with H_2 and subsequently described initial results of the extension of this work toward methane as a substrate. R. A. Periana (USC, Los Angeles, USA) reported the use of CH_4 to generate acetic acid in the metal-catalyzed oxidation with O_2 as well as the first efforts toward the establishment of a catalytic cycle for the O_2 -oxidation of hydrocarbons starting from Ir alkoxides.

A further important area of oxidation chemistry (especially within the detergent industry) is bleaching catalysis, to which an entire section of lectures was devoted. There is great interest in the development of active metal catalysts, and the most prominent representative of these is $[(\text{Me}_3\text{tacn})\text{Mn}(\mu\text{-O})_3\text{Mn}(\text{Me}_3\text{tacn})]^{2+}$ ($\text{tacn} = 1,3,7$ -triazacyclononane). The talk given by J. R. Lindsay-Smith (University of York, UK) dealt with mechanistic investigations of this system, and R. Hage (Unilever, UK) introduced the general development of metal-mediated bleaching. The lecture given by G. Reinhardt (Clariant, Germany) made it clear that there is not, and never will be a panacea for the bleaching industry. Additional talks on this subject were given by G. Miracle (P&G, USA) and J. J. Dannacher (University of Basel, Switzerland).

Efficient systems for the oxidation of prochiral thioethers to enantiomerically pure sulfoxides were introduced by R. F. W. Jackson (University of Sheffield, UK) and C. Bolm (RWTH Aachen, Germany). Through systematic variation of the ligand, metal, and additives, enantiomeric excesses of up to

99.5% could be reached, making the procedure suitable for the synthesis of biologically active compounds. Y. Shi (CSU, Fort Collins, USA) reported equally impressive *ee* values and yields in his investigation of organocatalyzed epoxidations. His research group succeeded in finding chiral ketone catalysts, which are converted in situ by an external oxidant into dioxiranes, which in turn, effect an enantioselective oxygen transfer to olefin substrates. M. Beller (Leibniz Institute for Organic Catalysis (IFOK), Rostock, Germany) presented a novel chiral pyridine bisimidazoline ligand system, in which Ru complexes in conjunction with pyridine dicarboxylic acid give the highest reported *ee* values for a transition-metal-mediated epoxidation with H_2O_2 . The talk by I. Hermans (University of Leuven, Belgium) gave rise to controversial discussions, as it dealt with autoxidation of hydrocarbons. The validity of the conventionally accepted mechanistic model of alcohol and ketone formation, was put into question based on current experimental and theoretical data; a new proposal was presented in which cyclohexylperoxyl radicals, for example, do not abstract hydrogen atoms from cyclohexane, but instead from cyclohexylhydroperoxide (\rightarrow ketone).

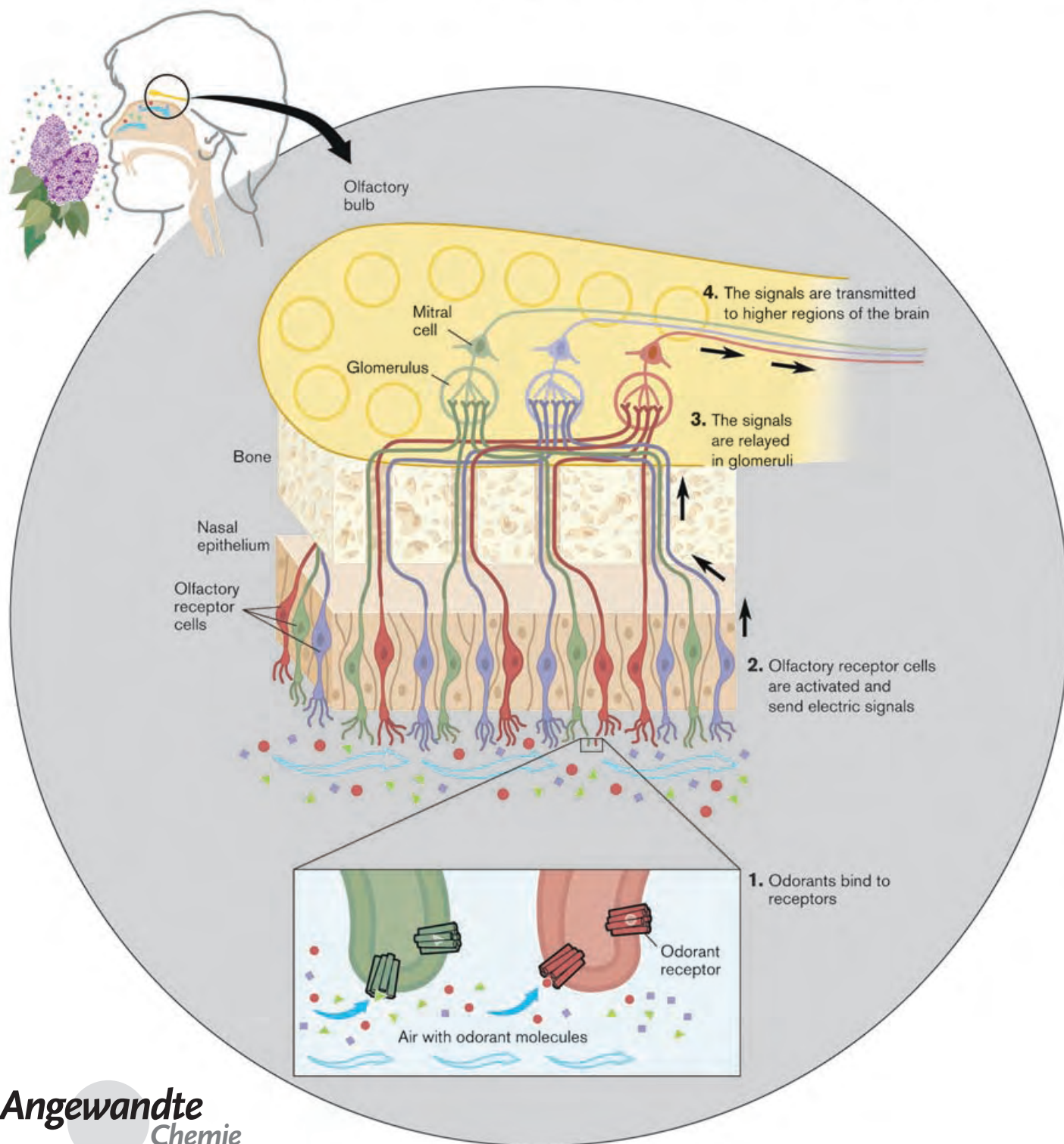
There were many other interesting talks regarding mechanistic and preparative aspects of oxidation catalysts the discussion of which would significantly expand the scope of this report [A. Llobet (University of Barcelona, Spain), Y. Naruta (Kyushu University, Fukuoka, Japan), T. Geller (Bayer CropScience, Germany), J. P. Roth (Johns Hopkins University, Baltimore,

USA), W. R. Thiel (University of Kaiserslautern, Germany), T. Funabiki (Doshisha University, Japan), C. Punta (University of Milan, Italy), I. Weinstock (City College New York, USA), Z. Gross (Technion, Haifa, Israel), C. Limberg (HU Berlin, Germany)]. The closing talk was given by R. A. Sheldon (TU Delft, The Netherlands), in which he discussed the imposing range of oxidation reactions that can be catalyzed by nitroxyl radicals.

Overall, the conference demonstrated that through the intense efforts of the past few years in the area of oxidation chemistry, many breakthroughs were made which, of course, have given rise to new questions and challenges. Among these, for example, the application of atmospheric oxygen for the selective oxidation of hydrocarbons remains an important goal. The mechanistic understanding was broadened, refined, and even renewed, and many novel systems can be developed from this. That oxidation chemistry—regardless of whether fundamental or technical questions are examined—is, as always, a very lively and rapidly developing research area was demonstrated impressively at ADHOC 2005. The pronounced emphasis on application was underscored by the fact that this year's meeting was, for the first time, organized jointly by both the industrial and academic spheres, and through the strong participation and generous support of industry (especially BASF).

DOI: 10.1002/anie.200502936

Odorant Receptors and the Organization of the Olfactory System



Scents and Sensibility: A Molecular Logic of Olfactory Perception (Nobel Lecture)**

Richard Axel*

Keywords:

brain research · fluorescence · Nobel Lecture · olfactory cells · receptors

From the Contents

Biography	6111
1. Introduction	6115
2. A Large Family of Odorant Receptor Genes	6116
3. A Topographic Map in the Olfactory Bulb	6117
4. Receptor Choice and the Topographic Map	6117
5. The Singular and Stable Choice of Receptor	6119
6. Cloning a Mouse from an Olfactory Sensory Neuron	6121
7. Olfaction in the Fly: A Functional Map in the Antennal Lobe	6122
8. Spatial Representations and Innate Behavior	6123
9. How is the Map Read?	6124
10. Concluding Remarks	6125

Biography

New York City is my world. I was born in Brooklyn, the first child of immigrant parents whose education was disrupted by the Nazi invasion of Poland. Although not themselves learned, my parents shared a deep respect for learning. I grew up in a home rich in warmth, but empty of books, art, and music. My early life and education were centered on the streets of Brooklyn. Stickball—baseball with a pink ball and broom handle—and schoolyard basketball were my culture. In stickball, a ball hit the distance to one manhole cover was a single, and four manhole covers, a home run, a “Nobel Prize”. My father was a tailor. My mother, although quick and incisive, did not direct her mind to intellectual pursuits and I had not even the remotest thought of a career in academia. I was happy on the courts. In those days, we worked at a relatively young age. At eleven, I was a messenger, delivering false teeth to dentists. At twelve, I was laying carpets, and at thirteen, I was serving corned beef and

pastrami in a local delicatessen. Vladimir, the Russian chef, was the first to expose me to Shakespeare, which he recited as we sliced cabbage heads for coleslaw.

My local high-school had the best basketball team in Brooklyn, but the Principal of my grade school had a vision different from my own and insisted that I attend Stuyvesant High-School, far away in Manhattan. Stuyvesant High advertised itself as a school for intellectually gifted boys but had the worst basketball team in the city. I was unhappy about the prospect of attending, for it seemed antithetical to my self-image. Shortly after I entered, however, my world changed. I

[*] Prof. R. Axel

Howard Hughes Medical Institute
Columbia University College of Physicians and Surgeons
New York, NY 10032 (USA)
Fax: (+1) 212-923-7249
E-mail: ra27@columbia.edu

[**] Copyright© The Nobel Foundation 2004. We thank the Nobel Foundation, Stockholm, for permission to print this lecture.

embraced the culture and aesthetics of Manhattan. The world of art, books, and music opened before me and I devoured it. In school, I heard bits of an opera for the first time. I remember it distinctly, the Letter Duet from Mozart's *Marriage of Figaro*. The next night I attended *Tannhauser* at the Metropolitan Opera and thus began a love affair, bordering on an obsession, that has had no end. Twice a week, I stood in line for standing room tickets at the Metropolitan Opera where I was exposed to a cult of similarly obsessed but far more knowledgeable aficionados who taught me the intricate nuances of this rich genre. The great Italian tenor, Franco Corelli, would serve us coffee as we waited, and the diva, Joan Sutherland, would invite us backstage.



Richard Axel

On other days, I would read in a most beautifully appointed place, the Reading Room of the Central New York Public Library on 42nd Street. One passes the pair of sculpted lions, ascends a flight of stairs into a huge high-ceilinged room of impressive silence where I read incessantly without direction but with a new-found fascination that made up for years of illiteracy. I met a coterie of library dwellers, men and women of New York, who spent all of their days in the Reading Room. I did not know who they were or how they came to be there, but they had an insight and understanding of literature that amazed and still perplexes me, and they were my teachers. This was New York for me, a city of the culturally obsessed that opened up before me and framed my new world.

To support a seemingly extravagant life for a young high-school student, I worked. I used my skills as a waiter in a delicatessen in Brooklyn, to wait tables in the cafes and nightspots of Greenwich Village. In the sixties, the Village was the home of the beat generation that, through music and poetry and ultimately protest, translated discord into meaningful changes in both America and the world. Stuyvesant High School was on the fringe of Greenwich Village and some of its teachers were artists, writers, and performers who fueled

the politically fired student body, many the sons of Marxist immigrants. With this array of artistic faculty, Stuyvesant nourished my new and voracious appetite.

But old worlds die hard. I continued to play basketball in high-school and this led to a most memorable and humbling experience. I came onto the court as the starting center, and the center on the opposing team from Power Memorial High School lumbered out on the court, a lanky 7 foot 2 inch sixteen year old. When I was first passed the ball, he put his hands in front of my face, looked at me and asked, "What are you going to do, Einstein?" I did rather little. He scored 54 points and I scored two. He was the young Lew Alcindor, later known as Karim Abdul Jabbar, who went on to be among the greatest basketball legends, and I became a neurobiologist.

My decision to remain in New York and attend Columbia College revealed the provincial but endearing quality of my family. When I chose to accept a gracious scholarship offered by Columbia, my father was disappointed. It was a well known fact that the brightest children of Brooklyn immigrants attended City College. My freshman year at Columbia, I lived with abandon. The opera, the arts, the freedom, the protest left little time for study. In the first semester, I met a student from Tennessee, Kevin Brownlee, who remains a dear friend and is now a Professor of Medieval French at the University of Pennsylvania. Brownlee urged me to redirect this intensity to learning. The world of the arts will remain, but my time at Columbia University was limited. Once again, a new world opened before me. With Kevin as my guide, I became a dedicated, even obsessed, student. My life was spent in a small room lined with volumes of Keats' poetry at the Columbia Library and I immersed myself in my studies. The study of literature at Columbia in the sixties was exciting in the presence of the poet, Kenneth Koch, the critics, Lionel Trilling, Moses Hadas, and Jacques Barzun. It was largely chance, however, that led me to biology.

To support myself in college, I obtained a job washing glassware in the laboratory of Bernard Weinstein, a Professor of Medicine at Columbia University. Bernie was working on the universality of the genetic code. The early sixties was a time shortly after the elucidation of the structure of DNA and the realization that DNA is the repository of all information and from which all information flows. The genetic code had just been deciphered and the central dogma was complete. I was fascinated by the new molecular biology with its enormous explanatory power. I was a terrible glassware washer because I was far more interested in experiments than dirty flasks. I was fired and was rehired as a Research Assistant and Bernie spent endless hours patiently teaching this scientifically naïve, but intensely interested young student. I was torn between literature and science. Dubious about my literary ambitions and fascinated by molecular biology, I decided to attend graduate school in genetics.

My plans were thwarted by an unfortunate war and to assure deferment from the military, I found myself a misplaced medical student at Johns Hopkins University School of Medicine. I entered medical school by default. I was a terrible medical student, pained by constant exposure to

the suffering of the ill and thwarted in my desire to do experiments. My clinical incompetence was immediately recognized by the faculty and deans. I could rarely, if ever, hear a heart murmur, never saw the retina, my glasses fell into an abdominal incision and finally, I sewed a surgeon's finger to a patient upon suturing an incision. It was during this period of incompetence and disinterest that I met another extremely close friend, Frederick Kass, now a Professor of Psychiatry at Columbia University. Fred was an unusual medical student, a Texan with a degree in art history from Harvard, who remains a kindred spirit.

It was a difficult time, but I was both nurtured and protected by Howard Dintzis, Victor McCusick, and Julie Krevins, three professors at Johns Hopkins who somehow saw and respected my conflict. Without them, there is little question that I would not have been tolerated but they urged the deans to come up with a solution. I was allowed to graduate medical school early with an MD if I promised never to practice medicine on live patients. I returned to Columbia as an intern in Pathology where I kept this promise by performing autopsies. After a year in Pathology, I was asked by Don King, the Chairman of Pathology, never to practice on dead patients.

Finally, I was afforded the opportunity to pursue molecular biology in earnest. I joined the laboratory of Sol Spiegelman in the Department of Genetics at Columbia University. Spiegelman was a short, incisive, witty man with a tongue as sharp as his mind. Spiegelman was the first to synthesize infectious RNA *in vitro* and this led to a series of extremely interesting and clever experiments revealing Darwinian selection at the level of molecules in a test tube. Sol recognized the importance of the early RNA world in the evolution of life and had recently turned his laboratory to a study of RNA tumor viruses. An immediate bond formed between us, and Sol taught me how to think about science, to identify important problems, and how to effect their solution.

Although I felt a growing confidence in my abilities in molecular biology, I was naïve in other areas of biology, notably biophysics. Importantly, I had a sense early in my career that my interest in biology was eclectic and that I would need a concomitantly broad background to embrace the different areas of biology without trepidation. I left to begin a second postdoctoral fellowship at the National Institutes of Health, working with Gary Felsenfeld on DNA and chromatin structure. Since I entered medical school to avoid the draft, I had a military obligation that was fulfilled by my years at the NIH and was endearingly termed a "yellow beret." Gary was great, but the NIH was alien, a government reservation with a fixed workday. As a night person, I found it strange and at some level difficult since I arrived at noon after all the parking spaces were occupied, left at midnight and accumulated an increasing number of parking tickets. In the midst of a molecular hybridization reaction, I was arrested by two FBI agents (the NIH is a federal reservation) for 100 summonses for parking violations.

As a fellow in Felsenfeld's lab studying how chromatin serves to regulate gene expression, I formed close friendships that continue to the present. On the beach at Cold Spring

Harbor, I sat with Tom Maniatis and Harold Weintraub and talked about chromosome replication and gene expression and within a few hours a bond formed, a respect for one another and for one another's thinking, that has lasted for thirty years. Hal, unfortunately, died ten years ago of a brain tumor, but his warmth, his creativity persist.

Sol Spiegelman invited me to return to Columbia as an Assistant Professor in 1974 at the Institute of Cancer Research. I was ecstatic to occupy a lab and office adjacent to his. Sol had many visitors in those years, and when he felt bored in a meeting he would excuse himself and hide in my office where we talked science until his visitors finally gave up and left. I was studying the structure of genes in chromatin and had the good fortune of participating in a revolution made possible by recombinant DNA technology. I spent a great deal of time with Tom Maniatis, who pioneered many of the techniques in recombinant DNA. Tom left Harvard for Caltech, because he was restricted from performing recombinant DNA experiments in Cambridge, Massachusetts. We learned how to cut and paste DNA, to isolate genes, and to analyze their anatomy down to the last detail. We recognized that to understand gene control and gene function, however, required a functional assay. Within months of establishing my own laboratory in 1974, Michael Wigler, my first graduate student along with Sol Silverstein, a Professor at Columbia, developed novel procedures that allowed DNA-mediated transformation of mammalian cells. Michael, even at this very early stage in his career, was conceptually and technically masterful and within a few years he devised procedures that permitted the introduction of virtually any gene into any cell in culture. He developed a system that not only allowed for the isolation of genes, but also for detailed analysis of how they worked. We now had a facile assay to study the sequences regulating gene expression as well as gene function.

Michael went off to the Cold Spring Harbor Laboratories and, simultaneous with Bob Weinberg at MIT, identified the mutant *ras* gene as the gene responsible for malignant transformation in many cancer cells. My laboratory went off in many directions, first identifying the regulatory sequences responsible for control of specific gene expression. At the same time, a research fellow, Dan Littman, now a Professor at NYU, joined the lab and was interested in two molecules that characterize the major classes of T cells. Dan, along with a student, Paul Maddon, succeeded in exploiting the gene transfer to isolate these two molecules. As often in science, serendipity heightened the interest in these molecules: we demonstrated that one of these receptors, CD4, was the high-affinity receptor for HIV, allowing attachment and infection of immune cells.

This early work on recombinant DNA was a period of enormous excitement, for it led to a revolution in both thinking and technology in biology. It provided a new tool for the study of fundamental problems and spurred a new and valuable industry: biotechnology. We, who were involved at its inception, were perhaps a bit haughty, aggressive, and proud, and were accused by many of playing "God." As evidence, the press noted that "I baptized my first child, Adam."

Recombinant DNA aroused a good deal of passion and hostility. The notion of tinkering with life was thought to endanger life and this cry became one of the major indictments of modern biology. These experiments raised endless debate because the idea that genes can be taken out of one organism and introduced into the chromosome of another is by itself upsetting. The very notion of the performance of recombinant DNA was linked with the mysterious and supernatural. This conjured up myths that elicited intense anxiety. Recombinant DNA, it was feared, would permit biologists to alter individual species as well as the evolution of species. This controversy emphasized the fact that advances in science may indeed bring harm as well as benefit. In the case of recombinant DNA, as Francois Jacob said, "Apocalypse was predicted but nothing happened." In fact, with recombinant DNA, only good things happened. At a practical level, the ability to construct bacteria-replicating eucaryotic genes has allowed for the production of an increasingly large number of clinically important proteins. At a conceptual level, gene cloning has permitted a detailed look at the molecular anatomy of individual genes, and from a precise analysis of these genes we have deduced the informational potential of the gene and the way in which it dictates the properties of an organism.

At a personal level, the emergence of a new discipline, biotechnology, introduced me to a world outside of academia. This important excursion showed me that brilliance is not limited to universities. I met and remain very close to two dynamic leaders of technology development, Fred Adler and Joe Pagano. Despite disparate histories, we remain very close and they continue to fascinate me with lives quite different from that of a university professor.

In 1982, I began to think about the potential impact of the new molecular biology and recombinant DNA technology on problems in neuroscience. Molecular biology was invented to solve fundamental problems in genetics at a molecular level. With the demystification of the brain, with the realization that the mind emerges from the brain and that the cells of the brain often use the very same principles of organization and function as a humble bacterium or a liver cell, perhaps molecular biology and genetics could now interface with neuroscience to approach the tenuous relationship between genes and behavior, cognition, memory, emotion, and perception. This thinking was the result of a faculty meeting at which Eric Kandel and I overcame our boredom with administration by talking science. Eric was characteristically exuberant about his recent data that revealed a correlation between a simple form of memory in the marine snail *Aplysia* and cellular memory at the level of a specific synapse. Molecular biologists had encountered cellular memory before in the self-perpetuating control of gene expression. This led to the realization that this was the moment to begin to apply the techniques of molecular biology to brain function and I would attempt to recruit Eric Kandel as my teacher.

A courageous new postdoctoral fellow in my laboratory, Richard Scheller, now Director of Research for Genentech, was excited about embarking on an initial effort in molecular neurobiology in a laboratory with absolutely no expertise in

neuroscience. Together with Richard and Eric, we set out to isolate the genes responsible for the generation of stereotyped patterns of innate behaviors. All organisms exhibit innate behaviors that are shaped by evolution and inherited by successive generations that are largely unmodified by experience or learning. It seemed reasonable to assume that this innate behavior was dictated by genes that might be accessible to molecular cloning. It was an exciting and amusing time, with myself unfamiliar with action potentials and Kandel uncomfortable with central dogma. Richard Scheller exploited the techniques of recombinant DNA to identify a family of genes encoding a set of related neuropeptides whose coordinated release was likely to govern the fixed action pattern of behaviors associated with egg laying. A single gene, the ELH gene, specifies a polypeptide that is cut into small biologically active peptides such that individual components of the behavioral array may be mediated by peptides encoded by one gene.

Watching the story unfold, observing the interface of molecular biology and neuroscience, provided great pleasure. More importantly, this collaboration formed the basis of a continuing relationship with Eric Kandel, with his incisive mind, inimitable laugh, and boundless energy. In 1986 neuroscience for me was made even richer when Tom Jessell came along. Tom joined the faculty at Columbia and was to occupy a lab adjacent to my own. Not surprisingly, the lab was not ready and I had the great pleasure of hosting Tom in my own laboratory, and this forged a long-lasting scientific and personal relationship. Jessell, the understated British scientist with a wry wit and piercing mind, joined a fellow in my laboratory, David Julius, now at the University of California at San Francisco, and together they devised a clever assay for the isolation of genes encoding the neurotransmitter receptors. These experiments, which might have been the last performed by the hands of Jessell, led to the isolation of genes encoding the seven transmembrane domain serotonin receptor 5HT_{1C}, and more generally provided an expression system that permitted the identification of functional genes that encode receptors in the absence of any information on the nature of the protein sequence. With Kandel one floor above, and Jessell next door, there was no departure from neuroscience. I was surrounded and I did not want to escape. I was beginning to feel that neuroscience was indeed an appropriate occupation for a molecular biologist. To quote Woody Allen, a fellow New Yorker, "The brain is my second favorite organ."

In the late 1980s I became fascinated in the problem of perception: how the brain represents the external world. I was struck by observations from animal behavior that what an organism detects in its environment is only part of what is around it and that part can differ in different organisms. The brain functions then not by recording an exact image of the world, but by creating its own selective picture. Biological reality will therefore reflect the particular representation of the external world that a brain is able to build, and a brain builds with genes. If genes are indeed the arbiters of what we perceive from the outside world, then it follows that an understanding of the function of these genes could provide

insight into how the external world is represented in the brain. Together with Linda Buck, a creative research fellow in the lab, we began to consider how the chemosensory world is represented in the brain. The problem of olfaction was a perfect intellectual target for a molecular biologist. How we recognize the vast diversity of odorous molecules posed a fascinating problem. We assumed that the solution would involve a large family of genes and Linda Buck devised a creative approach that indeed identified the genes encoding the receptors that recognize the vast array of odorants in the environment. Linda came to me with the experimental data late one night, exuberant, and I felt uncharacteristically silent. There were 1000 odorant receptor genes in the rat genome, the largest family of genes in the chromosome, and this provided the solution to the problem of the diversity of odor recognition. More importantly, the identification of these 1000 genes and their expression revealed an early and unanticipated logic of olfaction. Indeed, the subsequent use of these genes to manipulate the genome of mice has afforded a view of how the olfactory world could be represented in the brain and how genes shape our perception of the sensory environment. From that late night moment to the present, it has been a joy to watch this story unfold.

It is this work for which Linda Buck and I share the profound honor and good fortune of having been awarded the Nobel Prize in Physiology or Medicine. But there are, deeper,

more human joys, two sons, Adam and Jonathan, my sister, Linda, a very close coterie of friends, and a new love. Watching, contributing to the growth of my children is not only moving but humbling and puts my intense life in science in perspective. Often this intensity, bordering on obsession, distracted me from fathering and this is a regret. But my sons have emerged from a frenetic teenage into very human college students, extremely unlikely to pursue a career in science. My sister remains a close and dedicated member of an increasingly small family. A new love, Cori Bargmann, a behavioral geneticist now at Rockefeller University, has entered my world. Her intensity for science hides a knowledge and passion for books, music, and art. I have learned much from her, but most importantly Cori has shown me how to combine intellectual intensity with humanity and warmth.

Finally, the Nobel Prize was awarded to me not as a man, but for my work, a work of science that derives from the efforts of many brilliant students as well as from the incisive teachings of devoted colleagues. I take equal pride in the science that has been accomplished in the laboratory as in the scientists that have trained with me and are now independently contributing to our understanding of biology. I therefore feel that I can only accept the Nobel Prize in trust, as a representative of a culture of science in my laboratory and at Columbia University. I am deeply grateful for this culture.

1. Introduction

The image in the painting *La Bonne Aventure* is not a nose (Figure 1). It is a portrayal by the surrealist René Magritte of his own brain's representation of the external world. It is a



Figure 1. The painting *La Bonne Aventure* (Fortune Telling), by René Magritte (1937) portrays a monumental nose. I have added the inscription “Ceci n’est pas un nez” (“This is not a nose”) in Magritte’s script to emphasize the tension between image and reality, a conflict inherent in much of his art as well as in the science of perception.

vignette that reveals a tension between image and reality, a tension that is a persistent source of creativity in art, brought to its culmination by the surrealists. The problem of how the brain represents the external world is not only a central theme in art but is at the very core of philosophy, psychology, and neuroscience. We are interested in how the chemosensory world is represented in the brain.

All organisms have evolved a mechanism to recognize sensory information in the environment and transmit this information to the brain where it then must be processed to create an internal representation of the external world. There are many ways for organisms to probe the external world: some smell it, others listen to it, many see it. Each species therefore lives in its own unique sensory world of which other species may be partially or totally unaware. A whole series of specific devices alien to human perception have evolved: biosonar in bats, infrared detectors in snakes, electrosensitive organs in fish, and a sensitivity to magnetic fields in birds. What an organism detects in its environment is only part of what is around it and that part differs in different organisms. The brain functions, then, not by recording an exact image of the world, but by creating its own selective picture—a picture largely determined by what is important for the survival and reproduction of the species.

Sensory impressions, therefore, are apprehended through the lens of the particular perceiving brain, and the brain must therefore be endowed with an a priori potential to recognize the sensory world.^[1] Our perceptions are not direct recordings of the world around us, rather they are constructed internally

according to innate rules. Colors, tones, tastes, and smells are active constructs created by our brains out of sensory experience. They do not exist as such outside of sensory experience.^[2] Biological reality, I argue, therefore reflects the particular representation of the external world that a brain is able to build, and a brain builds with genes.

If our genes are indeed the arbiters of what we perceive from the outside world, then it follows that an understanding of the function of these genes could provide insight into how the external world is represented in our brain. But what can molecular biology really tell us about so elusive a brain function as perception? Molecular biology was invented to solve fundamental problems in genetics at a molecular level. With the demystification of the brain, with the realization that the mind emerges from the brain, and that the cells of the brain often use the very same principles of organization and function as a humble bacterium or a liver cell, molecular biology and genetics could now interface with neuroscience to approach the previously tenuous relationship between genes and behavior, cognition, memory, emotion, and perception.

Why would a molecular neuroscientist interested in perception choose to focus on the elusive sense of smell? In humans, smell is often viewed as an aesthetic sense, as a sense capable of eliciting enduring thoughts and memories. Smell, however, is the primal sense. It is the sense that affords most organisms the ability to detect food, predators, and mates. Smell is the central sensory modality by which most organisms communicate with their environment. Second, humans are capable of recognizing hundreds of thousands of different odors. For molecular neuroscientists studying the brain, the mechanism by which an organism can interact with the vast universe of molecular structures defined as odors provides a fascinating problem in molecular recognition and perceptual discrimination. Finally, the problem of perception necessarily involves an understanding of how sensory input is ultimately translated into meaningful neural output: thoughts and behavior. In olfaction, the sensory input is extremely well defined and consists of chemicals of precise molecular structure. The character of the input in olfaction is far simpler than that of a visual image, for example, which consists of contours, texture, color, movement, and form of confounding complexity. Representation of an olfactory image is simpler and reduces to the problem of how precisely defined chemical structures are transformed in brain space.

As molecular neurobiologists, Linda Buck and I approached olfactory sensory perception by dividing it into two problems: First, what mechanisms have evolved to allow for the recognition of the vast array of molecular structures we define as odorants? Clearly, there must be receptors in the sensory neurons of the nose capable of associating with odor molecules. Do we have a relatively small number of “promiscuous” receptors, each capable of interacting with a large number of odorous molecules? Alternatively, olfactory recognition may involve a very large number of “chaste” receptors each capable of interacting with a limited set of odor molecules. The second problem is conceptually more difficult: how does the olfactory sensory system discriminate among the vast array of odorous molecules that are recognized by the nose? Put simply, how does the brain know what

the nose is smelling? This question will ultimately require knowledge of how the different odors are represented and encoded in the brain.

2. A Large Family of Odorant Receptor Genes

We approached the problem of odor recognition directly by isolating the genes encoding the odorant receptors.^[3] The experimental design we employed to isolate these genes was based on three assumptions: 1) the odorant receptors were likely to belong to the superfamily of receptors, the G-protein coupled receptors (GPCRs), that transduce intracellular signals by coupling to GTP-binding proteins.^[4–7] 2) The large repertoire of structurally distinct, odorous molecules suggests that the odorant receptors themselves must exhibit significant diversity and are therefore likely to be encoded by a multigene family. 3) The expression of the odorant receptors should be restricted to the olfactory epithelium. Experimentally, we used the polymerase chain reaction (PCR) to amplify members of the GPCR gene superfamily expressed in olfactory sensory neurons. We then investigated whether any of the PCR products were indeed members of a large multigene family. We observed that restriction-enzyme cleavage of a single PCR band generated a set of DNA fragments whose molecular weight summed to a value significantly greater than that of the original PCR product.^[3] In this manner, we identified a multigene family that encodes a large number of GPCRs whose expression is restricted to the olfactory sensory neurons. The receptors were subsequently shown to interact with odors, translating the energy of odor binding into alterations in membrane potential.^[8–11]

The completed sequence of both the murine and human genome ultimately identified 1300 odorant receptors in the mouse^[12,13] and 500 in humans.^[14–16] If mice possess 20000 genes, then as much as 5 % of the genome (one in 20 genes) encodes the odorant receptors. A large family of odorant receptors is observed not only in vertebrates, but in the far simpler sensory systems of invertebrates. A somewhat smaller but highly diverse family of about 80 odorant receptor genes has been identified in the *Drosophila* genome.^[17–19, 50, 67] The invertebrate, *C. elegans*, with only 302 neurons and 16 olfactory sensory neurons expresses about 1000 odorant receptor genes.^[20,21] These experiments provide a solution to the first question: we recognize the vast array of molecular structures defined as odorants by maintaining in our genome a large number of genes encoding odorant receptors.

The observation that over 1000 receptors are required to accommodate the detection of odors suggests a conceptual distinction between olfaction and other sensory systems. Color vision in humans, for example, allows the discrimination of several hundred hues with only three different photoreceptors.^[22,23] These photoreceptors each have distinct but overlapping absorption spectra. Discrimination of color is thought to result from comparative processing of the information from these three classes of photoreceptors. Whereas three photoreceptors can absorb light across the entire visible spectrum, our data suggest that a small number of odorant receptors cannot recognize the full spectrum of distinct

molecular structures perceived by the mammalian nose. Rather, olfactory perception requires a large number of receptors, each capable of recognizing a small number of odorous ligands.

The large number of odorant receptor genes when compared with receptor numbers in other sensory systems perhaps reflects the fact that in vision and hearing the character of the sensory stimulus is continuously variable. Color is distinguished by quantitative differences in a single parameter, the wavelength of light. Similarly, one important parameter of hearing, the frequency of sound, is continuously variable. The diversity of chemical structures of odors do not exhibit continuous variation of a single parameter and therefore cannot be accommodated by a small number of receptors. Rather, the full spectrum of distinct molecular structures perceived by the olfactory system requires a large number of receptors, each capable of interacting with a small number of specific odorous ligands.

3. A Topographic Map in the Olfactory Bulb

We next turned to the question of olfactory discrimination: how does the brain know what the nose is smelling? The identification of a large family of receptor genes allowed us to pose this question in molecular terms. We could now ask how the brain knows which of the numerous receptors have been activated by a given odor. The elucidation of a mechanism by which the brain distinguishes the different combinations of receptors activated by different odors would provide a logic of odor discrimination. This problem was further simplified by the demonstration that an individual sensory neuron expresses only one of the 1000 receptor genes.^[10,24] This observation emerged from single-neuron cDNA cloning experiments, and allowed us to translate the problem of how the brain determines which receptor has been activated to a far simpler problem: how does the brain know which neuron has been activated by a given odor? As in other sensory systems, an invariant spatial pattern of olfactory sensory projections could provide a topographic map of receptor activation that defines the quality of a sensory stimulus.

In other sensory systems, spatially segregated afferent input from peripheral sensory neurons generates a topographic map that defines the location of a sensory stimulus within the environment as well as the quality of the stimulus itself. Olfactory sensory processing does not extract spatial features of the odorant stimulus. Relieved of the requirement to map the position of an olfactory stimulus in space, we asked whether the olfactory system might employ spatial segregation of sensory input to encode a quality of an odorant. Robert Vassar in my lab and Kerry Ressler in Linda Buck's lab therefore analyzed the spatial patterns of receptor expression in the olfactory epithelium by *in situ* hybridization and observed that cells expressing a given receptor are restricted to one of four broad but circumscribed zones.^[25,26] The overriding feature of this organization, however, is that within a zone, neurons expressing a given receptor are not topographically segregated, rather they appear randomly

dispersed. When they performed *in situ* hybridization experiments to the bulb, the first relay station for olfactory sensory neurons in the brain, they observed that topographic order was restored.^[27,28] Neurons expressing a given receptor, although randomly distributed in the epithelium, project to spatially invariant glomeruli in the olfactory bulb, thus generating a topographic map.

Peter Mombaerts, then a research fellow in the lab, developed a genetic approach to visualize axons from olfactory sensory neurons, thereby expressing a given odorant receptor as they project to the brain.^[29] We modified receptor genes by targeted mutagenesis in the germ line of mice. These genetically altered receptor genes now encoded a bicistronic mRNA that allows the translation of receptor along with tau-lacZ, a fusion of the microtubule-associated protein tau with β -galactosidase. In these mice, olfactory neurons that transcribe a given receptor also express tau-lacZ in their axons, permitting the direct visualization of the pattern of projections in the brain (Figure 2).

We observe that neurons expressing a receptor project to only two topographically fixed loci, or glomeruli, in the bulb, thus creating mirror-image maps in each bulb. Neurons expressing different receptors project to different glomeruli. The position of the individual glomeruli is topographically defined and is similar for all individuals in a species (Figure 3). Individual odors could activate a subset of receptors that would generate specific topographic patterns of activity within the olfactory bulb such that the quality of an olfactory stimulus could be encoded by spatial patterns of glomerular activity.

The identification of an anatomic olfactory sensory map poses four questions. The first addresses the singularity of receptor gene choice. What mechanism assures that a sensory neuron expresses only a single receptor and then projects with precision to one of 1000 topographically fixed glomerular loci? Second, does the anatomic map translate into a functional map such that different odors elicit different patterns of activity? Third, can we relate specific spatial patterns of glomerular activity to specific behaviors? Finally how is the map read? How does the brain look down upon a spatial pattern of activity and associate this pattern with a particular odor?

4. Receptor Choice and the Topographic Map

The topographic map in the olfactory system differs in character from the orderly representation inherent in the retinotopic, tonotopic, or somatotopic sensory maps. In these sensory systems, the peripheral receptor sheet is represented in the central nervous system (CNS), such that neighboring relations in the periphery are preserved in the CNS (for reviews, see Refs. [30,31]). In this manner, peripheral receptor cells may acquire a distinct identity that is determined by their spatial position in the receptor sheet. Spatial patterning in the periphery can therefore endow individual neurons with positional information that directs their orderly representation in the brain.

The olfactory system, however, does not exhibit an orderly representation of receptor cells in the periphery.

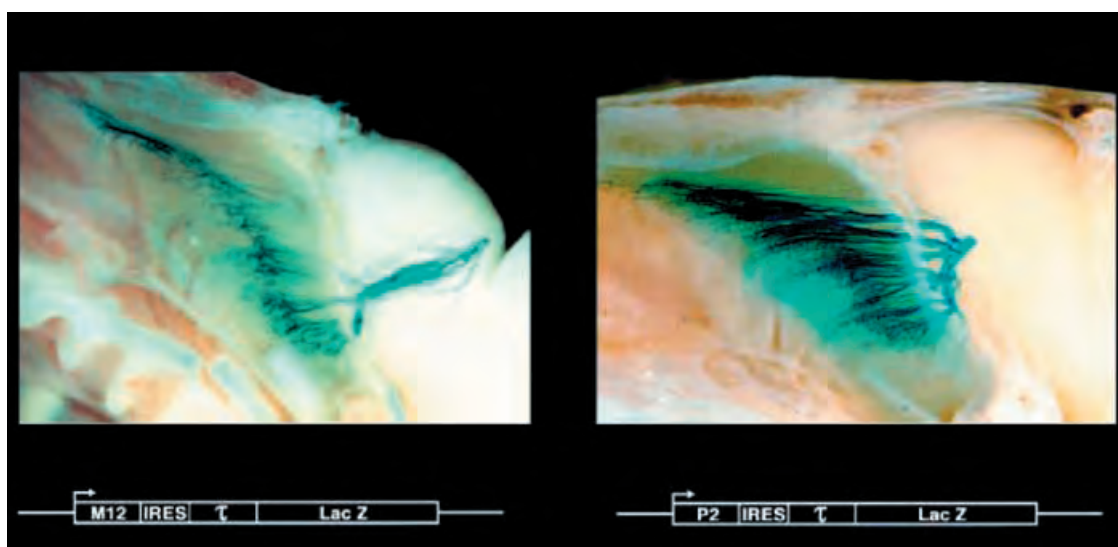


Figure 2. Convergence of axons from neurons expressing a given receptor. Odorant receptor loci were modified by homologous recombination in ES cells to generate strains of mice in which cells expressing a given receptor also express a fusion of the microtubule-associated protein tau with β -galactosidase. These photographs reveal neurons expressing either the M12 (left) or P2 (right) receptors along with their axons as they course through the cribriform plate to a single locus in the olfactory bulb. Neurons expressing different receptors converge on different glomeruli. The genetic modifications that assure the coordinate expression of receptor and tau-lacZ are shown beneath the photographs.

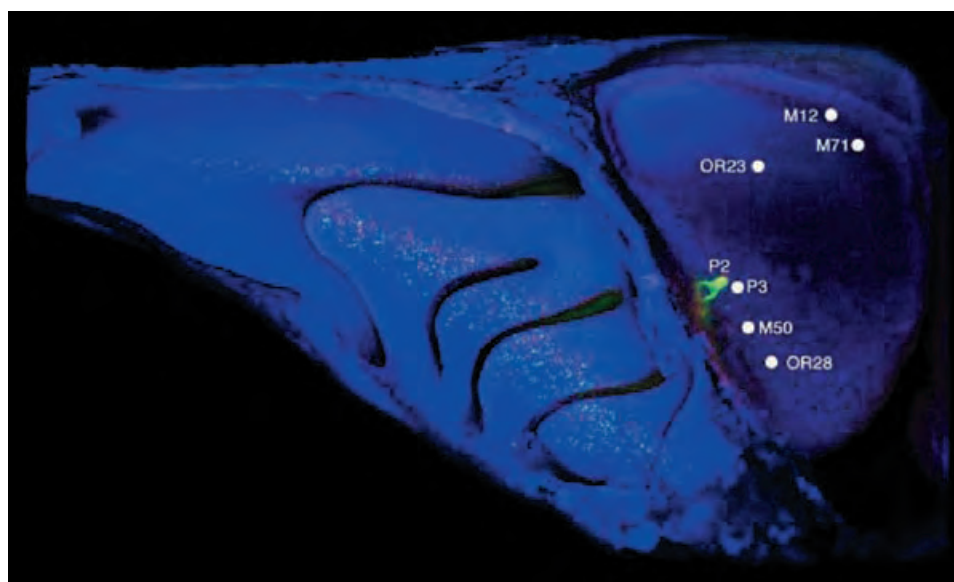


Figure 3. A Topographic map of olfactory sensory axons in the bulb. The picture reveals neurons expressing two modified P2 alleles: P2-IRES-tau-lacZ (red) or P2-IRES-GFP (green). These neurons send axons that co-converge on the same glomerulus in the olfactory bulb. Neurons expressing other receptors converge on different glomerular loci that are shown schematically. All nuclei are stained blue with TOTO-3. The relative positions of the different glomeruli are maintained in different mice, thus revealing an invariant topographic map in the olfactory bulb.

Neurons expressing a given receptor are randomly dispersed within a given zone and order is restored in the bulb where neurons expressing a given receptor converge on discrete loci to create a topographic map. Olfactory neurons differ from one another not by virtue of their position in a receptor sheet, but rather by the nature of the receptor they express. The tight linkage between the choice of an odorant receptor and the site of axon convergence suggests a model in which the odorant receptor is expressed on dendrites, where it recognizes odors in the periphery, and also on axons, where it

governs target selection in the bulb. In this manner, an olfactory neuron would be afforded a distinct identity that dictates the nature of the odorant to which it responds as well as the glomerular target to which its axon projects. If the odorant receptor also serves as a guidance molecule, this leads to two experimental predictions. First, the receptor should be expressed on axons as well as on dendrites, and second, genetic modifications in the receptor sequence might alter the topographic map.

The first prediction was tested by Gilad Barnea, who generated specific antibodies against two odorant receptors and examined the sites of receptor expression on sensory neurons.^[32] Antibodies were raised against extracellular and cytoplasmic epitopes of the mouse odorant receptors MOR28 and MOR11-4. In the sensory epithelium, we observe intense staining in the dendritic knobs, the site of odor binding. In the olfactory bulb, antibody stains axon termini whose arbors are restricted to two glomeruli (Figure 4). Antibody-staining of the bulb from mice bearing the MOR28-IRES-tau-lacZ allele reveals that the glomeruli stained by antibodies to MOR28 also receives the tau-lacZ fibers. Thus, the receptor is expressed on both dendrites and the axons of sensory neurons.

In a second series of experiments performed by my student, Fan Wang, we provided genetic evidence suggesting that the receptor on axons is indeed a guidance molecule. We modified our gene-targeting approach to ask whether substitutions of the P2 receptor coding sequence alter the projections of neurons that express this modified allele.^[33] We replaced the coding region of the P2 gene with the coding regions of several other receptors, and examined the consequences on the formation of the topographic map. Substitution of the P2 coding region with that of the P3 gene, a linked receptor gene homologous to P2 and expressed in the same epithelial zone, results in the projection of axons to a glomerulus distinct from P2 that resides immediately adjacent to the wild-type P3 glomerulus. Other substitutions that replace the P2 coding sequences with receptor sequences expressed either in different zones or from different chromo-

somal loci also result in the convergence of fibers to glomeruli distinct from P2. These observations, along with recent experiments involving more extensive genetic modifications^[34,35] provide support for the suggestion that the olfactory receptor plays an instructive role in axon targeting as one component of the guidance process.

How may the odorant receptors participate in the guidance process? In one model, the odorant receptor is expressed on the axon termini along with other guidance receptors where it recognizes positional cues elaborated by the bulb. Each of the 1000 distinct types of sensory neuron will therefore bear a unique combination of guidance receptors that define a code dictating the selection of a unique glomerular target. Such a model does not necessarily imply that there are 1000 distinct cues, each spatially localized within the bulb. Rather, a small number of graded cues may cause the differential activation of the different odorant receptors on axon termini. In this manner, the different affinities of individual receptors for one or a small number of cues, and perhaps different levels of receptor, might govern target selection. Such a model is formally equivalent to models of retinotopy in which a gradient of guidance receptors on retinal axons is matched by a positional gradient of guidance cues in the tectum (for a review see Ref. [31]).

5. The Singular and Stable Choice of Receptor

If the odorant receptor defines the functional identity of a sensory neuron and also determines the site of projection in

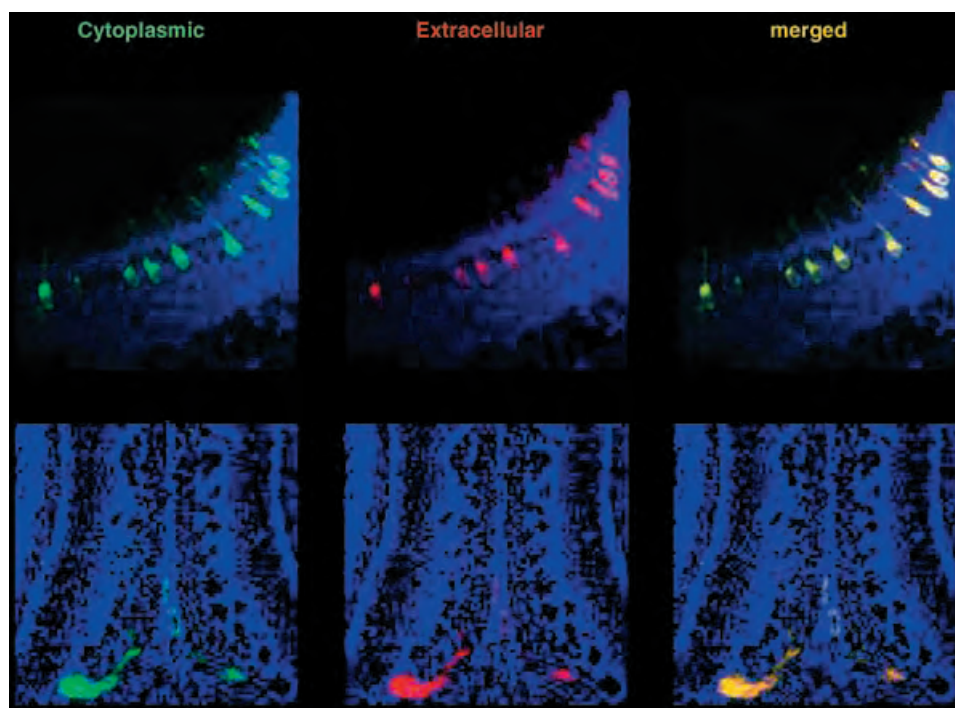


Figure 4. The odorant receptor gene is expressed on both dendrites and axons of olfactory sensory neurons. The mouse sensory epithelium (top picture) or olfactory bulb (bottom picture) was stained with antibody to either an extracellular (middle) or cytoplasmic (left) epitope of the MOR28 receptor. These experiments reveal the expression of odorant receptor in the cell body and dendrites in the epithelium as well as on axon termini within a defined glomerulus in the bulb. Antibody staining in the olfactory bulb coincides with the site of convergence of MOR28 axons. Adapted with permission from Ref. [32].

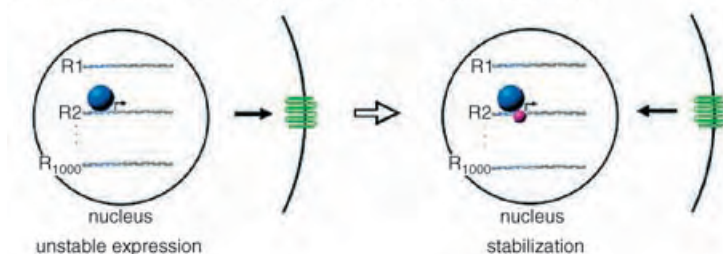
the brain, then the expression of a single receptor gene in a neuron is an essential feature in models of olfactory perception. This immediately poses the question as to what mechanism has evolved to assure the expression of a single receptor gene from the family of 1000 genes in the chromosome. One model for the control of olfactory receptor expression invokes the existence of 1000 different sensory neurons, each expressing a unique combination of regulatory factors that governs the choice of a different olfactory receptor gene. This deterministic model predicts that all olfactory receptor genes will contain different *cis*-regulatory sequences that are recognized by unique sets of transcription factors. An alternative, stochastic model of receptor gene selection suggests that all odorant receptor genes within a zone contain the same *cis*-regulatory information and are controlled by the same set of transcription factors. In this model, a special mechanism must exist to assure that only one receptor gene is chosen. Moreover, once a specific receptor is chosen for expression, this transcriptional choice must be stable for the life of the cell, because receptor switching after stable synapse formation would seriously perturb odor discrimination.

A series of transgene experiments performed by Ben Shykind in my own laboratory, as well as by other researchers, provide evidence for a mechanism of receptor choice that is stochastic.^[36,37] We have generated mice in which the endogenous P2 allele has been replaced with the P2-IRES-tau-lacZ allele. We have also introduced a randomly integrated P2-IRES-GFP transgene into the chromosome of this strain. In a deterministic model, we predict that a unique combination of transcription factors would activate both the endogenous and

transgenic P2 alleles such that cells that express lacZ from the endogenous P2-IRES-tau-lacZ allele should also express GFP from the P2 transgene. Examination of the sensory epithelium in these mice, however, reveals a singularity of P2 expression. Cells that express the endogenous P2 allele never express the transgene. In a conceptually similar experiment, we generated transgenic mice that harbor an integrated array of multiple P2 transgenes that include P2-IRES-tau-lacZ and P2-IRES-GFP linked at the same chromosomal locus. In these strains, we also observe a singularity of transgene expression. Neurons that express the P2-IRES-tau-lacZ transgene do not express the linked P2-IRES-GFP gene. Taken together, these experiments provide support for a model in which receptor choice is not deterministic, rather it is stochastic.

Once a single receptor gene is chosen for expression, this transcriptional choice must be stable for the life of the cell because receptor switching after stable synapse formation would seriously perturb odor discrimination. In recent experiments, Ben Shykind in my lab along with the research groups of Randall Reed and Hitoshi Sakano devised genetic strategies that permit the analysis of the stability of receptor choice.^[38–40] We have employed a lineage tracer to map the fate of sensory neurons that express either an intact or a nonfunctional deletion of the MOR28 gene. Mature neurons that express an intact MOR28 receptor, but have not yet formed stable synapses in the brain, can switch receptor expression, albeit at low frequency. Thus, we observe that switching is an inherent property of wild-type receptor gene choice. Neurons that choose to express a mutant MOR28 receptor subsequently extinguish its expression and switch at

A Choice of functional receptor leads to feedback stabilization:



B Choice of nonfunctional receptor leads to switching:

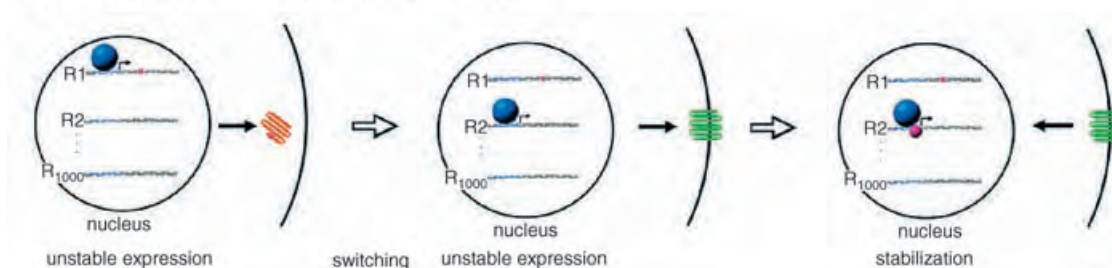


Figure 5. A feedback model assuring the stable expression of a functional receptor. A) The transcriptional machinery (blue sphere) expresses only one of 1000 odorant receptor genes (in this case, R2). R2 encodes a functional receptor that elicits a feedback signal that leads to the stabilization of receptor choice (purple sphere). B) If the transcriptional machinery chooses the nonfunctional receptor R1, which is not competent to mediate feedback stabilization, switching occurs. The transcriptional machine is then free to select a second receptor for expression that will ultimately mediate feedback stabilization. This model provides a mechanism to assure that a neuron expresses a functional odorant receptor.

high frequencies to express alternate receptors such that a given neuron stably transcribes only a single receptor gene. These observations suggest a mechanism of olfactory receptor gene choice in which a cell selects only one receptor allele but can switch at low frequency. Expression of a functional receptor would then elicit a signal that suppresses switching and stabilizes odorant receptor expression. Neurons that initially express a mutant receptor fail to receive this signal and switch genes until a functional receptor is chosen (Figure 5).

The mouse genome contains 340 olfactory receptor pseudogenes, whereas the human genome contains 550 pseudogenes, several of which continue to be transcribed.^[12,16] Expression of a pseudogene would result in the generation of sensory neurons incapable of odor recognition. A mechanism that allows switching provides a solution to the pseudogene problem such that if pseudogenes are chosen, another transcriptional opportunity is provided, thus assuring that each neuron expresses a functional receptor. This model of serial monogamy assures that neurons will express a single receptor throughout their life. This feedback model in which expression of a functional odorant receptor suppresses switching to other olfactory receptor genes is reminiscent of one mechanism of allelic exclusion in T and B lymphocytes.

6. Cloning a Mouse from an Olfactory Sensory Neuron

What mechanism assures that a single receptor gene is chosen stochastically in a sensory neuron? One model invokes DNA recombination of odorant receptor genes at a single active expression site in the chromosome. DNA recombination provides *Saccharomyces cerevisiae*,^[41] trypanosomes,^[42] and lymphocytes^[43] with a mechanism to stochastically express one member of a set of genes that mediate cellular interactions with the environment. One attractive feature shared by gene rearrangements in trypanosomes and lymphocytes is that gene choice is a random event, a feature of receptor gene selection in olfactory sensory neurons. However, efforts to demonstrate a recombination event involving receptor genes have been seriously hampered by the inability to obtain populations of neurons or clonal cell lines that express the same receptor. Kristin Baldwin in my laboratory, in a collaboration with Rudy Jaenisch, Kevin Eggan, and Andy Chess at MIT, addressed this problem by generating ES cell lines and cloned mice derived from the nuclei of olfactory sensory neurons expressing the P2 receptor (Figure 6).^[44] The generation of cloned mice from cells of the nose derives from an initial insight of Woody Allen in his 1978 futuristic comedy, *Sleeper*. In this film, efforts are made to resurrect a totalitarian leader by cloning from his only surviving body part, his nose. Twenty-five years later, science successfully imitated art with the generation of mice cloned from a single sensory neuron from the nose.

We would predict that if DNA recombination accompanies receptor gene choice, then the olfactory epithelium from cloned mice derived from a sensory neuron expressing the P2 gene should be clonal with respect to receptor expression,

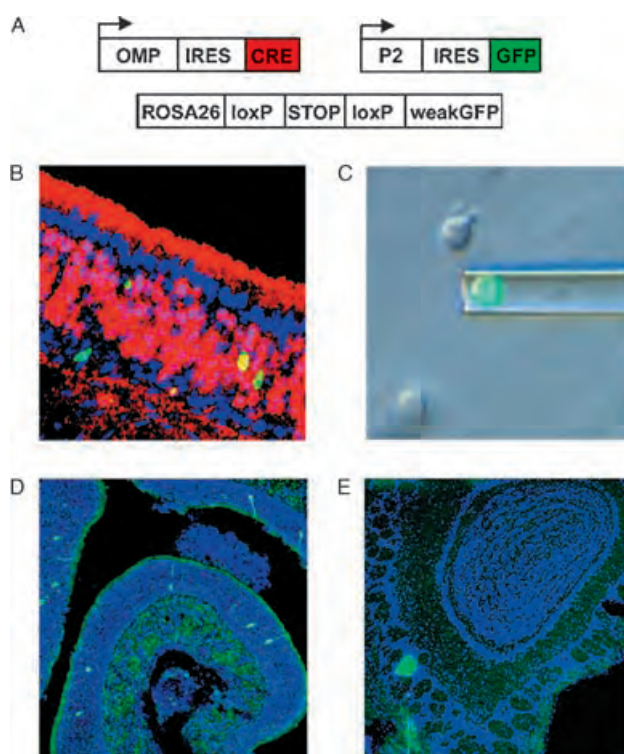


Figure 6. Cloning a mouse from olfactory sensory neurons expressing the P2 odorant receptor. A) A genetic strategy to label P2-expressing sensory neurons with GFP as well as to mark olfactory sensory neurons by virtue of a unique deletion in DNA. B) The olfactory epithelium of a mouse with the genetic modifications described in (A). A single nucleus expressing the P2 odorant receptor gene was picked and introduced into an enucleated oocyte. The epithelium was stained with antibody to Cre recombinase (red) to mark sensory neurons and GFP (green) to identify P2-expressing cells. C) A green neuron expressing P2-IRES-GFP was picked from dissociated olfactory epithelium of donor animals. D) The olfactory epithelium from a mouse cloned from a nucleus expressing the P2 receptor gene shows the normal distribution of P2-expressing cells. Axons from these neurons converge on a single glomerulus in the olfactory bulb (E). All nuclei are stained with TOTO-3 blue. The observation that mice cloned from a nucleus expressing the P2 receptor gene do not preferentially express this gene in the sensory epithelium suggests that DNA recombination events do not accompany receptor gene choice. Adapted with permission from Ref. [44].

such that all cells transcribe the rearranged P2 allele. Analysis of the sequence and organization of the DNA surrounding the P2 allele expressed in cloned mice revealed no evidence for either gene conversion or local transposition at the P2 locus. In addition, the pattern of receptor gene expression in the sensory epithelium of cloned mice was normal. Multiple odorant receptor genes are expressed without preference for the P2 allele transcribed in the donor nucleus (Figure 6). These data, along with similar experiments by Peter Mombaerts,^[45] demonstrate that the mechanism responsible for the choice of a single odorant receptor gene does not involve irreversible changes in DNA. In a broader context, the generation of fertile cloned mice that are anatomically and behaviorally indistinguishable from wild-type indicates that the genome of a postmitotic, terminally differentiated olfactory neuron can re-enter the cell cycle and be reprogrammed

to a state of totipotency after nuclear transfer. The stochastic choice of a single olfactory receptor gene is therefore not accomplished by DNA recombination but rather by a rate-limiting transcriptional process, perhaps involving a single transcriptional machine capable of stably accommodating only one olfactory receptor gene.

7. Olfaction in the Fly: A Functional Map in the Antennal Lobe

The identification of an anatomic map in the olfactory bulb immediately poses the question as to whether this map provides a meaningful representation of odor quality that is translated into appropriate behavioral output. Recently, we have become interested in how the olfactory world is represented in the brain of the fruit fly. *Drosophila* provides an attractive system to understand the logic of olfactory perception. Fruit flies exhibit complex behaviors controlled by an olfactory system that is anatomically and genetically simpler than that of vertebrates. Genetic analysis of olfaction in *Drosophila* may therefore provide a facile system to understand the mechanistic link between behavior and the perception of odors. The recognition of odors in *Drosophila* is accomplished by sensory hairs distributed over the surface of the third antennal segment and the maxillary palp. Olfactory neurons within sensory hairs send projections to one of the multiple glomeruli within the antennal lobe of the brain.^[46,47] Leslie Vosshall and Allan Wong showed that most sensory neurons express only one of about 80 odorant receptor genes. Neurons expressing the same receptor project with precision to one or rarely two spatially invariant glomeruli in the antennal lobe, the anatomic equivalent of the olfactory bulb of mammals (Figure 7).^[48–50]

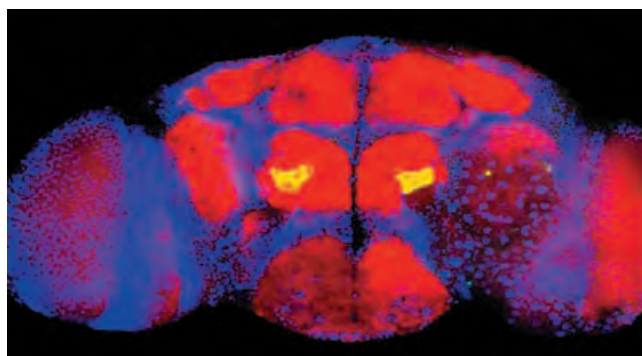


Figure 7. An olfactory sensory map in the fly antennal lobe. Neurons expressing the odorant receptor gene OR47b, also express the transgene synaptobrevin GFP, thus revealing convergence on a single spatially invariant glomerulus that is bilaterally symmetric in the antennal lobe.

The anatomic organization in *Drosophila* is therefore remarkably similar to that of the olfactory system of mammals, suggesting that the mechanism of odor discrimination has been shared despite the 600 million years of evolution separating insects from mammals. This conservation may reflect the maintenance of an efficient solution to

the complex problem of recognition and discrimination of a vast repertoire of odors in the environment. In both flies and mice, the convergence of like axons into discrete glomerular structures provides a map of receptor activation in the first relay station for olfactory information in the brain, such that the quality of an odorant may be reflected by spatial patterns of activity, first in the antennal lobe or olfactory bulb and ultimately in higher olfactory centers.

An understanding of the logic of odor perception requires functional analysis to identify odor-evoked patterns of activity in neural assemblies and ultimately the relevance of these patterns to odor discrimination. We have performed two-photon calcium imaging to examine the relationship between the anatomic map and the functional map in the antennal lobe.^[51] Jing Wang and Allan Wong in my lab developed an isolated *Drosophila* brain preparation that is amenable to two-photon imaging and is responsive to odor stimulation for up to five hours. We expressed the calcium-sensitive fluorescent protein G-CaMP in primary olfactory sensory neurons and projection neurons. G-CaMP consists of a circularly permuted EGFP flanked at the N-terminus by the calcium-binding site of calmodulin and at the C-terminus by the M13 fragment of myosin light chain kinase.^[52] In the presence of calcium, calmodulin interacts with the M13 fragment and elicits a conformation change in EGFP. The resulting elevations in fluorescent intensity reflect changes in the intracellular calcium concentration, a presumed mirror of electrical activity. Moreover, the ability to express G-CaMP in genetically defined populations of neurons allowed us to determine with certainty the locus of neural activity. Odor-evoked changes in fluorescence intensity within the antennal lobe are monitored by a laser-scanning two-photon microscope.^[53]

This imaging technique has allowed us to measure the responsivity of 23 glomeruli to 16 different odors.^[51] A number of interesting features of the glomerular response to odors are revealed by these experiments. First, different odors elicit different patterns of glomerular activation and these patterns are conserved among different animals (Figure 8). At odor concentrations likely to be encountered in nature, the map is sparse and glomeruli are narrowly tuned.

Second, the patterns of activity are insular, such that neighboring glomeruli do not necessarily respond together to a given odor. Each glomerulus visualized anatomically appears to be a functional unit. Third, the patterns of glomerular activity are qualitatively similar upon imaging either sensory or projection neurons. These observations suggest the faithful transmission of sensory input to higher brain centers. Fourth, we have coupled genetic experiments with imaging to demonstrate that the odor-evoked profile for a given glomerulus directly reflects the responsivity of an individual odorant receptor. This finding is consistent with previous molecular and anatomic studies that reveal that neurons that express only a single receptor in like axons converge on a single glomerulus. Thus these studies, along with other imaging approaches in insects,^[54,55] demonstrate that the anatomic map is indeed functional and suggests that each odor elicits a sparse pattern of glomerular activation that may confer a signature for different odors in the brain.

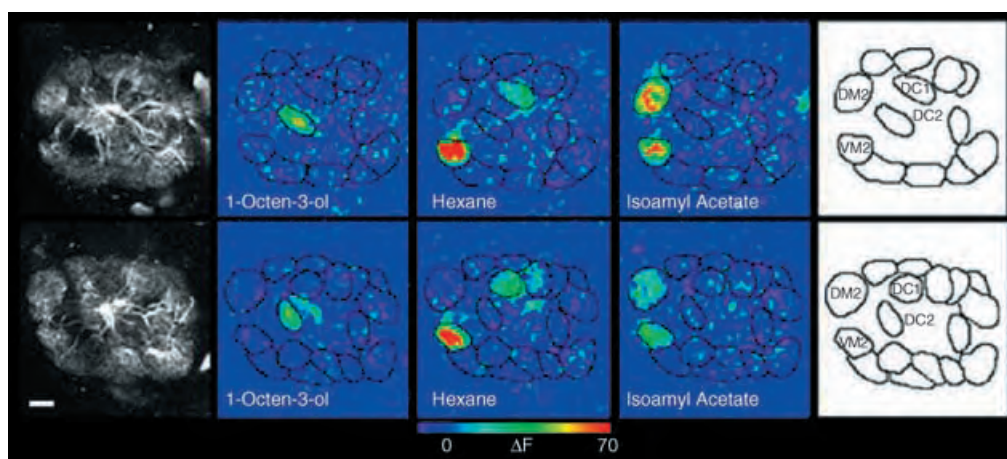


Figure 8. Different odors elicit different patterns of glomerular activation that are conserved among different organisms. Two different flies (top and bottom panels) bearing the GH146-Gal4 and UAS-G-CaMP transgenes were exposed to three odors. Glomerular responses reveal different patterns of activity for the different odors that are conserved in different animals. The pre-stimulation images (left) shows the glomerular structure and the images on the right show the specific glomeruli schematically.

Imaging experiments in vertebrates similarly reveal a functional representation of the anatomic map.^[56–58]

8. Spatial Representations and Innate Behavior

All animals exhibit innate behaviors in response to specific sensory stimuli that are likely to result from the activation of developmentally programmed circuits. Allan Wong and Jing Wang in my lab, in collaboration with Greg Suh, David Anderson, and Seymour Benzer at Caltech, asked whether we can relate patterns of glomerular activity elicited by an odor to a specific behavior.^[59] Some time ago Benzer observed that *Drosophila* exhibits robust avoidance to odors released by stressed flies. Gas chromatography and mass spectrometry identified one component of this “*Drosophila* stress odorant (DSO)” as CO₂. Exposure of flies to CO₂ alone also elicits an avoidance behavior at levels of CO₂ as low as 0.1 % (Figure 9).

We therefore performed imaging experiments with the calcium-sensitive fluorescent indicator G-CaMP and two-photon microscopy to ask whether we could discern a pattern of glomerular activity in response to DSO and CO₂. We first examined flies in which the G-CaMP indicator is driven in all neurons by the pan-neural activator Elav-Gal4. DSO activates only two glomeruli, DM2 and the V glomerulus, whereas CO₂ activates only the V glomerulus. Activation of the V glomerulus was detected at CO₂ levels as low as 0.05 % and this glomerulus was not activated by any of 26 other odorants tested (Figure 9).

We demonstrated that axonal projections to the V glomerulus originate from sensory neurons expressing the receptor GR21A.^[50] We therefore performed calcium imaging with flies in which the UAS G-CaMP reporter was driven by a GR21A promoter Gal4 activator. CO₂, as well as DSO, activated GR21A sensory termini in the V glomeruli. We next asked whether the GR21A sensory neurons are necessary for the avoidance response to CO₂. Inhibition of synaptic trans-

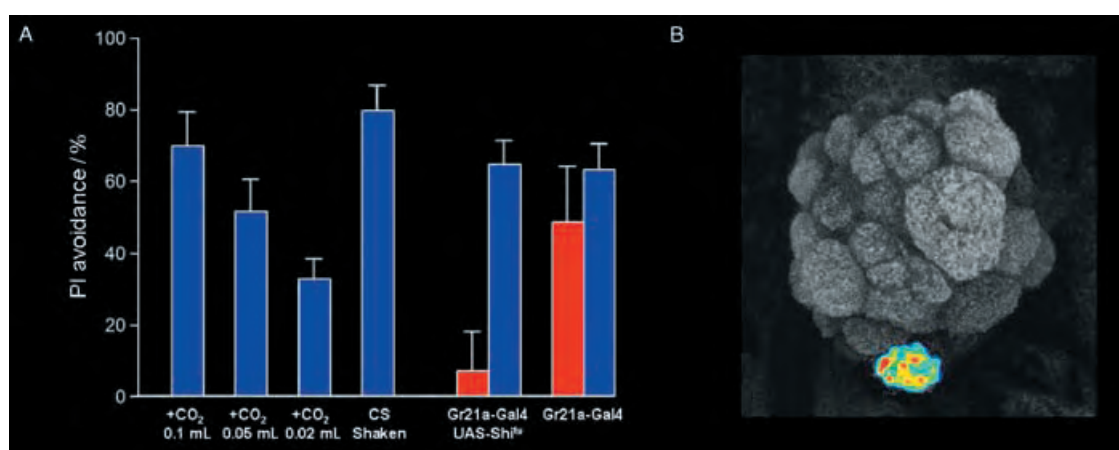


Figure 9. CO₂ activates a single glomerulus and elicits avoidance behavior. A) Avoidance of air from stressed flies (CS) as well as of increasing concentrations of CO₂. Inhibition of synaptic transmission in GR21A neurons that project to the V glomerulus using *shi^{ts}* blocks CO₂ avoidance. Red and blue bars indicate avoidance behavior at the nonpermissive (28 °C) and permissive (21 °C) temperatures, respectively. B) Two-photon imaging in a strain harboring GR21A-Gal4 and UAS G-cAMP reveals robust activation of the V glomerulus.

mission in the GR21A sensory neurons that innervate the V glomerulus, using the temperature-sensitive *shibire* gene shi^{ts} ^[60] blocks the avoidance response to CO₂ (Figure 9). Inhibition of synaptic release in the vast majority of other olfactory sensory neurons or in projection neurons other than those that innervate the V glomerulus had no effect on this behavior.

The identification of a population of olfactory sensory neurons innervating a single glomerulus that mediates robust avoidance to a naturally occurring odorant provides insight in the neural circuitry that underlies this innate behavior. These observations suggest that a dedicated circuit that involves a single population of olfactory sensory neurons mediates detection of CO₂ in *Drosophila*. The simplicity of this initial olfactory processing offers the possibility of tracing the circuits that translate odor detection into an avoidance response.

9. How is the Map Read?

Our experiments indicate that different odors elicit different patterns of glomerular activity within the antennal lobe and moreover that defined patterns of activity can be associated with specific behaviors. We can look at the pattern of activity in the fly antennal lobe with a two-photon microscope and discern, with a reasonable degree of accuracy, what odorant the fly has encountered in nature. Thus, we can determine with our eyes (and our brain) what odors the fly has encountered, but how does the fly brain read the sensory map?

A topographic map in which different odors elicit different patterns of activity in the antennal lobe suggests that these spatial patterns reflect a code defining odor quality. However, the mere existence of a map, whether anatomic or functional, does not prove that spatial information is the underlying parameter of an odor code. It has been suggested, for example, that the quality of an odor is reflected in temporal dynamics of a distributed ensemble of projection neurons.^[61,62] In this model, a given odor might activate a small number of glomeruli and a large ensemble of projection neurons such that different odors elicit different temporal patterns of activity in the same projection neuron. This temporal hypothesis in its simplest form postulates that the brain exploits circuit dynamics to create spatiotemporal patterns of neuronal activation to achieve a larger coding space. Whatever the code, patterns of activity in the antennal lobe must be translated by higher sensory centers to allow the discrimination of complex olfactory information. If odor quality is encoded by spatial patterns, we might expect that a representation of the glomerular map is retained in the protocerebrum.

We have begun to address the question of how the map in the antennal lobe is represented in higher olfactory centers by examining the pattern of projections of the neurons that connect the glomeruli to the protocerebrum. Allan Wong and Jing Wang randomly labeled individual projection neurons to visualize their processes that connect defined glomeruli with their targets in the mushroom body and protocerebrum. We

have used an enhancer trap line in which Gal4 is expressed in a subpopulation of projection neurons along with the “FLP-out” technique to label single projection neurons with a CD8 GFP reporter.^[63] A similar experimental approach has been used to determine the lineage relationship of individual projection neurons and to examine their pattern of axonal projections.^[64,65] We observe that most projection neurons send dendrites to a single glomerulus. Projection neurons that receive input from a given glomerulus extend axons that form a spatially invariant pattern in the protocerebrum (Figure 10).

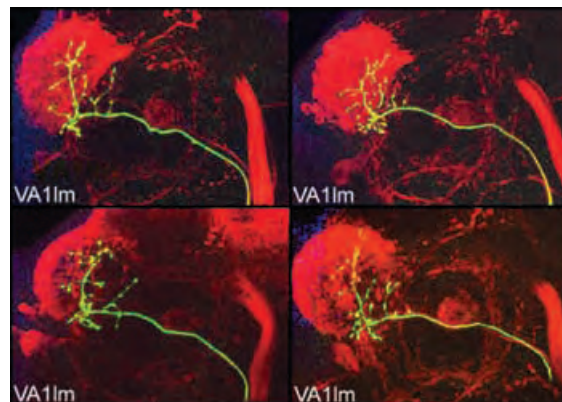


Figure 10. Projection neurons that innervate to the same glomerulus have similar axonal projection patterns. Individual projection neurons that connect to the VA1Lm glomeruli are visualized in the protocerebrum in different flies. These images reveal a striking constancy in the projection pattern among projection neurons that project to a given glomerulus. These observations reveal an invariant topographic map in the protocerebrum that differs in character from the map in the antennal lobe (printed with permission from Ref. [63]).

Projection neurons from different glomeruli exhibit patterns of axonal projections that are distinct, but often interdigitated (Figure 11). Our data reveal a striking invariance in the spatial patterns of axon arbors of projection neurons that

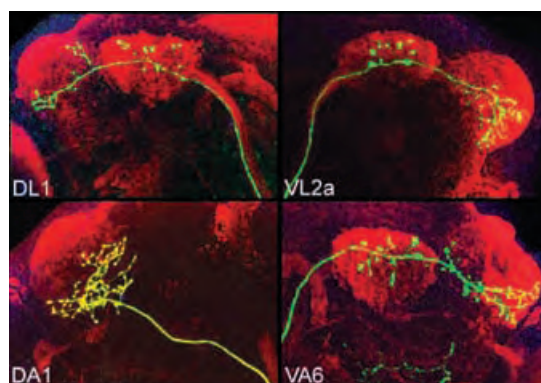


Figure 11. Axonal projections from single projection neurons can be visualized as they branch in the mushroom body and ultimately arborize in the protocerebrum. Projections neurons that connect to different glomeruli exhibit different patterns of axonal projections. The axon arbors in the protocerebrum are dispersed unlike the insular segregated arbors in the glomerulus, affording the possibility for integration in higher olfactory centers (printed with permission from Ref. [63]).

innervate a given glomerulus, a precision of connectivity that assures the specificity of information transfer.

The precision of projections of projection neurons reveals a spatial representation of glomerular activity in higher brain centers, but the character of the map differs from that observed in the antennal lobe. Axon arbors in the protocerebrum are diffuse and extensive, often extending over the entire dimension of the brain hemisphere (Figures 10, 11). This is in sharp contrast to the tight convergence of primary sensory axons, whose arbors are restricted to a small 5–10 μm spherical glomerulus. As a consequence, the projections from different glomeruli, although spatially distinct, often interdigitate. Thus, the point-to-point segregation observed in the antennal lobe is degraded in the second order projections to the protocerebrum. This affords an opportunity for the convergence of inputs from multiple different glomeruli essential for higher order processing. Third-order neurons in the protocerebrum might synapse on projection neurons from multiple distinct glomeruli, a necessary step in decoding spatial patterns to allow the discrimination of odor and behavioral responses.

10. Concluding Remarks

These data suggest a model in which the convergence of information from deconstructed patterns in the antennal lobe are reconstructed by “cardinal cell assemblies” that sit higher up in a hierarchical perceptual system in the protocerebrum. Olfactory processing will initially require that the structural elements of an odor activate a unique set of receptors that in turn result in the activation of a unique set of glomeruli. The odorous stimuli must then be reconstructed in higher sensory centers that determine which of the numerous glomeruli have been activated. The identification of a spatially invariant sensory map in the protocerebrum that is dispersive affords an opportunity for integration of multiple glomerular inputs by higher odor neurons.

The elucidation of an olfactory map in both the olfactory bulb or antennal lobe and in higher olfactory centers leaves us with a different order of problems. Though we may look at these odor-evoked images with our brains and recognize a spatial pattern as unique and can readily associate the pattern with a particular stimulus, the brain does not have eyes. How does the brain perceive the olfactory image? How is the map read? How are spatially defined bits of electrical information in the brain decoded to allow the perception of an olfactory image? We are left with an old problem, the problem of the ghost in the machine.

Finally, how do we explain the individuality of olfactory perception? The innately configured representation of the sensory world, the olfactory sensory maps that I have described, must be plastic. Our genes create only a substrate upon which experience can shape how we perceive the external world. Surely the smell of a madeleine does not elicit in all of us that “vast structure of recollection” it evoked for Marcel Proust. For Proust, smell is the evocative sense, the sense that brings forth memory and associations with a richness not elicited by other sensory stimuli. Nowhere is this

more apparent than in the eloquent words recalling the madeleine incident from “*Remembrance of Things Past*”.^[66]

“... But when from a long distant past nothing subsists, after the people are dead, after the things are broken and scattered, still alone, more fragile but with more vitality, more unsubstantial, more persistent, more faithful, the smell and taste of things remain, poised a long time, like souls ready to remind us, waiting and hoping for their moment, amid the ruins of all the rest; and bear unfaltering in the tiny and impalpable drop of their essence, the vast structure of recollection.”

This lecture encompasses the efforts in my laboratory over the past 13 years to provide further insight into the molecular logic of olfactory sensory perception. I wish to thank the Howard Hughes Medical Institute, the National Institutes of Health, and the Mathers Foundation for their continued gracious support of our research. The Howard Hughes Medical Institute provided an opportunity to interface molecular biology with neuroscience and has consistently encouraged and supported the efforts of the laboratory in novel directions. It is this work for which Linda Buck and I share the profound honor and good fortune of having been awarded the Nobel Prize in Physiology or Medicine. This award was not made to me as a man but for my work, a science that derives from the efforts of many brilliant students and from the incisive teachings of my colleagues. I take equal pride in the science that has been accomplished in the laboratory and in the scientists that have trained with me and have contributed to our efforts. I therefore feel that I accept this prize in trust as a representative of a culture of science in my laboratory and at Columbia University. I am deeply grateful for this culture. Over the past 30 years, Columbia has provided an atmosphere that fosters intellectual rigor and creativity and at the same time is imbued with a spirit of warmth and collaboration.

Received: May 19, 2005

- [1] I. Kant [1781/1787], *Critique of Pure Reason* (transl. N. K. Smith), MacMillan, London, **1961**.
- [2] *Principles of Neural Science*, 4th ed. (Eds.: E. Kandel, J. H. Schwartz, T. M. Jessell), McGraw Hill, New York, **2000**.
- [3] “A novel multigene family may encode odorant receptors: A molecular basis for odor recognition”: L. Buck, R. Axel, *Cell* **1991**, 65, 175–187.
- [4] “Odorant-sensitive adenylate cyclase may mediate olfactory reception”: U. Pace, Hanski, E. Y. Salomon, D. Lancet, *Nature* **1985**, 316, 255–258.
- [5] “The odorant-sensitive adenylate cyclase of olfactory receptor cells: differential stimulation by distinct classes of odorants”: P. B. Sklar, R. R. H. Anholt, S. H. Snyder, *J. Biol. Chem.* **1986**, 261, 15536–15543.
- [6] “G_{olf}, an olfactory neuron-specific G-protein involved in odorant signal transduction”: D. T. Jones, R. R. Reed, *Science* **1989**, 244, 790–795.
- [7] “Rapid kinetics of second messenger formation in olfactory transduction”: H. Breer, L. Boekhoff, E. Tarelius, *Nature* **1990**, 345, 65–68.
- [8] “Functional expression of a mammalian odorant receptor”: H. Zhao, L. Ivic, J. M. Otaki, M. Hashimoto, K. Mikoshiba, S. Firestein, *Science* **1998**, 279, 237–242.

- [9] "Identification of ligands for olfactory receptors by functional expression of a receptor library": D. Krautwurst, K.-W. Yau, R. R. Reed, *Cell* **1998**, 95, 917–926.
- [10] "Combinatorial receptor codes for odors": B. Malnic, J. Hirono, T. Sato, L. B. Buck, *Cell* **1999**, 96, 713–723.
- [11] "Functional identification and reconstitution of an odorant receptor in single olfactory neurons": K. Touhara, S. Sengoku, K. Inaki, A. Tsuboi, J. Hirono, T. Sato, H. Sakano, T. Haga, *Proc. Natl. Acad. Sci. USA* **1999**, 96, 4040–4045.
- [12] "The olfactory receptor gene superfamily of the mouse": X. Zhang, S. Firestein, *Nat. Neurosci.* **2002**, 5, 124–133.
- [13] "The mouse olfactory receptor gene family": P. A. Godfrey, B. Malnic, L. B. Buck, *Proc. Natl. Acad. Sci. USA* **2004**, 101, 2156–2161.
- [14] "The complete human olfactory subgenome": G. Glusman, I. Yanai, I. Rubin, D. Lancet, *Genome Res.* **2001**, 11, 685–702.
- [15] "The human olfactory receptor repertoire": S. Zozulya, F. Echeverri, T. Nguyen, *Adv. Genome Biol.* **2001**, 2, 0018.1–0018.12.
- [16] "The sense of smell: genomics of vertebrate odorant receptors": J. M. Young, B. J. Trask, *Hum. Mol. Genet.* **2002**, 11, 1153–1160.
- [17] "A novel family of divergent seven-transmembrane proteins: candidate odorant receptors in *Drosophila*": P. J. Clyne, C. G. Warr, M. R. Freeman, D. Lessing, J. Kim, J. R. Carlson, *Neuron* **1999**, 22, 327–338.
- [18] "Identification of candidate *Drosophila* olfactory receptors from genomic DNA sequence": Q. Gao, A. Chess, *Genomics* **1999**, 60, 31–39.
- [19] "A spatial map of olfactory receptor expression in the *Drosophila* antenna": B. L. Vosshall, H. Amrein, P. S. Morozov, A. Rzetsky, R. Axel, *Cell* **1999**, 96, 725–736.
- [20] "Divergent seven transmembrane receptors are candidate chemosensory receptors in *C. elegans*": E. R. Troemel, J. H. Chou, N. D. Dwyer, H. A. Colbert, C. I. Bargmann, *Cell* **1995**, 83, 207–218.
- [21] "*odr-10* encodes a seven transmembrane domain olfactory receptor required for responses to the odorant diacetyl": P. Sengupta, J. H. Chou, C. I. Bargmann, *Cell* **1996**, 84, 899–909.
- [22] "Iodopsin": G. Wald, P. K. Brown, P. H. Smith, *J. Gen. Physiol.* **1955**, 38, 623–681.
- [23] "Molecular genetics of human color vision: the genes encoding blue, green, and red pigments": J. Nathans, D. Thomas, D. S. Hogness, *Science* **1986**, 232, 193–202.
- [24] "Allelic inactivation regulates olfactory receptor gene expression": A. Chess, I. Simon, H. Cedar, R. Axel, *Cell* **1994**, 78, 823–834.
- [25] "A zonal organization of odorant receptor gene expression in the olfactory epithelium": K. J. Ressler, S. L. Sullivan, L. B. Buck, *Cell* **1993**, 73, 597–609.
- [26] "Spatial segregation of odorant receptor expression in the mammalian olfactory epithelium": R. Vassar, J. Ngai, R. Axel, *Cell* **1993**, 74, 309–318.
- [27] "Information coding in the olfactory system: evidence for a stereotyped and highly organized epitope map in the olfactory bulb": K. J. Ressler, S. L. Sullivan, L. B. Buck, *Cell* **1994**, 79, 1245–1255.
- [28] "Topographic organization of sensory projections to the olfactory bulb": R. Vassar, S. K. Chao, R. Sitcheran, J. M. Nunez, L. B. Vosshall, R. Axel, *Cell* **1994**, 79, 981–991.
- [29] "Visualizing an olfactory sensory map": P. Mombaerts, F. Wang, C. Dulac, S. K. Chao, A. Nemes, M. Mendelsohn, J. Edmondson, R. Axel, *Cell* **1996**, 87, 675–686.
- [30] "Development of inner ear afferent connections: forming primary neurons and connecting them to the developing sensory epithelia": B. Fritsch, *Brain Res. Bull.* **2003**, 60, 423–433.
- [31] "Regulation of axial patterning of the retina and its topographic mapping in the brain": T. McLaughlin, R. Hindges, D. M. O'Leary, *Curr. Opin. Neurobiol.* **2003**, 13, 57–69.
- [32] "Odorant receptors on axon termini in the brain": G. Barnea, S. O'Donnell, F. Mancia, X. Sun, A. Nemes, M. Mendelsohn, R. Axel, *Science* **2004**, 304, 1468.
- [33] "Odorant receptors govern the formation of a precise topographic map": F. Wang, A. Nemes, M. Mendelsohn, R. Axel, *Cell* **1998**, 93, 47–60.
- [34] "Axon guidance of mouse olfactory sensory neurons by odorant receptors and the β_2 adrenergic receptor": P. Feinstein, T. Bozza, I. Rodriguez, A. Vassali, P. Mombaerts, *Cell* **2004**, 117, 833–846.
- [35] "A contextual model for axonal sorting into glomeruli in the mouse olfactory system": P. Feinstein, P. Mombaerts, *Cell* **2004**, 117, 817–831.
- [36] "Mutually exclusive expression of odorant receptor transgenes": S. Serizawa, T. Ishii, H. Nakatani, A. Tsuboi, F. Nagawa, M. Asano, K. Sudo, J. Sakagami, H. Sakano, T. Iijiri, et al., *Nat. Neurosci.* **2000**, 3, 687–693.
- [37] "Minigenes impart odorant receptor-specific axon guidance in the olfactory bulb": A. Vassali, A. Rothman, P. Feinstein, M. Zapotocky, P. Mombaerts, *Neuron* **2002**, 35, 681–696.
- [38] "Negative feedback regulation ensures the one receptor-one olfactory neuron rule in mouse": S. Serizawa, K. Miyamichi, H. Nakatani, M. Suzuki, M. Saito, Y. Yoshihara, H. Sakano, *Science* **2003**, 302, 2088–2094.
- [39] "A feedback mechanism regulates monoallelic odorant receptor expression": J. L. Lewcock, R. R. Reed, *Proc. Natl. Acad. Sci. USA* **2004**, 101, 1069–1074.
- [40] "Gene switching and the stability of odorant receptor gene choice": B. Shykind, C. Rohani, S. O'Donnell, A. Nemes, M. Mendelsohn, Y. Sun, R. Axel, G. Barnea, *Cell* **2004**, 117, 801–815.
- [41] "Transposable mating type genes in *Saccharomyces cerevisiae*": J. Hicks, J. N. Strathern, A. J. Klar, *Nature* **1979**, 282, 478–483.
- [42] "Gene conversion as a mechanism for antigenic variation in trypanosomes": E. Pays, S. Van Assel, M. Laurent, M. Darville, T. Vervoort, N. Van Meirvenne, M. Steinart, *Cell* **1983**, 34, 371–381.
- [43] "A complete immunoglobulin gene is created by somatic recombination": C. Brack, M. Hiram, R. Lenhard-Schuller, S. Tonegawa, *Cell* **1978**, 15, 1–14.
- [44] "Mice cloned from olfactory sensory neurons": K. Eggan, K. Baldwin, M. Tackett, J. Osborne, J. Gogos, A. Chess, R. Axel, R. Jaenisch, *Nature* **2004**, 428, 44–49.
- [45] "Odorant receptor gene choice is reset by nuclear transfer from mouse olfactory sensory neurons": J. Li, T. Ishii, P. Feinstein, P. Mombaerts, *Nature* **2004**, 428, 393–399.
- [46] "The organization of the chemosensory system in *Drosophila melanogaster*: a review": R. F. Stocker, *Cell Tissue Res.* **1994**, 275, 3–26.
- [47] "Three-dimensional reconstruction of the antennal lobe in *Drosophila melanogaster*": P. P. Laissue, C. Reiter, P. R. Hiesinger, S. Halter, K. F. Fischbach, R. F. Stocker, *J. Comp. Neurol.* **1999**, 405, 543–552.
- [48] "Convergent projections of *Drosophila* olfactory neurons to specific glomeruli in the antennal lobe": Q. Gao, B. Yuan, A. Chess, *Nat. Neurosci.* **2000**, 3, 780–785.
- [49] "An olfactory sensory map in the fly brain": L. B. Vosshall, A. M. Wong, R. Axel, *Cell* **2000**, 102, 147–159.
- [50] "A chemosensory gene family encoding candidate gustatory and olfactory receptors in *Drosophila*": K. Scott, R. Brady, Jr., A. Cravchik, P. Morozov, A. Rzhetsky, C. Zuker, R. Axel, *Cell* **2001**, 104, 661–673.
- [51] "Two-photon calcium imaging reveals an odor-evoked map of activity in the fly brain": J. W. Wang, A. M. Wong, J. Flores, L. B. Vosshall, R. Axel, *Cell* **2003**, 112, 271–282.

- [52] "A high signal-to-noise Ca^{2+} probe composed of a single green fluorescent protein": J. Nakai, M. Ohkura, K. Imoto, *Nat. Biotechnol.* **2001**, *19*, 137–141.
- [53] "Two photon laser scanning fluorescence microscopy": W. Denk, J. H. Strickler, W. W. Webb, *Science* **1990**, *248*, 73–76.
- [54] "Representations of odours and odour mixtures visualized in the honeybee brain": J. Joerges, A. Jüttner, C. G. Galizia, R. Menzel, *Nature* **1997**, *387*, 285–287.
- [55] "Transmission of olfactory information between three populations of neurons in the antennal lobe of the fly": M. Ng, R. D. Roorda, S. Q. Lima, B. V. Zemelman, P. Morcillo, G. Miesenböck, *Neuron* **2002**, *36*, 463–474.
- [56] "Optical imaging of odorant representations in the mammalian olfactory bulb": B. D. Rubin, L. C. Katz, *Neuron* **1999**, *23*, 499–511.
- [57] "Odor maps in the mammalian olfactory bulb: domain organization and odorant structural features": N. Uchida, Y. K. Takahashi, M. Tanifuji, K. Mori, *Nat. Neurosci.* **2000**, *3*, 1035–1043.
- [58] "Tuning and topography in an odor map on the rat olfactory bulb": M. Meister, T. Bonhoeffer, *J. Neurosci.* **2001**, *21*, 1351–1360.
- [59] "A single population of olfactory neurons mediates an innate avoidance behavior in *Drosophila*": S. B. Suh, A. M. Wong, A. C. Hergarden, J. W. Wang, A. Simon, S. Benzer, R. Axel, D. J. Anderson, *Nature* **2004**, *431*, 854–859.
- [60] "Conditional modification of behavior in *Drosophila* by targeted expression of a temperature-sensitive *shibire* allele in defined neuron": T. Kitamoto, *J. Neurobiol.* **2001**, *47*, 81–92.
- [61] "A systems perspective on early olfactory coding": G. Laurent, *Science* **1999**, *286*, 723–728.
- [62] "Transformation of olfactory representations in the *Drosophila* antennal lobe": R. I. Wilson, G. Laurent, *Science* **2004**, *303*, 366–370.
- [63] "Spatial representation of the glomerular map in the *Drosophila* protocerebrum": A. M. Wong, J. W. Wang, R. Axel, *Cell* **2002**, *109*, 229–241.
- [64] "Target neuron prespecification in the olfactory map of *Drosophila*": G. S. Jefferis, E. C. Marin, R. F. Stocker, L. Luo, *Nature* **2001**, *414*, 204–208.
- [65] "Representation of the glomerular olfactory map in the *Drosophila* brain": E. C. Marin, G. S. Jefferis, T. Komiyama, H. Zhu, L. Luo, *Cell* **2002**, *109*, 243–255.
- [66] "Swann's Way": M. Proust, *Remembrance of Things Past, Vol. I*, Random House, New York, **1913**, pp. 50–51.
- [67] "Spatially restricted expression of candidate taste receptors in the *Drosophila* gustatory system": L. Dunipace, S. Meister, C. McNealy, H. Amrein, *Curr Biol.* **2001**, *11*, 822–835.

Unraveling the Sense of Smell (Nobel Lecture)**

Linda B. Buck*

Keywords:

brain research · fluorescence · Nobel Lecture · olfactory cells · receptors

From the Contents

Biography	6128
1. Introduction	6132
2. Odorant Receptors	6133
3. Organization of Odorant Receptors in the Olfactory Epithelium	6134
4. Combinatorial Receptor Codes for Odors	6135
5. A Stereotyped Map of Odorant Receptor Inputs in the Olfactory Bulb	6136
6. Odor Coding in the Olfactory Epithelium and Bulb	6137
7. Stereotypy, Divergence, and Convergence in Olfactory Cortex	6137

Biography

SEATTLE

I was born in 1947 in Seattle, Washington, a city surrounded by mountains, forests, and the sea. My mother was the daughter of Swedish immigrants who had come to the US in the late nineteenth century while my father's family had Irish roots on one side and ancestors extending back to the American Revolution on the other. I was the second of three children, all girls. My mother was a homemaker who was exceptionally kind and witty and loved word puzzles. My father was an electrical engineer who, at home, spent much of his time inventing things and building them in our basement. It may be that my parents' interest in puzzles and inventions planted the seeds for my future affinity for science, but I never imagined as a child that I would someday be a scientist.

During my childhood, I did the things that girls often do, such as playing with dolls. I was also curious and easily bored though, so I frequently embarked on what were to me new adventures. Aside from school and music lessons, my life was relatively unstructured and I was given considerable independence. I learned to appreciate music and beauty from my mother and my father taught me how to use power tools and build things. I spent a lot of time with my maternal grandmother, who told me magical stories about her childhood in Sweden and, to my delight, taught me how to sew clothes for my dolls. I was fortunate to have wonderfully supportive

parents who told me that I had the ability to do anything I wanted with my life. They taught me to think independently and to be critical of my own ideas, and they urged me to do something worthwhile with my life, in my mother's words, to "not settle for something mediocre". I realize now that I internalized those lessons and that they have influenced my work as a scientist.

I received my undergraduate education at the University of Washington, which was only a few miles from our home. I had always wanted to have a career in which I would help others, so I initially decided to major in psychology, thinking that I would become a psychotherapist. Over time, my interests expanded and I entertained a variety of different career possibilities. However, none seemed ideal and I was reluctant to embark on something that might prove to be inappropriate. Over the next several years, I intermittently traveled, lived on a nearby island, and took more classes in Seattle. I finally found my direction when I took a course in immunology, which I found fascinating. I would be a biologist.

[*] Dr. L. B. Buck

Howard Hughes Medical Institute
Fred Hutchinson Cancer Research Center
1100 Fairview Avenue North, Seattle, WA 98109-1024 (USA)
Fax: (+1) 206-667-1031
E-mail: lbuck@fhcrc.org

[**] Copyright© The Nobel Foundation 2004. We thank the Nobel Foundation, Stockholm, for permission to print this lecture.

DALLAS

In 1975, I began graduate school in the Microbiology Department at the UT Southwestern Medical Center in Dallas. The department had recently undergone an expansion in the area of immunology, making it a major center in this still young area and a stimulating place to learn. I had done a small amount of research at the University of Washington, first in psychology with Walter Makous and then in immunology with Ursula Storb, but it was in Texas that I truly learned to be a scientist. I had a wonderful thesis advisor, Ellen Vitetta, who demanded excellence and precision in research, habits that I believe are important to learn as a student. For my thesis, I compared the functional properties of subsets of B lymphocytes that differed in the class of cell-surface immunoglobulin that they used as antigen receptors. In this work and much of my subsequent work, I thought in terms of molecules and the molecular mechanisms underlying biological systems, and sought to gain insight into those mechanisms in my experiments.

NEW YORK

In 1980, I moved to Columbia University in New York City to do postdoctoral work in immunology with Benvenuto Pernis. As a graduate student, I had become fascinated with the unexplained requirement for major histocompatibility complex (MHC) proteins in immune responses, a mystery that was later solved. I decided to explore this puzzle, focusing on class II MHC proteins found on the surface of B lymphocytes. I found that, contrary to expectation, the MHC proteins rapidly accumulated inside these cells when they were activated. My further experiments indicated that they were being internalized from the cell surface and were probably being recycled to it. It was known that antigens are endocytosed with antigen receptors and then degraded. One possibility raised by the internalization and apparent recycling of MHC molecules was that, following internalization, they might be targeted to a specialized microenvironment where they could interact with degraded antigen. The MHC–antigen complexes might then be exported to the cell surface for co-recognition by T-helper cells.

By this time, it had become clear to me that to study molecular mechanisms underlying biological systems, which is what interested me, I needed to learn the recently developed techniques of molecular biology. To this end, I moved to the laboratory of Richard Axel, at Columbia University. Richard had begun to work in the area of neuroscience several years earlier through collaboration with Eric Kandel, who was also at Columbia. Their collaboration had focused on molecular studies on the nervous system of *Aplysia*, a sea snail. This was the model organism that Eric had used in many of his studies of learning and memory, for which he received a Nobel Prize in 2000. Perhaps not surprisingly, I was interested in searching for genes encoding neuronal cell surface receptors. However, at that time, Richard wanted to continue studying *Aplysia*, so I agreed to a project in which I would try to develop a

technique for cloning genes expressed in one *Aplysia* neuron, but not another. After spending a short time learning molecular techniques from Jim Roberts, a student in the lab, I started my *Aplysia* project. Eric Kandel's group showed me how to isolate giant *Aplysia* neurons that had been assigned names and could be identified by their locations and, within a relatively short time, I began to uncover genes that were differentially expressed among *Aplysia* neurons.

While studying a neuropeptide gene expressed in neuron number R15, I discovered that the gene was also expressed in some other neurons, but that its primary transcript was alternatively spliced in different neurons to give different polyproteins. The two polyproteins could generate two different combinations of peptides in different neurons, thus suggesting a way to produce physiological or behavioral programs with partially overlapping components. While working on the neuropeptide gene, I encountered numerous technical challenges that increased my knowledge of molecular biology and honed my abilities. During this period, I learned a lot of molecular biology from Richard and other members of his lab. I also got to know Eric Kandel, who has continued to be a wonderful source of inspiration and encouragement for me over the years.

From my first introduction to neuroscience, I had been fascinated by the brain's cellular and connective diversity. In parallel with my *Aplysia* experiments, I sporadically tried to find a way to scan the genome for genes that had undergone gene rearrangement or gene conversion in neurons, thinking that genes that showed this characteristic might be involved in the generation of neuronal diversity. One method that I devised showed promise in *Drosophila*, but was not sensitive enough for the much larger genome of a mammal, which is what interested me. Nonetheless, these efforts were a great source of creative enjoyment for me as I proceeded with the more mundane task of searching for minute alternative exons in the *Aplysia* genome.

I was grateful that Richard was tolerant of my high-risk endeavors. He was an unusual mentor in that he gave people in his lab extensive independence in charting their own course once they had established themselves. During this time, I had many colleagues at Columbia with whom I enjoyed long discussions about science. Among these were George Gaitanaris, who has remained a close friend over the years, as well as Tom Jessell and Jane Dodd, neuroscientists from whom I learned a great deal about neural development.

As I was nearing the end of my *Aplysia* project, I read a paper that changed my life. It was a 1985 publication from Sol Snyder's group that discussed potential mechanisms underlying odor detection. This was the first time I had ever thought about olfaction and I was fascinated. How could humans and other mammals detect 10 000 or more odorous chemicals, and how could nearly identical chemicals generate different odor perceptions? In my mind, this was a monumental puzzle and an unparalleled diversity problem. It was obvious to me that the first step to solving the puzzle was to determine how odorants are initially detected in the nose. This meant finding odorant receptors, a class of molecules that had been proposed to exist, but had not been found. I decided that

this is what I had to do as soon as my neuropeptide work was completed.

In 1988, I embarked on a search for odorant receptors, staying on in Richard's lab for this purpose. In a recent commentary in the journal *Cell*, I described what was known about odor detection at that time and the approaches that I tried in the quest to find the elusive odorant receptors. In short, it was known that odorants depolarize, and thereby activate, olfactory sensory neurons in the nose. Although there were varied proposals as to what kind of molecules might interact with odorants, there was compelling evidence that olfactory transduction involved G-protein-induced increases in cAMP. After trying several different approaches, I identified the odorant receptor family by designing experiments based on three assumptions: First, since odorants vary in structure and can be discriminated, there would be a family of varied, but related odorant receptors, which would be encoded by a multigene family. Second, odorant receptors would be at least distantly related to the relatively small set of G-protein-coupled receptors whose sequences were known at that time. Finally, odorant receptors would be selectively expressed in the olfactory epithelium, where olfactory sensory neurons are located. It took some time to devise and develop the methods I used in my search, but in the end they succeeded. Looking at the first sequences of odorant receptors obtained from rats, I was moved by nature's marvelous invention. This work showed that the rat has a multigene family that codes for in excess of one hundred different odorant receptors, all related, but each one unique. The unprecedented size and diversity of this family explained the ability of mammals to detect a vast array of diverse chemicals as having distinct odors. In 1991, Richard Axel and I published the identification of odorant receptors.

BOSTON

In 1991, I departed for Boston to be an assistant professor in the Neurobiology Department at Harvard Medical School. There, I was immersed in an environment in which I could broaden my understanding of the nervous system. I received excellent support from my chairman, Gerry Fischbach, as I set up my lab. I also acquired many excellent colleagues, including David Hubel, whose pioneering studies of the visual system with Torsten Wiesel (for which they received a Nobel Prize in 1981) had always been an inspiration to me. In 1994, I became an Investigator of the Howard Hughes Medical Institute, which has generously supported our work for the past 11 years. Over the next decade, I remained at Harvard, gradually rising through the ranks to become associate and then full professor. In 1994, I met Roger Brent, a marvelous intellect and fellow scientist who has been my partner and an important part of my life ever since.

The discovery of odorant receptors had explained how the olfactory system detects odorants. My next goal was to learn how signals from those receptors are organized in the brain to generate diverse odor perceptions. I was joined in this endeavor by a series of excellent students and postdoctoral



(Photo: Roland Morgan)

fellows. The discoveries on the organization of the olfactory system that were cited by the Nobel Foundation were made over a period of ten years, during which I was a faculty member at Harvard.

The first question we asked was how odorant receptors are organized in the olfactory epithelium of the nose. This work was begun by Kerry Ressler, an MD/PhD student who came to the laboratory for a few months just as the equipment and supplies I had ordered began to arrive in January 1992. I had decided to switch from the rat to the mouse as a model organism because of the advantage of using isogenic inbred strains for dissecting a multigene family, and the possibility of generating transgenic mice. After cloning and sequencing a series of mouse odorant receptor genes, Kerry did our first *in situ* hybridization experiments to examine patterns of receptor gene expression. By June, Kerry had returned as a full-time student and Susan Sullivan had joined the lab as a postdoctoral fellow. At this point, we began to precisely analyze gene-expression patterns and to compare them in different individuals. Prior to the present era of digital photographs that can be stored and analyzed on a computer, this was painstaking work that involved displaying photographic slides on a desktop viewer and recording, on transparencies, the locations of individual labeled cells in different animals. Our studies showed that each receptor gene is expressed in about 1/1000 olfactory sensory neurons, that the olfactory epithelium has several spatial zones that express non-overlapping sets of odorant receptor genes, and that neurons with the same odorant receptor are randomly scattered throughout one zone. This indicated that signals derived from different odorant receptors are segregated in different sensory neurons and in the information they transmit to the brain. It further indicated that, in the olfactory epithelium, neurons that detect the same odorant are dispersed and those that detect different odorants are interspersed. Thus, there is a broad organization of sensory information into several zonal sets in the epithelium, but, overall, information is encoded in a highly distributed manner. We published these findings in 1993. Similar

observations in rats by Richard Axel and his colleagues were also reported that year.

Having determined how inputs from different odorant receptors are organized in the nose, we asked how they are arranged at the next structure in the olfactory pathway, the olfactory bulb. In the bulb, the axons of olfactory sensory neurons synapse in about 2000 spherical structures, called glomeruli. Kerry began to use retroviral vectors to investigate how the axons of neurons expressing specific receptors are organized in the bulb, but then we inadvertently found another way to address the question. While using *in situ* hybridization to identify a number of receptor genes expressed in each epithelial zone for chromosomal mapping studies, Susan found that, in one tissue section, a receptor probe labeled a single spot in the bulb, which proved to be a glomerulus. Using probes that recognized single receptor genes rather than subfamilies of related receptor genes, we found that each probe labeled odorant receptor mRNAs in sensory axons that were confined to one or a few glomeruli at only two sites, one on either side of the bulb. Different probes labeled different glomeruli and those glomeruli had virtually identical locations in different individuals. I still remember a meeting with Kerry and Susan in my office in which I asked Kerry how many sections separated different labeled glomeruli in different bulbs. All of us were stunned by his answer, because it provided the first hint that the bulb might have a stereotyped map of receptor inputs and we could not imagine how this could be generated given the organization of receptor gene expression in the epithelium. This mystery still has not been solved. These studies indicated that while thousands of neurons expressing the same receptor are highly dispersed in the epithelium, their axons all converge in a few specific olfactory bulb glomeruli. The result is a stereotyped map of receptor inputs in which signals derived from different receptors are segregated in different glomeruli and in the bulb projection neurons whose dendrites innervate those glomeruli. Remarkably, Bob Vassar in Richard Axel's lab had concurrently found that different receptor probes labeled different glomeruli in the rat bulb. Our two groups published these findings in 1994.

Several years later, we began to investigate how the receptor family and the patterning of receptor inputs encode the identities of different odorants. By using single-cell RT-PCR (reverse transcriptase–polymerase chain reaction), Bettina Malnic, a fellow in the lab, had been comparing gene expression in single olfactory sensory neurons. Her work demonstrated that each neuron expresses only a single receptor gene, something that we had previously suspected, but that needed to be verified. Bettina was initially focused on the identification of genes that might be involved in receptor gene choice or axon targeting in the bulb, but we decided to change course when Takaaki Sato visited our lab and told us about his calcium imaging studies of odor responses in the olfactory epithelium. This was the beginning of a highly successful collaboration in which Takaaki used calcium imaging to define the odor response profiles of individual neurons and Bettina then used RT-PCR to identify the receptor expressed by each responsive neuron. These studies

demonstrated that the receptor family is used in a combinatorial manner. Different neurons are recognized, and thereby encoded, by different combinations of receptors, but each receptor is used as one component of the combinatorial receptor codes for many different odorants. These studies also provided explanations for several intriguing features of human odor perception, including how a slight change in the structure of an odorant can dramatically change its perceived odor quality.

As soon as we had determined how receptor inputs are organized in the olfactory bulb, we began to explore how they are arranged at the next structure in the olfactory pathway, the olfactory cortex. Lisa Horowitz, an MD/PhD student in the lab, initially investigated connections between the bulb and cortex using classical anatomical techniques. By depositing different tracers in the dorsal and ventral bulb, she determined that these areas project axons to the same regions of the cortex. In agreement with previous findings, this indicated that there could not be a point-to-point patterning of connections between the bulb and cortex. We decided to abandon traditional approaches and to instead ask whether we could chart neural pathways genetically by expressing a gene encoding a transneuronal tracer in olfactory sensory neurons. Lisa found that this was indeed possible. When she made transgenic mice that expressed barley lectin in all olfactory sensory neurons, the lectin crossed two synapses, labeling second-order neurons in the bulb, and then third-order neurons in the cortex. This work, which we published in 1999, opened the way to investigating a wide array of questions concerning neural circuits, including those that carry olfactory information.

We then went on to use the genetic tracer to examine how inputs from individual types of receptors are organized in the olfactory cortex. To do this we used gene targeting to generate mice that coexpressed barley lectin with a single receptor gene. Lisa, together with a fellow in the lab, Jean-Pierre Montmayeur, prepared the DNA constructs for gene targeting. Zhihua Zou, another fellow, then generated and analyzed mice that coexpressed the tracer with different receptor genes. The approach worked, but was difficult, with Zhihua investing almost a year in perfecting the conditions needed to detect minute amounts of the tracer in cortical neurons. These studies revealed that the olfactory cortex has a stereotyped map of receptor inputs, but one that is radically different from that in the bulb. The segregation of receptor inputs in different glomeruli and neurons in the bulb gives way in the cortex to a complex array of receptor inputs in which signals from different receptors partially overlap and single cortical neurons appear to receive signals from combinations of different receptors. This offers a means by which the individual components of an odorant's receptor code could be integrated at the level of single neurons. This could serve as an initial step in the reconstruction of an odor image from its deconstructed features, which are conveyed by the receptor elements of the receptor code. We published our findings on the cortex in 2001.

During the ten-year period at Harvard in which we did the work described above, my laboratory also investigated a

number of other questions. These included studies of the chromosomal organization of receptor genes and the evolution of the receptor gene family by Susan Sullivan, studies of the development of receptor gene expression patterns by Susan and Staffan Bohm, and bioinformatic studies by Bettina Malnic and Paul Godfrey that defined and compared the receptor gene repertoires of humans and mice. We also conducted a series of studies on the detection of pheromones in the vomeronasal organ, including studies by Emily Liman and Anna Berghard that revealed differences between transduction molecules involved in odor versus pheromone detection, the discovery of zonal patterns of transduction molecules likely to be involved in pheromone detection by Anna, analyses of vomeronasal responses to pheromones and odorants by Mehran Sam, and the discovery, by Hiroaki Matsunami, of a family of candidate pheromone receptors. During the latter part of this period, Hiroaki Matsunami, Jean-Pierre Montmayeur, and Stephen Liberles also began to explore the mechanisms underlying taste detection, in the process discovering candidate receptors for both bitter and sweet tastes, both of which were also found by other groups at about the same time.

SEATTLE

In 2002, I returned to Seattle to be a Member of the Division of Basic Sciences at the Fred Hutchinson Cancer Research Center and Affiliate Professor of Physiology and Biophysics at the University of Washington. I had always intended to someday return to the West Coast and had already stayed longer in Boston than I had anticipated. When Mark Groudine, then Director of the Basic Sciences Division at Fred Hutchinson, offered me a faculty position there, I gladly accepted. The Hutchinson Center had a reputation for cutting-edge science as well as a high level of collegiality, both of which were important to me. In addition, by moving to Seattle, I would be closer to my partner, Roger, who lived in Berkeley, and to my family and friends in Seattle.

In Seattle, we are continuing to explore the mechanisms underlying odor perception as well as the means by which

pheromones elicit instinctive behaviors. We have also become interested in the neural circuits that underlie innate behaviors and basic drives, such as fear, appetite, and reproduction. We are currently developing molecular techniques to uncover those circuits and to define their composite neurons and the genes they express. In a different vein, we have developed a high-throughput approach in which we are using chemical libraries to identify genes that control aging and lifespan, our chief interest being whether there might be a central mechanism that determines lifespan and regulates the aging of cells throughout the body.

LOOKING BACK

Since Richard Axel and I published the discovery of odorant receptors in 1991, it has been immensely satisfying for me to see many laboratories using these receptors in a large-scale effort to dissect the mechanisms that underlie the sense of smell and the developmental processes that shape the organization of the olfactory system. Molecular approaches to studying olfaction have extended to other vertebrates as well as to invertebrate species, with Cori Bargmann's group discovering a large variety of chemosensory receptors in the nematode worm *C. elegans*, and several groups, including Richard Axel's, identifying families of odorant and taste receptors in the fruit fly *D. melanogaster*.

Looking back over my life, I am struck by the good fortune I have had to be a scientist. Very few in this world have the opportunity to do everyday what they love to do, as I have. I have had wonderful mentors, colleagues, and students with whom to explore what fascinates me, and have enjoyed both challenges and discoveries. I am grateful for all of these things and look forward to learning what nature will next reveal to us.

As a woman in science, I sincerely hope that my receiving a Nobel Prize will send a message to young women everywhere that the doors are open to them and that they should follow their dreams.

1. Introduction

The subject of my lecture is the sense of smell, one of the five senses through which we perceive the world. Through the sense of smell, humans and other mammals can perceive a vast number and variety of chemicals in the external world. It is estimated that humans can sense as many as 10 000 to 100 000 chemicals as having a distinct odor. All of these "odorants" are small, volatile molecules. However, they have diverse structures and somehow those different structures are perceived as having different odors (Figure 1).

The sense of smell is mediated by the olfactory system, a system that is characterized by exquisite sensitivity and discriminatory power. Even a slight change in the structure

of an odorant can change its perceived odor. For example, the close relative of a chemical that is perceived as pear can have the scent of an apple. In addition to odorants, the olfactory system detects pheromones, chemicals that are released from animals and act on members of the same species, stimulating hormonal changes or instinctive behaviors, such as mating or aggression. The olfactory system also detects predator odors, which can elicit innate fear responses.

Over the past 16 years, our work has focused on two questions: First, how do mammals detect so many different environmental chemicals? And second, how does the brain translate those chemicals into diverse odor perceptions and behaviors?

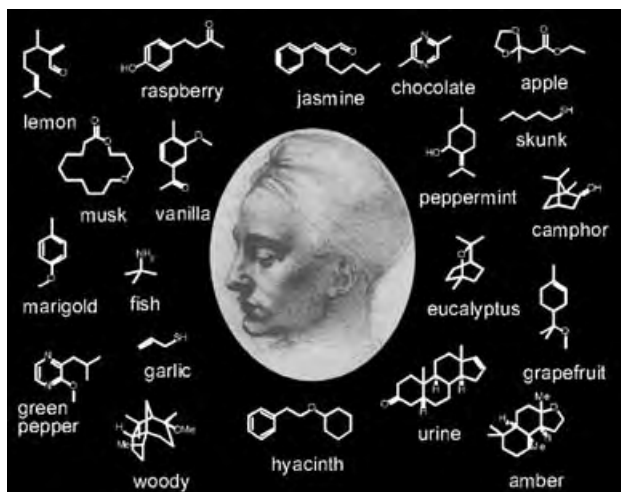


Figure 1. Humans and other mammals perceive a vast number of chemicals as having distinct odors.

Odorants are initially detected by olfactory sensory neurons, which are located in the olfactory epithelium lining the nasal cavity (Figure 2). These neurons transmit signals to

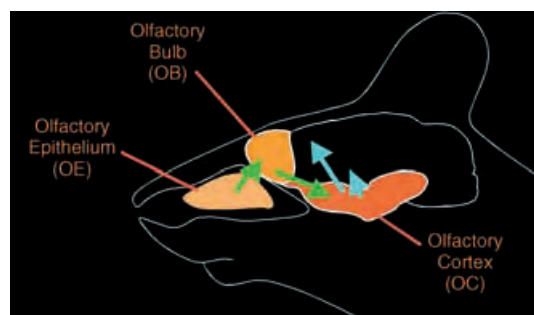


Figure 2. The olfactory pathway. Odorants are detected by olfactory sensory neurons in the olfactory epithelium. Signals generated in those neurons are relayed through the olfactory bulb to the olfactory cortex and then sent to other brain areas.

the olfactory bulb of the brain, which then relays those signals to the olfactory cortex. From there, olfactory information is sent to a number of other brain areas. These include higher cortical areas thought to be involved in odor discrimination as well as deep limbic areas of the brain, which are thought to mediate the emotional and physiological effects of odors. In contrast to odorants, pheromones are detected primarily in the vomeronasal organ (VNO), a separate olfactory structure in the nasal septum. From VNO neurons, signals are relayed through the accessory bulb to the medial amygdala and then the hypothalamus, areas implicated in hormonal and behavioral responses to pheromones.

The olfactory epithelium contains millions of olfactory sensory neurons. It also contains supporting cells and a basal layer of stem cells. Olfactory sensory neurons are short-lived cells that are continuously replaced from the stem-cell layer. At the surface of the epithelium, each neuron extends cilia into the nasal lumen, allowing it to come in contact with

odorants dissolved in the nasal mucus. Each neuron communicates with the brain through a single axon that it extends to the olfactory bulb.

2. Odorant Receptors

In our initial experiments, Richard Axel and I asked how it is that these neurons detect odorants. Beginning in 1965 with the work of Robert Gesteland,^[1] numerous electrophysiological studies had shown that different olfactory sensory neurons are depolarized, or activated, by different odorants. John Amoore proposed that these neurons had odorant receptor proteins that varied in their affinity for different odorants.^[2,3] In the mid 1980s, hints started to emerge about signal transduction in the cilia of the olfactory neurons. Doron Lancet, Sol Snyder, and their colleagues showed that odorants induce GTP-dependent increases in adenylyl cyclase activity in the cilia, thus suggesting the involvement of intracellular G proteins,^[4,5] and Randy Reed identified $G_{\alpha\text{olf}}$, a G protein that could mediate this response and was highly expressed in olfactory sensory neurons.^[6]

In 1988, Richard Axel and I embarked on a search for odorant receptors. The strategy we devised was based on three assumptions. First, odorant receptors would be selectively expressed in the olfactory epithelium. Second, since odorants vary in structure, there would be a family of varied, but related receptors, and those receptors would be encoded by a multigene family. Third, odorant receptors would be related to other types of receptors that interact with intracellular G proteins. By 1989, molecular cloning had revealed the structures of about 20 of these G-protein-coupled receptors (GPCRs). All of these receptors had seven potential transmembrane domains and they shared a few amino acid sequence motifs.

On the basis of these assumptions we set out to search for a family of GPCRs expressed in the rat olfactory epithelium.^[7] To do this, we first used the polymerase chain reaction (PCR) to look for receptors expressed in the olfactory epithelium that were related to known GPCRs. We designed 11 degenerate oligonucleotide primers that matched amino acid sequences in transmembrane domains 2 and 7 of known GPCRs. We then used these primers in all 30 pairwise combinations to amplify related sequences in cDNA prepared from rat olfactory epithelium RNA. From the 30 PCR reactions, we obtained 64 different PCR products in the appropriate size range. Each of these appeared as a distinct band by agarose gel electrophoresis.

We then asked whether any of the 64 PCR products contained multiple members of a multigene family. To do this we cut the DNA in each PCR product with a restriction enzyme. Most of the bands were cut into a small number of fragments that added up to the original in size. However, one band, no. 13, was cut into a large number of fragments, thus suggesting that it might contain multiple members of a multigene family. When we cloned and sequenced five of the DNAs in this band, we found what we had been looking for: all five encoded novel proteins with the hallmarks of GPCRs. Moreover, all five were related, but each one was unique.

By using these DNAs as probes, we isolated a series of related cDNAs from an olfactory epithelium cDNA library. We initially examined the proteins encoded by ten of the cDNAs. All ten proteins had the seven potential transmembrane domains characteristic of GPCRs. In addition, they had several amino acid sequence motifs seen in other GPCRs. However, the ten receptors all shared sequence motifs not seen in any other GPCRs, thus indicating that they were members of a novel receptor family.

Figure 3 shows a model of one of these receptors in the membrane with individual amino acids represented as balls. Red balls indicate amino acids that were especially variable

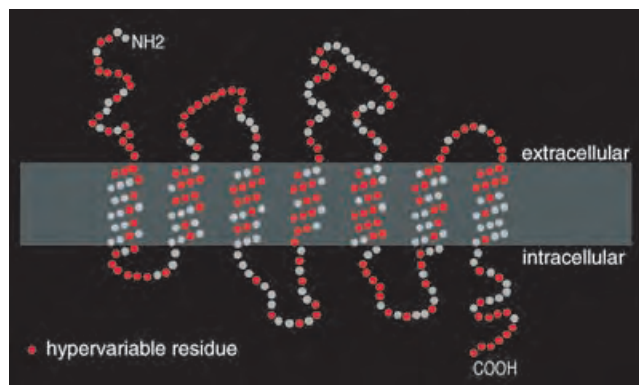


Figure 3. Topology of an odorant receptor in the membrane. Individual amino acid residues are indicated by balls. Red balls indicate residues that were hypervariable among ten odorant receptors. Adapted from Ref. [7].

among the ten receptors. Importantly, though related, the ten olfactory receptors varied extensively in amino acid sequence. This hypervariability was consistent with an ability of the receptors to interact with odorants of different structures.

Consistent with the selective expression of these receptors in the olfactory epithelium, a mixed olfactory receptor DNA probe hybridized to RNA from the olfactory epithelium, but not other tissues. Moreover, enriching for olfactory sensory neurons also enriched for receptor RNAs, thus suggesting that the receptors were expressed predominantly or exclusively by olfactory sensory neurons.

On Southern blots of genomic DNA, single receptor probes hybridized to multiple bands, and a mixed receptor probe hybridized to a large number of bands. This further indicated that the receptors we had found were encoded by a large multigene family. Genomic library screens indicated that the multigene family contained in excess of 100 members. In later studies, we obtained evidence for about 1000 different olfactory receptor genes in mice.

On the basis of these results, we concluded that the receptor family we had identified coded for odorant receptors

(ORs) expressed by olfactory sensory neurons in the nose.^[7] Subsequent studies showed that homologous families of odorant receptors are present in vertebrate species ranging from fish to humans.^[8] In 1991, after publishing our work on odorant receptors,^[7] I left Richard Axel's lab to join the faculty of Harvard Medical School.

A decade later, the sequencing of human and mouse genomes made it possible to determine the number of OR genes in these species. This was done by Lancet and Zozulya for human^[9,10] and by Firestein and Trask for mouse,^[11,12] and in my lab it was done for both species by Bettina Malnic and Paul Godfrey.^[13,14] These studies indicate that humans have about 350 different ORs and mice have about 1000. This result indicates that roughly 1–5 % of the genes in the genome are devoted to the detection of odorants. Odorant receptor genes are highly distributed across the genome. In our studies of the human genome, we found OR genes on 21 different chromosomes and at 51 different chromosomal loci, where they are found singly or in clusters (Figure 4).^[14]

In the mid 1990s, two additional families of receptors were found in the olfactory system. These receptors, called V1Rs and V2Rs, are unrelated to ORs in protein sequence, but both types have the characteristic seven-transmembrane domain structure of GPCRs. V1R and V2R genes are selectively expressed in the VNO, thus suggesting that they might be pheromone receptors. Both receptor families have more than 100 members. The V1R family was identified in 1995 by Dulac and Axel,^[15a] and the V2R family was identified in 1997 by Hiroaki Matsunami in my lab and also by the laboratories of Catherine Dulac and Nicholas Ryba.^[15b,16,17]

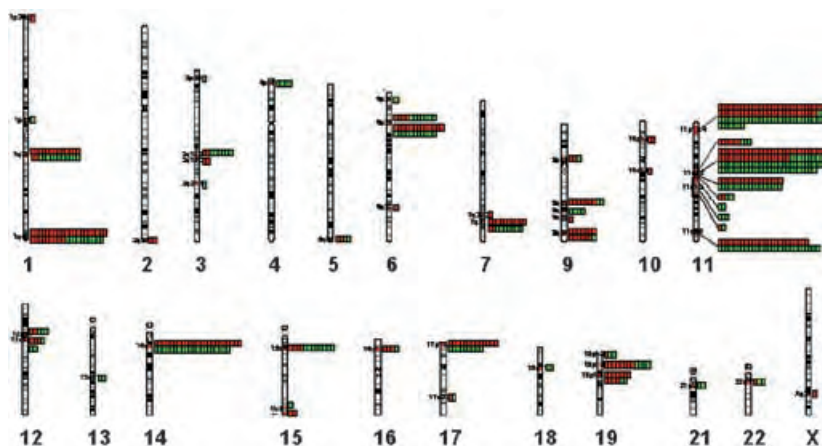


Figure 4. The chromosomal distribution of human odorant receptor genes. Intact receptor genes are shown in red and pseudogenes in green. Adapted from Ref. [14].

3. Organization of Odorant Receptors in the Olfactory Epithelium

The discovery of odorant receptors explained how the olfactory system detects a vast array of chemicals in the external world. It also did something else that was important: it provided a set of molecular tools to explore how the nervous system translates chemical structures into odor

perceptions. This is what we set out to do in my lab at Harvard.

In the mouse, we found evidence for as many as 1000 different OR genes. We first asked how information from different ORs is organized in the olfactory epithelium.^[18] In these experiments, Kerry Ressler, a graduate student in the lab, and Susan Sullivan, a postdoctoral fellow, hybridized labeled OR gene probes to sections through the mouse nose (Figure 5). These studies showed that the olfactory epithelium

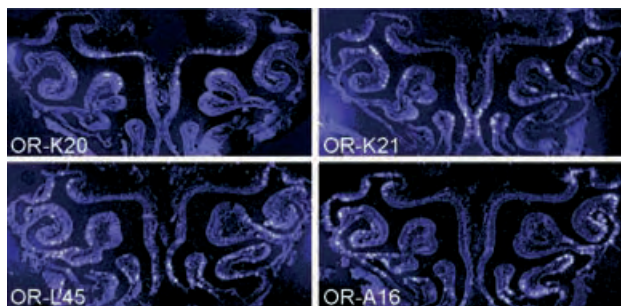


Figure 5. Expression patterns of odorant receptor genes in the mouse olfactory epithelium. Tissue sections through the mouse nose were hybridized to four different receptor gene probes. Adapted from Refs. [18, 30].

has distinct spatial zones that express non-overlapping sets of OR genes (Figure 6). Each OR gene is expressed in about 1/1000 neurons and those neurons are randomly scattered within one zone. Similar findings were made in Richard Axel's lab in rats.^[19] The OR expression zones form stripes that extend along the anterior–posterior axis of the nasal cavity.

These findings told us two important things. First, input from one type of OR is highly distributed in the epithelium. Therefore, neurons with receptors for one odorant (for example, a strawberry odorant) must be interspersed with neurons that have receptors for another odorant (such as a

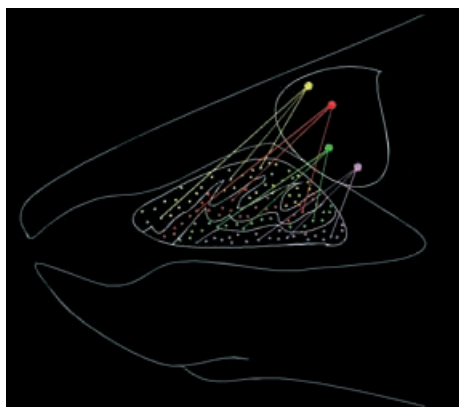


Figure 6. The organization of odorant receptor inputs in the olfactory epithelium and olfactory bulb. Sensory neurons expressing the same receptor are scattered within one epithelial zone, but their axons converge in specific glomeruli in the olfactory bulb. Adapted from Refs. [18, 22, 30].

lemon one). Second, each neuron may express only one OR gene. We later confirmed this by examining gene expression in single neurons.^[20] Thus, in the nose, inputs from different ORs are segregated in different neurons, and the information that each neuron transmits to the brain is derived from a single receptor type.

4. Combinatorial Receptor Codes for Odors

In later studies, we asked how the OR family encodes the identities of different odorants. To explore this question, we searched for ORs that recognize specific odorants.^[20] This work was done by Bettina Malnic in my lab in collaboration with Takaaki Sato and Junzo Hirono at the Life Electronics Research Center in Japan. We first exposed single mouse olfactory sensory neurons to a series of odorants, using calcium imaging to visualize their responses. We then isolated each responsive neuron and used reverse transcriptase–PCR (RT–PCR) to determine the OR gene it expressed. In every case, we identified only one expressed OR per neuron, thus confirming that each neuron expresses a single OR gene.

For test odorants, we used four different classes of linear aliphatic odorants with different functional groups and carbon chains ranging in length from four to nine carbon atoms. Each neuron was imaged as it was exposed sequentially to different odorants (Figure 7). If a response was seen, the neuron was retested with a lower concentration of the same odorant.

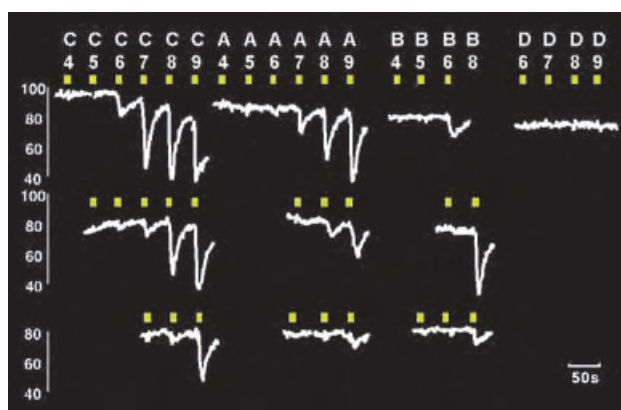


Figure 7. Responses of a single olfactory sensory neuron to different odorants. Fluorescence emission was monitored during sequential exposure of a neuron containing an indicator dye (Fura-2) to a series of odorants (C4–D9). Responses to lower odorant concentrations are shown below. Adapted from Ref. [20].

Figure 8 shows the response profiles of 14 neurons and therefore the recognition properties of the ORs expressed in those neurons. These data make three important points. First, each OR can recognize multiple odorants, something previously shown by Stuart Firestein for one rat OR.^[21] Second, each odorant can be detected by multiple different ORs. Finally, and most importantly, different odorants are recognized by different combinations of ORs.

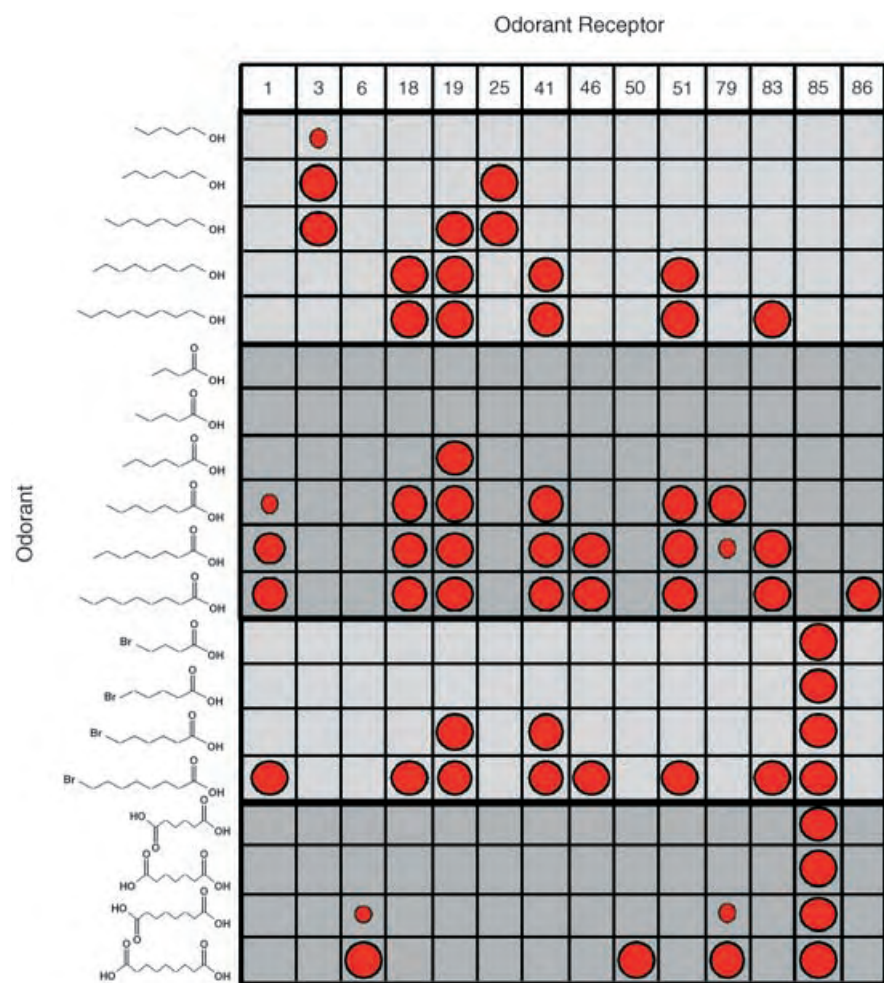


Figure 8. Odorant receptors are used combinatorially to detect odorants and encode their identities. The recognition profiles of individual odorant receptors to a series of odorants were determined by calcium imaging and single-cell RT-PCR. The sizes of circles reflect response intensity. Adapted from Ref. [20].

These results indicated that ORs are used combinatorially to encode odor identities.^[20] Different odorants are detected and thereby encoded by different combinations of ORs. However, each OR serves as one component of the codes for many odorants. Different odorants have different “receptor codes”. Given the number of possible combinations of 1000

ODORANT	ODORANT RECEPTOR														ODOR
	1	3	6	18	19	25	41	46	50	51	79	83	85	86	
Hexanoic Acid															rancid, sour, goat-like
Hexanol															sweet, herbal, woody
Heptanoic Acid															rancid, sour, sweaty
Heptanol															violet, sweet, woody
Octanoic Acid															rancid, sour, repulsive
Octanol															sweet, orange, rose
Nonanoic Acid															waxy, cheese, nut-like
Nonanol															fresh, rose, oily floral

Figure 9. Closely related odorants with different perceived odors are detected by different combinations of receptors. Adapted from Ref. [20].

different ORs, this combinatorial coding scheme could allow for the discrimination of an almost unlimited number of odorants. Even if each odorant were detected by only three ORs, this scheme could potentially generate almost one billion different odor codes.

These studies also provided insight into several puzzling features of human odor perception.^[20] Changing the structure of an odorant even slightly can alter its perceived odor. Sometimes the change in odor can be dramatic. The aliphatic acids and alcohols that we used in our studies are excellent examples of this phenomenon (Figure 9). All of the acids have unpleasant odors, such as rancid, sour, or sweaty. In contrast, all of the alcohols have pleasant odors, such as herbal, woody, or orange. In our studies, pairs of acids and alcohols that differed by a single functional group invariably had different receptor codes (Figure 9).

Our studies showed that a change in the concentration of an odorant can also change its receptor code. At higher concentrations, additional ORs were invariably recruited into the odor response. This may explain why changing the concentration of an odorant can alter its perceived odor.

5. A Stereotyped Map of Odorant Receptor Inputs in the Olfactory Bulb

These studies indicated that, in the nose, different odorants are detected by different combinations of ORs, and that the different combinations of ORs ultimately generate different odor perceptions. How is this accomplished? How does the brain translate an odorant's combinatorial receptor code into a perception?

Each olfactory sensory neuron in the olfactory epithelium sends a single axon to the olfactory bulb of the brain. Here the sensory axon enters a spherical structure called a glomerulus, where it synapses with the dendrites of bulb neurons. The mouse olfactory bulb has about 2000 glomeruli, each of which receives input from several thousand olfactory sensory neurons. Each sensory neuron synapses in only one glomerulus. Similarly, each mitral cell in the bulb receives input from a single glomerulus. Mitral cells are relay neurons that transmit signals to the olfactory cortex.

In the bulb, we found something very different from what we had seen in the nose.^[22] Here, single receptor probes labeled receptor mRNA in sensory axons in only a few glomeruli, and those glomeruli were located at only two spots, one on either side of the bulb (Figure 10A). We found that different receptor probes labeled different glomeruli, and surprisingly, those glomeruli had nearly identical locations in different individuals (Figure 10B). These findings were made

by Kerry Ressler and Susan Sullivan in my lab. In independent experiments in rats, Vassar and Axel obtained similar results, although individual receptor probes generally labeled a larger number of glomeruli at more locations in the bulb in their studies.^[23]

Our studies in mice indicated that the axons of thousands of sensory neurons with the same OR converge in only 2–4 glomeruli, each of which is likely to be dedicated to one OR (Figure 10).^[22] They further indicated that sensory informa-

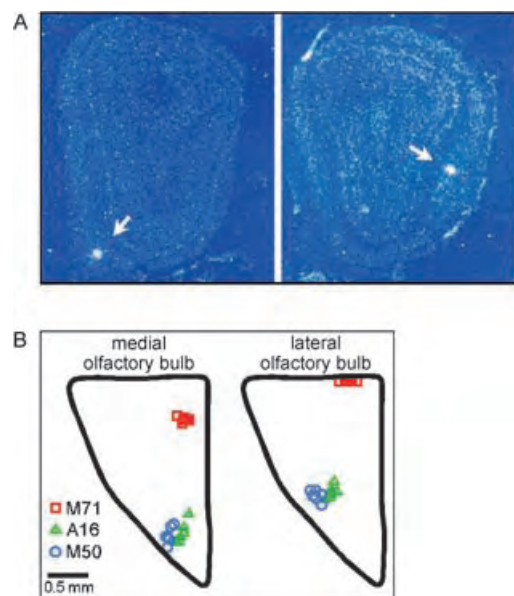


Figure 10. The olfactory bulb has a stereotyped map of OR inputs. A) A single OR gene probe hybridized to sensory axons in only one or two glomeruli on either side of the olfactory bulb. B) Different OR probes (A16, M50, M71) hybridized to different glomeruli and those glomeruli had similar locations in six different bulbs.

tion that is broadly organized into four zonal sets in the nose is transformed in the bulb into a stereotyped sensory map (Figure 6). In this map, inputs from different ORs are targeted to different glomeruli and the bulb neurons associated with those glomeruli. Remarkably, this map is virtually identical in different individuals.

The olfactory epithelium and bulb have one important thing in common, however: At both sites, inputs from different ORs are segregated. Each sensory neuron in the epithelium, and each glomerulus and relay neuron in the bulb, appears to be dedicated to only one type of OR.

The structure of the bulb map is likely to be important in at least two respects. First, it is likely to maximize sensitivity to low concentrations of odorants. Signals from 5000 or so neurons with the same OR converge on 2–4 glomeruli and about 50 mitral cells, thus allowing a high degree of signal integration. Second, the bulb map is likely to be important for the stimulation of odor memories. Sensory neurons in the epithelium are short lived and are continuously replaced. However, the bulb map remains constant over time. Thus, the neural code for an odor remains intact, assuring that odorants can elicit distant memories.

6. Odor Coding in the Olfactory Epithelium and Bulb

Given our finding that each odorant is recognized by a combination of ORs,^[20] these results imply that the code for an odor in the nose is a dispersed ensemble of neurons, each expressing one OR component of the odorant's receptor code (Figure 11). In the bulb, the code is a specific combination of

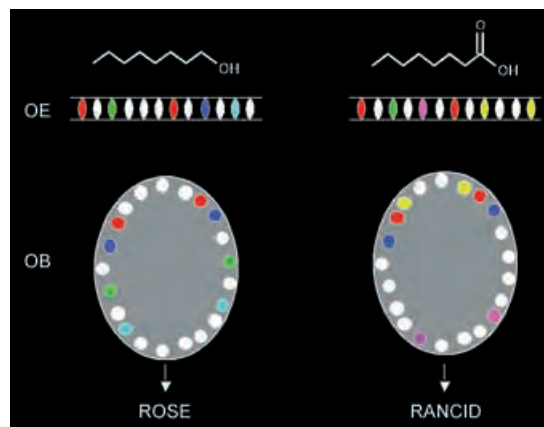


Figure 11. Odor coding in the olfactory epithelium and olfactory bulb. In this schematic representation, inputs from different ORs that recognize an odorant are indicated by different colors. In the olfactory epithelium (OE), the code for an odorant is a dispersed ensemble of neurons, each expressing one component of the odorant's receptor code. In the olfactory bulb (OB), it is a specific combination of glomeruli whose spatial arrangement is similar among individuals. Partially overlapping combinations of OR inputs generate distinct odor perceptions.

glomeruli that receive inputs from those ORs and have a similar spatial arrangement in different individuals. This arrangement is consistent with many studies of odor-induced activity in the epithelium and bulb, beginning in the 1950s with the studies of Lord Adrian, who discovered that different mitral cells in the rabbit bulb respond to different sets of odorants.^[24–26]

7. Stereotypy, Divergence, and Convergence in Olfactory Cortex

What happens to this information at higher levels of the nervous system to ultimately generate diverse odor perceptions?

Mitral cell relay neurons in the bulb extend axons to the olfactory cortex, a large area that stretches along the ventral–lateral part of the brain. The olfactory cortex is composed of a number of distinct anatomical areas, at least some of which are likely to have different functions. The largest area is the piriform cortex, which itself has morphologically distinct anterior and posterior halves.

In the 1980s, Lewis Haberly and others showed that a tracer placed in one small region of this cortex would back-label mitral cells in many parts of the bulb.^[27] This clearly

indicated that the organization of sensory information in the olfactory bulb could not be recapitulated in the cortex, but how olfactory information is organized in the olfactory cortex was a mystery.

We were initially interested in three questions regarding the olfactory cortex. First, do different areas of the olfactory cortex, which may have different functions, receive signals derived from different subsets of ORs or, alternatively, does each area receive input from the entire OR repertoire? Second, is input from one OR scattered in the cortex (as in the nose), is it targeted to unique, stereotyped sites (as in the bulb) or is it organized in some other way? Finally, given that each odorant is recognized by multiple ORs, are inputs from different ORs combined in individual cortical neurons, or are they segregated in different neurons as in the nose and bulb?

To determine how OR inputs are organized in the cortex, we first asked whether it would be possible to trace neural circuits genetically. In those studies, Lisa Horowitz, a graduate student in the lab, made transgenic mice that expressed a plant protein, barley lectin, in all olfactory sensory neurons in the nose. In those mice, the expression of barley lectin (BL) was controlled by the promoter of the OMP gene, a gene that is selectively expressed by olfactory sensory neurons.

Using BL-specific antibodies, we detected BL in olfactory sensory neurons in the olfactory epithelium, glomeruli, and relay neurons in the bulb, and also in neurons in the olfactory cortex.^[28] This indicated that BL produced by olfactory sensory neurons in the nose could travel across two synapses to label connected neurons first in the olfactory bulb and then in the olfactory cortex.

Having developed a genetic method for charting neural circuits, we were able to move to the next step. That was to ask how inputs from individual ORs are organized in the cortex. Our goal was to coexpress BL with only one of the 1000 different OR genes. To do this, Lisa Horowitz and Jean-Pierre Montmayeur in our lab altered individual OR genes by inserting, 3' to their coding regions, an internal ribosome entry site (IRES) sequence followed by a BL coding sequence. Using gene targeting in embryonic stem cells, Zhihua Zou, a postdoctoral fellow in the lab, then made "knockin" mice that contained an altered allele of either the M5 or M50 OR gene.^[29] In these knockin mice, BL was produced only in neurons that expressed the M5 or M50 OR.

In the olfactory cortex, the axons of bulb neurons branch and form synapses in layer Ia with the dendrites of pyramidal neurons located in layers II and III. In PompBL mice, which express BL in all olfactory sensory neurons,^[28] we saw labeled neurons in layers II and III throughout the olfactory cortex (Figure 12). In the M5 and M50 knockin mice, we also detected labeled cortical neurons, but they were located in distinct clusters (Figure 12).^[29] Moreover, the clusters appeared to have similar locations in different individuals.

In each knockin strain, we detected 2–3 clusters of labeled neurons in the anterior piriform cortex (Figure 12). Most of

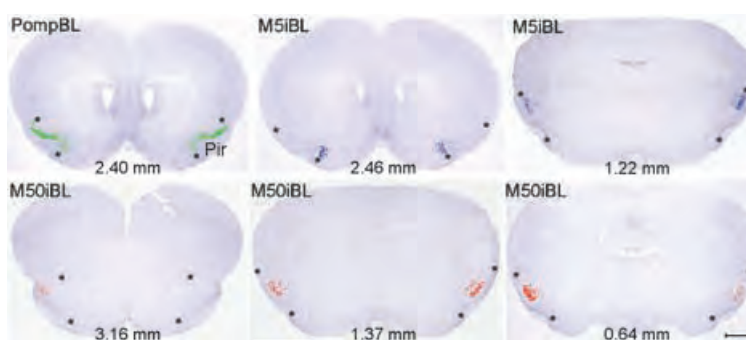


Figure 12. Inputs from one OR are targeted to two to three clusters of neurons in the anterior piriform cortex. Coronal sections through the anterior piriform cortex of mice in which barley lectin was expressed in all olfactory sensory neurons (PompBL) or only in neurons expressing the M5 (M5iBL) or M50 (M50iBL) odorant receptor. Asterisks indicate the outer limits of the piriform cortex (Pir). The distance from an anterior–posterior landmark is shown in mm. Adapted from Ref. [29].

these clusters were bilaterally symmetrical in the left and right brain. We also found clusters of labeled neurons in several other areas of the olfactory cortex. In each cluster, the highest density of labeled neurons was in the center, but even in the center, only about half of the resident pyramidal neurons were labeled with the BL tracer.

Detailed analysis of the clusters in the anterior piriform cortex revealed that they had similar locations and similar dimensions in different individuals and, in most cases, they were bilaterally symmetrical.^[29] The clusters had different locations in the two knockin strains, but one of the M5 clusters appeared to partially overlap with one of the M50 clusters.

These results showed that the olfactory cortex has a stereotyped map of OR inputs (Figure 13). In this map, signals derived from one type of OR are targeted to several loose clusters of cortical neurons. The clusters of neurons that receive input from a particular OR are found at specific locations, which are virtually identical among individuals.

These studies clearly indicated that input from one OR diverges to multiple areas of the olfactory cortex. This

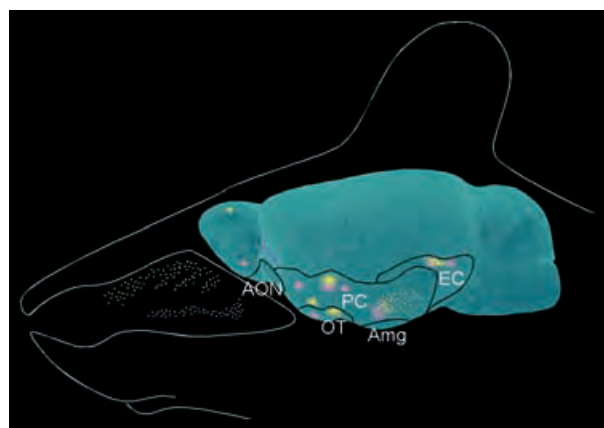


Figure 13. The olfactory cortex has a stereotyped map of OR inputs. Organization of inputs from the M5 (yellow) and M50 (pink) odorant receptors in the olfactory epithelium, bulb, and cortex. Black lines and abbreviations indicate different areas of the olfactory cortex. AON: anterior olfactory nucleus; PC: piriform cortex; OT: olfactory tubercle; Amg: olfactory nuclei of amygdala; EC: lateral entorhinal cortex.

divergence of OR inputs may allow a parallel processing of OR signals in which signals from the same ORs are combined or modulated in different ways prior to transmission to other brain regions that have different functions.

We found that in the anterior piriform cortex, the clusters of neurons that receive input from one OR occupy about five percent of the total area along the anterior–posterior and dorsal–ventral axes.^[29] In PomPBL mice, which express BL in all olfactory sensory neurons, there were about 180 000 BL-labeled neurons in the anterior piriform cortex. If each cortical neuron received input from only one of 1000 different ORs, one might expect to see about 180 labeled neurons in this area in each knockin mouse. However, we detected about 4000–6000 BL-labeled neurons in the anterior piriform cortex in each knockin strain.^[29]

These results indicated that the map of OR inputs in the olfactory cortex is markedly different from that in the olfactory bulb. First, while inputs from different ORs are spatially segregated in different glomeruli in the bulb, they are likely to overlap extensively in the cortex (Figure 14A).

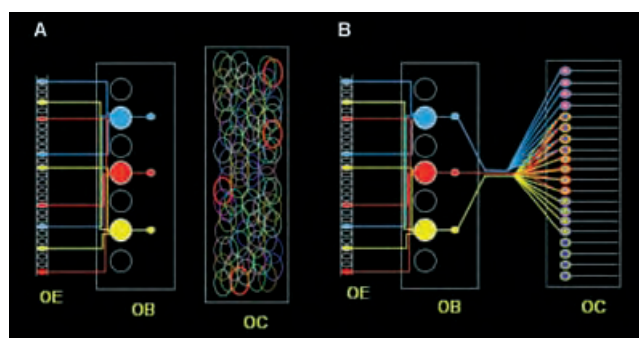


Figure 14. Schematic diagrams showing the organization of odorant receptor inputs in the olfactory epithelium (OE), olfactory bulb (OB), and olfactory cortex (OC). Inputs from different ORs are segregated in different neurons and glomeruli in the OE and OB. In contrast, it appears that different receptor inputs overlap extensively in the OC (A) and that single cortical neurons receive signals from a combination of receptors (B).

Second, while signals from different ORs are segregated in different neurons in both the nose and bulb, each cortical neuron is likely to receive signals derived from multiple different ORs (Figure 14B). Since each odorant is recognized by a combination of ORs, this may permit an initial integration of multiple components of an odorant's receptor code that is critical to the generation of diverse odor perceptions.

These findings raise the possibility that neurons in the olfactory cortex function as coincidence detectors that are activated only by correlated combinatorial inputs from different ORs. For example, in a simple model, signals from different ORs that recognize vanillin would be targeted to partially overlapping locations in the cortex, but the only neurons activated by vanillin would be those that receive coincident signals derived from more than one of the vanillin ORs.

In sensory systems, environmental stimuli are deconstructed and then reconstructed in the brain to create

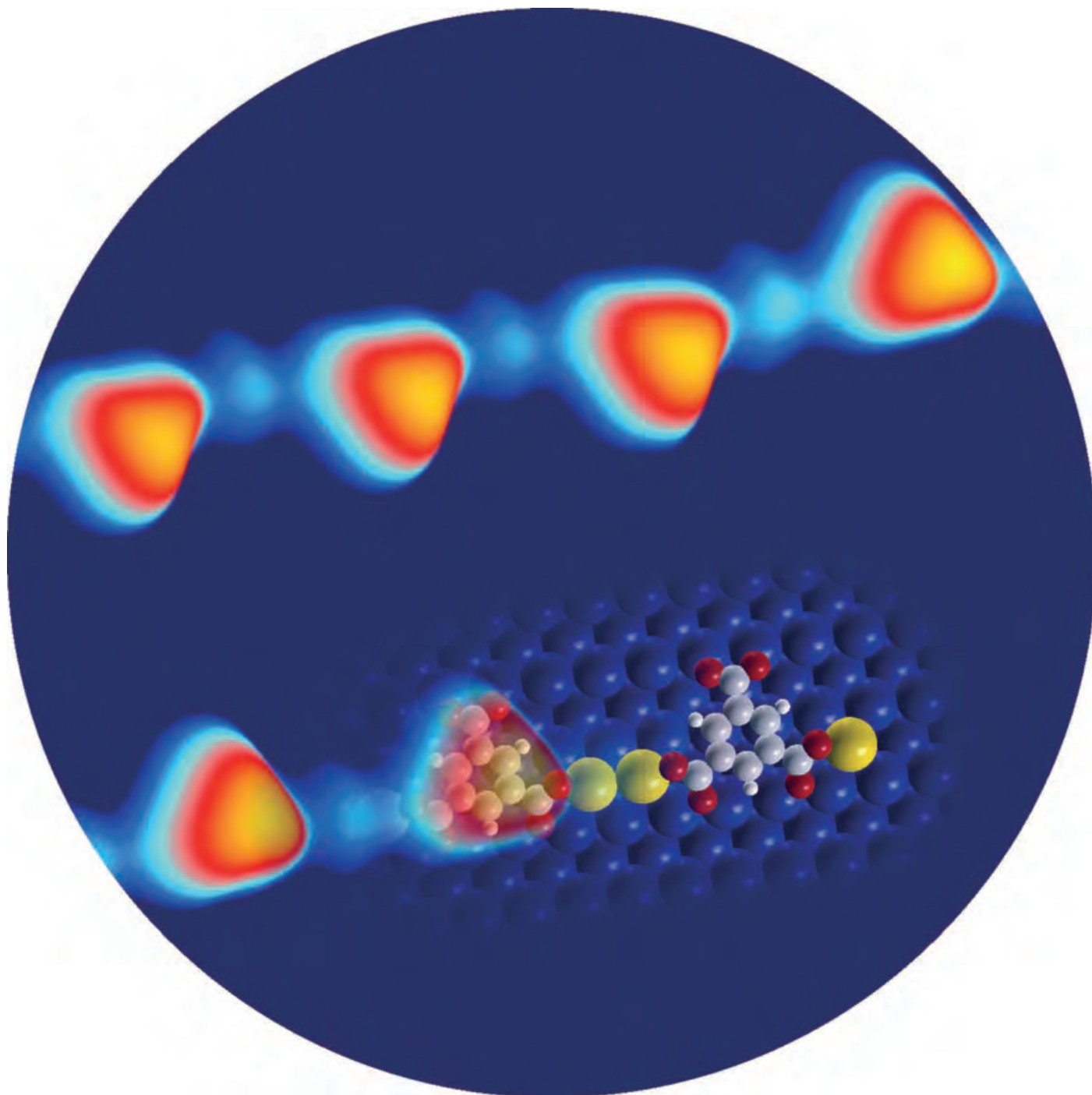
perceptions. The organization of receptor inputs seen in the olfactory cortex may serve as an initial step in the reconstruction of an odor image from its deconstructed features.

I would like to acknowledge the very talented students and postdoctoral fellows in my lab who did the experiments that I discussed today. Kerry Ressler and Susan Sullivan did all of the early studies on OR inputs in the olfactory epithelium and bulb. Hiroaki Matsunami identified and characterized the V2R family of candidate pheromone receptors. Bettina Malnic conducted the studies of OR specificities in collaboration with Takaaki Sato and Junzo Hirono at the Life Electronic Research Center in Japan. Bettina and Paul Godfrey defined the OR gene repertoires of humans and mice. Lisa Horowitz developed the genetic method for tracing neural circuits, and Zhihua Zou, in collaboration with Lisa and Jean-Pierre Montmayeur, conducted the studies of OR inputs in the olfactory cortex.

Received: March 30, 2005

- [1] "Chemical transmission in the nose of the frog": R. C. Gesteland, J. Y. Lettvin, W. H. Pitts, *J. Physiol.* **1965**, *181*, 525–559.
- [2] J. E. Amoore, *Molecular basis of odor*, Charles C. Thomas, Springfield, **1970**.
- [3] "Specific anosmia and the concept of primary odors": J. E. Amoore, *Chem. Senses Flavour* **1977**, *2*, 267–281.
- [4] "Odorant-sensitive adenylate cyclase may mediate olfactory reception": U. Pace, E. Hanski, Y. Salomon, D. Lancet, *Nature* **1985**, *316*, 255–258.
- [5] "The odorant-sensitive adenylate cyclase of olfactory receptor cells. Differential stimulation by distinct classes of odorants": P. B. Sklar, R. R. Anholt, S. H. Snyder, *J. Biol. Chem.* **1986**, *261*, 15538–15543.
- [6] "Golf: an olfactory neuron specific G-protein involved in odorant signal transduction": D. T. Jones, R. R. Reed, *Science* **1989**, *244*, 790–795.
- [7] "A novel multigene family may encode odorant receptors: a molecular basis for odor recognition": L. Buck, R. Axel, *Cell* **1991**, *65*, 175–187.
- [8] "Molecular biology of odorant receptors in vertebrates": P. Mombaerts, *Annu. Rev. Neurosci.* **1999**, *22*, 487–509.
- [9] "The complete human olfactory subgenome": G. Glusman, I. Yanai, I. Rubin, D. Lancet, *Genome Res.* **2001**, *11*, 685–702.
- [10] "The human olfactory receptor repertoire": S. Zozulya, F. Echeverri, T. Nguyen, *Adv. Genome Biol.* **2001**, *2*, RESEARCH0018.
- [11] "Different evolutionary processes shaped the mouse and human olfactory receptor gene families": J. M. Young, C. Friedman, E. M. Williams, J. A. Ross, L. Priddy-Tonnes, B. J. Trask, *Hum. Mol. Genet.* **2002**, *11*, 535–546.
- [12] "The olfactory receptor gene superfamily of the mouse": X. Zhang, S. Firestein, *Nat. Neurosci.* **2002**, *5*, 124–133.
- [13] "The mouse olfactory receptor gene family": P. A. , Godfrey, B. Malnic, L. B. Buck, *Proc. Natl. Acad. Sci. USA* **2004**, *101*, 2156–2161.
- [14] "The human olfactory receptor gene family": B. Malnic, P. A. Godfrey, L. B. Buck, *Proc. Natl. Acad. Sci. USA* **2004**, *101*, 2584–2589.
- [15] a) "A novel family of genes encoding putative pheromone receptors in mammals": C. Dulac, R. Axel, *Cell* **1995**, *83*, 195–206; b) "A novel family of putative pheromone receptors in

- mammals with a topographically organized and sexually dimorphic distribution”: G. Herrada, C. Dulac, *Cell* **1997**, *90*, 763–773.
- [16] “A multigene family encoding a diverse array of putative pheromone receptors in mammals”: H. Matsunami, L. B. Buck, *Cell* **1997**, *90*, 775–784.
- [17] “A new multigene family of putative pheromone receptors”: N. J. Ryba, R. Tirindelli, *Neuron* **1997**, *19*, 371–379.
- [18] “A zonal organization of odorant receptor gene expression in the olfactory epithelium”: K. J. Ressler, S. L. Sullivan, L. B. Buck, *Cell* **1993**, *73*, 597–609.
- [19] “Spatial segregation of odorant receptor expression in the mammalian olfactory epithelium”: R. Vassar, J. Ngai, R. Axel, *Cell* **1993**, *74*, 309–318.
- [20] “Combinatorial receptor codes for odors”: B. Malnic, J. Hirono, T. Sato, L. B. Buck, *Cell* **1999**, *96*, 713–723.
- [21] “Functional expression of a mammalian odorant receptor”: H. Zhao, L. Ivic, J. M. Otaki, M. Hashimoto, K. Mikoshiba, S. Firestein, *Science* **1998**, *279*, 237–242.
- [22] “Information coding in the olfactory system: evidence for a stereotyped and highly organized epitope map in the olfactory bulb”: K. J. Ressler, S. L. Sullivan, L. B. Buck, *Cell* **1994**, *79*, 1245–1255.
- [23] “Topographic organization of sensory projections to the olfactory bulb”: R. Vassar, S. K. Chao, R. Sitcheran, J. M. Nunez, L. B. Vosshall, R. Axel, *Cell* **1994**, *79*, 981–991.
- [24] “Sensory discrimination with some recent evidence from the olfactory organ”: E. D. Adrian, *Br. Med. Bull.* **1950**, *6*, 330–333.
- [25] “The action of the mammalian olfactory organ”: L. Adrian, *J. Laryngol. Otol.* **1956**, *70*, 1–14.
- [26] “Information coding in the vertebrate olfactory system”: L. B. Buck, *Annu. Rev. Neurosci.* **1996**, *19*, 517–544.
- [27] “The olfactory cortex”: L. B. Haberly in *The synaptic organization of the brain* (Ed.: G. M. Shepherd), Oxford University Press, New York, **1998**, pp. 377–41.
- [28] “A genetic approach to trace neural circuits”: L. F. Horowitz, J. P. Montmayeur, Y. Echelard, L. B. Buck, *Proc. Natl. Acad. Sci. USA* **1999**, *96*, 3194–3199.
- [29] “Genetic tracing reveals a stereotyped sensory map in the olfactory cortex”: Z. Zou, L. F. Horowitz, J. P. Montmayeur, S. Snapper, L. B. Buck, *Nature* **2001**, *414*, 173–179.
- [30] “The chromosomal distribution of mouse odorant receptor genes”: S. L. , Sullivan, M. A. Adamson, K. J. Ressler, C. A. Kozak, L. B. Buck, *Proc. Natl. Acad. Sci. USA* **1996**, *93*, 884–888.
-



Highly anisotropic metal surfaces can drive the formation of metal–organic coordination chains, as shown by scanning tunneling microscopy analysis and density functional calculations. For details about the templated coordination of Cu and Fe atoms with trimesitylic acid on a Cu(110) surface, see the Communication by T. Classen, S. Fabris, K. Kern, and co-workers on the following pages.

Templated Growth of Metal–Organic Coordination Chains at Surfaces**

Thomas Classen,* Guido Fratesi, Giovanni Costantini, Stefano Fabris,* Frank Louis Stadler, Cheolkyu Kim, Stefano de Gironcoli, Stefano Baroni, and Klaus Kern*

Metal–organic coordination networks (MOCNs) formed by coordination bonding between metallic centers and organic ligands can be efficiently engineered to exhibit specific magnetic, electronic, or catalytic properties.^[1–6] Instead of depositing prefabricated MOCNs onto surfaces, it has been recently shown that two-dimensional (2D) MOCNs can be directly grown at metal surfaces under ultrahigh vacuum (UHV), thus creating highly regular 2D networks of metal atoms.^[7–12] These grids have been pointed out to be potentially relevant for devices that involve sensing, switching, and information storage.^[13,14] We show here that this approach offers the additional advantage to predefine the geometry of the MOCN by using the substrate as a template to direct the formation of novel 1D metal–organic coordination chains (MOCCs).

The templating role of substrates is well known in the field of surface epitaxial growth.^[15–19] Among the highly anisotropic substrates, the Cu(110) surface is one of the most commonly used (Figure 1 a and b). To demonstrate its strong 1D templating effect on organic molecules, a ligand with a triangular symmetry was selected, namely 1,3,5-benzenetricarboxylic acid (trimesic acid, TMA; Figure 1 c). The three-

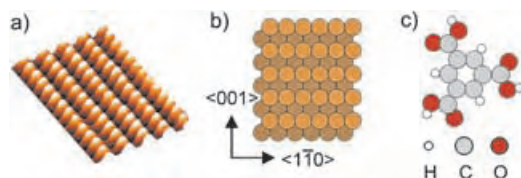


Figure 1. a) High-resolution STM image in 3D representation and b) structural model of the Cu(110) surface. c) Trimesic acid (TMA).

fold rotation symmetry of TMA supports the formation of hexagonal 2D and 3D architectures,^[20–22] therefore strongly disfavoring the linear geometry. On the isotropic Cu(100) surface, TMA forms 0D carboxylate complexes and 2D networks.^[9,10]

The deposition of TMA on Cu(110) under UHV at 300 K results in the formation of 1D chains along the <110> direction, as observed by scanning tunneling microscopy (STM). This deposition temperature is high enough to provide mobile Cu adatoms through evaporation from kinks and steps onto the terraces.^[23] Analysis of similar systems by X-ray photoelectron spectroscopy^[24,25] showed that these adatoms catalyze the deprotonation of molecular carboxylate groups. The adatoms are furthermore necessary for the formation of copper carboxylate complexes.^[23,24,26] Deposition at lower temperatures, 210 K and 250 K, resulted in disordered structures with a tip-to-tip bonding motif. This signature, which is never observed above 300 K, is characteristic for intermolecular dimeric hydrogen bonds of carboxylate groups,^[20–22,24] thus indicating that the carboxylate groups are protonated at temperatures below 300 K. Upon annealing to 300 K, these structures yield to the same 1D chains described above. The chains formed at 300 K typically show irregular kinks and poor long-range order. These inhomogeneities are removed by post-annealing to 380–410 K to yield straight and highly periodic chains, referred to as MOCC-I hereafter (Figure 2). At low coverage, chains predominantly attach to step edges, whereas upon increasing the coverage chain nucleation takes place also on terraces.

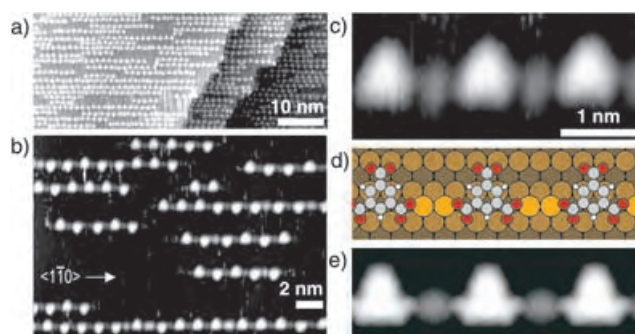


Figure 2. Representative STM images of [Cu-TMA-Cu]_n chains (MOCC-I) on Cu(110) for TMA coverages of a) 0.36 and b) 0.13 monolayers (ML), respectively. Comparison of c) the high-resolution STM image of MOCC-I, d) the atomistic MOCC-I model, and e) the corresponding simulated STM image.

These findings allow the substrate templating effect to be rationalized as follows: Upon deprotonation, the molecule–molecule interaction (favoring hexagonal geometries) is overcome by the molecule–substrate interaction, which effectively controls the 1D character of these MOCCs.

The chains consist of triangles alternating with round protrusions (Figure 2 b and c). The apparent height of the two units is significantly different, 140 ± 30 pm and 75 ± 20 pm, respectively, when scanning at -1 V and 1 nA. Following previous analysis,^[9,10,20–22] the triangles are identified as flat-lying TMA molecules. The round protrusions can be attrib-

[*] T. Classen, Dr. G. Costantini, Dr. F. L. Stadler, Dr. C. Kim, Prof. K. Kern
Max-Planck-Institut für Festkörperforschung
Heisenbergstr. 1, 70569 Stuttgart (Germany)
Fax: (+49) 711-689-1662
E-mail: t.classen@fkf.mpg.de
k.kern@fkf.mpg.de

G. Fratesi, Dr. S. Fabris, Prof. S. de Gironcoli, Prof. S. Baroni
SISSA and INFN-CNR DEMOCRITOS National Simulation Center
Via Beirut 2–4, 34014 Trieste (Italy)
Fax: (+39) 040-3787-528
E-mail: fabris@democritos.it

[**] The authors wish to acknowledge Nian Lin, Magali Lingenfelder, Alexander Schneider, and Giacinto Scoles for fruitful discussions, as well as HPC-EUROPA (project #506079) and INFN Progetto Calcolo Parallelo for computer resources.

uted to Cu adatoms,^[7,9,10] coordinated by two of the carboxylate groups of the TMA molecule. The third functional group of TMA is pointing out of the chain with no preferential up or down orientation (Figure 2b).

The periodicity of MOCC-I along $\langle 1\bar{1}0 \rangle$ is five Cu lattice spacings (12.70 ± 0.15 Å). High-resolution STM images indicate that the distance between the Cu protrusions and the oxygen atom of the molecular carboxylate groups is approximately 2.8 Å, a rather large value when compared to the typical Cu–O bond length of 1.9–2.2 Å.^[27] The simplest $[-\text{TMA-Cu-}]_n$ chain model for the adsorption geometry of MOCC-I seems therefore to be outruled by these observations.

Indeed, the lowest energy structure of MOCC-I as predicted by density functional theory (DFT) calculations is a $[-\text{Cu-TMA-Cu-}]_n$ chain in which a dimer of Cu metal adatoms forms unidentate Cu–carboxylate bonds with adjacent TMA molecules (Figure 2d). The dimer binds to the surface by 6.3 eV with respect to isolated Cu atoms, and each adatom is fivefold coordinated to the substrate. This structure has the correct $5 \times$ periodicity. Its simulated STM image (Figure 2e) closely agrees with that found experimentally, with the Cu–Cu dimer imaged as a single spot centered between the adatoms. The resulting Cu–O distance is 2.02 Å, which lies in the range of typical Cu–O bond lengths. Also the calculated apparent heights, 170 pm for the TMA unit and 90 pm for the Cu adatom unit, are in good agreement with those determined experimentally.

The theoretical analysis provides an unprecedented level of insight into the adsorption geometry of surface MOCNs. The phenyl ring of TMA and the Cu adatoms are located on the short-bridge and hollow sites, respectively (Figure 2d). The molecule stands 1.14 Å above the outermost Cu layer, with the carboxylate groups bending towards the surface by as much as 0.69 Å. With respect to a neutral Cu atom, surface complexation of Cu weakly reduces the metal center occupations of both the s and d electronic states by approximately 0.2 electrons.

$[-\text{Cu-TMA-Cu-}]_n$ chains are the intrinsic nanostructures on Cu(110), but functional MOCCs also require different elements than Cu as metallic centers. Extrinsic $[-\text{TMA-Fe-}]_n$ chains (MOCC-II) were created by holding the Cu(110) crystal at 230 K—thus preventing the formation of Cu–TMA complexes—and by depositing first TMA and then Fe at coverages higher than 0.04 ML. The sample was then annealed to 390 K for one minute. The number of chains increased with the amount of deposited Fe and saturation was reached for a coverage of around 0.08 ML of Fe. Further deposition of Fe results in the nucleation of Fe islands.

The $4 \times$ in-chain periodicity of these chains (Figure 3) leaves space for just one Fe metal center between TMA molecules. The TMA–TMA distances are therefore shorter when linked by Fe than when linked by Cu, similar to that reported for 2D MOCNs on the Cu(001) surface.^[9,10] According to DFT calculations the geometry of the adsorbed TMA molecule is weakly dependent on the metal center, with the phenyl ring lying 0.09 Å higher in the case of Fe. The metal–carboxylate bond is still unidentate and the Fe–O distance is 1.95 Å, thus 0.07 Å shorter than the Cu–O distance in

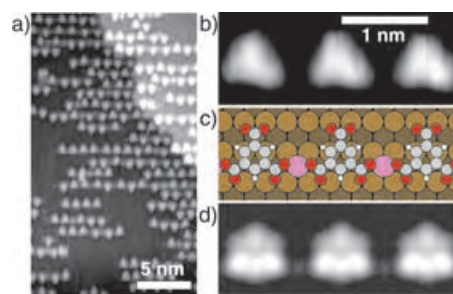


Figure 3. $[-\text{TMA-Fe-}]_n$ chains (MOCC-II): a) Overview image of the coordination chains formed upon deposition of 0.04 ML Fe and 0.40 ML TMA. Comparison of b) the high-resolution STM image, c) the atomistic MOCC-II model, and d) the corresponding simulated STM image.

MOCC-I. Single metal centers lead to very weak features in the simulated STM image (Figure 3d), in agreement with experiment (Figure 3b). With respect to a neutral Fe atom, surface complexation of Fe strongly reduces the occupations of the Fe s states by 1.3 electrons while it increases that of the d states by 0.5 electrons.

Insight into the potentially interesting magnetic properties of Fe-complexed MOCC-II can be gained by projecting the electron density on the atomic Fe d orbitals (Figure 4b).

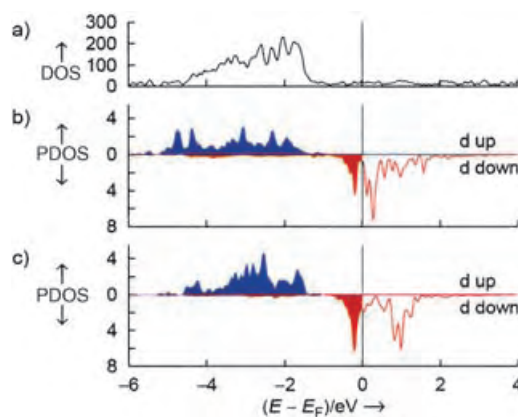


Figure 4. a) Total density of electronic states (DOS, in [eV] with respect to the Fermi energy E_F) of the $[-\text{TMA-Fe-}]_n$ chain (MOCC-II). Projected DOS (PDOS) on the atomic d states of b) the Fe center in MOCC-II and c) an Fe atom isolated on the Cu(110) surface.

The projected density of electronic states (DOS) displays a large splitting between the majority spin-up and minority spin-down electronic d states. The former are completely filled and well hybridized with the substrate Cu d states, extending from -5 to -1 eV in the total DOS of the $[-\text{TMA-Fe-}]_n$ chain (Figure 4a). The latter spin-down states are only partially filled and extend in the energy region dominated by the substrate s states. As a consequence, the Fe atoms are strongly magnetized with a spin polarization of $3.3 \mu_B$ per Fe atom. The polarization of a Fe adatom isolated on the Cu(110) surface is very similar, $3.2 \mu_B$, and the corresponding projected DOS is shown in Figure 4c. The comparison shows that the coordination with the carboxylate group does not affect the electron localization at the Fe adatoms and thus

does not produce any relevant quenching of the spin magnetic moment. This is a necessary (although not sufficient) condition for the emergence of intriguing magnetic properties induced by the low dimensionality, such as a giant magnetic anisotropy.^[28,29] Because of their high thermal stability, MOCNs similar to those presented here could thus be convenient model systems to explore the occurrence of low-dimensional magnetism.

In conclusion, metal–organic coordination chains were created in situ by self-organized growth at a metal surface under UHV. The 1D anisotropy of the substrate was effectively transferred to the resulting metal–organic coordination chains. This strategy was shown to work for intrinsic as well as for extrinsic metal–carboxylate systems. The precise atomic configuration of the structures was revealed by a combined use of STM and DFT. Spin-polarized DFT suggests that Fe centers within the 1D chains have magnetic properties similar to those of isolated Fe adatoms. This renders such regular and unidirectional arrangement of magnetic centers attractive candidates for the investigation of low-dimensional magnetism in thermally stable structures.

Experimental Section

Methods: The sample was prepared in a standard UHV preparation chamber with a base pressure of less than 2×10^{-10} mbar. The Cu(110) single crystal was cleaned by cycles of Ar⁺ sputtering (900 eV) and annealing to 830–850 K. Commercially available TMA (Fluka Chemie AG, purity > 97%) was evaporated from a ceramic crucible at 460 K for sample temperatures between 130 K and 300 K. The sample was then transferred under UHV conditions to a STM chamber (base pressure of 6×10^{-11} mbar) that comprised a commercial variable-temperature STM apparatus. Measurements were carried out at 300 K and 130 K with typical tunneling conditions of -1 V and 1 nA (filled-state imaging).

The computer simulations were based on DFT, in the generalized gradient approximation of Perdew–Burke–Ernzerhof.^[30] The calculations were performed in the pseudopotential plane-wave framework (plane-wave cutoff of 326.4 eV) using ultrasoft pseudopotentials^[31] as implemented in the PWscf simulation package.^[32] A three-layer slab provided a simplified model of the Cu(110) surface. The atomic positions were determined by relaxing the upper layer and keeping the distance between the others fixed at the bulk value. Metal adatoms and deprotonated TMA molecules were positioned on the upper surface of the slab and were structurally relaxed according to the Hellmann–Feynman forces. STM images were simulated by means of the Tersoff–Hamann method,^[33] that is, by a spatially resolved DOS integrated in energy from a bias potential (-1.0 eV) to the Fermi energy.

Received: June 10, 2005

Keywords: coordination modes · density functional calculations · nanostructures · scanning probe microscopy · self-assembly

- [1] O. M. Yaghi, M. O’Keeffe, N. W. Ockwig, H. K. Chae, M. Eddaoudi, J. Kim, *Nature* **2003**, 423, 705.
- [2] G. F. Swiegers, T. J. Malefetse, *Chem. Rev.* **2000**, 100, 3483.
- [3] B. J. Holliday, C. A. Mirkin, *Angew. Chem.* **2001**, 113, 2076; *Angew. Chem. Int. Ed.* **2001**, 40, 2022.

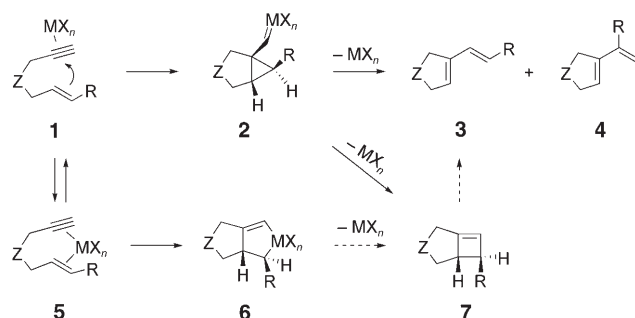
- [4] C. Copéret, M. Chabanas, R. P. Saint-Arroman, J.-M. Basset, *Angew. Chem.* **2003**, 115, 164; *Angew. Chem. Int. Ed.* **2003**, 42, 156.
- [5] C. Nozaki, C. G. Lugmair, A. T. Bell, T. Don Tilley, *J. Am. Chem. Soc.* **2002**, 124, 13194.
- [6] H. Srikanth, R. Hajndl, B. Moulton, M. J. Zaworotko, *J. Appl. Phys.* **2003**, 93, 7089.
- [7] A. Dmitriev, H. Spillmann, N. Lin, J. V. Barth, K. Kern, *Angew. Chem.* **2003**, 115, 2774; *Angew. Chem. Int. Ed.* **2003**, 42, 2670; S. Stepanow, M. Lingenfelder, A. Dmitriev, H. Spillmann, E. Delvigne, N. Lin, X. Deng, C. Cai, J. V. Barth, K. Kern, *Nat. Mater.* **2004**, 3, 229.
- [8] D. G. Kurth, N. Severin, J. P. Rabe, *Angew. Chem.* **2002**, 114, 3833; *Angew. Chem. Int. Ed.* **2002**, 41, 3681.
- [9] N. Lin, A. Dmitriev, J. Weckesser, J. V. Barth, K. Kern, *Angew. Chem.* **2002**, 114, 4973; *Angew. Chem. Int. Ed.* **2002**, 41, 4779.
- [10] P. Messina, A. Dmitriev, N. Lin, H. Spillmann, M. Abel, J. V. Barth, K. Kern, *J. Am. Chem. Soc.* **2002**, 124, 14000.
- [11] S. De Feyter, M. M. S. Abdel-Mottaleb, N. Schuurmans, B. J. V. Verkuijl, J. H. van Esch, B. L. Feringa, F. C. De Schryver, *Chem. Eur. J.* **2004**, 10, 1124.
- [12] M. Ruben, *Angew. Chem.* **2005**, 117, 1620; *Angew. Chem. Int. Ed.* **2005**, 44, 1594.
- [13] J.-M. Lehn, *Supramolecular Chemistry*, VCH, Weinheim, **1995**, chap. 9, p. 200.
- [14] M. Ruben, J. Rojo, F. J. Romero-Salguero, L. H. Uppadine, J.-M. Lehn, *Angew. Chem.* **2004**, 116, 3728; *Angew. Chem. Int. Ed.* **2004**, 43, 3644.
- [15] H. Röder, E. Hahn, H. Brune, J.-P. Bucher, K. Kern, *Nature* **1993**, 366, 141.
- [16] S. Lukas, G. Witte, C. Wöll, *Phys. Rev. Lett.* **2002**, 88, 028301.
- [17] A. Kühnle, L. M. Molina, T. R. Linderth, B. Hammer, F. Besenbacher, *Phys. Rev. Lett.* **2004**, 93, 086101.
- [18] P. Gambardella, M. Blanc, H. Brune, K. Kuhnke, K. Kern, *Phys. Rev. B* **2000**, 61, 2254.
- [19] P. W. Murray, I. M. Brookes, S. A. Haycock, G. Thornton, *Phys. Rev. Lett.* **1998**, 80, 988.
- [20] S. Griessl, M. Lackinger, M. Edelwirth, M. Hietschold, W. M. Heickl, *Single Mol.* **2002**, 3, 25.
- [21] Y. Ishikawa, A. Ohira, M. Sakata, C. Hirayama, M. Kunitake, *Chem. Commun.* **2002**, 22, 2652.
- [22] G.-J. Su, H.-M. Zhang, L.-J. Wan, C.-L. Bai, T. Wandlowski, *J. Phys. Chem. B* **2004**, 108, 1931.
- [23] C. C. Perry, S. Haq, B. G. Frederick, N. V. Richardson, *Surf. Sci.* **1998**, 409, 512.
- [24] N. Lin, D. Payer, A. Dmitriev, T. Strunskus, C. Wöll, J. V. Barth, K. Kern, *Angew. Chem.* **2005**, 117, 1512; *Angew. Chem. Int. Ed.* **2005**, 44, 1488.
- [25] S. Stepanow, T. Strunskus, M. Lingenfelder, A. Dmitriev, H. Spillmann, N. Lin, J. V. Barth, C. Wöll, K. Kern, *J. Phys. Chem. B* **2004**, 108, 19392.
- [26] D. S. Martin, R. J. Cole, S. Haq, *Phys. Rev. B* **2002**, 66, 155427.
- [27] A. Doyle, J. Felcman, M. T. do Prado Gambardella, C. N. Verani, M. L. Bragança Tristão, *Polyhedron* **2000**, 19, 2621.
- [28] P. Gambardella, A. Dallmeyer, K. Maiti, M. C. Malagoli, W. Eberhardt, K. Kern, C. Carbone, *Nature* **2002**, 416, 301.
- [29] P. Gambardella, S. Rusponi, M. Veronese, S. S. Dhessi, C. Grazioli, A. Dallmeyer, I. Cabria, R. Zeller, P. H. Dederichs, K. Kern, C. Carbone, H. Brune, *Science* **2003**, 300, 1130.
- [30] J. P. Perdew, K. Burke, M. Ernzerhof, *Phys. Rev. Lett.* **1996**, 77, 3865.
- [31] D. Vanderbilt, *Phys. Rev. B* **1990**, 41, 7892.
- [32] S. Baroni, A. Dal Corso, S. de Gironcoli, P. Giannozzi, <http://www.pwscf.org>.
- [33] J. Tersoff, D. R. Hamann, *Phys. Rev. Lett.* **1983**, 50, 1998.

DOI: 10.1002/anie.200501937

Divergent Mechanisms for the Skeletal Rearrangement and [2+2] Cycloaddition of Enynes Catalyzed by Gold**

Cristina Nieto-Oberhuber, Salomé López,
M. Paz Muñoz, Diego J. Cárdenas, Elena Buñuel,
Cristina Nevado, and Antonio M. Echavarren*

Transition-metal-catalyzed reactions of 1,6-enynes proceed via two general pathways (Scheme 1).^[1,2] If the metal coordinates selectively to the alkyne **1**, cyclopropyl-metal

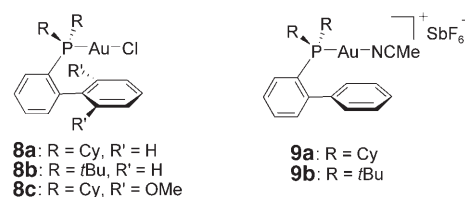


Scheme 1.

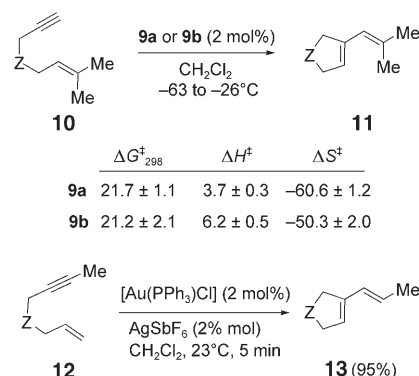
carbenes **2** are initially formed, which can react with alcohols or water to give products of alkoxy- or hydroxycyclization,^[1,2] whereas in the absence of nucleophiles, skeletal rearrangement forms dienes **3** (*single cleavage*) and/or **4** (*double cleavage*).^[1,3] Alternatively, coordination of MX_n to the alkyne and the alkene (as in **5**) is followed by oxidative cyclometalation to form **6**, which usually evolves by β -hydrogen elimination to give Alder-ene-type products.^[2] Formation of products **3** could also occur by conrotatory ring-opening of cyclobutenes **7**,^[4,5] which are formed either from **2** or by reductive elimination of **6**.

A pathway for the formation of **3** via ring-opening of **7** is favored by most authors.^[4,6] However, the formation of dienes **4** requires a different mechanistic rationalization. An earlier mechanistic proposal by Oi et al.^[3] suggested a direct pathway for the skeletal rearrangement via intermediates of type **2**. Herein we report experimental and theoretical results that shed new light into this complex mechanistic issue. In particular, this work strongly suggests that cyclobutenes **7** are not necessary intermediates in the skeletal rearrangement of enynes.

Alder-ene-type products have not been observed in Au^I -catalyzed reactions, which is consistent with the selective coordination of cationic $[Au(L)]^+$ complexes to the alkyne.^[2c,7,8] In the presence of catalysts formed from **8a-c** and $AgSbF_6$,^[7b] or new cationic complexes **9a,b**, enyne **10**



undergoes a *single cleavage rearrangement* to form **11** quantitatively at a temperature as low as -63°C (Scheme 2). On the other hand, enyne **12** undergoes a



Scheme 2. Z = $C(CO_2Me)_2$. ΔG^\ddagger_{298} and ΔH^\ddagger in kcal mol^{-1} ; ΔS^\ddagger in $\text{cal K}^{-1} \text{mol}^{-1}$.

double cleavage rearrangement with $[Au(PPh_3)]SbF_6$ to give exclusively **13**.^[3,9] These are the skeletal rearrangements occurring at the lowest temperatures. Reaction of enyne **10** with catalyst **9a** (-63 to -26°C) or **9b** (-43 to -28°C) was monitored by ^1H NMR spectroscopy in CD_2Cl_2 . Under these conditions, smooth and quantitative formation of diene **11** was observed without the build up of any intermediate. The rearrangement is pseudo-first order in **10**, which allowed us to determine the thermodynamic parameters shown in Scheme 2.

The large and negative activation entropies suggest that an associative ligand substitution^[10] (diene **11** by incoming enyne **10**) is the rate-determining step of the process. These results establish a very low activation energy (E_a) for the

[*] C. Nieto-Oberhuber, Dr. S. López, Prof. Dr. A. M. Echavarren
Institute of Chemical Research of Catalonia (ICIQ)
Av. Països Catalans, 16,
43007 Tarragona (Spain)
Fax: (+34) 977-920-225
E-mail: aecharren@iciq.es

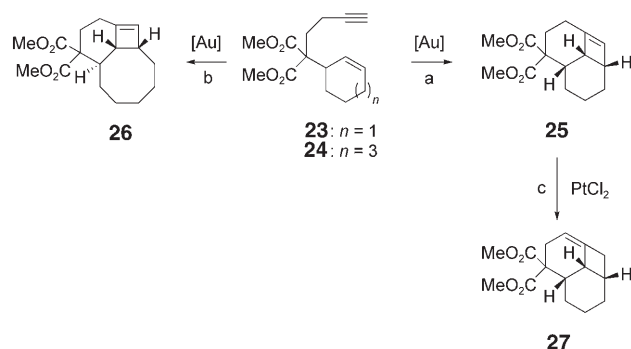
C. Nieto-Oberhuber, M. P. Muñoz, Dr. D. J. Cárdenas, Dr. E. Buñuel,
C. Nevado, Prof. Dr. A. M. Echavarren
Departamento de Química Orgánica
Universidad Autónoma de Madrid
Cantoblanco, 28049 Madrid (Spain)

[**] This work was supported by the MEC (project CTQ2004-02869, predoctoral fellowships to C.N.-O. and M.P.M., and a Torres Quevedo contract to S.L.), the CAM (predoctoral fellowship to C.N.), and the ICIQ Foundation. We also thank the Centro de Computación Científica (UAM), and Johnson Matthey PLC.

Supporting information for this article is available on the WWW under <http://www.angewandte.org> or from the author.

react with complexes $[\text{Au}(\text{L})]^+$ at room temperature to give **25** and **26**,^[4b,d] respectively (Scheme 5).

Tricycles **25** and **26** do not undergo ring-opening at 120–150 °C to form 1,3-dienes.^[15] To study the possible effect of transition metals in the ring-opening of the cyclobutene,^[16] **25**



Scheme 5. Reactions of **23** and **24**: a) **9b** (2 mol %), CH_2Cl_2 , room temp., 14 h (80%); b) **8c** (2 mol %), AgSbF_6 (2 mol %), CH_2Cl_2 , room temp., 45 min (67%); c) PtCl_2 (5 mol %), MeCN, 120 °C, 20 h (67%).

was heated in MeCN at 120 °C in the presence of 5 mol % PtCl_2 (Scheme 5). Interestingly, under these conditions, Pt^{II} ,^[1,3,4d,f,g] which is a known catalyst for the skeletal rearrangement, does not promote the ring-opening of the cyclobutene but rather promotes isomerization to form the less-strained tricycle **27**.^[17]

In summary, calculations on the Au^{I} -catalyzed skeletal rearrangement of enynes support the earlier proposals suggested by Oi et al.^[3] and others,^[1,4] although Scheme 3 provides a more rigorous and concise mechanistic picture. An alternative pathway has been found for the formation of cyclobutenes via *syn*-cyclopropyl–metal carbenes, formed by a *syn* electrophilic addition of the metal and the alkene to the alkyne. Kinetic experiments indicate that if a conrotatory ring-opening of a cyclobutene intervenes in the skeletal rearrangement, its E_a value would be unreasonably low.

Received: June 3, 2005

Published online: September 7, 2005

Keywords: alkynes · cyclization · density functional calculations · gold · rearrangement

3647–3650; c) B. M. Trost, M. Yanai, K. Hoogsteed, *J. Am. Chem. Soc.* **1993**, *115*, 5294–5295; d) A. Fürstner, F. Stelzer, H. Szillat, *J. Am. Chem. Soc.* **2001**, *123*, 11863–11869; e) N. Chatani, H. Inoue, T. Kotsuna, S. Murai, *J. Am. Chem. Soc.* **2002**, *124*, 10294–10295; f) F. Marion, J. Coulomb, C. Courillon, L. Fensterbank, M. Malacria, *Org. Lett.* **2004**, *6*, 1509–1511; g) G. B. Bajracharya, I. Nakamura, Y. Yamamoto, *J. Org. Chem.* **2005**, *70*, 892–897.

- [5] For formation of a different type of cyclobutene, see: a) A. Fürstner, P. W. Davies, T. Gress, *J. Am. Chem. Soc.* **2005**, *127*, 8244–8245; b) see also ref. [7b].
- [6] E. Soriano, P. Ballesteros, J. Marco-Contelles, *Organometallics* **2005**, *24*, 3172–3181.
- [7] a) C. Nieto-Oberhuber, M. P. Muñoz, E. Buñuel, C. Nevado, D. J. Cárdenas, A. M. Echavarren, *Angew. Chem. Int. Ed.* **2004**, *43*, 2402–2406; b) C. Nieto-Oberhuber, S. López, A. M. Echavarren, *J. Am. Chem. Soc.* **2005**, *127*, 6178–6179.
- [8] a) V. Mamane, T. Gress, H. Krause, A. Fürstner, *J. Am. Chem. Soc.* **2004**, *126*, 8654–8655; b) L. Zhang, S. A. Kozmin, *J. Am. Chem. Soc.* **2004**, *126*, 11806–11807; c) M. R. Luzung, J. P. Markham, F. D. Toste, *J. Am. Chem. Soc.* **2004**, *126*, 10858–10859.
- [9] a) N. Chatani, H. Inoue, T. Morimoto, T. Muto, S. Murai, *J. Org. Chem.* **2001**, *66*, 4433–4436; b) C. H. Oh, S. Y. Bang, C. Y. Rhim, *Bull. Korean Chem. Soc.* **2003**, *24*, 887–888.
- [10] P. N. Dickson, A. Wehrli, G. Geier, *Inorg. Chem.* **1988**, *27*, 2921–2925.
- [11] P. S. Lee, S. Sakai, P. Hörstermann, W. R. Roth, E. A. Kallel, K. N. Houk, *J. Am. Chem. Soc.* **2003**, *125*, 5839–5848.
- [12] W. F. Maier, P. von R. Schleyer, *J. Am. Chem. Soc.* **1981**, *103*, 1891–1900.
- [13] G. Oba, G. Moreira, G. Manuel, M. Koenig, *J. Organomet. Chem.* **2002**, *643–644*, 324–330.
- [14] Calculations at the B3LYP/6-31G(d) (C,H,P), LANL2DZ (Au) level.
- [15] The thermal ring-opening of a cyclobutene formed in a reaction of an enyne catalyzed by PtBr_2 has been shown to take place at 120 °C in acetonitrile: G. B. Bajracharya, I. Nakamura, Y. Yamamoto, *J. Org. Chem.* **2005**, *70*, 892–897.
- [16] D. J. Tantillo, R. Hoffmann, *J. Am. Chem. Soc.* **2001**, *123*, 9855–9859.
- [17] Tricycle **27** is 7.9 kcal mol^{−1} more stable than **25** (PM3 calculation).

[1] Reviews: a) G. C. Lloyd-Jones, *Org. Biomol. Chem.* **2003**, *1*, 215–236; b) C. Aubert, O. Buisine, M. Malacria, *Chem. Rev.* **2002**, *102*, 813–834; c) S. T. Diver, A. J. Giessert, *Chem. Rev.* **2004**, *104*, 1317–1382; d) A. M. Echavarren, C. Nevado, *Chem. Soc. Rev.* **2004**, *33*, 431–436.

[2] a) M. Méndez, M. P. Muñoz, C. Nevado, D. J. Cárdenas, A. M. Echavarren, *J. Am. Chem. Soc.* **2001**, *123*, 10511–10520; b) C. Nevado, D. J. Cárdenas, A. M. Echavarren, *Chem. Eur. J.* **2003**, *9*, 2627–2635; c) M. P. Muñoz, J. Adrio, J. C. Carretero, A. M. Echavarren, *Organometallics* **2005**, *24*, 1293–1300.

[3] S. Oi, I. Tsukamoto, S. Miyano, Y. Inoue, *Organometallics* **2001**, *20*, 3704–3709.

[4] a) B. M. Trost, G. J. Tanoury, *J. Am. Chem. Soc.* **1988**, *110*, 1636–1638; b) B. M. Trost, M. K. Trost, *Tetrahedron Lett.* **1991**, *32*,

Real-Time Observation of Ionization-Induced Hydrophobic→Hydrophilic Switching**

Shun-ichi Ishiuchi, Makoto Sakai, Yuji Tsuchida, Akihiro Takeda, Yasutake Kawashima, Masaaki Fujii,* Otto Dopfer,* and Klaus Müller-Dethlefs*

Noncovalent interactions are responsible for fundamental properties of complex molecular systems that occur in our macroscopic world.^[1] In particular, the structure, dynamics, and function of supramolecular systems such as DNA are entirely governed by noncovalent interactions.^[2,3] Most of our understanding of noncovalent forces has come from quantum chemical calculations.^[1,2] For example, a sophisticated *ab initio* treatment of intermolecular interactions in DNA base pairs has elucidated the competition between specific hydrogen-bonding and aromatic π -stacking interactions.^[2] For the total stabilization energy of DNA, the stacking contribution was estimated to be about two-thirds of that of the hydrogen-bond contributions, substantially higher than it was previously thought.^[2] This competition between hydrogen bonding and π stacking^[4] can also be viewed as competition between hydrophilic and hydrophobic binding sites. Experimental work in the area of intermolecular forces is challenging and employs specific model systems to provide the detailed answers required to understand complex noncovalent interactions at the molecular level. Molecular clusters are one such model system,^[5] and their spectroscopic characterization in molecular beams provides currently the most direct and most

detailed experimental access to the intermolecular interaction potential^[1,6] and excited-state dynamics.^[7] In particular, clusters of acidic aromatic molecules with rare-gas atoms, such as phenol...Ar, constitute the simplest model systems to study the competition between hydrophobic and hydrophilic binding motifs, as they exhibit both dispersion interactions (binding to the π ring) and hydrogen bonding to the acidic functional group, which are essential forces for chemical and biological recognition.^[2,3] As an example of such a chemical recognition process at the molecular level, we report here the first direct observation of a hydrophobic→hydrophilic site-switching process induced by ionization. This switching is initiated in the phenol...Ar₂ trimer by resonant photoionization. When the cation is prepared by photoionization, it is produced in the π -bound geometry of the neutral precursor, with argon binding to the hydrophobic ring site. On the timescale of a few picoseconds, one of the Ar atoms switches from the hydrophobic ring site to the hydrophilic OH site and creates a hydrogen bond. The dynamics of this isomerization process is monitored in real time by a change in the OH stretch vibrational wavenumber using time-resolved picosecond UV/IR pump-probe ionization depletion spectroscopy.

The competition between π bonding and hydrogen bonding in the phenol...Ar dimer cluster has been studied in the neutral ground electronic state (S_0), the electronically excited state (S_1), and the cation ground state (D_0).^[4,8] In the neutral S_0 state, only the π -bound isomer is observed because dispersion forces between Ar and the aromatic π -electron system dominate the attraction. In contrast, in the ionic D_0 state the hydrogen-bound isomer is more stable, as the additional induction forces between Ar and the acidic OH group that arise from the excess charge override dispersion. Hence, Ar binds preferentially to the hydrophobic site in the neutral cluster and to the hydrophilic site in the cationic cluster. Figure 1 shows the two binding sites for the argon atom and the relevant potential energy diagrams along with the available energetic data.^[4,8]

How does the system switch between the hydrophobic and hydrophilic sites? When the cation is prepared by photoionization, it is produced in the geometry of the neutral precursor (Franck–Condon principle), that is, argon binds to the hydrophobic site. Energetically, this π -bound cation is a metastable local minimum and could, in principle, switch by itself to the hydrogen-bound global minimum. However, the substantial energetic barrier between both minima^[4] prevents this isomerization for the phenol...Ar dimer. In contrast, in the phenol...Ar₂ trimer the energetics change in a subtle way that enables us to present the first direct evidence for ionization-induced hydrophobic→hydrophilic site switching. The spectroscopic method employed is a sophisticated extension of the IR hole-burning technique^[9] using three tuneable picosecond lasers. The excitation/ionization/depletion scheme is shown in Figure 2. Two UV lasers provide resonant ionization of phenol...Ar₂ via the S_1 state.^[8] The first UV photon (UV1) excites the phenol...Ar₂ complex from the neutral S_0 state to its excited S_1 state. The second UV photon (UV2) ionizes phenol...Ar₂ from the excited S_1 state, thus producing the phenol...Ar₂ cation in its electronic ground

[*] Dr. S. Ishiuchi, Dr. M. Sakai, Y. Tsuchida, A. Takeda, Y. Kawashima, Prof. M. Fujii
Chemical Resources Laboratory, Tokyo Institute of Technology
4259 Nagatsuta-cho, Midori-ku, Yokohama 226-8503 (Japan)
Fax: (+81) 45-924-5250
E-mail: mfujii@res.titech.ac.jp
Priv.-Doz. Dr. O. Dopfer
Heisenberg Stipendiat der DFG, Institut für Physikalische Chemie
Universität Würzburg
Am Hubland, 97074 Würzburg (Germany)
Fax: (+49) 931-888-6378
E-mail: dopfer@phys-chemie.uni-wuerzburg.de
Prof. Dr. K. Müller-Dethlefs
The Photon Science Institute, Simon Building
The University of Manchester, Manchester, M13 9PL (UK)
Fax: (+44) 161-275-1001
E-mail: k.muller-dethlefs@manchester.ac.uk

[**] O.D. and M.F. thank the Japan Society for Promotion of Science for support of the international collaboration. K.M.-D. gratefully acknowledges support from the Royal Society for a joint UK–Japan research project. This work is supported in part by a Grant-in-Aid for Scientific Research (KAKENHI) in the priority area “Molecular Nano Dynamics” from the Ministry of Education, Culture, Sports, Science and Technology, Japan.



Supporting information for this article is available on the WWW under <http://www.angewandte.org> or from the author.

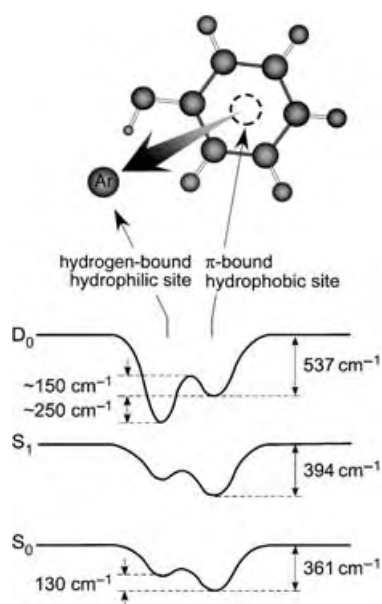


Figure 1. Hydrophobic ring site (π bonding) and hydrophilic OH site (hydrogen bonding) in the phenol...Ar cluster, along with potential diagrams^[4,8] for the neutral S_0 ground state, the S_1 excited state, and the D_0 cation ground state.

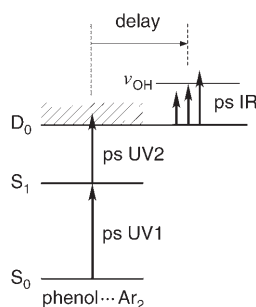


Figure 2. Excitation scheme for time-resolved picosecond UV-UV-(pump)-IR(probe) ionization depletion spectroscopy of phenol...Ar₂.

state, D_0 . Two different colors for the UV photons are required to prevent the dissociation of the cluster cation upon ionization. The energy of the second photon results in an excess energy of less than 300 cm^{-1} , which is sufficiently small to prevent direct dissociation of the doubly π -bonded phenol...Ar₂ trimer cation. After an adjustable delay, the IR laser is fired to probe if one of the Ar atoms of the cation produced by the two UV lasers has moved from the ring to the OH group. To this end, the IR laser is tuned from 3400 to 3600 cm^{-1} through the range of the OH stretch wavenumber, $\tilde{\nu}_{\text{OH}}$, to distinguish between the free OH ($\tilde{\nu}_{\text{OH}} = 3537\text{ cm}^{-1}$) and the hydrogen-bonded OH...Ar vibration ($\tilde{\nu}_{\text{OH}} = 3467\text{ cm}^{-1}$).^[4] The ν_{OH} wavenumber is substantially reduced by hydrogen bonding of argon to the OH group, whereas π -bound ligands have virtually no effect.^[4] When the IR laser is resonant to the OH stretch vibration, the trimer is vibrationally excited and subsequently dissociated. Thus, the wavenumber of the OH stretch vibration, that is, the spectroscopic signature of the binding site of the Ar atom, is detected in the experiment by the depletion of the signal of the parent ion.

Figure 3 shows the results of the UV-UV(pump)-IR-(probe) experiment for pump-probe delay times between 1 and 50 ps. Because ionization occurs in the geometry of the neutral cluster, in which the OH bond is free (both Ar atoms are π -bound), the cation is initially produced in the same

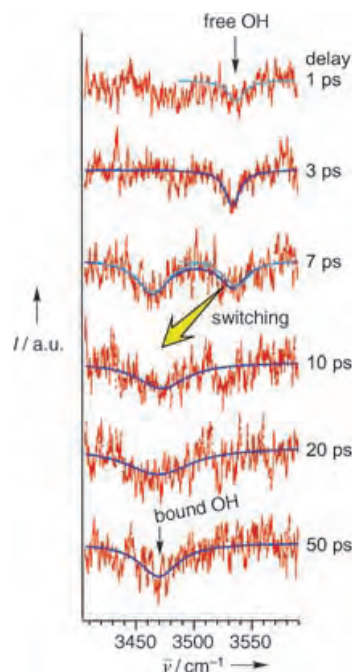


Figure 3. Time-resolved IR spectra of phenol...Ar₂ at various pump-probe delay times as indicated beside each spectrum. The vertical axis shows the signal for the phenol...Ar₂ ion, while the horizontal axis presents the wavenumber of the IR laser. When the IR laser is resonant to the OH stretch vibration, the ion signal is depleted because of vibrational predissociation of the parent cluster. Least-squares fits to the experimental data are included to guide the eyes.

geometry (Franck–Condon principle). This “free OH” structure is indeed detected immediately after ionization for IR probe delay times of up to 3 ps, for which only the free OH band is observed at $\tilde{\nu} = 3537\text{ cm}^{-1}$. With increasing probe delay, from around 7 ps onwards, an additional peak is observed at $\tilde{\nu} = 3467\text{ cm}^{-1}$. This peak corresponds to hydrogen-bonded OH...Ar and it grows with delay time, whereas the free OH band disappears. For delay times of 10, 20, and 50 ps, only the “bound OH” structure is seen. This result can only be explained by switching of one Ar atom from the π -bonding hydrophobic to the hydrogen-bonding hydrophilic site, which has been initiated by the ionization and is completed after around 10 ps. Such a timescale for the π -to-hydrogen-bonding isomerization is consistent with a (nearly) barrierless intermolecular isomerization process.

This first observation in real time of the dynamics of a molecular hydrophobic→hydrophilic switch represents a fundamental example of molecular recognition dynamics. The direct observation of this intermolecular reorganization process has been possible because the change in the charge state of the aromatic molecule phenol from 0 to +1 induces the switch in the preferred aromatic solvent recognition motif

from π bonding to hydrogen bonding.^[10] Thus, these experiments represent a milestone in the characterization of dynamical processes of noncovalent interactions and solute–solvent binding-site specificity. The experimental approach will be used to investigate the dynamics of other molecular recognition mechanisms, such as the ionization-triggered π -to-hydrogen-bonding switch in the fundamental benzene–water interaction.^[10,11]

Experimental Section

Phenol \cdots Ar₂ complexes were produced in a supersonic molecular beam expansion of phenol seeded in Ar carrier gas. The UV1 and UV2 lasers were tuned to 36280 and 32260 cm⁻¹ to prepare phenol \cdots Ar₂ cations through resonant ionization via the S₁ origin with an excess energy of ca. 300 cm⁻¹ above the ionization threshold. After an adjustable delay time, the phenol \cdots Ar₂ cations interacted with a tuneable IR laser. Resonant vibrational excitation induces cleavage of one of the intermolecular bonds, leading to a depletion of the phenol \cdots Ar₂ ion current. Ions were extracted in a time-of-flight (TOF) mass spectrometer and monitored as a function of the IR laser wavenumber to obtain the IR depletion spectrum. Further details of the experimental setup and the three-color picosecond laser system are provided in the Supporting Information.

Received: April 26, 2005

Published online: August 30, 2005

Keywords: hydrogen bonds · isomerization · noncovalent interactions · pi interactions · time-resolved spectroscopy

- [1] K. Müller-Dethlefs, P. Hobza, *Chem. Rev.* **2000**, *100*, 143–167.
- [2] P. Jurecka, P. Hobza, *J. Am. Chem. Soc.* **2003**, *125*, 15 608–15 613.
- [3] E. A. Meyer, R. K. Castellano, F. Diederich, *Angew. Chem.* **2003**, *115*, 1244–1287; *Angew. Chem. Int. Ed.* **2003**, *42*, 1210–1250; Erratum: E. A. Meyer, R. K. Castellano, F. Diederich, *Angew. Chem.* **2003**, *115*, 4254; *Angew. Chem. Int. Ed.* **2003**, *42*, 4120.
- [4] a) N. Solcá, O. Dopfer, *J. Phys. Chem. A* **2001**, *105*, 5637–5645; b) N. Solcá, O. Dopfer, *J. Mol. Struct.* **2001**, *563–564*, 241–244.
- [5] B. Brutschy, P. Hobza, Guest Editors, Special Issue No. 11 “van der Waals III”: *Chem. Rev.* **2000**, *100*, 3861–4264.
- [6] M. Mons, I. Dimicoli, F. Piuze, *Int. Rev. Phys. Chem.* **2002**, *21*, 101–135.
- [7] A. Stolow, A. E. Bragg, D. M. Neumark, *Chem. Rev.* **2004**, *104*, 1719–1757.
- [8] a) S. R. Haines, C. E. H. Dessent, K. Müller-Dethlefs, *J. Electron Spectrosc. Relat. Phenom.* **2000**, *108*, 1–11; b) C. E. H. Dessent, S. R. Haines, K. Müller-Dethlefs, *Chem. Phys. Lett.* **1999**, *315*, 103–108.
- [9] S. Ishiuchi, M. Sakai, K. Daigoku, T. Ueda, T. Yamanaka, K. Hashimoto, M. Fujii, *Chem. Phys. Lett.* **2001**, *347*, 87–92.
- [10] O. Dopfer, *Z. Phys. Chem.* **2005**, *219* 125–168.
- [11] a) S. Suzuki, P. G. Green, R. E. Bumgarner, S. Dasgupta, W. A. Goddard III, G. A. Blake, *Science* **1992**, *257*, 942–945; b) R. N. Pribble, T. Zwieter, *Science* **1994**, *265*, 75–79; c) H. Tachikawa, M. Igarashi, *J. Phys. Chem. A* **1998**, *102*, 8648–8656; d) M. Miyazaki, A. Fujii, T. Ebata, N. Mikami, *Chem. Phys. Lett.* **2001**, *349*, 431–436; e) M. Miyazaki, A. Fujii, T. Ebata, N. Mikami, *Phys. Chem. Chem. Phys.* **2003**, *5*, 1137–1148; f) N. Solcá, O. Dopfer, *Chem. Phys. Lett.* **2001**, *347*, 59–64; g) N. Solcá, O. Dopfer, *J. Phys. Chem. A* **2001**, *105*, 5637–5645.

DOI: 10.1002/anie.200501884

SOLARIA: A Protocol for Automated Cross-Peak Assignment and Structure Calculation for Solid-State Magic-Angle Spinning NMR Spectroscopy

Michele Fossi, Federica Castellani, Michael Nilges, Hartmut Oschkinat,* and Barth-Jan van Rossum*

Recently, it has been shown that structures of proteins can be determined by magic-angle-spinning (MAS) solid-state NMR spectroscopy.^[1,2] Central to most structure-determination procedures is the collection of a set of distance restraints that is sufficiently large to achieve convergence in the calculations. In our previous solid-state NMR spectroscopic structure investigation on a microcrystalline preparation of the α -spectrin SH3 domain these distance restraints were obtained by manual assignment of cross-peaks from 2D and 3D proton-driven spin diffusion (PDSF) correlation experiments.^[1,3] Extensively ^{13}C -labeled preparations obtained by protein expression on a medium containing either [1,3- ^{13}C]glycerol or [2- ^{13}C]glycerol as the carbon source were used for all the experiments. In such preparations, only a few amino acid types have ^{13}C labels in adjacent positions, which led to a substantial suppression of dipolar attenuation effects^[4,5] and enabled a straightforward detection of long-range ^{13}C - ^{13}C correlations (Figure 1). The spectra used in these studies displayed a high level of resonance overlap, which resulted in many assignment options per signal and led to the exclusion of a large fraction of ambiguous cross-peaks that could not be assigned manually. Automation of the cross-peak assignment would be beneficial to avoid this problem and to speed-up the structure-determination process.

In liquid-state NMR spectroscopy, software packages such as ARIA,^[6–10] CANDID,^[11] DYANA,^[12] KNOWNOE,^[13] NOAH,^[14,15] and AUTOSTRUCTURE^[16,17] have provided a way to handle ambiguous cross-peaks to derive distance restraints in an automated fashion. In ARIA, ambiguous NOE interactions are handled by treating them as “ambiguous distance restraints” (ADR).^[18,19] The calculated structures are then refined in an iterative manner, each time using the structures of the latest round of calculations to find new assignments as the input for the next round.

We developed SOLARIA,^[†] a MAS NMR-dedicated version of ARIA for solid-state NMR spectroscopic studies.

[*] M. Fossi, Dr. F. Castellani, Prof. Dr. H. Oschkinat, Dr. B.-J. van Rossum
Forschungsinstitut für Molekulare Pharmakologie (FMP)
Robert-Rössle-Strasse 10, Berlin (Germany)
Fax: (+49) 3094793169
E-mail: Oschkinat@fmp-berlin.de
brossum@fmp-berlin.de

Prof. Dr. M. Nilges
Institut Pasteur, 25–28 Rue du Docteur Roux
75015 Paris (France)

[†] Available from www.fmp-berlin.de.

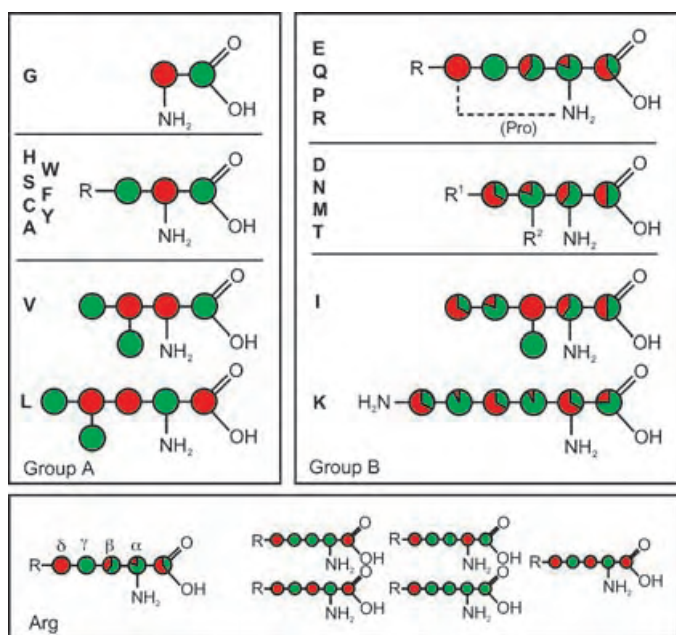


Figure 1. Labeling patterns for the different amino acids in the α -spectrin SH3 domain preparations used in these studies. Schematic representation of the effective ^{13}C enrichment for the different residues, as obtained by protein expression in *E. coli* BL21 (DE3). The green color corresponds to the degree of ^{13}C labeling obtained by growth of the bacteria on [1,3- ^{13}C]glycerol; the opposite labeling pattern, obtained by growth on [2- ^{13}C]glycerol, is represented in red. There are two groups of amino acids (A and B). In group A, the various carbon sites are either approximately 100% or 0% labeled, in group B the residues show fractional labeling. This fractional labeling is the result of the production of isotopomers of residues with different labeling patterns, as illustrated for arginine at the bottom. These percentages were estimated from extensive solution NMR studies using 2D and 3D heteronuclear NMR techniques.

The two programs share the same overall architecture consisting of nine iterations of cross-peak assignment and structure calculations. However, there are also significant differences. First, SOLARIA can handle peak lists containing not only ^1H - ^1H , but also typical solid-state ^{13}C - ^{13}C , ^{15}N - ^{15}N , and ^{13}C - ^{15}N correlations. Second, in contrast to solution NMR spectroscopy, it is very difficult to find a satisfying relationship between experimental volumes and distances in solid-state NMR spectroscopy. Peak volumes do not depend exclusively on the distance; they are strongly affected by mobility, which interferes with dipolar couplings. This situation can significantly alter the dipolar polarization transfer efficiency and often makes it difficult to achieve a uniform excitation of all the relevant spins. The proton environment may also influence the efficiency of mixing. Further complications may arise through offset-dependent transfer processes, interference with heteronuclear decoupling schemes, and sample heterogeneity. Finally, even with the reduced label-

ing, dipolar attenuation effects are not fully suppressed and the transfer efficiency between two spins can still be largely affected by coupling to other nearby spin systems. For these reasons, the program does not use volumes to set the boundaries for distance restraints, as done in ARIA. Therefore, all distance constraints are represented by the same lower boundary and the same generous upper boundary, and input peak lists do not require the presence of cross-peak volumes or intensities. Third, the labeling pattern in samples made by using 2- or 1,3-labeled glycerol is exploited by SOLARIA for better convergence of the automated assignment process. This is achieved by removal of all assignment options which are not allowed according to the labeling pattern. In principle, other labeling patterns can be easily implemented, for example, for proteins obtained from growth media containing selectively ^{13}C -labeled succinic acid as a precursor.^[20]

We tested SOLARIA on lists with the coordinates of manually picked peaks from PDS-type spectra of the α -spectrin SH3 domain. Intermolecular cross-peaks were identified previously on an experimental basis^[1] and removed from the lists. To face the computational difficulties inherent to the use of highly ambiguous solid-state peak lists (the average number of assignment candidates per signal was approximately 6 for the two 3D spectra, and 16 and 19 for the 2-CC and 1,3-CC 2D spectra, respectively) and very loose boundaries (all constraints are restrained between 2.5 and 6.5 Å, independent of the peak volume), we decided to enhance the convergence capability of the software by substantially increasing the number of cooling steps.^[21] We raised the number from 9000, which is the commonly used value, to 100000. Under these conditions and using standard ARIA1.2 input values for all other parameters SOLARIA produced convergent results. The 11 lowest-energy structures (blue) overlaid with the X-ray structure (red) as reference are shown in Figure 2. Despite the use of extremely generous boundaries for the distance restraints, well-defined (0.73-Å ensemble backbone rmsd) and accurate (1.3-Å backbone rmsd to the X-ray reference) structures could be obtained.

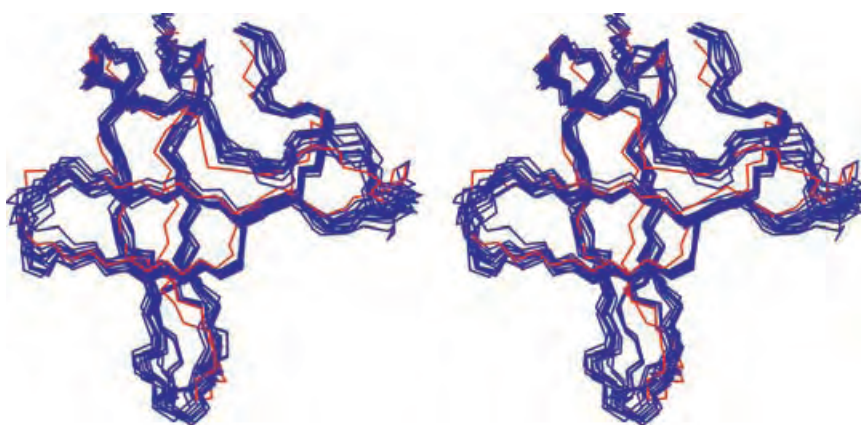


Figure 2. Stereoview of the 11 lowest-energy solid-state NMR structures of the α -spectrin SH3 domain calculated by SOLARIA (blue). For comparison, the X-ray reference structure is included (PDB entry: 1SHG; red) and overlaid with the family of solid-state structures by fitting the backbone atoms to the average solid-state structure. The calculations were performed on peak lists where intermolecular cross-peaks were manually removed.

These structures were calculated in approximately 12 h, which is in striking contrast to the several months required in our previous work for the manual assignment of the same spectra.^[1] More importantly, SOLARIA allowed the assignment of approximately 20% more cross-peaks than in the previous manual assignment procedure (Figure 3). All

represents an important step forward for the rapidly developing MAS NMR technique.

Experimental Section

Sample preparation and solid-state MAS NMR spectroscopy: The main characteristics of the SH3 domain and the spectra used in this work are summarized in Table 1. The sample preparation is described

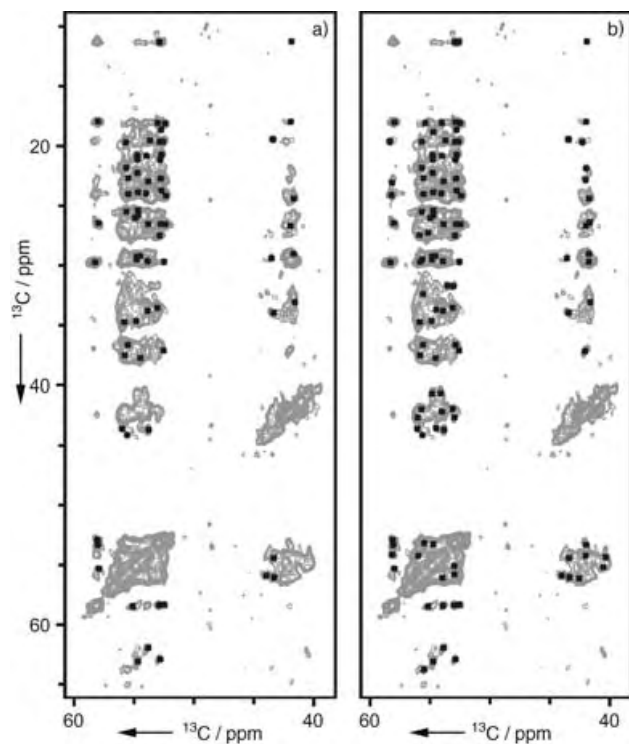


Figure 3. Visualization of the assignments. A strip of a two-dimensional PDSD spectrum recorded using [1,3-¹³C]glycerol-grown α -spectrin SH3 domain sample is shown.^[1] In (a), the cross-peaks that could be assigned manually using 2D and 3D data are indicated. In (b), cross-peaks assigned and used for the structure calculations by SOLARIA using the same dataset are indicated.

manual assignments obtained from the evaluation of 2D and 3D spectra are indicated in Figure 3a, displayed in a region of a 2D experiment, and all automatically assigned peaks are indicated in Figure 3b.

In summary, the program SOLARIA produced, in a few hours, accurate structures (1.3 Å rmsd to the X-ray reference) using unassigned peak lists from 2D and 3D MAS-NMR spectra of the α -spectrin SH3 domain, where intermolecular cross-peaks were discarded prior to the calculation. These structures exemplify a first successful attempt to introduce automation to structure determination of solid proteins by MAS NMR spectroscopy. The automation of the cross-peak assignment resulted in a dramatic speed-up of the whole procedure and, most importantly, provided a way to handle ambiguous cross-peaks in MAS NMR spectra. Hence, we expect that this work will open new possibilities for the use of MAS NMR to determine the structures of larger systems, such as membrane proteins, where the number of cross-peaks may become unmanageably large for manual assignment methods. For these reasons, we believe that SOLARIA

Table 1: Spectra used in the calculation.^[a]

Spectrum	Dimensionality	Labeling	Number of peaks
1,3-CC	2D	1,3-glycerol	566
2-CC	2D	2-glycerol	461
1,3-NCOCX	3D	1,3-glycerol	477
2-NCACX	3D	2-glycerol	377

[a] Peaks were picked manually. The numbers in parenthesis refer to the total number of peak list entries after the manual removal of intermolecular cross-peaks. No manual assignment was included in the lists.

in detail elsewhere.^[22] Peak lists for the structure calculations were generated from solid-state 2D ¹³C-¹³C and 3D ¹⁵N-¹³C-¹³C correlation spectra.^[1,3]

Structure calculations: The software SOLARIA was used to perform the automatic assignment of manually picked cross-peaks and to generate structures. The calculations were performed on a SGI Origin 2100 cluster at the FMP, Berlin. The chemical shift tolerances were set to 0.4 ppm for carbon and 0.5 ppm for nitrogen dimensions. The number of calculated structures was 20 for the first eight iterations and 100 for the final one. The results of the calculations were evaluated by computing a pairwise backbone rmsd (precision) and a backbone rmsd (accuracy) to the X-ray reference-structure^[23] (PDB entry: 1SHG) of the 15 lowest-energy structures.

Received: May 31, 2005

Keywords: computer chemistry · NMR spectroscopy · proteins · solid-state structures · structure elucidation

- [1] F. Castellani, B. van Rossum, A. Diehl, M. Schubert, K. Rehbein, H. Oschkinat, *Nature* **2002**, 420, 98–102.
- [2] A. E. McDermott, *Curr. Opin. Struct. Biol.* **2004**, 14, 554–561.
- [3] F. Castellani, B. J. van Rossum, A. Diehl, K. Rehbein, H. Oschkinat, *Biochemistry* **2003**, 42, 11476–11483.
- [4] P. Hodgkinson, L. Emsley, *J. Magn. Reson.* **1999**, 139, 46–59.
- [5] S. Kiihne, M. A. Mehta, J. A. Stringer, D. M. Gregory, J. C. Shiels, G. P. Drobny, *J. Phys. Chem. A* **1998**, 102, 2274–2282.
- [6] J. P. Linge, S. I. O'Donoghue, M. Nilges, *Nucl. Magn. Reson. Biol. Macromol. Part B* **2001**, 339, 71–90.
- [7] J. P. Linge, M. Habeck, W. Rieping, M. Nilges, *Bioinformatics* **2003**, 19, 315–316.
- [8] M. Nilges, M. J. Macias, S. I. O'Donoghue, H. Oschkinat, *J. Mol. Biol.* **1997**, 269, 408–422.
- [9] M. Nilges, S. I. O'Donoghue, *Prog. Nucl. Magn. Reson. Spectrosc.* **1998**, 32, 107–139.
- [10] A. Kharrat, M. J. Macias, T. J. Gibson, M. Nilges, A. Pastore, *EMBO J.* **1995**, 14, 3572–3584.
- [11] T. Herrmann, P. Guntert, K. Wuthrich, *J. Mol. Biol.* **2002**, 319, 209–227.
- [12] P. Guntert, C. Mumenthaler, K. Wuthrich, *J. Mol. Biol.* **1997**, 273, 283–298.

- [13] W. Gronwald, S. Moussa, R. Elsner, A. Jung, B. Ganslmeier, J. Trenner, W. Kremer, K. P. Neidig, H. R. Kalbitzer, *J. Biomol. NMR* **2002**, 23, 271–287.
- [14] C. Mumenthaler, W. Braun, *J. Mol. Biol.* **1995**, 254, 465–480.
- [15] C. Mumenthaler, P. Guntert, W. Braun, K. Wuthrich, *J. Biomol. NMR* **1997**, 10, 351–362.
- [16] H. N. Moseley, D. Monleon, G. T. Montelione, *Methods Enzymol.* **2001**, 339, 91–108.
- [17] H. N. Moseley, G. T. Montelione, *Curr. Opin. Struct. Biol.* **1999**, 9, 635–642.
- [18] M. Nilges, *J. Mol. Biol.* **1995**, 245, 645–660.
- [19] M. Nilges, *Proteins Struct. Funct. Genet.* **1993**, 17, 297–309.
- [20] A. J. van Gammeren, F. B. Hulsbergen, J. G. Hollander, H. J. de Groot, *J. Biomol. NMR* **2004**, 30, 267–274.
- [21] M. Fossi, H. Oschkinat, M. Nilges, L. J. Ball, *J. Magn. Reson.* **2005**, 175, 92–102.
- [22] J. Pauli, B. van Rossum, H. Forster, H. J. de Groot, H. Oschkinat, *J. Magn. Reson.* **2000**, 143, 411–416.
- [23] A. Musacchio, M. Noble, R. Pauptit, R. Wierenga, M. Saraste, *Nature* **1992**, 359, 851–855.

Molecular Recognition

DOI: 10.1002/anie.200501886

AFM Snapshots of Synthetic Multifunctional Pores with Polyacetylene Blockers: Pseudorotaxanes and Template Effects**

Jiro Kumaki,* Eiji Yashima, Guillaume Bollot,
Jiri Mareda, Svetlana Litvinchuk, and Stefan Matile*

Synthetic multifunctional pores are constructed from abiotic scaffolds and not only mediate molecular translocation across the membranes of lipid bilayers but also act as hosts or as catalysts.^[1,2] Synthetic multifunctional pores became accessible with the discovery of synthetic access to artificial, rigid-

rod β barrels. Their practical usefulness as detectors of chemical reactions has been demonstrated,^[1,2] and applications toward multicomponent sensing in complex matrixes are in progress.^[3] Structural studies naturally have low priority in research focusing on the creation and application of advanced function.^[4] Nevertheless, structural studies on molecular recognition by synthetic multifunctional pores under conditions relevant for function indicated that pore blockage occurs by the physical insertion of the guest into the transmembrane host.^[4] These findings implied the formation of inclusion complexes with small guests and of pseudorotaxanes^[5–11] with macromolecular guests. Herein, we report on atomic force microscopy (AFM) studies in which single polyacetylene-blocked rigid-rod β -barrel pores were imaged as giant, supramacromolecular pseudorotaxanes.

AFM imaging of molecular recognition by synthetic multifunctional pores became a realistic prospect only because of steady progress made in terms of both pores and blockers. The availability of a fine-tuned set of pores covering the complete spectrum of thermodynamic and kinetic stabilities,^[12] for example, promised a rapid identification of the optimal characteristics for the self-assembly of barrels on mica during drying from a buffer solution. As in the formation of synthetic multifunctional pores,^[12] the unstable but inert, namely, “self-repairing”, rigid-rod β -barrel **1** with internal KH dyads and external LLL triads (Figures 1 and 2a) gave the best AFM images rather than stable/inert barrels with internal RH dyads or stable/labile barrels with internal HH dyads.^[13] Consistent with previous AFM results,^[13] the obtained objects had an average height of approximately 3.6 nm that matched the height of the barrels standing on the mica surface. The heterogeneous height distribution of 2.3–4.1 nm was suggestive of the additional presence of barrels lying sideways on the surface. In this case, barrel widths of up to about 4 nm were conceivable for the “square-type” conformation **1^S** that was presumed to be observed in single-channel measurements.^[12] However, a “diamond-type” conformation **1^D** could exhibit a barrel width down to about 2 nm. The flattened appearance of vesicles, for example, in tapping-mode AFM images^[14] suggests that it was conceivable that external pressure by the AFM tip could compress the square **1^S** conformation into the local energy minimum of the diamond **1^D** conformation. Possible stabilization of diamond-like conformations **1^D** by interactions with the mica surface could neither be excluded nor confirmed.

Previously, anionic polyacetylene blockers such as **2** have served as probes to study molecular recognition by synthetic multifunctional pores in lipid bilayer membranes by circular dichroism (CD) spectroscopy.^[15] It now transpires that problems of imaging extended linear polymers on mica with classical blockers such as α -helical or random-coil polyglutamate could also be solved by using the more shape-persistent polyacetylene blockers. Poly(ethyl(4-ethynylphenyl)phosphonate)s **2**^[16] were detected as wormlike objects with an average height of 0.66 nm and a local maximal height of 1.1–1.5 nm (Figure 2b). Both values were independent of the molecular-weight distribution, whereas the average length found of course increased from low- to high-molecular-weight polymers.

[*] Dr. J. Kumaki, Prof. E. Yashima
Yashima Super-structured Helix Project, ERATO, JST
Creation Core Nagoya 101, Moriyama-ku
Nagoya 463-0003 (Japan)
Fax: (+81) 52-739-2083
E-mail: kumaki@yp-jst.jp

G. Bollot, Dr. J. Mareda, S. Litvinchuk, Prof. S. Matile
Department of Organic Chemistry
University of Geneva
Geneva, Switzerland
Fax: (+41) 22-379-5123
E-mail: stefan.matile@chiorg.unige.ch

[**] We thank Nathalie Sordé and Duy-Hien Tran for assistance in organic synthesis and the Swiss NSF for financial support (including the National Research Program “Supramolecular Functional Materials” 4047-057496).

Supporting information (experimental details) for this article is available on the WWW under <http://www.angewandte.org> or from the author.

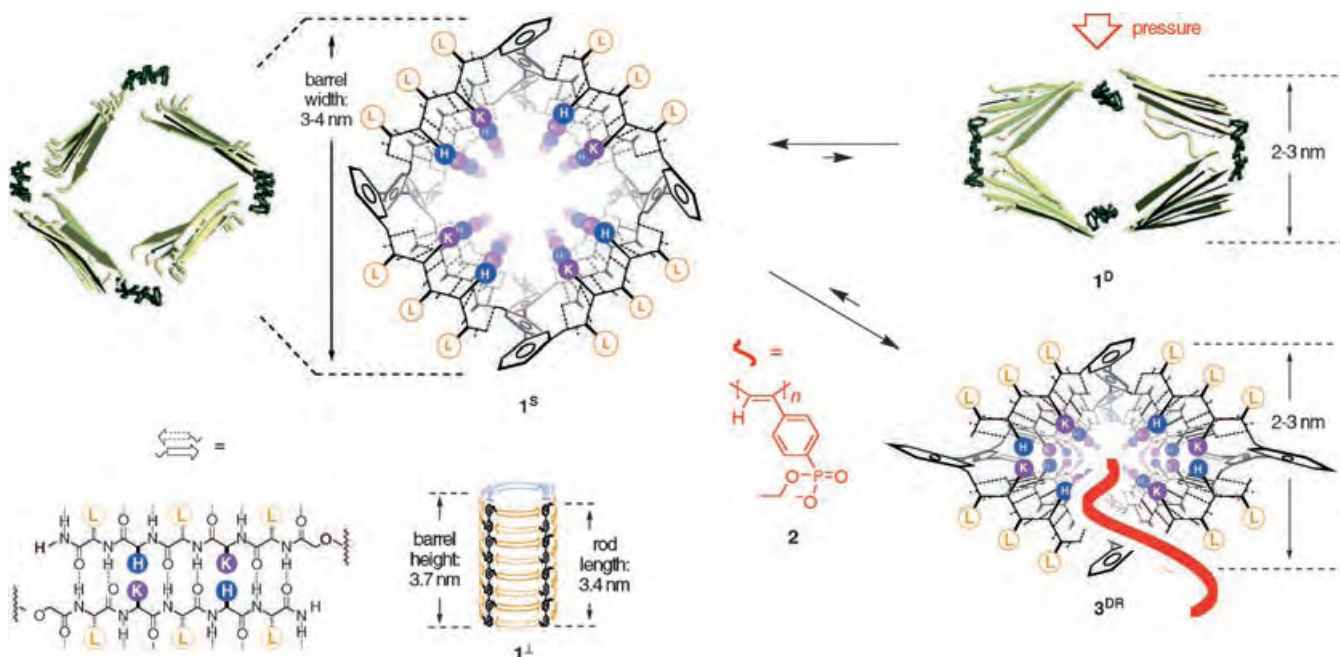


Figure 1. Notional structures and geometry-minimized models of pore **1** in a vertical (\perp) and horizontal position relative to a mica surface in open, “square-like” (1^S) and closed, “diamond-like” conformations (1^D) with pseudorotaxane 3^{DR} , and indication (red) of the expected $S \rightarrow D$ contraction by external pressure from the AFM tip and internal templation by blocker **2**. β Sheets are given as solid (backbone) and dotted lines (hydrogen bonds, 1^S , 1^D , 3^{DR}) or as arrows ($N \rightarrow C$, 1^\perp). External amino acid residues are shown in white circles, internal ones in dark circles (single-letter abbreviations).

These characteristics suggested that molecular recognition by synthetic multifunctional pores could be studied by AFM using barrel **1** and polymer **2**. The ability of polymer **2** to block pore **1** in lipid bilayers was confirmed by using methods described previously. The dose/response curve revealed an effective inhibitory concentration (IC_{50}) of 40 nM for a low-molecular-weight polymer **2**. This excellent molecular recognition was confirmed in AFM images of mixtures of pore **1** and blocker **2**. The ratio of bound to free barrels in the above example was 8:1 (Figure 2c); at higher polymer concentrations all the barrels were bound. On average, every second barrel was located at the end of the polymers (Figure 2c, e). Although the probability of observing pseudorotaxane motifs with barrels located more than half of the average polymer length from one terminus should decrease rapidly, the value was still far above the low number of end-on complexes expected for statistical ion pairing along the polymer template (Figure 2e). Under the studied conditions, excluding, for example, the experimentally inaccessible excess barrels, only a few examples with more than one barrel per polymer were found (see, for example, Figure 3, panels d1–d3 and c2).

End-on preference over rotaxane motifs suggested that molecular recognition occurs within the hollow supramolecule and that it is strong enough to hinder the continuing motion of the sticky polymer through the barrel. Consistent with earlier results on blockage and catalysis^[12] by synthetic multifunctional pores in bilayer membranes,^[4] this result

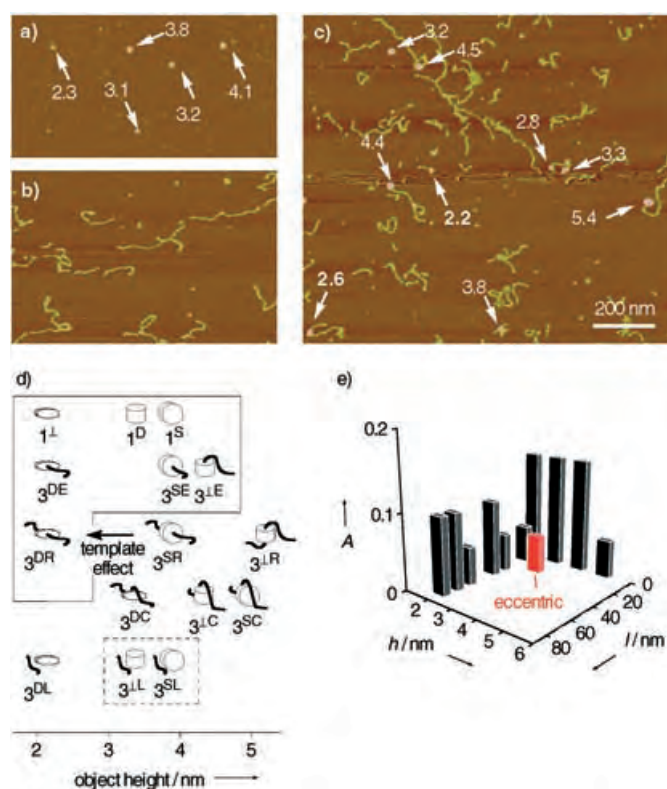


Figure 2. AFM images of a) barrel **1**, b) polymer **2**, and c) **1** and **2** together with object heights indicated in nm. d) Collection of possible structures as a function of their object height. Detected motifs are shown in a solid box, possibly detected in a dotted box, and undetected without a frame. For **1**, **3**, \perp , **S** (square-like), **D** (diamond-like), and **R** (pseudorotaxane), see Figure 1; **E**: “end-on” complexes, **L**: “lateral” complexes, **C**: crossovers. e) 2D Histogram with the relative abundance A as a function of object height h and distance l from the nearest polymer terminus ($n = 20$); red: eccentric barrel position, see Figure 3e.

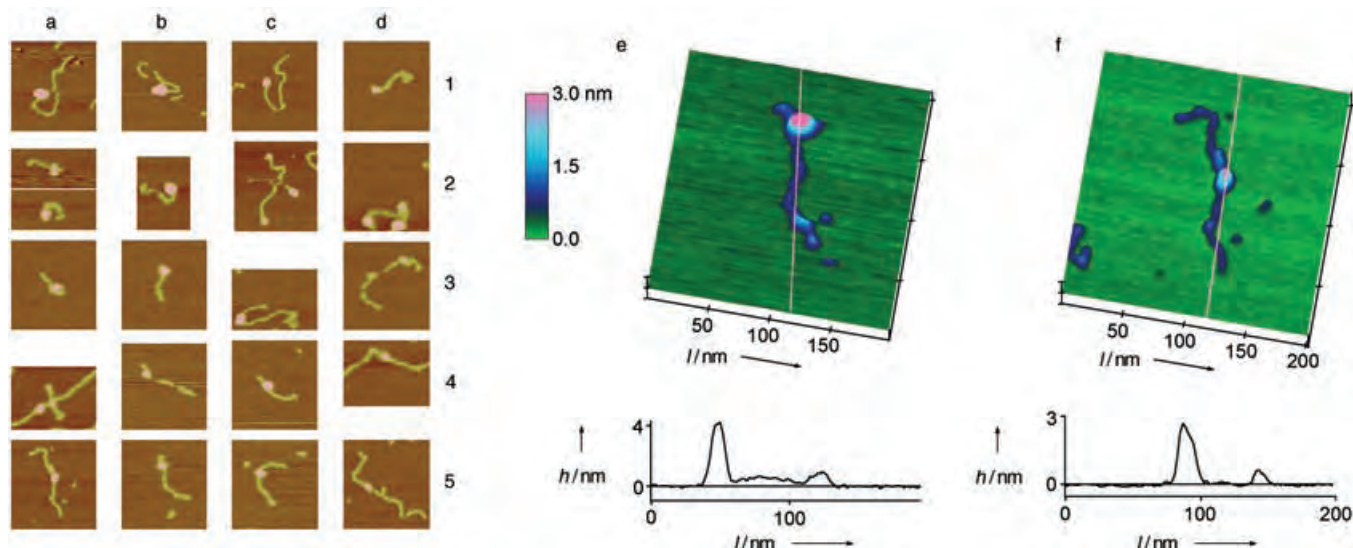


Figure 3. Gallery of rotaxane and “end-on” motifs (a–d, arbitrary scales) with magnification and height profile for eccentric (e) and centered rotaxanes (f).

demonstrated that molecular recognition by synthetic multifunctional pores occurs by threading of the polymer guest through the barrel host to form supramolecular pseudorotaxane complexes 3^R . This key finding explained the absence of polyrotaxanes under the studied conditions (namely, more than two barrels per polymer; Figure 3, panels d1–d3 and c2).^[5–11] Moreover, it excluded the existence of nonspecific interactions with monomeric rods and at the external barrel surface (that is, lateral complexes 3^{DL} , 3^{LL} , and 3^{SL} as well as crossover motifs 3^{DC} , 3^{SC} , and 3^{LC} , Figure 2d).

On average, barrels at the end of the polymer were clearly higher than barrels in the middle (Figure 2c, e). The height distribution of end-on objects 3^E implied that different conformers are likely to exist in different orientations relative to the mica surface (for example, vertical in 3^{LE} , horizontal in 3^{DE} , and perhaps the square-type 3^{SE} , Figure 2d). The accumulation of pseudorotaxane motifs with low object height in the middle of the polymer (Figure 2e) excluded the existence of crossover motifs (3^{DC} , 3^{SC} , 3^{LC}) as well as pseudorotaxanes with vertical (3^{LR}) and horizontal barrels in a square-type conformation (3^{SR} , Figure 2d). Pseudorotaxane 3^{DR} remained as the only meaningful suprastructure of the frequently found rotaxane-type objects with low height (Figure 2d).

The formation of pseudorotaxane 3^{DR} suggested that template effects^[5–11] may contribute to molecular recognition by synthetic multifunctional pores. Namely, as a polymer guest **2** enters into an open pore **1^S**, the square-type barrel **1^S** may flip into the energetically higher local minimum of the diamond-type barrel **1^D** to firmly bite into the internal thread. This experimental evidence for guest templation could, however, not be considered as unambiguous because contributions from the external pressure of the AFM tip to the low barrel width in most rotaxane motifs could not be excluded. However, optimizations of the average geometries obtained during the last 50 ps of a short molecular dynamics simulation revealed the separate local minima of the square- and

diamond-shaped conformers of β barrels and of rotaxanes. The conformational change of the square- to diamond-shaped barrel was associated with a pronounced shrinkage of the rod–rod barrel width from 3.5 nm for **1^S** to 1.8 nm in the optimized structure of **1^D**. In the computed structure of the diamond-shaped rotaxane 3^{DR} (Figure 4), the rod–rod width

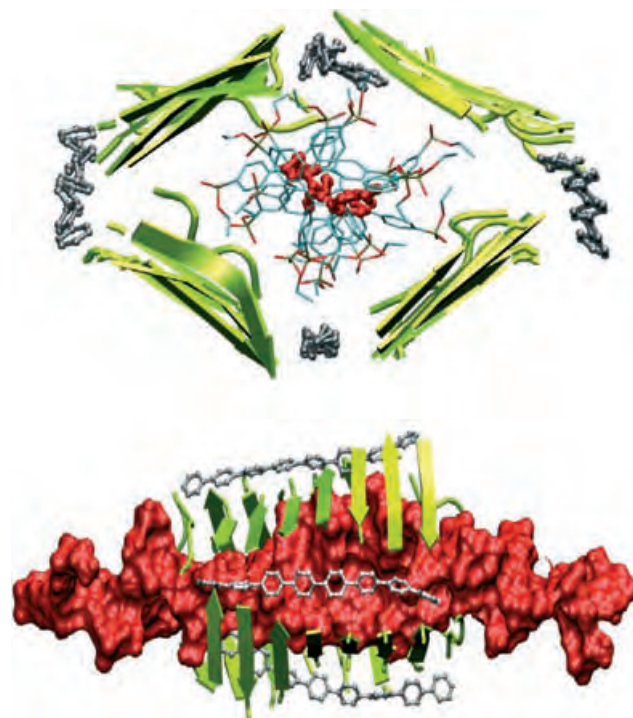


Figure 4. Fully optimized cutaway structures of diamond-shaped pseudorotaxane 3^{DR} in axial view (top, **2**: 20-mer, backbone in red) and in side view (bottom: **2**: 40-mer, Connolly surface in red). β Sheets are highlighted as arrows (green), *p*-octaphenyl groups as ball-and-stick models (silver); 100% phosphonate deprotonation, 100% K and 0% H protonation.

was also reduced to 2.2 nm. This finding corroborated the proposal of guest templation and was in agreement with the nonstatistical height distribution in the AFM images (Figure 2e). Similar guest templation has been observed in previous molecular dynamics simulations with α -helical blockers.^[4]

The few rotaxane motifs observed with object heights exceeding the range of 2–3 nm expected for diamond-type pseudorotaxanes **3^{DR}** could not be interpreted convincingly (Figure 2e). The eccentric position of the barrel with respect to the polymer was consistent with lateral complexes **3^{LL}** or **3^{SL}** (Figures 2d, 3e). The existence of nonspecific surface-to-surface association was, however, incompatible with the observed nonstatistical location of the barrel on the polymer. These infrequent rotaxane motifs with eccentric and high barrels may, therefore, be considered either as diamond-type pseudorotaxanes **3^{DR}** with imperfect barrel positioning or as an “accidental” detection of unfavored lateral complexes **3^{LL}**/**3^{SL}** at the single-molecule level without relevance to the average of the ensemble. The interpretation and significance of this exception—but not of the more important and unambiguous end-on preference and low-height pseudorotaxanes—deserve further reservation considering the low number of complexes observed as well as unexplored alternative conditions.

In summary, AFM snapshots of molecular recognition by synthetic multifunctional pores provide experimental evidence that the host–guest complexes formed between rigid-rod β -barrel pore and polymer blockers are pseudorotaxanes. The nonstatistical location of the barrel on the polymer indicates that entry of the polymer into the pore is favored over the motion of the polymer through the sticky pore. Although the clearly different conditions call for cautious interpretation,^[4] it can be considered as structural support for the possibility of blocker efflux through blocked, “blocker-selective” pores, a concept central to the understanding of synthetic multifunctional pores that has been verified previously at the functional level.^[17] Predicted^[4] and supported in silico, the nonstatistical object height distribution can be considered, with similar caution, as the so far elusive structural evidence for guest templation during molecular recognition by synthetic multifunctional pores.

Received: May 31, 2005

Published online: August 26, 2005

Keywords: bioorganic chemistry · ion channels · molecular recognition · scanning probe microscopy · supramolecular chemistry

- [5] *Molecular Catenanes, Rotaxanes and Knots* (Eds.: J.-P. Sauvage, C. Dietrich-Buchecker), Wiley-VCH, Weinheim, **1999**.
- [6] A. Harada, *Acc. Chem. Res.* **2001**, *34*, 456–464.
- [7] V. Balzani, A. Credi, F. M. Raymo, J. F. Stoddart, *Angew. Chem.* **2000**, *112*, 3484–3530; *Angew. Chem. Int. Ed.* **2000**, *39*, 3348–3391.
- [8] J. K. M. Sanders, *Pure Appl. Chem.* **2000**, *72*, 2265–2274.
- [9] O. Lukin, F. Vögtle, *Angew. Chem.* **2005**, *117*, 1480–1501; *Angew. Chem. Int. Ed.* **2005**, *44*, 1456–1477.
- [10] A. M. Brouwer, C. Frochot, F. G. Gatti, D. A. Leigh, L. Mottier, F. Paolucci, S. Roffia, G. W. H. Wurpel, *Science* **2001**, *291*, 2124–2128.
- [11] J. W. Lee, S. Samal, N. Selvapalam, H.-J. Kim, K. Kim, *Acc. Chem. Res.* **2003**, *36*, 621–630.
- [12] S. Litvinchuk, G. Bollot, J. Mareda, A. Som, D. Ronan, M. R. Shah, P. Perrottet, N. Sakai, S. Matile, *J. Am. Chem. Soc.* **2004**, *126*, 10067–10075.
- [13] G. Das, L. Ouali, M. Adrian, B. Baumeister, K. J. Wilkinson, S. Matile, *Angew. Chem.* **2001**, *113*, 4793–4797; *Angew. Chem. Int. Ed.* **2001**, *40*, 4657–4661.
- [14] Y. Tanaka, M. Miyachi, Y. Kobuke, *Angew. Chem.* **1999**, *111*, 565–567; *Angew. Chem. Int. Ed.* **1999**, *38*, 504–506.
- [15] G. Das, H. Onouchi, E. Yashima, N. Sakai, S. Matile, *ChemBioChem* **2002**, *3*, 1089–1096.
- [16] H. Onouchi, D. Kashiwagi, K. Hayashi, K. Maeda, E. Yashima, *Macromolecules* **2004**, *37*, 5495–5503.
- [17] D. Ronan, N. Sordé, S. Matile, *J. Phys. Org. Chem.* **2004**, *17*, 978–982.

[1] N. Sakai, J. Mareda, S. Matile, *Acc. Chem. Res.* **2005**, *38*, 79–87.

[2] N. Sakai, S. Matile, *Chem. Commun.* **2003**, 2514–2523.

[3] S. Litvinchuk, N. Sordé, S. Matile, *J. Am. Chem. Soc.* **2005**, *127*, 9316–9317.

[4] Y. Baudry, G. Bollot, V. Gorteau, S. Litvinchuk, J. Mareda, M. Nishihara, D. Pasini, F. Perret, D. Ronan, N. Sakai, M. R. Shah, A. Som, N. Sordé, P. Talukdar, D.-H. Tran, S. Matile, *Adv. Funct. Mater.*, in press.

Synthetic Methods

DOI: 10.1002/anie.200501925

**Rapid Two-Directional Synthesis of the F–J
Fragment of the Gambieric Acids by Iterative
Double Ring-Closing Metathesis****

J. Stephen Clark, Marc C. Kimber, Jerod Robertson,
Christopher S. P. McErlean, and Claire Wilson*

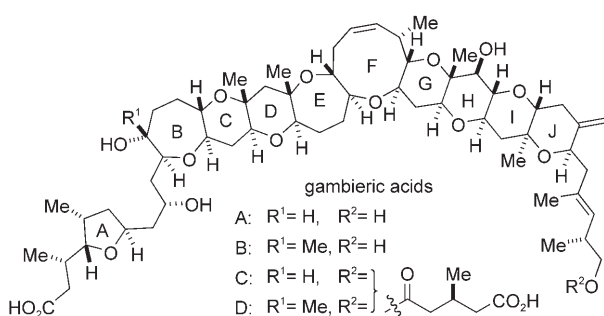
The gambieric acids A–D are potent antifungal agents, first isolated by Yasumoto and co-workers from a culture of the marine dinoflagellate *Gambierdiscus toxicus* (GII1 strain) collected near the Gambier Islands in French Polynesia (Scheme 1).^[1] The structures of these complex fused poly-ether natural products and the relative stereochemistry of the

[*] Prof. Dr. J. S. Clark, Dr. M. C. Kimber, Dr. J. Robertson,
Dr. C. S. P. McErlean, Dr. C. Wilson
School of Chemistry
University of Nottingham
University Park, Nottingham NG72RD (UK)
Fax: (+44) 115-951-3564
E-mail: j.s.clark@nottingham.ac.uk

[**] This work was funded by the Engineering and Physical Sciences
Research Council, UK (grant numbers GR/M30654/01 and GR/
S15761/01).



Supporting information for this article is available on the WWW
under <http://www.angewandte.org> or from the author.



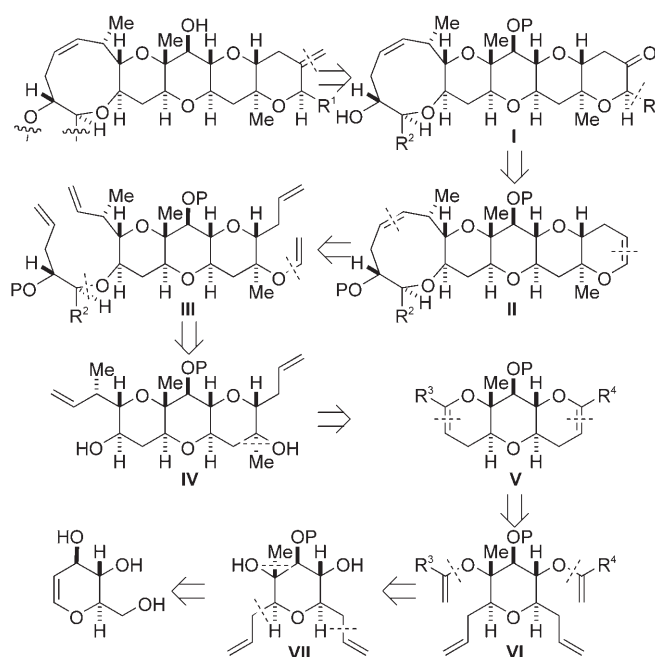
Scheme 1. The structures of the gambieric acids A–D.

trans-fused ring system (rings B–J) were determined by using NMR spectroscopic analysis in conjunction with mass-spectrometric analysis.^[1b] Absolute stereochemical assignments were later established by NMR spectroscopic analysis of compounds obtained by derivatization as the Mosher ester followed by oxidative cleavage of the side chain attached to the J ring, and by functionalization of the carboxylic acid functionality by using a chiral anisotropic reagent.^[1c]

The gambieric acids are potent and selective antifungal agents—they display significant activity against filamentous fungi but are inactive against yeasts—that exhibit up to 2000-fold higher activity against some fungi than amphotericin B in certain assays.^[2] The gambieric acids are also cytotoxic, but they do not possess the significant neurotoxicity associated with most other large marine fused-polyether natural products, such as the brevetoxins, ciguatoxins, yessotoxins, and maitotoxins.^[2] Interestingly, although the gambieric acids do not function as potent neurotoxins, gambieric acid A does inhibit binding of the brevetoxin B derivative PbTx-3 to site 5 of voltage-gated sodium channels of excitable membranes.^[3]

The obvious synthetic challenges presented by the gambieric acids, coupled with their potent antifungal activity, make them alluring targets for total synthesis. Recently, elegant total syntheses of the related marine polyether natural products brevetoxin A,^[4] brevetoxin B,^[5] ciguatoxin CTX-3,^[6] gambierol,^[7] and gymnocin^[8] have been reported. In contrast, there is a paucity of published work that concerns the synthesis of the polycyclic ether framework of the gambieric acids or even small subunits of these natural products.^[9]

We recently initiated a program to synthesize the gambieric acids based on the ring-closing metathesis (RCM) methodology that we had developed to address the general problem of fused-polyether construction^[10] and have recently described a concise synthesis of the A ring fragment of the gambieric acids by using copper-carbenoid chemistry.^[11] To construct the full ten-ring polyether system of the gambieric acids, we intend to pursue a highly convergent synthetic strategy in which the target will be constructed by the union of a tetracyclic A–D fragment and a pentacyclic F–J fragment followed by final closure of the E ring. Retrosynthetic disconnection of the F–J fragment **I** by removal of the side chain (R^1) and functional group interconversion suggests the enol ether **II** as an advanced precursor (Scheme 2). Scission of the F and J rings then leads to the tricyclic intermediate **III**, and removal of the acyclic ether substituents leads to the diol

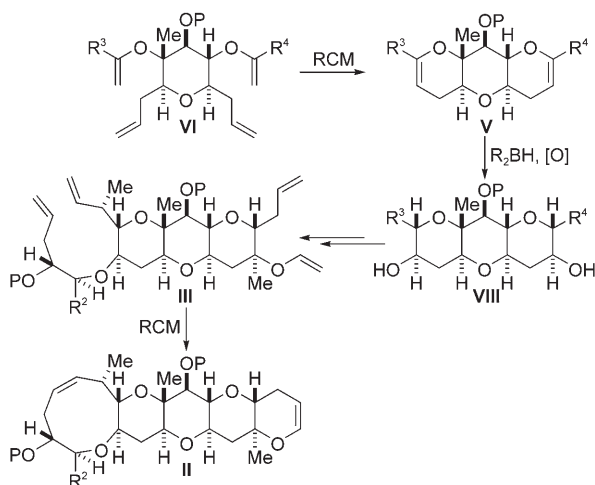


Scheme 2. Retrosynthetic analysis of the F–J fragment of the gambieric acids.

IV. Removal of the methyl group and retrosynthetic dehydration then reveals the bis(enol ether) **V**, and scission of the G and I rings leads to the monocyclic intermediate **VI**, which corresponds to the H ring. The tetrahydropyran unit can then be straightforwardly disconnected through the diol **VII** to reveal D-glucal as the chiral-pool starting material.

The use of a two-directional double-RCM reaction twice in the synthetic sequence to construct the tetrahydropyran G and I rings simultaneously and then the nine-membered F ring and the six-membered F ring and the six-membered J ring simultaneously is intrinsic to the retrosynthetic analysis shown in Scheme 2. In the forward direction, this approach would involve double RCM of a bis(enol ether) **VI** and then hydroboration of the tricyclic product **V** to give the diol **VIII** after oxidative work-up (Scheme 3).^[10a,c,12] The diol **VIII** would then be converted into the triene enol ether **III**; a second double two-directional RCM reaction would then deliver the pentacyclic F–J fragment to which the requisite side chain could be attached.

The anticipated strategy involves two-directional synthesis by iterative double simultaneous (as opposed to sequential) ring closure. Although there have been some early examples of two-directional synthesis, the potential of simultaneous two-directional homologation has only been fully appreciated within last decade.^[13] Some of the most elegant examples of this approach have been reported by Schreiber and co-workers in connection with their syntheses of the polyol-containing natural products mycotycins and hizikimycin.^[14] The implementation of a synthetic strategy that involves simultaneous two-directional homologation is attractive because such a reflexive approach can, in principle, improve the efficiency of both linear and convergent syntheses.^[15] However, unless the target molecule is entirely symmetrical, it must be possible to perform reactions simulta-

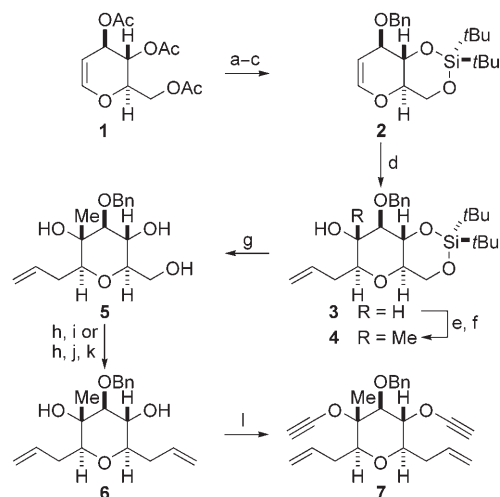


Scheme 3. The use of iterative double-RCM reactions to construct the F–J fragment of the gambieric acids.

neously at both ends of the molecule while being able to differentiate the termini at various stages along the synthetic route.

We have recently demonstrated that it is possible to construct tricyclic polyether fragments that possess a variety of ring sizes in good-to-excellent yield by performing simultaneous double ring construction by using RCM.^[16] Substrates bearing enol ethers, allylic ethers, and alkynyl ethers or mixtures of these functional groups were employed as substrates for the double-RCM reactions. The objective of the investigation described herein was to demonstrate that the F–J fragment of the gambieric acids could be assembled by a two-directional approach, in which simultaneous double-RCM reactions are used twice, and that many of the other reactions used to assemble the pentacyclic unit could be performed in a simultaneous or sequential two-directional fashion.

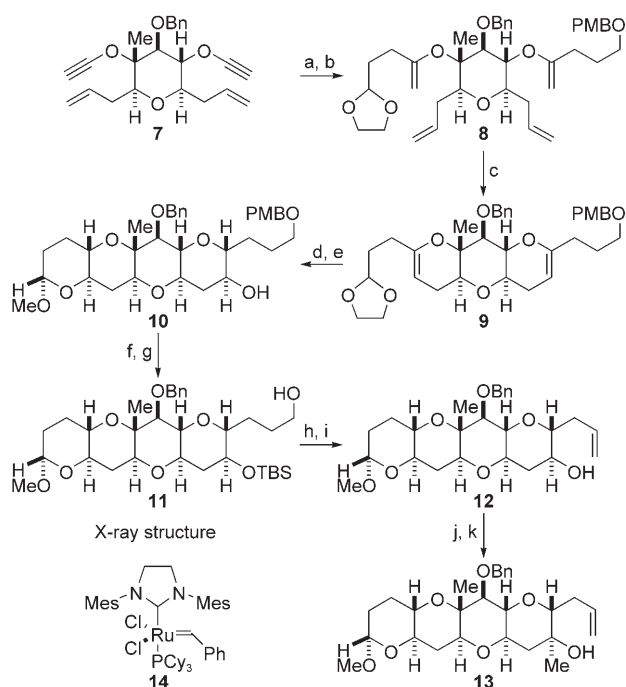
The two-directional synthesis of the F–J fragment of the gambieric acids commenced with deacetylation of the commercially available triacetate **1** (Scheme 4). Conversion of the resulting D-glucal into ether **2** was accomplished by protection of the primary and proximal secondary hydroxy groups with a di-*tert*-butylsilylene group and benzoylation of the remaining hydroxy group.^[16,17] The enol ether **2** was then subjected to highly diastereoselective oxidation with dimethyldioxirane^[18] and the resulting anomeric epoxide underwent ring opening with allylmagnesium chloride to give the alcohol **3** in good yield.^[19] Swern oxidation followed by treatment of the resulting ketone with methyl lithium at low temperature afforded the tertiary alcohol **4** in good yield and with a reasonable level of diastereocontrol (d.r. = 6:1). Subsequent removal of the di-*tert*-butylsilylene protecting group afforded the corresponding triol **5** in high yield, and sequential treatment of this triol with trifluoromethanesulfonic anhydride and triethylsilyl trifluoromethanesulfonate in the presence of 2,6-lutidine in a one-pot procedure gave the primary triflate with concomitant protection of the secondary hydroxy group. Introduction of the alkene side chain was then accomplished in a single operation by displacement of the



Scheme 4. Synthesis of the armed H-ring fragment **7**. a) NaOMe, MeOH, RT; b) *t*Bu₂Si(OTf)₂, DMF, pyridine, –40 °C; c) NaH, BnBr, THF/DMF, 0 °C → RT (85 %, 3 steps); d) DMDO, CH₂Cl₂, 0 °C, then CH₂CHCH₂MgCl, THF, 0 °C (82 %); e) (COCl)₂, DMSO, Et₃N, CH₂Cl₂, –78 °C → RT; f) MeLi, PhMe, –78 °C (76 %, 2 steps); g) (HF)₃·NEt₃, THF, 0 °C (98 %); h) Tf₂O then Et₃SiOTf, 2,6-lutidine, CH₂Cl₂, –78 °C (88 %); i) *n*Bu₃SnCHCH₂, *n*BuLi, CuCN, THF, –78 °C then TBAF, THF, 0 °C (78 %); j) HCCSiMe₃, *n*BuLi, DMPU, THF, 0 °C, then TBAF, THF, 0 °C (96 %); k) H₂, the Lindlar catalyst, quinoline, EtOAc, RT (82 %); l) KH, Cl₂CCHCl, THF, 0 °C then *n*BuLi, Et₂O, –78 → –40 °C (88 %). DMF = dimethylformamide, DMDO = dimethyldioxirane, DMSO = dimethyl sulfoxide, TBAF = tetrabutylammonium fluoride, DMPU = *N,N'*-dimethyl-*N,N'*-propyleneurea.

triflate group with the higher-order cyanocuprate, generated from vinyl lithium (formed in situ by transmetalation from tri-*n*-butylvinylstannane) and copper(I) cyanide at low temperature,^[20] and the diol **6** was obtained in good yield thereafter by desilylation of the secondary hydroxy site. The alkenyl side chain was also constructed by displacement of the triflate with lithium trimethylsilylacetylide followed by treatment of the alkyne product with fluoride and partial hydrogenation using the Lindlar catalyst in the presence of quinoline. The overall yield of the diol **6** obtained by using the less-direct route was similar to that obtained by using the higher-order cyanocuprate to displace the triflate directly. Diol **6** was then converted into the bis(alkynyl ether) **7** by using the one-pot alkylation procedure developed by Greene and co-workers.^[21] The alkylation reaction was the first two-directional reaction in our synthetic sequence, and it is noteworthy that both alkynyl ethers were generated simultaneously in excellent yield and that the highly hindered tertiary alcohol underwent reaction cleanly.

The bis(enol ether) required for the first double-RCM reaction was prepared from the bis(alkynyl ether) **7** by using sequential carbocupration reactions (Scheme 5).^[22] The first side chain was introduced by a completely regioselective addition of a homocuprate reagent at the less sterically encumbered alkynyl ether. An acetal-containing side chain was then installed by reaction of the remaining hindered alkynyl ether with an excess of the cyanocuprate generated from equimolar amounts of the Grignard reagent 1,3-dioxolan-2-ylethylmagnesium bromide and copper(I) cy-



Scheme 5. Synthesis of the tricyclic G-I fragment **13**. a) PMBO- $(\text{CH}_2)_3\text{MgBr}$, CuBr, LiBr, THF, $-95 \rightarrow -78^\circ\text{C}$ (85 %); b) $(\text{OCH}_2\text{CH}_2\text{O})\text{CH}(\text{CH}_2)_2\text{MgBr}$, CuCN, LiCl, THF, -78°C (84 %); c) catalyst **14** (10 mol %), PhMe, 70°C (89 %); d) thexyl borane, THF, $0^\circ\text{C} \rightarrow \text{RT}$ then $\text{NaBO}_3 \cdot 4\text{H}_2\text{O}$, pH 7 buffer (62 %); e) TsOH, MeOH, RT (71 %); f) $t\text{BuMe}_2\text{SiCl}$, DMAP, Et_3N , CH_2Cl_2 , RT; g) CAN, MeCN, H_2O , RT (56 %, 2 steps); h) $o\text{-O}_2\text{NC}_6\text{H}_4\text{SeCN}$, $n\text{Bu}_3\text{P}$, THF, RT then H_2O_2 , NaHCO_3 aq., 40°C ; i) TBAF, THF, RT (83 %, 2 steps); j) Dess–Martin periodinane, CH_2Cl_2 , 0°C ; k) MeMgI , PhMe, -78°C (83 %, 2 steps). PMB = pentamethylbenzyl, Cy = cyclohexyl, Mes = mesityl, Bn = benzyl, TBS = *tert*-butyldimethylsilyl, Ts = *para*-toluenesulfonyl, DMAP = 4-dimethylaminopyridine, CAN = cerium(IV) ammonium nitrate.

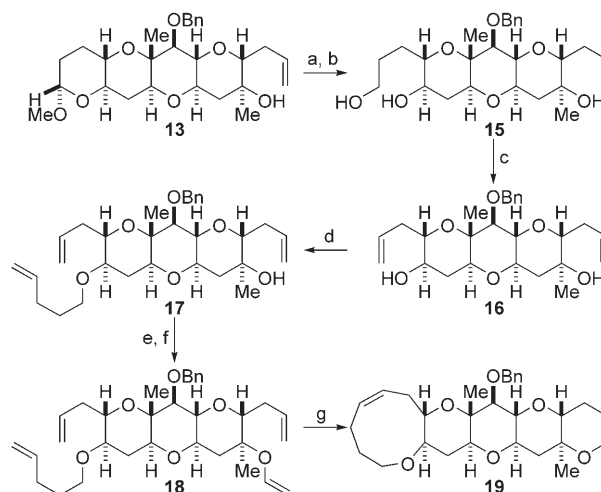
nide.^[23] The yields for both carbocupration reactions were excellent and the exceptionally high level of regiocontrol obtained during the first carbocupration reaction of the sequence is remarkable.

The bis(enol ether) **8** was subjected to double RCM by treatment with ruthenium catalyst **14**,^[24] and the tricyclic product **9** was obtained in excellent yield from this two-directional ring-closure reaction (Scheme 5).^[16] Double hydroboration of the metathesis product **9** was accomplished by using an excess of thexylborane, and mild oxidation of the intermediate organoborane with sodium perborate delivered the required diol in 62 % yield.^[25] Treatment of the diol with *para*-toluenesulfonic acid in methanol yielded the tetracyclic acetal **10** in excellent yield and resulted in differentiation of the two secondary hydroxy groups. The free secondary alcohol was then protected as its *tert*-butyldimethylsilyl ether and the *para*-methoxybenzyl ether side chain was cleaved with CAN. The resulting alcohol **11** was a crystalline solid, and both the structure and relative stereochemistry of this tetracyclic intermediate were confirmed by X-ray crystallographic analysis.^[26]

The alkene required for the second double-RCM reaction was installed by dehydration of the side chain (Scheme 5). Thus, the primary alcohol **11** was treated with *ortho*-nitro-

phenyl selenocyanate and tri-*n*-butylphosphine followed by oxidation of the intermediate selenide with buffered hydrogen peroxide and thermal elimination of selenoxide in situ.^[27] Removal of the silicon protecting group afforded the alcohol **12**, and subsequent oxidation and stereoselective addition of methylmagnesium iodide to the intermediate ketone delivered the tertiary alcohol **13** in a highly diastereoselective manner.

Acetal **13** was then elaborated to give the F–J ring fragment of the gambieric acids by using the sequence shown in Scheme 6. Acetal **13** was converted into the corresponding



Scheme 6. Completion of the pentacyclic F–J fragment **19**. a) HCl aq., THF, 60°C ; b) NaBH_4 , MeOH, 0°C (84 %, 2 steps); c) $o\text{-O}_2\text{NC}_6\text{H}_4\text{SeCN}$, $n\text{Bu}_3\text{P}$, THF, RT then H_2O_2 , NaHCO_3 aq., 40°C (96 %); d) $\text{CH}_2\text{CH}(\text{CH}_2)_3\text{Br}$, $n\text{Bu}_4\text{NI}$, THF/DMF, reflux (66 % (81 % brsm)); e) KH, Cl_2CHCl , THF, 0°C then $n\text{BuLi}$, Et_2O , $-78 \rightarrow -40^\circ\text{C}$; f) H_2 , Lindlar catalyst, quinoline, EtOAc, RT (49 %, 2 steps); g) catalyst **14** (10 mol %), PhMe, 80°C (60 %).

cyclic hemiacetal by treatment with aqueous acid, and subsequent reduction with sodium borohydride gave diol **15**. Dehydration of the side chain was effected by formation of selenide, oxidation, and elimination of selenoxide (cf. **11** \rightarrow **12**, Scheme 5), but protection of the secondary alcohol was not required in this case. Selective monoalkylation of the secondary hydroxy group of diene **16** was accomplished by sequential treatment with sodium hydride and 5-bromo-1-pentene in the presence of tetra-*n*-butylammonium iodide. The remaining hydroxy group of triene **17** was then converted into the requisite vinyl ether by sequential alkynyl ether formation and Lindlar reduction,^[16] thus giving the second double-RCM precursor **18** in reasonable yield. The final crucial double-RCM reaction to give the required nine- and six-membered cyclic ethers was then effected by treatment of the tricyclic compound **18** with the ruthenium complex **14**.^[24] The pentacyclic array **19**, which corresponds to the F–J ring fragment of the gambieric acids, was obtained from the reaction in 60 % yield. Analysis of partially cyclized material isolated from the reaction suggested that ring closure of the enol ether proceeds at a much faster rate than formation of the nine-membered ring.

In summary, we have demonstrated that the F–J fragment of the gambieric acids can be assembled by a rapid and efficient two-directional approach in which simultaneous double-RCM reactions are employed in an iterative manner. The formation of alkynyl ethers and carbocupration have also been performed in a two-directional manner, and it should be noted that by reordering some of the steps in the synthetic sequence, other reactions (e.g., the formation of selenide, oxidation, and elimination of selenoxide) could also be performed simultaneously, thus leading to an even more efficient route. The synthesis of the F–J fragment with the appropriate functionalities for the attachment of the A–D fragment is currently in progress, and results of these synthetic studies will be reported in due course.

Received: June 2, 2005

Published online: August 31, 2005

Keywords: cyclization · metathesis · natural products · polyethers

- [1] a) H. Nagai, K. Torigoe, M. Satake, M. Murata, T. Yasumoto, H. Hirota, *J. Am. Chem. Soc.* **1992**, *114*, 1102–1103; b) H. Nagai, M. Murata, K. Torigoe, M. Satake, T. Yasumoto, *J. Org. Chem.* **1992**, *57*, 5448–5453; c) A. Morohashi, M. Satake, H. Nagai, Y. Oshima, T. Yasumoto, *Tetrahedron* **2000**, *56*, 8995–9001.
- [2] H. Nagai, Y. Mikami, K. Yazawa, T. Gono, T. Yasumoto, *J. Antibiot.* **1993**, *46*, 520–522.
- [3] M. Inoue, M. Hiram, M. Satake, K. Sugiyama, T. Yasumoto, *Toxicon* **2003**, *41*, 469–474.
- [4] a) K. C. Nicolaou, Z. Yang, G.-Q. Shi, J. L. Gunzner, K. A. Agrios, P. Gärtner, Z. Yang, *Nature* **1998**, *392*, 264–269; b) K. C. Nicolaou, M. E. Bunnage, D. G. McGarry, S. Shi, P. K. Somers, P. A. Wallace, X.-J. Chu, K. A. Agrios, J. L. Gunzner, Z. Yang, *Chem. Eur. J.* **1999**, *5*, 599–617; c) K. C. Nicolaou, P. A. Wallace, S. Shi, M. A. Ouellette, M. E. Bunnage, J. L. Gunzner, K. A. Agrios, G.-Q. Shi, P. Gärtner, Z. Yang, *Chem. Eur. J.* **1999**, *5*, 618–627; d) K. C. Nicolaou, G.-Q. Shi, J. L. Gunzner, P. Gärtner, P. A. Wallace, M. A. Ouellette, S. Shi, M. E. Bunnage, K. A. Agrios, C. A. Veale, C.-K. Hwang, J. Hutchinson, C. V. C. Prasad, W. W. Ogilvie, Z. Yang, *Chem. Eur. J.* **1999**, *5*, 628–645; e) K. C. Nicolaou, J. L. Gunzner, G.-Q. Shi, K. A. Agrios, P. Gärtner, Z. Yang, *Chem. Eur. J.* **1999**, *5*, 646–658.
- [5] a) K. C. Nicolaou, C.-K. Hwang, M. E. Duggan, D. A. Nugiel, Y. Abe, K. B. Reddy, S. A. DeFrees, D. R. Reddy, R. A. Awartani, S. R. Conley, F. P. J. T. Rutjes, E. A. Theodorakis, *J. Am. Chem. Soc.* **1995**, *117*, 10227–10238; b) K. C. Nicolaou, E. A. Theodorakis, F. P. J. T. Rutjes, M. Sato, J. Tiebes, X.-Y. Xiao, C.-K. Hwang, M. E. Duggan, Z. Yang, E. A. Couladouros, F. Sato, J. Shin, H.-M. He, T. Bleckman, *J. Am. Chem. Soc.* **1995**, *117*, 10239–10251; c) K. C. Nicolaou, F. P. J. T. Rutjes, E. A. Theodorakis, J. Tiebes, M. Sato, E. Untersteller, *J. Am. Chem. Soc.* **1995**, *117*, 10252–10263; d) K. C. Nicolaou, E. A. Theodorakis, F. P. J. T. Rutjes, J. Tiebes, M. Sato, E. Untersteller, X.-Y. Xiao, *J. Am. Chem. Soc.* **1995**, *117*, 1171–1172; e) K. C. Nicolaou, F. P. J. T. Rutjes, E. A. Theodorakis, J. Tiebes, M. Sato, E. Untersteller, *J. Am. Chem. Soc.* **1995**, *117*, 1173–1174; f) K. C. Nicolaou, *Angew. Chem.* **1996**, *108*, 644–664; *Angew. Chem. Int. Ed. Engl.* **1996**, *35*, 589–607.
- [6] a) M. Hiram, T. Oishi, H. Uehara, M. Inoue, M. Maruyama, H. Oguri, M. Satake, *Science* **2001**, *294*, 1904–1907; b) M. Inoue, H. Uehara, M. Maruyama, M. Hiram, *Org. Lett.* **2002**, *4*, 4551–4554; c) M. Inoue, M. Hiram, *Acc. Chem. Res.* **2004**, *37*, 961–968; d) M. Inoue, M. Hiram, *Synlett* **2004**, 577–595; e) M. Inoue, K. Miyazaki, H. Uehara, M. Maruyama, M. Hiram, *Proc. Natl. Acad. Sci. USA* **2004**, *101*, 12013–12018.
- [7] a) H. Fuwa, M. Sasaki, M. Satake, K. Tachibana, *Org. Lett.* **2002**, *4*, 2981–2984; b) H. Fuwa, N. Kainuma, K. Tachibana, M. Sasaki, *J. Am. Chem. Soc.* **2002**, *124*, 14983–14992; c) I. Kadota, H. Takamura, K. Sato, A. Ohno, K. Matsuda, Y. Yamamoto, *J. Am. Chem. Soc.* **2003**, *125*, 46–47; d) I. Kadota, H. Takamura, K. Sato, A. Ohno, K. Matsuda, M. Satake, Y. Yamamoto, *J. Am. Chem. Soc.* **2003**, *125*, 11893–11899; e) H. W. B. Johnson, U. Majumder, J. D. Rainier, *J. Am. Chem. Soc.* **2005**, *127*, 848–849.
- [8] a) C. Tsukano, M. Sasaki, *J. Am. Chem. Soc.* **2003**, *125*, 14294–14295; b) C. Tsukano, M. Ebine, M. Sasaki, *J. Am. Chem. Soc.* **2005**, *127*, 4326–4335.
- [9] a) I. Kadota, N. Oguro, Y. Yamamoto, *Tetrahedron Lett.* **2001**, *42*, 3645–3647; b) I. Kadota, H. Takamura, Y. Yamamoto, *Tetrahedron Lett.* **2001**, *42*, 3649–3651.
- [10] a) J. S. Clark, J. G. Kettle, *Tetrahedron Lett.* **1997**, *38*, 123–126; b) J. S. Clark, J. G. Kettle, *Tetrahedron Lett.* **1997**, *38*, 127–130; c) J. S. Clark, O. Hamelin, R. Hufton, *Tetrahedron Lett.* **1998**, *39*, 8321–8324; d) J. S. Clark, G. P. Trevitt, D. Boyall, B. Stammen, *Chem. Commun.* **1998**, 2629–2630; e) J. S. Clark, J. G. Kettle, *Tetrahedron* **1999**, *55*, 8231–8248; f) J. S. Clark, F. Elustondo, G. P. Trevitt, D. Boyall, J. Robertson, A. J. Blake, C. Wilson, B. Stammen, *Tetrahedron* **2002**, *58*, 1973–1982; g) J. S. Clark, F. Elustondo, M. C. Kimber, *Chem. Commun.* **2004**, 2470–2471.
- [11] J. S. Clark, T. C. Fessard, C. Wilson, *Org. Lett.* **2004**, *6*, 1773–1776.
- [12] For other examples of the polyether construction by RCM of enol ethers, see: a) J. D. Rainier, S. P. Allwein, *J. Org. Chem.* **1998**, *63*, 5310–5311; b) J. D. Rainier, J. M. Cox, S. P. Allwein, *Tetrahedron Lett.* **2001**, *42*, 179–181; c) J. D. Rainier, S. P. Allwein, J. M. Cox, *J. Org. Chem.* **2001**, *66*, 1380–1386.
- [13] For a review of two-directional approaches to natural-product synthesis, see: S. R. Magnuson, *Tetrahedron* **1995**, *51*, 2167–2213.
- [14] a) S. L. Schreiber, M. T. Goulet, *J. Am. Chem. Soc.* **1987**, *109*, 8120–8122; b) N. Ikemoto, S. L. Schreiber, *J. Am. Chem. Soc.* **1992**, *114*, 2524–2536; c) C. S. Poss, S. D. Rychnovsky, S. L. Schreiber, *J. Am. Chem. Soc.* **1993**, *115*, 3360–3361; d) C. S. Poss, S. L. Schreiber, *Acc. Chem. Res.* **1994**, *27*, 9–17.
- [15] S. H. Bertz, *New J. Chem.* **2003**, *27*, 870–879.
- [16] J. S. Clark, O. Hamelin, *Angew. Chem.* **2000**, *112*, 380–382; *Angew. Chem. Int. Ed.* **2000**, *39*, 372–374.
- [17] J. O. Hoberg, *Carbohydr. Res.* **1997**, *300*, 365–367.
- [18] R. L. Halcomb, S. J. Danishefsky, *J. Am. Chem. Soc.* **1989**, *111*, 6661–6666.
- [19] a) W. M. Best, V. Ferro, J. Harle, R. V. Stick, D. M. G. Tilbrook, *Aust. J. Chem.* **1997**, *50*, 463–472; b) D. A. Evans, B. W. Trotter, B. Côté, *Tetrahedron Lett.* **1998**, *39*, 1709–1712; c) J. D. Rainier, S. P. Allwein, *J. Org. Chem.* **1998**, *63*, 5310–5311.
- [20] H. Tanaka, K. Kawai, K. Fujiwara, A. Murai, *Tetrahedron* **2002**, *58*, 10017–10031.
- [21] A. Moyano, F. Charbonnier, A. E. Greene, *J. Org. Chem.* **1987**, *52*, 2919–2922.
- [22] S. E. Denmark, V. Guagnano, J. A. Dixon, A. Stolle, *J. Org. Chem.* **1997**, *62*, 4610–4628.
- [23] D. Liu, L. M. Stuhmiller, T. C. McMorris, *J. Chem. Soc. Perkin Trans. 1* **1988**, 2161–2167.
- [24] M. Scholl, S. Ding, C. W. Lee, R. H. Grubbs, *Org. Lett.* **1999**, *1*, 953–956.
- [25] a) D. S. Matteson, R. J. Moody, *J. Org. Chem.* **1980**, *45*, 1091–1095; b) G. W. Kabalka, J. T. Maddox, T. Shoup, K. R. Bowers, *Org. Synth.* **1996**, *73*, 116–122; c) A. McKillop, W. R. Sanderson, *J. Chem. Soc. Perkin Trans. 1* **2000**, 471–476.
- [26] Crystal data for the acetal **11**: C₃₂H₅₂O₈Si, *M_r* = 592.85, colorless block cut from lath, crystal dimensions 0.52 × 0.48 × 0.32 mm³,

orthorhombic, space group $P2_12_12_1$, $a = 9.287(4)$, $b = 24.984(11)$, $c = 43.067(19)$ Å, $V = 9993(8)$ Å³, $Z = 12$, $\rho_{\text{calcd}} = 1.182$ Mg m⁻³, $\mu(\text{Mo K}\alpha) 0.117$ mm⁻¹, $T = 150(2)$ K; 28 321 reflections collected of which 15 595 independent, $2\theta_{\text{max}} = 50^\circ$, absorption correction made using multi-scan method (SADABS), $T_{\text{min/max}} = 0.562/1.00$. Structure solved by direct methods (SHELXS-97) and refined by full-matrix least squares against F^2 (SHELXTL), $R_1 = 0.106$, $wR_2 = 0.248$, 1101 parameters. One *t*BuMe₂Si group showed disorder and was modeled over two sites with occupancies 0.577(7) and 0.423(7) and isotropic atomic displacement parameters. All hydrogen atoms were placed in geometrically calculated positions, except those of OH groups which were located from difference Fourier syntheses and refined as rigid rotors. Maximum and minimum residual electron density = 0.66 and -0.50 e Å⁻³. CCDC-273286 contains the supplementary crystallographic data for this paper. These data can be obtained free of charge from the Cambridge Crystallographic Data Centre via www.ccdc.cam.ac.uk/data_request/cif.

- [27] P. A. Grieco, S. Gilman, M. Nishizawa, *J. Org. Chem.* **1976**, *41*, 1485–1486.

Enzyme Modeling

DOI: 10.1002/anie.200500814

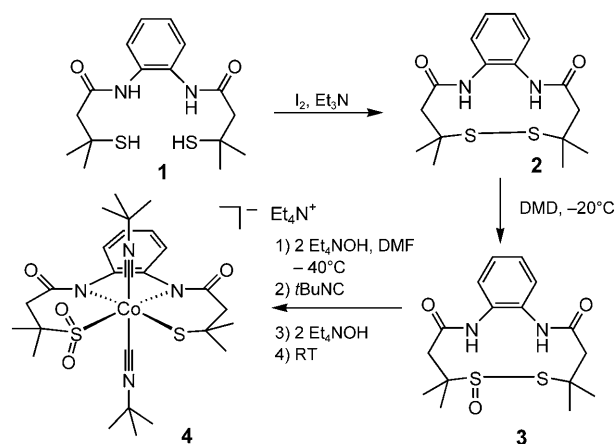
Direct Synthesis of a Thiolato-S and Sulfinato-S Co^{III} Complex Related to the Active Site of Nitrile Hydratase: A Pathway to the Post-Translational Oxidation of the Protein**

Emilie Bourles, Rodolphe Alves de Sousa,
Erwan Galardon, Michel Giorgi, and Isabelle Artaud*

A group of sulfur-oxidized species found in biological systems includes sulfenic, sulfinic, and sulfonic acids derived from cysteine.^[1,2] Currently “sulfur-oxidized” proteins are known to carry only one type of modification at a time, except for nitrile hydratase (NHase), which is the only system known to contain thiolate, sulfenate, and sulfinate groups in close proximity through coordination to a metal center.^[3] Despite

intense studies,^[4] the origin of the post-translational modification of NHase remains unclear. The prevalent hypothesis for cysteine sulfur oxidation involves a two-step reaction in which iron or cobalt is bound by the protein ligands within the consensus sequence Cys-X-Y-Cys-Ser-Cys. This results in the formation of an $[\text{Fe}(\text{N}_2\text{S}_3)]^{2-}$ or a $[\text{Co}(\text{N}_2\text{S}_3)]^{2-}$ species which is followed by oxidation of the two bound thiolate groups in the equatorial plane *trans* to two deprotonated amides to give sulfinate and sulfenate. The design of all models synthesized to mimic the NHase active site follows this hypothesis.^[5] The result is that only a few iron^[6] or cobalt^[7,8] complexes show dissymmetrically oxidized thiolate groups, and most of these contain two sulfinate groups irrespective of whether the oxidant used is O_2 ,^[5,9–11b] H_2O_2 ,^[5,11c,d] or dimethyl dioxirane.^[11a] This prompted us to find another route to prepare a dissymmetrically oxidized complex. Herein, we describe a new and simple strategy toward mixed thiolate/sulfinate complexes which involves the metalation of a thiosulfinate following cleavage of the S–S bond with HO^- . By using a cyclic pseudopeptidic thiosulfinate, we prepared and structurally characterized a six-coordinate Co^{III} bisamidato/thiolato/sulfinato complex with two axial isonitrile ligands. This enables us to propose an alternate pathway for the post-translational modification of the cysteine residues in NHase, thus extending the implication of disulfide *S*-oxides, a second emerging group of sulfur-oxidized species, in biological systems.^[2]

The cyclic disulfide *S*-monoxide **3** shown in Scheme 1 was synthesized in two steps from dithiol **1**, which was previously used to prepare both dithiolato $[\text{CoN}_2\text{S}_2](\text{Et}_4\text{N})$ and disul-



Scheme 1. Synthesis and Co metalation of a cyclic thiosulfinate. DMD = 2,2-dimethyl dioxirane, DMF = *N,N*-dimethyl formamide.

finato $[\text{CoN}_2(\text{SO}_2)_2(\text{tBuNC})_2](\text{Et}_4\text{N})$ complexes.^[11a] Oxidative cyclization of dithiol **1** with iodine in the presence of triethylamine^[12] afforded the cyclic disulfide **2**. Oxidation of **2** with 1 equivalent of 2,2-dimethyl dioxirane (DMD) in acetone at -20°C afforded the thiosulfinate **3** selectively and in high yield.

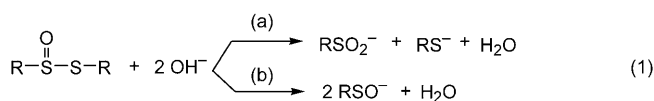
Thiosulfonates are very sensitive to nucleophiles, which cleave the S(O)–S bond, and nucleophilic attack can occur at the sulfenyl or sulfinyl sulfur atom.^[13] However, alkaline

[*] E. Bourles, R. Alves de Sousa, Dr. E. Galardon, Dr. I. Artaud
Laboratoire de Chimie et Biochimie Pharmacologiques
et Toxicologiques
UMR8601 CNRS, Université René Descartes
45 rue des Sts pères, 75270 Paris Cedex 06 (France)
Fax: (33) 1-42-86-83-87
E-mail: isabelle.artaud@univ-paris5.fr

Dr. M. Giorgi
Service Commun de Cristallographie
Faculté des Sciences et Techniques
Université Paul Cézanne (Aix-Marseille 3)
avenue Escadrille Normandie-Niemen, 13397 Marseille Cedex 20
(France)

[**] We thank Dr. Philippe Leduc for his help with the electrochemistry.
Supporting information for this article is available on the WWW
under <http://www.angewandte.org> or from the author.

hydrolysis of thiosulfinate has been described as quite selective for sulfinyl sulfur to afford a thiolate and a sulfinate as the predominant products [Eq. (1), route (a)].^[13a] We used



a combination of alkaline hydrolysis of compound **3** and metalation with a Co^{III} salt, Na₃[Co(NO₂)₆], to trap the open species. Incorporation of a Co^{II} salt followed by a single-electron oxidation with 2,3-dichloro-5,6-dicyano-1,4-benzoquinone is also possible, but the final purification of the complex is very tedious. This is why the use of the new hexanitrocobalt(III) sodium salt is much more convenient. Typically, the addition of 2 equivalents of Et₄NOH to a solution of **3** in DMF at −40 °C is followed by 1 equivalent of the Co^{III} salt. At this stage, the amide nitrogen atoms are likely coordinated in their imine tautomer form. After the addition of *tert*-butylisocyanide in excess, two other base equivalents are required to deprotonate the amides. The final complex is stable as a six-coordinate species with two isonitrile groups as axial ligands as previously observed for the disulfinate complex.^[11a]

Complex **4** (Scheme 1) was thoroughly characterized. All the spectroscopic data are in agreement with a dissymmetrical thiolate/sulfinate structure, [CoN₂(SO₂)(*t*BuNC)₂](Et₄N), with an S-bonded sulfinate, as in Co-NHase.^[3b] There is no evidence for a disulfinate species resulting from the cleavage of the S(O)–S bond by HO[−] group attack at the sulfinyl sulfur atom [Eq. (1), route (b)]. The IR spectrum of **4** (Supporting Information) exhibits the two SO₂ stretching frequencies expected for an S-bound sulfinate at 1185 ($\tilde{\nu}_{\text{as}}(\text{SO}_2)$) and 1047 cm^{−1} ($\tilde{\nu}_{\text{s}}(\text{SO}_2)$). There is no strong absorption around 950 cm^{−1} that could be attributed to the stretching frequency of a disulfinate species.^[11c] ESI MS (negative ion) analysis of **4** shows a molecular peak at *m/z* = 426.9, which corresponds to the mass of the anion of **4** with loss of the two isonitrile axial ligands. Further MS–MS analysis of this peak gives a daughter peak at *m/z* = 363.1 resulting from the loss of SO₂. As with all six-coordinate Co^{III} complexes in this series, **4** is diamagnetic. In contrast to the previously characterized [CoN₂(SO₂)₂(*t*BuNC)₂](Et₄N) species, which is completely symmetrical and exhibits only one resonance in its ¹H NMR spectrum for the methyl groups and another for the CH₂ protons,^[11a] both the methyl and the CH₂ protons of **4** are split and each appears at two different chemical shifts. The cyclic voltammogram of **4** in CH₃CN with NBu₄BF₄ as supporting electrolyte exhibits an oxidation step at +510 mV versus standard calomel electrode (SCE). This oxidation wave is located between that observed for [CoN₂(SO₂)₂(*t*BuNC)₂](Et₄N) (*E*_{pa} = +640 mV (vs. SCE)) and [CoN₂S₂(*t*BuNC)₂](Et₄N) (*E*_{pa} = +390 mV (vs. SCE)).^[11a] The anodic shift is about 125 mV for each addition of two oxygen atoms. The same trend has been observed upon sequential thiolate oxygenation of Ni complexes.^[14]

The dissymmetry of the coordination sphere is further supported by the crystal structure of the anion of **4** (Figure 1)

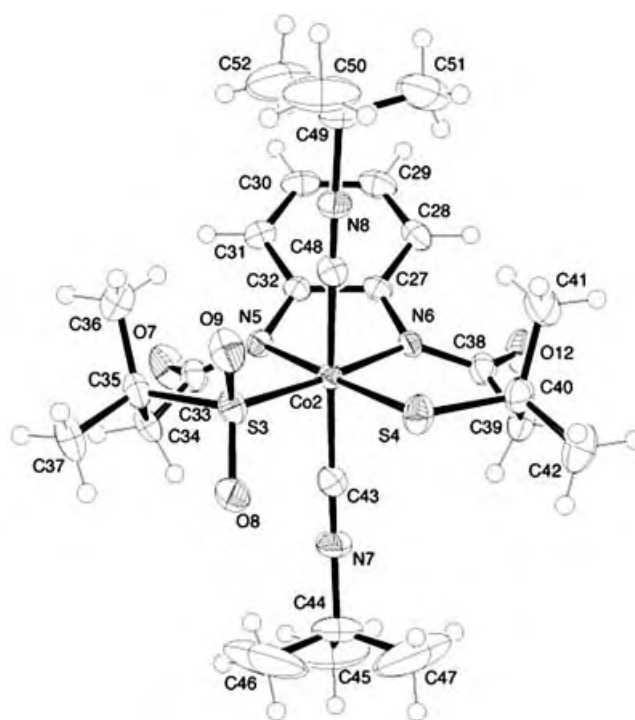
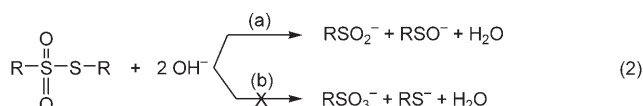


Figure 1. Thermal ellipsoid plot (50% probability level) of the anion of **4**. The hydrogen atoms, counterion, and solvent molecules have been omitted for clarity. Only one anionic enantiomer is shown. Selected bond lengths [Å]: Co2–C43 1.872(4), Co2–C48 1.870(4), Co2–N5 1.980(3), Co2–N6 1.997(3), Co2–S3 2.2205(11), Co2–S4 2.2505(12), S3–O8 1.463(4), S3–O9 1.467(4), N7–C43 1.143(5), N8–C48 1.142(5). Selected bond angles [°]: C48–Co2–C43 177.31(18), C48–Co2–N5 89.84(15), C48–Co2–N6 87.55(15), C43–Co2–N5 92.84(15), N5–Co2–N6 81.90(13), N5–Co2–S3 95.53(10), N5–Co2–S4 178.63(10), N6–Co2–S4 96.87(10), O8–S3–O9 113.9(2).

and by comparison with the disulfinate complex.^[11a] The Co^{III} center exhibits an octahedral geometry as does the disulfinate complex, but with one thiolate group and one S-bonded sulfinate group *trans* to the two carboxamido nitrogen atoms in the equatorial plane. The Co–S distances show significant variation (2.221–2.259 Å), which underscores the inequivalence of the two sulfur sites; these distances are almost equal in the disulfinate complex owing to the equivalence of the sulfur atoms. Whereas ¹H NMR analysis reveals a plane of symmetry in solution, the aromatic ring and the lateral chains relating N5 to S3 and N6 to S4 are on either side of the N₂S₂ plane, and the molecule is asymmetrical in the solid state. This can be related to the fact that the complex crystallizes with two enantiomers in the asymmetric unit (Experimental Section). The crystal structure of **4** also reveals the presence of hydrogen bonds between the co-crystallized water molecules and the oxygen atoms of the amides and one sulfinate, as previously observed in the crystal structure of the disulfinate complex.

Our results show that cyclic pseudopeptidic thiosulfonates can be efficiently trapped by a metallic cation under basic conditions. The alkaline cleavage occurs upon reaction of HO[−] at the sulfinyl sulfur atom to give the selective formation of the thiolate/sulfinate complex. As in other six-coordinate Co^{III} complexes,^[9,11] the sulfinate has a strong preference for a

sulfur-to-cobalt binding mode. Clearly, this is the only route to selectively prepare such a complex, as H_2O_2 oxidation of the dithiolate $[\text{CoN}_2\text{S}_2(\text{tBuNC})_2](\text{Et}_4\text{N})$ affords a mixture of sulfur-oxygenated species, whereas DMD oxidation gives the S-bonded disulfinate complex.^[11a] Such a reaction could be biologically relevant and could probably be extended to alkaline hydrolysis and metalation of cyclic pseudopeptidic thiosulfonates. Disulfide *S*-dioxides are much more sensitive to nucleophiles such as oxy anions than are disulfide *S*-monoxides; their alkaline hydrolysis has been described as selective for the sulfenyl sulfur atom [Eq. (2), route (a)].^[13]



The higher selectivity of thiosulfonates towards hydrolysis relative to thiosulfonates results from the fact that the sulfenyl sulfur is much more readily accessed than is the sulfonyl sulfur, and from the fact that a sulfinate is a better leaving group than a thiolate.^[13]

X-ray analysis of both Fe- and Co-NHases,^[3] as well as enzymatic inhibition studies^[4c] support the presence of a sulfenate group in the metal environment of NHase. Moreover, a Co complex with two S-bonded sulfenates has been shown recently to promote nitrile hydration.^[11d] With the aim of isolating a mixed sulfinate/sulfenate complex, the reactivity of **4** toward oxidants was studied. The products were identified by ^1H NMR spectroscopy. Oxidation of **4**, even at low temperature and with less than 1 equivalent of H_2O_2 or DMD, provides the previously isolated S-bonded disulfinate species, either alone or as a mixture with the starting product.^[11a]

On the basis of our results with a thiosulfinate, we can propose an alternate pathway for the specific thiolate oxidation of NHases into sulfinate and sulfenate species (Scheme 2). This sequence involves a post-translational modification of the protein prior to metal insertion as follows: the two cysteine residues of the consensus sequence that are

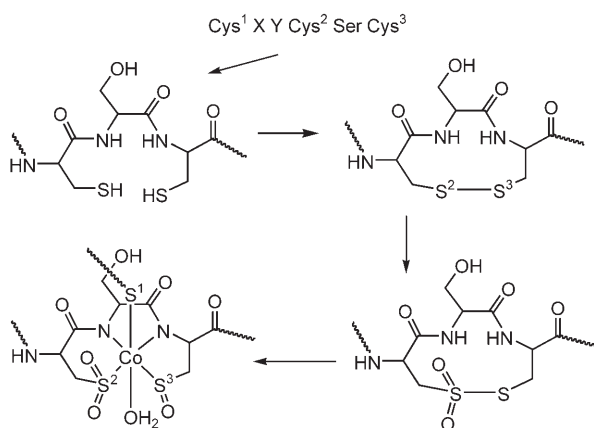
separated by a serine residue are initially oxidized to a disulfide, then to a disulfide *S*-dioxide. This is followed by alkaline hydrolysis and then by iron or cobalt insertion. A selective HO^- attack at the sulfenyl sulfur should directly afford the mixed sulfenate/sulfinate in the mean plane of the active site. Indeed, there is now clear evidence that disulfide *S*-oxides have important biological implications.^[2] Their production is either mediated by reactive oxygen, nitrogen species generated under oxidative stress conditions,^[2] or catalyzed by monooxygenases^[15a] or dioxygenases.^[15b] These disulfide oxides, mainly studied as the glutathione derivatives, lead to (gluta)thionylation of proteins or metallothionein by reaction of the free or zinc-bound cysteine group at the sulfenyl sulfur atom of the disulfide *S*-oxide.^[16] We suggest that these disulfide oxides might also result from a post-translational oxidation of proteins, with NHase possibly being the first example. Finally, we have shown that the reactivity of disulfide *S*-oxides is not limited to reaction with thiolates in proteins, but that they can also react with metallic cations after hydrolytic cleavage of the S–S bond. A more complete study of such reactions of thiosulfonates and thiosulfonates is in progress.

Experimental Section

All procedures were carried out under argon with standard Schlenk techniques. Solvents were dried following standard procedures and stored under argon.

3: Elemental analysis (%) calcd for $\text{C}_{16}\text{H}_{22}\text{N}_2\text{O}_3\text{S}_2 \cdot 0.33\text{H}_2\text{O}$ (360.49): C 53.31, H 6.34, N 7.77; found: C 53.50, H 6.21, N 7.48. ^1H NMR (250 MHz, CDCl_3): δ = 1.52 (s, 3H), 1.63 (s, 3H), 1.67 (s, 3H), 1.79 (s, 3H), 2.66–2.74 (m, 2H), 2.92–2.99 (m, 2H), 7.23 (m, 2H), 7.41 (m, 2H), 8.02 (s, 1H), 8.33 ppm (s, 1H). IR (neat): $\tilde{\nu}$ = 3253 (N–H), 1665 (C=O), 1069 cm^{-1} (S=O).

4: The sodium hexanitrocobaltate(III) salt is not soluble in DMF, but a solution was prepared as follows: DMF (3 mL) and trimethylorthoformate (10 mL) as a dehydrating agent were added to an aqueous solution (1.5 mL) of $\text{Na}_3[\text{Co}(\text{NO}_2)_6]$ (114 mg, 0.282 mmol). After stirring for 30 min, excess orthoformate as well as CH_3OH and HCOOCH_3 (products derived from the reaction of $\text{HC}(\text{OMe})_3$ with H_2O) were removed under controlled vacuum to prevent the complete evaporation of DMF. Then, Et_4NOH (1.4 M in MeOH, 405 μL , 2 equiv) and the Co^{III} solution were added to a solution (2 mL) of **3** (100 mg, 0.282 mmol) in DMF at -40°C . After stirring for a few minutes, a large excess of *t*BuNC (1 mL in 1 mL DMF) and 2 further equivalents of Et_4NOH (405 μL) were added to the mixture. The solution was then allowed to warm to room temperature. After evaporating to dryness in vacuo, the residue was dissolved in CH_3CN (1 mL) and a powder containing **4**, NaNO_2 , and Et_4NNO_2 was isolated upon precipitation with Et_2O . This powder was dissolved in acetone (2 mL) and nitrite salts were removed through careful precipitation by dropwise addition of Et_2O . After centrifugation, the supernatant was slowly poured into Et_2O while stirring to afford **4** as a brown powder. Yield: 130 mg (60%). Crystals suitable for X-ray crystallographic analysis were grown by diffusion of Et_2O into a CH_3CN solution of **4**. Elemental analysis (%) calcd for $\text{C}_{34}\text{H}_{58}\text{CoN}_5\text{O}_4\text{S}_2 \cdot 3\text{H}_2\text{O}$ (777.96): C 52.49, H 8.29, N 9.00; found: C 52.77, H 8.17, N 9.29. ^1H NMR (250 MHz, CD_3CN): δ = 1.01 (m, 12H, CH_3), 1.15 (s, 6H, CH_3), 1.3 (s, 18H, *t*BuNC), 1.39 (s, 6H, CH_3), 2.55 (s, 2H, CH_2), 2.69 (s, 2H, CH_2), 2.95 (m, 8H, CH_2 , Et_4N), 6.54 (m, 2H_{ar}), 7.94 ppm (m, 2H_{ar}). IR (neat): $\tilde{\nu}$ = 2200 (C=N), 1538 (C=O), 1185 and 1047 ($\tilde{\nu}_s$ and $\tilde{\nu}_{as}$ SO_2), 1173, 1002 cm^{-1} (Et_4N^+). Cyclic voltammetry (vs. SCE, $n\text{Bu}_4\text{NBF}_4$ (0.1 M), 20 mV s^{-1} , CH_3CN): E_{pc} = -1860 mV, E_{pa} = $+510$ mV. FAB MS (positive ion): m/z (%) = 853.39 (100) [CoN_2S



Scheme 2. Alternate pathway to the post-translational oxidation of nitrile hydratase.

(SO₂)(tBuNC₂)(Et₄N)₂⁺; ESI MS (negative ion): *m/z* (%) = 426.9 (40) [CoN₂S(SO₂)⁻, 363.1 (100) [M-SO₂]⁻.

Crystal data for complex **4**: (C₂₆H₃₈CoS₂O₄N₄)₂(C₈H₂₀N)₂·(C₂H₅N)₂(H₂O)₃, *M_w* = 1583.96, pale-yellow crystal (0.6 × 0.4 × 0.15 mm³), triclinic, space group *P* $\bar{1}$, *a* = 11.727(4), *b* = 20.031(9), *c* = 20.614(9) Å, α = 116.804(2)°, β = 90.384(3)°, γ = 95.913(3)°, *V* = 4291.3(3) Å³, *Z* = 2, ρ = 1.226 g cm⁻³, μ (Mo *K_α*) = 5.43 cm⁻¹, *T* = 223 K, θ = 1.18–28.62°. 47639 reflections measured at on a Bruker–Nonius Kappa CCD diffractometer, 20515 unique reflections, 946 parameters refined on *F*² (20515 reflections) using SHELXL-97 to final indices *R*[*F*² > 4σ(*F*²)] = 0.099, *wR* = 0.149 [*w* = 1/(σ²(*F*_o²) + (0.0001 *P*)² + 12.4629 *P*)] in which *P* = (*F*_o² + 2 *F*_c²)/3. Compound **4** crystallized as two independent anionic monomers in the asymmetric unit, with two Et₄N cations, two molecules of acetonitrile, and three water molecules. The anionic moiety was found to be a disordered mixture of two isomers corresponding to the two possible sulfur oxidation sites that afford sulfinates. The refinement was therefore carried out by considering two positions for the sulfinate group on each monomer: the occupancy factors for both the oxygen atoms of the sulfinate group were fixed to 0.8 and 0.2 on the two sites for the first monomer and to 0.2 and 0.8 on the two sites for the second monomer. Most of the H atoms, including one hydrogen of one water molecule, were found experimentally. The remaining H atoms (excluding those on the water molecules) were introduced in theoretical positions. They were all included in the calculations but not refined. The final residual Fourier positive and negative peaks were equal to 0.91 and –0.804 e Å⁻³, respectively. CCDC-262627 contains the supplementary crystallographic data for this paper. These data can be obtained free of charge from The Cambridge Crystallographic Data Centre via www.ccdc.cam.ac.uk/data_request/cif.

Received: March 4, 2005

Revised: May 17, 2005

Published online: September 1, 2005

Keywords: bioinorganic chemistry · cobalt · enzymes · oxidation · S ligands

- [5] a) T. C. Harop, P. K. Mascharak, *Acc. Chem. Res.* **2004**, *37*, 253–260; b) P. K. Mascharak, *Coord. Chem. Rev.* **2002**, *225*, 201–214; c) J. A. Kovacs, *Chem. Rev.* **2004**, *104*, 825–848.
- [6] L. Heinrich, Y. Li, J. Vaissermann, G. Chottard, J. C. Chottard, *Angew. Chem.* **1999**, *111*, 3736–3738; *Angew. Chem. Int. Ed.* **1999**, *38*, 3526–3528.
- [7] L. A. Tyler, J. C. Noveron, M. M. Olmstead, P. K. Mascharak, *Inorg. Chem.* **2003**, *42*, 5751–5761.
- [8] I. Kung, D. Schweitzer, J. Shearer, W. D. Taylor, H. L. Jackson, S. Lovell, J. A. Kovacs, *J. Am. Chem. Soc.* **2000**, *122*, 8299–8300.
- [9] a) L. A. Tyler, J. C. Noveron, P. K. Mascharak, *J. Am. Chem. Soc.* **1999**, *121*, 616–617; b) J. C. Noveron, M. M. Olmstead, P. K. Mascharak, *J. Am. Chem. Soc.* **2001**, *123*, 3247–3259.
- [10] E. Galdard, M. Giorgi, I. Artaud, *Chem. Commun.* **2004**, 286–287.
- [11] a) M. Rat, R. Alves de Sousa, J. Vaissermann, P. Leduc, D. Mansuy, I. Artaud, *J. Inorg. Biochem.* **2001**, *84*, 207–213; b) M. Rat, R. Alves de Sousa, A. Tomas, Y. Frapart, J. P. Tuchagues, I. Artaud, *Eur. J. Inorg. Chem.* **2003**, 759–765; c) L. Heinrich, Y. Li, J. Vaissermann, J. C. Chottard, *Eur. J. Inorg. Chem.* **2001**, 1407–1409; d) L. Heinrich, A. Mary-Verla, Y. Li, J. Vaissermann, J. C. Chottard, *Eur. J. Inorg. Chem.* **2001**, 2203–2206.
- [12] M. H. Goodrow, W. K. Musker, *Synthesis* **1981**, *6*, 457–459.
- [13] a) J. L. Kice, T. Rogers, *J. Am. Chem. Soc.* **1974**, *96*, 8009–8015; b) J. L. Kice, C. C. A. Liu, *J. Org. Chem.* **1979**, *44*, 1918–1923.
- [14] C. A. Grapperhaus, M. Y. Darensbourg, *Acc. Chem. Res.* **1998**, *31*, 451–459.
- [15] a) C. Teyssier, L. Guenot, M. Suschetet, M. A. Siess, *Drug Metab. Dispos.* **1999**, *27*, 835–841; b) D. R. Boyd, N. D. Sharma, M. A. Kennedy, S. D. Shepherd, J. F. Malone, A. Alves-Areias, R. Holt, S. G. Allenmark, M. A. Lemurell, H. Dalton, H. Luckarift, *Chem. Commun.* **2002**, 1452–1453.
- [16] a) J. Li, L. Huang, K. P. Huang, *J. Biol. Chem.* **2001**, *276*, 3098–3105; b) K. P. Huang, F. L. Huang, *Biochem. Pharmacol.* **2002**, *64*, 1049–1056; c) G. I. Giles, K. M. Tasker, C. Collins, N. M. Giles, E. O'Rourke, C. Jacob, *Biochem. J.* **2002**, *364*, 579–585.

- [1] L. B. Poole, P. A. Karplus, Al. Claiborne, *Annu. Rev. Pharmacol. Toxicol.* **2004**, *44*, 325–347.
- [2] a) C. Jacob, J. R. Lancaster, G. I. Giles, *Biochem. Soc. Trans.* **2004**, *32*, 1015–1017; b) C. Jacob, A. L. Holme, F. H. Fry, *Org. Biomol. Chem.* **2004**, *2*, 1953–1956; c) C. Jacob, G. I. Giles, N. M. Giles, H. Sies, *Angew. Chem.* **2003**, *115*, 4890–4907; *Angew. Chem. Int. Ed.* **2003**, *42*, 4742–4758; d) G. I. Giles, C. Jacob, *Biol. Chem.* **2002**, *383*, 375–388.
- [3] a) S. Nagashima, M. Nakasako, N. Dohmae, M. Tsujima, K. Takio, M. Odaka, M. Yohda, N. Kamiya, I. Endo, *Nat. Struct. Biol.* **1998**, *5*, 347–351; b) A. Miyanaga, S. Fushinobu, K. Ito, T. Wakagi, *Biochem. Biophys. Res. Commun.* **2001**, *288*, 1169–1174.
- [4] a) M. Nojiri, M. Yohda, M. Odaka, Y. Matsushita, M. Tsujimura, T. Yoshida, M. Dohmae, K. Takio, I. Endo, *J. Biochem. (Tokyo)* **1999**, *125*, 696–704; b) T. Murakami, M. Nojiri, H. Nakayama, M. Odaka, M. Yohda, K. Takio, T. Nagamune, I. Endo, *Protein Sci.* **2000**, *9*, 1024–1030; c) J. M. Stevens, M. Belghazi, M. Jaouen, D. Bonnet, J. M. Schmitter, M. A. Sari, D. Mansuy, I. Artaud, *J. Mass Spectrom.* **2003**, *38*, 955–961; d) J. M. Stevens, N. R. Saroja, M. Jaouen, M. Belghazi, J. M. Schmitter, D. Mansuy, I. Artaud, M. A. Sari, *Protein Expr. Purif.* **2003**, *29*, 70–76; e) M. Tsujimura, M. Odaka, H. Nakayama, N. Dohmae, H. Koshino, T. Asami, M. Hoshino, K. Takio, S. Yoshida, M. Maeda, I. Endo, *J. Am. Chem. Soc.* **2003**, *125*, 11532–11538; f) A. Miyanaga, S. Fushinobu, K. Ito, H. Shoun, T. Wakagi, *Eur. J. Biochem.* **2004**, *271*, 429–438.

DOI: 10.1002/anie.200501582

Tetraarylphosphonium Halides as Arylating Reagents in Pd-Catalyzed Heck and Cross-Coupling Reactions**

Lee Kyoung Hwang, Youngim Na, Junseong Lee, Youngkyu Do, and Sukbok Chang*

Transition-metal-catalyzed olefination and cross-coupling reactions have become one of the most powerful tools in organic synthesis.^[1] While aryl, alkenyl, alkynyl, and, more recently, alkyl halides are typically employed as coupling reagents, a variety of different types of pseudohalide species have been also investigated as useful electrophiles. Among these, representative recent examples are carboxylic acids,^[2] acid anhydrides,^[3] aryl esters,^[4] sulfonates,^[5] phosphonic acids,^[6] sulfonium ions,^[7] and ammonium salts.^[8] Although metal-mediated C–P bond cleavage of organophosphorus species was previously investigated,^[9] the use of such compounds in cross-coupling reactions has been relatively underdeveloped. Yamamoto and co-workers suggested that quaternary phosphonium iodide ($\text{Ph}_4\text{P}^+\text{I}^-$) oxidatively adds to Pd^0 complexes through P-aryl bond cleavage and they showed briefly that one phenyl group was transferred to react with activated olefins, although in low yields (32–36 %).^[10] Reetz et al. reported that the efficiency of the Heck reaction with normally unreactive aryl halides was significantly improved by the presence of phosphonium halides.^[11] Additionally, several research groups described mechanistic details for the observed aryl–aryl interchange process between phosphinyl- and Pd-bound aryl groups in cross-coupling reactions that relied on the composition of the products^[12] and theoretical considerations.^[13] Herein, we describe our recent studies on the utility of tetraarylphosphonium halides as arylating reagents in Heck and cross-coupling reactions, as well as providing spectroscopic details on the activation process.^[14]

At the outset of our studies, we attempted to optimize the reaction conditions for the Pd-catalyzed olefination reaction using tetraarylphosphonium ions. When tetraphenylphosphonium chloride (**1**) was treated with *n*-butyl acrylate (3.0 equiv) in the presence of $\text{Pd}(\text{OAc})_2$ (10 mol %) and sodium acetate (3.0 equiv), *n*-butyl *trans*-cinnamate was isolated in 85 % yield [Eq. (1)], which thus clearly suggested that the C–P bond of **1**

is activated catalytically in agreement with the previous report.^[10] We envisioned that the employment of electrospray ionization mass spectrometry (ESI-MS) could lead us to trace the activation process because it allows facile detection of highly unstable and/or sensitive metal-containing intermediates.^[15]



When **1** was treated with 0.5 equivalents of $[\text{Pd}_2(\text{dba})_3]$ (dba = *trans,trans*-dibenzylideneacetone) at 100 °C, a set of ion peaks were detected in the ESI-mass spectra which were attributed to transient metal species resulting from the activation of the P–phenyl bond of **1** (Figure 1). It was observed that a dba ligand in the complex was gradually displaced by acetonitrile to give a series of peaks for $[(\text{PPh}_3)_2\text{PhPd}(\text{CH}_3\text{CN})_m] (m=1-3)$ at the expense of phosphonium ion (Figure 1, all *m/z* values are reported on the basis of the ¹⁰⁶Pd isotope).^[16] When $\text{Pd}(\text{OAc})_2$ was employed instead of $[\text{Pd}_2(\text{dba})_3]$, the activation process occurred more slowly and the corresponding peaks started to appear only after a few hours under the same conditions. The fact that a complex of Pd^0 is more active than a Pd^{II} species for the activation is in a good agreement with the generally accepted assumption that Pd^{II} precursors are reduced initially into Pd^0 complexes, which are catalytically active in most cross-coupling reactions.^[17]

Pd-mediated cleavage of the P–C bond of tetraarylphosphonium ions was further supported by the isolation and characterization of an oxidatively inserted palladium species. When $\text{Ph}_4\text{P}^+\text{Cl}^-$ (**1**) was treated with 0.5 equivalents of $[\text{Pd}_2(\text{dba})_3]$ in the presence of PPh_3 , a transparent solid **2** was isolated (54 %) that revealed a square-planar geometry with two triphenylphosphine groups positioned *trans* to each other (Figure 2). The bond lengths and angles of **2** are within comparable range of those previously reported, although the same palladium species was prepared starting from a different precursor by a ligand-exchange method.^[18] When the isolated Pd complex **2** was treated with *n*-butyl acrylate,^[19] reaction occurred readily in the presence of sodium acetate at temperatures over 80 °C to afford butyl cinnamate in 55 %.^[20] This result led us to postulate that phosphonium species play a dual role, as a source of the arylating group and as a stabilizing ligand on palladium complexes, upon release of phosphine from the phosphonium ions.

During the course of optimization of the conditions for olefination with phosphonium halides, it was found that higher yields (ca. 20 %) were obtained when the reaction was carried out under atmospheric oxygen relative to those performed under N_2 .^[21] It is thought that oxygen oxidizes liberated triphenylphosphine into its oxide, thus driving the reaction to completion more readily. Indeed, a side product of triphenylphosphine oxide was seen to be generated (> 80 %) during the olefination reaction under an O_2 atmosphere

[*] L. K. Hwang, Y. Na, J. Lee, Prof. Y. Do, Prof. S. Chang
Center for Molecular Design and Synthesis (CMDS)
Department of Chemistry and School of Molecular Science (BK 21)
Korea Advanced Institute of Science and Technology (KAIST)
Daejeon 305-701 (Korea)
Fax: (+82) 42-869-2810
E-mail: sbchang@kaist.ac.kr

[**] This research was supported by the Center for Molecular Design and Synthesis at KAIST.

Supporting information for this article is available on the WWW under <http://www.angewandte.org> or from the author.

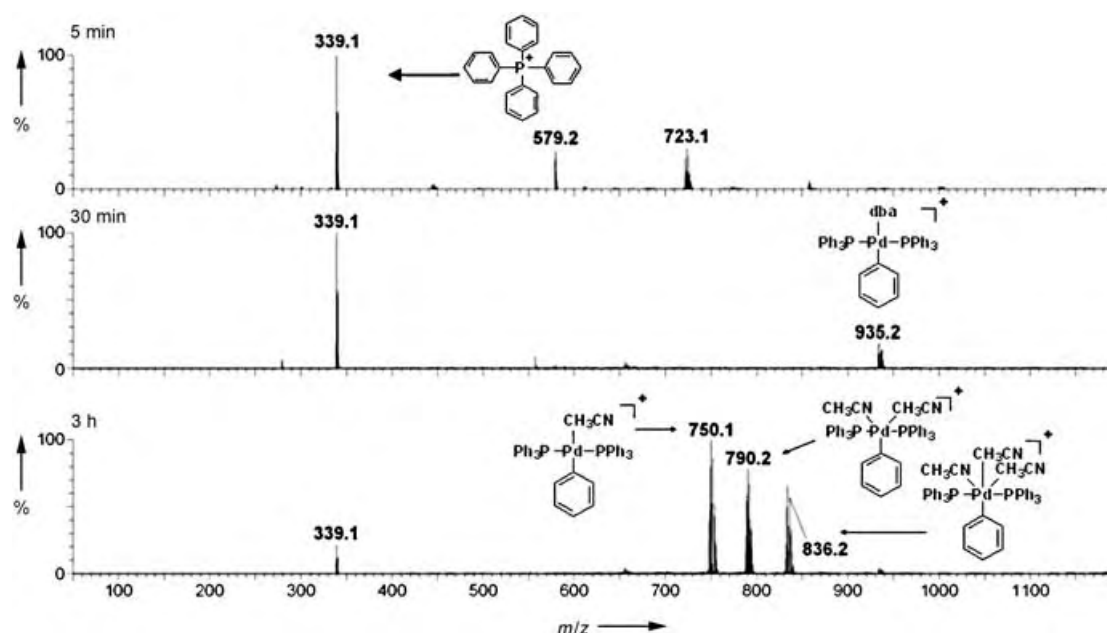


Figure 1. ESI mass spectra obtained from the treatment of tetraphenylphosphonium chloride (**1**) with $[\text{Pd}_2(\text{dba})_3]$ (0.5 equiv) at 100 °C.

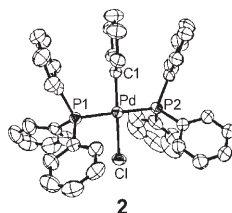
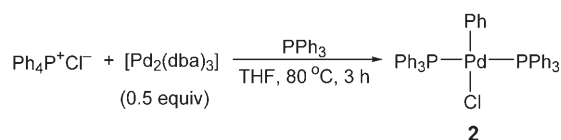
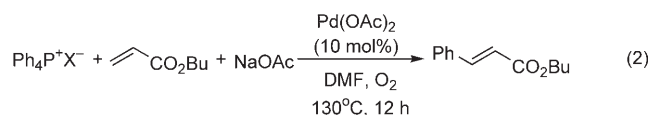
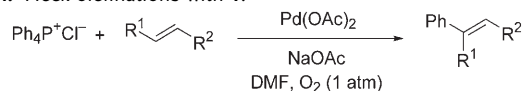


Figure 2. Preparation and X-ray crystal structure of **2**.



X = Cl: 85%
I: 57%
Br: 57%
Br: 82% (2 equiv of LiCl)

Table 1: Heck olefinations with **1**.^[a]



Entry	Alkene	Yield [%] ^[b]
1	$\text{CH}_2=\text{CHCO}_2\text{Et}$	72
2	$\text{CH}_2=\text{CHCO}_2\text{Bu}$	85
3	$\text{CH}_2=\text{CHCO}_2\text{NMe}_2$	98
4	$\text{CH}_2=\text{CHSO}_2\text{Ph}$	74
5 ^[c]	$\text{CH}_2=\text{CHPO}(\text{OEt})_2$	76
6	$\text{CH}_2=\text{CHCN}$	70 ^[d]
7	$\text{CH}_2=\text{CHCO}_2\text{H}$	71
8	$\text{CH}_2=\text{CHCO}_2\text{Et}$	59
9	$\text{CH}_2=\text{CHCOCH}_3$	70

[a] Reaction conditions: alkenes (3.0 equiv), catalyst (10 mol %), NaOAc (3.0 equiv), 130 °C, 12 h under O_2 (1 atm). [b] Yield of isolated product. [c] 3.0 equivalents of Cs_2CO_3 was used instead of NaOAc. [d] $E/Z = 4:1$.

[Eq. (1)]. Whereas sodium acetate turned out to be most effective of the various bases examined, it was interesting to observe that olefination proceeds even in the absence of an external base, albeit with moderate yields (53% from the reaction of Equation (1) under such conditions).^[22] Additionally, the efficiency of the reaction was dependent on the nature of the counteranions of the phosphonium salts [Eq. (2)]. Whereas reactions with phosphonium species that bear chloride ions gave the highest yield, other halide salts such as bromide and iodide resulted in reduced yields. However, upon addition of LiCl (2.0 equiv) in a reaction with $\text{Ph}_4\text{P}^+\text{Br}^-$, the efficiency was recovered to the same level as with $\text{Ph}_4\text{P}^+\text{Cl}^-$.

Under the optimized conditions, the olefination of **1** was examined with a range of alkenes (Table 1).^[23] Whereas reactions with acrylic esters, amides, vinyl sulfone, and vinyl phosphonate proceeded efficiently to afford the corresponding olefinated products exclusively in the *E* form, olefination with acrylonitrile produced cinnamionitrile with modest

selectivity ($E/Z = 4:1$). Notably, acrylic acid was also readily coupled with **1** to afford (*E*)-cinnamic acid in good yield.^[24]

The use of phosphonium species in the Suzuki–Miyaura reaction was next investigated (Table 2). While electronic and steric variations on organoboron compounds have negligible

Table 2: Suzuki coupling reactions with **1**.^[a]

$$\text{Ph}_4\text{P}^+\text{Cl}^- + \text{R}-\text{B}(\text{OR}')_2 \xrightarrow[\text{DMF, N}_2]{\text{Pd}(\text{OAc})_2, \text{NaOAc}} \text{Ph}-\text{R}$$

Entry	Organoborane	Yield [%] ^[b]
1	C ₆ H ₅ -B(OH) ₂	77
2	4-Ac-C ₆ H ₄ -B(OH) ₂	80
3	4-MeO-C ₆ H ₄ -B(OH) ₂	95
4	2-Me-C ₆ H ₄ -B(OH) ₂	83
5	4-Br-C ₆ H ₄ -B(OH) ₂	70
6	4-CHO-C ₆ H ₄ -B(OH) ₂	75
7	Ph-CH=CH-B(OH) ₂	91
8	nBu-CH=CH-B(OH) ₂	63
9	C ₆ H ₅ -B(O-C ₆ H ₃ (OH) ₂) ₂	70

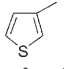
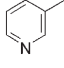
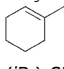
[a] Reaction conditions: organoboranes (1.5 equiv), catalyst (10 mol %), NaOAc (3.0 equiv), 100 °C, 12 h under N₂. [b] Yield of isolated product.

effects on efficiency, several functional groups were tolerated under the reaction conditions. As demonstrated in entry 9, a boronic ester derived from catechol was also employed as an efficient coupling partner with **1**. Although the exact reason is not clear at present, the effect of oxygen observed in the Heck olefination was not observed in case of Suzuki and Sonogashira reactions (see below).^[25]

In the Sonogashira-type reaction, tetraarylphosphonium halides were also readily employed as efficient arylating reagents with a wide range of alkynes (Table 3). In a similar

Table 3: Sonogashira coupling reactions with **1**.^[a]

$$\text{Ph}_4\text{P}^+\text{Cl}^- + \text{R}-\text{C}\equiv\text{C}-\text{R}' \xrightarrow[\text{Et}_3\text{N, DMF, N}_2]{\text{Pd}(\text{OAc})_2} \text{Ph}-\text{C}\equiv\text{C}-\text{R}'$$

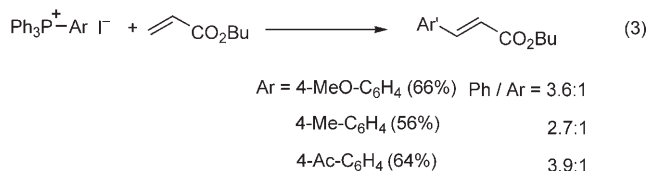
Entry	Alkyne	Yield [%] ^[b]
1	C ₆ H ₅	99
2	4-F-C ₆ H ₄	86
3	4-Me-C ₆ H ₄	62
4	4-PhO-C ₆ H ₄	99
5		62
6		77
7	HO(CH ₂) ₃	64
8	CH ₃ CH(OH)CH ₂	63
9		77
10	(iPr) ₃ Si	99

[a] Reaction conditions: alkynes (3.0 equiv), catalyst (5 mol %), Et₃N (2.0 equiv), 100 °C, 12 h under N₂. [b] Yield of isolated product.

manner as observed in Heck and Suzuki reactions, the alkynylation was not significantly affected by aryl substituents. Note that coupling of **1** with 1-phenyl-2-(trimethylsilyl)-acetylene, an internal alkyne, was also carried out efficiently (98 % yield) when 1,3-bis(2,4,6-trimethylphenyl)imidazolium chloride was employed as an additive (10 mol %).

When differently substituted tetraarylphosphonium halides^[26] were used in olefinations, a selective aryl transfer was

not observed [Eq. (3)]. Independent of the electronic nature of the aryl substituents, a mixture of unsubstituted (major) and substituted cinnamates (minor) were produced with a ratio of 3–4:1. The rather statistical aryl transfer in the Heck olefination was also observed in Suzuki and Sonogashira reactions. These results can be presumably attributed to fast aryl–aryl interchange processes between phosphinyl- and Pd-bound aryl groups that are generated upon cleavage of the C–aryl bond of the heterogeneously substituted phosphonium species.



In summary, conditions have been optimized for the Pd-catalyzed reactions of tetraarylphosphonium halides with olefins, organoborons, and alkynes that demonstrate the utility of the phosphonium species as facile arylating reagents. Characterization of reaction intermediates by ESI mass spectrometry and X-ray crystallography add important knowledge to the Pd-mediated activation pathway of the C–P bond of phosphonium precursors.

Received: May 10, 2005

Revised: June 13, 2005

Keywords: C–P activation · cross-coupling · mass spectrometry · olefination · phosphorus

- [1] a) R. F. Heck in *Comprehensive Organic Synthesis*, Vol. 4 (Eds.: B. M. Trost, I. Fleming), Pergamon, Oxford, **1991**; b) N. Miyauchi, A. Suzuki, *Chem. Rev.* **1995**, 95, 2457.
- [2] A. G. Myers, D. Tanaka, M. R. Mannion, *J. Am. Chem. Soc.* **2002**, 124, 11250.
- [3] M. S. Stephan, A. J. J. M. Teunissen, G. K. M. Verzijl, J. G. de Vries, *Angew. Chem.* **1998**, 110, 688; *Angew. Chem. Int. Ed.* **1998**, 37, 662.
- [4] L. J. Gooßen, J. Paetzold, *Angew. Chem.* **2002**, 114, 1285; *Angew. Chem. Int. Ed.* **2002**, 41, 1237.
- [5] C. Bolm, J. P. Hildebrand, J. Rudolph, *Synthesis* **2000**, 911.
- [6] A. Inoue, H. Shinokubo, K. Oshima, *J. Am. Chem. Soc.* **2003**, 125, 1484.
- [7] J. Srogl, G. D. Allred, L. S. Liebeskind, *J. Am. Chem. Soc.* **1997**, 119, 12376.
- [8] S. B. Blakey, D. W. C. MacMillan, *J. Am. Chem. Soc.* **2003**, 125, 6046.
- [9] a) P. E. Garrou, *Chem. Rev.* **1985**, 85, 171; b) H. Nakazawa, Y. Matsuoka, I. Nakagawa, K. Miyoshi, *Organometallics* **1992**, 11, 1385; c) X.-M. Zhang, A. J. Fry, *J. Org. Chem.* **1996**, 61, 4101; d) V. V. Grushin, *Organometallics* **2000**, 19, 1888.
- [10] M. Sakamoto, I. Shimizu, A. Yamamoto, *Chem. Lett.* **1995**, 1101.
- [11] M. T. Reetz, G. Lohmer, R. Schwickardi, *Angew. Chem.* **1998**, 110, 492; *Angew. Chem. Int. Ed.* **1998**, 37, 481.
- [12] a) V. Farina, B. Krishnan, *J. Am. Chem. Soc.* **1991**, 113, 9585; b) W. A. Herrmann, C. Broßmer, T. Priemermeier, K. Öfele, *J. Organomet. Chem.* **1994**, 481, 97; c) D. K. Morita, J. K. Stille, J. R. Norton, *J. Am. Chem. Soc.* **1995**, 117, 8576; d) F. E.

- Goodson, T. I. Wallow, B. M. Novak, *J. Am. Chem. Soc.* **1997**, *119*, 12441; e) G. de La Torre, A. Gouloumis, P. Vázquez, T. Torres, *Angew. Chem.* **2001**, *113*, 2979; *Angew. Chem. Int. Ed.* **2001**, *40*, 2895; f) F. Y. Kwong, K. S. Chan, *Organometallics* **2001**, *20*, 2570.
- [13] J. V. Ortiz, Z. Havlas, R. Hoffmann, *Helv. Chim. Acta* **1984**, *67*, 1.
- [14] For recent results on cross-coupling reactions from this laboratory, see: a) S. Chang, S. H. Yang, P. H. Lee, *Tetrahedron Lett.* **2001**, *42*, 4833; b) S. Chang, M. Lee, S. Kim, *Synlett* **2001**, 1557; c) Y. Na, S. Park, S. B. Han, H. Han, S. Ko, S. Chang, *J. Am. Chem. Soc.* **2004**, *126*, 250; d) S. Park, M. Kim, D. H. Koo, S. Chang, *Adv. Synth. Catal.* **2004**, *346*, 1638.
- [15] a) A. O. Aliprantis, J. W. Canary, *J. Am. Chem. Soc.* **1994**, *116*, 6985; b) J. M. Brown, K. K. Hii, *Angew. Chem.* **1996**, *108*, 679; *Angew. Chem. Int. Ed. Engl.* **1996**, *35*, 657; c) A. A. Sabino, A. H. L. Machado, C. R. D. Correia, M. N. Eberlin, *Angew. Chem.* **2004**, *116*, 2568; *Angew. Chem. Int. Ed.* **2004**, *43*, 2514.
- [16] See Supporting Information for a comparison of the distribution of isotopic ratios between the calculated and obtained spectra.
- [17] a) F. Ozawa, A. Kubo, T. Hayashi, *Chem. Lett.* **1992**, 2177; b) C. Amatore, A. Jutand, M. A. M'Barki, *Organometallics* **1992**, *11*, 3009.
- [18] A. Mentès, R. D. W. Kemmitt, J. Fawcett, D. R. Russeli, *Polyhedron* **1999**, *18*, 1141.
- [19] It was reported that some $[\text{ArPdCl}(\text{PPh}_3)_2]$ complexes react with olefins in the presence of Et_3N as base; see: a) H. A. Dieck, R. F. Heck, *J. Am. Chem. Soc.* **1974**, *96*, 1133; b) C.-M. Andersson, A. Hallberg, G. D. Daves, *J. Org. Chem.* **1987**, *52*, 3529.
- [20] Amatore et al. established that acetate ions substitute the iodide ion from $[\text{PhPdI}(\text{PPh}_3)_2]$ to afford $[\text{PhPd}(\text{OAc})(\text{PPh}_3)_2]$, which is determined to be an essential intermediate in the Heck reaction; see: C. Amatore, E. Carré, A. Jutand, M. A. M'Barki, G. Meyer, *Organometallics* **1995**, *14*, 5605.
- [21] Although the intermediate $[\text{Pd}^0(\text{PPh}_3)_2]$ species that is generated at the end of the catalytic cycle is known to be very sensitive to oxygen,^[1] the present results suggest that its oxidative addition with the phosphonium salts might be faster than its reaction with oxygen. We thank one reviewer for indicating this.
- [22] One reviewer suggested that triphenylphosphine, which is liberated during the reaction, may serve as a base, although the same role by chloride ion cannot be ruled out at present.
- [23] Although the reported yields were obtained from reactions with $\text{Pd}(\text{OAc})_2$ catalyst (10 mol %), use of $[\text{Pd}_2(\text{dba})_3]$ (5 mol %) resulted in almost comparable results.
- [24] When tetra-*p*-tolylphosphonium chloride was employed, *n*-butyl *trans*-3-(4-methylphenyl)acrylate was obtained in 99% yield.
- [25] Suzuki and Sonogashira reactions under oxygen atmosphere afforded significantly lower yields relative to those obtained under N_2 ; see the Supporting Information for details.
- [26] T. Migita, T. Nagai, K. Kiuchi, M. Kosugi, *Bull. Chem. Soc. Jpn.* **1983**, *56*, 2869.

DOI: 10.1002/anie.200500923

Highly Diastereoselective Alkylation of Aziridine-2-carboxylate Esters: Enantioselective Synthesis of LFA-1 Antagonist BIRT-377**

Aniruddha P. Patwardhan, V. Reddy Pulgam, Yu Zhang, and William D. Wulff*

Aziridines are important synthons in organic chemistry as they provide convenient entry to optically pure amines, α -amino acids, amino alcohols, diamines, and a variety of other amino compounds that are useful both in industrial and academic endeavors. In the past, most optically pure aziridines were derived from acyclic members of the chiral pool, however, methods are emerging for the direct synthesis of optically pure aziridines through catalytic asymmetric reactions.^[1] We have developed a process for the catalytic asymmetric synthesis of aziridines from the reaction of benzhydryl imines with diazo compounds mediated by a chiral boron Lewis acid prepared from the VAPOL and VANOL ligands.^[2–4] This asymmetric aziridination (AZ) proved general for a range imines including those prepared from a variety of aryl aldehydes and also from primary, secondary, and tertiary aliphatic aldehydes (90–99% *ee*). Much lower enantioselectivities were observed with *N*-benzyl imines.^[2d]

α -Amino acids which are tetrasubstituted at the α -carbon are very popular tools that are used to control conformation in peptides, and hence their biological and pharmaceutical properties. A large number of methods have been developed for the synthesis of tetrasubstituted α -amino acids, and this subject has been reviewed.^[5] Interestingly, aziridines have rarely been used for the synthesis of tetrasubstituted α -amino acids and this may be partly due to the fact that the alkylation of aziridine-2-carboxylates is virtually an unknown reaction. Typically, attempts to alkylate aziridine-2-carboxylate esters leads to either ring opening or to self-condensation.^[6,7] The only known examples involve the use of either thioesters of aziridine-2-carboxylates^[6] or the use of a nitrogen substituent on the aziridine that can chelate a metal enolate.^[7]

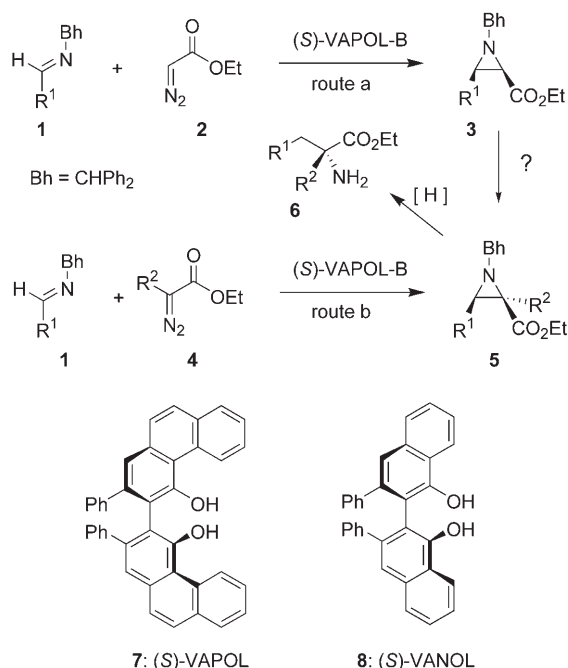
A direct application of the AZ reaction to the synthesis of tetrasubstituted α -amino acids could be envisioned through the asymmetric aziridination of imine **1** with diazo compound

[*] Dr. A. P. Patwardhan, Dr. V. R. Pulgam, Y. Zhang, Prof. W. D. Wulff
Department of Chemistry
Michigan State University
East Lansing, MI 48824 (USA)
Fax: (+1) 517-353-1793
E-mail: wulff@cem.msu.edu

[**] This work was supported by a grant from the NIH (NIGMS 63019). We thank Dr. Rui Hang for his help with the X-ray analysis.



Supporting information for this article, including preparative procedures and spectral data for all new compounds and X-ray diffraction data for **5a** and **10**, is available on the WWW under <http://www.angewandte.org> or from the author.



Scheme 1. Application of the AZ reaction to the synthesis of tetrasubstituted α -amino acids.

4 followed by the reductive opening of the aziridine ring (route a, Scheme 1). However, we found that substituted diazoesters of the type **4** ($\text{R}^2 \neq \text{H}$) are sluggish substrates in the AZ reaction. Thus route B, which involves the less readily available and sterically hindered diazo compound **4**, is not viable. Herein, we report the development of an alternative method (route A, Scheme 1) that utilizes commercially available ethyl diazoacetate and a subsequent stereoselective alkylation of an aziridine-2-carboxylate. This strategy has led to the first examples of alkylations of aziridine-2-carboxylate esters with nonchelating N substituents. The synthetic utility of the sequential AZ reaction and aziridine alkylation is illustrated in the asymmetric catalytic synthesis of the leukointegrin LFA-1 antagonist BIRT-377.^[8]

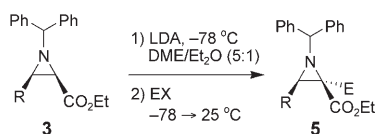
Aside from thioesters,^[6] the only known examples of aziridine-2-carboxylate alkylations employ a 2-methoxy-1-phenylethyl substituent on nitrogen to stabilize the metal enolate intermediate.^[7] Thus it was not clear if the desired alkylation of **3** to **5** would be feasible. Indeed, initial attempts to alkylate the aziridine **3a** with methyl iodide met with failure. Both the lithium and potassium amides of hexamethyldisilazane failed to deprotonate aziridine **3a**. Methylation was successful with lithium diisopropyl-

lamide (LDA). The optimal conditions involved the treatment of **3a** with 2.0 equivalents of LDA at -78°C followed by addition of 3 equivalents of methyl iodide, and then allowing the reaction mixture to warm to room temperature to give **5a** in 82% yield (1.1 equiv of LDA gave a 48% yield of **5a**). We screened the reactions in Table 1 with a mixture of DME (1,2-dimethoxyethane) and diethyl ether (5:1) as solvent,^[7] but have subsequently found that comparable yields of **5a** can be achieved with either DME (79%) or THF (85%). Interestingly, the use of diethyl ether led to a complicated reaction mixture with the formation of only a trace amount of the product. The aziridine **5a** was formed as a single diastereomer, as determined by ^1H NMR spectroscopy (>99% d.r.). The assignment of the stereochemistry of **5a** was made on the basis of NOE experiments and by an X-ray diffraction analysis of a single crystal of **5a**.

The scope of the alkylation reaction was investigated with a number of different aziridines and electrophiles (Table 1). In all cases a single C2 epimer was observed and, on the basis of the structure of **5a**, was assigned as that formed from retention at the 2-position. Attempts to epimerize the enolate of **3a** failed. Deprotonation of **3a** at -78°C and then warming to 0°C for 2 h before quenching with water at -78°C led to 98% recovery of **3a** with complete retention of stereochemistry. Primary alkyl iodides gave moderate yields, while aldehydes gave high yields but with no selectivity at the alcohol stereogenic center. The only electrophile that gave a mixture of isomers at the aziridine was tributyltin chloride, and in this case the minor product was assigned as the *O*-alkylated product.

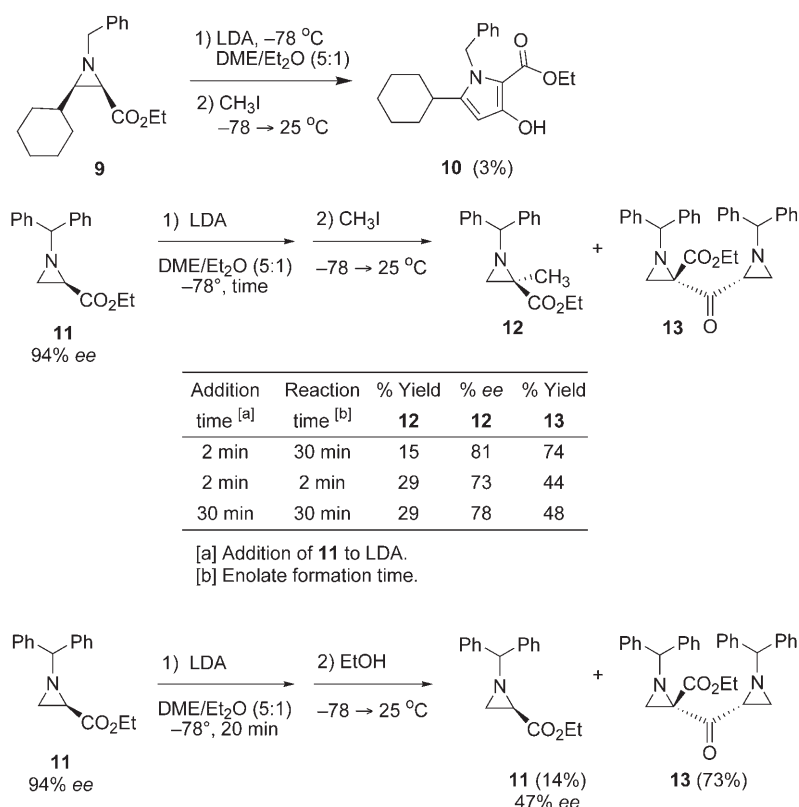
The alkylations of aziridine-2-carboxylates with a benzhydryl group on the nitrogen have never been reported, nor have the alkylations of aziridine-2-carboxylates with a

Table 1: Alkylation of **3**.^[a]



Entry	R	Substrate	EX	Product	Yield [%]
1	Ph	3a	H_2O	3a	98
2	Ph	3a	H_2O	3a	98 ^[b]
3	Ph	3a	CH_3I	5a	82
4	Ph	3a	$n\text{-C}_8\text{H}_{17}\text{I}$	5b	50
5	Ph	3a	$\text{CH}_2=\text{CHCH}_2\text{Br}$	5c	61
6	Ph	3a	PhCH_2Br	5d	33
7	Ph	3a	MOMCl	5e	63
8	Ph	3a	PhCHO	5f	95 ^[c]
9	Ph	3a	$n\text{-C}_3\text{H}_7\text{CHO}$	5g	89 ^[c]
10	Ph	3a	Bu_3SnCl	5h	73 ^[d]
11	2-naphthyl	3b	CH_3I	5i	70
12	$p\text{-PhC}_6\text{H}_4$	3c	CH_3I	5j	64
13	$p\text{-BrC}_6\text{H}_4$	3d	CH_3I	5k	86
14	$c\text{-C}_6\text{H}_{11}$	3e	CH_3I	5l	70
15	$t\text{Bu}$	3f	MOMCl	5m	66

[a] Unless otherwise specified, the reaction was performed with 2 equivalents of LDA in a solution of **3** (0.06 M) in DME/ Et_2O (5:1). Only one isomer of **5** was observed except for entries 8–10. [b] Reaction mixture warmed to 0°C for 2 h and then quenched at -78°C . [c] A 1:1 mixture of diastereomers at the carbinol carbon. [d] Includes an 18% yield of a product tentatively assigned as an *O*-alkylated isomer. MOM = methoxymethyl.

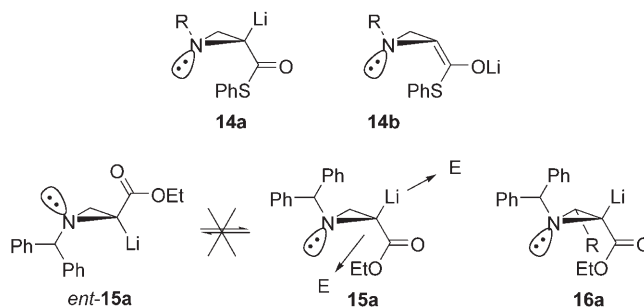


Scheme 2. Influence of substituents on aziridine-2-carboxylates in alkylation reactions.

substituent in the 3-position. Thus, we decided to investigate the alkylations of aziridines **9** and **11** in an effort to see which has the greater influence (Scheme 2). The results indicate that the benzhydryl group has the most significant impact. Whereas the cyclohexyl-substituted aziridine **3e** is methylated cleanly in 70% yield with methyl iodide (Table 1, entry 14), the benzyl analogue **9** gives a complicated reaction mixture under the same conditions and none of the expected alkylated aziridines could be detected or isolated from the crude reaction mixture (all starting material was consumed). The only product that was isolated and identified from this reaction mixture was the pyrrole **10**, whose origin is unclear but whose structure was confirmed by X-ray diffraction analysis. It is also clear that the presence of a substituent at the 3-position of the aziridine is important. Aziridine **11** which has no substituent in the 3-position gives only a 15% yield of the alkylated aziridine **12** while all of the aziridines in Table 1 can be alkylated with methyl iodide in 64–82% yield under the same conditions. The major product in the methylation of **11** is the Claisen condensation product **13**, which is the only product that has been seen from the attempted alkylation of ethyl esters of aziridine-2-carboxylates.^[7]

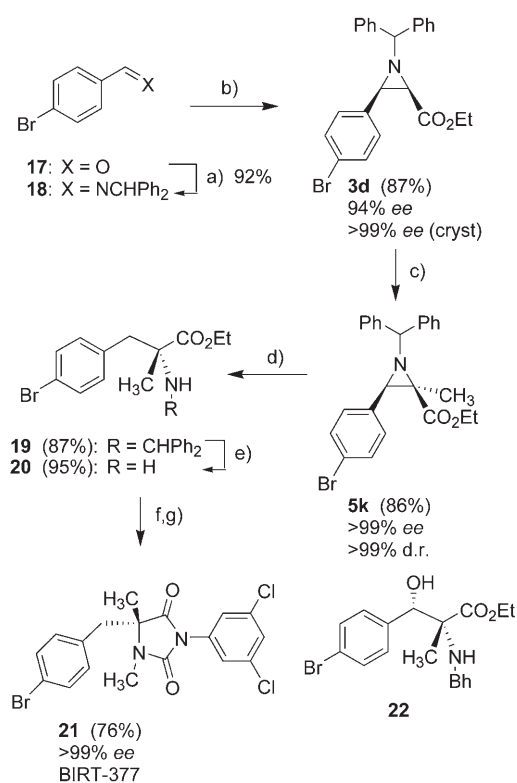
Interestingly, the optical purity of the methylated aziridine **12** (81% *ee*) is less than the starting aziridine **11** (94% *ee*). The loss of optical activity (47% *ee*) is greater for the protonation of the enolate of **11** which occurs with retention of configuration. This result suggests that the loss of optical activity is dependent on the electrophile. The enolate of **11** was allowed to age for only 2 minutes before methyl iodide was added, and the optical purity of **12** was found to be

73% *ee*. Thus, there does not seem to be a time dependence on the loss of optical activity. The normal aging time of the enolate is 30 minutes, and in this case its optical purity is not lower but in fact slightly higher (81% *ee*). Increasing the time of addition of **11** to LDA leads to only a slight increase in the proportion of the alkylated product **12** to the Claisen product **13**. Seebach and co-workers previously observed that the enolates of aziridine thioesters can also be alkylated with retention and that the enolate must either exist as the *C*-metalloenolate **14a** or the *O*-metalloenolate **14b**, which is substantially pyramidal at the enolate carbon (Scheme 3).^[6b] We interpret the above results as involving a configurationally stable enolate (drawn as the *C*-enolate **15a** but could also be the pyramidal *O*-enolate **15b**) that does not epimerize with time but rather reacts with either retention or inversion, the proportion of which is electrophile dependent. This would be consistent with the observation that all of the *cis*-3-substituted aziridines shown in Table 1 give exclusively alkylated products with retention of configuration. The R group in enolate **16a** would be expected to disfavor alkylation with inversion by approach of the electrophile from the rear side.



Scheme 3. Alkylation of aziridine thioesters. E = electrophile.

The utility of the alkylation of aziridine-2-carboxylates in the synthesis of tetrasubstituted α -amino acids is demonstrated in the synthesis of BIRT-377 (Scheme 4). BIRT-377 has been developed as an agent for the treatment of inflammatory and immune disorders.^[8] The asymmetric synthesis was achieved through the aziridine **3d**, which was prepared by the AZ reaction with 1 mol% catalyst in 87% yield and with 94% *ee* with greater than 50:1 selectivity for the *cis* isomer. A single recrystallization gave material with over 99% *ee* (72% recovery, first crop). The methylation of **3d** followed from the above procedure to give **5k** in 86% yield as a single diastereomer. Reductive ring opening was performed with borane–trimethylamine complex in the presence of trifluoroacetic acid (TFA) to give the amino ester **19** in 87% yield ($\text{BH}_3\cdot\text{Me}_3\text{N}$ with TFA gave a 6:1 mixture of **19** and **22**).^[9] Ring opening by hydrogenolysis under a variety of conditions including Pd/C/ HCO_2H occurred with simultaneous bromide reduction. Surprisingly, the



Scheme 4. Reagents and conditions: a) Ph₂CHNH₂ (1.0 equiv), CH₂Cl₂, MgSO₄, room temperature, 24 h; b) ethyl diazoacetate (1.1 equiv), (S)-VAPOL-B catalyst (1 mol%; see footnote 3), CCl₄, room temperature, 20 h; c) LDA (2 equiv), DME/Et₂O (5:1), −78 °C, 0.5 h; MeI (3 equiv), −78 to RT; d) BH₃·Me₂N (12 equiv), TFA (9 equiv), CH₂Cl₂, 0° to RT, 36 h; e) Et₃SiH (3 equiv), TFA, reflux, 5 h; f) 3,5-dichloro-phenyl isocyanate (1.1 equiv), DMSO, Na₂CO₃, 120 °C, 1.5 h; g) NaHMDS (1.2 equiv), DMF, room temperature; MeI (1.2 equiv), 2 h. DMSO = dimethyl sulfoxide; HMDS = hexamethyldisilazide; DMF = N,N-dimethylformamide.

reductive ring opening of **5k** with triethylsilane and TFA gave mainly the amino alcohol **22**, which results from ring opening with trifluoroacetate. Cleavage of the benzhydryl group in **19** with triethylsilane in the presence of trifluoroacetic acid gave the amine **20** in 95% yield. The conversion of amine **20** into BIRT-377 (**21**) follows methods employed in previous syntheses.^[8d]

The fact that benzhydryl-protected aziridine-2-carboxylates can be readily alkylated at the 2-position greatly enhances the synthetic utility of the asymmetric aziridination (AZ) reaction, as illustrated by the synthesis of BIRT-377. Additional studies with other electrophiles and applications in other syntheses will be reported in due course.

Received: March 11, 2005

Published online: August 24, 2005

Keywords: asymmetric catalysis · aziridines · BIRT-377 · enols · synthetic methods

[1] P. Müller, C. Fruit, *Chem. Rev.* **2003**, *103*, 2905–2920.

[2] a) J. C. Antilla, W. D. Wulff, *J. Am. Chem. Soc.* **1999**, *121*, 5099–5100; b) J. C. Antilla, W. D. Wulff, *Angew. Chem.* **2000**, *112*, 4692–4695; *Angew. Chem. Int. Ed.* **2000**, *39*, 4518–4521; c) C. Loncaric,

W. D. Wulff, *Org. Lett.* **2001**, *3*, 3675–3678; d) J. Antilla, W. D. Wulff, Y. Zhang, unpublished results.

[3] The catalyst is prepared by heating a solution of (S)-VAPOL and triphenylborate (3 equiv) in CCl₄ at 85 °C for 1 h and then by removing the volatiles under a high vacuum at 85 °C for 30 minutes.

[4] For other examples of aziridines from the reactions of imines with diazo compounds, see references [2a], [2b], and references therein, and the following: a) S. H. Lee, I. W. Song, *Bull. Korean Chem. Soc.* **2005**, *26*, 223–224; b) M. Redlich, M. M. Hossain, *Tetrahedron Lett.* **2004**, *45*, 8987–8990; c) B. Vanderhoydonck, C. V. Stevens, *Synthesis* **2004**, 722–734; d) A. L. Williams, J. N. Johnston, *J. Am. Chem. Soc.* **2004**, *126*, 1612–1613; e) Y. Li, P. W. H. Chan, N.-Y. Zhu, C.-M. Che, H.-L. Kwong, *Organometallics* **2004**, *23*, 54–66; f) J. R. Krumper, M. Gerisch, J. M. Suh, R. G. Bergman, T. D. Tilley, *J. Org. Chem.* **2003**, *68*, 9705–9710; g) J. S. Yadav, B. V. S. Reddy, P. N. Reddy, M. S. Rao, *Synthesis* **2003**, 1387–1390; h) T. Akiyama, S. Ogi, K. Fuchibe, *Tetrahedron Lett.* **2003**, *44*, 4011–4013; i) J. S. Yadav, B. V. S. Reddy, M. S. Rao, P. N. Reddy, *Tetrahedron Lett.* **2003**, *44*, 5275–5278; j) W. Sun, C.-G. Zia, H.-W. Wang, *Tetrahedron Lett.* **2003**, *44*, 2409–2411; k) E. Hevia, J. Perez, V. Riera, D. Miguel, S. Kassel, A. Rheingold, *Inorg. Chem.* **2002**, *41*, 4673–4679; l) M. F. Mayer, M. M. Hossain, *J. Organomet. Chem.* **2002**, *654*, 202–209; m) V. K. Aggarwal, E. Alonso, M. Ferrara, S. E. Spey, *J. Org. Chem.* **2002**, *67*, 2335–2344; n) D. Morales, J. Perez, L. Riera, V. Riera, R. Corzo-Suarez, S. Garcia-Granda, D. Miguel, *Organometallics* **2002**, *21*, 1540–1545; o) M. P. Spanedda, B. Crousse, S. Narizuka, D. Bonnet-Delphon, J.-P. Begue, *Collect. Czech. Chem. Commun.* **2002**, *67*, 1359–1365; p) K.-D. Lee, J.-M. Suh, J.-H. Park, H.-J. Ha, H. G. Choi, C. S. Park, J. W. Chang, W. K. Lee, Y. Dong, H. Yun, *Tetrahedron* **2001**, *57*, 8267–8276; q) V. K. Aggarwal, M. Ferrara, C. J. O'Brien, A. Thompson, R. V. H. Jones, R. Fieldhouse, *J. Chem. Soc. Perkin Trans. 1* **2001**, 1635–1643; r) B. Crousse, S. Narizuka, D. Bonnet-Delphon, J.-P. Begue, *Synlett* **2001**, 5, 679–681; s) M. P. Doyle, W. Hu, D. J. Timmons, *Org. Lett.* **2001**, *3*, 933–935; t) M. F. Mayer, Q. Wang, M. M. Hossain, *J. Organomet. Chem.* **2001**, *630*, 78–83; u) V. K. Aggarwal, E. Alonso, G. Fang, M. Ferrara, G. Hynd, M. Porcelloni, *Angew. Chem.* **2001**, *113*, 1482–1485; *Angew. Chem. Int. Ed.* **2001**, *40*, 1433–1436; v) S. H. Lee, T. D. Han, K. Yu, K. H. Ahn, *Bull. Korean Chem. Soc.* **2001**, *22*, 449–450; w) V. K. Aggarwal, M. Ferrara, *Org. Lett.* **2000**, *2*, 4107–4110; x) R. Hori, T. Aoyama, T. Shioiri, *Tetrahedron Lett.* **2000**, *41*, 9455–9458; y) S. Sengupta, S. Mondal, *Tetrahedron Lett.* **2000**, *41*, 6245; z) T. Kubo, S. Sakaguchi, Y. Ishii, *Chem. Commun.* **2000**, 625–626; aa) W. Xie, J. Fang, J. Li, P. G. Wang, *Tetrahedron* **1999**, *55*, 12929–12938; ab) D. L. Wright, M. C. McMills, *Org. Lett.* **1999**, *1*, 667–670; ac) K. Juhl, R. G. Hazell, K. A. Jorgensen, *J. Chem. Soc. Perkin Trans. 1* **1999**, 2293–2297.

[5] a) C. Cativiela, M. D. Diaz-de-Villegas, *Tetrahedron: Asymmetry* **1998**, *9*, 3517–3599; b) C. Cativiela, M. D. Diaz-de-Villegas, *Tetrahedron: Asymmetry* **2000**, *11*, 645–732.

[6] a) D. Seebach, R. Häner, *Chem. Lett.* **1987**, 49–52; b) R. Häner, B. Olano, D. Seebach, *Helv. Chim. Acta* **1987**, *70*, 1676–1691.

[7] a) V. Alezra, M. Bonin, L. Micouin, H.-P. Husson, *Tetrahedron Lett.* **2000**, *41*, 651–654; b) V. Alezra, M. Bonin, L. Micouin, C. Policar, H.-P. Husson, *Eur. J. Org. Chem.* **2001**, 2589–2594.

[8] a) N. K. Yee, *Org. Lett.* **2000**, *2*, 2781–2784; b) E. Napolitano, V. Farina, *Tetrahedron Lett.* **2001**, *42*, 3231–3234; c) R. P. Frutos, S. Stehle, L. Nummy, N. Yee, *Tetrahedron: Asymmetry* **2001**, *12*, 101–104; d) S. R. Kapadia, D. M. Spero, M. Eriksson, *J. Org. Chem.* **2001**, *66*, 1903–1905; e) N. S. Chowdari, C. F. Barbas III, *Org. Lett.* **2005**, *7*, 867–870.

[9] a) E. Vedejs, A. Klapars, D. L. Warner, A. H. Weiss, *J. Org. Chem.* **2001**, *66*, 7542–7546; b) B. Carboni, L. Monnier, *Tetrahedron* **1999**, *55*, 1197–1248.

General Catalysts for the Suzuki–Miyaura and Sonogashira Coupling Reactions of Aryl Chlorides and for the Coupling of Challenging Substrate Combinations in Water**

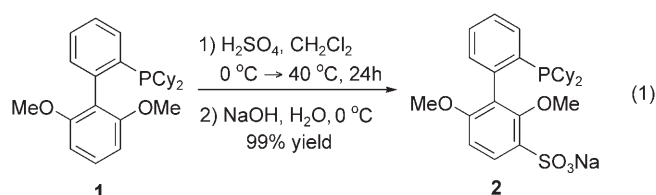
Kevin W. Anderson and Stephen L. Buchwald*

Metal-catalyzed cross-coupling methodology to form carbon–carbon bonds has inarguably advanced organic synthesis.^[1] The Suzuki–Miyaura coupling is one of the preeminent methods for formation of carbon–carbon bonds and has been used in numerous synthetic ventures.^[2] We recently reported a new catalyst system that manifested high activity paired with extremely broad scope.^[3] There remained, however, a need to develop reaction conditions for the coupling of water-soluble aryl chlorides and for the combination of difficult coupling partners in aqueous conditions. Additionally, substrates containing hydrophilic functional groups, which are insoluble in organic solvents and are present in many pharmaceutically interesting compounds, may be transformed, obviating the need for additional protection/deprotection steps. Furthermore, reactions conducted in water are attractive as water is nontoxic, nonflammable, and inexpensive, and is easily separated from organic products.^[4]

Very few examples have been reported concerning palladium-catalyzed cross-coupling reactions of hydrophilic aryl chlorides with aryl boronic acids using purely aqueous reaction conditions.^[5–9] Several sulfonated phosphine derivatives have been prepared and used in cross-coupling reactions conducted in water or water/organic biphasic solvent systems.^[10,11] Shaughnessy and coworkers reported that use of sterically demanding, water-soluble, alkylphosphine salts in the Suzuki–Miyaura, Sonogashira, and Heck coupling reactions of unactivated aryl bromides provided products derived from carbon–carbon bond formation in excellent yields.^[12] Limitations to this methodology include a lengthy synthesis and poor thermal and air stability of the ligand. Furthermore, only a single example of a substituted aryl chloride was described. The activated aryl chloride 4-chlorobenzonitrile was combined with phenylboronic acid in a reaction that

required 4 mol % of the palladium catalyst. Very recently, a Pd/glucosamine-based dicyclohexylarylphosphine catalyst was reported that displayed modest activity in Suzuki–Miyaura couplings of activated aryl chlorides when conducted in a mixture of water, toluene, and ethanol.^[13] This system, as reported, was not general and the ligand was not readily available.

We felt that the electron-rich lower aromatic ring on **1** would be readily amenable to the incorporation of a water-solubilizing sulfonate group. In fact, treatment of **1** with concentrated H₂SO₄ at 40 °C for 24 h gave **2** with exclusive monosulfonation at the 3'-position in 99% yield after treatment with NaOH and workup [Eq. (1)]. With **2**, excellent yields were obtained in Suzuki–Miyaura couplings of highly functionalized aryl chlorides or heterocyclic chlorides/bromides (containing carboxy, amino, hydroxy, sulfonamide, or sulfonate groups) and aryl or alkyl boronic acids in aqueous media.



Using a catalyst system based on **2**, we investigated the coupling of hydrophobic and hydrophilic substrates (Table 1). The coupling of electronically neutral 1-chloro-3,4-dimethylbenzene and phenylboronic acid at room temperature using water as the solvent provided the corresponding biaryl product in 99% yield (Table 1, entry 1). A temperature of 100 °C was necessary for successful coupling of 3-chlorobenzamide and hindered 2,6-dimethylphenylboronic acid resulting in 99% yield of the biaryl amide (Table 1, entry 2). Using microwave irradiation (150 °C), the same coupling product was obtained in 94% yield in 10 minutes.^[14,15] This result indicates that the catalyst system based on **2** exhibits high thermal stability. We found that coupling of 3-chlorobenzoic acid with phenylboronic acid proceeds at room temperature using 0.5% Pd and at 100 °C using 0.1% Pd to provide the coupled product in 97% yield in both cases (Table 1, entry 3). Similar catalytic activity was observed in the coupling of 3-chlorobenzoic acid and 2-methylphenylboronic acid using 0.5% Pd at room temperature and 0.1% Pd at 100 °C to give the desired product in yields of 95% and 96%, respectively (Table 1, entry 4). Using microwave irradiation (150 °C) and 0.1% Pd, the same coupling product was obtained in 98% yield in 10 minutes. The combination of 5-chloro-2-hydroxybenzoic acid and 2-methylphenylboronic acid, while slower, provided an excellent yield of the biaryl product using 2% Pd (room temperature) or 0.1% Pd (100 °C; Table 1, entry 5).

The Suzuki–Miyaura coupling of hydrophobic aryl bromides in aqueous media has been reported to occur with an assortment of catalysts including those that operate without a supporting ligand. Successful application to moderately hindered substrate combinations, however, has not been

[*] K. W. Anderson, Prof. Dr. S. L. Buchwald
Department of Chemistry
Room 18–490
Massachusetts Institute of Technology
Cambridge, MA 02139 (USA)
Fax: (+1) 617-253-3297
E-mail: sbuchwal@mit.edu

[**] We thank the National Institutes of Health (GM 46059 and GM 1S10RR13886-01) and the National Cancer Institute (Cancer Training Grant GM 5-T32-CA09112-30) for support of this work. We are grateful to Merck, Englehard (Pd(OAc)₂), and CEM (microwave reactor and supplies) for additional support.

Supporting information for this article is available on the WWW under <http://www.angewandte.org> or from the author.

Table 1: Suzuki–Miyaura coupling of aryl halides using ligand **2**.^[a]

Entry	Halide	Boronic acid	Product	Pd [mol %]	Conditions	Yield [%] ^[b]
1				2	RT, 10 h	99
2				1 1	100°C, 8 h 150°C, 10 min	99 94 ^[c]
3				2 0.5 0.1 0.1	RT, 2 h RT, 8 h 100°C, 5 h 150°C, 10 min	96 97 97 98 ^[c]
4				0.5 0.1	RT, 8 h 100°C, 6 h	95 96
5				2 0.1	RT, 12 h 100°C, 12 h	99 ^[d] 96 ^[d]
6				2	RT, 22 h	94
7				2	RT, 22 h	97

[a] Reaction conditions: 1.0 equiv aryl chloride, 1.2 equiv boronic acid, 3.0 equiv K₂CO₃, degassed water (1.5 mL mmol⁻¹), cat. Pd(OAc)₂, ligand **2**, L/Pd = 2:1. [b] Yield of isolated product (average of two runs). [c] Conducted using microwave irradiation with cooling. [d] 4.0 equiv K₂CO₃ was used.

disclosed or possible.^[11,12,15] To ascertain whether our Pd(OAc)₂/**2** catalyst system could address this limitation, we examined two reasonably hindered substrate combinations using water as the solvent at room temperature: the reactions of 2-bromomesitylene with 2-methylphenylboronic acid and 2-bromotoluene with 2,6-dimethylphenylboronic acid to form biaryl products that contain three substituents *ortho* to the aryl–aryl connection (Table 1, entries 6, 7).^[16] To our knowledge, this represents the first successful coupling of a hindered substrate combination conducted using a water or water/organic biphasic solvent at room temperature.

To determine the scope of this process, we examined the reaction of chlorobenzoic acids with 3-carboxyphenylboronic acid, 2-hydroxyphenylboronic acid, 2-aminophenylboronic acid, 2-acetylphenylboronic acid, and 2-formylphenylboronic acid. These coupling processes all proceeded in excellent yields using 1 % catalyst (Table 2, entries 1–3). Using microwave irradiation (150°C), 4-chlorobenzoic acid and 3-carboxyphenylboronic acid were coupled in 10 minutes with 1 % Pd to provide the product in 95 % yield (Table 2, entry 1), again demonstrating catalyst stability at higher temperatures.

We next turned our attention to Suzuki–Miyaura couplings of functionalized hydrophilic aryl chlorides and substituted arylboronic acids. Chlorobenzoic acids containing

hydroxy (Table 2, entry 4) and amino (Table 2, entry 5) groups on the aromatic ring were effectively coupled with substituted arylboronic acids (4-cyanophenylboronic acid and 3-aminophenylboronic acid, respectively) to generate the biaryl products in high yields (92 % and 99 %, respectively). 4-Chlorobenzenesulfonic acid successfully coupled with methylboronic acid to give the sulfonic acid derivative in 96 % yield, (Table 2, entry 6). To the best of our knowledge, this is the first reported Suzuki–Miyaura coupling of an aryl halide bearing an unprotected sulfonic acid.^[17]

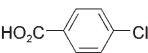
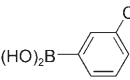
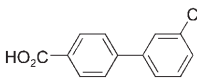
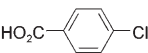
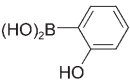
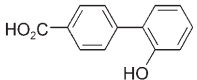
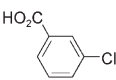
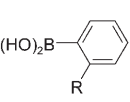
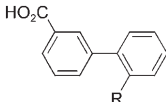
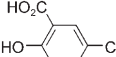
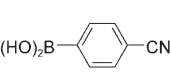
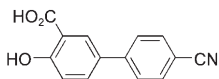
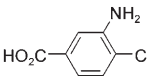
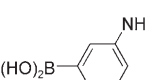
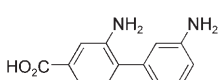
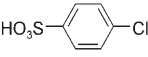
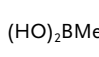
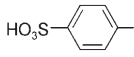
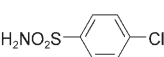
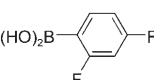
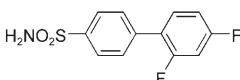
Applications of heterocyclic compounds in cross-coupling processes remain a challenge. To the best of our knowledge, very few examples of aqueous-phase Suzuki couplings of water-soluble heterocyclic halides have been published.^[18] We have examined the use of **2** as a supporting ligand in the Suzuki–Miyaura coupling with a variety of challenging hydrophilic heterocyclic halides (Table 3). As is shown, the method worked well for a number of different carboxy-group-containing heterocyclic chlorides and bromides, including indole (with a free N–H bond), pyridine, and thiophene derivatives (Table 3, entries 2, 3, 5). Even 2-amino-5-chloropyridine, which can potentially chelate to metal centers such as Pd^{II}, was successfully coupled with 3-pyridylboronic acid in 93 % yield (Table 3, entry 4).^[19]

The Suzuki–Miyaura coupling of 3-chlorobenzoic acid and phenylboronic acid employing **1** provided efficient conversion and yield of the desired product using a water/organic biphasic solvent system at 100 °C (Table 4, entries 3, 4). However, at room temperature this reaction was sluggish (Table 4, entry 5). A dramatic increase in activity was observed when using the amphiphilic ligand **2** in water at room temperature, which provided the biaryl product in 97 % yield (Table 4, entry 7). Although a catalyst system using **1** in a similar biphasic solvent system may work in many instances, this has not yet been explored.

Recently, we disclosed that a catalyst system based on $[\text{PdCl}_2(\text{CH}_3\text{CN})_2]/\mathbf{3}$ provided excellent reactivity in the copper-free Sonogashira coupling of aryl chlorides or tosylates and terminal alkynes.^[20] This catalyst system was successful in coupling aryl alkynes only when the alkyne was added slowly over the course of the reaction. This is presumably due to competing oligomerization of the alkyne at higher concentrations in the presence of the catalyst. We felt that incorporation of a water-solubilizing sulfonate group on **3** would provide an amphiphilic Sonogashira catalyst which might address the limitations that were previously reported and allow for the coupling of hydrophilic substrate combinations.^[21] We found that treatment of **3** with fuming sulfuric acid ($\text{H}_2\text{SO}_4/20\% \text{SO}_3$) at room temperature for 24 h provided **4**, with selective monosulfonation at the 4'-position, in 93 % yield after treatment with NaOH and workup [Eq. (2)].^[22]

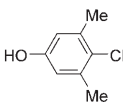
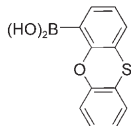
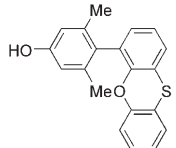
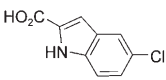
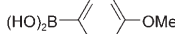
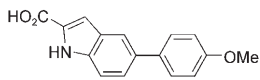
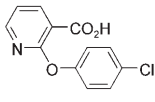
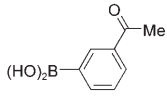
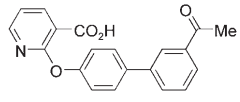
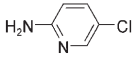
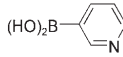
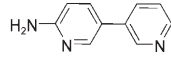
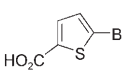
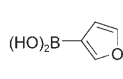
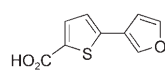
For the first time, by using a catalyst system based on $[\text{PdCl}_2(\text{CH}_3\text{CN})_2]/\mathbf{4}$ and a water/acetonitrile biphasic solvent system, propiolic acid was successfully coupled with 3-bromoaniline and 3-bromobenzoic acid to provide aryl alkynoic acids in yields of 70 % and 69 %, respectively (Table 5, entries 1, 2). This result represents a significant advancement in Sonogashira coupling reactions, as electron-deficient propiolate esters have been problematic coupling partners due to their increased reactivity towards nucleophilic attack and their propensity to polymerize in the presence of Pd catalysts.^[23] Good yields were obtained for the coupling of hydrophilic aryl chlorides bearing carboxy groups (Table 5, entries 3, 5) and an alkyne derived from an aliphatic carboxylic acid (Table 5, entry 4). Interestingly, by using **4** and a water/acetonitrile solvent system, the coupling of aryl chlorides and aryl alkynes

Table 2: Suzuki–Miyaura coupling of aryl chlorides using ligand **2**.^[a]

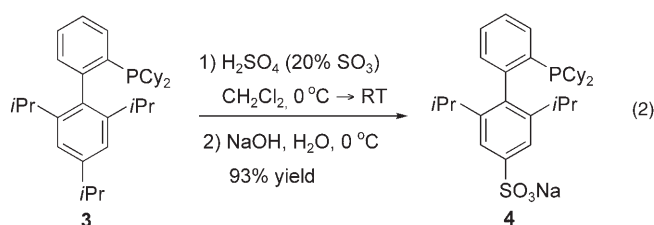
Entry	Halide	Boronic acid	Product	Yield [%] ^[b]
1				99 ^[c] 95 ^[d]
2				99
3				94 (R = NH ₂) 97 (R = C(O)Me) 87 ^[e] (R = CHO)
4				92 ^[e]
5				93
6				97
7				96

[a] Reaction conditions: 1.0 equiv aryl chloride, 1.3–1.5 equiv boronic acid, 3.0 equiv K_2CO_3 , degassed water (2.0 mL mmol⁻¹), $\text{Pd}(\text{OAc})_2$ (1.0 mol %), ligand **2** (2.0 mol %), 100 °C, 2–8 h. Reaction times and temperatures were not optimized. [b] Yield of isolated product (average of two runs). [c] The reaction was conducted at 50 °C. [d] Conducted using microwave irradiation with cooling, 150 °C for 10 min. [e] The reaction was conducted at 80 °C.

Table 3: Suzuki–Miyaura coupling of heterocyclic halides using ligand **2**.^[a]

Entry	Halide	Boronic acid	Product	Yield [%] ^[b]
1				93
2				93 ^[c]
3				92 ^[c]
4				93
5				97 95 ^[d]

[a] Reaction conditions: 1.0 equiv aryl halide, 1.3–1.5 equiv boronic acid, 3.0 equiv K_2CO_3 , degassed water (4.0 mL mmol⁻¹), $\text{Pd}(\text{OAc})_2$ (1.0 mol %), ligand **2** (2.0 mol %), 100 °C, 10–12 h. Reaction times and temperatures were not optimized. [b] Yield of isolated product (average of two runs). [c] The reaction was conducted at 80 °C. [d] The reaction was conducted using microwave irradiation with cooling, 150 °C for 10 min.



proceeds and obviates the need to employ slow addition of the aryl alkyne (Table 5, entries 6–8). This result may be attributed to the lower effective concentration of the alkyne in proximity to the catalyst, which resides at the water/organic interface.

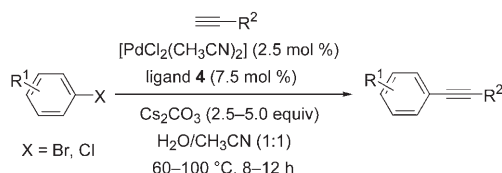
We have demonstrated that use of sulfonated ligands **2** and **4** provides highly active catalyst systems for Suzuki–Miyaura and Sonogashira cross-coupling reactions, with unprecedented scope, reactivity, and stability for aqueous-phase processes. Further work to apply sulfonated biaryl-

Table 4: Screening of conditions for Suzuki–Miyaura coupling with **1** and **2**.

Entry	Ligand	Solvent	T [°C]	Conv. [%]	Yield [%] ^[b]
1	1	<i>n</i> BuOH	100	77	75
2	1	<i>n</i> BuOH/H ₂ O (5:1)	100	27	26
3	1	CH ₃ CH ₂ CN/H ₂ O (1:1)	100	> 99	96
4	1	DMF/H ₂ O (1:1)	100	> 99	94
5	1	CH ₃ CN/H ₂ O (1:1)	RT	17	12
6	1	H ₂ O	100	22	20
7	2	H ₂ O	RT	> 99	97 ^[c]

[a] Reaction conditions: 1.0 equiv aryl chloride, 1.2 equiv boronic acid, 3.0 equiv K₂CO₃, solvent (2.0 mL mmol⁻¹), cat. Pd(OAc)₂, ligand **1** or **2**, L/Pd = 2:1, 14 h. [b] Yield of product determined by NMR spectroscopy. [c] The reaction was complete in 2 h.

Table 5: Sonogashira coupling of aryl halides using ligand **4**.^[a]



Entry	Halide	Alkyne	Product	Yield [%] ^[b]
1		$\equiv\text{CO}_2\text{H}$		70 ^[c,d]
2		$\equiv\text{CO}_2\text{H}$		69 ^[c,d]
3		$\equiv\text{C}_8\text{H}_{17}$		86
4		$\equiv(\text{CH}_2)_3\text{CO}_2\text{H}$		85 ^[d]
5		$\equiv\text{C}_8\text{H}_{17}$		71
6				88
7				93
8				96 ^[d]

[a] Reaction conditions: 1.0 equiv aryl halide, 1.3–1.5 equiv terminal alkyne, 2.5–5.0 equiv Cs₂CO₃, degassed water (2.0 mL mmol⁻¹), CH₃CN (2.0 mL mmol⁻¹), [PdCl₂(CH₃CN)₂] (2.5 mol %), ligand **4** (7.5 mol %), 100 °C, 8–12 h. Reaction times were not optimized. [b] Yield of isolated product (average of two runs). [c] The alkyne was added to the reaction at 0 °C and the mixture was heated to 60 °C. [d] To ease in purification, the product was converted to the methyl ester using trimethylsilyldiazomethane.

phosphines in other transition-metal-catalyzed processes is underway in our laboratories.

Received: June 11, 2005

Published online: August 12, 2005

Keywords: alkynes · aryl chlorides · boronic acids · cross-coupling · water

- [1] *Metal-Catalyzed Cross-Coupling Reactions*, Vol. 2 (Eds.: A. de Meijere, F. Diederich), Wiley-VCH, Weinheim, **2004**.
- [2] a) N. Miyaura, *Top. Curr. Chem.* **2002**, 219, 11; b) A. Suzuki, *J. Organomet. Chem.* **1999**, 576, 147.
- [3] a) T. E. Barder, S. D. Walker, J. R. Martinelli, S. L. Buchwald, *J. Am. Chem. Soc.* **2005**, 127, 4685; b) T. E. Barder, S. L. Buchwald, *Org. Lett.* **2004**, 6, 2649; c) S. D. Walker, T. E. Barder, J. R. Martinelli, S. L. Buchwald, *Angew. Chem.* **2004**, 116, 1907; *Angew. Chem. Int. Ed.* **2004**, 43, 1871.
- [4] a) C.-J. Li, T.-H. Chan, *Organic Reactions in Aqueous Media*, Wiley, New York, **1997**; b) *Organic Synthesis in Water* (Ed.: P. A. Grieco), Academic Press, Dordrecht, The Netherlands, **1997**; c) *Aqueous-Phase Organometallic Catalysis*, 2nd ed. (Eds.: B. Cornils, W. A. Herrmann), Wiley-VCH, Weinheim, **2004**; d) K. H. Shaughnessy, R. B. DeVasher, *Curr. Org. Chem.* **2005**, 9, 585; e) N. E. Lead-

- beater, *Chem. Commun.* **2005**, 2881.
- [5] For a NiCl₂/dppe/trisulfonated triphenylphosphine system, see: J.-C. Galland, M. Savignac, J. P. Genet, *Tetrahedron Lett.* **1999**, 40, 2323.
- [6] For oxime-derived palladacycles, see: a) L. Botella, C. Najera, *Angew. Chem.* **2002**, 114, 187; *Angew. Chem. Int. Ed.* **2002**, 41, 179; b) L. Botella, C. Najera, *J. Organomet. Chem.* **2002**, 663, 46.
- [7] For di-2-pyridylmethylamine-based palladium complexes, see: C. Najera, J. Gil-Molto, S. Karlstrom, L. R. Falvello, *Org. Lett.* **2003**, 5, 1451.
- [8] For palladium N-heterocyclic carbene complexes, see: a) I. Ozdemir, Y. Gok, N. Gurbuz, E. Cetinkaya, B. Cetinkaya, *Heteroat. Chem.* **2004**, 15, 419; b) I. Özdemir, S. Demir, S. Yaser, B. Cetinkaya, *Appl. Organomet. Chem.* **2005**, 19, 55.
- [9] For TBAB–water mixtures, see: R. B. Bedford, M. E. Blake, C. P. Butts, D. Holder, *Chem. Commun.* **2003**, 466.
- [10] a) H. Gulyas, A. Szollosy, P. Szabo, P. Halmos, J. Bakos, *Eur. J. Org. Chem.* **2003**, 2775; b) W. P. Mul, K. Ramkisoensing, P. C. J. Kamer, J. N. H. Reek, A. J. van der Linder, A. Marson, P. W. N. M. van Leeuwen, *Adv. Synth. Catal.* **2002**, 344, 293; c) H. Gulyas, A. Szollosy, B. E. Hanson, J. Bakos, *Tetrahedron Lett.* **2002**, 43, 2543; d) E. Schwab, S. Mecking, *Organometallics* **2001**, 20, 5504.
- [11] a) L. R. Moore, K. H. Shaughnessy, *Org. Lett.* **2004**, 6, 225; b) E. C. Western, J. R. Daft, E. M. Johnson II, P. M. Gannett, K. H. Shaughnessy, *J. Org. Chem.* **2003**, 68, 6767; c) A. E. Sollewijn Gelpke, J. J. N. Veerman, M. S. Goedheijt, P. C. J. Kamer, P. W. N. M. van Leeuwen, H. Hiemstra, *Tetrahedron* **1999**, 55, 6657; d) H. Bahrmann, K. Bergrath, H.-J. Kleiner, P. Lappe, C. Naumann, D. Peters, D. Regnat, *J. Organomet. Chem.* **1996**, 520, 97; e) J. P. Genet, A. Linquist, E. Blart, V. Mouries, M. Savignac, *Tetrahedron Lett.* **1995**, 36, 1443.
- [12] a) R. B. DeVasher, L. R. Moore, K. H. Shaughnessy, *J. Org. Chem.* **2004**, 69, 7919; b) R. B. DeVasher, J. M. Spruell, D. A. Dixon, G. A. Broker, S. T. Griffin, R. D. Rogers, K. H. Shaughnessy, *Organometallics* **2005**, 24, 962.
- [13] A. Konovets, A. Penciu, E. Framery, N. Percina, C. Goux-Henry, D. Sinou, *Tetrahedron Lett.* **2005**, 46, 3205.
- [14] R. K. Arvela, N. E. Leadbeater, *Org. Lett.* **2005**, 7, 2101.
- [15] For an excellent review on catalyst systems used in Suzuki–Miyaura couplings conducted in aqueous media and using microwave irradiation, see references [4d] and [4e], and references therein.
- [16] Our attempts to effect the coupling of 2-bromomesitylene with 2,6-dimethylphenylboronic acid in water at 100°C to form a biaryl with four substituents *ortho* to the aryl–aryl connection provided none of the desired product. This is in contrast to what is observed with a catalytic system using **1**. See ref. [2c].
- [17] The sulfonic acid is undoubtedly rapidly transformed to the sulfonate under the reaction conditions. For examples of Suzuki–Miyaura couplings of aryl halides with protected sulfonic acids, see: a) B. G. Avitabile, C. A. Smith, D. B. Judd, *Org. Lett.* **2005**, 7, 843; b) A. Hari, B. L. Miller, *Org. Lett.* **1999**, 1, 2109; c) E. W. Baxter, J. K. Rueter, S. O. Nortey, A. B. Reitz, *Tetrahedron Lett.* **1998**, 39, 979.
- [18] See references [4] and [10b].
- [19] The authors report that monodentate phosphines are poor ligands for the Suzuki–Miyaura coupling of 2-amino-pyridines and pyrimidines. This result suggests that use of a highly active catalyst system such as Pd/**2** at least in some instances overcomes this limitation; see: T. Itoh, T. Mase, *Tetrahedron Lett.* **2005**, 46, 3573.
- [20] D. Gelman, S. L. Buchwald, *Angew. Chem.* **2003**, 115, 6175; *Angew. Chem. Int. Ed.* **2003**, 42, 5993.
- [21] For recent reports of Sonogashira coupling reactions conducted in water or water/organic biphasic solvents, see: a) B. Liang, M. Dai, J. Chen, Z. Yang, *J. Org. Chem.* **2005**, 70, 391; b) G. Zhang, *Synlett* **2005**, 4, 619; c) M. S. Mohamed Ahmed, A. Mori, *Tetrahedron* **2004**, 60, 9977; d) C. Wolf, R. Lerebours, *Org. Biomol. Chem.* **2004**, 2, 2161; e) S. Bhattacharya, S. Sengupta, *Tetrahedron Lett.* **2004**, 45, 8733.
- [22] Choice of the palladium source and ligands **2** and **4** was made on the basis of our previous reports. See references [3] and [20].
- [23] a) Use of electron-deficient zinc acetylides allows coupling with aryl halides; see: E.-I. Negishi, L. Anastasia, *Chem. Rev.* **2003**, 103, 1979, and references therein. b) Use of K₂CO₃ allows the coupling of electron-deficient terminal alkynes and electron-deficient or neutral aryl iodides; see: T. Eckert, J. Ipaktschi, *Synth. Commun.* **1998**, 28, 327. c) Use of K₂CO₃ allows the coupling of electron-deficient terminal alkynes and diphenyliodonium salts; see: U. Radhakrishnan, P. J. Stang, *Org. Lett.* **2001**, 3, 859. d) Water was essential to the coupling reaction of aryl iodides and various alkynoates; see: Y. Uozumi, Y. Kobayashi, *Heterocycles* **2003**, 59, 71.

Stereoselective Butenolide Reduction

DOI: 10.1002/anie.200501890

Dynamic Kinetic Resolution of α,β -Unsaturated Lactones through Asymmetric Copper-Catalyzed Conjugate Reduction: Application to the Total Synthesis of Eupomatilone-3**

Matthew P. Rainka, Jacqueline E. Milne, and
Stephen L. Buchwald*

Eupomatilones 1–7 are a family of lignans^[1] isolated from the Australian shrub *Eupomatia bennettii*, found in the tropical and subtropical forests of New South Wales and Queensland.^[2] All seven members of this family contain a highly oxygenated biaryl motif, as well as a *cis* orientation of the substituents at C4 and C5 of the butyrolactone ring. Of all the members of the eupomatilone family, there have only been three for which a total synthesis has been reported: eupomatilone-6, eupomatilone-4, and 3-*epi*-eupomatilone-6.^[3] Despite this work, the total synthesis of enantiomerically enriched members of the eupomatilone family has remained an unsolved problem. Herein, we report the first asymmetric

[*] M. P. Rainka, J. E. Milne, Prof. S. L. Buchwald
Department of Chemistry, Room 18-490
Massachusetts Institute of Technology
Cambridge, MA 02139 (USA)
Fax: (+1) 617-253-3297
E-mail: sbuchwal@mit.edu

[**] We thank the National Institutes of Health (GM 46059) for support of this work. We are grateful to Merck for additional support. We thank Englehard for the generous supply of palladium compounds and Dr. Rudy Schmid of Roche Basel for the donation of MeO-BIPHEP. We also thank Dr. Lei Jiang for helpful discussions.

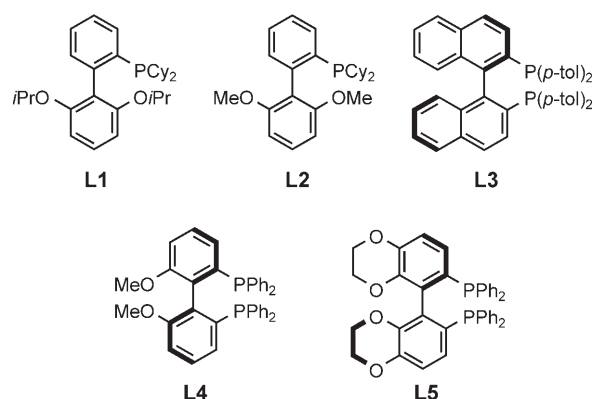


Supporting information for this article is available on the WWW under <http://www.angewandte.org> or from the author.

total synthesis of one member of the family, eupomatilone-3. The success of the synthesis was based on a highly efficient Suzuki–Miyaura cross-coupling,^[4] along with a dynamic kinetic resolution^[5] of an unsaturated lactone.

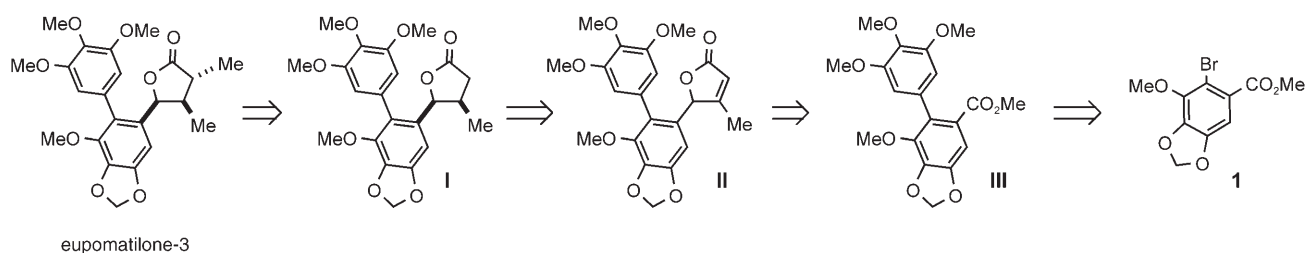
Our interest in the synthesis of eupomatilone-3 emanated from the compound's interesting structural features, in particular the biaryl motif, along with the *cis* orientation of the substituents at C4 and C5 of the lactone portion of the molecule. Our retrosynthetic analysis of eupomatilone-3 is shown in Scheme 1. On the basis of our recent work in the area of palladium-catalyzed cross-coupling reactions,^[6] it was believed we could assemble the highly oxygenated biaryl portion of the molecule **III** by utilizing either a Negishi or Suzuki–Miyaura coupling. Furthermore, we envisioned generating the desired lactone stereochemistry in **I** through either a diastereoselective or an enantioselective copper-catalyzed conjugate reduction reaction.^[7]

The synthesis was begun by investigating the cross-coupling of known aryl bromide **1**^[8] with organometallic reagents derived from bromo-3,4,5-trimethoxybenzene. By employing reaction conditions found to be optimal with palladium catalysts derived from the bulky phosphanylbiaryl ligands RuPhos **L1** (Negishi)^[6b] or SPhos **L2** (Suzuki–Miyaura)^[6a,c] allowed for efficient production of biaryl **2** (Scheme 2). The Negishi coupling produced **2** in 93% yield at a catalyst loading of 1 mol% palladium. With the corresponding Suzuki–Miyaura reaction, it was found that **2** could be obtained in 93% yield even when the catalyst

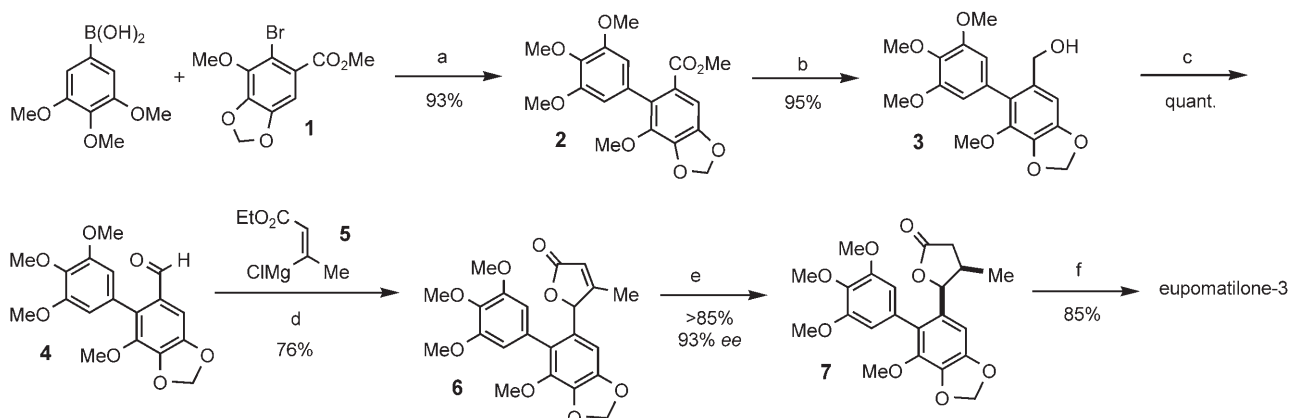


loading was lowered to 0.005 mol% palladium (0.00025 mol% [Pd₂(dba)₃]; dba = dibenzylideneacetone).

With a means to rapidly construct the biaryl portion of eupomatilone-3, investigation began into the preparation of the butenolide **6**. When examining this motif, we turned to Knochel's method for the synthesis of butenolides by the reaction of stabilized vinyl Grignard reagents with aldehydes.^[9] To apply this method to this synthesis, the methyl ester **2** first needed to be transformed to the corresponding aryl aldehyde **4**. Conversion of **2** into the benzyl alcohol **3** was accomplished by borane reduction in THF. Intermediate **3** was oxidized with MnO₂ to give the desired benzaldehyde derivative **4** in essentially quantitative yield. Treatment of this



Scheme 1. Retrosynthetic analysis of eupomatilone-3.



Scheme 2. Synthesis of eupomatilone-3 (yields are the average of two runs determined to be > 95% pure by ¹H NMR or GC). a) [Pd₂(dba)₃] (0.0025 mol%), SPhos **L2** (0.02 mol%), K₃PO₄ (2 equiv), THF, 80 °C. b) BH₃·THF, THF, 60 °C. c) MnO₂, CH₂Cl₂, RT. d) THF, –40 °C. e) CuCl₂·2 H₂O (5 mol%), MeO-BIPHEP **L4** (5 mol%), NaOtBu (1.2 equiv), PMHS (6 equiv), *t*BuOH, THF, CH₂Cl₂, RT. f) NaHMDS, THF, 0 °C, then MeI. PMHS: polymethylhydrosiloxane; NaHMDS: sodium hexamethyldisilazide.

aldehyde with the vinyl Grignard reagent **5** (formed in situ from the corresponding vinyl iodide^[10]) according to Knochen's procedure provided the desired unsaturated lactone in 76% yield.

The next hurdle in the synthesis was the conversion of butenolide **6** into *cis*-4,5-disubstituted lactone **7**. The installation of this stereochemistry was explored by using an asymmetric conjugate reduction reaction.^[11,12] We have previously demonstrated the asymmetric reduction of unsaturated lactones using a chiral copper-hydride catalyst.^[12b] Furthermore, we have succeeded in carrying out both kinetic as well as dynamic kinetic resolutions of 3,5-disubstituted cyclopentenones by employing similar catalysts.^[12d] Despite unsatisfactory results when reducing 3,4-disubstituted cyclopentenones,^[12d] we decided to attempt the kinetic resolution of **6** under our standard conjugate reduction conditions^[12] at -30°C in a 1:1 mixture of THF/ CH_2Cl_2 (dichloromethane was necessary due to the poor solubility of the lactone in THF). After 50% conversion of **6**, the desired *cis* compound **7** was isolated in 46% yield and with 87% *ee*. Interestingly, the process was completely diastereoselective: none of the *trans* isomer was ever detected.

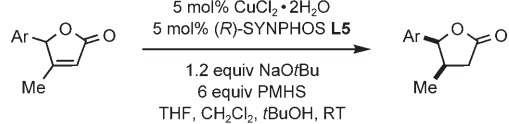
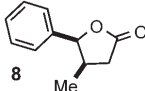
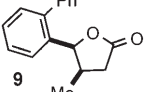
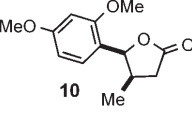
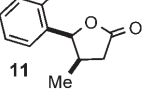
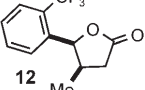
With this promising result, we sought to extend the method to the dynamic kinetic resolution of unsaturated lactones. We felt that performing the reaction in the presence of excess base (NaOtBu) should allow for racemization of the starting material such that complete conversion may be effected. Unfortunately, no racemization occurred when 1.2 equivalents of NaOtBu was used at -30°C , even after prolonged reaction times. When the same experiment, however, was conducted at room temperature, complete conversion of the starting material into the desired product was observed. As in the case of the simple kinetic resolution, the product was obtained as a single diastereomer and with 83% *ee*. This represents the first copper-catalyzed dynamic kinetic resolution of an unsaturated lactone.

In an attempt to improve the enantioselectivity of the reaction, other chiral bisphosphine ligands were used. It was found that replacing *p*-tol-BINAP **L3** with MeO-BIPHEP **L4** while still performing the reaction at room temperature provided the desired compound, again as a single diastereomer, but now with 93% *ee* (when the kinetic resolution was carried out at -30°C with **L4**, the product was obtained with 95% *ee*). With the *cis* lactone prepared, all that remained to complete the synthesis was to install the final methyl group in the α position on the lactone ring. This was accomplished by enolization of lactone **7** with NaHMDS followed by alkylation with iodomethane to give synthetic eupomatilone-3 in 85% yield; its spectra were in agreement with those published for material obtained from the natural source.^[2,13]

On the basis of the success of the dynamic kinetic resolution reaction described above, we briefly examined the scope of this process by using other γ -aryl-containing unsaturated lactones. Initial results employing **L4** as the supporting ligand provided poor enantioselectivity for substrates other than the natural product, however the diastereoselectivity remained high. A brief survey of the efficiency of ligands for this process was undertaken and it was observed that the commercially available SYNPHOS ligand **L5** pro-

vided the highest enantioselectivities (except in the case of the natural product, in which **L4** gave the best result).^[14] The scope of the reaction was examined and the results are shown in Table 1. Aside from **8**, all products were formed with enantioselectivities ranging from 77 to 87%. Thus, no clear

Table 1: Dynamic kinetic resolution of unsaturated lactones.

<div style="text-align: center;">  </div>		
Product	<i>ee</i> [%]	Yield [%] ^[a]
	67	95
	81	92
	87	85
	77	91
	78	94

[a] Yields are the average of two runs determined to be greater than 95% pure by ^1H NMR spectroscopy or GC.

dependence on steric or electronic factors could be ascertained.

Unfortunately, use of the same reaction conditions for the dynamic kinetic resolution of lactones that contain simple alkyl substituents in the γ position failed to give more than 50% conversion of the starting material. This is presumably due to poor racemization of the starting lactone. Additionally, the reaction provided both the *cis* and *trans* isomers of the product, and the enantiomeric enrichment of the *cis* product was found to be low (<25% *ee*).

In conclusion, the total synthesis of eupomatilone-3 was achieved in six steps and in 48% overall yield. The key to the success of the synthesis was the development of a dynamic kinetic resolution that allowed the α,β -unsaturated butenolide **6** to be reduced in high yield and with both high enantiomeric and diastereomeric excess. This is the first example of a copper-catalyzed dynamic kinetic resolution of an unsaturated lactone. The method was then applied to several γ -aryl containing α,β -unsaturated butenolides. While a number of catalysts based on chiral bisphosphines were found to successfully promote this transformation, optimal

enantioselectivity was obtained when employing the commercially available SYNPHOS ligand **L5**.

Received: May 31, 2005

Published online: August 30, 2005

Keywords: cross-coupling · eupomatilones · kinetic resolution · reduction · total synthesis

- [1] For a review on lignans, see: R. S. Ward, *Nat. Prod. Rep.* **1997**, *14*, 43.
- [2] A. R. Carroll, W. C. Taylor, *Aust. J. Chem.* **1991**, *44*, 1705.
- [3] For recent synthetic efforts, see: a) S.-P. Hong, M. C. McIntosh, *Org. Lett.* **2002**, *4*, 19; b) J. M. Hutchison, S. P. Hong, M. C. McIntosh, *J. Org. Chem.* **2004**, *69*, 4185; c) M. K. Gurjar, J. Cherian, C. V. Ramana, *Org. Lett.* **2004**, *6*, 317; d) R. S. Coleman, S. R. Gurralla, *Org. Lett.* **2004**, *6*, 4025.
- [4] For reviews, see: a) N. Miyaura, A. Suzuki, *Chem. Rev.* **1995**, *95*, 2457; b) N. Miyaura in *Metal-Catalyzed Cross-Coupling Reactions*, Vol. 1, 2nd ed. (Eds.: A. de Meijere, F. Diederich), Wiley-VCH, Weinheim, **2004**, chap. 2, pp. 41–123; c) S. P. Stanforth, *Tetrahedron* **1998**, *54*, 263; d) A. Suzuki, *J. Organomet. Chem.* **1999**, *576*, 147; e) M. Miura, *Angew. Chem.* **2004**, *116*, 2251; *Angew. Chem. Int. Ed.* **2004**, *43*, 2201; f) F. Bellina, A. Carpita, R. Rossi, *Synthesis* **2004**, 2419.
- [5] For reviews, see: a) H. Pellissier, *Tetrahedron* **2003**, *59*, 8291; b) R. S. Ward, *Tetrahedron: Asymmetry* **1995**, *6*, 1475; c) R. Noyori, T. Ikeda, T. Ohkuma, M. Widhalm, M. Kitamura, H. Takaya, S. Akutagawa, N. Sayo, T. Saito, T. Taketomi, H. Kumobayashi, *J. Am. Chem. Soc.* **1989**, *111*, 9134.
- [6] a) T. E. Barder, S. D. Walker, J. R. Martinelli, S. L. Buchwald, *J. Am. Chem. Soc.* **2005**, *127*, 4685; b) J. E. Milne, S. L. Buchwald, *J. Am. Chem. Soc.* **2004**, *126*, 13028; c) S. D. Walker, T. E. Barder, J. R. Martinelli, S. L. Buchwald, *Angew. Chem.* **2004**, *116*, 1907; *Angew. Chem. Int. Ed.* **2004**, *43*, 1871.
- [7] O. Riant, N. Mostefaï, J. Courmarcel, *Synthesis* **2004**, 2943.
- [8] a) A. Alam, Y. Takaguchi, H. Ito, T. Yoshida, S. Tsuboi, *Tetrahedron* **2005**, *61*, 1909; b) G. M. Keseru, M. Nogradi, M. Kajtar-Peredy, *Liebigs Ann. Chem.* **1994**, 361; c) J. Chang, X. Guo, S. Cheng, R. Guo, R. Chen, K. Zhao, *Bioorg. Med. Chem. Lett.* **2004**, *14*, 2131; d) J. Chang, R. Chen, R. Guo, C. Dong, K. Zhao, *Helv. Chim. Acta* **2003**, *86*, 2239.
- [9] I. Sapountzis, W. Dohle, P. Knochel, *Chem. Commun.* **2001**, 2068.
- [10] E. Piers, T. Wong, P. D. Coish, C. Rogers, *Can. J. Chem.* **1994**, *72*, 1816.
- [11] For related work involving chiral copper-hydride catalysts, see: a) B. H. Lipshutz, H. Shimizu, *Angew. Chem.* **2004**, *116*, 2278; *Angew. Chem. Int. Ed.* **2004**, *43*, 2228; b) B. H. Lipshutz, J. M. Servesko, *Angew. Chem.* **2003**, *115*, 4937; *Angew. Chem. Int. Ed.* **2003**, *42*, 4789; c) B. H. Lipshutz, C. C. Caires, P. Kuipers, W. Chrisman, *Org. Lett.* **2003**, *5*, 3085; d) C. Czekelius, E. M. Carreira, *Angew. Chem.* **2003**, *115*, 4941; *Angew. Chem. Int. Ed.* **2003**, *42*, 4793; e) B. H. Lipshutz, J. M. Servesko, B. R. Taft, *J. Am. Chem. Soc.* **2004**, *126*, 8352.
- [12] a) M. P. Rainka, Y. Aye, S. L. Buchwald, *Proc. Natl. Acad. Sci. USA* **2004**, *101*, 5821; b) G. Hughes, M. Kimura, S. L. Buchwald, *J. Am. Chem. Soc.* **2003**, *125*, 11253; c) V. Jurkauskas, J. P. Sadighi, S. L. Buchwald, *Org. Lett.* **2003**, *5*, 2417; d) V. Jurkauskas, S. L. Buchwald, *J. Am. Chem. Soc.* **2002**, *124*, 2892; e) Y. Moritani, D. H. Appella, V. Jurkauskas, S. L. Buchwald, *J. Am. Chem. Soc.* **2000**, *122*, 6797; f) D. H. Appella, Y. Moritani, R. Shintani, E. M. Ferreira, S. L. Buchwald, *J. Am. Chem. Soc.* **1999**, *121*, 9473; g) J. Yun, S. L. Buchwald, *Org. Lett.* **2001**, *3*, 1129.
- [13] While the absolute configuration of the natural material is unknown, the optical rotation measurements on the synthetic material were in agreement with those on material from the natural source.
- [14] a) C.-C. Pai, Y.-M. Li, Z.-Y. Zhou, A. S. C. Chan, *Tetrahedron Lett.* **2002**, *43*, 2789; b) S. D. de Paule, S. Jeulin, V. Ratovelomana-Vidal, J.-P. Genêt, N. Champion, P. Dellis, *Tetrahedron Lett.* **2003**, *44*, 823; c) SYNPHOS was purchased from Strem Chemicals, Inc.; d) While SEGPhos (another common ligand employed in conjugate reduction chemistry with copper) is not commercially available, in the near future we hope to test this ligand in the dynamic kinetic resolution process.

Helical Structures

DOI: 10.1002/anie.200500806

High Thermal Stability Imparted by a Designed Tandem Arg–Trp Stretch in an α -Helical Coiled Coil***Yuuki Sakurai, Toshihisa Mizuno, Hidekazu Hiroaki, Keigo Gohda, Jun-ichi Oku, and Toshiki Tanaka**

Studies on de novo designed proteins involve the construction of unique tertiary structures and the creation of novel functions. Protein structures are mainly formed by various interactions, such as ion-pair, hydrogen-bonding, and hydrophobic interactions. Recently, the cation– π interaction was noted as one of the effective interactions judging from various protein structures in the PDB (protein data bank) databases,^[1] and it is thought to contribute to protein structure stabilization and protein–ligand interactions.^[2–4] The cation– π interaction is formed between aromatic rings and cationic groups.^[1b,5] In proteins, Trp, Tyr, Phe, and His are aromatic residues, while Lys and Arg are cationic residues, and the interaction between Trp and Arg is considered to be the best combination.^[1c,6] The cation– π interaction is favored several-

[*] Y. Sakurai, T. Mizuno, J.-i. Oku, T. Tanaka
Department of Material Sciences, Graduate School of Engineering
Nagoya Institute of Technology
Gokiso-chou, Nagoya 466-8555 (Japan)
Fax: (+81) 527-355-210
E-mail: ttanaka@nitech.ac.jp

H. Hiroaki
Science of Biological Supramolecular Systems
Graduate School of Integrated Science, Yokohama City University
1-7-29 Suehirocho, Tsurumi, Yokohama, Kanagawa 230-0045
(Japan)

K. Gohda
CAMM-Kansai
Higashinada, Kobe 658-0046 (Japan)

[**] This work was supported by the Nagase Science and Technology Foundation.

fold over the formation of a salt bridge in water, in terms of the desolvation energy penalty of the ionic residues. A cation- π interaction stabilizes proteins by 2–3 kcal mol⁻¹ more than an ion-pair interaction, which is estimated to contribute 1–3 kcal mol⁻¹.^[7] Thus, the cation- π interaction provides strong and specific interactions, and therefore it should be considered in protein design.

Designed cation- π interactions have been assessed using the solvent-exposed sites of the short α helices, turn structure, and coiled-coil structure.^[8] These data suggested that the contributions of the cation- π interactions to the stability depend on the species and the positions of aromatic and cationic amino acids. However, the effects of the cation- π interactions on the structural stability are quantitatively lower than the values obtained from calculations, probably as a result of the flexibility of the amino acid side chains on the freely exposed sites of the α helix.

The location of the cation- π interaction is neither completely solvent-exposed nor deeply buried within the protein.^[6] It is often found between a solvent-exposed site and a completely buried site. We designed a cation- π interaction to reside at the interface between two α helices of a coiled-coil structure. The coiled coil consists of several α helices wrapped around each other, and it represents a heptad repeat sequence designated by *abcdefg* from each position.^[9] The *e* and *g'* positions exist between the hydrophobic-hydrophilic interfaces and are close to each other between two adjacent α helices. Glu and Lys at these positions are close and form an ion pair, which contributes to the stabilization and configuration of the coiled-coil structure. Therefore, the *e* and *g'* positions of the coiled coil might be suitable places to design a cation- π interaction. We designed a cation- π interaction at the *e* and *g'* positions and compared the ion-pair interaction between Glu and Lys at the same positions. Our results support the existence of the cation- π interaction.

A de novo designed peptide (IZ), [YGG(IEKKIEA)₄](*defgabc*), forms a parallel triple-stranded α -helical coiled-coil structure.^[10] The IZ peptide has a melting temperature (*T_m*) of more than 95 °C, which makes it difficult to compare the thermal stabilities of coiled-coil structures. Therefore, the amino acid at the *a* position of the second heptad was substituted with Gln to adjust the stability and to increase the uniqueness of the structure.^[11] We also mutated the amino acid residues on the IZ derivatives, where Lys at the *g* position and Glu at the *e* position were reversed. The prepared peptides are listed in Table 1. There are three possible sites

for interactions using the *e* and *g'* positions after homotrimerization. Trp and Arg were placed in the middle of the peptide. The rest of the *e* and *g'* positions contained Glu and Lys, respectively, for the ion-pair interactions. A series of cation- π interactions was designed, and the peptides containing Trp and Arg were named WR1, WR2, and WR3, depending on the number of Trp-Arg sets. The *e* position of one peptide and the *g'* position of the other peptide were alternated between the two α helices, and therefore Trp and Arg were designed to generate an extended array of cation- π interactions, formed by two and three Trp-Arg sets for WR2 and WR3, respectively. WRRW has two Trp-Arg sets; however, because of the repulsive positive charge from Arg, the two Trp-Arg interactions should work separately.

Molecular modeling of WR3 was performed by using molecular mechanics calculations to obtain the preferable spatial position of Trp and Arg residues in the α -helical coiled-coil structures.^[12] The energy-minimized WR3 model suggested that the designed three Trp-Arg sets were placed close enough together for cation- π interactions (Figure 1).

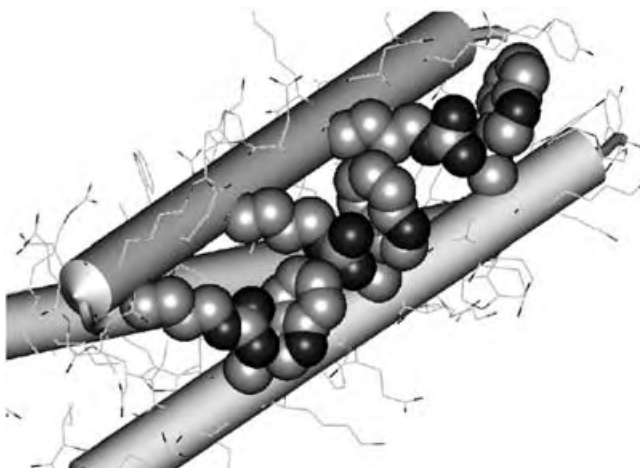


Figure 1. Energy-minimized model of WR3, which was constructed on the basis of a leucine-zipper coiled-coil structure (PDB ID: 1GCM) as template, followed by energy minimization with the OPLS-AA force field and GB/SA solvation model. Trp and Arg residues are illustrated by space-filling molecular graphics.

Circular dichroism (CD) spectroscopy was performed to characterize the secondary structures of the designed peptides (Figure 2). All of the peptides exhibited the spectra of typical α -helical structures, with the characteristic minima at 208 and 222 nm. To analyze the stoichiometry of the peptide aggregates, they were subjected to gel filtration on Sephadex G-50. The peptides eluted at the same position as the standard triple-stranded coiled-coil peptide with a similar amino acid length. These results indicate that the peptides assembled into the trimer with a coiled-coil structure.

The thermal stabilities of the peptides were analyzed by monitoring $[\theta]_{222}$ as a function of temper-

Table 1: Amino acid sequences of the designed coiled-coil peptides and their *T_m*, ΔT_m [°C], and ΔG [kcal mol⁻¹] values after homotrimerization.

Peptide	Sequence					<i>T_m</i>	ΔT_m	ΔG
	1	2	3	4				
EK	YGG	IKKEIEA	IKKEQEA	IKKEIEA	IKKEIEA	52	0	-15.3
WR1	--	---	--W--	-R--	---	58	6	-15.8
WR2	--	--W--	-R-W--	-R--	---	75	23	-16.7
WR3	--	--W--	-R-W--	-R-W--	-R--	> 95	n.d.	n.d.
WRRW	--	--W--	-R-R--	-W--	---	65	-	-
AA	--	---	--A--	-A--	---	42	-	-14.6
WA	--	---	--W--	-A--	---	48	-	-14.8
AR	--	---	--A--	-R--	---	45	-	-14.7

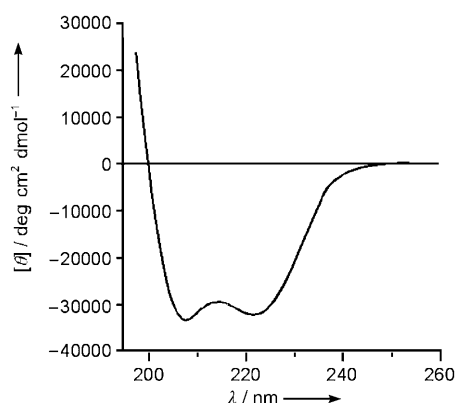


Figure 2. CD spectrum of WR3. EK, WR1, WR2, and WRRW exhibited the same CD spectra as WR3. The measurement was performed in sodium phosphate (20 mM, pH 7.0) containing NaCl (0.1 M) at 20 °C. The peptide concentration was 20 μ M.

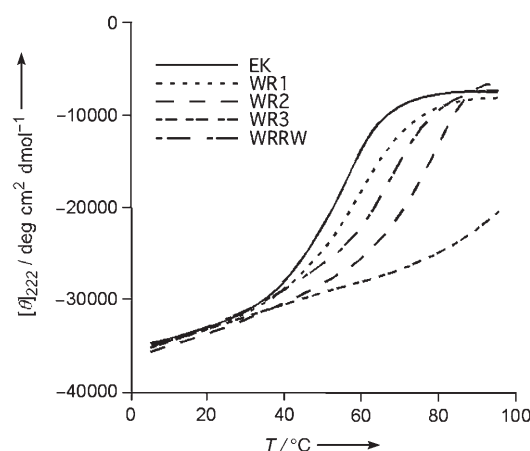


Figure 3. Thermal denaturation curves for EK, WR1, WR2, WR3, and WRRW. The curves were recorded in sodium phosphate (20 mM, pH 7.0) containing NaCl (0.1 M), with a peptide concentration of 20 μ M.

ature (Figure 3). EK exhibited a T_m of 52 °C. When one Glu–Lys set was changed to Trp–Arg, the T_m was increased to 58 °C (WR1), which is 6 K higher than that of EK, in spite of the removal of one of the ion pairs. This finding implies the presence of an interaction between Trp and Arg which is stronger than that of the ion pair. The effect on the thermal stability was more remarkable when a couple of Trp–Arg sets were placed at the *e* and *g* positions. WR2 exhibited a T_m of 75 °C, which is 23 K higher than that of EK. On the other hand, WRRW had a T_m of 65 °C, which is 13 K higher than that of EK. This 13-K increase is almost twice the ΔT_m between EK and WR1, which indicates that the two sets of Trp–Arg in WRRW do not interact cooperatively but separately, and that the orientation of WR (N→C or C→N) does not affect the stability of the coiled-coil structure. WR2 has an even higher T_m value, which is 10 K more than that of WRRW. Furthermore, when three Trp–Arg sets were used, the α -helical conformation was significantly more stable, leading to a T_m value greater than 95 °C for WR3. These results suggest that when Trp and Arg are aligned contigu-

ously between two α helices, they interact cooperatively. It is apparent that the alternating alignment of aromatic and cationic side chains multiplies their effects on the thermal stability.

The fluorescence maximum of Trp is 327–332 nm under hydrophobic conditions and 354 nm in solvent-exposed sites.^[13] We placed Trp at the *g* position, at the edge of the hydrophobic and hydrophilic environments. Trp might participate in the hydrophobic interaction, rather than the interaction with Arg, because the aromatic residues tend to be buried in the proteins. Therefore, we measured the fluorescence spectrum of the Trp residue. All of the peptides exhibited fluorescence maxima at 347–351 nm, with their intensities depending on the number of Trp residues. This finding indicates that the Trp residues exist at the solvent-exposed sites, and do not contribute to the hydrophobic interactions. The Trp residues in both WR2 and WRRW reside at solvent-exposed sites; however, WR2 is thermally more stable than WRRW. This result also supports the conclusion that the contiguous alignment of Trp and Arg augments the structural stability.

To obtain further physicochemical information concerning the Trp–Arg interaction, we prepared three more derivative peptides, AA, WA, and AR (see Table 1). These peptides formed triple-stranded coiled-coil structures. We carried out Gdn·HCl (guanidine hydrochloride) denaturation experiments to calculate the stabilization energy ΔG . The ΔG values obtained for AA, WA, and AR were similar at –14.6, –14.8, and –14.7 kcal mol^{–1}, respectively. Thus, the side chain of Trp or Arg alone does not contribute to the structural stability. The fact that the stabilization energies of EK and WR1 were –15.3 and –15.8 kcal mol^{–1}, respectively, indicates that an interhelical interaction between Glu and Lys, or Trp and Arg, was formed, and that one Trp–Arg interaction is stronger than one Glu–Lys ion-pair interaction by 0.17 kcal mol^{–1}. WR2 is even more stable, with a ΔG value of –16.7 kcal mol^{–1}, which shows that the stabilization energy of one Trp–Arg interaction is more than 0.23 kcal mol^{–1} higher than that of one Glu–Lys ion pair. Thus, one continuous Trp–Arg interaction stabilizes the structure even more, by 0.06 kcal mol^{–1}.

In conclusion, we have designed a cation– π interaction at the interface between two α helices. Physicochemical experiments suggested the existence of an interaction between Trp and Arg, and showed that its contribution to stabilizing the protein structure is greater than that of an ion pair. In particular, the tandem repeats of Trp and Arg alignment, which imply a network of cation– π interactions, substantially stabilize the structure. The extended cation– π interaction is observed in natural proteins, such as the human growth hormone receptor extracellular domain.^[1a,14] Although the role of the interaction was not revealed by the amino acid mutation, it may function to increase the protein stability. Our design strategy using the Trp–Arg interaction should contribute to increase protein stability and specificity.

Received: March 4, 2005

Revised: June 24, 2005

Published online: August 26, 2005

Keywords: amino acids · helical structures · peptides ·
pi interactions · protein structures

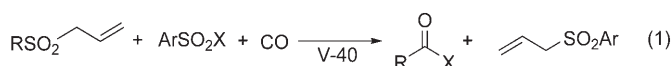
-
- [1] a) N. S. Scrutton, A. R. C. Raine, *Biochem. J.* **1996**, 319, 1–8; b) J. C. Ma, D. A. Dougherty, *Chem. Rev.* **1997**, 97, 1303–1324; c) J. P. Gallivan, D. A. Dougherty, *Proc. Natl. Acad. Sci. USA* **1999**, 96, 9459–9464.
- [2] a) M. P. Kavanaugh, R. S. Hurst, J. Yakel, M. D. Varnum, J. P. Adelman, R. A. North, *Neuron* **1992**, 8, 493–497; b) L. Satin, J. W. Kyle, M. Chen, P. Bell, L. L. Cribbs, H. A. Fozzard, R. B. Rogart, *Science* **1992**, 256, 1202–1205; c) W. Zhong, J. P. Gallivan, Y. Zhang, L. Li, H. A. Lester, D. A. Dougherty, *Proc. Natl. Acad. Sci. USA* **1998**, 95, 12088–12093; d) S. R. Hubbard, L. Wei, L. Ellis, W. A. Hendrickson, *Science* **1994**, 372, 746–753; e) O. Livnah, E. A. Stura, D. L. Johnson, S. A. Middleton, L. S. Mulcahy, N. C. Wrighton, W. J. Dower, L. K. Jolliffe, I. A. Wilson, *Science* **1996**, 273, 464–471; f) A. D. Kline, W. Braun, K. Wüthrich, *J. Mol. Biol.* **1986**, 189, 377–382; g) P. D. Kwong, R. Wyatt, J. Robinson, R. W. Sweet, J. Sodroski, W. A. Hendrickson, *Nature* **1998**, 393, 648–659.
- [3] S. Chakravarty, R. Varadarajan, *Biochemistry* **2002**, 41, 8152–8161.
- [4] a) Y. Satow, G. H. Cohen, E. A. Padlan, D. R. Davies, *J. Mol. Biol.* **1986**, 190, 593–604; b) A. R. C. Raine, C. C. Yang, L. C. Packman, S. A. White, F. S. Mathews, N. S. Scrutton, *Protein Sci.* **1995**, 4, 2625–2628; c) G. Waksman, D. Kominos, S. C. Robertson, N. Pant, D. Baltimore, R. B. Birge, D. Cowburn, H. Hanafusa, B. J. Mayer, M. Overduin, M. D. Resh, C. B. Rios, L. Silverman, J. Kuriyan, *Nature* **1992**, 358, 646–653.
- [5] S. K. Burley, G. A. Petsko, *FEBS Lett.* **1986**, 203, 139–143.
- [6] T. J. Shepodd, M. A. Petti, D. A. Dougherty, *J. Am. Chem. Soc.* **1988**, 110, 1983–1985.
- [7] J. P. Gallivan, D. A. Dougherty, *J. Am. Chem. Soc.* **2000**, 122, 870–874.
- [8] a) C. A. Olson, Z. S. Shi, N. R. Kallenbach, *J. Am. Chem. Soc.* **2001**, 123, 6451–6452; b) Z. S. Shi, C. A. Olson, N. R. Kallenbach, *J. Am. Chem. Soc.* **2002**, 124, 3284–3291; c) L. K. Tsou, C. D. Tatko, M. L. Waters, *J. Am. Chem. Soc.* **2002**, 124, 14917–14921; d) E. V. Pletneva, A. T. Laederach, D. B. Fulton, N. M. Kostic, *J. Am. Chem. Soc.* **2001**, 123, 6232–6245; e) M. M. Slutsky, E. N. G. Marsh, *Protein Sci.* **2004**, 13, 2244–2251.
- [9] C. Cohen, D. A. D. Parry, *Proteins Struct. Funct. Genet.* **1990**, 7, 1–15.
- [10] K. Suzuki, H. Hiroaki, D. Kohda, T. Tanaka, *Protein Eng.* **1998**, 11, 1051–1055.
- [11] a) S. Nautiyal, D. N. Woolfson, D. S. King, T. Alber, *Biochemistry* **1995**, 34, 11645–11651; b) D. M. Eckert, V. N. Malashkevich, P. S. Kim, *J. Mol. Biol.* **1998**, 284, 859–865.
- [12] a) P. B. Harbury, P. S. Kim, T. Alber, *Nature* **1994**, 371, 80–83; b) W. L. Jorgensen, D. S. Maxwell, J. Tirado-Rives, *J. Am. Chem. Soc.* **1996**, 118, 11225–11236; c) W. C. Still, A. Tempezyk, R. C. Hawley, T. Hendrickson, *J. Am. Chem. Soc.* **1990**, 112, 6127–6129.
- [13] a) C. N. Pace, *Methods Enzymol.* **1986**, 131, 266–269; b) T. M. Handel, S. A. Williams, D. Menyhard, W. F. DeGrado, *J. Am. Chem. Soc.* **1993**, 115, 4455–4460.
- [14] A. M. de Vos, M. Ultsch, A. A. Kossiakoff, *Science* **1992**, 255, 306–312.
-

DOI: 10.1002/anie.200501606

Tin-Free Radical Carbonylation: Thiol Ester Synthesis Using Alkyl Allyl Sulfone Precursors, Phenyl Benzenethiosulfonate, and CO**

Sangmo Kim, Sungak Kim,* Noboru Otsuka, and Ilhyong Ryu*

Free-radical carbonylation is synthetically very useful in preparing various carbonyl compounds.^[1] Synthetic methods based on free-radical carbonylation utilize mainly highly toxic organotin reagents as mediators.^[2] In our efforts to address the problems associated with toxic organotin reagents, we reported that the use of alkyl allyl sulfone precursors is one of the most useful and reliable methods for the generation of alkyl radicals under tin-free conditions and are very effective in radical carbon–carbon bond-formation reactions.^[3,4] In our continued efforts to achieve tin-free radical carbon–carbon bond formations,^[5] we have recently focused on tin-free radical carbonylations that use alkyl allyl sulfone precursors to prepare thiol esters [Eq. (1)].



Radical carboxylations were reported by Kharasch et al. in the 1940s,^[6] but no significant progress in this area was made in the subsequent 50 years. Direct radical carboxylation of alkyl radicals with carbon dioxide is an extremely difficult process because decarboxylation is a greatly favored process.^[7] Thus, radical carboxylations using highly reactive radical trapping agents such as oxalyl acid derivatives^[8] and *S*-phenyl chlorothioformate^[9] have recently been reported along with an indirect approach involving carbonylation and iodine atom transfer.^[10] For the synthesis of thiol esters, radical reactions of aldehydes with disulfides are used.^[11]

[*] S. Kim, Prof. Dr. S. Kim
Center for Molecular Design & Synthesis
and Department of Chemistry, School of Molecular Science (BK21)
Korea Advanced Institute of Science and Technology
Daejeon 305-701 (Korea)
Fax: (+82) 42-869-8370
E-mail: skim@kaist.ac.kr
N. Otsuka, Prof. Dr. I. Ryu
Department of Chemistry, Graduate School of Science
Osaka Prefecture University, Sakai, Osaka 599-8531 (Japan)
Fax: (+81) 72-254-9695
E-mail: ryu@c.s.osakafu-u.ac.jp

[**] S.K. is grateful to the CMDS and the Korea Electric Power Cooperation (KEPCO) for financial support. I.R. thanks JSPS and a Grant-in-Aid for Scientific Research on Priority Areas (A) "Reaction Control of Dynamic Complexes" from MEXT (Japan), for financial support.



Supporting information for this article is available on the WWW under <http://www.angewandte.org> or from the author.

To uncover efficient radical-trapping agents of acyl radicals,^[12,13] we screened several phenylsulfonyl derivatives as shown in Table 1. When 4-phenoxybutyl allyl sulfone (**1**) was treated with phenylsulfonyl bromide (**2b**) in the presence of V-40 (1,1'-azobis(cyclohexane-1-carbonitrile)) as initiator

Table 1: Radical carbonylation of alkyl allyl sulfone **1** (R = PhO(CH₂)₄) with arylsulfonyl derivatives **2**.

$\text{RSO}_2\text{CH}_2\text{CH=CH}_2 + \text{PhSO}_2\text{X} \xrightarrow[\text{V-40, 100 } ^\circ\text{C, 12 h}]{50 \text{ atm CO, 0.03 M heptane}} \text{R-C(=O)-X} + \text{R-X}$			
1	2	3	4
2: X =			
	3	4	1
a: Cl	10 ^[a]	0	76
b: Br	0	75	20
c: SePh	0	84	0
d: SPh	75	12	7

[a] Isolated as the methyl ester.

under pressurized CO (50 atm, 0.03 M, autoclave) in heptane at 100 °C for 12 h, 4-phenoxybutyl bromide (**4b**) was obtained in 75 % yield along with recovery of the starting material **1** (20 %) while no acid bromide was obtained. The use of phenyl benzeneselenosulfonate (**2c**) gave 4-phenoxybutyl phenyl selenide (**4c**) in 84 % yield, whereas the use of phenylsulfonyl chloride (**2a**) yielded a small amount of the acid chloride (10 %). Apparently, phenylsulfonyl bromide and phenyl benzeneselenosulfonate react with the alkyl radical prior to the carbonylation of the alkyl radical, whereas phenylsulfonyl chloride is too unreactive toward the alkyl radical. When the reaction was attempted using phenyl benzenethiosulfonate (**2d**) under the same conditions, a mixture of thiol ester **3d** (75 %) and alkyl sulfide **4d** (12 %) was isolated along with some starting material (7 %). Furthermore, the use of diphenyl disulfide as a trapping agent under the same conditions was not effective and **3d** was obtained in 15 % yield along with 80 % recovery of **1**.

As shown in Scheme 1, the addition of a phenylsulfonyl radical to **1** produces an alkyl radical through the thermal

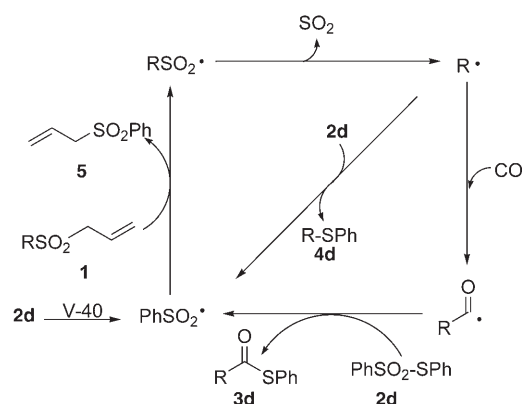
desulfonylation of the initially generated alkyl sulfonyl radical along with formation of phenyl allyl sulfone (**5**). The alkyl radical can react with CO and/or phenyl benzenethiosulfonate (**2d**) to yield the acyl radical and/or alkyl sulfide **4d**. Therefore, the success of this approach depends critically on obviating the formation of **4d**. To optimize the reaction conditions, the effect of the pressure of CO and the concentration of **1** were investigated (Table 2). As expected, the yield

Table 2: Effect of concentration of **1** (R = PhO(CH₂)₄) and pressure of CO on the tin-free radical carbonylation with **2d**.

$\text{RSO}_2\text{CH}_2\text{CH=CH}_2 + \text{PhSO}_2\text{SPh} \xrightarrow[\text{100 } ^\circ\text{C, 12 h, heptane}]{\text{CO, V-40}} \text{R-C(=O)-SPh} + \text{R-SPh}$				
1	2d		3d	4d
[1] [M]	<i>p</i> CO [atm]		Yield [%]	
			3d	4d
0.05	95		82	11
0.02	95		77	3
0.02	50		81	8
0.01	50		61	3
0.01	95		70	0
0.01	95 ^[a]		92	0

[a] Reaction time: 18 h.

of thiol ester **3d** was increased at the higher pressure of CO while a lower concentration of **1** led to a reduced yield of alkyl sulfide **4d**. The best result was obtained when the reaction was carried out with **2d** (1.5 equiv) and V-40 (0.2 equiv) as initiator in a pressurized autoclave (95 atm of CO) in heptane (0.01 M) at 100 °C for 18 hours. Furthermore, when the effectiveness of alkyl benzenethiosulfonates relative to **2d** was briefly studied, methyl benzenethiosulfonate was found to be equally effective and slightly more reactive than **2d** [Eq. (2)]. Additionally, we explored the application of the present method to synthetically useful pentafluorophenyl thiol esters [Eq. (3)].^[14] Treatment of **1** with pentafluorophenyl benzenethiosulfonate (**7**)^[15] under the same conditions afforded pentafluorophenyl thiol ester **8** in 82 % yield along with pentafluorophenyl sulfide **9** (16 %). A similar result was also obtained with **6**.



Scheme 1. Tin-free radical carbonylation of alkyl allyl sulfone **1** (R = PhO(CH₂)₄) with phenyl benzenethiosulfonate (**2d**).

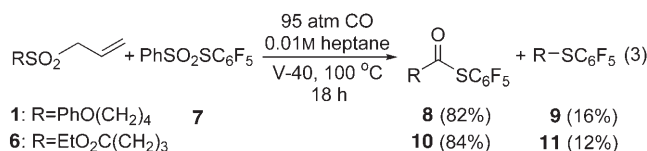
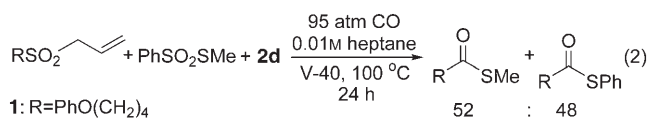


Table 3 illustrates the efficiency and the scope of the present method. Primary alkyl radicals worked well, yielding the corresponding thiol esters in high yields under the present

Table 3: Synthesis of thiol esters through tin-free radical carbonylation.

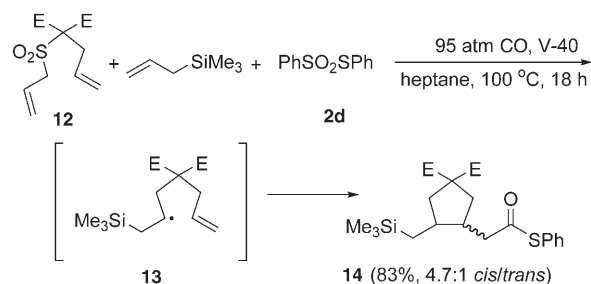
Entry	Alkyl allyl sulfone Y = SO ₂ CH ₂ CH=CH ₂	Conditions ^[a]	Thiol ester	Yield [%] ^[b]
1		A		97
2		A		98
3		A		94
4		A		83
5		A		95
6		A		84 ^[c]
7		A		64 (26)
8		B		80 (11)
9		A		87 (10)
10		A		83 (13)
11		A		33 (57)
12		A		72 (24)
13		A		– (51) ^[d]
14		A		90
15		A		24
				59

[a] A: **2d** (1.5 equiv), CO (95 atm), heptane, 100°C, 18 h; B: **2d** (1.5 equiv), CO (130 atm), heptane, 100°C, 18 h. TBDPS = *tert*-butyldiphenylsilyl. [b] The numbers in parentheses indicate isolated yields of alkyl phenyl sulfides. [c] Starting material (12%) was recovered. [d] Some starting material (46%) was also recovered.

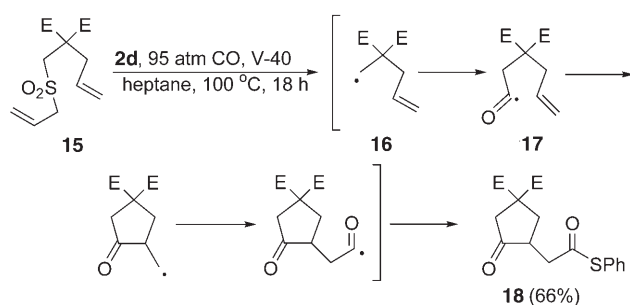
conditions (95 atm of CO, 0.01M solution of **1**). There was no indication of the formation of alkyl sulfide **4d**. In one case, a small amount of the starting material was recovered (entry 6). However, secondary alkyl radicals led to a significant amount of formation of **4d**. As the radical carbonylation of secondary alkyl radicals is less efficient than that of primary alkyl radicals, secondary alkyl radicals would have more chance to react with **5** prior to carbonylation. At 95 atm of CO, a 64:26 mixture of the thiol ester and the alkyl phenyl sulfide was isolated (entry 7). When the same reaction was repeated at a higher pressure of CO (130 atm) for 18 h, the formation of the

alkyl phenyl sulfide was reduced to some extent to yield an 80:11 mixture of **3d** and **4d** (entry 8). As we anticipated, tertiary alkyl radicals gave more direct addition products (entries 11 and 12). The benzylic radical did not undergo carbonylation and reacted with **2d** to give a benzyl phenyl sulfide in 51 % yield together with the recovery of some starting material (46%; entry 13). Sequential radical reaction involving cyclization and phenylthio carbonylation afforded the desired product in 90 % yield (entry 14). However, in the case of 6-*exo* ring closure, a 24:59 mixture of two products was obtained in favor of the direct carbonylation product, apparently as a result of the competition between 6-*exo* ring closure and the direct carbonylation (entry 15).^[16] When a four-component coupling reaction using **12**, allyl trimethylsilane, CO, and **2d** was carried out under the same conditions, a 4.7:1 diastereomeric mixture of the desired product **14** was isolated in 83 % yield (Scheme 2).^[17] Evidently, the electrophilic alkyl radical generated from **12** failed to undergo carbonylation and reacted with allyl trimethylsilane to yield intermediate **13**.

Next, the possibility of a double carbonylation was explored.^[18] Reaction of **15** with **2d** and CO yielded acyl radical **17** through carbonylation of the radical intermediate **16**. The subsequent 5-*exo* ring closure of **17** and CO trapping followed by quenching with **2d** afforded thiol ester **18** according to the scheme proposed (Scheme 3). When **15** was subjected to the



Scheme 2. E = CO₂Et.



Scheme 3. E = CO₂Et.

standard carbonylation conditions, **18** was isolated in 66 % yield.

In conclusion, we have reported that tin-free radical carbonylation is successfully achieved using alkyl allyl sulfone precursors and have developed a highly efficient method for the synthesis of thiol esters using phenyl benzenethiosulfonate as a trapping agent. This approach provides ready access to other related carbonyl derivatives.

Experimental Section

Typical procedure: Heptane (12 mL), 4-(prop-2-ene-1-sulfonyl)butyric acid ethyl ester (26 mg, 0.12 mmol), phenyl benzenethiosulfonate (**2d**; 45 mg, 0.18 mmol), and V-40 (8 mg, 0.03 mmol) were placed in a 50-mL stainless steel autoclave. The autoclave was sealed and purged with CO (3 × 10 atm). The autoclave was then pressurized with CO (95 atm) and heated, with stirring, at 100 °C for 18 h. After excess CO was discharged at room temperature, the solvent was evaporated, and the residue was purified by column chromatography on silica gel using ethyl acetate and *n*-hexane (1:20) as eluant to give 4-phenylsulfanyl-carbonylbutyric acid ethyl ester (28 mg, 94 %). ¹H NMR (CDCl₃, 400 MHz): δ = 1.24 (t, *J* = 7.1 Hz, 3 H), 2.01 (quin, *J* = 7.3 Hz, 2 H), 2.38 (t, *J* = 7.3 Hz, 2 H), 2.72 (t, *J* = 7.3 Hz, 2 H), 4.12 (q, *J* = 7.1 Hz, 2 H), 7.39 ppm (s, 5 H); ¹³C NMR (CDCl₃, 100 MHz): δ = 14.2, 20.6, 33.0, 42.5, 60.5, 127.6, 129.2, 129.4, 134.5, 172.7, 196.8 ppm; IR (polymer): $\tilde{\nu}$ = 749, 1026, 1187, 1442, 1479, 1708, 1735, 1963, 2983 cm⁻¹; HRMS [*M*⁺] calcd for C₁₃H₁₆O₃S: 252.0820; found: 252.0815.

Received: May 11, 2005

Published online: August 31, 2005

Keywords: carbonylation · radical reactions · radicals · synthetic methods

- [1] For reviews, see: a) I. Ryu, N. Sonoda, *Angew. Chem.* **1996**, *108*, 1140–1157; *Angew. Chem. Int. Ed. Engl.* **1996**, *35*, 1050–1066; b) I. Ryu, N. Sonoda, D. P. Curran, *Chem. Rev.* **1996**, *96*, 177–194; c) I. Ryu, *Chem. Soc. Rev.* **2001**, *30*, 16–25; d) I. Ryu, *Chem. Rec.* **2002**, 249–258.
- [2] For a review, see: P. A. Baguley, J. C. Walton, *Angew. Chem.* **1998**, *110*, 3272–3283; *Angew. Chem. Int. Ed.* **1998**, *37*, 3072–3082, and references therein.
- [3] a) B. Quiclet-Sire, S. Z. Zard, *J. Am. Chem. Soc.* **1996**, *118*, 1209–1210; b) F. L. Guyader, B. Quiclet-Sire, S. Seguin, S. Z. Zard, *J. Am. Chem. Soc.* **1997**, *119*, 7410–7411; c) J. Xiang, W. Jiang, J. Gong, P. L. Fuchs, *J. Am. Chem. Soc.* **1997**, *119*, 4123–4129; d) B. Quiclet-Sire, S. Seguin, S. Z. Zard, *Angew. Chem.* **1998**, *110*,

- 3056–3058; *Angew. Chem. Int. Ed.* **1998**, *37*, 2864–2866; e) F. Bertrand, B. Quiclet-Sire, S. Seguin, S. Z. Zard, *Angew. Chem.* **1999**, *111*, 2135–2138; *Angew. Chem. Int. Ed.* **1999**, *38*, 1943–1946;
- [4] a) S. Kim, C. J. Lim, *Angew. Chem.* **2002**, *114*, 3399–3401; *Angew. Chem. Int. Ed.* **2002**, *41*, 3265–3267; b) S. Kim, C. J. Lim, *Bull. Korean Chem. Soc.* **2003**, *24*, 1219–1222.
- [5] a) S. Kim, H.-J. Song, T.-L. Choi, J.-Y. Yoon, *Angew. Chem.* **2001**, *113*, 2592–2594; *Angew. Chem. Int. Ed.* **2001**, *40*, 2524–2526; b) S. Kim, C. J. Lim, C. Song, W.-j. Chung, *J. Am. Chem. Soc.* **2002**, *124*, 14306–14307; c) S. Lee, C. J. Lim, S. Kim, *Bull. Korean Chem. Soc.* **2004**, *25*, 1611–1612.
- [6] a) M. S. Kharasch, S. S. Kane, H. C. Brown, *J. Am. Chem. Soc.* **1942**, *64*, 1621–1624; b) M. S. Kharasch, H. C. Brown, *J. Am. Chem. Soc.* **1942**, *64*, 329–333.
- [7] a) J. Fossey, D. Lefort, J. Sorba, *Free Radicals in Organic Chemistry*, Wiley, New York, **1995**; b) S. Hadida, M. S. Super, E. J. Beckman, D. P. Curran, *J. Am. Chem. Soc.* **1997**, *119*, 7406–7407.
- [8] a) S. Kim, *Adv. Synth. Catal.* **2004**, *346*, 19–32; b) S. Kim, S. Y. Jon, *Chem. Commun.* **1998**, 815–816.
- [9] S. Kim, S. Y. Jon, *Tetrahedron Lett.* **1998**, *39*, 7317–7320.
- [10] a) K. Nagahara, I. Ryu, M. Komatsu, N. Sonoda, *J. Am. Chem. Soc.* **1997**, *119*, 5465–5466; b) M. Sugiura, H. Hagio, S. Kobayashi, *Chem. Lett.* **2003**, 898–899.
- [11] a) M. Takagi, S. Goto, T. Matsuda, *J. Chem. Soc. Chem. Commun.* **1976**, 92–93; b) M. Takagi, S. Goto, M. Tazaki, T. Matsuda, *Bull. Chem. Soc. Jpn.* **1980**, *53*, 1982–1987; c) H. Nambu, K. Hata, M. Matsugi, Y. Kita, *Chem. Commun.* **2002**, 1082–1083; d) H. Nambu, K. Hata, M. Matsugi, Y. Kita, *Chem. Eur. J.* **2005**, *11*, 719–727.
- [12] For a review on acyl radicals, see: C. Chatgililoglu, D. Crich, M. Komatsu, I. Ryu, *Chem. Rev.* **1999**, *99*, 1991–2070.
- [13] a) D. Crich, C. Chen, J.-T. Hwang, H. Yuan, A. Papadatos, R. I. Walter, *J. Am. Chem. Soc.* **1994**, *116*, 8937–8951; b) I. Ryu, T. Okuda, K. Nagahara, N. Kambe, M. Komatsu, N. Sonoda, *J. Org. Chem.* **1997**, *62*, 7550–7551.
- [14] a) A. P. Davis, J. J. Walsh, *Tetrahedron Lett.* **1994**, *35*, 4865–4869; b) A. P. Davis, J. J. Walsh, *Chem. Commun.* **1996**, 449–451; c) Z.-H. Huang, J. Wu, K. D. W. Roth, Y. Yang, D. A. Gae, J. T. Watson, *Anal. Chem.* **1997**, *69*, 137–144.
- [15] a) A. Haas, *J. Fluorine Chem.* **1986**, *32*, 415–439; b) T. Billard, B. R. Langlois, S. Large, D. Anker, N. Roidot, P. Roure, *J. Org. Chem.* **1996**, *61*, 7545–7550; c) K. Fujiki, N. Tanifuji, Y. Sasake, T. Yokoyama, *Synthesis* **2002**, 343–348.
- [16] K. Nagahara, I. Ryu, N. Kambe, M. Komatsu, N. Sonoda, *J. Org. Chem.* **1995**, *60*, 7384–7385.
- [17] a) A. L. J. Beckwith, G. Phillipou, A. K. Serelis, *Tetrahedron Lett.* **1981**, *22*, 2811–2814; b) T. V. Rajan Babu, *Acc. Chem. Res.* **1991**, *24*, 139–145; c) S. Kim, I. Y. Lee, J.-Y. Yoon, D. H. Oh, *J. Am. Chem. Soc.* **1996**, *118*, 5138–5139.
- [18] a) S. Tsunoi, I. Ryu, S. Yamasaki, H. Fukushima, M. Tanaka, M. Komatsu, N. Sonoda, *J. Am. Chem. Soc.* **1996**, *118*, 10670–10671; b) I. Ryu, S. Krimmerman, F. Araki, S. Nishitani, Y. Oderaotoshi, S. Minakata, M. Komatsu, *J. Am. Chem. Soc.* **2002**, *124*, 3812–3813.

DOI: 10.1002/anie.200502308

Lewis Acid Catalyzed Asymmetric Cycloadditions of Nitrones: α' -Hydroxy Enones as Efficient Reaction Partners**

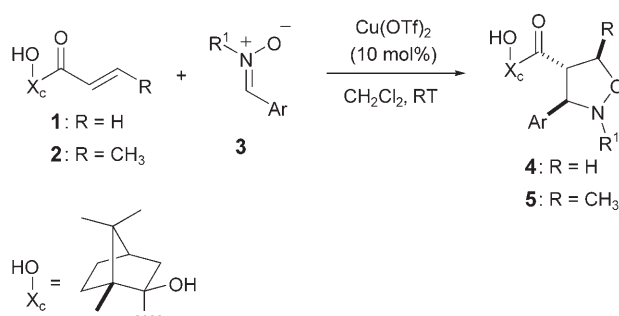
Claudio Palomo,* Mikel Oiarbide, Elena Arceo, Jesús M. García, Rosa López, Alberto González, and Anthony Linden

Dedicated to Professor J. Plumet on the occasion of his 60th birthday

The 1,3-dipolar cycloaddition of nitrones to alkenes^[1] is an atom-economic method for the construction of isoxazolidines, which are important precursors of, for example, alkaloids, amino acids, β -lactams, and amino sugars.^[2] Typically, an electron-deficient alkene is involved, with the interaction between the LUMO of the alkene and the HOMO of the nitrone being the determinant for the relative orientation of the reactants. However, steric factors often counterbalance the electronic preferences, particularly in β -unsubstituted enoyl (acryloyl) systems, and make regiocontrol challenging.^[3,4] Additionally, both *endo/exo* and π -facial selectivity have to be addressed. Although amine activation of enals^[5] has emerged as an attractive approach, most methods rely on the use of Lewis acids to activate the enoyl system toward the nitrone counterpart.^[3,4,6] However, despite the many applications, success in asymmetric nitrone cycloadditions remains very scarce compared to that reached in the parent Diels–Alder cycloaddition and only a limited number of alkene templates such as *N*-enoyl derivatives of oxazolidinone,^[4a–c,6c–6g] thiazolidinethione,^[6a] pyrrolidinone,^[6b] and pyrazolidinone,^[6h] as well as certain alkylidene malonates^[6i] have been employed to fulfill this gap. In metal-catalyzed nitrone

cycloadditions, not only are bidentate alkene substrates required but also metal–substrate coordination needs to be notably efficient for optimum selectivity.^[7] We report herein that excellent combined levels of regio-, *endo/exo*-, and enantioselectivity may be achieved by using α' -hydroxy enones as new partners for this reaction.

Recent observations from these laboratories in the context of Diels–Alder and conjugate addition reactions have shown the role of α' -hydroxy enones in metal-assisted activation, which likely occurs through formation of 1,4-metal-chelated species as the reactive intermediates.^[8] It was argued that such a complexation pattern might be effective in nitrone cycloadditions and hence increase the pool of available templates for this reaction. To evaluate this assumption, initial screening reactions were carried out with the chiral α' -hydroxy enone **1**^[9] and nitrone **3a** in the presence of several metal triflates (Scheme 1 and Table 1). Data



Scheme 1. Regio- and stereocontrolled 1,3-dipolar cycloadditions of nitrones to α' -hydroxy enones **1** and **2**. OTf=trifluoromethylsulfonyl.

Table 1: Screening of the catalyst for the reaction of enone **1** with nitrone **3a** ($R^1 = \text{Bn}$; $\text{Ar} = \text{Ph}$) to give **4a**.^[a]

Lewis acid	<i>t</i> [h]	Conversion [%]	Regioisomer ratio ^[b]
Mg(OTf) ₂	72	68 ^[c]	12:88 ^[d]
Zn(OTf) ₂	48	81 ^[c]	89:11 ^[e]
Cu(OTf) ₂	4	> 99	≥ 98:2 ^[e]
La(OTf) ₃	15	50	98:2 ^[e]
Yb(OTf) ₃	48	92 ^[c]	85:15 ^[e]

[a] Reactions conducted at room temperature in dry CH_2Cl_2 , with 1:1:0.1 molar ratio of enone **1**/**3a**/Lewis acid. [b] Determined by ¹H NMR spectroscopy. [c] By-products from nitrone and enone decomposition were detected. [d] Minor isomer corresponds to **4a**; configuration of the major isomer not established. [e] Configuration of the minor isomer not established.

revealed that Cu(OTf)₂ gave the best results and isoxazolidine **4a** could indeed be obtained in high yield and, most notably, with essentially perfect regio- and diastereoselectivity.

Gratifyingly, the chemical efficiency and the high degree of regio- and stereocontrol for this Cu(OTf)₂-mediated reaction was found to be quite general over the range of nitrones **3a–k** examined (Table 2). Nitrones bearing electron-rich, electron-neutral, or electron-poor aryl substituents were tolerated with almost equal efficiency to give isoxazolidines **4a–k** in good yields and with diastereomeric ratios ranging

[*] Prof. Dr. C. Palomo, Prof. Dr. M. Oiarbide, Dr. R. López
Departamento de Química Orgánica I
Facultad de Química
Universidad del País Vasco
Apdo. 1072, 20080 San Sebastián (Spain)
Fax: (+34) 943-015-270
E-mail: qoppanic@sc.ehu.es

E. Arceo, Dr. J. M. García, Prof. Dr. A. González
Departamento de Química Aplicada
Universidad Pública de Navarra (UPNA)
Campus de Arrosadía, 31006 Pamplona (Spain)

Dr. A. Linden
Organisch-Chemisches Institut
Universität Zürich
Winterthurerstrasse 190, 8057 Zürich (Switzerland)

[**] This work was financially supported by the University of the Basque Country and the Ministerio de Educación y Ciencia (MEC, Spain). A Ramón y Cajal contract to R.L. from the MEC, and a grant to E.A. from the UPNA are acknowledged. Crystal structure analyses were performed by A.L.

Supporting information for this article is available on the WWW under <http://www.angewandte.org> or from the author.

Table 2: Asymmetric 1,3-dipolar cycloadditions of enones **1** and **2** with nitrones **3**.^[a]

	Nitrone 3	R ¹	R	Product	t [h]	Yield [%] ^[b]	d.r. ^[c]
Ar							
3a	Ph	PhCH ₂	H	4a	4	88	≥ 98:2
		PhCH ₂	CH ₃	5a	22 ^[d]	84	≥ 98:2
3b	4-MeO-C ₆ H ₄	PhCH ₂	H	4b	24	68	≥ 98:2
3c	4-Me-C ₆ H ₄	PhCH ₂	H	4c	30 ^[e]	70	≥ 98:2
		CH ₃	CH ₃	5c	50 ^[d]	70	≥ 98:2
3d	3-Me-4-Me-C ₆ H ₃	PhCH ₂	H	4d	8	83	≥ 98:2
3e	4-Cl-C ₆ H ₄	PhCH ₂	H	4e	9 ^[e]	89	≥ 98:2
		CH ₃	CH ₃	5e	48 ^[d]	71	≥ 98:2
3f	3-Cl-C ₆ H ₄	PhCH ₂	H	4f	0.5	91	≥ 98:2
3g	3-Cl-4-MeO-C ₆ H ₃	PhCH ₂	H	4g	2	90	≥ 98:2
3h	4-CN-C ₆ H ₄	PhCH ₂	H	4h	28	76	94:6 ^[f]
3i	3-NO ₂ -4-Me-C ₆ H ₃	PhCH ₂	H	4i	2	89	≥ 98:2
3j	Ph	Ph ₂ CH	H	4j	8	70	90:10 ^[f]
3k	Ph	2-MeO-PhCH ₂	H	4k	10	84	≥ 98:2

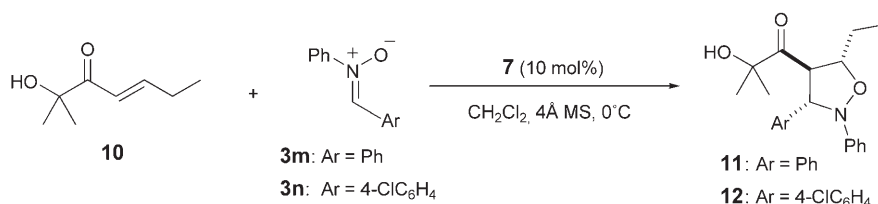
[a] Reactions conducted on 0.5-mmol scale in dry CH₂Cl₂, with 1:1:0.1 molar ratio of enone/nitrone/catalyst. [b] Yield of isolated product after column chromatography. [c] Determined by ¹³C NMR spectroscopy. [d] In the presence of 4-Å molecular sieves and a 1:2:0.2 molar ratio of enone/nitrone/catalyst. [e] Using 5 mol % of Cu(OTf)₂. [f] Configuration of the minor isomer not determined.

from 90:10 to greater than 98:2. The reactions were typically carried out in dichloromethane as solvent using 10 mol % catalyst, although a loading of 5 mol % catalyst led to similar results (products **4c** and **4e**). β-Substituted enones also behaved well in terms of both chemical and stereochemical efficiency, although longer reaction times were required.^[10] For example, the reaction of enone **2** with nitrones **3a**, **3c**, and **3e** provided cycloadducts **5a**, **5c**, and **5e** in good yields and with remarkable diastereoselectivity.

The scope of the model is further demonstrated in the catalytic, enantioselective 1,3-dipolar cycloaddition of nitrones to simple α'-hydroxy enone **6**^[8] (Table 3). A preliminary survey of combinations of privileged ligands and metal salts^[11,12] showed that the Evans bis(oxazoline)-Cu^{II} complex **7**

(tBOX/Cu) was most successful in providing the nitrone cycloadducts **8/9** with very high stereoselectivity and with regioisomeric ratios equal to or greater than 90:10. To the best of our knowledge, this represents the highest combined regio- and enantioselectivity observed for β-unsaturated enoyl substrates.^[4,13] As an apparent limitation, however, the reaction of **6** with nitrone **3m** provided low *endo/exo* selectivity, although excellent regio- and enantiocontrol were still attained.

As differently β-substituted, simple hydroxy enones are readily available,^[8] the method constitutes a straightforward route to 3,4,5-trisubstituted isoxazolidines of high diastereo- and enantiopurity. For instance, enone **10** reacted with nitrones **3m** and **3n** to give the respective isoxazolidines **11** and **12** with diastereomeric ratios of about 98:2 and enantioselectivities higher than 99 % (Scheme 2).



Scheme 2. Enantioselective approach for β-substituted hydroxy enone substrates.

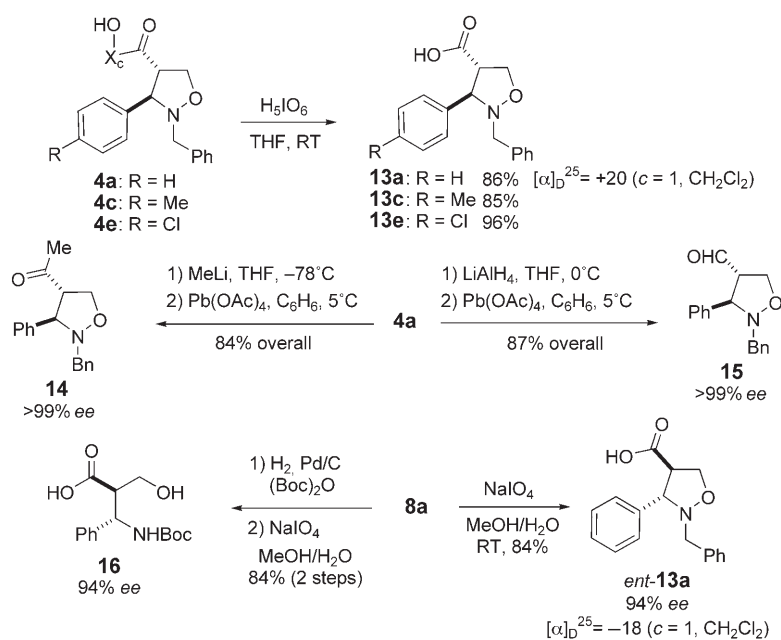
The assigned configuration of adducts **4**, **8**, **5**, and **9** was established by single-crystal X-ray analyses^[14] of adducts **4a**, **5a**, **8m**, and **9a** (the configurations of the remaining adducts were assigned by analogy). Additionally, the absolute configuration of **8a** was deduced from comparison of the optical rotation values of elaborated adducts (see below) and by assuming a uniform reaction mechanism.

The potential utility of the method is illustrated in Scheme 3. For example, treatment of adducts **4a**, **4c**, and **4e** with periodic acid afforded the corresponding carboxylic acids **13** in high yields and essentially enantiopure form. Likewise, after addition of methyl lithium to **4a** and subsequent cleavage of the diol with lead tetraacetate, enantiopure acetylisoxazolidine **14** was obtained in 84 % yield. Similarly, reduction of **4a** and further scission led to isoxazolidine carbal-

Table 3: Catalytic enantioselective 1,3-dipolar cycloadditions of nitrones and α'-hydroxy enone **6**.^[a]

3	Ar	R ¹	Yield [%]	Ratio 8:9 ^[b]	Product 8 <i>endo/exo</i> ^[c]	<i>ee</i> [%] ^[d]
3a	Ph	PhCH ₂	85	93:7	≥ 98:2	94
3b	4-MeO-C ₆ H ₄	PhCH ₂	99	92:8	≥ 98:2	92
3c	4-Me-C ₆ H ₄	PhCH ₂	81	92:8	≥ 98:2	92
3d	3-Me-4-Me-C ₆ H ₃	PhCH ₂	94	≥ 98:2	≥ 98:2	90
3e	Ph	CH ₃	55	90:10	≥ 98:2	96
3f	Ph	Ph	98	≥ 98:2 ^[e]	76:24	≥ 99

[a] Reactions conducted at 0.5-mmol scale in CH₂Cl₂ with a 2:1 molar ratio of **6/3**. [b] Determined by ¹³C NMR spectroscopy; absolute configuration of **9** not determined. [c] Determined by ¹H NMR spectroscopy. [d] Determined by HPLC. [e] Reaction conducted at -40 °C.



Scheme 3. Chemical elaboration of cycloadducts with detachment of the auxiliary X_c –OH. Bn = benzyl; Boc = *tert*-butoxycarbonyl.

dehyde **15**. In all the above examples, the starting (1*R*)-(+)-camphor was recovered after scission, ready for reuse. On the other hand, the oxidative elaboration of adduct **8a** gave *ent*-**13a** along with acetone as the only by-product, whereas hydrogenolytic opening of **8a** with concomitant *N*-protection (Boc) and further cleavage of the ketol afforded homoserine derivative **16** in two high-yielding steps. Of practical interest, both enantiomers of each isoxazolidine product are readily accessible by appropriate choice of the corresponding approach.

In conclusion, α' -hydroxy enones considerably expand the range of metal-catalyzed 1,3-dipolar cycloadditions of nitrones. Conditions have been set that produce the cycloadducts with very high combined levels of regio- and stereoselectivity. The potential of the method has been demonstrated using camphor-derived α' -hydroxy enone **1** in combination with catalytic $\text{Cu}(\text{OTf})_2$, or achiral enones **6** and **10** in combination with the Evans bis(oxazoline)– Cu^{II} catalyst, and by the easy elaboration of the cycloadducts to diversely functionalized di- and trisubstituted isoxazolidines in essentially enantiopure form.

Experimental Section

General procedure for Cu^{II} /tBOX (**7**)-catalyzed 1,3-dipolar cycloadditions of nitrones to **6**: A flame-dried flask was charged with 2-hydroxy-2-methylpent-4-en-3-one (**6**; 0.114 g, 1.0 mmol) and dry CH_2Cl_2 (1.5 mL) under N_2 . The solution was cooled to -20°C , and then freshly dried, powdered molecular sieves (4 Å; 250 mg), a solution of the corresponding nitrone (0.5 mmol) in CH_2Cl_2 (1 mL), and a solution of **7** in CH_2Cl_2 (0.05 M, 1 mL) were added consecutively. The resulting mixture was stirred at -20°C until completion of reaction. The reaction mixture was then diluted with 5 mL of ethyl acetate/hexane (1:1), and the solution was directly applied to a short column of silica gel (1.5 cm \times 1.5 cm). Elution with a mixture of ethyl

acetate and hexane (1:1), followed by concentration of the collected solution and subsequent purification by column chromatography (silica gel, 1:15 ethyl acetate/hexane), afforded the corresponding cycloadduct.

Received: July 1, 2005

Published online: September 1, 2005

Keywords: asymmetric catalysis · cycloaddition · hydroxy enones · Lewis acids · synthetic methods

- [1] For reviews, see: a) K. V. Gothelf, K. A. Jørgensen, *Chem. Rev.* **1998**, 98, 863–909; b) K. V. Gothelf, K. A. Jørgensen, *Chem. Commun.* **2000**, 1449–1458; c) S. Kanemasa, *Synlett* **2002**, 1371–1387; d) K. V. Gothelf in *Cycloaddition Reactions in Organic Synthesis* (Eds.: S. Kobayashi, K. A. Jørgensen), Wiley-VCH, Weinheim, **2002**, pp. 211–247; e) K. V. Gothelf, K. A. Jørgensen in *Synthetic Applications of 1,3-Dipolar Cycloaddition, Chemistry toward Heterocycles and Natural Products*, (Eds.: A. Padwa, W. H. Pearson), Wiley, Hoboken, NJ, **2003**, pp. 817–900.
- [2] a) J. N. Martin, R. C. F. Jones in *Synthetic Applications of 1,3-Dipolar Cycloaddition, Chemistry toward Heterocycles and Natural Products*, (Eds.: A. Padwa, W. H. Pearson), Wiley, Hoboken, NJ, **2003**, pp. 1–82; b) S. Karlsson, H.-E. Högborg, *Org. Prep. Proc. Int.* **2001**, 33, 103–172.
- [3] For illustrative examples using stoichiometric chiral auxiliaries, see: a) T. Gefflaut, U. Bauer, K. Airola, A. M. P. Koskinen, *Tetrahedron: Asymmetry* **1996**, 7, 3099–3102; b) A. Carriere, A. Virgili, M. Figueredo, *Tetrahedron: Asymmetry* **1996**, 7, 2793–2796; c) T. Tejero, A. Dondoni, I. Rojo, F. L. Merchán, P. Merino, *Tetrahedron* **1997**, 53, 3301–3318; d) P. Merino, S. Anoro, S. Franco, F. L. Merchán, T. Tejero, V. Tuñón, *J. Org. Chem.* **2000**, 65, 1590–1596; e) O. Tamura, A. Kanoh, M. Yamashita, H. Ishibashi, *Tetrahedron* **2004**, 60, 9997–10003.
- [4] For illustrative examples using chiral catalysts, see: a) K. V. Gothelf, R. G. Hazell, K. A. Jørgensen, *J. Org. Chem.* **1998**, 63, 5483–5488, and references therein; b) T. Saito, T. Yamada, S. Miyazaki, T. Otani, *Tetrahedron Lett.* **2004**, 45, 9585–9587; c) G. Desimoni, G. Faita, M. Mella, M. Boiocchi, *Eur. J. Org. Chem.* **2005**, 1020–1027; d) F. Viton, G. Bernardinelli, E. P. Küding, *J. Am. Chem. Soc.* **2002**, 124, 4968–4969; e) M. Shirahase, S. Kanemasa, Y. Oderaotoshi, *Org. Lett.* **2004**, 6, 675–678; f) D. Carmona, M. P. Lamata, F. Viguri, R. Rodríguez, L. A. Oro, A. I. Balana, F. J. Lahoz, T. Tejero, P. Merino, S. Franco, I. Montes, *J. Am. Chem. Soc.* **2004**, 126, 2716–2717.
- [5] a) W. S. Jen, J. J. M. Wiener, D. W. C. MacMillan, *J. Am. Chem. Soc.* **2000**, 122, 9874–9875; b) S. Karlsson, H.-E. Högborg, *Eur. J. Org. Chem.* **2003**, 2782–2791.
- [6] For complexes of Ni^{II} : a) H. Suga, T. Nakajima, K. Itoh, A. Kakehi, *Org. Lett.* **2005**, 7, 1431–1434; b) S. Iwasa, H. Maeda, K. Nishiyama, S. Tsushima, Y. Tsukamoto, H. Nishiyama, *Tetrahedron* **2002**, 58, 8281–8287; c) S. Kanemasa, Y. Oderaotoshi, J. Tanaka, E. Wada, *J. Am. Chem. Soc.* **1998**, 120, 12355–12356; for complexes of Pd^{II} : d) K. Hori, H. Kodama, T. Ohta, I. Furukawa, *J. Org. Chem.* **1999**, 64, 5017–5023; for complexes of Mg^{II} and Mn^{II} : e) S. Iwasa, Y. Ishima, H. S. Widagdo, K. Aoki, H. Nishiyama, *Tetrahedron Lett.* **2004**, 45, 2121–2124; for complexes of lanthanides: f) H. Kodama, J. Ito, K. Hori, T. Ohta, I. Furukawa, *J. Organomet. Chem.* **2000**, 603, 6–12; g) S. Kobayashi, M. Kawamura, *J. Am. Chem. Soc.* **1998**, 120, 5840–5841; for complexes of Cu^{II} : h) M. P. Sibi, Z. Ma, C. P. Jasperse, *J. Am. Chem. Soc.* **2004**, 126, 718–719; for complexes of Co^{II} : i) Z.-Z. Huang, Y.-B. Kang, J. Zhou, M.-C. Ye, Y. Tang, *Org. Lett.* **2004**, 6, 1677–1679.

- [7] Nitrones are basic in nature and may show competitive coordination to the metal, thus provoking inactivation of the Lewis acid; for more information on this subject, see: S. Kanemasa, T. Uemura, E. Wada, *Tetrahedron Lett.* **1992**, 33, 7889–7892.
- [8] For Diels–Alder reactions, see: a) C. Palomo, M. Oiarbide, J. M. García, A. González, E. Arceo, *J. Am. Chem. Soc.* **2003**, 125, 13942–13943; for conjugate additions of carbamates, see: b) C. Palomo, M. Oiarbide, R. Halder, M. Kelso, E. Gómez-Bengoa, J. M. García, *J. Am. Chem. Soc.* **2004**, 126, 9188–9189; for Friedel–Crafts reactions, see: c) C. Palomo, M. Oiarbide, B. G. Kardak, J. M. García, A. Linden, *J. Am. Chem. Soc.* **2005**, 127, 4154–4155.
- [9] Compound **1** is readily prepared in two steps (75 %) from (1*R*)-(+)-camphor and methoxyallene, two commodity chemicals that are available in bulk; see: C. Palomo, M. Oiarbide, J. M. García, A. González, A. Lecumberri, A. Linden, *J. Am. Chem. Soc.* **2002**, 124, 10288–10289.
- [10] To avoid decomposition of the nitron and ensure good yields and high selectivities, the presence of 4-Å molecular sieves was required in these instances; for the first observation and discussion of the effect of molecular sieves in Lewis acid catalyzed nitron cycloadditions, see: a) K. V. Gothelf, R. G. Hazell, K. A. Jørgensen, *J. Org. Chem.* **1996**, 61, 346–355; b) See Ref. [6g].
- [11] For the concept of privileged chiral catalysts, see: T. P. Yoon, E. N. Jacobsen, *Science* **2003**, 299, 1691–1693.
- [12] For other systems examined, see the Supporting Information.
- [13] a) For an exception using Ni^{II} complexes, see Ref. [6b]; b) in Ref. [4c], it is reported that the Mg^{II}-promoted reaction of diphenyl nitron with *N*-acryloyl oxazolidinone leads to a regioselectivity of greater than 98:2, an *endo/exo* ratio of 97:3, and 86 % *ee* for the *endo* isomer.
- [14] CCDC-280037–280040 contain the supplementary crystallographic data for this paper. These data can be obtained free of charge from the Cambridge Crystallographic Data Centre via www.ccdc.cam.ac.uk/data_request/cif.

DOI: 10.1002/anie.200502263

Tandem Radical-Addition–Aldol-Type Reaction of an α,β -Unsaturated Oxime Ether***Masafumi Ueda, Hideto Miyabe, Hisako Sugino, Okiko Miyata, and Takeaki Naito**

Conjugate addition of radical species has been recognized as a versatile tool for introducing an alkyl group into the β position of α,β -unsaturated carbonyl compounds,^[1] and the subsequent trapping of the intermediate radical species with allyltin compounds has been widely studied.^[2,3] Tandem reactions are among the most efficient synthetic methods. However, those that proceed sequentially through ionic species sometimes exhibit problematic drawbacks such as the need for exacting reaction conditions, whereas undesired polymerization may result from tandem radical reactions. A combination of radical and ionic processes may alleviate these problems and could thus be a promising approach. Oshima and co-workers first demonstrated that a tandem radical addition–aldol condensation of enones or enals could be performed via the formation of an intermediate boryl enolate.^[4] Other groups have recently reported tandem reactions involving radical and ionic processes for the convenient synthesis of highly complex molecules.^[5] However, there are only limited examples which employ enolate intermediates formed by a radical addition reaction. The goal of our work is to develop a highly efficient carbon–carbon bond-construction method by taking advantage of a novel hybrid radical–ionic reaction involving the radical addition to α,β -unsaturated oxime ethers and subsequent ionic trapping of the resulting *N*-boryl enamine by aldehydes.

Building upon our syntheses of α - and β -amino acids by radical addition to oxime ethers,^[6] we extended our use of α,β -unsaturated oxime ether **1** bearing Oppolzer's camphorsultam to the synthesis of γ -amino acids (Figure 1). Recent studies on the radical addition to imines showed that amino-boranes were effectively formed by trapping of intermediate aminyl radicals with triethylborane.^[7–10] Thus, we expected

[*] M. Ueda, H. Sugino, Dr. O. Miyata, Prof. T. Naito
Kobe Pharmaceutical University
Motoyamakita, Higashinada, Kobe 658-8558 (Japan)
Fax: (+81) 78-441-7556
E-mail: taknaito@kobepharm-u.ac.jp
Dr. H. Miyabe
Graduate School of Pharmaceutical Sciences
Kyoto University
Yoshida, Sakyo-ku, Kyoto 606-8501 (Japan)

[**] This work was supported in part by a Grant-in-Aid for Scientific Research on Priority Areas 17035088 and for Young Scientists (B) (M.U. and H.M.) from the Ministry of Education, Culture, Sports, Science, and Technology of Japan and the Science Research Promotion Fund of the Japan Private School Promotion Foundation for research grants. M.U. is grateful for a Fuji Photo Film Award in Synthetic Organic Chemistry, Japan.

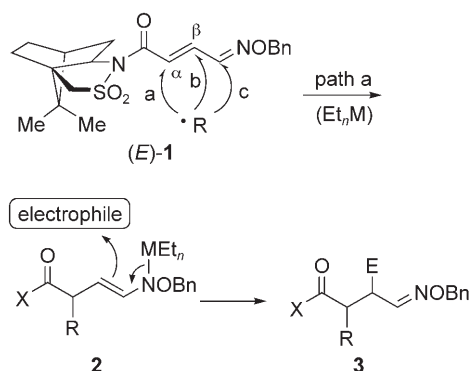
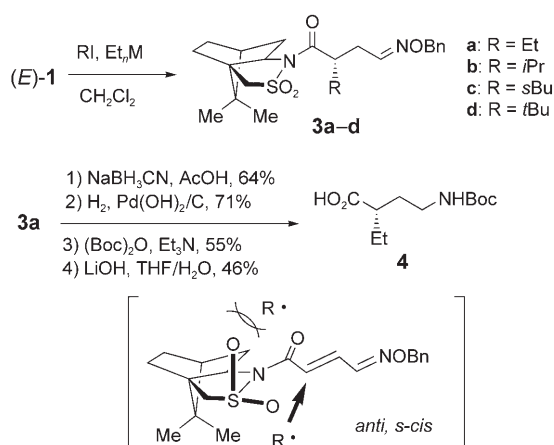


Figure 1. Tandem reaction involving both radical and ionic processes ($\text{X} = (1R)$ -camphorsultam). Bn = benzyl.

that the boryl enamine **2** could be formed by the triethylborane-promoted radical addition to (E) -1, if the reaction proceeds regioselectively by path a.

Prior to exploring issues of the tandem process, we first investigated the regioselectivity in the carbon-radical addition to conjugated oxime ether (E) -1, which possesses three radicophilic centers (Scheme 1). The addition of ethyl radical



Scheme 1. Radical addition to conjugated oxime ether (E) -1. Boc = *tert*-butoxycarbonyl.

to (E) -1 was performed in CH_2Cl_2 at 20°C for 20 min with triethylborane (Table 1, entry 1). The reaction took place regioselectively at the α position of the carbonyl group (path a as shown in Figure 1) to give the desired product **3a**

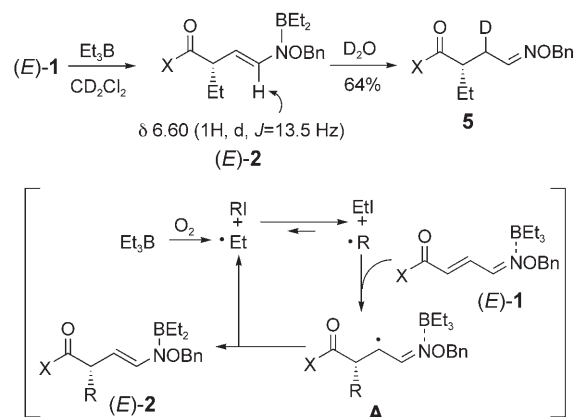
Table 1: Alkyl-radical addition to conjugated oxime ether (E) -1.^[a]

Entry	Initiator	RI	Product	Yield [%] ^[b]	d.r. ^[c]
1	Et_3B	none	3a	97	> 97.5:2.5
2	Et_2Zn	none	—	ND	
3	Et_3B	$i\text{PrI}$	3b	56	> 97.5:2.5
4	Et_3B	$s\text{BuI}$	3c	69	> 97.5:2.5
5	Et_3B	$t\text{BuI}$	3d	28	> 97.5:2.5

[a] Reactions were carried out using RI (30 equiv) and Et_3B or Et_2Zn in hexane (1.0 M, 5 equiv) in CH_2Cl_2 for 20 min. [b] Isolated yield of the desired alkylated product (ND = not detected). [c] Diastereomeric ratios were determined by ^1H NMR analysis.

in 97% yield without formation of other regioisomers (paths b or c). This is the first example of a regioselective radical addition to a conjugated oxime ether that involves four electrophilic positions. The diastereomeric purity of **3a** was found to be no less than 97.5:2.5 d.r. by ^1H NMR spectroscopic analysis of the crude product. The absolute configuration at the newly formed stereocenter was determined to be *S* by converting the adduct **3a** into the authentic γ -amino acid **4**.^[11] The stereochemical preference of this reaction can be rationalized as follows. With regard to the conformation of (E) -1, the *anti* (sulfonyl and carbonyl groups) and *s-cis* (carbonyl group and $\text{C}=\text{C}$ bond) planar rotamer shown in Scheme 1 should be favored over other rotamers. Therefore, the alkyl-radical addition to the *re* (bottom) face is favored, presumably resulting from steric interactions with the axial oxygen of the sulfonyl group.^[6c] In marked contrast, the ethylated product **3a** was not formed with the use of diethylzinc as a radical initiator (Table 1, entry 2).^[12] The high diastereoselectivities and good chemical yields were observed in the addition of secondary alkyl radicals to (E) -1 (Table 1, entries 3 and 4). A lower chemical yield was attained with a bulky *tert*-butyl radical, but the reaction still proceeded with high d.r. (> 97.5:2.5; Table 1, entry 5). These observations indicate that triethylborane acts as an effective reagent for trapping the intermediate enaminy radical to form the boryl enamine **2**.

To confirm the formation of boryl enamine **2**, we studied the ^1H NMR spectra and the trapping reaction of boryl enamine **2** with D_2O (Scheme 2). The ^1H NMR spectra of the

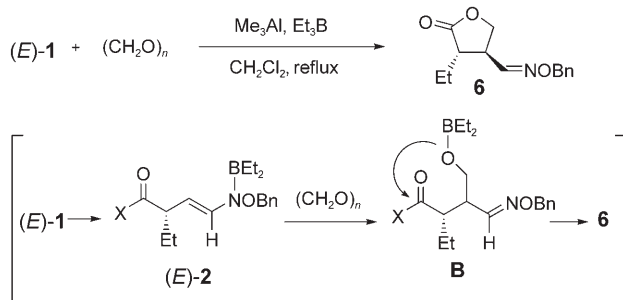


Scheme 2. Trapping reaction of boryl enamine with D_2O ($\text{X} = (1R)$ -camphorsultam).

reaction mixture of **1** with triethylborane in CD_2Cl_2 suggested the formation of (E) -enamine **2** as shown in Scheme 2. The deuteration of boryl enamine **2** took place at the β position (relative to the carbonyl group) to give the product **5** in 64% yield. Thus, the rationale of the reaction pathway is that the alkyl radical adds to the α position of the carbonyl group in (E) -1 to form the intermediate radical **A**, which is captured by triethylborane to afford the (E) -boryl enamine **2** and regenerate an ethyl radical.

With these results in mind, we next investigated the tandem radical-addition–aldol-type reaction of an α,β -unsaturated

turated oxime ether by using paraformaldehyde (Scheme 3). Triethylborane was added to a mixture of **1** and paraformaldehyde. The resulting products were the ethylated product **3a** and *trans*- γ -butyrolactone **6** in 53 and 44 % yields, respectively (Table 2, entry 1). The γ -butyrolactone **6** was presumably



Scheme 3. Tandem radical-addition-trapping reaction of boryl enamine with paraformaldehyde (X = (1*R*)-camphorsultam).

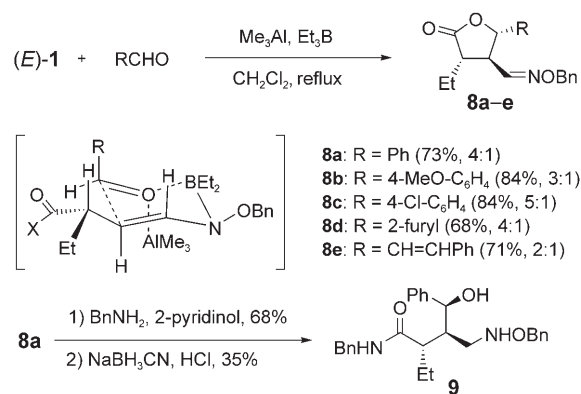
Table 2: Radical-aldol-type reaction of (*E*)-**1** with paraformaldehyde.^[a]

Entry	Lewis acid	<i>T</i> [°C]	Yield [%] ^[b]		Selectivity ^[c] <i>trans:cis</i>
			6	3a	
1	None	reflux	44	53	10:2
2	Me ₃ Al	20	41	42	10:3
3	Me ₃ Al	reflux	72	–	10:3 ^[d]

[a] Reactions were carried out with Et₃B in hexane (1.0 M, 5 equiv), Me₃Al in hexane (1.0 M, 1.2 equiv), and (CH₂O)_n (1.2 equiv) in CH₂Cl₂. [b] Isolated yield. [c] Determined by ¹H NMR analysis. [d] Enantiomeric purity of the *trans* isomer was found to be 90% *ee* by HPLC analysis.

formed through the diastereoselective addition of ethyl radical to **1**, trapping of boryl enamine **2** with paraformaldehyde, and intramolecular lactonization with concomitant removal of the chiral auxiliary. The relative configuration of the two substituents on lactone **6** was determined by NOE interaction experiments. To the best of our knowledge, this reaction represents the first reported example of the electrophilic trapping reaction of an unstable *N*-boryl enamine generated through a radical process. This tandem reaction was promoted in the presence of Me₃Al (1.2 equiv) as a Lewis acid. The reaction using Me₃Al under reflux gave the desired lactone **6** exclusively in 72 % yield (Table 2, entry 3). The enantiomeric purity of *trans*- γ -butyrolactone **6** was found to be 90% *ee* by chiral HPLC analysis. The lower stereoselectivity of the tandem reaction (90% *ee*) than that of the simple ethyl-radical addition (>97.5:2.5 d.r.) was attributed to the higher reaction temperature (reflux) used in the initial radical reaction step.

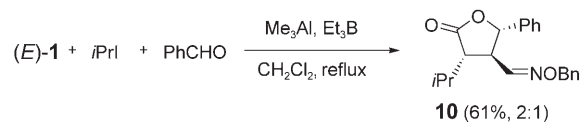
The utility of this new tandem radical-ionic reaction was tested in the asymmetric synthesis of various types of γ -butyrolactones. Thus, we investigated the reaction with different kinds of aldehydes (Scheme 4). The trapping reaction of boryl enamine **2** with benzaldehyde gave the *trans,trans* isomer **8a** as the major product, accompanied by small amounts of other diastereomers. γ -Butyrolactone **8a** was easily converted into γ -amino acid derivative **9**. Treat-



Scheme 4. Radical-addition-aldol-type reaction of (*E*)-**1** (ratio in parentheses is for the yield of the major isomer to that of all other isomers combined; X = (1*R*)-camphorsultam).

ment of **8a** with benzylamine in the presence of 2-pyridinol gave an acyclic oxime ether which was reduced to the amino acid derivative **9**.^[13] The electron-donating and electron-withdrawing substituents on the aromatic ring of the aldehyde exhibited no apparent effects on either the chemical yield or the stereoselectivity, and good yields were attained for both **8b** and **8c**. 2-Furfural and cinnamaldehyde also worked well under similar reaction conditions. The *trans,trans* stereoselectivity observed for the reaction can be explained by invoking a six-membered-ring transition state. The sterically more stable conformer of (*E*)-boryl enamine reacted with the Me₃Al-activated aldehyde in such a way that 1,3-diaxial interactions were minimized, and an unfavorable steric interaction with allylic substituents was avoided.^[14]

Finally, we examined the tandem reaction involving an addition of isopropyl radical, which occurred by way of an iodine atom-transfer process, followed by an aldol-type reaction (Scheme 5). With the use of isopropyl iodide



Scheme 5. Isopropyl-radical-addition-aldol-type reaction of (*E*)-**1** (ratio in parentheses is for the yield of the major isomer to that of all other isomers combined).

(20 equiv) as radical precursor and benzaldehyde as trapping agent, the tandem reaction of (*E*)-**1** proceeded smoothly to give isopropyl-substituted γ -butyrolactone **10** in 61 % yield.

In conclusion, we have developed a hybrid type of reaction that involves a radical addition and an aldol condensation. This tandem reaction of an α,β -unsaturated oxime ether provides a powerful synthetic approach to chiral γ -butyrolactones and γ -amino acids.

Experimental Section

General procedure for radical-addition-aldol-type reaction of α,β -unsaturated oxime ether (*E*)-**1**: Aldehyde (0.148 mmol) and Me₃Al

(1.0 M in hexane, 0.148 mL, 0.148 mmol) were added to a solution of (*E*)-**1** (50 mg, 0.124 mmol) in CH₂Cl₂ (5 mL) at room temperature under a N₂ atmosphere. Et₃B (1.0 M in hexane, 0.62 mL, 0.62 mmol) was then added dropwise to the reaction mixture at reflux. After stirring at reflux for 3 h, the reaction mixture was diluted with saturated aqueous NaHSO₃ and then extracted with EtOAc. The organic phase was washed with saturated aqueous NaHCO₃ and brine, dried over MgSO₄, and concentrated at decreased pressure. Purification of the residue by preparative TLC (hexane/EtOAc 5:1) afforded the desired γ -butyrolactones.

Received: June 28, 2005

Published online: August 26, 2005

Keywords: asymmetric synthesis · boranes · enamines · oxime ethers · radical reactions

- [1] a) P. Renaud, M. Gerster, *Angew. Chem.* **1998**, *110*, 2704; *Angew. Chem. Int. Ed.* **1998**, *37*, 2562; b) M. P. Sibi, N. A. Porter, *Acc. Chem. Res.* **1999**, *32*, 163; c) *Radicals in Organic Synthesis, Vols. 1 and 2* (Eds.: P. Renaud, M. P. Sibi), Wiley-VCH, Weinheim, **2001**; d) M. P. Sibi, S. Manyem, J. Zimmerman, *Chem. Rev.* **2003**, *103*, 3263; e) M. P. Sibi, S. Manyem, *Tetrahedron* **2000**, *56*, 8033.
- [2] For selected examples of tandem radical allylation, see: a) D. P. Curran, W. Shen, J. Zhang, T. A. Heffner, *J. Am. Chem. Soc.* **1990**, *112*, 6738; b) B. Giese, M. Zehnder, M. Roth, H.-G. Zeitz, *J. Am. Chem. Soc.* **1990**, *112*, 6741; c) N. A. Porter, I. J. Rosestein, R. A. Breyer, J. D. Bruhnke, W.-X. Wu, A. T. McPhail, *J. Am. Chem. Soc.* **1992**, *114*, 7664; d) J. H. Wu, R. Radinov, N. A. Porter, *J. Am. Chem. Soc.* **1995**, *117*, 11029; e) M. P. Sibi, J. Ji, *J. Org. Chem.* **1996**, *61*, 6090; f) M. P. Sibi, J. Chen, *J. Am. Chem. Soc.* **2001**, *123*, 9472.
- [3] For selected examples of tandem radical reaction, see: a) D. P. Curran, M.-H. Chen, E. Spletzer, C. M. Seong, C.-T. Chang, *J. Am. Chem. Soc.* **1989**, *111*, 8872; b) J. Marco-Contelles, *Chem. Commun.* **1996**, 2629; c) K. Takai, N. Matsukawa, A. Takahashi, T. Fujii, *Angew. Chem.* **1998**, *110*, 160; *Angew. Chem. Int. Ed.* **1998**, *37*, 152; d) C. Aïssa, A.-L. Dhimane, M. Malacria, *Angew. Chem.* **2002**, *114*, 3418; *Angew. Chem. Int. Ed.* **2002**, *41*, 3284; e) S. Yamago, M. Miyoshi, H. Miyazoe, J. Yoshida, *Angew. Chem.* **2002**, *114*, 1465; *Angew. Chem. Int. Ed.* **2002**, *41*, 1407; f) K. Takasu, H. Ohsato, J. Kuroyanagi, M. Ihara, *J. Org. Chem.* **2002**, *67*, 6001; g) A. Demircan, P. J. Parsons, *Eur. J. Org. Chem.* **2003**, 1729; h) K. Tsuchii, M. Doi, T. Hirao, A. Ogawa, *Angew. Chem.* **2003**, *115*, 3614; *Angew. Chem. Int. Ed.* **2003**, *42*, 3490; i) F. Denes, F. Chemla, J. F. Normant, *Angew. Chem.* **2003**, *115*, 4177; *Angew. Chem. Int. Ed.* **2003**, *42*, 4043; j) K. Miura, M. Tojino, N. Fujisawa, A. Hosomi, I. Ryu, *Angew. Chem.* **2004**, *116*, 2477; *Angew. Chem. Int. Ed.* **2004**, *43*, 2423; k) M. Tojino, Y. Uenoyama, T. Fukuyama, I. Ryu, *Chem. Commun.* **2004**, 2482; l) Y. Uenoyama, T. Fukuyama, O. Nobuta, H. Matsubara, I. Ryu, *Angew. Chem.* **2005**, *117*, 1099; *Angew. Chem. Int. Ed.* **2005**, *44*, 1075.
- [4] a) K. Nozaki, K. Oshima, K. Utimoto, *Tetrahedron Lett.* **1988**, *29*, 1041; b) K. Nozaki, K. Oshima, K. Utimoto, *Bull. Chem. Soc. Jpn.* **1991**, *64*, 403.
- [5] a) S. Bazin, L. Feray, D. Siri, J.-V. Naubron, M. P. Bertrand, *Chem. Commun.* **2002**, 2506; b) S. Chandrasekhar, C. Narsihmulu, N. R. Reddy, M. S. Reddy, *Tetrahedron Lett.* **2003**, *44*, 2583; c) H. Miyabe, R. Asada, K. Yoshida, Y. Takemoto, *Synlett* **2004**, 540; d) Y. Yamamoto, S. Nakano, H. Maekawa, I. Nishiguchi, *Org. Lett.* **2004**, *6*, 799; e) S. Bazin, L. Feray, N. Vanthuyne, M. P. Bertrand, *Tetrahedron* **2005**, *61*, 4261.
- [6] a) H. Miyabe, C. Ushiro, T. Naito, *Chem. Commun.* **1997**, 1789; b) H. Miyabe, K. Fujii, T. Naito, *Org. Lett.* **1999**, *1*, 569; c) H. Miyabe, C. Ushiro, M. Ueda, K. Yamakawa, T. Naito, *J. Org. Chem.* **2000**, *65*, 176; d) H. Miyabe, K. Fujii, T. Naito, *Org. Biomol. Chem.* **2003**, *1*, 381; e) M. Ueda, H. Miyabe, H. Sugino, T. Naito, *Org. Biomol. Chem.* **2005**, *3*, 1124.
- [7] a) H. Miyabe, R. Shibata, C. Ushiro, T. Naito, *Tetrahedron Lett.* **1998**, *39*, 631; b) H. Miyabe, M. Ueda, N. Yoshioka, T. Naito, *Synlett* **1999**, 465; c) H. Miyabe, M. Ueda, T. Naito, *Chem. Commun.* **2000**, 2059.
- [8] For reviews, see: a) G. K. Friestad, *Tetrahedron* **2001**, *57*, 5461; b) H. Miyabe, M. Ueda, T. Naito, *Synlett* **2004**, 1140.
- [9] a) M. P. Bertrand, L. Feray, R. Nougier, L. Stella, *Synlett* **1998**, 780; b) M. P. Bertrand, L. Feray, R. Nougier, P. Perfetti, *J. Org. Chem.* **1999**, *64*, 918; c) M. P. Bertrand, S. Coantic, L. Feray, R. Nougier, P. Perfetti, *Tetrahedron* **2000**, *56*, 3951.
- [10] a) G. K. Friestad, J. Qin, *J. Am. Chem. Soc.* **2000**, *122*, 8329; b) G. K. Friestad, J. Qin, *J. Am. Chem. Soc.* **2001**, *123*, 9922; c) G. K. Friestad, Y. Shen, E. L. Ruggles, *Angew. Chem.* **2003**, *115*, 5215; *Angew. Chem. Int. Ed.* **2003**, *42*, 5061.
- [11] S. Azam, A. A. D'Souza, P. B. Wyatt, *J. Chem. Soc. Perkin Trans. 1* **1996**, 621.
- [12] Ryu and Komatsu reported that Et₂Zn can serve as a radical initiator in the absence of O₂. See: I. Ryu, F. Araki, S. Minakata, M. Komatsu, *Tetrahedron Lett.* **1998**, *39*, 6335.
- [13] a) D. S. Tan, M. A. Foley, M. D. Shair, S. L. Schreiber, *J. Am. Chem. Soc.* **1999**, *121*, 9073; b) H. T. Openshaw, N. Whittaker, *J. Chem. Soc. C* **1969**, 89.
- [14] Bahmanyar and Houk reported a theoretical study of the aldol reaction of an enamine with acetaldehyde. Although there are two possible conformations of the six-membered ring transition state involving an equatorial or axial methyl group on acetaldehyde, the two conformations are predicted to be equal in energy. See: S. Bahmanyar, K. N. Houk, *J. Am. Chem. Soc.* **2001**, *123*, 11273.

Catalytic Oxidation

DOI: 10.1002/anie.200501688

**Versatile Hypervalent-Iodine(III)-Catalyzed
Oxidations with *m*-Chloroperbenzoic Acid as a
Cooxidant****

*Toshifumi Dohi, Akinobu Maruyama,
Misaki Yoshimura, Koji Morimoto, Hirofumi Tohma,
and Yasuyuki Kita**

As oxidants, hypervalent iodine(III) reagents are widely recognized as alternatives to highly toxic heavy-metal oxi-

[*] Dr. T. Dohi, A. Maruyama, M. Yoshimura, K. Morimoto,
Dr. H. Tohma, Prof. Dr. Y. Kita
Graduate School of Pharmaceutical Sciences, Osaka University
1-6 Yamada-oka, Suita, Osaka 565-0871 (Japan)
Fax: (+81) 6-6879-8229
E-mail: kita@phs.osaka-u.ac.jp

[**] This work was financially supported by a Grant-in-Aid for Scientific Research (S) from the Ministry of Education, Science, Sports and Culture (Japan).

dizers such as lead, mercury, and thallium reagents (Figure 1).^[1] They are generally used as stoichiometric oxidants, though it may be possible to carry out oxidations under catalytic conditions. Indeed, oxidative fluorination reactions with a catalytic amount of iodobenzene difluoride

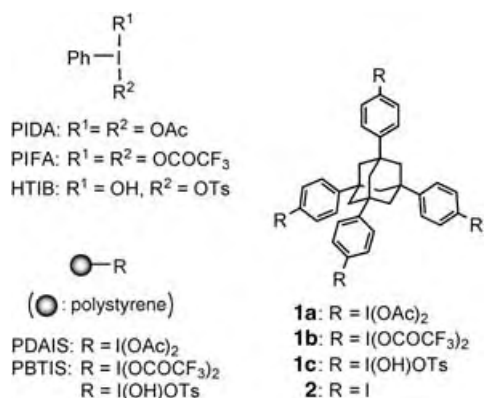


Figure 1. Hypervalent iodine(III) reagents. PIDA = phenyliodine diacetate; PIFA = phenyliodine bis(trifluoroacetate); HTIB = (hydroxy-(tosyloxy)iodo)benzene; PDAIS = poly(diaceotoxyiodo)styrene; PBTIS = poly(bis(trifluoroacetoxy)iodo)styrene.

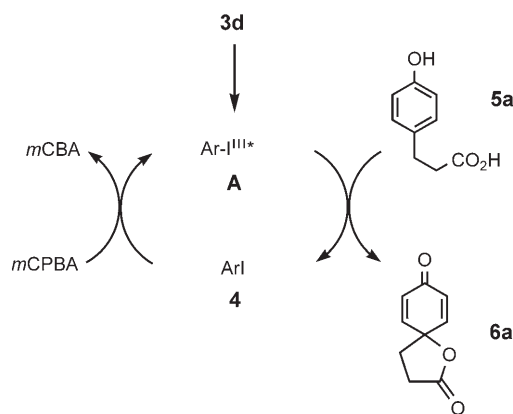
or 4-iodotoluene difluoride were reported in which the reoxidation of the iodine groups of iodoarenes was carried out electronically.^[2,3] However, to our knowledge, a catalytic system for the formation of other bond types has not yet been reported. This is probably due to the lack of efficient procedures for the reoxidation of organoiodine(I) to hypervalent iodine(III) species^[4–8] in the reaction system. Although new preparative methods that use sodium periodate (NaIO_4),^[6] chromium trioxide (CrO_3),^[7] and dimethyldioxirane^[8] have been reported, they remain unsatisfactory in terms of product yield, ease of operation, and other aspects.

We have recently developed environmentally friendly, recyclable hypervalent iodine(III) reagents **1a–c** with high reactivities.^[9] In its synthesis, we realized the need to prepare **1a** with nearly quantitative yield to make it a practical recyclable reagent; we also found that only an oxidation system using *meta*-chloroperbenzoic acid (*m*CPBA)^[10] in dilute acetic acid/dichloromethane was suitable for this purpose. This interesting aspect prompted us to explore the possibility of these adamantane-based recyclable reagents as catalysts by combination with *m*CPBA as a stoichiometric chemical oxidant.

Herein, we demonstrate oxidative transformations with catalytic amounts of hypervalent iodine(III) reagents, which enable versatile C–O and even C–C bond formations. Relying on the previous conditions

to synthesize **1a**, we first examined the oxidative spirocyclization reaction of the phenol **5a**^[11] with 0.1 equivalent of phenyliodine diacetate (PIDA), which gave disappointing results (Table 1, entry 1). Therefore, the reaction conditions were optimized. With **3a** instead of PIDA, a catalytic reaction was observed (entry 2). As the amount of trifluoroacetic acid ($\text{CF}_3\text{CO}_2\text{H}$) increased, the catalytic efficiency increased (entries 2 and 3). In the absence of **3a**, no reaction was observed. Interestingly, the rapid conversion of **5a** was observed in these cases. The nature of the acids and the presence of water were also influential (entries 4–7). The hypervalent iodine(III) reagent **3d** gave the best results of those examined (entries 10 and 11). It was possible to decrease the amount of **3d** to as low as 0.01 equivalent without a significant loss in catalytic efficiency (entry 11). The spirocyclization of **5a** using **3d** with other cooxidants such as peracetic acid,^[4] sodium perborate,^[5] NaIO_4 ,^[6] and CrO_3 ^[7] were not successful.

A proposed catalytic cycle is depicted in Scheme 1. First, **3d** forms the hypervalent iodine(III) active species **A** (which occurs under the stated reaction conditions, although a certain



Scheme 1. A possible catalytic cycle for oxidation by hypervalent iodine(III) species. Ar = 4-MeC₆H₄; *m*CBA = *meta*-chlorobenzoic acid.

Table 1: Optimization of the hypervalent-iodine(III)-catalyzed spirocyclization reaction of **5a**.

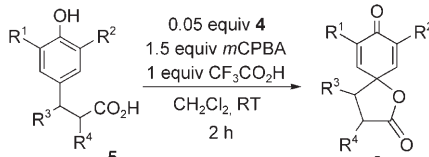
Entry	Ar	Equiv	Additive	<i>t</i> [h]	Yield [%]
1 ^[a]	–	0.1	none	4	15
2	C ₆ H ₅ (3a)	0.1	none	3	56
3	C ₆ H ₅ (3a)	0.1	CF ₃ CO ₂ H	2	66
4	C ₆ H ₅ (3a)	0.1	AcOH	3	49
5	C ₆ H ₅ (3a)	0.1	BF ₃ ·Et ₂ O	2	73
6	C ₆ H ₅ (3a)	0.1	TMSOTf	2	16
7	C ₆ H ₅ (3a)	0.1	4 Å MS ^[b]	3	35
8	2,4-F ₂ -C ₆ H ₃ (3b) ^[c]	–	CF ₃ CO ₂ H	17	60
9	4-MeO-C ₆ H ₄ (3c) ^[d]	–	CF ₃ CO ₂ H	2	21
10	4-Me-C ₆ H ₄ (3d)	0.05	CF ₃ CO ₂ H	2.5	67
11	4-Me-C ₆ H ₄ (3d)	0.01	CF ₃ CO ₂ H ^[e]	2	71

[a] 0.1 equiv PIDA was used. [b] 1 g mmol^{–1} **5a**. [c] Prepared from 0.1 equiv 2,4-difluoroiodobenzene in situ. [d] Prepared from 0.1 equiv 4-iodoanisole in situ. [e] 50 equiv CF₃CO₂H was used.

degree of **3d** formation was observed in the absence of these phenol derivatives). The intermediate **A** transforms phenol **5a** into **6a** with concomitant formation of 4-iodotoluene (**4**), which then regenerates **A** by the action of *m*CPBA. The effect of the methyl group in the aryl substituent of **3d** might be to accelerate the conversion of **4** into **A**. With 0.05 equivalent of **4** instead of **3d**, the spirocyclization of **5a** also occurred with nearly the same efficiency (2 h, 72 % yield). This result strongly supports the formation of **4** during the catalytic cycle.

The results of the oxidation of a series of phenol

Table 2: Spirocyclization reaction of various phenol derivatives with a catalytic amount of **4**.



Entry	Substrate	R ¹	R ²	R ³	R ⁴	Product	Yield [%]
1	5a	H	H	H	H	6a	72
2 ^[a,b]	5a	H	H	H	H	6a	74
3	5b	Br	H	H	H	6b	77
4	5c	Me	H	H	H	6c	66
5	5d	H	H	Me	H	6d	76
6	5e	H	H	H	Me	6e	73
7	5f	Br	Br	Me	H	6f	91
8	5g	Br	Me	Me	H	6g	80
9	5h	H	H	=CH-CH=CH-CH=	H	6h	79

[a] 0.05 equiv **1b** was used instead of **4**. [b] 1.05 equiv *m*CPBA was used.

derivatives with a catalytic quantity of **4** are shown in Table 2. This procedure imparts more versatility to the catalytic reaction, as the initial preparation of hypervalent iodine(III) reagents could be avoided. Thus, the oxidative transformations of various phenol derivatives proceeded smoothly in good yields with short reaction times. The recyclable reagent **1b** was also usable in this catalytic reaction (entry 2). After reaction completion, **2** was recovered nearly quantitatively in this case by taking advantage of its insolubility in methanol. Although further exploration is required, this catalytic approach was extended to other

ature by using *m*CPBA as an effective chemical cooxidant. These catalytic approaches have the following characteristics: rapid conversion (short reaction time), high catalytic efficiency, and no need for the preparation of hypervalent iodine(III) reagents. As **2** was also usable in the catalytic reaction, it has the advantage of the net recycling capacity of **1b**, considering the loss in the preparation of **1b** from **2**. The catalytic use of hypervalent iodine(III) reagents is our highly desirable goal. The application of other effective cooxidants with these hypervalent iodine(III)-catalyzed reactions is now in progress.

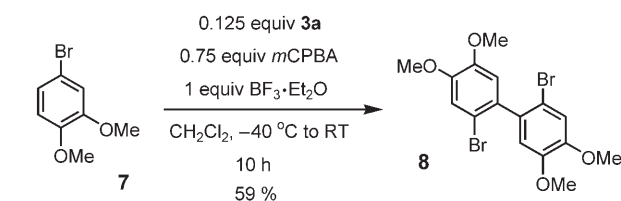
Experimental Section

Typical experimental procedure with **1b**: Compound **1b** (92.4 mg, 0.05 mmol) was added to a stirred solution of 3-(4-hydroxyphenyl)-propionic acid (**5a**; 166 mg, 1.0 mmol), trifluoroacetic acid (114 mg, 1.0 mmol), and *meta*-chloroperbenzoic acid ($\approx 69\%$ purity, 224 mg, ≈ 1.05 mmol), in CH_2Cl_2 (3 mL) at ambient temperature under a nitrogen atmosphere. The mixture was stirred for 2 h under the same reaction conditions while the reaction was monitored by TLC. The aqueous work-up was successive with saturated NaHCO_3 (20 mL), sodium thiosulfate (15 mL), and then the organic phase was evaporated to dryness. MeOH (10 mL) was added to the residue, and the resulting suspension was filtered to separate **2** from the product. The recovery of **2** was nearly quantitative. The filtrate was evaporated and subject to column chromatography (SiO_2/n -hexane/ AcOEt) to give 1-oxaspiro[4.5]deca-6,9-diene-2,8-dione (**6a**)^[11c] as a white powder (121 mg, 74 %).

Received: May 17, 2005

Published online: August 25, 2005

Keywords: homogeneous catalysis · hypervalent compounds · iodine · oxidation · synthetic methods



Scheme 2. Intermolecular C–C bond-formation reaction catalyzed by **3a**.

oxidative bond-formation reactions such as those of C–C bond formation^[12] (Scheme 2).

In summary, we have established the efficient catalytic reactions of hypervalent iodine(III) reagents at room temper-

- [1] For recent reviews, see: a) P. J. Stang, V. V. Zhdankin, *Chem. Rev.* **1996**, 96, 1123; b) Y. Kita, T. Takada, H. Tohma, *Pure Appl. Chem.* **1996**, 68, 627; c) A. Varvoglis, *Hypervalent Iodine in Organic Synthesis* Academic Press, San Diego, **1997**; d) T. Kitamura, Y. Fujiwara, *Org. Prep. Proced. Int.* **1997**, 29, 409; e) V. V. Zhdankin, P. J. Stang, *Chem. Rev.* **2002**, 102, 2523; f) *Hypervalent Iodine Chemistry* (Ed.: T. Wirth), Springer, Berlin, **2003**; g) R. M. Moriarty, *J. Org. Chem.* **2005**, 70, 2893; h) T. Wirth, *Angew. Chem.* **2005**, 117, 3722; *Angew. Chem. Int. Ed.* **2005**, 44, 3656.
- [2] a) T. Fuchigami, T. Fujita, *J. Org. Chem.* **1994**, 59, 7190; b) T. Fujita, T. Fuchigami, *Tetrahedron Lett.* **1996**, 37, 4725.
- [3] S. Hara, T. Hatakeyama, S.-Q. Chen, K. Ishii, M. Yoshida, M. Sawaguchi, T. Fukuhara, N. Yoneda, *J. Fluorine Chem.* **1998**, 87, 189.
- [4] J. G. Sharefkin, H. Salzman, *Org. Synth. Coll.* **1973**, 5, 660.
- [5] A. McKillop, D. Kemp, *Tetrahedron* **1989**, 45, 3299.
- [6] P. Kazmierczak, L. Skulski, L. Kraszkiewicz, *Molecules* **2001**, 6, 881.
- [7] P. Kazmierczak, L. Skulski, *Synthesis* **1998**, 1721.
- [8] A. Bravo, F. Fontana, G. Fronza, F. Minisci, A. Serri, *Tetrahedron Lett.* **1995**, 36, 6945.
- [9] a) T. Tohma, A. Maruyama, A. Maeda, T. Maegawa, T. Dohi, M. Shiro, T. Morita, Y. Kita, *Angew. Chem.* **2004**, 116, 3679; *Angew. Chem. Int. Ed.* **2004**, 43, 3595; b) T. Dohi, A. Maruyama, M. Yoshimura, K. Morimoto, H. Tohma, M. Shiro, Y. Kita, *Chem. Commun.* **2005**, 2205.

- [10] D. G. Morris, A. G. Shepherd, *J. Chem. Soc. Chem. Commun.* **1981**, 1250.
- [11] a) Y. Tamura, T. Yakura, J. Haruta, Y. Kita, *J. Org. Chem.* **1987**, 52, 3927; b) Y. Tamura, T. Yakura, J. Haruta, Y. Kita, *Synthesis* **1989**, 126; c) Y. Kita, H. Tohma, K. Kikuchi, M. Inagaki, T. Yakura, *J. Org. Chem.* **1991**, 56, 435; d) H. Tohma, Y. Harayama, M. Hashizume, M. Iwata, Y. Kiyono, M. Egi, Y. Kita, *J. Am. Chem. Soc.* **2003**, 125, 11235, and references therein.
- [12] H. Tohma, H. Morioka, S. Takizawa, M. Arisawa, Y. Kita, *Tetrahedron* **2001**, 57, 345, and references therein.

Phosphorus Cations

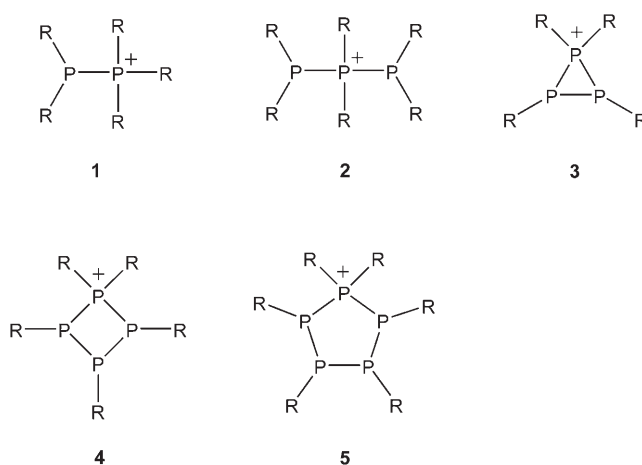
DOI: 10.1002/anie.200501850

Small Cyclopolyphosphinophosphonium Cations: Systematic Development of Fundamental *catena*-Phosphorus Frameworks**

Neil Burford,* C. Adam Dyker, Mike Lumsden, and Andreas Decken

Recognizing that catenation of carbon is principally responsible for the diversity and extent of organic chemistry, the “diagonal relationship” between carbon and phosphorus in the Periodic Table is often quoted^[1,2] in the discussion of the numerous catenated polyphosphines^[2–6] and polyphosphorus anions.^[2–4,7–12] *catena*-Phosphorus cation systems are less well developed despite the classical chemistry of phosphonium salts, but the pioneering contributions of Schmidpeter and co-workers^[13–15] and Schmutzler et al.^[16] have highlighted new aspects of structure and bonding that prompt the establishment of a comprehensive polyphosphinophosphonium series. Our high-yielding and facile methods for the synthesis of the prototypical phosphinophosphonium **1**,^[17] diphosphinophosphonium **2**,^[18] and cyclotetraphosphinophosphonium **5**^[18] cations have now been applied to the preparation of the

first examples of cyclodiphosphinophosphonium **3** and cyclotriphosphinophosphonium **4** cations (Scheme 1). Isolation of these new frameworks is surprising in light of the exclusive formation of **5** over possible tetra- and hexaphosphorus derivatives with phenyl substituents at the phosphorus



Scheme 1. Prototypical *catena*-polyphosphinophosphonium cation frameworks.

centers.^[18] Derivatives of **3** and **4** provide representative frameworks that complete a series of the smallest cyclopolyphosphinophosphonium cations **3–5**, and their characterization is pivotal in the systematic development of fundamental phosphorus chemistry.

³¹P NMR spectra of reaction mixtures containing (PrBu)₃ (**6a**) with excess MeOTf show quantitative formation of [(PrBu)₃Me][OTf] (**3a-OTf**; Figure 1a and Scheme 2a). The spectrum can be approximated as an AMX^[19] spin system and is consistent with the solid-state structure of **3a-OTf** (Figure 2a), thus demonstrating stereoselective methylation of **6a** at either of the *syn*-configured centers to give a racemic

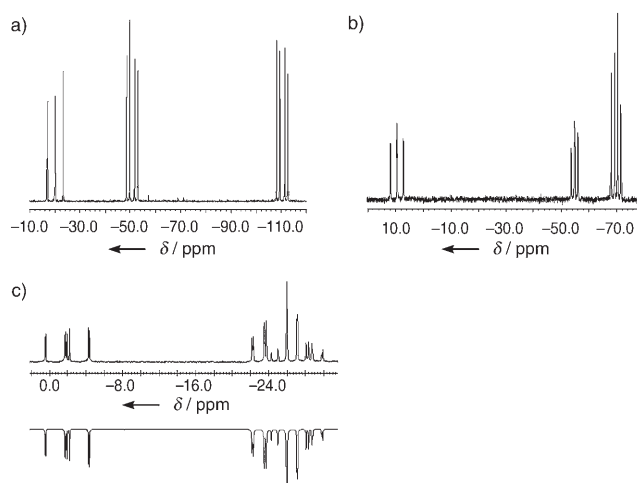
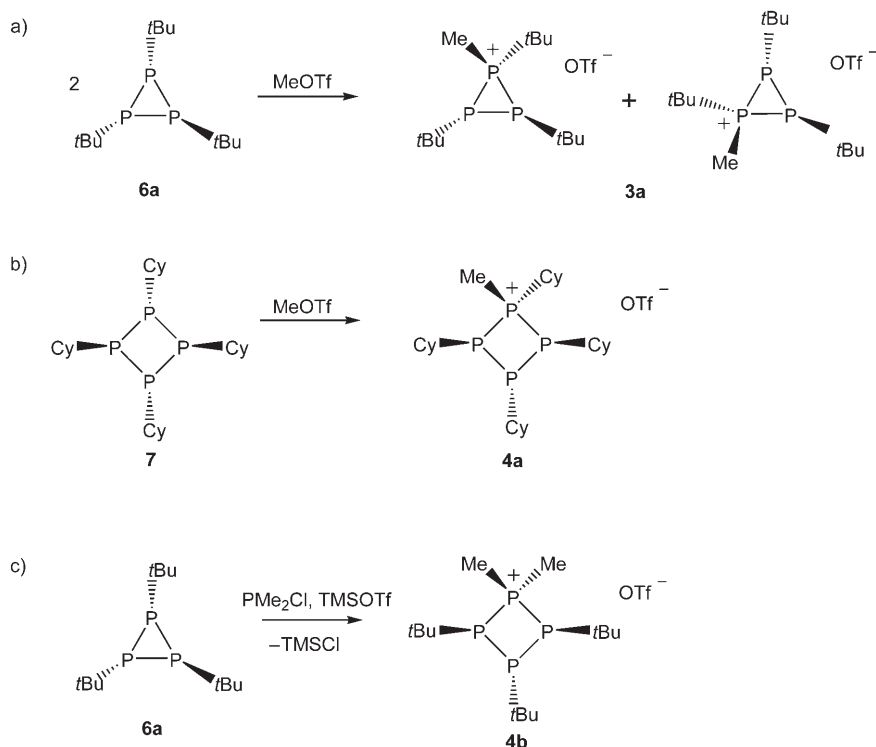


Figure 1. ³¹P NMR spectra at 101.3 MHz: a) mixture of MeOTf (2 equiv) and (PrBu)₃, which shows the approximate AMX pattern of **3a-OTf**; b) mixture of MeOTf (2 equiv) and (PCy)₄, which shows the approximate A₂MX pattern of **4a-OTf**; c) experimental (top) and simulated (inverted) AB₂X pattern of pure **4b-OTf**.

[*] Prof. N. Burford, C. A. Dyker
Department of Chemistry
Dalhousie University
Halifax, NS, B3H 4J3 (Canada)
Fax: (+1) 905-494-1310
E-mail: neil.burford@dal.ca

Dr. M. Lumsden
Atlantic Region Magnetic Resonance Center
Dalhousie University
Halifax, NS, B3H 4J3 (Canada)
Dr. A. Decken
Department of Chemistry
University of New Brunswick
Fredericton, NB, E3A 6E2 (Canada)

[**] We thank the Natural Sciences and Engineering Research Council of Canada, the Killam Foundation, the Canada Research Chairs Program, the Canada Foundation for Innovation, the Nova Scotia Research and Innovation Trust Fund, and the Walter C. Sumner Foundation for funding.



Scheme 2. Preparation of cyclopolyphosphinophosphonium cations. OTf = trifluoromethanesulfonate, Cy = cyclohexyl, TMS = trimethylsilyl.

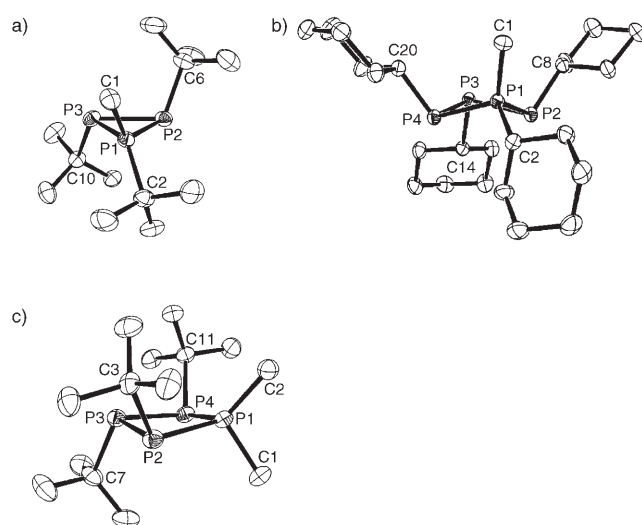


Figure 2. Representative structural views of the cations in a) **3a-OTf**, b) **4a-OTf**, and c) **4b-OTf**. Ellipsoids are given at the 50% probability level. Hydrogen atoms are omitted for clarity.

mixture rather than the *meso* isomer. Similarly, the homocyclic tetraphosphorus core is maintained in the formation of $[(\text{PCy})_4\text{Me}][\text{OTf}]$ (**4a-OTf**) from $(\text{PCy})_4$ (**7**) and MeOTf (Scheme 2b), and the ^{31}P NMR spectrum of the reaction mixture can be approximated as an A_2MX spin system (Figure 1b). Thus, methylation occurs at one of the four equivalent phosphorus atoms in the all-*trans* configuration of **7**, which is confirmed by the solid-state structure of the

meso isomer **4a** (Figure 2b). The reaction of **6a** with 1.5 equivalents of PMe_2^+ (formed in situ from Me_2PCl and TMSOTf, see Scheme 2c) gives $[(\text{PtBu})_3\text{PMe}_2][\text{OTf}]$ (**4b-OTf**) almost quantitatively through a PMe_2^+ bond insertion/ring expansion process. The complicated ^{31}P NMR spectrum of **4b-OTf** (Figure 1c) was simulated at 101.3 MHz (Figure 1c, inverted) and at 202.6 MHz as a second-order AB_2X spin system and is consistent with the symmetric *meso* structure of **4b** observed in the solid state (Figure 2c). There is no evidence for the existence of the diastereomeric isomers of **4b**, thus indicating a stereospecificity of the reaction that can be rationalized in terms of “ PMe_2^+ ” insertion into the *syn*-configured P–P bond at the less-hindered face of **6a**,^[20] as observed in similar insertions of “ PCl ” and “ PBr ”.^[21]

Examples of cations based on framework **4** have been previously postulated on the basis of elemental analysis^[22,23] and ^{31}P NMR data;^[24] however, we provide herein the first con-

firmation of structural types **3** and **4**. The solid-state structural features of **3a-OTf**, **4a-OTf**, and **4b-OTf** are listed in Table 1 along with the comparative parameters of $[\text{P}_5\text{Ph}_6][\text{OTf}]$ (**5a-OTf**), **6a**, **7**, and $(\text{PPh})_5$. The methylated, four-coordinate P1 center in **3a** is significantly distorted with the C–P1–P angles exhibiting the widest range (108.6–133.2°) of the compounds listed in Table 1 (Figure 2a). Whereas the endocyclic angles in **3a** are similar to those in the neutral precursor **6a**, the plane defined by C1, P1, C2 is twisted by 72.49(6)° with respect to the plane of the three phosphorus atoms (ideally 90°) because of the steric interactions of the *syn* substituents. The greater steric imposition of the *tert*-butyl substituents in **4b** relative to that of the cyclohexyl substituents in **4a** is indicated by both the greater planarity of the P_4 ring in **4b** (P–P–P–P torsional angles: **4a**: 23.6–24.2°, **4b**: 10.3–10.5°; c.f. $(\text{PtBu})_4$: 24.5°, **7**: 31.4°) and a greater distortion of the tetrahedral geometry at P1 in **4b**, in which a larger range of C–P1–P angles and a smaller C–P–C angle are adopted (Table 1). In this context, the cyclohexyl substituent at P1 in **4a** minimizes steric interactions by twisting to enable a *gauche* conformation of the α -hydrogen atom of C2 and the methyl substituent (C1).

The P–P distances are remarkably regular in neutral, anionic, and cationic compounds, although the four-coordinate phosphorus centers of the cations typically form slightly shorter P–P bonds (bold values in column 3 of Table 1). Interestingly, the P–P distances between the three-coordinate phosphorus centers in the cations are somewhat longer than those in the neutral cyclopolyphosphines. Consistent with the trend in P–P distances, the shortest P–C bonds within a given cation involve the phosphonium center (bold values in column 2 of Table 1).

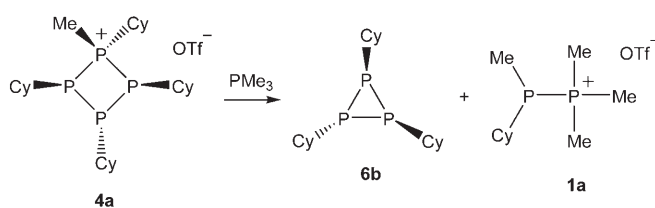
Table 1: Selected distances [Å] and angles [°] for **3a**-OTf, **4a**-OTf, and **4b**-OTf, and the comparative features of **5a**-OTf, **6a**, **7**, and (PPh)₅.^[a]

Compound	P–C	P–P	C–P–P	C–P–C	P–P–P	Ref.
[(PtBu) ₃ Me][OTf] (3a -OTf)	1.858(2) [1,2] 1.806(2) [1,1] 1.886(2) [2,6] 1.894(2) [3,10]	2.1465(6) [1,2] 2.1652(6) [1,3] 2.2306(6) [2,3]	123.15(7) [1,1,2] 108.62(7) [1,1,3] 112.97(6) [2,1,2] 133.21(6) [2,1,3]	110.41(9) [1,1,2]	62.31(2) [2,1,3] 59.26(2) [1,2,3] 58.43(2) [1,3,2]	[b]
[(PCy) ₄ Me][OTf] (4a -OTf)	1.822(2) [1,2] 1.797(2) [1,1] 1.867(2) [2,8] 1.871(2) [3,14] 1.858(2) [4,20]	2.1952(6) [1,2] 2.1896(6) [1,4] 2.2387(6) [2,3] 2.2378(6) [3,4]	114.45(7) [1,1,2] 115.54(7) [1,1,4] 113.68(6) [2,1,2] 113.03(6) [2,1,4]	108.44(8) [1,1,2]	91.05(2) [4,1,2] 84.92(2) [1,2,3] 88.68(2) [4,3,2] 85.07(2) [1,4,3]	[b]
[(PtBu) ₃ PMe ₂][OTf] (4b)	1.800(2) [1,2] 1.802(2) [1,1] 1.890(2) [2,3] 1.890(2) [3,7] 1.885(2) [4,11]	2.2032(5) [1,2] 2.1983(6) [1,4] 2.2385(6) [2,3] 2.2307(6) [3,4]	106.33(6) [1,1,2] 105.12(6) [1,1,4] 120.56(6) [2,1,4] 122.72(6) [2,1,2]	105.99(9) [2,1,1]	94.33(2) [4,1,2] 85.50(2) [1,2,3] 92.47(2) [4,3,2] 85.80(2) [1,4,3]	[b]
[P ₅ Ph ₆][OTf] (5a)	1.798(2) 1.799(2) 1.829(2) 1.843(2) 1.842(2) 1.827(2)	2.2221(6) 2.2072(6) 2.2318(6) 2.2392(6) 2.2251(6)	106.08(6) 113.22(6) 111.57(6) 107.03(6)	111.59(8)	107.36(2) 96.52(2) 93.59(2) 89.56(2) 91.64(2)	[18]
(PtBu) ₃ (6a) ^[c]	1.874(5) 1.915(5) 1.897(5)	2.188(2) 2.186(2) 2.216(2)	105.0–123.7 av. 112.1	–	60.8(1) 59.6(1) 59.6(1)	[20]
(PCy) ₄ (7)	1.874(2)	2.224(2)	102.8(1) 102.6(1)	–	85.47(6)	[25]
(PPh) ₅	1.83(1)–6(1) av. 1.84	2.207(5)–23(5) av. 2.217	96.4(4)–109.8(4) av. 102.0	–	94.0(2)–107.2(2) av. 100.0	[26]

[a] Numbers in square brackets denote atom labels and the values in bold are those that involve the four-coordinate phosphorus center (av. = average value). [b] This work. [c] The average of two crystallographically independent molecules.

In a preliminary study of reactivity, reaction mixtures that contain **4a**-OTf and PMe₃ show the characteristic A₂B pattern of (PCy)₃ (**6c**) in the ³¹P NMR spectra.^[27] In addition, two new doublets (δ = 15.4 and –38.2 ppm, ¹J(P–P) = 295 Hz) are assigned to the new phosphinophosphonium cation in [Me₃P–PMeCy][OTf] (**1a**-OTf), and a low-intensity sharp signal at δ = –67 ppm is assigned to **7** (Scheme 3). The

of cyclodiphosphinophosphonium **3** and cyclotriphosphinophosphonium **4** cations are facilitated by the appropriate imposition of substituent steric strain in the starting cyclopolyposphines. The phosphonium abstraction induced by PMe₃ and ring contraction provides further systematic development of these fundamentally important *catena*-phosphorus frameworks.



Scheme 3. Phosphenium abstraction from **4a**.

abstraction of MeCyP⁺ from **4a** by PMe₃ effects a ring contraction and, in conjunction with a previous methylation step, highlights a synthetically viable transformation from cyclotetraphosphine (PR)₄ to cyclotriphosphine (PR)₃. In addition, the reversibility of the phosphonium P–P insertion is observed (by ³¹P NMR spectroscopic analysis) in the reaction of **4b** with PMe₃, which slowly gives **6a** and [Me₃P–PMe₂][OTf] (**1b**-OTf).

In summary, the application of methylation or phosphonium insertion reactions to cyclopolyposphines has enabled the characterization of a family of small cyclopolyposphinophosphonium monocations. The high-yielding preparations

Experimental Section

Small-scale reactions were carried out in a glove box with an inert N₂ atmosphere. Solvents were dried on an MBraun solvent-purification system and stored over molecular sieves prior to use. (PtBu)₃^[28] and (PCy)₄^[29] were prepared according to literature methods. All the reported ³¹P NMR parameters were derived by computer simulation, as all compounds exhibited some degree of second-order character.

3a-OTf: MeOTf (0.08 mL, 0.71 mmol) was added dropwise to a solution of (PtBu)₃ (0.096 g, 0.36 mmol) in fluorobenzene (4 mL). The reaction mixture was filtered after 15 min. Slow diffusion of hexane vapors into the filtrate at –25 °C gave colorless crystals; yield = 0.14 g (0.32 mmol, 87 %). M.p. 121–125 °C; elemental analysis (%) calcd for C₁₄H₃₀F₃O₃P₃S: C 39.3, H 7.1; found: C 39.5, H 7.0; ¹H NMR (500.1 MHz, CDCl₃, 298 K): δ = 3.6 (dd, ¹J(P,H) = 13 Hz, ¹J(P,H) = 8 Hz, 1H), 1.6 (d, ³J(P,H) = 22 Hz, 3H), 1.4 (d, ³J(P,H) = 17 Hz, 3H), 1.6 ppm (d, ³J(P,H) = 17 Hz, 3H); ³¹P NMR (101.3 MHz, CDCl₃, 298 K): AMX spin system, δA = –110.3, M = –50.8, X = –20.4 ppm, ¹J(A,M) = –123, ¹J(A,X) = –334, ¹J(M,X) = –317 Hz; FTIR (nujol, ranked intensities): $\tilde{\nu}$ = 1399 (9), 1260 (1), 1151 (2), 1030 (4), 904 (5), 800 (10), 751 (8), 638 (3), 572 (7), 516 (6) cm^{–1}.

4a-OTf: MeOTf (0.095 mL, 0.84 mmol) was added dropwise to a mixture of (PCy)₄ (0.25 g, 0.55 mmol) in CH₂Cl₂ (5 mL). The reaction mixture was filtered after 90 min, and removal of the solvent in vacuo gave a white solid that was recrystallized at –25 °C from fluoroben-

zene by vapor diffusion of hexane over 3 days; yield = 0.15 g (0.23 mmol, 43 %). M.p. 175–177 °C; elemental analysis (%) calcd for $C_{26}H_{47}F_3O_3P_4S$: C 50.3, H 7.6; found: C 50.4, H 7.3; 1H NMR (500.1 MHz, $CDCl_3$, 298 K): δ = 2.6 (m, 1H) 2.4 (d, $J(P,H)$ = 12 Hz, 3H), 2.4 (m, 2H), 1.7–2.1 (m, 20H), 1.1–1.5 ppm (m, 21H); ^{31}P NMR (202.6 MHz, $CDCl_3$, 298 K): A_2MX spin system, δA = –69.8, M = –56.2, X = 10.1 ppm, $^1J(A,M)$ = –122, $^1J(A,X)$ = –230, $^2J(M,X)$ = –17 Hz; FTIR (nujol, ranked intensities): $\tilde{\nu}$ = 1284 (4), 1246 (1), 1158 (5), 1083 (3), 926 (9), 883 (8), 754 (10), 636 (2), 572 (7), 527 (6) cm^{-1} . Crystals suitable for X-ray diffraction were obtained by vapor diffusion of fluorobenzene/hexane at room temperature.

4b-OTf: A solution of PMe_2Cl (0.044 mL, 0.55 mmol) and $TMSOTf$ (0.10 mL, 0.67 mmol) in CH_2Cl_2 (3 mL) was added dropwise to a solution of $(PrBu)_3$ (0.098 g, 0.37 mmol) in CH_2Cl_2 (3 mL). The solvent was removed in vacuo after stirring of the reaction mixture for 45 min, and the resulting white solid was washed with portions of hexane (2 \times 4 mL). The product was recrystallized from fluorobenzene by diffusion of hexane vapor into the solution at room temperature over 5 days; yield = 0.095 g (0.20 mmol, 54 %). M.p. 112–114 °C; elemental analysis (%) calcd for $C_{15}H_{33}F_3O_3P_4S$: C 38.0, H 7.0; found: C 38.5, H 6.9; 1H NMR (500.1 MHz, $CDCl_3$, 298 K): δ = 2.7 (d, $^2J(P,H)$ = 14 Hz, 1H), 2.4 (dt, $J(P,H)$ = 13 Hz, $J(P,H)$ = 8 Hz, 1H), 1.5 (m, 6H), 2.7 ppm (d, $^3J(P,H)$ = 14 Hz, 3H); ^{31}P NMR (101.3 MHz, $CDCl_3$, 298 K): AB_2X spin system, δA = –28.2, B = –24.2, X = –2.1 ppm, $^1J(A,B)$ = –143, $^1J(B,X)$ = –251, $^2J(A,X)$ = 28 Hz; FTIR (nujol, ranked intensities): $\tilde{\nu}$ = 1304 (6), 1267 (2), 1224 (7), 1155 (3), 1032 (4), 957 (8), 914 (9), 638 (1), 573 (10), 517 (5) cm^{-1} .

X-ray crystallographic analysis: Data was collected on Bruker AXS P4/SMART 1000 diffractometer using ω and θ scans with a width of 0.3°, a exposure time of 10 s at 173 K, and a detector distance of 5 cm. The data were reduced (SAINT)^[30] and corrected for absorption (SADABS).^[31] Structures were solved by direct methods and refined by full-matrix least squares on F^2 (SHELXL).^[32] All non-hydrogen atoms were refined anisotropically. **3a-OTf**: $C_{14}H_{30}F_3O_3P_4S$; colorless, plates, crystal size 0.40 \times 0.40 \times 0.10 mm³, monoclinic, space group $P2_1/n$, a = 13.6318(9), b = 10.5918(7), c = 15.487(1) Å³, β = 104.084(1)°, V = 2168.9(2) Å³, Z = 4, μ = 0.405 mm^{–1}; $\lambda(Mo_{K\alpha})$ = 0.71073 Å, $2\theta_{max}$ = 53.8°, collected (independent) reflections = 14 573 (4869), R_{int} = 0.0213; 337 refined parameters, R_1 = 0.0487, wR_2 = 0.1056 for all data, max./min. residual electron density = 0.646/–0.476 e Å^{–3}. **4a-OTf**: $C_{26}H_{47}F_3O_3P_4S$, colorless parallelepiped, crystal size 0.275 \times 0.20 \times 0.175 mm³, triclinic, space group $P\bar{1}$, a = 11.4946(7), b = 11.5640(7), c = 14.0822(9) Å³, α = 110.984(1), β = 102.476(1), γ = 106.868(1)°, V = 1561.62(17) Å³, Z = 2, μ = 0.352 mm^{–1}; $\lambda(Mo_{K\alpha})$ = 0.71073 Å, $2\theta_{max}$ = 52.2°, collected (independent) reflections = 10 965 (6795), R_{int} = 0.0195; 522 refined parameters, R_1 = 0.0475, wR_2 = 0.0964 for all data, max./min. residual electron density = 0.491/–0.247 e Å^{–3}. **4b-OTf**: $C_{15}H_{33}F_3O_3P_4S$, colorless parallelepiped, crystal size 0.40 \times 0.275 \times 0.25 mm³, tetragonal, space group $I4_1/a$, a = 25.6452(11), b = 25.6452(11), c = 14.7549(8) Å³, V = 9703.9(8) Å³, Z = 16, μ = 0.432 mm^{–1}; $\lambda(Mo_{K\alpha})$ = 0.71073 Å, $2\theta_{max}$ = 54.7°, collected (independent) reflections = 33 323 (5547), R_{int} = 0.0293; 367 refined parameters, R_1 = 0.0445, wR_2 = 0.0809 for all data, max./min. residual electron density = 0.414/–0.237 e Å^{–3}.

CCDC-271727–271729 (**3a**, **4a**, and **4b**, respectively) contain the supplementary crystallographic data for this paper. These data can be obtained free of charge from the Cambridge Crystallographic Data Centre via www.ccdc.cam.ac.uk/data_request/cif.

Received: May 27, 2005

Published online: August 31, 2005

Keywords: catenation · cations · phosphines · phosphorus · polycations

- [1] K. B. Dillon, F. Mathey, J. F. Nixon, *Phosphorus: The Carbon Copy*, Wiley, New York, **1997**.
- [2] M. Baudler, *Angew. Chem.* **1982**, 94, 520; *Angew. Chem. Int. Ed. Engl.* **1982**, 21, 492–512.
- [3] M. Baudler, *Angew. Chem.* **1987**, 99, 429; *Angew. Chem. Int. Ed. Engl.* **1987**, 26, 419–441.
- [4] M. Baudler, K. Glinka, *Chem. Rev.* **1993**, 93, 1623–1667.
- [5] M. Baudler, K. Glinka, *Chem. Rev.* **1994**, 94, 1273–1297.
- [6] A. Schisler, P. Lonnecke, T. Gelbrich, E. Hey-Hawkins, *Dalton Trans.* **2004**, 2895–2898.
- [7] A. Schisler, P. Lonnecke, U. Huniar, R. Ahlrichs, E. Hey-Hawkins, *Angew. Chem.* **2001**, 113, 4345–4348; *Angew. Chem. Int. Ed.* **2001**, 40, 4217–4219.
- [8] R. Wolf, E. Hey-Hawkins, *Chem. Commun.* **2004**, 2626–2627.
- [9] R. Wolf, A. Schisler, P. Lonnecke, C. Jones, E. Hey-Hawkins, *Eur. J. Inorg. Chem.* **2004**, 3277–3286.
- [10] H.-W. Lerner, G. Margraf, L. Kaufmann, J. W. Bats, M. Bolte, M. Wagner, *Eur. J. Inorg. Chem.* **2005**, 1932–1939.
- [11] H.-W. Lerner, M. Bolte, K. Karaghiosoff, M. Wagner, *Organometallics* **2004**, 23, 6073–6076.
- [12] N. Wiberg, A. Wörner, H.-W. Lerner, K. Karaghiosoff, D. Fenske, G. Baum, A. Dransfeld, P. v. R. Schleyer, *Eur. J. Inorg. Chem.* **1998**, 833–841.
- [13] A. Schmidpeter, S. Lochschmidt, W. S. Sheldrick, *Angew. Chem.* **1985**, 97, 214; *Angew. Chem. Int. Ed. Engl.* **1985**, 24, 226–227.
- [14] A. Schmidpeter, S. Lochschmidt, K. Karaghiosoff, W. S. Sheldrick, *J. Chem. Soc. Chem. Commun.* **1985**, 1447–1448.
- [15] A. Schmidpeter, S. Lochschmidt, *Angew. Chem.* **1986**, 98, 271; *Angew. Chem. Int. Ed. Engl.* **1986**, 25, 253–254.
- [16] L. Heuer, L. Ernst, R. Schmutzler, D. Schomburg, *Angew. Chem.* **1989**, 101, 1549; *Angew. Chem. Int. Ed. Engl.* **1989**, 28, 1507–1509.
- [17] N. Burford, P. J. Ragogna, R. McDonald, M. Ferguson, *J. Am. Chem. Soc.* **2003**, 125, 14404–14410.
- [18] N. Burford, C. A. Dyker, A. Decken, *Angew. Chem.* **2005**, 117, 2416–2419; *Angew. Chem. Int. Ed.* **2005**, 44, 2364–2367.
- [19] Spin systems are labeled from the lowest frequency excitation (designated A) to the highest (designated X).
- [20] J. Hahn, M. Baudler, C. Kruger, Y.-H. Tsay, *Z. Naturforsch. B* **1982**, 37, 797–805.
- [21] B. Riegel, A. Pfizner, G. Heckmann, H. Binder, E. Fluck, *Z. Anorg. Allg. Chem.* **1995**, 621, 1365–1372.
- [22] R. Appel, R. Milker, *Z. Anorg. Allg. Chem.* **1975**, 417, 161–170.
- [23] K. Issleib, C. Rockstroh, I. Ducheck, E. Fluck, *Z. Anorg. Allg. Chem.* **1968**, 360, 77–87.
- [24] K. K. Laali, B. Geissler, M. Regitz, *J. Org. Chem.* **1995**, 60, 3149–3154.
- [25] J. C. J. Bart, *Acta Crystallogr. Sect. B* **1969**, 25, 762.
- [26] J. J. Daly, *J. Chem. Soc. Suppl.* **1964**, 6147–6166.
- [27] M. Baudler, C. Pinner, C. Gruner, J. Hellmann, M. Schwamborn, B. Kloth, *Z. Naturforsch. B* **1977**, 32, 1244–1251.
- [28] M. Baudler, K. Glinka, *Inorg. Synth.* **1989**, 25, 1–5.
- [29] W. A. Henderson, M. Epstein, F. S. Seichter, *J. Am. Chem. Soc.* **1963**, 85, 2462–2466.
- [30] SAINT 6.02, Bruker AXS, Inc., Madison, Wisconsin, USA, **1997–1999**.
- [31] SADABS George Sheldrick, Bruker AXS, Inc., Madison, Wisconsin, USA, **1999**.
- [32] SHELXTL 6.14, Bruker AXS, Inc., Madison, Wisconsin, USA, **2000–2003**.

Optical Absorption and Structure of a Highly Symmetrical Neptunium(V) Diamide Complex**

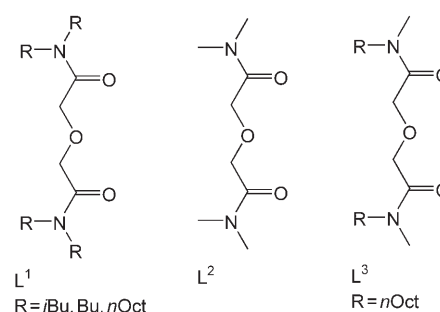
Guoxin Tian, Jide Xu, and Linfeng Rao*

The neptunium(V) cation, NpO_2^+ , contains Np in its most stable oxidation state under a wide range of conditions in aqueous media. Because of its low positive charge, NpO_2^+ does not form strong complexes with ligands so it is difficult to separate neptunium from high-level nuclear wastes by using traditional extracting agents that are effective for separating other actinides.^[1] Also, the low tendency of NpO_2^+ to undergo hydrolysis and sorption makes it highly mobile in the subsurface, raising concern in the migration of this radionuclide in the environment.^[2]

The absorption spectrum of NpO_2^+ is dominated by a band in the near-IR region with a fairly high intensity ($\epsilon \approx 390 \text{ M}^{-1} \text{ cm}^{-1}$ at 980.2 nm). This band, as well as a weaker band at 1024 nm, follows Beer–Lambert behavior and is often used to quantitatively determine the concentration of NpO_2^+ in solution.^[3] The position and intensity of these bands are also affected by the coordination environment of NpO_2^+ and are frequently used to study the complexation behavior of NpO_2^+ .^[4,5] The absorption band of the free $[\text{NpO}_2(\text{H}_2\text{O})_n]^+$ ion at 980.2 nm is usually shifted to longer wavelengths when NpO_2^+ forms complexes with ligands that replace the water molecules in the primary hydration sphere. For a series of structurally related ligands, the magnitude of the shifts in the wavelength appears to increase as the binding strength of the ligand is increased. For example, in the 1:1 complexes of NpO_2^+ with dicarboxylates, the stability constants and the shifts in wavelength ($\log \beta$ and $\Delta \lambda$ in nm) are 1.29 and 3.7 for glutarate,^[6] 1.47 and 4.5 for succinate,^[6] 2.63 and 7.2 for malonate,^[7] and 3.79 and 8.4 for oxalate.^[7] Formation of 1:2 complexes with these ligands shifts the absorption band to even longer wavelengths.^[4,6,7] The molar absorptivities of the bands vary in the range from 250 to $390 \text{ M}^{-1} \text{ cm}^{-1}$.^[4,6,7] The underlying mechanism that allows the transitions and the

origin of the intensities remain unclear. Theoretical calculations suggest that the absorption band at 980 nm is a $5f \rightarrow 5f$ electric-dipole transition, which is forbidden by Laporte's rule, and that the intensity of the transition depends on the symmetry of the Np^{V} species.^[8] The results of theoretical calculations are enlightening but need to be tested by comparison with experimentally observed spectra of Np^{V} complexes with different ligands.

In an effort to develop efficient extractants for the separation of actinide ions including Np^{V} , we have found that tetraalkyl-3-oxa-glutaramide, L^1 , displays a good ability



to extract Np^{V} ions.^[9] To obtain insight into the complexation of Np^{V} with diamide ligands, a simple water-soluble homologue of L^1 , tetramethyl-3-oxa-glutaramide (L^2), was synthesized and studied by optical absorption spectroscopy in aqueous solution.

Figure 1a shows the absorption spectra obtained during spectrophotometric titrations of Np^{V} with L^2 . As the concentration of L^2 was increased, the intensities of the absorption bands at 980 and 1024 nm that belong to the free NpO_2^+ cation decreased and new bands appeared at 987 and 1037 nm, which correspond to the formation of a 1:1 complex of Np^{V} with L^2 , $[\text{NpO}_2(\text{L}^2)]^+$. As the concentration of L^2 was further increased, the intensities at 987 and 1037 nm decreased but no new absorption peaks appeared at longer wavelengths. These changes in the spectra are different from those for Np^{V} complexes with many other ligands for which the decrease of the absorbance of the first complex is accompanied by the appearance of new absorption band(s) of successive complexes at longer wavelengths.

The variation of the spectra in Figure 1a is interpreted with the assumption that two complexes of Np^{V} with L^2 form in solution successively but that the second complex, $[\text{NpO}_2(\text{L}^2)_2]^+$, does not absorb in that wavelength region. This assumption is consistent with the factor analysis of the spectra using the Hyperquad2000 program;^[10] the formation constants of the $[\text{NpO}_2(\text{L}^2)]^+$ and $[\text{NpO}_2(\text{L}^2)_2]^+$ complexes are calculated to be $23.7 \pm 0.5 \text{ M}^{-1}$ and $295 \pm 6 \text{ M}^{-2}$, respectively. The deconvoluted spectra for free NpO_2^+ and the $[\text{NpO}_2(\text{L}^2)]^+$ complex are shown in Figure 1b.

The $[\text{NpO}_2(\text{H}_2\text{O})_n]^+$ ion also has absorption bands of much lower intensity in the visible region that render its usual green-blue color. Figure 2 shows that the intensities of the bands at 430, 476, and 616 nm decrease and the spectra tend to become flat and featureless as the concentration of L^2 increases, which suggests that the $[\text{NpO}_2(\text{L}^2)_2]^+$ complex does

[*] Dr. G. Tian, Dr. L. Rao
Lawrence Berkeley National Laboratory
Berkeley, California 94720 (USA)
Fax: (+1) 510-486-5596
E-mail: lrhao@lbl.gov

Dr. J. Xu
Department of Chemistry, University of California
Berkeley, California 94720 (USA)

[**] This work was supported by the Director, Office of Science, Office of Basic Energy Sciences of the U.S. Department of Energy (DOE) under Contract No. DE-AC02-05CH 11231 at the Lawrence Berkeley National Laboratory (LBNL). The Advanced Light Source (ALS) is operated by LBNL for the DOE. The authors thank Drs. D. Shuh and A. Gordon for developing the procedures for handling small crystals of actinides at Beamline 11.3.1 of the ALS, and Dr. Allen Oliver for collecting the X-ray diffraction data at the ALS.

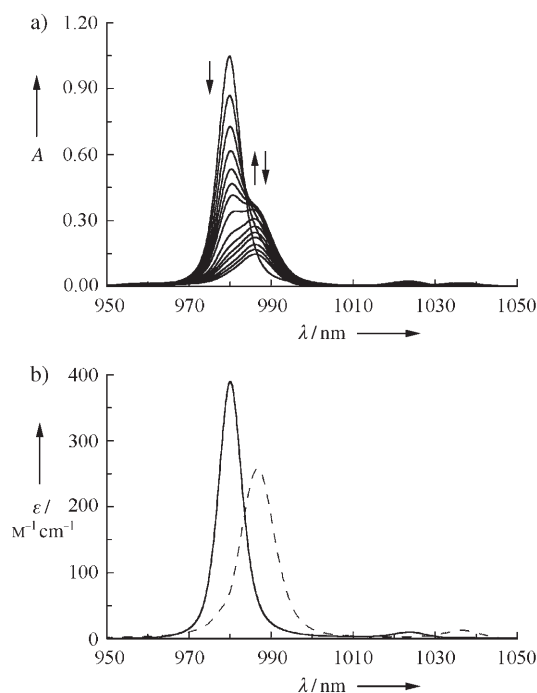


Figure 1. a) Spectrophotometric titrations in the near-IR region of Np^{V} with L^2 . $[\text{Np}] = 2.66 \text{ mM}$; $[\text{L}^2] = 0\text{--}336 \text{ mM}$; optical path: 1.0 cm. b) Deconvoluted absorption spectra of NpO_2^+ (—) and the $[\text{NpO}_2(\text{L}^2)]^+$ complex (----); $[\text{NpO}_2(\text{L}^2)_2]^+$ does not absorb in this region.

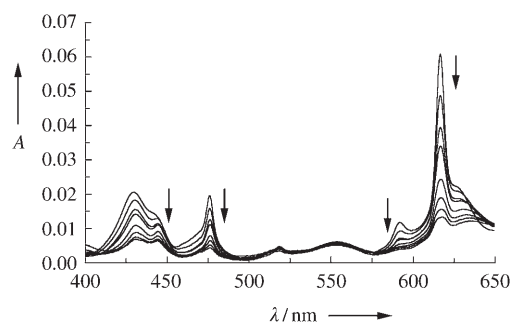


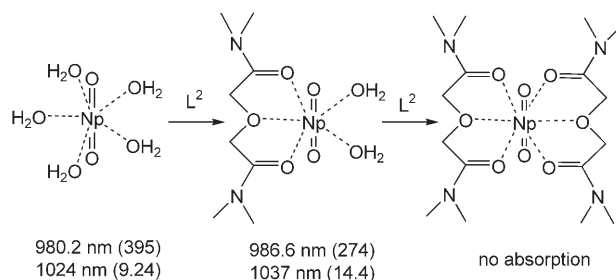
Figure 2. Spectrophotometric titrations of Np^{V} with L^2 in the visible region. $[\text{Np}] = 2.66 \text{ mM}$; $[\text{L}^2] = 0\text{--}336 \text{ mM}$; optical path: 1.0 cm.

not absorb in the visible region. In fact, the initial green-blue color of the solution of $[\text{NpO}_2(\text{H}_2\text{O})_n]^+$ gradually faded as the concentration of L^2 was increased and became almost colorless at the end of titration.

These results are consistent with the theoretical calculations by Matsika et al.^[8] For the f^2 electronic configuration of NpO_2^+ , all of the excited states up to 23000 cm^{-1} (corresponding to $\lambda \approx 430 \text{ nm}$) contain two f electrons and display the gerade parity in the ground state.^[8] Thus, all the excitations at low energies should be electric-dipole forbidden by Laporte's rule. This rule is followed if NpO_2^+ is in a coordination environment where a center of inversion exists. However, if the ligands that surround the NpO_2^+ are arranged so that the center of inversion is destroyed, Laporte's rule does not apply and the $f \rightarrow f$ transitions are allowed. The successive complexation of Np^{V} with L^2 and the accompany-

ing changes in symmetry and absorption spectra are best illustrated by Scheme 1.

The free NpO_2^+ cation contains five molecules of H_2O in the equatorial plane^[11] to result in a structure without a center of inversion. As a result, the $f \rightarrow f$ transitions are allowed and



Scheme 1. Successive complexation of $[\text{Np}^{\text{V}}\text{O}_2(\text{H}_2\text{O})_5]^+$ with L^2 and the accompanying changes in symmetry and absorption bands (corresponding ϵ values in $\text{M}^{-1} \text{ cm}^{-1}$ are given in parentheses).

absorption bands at 980 and 1024 nm are observed. For the same reason of absence of a center of inversion, the first complex, $[\text{NpO}_2(\text{L}^2)]^+$, does absorb light, but the energies of the absorption bands are red-shifted (987 and 1037 nm). However, the second complex, $[\text{NpO}_2(\text{L}^2)_2]^+$, could be highly symmetrical with a center of inversion, wherein each L^2 ligand supplies three oxygen atoms to coordinate NpO_2^+ in the equatorial plane. This complex is expected to display no absorption in the near-IR region (Figure 1). The same discussions apply to the change of absorption bands in the visible region (Figure 2) because all the bands up to 23000 cm^{-1} originate from $f \rightarrow f$ transitions as shown by the theoretical calculations by Matsika et al.^[8]

A comparison of the absorption spectra between the complexes of Np^{V} and L^2 (Figures 1 and 2) and those between Np^{V} and oxalate ($\text{C}_2\text{O}_4^{2-}$) complexes (Figure 3) further demonstrates the dependence of $f \rightarrow f$ transitions on the symmetry of the coordination environment of Np^{V} . It is known that the Np^{V} oxalate complexes, $[\text{NpO}_2(\text{C}_2\text{O}_4)]^-$ and $[\text{NpO}_2(\text{C}_2\text{O}_4)_2]^{3-}$, with a coordination number of five in the equatorial plane of NpO_2^+ , do not have inversion centers.^[12] There are three water molecules and one bidentate oxalate ligand in $[\text{NpO}_2(\text{C}_2\text{O}_4)]^-$, and one water molecule and two bidentate oxalate ligands in $[\text{NpO}_2(\text{C}_2\text{O}_4)_2]^{3-}$. As a result, the $f \rightarrow f$ transitions in both complexes should be allowed. This is indeed the case as shown by the absorption spectra in Figure 3. For the spectra in both the near-IR and visible regions, distinctive absorption bands are seen for $[\text{NpO}_2(\text{H}_2\text{O})_n]^+$, $[\text{NpO}_2(\text{C}_2\text{O}_4)]^-$, and $[\text{NpO}_2(\text{C}_2\text{O}_4)_2]^{3-}$. The successive complexation of Np^{V} ion with oxalate ion and the accompanying changes in symmetry and absorption spectra are illustrated in Scheme 2.

To obtain structural information for the $[\text{NpO}_2(\text{L}^2)_2]^+$ complex and test the assumption based on the theoretical calculations discussed above, single crystals of the complex were prepared from solution and X-ray diffraction data were collected (Figure 4).^[13] The perchlorate salt, $[\text{NpO}_2(\text{L}^2)_2]\text{ClO}_4$, crystallized in a highly symmetrical tetragonal space group, $I4/mcm$. The neptunium atom sits at the crossover

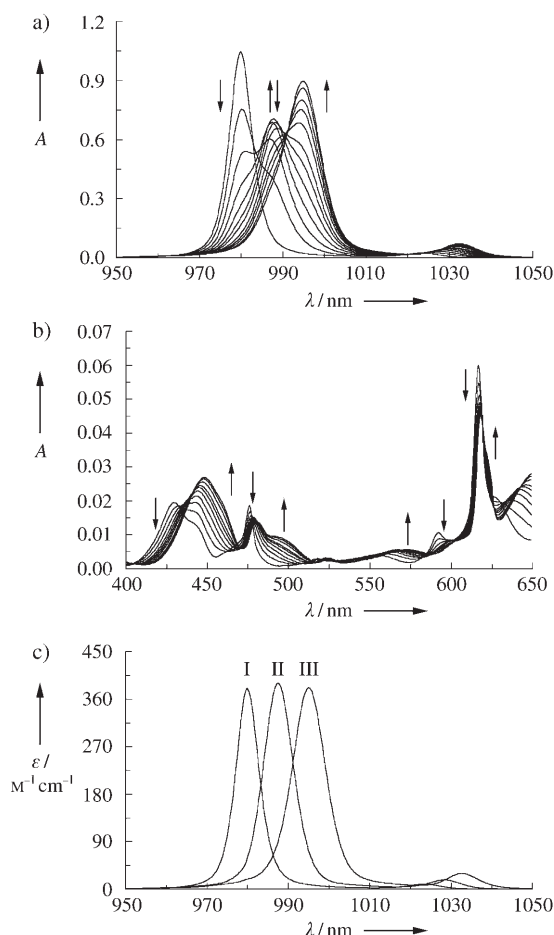
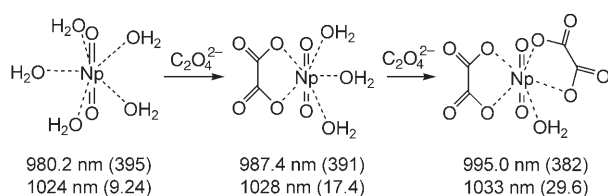


Figure 3. Spectrophotometric titrations of Np^{V} with oxalate ($[\text{Np}] = 2.66 \text{ mM}$; $[\text{C}_2\text{O}_4^{2-}] = 0\text{--}28.6 \text{ mM}$; optical path: 1.0 cm): a) in the near-IR region and b) in the visible region. c) Deconvoluted absorption spectra of $[\text{NpO}_2(\text{H}_2\text{O})_5]^+$ (I), $[\text{NpO}_2(\text{C}_2\text{O}_4)]^-$ (II), and $[\text{NpO}_2(\text{C}_2\text{O}_4)_2]^{3-}$ (III).



Scheme 2. Successive complexation of $[\text{Np}^{\text{V}}\text{O}_2(\text{H}_2\text{O})_5]^+$ with oxalate ion and the accompanying changes in symmetry and absorption bands (corresponding ϵ values in $\text{M}^{-1} \text{ cm}^{-1}$ are given in parentheses).

point of three mirror planes that lie perpendicular to each other. The two L^2 ligands are coplanar and are mirror images of each other. The $\text{O}=\text{Np}=\text{O}$ moiety is perfectly linear and symmetrical, with an angle of 180° and $\text{Np}=\text{O}$ distances of 1.729 \AA . The $f \rightarrow f$ transition in this highly symmetrical complex with a center of inversion is forbidden according to the theoretical calculations. In fact, the crystals and solutions of $[\text{NpO}_2(\text{L}^2)_2]\text{ClO}_4$ are almost colorless, drastically different from the green-blue colors of most reported Np^{V} compounds. We believe that the $[\text{NpO}_2(\text{L}^2)_2]^+$ complex in solution has the structure shown in Figure 4. Attempts to collect the diffuse reflectance spectra of $[\text{NpO}_2(\text{L}^2)_2]\text{ClO}_4$ in the solid state were

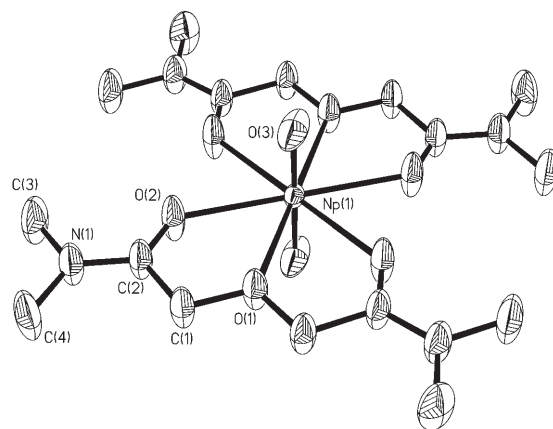


Figure 4. ORTEP drawing (30% probability ellipsoids) of $[\text{NpO}_2(\text{L}^2)_2]^+$. For clarity, the perchlorate anion is not shown.

unsuccessful owing to the limited availability of the solids and the complications involved in the experimental setup for handling the transuranic elements.

The structure of $[\text{NpO}_2(\text{L}^2)_2]^+$ (Figure 4) provides guidance in the design of better ligands to complex Np^{V} . The distance between the two carbon atoms of the terminal methyl groups is 4.01 \AA , implying that significant steric hindrance would be present if the methyl groups are replaced by bigger and/or bulkier alkyl groups such as the octyl or *iso*-butyl groups in L^1 , which is used as an extractant for the separation of actinides. The bigger alkyl groups in L^1 are mainly for enhancing its solubility in organic solvents. However, the structure of $[\text{NpO}_2(\text{L}^2)_2]^+$ suggests that asymmetric amide groups such as *N*-methyl-*N*-octyl (L^3) could be used, guaranteeing the solubility of the ligand in organic solvents as well as improving the complexation and thus the extraction of Np^{V} by reducing the steric hindrance in the Np^{V} complex. Also, the structural parameters of $[\text{NpO}_2(\text{L}^2)_2]^+$ help with the design of hexadentate amide ligands with a rigid backbone connecting the diamide ligands. Complexation of such ligands with Np^{V} should be enhanced due to a lower preorganization energy and a larger entropy effect.

In conclusion, we have synthesized, studied the optical absorption properties, and characterized the molecular structure of a highly symmetrical Np^{V} diamide complex, $[\text{NpO}_2(\text{L}^2)_2]^+$. This is the first neptunium complex that has been characterized by single-crystal X-ray diffraction with a synchrotron radiation source. The correlation between the optical absorption properties and the symmetry of Np^{V} complexes in solution was experimentally demonstrated and confirms the theoretical calculations of the optical spectra of $5f$ elements. The identified structure of $[\text{NpO}_2(\text{L}^2)_2]^+$, while helping to interpret the optical absorption spectra also suggests approaches for the rational design of ligands to improve the binding ability with Np^{V} and the separation of neptunium from nuclear wastes.

Experimental Section

Spectrophotometric titrations were performed on a Cary 5G UV-Vis-NIR spectrophotometer (Varian). Initial solutions of $[\text{NpO}_2](\text{ClO}_4)$ ($V_0 = 2.50 \text{ mL}$, $[\text{Np}] = 0.5\text{--}3 \text{ mM}$, $I = 1 \text{ M NaClO}_4$, pH 5–7) in a 1-cm

quartz cuvette were titrated with solutions of L^2 or oxalate ion (0.2–1 M). After each addition of the titrant (0.05–0.140 mL), the absorption spectrum was collected from $\lambda = 400$ –1150 nm at 0.2-nm intervals.

Single crystals of $[\text{NpO}_2(\text{L}^2)_2]\text{ClO}_4$ were prepared from 0.05 M $(\text{NpO}_2)(\text{ClO}_4)$ (0.2 mL) and 0.5 M L^2 by slow evaporation in a hood. A small crystal (20–80 μm) was immersed in Paratone-N oil and sealed inside a quartz capillary (i.d. = 0.3 mm). Precautions, including coating the capillary with a thin layer of protective resin, were taken to ensure the containment of radioactive neptunium. The capillary was mounted in a brass pin on the goniometer, which was then transported from the radiochemistry laboratory in a closed container to the Advanced Light Source (ALS), thus minimizing the amount of alignment required once at the diffractometer. Crystallographic data were collected at 255 K in less than one hour using a Bruker Platinum 200 detector at the Small-Crystal Crystallographic Beamline 11.3.1 at the ALS of Lawrence Berkeley National Laboratory.

Received: April 12, 2005

Revised: June 24, 2005

Published online: August 30, 2005

Keywords: absorption · amides · coordination modes · neptunium · X-ray diffraction

refinement, and data reduction were performed using the Bruker SAINT software package.^[16] Dispersion factors (f and f') at 16 keV for C, N, O, and Cl atoms were included using values from CROMER for Windows. Dispersion factors for Np were interpolated and imported for use in SHELXS using reported data.^[17] No decay corrections were applied. The structure was solved with direct methods using SHELXS^[18] and expanded using Fourier techniques.^[19] Non-hydrogen atoms were refined anisotropically; hydrogen atoms were included at calculation positions but not refined. All calculations were performed using SHELXL-97,^[19] the crystallographic software package of Bruker Analytical X-ray System. CCDC 268309 contains the supplementary crystallographic data for this paper. These data can be obtained free of charge from the Cambridge Crystallographic Data Centre via www.ccdc.cam.ac.uk/data_request/cif.

[14] R. H. Blessing, *Acta Crystallogr. Sect. A* **1995**, *51*, 33.

[15] ApexII: Bruker Analytical X-ray Systems Inc., Madison, WI, **2003**.

[16] SAINT: SAX Area-Detector Integration Program v6.40. Bruker Analytical X-ray Systems, Inc., Madison, WI, **2003**.

[17] A. J. C. Wilson, *International Tables of Crystallography, Vol. C*, Klumer Academic Publishers, London, **1995**.

[18] SHELXS-97: G. M. Sheldrick, Universität Göttingen, **1997**.

[19] SHELXL-97: G. M. Sheldrick, Universität Göttingen, **1997**.

- [1] "Neptunium": J. A. Fahey in *The Chemistry of the Actinide Elements*, 2nd ed. (Eds.: J. J. Katz, G. T. Seaborg, L. R. Morss), Chapman and Hall, London, **1986**, chap. 6, pp. 443–498.
- [2] G. R. Choppin, K. L. Nash, *Radiochim. Acta* **1995**, *70/71*, 225.
- [3] R. Sjöblom, J. C. Hindman, *J. Am. Chem. Soc.* **1951**, *73*, 1744.
- [4] D. M. Gruen, J. J. Katz, *J. Am. Chem. Soc.* **1953**, *75*, 3772.
- [5] J. Cooper, W. D. Reents, M. Woods, R. Sjöblom, J. C. Sullivan, *Inorg. Chem.* **1977**, *16*, 1030.
- [6] B. E. Stout, M. S. Caceci, F. Nectoux, M. Pages, *Radiochim. Acta* **1989**, *46*, 181.
- [7] M. P. Jensen, K. L. Nash, *Radiochim. Acta* **2001**, *89*, 557.
- [8] a) S. Matsika, R. M. Pitzer, *J. Phys. Chem. A* **2000**, *104*, 4064; b) S. Matsika, R. M. Pitzer, D. T. Reed, *J. Phys. Chem. A* **2000**, *104*, 11983.
- [9] G. Tian, P. Zhang, J. Wang, L. Rao, *Solvent Extr. Ion Exch.*, in press.
- [10] P. Gans, A. Sabatini, A. Vacca, *Talanta* **1996**, *43*, 1739–1753.
- [11] a) J.-M. Combes, C. J. Chisholm-Brause, G. E. Brown, Jr., G. A. Parks, S. D. Conradson, P. G. Eller, I. R. Triay, D. E. Hobart, A. Meijer, *Environ. Sci. Technol.* **1992**, *26*, 376; b) P. G. Allen, J. J. Bucher, D. K. Shuh, N. M. Edelstein, T. Reich, *Inorg. Chem.* **1997**, *36*, 4676.
- [12] a) S. V. Tomilin, Y. F. Volkov, G. I. Visyashcheva, I. I. Kapshukov, *Sov. Radiochem.* **1984**, *26*, 696; b) M. S. Grigor'ev, N. A. Baturin, L. L. Regel', N. N. Krot, *Sov. Radiochem.* **1991**, *33*, 121.
- [13] Crystal data: $\text{NpC}_{16}\text{H}_{32}\text{ClN}_4\text{O}_{12}$, $M_r = 744.91$, crystal dimensions $0.25 \times 0.20 \times 0.16 \text{ mm}^3$, tetragonal, $I4/mcm$, $a = 11.1785(16)$, $b = 11.1785(16)$, $c = 24.6937(81) \text{ Å}$, $\alpha = 90^\circ$, $\beta = 90^\circ$, $\gamma = 90^\circ$, $V = 3085.7(12) \text{ Å}^3$, $Z = 4$, $\rho_{\text{calcd}} = 1.603 \text{ g cm}^{-3}$, $2\theta_{\text{max}} = 62.20^\circ$, $T = 255 \text{ K}$, 8874 reflections collected, 1053 independent ($I > 2.00\sigma(I)$), $R_{\text{int}} = 0.0407$, $\mu = 5.856 \text{ mm}^{-1}$, absorption correction with SADABS,^[14] refinement against $|F^2|$, data/restraints/parameters of 1053/4/72, $R_1 = 0.0215$ ($wR_2 = 0.0671$, $I > 2\sigma(I)$), $R_1 = 0.0294$ ($wR_2 = 0.0910$, all data), $\text{GoF} = 1.096$, shift/esd in final cycle = 0.00, largest difference peaks $1.150/-0.646 \text{ e Å}^{-3}$. Crystallographic data were collected using a Bruker Platinum 200 detector at the Small-Crystal Crystallographic Beamline 11.3.1 at a wavelength of 0.77490 Å at the ALS of LBNL. The goniometer was mounted vertically and has a chi angle of 54.7° degrees. Intensity data were collected in less than one hour using Bruker Apex II software.^[15] Intensity data integrations, cell

Imido Complexes

DOI: 10.1002/anie.200462647

On the Mechanism of the Reaction of Organic Azides with Transition Metals: Evidence for Triplet Nitrene Capture**

Mahdi M. Abu-Omar, Catherine E. Shields,
Nicola Y. Edwards, and Rebecca A. Eikey*

Organic azides (RN_3) have received extensive attention recently because of their central role in several “spring-loaded” reactions that have been dubbed “click chemistry”.^[1–4] In organometallic chemistry, azides have been used

[*] Prof. Dr. M. M. Abu-Omar, C. E. Shields
Department of Chemistry
Purdue University
560 Oval Drive
West Lafayette, IN 47907 (USA)
Fax: (+1) 765-494-0238
E-mail: mabuomar@purdue.edu
N. Y. Edwards, Dr. R. A. Eikey
Department of Chemistry and Biochemistry
University of California
Los Angeles, CA 90095 (USA)

[**] This work was supported by the Department of Chemistry at Purdue University, the National Science Foundation, and the Beckman Foundation. We are grateful to Professors Matthew Platz and Kendall Houk for helpful discussions.

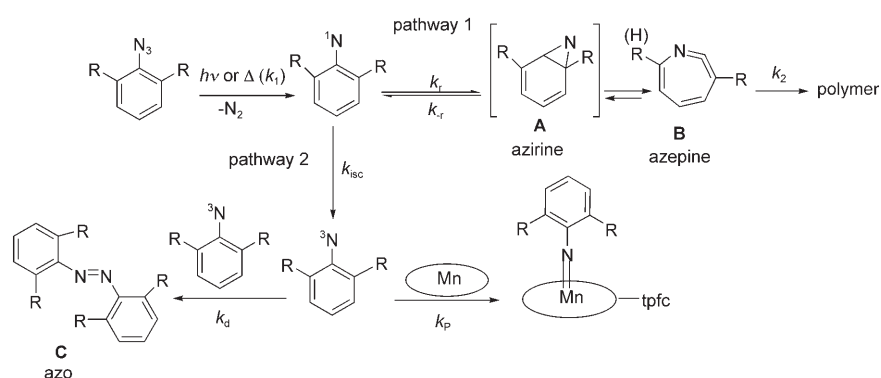


Supporting information for this article is available on the WWW under <http://www.angewandte.org> or from the author.

extensively for the preparation of imido ($M=NR$) complexes, in which dinitrogen is released as byproduct.^[5,6] As part of our interest in developing nitrene (NR) transfer to organic substrates by transition-metal catalysis, we have used aryl azides, which are quite stable and easy to make,^[7,8] to prepare mononuclear terminal imido complexes of manganese(v) and chromium(v) corroles.^[9,10] Despite many known reactions of organic azides with transition metals, little is known about the reaction mechanism. Organoazido metal complexes have been proposed to initially form for coordinatively unsaturated metal complexes.^[11–14] However, only in two instances have such complexes been characterized and shown to proceed to the imido product upon heating or photolysis, presumably via a four-membered metallacycle.^[15–17] Herein we report a novel mechanism for the reaction of aryl azides with manganese corroles in which the metal does not form an organoazido complex.

Encouraged by the successful synthesis of terminal imido manganese(v) complexes from mesityl azide and trichlorophenyl azide,^[9] we explored the utility and generality of this reaction (Scheme 1). We noted that *ortho* substitution is mandatory, as is thermal or photochemical activation. Phenyl azide with substituents in the *para* position as well as the electron-withdrawing sulfonyl azide did not produce imido metal complexes.

Results presented herein and the scope of the reaction (Scheme 1) gave valuable insight into the mechanism of the reaction of organic azides with transition-metal corroles. Our mechanistic proposal is presented in Scheme 2. On thermal or photochemical decomposition of aryl azide, singlet nitrene is formed and dinitrogen extruded.^[18,19] The singlet nitrene then decomposes along two pathways. The first is cyclization to azepine **B** via azirine **A** as a steady-state intermediate.^[20] The

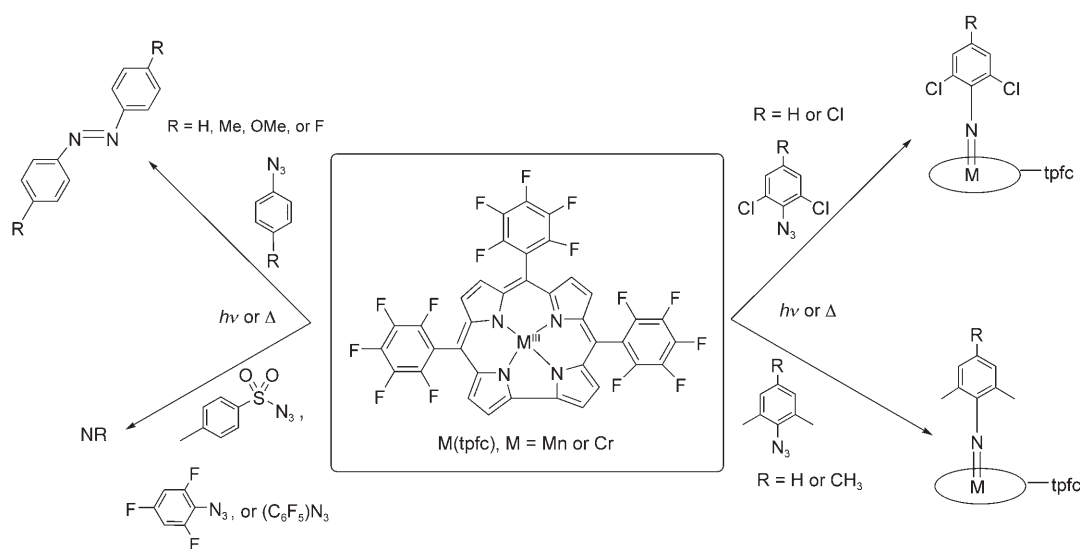


Scheme 2. Mechanism of the reaction of organic azides with $[Mn^{III}(tpfc)]$.

ultimate fate of the azepine is polymerization.^[19] However, in highly dilute solutions, polymerization of **B** is suppressed and it reverts to singlet nitrene, which relaxes by intersystem crossing (*isc*) to the lower-energy triplet state.^[21] The final thermodynamic product is azo compound **C**, assumed to form by dimerization of triplet nitrene.^[22] This second pathway, *isc* of singlet nitrene to triplet, is responsible for the formation of the imido manganese complex in our system and is most consistent with the observed scope of the reaction (Scheme 1) and kinetic data, as detailed below.

Ortho substituents are mandatory for the formation of imido metal complexes in this system. This is in agreement with results showing that singly *ortho*-substituted singlet aryl nitrenes cyclize away from the substituent,^[23] and *ortho* methylation increases the rate of intersystem crossing.^[21] Furthermore, the lack of reaction with fluorinated phenyl azides and sulfonyl azide is consistent with these substituents destabilizing the open-shell singlet nitrene.^[24] Indeed, under our reaction conditions only starting material was recovered with these substrates (Scheme 1).

The kinetics of imido metal formation were studied in detail for the reaction of mesityl azide ($MesN_3$) with $[Mn^{III}(tpfc)]$. Changes in the UV/Vis spectra for a typical reaction are displayed in Figure 1. The disappearance of the bands at



Scheme 1. Scope of the reaction of aryl azides with transition-metal corroles.

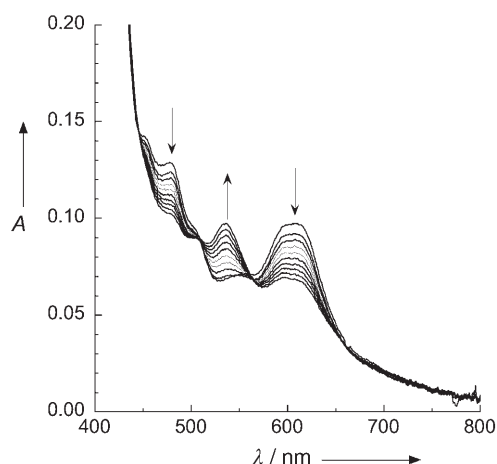


Figure 1. UV/Vis spectral changes for the reaction of $[\text{Mn}^{\text{III}}(\text{tpfc})]$ ($15\ \mu\text{M}$) with mesityl azide ($2.1\ \text{mM}$) in toluene at 80°C recorded every 6 min.

479 and 609 nm and appearance of the band at 536 nm are indicative of a change in the oxidation state from Mn^{III} to Mn^{V} . The tight isosbestic points at 510 and 565 nm demonstrate clean conversion without significant accumulation of an intermediate.

The progress of the reaction was monitored at 536 nm with $[\text{Mn}^{\text{III}}(\text{tpfc})]$ limiting and MesN_3 in excess. The experimental reaction rate was found to be first-order in mesityl azide (Figure 2) and exhibited a complex dependence on the concentration of the manganese complex. A simplified rate law that includes the reaction steps described in Scheme 2 is given in Equation (1).

$$\frac{d[\text{Mn}^{\text{V}}\text{imide}]}{dt} = \frac{k_1 k_{\text{PC}} [\text{Mn}(\text{tpfc})] C_{\text{MesN}_3}}{k_{\text{PC}} [\text{Mn}(\text{tpfc})] + k_{\text{d}} C_{\text{NMes}}} \quad (1)$$

Under conditions where $k_{\text{PC}} [\text{Mn}(\text{tpfc})] \gg k_{\text{d}} C_{\text{NMes}}$, the rate law simplifies to $d[\text{Mn}^{\text{V}}\text{imide}]/dt = k_1 C_{\text{MesN}_3}$ and the rate is zeroth-order in the concentration of the manganese corrole. However, as the reaction proceeds and $[\text{Mn}(\text{tpfc})]$ is consumed, the above assumption is no longer valid and the kinetics divert from zeroth order. This expectation is consistent with the time profiles shown in Figure 2A, which are linear over the initial 30% of the reaction (ca. $0.02\ \Delta\text{OD}$) and deviate from zeroth order in the later stages. The experimental time profiles do not fit an exponential pseudo-first-order equation (see Supporting Information). Furthermore, under no circumstance would the reaction rate be independent of the metal concentration if an organoazido adduct was formed initially or the metal corrole reacted directly with the organic azide. Similar kinetic behavior was observed when reaction progress was followed at 479 nm, which corresponds to the disappearance of the Mn^{III} reactant (see Supporting Information).

The observed kinetics were successfully modeled with the kinetic simulation program KINSIM.^[25,26] Figure 3A shows the simulated time profiles for $[\text{Mn}^{\text{III}}(\text{tpfc})]$, $[\text{Mn}^{\text{V}}(\text{tpfc})]$, azo compound, azepine, and polymer arising from the azepine. The rate constants used in association with Scheme 2 as the reaction mechanism are given in the caption of Figure 3. The rate constant for the thermal decomposition of mesityl azide

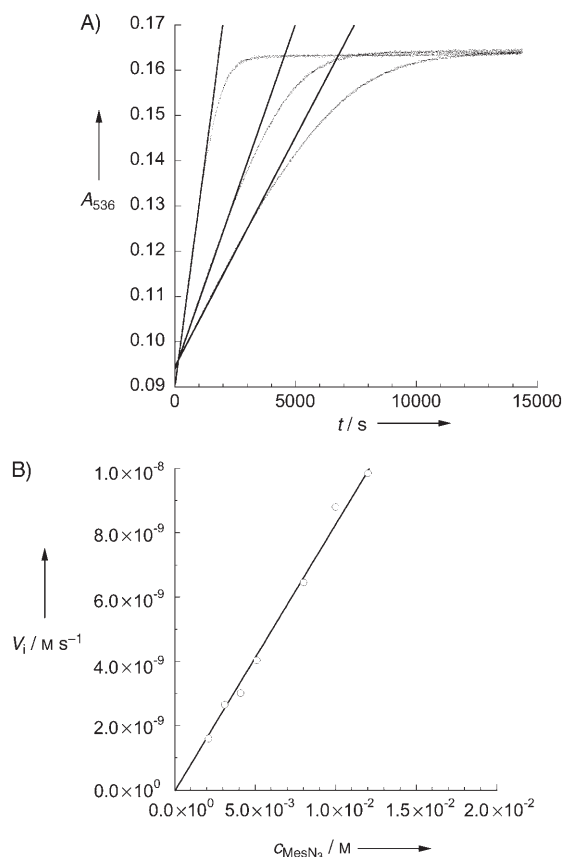


Figure 2. A) Time profiles for the reaction of $[\text{Mn}(\text{tpfc})]$ ($15\ \mu\text{M}$) and mesityl azide (3, 5, and $12\ \text{mM}$) in toluene at $(80.0 \pm 0.2)^\circ\text{C}$. The linear fit is over the initial 30% of the reaction to illustrate zeroth-order kinetics that deviate from linearity in the later stages of the reaction. B) A plot of the initial rate V_i versus the mesityl azide concentration showing first-order dependence on the azide concentration.

(k_1) was determined experimentally herein (Figure 2B); the rate constant for intersystem crossing (k_{isc}) was taken from published data,^[27] and the rate constants for triplet nitrene dimerization to give the azo compound (k_{d}) and for polymerization of azepine (k_2) were set to the diffusion limit ($8.0 \times 10^9\ \text{M}^{-1}\text{s}^{-1}$). The remaining three rate constants were floated to give the best fit to the experimental profiles. The agreement between experimental and simulated kinetics is illustrated in Figure 3B and the Supporting Information. It is worth noting that formation of the azo compound sets in after the initial 30% of reaction, which agrees with the observed kinetic behavior (see above). Nevertheless, GC-MS analyses of reaction mixtures at the end of the reaction show only azide, and only at longer decomposition times is the azo compound detected (see Supporting Information). This apparent contradiction is most likely due to low concentrations of the azo compound (below the GC-MS detection threshold) on the reaction timescale (2 h).

To date, the reaction of organic azides with transition-metal complexes to give imido metal compounds has been accepted to proceed via an organoazido metal intermediate. While this mechanism holds true in many instances and has been demonstrated in a couple of reaction systems, it is not exclusive.^[15–17] We have described herein a new mechanism

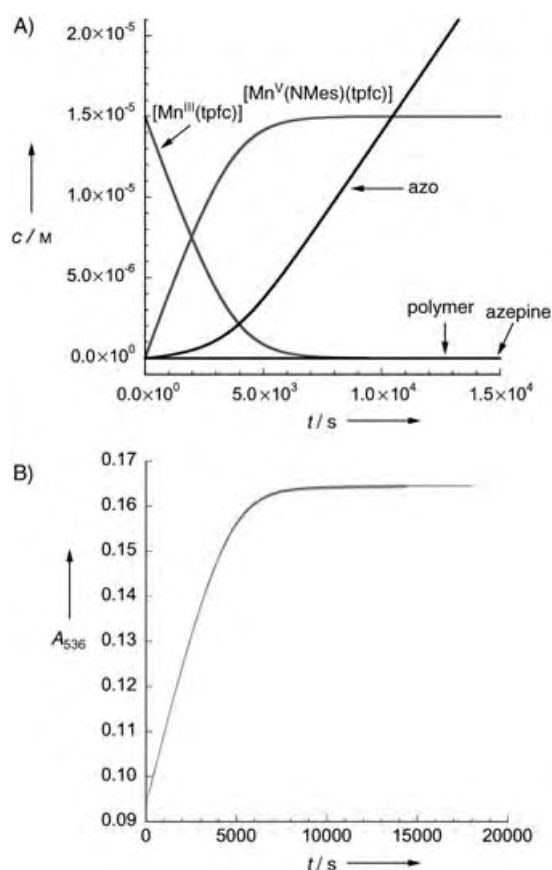


Figure 3. A) Time profiles simulated by the program KINSIM for the reaction of $[\text{Mn}^{\text{III}}(\text{tpfc})]$ with mesityl azide according to Scheme 2. Simulation conditions: $c_{[\text{Mn}^{\text{III}}(\text{tpfc})]} = 15 \mu\text{M}$, $c_{\text{MesN}_3} = 5.3 \text{ mM}$, $k_1 = 8.3 \times 10^{-7} \text{ s}^{-1}$, $k_{\text{isc}} = 2.0 \times 10^7 \text{ s}^{-1}$,^[27] $k_r = 1.0 \times 10^{10} \text{ s}^{-1}$, $k_{-r} = 1.0 \times 10^7 \text{ s}^{-1}$, $k_2 = k_d = 8.0 \times 10^9 \text{ M}^{-1} \text{ s}^{-1}$, $k_p = 2.0 \times 10^6 \text{ M}^{-1} \text{ s}^{-1}$. B) Simulated (gray) and experimental (black) data for the formation of $[\text{Mn}^{\text{V}}(\text{NMes})(\text{tpfc})]$ from the reaction of $15 \mu\text{M}$ $[\text{Mn}(\text{tpfc})]$ and 5 mM mesityl azide.

for the reaction of a manganese corrole with aryl azides to give imido metal complexes. In this mechanism, the transition-metal complex captures a triplet nitrene formed by thermal or photochemical activation of the organic azide. The compelling evidence presented for this mechanism is 1) complex dependence of the kinetics on metal concentration with zeroth order over 30 % of the reaction), 2) the kinetics have been modeled successfully for the reaction mechanism described in Scheme 2, and 3) substituents in both *ortho* positions (Me or Cl, but not F) are required. Contrary to conventional wisdom that highly reducing metal complexes are needed for a reaction with organic azides, we have demonstrated that effective imido metal formation via nitrene capture does not require a highly reducing center. Investigations into harnessing this mechanistic paradigm for selective nitrene transfer under thermal or photochemical catalysis are in progress.

Experimental Section

Compounds were prepared and handled by standard vacuum-line and glove-box techniques. Toluene and acetonitrile were predried over

molecular sieves and distilled over CaH_2 prior to use. When required, solvents were deoxygenated by freeze/pump/thaw cycles. Deuterated solvents were purchased from Cambridge Isotopes and used without further purification. All other solvents and reagents were of reagent grade and used as received. The syntheses of $\text{H}_3(\text{tpfc})$,^[28,29] $[\text{Mn}(\text{tpfc})]$,^[30] $[\text{Cr}(\text{tpfc})(\text{py}_2)]$,^[31] $[\text{Mn}(\text{tpfc})(\text{NMes})]$,^[9] (Mes = 2,4,6- $(\text{CH}_3)_3\text{C}_6\text{H}_2$), $[\text{Mn}(\text{tpfc})(\text{NAr})]$,^[9] (Ar = 2,4,6- $\text{Cl}_3\text{C}_6\text{H}_2$), $[\text{Mn}(\text{tpfc})(\text{NAr})]$,^[10] (Ar' = 2,6- $\text{Cl}_2\text{C}_6\text{H}_3$), $[\text{Cr}(\text{tpfc})(\text{NMes})]$,^[10] and $[\text{Cr}(\text{tpfc})(\text{NAr})]$,^[10] followed previously described methods. All azides were prepared by using the Sandmeyer reaction or slight variations thereof.^[7,8] Azo compounds were compared to authentic samples. Photolysis experiments were carried out with a Hanovia Model 673A-0360 550 W medium-pressure mercury arc lamp. Rate measurements were carried out by conventional UV/Vis spectroscopy on a Shimadzu UV-2501 spectrophotometer equipped with a temperature-controlled cell holder. Formation of $[\text{Mn}^{\text{V}}(\text{NMes})(\text{tpfc})]$ was monitored at 536 nm, $c_{[\text{Mn}(\text{tpfc})]} = 15$ or $30 \mu\text{M}$, and $c_{\text{MesN}_3} = 2.0\text{--}12.0 \text{ mM}$ at $(80 \pm 0.2)^\circ\text{C}$.

Received: November 17, 2004

Revised: June 13, 2005

Published online: August 29, 2005

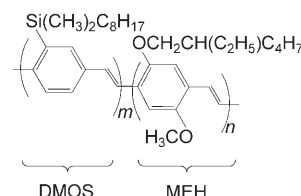
Keywords: azides · imido ligands · kinetics · macrocyclic ligands · manganese

- [1] H. C. Kolb, M. G. Finn, K. B. Sharpless, *Angew. Chem.* **2001**, *113*, 2056; *Angew. Chem. Int. Ed.* **2001**, *40*, 2004.
- [2] R. Huisgen, J. Sauer, H. J. Sturm, J. H. Markgraf, *Chem. Ber.* **1960**, *93*, 2106.
- [3] Z. P. Demko, K. B. Sharpless, *Angew. Chem.* **2002**, *114*, 2117; *Angew. Chem. Int. Ed.* **2002**, *41*, 2113.
- [4] Z. P. Demko, K. B. Sharpless, *Angew. Chem.* **2002**, *114*, 2114; *Angew. Chem. Int. Ed.* **2002**, *41*, 2110.
- [5] R. A. Eikey, M. M. Abu-Omar, *Coord. Chem. Rev.* **2003**, *243*, 83.
- [6] D. E. Wigley, *Prog. Inorg. Chem.* **1994**, *42*, 239.
- [7] S. Murata, S. Abe, H. Tomioka, *J. Org. Chem.* **1997**, *62*, 3055.
- [8] E. Leyva, D. Munoz, M. S. Platz, *J. Org. Chem.* **1989**, *54*, 5983.
- [9] R. A. Eikey, S. I. Khan, M. M. Abu-Omar, *Angew. Chem.* **2002**, *114*, 3743; *Angew. Chem. Int. Ed.* **2002**, *41*, 3591.
- [10] N. Y. Edwards, R. A. Eikey, M. I. Loring, M. M. Abu-Omar, *Inorg. Chem.* **2005**, *44*, 3700–3708.
- [11] G. LaMonica, S. Cenini, *J. Chem. Soc. Dalton Trans.* **1980**, 1145.
- [12] G. L. Hillhouse, J. E. Bercaw, *Organometallics* **1982**, *1*, 1025.
- [13] J. H. Osborne, A. L. Rheingold, W. C. Troglor, *J. Am. Chem. Soc.* **1985**, *107*, 7945.
- [14] D. M. Antonelli, W. P. Scafer, G. Parkin, J. E. Bercaw, *J. Organomet. Chem.* **1993**, *462*, 213.
- [15] G. Proulx, R. G. Bergman, *J. Am. Chem. Soc.* **1995**, *117*, 6382.
- [16] G. Proulx, R. G. Bergman, *Organometallics* **1996**, *15*, 684.
- [17] M. G. Fickes, W. M. Davis, C. C. Cummins, *J. Am. Chem. Soc.* **1995**, *117*, 6384.
- [18] S. Patai, Z. Rappoport in *The Chemistry of Azides* (Eds.: S. Patai, Z. Rappoport), Wiley-Interscience, New York, **1995**.
- [19] W. T. Borden, N. P. Gristan, C. M. Hadad, W. L. Karney, C. R. Kemnitz, M. S. Platz, *Acc. Chem. Res.* **2000**, *33*, 765.
- [20] N. P. Gristan, Z. Zhu, C. M. Hadad, M. S. Platz, *J. Am. Chem. Soc.* **1999**, *121*, 1202.
- [21] N. P. Gristan, D. Tigelaar, M. S. Platz, *J. Phys. Chem. A* **1999**, *103*, 4465.
- [22] E. Leyva, M. S. Platz, G. Persy, J. Wirz, *J. Am. Chem. Soc.* **1986**, *108*, 3783.
- [23] R. J. Sundberg, S. R. Sutar, M. Brenner, *J. Am. Chem. Soc.* **1972**, *94*, 513.
- [24] W. L. Karney, W. T. Borden, *J. Am. Chem. Soc.* **1997**, *119*, 3347.

- [25] B. A. Barshop, R. F. Wrenn, C. Frieden, *Anal. Biochem.* **1983**, *130*, 134.
- [26] C. T. Zimmerle, C. Frieden, *Biochem. J.* **1989**, *258*, 381.
- [27] N. P. Gritsan, A. D. Gudmundsdottir, D. Tigelaar, M. S. Platz, *J. Phys. Chem. A* **1999**, *103*, 3458.
- [28] Z. Gross, N. Galili, I. Saltsman, *Angew. Chem.* **1999**, *111*, 1530; *Angew. Chem. Int. Ed.* **1999**, *38*, 1427.
- [29] Z. Gross, N. Galili, L. Simkhovich, I. Saltsman, M. Botoshansky, D. Blaser, R. Boese, I. Goldberg, *Org. Lett.* **1999**, *1*, 599.
- [30] Z. Gross, G. Golubkov, L. Simkhovich, *Angew. Chem.* **2000**, *112*, 4211; *Angew. Chem. Int. Ed.* **2000**, *39*, 4045.
- [31] A. E. Meirer-Callahan, A. J. DiBilio, L. Simkhovich, A. Mahammed, I. Goldberg, H. B. Gray, Z. Gross, *Inorg. Chem.* **2001**, *40*, 6788.

done little to unravel the role of morphology in the energy-transfer process. Even nearfield scanning optical microscopy, which has been used to study polymer blends at the sub-100-nm scale,^[10,11] lacks the spatial resolution in most cases to study individual morphological regions that can be as small as a few nanometers.

Herein, we take an alternative approach by using single-molecule spectroscopy (SMS) to study energy transfer across a molecular interface in isolated, single diblock polymer DMOS-co-MEH chains (DMOS = 2-dimethyloctylsilyl-1,4-



Conjugated Polymers

DOI: 10.1002/anie.200501388

Single-Molecule Studies of Electronic Energy Transfer in a Diblock Conjugated Polymer^{*,**}

John K. Grey, Doo Young Kim, Young Jong Lee,
Jose J. Gutierrez, Nam Luong, John P. Ferraris, and
Paul F. Barbara^{*}

Electronic energy transfer across a molecular interface between two dissimilar conjugated polymers in a blend is a critical process for many promising optoelectronic device strategies.^[1–9] Owing to the short range of electronic energy transfer, this process should in principle be strongly modulated by molecular-scale morphology in the interfacial regions of polymer blends. The most common approach for characterizing energy transfer in polymer blends, namely, ensemble fluorescence measurements, is obscured by morphological and kinetic heterogeneity of these materials and thus has

phenylenevinylene; MEH = 2-methoxy-5-(2'-ethylhexyloxy)-1,4-phenylenevinylene) comprised of an energy-donor block (DMOS, $\lambda_{\text{max}}^{\text{em}} = 490$ nm) and an energy-acceptor block (MEH, $\lambda_{\text{max}}^{\text{abs}} = 500$ nm). The sizes of these molecules (≈ 10 nm) make them excellent models for developing a detailed understanding at the molecular level of energy transfer between a molecular interface of two dissimilar polymers. SMS has been used effectively to study intramolecular energy transfer in bi- and multichromophoric dendrimers,^[12–15] end-capped polymers,^[16,17] and conjugated homopolymers.^[18,19] The SMS approach reported here provides detailed information at the molecular level on how energy transfer is influenced by polymer morphology within a single diblock polymer chain.

Figure 1 shows ensemble fluorescence spectra (solid lines) for DMOS (a) and MEH (b) homopolymers at $T = 298$ K dissolved at high dilution in a polymethyl methacrylate (PMMA) polymer host. These spectra were obtained by summing single-molecule spectra for isolated polymer chains. For comparison we also show absorption spectra (dotted lines) for the homopolymers which were acquired in dilute liquid solutions (solvent) rather than in polymer thin films because of the weak absorption of the latter. These data indicate that excitation wavelengths of 415 nm and 488 nm selectively excite DMOS and MEH, respectively, and also demonstrate a good spectral overlap of the emission bands of DMOS and the absorption bands of MEH which is important for promoting energy transfer by the Förster mechanism (the dominant mechanism for conjugated polymers).^[20,21]

Analogous ensemble spectra for the DMOS-co-MEH diblock polymer are shown in Figure 1c. The emission spectra of DMOS-co-MEH (single molecules and ensembles) are well-modeled by a sum of MEH- and DMOS-like spectral components and do not show evidence of excimer emission between the two blocks. It is apparent from the spectrum of the diblock polymer in Figure 1c (solid line, $\lambda_{\text{ex}} = 415$ nm) that energy transfer occurs from the DMOS block to the MEH block with an overall efficiency of approximately 75%. The spectrum obtained upon excitation at 488 nm (dashed line) in Figure 1c demonstrates, as expected, that direct

[*] Dr. J. K. Grey, D. Y. Kim, Dr. Y. J. Lee, Prof. Dr. P. F. Barbara
Center for Nano- and Molecular Science and Technology and
Department of Chemistry and Biochemistry
University of Texas at Austin
Austin TX 78712 (USA)
Fax: (+1) 512-471-3389
E-mail: p.barbara@mail.utexas.edu

Prof. Dr. J. J. Gutierrez, N. Luong, Prof. Dr. J. P. Ferraris
Department of Chemistry
University of Texas at Dallas
Richardson TX 75083 (USA)

[**] We gratefully acknowledge financial support from the Basic Energy Sciences Program of the Department of Energy, the Keck Foundation, the Robert A. Welch Foundation, and SPRING. J.K.G. thanks the Petroleum Research Fund of the American Chemical Society for a fellowship. J.J.G., N.L., and J.P.F. acknowledge support from Los Alamos National Laboratory.

Supporting information for this article is available on the WWW under <http://www.angewandte.org> or from the author.

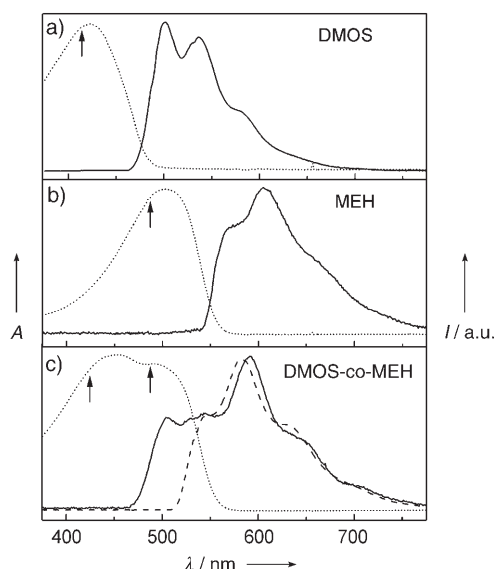


Figure 1. Absorption spectra recorded on dilute solutions (.....) and emission spectra from dilute thin-film ensembles (—) of a) DMOS, b) MEH, and c) DMOS-co-MEH. Ensemble spectra were obtained by summing single-molecule spectra for each polymer. Excitation wavelengths are indicated by arrows on the respective absorption bands (DMOS $\lambda_{\text{ex}} = 415$ nm; MEH $\lambda_{\text{ex}} = 488$ nm). Part (c) shows the dependence of the emission spectra from the DMOS-co-MEH ensemble at 298 K on the excitation wavelength: $\lambda_{\text{ex}} = 415$ nm (—); $\lambda_{\text{ex}} = 488$ nm (-----).

excitation of the MEH block does not lead to uphill energy transfer from the MEH block to the DMOS block.

Further insight into the energy-transfer process was gained in a molecule-by-molecule analysis of the spectroscopy of DMOS-co-MEH. Typical spectra for single isolated DMOS-co-MEH molecules excited in the donor DMOS block at 415 nm are shown in Figure 2a. Single-molecule spectra were acquired individually over approximately 3-minute periods, during which time the spectra did not vary, which indicates that spectral diffusion and photochemistry are not complicating factors for these measurements. A histogram (Figure 2b) of the peak wavelength for the DMOS-co-MEH molecules reveals three distinct classes: 1) 490–530 nm, 2) 535–560 nm, and 3) 570–605 nm. Sub-ensemble spectra (Figure 2c) for the different classes were generated by sorting the spectra according to the peak wavelength. Class 1 corresponds to almost pure DMOS-like emission ($\lambda_{\text{max}}^{\text{em}} = 505$ nm). Class 2 ($\lambda_{\text{max}}^{\text{em}} = 550$ nm) and 3 ($\lambda_{\text{max}}^{\text{em}} = 590$ nm), in contrast, closely correspond to the previously reported blue- and red-light-emitting morphological forms of the MEH homopolymer^[19,22] and thus imply efficient DMOS-to-MEH energy transfer.

It is informative to directly calculate the distribution of apparent energy-transfer efficiencies for the diblock single molecules. This has been determined by fitting the blue edge of each spectrum to a model DMOS spectrum and then using the amplitude of the donor spectrum to determine the fraction (f_D) of the donor intensity for each spectrum. Figure 3a shows a histogram of apparent energy-transfer efficiencies $(1-f_D)^{[23]}$ for all DMOS-co-MEH single molecules excited at 415 nm. The results clearly demonstrate that

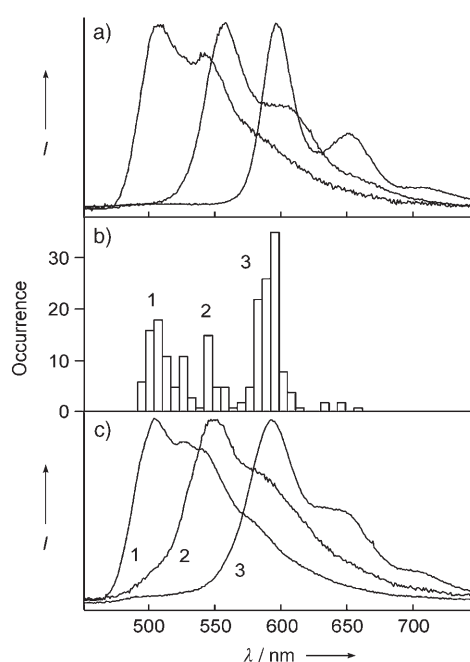


Figure 2. a) Typical single-molecule spectra for DMOS-co-MEH excited at 415 nm, b) histogram of peak wavelengths of 210 single DMOS-co-MEH molecules, and c) sub-ensemble spectra excited at 415 nm. Sub-ensemble spectra were sorted according to their wavelength distribution ranges (labeled 1, 2, and 3), which correspond to 1) DMOS (500–530 nm), 2) blue MEH (540–560 nm), and 3) red MEH (570–600 nm).

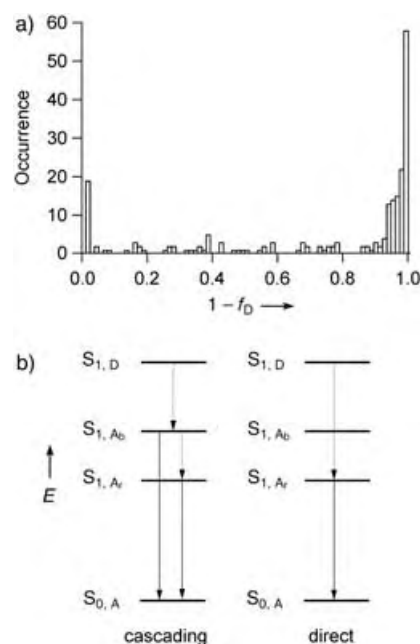


Figure 3. a) Apparent energy-transfer efficiencies $(1-f_D)$ for single DMOS-co-MEH molecules excited at 415 nm. b) Schematic diagrams illustrating energy transfer to red-light-emitting MEH sites in the diblock polymer: left) cascading energy transfer to blue-light-emitting MEH followed by emission and intrachain energy funneling to red-light-emitting MEH sites; right) direct energy transfer to red MEH. Spectroscopic states are represented by solid horizontal lines, and energy-transfer and emission transitions are shown as vertical dotted and solid lines with arrows, respectively.

the energy-transfer process in the diblock conjugated polymer sample is highly heterogeneous. The molecules that show a low energy-transfer efficiency (< 0.1) in the histogram consist mostly of diblocks that exhibit DMOS-only emission and closely correspond to class 1 in Figure 2c. Successive SMS scans of the same region of the sample using excitation alternatively at 415 and 488 nm demonstrated that these molecules contain extremely short MEH blocks, which lead to the lower efficiency of energy transfer. Thus, the major factor responsible for the low efficiency of energy transfer for a diblock molecule is a short MEH (acceptor) block. Presumably, energy transfer is slower for the shorter MEH block molecules owing to a smaller number of effective acceptor chromophores.

Two-color (415 nm/488 nm) excitation experiments were also carried out on the individual homopolymers to measure the contribution of “cross-talk” to the observed energy-transfer efficiencies by exciting MEH at 415 nm. The relative excitation efficiency of DMOS and MEH blocks excited at 415 nm was found to be greater than 9:1, which demonstrates that energy transfer rather than direct excitation is the dominant mechanism for the excitation of MEH. The data were not corrected for the small contribution from direct excitation.

It has recently been shown that MEH homopolymer chains can be roughly classified into blue- and red-light-emitting chains. The red-light-emitting single molecules have been shown to comprise a small number of low-energy “red” chromophores, due to chain–chain contacts, which act as acceptors of electronic energy from the much greater number of blue chromophores.^[19,24] In contrast, the blue-light-emitting morphological forms of MEH lack red chromophores and thus directly emit from the blue chromophores. One of the main results of this study is that the presence of the DMOS block induces folding of the MEH block which leads to a larger fraction of red-light-emitting MEH sites in the diblock polymer, as compared to the MEH homopolymer. Over 70 % of all single diblock polymer molecules studied exhibit high apparent efficiencies of energy transfer (> 0.8), with the MEH red-light-emitting form (class 3 in Figure 2c) being the dominant emitting species. It should be emphasized that the efficiency of energy transfer from DMOS to MEH is close to unity for a majority of both red- and blue-light-emitting molecules. The red and blue forms differ, however, in the ultimate sink for excitation energy, that is, the red or blue MEH chromophores. The reason for a larger fraction of red sites in the diblock case has not been established, but we speculate that it may be due to a co-collapse of both blocks to favor a more collapsed chain conformation, and hence a larger number of chain–chain contacts.

The possible photophysical processes pathways following excitation of the donor block at 415 nm which lead to the red-light-emitting forms are illustrated in Figure 3b. $S_{n,D}$ ($n = 0, 1$) represent the donor states and $S_{n,A}$ represent acceptor states, with the blue and red forms denoted with b and r subscripts, respectively. Interestingly, the fraction of red-light-emitting molecules is a factor of four greater than that observed for an MEH homopolymer of the same molecular weight as the MEH block in the DMOS-co-MEH diblock polymer

(Figure 4). The origin of the greater number of red-light-emitting molecules for the diblock sample relative to the homopolymer samples is revealed in low-temperature SMS studies on diblock and homopolymer samples. Figure 4 shows the distributions of peak wavelengths and sorted sub-ensemble spectra

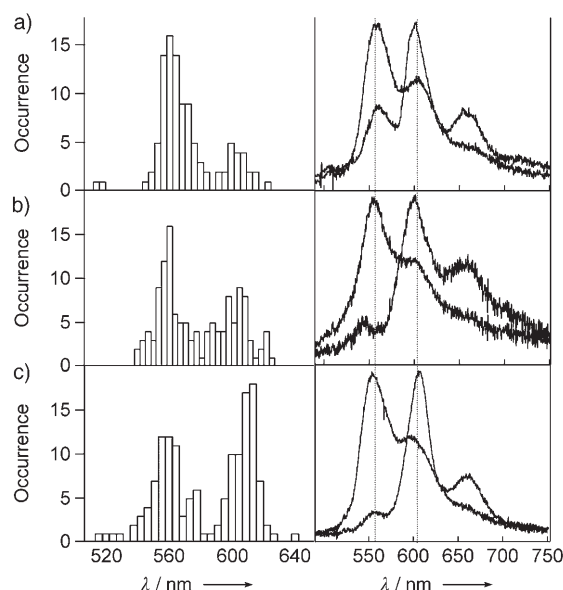


Figure 4. Histograms of peak wavelengths (left) and sorted sub-ensemble spectra (right) for a) MEH ($M_w = 186$ kDa), b) MEH ($M_w = 1000$ kDa), and c) DMOS-co-MEH (MEH block $M_w = 186$ kDa), excited at 488 nm at around 20 K. The dotted vertical lines show the peak wavelength positions of the red- and blue-light-emitting forms of MEH in the diblock polymer as well as the polymers of different molecular weights.

ble spectra of blue- and red-light-emitting species for MEH homopolymer samples ($M_w = 186$ kDa and 1000 kDa, panels a and b, respectively) and single DMOS-co-MEH molecules (MEH block $M_w = 186$ kDa, panel c) excited at 488 nm at around 20 K. Blue-to-red ratios for the 186-kDa MEH homopolymer and the DMOS-co-MEH diblock polymer are around 4:1 and 1:1, respectively, with the latter being similar to the high-molecular-weight MEH homopolymer sample ($M_w = 1000$ kDa, Figure 4b). This establishes that the MEH region of the diblock in fact contains higher number of red sites on average than an MEH homopolymer of the same length. The significantly better spectral resolution achieved at low temperature allowed for a precise, quantitative determination of the relative yields of the blue and red emission bands for MEH.

Unfortunately, the experimental data did not allow us to establish whether energy transfer from DMOS to red chromophores of MEH proceeds predominantly by a cascading or a direct mechanism (see Figure 3). If the MEH block has very few red chromophores per MEH block, as suggested by experiments on pure MEH,^[19] the cascading mechanism would be expected to be more rapid as it involves energy transfer from DMOS to blue chromophores in the first step.

In this report, single-molecule spectroscopy on diblock donor/acceptor polymers has been used to show that energy

transfer across a polymer–polymer interface can be highly heterogeneous as a result of morphological features at the interface. Furthermore, the results demonstrate that the morphology of the chains that comprise the diblock can differ substantially from the morphology of the separate homopolymers.

Experimental Section

Dilute thin-film samples of poly(2-methoxy,5-(2'-ethylhexyloxy)-*p*-phenylenevinylene)-co-poly(2-dimethyloctylsilyl-*p*-phenylenevinylene) (DMOS-co-MEH; $M_w = 312$ kDa, polydispersity index: 1.18) were prepared according to a reported procedure,^[19] and the synthesis and characterization of DMOS/MEH are described in detail in the Supporting Information. Typically, samples were diluted in a solution of PMMA (3 % w/w) in toluene and spin-cast onto glass substrates to yield films of approximately 100-nm thickness. Samples were then coated with either gold or aluminum (≈ 200 nm) to prevent oxygen and water from diffusing into the PMMA layer. Single molecules were excited with the doubled output (415 nm) of a Ti:sapphire laser centered at 830 nm, and the 457.9 nm and 488 nm lines of an argon-ion laser and images and spectra were obtained from a confocal scanning microscope apparatus described elsewhere.^[19] Excitation intensities were approximately 200 W cm^{-2} .

Received: April 21, 2005

Revised: June 15, 2005

Published online: September 1, 2005

Keywords: energy transfer · fluorescence · interfaces · polymers · single-molecule studies

- [14] R. Gronheid, J. Hofkens, F. Köhn, T. Weil, E. Reuther, K. Müllen, F. De Schryver, *J. Am. Chem. Soc.* **2002**, *124*, 2418.
- [15] R. Métivier, F. Kulzer, T. Weil, K. Müllen, T. Basché, *J. Am. Chem. Soc.* **2004**, *126*, 14364.
- [16] D. Beljonne, G. Pourtois, C. Silva, E. Hennebicq, L. M. Herz, R. H. Friend, G. D. Scholes, S. Setayesh, K. Müllen, J.-L. Brédas, *Proc. Natl. Acad. Sci. USA* **2002**, *99*, 10982.
- [17] E. Hennebicq, G. Pourtois, G. D. Scholes, L. Herz, D. Russell, C. Silva, S. Setayesh, A. C. Grimsdale, K. Muellen, J. L. Brédas, D. Beljonne, *J. Am. Chem. Soc.* **2005**, *127*, 4744.
- [18] D. Hu, J. Yu, K. Wong, B. Bagchi, P. J. Rossky, P. F. Barbara, *Nature* **2000**, *405*, 1030.
- [19] J. Yu, D. Hu, P. F. Barbara, *Science* **2000**, *289*, 1327.
- [20] J.-L. Brédas, D. Beljonne, V. Coropceanu, J. Cornil, *Chem. Rev.* **2004**, *104*, 4971.
- [21] a) G. D. Scholes, *Annu. Rev. Phys. Chem.* **2003**, *54*, 57; b) B. J. Schwartz, *Annu. Rev. Phys. Chem.* **2003**, *54*, 141.
- [22] Z. Yu, P. F. Barbara, *J. Phys. Chem. B* **2004**, *108*, 11321.
- [23] The expression for energy-transfer efficiency is given by: $E_{ET} = 1 - \frac{\varphi_{DA}}{\varphi_D}$, where φ_D and φ_{DA} are the quantum yields of the donor and donor-acceptor ensemble, respectively. Owing to lack of experimental data on the emission quantum yields, apparent efficiencies of energy transfer ($1 - f_D$) were determined here using relative intensities.
- [24] D. Hu, J. Yu, P. F. Barbara, *J. Am. Chem. Soc.* **1999**, *121*, 6936.

- [1] J. J. M. Halls, K. Pichler, R. H. Friend, S. C. Moratti, A. B. Holmes, *Appl. Phys. Lett.* **1996**, *68*, 3120.
- [2] J.-I. Lee, I.-N. Kang, D.-H. Hwang, H.-K. Shim, S. C. Jeoung, D. Kim, *Chem. Mater.* **1996**, *8*, 1925.
- [3] J. J. M. Halls, J. Cornil, D. A. dos Santos, R. Silbey, D.-H. Hwang, A. B. Holmes, J.-L. Brédas, R. H. Friend, *Phys. Rev. B* **1999**, *60*, 5721.
- [4] M. A. Stevens, C. Silva, D. M. Russell, R. H. Friend, *Phys. Rev. B* **2001**, *63*, 165213.
- [5] A. C. Arias, J. D. MacKenzie, R. Stevenson, J. J. M. Halls, M. Inbasekaran, E. P. Woo, D. Richards, R. H. Friend, *Macromolecules* **2001**, *34*, 6005.
- [6] A. R. Buckley, M. D. Rahn, J. Hill, J. Cabanillas-Gonzalez, A. M. Fox, D. D. C. Bradley, *Chem. Phys. Lett.* **2001**, *339*, 331.
- [7] H. J. Snaith, A. C. Arias, A. C. Morteani, C. Silva, R. H. Friend, *Nano Lett.* **2002**, *2*, 1353.
- [8] Y. J. Ahn, G. W. Kang, C. H. Lee, I. S. Yeom, S. H. Jin, *Synth. Met.* **2003**, *137*, 1447.
- [9] A. C. Morteani, P. Sreearunothai, L. Herz, R. H. Friend, C. Silva, *Phys. Rev. Lett.* **2004**, *92*, 247402.
- [10] J. Chappell, D. G. Lidzey, P. C. Jukes, A. M. Higgins, R. L. Thompson, S. O'Connor, I. Grizzi, R. Fletcher, J. O'Brien, M. Geoghegan, R. A. L. Jones, *Nat. Mater.* **2003**, *2*, 616.
- [11] R. Stevenson, M. Granstrom, D. Richards, *Appl. Phys. Lett.* **1999**, *75*, 1574.
- [12] M. Maus, R. De, M. Lor, T. Weil, S. Mitra, U.-M. Wiesler, A. Herrmann, J. Hofkens, T. Vosch, K. Müllen, F. De Schryver, *J. Am. Chem. Soc.* **2001**, *123*, 7668.
- [13] M. Cotlet, R. Gronheid, S. Habuchi, A. Stefan, A. Barbafina, K. Müllen, J. Hofkens, F. De Schryver, *J. Am. Chem. Soc.* **2003**, *125*, 13609.

DNA Cleavage

DOI: 10.1002/anie.200501956

2-Deoxyribonolactone Lesions in X-ray-Irradiated DNA: Quantitative Determination by Catalytic 5-Methylene-2-furanone Release**

*Marina Roginskaya, Yuriy Razskazovskiy, and William A. Bernhard**

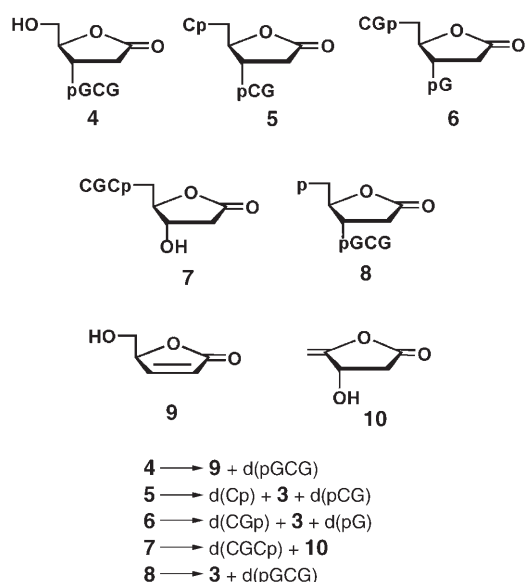
The C1'-oxidized abasic DNA lesion 2-deoxyribonolactone (dL, **1**) has attracted significant attention in recent years owing to its potential mutagenicity, which is associated with

[*] M. Roginskaya, Prof. W. A. Bernhard
Department of Biochemistry and Biophysics
University of Rochester
Rochester, NY 14642 (USA)
Fax: (+1) 585-275-6005
E-mail: William_Bernhard@urmc.rochester.edu
Prof. Y. Razskazovskiy
Department of Physics
East Tennessee State University,
Johnson City, TN 37614 (USA)

[**] We thank Prof. David M. Close for helpful discussions. We are grateful for support from PHS Grant 2-RO1-CA32546, awarded by NCI of DHHS, and from Grant CC5956 awarded by Research Corporation.



Supporting information for this article is available on the WWW under <http://www.angewandte.org> or from the author.



Scheme 2. Structures and decomposition patterns of dL-containing oligonucleotides isolated from X-irradiated d(CGCG) and d(pGCGGp) films.

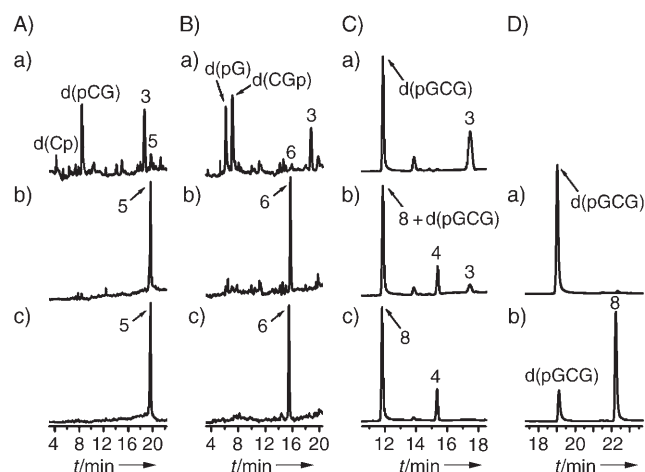


Figure 2. Thermal decomposition of **5**, **6**, and **8**. Reaction mixtures contained 50 mM sodium acetate buffer, pH 5.2, 10 mM spermine (added before or after heating). A–C: RP HPLC; a) 20 min at 90°C with spermine; b) as a) but heated without spermine; c) no heat. HPLC conditions: Gemini C18 4.6 mm×250 mm analytical column (Phenomenex) washed with ammonium acetate (40 mM) as running phase and acetonitrile as eluent (1–8% acetonitrile over 20 min, nonlinear gradient type 5 in the original Water's definition). D: Ion-exchange HPLC; a) 20 min at 90°C with spermine; b) no heat. HPLC conditions: Dionex DNAPac PA-100 column washed with ammonium acetate (40 mM)/ acetonitrile (10%) running phase and a solution of NaCl as eluent (5–250 mM NaCl over 20 min, linear gradient, 1 mL min^{−1}).

All dLs shown in Figure 2 (**5**, **6**, and **8**) are heat-resistant at pH 5.2 in the absence of a catalyst (see panels b of Figure 2 A–C). Furthermore, **5**, **6**, and **8** readily decompose with release of **3** upon heating under the same conditions but with spermine (10 mM) added. Thus these dLs show decomposition patterns analogous to irradiated calf thymus DNA.^[8] All dLs in

Figure 2 undergo quantitative decomposition; **3** and its corresponding phosphate fragments are formed in nearly stoichiometric ratios (with the exception of d(Cp) for **5**). These results show that the yield of **3**, released upon catalytic treatment of dL-containing oligonucleotides, correlates well with the yield of its dL precursor.

The 5'-terminal dL **4** undergoes about 80% conversion upon heating for 20 min at 90°C with spermine (10 mM) at pH 5.2 (Figure 3 A a), while its 3'-terminal analogue **7** is stable

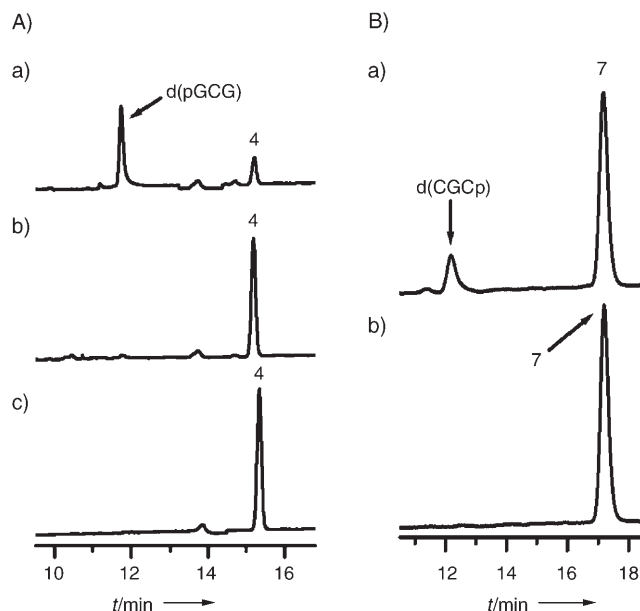


Figure 3. Thermal decomposition of **4** (A) and **7** (B). A) sodium acetate buffer (50 mM), pH 5.2, spermine (10 mM); a) 20 min at 90°C with spermine; b) as a) but heated without spermine; c) no heat; HPLC conditions: as in Figure 2 A–C. B) ammonium acetate (40 mM) buffer, pH 6.8, spermine (50 mM) a) 30 min at 90°C with spermine; b) no heat; HPLC conditions: Luna C18 4.6 mm×250 mm analytical column (Phenomenex) washed with ammonium acetate (40 mM) and acetonitrile as eluent (1–9.6% acetonitrile over 20 min, linear gradient, 1 mL min^{−1}).

under these conditions (results not shown). Significant decomposition of **7** required more prolonged heating at pH 6.8 (30 min or more, Figure 3 B, a). The optical absorption of the butenolides **9** and **10** (see Scheme 2) supposedly formed upon decomposition of **4** and **7** respectively, is apparently too weak at 254 nm to be detected under the conditions of this study.

The total yield of dL was estimated for the X-irradiated films of d(pGCGGp) (Figure 4). All four types of dL formed from d(pGCGGp) release **3** upon thermal catalytic decomposition; the yield of **3** therefore, is assumed to correlate with the total yield of dL. This assumption is justified by the quantitative release of **3** upon decomposition of phosphorylated dL-containing tetramers and by the stability of **3** under the experimental conditions employed (at slightly acidic pH values).^[8] The inset in Figure 4 shows the dose dependence for the formation of **3**; the radiation yield of **3**, $0.0103 \pm 0.0004 \mu\text{mol J}^{-1}$, was obtained from the slope of the linear fit to the experimental data. This yield is 3.4-fold lower than the

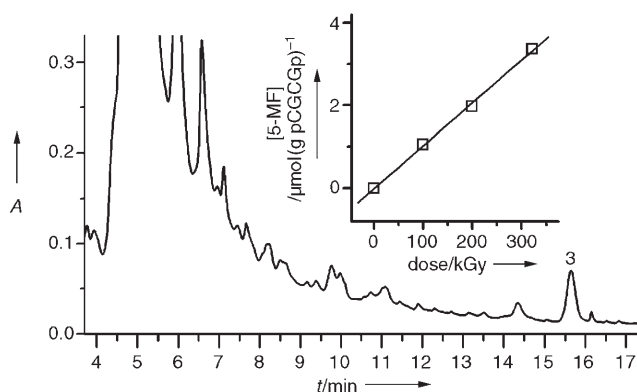


Figure 4. Release of **3** from the solution of the X-irradiated d(pCGCGp) film. The reaction mixture containing ammonium acetate buffer (40 mM), pH 6.8, and spermine (10 mM) was heated 25 min at 90 °C. The inset shows the dose dependence of the release of **3**. HPLC conditions: Gemini C18 4.6 mm × 250 mm analytical column (Phenomenex) washed with 40 mM ammonium acetate as a running phase, with acetonitrile as eluent (4–9.6% acetonitrile over 20 min, gradient type 5, 1 mL min^{−1}).

yield of **3** obtained for the X-irradiated films of calf thymus DNA^[8] subjected to analogous post-irradiation treatment. This degree of variation is not surprising given the large differences in the primary and tertiary structures of d(pCGCGp) when compared with genomic DNA.

In conclusion, we have demonstrated that catalytic decomposition of dL isolated from X-irradiated d(CGCG) and d(pCGCG) films quantitatively produces **3**. This finding supports our earlier hypothesis that **1** is the major, perhaps only, precursor of **3** released from X-irradiated highly polymerized DNA.^[8] Our data suggest that quantification of the yield of **3** released upon catalytic decomposition of dL can be applied as a method for selective quantitative detection of lesion **1** in DNA.

Experimental Section

Details of the isolation and characterization of dL-containing oligonucleotides are included in the Supporting Information. The product **3** used as a reference compound in HPLC experiments was synthesized according to a published procedure.^[13] All the DNA oligonucleotides used in this study were purified by semipreparative RP HPLC. The “dry” films containing the oligonucleotides (≈500 μg) were prepared from aqueous solution (200 μL) dried over saturated NaOH (5% relative humidity) on a microscope glass slide and then subjected to vacuum overnight.

X-irradiation of the films: A Phillips tube (tungsten anode) operated at 55 kV and 20 mA, giving a dose rate of 163 kGy h^{−1}, was used as the X-ray source. The dose rate was measured with radiochromic films (Far West Technology, Inc.). Typically, the DNA films were irradiated to a dose of ≈330 kGy. For the measurements of the radiation yield of **3** released from d(pCGCGp), the d(pCGCGp) films were irradiated to doses from 100 to 326 kGy. Immediately upon irradiation, the films were dissolved in H₂O (200 μL), transferred into microcentrifuge tubes, and stored at −20 °C until used.

HPLC analysis: Typically, the reaction mixture (200 μL) containing the oligonucleotide (50–200 μg) was injected. All HPLC experiments were performed at 30 °C and pH 6.8, with UV detection at λ = 254 nm. The retention times of the products were determined by

coinjection of a corresponding reference compound. The yields of released products were quantified from HPLC peak areas as previously described.^[14] For the measurements of the radiation yield of **3** released from d(pCGCGp), the yield of **3** was quantified by coinjection of a known amount of authentic **3**.

Thermal decomposition of 2-deoxyribonolactones: Typically, the reaction mixture (200 μL) of the dL-containing tetramer (50 μL), (≈20–50 μM final concentration), sodium acetate (50 mM), and spermine (10 mM) at pH 5.2 was heated for 20 min (unless otherwise stated) at 90 °C and then cooled to 4 °C. For thermal decomposition without spermine, the spermine was added after the reaction mixture was heated and cooled. These conditions have been optimized in our previous work for the maximum release of **3**.^[8] As shown herein, the loss of **3** owing to its decomposition and/or side reactions does not exceed 10% under the experimental conditions employed.

Received: June 6, 2005

Published online: September 1, 2005

Keywords: DNA cleavage · DNA · oligonucleotides · X-rays

- [1] a) N. Berthet, Y. Roupioz, J.-F. Constant, M. Kotera, J. Lhomme, *Nucleic Acids Res.* **2001**, *29*, 2725–2732; b) K. M. Kroeger, Y. L. Jiang, Y. W. Kow, M. F. Goodman, M. M. Greenberg, *Biochemistry* **2004**, *43*, 6723–6733; c) V. Faure, J. F. Constant, P. Dumy, M. Saparbaev, *Nucleic Acids Res.* **2004**, *32*, 2937–2946; d) M. M. Greenberg, Y. N. Weledji, J. Kim, B. C. Bales, *Biochemistry* **2004**, *43*, 8178–8183.
- [2] a) M. Kuwabara, C. Yoon, T. Goyne, T. Thederahn, D. S. Sigman, *Biochemistry* **1986**, *25*, 7401–7408; b) T. E. Goyne, D. S. Sigman, *J. Am. Chem. Soc.* **1987**, *109*, 2846–2848; c) M. M. Meijler, O. Zelenko, D. S. Sigman, *J. Am. Chem. Soc.* **1997**, *119*, 1135–1136; d) T. Chen, M. M. Greenberg, *J. Am. Chem. Soc.* **1998**, *120*, 3815–3816; e) B. C. Bales, M. Pitie, B. Meunier, M. M. Greenberg, *J. Am. Chem. Soc.* **2002**, *124*, 9062–9063.
- [3] a) R. N. Bose, S. Moghaddas, P. A. Mazzer, L. P. Dudones, L. Joudah, D. Stroup, *Nucleic Acids Res.* **1999**, *27*, 2219–2226; b) M. Pitie, J. Bernadou, B. Meunier, *J. Am. Chem. Soc.* **1995**, *117*, 2935–2936; c) G. A. Neyhart, C. C. Cheng, H. H. Thorp, *J. Am. Chem. Soc.* **1995**, *117*, 1463–1471.
- [4] L. S. Kappen, I. H. Goldberg, *Proc. Natl. Acad. Sci. USA* **1992**, *89*, 6706–6710.
- [5] H. Urata, K. Yamamoto, M. Akagi, H. Hiroaki, S. Uesugi, *Biochemistry* **1989**, *28*, 9566–9569.
- [6] a) C. Decarroz, J. R. Wagner, J. Cadet, *Free Radical Res. Commun.* **1987**, *2*, 295–301; b) G. W. Buchko, J. Cadet, *Can. J. Chem.* **1992**, *70*, 1827–1832.
- [7] a) J. Cadet, R. Teoule, *Bull. Soc. Chim. Fr.* **1975**, 891–895; b) M. Dizdaroglu, D. Schulte-Frohlinde, C. von Sonntag, *Int. J. Radiat. Biol. Relat. Stud. Phys. Chem. Med.* **1977**, *32*, 481–483; c) C. von Sonntag, *The Chemical Basis of Radiation Biology*, Taylor and Francis, New York, **1987**; d) A. A. Shaw, J. Cadet, *Int. J. Radiat. Biol.* **1996**, *70*, 1–6.
- [8] M. Roginskaya, W. A. Bernhard, R. T. Marion, Y. Razskazovskiy, *Radiat. Res.* **2005**, *163*, 85–89.
- [9] K. Sato, M. M. Greenberg, *J. Am. Chem. Soc.* **2005**, *127*, 2806–2807.
- [10] Y. Roupioz, J. Lhomme, M. Kotera, *J. Am. Chem. Soc.* **2002**, *124*, 9129–9135.
- [11] T. Oyoshi, H. Sugiyama, *J. Am. Chem. Soc.* **2000**, *122*, 6313–6314.
- [12] Y. Zheng, T. L. Sheppard, *Chem. Res. Toxicol.* **2004**, *17*, 197–207.
- [13] C. Grundmann, E. Kober, *J. Am. Chem. Soc.* **1955**, *77*, 2332–2333.
- [14] Y. Razskazovskiy, *Radiat. Res.* **2003**, *159*, 543–549.

DOI: 10.1002/anie.200502118

Ruthenium(II) Terdentate CNN Complexes: Superlative Catalysts for the Hydrogen-Transfer Reduction of Ketones by Reversible Insertion of a Carbonyl Group into the Ru–H Bond**

Walter Baratta,* Giorgio Chelucci, Serafino Gladiali, Katia Siega, Micaela Toniutti, Matteo Zanette, Ennio Zangrando, and Pierluigi Rigo

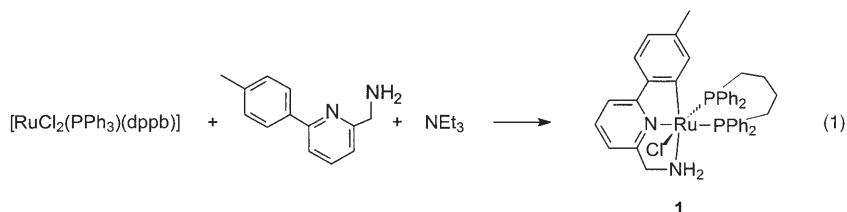
Dedicated to Professor Fausto Calderazzo on the occasion of his 75th birthday

Pincer ECE (E = N, P) transition-metal complexes, in which the terdentate ligands contain two stable five-membered cyclometalated rings, have reached a high level of sophistication and appear extremely attractive for both catalytic and stoichiometric reactions.^[1] The great interest in pincer ligands arises from the high level of control over the reactivity and the stereochemistry that they impose around the metal center as a result of their electronic properties and geometric restrictions. These factors afford highly selective transformations and lead to some unique species of relevance for the investigation of elementary processes.^[2] In spite of the great attention afforded to ruthenium for its versatility in catalysis,^[3] no examples of terdentate ruthenium CNN catalysts have been reported thus far. It is worth noting that CNN complexes are expected to have significantly different reactivity compared to the NCN analogues, mainly because of the different geometrical disposition of the σ -donor carbon atom.

Recently, we have shown that 2-(aminomethyl)pyridine (ampy) shows a high ligand acceleration effect in transfer hydrogenation^[4] catalyzed by ruthenium(II) complexes with phosphane ligands. Thus, complete reduction of many ketones in 2-propanol is quickly achieved with the cyclometalated

complex $[\text{RuCl}(\text{CO})(\text{CP})(\text{ampy})]$ (CP = (2-CH₂-6-MeC₆H₃)PPh₂), with turnover frequencies (TOF values) up to $6.3 \times 10^4 \text{ h}^{-1}$, whereas the derivatives *cis*-[RuCl₂(PP)-(ampy)] (PP = diphosphane) lead to TOF values up to $4.0 \times 10^5 \text{ h}^{-1}$ and *ee* values up to 94% by using chiral diphosphanes.^[5] Since it is well known that 2-phenylpyridine readily gives access to orthometalated CN ruthenium complexes,^[6] we decided to investigate the coordination chemistry of the related 6-(4'-methylphenyl)-2-pyridylmethylamine with the aim of obtaining terdentate CNN complexes. We report herein on novel complexes of formula [RuX(CNN)(dppb)] (X = Cl, H; dppb = Ph₂P(CH₂)₄PPh₂), which are remarkably active catalysts for transfer hydrogenation that afford TOF values up to $2.5 \times 10^6 \text{ h}^{-1}$ with very low loading of catalysts (0.005–0.001 mol%) compared to the most active systems reported.^[2f,7] Evidence is provided that the reduction of the ketone proceeds through the formation of a Ru^{II}-alkoxide complex by insertion of the carbonyl group of the substrate into the Ru–H bond of a ruthenium(II) hydride formed as an intermediate from the chloride complex **1**.

Treatment of [RuCl₂(PPh₃)(dppb)] with an equimolar amount of 6-(4'-methylphenyl)-2-pyridylmethylamine in 2-propanol at reflux in the presence of NEt₃ affords the thermally stable orthometalated ruthenium(II) complex **1**^[8] in high yield [Eq. (1)].



The signals for the diastereotopic NCH₂ protons in the ¹H NMR spectrum are at $\delta = 4.12$ and 3.72 ppm with $^2J(\text{H,H}) = 15.5 \text{ Hz}$. The doublet at $\delta = 52.5 \text{ ppm}$ with a $^3J(\text{C,P}) = 2.7 \text{ Hz}$ in the ¹³C NMR spectrum corresponds to the CH₂N group which is shifted downfield relative to the free ligand ($\delta = 48.2 \text{ ppm}$), thus indicating coordination of the NH₂ group to the metal center. Finally, the signal for the orthometalated carbon atom appears as a doublet of doublets at $\delta = 181.8 \text{ ppm}$ with $^2J(\text{C,P}) = 16.3$ and 7.8 Hz , which is strongly shifted downfield^[6a,9] relative to the free ligand ($\Delta\delta = 54.8$), thus allowing the former formulation to be established unambiguously in solution. The X-ray analysis carried out on a single crystal of **1** shows a severely distorted octahedral environment around the ruthenium center comprising the orthometalated terdentate pyridine ligand, the diphosphane, and a chloride ligand (Figure 1).^[10]

The two N1–Ru–C1 and N1–Ru–N2 bond angles in the five-membered rings are rather small, $80.32(13)$ and $76.45(12)^\circ$, respectively) because of the geometrical constraints of the terdentate ligand. The Ru–N2 bond length of $2.246(3) \text{ \AA}$ is significantly longer than the Ru–N1 bond ($2.046(3) \text{ \AA}$) because of the *trans* influence exerted by the aryl group. The terdentate ligand presents coplanar atoms with the exception of the CH₂NH₂ group, the carbon and amino nitrogen atoms of which are displaced by -0.13 and 0.53 \AA ,

[*] Prof. W. Baratta, Dr. K. Siega, Dr. M. Toniutti, Dr. M. Zanette, Prof. P. Rigo

Dipartimento di Scienze e Tecnologie Chimiche
Università di Udine

Via Cotonificio 108, 33100 Udine (Italy)

Fax: (+39) 0432-558-803

E-mail: inorg@dstc.uniud.it

Dr. G. Chelucci, Prof. S. Gladiali

Dipartimento di Chimica

Università di Sassari

Via Vienna 2, 07100 Sassari (Italy)

Prof. E. Zangrando

Dipartimento di Scienze Chimiche

Università di Trieste

Via L. Giorgieri 1, 34127 Trieste (Italy)

[**] This work was supported by the Ministero della Ricerca Scientifica e Tecnologica (MURST).

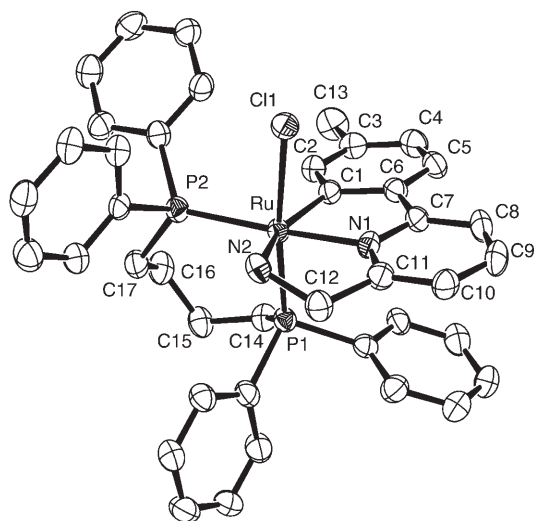
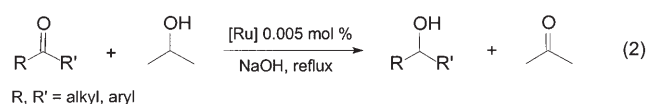


Figure 1. ORTEP representation of complex **1**. Thermal ellipsoids are at 40% probability, the labeling scheme of the phenyl carbon atoms is omitted for clarity. Selected coordination bond lengths [Å] and angles [°]: Ru–C1 2.057(4), Ru–N1 2.046(3), Ru–N2 2.246(3), Ru–P1 2.252(1), Ru–P2 2.287(1), Ru–Cl1 2.495(1); N1–Ru–C1 80.32(13), N1–Ru–N2 76.45(12), N2–Ru–P1 102.59(8), N1–Ru–P2 173.00(8), C1–Ru–P2 103.60(10), N2–Ru–P2 98.74(8), P1–Ru–P2 94.85(4), P1–Ru–Cl1 173.29(3), C1–Ru–N2 155.40(12), C1–Ru–P1 85.78(9), N1–Ru–P1 91.20(8).

respectively, from the mean plane. Related terdentate Pt^{II} and Pd^{II} complexes obtained from 6-phenyl-2-(2-aminoisopropyl)pyridine have recently been reported.^[11]

Complex **1** has been found to display an exceptionally high catalytic activity in the reduction of a large number of ketones (0.1M) with 2-propanol as the hydrogen donor and in the presence of NaOH (2 mol%) [Eq. (2)].

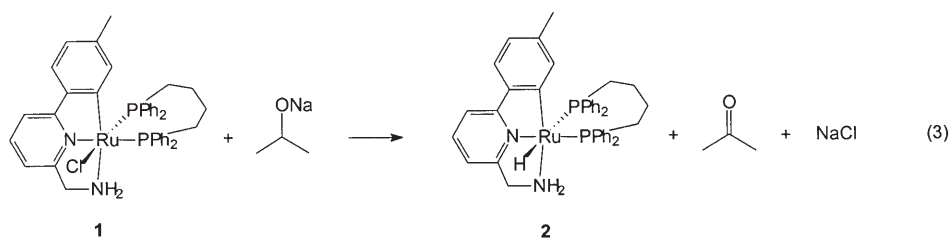


Acetophenone is quantitatively reduced to 1-phenylethanol in five minutes using a substrate/**1** ratio of 20 000:1 with a remarkably high TOF value of $1.1 \times 10^6 \text{ h}^{-1}$ at 50% conversion (Table 1). Subsequent addition of further amounts of the ketone (two times) results in complete reduction, thus suggesting that the stability of the complex results from the rigid framework built up by the association of the robust terdentate ligand with the chelating diphosphane, and consequently catalyst deactivation is significantly retarded.

Complex **1** can also be generated in situ from $[\text{RuCl}_2(\text{PPh}_3)_2(\text{dppb})]$ and the functionalized pyridine ligand (1:2 molar ratio) in 2-propanol and it shows the same activity as the isolated compound. In contrast, the in situ prepared analogue of **1** bearing $\text{N}(\text{CH}_3)_2$ instead of the NH_2 group

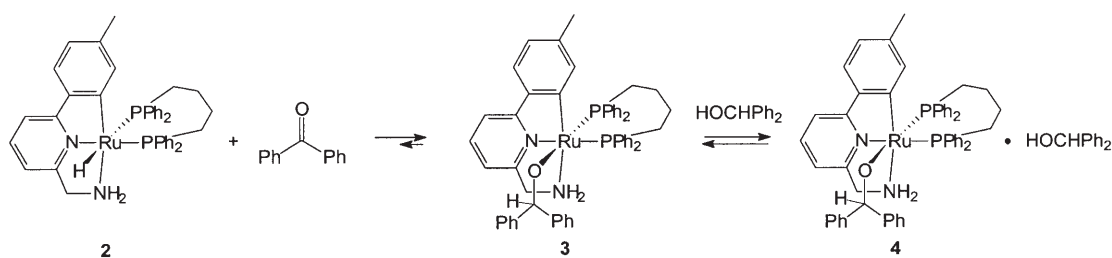
shows low activity for acetophenone (Ru 0.005 mol%, NaOH 2 mol%, 7% conversion after 1 h) under identical experimental conditions, thus suggesting that the high performance of **1** is in some way related to an assistance of the NH group in the catalytic cycle. Interestingly, complete reduction (98%) is achieved in 1 h with a substrate/**1** ratio of 100 000:1 ($\text{TOF} = 5.2 \times 10^5 \text{ h}^{-1}$), and experiments at lower catalyst loading (0.0005 mol%) led to a turnover number (TON) of 1.7×10^5 . These results are of particular relevance for large-scale synthesis since hydrogen-transfer catalysts are usually used in the range of 1–0.01 mol% as a consequence of their easy deactivation, with TOF values lower than 10^5 h^{-1} . As shown in Table 1, alkyl–aryl, dialkyl (cyclic and linear), and diaryl ketones are rapidly (minutes), quantitatively, and chemoselectively reduced to alcohols with TOF values in the range 5.0×10^5 to $2.5 \times 10^6 \text{ h}^{-1}$ with 0.005 mol% of **1**. The high performance of **1** means that this protocol allows the preparation of alcohols on a gram scale using very low amounts of catalyst.^[12]

It is generally accepted that the role of the base in ruthenium-catalyzed hydrogen-transfer reactions is to generate hydrides, which are the catalytic active species.^[13] In agreement with this, we have found that reaction of **1** with sodium isopropoxide in a 2-propanol/toluene solution affords the orange hydride complex **2**^[14] through elimination of acetone on evaporation of the medium [Eq. (3)].



The ^{31}P NMR spectrum of **2** displays two doublets at $\delta = 65.7$ and 34.6 ppm with a relatively small $^2J(\text{P,P})$ coupling constant of 17.2 Hz. The resonance of the hydride in the ^1H NMR spectrum appears as a doublet of doublets at $\delta = -5.58$ ppm with $^2J(\text{H,P}) = 89.1$ and 26.4 Hz, which is consistent with the presence of *trans* and *cis* phosphorus atoms.^[15] An IR band of medium intensity appears at $\tilde{\nu} = 1743 \text{ cm}^{-1}$ corresponding to the Ru–H species and this low-frequency shift is in agreement with the strong *trans* influence of the phosphane ligand.^[16] It is noteworthy that addition of hydride **2** (1 mol%) to acetophenone and 2-propanol (1:1 molar ratio) in C_6D_6 leads, at room temperature and within a few minutes, to an equilibrium mixture in which 1-phenylethanol and acetone are formed. Hydride **2** is a catalyst of impressive activity in 2-propanol at reflux which leads to complete conversion of acetophenone in a few minutes with TOF values ranging from $4.8 \times 10^4 \text{ h}^{-1}$ (**2** 0.01 mol%, in the absence of any additional base) to $8.0 \times 10^5 \text{ h}^{-1}$ (in the presence of a tenfold excess of $\text{NaO}i\text{Pr}$).

Complex **2** reacts promptly with an equimolar amount of benzophenone in C_6D_6 at 20°C to give the alkoxide–amine complex **3**^[17] through insertion of the ketone into the Ru–H bond (Scheme 1).



Scheme 1.

Table 1: Catalytic reduction of ketones (0.1 M) with **1** (0.005 mol%) and NaOH (2 mol%) in 2-propanol at 82 °C.

Ketone	Alcohol	Conversion [%] ^[a]	min	TOF [h ⁻¹] ^[b]
		98	5	1.1 × 10 ⁶
		98	2	1.9 × 10 ⁶
		99	1	2.5 × 10 ⁶
		99	5	1.2 × 10 ⁶
		97	2	1.5 × 10 ⁶
		99	10	5.0 × 10 ⁵
		97	5	7.0 × 10 ⁵
		98	10	5.3 × 10 ⁵

[a] The conversion was determined by GC or ¹H NMR analysis. [b] Turnover frequency (mol of ketone converted into alcohol per mol of catalyst per hour) at 50% conversion.

The ³¹P NMR spectrum of **3** shows two doublets at $\delta = 57.0$ and 37.3 ppm with $^2J(\text{P,P}) = 34.2$ Hz; this coupling constant is slightly smaller than that of **1** ($^2J(\text{P,P}) = 38.3$ Hz). The proton signal for the RuOCH moiety appears as a doublet at $\delta = 4.80$ ppm (0 °C in [D₈]toluene) with $^4J(\text{H,P}) = 3.7$ Hz, whereas one broad resonance shifted downfield to $\delta = 5.30$ ppm arises from one proton of the amine group, which may suggest an NH...O hydrogen bond interaction that stabilizes the alkoxide **3**. The ¹³C NMR peak of the OCH moiety in C₆D₆ appears at $\delta = 80.1$ ppm and it is shifted downfield relative to free benzhydrol ($\delta = 76.1$ ppm), a result

which is in agreement with other metal alkoxides.^[18] NMR spectroscopic studies show that heating a solution of **3** in [D₈]toluene above 70 °C results in reversible generation of both the ketone and the hydride **2**.

The alkoxide **3** is sensitive to protic compounds and the corresponding alcohol adducts are observed in the presence of alcohols.^[19] Addition of benzhydrol (2 equivalents) to **3** results in the formation of the species **4** (³¹P NMR: $\delta = 55.0$ and 42.8 ppm, with $^2J(\text{P,P}) = 34.2$ Hz), according to the equilibrium shown in Scheme 1 (**3/4** ca. 1.5:1). Heating the solution results in an increase of **3**, and coalescence of the signals for **3** and **4** is observed at about 60 °C. Elimination of benzhydrol has been observed with more acidic compounds such as water or carboxylic acids.^[20] It is worth noting that a ³¹P NMR spectroscopic study of the reaction of **1** with NaⁱOPr in 2-propanol/toluene to give the hydride **2** shows two doublets at $\delta = 54.3$ and 44.6 ppm, with $^2J(\text{P,P}) = 34.2$ Hz. These values are close to those of **4**, thus suggesting the formation of a similar adduct between the ruthenium isopropoxide and 2-propanol. A variable temperature NMR study shows that

heating this solution above 40 °C leads to an equilibrium reaction between the Ru-isopropoxide and the hydride **2**, whose concentration can also be increased by elimination of acetone through evaporation (in agreement with the reaction of benzophenone shown in Scheme 1).

While the insertion of unsaturated compounds into the Ru–H bond has been thoroughly studied, examples of the formation of Ru–alkoxides by reaction of ketones are rare and restricted to ketoesters or to substrates containing an additional electron-withdrawing group.^[21] The reverse reaction, that is, β -hydrogen elimination,^[22] provides one of the

most practical routes to metal hydrides. The reversibility of this process, however, has been clearly established only for $[\text{Re}_3(\mu\text{-O}i\text{Pr})_3(\text{O}i\text{Pr})_6]$,^[23a] although spectroscopic evidence has been collected at low temperature for $[\text{OsCl}(\text{OCH}(\text{CD}_3)_2)(\text{CO})(\text{P}i\text{Pr}_3)_2]$.^[23b] Recently, the NH-assisted reversible insertion of CO_2 into the Ru–H bond to give the formate–amine species has been reported by Koike and Ikariya.^[24] Interestingly, spectroscopic evidence of ruthenium–alkoxide–amine species has been obtained starting from ruthenium–amide complexes and alcohols.^[25]

The results of the study on the stoichiometric reactions of the CNN complexes, together with the influence of the alkoxide concentration on the catalytic activity of the hydride **2**, provide strong support to the formation of a discrete intermediate Ru–alkoxide species in the course of the catalytic transfer hydrogenation of ketones. As this fact cannot be explained by the concerted outer-sphere mechanism first proposed by Noyori and co-workers for ruthenium catalysts containing ligands with NH donor groups (metal–ligand bifunctional catalysis),^[4b,26] an alternative mechanism for this process may be envisioned as follows. The catalytically active Ru–isopropoxide species, which is formed from **1** and sodium isopropoxide, equilibrates with hydride **2**. Insertion of the ketone into the Ru–H bond of **2** provides a new ruthenium alkoxide, such as **3**. The latter, on exchange with 2-propanol, delivers the reaction product and regenerates the Ru–isopropoxide complex, thus closing the catalytic cycle. Although the classical ketone insertion into the metal–hydride bond and the β -hydrogen elimination pathways,^[4e,27] involving a *cis* vacant site (that is, through dissociation of the NH_2 moiety), cannot be ruled out, it is more likely that both elementary steps occur through hydrogen-bond assistance of the NH_2 group, without NH proton transfer. For example, the development of an $\text{NH}\cdots\text{O}=\text{C}$ interaction between the amine and the incoming ketone may at the same time activate the substrate towards the nucleophilic attack and provide the ketone with the correct orientation for the hydride transfer to be feasible. The resulting alkoxide anion might then migrate from the hydrogen to the metal center, possibly through a three-centered reaction mechanism, to afford the Ru–alkoxide intermediate. Thus, the formation of the Ru hydride from the Ru alkoxide may occur through the reverse pathway. Strong hydrogen bonding between the substrate, catalyst, and solvent probably plays a key role in the overall process. Theoretical studies on the mechanism of the transfer hydrogenation with Ru/NH catalysts show that ruthenium methoxide–amine complexes are the most stable species along the reaction pathways.^[26b,28]

Finally, it is worth noting that our approach can be easily extended to the high-speed enantioselective transfer hydrogenation. Thus, when $[\text{RuCl}_2(\text{PPh}_3)(\text{dppb})]$ is treated with the chiral derivative of 6-phenyl-2-pyridylmethylamine with a *t*Bu group on the CHNH_2 arm (*R* enantiomer), rapid conversion of *o*-methoxyacetophenone into (*S*)-*o*-methoxy- α -phenylethanol is observed (Ru 0.05 mol %, TOF = $6.0 \times 10^5 \text{ h}^{-1}$, *ee* = 87%), in agreement with the non-hemilabile behavior of the NH_2 function of the CNN ligand.

In summary, we have shown that terdentate $[\text{RuX}(\text{CNN})(\text{PP})]$ ($\text{X} = \text{Cl}, \text{H}$) complexes are highly efficient

catalysts in transfer hydrogenation involving 2-propanol to afford quantitative reduction of different ketones with very low loading and in a short time. Reduction of ketones apparently takes place by insertion of the substrate into the Ru–H bond, thus leading to a Ru^{II} alkoxide. The reversibility of this step has been observed in the case of the stoichiometric reaction of complex **2** with benzophenone. This fact provides strong evidence that a Ru alkoxide derivative is most probably an intermediate in the formation of the hydride **2**, the putative active catalyst, from the relevant chloride **1**. As the structure of the terdentate pyridine ligand is well suited for a modular synthetic approach, which allows for a fine tuning of the stereoelectronic properties of the CNN complexes, this new class of ruthenium derivatives holds the promise for a broad application in organometallic chemistry and in homogeneous asymmetric catalysis.

Experimental Section

1: $[\text{RuCl}_2(\text{PPh}_3)(\text{dppb})]$ (1.17 g, 1.36 mmol) was added to a solution of 2-propanol (15 mL) containing 6-(4'-methylphenyl)-2-pyridylmethylamine (300 mg, 1.51 mmol) and NEt_3 (1.9 mL, 13.6 mmol). The mixture was refluxed for 2 h and the yellow precipitate was filtered, washed with methanol, and dried under reduced pressure. Yield: 810 mg (78%).

2: Compound **1** (516 mg, 0.679 mmol) was suspended in toluene (10 mL) and a solution of $\text{NaO}i\text{Pr}$ (0.1M, 1.00 mmol) in 2-propanol (10 mL) was added. The solution was concentrated after 1 h at 60°C, stirred at room temperature, and after addition of toluene, filtered over celite. The filtrate was evaporated and the solid was precipitate from toluene and filtered, to afford a bright orange product which was dried under reduced pressure. Yield: 395 mg (80%).

3: Benzophenone (45 mg, 0.247 mmol) was added to a suspension of **2** (160 mg, 0.220 mmol) in toluene (2 mL), and the solution was stirred for 15 min. The solution was then concentrated and pentane added. This afforded a dark yellow precipitate which was filtered and dried under reduced pressure. Yield: 140 mg (70%).

Typical procedure for the catalytic hydrogen-transfer reaction: Complex **1** (3.0 mg, 4.0 μmol) was dissolved in 2-propanol (8 mL). The ketone (2 mmol) was dissolved in 2-propanol (19 mL) and the solution heated to reflux under argon. Addition of NaOH (0.1M, 400 μL) and the solution containing the catalyst **1** (200 μL) resulted in the reduction of the ketone starting immediately. The yield was determined by GC or NMR analysis (ketone:1: NaOH = 20000:1:400; ketone 0.1M).

Received: June 17, 2005

Published online: September 1, 2005

Keywords: homogeneous catalysis · hydride · hydrogenation · orthometalation · ruthenium

- [1] a) M. H. P. Rietveld, D. M. Grove, G. van Koten, *New J. Chem.* **1997**, 21, 751; b) M. Albrecht, G. van Koten, *Angew. Chem.* **2001**, 113, 3866; *Angew. Chem. Int. Ed.* **2001**, 40, 3750; c) M. E. van der Boom, D. Milstein, *Chem. Rev.* **2003**, 103, 1759; d) J. T. Singleton, *Tetrahedron* **2003**, 59, 1837.
- [2] a) M. Ohff, A. Ohff, M. E. van der Boom, D. Milstein, *J. Am. Chem. Soc.* **1997**, 119, 11687; b) F. Miyazaki, K. Yamaguchi, M. Shibasaki, *Tetrahedron Lett.* **1999**, 40, 7379; c) S. Gibson, D. F. Foster, G. R. Eastham, R. P. Tooze, D. J. Cole-Hamilton, *Chem. Commun.* **2001**, 779; d) M. Gupta, C. Hagen, W. C. Kaska, R. E. Cramer, C. M. Jensen, *J. Am. Chem. Soc.* **1997**, 119, 840; e) F.

- Liu, E. B. Pak, B. Singh, C. M. Jensen, A. S. Goldman, *J. Am. Chem. Soc.* **1999**, *121*, 4086; f) P. Dani, T. Karlen, R. A. Gossage, S. Gladiali, G. van Koten, *Angew. Chem.* **2000**, *112*, 759; *Angew. Chem. Int. Ed.* **2000**, *39*, 743; g) D. Conner, K. N. Jayaprakash, T. R. Cundari, T. B. Gunnoe, *Organometallics* **2004**, *23*, 2724; h) D. Amoroso, A. Jabri, G. P. A. Yap, D. G. Gusev, E. N. dos Santos, D. E. Fogg, *Organometallics* **2004**, *23*, 4047.
- [3] T. Naota, H. Takaya, S.-I. Murahashi, *Chem. Rev.* **1998**, *98*, 2599.
- [4] a) G. Zassinovich, G. Mestroni, S. Gladiali, *Chem. Rev.* **1992**, *92*, 1051; b) R. Noyori, S. Hashiguchi, *Acc. Chem. Res.* **1997**, *30*, 97; c) S. Gladiali, G. Mestroni in *Transition Metals for Organic Synthesis*, Vol. 2 (Eds.: M. Beller, C. Bolm), Wiley-VCH, Weinheim, **1998**, p. 97; d) R. Noyori, M. Yamakawa, S. Hashiguchi, *J. Org. Chem.* **2001**, *66*, 7931; e) O. Pàmies, J. E. Bäckvall, *Chem. Eur. J.* **2001**, *7*, 5052; f) J. E. Bäckvall, *J. Organomet. Chem.* **2002**, *652*, 105; g) S. E. Clapham, A. Hadzovic, R. H. Morris, *Coord. Chem. Rev.* **2004**, *248*, 2201.
- [5] a) W. Baratta, P. Da Ros, A. Del Zotto, A. Sechi, E. Zangrando, P. Rigo, *Angew. Chem.* **2004**, *116*, 3668; *Angew. Chem. Int. Ed.* **2004**, *43*, 3584; b) W. Baratta, A. Del Zotto, G. Esposito, A. Sechi, M. Toniutti, E. Zangrando, P. Rigo, *Organometallics* **2004**, *23*, 6264; c) W. Baratta, E. Herdtweck, K. Siega, M. Toniutti, P. Rigo, *Organometallics* **2005**, *24*, 1660.
- [6] a) A. J. Toner, S. Gründemann, E. Clot, H. H. Limbach, B. Donnadié, S. Sabo-Etienne, B. Chaudret, *J. Am. Chem. Soc.* **2000**, *122*, 6777; b) A. M. Clark, C. E. F. Rickard, W. R. Roper, L. J. Wright, *Organometallics* **1999**, *18*, 2813, and references therein.
- [7] a) P. Braunstein, M. D. Fryzuk, F. Naud, S. J. Rettig, *J. Chem. Soc. Dalton Trans.* **1999**, 589; b) H. Yang, M. Alvarez, N. Lugan, R. Mathieu, *J. Chem. Soc. Chem. Commun.* **1995**, 1721; c) H. Yang, M. Alvarez-Gressier, N. Lugan, R. Mathieu, *Organometallics* **1997**, *16*, 1401.
- [8] **1**: ¹H NMR (200.1 MHz, CD₂Cl₂, 20 °C, TMS): δ = 8.10–6.57 (m, 24H; ArH), 6.00 (t, *J*(H,H) = 8.1 Hz, 2H; *m*-Ph), 4.12 (dd, *J*(H,H) = 15.5, 4.4 Hz, 1H; CH₂N), 3.72 (td, *J*(H,H) = 15.5, 4.1 Hz, 1H; CH₂N), 3.41 (m, 1H; NH₂), 3.05 (m, 2H; CH₂P), 2.46–0.90 (m, 7H; NH and CH₂), 2.23 ppm (s, 3H; CH₃); ¹³C{¹H} NMR (50.3 MHz, CD₂Cl₂, 20 °C, TMS): δ = 181.8 (dd, *J*(C,P) = 16.3, 7.8 Hz; CRu), 163.2 (s; NCC), 155.9 (s; NCCH₂), 149.2–116.0 (m; Ar), 52.5 (d, *J*(C,P) = 2.7 Hz; CH₂N), 33.4 (d, *J*(C,P) = 26.3 Hz; CH₂P), 30.7 (d, *J*(C,P) = 31.6 Hz; CH₂P), 26.8 (s; CH₂), 22.1 (s; CH₂), 21.8 ppm (s, CH₃); ³¹P{¹H} NMR (81.0 MHz, CD₂Cl₂, 20 °C, H₃PO₄): δ = 57.3 (d, *J*(P,P) = 38.3 Hz), 42.6 ppm (d, *J*(P,P) = 38.3 Hz); elemental analysis (%) calcd for C₄₁H₄₁N₂ClP₂Ru: C 64.77, H 5.44, N 3.68; found: C 64.36, H 5.52, N 3.70.
- [9] T. Koizumi, T. Tomon, K. Tanaka, *Organometallics* **2003**, *22*, 970, and references therein.
- [10] Crystal structure analysis of **1**: 2C₆H₆, C₅₃H₅₃N₂ClP₂Ru, *M*_r = 916.43, triclinic, space group *P* $\bar{1}$, *a* = 11.547(3), *b* = 13.307(3), *c* = 16.400(4) Å, *α* = 84.38(3), *β* = 74.29(3), *γ* = 69.38(2)°, *V* = 2270.4(10) Å³, *Z* = 2, *ρ*_{calcd} = 1.341 g cm⁻³, *μ* = 4.285 mm⁻¹, *F*(000) = 952, *θ* = 3.55–64.82°. Final *R*₁ = 0.0487, *wR*₂ = 0.1262, *S* = 1.087 for 533 parameters and 6542 reflections (of which 6251 with *I* > 2σ(*I*)), max positive and negative peaks in Δ*F* map 0.547 and –0.689 e Å⁻³. Data were collected at 160(2) K on a Nonius FR590 rotating anode (CuKα radiation, λ = 1.54178 Å) equipped with KappaCCD detector. CCDC-265691 contains the supplementary crystallographic data for this paper. These data can be obtained free of charge from the Cambridge Crystallographic Data Centre via www.ccdc.cam.ac.uk/data_request/cif.
- [11] D. Song, R. H. Morris, *Organometallics* **2004**, *23*, 4406.
- [12] For example, 1.97 g of the pharmaceutical intermediate 4-chlorobenzhydrol (90% yield) was obtained from 4-chlorobenzophenone in 2-propanol (NaOH 2 mol%) after 2 h at reflux and using **1** (0.076 mg from a standard solution) (ketone/catalyst = 100000:1).
- [13] H. Jacobsen, H. Berke in *Recent Advances in Hydride Chemistry* (Eds.: M. Peruzzini, R. Poli), Elsevier, Amsterdam, **2001**, p. 89.
- [14] **2**: ¹H NMR (200.1 MHz, C₆D₆, 20 °C, TMS): δ = 8.55–5.90 (m, 26H; ArH), 3.10–0.90 (m, 12H; CH₂ and NH₂), 2.30 (s, 3H; CH₃), –5.58 ppm (dd, *J*(H,P) = 89.1, 26.4 Hz, 1H; RuH); ¹³C{¹H} NMR (50.3 MHz, C₆D₆, 45 °C, TMS): δ = 189.1 (s; CRu), 163.0 (s; NCC), 154.8 (s; NCCH₂), 149.2–113.2 (m; Ar), 52.1 (d, *J*(C,P) = 2.8 Hz; CH₂N), 32.5 (d, *J*(C,P) = 13.8 Hz; CH₂P), 30.0 (d, *J*(C,P) = 21.3 Hz; CH₂P), 27.0 (s; CH₂), 22.8 (s; CH₂), 22.0 ppm (s, CH₃); ³¹P{¹H} NMR (81.0 MHz, C₆D₆, 20 °C, H₃PO₄): δ = 65.7 (d, *J*(P,P) = 17.2 Hz), 34.6 ppm (d, *J*(P,P) = 17.2 Hz); IR (Nujol): $\tilde{\nu}$ = 1743 cm⁻¹ (br, RuH); elemental analysis (%) calcd for C₄₁H₄₂N₂P₂Ru: C 67.85, H 5.83, N 3.86; found: C 66.80, H 5.63, N 3.57.
- [15] a) S. D. Drouin, D. Amoroso, G. P. A. Yap, D. E. Fogg, *Organometallics* **2002**, *21*, 1042; b) C. Bianchini, P. Frediani, D. Masi, M. Peruzzini, F. Zanobini, *Organometallics* **1994**, *13*, 4616; c) G. C. Hsu, W. P. Kosar, W. D. Jones, *Organometallics* **1994**, *13*, 385.
- [16] a) T. G. Appleton, H. C. Clark, L. E. Manzer, *Coord. Chem. Rev.* **1973**, *10*, 335; b) J. P. Collman, L. S. Hegeudus, J. R. Norton, R. G. Finke in *Principles and Application of Organotransition Metal Chemistry*, University Science Books, Mill Valley, CA, **1987**; c) J. C. Toledo, B. S. Lima Neto, D. W. Franco, *Coord. Chem. Rev.* **2005**, *249*, 419.
- [17] **3**: ¹H NMR (200.1 MHz, C₆D₆, 20 °C, TMS): δ = 8.40–5.80 (m, 35H; ArH), 5.58 (d, *J*(H,H) = 7.2 Hz, 1H; ArH), 5.35 (brs, 1H; NH₂), 4.86 (s, 1H; OCH), 3.20–2.60 (m, 5H), 2.25 (s, 3H; CH₃), 2.10–0.9 ppm (m, 6H); ¹³C{¹H} NMR (50.3 MHz, C₆D₆, 20 °C, TMS): δ = 187.6 (s; CRu), 163.8 (s; NCC), 157.4 (s; NCCH₂), 155.7–112.4 (m; Ar), 80.1 (s, OCH), 52.0 (s; CH₂N), 31.6 (d, *J*(C,P) = 29.2 Hz; CH₂P), 30.9 (d, *J*(C,P) = 26.7 Hz; CH₂P), 27.0 (s; CH₂), 22.6 (s; CH₂), 22.1 ppm (s, CH₃); ³¹P{¹H} NMR (81.0 MHz, C₆D₆, 20 °C, H₃PO₄): δ = 57.0 (d, *J*(P,P) = 34.2 Hz), 37.3 ppm (d, *J*(P,P) = 34.2 Hz); elemental analysis (%) calcd for C₅₄H₅₂N₂OP₂Ru: C 71.43, H 5.77, N 3.09; found: C 70.51, H 5.39, N 2.81.
- [18] a) M. S. Sanford, L. M. Henling, M. W. Day, R. H. Grubbs, *Angew. Chem.* **2000**, *112*, 3593; *Angew. Chem. Int. Ed.* **2000**, *39*, 3451; b) F. Liang, H. W. Schmalle, T. Fox, H. Berke, *Organometallics* **2003**, *22*, 3382; c) Z. Chen, H. W. Schmalle, T. Fox, H. Berke, *Dalton Trans.* **2005**, 580.
- [19] a) J. R. Fulton, A. W. Holland, D. J. Fox, R. G. Bergman, *Acc. Chem. Res.* **2002**, *35*, 44; b) H. E. Bryndza, W. Tam, *Chem. Rev.* **1988**, *88*, 1163; c) Y. J. Kim, K. Osakada, A. Takenaka, A. Yamamoto, *J. Am. Chem. Soc.* **1990**, *112*, 1096; d) K. Osakada, K. Ohshiro, A. Yamamoto, *Organometallics* **1991**, *10*, 404; e) S. E. Kegley, C. J. Schaverien, J. H. Freudenberger, R. G. Bergman, S. P. Nolan, C. D. Hoff, *J. Am. Chem. Soc.* **1987**, *109*, 6563.
- [20] With acetic acid the formation of the corresponding ruthenium acetate has been established and it will be described elsewhere.
- [21] a) C. J. A. Daley, S. H. Bergens, *J. Am. Chem. Soc.* **2002**, *124*, 3680; b) Y. Hayashi, S. Komiya, T. Yamamoto, A. Yamamoto, *Chem. Lett.* **1984**, 1363.
- [22] a) S. P. Nolan, T. R. Belderrain, R. H. Grubbs, *Organometallics* **1997**, *16*, 5569; b) M. A. Esteruelas, E. Sola, L. A. Oro, H. Werner, U. Meyer, *J. Mol. Catal.* **1988**, *45*, 1; c) B. N. Chaudret, D. J. Cole-Hamilton, R. S. Nohr, G. Wilkinson, *J. Chem. Soc. Dalton Trans.* **1977**, 1546.
- [23] a) D. M. Hoffman, D. Lappas, D. A. Wierda, *J. Am. Chem. Soc.* **1993**, *115*, 10538; b) M. A. Esteruelas, C. Valero, L. A. Oro, U. Meyer, H. Werner, *Inorg. Chem.* **1991**, *30*, 1159.
- [24] T. Koike, T. Ikariya, *Adv. Synth. Catal.* **2004**, *346*, 37.
- [25] a) K. Abdur-Rashid, S. E. Clapham, A. Hadzovic, J. N. Harvey, A. J. Lough, R. H. Morris, *J. Am. Chem. Soc.* **2002**, *124*, 15104; b) T. Koike, T. Ikariya, *Organometallics* **2005**, *24*, 724.

- [26] a) K.-J. Haack, S. Hashiguchi, A. Fujii, T. Ikariya, R. Noyori, *Angew. Chem.* **1997**, *109*, 297; *Angew. Chem. Int. Ed. Engl.* **1997**, *36*, 285; b) M. Yamakawa, H. Ito, R. Noyori, *J. Am. Chem. Soc.* **2000**, *122*, 1466.
- [27] A. Aranyos, G. Csjernyk, K. J. Szabó, J. E. Bäckvall, *Chem. Commun.* **1999**, 351.
- [28] J. W. Handgraaf, J. N. H. Reek, E. J. Meijer, *Organometallics* **2003**, *22*, 3150.

Synthetic Methods

DOI: 10.1002/anie.200502134

Organocatalytic Asymmetric α -Halogenation of 1,3-Dicarbonyl Compounds**

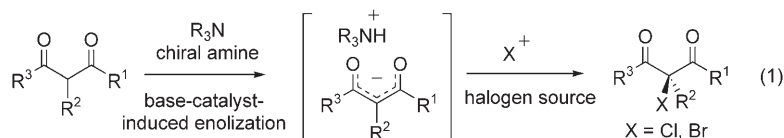
Giuseppe Bartoli,* Marcella Bosco, Armando Carlone, Manuela Locatelli, Paolo Melchiorre,* and Letizia Sambri

The enantioselective construction of carbon–halogen stereogenicity belongs to the topical area of current asymmetric catalysis^[1] by virtue of the fact that halogen atoms attached to a chiral stereocenter can serve as a linchpin for further stereospecific manipulations.^[2] Moreover, optically active halogen-containing compounds are increasingly important targets in drug discovery and material sciences.^[3] Despite this, different efficient catalytic asymmetric halogenation strategies have been developed only in the last few years.^[1a,b] To date, the most notable advances have been made in the α -halogenation of carbonyl compounds by using mild and stable sources of electrophilic halogens. All the reported asymmetric catalytic methodologies, from the first Lewis acid catalyzed asymmetric α -fluorination of β -keto esters reported by Hintermann and Togni,^[4] to several highly practical metal-free (organocatalytic)^[5] approaches, involve

the transient formation of an enolate (enol) that can be halogenated to generate the desired product. The crucial enolization process can be efficiently promoted through 1) coordination of chiral Lewis acids with 1,3-dicarbonyl compounds;^[6] 2) formation of an enamine intermediate derived from the reaction between a secondary chiral amine and enolizable aldehydes and ketones;^[7] 3) attack of a chiral nucleophile on a ketene intermediate to generate a zwitterionic enolate;^[8] and 4) ionic association of a phase-transfer catalyst with the enolate.^[9]

Recently, chiral tertiary amines have been successfully applied in various organocatalytic transformations, acting as chiral-base catalysts.^[10] However, this concept has not yet been applied to asymmetric halogen–carbon bond-forming reactions. Herein, we describe a new effective approach that uses a cinchona alkaloid derivative as a chiral base for promoting the enolization of 1,3-dicarbonyl compounds and the subsequent highly enantioselective electrophilic α -chlorination and α -bromination of the enol derivative [Eq. (1)].

Despite the considerable recent advances, the development of a novel halogenation system of 1,3-dicarbonyl compounds that displays satisfactory selectivity as well as generality is still in high demand, as the reported Lewis acid catalyzed asymmetric chlorinations and brominations of β -



keto esters are efficient only with selected substrates.^[6a–c] The organocatalytic halogenation presented herein is effective with both cyclic and acyclic β -keto esters and with cyclic β -diketones to afford highly optically enriched α -halogenated compounds (up to 96% *ee*) in good yields using inexpensive benzoylquinidine (BQd) as the catalyst and easy-to-prepare polyhalogenated quinolinones as new sources of the halogen.

To verify the feasibility of such an organocatalytic asymmetric halogenation strategy, we examined the reaction of ethyl 2-oxo-cyclopentanecarboxylate **1a** with *N*-chlorosuccinimide (NCS, **3a**) as the halogen source in the presence of some cinchona alkaloid derivatives as the chiral-base catalyst. Representative results of the extensive screening of reaction conditions are listed in Table 1. Several solvents were inves-

[*] Prof. G. Bartoli, Prof. M. Bosco, Dr. A. Carlone, Dr. M. Locatelli, Dr. P. Melchiorre, Dr. L. Sambri
Department of Organic Chemistry “A. Mangini”
Alma Mater Studiorum
Bologna University
Viale Risorgimento, 4, 40136 Bologna (Italy)
Fax: (+39) 051-209-3654
E-mail: giuseppe.bartoli@unibo.it
pm@ms.fci.unibo.it

[**] This work was carried out in the framework of the National Project “Stereoselezione in Sintesi Organica: Metodologie e Applicazioni” supported by the MIUR, Rome, and the FIRB National Project “Progettazione, preparazione e valutazione biologica e farmacologica di nuove molecole organiche quali potenziali farmaci innovativi”.



Supporting information for this article is available on the WWW under <http://www.angewandte.org> or from the author.

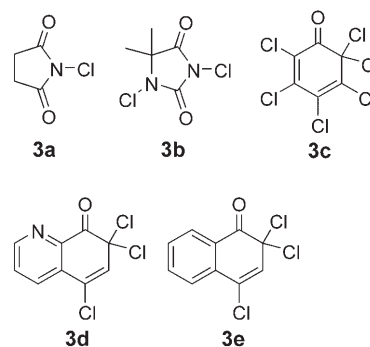


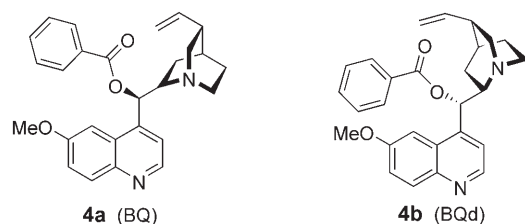
Table 1: Screening of reaction conditions for the organocatalytic asymmetric chlorination of **1a**.^[a]

Entry	Catalyst ^[b]	3	<i>t</i> [h]	<i>T</i> [°C]	Conv. [%] ^[c]	<i>ee</i> [%] ^[d]
1	(DHQ) ₂ PYR	3a	2	RT	> 95	21 (<i>R</i>)
2	(DHQD) ₂ PHAL	3a	2	RT	> 95	33 (<i>S</i>)
3	(DHQ) ₂ AQN	3a	2	RT	> 95	46 (<i>R</i>)
4	cinchonidine	3a	2	RT	> 95	10 (<i>R</i>)
5	quinine	3a	2	RT	> 95	18 (<i>R</i>)
6	4a	3a	2	RT	> 95	60 (<i>R</i>)
7	4a	3a	3	−78	> 95	58 (<i>R</i>)
8	4a	3b	3	RT	> 95	36 (<i>R</i>)
9	4a	3c	3	RT	> 95	57 (<i>R</i>)
10	4a	3d	3	RT	> 95 (98) ^[e]	79 (<i>R</i>)
11	4a	3e	3	RT	58	78 (<i>R</i>)
12	4a	3d	24	−78	70	95 (<i>R</i>)
13 ^[f]	4a	3d	24	−78	74	95 (<i>R</i>)
14 ^[g]	4a	3d	24	−78	80 (68) ^[e]	95 (<i>R</i>)
15 ^[g]	4b	3d	3	RT	> 95 (96) ^[e]	85 (<i>S</i>)
16 ^[g]	4b	3d	24	−40	> 95 (98) ^[e]	95 (<i>S</i>)

[a] Experimental conditions (0.4-mmol scale): open-air reactions run in undistilled solvent (0.1 M) using a 1:1.2 ratio of **1a** to **3**, and 5 mol % of catalyst. [b] (DHQ)₂PYR = hydroquinine 2,5-diphenyl-4,6-pyrimidinediyl diether, (DHQD)₂PHAL = hydroquinidine 1,4-phthalazinediyl diether, (DHQ)₂AQN = hydroquinine anthraquinone-1,4-diyl diether. See Supporting Information for structures of catalysts. [c] Conversion determined by ¹H NMR spectroscopy of the crude mixture. [d] Determined by GC analyses on commercially available chiral stationary phases; the absolute configuration reported in parentheses was determined by comparison of values of optical rotation with those reported in the literature. [e] Number in parenthesis indicates yield of the isolated product **2a**. [f] Reaction carried out with 1 equivalent of NaHCO₃. [g] Reaction carried out with 1 equivalent of NaHCO₃ in toluene (0.25 M).

tigated, and toluene was selected as the solvent of choice, although ethereal solvents afforded analogous results (see Supporting Information for details).

In the initial studies, benzoylquinine (BQ, **4a**) proved to be the most promising catalyst among the chiral amines tested by affording the *R* chloro derivative **2a** in moderate enantio-



meric excess (60% *ee*, Table 1, entry 6). However, a slight decrease in enantioselectivity was observed when the BQ-catalyzed reaction was performed at −78°C (entry 7). We speculated that, under these reaction conditions, the uncatalyzed background reaction of the enol form effectively competes with the stereoselective pathway, even at low temperature. Thus, the primary goal was to employ a less-reactive, finely tuned chlorinating agent that displays a minimal rate of background reaction with the substrate **1a**.

Along these lines, a series of electrophilic halogens was screened, employing BQ (**4a**) as the catalyst (entries 8–11). The trichloroquinolinone **3d**, which is easily prepared from 8-hydroxyquinoline and 3 equivalents of *tert*-butylhypochlorite, gave the best result, with the product **2a** obtained in 79% *ee*. The structurally related chlorinating agent **3e** provided the same stereochemical outcome with a significant decrease in reactivity. Performing the reaction at −78°C in the presence of **3d** led to a dramatic increase in enantioselectivity, albeit at the expense of reactivity (95% *ee*, entry 12), which indicates that under these conditions the discrimination between the background reaction and the asymmetric catalyzed chlorination was maximized.^[11] Importantly, the capacity of the trichloroquinolinone **3d** to function in highly enantioselective enolate halogenations is disclosed here for the first time.^[12]

Halogen transfers involving quinolinone **3d** are expected to release stabilized aromatic phenolate anion **5** in a thermodynamically favorable process (Figure 1). We envis-

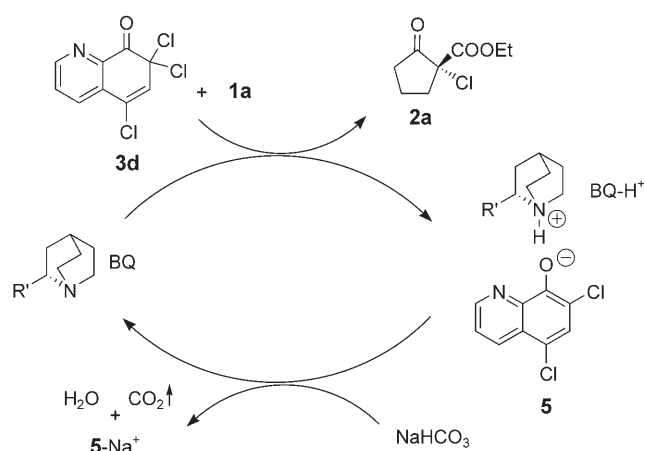


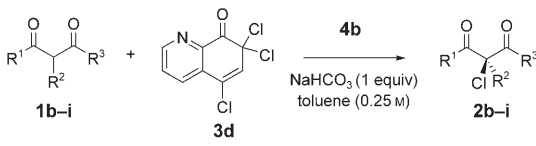
Figure 1. Halogen transfer from quinolinone **3d** to **1a** catalyzed by BQ (**4a**).

aged that the plausible tight ionic association of **5** with the protonated chiral amine catalyst may affect the efficiency of the system. We reasoned that an inorganic base that is able to facilitate the proton transfer from the protonated chiral amine (BQ-H⁺) to thus regenerate the active catalyst without promoting a racemic chlorination path could have a beneficial effect on the reaction rate.^[13] With this consideration in mind, a survey of reaction conditions was performed which revealed that the BQ-catalyzed asymmetric chlorination of **1a** was accelerated by using 1 equivalent of NaHCO₃ in a more concentrated solution (toluene, 0.25 M; Table 1, entries 13–14).^[14] Noteworthy, when the “pseudoenantiomeric” BQd (**4b**) was used as catalyst the opposite enantiomer (*S*)-**2a** was obtained in significantly higher enantiomeric excess (entry 15). Such a selectivity allowed the reaction to be performed at higher temperature without affecting the optical purity of the product, which was isolated in quantitative yield (95% *ee*, entry 16).

The superior levels of induction and efficiency exhibited by BQd (**4b**) in the presence of NaHCO₃ (1 equiv) and toluene (0.25 M), prompted us to select these conditions to

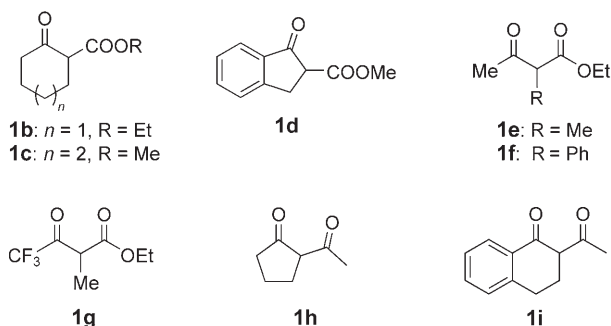
examine the scope of the 1,3-dicarbonyl substrates in this asymmetric chlorination protocol. As highlighted in Table 2, cyclic β -keto esters **1b–d** were all converted into the corresponding chloro derivatives in fairly good yields and with excellent optical purity (Table 2, entries 1–3). The

Table 2: Organocatalytic asymmetric chlorinations of β -keto esters and β -diketones.^[a]



Entry	Product	4b [mol%]	T [°C]	t [h]	Yield [%] ^[b]	ee [%] ^[c]
1	2b	15	−40	40	83	96
2	2c	15	−40	52	48 ^[d]	90
3	2d	5	−78	36	80 (75)	93 (91)
4	2e	20	RT	48	75	76 (69)
5	2f	15	−10	36	99	80
6 ^[e]	2g	15	−78	52	44 ^[f]	89
7 ^[e]	2h	5	−78	30	90 (87)	51 (56)
8 ^[e]	2i	15	−40	48	74 (78)	59 (58)

[a] Experimental conditions (0.4-mmol scale): open-air reactions run in undistilled toluene (0.25 M) using a 1:1.2 ratio of **1** to **3d**, 1 equivalent of NaHCO₃, and benzoylquinidine (**4b**) as catalyst. Results in parentheses were obtained by using BQ (**4a**) as catalyst to give the opposite enantiomer. [b] Yield of isolated products **2**. [c] ee values of **2** were determined by HPLC or by GC analyses on commercially available chiral stationary phases (see Supporting Information for details). [d] Conversion = 65%. [e] Reaction carried out in *tert*-butyl methyl ether. [f] Conversion = 80%; the lower yield is due to the volatility of **2g**. [g] Performed in the absence of NaHCO₃.



asymmetric chlorination of different substituted acyclic β -keto esters also afforded the desired products with good enantioselectivity, although a decreased reactivity was observed (entries 4–6). In the presence of a more-reactive substrate such as **1g**, the possibility to perform the reaction at low temperature allowed the generation of the chlorinated adduct **2g** in high optical purity (89% ee, entry 6).^[15]

We next investigated the efficiency of the method with β -diketones, a particularly challenging class of substrates for which, to our knowledge, just one example of low-enantioselective chlorination has been reported.^[6b] Reactions of cyclic diketones **1h–i** proceeded smoothly to give the expected products with moderate enantioselectivity (entries 7–8).

Last, the extension of the presented organocatalytic protocol to asymmetric brominations was evaluated. We presumed that the newly synthesized tribromoquinolinone **6** (Figure 2), structurally related to the chlorinating agent **3d**, might have been a useful source of bromine for the organo-

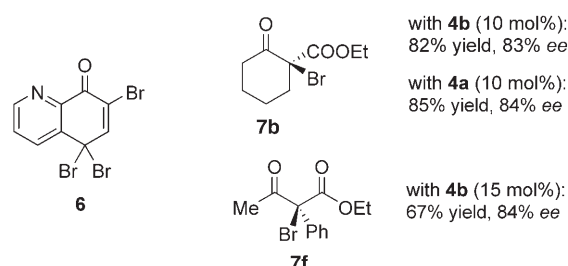


Figure 2. The organocatalytic asymmetric bromination of β -keto esters **1b,f** in the presence of 1.2 equivalents of **6** as the halogen source (toluene (0.25 M), −78 °C, 30 h) to afford **7b** and **7f**.

catalytic enantioselective α -bromination. Proof-of-principle was provided through BQd-catalyzed reactions of β -keto esters **1b** and **1f**: the corresponding bromo derivatives **7b** and **7f** were obtained in good yields and with good enantioselectivity (up to 84% ee, Figure 2).^[16] Further studies to improve the efficiency and the applicability of the organocatalytic enantioselective bromination reaction are ongoing in our laboratories.

In summary, we have developed the first organocatalytic asymmetric α -chlorination and α -bromination reactions of 1,3-dicarbonyl compounds by using an inexpensive chiral amine as the catalyst and a mild, operationally simple protocol that allows direct access to highly enantiomerically enriched halogen-containing compounds. The use of poly-halogenated quinolinones as new sources of halogen electrophiles was essential to achieve high enantioselectivity.

Received: June 20, 2005

Published online: September 1, 2005

Keywords: asymmetric catalysis · 1,3-dicarbonyl compounds · electrophilic substitution · halogenation · organocatalysis

- [1] For recent reviews on asymmetric halogenation reactions, see: a) M. Oestreich, *Angew. Chem.* **2005**, *117*, 2376; *Angew. Chem. Int. Ed.* **2005**, *44*, 2324; b) S. France, A. Weatherwax, T. Lectka, *Eur. J. Org. Chem.* **2005**, 475; c) H. Ibrahim, A. Togni, *Chem. Commun.* **2004**, 1147.
- [2] a) J. March, *Advanced Organic Chemistry: Reactions, Mechanism and Structure*, 4th ed., Wiley, New York, **1992**; b) N. De Kimpe, R. Verhé, *The Chemistry of α -Haloketones, α -Haloaldehydes, and α -Haloamines*, Wiley, New York, **1990**.
- [3] G. Thomas, *Medicinal Chemistry: An Introduction*, Wiley, New York, **2000**.
- [4] L. Hintermann, A. Togni, *Angew. Chem.* **2000**, *112*, 4530; *Angew. Chem. Int. Ed.* **2000**, *39*, 4359.
- [5] For general reviews on organocatalysis, see: a) *Asymmetric Organocatalysis* (Eds.: A. Berkessel, H. Gröger), Wiley-VCH, Weinheim, **2004**; b) *Acc. Chem. Res.* **2004**, *37*(8), special issue

- (Eds.: K. N. Houk, B. List); c) P. I. Dalko, L. Moisan, *Angew. Chem.* **2004**, *116*, 5248; *Angew. Chem. Int. Ed.* **2004**, *43*, 5138.
- [6] For catalytic asymmetric chlorinations and brominations of β -keto esters, see: a) L. Hintermann, A. Togni, *Helv. Chim. Acta* **2000**, *83*, 2425; b) M. Marigo, N. Kumaragurubaran, K. A. Jørgensen, *Chem. Eur. J.* **2004**, *10*, 2133; c) H. Ibrahim, F. Kleinbeck, A. Togni, *Helv. Chim. Acta* **2004**, *87*, 605; for catalytic asymmetric fluorination reactions, see: d) Y. Hamoshima, K. Yagi, H. Takano, L. Tamàs, M. Sodeoka, *J. Am. Chem. Soc.* **2002**, *124*, 14530; e) J.-A. Ma, D. Cahard, *Tetrahedron: Asymmetry* **2004**, *15*, 1007; f) L. Bernardi, K. A. Jørgensen, *Chem. Commun.* **2005**, 1324. See also reference [4].
- [7] For chlorination reactions, see: a) M. P. Brochu, S. P. Brown, D. W. C. MacMillan, *J. Am. Chem. Soc.* **2004**, *126*, 4108; b) N. Halland, A. Braunton, S. Bachmann, M. Marigo, K. A. Jørgensen, *J. Am. Chem. Soc.* **2004**, *126*, 4790; c) M. Marigo, S. Bachmann, N. Halland, A. Braunton, K. A. Jørgensen, *Angew. Chem.* **2004**, *116*, 5623; *Angew. Chem. Int. Ed.* **2004**, *43*, 5507; for fluorination reactions, see: d) M. Marigo, D. Fielenbach, A. Braunton, A. Kjærsgaard, K. A. Jørgensen, *Angew. Chem.* **2005**, *117*, 3769; *Angew. Chem. Int. Ed.* **2005**, *44*, 3703; e) D. D. Steiner, N. Mase, C. F. Barbas III, *Angew. Chem.* **2005**, *117*, 3772; *Angew. Chem. Int. Ed.* **2005**, *44*, 3706; f) T. D. Beeson, D. W. C. MacMillan, *J. Am. Chem. Soc.* **2005**, *127*, 8826.
- [8] a) H. Wack, A. E. Taggi, A. M. Hafez, W. J. Drury III, T. Lectka, *J. Am. Chem. Soc.* **2001**, *123*, 1531; b) S. France, H. Wack, A. E. Taggi, A. M. Hafez, T. R. Wagerle, M. H. Shah, C. L. Dusich, T. Lectka, *J. Am. Chem. Soc.* **2004**, *126*, 4245.
- [9] For a phase-transfer catalyzed fluorination of β -keto esters, see: D. Y. Kim, E. J. Park, *Org. Lett.* **2002**, *4*, 545.
- [10] For recent examples, see: a) T. B. Poulsen, C. Alemparte, S. Saaby, M. Bella, K. A. Jørgensen, *Angew. Chem.* **2005**, *117*, 2956; *Angew. Chem. Int. Ed.* **2005**, *44*, 2896; b) H. Li, Y. Wang, L. Tang, F. Wu, X. Liu, C. Guo, B. M. Foxman, L. Deng, *Angew. Chem.* **2005**, *117*, 107; *Angew. Chem. Int. Ed.* **2005**, *44*, 105; c) S. Saaby, M. Bella, K. A. Jørgensen, *J. Am. Chem. Soc.* **2004**, *126*, 8120; d) M. Bella, K. A. Jørgensen, *J. Am. Chem. Soc.* **2004**, *126*, 5672; e) H. Li, Y. Wang, L. Tang, L. Deng, *J. Am. Chem. Soc.* **2004**, *126*, 9906.
- [11] The uncatalyzed background chlorination reaction of **1a** was demonstrated to proceed to different extents depending on the chlorinating agent; that is, under conditions of 1:1 **1a/3**, in toluene for 3 h at room temperature, the conversion of **1a** is 100% with **3a**, 58% with **3c**, and 12% with **3d**.
- [12] It was reported that the use of trichloroquinolinone **3d** in the asymmetric catalytic α -chlorination of acid halides resulted in poor chemical and optical yields; see reference [8b].
- [13] For a similar system in which the proton transfer from the protonated benzoylquinine to NaHCO_3 represents a key step of catalysis, see the α -chlorination of acid halides in reference [8b].
- [14] The beneficial effect of NaHCO_3 on reactivity is more appreciable with less-reactive substrates such as linear β -keto esters. The effects of various bases on the asymmetric halogenation were evaluated (see Supporting Information).
- [15] The absolute configurations of **2a–b** and **2e** were determined to be *S* by comparison of the specific optical rotations with those reported in the literature. All other absolute configurations were assigned by analogy. Although it is premature to provide a detailed mechanistic explanation at this level, the sense of stereochemical induction suggests the formation of a BQd-enolate ionic complex in which the *Re* face is effectively shielded by the chiral organocatalyst.
- [16] The use of different brominating agents such as *N*-bromosuccinimide and 2,4,4,6-tetrabromo-2,5-cyclohexadione resulted in very low enantioselectivities.

DOI: 10.1002/anie.200501018

**Structural Dualism in the Zwitterionic
7-RR'NH-*nido*-7,8,9-C₃B₈H₁₀ Tricarbollide
Series: An Example of Absolute Tautomerism****

Mario Bakardjiev, Josef Holub, Drahomír Hnyk,
Ivana Císařová, Michael G. S. Londesborough,
Dmitry S. Perekalin, and Bohumil Štíbr*

Tautomerism, which is a dynamic equilibrium between two or more alternative structures of a single species, has been observed for many organic compounds. The commonest case of tautomerism, known as prototropy, is when the electrofuge (a leaving group that does not carry away the bonding electron pair) is a proton. This phenomenon is typical for compounds that contain a functional group that is able to donate a proton, and another functional group which is able to accept it, the functional groups must be in the same molecule and in close enough proximity to one another. The tautomerisation equilibrium is in all cases transmitted by a common anion. The most renowned textbook example of tautomerism is the equilibrium between the keto and enol forms of acetylacetone (Scheme 1).^[1] The tautomerisation constant, defined as $K_T = [\text{enol}]/[\text{keto}]$, is in this case 3.6 for neat acetylacetone.^[1]

Herein we report a unique example of what we would like to term “absolute tautomerism” in the “zwitterionic” tricarbollide series in which a compound adopts one of two different tautomeric forms, either zwitterionic 7-RR'NH-7,8,9-C₃B₈H₁₀ (**Z1**) or neutral 7-RR'N-7,8,9-C₃B₈H₁₁ (**N1**; where R,R' = H or alkyl groups), depending on the properties of the solvent used.

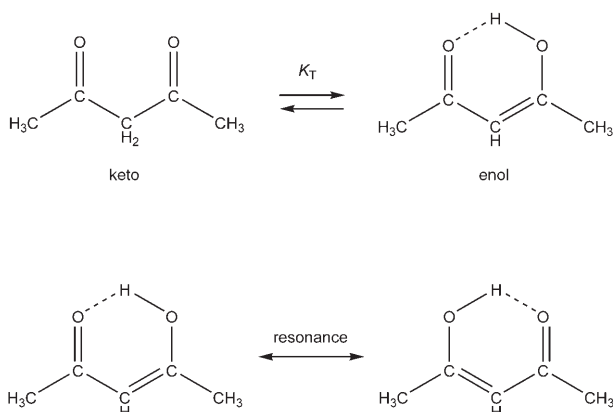
Almost a decade ago we reported the synthesis of the zwitterionic (**Z**) compounds 7-RR'NH-7,8,9-C₃B₈H₁₀ (**Z1**) (where R,R' = H,H (**1a**); H,*t*Bu (**Z1b**); Me,Me (**Z1c**); Me,*t*Bu (**Z1d**)). The NMR spectra for this series in CD₃CN

[*] Dr. M. Bakardjiev, Dr. J. Holub, Dr. D. Hnyk,
Dr. M. G. S. Londesborough, Prof. Dr. B. Štíbr
Institute of Inorganic Chemistry
Academy of Sciences of the Czech Republic
250 68 Řež (Czech Republic)
Fax: (+420) 2-2094-1502
E-mail: stibr@iic.cas.cz

Dr. I. Císařová
Faculty of Natural Sciences of Charles University
Hlavova 2030, 128 42 Prague 2 (Czech Republic)
Fax: (+420) 2-296-084
E-mail: cisarova@natur.cuni.cz

D. S. Perekalin
Institute of Organoelement Compounds
Russian Academy of Sciences
28 ul. Vavilova, 119991, Moscow GSP-1 (Russian Federation)

[**] The work was supported by the Grant Agency of the Czech Republic (project 203/05/2646), Ministry of Education of the Czech Republic (project LC 523), and INTAS project YSF no. 04-83-3848 (to D.S.P.)



Scheme 1. Equilibrium between the tautomeric keto and enol forms of acetylacetone.^[1]

show typical patterns consistent with the structural formulation **Z1**.^[2] Having the zwitterionic character of these compounds in mind, we initially did not attempt NMR spectroscopic measurements in proton nontransferring (PNT) solvents (such as CDCl_3) because of suspected insolubility. Serendipitously, however, we ventured to do so and to our surprise we found that not only are these compounds soluble in CH_2Cl_2 or CHCl_3 , but that their NMR spectra (in CDCl_3) show entirely different NMR patterns (for compounds **N1b** and **Z1b** see Figure 1) that are fully consistent with the

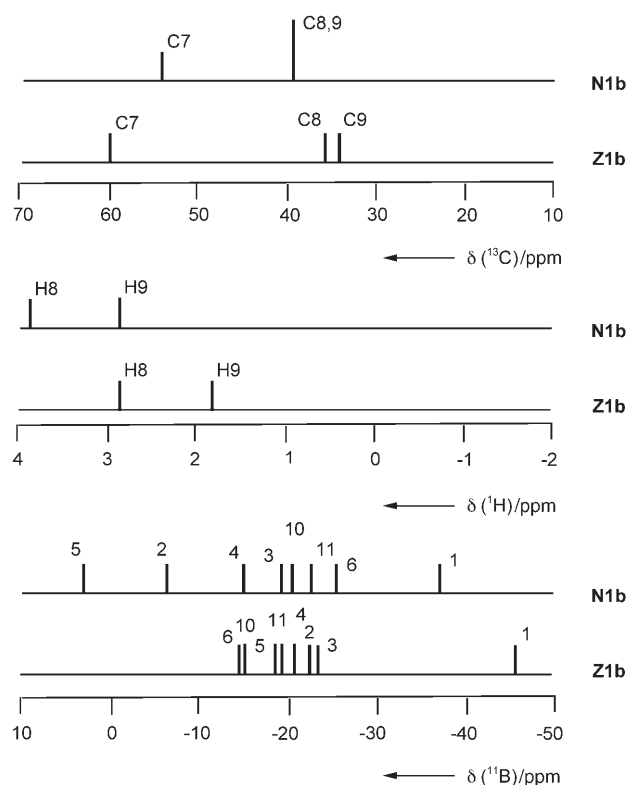
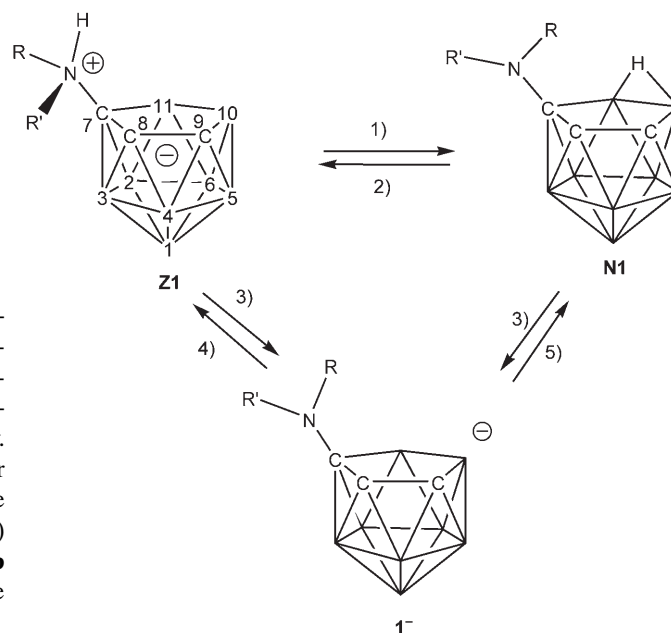


Figure 1. Stick diagrams showing chemical shifts and relative intensities in the ^{11}B (all signals), ^1H (signals from cage CH groups), and ^{13}C NMR (signals cage C atoms) spectra for the tautomeric pair 7-*t*BuNH₂-7,8,9- $\text{C}_3\text{B}_8\text{H}_{10}$ (**Z1b**) and 7-*t*BuNH-7,8,9- $\text{C}_3\text{B}_8\text{H}_{11}$ (**N1b**). For numbering scheme see **Z1** in Scheme 2

neutral tautomeric form of constitution 7-RR'N-7,8,9- $\text{C}_3\text{B}_8\text{H}_{11}$ (**N1**). It should be emphasized that in homogeneous solvent solutions all **Z1**→**N1** conversions are quantitative (at least K_T approaches infinity) with no sign of equilibrium between individual **Z1** and **N1** tautomers detectable in the NMR spectra. As shown in Scheme 2 (path 1) the tautomeric



Scheme 2. The formation and interconversions of the 7-RR'NH-7,8,9- $\text{C}_3\text{B}_8\text{H}_{10}$ (**Z1a**–**Z1d**) and the corresponding 7-RR'N-7,8,9- $\text{C}_3\text{B}_8\text{H}_{11}$ tautomers (**N1a**–**N1d**). 1) dissolution in PNT solvents (such as, CHCl_3 , CH_2Cl_2 , C_6H_6); 2) crystallization from PT solvents (EtOH/water, acetone/water); 3) proton sponge/ CH_2Cl_2 or NaH/ Et_2O ; 4) protonation (H_2SO_4 , CF_3COOH , HCl) in PT solvents; 5) protonation (H_2SO_4 , CF_3COOH , HCl) in PNT solvents. See text for details. C is CH (for C8 and C9), vertices without letters are BH.

conversion is achieved by a simple transfer of an N–H proton to a position bridging B10–B11. Conversely, the **N1** tautomers can also be quantitatively converted into **Z1** tautomers by simple crystallization from proton transferring (PT) solvents (such as EtOH/ H_2O , acetone/ H_2O) or by dissolution in acetonitrile (path 2).

In the case of nonhomogeneous solvent mixtures (see Figure 2) the addition of CH_3CN to a CDCl_3 solution of **N1b** expectedly leads to a classical equilibrium between the **Z1b** and **N1b** tautomers, the equilibrium being defined by the tautomeric constant $K_T = [\text{Z1b}]/[\text{N1b}]$ (where $[\text{Z1b}]$ and $[\text{N1b}]$ are equilibrium concentrations of the zwitterionic and neutral tautomers, respectively). It can be seen from Figure 2 that by adding CH_3CN to a CDCl_3 solution of **N1b** the concentration of the **Z1b** tautomer rapidly grows, and at a CH_3CN volume fraction of approximately 0.25, the **N1b** tautomer disappears from the solution ($[\text{N1b}] = 0$), there are no signals corresponding to the **N1b** tautomer in the ^{11}B and ^1H NMR spectra. This result suggests that at that critical CH_3CN concentration K_T is equal to or approaching infinity.

It is reasonable to suppose that in these tautomeric conversions the proton transfer between the two proton

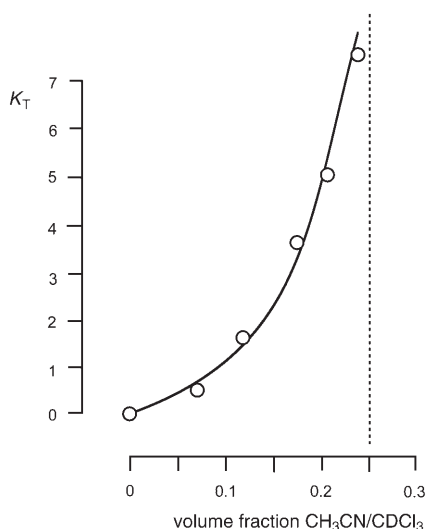


Figure 2. Plot of experimental K_T values versus volume fraction $\text{CH}_3\text{CN}/\text{CDCl}_3$ for the equilibrium between **Z1b** and **N1b** tautomers. At around 0.25 (dotted line) K_T approaches infinity and only one tautomer (**Z1b**) is present in the solution. $K_T = [\text{Z1b}]/[\text{N1b}]$.

accepting centers, the N-atom and the cage B10–B11 bond, occurs through common anions of type $[\text{7-RR}'\text{NH-7,8,9-C}_3\text{B}_8\text{H}_{10}]^-$ (**1**[−]). These anions can be prepared independently by treatment of both tautomers, **Z1** and **N1**, with NaH in Et_2O or proton sponge (PS) in $\text{CH}_2\text{Cl}_2/\text{hexane}$ mixtures (Scheme 2 (path 3)). Conversely, acidification (HCl, CF_3COOH) of the anions **1**[−] (Na^+ salts) in PT solvents (water, acetonitrile) generates tautomers **Z1** (path 4), while acidification of the PS^+ salts with H_2SO_4 in CH_2Cl_2 leads exclusively to tautomers **N1** (path 5)).

Figure 1 summarizes the NMR patterns for the tautomeric pair **Z1b/N1b**. The remaining compounds from the corresponding **Z1/N1** series exhibit very similar NMR spectroscopic behavior, which we will report elsewhere in a full paper.

The **Z1**-type compounds are derivatives of the $[\text{7,8,9-C}_3\text{B}_8\text{H}_{11}]^-$ ion, while their **N1** tautomers are derivatives of the neutral tricarbolide $\text{7,8,9-C}_3\text{B}_8\text{H}_{12}$.^[2,3] Significant differences between the **Z1** and **N1** tautomers are seen in their ^{11}B NMR spectra, and arise from the presence of the hydrogen atom bridging the B10–B11 bond in **N1**. However, the ^1H and ^{13}C NMR spectra for cage CH and C units are also remarkably different.

The different **Z1** and **N1** tautomers can also be isolated in the solid state. For example, **Z1b** and **N1b** differ in their melting points (148/136°C, respectively) and, moreover, the structure of pure **Z1b** (Figure 3^[4]) and **Z1d**. OCMe_2 ^[2] tautomers were determined by single-crystal X-ray diffraction analysis.

Unfortunately, we have not been able to grow crystals of **N1** compounds, therefore the structures for the simplest tautomeric pair, **Z1a** and **N1a**, were geometrically optimized^[5,6] at the RMP2(fc)/6-31G* level (see Figure 4 and Figure 5). Ignoring variances in H–N–H angles, the main difference (0.094 Å) between them was found for the respective B10–B11 bonds.

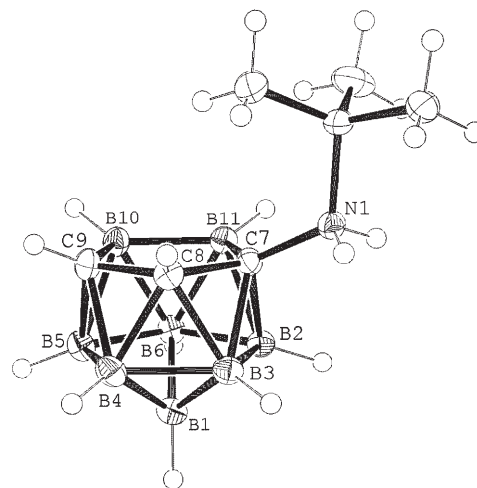


Figure 3. ORTEP representation of the crystallographically determined molecular structure of 7-*tert*-BuNH₂-7,8,9- $\text{C}_3\text{B}_8\text{H}_{10}$ (**Z1b**). Selected bond lengths [Å] and angles [°]: B1–B2 1.792(2), B1–B3 1.737(2), B1–B4 1.758(2), B1–B5 1.795(2), B1–B6 1.811(2), B2–B3 1.776(2), B2–B6 1.756(2), B2–C7 1.743(2), B2–B11 1.799(2), B3–B4 1.758(2), B3–C7 1.757(2), B3–C8 1.731(2), B4–B5 1.770(2), B4–C8 1.728(2), B4–C9 1.733(2), B5–B6 1.753(2), B5–C9 1.732(2), B5–B10 1.788(2), B6–B10 1.788(2), B6–B11 1.790(2), C7–C8 1.513(2), C7–B11 1.618(2), C8–C9 1.516(2), C9–B10 1.616(2), B10–B11 1.733(2), N1–C7 1.496(2), N1–C1 1.557(2); B11–C7–C8 112.2(1), C7–C8–C9 110.1(1), C8–C9–B10 110.8(1), C9–B10–B11 104.4(1), C7–B11–B10 102.4(1).

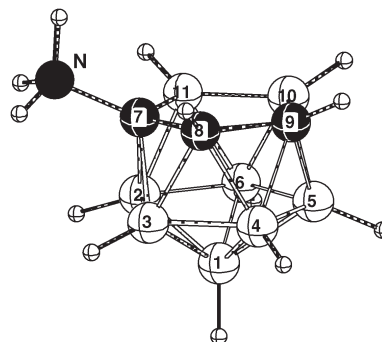


Figure 4. RMP2(fc)/6-31G* optimized geometry of 7-NH₂-7,8,9- $\text{C}_3\text{B}_8\text{H}_{10}$ (**Z1a**). White spheres B, black spheres C. Selected bond lengths [Å] and angles [°]: B1–B2 1.775, B1–B3 1.733, B1–B4 1.761, B1–B5 1.790, B1–B6 1.822, B2–B3 1.779, B2–B6 1.760, B2–C7 1.710, B2–B11 1.804, B3–B4 1.754, B3–C7 1.744, B3–C8 1.739, B4–B5 1.766, B4–C8 1.731, B4–C9 1.737, B5–B6 1.761, B5–C9 1.720, B5–B10 1.788, B6–B10 1.790, B6–B11 1.785, C7–C8 1.508, C7–B11 1.602, C8–C9 1.516, C9–B10 1.625, B10–B11 1.729, C7–N 1.491; C7–C8–C9 108.3, C8–C7–N 117.9, H–N–H (mean) 108.3, H–N–C7 (mean) 110.3. Calculated $\delta(^{11}\text{B})$ chemical shifts (B3LYP/6-31G*//RMP2(fc)/6-31G*) versus experimental (CD_3CN , data from ref. [2]): calcd/exp: B6 −10.8/−15.5, B10 −13.7/−15.5, B11 −19.7/−17.8, B5 −20.8/−18.5, B4 −20.8/−20.2, B2 −23.1/−23.1, B3 −23.8/−23.1, B1 −44.7/−47.1 ppm.

Considering the readiness of interconversion between the **Z1** and **N1** tautomers, a minimal difference in their calculated structure energies might be anticipated. However, the RMP2(fc)/6-31G* calculations on the “free” molecules of **Z1a** and **N1a** in vacuo reveal that the neutral **N1a** tautomer is 22.34 kcal mol^{−1} more stable than **Z1a**. Including the solvent

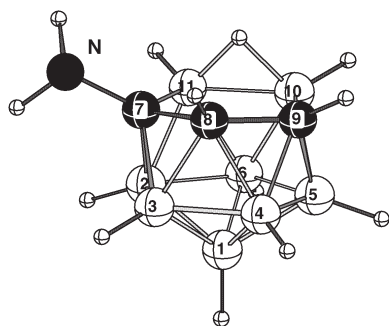


Figure 5. RMP2(fc)/6-31G* optimized geometry of 7-NH₂-7,8,9-C₃B₈H₁₁ (**N1a**). White spheres B, black spheres C. Selected bond lengths [Å] and angles [°]: B1-B2 1.756, B1-B3 1.772, B1-B4 1.777, B1-B5 1.760, B1-B6 1.800, B2-B3 1.753, B2-B6 1.780, B2-C7 1.689, B2-B11 1.796, B3-B4 1.765, B3-C7 1.700, B3-C8 1.720, B4-B5 1.753, B4-C8 1.730, B4-C9 1.695, B5-B6 1.777, B5-C9 1.685, B5-B10 1.804, B6-B10 1.793, B6-B11 1.792, C7-C8 1.532, C7-B11 1.667, C8-C9 1.515, C9-B10 1.657, B10-B11 1.823, C7-N 1.438; C7-C8-C9 116.7, C8-C7-N 115.6, H-N-H (mean) 107.6, H-N-C7 (mean) 110.3, B10-H_b and B11-H_b 1.312. Calculated $\delta(^{11}\text{B})$ chemical shifts (B3LYP/6-31G*/RMP2(fc)/6-31G*) versus experimental (CDCl₃): calcd/exp: B2 3.6/3.9, B5 -5.3/-5.7, B3 -16.9/-16.0, B11 -19.4/-19.5, B4 -21.6/-21.0, B10 -22.2/-22.1, B6 -26.2/-27.0, B1 -35.0/-36.2.

polarity effects in the calculations shows a gradual decrease in the difference between the two tautomers from 6.31 in CHCl₃ to 3.32 in CH₂Cl₂, to 0.15 kcal mol⁻¹ in MeCN. Nevertheless, the experimental observation of a rapid conversion of **N1a** into **Z1a** upon only small polarity change indicates that **Z1a** is stabilized by some specific interaction with acetonitrile (most probably, hydrogen bonding). The mass spectra of both **Z1** and **N1** show essentially the same fragmentation patterns, which indicates that the **Z1**→**N1** conversions proceed under the conditions of the mass-spectrometric experiment.

As far as we are aware, the isolation of pure tautomers of type **1** represents the first example of absolute tautomerism, and thus introduces a new type of structural dualism to chemistry.

Experimental Section

Typical experiments outlined below for compound **1b** are generally applicable to all compounds of constitution **1**.

Z1b: Compounds **Z1b** (102 mg, 0.5 mmol, prepared as reported earlier^[2]) and **N1b** (102 mg, 0.5 mmol) were re-crystallized from a hot EtOH/H₂O mixture to give 100 mg (98%) of **Z1b**. For **Z1b**: For ¹¹B and ¹H NMR spectra see ref. [2] ¹³C NMR (125.8 MHz, CD₃CN, 295 K): δ = 65.0 (s, 1 C, *t*Bu), 60.9 (br, s, 1 C, C7), 35.6 (br, s, 1 C, C8), 34.1 (br, s, 1 C, C9), 27.4 ppm (q, ¹J(C,H) = 129 Hz, 3 C, *t*Bu).

N1b: Compound **Z1b** (205 mg, 1 mmol) was dissolved in CH₂Cl₂ or CHCl₃ (10 mL). Diffusion in of hexane vapors led to crystallization to yield 158 mg (77%) of crystalline **N1b**. Further amount of **N1b** (42 mg, 21%, total yield of **N1b** 98%) was obtained by evaporation of mother liquors. For **N1b**: m.p. 136°C; ¹¹B NMR (128.3 MHz, 25°C, CDCl₃): δ = 2.8 (d, ¹J(B,H) = 159 Hz, 1 B; B2), -6.2 (d, ¹J(B,H) = 162 Hz, 1 B; B5), -15.2 (d, ¹J(B,H) = 171 Hz, 1 B; B3), -19.7 (d, ¹J(B,H) ≈ 170 Hz, 1 B; B4), -20.7 (d, ¹J(B,H) ≈ 140 Hz, 1 B; B11), -22.1 (d, ¹J(B,H) ≈ 150 Hz, 1 B; B10), -25.9 (d, ¹J(B,H) = 150 Hz, 1 B; B6), -37.2 ppm (d, ¹J(B,H) = 152 Hz, 1 B; B1), all theoretical [¹¹B-¹H] cross-peaks are observed; ¹H{¹¹B} NMR (400 MHz, 25°C, CDCl₃): δ = 3.88 (s, 1 H; H8), 3.01 (s, 1 H; H2), 2.73 (s, 1 H; H9), 2.48

(s, 1 H; H5), 2.17 (s, 1 H; H11), 2.00 (s, 1 H; H4), 1.89 (s, 1 H; H3), 1.83 (s, 1 H; H10), 1.1 (s, 2 H; H1, H6), -2.27 ppm (s, 1 H; μ H); ¹³C{¹H} NMR (100.2 MHz, CDCl₃, 295 K): δ = 69.1 (s, 1 C, *t*Bu), 54.9 (br, s, 1 C, C7), 39.2 (br, s, 2 C, C8, C9), 31.1 (s, 3 C, *t*Bu); C₇H₂₁B₈N (205.73): elemental analysis calcd (%) C 40.87, H 10.29; found C 40.64, H 10.12. A solution of PSH⁺**1b**⁻ (50 mg, 0.12 mmol; PS = proton sponge) in CH₂Cl₂ (10 mL) was treated dropwise with concentrated H₂SO₄ (0.5 mL) under cooling and stirring. The CH₂Cl₂ layer was collected, shaken with water (2 × 20 mL), dried over CaCl₂, and evaporated to afford 12 mg (84%) of **N1b**, which was identified by NMR spectroscopy.

1b⁻: A solution of compounds **Z1b** or **N1b** (102 mg, 0.5 mmol) in Et₂O (20 mL) was treated with NaH (ca. 50 mg, 2 mmol) under stirring at room temperature for 12 h. The mixture was then filtered under anaerobic conditions, the filtrate evaporated, and the residual solid dried at room temperature for 24 h to give Na⁺**1b**⁻·OEt₂ (145 mg, 96%) as white crystals. For Na⁺**1b**⁻·OEt₂: m.p. > 350°C (decomp.); ¹¹B NMR (128.3 MHz, 25°C, CD₃CN): δ = -15.4 (d, -, 1 B; B6), -16.8 (d, -, 2 B; B10,11), -17.7 (d, -, 1 B; B5), -18.9 (d, -, 1 B; B4), -23.5 (d, ¹J(B,H) = 161 Hz, 1 B; B3), -25.3 (d, ¹J(B,H) = 146 Hz, 1 B; B2), -48.0 ppm (d, ¹J(B,H) = 138 Hz, 1 B; B1), all theoretical [¹¹B-¹H] cross-peaks observed; - indicates couple constants that could not be determined ¹H{¹¹B} NMR (400 MHz, 25°C, CD₃CN): δ = 3.61 (s, 1 H; NH), 3.39 (t, 2 H; Et₂O), 2.31 (s, 1 H; H9), 1.77 (s, 1 H; H8), 1.45 (s, 1 H; H3), 1.38 (s, 1 H; H4), 1.30 (q, 3 H; Et₂O), 1.29 (s, 1 H; H10 or H11), 1.12 (s, 9 H; *t*Bu), 0.96 (s, 1 H; H5), 0.93 (s, 1 H; H6), 0.92 (s, 1 H; H10 or H11), 0.77 (s, 1 H; H2), -0.16 ppm (s, 1 H; H1); C₁₁H₃₀NB₈ONa (301.83): elemental analysis calcd (%) Na 7.62; found Na 7.56. A solution of compound **N1b** (50 mg, 0.24 mmol) in CH₂Cl₂ (10 mL) was treated with proton sponge (ca. 50 mg, 2 mmol) hexane (20 mL) was carefully layered onto the surface of the solution. After allowing the solution to stand for 24 h, the crystals were isolated by filtration, washed with hexane, and vacuum dried to give 91 mg (90%) of PSH⁺**1b**⁻, which was identified by NMR spectroscopy.

Received: March 21, 2005

Published online: August 11, 2005

Keywords: boron · carboranes · density functional theory · structural dualism · tautomerism

- [1] See, for example: J. D. Roberts, M. C. Caseiro, *Basic Principles of Organic Chemistry*, W. A. Benjamin, New York, 1965, pp. 496–498.
- [2] a) B. Štíbr, J. Holub, F. Teixidor, C. Viñas, *J. Chem. Soc. Chem. Commun.* **1995**, 795–796; B. Štíbr, J. Holub, I. Cířová, F. Teixidor, C. Viñas, J. Fusek, Z. Plzák, *Inorg. Chem.* **1996**, 35, 3635–3642; b) B. Štíbr, J. Holub, J. Plešek, T. Jelínek, B. Grüner, F. Teixidor, C. Viñas, *J. Organomet. Chem.* **1999**, 582, 282–285.
- [3] J. Holub, B. Štíbr, D. Hnyk, J. Fusek, I. Cířová, F. Teixidor, C. Viñas, Z. Plzák, P. v. R. Schleyer, *J. Am. Chem. Soc.* **1997**, 119, 7750–7759.
- [4] a) Crystal structure data for C₇H₂₁B₈N (**Z1b**): *M*_r = 205.73, colorless crystal, size 0.45 × 0.40 × 0.05 mm³, monoclinic, space group *P*2₁/*c*, *a* = 9.2840(3), *b* = 10.1030(2), *c* = 13.4830(5) Å, β = 106.544(2)°, *V* = 1212.3 Å³, *T* = 150(2) K, *Z* = 4, ρ_{calcd} = 1.127 Mg m⁻³, Data collected on NoniusKappaCCD four-circle diffractometer (MoK α radiation λ = 0.71073 Å, graphite monochromator); θ_{max} = 27.5°. A total of 16478 reflections were measured, 2771 unique (*R*_{int} = 0.044). Absorption was neglected ($\mu(\text{MoK}\alpha)$ = 0.055 mm⁻¹), GoF on *F*² was 1.045, *R*1 (*I* > 2 σ (*i*)) = 0.043, *wR*2 = 0.129. Largest difference Fourier peak and hole 0.219 and -0.211 e Å⁻³. Refinement used SHELXL97 (G. M. Sheldrick, **1997**). CCDC-266543 contains the supplementary crystallographic data for this paper. These data can be obtained

free of charge from the Cambridge Crystallographic Data Centre via www.ccdc.cam.ac.uk/data_request/cif.

- [5] The calculations used the Gaussian03 program package (ref. [6]) and were performed on a PC (FujitsuSiemens). The structures were optimized first at the RHF/6-31G* level without symmetry restrictions (C_1). Second-derivative analysis, carried out at the same level, determined the nature of the stationary points. The minima were characterized with zero imaginary frequencies. Final optimization at the RMP2/6-31G* included the effect of electron correlation. The calculation of the solvation effects on energy were performed for these geometries at the same level of theory using the PC (personal computer) model. The ^{11}B NMR spectroscopy chemical shifts were calculated at B3LYP/6-31G* level by the GIAO method. The complete data are available from the authors.
- [6] Gaussian03 (Revision B.03), M. J. Frisch, G. W. Trucks, H. B. Schlegel, G. E. Scuseria, M. A. Robb, J. R. Cheeseman, J. A. Montgomery, Jr., T. Vreven, K. N. Kudin, J. C. Burant, J. M. Millam, S. S. Iyengar, J. Tomasi, V. Barone, B. Mennucci, M. Cossi, G. Scalmani, N. Rega, G. A. Petersson, H. Nakatsuji, M. Hada, M. Ehara, K. Toyota, R. Fukuda, J. Hasegawa, M. Ishida, T. Nakajima, Y. Honda, O. Kitao, H. Nakai, M. Klene, X. Li, J. E. Knox, H. P. Hratchian, J. B. Cross, C. Adamo, J. Jaramillo, R. Gomperts, R. E. Stratmann, O. Yazyev, A. J. Austin, R. Cammi, C. Pomelli, J. W. Ochterski, P. Y. Ayala, K. Morokuma, G. A. Voth, P. Salvador, J. J. Dannenberg, V. G. Zakrzewski, S. Dapprich, A. D. Daniels, M. C. Strain, O. Farkas, D. K. Malick, A. D. Rabuck, K. Raghavachari, J. B. Foresman, J. V. Ortiz, Q. Cui, A. G. Baboul, S. Clifford, J. Cioslowski, B. B. Stefanov, G. Liu, A. Liashenko, P. Piskorz, I. Komaromi, R. L. Martin, D. J. Fox, T. Keith, M. A. Al-Laham, C. Y. Peng, A. Nanayakkara, M. Challacombe, P. M. W. Gill, B. Johnson, W. Chen, M. W. Wong, C. Gonzalez, J. A. Pople, Gaussian, Inc., Pittsburgh, PA, **2003**.

Synthesis of Enantiopure Carbohydrate Mimetics by Lewis Acid Catalyzed Rearrangement of 1,3-Dioxolanyl-Substituted 1,2-Oxazines**

Ahmed Al-Harrasi and Hans-Ulrich Reißig*

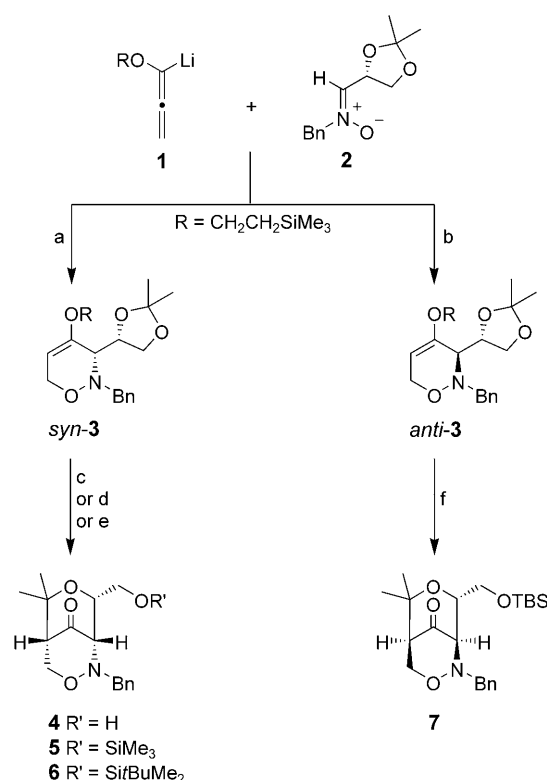
Dedicated to Professor Helmut Vorbrüggen on the occasion of his 75th birthday

Enantiomerically pure 3,6-dihydro-2*H*-1,2-oxazines, which are easily available by [3+3] cyclization of lithiated alkoxyallenes with aldonitrone,^[1] are versatile intermediates for the stereoselective synthesis of a range of highly functionalized compounds. All these products, including polyhydroxylated pyrrolidines, stereodefined amino polyols, and substituted tetrahydrofuran derivatives,^[2] are interesting because of their potential biological activities, for example, as glycosidase inhibitors.^[3] While trying to deprotect 1,2-oxazine *syn*-**3** with Lewis acids we found that a rearrangement to tetrahydropyran-bridged bicyclic 1,2-oxazine **4** occurred in moderate yield (Scheme 1).^[2b] Thereby the acetonide protecting group of *syn*-**3** was incorporated into product **4**. Herein we report that:

- this reaction proceeds quite generally with suitably substituted 3,6-dihydro-2*H*-1,2-oxazines as starting materials,
- the obtained enantiopure bicyclic products can be converted stereoselectively into numerous polyhydroxylated amino-substituted pyran derivatives,
- in a similar manner, highly functionalized oxepane derivatives are accessible.

The resulting products may be regarded as carbohydrate mimetics,^[4] which are potentially important building blocks for the synthesis of biologically active compounds, for example, oligosaccharide analogues.

The stereodivergent addition of lithiated alkoxyallene **1** to the D-glyceraldehyde-derived nitrone **2** gives either *syn*- or *anti*-configured **3** in excellent yield (Scheme 1).^[1] The unex-



Scheme 1. Reaction conditions: a) THF, −78 °C, 2 h (*syn*-**3**: 76%); b) **2** + Et₂AlCl, Et₂O, then add to **1**, −78 °C, 2 h (*anti*-**3**: 84%); c) SnCl₄ (3 equiv), CH₃CN, −30 °C → RT, 6 h (**4**: quant.); d) Me₃SiOTf (0.05 equiv), CH₂Cl₂, −30 °C → RT, 6 h (**5**: 79%); e) *t*BuMe₂SiOTf (3 equiv), CH₂Cl₂, room temperature, 20 h, then NEt₃, 0 °C, 15 min (**6**: quant.); f) *t*BuMe₂SiOTf (3 equiv), CH₂Cl₂, room temperature, 20 h, then NEt₃, 0 °C, 15 min (**7**: 93%). Bn = benzyl; TBS = *tert*-butyldimethylsilyl; Tf = trifluoromethanesulfonyl.

pected cyclization of *syn*-**3** to **4**, which was first observed in moderate yields in the presence of BF₃·OEt₂, was optimized by using a range of Lewis acids and screening the reaction conditions. Although the rearrangement could be accomplished with different Lewis acids, dibutylboron triflate, trimethylsilyl triflate, and tin tetrachloride proved to be the best promoters.^[5] The conversion of *syn*-**3** into bicyclic product **4** proceeded quantitatively with SnCl₄ in acetonitrile.

We propose that the mechanism of this reaction involves the coordination of the Lewis acid to the “outer” dioxolane oxygen atom (O-1) of *syn*-**3**, followed by ring opening of the acetonide unit and intramolecular attack of the generated carbenium ion at the enol ether unit of the 1,2-oxazine ring. Cleavage of the (trimethylsilyl)ethyl group—most probably to give ethene and Me₃SiX species^[6]—affords the central carbonyl group of the resulting bicyclic compound **4**. This rearrangement can be classified as an intramolecular aldol-type addition of an acetal to an enol ether^[7] or as a Prins reaction.^[8]

The rearrangement can also be triggered by catalytic amounts of trimethylsilyl (TMS) triflate.^[9] Treatment of *syn*-**3** with 0.05 equivalents of this mild Lewis acid led to TMS-protected derivative **5** in 79% yield. To introduce the more stable *tert*-butyldimethylsilyl protecting group, *syn*-**3** was treated with *t*BuMe₂SiOTf (3 equiv) and then with triethyl-

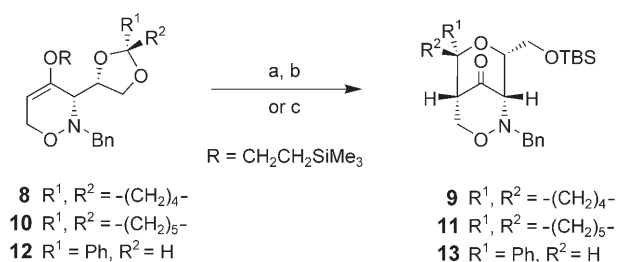
[*] A. Al-Harrasi, Prof. Dr. H.-U. Reißig
Institut für Chemie und Biochemie
Freie Universität Berlin
Takustrasse 3, 14195 Berlin (Germany)
Fax: (+49) 30-8385-5367
E-mail: hans.reissig@chemie.fu-berlin.de

[**] This work was generously supported by the Deutsche Forschungsgemeinschaft, the Deutscher Akademischer Austauschdienst (fellowship for A.A.H.), the Fonds der Chemischen Industrie, and Schering AG. We thank B. Bressel and Dr. R. Zimmer for help during the preparation of this manuscript, W. Münch for HPLC separations, as well as M. Wiecko and J. Gebers for experimental assistance.

Supporting information for this article is available on the WWW under <http://www.angewandte.org> or from the author.

amine to generate bicyclic product **6**. In a similar manner the rearrangement of diastereomeric 1,2-oxazine *anti*-**3** led to protected bicyclic 1,2-oxazine **7** (Scheme 1). This compound can also be obtained by SnCl₄-induced rearrangement followed by silylation (80% yield). As diastereomeric heterocycles *syn*- and *anti*-**3** are enantiopure,^[10] this should also hold for the corresponding bicyclic products **4–7**.

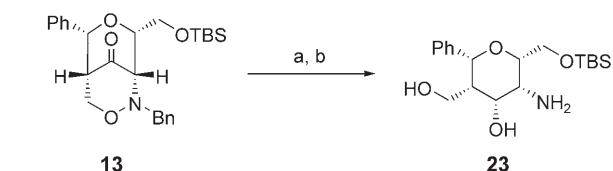
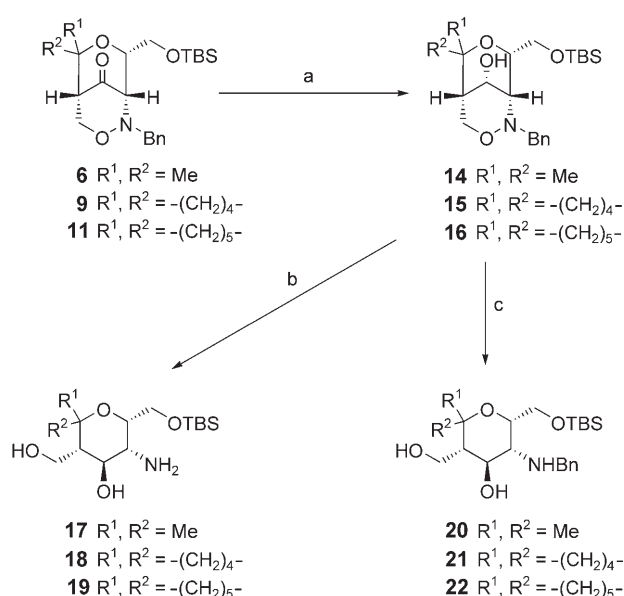
The incorporation of the acetonide unit into products **4–7** suggested that other “protecting” groups can be employed in the starting material to obtain differently substituted bicyclic compounds. Therefore *syn*-configured 1,2-oxazines **8**, **10**, and **12**, which contain cyclopentanone-, cyclohexanone-, and benzaldehyde-derived acetals, were synthesized in analogous procedures (Scheme 2).^[11] As expected, treatment of **8** with



Scheme 2. Reaction conditions: a) SnCl₄ (3 equiv), CH₃CN, $-30^\circ\text{C} \rightarrow \text{RT}$, 6 h; b) *t*BuMe₂SiOTf (3 equiv), NEt₃, CH₂Cl₂, 0°C , 1 h, (yields over two steps: **9**: 86%, **11**: 70%, **13**: 77%); c) *t*BuMe₂SiOTf (3 equiv), CH₂Cl₂, room temperature, 20 h, then NEt₃, 0°C , 15 min, (**11**, **13**: quant.).

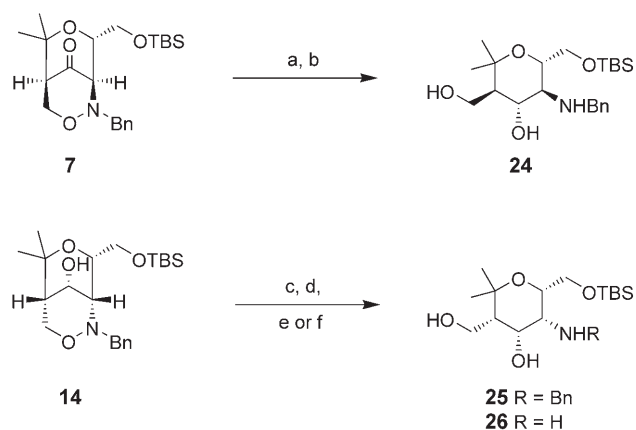
tin tetrachloride followed by *O*-silylation gave spiro compound **9** in very good overall yield. For 1,2-oxazines **10** and **12** the one-step procedure with *tert*-butyldimethylsilyl triflate as promoter was chosen, leading directly to the protected rearrangement products **11** and **13** in excellent yields. The configuration at the acetal carbon atom of compound **12** did not affect the outcome: the pure *R*-configured bicyclic product **13** was obtained from both diastereoisomers (or a mixture of the two).^[12] This can be expected if a carbenium ion with an equatorial aryl group is involved in the cyclization process. The *anti*-configured compounds underwent similarly efficient rearrangements.^[5]

The bicyclic products presented contain an N–O bond whose cleavage should give access to highly functionalized enantiopure pyran derivatives. With ketones such as **6** this ring fission was not successful. However, after reduction of the carbonyl group of **6**, **9**, or **11** with NaBH₄ the resulting diastereomerically pure alcohols **14–16**, respectively (or their *O*-protected derivatives),^[5] could be opened smoothly. Hydrogenolysis with hydrogen and palladium on charcoal did not only cleave the ring of the 1,2-oxazine but also removed the *N*-benzyl group to give primary amines **17–19** in good to very good yields (Scheme 3).^[13] Debenzylation can be avoided by using the milder reducing agent samarium diiodide.^[14] Secondary amines **20–22** were obtained after short reaction time in almost quantitative yields. These two reduction steps were used to convert phenyl-substituted bicyclic compound **13** into pyran derivative **23**, which contains five stereogenic centers.^[15]



Scheme 3. Reaction conditions: a) NaBH₄, EtOH, 0°C , 4 h, (**14**: 97%, **15**: 98%, **16**: 70%); b) H₂, Pd/C, MeOH, room temperature, 1 d, (**17**: 72%, **18**: 96%, **19**: 99%, **23**: 64% over two steps); c) SmI₂, THF, room temperature (**20**: quant., **21**: 93%, **22**: 95%).

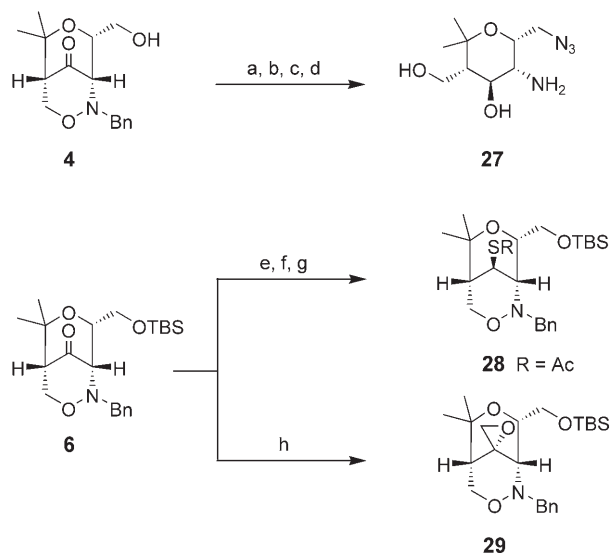
Several options are available to generate different configurations of the tetrahydropyran derivatives. Bicyclic 1,2-oxazine **7** (derived from *anti*-**3**) was reduced with NaBH₄ and subsequent ring opening with samarium diiodide led to *trans,trans,trans*-**24** (Scheme 4). Hydrogenolysis gave the



Scheme 4. Reaction conditions: a) NaBH₄, EtOH, 0°C , 4 h (82%); b) SmI₂, THF, room temperature (72%); c) DEAD, PPh₃, *p*-nitrobenzoic acid, benzene, room temperature, 6 h, (81%); d) NaN₃, MeOH, 55°C , 2 d, (78%); e) SmI₂, THF, room temperature (**25**: 81%); f) H₂, Pd/C, MeOH, room temperature (**26**: quant.). DEAD = diethylazodicarboxylate.

expected *N*-debenzylated product.^[5] With bicyclic compound **14** as an example, it was demonstrated that Mitsunobu reaction^[16] allows an inversion of configuration of the secondary hydroxy group and hence the synthesis of *all-cis*-substituted carbohydrate mimetics. Both methods of reduction provided the expected products **25** and **26** in good yields.

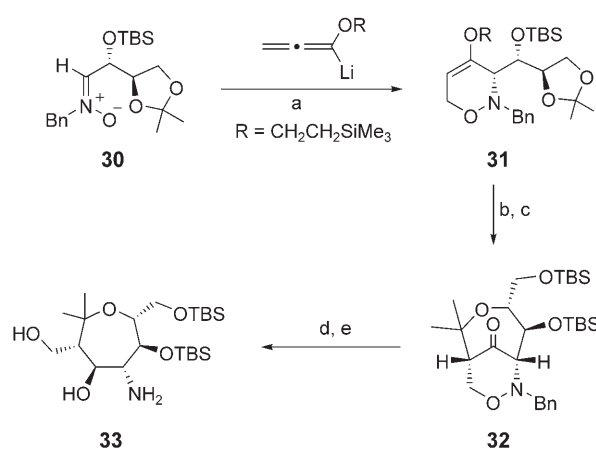
Further stereodefined pyran derivatives synthesized from bicyclic compounds **4** and **6** are presented in Scheme 5.



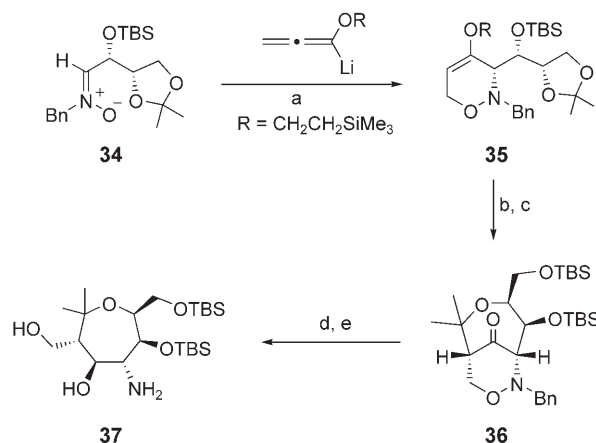
Scheme 5. Reaction conditions: a) MsCl, NEt₃, CH₂Cl₂, 0°C, 4 h, (quant.); b) NaBH₄, EtOH, room temperature, 3 h, (85%); c) NaN₃, DMF, 90°C, 6 h, (73%); d) H₂, Pd/C, MeOH, room temperature, 3 days, (**27**: 81%); e) NaBH₄, EtOH, 0°C, 4 h, (97%); f) MsCl, NEt₃, CH₂Cl₂, 0°C, 4 h, (quant.); g) KSAc, DMF/toluene, 60°C, 6 h, (**28**: 64%); h) Me₃SO⁺t[−], *n*BuLi, −78°C → RT, 12 h, (**29**: 70%). Ms = mesyl, DMF = *N,N*-dimethylformamide.

Mesylation of the primary hydroxy group of **4**, followed by reduction of the carbonyl group with NaBH₄ and introduction of an azido group, generated a new precursor for the reductive ring opening. Hydrogenolysis furnished pyran derivative **27** with an intact azido functionality which may be used for further transformations.^[17] Starting from **6**, a thioacetate group can be installed by nucleophilic attack at the corresponding mesylate, resulting in the bicyclic 1,2-oxazine **28** in good overall yield. Treatment with trimethylsulfoxonium iodide stereoselectively transformed **6** into tricyclic compound **29**, which contains an epoxide moiety. Products **27**–**29** and their precursors offer new options for the preparation of highly functionalized enantiopure tetrahydropyran derivatives that can serve as carbohydrate mimetics.

In first experiments we examined whether rings larger than pyrans can be formed by using the rearrangement presented herein. Schemes 6 and 7 show the reaction pathways that led to enantiopure oxepane derivatives in a highly diastereoselective and surprisingly effective manner. The reaction of nitrone **30** (which was easily prepared from D-isoascorbic acid^[18]) with lithiated alkoxyallene **1** provided compound **31** with high *syn/anti* selectivity. In the presence of SnCl₄ in acetonitrile, 1,2-oxazine **31** afforded the desired rearrangement product, which after protection of the primary



Scheme 6. Reaction conditions: a) THF, −78°C, 2 h, (**31**: 49%, *syn/anti* = 97:3); b) SnCl₄ (3 equiv), CH₃CN, −30°C → RT, 6 h, (76%); c) *t*BuMe₂SiOTf (3 equiv), NEt₃, CH₂Cl₂, 0°C, 1 h, (**32**: 92%); d) NaBH₄, EtOH, 0°C, 4 h, (71%); e) H₂, Pd/C, MeOH, room temperature, 1 day, (**33**: 82%).



Scheme 7. Reaction conditions: a) THF, −78°C, 2 h, (**35**: 71%, *syn/anti* > 97:3); b) SnCl₄ (3 equiv), CH₃CN, −30°C → RT, 6 h, (55%); c) *t*BuMe₂SiOTf (3 equiv), NEt₃, CH₂Cl₂, 0°C, 1 h, (**36**: 97%); d) NaBH₄, EtOH, 0°C, 4 h, (93%); e) H₂, Pd/C, MeOH, room temperature, 1 day, (**37**: 70%).

hydroxy group gave bicyclic product **32** in good overall yield. Reduction with NaBH₄ followed by hydrogenolysis yielded oxepane derivative **33**, whose constitution and configuration was confirmed by X-ray crystallographic analysis. In the same manner, the stereoisomeric oxepane derivative **37** was prepared from the diastereomeric nitrone **34** (derived from L-ascorbic acid)^[18] via intermediates **35** and **36**.^[19] Preliminary experiments proved that suitably substituted 1,2-oxazines as precursors opened a route to oxacyclooctane derivatives (oxocanes) in moderate yields.^[5]

Our results show that Lewis acid induced rearrangements of 3,6-dihydro-2*H*-1,2-oxazines with 1,3-dioxolanyl substituents and subsequent transformations lead to a variety of polyhydroxylated amino-substituted pyran and oxepane derivatives in an efficient and stereocontrolled manner.^[20] The obtained enantiopure oxygen-containing heterocycles can easily be protected selectively (and orthogonally). There-

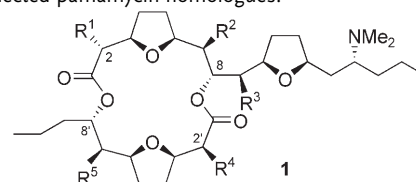
fore these analogues of aminodesoxy sugars should be of high interest for integration into oligosaccharides.^[4,21] Their lipophilicity should be strongly influenced by the nature of alkyl groups R¹ and R² (Scheme 2). These compounds also have potential as starting materials for the synthesis of carbohydrate-based β - or γ -amino acids (sugar amino acids) and they can therefore provide novel peptide analogues.^[22] The pyran derivatives **6** and **7** can be easily prepared in gram scale and hence they are also candidates for stereodefined scaffolds for the synthesis of polyfunctionalized compounds. This concept has been successfully applied to several carbohydrate derivatives.^[23]

Received: March 30, 2005

Keywords: carbohydrates · heterocycles · rearrangement · reduction

- [1] a) W. Schade, H.-U. Reissig, *Synlett* **1999**, 632–634; b) M. Helms, W. Schade, R. Pulz, T. Watanabe, A. Al-Harrasi, L. Fisera, I. Hlobilová, G. Zahn, H.-U. Reissig, *Eur. J. Org. Chem.* **2005**, 1003–1019.
- [2] a) R. Pulz, T. Watanabe, W. Schade, H.-U. Reissig, *Synlett* **2000**, 983–986; b) R. Pulz, A. Al-Harrasi, H.-U. Reissig, *Synlett* **2002**, 817–819; c) R. Pulz, A. Al-Harrasi, H.-U. Reissig, *Org. Lett.* **2002**, 4, 2353–2355; d) R. Pulz, W. Schade, H.-U. Reissig, *Synlett* **2003**, 405–407; e) R. Pulz, S. Cicchi, A. Brandi, H.-U. Reissig, *Eur. J. Org. Chem.* **2003**, 1153–1156; f) M. Helms, H.-U. Reissig, *Eur. J. Org. Chem.* **2005**, 998–1001.
- [3] For selected publications, see: a) *Iminosugars as Glycosidase Inhibitors* (Ed.: A. E. Stütz), Wiley-VCH, Weinheim, **1999**; b) T. D. Heightman, A. T. Vasella, *Angew. Chem.* **1999**, 111, 794–815; *Angew. Chem. Int. Ed.* **1999**, 38, 750–770; c) V. H. Lillelund, H. H. Jensen, X. Liang, M. Bols, *Chem. Rev.* **2002**, 102, 515–553; d) S. Gerber-Lemaire, F. Popowycz, E. Rodríguez-García, A. T. C. Asenjo, I. Robina, P. Vogel, *ChemBioChem* **2002**, 3, 466–470.
- [4] For reviews, see: *Carbohydrate Mimics—Concepts and Methods* (Ed.: Y. Chapleur), Wiley-VCH, Weinheim, **1998**; P. Sears, C.-H. Wong, *Angew. Chem.* **1999**, 111, 2446–2471; *Angew. Chem. Int. Ed.* **1999**, 38, 2301–2324; C.-H. Wong, *Acc. Chem. Res.* **1999**, 32, 376–385; B. Werschkun, J. Thiem, *Top. Curr. Chem.* **2001**, 215, 293–325; M. H. Postema, J. L. Piper, R. L. Betts, *Synlett* **2005**, 1345–1358. Selected recent original reports: C. Kieburg, K. Sadalapure, T. K. Lindhorst, *Eur. J. Org. Chem.* **2000**, 2035–2040; E. R. Palmacci, P. H. Seeberger, *Org. Lett.* **2001**, 3, 1547–1550; P. Compain, O. R. Martin, *Bioorg. Med. Chem.* **2001**, 9, 3077–3092; G. Hummel, L. Jobron, O. Hindsgaul, *J. Carbohydr. Chem.* **2003**, 22, 781–800; R. B. Hossany, M. A. Johnson, A. A. Eniade, B. M. Pinto, *Bioorg. Med. Chem.* **2004**, 12, 3743–3754; P. Wipf, J. G. Pierce, N. Zhuang, *Org. Lett.* **2005**, 7, 483–485, and references therein.
- [5] A. Al-Harrasi, H.-U. Reissig, unpublished results.
- [6] Ethene was trapped with bromine during this conversion.^[5] The rapid fragmentation of the residue R seems to be quite important for the smooth cyclization to compounds **4–7**. With the 4-methoxy-substituted analogue of *syn-3* similar reactions were observed but owing to the persistence of the methyl group the outcome was more complicated. Details will be presented in a future publication.
- [7] For reviews, see: F. Effenberger, *Angew. Chem.* **1969**, 81, 374–391; *Angew. Chem. Int. Ed. Engl.* **1969**, 8, 295–312; T. H. Chan in *Comprehensive Organic Synthesis*, Vol. 2 (Eds.: B. M. Trost, I. Fleming, C. H. Heathcock), Pergamon, Oxford, **1991**, pp. 595–628; for recent original reports on intramolecular reactions forming pyran derivatives, see: S. Das, L.-S. Li, S. C. Sinha, *Org. Lett.* **2004**, 6, 123–126; X. Gao, P. P. Seth, J. K. Bitok, N. I. Totah, *Synlett* **2005**, 819–823; K. N. Cossey, R. L. Funk, *J. Am. Chem. Soc.* **2004**, 126, 12216–12217.
- [8] For a review on Prins reactions, see: B. B. Snider in *Comprehensive Organic Synthesis*, Vol. 2, (Eds.: B. M. Trost, I. Fleming, C. H. Heathcock), Pergamon, Oxford, **1991**, pp. 527–561; for recent studies on intramolecular Prins reactions leading to bicyclic pyran derivatives, see: Y. S. Cho, H. Y. Kim, J. H. Cha, A. N. Pae, H. Y. Koh, J. H. Choi, M. H. Chang, *Org. Lett.* **2002**, 4, 2025–2028; V. K. Yadav, N. V. Kumar, *J. Am. Chem. Soc.* **2004**, 126, 8652–8653; R. Jasti, J. Vitale, S. D. Rychnovsky, *J. Am. Chem. Soc.* **2004**, 126, 9904–9905.
- [9] H. Vorbrüggen, *Silicon-mediated Transformations of Functional Groups*, Wiley-VCH, Weinheim, **2004**.
- [10] The enantiomeric purity of *syn-3* was proved in earlier studies: R. Pulz, Dissertation, Freie Universität Berlin, **2002**.
- [11] The corresponding nitrones were prepared analogously to **2**, starting from D-mannitol: A. Dondoni, S. Franco, F. Merchán, P. Merino, R. Tejero, *Synth. Commun.* **1994**, 24, 2537–2550.
- [12] The constitution and configuration of products presented herein were confirmed by 2D NMR spectra, associated with NOE studies; X-ray crystallographic analyses of key compounds **23**, **33**, and **35** as well as of the precursor of the ring-opened product **27** are available. Details will be presented in a future full publication.
- [13] Detailed studies showed that during hydrogenolyses of 1,2-oxazines similar to *syn*- or *anti-3*, at first the *N*-benzyl group was rapidly removed. Thereafter the N–O bond was cleaved. See reference [10] and M. Helms, Dissertation, Freie Universität Berlin, **2005**.
- [14] For the cleavage of N–O bonds with SmI₂, see: G. E. Keck, S. F. McHardy, T. T. Wager, *Tetrahedron Lett.* **1995**, 36, 7419–7422; J. L. Chiara, C. Destabel, P. Gallego, J. Marco-Contelles, *J. Org. Chem.* **1996**, 61, 359–360; see also reference [2c].
- [15] In this case the hydride reagent attacks the bicyclic compound **13** from the other face; in contrast to **6**, **9**, or **11**, there is no shielding alkyl group. The configuration was undoubtedly proven by X-ray crystallographic analysis at the stage of **23**.
- [16] For reviews, see: O. Mitsunobu, *Synthesis* **1981**, 1–28; B. R. Castro, *Org. React.* **1983**, 29, 1–162; for the method applied in this case (cleavage of the ester with sodium azide), see: J. A. Gómez-Vidal, M. T. Forrester, R. B. Silverman, *Org. Lett.* **2001**, 3, 2477–2479.
- [17] This azido group should offer excellent possibilities for the connection to other carbohydrate units, for example, by 1,3-dipolar cycloaddition with alkynes: A. Dondoni, P. P. Giovannini, A. Massi, *Org. Lett.* **2004**, 6, 2929–2932.
- [18] Several known procedures were combined: C. André, J. Bolte, C. Demuynck, *Tetrahedron: Asymmetry* **1998**, 9, 1359–1367; E. Abushanab, P. Vemishetti, R. W. Leiby, H. K. Singh, A. B. Mikkilineni, D. C.-J. Wu, R. Saibaba, R. P. Panzica, *J. Org. Chem.* **1988**, 53, 2598–2602; see also reference [11].
- [19] The oxepane derivatives may be regarded as aminoseptanose analogues; for septanoses, see: Z. Pakulski, *Pol. J. Chem.* **1996**, 70, 667–707; M. R. DeMatteo, N. L. Snyder, M. Morton, D. M. Baldisseri, C. M. Hadad, M. W. Pecuh, *J. Org. Chem.* **2005**, 70, 24–38, and references therein.
- [20] Carbohydrate derivatives that contain a 2,2-dimethyl group in the pyran ring are also part of antitumor substrates such as novobiocin: X. M. Yu, G. Shen, B. S. J. Blagg, *J. Org. Chem.* **2004**, 69, 7375–7378, and references therein.
- [21] Amino glycosides and their analogues are of interest as ligands for ribosomal RNA: D. M. Ratner, E. W. Adams, M. D. Disney, P. H. Seeberger, *ChemBioChem*, **2004**, 5, 1375–1383.

- [22] For reviews, see: S. A. W. Gruner, E. Locardi, E. Lohof, H. Kessler, *Chem. Rev.* **2002**, *102*, 491–514; A. Dondoni, A. Marra, *Chem. Rev.* **2000**, *100*, 4395–4421; for the use of sugar diaminocarboxylic acids, see: F. Sicherl, V. Wittmann, *Angew. Chem.* **2005**, *117*, 2133–2136; *Angew. Chem. Int. Ed.* **2005**, *44*, 2096–2099.
- [23] U. Hüniger, J. Ohnsmann, H. Kunz, *Angew. Chem.* **2004**, *116*, 1125–1128; *Angew. Chem. Int. Ed.* **2004**, *43*, 1104–1107.

Table 1: Selected pamamycin homologues.


	R ¹	R ²	R ³	R ⁴	R ⁵	Pamamycin
1a	Me	Me	Me	Me	H	607
1b	Me	Me	Me	Me	Me	621A
1c	Et	H	Me	Me	Me	621B
1d	Me	Me	Et	Me	Me	635A
1e	Me	Me	Me	Et	Me	635B
1f	Et	Me	Me	Me	Me	635C
1g	Et	Me	Et	Me	Me	649B

Natural Product Synthesis

DOI: 10.1002/anie.200501511

A General Sultone Route to the Pamamycin Macrodilides—Total Synthesis of Pamamycin-621A and Pamamycin-635B**

Petra Fischer, Ana Belén García Segovia,
Margit Gruner, and Peter Metz*

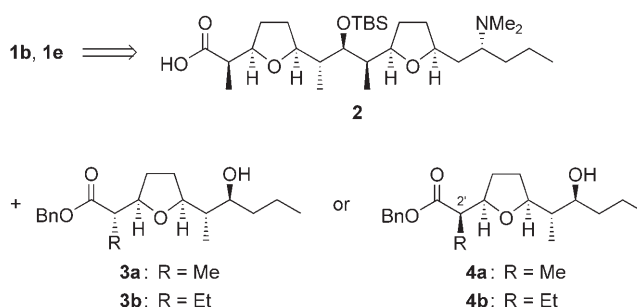
In memory of Udo Gräfe

The pamamycins (**1**) are a class of 16-membered macrodilide homologues that have been isolated from various *Streptomyces* species (Table 1).^[1,2] Besides displaying pronounced autoregulatory, anionophoric, and antifungal activities, several members of this family have been shown to be highly active against Gram-positive bacteria including multiple antibiotic-resistant strains of *Mycobacterium tuberculosis*.^[1a,3]

We have recently accomplished a total synthesis of pamamycin-607 (**1a**)^[4,5] by extensive application of sultone methodology.^[6] To facilitate more detailed studies of structure–activity relationships with respect to the antimycobacterial action of the pamamycins, we decided to utilize our sultone route to (n)actic acids and analogues^[7] for the preparation of selected higher homologues of **1a** as well. A major problem that had to be addressed in this context was the enantioselective synthesis of the smaller hydroxy acids incorporated in **1** featuring R⁵ ≠ H. Whereas the smaller fragment of pamamycin-607 (**1a**) with R⁵ = H could be

readily assembled by regioselective opening of an enantiomerically pure terminal epoxide with lithiated furan,^[4,8,9] an alternative protocol was required for efficiently securing the key hydroxyalkylfuran needed for targets with R⁵ ≠ H. Here we report a solution to this problem that eventually led to a straightforward route to pamamycin-621A (**1b**)^[10–13] and pamamycin-635B (**1e**)^[13a,14] using a sultone approach.

Following the strategy that was successful for **1a**,^[4] the pamamycins **1b** and **1e** were at first retrosynthetically disconnected to give the silylated larger hydroxy acid **2** and benzyl esters **3a** and **3b**, respectively (Scheme 1). Acid **2** had

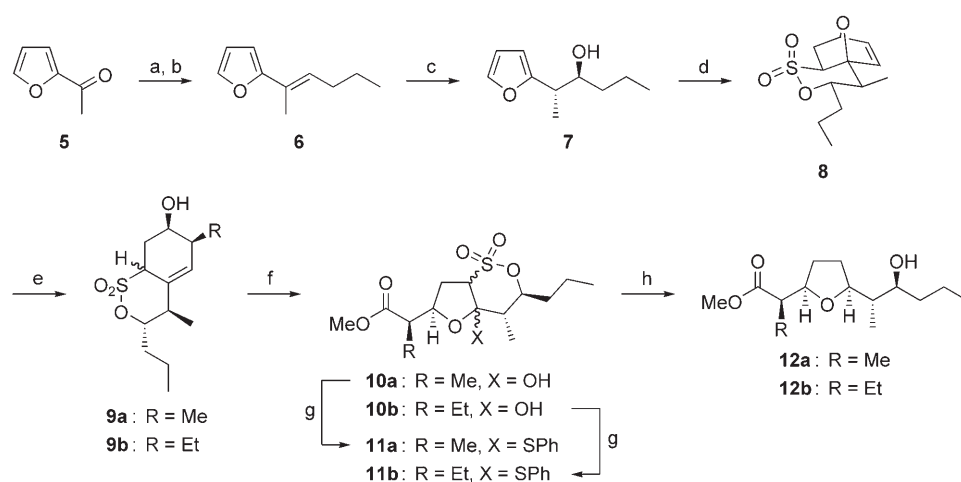

Scheme 1. Retrosynthetic analysis of **1b** and **1e**. TBS = *tert*-butyldimethylsilyl

already been used as the larger fragment in our synthesis of **1a**, and the smaller hydroxy acid corresponding to **3a** also occurs in the pamamycins **1c**, **1d**, **1f**, and **1g**. Very recently, we found that our published route to **1a**^[4] can be further streamlined by employing the more easily accessible benzyl ester of the smaller fragment epimeric at C2', since the final macrolactonization is accompanied by complete epimerization at C2'.^[2] As a consequence, we felt that use of **4a,b** instead of **3a,b** might be a viable alternative for a related route to pamamycin-621A (**1b**) and pamamycin-635B (**1e**) as well.

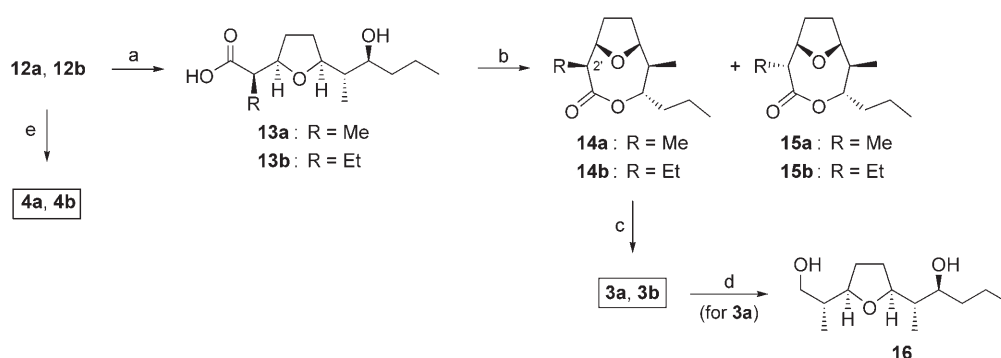
Benzyl esters **3a,b** and **4a,b** were synthesized enantioselectively as illustrated in Scheme 2 and Scheme 3. Addition of butyl Grignard to 2-acetylfuran (**5**) followed by acid-catalyzed dehydration of the resulting tertiary alcohol under

[*] Dipl.-Chem. P. Fischer, MSc A. B. García Segovia, Dr. M. Gruner, Prof. Dr. P. Metz
Institut für Organische Chemie
Technische Universität Dresden
Bergstrasse 66, 01069 Dresden (Germany)
Fax: (+49) 351-4633-3162
E-mail: peter.metz@chemie.tu-dresden.de

[**] This work was supported by the Deutsche Forschungsgemeinschaft (Graduierten-Kolleg "Struktur-Eigenschafts-Beziehungen bei Heterocyclen") and the Fonds der Chemischen Industrie. A.B.G.S. acknowledges a fellowship from the Spanish Ministry of Science and Technology. We thank Prof. Dr. U. Gräfe,[†] Hans-Knöll-Institut für Naturstoff-Forschung, Jena, for a sample of natural pamamycin-621A and Prof. Dr. M. Natsume, Tokyo University of Agriculture and Technology, for ¹H NMR spectra of natural pamamycin-635B.



Scheme 2. Sultone route to hydroxy esters **12a,b**. a) BuMgBr, Et₂O, reflux; b) cat. HCl, CH₂Cl₂, reflux, 58% from **5**, *E/Z* = 93:7; c) 1. IpcBH₂, THF, −25 °C, 2. H₂O₂, NaOH, 70 °C, 76% **7** (81% *ee*) + *syn* isomer; d) 1. CH₂=CHSO₂Cl, NEt₃, THF, 0 °C → RT, 2. recrystallization, 74% (≥ 99% *ee*); e) 1. 2 MeLi (for **9a**) or 2 EtLi (for **9b**), THF, −78 °C → RT, 2. NH₄Cl, H₂O, −78 °C → RT, 53% **9a**, 68% **9b**; f) 1. O₃, NaHCO₃, CH₂Cl₂, MeOH, −78 °C, 2. Ac₂O, pyridine, CH₂Cl₂, RT → reflux, 87% **10a**, 86% **10b**; g) PhSH, BF₃·Et₂O, CH₂Cl₂, RT, 79% **11a**, 80% **11b**; h) Raney Ni (W2), 50 bar H₂, EtOH, RT, 59% **12a**, 58% **12b**. IpcBH₂ = monoisopinocampheylborane.



Scheme 3. Synthesis of the smaller fragment surrogates **3a,b** and **4a,b**. a) 2 N NaOH, RT (for **13a**) or 90 °C (for **13b**), 100% **13a**, 79% **13b**; b) 1. 2,4,6-trichlorobenzoyl chloride, Et₃N, THF, RT, 2. DMAP, toluene, reflux, 65% **14a**, 11% **15a**, 68% **14b**, 14% **15b**; c) BnOLi, BnOH, THF, RT, 59% **3a**, 40% **3b** (yield based on recovered starting material); d) LiAlH₄, Et₂O, RT → reflux, 70% from **3a**; e) BnOH, 10 mol% Bu₂SnO, 160 °C, 93% **4a**, 100% **4b**. DMAP = 4-(*N,N*-dimethylamino)pyridine.

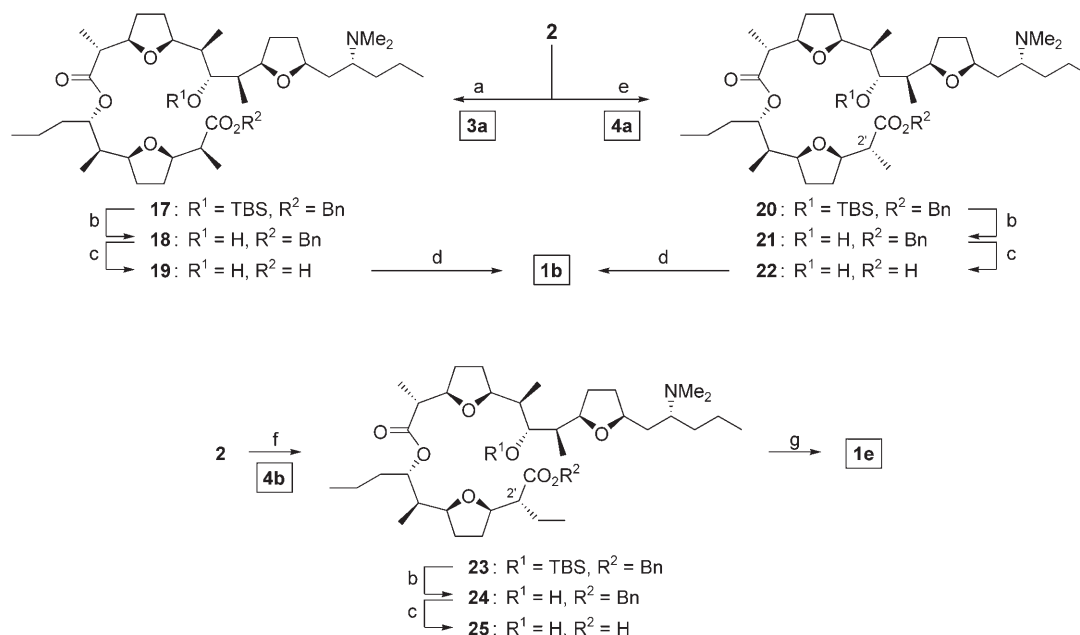
equilibrating conditions delivered olefin **6** as a mixture of isomers (*E/Z* = 93:7, Scheme 2). Asymmetric hydroboration^[15] of this mixture with monoisopinocampheylborane derived from (+)- α -pinene (91% *ee*) followed by oxidative workup led to the desired *anti* alcohol **7** (81% *ee* according to chiral GC) and some of the *syn* isomer in 76% combined yield. Treatment of this mixture with vinylsulfonyl chloride induced a smooth domino esterification/intramolecular Diels–Alder reaction^[6,8,16,17] to give the pure *exo* sultone **8** (≥ 99% *ee* according to chiral HPLC) after chromatographic purification and recrystallization. Application of the reaction sequence^[7,8,18] domino elimination/alkoxide-directed 1,6-addition,^[19] sequential ozonolysis/cyclization, Lewis acid catalyzed hydroxy/phenylthio exchange, and domino reductive elimination/hydrogenation converted sultone **8** to methyl esters **12a,b**.

Benzyl esters **3a,b** featuring the relative configuration at C2' present in **1b** and **1e** were prepared in a three-step sequence^[9] from methyl esters **12a,b** (Scheme 3). After saponification of **12a,b** and Yamaguchi lactonization^[20,21] of hydroxy acids **13a,b**, the C2'-epimerized lactones **14a,b** were isolated as the major products, which was revealed by 2D NOESY investigation of both lactone diastereomers. Lactone **14a** was recently isolated from *Streptomyces globisporus* and exhibited significant antibacterial activity.^[22] Subsequent cleavage of the medium-sized lactones **14a,b** with the lithium alkoxide prepared from benzyl alcohol^[4,23] gave isomerically pure **3a,b**.

The absolute configuration of **3a** and hence **3b** was proven by comparison of the optical rotation data of the known diol **16**,^[13a] which was derived from **3a**, with literature values.^[24] On the other hand, dibutyltin oxide catalyzed transesterification^[25] of **12a,b** with benzyl alcohol directly provided **4a,b** in excellent yields.

Yamaguchi coupling^[20] of the silylated larger hydroxy acid **2** with the naturally configured smaller building block **3a** (1.2 equiv) for **1b** effi-

ciently furnished the doubly protected seco acid **17** (Scheme 4). After desilylation and reductive debenzoylation, modified Yamaguchi macrolactonization^[23] of **19** (1.3 × 10^{−3} M) at room temperature in dichloromethane gave a high yield of pamamycin-621A (**1b**).^[11,26,27] Since utilization of **4a** instead of **3a** for fragment coupling promised a shortcut to **1b**, we decided to explore such a simplified approach as well. Intermolecular Yamaguchi esterification of **2** with **4a** (1.2 equiv) provided the coupling product **20** in high yield. Desilylation followed by debenzoylation proceeded uneventfully to give seco acid **22**. Most gratifyingly, Yamaguchi macrolactonization of **22** (1.2 × 10^{−3} M) under Fleming conditions^[23] again afforded pamamycin-621A (**1b**)^[11,26,27] as the single macrolide product in 64% yield. Thus, as was noted for the corresponding ring closure to give **1a**,^[2] the cyclization of **22** is accompanied by complete epimerization at C2' under



Scheme 4. Final steps of the synthesis of pamamycin-621A (**1b**) and pamamycin-635B (**1e**). a) 1. 2,4,6-trichlorobenzoyl chloride, Et₃N, THF, 0°C→RT, 2. **3a**, DMAP, toluene, RT, 94%; b) aq. HF, MeCN, RT, 97% **18**, 95% **21**, 95% **24**; c) H₂, 10% Pd/C, THF, RT, 100% **19**, 84% **22**, 100% **25**; d) 2,4,6-trichlorobenzoyl chloride, DMAP, MS 4 Å, CH₂Cl₂, RT, 78% **1b** from **19**, 64% **1b** from **22**; e) 1. 2,4,6-trichlorobenzoyl chloride, Et₃N, THF, 0°C→RT, 2. **4a**, DMAP, toluene, RT, 88%; f) 1. 2,4,6-trichlorobenzoyl chloride, Et₃N, THF, 0°C→RT, 2. **4b**, DMAP, toluene, RT, 78%; g) 1. 2,4,6-trichlorobenzoyl chloride, Et₃N, THF, 0°C→RT, 2. DMAP, toluene, reflux, 57%. MS=molecular sieves.

these conditions. Encouraged by the facile lactonization of **22** to **1b**, we directly applied such a streamlined sequence to access pamamycin-635B (**1e**). However, seco acid **25** readily obtained after coupling of **2** with the non-naturally configured smaller building block **4b** (1.4 equiv) and subsequent deblocking proved to be reluctant to cyclization under the modified Yamaguchi conditions used for **1b**. This is probably a result of the increased steric shielding imparted by the C2' ethyl group. To our delight, Yamaguchi macrolactonization^[20,21] of **25** performed by separate mixed-anhydride activation of the acid function and subsequent reflux in toluene under high dilution in the presence of 4-(*N,N*-dimethylamino)pyridine eventually afforded pamamycin-635B (**1e**)^[14,27,28] as the sole macrodiolide product in 57% yield.

In summary, a short and highly stereoselective access to the smaller fragment surrogates **3a,b** and **4a,b** of the pamamycins **1b-g** has been developed by means of asymmetric hydroboration and application of sultone methodology. Using benzyl esters **3a** and **4a**, the first total synthesis of the macrodiolide antibiotic pamamycin-621A (**1b**) has been accomplished, while the first total synthesis of pamamycin-635B (**1e**) was achieved using benzyl ester **4b**. Further synthetic work in this area and investigations on the biological activity of the pamamycins will be reported in due course.

Received: May 2, 2005

Published online: September 7, 2005

Keywords: antibiotics · domino reactions · natural products · sulfur heterocycles · total synthesis

- Reviews: a) B. M. Pogell, *Cell. Mol. Biol.* **1998**, *44*, 461–463; b) M. Natsume, *Recent Res. Dev. Agric. Biol. Chem.* **1999**, *3*, 11–22.
- Review on synthetic studies toward the pamamycins: P. Metz, *Top. Curr. Chem.* **2005**, *244*, 215–249.
- P. Lefèvre, P. Peirs, M. Braibant, M. Fauville-Dufaux, R. Vanhoof, K. Huygen, X.-M. Wang, B. Pogell, Y. Wang, P. Fischer, P. Metz, J. Content, *J. Antimicrob. Chemother.* **2004**, *54*, 824–827.
- Y. Wang, H. Bernsmann, M. Gruner, P. Metz, *Tetrahedron Lett.* **2001**, *42*, 7801–7804.
- Total syntheses of **1a** reported by other groups: a) O. Germa, N. Kumar, E. J. Thomas, *Tetrahedron Lett.* **2001**, *42*, 4969–4974; b) E. Lee, E. J. Jeong, E. J. Kang, L. T. Sung, S. K. Hong, *J. Am. Chem. Soc.* **2001**, *123*, 10131–10132; c) S. H. Kang, J. W. Jeong, Y. S. Hwang, S. B. Lee, *Angew. Chem.* **2002**, *114*, 1450–1453; *Angew. Chem. Int. Ed.* **2002**, *41*, 1392–1395; d) E. J. Jeong, E. J. Kang, L. T. Sung, S. K. Hong, E. Lee, *J. Am. Chem. Soc.* **2002**, *124*, 14655–14662.
- Review on sultone chemistry: P. Metz, *J. Prakt. Chem.* **1998**, *340*, 1–10.
- U. Meiners, E. Cramer, R. Fröhlich, B. Wibbeling, P. Metz, *Eur. J. Org. Chem.* **1998**, 2073–2078.
- H. Bernsmann, B. Hungerhoff, R. Fechner, R. Fröhlich, P. Metz, *Tetrahedron Lett.* **2000**, *41*, 1721–1724.
- H. Bernsmann, M. Gruner, R. Fröhlich, P. Metz, *Tetrahedron Lett.* **2001**, *42*, 5377–5380.
- First isolation of a mixture of pamamycins with a homologue of molecular weight 621 as the major component: P. A. McCann, B. M. Pogell, *J. Antibiot.* **1979**, *32*, 673–678.
- Isolation and structural elucidation of pamamycin-621A: a) U. Gräfe, R. Schlegel, K. Dornberger, W. Ihn, M. Ritzau, C. Stengel, M. Beran, W. Günther, *Nat. Prod. Lett.* **1993**, *3*, 265–271; b) M. Natsume, J. Tazawa, K. Yagi, H. Abe, S. Kondo, S. Marumo, *J. Antibiot.* **1995**, *48*, 1159–1164.

- [12] Bioactivities of pamamycin-621A: a) W.-G. Chou, B. M. Pogell, *Antimicrob. Agents Chemother.* **1981**, 20, 443–454; b) W.-G. Chou, B. M. Pogell, *Biochem. Biophys. Res. Commun.* **1981**, 100, 344–350; c) C. Stengel, G. Reinhardt, U. Gräfe, *J. Basic Microbiol.* **1992**, 32, 339–345; d) U. Gräfe, C. Stengel, U. Möllmann, L. Heinisch, *Pharmazie* **1994**, 49, 343–346; e) P. Grigoriev, A. Berg, R. Schlegel, U. Gräfe, *Bioelectrochem. Bioenerg.* **1996**, 39, 295–298.
- [13] Further synthetic approaches: a) R. D. Walkup, S. W. Kim, *J. Org. Chem.* **1994**, 59, 3433–3441; b) L. Arista, M. Gruttadauria, E. J. Thomas, *Synlett* **1997**, 627–628; c) M. A. Calter, F. C. Bi, *Org. Lett.* **2000**, 2, 1529–1531; d) A. Miura, H. Kiyota, S. Kuwahara, *Tetrahedron* **2005**, 61, 1061–1067.
- [14] Isolation, structural elucidation, and bioactivities of pamamycin-635B: M. Natsume, K. Yasui, S. Kondo, S. Marumo, *Tetrahedron Lett.* **1991**, 32, 3087–3090.
- [15] a) H. C. Brown, A. K. Mandal, N. M. Yoon, B. Singaram, J. R. Schwier, P. K. Jadhav, *J. Org. Chem.* **1982**, 47, 5069–5074; b) H. C. Brown, P. K. Jadhav, A. K. Mandal, *J. Org. Chem.* **1982**, 47, 5074–5083.
- [16] H. Bernsmann, R. Fröhlich, P. Metz, *Tetrahedron Lett.* **2000**, 41, 4347–4351.
- [17] J. Merten, R. Fröhlich, P. Metz, *Angew. Chem.* **2004**, 116, 6117–6120; *Angew. Chem. Int. Ed.* **2004**, 43, 5991–5994.
- [18] H. Bernsmann, M. Gruner, P. Metz, *Tetrahedron Lett.* **2000**, 41, 7629–7633.
- [19] P. Metz, U. Meiners, R. Fröhlich, M. Grehl, *J. Org. Chem.* **1994**, 59, 3687–3689.
- [20] J. Inanaga, K. Hirata, H. Saeki, T. Katsuki, M. Yamaguchi, *Bull. Chem. Soc. Jpn.* **1979**, 52, 1989–1993.
- [21] J. Mulzer, H. M. Kirstein, J. Buschmann, C. Lehmann, P. Luger, *J. Am. Chem. Soc.* **1991**, 113, 910–923.
- [22] T. Řezanka, J. Spížek, V. Přikrylová, V. M. Dembitsky, *Eur. J. Org. Chem.* **2004**, 4239–4244.
- [23] I. Fleming, S. K. Ghosh, *J. Chem. Soc. Perkin Trans. 1* **1998**, 2733–2747.
- [24] Compound **16** prepared by reduction of **3a** with LiAlH_4 : $[\alpha]_{\text{D}}^{25} = -19.1$ ($c = 1.03$, benzene); ref. [13a]: $[\alpha]_{\text{D}}^{25} = -19.1$ ($c = 6$, benzene).
- [25] P. Baumhof, R. Mazitschek, A. Giannis, *Angew. Chem.* **2001**, 113, 3784–3786; *Angew. Chem. Int. Ed.* **2001**, 40, 3672–3674.
- [26] Analytical data of synthetic **1b** match exactly those of the natural product obtained by flash chromatography from a mixture of natural pamamycin-621A (**1b**) and pamamycin-607 (**1a**) (ca. 2:1), which was kindly provided by Prof. Dr. U. Gräfe,† Hans-Knöll-Institut für Naturforschung, Jena.
- [27] Detailed 2D NMR analyses (COSY, HSQC, HMBC, NOESY) confirmed the depicted relative configuration, in particular at C2 and C2'.
- [28] ^1H NMR data of synthetic **1e** are identical to those of the natural product kindly provided by Prof. Dr. M. Natsume, Tokyo University of Agriculture and Technology.

DOI: 10.1002/anie.200501899

Activation of a Zinc-Bound Ethyl Group by Formation of a Zn-C_{Et}-Ba Moiety and Crystal Structure of $[(\text{Me}_3\text{Si})_2\text{N})\text{Ba}(\text{thf})\text{Zn}_2(\mu\text{-Et})(\mu_3\text{-PSi}t\text{Bu}_3)_2]$ with Bridging Ethyl Substituents***Matthias Westerhausen,* Gerhard Sapelza, and Peter Mayer*

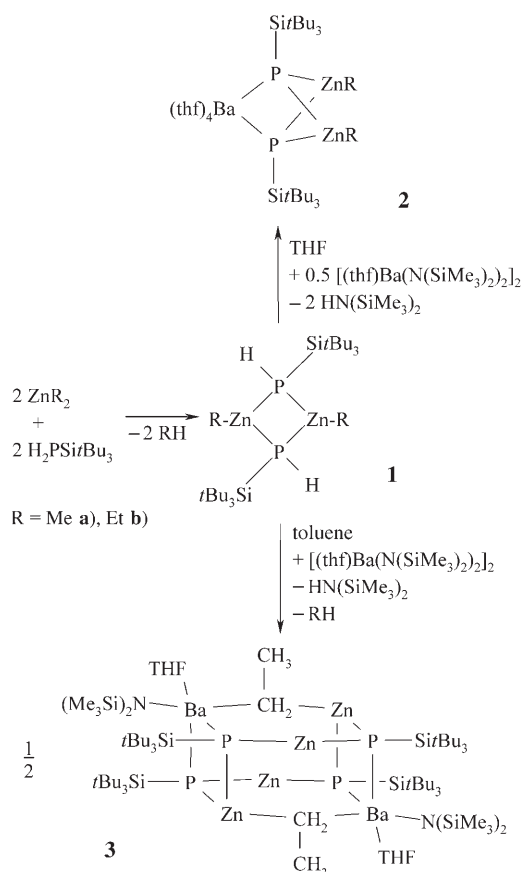
The organometallic chemistry of the heavy alkaline-earth metals has been studied for many decades. However, despite the enormous efforts to prepare and structurally characterize such compounds only very few crystal structures of organo-barium compounds are known. More than 60 years ago Gilman and Woods reported that the addition of diethylzinc drastically increases the reactivity of dialkylbarium towards benzonitrile.^[1] However, up to now most of these compounds remain poorly characterized because of their poor solubility in common organic solvents (highly ionic metal–carbon bond), poor yields (side reactions, necessity of metal activation prior to use), poor purity, and reactions with the solvent (ether cleavage). Within the last decades several procedures have been developed for the preparation of σ -bonded alkylbarium compounds.^[2] The majority of these derivatives contain α -bound aryl^[3] and trialkylsilyl groups^[4] for stabilization. These compounds found wide use as polymerization initiators,^[5] but their structures were determined only quite recently.^[6,7] In order to avoid side reactions the substituents bear no β -hydrogen atoms. In addition ab initio calculations predict bent structures for solvent-free monomeric dimethylbarium.^[8] Even though Cherkasov and co-workers^[9] reported reactions of diethylbarium with vinylalkynes, the resulting products were identified solely after protolysis reactions. Here we present an example of activation of a zinc-bound alkyl group by formation of an interaction with a barium center.

The reaction of dialkylzinc with tri(*tert*-butyl)silylphosphane in an equimolar ratio yields quantitatively dimeric alkylzinc tri(*tert*-butyl)silylphosphanide (**1**; Scheme 1). The deprotonation of **1** in THF by addition of $[(\text{thf})\text{Ba}\{\text{N}(\text{SiMe}_3)_2\}_2]$ yields $(\text{thf})_4\text{Ba}[(\text{RZn})_2(\text{PSi}t\text{Bu}_3)_2]$ (**2**) (metalation). Also the reaction of **1** with barium metal in THF gives **2** (transmetalation reaction). However, if the reaction is

[*] Prof. M. Westerhausen, G. Sapelza
Institute of Inorganic and Analytical Chemistry
Friedrich-Schiller-Universität Jena
August-Bebel-Strasse 2, 07743 Jena (Germany)
Fax: (+49) 3641-948-102
E-mail: m.we@uni-jena.de

Dr. P. Mayer
Department of Chemistry and Biochemistry
Ludwig-Maximilians-Universität München
Butenandtstrasse 9, 81377 Munich (Germany)

[**] We thank the Deutsche Forschungsgemeinschaft (DFG) for financial support.



Scheme 1.

performed in toluene and an excess of THF is avoided, the barium atom must be sterically saturated intramolecularly, and the reaction of **1** (R = Me, Et) with [(thf)Ba[N(SiMe₃)₂]₂]₂ leads to compound **3** (Scheme 1). The main difference between these reactions is that in the synthesis of **2** all bis(trimethylsilyl)amido groups react as the deprotonation reagent, whereas for the formation of **3** two ethyl and two amido groups deprotonate the phosphanides. This observation can be explained by a prior activation of the ethyl substituents by formation of Ba-C_{Et}-Zn three-center two-electron bonds or by agostic interactions between the C-H σ bonds and the barium cation as observed in **3**. In contrast to the reaction performed in toluene, the formation of such bonds in **2** is not necessary because in THF the barium atom always remains sterically saturated by solvent molecules.

Whereas in **2** the distorted octahedral coordination sphere of the heavy alkaline-earth metal atom is completed by four THF molecules (Figure 1), in **3** the barium atom displays the coordination number of 5. Here, the Ba atom is shielded by the bulky bis(trimethylsilyl)amido group, one THF ligand, and the neighboring P-bound tri(*tert*-butyl)silyl substituents (Figure 2). Furthermore, a zinc-bound ethyl group assumes a bridging position. Thus the central cage consists of a distorted Ba₂C₂P₄Zn₄ cuboid. The distortions result from the nearly trigonal-planar environment of the zinc atom (angle sum 348.8°. The other two-coordinate zinc atom, Zn1, shows short Zn1-P bonds 224 pm in length.

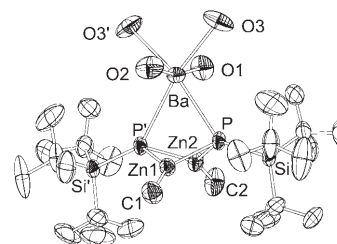


Figure 1. Molecular structure of **2a**. Symmetry-related atoms ($x, 0.5-y, z$) are marked with apostrophes. The ellipsoids are set at a probability of 50%. For clarity reasons the CH₂ groups of the THF ligands and all hydrogen atoms are omitted. Selected bond lengths (pm): Ba-P 313.9(1), Ba-O1 272.9(6), Ba-O2 269.4(6), Ba-O3 275.1(5), Zn1-P 235.8(1), Zn1-C1 197.5(8), Zn2-P 237.2(1), Zn2-C2 199.3(7), P-Si 220.9(2).

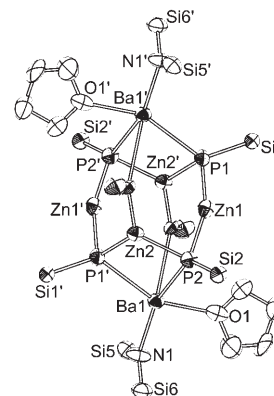


Figure 2. Molecular structure of **3**. Symmetry-related atoms ($1-x, -y, -z$) are marked with apostrophes. The ellipsoids are set at a probability of 50%. For clarity both the Si-bound alkyl groups and the hydrogen atoms are omitted. Selected bond lengths (pm): Ba1-P1' 323.2(5), Ba1-O1 269(2), Ba1-N1 255(1), Ba1-P2 333.9(4), Si5-N1 167(1), Si6-N1 171(1), Zn1-P2 224.1(5), Zn1-P1 223.8(5), Zn2-P2 242.6(5), Zn2-P1' 242.7(4), Zn2-C49 204(1), P1-Si1 226.7(7), P2-Si2 226.4(6).

The Ba-C bond length of 337.9(5) pm in **3** is very large compared to those of known organobarium compounds; also the Zn-C bond of 204 pm is elongated. In zincates such as (η^6 -toluene)₂Ba[Zn(CH₂SiMe₃)₃]₂^[10] and its thermolysis product [Ba₄Zn₆(CH₂SiMe₃)₈(CHSiMe₃)₆]^[11] shorter Ba-C bonds of 302.8(5)/305.5(5) pm and 299.4(4)/320.0(4) pm, respectively, have been observed. For ([18]crown-6)Ba(C \equiv C-SiPh₃)₂ extremely short Ba-C distances of 285.3(3) pm have been reported,^[12] whereas in (dme)Ba[C(SiMe₃)₂(SiMe₂OMe)]₂ values of 304.9(2) pm were found.^[7] The Ba-C distances in **3** are in the upper range of those in molecules with π -bonded ligands having significant charge delocalization^[13,14] or with side-on coordinated alkene moieties.^[15]

A comparison of the Ba-P distances of **3** (323.2(5) and 333.9(5) pm) with those of **2a** (313.9(1) pm) shows elongated bonds despite the smaller coordination number. This fact can be attributed to the bulkiness of the substituents. However, the Ba-O distances of the two compounds are similar.

The importance of such an activation of the alkylzinc moiety can be seen from the observation that, for example, alkylzinc amides and phosphanides are stable and form amine

and phosphane adducts rather than undergo deprotonation reactions.^[16] The enhancement of the reactivity of organometallic compounds by formation of heterobimetallic derivatives has often been observed.^[1,17] In **3** a kinetic stabilization by shielding of the Ba-C_{Et}-Zn moiety of the barium-bound ethyl group with large substituents enabled the structure elucidation by X-ray diffraction. Thus far, the characterization of compounds with alkylbarium moieties has been limited to α -phenyl- and α -trialkylsilyl-substituted derivatives and to the identification of protolysis products. It is very likely that the structural feature described here plays a key role in the activation of zinc-bound alkyl groups. In ether solvents where the alkaline-earth metal atom remains coordinatively saturated by Lewis bases throughout the reaction the alkylzinc moiety shows a strongly reduced reactivity towards H-acidic substrates.

Experimental Section

All manipulations were carried out in an anhydrous argon atmosphere. The solvents were thoroughly dried and distilled under argon. The starting compounds H₂PSi^tBu₃^[18] and [(thf)Ba(N(SiMe₃)₂)₂]^[19] were prepared according to literature procedures. In the elemental analysis the carbon content is low as a result of carbonate formation during combustion.

2a (Procedure 1): A solution of H₂PSi^tBu₃ (0.47 g) in 10 mL of toluene was treated with 1 mL of a 2 M solution of dimethylzinc in toluene. A solid precipitate of **1a** formed (m.p. 174 °C; ν (P-H) = 2308 cm⁻¹; ³¹P NMR (109.365 MHz, [D₈]toluene, -80 °C, AA'XX'): δ (³¹P) = -232.4, ¹J(P,H) = 257, ²J(P,P) = 60, ³J(P,H) = 5, ⁴J(H,H) < 1 Hz). This compound was dissolved by addition of 5 mL of THF. After addition of [(thf)Ba(N(SiMe₃)₂)₂] (0.6 g, 1 mmol) in 10 mL of THF, this solution was stirred for several hours at room temperature. Then all volatile materials were removed under vacuum, and the residue was dissolved in 3 mL of THF. At 5 °C colorless crystals of **2a** (0.3 mmol, 30 %) precipitated.

2a (Procedure 2): Compound **1a** was prepared as described above and dissolved by addition of 5 mL of THF. After the addition of barium metal (0.17 g, 1.2 mmol), the solution was stirred for three days. Then the volume was reduced to a third of the original volume. At 5 °C colorless crystals of **2a** (0.21 mmol; 21 %) formed. No melting point was observed. ¹H NMR (270.166 MHz, [D₆]benzene, 20 °C): δ = -0.13 (s, ZnCH₃), 1.34 ppm (s, *t*Bu); ¹³C NMR (100.526 MHz, [D₆]benzene, 20 °C): δ = -3.5 (ZnCH₃), 24.4 (s, CMe₃), 32.4 ppm (s, CMe₃); ²⁹Si NMR (53.674 MHz, [D₆]benzene, 20 °C): δ = 26.7 ppm (pseudo-t, AA'X, |J(AX) + J(A'X)| = 25.0 Hz); ³¹P NMR (109.365 MHz, [D₆]benzene, 20 °C): δ = -183.8 (s); IR: $\tilde{\nu}$ [cm⁻¹] = 1495 w, 1479 vs, 1441 w, 1419 vw, 1390 s, 1366 m, 1300 vw, 1260 vw, 1246 vw, 1185 m, 1073 vs, 1005 s, 965 w, 934 w, 867 vw, 844 vw, 819 vs, 727 vw, 694 vw, 671 vw, 628 m, 615 m, 567 w, 508 w, 469 m, 460 m; Elemental analysis (C₄₂H₉₂BaO₄P₂Si₂Zn₂, 1047.34 g mol⁻¹): calcd: C 48.16, H 8.85; found: C 47.10, H 8.47.

Crystal data for **2a**-toluene:^[20] C₄₉H₁₀₀BaO₄P₂Si₂Zn₂, 1139.54 g mol⁻¹, monoclinic, *P*₂/*m* (no. 11), *a* = 1100.96(8), *b* = 2543.8(1), *c* = 1117.98(7) pm, β = 104.984(8)°, *Z* = 2, ρ_{calcd} = 1.251 g cm⁻³, μ = 1.558 mm⁻¹, λ = 0.71073 Å, *T* = 200(2) K, 3.8° < 2 θ < 51.8°, 5734 independent reflections, *R*_{int} = 0.072, 3346 observed reflections (*I* > 2 σ (*I*)), 285 parameters, *wR*₂ = 0.1010, *s* = 0.84, min./max. residual electron density -0.44/0.61 e Å⁻³.

3: For the preparation of **1b** a 1 M solution of diethylzinc in hexane (2.0 mL, 2.0 mmol) was added to a solution of H₂PSi^tBu₃ (0.47 g, 2.0 mmol) in 15 mL of toluene. (**1b**: m.p. 181 °C; ν (P-H) = 2304 cm⁻¹; ³¹P{¹H} NMR ([D₈]toluene): δ (³¹P) = -231.5). [(thf)Ba(N(SiMe₃)₂)₂] (0.6 g, 1 mmol) was added and the solution stirred for an additional

three days. After reduction of the volume and storage at 5 °C yellow crystals of **3** (0.32 mmol; 65 %) precipitated. No melting point was detectable. ¹H NMR: (270.166 MHz, [D₆]benzene, 20 °C): δ = 0.32 (s, SiMe₃); 0.34 (q, CH₂, ²J(H,H) = 7.3), 1.28 (s, *t*Bu); 1.37 ppm (t, CH₃); ¹³C NMR (67.933 MHz, [D₆]benzene, 20 °C): δ = 5.3 (s, SiMe₃ and ZnCH₂), 6.0 (s, CH₃), 24.0 (s, C_q), 32.1 ppm (t, *t*Bu, ²J_{PC} = 20.0 Hz); ³¹P NMR (109.365 MHz, [D₆]benzene, 20 °C): δ = -245.0 ppm (s); IR: $\tilde{\nu}$ [cm⁻¹] = 1477 m, 1441 vw, 1415 vw, 1384 m, 1357 vw, 1249 s, 1179 w, 1012 s, 932 s, 876 s, 817 vs, 758 m, 665 w, 603 m, 564 m, 506 m, 479 w, 459 m. Elemental analysis (C₈₆H₁₈₆O₂N₂P₄Si₈Ba₂Zn₄, 2165.2 g mol⁻¹): calcd: C 47.70, H 8.65, N 1.38; found: C 45.43, H 8.62, N 1.45.

Crystal data for **3**:^[20] C₈₆H₁₈₆Ba₂N₂O₂P₄Si₈Zn₄, 2165.20 g mol⁻¹, triclinic, *P* $\bar{1}$ (no. 2), *a* = 1194.19(6), *b* = 1788.8(1), *c* = 2711.7(2) pm, α = 90.325(3), β = 90.773(3), γ = 105.701(3)°, *Z* = 2, ρ_{calcd} = 1.290 g cm⁻³, μ = 1.724 mm⁻¹, λ = 0.71073 Å, *T* = 200(2) K, 7.2° < 2 θ < 48°, 11 723 independent reflections, *R*_{int} = 0.057, 9248 observed reflections (*I* > 2 σ (*I*)), 903 parameters, *wR*₂ = 0.2280, *s* = 1.10, min./max. residual electron density -1.27/1.65 e Å⁻³.

Received: June 1, 2005

Published online: September 7, 2005

Keywords: barium · bond activation · metalation · P ligands · zinc

- [1] H. Gilman, L. A. Woods, *J. Am. Chem. Soc.* **1945**, 67, 520–522.
- [2] T. P. Hanusa, *Polyhedron* **1990**, 9, 1345–1362; T. P. Hanusa, *Chem. Rev.* **1993**, 93, 1023–1036; T. P. Hanusa, *Coord. Chem. Rev.* **2000**, 210, 329–367; M. Westerhausen, *Angew. Chem.* **2001**, 113, 3063–3065; *Angew. Chem. Int. Ed.* **2001**, 40, 2975–2977; J. S. Alexander, K. Ruhlandt-Senge, *Eur. J. Inorg. Chem.* **2002**, 2761–2774.
- [3] H. Gilman, A. H. Haubein, G. O'Donnell, L. A. Woods, *J. Am. Chem. Soc.* **1945**, 67, 922–926; Z. M. Baidakova, B. I. Nakhmanovich, A. A. Arest-Yakubovich, *Dokl. Akad. Nauk SSSR* **1976**, 230, 114–116; K. Takahashi, Y. Kondo, R. Asami, *J. Chem. Soc. Perkin Trans. 2* **1978**, 577–580; B. I. Nakhmanovich, E. V. Kristal'nyi, R. V. Basova, Z. M. Baidakova, A. A. Arest-Yakubovich, *Dokl. Akad. Nauk SSSR* **1980**, 255, 364–366; R. V. Basova, Z. M. Baidakova, E. V. Kristal'nyi, B. I. Nakhmanovich, A. A. Arest-Yakubovich, *Metalloorg. Khim.* **1988**, 1, 776–778; S. R. Drake, D. J. Otway, *Polyhedron* **1992**, 11, 745–758; M. Westerhausen, M. H. Digeser, H. Nöth, T. Seifert, A. Pfitzner, *J. Am. Chem. Soc.* **1998**, 120, 6722–6725; J. S. Alexander, K. Ruhlandt-Senge, H. Hope, *Organometallics* **2003**, 22, 4933–4937.
- [4] A. D. Frankland, M. F. Lappert, *J. Chem. Soc. Dalton Trans.* **1996**, 4151–4152; M. Westerhausen, C. Gückel, T. Habereeder, M. Vogt, M. Warchhold, H. Nöth, *Organometallics* **2001**, 20, 893–899; M. Westerhausen, C. Gückel, S. Schneiderbauer, H. Nöth, N. S. Hosmane, *Angew. Chem.* **2001**, 113, 1959–1961; *Angew. Chem. Int. Ed.* **2001**, 40, 1902–1904.
- [5] R. Masthoff, H. Wirth, Ger. Patent DD 76975, **1970**; R. R. Smith, S. D. Nielsen, Ger. Patent DE 2202262, **1972**; I. G. Hargis, R. A. Livigni, U.S. Patent US 3966638, **1976**; I. G. Hargis, A. Russell, U.S. Patent US 3965080, **1976**; W. E. Lindesell, F. C. Robertson, I. Soutar, *Eur. Polym. J.* **1983**, 19, 115–120; A. Weeber, S. Harder, H. H. Brintzinger, K. Knoll, *Organometallics* **2000**, 19, 1325–1332; B. I. Nakhmanovich, Y. G. Urman, A. A. Arest-Yakubovich, *Macromol. Chem. Phys.* **2001**, 202, 1327–1330; A. A. Arest-Yakubovich, B. I. Nakhmanovich, G. I. Litvinenko, *Polymer* **2002**, 43, 7093–7100.
- [6] J. S. Alexander, K. Ruhlandt-Senge, *Angew. Chem.* **2001**, 113, 2732–2734; *Angew. Chem. Int. Ed.* **2001**, 40, 2658–2660; J. S.

- Alexander, K. Ruhlandt-Senge, *Chem. Eur. J.* **2004**, *10*, 1274–1280.
- [7] K. Izod, S. T. Liddle, W. Clegg, *J. Am. Chem. Soc.* **2003**, *125*, 7534–7535.
- [8] M. Kaupp, P. von R. Schleyer, *J. Am. Chem. Soc.* **1992**, *114*, 491–497.
- [9] L. N. Cherkasov, G. I. Pis'mennaya, K. V. Bal'yan, A. A. Petrov, *Zh. Org. Khim.* **1971**, *7*, 2437; L. N. Cherkasov, *Zh. Org. Khim.* **1973**, *9*, 15–16; V. N. Cherkasov, L. N. Cherkasov, *Metalloorg. Khim.* **1989**, *2*, 314–316.
- [10] M. Westerhausen, C. Gückel, T. Haberer, M. Vogt, M. Warchhold, H. Nöth, *Organometallics* **2001**, *20*, 893–899.
- [11] M. Westerhausen, C. Gückel, P. Mayer, *Angew. Chem.* **2001**, *113*, 2736–2739; *Angew. Chem. Int. Ed.* **2001**, *40*, 2666–2668.
- [12] D. C. Green, U. Englich, K. Ruhlandt-Senge, *Angew. Chem.* **1999**, *111*, 365–367; *Angew. Chem. Int. Ed.* **1999**, *38*, 354–357.
- [13] M. G. Gardiner, C. L. Raston, H. Viebrock, *Chem. Commun.* **1996**, 1795–1796.
- [14] S. Harder, M. Lutz, A. W. G. Straub, *Organometallics* **1997**, *16*, 107–113; S. Harder, M. Lutz, *Organometallics* **1997**, *16*, 225–230.
- [15] H. Schumann, S. Schutte, H.-J. Kroth, D. Lentz, *Angew. Chem.* **2004**, *116*, 6335–6338; *Angew. Chem. Int. Ed.* **2004**, *43*, 6208–6211.
- [16] M. G. Davidson, A. J. Edwards, M. A. Paver, P. R. Raithby, C. A. Russell, A. Steiner, K. L. Verhorevoort, D. S. Wright, *J. Chem. Soc. Chem. Commun.* **1995**, 1989–1990; M. Westerhausen, T. Bollwein, A. Pfitzner, T. Nilges, H.-J. Deiseroth, *Inorg. Chim. Acta* **2001**, *312*, 239–244.
- [17] R. E. Mulvey, *Chem. Commun.* **2001**, 1049–1056.
- [18] N. Wiberg, H. Schuster, *Chem. Ber.* **1991**, *124*, 93–95; N. Wiberg, A. Wörner, H.-W. Lerner, K. Karaghiosoff, D. Fenske, G. Baum, A. Dransfeld, P. v. R. Schleyer, *Eur. J. Inorg. Chem.* **1998**, 833–841.
- [19] M. Westerhausen, *Inorg. Chem.* **1991**, *30*, 96–101. See also: M. Westerhausen, *Coord. Chem. Rev.* **1998**, *176*, 157–210.
- [20] CCDC-273568 (**2a**) and -273569 (**3**) contain the supplementary crystallographic data for this paper. These data can be obtained free of charge from the Cambridge Crystallographic Data Centre via www.ccdc.cam.ac.uk/data_request/cif.

DOI: 10.1002/anie.200462515

Metal@MOF: Loading of Highly Porous Coordination Polymers Host Lattices by Metal Organic Chemical Vapor Deposition**

Stephan Hermes, Marie-Katrin Schröter,
Rochus Schmid, Lamma Khodeir, Martin Muhler,
Arno Tissler, Richard W. Fischer, and
Roland A. Fischer*

Standing out from the vast majority of metal organic coordination polymers is the class of highly porous basic zinc carboxylates developed by Yaghi and co-workers.^[1] Its prototype is MOF-5 (MOF = metal organic framework), in which {Zn₄O} building blocks are linked together by terephthalate bridges to form a zeolite-like, cubic framework.^[2] The extremely high specific surface area^[2] of up to 4500 m² g⁻¹ and a pore volume of 0.69 cm³ cm⁻³ (for MOF-177), which has not been surpassed by any other crystalline substance, and thermal stability (up to 350 °C) opens up fascinating perspectives for the supramolecular host-guest chemistry.^[3] Applications for these materials in miniaturized fuel cells and convenient gas-storage devices (for H₂, CH₄), as gas sensors and for gas separation, as catalyst materials, and also for molecular electronics are emerging.^[4]

A report on the quantitative inclusion of C₆₀ and large polycyclic dye molecules (e.g. Astrazon Orange R) into the cavities of MOF-177 single crystals attracted our attention.^[5] Could these MOF host lattices also be suitable to efficiently and selectively absorb typical metal organic chemical vapor deposition (CVD) precursors, provided these were volatile (gas absorption) or very soluble in nonpolar hydrocarbons and had matching size and shape to fit into the cavity? The release of the metal atoms of the precursors imbedded in the

[*] S. Hermes, M.-K. Schröter, R. Schmid, Prof. Dr. R. A. Fischer
Lehrstuhl für Anorganische Chemie II
Organometallics & Materials Chemistry
Ruhr-Universität Bochum
44780 Bochum (Germany)
Fax: (+49) 234-32-14174
E-mail: roland.fischer@ruhr-uni-bochum.de
L. Khodeir, Prof. Dr. M. Muhler
Lehrstuhl für Technische Chemie
Ruhr-Universität Bochum
44780 Bochum (Germany)
Dr. A. Tissler, Dr. R. W. Fischer
Süd-Chemie AG
Waldheimer Strasse 13, 83052 Bruckmühl (Germany)

[**] The authors thank the German Research Foundation (DFG) for support within the framework of the Priority Programme 1119 "CVD Materials" as well as for support within the Collaborative Research Centre SFB 558 "Metal substrate interaction in heterogeneous catalysis". M.-K.S. is grateful to the Evangelische Studienwerk for a PhD grant.



Supporting information for this article is available on the WWW under <http://www.angewandte.org> or from the author.

cavities should then lead to “naked” metal-nanoclusters of a size regime otherwise difficult to access (1–2 nm) that are trapped in a novel and presumably only weakly interacting chemical environment.

When pure, freshly synthesized MOF-5 gently dried at 110 °C (to remove embedded solvents)^[2] was exposed to the vapor of the auburn palladium-precursor $[(\eta^5\text{-C}_5\text{H}_5)\text{Pd}(\eta^3\text{-C}_3\text{H}_5)]$ (**1**)^[6] in static vacuum (1 Pa) at 293 K in a tightly sealed Schlenk-tube, the originally colorless to light beige micro-crystalline MOF-5 material turned dark red within 5 min. Surprisingly, while the palladium adsorption is not reversible, the corresponding charging with pentacarbonyl iron $[\text{Fe}(\text{CO})_5]$ is. The quantitative desorption occurs at 0.01 Pa (dynamic vacuum, 298 K, IR control).

The three-dimensional crystalline order of the MOF-host lattice remains unchanged after loading with **1**, as shown by the comparison of the powder X-ray diffraction (XRD) pattern before and after adsorption. The analysis of the IR and ^{13}C magic-angle spinning (MAS) NMR solid-state spectra (see Supporting Information) reveal the presence of intact molecules of **1** in the MOF. The elemental analysis data suggest a formal inclusion of exactly four molecules per cavity (Figure 1, Table 1).

The molecular volume of the precursor can be calculated from the structural data^[6] with Gaussian98^[7] as 196.6 Å³. The palladium precursors **1** thus fill 36.3% of the elemental cell, which amounts to 45.3% of the pore volume. Analogously, other typical metal organic precursors for metal deposition

are absorbed unchanged, for example, $[(\eta^5\text{-C}_5\text{H}_5)\text{Cu}(\text{PMe}_3)]$ (**2**)^[8] and $[(\text{CH}_3)_3\text{Au}(\text{PMe}_3)]$ (**3**)^[9]

As expected, size and form selectivity are very high. For example, with **2** which is only slightly more space demanding than **1** and **3** only two instead of four embedded molecules are found, even though then only 28% of the pore volume is filled with precursor molecules **2**. The only slightly larger copper precursor $[\text{Cu}(\text{OR})_2]$ ($\text{R} = \text{CH}(\text{CH}_3)\text{CH}_2\text{NMe}_2$)^[10] with a volume of 327.5 Å³ (principal axes of the circumscribed ellipsoids 8.3, 10.4, 6.4 Å) is not absorbed by MOF-5 in which the pore opening diameter is 8 Å, whereas it will be absorbed by isoreticular IR-MOF-8^[4] in which the pore opening diameter is approximately 9.5 Å.

As the partial pressure of the precursors is comparatively very low (< 1 Pa at 298 K) the question of maximum loading of the cavities remains open. Solution penetration proved to be far less efficient than loading the empty cavities through the gas phase. The driving force for the exchange by diffusion of the solvent molecules in the cavity against the precursor molecules is weak. Note that highly reactive precursors such as ZnEt_2 or TiCl_4 will destroy the MOF-5 material immediately upon contact at room temperature.

If the inclusion compound **1**@MOF-5 is treated with H₂ gas, the reddish powder will turn to black immediately at –35 °C, indicating the reduction to palladium. GC/MS analysis of the components desorbed into the H₂ stream (293 K, 2 h) that are condensable at 77 K indicates the presence of cyclopentane and propane as the expected by-products (catalytic hydrogenation of the ligands). Furthermore, we found plenty of other species formed as a result of C–C couplings, C–H activation, isomerization, and (partial) hydrogenation of the ligands and their C–C coupling products. The obtained material Pd@MOF-5 is thus highly reactive and extremely air sensitive (glowing/calcination).

The XRD pattern (Figure 2) of a capillary probe prepared under argon displays a broad reflection (full width at half maximum (FWHM) = 5.4°) at 40.99° 2θ, which indicates palladium nanocrystallites of the dimension 1.4 (± 0.1) nm (profile analysis with Topas P 1.0, Pseudo Voigt). The shift of the 2θ angle to slightly bigger values, corresponding to a shrinking of the Pd–Pd distance, is also characteristic for small metal particles.^[11] The particle size is also confirmed by TEM data (Figure 2).

The characteristic reflections for the MOF-5 framework in the XRD of the Pd@MOF-5 samples prepared by H₂ reduction (Figure 3) are significantly reduced or completely missing, whereas the typical high Langmuir surface areas of approximately 1600 m²g^{–1} are still obtained. A noteworthy hydrogenation of the terephthalate ligands of the lattice

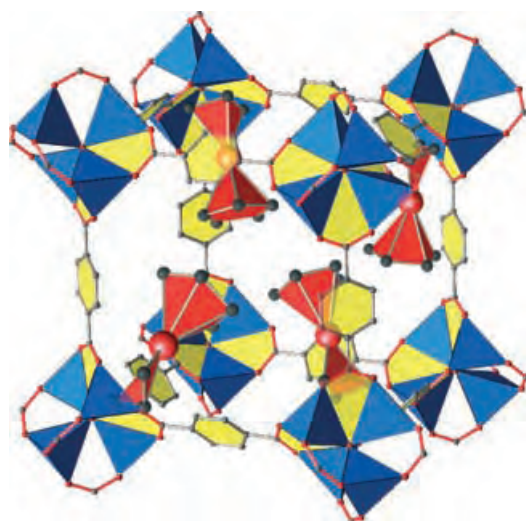


Figure 1. MOF-5 cage (blue/yellow) with four incorporated $[(\eta^5\text{-C}_5\text{H}_5)\text{Pd}(\eta^3\text{-C}_3\text{H}_5)]$ (**1**) precursors (red). The elemental cell of the crystalline MOF-5 contains eight cavities of this kind.

Table 1: Loading parameters of precursors **1–3** in MOF-5.

Precursor	Molecules per cavity	Elemental analysis [measured/calculated]			Volume precursor [Å ³] ^[a]		Allocation of pore volume [%] ^[c]
		M [%]	C [%]	H [%]	Per molecule	Per elemental cell MOF-5 ^[b]	
1	4	26.4/26.3	41.5/41.5	3.14/3.2	196.6	6291	45.3
2	2	10.7/10.8	40.4/40.7	3.4/3.4	242.6	3882	28.0
3	4	40.8/41.0	23.4/24.9	3.4/3.1	159.3	5098	36.7

[a] Calculated with Gaussian98^[14] (B3 LYP/SDD). [b] The elemental cell of MOF-5 consists of eight cavities. [c] The framework of MOF-5 occupies only 20% of the volume of the elemental cell ($V = 17343.6 \text{ Å}^3$).^[2]

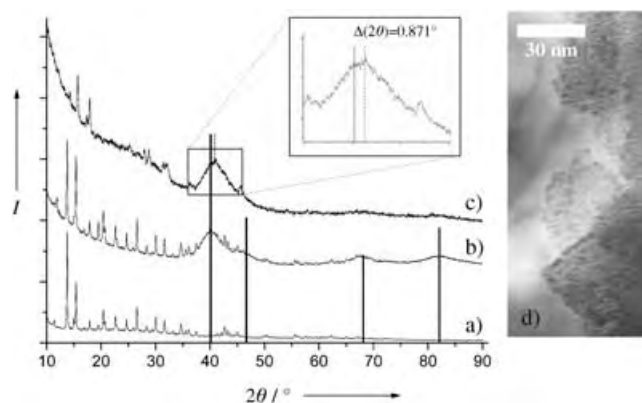


Figure 2. Powder diffraction patterns of a) MOF-5, b) photolytically generated Pd@MOF-5, c) Pd@MOF-5 (reduction by H₂). The 2θ values characteristic for palladium are highlighted. The enlargement shows the shift to higher 2θ values, typical of small particles; d) TEM image of photolytically generated Pd@MOF-5.

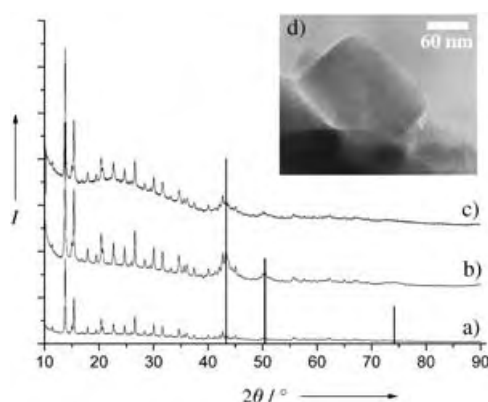


Figure 3. Powder diffraction patterns of a) MOF-5 b) photolytically generated Cu@MOF-5, c) Cu@MOF-5 (after methanol catalysis test, reduction by H₂), d) TEM image of Cu@MOF-5 (sample in (b)).

structure can be excluded on the basis of the IR data. We assume that only the long-range order of the host lattice is faulty. The existence of, for example, a defect or layer structure with 2D-order could be possible. The compound Pd@MOF-5 proved to be a moderately active catalyst for the hydrogenation of cyclooctene (coe) which was chosen as test reaction^[12] (Table 2).

We also found catalytic activity for the material Cu@MOF-5 which was obtained by reduction of **2**@MOF-5 in hydrogen stream at 150°C (1 h). With 70 μmol_{MeOH} g_{cat.}⁻¹ h⁻¹ methanol production from synthesis gas (rapid test at normal pressure^[13]) Cu@MOF-5 matches the standard of our recently reported novel supported mesoporous catalysts Cu/ZnO@MCM-41/48 (Table 2) prepared by metal organic CVD.^[14] The specific copper surface of approximately 6 m² g⁻¹ (at 13.8 wt % Cu) proved to be stable. According to the XRD data (Figure 3) there are copper particles in the range of 3–4 nm as well as an intact MOF-5 framework. The Langmuir surface area was determined to be 1100 m² g⁻¹ (after catalysis tests). This activity of Cu@MOF-5 is surprising as the promotion of copper by zinc or ZnO_x species^[13,15] normally essential for catalysis is, in this case, apparently not necessary, or is provided in a novel way by the MOF-5 framework stabilizing the copper particles and not collapsing under the catalysis conditions (220°C, CO/H₂). These observations confirm our earlier assumption, namely that the complicated metal–support interaction in the case of Cu/ZnO could imply a local interfacial phenomenon of Cu–O–Zn species that apparently does not require a well-developed (nano)crystalline ZnO phase.^[14]

Thermal transformation of **3**@MOF-5 (190°C, 4 h, H₂ stream) into Au@MOF-5 leaves the crystalline host lattice completely intact (XRD and Langmuir) as also found for Cu@MOF-5 but in contrast to Pd@MOF-5. TEM data (Figure 4) show polydisperse gold particles in a range of 5 to 20 nm. Apparently the gold atoms or gold clusters (or nuclei) primarily formed by decomposition of **3** are more mobile in the open MOF structure than the copper or palladium clusters and thus bigger aggregates are formed within the pores and a diffusion of gold particles to the outer surface also takes place, which accounts for the large gold particles of around 20 nm found outside the pores. Analogously this phenomenon was found for Au@MCM-41 and, as in our case, attributed to a very weak gold-particle–support or wall interaction.^[16]

The highly porous Au@MOF-5 material proved to be inactive for catalytic CO oxidation. The gold nanoparticles spread through the intact MOF-5 lattice and at the surface of the MOF-crystallites apparently lack the strong metal–support interaction or promotion (Au/TiO₂, Au/ZnO)^[17] necessary for this catalytic effect.

Table 2: Catalytic performance of different metal@MOF-5 systems.

Catalyst	Production rate		Metal surface	wt% metal	
	[μmol _{MeOH} g _{cat.} ⁻¹ h ⁻¹]	[μmol _{MeOH} m _{cat.} ⁻² h ⁻¹]		wt% Cu	wt% Zn
Cu@MOF-5	70	11.1	6.3	13.8	29.0 ^[a]
Cu/ZnO@MCM-41	19	4.1	4.6	6.9	10.4
Cu/ZnO@MCM-48	130	22.4	5.8	10.6	21.9
Pd@MOF-5	[mmol _{COA} g _{cat.} ⁻¹ h ⁻¹] ^[b]	[mmol _{COA} m _{cat.} ⁻² h ⁻¹] ^[b]	[m _{Pd} g _{cat.} ⁻¹]	wt% Pd	
	47.34	1.42	33.3	35.6	
Au@MOF-5	[μmol _{CO₂} g _{cat.} ⁻¹ h ⁻¹]	[μmol _{CO₂} m _{cat.} ⁻² h ⁻¹]	[m _{Au} g _{cat.} ⁻¹]	wt% Au	
	–	–	–	48	

[a] Zinc content of the MOF lattice and not additionally incorporated into MOF-5. [b] COA = cyclooctane.

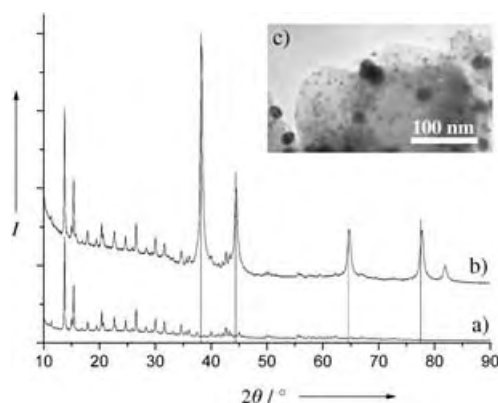


Figure 4. Powder diffraction patterns of the systems a) MOF-5 b) Au@MOF-5 (after reductive treatment with hydrogen at 190°C) c) TEM image of Au@MOF-5.

An alternative, and very gentle path to metal@MOF materials with a persistent, crystalline host lattice is the UV photolysis of the intermediate inclusion compounds **1–3**@MOF-5 at room temperature (water cooling) under inert gas (Ar, He) or vacuum. GC/MS analysis of the gaseous by-products in the case of photochemically generated Pd@MOF-5 merely shows cyclopentadiene as well as three further products of composition C_8H_{10} and $C_{10}H_{12}$. For Cu@MOF-5 $C_{10}H_{12}$ (fulvalen) as well as PMe_3 are found. TEM images (Figure 2 and Figure 3) reveal very small palladium and copper clusters (1–2 nm).

Our results show that metal organic chemical vapor deposition offers novel perspectives for the host–guest chemistry of porous coordination polymers. Nonaqueous colloid chemistry of metal and semiconductor nanoparticles is likewise based on metal organic precursor chemistry.^[18,19] Thus, MOF-5 and related solid-state materials will have lots to offer as moderately temperature stable “crystalline solvent cages” for the analysis of the chemical and physical properties of “naked” inorganic nanoparticles of all kinds, even beyond the scope of heterogeneous catalysis.

Experimental Section

Metal@MOF-5: Thermal metal organic CVD (MOCVD) loading: a sample of the freshly synthesized,^[2,4] pure solvent free MOF-5 template (50 mg) was placed in a Schlenk tube together with precursor (**1–3**; 100.0 mg) in a separate glass boat and warmed in static vacuum (1 Pa) for 3 h to 343 K (for **2** and **3**), or left at room temperature (for **1**). Samples of the thus obtained well defined intermediates **1–3**@MOF-5 (40 mg) were then reduced under H_2 at 23°C (30 min) for Pd@MOF-5 or at 150°C (1 h) for Cu@MOF-5 and 190°C (2 h) for Au@MOF-5. Cooling in vacuum (10^{-3} mbar) to room temperature (2 h) removed traces of the gaseous decomposition products (control by IR and ^{13}C -/ ^{31}P -MAS-NMR).

Photo MOCVD loading: Samples of the intermediates **1–3**@MOF-5 (30 mg) synthesized as described above where photolysed in an inert gas stream (Ar, He) for 2 h at 25–30°C (Hg high-pressure lamp, 500 W, Normag TQ718) and traces of remaining ligand fragments were removed in vacuum as described above.

The specific surface ($S_{Langmuir}$) of the empty MOF-5 and the samples metal@MOF-5 was determined by application of the Langmuir surface model in the pressure range $p/p_0 = 0.1–0.3$ at $T =$

77.36 K. The copper surface area of Cu@MOF-5 and its methanol synthesis activity was determined as described elsewhere in detail.^[16] A mixture of 72% H_2 , 10% CO, 14% CO_2 , and 14% He was used as synthesis gas. For tests on Au-catalyzed CO oxidation see ref. [20]. For the determination of the Pd surface and details on cyclooctene hydrogenation see ref. [21].

Further experimental details can be found in the Supporting Information.

Received: November 4, 2004

Revised: March 18, 2005

Published online: August 30, 2005

Publication delayed at author's request

Keywords: coordination polymers · chemical vapor deposition · heterogeneous catalysis · methanol synthesis · nanoparticles

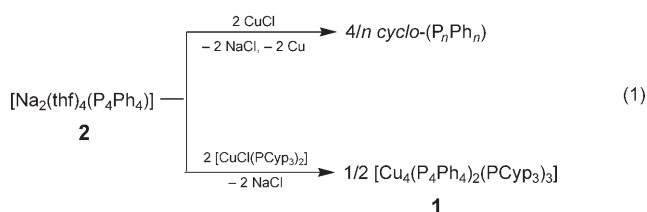
- [1] O. M. Yaghi, M. O'Keeffe, N. W. Ockwig, H. K. Chae, M. Eddaoudi, J. Kim, *Nature* **2003**, 423, 705–714.
- [2] a) H. Li, M. Eddaoudi, M. O'Keeffe, O. M. Yaghi, *Nature* **1999**, 402, 276–279; b) Surface determination was carried out using nitrogen adsorption and adapting to the Langmuir surface model.
- [3] C. Janiak, *Dalton Trans.* **2003**, 2781–2804.
- [4] a) A. Stein, *Adv. Mater.* **2003**, 15, 763–775; b) N. L. Rosi, J. Eckert, M. Eddaoudi, D. T. Vodak, J. Kim, M. L. O'Keeffe, O. M. Yaghi, *Science* **2003**, 300, 1127–1129; c) U. Müller, L. Lobree, M. Hesse, O. M. Yaghi, M. Eddaoudi (BASF AG, The Regents of the University of Michigan), US6624318, **2003** and US2004081611, **2004**.
- [5] H. K. Chae, D. Y. Siberio-Pérez, J. Kim, Y.-B. Go, M. Eddaoudi, A. J. Matzger, M. O'Keeffe, O. M. Yaghi, *Nature* **2004**, 427, 523–527.
- [6] a) Y. Zhang, Z. Yuan, R. J. Puddephatt, *Chem. Mater.* **1998**, 10, 2293–2300; b) J. E. Gozum, D. M. Pollina, J. A. Jensen, G. S. Girolami, *J. Am. Chem. Soc.* **1988**, 110, 2688–2689; c) R. R. Thomas, J. M. Park, *J. Electrochem. Soc.* **1989**, 136, 1661–1666.
- [7] Gaussian 98 (Revision A.11.1), Gaussian, Inc., Pittsburgh, PA, **2001**, M. J. Frisch et al., see Supporting Information.
- [8] a) H. Werner, H. Otto, Tri Ngo-Khac, Ch. Burschka, *J. Organomet. Chem.* **1984**, 262, 123–136; b) M. J. Hampden-Smith, T. T. Kodas, M. Paffett, J. D. Farr, H.-K. Shin, *Chem. Mater.* **1990**, 2, 636–639; c) D. B. Beach, F. K. LeGoues, Ch.-K. Hu, *Chem. Mater.* **1990**, 2, 216–219.
- [9] a) H. Schmidbaur, A. Shiotani, *Chem. Ber.* **1971**, 104, 2821–2830; b) J. L. Davidson, P. John, P. G. Roberts, M. G. Jubber, J. I. B. Wilson, *Chem. Mater.* **1994**, 6, 1712–1718; c) H. Uchida, N. Saito, M. Sato, M. Take, K. Ogi, *Jpn. Kokai Tokkyo Koho* **1995**, 6.
- [10] R. Becker, A. Devi, J. Weiss, U. Weckenmann, M. Winter, C. Kiener, H. W. Becker, R. A. Fischer, *Chem. Vap. Deposition* **2003**, 9, 149–156.
- [11] R. Lamber, S. Wetjen, N. I. Jaeger, *Phys. Rev. B* **1995**, 51, 10968–10971.
- [12] X. Mu, U. Bartmann, A. Guraya, G. W. Busser, U. Weckenmann, R. Fischer, *M. Muhler, Appl. Catal. A* **2003**, 248, 85–95.
- [13] M. Kurtz, N. Bauer, C. Buscher, H. Wilmer, O. Hinrichsen, R. Becker, S. Rabe, K. Merz, M. Driess, R. A. Fischer, M. Muhler, *Catal. Lett.* **2004**, 92, 49–52.
- [14] R. Becker, H. Parala, F. Hipler, A. Birkner, C. Wöll, O. Hinrichsen, O. P. Tkachenko, K. V. Klementiev, W. Grünert, S. Schäfer, H. Wilmer, M. Muhler, R. A. Fischer, *Angew. Chem.* **2004**, 116, 2899–2903; *Angew. Chem. Int. Ed.* **2004**, 43, 2839–2842.
- [15] a) P. L. Hansen, J. B. Wagner, S. Helveg, J. R. Rostrup-Nielsen, B. S. Clausen, H. Topsøe, *Science* **2002**, 295, 2053–2055;

- b) M. M. Günter, T. Ressler, B. Bems, C. Büscher, T. Genger, O. Hinrichsen, M. Muhler, R. Schlögl, *Catal. Lett.* **2001**, *71*, 37–44;
c) T. Fujitani, J. Nakamura, *Appl. Catal. A* **2000**, *191*, 111–129.
- [16] a) F. Schüth, personal communication; b) R. Kumar, A. Ghosh, C. R. Patra, P. Mukherjee, M. Sastry, *Nanotechnol. Catal.* **2004**, *1*, 111–136.
- [17] a) J. M. C. Soares, P. Morrall, A. Crossley, P. Harris, M. Bowker, *J. Catal.* **2003**, *219*, 17–24; b) Y. Iizuka, T. Tode, T. Takao, K.-I. Yatsu, T. Takeuchi, S. Tsubota, M. Haruta, *J. Catal.* **1999**, *187*, 50–58; c) F. Boccuzzi, A. Chiorino, S. Tsubota, M. Haruta, *J. Phys. Chem.* **1996**, *100*, 3625–3631.
- [18] a) F. Dumestre, B. Chaudret, C. Amiens, Ph. Renaud, P. Fejes, *Science* **2004**, *303*, 821–823; b) F. Dumestre, B. Chaudret, C. Amiens, M. Respaud, P. Fejes, Ph. Renaud, P. Zurcher, *Angew. Chem.* **2003**, *115*, 5371–5374; *Angew. Chem. Int. Ed.* **2003**, *42*, 5213–5216; c) S. Jansat, M. Gómez, K. Philippot, G. Muller, E. Guieu, C. Claver, S. Castillón, B. Chaudret, *J. Am. Chem. Soc.* **2004**, *126*, 1592–1593.
- [19] a) J. Hambrock, R. Becker, A. Birkner, J. Weiß, R. A. Fischer, *Chem. Commun.* **2002**, 68–69; b) J. Hambrock, M.-K. Schröter, A. Birkner, C. Wöll, R. A. Fischer, *Chem. Mater.* **2003**, *15*, 4217–4222; c) M. K. Schröter, L. Khodeir, E. Löffler, M. Muhler, R. A. Fischer, *Langmuir* **2004**, *20*, 9453–9455.
- [20] J. Assmann, V. Narkhede, L. Khodeir, E. Löffler, O. Hinrichsen, A. Birkner, H. Over, M. Muhler, *J. Phys. Chem. B* **2004**, *108*, 14634–14642.
- [21] J. E. Benson, H. S. Wang, M. Boudart, *J. Catal.* **1973**, *30*, 146–153.

The linear dianionic $(P_nR_n)^{2-}$ species were first obtained by Issleib et al. by reduction of cyclooligophosphanes *cyclo*-(P_nR_n) with alkali metals.^[1] The chain length of the $(P_nR_n)^{2-}$ fragments can be controlled by the stoichiometry of the reaction.^[1,2] Subsequently, it was shown that ^{31}P NMR spectroscopy can serve as a valuable tool to establish the identity of the resulting alkali metal salts $M_2(P_nR_n)$.^[3,4] Moreover, the alkali metal compounds $K[\text{cyclo}-(P_3t\text{Bu}_2)]$,^[2] $K[\text{cyclo}-(P_5\text{Ph}_4)]$,^[5] and $\text{Li}[\text{cyclo}-(P_n t\text{Bu}_{n-1})]$ ($n=3-5$)^[6,7] have also been described. However, these compounds were not isolated in pure form.

In spite of the established syntheses of alkali metal oligophosphanides, they have only been used sporadically in the synthesis of main group or transition metal complexes.^[8-13] Significantly, transmetalation of $K_2(P_4t\text{Bu}_4)$ with halides of Si^{IV} , Ge^{IV} , and Sn^{IV} leads to five-membered cyclic species *cyclo*-($P_4t\text{Bu}_4\text{ER}_2$) (R = organic substituent or Cl ; $E = \text{Si}, \text{Ge}, \text{Sn}$).^[8] In contrast, the $(P_nR_n)^{2-}$ chains do not remain intact in transmetalations of $K_2(P_2t\text{Bu}_2)$ with $[\text{NiCl}_2(\text{PMe}_3)_2]$, and of $M_2(P_n\text{Ph}_n)$ ($n=2-4$) with $[\text{Cp}_2\text{M}'\text{Cl}_2]$ ($M' = \text{Ti}, \text{Zr}, \text{Hf}$).^[9,10] Recently, the renaissance of oligophosphanide chemistry has been spurred by the targeted synthesis of $\text{Na}[\text{cyclo}-(P_5t\text{Bu}_4)]$, which displays highly versatile coordination chemistry,^[14,15] and by the simplified syntheses of alkali metal oligophosphanediides $M_2(P_nR_n)$ ($n=2-4$),^[16-18] which have enabled detailed structural investigations thereof.^[16-20] In the context of our ongoing studies on the synthesis of metal complexes containing oligophosphanide ligands,^[14-21] we now report the synthesis and structural characterization of $[\text{Cu}_4(P_4\text{Ph}_4)_2(\text{PCyp}_3)_3]$ (**1**; $\text{Cyp} = \text{cyclo-C}_5\text{H}_9$), which to our knowledge is the first copper(I) complex with an oligophosphanediide ligand.

One major difficulty in the transmetalation of alkali metal oligophosphanediides is their high reducing ability, which often leads to reduction of the metal halide employed and the formation of thermodynamically stable neutral cyclooligophosphanes. Thus, only a black precipitate, consisting of elemental copper and NaCl according to X-ray powder diffraction, and the cyclophosphanes *cyclo*-($P_n\text{Ph}_n$) ($n=4-6$) or *cyclo*-($P_4t\text{Bu}_4$), respectively, were formed in the reaction of two equivalents of CuCl with $[\text{Na}_2(\text{thf})_4(P_4\text{Ph}_4)]$ (**2**) or $K_2(P_4t\text{Bu}_4)$. However, no reduction was observed in the reaction of **2** with $[\text{CuCl}(\text{PCyp}_3)_2]$ [1:2; Eq. (1)]. Instead, $[\text{Cu}_4(P_4\text{Ph}_4)_2(\text{PCyp}_3)_3]$ (**1**) was isolated as air-sensitive orange crystals in 66 % yield.



An X-ray crystal structure analysis revealed that **1** exists in the solid state as a solvate with 3.5 molecules of toluene in the asymmetric unit. A tetranuclear aggregate of four Cu^+ ions with two $(P_4\text{Ph}_4)^{2-}$ dianions is observed (Figure 1),^[22] and

Copper Oligophosphanides

DOI: 10.1002/anie.200501607

Synthesis and Molecular Structure of the Cu_4P_8 Cage Compound $[\text{Cu}_4(\text{P}_4\text{Ph}_4)_2(\text{PCyp}_3)_3]$ **

Robert Wolf and Evamarie Hey-Hawkins*

Linear and cyclic oligophosphanide anions $(P_nR_n)^{2-}$ ($n=2-4$) and *cyclo*-(P_mR_{m-1})⁻ ($m=3-5$) are an attractive class of ligands displaying a plethora of potential coordination modes.

[*] M. Phil. R. Wolf, Prof. Dr. E. Hey-Hawkins
Institut für Anorganische Chemie der Universität Leipzig
Johannisallee 29, 04103 Leipzig (Germany)
Fax: (+49) 341-9739319
E-mail: hey@rz.uni-leipzig.de

[**] We thank Dr. Peter Lönnecke for assistance with the X-ray structure determination of **1**, Dr. Volker Gottschalch for X-ray powder diffraction, and Dipl.-Chem. Corinna Sykora, Dipl.-Chem. Tobias Langrock, and Dr. Diana Hofmann for mass spectrometric measurements. Support from the Studienstiftung des deutschen Volkes (PhD grant for R.W.) and the company CYTEC (generous donation of tricyclopentylphosphane) is gratefully acknowledged.
 $\text{Cyp} = \text{cyclo-C}_5\text{H}_9$.

Supporting information for this article is available on the WWW under <http://www.angewandte.org> or from the author.

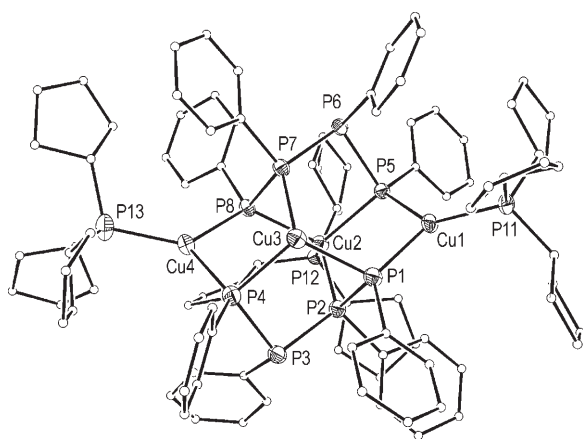


Figure 1. Solid-state molecular structure of **1** (without hydrogen atoms and toluene molecules).

three of the Cu^+ cations are additionally coordinated by tricyclopentylphosphane ligands. Thus, three distinct coordination environments can be distinguished for copper. Two of the cations (Cu1 and Cu4) are each coordinated by two terminal phosphorus atoms of different $(\text{P}_4\text{Ph}_4)^{2-}$ chains and a tricyclopentylphosphane molecule. These attain a trigonal-planar coordination geometry (sum of angles around Cu1 : 359.28° ; around Cu4 : 359.16°). This results in the formation of a “crownlike” ten-membered $[\text{Cu}_2(\text{P}_4\text{Ph}_4)_2]^{2-}$ macrocycle which coordinates two further copper ions through two terminal phosphorus atoms of the same P_4 chain and one internal phosphorus atom of the other P_4 chain. Thus, a unique Cu_4P_8 cage arrangement is formed (Figure 2).

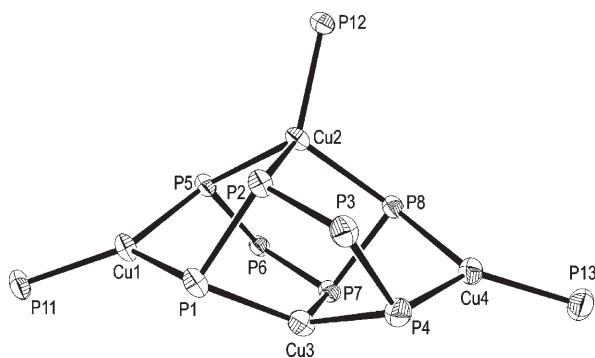


Figure 2. Core structure of **1** (only Cu and P atoms are shown).

In contrast, the formation of four- to eight-membered Cu_nP_n rings is generally observed in other Cu^{I} phosphanido complexes.^[23,24] Of the two remaining copper ions, Cu2 is additionally coordinated by a tricyclopentylphosphane molecule and therefore displays a distorted tetrahedral coordination environment, while the fourth copper cation (Cu3) is coordinated in a trigonal-pyramidal fashion (sum of angles around Cu3 : 343.60°). The higher coordination number of Cu2 is reflected in its rather long Cu–P bonds ($d(\text{Cu2}-\text{P2}, \text{P5}, \text{P8}, \text{P12}) = 2.316(2)–2.403(2) \text{ \AA}$) compared to the remaining Cu–P bond lengths ($d(\text{Cu}-\text{P}) = 2.239(2)–2.320(2) \text{ \AA}$). These differences apart, the Cu–P bond lengths

of the anionic and the neutral P donors are in a similar range and compare well with those found in other copper phosphanides,^[23,24] copper polyphosphides,^[25] and related Cu^{I} coordination compounds.^[26]

The P–P bond lengths are in the usual range for single bonds [$d(\text{P}-\text{P}) = 2.180(2)–2.241(2) \text{ \AA}$].^[27] Although the P_4 chains are in a *syn* arrangement they display rather large torsion angles compared to the structure of $[\text{Na}_2(\text{thf})_5(\text{P}_4\text{Ph}_4)]$ (**2**·thf) (**1**: $\text{P1}-\text{P2}-\text{P3}-\text{P4}$ 62.90° , $\text{P5}-\text{P6}-\text{P7}-\text{P8}$ -67.17° ; cf. $\text{P1}-\text{P2}-\text{P2}'-\text{P1}'$ 32.1° in **2**·thf).^[16] This appears to be a consequence of the coordination of an internal phosphorus atom to copper in each of the ligands, and underlines the structural flexibility of the $(\text{P}_4\text{Ph}_4)^{2-}$ ligands as they adapt to the coordination requirements of the metal atoms.

The composition of **1** is additionally supported by NMR spectroscopic investigations, C,H analysis, and mass spectrometric measurements. Due to its high mass the molecular ion was not observed in the LDI-MS spectrum, but dominant fragment ions were reproducibly detected which, according to their characteristic isotopic patterns, are derived from the parent molecule by loss of organic substituents (Ph, Cyp) and tricyclopentylphosphane units. As expected, the ^1H NMR spectrum of **1** displays overlapping resonances for the cyclopentyl groups, the phenyl substituents, and the toluene molecules, which are also present in the solid-state structure of **1**. After drying in vacuum it still contains about 1.5 equivalents of toluene. This is indicated both by the C, H analyses and by the ratio of aliphatic and aromatic resonances in the ^1H NMR spectrum.

The room-temperature $^{31}\text{P}\{^1\text{H}\}$ NMR spectrum is extremely complex, displaying several broad peaks of varying intensity. This is not entirely surprising considering that an unsymmetric spin system of 11 different phosphorus nuclei would be expected if the solid-state structure of **1** were to remain in solution. However, the spectrum becomes even more complicated at -80°C and shows numerous severely broadened multiplets in the regions between $\delta = +20$ and 0 ppm , -10 and -30 ppm , -70 and -105 ppm , as well as a broad symmetric multiplet at $+44.1 \text{ ppm}$. This indicates that line broadening at higher temperatures is not exclusively caused by coupling between phosphorus and the quadrupolar $^{63}\text{Cu}/^{65}\text{Cu}$ nuclei, but that a fluxional process also plays a key role. Although the exact nature of this process is still unclear, it appears unlikely that the molecular structure of **1** is retained in solution. This is in contrast to the behavior of alkali metal tetraphosphanediides, the solid-state structures of which are generally retained in solution.^[16,17]

In summary, the copper(I) tetraphosphanediide complex $[\text{Cu}_4(\text{P}_4\text{Ph}_4)_2(\text{PCyp}_3)_3]$ (**1**) has been synthesized and structurally characterized. In the solid state, it displays a twelve-membered Cu_4P_8 cage arrangement with an unprecedented coordination mode of the $(\text{P}_4\text{Ph}_4)^{2-}$ ligands involving one internal and two terminal phosphorus atoms of the P_4 chain. The synthesis of **1** demonstrates that in principal such complexes are readily accessible by transmetalation of the respective alkali metal tetraphosphanediides. In future work, the preparation of other copper oligophosphanido complexes will give further insight into the solution structures of such species. Furthermore, it is well known that Cu^{I} phosphanido

complexes often react differently to their alkali metal counterparts.^[24] Therefore, it will be of great interest to explore the reactivity of **1** with electrophiles and its utility in the synthesis of other homo- and heterometallic oligophosphanido complexes.

Experimental Section

All experiments were performed under an atmosphere of dry argon. The NMR spectra were recorded on a Bruker AVANCE-DRX-400 spectrometer. The mass spectra were recorded on an Applied Biosystems 4700 spectrometer by using the laser desorption ionization (LDI) technique. The IR spectra were recorded on an Perkin-Elmer System 2000 FTIR spectrometer in the range 350–4000 cm⁻¹. All solvents were purified by distillation, dried, saturated with argon, and stored over potassium mirror. [Na₂(thf)₄(P₄Ph₄)] (**2**) was synthesized according to the literature procedure;^[16] all other reagents were obtained from commercial sources and used as supplied.

1: A colorless solution of [CuCl(PCyp₃)₂] (0.99 g, 1.72 mmol), prepared from CuCl and 2 equiv of PCyp₃ in toluene (10 mL), was added to a yellow to orange solution of **2** (0.66 g, 0.86 mmol) in THF (6 mL) at -80°C. The resulting orange suspension was allowed to warm to room temperature. A clear orange solution formed on stirring overnight. This was concentrated to ca. 10 mL and layered with 20 mL of *n*-hexane. A fine, colorless powder (NaCl) formed on storage at +5°C for several days. This was removed by filtration and the filtrate was evaporated to dryness. The orange residue was carefully dissolved in 6 mL of warm toluene. Orange, crystalline needles formed on storing the clear orange solution at +5°C for several days. This solid was isolated and dried in vacuo. Under vacuum the compound loses toluene and contains ca. 1.5 equiv of toluene after evacuating for ca. 25 min at 10⁻²–10⁻³ torr. Yield: 0.56 g (66% ref. to 1·1.5C₇H₈); m.p. 152–153°C (red oil); ¹H NMR (400.13 MHz, C₆D₆, 25°C, TMS): δ = 0.85 (br, 1.5H, C₅H₉), 1.2–1.8 (brm, 79.5H, C₅H₉), 2.11 (s, 4.5H, CH₃ from toluene), 6.8–8.8 ppm (m, 47.5H, Ph); ¹³C{¹H,³¹P} NMR (100.16 MHz, C₆D₆, 25°C, TMS): δ = 21.08 (s, CH₃ in toluene), 25.16–30.47 (s, CH₂ in C₅H₉), 34.83–35.49 (s, CH in C₅H₉), 123.58–149.09 ppm (s, Ph); ³¹P{¹H} NMR (161.9 MHz, C₆D₆, 25°C): δ = +32.5 (brs), +18.2 (t, J_{PP} = ±72 Hz), +10.0 (brs), +5.35 (t, J_{PP} = ±48.0 Hz), +2.9 (brs), -20.4 (brm), -23.8 (brm), -71.2 (brm), -88.8 ppm (brm); IR (KBr): ν̄ = 3129 (vw), 3046 (m), 2951 (s), 2865 (s), 1941 (w), 1871 (w), 1801 (w), 1649 (w), 1576 (m), 1474 (m), 1448 (m), 1430 (m), 1299 (m), 1261 (m), 1179 (w), 1125 (m), 1089 (m), 1066 (m), 1024 (m), 908 (m), 804 (m), 736 (s), 694 (m), 485 cm⁻¹ (m); MS (LDI): *m/z* (%): 1061.7 (100) [M-2PCyp₃-2Cyp-2Ph-2H]⁺, 963.5 (50) [M-3PCyp₃-2Ph]⁺; elemental analysis (%) for C_{103.5}H₁₃₃Cu₄P₁₁ (*M* = 1972.10): calcd: C 63.04, H 6.80; found: C 63.12, H 6.69.

Received: May 11, 2005

Published online: September 7, 2005

Keywords: cage compounds · copper · P ligands · phosphorus

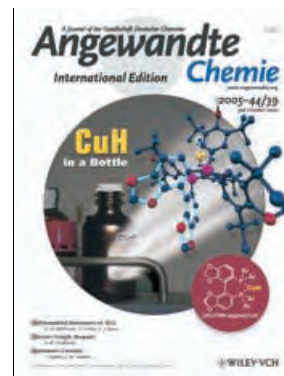
- [1] a) K. Issleib, K. Krech, *Chem. Ber.* **1965**, *98*, 2545; b) K. Issleib, E. Fluck, *Z. Anorg. Allg. Chem.* **1965**, *339*, 274; c) K. Issleib, K. Krech, *Chem. Ber.* **1966**, *99*, 1310; d) K. Issleib, M. Hoffmann, *Chem. Ber.* **1966**, *99*, 1320; e) K. Issleib, C. Rockstroh, I. Duchek, E. Fluck, *Z. Anorg. Allg. Chem.* **1968**, *360*, 77; f) K. Issleib, K. Krech, *J. Prakt. Chem.* **1969**, *311*, 463.
- [2] M. Baudler, C. Gruner, G. Fürstenberg, B. Kloth, F. Saykowski, U. Özer, *Z. Anorg. Allg. Chem.* **1978**, *446*, 169.
- [3] a) M. Baudler, D. Koch, E. Tolls, K. M. Diederich, B. Kloth, *Z. Anorg. Allg. Chem.* **1976**, *420*, 146; b) P. R. Hoffmann, K. G. Caulton, *J. Am. Chem. Soc.* **1975**, *97*, 6370.
- [4] M. Baudler, D. Koch, *Z. Anorg. Allg. Chem.* **1976**, *425*, 227.
- [5] A. Schmidpeter, G. Burget, *Phosphorus Sulfur* **1985**, *22*, 323.
- [6] G. Fritz, K. Stoll, *Z. Anorg. Allg. Chem.* **1986**, *538*, 782.
- [7] G. Fritz, R. Biastoch, K. Stoll, T. Vaahs, D. Hanke, H. W. Schneider, *Phosphorus Sulfur* **1987**, *30*, 385.
- [8] a) B. Riegel, A. Pfitzner, G. Heckmann, E. Fluck, H. Binder, *Phosphorus Sulfur Silicon Relat. Elem.* **1994**, *93*, 173; b) B. Riegel, A. Pfitzner, G. Heckmann, H. Binder, E. Fluck, *Z. Anorg. Allg. Chem.* **1994**, *620*, 8; c) B. Riegel, A. Pfitzner, G. Heckmann, H. Binder, E. Fluck, *Z. Anorg. Allg. Chem.* **1995**, *621*, 1989; d) D. Bongert, G. Heckmann, W. Schwarz, H. D. Hausen, H. Binder, *Z. Anorg. Allg. Chem.* **1995**, *621*, 1358; e) D. Bongert, G. Heckmann, W. Schwarz, H. D. Hausen, H. Binder, *Z. Anorg. Allg. Chem.* **1996**, *622*, 1167; f) D. Bongert, G. Heckmann, H. D. Hausen, W. Schwarz, H. Binder, *Z. Anorg. Allg. Chem.* **1996**, *622*, 1793; g) H. Binder, B. Schuster, W. Schwarz, K. W. Klinkhammer, *Z. Anorg. Allg. Chem.* **1999**, *625*, 699.
- [9] H. Köpf, R. Voigtländer, *Chem. Ber.* **1981**, *114*, 2731.
- [10] R. A. Jones, M. H. Seeberger, B. R. Whittlesey, *J. Am. Chem. Soc.* **1985**, *107*, 6424.
- [11] a) M. Baudler, S. Klautke, *Z. Naturforsch.* **1981**, *36*, 527; b) M. Baudler, S. Klautke, *Z. Naturforsch.* **1983**, *38*, 121.
- [12] M. Baudler, L. De Riese-Meyer, U. Schings, *Z. Anorg. Allg. Chem.* **1984**, *519*, 24.
- [13] a) A. H. Cowley, R. A. Jones, M. A. Maroones, J. L. Atwood, S. G. Bott, *Angew. Chem.* **1991**, *103*, 1163; *Angew. Chem. Int. Ed. Engl.* **1991**, *30*, 1141; b) G. Linti, R. Frey, W. Köstler, H. Schwenk, *Chem. Ber./Recueil* **1997**, *130*, 663; c) W. Köstler, G. Linti, *Eur. J. Inorg. Chem.* **2001**, 1841.
- [14] A. Schisler, Dissertation, Universität Leipzig, **2003**.
- [15] a) A. Schisler, U. Huniar, P. Lönnecke, R. Ahlrichs, E. Hey-Hawkins, *Angew. Chem.* **2001**, *113*, 4345; *Angew. Chem. Int. Ed.* **2001**, *40*, 4217; b) A. Schisler, P. Lönnecke, T. Gelbrich, E. Hey-Hawkins, *Dalton Trans.* **2004**, 2895; c) A. Schisler, P. Lönnecke, E. Hey-Hawkins, *Inorg. Chem.* **2005**, *44*, 461; d) A. Schisler, P. Lönnecke, E. Hey-Hawkins, unpublished results.
- [16] R. Wolf, A. Schisler, P. Lönnecke, C. Jones, E. Hey-Hawkins, *Eur. J. Inorg. Chem.* **2004**, 3277.
- [17] R. Wolf, Dissertation, Universität Leipzig, **2005**.
- [18] J. Geier, H. Rügger, M. Wörle, H. Grützmacher, *Angew. Chem.* **2003**, *115*, 4081; *Angew. Chem. Int. Ed.* **2003**, *42*, 3951.
- [19] a) J. Geier, J. Harmer, H. Grützmacher, *Angew. Chem.* **2004**, *116*, 4185; *Angew. Chem. Int. Ed.* **2004**, *43*, 4093; b) J. Geier, Dissertation, ETH Zürich, **2004**.
- [20] M. Kaupp, A. Patrakov, R. Reviakine, O. L. Malkina, *Chem. Eur. J.* **2005**, *11*, 2773.
- [21] R. Wolf, E. Hey-Hawkins, *Chem. Commun.* **2004**, 2626.
- [22] Structural data of **1**: C_{117.5}H₁₄₉Cu₄P₁₁, *M* = 2156.20, triclinic, space group *P* $\bar{1}$, *a* = 16.165(1), *b* = 17.199(2), *c* = 21.460(2) Å, *a* = 91.475(9), *β* = 91.334(9), *γ* = 110.077(7)°, *V* = 5599.0(7) Å³, *Z* = 2, *ρ*_{calcd} = 1.279 Mg m⁻³, *μ* = 0.953 mm⁻¹, *θ*_{max} = 26.03°, *R* = 0.0508, *R*_w = 0.1229. The data were collected on a STOE IPDS diffractometer (*λ*_{MoKα} = 0.71073 Å, *T* = 207(2) K), 20 533 independent reflections, 1154 parameters, 94 restraints, max. residual electron density 1.168 e Å⁻³. A numerical absorption correction was carried out with X-red (STOE & Cie GmbH, Darmstadt), and the structure solution with direct methods (G. M. Sheldrick, SHELXS-97, Program for Crystal Structure Solution, University of Göttingen, **1997**). Cu, P, and C atoms were refined anisotropically (G. M. Sheldrick, SHELXL-97, Program for the Refinement of Crystal Structures, University of Göttingen, **1997**). The structure contains 3.5 molecules of toluene in the asymmetric unit, some of which are heavily disordered. One toluene molecule that could not be refined satisfactorily was eliminated by using the program SQUEEZE implemented in PLATON (P. V. D. Sluis, A. L. Spek, *Acta Crystallogr. Sect. A* **1990**, *46*,

- 194). The positions of the H atoms were partially located on the Fourier difference map and partially calculated on idealized positions. CCDC 270972 contains the supplementary crystallographic data for this paper. These data can be obtained free of charge from the Cambridge Crystallographic Data Centre via www.ccdc.cam.ac.uk/data_request/cif.
- [23] For example, a) T. Greiser, E. Weiss, *Chem. Ber.* **1978**, *111*, 516; b) G. van Koten, J. G. Noltes, A. L. Spek, *J. Organomet. Chem.* **1978**, *159*, 441; c) A. H. Cowley, D. M. Giolando, R. A. Jones, C. M. Nunn, J. M. Power, *J. Chem. Soc. Chem. Commun.* **1988**, 208; d) T. A. Annan, R. Kumar, D. G. Tuck, *J. Chem. Soc. Chem. Commun.* **1988**, 446; e) D. J. Brauer, G. Hessler, P. C. Knüppel, O. Stelzer, *Inorg. Chem.* **1990**, *29*, 2370; f) D. J. Brauer, P. C. Knüppel, O. Stelzer, *Phosphorus Sulfur Silicon Relat. Elem.* **1990**, *49*, 449; g) T. A. Annan, R. Kumar, D. G. Tuck, *J. Chem. Soc. Dalton Trans.* **1991**, 11; h) A. Eichhöfer, D. Fenske, W. Holstein, *Angew. Chem.* **1993**, *105*, 257; *Angew. Chem. Int. Ed. Engl.* **1993**, *32*, 242; i) M. Faulhaber, M. Driess, K. Merz, *Chem. Commun.* **1998**, 1887.
- [24] C. Meyer, H. Grützmacher, *Angew. Chem.* **1997**, *109*, 2576; *Angew. Chem. Int. Ed. Engl.* **1997**, *36*, 2471.
- [25] a) O. Olofsson, *Acta Chem. Scand.* **1965**, *18*, 217; b) H. Schlenger, H. Jacobs, R. Juza, *Z. Anorg. Allg. Chem.* **1971**, 385, 177; c) E. Amberger, P. A. Rauh, *Acta Crystallogr. B* **1974**, *30*, 2549; d) M. H. Möller, W. Jeitschko, *Z. Anorg. Allg. Chem.* **1982**, *491*, 225.
- [26] A CCD search (November 2004) reveals that for 38 Cu^I complexes of the closely related ligand P(*cyclo*-C₆H₁₁)₃ the Cu–P distances lie in the range 2.145–2.311 Å (av 2.236 Å).
- [27] R. Blom, A. Haaland, *J. Mol. Struct.* **1985**, *128*, 21.

Cover Picture

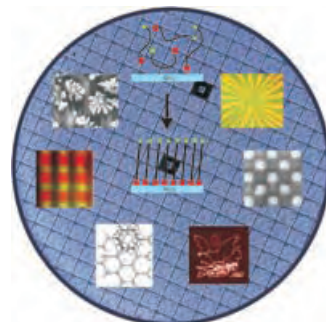
Bruce H. Lipshutz* and Bryan A. Frieman

The innate stability of the extraordinarily reactive and enantioselective reagent $[(R)\text{-(–)-DTBM-segphos}]\text{CuH}$ (whose structure is shown in the cover picture) is revealed in the Communication by Lipshutz and Frieman on page 6345 ff. Although there have been many advances in ligand-accelerated catalysis of hydrosilylations, these reactions invariably require the preparation of the catalyst prior to use owing to their limited shelf-life. This new reagent represents the first asymmetric “CuH in a Bottle”.



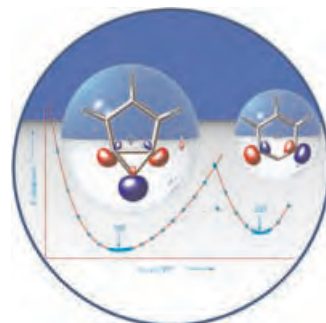
Monolayers on SiO₂

Self-assembled monolayers offer an ideal platform for the functionalization of silicon oxide surfaces. Their formation and modification as well as the generation of patterns are the themes of the Review by B. J. Ravoo, D. N. Reinhoudt, and S. Onclin on page 6282 ff.



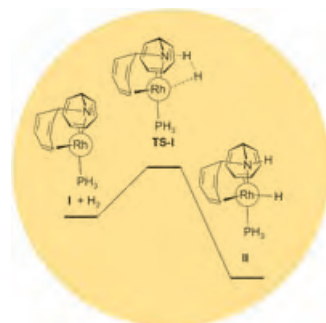
Tridehydrobenzenes

In their Communication on page 6306 ff., W. Sander et al. discuss the matrix isolation and spectroscopic characterization of 1,2,3-tridehydrobenzene. The triradical has a 2A_1 ground state.



Hydrogenation Catalysts

H. Grützmacher et al. present a four-coordinate rhodium(I)amide in their Communication on p. 6318 ff. The complex heterolytically cleaves H₂ activating it for the hydrogenation of ketones and imines.





The following Communications have been judged by at least two referees to be “very important papers” and will be published online at www.angewandte.org soon:

S. Klaus, H. Neumann, A. Zapf, D. Strübing, S. Hübner, J. Almerna,*
T. Riermeier, P. Groß, M. Sarich, W.-R. Krahner, K. Rossen,
M. Beller*

A General and Efficient Method for the Formylation of Aryl and Heteroaryl Bromides

N. Martín,* Á. Martín-Domenech, S. Filippone, M. Altable,
L. Echegoyen,* C. M. Cardona

Retro-Cycloaddition Reactions of Pyrrolidinofullerenes

C. Höbartner, S. K. Silverman*

Modulation of RNA Tertiary Folding by Incorporation of Caged Nucleotides

M. Nakamura,* A. Hajra, K. Endo, E. Nakamura*

Synthesis of Chiral α -Fluoroketones through Catalytic Enantioselective Decarboxylation

J. M. Macak, H. Tsuchiya, L. Taveira, S. Aldabergerova, P. Schmuki*
Smooth Anodic TiO₂ Nanotubes

Y. Yamaguchi,* S. Kobayashi, T. Wakamiya, Y. Matsubara,
Zen-ichi Yoshida*

Banana-Shaped Oligo(aryleneethynylenes): Synthesis and Light-Emitting Characteristics

Obituary

Christopher S. Foote (1935–2005): Singlet Oxygen

F. Jensen, P. Ogilby _____ **6268**

Books

Ruthenium in Organic Synthesis

Shun-Ichi Murahashi

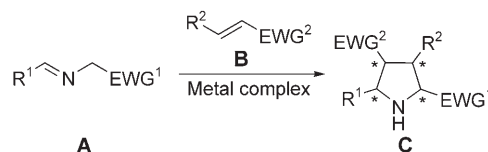
reviewed by W. Tam _____ **6269**

Highlights

Asymmetric Catalysis

C. Nájera,* J. M. Sansano* - **6272–6276**

Catalytic Enantioselective 1,3-Dipolar Cycloaddition Reaction of Azomethine Ylides and Alkenes: The Direct Strategy To Prepare Enantioenriched Highly Substituted Proline Derivatives



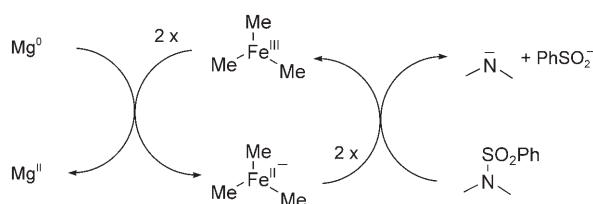
A direct hit! The asymmetric 1,3-dipolar cycloaddition of azomethine ylides (from imines **A**; EWG = electron-withdrawing group) and electrophilic alkenes **B** using chiral metal complexes in substoichiometric amounts provides a direct stereo-

selective synthesis of pyrrolidine or proline derivatives. The successful ligand/metal cation couples are rationalized on the basis of recently published results.

Electron-Transfer Reagents

R. W. Hoffmann* _____ **6277–6279**

Redox Catalysts for Reduction with Base Metals



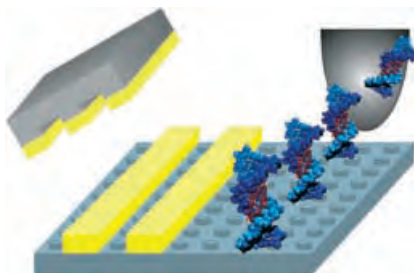
A question of potential! Clean reduction by dissolving base metals can be effected by employing redox catalysts of appropriate oxidation potential. The traditional use of aromatic hydrocarbons as redox catalysts has now been expanded by applica-

tion of Me₃Fe^{II}Li and related ate complexes. The scheme shows, for example, the catalytic cycle for the reductive cleavage of phenylsulfonamides with magnesium.

Reviews

Engineering on the nanometer scale:

Nanoscale control over surface properties is of paramount importance in bottom-up approaches to nanofabrication, which will revolutionize nanoelectronics and biotechnology in the near future. Self-assembled monolayers can form an ideal platform for nanofabrication on silicon oxide (see picture). Their formation, derivatization, and patterning are discussed.



Self-Assembled Monolayers

S. Onclin, B. J. Ravoo,*
D. N. Reinhoudt* ————— 6282 – 6304

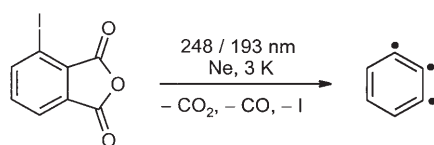
Engineering Silicon Oxide Surfaces Using Self-Assembled Monolayers

Communications

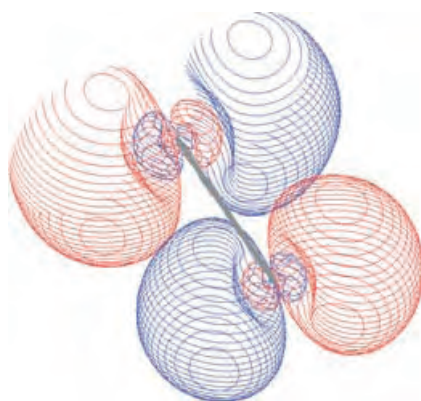
Tridehydrobenzenes

S. Venkataramani, M. Winkler,
W. Sander* ————— 6306 – 6311

1,2,3-Tridehydrobenzene



The first representative of the tridehydrobenzenes that could be spectroscopically characterized and isolated in cryogenic matrices is 1,2,3-tridehydrobenzene. Comparison of the measured IR spectrum with high-level ab initio calculations allows the assignment of a 2A_1 ground state to this unusual radical.



Joining the jet set: High-resolution, pure rotational spectra are obtained from a supersonic jet of TeSe prepared by laser ablation. The spectra give access to the internuclear potential, electronic structure (see picture), and details of the chemical bond of the first intermetallic $^3\Sigma$ compound observed by microwave spectroscopy.

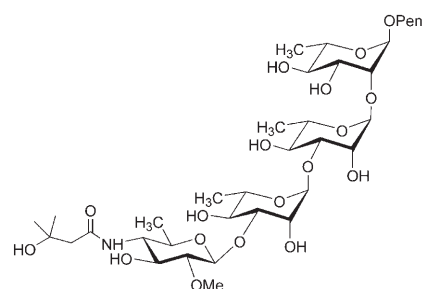
Rotational Spectroscopy

D. Baner, M. Schnell, J.-U. Grabow,*
E. J. Cocinero, A. Lesarri,
J. L. Alonso ————— 6311 – 6315

The Internuclear Potential, Electronic Structure, and Chemical Bond of Tellurium Selenide

Fighting Anthrax by recognizing its coat:

The spores of *Bacillus anthracis* bear unique oligosaccharides on their surface for interaction with a host. These specific oligosaccharides may prove useful in the development of vaccines against this major biowarfare threat. The total synthesis of such a vaccine candidate (see picture, Pent = 4-pentenyl) is reported.



Vaccines

D. B. Werz,
P. H. Seeberger* ————— 6315 – 6318

Total Synthesis of Antigen *Bacillus Anthracis* Tetrasaccharide—Creation of an Anthrax Vaccine Candidate

For the USA and Canada:

ANGEWANDTE CHEMIE International Edition (ISSN 1433-7851) is published weekly by Wiley-VCH PO Box 191161, D 69451 Weinheim, Germany. Air freight and mailing in the USA by Publications Expediting Inc. 200 Meacham Ave., Elmont, NY 11003. Periodicals

postage paid at Jamaica NY 11431. US POSTMASTER: send address changes to *Angewandte Chemie*, Wiley-VCH, 111 River Street, Hoboken, NJ 07030. Annual subscription price for institutions: US\$ 4948.00/4498.00 (valid for print and electronic / print or electronic delivery); for individuals who are personal members of a

national chemical society, or whose institution already subscribes, or who are retired or self-employed consultants, print only: US\$ 394.00. Postage and handling charges included. All Wiley-VCH prices are exclusive VAT.

The best in chemistry – for more than a hundred years



A Journal of the Gesellschaft Deutscher Chemiker
Angewandte
International Edition **Chemie**

www.angewandte.org

1888: The beginning
of a success story

Constant Innovations

- 1962:** First issue of the International Edition
- 1976:** Graphical abstracts
- 1979:** Cover pictures
- 1988:** Centenary of Angewandte
- 1989:** Routine use of color
- 1991:** New section: Highlights
- 1992:** Computerized editorial tracking system
- 1995:** Internet service for readers
- 1998:** Regular press service; full-text online
- 2000:** New section: Essays; EarlyView: Communications available online ahead of the printed version
- 2001:** New section: Minireviews
- 2002:** Online submission of manuscripts
- 2003:** Weekly publication; new section: News; new layout
- 2004:** Backfiles (1962-1997); ManuscriptXpress: Online system for authors and referees



Angewandte's advisors...

E. W. "Bert" Meijer
Technische Universiteit
Eindhoven

»» *Angewandte Chemie*, in its way of publishing, is as original as the chemistry described in the journal. It serves our society in a superb and attractive way. Many leading communications and comprehensive reviews have been published through the years and many of them are used in my teaching and cited in my own papers. It is a privilege to publish in and to be connected to a journal that is the trendsetter in chemistry of the highest standards. ««

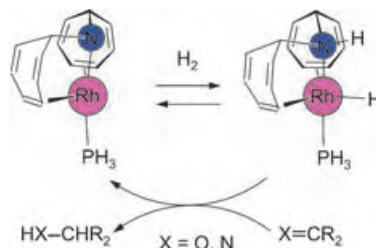
Angewandte Chemie International Edition is
a journal of the German Chemical Society (GDCh)

GDCh

 **WILEY**
InterScience®
DISCOVER SOMETHING GREAT

 **WILEY-VCH**

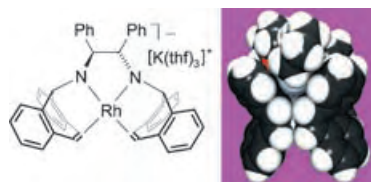
A split decision: Efficient heterolytic hydrogen splitting is achieved with novel tetracoordinate rhodium(I) amides. This reaction is reversible, and DFT calculations imply that the cleavage is a one-step process with a relatively low activation barrier. Ketones and imines are hydrogenated by the amide complexes without the need for further additives.



Hydrogenation Catalysts

P. Maire, T. Büttner, F. Breher, P. Le Floch, H. Grützmacher* 6318–6323

Heterolytic Splitting of Hydrogen with Rhodium(I) Amides



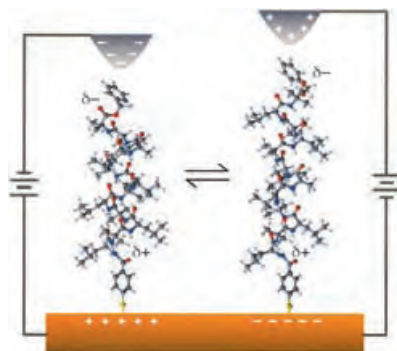
The filled/filled repulsion model can be used to explain qualitatively the trends in the acidity of the coordinated NH groups,

the redox potentials of the amides, and the UV/Vis absorptions in different aggregates between a counter cation, $[M(soln)_n]^+$, and the first stable diamido rhodate(1–) anion (see structure and space-filling model), which was synthesized by using the tetradentate diamino diolefin ligand (*S,S*)-trop₂dpn.

Rhodium Complexes

P. Maire, F. Breher, H. Grützmacher* 6325–6329

Diamido Rhodates(1–)

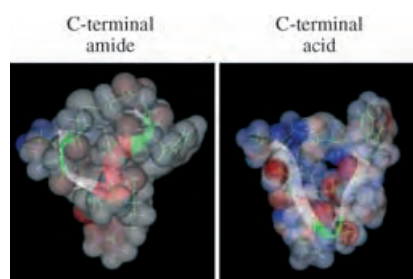


Outstanding in the electric field: Bundles of helical peptides undergo stochastic switching in response to the applied bias polarity as observed by STM. This behavior results from a conformational change between the α -helical (left) and 3_{10} -helical (right) states and affects the overall helix length. The interaction of the helical dipole moment with the applied electric field determines the preferred conformation of the peptides.

Molecular Switches

K. Kitagawa, T. Morita, S. Kimura* 6330–6333

A Helical Molecule That Exhibits Two Lengths in Response to an Applied Potential



Building bridges: α -Conotoxins (C1–C3, C2–C4 disulfide pairing) adopt a globular conformation, whereas γ/λ -conotoxins (C1–C4, C2–C3 disulfide pairing) fold into a ribbon conformation. Amidation of the peptide C terminus has been shown to influence the folding (see picture) and hence the biological activity of conotoxins.

Peptide Conformations

T. S. Kang, S. Vivekanandan, S. D. S. Jois, R. M. Kini* 6333–6337

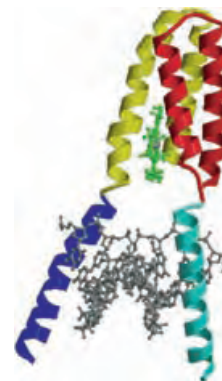
Effect of C-Terminal Amidation on Folding and Disulfide-Pairing of α -Conotoxin Iml

DNA Recognition

D. D. Jones, P. D. Barker* — 6337–6341

Controlling Self-Assembly by Linking Protein Folding, DNA Binding, and the Redox Chemistry of Heme

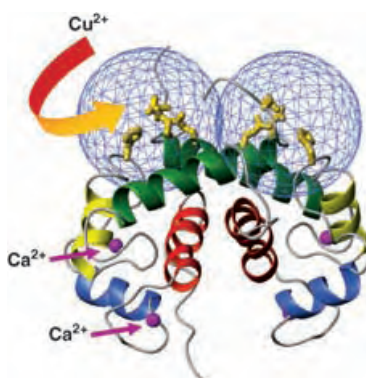
Heme recognizes genes: As a step towards the electronic control of reading DNA code at a molecular level, heme and DNA recognition can be linked through protein folding (see picture). Through the conversion of an engineered DNA-binding cytochrome into a heterodimer, the sequence-specific DNA recognition can be controlled by heme recognition and the oxidation state of the iron center.



Protein Structures

F. Arnesano, L. Banci, I. Bertini,*
A. Fantoni, L. Tenori,
M. S. Viezzoli — 6341–6344

Structural Interplay between Calcium(II) and Copper(II) Binding to S100A13 Protein

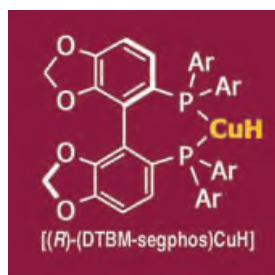


New binding sites: Calcium(II) binding to the dimeric protein S100A13 triggers key conformational changes, thus creating two symmetrical copper(II)-binding sites between the helices of the monomers (see picture). These solvent-exposed binding sites are unique among the S100 proteins.

Hydride Reagents

B. H. Lipshutz,*
B. A. Frieman — 6345–6348

CuH in a Bottle: A Convenient Reagent for Asymmetric Hydrosilylations

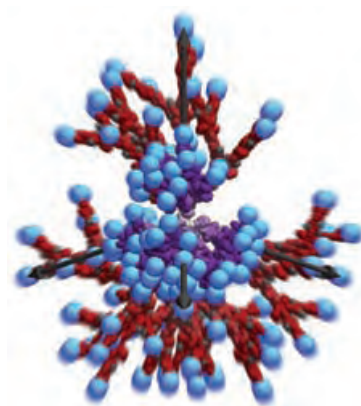


Bottled for freshness: [(R)-(DTBM-segphos)CuH] (see formula; DTBM = 3,5-di-*tert*-butyl-4-methoxy) generated in situ represents the first reported copper hydride reagent that can be stored and used over time without loss of activity in several types of asymmetric hydrosilylation reactions.

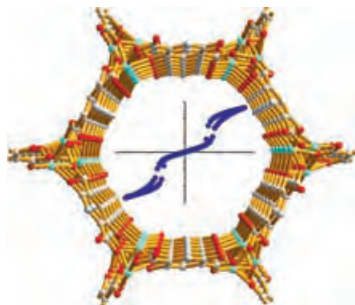
Dendrimers

E. V. Andreitchenko, C. G. Clark, Jr.,
R. E. Bauer, G. Lieser,
K. Müllen* — 6348–6354

Pushing the Synthetic Limit: Polyphenylene Dendrimers with “Exploded” Branching Units—22-nm-Diameter, Monodisperse, Stiff Macromolecules



Structural perfection up to the fifth generation of a polyphenylene dendrimer has been achieved by inserting *p*-terphenyl spacers into the arms of each branching unit (see picture). The stiff, monodisperse macromolecules with diameters up to 22 nm were synthesized in a stepwise manner, during which the topology of the branching units was controlled. Dendrimers containing up to 1368 phenyl rings with high porosity were generated.



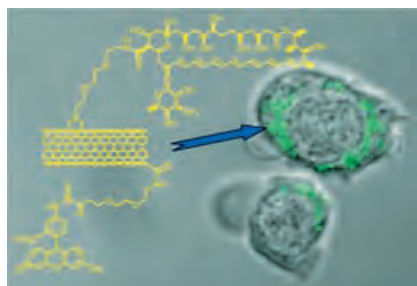
The arrangement of the spins of adjacent helical cobalt–oxygen chains that form the backbone of the framework (see figure) of a microporous coordination polymer lead to metamagnetic behavior. When the polymer is heated, the metal center loses a coordinated water molecule and alters its coordination geometry from octahedral to square-pyramidal, although the framework remains stable.

Metal–Organic Frameworks

P. D. C. Dietzel,* Y. Morita, R. Blom, H. Fjellvåg ————— **6354–6358**

An In Situ High-Temperature Single-Crystal Investigation of a Dehydrated Metal–Organic Framework Compound and Field-Induced Magnetization of One-Dimensional Metal–Oxygen Chains

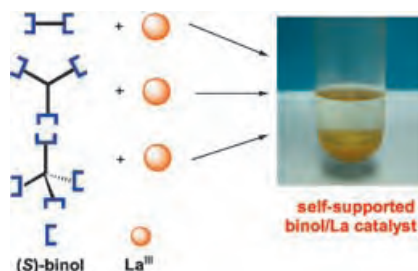
Tasty tubes: Multiwalled carbon nanotubes functionalized with fluorescein isothiocyanate and amphotericin B (AmB) have been shown to be rapidly internalized by mammalian cells (see picture) without the toxic effects typically displayed upon treatment with AmB. Furthermore, the modified drug exhibits a higher antifungal activity than native AmB.



Functionalized Nanotubes

W. Wu, S. Wieckowski, G. Pastorin, M. Benincasa, C. Klumpp, J.-P. Briand, R. Gennaro, M. Prato, A. Bianco* ————— **6358–6362**

Targeted Delivery of Amphotericin B to Cells by Using Functionalized Carbon Nanotubes

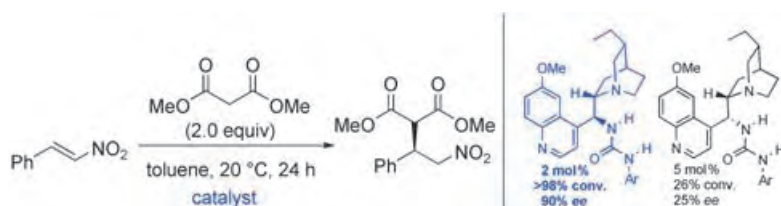


Bridging the gap: Heterogenized Shibasaki's binol/La catalyst is synthesized by a self-supporting strategy through the reactions of multitopic ligands with La(OiPr)₃ (see picture). The catalyst shows high activity and enantioselectivity, and can be reused in the asymmetric epoxidation of α,β -unsaturated ketones.

Asymmetric Catalysis

X. Wang, L. Shi, M. Li, K. Ding* ————— **6362–6366**

Heterogenization of Shibasaki's Binol/La Catalyst for Enantioselective Epoxidation of α,β -Unsaturated Ketones with Multitopic Binol Ligands: The Impact of Bridging Spacers



Natural not always best: Novel *N*-aryl urea and thiourea derivatives of dihydrocinchona alkaloids serve as efficient catalysts for the asymmetric addition of dimethyl malonate to a range of nitroalkenes. Catalytic activity and selectivity

depend strongly on the relative configuration at C8/C9. Catalysts with “non-natural” inverted configuration at C9 display excellent activity and enantioselectivity at loadings as low as 0.5 mol %.

Organocatalysis

S. H. McCooley, S. J. Connon* ————— **6367–6370**

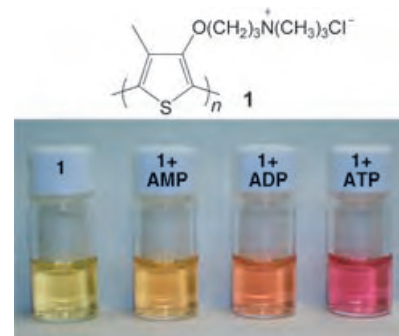
Urea- and Thiourea-Substituted Cinchona Alkaloid Derivatives as Highly Efficient Bifunctional Organocatalysts for the Asymmetric Addition of Malonate to Nitroalkenes: Inversion of Configuration at C9 Dramatically Improves Catalyst Performance.

Biosensors

C. Li, M. Numata, M. Takeuchi,
S. Shinkai* ————— **6371–6374**

A Sensitive Colorimetric and Fluorescent
Probe Based on a Polythiophene
Derivative for the Detection of ATP

From amber to red: The water-soluble polythiophene derivative **1** forms a supramolecular complex with ATP (adenosine triphosphate) through electrostatic and hydrophobic cooperative interactions which results in a color change of the aqueous solution from yellow to pink-red (see photo; AMP/ADP = adenosine mono-/diphosphate). Besides naked-eye detection of ATP, the detection limit may be extended to 10^{-8} M by using fluorometry.

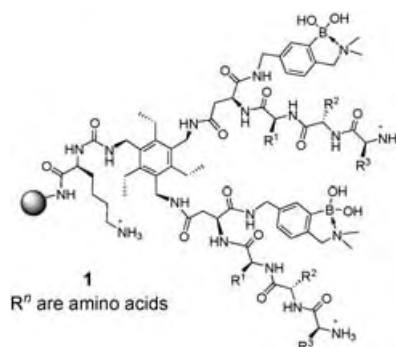


Protein Analysis

A. T. Wright, M. J. Griffin, Z. Zhong,
S. C. McCleskey, E. V. Anslyn,*
J. T. McDevitt* ————— **6375–6378**

Differential Receptors Create Patterns
That Distinguish Various Proteins

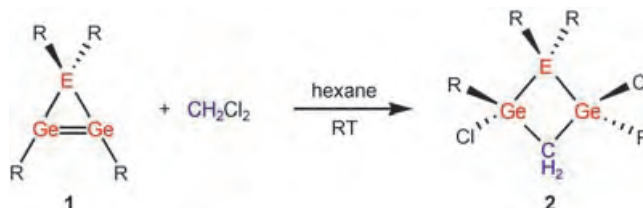
Pattern formation: Analysis with an array of differential receptors such as **1** rather than specific receptors leads to patterns for various proteins and glycoproteins that can be examined by principal component analysis. This allows for the direct recognition of large substrates for which the creation of synthetic specific receptors would be very difficult.



Organometallic Chemistry

V. Ya. Lee, H. Yasuda, M. Ichinohe,
A. Sekiguchi* ————— **6378–6381**

$SiGe_2$ and Ge_3 : Cyclic Digermenes That
Undergo Unexpected Ring-Expansion
Reactions



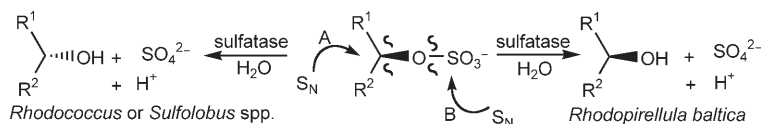
The heavy cyclopropene analogues $1H$ -siladigermirene R_4SiGe_2 (**1a**) and $1H$ -trigermirene R_4Ge_3 (**1b**) have been obtained, and the X-ray crystal structure of **1a** shows that it forms an isosceles triangle with a highly *trans*-bent endocyclic

$Ge=Ge$ bond (bending angle $51.0(2)^\circ$). The interaction of **1a** and **1b** with CH_2Cl_2 unexpectedly affords the unusual four-membered-ring compounds **2a** and **2b** as a result of ring expansion (see scheme: $E = Si, Ge$; $R = SiMe_2Bu_2$).

Sulfatases

S. R. Wallner, M. Bauer, C. Würdemann,
P. Wecker, F. O. Glöckner,
K. Faber* ————— **6381–6384**

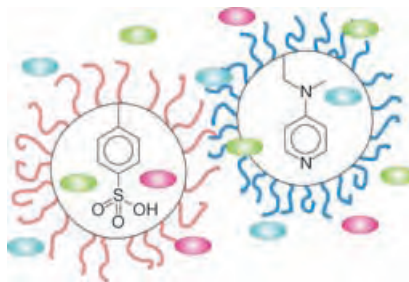
Highly Enantioselective *sec*-Alkyl Sulfatase
Activity of the Marine Planctomycete
Rhodopirellula baltica Shows Retention of
Configuration



Hydrolytic enzymes: The marine planctomycete *Rhodopirellula baltica* DSM 10527 displays high stereo- and enantioselective alkyl sulfatase activity towards (\pm) -*sec*-alkyl sulfates with retention of configura-

tion through cleavage of their S–O bond (see scheme; pathway B), whereas inversion of configuration is observed upon cleavage of the C–O bond (pathway A).

My stars! Star polymers that contain otherwise incompatible acid or base catalysts, such as *para*-toluenesulfonic acid or 4-(dialkylamino)pyridines moieties, at their sterically restricted cores (see scheme) are readily prepared. Homogeneous catalysis using these star polymers can perform reaction cascades in the same pot and is demonstrated with an acid-catalyzed deprotection and the nucleophilic amine-catalyzed Baylis–Hillman reaction.

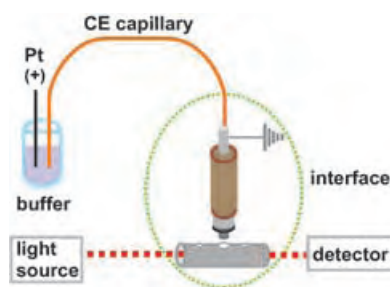


Homogeneous Catalysis

B. Helms, S. J. Guillaudeu, Y. Xie,
M. McMurdo, C. J. Hawker,*
J. M. J. Fréchet* — 6384–6387

One-Pot Reaction Cascades Using Star
Polymers with Core-Confined Catalysts

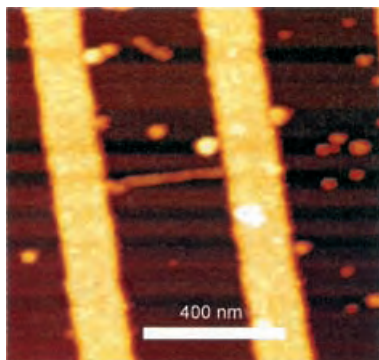
Happy couples: A new hybrid technique, capillary electrophoresis combined with online detection through electrothermal atomic absorption spectroscopy, allows the study of metal speciation and metal–biomolecule interactions, important aspects of metallomics. Advantages include complete sample introduction, nanoliter sample and reagent consumption, real-time detection, high sensitivity, and low cost.



Analytical Methods

Y. Li, X.-P. Yan,* Y. Jiang — 6387–6391

Interfacing Capillary Electrophoresis and
Electrothermal Atomic Absorption
Spectroscopy To Study Metal Speciation
and Metal–Biomolecule Interactions

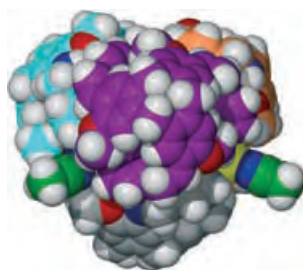


Conductive polypyrrole (Ppy) nanowires (see picture) can be grown from single adsorbed synthetic polyelectrolyte molecules by oxidative polycondensation of pyrrole. The location and length of the Ppy nanowires are defined by the location and length of the adsorbed single-molecule templates. The diameter of the Ppy nanowires varies from a few to hundreds of nanometers and can be adjusted by varying the reaction conditions.

Polypyrrole Nanowires

V. Bocharova, A. Kiriya,* H. Vinzelberg,
I. Mönch, M. Stamm — 6391–6394

Polypyrrole Nanowires Grown from Single
Adsorbed Polyelectrolyte Molecules



A flexible host: The use of pyridyl-substituted cyclotrimeratrylene ligands coupled with geometrically accommodating silver centers has resulted in the isolation and structural characterization of a compact $[M_2L_2]$ molecular capsule and an $[M_4L_4]$ tetrahedral prism (see structure). The former incarcerates two coordinated CH_3CN molecules while the latter has an unusual star-burst shape and also acts as host for CH_3CN molecules.

Host–Guest Systems

C. J. Sumby, M. J. Hardie* — 6395–6399

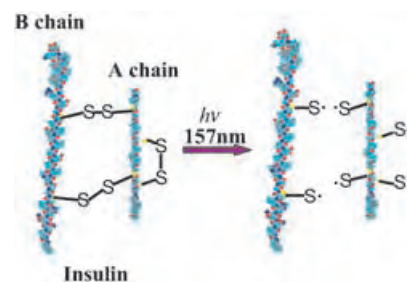
Capsules and Star-Burst Polyhedra: An
 $[Ag_2L_2]$ Capsule and a Tetrahedral $[Ag_4L_4]$
Metallosupramolecular Prism with
Cyclotrimeratrylene-Type Ligands

Structure Elucidation

Y. M. E. Fung, F. Kjeldsen,* O. A. Silivra,
T. W. D. Chan,
R. A. Zubarev* ————— **6399–6403**

Facile Disulfide Bond Cleavage in
Gaseous Peptide and Protein Cations by
Ultraviolet Photodissociation at 157 nm

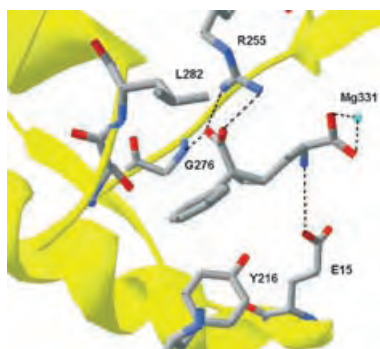
Overall charge unchanged: Disulfide bonds in gaseous polypeptide cations can be cleaved efficiently by ultraviolet photodissociation (UVPD) at 157 nm (see scheme). Unlike electron-capture dissociation, UVPD cleaves S–S bonds without overall charge reduction in the product ions. This cleavage is suggested to be a result of electronic excitation caused by the absorption of photons of 7.9 eV.



Enzyme Inhibitors

G. E. Besong, J. M. Bostock, W. Stubbings,
I. Chopra, D. I. Roper, A. J. Lloyd,
C. W. G. Fishwick,*
A. P. Johnson* ————— **6403–6406**

A De Novo Designed Inhibitor of
D-Ala–D-Ala Ligase from *E. coli*

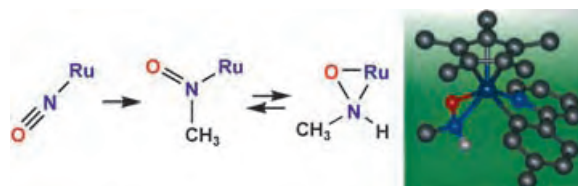


Blueprints for an inhibitor: The de novo molecular design program SPROUT was used in conjunction with the X-ray crystal structures of the bacterial enzymes DdlB and VanA to produce a novel enzyme-selective inhibitor template. Following short and efficient synthesis and in keeping with the design predictions, the resulting inhibitor showed useful levels of enzyme-selective inhibition.

Bioinorganic Chemistry

S. Kura, S. Kuwata,*
T. Ikariya* ————— **6406–6409**

N-Methylhydroxylamido(1–)- and
Nitrosomethaneruthenium Complexes
Derived from Nitrosyl Complexes:
Reversible N-Protonation of an
N-Coordinated Nitrosoalkane



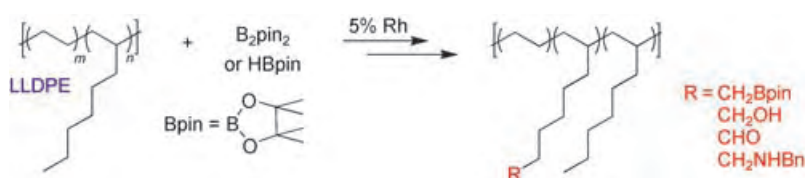
Interconversion of organonitrogen oxides: Nitrosyl, nitrosoalkane, and hydroxylamido(1–) ligands are interconverted on an organoruthenium platform (see structure and scheme). These stepwise and sequential reactions provide insights

into the mechanism of the biological nitrite–ammonia interconversion, a major process in the inorganic nitrogen cycle in which nitric oxide, nitroxyl, and hydroxylamine have been invoked as intermediates.

Polymer Chemistry

C. Bae, J. F. Hartwig,* H. Chung,
N. K. Harris, K. A. Switek,
M. A. Hillmyer* ————— **6410–6413**

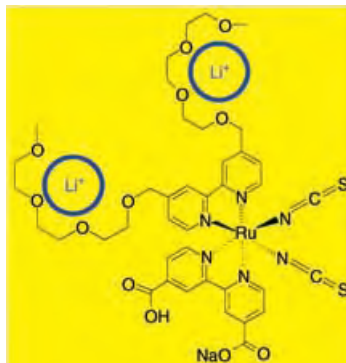
Regiospecific Side-Chain
Functionalization of Linear Low-Density
Polyethylene with Polar Groups



The tail end: The Rh-catalyzed selective functionalization of commercial linear low-density polyethylene (LLDPE) with boron reagents is demonstrated. Subsequent oxidation and transformations of

the boron-containing polymer yields materials that contain a variety of polar functionalities, such as hydroxy, amino, and formyl groups, at the termini of the side chains (see scheme).

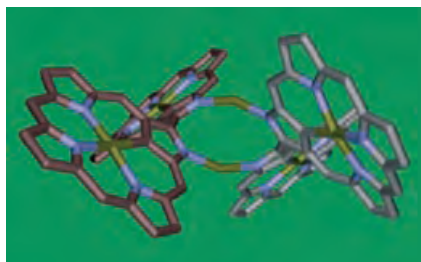
Sun sensitivity: A charge-transfer sensitizer with an ion-complexing moiety formed by oxyethylene side groups (see picture) is used in a solid-state dye-sensitized solar cell. Lithium coordination to the dye backbone produces under realistic conditions photovoltages of nearly 900 mV and efficiencies of 3.8 %.



Solar Cells

H. J. Snaith,* S. M. Zakeeruddin,
L. Schmidt-Mende, C. Klein,
M. Grätzel _____ **6413 – 6417**

Ion-Coordinating Sensitizer in Solid-State Hybrid Solar Cells



Four-gone confusion! An assembly of four N-confused porphyrinatosilver(I) subunits (see structure; N blue, Ag olive-colored, C silver/red) placed on the perimeter of a cyclic structure that comprises two silver(I) ions is effectively formed from a bis(N-confused porphyrin) free base and a silver(I) salt.

Metalloporphyrinoids

P. J. Chmielewski* _____ **6417 – 6420**

Synthesis and Characterization of a Cyclic Bis-silver(I) Assembly of Four 2-Aza-21-carbaporphyrinatosilver(III) Subunits

Looking for outstanding employees?

Do you need another expert for your excellent team?

... Chemists, PhD Students, Managers, Professors, Sales Representatives...

Place an advert in the printed version and have it made available online for 1 month, free of charge!

Angewandte Chemie International Edition

Advertising Sales Department: Marion Schulz

Phone: 0 62 01 - 60 65 65

Fax: 0 62 01 - 60 65 50

E-Mail: MSchulz@wiley-vch.de

Service

Keywords _____ **6422**

Authors _____ **6423**

Preview _____ **6425**



Fast, Individual, Popular...
REPRINTS
Available to order anytime!
Contact Carmen Leitner (e-mail: cleitner@wiley-vch.de)

Christopher S. Foote (1935–2005): Singlet Oxygen

Christopher Spencer Foote, professor of chemistry at the University of California, Los Angeles (UCLA), passed away at the age of 70 on June 13, 2005.



Born in Hartford, Connecticut, Foote grew up in an intellectual environment. His father was the editor of the local newspaper, while his mother was a descendant of the Benjamin Sillimans (father and son), who were eminent chemists at Yale University. Foote graduated from Kingswood School in West Hartford, Connecticut, and obtained a Bachelors degree in chemistry from Yale University in 1957. He spent the following year as a Fulbright scholar with G. O. Schenck at the University of Göttingen in Germany. In retrospect, this year in Germany clearly set the stage for his life's work. Foote's first scientific paper, on the "Photosensitized Autooxidation of Menthofuran", with Schenck as a coauthor, was published in *Angewandte Chemie* in 1958.^[1]

Foote took "time off" from the study of photooxygenation reactions to obtain a PhD: He joined the research group of R. B. Woodward at Harvard University in 1958 and graduated in 1962 with a thesis entitled "Angle Strain and Solvolytic Reactivity in Bridged Bicyclic Systems." Immediately after leaving Harvard, Foote joined the chemistry faculty at UCLA. It was here that he returned to the study of photooxygenation reactions, establishing the lifelong program for which he is now recognized. Foote was associated with UCLA throughout his entire academic career. He attained the rank of full professor in 1969 and served as department chairman from 1978 to 1981.

Foote arguably established his career with two communications of his results that appeared in *J. Am. Chem. Soc.* in 1964.^[2] In these reports, he proposed that the lowest excited electronic state of molecular oxygen, singlet molecular oxygen, $O_2(a^1\Delta_g)$, was the pertinent reactive intermediate in a sol-

ution-phase dye-sensitized photooxygenation reaction. In effect, Foote was confirming a hypothesis originally made by H. Kautsky in 1931 which was subsequently dismissed by, among others, G. O. Schenck. The final sentence in the latter of these two communications was, "Further experiments are in progress"; a statement that essentially presaged the next 40 years of his life.

Foote's primary research interest centered on reactive oxygen species, with singlet oxygen being the most prominent.^[3,4] Despite its reactivity and short lifetime in condensed phases, singlet oxygen displays many selective reactions, some of which are synthetically useful. The reaction with dienes to form endoperoxides is still one of the most selective and mild reactions to form these types of compounds. The singlet-oxygen-mediated formation of allylic hydroperoxides from unsaturated hydrocarbons and the oxidation of sulfur-, nitrogen-, and phosphorus-containing compounds have important biological ramifications. Indeed, singlet oxygen is an acknowledged intermediate in processes that result in cell death, a phenomenon that forms the basis for photodynamic therapy, a medical procedure used to destroy undesired tissue in the treatment of cancer, for example. Likewise, the process of ageing involves the destruction of key biochemical compounds by reactive oxygenating species.

The mechanistic aspects of these oxygenation reactions are often complex, involving one or more reactive intermediates. One of Foote's scientific achievements was to methodically elucidate many of these reaction mechanisms. It was through these studies that he established his reputation as the foremost authority on the reactions of singlet oxygen. In his latter years, Foote expanded his research program to include studies on the photophysical properties of fullerenes.

Foote's research covered a broad spectrum of science. Although formally an organic chemist, his interests and tools ranged from biology to physics and from experimental to computational. He was a cross-disciplinary chemist of the highest level. In addition to an extensive list of research publica-

tions, Foote was coauthor of a textbook now in its fourth edition.^[5] He was president of the American Society for Photobiology during 1988–89 and was a senior editor of *Accounts of Chemical Research* during the last 10 years of his life. In 1994, the American Chemical Society acknowledged his contributions with the Arthur C. Cope Scholar Award.

Foote always allowed members of his research group to pursue their own ideas, thereby creating a stimulating environment for the large number of graduate students and postdoctoral fellows for whom he served as mentor (the authors of this article are two of his former PhD students). He was very tolerant and patient when listening to research presentations, but always asked sharp questions at the end. In his private life, Foote particularly enjoyed music. He was a noted fan of Bach and never tired of Wagner's "Der Ring des Nibelungen". He had the amazing nose of a good old-fashioned qualitative organic chemist; one that could readily distinguish an aldehyde from a ketone. This characteristic was frequently put to good use in distinguishing a good merlot from a bad merlot.

It was a privilege and a pleasure to have known and worked with Chris. His brilliance, insight, companionship, and warmth will be missed. Christopher S. Foote passed away having earned the deep-seated respect of his colleagues. No higher award can be achieved.

Frank Jensen

University of Southern Denmark

Peter R. Ogilby

University of Aarhus (Denmark)

- [1] G. O. Schenck, C. S. Foote, *Angew. Chem.* **1958**, 70, 505.
- [2] C. S. Foote, S. Wexler, *J. Am. Chem. Soc.* **1964**, 86, 3879; C. S. Foote, S. Wexler, *J. Am. Chem. Soc.* **1964**, 86, 3880.
- [3] C. S. Foote, *Acc. Chem. Res.* **1968**, 1, 104; C. S. Foote, *Science* **1968**, 162, 963.
- [4] C. S. Foote, E. L. Clennan in "Active Oxygen in Chemistry" (Eds.: C. S. Foote, J. S. Valentine, A. Greenberg, J. F. Liebman), Chapman and Hall, London **1995**, p. 105.
- [5] W. H. Brown, C. S. Foote, B. L. Iverson, *Organic Chemistry*, 4th ed., Brooks/Cole, **2005**.

DOI: 10.1002/anie.200502934

Catalytic Enantioselective 1,3-Dipolar Cycloaddition Reaction of Azomethine Ylides and Alkenes: The Direct Strategy To Prepare Enantioenriched Highly Substituted Proline Derivatives**

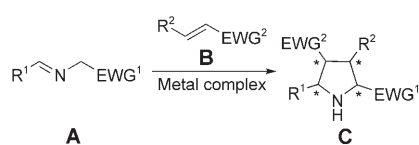
Carmen Nájera* and José M. Sansano*

Keywords:

asymmetric catalysis · azomethine ylides · chiral ligands · cycloaddition · Lewis acids

The interest in asymmetric synthesis is continuously increasing owing to the continuous demand for enantiomerically enriched molecules. The main challenge in this area is to create the maximum number of stereogenic centers in one reaction step by employing the minimum number of reagents. From both an economic and a synthetic point of view, asymmetric catalysis^[1] can constitute a powerful tool, especially for pericyclic reactions, where the relative and absolute configuration of several carbon atoms can be established almost simultaneously.

One example is the 1,3-dipolar cycloaddition of azomethine ylides (from imines **A**) and alkenes **B**,^[2] which allows the stereoselective synthesis of pyrrolidines or proline derivatives **C** (Scheme 1). Among such molecules of type **C**, which can be obtained through longer and more sophisticated routes, are very important pharmaceuticals and natural alkaloids, organocatalysts, and building blocks in organic synthesis.^[3] In this cycloaddition, the particular struc-

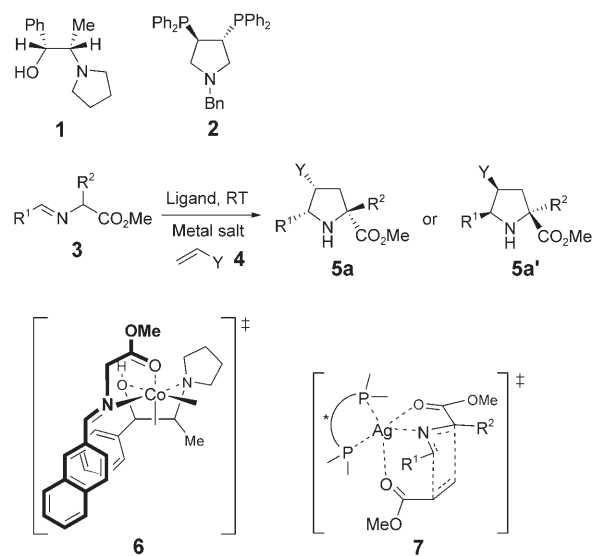


Scheme 1. EWG = electron-withdrawing group.

ture of the azomethine ylide promotes a characteristic frontier molecular orbital (FMO) controlled reactivity with alkenes, which can lead to the formation of four stereocenters with high stereoselectivity. There are several procedures for generating azomethine ylides, of which the metalation of imino esters **A** is the most widely used in organic chemistry.^[2a,c] The benefits of the in situ preparation of metalloazomethine dipoles from α -imino esters **A** in basic media, such as working at room temperature with a highly coordinated transition state and starting from easily available compounds, make this reaction much more attractive (Scheme 1).

The asymmetric version of this 1,3-dipolar cycloaddition reaction can be accomplished following different strategies: a) by attaching a chiral auxiliary to the imino (R^1) or to the electron-withdrawing group (EWG^1) of the

dipole **A**; b) by attaching a chiral auxiliary to the EWG^2 of the alkene **B**; c) by employing a chiral Lewis acid capable of chelating both components **A** and **B**. According to the last strategy, and considering all of the previous advantages of these metalloazomethine ylides, Grigg and co-workers employed a stoichiometric amount of the catalytic system ephedrine derivative **1**/cobalt(II) chloride in the reaction of the dipole precursor **3** with the dipolarophile **4** ($Y = CO_2Me$, used as solvent) giving an excellent *ee* in the case of the enantiomer **5a** with total *endo*-selectivity (Scheme 2, Table 1).^[4,5] However, the stoichiometric catalyst formed by bisphosphine **2**/AgOTf (Tf = trifluoro-



Scheme 2. R^1 = 2-naphthyl, R^2 : see Table 1; **4** as solvent when $Y = CO_2Me$, Bn = benzyl.

[*] Prof. Dr. C. Nájera, Dr. J. M. Sansano
Departamento de Química Orgánica
Universidad de Alicante
Apartado 99, 03080 Alicante (Spain)
Fax: (+34) 965-903-549
E-mail: cnajera@ua.es
jmsansano@ua.es

[**] We thank the Spanish Ministerio de Ciencia y Tecnología (BQU2001-0724-CO2 and CTQ 2004-00808/BQU), the Generalitat Valenciana (CTIOIB/2002/320 and GRU-POS 03/134), and the University of Alicante for financial support.

Table 1: Asymmetric catalytic 1,3-dipolar cycloaddition using stoichiometric catalyst systems (see Scheme 2).

R ²	Y	Lig. ^[a]	Metal salt ^[a]	Yield [%]	5, ee [%]
H	CO ₂ Me	1	CoCl ₂	84	5a , 96
Me	COMe	2	AgOTf	83	5a' , 70
Me	SO ₂ Ph	2	AgOTf	84	5a' , 70

[a] 100 mol %.

methanesulfonyl) afforded the other enantiomer, *endo*-**5a'**, albeit with lower enantioselection.^[5] The high enantiomeric excesses obtained in these examples can be justified, presumably, by the presence of the compact transition states **6** and **7**, respectively.

Despite these attractive precedents, the first asymmetric catalytic 1,3-dipolar cycloaddition reaction, in which substoichiometric amounts of a chiral metallic complex were used, was not described until 2002.^[6] Zhang and co-workers screened several chiral bisphosphine ligands such as binap ((*R*-) or (*S*)-2,2'-bis(diphenylphosphanyl)-1,1'-binaphthyl), Me-DuPhos [(*S*)-1,2-bis-(2*R*,5*R*-2,5-dimethylphospholano)benzene], PennPhos (*P,P'*-1,2-phenylenebis(*endo*-2,5-dialkyl-7-phosphobicyclo[2.2.1]heptane) and bicip ((*R,R*)- or (*S,S*)-2,2'-bis(diphenylphosphanyl)dicyclopentane), with silver acetate, and obtained very poor enantioselectivities and even diastereoselectivities, in the cyclization reaction of imino esters **3** and dimethyl maleate.^[6] However, Trost's ligand **8**^[7] provided a promising higher enantioselectivity; the weak interaction of the nitrogen atom of the bisamide seems to be very important in the assembly of the

chiral ligand with the silver cation (Scheme 3).^[6]

A similar ligand **9**, which incorporates an additional element of planar chirality (two ferrocene units), was designed to impart different steric and stereoelectronic properties on the product (Scheme 3). The best results for the *endo*-**10** adducts were obtained with these ligands when the aryl group was 3,5-dimethylphenyl and dimethyl maleate was used (Table 2).^[6] Surprisingly, the adduct **10** was also formed in good yield and noticeable enantiomeric purity when the substituent R¹ of the

Table 2: Asymmetric catalytic 1,3-dipolar cycloaddition using substoichiometric amounts of a chiral metal complex (see Scheme 3).

R ¹	Dipolarophile	Yield [%]	ee [%]
Ph	methyl maleate	87	87
4-(NC) ₆ H ₄	methyl maleate	90	86
2-Naph ^[a]	methyl maleate	98	97
<i>i</i> Pr	methyl maleate	82	70
Cy ^[b]	methyl maleate	82	81
Ph	methyl acrylate	90	60
Ph	<i>tert</i> -butyl acrylate	85	93
Ph	NMM ^[c]	87	79

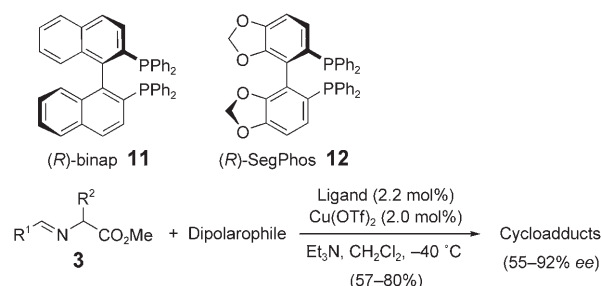
[a] Naph = naphthyl, [b] Cy = cyclohexyl, [c] NMM = *N*-methyl maleimide.

precursor **3** was a cyclohexyl or isopropyl group. In previous work, it has been pointed out that the Michael-type addition reaction of the dipole to the electrophilic alkene is the expected pathway and, normally, no further cyclization occurred when R¹ is an alkyl substituent.^[8] Very good enantioselection was also exhibited by the

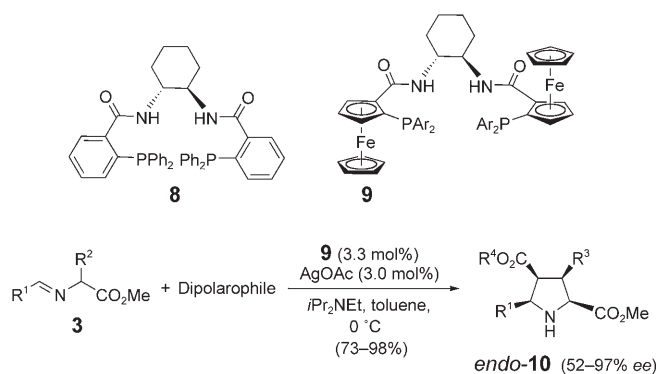
dipolarophile *tert*-butyl acrylate (Table 2).^[6]

However, it has been demonstrated that chiral bisphosphine ligands form a more suitable complex with copper triflate than with silver acetate. Komatsu and co-workers observed reverse *exo*-selectivity using chiral bisphosphine/copper(II) triflate at -40 °C.^[9] In most of the cases, the *exo/endo* ratio exceeded 95:5 using *N*-phenylmaleimide (NPM), the higher enantioselection being achieved with the catalytic systems formed by (*R*)-binap **11** or (*R*)-SegPhos **12**/copper(II) triflate (Scheme 4). With other dipolarophiles, such as dimethyl fumarate or fumaronitrile, the *endo*-adduct (e.g. **14**) was formed in higher proportion (Table 3).

The authors proposed a plausible mechanism for the cycloaddition reaction and for the explanation of the obtained diastereoselection (Scheme 2) by which the azomethine ylide **15** would be generated under basic media, and in turn this would react with NPM to give the *exo*-



Scheme 4. R¹: see Table 3, R² = H; SegPhos = (4,4'-bi-1,3-benzodioxole)-5,5'-diylbis(diphenylphosphane).

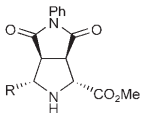
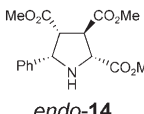


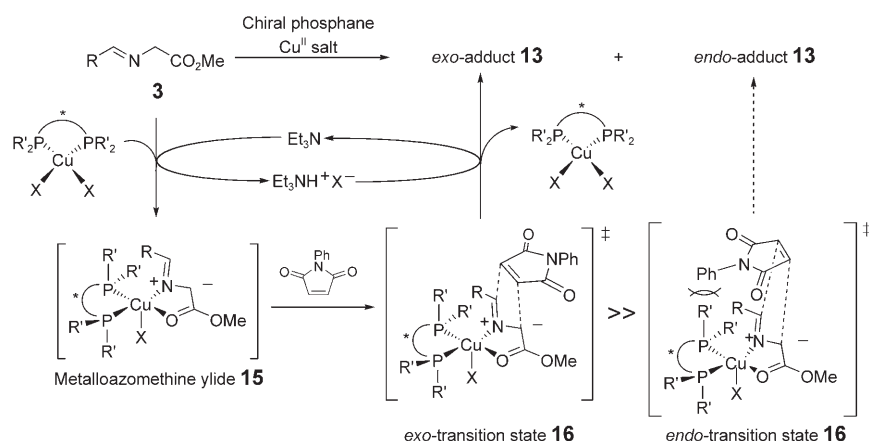
Scheme 3. R¹: see Table 2, R² = H, R³, R⁴: see dipolarophiles listed in Table 2, Ar = 3,5-dimethylphenyl.

transition state **16**, because here the steric interactions between NPM and the bisphosphine ligand are less than in the *endo*-transition state **16** (Scheme 5). This hypothesis was also supported by ZINDO calculations.^[9]

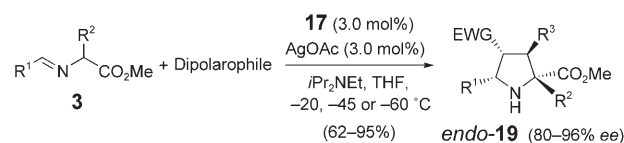
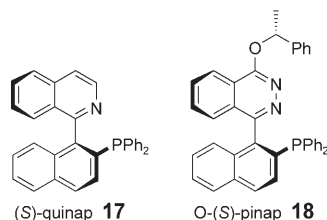
Focusing on the silver(I)-catalyzed enantioselective cycloaddition developed by Zhang and co-workers, Schreiber and co-workers studied the catalytic 1,3-dipolar cycloaddition reaction of azomethine ylides with a series of chiral monophosphines bearing a donor group; the P,N-ligand quinap **17** is an

Table 3: Asymmetric catalytic 1,3-dipolar cycloaddition with catalyst systems comprising the chiral bisphosphines **11** and **12** and Cu(OTf)₂ (see Scheme 4).

R ¹	Ligand	Dipolarophile	Yield [%]	Cycloadduct	exo/endo	ee _{exo} [%]
4-(MeO)C ₆ H ₄	11	NPM	83	 exo- 13	> 95:5	87
Ph	12	NPM	78		89:11	72
Ph	11	dimethyl fumarate	80	 endo- 14	36:64	77



Scheme 5.



Scheme 6. R¹, R², R³: see Table 4; (S)-pinap = (S)-1-[2-(diphenylphosphanyl)-1-naphthyl]phthalazine, (S)-quinap = (S)-1-[2-(diphenylphosphanyl)-1-naphthyl]isoquinoline.

Table 4: Asymmetric catalytic 1,3-dipolar cycloaddition with catalyst systems comprising the P,N-ligands **17** and **18** and Ag^I (see Scheme 6).

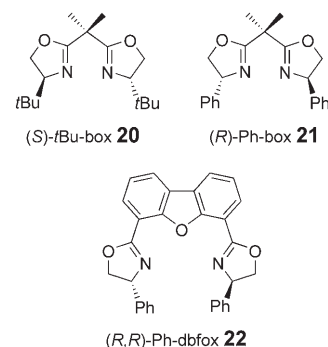
R ¹	R ²	R ³	Ligand	T [°C]	Dipolarophile	Yield [%]	ee [%]
Ph	H	Me	17	−20	<i>tert</i> -butyl crotonate	97	84
Ph	Me	H	17	−20	<i>tert</i> -butyl acrylate	98 ^[a]	80
Ph	<i>i</i> Bu	H	17	−20	<i>tert</i> -butyl acrylate	97 ^[a]	84
4-(NC) ₆ H ₄	H	H	17	−45	<i>tert</i> -butyl acrylate	92	96
4-(NC) ₆ H ₄	H	H	18	−40	<i>tert</i> -butyl acrylate	94	95

[a] By using 10 mol% of the catalyst system **17**/Ag^I.

excellent chelating molecule for the silver cation (see chelate **7** in Scheme 2).^[10] The catalyst loading (3 mol %) was very similar to that reported in previous examples (see above). When substrates **3** were allowed to react with *tert*-butyl acrylate, *tert*-butyl crotonate, and *tert*-butyl cinnamate (Scheme 6, Table 4), the enantioselectivities achieved were very high. Nevertheless, the reaction between the imino ester **3** and dimethyl maleate furnished compound **19** in 60% ee. In all these cycloadditions the *endo*-selectivity was overwhelmingly predominant, except when *tert*-butyl cinnamate was employed as dipolarophile. In addition, α -substituted esters **3** (incorporating methyl, isobutyl, benzyl, and 3-indolylmethyl groups) were also evaluated in this transformation using a catalyst loading of 10 mol %; proline derivatives **19** with a quaternary carbon atom in the α -position were obtained in high yields and very good ee values.

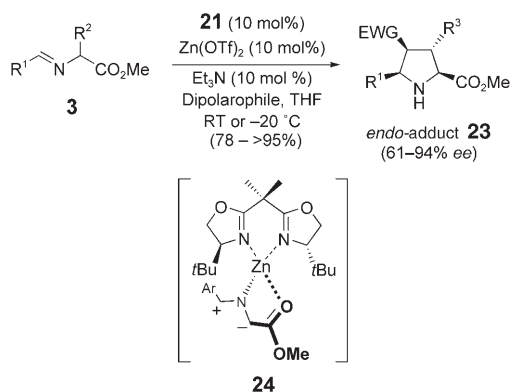
The same enantioselection and yields were achieved by Carreira and co-workers with the ligand O-(S)-pinap **18** under the reaction conditions detailed in Table 4 (R¹ = 4-(NC)₆H₄),^[11] namely 3 mol % of the catalytic mixture **18**/AgOAc was employed at −40 °C. This result also confirmed the efficient coordination of the silver cation to the chiral moiety of (S)-quinap **17** and O-(S)-pinap **18**, as was shown in the model **7** (Scheme 2).

Jørgensen and co-workers demonstrated that chiral bisoxazolines **20–22** (Scheme 7) were suitable ligands for the standard 1,3-dipolar cycloaddition reac-



Scheme 7. Ph-box = 2,2'-isopropylidene-bis[(4S)-4-phenyl-2-oxazoline], Ph-dbox = (R,R)-4,6-dibenzofurandiyl-2,2'-bis(4-phenyloxazoline), tBu-box = 2,2'-isopropylidenebis[(4S)-4-*tert*-butyl-2-oxazoline].

tions of azomethine ylides and electrophilic alkenes when zinc(II) triflate, rather than copper(II) triflate, was used as Lewis acid.^[12] The reaction of the imino ester **3** in basic media with several dipolarophiles occurred at room temperature with excellent diastereoselectivity (*endo*-products **23** were exclusively formed) in very good yields and very high *ee* values, although an improvement of the enantioselectivity was observed when the reaction was carried out at -20°C (Scheme 8, Table 5). The



Scheme 8. R^1, R^3 : see Table 5, $R^2 = \text{H}$.

catalyst loading employed in this reaction is higher than that employed in the previously described cases. These reaction conditions were independent of the quantity of base used and were very sensitive to the bulkiness of the substituents anchored to the dipolarophile (the *ee* value decreased when *tert*-butyl acrylate was used as the dipolarophile). Based on the absolute configuration of the *N*-tosylated adducts **23** (determined by X-ray structure analysis), the authors proposed an intermediate **24** in which the azomethine ylide coordinates with the Zn^{II} -*t*Bu-box catalyst to form an 18-electron complex with a tetrahedral arrangement of the ligand around the metal center (Scheme 8).^[12]

In summary, if we evaluate all these aspects we determine that the metal-catalyzed 1,3-dipolar cycloaddition re-

action of azomethine ylides is a very difficult reaction because too many parameters have to be controlled. For example, the coordination between the metal center and the chiral ligand has to be stronger than the coordination of the metal center and the 1,3-dipole; however, the interaction with the final pyrrolidine should be weaker to allow the regeneration of the chiral catalyst. The chiral domain must differentiate the two enantiotopic faces of the 1,3-dipole on attack of the dipolarophile. The substituents of the imine and the ester groups, as well as the structure of the electron-deficient olefin are crucial for the course of the enantioselection. Finally, the solvent and the temperature play important roles in fine-tuning this asymmetric reaction and have to be considered carefully.

The five contributions described previously^[6,9–12] constitute very good pieces of chemistry, each of which has some intrinsic drawbacks that need to be corrected. Which ligand/metal cation couple can ensure a very good enantioselection? From the work done so far, it is seen that N,P-ligands/ Ag^{I} , P,P-ligands/ Cu^{II} , and N,N-ligands/ Zn^{II} are, a priori, suitable combinations for this enantioselective cycloaddition. The perfect asymmetric reaction, for which yields and enantiomeric enrichment are excellent, independent of the structure of the 1,3-dipole and dipolarophile, has not been reported yet. A fast reaction, at room temperature, in the presence of a recoverable chiral ligand without any significant loss of efficiency or activity of the catalyst system, is very desirable. Thus, this area remains fascinating and much work still has to be done in the pursuit of the perfect catalytic system.^[13]

Published online: September 19, 2005

Table 5: Asymmetric catalytic 1,3-dipolar cycloaddition with a catalyst system comprising chiral bisoxazoline **21** and $\text{Zn}(\text{OTf})_2$ (see Scheme 8).

R^1	R^3	T [$^{\circ}\text{C}$]	Dipolarophile	Yield [%]	<i>ee</i> [%]
Ph	H	0	methyl acrylate	95	78
4-BrC ₆ H ₄	H	-20	methyl acrylate	89	94
2-Naph	H	-20	methyl acrylate	84	91
Ph	CO ₂ Me	-20	dimethyl fumarate	78	76
2-Naph	CO ₂ Me	0	dimethyl fumarate	84	90

- [1] *Comprehensive Asymmetric Catalysis*, Vol. 1–3, Suppl. 1–2 (Eds.: E. N. Jacobsen, A. Pfaltz, H. Yamamoto), Springer, Heidelberg, **2004**.
- [2] For recent reviews of 1,3-dipolar cycloaddition reactions of azomethine ylides, see: a) C. Nájera, J. M. Sansano, *Curr. Org. Chem.* **2003**, *7*, 1105–1150; b) *Synthetic Applications of 1,3-Dipolar Cycloaddition Chemistry Towards Heterocycles and Natural Products* (Eds.: A. Padwa, W. H. Pearson), Wiley, New York, **2003**; c) S. Kanemasa, *Synlett* **2002**, 1371–1387; d) K. V. Gothelf in *Cycloaddition Reactions in Organic Synthesis* (Eds.: S. Kobayashi, K. A. Jørgensen), Wiley-VCH, Weinheim, **2002**, pp. 211–245.
- [3] For reviews about synthesis an applications of pyrrolidine derivatives, see: a) Y. Cheng, Z.-T. Huang, M.-X. Wang, *Curr. Org. Chem.* **2004**, *8*, 325–351; b) W. Notz, F. Tanaka, C. F. Barbas III, *Acc. Chem. Res.* **2004**, *37*, 580–591; c) F.-X. Felpin, J. Lebreton, *Eur. J. Org. Chem.* **2003**, 3693–3712; d) W. H. Pearson, P. Stoy, *Synlett* **2003**, 903–921; e) W. H. Pearson, *Pure Appl. Chem.* **2002**, *74*, 1339–1347; f) *Pharmaceuticals*, Vol. 1–4 (Ed.: J. L. McGuire), Wiley-VCH, Weinheim, **2000**.
- [4] P. Allway, R. Grigg, *Tetrahedron Lett.* **1991**, *32*, 5817–5820.
- [5] R. Grigg, *Tetrahedron: Asymmetry* **1995**, *6*, 2475–2486.
- [6] J. M. Longmire, B. Wang, X. Zhang, *J. Am. Chem. Soc.* **2002**, *124*, 13400–13401.
- [7] B. M. Trost, D. L. Van Vranken, C. Bingle, *J. Am. Chem. Soc.* **1992**, *114*, 9327–9329.
- [8] J. Casas, R. Grigg, C. Nájera, J. M. Sansano, *Eur. J. Org. Chem.* **2001**, 1971–1982.
- [9] a) Y. Oderaotoshi, W. Cheng, S. Fujitomi, Y. Kasano, S. Minakata, M. Komatsu, *Org. Lett.* **2003**, *5*, 5043–5046; b) ZINDO: Modified INDO (intermediate neglect of the differential overlap) program. It is a semiempirical molecular orbital program for studying the spectroscopic properties of a wide range of compounds, such as organic and inorganic molecules, polymers, and organometallic complexes.
- [10] C. Chen, X. Li, S. L. Schreiber, *J. Am. Chem. Soc.* **2003**, *125*, 10174–10175.
- [11] T. F. Knöpfel, P. Aschwanden, T. Ichikawa, T. Watanabe, E. M. Carreira, *Angew. Chem.* **2004**, *116*, 6097–6099; *Angew. Chem. Int. Ed.* **2004**, *43*, 5971–5973.
- [12] A. S. Gothelf, K. V. Gothelf, R. G. Hazell, K. A. Jørgensen, *Angew. Chem.* **2002**, *114*, 4410–4412; *Angew. Chem. Int. Ed.* **2002**, *41*, 4236–4238.

[13] Note added in proof: After this Highlight had been written, Pfaltz and co-workers reported the catalytic enantio- and diastereoselective [3+2] cycloaddi-

tion of azomethine ylides **3** using a chiral phosphanylazoline–Ag^I complex as the catalyst. Inter- and intramolecular cyclizations were achieved with up to

99% *ee*; R. Stohler, F. Wahl, A. Pfaltz, *Synthesis* **2005**, 1431–1436.

Quality counts...

The best of chemistry every week



Wiley-VCH

P.O. Box 10 11 61

69451 Weinheim

Germany

Phone +49 (0) 6201–606-400

Fax +49 (0) 6201–606-184

e-mail: angewandte@wiley-vch.de

www.angewandte.org

Angewandte Chemie International Edition is a journal of the GDCh, the German Chemical Society

GDCh



WILEY-VCH

Redox Catalysts for Reduction with Base Metals

Reinhard W. Hoffmann*

Keywords:

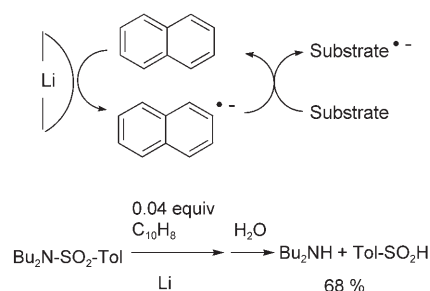
ate complexes · electron transfer · homogeneous catalysis · reduction

Reduction of organic compounds by dissolving base metals (short: dissolving metal reduction) is one of the established methods in functional group interconversion.^[1] Organic chemists traditionally use lithium ($E^\circ = -3.28$ V),^[+] sodium ($E^\circ = -2.95$ V), magnesium ($E^\circ = -2.60$ V), sodium amalgam ($E^\circ = -1.80$ V), or zinc ($E^\circ = -1.00$ V) as reductants, which allows a rather coarse differentiation between various reducible groups in a substrate. A major step forward in the field of dissolving metal reduction was the development and progress made by Yus and Ramon^[2] on the redox catalysis^[3,4] by naphthalene ($E^\circ = -2.50$ V) or di-*tert*-butylbiphenyl ($E^\circ = -2.70$ V) of reductive metalations with lithium metal. This provided convenient reduction procedures,^[5] at potentials less negative than those of sodium or lithium metal (Scheme 1).^[6]

In fact, the metal reductions with naphthalene or di-*tert*-butylbiphenyl were so convenient, that different redox catalysts, which might allow access to other regimes of redox potentials have hardly been explored. In this regard the report^[7] is remarkable that organometallic ate complexes such as Me_3FeLi , Me_3CoLi , or Me_3MnLi are useful catalysts for the reduction of various functional groups by magnesium metal. Their oxidation potentials ($E^\circ = -2.55$ to -2.65) fall in between those of naphthalene and di-*tert*-butylbiphenyl.

[*] Prof. Dr. R. W. Hoffmann
Fachbereich Chemie
Philipps-Universität Marburg
Hans-Meerwein-Strasse
35032 Marburg (Germany)
Fax: (+49) 6421-282-5677
E-mail: rwho@chemie.uni-marburg.de

[†] The redox potentials given herein are all relative to the saturated calomel electrode, SCE.



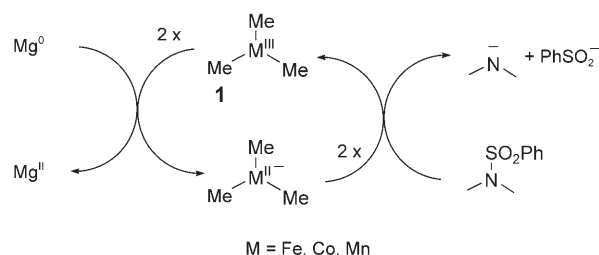
Scheme 1. Reductive cleavage of *p*-toluenesulfonamides with naphthalene as electron transfer catalyst.

These compounds have for example, been applied (10 mol% in THF) to mediate the reductive cleavage of sulfonamides by magnesium metal (Table 1).

This reduction reaction is apparently based on the catalytic cycle given in Scheme 2. This and related reductive cleavage reactions^[7] appear to proceed by electron transfer and not by group transfer,^[8] other-

wise rapid turnover in a catalyzed reaction would be difficult to explain. It is fortunate that the trimethyl metal(III) intermediate **1** is sufficiently long-lived to maintain the catalytic cycle, rather than to decompose by homolysis of the metal-carbon bond^[9] or by reductive elimination.^[10]

But what could be important about the use of metal ate complexes as electron transfer catalysts? First of all, it underscores that efficient catalysts for electron transfer reactions may be found outside the trodden paths of aromatic and heteroaromatic compounds.^[11] When redox catalysts with a rather negative oxidation potential had to be sought, it seems quite rational to look

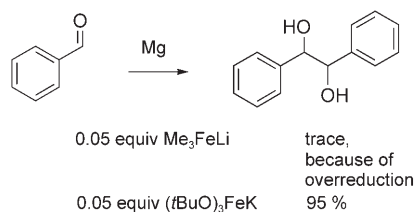


Scheme 2. Proposed catalytic cycle for the reductive cleavage of phenylsulfonamides.

Table 1: Reductive cleavage of phenylsulfonamides with magnesium and trimethyl metalates as electron transfer catalysts. Yields refer to amines obtained.

Reaction	Yield [%]		
	Mg/Me ₃ CoLi	Mg/Me ₃ MnLi	Mg/Me ₃ FeLi
	100	100	89
	94	82	80
	100	83	83

among the electron-rich organometallic compounds and ate complexes.^[12] It was, however, by no means obvious to examine the trialkyl ferrates(II)^[13] or the related manganates(II) or cobaltates, which had hitherto not attracted much attention in chemistry. The fortunate aspect of this choice is that the reactivity of these reagents can be tuned by way of the metal and ligand.^[14] Thus, a change from Me₃FeLi to (tBuO)₃FeK provides a catalyst with a more positive oxidation potential ($E^\circ = -1.90$ V), which allowed a high-yielding pinacol coupling of aromatic aldehydes (Scheme 3).^[17]

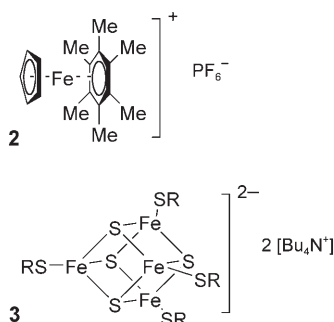


Scheme 3. Example of ligand tuning in the metalate-catalyzed reduction of benzaldehyde by magnesium metal.

The unexpected move from aromatic systems to the metal ate complexes as redox catalysts for dissolving metal reduction leads one to ask, which molecular properties besides possessing the “right” oxidation potential a compound should have to function as an efficient electron transfer catalyst.^[3] In the end, the catalyzed process should be faster than the noncatalyzed direct electron transfer from the stoichiometric metal to the substrate. The catalyst is therefore required to provide a fast two-stage electron transfer, that is, the electron transfer rates to and from the catalyst should be high. This brings the Marcus theory into focus.^[15] The electron transfer rate is increased when the reorganization energy on electron transfer remains small. Hence systems, in which the reduced and oxidized state have essentially the same molecular geometry, are favored.^[16] In fact, BP86/SV(P) calculations indicate for the trimethylferrate system **1** that upon electron transfer changes in bond length remain less than 0.01 Å and changes in bond angles less than 2°. ^[17] As far as solvent reorganization goes, the valence electrons in the redox catalyst should be in

delocalized orbitals which do not cause a marked solvation in either the reduced or the oxidized state. The shape of the frontier orbitals is also of consequence: spatially extended and spatially directed frontier orbitals allow a better overlap between the partners during electron transfer and affect, via the electronic matrix coupling element H_{AB} , the rate of the electron transfer.^[18] Besides these intrinsic factors that make a good electron transfer catalyst, there are also nontrivial external factors of importance: Obviously both the oxidized and reduced state should have sufficient kinetic stability that they persist long enough to permit reversible electron transfer and turnover. Second, reducing agents with a high-lying HOMO are likely not only to be strong reductants but also good nucleophiles. A reagent with a predominant nucleophilic reactivity such as [Na₂Fe(CO)₄]^[19] might therefore have a handicap if considered as an electron transfer catalyst.

From these considerations it becomes clear that the trimethylferrates(II) will not be the only candidates for efficient redox catalysts in dissolving metal reductions. Just staying with iron, inorganic chemistry has provided remarkable redox catalysts such as **2** or **3** (Scheme 4), which appear to have so far been overlooked by the organic chemistry community.

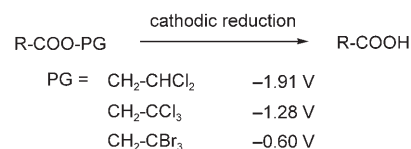


Scheme 4. Examples of potential redox catalysts for metal reductions by sodium or magnesium.

The cyclopentadienyl-Fe^{II}-arene complexes (**2**) are readily prepared and soluble in organic solvents.^[20] They are reversibly reduced to neutral cyclopentadienyl-Fe^I-arene complexes at potentials between -1.1 to -1.9 V,^[21] and have already been applied as redox

catalysts in the reduction of nitrate ions.^[22] This bodes well for their application as redox catalysts in the dissolving metal reduction of a variety of organic substrates.

The iron-sulfur cubane clusters^[23] **3** are perhaps a little bit more difficult to handle on account of their air-sensitivity. These^[24] and the related MoFe₃S₄ double cubane clusters^[25] offer reversible redox systems that span redox potentials in the $+0.13$ to -1.61 and the -0.7 to -2.1 V range. The clusters **3** have been applied as redox catalysts in the reduction of acridine derivatives by sodium dithionite.^[26] Overall the series of compounds **2** and **3** should allow the choice of an appropriate redox catalyst anywhere in the potential range of interest for group selective reduction in organic chemistry. Potential applications have been delineated by Semmelhack and Heinsohn,^[27] who devised a series of different ester protecting groups, which can be removed selectively by controlled potential electrolysis in the -0.6 to -2.1 V range (Scheme 5).



Scheme 5. Chemoselective cleavage of reducible esters by controlled potential electrolysis.

Rather than relying on controlled potential electrolysis, which many organic chemists consider as inconvenient, dissolving metal reduction with a redox catalyst of appropriate reduction potential should effect the same results. A cautionary word regarding chemoselectivity by electrochemical methods (or catalyzed metal reduction) should be added. Electrochemical reduction will not only occur when it is thermodynamically downhill. Rather an uphill reduction may occur, when the substrate is reduced to a radical anion that undergoes a rapid follow-up reaction such as an irreversible decomposition. This particularly holds for the reductive cleavage of protective groups that occurs by bond breaking in the intermediary radical anion.

The results and possibilities referred to here suggest that the field of dissolving metal reduction no longer should be considered as a static and ripe technology. Rather it appears that a renaissance in the development of versatile synthetic methods is forthcoming in this area of chemistry.

Published online: July 26, 2005

- [1] a) H. O. House in *Modern Synthetic Reactions*, 2nd ed., W. A. Benjamin, London, **1972**, pp. 145–227; b) H. Muth, M. Sauerbier in *Houben Weyl, Methoden der Organischen Chemie, Vol. 4/1c* (Ed.: H. Kropf), Thieme, Stuttgart, **1980**, pp. 613–743; c) J. W. Huffman in *Comprehensive Organic Synthesis, Vol. 8* (Eds.: B. M. Trost, I. Fleming), Pergamon, Oxford, **1991**, pp. 107–127; d) J. Clayden in *Organolithiums: Selectivity for Synthesis*, Pergamon, Amsterdam, **2002**, pp. 149–168.
- [2] a) M. Yus, D. J. Ramon, *J. Chem. Soc. Chem. Commun.* **1991**, 398–400; b) M. Yus, *Chem. Soc. Rev.* **1996**, 25, 155–161; c) M. Yus, R. P. Herrera, A. Guijarro, *Chem. Eur. J.* **2002**, 8, 2574–2584.
- [3] D. Astruc in *Electron Transfer and Radical Processes in Transition-Metal Chemistry*, VCH, Weinheim, **1995**, pp. 479–566.
- [4] D. Astruc *Electron-transfer reactions of Electron-reservoir Complexes and other Monoelectronic Redox Reagents in Transition-metal Chemistry in Electron Transfer in Chemistry, Vol. 2* (Ed.: V. Balzani), Wiley-VCH, Weinheim, **2001**, pp. 714–803.
- [5] a) D. J. Ramon, M. Yus, *Eur. J. Org. Chem.* **2000**, 225–237; b) M. Yus, *Synlett* **2001**, 1197–1205.
- [6] E. Alonso, J. Ramón, M. Yus, *Tetrahedron* **1997**, 53, 14355–14368.
- [7] M. Uchiyama, Y. Matsumoto, S. Nakamura, T. Ohwada, N. Kobayashi, N. Yamashita, A. Matsumiya, T. Sakamoto, *J. Am. Chem. Soc.* **2004**, 126, 8755–8759.
- [8] R. S. Wade, C. E. Castro, *J. Am. Chem. Soc.* **1973**, 95, 226–230.
- [9] a) J. Halpern, *Acc. Chem. Res.* **1982**, 15, 238–244; b) B. G. Daikh, R. G. Finke, *J. Am. Chem. Soc.* **1992**, 114, 2938–2943.
- [10] W. Lau, J. C. Huffman, J. K. Kochi, *Organometallics* **1982**, 1, 155–169.
- [11] J. Simonet, J. F. Pilard *Use of indirect electrochemical reactions in synthesis in Organic Electrochemistry*, 4th ed. (Eds.: H. Lund, O. Hammerich), M. Dekker, New York, **2001**, pp. 1171–1180.
- [12] W. Tochtermann, *Angew. Chem.* **1966**, 78, 355–375; *Angew. Chem. Int. Ed. Engl.* **1966**, 5, 351–371.
- [13] T. Kauffmann, *Angew. Chem.* **1996**, 108, 401–418; *Angew. Chem. Int. Ed. Engl.* **1996**, 35, 386–403.
- [14] M. T. Reetz, *Pure Appl. Chem.* **1992**, 64, 351–359.
- [15] R. A. Marcus, *Angew. Chem.* **1993**, 105, 1161–1280; *Angew. Chem. Int. Ed. Engl.* **1993**, 32, 1111–1121.
- [16] D. Astruc in *Electron Transfer and Radical Processes in Transition-Metal Chemistry*, VCH, Weinheim, **1995**, pp. 23–26.
- [17] M. C. Holthausen, Marburg, personal communication 2004.
- [18] N. Sutin, *Acc. Chem. Res.* **1982**, 15, 275–282.
- [19] J. P. Collman, *Acc. Chem. Res.* **1975**, 8, 342–347.
- [20] D. Astruc, *Acc. Chem. Res.* **1986**, 19, 377–383.
- [21] a) J.-R. Hamon, D. Astruc, P. Michaud, *J. Am. Chem. Soc.* **1981**, 103, 758–766; b) M.-H. Delville, *Inorg. Chim. Acta* **1999**, 291, 1–19.
- [22] S. Rigaut, M.-H. Delville, J. Losada, D. Astruc, *Inorg. Chim. Acta* **2002**, 334, 225–242.
- [23] R. H. Holm, *Chem. Soc. Rev.* **1981**, 10, 455–490.
- [24] B. V. DePamphilis, B. A. Averill, T. Herskovitz, jr. L. Que, R. H. Holm, *J. Am. Chem. Soc.* **1974**, 96, 4159–4182.
- [25] G. Christou, P. K. Mascharak, W. H. Armstrong, G. C. Papaefthymiou, R. B. Frankel, R. H. Holm, *J. Am. Chem. Soc.* **1982**, 104, 2820–2831.
- [26] I. Tabushi, Y. Kuroda, Y. Sasaki, *J. Chem. Soc. Chem. Commun.* **1987**, 1622–1623.
- [27] M. F. Semmelhack, G. E. Heinsohn, *J. Am. Chem. Soc.* **1972**, 94, 5139–5140.

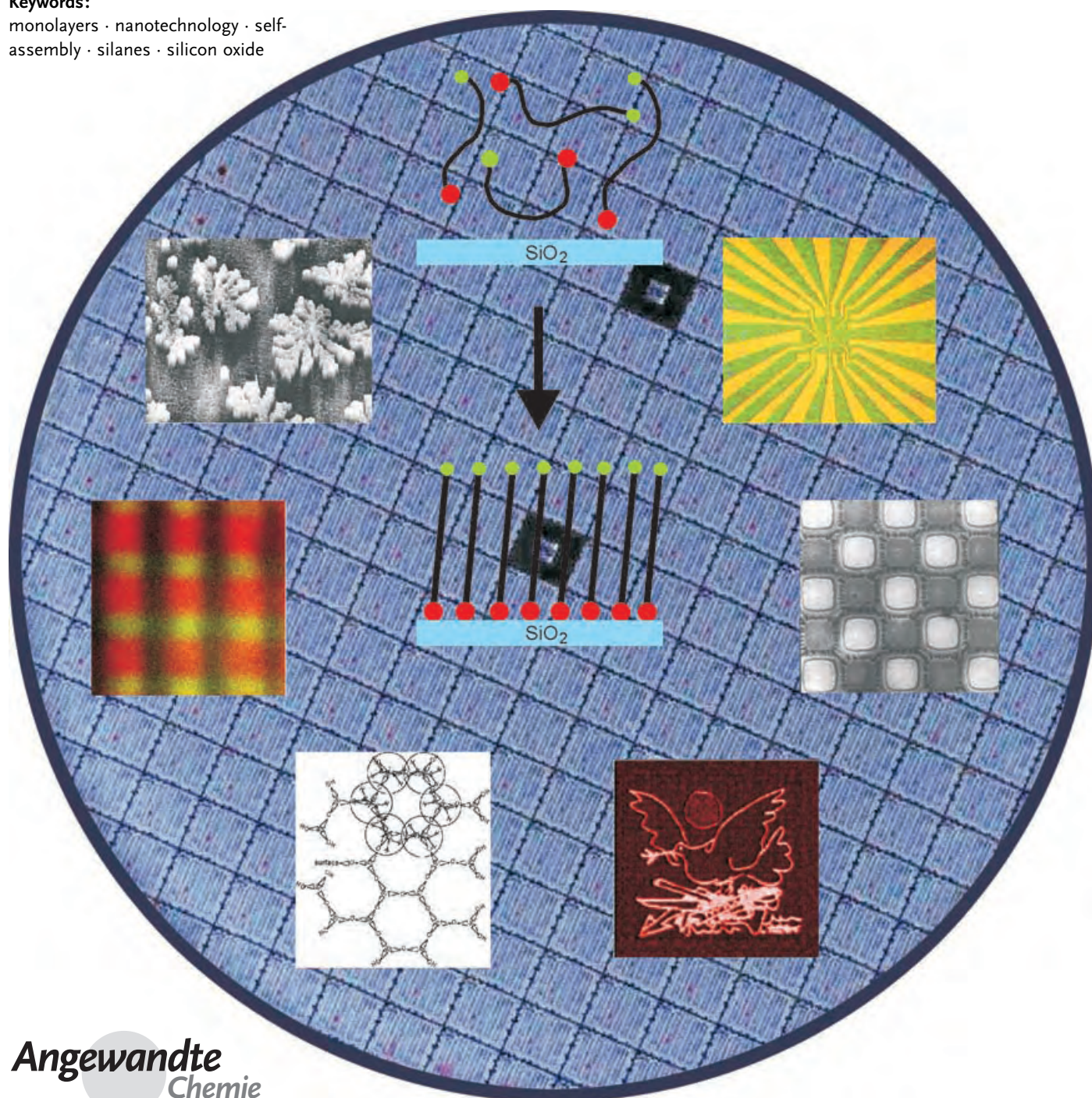
Self-Assembled Monolayers

Engineering Silicon Oxide Surfaces Using Self-Assembled Monolayers

Steffen Onclin, Bart Jan Ravoo,* and David N. Reinhoudt*

Keywords:

monolayers · nanotechnology · self-assembly · silanes · silicon oxide



Although a molecular monolayer is only a few nanometers thick it can completely change the properties of a surface. Molecular monolayers can be readily prepared using the Langmuir–Blodgett methodology or by chemisorption on metal and oxide surfaces. This Review focuses on the use of chemisorbed self-assembled monolayers (SAMs) as a platform for the functionalization of silicon oxide surfaces. The controlled organization of molecules and molecular assemblies on silicon oxide will have a prominent place in “bottom-up” nanofabrication, which could revolutionize fields such as nanoelectronics and biotechnology in the near future. In recent years, self-assembled monolayers on silicon oxide have reached a high level of sophistication and have been combined with various lithographic patterning methods to develop new nanofabrication protocols and biological arrays. Nanoscale control over surface properties is of paramount importance to advance from 2D patterning to 3D fabrication.

1. Introduction

The term “self-assembling monolayer” was coined in 1983 in *New Scientist*^[1] in an anonymous report describing the work of Lucy Netzer and Jacob Sagiv on the chemically controlled layer-by-layer self-assembly of multilayer films.^[2] The self-assembly of adsorbates on an appropriate surface has been known since 1946, when Zisman and co-workers reported the formation of monomolecular films of long-chain hydrocarbons carrying polar groups on a variety of polar surfaces.^[3,4] Although these films are extremely thin (typically ca. 2 nm), they are able to completely change the surface properties. However, the versatility of these adsorbed monolayers was not realized until 1978, when Polymeropoulos and Sagiv proposed their use for measuring electrical conduction between two metal surfaces.^[5] In 1980, Sagiv published the first article demonstrating the formation of well-defined organosilane monolayers on SiO₂ by direct adsorption (that is, self-assembly) from solution.^[6]

Self-assembled monolayers (SAMs) are highly ordered two-dimensional structures that form spontaneously on a variety of surfaces. Several reviews have discussed this subject.^[7–10] The most common adsorbate/substrate combinations are alkylsilanes on oxide surfaces,^[6] and sulfur-containing molecules on gold.^[11] Although the latter combination has received the most attention, presumably because of the ease of preparation, alkylsilane monolayers on oxide surfaces such as SiO₂ possess some advantageous features. The covalent nature of the assembly process results in them displaying superior stability, which allows extensive handling and further modification steps without deterioration of the monolayer. Moreover, these SAMs are compatible with silicon technology and permit the use of optical techniques, such as fluorescence spectroscopy, as read-out methods.

Since the pioneering work of Sagiv and co-workers in the 1980s,^[2,6,12–19] the field of SAMs on SiO₂ surfaces has grown exponentially. SAMs are not merely a method to passivate surfaces, but constitute ordered molecular platforms that can

From the Contents

1. Introduction	6283
2. Self-Assembled Monolayers on Silicon Oxide	6283
3. Chemical Diversity of Self-Assembled Monolayers on Silicon Oxide	6287
4. Engineering the Silicon Oxide Surface Using Self-Assembled Monolayers	6292
5. Summary and Outlook	6299

be employed in surface patterning and bottom-up nanofabrication techniques. However, in contrast to the

increasing sophistication of the molecular architectures based on SAMs, the actual mechanism of monolayer formation remains a subject of debate. Many studies have been carried out to elucidate this process, but the results are often conflicting.

In this Review the mechanism of monolayer formation will be discussed, followed by an overview of the chemistry that has become available to derivatize monolayers. Much of this chemistry is exploited for applications, such as (bio)-chemical sensing. Particularly important for the application of SAMs in areas such as nanotechnology and biological array formation has been the development of (soft) lithographic methods, which can be used to address and modify selected parts of the surface in a controlled manner. These methods greatly facilitate the preparation of high-density chemical patterns on a surface, which in turn are available for further functionalization by, for example, self-assembly. In this way, SAMs form well-defined platforms for nanofabrication, where a 2D pattern is expressed and amplified in a 3D functional structure. An overview of the techniques available for surface patterning is presented and future applications of SAMs are discussed.

2. Self-Assembled Monolayers on Silicon Oxide

The development of analytical tools for the study of SAMs has been impressive in the last two decades. The methods that are used most frequently are listed briefly here. It should be

[*] Dr. Ir. S. Onclin, Dr. B. J. Ravoo, Prof. Dr. Ir. D. N. Reinhoudt
Laboratory of Supramolecular Chemistry and Technology
MESA⁺ Institute for Nanotechnology
University of Twente
P. O. Box 217, 7500 AE Enschede (The Netherlands)
Fax: (+31) 53-4894645
E-mail: b.j.ravoo@utwente.nl
d.n.reinhoudt@utwente.nl

noted that a satisfactory characterization of films with a thickness of just a few nanometers can only be obtained by combining several of these techniques, each providing specific information. Contact angle goniometry provides information on the polarity, roughness, and order of a SAM.^[7] Ellipsometry is a common optical technique for the determination of the thickness of thin films.^[7,20] Detailed information on the elemental composition of SAMs can be gathered by X-ray photoelectron spectroscopy (XPS),^[21] which probes the kinetic energy of the inner or valence electrons ejected by an incident photon with a known energy $h\nu$. An alternative technique to study the composition of a monolayer is secondary ion mass spectrometry (SIMS).^[22,23] SIMS uses a beam of high-energy “primary” particles (ions) to bombard the SAM and analyses the ionized “secondary” particles that are emitted. Fourier transform infrared spectroscopy (FT-IR) can be employed to determine the molecular packing and orientation as well as to identify functional groups in SAMs.^[22] It is mainly used in three spectroscopy modes: attenuated total reflection,^[24] grazing angle,^[25] and Brewster angle.^[25] The electron-density profile of thin films can be probed by X-ray reflectivity, which can be used to determine the film thickness.^[26] The technique of choice to measure surface topology, nanoscale structures, and molecular as well as atomic scale lattices is atomic force microscopy (AFM),^[27] which measures the repulsive and attractive forces between a very sharp tip (radius 10–100 nm) and the sample surface.

2.1. Mechanism of Formation

There has been considerable debate on how SAMs are formed on SiO₂. Especially in the late 1980s and 1990s, when the field started to grow rapidly, many fundamental studies were performed to establish a clear picture of the mechanism of monolayer formation and to formulate procedures that would guarantee reproducibility. It soon became apparent that several parameters are important in monolayer formation and, in particular, the role of water has been investigated thoroughly. The first SAM of octadecyltrichlorosilane (OTS) molecules was reported by Sagiv.^[6] He recognized that water adsorbed on the surface was necessary to hydrolyze the chlorosilane and assumed that the hydrolyzed molecules

would undergo condensation reactions with the surface hydroxy groups^[28] and other OTS molecules to form a polymerized network of molecules in which each OTS molecule is covalently anchored to the surface.

This view on the self-assembly process had to be adjusted when Finklea et al. discovered that organized monolayers of OTS could also be formed on a gold surface, that is, a surface devoid of hydroxy groups.^[29] They concluded that self-assembly occurs on the adsorbed water film on the gold substrate and that the silane head groups are incorporated into a two-dimensional cross-linked network of Si-O-Si bonds. This view was later confirmed by Allara et al.^[30] The observation of a lower roughness of silanized wafers compared to unmodified wafers, as observed in X-ray reflectivity experiments by Silberzan et al., also indicated that not all molecules are individually linked to the surface, but rather form a cross-polymerized network of molecules with only a few bonds to the surface.^[31] This scenario was supported by the IR studies of Tripp and Hair:^[32,33] they found in a low-frequency IR study that the adsorbed species form few, if any, Si-O-Si bonds with the surface.

Commonly, the surface is activated prior to the self-assembly to clean the surface and maximize the number of silanol groups at the surface.^[28] There are several methods to achieve this, but usually strong acids or an oxygen plasma are employed. This procedure renders the surface hydrophilic and prone to the formation of a thin water layer. There is a general consensus that trace amounts of water are essential for the formation of well-packed monolayers. Several studies even reported that the quality of SAMs increases with the degree of hydration of the substrate.^[24,32,34–36] SAMs formed on dry SiO₂ surfaces are generally of poor quality. IR data suggested that a uniform film containing disordered alkyl chains was formed.^[24] Tripp and Hair showed that a solution of OTS in carbon tetrachloride does not react at all with the surface in the absence of moisture.^[32,37] Rye et al. compared the saturation coverage of octadecyldimethylchlorosilane (ODMS) and OTS.^[38] The ODMS coverage on hydrated surfaces was approximately one third of the OTS coverage. In contrast, when the substrates were vacuum-baked prior to self-assembly the saturation coverages were comparable. Rye et al. attributed this to coupling reactions being limited to the surface hydroxy groups.



Steffen Onclin was born in 1975 and studied chemical engineering at the University of Twente (The Netherlands). From 2000 to 2004 he worked in the Laboratory of Supramolecular Chemistry and Technology on his PhD Thesis on supramolecular nanotechnology. In October 2004 he received his PhD from the University of Twente. Since February 2005 he has been working as a project manager at Ciba Specialty Chemicals.



Bart Jan Ravoo was born in 1970 and obtained his graduate and postgraduate degrees in chemistry from the University of Groningen (The Netherlands). From 1999 to 2002 he held a Newman Scholarship at the University College Dublin (Ireland). In 2002 he was appointed as assistant professor at the University of Twente. His main research interest is self-assembly and molecular recognition in water and at the dynamic interface between water and (soft) surfaces. His research interests include the development of functional SAMs, soft lithography, and nanofabrication.

The same authors proposed a model of a growing crystallite resulting from the reaction of an alkyltrichlorosilane with oxidized silicon covered by a thin water layer.^[38,39] The model, shown in Figure 1, is controversial. The model

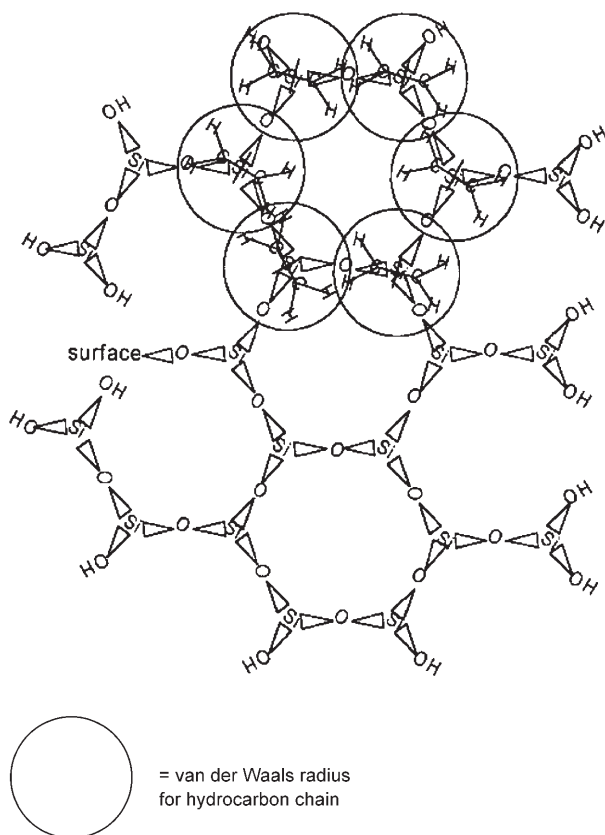


Figure 1. Model of a growing monolayer crystallite resulting from the reaction of an alkyltrichlorosilane with a silicon oxide surface.^[39]

shows alkyl chains that are forced into proximity by the covalent bonds of the Si-O-Si framework and not by the interaction of the alkyl chains. A distance of 3.5 Å between nearest neighbor Si atoms was used in the construction of the model and the circles around the hydrocarbon chains represent the van der Waals radius for linear hydrocarbons

(2 Å). Rye et al. claimed that the steric crowding imposed on the alkane chains can be reduced by a tilt of the chains relative to the surface normal. However, in a modeling study by Stevens it was shown that cross-polymerization, which was considered an essential element in the formation of stable SAMs on SiO₂, cannot occur for monolayers at full surface coverage.^[40] The reason for this is because of steric effects.

A fundamental inconsistency in the organization in a monolayer as proposed in Figure 1 is that the covalent bonds in the Si-O-Si network (3.2 Å) are substantially shorter than the van der Waals diameters for C atoms (3.5 Å). The steric overlap is even larger when the hydrogen atoms of the hydrocarbon chain are also taken into account. Moreover, complete cross-polymerization would yield an area per chain of around 11 Å², which is not possible and not observed. Instead, the experimentally observed area per chain of 21–25 Å²^[26,41–45] is more consistent with the area per chain of 20–24 Å² that was found for hexagonally close-packed Langmuir–Blodgett layers of OTS,^[46,47] thus indicating that SAMs on SiO₂ are very similar to Langmuir–Blodgett layers.

Kajiyama and co-workers compared OTS monolayers prepared by the Langmuir–Blodgett method and the chemisorption method,^[48] and found that OTS molecules in the Langmuir monolayer were less tilted (ca. 8–10°) than in the chemisorbed layers (15–17°). The Langmuir monolayers are also slightly better ordered, as concluded from the spacing of the molecules. The molecular packing of chemisorbed monolayers was discussed earlier.^[49] Taking into account the overall experimental evidence furnished by IR and X-ray scattering data collected strictly from the same film specimens, they proposed a dynamic structural model that can reconcile the steric limitations imposed by the packing of perpendicularly oriented hydrocarbon tails with the apparent formation of extended lateral siloxane (-Si-O-Si-O-) chains. More recently, further evidence in support of this model was put forward in a semiquantitative experimental evaluation of the intra- and interlayer modes of bonding in organosilane multilayers.^[50] The hydrocarbon chains in these highly ordered multilayers adopt an essentially perpendicular orientation (that is, no significant tilt) with a maximum molecular area of 20 Å². Thus, it seems reasonable to conclude that SAMs of alkylsilanes on SiO₂ are very similar to Langmuir–Blodgett layers and that the reduced ordering of the SAMs can be explained by a certain degree of cross-polymerization. This most likely accounts for the fact that no long-range order is observed.

Recently, Wang et al. reported a method to grow ultra-smooth OTS monolayers on native SiO₂.^[51] By comparing the deposition of OTS under “dry” and “wet” conditions, they concluded that growth occurs by different mechanisms. In dry, hydrophobic solvents, when water is only present as a thin layer on the surface and not in solution, true monolayers could be grown with a root-mean-square roughness of about 1 Å in two days, which is a much longer deposition time than usually applied. Under “wet” conditions OTS condensed onto flat aggregates in solution which subsequently adsorbed onto the substrate. Since the aggregates are preformed in solution, they cover the substrate much faster than under “dry” conditions, but are not able to form a smooth monolayer.



David N. Reinhoudt was born in 1942 in The Netherlands and obtained a PhD in chemistry in Delft in 1969. From 1970 to 1975 he worked at Shell on the crown ether research program. He was appointed as a part-time professor at the University of Twente in 1975 and as a full professor in 1978. He is now in charge of the Laboratory of Supramolecular Chemistry and Technology, scientific director of the MESA⁺ Institute for Nanotechnology, and chairman of the Board of NanoNed, the Dutch program for Nanotechnology. He is the author of more than 750 scientific publications and patents.

The role of solvents on the self-assembly process was systematically investigated by McGovern et al.,^[52] and by Hoffmann et al.^[20] McGovern et al. found that aromatic solvents such as toluene, which are able to extract significant amounts of water from the substrate, yielded the densest OTS films in one hour and postulated that hydrolysis of OTS took place in solution rather than at the surface, as had commonly been assumed until then. In the second study, kinetic information on the monolayer growth in different solvents was obtained by in situ ellipsometry measurements. Different solvents resulted in differences in the rate of monolayer growth of up to a factor of 50.

The study of partially formed monolayers is helpful to understand the self-assembly process and was a topic of controversy during the 1980s and early 1990s. Sagiv and co-workers proposed that monolayers are formed through islands, as suggested by IR data on partially formed SAMs,^[14,17] while others concluded that disordered, homogeneous, but incomplete monolayers are formed.^[26,42,53–55] Both processes are illustrated in Figure 2.

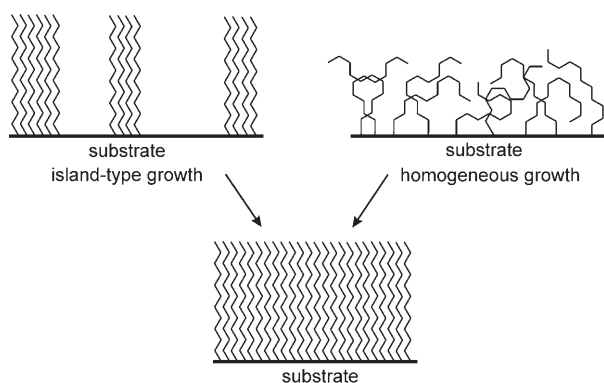


Figure 2. Schematic representation of island-type growth and homogeneous growth of SAMs.

Eventually, it was shown by AFM that OTS monolayers grow via islands that are virtually perpendicular to the substrate surface.^[56] Perfluorinated trichlorosilanes also grow via island formation,^[57] and alternate phases depending on the deposition conditions.^[58] In contrast, shorter-chain molecules do not show island growth.^[56] Several AFM studies revealed that the deposition process strongly depends on parameters such as solvent,^[59] solution age,^[60–62] water content,^[51,60,61,63] deposition time,^[62–64] and temperature.^[65–68] Vallant et al. observed both homogeneous growth and island-type growth depending on the water content and age of the silane solution.^[60] Island-type growth was found to be strongly favored with increasing water content or age of the solution. This result is indicative of the formation of larger preorganized aggregates of siloxanes in solution. However, Wang and Lieberman recently showed that even in the absence of traces of water in solution, the self-assembly process still proceeds via island-type growth.^[51] The reason that this was not observed in other studies is probably the slow kinetics. Wang et al. claim that they observed monolayer islands after 18 h of deposition time in the absence of water,

while deposition times of only seconds to a few hours are common. Figure 3 shows a tapping-mode AFM image of a partial OTS film on oxidized silicon, which clearly shows the growth of an OTS monolayer via islands.

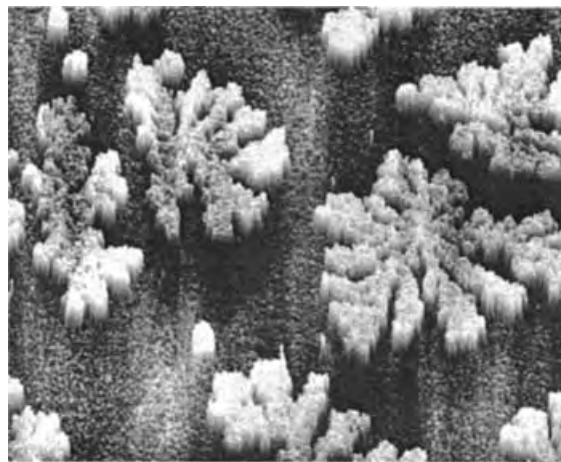


Figure 3. Tapping mode AFM image ($20 \times 20 \mu\text{m}^2$) of a partial OTS film on oxidized silicon.^[67]

The formation of monolayers appears to proceed through a number of stages. A combined lateral force microscopy (LFM) and sum-frequency generation (SFG) spectroscopy study by Liu et al. showed OTS adsorption from solution and the beginning of island formation during the initial stage. This process was followed by a dramatic change in the conformation of the alkyl chain within the film from a disordered to an ordered, mainly all-*trans* conformation, with only a small increase in surface coverage.^[63] The final stage is a much slower adsorption process to form a complete monolayer. Balgar et al. observed two regimes: a nearly linear growth up to a coverage of about 75 %, followed by slow saturation at higher coverages.^[64]

Despite the complex mechanism of monolayer formation, and its dependence on many parameters, several studies reported first-order Langmuir adsorption kinetics by using analytical techniques such as in situ attenuated total reflection infrared spectroscopy (ATR-IR),^[69] in situ AFM,^[61] X-ray reflectivity,^[70] and in situ ellipsometry.^[20] Recently, a simple two-dimensional model for the growth of alkylsilane monolayers on hydroxylated surfaces was proposed.^[71] The model, which takes into account the weak and strong bonding interactions of the aggregating species, was able to reproduce characteristics such as island-type growth and first-order Langmuir adsorption kinetics. In addition, it provides an explanation for the observed deviations from the first-order Langmuir adsorption kinetics in various ex situ studies.^[64,72]

The observation that monolayer formation depends on temperature was reported in the very first paper on monolayer self-assembly.^[3] A thorough account reporting the existence of a critical temperature above which monolayers are not produced followed as early as 1947, in the second classic paper published by Zisman and co-workers on the formation of such monolayers.^[4] These observations were

“rediscovered” 45 years later by Silberzan et al.^[31] who also found that lower temperatures favor the chemisorption, which may seem paradoxical at first sight. Several research groups have studied this phenomenon by monitoring the surface tension and confirmed that a critical temperature, close to ambient temperature for OTS, exists for the formation of high-quality SAMs.^[73–75] As the critical temperature was found to depend on the length of the alkyl chain, these studies related the critical temperature to the triple point observed in the phase diagram of Langmuir layers at the air–water interface. Silberzan and co-workers confirmed the analogy to Langmuir films by AFM studies.^[65,72] Island-type growth takes place below the critical temperature, while islands were not observed for depositions above the critical temperature. However, Rye reported that a much simpler and more straightforward correlation exists between the melting points of alkanes and the observed critical temperature.^[39]

Time-resolved AFM studies by Carraro et al. indicated three distinct mechanisms, depending on deposition temperature: island growth at low temperatures, homogeneous growth at high temperatures, and a mixed regime at intermediate temperatures.^[66] Later, they reported an experiment that showed reversible structural change of the same partial OTS monolayer as a function of temperature at constant coverage.^[67] They concluded that the highly mobile monolayer exists in a hydrogen-bonded state at the surface and is closely related to the equilibrium state of Langmuir films at the air–water interface.

Recently, the interplay between water and temperature on the growth of OTS submonolayers was investigated.^[76] Dynamic light scattering studies revealed the formation of aggregates in solution with a hydrodynamic radius of approximately 200 nm for all examined water concentrations and temperatures. However, formation of the aggregates was faster at higher water contents and lower temperatures. In addition, a characteristic temperature was found above which such aggregates could no longer be detected, and which was higher for higher water concentrations.

2.2. Stability of the Self-Assembled Monolayers

Part of the attractiveness of SAMs on SiO₂ stems from their stability, which is a vital issue in applications. The stability is caused by partial in-plane cross-linkage of the molecules and possible covalent anchoring to the substrate. SAMs of OTS are stable in air up to about 150 °C,^[17,77–80] after which irreversible changes occur in the monolayer structure. Perfluorinated SAMs appear to be even more resistant towards thermal decomposition.^[78,81] Srinivasan et al. reported that 1H,1H,2H,2H-perfluorodecyltrichlorosilane coatings remain intact even up to 400 °C.^[78] The stability toward various chemicals is also remarkable: OTS SAMs can be washed with organic solvents, hot (tap) water, or detergent solutions without detectable damage to the layer.^[82,83] Their stability in boiling solvents such as chloroform and water is good,^[84] but when exposed to 2.5 M sulfuric acid in boiling dioxane or 48 % aqueous HF the layers were damaged significantly, as witnessed by reduced ellipsometric thick-

nesses.^[85] Wasserman et al. found that exposure of tetradecyltrichlorosilane SAMs to 0.1 N HCl for more than 40 h did not affect the monolayer, but immersion in 0.1 N NaOH resulted in immediate degradation.^[86] This lack of stability in basic media was attributed to the hydrolysis of Si–O bonds close to the surface.

One of the first applications where SAMs on SiO₂ were thought to play a key role was in boundary lubrication in, for example, magnetic storage devices. As early as in 1993, the tribological properties of alkylsilane films on solid substrates were investigated.^[87] The friction of coated interfaces was lower compared to the friction of bare interfaces, and the lifetime of the lubricated interfaces increased with increasing chain length.^[87,88] Srinivasan et al. examined the potential of SAMs for the reduction of adhesion in microelectromechanical systems.^[78] They found a reduction in adhesion by more than three orders of magnitude upon applying an OTS coating, while fluorinated SAMs reduced it further by a factor of four. The mechanical strength of octadecyltriethoxysilane (OTE) layers on mica has been investigated by scratching studies with an AFM tip.^[89] No mechanical wear was observed for loads up to 300 nN when a large tip radius was used. When sharper tips were used a load of about 10 nN was sufficient to displace the OTE monolayer. *n*-Alkanethiols on Au were removed with a smaller force (ca. 5 nN) using the same sharp tip. However, a more recent study questioned the mechanical stability of OTS SAMs on SiO₂.^[90] Lower friction coefficients for monolayer-coated surfaces were reported, as well as a poor load-carrying capacity and antiwear ability. This report concluded that OTS SAMs could only be potential boundary lubricants at low loads.

3. Chemical Diversity of Self-Assembled Monolayers on Silicon Oxide

SAMs on SiO₂ provide molecularly defined platforms for chemical derivatization. Potential applications range from the control of surface properties to the fabrication of sensors and biochips as well as their use in nanotechnology. Progress in the development of these fields partly depends upon the ability to functionalize SAM surfaces with suitable groups. Two constraints determine the utility of SAMs on SiO₂ for the creation of functionalized surfaces: 1) the range of functionalities that can be tolerated in the self-assembly process to yield stable and ordered SAMs, and 2) the scope of chemical modifications of the monolayer that can be achieved.

An efficient reaction in solution is not necessarily successful on a solid substrate. The reactivity of immobilized reactants can be significantly reduced as a consequence of steric constraints, transport limitations, solvation effects, charge, and dipole effects.^[91] Therefore, the extent of reaction in a SAM depends strongly on the location of the reaction center: When it is located on the incoming reagent, the transition state does not experience much steric limitation, while if it is confined to the surface the reaction center is severely crowded by immobilized neighbors. Acid/base properties of surface-confined molecules can also differ significantly from those in solution.^[92–95] Important factors might be

the polarity of the surface, interfacial electrostatic fields, and the local structure of the solvent.

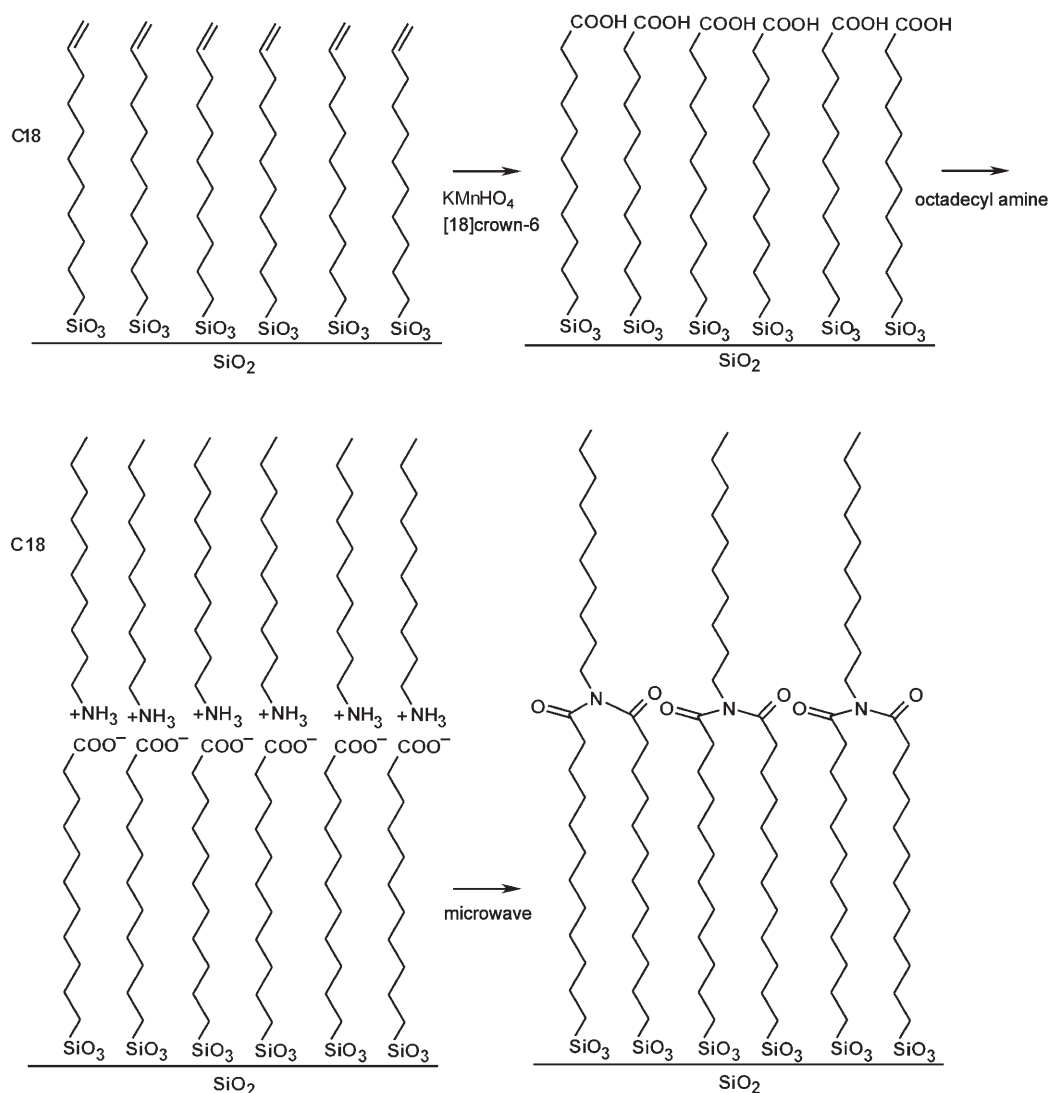
3.1. Self-Assembly of Functionalized Alkylsilanes and Chemical Transformations at the Monolayer Surface

The most straightforward way to prepare a functionalized SAM is by using an ω -substituted alkylsilane. In general, chlorosilanes are preferred over alkoxysilanes since they are more reactive. However, the reactivity of chlorosilanes severely limits the range of functional groups that can be introduced in this manner. The preparation of ω -functionalized alkyltrichlorosilanes is facilitated by using trialkoxysilanes as synthetic intermediates, as was reported by Barness et al.^[96] These offer superior stability with respect to synthetic operations and can be converted into trichlorosilanes by reaction with trichloroacetyl chloride.

The first functionalized SAM was reported by Netzer and Sagiv, and contained vinyl groups that could be transformed into terminal hydroxy groups by hydroboration and oxida-

tion.^[2] Other reactions on these layers generated carboxylic acid, and bromo-terminated films.^[86] A nice example of surface chemistry with these carboxylic acid monolayers was shown by Sagiv et al.^[97] The carboxylic acids were used to form a bilayer with octadecylamine through electrostatic/hydrogen-bonding interactions. Exposure of the bilayer to microwaves resulted in the formation of imides (Scheme 1).

More recently, vinyl SAMs have been covalently coupled to zwitterionic phosphorylcholine groups.^[98] Such monolayers are biocompatible and prohibit the deposition of enzymes and proteins. In addition, vinyl monolayers can be modified with adenine, and subsequently zeolite crystals functionalized with thymine were assembled at that surface through adenine–thymine hydrogen bonding.^[99] Tillman et al. prepared monolayers incorporating phenoxy groups and methyl esters, of which the latter were reduced to the corresponding alcohols by LiAlH_4 .^[82,83,100] Other functional groups incorporated into monolayers include methyl ether,^[101] acetate,^[101] thiocyanate,^[102] α -haloacetate,^[103] (trimethylsilyl)ethynyl,^[104] and thioacetate,^[102] which can be reduced to thiols.^[105]



Scheme 1. Microwave-induced imide formation in SAMs.^[97]

A convenient starting point for chemistry on monolayers is provided by bromo-terminated SAMs.^[69,101,106,107] Bromides can be quantitatively replaced by azide groups, which in turn are reduced to ω -amino SAMs,^[102,108] or can be used to tether to a fullerene molecule.^[109] In addition, bromides have also been replaced by other anionic nucleophiles such as thiocyanate and thiolate.^[110] These reactions did not go to completion, most likely because of steric congestion and because thiocyanates and thiolates are less nucleophilic than azides.

An alternative method to obtain amino-terminated SAMs is by self-assembly of cyanide monolayers.^[69,102] These SAMs can be reduced in one step using LiAlH₄ or BH₃.^[102] Such amino-terminated SAMs form an important platform for reaction with functionalized molecules. Ordered and well-defined layers are obtained when amino-terminated SAMs are prepared by reduction of azides or cyanides.^[102,108,111] Aminosilane films prepared in one step, on the other hand, are completely disordered.^[112] XPS and IR measurements indicated that this is probably a result of interaction of the amino group with the SiO₂ surface.^[112,113] Nevertheless, aminosilanes, and particularly 3-aminopropyltrialkoxysilanes (APS), have been used extensively as adhesion promoters and the well-known reactivity of amines has been exploited for the introduction of various functionalized molecules. APS layers were used to covalently bind fullerenes,^[114,115] chromophores,^[116,117] and fluorophores,^[118,119] and to coordinate to a zinc porphyrin.^[120] In addition, photoresponsive spiropyran molecules were covalently attached to an APS layer and used to induce reversible changes in wettability upon switching to a more polar zwitterionic merocyanine isomer, triggered by the absorption of UV light.^[121,122] Other reactions on amino-terminated SAMs will be discussed in Sections 3.3 and 3.4.

SAMs exposing sulfanyl groups are potentially interesting because of their ability to coordinate to noble metals. The self-assembly of (mercaptopropyl)trimethoxysilane (MPTMS) has been reported,^[91,123] and the preparation of colloidal gold multilayers using MPTMS as a linker molecule has been investigated.^[124] This layer-by-layer growth method yields uniform colloidal Au multilayers. More recently, MPTMS layers have been oxidized to produce sulfonic acid functionalized silica that can be used as a catalyst in esterification reactions,^[125] and MPTMS monolayers have also been used for electroless plating of Ag.^[126]

Homogeneous epoxy-terminated SAMs have been reported by Luzinov et al. to serve as templates for the chemical tethering of polymer layers.^[127] These layers can serve as functionalized surfaces and react with various amino-derivatized molecules. Kulak et al. attached an APS layer to zeolite crystals and found that the modified crystals assembled as monolayers on an epoxide SAM.^[128] The zeolite layer remained intact after sonication, thus indicating that strong linkages were formed between each crystal and the substrate. Furthermore, epoxide layers were used to immobilize per-6-amino- β -cyclodextrin on SiO₂, which led to a surface exposing host molecules.^[129]

The immobilization of polymers at a surface is a convenient way to tailor the surface properties of inorganic materials. One way to accomplish this is by the immobilization of

initiators for the in situ generation of grafted polymers. R  he and co-workers prepared layers of polystyrene and a perfluorinated polymer in a controlled manner and with high graft densities by using SAMs carrying azo initiators.^[130,131] A particular interesting development in this area has been the use of a "living" free-radical process at the surface to prepare accurately controlled polymer brushes.^[132–135] Advantages of this "living" polymerization include the control of molecular weight and polydispersity and the wide variety of monomers amenable to the process. In this way, surface-attached block and random copolymers can be formed for applications such as the precise tuning of surface properties and the preparation of responsive surfaces.^[133,135]

Tailoring surface properties using SAMs does not necessarily require polymers. Surfaces with very low surface free energies are generated by self-assembly of fluorinated silanes,^[57,101,136,137] while poly(ethylene glycol)-carrying silanes are widely used to prepare SAMs that resist the nonspecific adsorption of biomolecules.^[138–140]

3.2. Formation of Multilayers

Whereas a SAM is only a few nanometers thick, many practical devices require the formation of high-quality, close-packed, and highly ordered films with thicknesses of a few hundred nanometers to several micrometers.^[83] The growth of highly ordered multilayers is necessary to extend the two-dimensional structure of SAMs to the third dimension. Multilayer formation was studied for the first time by Netzer and Sagiv.^[2] They described the conversion of an olefin-terminated SAM into a hydroxy-terminated surface, which could be used to deposit a second layer of olefinic silanes. However, hydroboration of the olefin was not quantitative and led to increasing disorder in the subsequent layers. An improvement of this strategy was reported in which the reduction of methyl esters to alcohols by LiAlH₄ was used,^[83] which led to the construction of ordered assemblies of up to 25 discrete monolayers. A methodology to produce hydroxy-terminated siloxane-anchored SAMs and multilayers, which takes advantage of the photolysis of a nitrate-functionalized SAM for the formation of surface hydroxy groups without any reagents, was later reported.^[141] This photoconversion allowed the photopatterning of films and subsequent construction of multilayers.

An alternative procedure to yield multilayer assemblies involves the immobilization of a boronate-protected trichlorosilane, which can be hydrolyzed conveniently with water/ethanol to a diol, after which the process can be repeated.^[142] A different approach, reported by Yam and Kakkar,^[143] involved acid-base hydrolysis of aminosilanes with dihydroxy-terminated molecules. The layer-by-layer construction methodology used Si(NEt₂)₄ and rigid, rodlike diols, and led to relatively close-packed multilayered structures.

Hydrogen bonds can also be used instead of covalent coupling to stabilize the three-dimensional structure of the multilayer. Maoz et al. oxidized an olefinic SAM to the corresponding carboxylic acid before the next silane layer was assembled on top.^[49,144,145] Lateral cross-coupling of the silane

head-groups provided structural robustness and a self-healing capability to the films. Noncovalent multilayers were also reported by Mallouk and co-workers.^[146,147] They used the strong electrostatic and coordinative interaction between phosphonates and Zr^{4+} ions for the formation of multilayers.

Marks and co-workers prepared thin-film nonlinear optical (NLO) materials consisting of self-assembled chromophore-containing multilayer structures.^[148–154] They reported the formation of an acentric monolayer by self-assembly of a trimethoxysilane-functionalized azobenzene chromophore from solution. A siloxane capping layer was subsequently formed, which stabilized the structure by cross-linking and provided hydroxy groups to start a new cycle (Figure 4). The advantages of this approach to prepare NLO materials are the high chromophore concentration of the SAM and its robustness as a consequence of the covalent bonds.

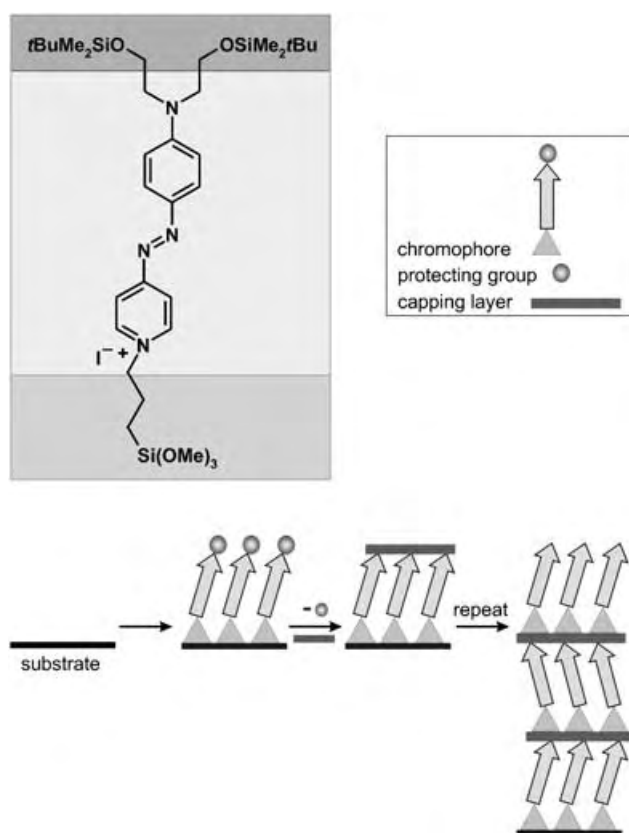


Figure 4. NLO materials obtained by self-assembly of chromophoric superlattices.^[154] Self-assembly of the chromophore yields a hydrophobic surface. Treatment with octachlorotrisiloxane ($\text{Si}_3\text{O}_2\text{Cl}_8$) results in deprotection and in the formation of a robust polysiloxane capping layer approximately 0.8 nm thick.

3.3. Sensor Layers

One field of increasing interest in which SAMs are employed extensively is (bio)chemical sensing. Immobilization of sensor systems implies the transition from solution to the solid state, which offers a convenient way to couple

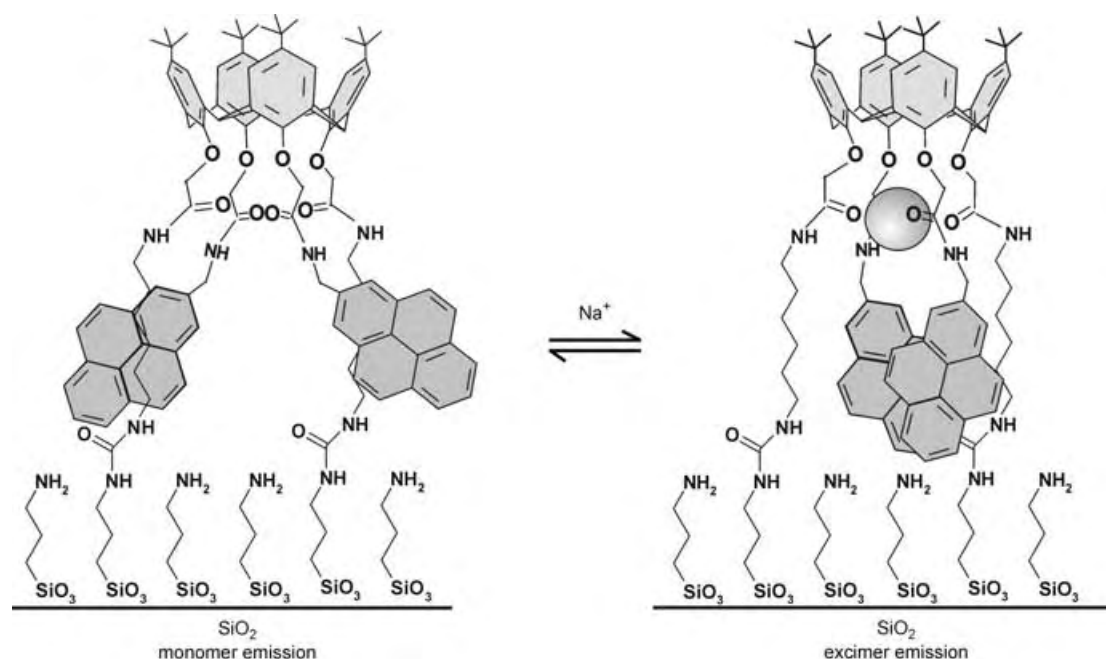
sensing systems to the macroscopic world through read-out functions. Furthermore, immobilized sensors usually have faster response times, are easier to handle, and may be recycled. Most sensor functionalities in SAMs were developed for gold surfaces, with read-out techniques such as electrochemistry, surface plasmon resonance, and AFM.^[25]

Fluorescence spectroscopy has advantages over electrochemical methods, as there is no need for reference electrodes or additional electrolytes.^[155] Moreover, molecules labeled with fluorescent probes are easily prepared or commercially available and can even be visualized individually. Fluorescence spectroscopy is extensively used in biological sensing (see Section 3.4), where it is applied in, for example, DNA chips and protein microarrays to gain information at the nucleic acid or protein level. The reason for the limited use of fluorescence spectroscopy on gold lies in the strong quenching effect of the gold substrate on the fluorescence of nearby molecules,^[156] thus making oxide surfaces such as SiO_2 the surface of choice for the immobilization of fluorescent sensing molecules.^[157–161]

One of the first immobilized sensors was reported by de Silva et al.^[162] The sensor consisted of an anthracene fluorophore covalently connected to an APS layer. The fluorophore could behave as a pH probe depending on the protonation state of the amino group. Porphyrins linked to an APS layer were reported by McCallien et al.^[163] After attachment to the substrate, zinc was inserted and the interaction of the zinc porphyrins with amino ligands was investigated by UV/Vis spectroscopy. Porphyrins could also be immobilized through reaction of a vinyl or hydroxyethyl group of a porphyrin with a sulfanyl-terminated monolayer, thus providing a simple and direct method for attaching porphyrins on solid substrates.^[164] UV/Vis measurements were used to monitor the coordination of carbon monoxide to various metal porphyrins.

Sensing by host–guest interactions on the SiO_2 surface has been reported by several research groups. Fullerenes were attached to silica gel to investigate binding affinities of potential hosts such as calixarenes and cyclodextrins.^[165] Cyclodextrins (CDs) constitute a class of receptor molecules that have been studied extensively in solution. CD films were prepared to monitor the interactions with various guest molecules,^[129,166,167] and in an elegant experiment Flink et al. monitored the interaction of β -CD hosts with monolayers of dansyl adsorbates by polarity-dependent fluorescence.^[168] Recently, we reported a procedure that yields densely packed β -CD monolayers, and it was shown that the binding properties of the CDs were retained when they were assembled at a surface.^[111] A monolayer bearing preorganized binding sites for metal ions was reported by van der Veen et al. (Scheme 2).^[155] They used a calix[4]arene receptor modified with ligating groups and two pyrene fluorophores. The immobilized receptor site showed selectivity for Na^+ over other alkali-metal ions. The complexation of Na^+ ions could be monitored by a decrease in monomer emission and an increase in excimer emission.

Although the fluoroionophore shown in Scheme 2 was found to be a good receptor for Na^+ ions, the use of preorganized recognition sites brings forth certain disadvan-



Scheme 2. Immobilized Na⁺-selective fluoro-ionophore which shows a change from the monomer emission to excimer emission upon complexation of Na⁺ ions.^[155]

tages: It requires lengthy syntheses and results in disordered monolayers as a result of the bulkiness of the receptor molecule. Therefore, a new approach was developed more recently.^[169,170] It relies on the immobilization of ligating functionalities on an amino-terminated SAM, without any preorganization. A small library containing various simple ligating and reporter molecules was made, and the response to different metal ions was measured. The results showed that selectivity for different metal ions depended on the surface functionalization. The same approach was used by Brasola et al. to develop a fluorescence nanosensor for Cu²⁺ ions on silica particles, the only difference being the immobilization of ligating and reporter molecules in one step, instead of linking them to a preformed monolayer.^[171]

3.4. Immobilization of Biomolecules

The attachment of biologically active molecules to surfaces is of considerable importance for the development of biological microarrays, such as DNA chips and protein microarrays.^[172,173] DNA chips are promising for obtaining information on nucleic acid levels and sequences in a fast, simple, and cheap way, and are developed for use in large-scale genotyping and gene-expression profiling.^[172] Protein microarray technology is valuable in the pharmaceutical industry for the acceleration of drug target and diagnostic biomarker discovery.^[173] Crucial to the development of these small-molecule microarrays is the ability to selectively attach molecules to the surface under mild conditions and at the same time avoid nonspecific interactions. Moreover, the reactions should be compatible with a wide variety of functional groups that occur in biologically relevant molecules. To meet these requirements, extensive research has

been performed to expand the immobilization techniques on surfaces. Recently, an overview of different reactions that have been studied with monolayers on Au and SiO₂, with the emphasis on immobilization of biomolecules, was reported.^[174]

The formation of amine-terminated SAMs on glass surfaces allows immobilization of biologically important molecules in both a covalent and a noncovalent way. Cells stick to the SAMs through electrostatic interactions between the positively charged ammonium groups and the negatively charged cell membrane.^[175] This simple electrostatic adsorption has also been used to link short oligonucleotides to a positively charged amino-functionalized SAM.^[176] This method produced a stable oligonucleotide monolayer with a density that approached a two-dimensional close-packed array.

Several mild methods have been developed to covalently couple biological molecules to the glass surface. Successful reactions include *N,N'*-dicyclohexylcarbodiimide (DCC) coupling of pepsin,^[91] 1-ethyl-3-(3-dimethylaminopropyl)carbodiimide (EDC) coupling of DNA,^[177] the immobilization of *p*-nitrophenyl chloroformate activated dextrans,^[178] reaction of compounds containing acidic protons with diazobenzilidene-functionalized glass slides,^[179] and a photoaffinity reaction.^[180] Many research groups have employed a two-step approach, where the amine-functionalized SAM was derivatized with a linker molecule after self-assembly to increase the reactivity of the monolayer. Heterobifunctional reagents such as *N*-succinimidyl-6-maleimidocaproate react with APS monolayers to expose the maleimide functionality, which in turn can be used in a Michael addition with sulfanyl groups.^[181–183] A critical feature of this methodology is the resistance to nonspecific adsorption, which was attributed to the hydrophilicity of the maleimide functionality.^[183] It has also been

shown that the same heterobifunctional molecule could be attached to a sulfanyl-terminated SAM.^[184] In this case it was utilized to link an amine-containing, fluorescently labeled oligodeoxynucleotide probe to the surface for hybridization experiments. A slightly different approach to attach DNA covalently to glass surfaces was reported by O'Donnel et al.^[185] They applied a heterobifunctional cross-linking agent to incorporate an iodoacetamido group, which was treated with a reduced oligodeoxynucleotide presenting free sulfanyl groups.

As was mentioned before, resistance to nonspecific adsorption is a critical issue when designing microarrays. Sekal et al. described a method to prepare monolayers that are resistant to nonspecific protein adsorption and present primary amino groups for derivatization.^[186] By treating an APS layer with glutaraldehyde and subsequently with 2,2'-(ethylenedioxy)bis(ethylenediamine) they were able to incorporate ligands and protein-sensitive fluorescent reporter groups, and used these monolayers for the detection of protein–ligand interactions.

Efficient surface silylation reactions can be complicated by formation of inhomogeneous layers, poor surface coverage, and instability to frequent regeneration steps.^[187] To overcome these problems, Benders et al. developed a method for generating highly homogeneous activated silicon oxide surfaces that can be applied to the efficient coupling of oligonucleotides to produce DNA microarrays.^[187] The method involves the initial formation of an APS layer, which is activated by a homobifunctional linker such as 1,4-phenylenediisothiocyanate (DITC), and then allowed to react with a starburst dendrimer containing 64 primary amino groups at the periphery. The attached dendritic molecules are subsequently activated and cross-linked with a homobifunctional spacer to display a surface with high coverage and decreased steric hindrance, and that is resistant against repeated regeneration procedures. Recently, layers obtained by this procedure and APS layers were derivatized with appropriate phosphane groups to immobilize azido-functionalized biomolecules by Staudinger ligation.^[188,189] This coupling strategy affords rapid immobilization and offers the advantage that it is compatible with unprotected functional groups, which are often required for interactions in biological systems.

Epoxy-terminated SAMs can react with molecules bearing amino groups. In this way it was possible to bind cyclopeptides to the glass surface for use as a molecular receptor^[190] and to determine binding constants between an immobilized tripeptide and vancomycin using confocal fluorescence detection.^[191] Hydrolysis of an epoxide-functionalized SAM yields a diol-functionalized SAM, which was used to develop a biosensor of immobilized nucleic acid aptamers to detect nonlabeled targets such as proteins.^[192]

Another relatively simple coupling strategy involves the reaction of aldehyde-modified glass surfaces with amine-containing molecules. The aldehydes react readily with primary amines of proteins or DNA to form a Schiff base linkage.^[177,193] This strategy was applied to prepare libraries of peptidyl coumarins in microarrays. It was demonstrated that

the immobilized peptides were accessible for proteolytic cleavage.^[194]

Other reported strategies to attach biological molecules to SiO₂ surfaces involve the reactions of sulfanyl-terminated SAMs with disulfide-modified oligonucleotides or heme proteins,^[195,196] iodopropyl monolayers with sulfanyl-containing proteins,^[197] alcohols with a silyl chloride surface,^[198] and bromoacetamide SAMs with phosphorothioate-functionalized oligonucleotides.^[199]

4. Engineering the Silicon Oxide Surface Using Self-Assembled Monolayers

The development of methods to control surface chemistry on the 1–100-nm length scale is a fundamental challenge in nanoscience and nanotechnology because it opens up new possibilities in fields ranging from molecular electronics to biomedicine and catalysis.^[200] SAMs offer an ideal platform for engineering surfaces on a molecular level, provided that techniques are developed to pattern or assemble SAMs with high resolution and fidelity.

4.1. Spacing of Chemical Functionalities

The positioning of chemical groups at regular intervals on a surface is of technological importance to localize adsorption and tune surface coverage, for example. The density of probe molecules is a critical issue in the design of DNA and protein chips. A facile method to achieve low surface coverage of functional groups is by preparing multicomponent SAMs so that chemical functionalities are diluted in an “inert” matrix of other molecules, which might be either unfunctionalized or carry a different functionality. Several approaches have been described in the literature, of which the most widely used involves competitive chemisorption, that is, the treatment of a surface with a mixture of adsorbates. Although the composition and properties of mixed monolayers are not at all straightforward, numerous binary monolayers have been prepared, as listed by Fadeev and McCarthy in Ref. [201].

Fan et al. stimulated phase separation in a binary monolayer by using two very different alkylsilane amphiphiles—one with strong cohesive interactions and one able to form hydrogen bonds—to generate a surface with nano-islands of a chemical functionality.^[202] The surface composition was analyzed by AFM, which showed pronounced differences in height and friction for the two components. The phase behavior of multicomponent SAMs could be used as an effective “latent image” to generate features on the surface by wet etching.^[203] This difference in etch resistance was achieved by the assembly of molecules with different chain length, and it was proposed that regions of more densely packed molecules were more etch resistant than regions of less coherent packing. Mixed SAMs can be conveniently used to control the surface free energy, as was shown in an elegant experiment by Lee et al.^[204] They used different ratios of hydroxy and methyl groups to tailor the surface free energy of silicon substrates, and found that in this way they could

light to remove photolabile protecting groups from selected areas, determines which regions of the surface are activated for coupling. The first set of building blocks, each bearing a photolabile group, is exposed to the surface but reacts only with the patterned areas. The substrate is subsequently illuminated through another mask for deprotection and coupling with a second building block. The steps of masking/irradiation and coupling are repeated to introduce various oligomers. The patterns of the masks and the sequence of reagents define the ultimate sequences synthesized, and their locations on the surface are known.

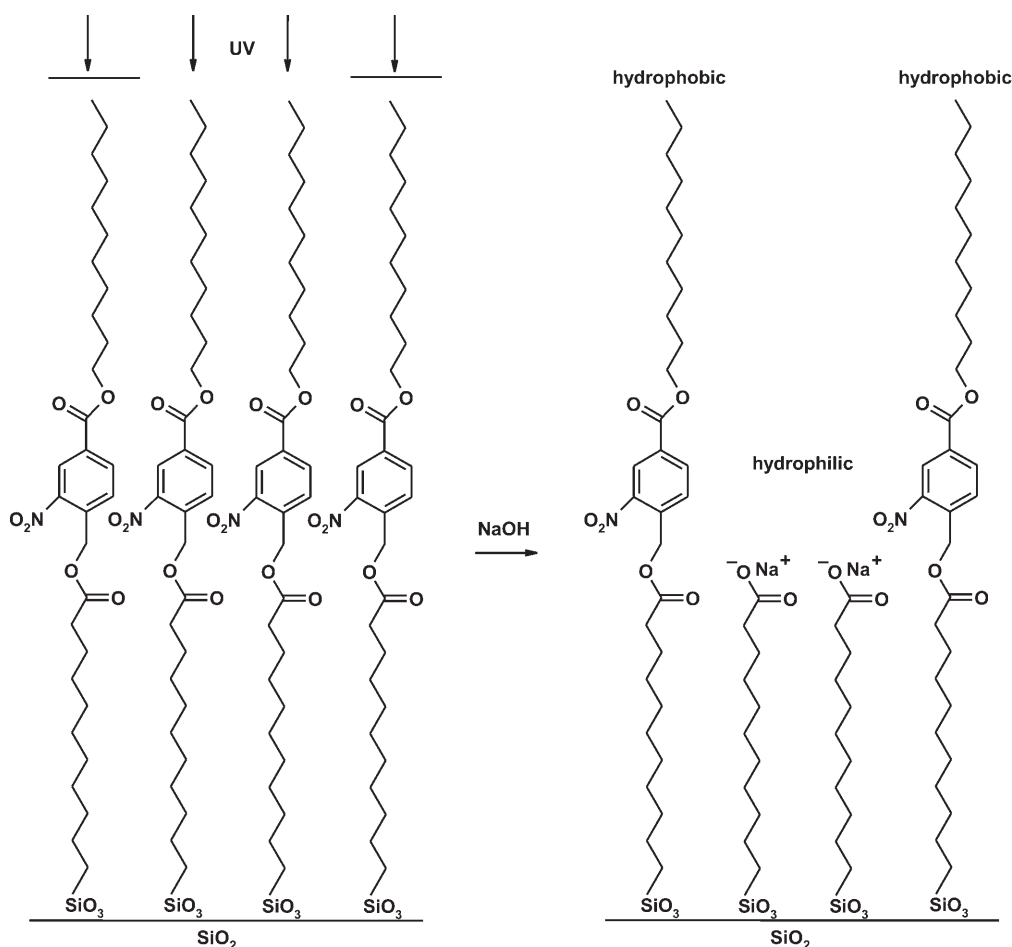
Other chemical transformations have been shown by the research groups of Dressick and Sugimura. Dressick and co-workers were able to transform 4-(chloromethyl)phenyl chromophores into phenylaldehyde groups, which in turn could be reduced to amines.^[226] Sugimura et al. showed that OTS SAMs decomposed gradually upon exposure to UV light in a vacuum to generate carboxylic acid groups that were successfully treated with functionalized and fluorinated silanes.^[214,215] Surface wettability could also be controlled using photolithographic methods. In a series of publications Beebe and co-workers reported cunning experiments to control liquid flow inside microchannels.^[227–229] Surface free energies were patterned by use of SAMs in combination with photolithography (Scheme 3). They could confine the flow of

aqueous liquids to the hydrophilic pathways, provided that the pressure was maintained below a critical value.

Photolithography has recently been applied in a constructive procedure.^[230] Direct writing with a laser allowed the formation of sub-200 nm oxide patterns on H-terminated Si. Exposing these substrates to a solution containing OTS molecules resulted in selective growth on the oxide patterns.

4.2.2. Electron Beam Lithography

SAMs are candidates for very high resolution resists in electron beam lithography. Since the feature size generated with electron beam lithography depends on the thickness of the resist, the monomolecular thickness of SAMs could reduce back scattering of electrons and provide ultrahigh-resolution electron beam patterning. It has been shown that patterns of several tens of nanometers could be created in OTS and perfluorinated SAMs on SiO₂, and that the patterns could be transferred into the substrate by wet-etching techniques.^[231–233] Patterns smaller than 10 nm could also be attained by using scanning electron microscopy (SEM) with a small beam diameter.^[234] A different development of the created patterns was reported by Marrian et al.^[235] Low voltage electron beam lithography was used to pattern films and the patterns were applied as templates for the electrodeless



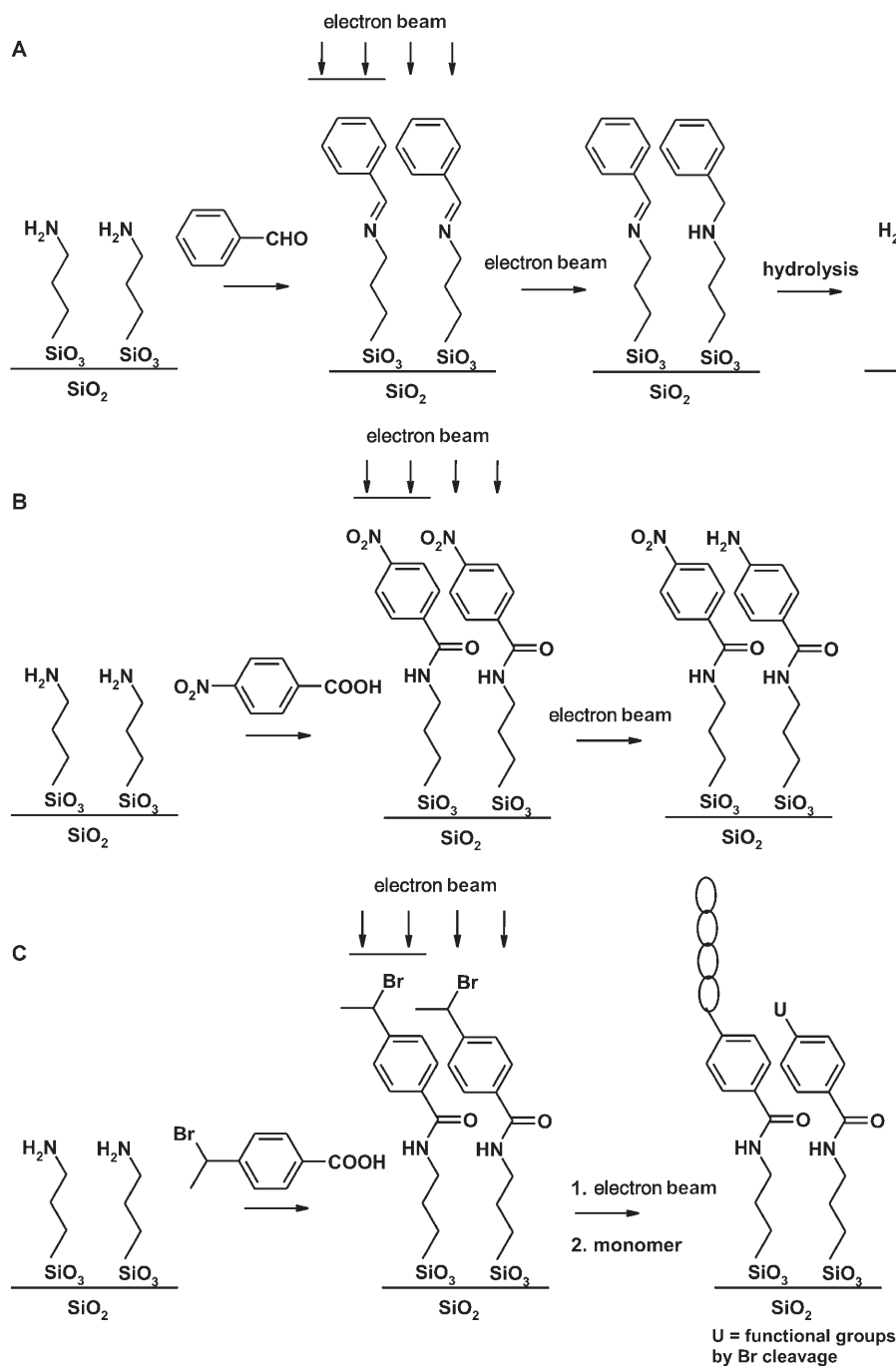
Scheme 3. UV photolithography to fabricate hydrophilic patterns inside microchannels.^[227]

plating of thin Ni films. Linewidths down to about 20 nm were observed after plating.

There have been several reports that combine electron beam lithography with functionalized SAMs. Craighead and co-workers patterned amino-terminated SAMs and developed the patterns by exposing them to palladium colloids and coated polystyrene fluorescent spheres.^[236] The colloids and spheres adhered only to unexposed areas of the monolayers. Other studies employed the deposition of aminosilanes through a poly(methylmethacrylate) (PMMA) mask or an unfunctionalized SAM that was patterned by electron beam lithography.^[237–239] In this way colloidal particles and carbon

nanotubes were deposited selectively on the amine-modified parts of the substrate.

Recently, electron beam irradiation was used to induce chemical transformations in monolayers. Park and co-workers studied several procedures to prepare patterned amino- and bromo-terminated SAMs, and verified the reactivity by attaching biotin/streptavidin groups,^[240] or amplified the patterns vertically by radical polymerization.^[241] The transformations are shown in Scheme 4. The induced transformations have been employed to direct adsorption of gold nanoparticles.^[242] In addition, sub-50 nm patterns were prepared in SAMs with embedded disulfide bonds.^[243] Phenyl-3-



Scheme 4. Chemical transformations of SAMs with a low-energy electron beam.^[240,241]

(trimethoxysilylpropyl)disulfide monolayers were patterned with electron beam lithography, which generated 3–4-Å deep and 30-nm wide trenches. XPS indicated the cleavage of the disulfide bonds to sulfhydryl groups, and the resulting chemical patterns could be developed by reaction with *N*-(1-pyrene)maleimide. Even smaller chemical patterns were obtained by a combination of electron beam lithography and gas-phase silanization.^[244] It was shown that monolayers with varying chemical functionalities could be formed through nanoholes in a PMMA mask. After removing the mask, a monolayer of different functionality was deposited, and generated well-defined nano-islands as small as 20 nm of one chemical functionality in a matrix of another.

4.2.3. Ion-beam and X-ray Lithography

Ion-beam and X-ray lithography are methods that have been less frequently used to pattern SAMs on SiO₂. Patterning with low-energy ion beams usually employs shadow masks because of the difficulty of focusing such sources. However, high-energy focused ion beams (FIBs) should result in nanometer-scale patterns, as it is possible to attain beam diameters as small as 8 nm.^[245] FIBs have already been used to write 10-nm wide features in thin PMMA films.^[246] A vinyl-terminated monolayer was selectively deposited in ion-beam-etched regions of a methyl-terminated SAM with a resolution of 1–3 μm.^[247] Ada et al. have studied in detail the interaction of low-energy ions with organosilane SAMs, and were able to create 300-nm wide gaps by employing FIB.^[248] Smaller feature sizes were reported by exposing monolayers to low doses of slow, highly charged ions, such as Xe⁴¹⁺ and Th⁷³⁺.^[249] AFM images showed craters from single ion impacts with diameters of 50–63 nm. Equally small features have also been reported by Whitesides and co-workers by utilizing a beam of neutral Cs atoms.^[250]

Irradiation with soft X-rays through a mask can be a convenient method for chemical patterning of monolayers. Reported transformations include the loss of halogens in halogenmethylphenylsilyl layers,^[251,252] and the cleavage of nitro groups in nitro-substituted aromatic SAMs.^[253] La et al. used masks with nanometer-sized features to develop sub-100 nm patterns, as evidenced by AFM.^[254] The patterns could be derivatized by attachment of fluorescently labeled oligonucleotides. Irradiation of OTS layers resulted in the formation of oxygen-containing groups such as OH and C(O)H.^[255] Pattern transfer of features with dimensions as small as 150 nm into the underlying substrate were obtained by reactive ion etching using thin films of Ni selectively deposited onto the exposed areas of the OTS SAM.

Recently, it was shown that hybrid patterning strategies allow for the fabrication of defect-free nanopatterns of block copolymers.^[256] A photoresist on top of a phenylethyl monolayer was patterned with 45–55-nm-sized features by interferometric lithography using extreme UV light, and the pattern was transferred into the underlying SAM by chemical modification using soft X-rays. After removing the photoresist, poly(styrene-*block*-methylmethacrylate) (PS-*b*-PMMA) was spin-coated onto the patterned SAM and annealed. It was found that the PMMA block preferentially

wetted the modified regions of the surface, and thus domain structures were formed analogous to the SAM patterns, as observed by SEM (Figure 7).

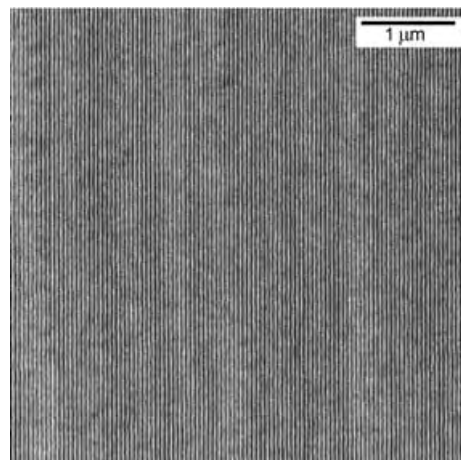


Figure 7. SEM image of 48-nm wide PS and PMMA domains formed by selective absorption on a SAM patterned by a combination of UV and X-ray lithography.^[256]

4.3. Soft Lithography

Soft lithography^[257] is the collective name for a set of lithographic methods including replica molding, microcontact printing (μCP), and micromolding using a patterned elastomer as a mold, stamp, or mask to transfer a pattern.^[258] Soft lithography offers advantages over other lithographic methods for the patterning of nonplanar substrates, unusual materials, or large areas.^[258] Of these techniques, μCP has been employed most frequently for the facile (sub)micron patterning of surfaces. μCP relies on the inking of an elastomeric (usually PDMS) stamp with suitable molecules. When the stamp is brought into contact with a substrate, the molecules are transferred from the stamp to the substrate in the regions of contact. μCP was initially developed for the patterning of gold surfaces with alkanethiols, and even today the bulk of the literature comprises patterning of this surface with these adorbates.

Reports regarding μCP on SiO₂ surfaces have been rather limited. This situation might be explained by the inherent sensitivity of trialkoxy- and especially trichlorosilanes, and the lower edge resolution of silanes on SiO₂ relative to thiols on gold.^[259] Although Whitesides and co-workers reported that printed OTS SAMs were only partly etch resistant, later studies showed that printed patterns could be transferred into the underlying silicon substrate,^[260] even with feature sizes as small as 80 nm.^[261] Detailed studies by Nuzzo and co-workers indicated that close-packed OTS monolayers were formed after only 30 s of printing while it took minutes to form a densely packed monolayer by deposition from solution.^[262] They also found that stable SAMs were formed, but that patterning at dimensions less than a few micrometers resulted in the spreading of OTS in regions that had not been in

contact with the stamp. μ CP with docosyltrichlorosilane resulted in more accurate transfer to the substrate, and these films had an improved etch-resistance.^[263]

Amplification of a printed pattern can also be achieved in a different manner. Harada et al. amplified a printed vinyl-terminated pattern by selectively attaching a Ru complex, which reacted with norbornene derivatives to give thin polymer films.^[264] The contrast in wettability between clean SiO₂ and a printed OTS pattern enabled the confinement and alignment of molecules.^[265] After printing, the remaining hydrophilic parts of the substrate were covered with a thin polyelectrolyte layer, onto which biological macromolecules and liquid crystals could be confined. This process afforded a straightforward way to create microchannels on a surface.

The majority of the work concerning μ CP of SAMs on SiO₂ involves deposition of metals. Printed monolayers can serve as a resist for chemical vapor deposition of copper,^[266] or deposition of SnCl₂ from solution, which serves as a nucleation point for electroless plating of Ag.^[267]

Instead of printing a monolayer, it is also possible to print onto a monolayer assembled from solution. Hidber et al. used an amino-terminated SAM as an adhesion promoter to print (sub)micron patterns of Pd colloids.^[268] The immobilized colloids served as a catalyst for the electroless deposition of copper, and yielded (sub)micrometer-scale copper lines on an insulating surface. Recently, Reinhoudt and co-workers introduced supramolecular μ CP, which is shown schematically

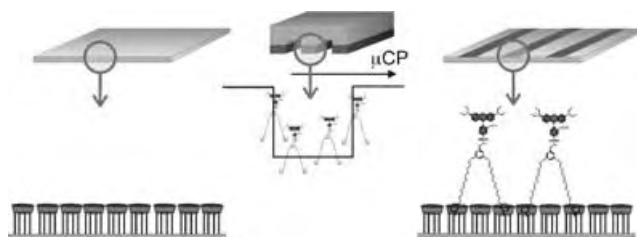


Figure 8. Schematic representation of supramolecular microcontact printing (μ CP). Cyclodextrin host monolayers are patterned by μ CP of suitable guest molecules.^[269,270]

in Figure 8.^[269–271] In this method, guest molecules that bind through multiple supramolecular interactions were printed onto a densely packed monolayer of cyclodextrin receptor molecules on SiO₂ (or gold). The patterns were characterized by AFM, XPS, and confocal microscopy. Control experiments showed that the ink molecules bind to the receptor surface

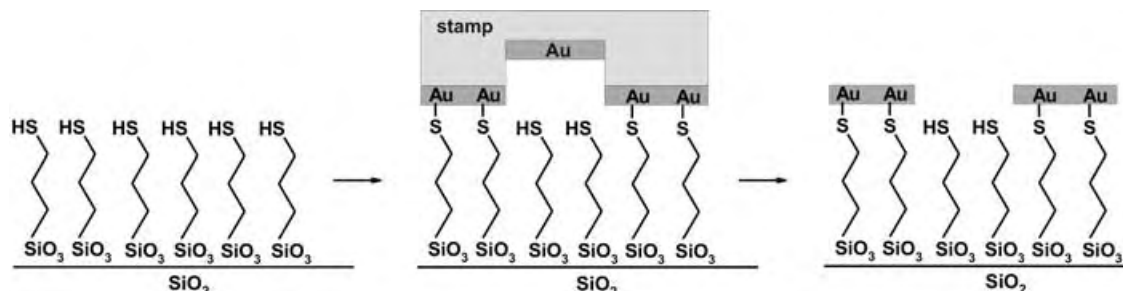
through specific host–guest interactions. One advantage of this method is that the stability of the assemblies can be tuned by the number of interactions between the guest molecules and host monolayer.

Sulfanyl-terminated MPTMS SAMs can be employed as adhesion promoters for noble metals.^[272] In nanotransfer lithography a gold-coated PDMS stamp is used to transfer thin but stable gold layers onto the monolayer (Scheme 5). In a series of publications Delamarche et al. described an elegant process to produce NiB structures and metal nanowires on glass substrates.^[273–277] They combined the adhesive properties of an amino-terminated SAM to bind Pd/Sn colloids, which were used to initiate electroless deposition of NiB. Then, copper was electroplated and patterned by μ CP using a protective layer of thiol molecules. The pattern was subsequently etched into the copper and NiB by two wet etching techniques. This process was developed to provide a new and potentially cost-effective way for the fabrication of gate layers in thin-film transistor (TFT) LCDs, and could even be applied on a macro (38 cm) scale.

Nanoimprint lithography (NIL)^[278] was recently advocated as a powerful alternative to μ CP of organosilanes.^[279] A PMMA polymer template obtained by NIL directs the assembly of a SAM from the gas phase to the uncovered area of the substrate while preventing the formation of a SAM in the covered area. After removal of the polymer, SAM patterns are obtained that may be filled with other silanes. NIL-patterned SAMs are useful in nanofabrication, for example, to direct adsorption of particles or deposition of metal electrodes on SAMs (Figure 9).

4.4. Scanning Probe Lithography

Scanning probe microscopy can visualize surface topography and surface chemistry at the submolecular level. In addition, probe tips can be used to manipulate atoms and molecules on surfaces, and in this mode the technique is often referred to as scanning probe lithography.^[280] Sugimura et al. were among the first to combine a scanning probe tip with self-assembly on SiO₂ surfaces to create nanoscale patterns. They have used a scanning tunneling microscope tip for local anodization of a Si-H surface to SiO₂ in the presence of an organosilane vapor.^[281] This resulted in the formation of monolayer features of 20 nm that showed a resistance to chemical etching. Other studies from the same authors reported patterning of a homogeneous monolayer by apply-



Scheme 5. Metal structures prepared on adhesive SAMs by nanotransfer printing.^[272]

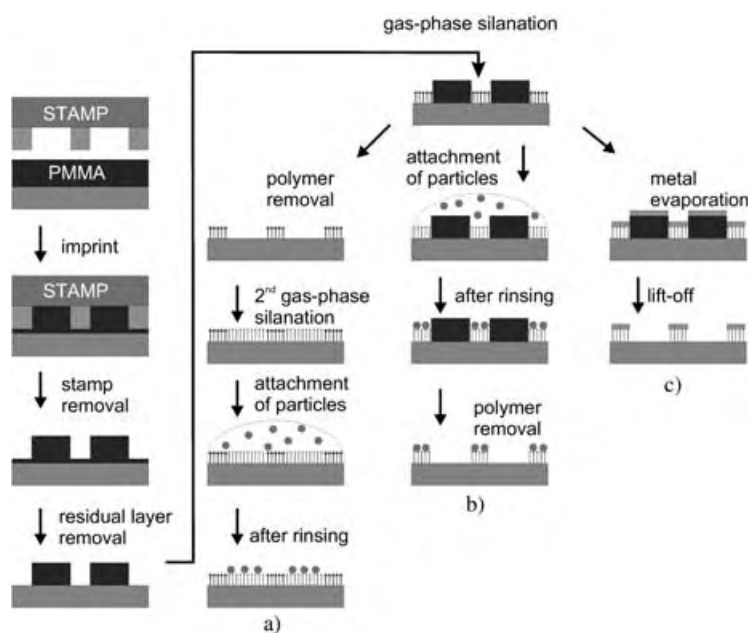


Figure 9. Nanofabrication using SAMs patterned by nanoimprint lithography. Applications: a) Polymer removal, evaporation of a second silane, and selective attachment of functionalized particles. b) Selective attachment of functionalized particles, and polymer removal. c) Metal evaporation and metal lift-off.^[279]

ing a bias voltage to the probe tip, effectively removing the monolayer from the probe-scanned regions. Next, the exposed regions were filled with SAMs of different chemical composition to regulate the surface potential or selectively assemble proteins at a spatial resolution on the nanometer scale.^[282,283] A different method for nanometer-scale patterning was obtained by field-induced oxidation (FIO) using a conductive cantilever.^[284] Surface hydroxy groups, necessary for monolayer formation, were removed and monolayer formation was suppressed when FIO was employed locally on an oxide surface in a dry nitrogen atmosphere. In this way, a line structure of an OTS SAM as narrow as 22 nm could be fabricated. In contrast, OTS SAMs formed on the entire surface when FIO was performed under humid conditions.

4.4.1. Constructive-Nanolithography

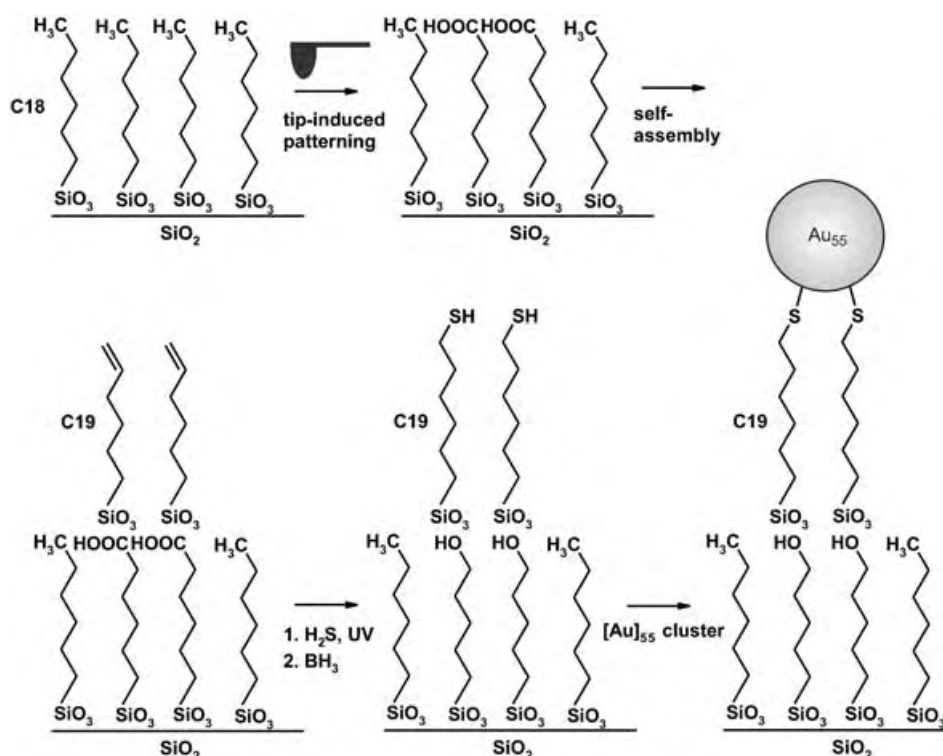
Constructive nanolithography was introduced by Sagiv and co-workers.^[285] It involves nondestructive surface patterning by means of an electrical

bias to a conducting AFM tip operated under ambient conditions, followed by template-controlled self-assembly. The versatility of this approach was demonstrated in several systems where vinyl-terminated and OTS SAMs were locally electrooxidized to prepare patterned bilayers,^[286] self-assembled metal islands,^[285,287] metal nanoparticles,^[288–290] and nanowires.^[289] Features with sub-50 nm dimensions could be fabricated by using this method. A schematic representation of the organosilane template pattern and the self-assembly of $[\text{Au}_{55}]$ clusters on the template is displayed in Scheme 6. This methodology could be used for the nanometer to millimeter range by employing electrooxidation with a rigid metallic stamp.^[291] Recently, other research groups have applied local probe oxidation of SAMs for functionalization with cationic gold nanoparticles, quaternary ammonium salts, and polymers.^[292,293]

A few years before Sagiv and co-workers introduced constructive nanolithography, a similar approach was presented by Schultz and co-workers, who made use of a catalytic probe.^[294] In this elegant experiment an alkylazide monolayer was reduced to its corresponding amine by a catalytic Pt coated AFM tip. The amino groups were then covalently modified with fluorescently labeled beads and imaged under a confocal microscope.

4.4.2. Dip-Pen Nanolithography

Dip-pen nanolithography (DPN)^[200,295] uses an inked AFM tip to deposit molecules on a substrate. This technique, which is believed to rely on the transport of molecules from



Scheme 6. Schematic representation of constructive nanolithography, in which tip-induced electrooxidation and subsequent self-assembly on the written template are employed. In this case $[\text{Au}_{55}]$ clusters were assembled.^[288]

the tip to a surface through a water meniscus, has been used to generate structures with line widths as small as about 10 nm (Figure 10a). Reported examples have dealt almost exclusively with the writing of thiol inks on gold substrates, or the use of metal salts for the electrostatical assembly on appropriately biased silicon substrates.

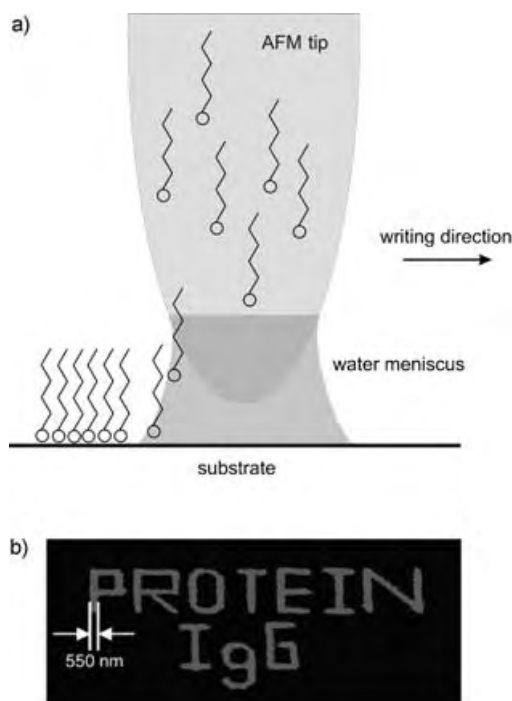


Figure 10. a) Schematic representation of dip-pen lithography (DPN). b) Fluorescence image of DPN-generated labeled antirabbit IgG structure on SiO₂.^[301]

Thus far, silane-based inks have rarely been used, mainly because of the incompatibility of chloro- and alkoxy silane groups with the water meniscus that mediates ink transport. Ivanisevic and Mirkin used hexamethyldisilazane to write organic patterns on SiO₂ with sub-100 nm dimensions.^[296] Two recent articles, however, demonstrated that it is possible to write with trialkoxysilane-based inks. Pena et al. wrote APS and MPTMS lines of nanometer dimensions, but were not able to further derivatize the formed structures.^[297] They explained this lack of reactivity by the formation of multilayers through hydrogen bonding. These results were contradicted in a study by Jung et al.,^[298] who claimed that DPN with reactive silanes is possible if proper measures against polymerization are taken. Writing at low humidity resulted in the formation of 110-nm-wide MPTMS lines, which were successfully treated with biotin and fluorescently labeled streptavidin.

An alternative method to write functionalized structures on the SiO₂ surface constitutes writing on functional monolayers. Reinhoudt and co-workers recently demonstrated supramolecular DPN where an AFM tip is inked with suitable guest molecules and the substrate is a β -cyclodextrin host monolayer.^[270] Sub-500 nm patterns, based on host–guest interactions, were written and imaged by confocal microscopy

and AFM. Covalently anchored nanoscale patterns of oligonucleotides and maleimide-linked biotin were written onto MPTMS SAMs.^[299,300] It was found that nanoscale patterning of maleimide-linked biotin was facilitated by the addition of small amounts of non-ionic surfactant to the biotin ink. An increase in the wettability of the substrate is thought to cause this phenomenon.

The direct writing of proteins on modified SiO₂ surfaces has been reported.^[301] A negatively charged surface was used to bind proteins electrostatically (Figure 10b), and proteins were covalently bound by writing on a preformed aldehyde-terminated monolayer. Some modifications to the writing process had to be made. First, an AFM tip coated with poly(ethylene glycol) (PEG) was used to minimize protein adsorption and to reduce the activation energy required for protein transport from the tip to the surface. In addition, it protects the protein from denaturation on the tip surface. Second, it was found that high humidity is a prerequisite for writing with high-molecular-weight molecules. Patterning was performed at relative humidities between 60 and 90%, whereas low humidities were sufficient for writing with low-molecular-weight trialkoxysilanes.

5. Summary and Outlook

Since the first report on SAMs on SiO₂ in 1980, many studies have investigated the mechanism of monolayer formation, which has led to a better understanding of the principles underlying this self-assembly process. It has become clear that factors such as solvent, temperature, water content, deposition time, and age of the adsorbate solution play a crucial role in the self-assembly process. Small variation of one or more of these factors can result in very different assembly properties, and several studies appear to have conflicting outcomes. An illustrative example is the temperature at which the self-assembly takes place: Lower temperatures favor island growth, while at higher temperature homogeneous growth has been observed. In addition, several studies have shown that the assembly process is not so much covalent in nature as had been assumed for a long time. Adsorbate molecules that covalently attach to the surface are scarce, and in-plane polymerization of the adsorbates might lead to decreased order instead of a close-packed monolayer. These results indicate that the monolayers have Langmuir-like features, as was elegantly demonstrated by reversible temperature-dependent island-growth formation of sub-monolayers.^[67]

Chemical derivatization of SAMs on SiO₂ is essential for many potential applications. Two factors determine the versatility of functional SAMs on SiO₂: the range of functionalities that are tolerated in the self-assembly of stable and ordered SAMs, and the scope of chemical post-modifications that can be achieved. Not all functional groups can be conveniently introduced in the self-assembly process because of the inherent reactivity of the trichloro- or trialkoxysilanes that are used for chemisorption. In addition, functional groups might interact with the polar surface, thus resulting in the formation of disordered monolayers. For these

reasons chemical postmodifications have been studied in depth and a wide range of surface chemistry is nowadays available for further derivatization of the SAMs. Selective attachment of compounds to the surface under mild conditions, while avoiding nonspecific interactions, is crucial particularly for the development of bioanalytical surfaces. These reactions should be compatible with a wide variety of functional groups that occur in biologically relevant molecules. Bifunctional coupling agents are often used to meet these requirements.

Positional control of surface chemistry on the nanoscale allows the development of arrays containing a high density of chemical information. The chemical information can then be translated into high-density functional surfaces, such as proteins or DNA chips, or be exploited as a platform for building nanosized functional materials (for example, by self-assembly). The ability to pattern surfaces with chemical information is therefore of prime importance. Electron beam lithography, and especially photolithography, have been the principal techniques for the patterning of surfaces for many years, but soft and probe lithographic techniques have recently witnessed a tremendous development. The main advantages of these methods include the use of inexpensive equipment, the high (sub-100 nm) resolution, and the possibility to prepare positive patterns under mild conditions.

The logical extension of surface patterning is to express and amplify a 2D pattern into a 3D structure. This is a requirement for the bottom-up fabrication of nanoscale devices. Taking nature as a source of inspiration, it is expected that self-assembly techniques will play a major role in nanofabrication. Striking examples of this trend have already been published by Sagiv and co-workers, who used self-assembly techniques to translate a chemical pattern into nanostructures of colloidal gold,^[288] and by Mirkin and co-workers, who employed an AFM tip to write protein structures on a SAM.^[301] It is expected that this trend from 2D to 3D will be continued in the next decade, while the focus of research in this area will shift more and more toward the nanofabrication of devices.

The authors are grateful to Jacob Sagiv for helpful suggestions. The Microchemical Systems (MiCS) program of the MESA⁺ Institute for Nanotechnology is acknowledged for financial support.

Received: February 21, 2005

Published online: September 19, 2005

- [1] *New Scientist* **1983**, 98, 20.
- [2] L. Netzer, J. Sagiv, *J. Am. Chem. Soc.* **1983**, 105, 674.
- [3] W. C. Bigelow, D. L. Pickett, W. A. Zisman, *J. Colloid Sci.* **1946**, 1, 513.
- [4] W. C. Bigelow, E. Glass, W. A. Zisman, *J. Colloid Sci.* **1947**, 2, 563.
- [5] E. E. Polymeropoulos, J. Sagiv, *J. Chem. Phys.* **1978**, 69, 1836.
- [6] J. Sagiv, *J. Am. Chem. Soc.* **1980**, 102, 92.
- [7] A. Ulman, *An Introduction to Ultrathin Organic Films*, Academic Press, Boston, **1991**.
- [8] A. Ulman, *Chem. Rev.* **1996**, 96, 1533.

- [9] D. K. Schwartz, *Annu. Rev. Phys. Chem.* **2001**, 52, 107.
- [10] J. C. Love, L. A. Estroff, J. K. Kriebel, R. G. Nuzzo, G. M. Whitesides, *Chem. Rev.* **2005**, 105, 1103.
- [11] R. G. Nuzzo, D. Allara, *J. Am. Chem. Soc.* **1983**, 105, 4481.
- [12] L. Netzer, R. Iscovici, J. Sagiv, *Thin Solid Films* **1983**, 99, 235.
- [13] L. Netzer, R. Iscovici, J. Sagiv, *Thin Solid Films* **1983**, 100, 67.
- [14] R. Maoz, J. Sagiv, *J. Colloid Interface Sci.* **1984**, 100, 465.
- [15] J. Gun, R. Iscovici, J. Sagiv, *J. Colloid Interface Sci.* **1984**, 101, 201.
- [16] J. Gun, J. Sagiv, *J. Colloid Interface Sci.* **1986**, 112, 457.
- [17] S. R. Cohen, R. Naaman, J. Sagiv, *J. Phys. Chem.* **1986**, 90, 3054.
- [18] R. Maoz, J. Sagiv, *Langmuir* **1987**, 3, 1034.
- [19] R. Maoz, J. Sagiv, *Langmuir* **1987**, 3, 1045.
- [20] H. Brunner, M. Vallant, U. Mayer, H. Hoffmann, *J. Colloid Interface Sci.* **1999**, 212, 545.
- [21] V. I. Nefodov, *X-ray Photoelectron Spectroscopy of Solid Surfaces*, VSP, Utrecht, **1988**.
- [22] J. C. Vickerman, *Surface Analysis—The Principal Techniques*, Wiley, Chichester, **1997**.
- [23] B. Hagenhoff, A. Benninghoven, K. Stoppeklanger, J. Grobe, *Adv. Mater.* **1994**, 6, 142.
- [24] D. L. Angst, G. W. Simmons, *Langmuir* **1991**, 7, 2236.
- [25] S. Flink, F. C. J. M. van Veggel, D. N. Reinhoudt, *Adv. Mater.* **2000**, 12, 1315.
- [26] S. R. Wasserman, G. M. Whitesides, I. M. Tidswell, B. M. Ocko, P. S. Pershan, J. D. Axe, *J. Am. Chem. Soc.* **1989**, 111, 5852.
- [27] S. N. Magonov, M.-H. Whangbo, *Surface Analysis with STM and AFM*, VCH, Weinheim, **1996**.
- [28] L. T. Zhuravlev, *Langmuir* **1987**, 3, 316.
- [29] H. O. Finklea, L. R. Robinson, A. Blackburn, B. Richter, D. Allara, T. Bright, *Langmuir* **1986**, 2, 239.
- [30] D. L. Allara, A. N. Parikh, F. Rondelez, *Langmuir* **1995**, 11, 2357.
- [31] P. Silberzan, L. Leger, D. Ausserre, J. J. Benattar, *Langmuir* **1991**, 7, 1647.
- [32] C. P. Tripp, M. L. Hair, *Langmuir* **1992**, 8, 1120.
- [33] C. P. Tripp, M. L. Hair, *Langmuir* **1995**, 11, 1215.
- [34] J. D. Legrange, J. L. Markham, C. R. Kurkjian, *Langmuir* **1993**, 9, 1749.
- [35] R. W. P. Fairbank, M. J. Wirth, *J. Chromatogr. A* **1999**, 830, 285.
- [36] R. W. Wang, S. L. Wunder, *Langmuir* **2000**, 16, 5008.
- [37] M. L. Hair, C. P. Tripp, *Colloids Surf. A* **1995**, 105, 95.
- [38] R. R. Rye, G. C. Nelson, M. T. Dugger, *Langmuir* **1997**, 13, 2965.
- [39] R. R. Rye, *Langmuir* **1997**, 13, 2588.
- [40] M. J. Stevens, *Langmuir* **1999**, 15, 2773.
- [41] R. Banga, J. Yarwood, A. M. Morgan, B. Evans, J. Kells, *Thin Solid Films* **1996**, 285, 261.
- [42] I. M. Tidswell, B. M. Ocko, P. S. Pershan, S. R. Wasserman, G. M. Whitesides, J. D. Axe, *Phys. Rev. B* **1990**, 41, 1111.
- [43] I. M. Tidswell, T. A. Rabedeau, P. S. Pershan, S. D. Kosowsky, J. P. Folkers, G. M. Whitesides, *J. Chem. Phys.* **1991**, 95, 2854.
- [44] M. Fujii, S. Sugisawa, K. Fukada, T. Kato, T. Seimiya, *Langmuir* **1995**, 11, 405.
- [45] Fujii et al. reported an occupied area of 0.43 nm² per OTS chain, but extensively dried the substrate prior to self-assembly. This could explain the high surface area per OTS chain and the observed low ellipsometric thickness.
- [46] S. W. Barton, A. Goudot, F. Rondelez, *Langmuir* **1991**, 7, 1029.
- [47] K. Kojio, S. R. Ge, A. Takahara, T. Kajiyama, *Langmuir* **1998**, 14, 971.
- [48] K. Kojio, A. Takahara, K. Omote, T. Kajiyama, *Langmuir* **2000**, 16, 3932.
- [49] R. Maoz, J. Sagiv, D. Degenhardt, H. Mohwald, P. Quint, *Supramol. Sci.* **1995**, 2, 9.
- [50] A. Baptiste, A. Gibaud, J. F. Bardeau, K. Wen, R. Maoz, J. Sagiv, B. M. Ocko, *Langmuir* **2002**, 18, 3916.

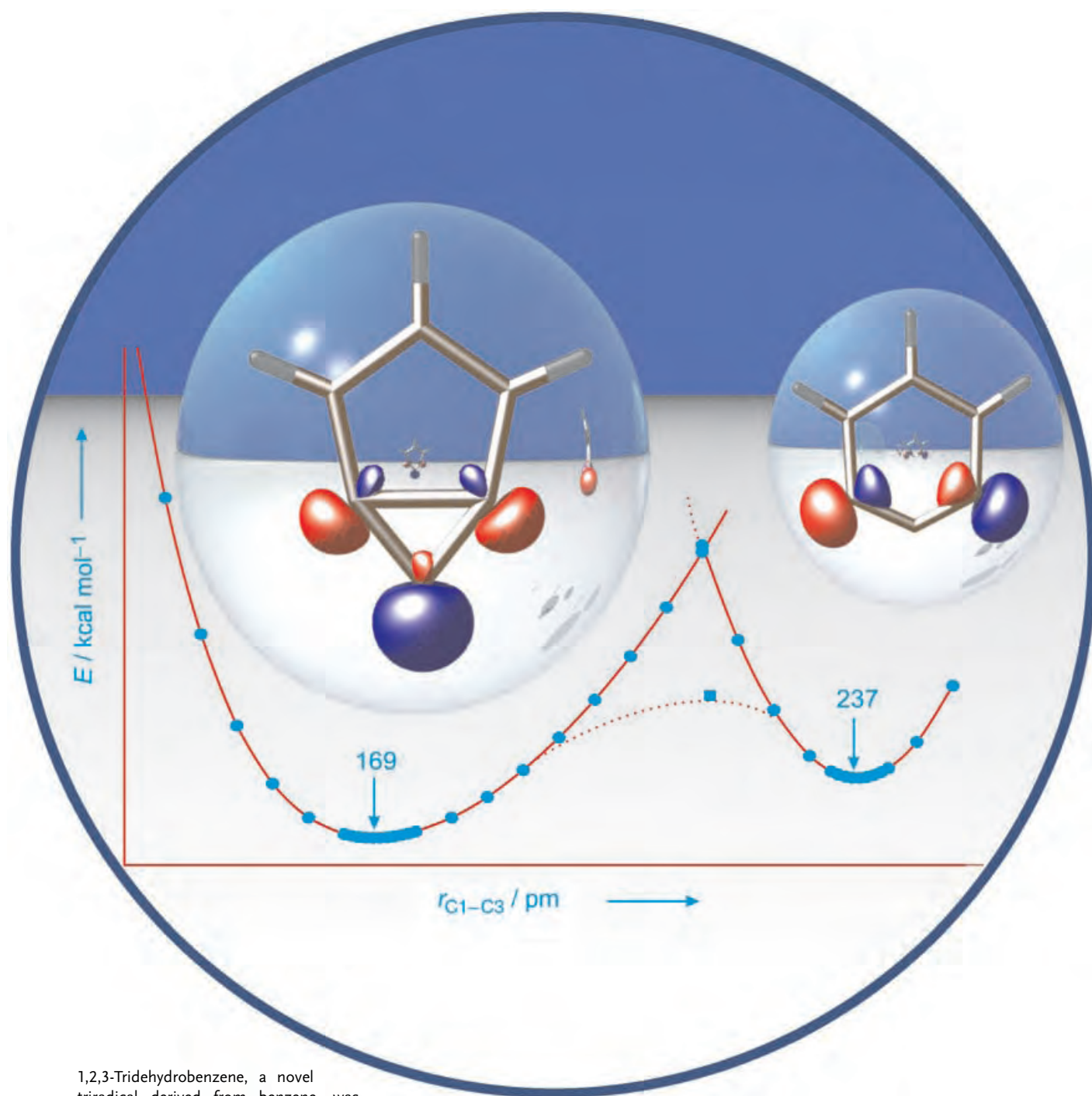
- [51] Y. L. Wang, M. Lieberman, *Langmuir* **2003**, *19*, 1159.
- [52] M. E. McGovern, K. M. R. Kallury, M. Thompson, *Langmuir* **1994**, *10*, 3607.
- [53] T. Ohtake, N. Mino, K. Ogawa, *Langmuir* **1992**, *8*, 2081.
- [54] K. Mathauer, C. W. Frank, *Langmuir* **1993**, *9*, 3002.
- [55] K. Mathauer, C. W. Frank, *Langmuir* **1993**, *9*, 3446.
- [56] K. Bierbaum, M. Grunze, A. A. Baski, L. F. Chi, W. Schrepp, H. Fuchs, *Langmuir* **1995**, *11*, 2143.
- [57] R. Banga, J. Yarwood, A. M. Morgan, B. Evans, J. Kells, *Langmuir* **1995**, *11*, 4393.
- [58] B. C. Bunker, R. W. Carpick, R. A. Assink, M. L. Thomas, M. G. Hankins, J. A. Voigt, D. Sipola, M. P. de Boer, G. L. Gulley, *Langmuir* **2000**, *16*, 7742.
- [59] N. Rozlosnik, M. C. Gerstenberg, N. B. Larsen, *Langmuir* **2003**, *19*, 1182.
- [60] T. Vallant, H. Brunner, U. Mayer, H. Hoffmann, T. Leitner, R. Resch, G. Friedbacher, *J. Phys. Chem. B* **1998**, *102*, 7190.
- [61] T. Leitner, G. Friedbacher, T. Vallant, H. Brunner, U. Mayer, H. Hoffmann, *Mikrochim. Acta* **2000**, *133*, 331.
- [62] M. Reiniger, B. Basnar, G. Friedbacher, M. Schleberger, *Surf. Interface Anal.* **2002**, *25*, 85.
- [63] Y. Liu, L. K. Wolf, M. C. Messmer, *Langmuir* **2001**, *17*, 4329.
- [64] T. Balgar, R. Bautista, N. Hartmann, E. Hasselbrink, *Surf. Sci.* **2003**, *532*, 963.
- [65] J. V. Davidovits, V. Pho, P. Silberzan, M. Goldmann, *Surf. Sci.* **1996**, *352*, 369.
- [66] C. Carraro, O. W. Yauw, M. M. Sung, R. Maboudian, *J. Phys. Chem. B* **1998**, *102*, 4441.
- [67] M. M. Sung, C. Carraro, O. W. Yauw, Y. Kim, R. Maboudian, *J. Phys. Chem. B* **2000**, *104*, 1556.
- [68] A. Glaser, J. Foisner, G. Friedbacher, H. Hoffmann, *Anal. Bioanal. Chem.* **2004**, *379*, 653.
- [69] T. Vallant, J. Kattner, H. Brunner, U. Mayer, H. Hoffmann, *Langmuir* **1999**, *15*, 5339.
- [70] A. G. Richter, C. J. Yu, A. Datta, J. Kmetko, P. Dutta, *Colloids Surf. A* **2002**, *198*, 3.
- [71] R. Bautista, N. Hartmann, E. Hasselbrink, *Langmuir* **2003**, *19*, 6590.
- [72] M. Goldmann, J. V. Davidovits, P. Silberzan, *Thin Solid Films* **1998**, *329*, 166.
- [73] J. B. Brzoska, N. Shahidzadeh, F. Rondelez, *Nature* **1992**, *360*, 719.
- [74] J. B. Brzoska, I. Benazouz, F. Rondelez, *Langmuir* **1994**, *10*, 4367.
- [75] A. N. Parikh, D. L. Allara, I. B. Azouz, F. Rondelez, *J. Phys. Chem.* **1994**, *98*, 7577.
- [76] A. Glaser, J. Foisner, H. Hoffmann, G. Friedbacher, *Langmuir* **2004**, *20*, 5599.
- [77] M. CalistriYeh, E. J. Kramer, R. Sharma, W. Zhao, M. H. Rafailovich, J. Sokolov, J. D. Brock, *Langmuir* **1996**, *12*, 2747.
- [78] U. Srinivasan, M. R. Houston, R. T. Howe, R. Maboudian, *J. Microelectromech. Syst.* **1998**, *7*, 252.
- [79] R. W. Wang, G. Baran, S. L. Wunder, *Langmuir* **2000**, *16*, 6298.
- [80] R. W. Wang, S. L. Wunder, *J. Phys. Chem. B* **2001**, *105*, 173.
- [81] D. Devaprakasam, S. Sampath, S. K. Biswas, *Langmuir* **2004**, *20*, 1329.
- [82] N. Tillman, A. Ulman, J. S. Schildkraut, T. L. Penner, *J. Am. Chem. Soc.* **1988**, *110*, 6136.
- [83] N. Tillman, A. Ulman, T. L. Penner, *Langmuir* **1989**, *5*, 101.
- [84] M. R. Linford, C. E. D. Chidsey, *J. Am. Chem. Soc.* **1993**, *115*, 12631.
- [85] M. R. Linford, P. Fenter, P. M. Eisenberger, C. E. D. Chidsey, *J. Am. Chem. Soc.* **1995**, *117*, 3145.
- [86] S. R. Wasserman, Y. T. Tao, G. M. Whitesides, *Langmuir* **1989**, *5*, 1074.
- [87] J. R  he, V. J. Novotny, K. K. Kanazawa, T. Clarke, G. B. Street, *Langmuir* **1993**, *9*, 2383.
- [88] X. D. Xiao, J. Hu, D. H. Charych, M. Salmeron, *Langmuir* **1996**, *12*, 235.
- [89] X. D. Xiao, G. Y. Liu, D. H. Charych, M. Salmeron, *Langmuir* **1995**, *11*, 1600.
- [90] S. Ren, S. R. Yang, Y. P. Zhao, J. F. Zhou, T. Xu, W. M. Liu, *Tribol. Lett.* **2002**, *13*, 233.
- [91] D. G. Kurth, T. Bein, *Langmuir* **1993**, *9*, 2965.
- [92] T. T.-T. Li, M. J. Weaver, *J. Am. Chem. Soc.* **1984**, *106*, 6107.
- [93] B. Zhao, D. Mulkey, W. J. Brittain, Z. H. Chen, M. D. Foster, *Langmuir* **1999**, *15*, 6856.
- [94] O. Gershevit, C. N. Sukenik, *J. Am. Chem. Soc.* **2004**, *126*, 482.
- [95] C. T. Konek, M. J. Musorrafiti, H. A. Al-Abadleh, P. A. Bertin, S. T. Nguyen, F. M. Geiger, *J. Am. Chem. Soc.* **2004**, *126*, 11754.
- [96] Y. Barnes, O. Gershevit, M. Sekar, C. N. Sukenik, *Langmuir* **2000**, *16*, 247.
- [97] R. Maoz, H. Cohen, J. Sagiv, *Langmuir* **1998**, *14*, 5988.
- [98] Y. L. Wang, T. J. Su, R. Green, Y. Q. Tang, D. Styrkas, T. N. Danks, R. Bolton, J. R. Liu, *Chem. Commun.* **2000**, 587.
- [99] J. S. Park, G. S. Lee, Y. J. Lee, Y. S. Park, K. B. Yoon, *J. Am. Chem. Soc.* **2002**, *124*, 13366.
- [100] N. Tillman, A. Ulman, J. F. Elman, *Langmuir* **1989**, *5*, 1020.
- [101] M. K. Chaudhury, G. M. Whitesides, *Science* **1992**, *255*, 1230.
- [102] N. Balachander, C. N. Sukenik, *Langmuir* **1990**, *6*, 1621.
- [103] Y. W. Lee, J. Reedmundell, C. N. Sukenik, J. E. Zull, *Langmuir* **1993**, *9*, 3009.
- [104] K. Ogawa, N. Mino, H. Tamura, M. Hatada, *Langmuir* **1990**, *6*, 1807.
- [105] L. A. Wenzler, G. L. Moyes, G. N. Raikar, R. L. Hansen, J. M. Harris, T. P. Beebe, L. L. Wood, S. S. Saavedra, *Langmuir* **1997**, *13*, 3761.
- [106] J. A. Chupa, S. T. Xu, R. F. Fischetti, R. M. Strongin, J. P. McCauley, A. B. Smith, J. K. Blasie, L. J. Peticolas, J. C. Bean, *J. Am. Chem. Soc.* **1993**, *115*, 4383.
- [107] M. V. Baker, J. D. Watling, *Langmuir* **1997**, *13*, 2027.
- [108] M. T. Lee, G. S. Ferguson, *Langmuir* **2001**, *17*, 762.
- [109] V. V. Tsukruk, L. M. Lander, W. J. Brittain, *Langmuir* **1994**, *10*, 996.
- [110] G. E. Fryxell, P. C. Rieke, L. L. Wood, M. H. Engelhard, R. E. Williford, G. L. Graff, A. A. Campbell, R. J. Wiacek, L. Lee, A. Halverson, *Langmuir* **1996**, *12*, 5064.
- [111] S. Onclin, A. Mulder, J. Huskens, B. J. Ravoo, D. N. Reinhoudt, *Langmuir* **2004**, *20*, 5460.
- [112] K. Bierbaum, M. Kinzler, C. W  ll, M. Grunze, G. H  hner, S. Heid, F. Effenberger, *Langmuir* **1995**, *11*, 512.
- [113] S. P. Zhdanov, L. S. Kosheleva, T. I. Titova, *Langmuir* **1987**, *3*, 960.
- [114] K. M. Chen, W. B. Caldwell, C. A. Mirkin, *J. Am. Chem. Soc.* **1993**, *115*, 1193.
- [115] D. Q. Li, B. I. Swanson, *Langmuir* **1993**, *9*, 3341.
- [116] P. A. Heiney, K. Gruneberg, J. Y. Fang, C. Dulcey, R. Shashidhar, *Langmuir* **2000**, *16*, 2651.
- [117] J. Y. Fang, M. S. Chen, R. Shashidhar, *Langmuir* **2001**, *17*, 1549.
- [118] S. Flink, F. C. J. M. van Veggel, D. N. Reinhoudt, *J. Phys. Org. Chem.* **2001**, *14*, 407.
- [119] A. V. Krasnoslobodtsev, S. N. Smirnov, *Langmuir* **2002**, *18*, 3181.
- [120] Z. Zhang, R. Hu, Z. Liu, *Langmuir* **2000**, *16*, 1158.
- [121] R. Rosario, D. Gust, M. Hayes, F. Jahnke, J. Springer, A. A. Garcia, *Langmuir* **2002**, *18*, 8062.
- [122] B. C. Bunker, B. I. Kim, J. E. Houston, R. Rosario, A. A. Garcia, M. Hayes, D. Gust, S. T. Picraux, *Nano Lett.* **2003**, *3*, 1723.
- [123] M. H. Hu, S. Noda, T. Okubo, Y. Yamaguchi, H. Komiyama, *Appl. Surf. Sci.* **2001**, *181*, 307.
- [124] J. Y. Tseng, M. H. Lin, L. K. Chau, *Colloids Surf. A* **2001**, *182*, 239.

- [125] E. Cano-Serrano, J. M. Campos-Martin, J. L. G. Fierro, *Chem. Commun.* **2003**, 246.
- [126] Z. C. Liu, Q. G. He, P. F. Xiao, B. Liang, J. X. Tan, N. Y. He, Z. H. Lu, *Mater. Chem. Phys.* **2003**, *82*, 301.
- [127] I. Luzinov, D. Julthongpiput, A. Liebmman-Vinson, T. Cregger, M. D. Foster, V. V. Tsukruk, *Langmuir* **2000**, *16*, 504.
- [128] A. Kulak, Y. J. Lee, Y. S. Park, K. B. Yoon, *Angew. Chem.* **2000**, *112*, 980; *Angew. Chem. Int. Ed.* **2000**, *39*, 950.
- [129] S. Busse, M. DePaoli, G. Wenz, S. Mittler, *Sens. Actuators B* **2001**, *80*, 116.
- [130] O. Prucker, J. R  he, *Macromolecules* **1998**, *31*, 592.
- [131] D. H. Jung, I. J. Park, Y. K. Choi, S. B. Lee, H. S. Park, J. R  he, *Langmuir* **2002**, *18*, 6133.
- [132] B. Zhao, W. J. Brittain, *J. Am. Chem. Soc.* **1999**, *121*, 3557.
- [133] M. Husseman, E. E. Malmstrom, M. McNamara, M. Mate, D. Mecerreyes, D. G. Benoit, J. L. Hedrick, P. Mansky, E. Huang, T. P. Russel, C. J. Hawker, *Macromolecules* **1999**, *32*, 1424.
- [134] X. Huang, M. J. Wirth, *Macromolecules* **1999**, *32*, 1694.
- [135] K. Matyjaszewski, P. J. Miller, N. Shukla, B. Immraporn, A. Gelman, B. B. Luokala, T. M. Siclovan, G. Kickelbick, T. Vallant, H. Hoffmann, T. Pakula, *Macromolecules* **1999**, *32*, 8716.
- [136] E. Lindner, E. Arias, *Langmuir* **1992**, *8*, 1195.
- [137] C. P. Tripp, R. P. N. Veregin, M. L. Hair, *Langmuir* **1993**, *9*, 3518.
- [138] A. Papra, N. Gadegaard, N. B. Larsen, *Langmuir* **2001**, *17*, 1457.
- [139] Z. Yang, J. A. Galloway, H. Yu, *Langmuir* **1999**, *15*, 8405.
- [140] Y.-H. M. Chan, R. Schweiss, C. Werner, M. Grunze, *Langmuir* **2003**, *19*, 7380.
- [141] R. J. Collins, I. T. Bae, D. A. Scherson, C. N. Sukenik, *Langmuir* **1996**, *110*, 618.
- [142] S. Kato, C. Pac, *Langmuir* **1998**, *14*, 2372.
- [143] C. M. Yam, A. K. Kakkar, *Langmuir* **1999**, *15*, 3807.
- [144] R. Maoz, S. Matlis, E. DiMasi, B. M. Ocko, J. Sagiv, *Nature* **1996**, *384*, 150.
- [145] R. Maoz, J. Sagiv, *Adv. Mater.* **1998**, *10*, 580.
- [146] H. Lee, L. J. Kepley, H. G. Hong, T. E. Mallouk, *J. Am. Chem. Soc.* **1988**, *110*, 618.
- [147] H. Lee, L. J. Kepley, H. G. Hong, S. Akhter, T. E. Mallouk, *J. Phys. Chem.* **1988**, *92*, 2597.
- [148] D. Q. Li, M. A. Ratner, T. J. Marks, C. H. Zhang, J. Yang, G. K. Wong, *J. Am. Chem. Soc.* **1990**, *112*, 7389.
- [149] A. K. Kakkar, S. Yitzchaik, S. B. Roscoe, F. Kubota, D. S. Allan, T. J. Marks, W. P. Lin, G. K. Wong, *Langmuir* **1993**, *9*, 388.
- [150] S. Yitzchaik, S. B. Roscoe, A. K. Kakkar, D. S. Allan, T. J. Marks, Z. Y. Xu, T. G. Zhang, W. P. Lin, G. K. Wong, *J. Phys. Chem.* **1993**, *97*, 6958.
- [151] S. B. Roscoe, S. Yitzchaik, A. K. Kakkar, T. J. Marks, *Langmuir* **1994**, *10*, 1337.
- [152] S. Yitzchaik, T. J. Marks, *Acc. Chem. Res.* **1996**, *29*, 197.
- [153] S. B. Roscoe, A. K. Kakkar, T. J. Marks, A. Malik, M. K. Durbin, W. P. Lin, G. K. Wong, P. Dutta, *Langmuir* **1996**, *12*, 4218.
- [154] M. E. van der Boom, G. Evmenenko, C. J. Yu, P. Dutta, T. J. Marks, *Langmuir* **2003**, *19*, 10531.
- [155] N. J. van der Veen, S. Flink, M. A. Deij, R. J. M. Egberink, F. C. J. M. van Veggel, D. N. Reinhoudt, *J. Am. Chem. Soc.* **2000**, *122*, 6112.
- [156] W. Dulkeith, A. C. Morteau, T. Niedereichholtz, T. A. Klar, J. Feldmann, S. A. Levi, F. C. J. M. van Veggel, D. N. Reinhoudt, M. M  ller, D. Gittins, *Phys. Rev. Lett.* **2002**, *89*, 203002.
- [157] R. Chance, A. Prock, R. Silbey, *Adv. Chem. Phys.* **1978**, *37*, 1.
- [158] J. Kummerlen, A. Leitner, H. Brunner, F. R. Aussenegg, A. Wokaun, *Mol. Phys.* **1993**, *80*, 1031.
- [159] J. Enderlein, *Chem. Phys.* **1999**, *247*, 1.
- [160] S. Reese, M. A. Fox, *J. Phys. Chem. B* **1998**, *102*, 9820.
- [161] L. N. Gao, Y. Fang, X. P. Wen, Y. G. Li, D. D. Hu, *J. Phys. Chem. B* **2004**, *108*, 1207.
- [162] M. Ayadim, J. L. H. Jiwan, A. P. de Silva, J. P. Soumillion, *Tetrahedron Lett.* **1996**, *37*, 7039.
- [163] D. W. J. McCallien, P. L. Burn, H. L. Anderson, *J. Chem. Soc. Perkin Trans. 1* **1997**, 2581.
- [164] D. L. Pilloud, C. C. Moser, K. S. Reddy, P. L. Dutton, *Langmuir* **1998**, *14*, 4809.
- [165] A. Bianco, F. Gasparrini, M. Maggini, D. Misiti, A. Polese, M. Prato, G. Scorrano, C. Toniolo, C. Villani, *J. Am. Chem. Soc.* **1997**, *119*, 7550.
- [166] D. Q. Li, M. Ma, *Sens. Actuators B* **2000**, *69*, 75.
- [167] C. M. Rudzinski, A. M. Young, D. G. Nocera, *J. Am. Chem. Soc.* **2002**, *124*, 1723.
- [168] S. Flink, F. C. J. M. van Veggel, D. N. Reinhoudt, *Chem. Commun.* **1999**, 2229.
- [169] M. Crego-Calama, D. N. Reinhoudt, *Adv. Mater.* **2001**, *13*, 1171.
- [170] L. Basabe-Desmonts, J. Beld, R. S. Zimmerman, J. Hernando, P. Mela, M. F. Garc  a Paraj  , N. F. Van Hulst, A. Van den Berg, D. N. Reinhoudt, M. Crego-Calama, *J. Am. Chem. Soc.* **2004**, *126*, 7293.
- [171] E. Brasola, F. Mancin, E. Rampazzo, P. Tecilla, U. Tonellato, *Chem. Commun.* **2003**, 3026.
- [172] M. C. Pirrung, *Angew. Chem.* **2002**, *114*, 1326; *Angew. Chem. Int. Ed.* **2002**, *41*, 1276.
- [173] D. S. Wilson, S. Nock, *Angew. Chem.* **2003**, *115*, 510; *Angew. Chem. Int. Ed.* **2003**, *42*, 494.
- [174] T. P. Sullivan, W. T. S. Huck, *Eur. J. Org. Chem.* **2003**, 17.
- [175] S. Margel, O. Sivan, Y. Dolitzky, *Langmuir* **1991**, *7*, 2317.
- [176] Y. Belosludtsev, B. Iverson, S. Lemesko, R. Eggers, R. Wiese, S. Lee, T. Powdrill, M. Hogan, *Anal. Biochem.* **2001**, *292*, 250.
- [177] N. Zammateo, L. Jeanmart, S. Hamels, S. Courtois, P. Louette, L. Hevesi, J. Remacle, *Anal. Biochem.* **2000**, *280*, 143.
- [178] S. Tasker, G. Matthijs, M. C. Davies, C. J. Roberts, E. H. Schacht, S. J. B. Tandler, *Langmuir* **1996**, *12*, 6436.
- [179] D. Barnes-Seeman, S. B. Park, A. N. Koehler, S. L. Schreiber, *Angew. Chem.* **2003**, *115*, 2478; *Angew. Chem. Int. Ed.* **2003**, *42*, 2376.
- [180] N. Kanoh, S. Kumashiro, S. Simizu, Y. Kondoh, S. Hatakeyama, H. Tashiro, H. Osada, *Angew. Chem.* **2003**, *115*, 5742; *Angew. Chem. Int. Ed.* **2003**, *42*, 5584.
- [181] H. G. Hong, P. W. Bohn, S. G. Sligar, *Anal. Chem.* **1993**, *65*, 1635.
- [182] H. G. Hong, M. Jiang, S. G. Sligar, P. W. Bohn, *Langmuir* **1994**, *10*, 153.
- [183] G. MacBeath, A. N. Koehler, S. L. Schreiber, *J. Am. Chem. Soc.* **1999**, *121*, 7967.
- [184] V. Benoit, A. Steel, M. Torres, Y. Y. Lu, H. J. Yang, J. Cooper, *Anal. Chem.* **2001**, *73*, 2412.
- [185] M. J. O'Donnell, K. Tang, H. Koster, C. L. Smith, C. R. Cantor, *Anal. Chem.* **1997**, *69*, 2438.
- [186] M. B. A. Sekar, P. D. Hampton, T. Buranda, G. P. Lopez, *J. Am. Chem. Soc.* **1999**, *121*, 5135.
- [187] R. Benders, C. M. Niemeyer, D. W  hrle, *ChemBioChem* **2001**, *2*, 686.
- [188] M. K  hn, R. Wacker, C. Peters, H. Schr  der, L. Sou  re, R. Breinbauer, C. M. Niemeyer, H. Waldmann, *Angew. Chem.* **2003**, *115*, 6010; *Angew. Chem. Int. Ed.* **2003**, *42*, 5830.
- [189] M. B. Soellner, K. A. Dickson, B. L. Nilsson, R. T. Raines, *J. Am. Chem. Soc.* **2003**, *125*, 11790.
- [190] D. Leipert, D. Nopper, M. Bauser, G. Gauglitz, G. Jung, *Angew. Chem.* **1998**, *110*, 3503; *Angew. Chem. Int. Ed.* **1998**, *37*, 3308.
- [191] M. Elbs, R. Brock, *Anal. Chem.* **2003**, *75*, 4793.
- [192] R. A. Potyrailo, R. C. Conrad, A. D. Ellington, G. M. Hieftje, *Anal. Chem.* **1998**, *70*, 3419.
- [193] G. MacBeath, S. L. Schreiber, *Science* **2000**, *289*, 1760.

- [194] C. M. Salisbury, D. J. Maly, J. A. Ellman, *J. Am. Chem. Soc.* **2002**, *124*, 14868.
- [195] D. L. Pilloud, F. Rabanal, B. R. Gibney, R. S. Farid, P. L. Dutton, C. C. Moser, *J. Phys. Chem. B* **1998**, *102*, 1926.
- [196] Y. H. Rogers, P. Jiang-Baucom, Z. J. Huang, V. Bogdanov, S. Anderson, M. T. Boyce-Jacino, *Anal. Biochem.* **1999**, *266*, 23.
- [197] P. S. Stayton, J. M. Olinger, M. Jiang, P. W. Bohn, S. G. Sligar, *J. Am. Chem. Soc.* **1992**, *114*, 9298.
- [198] P. J. Hergenrother, K. M. Depew, S. L. Schreiber, *J. Am. Chem. Soc.* **2000**, *122*, 7849.
- [199] M. C. Pirrung, J. D. Davis, A. L. Odenbaugh, *Langmuir* **2000**, *16*, 2185.
- [200] D. S. Ginger, H. Zhang, C. A. Mirkin, *Angew. Chem.* **2004**, *116*, 30; *Angew. Chem. Int. Ed.* **2004**, *43*, 30.
- [201] A. Y. Fadeev, T. J. McCarthy, *Langmuir* **1999**, *15*, 7238.
- [202] F. Q. Fan, C. Maldarelli, A. Couzis, *Langmuir* **2003**, *19*, 3254.
- [203] K. R. Finnie, R. G. Nuzzo, *Langmuir* **2001**, *17*, 1250.
- [204] J. P. Lee, Y. J. Jang, M. M. Sung, *Adv. Funct. Mater.* **2003**, *13*, 873.
- [205] N. Kumar, C. Maldarelli, C. Steiner, A. Couzis, *Langmuir* **2001**, *17*, 7789.
- [206] J. Buseman-Williams, J. C. Berg, *Langmuir* **2004**, *20*, 2026.
- [207] Z. D. Xiao, C. Z. Cai, A. Mayeux, A. Milenkovic, *Langmuir* **2002**, *18*, 7728.
- [208] C. M. Yam, A. Mayeux, A. Milenkovic, C. Z. Cai, *Langmuir* **2002**, *18*, 10274.
- [209] B. J. Hong, J. Y. Shim, S. J. Oh, J. W. Park, *Langmuir* **2003**, *19*, 2357.
- [210] C. S. Dulcey, J. H. Georger, V. Krauthamer, D. A. Stenger, T. L. Fare, J. M. Calvert, *Science* **1991**, *252*, 551.
- [211] D. A. Stenger, J. H. Georger, C. S. Dulcey, J. J. Hickman, A. S. Rudolph, T. B. Nielsen, S. M. McCort, J. M. Calvert, *J. Am. Chem. Soc.* **1992**, *114*, 8435.
- [212] N. Saito, K. Hayashi, H. Sugimura, O. Takai, N. Nakagiri, *Chem. Phys. Lett.* **2001**, *349*, 172.
- [213] K. Hayashi, N. Saito, H. Sugimura, O. Takai, N. Nakagiri, *Langmuir* **2002**, *18*, 7469.
- [214] H. Sugimura, K. Ushiyama, A. Hozumi, O. Takai, *Langmuir* **2000**, *16*, 885.
- [215] H. Sugimura, T. Hanji, O. Takai, T. Masuda, H. Misawa, *Electrochim. Acta* **2001**, *47*, 103.
- [216] N. Saito, H. Haneda, T. Sekiguchi, N. Ohashi, I. Sakaguchi, K. Koumoto, *Adv. Mater.* **2002**, *14*, 418.
- [217] Y. Masuda, W. S. Seo, K. Koumoto, *Langmuir* **2001**, *17*, 4876.
- [218] J. P. Lee, M. M. Sung, *J. Am. Chem. Soc.* **2004**, *126*, 28.
- [219] U. Jonas, A. del Campo, C. Krüger, G. Glasser, D. Boos, *Proc. Natl. Acad. Sci. USA* **2002**, *99*, 5034.
- [220] M. Nakagawa, K. Ichimura, *Colloids Surf. A* **2002**, *204*, 1.
- [221] M. C. Pirrung, *Chem. Rev.* **1997**, *97*, 473.
- [222] S. P. A. Fodor, J. L. Read, M. C. Pirrung, L. Stryer, A. T. Lu, D. Solas, *Science* **1991**, *251*, 767.
- [223] A. Pease, D. Solas, E. Sullivan, M. Cronin, C. Holmes, S. Fodor, *Proc. Natl. Acad. Sci. USA* **1994**, *91*, 5022.
- [224] G. McGall, J. Labadie, P. Brock, G. Wallraff, T. Nguyen, W. Hinsberg, *Proc. Natl. Acad. Sci. USA* **1996**, *93*, 13555.
- [225] G. H. McGall, A. D. Barone, M. Diggelmann, S. P. A. Fodor, E. Gentalen, N. Ngo, *J. Am. Chem. Soc.* **1997**, *119*, 5081.
- [226] S. L. Brandow, M. S. Chen, R. Aggarwal, C. S. Dulcey, J. M. Calvert, W. J. Dressick, *Langmuir* **1999**, *15*, 5429.
- [227] B. Zhao, J. S. Moore, D. J. Beebe, *Science* **2001**, *291*, 1023.
- [228] B. Zhao, J. S. Moore, D. J. Beebe, *Anal. Chem.* **2002**, *74*, 4259.
- [229] B. Zhao, N. O. L. Viernes, J. S. Moore, D. J. Beebe, *J. Am. Chem. Soc.* **2002**, *124*, 5284.
- [230] T. Balgar, S. Franzka, N. Hartmann, E. Hasselbrink, *Langmuir* **2004**, *20*, 3525.
- [231] M. J. Lercel, R. C. Tiberio, P. F. Chapman, H. G. Craighead, C. W. Sheen, A. N. Parikh, D. L. Allara in *Proceedings of the 16th international symposium on electron, ion, and photon beams*, Vol. 11, AVS, San Diego, California (USA), **1993**, 2823.
- [232] M. J. Lercel, G. F. Redinbo, F. D. Pardo, M. Rooks, R. C. Tiberio, P. Simpson, H. G. Craighead, C. W. Sheen, A. N. Parikh, D. L. Allara, *J. Vac. Sci. Technol. B* **1994**, *12*, 3663.
- [233] P. M. StJohn, H. G. Craighead, *J. Vac. Sci. Technol. B* **1996**, *14*, 69.
- [234] M. J. Lercel, H. G. Craighead, A. N. Parikh, K. Seshadri, D. L. Allara, *Appl. Phys. Lett.* **1996**, *68*, 1504.
- [235] C. R. K. Marrian, F. K. Perkins, S. L. Brandow, T. S. Koloski, E. A. Dobisz, J. M. Calvert, *Appl. Phys. Lett.* **1994**, *64*, 390.
- [236] C. K. Harnett, K. M. Satyalakshmi, H. G. Craighead, *Appl. Phys. Lett.* **2000**, *76*, 2466.
- [237] T. Sato, D. G. Hasko, H. Ahmed, *J. Vac. Sci. Technol. B* **1997**, *15*, 45.
- [238] K. H. Choi, J. P. Bourgoin, S. Auvray, D. Esteve, G. S. Duesberg, S. Roth, M. Burghard, *Surf. Sci.* **2000**, *462*, 195.
- [239] R. Krupke, S. Malik, H. B. Weber, O. Hampe, M. M. Kappes, H. von Löhneysen, *Nano Lett.* **2002**, *2*, 1161.
- [240] Y. J. Jung, Y. H. La, H. J. Kim, T. H. Kang, K. Ihm, K. J. Kim, B. Kim, J. W. Park, *Langmuir* **2003**, *19*, 4512.
- [241] I. S. Maeng, J. W. Park, *Langmuir* **2003**, *19*, 4519.
- [242] P. M. Mendes, S. Jacke, K. Critchley, J. Plaza, Y. Chen, K. Nikitin, R. E. Palmer, J. A. Preece, S. D. Evans, D. Fitzmaurice, *Langmuir* **2004**, *20*, 3766.
- [243] X. J. Wang, W. C. Hu, R. Ramasubramaniam, G. H. Bernstein, G. Snider, M. Lieberman, *Langmuir* **2003**, *19*, 9748.
- [244] A. Pallandre, K. Glinel, A. M. Jonas, B. Nysten, *Nano Lett.* **2004**, *4*, 365.
- [245] R. L. Kubena, J. W. Ward, F. P. Stratton, R. J. Joyce, G. M. Atkinson, *J. Vac. Sci. Technol. B* **1991**, *9*, 3079.
- [246] R. L. Kubena, R. J. Joyce, J. W. Ward, H. L. Garvin, F. P. Stratton, R. G. Brault, *J. Vac. Sci. Technol. B* **1988**, *6*, 353.
- [247] P. C. Rieke, B. J. Tarasevich, L. L. Wood, M. H. Engelhard, D. R. Baer, G. E. Fryxell, C. M. John, D. A. Laken, M. C. Jaehrig, *Langmuir* **1994**, *10*, 619.
- [248] E. T. Ada, L. Hanley, S. Etchin, J. Melngailis, W. J. Dressick, M.-S. Chen, J. M. Calvert, *J. Vac. Sci. Technol. B* **1995**, *13*, 2189.
- [249] T. Schenkel, M. Schneider, M. Hattass, M. W. Newman, A. V. Barnes, A. V. Hamza, D. H. Schneider, R. L. Cicero, C. E. D. Chidsey, *J. Vac. Sci. Technol. B* **1998**, *16*, 3298.
- [250] R. Younkin, K. K. Berggren, K. S. Johnson, M. Prentiss, D. C. Ralph, G. M. Whitesides, *Appl. Phys. Lett.* **1997**, *71*, 1261.
- [251] D. Suh, J. K. Simons, J. W. Taylor, T. S. Koloski, J. M. Calvert in *Proceedings of the 16th international symposium on electron, ion, and photon beams*, Vol. 11, AVS, San Diego, California (USA), **1993**, 2850.
- [252] W. J. Dressick, C. S. Dulcey, S. L. Brandow, H. Witschi, P. F. Neeley, *J. Vac. Sci. Technol. A* **1999**, *17*, 1432.
- [253] Y. H. La, H. J. Kim, I. S. Maeng, Y. J. Jung, J. W. Park, K. J. Kim, T. H. Kang, B. Kim, *Langmuir* **2002**, *18*, 2430.
- [254] Y. H. La, Y. J. Jung, H. J. Kim, T. H. Kang, K. Ihm, K. J. Kim, B. Kim, J. W. Park, *Langmuir* **2003**, *19*, 4390.
- [255] X. M. Yang, R. D. Peters, T. K. Kim, P. F. Nealey, S. L. Brandow, M. S. Chen, L. M. Shirey, W. J. Dressick, *Langmuir* **2001**, *17*, 228.
- [256] S. O. Kim, H. H. Solak, M. P. Stoykovich, N. J. Ferrier, J. J. de Pablo, P. F. Nealey, *Nature* **2003**, *424*, 411.
- [257] Y. N. Xia, G. M. Whitesides, *Angew. Chem.* **1998**, *110*, 568; *Angew. Chem. Int. Ed.* **1998**, *37*, 551.
- [258] Y. N. Xia, J. A. Rogers, K. E. Paul, G. M. Whitesides, *Chem. Rev.* **1999**, *99*, 1823.
- [259] Y. N. Xia, M. Mrksich, E. Kim, G. M. Whitesides, *J. Am. Chem. Soc.* **1995**, *117*, 9576.
- [260] P. M. S. John, H. G. Craighead, *Appl. Phys. Lett.* **1996**, *68*, 1022.
- [261] D. Wang, S. G. Thomas, K. L. Wang, Y. Xia, G. M. Whitesides, *Appl. Phys. Lett.* **1997**, *70*, 1593.

- [262] N. L. Jeon, K. Finnie, K. Branshaw, R. G. Nuzzo, *Langmuir* **1997**, *13*, 3382.
- [263] K. R. Finnie, R. Haasch, R. G. Nuzzo, *Langmuir* **2000**, *16*, 6968.
- [264] Y. Harada, G. S. Girolami, R. G. Nuzzo, *Langmuir* **2003**, *19*, 5104.
- [265] T. Pfohl, J. H. Kim, M. Yasa, H. P. Miller, G. C. L. Wong, F. Bringezu, Z. Wen, L. Wilson, M. W. Kim, Y. Li, C. R. Safinya, *Langmuir* **2001**, *17*, 5343.
- [266] N. L. Jeon, P. G. Clem, D. A. Payne, R. G. Nuzzo, *Langmuir* **1996**, *12*, 5350.
- [267] C. E. Moran, C. Radloff, N. J. Halas, *Adv. Mater.* **2003**, *15*, 804.
- [268] P. C. Hidber, W. Helbig, E. Kim, G. M. Whitesides, *Langmuir* **1996**, *12*, 1375.
- [269] T. Auletta, B. Dordi, A. Mulder, A. Sartori, S. Onclin, C. M. Bruinink, M. Péter, C. A. Nijhuis, H. Beijleveld, H. Schönher, G. J. Vancso, A. Casnati, R. Ungaro, B. J. Ravoo, J. Huskens, N. F. Van Hulst, D. N. Reinhoudt, *Angew. Chem.* **2004**, *116*, 373; *Angew. Chem. Int. Ed.* **2004**, *43*, 369.
- [270] A. Mulder, S. Onclin, M. Péter, J. P. Hoogenboom, H. Beijleveld, J. ter Maat, M. F. García Parajó, B. J. Ravoo, J. Huskens, N. F. van Hulst, D. N. Reinhoudt, *Small* **2005**, *1*, 242.
- [271] V. Mahalingam, S. Onclin, M. Péter, B. J. Ravoo, J. Huskens, D. N. Reinhoudt, *Langmuir* **2004**, *20*, 11756.
- [272] Y. L. Loo, R. L. Willett, K. W. Baldwin, J. A. Rogers, *J. Am. Chem. Soc.* **2002**, *124*, 7654.
- [273] E. Delamarche, M. Geissler, R. H. Magnuson, H. Schmid, B. Michel, *Langmuir* **2003**, *19*, 5892.
- [274] E. Delamarche, M. Geissler, J. Vichiconti, W. S. Graham, P. A. Andry, J. C. Flake, P. M. Fryer, R. W. Nunes, B. Michel, E. J. O'Sullivan, H. Schmid, H. Wolf, R. L. Wisnieff, *Langmuir* **2003**, *19*, 5923.
- [275] M. Geissler, H. Kind, P. Schmidt-Winkel, B. Michel, E. Delamarche, *Langmuir* **2003**, *19*, 6283.
- [276] M. Geissler, H. Wolf, R. Stutz, E. Delamarche, U. W. Grummt, B. Michel, A. Bietsch, *Langmuir* **2003**, *19*, 6301.
- [277] E. Delamarche, J. Vichiconti, S. A. Hall, M. Geissler, W. Graham, B. Michel, R. Nunes, *Langmuir* **2003**, *19*, 6567.
- [278] S. Y. Chou, P. R. Krauss, P. J. Renstrom, *Science* **1996**, *272*, 85.
- [279] P. Maury, M. Péter, V. Mahalingam, D. N. Reinhoudt, J. Huskens, *Adv. Funct. Mater.* **2005**, *15*, 451.
- [280] S. Kramer, R. R. Fuieler, C. B. Gorman, *Chem. Rev.* **2003**, *103*, 4367.
- [281] H. Sugimura, N. Nakagiri, N. Ichinose, *Appl. Phys. Lett.* **1995**, *66*, 3686.
- [282] H. Sugimura, N. Nakagiri, *J. Am. Chem. Soc.* **1997**, *119*, 9226.
- [283] H. Sugimura, T. Hanji, K. Hayashi, O. Takai, *Adv. Mater.* **2002**, *14*, 524.
- [284] A. Inoue, T. Ishida, N. Choi, W. Mizutani, H. Tokumoto, *Appl. Phys. Lett.* **1998**, *73*, 1976.
- [285] R. Maoz, E. Frydman, S. R. Cohen, J. Sagiv, *Adv. Mater.* **2000**, *12*, 424.
- [286] R. Maoz, S. R. Cohen, J. Sagiv, *Adv. Mater.* **1999**, *11*, 55.
- [287] R. Maoz, E. Frydman, S. R. Cohen, J. Sagiv, *Adv. Mater.* **2000**, *12*, 725.
- [288] S. T. Liu, R. Maoz, G. Schmid, J. Sagiv, *Nano Lett.* **2002**, *2*, 1055.
- [289] S. Hoepfner, R. Maoz, S. R. Cohen, L. F. Chi, H. Fuchs, J. Sagiv, *Adv. Mater.* **2002**, *14*, 1036.
- [290] C. S. Liu, R. Maoz, J. Sagiv, *Nano Lett.* **2004**, *4*, 845.
- [291] S. Hoepfner, R. Maoz, J. Sagiv, *Nano Lett.* **2003**, *3*, 761.
- [292] D. Wouters, U. S. Schubert, *Langmuir* **2003**, *19*, 9033.
- [293] Z. M. Fresco, I. Suez, S. A. Backer, J. M. J. Frechet, *J. Am. Chem. Soc.* **2004**, *126*, 8374.
- [294] W. T. Müller, D. L. Klein, T. Lee, J. Clarke, P. L. McEuen, P. G. Schultz, *Science* **1995**, *268*, 272.
- [295] R. D. Piner, J. Zhu, F. Xu, S. H. Hong, C. A. Mirkin, *Science* **1999**, *283*, 661.
- [296] A. Ivanisevic, C. A. Mirkin, *J. Am. Chem. Soc.* **2001**, *123*, 7887.
- [297] D. J. Pena, M. P. Raphael, J. M. Byers, *Langmuir* **2003**, *19*, 9028.
- [298] H. Jung, R. Kulkarni, C. P. Collier, *J. Am. Chem. Soc.* **2003**, *125*, 12096.
- [299] L. M. Demers, D. S. Ginger, S.-J. Park, Z. Li, S.-W. Chung, C. A. Mirkin, *Science* **2002**, *296*, 1836.
- [300] H. Jung, C. K. Dalal, S. Kuntz, R. Shah, C. P. Collier, *Nano Lett.* **2004**, *4*, 2171.
- [301] J. H. Lim, D. S. Ginger, K. B. Lee, J. Heo, J. M. Nam, C. A. Mirkin, *Angew. Chem.* **2003**, *115*, 2411; *Angew. Chem. Int. Ed.* **2003**, *42*, 2309.

Communications



1,2,3-Tridehydrobenzene, a novel triradical derived from benzene, was isolated and spectroscopically characterized in cryogenic neon matrices. The IR spectra are in accordance with a 2A_1 ground state, whereas the 2B_2 excited state is 1–2 kcal mol $^{-1}$ higher in energy and not observed under these conditions. For more information, see the Communication by W. Sander and co-workers on the following pages.

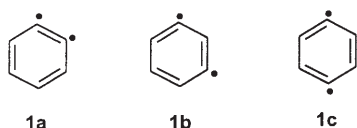
DOI: 10.1002/anie.200501912

1,2,3-Tridehydrobenzene**

Sugumar Venkataramani, Michael Winkler, and
Wolfram Sander*

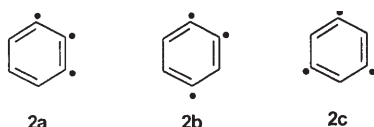
In memory of Orville Chapman

Didehydrobenzenes (benzynes) **1** are well-established reactive intermediates in organic synthesis that have been the target of a large number of mechanistic studies.^[1–3] The singlet–triplet splittings in the three isomers **1a–c** were



determined by negative-ion photoelectron spectroscopy to be 37.5 ± 0.3 , 21.0 ± 0.3 , and 3.8 ± 0.5 kcal mol^{−1}, respectively.^[4] These values indicate that the stabilizing interactions of the radical centers in the singlet ground states of **1** decrease in the order *ortho* > *meta* > *para*. This bonding interaction results in a shortening of the 1,2-bond (the formal triple bond) in **1a** and a trapezoid deformation with a comparatively short C1–C3 distance (205 ± 5 pm) in **1b**.^[5–8]

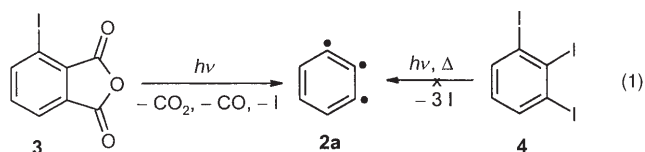
The addition of a third radical center to form tridehydrobenzenes **2** results in more-complicated electronic structures with several close-lying low-spin (doublet) and high-spin (quartet) states. In a recent computational study, Krylov and co-workers found that all three isomers **2a–c** prefer low-spin



doublet ground states with partial bonds between the radical centers.^[9] Again, the adiabatic energy difference between high-spin and low-spin states (i.e. the doublet–quartet splitting) can be taken as a measure of the interaction between the three unpaired electrons in the low-spin states. According to these calculations, **2a** has a ²B₂ ground state, and the doublet–

quartet splitting is as high as 2.1–2.2 eV, the largest in the series of the tridehydrobenzenes.^[9]

Thermodynamic data for 1,3,5-tridehydrobenzene **2c** were determined by Wenthold and co-workers by means of collision-induced dissociation in a flowing afterglow apparatus.^[10] According to these measurements, **2c** is best described as a phenyl radical that interacts only weakly with a *meta*-didehydrobenzene unit on the opposite side of the ring. None of the three isomers had so far been isolated or spectroscopically characterized. Herein we describe the matrix isolation and IR spectroscopic characterization of 1,2,3-tridehydrobenzene (**2a**). We selected 3-iodophthalic anhydride (**3**) and 1,2,3-triiodobenzene (**4**) as photochemical precursors for **2a** [Eq. (1)].^[11,12]



Phthalic anhydrides have frequently been used to generate **1a** and its derivatives in inert gas matrices.^[13–15] Iodoarenes, on the other hand, undergo photochemical or thermal cleavage of the C–I bond and are thus precursors for aryl radicals and diradicals.^[15–17] A general problem in the matrix photolysis of iodoarenes is the rapid thermal recombination of the aryl radicals with the iodine atoms which thus lowers the yield of the radicals. In several instances the yields of radicals increased when the photolysis was carried out in neon matrices at 3 K instead of in the more-common argon matrices at 10 K. As this matrix effect is as yet not well understood or predictable, we investigated the photolysis of **3** and **4** in argon, nitrogen, and neon matrices.

Photolysis of **3**, matrix-isolated in argon at 10 K, with the 308-nm light of a XeCl excimer laser produced CO₂, CO, and 3-iodo-1,2-didehydrobenzene **5** as the major product [Eq. (2)]. The latter exhibits strong IR absorptions at $\tilde{\nu} = 1387$, 1076, 848, 754, and 473 cm^{−1}, in good agreement with the values calculated at the B3LYP/6-311G(d,p) level of theory (Table 1). A further product is 3-dehydrophthalic anhydride (**6**), which again was identified by comparison of its IR spectrum with DFT calculations. In nitrogen the yield of radical **6** is lower, and benzyne **5** is formed almost exclusively (besides CO₂ and CO).

Continuous irradiation at $\lambda = 308$ nm in argon or nitrogen at 10 K did not lead to **2a** or other C₆H₃ isomers. Irradiation at shorter wavelength ($\lambda = 248$ nm) resulted in the formation of several ring-opened alkyne products with characteristic C≡C–H stretching vibrations at $\tilde{\nu} \approx 3300$ cm^{−1}. Hexatriyne (**7**) was tentatively identified as one of these products.

Irradiation of **3** in neon at 3 K with $\lambda = 308$ nm produced the same major products **5** and **6** as in argon. However, the yield of radical **6** was now higher than in argon. Irradiation of this matrix, which contained **5** and **6**, at shorter wavelength (248-nm KrF or 193-nm ArF excimer lasers) resulted in a decrease in the intensity of all the IR bands assigned to these species and in the appearance of several new absorptions.^[18] Three of these bands ($\tilde{\nu} = 1698$, 753, and 524 cm^{−1}; Table 2)

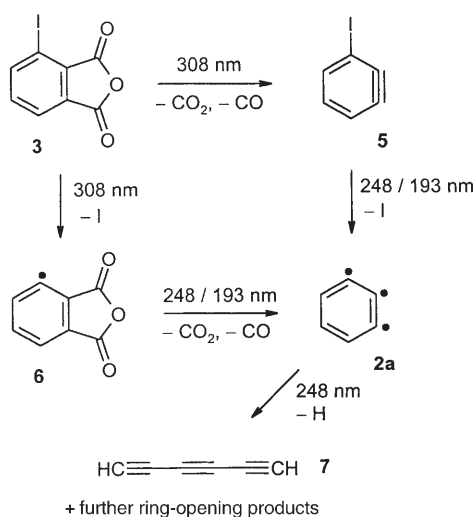
[*] S. Venkataramani, Dr. M. Winkler, Prof. Dr. W. Sander
Lehrstuhl für Organische Chemie II
Ruhr-Universität Bochum
44 780 Bochum (Germany)
Fax: (+49) 234-321-4353
E-mail: wolfram.sander@rub.de

[**] This work was financially supported by the Deutsche Forschungsgemeinschaft and the Fonds der Chemischen Industrie.

Table 1: Calculated and measured (Ne, 3 K) IR data of **5** and **6**.

5						6					
Mode	Sym.	ν_{calcd} [cm ⁻¹] ^[a]	$I_{\text{rel,calcd}}$ ^[b]	ν_{exp} [cm ⁻¹]	$I_{\text{rel,exp}}$ ^[b]	Mode	Sym.	ν_{calcd} [cm ⁻¹] ^[a]	$I_{\text{rel,calcd}}$ ^[b]	ν_{exp} [cm ⁻¹]	$I_{\text{rel,exp}}$ ^[b]
4	<i>a'</i>	440.9	100	475	70	8	<i>a'</i>	534	1	528	10
8	<i>a'</i>	666.5	13	652	20	9	<i>a'</i>	545	1	538	10
9	<i>a''</i>	770.7	38	760	20	10	<i>a'</i>	638	1	631	5
10	<i>a'</i>	848.0	58	850	100	11	<i>a''</i>	646	1	637	5
13	<i>a'</i>	1032.3	4	1013	< 5	12	<i>a'</i>	682	1	672	5
14	<i>a'</i>	1098.3	33	1078	35	13	<i>a''</i>	737	12	723	40
16	<i>a'</i>	1182.4	6	1163	5	16	<i>a''</i>	801	2	770	5
18	<i>a'</i>	1420.4	47	1390	45	17	<i>a'</i>	834	1	828	< 5
20	<i>a'</i>	1461.5	9	1443	15	18	<i>a'</i>	910	38	915	100
21	<i>a'</i>	2000.9	23	1840	5	21	<i>a'</i>	1049	1	1027	5
						22	<i>a'</i>	1087	1	1064	5
						23	<i>a'</i>	1138	10	1122	30
						25	<i>a'</i>	1232	8	[c]	
						26	<i>a'</i>	1262	35	1251	90
						27	<i>a'</i>	1359	6	1325	40
						28	<i>a'</i>	1454	1	1430	5
						32	<i>a'</i>	1858	100	[c]	
						33	<i>a'</i>	1915	36	[c]	

[a] Unscaled frequencies calculated at the (U)B3LYP/6-311G(d,p) level of theory. [b] Relative intensity based on the most intense absorption. [c] Peaks coincide with absorptions of the precursor.



disappeared upon warming the neon matrix from 3 K to 8 K (annealing to allow diffusion of small trapped species) or upon broad-band UV irradiation at $\lambda > 350 \text{ nm}$ (Figure 1). Simultaneously, iodobenzene (**5**) was formed as the principal product. Furthermore, radical **6** disappeared and some starting material **3** was reformed, thus confirming that radical recombination with iodine atoms takes place under these conditions. Prolonged irradiation at $\tilde{\nu} = 193 \text{ nm}$ also led to the disappearance of the newly formed

IR signals. However, the principal products are now terminal alkynes formed by opening of the benzene ring. These results clearly indicate that a new, labile compound with properties expected for triradical **2a** was generated and isolated in a neon matrix at 3 K.

To assign the three IR signals conclusively to **2a**, extensive quantum-chemical calculations at various levels of theory were performed (Table 3).^[19] Two low-lying doublet states have to be considered that arise from single occupation of the

Table 2: IR spectroscopic data of **2a** (Ne, 3 K). Calculated vibrational spectra of the 2A_1 -**2a** and 2B_2 -**2a**.

Mode	Sym.	² A ₁		Ne, 3 K		Sym.	² B ₂	
		$\tilde{\nu}$ [cm ⁻¹] ^[a]	<i>I</i> _{rel} ^[b]	$\tilde{\nu}$ [cm ⁻¹]	<i>I</i> _{rel} ^[b]		$\tilde{\nu}$ [cm ⁻¹] ^[a]	<i>I</i> _{rel} ^[b]
1	<i>b</i> ₁	356.2	0	524	85	<i>b</i> ₁	388.8	2
2	<i>a</i> ₁	399.3	17			<i>a</i> ₂	433.9	0
3	<i>b</i> ₂	521.8	94			<i>b</i> ₂	440.8	65
4	<i>a</i> ₂	548.3	0			<i>b</i> ₁	533.7	5
5	<i>b</i> ₁	555.4	2	753	100	<i>a</i> ₁	565.0	3
6	<i>b</i> ₁	742.4	100			<i>b</i> ₁	738.1	100
7	<i>a</i> ₂	778.5	0			<i>a</i> ₁	816.7	4
8	<i>a</i> ₁	809.2	0			<i>a</i> ₂	838.3	0
9	<i>b</i> ₂	893.9	14	1698	30	<i>b</i> ₁	915.1	0
10	<i>b</i> ₁	902.8	1			<i>a</i> ₁	992.6	0
11	<i>a</i> ₁	1041.3	4			<i>b</i> ₂	1084.6	19
12	<i>a</i> ₁	1048.7	4			<i>a</i> ₁	1090.3	24
13	<i>b</i> ₂	1076.3	3			<i>b</i> ₂	1138.3	4
14	<i>b</i> ₂	1256.4	0			<i>b</i> ₂	1256.9	2
15	<i>b</i> ₂	1319.1	3			<i>a</i> ₁	1364.1	0
16	<i>a</i> ₁	1375.8	5			<i>b</i> ₂	1384.9	6
17	<i>b</i> ₂	1468.7	18			<i>b</i> ₂	1483.2	5
18	<i>a</i> ₁	1711.6	39			<i>a</i> ₁	1518.8	0
19	<i>a</i> ₁	3075.3	22			<i>a</i> ₁	3085.1	1
20	<i>b</i> ₂	3142.4	3			<i>b</i> ₂	3107.2	10
21	<i>a</i> ₁	3145.3	4	<i>a</i> ₁	3113.1	15		

[a] Unscaled frequencies calculated at the UBLYP/cc-pVTZ level of theory. [b] Relative intensity based on the most intense absorption.

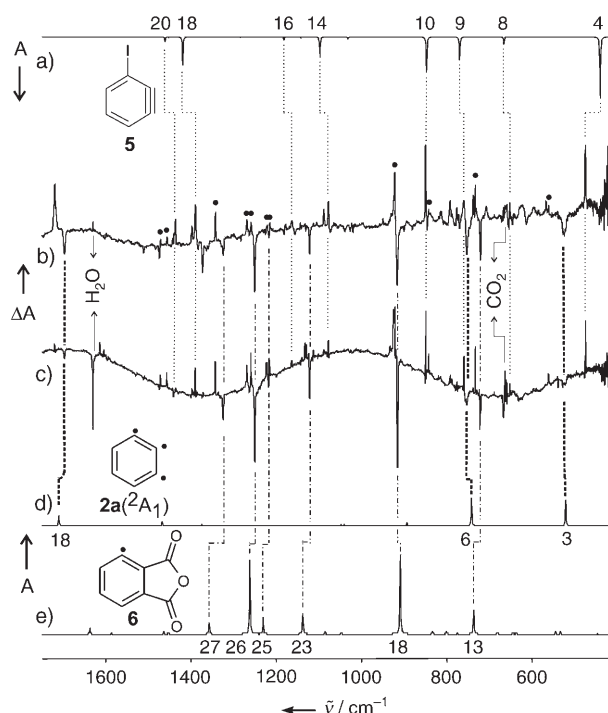


Figure 1. a) Calculated IR spectrum (B3LYP/6-311G(d,p)) of **5**. b) Difference IR spectrum of a matrix containing the photolysis products of **3** (Ne, 3 K). Bands pointing downwards decrease in intensity during broad band irradiation (350–450 nm). Black dots indicate bands assigned to **3**. c) Difference IR spectrum of a matrix containing the photolysis products ($\lambda = 308, 248$ nm) of **3** (Ne, 3 K). Bands pointing downwards decrease in intensity upon warming the matrix to 8 K. d) Calculated IR spectrum (UBLYP/cc-pVTZ) of **2a** (2A_1). e) Calculated IR spectrum (B3LYP/6-311G(d,p)) of **6**.

$11a_1$ or $7b_2$ orbitals at small and large C1–C3 distances, respectively (Figure 2). The 2A_1 state resembles a bicyclo-[3.1.0]hexatriene system with a relatively short C1–C3

Table 3: Relative stabilities of the 2A_1 and 2B_2 states of **2a** [$E_0(^2A_1) - E_0(^2B_2)$].^[a]

Method	cc-pVDZ	cc-pVTZ	cc-pVQZ
UB3PW91	5.6 (5.6)	4.5 (4.4)	(4.4)
UBPW91	5.5 (5.6)	4.1 (4.1)	(4.0)
UB3LYP	3.4 (3.3)	1.8 (1.7)	(1.6)
UBLYP	2.7 (2.7)	0.9 (0.8)	(0.6)
CCSD ^[b]	4.5 (4.4)	4.5 (4.3)	4.4 (4.2)
CCSD ^[c]	5.1 (5.0)	5.3 (5.2)	5.2 (5.1)
CCSD(T) ^[b]	2.1 (2.0)	2.0 (1.8)	1.9 (1.7)
CCSD(T) ^[c]	2.3 (2.2)	2.3 (2.2)	2.3 (2.1)
CAS(9,9)-SCF ^[b]	−14.7 (−14.9)	−15.1 (−15.3)	−15.3 (−15.4)
CAS(9,9)-SCF ^[c]	−15.1 (−15.2)	−15.5 (−15.6)	−15.6 (−15.7)
CAS(9,9)-RS2 ^[b]	0.5 (0.3)	0.8 (0.6)	0.9 (0.7)
CAS(9,9)-RS2 ^[c]	0.6 (0.5)	0.9 (0.8)	1.1 (1.0)
CAS(9,9)-RS3 ^[b]	0.4 (0.2)	0.4 (0.2)	0.4 (0.3)
CAS(9,9)-RS3 ^[c]	0.9 (0.7)	1.1 (0.9)	1.2 (1.1)

[a] A negative value indicates that the 2B_2 level lies below 2A_1 . Electronic contributions [$E_e(^2A_1) - E_e(^2B_2)$] are given in parenthesis. [b] UBLYP/cc-pVTZ geometries and ZPVE corrections. [c] UB3LYP/cc-pVTZ geometries and ZPVE corrections.

distance of 169 pm, whereas the 2B_2 state exhibits a C1–C3 distance of 237 pm, as expected for a benzene derivative. As noted previously,^[9] both states exhibit only modest multi-configurational character.^[20] Accordingly, the relative energies of both isomers calculated at the DFT level agree favorably with CCSD(T), CAS(9,9)RS2, and CAS(9,9)RS3 calculations. All correlated ab initio calculations as well as DFT indicate a small preference for the 2A_1 state, whereas the 2B_2 state lies in a shallow minimum slightly higher in energy. Interconversion of both isomers requires a distortion to C_s

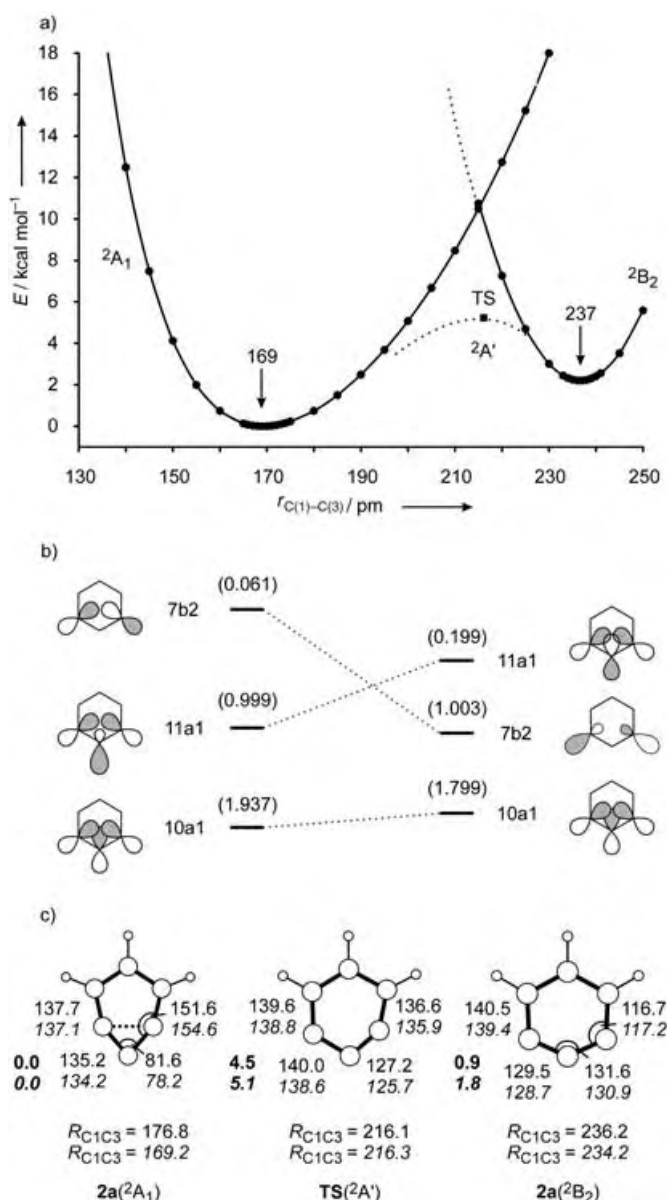


Figure 2. a) Energy as a function of the distance of radical centers C1 and C3 calculated at the CCSD(T)/cc-pVTZ//UBLYP/cc-pVTZ level of theory. b) Qualitative orbital energy diagram of the leading configurations of **2a** (CASSCF(9,9)/cc-pVTZ//UBLYP/cc-pVTZ) in the 2A_1 ground and 2B_2 excited state. Occupation numbers of natural orbitals are given in parenthesis. c) Selected structural parameters (bond lengths in pm, bond angles in degrees) of **2a** (2A_1), **2a** (2B_2), and the transition state TS ($^2A'$) connecting both isomers (normal print: UBLYP/cc-pVTZ; italics: UB3LYP/cc-pVTZ; bold: relative energies E_0 in kcal mol^{−1}).

symmetry. The barrier for this process amounts to only 4–5 kcal mol⁻¹ (relative to the ²A₁ ground state).

A comparison of the three IR signals tentatively assigned to **2a** with the values calculated for the ²B₂ and ²A₁ isomers at different levels of theory indicates that indeed the more stable ²A₁ state of **2a** is formed under the conditions of matrix isolation (Table 2).^[21] Vibrational mode 3 at $\tilde{\nu}=524\text{ cm}^{-1}$ is in better agreement with $\tilde{\nu}=522\text{ cm}^{-1}$ calculated for ²A₁-**2a** than $\tilde{\nu}=441\text{ cm}^{-1}$ for ²B₂-**2a**. Mode 18 at $\tilde{\nu}=1698\text{ cm}^{-1}$ is predicted to have no intensity for ²B₂-**2a**, but significant intensity (40% relative to the most intense signal) for ²A₁-**2a**. Displacement vectors for the three experimentally accessible normal modes of **2a** are shown schematically in Figure 3. Mode 3 corresponds to the intense absorption at around 550 cm⁻¹ characteristic of *meta*-didehydrobenzenes which was measured for **1b** (exp.: $\tilde{\nu}=547\text{ cm}^{-1}$; BLYP/cc-pVTZ: $\tilde{\nu}=535\text{ cm}^{-1}$),^[7] for various substituted derivatives, and for 3,5-didehydropyridine.^[15–17,22]

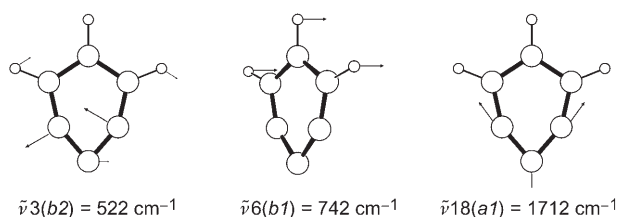


Figure 3. Displacement vectors corresponding to the three experimentally accessible normal modes of ²A₁-**2a** (UBLYP/cc-pVTZ).

The photolysis of matrix-isolated **4** as an alternative precursor resulted in only very low yields of products. Flash vacuum pyrolysis (FVP) of **4** at 690 °C with subsequent trapping of the thermolysis products in argon at 10 K gave **5** and several ring-fragmentation products such as acetylene and diacetylene. 1,2,3-Tridehydrobenzene was not detected under these conditions.

In summary, our experiments and calculations indicate that 1,2,3-tridehydrobenzene (**2a**) has been isolated and spectroscopically characterized in cryogenic neon matrices at 3 K. The IR spectra are in accordance with a ²A₁ ground state, whereas the ²B₂ excited state is 1–2 kcal mol⁻¹ higher in energy and not observed under these conditions.

Received: June 2, 2005

Keywords: ab initio calculations · dehydrobenzenes · IR spectroscopy · matrix isolation · radicals

- [1] a) W. Sander, *Acc. Chem. Res.* **1999**, 32, 669; b) H. H. Wenk, M. Winkler, W. Sander, *Angew. Chem.* **2003**, 115, 518; *Angew. Chem. Int. Ed.* **2003**, 42, 502; c) M. Winkler, H. H. Wenk, W. Sander in *Reactive Intermediate Chemistry* (Eds.: R. A. Moss, M. S. Platz, M. Jones, Jr.), Wiley, New York, **2004**.
- [2] R. W. Hoffmann, *Dehydrobenzene and Cycloalkynes*, Academic Press, New York, **1967**.
- [3] H. Pellissier, M. Santelli, *Tetrahedron* **2003**, 59, 701.
- [4] P. G. Wenthold, R. R. Squires, W. C. Lineberger, *J. Am. Chem. Soc.* **1998**, 120, 5279.

- [5] E. Kraka, D. Cremer, G. Bucher, H. Wandel, W. Sander, *Chem. Phys. Lett.* **1997**, 268, 313.
- [6] E. Kraka, J. Anglada, A. Hjerpe, M. Filatov, D. Cremer, *Chem. Phys. Lett.* **2001**, 348, 115.
- [7] W. Sander, M. Exner, M. Winkler, A. Balster, A. Hjerpe, E. Kraka, D. Cremer, *J. Am. Chem. Soc.* **2002**, 124, 13072.
- [8] M. Winkler, W. Sander, *J. Phys. Chem. A* **2001**, 105, 10422.
- [9] A.-M. C. Cristian, Y. Shao, A. I. Krylov, *J. Phys. Chem. A* **2004**, 108, 6581.
- [10] A. Lardin Harvey, J. J. Nash, P. G. Wenthold, *J. Am. Chem. Soc.* **2002**, 124, 12612.
- [11] C. Soucy, D. Favreau, M. M. Kayser, *J. Org. Chem.* **1987**, 52, 129.
- [12] a) D. L. Mattern, X. Chen, *J. Org. Chem.* **1991**, 56, 5903; b) L. Kalb, F. Schweizer, H. Zellner, E. Berthold, *Ber. Dtsch. Chem. Ges.* **1926**, 59, 1860.
- [13] O. L. Chapman, K. Mattes, C. L. McIntosh, J. Pacansky, G. V. Calder, G. Orr, *J. Am. Chem. Soc.* **1973**, 95, 6134.
- [14] a) J. G. Radziszewski, B. A. Hess, R. Zahradnik, *J. Am. Chem. Soc.* **1992**, 114, 52; see also: b) A. M. Orendt, J. C. Facelli, J. G. Radziszewski, J. W. Horton, D. M. Grant, J. Michl, *J. Am. Chem. Soc.* **1996**, 118, 846; c) S. G. Kukolich, C. Tanjaro, M. C. McCarthy, P. Thaddeus, *J. Chem. Phys.* **2003**, 119, 4353.
- [15] H. H. Wenk, W. Sander, *Chem. Eur. J.* **2001**, 7, 1837.
- [16] H. H. Wenk, W. Sander, *Eur. J. Org. Chem.* **2002**, 3927.
- [17] M. Winkler, B. Cakir, W. Sander, *J. Am. Chem. Soc.* **2004**, 126, 6135.
- [18] One or more by-products with absorptions at $\tilde{\nu}=2157$, 1721, 1399, and 777 cm⁻¹ are only formed upon irradiation at $\lambda=308$ or 248 nm in neon matrices, but are not observed in experiments with irradiation at $\lambda=193\text{ nm}$. The bands for **2a**, **5**, and **6** can clearly be distinguished from each other and from these by-products by their different increase/decrease rates upon irradiation at different wavelengths in different matrices or upon annealing.
- [19] DFT calculations were carried out with Gaussian 98: a) Gaussian 98 (Revision A.7), M. J. Frisch, G. W. Trucks, H. B. Schlegel, G. E. Scuseria, M. A. Robb, J. R. Cheeseman, V. G. Zakrzewski, J. A. Montgomery, R. E. Stratmann, J. C. Burant, S. Dapprich, J. M. Millam, A. D. Daniels, K. N. Kudin, M. C. Strain, O. Farkas, J. Tomasi, V. Barone, M. Cossi, R. Cammi, B. Mennucci, C. Pomelli, C. Adamo, S. Clifford, J. Ochterski, G. A. Petersson, P. Y. Ayala, Q. Cui, K. Morokuma, D. K. Malick, A. D. Rabuck, K. Raghavachari, J. B. Foresman, J. Cioslowski, J. V. Ortiz, B. B. Stefanov, G. Liu, A. Liashenko, P. Piskorz, I. Komaromi, R. Gomperts, R. L. Martin, D. J. Fox, T. Keith, M. A. Al-Laham, C. Y. Peng, A. Nanayakkara, C. Gonzalez, M. Challacombe, P. M. W. Gill, B. G. Johnson, W. Chen, M. W. Wong, J. L. Andres, M. Head-Gordon, E. S. Replogle, J. A. Pople, Gaussian, Inc., Pittsburgh, PA, **1998**. Tight convergence criteria for gradients and a full (99, 590) integration grid were used throughout. The 6-311G(d,p) basis set for iodine was obtained from the Extensible Computational Chemistry Environment Basis Set Database; ab initio calculations were carried out with Molpro 2000.1: b) H.-J. Werner, P. J. Knowles, Molpro 2000.1, Birmingham, **1999**; CCSD(T) calculations employed the partially spin-restricted open-shell coupled cluster (RHF-RCCSD(T)) program as described in: c) P. J. Knowles, C. Hampel, H.-J. Werner, *J. Chem. Phys.* **1993**, 99, 5219; d) P. J. Knowles, C. Hampel, H.-J. Werner, *J. Chem. Phys.* **2000**, 112, 3106; In multireference Rayleigh Schrödinger perturbation theory calculations to second (RS2) or third order (RS3) the doubly external configurations were internally contracted whereas singles were left uncontracted; e) H.-J. Werner, *Mol. Phys.* **1996**, 89, 645; the (9,9) active space for CASSCF calculations of **2a** covers the six valence π orbitals of the arene and the three σ orbitals depicted in Figure 2b. The core orbitals were kept frozen in post-(CAS)SCF calculations; Dunning's correlation-consistent basis sets were

- used for all computations on **2**: f) D. E. Woon, T. H. Dunning, *J. Chem. Phys.* **1993**, 98, 1358; g) R. A. Kendall, T. H. Dunning, R. J. Harrison, *J. Chem. Phys.* **1992**, 96, 6796; h) T. H. Dunning, *J. Chem. Phys.* **1989**, 90, 1007.
- [20] The CI coefficients of the $|(10a_1)^2(11a_1)^1\rangle$ and $|(10a_1)^2(7b_2)^1\rangle$ configurations at the CASSCF(9,9)/cc-pVTZ//UBLYP/cc-pVTZ level are 0.925 and 0.861 for the 2A_1 and 2B_2 wave-functions, respectively.
- [21] The structures and IR spectra for both states of **2a** show little dependence on the density functional employed. For consistency with earlier work on 1,3-biradicals, the UBLYP/cc-pVTZ level is discussed. The absolute intensities of the most-intense absorptions for both states (74 kmol^{-1} for mode 6 of 2A_1 -**2a**, 66 kmol^{-1} for the same mode of 2B_2 -**2a**) are similar, so that the formation of a mixture of both isomers is unlikely. IR spectra of numerous other potential by-products (carbonyl compounds, ring-contraction products, etc.) have been calculated and can be excluded as the carrier of the three traces assigned to **2a**.
- [22] W. Sander, M. Exner, *J. Chem. Soc. Perkin Trans. 2* **1999**, 2285.

Rotational Spectroscopy



DOI: 10.1002/anie.200501658

The Internuclear Potential, Electronic Structure, and Chemical Bond of Tellurium Selenide**

Deike Banser, Melanie Schnell, Jens-Uwe Grabow,*
Emilio J. Cocinero, Alberto Lesarri, and José L. Alonso

With the advances in micro- and nanoelectronics,^[1] interest in the electronic and structural properties of small metal and semimetal particles is increasing, this is because the concen-

trations of free valences as well as quantum size effects are more important once the number of atoms falls below a few ten thousand. The preparation and examination of these aggregates is quite challenging because of their high instability.^[2] The collision-free environment of a supersonic jet, which provides a “matrix” without effects that arise from the interaction with stabilizing materials, is appealing for the investigation and isolation of pure and mixed-metal or semimetal species. An intense laser-beam can vaporize almost every solid^[3] and, in particular, pulsed laser sources can be excellently adapted to pulsed supersonic expansions. Precise information on the geometrical structure as well as the electronic and nuclear magnetic properties of small particles and inorganic clusters formed in the laser-generated plasma can be gained from high-resolution rotational analysis. Fourier-transform microwave (FTMW) spectroscopy combines ideally with pulsed-jet techniques.^[4]

Even though laser-ablation of metals and semimetals has found extensive use in mass spectrometry, its combination with rotational spectroscopy is rare: The first attempts using single-target laser-ablation molecular beam FTMW spectroscopy were limited to small inorganic compounds such as metal oxides,^[5] halides,^[6] and sulfides.^[7] Somewhat later, solid organic species such as amino acids^[8] or urea were used.^[9] However, the study of intermetallic systems is new, to date only one mixed-metal cluster, PtSi^[10] in a $^1\Sigma$ closed-shell ground state, has been studied using this combination of techniques. Group 14 selenides and tellurides^[11] have only been analyzed by rotational spectroscopy in very hot vapors.

To generate aggregates such as mixed-metal clusters from two solid precursors we designed a new twin-laser ablation source and combined it with a state-of-the-art ultra broadband (2–26.5 GHz) FTMW spectrometer as shown in Figure 1, allowing low frequency measurements to cover the rotational spectra of heavier clusters. This apparatus utilizes a coaxially oriented beam resonator arrangement (COBRA)^[13] which provides exceptional (sub-Doppler) resolution and unrivalled sensitivity. Virtually any stable solid compound, even very ductile and reactive alkali metals,^[14] can be vaporized by laser-ablation from a pressed target rod and expanded in the supersonic jet.^[15] Consequently, the coaxial ablation twin source (CATS) allows the production of a huge variety of clusters by secondary reactions in the plasma prior to the supersonic expansion.

Tellurium selenide is a photoconducting semimetal material that is widely used for optoelectronic devices such as liquid crystal light valves (LCLV).^[16] The preparation, study, and application of nanowires, nanotubes, and semiconductor heterojunction nanorods prepared from this material are of current research interest.^[17] A prototype building unit in these structures—the diatomic cluster TeSe—is a heteroatomic homologue of the oxygen molecule. In contrast to the oxygen molecule, little is known about TeSe. Thermodynamic properties of TeSe were derived from Knudsen-cell mass spectrometric experiments.^[18] Fink et al. observed the rotationally resolved IR-chemiluminescence spectrum in the gaseous state^[19] while laser-induced fluorescence experiments on TeSe in the gas phase as well as in inert gas matrices were performed by Ahmed et al.^[20] However, precise data on the

[*] Dr. D. Banser, Dr. M. Schnell, Priv.-Doz. Dr. J.-U. Grabow
Institut für Physikalische Chemie, Lehrgebiet A
Universität Hannover
Callinstrasse 3–3A, 30167 Hannover (Germany)
Fax: (+49) 511-7624009
E-mail: jens-uwe.grabow@pci.uni-hannover.de

E. J. Cocinero, Prof. Dr. A. Lesarri, Prof. Dr. J. L. Alonso
Grupo Espectroscopía Molecular (GES)
Departamento de Química Física y Química Inorgánica
Facultad de Ciencias, Universidad de Valladolid
Prado de la Magdalena, s/n, 47005 Valladolid (Spain)

[**] We would like to thank the Deutscher Akademischer Austauschdienst (PPP D/0246239) as well as the Spanish ministry of education (Acciones Integradas HA-2002-0014) for funding a bilateral exchange program. M.S. thanks the Fonds der Chemischen Industrie (FCI) for support. J.-U.G. thanks the Deutsche Forschungsgemeinschaft (DFG) and the Land Niedersachsen, A.L. and J.L.A. thank the Spanish Ministry of Science and Technology (BQU2003-03275). We are indebted to R. LeRoy, Waterloo, and S. Cooke, Vancouver, for fruitful discussions.



Supporting information for this article is available on the WWW under <http://www.angewandte.org> or from the author.

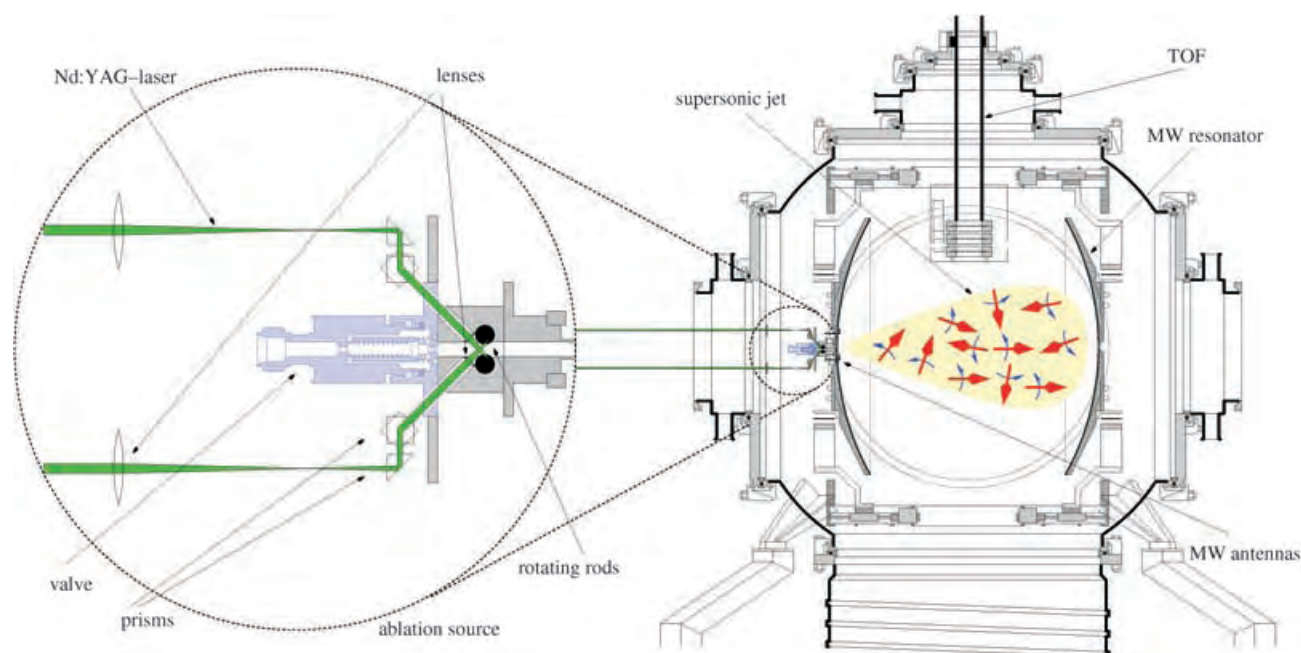


Figure 1. FTMW impulse experiment: Species are generated and expanded into a supersonic jet from a coaxial ablation twin source (CATS). Using a coaxially oriented beam-resonator arrangement (COBRA), the molecular systems are coherently excited by an MW pulse and their response is recorded in the time domain. Subsequent discrete Fourier transformation yields the frequency domain. A time-of-flight (TOF) mass spectrometer reassembling the principle Wiley–McLaren arrangement^[12] can be lowered onto the jet axis for efficient real-time source optimization towards the desired cluster species.

internuclear potential and quantitative details of the chemical bond, which can be obtained from high-resolution spectroscopy, are unavailable to date.

The study of TeSe started with a coaxial single-target laser-ablation source^[6] spectrometer in Valladolid described elsewhere^[21] and was continued with the CATS spectrometer in Hannover presented herein. Owing to the extraordinary sensitivity of this technique, it was possible to characterize 43 of the existing 48 isotopologues of TeSe in their natural abundances. 350 rotational transitions $J+1, v \leftarrow J, v$ for $J=0-6$ in the vibrational states $v=0-6$ were recorded and analyzed (see Supporting Information). The extensive analysis of this huge dataset, using the approach of Dunham^[22] and Watson^[23] for a diatomic vibrating rotor as implemented by LeRoy,^[24] will be given in detail in a subsequent publication. From the multi-isotopologue analysis, the rotational constants B_e , the vibration–rotation interaction coefficients $-a_e$, γ_e , and ϵ_e , and the fourth-order centrifugal distortion constants $-D_e$ can be derived for all isotopologues. With these parameters and using the Bohr theory expansion^[25] the individual spectra can be described by Equation (1):

$$\nu_{J+1, v \leftarrow J, v} = 2 \left[B_e - \frac{2P^2}{W_{X1} - W_{X0}} - a_e \left(v + \frac{1}{2} \right) + \gamma_e \left(v + \frac{1}{2} \right)^2 + \epsilon_e \left(v + \frac{1}{2} \right)^3 - D_e (J+1)^2 \right] (J+1) \quad (1)$$

The additional term $P = \langle v, J_a, \Omega=1 | B(J_a)_+ | v', J_a, \Omega=0 \rangle$ accounts^[26] for the interaction between the two levels of positive parity, $\Omega=0^+, 1^+$, in a $^3\Sigma$ state separated in energy by $W_{X1} - W_{X0}$, which is accurately described for heavy diatomic

species such as TeSe by Hund's case (c).^[27] Since finite nuclear-size effects, known for Pb and Tl,^[28] should be negligible in this case, such terms are not included. From the spectroscopic constants the equilibrium bond lengths r_e can be calculated and the harmonic vibration frequency ω_e as well as the first anharmonicity constant $-\omega_e x_e$ can be estimated by Equations (2)–(4), with the reduced mass μ :^[29]

$$r_e = \sqrt{\frac{h}{8\pi^2 B_e \mu}} \quad (2)$$

$$\omega_e \cong 2\sqrt{-\frac{B_e^3}{D_e}} \quad (3)$$

$$-\omega_e x_e \cong -\left(\frac{-a_e}{3\sqrt{-D_e}} + \sqrt{B_e} \right)^2 \quad (4)$$

The constants ω_e and $-\omega_e x_e$ allow the determination of the Morse potential parameter a and the Morse dissociation energy D [Eq. (5) and Eq. (6)]^[30]

$$D \cong \frac{h\omega_e^2}{4(-\omega_e x_e)} \quad (5)$$

$$a = \sqrt{\frac{-\omega_e x_e}{B_e}} \quad (6)$$

The results for the most abundant isotopologue are compared to those from Fink et al.^[19] in Table 1. As shown, the accuracy for the rotational constants from microwave spectroscopy is two to four orders of magnitude higher. Even the uncertainty in the indirectly determined vibrational

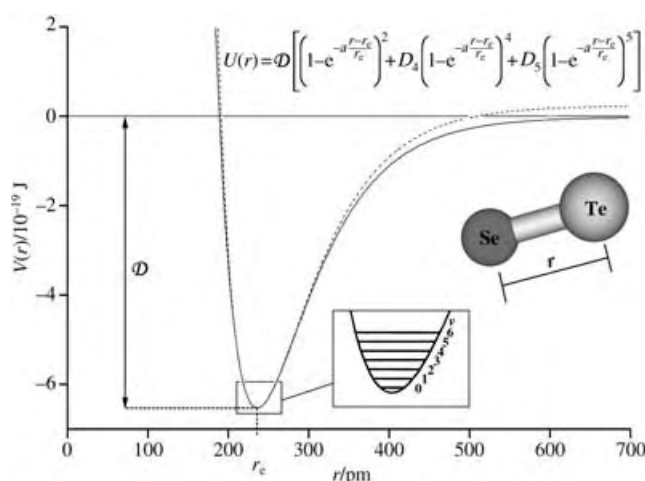
Table 1: Equilibrium parameters and vibrational ground-state constants of the main isotopologue $^{130}\text{Te}^{80}\text{Se}$.

	This work	Ref. [19]
B_e [MHz] ^[a]	1834.980709(54) ^[c]	
$-\alpha_e$ [MHz]	-5.352710(80)	
γ_e [kHz]	-4.762(39)	
ε_e [Hz]	-47.0(46)	
$-D_e$ [kHz]	-0.28060(41)	
ω_e [GHz]	9385.0(69)	
$-\omega_e x_e$ [MHz]	-22.306(35)	
$B_{v=0}$ [MHz]	1832.303158(178)	1832.21(75)
$-D_{v=0}$ [kHz]	-0.28060(41)	-0.300(63)
$r_{v=0}$ [pm]	236.10380(15)	236.11(5)
ω_e [GHz]	9385.0(69)	9384(24)
$-\omega_e x_e$ [MHz]	-22.306(35)	-21.6
derived Morse potential parameters		
D [kJ mol ⁻¹] ^[b]	393.9(12) ^[c]	
a	3.4861(28)	
r_e [pm]	235.93148(15)	

[a] The rotational constant B , the vibration-rotation-interaction coefficients $-\alpha_e$, γ_e , ε_e , the fourth-order centrifugal distortion constant $-D$, the bond length r , the harmonic frequency ω_e , and the first anharmonicity constant $-\omega_e x_e$. [b] The Morse dissociation energy D , the Morse parameter a , and the equilibrium bond length r_e . [c] Standard deviations in parentheses are given in units of the last digit.

parameters is improved, which is generally the case when microwave data, rather than infrared studies, are used for the characterization of heavier diatomics.

The dissociation energy of 293.3 kJ mol⁻¹ obtained from Knudsen-cell mass spectrometric experiments is about 25 % lower than the Morse dissociation energy D , this is consistent with observations in other systems.^[31] Using the higher order anharmonicity contributions that are made available by the spectroscopic data in Table 1, the potential function can be expanded further^[22] as shown in Figure 2 where the first term represents the Morse potential. Since the first term is already a good representation and the D_n values are quite small, the


Figure 2. Morse potential (—) and expanded Morse-based potential (----) functions of tellurium selenide for the main isotopologue $^{130}\text{Te}^{80}\text{Se}$.

potential converges rapidly about r_e . However, the corrected dissociation energy $D(1+D_4+D_5) = 409.6$ kJ mol⁻¹ is still not supposed to be very reliable since the spectroscopic data sample only the lower region of the potential, where high-order anharmonicities do not contribute. However, in the absence of experiments on near-dissociative states, the Morse dissociation energy D is still valuable as maximum estimate for the dissociation limit.

Omitting contributions from the second term of Equation (1) in the multi-isotopologue analysis was quite unsatisfactory in terms of experimental accuracy, that is, the breakdown of the Born–Oppenheimer approximation is important in this case. This situation strongly indicates the bi-radical nature of the electronic ground state of this cluster, this nature was also discussed for the reasonable large corrections found for PtS.^[7] The terms in Equation (1) might be compared with the expression discussed by Watson.^[23] The equations are essentially the same giving the relation in Equation (7) with the electron mass m_e , the atomic masses M_i ($i = \text{Se, Te}$), and the isotopologue invariant Born–Oppenheimer breakdown (BOB) mass-scaling correction constants $\Delta_{0,1}^i$ ($i = \text{Se, Te}$).^[23]

$$-\frac{2P^2}{B_e(W_{X1}-W_{X0})} = \frac{m_e}{M_A} \Delta_{0,1}^A + \frac{m_e}{M_B} \Delta_{0,1}^B \quad (7)$$

Both parameters, $\Delta_{0,1}^{\text{Te}}$ and $\Delta_{0,1}^{\text{Se}}$, have relatively large values as seen in Table 2. By means of Equation (2)–(4) and using

Table 2: BOB parameters of TeSe and related compounds.

AB	$\Delta_{0,1}^A$ [a]	$\Delta_{0,1}^B$	Ref.
TeSe	-20.9787(71) ^[b]	-20.9541(32)	this work
GeSe	-1.612(46)	-2.014(69)	[11]
SnSe	-1.555(84)	-2.124(50)	[11]
SnTe	-1.749(97)	-2.120(76)	[11]
PbSe	-11.86(92)	-1.653(97)	[11]
PbTe	-11.98(81)	-1.794(110)	[11]

[a] BOB correction parameter $\Delta_{0,1}^i$ for atom $i = A, B$. [b] Standard deviations in parentheses are given in units of the last digit.

the pure precession approximation $P \approx B_e \sqrt{J_a(J_a + 1)}$ with $J_a = S + L = 1$, the BOB analysis of pure rotational spectra provides an estimate for the separation of the $^3\Sigma$ -state that is split into a $X0$ - and a $X1$ -sublevel, or by using Verseth's expression $P \approx B_e \sqrt{2} - \gamma/\sqrt{2}$ can give an estimate of the electron spin-rotation coupling constant γ , provided that the energy separation is known [Eq. (8) and Eq. (9)].^[25] This approach gives $W_{X1} - W_{X0} = 1059$ cm⁻¹, which is in fair agreement with the energy separation of 1233.49 cm⁻¹ determined from the IR-chemiluminescence spectrum,^[19] or $\gamma = -0.01008$ cm⁻¹:

$$W_{X1} - W_{X0} \approx -\frac{4B_e}{\frac{m_e}{M_{\text{Se}}} \Delta_{0,1}^{\text{Se}} + \frac{m_e}{M_{\text{Te}}} \Delta_{0,1}^{\text{Te}}} \quad (8)$$

$$\gamma \approx 2B_e - \sqrt{-B_e(W_{X1} - W_{X0}) \left(\frac{m_e}{M_{\text{Se}}} \Delta_{0,1}^{\text{Se}} + \frac{m_e}{M_{\text{Te}}} \Delta_{0,1}^{\text{Te}} \right)} \quad (9)$$

Owing to the very high resolution of the COBRA-FTMW technique, it is feasible to analyze the narrow hyperfine structure of isotopologues having one or two nuclear spins $I = 1/2$, thereby gaining some quantitative insight of the chemical bond. For the $\Omega = 0^+$ component of a $^3\Sigma$ state in the Hund's case (c) limit, the interaction energy^[32] for one nucleus in a diatomic molecule ($F = J + I$, $|J - I|$) is given by Equation (10) and Equation (11) in the pure precession approximation. In this case, the unperturbed nuclear spin-rotation interaction constant f is altered by the low lying $\Omega = 1^+$ state. The constant b is averaged over each unpaired electron [Eq. (12) and Eq. (13)] with the molecular g_J -factor on the order of unity and $g_N = \mu/I\mu_N$ being proportional to the magnetic moment μ of the coupling nucleus and the probability $|\psi^2(0)|$ of the electron being found at the nucleus.

$$W_{\text{hfs}} = \frac{1}{2} C_I \{F(F+1) - J(J+1) - I(I+1)\} \quad (10)$$

$$C_I = f + (b-f) \frac{4B_e}{W_{X1} - W_{X0}} \quad (11)$$

$$f = 2g_J g_N \mu_N^2 \left(\frac{1}{r^3} \right)_{\text{av}} \quad (12)$$

$$b = g_N \mu_N \mu_B \left[\frac{16\pi}{3} |\psi^2(0)| - \frac{3\cos^2\theta - 1}{r^3} \right]_{\text{av}} \quad (13)$$

In Equation (13) the angle θ is taken between the internuclear axis and the radius r from the nucleus to the electron. Our CAS-SCF calculations show that the unpaired electrons in the π^* orbital have contributions of $-0.842p$ and $-0.059d$ from Te and $+0.699p$ and $0d$ from Se. The lack of s character for both nuclei makes $|\psi^2(0)|$ essentially zero, since this probability is negligibly small for p - and d -orbitals. The parameter b is dominated by the second term, which can either be positive or negative or vanishes for a spherical distribution, thus b can become of opposite sign to f , with f assuming the sign of μ . Values of $|b| = 1000$ MHz are not unlikely.^[32] However, the measured spin-rotation constants, for example, $C_I(^{125}\text{Te}^{77}\text{Se}) = 45.80(19)$ kHz given in Table 3, are rather large and bear the sign of μ for all isotopologues. An estimate for $f(^{77}\text{Se})$ might be the recently determined $C_I(^{208}\text{Pb}^{77}\text{Se}) = 9.61(30)$ kHz in a $^1\Sigma$ state.^[33] Consequently, with $4B_e/(W_{X1} - W_{X0}) \approx 2 \times 10^{-4}$, $b(^{77}\text{Se})$ is estimated to be of the order of 180 MHz, thereby indicating large average values θ for the unpaired electrons in the antibonding π^* orbitals.

Table 3: Hyperfine constants of abundant TeSe isotopologues and related compounds.

	$C_I(^{125}\text{Te})$ [MHz] ^[a]	$C_I(^{77}\text{Se})$ [MHz]	Ref.
$^{125}\text{Te}^{80}\text{Se}$	$-0.06958(25)^{[b]}$		this work
$^{130}\text{Te}^{77}\text{Se}$		0.04580(19)	this work
$^{208}\text{Pb}^{125}\text{Te}$	$-0.01177(29)$		[33]
$^{208}\text{Pb}^{77}\text{Se}$		0.00961(30)	[33]

[a] Nuclear magnetic spin-rotation coupling constant C_I . [b] Standard deviations in parentheses are given in units of the last digit.

In conclusion, this investigation on TeSe proves the power of supersonic-jet FTMW spectroscopy in combination with laser-ablation for research on intermetallic species. Not only spectroscopic parameters and structural information are accessible, but also information on the internuclear potential, electronic structure, and details of the chemical bond of the compound can be gained from high-resolution multi-isotopologue rotational spectra determined with high sensitivity. Even the energy separation of interacting triplet states can be estimated from pure rotational spectra instead of by electronic spectroscopy. Such studies are generally applicable to various metal or semimetal systems. The ability to prepare supersonic jets of these samples and to obtain high-resolution rotational spectra extends the horizon for investigations on the building units of small particles and inorganic clusters that form new materials.

Experimental Section

A stoichiometric mixture of tellurium and selenium powders (Alfa Aesar, 99.96%) was sealed in quartz ampoules under reduced pressure and heated at 800 °C for 24 h. Some grams of the ground alloy were mixed with a few drops of acrylic acid based glue, pressed to a rod and dried. Material was ablated from the samples at a repetition rate of 5–20 Hz by the beams of pulsed Nd:YAG-lasers ($\lambda = 1064$ nm, 500 mJ or $\lambda = 532$ nm, 90 mJ) focused on the rod surface in neon (Linde, 3.5) at a stagnation pressure of 5–8 bar. The accuracy of the transition frequencies varies from better than 1 kHz (Hannover) to 5 kHz (Valladolid). For the microwave excitation, a radiation power -8 dBm at 0.4 μ s pulse duration was needed to obtain maximum signal-to-noise ratios.

Received: May 13, 2005

Published online: September 16, 2005

Keywords: Born–Oppenheimer breakdown · chalcogens · laser ablation · rotational spectroscopy · supersonic jets

- [1] a) M. Forshaw, R. Stadler, D. Crawley, K. Nikolić, *Nanotechnology* **2004**, *15*, S220–S224; b) P. J. Burke, *Sol. State Electr.* **2004**, *48*, 1981–1986.
- [2] W. A. de Heer, *Rev. Mod. Phys.* **1993**, *65*, 611–676.
- [3] M. Smits, C. A. de Lange, S. Ullrich, T. Schultz, M. Schmitt, J. G. Underwood, J. P. Shaffer, D. M. Rayner, A. Stolow, *Rev. Sci. Instrum.* **2003**, *74*, 4812–4817.
- [4] J.-U. Grabow, W. Stahl, H. Dreizler, *Rev. Sci. Instrum.* **1996**, *67*, 4072–4084.
- [5] R. D. Suenram, F. J. Lovas, G. Fraser, K. Matsumura, *J. Chem. Phys.* **1990**, *92*, 4724–4733.
- [6] K. D. Hensel, C. Styger, W. Jäger, A. J. Merer, M. C. L. Gerry, *J. Chem. Phys.* **1993**, *99*, 3320–3328.
- [7] K. A. Walker, M. C. L. Gerry, *J. Mol. Spectrosc.* **1997**, *182*, 178–183.
- [8] F. J. Lovas, Y. Kawashima, J.-U. Grabow, R. D. Suenram, G. T. Fraser, E. Hirota, *Astrophys. J. Lett.* **1995**, *455*, L201–L204.
- [9] U. Kretschmer, D. Consalvo, A. Knaack, W. Schade, W. Stahl, H. Dreizler, *Mol. Phys.* **1996**, *87*, 1159–1168.
- [10] S. A. Cooke, M. C. L. Gerry, D. J. Brugh, R. D. Suenram, *J. Mol. Spectrosc.* **2004**, *223*, 185–194.
- [11] E. Tiemann, H. Arnst, W. U. Stieda, T. Törring, J. Hoeft, *Chem. Phys.* **1982**, *67*, 133–138.
- [12] W. C. Wiley, I. H. McLaren, *Rev. Sci. Instrum.* **1955**, *26*, 1150–1157.

- [13] J.-U. Grabow, W. Stahl, *Z. Naturforsch. A* **1990**, 45, 1043–1044.
- [14] C. Herwig, D. Banser, M. Schnell, J. A. Becker, *J. Phys. Chem. A* **2004**, 108, 6151–6155.
- [15] A. Lesarri, S. Mata, E. J. Cocinero, S. Blanco, J. C. López, J. L. Alonso, *Angew. Chem.* **2002**, 114, 4867–4870; *Angew. Chem. Int. Ed.* **2002**, 41, 4673–4676.
- [16] S. Yohikawa, M. Horie, H. Takahashi, *Fujitsu Sci. Tech. J.* **1976**, 12, 57–72.
- [17] X. Jian, L. Yadong, *Mater. Chem. Phys.* **2003**, 82, 515–519, and references therein.
- [18] J. Drowart, S. Smoes, *J. Chem. Soc. Faraday Trans. 2* **1977**, 73, 1755–1767.
- [19] E. H. Fink, K. D. Setzer, D. A. Ramsay, M. Vervolet, G. Z. Xu, *J. Mol. Spectrosc.* **1989**, 136, 218–221.
- [20] a) F. Ahmed, E. R. Nixon, *J. Mol. Spectrosc.* **1981**, 87, 101–109; b) F. Ahmed, R. F. Barrow, K. K. Yee, *J. Phys. B* **1975**, 8, 649–658.
- [21] A. Lesarri, S. Mata, J. C. Lopez, J. L. Alonso, *Rev. Sci. Instrum.* **2003**, 74, 4799–4804.
- [22] J. L. Dunham, *Phys. Rev.* **1932**, 41, 721–731.
- [23] J. K. G. Watson, *J. Mol. Spectrosc.* **1980**, 80, 411–421.
- [24] R. J. LeRoy, *DParFit 3.1* **2003**, available from <http://scienide.u-waterloo.ca/~leroy/>.
- [25] a) G. Herzberg, *Molecular Spectra and Molecular Structure, Vol. 1: Spectra of Diatomic Molecules*, 2nd ed., Van Nostrand, New Jersey, **1950**; b) L. Veseth, *J. Phys. B* **1973**, 6, 1473.
- [26] P. Kuipers, T. Törring, A. Dymanus, *Chem. Phys.* **1976**, 12, 309.
- [27] C. H. Townes, A. L. Shawlow, *Microwave Spectroscopy*, Dover, New York, **1975**.
- [28] J. Schlembach, E. Tiemann, *Chem. Phys.* **1982**, 68, 21–28.
- [29] C. L. Pekeris, *Phys. Rev.* **1934**, 45, 98–103.
- [30] P. M. Morse, *Phys. Rev.* **1929**, 34, 57–64.
- [31] R. T. Birge, H. Sponer, *Phys. Rev.* **1926**, 28, 259–283.
- [32] R. Tischer, K. Möller, T. Törring, *Chem. Phys.* **1981**, 62, 115–121.
- [33] L. Bizzocchi, B. M. Giuliano, D. Banser, J. Fritzsche, M. Hess, J.-U. Grabow, *19th Colloquium on High Resolution Molecular Spectroscopy*, H8, Salamanca, **2005**.

DOI: 10.1002/anie.200502615

Total Synthesis of Antigen *Bacillus Anthracis* Tetrasaccharide—Creation of an Anthrax Vaccine Candidate**

Daniel B. Werz and Peter H. Seeberger*

A few letters containing a seemingly inconspicuous white powder killed four innocent people, instilled fear in most Americans for several weeks, and brought the US Postal Service to the brink of collapse shortly after the events of September 11, 2001. The white powder was identified as dormant spores of the Gram-positive soil bacterium *Bacillus anthracis*,^[1,2] which are highly resistant to extreme temperatures, radiation, harsh chemicals, desiccation, and physical damage. These properties allow them to persist in the soil for many years.^[3] These spores cause anthrax, a serious infection of herbivores and cattle, but infects humans only rarely, except when specially prepared and dispensed as biowarfare agents. If the spores are inhaled, the host is usually killed within days. Three polypeptides that comprise the anthrax toxin play a major role in all stages of infection, from germination to the induction of vascular collapse leading to host death.^[4]

Bacillus anthracis, like most bacteria, bears unique oligosaccharides on the surface of the spore for interaction with the host. Specific oligosaccharide antigens can be used to design an antibacterial vaccine for the induction of an immune response.^[5] Carbohydrates are evolutionarily more stable than proteins and have been exploited in a series of commonly employed vaccines.^[6] Synthetic oligosaccharide vaccines have shown very encouraging results against cancer,^[7] malaria,^[8] and *Haemophilus influenzae* type b^[9] to name just a few.

The structure of tetrasaccharide **1**, which is found on the surface of the exosporium glycoprotein BC1A of *Bacillus anthracis* was elucidated in 2004 (Figure 1).^[10] A unique characteristic of this antigen is the nonreducing terminal sugar, the so-called anthrose, which is not even found in closely related species.^[10] Tetrasaccharide **1** is therefore a very attractive target for vaccine development and the elucidation

[*] Dr. D. B. Werz, Prof. Dr. P. H. Seeberger
Laboratory for Organic Chemistry
Swiss Federal Institute of Technology (ETH) Zürich
ETH Hönggerberg, HCI F 315
Wolfgang-Pauli-Strasse 10, 8093 Zürich (Switzerland)
Fax: (+41) 44-633-1235
E-mail: seeberger@org.chem.ethz.ch

[**] This research was supported by the ETH Zürich, by a Feodor Lynen Research Fellowship of the Alexander von Humboldt Foundation, and by an Emmy Noether Fellowship of the Deutsche Forschungsgemeinschaft (to D.B.W.). We thank Prof. Dr. B. Jaun and B. Brandenburg for NMR measurements.



Supporting information for this article is available on the WWW under <http://www.angewandte.org> or from the author.

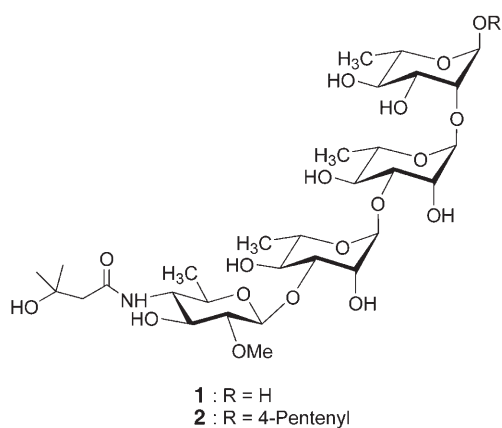


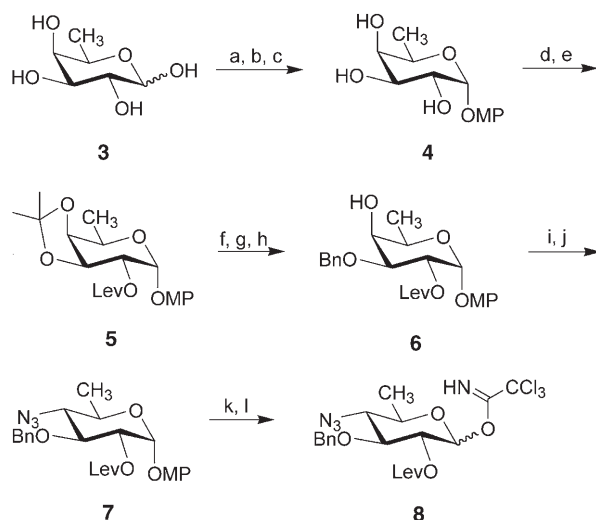
Figure 1. Structure of the terminal tetrasaccharide **1** of the major surface glycoprotein of *Bacillus anthracis* and analogue **2** ready for conjugation.

of a highly specific immune response against *Bacillus anthracis*.

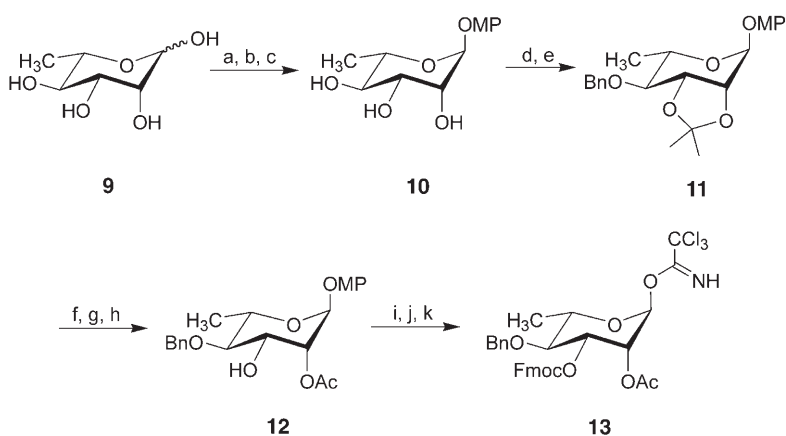
Herein, we describe the first total synthesis of tetrasaccharide **2** through a convergent [2+2] approach that facilitates access to analogues and shorter sequences. The terminal pentenyl group can serve as a point of attachment during conjugation to a carrier protein in vaccine development. A straightforward synthesis of the unique monosaccharide anthrose is part of this total synthesis.

Synthesis of the terminal anthrose^[10] started from commercially available D-fucose (**3**) (Scheme 1). Acetylation of **3**, followed by immediate protection of the anomeric center with *para*-methoxyphenol (MPOH) and subsequent cleavage of the acetates furnished **4**. A levulinyl group proved to be the best choice to protect the C2 hydroxy group during installation of the β (1→3) glycosidic linkage in anticipation of its selective removal prior to methylation of O2. Thus, reaction of **4** with 2,2-dimethoxypropane and introduction of the levulinic ester at C2 furnished **5**. Removal of the isopropylidene and tin-mediated selective benzylation of the hydroxy group at C3 afforded **6**. The configuration of C4 was inverted by reaction of the hydroxy group with triflic anhydride to install a triflate, which was displaced by sodium azide in an S_N2 -type fashion to give **7**.^[11] Removal of the anomeric *p*-methoxyphenyl group with wet cerium ammonium nitrate was followed by the formation of the anthrose trichloroacetimidate **8** by treatment with trichloroacetonitrile and a catalytic amount of sodium hydride. A completely different, more lengthy approach to the synthesis of an anthrose monosaccharide was reported recently.^[12]

Rhamnose building block **13**, which is equipped with a robust participating group at C2 to ensure α selectivity and a readily removable temporary protecting group (Fmoc) at 3-OH was synthesized next (Scheme 2). First, the anomeric



Scheme 1. Synthesis of anthrose building block **8**. Reagents and conditions: a) Ac_2O , pyridine, 12 h, quant.; b) MPOH, $\text{BF}_3 \cdot \text{OEt}_2$, acetone, $0^\circ\text{C} \rightarrow 25^\circ\text{C}$, 12 h, 71%; c) NaOMe, MeOH, 6 h, quant.; d) 2,2-dimethoxypropane, $\text{BF}_3 \cdot \text{OEt}_2$, acetone, $0^\circ\text{C} \rightarrow 25^\circ\text{C}$, 12 h, 96%; e) LevOH, DMAP, DIPC, CH_2Cl_2 , 0°C , 3 h, 92%; f) HCl (pH 3), MeOH, 50°C , 18 h, 85%; g) $n\text{Bu}_4\text{Sn}$, toluene, Dean–Stark apparatus, reflux, 2 h; h) BnBr, TBAI, toluene, reflux, 3 h, 95% (two steps); i) TiCl_4 , pyridine, 0°C , 90 min; j) NaN_3 , DMF, 25°C , 10 h, 80% (two steps); k) CAN, $\text{H}_2\text{O}/\text{CH}_3\text{CN}$, 25°C , 1 h; l) Cl_3CCN , NaH, CH_2Cl_2 , 25°C , 45 min, 78% (two steps). MPOH = *para*-methoxyphenol, LevOH = levulinic acid, DMAP = 4-dimethylaminopyridine, DIPC = diisopropyl carbodiimide, Bn = benzyl, TBAI = tetrabutylammonium iodide, CAN = cerium ammonium nitrate.



Scheme 2. Synthesis of rhamnose building block **13**. Reagents and conditions: a) Ac_2O , pyridine, 12 h, quant.; b) MPOH, $\text{BF}_3 \cdot \text{OEt}_2$, acetone, $0^\circ\text{C} \rightarrow 25^\circ\text{C}$, 12 h, 80%; c) NaOMe, MeOH, 12 h, 96%; d) 2,2-dimethoxypropane, $\text{BF}_3 \cdot \text{OEt}_2$, acetone, $0^\circ\text{C} \rightarrow 25^\circ\text{C}$, 12 h, 84%; e) NaH, BnBr, DMF, $0^\circ\text{C} \rightarrow 25^\circ\text{C}$, 4 h, quant.; f) HCl (pH 3), MeOH, 50°C , 89%; g) 1,1,1-triethoxyethane, *p*-TsOH (cat.), DMF, 50°C , 50 min; h) $\text{AcOH}/\text{H}_2\text{O}$ (4/1, v/v), 10°C , 10 min, 98% (two steps); i) FmocCl, pyridine, 25°C , 2 h, 88%; j) CAN, $\text{H}_2\text{O}/\text{CH}_3\text{CN}$, 25°C , 1 h, 76%; k) Cl_3CCN , NaH, CH_2Cl_2 , 25°C , 1 h, 94%. TsOH = *para*-toluenesulfonic acid, DMF = *N,N*-dimethylformamide, Fmoc = fluorenylmethoxycarbonyl.

center was protected with a *para*-methoxyphenol group under the conditions described above to give **10**.^[13] Formation of the *cis*-fused acetal and subsequent benzylation afforded **11**. The transformation of the acetal into the corresponding

orthoester and ring opening resulted in the kinetically preferred axial acetate in **12**. The remaining hydroxyl function was protected with an Fmoc group, and the *para*-methoxyphenyl glycoside was cleaved. Subsequent reaction with trichloroacetonitrile in the presence of traces of sodium hydride afforded building block **13**.

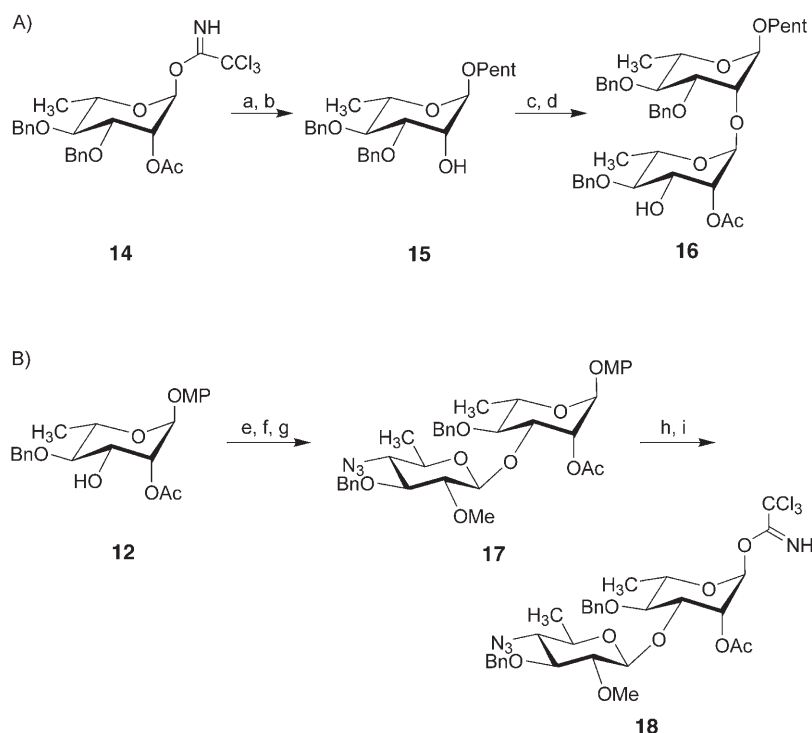
The assembly of the tetrasaccharide through a [2+2] approach commenced with the reaction of known building block **14**^[14] with 4-penten-1-ol (Scheme 3). The pentenyl

moiety serves at a later stage as a handle for conjugation to a carrier protein in the preparation of the vaccine candidate. Cleavage of the acetate at C2, further glycosylation with **13**, and subsequent removal of Fmoc yielded disaccharide **16**. During the cleavage of the Fmoc group, minor acetate migration ($\approx 10\%$) from the 2-OH to the 3-OH group was observed, but the undesired product was easily removed by column chromatography.

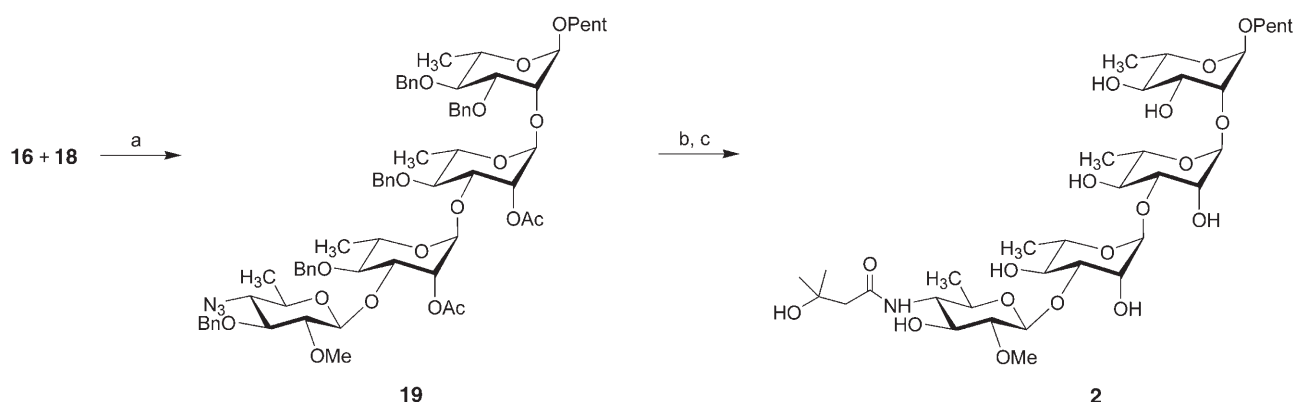
The second disaccharide (Scheme 3B) was assembled by glycosylation of rhamnose **12**, an intermediate in the synthesis of building block **13**, with the anthrose unit **8**. The levulinoyl group, which ensured β selectivity, was replaced by the final methoxy substituent at C2. The methylation in the presence of acetate proved to be challenging. Even powerful methylating agents such as methyl triflate and diazomethane failed to facilitate the transformation. Satisfying yields were only possible with MeI/Ag₂O in the presence of catalytic amounts of dimethyl sulfide. The commonly used maneuver to convert the methoxyphenyl glycoside into the corresponding trichloroacetimidate furnished disaccharide unit **18**.

To complete the total synthesis, the two disaccharide units **16** and **18** were coupled to afford tetrasaccharide **19** (Scheme 4). Sodium in liquid ammonia removed all permanent protecting groups and transformed the azide moiety into an amine, thus achieving global deprotection. The formation of the amide with 3-hydroxy-3-methylbutanoic acid under peptide-coupling conditions^[15] led to tetrasaccharide **2**, whose structure was confirmed by comprehensive spectroscopic analysis and comparison with the reported analytical data for **1**.

In conclusion, we have reported a convergent total synthesis of a *Bacillus anthracis* tetrasaccharide antigen ready for conjugation



Scheme 3. Syntheses of disaccharide building blocks **16** (A) and **18** (B). Reagents and conditions: a) 4-pentenol, TMSOTf, CH₂Cl₂, -20°C , 45 min, 79%; b) NaOMe, MeOH, 4 h, 96%; c) **13**, TMSOTf, CH₂Cl₂, 0°C , 1 h, 91%; d) piperidine, DMF, 25°C , 30 min, 89%; e) **8**, TMSOTf, CH₂Cl₂, 0°C , 1 h, 90%; f) hydrazinium acetate, CH₂Cl₂, MeOH, 25°C , 12 h, quant.; g) MeI, Ag₂O, THF, Me₂S (cat.), 25°C , 8 h, 73%; h) CAN, H₂O/CH₃CN, 25°C , 1 h; i) Cl₃CCN, NaH, CH₂Cl₂, 25°C , 1 h 95% (two steps). TMSOTf = trimethylsilyl trifluoromethanesulfonate.



Scheme 4. Completion of the total synthesis. Reagents and conditions: a) TMSOTf, CH₂Cl₂, 0°C , 70 min, 73%; b) Na/NH₃(l), THF, -78°C , 60%; c) 3-hydroxy-3-methylbutanoic acid, HATU, DIPEA, DMF, 25°C , 2 h, 75%. HATU = *N*[(dimethylamino)-1*H*-1,2,3-triazolo[4,5-*b*]pyridin-1-yl]methyl-ene-*N*-methylmethanaminium hexafluorophosphate, DIPEA = diisopropylethylamine.

to carrier proteins. Immunological studies as well as the preparation of derivatives are currently under investigation.

Received: July 26, 2005

Published online: September 19, 2005

Keywords: anthrose · carbohydrates · oligosaccharides · total synthesis · vaccines

-
- [1] M. Mock, A. Fouet, *Annu. Rev. Microbiol.* **2001**, 55, 647–671.
 - [2] P. Sylvestre, E. Couture-Tosi, M. Mock, *Mol. Microbiol.* **2002**, 45, 169–178.
 - [3] W. L. Nicholson, N. Munakata, G. Horneck, H. J. Melosh, P. Setlow, *Microbiol. Mol. Biol. Rev.* **2000**, 64, 548–572.
 - [4] M. Moayeri, S. H. Leppla, *Curr. Opin. Microbiol.* **2004**, 7, 19–24, and references therein.
 - [5] B. Kuberan, R. J. Linhardt, *Curr. Org. Chem.* **2000**, 4, 653–677.
 - [6] R. Roy, *Drug Discovery Today Technol.* **2004**, 1, 327–336.
 - [7] S. J. Danishefsky, J. R. Allen, *Angew. Chem.* **2000**, 112, 882–911; *Angew. Chem. Int. Ed.* **2000**, 39, 836–863.
 - [8] L. Schofield, M. C. Hewitt, K. Evans, M.-A. Siomos, P. H. Seeberger, *Nature* **2002**, 418, 785–789.
 - [9] V. Verez-Bencomo, V. Fernández-Santana, E. Hardy, M. E. Toledo, M. C. Rodríguez, L. Heynngnezz, A. Rodríguez, A. Baly, L. Herrera, M. Izquierdo, A. Villar, Y. Valdés, K. Cosme, M. L. Deler, M. Montane, E. Garcia, A. Ramos, A. Aguilar, E. Medina, G. Toraño, I. Sosa, I. Hernandez, R. Martínez, A. Muzachio, A. Carmenates, L. Costa, F. Cardoso, C. Campa, M. Diaz, R. Roy, *Science* **2004**, 305, 522–525.
 - [10] J. M. Daubenspeck, H. Zeng, P. Chen, S. Dong, C. T. Steichen, N. R. Krishna, D. G. Pritchard, C. L. Turnbough, Jr., *J. Biol. Chem.* **2004**, 279, 30945–30953.
 - [11] J. Golik, H. Wong, B. Krishnan, D. M. Vyas, T. W. Doyle, *Tetrahedron Lett.* **1991**, 32, 1851–1854.
 - [12] R. Saksena, R. Adamo, P. Kováč, *Carbohydr. Res.* **2005**, 340, 1591–1600.
 - [13] K. Sarkar, I. Mukherjee, N. Roy, *J. Carbohydr. Chem.* **2003**, 22, 95–107.
 - [14] A. Fürstner, T. Müller, *J. Am. Chem. Soc.* **1999**, 121, 7814–7821.
 - [15] L. A. Carpino, A. El-Faham, *J. Org. Chem.* **1995**, 60, 3561–3564.
-

DOI: 10.1002/anie.200500773

Heterolytic Splitting of Hydrogen with Rhodium(I) Amides***Pascal Maire, Torsten Büttner, Frank Breher, Pascal Le Floch, and Hansjörg Grützmacher***Dedicated to Professor Gottfried Huttner on the occasion of his 68th birthday*

The classical mechanisms for the catalytic hydrogenation of C=C double bonds with rhodium(I) or iridium(I) complexes consist of six steps: 1) ligand dissociation from the catalyst precursor, 2) oxidative addition of H₂, 3) olefin coordination, 4) insertion of the coordinated C=C bond in a Rh–H bond, 5) isomerization, and 6) reductive elimination of the product.^[1] In the Halpern mechanism,^[2] the olefin insertion and in the Brown mechanism the reductive elimination of the alkane is rate-determining.^[3] In both mechanisms, a T-shaped 14-electron [ML₂X] complex is the key intermediate which adds H₂ oxidatively in an almost barrierless exothermic reaction. The heterolytic addition of hydrogen across a metal–nitrogen bond was first investigated systematically by Fryzuk and co-workers.^[4] In the meantime, this reaction has been recognized as a key step in the very efficient catalytic hydrogenation of unsaturated substrates RR¹C=X,^[5–7] especially of ketones (X=O), which became known as metal–ligand bifunctional catalysis through the work of Noyori and Morris. This mechanism is different and involves: 1) heterolytic addition of H₂ across the metal–amide bond as the rate-determining step, 2) binding of RR¹C=X in the second coordination sphere of the MH^{δ−}–NH^{δ+} unit, 3) “concerted” transfer of H^{δ−} from the metal atom to the C=X carbon atom and H^{δ+} from the nitrogen atom to the X center, and 4) product release. In this mechanism no change of the formal oxidation state and no major structural changes in the first coordination sphere of the metal center occur. Combined with the possibility to isolate the species that are directly involved in

[*] Dr. P. Maire, Dr. T. Büttner, Dr. F. Breher, Prof. Dr. P. Le Floch,^[†] Prof. Dr. H. Grützmacher
Department of Chemistry and Applied Biosciences
ETH-Hönggerberg, 8093 Zürich (Switzerland)
Fax: (+41) 1-633-1032
E-mail: gruetzmacher@inorg.chem.ethz.ch

[†] Permanent address:
Department of Chemistry
Laboratory “Hétéroéléments et Coordination”
UMR CNRS 7653, Ecole Polytechnique
91128 Palaiseau cedex (France)

[**] This work was supported by the LANXESS AG and the Swiss National Science Foundation. We thank our colleague A. Togni for fruitful discussions and the reviewers for valuable comments.

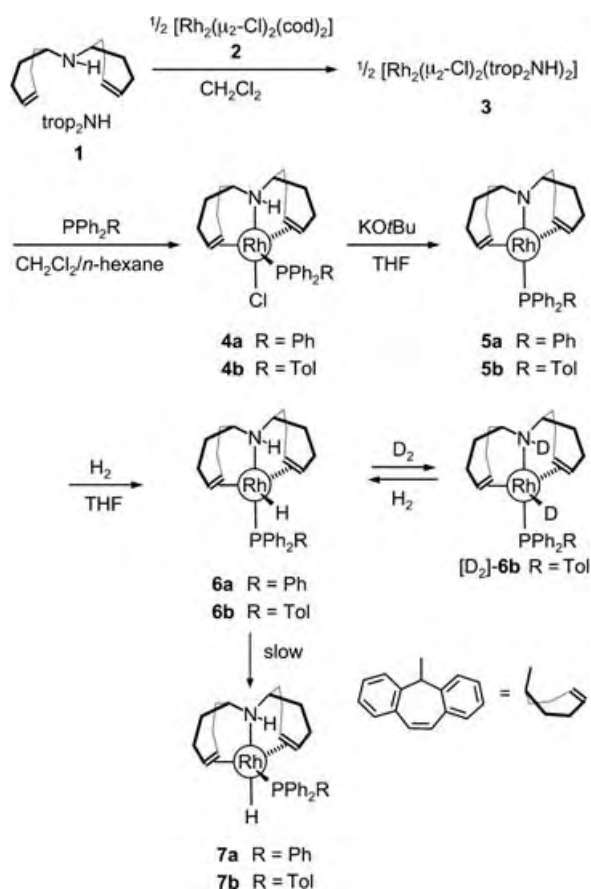


Supporting information for this article is available on the WWW under <http://www.angewandte.org> or from the author.

the catalytic cycle,^[7b,8] new possibilities for rational catalyst design emerge.

Recently, we isolated rhodium(i) amide olefin complexes with a rigid tetrahedrally distorted square-planar structure.^[9] In accord with a calculated high activation barrier ($> 29 \text{ kcal mol}^{-1}$), these compounds do not split H_2 heterolytically. Here we report the syntheses of rhodium amides with a novel structure. These complexes are easily prepared in a few steps, can be isolated, split H_2 heterolytically, and are directly active hydrogenation catalysts for ketones and imines without the need for any additives.

The reaction of bis(5-*H*-dibenzo[*a,d*]cyclohepten-5-yl)amine (**1**, bis(tropylidenyl)amine, trop_2NH)^[10a] with $[\text{Rh}_2(\mu_2\text{-Cl})_2(\text{cod})_2]$ (**2**) gives the dinuclear complex $[\text{Rh}_2(\mu_2\text{-Cl})_2(\text{trop}_2\text{NH})_2]$ (**3**, Scheme 1).



Scheme 1. Synthesis of rhodium bis(trop)amine complexes **4a,b**, **5a,b**, **6a,b**, and **7a,b**. cod = cycloocta-1,5-diene.

Subsequent reaction with a phosphane leads to the mononuclear complexes $[\text{RhCl}(\text{trop}_2\text{NH})(\text{PPh}_2\text{R})]$ **4a** ($\text{R} = \text{Ph}$) and **4b** ($\text{R} = 4\text{-MeC}_6\text{H}_4 = \text{Tol}$) in which the phosphane ligand is in the equatorial position and the chloro substituent is in the apical position (these stereochemical assignments are based on the NMR spectroscopic data). The complexes **3** (red crystals) and **4a,b** (yellow crystals) are obtained quantitatively and can be stored in air.

The NH function of the rhodium(i)-coordinated trop_2NH ligands is sufficiently acidic (pK_a 15–20 in DMSO)^[9,10] to be

fully deprotonated by addition of one equivalent of KOtBu to **4a,b** in THF; this is accompanied by an immediate color change of the reaction solution from orange-red to intense green. Deep green, highly air-sensitive crystals of **5a,b** grew from a 1:1 mixture of THF/toluene which was layered with *n*-hexane. The result of a structure analysis on a single crystal of **5b** is shown in Figure 1.^[11]

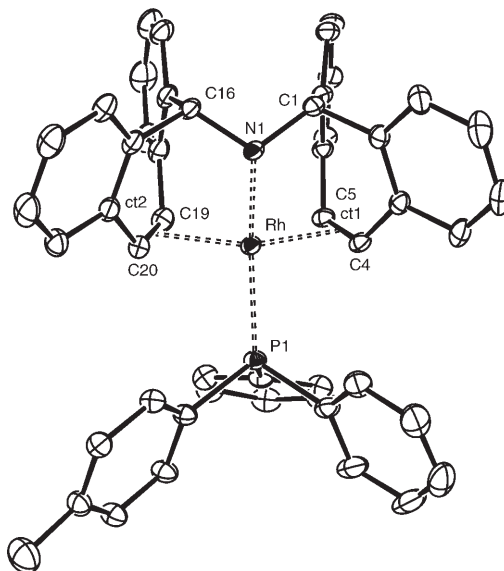


Figure 1. Structure of **5b**. Thermal ellipsoids are drawn at 30% probability; hydrogen atoms are omitted for clarity. Selected bond lengths [Å] and angles [°]: Rh–N1 2.007(1), Rh–P1 2.316(1), Rh–C5 2.165(2), Rh–C4 2.190(2), Rh–C19 2.174(2), Rh–C20 2.199(2), Rh–ct1 2.058(2), Rh–ct2 2.070(2), C4–C5 1.423(3), C19–C20 1.407(3); N1–Rh–P1 166.18(5), ct1–Rh–ct2 135.81(7), C16–N1–C1 109.5(1), C16–N1–Rh 118.5(1), C1–N1–Rh 119.0(1).

The structure of the neutral amide **5b** is unique among tetracoordinate d^8 rhodium complexes. However, a close relationship exists to the zero-valent 16 valence-electron (VE) $[\text{Ru}(\text{CO})_2(\text{PR}_3)_2]$ complexes studied by Caulton, Eisenstein, et al.^[12] and to the highly reactive transient carbonyls $[\text{M}(\text{CO})_4]$ ($\text{M} = \text{Fe}, \text{Ru}, \text{Os}$).^[13] Indeed, like these species, **5b** adopts a “sawhorse” structure with a N–Rh–P angle of $166.18(5)^\circ$ and a ct1–Rh–ct2 angle of $135.81(7)^\circ$ (ct = centroid of the coordinated C=C bond). Comparable angles in $[\text{Ru}(\text{CO})_2(\text{PtBu}_2\text{Me})_2]$ are: P–Ru–P $165.56(8)^\circ$, and C–Ru–C $133.3(4)^\circ$.

The amide nitrogen atom N1 has a pyramidal coordination sphere ($\Sigma = 347^\circ$). At temperatures below 220 K, sharp and distinct ^1H NMR resonances for the inequivalent protons at the olefinic carbon atoms C4/C20 and C5/C19, respectively, are observed, which demonstrates that the sawhorse structure corresponds to the ground-state structure. At room temperature, these NMR resonances collapse to give one broadened singlet, indicating inversion at the nitrogen and rhodium centers, probably via a planar transition state.

The rhodium amides **5a,b** react rapidly and quantitatively with H_2 (1 atm) even at -78°C to give the yellow rhodium hydride complexes $[\text{RhH}(\text{trop}_2\text{NH})(\text{PPh}_2\text{R})]$ (**6a,b**). This reaction is very likely reversible as **6b** reacts with D_2 to give

[D₂]-**6b** exclusively and, vice versa, [D₂]-**6b** reacts with H₂ to give **6b**. The latter reaction was monitored by ¹H NMR spectroscopy and shows that the intensities of the signals for the NH and RhH protons build up simultaneously. We have no evidence that deuterium labeling occurs at any other position in the molecule. The structure of **6b** was determined by X-ray diffraction (Figure 2).^[11]

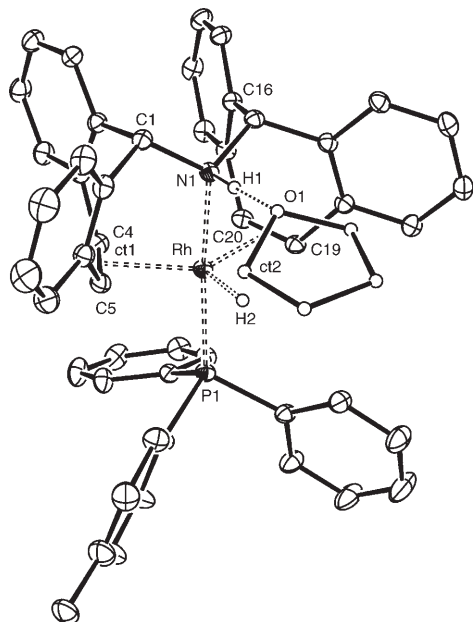


Figure 2. Structure of **6b**. Thermal ellipsoids are drawn at 30% probability; hydrogen atoms apart from H1 and H2 and one THF solvent molecule are omitted for clarity. One position of the disordered *para*-methyl substituent within the PPh₂Tol ligand is shown. Selected bond lengths [Å] and angles [°]: Rh–N1 2.178(1), Rh–P1 2.230(1), Rh–H2 1.59(3), Rh–C5 2.159(1), Rh–C4 2.199(1), Rh–C19 2.158(1), Rh–C20 2.203(1), Rh–ct1 2.057(1), Rh–ct2 2.059(1), C4–C5 1.437(2), C19–C20 1.436(2), N1–O1 3.02; N1–Rh–P1 169.95(3), ct1–Rh–ct2 132.54(5), C16–N1–C1 110.7(1), C16–N1–Rh 116.15(7), C1–N1–Rh 117.36(7).

The structural differences between **5b** and **6b** are very small. In **6b** the Rh–N bond is 9% longer and the Rh–P bond is 4% shorter than in **5b**; the ct1–Rh–ct2 angle is 2% more acute, whereas the N–Rh–P angle is 2% more open. Also the coordination sphere at N1 is not influenced very much ($\Sigma(\text{C–N–C}, 2 \times \text{C–N–Rh}) = 344.2^\circ$). A THF molecule is coordinated to the NH function (N1...O1 3.02 Å) and indicates, as does the high-frequency ¹H NMR shift (δ : 5.56 ppm (**6a**), 5.09 ppm (**6b**)), its acidic character. The hydride ligand H2 in the equatorial position of the trigonal-bipyramidal structure of **6b** causes the typical^[14] shift of the olefinic ¹³C resonances to low frequency (by about 20 ppm) and an elongation of the coordinated C=C bonds.

Solutions of the recrystallized hydrides **6a,b** in THF are stable for at least 24 h. However, impurities provoke the quantitative isomerization to the air-stable yellow complexes **7a,b** in which the hydride ligand adopts the axial position.

The assumption that the amide complexes **5a,b** split H₂ heterolytically is supported by DFT calculations with the model complex [Rh(cht₂N)(PH₃)] (**I**) (cht = cyclohepta-

trienyl, Figure 3).^[15] The formation of the hydride **II** is exothermic ($\Delta_R H = -15.8 \text{ kcal mol}^{-1}$) and proceeds in one step^[16] via the transition state **TS-I**. The calculated NBO charges show that the H₂ molecule is significantly polarized

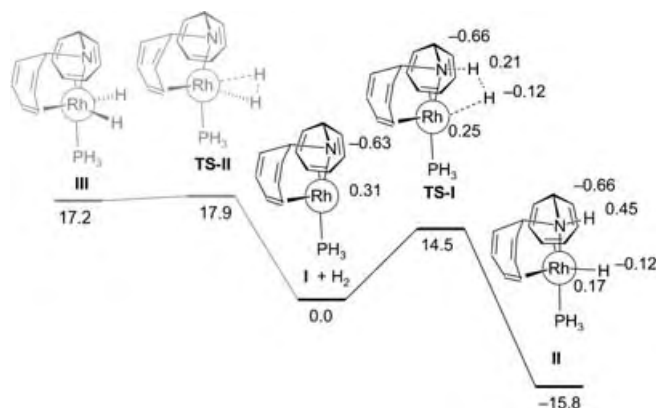


Figure 3. DFT^[15] computed energies for the heterolytic (shown in black) and oxidative addition (shown in gray) of H₂ to the model complex **I**. NBO charges are given for the Rh, N, and the adding H₂ molecule in **I**, **TS-I**, and **II**.

($\Delta q^{\text{NBO}} = 0.33 \text{ e}$) in the transition state (compare with $\Delta q^{\text{NBO}} = 0.57 \text{ e}$ in the product **II**). The polarity of the Rh^I–N bond varies little throughout this addition process ($\Delta q^{\text{NBO}} = 0.94 \text{ e}$ (**I**), 0.91 e (**TS-I**), 0.83 e (**II**)). The “classical” oxidative addition of H₂ leading to the rhodium(III) dihydride **III** is an unfavorable endothermic process ($\Delta_R H = 17.9 \text{ kcal mol}^{-1}$) and has to encompass the transition state **TS-II** which is higher in energy than **TS-I** by 3.4 kcal mol^{–1}.

The isolated crystalline amide **5b** and the hydride **6b** were used in catalytic hydrogenations without any further additives. The conditions and results are listed in Table 1. Under these (not yet optimized) conditions,^[17] alkyl- (**8**) and aryl-substituted ketones (**9**) and the imine **10** are completely converted to the corresponding hydrogenated products cyclohexanol, 1-phenylethanol, and *N*-phenylbenzylamine, respectively. The amide **5b** and the hydride **6b** are equally active (see Table 1, entries 2 and 3). Addition of an excess of phosphine does not significantly slow down the catalytic activity. However, at the end of each catalytic run, the axial

Table 1: Hydrogenation of the ketones **8** and **9** and the imine **10** with **5b** or **6b** as catalysts.^[a]

Entry	Substrate	Cat.	S/C ^[b]	t [h]	Conversion [%]
1	8	5b	100	16	> 97
2	9	5b	100	16	> 97
3	9	6b	100	16	> 97
4	9	5b	1000	1.5	22
5	9	5b	1000	16	65
6	10	5b	100	16	> 97

[a] THF, 100 bar H₂, T = 298 K. [b] Ratio substrate/catalyst.

hydride **7b** is the only detectable rhodium- and phosphorus-containing species and this hydride is catalytically inactive. We therefore assume that the formation of **7b** in course of the catalytic reaction is responsible for the incomplete conversion of **9** with low catalyst loadings (Table 1, entry 5).

In summary, rhodium amides with previously unreported structures can be prepared from readily available starting materials. These complexes react cleanly with H_2 which is heterolytically split in a one-step process across the polar Rh–N bond. Both, the amide and hydride can be used directly as catalysts for ketone or imine hydrogenations, which very likely proceed via the metal–ligand bifunctional mechanism.^[17] Given that the isomerization of the catalytically active hydride intermediate to an inactive one can be suppressed, efficient new catalysts for hydrogenations are in sight.

Experimental Section

The syntheses of **4a,b** can be performed without any particular precautions. In contrast, the amides **5a,b** must be handled under exclusion of moisture and oxygen. Detailed descriptions of the syntheses and spectroscopic data are given in the Supporting Information.

The reaction of **2** with two equivalents **1** in CH_2Cl_2 gave **3**· CH_2Cl_2 , which was obtained as red crystals from the reaction mixture (yield > 90 %). Subsequent reaction with PPh_2R ($R = Ph$ or Tol) gave yellow solutions, from which **4a,b** were precipitated by addition of n -hexane (yields > 80 %; **4a**: $R = Ph$, **4b**: $R = Tol$). The reaction of **4a,b** with one equivalent of $KOtBu$ in THF gave a deep green reaction solution, to which was added toluene (50 vol %). After all volatiles had been evaporated under vacuum, the green residue was extracted with THF, filtered, and concentrated. Layering this THF extract with toluene and n -hexane (THF/toluene/ n -hexane = 1:1:10) gave dark green microcrystals of **5a,b** (yields: 80 %). Deep green solutions of **5a,b** in THF were treated with H_2 (D_2) gas at 2 atm. Layering of the resulting yellow solutions with n -hexane led to the crystallization of the hydrides **6a,b** or $[D_2]$ -**6b** as yellow air-stable platelets (yields > 80 %).

NMR data were recorded at 298 K when not specified otherwise: **3**: M.p.: > 250 °C (decomp). 1H NMR (400.1 MHz, CD_2Cl_2): $\delta = 5.97$ (dd, $^3J_{H,H} = 9.4$ Hz, $^2J_{Rh,H} = 2.1$ Hz, 4H; CH_{olefin}), 6.20 ppm (d, $^3J_{H,H} = 9.4$ Hz, 4H; CH_{olefin}); ^{13}C NMR (100.6 MHz, CD_2Cl_2): $\delta = 71.4$ ppm (br s, 8C; CH_{olefin}); ^{103}Rh NMR (12.7 MHz, CD_2Cl_2): $\delta = 2992$ ppm (s); UV/Vis (CH_3CN): λ_{max} (ϵ) = 232 (sh), 289 (45 700), 329 nm (sh). **4a**: M.p.: > 260 °C (decomp). 1H NMR (300.1 MHz, $CDCl_3$): $\delta = 1.59$ (br, 1H; NH), 5.42 (dd, $^3J_{H,H} = 9.4$ Hz, $^3J_{P,H} = 7.4$ Hz, 2H; CH_{olefin}), 5.66 ppm (ddd, $^3J_{H,H} = 9.4$ Hz, $^3J_{P,H} = 5.8$ Hz, $^2J_{Rh,H} = 1.3$ Hz, 2H; CH_{olefin}); ^{31}P NMR (101.2 MHz, $CDCl_3$): $\delta = 7.7$ ppm (d, $^1J_{Rh,P} = 111$ Hz). **4b**: M.p.: > 260 °C (decomp). In $CDCl_3$ solution two conformations (likely due to hindered rotation around the Rh–P bond) in an approximate 2:1 ratio are observed. 1H NMR (300.1 MHz, $CDCl_3$): $\delta = 1.59$ (br s, 1H; NH_{maj}), 1.71 (br s, 1H; NH_{min}), 5.35–5.48 (m, 2H; $CH_{olefin,min}$; and 2H; $CH_{olefin,maj}$), 5.60–5.67 ppm (m, 2H; $CH_{olefin,min}$; and $CH_{olefin,maj}$); ^{31}P NMR (121.5 MHz, $CDCl_3$): $\delta = 6.9$ (d, $^1J_{Rh,P} = 111$ Hz, maj), 7.6 ppm (d, $^1J_{Rh,P} = 111$ Hz, min). **5a**: 1H NMR (400.1 MHz, $[D_8]THF$, 200 K): $\delta = 4.69$ (ddd, $^3J_{H,H} = 9.0$ Hz, $^3J_{P,H} = 6.2$ Hz, $^2J_{Rh,H} = 1.2$ Hz, 2H; CH_{olefin}), 5.62 ppm (ddd, $^3J_{H,H} = 9.0$ Hz, $^2J_{Rh,H} = 3.3$ Hz, $^3J_{P,H} = 2.9$ Hz, 2H; CH_{olefin}); ^{13}C NMR (100.6 MHz, $[D_8]THF$, 200 K): $\delta = 76.2$ (d, $^1J_{Rh,C} = 6.7$ Hz, 2C; CH_{olefin}), 84.5 ppm (d, $^1J_{Rh,C} = 14.7$ Hz, 2C; CH_{olefin}). ^{31}P NMR (162.0 MHz, $[D_8]THF$, 200 K): $\delta = 40.8$ ppm (d, $^1J_{Rh,P} = 124$ Hz); ^{103}Rh NMR (12.6 MHz, $[D_8]THF$, 200 K): $\delta = 838$ ppm (d, $^1J_{Rh,P} = 124$ Hz); UV/Vis (THF): λ_{max} (ϵ) = 301 (20 000), 352 (10 000), 438 (3000),

662 nm (1000). **5b**: 1H NMR (500.2 MHz, $[D_8]THF$, 190 K): $\delta = 4.74$ (dd, $^3J_{H,H} = 7.3$ Hz, $J = 7.3$ Hz, 2H; CH_{olefin}), 5.68 ppm (d, $^3J_{H,H} = 7.3$ Hz, 2H; CH_{olefin}); ^{13}C NMR (125.8 MHz, $[D_8]THF$, 190 K): $\delta = 75.7$ (s, 2C; CH_{olefin}), 83.9 ppm (d, $^1J_{Rh,C} = 15.1$ Hz, 2C; CH_{olefin}); ^{31}P NMR (121.5 MHz, $[D_8]THF$): $\delta = 38.7$ ppm (d, $^1J_{Rh,P} = 124$ Hz). **6a**: 1H NMR (400.1 MHz, $[D_8]THF$): $\delta = -8.15$ (dd, $^1J_{Rh,H} = 23.0$ Hz, $^2J_{P,H} = 23.0$ Hz, 1H; RhH), 3.55 (d, $^3J_{H,H} = 9.3$ Hz, 2H; CH_{olefin}), 3.91 (dd, $^3J_{H,H} = 9.3$ Hz, $^3J_{H,H} = 4.7$ Hz, 2H; CH_{olefin}), 5.56 ppm (d, $^3J_{P,H} = 4.9$ Hz, 1H; NH); ^{13}C NMR (100.6 MHz, $[D_8]THF$): $\delta = 57.8$ (d, $^1J_{Rh,C} = 8.0$ Hz, 2C; CH_{olefin}), 60.6 ppm (d, $^1J_{Rh,C} = 8.6$ Hz, 2C; CH_{olefin}); ^{31}P NMR (162.0 MHz, $[D_8]THF$): $\delta = 65.4$ ppm (d, $^1J_{Rh,P} = 144$ Hz); ^{103}Rh NMR (12.6 MHz, $[D_8]THF$, 230 K): $\delta = -187$ ppm (d, $^1J_{Rh,P} = 144$ Hz). **6b**: M.p.: > 100 °C (decomp). 1H NMR (300.1 MHz, $[D_8]THF$): $\delta = -8.19$ (dd, $^1J_{Rh,H} = 23.3$ Hz, $^2J_{P,H} = 23.3$ Hz, 1H; RhH), 3.65 (d, $^3J_{H,H} = 9.4$ Hz, 2H; CH_{olefin}), 3.97 (dd, $^3J_{H,H} = 9.4$ Hz, $^3J_{P,H} = 4.5$ Hz, 2H; CH_{olefin}), 5.09 ppm (d, $^3J_{P,H} = 5.5$ Hz, 1H; NH); ^{13}C NMR (75.5 MHz, $[D_8]THF$): $\delta = 57.0$ (d, $^1J_{Rh,C} = 7.9$ Hz, 2C; CH_{olefin}), 60.0 ppm (d, $^1J_{Rh,H} = 8.8$ Hz, 2C; CH_{olefin}); ^{31}P NMR (121.5 MHz, $[D_8]THF$): $\delta = 63.0$ ppm (d, $^1J_{Rh,P} = 145$ Hz); ATR IR: $\tilde{\nu} = 3169$ (m, NH), 1756 cm^{-1} (m, RhH). $[D_2]$ -**6b**: 2H NMR (46.1 MHz, THF): $\delta = -8.19$ (br s, RhD), 4.92 ppm (br s, ND); ^{31}P NMR (121.5 MHz, $[D_8]THF$): $\delta = 61.3$ ppm. The ND and RhD IR absorptions (expected at about 1580 and 880 cm^{-1}) are hidden by intense absorptions from the ligand. **7a**: M.p.: > 150 °C (decomp). 1H NMR (400.1 MHz, $[D_8]THF$): $\delta = -21.37$ (dd, $^1J_{Rh,H} = 17.4$ Hz, $^2J_{P,H} = 17.4$ Hz, 1H; RhH), 0.82 (s, 1H; NH), 4.40 (dd, $^3J_{H,H} = 9.0$ Hz, $^3J_{P,H} = 7.8$ Hz, 2H; CH_{olefin}), 5.15 ppm (dd, $^3J_{H,H} = 9.0$, $^3J_{P,H} = 5.1$ Hz, 2H; CH_{olefin}); ^{13}C NMR (100.6 MHz, $[D_8]THF$): $\delta = 57.1$ (dd, $^2J_{P,C} = 14.7$ Hz, $^1J_{Rh,C} = 9.8$ Hz, 2C; CH_{olefin}), 61.2 ppm (dd, $^1J_{Rh,C} = 8.6$ Hz, $^2J_{P,C} = 4.90$ Hz, 2C; CH_{olefin}); ^{31}P NMR (162.0 MHz, $[D_8]THF$): $\delta = 47.3$ ppm (d, $^1J_{Rh,P} = 138$ Hz); ^{103}Rh NMR (12.6 MHz, $[D_8]THF$): $\delta = -38$ ppm (d, $^1J_{Rh,P} = 138$ Hz). **7b**: 1H NMR (300.1 MHz, $[D_8]THF$): $\delta = -21.49$ (dd, $^1J_{Rh,H} = 17.3$ Hz, $^2J_{P,H} = 17.3$ Hz, 1H; RhH), 0.96 (s, 1H; NH), 4.47 (dd, $^3J_{H,H} = 8.8$ Hz, $^3J_{P,H} = 7.8$ Hz, 2H; CH_{olefin}), 5.20 ppm (dd, $^3J_{H,H} = 8.8$, $^3J_{P,H} = 5.0$ Hz, 2H; CH_{olefin}); ^{13}C NMR (75.5 MHz, $[D_8]THF$): $\delta = 56.4$ (dd, $^2J_{P,C} = 14.3$ Hz, $^1J_{Rh,C} = 9.4$ Hz, 2C; CH_{olefin}), 60.4 ppm (dd, $^1J_{Rh,C} = 8.8$ Hz, $^2J_{P,C} = 5.2$ Hz, 2C; CH_{olefin}); ^{31}P NMR (121.5 MHz, $[D_8]THF$): $\delta = 45.0$ ppm (d, $^1J_{Rh,P} = 138$ Hz).

Received: March 2, 2005

Revised: May 25, 2005

Published online: September 19, 2005

Keywords: amides · heterolytic H_2 splitting · homogeneous catalysis · hydrogenation · rhodium

- [1] For a review citing experimental and theoretical work see: M. Torrent, M. Solà, G. Frenking, *Chem. Rev.* **2000**, *100*, 439.
- [2] a) J. Halpern, *Inorg. Chim. Acta* **1981**, *50*, 11; b) For calculations see: C. Daniel, N. Koga, J. Han, X. Y. Fu, K. Morokuma, *J. Am. Chem. Soc.* **1988**, *110*, 3773.
- [3] a) J. M. Brown, *Chem. Soc. Rev.* **1993**, *22*, 25; b) For calculations see: “The Challenge of d and f Electrons: Theory and Computation”: N. Koga, K. Morokuma, *ACS Symp. Ser.* **1989**, *394*, 77.
- [4] a) M. D. Fryzuk, P. A. MacNeil, *Organometallics* **1983**, *2*, 682; b) M. D. Fryzuk, P. A. MacNeil, S. J. Rettig, *J. Am. Chem. Soc.* **1987**, *109*, 2803; c) M. D. Fryzuk, C. D. Montgomery, *Coord. Chem. Rev.* **1989**, *95*, 1. The heterolytic splitting of H_2 by metal complexes, for example $Cu^{2+} + H_2 \rightarrow CuH^+ + H^+$ was proposed much earlier: d) J. Halpern, *J. Organomet. Chem.* **1980**, *200*, 133, and references therein; it is one key step in the enzymatic H_2 activation by metal–sulfur clusters in hydrogenases: e) D. J. Evans, C. J. Pickett, *Chem. Soc. Rev.* **2003**, *32*, 268.

- [5] Recent reviews: a) S. E. Clapham, A. Hadzovic, R. H. Morris, *Coord. Chem. Rev.* **2004**, 248, 2201; b) R. Noyori, *Angew. Chem.* **2002**, 114, 2108; *Angew. Chem. Int. Ed.* **2002**, 41, 2008; ; c) R. Noyori, T. Ohkuma, *Angew. Chem.* **2001**, 113, 40; *Angew. Chem. Int. Ed.* **2001**, 40, 40; d) M. J. Palmer, M. Wills, *Tetrahedron: Asymmetry* **1999**, 10, 2045.
- [6] Mechanistic and theoretical work: a) C. A. Sandoval, T. Ohkuma, K. Muñiz, R. Noyori, *J. Am. Chem. Soc.* **2003**, 125, 13490, and references therein; b) K. Abdur-Rashid, S. E. Clapham, A. Hadzovic, J. N. Harvey, A. J. Lough, R. H. Morris, *J. Am. Chem. Soc.* **2002**, 124, 15104.
- [7] a) Hydrogenolysis of the iridium nitrogen bond is a key-step in the catalyzed hydrogenation of imines see: R. Dorta, D. Broggini, R. Kissner, A. Togni, *Chem. Eur. J.* **2004**, 10, 4546, and references therein. b) See also: Y. Ng, C. Chan, J. A. Osborn, *J. Am. Chem. Soc.* **1990**, 112, 9400.
- [8] Intermediates in the related catalytic cycle for the transfer hydrogenation of ketones with ruthenium arene complexes could be isolated and crystallized, see: K.-J. Haack, S. Hashiguchi, A. Fujii, T. Ikariya, R. Noyori, *Angew. Chem.* **1997**, 109, 297; *Angew. Chem. Int. Ed. Engl.* **1997**, 36, 285.
- [9] P. Maire, F. Breher, H. Schönberg, H. Grützmacher, *Organometallics* **2005**, 24, 3207.
- [10] a) T. Büttner, F. Breher, H. Grützmacher, *Chem. Commun.* **2004**, 2820; b) T. Büttner, J. Geier, G. Frison, J. Harmer, C. Calle, A. Schweiger, H. Schönberg, H. Grützmacher, *Science* **2005**, 307, 235.
- [11] Crystal structure of **5b**: C₄₉H₃₉NPRh, monoclinic, space group *P*2₁(1)/*c*; *a* = 11.897(1), *b* = 14.932(1), *c* = 20.862(1) Å, β = 104.046(1)°; *V* = 3595.3(2) Å³; *Z* = 4; ρ_{calc} = 1.433 Mg m⁻³; crystal dimensions 0.47 × 0.31 × 0.25 mm; diffractometer Bruker SMART Apex; MoK α radiation, 200 K, 2 θ_{max} = 80.16°; 97 685 reflections, 22 235 independent (*R*_{int} = 0.0537), direct methods; empirical absorption correction SADABS (version 2.03); refinement against full matrix (versus *F*²) with SHELXTL (version 6.12) and SHELXL-97,^[18] 471 parameters, *R*1 = 0.0560 and *wR*2 (all data) = 0.1471, max./min. residual electron density 1.900/−1.523 e Å⁻³. The hydrogen atoms were placed in idealized positions and included as riding atoms. Crystal structure of **6b**: C₄₉H₄₁NPRh·2THF, triclinic, space group *P* $\bar{1}$; *a* = 10.935(1), *b* = 11.864(1), *c* = 19.658(1) Å, α = 91.408(3)°, β = 100.019(3)°, γ = 109.948(3); *V* = 2350.8(3) Å³; *Z* = 2; ρ_{calc} = 1.301 Mg m⁻³; crystal dimensions 0.62 × 0.53 × 0.43 mm; diffractometer Bruker SMART Apex; MoK α radiation, 200 K, 2 θ_{max} = 82.46°; 61 525 reflections, 29 179 independent (*R*_{int} = 0.0239), direct methods; empirical absorption correction SADABS (ver. 2.03); refinement against full matrix (versus *F*²) with SHELXTL (ver. 6.12) and SHELXL-97,^[18] 471 parameters, *R*1 = 0.0471 and *wR*2 (all data) = 0.1465, max./min. residual electron density 2.757/−1.422 e Å⁻³. The hydrogen atoms were placed in idealized positions and included as riding atoms. The positions of the hydrogen atoms H1 (NH) and H2 (RhH) were obtained from a difference Fourier synthesis, they were refined isotropically. The *para*-methyl moiety of the PPh₂Tol ligand was “disordered” due to phenyl/tolyl interchange and had to be split over two positions, which were refined against each other (*F*VAR = 0.47). Consequently, one hydrogen atom in the *para*-position of a phenyl ring was not included in the refinement. CCDC-264482 (**5b**) and CCDC-264483 (**6b**) contain the supplementary crystallographic data for this paper. These data can be obtained free of charge from the Cambridge Crystallographic Data Centre via www.ccdc.cam.ac.uk/data_request/cif.
- [12] a) M. Ogasawara, S. A. Macgregor, W. E. Streib, K. Folting, O. Eisenstein, K. G. Caulton, *J. Am. Chem. Soc.* **1996**, 118, 10189; b) T. Gottschalk-Gaudig, J. C. Huffman, K. G. Caulton, H. Gérard, O. Eisenstein, *J. Am. Chem. Soc.* **1999**, 121, 3242; c) T. Gottschalk-Gaudig, J. C. Huffman, H. Gérard, O. Eisenstein, K. G. Caulton, *Inorg. Chem.* **2000**, 39, 3957.
- [13] [M(CO)₄]: a) M = Fe, Os: M. Poliakoff, J. J. Turner, *J. Chem. Soc. Dalton Trans.* **1974**, 2276; b) M = Ru: P. L. Bogdan, E. Weitz, *J. Am. Chem. Soc.* **1989**, 111, 3163; c) for calculations see: J. Li, G. Schreckenbach, T. Ziegler, *J. Am. Chem. Soc.* **1995**, 117, 486. For a general discussion of the isolobal relationship between d⁸ML₄ and CH₂, see: T. A. Albright, J. K. Burdett, M.-H. Whangbo, *Orbital Interactions in Chemistry*, Wiley, **1985**, pp. 360, 404.
- [14] C. Böhrer, N. Avarvari, H. Schönberg, M. Wörle, H. Rüegger, H. Grützmacher, *Helv. Chim. Acta* **2001**, 84, 3127.
- [15] All calculations were carried out within the framework of DFT using the Gaussian03^[15a] set of programs and the B3PW91 functional. This functional employs a combination of exchange terms: exact HF, the Becke 1988 nonlocal gradient correction^[15b] and the original Slater local exchange functional.^[15c] In addition, it uses the Perdew–Wang 1991 local correlation functional.^[15d] The 6-31 + G* basis set was employed for all the atoms connected to the Rh center as well as for the four CH olefinic protons. All the other atoms, except Rh, were calculated using the 6-31G* basis set. A quasirelativistic effective core potential operator was used to represent the 28 innermost electrons of the rhodium atom. The basis set for the metal was that associated with the pseudopotential, with a standard double- ζ LANL2DZ contraction.^[15e] Cartesian coordinates of the theoretical structures are given in the Supporting Information. The minimum energy structures were characterized by full vibration frequencies calculations. Natural charges were computed with the NBO program implemented in Gaussian03.^[15f] Gaussian03 (Revision B.04), M. J. Frisch, G. W. Trucks, H. B. Schlegel, G. E. Scuseria, M. A. Robb, J. R. Cheeseman, J. A. Montgomery, Jr., T. Vreven, K. N. Kudin, J. C. Burant, J. M. Millam, S. S. Iyengar, J. Tomasi, V. Barone, B. Mennucci, M. Cossi, G. Scalmani, N. Rega, G. A. Petersson, H. Nakatsuji, M. Hada, M. Ehara, K. Toyota, R. Fukuda, J. Hasegawa, M. Ishida, T. Nakajima, Y. Honda, O. Kitao, H. Nakai, M. Klene, X. Li, J. E. Knox, H. P. Hratchian, J. B. Cross, C. Adamo, J. Jaramillo, R. Gomperts, R. E. Stratmann, O. Yazyev, A. J. Austin, R. Cammi, C. Pomelli, J. W. Ochterski, P. Y. Ayala, K. Morokuma, G. A. Voth, P. Salvador, J. J. Dannenberg, V. G. Zakrzewski, S. Dapprich, A. D. Daniels, M. C. Strain, O. Farkas, D. K. Malick, A. D. Rabuck, K. Raghavachari, J. B. Foresman, J. V. Ortiz, Q. Cui, A. G. Baboul, S. Clifford, J. Cioslowski, B. B. Stefanov, G. Liu, A. Liashenko, P. Piskorz, I. Komaromi, R. L. Martin, D. J. Fox, T. Keith, M. A. Al-Laham, C. Y. Peng, A. Nanayakkara, M. Challacombe, P. M. W. Gill, B. Johnson, W. Chen, M. W. Wong, C. Gonzalez, J. A. Pople, Gaussian, Inc., Pittsburgh, PA, **2003**; b) A. D. Becke, *Phys. Rev. A* **1988**, 38, 3098; A. D. Becke, *J. Chem. Phys.* **1993**, 98, 5648; c) J. C. Slater, *Quantum Theory of Molecules and Solids*, McGraw-Hill, New York, **1974**; d) J. P. Perdew, J. A. Chevary, S. H. Vosko, K. A. Jackson, M. R. Pederson, D. J. Singh, C. Fiolhais, *Phys. Rev. B* **1992**, 46, 6671; e) P. J. Hay, W. R. Wadt, *J. Chem. Phys.* **1985**, 82, 299; f) A. E. Reed, L. A. Curtiss, F. Weinhold, *Chem. Rev.* **1988**, 88, 899.
- [16] We could not locate any minimum structure with a η^2 -bonded H₂ molecule as ligand. On the contrary, the heterolytic splitting of H₂ by ruthenium(II) phosphane amides is a two-step process including first the formation of a σ -bonded H₂ complex followed by an intramolecular proton transfer to the amide nitrogen atom (energy barrier (DFT) from the amide to the transition state for H₂ cleavage: 13.4 kcal mol⁻¹.^[7b]) A one-step heterolytic cleavage of H₂ has been calculated for ruthenium(II) arene amides with a transition state at 25.2 kcal mol⁻¹ (MP2): M. Yamakawa, H. Ito, R. Noyori, *J. Am. Chem. Soc.* **2000**, 122, 1466.
- [17] The complete catalytic cycle for the hydrogenation of H₂C=O with **I** was calculated. The results strongly support the assumption that this reaction follows the metal–ligand bifunctional

mechanism and that the heterolytic H₂-splitting is the rate-determining step. The transfer of H^{δ+}, H^{δ-} to the H₂C=O molecule, which is bonded in the second coordination sphere at the place where the THF molecule is in **6b**, has only a very small barrier ($E_a = 0.5 \text{ kcal mol}^{-1}$). However, our experimental set-up did not allow the stirring of the reaction mixtures, which should enhance considerably the turnover frequency. Details concern-

ing the calculation of the catalytic cycle are given in the Supporting Information.

- [18] SHELXTL, V. 6.12, Bruker AXS, Madison, Wisconsin, USA, **2002**; G. M. Sheldrick, SHELXL-97, Program for the Refinement of Crystal Structures, University of Göttingen, Germany, **1997**.

Rhodium Complexes

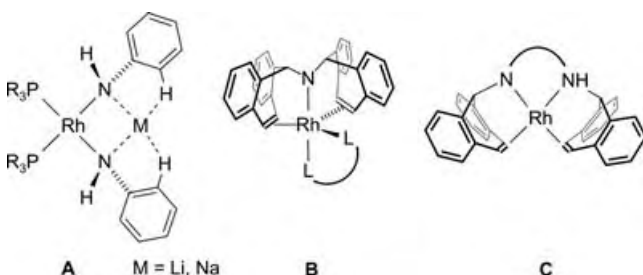
DOI: 10.1002/anie.200502036

Diamido Rhodates(1[−])**

Pascal Maire, Frank Breher, and
Hansjörg Grützmacher*

Dedicated to Professor Herbert W. Roesky
on the occasion of his 70th birthday

The M–N bond in late transition-metal amides^[1] is susceptible to a number of useful synthetic transformations.^[2] Some years ago, Brunet et al. reported the only known bis-(amido)rhodium(I) complexes, which were characterized in rather complex equilibria in the reaction of $[\text{Rh}_n\text{Cl}_m(\text{PR}_3)_l]$ compounds with anilide, MNHPh ($\text{M} = \text{Li}, \text{Na}$).^[3] Based on NMR data, the structure **A** was proposed for $[\text{Li}(\text{solv})_x - [\text{Rh}(\text{NHPh})_2(\text{PR}_3)_2]]$ (Scheme 1). In this intimate ion pair,



Scheme 1. The diamido rhodate(1[−]) **A** reported by Brunet et al.^[3], and isolated 18-electron and 16-electron rhodium(I) amides **B** and **C**, respectively ($\text{LNL} = \text{tropNH}_2$, bipy).

which is only stable in the presence of an excess of anilide in solution, the NHPh groups are likely rotated such that they are orientated perpendicular to the central plane, and the lone pairs are involved in the complexation of the alkali-metal cation.

Previously, we reported the stable neutral rhodium(I) amides **B** and **C**, which were isolated and fully characterized (see Table 1 for pertinent data). The pentacoordinate 18-electron complex **B** adopts the expected trigonal-bipyramidal structure with the nitrogen atom in an apical position.^[4,5] The $[\text{Rh}(\text{trop}_2\text{N})(\text{LNL})]$ amides **B** ($\text{trop}_2\text{N} = \text{bis}(5H\text{-dibenzo}[a,d]\text{cycloheptene-5-yl})\text{amide}$; $\text{LNL} = \text{tropNH}_2$, bipy) are reversibly oxidized at about -0.5 V (versus the ferrocenium/ferrocene, Fc^+/Fc , couple) to the aminyl radical complexes $[\text{Rh}(\text{trop}_2\text{N})(\text{LNL})]^{+\bullet}$. Their conjugated acids, $[\text{Rh}(\text{trop}_2\text{NH})(\text{LNL})]^{+\bullet}$, have pK_a values of about 19 in DMSO.^[5] In the neutral tetracoordinate 16-electron complex $[\text{Rh}(\text{trop}_2\text{-dach-H})]$, **C**, the NR_2 group is approximately coplanar with the central plane, which leaves the amide nitrogen lone pair in a perpendicular position ($\text{trop}_2\text{-dach} = (R,R)\text{-}N,N'\text{-bis}(5H\text{-dibenzo}[a,d]\text{cyclohepten-5-yl})\text{-1,2-diaminocyclohexane}$; the “ -H ” indicates mono-deprotonation).^[6] This complex is less readily oxidized (-0.34 V versus Fc^+/Fc) and the $\text{pK}_a^{\text{DMSO}}$ of the conjugated acid $[\text{Rh}(\text{trop}_2\text{-dach})]^{+\bullet}$ (15.7) is significantly lower than in **B**. We now report the first stable and fully characterized diamido rhodates(1[−]) and some of their properties. Interestingly, we observe different aggregates between the counteranion, $[\text{M}(\text{solv})_n]^{+}$ ($\text{solv} = \text{solvent molecules}$), and the diamido rhodate(1[−]) anion.

For this purpose, we used the chiral tetrachelating amino olefin $(S,S)\text{-}N,N'\text{-bis}(5H\text{-dibenzo}[a,d]\text{cyclohepten-5-yl})\text{-1,2-diphenyl-1,2-ethylenediamine}$ ($(S,S)\text{-trop}_2\text{dpen} = (S,S)\text{-1}$)^[6] as ligand (Scheme 2). The reaction of ligand $(S,S)\text{-1}$ with $[\text{Rh}(\text{cod})_2]\text{OTf}$ was straightforward and gave the orange-red

Table 1: Selected structural and physical data of **B**, **C**, $(S,S)\text{-3}$, $(S,S)\text{-4}$, $(S,S)\text{-5 hip}$, $(S,S)\text{-5 cip}$, and $(S,S)\text{-5 sip}$. Σ° denotes the sum of bond angles around the nitrogen atom. $\delta(^{103}\text{Rh})$ in ppm ($[\text{D}_8]\text{THF}$, 298 K).

	Rh–N1	Rh–N2	$\Sigma^\circ(\text{N1})^{[a]}$	$\Sigma^\circ(\text{N2})$	$\text{pK}_a^{\text{DMSO}[b]}$	$E_{\text{ox}}^\circ[\text{V}]^{[c]}$	$\lambda_{\text{max}}[\text{nm}]$	$\delta(^{103}\text{Rh})$
B	2.05	–	340.0	–	19	-0.5	≈ 380	> 1000
$(S,S)\text{-3}$	2.093(3)	2.083(3)	342.7(2)	339.8(3)	> 0.6	> 0.6	470	897
C	1.962(2)	2.110(2)	351.1(2)	337.4(2)	15.7(2)	-0.34	516	736
$(S,S)\text{-4}$	–	–	–	–	–	–	506	702
$(S,S)\text{-5 hip}$	1.955(2)	2.030(2)	358.8(2)	340.0(2)	–	–	545	577
$(S,S)\text{-5 cip}$	1.964(4)	2.002(4)	355.7(4)	343.8(4)	21–23	-1.09	598	665 ^[d]
$(S,S)\text{-sip}$	1.992(3)	1.976(3)	347.3(3)	350.9(3)	–	–	599	682

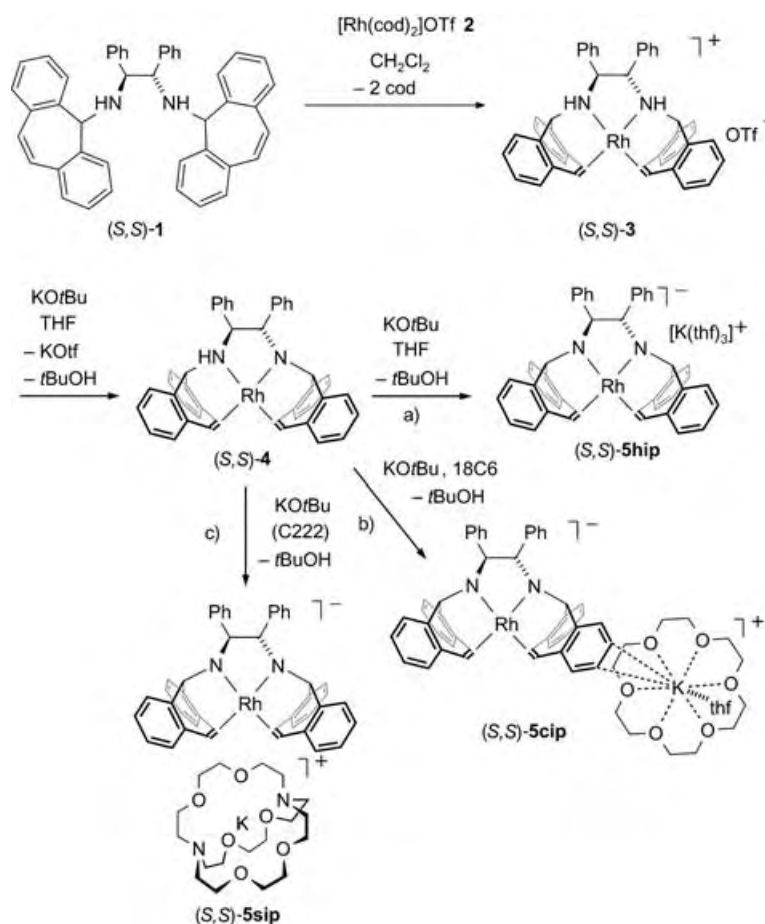
[a] N1 denotes the amido nitrogen center, N2 is NH in **C** and N-K in $(S,S)\text{-5 hip}$. [b] Data of the corresponding acids with the protonated ligand. [c] Potentials versus Fc^+/Fc in a $\text{THF}/n\text{Bu}_4\text{NPF}_6$ electrolyte at $T = 20^\circ\text{C}$, scan rate 100 mVs^{-1} , Pt working electrode. [d] $(S,S)\text{-5 sip}$ in $[\text{D}_6]\text{DMSO}$: $\delta(^{103}\text{Rh}) = 666$ ppm.

[*] Dr. P. Maire, Dr. F. Breher, Prof. Dr. H. Grützmacher
Department of Chemistry and Applied Biosciences
ETH-Hönggerberg
8093 Zürich (Switzerland)
Fax: (+41) 44-633-1032
E-mail: gruetzmacher@inorg.chem.ethz.ch

[**] This work was supported by the LANXESS AG and the Swiss National Science Foundation.

Supporting information for this article is available on the WWW under <http://www.angewandte.org> or from the author.

complex ($\lambda_{\text{max}} = 470 \text{ nm}$) $(S,S)\text{-3}$. When an orange solution of $(S,S)\text{-3}$ in THF was treated with one equivalent of KOtBu , the solution immediately turned red to furnish the amide $(S,S)\text{-4}$ quantitatively. This compound was not isolated but was characterized by NMR and UV/Vis spectroscopy, which show that it is very similar to **C** (see Table 1 for selected data). Subsequently, $(S,S)\text{-4}$ was further deprotonated under different reaction conditions: a) in THF, b) in the presence of three equivalents of $[\text{18}] \text{crown-6}$ (18C6), and c) in the presence of $[\text{2.2.2}] \text{cryptand}$ (C222) (see Scheme 2). In case (a), an



Scheme 2. Synthesis of the amidorhodium(I) complex (S,S)-4, and the various ion pairs (S,S)-5hip, (S,S)-5cip, and (S,S)-5sip.

intensely deep red solution was obtained. In cases (b) and (c), deep green solutions were obtained. Double deprotonation of (S,S)-3 in DMSO as solvent with two equivalents of KOtBu also gave green solutions. The ^1H NMR spectra indicated in each case, that the doubly deprotonated diamido rhodate(1 $^-$), (S,S)- $[\text{Rh}(\text{trop}_2\text{dpn}-2\text{H})]^-$ was obtained.

The products obtained under the conditions a)–c) in Scheme 2 were crystallized and the results of the X-ray diffraction studies are displayed in Figures 1–3, respectively.^[7] From experiment (a), dark red crystals of the composition (S,S)- $[\text{K}[\text{Rh}(\text{trop}_2\text{dpn}-2\text{H})](\text{thf})_3]$, (S,S)-5hip, precipitated (> 80% yield) after the reaction mixture had been layered with *n*-hexane. From experiments (b) and (c), dark green needles of the composition (S,S)- $[\text{K}(\text{18C6})(\text{thf})][\text{Rh}(\text{trop}_2\text{dpn}-2\text{H})]\cdot 0.5\text{Et}_2\text{O}$, (S,S)-5cip, and (S,S)- $[\text{K}(\text{C222})][\text{Rh}(\text{trop}_2\text{dpn}-2\text{H})]\cdot \text{Et}_2\text{O}\cdot 1.5\text{THF}$, (S,S)-5sip, were obtained from solutions of the respective complexes in THF layered with Et_2O ($\geq 80\%$ yield).

The structure of (S,S)-5hip is best described as an electrostatically enforced host–guest complex,^[8] in which the cationic $[\text{K}(\text{thf})_3]^+$ fragment is embedded in the ligand framework of the anion (see Figure 1b). The potassium ion has short contacts to the rhodium(I) atom, one amide nitrogen atom, one hydrogen atom in the ethylene bridge, and four carbon atoms of one of the adjacent benzo rings (see

Figure 1a). Such arene–potassium interactions were recently proposed to account for the performance of ruthenium(II) amides as hydrogenation catalysts.^[9] Note that the coordination of the K^+ ion to N2 causes the Rh–N2 bond (2.030(2) Å) to be significantly longer and the N2 coordination sphere to be more pyramidal (sum of angles $\Sigma^\circ = 340.0(2)^\circ$) compared to N1 which binds at a remarkable short distance (1.955(2) Å) to Rh and resides in an almost planar coordination sphere ($\Sigma^\circ = 358.8(2)^\circ$).

In the crown-ether complex (S,S)-5cip, the $[\text{K}(\text{18C6})(\text{thf})]^+$ and $[\text{Rh}(\text{trop}_2\text{dpn}-2\text{H})]^-$ form a loose contact ion pair; the potassium ion binds at about 3.2 Å in an η^2 -fashion to one benzo group from the outside of the anion (Figure 2). In the two crystallographically independent molecules in (S,S)-5cip the slightly shorter Rh–N bond lengths (1.968(4) Å) correlate with a larger sum of bond angles $\Sigma^\circ(\text{N}) = 354.5^\circ$ ($\Sigma^\circ(\text{N}) = 344.1^\circ$ for the longer Rh–N distances, 1.994(4) Å; averaged data).

In $[\text{K}(\text{C222})][\text{Rh}(\text{trop}_2\text{dpn}-2\text{H})]\cdot \text{Et}_2\text{O}\cdot 1.5\text{THF}$, (S,S)-5sip (Figure 3), the potassium ion has no direct contact to the anion and is encapsulated by the [2.2.2]cryptand. A “free” diamido rhodate(1 $^-$) ion is observed with short Rh–N distances (1.984(3) Å) and flattened coordination spheres at N1 and N2 ($\Sigma^\circ(\text{N}) = 349.1(3)^\circ$) compared to the situation in (S,S)-3 (Rh–N 2.09 Å, $\Sigma^\circ(\text{N}) = 341.2^\circ$). Taking the average over all structures, the Rh–N distance to an amido nitrogen atom, NR_2 , is about 5% shorter than to an amino nitrogen atom, NR_3 .

Figure 4 shows the UV/Vis spectra of the cationic complex (S,S)-3, the neutral rhodium amide (S,S)-4, the

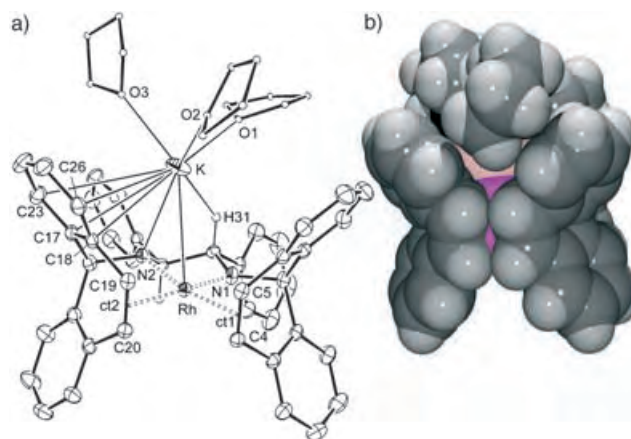


Figure 1. a) Structure of the complex (S,S)-5hip. Thermal ellipsoids are drawn at 30% probability; the three THF molecules are depicted as ball-and-stick models; hydrogen atoms apart from those in the ethylene bridge are omitted for clarity. Selected bond lengths [Å] and angles [°]: Rh–N1 1.955(2), Rh–N2 2.030(2), Rh–C4 2.141(3), Rh–C5 2.121(3), Rh–ct1 2.010(3), Rh–C19 2.126(3), Rh–C20 2.130(3), Rh–ct2 2.004(3), C4=C5_{trop} 1.418(4), C19=C20_{trop} 1.430(4), Rh–K 3.3596(9), K–N2 2.856(3), K–O1 2.727(3), K–O2 2.635(3), K–O3 2.736(4), K–C17 3.424(3), K–C18 3.387(3), K–C23 3.908(3), K–C26 3.797(3), K–H31 2.81; N1–Rh–N2 80.5(1), N1–Rh–ct1 90.8(1), N2–Rh–ct2 92.4(1), ct1–Rh–ct2 96.8(1); $\phi = 7.6^\circ$; (ct = centroids of the $\text{C}=\text{C}_{\text{trop}}$ units; ϕ is the intersection of the planes spanned by the rhodium atom, the N atom and ct of each bischolate ligand). b) Space-filling model of (S,S)-5hip.

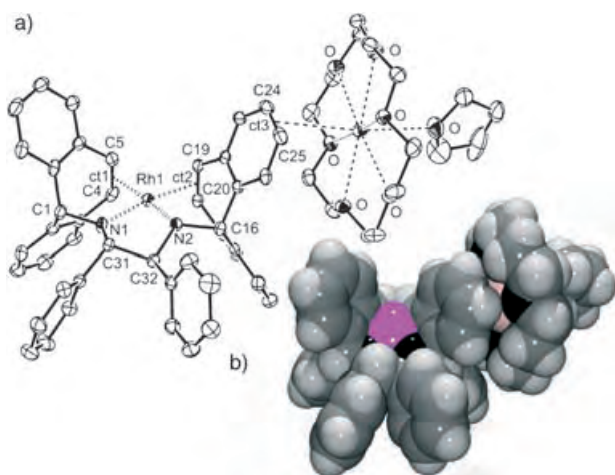
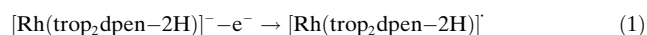


Figure 2. Structure of one of the two independent molecules in (S,S)-5cip. a) A diethyl ether molecule in the crystal lattice and hydrogen atoms are omitted for clarity. Thermal ellipsoids are drawn at 30% probability. Selected bond lengths [Å] and angles [°] (data for the second molecule are given in italics): Rh1–N1 1.964(4), Rh1–N2 2.002(4), Rh2–N3 1.986(4), Rh2–N4 1.972(4), Rh1–C4 2.144(5), Rh1–C5 2.134(5), Rh2–C53 2.156(5), Rh2–C54 2.109(5), Rh1–C19 2.135(4), Rh1–C20 2.120(5), Rh2–C68 2.159(5), Rh2–C69 2.144(5), Rh1–ct1 2.022(5), Rh1–ct2 2.006(5), Rh2–ct4 2.008(5), Rh2–ct5 2.028(5), Rh1–ct3 3.164(6), Rh2–ct6 3.217(6), C4=C5_{trop} 1.397(8), C19=C20_{trop} 1.416(8), C53=C54_{trop} 1.436(8), C68=C69_{trop} 1.439(8), K1–C24 3.179(6), K2–C62 3.255(6), K1–O_(18C6) 2.729(4)–2.861(4), K2–O_(18C6) 2.760(4)–2.833(4), N1–Rh1–N2 80.5(2), N3–Rh2–N4 81.0(2), N2–Rh1–ct2 91.9(2), N3–Rh2–ct4 91.9(2), N1–Rh1–ct1 90.5(2), N4–Rh2–ct5 91.6(2), ct1–Rh1–ct2 97.4(2), ct4–Rh2–ct5 97.8(2); $\phi = 6.4^\circ$, $\phi = 16.2^\circ$; (ct = centroids of C=C bonds; ϕ is the intersection of the planes spanned by the rhodium atom, the N atom and ct of each bischelatate ligand). b) Space-filling model of (S,S)-5cip.

intimate ion pair (S,S)-5hip, and the diamido rhodate(1–) salt (S,S)-5sip in THF. Note the progressively red-shifted absorption λ_{max} in the series: (S,S)-3 \rightarrow (S,S)-4 ($\Delta\lambda_{\text{max}} \approx 40$ nm), (S,S)-4 \rightarrow (S,S)-5hip ($\Delta\lambda_{\text{max}} \approx 40$ nm), and (S,S)-5hip \rightarrow (S,S)-5sip ($\Delta\lambda_{\text{max}} \approx 50$ nm).

We believe that the deep red color ($\lambda_{\text{max}} = 545$ nm) characterizes the host–guest ion pair (S,S)-5hip. Furthermore we assume that (S,S)-5cip and (S,S)-5sip both dissociate in solution and the green color ($\lambda_{\text{max}} = 598$ nm) indicates the presence of the solvent separated “free” anion [Rh(trop₂dpen–2H)][–]. ¹H NMR spectroscopy did not allow us to distinguish between both situations, but the ¹⁰³Rh NMR resonance signal of a red solution of (S,S)-5hip is observed at $\delta = 580$ ppm, whereas the green solutions of (S,S)-5cip and (S,S)-5sip showed $\delta(^{103}\text{Rh}) \approx 670$ ppm (Table 1).

A cyclic voltammogram (Pt electrode, 0.1M nBu₄NPF₆/THF electrolyte at $T = 20^\circ\text{C}$, scan rate 100 mV s^{–1}) of a green solution of (S,S)-5 in DMSO shows a reversible redox wave for the process (1) at a remarkably low oxidation potential (–1.09 V, versus Fc^{+/0}):



The relative differences between the pK_a values, redox potentials, E°_{ox} , and UV/Vis absorptions in the complexes **B**, **C**,

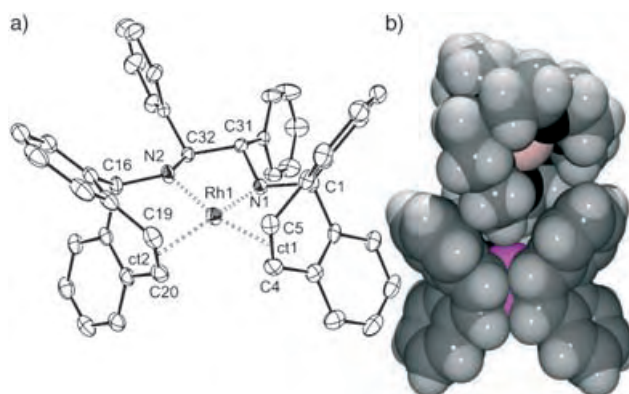


Figure 3. Structure of one of the two independent ion pairs in (S,S)-5sip. a) Structure of the anion, hydrogen atoms are omitted for clarity. Thermal ellipsoids are drawn at 30% probability. Selected bond lengths [Å] and angles [°] (data for the second molecule are given in italics): Rh1–N1 1.992(3), Rh1–N2 1.976(3), Rh2–N3 1.995(3), Rh2–N4 1.970(3), Rh1–C4 2.145(4), Rh1–C5 2.110(4), Rh2–C104 2.136(3), Rh2–C105 2.113(4), Rh1–C19 2.161(4), Rh1–C20 2.114(4), Rh2–C119 2.134(4), Rh2–C120 2.119(4), Rh1–ct1 2.004(4), Rh1–ct2 2.014(4), Rh2–ct3 2.001(4), Rh2–ct4 2.004(4), C4=C5_{trop} 1.429(6), C19=C20_{trop} 1.434(6), C104=C105_{trop} 1.427(5), C119=C120_{trop} 1.422(5), N1–Rh1–N2 81.9(1), N1–Rh1–ct1 91.4(2), N2–Rh1–ct2 91.2(2), ct1–Rh1–ct2 97.9(2), N3–Rh2–N4 82.0(1), N3–Rh2–ct3 92.0(2), N4–Rh2–ct4 91.3(2), ct3–Rh2–ct4 97.3(2); $\phi = 16.6^\circ$, $\phi = 17.1^\circ$; (ct = centroids of the C=C_{trop} units; ϕ is the intersection of the planes spanned by the rhodium atom, the N atom and ct of each bischelatate ligand). b) Space-filling model of (S,S)-5sip.

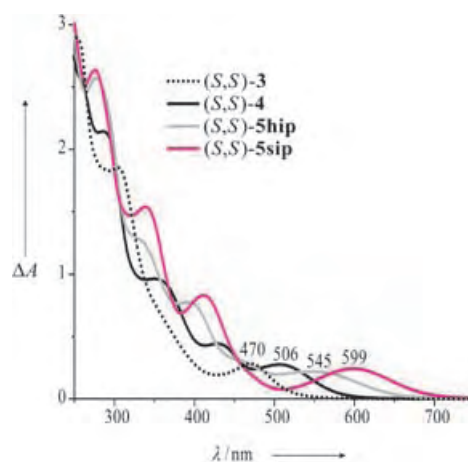


Figure 4. UV/Vis spectra of (S,S)-3, (S,S)-4, (S,S)-5hip, and (S,S)-5sip in solution in THF.

(S,S)-3, (S,S)-4, (S,S)-5hip, and (S,S)-5sip (Table 1) can be interpreted within the concept of filled/filled repulsions (FFR) elegantly developed by Caulton (see Figure 5).^[10,11]

In a pentacoordinate 18-electron rhodium amide **I**, the lone pair at the amide nitrogen atom undergoes a strong and repulsive two-center–four-electron interaction with the occupied d_{xz} orbital at the metal center. This orbital is directed towards the filled p-type orbital at the nitrogen center and is

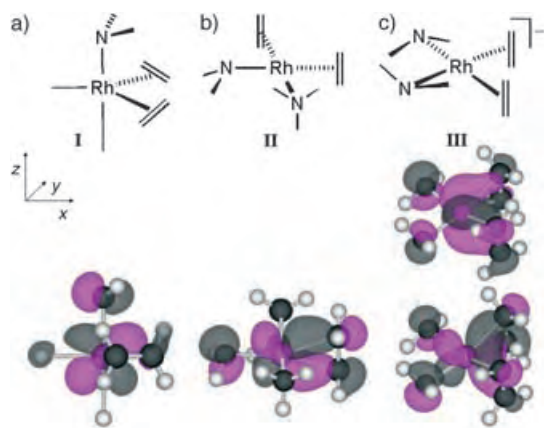


Figure 5. Schematic diagram showing the interaction of filled metal located and filled nitrogen located orbitals in a pentacoordinate 18-electron amido complex **I**, a tetracoordinate 16-electron amino amido complex **II**, and a bisamido complex **III** [filled/filled repulsion (FFR) model]. Only the energetically high-lying antibonding orbital interactions based on extended Hückel calculations are presented.

only slightly perturbed by the olefins which lie in the nodal plane (see Figure 5a). In a tetracoordinate 16-electron amino amido complex **II**, the lone pair at N also suffers from a repulsive interaction (seen in the red shift of λ_{\max} in (S,S)-**4** compared to that in (S,S)-**3**). However, less so because the filled d_{xz} and d_{yz} orbitals at the metal center are involved in $M \rightarrow L$ back-bonding into the $\pi^*(C=C)$ orbitals and are polarized towards the coordinated olefins (see Figure 5b). In that respect, the coordinated olefins contribute to the remarkable stability of late transition metal. Consequently, the strongly destabilized amide **I** is easy to oxidize and the NH function in its conjugated acid has a low acidity (large pK_a). On the other hand, the pK_a value of the NH function of a 16-electron amine complex such as (S,S)-**3**, which gives amide (S,S)-**4** upon deprotonation, is more acidic (by approximately four orders of magnitude). However, double deprotonation of a diamino complex to give a diamido complex **III** gives rise to two destabilizing interactions between the nitrogen lone pairs and the filled d_{xz} and d_{yz} orbitals at the metal center (see Figure 5c). Consequently, λ_{\max} is red-shifted to about 600 nm in compounds of type **III**. The facile oxidation of **III** can be taken as a further indication of this destabilization. The pK_a value of the NH function in the amine amide complex of type **II** falls in the region ($21 < pK_a^{\text{DMSO}} < 23$).^[12] In the host–guest ion pairs, the destabilizing interaction is diminished (blue shift of λ_{\max} ((S,S)-**5sip** \rightarrow (S,S)-**5hip**) by about 50 nm) because of the interaction of the nitrogen lone pair with the potassium cation.

Caulton's FFR concept qualifies nicely as a model to interpret the results presented here with a set of structurally very closely related and rare dialkylamine/amide complexes. On the other hand, the fact that the NH functions in d⁸ rhodium complexes are remarkably acidic^[13] (note that the diamide (S,S)-**5** is even stable in presence of small amounts of methanol or water) and that the Rh–N bond shortens upon deprotonation must await a more deep-sighted (computational) analysis.

Experimental Section

General: Solvents were freshly distilled under argon from sodium/benzophenone (THF, Et₂O) or from sodium/diglyme/benzophenone (*n*-hexane). Air-sensitive compounds were stored and weighed in a glovebox (Braun MB 150 B-G system), and reactions on small scales were performed directly in the glovebox. NMR spectra were recorded on Bruker Avance 400 or 500 systems. The chemical shifts are given as δ values and were referenced against tetramethylsilane (TMS) for ¹H and ¹³C. ¹⁰³Rh NMR spectra were calibrated with the frequency reference $\nu = 3.16$ MHz. IR spectra were measured with the attenuated total reflection technique (ATR) on a Perkin-Elmer 2000 FT-IR spectrometer in the range from 4000 cm⁻¹ to 600 cm⁻¹ using a KBr beam splitter. The UV/Vis spectra were measured with a Perkin-Elmer UV/Vis/NIR Lambda 19 spectrometer in 0.5-cm quartz cuvettes.

(S,S)-[K[Rh(trop₂dpen–2H)](thf)₃] ((S,S)-**5hip**): To an orange solution of (S,S)-[Rh(trop₂dpen)]SO₃CF₃ ((S,S)-**3**) (84 mg, 0.10 mmol) in THF (2 mL) was added KOtBu (25 mg, 0.22 mmol). The color turned immediately to dark red and the solution was layered with *n*-hexane (10 mL). Dark red crystals of (S,S)-**5hip** (80 mg, 0.84 mmol; 84%) suitable for x-ray structure analysis grew overnight. M.p. > 130 °C (decomp); ¹H NMR (400.1 MHz, [D₈]THF): δ = 3.30 (d, ³J_{H,H} = 8.9 Hz, 2H; CH_{olefin}), 3.91 (s, 2H; CH(Ph)(N)), 4.21 (d, ³J_{H,H} = 8.9 Hz, 2H; CH_{olefin}), 4.35 (s, 2H; CH_{benzyl}), 6.60–7.03 (m, 22H; CH_{ar}), 7.37–7.45 ppm (m, 4H; CH_{ar}); ¹³C NMR (100.6 MHz, [D₈]THF): δ = 68.4 (br, CH_{olefin}), 70.8 (CH_{benzyl}), 74.5 (d, ¹J_{Rh,C} = 13.0 Hz; CH_{olefin}), 83.4 (CH(Ph)(N)), 123.6–129.0 (CH_{ar}), 141.1–148.2 ppm (C_{quart}); ¹⁰³Rh NMR (12.7 MHz, [D₈]THF): δ = 577 (s); ATR-IR (neat): $\tilde{\nu}$ = 3061 w, 2972 m, 2866 m, 1594 m, 1482 m, 1466 s, 1404 m, 1259 m, 1052 s, 1016 m, 896 m, 750 s, 699 s cm⁻¹; UV/Vis (THF): λ_{\max} (ϵ) = 545 (2210), 339 (7760), 277 nm (25 680).

(S,S)-[[K([18]crown-6)(thf)][Rh(trop₂dpen)]] ((S,S)-**5cip**): To an orange solution of (S,S)-[Rh(trop₂dpen)]SO₃CF₃ ((S,S)-**3**) (84 mg, 0.10 mmol) in THF (2 mL) was added KOtBu (25 mg, 0.22 mmol) followed by [18]crown-6 (79 mg, 0.3 mmol). The resulting dark green solution was layered with Et₂O. Dark green crystals of (S,S)-**5cip** (101 mg, 0.080 mmol; 80%) grew overnight. M.p. > 155 °C (decomp); ¹H NMR (400.1 MHz, [D₈]THF): δ = 3.08 (d, ³J_{H,H} = 8.9 Hz, 2H; CH_{olefin}), 3.53 (m, 24H; OCH₂CH₂O), 3.96 (s, 2H; CH(Ph)(N)), 3.99 (d, ³J_{H,H} = 8.9 Hz, 2H; CH_{olefin}), 4.27 (d, ³J_{Rh,H} = 1.8 Hz, 2H; CH_{benzyl}), 6.56–6.59 (m, 4H; CH_{ar}), 6.67–6.94 (m, 18H; CH_{ar}), 7.30 (d, ³J_{H,H} = 7.4 Hz, 2H; CH_{ar}), 7.35 ppm (d, ³J_{H,H} = 7.4 Hz, 2H; CH_{ar}); ¹³C NMR (100.6 MHz, [D₈]THF): δ = 67.6 (d, ¹J_{Rh,C} = 10.5 Hz; CH_{olefin}), 70.5 (OCH₂CH₂O), 71.3 (CH_{benzyl}), 73.5 (d, ¹J_{Rh,H} = 12.8 Hz; CH_{olefin}), 84.6 (CH(Ph)(N)), 122.4–129.7 (CH_{ar}), 142.3–148.6 ppm (C_{quart}); ¹⁰³Rh NMR (12.7 MHz, [D₈]THF): δ = 665 ppm (s); ATR-IR (neat): $\tilde{\nu}$ = 2879 m, 1593 w, 1480 w, 1463 m, 1349 m, 1246 s, 1099 s, 960 m, 835 m cm⁻¹; UV/Vis (THF): λ_{\max} (ϵ) = 598 (2420), 412 (8310), 339 (15 360), 275 nm (26 370).

(S,S)-[[K(C222)][Rh(trop₂dpen–2H)]] ((S,S)-**5sip**): To an orange solution of (S,S)-[Rh(trop₂dpen)]SO₃CF₃ ((S,S)-**3**) (32 mg, 0.038 mmol) in THF (0.5 mL) was added KOtBu (9 mg, 0.08 mmol, 2.1 equiv) followed by [2.2.2]cryptand (30 mg, 0.08 mmol, 2.1 equiv). The resulting dark green solution was layered with Et₂O (2.5 mL). Dark green crystals of (S,S)-**5sip** (41 mg, 0.031 mmol; 80%) grew overnight. M.p. > 210 °C (decomp); ¹H NMR (500.1 MHz, [D₈]THF): δ = 2.55–2.57 (m, 12H; NCH₂CH₂O), 3.06 (d, ³J_{H,H} = 9.0 Hz, 2H; CH_{olefin}), 3.54–3.56 (m, 12H; NCH₂CH₂O), 3.60 (s, 12H; OCH₂CH₂O), 3.95 (d, ³J_{H,H} = 9.0 Hz, 2H; CH_{olefin}), 3.98 (s, 2H; CH(Ph)(N)), 4.27 (d, ³J_{Rh,H} = 2.2 Hz, 2H; CH_{benzyl}), 6.56–6.96 (m, 22H; CH_{ar}), 7.28–7.36 ppm (m, 4H; CH_{ar}); ¹³C NMR (125.8 MHz, [D₈]THF): δ = 54.3 (NCH₂CH₂O), 67.5 (d, ¹J_{Rh,C} = 10.0 Hz; CH_{olefin}), 67.9 (NCH₂CH₂O), 70.7 (OCH₂CH₂O), 71.3 (CH_{benzyl}), 73.3 (d, ¹J_{Rh,H} = 12.7 Hz; CH_{olefin}), 84.7 (CH(Ph)(N)), 122.2–129.8 (CH_{ar}), 142.8–149.7 ppm (C_{quart}); ¹⁰³Rh NMR (15.8 MHz, [D₈]THF): δ = 682 ppm (s); ATR-IR (neat): $\tilde{\nu}$ = 3055 w, 2965 w, 2868 s, 1593 m, 1479 m, 1461 m, 1352 m, 1256 m, 1100 s, 946 m, 747 s, 700 m cm⁻¹; UV/

Vis (THF): λ_{max} (ϵ) = 599 (2160), 412 (8300), 339 (15750), 275 nm (23160).

Received: June 13, 2005

Keywords: alkene ligands · amides · binding models · redox chemistry · rhodium

- [1] a) The first rhodium(I) amide was reported by: B. Cetinkaya, M. F. Lappert, S. Torroni, *J. Chem. Soc. Chem. Commun.* **1979**, 843; for reviews see: b) M. F. Lappert, P. P. Power, A. R. Sanger, R. C. Shrivastava, *Metal and Metalloid Amides*, Ellis Horwood, Chichester, UK, **1980**; c) H. E. Brynzda, W. Tam, *Chem. Rev.* **1988**, 88, 1163; d) M. D. Fryzuk, C. D. Montgomery, *Coord. Chem. Rev.* **1989**, 95, 1; e) J. R. Fulton, A. W. Holland, D. J. Fox, R. G. Bergman, *Acc. Chem. Res.* **2002**, 35, 44.
- [2] Selected recent reviews: a) S. E. Clapham, A. Hadzovic, R. H. Morris, *Coord. Chem. Rev.* **2004**, 248, 2201; b) F. Alonso, I. P. Beletskaya, M. Yus, *Chem. Rev.* **2004**, 104, 3079; c) R. Noyori, T. Ohkuma, *Angew. Chem.* **2001**, 113, 40; *Angew. Chem. Int. Ed.* **2001**, 40, 40.
- [3] a) J.-J. Brunet, G. Commenges, D. Neidbecker, K. Phillipot, L. Rosenberg, *Inorg. Chem.* **1994**, 33, 6373; b) J.-J. Brunet, G. Commenges, D. Neidbecker, K. Phillipot, L. Rosenberg, *J. Organomet. Chem.* **1996**, 522, 117; polyanionic amides of rhodium(III) have been reported: R. Zhou, C. Wang, Y. Hu, T. C. Flood, *Organometallics* **1997**, 16, 434.
- [4] T. Büttner, F. Breher, H. Grützmacher, *Chem. Commun.* **2004**, 2820.
- [5] T. Büttner, J. Geier, G. Frison, J. Harmer, C. Calle, A. Schweiger, H. Schönberg, H. Grützmacher, *Science* **2005**, 307, 235.
- [6] P. Maire, F. Breher, H. Schönberg, H. Grützmacher, *Organometallics* **2005**, 24, 3207.
- [7] Crystal structure of (S,S)-**5hip**: Red, highly air-sensitive crystals were obtained from a THF solution which was layered with *n*-hexane at room temperature; $\text{C}_{56}\text{H}_{58}\text{KN}_3\text{O}_3\text{Rh}$, orthorhombic, space group $P2(1)2(1)2(1)$; $a = 11.102(1)$, $b = 16.690(1)$, $c = 24.797(1)$ Å, $V = 4594.4(4)$ Å³; $Z = 4$; $\rho_{\text{calcd}} = 1.372$ Mg m⁻³; crystal dimensions $0.58 \times 0.23 \times 0.23$ mm; diffractometer Bruker SMART Apex; $\text{MoK}\alpha$ radiation, 200 K, $2\theta_{\text{max}} = 56.76^\circ$; 48252 reflections, 11474 independent ($R_{\text{int}} = 0.0779$), direct methods; refinement against full matrix (versus F^2) with SHELXTL (ver. 6.12) and SHELXL-97, 568 parameters, 36 restraints, $R1 = 0.0434$ and $wR2$ (all data) = 0.0914, max./min. residual electron density $0.980/-0.706$ e Å⁻³. Crystal structure of (S,S)-**5cip**: Dark green single crystals were obtained from a THF/Et₂O solution at room temperature; $\text{C}_{120}\text{H}_{132}\text{K}_2\text{N}_4\text{O}_{14}\text{Rh}_2 \cdot \text{Et}_2\text{O}$, monoclinic, space group $P2(1)$; $a = 12.842(1)$, $b = 23.010(1)$, $c = 18.969(1)$ Å, $\beta = 101.780(1)^\circ$; $V = 5487.1(5)$ Å³; $Z = 2$; $\rho_{\text{calcd}} = 1.339$ Mg m⁻³; crystal dimensions $0.60 \times 0.32 \times 0.30$ mm; diffractometer Bruker SMART Apex; $\text{MoK}\alpha$ radiation, 200 K, $2\theta_{\text{max}} = 52.74^\circ$; 40465 reflections, 21957 independent ($R_{\text{int}} = 0.0285$), direct methods; empirical absorption correction SADABS (ver. 2.03); refinement against full matrix (versus F^2) with SHELXTL (ver. 6.12) and SHELXL-97, 1326 parameters, 1 restraint, $R1 = 0.0457$ and $wR2$ (all data) = 0.1124, max./min. residual electron density $0.775/-0.429$ e Å⁻³. Crystal structure of (S,S)-**5sip**: Dark green single crystals were obtained from a THF solution which was layered with Et₂O at room temperature; $\text{C}_{124}\text{H}_{140}\text{K}_2\text{N}_5\text{O}_{12}\text{Rh}_2 \cdot 3\text{THF} \cdot 2\text{Et}_2\text{O}$, triclinic, space group $P1$; $a = 12.078(1)$, $b = 14.324(1)$, $c = 21.272(2)$ Å, $\alpha = 80.882(1)$, $\beta = 85.728(2)$, $\gamma = 68.406(1)^\circ$; $V = 3378.1(5)$ Å³; $Z = 1$; $\rho_{\text{calcd}} = 1.270$ Mg m⁻³; crystal dimensions $0.54 \times 0.48 \times 0.47$ mm; diffractometer Bruker SMART CCD1k; $\text{MoK}\alpha$ radiation, 200 K, $2\theta_{\text{max}} = 56.50^\circ$; 28372 reflections, 25863 independent, direct methods; empirical absorption correction SADABS (ver. 2.03); refinement against full matrix (versus F^2) with SHELXTL (ver. 6.12) and SHELXL-97, 1508 parameters, 22 restraints, $R1 = 0.0424$ and $wR2$ (all data) = 0.1106, max./min. residual electron density $0.660/-0.618$ e Å⁻³. For all reported x-ray crystal structures the non-hydrogen atoms were refined anisotropically. Only one carbon atom of a Et₂O solvent molecule in (S,S)-**5sip** had to be refined using the ISOR restraint. The contribution of the hydrogen atoms, in their calculated position, was included in the refinement using a riding model. Upon convergence, the final Fourier difference map showed no significant peaks. CCDC-267206 ((S,S)-**5hip**), CCDC-267207 ((S,S)-**5cip**), and CCDC-272867 ((S,S)-**5sip**) contain the supplementary crystallographic data for this paper. These data can be obtained free of charge from the Cambridge Crystallographic Data Centre via www.ccdc.cam.ac.uk/data_request/cif.
- [8] Because the coordination sphere of the unsaturated $[\text{K}(\text{thf})_3]^+$ fragment is completed by direct and close contacts within the cavity of the $[\text{Rh}(\text{trop}_2\text{dppe}-2\text{H})^-]$ ion, we denote (S,S)-**5hip** as a host-guest ion pair held together by electrostatic forces. Similarly, (S,S)-**5cip** is considered as contact ion pair because the one open coordination site in the $[\text{K}(\text{18C6})(\text{thf})]^+$ ion is completed by one contact with the anion, however, outside of its cavity. The ion pair (S,S)-**5sip** is denoted as a separated ion pair because of the lack of a direct contact between the potassium ion and the anion although the cryptand penetrates the anion in the solid state. For further definitions see, G. Boche, *Angew. Chem.* **1992**, 104, 742; *Angew. Chem. Int. Ed. Engl.* **1992**, 31, 731, and references therein. For a review on ion pairing in organometallics see: A. Macchioni, *Chem. Rev.* **2005**, 105, 2039.
- [9] R. Hartmann, P. Chen, *Angew. Chem.* **2001**, 113, 3693; *Angew. Chem. Int. Ed.* **2001**, 40, 3581.
- [10] K. G. Caulton, *New J. Chem.* **1994**, 18, 25.
- [11] D. Conner, K. N. Jayaprakash, T. B. Gunnoe, P. D. Boyle, *Inorg. Chem.* **2002**, 41, 3042, and references therein.
- [12] The $\text{p}K_{\text{a}}$ of (S,S)-**4** could not be determined exactly but was estimated by using indole ($\text{p}K_{\text{a}}^{\text{DMSO}} = 20.95$) and benzamide ($\text{p}K_{\text{a}}^{\text{DMSO}} = 23.35$) as reference substances. Green solutions of (S,S)-**5sip** in DMSO react with a slight excess ($\approx 10\%$) of indole to give red (S,S)-**4**, which can be deprotonated with lithium benzamide to give back the green solution characteristic for the diamido rhodate(1-), (S,S)-**5sip**.
- [13] For rather basic amide complexes ($\text{p}K_{\text{a}}^{\text{THF}} > 22$) see: D. Rais, R. G. Bergman, *Chem. Eur. J.* **2004**, 10, 3970; and references therein.

A Helical Molecule That Exhibits Two Lengths in Response to an Applied Potential**

Kazuya Kitagawa, Tomoyuki Morita, and Shunsaku Kimura*

Molecular devices are expected to play an important role in advanced electronics in the form of molecular diodes,^[1] molecular transistors,^[2] and molecular switches.^[3] However, the electron-transfer mechanism of organic molecules on metal surfaces—the most fundamental aspect of molecular devices—still awaits elucidation.^[4–6] In an effort to shed light on this issue, we applied helical peptides as mediators for long-range electron transfer,^[7] a scaffold for chromophores to accelerate electron transfer,^[8] and a viable system for molecular photodiodes.^[9]

Stochastic on–off switching phenomena of molecular conductance in organic molecules have been observed in numerous cases through careful observation by scanning tunneling microscopy (STM).^[10–13] These phenomena are considered to be caused by fluctuations in the hybridization of the sulfur atom that accompanies the change in molecular orientation. Our focus is on the use of this mechanism in a molecular memory device, because one bit may be recognized by a change in molecular length. For this purpose, however, the molecule should be able to exhibit two distinct lengths in response to outer stimuli. Herein, we propose helical peptides as an appropriate system for the controlled switching of molecular length on a bulk substrate.

Peptides that contain α -aminoisobutyric acid (Aib) have the unique ability to adopt two different helical structures: an α -helical conformation with a short overall length (1.5 Å for each amino acid residue) and a longer 3_{10} -helical conformation (2.0 Å for each amino acid residue).^[14,15] Whereas Boc-(Ala-Aib)₄-OCH₃ in crystalline form has been reported to adopt a 3_{10} -helical structure, crystals of Boc-(Ala-Aib)₈-OCH₃ favor an α -helical structure (Boc = *tert*-butoxycarbonyl).^[16] This suggests that an intermediate-length dodecapeptide could have dual α -helical and 3_{10} -helical character. The critical chain length which determines the favored helix type may be an octapeptide, because *para*-bromobenzoyl-

(Aib-Ala)₄-OCH₃ forms an α helix in the crystalline state.^[17] However, the critical chain length is expected to be longer (10 or 12 residues) for the present case, in which the peptides immobilized on gold are examined in air or under ultrahigh vacuum (UHV) because less-polar media tends to favor the formation of 3_{10} helices in peptides, whereas media of higher polarity favors the α -helical conformation, as discussed previously.^[16]

In an earlier study, we succeeded in single-molecule observations of upright helical peptides incorporated into an alkanethiolate self-assembled monolayer (SAM) by STM.^[18] Notably, these helical peptides display a large dipole moment parallel to the helical axis from the C terminus to the N terminus. Therefore, such peptides should be responsive to an applied electric field. Figure 1a illustrates our experimental design with a helical peptide in which the molecular length is modulated with the applied bias. The helical dodecapeptide is immobilized to the gold surface by the N terminus to expose the negatively charged C terminus at the top. The peptide can be contracted to the α helix by placing the STM tip of negative potential on the peptide C terminus. Alternatively, the peptide favors the 3_{10} -helical conformation by the extension force of the STM tip bearing a

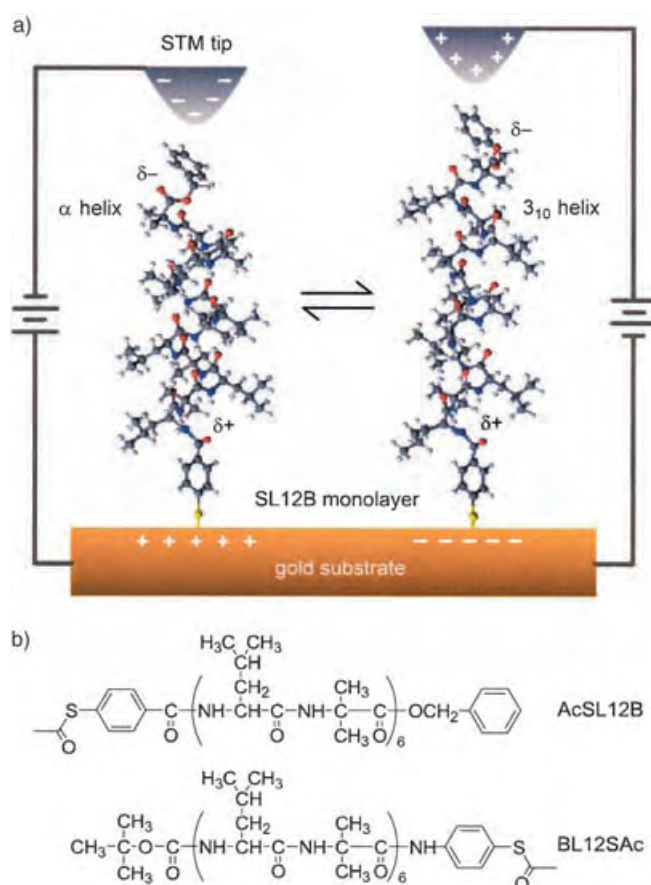


Figure 1. a) Conformational change of a dodecapeptide immobilized onto a gold surface by the N terminus. α Helices and 3_{10} helices are stabilized by applying a positive (left) and negative (right) bias, respectively. b) Structures of the two dodecapeptides used for the work reported herein.

[*] K. Kitagawa, Dr. T. Morita, Prof. S. Kimura
Department of Material Chemistry
Graduate School of Engineering, Kyoto University
Kyoto-Daigaku-Katsura, Nishikyo-ku, 615-8510 Kyoto (Japan)
Fax: (+81) 75-383-2401
E-mail: shun@scl.kyoto-u.ac.jp

[**] This work is partly supported by a Grant-in-Aid for Scientific Research B (15350068) from the Ministry of Education, Culture, Sports, Science, and Technology, Japan. K.K. acknowledges the Research Fellowships of the Japan Society for the Promotion of Science for Young Scientists.

Supporting information for this article is available on the WWW under <http://www.angewandte.org> or from the author.

positive potential. Indeed, we observed conductance switching for the first time in which the apparent molecular lengths are altered as a function of the polarity of the applied bias through the use of the two helical dodecapeptides (Figure 1b). For the experiments reported herein, benzyl ester was used instead of *tert*-butyl ester as the protecting group for the C terminus of the SL12B peptide for synthetic purposes. However, as the size of benzyl ester of SL12B is similar to that of a Boc group in the BL12S peptide, the different terminating groups are not expected to affect the length of the peptides on the substrate.

Conformational energies of the peptide Ac-(Leu-Aib)_n-OCH₃ (*n* = 4, 6, 8) in α -helical and 3_{10} -helical conformations are calculated semiempirically. The heats of formation (kcal mol⁻¹) are indicated in the parentheses as follows: Ac-(Leu-Aib)₄-OCH₃ α helix (−491.759), 3_{10} helix (−492.390); Ac-(Leu-Aib)₆-OCH₃ α helix (−699.056), 3_{10} helix (−697.146); Ac-(Leu-Aib)₈-OCH₃ α helix (−907.733), 3_{10} helix (−902.486). The dodecapeptide with the intermediate length exhibits a small energy difference between the α -helical and 3_{10} -helical conformations, which suggests that there is facile exchange between the two helical types.

Characterizations of BL12S in solution and in SAMs on gold were carried out similarly to those of the previous report on SL12B.^[18] Circular dichroism (CD) studies of BL12SAc in 2,2,2-trifluoroethanol and reflection–absorption spectroscopy (RAS) of the BL12S SAM revealed its α -helical conformation. From the RAS spectrum, the tilt angle of the helical axis from the surface normal was calculated to be 45° (Supporting Information).^[7,9,19,20]

We previously observed single molecules or bundles of SL12B incorporated into dodecanethiolate (C₁₂) SAMs as bright spots by STM under UHV.^[18] BL12S in a C₁₂ SAM is also observed as bright spots (Figure 2a). Notably, time-resolved STM images of the BL12S molecules clearly show switching. Each circle shown in Figure 2a represents a fixed observation point for the peptide helices. Peptides are observed as bright spots with apparent length differences of 5 Å from the surrounding dodecanethiolate SAM surface (ON state). However, these protrusions stochastically disappeared (OFF state) and reappeared (ON state) over a time span of three to four hours.

The effect of the density of the surrounding alkanethiolate matrix on switching was examined.^[10,13] Dodecanethiolate molecules were found to desorb from the gold surface if SAMs were left under UHV ($\approx 10^{-8}$ Pa) for a long period even at room temperature which resulted in a rearrangement of the SAM surface structure.^[21] Figure 2b shows a series of STM images of the SL12B/C₁₂ SAM after leaving the sample under UHV for a long period. The striped pattern of the matrix monolayer is clearly observable, indicating that the C₁₂ molecules lie down on the surface owing to low surface coverage. Under these conditions, the molecular motion of the peptides is allowed more freedom than that of tightly packed peptides in freshly prepared SAMs. The switching behaviors shown in Figure 2b, however, occur at a frequency similar to those shown in Figure 2a; these stochastic switching data are summarized in Table 1. The average number of switching events is nearly the same for the loosely packed

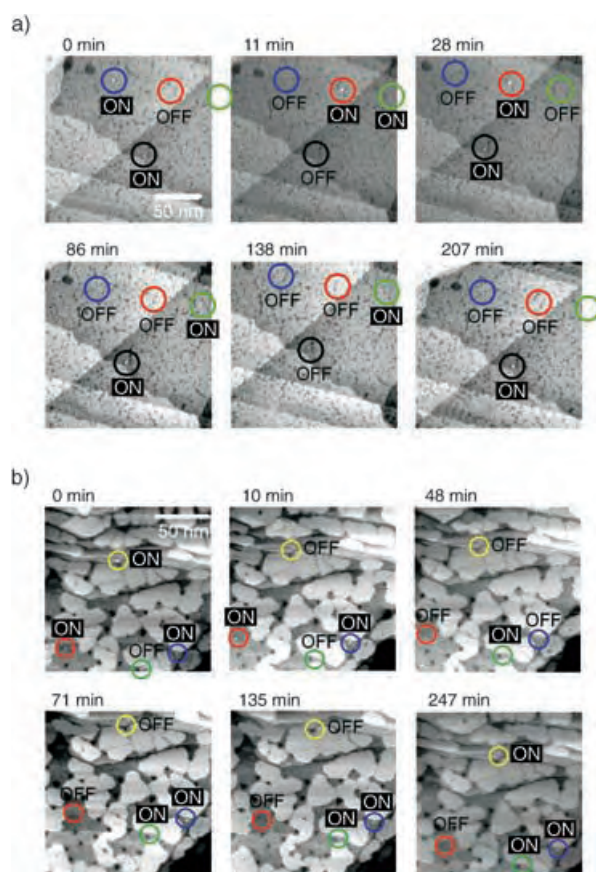


Figure 2. a) STM images of BL12S incorporated into the dodecanethiolate SAM. Images were obtained at a sample bias of 1.4 V and a set-point current of 2.5 pA. b) STM images of SL12B incorporated into the dodecanethiolate SAM after leaving the sample under UHV for a long period (several days). Images were obtained at a sample bias of −1.3 V and set-point current of 5.0 pA.

Table 1: Summary of stochastic conductance switching events.

Parameter	Peptide			
	SL12B		BL12S	
Alkanethiol density	tight	loose	tight	loose
Number of samples	9	6	6	9
Observation time [min]	305	306	207	211
Total number of switching events ^[a]	36	27	19	14
Average number of switching events [min ⁻¹ (500×500 nm ⁻²)]	0.50	0.85	0.55	0.47

[a] The total number of switching events was counted by all changes from ON to OFF and vice versa observed in the STM images between the two successive scans. Each scan required an average of ≈ 6 min. With an observation time of 305 min, ≈ 50 images were recorded.

SAM as it is for the tightly packed SAM. The surrounding C₁₂ molecules do not influence the switching behavior, which suggests that the apparent length change is not a result of the change of the molecular orientation as has been reported for oligo(phenylene ethynylene) groups in alkanethiolate SAMs.^[10,13]

The variation of the apparent molecular length of BL12S is plotted as a function of time (Figure 3a). The dodecapep-

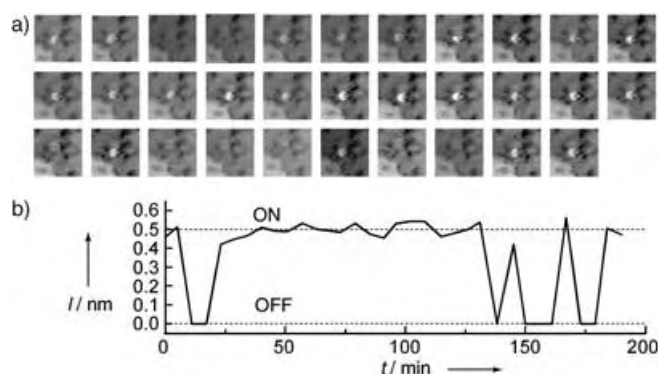


Figure 3. a) Time-lapse STM images (first image, upper left; final image, lower right) of BL12S peptide molecules incorporated into the dodecanethiolate SAM; conditions are the same as those reported in Figure 2. b) Measured molecular length (l) for each image in part a).

tion shows two apparent molecular lengths, and the switching occurs stochastically in transition between these two states. As the dodecapeptide is allowed to take both α -helical and 3_{10} -helical conformations, the two states may be explained by an α helix representing the ON state, and a 3_{10} helix corresponding to the OFF state. This interpretation is supported strongly by the length difference of 5 Å between the two states (Figure 3b), which is in agreement with the molecular-length difference between an α helix and a 3_{10} helix.

Because both helix types display a large dipole moment along the helical axis,^[22] it is expected that the polarity of the applied voltage between the STM tip and the gold substrate influences the STM image of the peptides.^[23,24] BL12S was observed by STM under application of the positive sample bias as described above. When the sample bias was inverted from positive to negative, the bright spots of BL12S disappeared within a few scans, but they reappeared with a return to the positive bias (Figure 4a).

If the interaction of the peptide dipole moment with the applied electric field is the origin of this conductance switch-

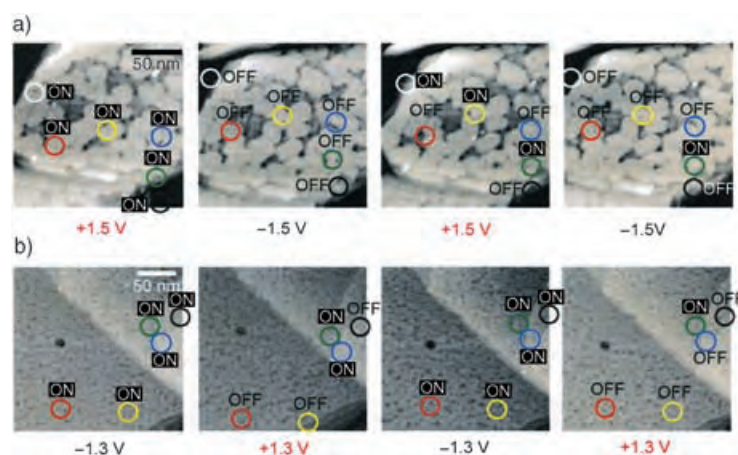


Figure 4. Sequential STM images of a) BL12S (set-point current of 4.5 pA) and b) SL12B (set-point current of 5.0 pA) incorporated into the dodecanethiolate SAM with alternation of the polarity of the applied sample bias voltage.

ing, then SL12B, which has an orientation opposite to that of BL12S and which was immobilized to the gold surface by the N terminus, should also show switching behavior, but with the opposite response to the applied bias polarity. Figure 4b shows the bias dependence of the STM images of SL12B. Indeed, SL12B helices were observed as bright spots at the negative sample bias, but nearly all peptides apparently disappeared from the STM image at the positive bias. Taken together, the dodecapeptides take on a physically elongated state upon application of an electric field in accordance with the direction of the dipole moment. The peptide adopts physically shortened state if the applied electric field is opposite in direction to the dipole moment. It is speculated that under a parallel electric field, the peptides are most stable in a 3_{10} -helical conformation (elongated), and under an opposing electric field direction, the peptides are most stable in an α -helical conformation (shortened; Figure 1a).

The dependence of helical peptide conductivity on the applied bias polarity was further investigated by scanning tunneling spectroscopy (STS) at 77 K. Current–voltage (I – V) curves of the C_{12} molecules and the peptide helices in the SAMs are shown in Figure 5. The I – V curve of the matrix C_{12}

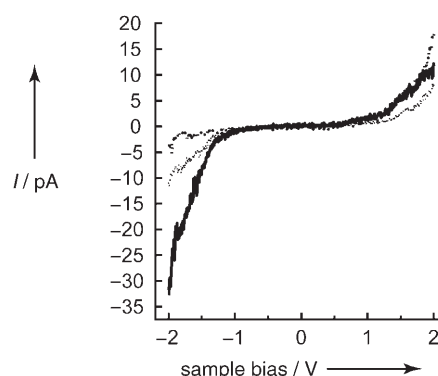


Figure 5. Current–voltage (I – V) curves of dodecanethiolate (thin dotted line), BL12S (thick dotted line), and SL12B (thick solid line) acquired at the temperature of liquid nitrogen (77 K). The lines represent the average of 20–30 individual responses.

molecules shows a featureless monotonic increase in the range from -2 to $+2$ V.^[25,26] On the contrary, asymmetric I – V responses are observed for the helices. In the case of BL12S, the current increased more dramatically at the positive sample bias than at the negative bias. On the other hand, the current through SL12B increased more strongly at the negative bias than that at the positive bias. Both results indicate that the current through the helix is enhanced by applying the bias voltage such that the direction of the electric field coincides with the helical dipole moment. Therefore, the I – V characteristics of the helices also support the interpretation that the helix dipole moment interacts with the external electric field to convert between α -helical and 3_{10} -helical conformations.

In conclusion, we observed conductance switching of peptide helix bundles by STM. The conductance and the

apparent molecular length were observed to undergo stochastic changes with time. The conductance of the helix alternated between two states by changing the polarity of applied bias. This novel behavior can be explained by the conformational change between an α helix and a 3_{10} helix. The helical structure is influenced by the applied electric field as a result of the interaction with the large dipole moment of the helix. This means that the apparent molecular length can be regulated by an external stimulus. The precise control of the switching of the helices is now under investigation.

Received: June 25, 2005

Keywords: electron transfer · helical structures · monolayers · peptides · scanning probe microscopy

- [1] R. M. Metzger, B. Chen, U. Hopfner, M. V. Lakshmikantham, D. Vuillaume, T. Kawai, X. L. Wu, H. Tachibana, T. V. Hughes, H. Sakurai, J. W. Baldwin, C. Hosch, M. P. Cava, L. Brehmer, G. J. Ashwell, *J. Am. Chem. Soc.* **1997**, *119*, 10455.
- [2] S. J. Tans, A. R. M. Verschueren, C. Dekker, *Nature* **1998**, *393*, 49.
- [3] C. P. Collier, E. W. Wong, M. Belohradsky, F. M. Raymo, J. F. Stoddart, P. J. Kuekes, R. S. Williams, J. R. Heath, *Science* **1999**, *285*, 391.
- [4] D. M. Adams, L. Brus, C. E. D. Chidsey, S. Creager, C. Creutz, C. R. Kagan, P. V. Kamat, M. Lieberman, S. Lindsay, R. A. Marcus, R. M. Metzger, M. E. Michel-Beyerle, J. R. Miller, M. D. Newton, D. R. Rolison, O. Sankey, K. S. Schanze, J. Yardley, X. Y. Zhu, *J. Phys. Chem. B* **2003**, *107*, 6668.
- [5] C. Joachim, J. K. Gimzewski, A. Aviram, *Nature* **2000**, *408*, 541.
- [6] A. Nitzan, M. A. Ratner, *Science* **2003**, *300*, 1384.
- [7] T. Morita, S. Kimura, *J. Am. Chem. Soc.* **2003**, *125*, 8732.
- [8] K. Yanagisawa, T. Morita, S. Kimura, *J. Am. Chem. Soc.* **2004**, *126*, 12780.
- [9] S. Yasutomi, T. Morita, Y. Imanishi, S. Kimura, *Science* **2004**, *304*, 1944.
- [10] Z. J. Donhauser, B. A. Mantooth, K. F. Kelly, L. A. Bumm, J. D. Monnell, J. J. Stapleton, D. W. Price, A. M. Rawlett, D. L. Allara, J. M. Tour, P. S. Weiss, *Science* **2001**, *292*, 2303.
- [11] G. K. Ramachandran, T. J. Hopson, A. M. Rawlett, L. A. Nagahara, A. Primak, S. M. Lindsay, *Science* **2003**, *300*, 1413.
- [12] R. A. Wassel, R. R. Fuiere, N. J. Kim, C. B. Gorman, *Nano Lett.* **2003**, *3*, 1617.
- [13] Z. J. Donhauser, B. A. Mantooth, T. P. Pearl, K. F. Kelly, S. U. Nanayakkara, P. S. Weiss, *Jpn. J. Appl. Phys. Part 1* **2002**, *41*, 4871.
- [14] E. Benedetti, B. Di Blasio, V. Pavone, C. Pedone, C. Toniolo, M. Crisma, *Biopolymers* **1992**, *32*, 453.
- [15] S. Mehdi, *Trends Biochem. Sci.* **1991**, *16*, 150.
- [16] K. Otoda, Y. Kitagawa, S. Kimura, Y. Imanishi, *Biopolymers* **1993**, *33*, 1337.
- [17] V. Pavone, E. Benedetti, B. Di Blasio, C. Pedone, A. Santini, A. Bavoso, C. Toniolo, M. Crisma, L. Sartore, *J. Biomol. Struct. Dyn.* **1990**, *8*, 1321.
- [18] K. Kitagawa, T. Morita, S. Kimura, *J. Phys. Chem. B* **2004**, *108*, 15090.
- [19] T. Morita, S. Kimura, S. Kobayashi, Y. Imanishi, *J. Am. Chem. Soc.* **2000**, *122*, 2850.
- [20] Y. Miura, S. Kimura, S. Kobayashi, Y. Imanishi, J. Umemura, *Biopolymers* **2000**, *55*, 391.
- [21] G. E. Poirier, *Chem. Rev.* **1997**, *97*, 1117.
- [22] W. G. J. Hol, *Prog. Biophys. Mol. Biol.* **1985**, *45*, 149.
- [23] C. G. Worley, R. W. Linton, E. T. Samulski, *Langmuir* **1995**, *11*, 3805.
- [24] Y. Miura, S. Kimura, S. Kobayashi, M. Iwamoto, Y. Imanishi, J. Umemura, *Chem. Phys. Lett.* **1999**, *315*, 1.
- [25] W. Y. Wang, T. Lee, M. A. Reed, *Phys. Rev. B* **2003**, *68*.
- [26] D. J. Wold, C. D. Frisbie, *J. Am. Chem. Soc.* **2001**, *123*, 5549.

Peptide Conformations

DOI: 10.1002/anie.200502300

Effect of C-Terminal Amidation on Folding and Disulfide-Pairing of α -Conotoxin ImI**

Tse Siang Kang, Subramanian Vivekanandan,
Seetharama D. S. Jois, and R. Manjunatha Kini*

α -Conotoxins are disulfide-rich neurotoxins isolated from the venom of the marine predatory cone snail. These structurally compact toxins form well-ordered three-dimensional structures through the formation of two crucial disulfide bridges. All currently identified members of the α -conotoxin family exhibit a highly conserved four-cysteine framework, with an absolute preference for folding into the globular form (C1–C3, C2–C4) as the native conformation.^[1–3] They specifically bind to nicotinic acetylcholine receptors. Recently, a new family of γ/λ -conotoxin was identified and shown to have conserved the positions of the cysteine residues characteristic of α -conotoxins. However, γ/λ -conotoxins revealed an alternative disulfide-pairing pattern (C1–C4, C2–C3) that results in the ribbon conformation^[4–6] and distinct biological activity such as inhibition of the noradrenaline transporter by MrIA conotoxin.^[6] Functional assays with the non-native conformations of both α -conotoxin and γ/λ -conotoxin resulted in a tenfold and three-order decrease in activities, respectively.^[4,7]

[*] T. S. Kang, Dr. S. Vivekanandan, Prof. R. M. Kini
Department of Biological Sciences
National University of Singapore
14 Science Drive 4, Block S3 #03–17,
Singapore 117543 (Singapore)
Fax: (+ 65) 6779–2486
E-mail: dbskinim@nus.edu.sg

Dr. S. D. S. Jois
Department of Pharmacy
National University of Singapore
Singapore 117543 (Singapore)

[**] This work is supported by the Biomedical Research Council, Agency for Science, Technology, and Research, Singapore. T.S.K. acknowledges the Singapore Millennium Foundation for granting the research scholarship. The authors thank the Sophisticated Instrument Facility at the Indian Institute of Science and the Chemical and Molecular Analysis Center, Department of Chemistry at the National University of Singapore for allowing the use of their NMR spectrometers.



Supporting information for this article is available on the WWW under <http://www.angewandte.org> or from the author.

These results indicate that the disulfide pairing and the consequent conformation play a crucial role in the biological potencies of native toxins. To identify the structural features that determine specific disulfide pairing, we analyzed the amino acid sequences of α -[8–19] and χ/λ -conotoxins.[4–6] The α -conotoxins, with the exception of GID conotoxin, have a conserved C-terminal amide, whereas all members of χ/λ -conotoxins bear a free carboxylic acid at the C terminus. Herein we report the influence of C-terminal amidation in the determination of the folding tendencies of ImI α -conotoxin in vitro.

Oxidation of the synthetic ImI conotoxin (termed ImI amide) and the corresponding deamidated analogue (termed ImI acid) was conducted in either folding buffer (100 mM Tris-HCl, 2 mM EDTA, pH 8.5) or denaturant buffer (100 mM Tris-HCl, 2 mM EDTA, 6 M GndCl, pH 8.5) by oxidation with air and a glutathione redox system (Gnd = guanidinium; for detailed protocols, see the Supporting Information). Upon oxidation, each of the synthetic variants folded into three monomeric isoforms that correspond to the three peaks observed in the HPLC chromatograms. Each band contained peptides that were completely oxidized as was verified by a decrease by four mass units, which corresponds to the formation of two disulfide bridges (1351.35 ± 0.47 Da and 1352.65 ± 0.04 Da for ImI amide and ImI acid, respectively). The folding experiments conducted in the presence of redox systems also generated isoforms in similar proportions (Table 1).

Table 1: Oxidation studies of peptide analogues under folding and denaturant conditions.^[a]

	% Total oxidized peptides		
	Globular	Ribbon	Beaded
A) Folding buffer			
ImI amide	54.0 \pm 0.4 (52.1 \pm 0.1)	43.0 \pm 1.0 (43.8 \pm 0.4)	3.0 \pm 0.6 (4.0 \pm 0.2)
ImI acid	30.1 \pm 0.6 (29.4 \pm 0.3)	67.2 \pm 0.4 (67.9 \pm 0.1)	2.7 \pm 0.5 (2.8 \pm 0.2)
ImI Gly	40.3 \pm 0.1 (41.5 \pm 0.3)	57.6 \pm 0.1 (54.0 \pm 0.8)	2.1 \pm 0.03 (4.5 \pm 0.5)
B) Denaturant buffer			
ImI amide	48.9 \pm 0.1 (48.3 \pm 0.5)	39.7 \pm 0.0 (38.0 \pm 0.4)	11.4 \pm 0.1 (13.7 \pm 0.1)
ImI acid	37.6 \pm 0.7 (50.3 \pm 0.3)	44.6 \pm 1.8 (39.8 \pm 1.1)	17.8 \pm 2.4 (9.9 \pm 0.1)

[a] The results shown in parentheses represent data acquired when the study was performed in the presence of a redox system.

The various isoforms were initially identified by comparison of the retention times of the conotoxin isoforms with the corresponding regiospecifically synthesized globular and ribbon conformations (Figure 1). The dominant isoform of ImI amide coelutes with the globular form. In contrast, the major isoform of the deamidated ImI acid has the same retention time as its ribbon conformation but not its globular form. In folding buffer, ImI amide shows a tendency to fold into the globular conformation. Substitution of the C-terminal amide to free carboxylic acid, however, resulted in

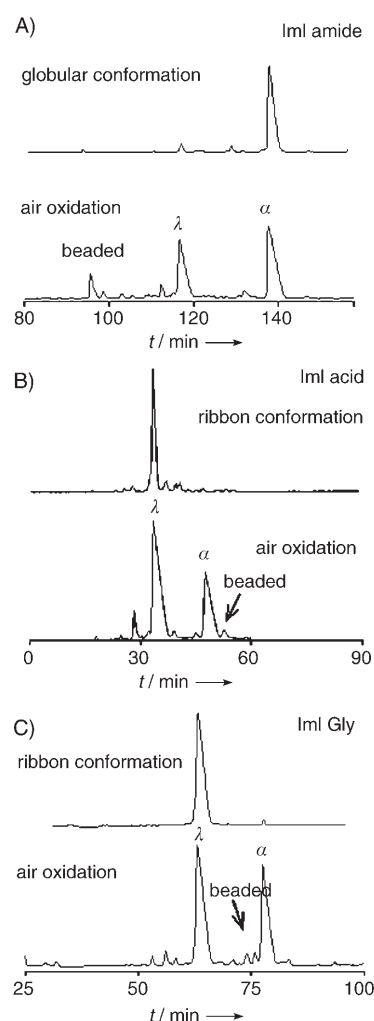


Figure 1. Chromatographic profiles of ImI conotoxin analogues. Comparison of the retention times for the dominant isoform of A) ImI amide B) ImI acid, and C) ImI Gly, with the corresponding regiospecifically synthesized isoforms.

a switch in folding preference of ImI acid to that of the ribbon conformation. Thus, it appears that C-terminal amidation plays a pivotal role in the folding tendencies of ImI conotoxin.

In the presence of a denaturant, the overall folding tendencies remained the same as when the peptides were oxidized with air. However, the amounts of disfavored beaded conformation in both variants were found to have increased, and the presence of guanidine resulted in a “normalizing” effect on the lead of the predominant isoform in both variants. We therefore concluded that side-chain interaction has a significant, but non-absolute, role in the folding to the final conformation of ImI peptides.

To further confirm the disulfide pairings and the folding of ImI amide and ImI acid isoforms, we determined their three-dimensional structure by NMR spectroscopy. Figure 2A shows the amide region in the 1D ^1H NMR spectrum of the dominant forms of the two variants. The 1D ^1H NMR spectrum of the major isoform of ImI amide matches well with that of the force-folded globular conformation. Con-

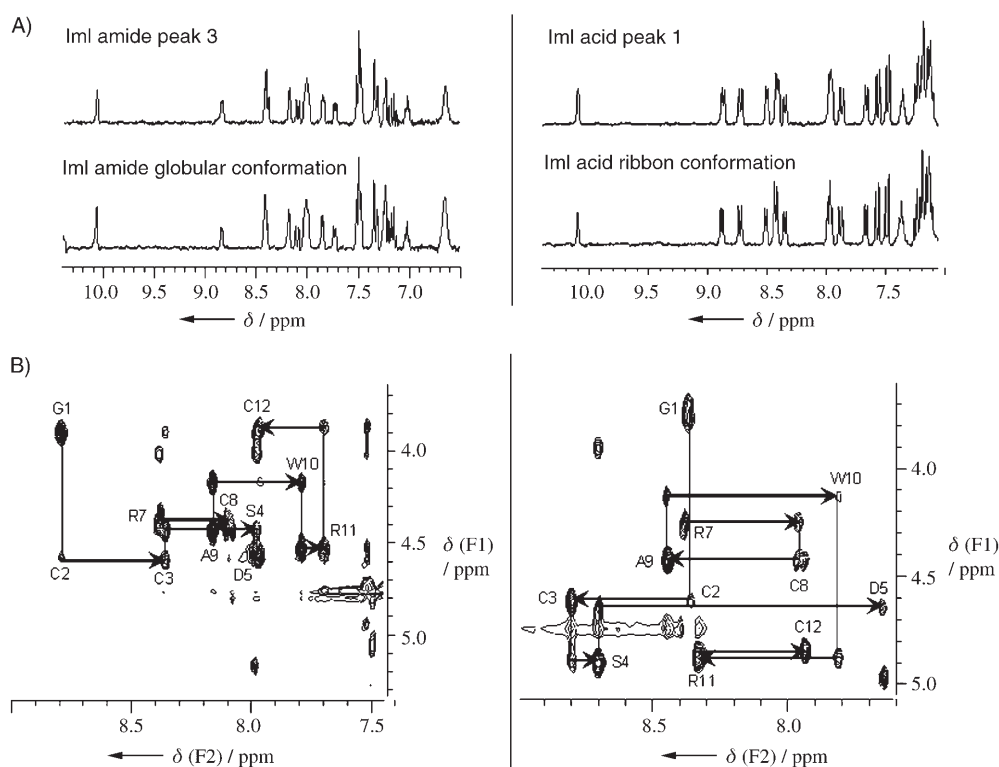


Figure 2. Structural differences between ImI amide and ImI acid. A) Comparison of 1D NMR spectra of the dominant isoforms of ImI amide and ImI acid with the corresponding globular or ribbon conformations. B) Sequential assignment of 2D NMR ROESY spectra of ImI amide (left) and ImI acid (right).

versely, the 1D ^1H NMR spectrum of the major isoform of ImI acid corresponds well to that of its ribbon form.

2D ^1H NMR spectroscopic experiments for ImI amide and ImI acid yielded good-quality spectra. The TOCSY spectrum obtained for ImI amide was similar to that reported earlier,^[20] and the 88 distance constraints derived from its ROESY spectrum fitted well with the reported structure of ImI conotoxin. The 2D NMR ROESY spectrum for ImI acid yielded 110 distance constraints of which the presence of a strong $\alpha\text{H}-\delta\text{H}$ ROE between Asp5–Pro6 suggests a *trans* peptide bond between these two residues. Identification of the $\text{C}\beta\text{H}-\text{C}\beta\text{H}$ ROEs between Cys3–Cys8 and Cys2–Cys12 is indicative of the disulfide-pairing characteristic of the ribbon conformation. The amide regions of the ROESY spectra revealed distinct chemical shift patterns between the globular form of ImI amide and the ribbon conformation that was seen with ImI acid (Figure 2B). Significant differences in chemical shift were observed despite the similarity in amino acid sequences between the analogues. These spectra further support the theory that ImI amide folds preferentially into the globular form and ImI acid into the ribbon conformation.

Figure 3A shows the three-dimensional structure of ImI acid calculated from 2D NMR constraints, the statistics of which are shown in Table 2. The solution structure clearly indicates that ImI acid folds into the ribbon conformation. As the ^1H NMR spectra for ImI amide were similar to those reported earlier, we used the structure previously published.^[21] Figure 3B shows the superimposition of the ribbon

conformation of ImI acid with that of the native globular conformation of ImI conotoxin (PBD accession code 1G2G). Based on ^1H NMR spectra, the solution structure of the isoforms, as well as coelution profiles, we concluded that ImI amide folds predominantly into the globular conformation with C1–C3, C2–C4 disulfide pairings, whereas ImI acid folds preferentially into the ribbon conformation with C1–C4, C2–C3 disulfide pairings. Thus the C-terminal amide has been shown to play a very important role in the determination of the disulfide pairing and resultant protein folding in these two classes of short conotoxins.

Amidation is caused by post-translational oxidative cleavage of a C-terminal glycine residue, and hence we also examined

the folding of the precursor peptide with a further C-terminal glycine (termed ImI Gly). ImI Gly, with its free carboxylic acid, folded predominantly into a ribbon conformation (Table 1). Thus, the presence of a negatively charged group appears to favor the ribbon conformation even in the presence of a further C-terminal residue. Although the three sets of peptides fold into different predominant isoforms, the excess of one form over the other is not drastically different, which therefore suggests that the folding may occur through independent pathways. Figures 3C and D show the proposed hydrogen-bonding interactions of the C-terminal regions of ImI amide and ImI acid, respectively. These noncovalent interactions were derived from the averaged 3D structures calculated. The two variants exhibit distinct hydrogen-bonding patterns. It is not clear whether *cis-trans* isomerization of proline or the postulated hydrogen bonds contribute to these folding pathways.

In several earlier studies, a number of bioactive peptides in nature were shown to have undergone amidation at the C terminus. Such a modification has been shown to have a substantial impact on the biological activities of several of these peptides, presumably owing to the neutralization of negative charges conferred by the carboxylic acid at the C terminus.^[22–26] In these cases, however, the C-terminal amide is not known to influence the conformation of the peptides. In earlier reports, post-translational modifications such as γ -carboxylation of glutamate residues have been shown to be important for the folding in P-superfamily

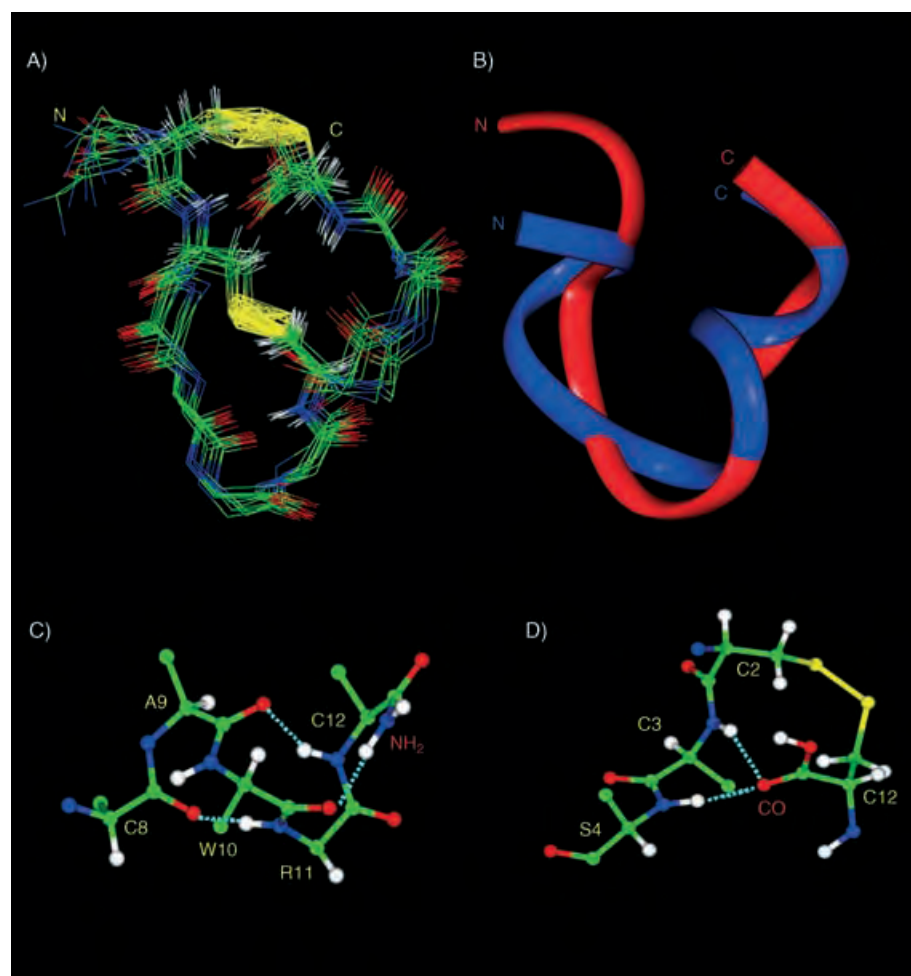


Figure 3. Comparison of solution structures of Iml amide and Iml acid. A) Backbone superimposition of 15 structures of Iml acid determined by NMR spectroscopy. B) Backbone overlay of Iml acid structure (red) with Iml amide (blue). Proposed hydrogen-bonding interactions in the C-terminal region of C) Iml amide and D) Iml acid. The hydrogen bonds are labeled with cyan broken lines, and the C-terminal amide and carbonyl groups are labeled in red.

Table 2: Summary of statistics for structure calculations.

Restraining NMR constraints	RMSD ^[a]
intra residue = 73	backbone atoms: 0.48 ± 0.10
short range (distance $ i-j =1$) = 23	heavy atoms: 0.70 ± 0.14
medium range (distance $1 < i \leq 2$) = 4	all atoms: 0.84 ± 0.13
long range (distance > 2) = 10	
total = 110	

[a] RMSD = root-mean-square deviation.

conotoxins.^[27,28] This is the first example in which amidation was shown to influence the folding tendencies and hence the biological activity of two-disulfide-bonded conotoxins.

Received: July 1, 2005

Revised: July 26, 2005

Published online: September 14, 2005

Keywords: amidation · neurotoxins · NMR spectroscopy · peptides · protein folding

- [1] H. R. Arias, M. P. Blanton, *Int. J. Biochem. Cell Biol.* **2000**, 32, 1017–1028.
- [2] J. M. McIntosh, A. D. Santos, B. M. Olivera, *Annu. Rev. Biochem.* **1999**, 68, 59–88.
- [3] H. Terlau, B. M. Olivera, *Physiol. Rev.* **2004**, 84, 41–68.
- [4] R. A. Balaji, A. Ohtake, K. Sato, P. Gopalakrishnakone, R. M. Kini, K. T. Seow, B. H. Bay, *J. Biol. Chem.* **2000**, 275, 39516–39522.
- [5] J. M. McIntosh, G. O. Corpuz, R. T. Layer, J. E. Garrett, J. D. Wagstaff, G. Bulaj, A. Vyazovkina, D. Yoshikami, L. J. Cruz, B. M. Olivera, *J. Biol. Chem.* **2000**, 275, 32391–32397.
- [6] I. A. Sharpe, J. Gehrmann, M. L. Loughnan, L. Thomas, D. A. Adams, A. Atkins, E. Palant, D. J. Craik, D. J. Adams, P. F. Alewood, R. J. Lewis, *Nat. Neurosci.* **2001**, 4, 902–907.
- [7] J. Gehrmann, P. F. Alewood, D. J. Craik, *J. Mol. Biol.* **1998**, 278, 401–415.
- [8] G. E. Cartier, D. Yoshikami, W. R. Gray, S. Luo, B. M. Olivera, J. M. McIntosh, *J. Biol. Chem.* **1996**, 271, 7522–7528.
- [9] M. Ellison, J. M. McIntosh, B. M. Olivera, *J. Biol. Chem.* **2003**, 278, 757–764.
- [10] M. Fainzilber, A. Hasson, R. Oren, A. L. Burlingame, D. Gordon, M. E. Spira, E. Zlotkin, *Biochemistry* **1994**, 33, 9523–9529.
- [11] W. R. Gray, A. Luque, B. M. Olivera, J. Barrett, L. J. Cruz, *J. Biol. Chem.* **1981**, 256, 4734–4740.
- [12] M. Loughnan, T. Bond, A. Atkins, J. Cuevas, D. J. Adams, N. M. Broxton, B. G. Livett, J. G. Down, A. Jones, P. F. Alewood, R. J. Lewis, *J. Biol. Chem.* **1998**, 273, 15667–15674.
- [13] M. L. Loughnan, A. Nicke, A. Jones, D. J. Adams, P. F. Alewood, R. J. Lewis, *J. Med. Chem.* **2004**, 47, 1234–1241.
- [14] S. Luo, J. M. Kulak, G. E. Cartier, R. B. Jacobsen, D. Yoshikami, B. M. Olivera, J. M. McIntosh, *J. Neurosci.* **1998**, 18, 8571–8579.
- [15] J. S. Martinez, B. M. Olivera, W. R. Gray, A. G. Craig, D. R. Groebe, S. N. Abramson, J. M. McIntosh, *Biochemistry* **1995**, 34, 14519–14526.
- [16] J. M. McIntosh, D. Yoshikami, E. Mahe, D. B. Nielsen, J. E. Rivier, W. R. Gray, B. M. Olivera, *J. Biol. Chem.* **1994**, 269, 16733–16739.
- [17] J. M. McIntosh, C. Dowell, M. Watkins, J. E. Garrett, D. Yoshikami, B. M. Olivera, *J. Biol. Chem.* **2002**, 277, 33610–33615.
- [18] A. Nicke, M. L. Loughnan, E. L. Millard, P. F. Alewood, D. J. Adams, N. L. Daly, D. J. Craik, R. J. Lewis, *J. Biol. Chem.* **2003**, 278, 3137–3144.
- [19] G. C. Zafaralla, C. Ramilo, W. R. Gray, R. Karlstrom, B. M. Olivera, L. J. Cruz, *Biochemistry* **1988**, 27, 7102–7105.
- [20] J. Gehrmann, N. L. Daly, P. F. Alewood, D. J. Craik, *J. Med. Chem.* **1999**, 42, 2364–2372.
- [21] H. Lamthanh, C. Jegou-Matheron, D. Servent, A. Menez, J. M. Lancelin, *FEBS Lett.* **1999**, 454, 293–298.
- [22] M. F. Ali, A. Soto, F. C. Knoop, J. M. Conlon, *Biochim. Biophys. Acta* **2001**, 1550, 81–89.
- [23] R. C. Fernandez, A. A. Weiss, *Antimicrob. Agents Chemother.* **1996**, 40, 1041–1043.
- [24] A. Mor, P. Nicolas, *J. Biol. Chem.* **1994**, 269, 1934–1939.

- [25] Y. Nakajima, X. M. Qu, S. Natori, *J. Biol. Chem.* **1987**, 262, 1665–1669.
- [26] M. L. Sforca, S. Oyama, Jr, F. Canduri, C. C. Lorenzi, T. A. Pertinhez, K. Konno, B. M. Souza, M. S. Palma, N. J. Ruggiero, W. F. Azevedo, Jr., A. Spisni, *Biochemistry* **2004**, 43, 5608–5617.
- [27] G. Bulaj, O. Buczek, I. Goodsell, E. C. Jimenez, J. Kranski, J. S. Nielsen, J. E. Garrett, B. M. Olivera, *Proc. Natl. Acad. Sci. USA* **2003**, 100 Suppl 2, 14562–14568.
- [28] M. B. Lirazan, D. Hooper, G. P. Corpuz, C. A. Ramilo, P. Bandyopadhyay, L. J. Cruz, B. M. Olivera, *Biochemistry* **2000**, 39, 1583–1588.

DNA Recognition

DOI: 10.1002/anie.200463035

Controlling Self-Assembly by Linking Protein Folding, DNA Binding, and the Redox Chemistry of Heme**

D. Dafydd Jones and Paul D. Barker*

Biological molecules are being used extensively as self-assembling materials for the “bottom-up” creation of useful nanoscale structures with non-natural functions.^[1–3] New proteins have been created that form linear, branched, and meshed “wires”,^[4–6] recognize inorganic surfaces,^[2,7] assemble and solubilize carbon nanotubes,^[8,9] create molecular wires by the organization of conducting materials,^[10,11] and generate organized protein networks.^[6] As a result of these functions, the ability to control self-assembly processes through an external signal would be very useful. Allowing added ligand molecules to direct assembly is one such method and is used extensively in nature to switch conformational states which then regulates the associated activity. Artificial systems have also been designed in which a small molecule acts as the link between two separate protein components. The problem with

such a system is that when the small molecule simply bridges the protein components, the signaling event is only dependent on the presence or absence of that small molecule. A system in which control is exerted by an external electron transfer or a photochemical event would be more useful for nanotechnology applications. Extending the principle of electron-transfer-triggered folding reactions^[17] and learning from natural heme-based sensors,^[18,19] we sought to create a macromolecular assembly system that can be controlled by the electronic state of the small molecule — a step towards true electronic control of macromolecular assembly and function.

Previously, we constructed a novel protein that incorporates both cytochrome *b*₅₆₂ (cyt *b*₅₆₂) and the DNA binding basic helix region (BHR) of the leucine zipper transcription factor (bZIP) GCN4.^[20] This design created a protein capable of being assembled on a designated template (DNA) that could potentially both carry and control current flow. The novel DNA-binding cytochrome (DBC) exhibits spectral characteristics and heme affinity that is comparable to those of the parent cyt *b*₅₆₂ and also has the ability to bind DNA sequences based around those recognized by GCN4. This new protein provides the starting point for the creation of a controllable protein-based assembly system in which the parent protein is split into two separate fragments. Each fragment contains one half of the heme binding site and one of the two DNA binding elements that is required for DNA recognition (Figure 1). The assembly of the two protein

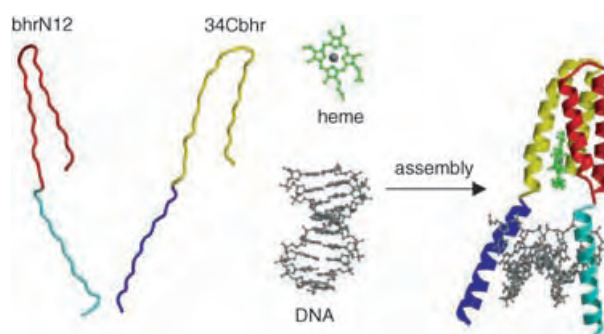


Figure 1. Schematic representation of each system component. The original DNA-binding cytochrome was fragmented to create bhrN12 (residues Met1 to Thr70) and 34Cbhr (residues Met84 to Arg156). DsNC1 is the optimum DNA binding sequence and corresponds to the DNA sequence 5'-caacgATGAcgATGAcggtt-3' (capital letters designate the potential recognition site).

components is dependent on heme and/or DNA. The oxidation-state-dependent affinity of heme for protein can then be exploited to control the assembly, and conditions can be identified under which DNA binding could be controlled by electron-transfer reactions.

The original design of the single-molecule scaffold^[20] has the BHR of GCN4, attached to the termini of the four-helix bundle of cyt *b*₅₆₂, thus creating a DBC. The design specifically arranges the conducting material (heme) on a template (DNA), and events that occur at the heme center can be transmitted to the DNA-binding region and vice versa, which

[*] D. D. Jones,^[†] P. D. Barker
University Chemical Laboratories and MRC Centre for Protein Engineering
University of Cambridge
Lensfield Road, Cambridge, CB21EW (UK)
Fax: (+44) 122-333-6362
E-mail: jonesdd@cardiff.ac.uk
pdb30@cam.ac.uk

[†] Present address:
School of Biosciences, Biomedical Sciences Building
Cardiff University
Museum Avenue, Cardiff, CF103US (UK)

[**] This work was supported by the BBSRC through Grant #SBD07575 and an Advanced Fellowship to P.D.B. We thank Alan Fersht for support and access to facilities, and Shankar Balasubramanian for critical reading of the manuscript.

Supporting Information for this article is available on the WWW under <http://www.angewandte.org> or from the author.

would allow the attenuation of current flow by DNA binding. The DBC binds to specific DNA sequences with a K_D value in the low nM range, but little change in DNA-binding affinity was observed in either the presence or absence of heme, and the affinity was seen to be independent of the oxidation state of heme. We have deconstructed the single protein to create two mutually compatible fragments, bhrN12 and 34Cbhr. Each of these contains one half of the heme-binding site together with one BHR that defines half of the DNA-recognition motif. The two residues that provide axial ligands to the heme iron center, Met7 and His102 (wild-type cyt b_{562} numbering), are separated into the two different molecules in this arrangement. The assembly of these two fragments can be driven by the binding of either heme or DNA and then regenerates an analogue of the original intact complex (Figure 1). The three classes of interaction that become thermodynamically linked in the assembly process are protein–protein, protein–DNA, and protein–heme interactions. As the latter is dependent on the oxidation state of heme, the oxidation state is therefore coupled to the DNA-binding process. The fragments should not self-assemble in the absence of heme or DNA, and the individual halves should not bind heme on their own but can have low affinity for DNA. (In the context of wild-type GCN4, a single BHR can bind its target DNA but with a much lower affinity than the dimeric forms.)^[21,22]

In the wild-type cyt b_{562} , the dissociation constant for reduced heme is in the pM range, but rises to 10 nM when the heme is oxidized.^[23] In the context of our fragments, the difference in free energy between the two states results in a redox-dependent complex assembly that can be used to influence DNA binding. Titration of bhrN12 and 34Cbhr with ferric heme (2 μ M) revealed a low affinity for the cofactor (Figure 2a); $K_D > 27000 \text{ nM} \pm 3000$ is at least 1000-fold higher than that observed for the intact DBC.^[20] Under reducing conditions, the bhrN12 and 34Cbhr fragments bind heme with an affinity ($K_D = 435 \text{ nM} \pm 85 \text{ nM}$) much lower than that of the oxidized form (Figure 2b). In both oxidation states, the spectrum was identical to that of wild-type cyt b_{562} , and the DBC was observed on the addition of 5 equivalents of bhrN12 and 34Cbhr (relative to heme), indicating that the helical bundle had assembled correctly (Supporting Information).

Circular dichroism (CD) spectra of bhrN12 and 34Cbhr suggest that there is little helical structure present when the domains are separated (Supporting Information). Upon mixing of the two components, the CD spectra suggest that no additional structure is induced (Figure 3). The addition of either an equimolar (data not shown) or excess amount of oxidized heme to the mixture of the two proteins, however, results in significant changes in the CD spectrum. The shift in the wavelength of the minimum at 205 nm to 208 nm and the increase in ellipticity at 222 nm are consistent with large increases in the helical content as a result of complex formation. It was not possible to perform the same experiments with the reduced state of heme owing to the absorbance of the reductant required to keep the heme in the reduced state.

To determine if DNA can influence complex assembly, the optimum double-stranded DNA sequence for the chimera^[20]

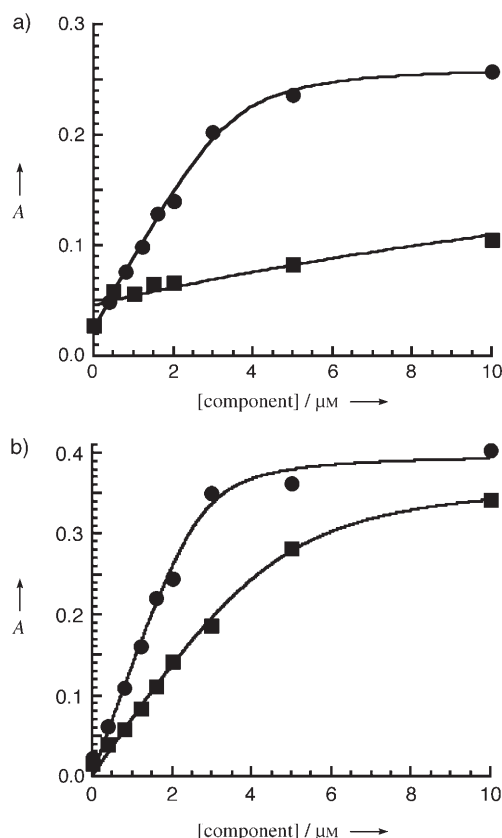


Figure 2. Determination of heme affinity for bhrN12 and 34Cbhr. Data were extracted at a) 417 nm (oxidizing conditions) and b) 427 nm (reducing conditions) in the absence (■) and presence (●) of dsNC1 DNA (Supporting Information). In all samples, heme concentration remains constant at 2 μ M in tris-HCl (20 mM), pH 7.5. BhrN12 and 34Cbhr were titrated in equimolar amounts of 0.4, 0.8, 1.2, 1.6, 2.0, 3.0, 5.0, and 10 μ M. When present, dsNC1 DNA was also at the same concentration as bhrN12 and 34Cbhr. Curve fitting was performed as described in the Supporting Information.

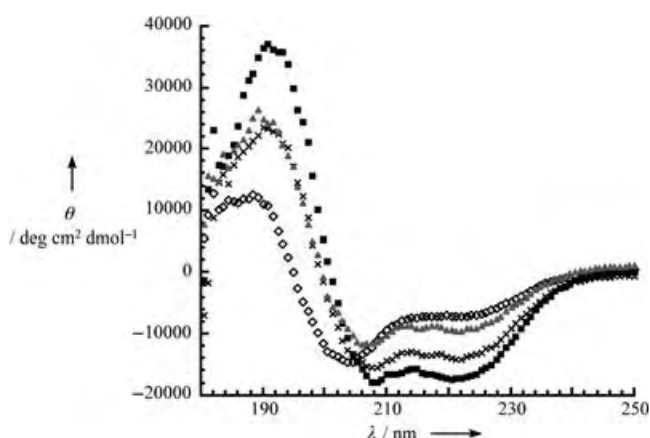


Figure 3. Effect of heme on the structure of the protein components. CD spectra of 5 μ M each of bhrN12 and 34Cbhr in the absence of any ligand (○) or in the presence of either 30 μ M heme (▲), 5 μ M dsNC1 DNA (×), or both 5 μ M dsNC1 DNA and 5 μ M heme (■). CD spectroscopy methods are outlined in the Supporting Information.

dsNC1 was employed to maximize potential binding. It has been observed that the presence of only one BHR region attached to either the N or C terminus of the intact cyt *b*₅₆₂ does not promote tight, specific DNA binding.^[20] However, the increase in helical content of the fragments in the presence of DNA (Supporting Information) suggests that both the bhrN12 and 34Cbhr fragments bind to DNA alone. This crucial difference should allow DNA to direct the assembly and so influence heme binding.

This is indeed the case, as in the presence of dsNC1 DNA, the affinity of bhrN12 and 34Cbhr for oxidized heme is 100-fold higher (K_D decreases to $207 \text{ nm} \pm 27$) than in the absence of DNA (Figure 2). Under reducing conditions, DNA again increased the affinity of bhrN12 and 34Cbhr for heme, to give $K_D < 3 \text{ nm}$, which is more than a 100-fold increase in affinity relative to that in the absence of DNA. It is therefore clear that DNA preassembles the bhrN12 and 34Cbhr fragments to generate a heme-binding site. In the presence of different DNA sequences (comparable length to dsNC1, but with no recognition site), tight binding of heme to the fragments was not observed, regardless of the oxidation state (data not shown). These observations suggest that specific DNA binding is required for optimum bundle-assembly enhancement and is reinforced by the changes observed in the CD spectra upon the addition of DNA to the protein fragments, which indicate an increase in helicity (Supporting Information). The increase in the helical signal is consistent with a coil-to-helix transition known to occur upon BHR binding DNA.^[24] The CD spectrum in the presence of both DNA and heme together with bhrN12 and 34Cbhr indicates that further structural events occur when the complete quaternary complex is formed (Figure 3). The final spectrum in either oxidation state closely resembles that of the wild-type cyt *b*₅₆₂, which suggests that the core of the four-helix-bundle structures are very similar. The specific protein–protein interactions allow precise assembly of the complex thus deterring “off pathway” assembly events such as bhrN12 or 34Cbhr binding heme, despite the presence of the appropriate ligands (Supporting Information). The reduction potential of the DNA-bound, monomeric NC*b*₅₆₂ protein is close to that of the wild-type cyt *b*₅₆₂ (180 mV vs. normal hydrogen electrode at pH 7^[25]). In general, the potential of cyt *b*₅₆₂ is very sensitive to the electrostatic environment, and hence the heme bound species in the thermodynamic scheme (Figure 4) may have different reduction potentials. The electrochemical properties of these assemblies are complicated by multiple equilibria and are being studied by direct electrochemical methods.

CD spectroscopy was also used to observe the binding properties of bhrN12 and 34Cbhr with DNA. The traditional gel-shift assay, as was employed for the intact DBC,^[20] is not useful when complexes can dissociate during electrophoresis.^[22] The changes in the CD spectrum as DNA was titrated against a solution of equimolar concentrations of bhrN12 and 34Cbhr are included in the Supporting Information. Maximum intensity was almost reached at 1 equivalent of DNA. The dissociation constant for DNA binding ($K_D = 186 \text{ nm}$) is about twofold higher than that observed for the intact apo-, chimeric DNA-binding cytochrome, but is still lower than that

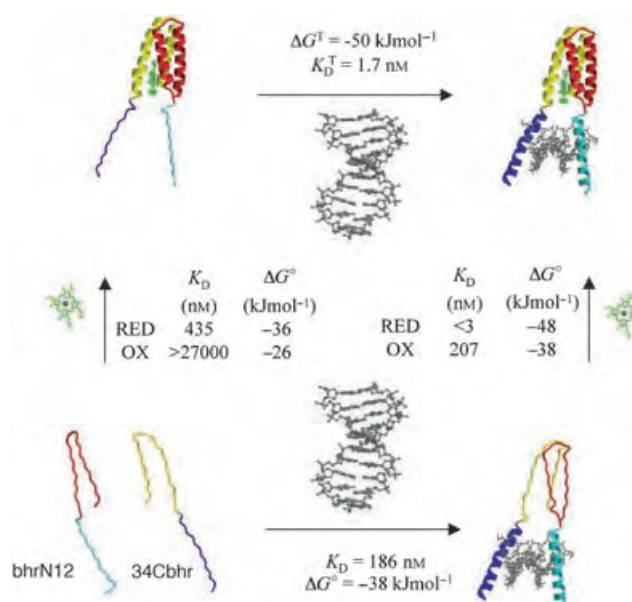


Figure 4. Thermodynamic square based on the calculated K_D values. The K_D values were converted into free energies by using the classical equation $\Delta G^\circ = -RT \ln K_D$. The terms ΔG° and K_D are theoretical values for the bhrN12-heme-34Cbhr complex binding to DNA, calculated by using the determined values of reduced heme for the other three binding equilibria.

observed for the intact DBC binding to a non-optimal DNA-binding sequence.^[20]

Measurement of the dissociation constant of DNA from the heme-bound complex has not yet been possible as measurements cannot be made at concentrations well above the K_D value required for the saturated ternary complex between ferric heme and the two fragments. Below the K_D value, binding experiments result in convolution of multiple equilibria, and there is no measurable signal that reports the contribution of each binding event. We are, however, pursuing the use of fluorescently labeled DNA to access this equilibrium constant. The K_D value can be estimated for bhrN12 \approx heme \approx 34Cbhr for DNA through the construction of a classical thermodynamic square (Figure 4). The sum of the free energies of the formation of the quaternary complex (DNA-bound bhrN12-heme-34Cbhr complex; top right corner of Figure 4) from bhrN12 and 34Cbhr should be equal, irrespective of the pathway taken. The calculated standard free energy for the formation of the bhrN12-heme-34Cbhr complex with DNA is -50 kJ mol^{-1} , which translates into $K_D = 1.7 \text{ nm}$ and is independent of the oxidation state of the heme. This value is very close to that of the intact DBC binding to dsNC1 in the absence of nonspecific DNA ($K_D \approx 10 \text{ nm}$).^[20] The magnitude of the changes in the DNA-binding affinity of our proteins in the absence and presence of heme is similar to the changes observed when naturally occurring GCN4 peptides dimerize upon DNA binding.^[22] Therefore, we relate heme binding in our system to leucine zipper dimerization in GCN4. The magnitude of the energy of the coupling between DNA and heme binding (two orders of magnitude in K_D) compares favorably with the coupling of small-molecule binding (by maltose-binding protein) with β -

lactamase activity, as was recently reported for a different chimeric protein.^[26,27]

To assess the influence of DNA on protein assembly, equimolar amounts of bhrN12 and 34Cbhr were incubated with varying concentrations of DNA prior to the addition of heme. As the DNA concentration increases to the equivalence point, so does absorbance at 417 nm, therefore indicating complex formation (Figure 5). After the equivalence

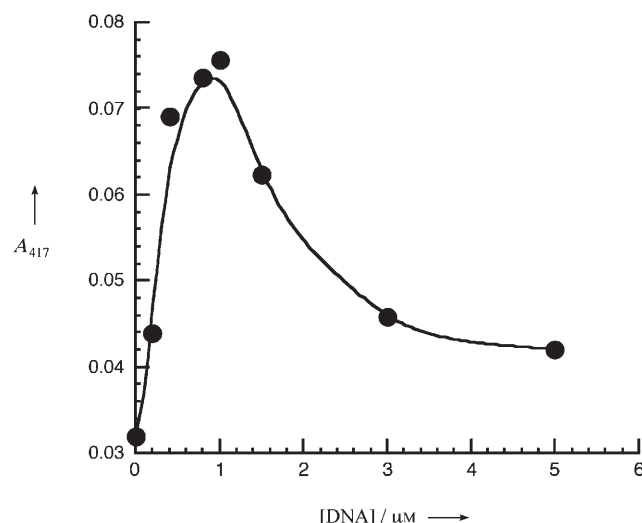


Figure 5. DNA as a competitive inhibitor to complex formation. The bhrN12 and 34Cbhr components were present at 1 μM , in the presence of 0.2, 0.4, 0.6, 0.8, 1.0, 1.5, 3.0, or 5.0 μM dsNC1 DNA. Oxidized heme (1 μM) was added as the last component of the mixture, and the system was allowed to equilibrate. Absorbance at 417 nm was used to determine complex assembly (Supporting Information).

lence point, the absorbance begins to decrease, suggesting a decrease in complex assembly. Increasing the DNA concentration beyond that of the protein concentration results in the binding of the protein fragments to different DNA molecules, inhibiting complex assembly. Together with the observation that the binding of DNA alone induces helical structure in bhrN12 and 34Cbhr (Supporting Information), these data suggest the binding of a monomeric BHR peptide to DNA. This is in contrast to our previous result that the complete cytochrome with only one BHR unit attached to either terminus cannot bind DNA.^[20] Although we currently have no explanation for this, it is interesting that the loop that links helices 2 and 3 of the wild-type cyt b_{562} is present in the intact DBC, but absent in our current work (having been deleted in making the fragments described herein). Modeling studies suggest that this loop may interact in a negative fashion with the DNA, and our initial study revealed a complex relationship between loop length and DNA affinity.^[20] Complete removal of the constraints imposed by this loop (as is the case in our current work) may promote the binding of the fragments to DNA.

The mechanism by which GCN4 binds DNA is dependent on how the whole complex assembles. It is known that GCN4 can bind DNA either as a monomer or as a dimer, but to

generate a stable, high-affinity protein–DNA complex, the dimeric form is required.^[22] GCN4 can form the dimer through the leucine zipper prior to binding, with the BHR disordered until it binds to DNA,^[24,28] but the dimerization event is thought to be rate-limiting with respect to DNA binding.^[22] It has also been reported that certain bZIP proteins bind sequentially as monomers to DNA and then assemble into dimers,^[21] whereas other studies have shown that bZIP proteins can bind as monomers.^[22,29] It is therefore not surprising that we have observed evidence of DNA binding of the individual fragments.

We have successfully taken the original design of the DNA-binding cytochrome (DBC) and converted it into a highly cooperative system in which heme and DNA binding influence the self-assembly of the complex. Splitting the complex into two fragments essentially mimics the original GCN4 mechanism, but in this case, a heme-binding domain replaces the leucine zipper. The result is that heme and DNA-binding processes are linked through protein conformation and assembly, which can be controlled electronically. This therefore adds an extra functional component to the toolbox of molecules that could be used in device construction.^[3,30] To avoid heme dissociation during the switching, a covalent linkage between the protein and the cofactor can be introduced into the system,^[31,32] though this will change the relative stabilities of the different assembled states. To compensate for this, heme-iron–ligand mutations^[33] will be needed to exaggerate the oxidation-state dependence of assembly. Direct electron transfer between cyt b_{562} and solid-state electrodes is facile,^[34] and we are currently investigating the DNA-promoted electrochemistry of these DBCs. Our system therefore has the properties required of a molecular transducer in an electronic device that can control an assembly process. The scaffold in its present forms represents the fundamental core of such a device and can be modified further to change or enhance its character.

Experimental Section

All the materials used are described in the Supporting Information. The bhrN12 and 34Cbhr genes were constructed by using the original DBC as the template. A more-detailed description of fragment construction and purification is in the Supporting Information. Heme-binding affinity was determined spectrophotometrically as outlined in both the figure legends and Supporting Information. Absorbance at 417 nm and 427 nm was used to monitor heme binding to bhrN12 and/or 34Cbhr under both oxidizing and reducing conditions (2 mM sodium ascorbate as the source of reducing equivalents). The heme-binding affinity for bhrN12 and 34Cbhr was determined by extracting the data at the above wavelengths and plotting against component concentration (bhrN12, 34Cbhr, and/or DNA). The data was then analyzed in a manner similar to that used by Bosshard and co-workers for dimeric derivatives of the GCN4 protein.^[22] DNA inhibition of complex formation was determined as described in the legend to Figure 5 and in the Supporting Information. CD spectroscopy methods are described in the Supporting Information.

Received: December 22, 2004

Revised: July 13, 2005

Published online: September 15, 2005

Keywords: cytochromes · DNA binding · heme · protein folding · self-assembly

- [1] T. O. Yeates, J. E. Padilla, *Curr. Opin. Struct. Biol.* **2002**, *12*, 464.
- [2] S. Zhang, *Nat. Biotechnol.* **2003**, *21*, 1171.
- [3] I. Willner, B. Willner, *Trends Biotechnol.* **2001**, *19*, 222.
- [4] M. G. Ryadnov, B. Ceyhan, C. M. Niemeyer, D. N. Woolfson, *J. Am. Chem. Soc.* **2003**, *125*, 9388.
- [5] M. G. Ryadnov, D. N. Woolfson, *Angew. Chem.* **2003**, *115*, 3129; *Angew. Chem. Int. Ed.* **2003**, *42*, 3021.
- [6] P. Ringler, G. E. Schulz, *Science* **2003**, *302*, 106.
- [7] M. Sarikaya, C. Tamerler, A. K. Jen, K. Schulten, F. Baneyx, *Nat. Mater.* **2003**, *2*, 577.
- [8] R. J. Chen, S. Bangsaruntip, K. A. Drouvalakis, N. W. Kam, M. Shim, Y. Li, W. Kim, P. J. Utz, H. Dai, *Proc. Natl. Acad. Sci. USA* **2003**, *100*, 4984.
- [9] G. R. Dieckmann, A. B. Dalton, P. A. Johnson, J. Razal, J. Chen, G. M. Giordano, E. Munoz, I. H. Musselman, R. H. Baughman, R. K. Draper, *J. Am. Chem. Soc.* **2003**, *125*, 1770.
- [10] T. Scheibel, R. Parthasarathy, G. Sawicki, X. M. Lin, H. Jaeger, S. L. Lindquist, *Proc. Natl. Acad. Sci. USA* **2003**, *100*, 4527.
- [11] E. Katz, I. Willner, *Angew. Chem.* **2004**, *116*, 6166; *Angew. Chem. Int. Ed.* **2004**, *43*, 6042.
- [12] J. C. Carlson, A. Kanter, G. R. Thuduppathy, V. Cody, P. E. Pineda, R. S. McIvor, C. R. Wagner, *J. Am. Chem. Soc.* **2003**, *125*, 1501.
- [13] J. D. Klemm, S. L. Schreiber, G. R. Crabtree, *Annu. Rev. Immunol.* **1998**, *16*, 569.
- [14] H. D. Mootz, T. W. Muir, *J. Am. Chem. Soc.* **2002**, *124*, 9044.
- [15] R. Pollock, T. Clackson, *Curr. Opin. Biotechnol.* **2002**, *13*, 459.
- [16] R. Pollock, M. Giel, K. Linher, T. Clackson, *Nat. Biotechnol.* **2002**, *20*, 729.
- [17] J. R. Telford, P. Wittungstafshede, H. B. Gray, J. R. Winkler, *Acc. Chem. Res.* **1998**, *31*, 755.
- [18] S. Aono, *Acc. Chem. Res.* **2003**, *36*, 825.
- [19] M. A. Gilles-Gonzalez, G. Gonzalez, *J. Appl. Physiol.* **2004**, *96*, 774.
- [20] D. D. Jones, P. D. Barker, *ChemBioChem* **2004**, *5*, 964.
- [21] S. J. Metallo, A. Schepartz, *Nat. Struct. Biol.* **1997**, *4*, 115.
- [22] S. Cranz, C. Berger, A. Baici, I. Jelesarov, H. R. Bosshard, *Biochemistry* **2004**, *43*, 718.
- [23] P. Garcia, M. Bruix, M. Rico, S. Ciofi-Baffoni, L. Banci, M. C. R. Shastry, H. Roder, T. D. Woodyear, C. M. Johnson, A. R. Fersht, P. D. Barker, *J. Mol. Biol.* **2005**, *346*, 331.
- [24] T. E. Ellenberger, *Curr. Opin. Struct. Biol.* **1994**, *4*, 12.
- [25] P. D. Barker, unpublished results.
- [26] G. Guntas, S. F. Mitchell, M. Ostermeier, *Chem. Biol.* **2004**, *11*, 1483.
- [27] G. Guntas, M. Ostermeier, *J. Mol. Biol.* **2004**, *336*, 263.
- [28] M. A. Weiss, T. Ellenberger, C. R. Wobbe, J. P. Lee, S. C. Harrison, K. Struhl, *Nature* **1990**, *347*, 575.
- [29] C. Park, J. L. Campbell, W. A. Goddard III, *J. Am. Chem. Soc.* **1996**, *118*, 4235.
- [30] I. Willner, *Science* **2002**, *298*, 2407.
- [31] P. D. Barker, E. P. Nerou, S. M. V. Freund, I. M. Fearnley, *Biochemistry* **1995**, *34*, 15191.
- [32] J. W. Allen, P. D. Barker, S. J. Ferguson, *J. Biol. Chem.* **2003**, *278*, 52075.
- [33] P. D. Barker, E. P. Nerou, M. R. Cheesman, A. J. Thomson, P. de Oliveira, H. A. O. Hill, *Biochemistry* **1996**, *35*, 13618.
- [34] P. D. Barker, J. Butler, P. de Oliveira, H. A. O. Hill, N. I. Hunt, *Inorg. Chim. Acta* **1996**, *250*, 71.

DOI: 10.1002/anie.200500540

Structural Interplay between Calcium(II) and Copper(II) Binding to S100A13 Protein**

Fabio Arnesano, Lucia Banci, Ivano Bertini,*
Adele Fantoni, Leonardo Tenori, and
Maria Silvia Viezzoli

S100s are dimeric proteins that constitute one of the largest groups in the EF-hand Ca^{II} -binding protein family.^[1] The relevance of S100 proteins is shown by their involvement in various human diseases, through a variety of networks of interacting proteins.^[1]

Human S100A13 is a ubiquitous protein of 98 amino acids which represents one of the latest members identified in the S100 protein family.^[2] S100A13 is involved in the cellular export of interleukin-1 α (IL-1 α), a potent proinflammatory cytokine, and of fibroblast growth factor-1 (FGF-1), which plays a crucial role in angiogenesis and tissue regeneration.^[3] Export is based on the Cu^{II} -dependent formation of multi-protein complexes containing the S100A13 protein, which assemble near the inner surface of the plasma membrane.

The primary sequence indicates that, like most S100 proteins, S100A13 contains a 12-residue canonical Ca^{II} -binding loop (site II) and a 14-residue “pseudo” Ca^{II} -binding loop (site I). The affinity of the two Ca^{II} -binding sites is 1.25×10^5 and $2.5 \times 10^3 \text{ M}^{-1}$, respectively.^[4] Consistent with its function and its intracellular location near the inner surface of the plasma membrane, the Ca^{II} -binding affinity of site I of S100A13 is lower ($\approx 10^3 \text{ M}^{-1}$) than that typically found for other S100 proteins ($\approx 10^5$ – 10^6 M^{-1}), as it is tuned for the higher local Ca^{II} ion concentration near the membrane.^[5]

Herein, we report the structural effects of Ca^{II} and Cu^{II} ion binding to S100A13, and show that binding of two Ca^{II} ions per monomer triggers key conformational changes leading to the creation of two identical and symmetrical Cu^{II} -binding sites on the surface of the protein, close to the interface between the two monomers. These Cu^{II} -binding sites are unique among the S100 proteins, which are reported to bind Cu^{II} or Zn^{II} ions in addition to Ca^{II} ions.^[6,7]

The expressed S100A13 was treated with ethylenediaminetetraacetic acid (EDTA) to remove all bound metal ions. Its molecular weight, as measured from electrospray

[*] Dr. F. Arnesano, Prof. L. Banci, Prof. I. Bertini, A. Fantoni, L. Tenori, Prof. M. S. Viezzoli
Magnetic Resonance Center CERM and Department of Chemistry
University of Florence
Via L. Sacconi 6, 50019 Sesto Fiorentino (Italy)
Fax: (+39) 055-457-4271
E-mail: bertini@cerm.unifi.it

[**] This work was supported by the European Commission (SPINE contract QL2-CT-2002-00988). The Italian MURST COFIN03 is acknowledged for financial support.



Supporting information for this article is available on the WWW under <http://www.angewandte.org> or from the author.

mass spectra (ES-MS), is $11\,340 \pm 1$ Da, which corresponds to residues 2–98 (with the N-terminal methionine residue cleaved). Gel-filtration chromatography gives an apparent molecular mass of $25\,500 \pm 500$ Da, which indicates that the protein is in a dimeric state. Addition of Ca^{II} to the apoprotein (apo), followed by electronic spectroscopy,^[4] produced a final species whose molecular weight was greater by 80 Da, thus confirming that the protein contains two bound Ca^{II} ions per monomer (Ca_2 -S100A13).

The ^1H , ^{15}N heteronuclear single-quantum coherence (HSQC) NMR spectra showed well-dispersed signals in both dimensions, indicative of a well-folded protein for both apo and Ca-loaded states, with a larger spectral dispersion for the latter (see Supporting Information). The ^{15}N relaxation measurements are consistent with a dimeric state of both forms of the protein in solution. They are characterized by overall rotational correlation times of 13.4 ± 1.2 and 15.0 ± 0.9 ns for the apo and Ca-loaded forms, respectively, and by the same rotational diffusion tensor ($D_{\parallel}/D_{\perp} = 1.2$).

Sequence-specific assignment was not complete for the backbone resonances of some of the residues at the C terminus ($\text{R}^{88}\text{KKKDLKIRKK}^{98}$) because of the high number of Lys and Arg residues determining extensive signals overlap. These residues experience negative $^{15}\text{N}\{^1\text{H}\}$ NOE values, which indicates a mobility faster than protein tumbling. The ^1H - ^{15}N cross-peaks of residues 22–27 (corresponding to the first Ca^{II} -binding loop between helices $\alpha 1$ and $\alpha 2$) are sensitive to pH and disappear at pH values higher than 6.5 in both forms of the protein. The signals for residues 22–27 appear at lower pH values, but in the apo form they are split in multiple lines, thus indicating multiple conformations in slow exchange on the NMR timescale. This is not the case for Ca_2 -S100A13, where residues 22–27 are stabilized toward a single conformation by calcium. Therefore, a complete dynamic characterization can be performed for the latter system. In total (residues 2–87), about 89 and 94% of carbon atoms, 90 and 95% of nitrogen atoms, and 86 and 91% of protons were assigned for apo- and Ca_2 -S100A13, respectively (see Supporting Information).

The structures have backbone root-mean-square deviation (RMSD) values to the mean monomeric structure (residues 8–86) of 0.94 ± 0.41 and 0.58 ± 0.09 Å for apo- and Ca_2 -S100A13, respectively. These values are 1.05 and 0.69 Å, respectively, for the dimer, for which the relative orientation of the two subunits has been experimentally determined through several intermonomer NOEs. The mean structures are shown in Figure 1a and b. A statistical analysis of the quality is reported in the Supporting Information. Both forms consist of homodimers, in which the two monomers are related by a twofold symmetry axis. Each monomer encompasses four α helices and two short β strands, in agreement with the chemical shift index. The two proposed Ca^{II} -binding sites are located between helices $\alpha 1$ and $\alpha 2$, and between helices $\alpha 3$ and $\alpha 4$, respectively (inset of Figure 1b), while a hinge region (residues 45–55) separates $\alpha 2$ from $\alpha 3$. A short antiparallel β sheet is identified within each monomer between residues S^{32} and S^{34} in Ca^{II} -binding site I, and residues E^{70} and K^{72} in site II. The ^1H , ^{15}N amide chemical-shift differences between apo- and Ca_2 -S100A13 are larger

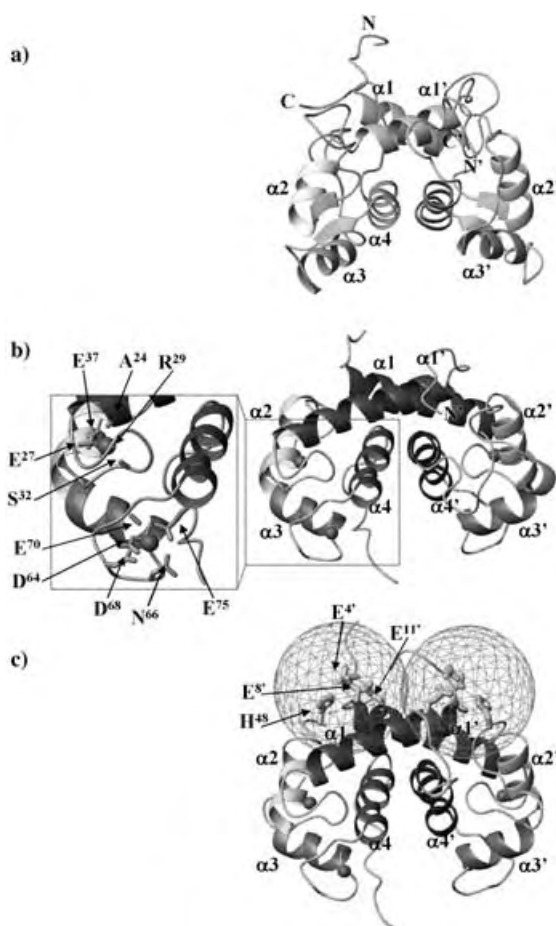


Figure 1. Dimeric structures of a) apo-S100A13 and b) Ca_2 -S100A13 in solution are represented as ribbons, where each helix within a monomer has a different gray scale. Secondary structure elements are indicated. The two Ca^{II} -binding sites and Ca^{II} ligands are shown in the inset of (b). Ca^{II} ions are represented as spheres. c) Two 10-Å spheres are drawn on the structure of Ca_2 -S100A13, which contain all residues whose signals are broadened beyond detection in the ^1H - ^{15}N HSQC spectrum of Ca_2 ,Cu-S100A13. The potential Cu^{II} ligands of one site are indicated.

than average ($\Delta\delta_{\text{av}}(\text{HN}) > 0.37$ ppm) for segments 23–35, 60–70, and 77–82 (see Supporting Information), that is, where the two proposed Ca^{II} -binding sites are located. The extreme N terminus and the last ten residues of the C terminus are poorly defined as a result of their fast internal mobility, revealed by the small or negative $^{15}\text{N}\{^1\text{H}\}$ NOE values, which determines the lack of long-range interproton NOE values. Mutational studies have shown that deletion of the basic residues at the C terminus dramatically alters the ability of S100A13 to associate with the acidic protein partner FGF-1,^[8] which suggests that the C terminus of S100A13 may become structured upon interaction with FGF-1.

Dimerization occurs through interactions between helices $\alpha 1$ and $\alpha 4$ of both monomers, which form an X-type bundle. At the dimer interface, residues in the hinge between $\alpha 2$ and $\alpha 3$ make contacts with residues near the N terminus of helix $\alpha 1'$ of the other monomer. The aromatic residues Y^{76} and W^{77} in helix $\alpha 4$ also make several contacts with helices $\alpha 1'$ and $\alpha 4'$ of the other monomer. All these interactions align $\alpha 1$

and $\alpha 4$ in opposite directions to $\alpha 1'$ and $\alpha 4'$, respectively, in the dimer. The angle between helices $\alpha 4$ and $\alpha 4'$ ($160 \pm 5^\circ$) in apo-S100A13 is larger than that in Ca_2 -S100A13 ($145 \pm 5^\circ$), while helices $\alpha 1$ and $\alpha 1'$ form a similar angle ($155 \pm 5^\circ$). Also, the relative orientation of helices $\alpha 1$ and $\alpha 2$ is similar in the two forms ($125 \pm 5^\circ$). In contrast, the angle between helices $\alpha 3$ and $\alpha 4$ changes by $\approx 40^\circ$. In combination with $\alpha 4$ – $\alpha 4'$ reorientation, this latter change has the dramatic effect of placing helix $\alpha 3$ nearly perpendicular to helix $\alpha 4$ ($110 \pm 5^\circ$) in the Ca^{II} -bound structure (Figure 1b), whereas they make an angle of $150 \pm 5^\circ$ in the apo form. The overall structure and the conformational changes induced by Ca^{II} binding are essentially the same as those observed for other S100 proteins.^[1,9–11]

One result of the reorientation of helices is the exposure of several residues (see Supporting Information). In the S100 proteins characterized up to now this reorientation exposes a hydrophobic surface,^[11] while in S100A13 the majority of the residues that become exposed are positively or negatively charged. They are located at the N termini (E^4 , P^5 , and E^{14}) and C termini (E^{86} , K^{89} , D^{92} , L^{93} , K^{94} , I^{95} , R^{96} , and K^{97}). Some residues in the hinge between helices $\alpha 2$ and $\alpha 3$ (P^{47} , H^{48} , K^{51} , and D^{52}) also become sizably exposed upon Ca^{II} binding. In particular, residue H^{48} increases its exposure by nearly 40 %. However, some residues (mostly hydrophobic) become more buried upon Ca^{II} binding. As a consequence of the decreased exposure of residues 23–27 in Ca_2 -S100A13, helix $\alpha 1$ becomes more extended at the C-terminal end, also resulting in a switch of residue packing. All these changes on the surface modify the electrostatic potential of the protein (Figure 2). The protein surface is highly charged in both forms, but the charge distribution appears quite different. In particular, at the dimer interface a more extended and continuous negative patch surrounded by positive charges is observable in Ca_2 -S100A13 on top of helices $\alpha 1$ and $\alpha 1'$.

Interaction with Cu^{II} is a key functional aspect of S100A13, as this protein is reported to interact with other proteins in the presence of Cu^{II} ions. Indeed, it is involved in the Cu^{II} -mediated release of FGF1-1 and IL-1 α .^[3] On addition of a solution of CuSO_4 to Ca_2 -S100A13 up to a ratio of 0.9:1, an absorption band appears at 720 nm and the ES-MS data indicate a mass increase of 63 Da, still maintaining the two Ca^{II} ions bound per monomer. The EPR spectrum of Ca_2 , Cu -S100A13 is characterized by parameters $g_{\parallel} = 2.35$, $g_{\perp} = 2.07$, and $A_{\parallel} = 148 \times 10^{-4} \text{ cm}^{-1}$. These data indicate a type II, pseudotetragonal coordination of Cu^{II} with N and O as donor atoms.^[12]

The coupling between the unpaired electron of a type II Cu^{II} , characterized by electronic relaxation times in the range of 10^{-8} – 10^{-9} s, and the nuclear spins has a dramatic effect on their nuclear relaxation and consequently on the NMR signal line widths.^[13] Addition of substoichiometric amounts of copper to Ca_2 -S100A13 results in the disappearance of a number of amide ^1H – ^{15}N cross-peaks (residues 3, 4, 7–9, 11, 15, 48, and 49; see Supporting Information). From the location of the disappearing signals and line broadening analysis of the surrounding NH resonances,^[13] the copper binding site can be located in a position equidistant from the hinge connecting helices $\alpha 2$ and $\alpha 3$ (residues 44–55) of one

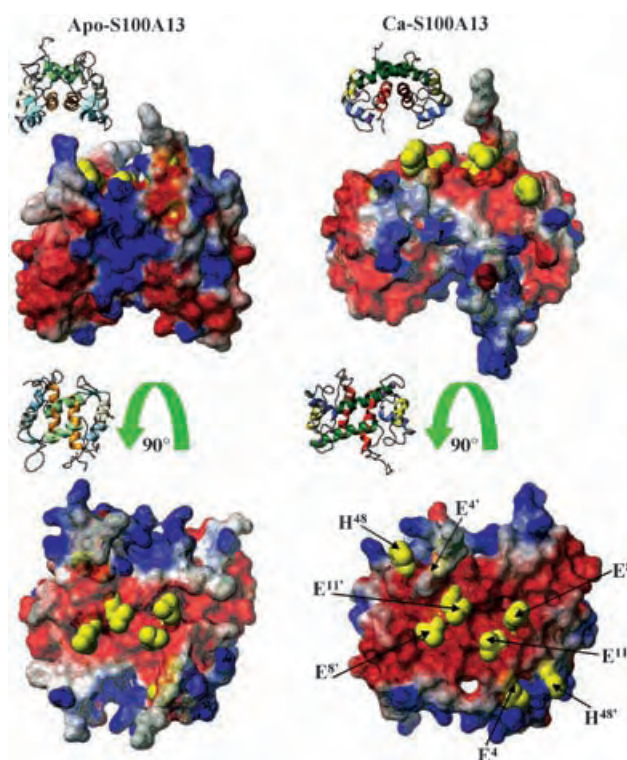


Figure 2. Rotated views of the electrostatic potential surface and ribbon representations of apo- and Ca_2 -S100A13. The positively charged, negatively charged, and neutral amino acids are represented in blue, red, and gray, respectively. The putative Cu^{II} ligands are shown in yellow to allow their different degrees of solvent exposure in apo- and Ca_2 -S100A13 to be observed.

monomer and the N-terminal region of the other monomer (Figure 1c). The ^{15}N and ^{13}C NMR spectral data, confined in a well-defined region, also clearly indicate that the protein structure is not affected by the copper binding, as it is a secondary structural element, and the overall protein fold is maintained. It might also be possible that there is not a single binding site in the absence of the partner proteins, as some signal broadening occurs on residues located in the C terminus and close to the C-terminal calcium-binding site.

In principle, direct ^{13}C NMR detection offers advantages for the study of paramagnetic proteins because the paramagnetic dipolar contributions to nuclear relaxation depend on the square of the gyromagnetic ratio of the observed nucleus. Thus, going from ^1H to ^{13}C detection guarantees a decrease in relaxation rates of a factor of about 16 ($\gamma_{\text{H}} = 2.67 \times 10^{-8} \text{ rads}^{-1} \text{ T}^{-1}$; $\gamma_{\text{C}} = 6.73 \times 10^{-7} \text{ rads}^{-1} \text{ T}^{-1}$), which therefore decreases the negative effects on the NMR signals arising from the paramagnetic nature of Cu^{II} ions.^[14] Also, ^{13}C spectra are more sensitive than ^{15}N and ^1H spectra to even minimal changes of their environment, thus determining their power in monitoring structural perturbations. However, the presence of exchange processes can dramatically affect the ^{13}C signals determining their disappearance. In the CBCACO and CACO experiments^[15] acquired on Ca_2 -S100A13 in the presence of 0.9 equivalents of Cu^{II} ions (see Supporting Information) it appears that most of the carboxylate side chains of acidic residues disappear, presumably because of

their interaction with a fractional amount of copper in quasi-slow exchange. The disappearing signals on the backbone, however, are fully consistent with the ^{15}N spectral data, thus confirming that the Cu^{II} ion-binding site involves the N terminus region which is rich in glutamates (disappearance of ^{13}C backbone resonances of 3, 4, 6–9, 11) of one subunit and H^{48} , located in the loop between helices $\alpha 2$ and $\alpha 3$ (disappearance of its $\text{C}\beta$ signal) of the other subunit.

The metal-binding site is completely different from that present in a few other S100 proteins where copper or zinc binding has been characterized.^[6,7] The sites are different in their location on the protein frame, the nature of the ligand, and accessibility. That of S100A13 is completely exposed to solvent, which is in contrast to the situation in the other proteins where the site is quite buried.^[6,7]

In conclusion, results of ^{15}N and ^{13}C NMR experiments have shown that Ca^{II} binding to S100A13 triggers sizable conformational changes, thus creating a novel binding site for Cu^{II} ions on a solvent-exposed location. The opening up of the interhelical angle $\alpha 3$ – $\alpha 4$ and the uncovering of H^{48} in Ca_2 -S100A13 (Figure 2) facilitate Cu^{II} binding at a site bridging the N terminus of one monomer with the hinge of the other monomer. This result suggests that Cu^{II} binding may trigger the interaction with biological partners and provide a mechanism for fine-tuning of the multiprotein complex that involves S100A13.

Experimental Section

The S100A13 recombinant protein was expressed in *Escherichia coli* by using cDNA from human brain, and purified by fast protein liquid chromatography. ^{15}N - and ^{13}C , ^{15}N -labeled samples were obtained from cultures grown in labeled Silantes medium. All NMR experiments used for resonance assignment and structure determination were performed on 1.5 mm ^{13}C , ^{15}N -S100A13 samples in sodium acetate buffer (20 mM, pH 5.6), and are summarized in the Supporting Information. Structure calculations were performed with DYANA,^[16] calculated by using distance and dihedral angle constraints. Restrained energy minimization was then applied to the 25 conformers with the lowest DYANA target function, by using the AMBER 6 package.^[17] The ^{15}N backbone longitudinal (R_1) and transverse (R_2) relaxation rates as well as heteronuclear $^{15}\text{N}\{^1\text{H}\}$ NOE values were measured as previously described.^[18,19] 2D IPAP-CBCACO and CACO experiments based on direct ^{13}C NMR detection^[15] were recorded for Ca_2 -S100A13 and Ca_2 , Cu -S100A13 on a 500-MHz spectrometer equipped with a TCI cryoprobe. Details on protein expression and characterization, NMR experiments, and structure calculations are available as Supporting Information.

Received: February 13, 2005

Revised: June 8, 2005

Published online: September 7, 2005

Keywords: calcium · copper · helical structures · NMR spectroscopy · protein structures

- [3] I. Prudovsky, A. Mandinova, R. Soldi, C. Bagala, I. Graziani, M. Landriscina, F. Tarantini, M. Duarte, S. Bellum, H. Doherty, T. Maciag, *J. Cell Sci.* **2003**, *116*, 4871–4881.
- [4] K. Ridinger, B. W. Schäfer, I. Durussel, J. A. Cox, C. W. Heizmann, *J. Biol. Chem.* **2000**, *275*, 8686–8694.
- [5] S. McLaughlin, *Annu. Rev. Biophys. Biophys. Chem.* **1989**, *18*, 113–136.
- [6] D. E. Brodersen, J. Nyborg, M. Kjeldgaard, *Biochemistry* **1999**, *38*, 1695–1704.
- [7] O. V. Moroz, A. A. Antson, S. J. Grist, N. J. Maitland, G. G. Dodson, K. S. Wilson, E. Lukanidin, *Acta Crystallogr. Sect. D* **2003**, *59*, 859–867.
- [8] M. Landriscina, R. Soldi, C. Bagala, I. Micucci, S. Bellum, F. Tarantini, I. Prudovsky, T. Maciag, *J. Biol. Chem.* **2001**, *276*, 22544–22552.
- [9] L. Otterbein, J. Kordowska, C. Witte-Hoffmann, C. L. Wang, R. Dominguez, *Structure* **2002**, *10*, 557–567.
- [10] L. Maler, M. Sastry, W. J. Chazin, *J. Mol. Biol.* **2002**, *317*, 279–290.
- [11] S. Bhattacharya, W. J. Chazin, *Structure* **2003**, *11*, 738–739.
- [12] J. Peisach, W. E. Blumberg, *Arch. Biochem. Biophys.* **1974**, *165*, 691–708.
- [13] L. Banci, I. Bertini, C. Luchinat, *Nuclear and Electron Relaxation: The Magnetic Nucleus–Unpaired Electron Coupling in Solution*, VCH, Weinheim, **1991**.
- [14] F. Arnesano, L. Banci, I. Bertini, I. C. Felli, C. Luchinat, A. R. Thompson, *J. Am. Chem. Soc.* **2003**, *125*, 7200–7208.
- [15] I. Bertini, L. Duma, I. C. Felli, M. Fey, C. Luchinat, R. Pierattelli, P. Vasos, *Angew. Chem.* **2004**, *116*, 2307–2309; *Angew. Chem. Int. Ed.* **2004**, *43*, 2257–2259.
- [16] P. Güntert, C. Mumenthaler, K. Wüthrich, *J. Mol. Biol.* **1997**, *273*, 283–298.
- [17] D. A. Case, D. A. Pearlman, J. W. Caldwell, T. E. Cheatham, W. S. Ross, C. L. Simmerling, T. A. Darden, K. M. Merz, R. V. Stanton, A. L. Cheng, J. J. Vincent, M. Crowley, V. Tsui, R. J. Radmer, Y. Duan, J. Pitner, I. Massova, G. L. Seibel, U. C. Singh, P. K. Weiner, P. A. Kollman, AMBER 6, University of California, San Francisco, **1999**.
- [18] L. Banci, I. Bertini, F. Cantini, M. D’Onofrio, M. S. Viezzoli, *Protein Sci.* **2002**, *11*, 2479–2492.
- [19] S. Grzesiek, A. Bax, *J. Am. Chem. Soc.* **1993**, *115*, 12593–12594.

[1] I. Marenholz, C. W. Heizmann, G. Fritz, *Biochem. Biophys. Res. Commun.* **2004**, *322*, 1111–1122.

[2] R. Wicki, B. W. Schäfer, P. Erne, C. W. Heizmann, *Biochem. Biophys. Res. Commun.* **1996**, *227*, 594–599.

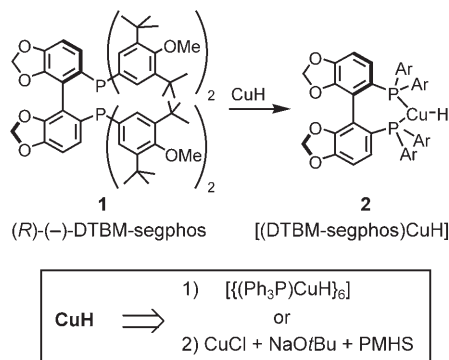
Hydride Reagents

DOI: 10.1002/anie.200500800

CuH in a Bottle: A Convenient Reagent for Asymmetric Hydrosilylations**

Bruce H. Lipshutz* and Bryan A. Frieman

Copper hydride (CuH), when complexed by the Takasago ligand (*R*)-(-)-DTBM-segphos, (**1**),^[1] as shown in Scheme 1



Scheme 1. Formation of [(DTBM-segphos)CuH].

(DTBM = 3,5-di-*tert*-butyl-4-methoxy), is a remarkably reactive yet selective reagent for effecting asymmetric hydrosilylations. Aromatic ketones,^[2a] hindered cyclic enones,^[2b] aryl imines,^[2c] and selected α,β -unsaturated esters and lactones^[2d] all react with [(*R*)-(-)-DTBM-segphos]CuH (**2**) in the presence of stoichiometric PMHS^[3] to afford the corresponding products of asymmetric reduction with excellent *ee* values. Substrate-to-catalyst (S/C) ratios typical of asymmetric hydrosilylations (<500:1) mediated by other metals (e.g., Rh, Ti, Ru)^[4] can be increased substantially, while reaction rates are comparable in many cases, even at much lower temperatures.

Preparation of **2** typically follows either of two procedures: 1) addition of ligand **1** to preformed [(Ph₃P)CuH]₆ (i.e., Stryker reagent)^[5] or 2) in situ formation^[6] by using CuCl, NaOtBu, and **1** in the presence of excess silane (PMHS). To simplify handling and to gauge reagent lifetime for potential storage and ease of use, alternatives to its

preparation have been investigated. Herein, we report our findings, which suggest that complex **2** is, indeed, quite robust.

Several copper salts were screened as alternatives to CuCl. In particular, those with counterions that are already oxygen-based are, in principle, ready for direct transmetalation with PMHS to CuH. The 1,4-reduction of hindered enone isophorone was used as a test case; results from several experiments are illustrated in Table 1. Each reaction was

Table 1: Survey of copper salt precursors to [(DTBM-segphos)CuH].

Entry	Copper source ^[a]	<i>t</i> [h]	Conversion [%]	<i>ee</i> [%] ^[b]
1	Cu(OAc) ₂ ·H ₂ O	1	100	99
2	CuOPh	1.5	100	99
3	CuCl	2	100	99
4	CuOAc	2	100	99
5	CuCl ₂ ·H ₂ O	20	17	98
6	Cu(O ₂ CCF ₃) ₂ ·H ₂ O	20	50	98
7	Cu(OTf) ₂	20	25	97
8	[Cu(acac) ₂]	20	44	99
9	[Cu(bzac) ₂]	20	5	86
10	[Cu(TMHD) ₂]	20	67	98
11	Cu(BHT)	20	81	99

[a] acac = acetoacetate; BHT = 2,6-di-*tert*-butyl-4-methylphenol; bzac = PhC(O)CH₂C(O)CH₃; Tf = trifluoromethanesulfonyl; TMHD = 2,2,6,6-tetramethyl-3,5-heptanedione. [b] By chiral capillary GC. [c] From CuCl + NaBHT.

performed under otherwise identical conditions, with a S/C ratio of 200:1. While the *ee* values for all but one case were > 96 %, the extent of conversion over time varied considerably as a function of the counterion. In principle, the counterion should not play a major role, but these data suggest that rates can indeed be affected by this reaction variable. Cu(OAc)₂·H₂O (Table 1, entry 1) appears to be the best choice to date for several reasons (see below), as also noted recently by others.^[7] Copper phenoxide (Table 1, entry 2) was roughly comparable in all respects, an unexpected result in light of prior work from Stryker and co-workers, who found that the replacement of NaOtBu with NaOPh did not lead to a useful catalytic system.^[8] The bulky phenoxide from BHT (Table 1, entry 11), on the other hand, in the form of Cu(BHT), led to a far less reactive albeit highly selective precursor to ligated CuH.

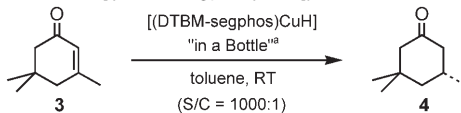
The catalyst **2** derived from Cu(OAc)₂·H₂O led to complete reduction of enone **3** to nonracemic ketone **4** in 1 h with > 99 % *ee*. Given the room temperature conditions and high enantioselectivity, this observation encouraged investigation of reagent shelf life, but now with catalyst **2** at a S/C ratio of 1000:1 (vs. 200:1; see Table 1, entry 1). Thus, a 0.001 M solution of **2** in toluene was prepared and stored in a bottle at room temperature. This stock solution stored in a refrigerator was monitored over time for yields of isolated product and levels of induction in the reaction of isophorone (1 mmol) added to **2** (1 mL). As shown in Table 2, over a 4-

[*] Prof. B. H. Lipshutz, B. A. Frieman
Department of Chemistry & Biochemistry
University of California
Santa Barbara, CA 93106 (USA)
Fax: (+1) 805-893-8265
E-mail: lipshutz@chem.ucsb.edu

[**] We warmly thank the NSF (CHE 0213522) for financial support and Takasago (Dr. Takao Saito and Mr. Hideo Shimizu) and Prof. Sannicola (University of Milan) for supplying the segphos and bitianp ligands, respectively, used in this study.

Supporting information for this article is available on the WWW under <http://www.angewandte.org> or from the author.

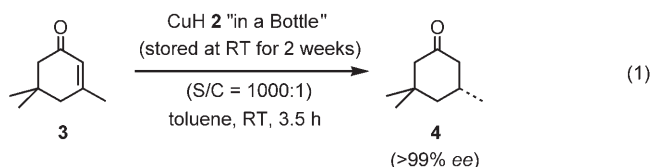
Table 2: Shelf life of [(DTBM-segphos)CuH]/PMHS.



<i>t</i> [days]	Yield [%] ^[b]	<i>ee</i> [%]
1	88	99
5	87	99
9	88	98
28	86	96
60	87	94

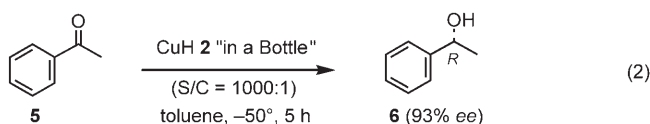
[a] Stored at 4 °C. [b] Yield of isolated product.

week period, the enantioselectivity dropped only slightly (from 99 to 96 % *ee*). After 2 months, the recorded enantioselectivity was still ≥ 94 % *ee*. To show that the decline in enantioselectivity was likely to be due to adventitious oxygen introduced over time as a result of normal use, a fresh solution of CuH was prepared and stored at room temperature for 14 days without puncturing the Sure/Seal. The CuH in a bottle was tested again on isophorone [Eq. (1)]; no loss in enantio-



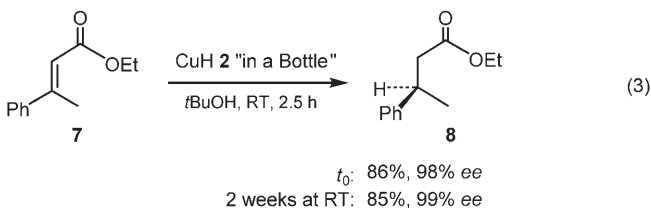
selectivity was observed. Thus, we have found that reagent degradation can be minimized by simply switching to a more efficient Oxford Sure/Seal Storage valve cap. With reagent integrity documented at room temperature for a 2-week period, prospects for routine storage and even commercialization now exist. Notably, whereas in prior applications the ratio of substrate-to-copper was about 100:1 (i.e., ≈ 1 % CuCl),^[2b] in the case at hand the amount of copper present is equal to the quantity of ligand, thus significantly decreasing the extent of transition metal involved.

Treatment of an aryl ketone, acetophenone (**5**), with Cu(OAc)₂-derived reagent **2** [Eq. (2)] led to the alcohol **6** with 93 % *ee*, essentially identical to that seen previously when using freshly prepared [(*R*)-(-)-DTBM-segphos]CuH derived from CuCl.^[2a]



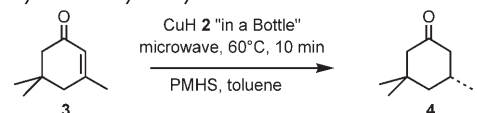
Cinnamate **7** was also exposed to [(DTBM-segphos)CuH] (S/C 1000:1, room temperature). Initially, product ester **8** was obtained with 98 % *ee* [86 % yield of isolated product; Eq. (3)]. A second experiment under identical conditions (room temperature, 2.5 h) in the presence of reagent **2** that had been stored on the shelf at room temperature over a 2-

week period afforded **8** with essentially the same enantioselectivity (99 % *ee*) and yield (85 %).



Asymmetric hydrosilylations with CuH under microwave conditions are unprecedented in the literature, and are made all the more interesting given the limited thermal stability of this species. Nonetheless, the increased rates normally observed when using this technique might allow rapid conjugate reduction to occur. In the event, even at 1000:1 S/C ratios, reactions run within a microwave reactor at 60 °C are close to complete within 10 min without erosion in enantioselectivity (Table 3).^[9]

Table 3: Asymmetric hydrosilylations under microwave irradiation.



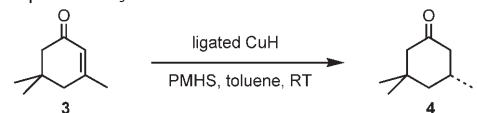
S/C	Conversion ^[a] [%]	<i>ee</i> [%]
500	98	99
1000	95	99

[a] By GC analysis.

The results of the reactions of enoates and cyclic enones at room temperature or above in the presence of the Stryker reagent as the catalytic source of CuH^[2b,d] raises the question as to the impact of Ph₃P. Achiral [(Ph₃P)CuH] could potentially compete in a background reaction, thereby lowering the *ee* values. The addition of Ph₃P (1 equiv) to a solution of [(DTBM-segphos)CuH]/PMHS stored in a bottle caused the *ee* value of the product ketone **4** from the hydrosilylation of isophorone to drop from 99 to 96 % (Table 4, entry 2). Alternatively, the addition of ligand **1** (2 equiv) to preformed [(Ph₃P)CuH] led to further erosion in enantioselectivity to 95 % *ee* (Table 4, entry 3). Thus, the presence of Ph₃P has a small but finite effect that detracts from the inherent enantioselectivity imparted by the DTBM-segphos ligand.

Although ¹H NMR spectral information on the Stryker reagent is available,^[10] the corresponding data for CuH

Table 4: Impact of Ph₃P on reactions of **3** with **2**.



Entry	Copper source	CuH/ 1	<i>t</i> [h]	<i>ee</i> [%]
1	[(segphos)CuH] in a bottle (2)	1:1	3	99
2	Cu(OAc) ₂ H ₂ O + 1 + Ph ₃ P (1 equiv)	1:1	5	96
3	[(Ph ₃ P)CuH] + 1 (2 equiv)	1:2	5	95

complexed by a nonracemic bisphosphine ligand has yet to be reported. The spectrum of $[(\text{Ph}_3\text{P})\text{CuH}]_6$ in C_6D_6 shows the hydride at $\delta = 3.52$ ppm.^[11] Individual spectra of PMHS (Figure 1a) and DTBM-segphos (Figure 1b) in this solvent are shown along with that of $\text{Cu}(\text{OAc})_2 \cdot \text{H}_2\text{O}$ in the presence of this ligand (Figure 1c). Upon addition of PMHS, a new peak at $\delta = 2.55$ ppm appears (Figure 1d), which is presumed

DTBM-segphos, has been prepared and documented to be a stable “CuH in a bottle” for easy access and use in asymmetric hydrosilylations.^[13,14] Just as our “cuprate in a bottle” (i.e., (2-thienyl)Cu(CN)Li) introduced two decades ago^[15] provides easy access to “higher-order” cuprate species, this reagent combination should encourage many future applications of ligand-accelerated asymmetric CuH chemistry.

Received: March 4, 2005

Revised: June 23, 2005

Published online: August 26, 2005

Keywords: asymmetric synthesis · copper · hydrides · hydrosilylation · P ligands

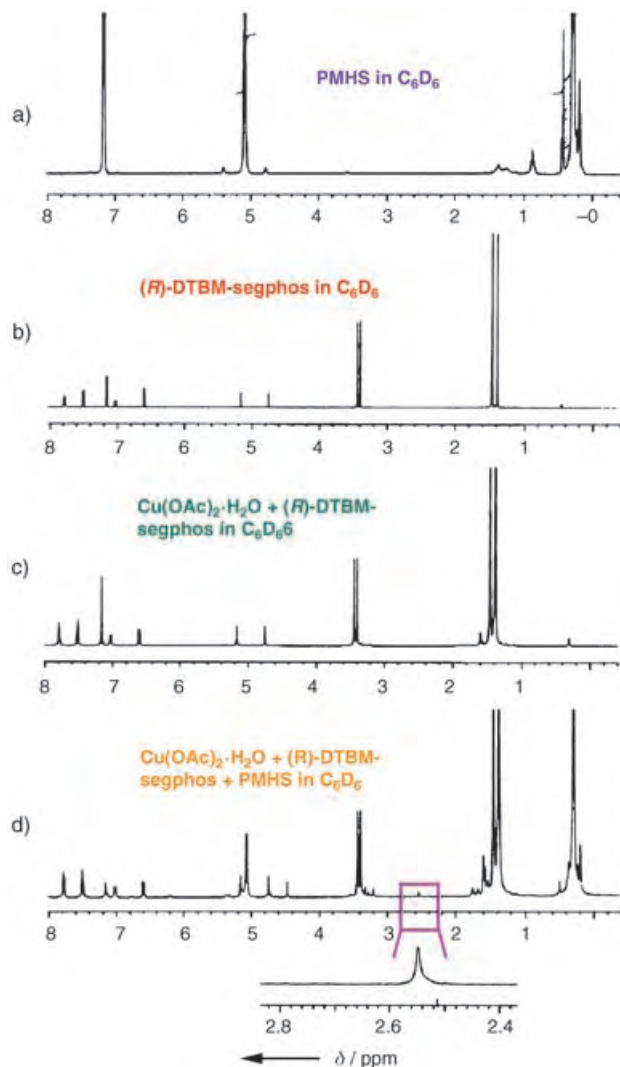


Figure 1. ^1H spectrum of $[(\text{R})\text{-DTBM-segphos}]\text{CuH}$.

to correspond to the hydride in reagent **2**. The identical chemical shift is observed for the corresponding reagent complexed with a bitianp ligand (see the Supporting Information).^[12] These spectra also show not only that a seemingly discrete species arises from the combination of CuH and DTBM-segphos (or bitianp), but that the presence of Ph_3P (as noted previously; see Table 4, entry 3, and the Supporting Information) in reactions at room temperature or above can alter enantioselectivities through competing background reactions that would not otherwise be observed in the presence of DTBM-segphos alone.

In summary, a powerful source of an asymmetric Stryker reagent, copper hydride complexed by Takasago's (R)-

- [1] T. Saito, T. Yokozawa, T. Ishizaki, T. Moroi, N. Sayo, T. Miura, H. Kumobayashi, *Adv. Synth. Catal.* **2001**, 343, 264.
- [2] a) B. H. Lipshutz, K. Noson, W. Chrisman, A. Lower, *J. Am. Chem. Soc.* **2003**, 125, 8779; b) B. H. Lipshutz, J. M. Servesko, T. B. Petersen, P. P. Papa, A. Lover, *Org. Lett.* **2004**, 6, 1273; c) B. H. Lipshutz, H. Shimizu, *Angew. Chem.* **2004**, 43, 2278; *Angew. Chem. Int. Ed.* **2004**, 43, 2228; d) B. H. Lipshutz, J. M. Servesko, B. R. Taft, *J. Am. Chem. Soc.* **2004**, 126, 8352.
- [3] PMHS = polymethylhydrosiloxane; N. J. Lawrence, M. D. Drew, S. M. Bushell, *J. Chem. Soc. Perkin Trans. 1* **1999**, 3381; we found that this silane, used as purchased from Lancaster, works well in all of the hydrosilylations reported by us to date. However, PMHS received from Acros, surprisingly, was totally ineffective in this CuH chemistry.
- [4] For representative examples, see: Rh: D. A. Evans, J. S. Tedrow, K. R. Campos, *J. Am. Chem. Soc.* **2003**, 125, 3534; B. Tao, G. C. Fu, *Angew. Chem.* **2002**, 41, 4048; *Angew. Chem. Int. Ed.* **2002**, 41, 3892; Ti: J. Yun, S. L. Buchwald, *J. Am. Chem. Soc.* **1999**, 121, 5640; Ru: a) G. Zhu, M. Terry, X. Zhang, *J. Organomet. Chem.* **1997**, 547, 97; b) Y. Nishibayashi, I. Takei, S. Uemura, M. Hidai, *Organometallics* **1998**, 17, 3420; Zn: H. Mimoun, J. Y. de Saint Laumer, L. Giannini, R. Scopelliti, C. Floriani, *J. Am. Chem. Soc.* **1999**, 121, 6158. For a review, see: “Asymmetric Hydrosilylation and Related Reactions”: H. Nishiyama, K. Itoh in *Catalytic Asymmetric Synthesis* (Ed.: I. Ojima), Wiley-VCH, New York, **2000**, chap. 2.
- [5] a) W. S. Mahoney, D. M. Brestensky, J. M. Stryker, *J. Am. Chem. Soc.* **1988**, 110, 291; b) D. M. Brestensky, J. M. Stryker, *Tetrahedron Lett.* **1989**, 30, 5677; c) W. S. Mahoney, J. M. Stryker, *J. Am. Chem. Soc.* **1989**, 111, 8818.
- [6] D. H. Appella, Y. Moritani, R. Shintani, E. M. Ferreira, S. L. Buchwald, *J. Am. Chem. Soc.* **1999**, 121, 9473.
- [7] For the first reported uses of this alternative precursor to nonracemically ligated CuH, see: M. P. Rainka, Y. Aye, S. L. Buchwald, *Proc. Natl. Acad. Sci. USA* **2004**, 101, 5821; D. Lee, J. Yun, *Tetrahedron Lett.* **2004**, 45, 5415.
- [8] J. M. Stryker, W. S. Mahoney, J. F. Daeuble, D. M. Brestensky in *Catalysis in Organic Synthesis* (Ed.: W. E. Pascoe), Marcel Dekker, New York, **1992**, pp. 29–44.
- [9] For a more detailed study on the use of microwave irradiation in reactions of ligated copper hydride, see: B. H. Lipshutz, B. A. Frieman, J. B. Unger, D. M. Nihan, *Can. J. Chem.* **2005**, 83, 606.
- [10] G. V. Goeden, K. G. Caulton, *J. Am. Chem. Soc.* **1981**, 103, 7354.
- [11] B. H. Lipshutz, W. Chrisman, K. Noson, P. Papa, J. A. Sclafani, R. W. Vivian, J. Keith, *Tetrahedron* **2000**, 56, 2779.
- [12] a) T. Benincori, E. Cesarotti, O. Piccolo, F. Sanniccolo, *J. Org. Chem.* **2000**, 65, 2043; b) T. Benincori, E. Brenna, F. Sanniccolo, L. Trimarco, P. Antognazza, E. Cesarotti, F. Demartin, T. Pilati, *J. Org. Chem.* **1996**, 61, 6244.

- [13] Preparation of [(DTBM-segphos)CuH] in a bottle (0.001M): An oven-dried poly-coated amber glass bottle equipped with a stirrer bar was purged under argon. Under an inert atmosphere (e.g., glove box), Cu(OAc)₂·H₂O (10 mg, 0.05 mmol) and (*R*)-(–)-DTBM-segphos (59 mg, 0.05 mmol) were added followed by dry toluene (44 mL), and the reaction mixture was allowed to stir for 2 h at room temperature. PMHS (6 mL, 100 mmol) was added dropwise, and the mixture was allowed to stir for 30 min. The amber bottle was then sealed by using a standard Oxford Sure/Seal top and stored at 0°C.
- [14] Typical procedure (isophorone): A solution of [(DTBM-segphos)CuH] “in a bottle” (1 mL, 0.001M) was added to a 10-mL round-bottomed flask that had been flame dried and purged with argon. Isophorone (**3**, 150 µL, 1 mmol) was added neat and the reaction was stirred at room temperature until complete (monitored by TLC; 1 h; 4:1 hexanes/EtOAc). The reaction was diluted with THF (5 mL) and then quenched with aqueous NaOH (5 mL, 3M), after which the mixture was allowed to stir at room temperature for 2 h. After a standard extractive workup, the residue was purified by flash chromatography (4:1 hexanes/EtOAc) to afford the product ketone (*R*)-**4** (123.6 mg, 88%) as a clear oil. The product was analyzed by chiral GC (BDM-75), which indicated an *ee* value of 99%. The spectral data matched those previously reported.^[2b]
- [15] B. H. Lipshutz, J. A. Kozlowski, D. A. Parker, S. L. Nguyen, K. E. McCarthy, *J. Organomet. Chem.* **1985**, 285, 437.

Dendrimers

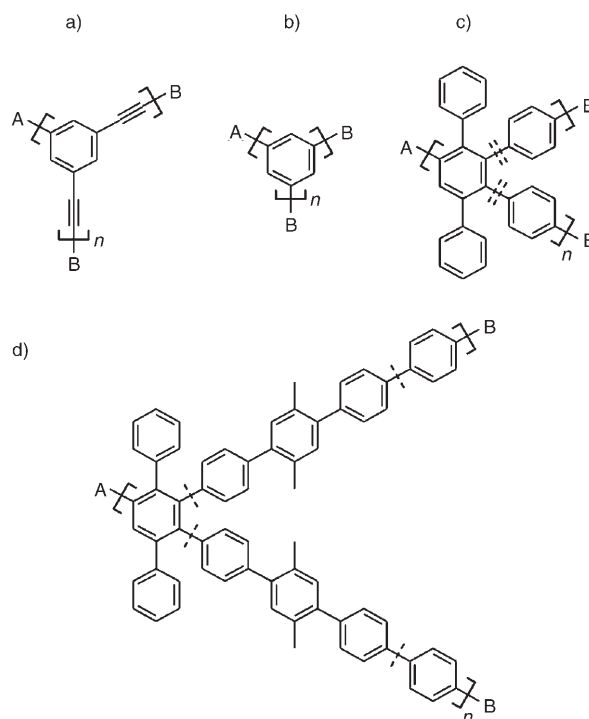
DOI: 10.1002/anie.200501368

Pushing the Synthetic Limit: Polyphenylene Dendrimers with “Exploded” Branching Units—22-nm-Diameter, Monodisperse, Stiff Macromolecules**

Ekaterina V. Andreitchenko, Christopher G. Clark, Jr., Roland E. Bauer, Günter Lieser, and Klaus Müllen*

The majority of effort in dendrimer chemistry has been devoted to constructions with flexible branching units, thereby introducing a variety of conformational aspects into

the molecule, such as the nature of the molecular density and the location and orientation of the chain ends.^[1] Rigidification of the dendrimer, and in some cases, control over the chain-end locations, has come from a variety of approaches,^[2] including the use of stiff building blocks such as that of poly(1-3,5-phenylene ethynylene),^[3] poly(1-3,5-phenylene),^[4] and polyphenylene dendrimers based on pentaphenylbenzene^[5] (Scheme 1 a, b, and c, respectively). Beyond a critical



Scheme 1. Stiff, dendritic AB₂ repeat units: a) poly(1-3,5-phenylene ethynylene), b) poly(1-3,5-phenylene), c) poly(4'-4,4''-(3',6'-diphenyl o-terphenylene)), and d) “exploded” polyphenylene by the extension of each arm by insertion of a linear terphenyl between each set of dashed lines of the general polyphenylene repeat unit shown in (c).

generation, the convergent synthesis of dendrimers necessitates the use of flexible building blocks or smaller dendrons.^[6] To circumvent this limitation, a gradient of branching unit lengths has been employed^[7] in the case of a dendrimer with 1-3,5-phenylene ethynylene branching points, thus installing greater volume at the interior of the molecule. A similar size-modulation approach to the branching unit is herein proposed for the enlargement of the parent, polyphenylene dendrimers. Linear enlargement of the arms of the general dendritic repeat unit (Scheme 1d) should directly translate into increased dendrimer radii without requiring a larger core moiety (Figure 1). The synthesis of polyphenylene dendrimers around a tetraphenylmethane core has thus far been limited to the fourth generation^[8] because of incomplete conversion at higher generations, presumably the prohibitive result of steric crowding at the chain ends.^[9] In light of this observation, a terphenyl spacer was introduced into each arm of the branching unit to decrease the congestion of the chain ends at higher generations (Figure 1). Since the connectivity of the branching points in the dendrimers with extended arms

[*] E. V. Andreitchenko, Dr. C. G. Clark, Jr., Dr. R. E. Bauer, Dr. G. Lieser, Prof. Dr. K. Müllen
Max-Planck-Institute for Polymer Research
Ackermannweg 10, 55128 Mainz (Germany)
Fax: (+49) 6131-379-100
E-mail: muellen@mpip-mainz.mpg.de

[**] The research was supported by the Deutsche Forschungsgemeinschaft (DFG) in the frame of the Sonderforschungsbereich (SFB) 625. C.G.C. is grateful for financial support from a US National Science Foundation MPS Distinguished International Postdoctoral Research Fellowship (MPS-DRF; Award: DMR-0207086). We would like to thank M. Wagner for NMR results and A. Rouhanipour and H.-J. Räder for mass spectrometric results and helpful discussions.

Supporting information for this article is available on the WWW under <http://www.angewandte.org> or from the author.

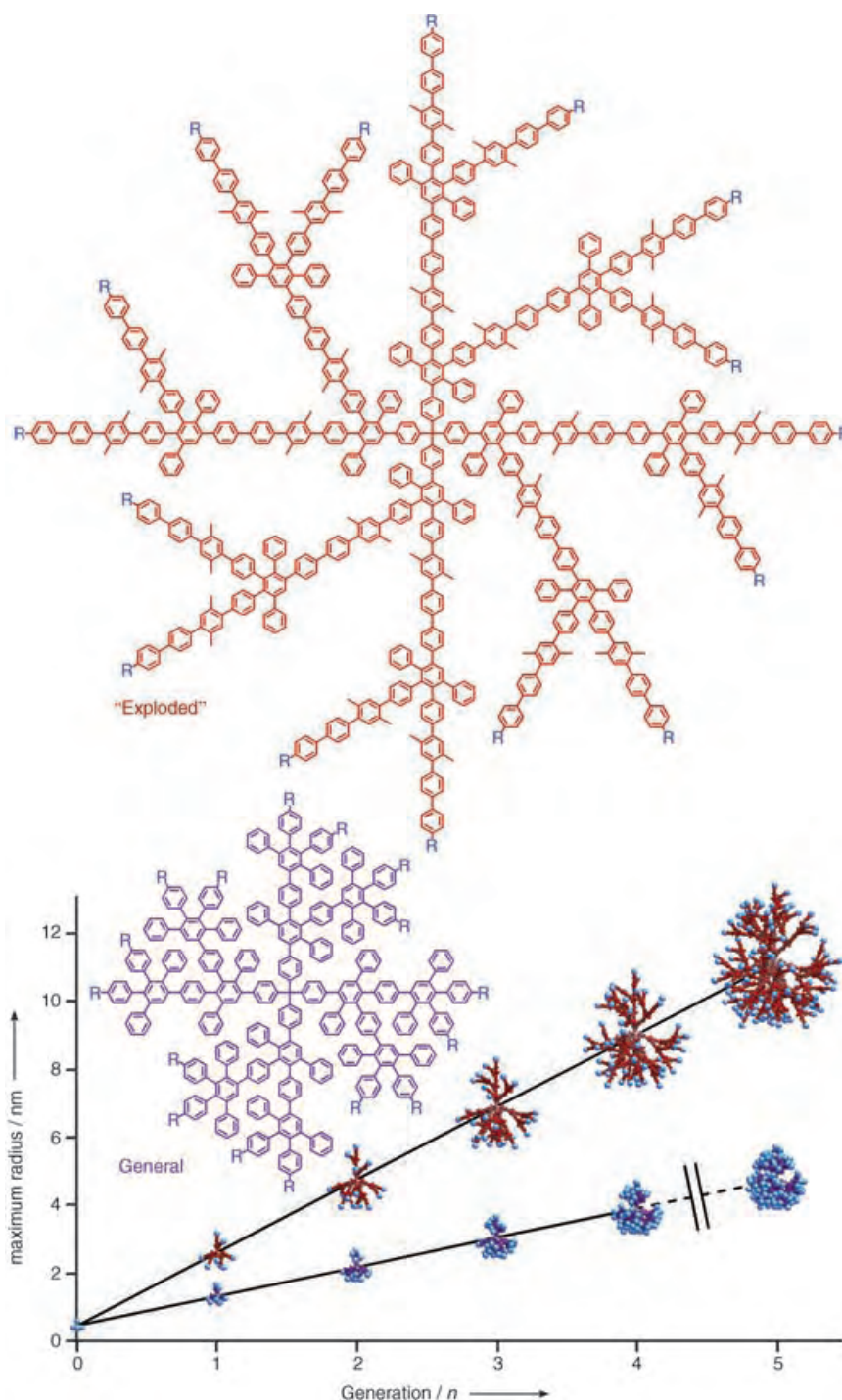


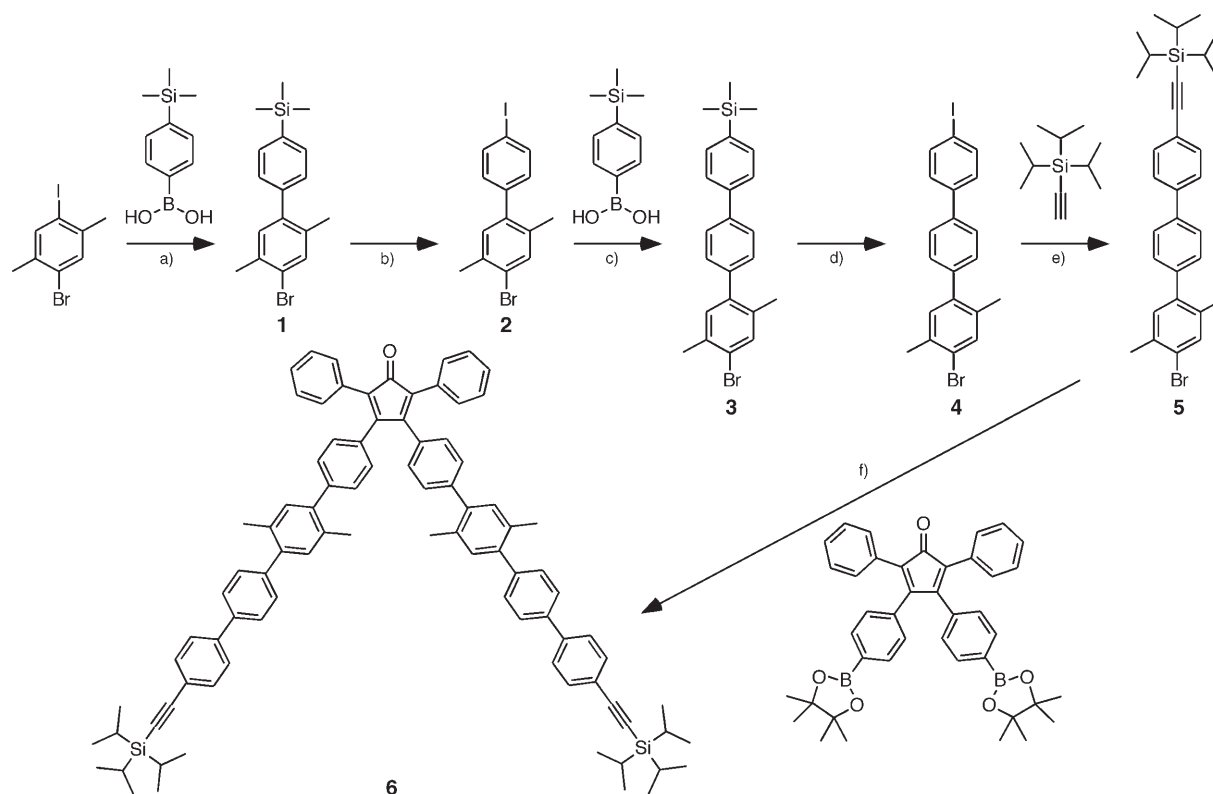
Figure 1. Scaling of the dendrimer radii for general polyphenylene dendrimers and new “exploded” polyphenylene dendrimers with identical branching-point connectivity but increased branching unit arm length through the use of a 2,5′-dimethyl-*p*-terphenyl spacer. Second-generation dendrimers for each type are illustrated in greater detail. The iterative illustrations were generated using POV-Ray and are qualitatively similar to the results of MMFF94 molecular mechanics calculations for generations 1–4. The maximum radius was determined by the length of the longest linear oligophenylene arm for each generation.

is the same as for the parent polyphenylene dendrimers, the radii should be 150 % greater than the comparable radii of the parent cases. This situation would enable the stepwise synthesis of a structurally perfect particle with a diameter greater

than 20 nm, which well exceeds the dimension of the narrowly disperse but not monodisperse particles that have been synthesized by self-assembly or multiphase approaches.^[10]

The key component in the dendrimer synthesis is the masked AB_2 building block 3,4-bis-(2,5′-dimethyl-4′′′-triisopropylsilyl)ethynyl-1,1′:4′,1′′:4′,1′′′-quaterphenyl-4-yl)-2,5-diphenylcyclopentadienone (**6**; Scheme 2) which bears an active tetraphenylcyclopentadienone and two terminal aryl acetylenes, or Diels–Alder dienophiles, protected with bulky triisopropylsilyl (TiPS) groups. While the solubilities of the final dendrimers were not anticipated to be poor, the solubilities of the *p*-terphenyl intermediates were expected to complicate the synthesis. As such, two methyl groups were introduced as side chains from the beginning by using 1-bromo-4-iodo-2,5-dimethylbenzene. An efficient, iterative, selective Suzuki coupling^[11] (Scheme 2) using the more-reactive aryl iodide, compared to the aryl bromide, with commercially available 4-trimethylsilylphenylboronic acid was performed to give 4-bromo-2,5-dimethyl-4′-trimethylsilylbiphenyl (**1**). Removal of the trimethylsilyl group with ICl ^[12] provided 4-bromo-4′-iodo-2,5-dimethylbiphenyl (**2**). The cycle was repeated to obtain 4-bromo-4′′-iodo-2,5-dimethyl-1,1′:4′,1′′-terphenyl (**4**). The aryl iodide was treated with trimethylsilylacetylene under Sonogashira/Hagihara conditions^[13] to afford **5**. The final step was the twofold Suzuki coupling of the remaining aryl bromide with 3,4-bis(4-(4,4,5,5-tetramethyl-1,3,2-dioxaborolan-2-yl)phenyl)-2,5-diphenylcyclopentadienone to furnish **6**.^[14] Chromatographic purification was performed for all steps.

The strategy for the synthesis of the new dendrimers with extended arms (Scheme 3) was directly analogous to the synthesis of the parent polyphenylene dendrimers. Fourfold Diels–Alder reactions of the masked AB_2 building block **6** with tetra(4-ethynylphenyl)methane^[8] produced the first-generation dendrimer **7** bearing eight TiPS chain end groups. Removal of excess **6** was accomplished by chromatographic purification. Removal of the TiPS groups with tetrabutylammonium fluoride trihydrate gave the first-generation dendrimer **8** with eight terminal ethynyl units

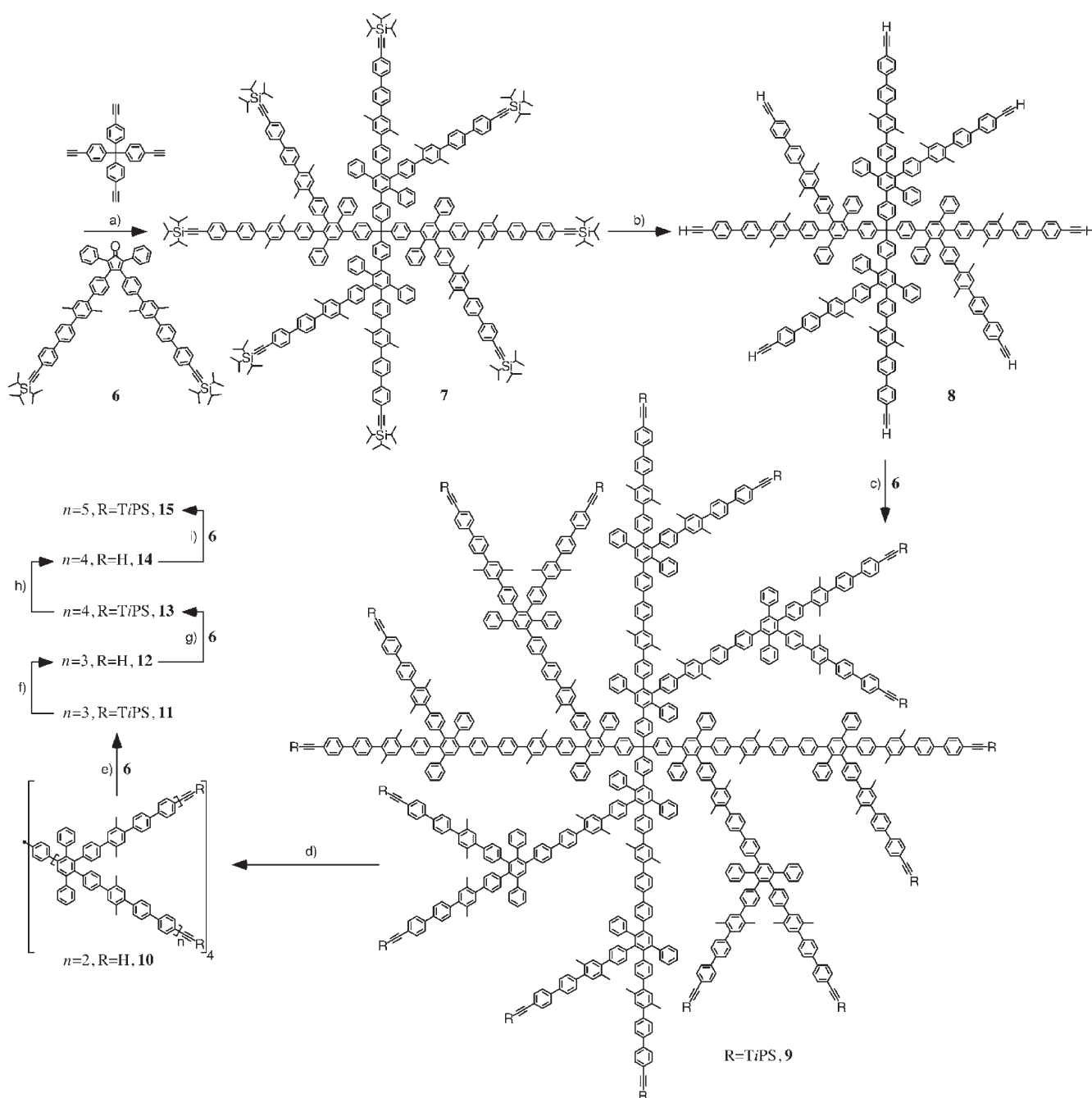


Scheme 2. Synthesis of the masked, AB₂ building block **6**: a) K₂CO₃, [Pd(PPh₃)₄], toluene, water, reflux, 62%; b) ICl, CCl₄, CH₂Cl₂, 0 °C, 96%; c) K₂CO₃, [Pd(PPh₃)₄], toluene, water, ethanol, reflux, 83%; d) ICl, CH₂Cl₂, 0 °C, 87%; e) [PdCl₂(PPh₃)₂], CuI, PPh₃, NEt₃, CH₂Cl₂, 80%; f) K₂CO₃, [Pd(PPh₃)₄], toluene, water, ethanol, reflux, 48%.

quantitatively. After quenching the reaction with water and precipitation in methanol, **8** was ready for subsequent generational growth. The cycle was repeated through to the fourth generation, and a final coupling yielded the fifth-generation dendrimer with 128 TiPS chain ends. Removal of excess **6** from the reaction mixture was achieved, beginning with the synthesis of the second-generation dendrimer **9**, by first adsorbing the dendrimer onto silica gel. The adsorbate was washed with acetone until the purple color of the eluent disappeared, and then the dendrimer was extracted with THF and reprecipitated in acetone. Synthetic details for all compounds presented here are included in the Supporting Information.

¹H NMR spectroscopic analysis (see Supporting Information) is consistent with the growth of each new generation of dendrimer (**7**, **9**, **11**, **13**, and **15**). The aromatic resonances for the third-, fourth-, and fifth-generation dendrimers (**11**, **13**, and **15**, respectively) were virtually identical, as the resonances from the tetraphenylmethane core were diluted. Resonances for the four inequivalent methyl groups (two closely spaced near $\delta = 2.3$ ppm and two others further separated at $\delta = 2.13$ and 2.10 ppm for **7**) of the repeat unit were nearly unchanged upon deprotection and growth to the next generations, as they are too far from sites of reactivity. Integration of the TiPS chain end resonances, relative to both the aromatic backbone resonances and the methyl side-chain resonances, is in agreement with complete conversion into the dendrimer product. Size-exclusion chromatography (SEC)

results (THF; Figure 2) showed a progressive decrease in the elution volume for each subsequent generation (**7**, **9**, **11**, **13**, and **15**), while the decrease in the elution volume was smaller going to the fifth-generation dendrimer **15**;^[15] the peak shape confirmed that **15** is smaller than the exclusion limit of the columns. A high-molecular-weight shoulder was present, which gave rise to a broader polydispersity than the earlier generation dendrimers. The shoulder, presumed to be the result of aggregation, has been observed for large generation dendrimers^[2c] and was further broadened at higher concentration. Neither ¹H NMR spectroscopy nor SEC, however, has the inherent dynamic range to determine whether the final coupling reactions go exclusively to completion (for example, whether the pure dendrimer or a mixture of the dendrimer and nearly complete conversions is produced). MALDI-TOF analysis (using dithranol as matrix, and in some cases, a suitable cationization agent was added) was relied upon to detect the presence of the final dendrimers. The Diels–Alder reactions were stopped when the product molecular ion was the only large molecular ion observed (Table 1). The molecular ions of the desired dendrimeric products were detected for the first three generations, **7**, **9**, and **11**. At higher generation (**13**, Figure 3) an ion corresponding to MALDI fragmentation at the core could be observed (calcd: m/z 16370, found: m/z 16339) in addition to the molecular ion (calcd: m/z 65494, found: m/z 65430). This fragmentation mechanism, removal of one dendron from the core, has been typically observed with polyphenylene den-



Scheme 3. Synthesis of the first- through to fifth-generation “exploded” polyphenylene dendrimers with a tetraphenylmethane core: a, c, e, g, i) *o*-xylene, reflux; b, d, f, h) tetrabutylammonium fluoride trihydrate, THF, RT; a) 85%, b) 76%, c) 96%, d) 75%, e) 87%, f) 75%, g) 64%, h) 58%, i) 65%.

drimers bearing a tetraphenylmethane core.^[16] No ions could be observed in the MALDI-TOF spectrum of the fifth-generation dendrimer **15** using dithranol as matrix; however, the MALDI-TOF spectrum obtained using DCTB^[17] as matrix (Figure 4) and sufficient laser power to observe any ions showed a weak signal for the molecular ion (calcd: m/z 134162, found: m/z 135290). Further proof of the existence of **15** came from the detected ions, which resulted from a large degree of fragmentation and coalescence of the highly reactive fragments with the molecular species. In addition to fragmentation at the core (m/z 33948, 67980, 101273), an

additional fragmentation pathway was identified at the first branching point away from the core (m/z 16975, 50971, 84626, 118281, and higher coalescence ions). Increasing the relative amount of matrix or the introduction of cationization agents did not improve the intensity of the molecular ion. The fragmentation is possibly a result of the spectral overlap between the nitrogen laser (337 nm) used for excitation of the matrix and the UV absorbance for the higher generation dendrimers ($\lambda_{\text{max}}=300$ nm). The fourth-generation dendrimer **13** appears to be the limit for efficient generation and detection of the molecular ion without substantial

Table 1: Summary and comparison of the size characteristics for new polyphenylene dendrimers **7**, **9**, **11**, **13**, and **15** compared with hydrogen end-capped general polyphenylene dendrimers **A**, **B**, and **C**.^[8,16] [a]

Compound	Molecular formula	Aryl rings	Chain ends	Molecular mass [g mol ⁻¹]	MALDI-TOF MS [g mol ⁻¹]	SEC M _p (PS) ^[b] [g mol ⁻¹]	SEC PDI	Theo. radius ^[c] [nm]	DLS radius ^[d] [nm]	TEM radius ^[e] [nm]	Dendrimer density ^[f] [g mL ⁻¹]
<i>"exploded" dendrimers</i>											
C(Ph([G1](C≡C-TiPS)) ₄) (7)	C ₃₉₃ H ₃₈₈ Si ₈	48	8	5336	5443 (Ag)	8000	1.04	2.5	2.0	—	0.26
C(Ph([G2](C≡C-TiPS)) ₄) (9)	C ₁₀₄₁ H ₉₆₄ Si ₁₆	136	16	13 924	13 935 (K)	22 000	1.05	4.2	3.6	—	0.12
C(Ph([G3](C≡C-TiPS)) ₄) (11)	C ₂₃₃₇ H ₂₁₁₆ Si ₃₂	312	32	31 101	31 168	38 900	1.03	6.9	5.2	—	0.09
C(Ph([G4](C≡C-TiPS)) ₄) (13)	C ₄₉₂₉ H ₄₄₂₀ Si ₆₄	664	64	65 454	65 430 (K)	83 200	1.05	9.0	9.0	—	0.04
C(Ph([G5](C≡C-TiPS)) ₄) (15)	C ₁₀₁₁₃ H ₉₀₂₈ Si ₁₂₈	1368	128	134 162	135 290	114 200	1.10	11.0	11.8	11	0.03
<i>general dendrimers</i>											
C(Ph([G2](H)) ₄) (A)	C ₃₈₅ H ₂₆₀	64	16	4886	4916 (K)	3900	1.04	1.8	1.5	—	0.57
C(Ph([G3](H)) ₄) (B)	C ₈₆₅ H ₅₈₀	144	32	10 974	11 113 (Ag)	7900	1.03	2.5	2.2	2.6	0.41
C(Ph([G4](H)) ₄) (C)	C ₁₈₂₅ H ₁₂₂₀	304	64	23 150	23 194 (K)	13 800	1.05	3.2	2.9	3.0	0.38

[a] All MALDI-TOF mass spectra were acquired by irradiating the 1:250 analyte/matrix mixture with a nitrogen laser (337 nm) using dithranol as matrix and optional cationization agent, a trifluoroacetate salt, if specified, except for that of **15** which was acquired using DCTB.^[17] [b] SEC was performed at room temperature in THF using SEC columns with 500, 10⁴, and 10⁶ Å porosities and calibrated against narrowly disperse, linear polystyrene (PS) standards. [c] Theoretical radii were determined using MMFF94 molecular mechanics calculations, by evaluating the distance between the central carbon atom and the chain end of the longest linear oligophenylene arm. [d] DLS experiments were performed using a krypton ion laser (647.1 nm), a toluene filled index matching bath, and detected at 60, 90, 120, and 150° with respect to the incident beam and were measured in THF for **7**, **9**, **11**, **13**, and **15** and in toluene for **A**, **B**, and **C**.^[8,16] The hydrodynamic radii were calculated using the Stokes–Einstein equation. [e] TEM samples were prepared by spin-coating 10⁻⁸–10⁻⁹ M CH₂Cl₂ solutions onto mica substrates and subsequently shadowed with a tungsten/tantalum alloy at high vacuum, followed by deposition of a thin carbon support. The films were floated off the mica substrates onto a water surface and transferred to 600-mesh hexagonal copper grids for imaging. [f] The dendrimer densities were calculated by dividing the molecular mass by the hydrodynamic volume determined from DLS studies, and are substantially lower for the new polyphenylene dendrimer series, which suggests much higher porosities for the same series than those of the general polyphenylene dendrimers.

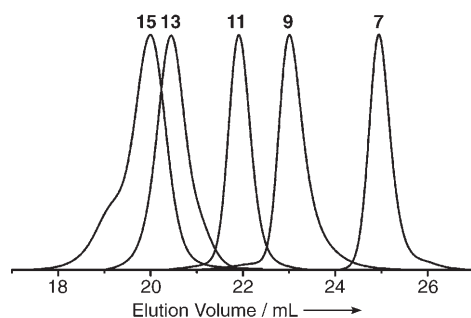


Figure 2. SEC traces for TiPS-ethynyl-functionalized polyphenylene dendrimers **7**, **9**, **11**, **13**, and **15** in THF with 500, 10⁴, and 10⁶ Å column porosities.

fragmentation for this family of dendrimers using these experimental conditions.^[18] While fragmentation from MALDI is generally regarded as undesired, the iterative nature of the dendrimer, and a clear fragmentation point (such as at the core) enables conclusive evidence to be drawn from such a “digestion.” All the detected ions from this MALDI “digestion,” combined with the ¹H NMR spectrum of the intact dendrimer **15** unequivocally prove the complete conversion into the fifth generation.

Transmission electron microscopy (TEM; Figure 5, Table 1) and dynamic light scattering (DLS) studies (Table 1) in THF were performed to gauge the sizes of the dendrimers. The TEM samples were obtained by spin-coating dilute CH₂Cl₂ solutions onto freshly cleaved mica substrates and subsequent shadowing with a tungsten/tantalum alloy by electron-beam evaporation at high vacuum, followed by deposition of a thin carbon support.^[8,19] The fourth-gener-

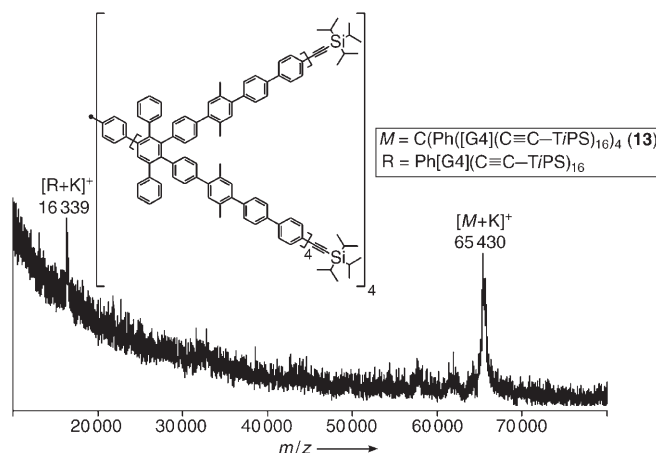


Figure 3. MALDI-TOF mass spectrum (dithranol, potassium trifluoroacetate) of C(Ph([G4](ethynyl-TiPS))₄) (**13**); G4 = fourth generation.

ation dendrimer **13** showed only filmlike aggregates, but the molecules of fifth-generation dendrimer **15** were well-separated with an average radius of 11.0 nm.^[20] There is agreement between the diffusional radius (11.8 nm) and the radius calculated by MMFF94 molecular mechanics (11.0 nm), thus suggesting that the chain ends are not appreciably backfolded and that the shape is preserved in solution. Such agreement, combined with surface accessibility of the chain ends, suggests that the rigid, pentaphenylbenzene branching units provide a conformational stiffness and directionality to the chain ends, similar to that of the parent case.^[21] The SEC elution behavior (Table 1) clearly indicates how much more compact the parent polyphenylene dendrimers (**A**, **B**, **C**)^[8,16] are than are the new dendrimers **7**, **9**, **11**, **13**, and **15**. The polystyrene (PS)-

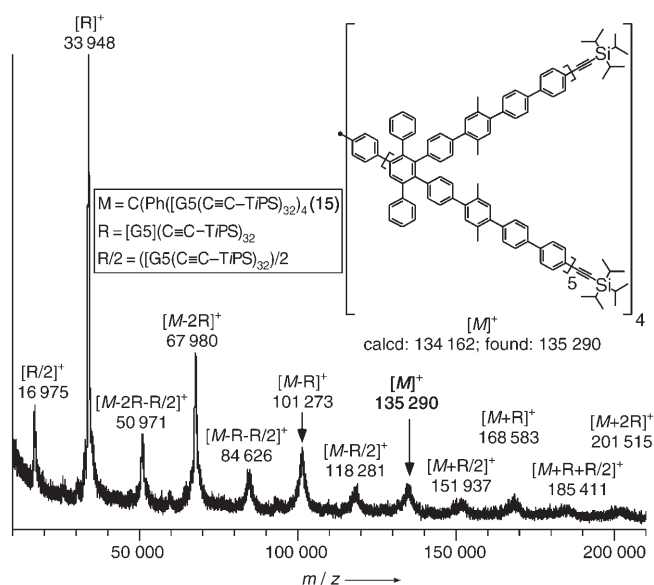


Figure 4. MALDI-TOF mass spectrum (DCTB) of $C(Ph([G5](ethynyl-TiPS)_{32})_4$ (**15**). G5 = fifth generation.

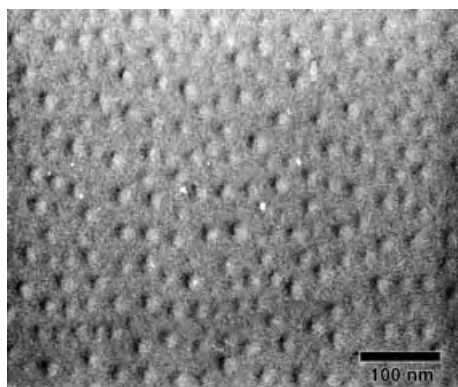


Figure 5. TEM image of tungsten/tantalum-shadowed $C(Ph([G5](ethynyl-TiPS)_{32})_4$ (**15**).

equivalent molecular weights (MWs) are less than the masses determined by MALDI-TOF for the former, and with the exception of the fifth-generation dendrimer, the PS-equivalent MWs are higher than the masses (MALDI-TOF) for the new series, thus indicating there is a very large amount of free volume occupied by solvent. Calculation of the dendrimer density (Table 1) from the hydrodynamic volume for each series revealed that a tenfold greater solvent volume is available in the new dendrimers. The significantly faster decrease in the dendrimer density with increasing generation for the new dendrimer series was the result of having used the same compact core from the general polyphenylene dendrimer series. The consequence of such a low dendrimer density could be a higher propensity for interdigitation, and thus aggregates which are difficult to separate.

Experimental and analytical conditions were found up to the fifth generation that demonstrated the complete conversion into the next generation. The limitations of generating molecular ions with MALDI techniques had precluded

evaluation of growth to a higher generation with complete certainty, but the results are highly encouraging using MALDI "digestion." Perhaps the most compelling synthetic observation is that, unlike the syntheses of the parent polyphenylene dendrimers which necessitated several weeks for the final growth reaction to go exclusively to completion, the reaction conversion for the fifth generation required less than 50 h. This result suggests that the steric demands at the chain ends required by the Diels–Alder cycloaddition are well below any critical threshold, completely unlike that of the parent polyphenylene dendrimers. The control over the topology of the branching units and the high porosity result in efficient growth cycles that lead to structural perfection, even for constructions containing 664 and 1368 phenyl rings (for the fourth- and fifth-generation dendrimers **13** and **15**, respectively). To the best of our knowledge, this is the first report of the stepwise chemical synthesis and proof of a truly monodisperse molecule with a diameter greater than 20 nm. Furthermore, no evidence was observed for the physical encapsulation of the branching unit within the dendrimers during the synthesis, thus suggesting that the cavities within the structures are large and may be exploited as novel hosts for large guests.^[22] Efforts are underway to evaluate the stiffness and to clarify the aggregate formation for the fifth-generation dendrimer **15**.

Received: April 20, 2005

Published online: September 7, 2005

Keywords: cycloaddition · dendrimers · mass spectrometry · nanostructures · structure elucidation

- [1] a) P. G. de Gennes, H. J. Hervat, *J. Phys. Lett.* **1983**, 44, L351–L360; b) T. C. Zook, G. T. Pickett, *Phys. Rev. Lett.* **2003**, 90, 015502; c) R. L. Lescanec, M. Muthukumar, *Macromolecules* **1990**, 23, 2280–2288; d) M. L. Mansfield, L. I. Klushin, *Macromolecules* **1993**, 26, 4262–4268; e) M. Murat, G. S. Grest, *Macromolecules* **1996**, 29, 1278–1285; f) T. H. Mourey, S. R. Turner, M. Rubinstein, J. M. J. Fréchet, C. J. Hawker, K. L. Wooley, *Macromolecules* **1992**, 25, 2401–2406; g) M. L. Mansfield, *Chemtracts: Macromol. Chem.* **1991**, 2, 364; h) D. Boris, M. Rubinstein, *Macromolecules* **1996**, 29, 7251–7260; i) K. L. Wooley, C. A. Klug, K. Tasaki, J. Schaefer, *J. Am. Chem. Soc.* **1997**, 119, 53–58; j) S. Rosenfeldt, N. Dingenouts, M. Ballauff, N. Werner, F. Vögtle, P. Lindner, *Macromolecules* **2002**, 35, 8098–8105.
- [2] a) Sterically bulky chain ends: H.-B. Meikelburger, K. Rissanen, F. Vögtle, *Chem. Ber.* **1993**, 126, 1161–1169; J. F. G. A. Jansen, E. W. Meijer, E. M. M. de Brabander-van den Berg, *J. Am. Chem. Soc.* **1995**, 117, 4417–4418; b) phase-segregating chain ends: J. H. Cameron, A. Facher, G. Lattermann, S. Diele, *Adv. Mater.* **1997**, 9, 398–403; V. Percec, W. D. Cho, M. Moller, S. A. Prokhorova, G. Ungar, D. J. P. Yeardley, *J. Am. Chem. Soc.* **2000**, 122, 4249–4250; c) incredibly high-generation dendrimers (not monodisperse): C. L. Jackson, H. D. Chanzy, F. P. Booy, B. J. Drake, D. A. Tomalia, B. J. Bauer, E. J. Amis, *Macromolecules* **1998**, 31, 6259–6265; M.-L. Lartigue, B. Donnadieu, C. Galliot, A.-M. Caminade, J.-P. Majoral, J.-P. Fayet, *Macromolecules* **1997**, 30, 7335–7337; M. Slany, M. Bardaji, M.-J. Casanove, A.-M. Caminade, J.-P. Majoral, B. Chaudret, *J. Am. Chem. Soc.* **1995**, 117, 9764–9765.

- [3] Z. Xu, M. Kahr, K. L. Walker, C. L. Wilkins, J. S. Moore, *J. Am. Chem. Soc.* **1994**, *116*, 4537–4550.
- [4] a) T. M. Miller, T. X. Neenan, *Chem. Mater.* **1990**, *2*, 346–349; b) T. M. Miller, T. X. Neenan, R. Zayas, H. E. Bair, *J. Am. Chem. Soc.* **1992**, *114*, 1018–1025.
- [5] a) F. Morgenroth, C. Kübel, K. Müllen, *J. Mater. Chem.* **1997**, *7*, 1207–1211; b) F. Morgenroth, E. Reuther, K. Müllen, *Angew. Chem.* **1997**, *109*, 647–649; *Angew. Chem. Int. Ed. Engl.* **1997**, *36*, 631–634.
- [6] Double-exponential dendrimer growth: T. Kawaguchi, K. L. Walker, C. L. Wilkins, J. S. Moore, *J. Am. Chem. Soc.* **1995**, *117*, 2159–2165.
- [7] J. S. Moore, Z. Xu, *Macromolecules* **1991**, *24*, 5893–5894.
- [8] U.-M. Wiesler, A. J. Berresheim, F. Morgenroth, G. Lieser, K. Müllen, *Macromolecules* **2001**, *34*, 187–199, and references therein.
- [9] M. Wind, K. Saalwachter, U.-M. Wiesler, K. Müllen, H. W. Spiess, *Macromolecules* **2002**, *35*, 10071–10086.
- [10] C. G. Clark, Jr., K. L. Wooley, *Curr. Opin. Colloid Interface Sci.* **1999**, *4*, 122–129.
- [11] P. Liess, V. Hensel, A.-D. Schlüter, *Liebigs Ann.* **1996**, 1037–1040.
- [12] B. C. Berris, G. H. Hovakeemian, Y.-H. Lai, H. Mestdagh, K. P. C. Vollhardt, *J. Am. Chem. Soc.* **1985**, *107*, 5670–5687.
- [13] a) P. Fitton, E. A. Rick, *J. Organomet. Chem.* **1971**, *28*, 287–291; b) G. W. Gray, M. Hird, D. Lacey, K. J. Toyne, *J. Chem. Soc. Perkin Trans. 2* **1989**, 2041–2053.
- [14] T. Weil, U.-M. Wiesler, A. Herrmann, R. Bauer, J. Hofkens, F. C. De Schryver, K. Mullen, *J. Am. Chem. Soc.* **2001**, *123*, 8101–8108.
- [15] During the review of this manuscript, the sixth-generation dendrimer was synthesized, and it continues the nonlinear elution trend for dendrimers higher than G5.
- [16] U.-M. Wiesler, Dissertation Johannes-Gutenberg-Universität, Mainz, **2001**.
- [17] 2-[(2*E*)-3-(4-*tert*-butylphenyl)-2-methylprop-2-enylidene]malononitrile (DCTB): L. Ulmer, J. Mattay, G. Torres-Garcia, H. Luftmann, *Eur. J. Mass Spectrom.* **2000**, *6*, 49–52.
- [18] J.-C. Blais, C.-O. Turrin, A.-M. Caminade, J.-P. Majoral, *Anal. Chem.* **2000**, *72*, 5097–5105.
- [19] Tungsten/tantalum shadowing provides for the finest grain of images possible.
- [20] Any polydispersity in observed particle size may be the result of the shadowing procedure and the high porosity of the particles.
- [21] S. Rosenfeldt, N. Dingenouts, D. Pötschke, M. Ballauff, A. J. Berresheim, K. Müllen, P. Lindner, *Angew. Chem.* **2004**, *116*, 111–114; *Angew. Chem. Int. Ed.* **2004**, *43*, 109–112.
- [22] M. Schlupp, T. Weil, A. J. Berresheim, U.-M. Wiesler, J. Bargon, K. Müllen, *Angew. Chem.* **2001**, *113*, 4124–4129; *Angew. Chem. Int. Ed.* **2001**, *40*, 4011–4015.

DOI: 10.1002/anie.200501508

An In Situ High-Temperature Single-Crystal Investigation of a Dehydrated Metal–Organic Framework Compound and Field-Induced Magnetization of One-Dimensional Metal–Oxygen Chains***Pascal D. C. Dietzel,* Yusuke Morita, Richard Blom, and Helmer Fjellvåg*

Metal–organic framework compounds have attracted considerable interest recently because of their eminently promising properties, which make them suitable for applications as gas-storage systems, sensors, and in ion exchange or catalysis,^[1] and, more seldom, because of their magnetic properties.^[2,3] The diversity of potential applications arises from the possibilities that the range of applicable metals and the appropriate choice of organic linking blocks offer for the intentional or inadvertent design of advantageous compounds. The common feature of most applications is that they necessitate the framework to have a sufficiently large and permanent porosity to be penetrated by guest molecules and ions. As such, coordination polymers have frequently been compared with zeolites, over which they offer a number of advantages. Among these are accessible volumes that are several times higher than for zeolites.^[4] A severe disadvantage of an organic–inorganic hybrid compound with respect to zeolites, however, is often the significantly lower thermal stability. For most applications, it is necessary to remove the solvent from the pores, which is usually only achieved at elevated temperatures, and this sometimes leads to the collapse of the long-range order of the framework. Thus, the investigation of the thermal behavior of any novel porous metal–organic framework compound lies at the core of determining its suitability for applications. There have been only a few reports of single-crystal investigations of desolvated microporous metal–organic frameworks,^[5] and in only one case was the study conducted in situ.^[6] In all of these cases, the connectivities of the framework of the desolvated compound remained unchanged. Here, we report the synthesis and characterization of a microporous cobalt(II)-

[*] Dr. P. D. C. Dietzel, Dr. R. Blom
SINTEF Materials and Chemistry
Postboks 124, Blindern, 0314 Oslo (Norway)
Fax: (+47) 2206-7350
E-mail: pascal.dietzel@sintef.no

Dr. Y. Morita, Prof. Dr. H. Fjellvåg
Centre for Materials Science and Nanotechnology
Department of Chemistry
University of Oslo
Postboks 1033, Blindern, 0315 Oslo (Norway)

[**] Support of this work by the Research Council of Norway (grants 153869/S10 and 165847/V30) is gratefully acknowledged.



Supporting information for this article is available on the WWW under <http://www.angewandte.org> or from the author.

containing metal–organic framework. The in situ single-crystal X-ray investigation of its dehydrated form reveals that a water molecule originally coordinated to the metal center is removed as well in the course of the solvent elimination. However, the framework remains stable, with the coordination environment of the cobalt atom changing from octahedral to square pyramidal. The as-synthesized compound orders antiferromagnetically below 8 K, but it subsequently passes through a metamagnetic phase transition to display field-induced ferromagnetic ordering.

The reaction of cobalt(II) acetate and 2,5-dihydroxyterephthalic acid ($\text{C}_8\text{H}_6\text{O}_6$) in a mixture of water and tetrahydrofuran (molar ratio 2:1:556:165) under autogenous pressure at 110 °C in a Teflon-lined autoclave (50% filling level) yielded the pink-red, needle-shaped crystalline substance $[\text{Co}_2(\text{C}_8\text{H}_2\text{O}_6)(\text{H}_2\text{O})_2] \cdot 8\text{H}_2\text{O}$ (**1**). The results of the elemental analysis confirm that the channels are occupied solely by water molecules even though a solvent mixture was used in the synthesis. The crystal structure analysis revealed a three-dimensional coordination polymer with honeycomb topology that contains one-dimensional, solvent-filled channels (Figure 1a). The cobalt atom is coordinated in a distorted octahedral fashion by six oxygen atoms. Five of the oxygen atoms are part of the organic ligand, which utilizes all of its oxygen atoms in coordinative bonds with the cobalt center. The sixth oxygen ligand at the cobalt center comes from a water molecule. Four of the Co–O distances are in the range between 2.03 and 2.06 Å, while the fifth Co–O distance is 2.190(5) Å. The water molecule is *trans* to this bond, and its Co–O bond is also elongated (2.158(7) Å). The hydroxide oxygen atom and one of the carboxylate oxygen atoms coordinate two cobalt atoms each, while the second carboxylate oxygen coordinates only one cobalt atom. This coordination arrangement results in cobalt–oxygen octahedra that are linked by *cis*-oriented edges (Figure 1b) such that the cobalt atoms form a threefold helix parallel to the *c* axis. The framework topology is identical to that recently described for $[\text{Zn}_2(\text{C}_8\text{H}_2\text{O}_6)(\text{dmf})_2] \cdot (\text{H}_2\text{O})_2$ (dmf = *N,N*-dimethylformamide).^[7]

After the hypothetical removal of the noncoordinating solvent molecules in the channels, the empty channels occupy 49% of the total volume of the unit cell, and the average cross-sectional channel dimensions are $11.08 \times 11.08 \text{ Å}^2$. The empty volume increases to 60% if the coordinating water is also removed. The water molecules excluding and including the coordinating water account for 29.2% and 36.6% of the mass, respectively. We found that it was possible to repeatedly dehydrate and hydrate compound **1** by heating to 100 °C in a dry argon gas stream and then cooling down and admixing water vapor with the inert gas stream. A dry gas stream at room temperature actually suffices to remove 90% of the water within 43 h. The amount of weight loss during the heating experiments indicates that the coordinatively bound water molecules are also removed. Indeed, this was confirmed by an in situ single-crystal structure determination at 95 °C which revealed that the three-dimensional framework actually remains intact upon dehydration. Because of the abscission of the coordinating water molecule, the cobalt center remains in a square-pyramidal coordination environ-

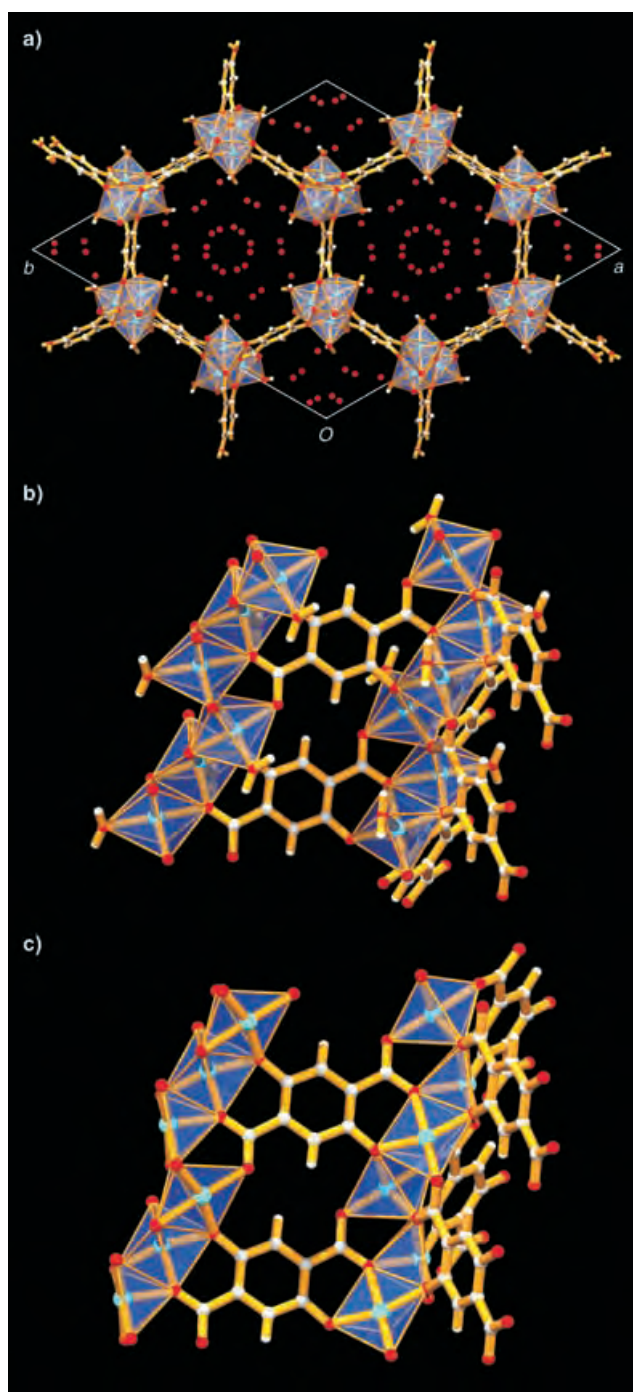


Figure 1. a) Packing diagram of **1** along [001]; b) chains of edge-connected cobalt oxygen octahedra in **1**. Neighboring chains are of opposite handedness; c) square-pyramidal environment of the cobalt center in **2** after removal of the water molecules.

ment (Figure 1c). At the apex of the pyramid is the oxygen atom that used to be *trans* to the vacated water position; the Co–O distance is now significantly shorter than before (2.067(5) Å). The empty coordination site is accessible for molecules from the channels, which is a necessary requirement for the metal to perform catalytic functions.^[8]

Plots of the projection of the electron density along the channel direction illustrate the change from the hydrated to the dehydrated framework (surface plots in Figure 2). The

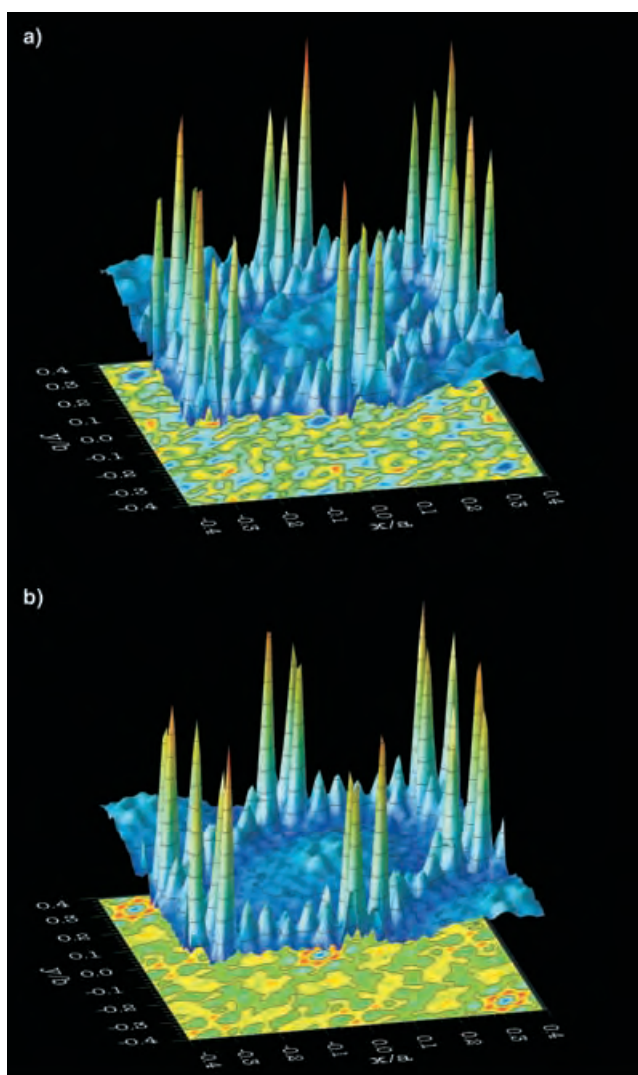


Figure 2. Projection of the electron density along [001] (surface plots) and the final difference electron maps (contour plots; line at 0.0 e Å^{-3}) at a) 25°C and b) 95°C . Observed reflections ($I > 2\sigma(I)$) were used for the calculation with the map function of WinGX.^[9]

cobalt atoms stand out as the most-intense peaks in groups of three at the corners of the hexagon. Connecting these are the rows of peaks due to the organic ligand. The water molecules in the channel and at the cobalt atoms are clearly distinguishable in Figure 2a, while they are absent in Figure 2b. Some electron density is observed in the center of the channel at 95°C . This might be due to the inert gas molecules that are bound to occupy the channels now, but the shape of the surface indicates that it is more likely a result of Fourier termination errors accumulating electron density around the element of symmetry. No atoms can be refined in these positions, and the final difference density maps (contour plots in Figure 2) agree well with the chosen structural models. In this context, it is noteworthy to mention that we also measured the crystal at 200°C and the results were congruent to those obtained at 95°C . A second crystal that had only been heated to 95°C yielded identical results to the first crystal. It was subsequently cooled down and stored in a water-vapor-saturated atmosphere, whereupon we could

again localize the coordinating water and bulk solvent water molecules.

We confirmed the stability of compound **2** in an inert atmosphere by thermogravimetry and thermogravimetry studies. The crystallinity of **2** starts to decrease above 200°C , and final decomposition occurs above 320°C . A sample heated at 200°C in argon for a total of 63 h can still take up the entire amount of water. Compound **2** is substantially less stable in air. Decomposition is observed at 234°C and proceeds rapidly, and the crystallinity of the sample diminishes already above 140°C . Concurrently, if a sample is dehydrated in air at 150°C , the amount of water that it can take up again diminishes with the time it has been exposed to this temperature. Apparently, the presence of the oxygen in air promotes the collapse of the framework.

In compound **1**, the shortest metal-to-metal distance within a helical metal–oxygen backbone chain is $3.059(2) \text{ Å}$, while the shortest distance between cobalt atoms in adjacent chains is $7.387(2) \text{ Å}$. Cobalt compounds with such a large anisotropy in metal-to-metal distances have frequently been found to behave as one-dimensional magnetic systems.^[10] While measurements of the magnetic susceptibility confirm the $+2$ oxidation state of the cobalt ($\mu = 4.67(13) \mu_B$, $\theta = -6(2) \text{ K}$), they do not show any noticeable deviation from three-dimensional behavior. The susceptibility drops off sharply below 8 K , which indicates antiferromagnetic ordering (Figure 3). However, on application of magnetic fields stronger than about 2 T , we observed a field-induced transition to a ferromagnetic-like ordered state.^[11] The superexchange pathway in the metal–oxygen chain suggests that the magnetic moments couple ferromagnetically in the chains. The antiferromagnetic long-range order in low magnetic fields then results from the antiparallel alignment of the spins of adjacent chains. It may be the aromatic system of the organic ligand that propagates this further to give a three-dimensional interaction.^[12] Stronger magnetic fields can overcome this interaction and induce the ferromagnetic-like state.

In conclusion, we would like to emphasize that metal–organic framework compounds may be very suitable systems to investigate magnetic interactions, even more so since materials with switchable magnetic properties promise to deliver the next revolution in information technology.^[13] We have shown that it is possible to remove the solvent from compound **1** whilst maintaining the framework structure intact, even though the cobalt atom also loses its coordinating water molecule and remains pentacoordinate. The resulting compound **2** is stable to above 200°C in an inert atmosphere.

The stability and the readily available coordination site at the metal atom indicate that it should be worthwhile to investigate the chemical properties of this compound further. This should encompass possible catalytic activity, while its magnetic properties suggest that a more detailed study of its magnetic structure needs to be performed.

Experimental Section

Crystals of compound **1** of a suitable size for a single-crystal structure determination were obtained by reducing the molar ratio of cobalt acetate to ligand to 1:1. They were obtained by combining a solution of cobalt(II) acetate (187 mg, 0.75 mmol) in water (10 mL) and a

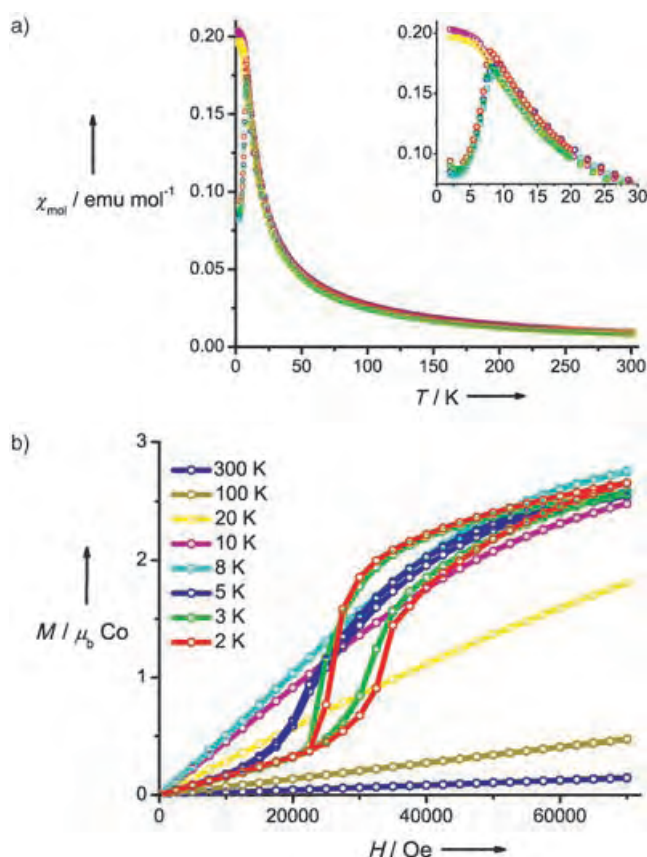


Figure 3. a) Molar magnetic susceptibility χ_{mol} as a function of the temperature for compound **1** and various fields (zero-field-cooled: 1000 Oe red, 10^4 Oe blue, 4×10^4 Oe magenta; field-cooled: 1000 Oe green, 10^4 Oe cyan, 4×10^4 Oe yellow); b) magnetization M per cobalt atom [μ_B] as a function of magnetic field and temperature.

solution of 2,5-dihydroxyterephthalic acid (149 mg, 0.75 mmol) in THF (10 mL) in a Teflon-lined steel autoclave and heating at 110 °C for three days. The crystals were isolated after filtration in 54 % yield (95 mg, 0.2 mmol) with respect to cobalt. Elemental analysis (%): calcd: C 19.52, H 4.47, Co 23.95, O 52.05; found: C 19.60, H 4.38, Co 23.95, O 52.06.

Single-crystal X-ray crystallography: A hemisphere of data was collected on a Bruker D8 diffractometer with an Apex II detector and an Oxford Cryosystems Cryostream Plus device. After data integration with SAINT and semiempirical absorption correction with SADABS,^[14] structures were solved by direct methods and refined on F^2 with the SHELX program suite.^[15]

Compound 1: Crystal dimensions $0.02 \times 0.02 \times 0.20$ mm³, trigonal, space group $R\bar{3}$ (no. 148), $a = 26.1102(19)$, $b = 26.1102(19)$, $c = 6.7192(10)$ Å, $V = 3967.1(7)$ Å³, $\rho_{\text{calcd}} = 1.793$ g cm⁻³, $Z = 18$, $2\theta_{\text{max}} = 50^\circ$, $\text{MoK}\alpha$ radiation, $\lambda = 0.71073$ Å, ω scans, $T = 293$ K, 12577 reflections collected, 1544 unique reflections, 1093 observed data ($I > 2\sigma(I)$), $R_{\text{int}} = 0.115$, $\mu = 1.959$ mm⁻¹, min/max transmission 0.712/0.962, 124 parameters, final $R_1(I > 2\sigma(I)) = 0.0626$, $wR_2(\text{all data}) = 0.1647$, $\text{GOF} = 1.15$, $\Delta\rho_{\text{min}} = -0.59$ e Å⁻¹, $\Delta\rho_{\text{max}} = 0.73$ e Å⁻¹. **Compound 2:** A crystal of dimensions of $0.03 \times 0.03 \times 0.30$ mm³ was attached carefully oriented and with a minimum of glue to the tip of a capillary to avoid obstructing the channels; it was then slowly heated at 20 °C h⁻¹ to 95 °C; trigonal, space group $R\bar{3}$ (no. 148), $a = 25.885(3)$, $b = 25.885(3)$, $c = 6.8058(17)$ Å, $V = 3949.0(12)$ Å³, $\rho_{\text{calcd}} = 1.181$ g cm⁻³, $Z = 18$, $2\theta_{\text{max}} = 50.6^\circ$, $\text{MoK}\alpha$ radiation, $\lambda = 0.71073$ Å, ω scans, $T = 368$ K, 6446 reflections collected, 1598 unique reflections, 1150 observed data ($I > 2\sigma(I)$), $R_{\text{int}} = 0.066$, $\mu = 1.89$ mm⁻¹, min/max

transmission 0.590/0.945, 73 parameters, final $R_1(I > 2\sigma(I)) = 0.058$, $wR_2(\text{all data}) = 0.209$, $\text{GOF} = 1.24$, $\Delta\rho_{\text{min}} = -0.76$ e Å⁻¹, $\Delta\rho_{\text{max}} = 1.30$ e Å⁻¹.

CCDC 270292 (**1**) and 270293 (**2**) contain the supplementary crystallographic data for this paper. These data can be obtained free of charge from the Cambridge Crystallographic Data Centre via www.ccdc.cam.ac.uk/data_request/cif.

Received: May 2, 2005

Published online: September 7, 2005

Keywords: cobalt · magnetic properties · microporous materials · organic–inorganic hybrid composites · X-ray diffraction

- [1] a) C. Janiak, *Dalton Trans.* **2003**, 2781–2804; b) C. N. R. Rao, S. Natarajan, R. Vaidyanathan, *Angew. Chem.* **2004**, *116*, 1490–1521; *Angew. Chem. Int. Ed.* **2004**, *43*, 1466–1496; c) S. Kitagawa, R. Kitaura, S. Noro, *Angew. Chem.* **2004**, *116*, 2388–2430; *Angew. Chem. Int. Ed.* **2004**, *43*, 2334–2375; d) J. L. C. Rowsell, O. M. Yaghi, *Microporous Mesoporous Mater.* **2004**, *73*, 3–14; e) M. J. Rosseinsky, *Microporous Mesoporous Mater.* **2004**, *73*, 15–30; f) W. Mori, S. Takamizawa, C. N. Kato, T. Ohmura, T. Sato, *Microporous Mesoporous Mater.* **2004**, *73*, 31–46; g) S. L. James, *Chem. Soc. Rev.* **2003**, *32*, 276–288.
- [2] a) M. A. Lawandy, X. Huang, R.-J. Wang, J. Li, J. Y. Lu, T. Yuen, C. L. Lin, *Inorg. Chem.* **1999**, *38*, 5410–5414; b) J.-M. Rueff, S. Pillet, N. Claiser, G. Bonaventure, M. Souhassou, P. Rabu, *Eur. J. Inorg. Chem.* **2002**, 895–900; c) J. R. Galán-Mascarós, K. R. Dunbar, *Angew. Chem.* **2003**, *115*, 2391–2395; *Angew. Chem. Int. Ed.* **2003**, *42*, 2289–2293; d) L. Li, Z. Liu, S. S. Turner, D. Liao, Z. Jiang, S. Yan, *Eur. J. Inorg. Chem.* **2003**, 62–65; e) M. Kurmoo, H. Kumagai, S. M. Hughes, C. J. Kepert, *Inorg. Chem.* **2003**, *42*, 6709–6722; f) K. Barthelet, D. Riou, M. Nogues, G. Férey, *Inorg. Chem.* **2003**, *42*, 1739–1743; g) M.-L. Tong, S. Kitagawa, H.-C. Chang, M. Ohba, *Chem. Commun.* **2004**, 418–419; h) S. G. Baca, S. T. Malinovsky, P. Franz, C. Ambrus, H. Stoeckli-Evans, N. Gerbeleu, S. Decurtins, *J. Solid State Chem.* **2004**, *177*, 2841–2849; i) M. Sanselme, J.-M. Grenèche, M. Riou-Cavellec, G. Férey, *Solid State Sci.* **2004**, *6*, 853–858.
- [3] a) J. A. Real, E. Andrés, M. C. Muñoz, M. Julve, T. Granier, A. Bousseksou, F. Varret, *Science* **1995**, *268*, 265–267; b) G. J. Halder, C. J. Kepert, B. Moubarak, K. S. Murray, J. D. Cashion, *Science* **2002**, *298*, 1762–1765; c) V. Niel, A. L. Thompson, M. C. Muñoz, A. Galet, A. E. Goeta, J. A. Real, *Angew. Chem.* **2003**, *115*, 3890–3893; *Angew. Chem. Int. Ed.* **2003**, *42*, 3760–3763; d) G. S. Matouzenko, G. Molnar, N. Bréfuel, M. Perrin, A. Bousseksou, S. A. Borshch, *Chem. Mater.* **2003**, *15*, 550–556; e) V. Niel, A. L. Thompson, A. E. Goeta, C. Enachescu, A. Hauser, A. Galet, M. C. Muñoz, J. A. Real, *Chem. Eur. J.* **2005**, *11*, 2047–2060; f) R. Bronisz, *Inorg. Chem.* **2005**, *44*, 4463–4465.
- [4] a) O. M. Yaghi, M. O’Keeffe, N. W. Ockwig, H. K. Chae, M. Eddaoudi, J. Kim, *Nature* **2003**, *423*, 705–714; b) H. K. Chae, D. Y. Siberio-Pérez, J. Kim, Y. Go, M. Eddaoudi, A. J. Matzger, M. O’Keeffe, O. M. Yaghi, *Nature* **2004**, *427*, 523–527; c) G. Férey, C. Serre, C. Mellot-Draznieks, F. Millange, S. Surblé, J. Dutour, I. Margiolaki, *Angew. Chem.* **2004**, *116*, 6456–6461; *Angew. Chem. Int. Ed.* **2004**, *43*, 6296–6301.
- [5] a) H. Li, M. Eddaoudi, M. O’Keeffe, O. M. Yaghi, *Nature* **1999**, *402*, 276–279; b) K. Biradha, Y. Hongo, M. Fujita, *Angew. Chem.* **2000**, *112*, 4001–4003; *Angew. Chem. Int. Ed.* **2000**, *39*, 3843–3845; c) Y. H. Liu, H. L. Tsai, Y. L. Lu, Y. S. Wen, J. C. Wang, K. L. Li, *Inorg. Chem.* **2001**, *40*, 6426–6431; d) J. Y. Lu, A. M. Babb, *Chem. Commun.* **2002**, 1340–1341; e) E. J. Cussen, J. B. Claridge, M. J. Rosseinsky, C. J. Kepert, *J. Am. Chem. Soc.*

- 2002**, 124, 9574–9581; f) B. Rather, M. J. Zaworotko, *Chem. Commun.* **2003**, 830–831.
- [6] C. J. Kepert, M. J. Rosseinsky, *Chem. Commun.* **1999**, 375–376.
- [7] N. L. Rosi, J. Kim, M. Eddaoudi, B. Chen, M. O’Keeffe, O. M. Yaghi, *J. Am. Chem. Soc.* **2005**, 127, 1504–1518.
- [8] K. Schlichte, T. Kratzke, S. Kaskel, *Microporous Mesoporous Mater.* **2004**, 73, 81–88.
- [9] L. J. Farrugia, *J. Appl. Crystallogr.* **1999**, 32, 837–838.
- [10] R. L. Carlin, *Magnetochemistry*, Springer, Berlin, **1986**.
- [11] E. Strykowski, N. Giordano, *Adv. Phys.* **1977**, 26, 487–650.
- [12] K. Barthelet, J. Marrot, D. Riou, G. Férey, *Angew. Chem.* **2002**, 114, 291–294; *Angew. Chem. Int. Ed.* **2002**, 41, 281–284.
- [13] a) O. Kahn, J. C. Martinez, *Science* **1998**, 279, 44–48; b) A. Bousseksou, G. Molnár, P. Demont, J. Menegotto, *J. Mater. Chem.* **2003**, 13, 2069–2071; c) D. C. Worledge, *Appl. Phys. Lett.* **2004**, 84, 4559–4561; d) A. Ney, J. S. Harris, *Appl. Phys. Lett.* **2005**, 86, 013502.
- [14] a) SAINT: Area-Detector Integration Software. V7.06 A; Bruker-Nonius, Inc., Madison, WI, **2003**; b) SADABS: Area-Detector Absorption Correction; Bruker-Nonius, Inc., Madison, WI, **2003**.
- [15] G. M. Sheldrick, SHELX97—Program suite for the solution and refinement of crystal structures (Release 97-2), University of Göttingen, Germany, **1998**.

Functionalized Nanotubes

DOI: 10.1002/anie.200501613

Targeted Delivery of Amphotericin B to Cells by Using Functionalized Carbon Nanotubes**

Wei Wu, Sébastien Wieckowski, Giorgia Pastorin, Monica Benincasa, Cédric Klumpp, Jean-Paul Briand, Renato Gennaro, Maurizio Prato, and Alberto Bianco*

Functionalized carbon nanotubes (f-CNTs) are attracting increasing attention as new vectors for the delivery of

therapeutic molecules.^[1–5] In fact, carbon nanotubes (CNTs) have been shown to cross cell membranes easily and to deliver peptides, proteins, and nucleic acids into cells.^[6–14] These innovative carriers present a lower toxicity, a fact that boosts their potential for biomedical applications.^[1–3,15]

The use of f-CNTs for drug delivery of small molecules (e.g. anticancer, antibacterial, or antiviral agents) is still unexplored. The development of nanovectors able to carry one or more therapeutic agents with recognition capacity, optical signals for imaging, and/or specific targeting is of fundamental advantage, for example, in the treatment of cancer and/or different types of infections.^[16] Theoretically, the use of f-CNTs in this approach would require the introduction of different functionalities on the external surface of the CNTs. Multiple functionalization of the tips of CNTs has been reported recently.^[17] Although the method is original and interesting, it does not exploit the full surface available on the CNTs for the linking of different molecules, nor has an application for drug delivery been envisaged. We decided to explore an alternative strategy for the introduction of two different and orthogonal functionalizations to CNTs. The orthogonal methodology, which is widely used in organic synthesis, would allow the selection and control of the attachment of active molecules to the sidewalls and tips of the CNTs. This approach enabled us to simultaneously link fluorescent probes to the CNTs for tracking the uptake of material as well as an antibiotic moiety as the active molecule. For this purpose we chose fluorescein and amphotericin B (AmB), respectively. AmB is considered to be the most effective antibiotic in the treatment of chronic fungal infections.^[18–20] However, the drug is highly toxic to mammalian cells,^[18] one reason for this toxicity can be attributed to the formation of aggregates as a result of the lower solubility of AmB in water.^[19] Conjugation of this drug to CNTs could have several advantages: 1) increased solubility of the molecule; 2) decrease in the aggregation phenomena; 3) improved efficacy owing to the internalization capacity of the CNTs; and 4) modulation of the antibiotic activity against different types of cells (mammalian, bacterial, and fungal). Herein we present the first case of AmB covalently linked to a polymeric carrier. Previously, the drug was encapsulated into colloidal or lipid systems owing to the need for slow release;^[21] however, high doses are required to elicit the same efficacy as that of AmB alone. The incorporation of CNTs could allow a reduction in the amount of AmB administered. It is easy to control their dimensions and the degree of functionalization. CNTs are particularly promising delivery systems as they are non-immunogenic.^[3,10]

The aim of the work described herein was first to explore a new strategy for the double functionalization of CNTs, second, to assess the characteristics of toxicity and uptake of CNTs functionalized with AmB and fluorescein towards mammalian cells, and thirdly, to evaluate the antifungal activity of CNT–AmB conjugates.

It is known that the exposure of CNTs to oxidative conditions (for example, sonication in a mixture of sulfuric and nitric acids) not only cuts the tubes and generates surface defects but can also provide abundant carboxylated sites along their sidewalls.^[22,23] To establish the effect of acidic

[*] Dr. W. Wu, S. Wieckowski, Dr. G. Pastorin, C. Klumpp, Dr. J.-P. Briand, Dr. A. Bianco
Institut de Biologie Moléculaire et Cellulaire
UPR9021 CNRS, Immunologie et Chimie Thérapeutiques
67084 Strasbourg (France)
Fax: (+33) 3-8861-0680
E-mail: a.bianco@ibmc.u-strasbg.fr

C. Klumpp, Prof. M. Prato
Dipartimento di Scienze Farmaceutiche
Università di Trieste
34127 Trieste (Italy)

Dr. M. Benincasa, Prof. R. Gennaro
Dipartimento di Biochimica, Biofisica e Chimica Macromolecolare
Università di Trieste
34127 Trieste (Italy)

[**] This work was financially supported by the CNRS, the University of Trieste, and the MIUR (PRIN 2004, prot. 2004035502). W.W. and G.P. are grateful to the French Ministry for Research and New Technologies for a post doctoral fellowship. The authors wish to thank Sylvie Fournel for critical reading of this manuscript.

Supporting information for this article is available on the WWW under <http://www.angewandte.org> or from the author.

and those of FITC at 517 nm (Figure 2). Upon subtraction of the contribution of CNTs to the UV/Vis spectrum of **4**, the ratio between AmB and FITC attached to the tubes was 1.5:1. A similar result was found for the conjugate dissolved in methanol (Supporting Information).

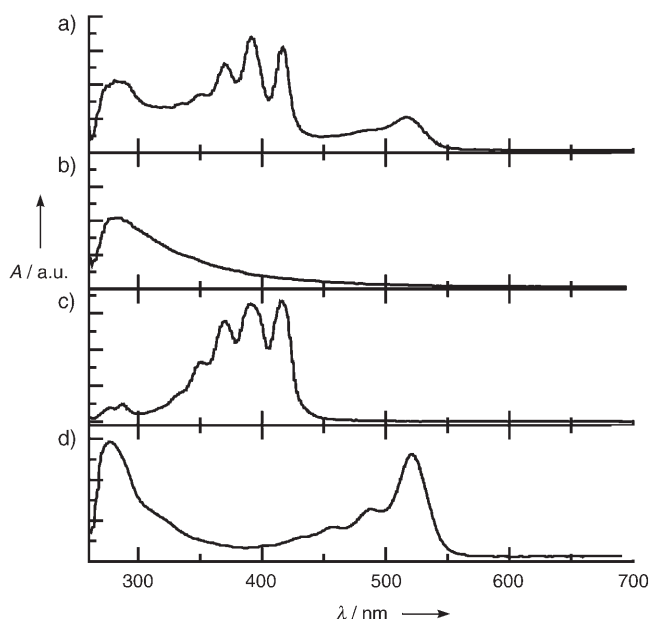


Figure 2. UV/Vis spectra of a) MWNTs **4**, b) **2**, c) AmB, d) FITC in DMF.

To assess the biological properties of the novel, doubly functionalized CNTs, we initially studied the toxicity effects of MWNTs **4** on mammalian cells, tracing its capacity to cross the cell membrane. Human Jurkat lymphoma T cells were incubated with either MWNTs **4** or AmB as the control. The cells were grown at 37 °C in RPMI medium and treated for 1 h with doses of MWNTs **4** increasing from 1 to 40 $\mu\text{g mL}^{-1}$. Cell viability was analyzed by flow cytometry by staining early and late apoptosis and necrosis with annexin V and propidium iodide (Figure 3). As a positive control, the cells were treated with AmB (10 $\mu\text{g mL}^{-1}$) alone. The dose of AmB used for the control experiment corresponded to the amount of drug covalently bound to 40 $\mu\text{g mL}^{-1}$ of MWNTs **4**. The conjugation of AmB to CNTs clearly reduces the toxic effects of the antibiotic on mammalian cells. At the highest doses, more than 40% of the cells died in the presence of AmB, whereas all the cells remained alive upon treatment with MWNTs **4**. We subsequently verified that longer incubation times do not increase the percentage of dead cells. Indeed, all the Jurkat cells remained alive after treatment with MWNTs **4** for 4 and 16 h (Supporting Information). Furthermore, cell uptake of MWNTs **4** was very fast as maximum fluorescence was observed after only 1 h of incubation. This result is in accordance with the behavior of single-walled CNTs previously used as transporters for peptides and proteins.^[6–8]

Attachment to CNTs modified the internalization properties of AmB. Jurkat cells incubated with MWNTs **4** at different doses and time points were analyzed by using epifluorescence and confocal microscopy. We found that the

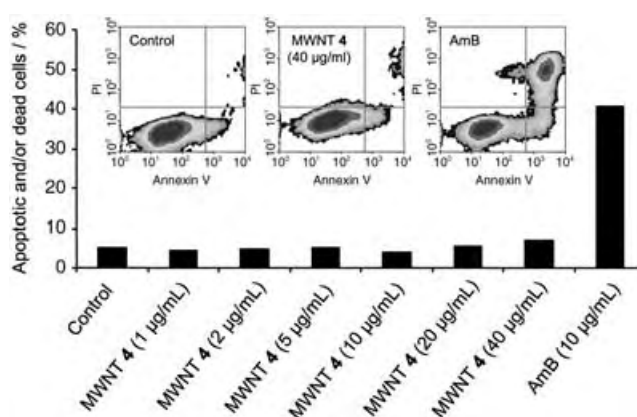


Figure 3. Percentage of early-apoptotic, late-apoptotic, and/or dead Jurkat cells after treatment with MWNTs **4** at different concentrations for 1 h. After incubation and washings, the cells were stained with annexin V and propidium iodide and analyzed by flow cytometry (inset).

internalization of AmB linked to the nanotubes was dose-dependent (Supporting Information). Figure 4 clearly shows that the conjugates pass into the cell cytoplasm. Notably, the MWNTs **4** is mainly localized around the nuclear membrane, but does not cross this barrier.

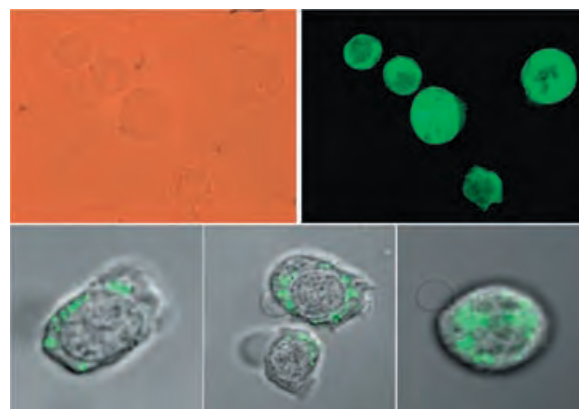


Figure 4. Epifluorescence (top) and confocal (bottom) microscopy images of Jurkat cells incubated for 1 h at 37 °C with 10 and 40 $\mu\text{g mL}^{-1}$ of MWNTs **4**, respectively. Jurkat cells have an average diameter of 10 μm .

The mechanism of penetration is not mediated by endocytosis because incubation in the presence of NaN_3 at 4 °C does not remarkably influence the penetration capacity of MWNTs **4** observed at 37 °C (Supporting Information).^[7] We demonstrated that f-CNTs are able to enter the cell by a spontaneous mechanism: they behave like nanoneedles and pass through the cell membrane without causing cell death.^[11] This mechanism was recently confirmed by Cai et al., who showed that the nanopenetration of cell membranes seems to be a unique feature of CNTs.^[28] Concerning the toxic effects of AmB on mammalian cells, it is thought that this antibiotic destabilizes the cell membrane in a manner similar to the cases of fungi and yeasts.^[20] Therefore, the ability of CNTs to internalize AmB rapidly into the cytoplasm of Jurkat cells

remarkably reduces the possibility of disruption of the membrane core. The covalent attachment of AmB to the nanotubes has another clear advantage: it prevents the aggregation phenomena that the drug typically displays in solution. AmB strongly self-associates in aqueous solution and increases the possibility of toxic effects to the cells. In UV/Vis spectra of MWNTs **4** in water and RPMI, we found that the aggregation is lower than that of AmB alone (Supporting Information).^[19,29]

Finally, we evaluated the antifungal activity of CNTs, functionalized with AmB, against three species of fungi that are either pathogenic or may opportunistically infect humans. These included collection strains (*Candida parapsilosis* ATCC 90118 and *Cryptococcus neoformans* ATCC 90112) and clinical isolates (*Candida albicans*). In these experiments we used AmB that was covalently linked to ammonium-functionalized multi- and single-walled carbon nanotubes (MWNT-AmB **18** and SWNT-AmB **19**) (Supporting Information). We explicitly chose these types of conjugates to compare the antifungal activity of AmB bound to CNTs directly with that of native AmB, in the absence of the fluorescent probe. The minimum inhibitory concentration (MIC) values were determined after 48 h of incubation with different doses of free AmB, unconjugated CNTs, or CNT-AmB conjugates. As shown in Table 2, ammonium-function-

appropriate conjugation can increase the effectiveness of AmB while decreasing its toxicity, as shown by the flow cytometric experiments with Jurkat cells (Figure 3). Such a development would increase the clinical use of AmB, which is, at present, limited by its narrow therapeutic index.^[30]

In summary, we were successful in preparing CNTs containing both fluorescein and amphotericin B. Our studies revealed that AmB covalently linked to CNTs is taken up by mammalian cells without presenting any specific toxic effect. Furthermore, AmB bound to CNTs preserves its high antifungal activity. Therefore, multifunctionalized CNTs can be envisaged for the delivery of antibiotics to different types of cells by selective transport through the membrane. Finally, the covalent linkage of different drugs to CNTs is an approach that may be used to modulate the therapeutic action of the agent, thus obtaining new conjugates with interesting properties.

Received: May 11, 2005

Revised: July 26, 2005

Published online: September 2, 2005

Keywords: antibiotics · drug delivery · nanotubes · nanovectors · toxicity

Table 2: Antifungal activity of CNT-AmB conjugates.

CNT	Minimum inhibitory concentration (MIC) ^[a] [$\mu\text{g mL}^{-1}$]		
	<i>C. parapsilosis</i> ATCC 90118	<i>C. albicans</i> (c.i.) ^[b]	<i>C. neoformans</i> ATCC 90112
AmB	20	> 80	5
SWNT-NH ₃ ⁺	> 80	> 80	> 80
MWNT-AmB ^[c] 18	1.6	6.4	0.8
SWNT-AmB ^[c] 19	1.6	13.8	0.8

[a] The MIC corresponds to the lowest concentration of compound that inhibited visible growth of the organism. Results given are mean values of two independent determinations performed in duplicate. [b] c.i., clinical isolate. [c] In this table, the MIC values for MWNT-AmB and SWNT-AmB refer to the amount of AmB in the conjugates (approximately one third by weight).

alized CNTs, free of AmB, were inactive up to the maximal concentration ($80 \mu\text{g mL}^{-1}$) used against all the microorganisms tested. Conversely, MWNT- and SWNT-AmB were highly effective, indicating that the activity of the drug was not prevented by its covalent binding to both single- and multiwalled CNTs. Interestingly, when equal amounts of free and bound drug are considered, (the actual amount of AmB bound to CNTs is approximately one third by weight), conjugated AmB is definitely more potent than the free drug, particularly against the *Candida* spp. The reason for this increased activity is at present unclear, although an increased solubility of the drug by conjugation to CNTs might explain, at least in part, this finding. Alternatively, or supplementary to an increased solubility, binding to CNTs and the presence of multiple copies of AmB per CNT molecule might favor the interaction of the drug with its target, the fungal membrane. Although further investigations are necessary in this respect, the in vitro results are very promising as they indicate that

- [1] A. Bianco, K. Kostarelos, C. D. Partidos, M. Prato, *Chem. Commun.* **2005**, 571–577.
- [2] K. Kostarelos, L. Lacerda, C. D. Partidos, M. Prato, A. Bianco, *J. Drug Delivery Sci. Technol.* **2005**, *15*, 41–47.
- [3] A. Bianco, *Expert Opin. Drug Delivery* **2004**, *1*, 57–65.
- [4] Y. Lin, S. Taylor, H. Li, K. Fernando, L. Qu, W. Wang, L. Gu, B. Zhou, Y.-P. Sun, *J. Mater. Sci.* **2004**, *14*, 527–541.
- [5] A. Bianco, M. Prato, *Adv. Mater.* **2003**, *15*, 1765–1768.
- [6] N. W. Shi Kam, T. C. Jessop, P. A. Wender, H. Dai, *J. Am. Chem. Soc.* **2004**, *126*, 6850–6851.
- [7] D. Pantarotto, J.-P. Briand, M. Prato, A. Bianco, *Chem. Commun.* **2004**, 16–17.
- [8] N. W. Shi Kam, H. Dai, *J. Am. Chem. Soc.* **2005**, *127*, 6021–6026.
- [9] D. Pantarotto, C. D. Partidos, R. Graff, J. Hoebeke, J.-P. Briand, M. Prato, A. Bianco, *J. Am. Chem. Soc.* **2003**, *125*, 6160–6164.
- [10] D. Pantarotto, C. D. Partidos, J. Hoebeke, F. Brown, E. Kramer, J.-P. Briand, S. Muller, M. Prato, A. Bianco, *Chem. Biol.* **2003**, *10*, 961–966.
- [11] D. Pantarotto, R. Singh, D. McCarthy, M. Erhardt, J.-P. Briand, M. Prato, K. Kostarelos, A. Bianco, *Angew. Chem.* **2004**, *116*, 5354–5358; *Angew. Chem. Int. Ed.* **2004**, *43*, 5242–5246.
- [12] R. Singh, D. Pantarotto, D. McCarthy, O. Chaloin, J. Hoebeke, C. D. Partidos, J.-P. Briand, M. Prato, A. Bianco, K. Kostarelos, *J. Am. Chem. Soc.* **2005**, *127*, 4388–4396.
- [13] A. Bianco, J. Hoebeke, S. Godefroy, O. Chaloin, D. Pantarotto, J.-P. Briand, S. Muller, M. Prato, C. D. Partidos, *J. Am. Chem. Soc.* **2005**, *127*, 58–59.
- [14] Q. Li, J. M. Moore, G. Huang, A. S. Mount, A. M. Rao, L. L. Larcom, P. C. Ke, *Nano Lett.* **2004**, *4*, 2473–2477.
- [15] V. L. Colvin, *Nat. Biotechnol.* **2003**, *21*, 1166–1170.
- [16] M. Ferrari, *Nat. Rev. Cancer* **2005**, *5*, 161–171.
- [17] K. M. Lee, L. Li, L. Dai, *J. Am. Chem. Soc.* **2005**, *127*, 4122–4123.
- [18] S. B. Zotchev, *Curr. Med. Chem.* **2003**, *10*, 211–223.
- [19] J. Szlinder-Richert, B. Cybulska, J. Grzybowski, J. Bolard, E. Borowski, *Farmaco* **2004**, *59*, 289–296.
- [20] A. Zumbuehl, D. Jeannerat, S. E. Martin, M. Sohrmann, P. Stano, T. Vigassy, D. D. Clark, S. L. Hussey, M. Peter, B. R.

- Peterson, E. Pretsch, P. Walde, E. M. Carreira, *Angew. Chem.* **2004**, *116*, 5293–5297; *Angew. Chem. Int. Ed.* **2004**, *43*, 5181–5185.
- [21] J. Brajburg, J. Bolard, *Clin. Microbiol. Rev.* **1996**, *9*, 512–531.
- [22] D. B. Mawhinney, V. Naumenko, A. Kuznetsova, J. T. Yates, J. Liu, R. E. Smalley, *Chem. Phys. Lett.* **2000**, *324*, 213–216.
- [23] H. Hu, P. Bhowmik, B. Zhao, M. A. Hamon, M. E. Itkis, R. C. Haddon, *Chem. Phys. Lett.* **2001**, *345*, 25–28.
- [24] J. Liu, A. G. Rinzler, H. Dai, J. H. Hafner, R. K. Bradley, P. J. Boul, A. Lu, T. Iverson, K. Shelimov, C. B. Huffman, F. Rodriguez-Macias, Y.-S. Shon, T. R. Lee, D. T. Colbert, R. E. Smalley, *Science* **1998**, *280*, 1253–1256.
- [25] Y. Qin, J. Shi, W. Wu, X. Li, Z.-X. Guo, D. Zhu, *J. Phys. Chem. B* **2003**, *107*, 12899–12901.
- [26] V. Georgakilas, K. Kordatos, M. Prato, D. M. Guldi, M. Holzinger, A. Hirsch, *J. Am. Chem. Soc.* **2002**, *124*, 760–761.
- [27] V. Georgakilas, N. Tagmatarchis, D. Pantarotto, A. Bianco, J.-P. Briand, M. Prato, *Chem. Commun.* **2002**, 3050–3051.
- [28] D. Cai, J. M. Mataraza, Z.-H. Qin, Z. Huang, J. Huang, T. C. Chiles, D. Carnahan, K. Kempa, Z. Ren, *Nat. Methods* **2005**, *2*, 449–454.
- [29] M. Gago, R. Koper, W. I. Gruszecki, *Biochim. Biophys. Acta* **2001**, *1511*, 90–98.
- [30] H. A. Gallis, R. H. Drew, W. W. Pickard, *Rev. Infect. Dis.* **1990**, *12*, 308–329.

Asymmetric Catalysis

DOI: 10.1002/anie.200501676

Heterogenization of Shibasaki's Binol/La Catalyst for Enantioselective Epoxidation of α,β -Unsaturated Ketones with Multitopic Binol Ligands: The Impact of Bridging Spacers**

Xingwang Wang, Lei Shi, Mingxing Li, and Kuiling Ding*

The use of homochiral metal–organic polymers^[1] as heterogeneous catalysts for asymmetric reactions has provided a new strategy for chiral catalyst immobilization,^[2–4] which

might overcome some drawbacks of traditional approaches, such as reduced enantioselectivity or decreased activity in comparison with their homogeneous counterparts.^[5–7] With this strategy, the bridged ligands spontaneously coordinate with metal ions to form homochiral metal–ligand assemblies, in which the bridged chiral ligands provide an enantiodiscrimination environment and the metal ions act as the catalytically active centers in asymmetric catalysis.^[4,5] In principle, the stereochemical characteristics of the multitopic ligands should have significant impact on the microstructures of the resulting homochiral metal–organic polymers, and thus may exert a profound influence on the enantioselectivity and activity of the catalysis in a given reaction. Therefore, the design and synthesis of multitopic chiral ligands with diverse geometrical features is a central issue in the generation of homochiral metal–organic polymers for heterogeneous asymmetric catalysis (Figure 1).

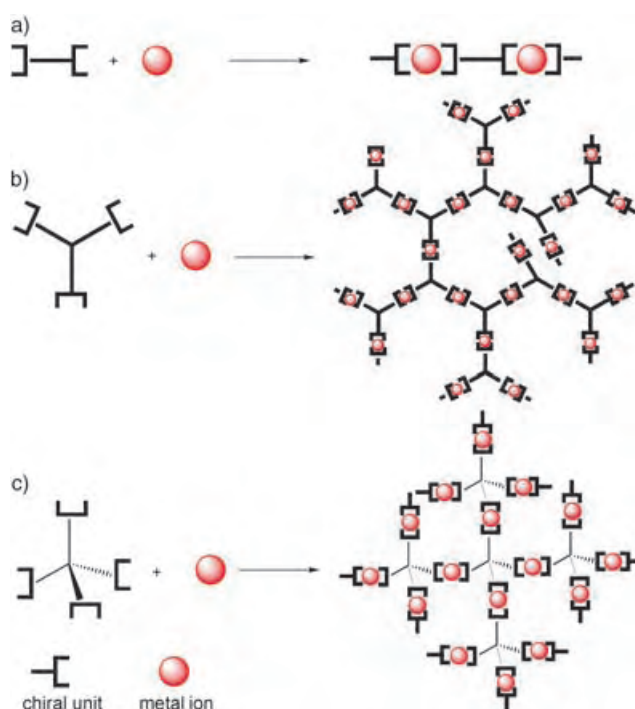


Figure 1. Schematic representation of the strategy for generation of self-supported enantioselective heterogeneous catalysts by using a) 1D, b) 2D, and c) 3D multitopic chiral ligands with metal ions.

The homogeneous catalytic asymmetric epoxidation of α,β -unsaturated ketones in the presence of Shibasaki's lanthanum catalyst,^[8–10] which is based on the 2,2'-dihydroxy-1,1'-binaphthyl (binol) ligand, has provided one of the most convenient approaches to α,β -epoxy ketones among various catalytic systems developed so far.^[11–15] Although excellent yields and enantioselectivity have been achieved, a catalyst loading of 5–20 mol % rendered the process less practical. However, the immobilization of this type of catalyst by an organic polymer support or stereoregular polymeric ligands often resulted in a drastic decrease of catalytic activity and enantioselectivity in the catalysis.^[16] Herein, we report preliminary results on the heterogenization of Shibasaki's

[*] X. Wang, L. Shi, Prof. Dr. K. Ding
State Key Laboratory of Organometallic Chemistry
Shanghai Institute of Organic Chemistry
Chinese Academy of Sciences, 354 Fenglin Road
Shanghai 200032 (China)
Fax: (+) 21-6416-6128
E-mail: kding@mail.sioc.ac.cn

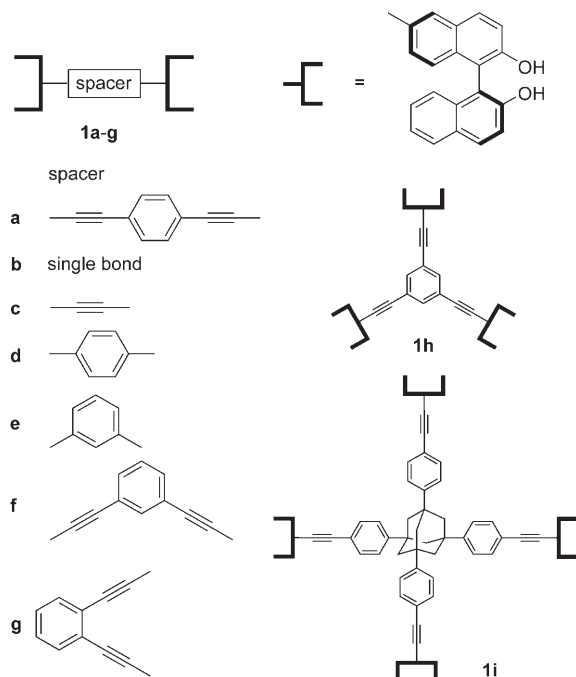
L. Shi, Prof. Dr. M. Li
Department of Chemistry
College of Sciences, Shanghai University
99 Shangda Road, Shanghai 200436 (China)

[**] Financial support from the National Natural Science Foundation of China, the Chinese Academy of Sciences, the Major Basic Research Development Program of China (Grant no. G2000077506), and the Ministry of Science and Technology of Shanghai Municipality is gratefully acknowledged. Binol = 2,2'-dihydroxy-1,1'-binaphthyl.

Supporting information for this article is available on the WWW under <http://www.angewandte.org> or from the author.

lanthanum catalyst by using multitopic binol ligands bridged by spacers with diverse shapes and sizes. These catalysts are used for the enantioselective epoxidation of α,β -unsaturated ketones, and afford optically active epoxy ketones in excellent yields and enantiomeric excesses.

Three types of multitopic ligands (**1a–i**; Scheme 1) containing different bridging linkers, including linear (**a–d**), bent



Scheme 1. Multitopic ligands employed for the generation of heterogeneous lanthanum catalysts.

(**e–g**), trigonal-planar (**h**), and tetrahedral (**i**) spacers, were designed to investigate the impact of the spatial arrangement of chiral units ((*S*)-binol) on the catalytic properties of their assemblies with the lanthanum ion. Ligands **1b**, **1d**, and **1e** were prepared by following a reported procedure.^[4d] The syntheses of other ligands (**1a**, **1c**, and **1f–i**) were achieved by the Pd-catalyzed Sonogashira reactions of a methoxymethyl (MOM)-protected, 6-ethynyl-substituted binol derivative with the corresponding aryl bromides or a MOM-protected, 6-bromo-substituted binol derivative with the corresponding aryl acetylenes, followed by deprotection of the MOM groups of the Sonogashira coupling products by acidic hydrolysis (see Supporting Information).

The heterogeneous catalyst was easily prepared by dropwise addition of a solution of the corresponding multitopic ligand in THF and triphenylphosphine oxide to a solution of $\text{La}(\text{O}i\text{Pr})_3$ under an argon atmosphere. The pale yellow or white (in the case of catalysts **2b**, **2d**, **2e**, and **2i**) solids precipitated immediately. After the mixture had been stirred at room temperature for two hours, the resulting solids were collected by filtration and washed with THF to remove trace amounts of soluble low-molecular-weight species. As exemplified by catalyst **2a** in Figure 2a, these polymeric solids were completely insoluble in THF, and accordingly fulfilled the

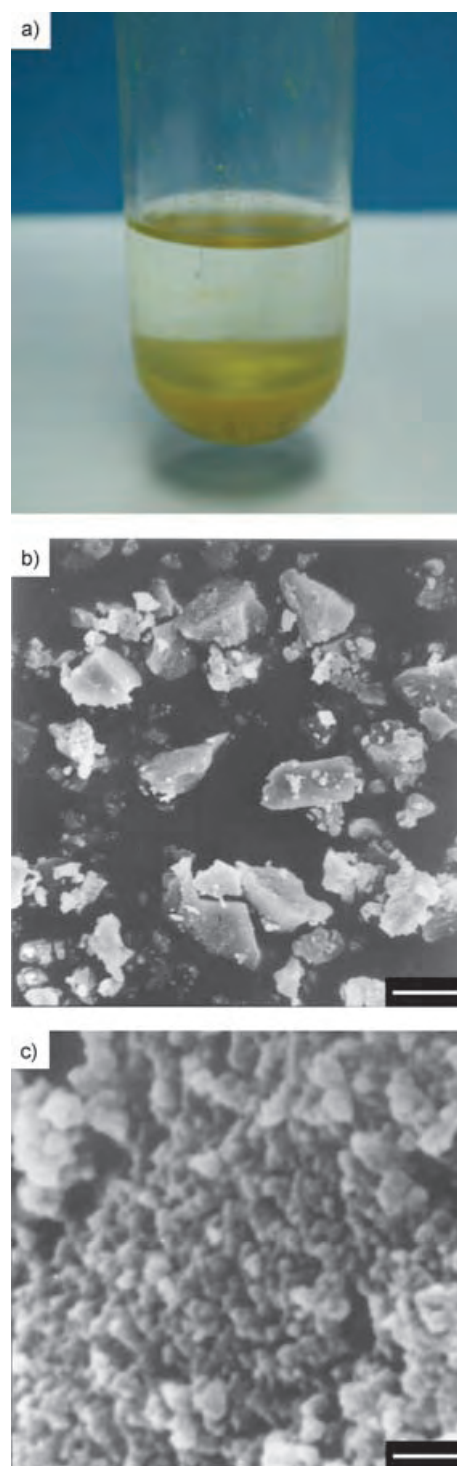


Figure 2. a) Self-supported chiral lanthanum catalyst **2a** (yellow solids at the bottom of the test tube) in THF. b) SEM image of the self-supported lanthanum catalyst **2a**; scale bar: 9.7 μm . c) Enlarged SEM image of the catalyst in (b); scale bar: 0.74 μm .

basic prerequisite for heterogeneous catalysis. SEM images showed that these solids were composed of micrometer-sized particles (Figure 2b), and the surface of the particles exhibited a microstructure with nanoscale noncrystalline species (Figure 2c). The powder X-ray diffraction patterns did not

show any obvious peaks in the scanning range of 5–70° (2 θ), which further confirmed the noncrystalline morphology of the catalysts (see Supporting Information).

To optimize the reaction conditions, the insoluble homo-chiral assembly **2a** was then tested as a self-supported heterogeneous catalyst for the enantioselective epoxidation of α,β -unsaturated ketone **3a**. The reaction was carried out at room temperature by using catalyst **2a** (5 mol %) with cumene hydroperoxide (CMHP, 88 %) as the oxidant, and THF was selected as the reaction solvent after a preliminary examination of the solvent effect (see Supporting Information). As shown in Table 1, the molar ratio between the chiral

prominent in terms of catalytic activity (Table 1, entry 2 versus entry 8). The use of *t*BuO₂H (TBHP) instead of CMHP as oxidant led to a degraded yield and enantioselectivity (Table 1, entry 9). Reduction of the catalyst loading to 1 mol % resulted in a slight drop of the enantioselectivity (Table 1, entry 2 versus entry 10) despite the high yield of product **4a**.

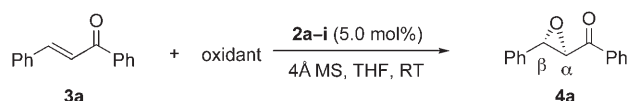
We then turned our attention to investigating the impact of the bridging spacers in the multitopic ligands on the enantioselectivity of the catalysis under the optimized reaction conditions. The heterogeneous catalysts **2b–i**, generated from the reactions of multitopic ligands **1b–i** and La(O*i*Pr)₃,

were subsequently applied to the epoxidation of **3a** with CMHP as the oxidant in the presence of Ph₃PO (15 mol %) and MS (4 Å). As shown in Table 1 (entries 11–18), all of the examined catalysts demonstrated excellent catalytic activity, and afforded **4a** in 99 % yields in 30 min. The influence of the structure of the spacer on the enantioselectivity of the catalysis was dramatic. For ligands with linear spacers (**1a–d**), shortening the length of the linker between two chiral units generally had a disadvantageous effect on the enantioselectivity (Table 1, entries 11–13 versus entry 2). However, the reduction of the extension angles of the spacers was clearly unfavorable for the enantioselectivity (Table 1, entries 15–16 versus 2; also entry 13 versus entry 14). The catalysts (**2h** and **2i**) composed of planar tritopic (**1h**) or tetrahedral tetratopic (**1i**) ligands with relatively longer spacers also demonstrated high activity and enantioselectivity (91.5–95 % *ee*; Table 1, entries 17 and 18). All these facts clearly indicate that both the length and the spatial orientation of the spacers in the multitopic ligands have a significant impact on the enantioselectivity of the heterogeneous epoxidation. It can be concluded that the structural variation of the spacer moieties in the ligands may alter the supramolecular

structures of the assemblies and, as a result, affect their catalytic behavior, particularly the enantioselectivity of the catalysis. Given the modular nature of the multitopic ligands, it can be envisioned that both the reactivity and enantioselectivity may be fine-tuned by judicious choice of the spacer part of the ligands.

Encouraged by these preliminary results, the heterogeneous catalysis of the enantioselective epoxidation of a variety of α,β -unsaturated ketones (**3a–h**) was then investigated by using catalyst **2a** with CMHP as oxidant. As shown in Table 2, the reactions proceeded efficiently to give the corresponding epoxides (**4a–g**) in 99 % yield with excellent enantioselectivities (94.3–97.6 % *ee*, Table 2, entries 1–7), although the electron-withdrawing group at the *para* position of chalcones (Table 2, entries 5 and 6) may reduce the reaction activities. The reactivity and enantioselectivity for

Table 1: Enantioselective epoxidation of α,β -unsaturated ketone (**3a**) catalyzed by self-supported catalyst **2a–i**.^[a]



Entry	Cat. ([mol %])	Additive ([mol %])	Oxidant	<i>t</i> [h]	Yield [%] ^[b]	<i>ee</i> [%] ^[c] (config.) ^[d]
1	2a (5)	–	CMHP	20	99	71.7 (<i>R,S</i>)
2	2a (5)	Ph ₃ PO (15)	CMHP	0.5	99	97.6 (<i>R,S</i>)
3	2a (5)	Ph ₃ PO (10)	CMHP	0.5	99	96.6 (<i>R,S</i>)
4	2a (5)	Ph ₃ PO (5)	CMHP	0.5	91	94.5 (<i>R,S</i>)
5	2a (5)	Ph ₃ AsO (15)	CMHP	1.0	94	60.9 (<i>R,S</i>)
6	2a (5)	Ph ₃ AsO (10)	CMHP	1.0	99	90.3 (<i>R,S</i>)
7	2a (5)	Ph ₃ AsO (5)	CMHP	0.5	99	96.0 (<i>R,S</i>)
8	2a (5) ^[e]	Ph ₃ PO (15)	CMHP	20	81	95.1 (<i>R,S</i>)
9	2a (5)	Ph ₃ PO (15)	TBHP	3	90	66.9 (<i>R,S</i>)
10	2a (1)	Ph ₃ PO (15)	CMHP	1	99	93.8 (<i>R,S</i>)
11	2b (5)	Ph ₃ PO (15)	CMHP	0.5	99	83.7 (<i>R,S</i>)
12	2c (5)	Ph ₃ PO (15)	CMHP	0.5	99	82.9 (<i>R,S</i>)
13	2d (5)	Ph ₃ PO (15)	CMHP	0.5	99	95.5 (<i>R,S</i>)
14	2e (5)	Ph ₃ PO (15)	CMHP	0.5	99	93.3 (<i>R,S</i>)
15	2f (5)	Ph ₃ PO (15)	CMHP	0.5	99	95.1 (<i>R,S</i>)
16	2g (5)	Ph ₃ PO (15)	CMHP	0.5	99	84.2 (<i>R,S</i>)
17	2h (5)	Ph ₃ PO (15)	CMHP	0.5	99	91.5 (<i>R,S</i>)
18	2i (5)	Ph ₃ PO (15)	CMHP	0.5	99	95.0 (<i>R,S</i>)

[a] All of the reactions were carried out at 25 °C with 1.5 equivalents of oxidant in **3a** (0.4 mmol) in the presence of MS (80 mg, 4 Å). The catalyst loading was based on the binol/La unit of the assemblies. [b] Yield of isolated product. [c] Determined by HPLC on a Chiralcel OB-H column. [d] Determined by comparison of their optical rotations with those reported in the literature.^[8d,10] [e] In the absence of MS (4 Å).

binol unit and La^{III} was critical for achieving high catalytic activity and enantioselectivity. The ratio of 1:1.05 (binol unit **1a**/La(O*i*Pr)₃) turns out to be optimal (for details, see the Supporting Information), and affords the corresponding epoxide (*R,S*)-**4a** in over 99 % yield and 97.6 % *ee* after a reaction time of 30 min (Table 1, entry 2). In the analogous homogeneous catalyst system, the employment of Ph₃PO or Ph₃AsO as additive in the reaction system dramatically enhanced the catalytic activity but scarcely influenced the enantioselectivity.^[8,9] In contrast to the homogeneous catalytic system, the addition of triphenylphosphine oxide to the heterogeneous catalytic system described herein had a significant impact on both the activity and enantioselectivity of the catalysis (Table 1, entries 2–7 versus entry 1). It seems that Ph₃PO is superior to Ph₃AsO (Table 1, entries 2–4 versus entries 5–7). The effect of molecular sieves (MS, 4 Å) was also

7.40 (m, 5H), 4.29 (d, $J = 1.8$ Hz, 1H), 4.05 ppm (d, $J = 1.8$ Hz, 1H); ^{13}C NMR (75 MHz, CDCl_3): $\delta = 192.9, 135.3, 135.2, 133.8, 128.9, 128.7, 128.6, 128.1, 125.6, 60.8, 59.2$ ppm. The *ee* value was determined to be 97.6% by HPLC on a Chiralcel OB-H column: UV detector, $\lambda = 254$ nm; 20°C, hexane/*i*PrOH = 60:40, flow rate 0.5 mL min $^{-1}$; $t_{\text{R}1} = 28.2$ min (minor isomer), $t_{\text{R}2} = 35.6$ min (major isomer).

Received: May 16, 2005

Published online: September 15, 2005

Keywords: asymmetric catalysis · epoxidation · heterogeneous catalysis · ketones · lanthanum

- [1] For a comprehensive review, see: O. M. Yaghi, M. O'Keeffe, N. W. Ockwig, H. K. Chae, M. Eddaoudi, J. Kim, *Nature* **2003**, *423*, 705–714.
- [2] J. S. Seo, D. Whang, H. Lee, S. I. Jun, J. Oh, Y. J. Jeon, K. Kim, *Nature* **2000**, *404*, 982–986.
- [3] For heterogenization of Noyori's catalyst by in situ formation of chiral porous hybrid solids, see: a) A. Hu, H. L. Ngo, W. Lin, *J. Am. Chem. Soc.* **2003**, *125*, 11490–11491; b) A. Hu, H. L. Ngo, W. Lin, *Angew. Chem.* **2003**, *115*, 6182–6185; *Angew. Chem. Int. Ed.* **2003**, *42*, 6000–6003. For use of homochiral porous hybrid solids in the catalysis of diethylzinc addition to aldehydes, see: c) C. Wu, A. Hu, L. Zhang, W. Lin, *J. Am. Chem. Soc.* **2005**, *127*, 8940–8941.
- [4] a) S. Takizawa, H. Somei, D. Jayaprakash, H. Sasai, *Angew. Chem.* **2003**, *115*, 5889–5892; *Angew. Chem. Int. Ed.* **2003**, *42*, 5711–5714; b) H. Guo, X. Wang, K. Ding, *Tetrahedron Lett.* **2004**, *45*, 2009–2012; c) X. Wang, K. Ding, *J. Am. Chem. Soc.* **2004**, *126*, 10524–10525; d) X. Wang, X. Wang, H. Guo, Z. Wang, K. Ding, *Chem. Eur. J.* **2005**, *11*, 4078–4088; e) Y. Liang, Q. Jing, X. Li, L. Shi, K. Ding, *J. Am. Chem. Soc.* **2005**, *127*, 7694–7695.
- [5] For a highlight, see: L.-X. Dai, *Angew. Chem.* **2004**, *116*, 5846–5850; *Angew. Chem. Int. Ed.* **2004**, *43*, 5726–5729.
- [6] *Chiral Catalyst Immobilization and Recycling* (Eds.: D. E. de Vos, I. F. Vankelecom, P. A. Jacobs), Wiley-VCH, Weinheim, **2000**.
- [7] For recent reviews, see: a) C. E. Song, S. Lee, *Chem. Rev.* **2002**, *102*, 3495–3524; b) Q. Fan, Y.-M. Li, A. S. C. Chan, *Chem. Rev.* **2002**, *102*, 3385–3466; c) D. E. de Vos, M. Dams, B. F. Sels, P. A. Jacobs, *Chem. Rev.* **2002**, *102*, 3615–3640; d) N. E. Leadbeater, M. Marco, *Chem. Rev.* **2002**, *102*, 3217–3274; e) D. E. Bergbreiter, *Chem. Rev.* **2002**, *102*, 3345–3384; f) L. Pu, *Chem. Rev.* **1998**, *98*, 2405–2494. For a comprehensive review of the use of linked binol in the intramolecular assembly of chiral catalysts, see: g) S. Matsunaga, T. Ohshima, M. Shibasaki, *Adv. Synth. Catal.* **2002**, *344*, 3–15. For catalyst immobilization using polymer-supported bisbinol ligands on the basis of the “catalyst analogue” concept, see: h) T. Arai, T. Sekiguti, K. Otsuki, S. Takizawa, H. Sasai, *Angew. Chem.* **2003**, *115*, 2194–2197; *Angew. Chem. Int. Ed.* **2003**, *42*, 2144–2147. For other strategies in binol-based catalyst immobilization, see: i) T. Sekiguti, Y. Iizuka, S. Takizawa, D. Jayaprakash, T. Arai, H. Sasai, *Org. Lett.* **2003**, *5*, 2647–2650; j) T. Arai, T. Sekiguti, Y. Iizuka, S. Takizawa, S. Sakamoto, K. Yamaguchi, H. Sasai, *Tetrahedron Asymmetry* **2002**, *13*, 2083–2087.
- [8] a) M. Bougauchi, S. Watanabe, T. Arai, H. Sasai, M. Shibasaki, *J. Am. Chem. Soc.* **1997**, *119*, 2329–2330; b) S. Watanabe, T. Arai, H. Sasai, M. Bougauchi, M. Shibasaki, *J. Org. Chem.* **1998**, *63*, 8090–8091; c) S. Watanabe, Y. Kobayashi, T. Arai, H. Sasai, M. Bougauchi, M. Shibasaki, *Tetrahedron Lett.* **1998**, *39*, 7353–7356; d) T. Nemoto, T. Ohshima, K. Yamaguchi, M. Shibasaki, *J. Am. Chem. Soc.* **2001**, *123*, 2725–2732; e) T. Ohshima, T. Nemoto, S. Y. Tosaki, V. Gnanadesikan, M. Shibasaki, *Tetrahedron* **2003**, *59*, 10485–10497; f) T. Nemoto, T. Ohshima, M. Shibasaki, *J. Am. Chem. Soc.* **2001**, *123*, 9474–9475; g) T. Kinoshita, S. Okada, S. R. Park, S. Matsunaga, M. Shibasaki, *Angew. Chem.* **2003**, *115*, 4828–4832; *Angew. Chem. Int. Ed.* **2003**, *42*, 4680–4684; h) S. Matsunaga, T. Kinoshita, S. Okada, S. Harada, M. Shibasaki, *J. Am. Chem. Soc.* **2004**, *126*, 7559–7570.
- [9] For excellent examples of modified Shibasaki's binol/La catalyst in epoxidation reactions, see: a) K. Daikai, M. Kamaura, J. Inanaga, *Tetrahedron Lett.* **1998**, *39*, 7321–7322; b) K. Daikai, T. Hayano, R. Kino, H. Furuno, T. Kagawa, J. Inanaga, *Chirality* **2003**, *15*, 83–88; c) R. Kino, K. Daikai, T. Kawanami, J. Inanaga, *Org. Biomol. Chem.* **2004**, *2*, 1822–1824.
- [10] R. Chen, C. Qian, J. G. de Vries, *Tetrahedron* **2001**, *57*, 9837–9842.
- [11] For chiral peptide catalysts, see: a) S. Colonna, S. Juliá, J. Masana, A. Alvarez, *Tetrahedron* **1983**, *39*, 1635–1641; b) S. Banfi, S. Colonna, S. Juliá, J. Guixer, *Tetrahedron* **1984**, *40*, 5207–5211; c) S. Juliá, J. Masana, J. C. Vega, *Angew. Chem.* **1980**, *92*, 968–969; *Angew. Chem. Int. Ed. Engl.* **1980**, *19*, 929–930; d) S. Juliá, S. Colonna, J. Guixer, J. Masana, *J. Chem. Soc. Perkin Trans. 1* **1982**, 1317–1324; e) W. P. Chen, A. L. Egar, M. B. Hursthouse, K. M. A. Malik, J. E. Mathews, S. M. Roberts, *Tetrahedron Lett.* **1998**, *39*, 8495–8498; f) M. B. Adger, J. V. Barkley, S. M. Roberts, *J. Chem. Soc. Perkin Trans. 1* **1997**, 3501–3507; g) R. J. J. Nel, H. van Rensburg, P. S. van Heerden, J. Coetzee, D. Ferreira, *Tetrahedron* **1999**, *55*, 9727–9736.
- [12] For chiral phase-transfer catalysts, see: a) G. Macdonald, L. Alcaraz, N. J. Lewis, R. J. K. Taylor, *Tetrahedron Lett.* **1998**, *39*, 5431–5436; b) S. Arai, M. Oku, M. Miura, T. Shioiri, *Synlett* **1998**, 1201–1202; c) S. Arai, H. Tsuge, T. Shioiri, *Tetrahedron Lett.* **1998**, *39*, 7563–7566; d) B. Lygo, P. G. Wainwright, *Tetrahedron Lett.* **1998**, *39*, 1599–1602; e) B. Lygo, P. G. Wainwright, *Tetrahedron* **1999**, *55*, 6289–6300; f) E. J. Corey, F. Y. Zhang, *Org. Lett.* **1999**, *1*, 1287–1290; g) S. Arai, H. Tsuge, M. Oku, M. Miura, T. Shioiri, *Tetrahedron* **2002**, *58*, 1623–1630.
- [13] For chiral dioxirane catalysts, see: a) Y. Shi, *Acc. Chem. Res.* **2004**, *37*, 488–496; b) D. Yang, *Acc. Chem. Res.* **2004**, *37*, 497–505.
- [14] For chiral Zn, Mg, and Ca catalysts, see: a) D. Enders, J. Zhu, G. Raabe, *Angew. Chem.* **1996**, *108*, 1727–1729; *Angew. Chem. Int. Ed. Engl.* **1996**, *35*, 1725–1728; b) C. L. Elston, R. F. W. Jackson, S. J. F. MacDonald, P. J. Murray, *Angew. Chem.* **1997**, *109*, 379–381; *Angew. Chem. Int. Ed. Engl.* **1997**, *36*, 410–412; c) D. Enders, L. Kramps, J. Zhu, *Tetrahedron Asymmetry* **1998**, *9*, 3959–3962; d) G. Kumaraswamy, M. N. V. Sastry, N. Jena, K. R. Kumar, M. Vairamani, *Tetrahedron Asymmetry* **2003**, *14*, 3797–3803; e) B. M. Chaudary, M. L. Kantam, K. V. Ranganath, B. Sreedhar, *J. Am. Chem. Soc.* **2004**, *126*, 3396–3397.
- [15] For recent reviews, see: a) M. J. Porter, S. M. Roberts, J. Skidmore, *Bioorg. Med. Chem.* **1999**, *7*, 2145–2156; b) M. J. Porter, J. Skidmore, *Chem. Commun.* **2000**, 1215–1225; c) T. Nemoto, T. Ohshima, M. Shibasaki, *J. Synth. Org. Chem. Jpn.* **2002**, *60*, 94–105.
- [16] a) H. B. Yu, X. F. Zheng, Z. M. Lin, Q. S. Hu, W. S. Huang, L. Pu, *J. Org. Chem.* **1999**, *64*, 8149–8155; b) D. Jayaprakash, Y. Kobayashi, S. Watanabe, T. Arai, H. Sasai, *Tetrahedron Asymmetry* **2003**, *14*, 1587–1592; c) D. Jayaprakash, Y. Kobayashi, T. Arai, Q. S. Hu, X. F. Zheng, L. Pu, H. Sasai, *J. Mol. Catal. A* **2003**, *196*, 145–149.

Urea- and Thiourea-Substituted Cinchona Alkaloid Derivatives as Highly Efficient Bifunctional Organocatalysts for the Asymmetric Addition of Malonate to Nitroalkenes: Inversion of Configuration at C9 Dramatically Improves Catalyst Performance.**

Séamus H. McCooey and Stephen J. Connon*

Inspired by the efficiency, elegance, and selectivity of enzymatic catalysis, the design of organic molecules capable of the efficient and enantioselective promotion of carbon–carbon bond-forming processes is a formidable challenge which is currently receiving considerable attention.^[1] In this context, one of the fundamental enzymatic catalyst competencies that is most difficult to engineer in synthetic systems is bifunctionality; that is, the ability of a catalyst to employ Lewis/Brønsted acidic and Lewis/Brønsted basic functionality synergistically to bring about the activation of both the nucleophilic and electrophilic components of a reaction simultaneously.^[2]

Over 20 years ago, Wynberg and Hiemstra^[3] reported that cinchona alkaloids were efficient (albeit only moderately selective) bifunctional organocatalysts for the 1,4-addition of thiophenol derivatives to cyclohexenones, and proposed catalyst participation in the deprotonation of the thiol (through the basic quinuclidine alkaloid nitrogen atom) and in the stabilization of the enolate resulting from the 1,4-addition step (through hydrogen bonding with the hydroxy moiety of the catalyst).^[4–6]

As Wynberg predicted,^[3] the derivitization of cinchona alkaloids^[7] with the goal of augmenting hydrogen-bond-donating ability has resulted in an expansion of catalyst scope: Hatakeyama and co-workers reported that the rigid phenolic quinidine derivative **1** promotes highly enantioselective (aza)-Baylis–Hillman reactions,^[8] and Deng and co-workers demonstrated that the readily available 6'-demethylated quinine and quinidine alkaloids are considerably more active and selective catalysts for the addition of 1,3-dicarbonyl compounds to β -nitrostyrenes than their natural 6'-methylated analogues.^[9,10]

The ability of chiral urea^[11] and thiourea derivatives to serve as powerful hydrogen-bond-donating organocatalysts was recently recognized by Jacobsen and co-workers, who developed a suite of thiourea catalysts that promote a diverse range of reactions with excellent enantioselectivity.^[12] The compatibility of (thio)ureas with Lewis basic functionality was also demonstrated recently: Takemoto and co-workers have introduced the bifunctional catalyst **2**, which promotes Michael-type^[13a,b] and aza-Henry^[13c] reactions with high enantioselectivity.^[14] Furthermore, we have found that bisaryl(thio)urea derivatives are significantly more efficient “mole-per-mole” promoters of the DABCO-catalyzed Baylis–Hillman reaction than either methanol or water.^[15]

We were therefore intrigued by the possibility of modifying the “privileged”^[16] cinchona alkaloid structural backbone by substituting the hydroxy group at C9 with an aryl(thio)urea moiety with the aim of augmenting the rigidity, tunability, and hydrogen-bond-donating proclivity of these materials. An additional advantage associated with this strategy is the opportunity to examine the (little studied) effect of inversion of configuration at C9 on catalyst performance. We therefore prepared 9-(3,5-bis(trifluoromethyl)phenyl)urea derivatives of dihydroquinine (DHQ) and dihydroquinidine (DHQD) (DHQU and DHQDU, respectively) together with their C9-inverted analogues (Scheme 1).^[17]

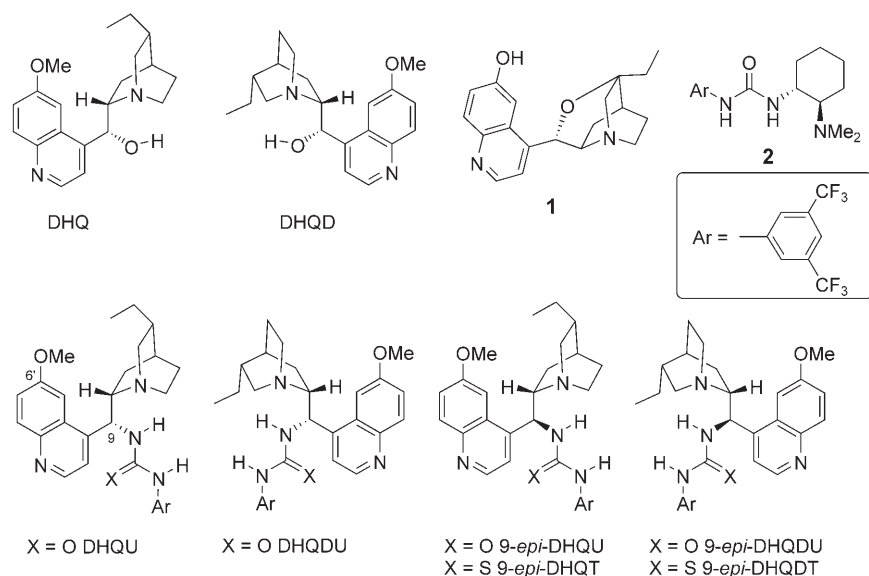
The asymmetric Michael addition of relatively acidic carbon pronucleophiles (such as malonates) to nitroolefins is an important C–C bond forming reaction that provides access to synthetically useful enantioenriched nitroalkanes.^[18,19] Current bifunctional organocatalytic systems such as **2**^[13] and 6'-demethylated quinidine^[9] are capable of promoting the reaction with high enantioselectivity at typical catalyst loadings of 10 mol %, and efficient metal-based systems (chiral Mg–bisoxazoline^[20a,b] and Ru–amido^[20c] complexes at 2–5 mol % loadings) have been reported which require more stringent control of the reaction conditions. This reaction therefore seemed to be an ideal test for the potential activity and selectivity of the novel urea-substituted cinchona alkaloid structures.

The results of initial investigations into the addition of dimethyl malonate to (*E*)- β -nitrostyrene (**3**) catalyzed by cinchona alkaloid derivatives are presented in Table 1. Initial screening studies identified toluene as the optimal solvent for the reaction. The urea-substituted analogues (DHQU and DHQDU) with the stereochemistry of the “natural” cinchona alkaloid were more-selective albeit significantly less-active catalysts than their respective dihydroalkaloid precursors DHQ and DHQD (Table 1, entries 1, 3 and 4, 5) at room temperature. Gratifyingly, the C9 diastereoisomers of these materials (9-epi-DHQU and 9-epi-DHQDU, Figure 1)^[21] exhibited decidedly superior activity and enantioselectivity (Table 1, entries 6–8); and gave complete conversion of **3** into nitroalkane **4** with high enantioselectivity at room temperature in the presence of only 2 mol % of catalyst. Further improvement was observed upon the synthesis and evaluation of their thiourea analogues (9-epi-DHQT and 9-epi-DHQDT, Figure 1). Below ambient temperature, **4** could be generated with quantitative conversion and excellent enantioselectivity (Table 1, entries 9–11) at low catalyst loadings. It is noteworthy that inversion of the absolute configuration at C9 in

[*] S. H. McCooey, Dr. S. J. Connon
Centre for Synthesis and Chemical Biology
Department of Chemistry
Trinity College, University of Dublin
Dublin 2 (Ireland)
Fax: (+353) 1-671-2826
E-mail: connon@tcd.ie

[**] Financial support from the Irish Research Council for Science Engineering and Technology is gratefully acknowledged. We would like to thank TopChem Laboratories Ltd. and the Gunnlaugsson group (TCD) for the use of their equipment.

Supporting information for this article is available on the WWW under <http://www.angewandte.org> or from the author.



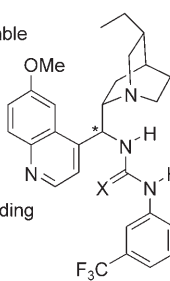
(thio)urea-substituted cinchona alkaloid catalysts: design rationale

C9 stereocenter

- synthetic route makes both diastereomers (epimers) available

(thio)urea N-aryl group

- relatively unhindered (facilitates selective substrate binding orientation)
- substitution (and hence pK_a /binding ability) variable
- CF_3 substituents serve as non Lewis basic electron withdrawing groups



quinclidine ring

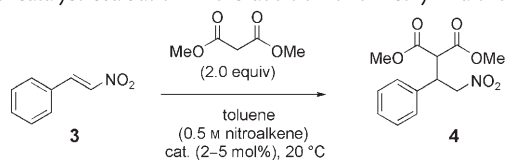
- activates the nucleophilic reaction component
- located in close proximity to the (thio)urea group
- variable absolute configuration at C8

(thio)urea moiety

- activates the electrophilic reaction component
- two coplanar protons available for H-bond donation: known to bind to a variety of Lewis basic functional groups
- rigid (minimal entropy loss on substrate binding)
- variable Lewis acidity ($X = O$ or S)

Scheme 1. Modified cinchona alkaloid derivatives.

Table 1: Catalyst evaluation in the addition of dimethyl malonate to **3**.



Entry	Catalyst	mol %	<i>t</i> [h]	Conv. [%] ^[a]	<i>ee</i> [%] ^[b]	Product config. ^[c]
1	DHQ	5	24	> 98	12	(S)
2	9- <i>epi</i> -DHQ	5	144	46	18	(R)
3	DHQD	5	24	> 98	1	(R)
4	DHQU	5	24	26	25	(S)
5	DHQDU	5	144	25	17	(R)
6	9- <i>epi</i> -DHQU	5	5	> 98	74	(S)
7	9- <i>epi</i> -DHQU	2	24	> 98	88	(S)
8	9- <i>epi</i> -DHQDU	2	30	> 98	79	(R)
9	9- <i>epi</i> -DHQT	2	24	> 98	90	(S)
10	9- <i>epi</i> -DHQDT	2	30	> 98	85	(R)
11	9- <i>epi</i> -DHQT	2	30	> 98 ^[d]	99 ^[e]	(S)

[a] Determined by 1H NMR spectroscopy. [b] Determined by chiral stationary phase (CSP)-HPLC (see Supporting Information). [c] Absolute configuration as determined by comparison with literature CSP-HPLC retention times and optical rotation data (references [9] and [13a]). [d] 93 % yield of isolated product. [e] Reaction at $-20^\circ C$.

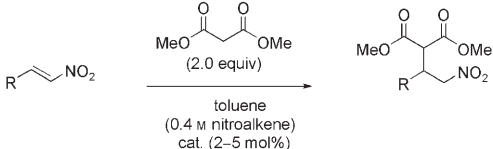
these (thio)urea-substituted systems dramatically improves catalyst activity and selectivity without altering the sense of stereoselection observed, that is, 9-*epi*-DHQU and 9-*epi*-DHQT promote the formation of the same antipode of **4** as DHQU (and DHQ), whereas 9-*epi*-DHQDU furnishes the same product enantiomer as DHQDU (and DHQD).

This is in marked contrast to the relative performance of the hydroxy-substituted DHQ and 9-*epi*-DHQ: epimerization of C9 of the parent dihydroalkaloid led to a marginal increase in enantioselectivity (with inversion of the sense of stereoselection) and a significant reduction of catalyst activity (Table 1, entries 1 and 2). It is therefore clear that although neither inversion of the C9 stereocenter nor (thio)urea substitution alone endow the parent alkaloids DHQ and DHQD with significantly improved catalytic properties (in the context of the addition reaction studied), a combination of both modifications results in a remarkable enhancement of catalyst efficacy and enantioselectivity.

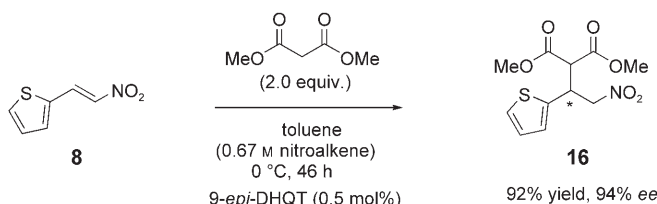
We then turned our attention to the question of catalyst scope. The use of either 9-*epi*-DHQT or 9-*epi*-DHQDT allowed the conversion of both activated (**6–8**) and deactivated (**9–11**) β -nitrostyrenes (Table 2, entries 1–10) into their corresponding Michael adducts **14–19** in excellent yields (91–95 %) and enantioselectivities (87–99 % *ee*) at convenient reaction temperatures between ambient temperature and $-20^\circ C$. Although we did not observe a strong correlation between the electronic properties of the substrate and the enantiopurity of the product, in general, relatively deactivated olefins gave rise to products of marginally higher enantiopurity than more-electrophilic analogues. Alkyl-substituted nitroolefins were also found to be compatible with 9-*epi*-DHQT; the unhindered **12** proved unproblematic and even the traditionally challenging substrate **13** (which is inert towards a binary bifunctional catalyst system, Table 2, entry 13)^[22] underwent conversion into **21** with attenuated enantioselectivity (75 % *ee*).

9-*epi*-DHQT and 9-*epi*-DHQDT are characterized by excellent catalytic activity at 2–5 mol % loadings and convenient reaction temperatures, and are also comparable in terms of efficacy, scope, and enantioselectivity to benchmark metal-based systems.^[20] At higher concentrations catalytic asymmetric addition can be conveniently carried out at unprecedented catalyst loadings without compromising either efficiency or enantioselectivity, as exemplified by the synthesis of **16** from **8** in excellent yield and enantioselectivity promoted by 9-*epi*-DHQT (0.5 mol %) at $0^\circ C$ (Scheme 2, compare with Table 2, entry 4).

Table 2: Catalyst scope for the conversion of both activated and deactivated β -nitrostyrenes.

									
Entry	Substr.	R	Catalyst	mol %	T [°C]	t [h]	Prod.	Yield [%] ^[a]	ee [%] ^[b]
1	6	4-BrC ₆ H ₄	9- <i>epi</i> -DHQT	2	20	17	14	92	87
2	6	4-BrC ₆ H ₄	9- <i>epi</i> -DHQT	2	−20	40	14	94	93
3	6	4-BrC ₆ H ₄	9- <i>epi</i> -DHQDT	2	−20	55	14	80	93
4	7	2-NO ₂ C ₆ H ₄	9- <i>epi</i> -DHQT	2	−20	69	15	91	90
5	8	2-thienyl	9- <i>epi</i> -DHQT	2	−20	23	16	94	95
6	9	2-MeC ₆ H ₄	9- <i>epi</i> -DHQT	5	20	25	17	93	93
7	9	2-MeC ₆ H ₄	9- <i>epi</i> -DHQT	5	0	30	17	95	94
8	10	1-naphthyl	9- <i>epi</i> -DHQT	2	0	31	18	94	93
9	11	4-MeOC ₆ H ₄	9- <i>epi</i> -DHQT	5	0	30	19	92	99
10	11	4-MeC ₆ H ₄	9- <i>epi</i> -DHQDT	5	0	38	19	90	91
11	12	<i>n</i> -hexyl	9- <i>epi</i> -DHQT	5	−20	69	20	88	86
12	13	cyclohexyl	9- <i>epi</i> -DHQT	5	20	147	21	63	75
13	13	cyclohexyl	quinuclidine ^[c]	20	20	72	21	0	–

[a] Refers to the yield of the isolated product after column chromatography. [b] Determined by CSP-HPLC (see Supporting Information).


Scheme 2. Catalysis by 9-*epi*-DHQT at low catalyst loading.

The dependence of catalytic efficiency and selectivity on both the presence of (thio)urea functionality and the relative stereochemistry at C8/C9 strongly implies that these modified cinchona alkaloid systems operate through a bifunctional mechanism, that is, quinuclidine-moiety-assisted generation of the deprotonated malonate nucleophile and its addition to a single face of the (thio)urea-bound nitroolefin electrophile. A preliminary selectivity principle based on the results presented in Table 1 is outlined in Figure 1. An examination of models and MM2 calculations^[23] indicate that **A** is a reasonable representation of the least strained conformation of the active and selective catalyst 9-*epi*-DHQU in which the bulky alkyl groups at the C9 stereogenic centre avoid steric interactions with each other and with the carbonyl group of the urea functionality.^[24] In this conformation it would be expected that the nitroolefin would bind (through both oxygen atoms)^[25] as shown in pretransition state (TS) assembly **B** (Figure 1) to minimize

contact with the large catalyst substituents, thus allowing the proximal Brønsted basic aliphatic heterocycle to bring about enolate generation at the *Si* face of the electrophile, leading to the formation of (*S*)-**4** (Figure 1, **B** and Table 1, entry 7).

A similar MM2 examination of DHQU identifies **C** as the minimum-energy conformer, which would clearly be ill suited to efficient bifunctional catalysis and would be expected to furnish the opposite enantiomer to that observed experimentally (Figure 1, **C** and Table 1, entry 4.). We therefore propose that bifunctional catalysis involving DHQU may proceed predominantly through a minor conformer represented by **D**, in which the bifunctional catalyst components are more suitably

oriented to cooperate catalytically and to generate the product enantiomer observed. The catalyst components, however, are still poorly situated relative to the catalytically active components of 9-*epi*-DHQU in terms of both proximity of the quinuclidine ring to the aryl urea and the ability of the catalyst to bind the nitroalkene selectively.^[26]

In summary we have developed a new class of highly active and selective (thio)urea-substituted cinchona alkaloid based catalysts for the addition of dimethyl malonate to nitroalkenes. A systematic investigation into the effects of the relative stereochemistry at C8 and C9 of these materials on catalyst performance has implicated bifunctional catalysis and revealed that C9 epimeric catalysts are remarkably more efficacious in terms of rate and selectivity than analogues of

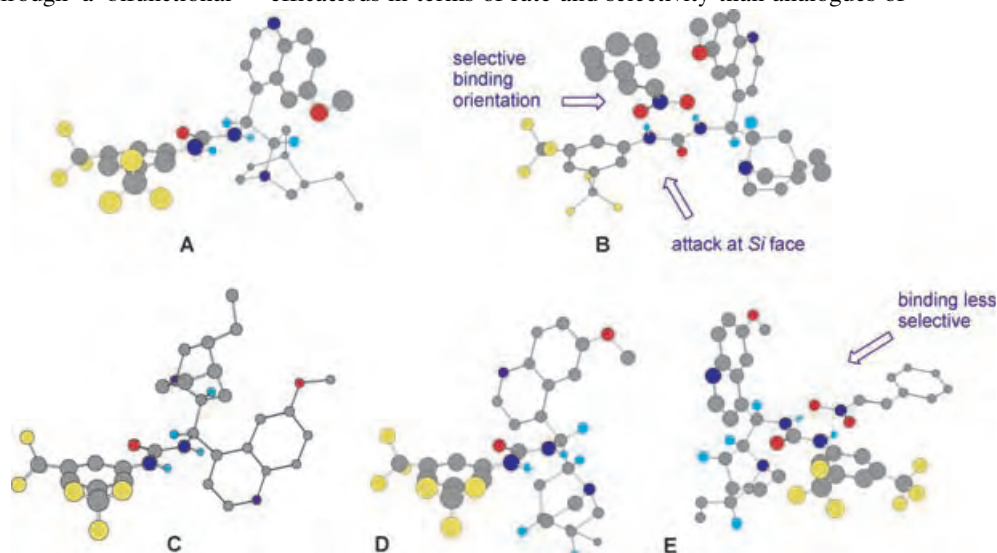


Figure 1. Selectivity model. A: Proposed catalytically active conformation of 9-*epi*-DHQU (MM2). B: Possible pre-TS assembly for enantioselective addition to **3** promoted by 9-*epi*-DHQU. C: Proposed lowest energy conformation (MM2) of DHQU. D: Proposed catalytically active conformation of DHQU. E: Possible pre-TS assembly for addition to **3** promoted by DHQU.

“natural” cinchona alkaloid stereochemistry. Highly active 9-*epi*-DHQT and 9-*epi*-DHQDT (which are readily available from DHQ and DHQD - see Supporting Information) have been identified as efficient and enantioselective catalysts with substrate-scope and selectivity profiles on a par with current benchmark literature systems and can be conveniently employed at relatively low catalyst loadings (0.5–5 mol %). Studies to determine the solution-state structure of these materials and to explore their potential as promoters of a variety of reactions susceptible to the influence of bifunctional catalysis are underway.

Received: May 19, 2005

Published online: September 1, 2005

Keywords: asymmetric catalysis · cinchona alkaloids · Michael addition · organocatalysis · ureas

- [1] For recent reviews, see: a) S. Jayasree, B. List, *Org. Biomol. Chem.* **2005**, 3, 719; b) P. I. Dalko, L. Moisan, *Angew. Chem.* **2004**, 116, 5248; *Angew. Chem. Int. Ed.* **2004**, 43, 5138; c) K. N. Houk, B. List, *Acc. Chem. Res.* **2004**, 37(8).
- [2] For reviews of bifunctional systems involving metals see: a) S. France, A. Weatherwax, A. E. Taggi, T. Lectka, *Acc. Chem. Res.* **2004**, 37, 592; b) M. Shibasaki, N. Yoshikawa, *Chem. Rev.* **2002**, 102, 2187; c) H. Gröger, *Chem. Eur. J.* **2001**, 7, 5247.
- [3] H. Hiemstra, H. Wynberg, *J. Am. Chem. Soc.* **1981**, 103, 417.
- [4] For a more recent study of this alkaloid-catalyzed reaction, see: P. McDaid, Y. Chen, L. Deng, *Angew. Chem.* **2002**, 114, 348; *Angew. Chem. Int. Ed.* **2002**, 41, 338.
- [5] For early examples of the use of chiral amines as nucleophilic organocatalysts, see: a) V. Prelog, H. Wilhelm, *Helv. Chim. Acta* **1954**, 37, 1634; b) H. Pracejus, *Justus Liebigs Ann. Chem.* **1960**, 634, 9; c) D. Borrmann, R. Wegler, *Chem. Ber.* **1967**, 100, 1575; d) H. Wynberg, R. Helder, *Tetrahedron Lett.* **1975**, 16, 4057.
- [6] For reviews concerning the use of cinchona alkaloid derivatives as organocatalysts, see: a) S.-K. Tian, Y. Chen, J. Hang, L. Tang, P. McDaid, L. Deng, *Acc. Chem. Res.* **2004**, 37, 621; b) S. France, D. J. Guerin, S. J. Miller, T. Lectka, *Chem. Rev.* **2003**, 103, 2985; c) K. Kacprzak, J. Gawronski, *Synthesis* **2001**, 961.
- [7] For a recent review of cinchona alkaloid chemistry, see: H. M. R. Hoffmann, J. Frakenpohl, *Eur. J. Org. Chem.* **2004**, 4293.
- [8] a) Y. Iwabuchi, M. Nakatani, N. Yokoyama, S. Hatakeyama, *J. Am. Chem. Soc.* **1999**, 121, 10219; b) S. Kawahara, A. Nakano, T. Esumi, Y. Iwabuchi, S. Hatakeyama, *Org. Lett.* **2003**, 5, 3103.
- [9] H. Li, Y. Wang, L. Tang, L. Deng, *J. Am. Chem. Soc.* **2004**, 126, 9906.
- [10] H. Li, Y. Wang, L. Tang, F. Wu, X. Liu, C. Cuo, B. M. Foxman, L. Deng, *Angew. Chem.* **2005**, 117, 107; *Angew. Chem. Int. Ed.* **2005**, 44, 105.
- [11] For early examples of the use of (thio)ureas as organocatalysts, see: a) D. P. Curran, L. H. Kuo, *J. Org. Chem.* **1994**, 59, 3259; b) D. P. Curran, L. H. Kuo, *Tetrahedron Lett.* **1995**, 36, 6647; c) P. R. Schreiner, A. Wittkopp, *Org. Lett.* **2002**, 4, 217; d) P. R. Schreiner, A. Wittkopp, *Chem. Eur. J.* **2003**, 9, 407; e) T. Okino, Y. Hoashi, Y. Takemoto, *Tetrahedron Lett.* **2003**, 44, 2817; f) Review: P. R. Schreiner, *Chem. Soc. Rev.* **2003**, 32, 289.
- [12] a) M. S. Sigman, E. N. Jacobsen, *J. Am. Chem. Soc.* **1998**, 120, 4901; b) M. S. Sigman, P. Vachal, E. N. Jacobsen, *Angew. Chem.* **2000**, 112, 1336; *Angew. Chem. Int. Ed.* **2000**, 39, 1279; c) P. Vachal, E. N. Jacobsen, *Org. Lett.* **2000**, 2, 867; d) P. Vachal, E. N. Jacobsen, *J. Am. Chem. Soc.* **2002**, 124, 10012; e) A. G. Wenzel, E. N. Jacobsen, *J. Am. Chem. Soc.* **2002**, 124, 12964; f) A. G. Wenzel, M. P. Lalonde, E. N. Jacobsen, *Synlett* **2003**, 1919; g) G. D. Joly, E. N. Jacobsen, *J. Am. Chem. Soc.* **2004**, 126, 4102; h) M. S. Taylor, E. N. Jacobsen, *J. Am. Chem. Soc.* **2004**, 126, 10558.
- [13] a) T. Okino, Y. Hoashi, Y. Takemoto, *J. Am. Chem. Soc.* **2003**, 125, 12672; b) T. Okino, Y. Hoashi, T. Furukawa, X. Xu, Y. Takemoto, *J. Am. Chem. Soc.* **2005**, 127, 119; c) T. Okino, S. Nakamura, T. Furukawa, Y. Takemoto, *Org. Lett.* **2004**, 6, 625.
- [14] For recent applications of **2** (and modified derivatives) in kinetic resolution, see: a) A. Berkessel, F. Cleemann, S. Mukherjee, T. N. Müller, J. Lex, *Angew. Chem.* **2005**, 117, 817; *Angew. Chem. Int. Ed.* **2005**, 44, 807; b) A. Berkessel, F. Cleemann, S. Mukherjee, T. N. Müller, J. Lex, *Chem. Commun.* **2005**, 1898.
- [15] D. J. Maher, S. J. Connon, *Tetrahedron Lett.* **2004**, 45, 1301.
- [16] T. P. Yoon, E. N. Jacobsen, *Science* **2003**, 299, 1691.
- [17] While this manuscript was being prepared, two reports detailing a similar strategy have appeared: a) for a report disclosing the synthesis of two C-1,2-didehydro cinchonidine/chinchonine-derived variants of 9-*epi*-DHQT (amongst others) which promoted the efficient addition to thiophenol to α - β -unsaturated imides with low selectivity (up to 17% *ee*), see: B.-J. Li, L. Jiang, M. Liu, Y.-C. Chen, L.-S. Ding, Y. Wu, *Synlett*, **2005**, 603; b) 9-*epi*-DHQT and C-1,2-didehydro analogues have been prepared for use in the efficient enantioselective addition of nitromethane to chalcones, and a clear dependence of catalyst activity and selectivity on the relative stereochemistry at C8/C9 has been demonstrated: B. Vakulya, S. Varga, A. Csámpai, T. Soós, *Org. Lett.* **2005**, 7, 1967.
- [18] For recent reviews concerning the asymmetric addition of nucleophiles to nitroalkenes, see: a) O. M. Berner, L. Tedeschi, D. Enders, *Eur. J. Org. Chem.* **2002**, 1877; b) N. Krause, A. Hoffmann-Röder, *Synthesis* **2001**, 171; c) M. P. Sibi, S. Manyem, *Tetrahedron* **2000**, 56, 8033.
- [19] For a recent review concerning the secondary-amine catalyzed addition of carbonyl compounds to nitroolefins, see: W. Notz, F. Tanaka, C. F. Barbas III, *Acc. Chem. Res.* **2004**, 37, 580.
- [20] a) J. Ji, D. M. Barnes, J. Zhang, S. A. King, S. J. Wittenberger, H. E. Morton, *J. Am. Chem. Soc.* **1999**, 121, 10215; b) D. M. Barnes, J. Ji, M. G. Fickes, M. A. Fitzgerald, S. A. King, H. E. Morton, F. A. Plagge, M. Preskill, S. H. Wagaw, S. J. Wittenberger, J. Zhang, *J. Am. Chem. Soc.* **2002**, 124, 13097; c) M. Watanabe, A. Ikagawa, H. Wang, K. Murata, T. Ikariya, *J. Am. Chem. Soc.* **2004**, 126, 11148.
- [21] The prefix “*epi*” usually refers only to inversion of configuration at a single stereocenter, that is, no functional-group interconversion is implied. The term is adopted in this case for convenient identification of the relative stereochemistry of the catalyst at C8/C9.
- [22] To the best of our knowledge only Deng et al. (ref. [9]) have thus far successfully selectively converted this hindered substrate by using 20 mol % 6'-demethylated quinine.
- [23] MM2 force-field energy-minimization calculations were carried out with CS Chem3D Std v.4.0 software. Conformers were minimized to a minimum RMS gradient of 0.02.
- [24] The catalysts were obtained as amorphous solids, and several attempts to recrystallize these materials were unsuccessful. Conformation **A** is in very good agreement with structural data associated with other (thio)urea-based catalysts in the literature which incorporate a chiral methine group adjacent to the (thio)urea functionality.^[12e, 13b]
- [25] B. J. Hay, T. K. Firman, B. A. Moyer, *J. Am. Chem. Soc.* **2005**, 127, 1810.
- [26] This would account for the observed product stereochemistry, and the decrease in catalyst efficiency and selectivity associated with DHQU relative to 9-*epi*-DHQU. However, it is acknowledged that alternative rationales are possible, for example, reversal of binding selectivity relative to 9-*epi*-DHQU, etc. It is envisaged that ongoing structural studies will provide more detailed insight into the catalytic behaviour of these C9 diastereomers.

DOI: 10.1002/anie.200501823

A Sensitive Colorimetric and Fluorescent Probe Based on a Polythiophene Derivative for the Detection of ATP

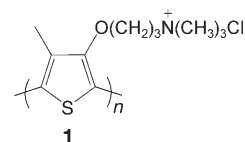
Chun Li, Munenori Numata, Masayuki Takeuchi, and Seiji Shinkai*

The design and construction of chemo- and biosensors for recognizing biologically important small molecules and anions has received considerable attention in recent years.^[1] The anion adenosine triphosphate (ATP) is known to be a key player in bioenergetics in all biological systems, and thus it is important to be able to monitor easily the concentration of ATP in aqueous solution. Although several intriguing strategies have been developed to detect ATP, such as synthetic host–guest receptors,^[2] peptides,^[3] and RNA aptamers,^[4] it remains a challenge to find new approaches that could improve the simplicity, selectivity, and sensitivity of ATP detection.

Recently, a new sensory technology based on conjugated polymers has been developed in view of their signal-amplification effect, and thus is sensitive to very minor perturbations.^[5] In particular, water-soluble conjugated polymers provide a unique platform for the development of chemosensors for biologically relevant targets.^[6] For example, we and others have successfully prepared interpolymer complexes between water-soluble polythiophene (PT) derivatives and biomacromolecules such as DNA,^[7] polypeptides,^[8] and polysaccharides.^[9] The induced conformational changes of PTs can be followed by absorption, emission, and circular dichroism (CD) spectroscopic methods, which provides the means for implementation of these systems as sensors. Moreover, nucleobases and ATP have been demonstrated to be versatile building blocks for the construction of supramolecular aggregates.^[10] Thus, we thought that if ATP can form some supramolecular complexes with conjugated polymers and induce changes in their conformation and mode of aggregation, the perceived structural changes of conjugated polymers would be useful not only for spectroscopic detection but also for rapid visual sensing. Herein, we report a water-soluble cationic polythiophene derivative that displays colorimetric and fluorescent responses to ATP through electrostatic and hydrophobic cooperative interactions. To the best of our knowledge, water-soluble conjugated polymers

have not been applied to ATP sensing previously; this is the first observation of a colorimetric probe based on a conjugated polymer for ATP that operates in aqueous solution at physiological pH.

Poly(3-alkoxy-4-methylthiophene) was chosen as a model conjugated polymer to study the viability of this approach because its conformation is sensitive to external stimuli as a result of the presence of sterically demanding side chains (i.e. the 4-methyl group).^[11] Therefore, the changes in the π – π^* transitions that arise from conformational alterations in the PT backbone upon the formation of a complex are convenient to monitor by using absorption and fluorescence spectroscopy. Water-soluble PT derivative, **1**, was synthesized as



reported previously.^[9] Titration of **1** with ATP in water at 20°C was monitored by absorption spectroscopy. As shown in Figure 1, the absorption maximum of **1** in water appears at

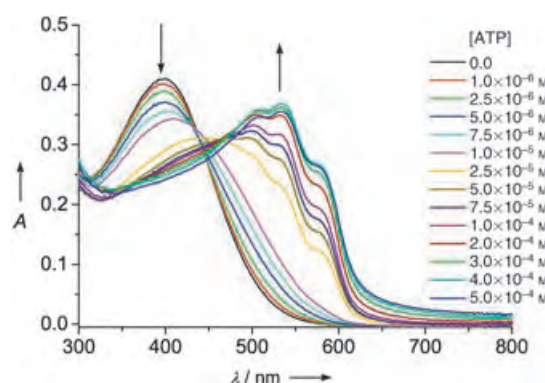


Figure 1. Variation in the absorption spectra of **1** (1.0×10^{-4} M) in water with increasing concentrations of ATP as indicated.

around 400 nm and is associated with a random-coil conformation of the PT derivatives.^[11] Upon adding increasing amounts of ATP, the absorption maximum is gradually red-shifted to 538 nm with an observed dramatic color change from yellow to pink-red. This distinct shift and the appearance of two vibronic bands are characteristic of the aggregation of the PT backbone.^[11,12] These results indicated promise that water-soluble **1** could be used as a colorimetric sensor for ATP.

To validate the specificity of the PT derivative toward anionic guests, the changes in the absorption spectra of **1** in water upon addition of biologically important anions such as adenosine monophosphate (AMP), adenosine diphosphate (ADP), and uridine triphosphate (UTP), as well as chloride, carboxylate, phosphate, and triphosphate ions (as sodium salts) were studied (see Supporting Information). After addition of an equimolar amount of these anions to aqueous

[*] Dr. C. Li, Dr. M. Numata, Dr. M. Takeuchi, Prof. Dr. S. Shinkai
Department of Chemistry and Biochemistry
Graduate School of Engineering
Kyushu University
Fukuoka 812-8581 (Japan)
Fax: (+81) 92-642-3611
E-mail: seijitcm@mbox.nc.kyushu-u.ac.jp

Supporting information for this article is available on the WWW under <http://www.angewandte.org> or from the author.

solutions of **1**, most of the solutions remained yellow with $\lambda_{\text{max}} < 435$ nm except for those that contained ADP and UTP, which gave orange solutions with shifts of the absorption maxima to 435 and 461 nm, respectively. The most remarkable effect was noted, however, upon addition of ATP, which gave a pink-red solution (Figure 2). Note, the dramatic color

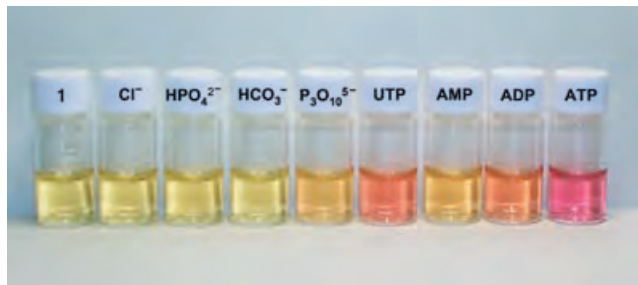


Figure 2. Changes in the color of solutions of **1** (1.0×10^{-4} M) in water induced by the addition of equimolar amounts of various anions.

change of **1** upon addition of ATP provides a very simple means for naked-eye detection of ATP in aqueous solution. Figure 3 shows the dependence of A_{535}/A_{400} , the ratio of the

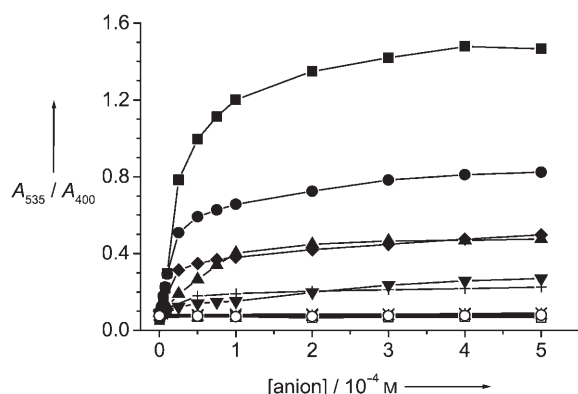


Figure 3. The dependence of the relative absorbance of **1** (1.0×10^{-4} M) at 535 and 400 nm (A_{535}/A_{400}) on the different anions at various concentrations in pure water. ATP (■); UTP (●); $P_3O_{10}^{5-}$ (▲); $P_2O_7^{4-}$ (▼); ADP (◆); AMP (+); Cl^- , $H_2PO_4^-$, HPO_4^{2-} , PO_4^{3-} , HCO_3^- , and CO_3^{2-} ions all have a negligible effect (see lowest line with overlapping unfilled symbols).

absorbance of **1** at 535 nm (π -stacked aggregates) and 400 nm (random coil), on the addition of different amount of various anions. It is clear from these results that the most striking effects are observed for ATP, and hence they confirm that the water-soluble derivative **1** is selectively responsive to ATP.

The analysis of ATP in biological systems is commonly carried out in the presence of alkali and alkali-earth metal cations. Therefore, we also studied the influence of the metal ions Na^+ , K^+ , Ca^{2+} , and Mg^{2+} (as their chloride salts) on the properties of **1** in solution (see Supporting Information). It was found that the absorption bands of **1** do not show any significant shift upon addition of these cations even when they are present in 20-fold excess. It is known that ATP has an

intrinsic metal-binding affinity with respective binding constants of $9554 M^{-1}$ (Mg^{2+}), $3722 M^{-1}$ (Ca^{2+}), $13 M^{-1}$ (Na^+), and $8 M^{-1}$ (K^+).^[13] To study the possibility of analytical interference from these cations, the influence of these cations (20-fold excess with respect to the repeating unit **1**) on the binding of ATP to **1** was also investigated (see Supporting Information). The introduction of monovalent cations (Na^+ , K^+) revealed little influence on the binding of ATP with **1**, whereas the presence of Mg^{2+} and Ca^{2+} suppressed to some extent the formation of the supramolecular complex as a result of their stronger binding (larger binding constants) with ATP relative to the monovalent cations. However, this does not interfere with the analytical determination of ATP by optical and visual detection.

To elucidate the mechanism behind the remarkable color change observed for **1** in the presence of ATP, the absorption spectra of **1** in the absence of anionic guest but in the presence of an equimolar amount of AMP, ADP, or ATP, or the presence of phosphate, pyrophosphate, triphosphate, UTP, or ATP were compared in Figure 4. As shown in Figure 4a, the absorption maximum at 400 nm of **1** is red-shifted to 416, 435, and 504 nm upon the stepwise addition of an equimolar amount of AMP, ADP, and ATP, which indicates that the number of negative charges on the anion plays a crucial role in promoting the formation of a supramolecular aggregate of **1**. However, only the presence of inorganic oligoanionic triphosphate ion does not induce a distinct change in the color of the solution of **1** and no supramolecular aggregate is

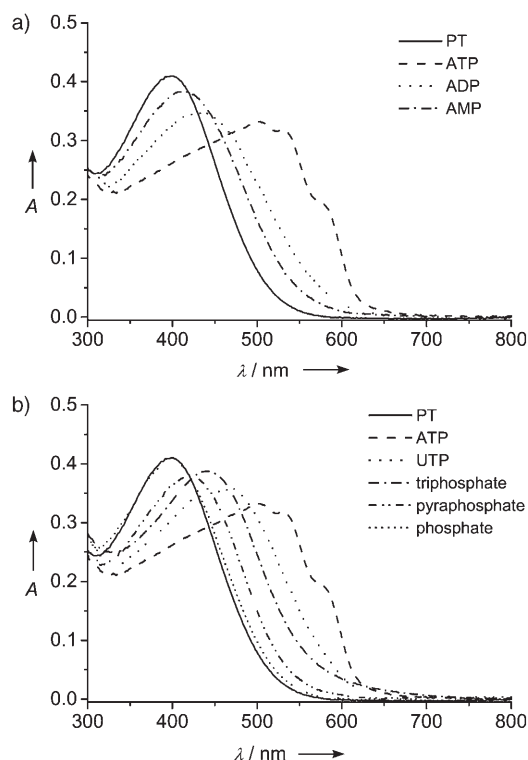


Figure 4. Absorption spectra of **1** (1.0×10^{-4} M) in water in the absence of anionic guest (—) and a) in the presence of an equimolar amount of AMP, ADP, or ATP, or b) in the presence of an equimolar amount of phosphate, pyrophosphate, triphosphate, UTP, or ATP. All spectra were extracted from the titration curves.

formed in this mixture (Figure 4b). It is also important to consider the effect of different nucleotides on the aggregation structure of **1**. As can be seen in Figure 4b, the presence of nucleotides uridine and adenosine is indispensable for accelerating the formation of a π -stacked supramolecular complex. In particular, the presence of the more hydrophobic nucleobase adenine leads to more efficient formation of supramolecular aggregates,^[14] and thus displays the most pronounced color change which is noticeable even to the naked eye. Although further studies will be needed to address the molecular mechanism behind this event, some preliminary considerations concerning the origin of the color are discussed next. The electrostatic interaction between the negative charges in the triphosphate group and the positive charge on the ammonium group in **1** promotes planarization of the PT backbone upon addition of increasing amounts of ATP, and above a critical concentration efficient π - π -stacking interaction between **1** backbones is induced by the synergistic effect that arises from the hydrophobic interaction between adenine units (see Supporting Information).^[15,16] Simultaneously, these interactions shift the π - π^* transition to longer wavelengths and lead to a color change from yellow to pink-red. To further confirm that the sensory response is due to interpolymer π -stacking aggregation, the absorption spectrum of **1** in the aggregated state (solid film cast from aqueous solution of **1**) was also measured (see Supporting Information). The resultant pink-red solid film exhibited characteristic absorption bands that are similar to those observed for **1** in aqueous solution in the presence of ATP, which supports the viewpoint that the addition of ATP promotes the aggregation of **1**.

To emphasize the biological importance and to assess the viability of this approach for the detection of ATP at physiological pH values, we subsequently examined the sensing ability of water-soluble **1** toward ATP in an aqueous solution containing HEPES (2-[4-(2-hydroxyethyl)-1-piperazinyl]ethanesulfonic acid) buffer (10 mM, pH 7.4; see Supporting Information). In the absence of anionic guest, the absorption maximum of **1** in HEPES buffered solution shows a slight red shift (12 nm) relative to that observed in unbuffered aqueous solution and appears at 412 nm. This difference may be due to the size-dependent effects of counterions as reported previously.^[17] Upon further addition of ATP, the absorption maximum is red-shifted gradually to 476 nm and is accompanied by the appearance of two shoulders at 536 and 583 nm. Unlike the large shift of 138 nm toward the red region as observed in aqueous solution, a relatively small red shift (64 nm) is detected in solution of **1** in HEPES buffer due to the competitive binding of HEPES anions with **1**. Despite this, it does not prevent the analytical determination of ATP with **1** (see Supporting Information) which indicates that **1** can be applied as a satisfactory ATP sensor in aqueous solution at physiological pH values.

It is known that conformational changes and interchain interactions play decisive roles in controlling the emissive properties of conjugated polymers that have been applied in some fluorescence sensory systems.^[18] Given the high sensitivity of fluorometric methods relative to absorption spec-

troscopy, it is expected that fluorometry will extend the detection limit of ATP. The yellow, random-coiled form of **1** is fluorescent and exhibits an emission band around 536 nm upon excitation at 445 nm (see Supporting Information). Upon addition of increasing amounts of ATP, the emission intensity decreases gradually and a slight red shift and broadening of the band is observed which indicates that fluorometric detection of ATP binding is possible. Of the analytes studied here, the fluorescence quenching of **1** (5.0×10^{-6} M in 10 mM HEPES buffer at pH 7.4) is most sensitive to binding with ATP; that is, an 84 % decrease in intensity at the emission maximum was observed in the presence of an equimolar amount of ATP, whereas only 12 % quenching of the fluorescence was detected upon addition of an equimolar amount of AMP (Figure 5). These results indicate that the

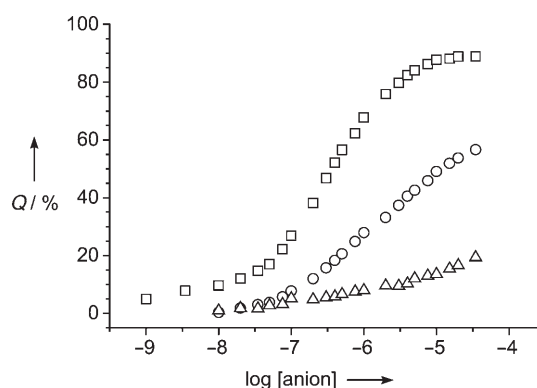


Figure 5. Fluorescence quenching of **1** (5.0×10^{-6} M) by AMP, ADP, and ATP at various concentrations in 10 mM HEPES buffered solution at pH 7.4. The fluorescence quenching $Q = [(I_0 - I)/I_0] \times 100\%$; I_0 is the fluorescence intensity at 529 nm of a solution of **1** (5.0×10^{-6} M); I is the fluorescence intensity at 529 nm of a solution of **1** (5.0×10^{-6} M) in the presence of different amounts of the analytes ATP (□; $\lambda_{\text{ex}} = 445$ nm), ADP (○; $\lambda_{\text{ex}} = 435$ nm), and AMP (△; $\lambda_{\text{ex}} = 435$ nm).

quenching of fluorescence is much more effective in the presence of ATP than with the use of AMP or ADP and that the detection limit can be extended to the order of 10^{-8} M.

In conclusion, we have developed a novel colorimetric and fluorescent sensor for ATP that operates in aqueous solution. The present findings will not only extend the application of water-soluble conjugated polymers but also provide a new approach for facile monitoring of ATP based on the different mechanisms discussed above. Therefore, we expect that the present system will be applicable to routine cellular assays after the rational design of the substituted groups (e.g. the introduction of zwitterionic groups or poly(ethylene glycol) groups) in polythiophenes to improve the membrane permeability of the probe, and further research along this line is currently in progress.

Received: May 26, 2005

Revised: June 20, 2005

Published online: September 19, 2005

Keywords: aggregation · anion binding · fluorescence · polymers · UV/Vis spectroscopy

- [1] a) T. D. James, K. R. A. S. Sandanayake, S. Shinkai, *Angew. Chem.* **1996**, *108*, 2038–2050; *Angew. Chem. Int. Ed. Engl.* **1996**, *35*, 1911–1922; b) A. P. de Silva, H. Q. N. Gunaratne, T. Gunnlaugsson, A. J. M. Huxley, C. P. McCoy, J. T. Rademacher, T. E. Rice, *Chem. Rev.* **1997**, *97*, 1515–1566; c) F. P. Schmidtchen, M. Berger, *Chem. Rev.* **1997**, *97*, 1609–1646; d) M. M. G. Antonisse, D. N. Reinhoudt, *Chem. Commun.* **1998**, 443–448; e) J. H. Hartley, T. D. James, C. J. Ward, *J. Chem. Soc. Perkin Trans. 1* **2000**, 3155–3184; f) P. D. Beer, P. A. Gale, *Angew. Chem.* **2001**, *113*, 502–532; *Angew. Chem. Int. Ed.* **2001**, *40*, 487–516; g) T. D. James, S. Shinkai, *Top. Curr. Chem.* **2002**, *218*, 159–200; h) R. Martínez-Máñez, F. Sancenón, *Chem. Rev.* **2003**, *103*, 4419–4476; i) L. Pu, *Chem. Rev.* **2004**, *104*, 1687–1716.
- [2] a) M. W. Hosseini, A. J. Blacker, J.-M. Lehn, *J. Am. Chem. Soc.* **1990**, *112*, 3896–3904; b) H. Fenniri, M. W. Hosseini, J. M. Lehn, *Helv. Chim. Acta* **1997**, *80*, 786–803; c) S. Patterson, B. D. Smith, R. E. Taylor, *Tetrahedron Lett.* **1997**, *38*, 6323–6326; d) Y. Kanekiyo, M. Sano, R. Iguchi, S. Shinkai, *J. Polym. Sci. Part A* **2000**, *38*, 1302–1310; e) F. Sancenón, A. B. Descalzo, R. Martínez-Máñez, M. A. Miranda, J. Soto, *Angew. Chem.* **2001**, *113*, 2710–2713; *Angew. Chem. Int. Ed.* **2001**, *40*, 2640–2643; f) A. Ojida, S.-K. Park, Y. Mito-oka, I. Hamachi, *Tetrahedron Lett.* **2002**, *43*, 6193–6195; g) S. Mizukami, T. Nagano, Y. Urano, A. Odani, K. Kikuchi, *J. Am. Chem. Soc.* **2002**, *124*, 3920–3925; h) N. Marcotte, A. Taglietti, *Supramol. Chem.* **2003**, *15*, 617–625; i) D. H. Lee, S. Y. Kim, J.-I. Hong, *Angew. Chem.* **2004**, *116*, 4881–4884; *Angew. Chem. Int. Ed.* **2004**, *43*, 4777–4780.
- [3] a) S. E. Schneider, S. N. O’Neil, E. V. Anslyn, *J. Am. Chem. Soc.* **2000**, *122*, 542–543; b) S. C. McCleskey, M. J. Griffin, S. E. Schneider, J. T. McDevitt, E. V. Anslyn, *J. Am. Chem. Soc.* **2003**, *125*, 1114–1115; c) S. M. Butterfield, M. L. Waters, *J. Am. Chem. Soc.* **2003**, *125*, 9580–9581; d) J. A. Cruz-Aguado, Y. Chen, Z. Zhang, N. H. Elowe, M. A. Brook, J. D. Brennan, *J. Am. Chem. Soc.* **2004**, *126*, 6878–6879.
- [4] a) P. L. Sazani, R. Larralde, J. W. Szostak, *J. Am. Chem. Soc.* **2004**, *126*, 8370–8371; b) M. N. Stojanovic, D. M. Kolpashchikov, *J. Am. Chem. Soc.* **2004**, *126*, 9266–9270; c) E. J. Cho, L. Yang, M. Levy, A. D. Ellington, *J. Am. Chem. Soc.* **2005**, *127*, 2022–2023.
- [5] a) T. M. Swager, *Acc. Chem. Res.* **1998**, *31*, 201–207; b) D. T. McQuade, A. E. Pullen, T. M. Swager, *Chem. Rev.* **2000**, *100*, 2537–2574.
- [6] a) L. Chen, D. W. McBranch, H.-L. Wang, R. Helgeson, F. Wudl, D. G. Whitten, *Proc. Natl. Acad. Sci. USA* **1999**, *96*, 12287–12292; b) M. R. Pinto, K. S. Schanze, *Proc. Natl. Acad. Sci. USA* **2004**, *101*, 7505–7510; c) B. Liu, G. C. Bazan, *Chem. Mater.* **2004**, *16*, 4467–4476; d) B. Liu, G. C. Bazan, *Proc. Natl. Acad. Sci. USA* **2005**, *102*, 589–593.
- [7] a) P. C. Ewbank, G. Nuding, H. Suenaga, R. D. McCullough, S. Shinkai, *Tetrahedron Lett.* **2001**, *42*, 155–157; b) H.-A. Ho, M. Boissinot, M. G. Bergeron, G. Corbeil, K. Doré, D. Boudreau, M. Leclerc, *Angew. Chem.* **2002**, *114*, 1618–1621; *Angew. Chem. Int. Ed.* **2002**, *41*, 1548–1551; c) H.-A. Ho, M. Bera-Aberem, M. Leclerc, *Chem. Eur. J.* **2005**, *11*, 1718–1724.
- [8] a) K. P. R. Nilsson, J. Rydberg, L. Baltzer, O. Inganäs, *Proc. Natl. Acad. Sci. USA* **2004**, *101*, 11197–11202; b) A. Herland, K. P. R. Nilsson, J. D. M. Olsson, P. Hammarström, P. Konradsson, O. Inganäs, *J. Am. Chem. Soc.* **2005**, *127*, 2317–2323; c) K. P. R. Nilsson, A. Herland, P. Hammarström, O. Inganäs, *Biochemistry* **2005**, *44*, 3718–3724.
- [9] C. Li, M. Numata, A.-H. Bae, K. Sakurai, S. Shinkai, *J. Am. Chem. Soc.* **2005**, *127*, 4548–4549.
- [10] a) M. Numata, S. Shinkai, *Chem. Lett.* **2003**, *32*, 308–309; b) R. Iwaura, K. Yoshida, M. Masuda, M. Ohnishi-Kameyama, M. Yoshida, T. Shimizu, *Angew. Chem.* **2003**, *115*, 1039–1042; *Angew. Chem. Int. Ed.* **2003**, *42*, 1009–1012; c) K. Sugiyasu, M. Numata, N. Fujita, S. M. Park, Y. J. Yun, B. H. Kim, S. Shinkai, *Chem. Commun.* **2004**, 1996–1997; d) S. Sivakova, S. J. Rowan, *Chem. Soc. Rev.* **2005**, *34*, 9–21; e) M. Morikawa, M. Yoshihara, T. Endo, N. Kimizuka, *J. Am. Chem. Soc.* **2005**, *127*, 1358–1359.
- [11] a) M. Chayer, K. Faïd, M. Leclerc, *Chem. Mater.* **1997**, *9*, 2902–2905; b) F. Brustolin, F. Goldoni, E. W. Meijer, N. A. J. M. Sommerdijk, *Macromolecules* **2002**, *35*, 1054–1059.
- [12] a) B. M. W. Langeveld-Voss, R. A. J. Janssen, M. P. T. Christiaans, S. C. J. Meskers, H. P. J. M. Dekkers, E. W. Meijer, *J. Am. Chem. Soc.* **1996**, *118*, 4908–4909; b) B. M. W. Langeveld-Voss, R. A. J. Janssen, E. W. Meijer, *J. Mol. Struct.* **2000**, *521*, 285–301; c) F. J. M. Hoebe, P. Jonkheijm, E. W. Meijer, A. P. H. J. Schenning, *Chem. Rev.* **2005**, *105*, 1491–1546.
- [13] J. E. Wilson, A. Chin, *Anal. Biochem.* **1991**, *193*, 16–19.
- [14] Guanosine triphosphate (GTP), which bears a purine base, can also form a supramolecular complex with **1**, which results in a similar change in color of the solution from yellow to pink-red. However, the presence of ATP can be efficiently distinguished from GTP by a chiroptical method as the two supramolecular complexes with **1** give opposite induced circular dichroism pattern (see Supporting Information).
- [15] H. Kobayashi, M. Amaike, K. Koumoto, S. Shinkai, *Bull. Chem. Soc. Jpn.* **2001**, *74*, 1311–1317.
- [16] The differences between the ¹H NMR spectra (D₂O) of the adenosine moiety in ATP and the complex ATP/**1** further support this conclusion. In the complex, the 8-H and 2-H protons in the adenine moiety and the 1'-H proton in the D-ribose moiety shift to higher field and is accompanied by broadening of these peaks relative to those for “free” ATP in solution, indicating the significant contribution of π–π stacking between adenosine moieties.
- [17] a) R. D. McCullough, P. C. Ewbank, R. S. Loewe, *J. Am. Chem. Soc.* **1997**, *119*, 633–634; b) P. C. Ewbank, R. S. Loewe, L. Zhai, J. Reddinger, G. Sauvé, R. D. McCullough, *Tetrahedron* **2004**, *60*, 11269–11275.
- [18] a) J. Kim, D. T. McQuade, S. K. McHugh, T. M. Swager, *Angew. Chem.* **2000**, *112*, 4026–4030; *Angew. Chem. Int. Ed.* **2000**, *39*, 3868–3872; b) H. A. Ho, M. Leclerc, *J. Am. Chem. Soc.* **2003**, *125*, 4412–4413.

Differential Receptors Create Patterns That Distinguish Various Proteins**

Aaron T. Wright, Michael J. Griffin, Zhenlin Zhong, Shawn C. McCleskey, Eric V. Anslyn,* and John T. McDevitt*

The term “protein-detecting array” has been coined to describe an analytical device consisting of a series of protein receptors.^[1] Classically, such an array consists of highly selective protein-binding agents. Unfortunately, the creation of synthetic receptors with high affinity and specificity for proteins is particularly challenging owing to their molecular complexity. However, there has been recent success in creating selective synthetic receptors for assorted peptides.^[2]

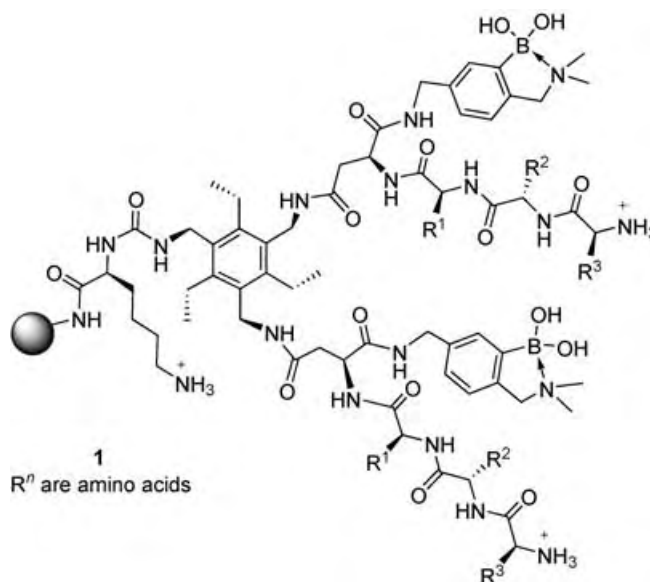
An alternative to the use of highly selective receptors is to employ differential receptors.^[3] This method uses an array of receptors having good affinity, but not necessarily high selectivity, for a particular target. When functioning in tandem the combined response of the receptors creates a pattern that is diagnostic for each analyte. Because the response of the receptor array does not necessarily rely on specific recognition interactions between substrate and analyte, highly challenging analytes can be targeted.

Very few groups have used differential receptors for the analysis of biomolecules.^[3] Hamilton et al. recently reported the use of a 35-member receptor library of tetraphenyl porphyrin derivatives, functionalized with different amino acids resulting in charges varying from +8 to −8, for the detection of charged proteins. Eight members of the library were used to detect four charged proteins, ranging from acidic ferredoxin (pI=2.75) to highly basic cytochrome C (pI=10.6). Fluorescence quenching patterns composed from the responses of the eight receptors correlated with the charge complementarity between the receptors and proteins.^[4] Until our current report, differential receptor arrays had not found use in distinguishing classes of proteins.

Our group's approach to differential sensing is to create libraries of receptors that are biased towards particular analyte classes. Using this approach, we have shown that a

microchip-based array incorporating a combinatorial library of receptors^[5] is effective in differentiating nucleotide phosphates with an indicator-displacement assay.^[6] We now report the development of a library of differential receptors biased towards proteins and glycoproteins. When combined with an indicator-uptake visualization assay and principal component analysis (PCA), the library gives differentiation of proteins and glycoproteins, as well as subtle differentiation within each protein class.^[7]

To differentiate proteins and glycoproteins, we designed and synthesized library **1**, which incorporates one of 19



natural amino acids (cysteine excluded) at each of three sites on two different binding arms, by using combinatorial chemistry.^[8] This created a library with 19³ (6859) unique members. The peptide arms provide sites for molecular recognition of proteins by means of ion pairing, hydrogen bonding, and the hydrophobic effect. The boronic acids provide effective sugar binding sites because these groups rapidly and reversibly form cyclic esters with diols in aqueous media.^[9] The hexasubstituted benzene scaffold acts as a spacer and assists in the creation of a binding cavity.^[10] Our expectation was that each receptor would show differential binding with proteins based on the variance in the peptide arms, and that the boronic acids would assist in differentiation of proteins from glycoproteins.

We used a 7 × 5 array consisting of 29 randomly selected resin beads from library **1** and six acylated resin blanks. Each bead was placed in a micromachined chip-based array platform (see the Supporting Information) that has been previously described.^[11] Protocols for the delivery of protein and indicator, and for acidic and basic washes? have been detailed previously. The patterns created by the array of receptors are obtained by measuring the intensity of transmitted red, green, and blue light for each bead using a charge-coupled device attached to a customized reader.^[12]

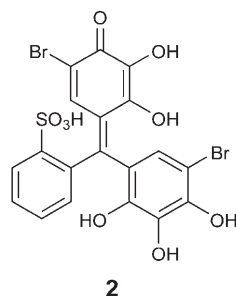
In order to create diagnostic patterns for each protein, a signaling protocol was incorporated. Previous work utilized

[*] A. T. Wright, M. J. Griffin, Dr. Z. Zhong, S. C. McCleskey, Dr. E. V. Anslyn, Dr. J. T. McDevitt
Department of Chemistry and Biochemistry
The University of Texas at Austin
Austin, TX 78712 (USA)
Fax: (+1) 512-471-8696
E-mail: Anslyn@ccwf.cc.utexas.edu
Mcdevitt@mail.utexas.edu

[**] We gratefully acknowledge support for this work from the U.S. NIH (EB00549-5). We thank Dr. Lara Mahal for her advice and insight. Thanks also to Dr. Klaus Linse and Michelle Gadush for their assistance in sequencing beads.

Supporting information for this article is available on the WWW under <http://www.angewandte.org> or from the author.

indicator-displacement assays; however, at the low protein concentrations used in this study it was more advantageous to evaluate the rate of indicator uptake. Our indicator-uptake signaling protocol allowed us to use protein concentrations (355 μM) nearly 60 times less than that in our previous work with nucleotide phosphates (20 mM).^[6] We incorporated the commercially available indicator bromopyrogallol red (**2**) for the indicator-uptake colorimetric analysis. This indicator forms reversible cyclic esters with the boronic acids of the receptor.



Our experimental protocol starts with a delivery of 5 mL of a protein solution (355 μM in HEPES buffer) at a flow rate of 0.25 mL min⁻¹. This is followed by washing with buffer for 3 min (25 mM HEPES, pH 7.4, 1.0 mL min⁻¹) and then delivery of **2** (3.0 μM in HEPES buffer, 1.0 mL min⁻¹). After each analysis, the protein and indicator were washed from the array with NaOH (150 mM) and HCl (300 mM) rinses. This allowed for repeated use of the array. A 12-bit image was captured every 2 s during indicator uptake. For each receptor bead in the array the green-channel absorbance ($\lambda = 550$ nm) was plotted versus time and a slope was garnered. Effective absorbance values were obtained by calculating the negative log of the ratio of the green-channel intensity of each bead to the green-channel intensity of a blank bead.^[11]

Ovalbumin, fetuin, lysozyme, bovine serum albumin (BSA), and elastin were used for this study. These choices were made to challenge our design principles by grouping proteins of similar properties. The characteristics of the proteins span a variety of molecular weights, glycosidic properties, and isoelectric points (pI). The molecular weights of ovalbumin and fetuin are similar, as are those of elastin and BSA. The pI of ovalbumin, BSA, and fetuin are similar, as are those of lysozyme and elastin (Table 1).

Table 1: Characteristic protein data.

Protein	M_w [kDa]	pI	Glycoprotein?
ovalbumin	44–45	4.6	yes
fetuin	48.4	4.5–4.9	yes
lysozyme	14	9.6–11	no
BSA	66	4.7–5.2	no
elastin	60	9.3–10.2	no

Four trials were performed for each protein.^[13] The indicator-uptake slopes were calculated for each receptor bead over the time during which the dye passed through the array (49 to 403 s). An illustration of the differences in indicator uptake from different resin-bound receptors can be seen in Figure 1. For each trial a slope was measured for each bead (blanks not included). Because of the large number of slopes calculated from each trial, the dimensionality of the data set was simplified using PCA.

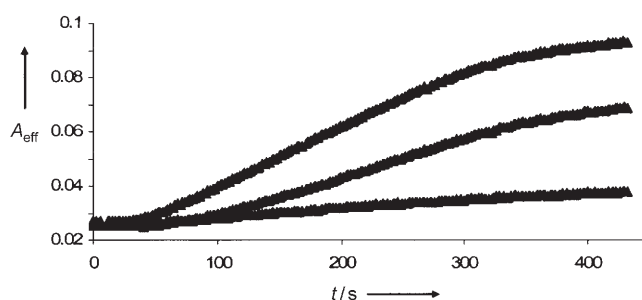


Figure 1. Indicator-uptake curves from three beads are represented from a trial with BSA. The slope from 49 to 403 s for each resin-bound receptor is taken as part of a cumulative slope pattern for each protein. A_{eff} is the effective absorbance. See the text for an explanation of the measurement procedure.

In PCA, the first principal component (PC) axis is calculated to lie along the line of maximum variance in the original data set. Subsequent orthogonal axes are calculated to lie along lines of diminishing levels of variance. In this study, the first four PC axes effectively satisfied the Kaiser criterion, which states that as many factors can be extracted as variables that have eigenvalues greater than one.^[14] Figure 2

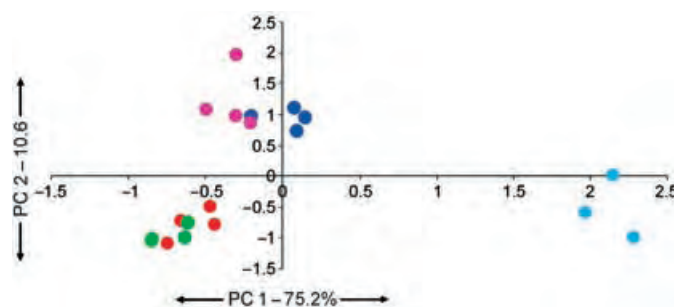


Figure 2. PCA score plot for each protein trial. Percentages on the PC axes define the weight of those axes to the overall pattern. Spacing between proteins demonstrates the recognition capability of the resin-bound receptors. (● lysozyme, ● elastin, ● ovalbumin, ● fetuin, ● BSA)

shows a two-dimensional PCA plot which effectively separates the different protein classes. As illustrated, there is differentiation between proteins and glycoproteins, which was a primary goal of this study. However, because four PC axes are outside the range of error it was possible to generate a three-dimensional PCA plot that further separates the proteins. Figure 3 shows an expanded PCA plot using PC axes 1–3. This demonstrates that the array of receptors adequately separated proteins from glycoproteins, and to a lesser extent even separates proteins within the classes. The fact that we used a random selection of receptors to achieve these results illustrates the power of our method. More than likely any one of these 29 receptors would not have been a good receptor for a particular protein; however, when functioning in tandem, the array works well. Further, any 29 receptors could presumably be used to obtain analogous patterns for the proteins. PC axis 4 (4.7%) could have also been used for further discrimination in another plot.

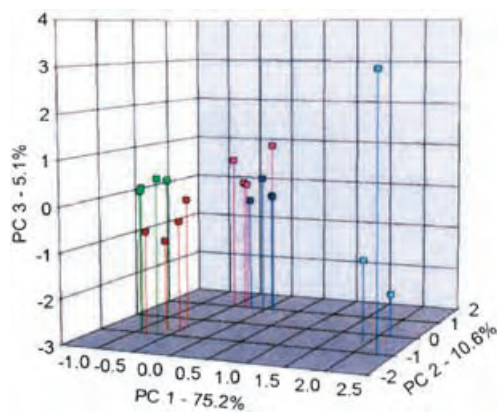


Figure 3. PCA score plot for each protein trial (● lysozyme, ● elastin, ● ovalbumin, ● fetuin, ● BSA). The additional dimension further separates the proteins.

A control was performed using a 7×5 array with six blanks and 29 resin beads derivatized only with tripeptides that were obtained from a combinatorial library synthesized with 19 natural amino acids (cysteine excluded). Using this array of tripeptide beads, no separation of analytes occurred. This control illustrates that some design must be incorporated into the receptors to bind certain analyte classes, and that simple random receptors are inefficient. These results do not strictly demonstrate that the boronic acids bind to glycoproteins and not standard proteins. More likely the boronic acids interact with surface epitopes on both protein classes but to different extents. Yet, if differential formation of covalent bonds with the boronic acids was the only factor in the discrimination between protein classes, then because they are the only binding moiety present in every receptor we would expect no differences within each protein class. Therefore, both the boronic acids and the variable peptide arms of the receptors are critical in the identification and discrimination of proteins and glycoproteins.

Though we significantly reduced the analyte concentrations from those in our previous report with nucleotide phosphates, the protein concentrations ($355 \mu\text{M}$) are still relatively high for practical analysis. Reduction to practical concentrations (nM) was accomplished with differential receptors of higher affinity. In other work we have also shown that an analysis cell that recycles the analyte solution through the array leads to extremely sensitive assays.^[15]

The PCA plot (Figure 2 and Figure 3) demonstrates similarities between ovalbumin and fetuin, and similarities between elastin and lysozyme. Yet, even the proteins in similar groups are separated. The proximity of ovalbumin and fetuin is reasonable as both are glycoproteins with similar pI values, and both likely interacted with the boronic acid moieties. Further, elastin and lysozyme have similar pI values. Therefore, the separation in our analysis is not simply a result of charge differences. Interestingly, molecular weight also did not play a large role in the patterns exhibited. BSA is likely separated from the others because it has a different pI than elastin and lysozyme and is not a glycoprotein. The differentiation between similar proteins is likely due to specific

contacts between the receptors and proteins that are cross-reactive and subtly discriminatory.

Factor loading values are calculated in PCA to determine the magnitude of the contribution of an original variable to the formation of a PC axis. Variables with loading values approaching -1 or 1 have a dominant role in the formation of a PC axis. Because PC axis 1 described the most variance, five beads with high loading values on PC 1 and two beads with low loading values were selected for receptor characterization (Table 2) using Edman degradation. The sequencing results do not show any obvious homologies. Yet, the lack of any homology is a lesson in itself: differential sensing schemes can be successful and may even benefit from a wide variety of structurally diverse receptors.

Table 2: Factor loadings and sequencing results for principal component 1.

Tripeptide sequence	Factor loadings (PC 1)	Bead number
Ala-Ser-Asp	0.984	12
Ser-Lys-Gly	0.963	9
Arg-Lys-Lys	0.951	15
Gly-Asp-Ser	0.932	2
Asp-Leu-Val	0.928	22
Lys-Arg-Met	0.774	23
Gly-Gln-Gln	0.722	6

In summary, we have shown that the use of an array of differential receptors can differentiate between classes of proteins, and even between very structurally similar proteins. This separation did not arise from charge differences or molecular weight differences, but rather from specific contacts between receptors and proteins giving discriminatory patterns. We plan to expand this general approach to the qualitative analysis of complex mixtures of proteins.

Received: March 30, 2005

Revised: June 6, 2005

Published online: September 12, 2005

Keywords: host–guest systems · proteins · receptors · supramolecular chemistry

- [1] T. Kodadek, *Chem. Biol.* **2001**, 8, 105–115.
- [2] a) A. T. Wright, E. V. Anslyn, *Org. Lett.* **2004**, 6, 1341; b) A. Buryak, K. Severin, *Angew. Chem.* **2004**, 116, 4875–4878; *Angew. Chem. Int. Ed.* **2004**, 43, 4771–4774; c) H. Wennemers, M. Conza, M. Nold, P. Krattiger, *Chem. Eur. J.* **2001**, 7, 3342–3347; d) M. W. Peczu, A. D. Hamilton, *Chem. Rev.* **2000**, 100, 2479–2494; e) W. C. Still, *Acc. Chem. Res.* **1996**, 29, 155–163.
- [3] a) A. Buryak, K. Severin, *J. Am. Chem. Soc.* **2005**, 127, 3700–3701; b) J. J. Lavigne, E. V. Anslyn, *Angew. Chem.* **2001**, 113, 3212–3225; *Angew. Chem. Int. Ed.* **2001**, 40, 3118–3130; c) S. L. Wiskur, P. N. Floriano, E. V. Anslyn, J. T. McDevitt, *Angew. Chem.* **2003**, 115, 2116–2118; *Angew. Chem. Int. Ed.* **2003**, 42, 2070–2072; d) K. J. Albert, N. S. Lewis, C. L. Schauer, G. A. Sotzing, S. E. Stitzel, T. P. Vaid, D. R. Walt, *Chem. Rev.* **2000**, 100, 2595–2626; e) N. A. Rakow, K. S. Suslick, *Nature* **2000**, 406,

- 710–713; f) T. Hirsch, H. Kettenberger, O. S. Wolfbeis, V. M. Mirsky, *Chem. Commun.* **2003**, 432–433.
- [4] L. Baldini, A. J. Wilson, J. Hong, A. D. Hamilton, *J. Am. Chem. Soc.* **2004**, *126*, 5656–5657.
- [5] S. L. Wiskur, H. Ait-Haddou, J. J. Lavigne, E. V. Anslyn, *Acc. Chem. Res.* **2001**, *34*, 963–972.
- [6] S. C. McCleskey, M. J. Griffin, S. E. Schneider, J. T. McDevitt, E. V. Anslyn, *J. Am. Chem. Soc.* **2003**, *125*, 1114–1115.
- [7] a) W. Carey, K. Beebe, B. Kowalski, *Anal. Chem.* **1986**, *58*, 149–153; b) P. Jurs, G. Bakken, H. McClelland, *Chem. Rev.* **2000**, *100*, 2649–2678.
- [8] Z. Zhong, E. V. Anslyn, *J. Am. Chem. Soc.* **2002**, *124*, 9014–9015.
- [9] a) H. G. Kuivila, A. H. Keough, E. J. Soboczenski, *J. Org. Chem.* **1954**, *19*, 780–783; b) J. P. Lorand, J. D. Edwards, *J. Org. Chem.* **1959**, *24*, 769–774; c) T. D. James, K. R. A. S. Sandanayake, S. Shinkai, *Angew. Chem.* **1996**, *108*, 2051–2053; *Angew. Chem. Int. Ed. Engl.* **1996**, *35*, 1910–1922; d) S. L. Wiskur, J. J. Lavigne, H. Ait-Haddou, V. Lynch, Y. H. Chiu, J. W. Canary, E. V. Anslyn, *Org. Lett.* **2001**, *3*, 1311–1314.
- [10] a) D. J. Iverson, G. Hunter, J. F. Blount, J. R. Damewood, K. Mislow, *J. Am. Chem. Soc.* **1981**, *103*, 6073–6083; b) K. V. Kilway, J. S. Siegel, *J. Am. Chem. Soc.* **1992**, *114*, 255–261; c) H. E. Gottlieb, C. Ben-Ary, A. Hassner, V. Marks, *Tetrahedron* **1999**, *55*, 4003–4114.
- [11] A. Goodey, J. J. Lavigne, S. Savoy, M. Rodriguez, T. Curey, A. Tsao, G. Simmons, S. Yoo, Y. Sohn, E. V. Anslyn, J. Shear, D. Niekirk, J. T. McDevitt, *J. Am. Chem. Soc.* **2001**, *123*, 2559–2570.
- [12] a) K. Niikura, A. Metzger, E. V. Anslyn, *J. Am. Chem. Soc.* **1998**, *120*, 8533–8534; b) J. J. Lavigne, E. V. Anslyn, *Angew. Chem.* **1999**, *111*, 3903–3906; *Angew. Chem. Int. Ed.* **1999**, *38*, 3666–3669; c) S. L. Wiskur, E. V. Anslyn, *J. Am. Chem. Soc.* **2001**, *123*, 10109–10110; d) See refs. [4] and [5].
- [13] One BSA trial was excluded because an air bubble skewed the CCD images.
- [14] H. F. Kaiser, *Educ. Psychol. Meas.* **1960**, *20*, 141–150.
- [15] N. Christodoulides, S. Mohanty, C. S. Miller, M. C. Langub, P. N. Floriano, P. Dharshan, M. F. Ali, B. Bernard, D. Romanovicz, E. Anslyn, P. C. Fox, J. T. McDevitt, *Lab on a Chip* **2005**, *5*, 261–269.

DOI: 10.1002/anie.200501885

SiGe₂ and Ge₃: Cyclic Digermenes that Undergo Unexpected Ring-Expansion Reactions***Vladimir Ya. Lee, Hiroyuki Yasuda, Masaaki Ichinohe, and Akira Sekiguchi**

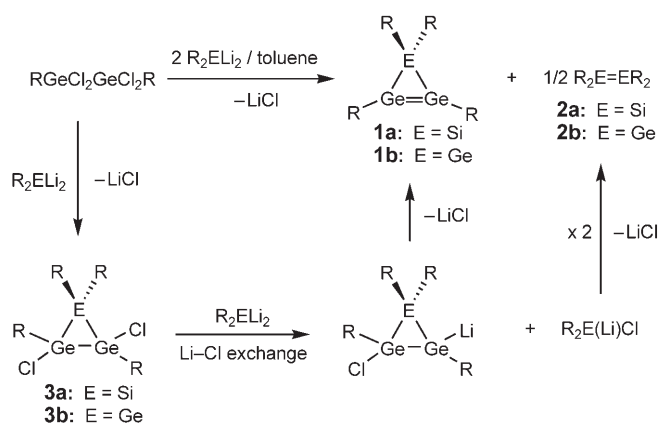
The chemistry of cyclic compounds composed of heavier Group 14 elements represents one of the most fascinating topics of modern organometallic chemistry. Since the first reports on the preparation of heavy cyclopropane analogues by Masamune et al. in 1982–1983,^[1] the chemistry of these unusual compounds has been greatly developed in all respects, including synthesis, structure, and reactivity. The first examples of heavy cyclopropene analogues were synthesized only recently, during the last decade.^[2] Since then, several representatives of these highly challenging compounds, which combine the properties of heavy cyclopropanes and heavy alkenes in one molecule, have been reported.^[3]

Apart from the homonuclear heavy cyclopropenes, consisting of identical Group 14 elements, several heteronuclear analogues containing different heavier Group 14 elements can also be imagined. However, of all the possible combinations only two heteronuclear heavy cyclopropenes have been synthesized by the Würtz-type coupling reaction, namely 3*H*- and 1*H*-disilagermirenes, which feature endocyclic Si=Si and Si=Ge bonds, respectively.^[4] Herein, we report the synthesis of two cyclic, three-membered-ring digermenes: the first 1*H*-siladigermirene, a heteronuclear cyclopropene with one Si and two Ge atoms, and a novel 1*H*-trigermirene derivative.

As the target compound 1*H*-siladigermirene, in contrast to 3*H*-disilagermirene,^[4] could not be prepared by the Würtz coupling reaction, we developed a new synthetic protocol that involves a coupling reaction of 1,1-dilithiosilane R₂SiLi₂^[5] with tetrachlorodigermene RCl₂Ge–GeCl₂R in toluene (R = SiMe₂tBu₂). This reaction quickly results in the formation of two products, tetrakis(di-*tert*-butylmethylsilyl)-1*H*-siladigermirene (R₄SiGe₂, **1a**) and disilene R₂Si=SiR₂ (**2a**),^[6] in a 2:1 ratio (Scheme 1). It is interesting that among the various compounds that one can imagine as the products of this reaction, namely 1,4-disila-2,3-digermabuta-1,3-diene, 2,4-disila-1,3-digermabicyclo[1.1.0]butane, and 1*H*-siladigermirene, only the last compound was formed. The isolation of disilene **2a** as the side product provides evidence for the

[*] Dr. V. Ya. Lee, H. Yasuda, Dr. M. Ichinohe, Prof. Dr. A. Sekiguchi
Department of Chemistry
Graduate School of Pure and Applied Sciences
University of Tsukuba
Tsukuba, Ibaraki 305-8571 (Japan)
Fax: (+81) 298-53-4314
E-mail: sekiguch@staff.chem.tsukuba.ac.jp

[**] This work was supported by Grants-in-Aid for Scientific Research (Nos. 14078204, 16205008, 17655014) from the Ministry of Education, Culture, Sports, Science, and Technology, and the COE (Center of Excellence) program.



Scheme 1. Synthesis of the 1*H*-siladigermirene **1a** and the 1*H*-trigermirene **1b**. E = Si, Ge; R = SiMe₂Bu₂.

initial formation of the intermediate cyclic 2,3-dichlorosila-digermirane (**3a**) followed by a rapid lithium–chlorine exchange reaction between **3a** and a second equivalent of R₂SiLi₂, finally resulting in the formation of **1a** and **2a** in a 2:1 ratio.^[7] The 1*H*-siladigermirene **1a** represents the first SiGe₂ hybrid heavy analogue of cyclopropene featuring a skeletal Ge=Ge double bond.

Compound **1a** exhibits very simple ¹H and ¹³C NMR spectra with only two sets of signals for the protons of the Me and *t*Bu groups. In the ²⁹Si NMR spectrum of **1a**, the skeletal Si atom resonates at high field (δ = −110.6 ppm), as expected for tetrahedral Si atoms incorporated in a three-membered-ring system. Dark red crystals of **1a** were isolated that were highly sensitive to air and moisture. The X-ray crystal structure analysis^[8] proved that **1a** was an unsaturated three-membered ring with a Ge=Ge double bond length of 2.2429(6) Å (Figure 1). The remaining two sides of the SiGe₂ isosceles triangle are made up of Si–Ge single bonds (2.4167(10) Å). These skeletal bond lengths are characteristic for three-membered rings of heavier Group 14 elements. As expected, the Ge=Ge double bond has a highly pronounced *trans*-bent configuration with a bending angle of 51.0(2)°.^[9]

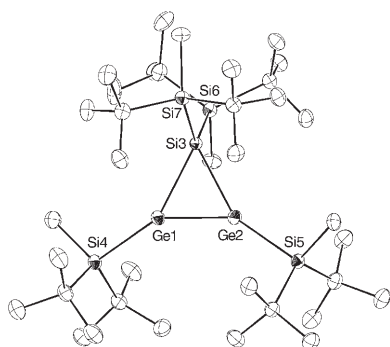
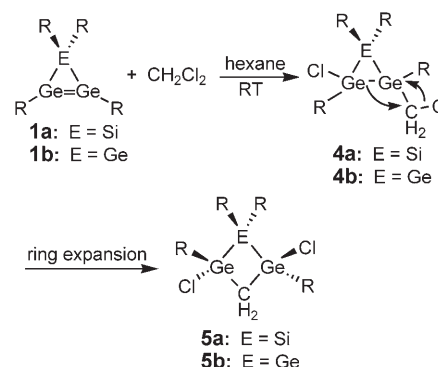


Figure 1. ORTEP plot of the crystal structure of **1a**; the thermal ellipsoids are shown at the 30% probability level and hydrogen atoms are omitted. Selected bond lengths [Å] and angles [°]: Ge1–Ge2 2.2429(6), Si3–Ge1 2.4168(10), Si3–Ge2 2.4165(10), Ge1–Si4 2.3995(11), Ge2–Si5 2.3943(11), Si3–Si6 2.3993(13), Si3–Si7 2.4033(13); Ge2–Ge1–Si3 62.34(11), Ge1–Ge2–Si3 62.36(3), Ge1–Si3–Ge2 55.30(2). The torsional angle Si4–Ge1–Ge2–Si5 is 51.0(2)°.

By employing the same synthetic approach, we were able to prepare the corresponding Ge₃ analogue, tetrakis(di-*tert*-butylmethylsilyl)-1*H*-trigermirene (**1b**), by the reaction of dilithiogermene R₂GeLi₂^[10] and tetrachlorodigermene RCl₂Ge–GeCl₂R in toluene (Scheme 1). As with **1a**, compound **1b** was formed along with R₂Ge=GeR₂ (**2b**) in a 2:1 ratio.

The reactivity of the new cyclic digermenes **1a** and **1b** proved to be very interesting. Compounds **1a** and **1b** readily react with an excess of CH₂Cl₂ at room temperature to produce the new four-membered-ring compounds, *trans*-2,4-dichloro-1,1,2,4-tetrakis(di-*tert*-butylmethylsilyl)[1,2,4]sila-digermetane (**5a**) and *trans*-1,3-dichloro-1,2,2,3-tetrakis(di-*tert*-butylmethylsilyl)[1,2,3]trigermetane (**5b**), respectively, as the result of ring expansion (Scheme 2).



Scheme 2. Reaction of **1a** and **1b** with CH₂Cl₂ along with the proposed mechanism for the formation of [1,2,4]siladigermetane **5a** and [1,2,3]trigermetane **5b**. R = SiMe₂Bu₂.

Surprisingly, the ¹H NMR spectra of **5a** and **5b** display markedly downfield-shifted resonances for the skeletal methylene protons: δ = 2.79 and 2.98 ppm, respectively.^[11] This unusual feature might be attributed to a hyperconjugative σ(C–H)–σ*(Ge–Cl) interaction, which would result in a downfield shift of the signal of the CH₂ protons. The crystal structure analysis of **5a**^[8] demonstrates a folded SiGe₂C four-membered ring (folding angle 33°) with long skeletal Si–Ge bonds of 2.475(2) and 2.547(3) Å (typical values 2.384–2.462 Å^[12]), which could be due to steric congestion around the Ge1–Si2–Ge3 unit (Figure 2). The long Ge–Cl bonds of 2.229(2)–2.236(2) Å are another interesting feature, as they exceed the normal values of 2.08–2.15 Å.^[12] The formation of **5a** and **5b** may involve initial 1,2-addition of a molecule of CH₂Cl₂ across the Ge=Ge bond of **1a** and **1b** to form the intermediate cyclopropane-type derivatives **4a** and **4b**,^[13] followed by intramolecular insertion of the methylene unit into the neighboring endocyclic Ge–Ge bond (Scheme 2). Indeed, calculations at the B3LYP/6-31G(d) level with the GAUSSIAN 98 program on model compounds of **5a** and **4a** with R=SiH₃ showed that the final four-membered ring **5a** is 41.7 kcal mol^{−1} more stable than the intermediate three-membered ring **4a**.

We found that CH₂Cl₂ is a unique reagent with respect to its reactivity toward the heavy cyclopropene analogues **1a** and **1b**. For example, CCl₄ reacts with **1a** and **1b** to form the

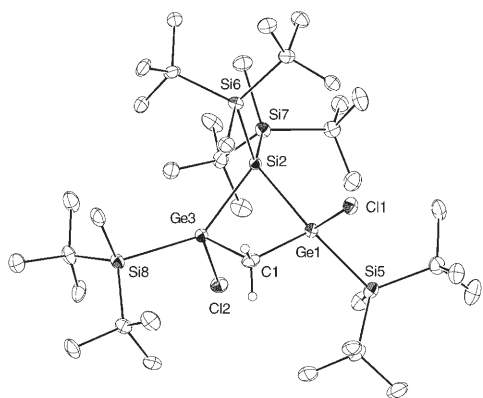
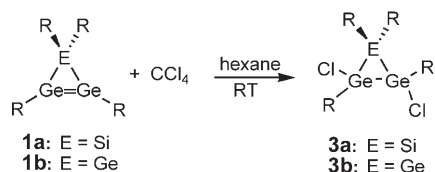


Figure 2. ORTEP plot of the crystal structure of **5a**; the thermal ellipsoids are shown at the 30% probability level and hydrogen atoms are omitted. Selected bond lengths [Å] and angles [°]: Si2–Ge1 2.547(3), Si2–Ge3 2.475(2), Ge1–C1 1.998(10), Ge3–C1 1.956(10), Ge1–Cl1 2.229(2), Ge3–Cl2 2.236(2); Ge1–Si2–Ge3 73.88(6), Si2–Ge3–C1 90.0(3), Ge3–C1–Ge1 99.5(4), C1–Ge1–Si2 87.0(3).

corresponding dichloro derivatives 2,3-dichloro-1,1,2,3-tetrakis(di-*tert*-butylmethylsilyl)siladigermirane (**3a**) and 1,2-dichloro-1,2,3,3-tetrakis(di-*tert*-butylmethylsilyl)trigermirane (**3b**), instead of the ring-expansion products (Scheme 3).^[14]



Scheme 3. Reaction of **1a** and **1b** with CCl_4 with formation of 2,3-dichlorosiladigermirane **3a** and 1,2-dichlorotrigermirane **3b**. $\text{R} = \text{SiMe}_2\text{Bu}_2$.

The reaction with CHCl_3 results in complicated product mixtures. The ring-expansion reaction with CH_2Cl_2 is general for all heavy cyclopropene analogues of the type $\text{R}_4\text{EE}'_2$ ($\text{R} = \text{SiMe}_2\text{Bu}_2$; $\text{E}, \text{E}' = \text{Si}, \text{Ge}$). Thus, the previously reported 1*H*-trisilirene R_4Si_3 ^[2b] as well as the 3*H*- and 1*H*-disiladigermirenes R_4GeSi_2 ^[4] smoothly react with CH_2Cl_2 to produce four-membered rings that are isostructural to **5a** and **5b**.

Experimental Section

1a: A mixture of $(t\text{Bu}_2\text{MeSi})_2\text{SiLi}_2$ —prepared from 1,1-bis(di-*tert*-butylmethylsilyl)-2,3-bis(trimethylsilyl)-1-silacycloprop-2-ene (500 mg, 0.98 mmol) and Li (35 mg, 5.00 mmol) in THF (4 mL)—and $t\text{Bu}_2\text{MeSi-GeCl}_2\text{-GeCl}_2\text{-SiMe}_2\text{Bu}_2$ (200 mg, 0.33 mmol) was placed in a reaction tube with a magnetic stirrer bar. Dry, oxygen-free toluene (4 mL) was introduced by vacuum transfer, and the dark green reaction mixture was stirred for 1 h at room temperature. After the inorganic salts were removed by filtration and the solvent was removed under vacuum, the residue was taken up in hexane and separated by column chromatography on silica gel (eluent: hexane) in a glove box. Recrystallization of the appropriate fraction from pentane at -30°C produced pure **1a** as dark red crystals (68 mg, 26%), m.p.: 193–195°C; ^1H NMR (300.1 MHz, $[\text{D}_6]\text{benzene}$, TMS): $\delta = 0.43$ (s, 6H), 0.53 (s, 6H), 1.21 (s, 36H), 1.30 ppm (s, 36H);

$^{13}\text{C}\{^1\text{H}\}$ NMR (75.5 MHz, $[\text{D}_6]\text{benzene}$, TMS): $\delta = -3.9, -2.1, 22.8, 23.4, 29.8, 31.2$ ppm; $^{29}\text{Si}\{^1\text{H}\}$ NMR (59.6 MHz, $[\text{D}_6]\text{benzene}$, TMS): $\delta = -110.6$ (cyclic Si), 5.8 and 40.8 ppm (substituent Si); UV/Vis (hexane): λ_{max} (ϵ) = 470 (1200), 403 (1000), 311 (2400), 236 nm ($21800 \text{ m}^{-1}\text{cm}^{-1}$); elemental analysis (%) calcd for $\text{C}_{36}\text{H}_{84}\text{Ge}_2\text{Si}_5$: C 53.87, H 10.55; found: C 54.06, H 10.33.

1b: Compound **1b** was prepared from $(t\text{Bu}_2\text{MeSi})_2\text{GeLi}_2$ and $t\text{Bu}_2\text{MeSi-GeCl}_2\text{-GeCl}_2\text{-SiMe}_2\text{Bu}_2$ in 22% yield as dark red crystals; m.p.: 188–190°C; ^1H NMR (300.1 MHz, $[\text{D}_6]\text{benzene}$, TMS): $\delta = 0.46$ (s, 6H), 0.54 (s, 6H), 1.23 (s, 36H), 1.29 ppm (s, 36H); $^{13}\text{C}\{^1\text{H}\}$ NMR (75.5 MHz, $[\text{D}_6]\text{benzene}$, TMS) $\delta = -3.8, -1.9, 22.7, 23.7, 29.8, 31.0$ ppm; $^{29}\text{Si}\{^1\text{H}\}$ NMR (59.6 MHz, $[\text{D}_6]\text{benzene}$, TMS): $\delta = 17.0, 39.1$ ppm; UV/Vis (hexane): λ_{max} (ϵ) = 457 (700), 407 (700), 324 (2400), 234 nm ($13600 \text{ m}^{-1}\text{cm}^{-1}$); elemental analysis (%) calcd for $\text{C}_{36}\text{H}_{84}\text{Ge}_3\text{Si}_4$: C 51.04, H 9.99; found: C 50.71, H 9.77.

5a: A mixture (319 mg) of 2-siladigermirane **1a** and disilene **2a** (2:1) was placed in a reaction tube with a magnetic stirrer bar. Dry, oxygen-free CH_2Cl_2 (1 mL) and hexane (1 mL) were introduced by vacuum transfer, and the reaction mixture was stirred for 3 h at room temperature to give a dark blue solution. After removal of the solvents under vacuum, the residue was separated by column chromatography on silica gel (eluent: hexane) in a glove box. Two fractions were collected: the first blue fraction (**2a**) and the second pale yellow fraction (**5a**). After removal of the solvent under vacuum, the second fraction was recrystallized from hexane at -30°C to give pure **5a** as colorless crystals (173 mg, 71%), m.p.: 152–154°C; ^1H NMR (300.1 MHz, $[\text{D}_6]\text{benzene}$, TMS): $\delta = 0.46$ (s, 6H), 0.79 (s, 6H), 1.20 (s, 18H), 1.21 (s, 18H), 1.24 (s, 18H), 1.31 (s, 18H), 2.79 ppm (s, 2H, CH_2); $^{13}\text{C}\{^1\text{H}\}$ NMR (75.5 MHz, $[\text{D}_6]\text{benzene}$, TMS): $\delta = -4.8, 1.1, 22.5, 23.1, 23.5, 24.3, 29.8, 30.0, 31.4, 31.8, 42.6$ ppm; $^{29}\text{Si}\{^1\text{H}\}$ NMR (59.6 MHz, $[\text{D}_6]\text{benzene}$, TMS): $\delta = 21.5$ and 28.6 (substituent Si), 30.7 ppm (cyclic Si); elemental analysis (%) calcd for $\text{C}_{37}\text{H}_{86}\text{Cl}_2\text{Ge}_2\text{Si}_5$: C 50.07, H 9.77; found: C 49.81, H 9.82.

5b: Compound **5b** was prepared from a mixture of **1b** and **2b** in 69% yield as colorless crystals; m.p.: 149–152°C; ^1H NMR (300.1 MHz, $[\text{D}_6]\text{benzene}$, TMS): $\delta = 0.46$ (s, 6H), 0.84 (s, 6H), 1.201 (s, 18H), 1.203 (s, 18H), 1.23 (s, 18H), 1.30 (s, 18H), 2.98 ppm (s, 2H, CH_2); $^{13}\text{C}\{^1\text{H}\}$ NMR (75.5 MHz, $[\text{D}_6]\text{benzene}$, TMS): $\delta = -4.9, 1.3, 22.9, 23.3, 23.5, 24.2, 29.8, 30.0, 31.2, 31.6, 44.9$ ppm; $^{29}\text{Si}\{^1\text{H}\}$ NMR (59.6 MHz, $[\text{D}_6]\text{benzene}$, TMS): $\delta = 27.7, 31.0$ ppm; elemental analysis (%) calcd for $\text{C}_{37}\text{H}_{86}\text{Cl}_2\text{Ge}_3\text{Si}_4$: C 47.68, H 9.30; found: C 47.74, H 9.32.

Received: May 31, 2005

Published online: September 7, 2005

Keywords: germanium · group 14 elements · ring expansion · silicon · small ring systems

- [1] a) S. Masamune, W. Hanzawa, S. Murakami, T. Bally, J. F. Blount, *J. Am. Chem. Soc.* **1982**, *104*, 1150; b) S. Masamune, W. Hanzawa, D. J. Williams, *J. Am. Chem. Soc.* **1982**, *104*, 6137; c) S. Masamune, L. R. Sita, D. J. Williams, *J. Am. Chem. Soc.* **1983**, *105*, 630.
- [2] a) Cyclotrigermene: A. Sekiguchi, H. Yamazaki, C. Kabuto, H. Sakurai, S. Nagase, *J. Am. Chem. Soc.* **1995**, *117*, 8025; b) Cyclo-trisilene: M. Ichinohe, T. Matsuno, A. Sekiguchi, *Angew. Chem.* **1999**, *111*, 2331; *Angew. Chem. Int. Ed.* **1999**, *38*, 2194; c) T. Iwamoto, C. Kabuto, M. Kira, *J. Am. Chem. Soc.* **1999**, *121*, 886; d) cyclotristannene: N. Wiberg, H.-W. Lerner, S.-K. Vasisht, S. Wagner, K. Karaghiosoff, H. Nöth, W. Ponikwar, *Eur. J. Inorg. Chem.* **1999**, 1211.
- [3] a) V. Ya. Lee, A. Sekiguchi in *The Chemistry of Organic Germanium, Tin, and Lead Compounds*, Vol. 2, Part 1 (Ed.: Z. Rappoport), Wiley, Chichester, UK, **2002**, chap. 14; b) A. Sekiguchi, V. Ya. Lee, *Chem. Rev.* **2003**, *103*, 1429.

- [4] V. Ya. Lee, M. Ichinohe, A. Sekiguchi, N. Takagi, S. Nagase, *J. Am. Chem. Soc.* **2000**, *122*, 9034.
- [5] M. Ichinohe, Y. Arai, A. Sekiguchi, N. Takagi, S. Nagase, *Organometallics* **2001**, *20*, 4141.
- [6] A. Sekiguchi, S. Inoue, M. Ichinohe, Y. Arai, *J. Am. Chem. Soc.* **2004**, *126*, 9626.
- [7] The dichloride **3a**, independently synthesized by the reaction of **1a** with CCl_4 , immediately reacts with an equivalent amount of R_2SiLi_2 to form exclusively **1a** and **2a** in a 2:1 ratio.
- [8] Crystal structure analyses of **1a** and **5a**: The single crystals were grown from saturated solutions in hexane. The diffraction data were collected at 120 K on a MacScience DIP2030 Image Plate Diffractometer employing graphite-monochromated $\text{MoK}\alpha$ radiation ($\lambda = 0.71070 \text{ \AA}$). Crystal data for **1a** ($\text{C}_{36}\text{H}_{84}\text{Ge}_2\text{Si}_5$): $M_r = 802.66$, monoclinic, space group $P2_1/c$, $a = 24.1020(6)$, $b = 11.6190(9)$, $c = 17.7300(16) \text{ \AA}$, $\beta = 110.206(4)^\circ$, $V = 4659.6(6) \text{ \AA}^3$, $Z = 4$, $\rho_{\text{calcd}} = 1.144 \text{ g cm}^{-3}$, $\text{GOF} = 1.008$. The final R factor was 0.0544 ($R_w = 0.1611$ for all data) for 7455 reflections with $I_o > 2\sigma(I_o)$. Crystal data for **5a** ($\text{C}_{37}\text{H}_{86}\text{Cl}_2\text{Ge}_2\text{Si}_5$): $M_r = 887.59$, monoclinic, space group Cc , $a = 23.1270(16)$, $b = 12.4550(14)$, $c = 17.8730(19) \text{ \AA}$, $\beta = 109.567(6)^\circ$, $V = 4850.9(8) \text{ \AA}^3$, $Z = 4$, $\rho_{\text{calcd}} = 1.215 \text{ g cm}^{-3}$, $\text{GOF} = 0.999$. The final R factor was 0.0580 ($R_w = 0.1548$ for all data) for 3834 reflections with $I_o > 2\sigma(I_o)$. The structures were solved by direct methods and refined by full-matrix least-squares methods using the SHELXL-97 program. CCDC 273374 (**1a**) and 273375 (**5a**) contain the supplementary crystallographic data for this paper. These data can be obtained free of charge from the Cambridge Crystallographic Data Centre via www.ccdc.cam.ac.uk/data_request/cif.
- [9] The Ge=Ge bond is typically *trans*-bent: P. P. Power, *Chem. Rev.* **1999**, *99*, 3463.
- [10] A. Sekiguchi, R. Izumi, S. Ihara, M. Ichinohe, V. Ya. Lee, *Angew. Chem.* **2002**, *114*, 1668; *Angew. Chem. Int. Ed.* **2002**, *41*, 1598.
- [11] This is in a sharp contrast to other known cyclobutane derivatives containing $-\text{RR}'\text{Si}-\text{CH}_2-\text{SiRR}'-$ fragments, which typically exhibit ^1H NMR resonances for CH_2 groups in the upfield region ($\delta = 0.18\text{--}0.89 \text{ ppm}$): a) J.-H. Hong, J. S. Han, G.-H. Lee, I. N. Jung, *J. Organomet. Chem.* **1992**, *437*, 265; b) J. Braddock-Wilking, M. Y. Chiang, P. P. Gaspar, *Organometallics* **1993**, *12*, 197.
- [12] K. M. Baines, W. G. Stibbs, *Coord. Chem. Rev.* **1995**, *145*, 157.
- [13] The 1,2-addition of chloroalkanes (CH_2Cl_2 , CHCl_3 , CCl_4) to stable tetrasilyldisilenes (M. Kira, T. Ishima, T. Iwamoto, M. Ichinohe, *J. Am. Chem. Soc.* **2001**, *123*, 1676) and some transient digermenes ($\text{Me}_2\text{Ge}=\text{GeMe}_2$: K. Mochida, T. Kayamori, M. Wakasa, H. Hayashi, M. P. Egorov, *Organometallics* **2000**, *19*, 3379; $\text{Me}_3\text{Ge}=\text{GeMe}_3$: M. S. Samuel, M. C. Jennings, K. M. Baines, *Organometallics* **2001**, *20*, 590) has been reported.
- [14] Similar dichloro derivatives were formed upon reaction of 1*H*-trisilirene $\text{R}_3\text{Si}_3^{[2b]}$ as well as the 3*H*- and 1*H*-disilagermirenes $\text{R}_4\text{GeSi}_2^{[4]}$ ($\text{R} = \text{SiMe}_2\text{Bu}$) with CCl_4 : V. Ya. Lee, T. Matsuno, M. Ichinohe, A. Sekiguchi, *Heteroat. Chem.* **2001**, *12*, 223.

DOI: 10.1002/anie.200501955

Highly Enantioselective *sec*-Alkyl Sulfatase Activity of the Marine Planctomycete *Rhodopirellula baltica* Shows Retention of Configuration**

Sabine R. Wallner, Marga Bauer, Chris Würdemann, Patricia Wecker, Frank O. Glöckner, and Kurt Faber*

The molecular mechanisms of the commonly employed hydrolases involve nucleophilic attack onto the carbonyl group of carboxylic acids or their derivatives.^[1,2] As this group is a planar entity, any stereochemical alterations of the substrate caused by enzymatic catalysis are impossible, and as a consequence, enantiomers of the transformed substrate and product are usually homochiral (with the exception of prochiral or *meso* esters), that is, they have the same absolute configuration. Although the stereochemical features of the substrate, such as stereogenic centers (in racemates) or enantiotopic groups (in prochiral or *meso* compounds), are “recognized” by the enzyme, which gives rise to differences in k_{cat} and/or K_{M} values, they remain unchanged during catalysis.

Biocatalysts, which elicit the more complex potential to affect the stereochemistry of the substrate in a controlled fashion during catalysis, are rather rare and encompass haloalkane dehalogenases,^[3] epoxide hydrolases,^[4] and (alkyl) sulfatases.^[5,6] In each case, a C(sp³) atom could potentially be involved in the catalysis and therefore open the possibility of stereocomplementary pathways. These enzymes do not only display enantioselectivity (through the transformation of one substrate enantiomer faster than the other) but also stereoselectivity (with retention or inversion of configuration). This therefore makes them important catalytic tools for the development of so-called enantioconvergent processes in which each enantiomer from a racemic mixture is transformed into the same product through independent pathways, that is, through retention and inversion of configuration.^[7] As a consequence, a racemate can be

[*] Dr. S. R. Wallner, Prof. K. Faber
Research Centre for Applied Biocatalysis
Department of Chemistry, Organic and Bioorganic Chemistry
University of Graz
Heinrichstrasse 28, 8010 Graz (Austria)
Fax: (+43) 316-380-9840
E-mail: Kurt.Faber@Uni-Graz.at
Dr. M. Bauer, C. Würdemann, P. Wecker, Dr. F. O. Glöckner
MPI Marine Microbiology
Celsiusstrasse 1, 28359 Bremen (Germany)

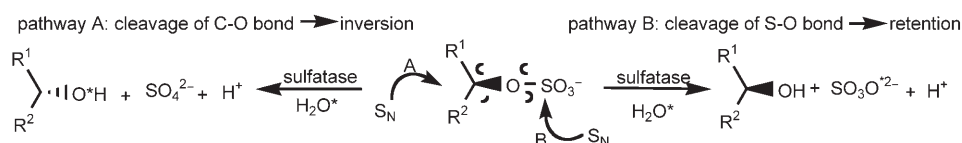
[**] This study was performed within the Research Centre for Applied Biocatalysis. Financial support by the FFG, the City of Graz, and the Province of Styria is gratefully acknowledged. L. Arbanas, T. Glieder, W. Kroutil, and U. Wagner (Graz) are thanked for their valuable contributions in sequence analysis.



Supporting information for this article is available on the WWW under <http://www.angewandte.org> or from the author.

converted, in principle, into a single stereoisomeric product without the occurrence of an undesired stereoisomer.

Sulfatases catalyze the hydrolytic cleavage of the sulfate ester bond (Scheme 1). Depending on the enzyme subtype, the stereochemical course of sulfate ester hydrolysis can be



Scheme 1. Enzymatic stereodivergent hydrolysis of sulfate esters catalyzed by sulfatases.

controlled by an appropriate enzyme. On the one hand, inverting sulfatases^[8,9] were shown to act on *sec*-alkyl sulfate esters by breaking the C–O bond of the sulfate ester, which resulted in inversion of configuration (Scheme 1, pathway A). However, nothing is known about their mechanism of action. Based on limited knowledge of the stereospecific and enantioselective hydrolysis of alkyl sulfate esters,^[8] we recently reported an inverting alkyl sulfatase (termed “RS2”) from *Rhodococcus ruber* DSM 44541.^[10–12] Although the enzyme exhibited absolute stereospecificity through strict inversion of configuration of simple *sec*-alkyl sulfate esters, its enantioselectivity was less than perfect and its substrate tolerance was rather narrow. These limitations could be circumvented through the use of aerobically grown sulfur metabolizers. In particular, *Sulfolobus* spp., which exhibited not only enhanced enantioselectivities but also a broader substrate spectrum,^[13] showed a stereoselectivity identical to that of “RS2”, that is, inversion of configuration was observed.

To exploit the full potential of the enzymatic hydrolysis of alkyl sulfate esters, stereocomplementary sulfatases that act with retention of configuration were needed. In contrast to inverting sulfatases, the mechanism of action of retaining sulfatases is well understood (Scheme 2).^[14,15] The mechanism

was elucidated during structural studies on human aryl sulfatase A^[16] and was shown to proceed through cleavage of the S–O bond.^[17] The latter is effected by nucleophilic attack of an aldehyde hydrate (formed from a Cys or Ser residue by post-translational modification^[18]) onto the sulfur atom; the result is liberation of the corresponding alcohol and retention of its stereochemistry (Scheme 2).^[19]

The same principle of catalysis was shown to occur in sulfatases from *Pseudomonas aeruginosa*^[20] and *Klebsiella pneumoniae*.^[21] As the natural substrates of these enzymes are believed to be glycosyl and aryl sulfate esters,^[16]

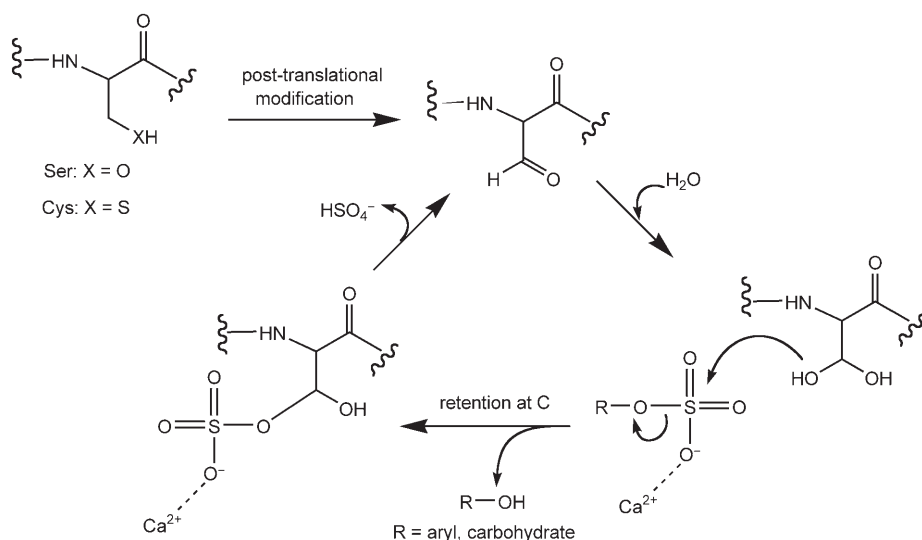
nothing is known about their enantioselectivities. Our search for a suitable microbial source for retaining (alkyl) sulfatase activity was led by the fact that all known sulfatases that act through the above-mentioned mechanism have the canonical sulfatase consensus motif C/S-X-P-X-R-X₄-T-G.^[18,22,23,27] This sequence motif encompasses sulfatases from mammals, lower eukaryotes, and prokaryotes,^[24] but is absent in the inverting alkyl sulfatase RS2 from *Rhodococcus ruber*.^[25]

A recently published complete genome sequence of the marine planctomycete *Rhodopirellula baltica* DSM 10527 (formerly denoted as *Pirellula* sp. 1)^[26,27] revealed the existence of an unexpectedly high number of 110 genes putatively encoding sulfatases. It is believed that, in *R. baltica*, these enzymes play a vital role in the metabolism of sulfated carbohydrates, such as chondroitin. Of the 110 potential sulfatase sequences, 85 show the conserved “core” of the sulfatase consensus motif C-X-P-X-R, which is required in post-translational modification to render activated sulfatase proteins. Furthermore, each of the 85 sequences contains the adjacent “auxiliary” part of the consensus motif, X₄-T-G, either fully conserved or only slightly modified. This part of the sulfatase consensus motif has been implicated in modulating the efficiency of the post-translational modification step.^[24] According to the sequence–function relationships

proposed for both eukaryotic and prokaryotic sulfatases,^[20,22,24] the 85 putative sulfatases from *R. baltica* were expected to act through retention of configuration.

To prove this hypothesis, a set of *sec*-alkyl sulfate esters, *rac*-**1a–9a** and the primary sulfate ester **10a** were screened by using resting whole cells of *R. baltica* DSM 10527 (Table 1). In general, the enantiopreference was shown to be *R*, that is, *R* enantiomers were preferentially hydrolyzed from the racemate, while *S* enantiomers remained untouched.

R. baltica displayed excellent activities on linear (ω -1)-sulfate esters *rac*-**1a–3a** (Table 2, entries 1–3), which were readily accepted as substrates. Surprisingly, even sterically demanding sulcatyl sulfate (*rac*-**4a**), which was accepted by neither sulfatase RS2 nor *Sulfolobus* spp., was converted with good rates. Concerning the



Scheme 2. Schematic representation of the mechanism of action of retaining (aryl) sulfatases.

Table 1: Enantioselective hydrolysis of *sec*-alkyl sulfates with retention of configuration.

Compound	R ¹	R ²
1a,b	CH ₃	<i>n</i> -C ₆ H ₁₃
2a,b	CH ₃	<i>n</i> -C ₅ H ₁₁
3a,b	CH ₃	<i>n</i> -C ₇ H ₁₅
4a,b	CH ₃	(CH ₃) ₂ C=CH(CH ₂) ₂
5a,b ^[a]	CH ₃	PhCH ₂
6a,b ^[a]	CH ₃	Ph(CH ₂) ₂
7a,b	<i>n</i> -C ₂ H ₅	<i>n</i> -C ₅ H ₁₁
8a,b	<i>n</i> -C ₃ H ₇	<i>n</i> -C ₄ H ₉
9a,b ^[b]	CH ₂ =CH	<i>n</i> -C ₅ H ₁₁
10a,b	H	<i>n</i> -C ₇ H ₁₅

[a] No conversion. [b] Opposite absolute configuration due to a switch in Cahn—Ingold priority (CIP) assignment of R¹ and R².

Table 2: Hydrolysis of sulfate esters using glucose-grown *Rhodopirellula baltica* DSM 10527.

Entry	Substrate	Conversion [%]	Product	<i>ee</i> [%]	Enantioselectivity (<i>E</i> value)
1	<i>rac</i> - 1a	16	(<i>R</i>)- 1b	> 99	> 200
2	<i>rac</i> - 2a	13	(<i>R</i>)- 2b	> 99	> 200
3	<i>rac</i> - 3a	18	(<i>R</i>)- 3b	> 99	> 200
4	<i>rac</i> - 4a	11	(<i>R</i>)- 4b	> 99	> 200
5	<i>rac</i> - 5a	n.c.	—	—	—
6	<i>rac</i> - 6a	n.c.	—	—	—
7	<i>rac</i> - 7a	3	(<i>R</i>)- 7b	48	3
8	<i>rac</i> - 8a	10	(<i>R</i>)- 8b	29	2
9	<i>rac</i> - 9a	6	(<i>S</i>)- 9b ^[a]	42	3
10	10a	26	10b	n.a.	n.a.

[a] Absolute configuration is *S* owing to a switch in CIP priority rules, however, it is homochiral to (*R*)-**1b–4b**, **7b**, **8b**. n.c. = no conversion; n.a. = not applicable. *E* values were calculated from $E = \{\ln[1 - c(1 + ee_p)]\} / \{\ln[1 - c(1 - ee_p)]\}$ where *c* = conversion and *ee_p* = enantiomeric excess of product.

enantioselectivities, all four substrates (Table 2, entries 1–4) showed perfect *E* values (> 200) and the corresponding *R* alcohols **1b–4b** were obtained with excellent *ee* values (> 99%). However, in the case of phenyl-substituted substrates (Table 2, entries 5 and 6), no conversion was observed. As R¹ and R² became similar in size, yielding near-symmetrical compounds (Table 2, entries 7–9), the enantioselectivities decreased as was observed in previous studies on inverting sulfatases.^[9,10,13] As *R. baltica* has more than 100 genes that encode putative sulfatases, it is not surprising that the primary sulfate ester **10a** was readily converted as well.

Stereochemical analysis of the products suggested that the hydrolysis pathway proceeded with retention of configuration. For unambiguous proof, enantiopure (*R*)-2-octyl sulfate was used as the substrate, which yielded (*R*)-2-octanol

without racemization in > 99% *ee*; analogously, enantiopure (*S*)-2-octyl sulfate remained untouched. Screening of the extracellular medium did not show any activity, which suggests that these sulfatases are intracellular. Using *R. baltica* grown on various C sources—glucose, chondroitin sulfate A,^[28] and chondroitin sulfate C—did not lead to significant differences in either activity or selectivity, thus indicating that no enzyme induction takes place. This suggests that the observed activity can, most likely, be associated with a “broad-spectrum sulfatase” rather than with separate primary- or *sec*-alkyl sulfatases.

In summary, the first highly enantioselective *sec*-alkyl sulfatase that acts with strict retention of configuration was detected in *R. baltica* DSM 10527 through a sequence-similarity approach. The use of this sulfatase in combination with a stereocomplementary inverting enzyme from *Sulfolobus* spp. in a deracemization strategy is currently being investigated.^[29]

Received: June 6, 2005

Published online: September 14, 2005

Keywords: enantioselectivity · hydrolysis · stereoselectivity · sulfatases · sulfate esters

- [1] This may be an ester, amide, lactone, hydantoin, lactam, or some thio derivative.
- [2] U. T. Bornscheuer, R. J. Kazlauskas, *Hydrolases in Organic Synthesis*, Verlag Chemie, Weinheim, 1999.
- [3] a) P. E. Swanson, *Curr. Opin. Biotechnol.* **1999**, *10*, 365–369; b) T. Kurihara, N. Esaki, K. Soda, *J. Mol. Catal. B* **2000**, *10*, 57–65; c) S. Fetzner, F. Lingens, *Microbiol. Rev.* **1994**, *58*, 641–685; d) D. B. Janssen, F. Pries, J. R. van der Ploeg, *Annu. Rev. Microbiol.* **1994**, *48*, 163–191.
- [4] a) E. J. de Vries, D. B. Janssen, *Curr. Opin. Biotechnol.* **2003**, *14*, 414–420; b) R. V. A. Orru, A. Archelas, R. Furstoss, K. Faber, *Adv. Biochem. Eng./Biotechnol.* **1999**, *63*, 145–167.
- [5] a) K. S. Dodgson, G. F. White, J. W. Fitzgerald, *Sulfatases of Microbial Origin, Vols. 1 and 2*, CRC Press, Boca Raton, FL, **1982**; b) S. R. Hanson, M. D. Best, C.-H. Wong, *Angew. Chem.* **2004**, *116*, 5858–5886; *Angew. Chem. Int. Ed.* **2004**, *43*, 5736–5763.
- [6] S. R. Wallner, M. Pogorevc, H. Trauthwein, K. Faber, *Eng. Life Sci.* **2004**, *4*, 512–516.
- [7] a) K. Faber, *Chem. Eur. J.* **2001**, *7*, 5004–5010; b) K. Faber, W. Kroutil, *Tetrahedron: Asymmetry* **2002**, *13*, 377–382; c) U. T. Strauss, U. Felfer, K. Faber, *Tetrahedron: Asymmetry* **1999**, *10*, 107–117; d) W. Kroutil, M. Mischitz, K. Faber, *J. Chem. Soc. Perkin Trans. 1* **1997**, 3629–3636; e) S. Pedragosa-Moreau, A. Archelas, R. Furstoss, *J. Org. Chem.* **1993**, *58*, 5533–5536.
- [8] a) D. J. Shaw, K. S. Dodgson, G. F. White, *Biochem. J.* **1980**, *187*, 181–196; b) B. Bartholomew, K. S. Dodgson, G. W. J. Matcham, D. J. Shaw, G. F. White, *Biochem. J.* **1977**, *165*, 575–580; c) G. F. White, *Appl. Microbiol. Biotechnol.* **1991**, *35*, 312–316.
- [9] M. Pogorevc, W. Kroutil, S. R. Wallner, K. Faber, *Angew. Chem.* **2002**, *114*, 4230–4231; *Angew. Chem. Int. Ed.* **2002**, *41*, 4052–4054.
- [10] M. Pogorevc, K. Faber, *Tetrahedron: Asymmetry* **2002**, *13*, 1435–1441.
- [11] M. Pogorevc, K. Faber, *Appl. Environ. Microbiol.* **2003**, *69*, 2810–2815.
- [12] M. Pogorevc, U. T. Strauss, T. Riermeier, K. Faber, *Tetrahedron: Asymmetry* **2002**, *13*, 1443–1447.

- [13] a) S. R. Wallner, B. M. Nestl, K. Faber, *Org. Lett.* **2004**, 6, 5009–5010; b) S. R. Wallner, B. M. Nestle, K. Farbe, *Org. Biomol. Chem.* **2005**, 3, 2652–2656
- [14] R. von Bülow, B. Schmidt, T. Dierks, K. von Figura, I. Uson, *J. Mol. Biol.* **2001**, 305, 269–277.
- [15] G. Lukatela, N. Krauss, K. Theis, T. Selmer, V. Gieselmann, K. von Figura, W. Saenger, *Biochemistry* **1998**, 37, 3654–3664.
- [16] Aryl sulfatases have often been wrongly annotated because they are able to hydrolyze “surrogate” aromatic sulfate esters such as 4-nitrophenyl sulfate or nitrocatechol sulfate; however, their natural substrates are aliphatic or carbohydrate sulfates.^[22]
- [17] I. Boltes, H. Czapinska, A. Kahnert, R. von Bülow, T. Dierks, B. Schmidt, K. von Figura, M. A. Kertesz, I. Uson, *Structure* **2001**, 9, 483–491.
- [18] T. Dierks, C. Miech, J. Hummerjohann, B. Schmidt, M. A. Kertesz, K. von Figura, *J. Biol. Chem.* **1998**, 273, 25560–25564.
- [19] a) E. J. Sampson, E. V. Vergara, J. M. Fedor, M. O. Funk, S. J. Benkovic, *Arch. Biochem. Biophys.* **1975**, 169, 372–383; b) V. Lillis, K. S. Dodgson, G. F. White, W. J. Payne, *Appl. Environ. Microbiol.* **1983**, 46, 988–994.
- [20] I. Boltes, H. Czapinska, A. Kahnert, R. von Bülow, T. Dierks, B. Schmidt, K. von Figura, M. A. Kertesz, I. Uson, *Structure* **2001**, 9, 483–491.
- [21] C. Miech, T. Dierks, T. Selmer, K. von Figura, B. Schmidt, *J. Biol. Chem.* **1998**, 273, 4835–4837.
- [22] M. A. Kertesz, *FEMS Microbiol. Rev.* **1999**, 24, 135–175.
- [23] K. von Figura, T. Dierks, B. Schmidt, *BIOspektrum* **1999**, 5, 191–194.
- [24] T. Dierks, M. R. Lecca, P. Schlotterhose, B. Schmidt, K. Von Figura, *EMBO J.* **1999**, 18, 2084–2091.
- [25] L. Arbanas, T. Glieder, U. Wagner, W. Kroutil, unpublished results.
- [26] H. Schlesner, C. Rensmann, B. J. Tindall, D. Gade, R. Rabus, S. Pfeiffer, P. Hirsch, *Int. J. Syst. Evol. Microbiol.* **2004**, 54, 1567–1580.
- [27] F. O. Glöckner, M. Kube, M. Bauer, H. Teeling, T. Lombardot, W. Ludwig, D. Gade, A. Beck, K. Borzym, K. Heitmann, R. Rabus, H. Schlesner, R. Amann, R. Reinhardt, *Proc. Natl. Acad. Sci. USA* **2003**, 100, 8298–8303.
- [28] Chondroitin sulfate A bears a *sec*-sulfate ester (at position 4 on the sugar moiety), whereas chondroitin sulfate C bears a primary sulfate ester at position 6.
- [29] For a preliminary communication on the proof of principle, see reference [6].

DOI: 10.1002/anie.200502095

One-Pot Reaction Cascades Using Star Polymers with Core-Confined Catalysts**

Brett Helms, Steven J. Guillaudeu, Yu Xie,
Meredith McMurdo, Craig J. Hawker,* and
Jean M. J. Fréchet*

An attractive feature of dendritic systems, and possibly other highly branched polymers, is their ability to encapsulate and isolate various functional groups within the interior of the molecule.^[1] In many applications, from light harvesting to catalysis, the benefit derived from site isolation is typically the preservation of both the structure and activity of moieties that would normally be sensitive to quenching or deactivation if used as small molecules.^[2] Site isolation as such has been used since the work of Patchornik and co-workers with so-called “wolf and lamb” reactions, in which otherwise incompatible reagents on large heterogeneous particulate solid supports were used in mixed-bed reactors to perform multiple steps of a reaction sequence.^[3] More recent investigations of sol-gels with encapsulated opposing reagents have made the concept of “wolf and lamb” reactions emerge as a powerful tool to probe site-isolation effects in cross-linked solid materials.^[4] To our knowledge, this concept has never been applied to soluble molecular reagents, such as star polymers, although their synthetic accessibility relative to dendrimers makes them attractive targets for practical applications. Herein, we report a one-pot reaction cascade performed with two different star polymers, each containing a different catalytic group confined in its core. To demonstrate the synthetic utility that site isolation affords, we have devised a “wolf and lamb” test, in which otherwise incompatible acid and base catalysts are employed to effect the overall transformation. Our results clearly show that encapsulation of both acidic and basic groups within highly branched, yet fully soluble, multiarm star polymers suppresses their mutual deactivation, thus allowing for a sequence of acid and base reactions to be performed in succession (Figure 1). Thus, the concept of “wolf and lamb”

[*] Prof. C. J. Hawker

Materials Research Laboratory
University of California
Santa Barbara, CA 93106 (USA)
Fax: (+1) 805-893-8797
E-mail: hawker@chem.ucsb.edu

B. Helms, S. J. Guillaudeu, Y. Xie, M. McMurdo, Prof. J. M. J. Fréchet
Department of Chemistry
University of California
Berkeley, CA 94720 (USA)
Fax: (+1) 510-643-3079
E-mail: frechet@berkeley.edu

[**] This work was funded through the National Science Foundation (NSF-DMR0317514) and the Department of Energy (DE-AC03-76SF00098). Dr. Jeffrey Pyun contributed to early exploratory work on this project.

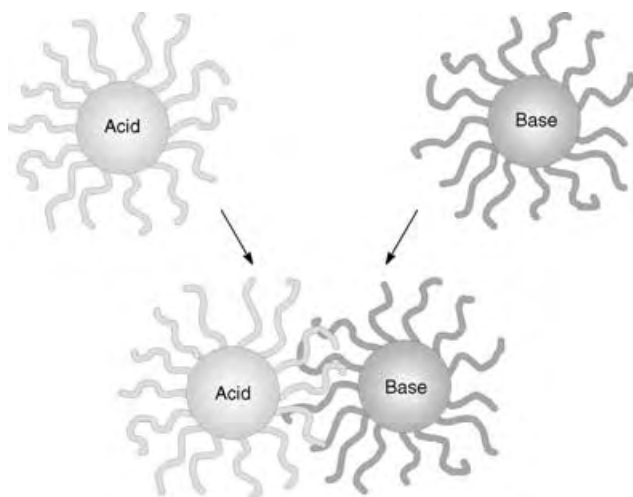


Figure 1. Acid- and base-containing star polymers with non-interpenetrating highly cross-linked cores.

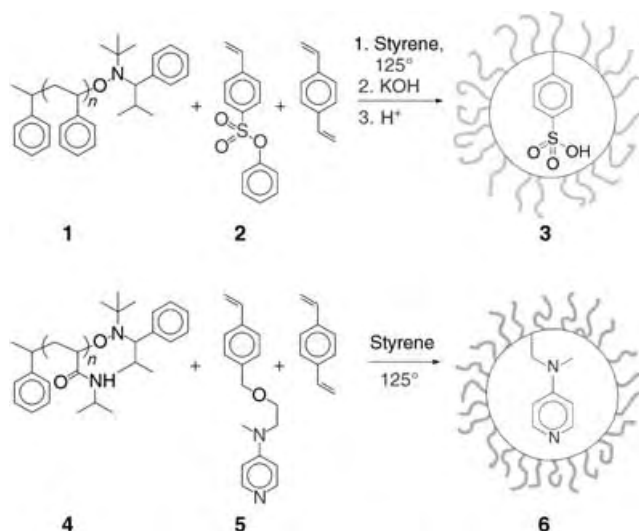
reactions, previously limited to immiscible solid reagents, has now been demonstrated successfully with reactive moieties attached to well-defined and sterically restricted locations within soluble synthetic macromolecules that are comparable in size to many proteins.

The preparation of highly branched multiarm star polymers with a narrow polydispersity has been an active area in polymer science as these materials provide quick access to globular macromolecules that bear some crude resemblance to the more structurally perfect dendrimers. Although syntheses of dendrimers have been well documented, it is only recently that techniques have been put forth to prepare well-defined star polymers without resorting to living anionic methods.^[5] We recently reported an “arm-first” approach based on nitroxide-mediated living free-radical polymerization.^[6]

Star polymers that contain analogues of *para*-toluenesulfonic acid (PTSA) groups at the core were prepared by using the arm-first approach. A low-molecular-weight polystyrene macroinitiator **1** was prepared in bulk from an α -hydridoalkoxyamine initiator and styrene at 125 °C (Scheme 1; size-exclusion chromatography (SEC) with THF: $M_n = 6250$, $M_w = 6730$, polydispersity index (PDI) = 1.07).^[7] Star polymers were then obtained by using a 1:4:10 ratio of **1**, divinylbenzene (DVB), and a mixture of co-monomers (styrene and the functional monomer phenyl 4-styrenesulfonate (**2**) in 3:2 ratio). The phenylsulfonate esters were saponified with KOH in methanolic THF and then acidified to generate the active form of the catalyst. The star polymers **3** thus obtained were of high molecular weight (SEC with THF: $M_n = 66150$, $M_w = 78530$; multiangle laser light scattering (MALLS): $M_n = 221200$, $M_w = 260200$) and narrow polydispersity (PDI = 1.19). Further examination of the SEC traces of **1** and **3** indicates clean conversion to the macromolecule without any low-molecular-weight polymer contaminants (Figure 2a), which is critical to achieve catalyst isolation. Elemental analysis of the sulfur content of **3** revealed 0.45 mmols of sulfonic acid groups per gram of polymer, or approximately 100 residues per star polymer. These values correspond to 3–4

acidic groups per arm for the 35–40-arm star polymer or 7–8 wt %.

Similarly, star polymer **6**, which contains amine moieties, was synthesized by the arm-first method from an *N*-isopropylacrylamide (NIPAAm) macroinitiator **4** (SEC with *N,N*-dimethylformamide (DMF): $M_n = 4450$, $M_w = 5890$, PDI = 1.32) and a styrene monomer **5** that contains a pendant 4-(dialkylamino)pyridine catalyst (Scheme 1). The same optimized ratio of 1:4:10 was used for the polymerization of **6** (SEC with DMF: $M_n = 59160$, $M_w = 110210$, PDI = 1.86; MALLS: $M_n = 526300$, $M_w = 640800$), with the co-monomer portion composed of styrene and **5** in a 1:1 ratio. Although the SEC data with DMF as the solvent (Figure 2b) indicate a less-controlled star polymerization and a higher molecular weight for **6** (approximately 100 arms per star) relative to **3**, we were satisfied with the absence of contamination by low-molecular-weight species and proceeded with the catalytic experiments. The catalyst loading for **6** was evaluated by using UV spectroscopy with 4-(dimethylamino)pyridine (DMAP) as the reference compound in CHCl_3 ($\lambda_{\text{max}} = 260 \text{ nm}$), with subtraction of any background absorbance from the poly-NIPAAm-core-(PS-co-DVB) star polymer. An upper value of 0.63 mmols of **5** per gram of polymer was measured which corresponds to approximately 350 catalytic groups per star polymer or 3 or 4 residues per arm. Therefore, the DMAP-



Scheme 1. Synthesis of star polymers that contain core-confined PTSA analogues or 4-(dialkylamino)pyridines.

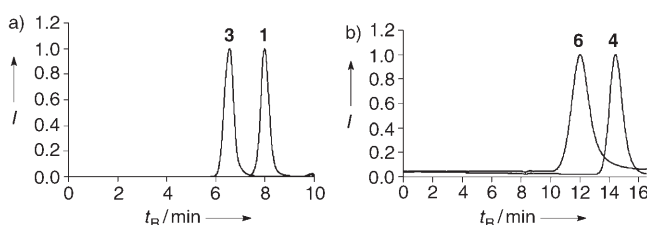
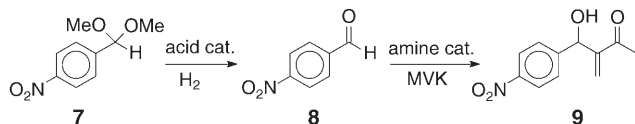


Figure 2. a) SEC traces with THF as the solvent for macroinitiator **1** and star polymer **3**; b) SEC traces with DMF as the solvent for macroinitiator **4** and star polymer **6**.

like residues constitute up to 5–7% of the weight in the polymer.

The chemical transformations targeted for this system were the acid-catalyzed deprotection of 4-nitrobenzaldehyde dimethyl acetal and the nucleophilic amine-catalyzed Baylis–Hillman reaction of 4-nitrobenzaldehyde with methyl vinyl ketone (MVK) (Scheme 2).^[8] As control experiments, reac-



Scheme 2. One-pot-reaction cascade involving sequential acid-catalyzed acetal hydrolysis followed by the amine-catalyzed Baylis–Hillman reaction.

tions were performed in the absence of any catalysts; with DMAP and PTSA; with non-polymer-bound DMAP and **3**; and with non-polymer-bound PTSA and **6** (Table 1).

Table 1: Catalytic results for the reaction cascade using acid and amine catalysts.

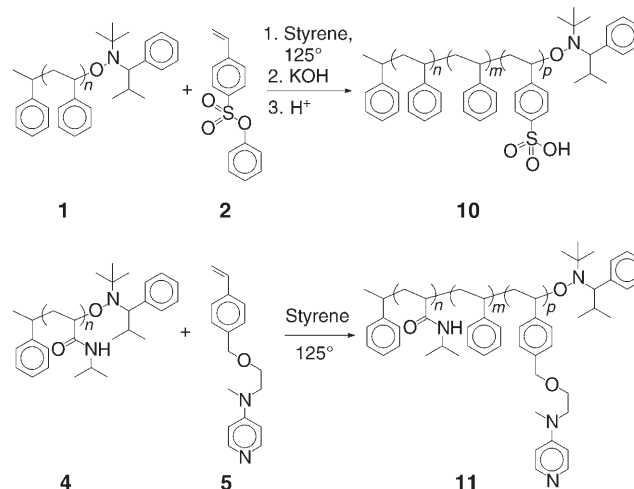
Entry	Acid catalyst ^[a]	Amine catalyst ^[a]	Yield of 8 [%] ^[b]	Yield of 9 [%] ^[b]
1	3	6	34	65
2	3	DMAP	9	0
3	PTSA	6	6	0
4	PTSA	DMAP	3	0
5	3	11	< 1	0
6	10	6	< 1	0
7	none	none	0	0

[a] Reaction conditions: 10 mol% acid and amine catalysts were used. $[7]_0 = 0.50$ M in DMF with H_2O (1 equiv) and MVK (4 equiv). The reaction mixtures were heated at 70 °C in sealed vials for 36 h. [b] Yields are based on GC-MS measurements with decane as the internal standard. The values represent an average of three runs.

Complete hydrolysis of the acetal was observed over the course of a few hours when the reaction was performed with **3** and **6**, and at the end of the experiment 65 % of the aldehyde had been converted into the Baylis–Hillman adduct. When either of the small-molecule catalysts DMAP or PTSA were added to **3** or **6**, respectively, only partial hydrolysis of the acetal was observed (Table 1, entries 2 and 3), which was also the case when PTSA and DMAP were added (entry 4). Finally, the acetal appears to be stable to hydrolysis when no catalysts are used (entry 7).

Given that a Baylis–Hillman adduct did not form in any of the entries except those in which both **3** and **6** were used, we reason that when the small molecules DMAP or PTSA are added to **3** and **6**, respectively, they can penetrate the cores of the star polymers and deactivate the acidic and basic groups through salt formation. The absence of reactivity for the resulting salt is confirmed by entry 4. The partial hydrolysis observed in entries 2 and 3 points to the difficulty of titrating the exact amount of catalyst in each internally cross-linked star polymer for a given reaction.

To examine further the site-isolation properties of these polymers, acid- or amine-containing diblock copolymers were synthesized from the same macroinitiators and functional monomers used in the preparation of **3** and **6** (Scheme 3). The



Scheme 3. Synthesis of diblock copolymers containing PTSA analogues or 4-(dialkylamino)pyridines.

acid-containing polymer **10** (SEC with THF: $M_n = 8170$, $M_w = 9090$, PDI = 1.11, 0.73 mmol of sulfur per gram polymer) and amine-containing polymer **11** (SEC with DMF: $M_n = 6980$, $M_w = 10050$, PDI = 1.44, 0.55 mmol of catalyst per gram polymer) were prepared to best resemble the star polymers in terms of composition but not architecture. When either of these diblock copolymer catalysts was used along with the complementary star polymer (namely, **3** with **11** or **10** with **6**, entries 5 and 6, respectively), the reaction cascade did not proceed. This result implies that the linear polymers can penetrate the corona of the star polymers with the same deleterious effects as either PTSA or DMAP, thus confirming our hypothesis that the catalysts must be confined to the sterically restricted core of the star polymers before the advantages of site isolation can be realized.

Thus, we have shown that core-confined groups in these high-molecular-weight, yet fully soluble, star polymers appear to be site isolated as is observed with moieties at the core of dendrimers. As a result of this site isolation, sequential catalysis of a “wolf and lamb” two-step reaction using catalytic species that are normally incompatible with each other is possible. This ability to generate a pathway by which a cascade of reactions is enabled is reminiscent of biological systems in which a series of discrete reactions performed by different enzymes is used to create a wide range of chemical functionality and diversity through the combination of a few simple steps.

Experimental Section

3: The polymerization mixture containing polystyrene macroinitiator **1** (1.93 g, 0.355 mmol; SEC with THF: $M_n = 6247$, $M_w = 6728$, PDI = 1.07), DVB (336 mg, 1.42 mmol; 55 wt %), styrene (221 mg, 2.13 mmol), and phenyl 4-styrenesulfonate (**2**; 369 mg, 1.42 mmol)

in DMF (7.28 g) was heated at 125 °C for 16 h. The reaction mixture was diluted with CH₂Cl₂ and precipitated on addition to *i*PrOH. Fractionation from benzene using methanol gave a solid, which was reprecipitated to give 2.54 g of the star polymer (89%). The star polymer (250 mg, 1.25 μmol) was treated with KOH (250 mg, 4.45 mmol) in MeOH/THF (9:1) at 50 °C for 16 h, acidified with H₂SO₄, and precipitated on addition to *i*PrOH to give a white solid (215 mg, 87%). ¹H NMR (500 MHz, CDCl₃): δ = 7.5–6.9 (br, Ar-H), 6.8–6.3 (br, Ar-H), 2.1–1.7 (br, -C(Ar)H-), 1.7–1.2 ppm (br, -CH₂-); IR (thin film): $\tilde{\nu}$ = 3600–3200, 3081, 3059, 3025, 2924, 2850, 1942, 1873, 1804, 1746, 1730, 1713, 1687, 1600, 1584, 1492, 1452, 1413, 1372, 1217, 1179, 1155, 1126, 1069, 1030, 1006, 907, 834, 758, 699, 667 cm⁻¹; SEC with THF: M_n = 66 150, M_w = 78 530, PDI = 1.19; MALLS: M_n = 221 200, M_w = 260 200.

6: The polymerization mixture containing polyNIPAAm macro-initiator **4** (280 mg, 69.4 μmol; SEC with DMF: M_n = 4453, M_w = 5888, PDI = 1.32), DVB (66 mg, 0.279 mmol; 55 wt %), styrene (36 mg, 0.344 mmol), and 4-(dialkylamino)pyridine monomer **5** (93 mg, 0.345 mmol) in DMF (1.35 g) was heated at 125 °C for 16 h. The reaction mixture was diluted with CH₂Cl₂ and precipitated on addition to cold diethyl ether. Fractionation from acetone using hexanes gave the solid, which then reprecipitated to give 120 mg of the star polymer (33%). ¹H NMR (500 MHz, CDCl₃): δ = 8.3–8.0 (br, Py-H; Py = pyridine), 7.1–6.2 (br, Ar-H, -NH-*i*Pr), 4.2–3.9 (br, -CH(Me)₂), 3.8–3.5 (br, N-CH₂-CH₂-O), 3.2–2.9 (br, N-CH₃), 2.5–2.3 (br, Ar-CH₂-O), 2.3–1.8 (br, -C(Ar)H-, -C(C=O)H-, -CH₂-), 1.8–1.5 (br, -CH₂-), 1.4–0.8 ppm (br, -CH(CH₃)₂); IR (thin film): $\tilde{\nu}$ = 2965, 2928, 1664, 1608, 1598, 1529, 1453, 1384, 1366, 1211, 1171, 1129, 989, 910, 804, 763, 701 cm⁻¹; SEC with DMF: M_n = 59 160, M_w = 110 210, PDI = 1.86; MALLS: M_n = 526 300, M_w = 640 800.

Received: June 16, 2005

Published online: September 14, 2005

Keywords: amines · dendrimers · homogeneous catalysis · polymers · reaction cascades

- [6] a) A. W. Bosman, R. Vestberg, A. Heumann, J. M. J. Fréchet, C. J. Hawker, *J. Am. Chem. Soc.* **2003**, *125*, 715–728; b) A. W. Bosman, A. Heumann, G. Klaerner, D. Benoit, J. M. J. Fréchet, C. J. Hawker, *J. Am. Chem. Soc.* **2001**, *123*, 6461–6462.
[7] D. Benoit, V. Chaplinski, R. Braslau, C. J. Hawker, *J. Am. Chem. Soc.* **1999**, *121*, 3904–3920.
[8] a) D. Basavaiah, A. J. Rao, T. Satyanarayana, *Chem. Rev.* **2003**, *103*, 811–891; b) J.-W. Huang, M. Shi, *Adv. Synth. Catal.* **2003**, *345*, 953–958.

- [1] S. Hecht, J. M. J. Fréchet, *Angew. Chem.* **2001**, *113*, 76–94; *Angew. Chem. Int. Ed.* **2001**, *40*, 74–91.
[2] a) C. Müller, L. J. Ackerman, J. N. H. Reek, P. C. J. Kamer, P. W. N. M. van Leeuwen, *J. Am. Chem. Soc.* **2004**, *126*, 14960–14963; b) L. F. Lee, A. Adronov, R. D. Schaller, J. M. J. Fréchet, R. J. Saykally, *J. Am. Chem. Soc.* **2003**, *125*, 536–540; c) E. M. Harth, S. Hecht, B. Helms, E. E. Malmström, J. M. J. Fréchet, C. J. Hawker, *J. Am. Chem. Soc.* **2002**, *124*, 3926–3938; d) D. Astruc, F. Chardac, *Chem. Rev.* **2001**, *101*, 2991–3023; e) R. M. Crooks, M. Zhao, L. Sun, V. Chechik, L. K. Yeung, *Acc. Chem. Res.* **2001**, *34*, 181–190; f) D.-L. Jiang, T. Aida, *Nature* **1997**, *388*, 454–456; g) P. Bhyrappa, J. K. Young, J. S. Moore, K. S. Suslick, *J. Am. Chem. Soc.* **1996**, *118*, 5708–5711.
[3] a) A. Patchornik, *Proc. IUPAC Macromol. Symp.* **1982**, *28*, 85; b) B. J. Cohen, M. A. Kraus, A. Patchornik, *J. Am. Chem. Soc.* **1981**, *103*, 7620–7629.
[4] a) F. Gelman, J. Blum, D. Avnir, *New J. Chem.* **2003**, *27*, 205–207; b) F. Gelman, J. Blum, D. Avnir, *Angew. Chem.* **2001**, *113*, 3759–3761; *Angew. Chem. Int. Ed.* **2001**, *40*, 3647–3649; c) F. Gelman, J. Blum, D. Avnir, *J. Am. Chem. Soc.* **2000**, *122*, 11 999–12 000.
[5] a) X. Hao, C. Nilsson, M. Jesberger, M. H. Stenzel, E. Malmström, T. P. Davis, E. Oestmark, C. Barner-Kowollik, *J. Polym. Sci. Part A* **2004**, *42*, 5877–5890; b) Y. Zhao, X. Shuai, C. Chen, F. Xi, *Macromolecules* **2004**, *37*, 8854–8862; c) M. Kamigaito, T. Ando, M. Sawamoto, *Chem. Rec.* **2004**, *4*, 159–175; d) V. Darcos, A. Dureault, D. Taton, Y. Gnanou, P. Marchand, A.-M. Caminade, J.-P. Majoral, M. Destarac, F. Leising, *Chem. Commun.* **2004**, *18*, 2110–2111; e) K. Matyjaszewski, P. J. Miller, J. Pyun, G. Kickelbick, S. Diamanti, *Macromolecules* **1999**, *32*, 6526–6535.

Analytical Methods

DOI: 10.1002/anie.200501245

Interfacing Capillary Electrophoresis and Electrothermal Atomic Absorption Spectroscopy To Study Metal Speciation and Metal–Biomolecule Interactions**

Yan Li, Xiu-Ping Yan,* and Yan Jiang

Metallomics is a new field in the study of biometals and is related to genomics, proteomics, and metabolomics.^[1] Trace metals in the environment may be adopted by biological systems to assist in the syntheses and metabolic functions of genes (DNA and RNA) and proteins. These metals may be beneficial or may pose a risk to humans and other life forms.^[1–9] To establish metallomics as an integral biometal science, more robust and information-rich trace- and ultra-trace-chemical speciation analyses are needed for adequate risk or benefit assessments and to determine distributions of metals in humans, human blood serum, seawater, and even biological cells. Metal speciation is an important research subject in metallomics because the bioavailability and toxicity of metals on a molecular basis depends on their chemical state. Different species of the same metal be considered as essential, innocuous, or toxic.^[1–9] Another important research subject in metallomics is the interaction between metal species and biomolecules, which is significant for biochemistry, biology, medicine, pharmacy, nutrition, agriculture, and environmental science.^[1–9]

[*] Y. Li, Dr. X.-P. Yan, Y. Jiang
Key Laboratory of Functional Polymer Materials of
the Ministry of Education of China
Research Center for Analytical Sciences
Department of Chemistry, Nankai University
Tianjin 300071 (China)
Fax: (+86) 22-2350-6075
E-mail: xpyan@nankai.edu.cn

[**] This work was supported by the National Basic Research Program of China (No. 2003CB415001), the National Natural Science Foundation of China (No. 20475028, 20437020), and the National Key Technologies R&D Program (2002A906A28-2).



Supporting information for this article is available on the WWW under <http://www.angewandte.org> or from the author.

Hybrid approaches are currently preferred for the study of metal speciation and metal–biomolecule interactions in numerous techniques developed to date.^[6–9] The use of high-resolution separation methods in combination with highly sensitive detection techniques is necessary to improve the accuracy of the detection of metal speciation and metal–biomolecule interactions. The importance of capillary electrophoresis (CE) for such purposes has grown rapidly in the past decade, primarily as a result of its potential flexibility and easy implementation, high resolution, minimal sample and reagent consumption, and rapid and efficient separations with only minor disturbances of the existing equilibrium between the different species.^[6,10–12] The use of inductively coupled plasma mass spectroscopy (ICP-MS) or optical emission spectroscopy (ICP-OES) as online detection techniques for CE promises substantial improvements in the sensitivity of the methods and in the identification and quantification of multispecies systems.^[6]

Herein we report a new hybrid technique for nanoliter trace-metal speciation and metal–biomolecule interaction studies based on online coupling of CE to electrothermal atomic absorption spectroscopy (ETAAS). ETAAS provides high detection capability with low instrumental and operational costs. However, the discontinuous nature of ETAAS makes it troublesome when used in combination with continuous-flow systems and departs from the concept of monitoring continuously the chromatographic eluent.^[13] We have developed a method for real-time ETAAS detection of the CE effluent by the direct interface of CE with ETAAS. The analysis was conducted on a laboratory-made thermospray interface, with no need for external heat sources or postcolumn derivatization steps. The features of this new hybrid technique are its simplicity, low instrument and running costs, easy operation, high sensitivity and selectivity, as well as its environmentally friendly nature.

The schematic setup of the CE–ETAAS hybrid system is shown in Figure 1. It includes a capillary electrophoresis system, a thermospray interface, and a graphite furnace. It is crucial for the interface to serve as a link that can harness the full potential of the separation method and the detector. ETAAS is sufficiently sensitive for speciation analysis, but graphite furnaces are not designed for continuous operation. Direct coupling of ETAAS to CE involves a number of problems because of the stepwise operational characteristic of the commercially available atomizers and because only a small volume can be injected into the furnace.

In view of above problems, a thermospray interface was designed to allow the real-time ETAAS monitoring of individual species separated by CE. A commercially available graphite tube and conventional ETAAS operating procedures were modified slightly to enable real-time detection of the CE effluent. First, the dosing hole of the graphite tube was enlarged to allow the tight attachment of a hollow graphite cap (1.0 mm i.d.), into which the thermospray vaporizer was inserted. The graphite cap behaved as a good heat-transfer medium for the vaporizer. A small gap was left between the vaporizer and the graphite capsule for carrier gas (argon) to flow through, thus enabling the delivery of the locally generated vapor into the graphite tube. Second, because the

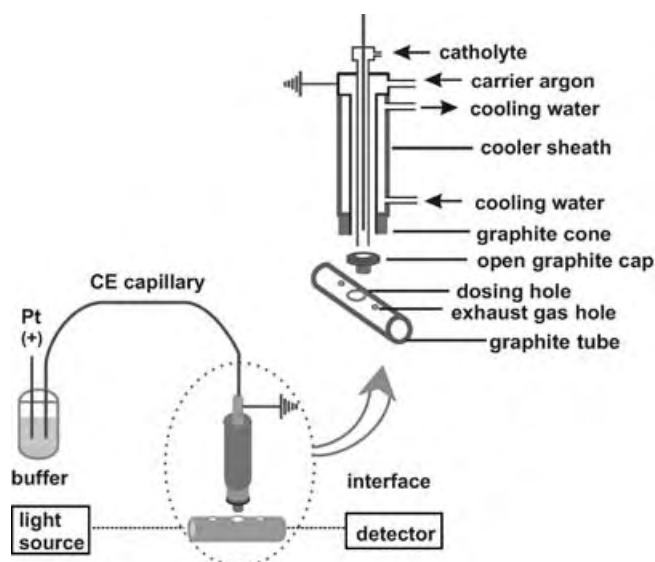


Figure 1. Schematic diagram for the new hybrid technique of capillary electrophoresis coupled online with electrothermal atomic absorption spectroscopy through a thermospray interface (not to scale).

original dosing hole of the graphite tube was blocked by the thermospray interface, two more holes (1.0 mm i.d.) were made symmetrically beside the original dosing hole in the graphite tube to serve as hole for exhaust gas. The distance between the dosing hole and the hole for exhaust gas was 6.0 mm.

To demonstrate the applicability of the developed hybrid technique for ultra-trace-element speciation, mercury and cadmium were chosen as target elements as they are highly dangerous metals, with an accumulative and persistent character in the environment. To ensure sufficient time for monitoring individual metal species in the CE effluent, the graphite furnace was programmed with seven successive thermostatic steps in the gas stop mode at an appropriate constant temperature for 99 s (the maximum time allowed) for each step. The temperature of the graphite furnace was set at 600 °C for the efficient atomization of mercury species. In this case, the lifetime of the graphite tube was 400 h. For cadmium speciation, the temperature of the graphite furnace was set at 1000 °C as a compromise between the lifetime of the graphite tube (≈ 70 h) and the sensitivity of the method. The lifetime of the graphite tube decreased markedly when the temperature of the graphite furnace rose above 1200 °C.

In view of the complete introduction of CE effluent into the graphite tube, running electrolyte may influence the real-time ETAAS detection, depending on the nature of the element of interest. The goal herein was to achieve adequate resolution of the target species and to ensure subsequent detection without interference. Phosphate and borate buffers were suitable for mercury, but led to serious interferences for real-time ETAAS detection of cadmium at 1000 °C. Ammonium acetate (NH_4Ac) was preferred for cadmium speciation owing to its easy decomposition. As a running electrolyte with higher salt content causes undesirable blocking at the tip of the thermospray vaporizer after continuous heating for a long time, the concentration of the electrolyte should be as low as

possible, but should be enough to ensure good resolution and reproducibility for CE separation.

As shown in Figure 2A, three mercury species of methylmercury (MeHg^{I}), phenylmercury (PhHg^{I}), and inorganic mercury (Hg^{II}) were treated by baseline separation with CE

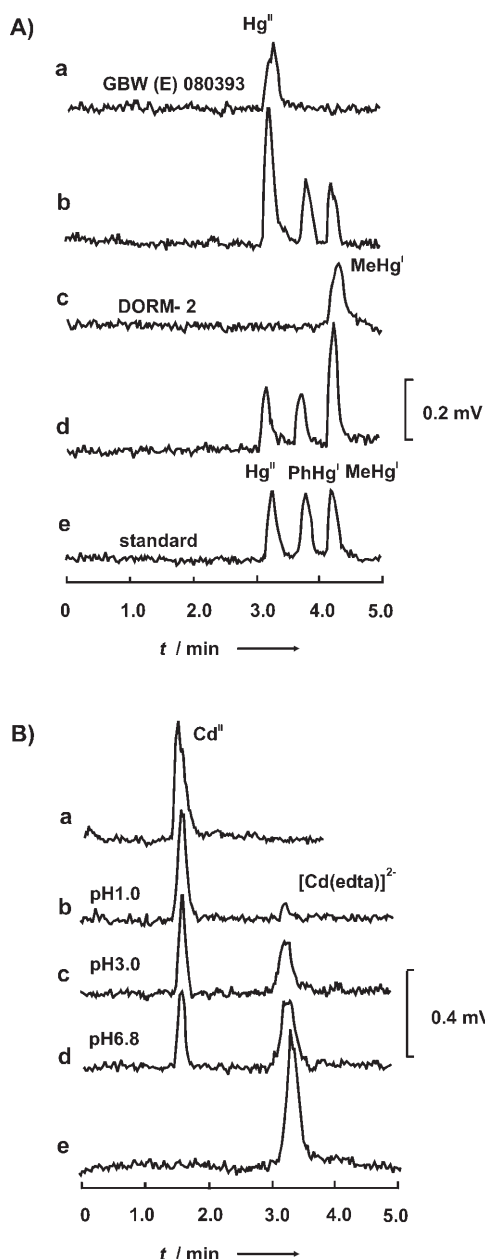


Figure 2. A) Electropherograms of a) GBW (E) 080393 (simulated natural water); b) GBW (E) 080393 spiked with of Hg^{II} , PhHg^{I} , and MeHg^{I} ($100 \mu\text{g L}^{-1}$ each); c) the extract of a certified reference material (DORM-2, dogfish muscle); d) the extract of DORM-2 spiked with of MeHg^{I} , PhHg^{I} , and Hg^{II} ($100 \mu\text{g L}^{-1}$ each); e) a standard mixture of MeHg^{I} , PhHg^{I} , and Hg^{II} ($100 \mu\text{g L}^{-1}$ each). B) Electropherograms of Cd^{II} and $[\text{Cd}(\text{edta})]^{2-}$ for a) Cd^{II} (89 nmol L^{-1}), pH 6.8; b) a standard mixture of Cd^{II} (89 nmol L^{-1}) and EDTA (40 nmol L^{-1}), pH 1.0; c) a standard mixture of Cd^{II} (89 nmol L^{-1}) and EDTA (40 nmol L^{-1}), pH 3.0; d) a standard mixture of Cd^{II} (89 nmol L^{-1}) and EDTA (40 nmol L^{-1}), pH 6.8; e) a standard mixture of Cd^{II} (89 nmol L^{-1}) and EDTA (160 nmol L^{-1}), pH 6.8.

in a $50 \text{ cm} \times 75 \mu\text{m}$ i.d. fused-silica capillary at 20 kV by using 15 mmol L^{-1} phosphate buffer at pH 6.8. The detection limit of the developed hybrid technique for mercury speciation was independent of mercury species. With an injection of 200 nL of sample solution in the hydrodynamic method, the detection limit ($S/N = 3$) of the mercury species was $14.8 \pm 0.7 \mu\text{g L}^{-1}$ (as Hg). The developed method was validated by analyzing two certified reference materials GBW (E) 080393 (simulated natural water, National Research Center for Standard Materials, Beijing, China) and DORM-2 (dogfish muscle, NRCC, Ottawa, Canada). Both the quantified Hg^{II} content ($97 \pm 2 \mu\text{g L}^{-1}$, $n = 5$) in GBW (E) 080393 and the methylmercury content ($4.28 \pm 0.21 \mu\text{g g}^{-1}$) in DORM-2 by using a simple external calibration method based on peak-area measurements are commensurate with the certified values ($100 \pm 4 \mu\text{g L}^{-1}$ for Hg^{II} in GBW (E) 080393, and $4.47 \pm 0.32 \mu\text{g g}^{-1}$ for methylmercury in DORM-2).

The developed hybrid technique was also applied to the study of the effect of the pH value on the reaction of Cd^{II} with disodium ethylenediaminetetraacetate (EDTA). As shown in Figure 2B, Cd^{II} and $[\text{Cd}(\text{edta})]^{2-}$ were well separated by CE in a $50 \text{ cm} \times 75 \mu\text{m}$ i.d. fused-silica capillary at 20 kV when using NH_4Ac buffer (5 mmol L^{-1}) at pH 8.0. The peak area of Cd^{II} increased, whereas that of $[\text{Cd}(\text{edta})]^{2-}$ decreased as the pH value decreased from 6.8 to 1.0 owing to the coalescence of H^+ with EDTA. The peak of Cd^{II} disappeared in the presence of excess EDTA at pH 6.8 (Figure 2Be).

The usefulness of the developed hybrid technique for the study of metal–biomolecule interactions was demonstrated by taking Cd^{II} /bovine serum albumin (BSA) and Hg^{II} /DNA as model systems. For this purpose, experiments were performed to obtain a series of incubation-time-dependent electropherograms of Cd^{II} and Cd–BSA adduct for a mixture solution of Cd^{II} ($0.2 \mu\text{mol L}^{-1}$) and BSA ($0.1 \mu\text{mol L}^{-1}$) (Figure 3A). Baseline separation of Cd^{II} and Cd–BSA adduct was carried out by CE in a $50 \text{ cm} \times 75 \mu\text{m}$ i.d. fused-silica capillary at 20 kV in the presence of 5 mmol L^{-1} of NH_4Ac -Tris buffer (pH 7.40) as running electrolyte. It was found from Figure 3A that about 55 % of the Cd^{II} was bound to BSA within 12 h and that the binding reaction between Cd^{II} and BSA reached equilibrium after 48 h. Hereafter no variations in the concentrations of Cd^{II} and Cd–BSA adduct were observed at various Cd^{II} /BSA molar ratios. The kinetics and binding constant for the interaction of Cd^{II} with BSA were evaluated from the time-dependent peak areas of Cd^{II} and Cd–BSA adduct. We assume that the interaction of Cd^{II} and BSA results in pseudo-first-order kinetic properties at the initial stage of incubation. The apparent kinetic rate constant (k) was then calculated by polynomial approximation of the concentration–time plots according to Equation (1).^[14]

$$\ln \frac{C_{\text{Cd}}^{\text{b}}}{C_{\text{Cd}}^{\text{0}}} = -kt \quad (1)$$

C_{Cd}^{0} and C_{Cd}^{b} are the initial molar concentration of Cd^{II} and the concentration of Cd–BSA adduct, respectively. The kinetic rate constant for the interaction of Cd^{II} and BSA was found to be independent of BSA concentration (zero-order kinetics for BSA). The value of k at various initial molar

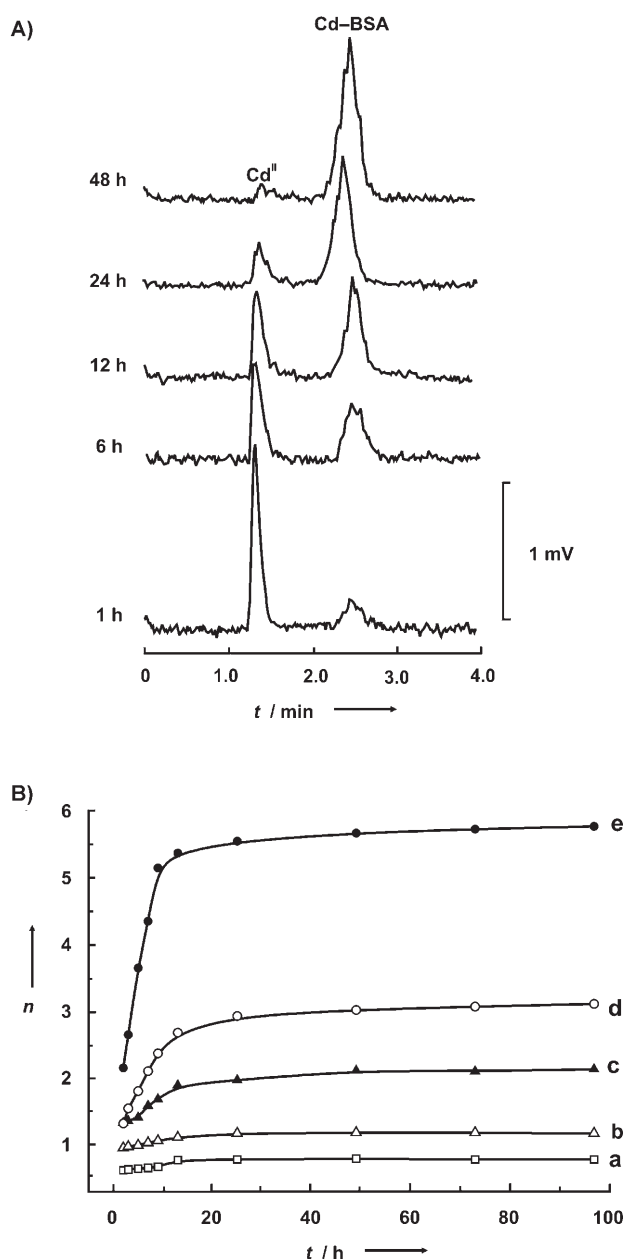


Figure 3. A) Incubation-time-dependent electropherograms of Cd^{II} and Cd-BSA adduct for the binding of Cd^{II} ($0.2 \mu\text{mol L}^{-1}$) with BSA ($0.1 \mu\text{mol L}^{-1}$). Baseline separation of Cd^{II} and Cd-BSA adduct was achieved by capillary electrophoresis in a fused-silica capillary ($50 \text{ cm} \times 75 \mu\text{m}$ i.d.) at 20 kV by using NH_4Ac -Tris buffer (pH 7.40; 5 mmol L^{-1}) as running electrolyte. B) Number of cadmium atoms binding per BSA molecule at variable incubation time. Initial Cd^{II} /BSA molar ratio (initial Cd^{II} concentration of $0.2 \mu\text{mol L}^{-1}$): a) 1:2; b) 1:1; c) 2:1; d) 4:1; e) 10:1.

ratios (0.5, 1, 2, 4, and 10) of Cd^{II} /BSA with an initial Cd^{II} concentration of $0.2 \mu\text{mol L}^{-1}$ at 37°C was determined to be $(1.108 \pm 0.065) \times 10^{-3} \text{ min}^{-1}$.

The determination of Cd-BSA binding constant (K_b) was based on the bimolecular reaction between the donor (Cd^{II}) and the acceptor (BSA). If the concentration of BSA was kept constant, but different concentrations of Cd^{II} were added in the mixture, the value of K_b could be estimated by using a

linear regression of a Scatchard plot.^[15] based on the following expression [Eq. (2)]:

$$\frac{C_{\text{Cd}}^{\text{b}}}{C_{\text{Cd}}^{\text{f}}} = -K_b C_{\text{Cd}}^{\text{b}} + C_{\text{BSA}} K_b \quad (2)$$

In Equation (2), C_{Cd}^{b} and C_{Cd}^{f} are the concentrations of bound Cd^{II} (i.e. Cd-BSA adduct) and Cd^{II} , and C_{BSA} is the concentration of the binding site on the BSA. The number of Cd atoms bound per BSA molecule (n) was calculated from the change in the peak areas of Cd^{II} and Cd-BSA adduct based on Equation (3):^[14]

$$n = \frac{C_{\text{Cd}}^0}{C_{\text{BSA}}^0} \frac{S_{\text{Cd}}^{\text{b}}}{S_{\text{Cd}}^{\text{f}} + S_{\text{Cd}}^{\text{b}}} \quad (3)$$

In Equation (3), C_{Cd}^0 and C_{BSA}^0 are the initial concentrations of Cd^{II} and BSA, respectively, S_{Cd}^{f} and S_{Cd}^{b} are the peak areas of Cd^{II} and Cd-BSA adduct, respectively. As such, the binding constant of Cd^{II} with BSA was estimated to be $2.68 \times 10^7 \text{ L mol}^{-1}$, and the number of binding sites was 3.4 after incubation for 12 h. The evolution of Cd-BSA binding as a function of incubation time at various initial molar ratios of Cd^{II} to BSA is illustrated in Figure 3B. In the presence of excess Cd^{II} , the reaction proceeds more rapidly and the protein is attached to Cd to a higher degree, as expressed by a growing number of Cd^{II} bound per BSA molecule. The number of Cd atoms bound per BSA molecule increased more rapidly with higher molar ratios of Cd^{II} to BSA as the incubation time increased to 12 h. The number of Cd^{II} species bound per BSA molecule increased very slowly with increase of incubation time over a 12-h period. These results indicate that both strong and weak binding sites on the BSA molecule might contribute to the interaction of Cd^{II} with BSA in the presence of excess Cd^{II} . It was found that BSA binds up to 5 mol of Cd^{II} per mol of the protein when incubated with Cd^{II} in tenfold excess. The Cd^{II} /BSA stoichiometry ratio is greater than 3.4:1 and might be ascribed to the high affinity of soft Cd^{II} to some potential binding sites on BSA.

Representative electropherograms of the mixture of Hg^{II} and salmon sperm DNA are shown in Figure 4. Hg^{II} was well resolved from Hg-DNA adduct. The electropherograms show that Hg^{II} decreased, whereas the bound Hg-DNA increased with increasing concentration of DNA, as was clearly reflected by the variations in peak areas of Hg^{II} and the Hg-DNA adduct. The K_b value for the binding of Hg^{II} with DNA is $5.12 \times 10^6 \text{ L mol}^{-1}$, and the number of binding sites is 0.2 for an initial DNA concentration of 2 mg L^{-1} (corresponding to a base-pair concentration of $3.4 \mu\text{mol L}^{-1}$) after incubation with various concentrations of Hg^{II} for 1 h. Detailed studies are underway in our laboratory to determine the interactions of different mercury species with DNA, improve our understanding of the kinetic and thermodynamic properties, and to evaluate the relevant binding parameters, the damage of different mercury species to DNA, and the potential toxicity and environmental effects.

In summary, ETAAS was employed for the first time as a real-time CE detector. The combination of species separation by CE with direct ETAAS detection is suitable for elemental speciation. The technique could be used in investigations of

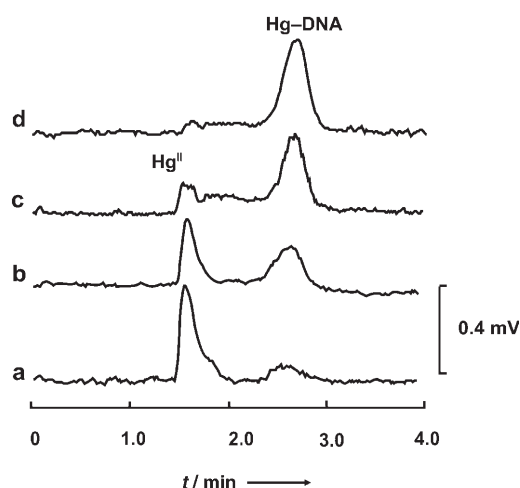


Figure 4. DNA-concentration-dependent electropherograms of Hg^{II} and Hg-DNA adduct for the binding of Hg^{II} ($1 \mu\text{mol L}^{-1}$) with DNA at various concentrations ($\mu\text{mol L}^{-1}$): a) 0.84; b) 1.7; c) 3.4; d) 6.8. Base-line separation of Hg^{II} and Hg-DNA adduct was achieved by capillary electrophoresis in a fused-silica capillary ($50 \text{ cm} \times 75 \mu\text{m}$ i.d.) at 20 kV by using Tris-HAc buffer ($\text{pH } 7.40$; 50 mmol L^{-1}) as running electrolyte.

the thermodynamic equilibrium between the coexisting species and to determine the kinetics and stoichiometry of the binding reaction between metal species and biomolecules with good selectivity and high sensitivity.

Experimental Section

Certified reference materials DORM-2 (dogfish muscle; NRCC, Ottawa, Canada) and GBW (E) 080393 (simulated natural water; NRCSM, Beijing, China) were analyzed to check the accuracy of the developed hybrid technique for speciation analysis. An acid-leaching procedure was employed for extraction of mercury species from biological materials.^[16] Briefly, hydrochloric acid (5 mL , 5 mol L^{-1}) was added to the certified reference material DORM-2 (0.3 g) in a 10-mL centrifuge tube. The mixture was then placed in an ambient ultrasonic bath for 10 min . After extraction, the suspension was centrifuged at 3500 rpm for 10 min , and the supernatant was transferred to a 10-mL flask. The supernatant was neutralized with $\text{NH}_3\text{H}_2\text{O}$ and adjusted to $\text{pH } 4.8\text{--}5.0$ with phosphate buffer, then diluted to volume with doubly deionized water.

To simulate physiological conditions, NH_4Ac -Tris buffer (5 mmol L^{-1}) containing 100 mmol L^{-1} NaCl at $\text{pH } 7.40$ was used as the incubation solution. For the kinetic experiment, the reaction mixtures were incubated at 37°C for more than 6 days, and aliquots were continuously taken from the same sample for analysis.

Received: April 9, 2005

Published online: September 15, 2005

Keywords: analytical methods · atomic absorption spectroscopy · electrophoresis · metal speciation · metallomics

- [6] *Comprehensive Analytical Chemistry, Vol. XXXIII Elemental Speciation* (Eds.: J. A. Caruso, K. L. Sutton, K. L. Ackley), Elsevier, Tokyo, **2000**, pp. 169–181.
- [7] *Element Speciation in Bioinorganic Chemistry* (Ed.: S. Caroli), Wiley, New York, **1996**.
- [8] *Chemical Speciation in the Environment* (Eds.: C. M. Davidson, A. M. Ure), Blackie Academic & Professional, London, **1995**.
- [9] J. A. Caruso, M. Montes-Bayon, *Ecotoxicol. Environ. Saf.* **2003**, *56*, 148–463.
- [10] S. Schäffer, P. Gareil, C. Dezael, D. Richard, *J. Chromatogr. A* **1996**, *740*, 151–157.
- [11] E. Dabek-Zlotorzynska, E. P. C. Lai, A. R. Timerbaev, *Anal. Chim. Acta* **1998**, *359*, 1–26.
- [12] X.-B. Yin, X.-P. Yan, Y. Jiang, X.-W. He, *Anal. Chem.* **2002**, *74*, 3720–3725.
- [13] X.-H. Zhang, D. Chen, R. Marquardt, J. A. Koropchak, *Microchem. J.* **2000**, *66*, 17–53.
- [14] A. R. Timerbaev, S. S. Aleksenko, K. Polec-Pawlak, R. Ruzik, O. Semenova, C. G. Hartinger, S. Oszwardowski, M. Galanski, M. Jarosz, B. K. Keppler, *Electrophoresis* **2004**, *25*, 1988–1995.
- [15] G. Scatchard, *Ann. N. Y. Acad. Sci.* **1949**, *51*, 660–672.
- [16] A. I. C. Ortiz, Y. M. Aibarrán, C. C. Rica, *J. Anal. At. Spectrom.* **2002**, *17*, 1595–1601.

- [1] H. Haraguchi, *J. Anal. At. Spectrom.* **2004**, *19*, 5–14.
- [2] C. Ash, R. Stone, *Science* **2003**, *300*, 925–925.
- [3] L. A. Finney, T. V. O'Hallaoran, *Science* **2003**, *300*, 931–936.
- [4] K. H. Thompson, C. Orvig, *Science* **2003**, *300*, 936–939.
- [5] F. M. M. Morel, N. M. Price, *Science* **2003**, *300*, 944–947.

Polypyrrole Nanowires

DOI: 10.1002/anie.200501354

Polypyrrole Nanowires Grown from Single Adsorbed Polyelectrolyte Molecules**
Vera Bocharova, Anton Kiriya, Hartmut Vinzelberg, Ingolf Mönch, and Manfred Stamm*

One-dimensional nanostructures of conductive polymers (CPs) have attracted a great deal of interest as building blocks for future miniaturized nanoelectronic devices^[1] and highly sensitive chemical^[2] or biological sensors.^[3] Several “template-less” approaches to 1D superstructures of CPs based on the self-assembly of conjugated polymers, oligomers, or monomers have been reported recently.^[4] Other methods for the synthesis of CP nanowires involve chemical or electrochemical oxidative polycondensation in “hard tem-

[*] V. Bocharova, Dr. A. Kiriya, Prof. Dr. M. Stamm
Leibniz Institute of Polymer Research Dresden
01069 Dresden (Germany)
Fax: (+49) 351-4658-284
E-mail: kiriya@ipfdd.de

Dr. H. Vinzelberg, Dr. I. Mönch
Leibniz Institute for Solid State and Materials Research
01069 Dresden (Germany)

[**] Financial support was provided by the DFG within the ESF EUROCORES/SONS program (02-PE-SONS-092-NEDSPE) and SFB-287 (project B1).



Supporting information for this article is available on the WWW under <http://www.angewandte.org> or from the author.

plates" (such as zeolites, track-etched polymeric membranes, and porous alumina),^[5] or "soft templates" (surfactant micelles or liquid-crystalline phases).^[6] However, for various applications, CP nanowires must be properly integrated into circuits. Therefore, at least one additional step is required, such as the release of the nanowires from the templates and/or their positioning in the device.

Polymer chemistry offers a fascinating world of structures of different architecture, composition, and functionality. The use of single polymer molecules as templates constitutes a highly promising strategy to generate nanoparticles with desired size, shape, location, and with specific properties.^[7] Like macroscopic objects, single molecules of polyelectrolyte (PE) can be stretched and aligned under external forces^[8] (such as centrifugal or capillary forces and electric or shear fields) and can be immobilized onto surfaces by simple procedures like casting or printing.^[9] Single DNA molecules have recently been used for the fabrication of metallic^[10] and conductive polymer (polyaniline, PANI) nanowires.^[11] In the latter case, DNA molecules were covalently attached to a Si surface and activated with aniline, which was then polymerized. However, the PANI nanowire networks produced in this way have rather low conductivity, even when doped.^[11] This low conductivity is the result of a very limited quantity of PANI being formed along the template. This restriction is governed by the quantity of aniline that can be attracted by DNA during the activation step owing to electrostatic and hydrophobic interactions. The oxidative degradation of DNA templates has been proposed by some authors^[11b] as a possible factor that decreases the continuity and thus the conductivity of the DNA-PANI nanowires. We therefore assumed that the use of chemically robust synthetic PE molecules might benefit the fabrication of more conductive nanowires. Herein, we report the use of single molecules of negatively charged synthetic polyelectrolyte (polystyrene sulfonic acid, PSA) to grow continuous and conductive polypyrrole (Ppy) nanowires through selective "electroless" deposition of Ppy along PSA molecules.

Spin-coating of a PSA solution onto mica or a thermally oxidized Si wafer at high rotation speed results in stretching and alignment of the PSA chains (Figure 1 a and Supporting Information). In initial experiments, mica-deposited PSA templates were incubated in pyrrole (Py) monomer solution, then rinsed with deionized water to remove unattached Py and placed in a solution of ammonium persulfate (APS) to polymerize the Py attached to the templates. The resulting product appears in AFM images as a 1D sequence of apparently separated clusters 2–4 nm in height (Figure 1 c). These structures are considerably higher than bare PSA molecules (≈ 0.5 nm),^[8] which clearly reflects the formation of Ppy clusters along the PSA molecules.

To produce more continuous and thicker Ppy nanowires, we performed electroless deposition of Ppy.^[12] PSA chains were deposited onto substrates in the stretched conformation and were then treated with aqueous solution of Py and APS for up to 60 s (for details, see Experimental Section and Supporting Information). AFM investigations revealed the successful formation of PSA-Ppy nanowires with diameters that vary from a few to hundreds of nanometers depending on

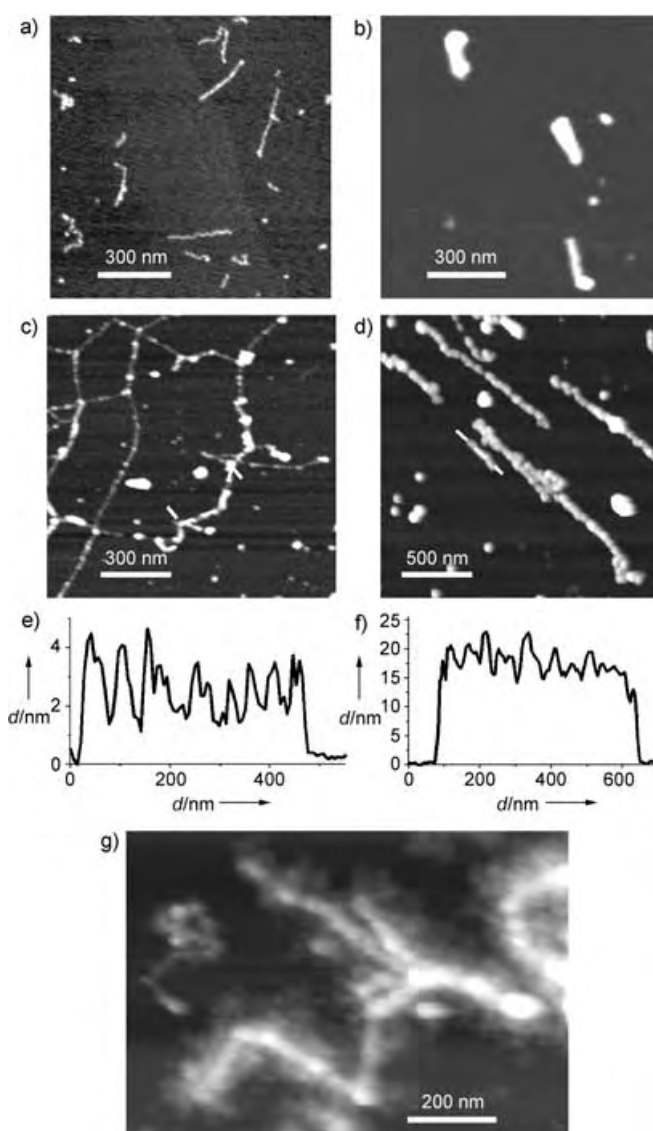


Figure 1. a) Topographic AFM image of short ($M_w = 403 \text{ kg mol}^{-1}$) PSA molecules. b) AFM image of Ppy nanoparticles formed from the placement of aqueous solutions of Py and APS onto mica-immobilized PSA templates ($M_w = 403 \text{ kg mol}^{-1}$) for 20 s. c) AFM image of Ppy nanoparticles formed from the incubation of mica-immobilized long ($M_w = 6940 \text{ kg mol}^{-1}$) PSA molecules in Py monomer solution followed by rinsing with water and oxidation with APS. d) Surface image from the same procedure as in b), but with the use of long ($M_w = 6940 \text{ kg mol}^{-1}$) PSA templates. e), f) Cross-sections along the dashed lines in c) and d), respectively. g) Surface image from the same procedure as in d), but with an APS concentration fivefold smaller.

the polymerization time (Figure 1 c,d). As expected for the template method, the aspect ratio of the nanowires (≈ 7 and ≈ 100 for the nanowires in Figures 1 b and d, respectively) is dependent on the contour length of the PSA molecules. The resulting nanowires, however, are somewhat shorter than the corresponding templates (usually by a factor of 1.5–3, depending on the polymerization time). The observed partial shrinkage of the nanowires is the result of attractive interactions between hydrophobic segments of Ppy, which

can be avoided if the PSA templates are properly fixed to the substrate.

Close inspection of the AFM images shows that thin nanowires ($\varnothing < 5$ nm) are still sequences of isolated Ppy clusters, although the nanowires become quasi-continuous (the clusters are closely packed) if their diameter exceeds 10 nm. The clusters are localized predominantly along the PSA chains, which indicates a rather high selectivity of the deposition.

In general, growth of Ppy nanowires can be realized according to two schemes: 1) precipitation of hydrophobic Ppy nanoparticles preformed in solution onto the hydrophobic PSA-Py complex, and 2) growth of Ppy from the PSA-Py complex.^[13] We performed a set of experiments to decide which scheme is realized in our case. For this, we prepared colloidal dispersions of Ppy by mixing solutions of Py and APS followed by quenching with excess sodium bisulfite (SBS) as a reducing agent. The colloids prepared in this manner were placed on a substrate with pre-adsorbed PSA template molecules. However, the formation of Ppy nanowires was never observed in these experiments regardless of the activation time, size, and concentration of Ppy colloids used. Thus, the prerequisite for nanowire growth is the presence of both Py monomer and oxidizing agent in solution. This result clearly excludes the “grafting-to” and supports the “grafting-from” scheme for Ppy nanowire formation.

Varying the reaction conditions influences the morphology of the Ppy nanowires. With excess oxidant, the resulting nanowires display a relatively smooth morphology (Figure 1c,d). In contrast, a lack of oxidant leads to the formation of “hairy nanowires” that resemble “molecular brushes”^[14] (Figure 1g). These observations are consistent with the “grafting-from” scheme of Ppy growth.^[15]

Electrical characterization was performed for the larger Ppy nanowires (Figure 2). For this, Ppy nanowires 50–60 nm thick were grown onto devices with gold micro-electrodes (the distance between the electrodes was 1 μ m). The amount of PSA-Ppy nanowires produced was adjusted to allow only a few Ppy nanowires to bridge the electrodes; the other nanowires remained disconnected. This allowed us to measure the dc conductivity of individual nanowires. After deposition, the device was carefully investigated by AFM, and the amount, location, and size of all nanowires was noted. These electrical measurements revealed the resistance of a single nanowire to be ≈ 0.6 –1.5 M Ω , which corresponds to a conductivity of ≈ 1 –3 S cm⁻¹. This rather high conductivity approaches the conductivity of Ppy in bulk.^[16] The nanowires display a linear current–voltage dependence (Figure 2h, inset), which reflects good contacts between the nanowires and the electrodes and good connectivity of the Ppy clusters along the PSA molecule. To break a certain nanowire, we slowly increased the potential between the electrodes until an abrupt increase in resistance was observed. The significant resistance increase after this procedure (from 1.1 to 21 M Ω for the nanowire in Figure 2b) proves that the measured conductance is indeed caused by this particular nanowire. On the other hand, AFM inspection of the broken nanowires reveals the formation of gaps (usually one or two per broken

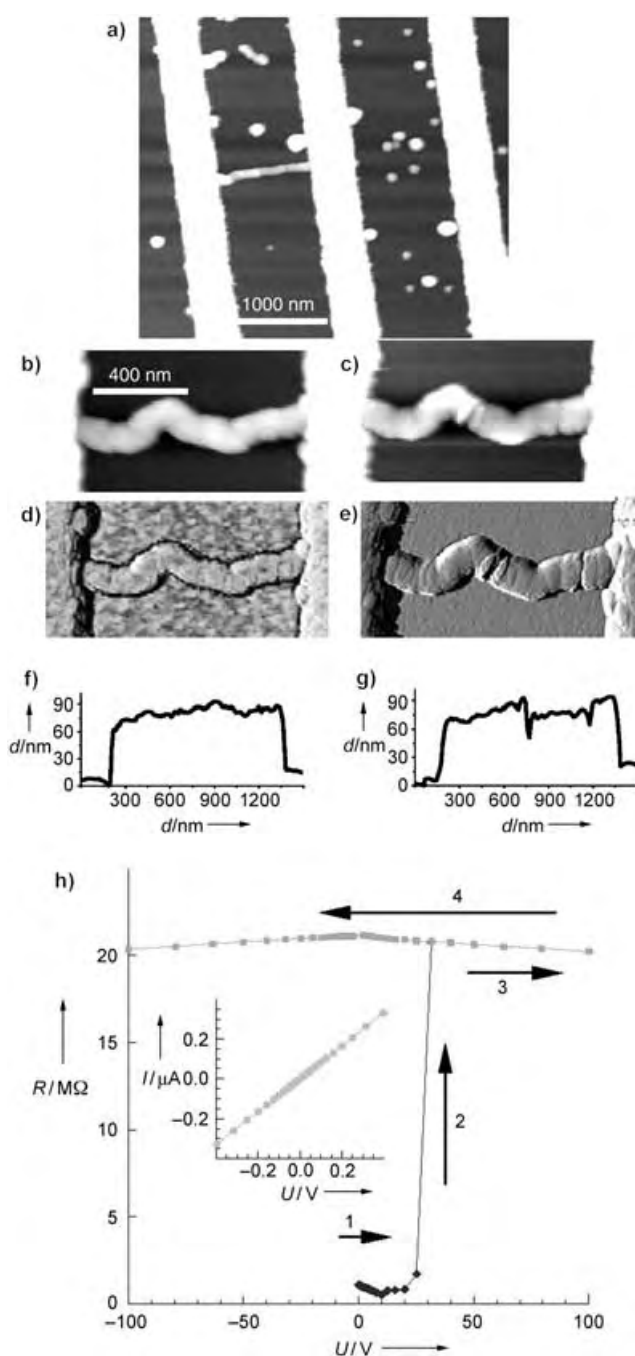


Figure 2. a) AFM topography image of a representative Ppy nanowire with a resistance of ≈ 1 M Ω . b), c) High-magnification topography and d), e) phase AFM images of the pristine Ppy nanowire bridging two microelectrodes. The intact nanowire shown in b) and d) was broken by applying a high voltage (25 V; c) and e), respectively. f), g) Cross section profiles of the nanowires in images b) and c), respectively. h) Room-temperature resistance–current characteristics of the pristine nanowire with a resistance of 1.1 M Ω ; numbered arrows indicate the sequence of increasing (1–3, \blacklozenge) and subsequent decreasing (4, \blacksquare) voltage. The same nanowire after breakage with high voltage displays a resistance of ≈ 21 M Ω . (Inset: demonstration of the linear I – U dependence of the pristine nanowire at low voltage.)

wire, Figure 2b–g). An even more pronounced decrease of the conductance (the resistance increased from a few M Ω to a

few G Ω) was observed when the nanowires were mechanically broken by movement of the AFM tip operating in contact mode (Supporting Information).

Finally, we evaluated the possibility of using Ppy nanowires as active elements in sensors. In general, the conductivity of Ppy can be modulated by changing the doping level: the conductivity is high in an oxidized (doped) state and low in a reduced (de-doped) form. Alternatively, Ppy in the reduced form can be doped by acids and de-doped by bases. As expected, the Ppy nanowires synthesized by oxidative polycondensation display a rather high conductivity that changes only slightly upon further exposure to acidic (HCl) or basic (NH₃) vapors. To make the conductivity of the Ppy nanowires sensitive to acids and bases, they were reduced by rinsing with an aqueous solution of NaBH₄ (1 g L⁻¹), which resulted in an increase in resistance from 1–5 M Ω for doped nanowires to more than 1 G Ω for the de-doped wires. In the reduced state, the nanowires reversibly change their resistance upon exposure to HCl and NH₃ vapors from several M Ω to a few G Ω .^[17]

In conclusion, we have developed a simple chemical route to conductive Ppy nanowires by the grafting of Ppy from isolated synthetic polyelectrolyte molecules. The location and length of the synthesized Ppy nanowires are defined by the location and length of adsorbed single-molecule templates. The diameter of the nanowires can be varied from a few nanometers to hundreds of nanometers by adjusting the polycondensation time and concentration of the reagents. The dc conductivity of individual Ppy nanowires approaches the conductivity of Ppy in bulk. This result opens up broad opportunities for the fabrication of electronic devices and sensors at a molecular level.

Experimental Section

Polystyrene sulfonic acid (PSA; M_w = 6940 kg mol⁻¹, PDI = 1.3; M_w = 403 kg mol⁻¹, PDI = 1.3) was purchased from the Polymer Standards Service, Mainz, Germany. Ammonium persulfate (APS), pyrrole (Py), and all other chemicals were purchased from Aldrich.

Ppy nanowires: Stretched PSA molecules were deposited from aqueous solution (0.01 g L⁻¹) onto clean Si wafers or freshly cleaved mica by spin-coating at high speed (10000 rpm). Py (3 g L⁻¹, 50 μ L) and APS (30 g L⁻¹, 50 μ L) in deionized water were placed for a limited time (10–60 s) onto the substrates with predeposited PSA molecules. Afterwards, the samples were rinsed with water, dried, and examined by AFM (NanoScope IV-D3100, Digital Instruments, Santa Barbara, USA) in tapping mode. The diameter of the Ppy nanowires was dependent on the polymerization time and was found to be < 10, 10–30, and 30–60 nm for polymerization times of 15, 30, and 60 s, respectively. "Hairy nanowires" were produced with a similar procedure in which the only difference was a lower concentration of APS (6 g L⁻¹).

For electrical measurements (Keithley 236 Source-Measure Unit), 18-finger gold micro-electrodes (step height: 50 nm; width: 500 nm; separation: 1 μ m) were fabricated by photolithography on a Si wafer with an insulating SiO₂ layer (300 nm).

Received: April 19, 2005

Revised: May 26, 2005

Published online: September 14, 2005

Keywords: conducting materials · nanostructures · nanotechnology · polymers · scanning probe microscopy

- [1] Y. Huang, X. Duan, Y. Cui, L. J. Lauhon, K.-H. Kim, C. M. Lieber, *Science* **2001**, 294, 1313.
- [2] S. Virji, J. Huang, R. B. Kaner, B. H. Weiller, *Nano Lett.* **2004**, 4, 491.
- [3] a) H.-H. Yang, S.-Q. Zhang, F. Tan, Z.-X. Zhuang, X.-R. Wang, *J. Am. Chem. Soc.* **2005**, 127, 1378; b) K. Ramanathan, M. A. Bangar, M. Yun, W. Chen, N. V. Myung, A. Mulchandani, *J. Am. Chem. Soc.* **2005**, 127, 496.
- [4] a) F. J. M. Hoebe, P. Jonkheijm, E. W. Meijer, A. P. H. J. Schenning, *Chem. Rev.* **2005**, 105, 1491; b) N. Kiriy, E. Jähne, H.-J. Adler, M. Schneider, A. Kiriy, G. Gorodyska, S. Minko, D. Jehnichen, P. Simon, A. A. Fokin, M. Stamm, *Nano Lett.* **2003**, 3, 707.
- [5] a) C. R. Martin, *Science* **1994**, 266, 1961; b) R. M. Hernandez, L. Richter, S. Semancik, S. Stranick, T. E. Mallouk, *Chem. Mater.* **2004**, 16, 3431; c) S. Park, S.-W. Chung, C. A. Mirkin, *J. Am. Chem. Soc.* **2004**, 126, 11772.
- [6] a) T. Hatano, A.-H. Bae, M. Takeuchi, N. Fujita, K. Kaneko, H. Ihara, M. Takafuji, S. Shinkai, *Angew. Chem.* **2004**, 116, 471; *Angew. Chem. Int. Ed.* **2004**, 43, 465; b) J.-J. Chiu, C.-C. Kei, T.-P. Perng, W.-S. Wang, *Adv. Mater.* **2003**, 15, 1361.
- [7] a) A. Kiriy, S. Minko, G. Gorodyska, M. Stamm, *J. Am. Chem. Soc.* **2002**, 124, 10192; b) G. Gorodyska, A. Kiriy, S. Minko, C. Tsitsilianis, M. Stamm, *Nano Lett.* **2003**, 3, 365; c) A. Kiriy, G. Gorodyska, S. Minko, C. Tsitsilianis, W. Jaeger, M. Stamm, *J. Am. Chem. Soc.* **2003**, 125, 11202.
- [8] N. Severin, J. Barner, A. A. Kalachev, J. P. Rabe, *Nano Lett.* **2004**, 4, 577.
- [9] H. Nakao, M. Gad, S. Sugiyama, K. Otobe, T. Ohtani, *J. Am. Chem. Soc.* **2003**, 125, 7162.
- [10] a) E. Braun, Y. Eichen, U. Sivan, G. Ben-Yoseph, *Nature* **1998**, 391, 775; b) J. Richter, M. Mertig, W. Pompe, I. Mönch, H. K. Schackert, *Appl. Phys. Lett.* **2001**, 78, 536.
- [11] a) Y. Ma, J. Zhang, G. Zhang, H. He, *J. Am. Chem. Soc.* **2004**, 126, 7097; b) P. Nickels, W. U. Dittmer, S. Beyer, J. P. Kotthaus, F. C. Simmel, *Nanotechnology* **2004**, 15, 1524.
- [12] X. Hong, J. C. Tyson, J. S. Middlecoff, D. M. Collard, *Macromolecules* **1999**, 32, 4232.
- [13] J. Stejskal, M. Trchova, S. Fedorova, I. Sapurina, J. Zemek, *Langmuir* **2003**, 19, 3013.
- [14] S. S. Sheiko, S. A. Prokhorova, K. L. Beers, K. Matyjaszewski, I. I. Potemkin, A. R. Khokhlov, M. Moller, *Macromolecules* **2001**, 34, 8354.
- [15] W.-L. Yuan, E. A. O'Rear, G. Cho, G. P. Funkhouser, D. T. Glatzhofer, *Thin Solid Films* **2001**, 385, 96.
- [16] C.-G. Wu, C.-Y. Chen, *J. Mater. Chem.* **1997**, 7, 1409.
- [17] For sensors based on PANI and Ppy fibers, see: a) J. Wang, S. Chan, R. R. Carlson, Y. Luo, G. Ge, R. S. Ries, J. R. Heath, H.-R. Tseng, *Nano Lett.* **2004**, 4, 1693; b) K. Ramanathan, M. A. Bangar, M. Yun, W. Chen, A. Mulchandani, N. V. Myung, *Nano Lett.* **2004**, 4, 1237; c) B. Dong, M. Kruschke, X. Zhang, L. Chi, H. Fuchs, *Small* **2005**, 1, 520.

Capsules and Star-Burst Polyhedra: An [Ag₂L₂] Capsule and a Tetrahedral [Ag₄L₄] Metallosupramolecular Prism with Cyclotrimeratrylene-Type Ligands**

Christopher J. Sumby and Michael J. Hardie*

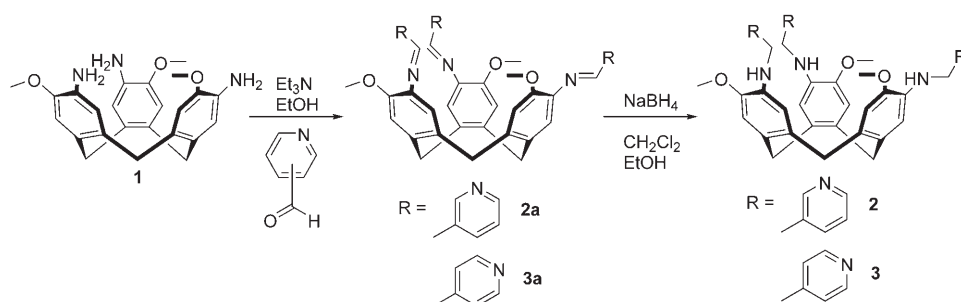
Cyclotrimeratrylene (CTV) is a macrocyclic host molecule that strongly favors a crown conformation, which gives it a bowl shape with a shallow molecular cavity.^[1] Indeed, despite CTV being known for over 40 years, the alternative saddle conformation has only recently been isolated by the rapid quenching of a hot solution or melt,^[2] or within a novel CTV-based cryptophane.^[3] The bowl-shaped CTV is a cyclic trimer which has a distinctly spiked, pyramidal aspect. We wish to exploit this characteristic to create self-assembled capsules and polyhedra through the formation of metallosupramolecular assemblies. These would likewise have a spiked aspect that allows for significantly more internal space than could be afforded from a similar flat or flexible ligand. A range of spectacular polyhedral structures have been reported from the self-assembly of metal salts with multifunctional ligands.^[4] CTV itself is not a good molecular component for such assemblies as it lacks predictable coordination sites for transition metals, hence we have synthesized a number of CTV analogues with pyridyl groups at the upper rim for use as ligands for these types of assemblies as well as coordination networks.^[5] Notably, a number of crystalline hydrogen-bonded assemblies feature tetrahedral clusters of CTV hosts arranged in a back-to-back fashion,^[6] which excludes the possibility of forming an assembly with internal space. Likewise a 3D coordination polymer with a C₃-substituted CTV derivative also shows this back-to-back stacking.^[7] Self-assembled complexes of CTV-related host molecules that do show an internal space would result from the head-to-head association of host molecules. Examples are currently restricted to a dimeric [Pd₃L₂] capsule that has been characterized in solution by Shinkai and co-workers.^[8] This

capsule results from the assembly of a trisubstituted CTV derivative possessing rigid pyridyl arms with *cis*-protected Pd salts. Covalently linked cryptophanes, where two CTV fragments are linked in a head-to-head fashion by organic spacers, are well established.^[9]

Other bowl-shaped host molecules have been shown to form both capsule assemblies and more complicated polyhedral structures. Capsule structures assembled from hydrogen bonds or coordination chemistry are known with calixarenes and calixresorcinarenes.^[10] Considerably more complicated assemblies such as a cyclic trimer,^[11] cyclic hexamers,^[12] a tetrahedron,^[11b] a snub cube,^[13] icosahedron,^[14] and a cuboctahedron^[15] have also been reported from similar tetrameric molecular hosts.

We report herein a new type of [M₂L₂] dimeric capsule with a CTV-related host molecule in the complex [Ag₂(tris(3-pyridylmethylamino)cyclotrimeratrylene)₂](CH₃CN)₂·2PF₆·4CH₃CN, along with the first example of a discrete polyhedral cluster larger than a dimeric capsule assembled with a CTV-related host molecule. This latter complex [Ag₄(tris(4-pyridylmethylamino)cyclotrimeratrylene)₄](CH₃CN)₄·4BF₄·7CH₃CN·2.8H₂O features a tetrahedral metallosupramolecular prism with a novel stellated “star-burst” aspect to the assembly.

The precursor 3,8,13-triamino-2,7,12-trimethoxy-10,15-dihydro-5*H*-tribenzo[*a,d,g*]cyclononene (**1**) has been previously reported,^[16] and can be converted into the tris(pyridylmethylamino)cyclotrimeratrylenes **2** and **3** in good yields by reaction with the appropriate pyridinecarboxaldehyde, followed by reduction with sodium borohydride (Scheme 1).



Scheme 1.

Reaction of ligand **2** dissolved in acetone with AgPF₆ in CH₃CN gives the crystalline complex [Ag₂(**2**)₂](CH₃CN)₂·2PF₆·4CH₃CN (**4**), whose structure was determined by X-ray crystallography.^[17] The metal complex [Ag₂(**2**)₂(CH₃CN)₂]²⁺ is a dinuclear, dimeric species with a capsulelike structure (Figure 1). The centrosymmetric capsule forms through the head-to-head coordination of two ligands to two Ag^I centers to give an [M₂L₂] capsule rather than the [M₃L₂] capsule reported by Shinkai and co-workers. The Ag^I center is coordinated by a terminal acetonitrile ligand at an Ag–N distance of 2.347(3) Å, and three pyridyl groups at Ag–N distances of 2.322(3), 2.346(2), and 2.247(2) Å in a distorted tetrahedral geometry.

The conformation and directionality of twist of the pyridyl arms of ligand **2** are all similar, and directed above the

[*] Dr. C. J. Sumby, Dr. M. J. Hardie
School of Chemistry
University of Leeds
Leeds LS29JT (UK)
Fax: (+44) 113-343-6565
E-mail: m.j.hardie@leeds.ac.uk

[**] We thank the EPSRC for financial support and Dr. Julie Fisher for helpful discussions.

Supporting information for this article is available on the WWW under <http://www.angewandte.org> or from the author.

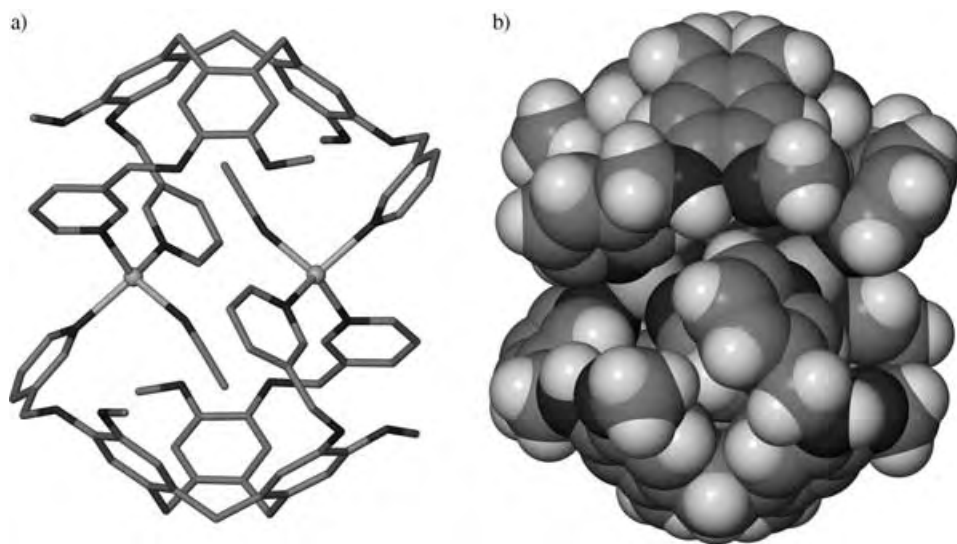


Figure 1. The capsule structure of $[\text{Ag}_2(\mathbf{2})_2(\text{CH}_3\text{CN})_2]^{2+}$ from the crystal structure of **4**. a) Stick representation, b) space-filling representation.

molecular cavity of the ligand. This arrangement means that the Ag^{I} centers are likewise located above the molecular cavity which results in the capsule having an equatorial region that is pinched inwards. Each coordinated acetonitrile ligand is directed into the cavity of a molecular host. Such host–guest associations between a host and coordinated acetonitrile have been previously observed for silver–CTV complexes.^[18] The two specific host–guest interactions observed in this structure may be a factor favoring the formation of an $[\text{M}_2\text{L}_2]$ capsule over the $[\text{M}_3\text{L}_2]$ species.

^1H NMR spectroscopic analysis of the dimeric capsule suggests a species related to the solid-state structure may be present in solution. Addition of one equivalent of a silver salt to a solution of **2** results in subtle, but significant, changes to the ^1H NMR spectrum: in particular, the splitting of the signal for the methylene spacer of the pyridyl arms of **2** into two doublets and the considerable upfield shift of the H2 proton of the pyridyl ring. The former change is likely to originate because of restricted rotation of the pyridyl arm of **2** upon coordination, while the latter may result from internalization of the pyridyl H2 within a capsule or related species. However, the $[\text{Ag}_2(\mathbf{2})_2(\text{CH}_3\text{CN})_2]^{2+}$ capsule characterized by X-ray crystallography has C_2 symmetry but in solution the ligand (**2**) possesses C_3 symmetry—that is, only one set of signals are observed. Thus, either a fluxional process which is fast on the NMR timescale is simplifying the expected spectrum for the $[\text{Ag}_2(\mathbf{2})_2(\text{CH}_3\text{CN})_2]^{2+}$ capsule, or another species such as an $[\text{Ag}_3(\mathbf{2})_2]^{3+}$ cage or an $[\text{Ag}(\mathbf{2})]^+$ complex where the ligand is a tripodal tridentate donor is present in solution. Rapid crystallization (ca. 20 min) of the $[\text{Ag}_2(\mathbf{2})_2(\text{CH}_3\text{CN})_2]^{2+}$ capsule occurs from acetonitrile solution when the silver salt used is silver(I) cobalt(III) bis(dicarbollide) ($\text{Ag}[\text{Co}(\text{C}_2\text{B}_9\text{H}_{11})_2]$) which indicates there is some form of preorganization of the structure in solution.

Titration of **2** with $\text{Ag}[\text{Co}(\text{C}_2\text{B}_9\text{H}_{11})_2]$ leads to a significant upfield shift of the pyridyl H2 signal when up to one equivalent of the silver salt is added. The upfield movement

of the resonance then stabilizes before undergoing a downfield shift as more than 1.5 equivalents of $\text{Ag}[\text{Co}(\text{C}_2\text{B}_9\text{H}_{11})_2]$ are added. The pyridyl H6 proton signal mimics this behavior, but undergoes a significantly less-pronounced upfield shift, while the signals for the more remote pyridyl H4 and H5 move progressively downfield throughout the titration. In an additional set of experiments, crystals of **4** prepared in acetonitrile were redissolved in $[\text{D}_6]\text{acetone}$ or CD_3NO_2 , but signals for the incarcerated acetonitrile, disappointingly, could not be observed. These results suggest that while a related $[\text{Ag}_2(\mathbf{2})_2]^{2+}$ capsule may be present in solution, other species, including the originally anticipated $[\text{Ag}_3(\mathbf{2})_2]^{3+}$ capsule, and possibly a 1:1 complex, are also likely solution structures. ES-MS results demonstrate the

presence of a 1:1 complex in solution, thus suggesting that the ligand may in fact act as a tripodal tridentate donor in solution. This 1:1 complex then dimerizes upon crystallization to generate the $[\text{M}_2\text{L}_2]$ capsule. Further solution studies will be discussed in a future full paper that demonstrates the generality of this capsule-related topology with other tetrahedral transition-metal ions.

Use of the 4-substituted ligand **3** in place of the 3-substituted ligand **2** has a profound effect on the type of metallosupramolecular prism isolated. Reaction of **3** with one equivalent of AgBF_4 in CH_3CN gives the crystalline complex $[\text{Ag}_4(\mathbf{3})_4(\text{CH}_3\text{CN})_4] \cdot 4\text{BF}_4 \cdot 7\text{CH}_3\text{CN} \cdot 2.8\text{H}_2\text{O}$ (**5**). The crystal structure of **5** was determined by single-crystal techniques.^[17] Complex **5** contains a $[\text{Ag}_4(\mathbf{3})_4(\text{CH}_3\text{CN})_4]^{4+}$ metallosupramolecular prism in which the Ag^{I} centers form the vertices of a slightly distorted tetrahedral prism, with $\text{Ag} \cdots \text{Ag}$ separations along the tetrahedron edges ranging from 8.29 to 10.33 Å. Four tris(4-pyridylmethylamino)cyclotriguaiacylene ligands form the faces of the $[\text{M}_4\text{L}_4]$ tetrahedral prism (Figure 2).

There are four independent ligands within complex **5**, and each shows a noncrystallographic C_3 symmetry. The conformation of each ligand is similar, with the plane of each pyridyl arm at approximately 90° to the plane of the core arene group to which it is attached. All pyridyl arms are directed inwards in relation to the ligand core. This conformation allows for formation of a convergent, discrete structure, rather than a polymeric structure which would result from an *exo* pyridyl arm conformation. Each molecule of **3** bridges between three Ag^{I} centers. There are four crystallographically independent Ag^{I} centers, and each is coordinated by pyridyl groups from three different molecules of **3** and an acetonitrile ligand. The $\text{Ag}-\text{N}_{\text{py}}$ and $\text{Ag}-\text{NCMe}$ interatomic distances range from 2.216(13) to 2.328(13) and 2.390(18) to 2.60(3) Å, respectively, and the metal geometries are distorted tetrahedral, distorted trigonal pyramidal, or have a geometry in-between these extremes. Three of the four Ag^{I} centers have their terminal acetonitrile ligand directed *exo* from the tetrahedral

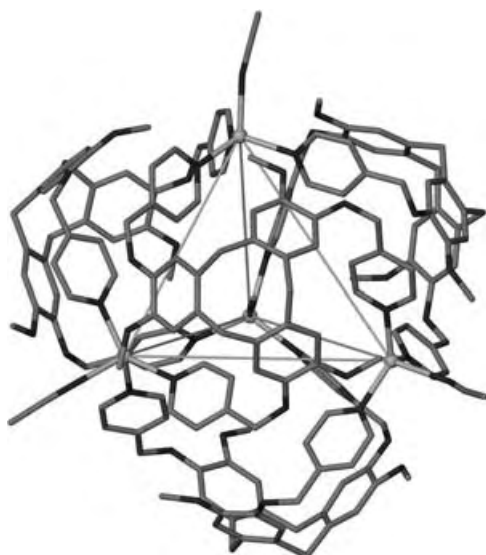


Figure 2. Tetrahedral metallocupramolecular prism $[\text{Ag}_4(\mathbf{3})_4(\text{CH}_3\text{CN})_4]^{4+}$ from the X-ray crystal structure of **5**. Thin lines highlight the tetrahedral prism formed by the Ag^{I} centers (shown as spheres).

prism, and one, $\text{Ag}(\mathbf{3})$, has the terminal acetonitrile molecule directed into the prism. The geometry of $\text{Ag}(\mathbf{3})$ is closest to trigonal pyramidal with the acetonitrile ligand forming a long bond ($\text{Ag}-\text{N}$: 2.60(3) Å) in the capping position.

Tetrahedral metallocupramolecular prisms have been reported by a number of researchers, with most examples having an $[\text{M}_4\text{L}_6]$ stoichiometry where the six ligands define the edges of the tetrahedron.^[19] There have been fewer examples of tetrahedral metallocupramolecular assemblies where the ligand defines a face of the tetrahedron. These are a $[\text{M}_8\text{L}_4]$ distorted tetrahedron from Fujita and co-workers,^[20] a distorted $[\text{M}_{12}\text{L}_4]$ tetrahedron reported by Robson and co-workers,^[21] a handful of $[\text{M}_4\text{L}_4]$ tetrahedra with triscatecholate ligands,^[22,23] an $[\text{M}_4\text{L}_4]$ tetrahedron formed from a disk-shaped tridentate ligand,^[24] and an $[\text{M}_4\text{L}_4]$ tetrahedron with a podand borate ligand.^[25] Additionally, a flattened tetrahedral

structure, in which the calixresorcinarene ligands act as the vertices of a metallocupramolecular tetrahedron, has been reported by Beer and co-workers.^[11b] Aside from the final two examples, these tetrahedra feature ligands with a flat trigonal core. Where the structure of **5** differs from these examples is in having a pyramidal ligand defining the triangular faces of the tetrahedron, which gives the assembly a spiked starlike aspect, somewhat akin to stellations of a prism.^[26] Figure 3a highlights this “star-burst” aspect of **5** and shows the tetrahedron of Ag^{I} ions and the centers of the lower rim $-(\text{CH}_2)_3-$ plane of the ligands. This “star-burst” topology engenders the structure with a greater internal volume than a tetrahedron of equivalent dimensions formed with a planar trigonal ligand.

Overall, the $[\text{Ag}_4(\mathbf{3})_4(\text{CH}_3\text{CN})_4]^{4+}$ prism is a molecular host for five molecules of acetonitrile. Four of these acetonitrile guests form host–guest interactions, each with an individual ligand, in which the hydrophobic methyl group is directed into the molecular cavity. Distances between the methyl carbon atom of the guest and the lower rim $-(\text{CH}_2)_3-$ plane of the host ligand range between 3.74 and 3.86 Å. The fifth acetonitrile molecule is disordered across two positions with 65 % occupancy as the *endo* CH_3CN molecule coordinated to $\text{Ag}(\mathbf{3})$ and 35 % occupancy as a guest in the middle of the assembly (Figure 3b).

The tetrahedral prisms pack together in the crystal lattice with various π -stacking interactions apparent. These include face-to-face interactions between core arene groups at centroid separations of 3.56 Å and edge-to-face interactions between pyridyl CH groups and core arene groups at C–H...centroid separations of 2.40 Å (C...centroid distance 3.3 Å). The additional solvent molecules and BF_4^- counterions fill spaces created by the packing of the prisms. These sites are approximations of the tetrahedral and octahedral interstitial holes displayed by close-packing spheres, which are created as $[\text{Ag}_4(\mathbf{3})_4(\text{CH}_3\text{CN})_4]^{4+}$ has a roughly spherical surface. Note that $[\text{Ag}_4(\mathbf{3})_4(\text{CH}_3\text{CN})_4]^{4+}$ does not genuinely close pack as it is not truly spherical; distortions are such that each $[\text{Ag}_4(\mathbf{3})_4(\text{CH}_3\text{CN})_4]^{4+}$ unit is in proximity to 11 others rather than the 12 expected of a genuinely close-packed array.

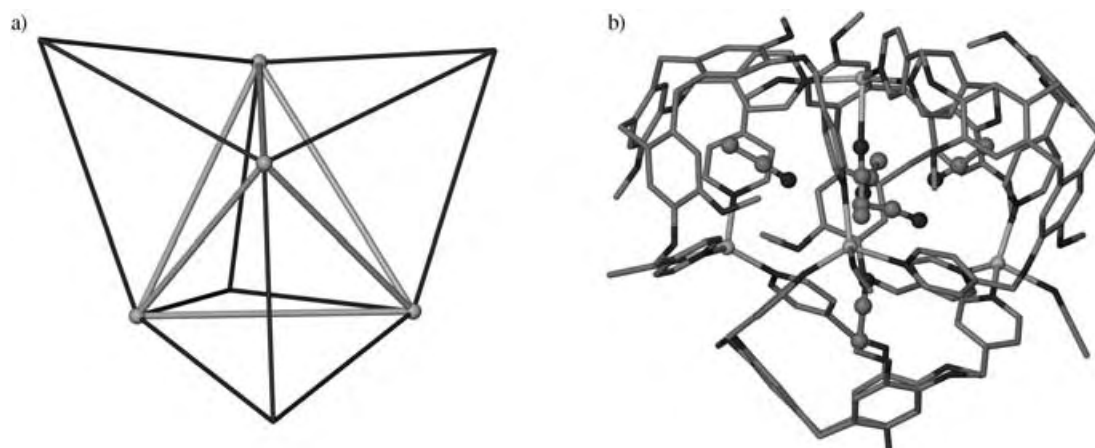


Figure 3. a) Star-burst aspect of $[\text{Ag}_4(\mathbf{3})_4(\text{CH}_3\text{CN})_4]^{4+}$ with Ag^{I} centers shown as spheres and the centers of the ligand's lower rim $-(\text{CH}_2)_3-$ plane shown as 3-connecting points. b) Host–guest associations within prism $[\text{Ag}_4(\mathbf{3})_4(\text{CH}_3\text{CN})_4]^{4+}$ with guest CH_3CN molecules inside the prism shown in ball-and-stick representation.

We have reported herein the first structural characterizations of metallosupramolecular cages incorporating ligands derived from the molecular host CTV. In the first case, the additional flexibility engineered into our ligand system over that reported by Shinkai and co-workers, coupled with the geometrically more accommodating silver centers have resulted in the isolation and structural characterization of a more compact $[M_2L_2]$ molecular capsule which incarcerates two coordinated CH_3CN guests. The utilization of the more-divergent 4-pyridyl ligand **3** led to the formation of a significantly expanded stellated tetrahedron with an internal space capable of accommodating five CH_3CN guest molecules. This dichotomy of structures observed presents the intriguing possibility that by tailoring the size of the guest we can control the formation of various metallosupramolecular cages with this ligand system.

Received: April 19, 2005

Published online: September 7, 2005

Keywords: coordination modes · host–guest systems · N ligands · silver · supramolecular chemistry

- [1] J. W. Steed, J. L. Atwood, *Supramolecular Chemistry*, Wiley, Chichester, **2000**.
- [2] H. Zimmermann, P. Tolstoy, H.-H. Limbach, R. Poupko, L. Z. Rappaport, *J. Phys. Chem. B* **2004**, *108*, 18772–18778.
- [3] S. T. Mough, J. C. Goeltz, K. T. Holman, *Angew. Chem.* **2004**, *116*, 5749–5753; *Angew. Chem. Int. Ed.* **2004**, *43*, 5631–5635; .
- [4] For reviews, see: a) S. R. Seidel, P. J. Stang, *Acc. Chem. Res.* **2002**, *35*, 972–983; b) M. Fujita, K. Umemoto, M. Yoshizawa, N. Fujita, T. Kusukawa, K. Biradha, *Chem. Commun.* **2001**, 509–518; c) G. F. Sweigert, T. J. Malefeste, *Chem. Rev.* **2000**, *100*, 3483–3537; d) D. L. Caulder, K. N. Raymond, *Acc. Chem. Res.* **1999**, *32*, 975–982.
- [5] M. J. Hardie, R. Mills, C. J. Sumby, *Org. Biomol. Chem.* **2004**, *2*, 2958–2964.
- [6] a) M. J. Hardie, C. L. Raston, A. Salinas, *Chem. Commun.* **2001**, 1850–1851; b) R. Ahmad, M. J. Hardie, *CrystEngComm* **2002**, *4*, 227–231; c) R. Ahmad, I. Dix, M. J. Hardie, *Inorg. Chem.* **2003**, *42*, 2182–2184.
- [7] C. J. Sumby, M. J. Hardie, *Cryst. Growth Des.* **2005**, *5*, 1321–1324.
- [8] Z. Zhong, A. Ikeda, S. Shinkai, S. Sakamoto, K. Yamaguchi, *Org. Lett.* **2001**, *3*, 1085–1087.
- [9] For a review, see: A. Collet, *Tetrahedron* **1987**, *43*, 5725–5759.
- [10] For example, see: a) R. Pinalli, V. Cristini, V. Sottili, S. Geremia, M. Campagnolo, A. Caneschi, E. Dalcanele, *J. Am. Chem. Soc.* **2004**, *126*, 6516–6517; b) M. J. Hardie and C. L. Raston, *J. Chem. Soc. Dalton Trans.* **2000**, 2483–2492; c) L. R. MacGillivray, P. R. Diamente, J. L. Reid, J. A. Ripmeester, *Chem. Commun.* **2000**, 359–360; d) J. Rebek, Jr., *Chem. Commun.* **2000**, 637–643.
- [11] a) O. D. Fox, M. G. B. Drew, E. J. S. Wilkinson, P. D. Beer, *Chem. Commun.* **2000**, 391–392; b) D. Fox, M. G. B. Drew, P. D. Beer, *Angew. Chem.* **2000**, *112*, 139–144; *Angew. Chem. Int. Ed.* **2000**, *39*, 135–140; .
- [12] a) G. W. V. Cave, J. Antesberger, L. J. Barbour, R. M. McKinlay, J. L. Atwood, *Angew. Chem.* **2004**, *116*, 5375–5378; *Angew. Chem. Int. Ed.* **2004**, *43*, 5263–5266; b) J. L. Atwood, L. J. Barbour, A. Jerga, *Chem. Commun.* **2001**, 2376–2377; c) T. Gerkenmeier, W. Iwanek, C. Agena, R. Fröhlich, S. Kotila, C. Näther, J. Mattay, *Eur. J. Org. Chem.* **1999**, 2257–2262.
- [13] L. R. MacGillivray, J. L. Atwood, *Nature* **1997**, *389*, 469–472.
- [14] G. W. Orr, L. J. Barbour, J. L. Atwood, *Science* **1999**, *285*, 1049–1052.
- [15] J. L. Atwood, L. J. Barbour, S. J. Dalgarno, M. J. Hardie, C. L. Raston, H. R. Webb, *J. Am. Chem. Soc.* **2004**, *126*, 13170–13171.
- [16] a) D. S. Bohle, D. J. Stasko, *Inorg. Chem.* **2000**, *39*, 5768–5770; b) C. Garcia, J. Malthête, A. Collet, *Bull. Soc. Chim. Fr.* **1995**, *132*, 52–58.
- [17] Crystal data for **4**: $C_{96}H_{102}Ag_2F_{12}N_{18}O_6P_2$, $M_r = 2109.64$, triclinic, $P\bar{1}$, $a = 12.789(3)$, $b = 13.779(3)$, $c = 15.735(3)$ Å, $\alpha = 98.26(3)$, $\beta = 110.38(3)$, $\gamma = 104.71(3)^\circ$, $V = 2430.1(8)$ Å³, $Z = 1$, $\rho_{\text{calcd}} = 1.442$ Mg cm⁻³, $\mu = 0.522$ mm⁻¹, $F(000) = 1084$, colorless block, $0.31 \times 0.23 \times 0.13$ mm³, $2\theta_{\text{max}} = 55.48^\circ$, $T = 150(1)$ K, 46790 reflections, 11104 unique (99.7% completeness), $R_{\text{int}} = 0.0888$, 658 parameters, $GOF = 1.037$, $wR2 = 0.1380$ for all data, $R_1 = 0.0477$ for 8477 data with $I > 2\sigma(I)$. CCDC-268973 contains supplementary crystal data for this structure. Crystal data for **5**: $C_{190}H_{196}Ag_4B_4F_{16}N_{35}O_{14.80}$, $M_r = 3985.34$, orthorhombic, $Pbca$, $a = 34.132(7)$, $b = 32.714(7)$, $c = 35.700(7)$ Å, $V = 39862(14)$ Å³, $Z = 8$, $\rho_{\text{calcd}} = 1.328$ Mg cm⁻³, $\mu = 0.469$ mm⁻¹, $F(000) = 16411$, colorless block, $0.18 \times 0.13 \times 0.07$ mm³, $2\theta_{\text{max}} = 42.08^\circ$, $T = 150(1)$ K, 116753 reflections, 21415 unique (99.5% completeness), $R_{\text{int}} = 0.1335$, 2361 parameters, $GOF = 1.086$, $wR2 = 0.3673$ for all data, $R_1 = 0.1096$ for 12572 data with $I > 2\sigma(I)$. CCDC-268974 contains the supplementary crystallographic data for this paper. These data can be obtained free of charge from the Cambridge Crystallographic Data Centre via www.ccdc.cam.ac.uk/data_request/cif.
- [18] R. Ahmad, M. J. Hardie, *Cryst. Growth Des.* **2003**, *3*, 493–499.
- [19] For example, see: a) T. Beissel, R. E. Powers, K. N. Raymond, *Angew. Chem.* **1996**, *108*, 1166–1168; *Angew. Chem. Int. Ed. Engl.* **1996**, *35*, 1084–1086; b) D. L. Caulder, R. E. Powers, T. N. Parac, K. N. Raymond, *Angew. Chem.* **1998**, *110*, 1940–1943; *Angew. Chem. Int. Ed.* **1998**, *37*, 1840–1843; c) M. Ziegler, A. V. Davis, D. W. Johnson, K. N. Raymond, *Angew. Chem.* **2003**, *115*, 689–692; *Angew. Chem. Int. Ed.* **2003**, *42*, 665–668; d) S. Mann, G. Huttner, L. Zsolnai, K. Heinze, *Angew. Chem.* **1996**, *108*, 2983–2984; *Angew. Chem. Int. Ed. Engl.* **1996**, *35*, 2808–2809; e) J. S. Fleming, K. L. Mann, C.-A. Carraz, E. Psillakis, J. C. Jeffery, J. A. McCleverty, M. D. Ward, *Angew. Chem.* **1998**, *110*, 1315–1318; *Angew. Chem. Int. Ed.* **1998**, *37*, 1279–1281; ; f) R. L. Paul, Z. R. Bell, J. C. Jeffery, J. A. McCleverty, M. D. Ward, *Proc. Natl. Acad. Sci. USA* **2002**, *99*, 4883–4888; g) R. L. Paul, S. P. Argent, J. C. Jeffery, L. P. Harding, J. M. Lynam, M. D. Ward, *Dalton Trans.* **2004**, 3453–3458; h) R. W. Saalfrank, A. Stark, K. Peters, H. G. Von Schnering, *Angew. Chem.* **1988**, *100*, 878–880; *Angew. Chem. Int. Ed. Engl.* **1988**, *27*, 851–853; ; i) E. J. Enemark, T. D. P. Stack, *Angew. Chem.* **1998**, *110*, 977–981; *Angew. Chem. Int. Ed.* **1998**, *37*, 932–935.
- [20] K. Umemoto, K. Yamaguchi, M. Fujita, *J. Am. Chem. Soc.* **2000**, *122*, 7150–7151.
- [21] I. M. Müller, R. Robson, F. Separovic, *Angew. Chem.* **2001**, *113*, 4519–4520; *Angew. Chem. Int. Ed.* **2001**, *40*, 4385–4386.
- [22] a) C. Brückner, R. E. Powers, K. N. Raymond, *Angew. Chem.* **1998**, *110*, 1937–1940; *Angew. Chem. Int. Ed.* **1998**, *37*, 1837–1839; b) D. L. Caulder, C. C. Brückner, R. E. Powers, S. König, T. N. Parac, J. A. Leary, K. N. Raymond, *J. Am. Chem. Soc.* **2001**, *123*, 8923–8938; c) R. W. Saalfrank, H. Glaser, B. Demleiter, F. Hampel, M. M. Chowdhry, V. Schünemann, A. X. Trautwein, G. B. M. Vaughan, R. Yeh, A. V. Davis, K. N. Raymond, *Chem. Eur. J.* **2002**, *8*, 493–497.
- [23] M. Albrecht, I. Janser, S. Meyer, P. Weis, R. Fröhlich, *Chem. Commun.* **2003**, 2854–2855.
- [24] S. Hiraoka, T. Yi, M. Shiro, M. Shionoya, *J. Am. Chem. Soc.* **2002**, *124*, 14510–14511.

- [25] A. J. Amoroso, J. C. Jeffery, P. L. Jones, J. A. McCleverty, P. Thornton, M. D. Ward, *Angew. Chem.* **1995**, *107*, 1577–1580; *Angew. Chem. Int. Ed. Engl.* **1995**, *34*, 1443–1445.
- [26] Stellations arise from extending the edges of a polyhedron so that they intersect to form a star. A tetrahedron cannot strictly show a stellation as the extended edges of a tetrahedron never meet. Often the overall effect of stellation is to produce pyramidal faces in place of flat faces; hence this prism is reminiscent of a stellated prism. For an example of a complex with a stellated structure, see: E. C. Constable, C. E. Housecroft, M. Neuburger, S. Reymann, S. Schaffner, *Chem. Commun.* **2004**, 1056–1057.

Structure Elucidation

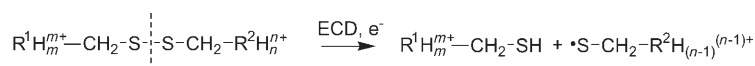
DOI: 10.1002/anie.200501533

Facile Disulfide Bond Cleavage in Gaseous Peptide and Protein Cations by Ultraviolet Photodissociation at 157 nm**

Y. M. Eva Fung, Frank Kjeldsen,* Oleg A. Silivra,
T. W. Dominic Chan, and Roman A. Zubarev*

Disulfide bonds formed between cysteine residues stabilize the native structure of many proteins.^[1] These covalent cross-linkages are part of the tertiary structure and introduce conformational constraints to the polypeptide architecture, thus improving the thermodynamic stability. Mass spectrometry has become increasingly important in the characterization and identification of proteins as a result of its capability for highly specific measurements on relatively small amounts of analyte. Protein characterization and identification relies on database searches using primary sequence information obtained by tandem mass spectrometry (MSⁿ or MS/MS). The top-down approach^[2] applied to intact protein ions is an efficient MS/MS method which is potentially suited for the high-throughput characterization

of proteins. The problems addressed by the top-down approach include verification of the protein sequence, localization of errors in DNA-predicted sequences, de novo sequencing, as well as the analysis of pre- or posttranslational modifications (PTMs). However, such PTMs as disulfide bonds still remain a challenge for traditional MS/MS techniques that utilize vibrational excitation (VE), as they break peptide bonds preferentially in protonated polypeptides and leave the disulfide bonds intact.^[3] As a result, information on the primary sequence is limited to parts of the protein that is not constrained by disulfide bonds. This restriction complicates primary sequence elucidation and limits the utility of automated database searches. The problem of disulfide bonds is solved conventionally by their reduction and alkylation^[4] prior to MS/MS measurements. However, the additional step involving solution-phase chemistry, including subsequent purification, greatly increases the analysis time and the risk of sample loss. Another approach is to use an alternative ion-dissociation strategy. Chrisman and McLuckey have shown that VE of deprotonated polypeptides induced by collisionally activated dissociation (CAD)^[5] breaks disulfide bonds with high efficiency.^[6] However, CAD of peptide anions often produces complicated mass spectra that, together with backbone cleavages, contain significant amounts of neutral mass losses and rearrangement products which make such MS/MS spectra of limited value for sequencing. Electron-capture dissociation (ECD)^[7] stands alone in its ability to cleave S–S bonds preferentially in peptide polycations (Scheme 1).^[3] A



Scheme 1. Charge reduction by cleavage of the disulfide bond with ECD.

drawback of this technique is that the capture of a low-energy electron by multiply charged polypeptides results in charge reduction prior to bond cleavage, which in turn leads to a charge decrease in one of the two fragments. As species need to contain at least one charge to be detectable in mass spectrometry, the charge reduction in ECD can lead to a loss of information.

Previously, when magnetic sector instruments were widely used, high-energy CAD (HE CAD) was utilized to produce cleavage of numerous disulfide bonds in peptides.^[8] The abundance of this fragmentation channel compared to low-energy CAD has been explained by electronic excitation. Today, HE CAD can only be found in TOF/TOF instruments that are more suitable for peptides than for proteins, and for which MSⁿ abilities are limited above $n=2$. Therefore, a fragmentation technique is needed that is suitable for MSⁿ of protein cations and that would not involve charge reduction.

We have assumed that if the HE CAD efficiency for cleavage of a disulfide bond is indeed a result of electronic excitation, a similar effect could be expected upon irradiation of polycations with ultraviolet (UV) light. Indeed, irradiation of desorbed cations with light of wavelength 337 nm in matrix-assisted laser desorption ionization (MALDI) studies^[9] results in partial reduction of the S–S bonds in situ.^[10] The

[*] Dr. F. Kjeldsen, Dr. O. A. Silivra, Prof. R. A. Zubarev
Laboratory for Biological and Medical Mass Spectrometry
BMC, Uppsala University
Box 583, 75123 Uppsala (Sweden)
Fax: (+46) 18-471-22-44
E-mail: frank.kjeldsen@bmms.uu.se
roman.zubarev@bmms.uu.se

Y. M. E. Fung, Prof. T. W. D. Chan
Department of Chemistry
The Chinese University of Hong Kong
H.K.S.A.R. (China)

[**] This work was supported by the Swedish Research Council and KAW Foundation (to R.Z.) as well as by the CUHK Postgraduate Student Grants for Overseas Academic Activities (grant no. 0680026 to Y.M.E.F.).



Supporting information for this article is available on the WWW under <http://www.angewandte.org> or from the author.

wavelength of maximum absorption for the S–S bond in, for example, cystine (Cys-S-S-Cys) is approximately 150 nm.^[11] Therefore, one may expect an efficient cleavage of the S–S bond upon UV photodissociation (UVPD) at 157 nm. This cleavage would compete with the backbone fragmentation of peptide monocations reported by Reilly and co-workers that resulted in unusual cleavage of the backbone C_α–C bonds (a, x-type fragments).^[12] The fragmentation of the peptide backbone in that study was explained as a result of electronic excitation of the polyamide bonds as a consequence of absorption of photons of 7.9 eV.

Herein, we have tested the above assumption and present evidence of a facile cleavage of both intra- and intermolecular disulfide bonds in peptide and protein polycations by UVPD at 157 nm. Figure 1 presents a comparison of the MS/MS spectra obtained with CAD, ECD, and consecutive UVPD and CAD (UVPD/CAD) of a peptide dimer linked by an intermolecular disulfide bridge. The CAD mass spectrum (Figure 1a) of the $[M+3H]^{3+}$ ions contains only a few (ten) b- and y-type fragment ions (in b ions, the charge is retained on the N-terminal side of the peptide, and in y ions on the C-terminal side).^[13] However, there was no evidence for cleavage of the disulfide bond. In contrast, ECD (Figure 1b) produced abundant signals corresponding to free monomers

and thus to cleavage of the S–S bond. Charge reduction meant that only singly charged peptide monomers were observed, thus rendering them useless for MS³ by ECD, as electron capture would neutralize them and their products. UVPD at 157 nm (Figure 1c) also cleaved the disulfide bond, and led to both singly and doubly charged peptide monomers. The efficiency of the dissociation of the S–S bond (defined as the ratio of the released monomer abundances divided by the total ion abundance) by UVPD at 157 nm was 1.2% compared to 2.3% with ECD. However, UVPD at 157 nm was implemented on a linear ion trap that was approximately 100 times more sensitive than the Fourier transform analyzer on which the ECD mass spectrum was obtained. Thus, the twofold loss of efficiency was more than compensated by the huge advantage in sensitivity. Furthermore, the efficiency of the S–S bond cleavage in UVPD increases as the positive charge decreases (data not shown).

Only limited information on the sequence of the peptide dimers was obtained in MS² with UVPD at 157 nm, as the S–S bond was cleaved at a higher rate than the peptide backbone. Therefore, the released doubly charged peptide monomers were isolated and subjected to MS³ by CAD (Figure 1d and e), which resulted in extensive fragmentation of the backbone (> 60% sequence coverage). The same procedure was carried

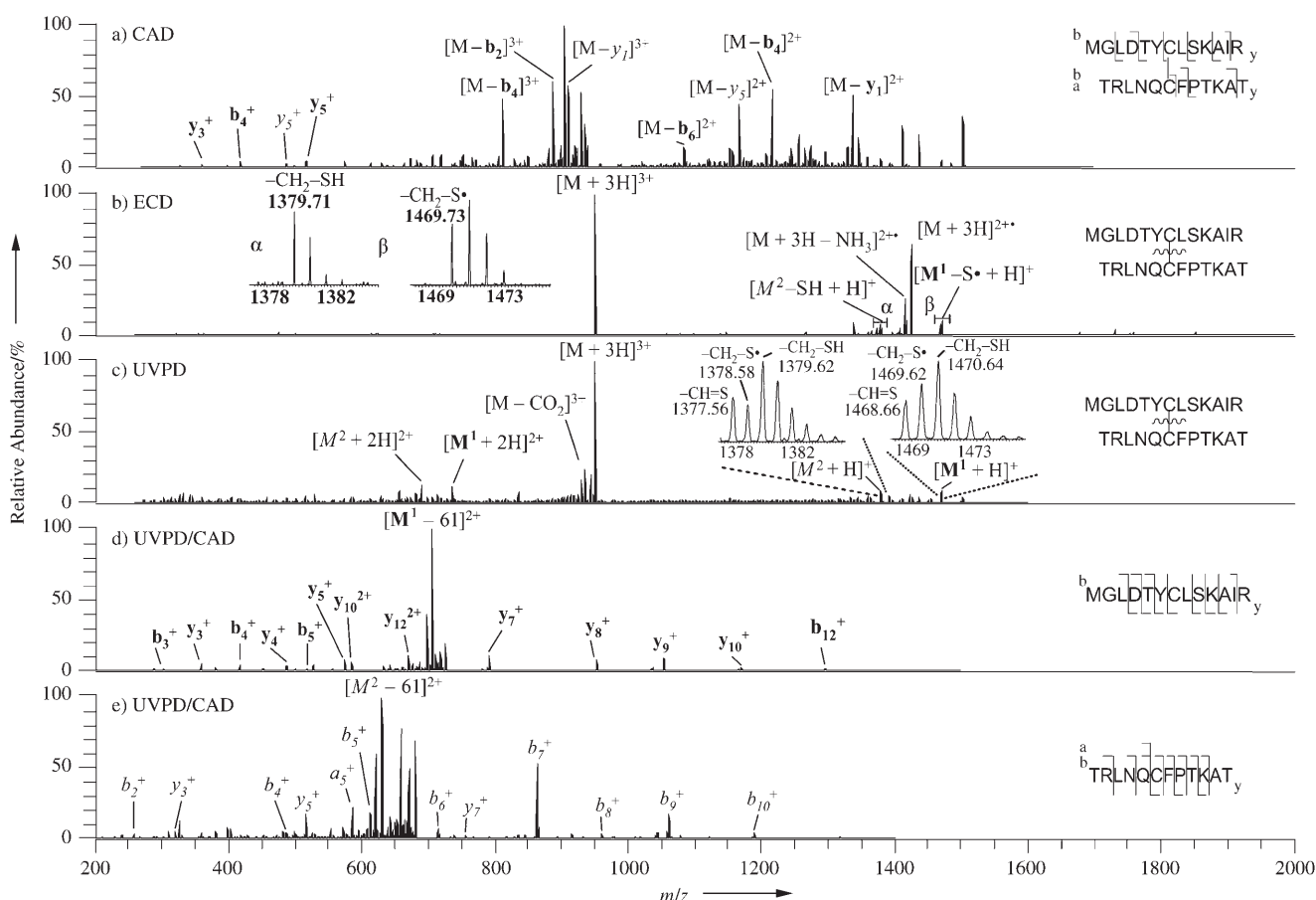


Figure 1. a)–c) Tandem mass spectra of a disulfide-bridged peptide dimer, M^1 -S-S- M^2 ; where M^1 = MGLDTYCLSKAIR and M^2 = TRLNQCFPTKAT. Fragments from M^1 are marked in bold and that from M^2 are marked in italics. The fragmentation techniques were: a) CAD, b) ECD, c) UVPD at 157 nm, d) CAD of isolated $[M^1+2H]^{2+}$ after UVPD at 157 nm of M^1 -S-S- M^2 trications; e) CAD of isolated $[M^2+2H]^{2+}$ after UVPD at 157 nm of M^1 -S-S- M^2 trications. The identities of the $[M^{1,2}-61]^{2+}$ peaks in (d) and (e) are currently under investigation.

out on singly charged peptide monomers, which increased the overall sequence coverage to 96 %, with only one interresidue bond not cleaved. The combined sequence information of all the disulfide-linked peptide dimers studied is summarized in Figure 2.



Figure 2. a) Fragmentation schemes of three trications of disulfide-bridged peptide dimers resulting from UVPD/CAD at 157 nm.

We hypothesize that UVPD breaks disulfide bonds by homolytic cleavage induced by electronic excitation. This process should result in two complementary fragments with radicals localized on each of the sulfur atoms ($R^1CH_2S^\bullet$ / $R^2CH_2S^\bullet$). However, the isotopic pattern observed for the sulfenyl radical (see inset of Figure 1c) was much broader than the theoretically calculated distribution. To investigate this effect further we isolated separately two isotope components of the UVPD-released doubly charged TRLNQCFPTKAT peptide monomer and fragmented them by CAD (Figure 3a and b, respectively). Only the cysteine-containing fragment ions exhibited a mass difference of 1 Da between the two spectra—other fragment ions were of the same mass. This result implies that the mass difference of 1 Da between the two monomeric ions was not exclusively the consequence of stable isotopes (for example, ^{12}C versus ^{13}C), but also the result of the presence of two different species ($R^1CH_2S^\bullet$ and R^1CH_2SH). Similarly, isolation and MS/MS of the isotope 1 Da below the monoisotopic signal confirmed the identity of these ions as $R^1CH=S$ (data not shown).

Thus, three mechanisms for the cleavage of disulfide bonds in UVPD at 157 nm were proposed (Scheme 2). Electronic excitation by photon absorption can lead to rapid cleavage of the disulfide bond and formation of two sulfenyl radicals $R^1CH_2S^\bullet$ and $R^2CH_2S^\bullet$ (path a). If fragment separation is delayed because of noncovalent bonds between the monomers, the proximity of the two radical peptide chains

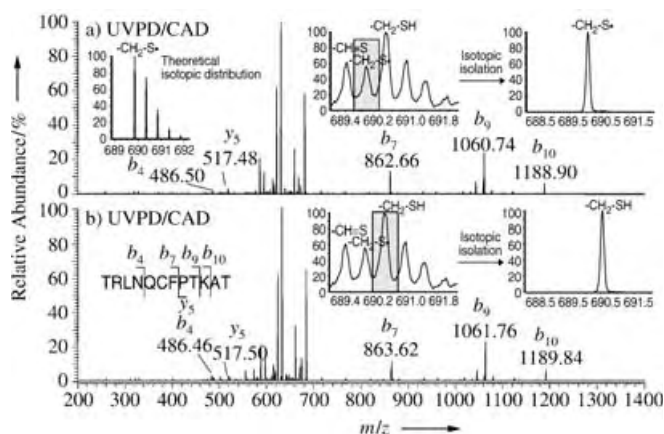
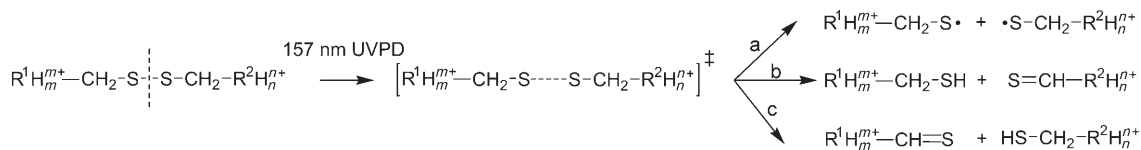


Figure 3. CAD mass spectra of isolated isotopic ions after UVPD at 157 nm of dications of the TRLNQCFPTKAT peptide corresponding to masses of a) monoisotopic signal and b) the first isotopic signal.

can result in intermolecular hydrogen transfer. This process leads to reactions (path b or path c) where either abstraction of a H atom by a peptide monomer from the other monomer forms sulphydryl or thioaldehyde ($-CH_2SH$ or $-CH=S$) functional groups. Alternatively, absorption of a photon by a dimer leads to intramolecular hydrogen rearrangement, with an H atom attacking the S–S bond, as has been suggested for ECD.^[3,14] Additional evidence for this latter mechanism comes from the observation of abundant loss of H atoms from irradiated precursor ions (data not shown), thus indicating that hydrogen abstraction and rearrangement do play a significant role in UVPD at 157 nm.

The ability of UVPD at 157 nm to cleave intramolecular disulfide bonds was tested on the peptide RLCADTPICGK with a disulfide bridge between the two cysteine residues. Figure 4 shows the CAD spectrum (Figure 4a) and the UVPD spectrum (Figure 4b) for comparison. While CAD yielded only three b and one y ions with no cleavage of the disulfide bond, UVPD generated a series of a-type (a_2 – a_{10}) fragment ions (a ions correspond to cleavage of a C_α –C backbone bond with the charge retained on the N-terminal side) and two d-type fragment ions (d_n ions form from radical a_n ions by loss of side-chains from the C-terminal residue), all as a consequence of cleavage of the disulfide bond. The observation of a-type fragment ions in UVPD at 157 nm was in agreement with the results obtained by Reilly and co-workers.^[12] Two other peptide ions with intramolecular disulfide bonds gave similar fragmentation (data not shown).

Moving from model peptides to biologically relevant proteins, we applied UVPD at 157 nm to human insulin, a 5.9-kDa molecule containing polypeptide chains A and B linked by two disulfide bonds, and with one S–S bond within the



Scheme 2. Suggested reaction pathways for the cleavage of the disulfide bond by UVPD at 157 nm.

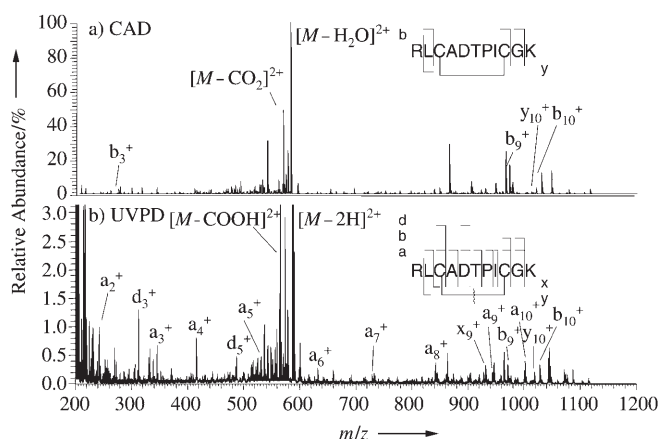


Figure 4. Tandem mass spectra of dications of the peptide RLCADTPICGK with an intramolecular disulfide bridge, obtained with: a) CAD and b) UVPD at 157 nm.

A chain (Figure 5). Previously, ECD of 6+ ions have released free A and B chains, but only the B chain gave a MS³ spectrum.^[3] Here, UVPD of [M+6H]⁶⁺ ions (Figure 5a) yielded predominantly the quadruply charged B chain and doubly charged A chain by simultaneous cleavage of both intermolecular disulfide bonds. CAD on the isolated 4+ charged B chain (Figure 5b) gave abundant *b* and *y* fragment ions covering 59% of the sequence. CAD was performed on 2+ charged A-chain ions (Figure 5c) to determine whether the intramolecular S–S bond in the A chain was also cleaved. This experiment yielded *b* and *y* ions covering 85% of the

sequence. Observation of seven fragments arising from backbone cleavages between the two cysteine residues confirmed the breakage of the intramolecular S–S bond. Thus, the UVPD/CAD combination provided the most complete top-down sequence verification of a protein with three S–S bonds to date.

In summary, we have demonstrated the ability of UVPD at 157 nm to cleave both intra- and intermolecular disulfide bonds without charge reduction in peptide and protein cations. This methodology is expected to be useful in de novo sequencing of polypeptides. As a note of caution, competition with backbone cleavages in UVPD complicates identification of complementary fragment pairs arising exclusively from cleavage of the S–S bond in de novo sequencing. This problem can be addressed by first performing CAD of the intact protein to reveal complementary pairs arising from cleavage of the backbone. While classical reduction of the S–S bond in solution may still provide a clearer answer, the faster UVPD approach that avoids time- and sample-consuming wet chemistry will be preferred in many cases. As photons are not affected by electromagnetic irradiation, UVPD can easily be adapted to different types of mass analyzers, which broadens the application range of this technique.

Experimental Section

Cysteine-containing peptides were synthesized by automated solid-phase synthesis using the 9-fluorenylmethoxycarbonyl (Fmoc) protection strategy on a research-scale ResPep peptide synthesizer (Intavis AG, Gladbach, Germany). The oxidation of the cysteine residues was performed on 0.5 mg of peptides in a solution of DMSO (20 µL) in 20 mM NH₄HCO₃ (aq, 80 µL) for two days at RT. Human insulin (Sigma, St Louis, MO) was used without further purification. Mass-spectrometric experiments were performed on a linear ion trap mass spectrometer (Thermo Electron, San Jose, CA) equipped with a nanoelectrospray interface operated in the positive ion mode. Oxidized peptides were diluted in a solvent containing acetic acid/methanol/water (2:49:49, v/v/v) to approximately 10^{−6} M and electrosprayed. An excimer F₂ UV laser at 157 nm (Excistar S500, Tuilaser, Germering, Germany) was connected with the mass spectrometer by means of a CaF₂ window on-axis with the ion trap. Unfocused laser pulses (15 ns, 1 mJ) with a repetition rate of 500 Hz were passed through a 1.5-mm collimator installed in front of the window. Isolated precursor ions were irradiated for 3 to 9 ms with UV light. ECD experiments were performed on a 7 Tesla FT mass spectrometer (Thermo Electron AG, Bremen, Germany) equipped with an indirectly heated cathode as an electron source. The electron irradiation in ECD lasted for 70 ms.

Received: May 4, 2005

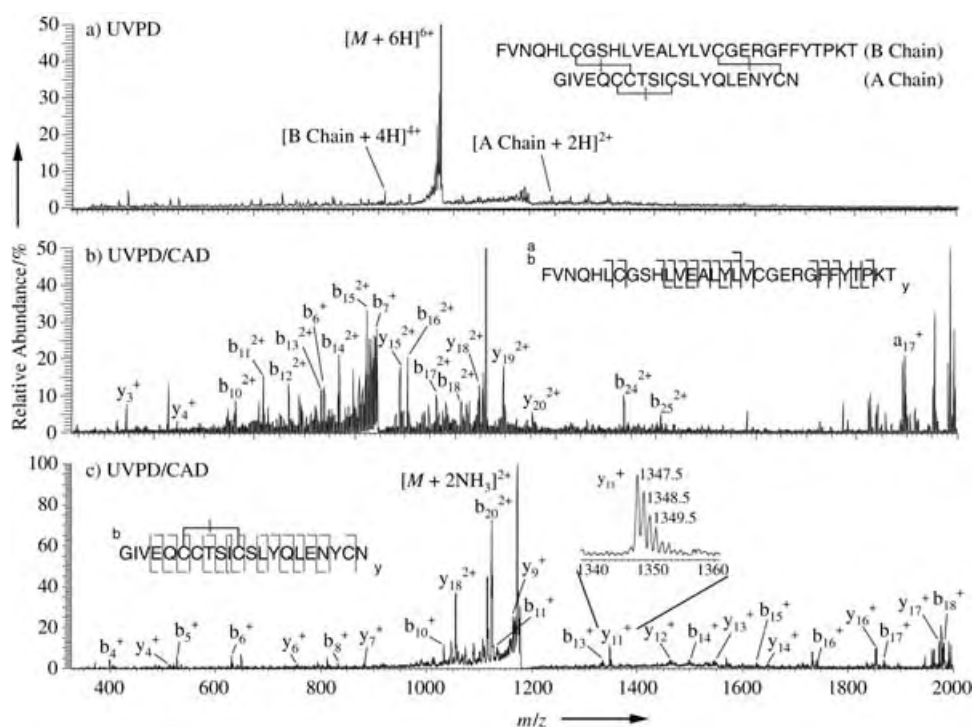


Figure 5. a) Mass spectrum of human insulin 6+ ions obtained by UVPD at 157 nm, b) CAD spectrum of [M+4H]⁴⁺ ions of the B chain released in UVPD at 157 nm from 6+ insulin ions, c) CAD spectrum of [M+2H]²⁺ ions of the A chain released in UVPD at 157 nm from 6+ insulin ions. The inset shows the isotopic distribution of *y*₁₁ ions (Ile–Cys bond cleaved) confirming breakage of the disulfide bond.

Keywords: mass spectrometry · photodissociation · proteins · radical chemistry · sequencing

-
- [1] M. Matsumura, G. Signor, B. W. Matthews, *Nature* **1989**, *342*, 291.
 - [2] N. L. Kelleher, H. Y. Lin, G. A. Valaskovic, D. J. Aaserud, E. K. Fridriksson, F. W. McLafferty, *J. Am. Chem. Soc.* **1999**, *121*, 806.
 - [3] R. A. Zubarev, N. A. Kruger, E. K. Fridriksson, M. A. Lewis, D. M. Horn, B. K. Carpenter, F. W. McLafferty, *J. Am. Chem. Soc.* **1999**, *121*, 2857.
 - [4] J. A. Loo, C. G. Edmonds, H. R. Udseth, R. D. Smith, *Anal. Chem.* **1990**, *62*, 693.
 - [5] W. F. Haddon, F. W. McLafferty, *J. Am. Chem. Soc.* **1968**, *90*, 4745.
 - [6] P. A. Chrisman, S. A. McLuckey, *J. Proteome Res.* **2002**, *1*, 549.
 - [7] R. A. Zubarev, N. L. Kelleher, F. W. McLafferty, *J. Am. Chem. Soc.* **1998**, *120*, 3265.
 - [8] J. T. Stults, J. H. Bourell, E. Canovadavis, V. T. Ling, G. R. Laramée, J. W. Winslow, P. R. Griffin, E. Rinderknecht, R. L. Vandlen, *Biomed. Environ. Mass Spectrom.* **1990**, *19*, 655.
 - [9] M. Karas, D. Bachmann, U. Bahr, F. Hillenkamp, *Int. J. Mass Spectrom. Ion Process.* **1987**, *78*, 53.
 - [10] J. Qin, B. T. Chait, *Anal. Chem.* **1997**, *69*, 4002.
 - [11] J. W. Preiss, R. Setlow, *J. Chem. Phys.* **1956**, *25*, 138.
 - [12] M. S. Thompson, W. D. Cui, J. P. Reilly, *Angew. Chem.* **2004**, *116*, 4895; *Angew. Chem. Int. Ed.* **2004**, *43*, 4791.
 - [13] P. Roepstorff, J. Fohlman, *Biomed. Mass Spectrom.* **1984**, *11*, 601.
 - [14] E. Uggerud, *Int. J. Mass Spectrom.* **2004**, *234*, 45.

covalent linear glycan polymer that consists of alternating *N*-acetylglucosamine (GlcNAc) and *N*-acetylmuramic acid (MurNAc) residues, the latter of which have an appended pentapeptide chain. In addition to the transglycosylase and transpeptidase enzyme families, the biosynthesis of peptidoglycan involves a number of ATP-dependant ligases (namely the Mur ligases). These catalyze the assembly of the pentapeptide moiety through the successive addition of L-Ala, D-Glu, *m*-dpm or L-Lys, and D-Ala–D-Ala to UDP-MurNAc by MurC, MurD, MurE, and MurF enzymes, respectively (*m*-dpm = *meso*-diaminopimelic acid; UDP = uridine-5'-diphosphoryl). An additional ATP-dependant enzyme, D-Ala–D-Ala ligase (DD-ligase) is responsible for supplying the D-Ala–D-Ala dipeptide, which is the substrate for MurF.

Inhibition of any of these essential enzymes in either Gram-positive or Gram-negative organisms leads to the loss of cell shape and integrity followed by bacterial death.^[2–4] The emergence of bacterial strains that are resistant to all antibiotics in current clinical use has created an urgent need for the development of new inhibitors of peptidoglycan biosynthesis enzymes and, in particular, those that act on targets that have not been previously exploited.

As part of a structure-based design and synthesis program for the discovery of new enzyme inhibitors, we previously described the computer-aided molecular design, synthesis, and biological evaluation of novel inhibitors of the ligase responsible for D-Glu attachment, MurD.^[5] Other research groups, using either library-screening methods or substrate-inspired approaches, have also reported useful inhibitors of the MurC^[6–8] and MurD^[6,9,10] ligases. A phosphinate-based transition-state isostere of DD-ligase has also been reported.^[10]

The structure-based design of small-molecule enzyme inhibitors is a powerful tool in drug discovery, particularly if an X-ray crystal structure of the target enzyme is available. For cases in which the X-ray crystal structure includes a substrate or a known inhibitor, a substrate-inspired approach can be adopted; classical molecular modeling techniques can be used to alter the structure of the co-crystallized substrate, and a new molecule with enhanced enzyme-binding affinity can be produced. To identify different inhibitor structure types, the technique of virtual high-throughput screening (VHTS) can also be applied to the crystal structure of the enzyme in an attempt to identify new “hits” by docking the 3D structures of molecules contained in a database.^[11]

However, both techniques have a number of drawbacks. The substrate-inspired approach requires a suitable enzyme–substrate co-crystal structure. Furthermore, the structures of the designed molecules will necessarily be biased toward that of the original co-crystallized small molecule, which, as is the case for many natural enzyme substrates, may not possess drug-like properties and may not be an ideal starting point. Although suitable databases allow the design of molecules by the VHTS method to focus on drug-like fragments, this technique is limited by the size and diversity of the small-molecule database; even databases that consist of millions of compounds constitute only a small fraction of the available “diversity space”.

Enzyme Inhibitors

DOI: 10.1002/anie.200501662

A De Novo Designed Inhibitor of D-Ala–D-Ala Ligase from *E. coli*

Gilbert E. Besong, Julianne M. Bostock,
Will Stubbings, Ian Chopra, David I. Roper,
Adrian J. Lloyd, Colin W. G. Fishwick,* and
A. Peter Johnson*

Peptidoglycan is an essential component of the bacterial cell wall and provides the structural integrity necessary to resist internal osmotic pressure and to prevent cell lysis.^[1] It is a

[*] G. E. Besong, Dr. C. W. G. Fishwick, Prof. Dr. A. P. Johnson
School of Chemistry, University of Leeds
Leeds, LS2 9JT (UK)
Fax: (+44) 113-343-6565
E-mail: c.w.g.fishwick@leeds.ac.uk
a.p.johnson@chem.leeds.ac.uk

Dr. J. M. Bostock, Dr. W. Stubbings, Prof. Dr. I. Chopra
Department of Biochemistry and Molecular Biology
University of Leeds
Leeds, LS2 9JT (UK)

Dr. D. I. Roper, Dr. A. J. Lloyd
Department of Biological Sciences, University of Warwick
Coventry, CV4 7AL (UK)

Recent reports involving the application of de novo design indicate that this approach is a powerful alternative to these classical drug discovery approaches.^[12–15] Through the use of only structural features present within the enzyme, new inhibitor designs can be built up sequentially according to the requirements of the targeted binding site. Therefore, in principle, de novo design should be a far more useful technique than VHTS, because a good de novo design program will examine structure space many orders of magnitude larger than that of most virtual libraries currently in use for this purpose. Herein, we report the application of the de novo molecular design program SPROUT^[16] to the design of a novel inhibitor of DD-ligase from *E. coli*. We also describe the development of an efficient synthesis of this novel inhibitor and the enzymological characterization of its interaction with DD-ligase and a related enzyme.

SPROUT^[16] is a powerful suite of software modules for de novo structure-based molecular design. SPROUT has modules for 1) characterizing regions within a protein, 2) detecting “hot-spots” in which ligand atoms are expected to form strong interactions with the protein, 3) docking molecular fragments to these sites, 4) joining these fragments with a molecular backbone to give a complete ligand, and 5) ranking the set of predicted ligands by criteria that include predicted binding energy, structural complexity, and synthetic accessibility.

In *E. coli*, there are two isoforms of DD-ligase (DdlA and DdlB) encoded by the genes *ddlA* and *ddlB*, with similar kinetic characteristics. The crystal structure of *E. coli* DdlB complexed with a phosphorylphosphinate inhibitor and resolved to 2.3 Å has been used to propose a catalytic mechanism for the formation of D-Ala-D-Ala.^[17] To use a de novo approach for the discovery of novel DD-ligase inhibitors, we applied SPROUT to the X-ray crystal structure^[18] of DD-ligase encoded by *ddlB* from *E. coli*.

The active site contains two distinct D-alanine binding sites; the N-terminal site is a high-affinity site with strict substrate specificity, whereas the C-terminal site is a lower-affinity site showing lower substrate specificity.^[19] A phosphonate-based transition-state isostere is included in the crystal structure of DdlB, located within the active site. It makes direct contacts with essentially all of the residues implied by the catalytic reaction mechanism^[17] (Figure 1).

To design a structurally simple inhibitor which was predicted to show high affinity for the enzyme, we wished to use only a small number of these contacts in our SPROUT design strategy. Examination of this active site with SPROUT indicated that use of the side chains of residues R255 and E15, the C α backbone N–H group of G276, and the magnesium ion Mg331 should result in relatively simple designed molecular templates. Additionally, SPROUT analysis revealed the presence of a small hydrophobic region (which is not used by the phosphonate isostere) between the phenolic ring of Y216 and the alkyl side chain of L282 that we also wished to use for inhibitor design. During this work, it became apparent that the design of a molecular template which allows good contacts to be made to all these sites would require a rigid small-ring framework; the cyclopropyl-based amino acid **1**

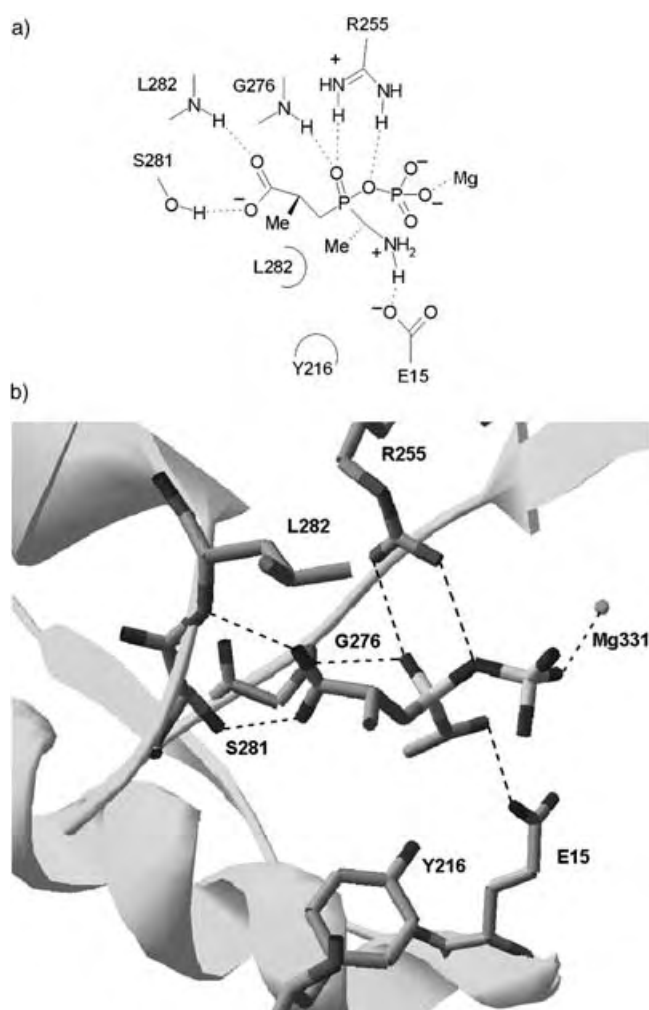


Figure 1. a) The bonding interactions between the phosphonate-based isostere and DdlB based on the crystal structure; b) view of the DdlB active site.

(Figure 2) was selected from the many suggestions that arose from the SPROUT design iterations.

One of us recently reported the X-ray crystal structure of the closely related ligase VanA co-crystallized with the same phosphinate-based isostere as described above for DdlB.^[20] In addition to the DD-ligases, VanA is present in certain vancomycin-resistant enterococci and is responsible for the formation of D-alanine-D-lactate. This unit is then incorporated into the pentapeptide chain, and it is the resulting lactate-containing peptide that binds poorly to vancomycin. We were aware that although the overall topology of the active sites of VanA and DdlB were very similar, there are also important differences, particularly in the hydrophobic region bordered by L282 and Y216 in DdlB (corresponding to R317 and H244 in VanA). We therefore used SPROUT to produce a model of our designed inhibitor **1** within the active site of VanA (Figure 3). This revealed that the three designed hydrogen-bonding contacts to E15 (E16 in VanA), R255 (R290 in VanA), and G276 (G311 in VanA) as well as binding to the magnesium ion were possible for the inhibitor **1** bound within the active site of VanA. However, VanA possesses a

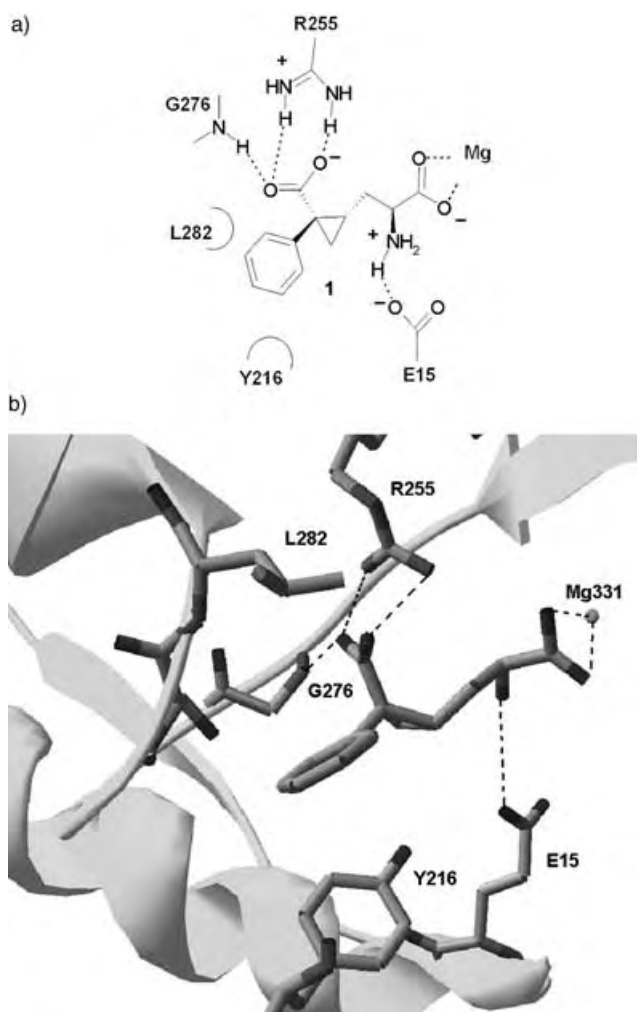


Figure 2. a) The bonding interactions of SPROUT-designed inhibitor **1**; b) view of inhibitor **1** within DdlB active site.

much narrower hydrophobic region between H244 and R317 than the equivalent region in DdlB (between L282 and Y216) due to protrusion of the imidazole ring of VanA H244 into the cavity (Figure 3). In fact, SPROUT analysis of the inhibitor **1**–VanA complex indicated that this inhibitor should bind only very poorly to VanA. Following synthesis, we therefore planned to measure the affinity of inhibitor **1** with both DdlB and VanA and test the selectivity of our inhibitor predicted by these computational studies.

A short synthesis of cyclopropane **1** was developed and is summarized below (Scheme 1). Ring opening of the readily available racemic lactone **2**^[21] followed by halogen exchange and oxidation afforded aldehyde **3**. Olefination with phosphorane **4** followed by catalytic reduction of the double bond with concomitant *N*-deprotection and final ester hydrolysis yielded the desired inhibitor **1** as an inseparable 1:1 mixture of diastereomers.^[22]

Enzymological evaluation^[23] of designed inhibitor **1** was performed with recombinant *E. coli* DdlB and VanA enzymes. In keeping with our modeling predictions, this molecule (as a diastereomeric mixture) inhibits the activity of DdlB with an apparent K_i value of $12.5(\pm 0.1) \mu\text{M}$, whereas it

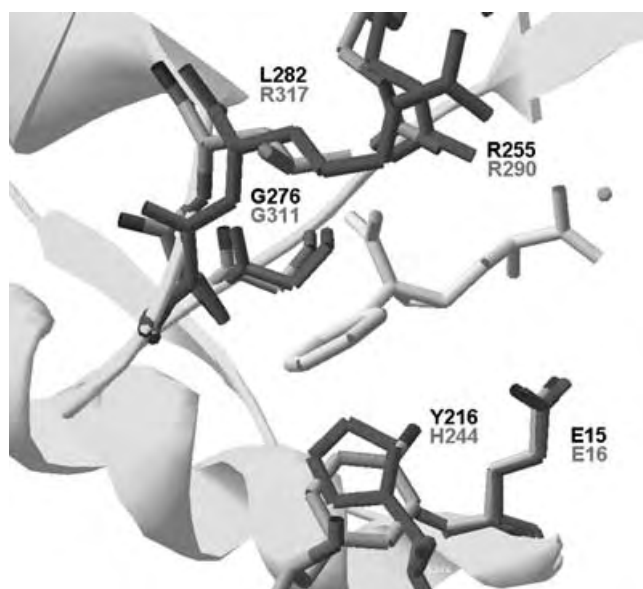
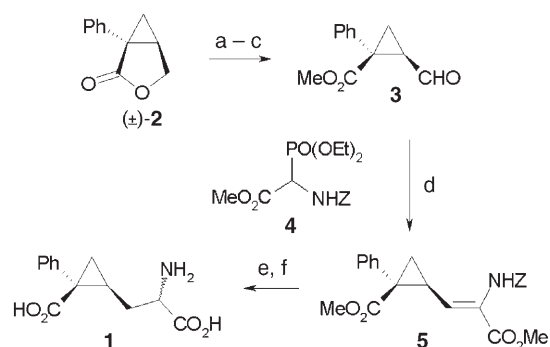


Figure 3. SPROUT-designed DdlB inhibitor **1** in the active site of VanA showing contacting residues. The corresponding residues in DdlB are superimposed (VanA residues in darker shading, DdlB numbering shown above VanA numbering).



Scheme 1. Synthesis of inhibitor **1**: a) SOBr_2 , MeOH, 93%; b) NaI, Me_2CO , 98%; c) DMSO, $i\text{Pr}_2\text{NEt}$, 63%; d) **4**, DBU, 87%; e) H_2 , Pd/C, MeOH, 33%; f) LiOH, MeOH, 63%. DBU = 1,8-diazabicyclo-[5.4.0]undec-7-ene.

had no inhibitory activity against VanA. The apparent K_i value of cycloserine for DdlB, a known inhibitor of this enzyme, was $1.4 \mu\text{M}$. Clearly, the designed template is for a single enantiomer of absolute stereochemistry shown in Figure 2. In these proof-of-principal studies, however, we chose to perform biological evaluation with a readily available diastereomeric mixture containing this designed template along with equimolar amounts of three other stereoisomeric versions of this inhibitor. Therefore, although the measured binding affinity of this mixture to DdlB is very encouraging, it is likely that the actual designed enantiomer **1** is an even more potent inhibitor of DdlB. It should be noted that the production of inhibitors that are active at the low micromolar concentration range after pure de novo design is quite typical of the current state of this approach; of course, inhibitors active at this level provide an excellent starting

point for further optimization. Development of more accurate functions for the estimation of binding affinity remains a key requirement for further progress in the de novo design of even more potent inhibitors.

In summary, it appears that SPROUT-based de novo design holds tremendous potential for the rapid discovery of selective inhibitors of DdlB and related enzymes. We believe that this approach is complementary to the use of high-throughput screening and is particularly attractive for cases in which such screening methodology is not available or in which access to large collections of library compounds of sufficient molecular diversity is limited.

Received: May 13, 2005

Revised: June 4, 2005

Published online: September 13, 2005

Keywords: inhibitors · ligases · medicinal chemistry · molecular modeling · molecular recognition

- [1] K. H. Schleifer, D. Kandler, *Bacteriol. Rev.* **1972**, 36, 407–412.
- [2] K. Isono, M. Uramoto, H. Kusakabe, K. Kimura, K. Izaki, C. C. Nelson, J. A. McCluskey, *J. Antibiot.* **1985**, 38, 1617–1620.
- [3] K. Kimura, Y. Ikeda, S. Kagami, M. Yoshihara, *J. Antibiot.* **1998**, 51, 1099–1103.
- [4] D. W. Green, *Expert Opin. Ther. Targets* **2002**, 6, 1–5.
- [5] J. R. Horton, J. M. Bostock, I. Chopra, L. Hesse, S. E. V. Phillips, D. J. Adams, A. P. Johnson, C. W. G. Fishwick, *Bioorg. Med. Chem. Lett.* **2003**, 13, 1557–1560.
- [6] Z. Li, G. D. Francisco, W. Hu, P. Labthavikul, P. J. Petersen, A. Severin, G. Singh, Y. J. Yang, B. A. Rasmussen, Y. I. Lin, J. S. Skotnicki, T. S. Mansour, *Bioorg. Med. Chem. Lett.* **2003**, 13, 2591–2594.
- [7] D. E. Ehmman, J. E. Demeritt, K. G. Hull, S. L. Fisher, *Biochim. Biophys. Acta Proteins Proteom.* **2004**, 1698, 167–174.
- [8] A. El Zoeiby, F. Sanschagrin, A. Darveau, J. R. Brisson, R. C. Levesque, *J. Antimicrob. Chemother.* **2003**, 51, 531–543.
- [9] M. E. Tanner, S. Vaganay, J. van Heijenoort, D. Blanot, *J. Org. Chem.* **1996**, 61, 1756–1760.
- [10] L. D. Gegnas, S. T. Waddell, R. M. Chabin, S. Reddy, K. K. Wong, *Bioorg. Med. Chem. Lett.* **1998**, 8, 1643–1648.
- [11] K. M. Branson, B. J. Smith, *Aust. J. Chem.* **2004**, 57, 1029–1037.
- [12] G. Schneider, O. Clement-Chomienne, L. Hilfiger, P. Schneider, S. Kirsch, H.-J. Bohm, W. Neidhart, *Angew. Chem.* **2000**, 112, 4305–4309; *Angew. Chem. Int. Ed.* **2000**, 39, 4130–4133.
- [13] Q. Han, C. Dominguez, P. F. W. Stouten, J. M. Park, D. E. Duffy, R. A. Gallemmo Jr., K. A. Rossi, R. S. Alexander, A. M. Smallwood, P. C. Wong, M. M. Wright, J. M. Luetzgen, R. M. Knabb, R. R. Wexler, *J. Med. Chem.* **2000**, 43, 4398–4415.
- [14] T. Honma, K. Haysashi, T. Aoyama, N. Hashimoto, T. Machida, K. Fukasawa, T. Iwama, C. Ikeura, M. Ikuta, I. Suzuki-Takahashi, Y. Iwasawa, T. Hayama, S. Nishimura, H. Morishima, *J. Med. Chem.* **2001**, 44, 4615–4627.
- [15] B. A. Grzybowski, A. V. Ishchenko, C.-Y. Kim, G. Topalov, R. Chapman, D. W. Christianson, G. M. Whitesides, E. I. Shakhnovich, *Biophysics* **2002**, 99, 1270–1273.
- [16] V. J. Gillet, W. Newell, P. Mata, G. Myatt, S. Sike, Z. Zsoldos, A. P. Johnson, *J. Chem. Inf. Comput. Sci.* **1994**, 34, 207–217.
- [17] C. Fan, P. C. Moews, C. T. Walsh, J. R. Knox, *Science* **1994**, 266, 439–443.
- [18] Brookhaven Protein Data Bank code 2DLN.
- [19] L. E. Zawadzke, T. D. H. Bugg, C. T. Walsh, *Biochemistry* **1991**, 30, 1673–1682.
- [20] D. I. Roper, T. Huyton, A. Vagin, G. Dodson, *Proc. Natl. Acad. Sci. USA* **2000**, 97, 8921–8925.
- [21] S. Shuto, H. Takada, D. Mochizuki, R. Tsujita, Y. Hase, S. Ono, N. Shibuya, A. Matsuda, *J. Med. Chem.* **1995**, 38, 2964–2968.
- [22] Diastereoisomer ratio determined by high-resolution NMR analysis. Attempts to separate the diastereomeric mixture under a variety of HPLC conditions proved unsuccessful.
- [23] Apparent K_i values were estimated with the method of Y. Cheng, W. H. Prusoff, *Biochem. Pharmacol.* **1973**, 22, 3099–3108. For DdlB assays (K_m for the first D-Ala site on DdlB = 3.3 μ M), activity was monitored by detection of orthophosphate using malachite green; see: P. A. Lanzetta, P. S. Alvarez, P. S. Reinach, O. A. Candia, *Biochemistry* **1979**, 18, 95–98. Assays were performed at 37°C with inhibitor **1** (between 0.003 mM and 32 mM), DdlB (0.32 mM), and enzyme substrate in reaction buffer: (HEPES (50 mM, pH 8), ATP (1 mM), $MgCl_2$ (10 mM), KCl (10 mM), D-Ala (2.5 mM)), malachite green-molybdate (50 μ M, malachite green hydrochloride (0.045 % w/v) and ammonium molybdate (4.2 % w/v) in 4-N HCl). VanA assays were performed with the same inhibitor concentration range as for DdlB by using the method of I. A. Lessard, V. L. Healy, I. S. Park, C. T. Walsh, *Biochemistry* **1999**, 38, 14006–14022, following the D-Ala and D-lactate dependent release of ADP.

Bioinorganic Chemistry

DOI: 10.1002/anie.200501916

N*-Methylhydroxylamido(1-)- and Nitrosomethaneruthenium Complexes Derived from Nitrosyl Complexes: Reversible N-Protonation of an N-Coordinated Nitrosoalkane*

Satoshi Kura, Shigeki Kuwata,* and Takao Ikariya*

Nitric oxide (NO), nitroxyl (HNO), and hydroxylamine have been invoked as key intermediates in the biological multi-electron reduction of nitrite to ammonia, which is a fundamental process in the inorganic nitrogen cycle in nature. The reaction is catalyzed by a certain type of nitrite reductase that contains heme moieties at its active site.^[1] Within this context,

[*] S. Kura, Prof. Dr. S. Kuwata, Prof. Dr. T. Ikariya
Department of Applied Chemistry
Graduate School of Science and Engineering
Frontier Collaborative Research Center
Tokyo Institute of Technology
O-okayama, Meguro-ku, Tokyo 152-8552 (Japan)
Fax: (+81) 3-5734-2637
E-mail: skuwata@apc.titech.ac.jp
tikariya@apc.titech.ac.jp

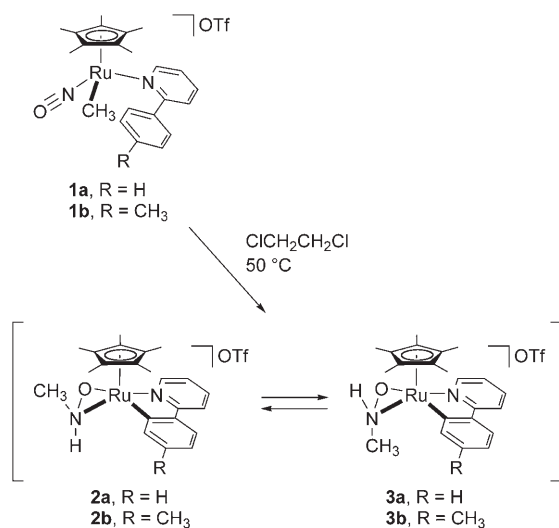
[**] This work was supported by a Grant-in-Aid for Scientific Research on Priority Areas (no. 14078209, "Reaction Control of Dynamic Complexes") from the Ministry of Education, Culture, Sports, Science, and Technology, Japan.



Supporting information for this article is available on the WWW under <http://www.angewandte.org> or from the author.

the electrochemical reduction of nitrite to ammonia by coordination compounds of iron and its congeners ruthenium and osmium has been studied extensively.^[2] In these systems, however, the exact formulation and coordination mode of the intermediary nitroxyl and hydroxylamine complexes are not known. Indeed, interconversion of these partially reduced nitrogenous species, including their organic derivatives such as nitrosoalkanes (RNO), on late transition-metal centers remains unexplored^[3–8] compared with that on the early transition metals.^[9,10] In an early example, Roper and co-workers^[3] reported the reversible protonation of the nitrosyl complex $[\text{Ir}(\text{NO})\{\text{P}(\text{C}_6\text{H}_5)_3\}_3]$ by HCl to afford the hydroxylamine complex $[\text{IrCl}_3(\text{NH}_2\text{OH})\{\text{P}(\text{C}_6\text{H}_5)_3\}_2]$. Although the nitroxyl complex $[\text{IrCl}(\text{HNO}-\kappa\text{N})\{\text{P}(\text{C}_6\text{H}_5)_3\}_3]$ has recently been characterized as an initial protonation product in this transformation,^[4] the second protonation site of the nitroxyl complex, for example, is still unclear. We now describe the stepwise transformation of nitrosylruthenium complexes to nitrosoalkane and *N*-alkylhydroxylamido(1–) complexes, as well as the facile interconversion of the latter two species.

The thermolysis of the linear nitrosyl complexes $[\text{Cp}^*\text{Ru}(\text{NO})(\text{CH}_3)(\text{NC}_5\text{H}_4\text{Ar}-2)](\text{OTf})$ (**1a**, Ar = C₆H₅; **1b**, Ar = 4-CH₃C₆H₄; Cp* = C₅Me₅)^[11] gave mixtures of the two isomeric *N*-methylhydroxylamido(1–)- $\kappa^2\text{N},\text{O}$ complexes **2** and **3** (Scheme 1). Fortunately, all of these isomers, except



Scheme 1. Synthesis of **2** and **3**.

for the phenylpyridine derivative **3a**, could be isolated by adjusting the reaction conditions and subsequent workup procedure. The solid-state structures of the tolylpyridine derivatives **2b** and **3b** are depicted in Figure 1.^[12] The two isomers **2b** and **3b** have the same stereochemistry around the Ru atom but are differentiated by the relative orientation of the Cp* and methyl groups with respect to the three-membered RuNO ring; these groups lie on the same side of the RuNO plane in **2** and on the opposite side in **3**. The N–O distances (1.380(5) and 1.377(4) Å) are unexceptional for hydroxylamido(1–) complexes.^[9,14,15] Although the hydroxylamido(1–) H atom could not be located in the difference Fourier map, close contacts (ca. 2.9 Å) of the N atom and the

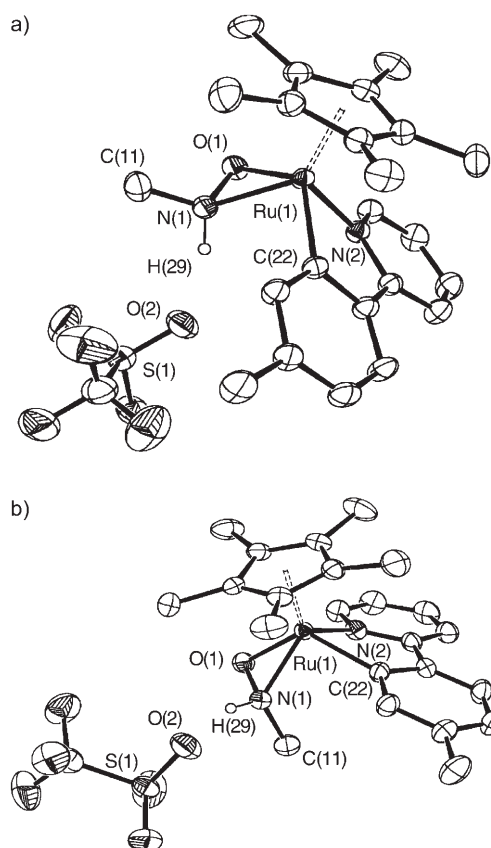
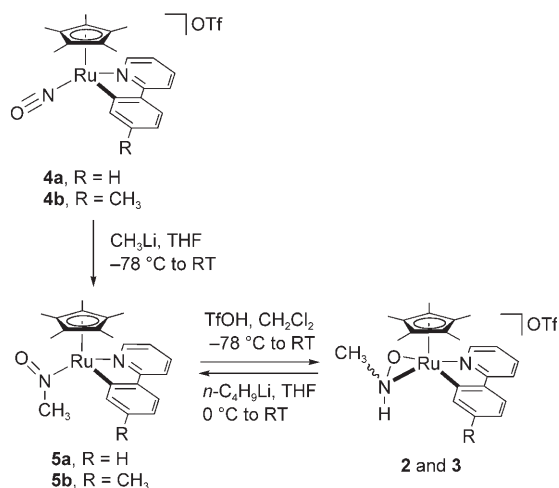


Figure 1. Structures of a) **2b** and b) **3b** with 30% ellipsoids. Hydrogen atoms except that for the hydroxylamido group are omitted for clarity. Selected interatomic distances [Å] for **2b**: Ru(1)–O(1) 2.042(3), Ru(1)–N(1) 2.057(3), Ru(1)–N(2) 2.081(3), Ru(1)–C(22) 2.075(4), N(1)–O(1) 1.379(4), N(1)–O(2) 2.869(5). For **3b**: Ru(1)–O(1) 2.040(2), Ru(1)–N(1) 2.042(2), Ru(1)–N(2) 2.087(3), Ru(1)–C(22) 2.073(3), N(1)–O(1) 1.370(3), N(1)–O(2) 2.982(4).

triflate O atom in both crystals clearly indicate the presence of an amine proton hydrogen-bonded to the OTf[–] counterion. The presence of the amine proton was also deduced from the IR spectra, which display an NH stretching band around 3140 cm^{–1}. In the ¹H NMR spectra, the amine proton in **3** is observed at around δ = 8.6 ppm as a quartet split by the *N*-methyl protons with a ³J_{H,H} coupling constant of 4.4 Hz;^[16] the corresponding signal of **2** is overlapped by the aryl resonances around δ = 7.8 ppm. These observations confirm the formulation of the Ru^{IV} hydroxylamido(1–) complexes **2** and **3**. To the best of our knowledge, **2** and **3** are the first fully characterized hydroxylamido(1–) complexes of a late transition metal.^[5,7]

It should be noted that samples of isolated **2** and **3** undergo slow isomerization to give mixtures of **2** and **3**. The disappearance of the ¹H NMR signal of the amine proton upon treatment of **2** or **3** with D₂O suggests that the isomerization takes place by a deprotonation–protonation sequence that involves the amine proton. Dissociation of the M–N bond followed by inversion at the N atom^[17] seems less plausible because **2** and **3** were found to be inert towards various two-electron donor ligands such as CO, phosphanes, and alkynes at room temperature.

In the formation of **2** and **3** from **1**, the nitrosyl ligand undergoes an intramolecular methylation and protonation coupled with the cyclometalation of the coordinated arylpyridine. Evidence for the stepwise transformation of the nitrosyl ligand was obtained from separate experiments. Treatment of the ruthenacyclic complexes $[\text{Cp}^*\text{Ru}(\text{NO})(\text{C}_6\text{H}_3\text{R}-\text{C}_5\text{H}_4\text{N}-\kappa^2\text{N},\text{C})](\text{OTf})$ (**4a**, $\text{R} = \text{H}$; **4b**, $\text{R} = \text{CH}_3$)^[11] with an equimolar amount of CH_3Li afforded the Ru^{II} nitrosomethane- κN complexes **5** as the main product, although the yields of isolated product were unsatisfactory due to the difficulty in separating them from small amounts of uncharacterized by-products (Scheme 2). The X-ray crystal structure analysis of



Scheme 2. Transformation of **4** into **2** and **3** via **5**.

the phenylpyridine derivative **5a** revealed the N-coordination of the nitrosomethane ligand (Figure 2).^[12] The N–O distance of 1.264(13) Å is much shorter than those in the hydroxylamido(1–) complexes **2b** and **3b**. The nitrosomethane ligand, the Ru atom, and the centroid of the Cp^* ligand are coplanar to maximize the π back-donation to the nitrosomethane

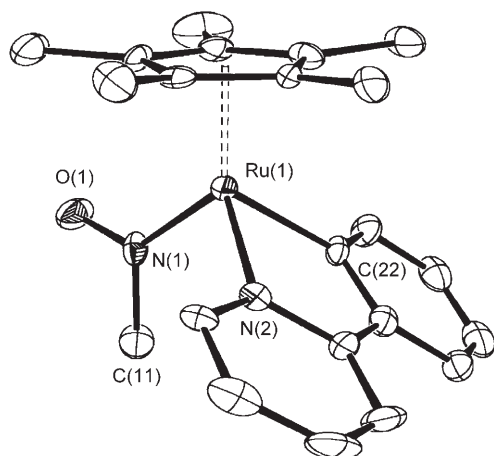
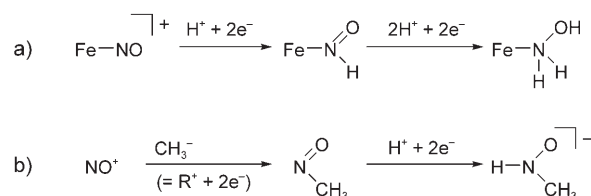


Figure 2. Structure of **5a** with 30% ellipsoids. Hydrogen atoms are omitted for clarity. Selected interatomic distances [Å] and angles [°]: $\text{Ru}(1)-\text{N}(1)$ 1.914(7), $\text{Ru}(1)-\text{N}(2)$ 2.067(7), $\text{Ru}(1)-\text{C}(22)$ 2.068(7), $\text{N}(1)-\text{O}(1)$ 1.27(1), $\text{N}(1)-\text{C}(11)$ 1.47(1); $\text{Ru}(1)-\text{N}(1)-\text{O}(1)$ 125.2(6), $\text{Ru}(1)-\text{N}(1)-\text{C}(11)$ 124.0(6), $\text{O}(1)-\text{N}(1)-\text{C}(11)$ 110.7(7).

ligand, as observed in the isoelectronic complex $[\text{Cp}^*\text{Ru}(\text{C}_6\text{H}_5)(\text{C}_2\text{H}_5\text{NO}-\kappa\text{N})\{\text{P}(\text{CH}_3)_2(\text{C}_6\text{H}_5)\}]$.^[18]

As expected, subsequent protonation of the nitrosomethane complexes **5** with a slight excess of triflic acid gave isomeric mixtures of the hydroxylamido(1–) complexes **2** and **3**. Despite the rich coordination chemistry of nitrosoalkane,^[19] protonation of well-defined nitrosoalkane (or nitroxyl) ligands on late transition-metal centers is extremely rare. The only precedent we are aware of is the *O*-protonation of the nitrosobenzene complex $[\text{Os}(\text{NO})\text{Cl}(\text{C}_6\text{H}_5\text{NO}-\kappa^2\text{N},\text{O})\{\text{P}(\text{C}_6\text{H}_5)_3\}_2]$, the product of which was characterized only by IR spectroscopy.^[7] Furthermore, the reverse reaction, namely deprotonation of isomeric mixtures of **2** and **3**, regenerated the nitrosomethane- κN complexes **5**. The formation of the nitroxyl- κN derivatives **5** contrasts sharply with the deprotonation of the hydroxylamido(1–)molybdenum complex $[\text{Mo}(\text{NO})(\text{terpy})(\text{H}_2\text{O})(\text{H}_2\text{NO}-\kappa^2\text{N},\text{O})]^{2+}$, which forms a nitroxyl- $\kappa^2\text{N},\text{O}$ complex.^[20]

The overall transformation shown in Scheme 2 has close relevance to the biological reduction of nitrite (Scheme 3). In the biological system, alternating proton and electron transfer



Scheme 3. a) Consecutive proton and electron transfer to the nitrosyl intermediate proposed for the mechanism of cytochrome *c* nitrite reductase. b) Sequential reduction of the nitrosyl ligand at the $\{\text{Cp}^*\text{Ru}(\text{C}_6\text{H}_3\text{R}-\text{C}_5\text{H}_4\text{N}-\kappa^2\text{N},\text{C})\}$ chromophore.

is thought to convert the nitrosyl intermediate into the heme-bound nitroxyl and hydroxylamine.^[1c] On the other hand, the nitrosyl ligand on the ruthenium complexes **4** is reduced upon methylation and subsequent protonation. The electrons for this reduction are formally supplied by the methyl anion in the first step, and by the Ru^{II} center in the nitrosomethane complexes **5** in the second step, to give the hydroxylamido(1–) ligand in the Ru^{IV} complexes **2** and **3**. Similarly, the reaction in Scheme 1 can be considered as the migratory insertion of the nitrosyl ligand in **1** into the $\text{Ru}-\text{CH}_3$ bond^[10,21] followed by an aromatic C–H bond activation and subsequent proton migration to the resultant nitrosomethane ligand. It should be emphasized that related electron–proton chemistry of the nitrosyl ligand has been observed only in some early transition-metal complexes.^[14,22]

In summary, we have demonstrated that organic derivatives of the possible intermediates in the inorganic nitrogen cycle, with various formal oxidation states of nitrogen ranging from +3 (NO^+) and +1 (RNO) to –1 (RNHO^-), can be stabilized, structurally characterized, and converted into each other on an organometallic platform. Reversible *N*-protonation of the nitrosoalkane ligand, which results in the formation of the unprecedented hydroxylamido(1–)ruthenium complexes **2** and **3**, is particularly noteworthy because it

sheds light on the detailed mechanism of the biological nitrite–ammonia conversion at a late transition-metal center. The reactions described herein also feature a facile aromatic C–H bond activation in **1** to give the high-valent, yet stable, Ru^{IV} center in **2** and **3**, and the isomerism of the novel *N*-methylhydroxylamido(1–) complexes of a late transition metal.

Received: June 2, 2005

Published online: September 12, 2005

Keywords: bioinorganic chemistry · C–H activation · N,O ligands · nitrogen oxides · ruthenium

- [1] a) B. C. Berks, S. J. Ferguson, J. W. B. Moir, D. J. Richardson, *Biochim. Biophys. Acta* **1995**, *1232*, 97–173; b) D. B. Knaff, M. Hirasawa, *Biochim. Biophys. Acta* **1991**, *1056*, 93–125; c) O. Einsle, A. Messerschmidt, R. Huber, P. M. H. Kroneck, F. Neese, *J. Am. Chem. Soc.* **2002**, *124*, 11737–11745; d) O. Einsle, A. Messerschmidt, P. Stach, G. P. Bourenkov, H. D. Bartunik, R. Huber, P. M. H. Kroneck, *Nature* **1999**, *400*, 476–480; e) O. Einsle, P. Stach, A. Messerschmidt, J. Simon, A. Kröger, R. Huber, P. M. H. Kroneck, *J. Biol. Chem.* **2000**, *275*, 39608–39616; f) S. Kuznetsova, D. B. Knaff, M. Hirasawa, B. Lagoutte, P. Sétif, *Biochemistry* **2004**, *43*, 510–517.
- [2] J. N. Younathan, K. S. Wood, T. J. Meyer, *Inorg. Chem.* **1992**, *31*, 3280–3285, and references therein.
- [3] K. R. Grundy, C. A. Reed, W. R. Roper, *J. Chem. Soc. Chem. Commun.* **1970**, 1501–1502.
- [4] R. Melenkivitz, G. L. Hillhouse, *Chem. Commun.* **2002**, 660–661.
- [5] A. R. Middleton, J. R. Thornback, G. Wilkinson, *J. Chem. Soc. Dalton Trans.* **1980**, 174–179.
- [6] a) D. Sellmann, T. Gottschalk-Gaudig, D. Häußinger, F. W. Heinemann, B. A. Hess, *Chem. Eur. J.* **2001**, *7*, 2099–2103; b) J. Lee, G. B. Richter-Addo, *J. Inorg. Biochem.* **2004**, *98*, 1247–1250.
- [7] M. Herberhold, A. F. Hill, *J. Organomet. Chem.* **1989**, *363*, 371–376.
- [8] a) R. D. Wilson, J. A. Ibers, *Inorg. Chem.* **1979**, *18*, 336–343; b) E. B. Boyar, A. Dobson, S. D. Robinson, B. L. Haymore, J. C. Huffman, *J. Chem. Soc. Dalton Trans.* **1985**, 621–627; c) S. J. Skoog, W. L. Gladfelter, *J. Am. Chem. Soc.* **1997**, *119*, 11049–11060; d) J. S. Southern, G. L. Hillhouse, A. L. Rheingold, *J. Am. Chem. Soc.* **1997**, *119*, 12406–12407; e) F. Ragaini, S. Cenini, S. Tollari, G. Tummolillo, R. Beltrami, *Organometallics* **1999**, *18*, 928–942; f) R. Lin, P. J. Farmer, *J. Am. Chem. Soc.* **2000**, *122*, 2393–2394; g) J.-L. Liang, J.-S. Huang, Z.-Y. Zhou, K.-K. Cheung, C.-M. Che, *Chem. Eur. J.* **2001**, *7*, 2306–2317; h) J. S. Southern, M. T. Green, G. L. Hillhouse, I. A. Guzei, A. L. Rheingold, *Inorg. Chem.* **2001**, *40*, 6039–6046; i) A. Llamazares, H. W. Schmalle, H. Berke, *Organometallics* **2001**, *20*, 5277–5288; j) R. Melenkivitz, J. S. Southern, G. L. Hillhouse, T. E. Concolino, L. M. Liable-Sands, A. L. Rheingold, *J. Am. Chem. Soc.* **2002**, *124*, 12068–12069; k) A. V. Marchenko, A. N. Vedernikov, D. F. Dye, M. Pink, J. M. Zaleski, K. G. Caulton, *Inorg. Chem.* **2004**, *43*, 351–360; l) P. J. Farmer, F. Sulc, *J. Inorg. Biochem.* **2005**, *99*, 166–184.
- [9] a) J. A. McCleverty, *Transition Met. Chem.* **1987**, *12*, 282–287; b) K. Wieghardt, *Adv. Inorg. Bioinorg. Mech.* **1984**, *3*, 213–274.
- [10] For reviews of the reactivities of nitrosyl complexes, see: a) T. W. Hayton, P. Legzdins, W. B. Sharp, *Chem. Rev.* **2002**, *102*, 935–991; b) P. C. Ford, I. M. Lorkovic, *Chem. Rev.* **2002**, *102*, 993–1017.
- [11] The detailed synthetic procedures and spectroscopic data for all the novel complexes **1–5** are provided as Supporting Information.
- [12] Crystal data for **2b**: monoclinic, $P2_1/c$, $a = 8.783(3)$, $b = 15.029(5)$, $c = 19.833(7)$ Å, $\beta = 99.106(6)^\circ$, $V = 2585.0(15)$ Å³, $Z = 4$, $\rho_{\text{calcd}} = 1.541$ g cm^{–3}, $F_{000} = 1224$, $\mu = 7.41$ cm^{–1}, transmission factors: 0.8592–1.0000, reflections measured 20196, independent reflections 5702, $R1 = 0.045$ [$I > 2\sigma(I)$], $wR2 = 0.116$ (all data), residual electron density 1.27/–0.57 e Å^{–3}. For **3b**: monoclinic, $P2_1/n$, $a = 8.287(4)$, $b = 15.301(6)$, $c = 21.140(9)$ Å, $\beta = 105.085(6)^\circ$, $V = 2588.1(19)$ Å³, $Z = 4$, $\rho_{\text{calcd}} = 1.539$ g cm^{–3}, $F_{000} = 1224$, $\mu = 7.40$ cm^{–1}, transmission factors: 0.7399–1.0000, reflections measured 20240, independent reflections 5868, $R1 = 0.036$ [$I > 2\sigma(I)$], $wR2 = 0.092$ (all data), residual electron density 0.57/–0.50 e Å^{–3}. For **5a**: orthorhombic, $Pna2_1$, $a = 17.493(3)$, $b = 8.510(2)$, $c = 13.009(2)$ Å, $V = 1936.5(6)$ Å³, $Z = 4$, $\rho_{\text{calcd}} = 1.494$ g cm^{–3}, $F_{000} = 896$, $\mu = 8.23$ cm^{–1}, transmission factors: 0.7993–1.0000, reflections measured 15411, independent reflections 4410, $R1 = 0.040$ [$I > 2\sigma(I)$], $wR2 = 0.143$ (all data), residual electron density 2.25/–2.22 e Å^{–3}. Data were collected at 193 K using a Rigaku Saturn CCD area detector with graphite-monochromated MoK α radiation ($\lambda = 0.7107$ Å) to a maximum 2θ value of 55°. Intensity data were corrected for Lorentz-polarization effects and for absorption. Structure solution and refinements were performed with the CrystalStructure program package.^[13] The structures were refined against F^2 with anisotropic temperature factors for all non-hydrogen atoms. All hydrogen atoms were added geometrically and refined by using a riding model. CCDC-265939 (**2b**), -265939 (**3b**), and -265940 (**5a**) contain the supplementary crystallographic data for this paper. These data can be obtained free of charge from the Cambridge Crystallographic Data Centre via www.ccdc.cam.ac.uk/data_request/cif.
- [13] CrystalStructure 3.6: Crystal Structure Analysis Package, Rigaku and Rigaku/MS, The Woodlands TX 77381 USA, **2000–2004**.
- [14] D. Sellmann, B. Seubert, F. Knoch, M. Moll, *Z. Naturforsch. B* **1991**, *46*, 1449–1458.
- [15] a) A. P. Dove, X. Xie, R. M. Waymouth, *Chem. Commun.* **2005**, 2152–2154; b) J. H. Doerrer, J. R. Galsworthy, M. L. H. Green, M. A. Leech, M. Müller, *J. Chem. Soc. Dalton Trans.* **1998**, 3191–3194; c) N. W. Mitzel, S. Parsons, A. J. Blake, D. W. H. Rankin, *J. Chem. Soc. Dalton Trans.* **1996**, 2089–2093.
- [16] The $^3J_{\text{H,H}}$ values in *N*-alkylhydroxylamido(1–) complexes fall in the range of 3.8–6.6 Hz: a) K. Wieghardt, E. Hofer, W. Holzbach, B. Nuber, J. Weiss, *Inorg. Chem.* **1980**, *19*, 2927–2932; b) K. Wieghardt, W. Holzbach, E. Hofer, J. Weiss, *Chem. Ber.* **1981**, *114*, 2700–2712; c) P. Legzdins, P. J. Lundmark, S. J. Rettig, *Organometallics* **1996**, *15*, 2988–2993.
- [17] E. Hofer, W. Holzbach, K. Wieghardt, *Angew. Chem.* **1981**, *93*, 303–304; *Angew. Chem. Int. Ed. Engl.* **1981**, *20*, 282–283.
- [18] J. Chang, M. D. Seidler, R. G. Bergman, *J. Am. Chem. Soc.* **1989**, *111*, 3258–3271.
- [19] a) J. Lee, L. Chen, A. H. West, G. B. Richter-Addo, *Chem. Rev.* **2002**, *102*, 1019–1065; b) M. Cameron, B. G. Gowenlock, G. Vasapollo, *Chem. Soc. Rev.* **1990**, *19*, 355–379; c) R. Wilberger, C. Krinninger, H. Piotrowski, P. Mayer, I.-P. Lorenz, *Eur. J. Inorg. Chem.* **2004**, 2488–2492.
- [20] K. Wieghardt, W. Holzbach, J. Weiss, *Z. Naturforsch. B* **1982**, *37*, 680–683.
- [21] a) W. P. Weiner, R. G. Bergman, *J. Am. Chem. Soc.* **1983**, *105*, 3922–3929; b) S. Niu, M. B. Hall, *J. Am. Chem. Soc.* **1997**, *119*, 3077–3086.
- [22] a) K. Wieghardt, U. Quilitzsch, *Z. Naturforsch. B* **1981**, *36*, 683–686; b) D. Sellmann, *J. Organomet. Chem.* **1989**, *372*, 99–107; c) P. Legzdins, S. J. Rettig, S. F. Sayers, *J. Am. Chem. Soc.* **1994**, *116*, 12105–12106; see also ref. [6].

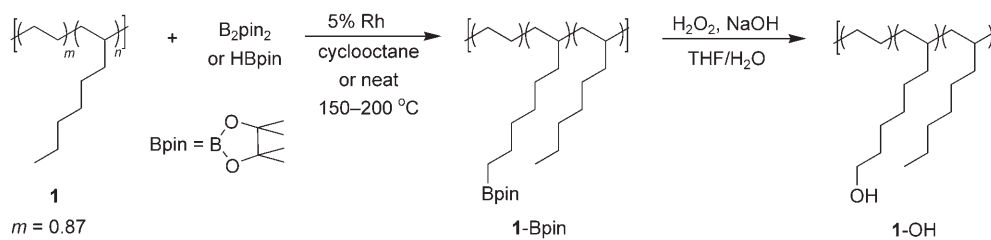
DOI: 10.1002/anie.200501837

Regiospecific Side-Chain Functionalization of Linear Low-Density Polyethylene with Polar Groups**

Chulsung Bae, John F. Hartwig,* Hoyong Chung, Nicole K. Harris, Karen A. Switek, and Marc A. Hillmyer*

The incorporation of polar functional groups along the backbone of polyolefins can significantly alter the physical properties and increase the utility of these commodity materials.^[1,2] A polar functionality can improve the interaction of these materials with other polymers and their adhesion to metals or glass. Moreover, functional groups in a polymer chain can serve as initiation sites for the formation of graft copolymers.^[2] Thus, polyolefins with polar groups have been a target for polymer synthesis.^[2–4]

We recently reported the synthesis of such materials by conducting selective, catalytic functionalization of the pendant methyl groups of a model atactic amorphous polybutene of moderate molecular weight^[5] and of commercial polypropylenes of various tacticities.^[6] Both polybutene and polypropylene contain an abundance of accessible methyl groups. In contrast, commercially important linear low-density polyethylenes (LLDPEs), generated from ethylene and an α -olefin, such as octene, contain a small population of methyl groups. Because the yields of the borylation of ali-



Scheme 1. Regiospecific functionalization and subsequent oxidation of linear low-density polyethylene (LLDPE).

phatic C–H bonds depend on the population of methyl groups in the system,^[7] the extension of the functionalization of polybutene and polypropylene to the functionalization of amorphous polybutene to LLDPE is challenging. Moreover, these polyolefins have been converted into materials with boronic esters and alcohols, but not into materials with groups such as amines or carbonyls which would be useful for generating ionic polymers or graft copolymers. We have recently met these challenges. Herein, we report the regio-specific functionalization of an ethylene–octene copolymer using pinacolborane (HBpin) or bis(pinacolato)diboron (B_2pin_2) as reagent in the presence of a rhodium catalyst, and the conversion of the resulting borylated polymer into a family of materials with hydroxy, amino, and formyl groups at the termini of the hexyl side chains.

As with the borylation of small alkanes,^[8] the rhodium-catalyzed reactions of HBpin and B_2pin_2 at 150–200 °C with a copolymer **1** of ethylene (87 mol %) and 1-octene (13 mol %) which has a number-average molecular weight (M_n) of 112 kgmol^{−1} and a polydispersity index ($PDI = M_w/M_n$) of 1.9,^[9] produced the corresponding polymer with boryl groups at the termini of the side chains. The isolated **1-Bpin** was then oxidized with NaOH/hydrogen peroxide in a mixture of THF and H₂O to give the corresponding polymer **1-OH** with hydroxy groups at the termini of the side chains (Scheme 1).

Both **1-Bpin** and **1-OH** were characterized by NMR spectroscopy. The borylated material **1-Bpin** gave rise to a

[*] Prof. C. Bae, Prof. J. F. Hartwig
Department of Chemistry, Yale University
P.O. Box 208107, New Haven, CT 06520-8107 (USA)
Fax: (+1) 203-432-6144
E-mail: john.hartwig@yale.edu

N. K. Harris, K. A. Switek, Prof. M. A. Hillmyer
Department of Chemistry, University of Minnesota
207 Pleasant Street SE, Minneapolis, MN 55455-0431 (USA)
Fax: (+1) 612-624-7029
E-mail: hillmyer@chem.umn.edu

Prof. C. Bae, H. Chung
Department of Chemistry, University of Nevada Las Vegas
4505 Maryland Parkway, Las Vegas, NV 89154-4003 (USA)

[**] We thank the National Science Foundation (CHE-0301907) and Frontier Scientific Co. for a gift of B_2pin_2 . C.B. thanks the UNLV Office of Research and Graduate Studies for support through the New Investigator Award, and Professor Byron L. Bennett for use of laboratory instrumentation.

Supporting information for this article is available on the WWW under <http://www.angewandte.org> or from the author.

broad peak in the ¹¹B NMR spectrum at $\delta = 34$ ppm for the alkyl–Bpin moiety and a resonance in the ¹H NMR spectrum at $\delta = 0.75$ ppm for the methylene groups adjacent to the Bpin units. The ¹³C NMR spectrum contained two signals of low intensity at $\delta = 24.9$ and 82.8 ppm from the Bpin groups. DEPT ¹³C NMR spectroscopy confirmed that these signals corresponded to methyl and quaternary carbon atoms.

After treatment of **1-Bpin** with basic hydrogen peroxide, no signals for an alkyl–Bpin moiety were observed in the ¹H and ¹³C NMR spectra, consistent with complete conversion of **1-Bpin** into the hydroxylated material **1-OH**. The ¹H NMR spectrum contained a triplet at $\delta = 3.64$ ppm, and the ¹³C NMR spectrum contained a singlet at $\delta = 63.2$ ppm for the methylene group that lies alpha to the hydroxy group. An attached proton test confirmed the assignment of the signal at $\delta = 63.2$ ppm as a methylene resonance. The relative intensities of the ¹H NMR signals of the hydroxymethyl methylene protons and of the unfunctionalized methyl groups of the side

chains were used to calculate the fraction of side chains that were functionalized with hydroxy groups (Table 1 and Table 2).

Data on the molecular weight and degree of functionalization of polymers generated from **1** are summarized in Table 1 (HBpin) and Table 2 (B_2pin_2). Size-exclusion chromatography (SEC) data show that the borylation and hydroxylation processes do not lead to a significant change in the molecular weight or polydispersity of the parent polymer **1**. Thus, the rhodium-catalyzed reaction and subsequent oxidation led to the addition of a polar functionality without causing significant chain scission or coupling between polymer chains as typically observed in the free-radical modification of polyolefins.^[10,11]

We defined the efficiency of the functionalization reaction as the ratio of hydroxy groups in the polymer to the boron reagent added initially. As complete conversion of **1**-Bpin into **1**-OH is supported by the disappearance of resonances for alkyl-Bpin in the NMR spectra, we assume that the reported OH efficiency is also representative of the initial efficiency of the addition of Bpin. Reactions of **1** with HBpin in the presence of $[Cp^*Rh(\eta^4-C_6Me_6)]$ and $[Cp^*Rh(C_2H_4)_2]$ (Cp^* = pentamethylcyclopentadiene) occurred with similar efficiencies, whereas reactions with $[Cp^*RhCl_2]_2$ led to incorporation of less boron into the polymer (Table 1, entries 1–3). Reactions of B_2pin_2 catalyzed by $[Cp^*Rh(\eta^4-C_6Me_6)]$ led to **1**-Bpin

with a higher concentration of boryl groups in the polymer than reactions catalyzed by $[Cp^*RhCl_2]_2$ or $[Cp^*Rh(C_2H_4)_2]$ under otherwise identical conditions (Table 2, entries 1–3) and showed more effective functionalization than those with HBpin as the boron reagent. Therefore, the combination of B_2pin_2 reagent and $[Cp^*Rh(\eta^4-C_6Me_6)]$ catalyst was chosen to study the effects of solvent, temperature, and the ratio of boron to hexyl side chains (Table 2, entries 3–11). Reactions performed at 150 °C in cyclooctane generated a polymer with the highest concentration of functionalized hexyl side chains, which could be controlled by varying the ratio of B_2pin_2 to side chain without adversely affecting the molecular parameters under the optimized conditions (Table 2, entries 3, 5, 7, and 10). For example, the degree of functionalization increased by a factor of two when the ratio of B_2pin_2 to hexyl groups was increased from 0.3 to 0.7, but a further increase in the ratio of diboron reagent to hexyl groups from 0.7 to 1.0 did not increase the percentage of functionalized side chains. The maximum percentage of side chains that we were able to functionalize with hydroxy groups was about 20 % (Table 2, entries 7 and 10).

We also explored the conversion of the selectively hydroxylated LLDPE into materials with other types of polar functionality. At this time, no method to directly convert an alkyl pinacolboronate into an alkylamine or aldehyde is known. Thus, we developed conditions to convert

Table 1: Molecular weight and degree of functionalization of LLDPE after selective modification with pinacolborane (HBpin).^[a]

Entry	Ratio ^[b]	Rh catalyst	T [°C]	1 -Bpin M_n [kg mol ⁻¹] ^[c]	PDI ^[c]	1 -OH M_n [kg mol ⁻¹] ^[c]	PDI ^[c]	OH [mol %] ^[d]	Efficiency [%] ^[e]
1	0.2	$[Cp^*RhCl_2]_2$	165	109	2.1	110	1.8	0.8	4
2	0.2	$[Cp^*Rh(C_2H_4)_2]$	165	87.9	1.8	115	1.9	2.5	13
3	0.2	$[Cp^*Rh(\eta^4-C_6Me_6)]$	165	110	1.9	103	1.6	2.5	13
4	0.5	$[Cp^*Rh(\eta^4-C_6Me_6)]$	150	87.0	1.6	101	1.9	3.6	7
5	1.0	$[Cp^*Rh(C_2H_4)_2]$	150	—	—	96.0	2.0	5.6	6
6	2.0	$[Cp^*Rh(\eta^4-C_6Me_6)]$	150	98.2	1.8	108	1.7	2.4	1

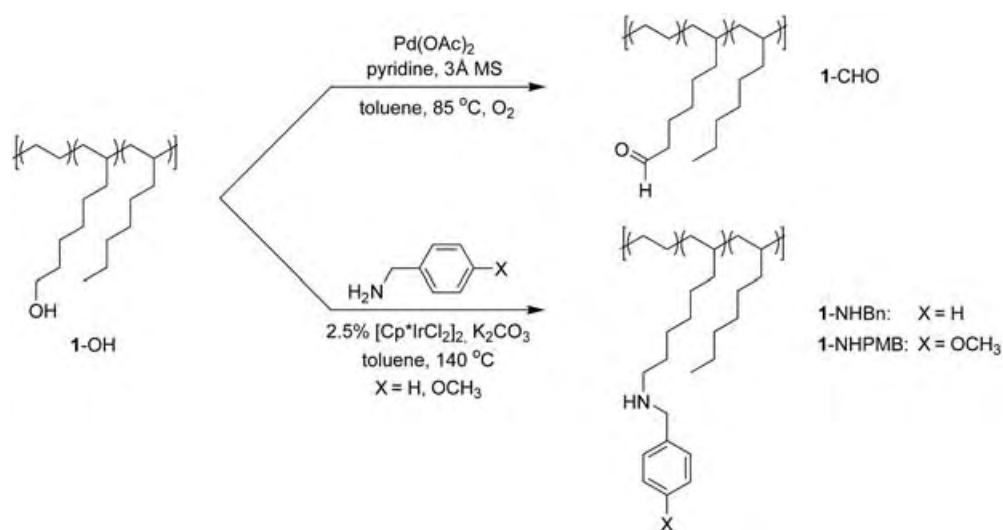
[a] Borylations were conducted on 150 mg of polymer with 5 mol % of Rh relative to HBpin in a sealed tube for 36 h. [b] Ratio of HBpin to hexyl side chains. [c] Measured by size-exclusion chromatography relative to polystyrene standards (THF as eluent at 40 °C); values for unfunctionalized LLDPE (**1**): M_n = 112 kg mol⁻¹; PDI = 1.9.^[9] [d] Ratio of -CH₂OH to -CH₃ groups in the functionalized polymer (× 100). [e] Molar ratio of hydroxy groups in the polymer to boron reagent added.

Table 2: Molecular weight and degree of functionalization of LLDPE after selective modification with bis(pinacolato)diboron (B_2pin_2).^[a]

Entry	Ratio ^[b]	Rh catalyst	T [°C]	1 -Bpin M_n [kg mol ⁻¹] ^[c]	PDI ^[c]	1 -OH M_n [kg mol ⁻¹] ^[c]	PDI ^[c]	OH [mol %] ^[d]	Efficiency [%] ^[e]
1	0.2	$[Cp^*RhCl_2]_2$	165	98.2	2.0	102	2.4	3.6	18
2	0.2	$[Cp^*Rh(C_2H_4)_2]$	165	92.7	2.1	121	2.1	4.9	25
3	0.2	$[Cp^*Rh(\eta^4-C_6Me_6)]$	165	97.6	2.1	114	2.1	6.8	34
4 ^[f]	0.3	$[Cp^*Rh(\eta^4-C_6Me_6)]$	200	—	—	—	—	5.4	18
5	0.3	$[Cp^*Rh(\eta^4-C_6Me_6)]$	150	101	2.1	102	2.1	10.0	33
6 ^[f]	0.3	$[Cp^*Rh(\eta^4-C_6Me_6)]$	150	—	—	—	—	5.9	20
7	0.7	$[Cp^*Rh(\eta^4-C_6Me_6)]$	150	—	—	—	—	19.0	27
8	1.0	$[Cp^*Rh(\eta^4-C_6Me_6)]$	200	95.6	1.9	101	1.9	14.4	14
9 ^[f]	1.0	$[Cp^*Rh(\eta^4-C_6Me_6)]$	200	83.1	1.7	85.2	1.9	12.0	12
10	1.0	$[Cp^*Rh(\eta^4-C_6Me_6)]$	150	96.5	2.0	94.1	2.1	19.2	19
11 ^[f]	1.0	$[Cp^*Rh(\eta^4-C_6Me_6)]$	150	107	1.8	102	1.9	15.5	16

[a] Borylations were conducted on 150 mg to 5 g of polymer with 5 mol % of Rh relative to B_2pin_2 in neat polymer or in cyclooctane under nitrogen for 36 h. [b] Ratio of B_2pin_2 to hexyl side chains. [c] Measured by size-exclusion chromatography relative to polystyrene standards (THF as eluent at 40 °C); values for unfunctionalized LLDPE (**1**): M_n = 112 kg mol⁻¹; PDI = 1.9.^[9] [d] Ratio of CH₂OH to CH₃ groups in the functionalized polymer (× 100). [e] Molar ratio of hydroxy groups in the polymer to diboron reagent added. [f] No solvent.

the hydroxylated polymers into materials with formyl and amino groups. Although several reactions of stoichiometric reagents are available for the oxidation of alcohols to aldehydes, we chose the catalytic route with water as the only byproduct as shown in Scheme 2. The conversion of **1-OH**



Scheme 2. Conversion of **1-OH** to formyl- (**1-CHO**) and amino-functionalized (**1-NHBn**, **1-NHPMB**) LLDPEs.

1-OH (Table 2, entry 5) into the aldehyde-containing polymer **1-CHO** proceeded with molecular oxygen in the presence of $\text{Pd}(\text{OAc})_2$ under the mild conditions reported for low-molecular-weight alcohols by Nishimura et al.^[12] and without adversely affecting the molecular parameters (Table 3). As

Table 3: Molecular weight data for formyl- and amino-functionalized LLDPEs.

Entry	M_n [kg mol ⁻¹] ^[a]	PDI
1-OH	102	2.1
1-CHO	105	1.8
1-NHBn ^[b]	67.0	2.1
1-NHPMB ^[b]	49.9	2.1

[a] Measured by SEC relative to polystyrene standards (THF as eluent at 40 °C). [b] M_n and PDI measured from an initial solution of polymer in toluene, eluted with THF at 40 °C.^[13]

with the hydroxy groups of **1-OH**, the aldehyde groups in **1-CHO** were easily identified by NMR spectroscopy. Resonances for a formyl hydrogen center and a methylene group alpha to an aldehyde were observed as a singlet at $\delta = 9.77$ ppm and a triplet at $\delta = 2.42$ ppm in the ¹H NMR spectrum and as resonances at $\delta = 202.4$ and 44.0 ppm, respectively, in the ¹³C NMR spectrum. The formyl group was also detected by the C=O stretching band at $\tilde{\nu} = 1711$ cm⁻¹ in the IR spectrum.

We converted the hydroxylated polymers into amino-substituted polymers by an iridium-catalyzed amination of alcohols.^[13] The reaction of polymer **1-OH** with benzylamine (BnNH_2) and *p*-methoxybenzylamine (PMBNH_2) in toluene at 140 °C for 48 h in the presence of 2.5 mol % of $[\text{Cp}^*\text{IrCl}_2]_2$,

relative to the hydroxy groups, and K_2CO_3 as the base (Scheme 2) formed a polymer with benzylamino and *p*-methoxybenzylamino groups in place of hydroxy groups at the termini of the functionalized side chains. The ¹H and ¹³C NMR spectra of the product polymers **1-NHBn** and **1-NHPMB** showed an absence of resonances from a methylene group alpha to the oxygen atom.

The ¹H NMR spectrum of **1-NHBn** contained new singlet and triplet methylene resonances at $\delta = 3.79$ and 2.62 ppm, and the ¹³C NMR spectrum contained two new resonances at $\delta = 54.1$ and 49.6 ppm for the methylene units of the benzyl group and the methylene unit of the side chain alpha to the nitrogen center. ¹H and ¹³C NMR data for **1-NHPMB** were similar but displayed a ¹H NMR resonance at $\delta = 3.77$ ppm and a ¹³C NMR resonance at $\delta = 55.4$ ppm for the methoxy groups.

Molecular-weight data from SEC of these amino-substituted polymers are included in Table 3.

The PDI values and peak shapes of **1-NHBn** and **1-NHPMB** are similar to those of **1-OH**, suggesting that chain scission and chain coupling have not occurred. However, the average molecular weights of the **1-NHR** polymers relative to polystyrene standards are significantly lower than those of the starting hydroxylated polymer **1-OH**. We presume that the M_n values of the amine-functionalized polymers are lower owing to a combination of changes in the solubility^[14] and the hydrodynamic volume of the polymer from the addition of the amino groups, and that unfunctionalized polystyrene standards do not provide an appropriate representation of the molecular weight of the material with basic groups.

In summary, we have demonstrated that functionalization of a commercial linear low-density polyethylene can be accomplished through the rhodium-catalyzed borylation of alkanes and subsequent oxidation without significantly altering the molecular weight of the starting polymer. Moreover, the hydroxy groups can be further modified to generate polymers with formyl and amino groups at the termini of the side chains.

Received: May 26, 2005

Published online: September 7, 2005

Keywords: boron · C–H activation · homogeneous catalysis · polymers · rhodium

[1] L. S. Boffa, B. M. Novak, *Chem. Rev.* **2000**, *100*, 1479.

[2] T. C. Chung, *Prog. Polym. Sci.* **2002**, *27*, 39.

[3] L. R. Rieth, R. F. Eaton, G. W. Coates, *Angew. Chem.* **2001**, *40*, 2211; *Angew. Chem. Int. Ed.* **2001**, *40*, 2153.

[4] N. K. Boan, M. A. Hillmyer, *Chem. Soc. Rev.* **2005**, *34*, 267.

- [5] Y. Kondo, D. García-Cuadrado, J. F. Hartwig, N. K. Boen, N. L. Wagner, M. A. Hillmyer, *J. Am. Chem. Soc.* **2002**, *124*, 1164.
- [6] C. Bae, J. F. Hartwig, N. K. B. Harris, R. O. Long, K. S. Anderson, M. A. Hillmyer, *J. Am. Chem. Soc.* **2005**, *127*, 767.
- [7] J. D. Lawrence, M. Takahashi, C. Bae, J. F. Hartwig, *J. Am. Chem. Soc.* **2004**, *126*, 15334.
- [8] H. Chen, S. Schlecht, T. C. Semple, J. F. Hartwig, *Science* **2000**, *287*, 1995.
- [9] Because **1** was significantly less soluble in THF than the functionalized polymers, a solution of **1** in toluene was injected into the SEC system with THF as the eluent.
- [10] N. G. Gaylord, M. K. Mishra, *J. Polym. Sci. Polym. Lett. Ed.* **1983**, *21*, 23.
- [11] K. E. Russell, *Prog. Polym. Sci.* **2002**, *27*, 1007.
- [12] T. Nishimura, T. Onoue, K. Ohe, S. Uemura, *J. Org. Chem.* **1999**, *64*, 6750.
- [13] K. Fujita, Z. Li, N. Ozeki, R. Yamaguchi, *Tetrahedron Lett.* **2003**, *44*, 2687.
- [14] Because the amino-functionalized polymers were significantly less soluble in THF than the other functionalized polymers, solutions of **1**-NHR in toluene were injected into the SEC system with THF as the eluent.

Solar Cells

DOI: 10.1002/anie.200502009

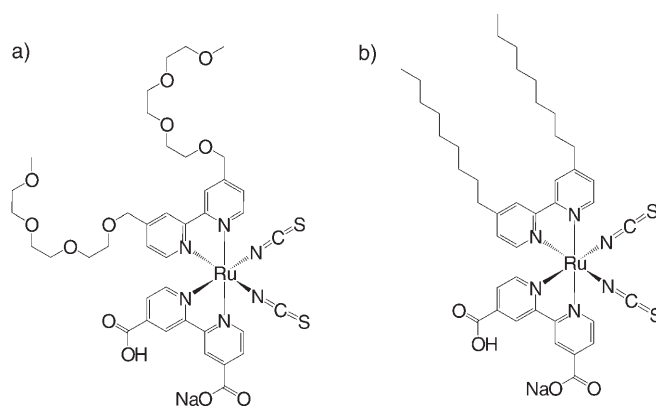
Ion-Coordinating Sensitizer in Solid-State Hybrid Solar Cells**

Henry J. Snaith,* Shaik M. Zakeeruddin,
Lukas Schmidt-Mende, Cédric Klein, and
Michael Grätzel

The solid-state dye-sensitized solar cell is one of the most promising organic-based device concepts which demonstrates solar-power conversion efficiencies in excess of 4%.^[1,2] The basic strategy of this hybrid system is that light is absorbed in a dye to form an excited electronic state, termed an exciton. Electron transfer takes place from the excited dye molecule to an inorganic semiconductor, where it is transported to and collected at an electrode. Subsequent hole transfer from the

oxidized dye to a hole-transporting organic molecule or polymer takes place, where the hole is transported to and collected at the counter electrode.^[3] The fundamental advantage of this system over two-component systems^[4–7] is that the electron- and hole-transporting components are spatially separated by the dye molecules, which hugely suppresses charge recombination and allows efficient charge collection through microns-thick material.^[8] Furthermore, the efficiency of such devices has been found to dramatically improve with the addition of various additives to the hole-transporting material, with the most efficient devices incorporating specific quantities of ionic salts and electrochemical dopants. This “cocktail” of additives has been fine-tuned and optimized for the current system.^[2] However, the precise function of each component is, as yet, not fully understood.^[9] Herein, we report a new charge-transfer sensitizer with an ion-complexing moiety formed by oxyethylene side groups. Lithium coordination to the backbone of this dye induces a striking improvement in the photovoltage and performance, with voltages of nearly 900 mV regularly achieved and efficiencies improved from 3.2 to 3.8% (under 100 mW cm^{−2} simulated air mass (AM) 1.5 solar conditions) for the lithium-coordinating sensitizer as compared with a noncoordinating analogue. A staggering record efficiency of 4.6% is achieved under 10 mW cm^{−2} simulated AM 1.5 illumination. Our supramolecular approach to the self-assembly of functional components^[10,11] opens new avenues to control charge separation and recombination at the interface, and gives us a more comprehensive understanding of the mechanisms occurring within this class of solar cells.

The chemical structures of the dyes used for sensitization are shown in Scheme 1. Z907 is an amphiphilic ruthenium



Scheme 1. Structures of the sensitizing dyes used: a) K51 (tetraethylene oxide side chains) and b) Z907 (nonyl side chains).

complex with one proton and one sodium ion,^[12] and K51 is an analogue of Z907, in which the hydrophobic alkyl chains have been replaced with ion-coordinating triethyleneglycol methyl ether (TEG) groups. A brief description of the synthetic procedure for this novel sensitizer (K51) is provided in the Supporting Information and will be published in detail elsewhere.^[13] The light absorption of the K51 and Z907 dyes is almost identical, both in solution and when adsorbed on a TiO₂ nanoporous film.

[*] Dr. H. J. Snaith, Dr. S. M. Zakeeruddin, Dr. L. Schmidt-Mende, Dr. C. Klein, Prof. M. Grätzel
Institut de Chimie Physique
École Polytechnique Fédérale de Lausanne
1015 Lausanne (Switzerland)
Fax: (+41) 21-6934111
E-mail: henry.snaith@epfl.ch

[**] This work was funded by the MOLYCELL European project. We thank Jacques E. Moser for the introduction and use of the transient photovoltage equipment and Michel Schaer and Libero Zuppiroli from the Laboratory of Optoelectronics of Molecular Materials at the EPFL for discussions, assistance with, and use of a low-temperature testing rig.

Supporting information for this article is available on the WWW under <http://www.angewandte.org> or from the author.

Figure 1a shows the current density–voltage (JV) curves in the dark for dye-sensitized solar cells. The dark current for the K51 device at 1.5 V bias is over ten-times larger in the presence of Li ions than in their absence. There is no color

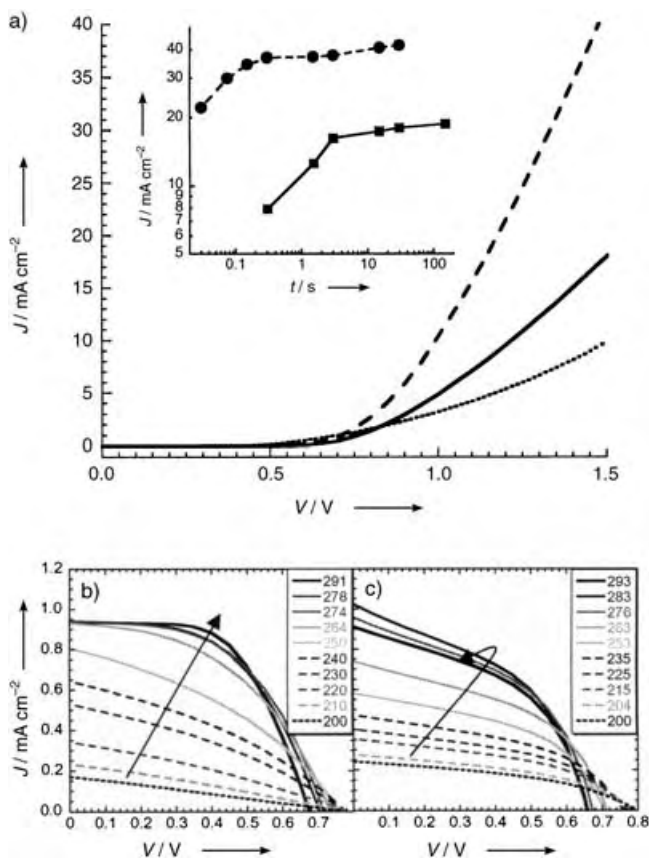


Figure 1. a) Current density (J) measured in the dark versus applied bias (V) for a dye-sensitized solar cell with K51 dye in the absence of Li triflate (....., $\times 10$), K51 dye with Li triflate (—), and Z907 dye with Li triflate (---). Inset: current density at 1.5-V applied bias versus scan time from 0 to 1.5 V with the Z907 device (---, \bullet) and the K51 device (—, \blacksquare). b, c) Current density–voltage characteristics for K51 device (b) and Z907 device (c) under illumination from a halogen lamp (20 mWcm⁻²) and at 200–300 K (see legends; the arrows indicate increasing temperatures). These measurements were performed in the Laboratory of Optoelectronics of Molecular Materials (LOMM), EPFL.

change of the hole-transporting material 2,2',7,7'-tetrakis(*N,N*-di-*p*-methoxyphenylamine)-9,9'-spirobifluorene (Spiro) upon the addition of Li salt, which suggests that no electronic doping takes place. The increased current density could be a consequence of the formation of a dipole at the Au electrode.^[14] However, this would require the bulky triflate anion (negatively charged) to migrate to the gold electrode to improve the hole-injection characteristics, which is unlikely. A more reasonable explanation is that the ions in the “electrolyte” can redistribute to balance the space charge, and higher current densities are sustainable as hole transport will no longer be under the “space-charge-limited” regime.^[15] In effect, the addition of the ionic salt dramatically improves the hole mobility in the organic material. Significantly, the

current density through the Li-doped Z907 device is approximately three times that of the Li-doped K51 device, although the initial ionic concentration in both devices is identical. The current density through Li-doped devices varies with the scan rate, with slower scans giving higher currents (this is constant for undoped devices). Notably, this is much more pronounced for the K51 device. The inset to Figure 1a shows the current density at 1.5 V versus scan time (from 0 to 1.5 V) for the K51 and Z907 Li-doped devices. The current for the Z907 device reaches a plateau after approximately 300 ms, whereas the K51 device does not plateau until after 3 s. The increase in current density with time is likely to be a result of the finite time taken for the ions to redistribute and balance the space charge within the device.^[15] The only difference between the Z907 and K51 devices is the ion-coordinating side chains, so this is direct evidence that a large proportion of the ions are immobilized on the surface of the K51 dye molecules.

Figure 1b and c show the JV characteristics of the K51 and Z907 devices over a range of temperatures under illumination. The short-circuit current increases with temperature up to around 280 K. The increase in short-circuit current over the lower temperature region is consistent with the temperature dependence expected for the hole mobility in an organic hole transporter,^[16] with the holes being “frozen” in the device at low temperatures. The fill factor increases with temperature over the entire range studied, but increases most rapidly from around 250 K. An increase in fill factor is consistent with reduced series resistance within the cell,^[17] this is likely to be because the ions become more mobile at these higher temperatures.^[18] This finding demonstrates that the function of the mobile ions in the hole-transporter material is to facilitate a low series resistance, fast charge extraction, and thus a large fill factor.

A striking difference between the two devices is that the short-circuit current remains high over the higher range of temperatures for the K51 device, whereas it drops for the Z907 device with a peak at approximately 280 K. There are two competing temperature-dependent factors which influence the short-circuit current. First, an increased charge mobility will increase the short-circuit current by increasing the charge-diffusion length^[19] and increase the fill factor through reducing the series resistance.^[17] Second, the charge-recombination rate increases with temperature.^[20] An increased charge-recombination rate will reduce the short-circuit current through reducing the charge-diffusion length^[19] and reduce the open-circuit voltage as it reduces the chemical potential gradient which is sustainable within the device.^[21,22] For the Z907 device, it appears that the increasing recombination rate becomes dominant at higher temperatures, which results in a drop in short-circuit current at these temperatures. However, for the K51 device the increased mobility appears to be dominant over the temperature range studied. The tethering of the Li ions to the interface is likely to “coulombically” retard recombination by screening the electrons in the TiO₂ from the holes in the Spiro, thus increasing the activation energy for recombination and retaining a high photocurrent at higher temperatures. This effect appears to be a dominant factor over the increased charge mobility in the Spiro, as the Z907 device, which incorporates the free Li ions,

exhibits much higher charge-transport characteristics. This finding has implications in the use of dual-conductive (ion and hole) materials in these solar cells, as the immobilization of ions at the surface seems beneficial.^[23,24]

Figure 2a shows the transient decay of the open-circuit voltage for various devices. An estimate of the overall charge

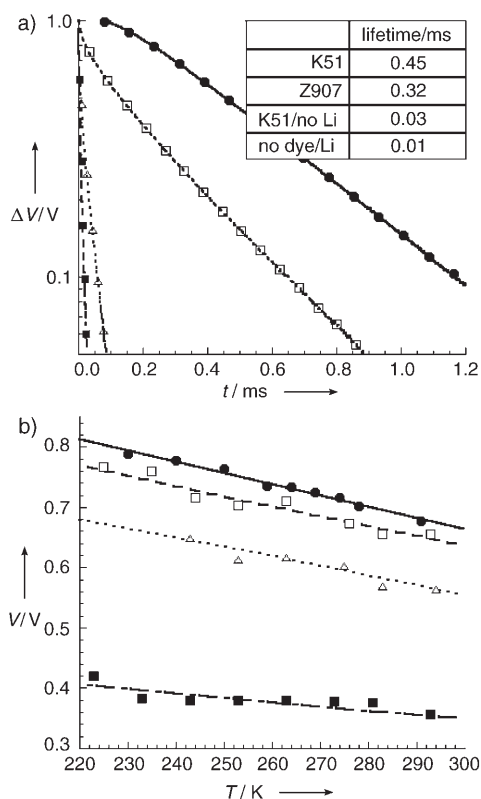


Figure 2. a) Transient open-circuit voltage measurements (normalized values) of a Li-doped K51 device (●, —), a Li-doped Z907 device (□, ----), a K51 device in the absence of both Li and tbp (Δ, ·····), and a device with only Sb-doped Spiro (no dye, Li, or tbp) (■, ---). The inserted table gives the charge lifetimes (τ_{rec}) calculated from the V_{oc} decay measurements by fitting the decays as $\exp(-t/\tau_{\text{rec}})$. b) Open-circuit voltage versus temperature for the same devices as in (a); the symbols are the data points and the lines are linear fits to the data. tbp = 4-tert-butylpyridine, rec = recombination, oc = open circuit.

lifetime in these devices can be obtained by simply fitting a monoexponential decay to the curves (see table inset to Figure 2a). Charge lifetimes derived in this manner have been shown to give very similar values to those obtained by intensity-modulated photovoltage spectroscopy.^[25,26] As we might expect, the presence of the dye at the interface increases the charge lifetime (from 10 to 30 μs) as compared to that of a pristine TiO_2 film coated with Spiro. Addition of free Li ions (Z907 device) dramatically increases the charge lifetime tenfold to 320 μs ; this effect has been observed by Kruger et al.^[9] with transient absorption spectroscopy. Furthermore, the charge lifetime is increased to 430 μs by tethering the ions to the dye backbone (K51 device). This result is consistent with the above analysis of the JV data.

Figure 2b shows the open-circuit voltage as a function of temperature for the same devices. The open-circuit voltage

drops with increasing temperature over the range studied for all devices. Koster et al. have derived the relationship between open-circuit voltage (V_{oc}) and absolute temperature (T) for organic PPV:PCBM (PPV = poly(*p*-phenylenevinylene); PCBM = [6,6]-phenyl- C_{60} -butyric acid methyl ester) bulk heterojunction photovoltaic devices.^[27] We believe the solid-state dye-sensitized solar cell to be a very similar system, with the only important difference being that there is a dye molecule at the interface between the two components where all excitons are formed. Koster et al. studied the metal-insulator-metal picture where the material composite is considered to be one intrinsic semiconductor, with the valance band corresponding to the highest occupied molecular orbital (HOMO) of the hole-transporting polymer, and the conduction band corresponding to the lowest unoccupied molecular orbital (LUMO) of the electron-withdrawing component (PCBM), with a corresponding energy gap (E_{gap}). The relationship is shown in [Eq (1)] where γ is the

$$V_{\text{oc}} = \frac{E_{\text{gap}}}{q} - \frac{kT}{q} \ln \left(\frac{(1-P)\gamma N_c^2}{PG} \right) \quad (1)$$

Langevin recombination constant, N_c is the effective density of states, G is the generation rate of bound electron-hole pairs, P is the dissociation probability of bound electron-hole pairs, and k is Boltzmann's constant. For the system studied herein, we consider G to be the rate of generation of electrons in the TiO_2 by electron transfer from the photoexcited dye molecule with the hole remaining on the dye, and P to be the probability of hole transfer from the dye molecule to the Spiro.

The linear fit to the data in Figure 2b is the relationship we would expect from Equation (1), with the y axis intercept at zero temperature giving E_{gap} . It is clear that if the active layer in the solid-state dye-sensitized solar cell can be considered as a single semiconductor material, the exact nature of the interface between the components is critical in determining the electronic structure of such a material. For a TiO_2 and Spiro composite E_{gap} should be approximately 0.6 eV.^[1,28] This value is close to that obtained for the device with no dye molecule (0.56 eV), which demonstrates that Equation (1) correctly describes the temperature dependence of the open-circuit voltage for this system. However, the derived value of E_{gap} rises to 1.0 eV when the TiO_2 is sensitized with dye molecules, and further to 1.1 eV when Li is added to the Z907 device, and to 1.2 eV with surface-tethered Li ions in the K51 device.

To understand this trend we must consider what the definition of an "energy gap" is in this nanocomposite material. There is no direct transition for an electron in the conduction band of TiO_2 to the HOMO level of Spiro, but there is a spatial and energetic barrier in the form of the dye molecule. For this material we should consider the energy gap to be the energy required to move an electron from the HOMO of the Spiro to the conduction band of TiO_2 , thus overcoming the barrier presented by the dye molecule. If this is so, the potential barrier is clearly susceptible to changes in local conditions, with the addition of Li and, more importantly, the coordination of Li ions to the dye molecule

increasing the barrier height. This results in a widening of the quasi energy gap, with the most important implication being that the fundamental limit of the open-circuit voltage ($qV_{oc,max} = E_{LUMO}(\text{electron transporter}) - E_{HOMO}(\text{hole transporter})$) is no longer true, as V_{oc} has an additional contribution (or at least the energy levels can be further offset) because of the exact nature of the interface. This further “energy-level offset” is likely to be influenced by the dipole moment which will be present at the interface; the ion-coordinating dye molecule will act as a dipole at the surface, and cause a downward shift in the vacuum level of the Spiro with respect to that of the TiO_2 .^[29–31] This shift will force the HOMO level of the Spiro further from the conduction band of the TiO_2 , thereby increasing the quasi energy gap and thus the open-circuit voltage. The introduction of a surface dipole in “flat-junction” TiO_2 solar cells has previously been shown to increase the open-circuit voltage in such devices.^[31]

Figure 3 shows the current density–voltage characteristics for the devices sensitized with the K51 and Z907 dyes, measured under simulated AM 1.5 sunlight at 100 mW cm^{-2} .

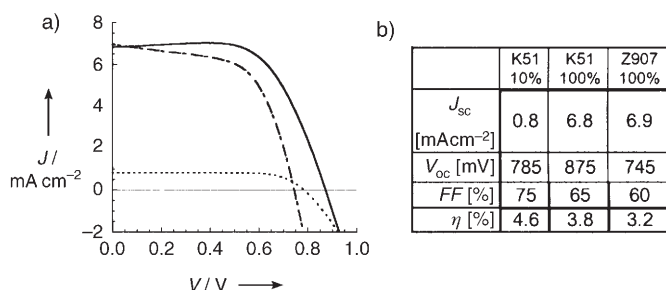


Figure 3. a) Current density–voltage characteristics under simulated AM 1.5 solar conditions (100 mW cm^{-2}) for a full device containing K51 sensitizing dye (—) and Z907 sensitizing dye (---). Also shown is the K51 device illuminated by 10 mW cm^{-2} simulated sunlight. b) The standard device performance parameters calculated from the JV data.

The current densities are similar for the two devices, but both the fill factor and open-circuit voltage are improved for the device sensitized with the K51 dye, which leads to an improved efficiency of 3.8% as opposed to 3.2% for the Z907 dye. Furthermore, at 10 mW cm^{-2} the efficiency of the K51 device is as high as 4.6%, which demonstrates the potential of this system.

In summary, the presence of mobile ions in the hole-transporting material is important as it enables hole transport to take place beyond the space-charge-limited current regime, dramatically improving the material characteristics. Control of the nature of the interface between the TiO_2 and the Spiro, by coordination of Li ions to the dye backbone, tailors the electronic structure of the composite system to be more favorable for photovoltaic operation. Our findings open new avenues to control charge separation and recombination at the interface of inexpensive bulk-junction solar cells, and this work will pave the way for a whole new class of multifunctional sensitizer molecules.

Experimental Section

The dye-sensitized solar cells were fabricated, and the standard device measurements were performed, by identical methods to those used by Schmidt-Mende et al.^[2] The additives and concentrations used in a full device were Li triflate ($1 \times 10^{20} \text{ cm}^{-3}$ in the solid film), 4-*tert*-butyl pyridine (tbp; $17 \mu\text{L mL}^{-1}$ in chlorobenzene), and antimony salt as the electrochemical dopant (0.03 M relative to Spiro). These additives were predissolved in the Spiro solution prior to coating of the sensitized TiO_2 film. Tbp was used to help dissolve the Li triflate in the Spiro solution. It has been shown to cause considerable changes to the operation of the device,^[9] however, here we always used tbp in conjunction with Li triflate and consider it as one additive for the purposes of analysis. Low-temperature current density–voltage measurements were performed under high vacuum in the dark and under illumination from an unfiltered halogen lamp with an optical output of 20 mW cm^{-2} . Transient photovoltage measurements were performed by illuminating the devices with a Nd:YAG laser filtered to give a low intensity (532 nm, 30 Hz, 6-ns pulse width), superimposed upon a large-bias, red-filtered ($> 630 \text{ nm}$), white-light illumination from a xenon lamp ($\approx 500 \text{ mW cm}^{-2}$), by a similar method to that described by O'Regan and Lenzmann.^[32]

Received: June 10, 2005

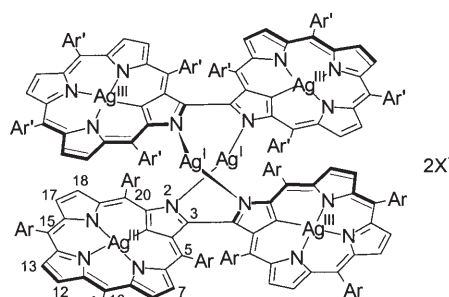
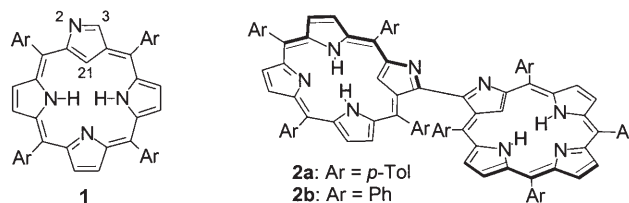
Published online: September 14, 2005

Keywords: charge transfer · dyes/pigments · sensitizers · solar cells · supramolecular chemistry

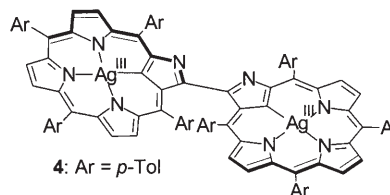
- [1] U. Bach, D. Lupo, P. Comte, J. E. Moser, F. Weissortel, J. Salbeck, H. Spreitzer, M. Grätzel, *Nature* **1998**, 395, 583.
- [2] L. Schmidt-Mende, S. M. Zakeeruddin, M. Grätzel, *Appl. Phys. Lett.* **2005**, 86, 013504.
- [3] B. O'Regan, M. Grätzel, *Nature* **1991**, 353, 737.
- [4] C. J. Brabec, N. S. Sariciftci, J. C. Hummelen, *Adv. Funct. Mater.* **2001**, 11, 15.
- [5] N. C. Greenham, X. G. Peng, A. P. Alivisatos, *Phys. Rev. B* **1996**, 54, 17628.
- [6] J. J. M. Halls, C. A. Walsh, N. C. Greenham, E. A. Marseglia, R. H. Friend, S. C. Moratti, A. B. Holmes, *Nature* **1995**, 376, 498.
- [7] G. Yu, A. J. Heeger, *J. Appl. Phys.* **1995**, 78, 4510.
- [8] L. Schmidt-Mende, J. E. Kroeze, J. R. Durrant, M. K. Nazeeruddin, M. Grätzel, *Nano Lett.* **2005**, 5, 1315.
- [9] J. Kruger, R. Plass, L. Cevey, M. Picirelli, M. Grätzel, U. Bach, *Appl. Phys. Lett.* **2001**, 79, 2085.
- [10] J. M. Lehn, *Proc. Natl. Acad. Sci. USA* **2002**, 99, 4763.
- [11] J. M. Lehn, *Science* **2002**, 295, 2400.
- [12] P. Wang, B. Wenger, R. Humphry-Baker, J. E. Moser, J. Teuscher, W. Kantelehner, J. Mezger, E. V. Stoyanov, S. M. Zakeeruddin, M. Grätzel, *J. Am. Chem. Soc.* **2005**, 127, 6850.
- [13] D. Kuang, C. Klein, H. J. Snaith, R. Humphry-Baker, J.-E. Moser, S. M. Zakeeruddin, M. Grätzel, **2005**, unpublished results.
- [14] F. Nuesch, K. Kamaras, L. Zuppiroli, *Chem. Phys. Lett.* **1998**, 283, 194.
- [15] J. C. de Mello, N. Tessler, S. C. Graham, R. H. Friend, *Phys. Rev. B* **1998**, 57, 12951.
- [16] P. W. M. Blom, M. J. M. de Jong, M. G. van Munster, *Phys. Rev. B* **1997**, 55, R656.
- [17] J. Nelson, *The Physics of Solar Cells*, Imperial College Press, London, **2003**.
- [18] J. Gao, G. Yu, A. J. Heeger, *Appl. Phys. Lett.* **1997**, 71, 1293.
- [19] T. Markvart, L. Castaner, *Solar Cells: Materials, Manufacture and Operation*, Elsevier, Oxford, **2005**.
- [20] J. Nelson, S. A. Haque, D. R. Klug, J. R. Durrant, *Phys. Rev. B* **2001**, 6320, 205321.

- [21] B. A. Gregg, M. C. Hanna, *J. Appl. Phys.* **2003**, 93, 3605.
- [22] C. M. Ramsdale, J. A. Barker, A. C. Arias, J. D. MacKenzie, R. H. Friend, N. C. Greenham, *J. Appl. Phys.* **2002**, 92, 4266.
- [23] S. A. Haque, Y. Tachibana, R. L. Willis, J. E. Moser, M. Grätzel, D. R. Klug, J. R. Durrant, *J. Phys. Chem. B* **2000**, 104, 538.
- [24] T. Park, S. A. Haque, R. J. Potter, A. B. Holmes, J. R. Durrant, *Chem. Commun.* **2003**, 2878.
- [25] N. Kopidakis, K. D. Benkstein, J. van de Lagemaat, A. J. Frank, *J. Phys. Chem. B* **2003**, 107, 11307.
- [26] G. Schlichthorl, S. Y. Huang, J. Sprague, A. J. Frank, *J. Phys. Chem. B* **1997**, 101, 8141.
- [27] L. J. A. Koster, V. D. Mihailetschi, R. Ramaker, P. W. M. Blom, *Appl. Phys. Lett.* **2005**, 86, 123509.
- [28] M. Grätzel, *Nature* **2001**, 414, 338.
- [29] D. M. Alloway, M. Hofmann, D. L. Smith, N. E. Gruhn, A. L. Graham, R. Colorado, V. H. Wysocki, T. R. Lee, P. A. Lee, N. R. Armstrong, *J. Phys. Chem. B* **2003**, 107, 11690.
- [30] S. Kera, Y. Yabuuchi, H. Yamane, H. Setoyama, K. K. Okudaira, A. Kahn, N. Ueno, *Phys. Rev. B* **2004**, 70, 085304.
- [31] J. Kruger, U. Bach, M. Grätzel, *Adv. Mater.* **2000**, 12, 447.
- [32] B. C. O'Regan, F. Lenzmann, *J. Phys. Chem. B* **2004**, 108, 4342.

phyrin **1**^[5] is particularly attractive owing to its unique structure, which allows multimodal coordination of the confused pyrrole to metal ions,^[6] and its reactivity. The exposed position of the external nitrogen atom (N2) makes this fragment of molecule susceptible to interactions with metal ions.^[7]



3a: Ar = Ar' = *p*-Tol, X[−] = BF₄[−], CF₃SO₃[−]
3b: Ar = Ar' = Ph, X[−] = BF₄[−]
3c: Ar = Ph, Ar' = *p*-Tol, X[−] = BF₄[−]



Recently, we reported the synthesis of the dimeric N-confused porphyrin **2** (Ar = phenyl, *p*-tolyl (*p*-Tol)),^[8] which is a unique isomer that preserves the basic skeleton of a directly β-β-linked bis(porphyrin).^[9] The cyclic assemblies **3**, whose synthesis and characterization are presented herein, exemplify a new type of carbaporphyrinoid array that consists of both covalent and coordinating links between the subunits. Owing to the steric factors imposed by *meso*-aryl substituents, the bipyrrrole fragment adopts a cisoid conformation in **2** but deviates strongly from planarity. Such an arrangement determines the coordination mode of this fragment, which, unlike the planar bipyrrrole system present in corroles,^[10] is preorganized to coordinate two metal ions rather than to form a chelate ring.

Reaction of bis(carbaporphyrinoid) **2** with AgX (X = BF₄[−] or CF₃SO₃[−]) was carried out at room temperature in THF for 30 minutes. After evaporation of the solvent, the residue was dissolved in CH₂Cl₂, and washed with water to remove the excess of silver(I) ions and the acid liberated upon insertion of the metal. The composition and molecular structure of **3** was established on the basis of ESI-MS, NMR

Metalloporphyrinoids

DOI: 10.1002/anie.200502208

Synthesis and Characterization of a Cyclic Bis-silver(I) Assembly of Four 2-Aza-21-carbaporphyrinatosilver(III) Subunits**

Piotr J. Chmielewski*

Porphyrins and metalloporphyrins constitute a class of building blocks for the construction of multicomponent 2D and 3D molecular arrays that are being considered as possible biomimetic models, catalysts, or materials for the transport of charge, molecules, and ions. Covalent^[1] as well as coordination linkages^[2] have been exploited in the design of a variety of discrete porphyrin assemblies. Recently, special attention has been given to systems built up of directly linked porphyrins with strongly interacting aromatic subunits,^[3] which represent some of the most promising candidates for potential applications.

Porphyrin analogues^[4] exhibit many distinct features that can be exploited in the construction of novel molecular and supramolecular systems. Among them, the N-confused por-

[*] Prof. P. J. Chmielewski
 Department of Chemistry
 University of Wrocław
 F. Joliot-Curie Street 14, 50 383 Wrocław (Poland)
 Fax: (+48) 713-282-348
 E-mail: pjc@wchuwr.chem.uni.wroc.pl

[**] This work was supported by the Polish Ministry of Scientific Research and Information Technology (Grant 3 T09A 16228).

Supporting information for this article is available on the WWW under <http://www.angewandte.org> or from the author.

spectroscopy, and single-crystal X-ray analyses. Owing to the dicationic character of the complex, the dominant peak in the mass spectrum corresponds to the dication ($m/z = 1657$, 100%) with a characteristic half-unit isotopic pattern. The fragmentation peak at $m/z = 1549.5$ (47%) reflects liberation of the dimeric fragment **4**.

The solid-state structure of **3a**-(OTf)₂ (OTf = CF₃SO₃[−]) presents an assembly of four 2-aza-21-carbaporphyrinosilver(III) subunits,^[11] which are organized on the perimeter of a ten-membered ring that contains two silver(I) ions (Figure 1). The assembly of the axially chiral^[8] dimeric subunits **4** on the bis-silver(I) template may lead to the formation of diastereomers. However, only *S,S* and *R,R* enantiomers are observed in the crystal structure (see Supporting Information). Although both monovalent silver centers are two-coordinate, the N-Ag-N fragments are far from linear, being bent outwards with an angle of 147.0(3)°. This is likely due to the geometric constraints imposed on the ring by the

structure of the bipyrrrolic moiety. The relatively short distance between the bridging silver atoms Ag3–Ag3* (3.107(2) Å) suggests that an “argentophilic” interaction^[12] stabilizes the assembly. Such interactions have been shown to influence the outcome of several supramolecular assemblies, and their importance has been crystallographically investigated.^[13] The distances within the macrocyclic core (Ag1–C21: 1.974(9); Ag1–N22: 2.030(9); Ag1–N23: 2.052(7); Ag1–N24: 2.027(8) Å) are slightly shorter than those observed in monomeric neutral silver(III) complexes of **1**,^[11] an O-confused porphyrin derivative,^[14] or the so-called “true” carbaporphyrin.^[15] The distances between the external nitrogen atoms and the bridging silver ions (Ag3–N2: 2.175(8); Ag3–N26: 2.169(8)) are typical for the monovalent silver complexes.^[13g]

As a consequence of the crystal-packing forces, the molecule displays only twofold symmetry in the solid state. In contrast, the effective symmetry of the molecule in solution is fourfold, as inferred from the ¹H NMR spectra which reveal only one set of signals (Figure 2a,b). The spectra support the stereoselectivity of the formation of the assembly, as diastereomers are expected to exhibit different ¹H NMR spectra. Owing to the nonplanar character of the system and freezing of rotation of the *meso*-aryl substituents, each proton of the subunit in **3** is represented by a unique signal and can be assigned on the basis of 2D NMR experiments (see Supporting Information). Analysis of the chemical shifts and interprotonic through-space interactions observed in NOESY or ROESY experiments allowed a model to be built that has the same molecular topology as the solid-state structure of **3a** but which displays fourfold symmetry.

A neutral diamagnetic bis-silver(III) complex **4** can be obtained by treating a solution of **3** in chloroform with either an aqueous solution of sodium halogenide or with a solution of tetraalkylammonium bromide in chloroform to remove bridging silver(I) ions.^[16] Protonation of **3** with one equivalent of trifluoroacetic acid or the addition of pyridine (500-fold excess) breaks the assembly reversibly. The process can be fully reversed upon addition of water or by evaporation of the solvents. Thus, reconstruction of **3** is possible as long as silver(I) ions are present in the solution.

A slow exchange reaction can be observed upon mixing of the solutions of **3a** and **3b** to result, after 20 h at room temperature, in an equilibrium of starting complexes and a mixed-ligand species **3c** that can be identified by ESI-MS (observed: $m/z = 1602.4$; calcd: $m/z = 1601.7$) and ¹H NMR spectroscopy (Figure 2d). Formation of **3c**, which exhibits twofold symmetry, indicates the lability of the system but also provides additional support for the preservation of the tetrameric structure in solution.

The charge on the external nitrogen atom of the confused pyrroles strongly influences redox properties of the metal ion that is coordinated in the macrocyclic core.^[7f,17] Thus, it can be expected that

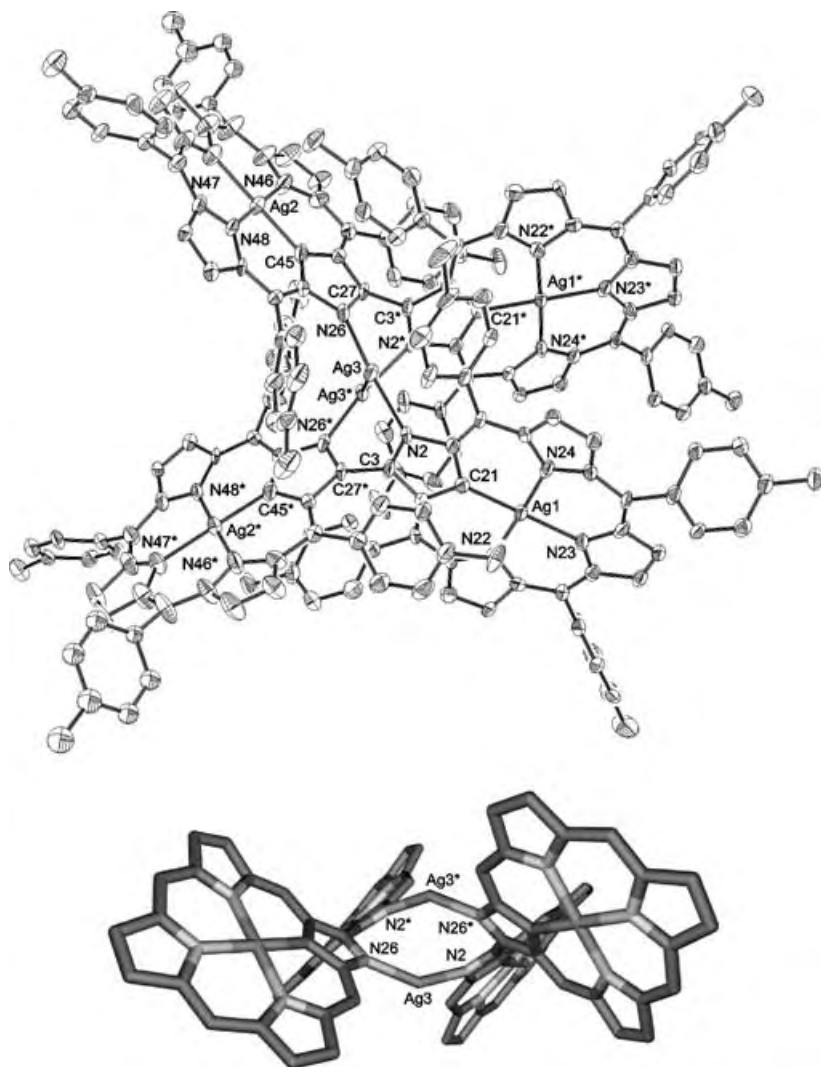


Figure 1. Molecular structure of the assembly **3a**. Top: ORTEP view with thermal ellipsoids scaled at the 30% probability level (hydrogen atoms, triflate anions, and solvent molecules are omitted); bottom: wire-frame representation of the structure with all aryl substituents omitted for clarity.

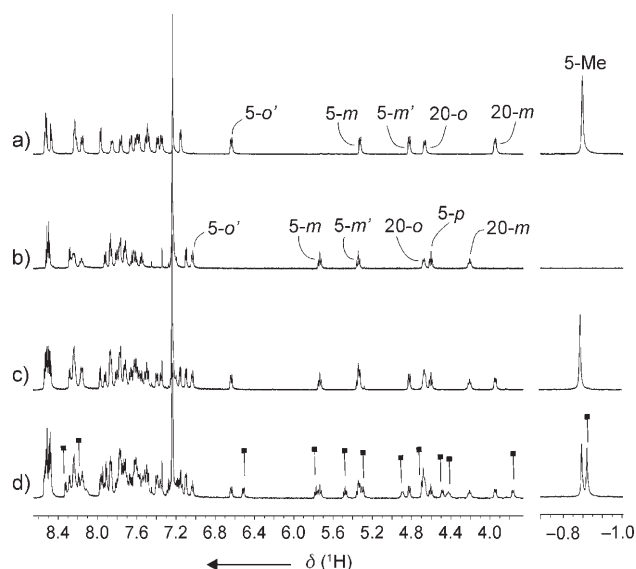


Figure 2. Fragments of the ^1H NMR spectra (CDCl_3 , 298 K) of the assemblies a) **3a**, b) **3b**, c) **3a** + **3b** immediately after mixing, and d) **3a** + **3b** 40 h after mixing (some of the new features, attributed to the mixed-ligand species **3c**, are indicated by ■). Signal assignments of the most upfield-shifted *meso*-aryl protons in **3a** and **3b** are presented in (a) and (b), with numbers indicating *meso* positions.

coordination of the Ag^{I} cation to the external nitrogen atom destabilizes the trivalent silver center in each subunit to allow the reduction of the metal. Such a reduction process has not been observed to date for any of the carbaporphyrinoid silver(III) complexes. In cyclic voltammograms of **3a** and **3b** (CH_2Cl_2 solutions; tetrabutylammonium perchlorate as the supporting electrolyte; glassy carbon as a working electrode; all data are referenced to ferrocene/ferrocenium internal standard), a pair of two-electron couples ($E_{1/2} = -1100$ mV, $\Delta E_{\text{ac}} = 40$ mV, $E_{1/2} = -1230$ mV, $\Delta E_{\text{ac}} = 46$ mV for **3a**; $E_{1/2} = -1055$ mV, $\Delta E_{\text{ac}} = 40$ mV, $E_{1/2} = -1175$ mV, $\Delta E_{\text{ac}} = 46$ mV for **3b**) is attributable to a stepwise reduction of silver(III) centers in the strongly interacting covalently linked subunits.^[8,18] Each reduction step takes place at the same potential in two nondirectly connected, and thus non-interacting subunits, which is accounted for by the two-electron character of the processes. Two overlapping couples observed for **3a** around -1425 mV and those better-resolved for **3b** ($E_{1/2} = -1330$ mV, $\Delta E_{\text{ac}} = 36$ mV, $E_{1/2} = -1440$ mV, $\Delta E_{\text{ac}} = 30$ mV) reflect reductions of the ligand. For **4** only ligand reductions represented by two couples at -1470 and -1600 mV are observed.

In conclusion, we have shown the very facile diastereoselective formation of a molecular assembly that consists of four carbaporphyrinoids and which is effectively formed despite steric overcrowding imposed by the substituents in the vicinity of the donor sites. It seems that access to the bridging silver–silver fragment is hindered which may stabilize the cyclic structure. Experiments are underway to explore the application of this novel coordination mode of the nonplanar bipyrrrolic moiety in the construction of larger redox-active assemblies that consist of covalently linked N-confused porphyrin derivatives.

Experimental Section

3a-(BF_4)₂: 3,3'-Bis(5,10,15,20-tetrakis(*p*-tolyl)-2-aza-21-carbaporphyrin) (**2a**; 20 mg, 0.015 mmol) was dissolved in THF (20 mL) and stirred with silver tetrafluoroborate (10 mg, 0.115 mmol) for 0.5 h. The solvent was then removed by evaporation, and the solid residue was dissolved in dichloromethane (10 mL). The solution was shaken with three portions of water (10 mL each). After separation of the organic phase, the solution was filtered and then the solvent was removed. The solid residue was dissolved in dichloromethane, and the solution was left to crystallize slowly after the addition of hexane to yield the olive-colored product **3a**-(BF_4)₂ (26 mg, 94%). A similar procedure using AgOTf instead of AgBF_4 or **2b** instead of **2a** yielded **3a**-(OTf)₂ or **3b**-(BF_4)₂, respectively. Spectral data recorded in the solution state were independent of the counteranion present in the complex. See Supporting Information for NMR spectroscopic data for **3a** and **3b**.

3a-(BF_4)₂: UV/Vis (CH_2Cl_2): λ_{max} ($\log \epsilon$) = 258 (5.23), 313 (5.00), 378 (5.08), 451 (sh), 472 (5.51), 533 (4.80), 596 (4.67), 636 (sh), 686 nm (4.52); ESI-MS: m/z calcd for $\text{C}_{192}\text{H}_{136}\text{N}_{16}\text{Ag}_6$: 1657.7 ($[M]^{2+}$); found: 1657.4; elemental analysis: calcd (%) for $\text{C}_{192}\text{H}_{136}\text{N}_{16}\text{Ag}_6\text{B}_2\text{F}_8 \cdot 2 \cdot (\text{CH}_2\text{Cl}_2)$: C 63.70, H 3.86, N 6.13; found: C 63.40, H 3.56, N 6.12.

3b-(BF_4)₂: UV/Vis (CH_2Cl_2): λ_{max} ($\log \epsilon$) = 256 (5.19), 323 (sh), 378 (5.08), 452 (sh), 471 (5.47), 531 (4.75), 594 (4.67), 641 (sh), 691 nm (4.48); ESI-MS: m/z calcd for $\text{C}_{176}\text{H}_{104}\text{N}_{16}\text{Ag}_6$: 1545.7 ($[M]^{2+}$); found: 1545.2; elemental analysis: calcd (%) for $\text{C}_{176}\text{H}_{104}\text{N}_{16}\text{Ag}_6\text{B}_2\text{F}_8 \cdot 2 \cdot (\text{CH}_2\text{Cl}_2)$: C 62.27, H 3.17, N 6.53; found: C 62.40, H 3.32, N 6.23.

Crystals of suitable quality for X-ray analysis were obtained by slow diffusion of hexane into a solution of **3a**-(OTf)₂ in toluene. Crystal data for **3a**-(OTf)₂: $\text{C}_{231.5}\text{H}_{172}\text{N}_{16}\text{Ag}_6 \cdot 2 \text{CF}_3\text{SO}_3$, $M_w = 4099.19$, $T = 100$ K, $\text{Cu}_{\text{K}\alpha}$ radiation, monoclinic, space group $C2/c$, $a = 24.208(4)$, $b = 34.279(4)$, $c = 24.175(4)$ Å, $\beta = 103.35(3)^\circ$, $V = 19519(5)$ Å³, $Z = 4$, $\rho_{\text{calcd}} = 1.395$ mg m⁻³, $\lambda = 1.54178$ Å, $\mu = 5.485$ mm⁻¹, $F(000) = 8356$, Oxford Diffraction Xcalibur PX with KM4CCD Sapphire detector, $3.19 \leq \theta \leq 68.00^\circ$, 15171 collected reflections, 8504 independent reflections with $I > 2\sigma(I)$, 1104 parameters, $R1(F) = 0.0827$, $wR2(F^2) = 0.2102$, $S = 1.064$, largest difference peak and hole 1.861 and -1.06 e Å⁻³. All non-hydrogen atoms were refined with anisotropic displacement parameters except for those of the disordered solvents, triflate anion, and one *meso*-tolyl ring. Hydrogen atoms were excluded from the geometry of molecules and refined isotropically. The asymmetric unit contains half of the molecule of **3a**, consisting of two subunits linked by a silver ion, one disordered triflate anion, a half molecule of hexane, and one and a half molecules of toluene displaced into six different sites. CCDC 276104 contains the supplementary crystallographic data for this paper. These data can be obtained free of charge from the Cambridge Crystallographic Data Centre via www.ccdc.cam.ac.uk/data_request/cif.

4: Complex **3a** (10 mg, 3 μmol) was dissolved in CH_2Cl_2 (20 mL), and the solution was stirred vigorously for 0.5 h with a 1M aqueous solution of NaBr (10 mL) until the originally olive-colored solution turned red-brown. The layers were then separated, and the organic phase was washed with two 10-mL portions of water. After drying over a small amount of anhydrous K_2CO_3 and filtration, the volume of the solution was reduced to 10 mL, and hexane (5 mL) was added which caused precipitation of **4** as a brown powder (6.1 mg, 65%). ^1H NMR: see Supporting Information; UV/Vis (CH_2Cl_2): λ_{max} ($\log \epsilon$) = 254 (5.20), 285 (sh), 323 (5.02), 384 (sh), 412 (sh), 450 (sh), 468 (5.50), 533 (4.88), 621 (sh), 661 nm (4.45); ESI-MS: m/z calcd for $\text{C}_{96}\text{H}_{68}\text{N}_8\text{Ag}_2$: 1549.4 ($[M+1]^+$); found: 1549.5; elemental analysis: calcd (%) for $\text{C}_{96}\text{H}_{68}\text{N}_8\text{Ag}_2 \cdot \text{CH}_2\text{Cl}_2 \cdot \text{C}_6\text{H}_{14}$: C 71.90, H 4.89, N 6.51; found: C 71.94, H 4.78, N 6.22.

Received: June 23, 2005

Published online: September 8, 2005

Keywords: nitrogen heterocycles · oligomers · porphyrinoids · silver · supramolecular chemistry

- [1] a) M. G. H. Vicente, L. Jaquinod, K. M. Smith, *Chem. Commun.* **1999**, 1771; b) A. K. Burrell, D. L. Officer, P. G. Plieger, D. C. W. Reid, *Chem. Rev.* **2001**, 101, 2751.
- [2] a) J. Wojaczyński, L. Latos-Grażyński, *Coord. Chem. Rev.* **2000**, 204, 113; b) S. Richeter, C. Jeandon, R. Ruppert, H. J. Callot, *Chem. Commun.* **2001**, 91; c) S. Richeter, C. Jeandon, C. Sauber, J.-P. Gisselbrecht, R. Ruppert, H. J. Callot, *J. Porphyrins Phthalocyanines* **2002**, 6, 423; d) S. Richeter, C. Jeandon, J.-P. Gisselbrecht, R. Ruppert, H. J. Callot, *J. Am. Chem. Soc.* **2002**, 124, 6; e) S. Richeter, C. Jeandon, R. Ruppert, H. J. Callot, *Chem. Commun.* **2002**, 266.
- [3] a) A. Osuka, H. Shimidzu, *Angew. Chem.* **1997**, 109, 93; *Angew. Chem. Int. Ed. Engl.* **1997**, 36, 135; b) T. Ogawa, Y. Nishimoto, N. Yoshida, N. Ono, A. Osuka, *Chem. Commun.* **1998**, 337; c) T. Ogawa, Y. Nishimoto, N. Yoshida, N. Ono, A. Osuka, *Angew. Chem.* **1999**, 111, 140; *Angew. Chem. Int. Ed.* **1999**, 38, 176; d) N. Yoshida, A. Osuka, *Tetrahedron Lett.* **2000**, 41, 9287; e) A. Tsuda, Y. Nakamura, A. Osuka, *Chem. Commun.* **2003**, 1096; f) Y. H. Kim, D. H. Jeong, D. Kim, S. C. Jeoung, H. S. Cho, S. K. Kim, N. Aratani, A. Osuka, *J. Am. Chem. Soc.* **2001**, 123, 76; g) A. Tsuda, A. Nakano, H. Furuta, H. Yamochi, A. Osuka, *Angew. Chem.* **2000**, 112, 572; *Angew. Chem. Int. Ed.* **2000**, 39, 558; h) A. Tsuda, A. Osuka, *Adv. Mater.* **2002**, 14, 75; i) A. Takagi, Y. Yanagawa, A. Tsuda, N. Aratani, T. Matsumoto, A. Osuka, T. Kawai, *Chem. Commun.* **2003**, 2986; j) N. Aratani, A. Osuka, Y. H. Kim, D. H. Jeong, D. Kim, *Angew. Chem.* **2000**, 112, 1517; *Angew. Chem. Int. Ed.* **2000**, 39, 1458; k) H. Segawa, Y. Senshu, J. Nakazaki, K. Susumu, *J. Am. Chem. Soc.* **2004**, 126, 1354; l) H. Segawa, D. Machida, Y. Senshu, J. Nakazaki, K. Hirakawa, F. Wu, *Chem. Commun.* **2002**, 3032.
- [4] L. Latos-Grażyński in *The Porphyrin Handbook*, Vol. 2 (Eds.: K. M. Kadish, K. M. Smith, R. Guilard), Academic Press, San Diego, CA **2000**, p. 361.
- [5] a) P. J. Chmielewski, L. Latos-Grażyński, K. Rachlewicz, T. Głowiak, *Angew. Chem.* **1994**, 106, 805; *Angew. Chem. Int. Ed. Engl.* **1994**, 33, 779; b) H. Furuta, T. Asano, T. Ogawa, *J. Am. Chem. Soc.* **1994**, 116, 767; c) G. R. Geier III, D. M. Haynes, J. S. Lindsey, *Org. Lett.* **1999**, 1, 1455.
- [6] J. D. Harvey, C. J. Ziegler, *Coord. Chem. Rev.* **2003**, 247, 1.
- [7] a) A. Srinivasan, H. Furuta, A. Osuka, *Chem. Commun.* **2001**, 1666; b) H. Furuta, T. Ishizuka, A. Osuka, *J. Am. Chem. Soc.* **2002**, 124, 5622; c) H. Furuta, K. Youfu, H. Maeda, A. Osuka, *Angew. Chem.* **2003**, 115, 2236; *Angew. Chem. Int. Ed.* **2003**, 42, 2186; d) H. Furuta, T. Morimoto, A. Osuka, *Inorg. Chem.* **2004**, 43, 1618; e) I. Schmidt, P. J. Chmielewski, Z. Ciunik, *J. Org. Chem.* **2002**, 67, 8917; f) P. J. Chmielewski, I. Schmidt, *Inorg. Chem.* **2004**, 43, 1885; g) C.-H. Hung, W.-C. Chen, G.-H. Lee, S.-M. Peng, *Chem. Commun.* **2002**, 1516; h) K. Rachlewicz, S.-L. Wang, J.-L. Ko, C.-H. Hung, L. Latos-Grażyński, *J. Am. Chem. Soc.* **2004**, 126, 4420; i) J. D. Harvey, C. J. Ziegler, *Chem. Commun.* **2002**, 1942.
- [8] P. J. Chmielewski, *Angew. Chem.* **2004**, 116, 5773; *Angew. Chem. Int. Ed.* **2004**, 43, 5655.
- [9] a) Y. Deng, C. K. Chang, D. G. Nocera, *Angew. Chem.* **2000**, 112, 1108; *Angew. Chem. Int. Ed.* **2000**, 39, 1066; b) H. Hata, H. Shinokubo, A. Osuka, *J. Am. Chem. Soc.* **2005**, 127, 8264.
- [10] a) L. Simkhovich, I. Luobeznova, I. Goldberg, Z. Gross, *Chem. Eur. J.* **2003**, 9, 201; b) C. Bruckner, Ch. A. Barta, R. P. Brinas, J. A. Krause-Bauer, *Inorg. Chem.* **2003**, 42, 1673.
- [11] H. Furuta, T. Ogawa, Y. Uwatoko, K. Araki, *Inorg. Chem.* **1999**, 38, 2676.
- [12] M. A. Rawashdeh-Omary, M. A. Omary, H. H. Patterson, *J. Am. Chem. Soc.* **2000**, 122, 10371.
- [13] a) S. Sailaja, M. V. Rajasekharan, *Inorg. Chem.* **2003**, 42, 5675; b) V. J. Catalano, H. M. Kar, B. L. Bennett, *Inorg. Chem.* **2000**, 39, 121; c) V. J. Catalano, S. J. Horner, *Inorg. Chem.* **2003**, 42, 8430; d) V. J. Catalano, M. A. Malwitz, *Inorg. Chem.* **2003**, 42, 5483; e) V. J. Catalano, M. A. Malwitz, A. O. Etogo, *Inorg. Chem.* **2004**, 43, 5714; f) O. Kristiansson, *Inorg. Chem.* **2001**, 40, 5058; g) S. M. Cortez, R. G. Raptis, *Coord. Chem. Rev.* **1998**, 169, 363; A. N. Khlobystov, A. J. Blake, N. R. Champness, D. A. Lemenovskii, A. G. Majouga, N. V. Zyk, M. Schröder, *Coord. Chem. Rev.* **2001**, 222, 155.
- [14] M. Pawlicki, L. Latos-Grażyński, *Chem. Eur. J.* **2003**, 9, 4650.
- [15] a) M. A. Muckey, L. F. Szczepura, G. M. Ferrence, T. D. Lash, *Inorg. Chem.* **2002**, 41, 4840; b) T. D. Lash, J. M. Rasmussen, K. M. Bergman, D. A. Colby, *Org. Lett.* **2004**, 6, 549.
- [16] After isolation from the solution, **4** is sparingly soluble in organic solvents, which may suggest its association leading to the formation of a polymer. Solid **4** is readily converted back into **3a** upon its treatment with a solution of a silver salt in THF or methanol.
- [17] a) H. Maeda, Y. Ishikawa, H. Matsueda, A. Osuka, H. Furuta, *J. Am. Chem. Soc.* **2003**, 125, 11822; b) I. Schmidt, P. J. Chmielewski, *Inorg. Chem.* **2003**, 42, 5579.
- [18] Probably as a result of the labile character of the assembly, an irreversible reduction of “free” silver(I) ion takes place to result in the deposition of metallic silver on the surface of the electrode. The appearance of an oxidation peak at 380 mV follows cathodic scans below –950 mV.

Cover Picture

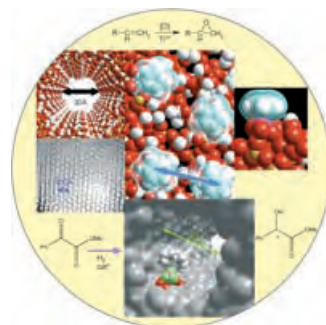
Marco Affronte,* Ian Casson, Marco Evangelisti, Andrea Candini, Stefano Carretta, Christopher A. Muryn, Simon J. Teat, Grigore A. Timco,* Wolfgang Wernsdorfer, and Richard E. P. Winpenny*

Linked paramagnetic cage complexes could potentially be used as quantum gates for quantum information processing. The cover picture shows such a supramolecular assembly, which consists of two heterometallic octagons (paramagnetic $\{\text{Cr}_7\text{Ni}\}$ cages) linked through a metal dimer. The white arrow represents the light input that switches the interaction between the two halves of the quantum gate. For more details see the Communication by M. Affronte, G. A. Timco, R. E. P. Winpenny et al. on page 6496 ff.



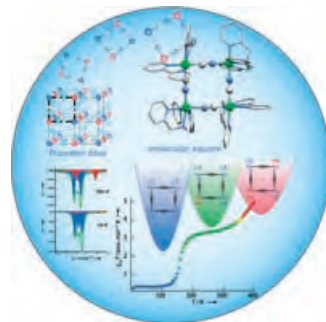
Heterogeneous catalysis

In their Review on page 6456 ff. J. M. Thomas et al. describe heterogeneous catalysts with isolated catalytic centers (single-site catalysts). The main focus is on strategically modified mesoporous and microporous structures.



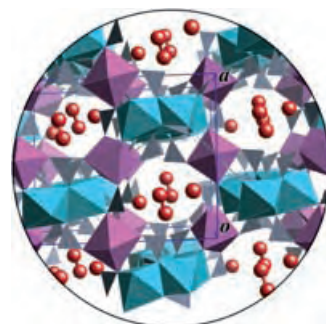
Molecular Switches

A thermally induced, two-step spin crossover in a cyanide-bridged molecular square is described in the Communication by H. Oshio and co-workers on page 6484 ff. Such molecules are suitable building blocks for multistep molecular switches.



Host–Guest Systems

The polarizable molecular system consisting of H_2O and CH_3OH in a porous crystal of $[\text{Mn}_3(\text{HCOO})_6]$ is changed into a nonpolarized one by lowering the temperature, as described by H. Kobayashi et al. in their Communication on page 6508 ff.





The following Communications have been judged by at least two referees to be “very important papers” and will be published online at www.angewandte.org soon:

S. Klaus, H. Neumann, A. Zapf, D. Strübing, S. Hübner, J. Almerna,*
T. Riermeier, P. Groß, M. Sarich, W.-R. Krahnert, K. Rossen,
M. Beller*

A General and Efficient Method for the Formylation of Aryl and Heteroaryl Bromides

N. Martín,* Á. Martín-Domenech, S. Filippone, M. Altable,
L. Echegoyen,* C. M. Cardona

Retro-Cycloaddition Reactions of Pyrrolidinofullerenes

C. Höbartner, S. K. Silverman*

Modulation of RNA Tertiary Folding by Incorporation of Caged Nucleotides

M. Nakamura,* A. Hajra, K. Endo, E. Nakamura*

Synthesis of Chiral α -Fluoroketones through Catalytic Enantioselective Decarboxylation

J. M. Macak, H. Tsuchiya, L. Taveira, S. Aldabergerova, P. Schmuki*

Smooth Anodic TiO₂ Nanotubes

Y. Yamaguchi,* S. Kobayashi, T. Wakamiya, Y. Matsubara,
Zen-ichi Yoshida*

Banana-Shaped Oligo(aryleneethynyls): Synthesis and Light-Emitting Characteristics

Meeting Reviews

A Feast of Supramolecular Chemistry

D.-P. Funeriu* _____ 6442

Books

Evaluation of Enzyme Inhibitors in Drug Discovery

Robert A. Copeland

reviewed by R. Breinbauer _____ 6445

Essential NMR

Bernhard Blümich

reviewed by A. Lützen _____ 6445

Highlights

Helical Structures

M. Albrecht* _____ 6448 – 6451

Artificial Molecular Double-Stranded Helices



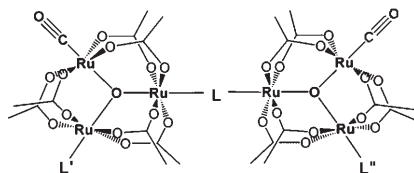
Not only aesthetically appealing: The motif of the double-stranded helix (see picture) is found in DNA, which is able to store and process “information”. It inspires scientists to search for ways to mimic not only its fascinating structure

but also to develop helical systems with different functionalities and properties, with which one day, likewise, information storage and processing could be achieved.

Electron Transfer

R. J. Crutchley* _____ 6452 – 6454

Charge-Transfer Isomers and Mixed-Valence Properties



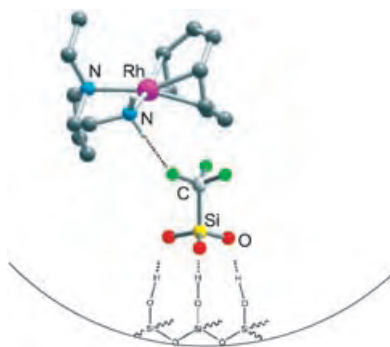
The unusual suspects: By using a series of ruthenium clusters of the type $[\{Ru_3O(\mu-CH_3COO)_6(CO)L'\}(\mu-L)\{Ru_3O(\mu-CH_3COO)_6(CO)L''\}]$ (see picture) it has been possible to identify the existence of charge-transfer isomers and establish them as identifiable chemical entities that exist in dynamic equilibrium.

Reviews

Heterogeneous Catalysts

J. M. Thomas,* R. Raja,
D. W. Lewis _____ 6456–6482

Single-Site Heterogeneous Catalysts



Living in isolation: Single-site heterogeneous catalysts offer a widely applicable strategic principle for the design of new mono- and bifunctional catalysts. They combine the merits of homogeneous and heterogeneous processes and permit the preparation of high activity regio-, shape-, and enantioselective solid catalysts. The picture shows a spatially constrained organometallic, Rh^I-based enantioselective catalyst.

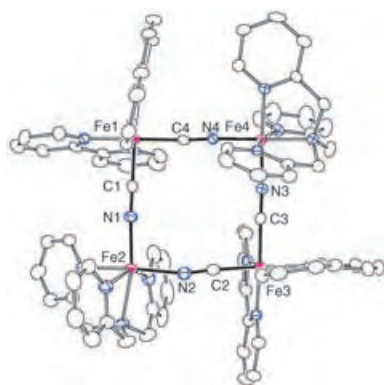
Communications

Molecular Switches

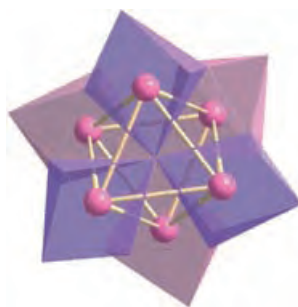
M. Nihei, M. Ui, M. Yokota, L. Han,
A. Maeda, H. Kishida, H. Okamoto,
H. Oshio* _____ 6484–6487

Two-Step Spin Conversion in a Cyanide-Bridged Ferrous Square

Spinning out: A cyanide-bridged molecular square (see picture) has been isolated and found to undergo thermally induced, two-step spin crossover. Molecules with more than one spin-crossover site are suitable building blocks for multistep molecular switches.



Unusual octahedral hexamers built up from triangular, corner-linked cobalt trimers (see figure), form the basis of a novel three-dimensional cobalt isophthalate obtained by a solvothermal route. This structure provides a new example of the concept of scale chemistry, in which an {Na₆Co₆O₂₆} “super octahedron” is connected in a classical ReO₃ architecture.



Supramolecular Chemistry

C. Livage,* N. Guillo, J. Chaigneau,
P. Rabu, M. Drillon,
G. Férey _____ 6488–6491

A Three-Dimensional Metal–Organic Framework with an Unprecedented Octahedral Building Unit

For the USA and Canada:

ANGEWANDTE CHEMIE International Edition (ISSN 1433-7851) is published weekly by Wiley-VCH PO Box 191161, D 69451 Weinheim, Germany. Air freight and mailing in the USA by Publications Expediting Inc. 200 Meacham Ave., Elmont, NY 11003. Periodicals

postage paid at Jamaica NY 11431. US POSTMASTER: send address changes to *Angewandte Chemie*, Wiley-VCH, 111 River Street, Hoboken, NJ 07030. Annual subscription price for institutions: US\$ 4948.00/4498.00 (valid for print and electronic / print or electronic delivery); for individuals who are personal members of a

national chemical society, or whose institution already subscribes, or who are retired or self-employed consultants, print only: US\$ 394.00. Postage and handling charges included. All Wiley-VCH prices are exclusive VAT.

The best in chemistry – for more than a hundred years



A Journal of the Gesellschaft Deutscher Chemiker
Angewandte
International Edition **Chemie**

www.angewandte.org

1888: The beginning
of a success story

Constant Innovations

- 1962:** First issue of the International Edition
- 1976:** Graphical abstracts
- 1979:** Cover pictures
- 1988:** Centenary of Angewandte
- 1989:** Routine use of color
- 1991:** New section: Highlights
- 1992:** Computerized editorial tracking system
- 1995:** Internet service for readers
- 1998:** Regular press service; full-text online
- 2000:** New section: Essays; EarlyView: Communications available online ahead of the printed version
- 2001:** New section: Minireviews
- 2002:** Online submission of manuscripts
- 2003:** Weekly publication; new section: News; new layout
- 2004:** Backfiles (1962-1997); ManuscriptXpress: Online system for authors and referees



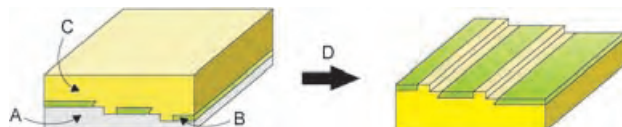
Angewandte's advisors...

Martin Quack
Physical Chemistry,
ETH Zürich

» **Angewandte Chemie** is my favourite journal covering all aspects of chemistry, from theoretical and physical chemistry to inorganic, organic, and biochemistry. It is by far the best journal worldwide for an overview of current research in chemistry as a whole. Beyond just publishing the best research in chemistry, it also helps us to fight the trend of too narrow specialization. «

Angewandte Chemie International Edition is
a journal of the German Chemical Society (GDCh)





The unique structure of a highly ordered pyrolytic-graphite (HOPG) surface is employed as a template to fabricate large random arrays of metal-nanoband electrodes. This process is achieved through

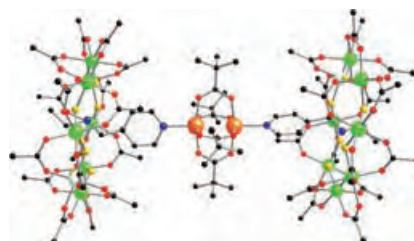
selective blocking of the basal-plane HOPG (A) with a polymer film (B), followed by metal coating (C) and cleavage of the metal layer from the HOPG substrate (D; see picture).

Nanotechnology

M. E. Hyde, T. J. Davies,
R. G. Compton* — 6491 – 6496

Fabrication of Random Assemblies of Metal Nanobands: A General Method

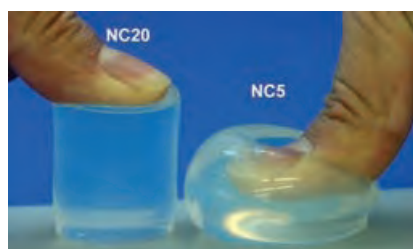
Gates leading from cages: Linked paramagnetic cage complexes could potentially be used as quantum gates for quantum information processing. Experiments demonstrate that it is possible to link octanuclear $\{\text{Cr}_7\text{Ni}\}$ rings through both organic and metal–organic fragments into supramolecular dimers (see structure; Cr green, Ni light green, Cu orange, F yellow, O red, N blue, C black).



Cage Compounds

M. Affronte,* I. Casson, M. Evangelisti,
A. Candini, S. Carretta, C. A. Muryn,
S. J. Teat, G. A. Timco,* W. Wernsdorfer,
R. E. P. Winpenny* — 6496 – 6500

Linking Rings through Diamines and Clusters: Exploring Synthetic Methods for Making Magnetic Quantum Gates

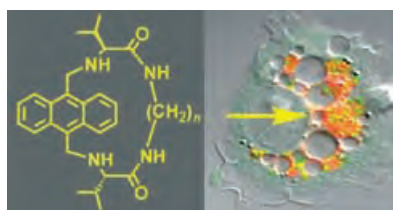


Polymer clay for chemists: High strengths and high fracture energies of polymeric hydrogels have been demonstrated by incorporating a substantial amount of nanodispersed inorganic clay during the in situ free-radical polymerization of *N*-isopropylacrylamide. By varying the amount of clay used, mechanical properties as well as the swelling and transparency of the nanocomposite (NC) could be controlled (see picture; NC20 contains more clay than NC5).

Polymers

K. Haraguchi,* H.-J. Li — 6500 – 6504

Control of the Coil-to-Globule Transition and Ultrahigh Mechanical Properties of PNIPA in Nanocomposite Hydrogels



Acid test: Macrocyclic compounds that comprise a 9,10-anthracene subunit linked by a C_2 -symmetric peptidomimetic

chain (see formula) are useful as fluorescent probes in a pH range of biomedical interest. Changes in the size of the macrocycle ($n = 3, 4, 6, 8$) produce a shift in the pK_a values. Experiments with live mouse macrophage cells show the selective localization of the probe in the acidic organelles (see differential interference contrast image).

Fluorescent Probes

F. Galindo,* M. I. Burguete, L. Vígara,
S. V. Luis,* N. Kabir, J. Gavrilovic,
D. A. Russell* — 6504 – 6508

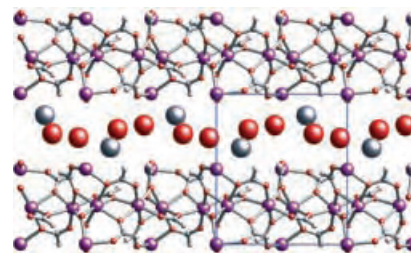
Synthetic Macrocyclic Peptidomimetics as Tunable pH Probes for the Fluorescence Imaging of Acidic Organelles in Live Cells

Host–Guest Systems

H.-B. Cui, K. Takahashi, Y. Okano,
H. Kobayashi,* Z. Wang,
A. Kobayashi ————— **6508–6512**

Dielectric Properties of Porous Molecular
Crystals That Contain Polar Molecules

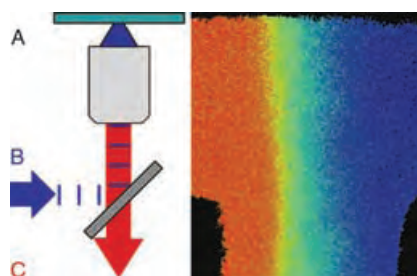
Simply lowering the temperature changes a polarizable molecular system, which consists of H_2O and CH_3OH inserted into the porous crystal $[\text{Mn}_3(\text{HCOO})_6]$ (see structure; Mn pink, C gray, O red), into a nonpolarizable one. Although a large drop in the dielectric constant was observed around 120 K, reminiscent of a liquid \leftrightarrow solid phase transition of the guest molecules, the anisotropy cannot be explained by a simple liquid model of the guest molecules.



Microfluidics

S. W. Magennis, E. M. Graham,
A. C. Jones* ————— **6512–6516**

Quantitative Spatial Mapping of Mixing in
Microfluidic Systems



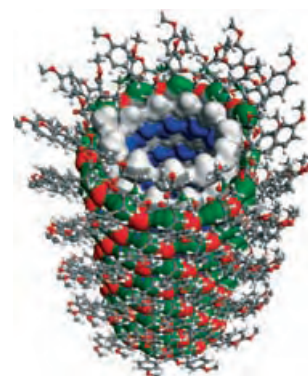
The problem of miniaturizing the mixing process is a barrier to the advance of microfluidic technology. Fluorescence lifetime imaging is a powerful technique for the quantitative mapping of mixing in microfluidic systems, providing information essential to the design and evaluation of next-generation devices. With the use of a pulsed laser (B), mixing in a microfluidic cell (A) can be measured with fluorescence (C); a sample image is shown (right).

Supramolecular Chemistry

V. Percec,* A. E. Dulcey, M. Peterca,
M. Ilies, J. Ladislaw, B. M. Rosen,
U. Edlund, P. A. Heiney — **6516–6521**

The Internal Structure of Helical Pores
Self-Assembled from Dendritic
Dipeptides is Stereochemically
Programmed and Allosterically Regulated

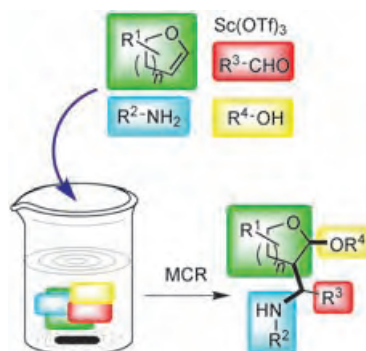
Keeping nature under control: The internal structure of helical porous protein mimics self-assembled from hybrid dendritic dipeptides is programmed by the stereochemistry of the dipeptide and regulated allosterically. This is the first example of a synthetic helical porous supramolecular structure that is stable both in solution and in the solid state, and that is created by a sequence of events related to those encountered in nature.



Synthetic Methods

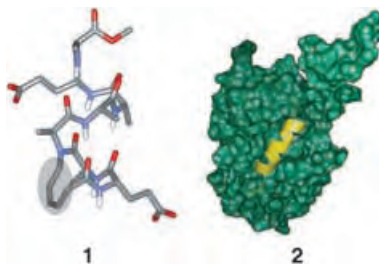
O. Jiménez, G. de la Rosa,
R. Lavilla* ————— **6521–6525**

Straightforward Access to a Structurally
Diverse Set of Oxacyclic Scaffolds through
a Four-Component Reaction



Just add CH_3CN and stir! Four building blocks taken in a multicomponent reaction (MCR, see picture; Tf = trifluoromethanesulfonyl) afford a β -aminoacetal adduct, which can be further diversified by post-condensation reactions. The modular character of this approach, the simplicity of the building blocks used, and the structural diversity attained render this process attractive for combinatorial as well as target- and diversity-oriented synthesis.

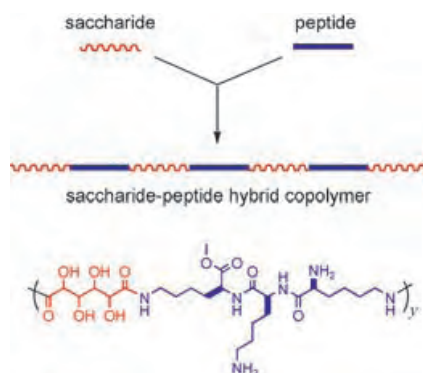
Artificial α helices prepared by the replacement of a hydrogen bond between residues i and $i+4$ with a carbon–carbon bond can stabilize biologically relevant peptides in helical conformations (**1**, internal constraint shaded in gray). α Helices based on hydrogen-bond surrogates that mimic Bak BH3 (**2**, yellow) can bind their expected protein receptor, Bcl-xL (**2**, green), with high affinity and resist proteolytic degradation.



Helical Structures

D. Wang, W. Liao,
P. S. Arora* _____ **6525–6529**

Enhanced Metabolic Stability and Protein-Binding Properties of Artificial α Helices Derived from a Hydrogen-Bond Surrogate: Application to Bcl-xL



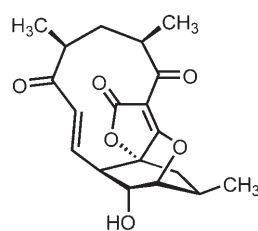
Au natural: A new class of synthesized biomaterials (saccharide–peptide hybrid copolymers shown) are biodegradable, nontoxic, and nonimmunogenic. The cationic saccharide–peptide hybrid copolymers were also shown to be effective in compacting and transferring plasmid DNA into cells.

Biomaterials

M. Metzke, N. O'Connor, S. Maiti,
E. Nelson, Z. Guan* _____ **6529–6533**

Saccharide–Peptide Hybrid Copolymers as Biomaterials

An efficient and highly diastereoselective intramolecular Diels–Alder reaction is the basis of a concise asymmetric synthesis of the potent antibacterial natural product abyssomicin C (see formula). The complexity of the target structure was reduced to three fragments and required two carbonyl addition reactions to achieve key bond formations.

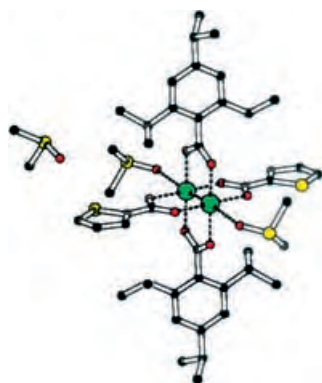


Abyssomicin C

Natural Product Synthesis

C. W. Zapf, B. A. Harrison, C. Drahl,
E. J. Sorensen* _____ **6533–6537**

A Diels–Alder Macrocyclization Enables an Efficient Asymmetric Synthesis of the Antibacterial Natural Product Abyssomicin C



Illuminating quadruple bonds: The polymeric materials $[M_2(O_2CC_6H_2-2,4,6-Me_3)_2(O_2C-(Thp)_n-CO_2)]_n$ ($M = Mo$ or W (green); Thp = thiophene (S atoms yellow); DMSO molecules also shown) incorporate metal–metal quadruple bonds and form thin films from THF solutions. These films show electroluminescence when deposited on an indium–tin oxide glass-coated plate followed by vapor deposition of aluminum or calcium.

Metal–Metal Bonds

M. H. Chisholm,* A. J. Epstein,*
J. C. Gallucci, F. Feil,
W. Pirkle _____ **6537–6540**

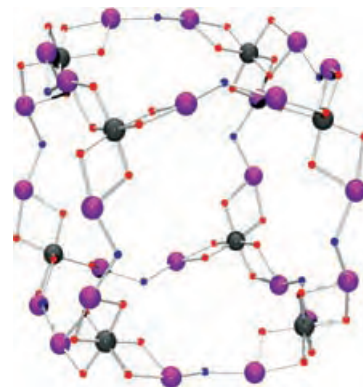
Oligothiophenes Incorporating Metal–Metal Quadruple Bonds

Magnetic Clusters

R. T. W. Scott, S. Parsons, M. Murugesu, W. Wernsdorfer, G. Christou, E. K. Brechin* — 6540–6543

Linking Centered Manganese Triangles into Larger Clusters: A $\{Mn_{32}\}$ Truncated Cube

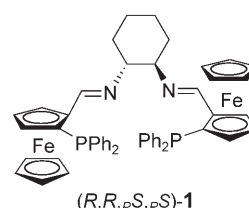
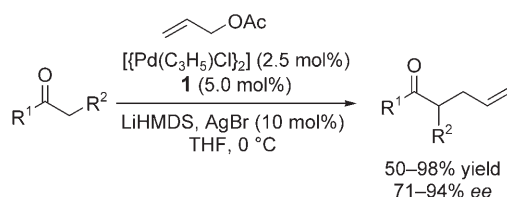
Cutting Corners: Elaborate triangular arrays of Mn ions are stabilized by the tripodal ligand 1,1,1-tris(hydroxymethyl)-ethane. The self-assembled $\{Mn_{32}\}$ truncated cube (see picture) is further stabilized by end-on-bridging azide ligands and acetate groups. Such stabilization could prove to be useful in the preparation of single-molecule magnets.



Asymmetric Synthesis

X.-X. Yan, C.-G. Liang, Y. Zhang, W. Hong, B.-X. Cao, L.-X. Dai, X.-L. Hou* — 6544–6546

Highly Enantioselective Pd-Catalyzed Allylic Alkylations of Acyclic Ketones



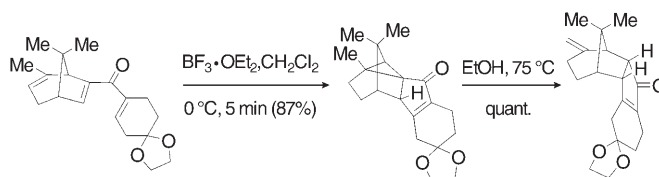
Pocket the difference: Highly enantioselective allylic alkylation of simple acyclic ketones is carried out by using a Pd catalyst with a “chiral pocket” ligand **1** (see scheme). The addition of a Lewis acid

such as AgBr and the selection of one enolate form over another dramatically affect the enantioselectivity of the reaction.

Domino Pericyclic Processes

S. Giese, R. D. Mazzola, Jr., C. M. Amann, A. M. Arif, F. G. West* — 6546–6549

Unexpected Participation of an Unconjugated Olefin during Nazarov Cyclization of Bridged Bicyclic Dienones



Surprising rearrangements in a rigid system: A cyclopropyl ring is formed unexpectedly when a trienone substrate is subjected to the Nazarov cyclization (see scheme). The participation of the unconjugated alkene unit present in the sub-

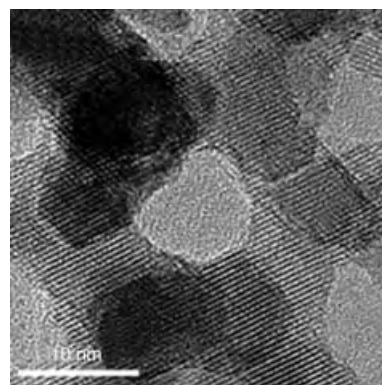
strate might be a consequence of the complete torquoselectivity of the initial electrocyclic closure. A subsequent rearrangement by a homo-1,5-hydrogen shift occurs cleanly to give the final product.

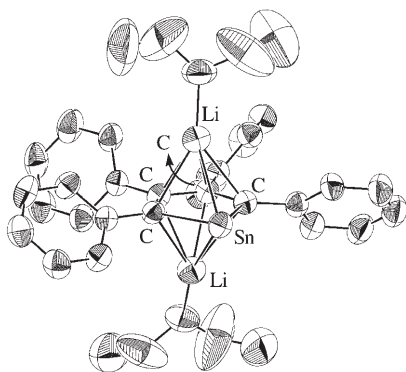
Electrode Materials

F. Jiao, K. M. Shaju, P. G. Bruce* — 6550–6553

Synthesis of Nanowire and Mesoporous Low-Temperature LiCoO_2 by a Post-Templating Reaction

Giving in to templation: Lithium-containing nanostructured transition metal oxides have been prepared by a templating route with preservation of the nanostructure. Both one-dimensional nanowire and three-dimensional mesoporous samples of low-temperature (LT)- LiCoO_2 with highly crystalline structures (see image) have been obtained, and these perform better than “normal” LT- LiCoO_2 as intercalation electrodes in lithium batteries.



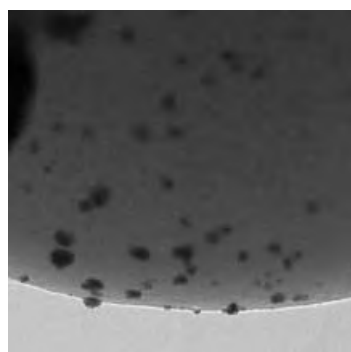


Delocalization in heterocycles: Reaction of hexaphenylstannole with excess lithium gives the dilithium stannole as deep-red crystals. The aromaticity of the dianion was examined by NMR spectroscopy, X-ray analysis (see picture), and calculations. The dianion has considerable aromatic character and is reported to be the first tin-containing carbocyclic aromatic compound.

Aromaticity

M. Saito,* R. Haga, M. Yoshioka, K. Ishimura, S. Nagase — 6553 – 6556

The Aromaticity of the Stannole Dianion

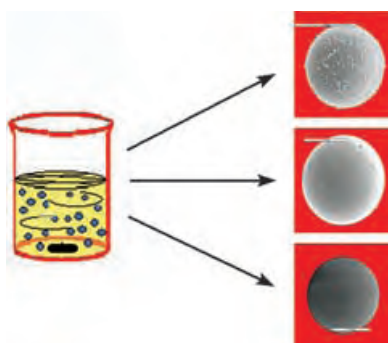


Thrifty catalysis: Tungsten carbide microspheres with high surface area and CO chemisorption capacity were prepared by heating mixtures of a resorcinol–formaldehyde polymer and ammonium metatungstate. Platinum supported on these microspheres (see electron micrograph) shows higher activity than the commercial catalyst with 20% Pt–Ru (1:1) on C for the electrooxidation of methanol.

Heterogeneous Catalysis

R. Ganesan, J. S. Lee* — 6557 – 6560

Tungsten Carbide Microspheres as a Noble-Metal-Economic Electrocatalyst for Methanol Oxidation

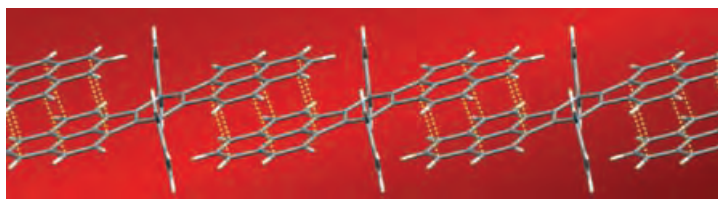


Take the rough with the smooth: Conducting silica microspheres with different morphologies—rough, dotted, and smooth (see picture)—have been rapidly synthesized in an ionic liquid under various experimental conditions. The conducting property of the silica particles is attributed to the presence of entrapped molecules of ionic liquid and water.

Conducting Materials

D. S. Jacob, A. Joseph, S. P. Mallenahalli, S. Shanmugam, S. Makhluf, J. Calderon-Moreno, Y. Koltypin, A. Gedanken* — 6560 – 6563

Rapid Synthesis in Ionic Liquids of Room-Temperature-Conducting Solid Microsilica Spheres



A phenalenyl-based Kekulé hydrocarbon with singlet biradical character has been isolated and characterized. Strong intra- and intermolecular interactions between the unpaired electrons lead to short π –

π contacts and formation of one-dimensional chains (see picture). Thus, wide valence and conduction bands are established, and the compound shows semiconductive behavior.

Radicals

T. Kubo,* A. Shimizu, M. Sakamoto, M. Uruichi, K. Yakushi, M. Nakano, D. Shiomi, K. Sato, T. Takui, Y. Morita, K. Nakasuji* — 6564 – 6568

Synthesis, Intermolecular Interaction, and Semiconductive Behavior of a Delocalized Singlet Biradical Hydrocarbon

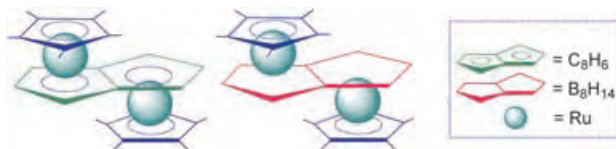
Metallaboranes

S. Ghosh,* B. C. Noll,
T. P. Fehlner* ————— 6568–6571

Borane Mimics of Classic Organometallic Compounds: $[(\text{Cp}^*\text{Ru})\text{B}_8\text{H}_{14}(\text{RuCp}^*)]^{0,+}$,
Isoelectronic Analogues of Dinuclear Pentalene Complexes

Body doubles: An isoelectronic borane analogue of a dinuclear ruthenium–pentalene (C_8H_6) π complex (see picture) has been prepared and isolated. It is found to

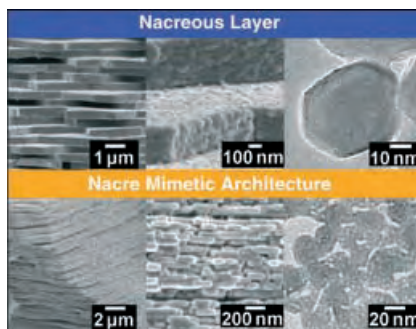
be an intermediate in the growth of the borane fragment of a diruthenaborane framework.



Bioinorganic Chemistry

Y. Oaki, H. Imai* ————— 6571–6575

The Hierarchical Architecture of Nacre and Its Mimetic Material

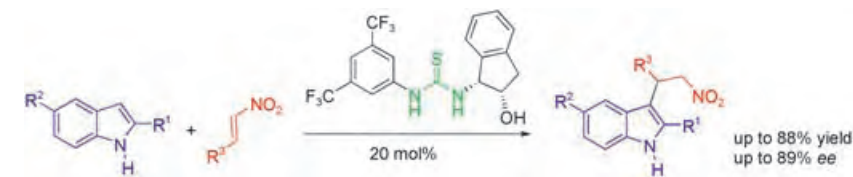


Mother-of-pearl has a three-level nano-
scopic-to-macroscopic hierarchical archi-
tecture, which provides storage for
organic molecules at the nanoscale. A
material that mimics the hierarchical
architecture and nanostorage properties
of nacre emerges from the simple crys-
tallization of potassium sulfate and
poly(acrylic acid) (see picture).

Asymmetric Synthesis

R. P. Herrera, V. Sgarzani, L. Bernardi,
A. Ricci* ————— 6576–6579

Catalytic Enantioselective Friedel–Crafts
Alkylation of Indoles with Nitroalkenes by
Using a Simple Thiourea Organocatalyst



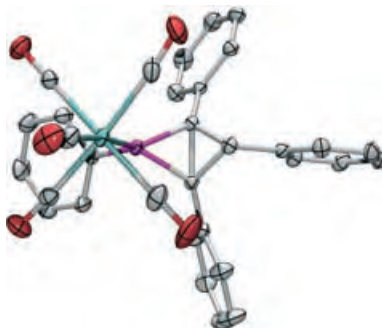
A facile access to optically active 2-indolyl-
1-nitro derivatives, which can be easily
transformed into highly valuable com-
pounds such as tryptamines and 1,2,3,4-
tetrahydro- β -carbolines, is provided by the

first catalytic enantioselective Friedel–
Crafts alkylation of indoles with nitro-
alkenes (see scheme; e.g. $\text{R}^1 = \text{R}^2 = \text{H}$,
 $\text{R}^3 = \text{Ph}$).

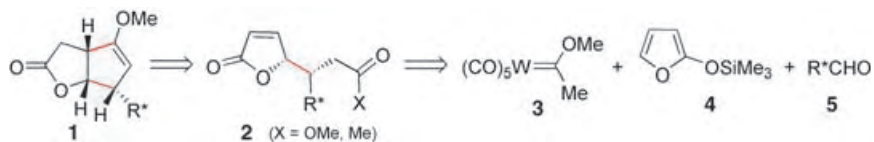
Bicyclobutanes

J. C. Slootweg, S. Krill, F. J. J. de Kanter,
M. Schakel, A. W. Ehlers, M. Lutz,
A. L. Spek,
K. Lammertsma* ————— 6579–6582

Valence Isomerization of 2-
Phosphabicyclo[1.1.0]butanes



Remarkably stable 2-phosphabicyclo-
[1.1.0]butanes (see picture; O red, P violet,
W turquoise) were synthesized from the
complexed phosphinidene $\text{Ph-P}=\text{W}(\text{CO})_5$
and cyclopropenes. These compounds
undergo valence isomerization to form 3-
phosphacyclobutenes via 1-phosphabuta-
dienes at elevated temperatures.



A simple start: A tungsten carbene **3**, 2-trimethylsilyloxyfuran (**4**), and an enantiopure aldehyde **5** provide easy access to enantiopure butenolides **2**. The metal

carbene increases the accepting character of the C=C bond and allows further transformations into butenolide structures such as **1**.

Conjugate Additions

J. Barluenga,* A. de Prado, J. Santamaría, M. Tomás — 6583–6585

Uncatalyzed Mukaiyama–Michael Reaction: Rapid Access to Simple and Complex Enantiopure γ -Butenolides



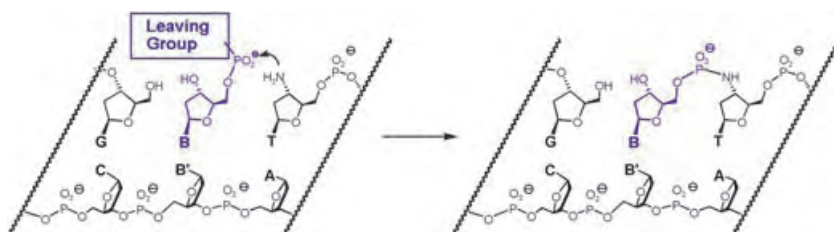
Enamine–imine transformations of guanine lead to tautomers that support valence anionic states which are adiabatically bound by as much as 8 kcal mol⁻¹ (see scheme). The valence anions might be formed by dissociative electron

attachment followed by attachment of a hydrogen atom to a carbon atom. Such tautomers might affect the structure and properties of DNA and RNA exposed to low-energy electrons.

Computational Chemistry

M. Harańczyk, M. Gutowski* — 6585–6588

Finding Adiabatically Bound Anions of Guanine through a Combinatorial Computational Approach



Rapid replication: Non-enzymatic primer extension has previously been studied in the context of prebiotic chemistry, but not for practical applications. Reactions with primers featuring a 3'-amino-2',3'-dideoxynucleotide can be rapid and selective for

all four templating nucleobases (see scheme). On a chip with immobilized capture strands, 500 fmol of template suffice for single-nucleotide determinations within 2.7 h.

DNA Replication

P. Hagenbuch, E. Kervio, A. Hochgesand, U. Plutowski, C. Richert* — 6588–6592

Chemical Primer Extension: Efficiently Determining Single Nucleotides in DNA

Angewandte

WILEY InterScience®

DISCOVER SOMETHING GREAT

"Hot Papers" are chosen by the Editors for their importance in a rapidly evolving field of high current interest. A preview with the graphical abstracts of these articles can be found on the *Angewandte Chemie* homepage in Wiley InterScience at www.angewandte.org.

All articles in *Angewandte Chemie* are published online several weeks ahead of print. They are found under the "EarlyView" link on the journal's homepage in Wiley InterScience.

Angewandte

Service

Keywords — 6594

Authors — 6595

Preview — 6597

Corrigendum

ADHOC 2005 in Cologne: The Latest in
Dioxygen Activation and Homogeneous
Catalytic Oxidation

C. Limberg* _____ **6102–6104**

Angew. Chem. Int. Ed. **2005**, *44*

DOI 10.1002/anie.200502936

Some sentences in the meeting review of ADHOC 2005 in Cologne were incorrect at the time of press.

Page 6102, column 1, line 11 should read: To gain better insights, model systems with well-defined active sites are being developed; on the other hand problems are approached with the aid of kinetic measurements, sophisticated isotope-labeling experiments, molecular probes, and especially computational chemistry which allows the discussion of structure–activity relationships and can either support or reject proposed mechanisms.

Page 6102, column 3, line 6 should read: On the other hand, A. Griesbeck (University of Cologne, Germany) described how $^1\text{O}_2$ with the aid of tetraarylporphyrin-loaded polystyrene can be used for ene reactions and [4+2] cycloadditions, and how it can even be “made chiral” through organocatalysts.

Page 6103, column 2, line 7 should read: these effect the oxidation of bromide to bromonium ions, which in turn can be reacted under nonacidic conditions with olefins and aromatic compounds.

Page 6103, column 3, line 5 should read: The latter, however, are apparently stabilized by POM ligands; their use recently afforded the synthesis of a $\text{Pt}=\text{O}$ complex as described by C. L. Hill (Emory University, Atlanta, USA), and now he reported the isolation and characterization of the first $\text{Pd}=\text{O}$ complex, $\text{K}_9\text{Na}_4[(\text{O}=\text{Pd}^{\text{IV}}\cdot\text{OH})\text{WO}(\text{OH}_2)\text{L}_2]$ ($\text{L}=[\text{PW}_9\text{O}_{34}]^{9-}$).

Page 6103, column 3, line 21 should read: Altogether, there is still great interest in the oxidation of methane, the simplest yet most resistant C1 hydrocarbon source.

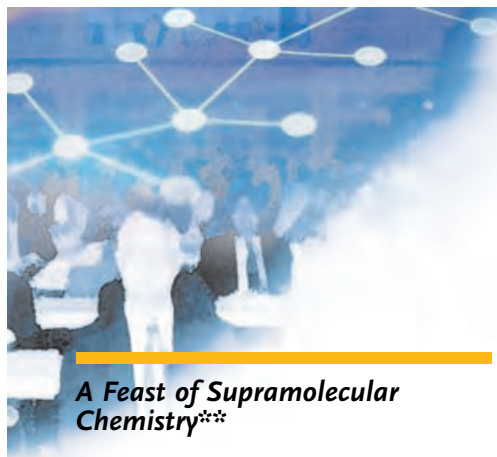
Page 6104, column 1, line 27 should read: ... R. Hage (Unilever, The Netherlands)...

Page 6104, column 1, line 29 should read: The lecture given by G. Reinhardt (Clariant, Germany) made it clear that there is not, and yet cannot be, a panacea for the bleaching industry.

Page 6104, column 3, line 22 should read: The mechanistic understanding was broadened, refined, and even renewed, and many novel systems have been developed.

Page 6104, column 3, last sentence: The pronounced relation to application was underscored by the fact that this year's meeting was, for the first time, organized jointly by both the industrial and academic spheres as well as through the strong participation and generous support of industry (especially BASF).

The Editorial Office apologizes for the oversight.



A Feast of Supramolecular Chemistry**

Daniel-Petru Funeriu*

Just before the distinctly French August holidays, the meeting “Advances in Supramolecular Chemistry” was held in Strasbourg, France, to celebrate the 40th anniversary of Jean-Marie Lehn’s laboratory. Eight plenary lectures, rich poster sessions, and a string of cultural and social events made attendance at this meeting memorable and inspiring for some 200 participants. With the contribution of numerous sponsors, the organizing team managed by Nicolas Giuseppone and expertly complemented by Jacline Claudon and Jean-Louis Schmitt succeeded in attracting an exceptional panel of speakers to the esthetic and functional surroundings of the newly built ISIS institute.

On the first day of the meeting, the participants gathered on the top level of the Museum of Modern Art—an inspired choice—where they had the pleasure to meet former colleagues and the invited speakers while enjoying a delightful view of Strasbourg.

The following day, Jean-Marie Lehn opened the scientific session by reviewing the results obtained in his laboratory over the last 40 years (which represents some 600 years worth of research in

total)! The first results from the group of the then 25-year-old Lehn were also among the first concerning ab initio studies on organic molecules, with the calculation of energetic barriers for nitrogen and phosphorus inversions and the study of stereoelectronic effects. This topic was followed by studies on ^{14}N nuclear quadrupole relaxation and its use in molecular dynamics. Notably, some of these pioneering results, such as the finding of a second-order transition of quinolein in the liquid phase at 15°C , were only confirmed and published some 20 years later.



Figure 1. Jean-Marie Lehn and his long-term administrative assistant (background).

In 1967, Lehn’s earlier interests in “*how a chemist might contribute to the study of [...] highest biological functions*” led to the development of the chemistry of cryptands and cryptates in the Strasbourg laboratory. The physical chemistry background of the laboratory was pivotal in the study of the properties of these compounds and, probably, in the genesis of concepts that evolved from these results. The idea that information stored into a molecule can be expressed through an interactional algorithm which is supramolecular in nature flowered into the notion that chemistry can (and should) be seen not only as the science of energy and matter but also as information science. On the basis of Emil Fischer’s lock-and-key model, the construction of anion recep-

tors, receptors with multiple binding sites, as well as receptors of organic molecules with transport and catalytic properties substantiated the ensuing, quite natural, emergence of the founding concepts of supramolecular chemistry. The early results in metal-ion-directed self-assembly further anchored this daring conceptualization, which it was at the time, and opened a field of supramolecular chemistry, among which helicates, cages, grids, and higher order assemblies represent many landmarks. Some devices constructed along these principles have had an important practical

impact, such as the europium cryptates that are used in screening technologies. The inaugural lecture concluded with a discussion of an area of research that first started in 1994 and is now the main focus of the laboratory: the further exploration of constitutionally dynamic chemical space. The earliest examples from Lehn’s laboratory in the field of dynamic combinatorial chemistry, in which the key to Fischer’s lock was now self-generated from a multitude of possibilities under the influence of the lock itself, have developed into the field of constitutional dynamic chemistry (CDC), in which reversible bonds (covalent and noncovalent) are used to generate a constitutional diversity that

responds in an adaptive process to the pressure of internal or external factors.

On the occasion of such an anniversary, one is usually tempted to look with admiration and sometimes nostalgia to achievements of the past rather than to those yet to emerge in the coming years. In that respect, Lehn’s inaugural talk is certainly better described as a scientific appetizer than the cherry on the cake!

In a typically inciting presentation, Helmut Ringsdorf (Mainz) discussed the role of scientists as exchange vectors between science and society, as well as the responsibilities, challenges, and opportunities that they should address in our world of rapid change. The meeting in Strasbourg on supramolecular chemistry, which has crossed the borders

[*] Dr. D.-P. Funeriu
Research Institute for Cell Engineering
National Institute of Advanced Industrial
Science and Technology (AIST)
3-11-46 Nakouji, Amagasaki
Hyogo 661-0974 (Japan)
E-mail: danielpetru-funeriu@aist.go.jp

[**] Advances in Supramolecular Chemistry,
Strasbourg, July 27–30, 2005. A full video
recording of the talks can be consulted at
<http://canalc2.u-strasbg.fr/video.asp?idEvenement=184>

of physics and biology to become supra-molecular science, was an ideal setting to discuss the theme of crossing borders between science and society. It was, therefore, only natural in the context of such a meeting to raise the question of “*why is not the responsibility that we, as scientists, feel towards the scientific truth and fairness, transferred to ‘the other side’, that is, society’s evolution?*” Poignant examples of the past, largely illustrating the lack of attitude of German scientists during the emergence of the third Reich, and worrying signs of the present could be considered the data on which Ringsdorf built the case for increased involvement of scientists in the future of society, such as to prevent a “*socio-economic brutalization of Europe and the world in the 21st century*”. In science, Ringsdorf advocated the need for young researchers to exit the gravity field of their mentors (or as he put it, “*to dig their own rivers rather than continuously fishing in their mentor’s*”) and take a more courageous approach towards interdisciplinarity. A difficult but also rewarding path, one may add.



Figure 2. Helmut Ringsdorf and Jean-Pierre Sauvage.

Next, David Leigh (Edinburgh) took the spotlight with a presentation of his laboratory’s work on rotaxanes and catenanes. Since the first controlled synthesis of these assemblies assisted by metal-ion complexation, templation by ion-pairing and hydrogen-bonding interactions have expanded the repertoire of interlocked molecules so much so that time is ripe to address whether there is more to the field of interlocked molecules than their exotic structure. Leigh

demonstrated how his group has succeeded in relating the unusual molecular-level mechanical features of catenanes and rotaxanes to the emergence of function, particularly the control of directional molecular motion induced by various stimuli. The generally used principle that Leigh’s group has brought to the level of art involves the construction of a template unit (a strand in the case of rotaxanes, or macrocycles in the case of catenanes) that contains “stations” with orthogonally modulable affinities for a threaded macrocycle. Then, starting from an initial state in which the threaded macrocycle is bound to the first station, an input signal (such as light or a change of solvent) modifies the relative affinities of the first and second stations which results in a net movement of the threaded macrocycle. By using this principle, his group has succeeded, for example, in moving macroscopic objects against gravity on surfaces.

Henri Kagan (Paris) reviewed the progress in the field of asymmetric amplification, illustrated with recent examples from his laboratory. Kagan disclosed the first example (predicted by the kinetic treatment of the reaction between two enantiopure reagents by Ugi in 1977) of a kinetic resolution in which a racemic reagent enhances the enantiomeric excess of a partially resolved substrate. By reacting one equivalent of an amine with 67% *ee* with 0.6 equivalents of a racemic acetylation reagent, Kagan’s group obtained 0.4 equivalents of the initial amine with 95% *ee* together with 0.6 equivalents of the acetylated compound with 50% *ee*. Kagan concluded a well-guided, in-depth journey into the labyrinths of asymmetric amplification with examples of recent work from his laboratory in combining distinct asymmetric amplification strategies within a single process.

The third day of the meeting was devoted to a visit of the city of Selestat and its humanist library (established in 1452), possibly the most representative humanist library to be preserved intact during the Renaissance. Among the collection of rare books is one of the few

copies of the “*Cosmographiae Introductio*”, produced in nearby Saint-Die, which for the first time coined the term “America”. This excursion into universal culture was complemented by a tasty incursion into the local culture: a visit and dinner in one of Alsace’s most famous vineyards. The wine-tasting session of the dinner was an enriching experience both for the participants and the wine-producer alike.

In the speech on the morning after the night before, Samuel Stupp (Evanston) presented spectacular examples of macromolecular self-assembled systems, in which an exquisite level of control can be achieved in the micron range by taking advantage of classical molecular recognition codes as well as more subtle ones, such as entropy-limited finite crystallization and steric-crowding-imposed torque. Particularly striking by its implications in medicine was the controlled formation of self-assembled bioactive nanofibers from peptide amphiphiles. The peptides, and thus the external surface of the resulting self-assembled nanofibers, can be engineered to display bioactive epitopes (such as the neurite-guiding epitope IKVAV). Injection of a solution of the IKVAV peptide amphiphile into mice at the site of a spinal-cord injury (where the axons typically cannot penetrate due to reasons of mechanical and chemical signaling) results in spontaneous nanofiber formation. By signaling through the conveniently exposed epitopes, the nanofibers lure the axons into (and through) the site of the injury, consequently re-establishing neuronal contacts. This improves the prognosis in mice that have suffered severe spinal-cord injury.

Javier de Mendoza (Tarragona) drew parallels between art and structural chemistry in describing the advances from his laboratory. Prominent among those are the recent further developments of guanidinium-based receptors for oxo-anion recognition, protein binding, as well as transport into cells. In particular, the binding of chiral bicyclic guanidinium oligomers to p53 protein may be especially important in the future. Other recent developments that Mendoza reported at this meeting were self-assembled rosettes in which ureido-pyrimidinones were used

as multiple-hydrogen-bonding connectors.

Are there unused strings on a supramolecular chemist's violin? Judging by the presentation given by François Diederich (Zürich) about the structural features of orthogonal multipolar interactions and their importance in recognition events, it certainly appears so. Indeed, these interactions (such as $C-X\cdots C=O$ ($X=F, Cl, Br, I, OH$), $C=O\cdots C=O$, and $CN\cdots CO$) appear to have been somehow overlooked and less exploited in the design of molecular interacting partners than hydrogen bonds and ion-ion, ion-dipole, and hydrophobic interactions. Diederich's group, in collaboration with scientists at Roche, undertook a statistical approach and compiled a detailed repertoire of such interactions found through data-mining of crystallographic databases. The results revealed numerous cases of $C-X\cdots CO$ contacts with $X\cdots C$ distances smaller than the sum of their $C+X$ van der Waals radii and $C-X\cdots C=O$ angles close to 90° . Can we predict these "contextual interactions"? Can we harness their proposed potential in molecular design? The answers to these important questions are likely to rely on their difficult but important quantification, for example, as performed by Diederich et al. for the $C-F(CF_3)\cdots CO(\text{amide})$ interaction.

David Reinhoudt (Twente) presented his group's latest results, which make imaginative use of the supra-

molecular chemistry of cyclodextrins, towards the construction of molecular printboards. By further expanding the knowledge gained in this endeavour, in an approach that combines layer-by-layer assembly with nanoimprint lithography, nanometric islands of Au could be efficiently patterned onto a flat surface. In this approach, Au is sublimed by laser deposition onto a poly(dimethylsiloxane) (PDMS) stamp and a monolayer of thioether-functionalized cyclodextrins is then formed on the Au surface. The resulting Au-cyclodextrin stamp is applied onto a flat surface functionalized with a ferrocene dendrimer. Through the multivalent cyclodextrin-ferrocene dendrimer interactions, the Au layer sandwiched between the PDMS and the cyclodextrin is transferred to the flat surface. Thus, the surface now exposes the Au replica of the stamp, and sandwiched between the surface and the Au lies a monolayer of ferrocene molecules. High-density field-effect transistors can now be fabricated and characterized by using the Au islands as electrical contacts and through the electrical properties of the ferrocenes.

Over the years, the concepts of supramolecular chemistry have been mainly used to build progressively more complex structures. The molecular toolbox that is now available makes it tempting as well as increasingly facile to continue this trend. However, and very importantly so, one common

theme of the speakers in the Strasbourg meeting was the emergence of function through structure engineering, both in the biological and the physical sciences. The fact is that function is no longer at the horizon of supramolecular chemistry but has become (at least in the hands of pioneers) its daily reality. As Reinhoudt stated: "*We are reaching in supramolecular chemistry a phase where structure is not enough: We have to show that we can obtain, by self-assembly, a function as well.*" Indeed, most of the speakers did exactly this and very convincingly so, one should add. During this meeting, the question that friends and foes alike have asked — "*What can we do with supramolecular chemistry?*" — received a comprehensive and clear answer, prefiguring a function-focused trend in supramolecular sciences.

With such an event, one could not talk about the science without talking about the people that made it happen. By perfectly illustrating the history and philosophy of the laboratory, and hinting to one of its main sources of success at both scientific and human level, Lehn's concluding remarks about science, art, as well as his former collaborators reinforced the global impression that science and the group, more than the man himself, were the celebrated ones.

DOI: 10.1002/anie.200503161

Artificial Molecular Double-Stranded Helices

Markus Albrecht*

Keywords:

coordination modes · helical structures · hydrogen bonds · self-assembly

Helicity is a topological motif that is highly attractive from an aesthetic point of view. It can be observed in huge objects like the spiral arms of galaxies and it plays an important role in the world of “string theory”.^[1] Helical structures, such as those found in the plant kingdom, have inspired architects and artists. For a chemist, helicity is important owing to the wide appearance of helical structures in, for example, quartz,^[2] proteins,^[3] collagens, and many more natural or artificial fiber-type derivatives.^[4]

Since the discovery of the double-stranded helical structure of DNA by Watson and Crick,^[5] chemists have been searching for simple linear molecules that are able to form artificial double helices through noncovalent interactions, such as π -stacking, electrostatic interactions, hydrogen bonding, or metal coordination.^[6] In naturally occurring DNA the stability of the double helix is attributed to hydrogen bonding between complementary oligonucleotide strands. As an additional stabilizing interaction, the aromatic base pairs display π - π interactions, which are optimized, if the double-strand adopts a helical twist^[7] (Figure 1^[8]).

In artificial analogues of DNA, the hydrogen bonding interaction between the two strands can be substituted by metal coordination. Shionoya et al. demonstrated this impressively by preparing a heptanucleotide strand with the GXXXXXC sequence (X = hydroxy-

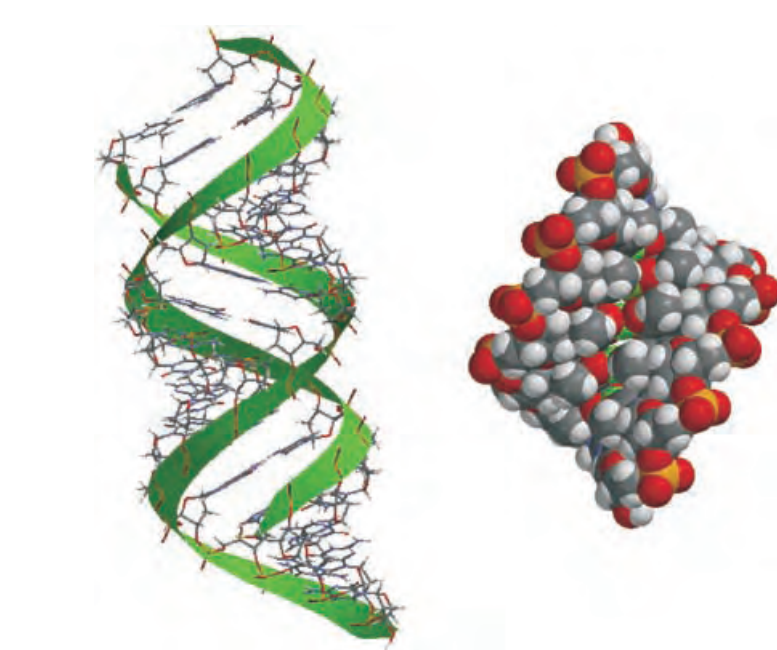


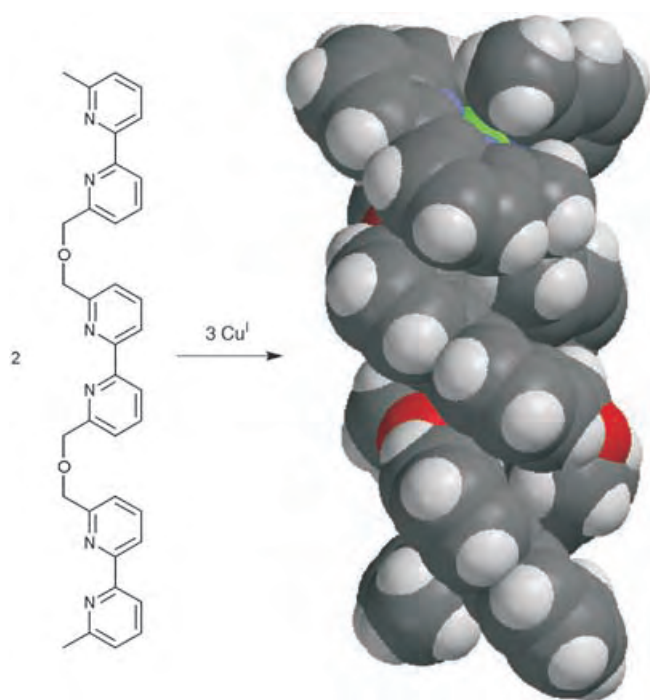
Figure 1. Double-helical DNA (left: C: gray; H: white; N: blue; P: orange; O: red) and a CPK model of the artificial pentanuclear metalla-DNA synthesized by Shionoya et al. (right: Cu: green).^[8]

pyridone). Upon addition of copper(II) ions, a double-stranded DNA-type structure is formed, in which the two strands are connected by five copper(II) ions, each possessing a square-planar coordination geometry (Figure 1, right).^[9] Metal coordination is frequently used to prepare artificial double helices. There are numerous reports on coordination polymers that exhibit double-helical motifs in the crystal.^[10] A special class of well-defined molecular double-stranded helical metal complexes was introduced in 1987 by J.-M. Lehn and was termed *double-stranded helicates*. In these complexes two linear oligodonor ligands wrap around two or more metal centers and thus form a double helix (Scheme 1).^[11]

In the first paper on helicates, Lehn and co-workers point out that helicates represent an “*inorganic double helix*, reminiscent of the double-helical structure of nucleic acid”.^[11] Although on first sight this seems to be a provocative statement, there is some analogy between helicates and DNA with regard to the cooperative self-assembly of the double helix, the noncovalent connection by cations (protons of DNA versus metal cations), and π - π interactions as additional stabilizing effects. If nothing else, at least the double-helical structures of DNA and of helicates are aesthetically appealing.

A class of single-stranded compounds with a helical structure are the helicenes (**A**, Scheme 2).^[12] Compound

[*] M. Albrecht
Institut für Organische Chemie
RWTH Aachen
Landoltweg 1, 52074 Aachen (Germany)
Fax: (+49) 241-8092385
E-mail:
markus.albrecht@oc.rwth-aachen.de



Scheme 1. A model of the first double-stranded helicate, which was formed by Lehn et al. from three copper(I) ions and two ligands, which each contain three 2,2'-bipyridyl units. C: gray; H: white; N: blue; O: red; Cu: green.

B (Scheme 2) represents an extended helicene, which, owing to the alkyl bridges, possesses some flexibility and which additionally bears some internal nitrogen-donor atoms. Compound **B** forms a double-stranded helicate-type complex upon addition of one or two equivalents of sodium ions.^[13] The oligo(pyridine amide) **D** (Scheme 2)

adopts a helical conformation owing to intramolecular hydrogen bonding between the amide protons and the pyridine-nitrogen atoms (**C**, Scheme 2). Depending on the concentration and on the temperature, foldamer **D** forms double-stranded compounds owing to attractive π - π interactions between two single strands.^[14] In hydrogen-bonded systems

with additional electrostatic attraction, the formation of double-stranded helices also can be achieved. As shown in Figure 2 (**E**), the chiral sulfur-bridged bisguanidinium strand assembles around dianionic tetrahedral sulfate ions and thus forms an “inverted” helicate-type structure.^[15]

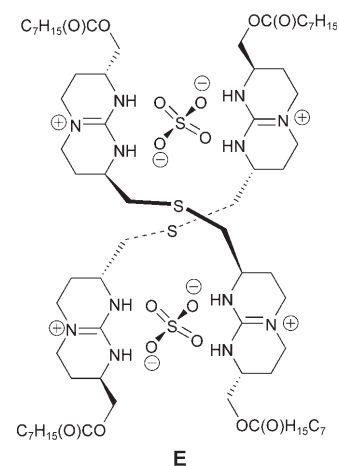
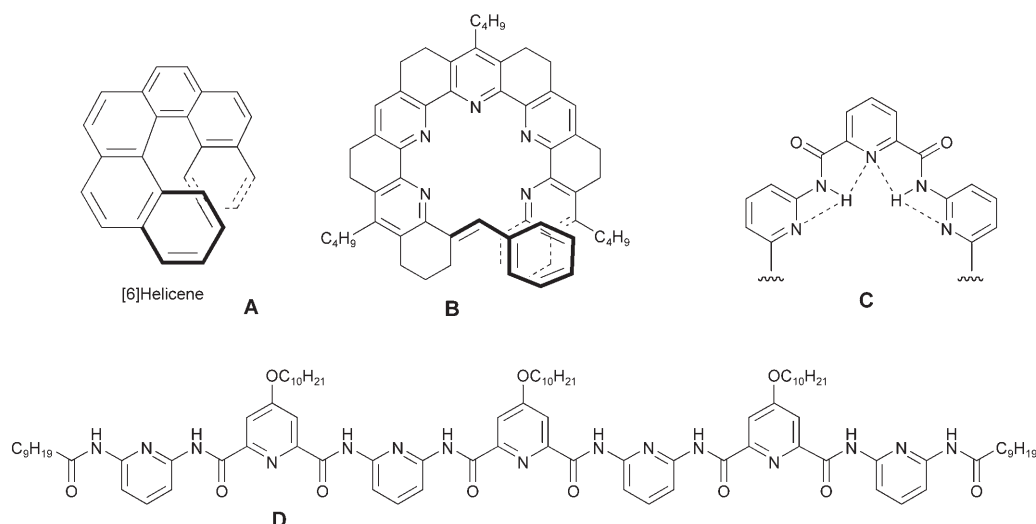


Figure 2. The “inverted” double-stranded helicate **E** described by de Mendoza et al.^[15]

The examples described to date of artificial double helices lack one important feature compared to the natural model DNA. They are not able to store information other than the stereochemistry in the double-strand—information



Scheme 2. Molecules that form helical structures: [6]helicene (**A**) adopts a single-stranded helical structure, whereas **B** yields a double-stranded helicate in the presence of sodium ions. The foldamer **D** forms a helical structure owing to intramolecular hydrogen bonding interactions. Compound **C** dimerizes in solution at high concentration and low temperatures.

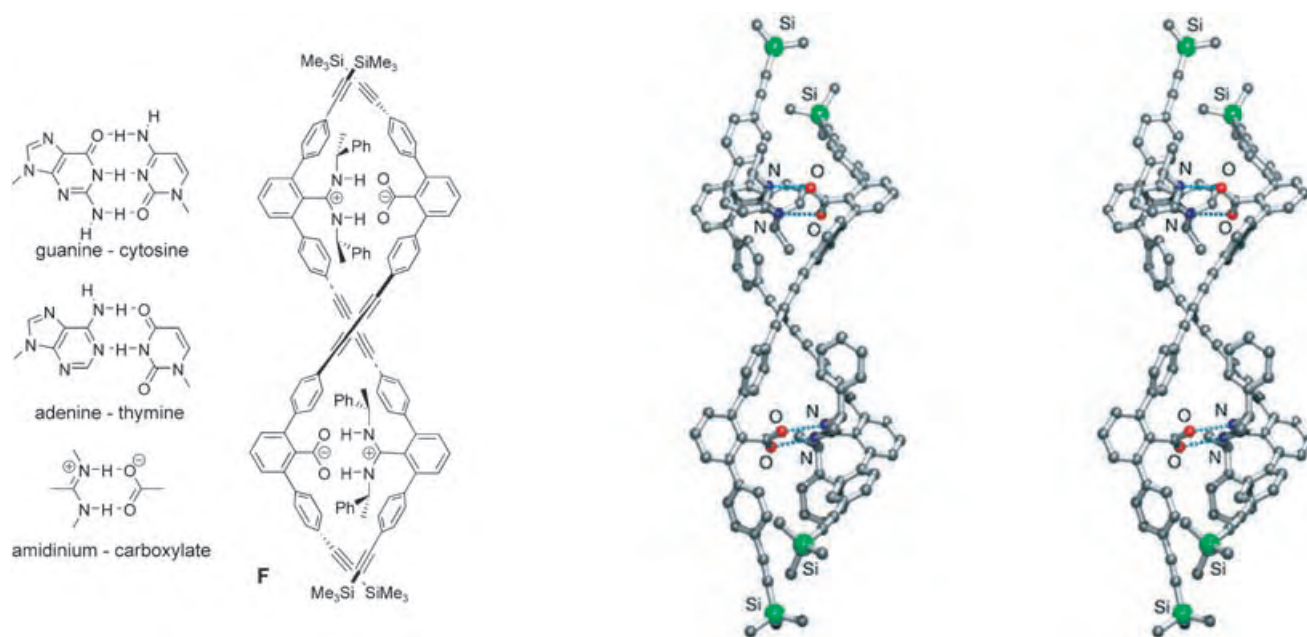


Figure 3. Left: The complementary pairs guanine–cytosine, adenine–thymine, amidinium–carboxylate, and the double-stranded helix with complementary amidinium–carboxylate pairing, which was described by Furusho and Yashima. Right: Stereoview of the X-ray structure taken from reference [16].

storage and processing is an important feature of DNA and occurs by a sequential arrangement of complementary base-pairs. The sequence in one strand dictates the sequence of the complementary one. To store information in artificial systems, we have to form the double helices from two strands with complementary binding sites. This can be achieved, for example, by substituting the natural base-pairs guanine–cytosine or adenine–thymine by simple analogues (e.g. amidinium–carboxylate).

Recently, the synthesis of the hetero-stranded double helix **F** was described, in which different but complementary binding sites were introduced in two different strands (Figure 3). Hereby, a bisamidinium strand and the complementary bicarboxylate strand were prepared by modular approaches. Mixing of the two strands led to the spontaneous formation of an enantiomerically pure double helix, which was characterized by NMR and CD spectroscopy in solution. X-ray structure analysis revealed that the double-helical structure is maintained in the solid state (Figure 3).^[16] Compound **F** is a new type of double-stranded helix, in which two different strands interact by salt bridges between complementary amidinium and carbox-

ylate units. Therefore, for the first time the complementarity between two strands, which is found in DNA, is an important aspect of the noncovalent formation of an artificial double-stranded system. In related future studies this might allow the preparation of sequential strands with complementary binding sites that are either self-complementary or that form hetero-duplexes (as shown in **F**). In the future, an artificial system might result, which contains not only stereochemical^[17] but also sequential information. Duplex formation combined with chemical ligation processes might then be able to transfer this information to a new strand. Complementary pairs such as amidinium and carboxylate might take the place held by guanine–cytosine or adenine–thymine in nature. Therefore the preparation of a self-complementary strand with one carboxylate and one amidinium group should be one of the next challenges.

As described herein, naturally occurring double-stranded DNA acts as a model for chemists and motivates us to develop routes to artificial molecular double-stranded helices. Possibilities have to be found to assemble linear molecules to form double-stranded systems with a helical twist. Ideally this

process should proceed stereoselectively. The obtained systems—including those described herein—are still relatively simple compared to nature's wonderful example of DNA. Information storage and processing in double-helical compounds is still a monopoly of nature. However, the introduction of sequential strands in artificial double helices^[18] and the use of complementary base-pairs^[16] are first steps towards breaking this monopoly in the future.

Published online: July 26, 2005

- [1] S. W. Hawking, *A Brief History of Time*, Bantam Books, New York, **1998**.
- [2] J. H. Jung, Y. Ono, S. Shinkai, *Chem. Eur. J.* **2000**, 6, 4552.
- [3] N. Sewald, H.-D. Jakubke, *Peptides: Chemistry and Biology*, Wiley-VCH, Weinheim, **2002**.
- [4] K. P. Meurer, F. Vögtle, *Top. Curr. Chem.* **1985**, 127, 1.
- [5] J. D. Watson, F. C. H. Crick, *Nature* **1953**, 171, 737.
- [6] I. E. Rowan, R. J. M. Nolte, *Angew. Chem.* **1998**, 110, 65; *Angew. Chem. Int. Ed.* **1998**, 37, 62.
- [7] G. Ebert, *Biopolymere*, Teubner, Stuttgart, **1992**.
- [8] All models were generated by using force field calculations implemented in

- the Spartan O2 software package: Spartan O2, Wavefunction Inc., **2002**.
- [9] K. Tanaka, A. Tengeiji, T. Kato, N. Toyama, M. Shionoya, *Science* **2003**, 299, 1212.
- [10] See for selected examples: a) O. Mamula, A. von Zelewsky, T. Bark, G. Bernardinelli, *Angew. Chem.* **1999**, 111, 3129; *Angew. Chem. Int. Ed.* **1999**, 38, 2945; b) A. Erxleben, *Inorg. Chem.* **2001**, 40, 2928.
- [11] J.-M. Lehn, A. Rigault, J. Siegel, J. Harrowfield, B. Chevrier, D. Moras, *Proc. Natl. Acad. Sci. USA* **1987**, 84, 2565.
- [12] M. S. Newman, D. Lednicer, *J. Am. Chem. Soc.* **1956**, 78, 4765.
- [13] T. W. Bell, H. Jousselin, *Nature* **1994**, 367, 441.
- [14] a) V. Berl, I. Huc, R. G. Khoury, M. J. Krische, J.-M. Lehn, *Nature* **2000**, 407, 721; b) I. Huc, *Eur. J. Org. Chem.* **2004**, 17.
- [15] J. Sánchez-Quesada, C. Seel, P. Prados, J. de Mendoza, *J. Am. Chem. Soc.* **1996**, 118, 277.
- [16] Y. Tanaka, H. Katagiri, Y. Furusho, E. Yashima, *Angew. Chem.* **2005**, 117, 3935; *Angew. Chem. Int. Ed.* **2005**, 44, 3867.
- [17] The first enantiomerically pure double-stranded helicate: W. Zarges, J. Hall, J.-M. Lehn, C. Bolm, *Helv. Chim. Acta* **1991**, 74, 1843.
- [18] For double-stranded helicates with sequential strands, see: a) B. Hasenknopf, J.-M. Lehn, G. Baum, D. Fenske, *Proc. Natl. Acad. Sci. USA* **1996**, 93, 1397; b) V. C. M. Smith, J.-M. Lehn, *Chem. Commun.* **1996**, 2733.


WILEY InterScience®
DISCOVER SOMETHING GREAT
 Access some of the finest full text journals, reference works, books, and databases from around the globe. It's just what you need to make some important discoveries of your own.

ABOUT US
VIEW DEMO
CONTACT US
HELP

Enter your saved titles, articles, queries and alerts in My Profile.

☐ Remember Me

[Register Now](#) | [Archives](#) | [Forgot My Password](#)

Manage your access easily with “MY PROFILE”

Simply register. Registration is fast and free to all internet users.



Easy Access

- Save Titles, Articles & Queries for quick access
- Set up roaming access to access content outside of your institutions network
- Get free online sample copies
- Get free online trial subscriptions
- View a complete list of your subscriptions and accessible products

Enhanced Tools

- Receive E-Mail Alerts when new content is available
- Purchase Article Select Tokens online
- Purchase individual articles online with Pay-Per-View


WILEY InterScience®
 DISCOVER SOMETHING GREAT

www.interscience.wiley.com

Angew. Chem. Int. Ed. **2005**, 44, 6448–6451

© 2005 Wiley-VCH Verlag GmbH & Co. KGaA, Weinheim

www.angewandte.org

6451

Charge-Transfer Isomers and Mixed-Valence Properties**

Robert J. Crutchley*

Keywords:

bridging ligands · charge-transfer isomers · cluster compounds · mixed-valence compounds · ruthenium

The recent studies of Kubiak and co-workers^[1,2] in which they were able to identify the existence of charge-transfer isomers are important contributions to the field of mixed-valence chemistry. The work establishes charge-transfer isomers as identifiable chemical entities that exist in dynamic equilibrium determined by electron transfer on the pico-second time scale.

Mixed-valence compounds are generally odd-electron systems and are composed of two or more reduction/oxidation (redox) centers. The odd electron is able to exchange between the two redox centers either by photoinduced or thermal electron transfer depending upon the extent of electronic coupling between the two redox centers. For thermal electron transfer, three absolute conditions arise: no coupling between redox sites and no electron transfer (Class I), weak coupling and electron transfer between redox sites that is dependent upon thermal activation (Class II), and finally strong coupling and activationless electron transfer between redox sites (Class III).^[3] Class II and Class III systems are also referred to as valence-trapped and delocalized mixed-valence states, respectively. For mixed-valence systems at the boundary between Class II and Class III behavior,

where electron transfer rates are on the order of solvent relaxation times ($< 10^{-12}$ s), the classification Class II–III has been proposed.^[4] The charge-transfer isomers studied by Kubiak and co-workers are of Class II–III.

Of the many mixed-valence systems that have been studied, the vast majority of molecular systems are dinuclear ruthenium complexes and that is because of the stability of the coordination sphere in either Ru^{II} or Ru^{III} oxidation states and the enormous literature resource of ruthenium-complex synthesis. Kubiak and co-workers have extended this series to ruthenium clusters of the type $[\{\text{Ru}_3\text{O}(\mu\text{-CH}_3\text{COO})_6(\text{CO})\text{L}'\}(\mu\text{-L})\{\text{Ru}_3\text{O}(\mu\text{-CH}_3\text{COO})_6(\text{CO})\text{L}''\}]$ (Figure 1).

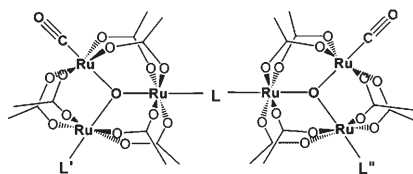


Figure 1. General diagram of the Ru₃ dimers, bridging ligand L, and monodentate ligands L' and L''.

For the above complexes in the neutral isolated state, each trinuclear Ru₃ moiety formally contains one Ru^{II} and two Ru^{III} centers (Ru₃^{III,III,II}) and the carbonyl ligand is coordinated to the formally divalent center. The cyclic voltammetry of these complexes shows two reversible two-electron oxidation waves at positive potentials and two reversible one-electron waves at negative potentials. The one-electron waves correspond formally to the Ru₃^{III,III,II}–Ru₃^{III,III,II}/Ru₃^{III,III,II}–Ru₃^{III,III,II} and

Ru₃^{III,III,II}–Ru₃^{III,III,II}/Ru₃^{III,III,II}–Ru₃^{III,III,II} one electron couples (i.e. the sequential reduction of one Ru^{III} center on each cluster unit) and are separated from each other in potential, ΔE , because of the stability of the Ru₃^{III,III,II}–Ru₃^{III,III,II} mixed-valence state that largely arises for a symmetric complex from the coupling between Ru₃ moieties. The Ru₃ moieties are separated by a distance that prevents direct orbital overlap and because of this the electronic coupling between Ru₃ moieties can only occur by mixing ruthenium orbitals with bridging ligand (L) orbitals in a process referred to as superexchange. As might be expected, the extent of orbital mixing and hence coupling is sensitive to the relative symmetry and energy of the interacting orbitals and this provides a means by which these complexes can be made extraordinarily useful probes of the mixed-valence state. In previous studies,^[5] Kubiak and co-workers changed the nature of the bridging ligand L and the monodentate ligands L' and L'' to purposefully vary the extent of superexchange coupling. Most importantly, the presence of a carbonyl ligand and the infrared spectroscopy of its carbonyl stretch $\nu(\text{CO})$ provided an independent probe of the valence state of each Ru₃ moiety in the mixed-valence state on the infrared time scale of 10^{-13} s. If the mixed-valence complex is Class III and symmetric (L' = L'' and L possesses a center of symmetry), the two carbonyl ligands will be in identical environments and so only one $\nu(\text{CO})$ band will be observed. For a Class II mixed-valence ion, the rate of electron transfer between redox sites is far slower than 10^{13} s⁻¹ and so two $\nu(\text{CO})$ bands will be

[*] Prof. R. J. Crutchley
Chemistry Department
Carleton University
1125 Colonel By Drive, Ottawa, Ontario
K1B5B6 (Canada)
Fax: (+1) 613-520-3749
E-mail: robert_crutchley@carleton.ca

[**] This work was supported by the Natural Sciences and Engineering Research Council of Canada

observed. With stronger coupling and faster electron transfer, the two $\nu(\text{CO})$ bands coalesce so that only one average band is observed. Kubiak and co-workers fitted the coalescence of the $\nu(\text{CO})$ bands^[5] according to an algorithm^[6] in which the electron-transfer rate constant was a variable. The studies convincingly showed that electron-transfer rates k_{et} approach the activationless limit ($k_{\text{et}} \approx 10^{12}$ to 10^{13} s^{-1}) in their most strongly coupled systems.

Charge-transfer isomers are mixed-valence complexes which differ only in the location of the odd electron. These isomers cannot be distinguished experimentally in symmetric mixed-valence systems but can be in asymmetric systems. However, the asymmetry in mixed-valence complexes biases the stability of one charge-transfer isomer over the other so that only the most stable charge-transfer isomer is normally observed. This bias in stability can be estimated from the difference in redox couples of isolated Ru_3 moieties (no coupling between moieties) and is referred to as the diabatic free-energy change.^[1] It can be accurately calculated by determining the charge-transfer isomer equilibrium constant and hence the adiabatic free-energy change.^[1] This latter value includes the effect of coupling on the energy difference between Ru_3 moieties. What Kubiak and co-workers were able to accomplish was to synthesize asymmetric mixed-valence complexes in which the difference in stability between charge-transfer isomers (the adiabatic free energy) was exceedingly small ($\leq 0.0248 \text{ eV}$) and the relative populations of charge-transfer isomers in equilibrium sufficiently large to be experimentally measurable. By slightly modifying the complexes in Figure 1, the population of charge-transfer isomers could be established by the asymmetric binding of $^{13}\text{C}^{18}\text{O}$ and $^{12}\text{C}^{16}\text{O}$ ligands. Energetic asymmetry was achieved by substituting different L' and L'' ligands or by binding an asymmetric bridging ligand L . The latter resulted in an elegant and unambiguous experimental identification of charge transfer isomers.

Figure 2 shows the structure and infrared spectroelectrochemistry of two complexes in which the asymmetric ligand, $\text{L} = \text{methylpyrazine}$, bridges two

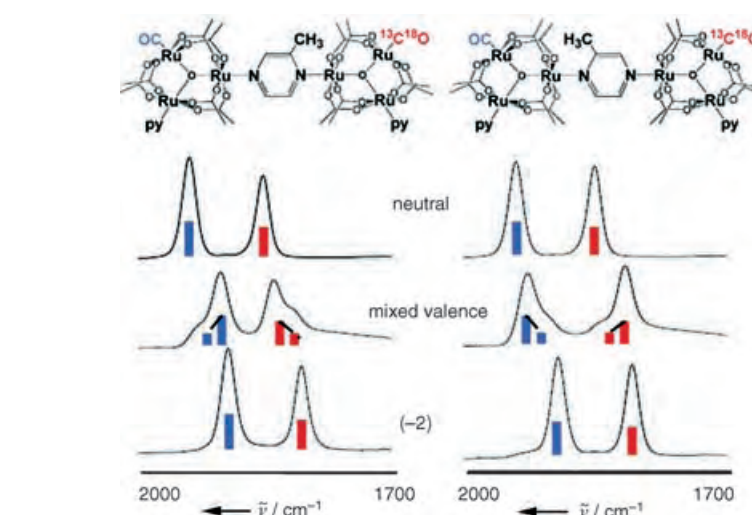


Figure 2. Infrared spectroelectrochemistry (at -30°C in a $0.1 \text{ M } n\text{Bu}_4\text{NPF}_6$ solution in CH_2Cl_2) of the two complex isomers $[\{\text{Ru}_3\text{O}(\mu\text{-CH}_3\text{COO})_6(^{12}\text{C}^{16}\text{O})\text{py}\}(\mu\text{-methylpyrazine})\{\text{Ru}_3\text{O}(\mu\text{-CH}_3\text{COO})_6(^{13}\text{C}^{18}\text{O})\text{py}\}]$ which differ only in the position of the pyrazine methyl group relative to $^{13}\text{C}^{18}\text{O}$. Spectra for the neutral (top), mixed-valence (middle), and doubly reduced (bottom) states are shown with a schematic of the exchanging populations. The CO groups and their corresponding IR bands are shown in the same color. See text for details. Reprinted from ref. [2].

Ru_3 moieties and $\text{L}' = \text{L}'' = \text{pyridine (py)}$.^[2] These complexes would be identical were it not for the selective substitution of $^{13}\text{C}^{18}\text{O}$. The IR spectrum of neutral and doubly reduced complexes shows only two $\nu(\text{CO})$ bands, the higher frequency band is assigned to $^{12}\text{C}^{16}\text{O}$ while the band at lower frequency is assigned to $^{13}\text{C}^{18}\text{O}$. A slight shifting to lower frequencies of both bands is seen upon reduction. However, the mixed-valence complex shows four $\nu(\text{CO})$ bands and this occurs because there are two charge-transfer isomers in equilibrium, each with $\nu(^{12}\text{C}^{16}\text{O})$ and $\nu(^{13}\text{C}^{18}\text{O})$ bands. The bands do not have equivalent intensity because the population of isomers in equilibrium is not the same. For the complex on the left in Figure 2, the basicities of the nitrogen atoms of the methylpyrazine bridging ligand suggest that the most stable charge-transfer isomer (the major population) will be the one with most of the electron density on the Ru_3 cluster bonded to $^{12}\text{C}^{16}\text{O}$. Thus, for the two $\nu(^{12}\text{C}^{16}\text{O})$ bands, the band at slightly lower frequency has the greater intensity while the higher frequency band, which appears as a shoulder, is associated with the minor isomer in which most of the electron density is on the Ru_3 cluster bonded to $^{13}\text{C}^{18}\text{O}$. Similar arguments can be used to rationalize the two $\nu(^{13}\text{C}^{18}\text{O})$ bands. Further convincing

proof of the existence of the charge-transfer equilibrium comes from the spectroelectrochemistry of the complex on the right in Figure 2. In this complex, the orientation of the bridging methylpyrazine has been switched so that now the most stable charge-transfer isomer is the one with most of the electron density on the Ru_3 cluster bonded to $^{13}\text{C}^{18}\text{O}$. This in turn switches charge-transfer isomer populations and $\nu(\text{CO})$ band intensities compared to that of the complex on the left in Figure 2.

In another study^[1] of mixed-valence complexes of the type shown in Figure 1, the charge-transfer equilibrium was perturbed by holding the bridging ligand $\text{L} = \text{pyrazine}$ fixed but varying L' and L'' . Three complexes were examined in which $\text{L}' = 4\text{-dimethylaminopyridine}$ and $\text{L}'' = \text{pyridine}$ (**1**), $\text{L}' = \text{pyridine}$ and $\text{L}'' = 4\text{-cyanopyridine}$ (**2**), and $\text{L}' = 4\text{-dimethylaminopyridine}$ and $\text{L}'' = 4\text{-cyanopyridine}$ (**3**). Cyclic voltammetry of the complexes gave values of ΔE which varied from 310 mV to 410 mV and were considerably larger than those predicted from the differences in intrinsic reduction potentials. This result was appropriately taken as evidence of significant electronic coupling. As discussed above, the substitution of $^{13}\text{C}^{18}\text{O}$ permitted the charge-transfer equilibrium to be characterized. The adiabatic free-energy differences of the charge-transfer equi-

bria varied from 9.3×10^{-3} to 0.025 eV and were considerably smaller although they followed the same trend as the diabatic free-energy differences which varied from 0.1 to 0.23 eV. The relatively small adiabatic free energy is a consequence of the magnitude of electronic coupling between Ru_3 moieties. Applying the potential energy surfaces developed by Sutin^[7] to the case of a diabatic free energy of 0.1 eV and reorganizational energy of 1.43 eV, Kubiak and co-workers estimated that the electronic coupling required to achieve a delocalized state is $H_{\text{ad}} = 4260 \text{ cm}^{-1}$. For this delocalized state the adiabatic free-energy difference was calculated to be 0.065 eV. This value is considerably larger than that found for mixed-valence complexes **1–3** which suggests that these complexes should undergo activationless electron-transfer rates. However, the experimental electron-transfer rates range from 0.4 to $8.5 \times 10^{11} \text{ s}^{-1}$ which is significantly less than that required for activationless electron-transfer. This result led to the suggestion that these systems are coupled to the solvent or

molecular normal modes and that this is an additional barrier to full delocalization. While this may be true, the magnitude of the calculated electronic coupling is also a concern. If $H_{\text{ad}} = 4260 \text{ cm}^{-1}$ or 530 mV, the difference in Ru_3 redox couples ΔE should be at least as large as 530 mV but the largest measured by cyclic voltammetry is only 410 mV. This disagreement may be due to antiferromagnetic exchange within the Ru_3 moieties which would reduce the stability of the mixed-valence state. If this is found to be unimportant the choice of parameters or the model itself should be re-examined.

Kubiak and co-workers have made a significant contribution to the field of mixed-valence complexes. By experimentally characterizing charge-transfer equilibria which are established on the picosecond time scale, these researchers have unprecedented access to the chemistry at the transition between localized and delocalized mixed-valence states. The elucidation of their properties has clear application to the purpose-

ful construction of electronic molecular devices.

Published online: August 30, 2005

-
- [1] T. Ito, N. Imai, T. Yamaguchi, T. Hamaguchi, C. H. Londergan, C. P. Kubiak, *Angew. Chem.* **2004**, *116*, 1400–1405; *Angew. Chem. Int. Ed.* **2004**, *43*, 1376–1381.
 - [2] J. C. Salsman, C. P. Kubiak, *J. Am. Chem. Soc.* **2005**, *127*, 2382–2383.
 - [3] M. B. Robin, P. Day, *Adv. Inorg. Chem. Radiochem.* **1967**, *10*, 247–422.
 - [4] K. D. Demadis, C. M. Hartshorn, T. J. Meyer, *Chem. Rev.* **2001**, *101*, 2655.
 - [5] a) T. Ito, T. Hamaguchi, H. Nagino, T. Yamaguchi, J. Washington, C. P. Kubiak, *Science* **1997**, *277*, 660–663; b) T. Ito, T. Hamaguchi, H. Nagino, T. Yamaguchi, H. Kido, I. S. Zavarine, T. Richmond, J. Washington, C. P. Kubiak, *J. Am. Chem. Soc.* **1999**, *121*, 4625–4632.
 - [6] F.-W. Grevels, K. Kerpen, W. E. Klotzbücher, R. E. McClung, G. Russel, M. Viotte, K. Schaffner, *J. Am. Chem. Soc.* **1998**, *120*, 10423–10433.
 - [7] N. Sutin, *Prog. Inorg. Chem.* **1983**, *30*, 441–498.

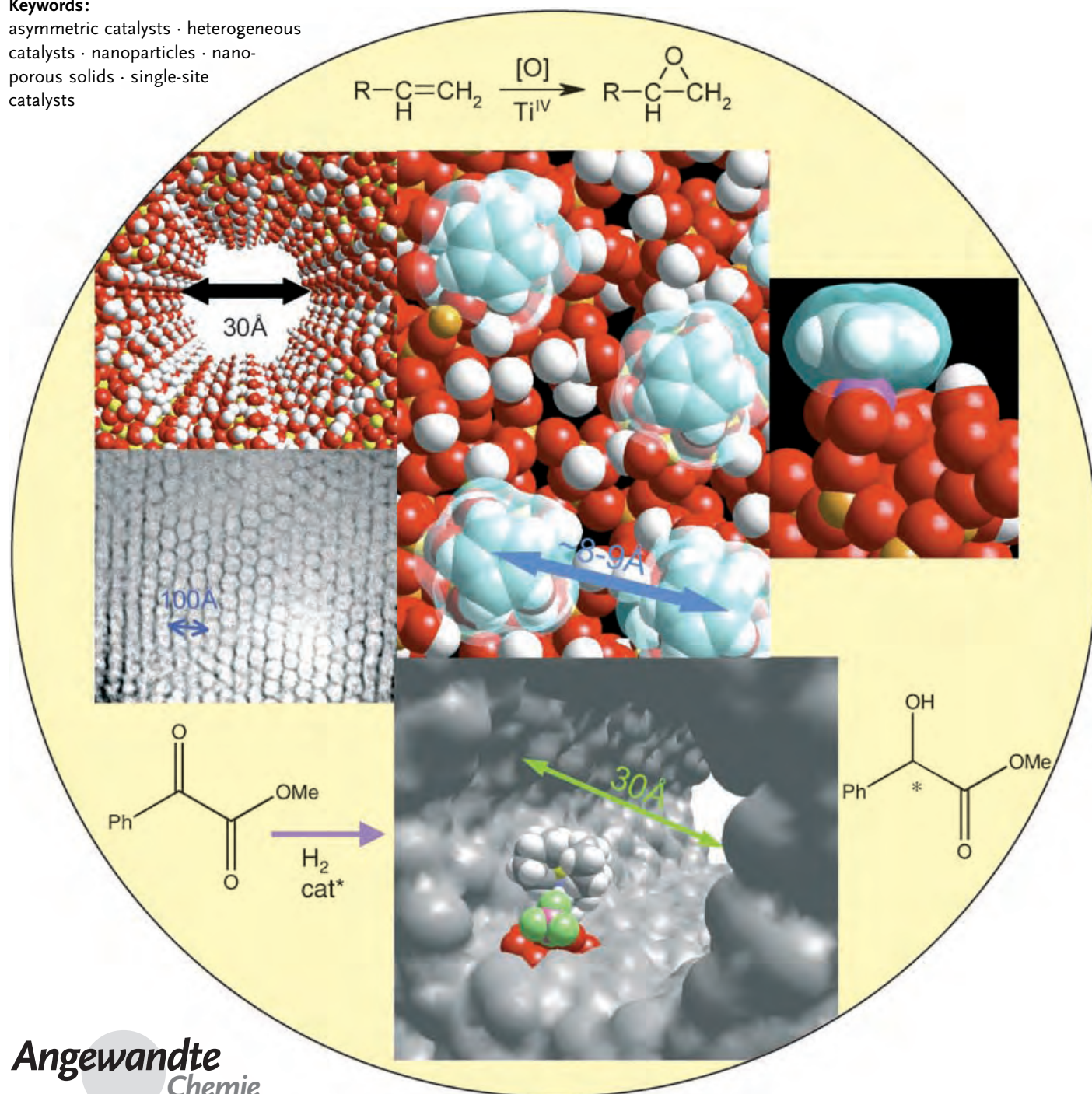
Heterogeneous Catalysts

Single-Site Heterogeneous Catalysts**

John Meurig Thomas,* Robert Raja, and Dewi W. Lewis

Keywords:

asymmetric catalysts · heterogeneous catalysts · nanoparticles · nanoporous solids · single-site catalysts



Intellectually, the advantages that flow from the availability of single-site heterogeneous catalysts (SSHC) are many. They facilitate the determination of the kinetics and mechanism of catalytic turnover—both experimentally and computationally—and make accessible the energetics of various intermediates (including short-lived transition states). These facts in turn offer a rational strategic principle for the design of new catalysts and the improvement of existing ones. It is generally possible to prepare soluble molecular fragments that circumscribe the single-site, thus enabling a direct comparison to be made, experimentally, between the catalytic performance of the same active site when functioning as a heterogeneous (continuous solid) as well as a homogeneous (dispersed molecular) catalyst. This approach also makes it possible to modify the immediate atomic environment as well as the central atomic structure of the active site. From the practical standpoint, SSHC exhibit very high selectivities leading to the production of sharply defined molecular products, just as do their homogeneous analogues. Given that mesoporous silicas with very large internal surface areas are ideal supports for SSHC, and that more than a quarter of the elements of the Periodic Table may be grafted as active sites onto such silicas, there is abundant scope for creating new catalytic opportunities.

1. Introduction

It is often explicitly stated, but far more frequently implied, that solid catalysts functioning heterogeneously possess a spectrum of active sites each with their own energetics, activity, and selectivity. The plausibility of this statement is reinforced if the topography of a metal surface such as that depicted in Figure 1 is examined. In this case, atoms located at surface steps or kinks are stereochemically different from one another and less fully coordinated to other atoms than those at terrace sites and flat exterior surfaces.^[1] But even at a flat exterior surface (typically the (111) face of a face-centered cubic (fcc) metal such as platinum), there are clearly three distinct adsorption sites—atop, bridge, and hollow—for small molecules such as carbon monoxide to be bound. It is not surprising, therefore, that the enthalpy of adsorption as a function of surface coverage falls, and that a temperature-programmed desorption has several peaks, as these reflect the variety of energetic situations associated with the adsorbed species.^[2] This is a situation that is encountered with all metal and alloy catalysts and with a very large number of other catalysts that are continuous solids, including close-packed oxides, halides, and chalcogenides.

Yet, the concept of the catalytically active site, introduced^[3] to the literature of catalysis by Taylor eighty years ago, is as widely used as ever; and it has spawned other, heuristically and practically, important notions such as

“active-site engineering” and “active-site modification”. Demonstrably, it is easy to comprehend what is meant by the structurally well-defined active site of a metalloenzyme (or any other enzyme) and also by the active site of members of the entire family of homogeneous (i.e. molecular) catalysts in which discrete molecular entities (encompassing the active

From the Contents

1. Introduction	6457
2. Four Principal Categories of Single-Site Heterogeneous Catalysts	6459
3. Individual Isolated Ions, Atoms, Molecular Complexes, and Bimetallic Clusters as Single-Site Heterogeneous Catalysts	6460
4. Single-Site Heterogeneous Organometallic Chiral Catalysts	6465
5. Single-Site, Ship-in-Bottle Catalysts	6466
6. Single-Site, Open-Structure Solid Catalysts	6468
7. A Selection of Examples Illustrating Practical Applications of SSHC	6471
8. Summary and Conclusions	6479

[*] Prof. Sir J. M. Thomas

The Royal Institution of Great Britain
Davy Faraday Research Laboratory
21 Albermarle Street, London W1S 4BS (UK)
and
Department of Materials Science and Metallurgy
New Museums Site
Pembroke Street
Cambridge CB2 3QZ (UK)
Fax: (+44) 1223-740360
E-mail: jmt@ri.ac.uk

Dr. R. Raja
Department of Chemistry
University of Cambridge
Lensfield Road, Cambridge CB2 1EW (UK)
Dr. D. W. Lewis
Department of Chemistry
University College London
20 Gordon Street, London WC1H 0AJ (UK)

[**] Based on the Sunner Memorial Lecture given (by J.M.T.) at Lund University, November 1, 2004.

site) are dispersed in a fluid phase, usually water. No intellectual or practical problems are encountered when these catalysts are referred to as being of the "single-site" variety.

So far as heterogeneous catalysts made of metal or alloy are concerned, the nature of the active sites is far less sharply defined than was originally envisaged by Taylor. Taylor advanced reasons for believing that preferential adsorption on a catalyst surface would take place at those atoms situated at peaks, fissures, and other crystalline discontinuities. (In Taylor's days the concepts of kinks, emergent dislocations, and even point-defects had not yet been formulated). Moreover, he inferred that such atoms would also have the highest catalytic activity. In the intervening years it has become clear that preferential adsorption does indeed occur (see Figure 1) at the step and kink sites of solid surfaces. But what is required in a good, catalytically active site is not a high



John Meurig Thomas, a former Head of the Department of Physical Chemistry, University of Cambridge and former Director of the Royal Institution of Great Britain, is now Honorary Professor at the Department of Materials Science, Cambridge. A solid-state, materials and surface scientist, he has focused mainly on the design of solid catalysts. For his work on *in situ* characterization and numerous discoveries in catalysis he has received several awards including the Davy Medal of the Royal Society and the Willard Gibbs medal of the ACS. In 1991, he was knighted for his services to chemistry and the popularization of science.



Robert Raja completed his Ph.D. at the National Chemical Laboratory, Pune, India. In 1997, he was awarded the prestigious 1851 Exhibition fellowship to pursue an independent research program, at the Royal Institution of Great Britain, with Prof. Sir J. M. Thomas. He is currently a Senior Research Associate at the Department of Chemistry, University of Cambridge, where he focuses on the discovery, design, and synthesis of novel microporous and mesoporous solids, for application as heterogeneous catalysts. His recent awards include the IACS "Young Scientist Award" (2004) and the "Barrer Award" (2005).



Dewi Wyn Lewis studied Computer-Aided Chemistry at the University of Surrey. After working for IBM for a year he completed a PhD at the Royal Institution of Great Britain with Prof. Richard Catlow, followed by a postdoctoral position with Prof. Catlow and Prof. Sir J. M. Thomas. He was then Oppenheimer Research Fellow at the University of Cambridge. He was appointed as lecturer (and subsequently senior lecturer) at the Department of Chemistry, University College London in 1998. His research interests encompass computer modeling of materials with an emphasis on microporous solids.

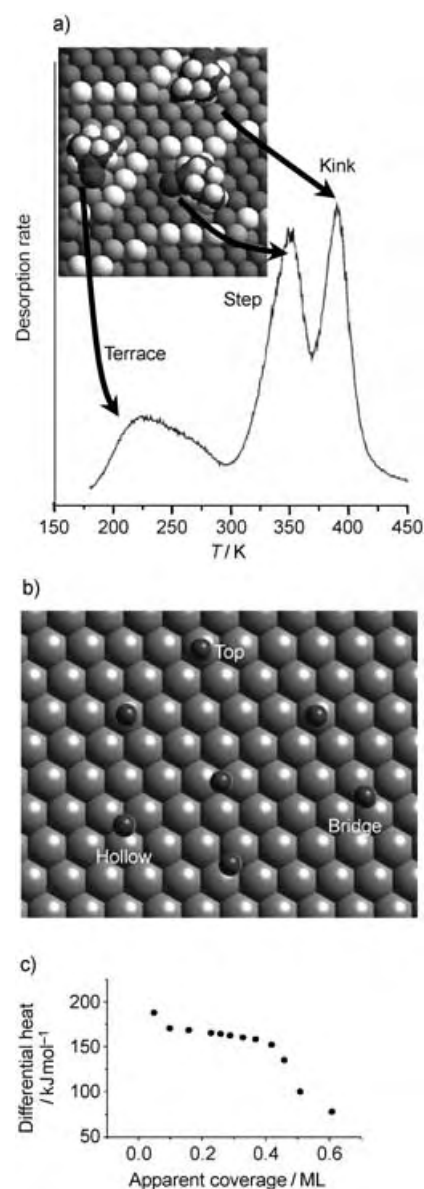


Figure 1. a) A temperature-programmed spectrum showing three peaks corresponding to progressively stronger bound states at terrace, step, and kink sites of an adsorbate molecule (methylcyclohexanone) at a roughened copper surface.^[1] b) Even on a flat surface, such as the (111) face of platinum, there are three distinct sites for a molecule such as CO to be adsorbed. c) The decline in the heat of adsorption with increasing coverage of a flat single-crystal surface arises because of the heterogeneity of sites and mutual repulsion of species adsorbed at neighboring sites (ML = monolayer).^[2]

binding energy; rather one of an intermediate value which is such that it optimizes both the residence time of the adsorbate and facilitates its conversion into desirable product species.

With strictly stoichiometric processes (rather than catalytic ones) such as adsorption in general or with surface reactions in a noncatalytic sense, such as thermal oxidation, decomposition, dissolution or gasification, crystalline discontinuities do indeed exhibit enhanced reactivity, and in that

context may legitimately be regarded as active centers.^[4] Somorjai's and others^[5] work have shown that surface steps and kinks on many metals may indeed function as favored sites for the activation of C–H, H–H, O=O, N≡N, or C≡O bonds under certain circumstances. A major advance in the notion of catalytically active centers in inorganic solids came with the Cossee–Arlman interpretation of Ziegler–Natta catalysts.^[6] Working on the plausible assumption that the prismatic faces of α -TiCl₃, a vital constituent of such catalysts, inevitably—for thermodynamic reasons—contain a minute fraction of chloride-ion vacancies and hence coordinatively unsaturated titanium ions, Cossee and Arlman showed that these ions are the active centers for the stereoregular polymerization of alkenes. But, for metals and alloys, it has become abundantly clear, thanks to the investigations of Ertl et al.,^[7,8] and others, that a great deal of surface mobility (even fluidity) exists under quite thermally mild catalytic conditions. Standing-wave patterns and periodic kinetic oscillations in the oxidation of CO on a Pt surface are pronounced;^[9] and chaotic phenomena involving spatio-temporal changes on quite rapid time-scales are frequent occurrences, as are pronounced surface morphological changes brought about as the surface catalytic reactions proceed.^[10] It is therefore clear that, at such catalyst surfaces—unlike the situations that prevail for solids in categories A to D in Table 1 (see Section 2)—the concept of a structurally fixed active site is of little value. For such catalysts it is more fruitful to picture them as energetically (and otherwise) multisite catalysts. But where, in other kinds of solid catalysts, one, or a small number of, metal atom(s) is firmly and uniformly anchored to a support (see category A in Table 1) the concept of a single-site catalyst is certainly valid.

There appears, therefore, to be a dichotomy—an ostensible contradiction of facts. On the one hand, it is profitable, for certain types of solid catalysts, to retain the notion of the active site; on the other, the idea of a well-defined active site at a metal surface (where they were conceived by Taylor) seems to be progressively less valid.^[11] One of the principal purposes of this Review is to resolve this apparent contradiction. More importantly, it is to identify and classify numerous examples of single-site heterogeneous catalysts—henceforth referred to as SSHC—as they are already playing a significant role in many industrially important chemical processes and are ever-more present in a variety of academic (laboratory-based) situations. Many new developments (and Patents) are continuing to emerge in this hitherto inadequately recognized branch of heterogeneous catalysis. Moreover, single-site heterogeneous catalysts (SSHC) are important for two other reasons which are of profound significance so far as the understanding of the nature of catalysis as well as the design of new catalysts is concerned. First, sophisticated and reliable theoretical computations of the structures, energetics, and kinetics of catalytic conversions may readily be performed on transformations that take place at single-sites, and these, in turn, enable quantitative comparisons to be made between homogeneous and heterogeneous catalysts involving essentially the same active centers. Second, equipped with such quantitative information it becomes possible to evolve strategic principles for the design of improved

catalysts. In other catalytic situations, notably catalysis by metals and most continuous solids, because of the perceived complexity of their mode of action, certain design possibilities cannot even be framed, let alone be constructively implemented.

To fix our ideas, it is prudent to elaborate briefly what we mean by a “single site” in the general context of heterogeneous (solid) catalysts. The “single site” (catalytically active center) may consist of one or more atoms—as will become clear in the discussion and examples given below. Such single sites are spatially isolated from one another, there is no spectroscopic or other cross-talk between such sites. Each site has the same energy of interaction between it and a reactant as every other single site; and each such site is structurally well-characterized, just as the single sites in homogeneous molecular catalysts are.

Herein we give examples of 1) the high regioselectivities of inorganic SSHC enzyme mimics which oxyfunctionalize terminal methyl groups in linear alkanes under mild conditions; 2) the marked shape-selectivity of SSHC in converting methanol (by Brønsted acid catalyzed dehydration) preferentially into ethene and propene; 3) numerous selective hydrogenations with high turnover frequencies (under solvent-free conditions) of polyenes, and also of several enantioselective hydrogenations characterized by high *ee* values; and 4) bifunctional open-structure forms of SSHC in which “isolated” acid centers and “isolated” redox centers cooperatively lead to the in situ production of hydroxylamine (from NH₃ and O₂), cyclohexanone oxime (from cyclohexanone), and ϵ -caprolactam (the precursor to nylon-6).

By identifying the reality and usefulness of categorizing certain kinds of solid catalysts as SSHC, a rational strategic principle for the design of new catalysts clearly emerges. Much progress has been made in the design of such catalysts in the past few years. The so-called “uniform heterogeneous catalysts” reviewed^[12] by one of us in 1988—where active sites are spatially distributed inside open-structure solids and are freely accessible to reactants—will be seen below to be a special case of the SSHC discussed herein.

2. Four Principal Categories of Single-Site Heterogeneous Catalysts

Table 1 enumerates the four main categories into which SSHC may be conveniently classified. There are subdivisions within some of these categories. For example, in category A, various kinds of supports, to which the catalytic entity containing the single-site are attached, may confer extra activity or selectivity to the SSHC. And both monofunctional and bifunctional catalytic performance may be exhibited by certain examples in category D.

In all four categories there exist structurally well-defined active sites, the precise atomic nature of which may be probed—increasingly nowadays under reaction conditions,^[13,14]—by a range of experimental and computational techniques. Such sites are amenable (by pre- or post-synthesis interruption) to controllable, subtle changes in structure that may have far-reaching catalytic repercussions.

Table 1: Four categories of single-site heterogeneous catalysts (SSHC).

A: Individual isolated 1) ions, 2) atoms, 3) molecular complexes, and 4) bimetallic clusters anchored to high-area supports (generally silica).

B: Immobilized asymmetric organometallic species at high-area mesoporous solids, of pore diameters in the range 15 to 500 Å).

C: "Ship-in-bottle" structures, in which isolated catalytic molecular entities (or organometallic complexes) are entrapped within zeolitic cages that are permeable to certain reactants and to some of the potential products.

D: Open-structure, microporous solids (molecular sieves) with pore diameters in the range 3.5 to approximately 10 Å. The isolated active sites, which are uniformly distributed spatially throughout the bulk, are located at or adjacent to ions that have replaced framework ions of the parent structure.

3. Individual Isolated Ions, Atoms, Molecular Complexes, and Bimetallic Clusters as Single-Site Heterogeneous Catalysts

In the four subcategories isolated ions, atoms, molecular complexes, and bimetallic clusters, quite distinct features can be distinguished. First, there are transition-metal-ions grafted on to high-area supports, silica being the most suitable and popular, thereby forming a kind of metal-oxo entity. Second, single atoms of a metal such as palladium may be anchored to a surface structural defect at an oxide support, typically magnesia (MgO). Third, isolated organometallic complexes anchored to silica or alumina surfaces also function as single-site catalysts. Finally, small clusters (all of the same size) of metal atoms or of bimetallic clusters or of their carbides may be anchored securely to mesoporous silica also exhibiting single-site but multinuclear behavior.

3.1. Single-Site Transition-Metal Ions Supported on Mesoporous Silica

From the early days of heterogeneous catalysis, silica has been widely used as a support. Its merits are numerous: it is robust, readily prepared (with high surface area), it does not swell in contact with organic solvents, it has considerable thermal stability as well as structural flexibility and it bonds rather readily to a large number of the elements of the Periodic Table. Moreover, soluble analogues of silica, the so-called silsesquioxanes^[15,16] (see, for example, Figure 2) are available, so that it becomes readily possible to characterize new functionalities that are attached to silica surfaces. In addition, the catalytic performance of a hetero ion (e.g. Ti, Fe, Cr) introduced to a silica may be studied both as a homogeneous and as a heterogeneous catalyst.^[17]

Twenty-five years ago Basset et al.,^[18] extending the earlier studies of others,^[19] began a systematic study, which has continued to blossom^[20] in which they deliberately set out to functionalize the surfaces of the so-called Aerosil silicas which are nonporous. Their work, often described as surface organometallic chemistry, produces SSHC by appropriately

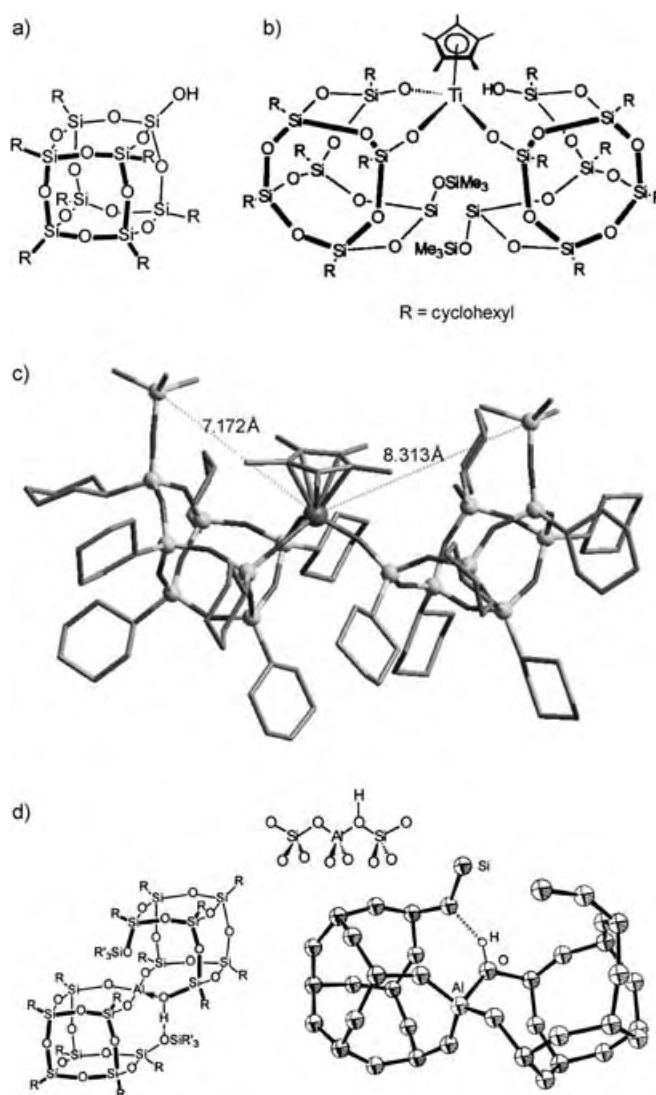


Figure 2. a) Silsesquioxanes (general formula $(\text{RSiO}_{1.5})_n$) are structurally similar to β -cristobalite and β -tridymite, (shown is the structure of $\text{Cy}_8\text{Si}_8\text{O}_{12}$ (Cy = cyclohexyl)). They are, effectively, soluble analogues of silica; and a heteroatom (usually transition metal or Ge) attached to the silsesquioxane simulates the behavior (in solution) of the same, grafted atom attached to mesoporous silica forming the corresponding heterogeneous catalyst. b) Fragment of the crystal structure (schematic) of a Ti^{IV} -cyclopentadienyl complex bound to two silsesquioxane moieties (after F. T. Edlmann et al. ref. [146]). c) Actual structure (shown in (b)), indicating the isolated nature of the Ti^{IV} center (hydrogen atoms have been omitted for clarity). d) A soluble Brønsted acid site formed from silsesquioxanes.^[15b]

functionalizing the residual pendant silanol groups ($\equiv \text{SiOH}$) on the Aerosil silica (surface area typically $200 \text{ m}^2 \text{ g}^{-1}$ and silanol surface concentration of 0.7 ± 0.2 per nm^2 , which is equivalent to $0.23 \text{ mol}(\text{OH}) \text{ g}^{-1}$). A specific example is the tripodally grafted zirconium hydride, which activates alkanes under mild conditions (Figure 3). Other transition-metal ions have been grafted on to silica by Basset et al.; and their work on grafted organometallic complexes as SSHC, is returned to again in Section 7.5.2.

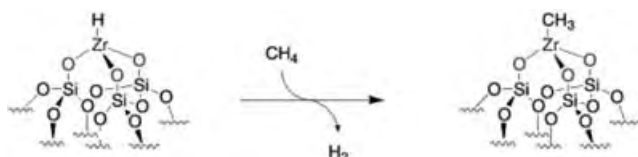


Figure 3. An isolated site, such as a tripodally bound zirconium hydride at a silica surface, readily activates methane at modest temperatures.^[20]

Great scope for the preparation of a variety of single-ion SSHC began once it became readily possible—thanks to discoveries at the Mobil Oil Co.^[21] and in Japan (Waseda University and the Toyota Co.)^[22]—to prepare mesoporous silica with pore diameters that may controllably fall in the range 20 to 100 Å or more. Later workers produced mesoporous silicas with pore diameters as large as 500 Å. Such silicas possess exceptionally high surface areas (typically 600 to 1000 m² g⁻¹) and their inner and outer surfaces have a profusion of pendant silanol groups (Figure 4), approximately 1–2 per nm².

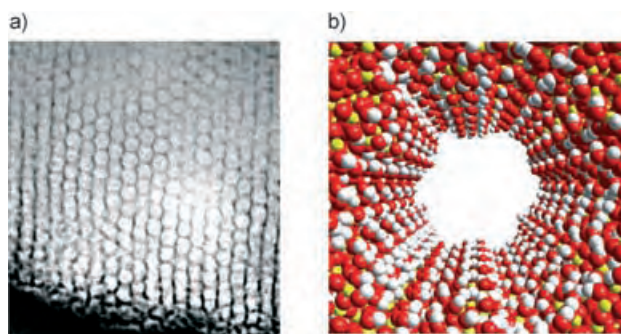


Figure 4. a) A high-resolution electron micrograph of an ordered mesoporous silica where the diameter of the pores is approximately 100 Å and the walls are only a few atoms thick. b) Each pore is lined with pendant silanol ($\equiv\text{Si-OH}$) groups; yellow Si, red O, white H.

Corma,^[23] Thomas,^[24,25] and others^[26] were quick to appreciate the advantages that large-pore silicas would confer in facilitating the preparation of single-site, ion-centered heterogeneous catalysts. A significant advance was made when Ti^{IV} active centers were grafted on to the inner walls of mesoporous silica using an organometallic precursor, in particular titanocene dichloride [$\text{Ti}(\text{Cp})_2\text{Cl}_2$] ($\text{Cp} = \text{C}_5\text{H}_5$) as was done by Maschmeyer et al.^[27] The key steps in the introduction of the isolated, single-site active centers on the inner walls of the so-called MCM-41 silica are shown in Figure 5. The detailed course of this “heterogenization” of a Ti^{IV} active center was followed by in situ X-ray absorption spectroscopy combined with in situ X-ray diffractometry.^[28] Density functional theory (DFT) calculations yield important supplementary information: in particular they show that the titanyl group ($>\text{Ti=O}$), once postulated^[29] as the active site for epoxidation of alkenes, is energetically unfavorable.

It is to be seen that a tripodally grafted $\text{Ti}(\text{OH})_3$ group constitutes the isolated active site, very resistant to leaching, in this instance. Note that the van der Waals envelopes of the

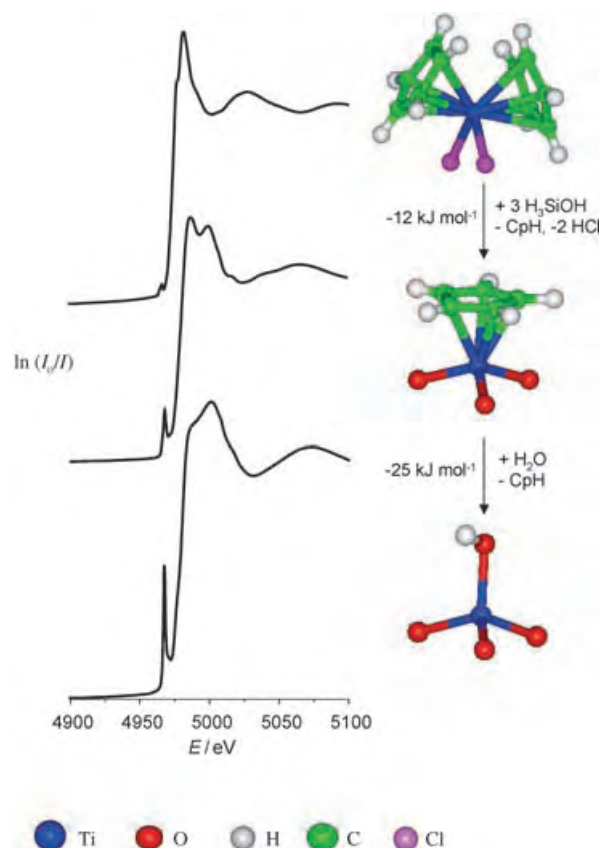


Figure 5. Experimentally, by in situ measurements,^[27a] the course of conversion of a free titanocene dichloride molecule (top right) into a tripodally bound isolated site of $\equiv\text{TiOH}$ (bottom right) may be followed by X-ray absorption spectroscopy.^[28] Note the pronounced “pre-edge” peak signifying four-coordinate Ti^{IV} (bottom left) of the XANES (Ti K-edge) spectra. Bond lengths are extracted from EXAFS spectra, whilst the energetics are from DFT calculations.^[27b]

cyclopentadienyl groups attached to the surface bound (“half-sandwich”) intermediate, shown in Figure 5, ensure that no two Ti^{IV} active centers are closer than approximately 7 Å (see Figure 6), thereby ensuring the generation of a genuine, isolated, single-site catalyst. (Other methods of introducing Ti^{IV} active centers, involving salts of titanium or in-grown titanium alkoxide additives to the siliceous precursor do not guarantee production of isolated, tetrahedral Ti^{IV} centers and a tendency to form Ti-O-Ti linkages exists with these methods). This catalyst is an exceptionally good epoxidation catalyst using alkyl hydroperoxides as we shall describe in Section 7.2.3.

Other transition-metal ions may be grafted on to mesoporous silicas using the metallocene route, and active centers composed of isolated Mo^{VI}, Cr^{VI}, and VO^{IV} have been described.^[30,31]

An altogether different, but equally effective approach has been pioneered by Tilley et al.^[32–35] in which a molecular precursor is taken to yield a series of active catalysts on mesoporous (and certain other) supports. The metal ions in question are those of Ti, Cr, Fe, and VO; and the essence of their preparation is that the desired atomic environment aimed at in the final catalyst (e.g. $\text{Ti}(\text{OSi})_4$ or $\text{Ti}(\text{OSi})_3$) is

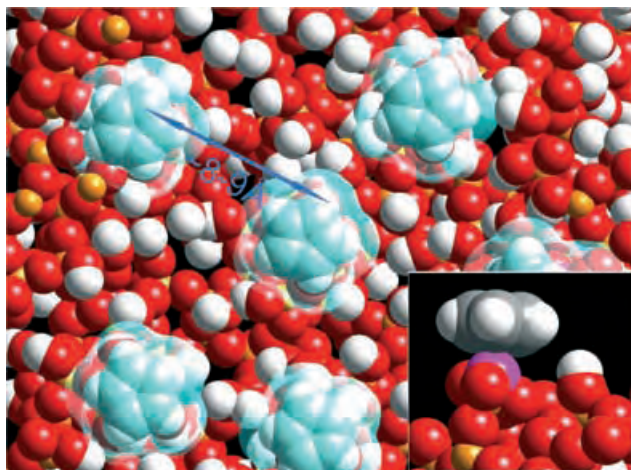


Figure 6. The “half-sandwich” surface intermediate (see middle right of Figure 5), with the van der Waals envelope (light blue) surrounding the cyclopentadienyl ligands which ensures that only spatially isolated, tripodal Ti^{IV} sites are formed. EXAFS data show the absence of Ti-O-Ti linkages. Inset: side view, purple Ti, gray C, white H, red O.

already present in the thermolytic precursor. Thus, by taking the tris(*tert*-butoxy)siloxy titanium complex $(i\text{PrO})\text{Ti}[\text{OSi}(\text{O}t\text{Bu})_3]_3$, the environment ultimately achieved in the single-site catalyst is $\text{Ti}(\text{OSi})_3$, and from $\text{Ti}[\text{OSi}(\text{O}t\text{Bu})_3]_4$ it is $\text{Ti}(\text{OSi})_4$. Typical supports used by Tilley were the high-area mesoporous silicas MCM-41 and SBA-15, the latter being distinctly more thermally stable than the former. The general picture, depicting the production of this type of SSHC is shown in Figure 7. The precursor is bonded to the hydroxy groups of the surface of the silica by protonolysis reactions (Figure 7). For the case of an alkoxy (siloxy) species of the type $\text{M}[\text{OSi}(\text{O}t\text{Bu})_3]_n$ (where $\text{M} = \text{Ti}, \text{Fe}, \text{Cr}, \dots$) this surface-attachment chemistry occurs with loss of $\text{HO}t\text{Bu}$ or $\text{HOSi}(\text{O}t\text{Bu})_3$, to result in bonding to the surface through M-O-(surface) or Si-O-(surface) linkages, respectively. (Calcination results in the loss of all the carbon and hydrogen, leading to the single-site catalyst of nominal composition $\text{MO}_x \cdot (n-1)\text{SiO}_2$. All the physical methods of analysis, such as diffuse reflectance UV (DRUV) and EPR spectroscopy carried out on the product suggest that the metal-ion sites (such as Fe^{III} sites) possess distorted tetrahedral geometry. When attempts are made to prepare isolated Fe^{III} sites using FeCl_3 , FePO_4 , or $\text{Fe}_2(\text{SO}_4)_3$ as precursors no success is achieved and calcination almost invariably leads to clusters of iron oxides). Isolated Cu^{I} species, which are good catalysts for the production of dimethyl carbonate from methanol and CO_2 ,^[34b] may be formed on silica using $[\text{CuOSi}(\text{O}t\text{Bu})_3]_4$ as precursor.

3.2. Supported Isolated Atoms as Single-Site Heterogeneous Catalysts

Recent experimental work has established beyond doubt that a single metal atom of palladium, supported on magnesia (MgO) facilitates the cyclotrimerization of acetylene^[36] and

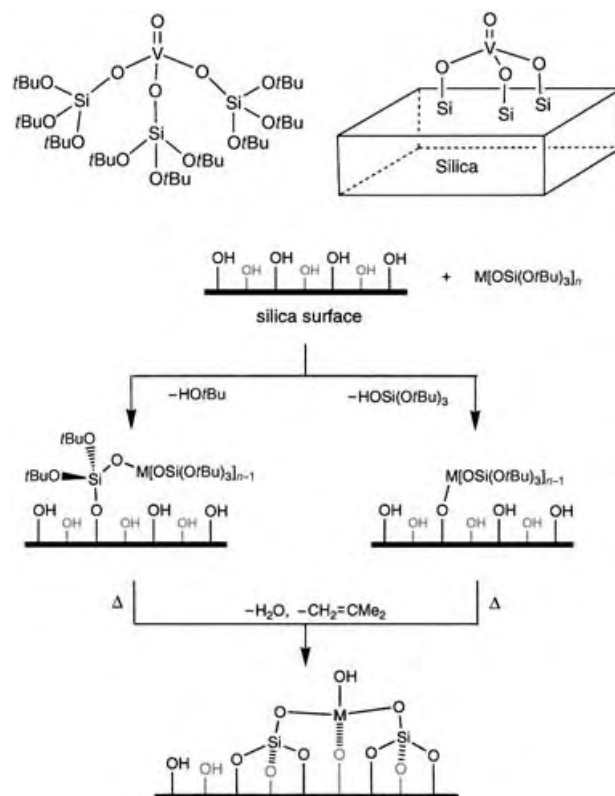


Figure 7. The Tilley method^[32,33] of preparing single-site catalysts on mesoporous silica through thermolytic molecular precursors such as $\text{M}[\text{OSi}(\text{O}t\text{Bu})_3]_n$.

the oxidation of CO by O_2 to CO_2 .^[37] Heiz and co-workers,^[36,37] using mass-selected techniques, prepared single-site active centers such as that shown in Figure 8, in which an F-

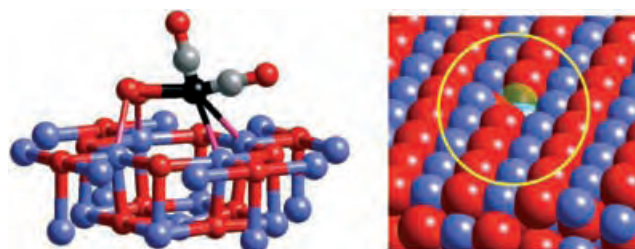


Figure 8. An isolated atom of palladium (black) when bound (by charge-transfer) to an F-center at the surface of MgO forms^[36] the stable complex $\text{Pd}(\text{CO})_2\text{O}_2$. Right: top view of F-center. Red O, blue Mg, gray C.

center (that is, an electron trapped at an oxygen anion vacancy) in MgO localizes a single palladium atom, with electronic charge being transferred to the palladium.

When this “single-atom” active site is first exposed to O_2 and then to CO (at 90 K) and then subjected to a linear temperature rise, conversion ensues, the adsorbed gases combine to yield CO_2 , and the surplus oxygen is taken up by the F-center, which thereby loses its ability to localize the

palladium. Ab initio computations reveal the optimized structure of the $\text{MgO-Pd}(\text{CO})_2\text{O}_2$ single-site active center with its bound reactants (Figure 9). Heiz et al.^[36] have also

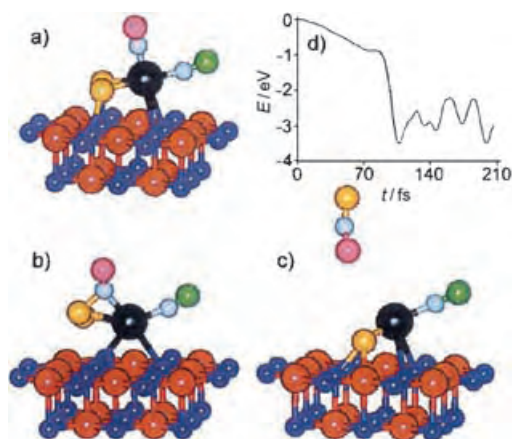


Figure 9. a) Computationally optimized structure of the $\text{MgO}(\text{F-center})\text{-Pd}(\text{CO})_2\text{O}_2$ complex.^[37] b), c) selected configurations, and d) the potential energy versus time, recorded in an ab initio molecular dynamics (MD) simulation where CO_2 is formed from the complex shown in (a). The simulation starts^[37] from the transition state shown in (b). The potential energy of the transition state is 0.84 eV above the optimized configuration shown in (a). c) A snapshot at 210 fs, where the formed CO_2 is desorbing and the remaining O atom from O_2 is moving towards the F-center; black Pd, blue Mg and red O (in MgO), adsorbed O_2 is yellow, carbon atoms are gray and their respective oxygen centers are purple and green.

completed a combined experimental and computational study of this model, single-atom version of a SSHC for the cyclotrimerization of acetylene to benzene. In each of these examples of SSHC it is to be noted that, because of the destruction of the F-center during reaction in the first case and the clustering of the Pd atoms to form larger units (Pd_n , $3 < n < 30$) in the second, there is no sustained catalytic turnover. In a sense, therefore, this admirable model study, like many in the literature, is concerned with a surface stoichiometric rather than a catalytic reaction.

3.3. Anchored Organometallic Complexes as SSHC

Using the surface organometallic approach, Basset et al.^[20] have produced a number of single-site catalysts at nonporous silica surfaces, the molecular complexes thereby anchored being fully characterized by both spectroscopic and chemical methods. Figure 10 shows the single-sites for three powerful examples of metathesis reactions. Basset's group, and especially that of Marks^[38–40] (see Section 7.5.2), have also produced single-site, heterogeneous catalysts derived from metallocenes for the polymerization of alkenes.

Microcrystalline $\alpha\text{-TiCl}_3$ Ziegler–Natta catalysts, because they have several non-identical atomic environments around the catalytically active centers—the chloride ion vacancy may be a regular site or at a step or corner site—yield polymers

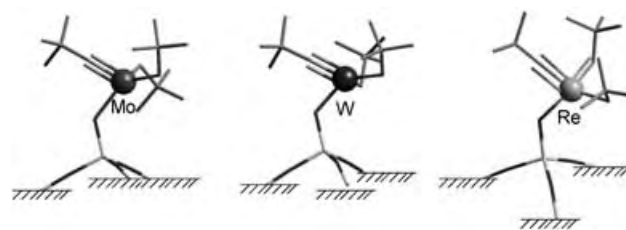
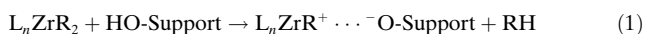


Figure 10. Single-site active centers designed by Basset et al.^[20] for heterogeneously catalyzed metathesis reactions.

with broad molecular-weight distributions. Homogeneous metallocene catalysts, on the other hand yield highly uniform homopolymers and copolymers; this arises because of the identical coordination environment of the active site in the homogeneous metallocene catalyst. If the metallocene-type polymerization catalysts could be so anchored as to have only a single kind of active site, this would unite the best qualities of the homogeneous and heterogeneous agents. Recent work, which we now briefly describe, has achieved this desirable goal.

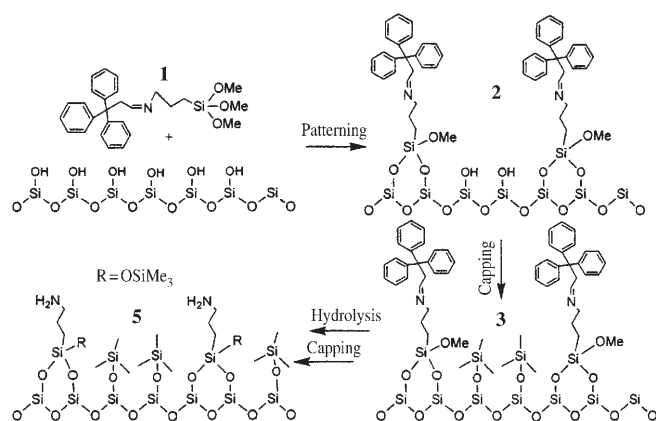
Take first the work of Marks et al.,^[38–40] who have used a variety of oxidic supports. Partially dehydroxylated alumina has approximately four Brønsted acidic OH groups, approximately 5.5 Lewis acidic Al^{III} centers, and around 5.5 Lewis basic oxide centers per nm^2 of surface area. The fully dehydroxylated alumina has a much lower Brønsted acidic surface concentration (approximately 0.12), though the concentrations of the other centers remain essentially the same. An even more strongly acidic surface is that of the so-called “superacidic sulfated zirconia.” (Recent evidence suggests that this surface is not “superacidic”). When a zirconocene of general formula L_nZrR_2 (L is a cyclopentadienyl ligand, and R an alkyl group) approaches the “superacidic” surface, a cationic-like-structure as schematized in Equation (1), forms.



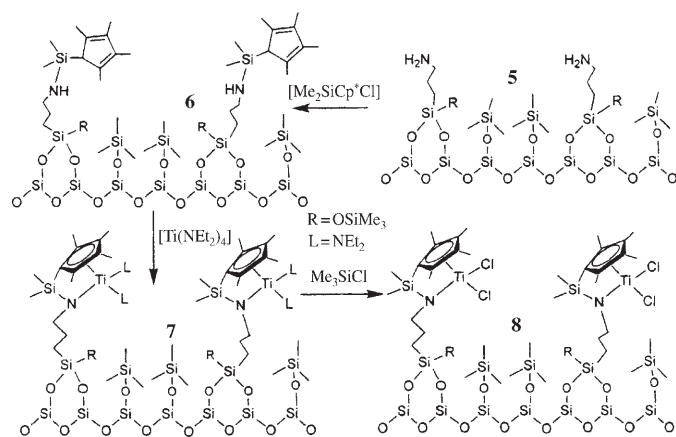
This cationic-like-structure, is in effect, an ion pair consisting of a cationic metallocene and a weak conjugate base of a strong Brønsted acid site. The negative charge of the conjugate base is so highly delocalized that coordination to the single-site cationic Zr center is minimal, thereby facilitating access of the alkene to the active site.

Marks et al.^[40] have elucidated other, related single-site organometallic electrophiles on “superacidic” sulfated zirconia, including $[\text{Cp}^*\text{Th}(\text{CH}_3)_2]$ and $[\text{CpTi}(\text{CH}_3)_2]$ ($\text{Cp}^* = \eta^5\text{-C}_5\text{Me}_5$). And on sulfated alumina, they have shown that protonolysis at the strong surface Brønsted (OH) acidic site again yields a “cation-like” highly reactive (in polymerization) zirconocenium electrophile $[\text{Cp}^*\text{ZrCH}_3]^+$. On a dehydroxylated silica surface no such “cation-like” single-site active center is formed.

Finally, a recent paper by McKittrick and Jones^[41] discloses a general method for preparing an isolated titanium-centered polymerization catalyst on porous silica. The essence of the preparation is shown in Scheme 1 and Scheme 2.



Scheme 1.



Scheme 2.

The catalytic performance of the final, site-isolated heterogeneous Ti-centered polymerization catalyst (**8** in Scheme 2) exceeds that of even the homogeneous analogue.

3.3.1. Single-Site Organometallic Complexes Anchored by Noncovalent Interaction

In addition to immobilizing single-site molecular catalysts to solid surfaces by covalent bonding (as done by McKittrick and Jones),^[41] it is also feasible, and indeed more convenient, to do so by noncovalent means. Bianchini et al.^[42] and we^[31, 43–45] have taken advantage of the strong hydrogen bonding that secures tripodal attachment of an ionic (or zwitterionic) complex to a silanol-rich silica surface through a triflate^[46] or a sulfonate tail (Figure 11, left).^[42]

The grafted Rh^I catalyst, [(sulfos)Rh(cod)] (cod = cyclooctadiene), on silica is an example of SSHC for the hydrogenation of alkenes (in either flow reactors or batch reactors) in hydrocarbon solvents. It also hydroformylates alkenes such as hex-1-ene under solid–liquid conditions. When, however the hydroformylation takes place under solid–gas conditions, the syngas (CO + H₂) converts the active catalyst into an inactive species (Figure 11, right), a dicarbonyl derivative is formed [(sulfos)Rh(CO)₂].^[42] de Rege et al.^[46] have also taken

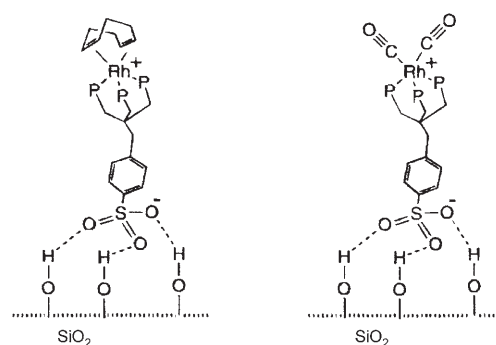


Figure 11. Left: noncovalently bound Rh^I based molecular complex for hydroformylation immobilized at a silica surface. Right: catalytically inactive species, it forms on prolonged exposure of the one on the left to syngas.^[42]

advantage of the hydrogen bonding of a triflate group to secure the active complex to a silica support.

3.4. Individual, Isolated, Bimetallic Clusters as Single-Site Heterogeneous Catalysts

Along with our colleagues, Johnson et al.^[47–50] we have shown that monodisperse mixed-metal cluster carbonylates may be uniformly incorporated inside mesoporous silica and gently decarbonylated to yield the naked clusters, which are anchored securely to the underlying silica (Figure 12). The key point in this case is to recognize that the method of preparation produces 1) clusters that are of the same stoi-

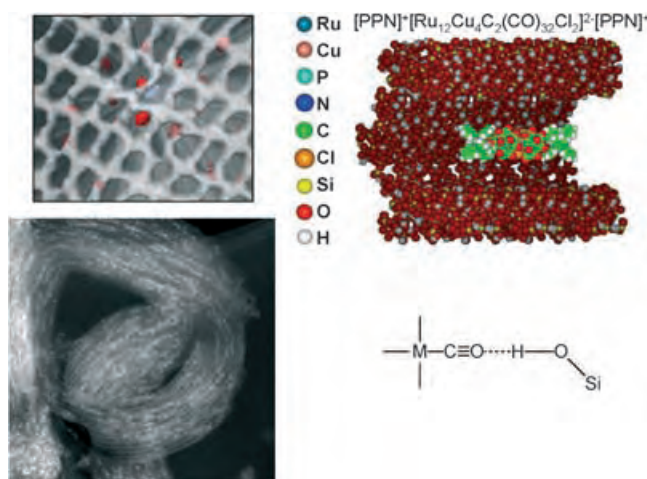


Figure 12. Top right: a mixed-metal cluster carbonylate $[\text{Ru}_{12}\text{Cu}_4\text{C}_2(\text{CO})_{32}\text{Cl}_2]^{2-}$ is readily sequestered within the mesopores of silica in the presence of the molecular cation PPN^+ (bis(triphenylphosphine)iminium). The carbonyl groups are held by hydrogen bonds (bottom right) to the silanol-rich inner surface. Upon gentle thermolysis, all the organic components are eliminated (as judged by in situ FTIR) leaving monodisperse mixed-metal $\text{Ru}_{12}\text{Cu}_4\text{C}_2$ clusters within the mesopores. Top left: individual mixed-metal clusters (shown in red) anchored inside pores (average diameter approximately 35 Å) of the silica support. Bottom left: high-resolution electron micrograph, where each white spot denotes a single mixed-metal cluster.^[51]

First, we recall the relevant background work on non-enantioselective conversions using immobilized organometallic catalysts, see Marks,^[38–40] Bianchini^[42] and Jones et al.^[57] All these cases are based on single-site heterogeneous reactions (polymerizations, hydrogenations, and hydroformylations). We also note the work of Hutchings^[58] who, by modifying zeolite-Y with chiral molecules (such as 1,3-dithiane-1-oxide) achieved an efficient chiral preference in the catalytic dehydration of racemic butan-2-ol. We shall see, in Section 7, how a single-site chiral Cr^{III} (Salen) complex anchored to a silica surface is an effective enantioselective catalyst in the asymmetric ring opening of epoxides.^[59]

It is therefore clearly established that single-site heterogeneous chiral catalysts, involving immobilized organometallic (or enantiomeric organic) species are viable propositions. We now show that, using mesoporous silica supports, high-performance single-site heterogeneous chiral catalysts may be conveniently prepared following methods that we have described fully elsewhere,^[43–45, 57] but which are summarized below. (The drive to prepare enantiomerically pure products for the pharmaceutical, agrochemical, and related industries, such as flavors and fragrances, is partly a response to tightening legislation, but it also reflects an attempt to develop efficient, recyclable catalysts such as SSHC).

We have shown repeatedly that, with mesoporous silica either of the highly ordered but thermally fragile kind (for example, MCM-41 and SBA-15) or non-ordered desiccant-grade commercially available robust (Davison) type^[44] each of which have pendant silanol groups, a range of sizeable chiral metal complexes and organometallic moieties may be tethered to the inner walls of the silica. This incorporation is carried out using alkylhalides, amines, carboxylates, or phosphines. The procedure to arrive at single-site, well-isolated asymmetric organometallic active centers on the inner walls only of the mesoporous silica is outlined^[49] in Figure 15, where we render the exterior surfaces “neutral” in the sense that the dichlorodiphenyl silane, which functionalizes all the silanol groups at the exterior surfaces, is used under conditions where it cannot diffuse to the interior. Silanols at the interior surfaces are functionalized using trichlorosilane propyl bromide, the ensuing reactions (Figure 16) to tether the chiral organometallic entities being effected through the bromine atom.

When certain kinds of organometallic, chiral catalysts are tethered to the inner walls of the mesoporous silica, it follows that the reactant's (substrate) interaction with both the pore walls and the chiral directing group will be distinct from the interaction it would experience if the chiral catalysts were free (as in the case of a homogeneous catalyst). The confinement of the reactant within the mesopore will lead to a larger influence of the chiral directing group on the orientation of the substrate relative to the reactive catalytic center when compared with the situation in solution. The validity of this strategic principle has been multiply attested in our work^[44, 57]—see, for example, our reports on allylic amination^[60] (of cinnamyl acetate and benzylamine) and on several instances of hydrogenation^[44, 61]—specific examples are cited later.

The reality of how tethering an asymmetric catalyst at a concave surface boosts the resulting enantioselectivity is

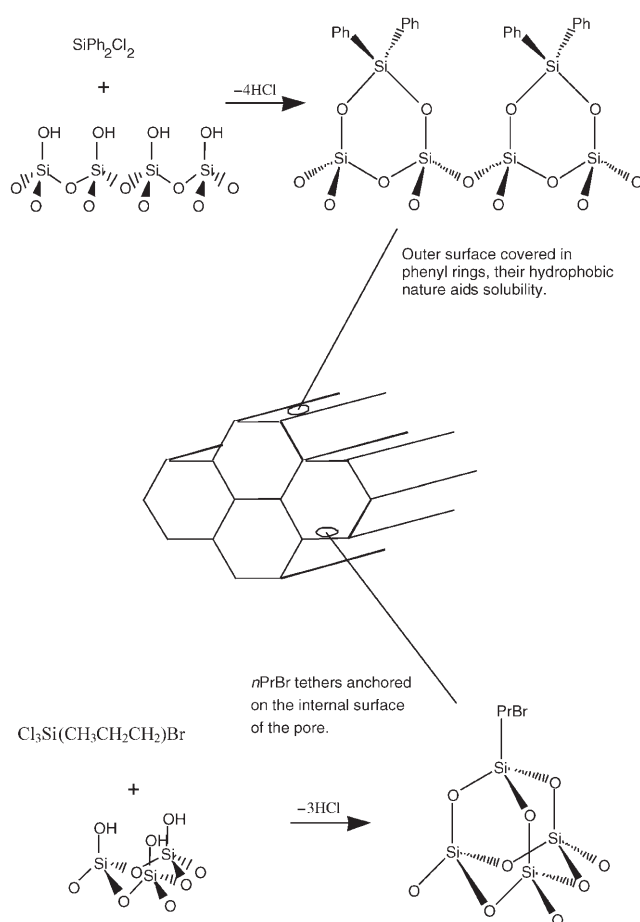


Figure 15. Sequence of steps illustrating how the exterior surface of the mesoporous silica support is rendered inactive and hydrophobic by the attachment of covalently bound $\text{Si}(\text{Ph})_2$ groups.^[49] Only the silanol groups at the interior surfaces are implicated in the support of the nanoparticles (compare Figure 12).

summarized in Figure 17 (see page 6468), where the results of a particular hydrogenation (of (*E*)- α -phenylcinnamic acid) are compared for the same catalyst ($\text{Rh}^{\text{I}}(\text{S})$ -(-)-2-amino-methyl-1-ethyl pyrrolidine) tethered in the one case on a concave, and in another on a convex silica.

It is clear that the catalytic performance is enhanced using a concave silica support. We have also shown^[44] that non-covalent attachment of the asymmetric catalyst as shown in Figure 18 (i.e. using hydrogen bonding and not covalent bonding; see page 6468) in the manner of Bianchini et al.^[42] and de Rege et al.^[46] is an effective method of generating well-defined, isolated, and readily accessible single-site active centers for enantioselective conversions (Scheme 3 and Figure 18).

The convenience of using noncovalently tethered chiral organometallic catalysts in the production of fine chemicals and pharmaceuticals has obvious practical merit.^[62]

5. Single-Site, “Ship-in-Bottle” Catalysts

Zeolitic supports for so-called “ship-in-bottle” catalysts of the types used by Herron,^[63] Raja and Ratnasamy,^[64, 65]

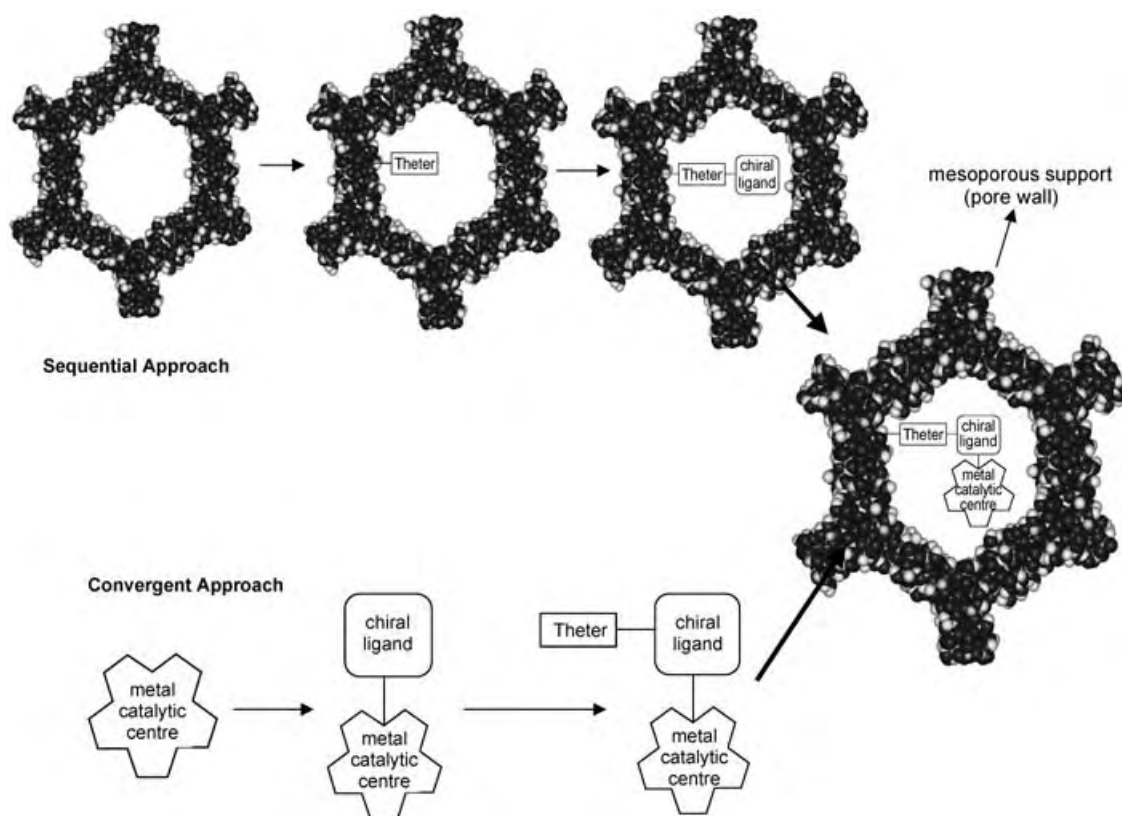


Figure 16. Two distinct approaches may be used to introduce an anchored chiral (asymmetric) organometallic inside the mesopores.^[49]

Vasudevan,^[66] Bäckvall,^[67] and Jacobs^[68] and exemplified in Figure 19 (see page 6469) have long been entertained as being important in situations where it is necessary to prevent an active site entity, such as a metalloporphyrin or metal-molecular complex, from losing its intrinsic catalytic performance because of dimerization or other complicating side-reactions. Such encapsulated catalysts, which are single site, also allow access of only those reactant molecules small enough to diffuse through the windows of the zeolitic cage, and prevent any of those products, which, if formed, are too large, from leaving the reaction environment. In general, however, it is preservation of the single-site (isolated state) catalytic activity that is of paramount importance.

These catalysts, frequently termed zeozymes or enzyme mimics, have yielded encouraging and patentable results in oxyfunctionalizing methane to methanol^[64] and propane to isopropanol^[65] using oxygen as the oxidant and copper hexadecachlorophthalocyanine ($\text{CuCl}_{16}\text{Pc}$) as the single-site active center. Because the zeolitic cage distorts the flat $\text{CuCl}_{16}\text{Pc}$ into a shallow bowl, the latter creates a hydrophobic environment^[66] around the central metal atom, thereby boosting catalytic activity.

Jacobs et al.^[69] encapsulated $\text{cis-}[\text{Mn}(\text{bpy})_2]^{2+}$ complexes (bpy = bipyridine) within the micropores of zeolite Y and used the resulting catalyst for the epoxidation of alkenes with H_2O_2 . These reactions proceeded without complications of competing processes, such as the decomposition of the peroxide. High yields of the epoxides of hex-1-ene, cyclohexene, dodec-1-ene, and cyclododecene were obtained.

These catalysts are quite robust, and may be repeatedly re-used without loss of activity. Electronic factors are thought to play a key role in the performance of the encapsulated $\text{cis-}[\text{Mn}(\text{bpy})_2]^{2+}$,^[69] it being argued that the H_2O_2 activates the Mn ions so as to produce a $\text{Mn}^{\text{IV}}=\text{O}$ group, which releases its oxygen in the critical act of addition across the double bond to form the epoxide. Bein et al.^[70] also used a “ship-in-bottle” alkene epoxidation catalyst formed inside the cages of zeolite Y when extraframework Mn^{II} cations were complexed with a trimethyl triazocyclononane ligand (tmtacn), the role of the methyl groups being chiefly to protect the amine against oxidation by H_2O_2 . In situ ESR measurements show that the catalytically active site is a $\text{Mn}^{\text{III}}\text{-Mn}^{\text{IV}}$ dinuclear complex.

The great practical advantages of “ship-in-bottle” SSHC are well illustrated in the recent work of Bäckvall et al.^[67] on ruthenium-catalyzed aerobic oxidation of alcohols (where encapsulated cobalt Salophen was the active, single-site catalyst: $\text{H}_2\text{Salophen} = 2,2'\text{-[benzene-1,2-diyl bis(nitrilomethylidyne)]diphenol}$). Apart from highlighting the usual advantages of being able to remove and re-use the “ship-in-bottle” catalyst by simple filtration, these workers showed that this SSH catalyst had a higher specific rate than the homogeneous analogue. Moreover the zeolite (bottle) serves as a water acceptor, so that there is no necessity to introduce a separate one, and the zeolite also exhibits shape-selectivity in the oxidation of secondary alcohols.

Although not strictly an example of “ship-in-bottle” catalysis in the sense described above, the recent ingenious

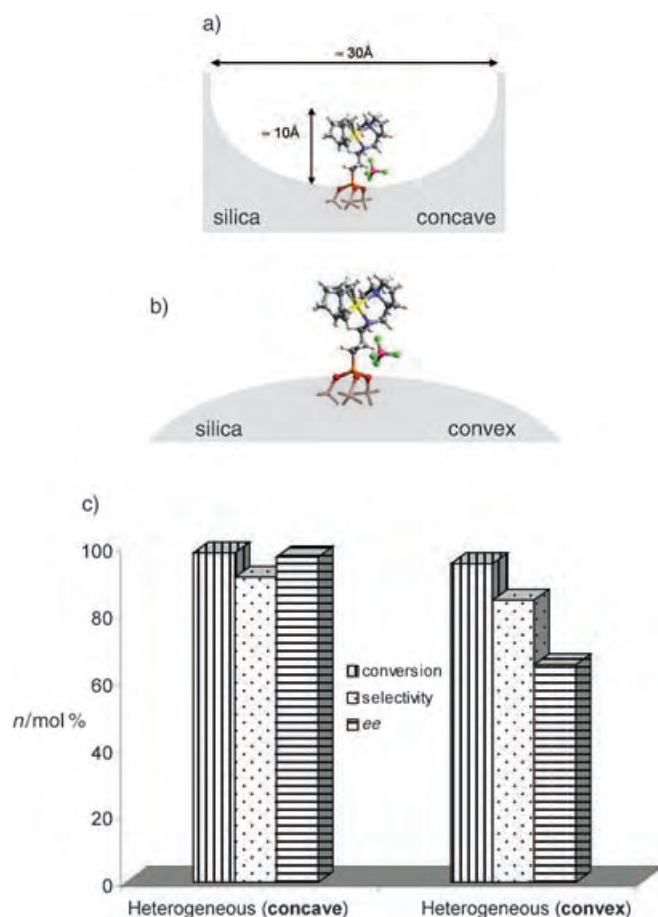
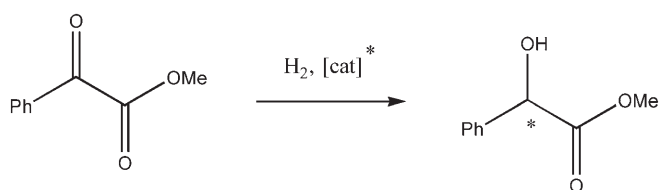


Figure 17. Illustration (to scale) of how a spatial constraint is imposed on the asymmetric catalyst when it is anchored at a) a concave surface in contrast to the situation when anchored at a b) convex one. c) The catalytic performance (selectivity and *ee* value in the hydrogenation of *E*-(α)-phenylcinnamic acid) of an asymmetric catalyst is greater in the spatially constrained (a) than in the less constrained (b).^[57]



Scheme 3.

strategy adopted by Strukul et al.,^[70b] in which they “micro-encapsulate” the enzyme chloroperoxidase within a micro-porous cage of silica gel, conforms to the principle of site isolation and single-site catalysis. Such catalysts are effective in the enantioselective oxidation of sulfides to sulfoxides with H_2O_2 .

6. Single-Site, Open-Structure Solid Catalysts

Unlike bulk metal, alloy, and other binary continuous solid catalysts, the open-structure aluminosilicates (embrac-

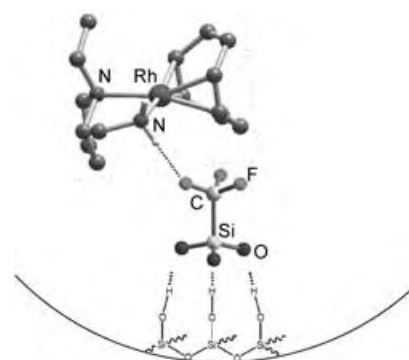
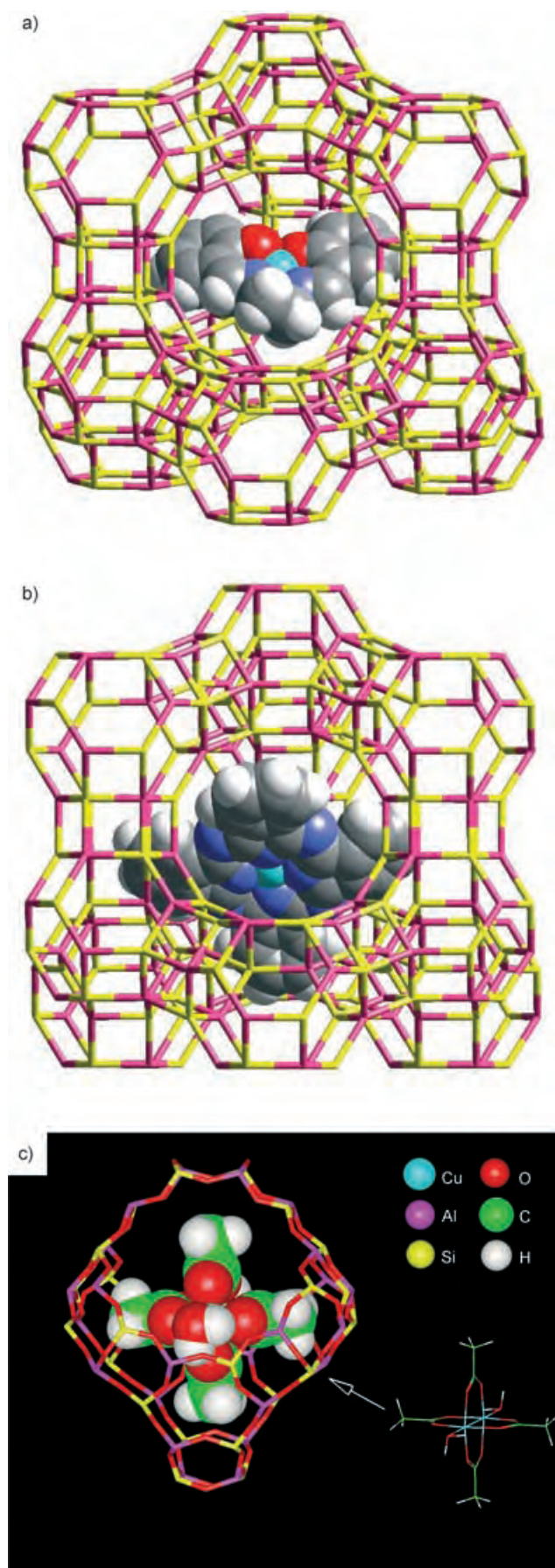


Figure 18. A triflate counterion, which is strongly hydrogen bonded to the silanol groups of the silica, holds securely (by ionic forces) the chiral organometallic Rh^I -based cation.^[44]

ing natural and synthetic zeolites) as well as open-structure aluminophosphates (AIPOs), particularly framework-substituted variants (MAIPOs where $M = Mg, Co, Mn, Zn, \dots$) are prime examples of uniform heterogeneous catalysts. Because the active sites in these catalysts are distributed in a spatially isolated and uniform manner^[12] they conform to Langmuir’s classic assumption in that the energy released upon the uptake of adsorbate species is constant up to monolayer coverage. This energetic uniformity is seen vividly in the calorimetric work^[71] shown in Figure 20 (see page 6470), where there is essentially a constant enthalpy of adsorption of pyridine on the Brønsted acid sites of the so-called pentasil zeolite H-ZSM-5 up until all the sites are neutralized (i.e. up to monolayer coverage of the catalytically active acid centers).

In zeolitic and MAIPO catalysts, the Brønsted active sites, which may be represented as $\equiv Si-O(H)-Al \equiv$ and $\equiv M^{II}-O(H)-P \equiv$, respectively, are so far apart spatially—and the higher the Si/Al ratio in the acidic zeolite, $H_xSi_{n-x}Al_xO_{2n}$, or the higher the P/M^{II} ratio in the acidic MAIPO the further apart they are—that they are essentially isolated within the molecular sieve structure, thereby behaving as SSHC as defined in Section 1. An illustration of the nature of the “isolated” Brønsted acid sites of the efficient methanol-dehydration catalyst (to produce light olefins) $Co^{II}AIPO-18$ is shown in Figure 21 (see page 6470).^[72] Also shown in Figure 21 is the isolated “redox” active site generated when the Co^{II} has been converted into the higher oxidation state, Co^{III} . The respective Co–O bond lengths of the acid and redox active centers were determined under in situ conditions by X-ray absorption spectroscopy (XAFS).^[28,72]

In the family of single-site acid catalysts MAIPO-18 ($M = Co^{II}, Mg^{II}, Zn^{II}, Mn^{II}, \dots$), which shape-selectively convert methanol into light olefins, ethene, propene and traces of butene,^[73] the active sites are the protons loosely attached to the oxygen atoms adjacent to the doubly charged M^{II} ions. These metal ions occupy a controllable small percentage (up to about 4 mol %) of the sites normally occupied by framework Al^{III} ions. Likewise, when the transition-metal-ion is raised to a higher oxidation state (e.g. $Co^{II} \rightarrow Co^{III}$), the “redox” active centers, which are efficient^[74,75] in activating C–H bonds in the presence of molecular oxygen, are again essentially isolated (as borne out by the XAFS data) and



therefore are, by definition, a clear-cut example of SSHC (Figure 22).

The widely used selective oxidation catalyst TS-1,^[76] in which some of the silicon atoms that occupy the tetrahedral sites in the siliceous analogue of ZSM-5 are isomorphously replaced by Ti^{IV} ions, is another archetypal example of a SSHC. So also is the (Fe)ZSM-5 catalyst that, in the hands of Panov et al.,^[77] has been developed for the selective oxidation of aromatics such as benzene. (In Section 7, we discuss the mechanistic features of TS-1 in the light of the performance of a Ti^{IV}-centered catalyst belonging to category D of Table 1).

6.1. Bifunctional Single-Site Open-Structure Catalysts

Whereas homogeneous catalysts are seldom bifunctional—a recent, unusual example involving allosteric regulation has, however, been reported^[78]—it is feasible to design single-site, open-structure catalysts in which a Brønsted acidic site is well-separated from a redox site in a shape-selective nanoporous matrix. The case in question involves^[13] another aluminophosphate matrix, known as MAIPO-36, which Raja et al.,^[79] were able to modify so as to create both strong Brønsted acid sites (loosely attached protons) adjacent to M^{II} ions such as Mg^{II} or Co^{II} as well as strong redox sites (where Al^{III} is replaced by Co^{III}). Such a catalyst designated M^{II}M^{III}AIPO-36 performs well in converting cyclohexanone into its oxime and then into ϵ -caprolactam in the presence of O₂ and ammonia (Scheme 4).

This sequence of consecutive conversions occurs freely because (see Figure 23, see page 6471): a) hydroxylamine (NH₂OH) is readily formed in situ inside the pores from NH₃ and O₂ at the M^{III} active sites; b) the NH₂OH converts cyclohexanone (**9**) into cyclohexanone oxime (**10**) both inside and outside the pores of the catalyst; and c) likewise, at the Brønsted acid sites **10** isomerizes to ϵ -caprolactam (**11**) inside the pores of the molecular sieve catalyst.

Recent work^[80] in which a systematic variation of the strength of the isolated Brønsted acid sites was introduced (by, for example, keeping a fixed redox site (Co^{III}) and vice versa (keeping a fixed acid site and changing the redox site) has led to a viable industrial method of producing ϵ -caprolactam, see ref. [148].

6.2. Open-Structure Chiral SSHC

It has not yet proved possible to prepare an open-structure, synthetic zeolite or open-structure MAIPO solid

Figure 19. Views of three examples of “ship-in-bottle” SSHC. a) Pictorial representation of the Co(Salen) adduct inside the supercage of zeolite Y. The complex as its pyridine adduct shows affinity for dioxygen; light blue Co, dark blue N, red O.^[63] b) Cobalt phthalocyanine housed within zeolite Y. Owing to spatial restrictions, the guest molecule is distorted, thereby increasing its reactivity and hydrophobicity (from ref. [66]). c) The dimer of copper acetate (in a compressed state with the Cu–Cu distance significantly reduced from its normal value) housed within zeolite Y.^[64,65]

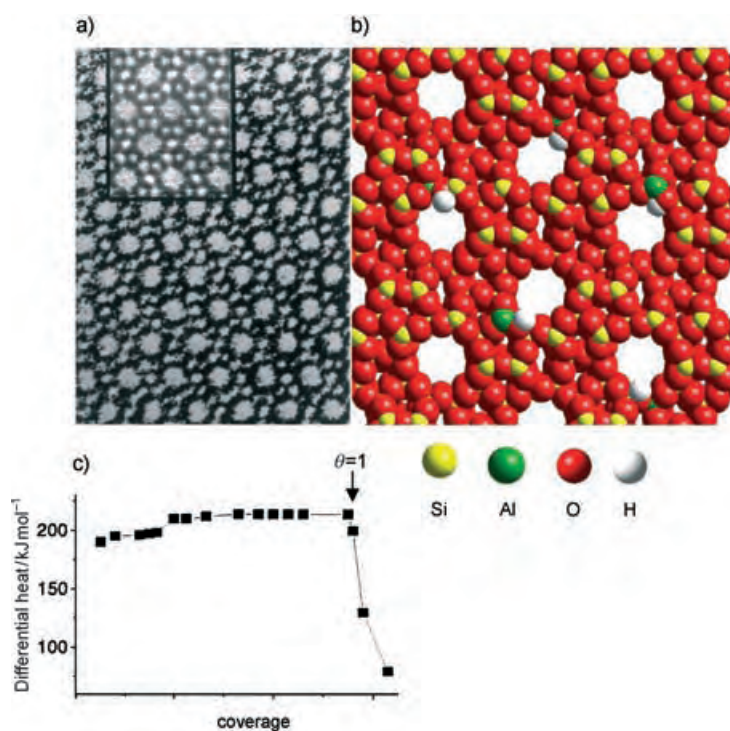


Figure 20. a) High-resolution electron micrograph of H⁺-ZSM-5 (Si:Al ratio approximately 25:1) inset: computed image. b) Scalar model of the H⁺-ZSM-5 open-structure, showing the isolated Brønsted acid sites (loosely attached hydrogen atoms adjacent to Al^{III} sites). c) The heat of adsorption of pyridine remains essentially constant until all the (single-site) acidic centers are neutralized.^[71]

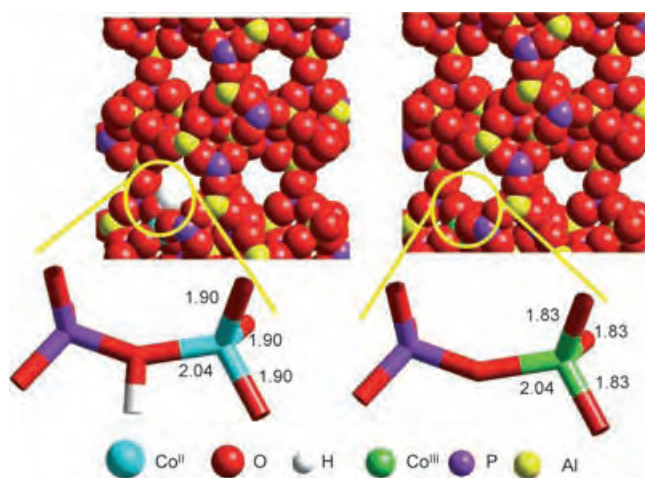


Figure 21. Left: in the open-structure aluminophosphate (AIPO-18) some of the Al^{III} framework ions have been replaced by cobalt ions in a spatially uniform fashion. In the resulting single-site catalyst, Co^{II}AIPO-18, there is Brønsted activity. Right: in the oxidized state Co^{III}AIPO-18 there is redox activity. The bond lengths were determined by in situ XAFS.^[72]

which possesses intrinsic chirality. It has, however, been possible, as first demonstrated by Hutchings et al.,^[58,81] to modify the supercage of an acidic zeolite catalyst (H-Y) so as to create the chiral environment required to favor the formation of one of a pair of diastereoisomeric transition states, which is a necessary condition for enantioselective

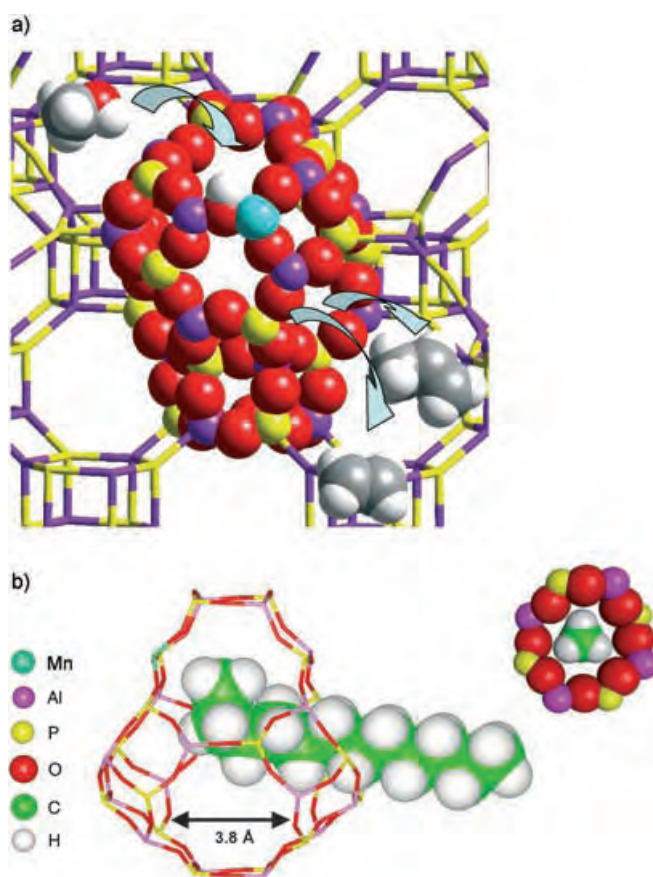
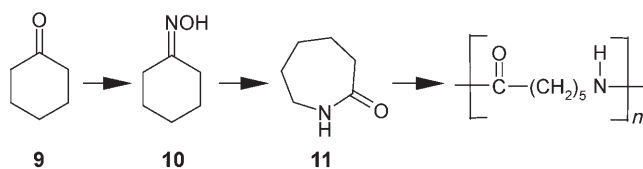


Figure 22. a) The Brønsted acidic sites in the open-structure AIPO-18 solid are the loosely attached protons adjacent either to Co^{II} ions that have replaced Al^{III} framework ions or Si^{IV} ions that have replaced P^V ions. Co^{II}AIPO-18 is a powerful shape-selective dehydration catalyst which converts methanol (top left) into a mixture of ethene and propene (bottom right), just as DAF-4 does.^[73b] b) M^{II}AIPO-18 (M^{II} = Mn^{II}, Co^{II}) is a regioselective oxidation catalyst that, in air or O₂, preferentially oxyfunctionalizes the terminal methyl group, as shown for n-dodecane.^[74]

conversion. Full details have been given by Hutchings in an earlier review.^[58] In essence, by adding a chiral agent (either *R* or *S*) 1,3-dithiane-1-oxide to a zeolite H-Y that has been mildly de-aluminated, a well-defined single-site (Figure 24, left) active center is created which, kinetically enantioselectively resolves (in a gas-phase, acid catalyzed dehydration) racemic butan-2-ol. Hutchings et al.,^[82] have also succeeded to effect enantioselective aziridination of alkenes (employing [*N*-(*p*-tolylsulfonyl)imino] phenyliodine {PhI=NTs}) as the



Scheme 4.

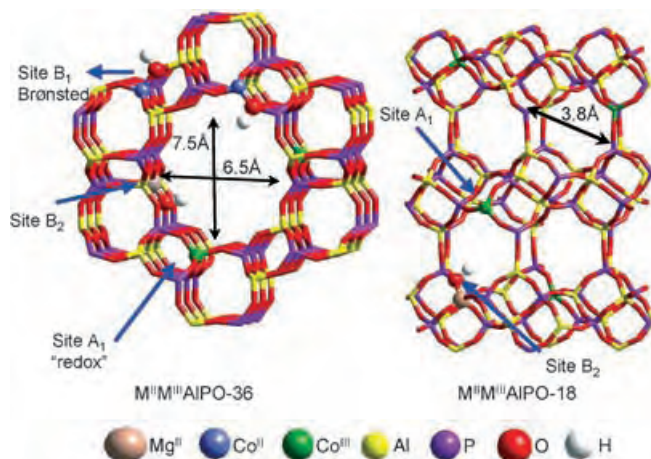


Figure 23. Left: In $M^{II}/M^{III}AlPO-36$ ($M = Co, Mn$), the framework M^{III} ions are the redox-active centers (A_1), whereas the $M^{II}OH$ ions that have ionizable $O-H$ bonds are the Brønsted (B_1) acid sites. Mg^{II} ions in the framework also have neighboring ionizable OH ions (the B_2 sites). Right: In $M^{II}/M^{III}AlPO-18$ all the framework M^{III} ions are again redox active centers: there are no Co^{II} (or Mn^{II}) framework sites. Mg^{II} framework ions again have neighboring (B_2) Brønsted sites.^[79]

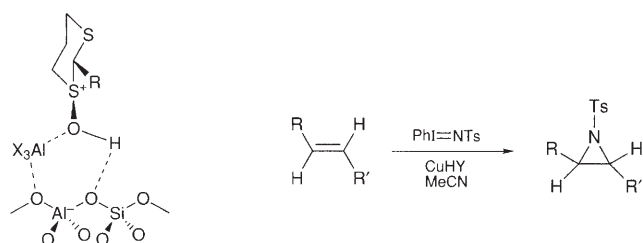


Figure 24. Left: Isolated active site for the enantioselective dehydration of butan-2-ol catalyzed by zeolite Y that has been premodified with bound dithiane oxide.^[58] Right: Aziridination of alkenes using $CuHY$ as catalyst.^[58]

nitrogen source, with a single-site Cu^{II} -exchanged zeolite H-Y (see Figure 24, right).

7. A Selection of Examples Illustrating Practical Applications of SSHC

In addition to the examples that have been cited earlier in the description of various categories (summarized in Table 1) of SSHC, we illustrate below further instances encompassing both laboratory (research) scale and industrially used solid catalysts where the single-site active centers are uniformly

distributed, in a spatial sense, over the two-dimensional or three-dimensional surfaces in question. Many of the examples highlighted are of particular value in the general quest for clean technology and green chemistry, with several instances in which the catalysts themselves are environmentally benign and the reactions that they facilitate (involving, for example, oxygen or air instead of nitric acid as an oxidant) even more so.

We shall also illustrate how, 1) recent computational chemical procedures, combined with in situ experimental studies of single-site catalysts, enable us to establish the mechanism of the Ti^{IV} -centered catalytic epoxidation of alkenes and, 2) using functionalized silsesquioxane fragments, direct measurements of catalytic performance may be made of the same active site in both homogeneous and heterogeneous situations.

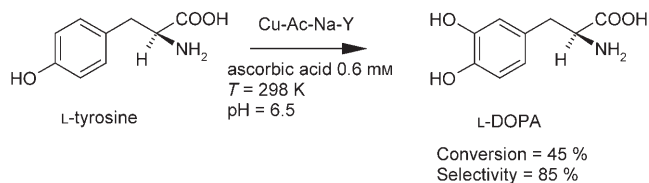
7.1. Enzyme Mimics

The analogy between the mode of action of enzymes on the one hand, and molecular sieve (open-structure) as well as “ship-in-bottle” catalysts on the other hand has frequently been drawn.^[83–87] In each case, cavities in the catalysts impose shape-selectivity that governs the “choice” of reactant species which is to be transformed, and the molecular complementarity and associated factors of the microenvironment at the active site facilitates ensuing chemical conversion. In designing inorganic enzyme mimics,^[88–90] the key targets are high activity coupled with high selectivity and an ability to function at ambient temperatures and pressures. In general, inorganic enzyme mimics are thermally and mechanically stable, robust, and are usually readily capable of being regenerated when (through “poisoning” of active sites, for example) their performance diminishes. Moreover, because much is now known about ways of designing the molecular dimensions,^[91,92] degree of hydrophobicity,^[66] and other features of open-structure inorganic catalysts, genuine inorganic mimics of certain enzymes may be prepared. In addition, a range of highly refined techniques has been evolved to probe, under operating conditions,^[13,14,93,94] the behavior of reactant species and the active sites inside the cavities of open-structure inorganic solids.

7.1.1. A Tyrosinase Mimic

Copper-containing monooxygenase enzymes, such as tyrosinase (EC 1.14.18.1) reversibly bind O_2 and catalyze two different reactions—the hydroxylation of monophenols to *ortho*-diphenols (monophenolase activity) and the oxidation of the *ortho*-diphenols to *ortho*-quinones (diphenolase activity) using molecular oxygen as the oxidant. The active site contains a pair of antiferromagnetically coupled copper ions. Even though several homogeneous models of tyrosinase have been proposed, none of them actually catalyzes the conversion of L-tyrosine into L-DOPA (the reaction the enzyme catalyzes), nor has a heterogeneous solid mimic of tyrosinase been reported to date. Raja and Ratnasamy^[95,96] have shown that dimeric copper acetate complexes, encapsu-

lated within the microcavities of porous solids (zeolites X, Y, and MCM-22), were effective in converting L-tyrosine into L-DOPA in air (Scheme 5). The catalysts (enzyme mimics) also displayed high substrate specificity (only monophenols were

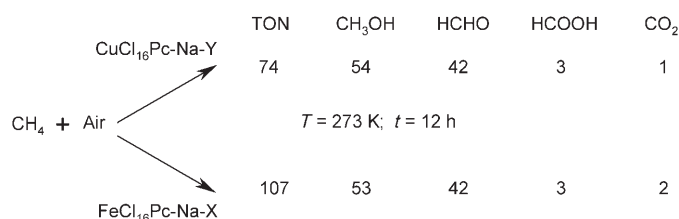


Scheme 5.

oxidized) and regioselectivity (hydroxylation always occurred at the position *ortho* to the -OH group). A linear correlation was obtained between the concentration of the encapsulated copper acetate dimers (estimated from the integrated intensity of the seven-line ESR spectra) and monophenol conversion, suggesting that these copper acetate dimers are the active sites in the activation of dioxygen.^[95] The turnover frequencies for the encapsulated catalysts are higher than their free analogues, suggesting that these copper dimers are well-isolated in the molecular sieve matrix.

7.1.2. Methane Monooxygenase Mimic

Methane monooxygenases are a group of enzymes (molecular mass ca. 300 kD) extractable from methanotropic bacteria. These enzymes are able to hydroxylate methane to yield methanol, an extremely valuable commodity chemical (produced mainly on an industrial scale by steam-reforming of natural gas). Raja and Ratnasamy^[64] have shown that “ship-in-bottle” SSHC, consisting of encapsulated complexes of iron and copper phthalocyanine (see Figure 19) in which all or most of the hydrogen atoms have been replaced by electron-withdrawing substituents (halogens or nitro groups) may convert methane in air at 273 K to methanol and formaldehyde as principal products (Scheme 6). The role of



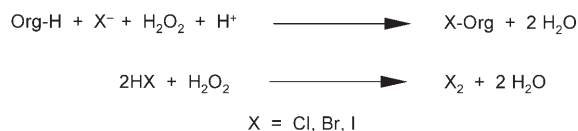
Scheme 6.

the solvent (acetonitrile) is quite important in this conversion, but detrimental to the commercial exploitation of this technology.

7.1.3. Haloperoxidase Mimic

Haloperoxidases, which occur widely in marine organisms, are enzymes which catalyze the oxidation of a halide (Cl^- ,

Br^- , or I^-), by hydrogen peroxide, in such a manner as to achieve concomitant halogenation of certain organic substrates. However, in the absence of organic substrates these enzymes convert the halide ions into the molecular halogen (see Scheme 7).^[97]



Scheme 7.

[CuCl₁₆Pc] complexes, encapsulated within the supercages of zeolites X and Y, are effective for the oxychlorination and oxybromination of a wide range of aromatic compounds, at ambient conditions, using molecular oxygen as the oxidant, in the presence of a suitable alkali halide, such as KBr (Table 2).

Table 2: Oxyhalogenation of aromatic compounds in air using CuCl₁₆Pc-Na-X and KBr.^[a]

Substrate	T [K]	Conv. [%]	Halogenated products [wt. %]			
			Mono	Di	Tri	Side-chain oxidation
Benzene	338	6.2	100	—	—	—
Toluene	338	16.8	69.5	5.5	—	25.0
Phenol	323	18.1	62.0	25.0	13.0	—
Aniline	338	10.3	63.0	15.5	21.5	—
Anisole	338	6.7	25.5	55.0	19.5	—
Resorcinol	323	18.2	100	—	—	—

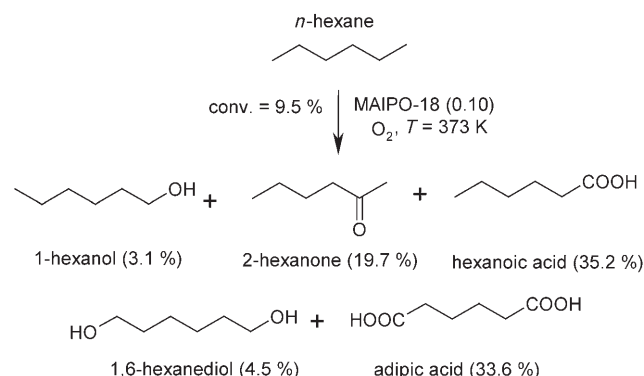
[a] Reaction conditions: Catalyst 0.5 g, $t = 10 \text{ h}$, halide = KBr, air over pressure = 400 psi ($1 \text{ psi} \approx 6.8 \times 10^{-2} \text{ atm}$), solvent $\text{CH}_3\text{CN}:\text{H}_2\text{O}$ 2:1 mol %, Initiator 2 mol % *tert*-butyl hydroperoxide.

The encapsulation of the [CuCl₁₆Pc] complex results in *ortho-para* substitution among the halogenated products with virtually no attack at the *meta*-position. Further, the in situ formation of Br₂ from KBr (established by spectroscopic methods), and, the pH dependence of the catalytic activity, suggests that the halogenating agent is an electrophilic species.^[97,98]

7.1.4. Hydroxylases

By virtue of their ability selectively to bind a linear alkane and to so orient it with respect to the active oxidant at the active site, the so-called ω -hydroxylases can achieve the remarkable regioselective hydroxylation of terminal methyl groups. Herron and Tolman^[99] made significant progress in designing a completely inorganic mimic of the alkane ω -hydroxylases by using encapsulated Pd⁰ and Fe^{II} entities inside zeolite A. This “ship-in-bottle” design succeeds in producing hydrogen peroxide from an O₂/H₂ mixture, but they were unable selectively to functionalize only the terminal methyl group of *n*-octane with this catalyst. Open-structure SSHC (such as M^{III}AlPO-18 where M = Co or Mn) are, however, very effective^[74,75,100] in preferentially hydroxylating

the terminal methyl groups of linear alkanes (C_nH_{2n+2} , $n = 6-12$) in air or oxygen (see Figure 22b). Indeed it is also possible with this category of SSHC, provided the degree of substitution of framework Al^{III} ions by M^{III} ions (Co or Mn) is large enough (ca. 10 atom percent), to convert *n*-hexane into adipic acid in air under mild conditions (Scheme 8).^[101]



Scheme 8.

7.2. SSHC for Sustainable Development and Clean Technology

Selective hydrogenation as well as selective oxidation catalysis nowadays loom progressively larger in the general area of clean (green) chemistry and sustainable development.^[102,103]

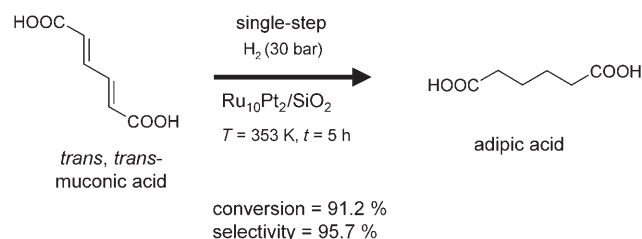
7.2.1. Solvent-Free Selective Hydrogenation Reactions as Candidates for the Production of Commodity Chemicals

The drive to minimize the use of volatile solvents or replace them with environmentally more benign ones (such as supercritical CO₂) has, as its logical conclusion, the development of catalysts that may effect conversions in a solvent-free

manner.^[45,49] Table 3 enumerates many of the selective hydrogenation processes, leading to much-used commodity chemicals, that are catalyzed by single-site, multinuclear bimetallic nanoparticles. (Note that the turnover frequencies (TOFs) are exceptionally high under relatively mild conditions of temperature and pressure). The selective hydrogenation of benzene to cyclohexene is particularly noteworthy as it opens up a new, environmentally benign route to adipic acid that dispenses with the need to use concentrated nitric acid as an oxidant (and the consequential production of massive quantities the greenhouse gas, N₂O). Cyclohexene, with the “right” catalyst is converted into adipic acid using H₂O₂ as oxidant.^[104,105]

7.2.2. Adipic Acid from Sustainable Sources by Using a Single-Site Supported Ru₁₀Pt₂ Nanoparticle Catalyst

With the aid of biocatalysts, muconic acid may be readily produced^[106a] from corn, a renewable feedstock. We have discovered^[106b] that a single-site Ru₁₀Pt₂ multinuclear nanoparticle catalyst supported on mesoporous silica is superior to a variety of comparable catalysts (e.g. Rh/Al₂O₃, Pt/SiO₂, Pd₆Ru₆/SiO₂) in converting muconic acid, in a single-step into adipic acid (see Scheme 9).^[106b]



Scheme 9.

Table 3: Single-step, highly active and selective nanoparticle catalysts for the solvent-free hydrogenation of polyenes.

Catalyst	Reaction	t [h]	TOF [h ⁻¹]	Commercial significance
Pd ₆ Ru ₆ /SiO ₂ Ru ₆ Sn/SiO ₂ Cu ₄ Ru ₁₂ /SiO ₂ Ag ₄ Ru ₁₂ /SiO ₂		8 8 8 8	2012 1980 690 465	Polymer intermediates, ketones, and polyesters
Pd ₆ Ru ₆ /SiO ₂ Ru ₆ Sn/SiO ₂		8 8	5350 1940	Lauroctam, copolyamides, nylon intermediates
Pd ₆ Ru ₆ /SiO ₂ Ru ₆ Sn/SiO ₂		8 8	11176 10210	Coatings, lactones, polymers
Ru ₅ Pt ₁ /SiO ₂ Ru ₁₀ Pt ₂ /SiO ₂ Pd ₆ Ru ₆ /SiO ₂		6 6 6	2625 1790 3216	Starting material in production of K-A oil

7.2.3. Commercially and Environmentally Important Selective Oxidation Processes that may be Effected by SSHC

A selection of the important selective oxidations that may be effected by a range of isolated (single-site) transition-metal ions grafted into mesoporous silica is shown in Figure 25.^[31,33,35,107] The reagents used for the selective oxidations vary according to the reaction and the catalyst in question. Sometimes H₂O₂ is the oxidant,^[108] sometimes alkyl hydroperoxides^[109] (such as *tert*-butyl hydroperoxide, TBHP) and occasionally oxygen itself (as in the case of the oxidative dehydrogenation of methanol to formaldehyde).

Epoxidation of alkenes with Ti/SiO_2 catalysts is of major industrial importance in the production of fine chemicals and several other commodities.^[110] For example, the catalytic conversion of propylene into propylene oxide over Ti/SiO_2 in the presence of alkyl hydroperoxides is an industrially important epoxidation process that accounts for an annual production of more than one million tons of propylene oxide world wide. As a result of recent research work,^[111,112] there are now real prospects that (renewable) vegetable oils and fats, which are good sources for two widely used unsaturated fatty methyl esters—methyl-(*Z*)-9-octadecanoate (methyl oleate (**12**)) and methyl-(*E*)-9-octadecanoate (methyl elaidate (**13**))—may be benignly epoxidized with TBHP using a silica (single-site) catalyst containing Ti^{IV} centers (Figure 26).

In the past, an environmentally unfriendly “peracid” method was used to epoxidize the naturally occurring compounds. Ravasio et al.^[112] have also shown that the Ti^{IV} -center single-site catalyst also effectively converts the doubly unsaturated components of soya bean oil into useful epoxides—another important step towards sustainable development.

Ravasio et al.^[112] have also shown that the Ti^{IV} -ion SSHC (on silica) is particularly good in epoxidizing terpenes such as

α -terpineol, carveol, and limonene under mild conditions (Table 4).

7.2.4. Other Economically Important Examples of Ti^{IV} -Catalyzed (Single-Site) Selective Oxidations

The open-structure microporous silica known as MFI (the accepted international notation for the framework ZSM-5),^[113] when it contains isolated Ti^{IV} ions replacing some of the Si^{IV} tetrahedral sites is known as TS-1, and is an exceptionally good single-site heterogeneous selective oxidation catalyst.^[114] Some key processes using H_2O_2 as oxidant are indicated in Scheme 10.

7.2.5. Mechanism and Energetics of Epoxidation and Comparison between the Heterogeneous and Homogeneous Processes.

Figure 27 shows the kinship that exists between the four-coordinate Ti^{IV} active site for both the corresponding microporous and mesoporous silica frameworks.^[115] Using a joint experimental (X-ray absorption) and computational study, in the course of which we could directly probe the environment

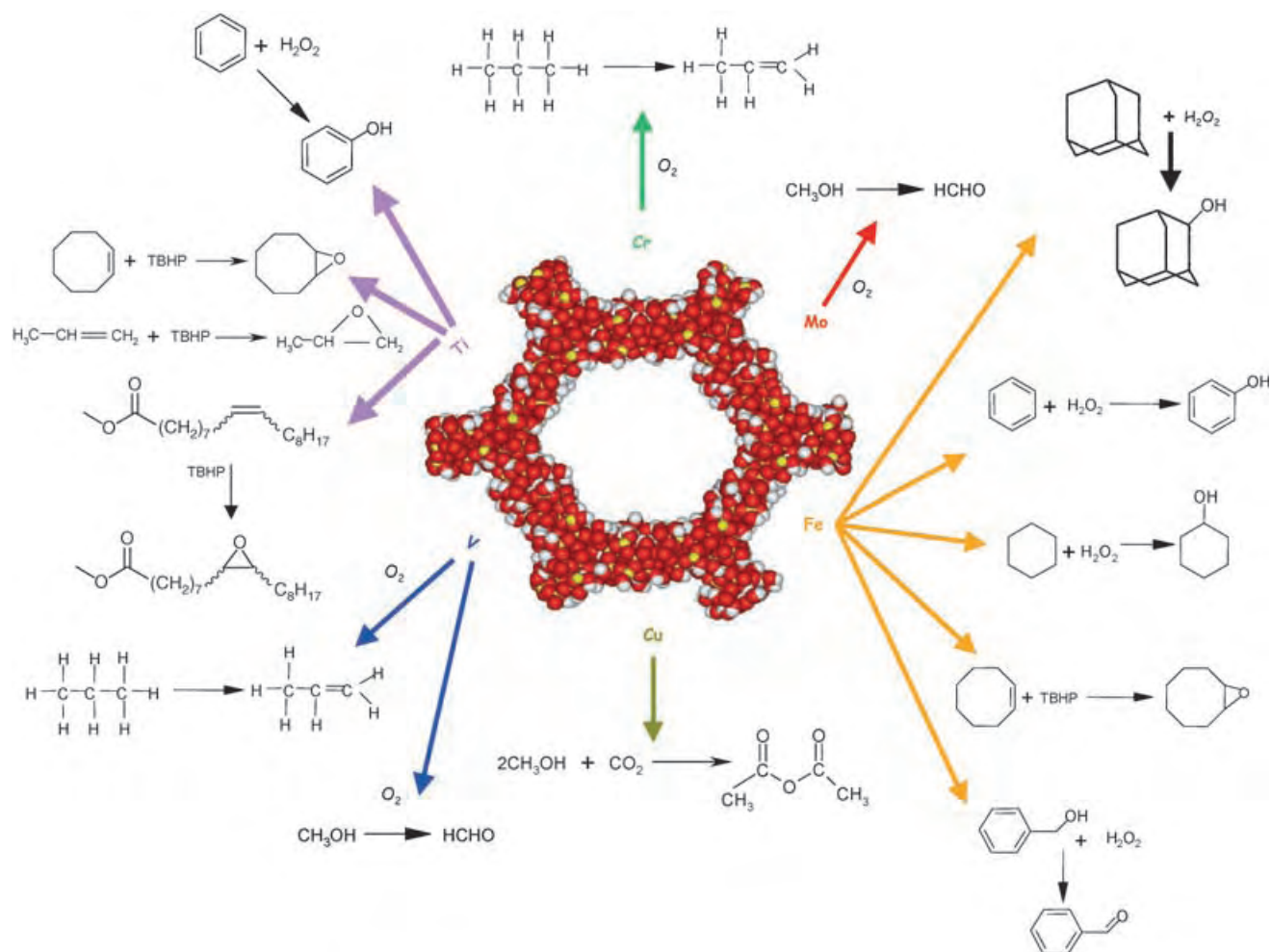


Figure 25. Illustration of some of the selective oxidations that may be effected by SSHC formed by anchoring various $\text{M}^{\text{n}+}$ ions at the surfaces of mesoporous silica.

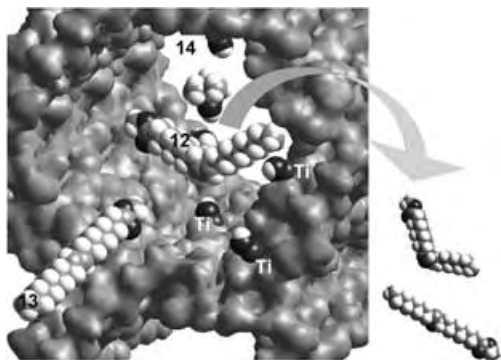
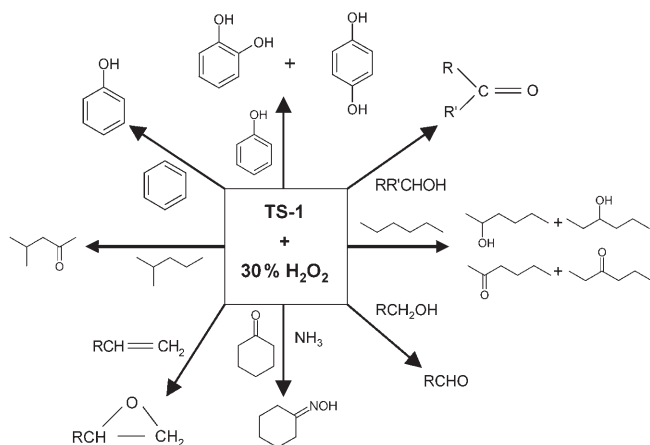


Figure 26. Both methyl oleate (**12**) and methyl elaidate (**13**) are completely epoxidized using single-site Ti^{IV} -mesoporous silica catalysts and *tert*-butyl hydroperoxide (**14**) as oxidant.^[111]

Table 4: Epoxidation of terpenes using Ti^{IV} SSHC on silica^[112] under mild conditions.^[a]

Substrate	TOF [h^{-1}] $\text{Ti} \rightarrow$	$\text{Ti} \uparrow$
α -terpineol	2	20
carveol	15	33
limonene	4	20

[a] $T = 85^\circ\text{C}$; CH_3CN (solvent); 30% wt catalyst; TBHP:terpene mol ratio = 1:1. $\text{Ti} \rightarrow$ indicates Ti^{IV} ions grafted in (and parallel to) the silica surface and $\text{Ti} \uparrow$ Ti^{IV} ions grafted perpendicular to the surface.



Scheme 10.

of the active Ti^{IV} center under steady-state conditions during the actual epoxidation, we could arrive at the pathway and associated energetics for the mechanism of the epoxidation. These are shown in Figure 28.

Coordination of the oxygen atoms of the peroxide to the Ti^{IV} center activates them by increasing their electrophilicity; and the computations reveal that the oxygen atoms may be readily abstracted by the nucleophilic alkenes to form the epoxides. As shown in Figure 28, subsequent loss of the water regenerates the original tripodal (four-coordinate) Ti^{IV} active center. In line with this mechanism, which harmonizes with the independent work of Roesky et al.^[116] (on the formation of titanium alkylhydroperoxide), it is not surprising that when

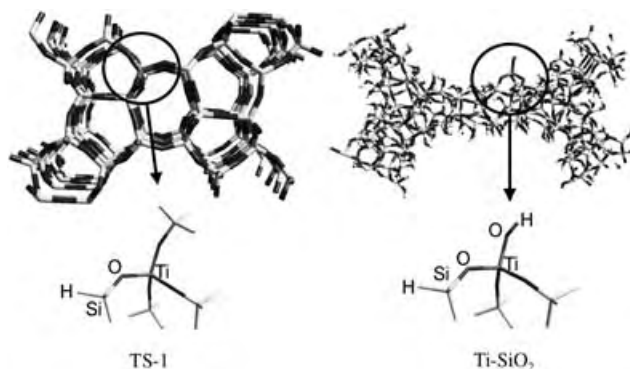


Figure 27. Left: TS-1, a single-site, open-structure selective oxidation catalyst (see Scheme 11) that has the same framework structure as H-ZSM-5 (see Figure 20), except that there are no Al^{III} ions in the framework, only isolated Ti^{IV} sites substitutionally replacing the Si^{IV} centers. Right: The tripodally anchored Ti^{IV} redox sites in a Ti-SiO_2 epoxidation catalyst (see Section 7.2.3) in mesoporous silica (compare Figure 5) are very similar to the Ti^{IV} active centers in TS-1.^[115]

one of the three silicon atoms, to which, through oxygen, the Ti^{IV} site is attached, is replaced by germanium, there is an increase in the rate of epoxidation.^[117]

Experiments with soluble, molecular (homogeneous) analogues of the heterogeneous Ti/SiO_2 epoxidation catalyst using the silsesquioxanes: $[(\text{C-C}_5\text{H}_9)_7\text{Si}_7\text{O}_{12}\text{TiOXPh}_3]$, where $\text{X} = \text{Si}, \text{Ge}, \text{or Sn}$ —in which XAFS and kinetic measurements could be carried out in solution—not only confirm that replacement of Si by Ge (or Sn) at the active site enhances the rate of epoxidation, they also show that the turnover frequencies for the “hetero” and “homo” active sites are numerically similar.^[117]

7.3. In Situ Generation of Hazardous Reagents by Using Open-Structure SSHC

The in situ production and containment of aggressive and hazardous reagents (as well as the avoidance of the use of ecologically harmful ones) has been much assisted by the design of appropriate open-structure SSHC, such as those consisting of metal-ion-framework-substituted aluminophosphates, MAIPOs (see Section 6). A range of such nanoporous catalysts designed by us has been described previously.^[13,100,118] We give two specific examples here: 1) a Baeyer–Villiger process (for the conversion of cyclic ketones to lactones; and 2) the generation of hydroxylamine in the intrapore cavities and channels of bifunctional SSHC (Scheme 11).

In (1), the aggressive permonosulfuric acid (used by Baeyer and Villiger) or methyl rhenium trioxide or any added peroxide is avoided and O_2 is used in the presence of (a sacrificial) benzaldehyde (Scheme 11).^[119] In (2), ammonia and oxygen generate hydroxylamine at the redox active sites of the bifunctional catalyst (Scheme 12).

The convenience of having a bifunctional open-structure SSHC, such as that shown in Figure 23, commends itself commercially, since this is an extremely direct way of

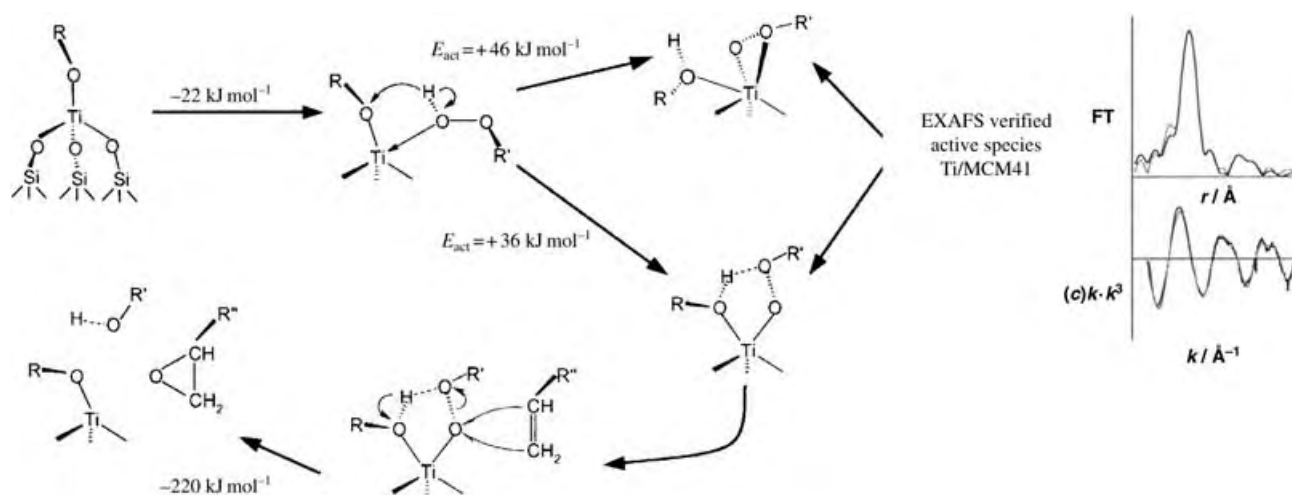
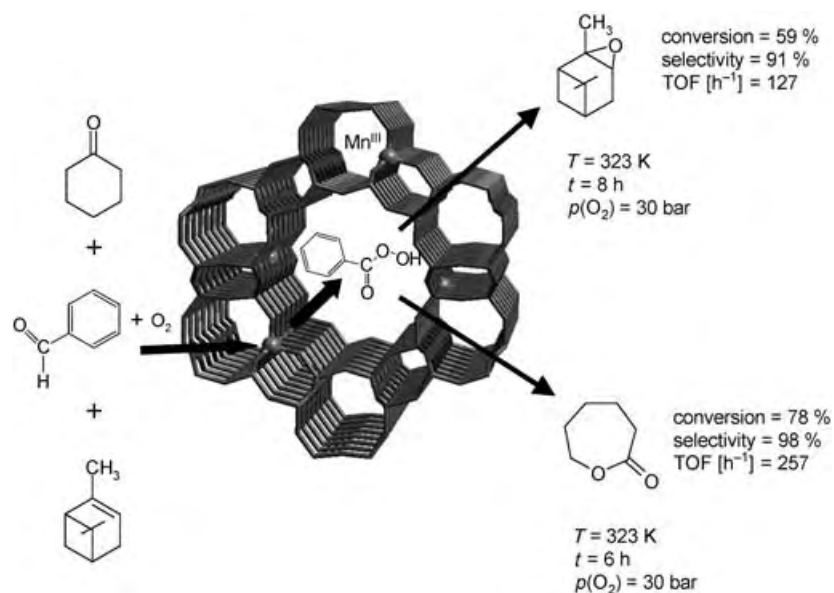


Figure 28. Catalytic cycle, including calculated energies for the epoxidation of alkenes by catalysts with Ti^{IV} centers. At the right are the observed and calculated radial distribution curve and X-ray absorption spectrum.^[115b]



Scheme 11.

generating cyclohexanone oxime, and its isomer, ϵ -caprolactam, which, on polymerization, yields nylon.^[120]

Another example where SSHC has proved valuable is that of the enzyme mimic for haloperoxidase, described in Section 7.1.3. With such a catalyst, the need to add neat halogen to the sphere of reaction is dispensed with.

7.4. Enantioselective Conversions with SSHC

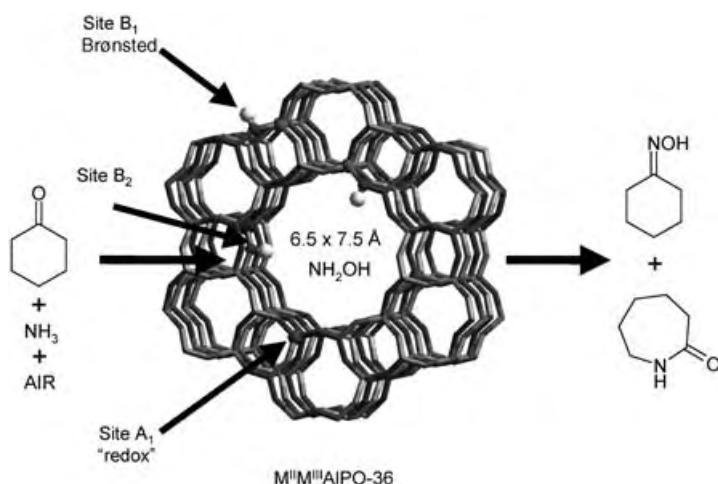
There is an ever-growing need for high-performance, heterogeneous, recyclable asymmetric catalysts, because, as with other areas of catalytic conversion^[121] they should surpass their homogeneous analogues so far as the important practical consideration of separation of products is con-

cerned. Of late, many new strategies have been proposed to accelerate the arrival of reliable, robust heterogeneous asymmetric catalysts, and a recent monograph^[56] along with other publications^[62, 122, 123] outline various possible strategies for “imprinting” a surface with chirality.

We have already alluded to the ingenious method of Hutchings et al.,^[58] who, in turn, refer to the elegant work of Bianchini^[42, 124] and others especially that of Corma and Garcia^[125] and Xiang et al.^[126] (who successfully immobilized the Sharpless titanium diethyltartrate system). Herein, for illustrative purposes, we focus on Jacobs’s work on the coordination of $\{\text{Cr}^{\text{III}}(\text{Salen})\}$ complexes on functionalized silica for the asymmetric ring opening (ARO) of epoxides^[127a] and on that of Maschmeyer and Sheldon^[127b] on the use of single-site, immobilized $[\text{Rh}(\text{MonoPhos})]$ (MonoPhos is a chiral monodentate ligand). We also summarize the practical advantages of our own approach^[43–45, 57] to designing constrained (single-site) chiral catalysts.

The heterogeneous ARO of *meso*-epoxides with trimethylsilylazide (TMSN_3) catalyzed by a $\{\text{Cr}^{\text{III}}(\text{Salen})\}$ moiety coordinated to an aminopropyl-functionalized (high-area) silica combines good enantioselectivity with high conversions and no tendency for the catalyst to be leached off its support. Thus, in the ring-opening of cyclohexene oxide, under the conditions given in Table 5, conversions are always in excess of 99 % and *ee* values range (in ten successive runs to test leachability) from a low of 65 to a high of 77 %.

Feringa and his colleagues demonstrated^[127c] that rhodium complexes with chiral monodentate ligands such as phosphoramidites (MonoPhos) are very powerful tools for reduction, and that homogeneous catalysts based on these ligands are highly enantioselective. Using the specially prepared mesoporous silica known as TUD-1,^[127b] into the framework of which isolated Al^{III} ions have replaced some Si^{IV} ions

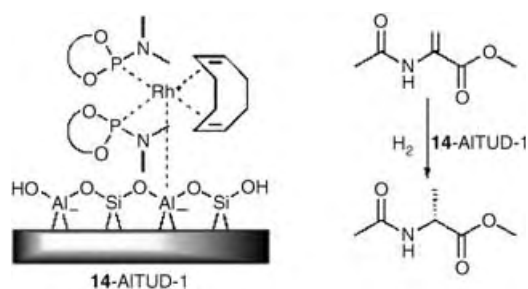


Scheme 12.

Table 5: Asymmetric ring opening of cyclohexene oxide in the presence of supported catalytically active Cr^{III}(Salen).

Run	<i>t</i> [h]	Conv. [%]	<i>ee</i> [%]	Leaching [%]
1	1	99.5	65.4	0.9
2	18	100	67.9	0.8
3	18	100	68.7	0.5
4	18	100	73.3	1.0
5	19	99.3	73.1	1.0

(thereby producing a high-area solid designated AITUD-1), Maschmeyer, Simons, and co-workers showed that ionically bound Rh-phosphoramidite exhibited excellent enantioselectivity in the asymmetric hydrogenation of methyl-2-acetamidoacrylate (Scheme 13).^[127b] The ionic binding procedure of Rege et al.,^[46] also used by us,^[44] is a rapid, convenient method of generating highly efficient, robust, and recyclable SSHC for enantioselective hydrogenations that may be carried out using water as solvent.



Scheme 13.

So far as the use of our own approach to constrained chiral catalysis is concerned, we emphasize that highly efficient enantioselective hydrogenations, of prochiral molecules that yield products of considerable commercial significance, have been achieved. The following advances have been reported:

1. Two distinct metal centers (Rh^I and Pd^{II}).
2. Three distinct diamino ligands (see Table 6).
3. Two methods of producing the single-site (covalent and ionic) immobilized organometallic centers.
4. Two specific examples of hydrogenation reactions.

The relevant catalytic activities, selectivities, and enantiomeric excesses (*ee* values) for the various homogeneous and heterogeneous Rh^I catalysts are summarized in Table 6 for the asymmetric hydrogenation of methylbenzoylformate (MBF); and the corresponding catalytic performance for the Pd^{II}-based asymmetric catalysts for the hydrogenation of both *E*-(α)-phenylcinnamic acid (PCA) and MBF are shown in Table 7. Several patents,^[128–130] based on these constrained, single-site, asymmetric heterogeneous catalysts, have been recently filed by German industry (on behalf of the Inventors).

7.5. Some Miscellaneous Examples

Already in this Review we have cited a number of important examples where single-site, open-structure heterogeneous catalysts hold sway. The majority of zeolites (as well as the growing number of metal-substituted aluminophosphates) used in industry have isolated, single-site active centers. They catalyze a large number of commercially important reactions and also offer ideal testing grounds for fundamental studies. Both these facets are dealt with in Section 7.5.1. In Sections 7.5.2, 7.5.3, and 7.5.4 potential large-scale operations involving hydroformylation, metathesis, and polymerization are outlined.

7.5.1. Solid Acid Catalysts

In all so-called pentasil^[83] zeolites (e.g. ZSM-5 and ZSM-11) where the Si:Al ratios are seldom less than 10:1 and often much in excess of this, and in numerous other aluminosilicate and aluminophosphate open-structure solids (such as faujasite (zeolite Y), ferrierite, erionite, and SAPO-34), a huge variety of (Brønsted) acid-catalyzed reactions may be carried out. Several Reviews^[131–135] of this vital class of reactions, that embrace both the petrochemical and fine-chemical world, are already available. Table 8 lists some of these reactions.

7.5.1.1. Shape-Selective, Solid-Acid, Single-Site Zeolitic Catalysts and Their Kinship with Enzymes

As mentioned in Section 7.1, the analogy between the mode of action of an enzyme on the one hand and a “ship-in-

Table 6: Activities, selectivity (for methyl mandelate), and enantiomeric excess (*ee*) for the various homogeneous and heterogeneous Rh^I catalysts for the asymmetric hydrogenation of methyl benzoyl formate.^[a]

Ligand	Phase	Tethering approach	Counterion	Conv. [%]	Sel. [%]	<i>ee</i> [%]
AMP	Homo	-	BF ₄ ⁻	79	63	0
AMP	Het	Covalent	BF ₄ ⁻	100	89	93
AMP	Homo	-	CF ₃ SO ₃ ⁻	95	79	0
AMP	Het	Ionic	CF ₃ SO ₃ ⁻	99	89	93
DED	Homo	-	CF ₃ SO ₃ ⁻	70	84	0
DED	Het	Ionic	CF ₃ SO ₃ ⁻	98	92	84
PMP	Homo	-	CF ₃ SO ₃ ⁻	96	91	0
PMP	Het	Ionic	CF ₃ SO ₃ ⁻	98	93	85

[a] Reaction conditions: substrate 0.5 g, solvent (methanol) 30 mL, homogeneous catalyst 10 mg, heterogeneous catalyst 50 mg, 20 bar, 313 K, 2 h. AMP = (S)-(-)-2-aminomethyl-1-ethylpyrrolidine, DED = (1R,2R)-(+)-2-diphenylethylenediamine, PMP = (S)-(+)-1-(2-pyrrolidinylmethyl)pyrrolidine.

bottle” SSHC on the other can be quite striking. It is also true that certain acid-catalyzed reactions in zeolitic solids also have a kinship with enzyme action. Thus, the Brønsted acid catalyzed cyclodimerization of 3-hydroxy-3-methylbutan-2-

Table 7: Asymmetric hydrogenation of *E*-(α)-phenylcinnamic acid (PCA) and methylbenzoylformate (MBF) with the Pd^{II} catalysts.^[a]

Ligand	Phase	Tethering approach	Counterion	Substrate	Conv. [%]	Sel. [%]	<i>ee</i> [%]
AMP	Homo	-	BF ₄ ⁻	PCA	100	87	76
AMP	Het	Covalent	BF ₄ ⁻	PCA	93	87	93
DED	Homo	-	BF ₄ ⁻	PCA	95	82	79
DED	Het	Covalent	BF ₄ ⁻	PCA	55	100	88
AMP	Homo	-	BF ₄ ⁻	MBF	100	93	0
AMP	Het	Covalent	BF ₄ ⁻	MBF	97	96	78
PMP	Homo	-	CF ₃ SO ₃ ⁻	MBF	99	89	0
PMP	Het	Ionic	CF ₃ SO ₃ ⁻	MBF	99	98	67

[a] The reactions were carried out for 24 h for PCA and 2 h for MBF (see Table 6 for reaction conditions).

Table 8: A summary of the economically significant catalytic conversions effected by single-site, open-structure aluminosilicate and aluminophosphate (zeolitic) solids.^[133]

Hydrocarbons produced (sometimes shape-selectively) from acid-catalyzed reactions

Ethyl benzene from benzene and ethene
 Xylenes from isomerizations and disproportionation of toluene
 Methanol to olefins and methanol to gasoline
 Cumene from benzene plus propene
 Oligomerization of olefins
 Detergent alkylate from benzene plus C₆ to C₁₄ olefins
 Aromatics from acetylene
 Isomerization of methyl naphthalenes
 Vinylcyclohexene from butadiene by dimerization

Reactions involving functionalized hydrocarbons

Alkylation of phenol
 Ester hydrolysis
 Chlorination of chlorobenzene
 Alkyl carboxylates from carboxylic acids and olefins
 Primary amines from ammonia and olefin
 Secondary amines by elimination of ammonia from primary amine
 Glycol ethers by ethoxylation of lower aliphatic alcohols
 Nitration of chlorobenzene^[137,138]

one (HMB)^[89] over a H⁺ form of (synthetic) ferrierite (Si:Al ratio of 40:1) yields only one product, whereas HMB in acidic solution generates a wide variety of products (Scheme 14 a).

Likewise, acetaldehyde^[90] is catalytically transformed in acidic solution to a broad distribution of products, whereas within the space-restricting cages of H⁺ ferrierite cyclotrimerization occurs with 100 % selectivity at ambient temperature (Scheme 14 b).

7.5.2. Hydroformylations, Metathesis, and Polymerization Reactions Using SSHC Assembled from Anchored Organometallic Species^[134, 136, 139]

Bianchini et al.^[42] have shown how to overcome the disadvantages that homogeneous Rh^I complexes possess by anchoring them, in a single-site fashion, on to a silica surface (see Figure 11). Although hydroformylation (metal-complex) catalysts have been successfully immobilized at silica surfaces their activities and selectivities have not yet reached values high enough to rival those registered by their homogeneous counterparts, which they surpass in ease of separation of products from reactants. The dinuclear rhodium(II) catalyst studied by Maschmeyer et al.^[139] is a case in point. In this case, it was possible to pin down the precise structure of the active catalyst from a crystallographic study of the soluble silsesquioxane derivative (Figure 29)

Coperét et al.,^[20] using nonporous silica supports were able to immobilize organometallic metathesis catalysts, in which the central atom was either Ta, Mo, W, or Re:

examples of such well-defined silica-supported metallocarbenes and carbynes are shown in Figure 10. It is noteworthy that, in contrast to the dirhodium catalyst for hydroformylation, the activities, selectivities, and lifetimes of these SSHC are close to—and in some instances superior—to those of the corresponding homogeneous catalysts.^[140–141]

The so-called constrained geometry-inspired catalysts (CGCs) of McKittrick and Jones,^[41,142] mentioned earlier—see Section 3.3 and Scheme 1 and Scheme 2—in which a titanium-based catalyst that is immobilized, site-isolated fashion, at a silica surface exhibits exceptionally good catalytic performance in the room-temperature polymerization of ethene (in the presence of an alkyl aluminum species and a pentafluorophenyl activator). And a text book example of polymerization at a SSHC of the Brønsted acid type is contained in the work of Zecchina et al.^[143] These workers showed (using in situ FTIR) that acetylene, methylacetylene, and ethylacetylene interact with the Brønsted acid sites of H-ZSM-5 with the formation of hydrogen-bonded (precursor) species characterized by well-defined IR properties (Scheme 15). These species are then protonated (by the catalyst) to give intensely colored carbocationic species.

5. They are generally amenable to sophisticated computational approaches (using DFT) so that direct comparisons with experiment are possible (e.g. reaction kinetics).
6. Most importantly, they offer a proven and widely applicable strategic principle for the design of new catalysts and the improvement of existing ones. This principle, applicable to almost all open-structure solids but especially metal-substituted mesoporous silicas and microporous aluminophosphates, applies both to monofunctional and bifunctional catalysts.

A multiplicity of examples, cited above and in earlier articles (see refs. [13,31,45,148]), encompassing a variety of selective oxidations (including the oxyfunctionalization of alkanes and the benign epoxidation of replenishable terpenes and the esters of naturally occurring unsaturated fatty acids), selective hydrogenation of polyenes and unsaturated (pro-chiral) ketoesters, dehydrations of alkanols, alkylations, allylic aminations, ammoximations, oxyhalogenations, isomerizations, oligomerizations, and polymerization of alkenes and aldehydes, as well as a proven “green” method for producing ϵ -caprolactam (th precursor of nylon 6)^[148] demonstrate the veracity of the above advances. A large fraction of these catalyzed conversions is achieved using open-structure solids, especially metal-substituted mesoporous (15 to 250 Å diameter) silica and microporous (3.8 to 7.5 Å diameter) aluminophosphates, into which, as isolated entities more than a quarter of the elements of the Periodic Table may be incorporated either as well-separated redox or acid–base (or both) active centers. The resulting high-area open-structure and molecularly accessible solids possess, in effect, three-dimensional surfaces over which the active sites are judiciously placed.

We are grateful to our colleague Prof. B. F. G. Johnson for his stimulating contributions to our endeavors, to other colleagues mentioned in the text, and to a variety of research sponsors including EPSRC, Bayer Chemicals, and BP. J.M.T. wishes to thank Prof. Viveka Alfredsson and her colleagues at Physical Chemistry I, University of Lund, for their hospitality.

Received: October 29, 2004

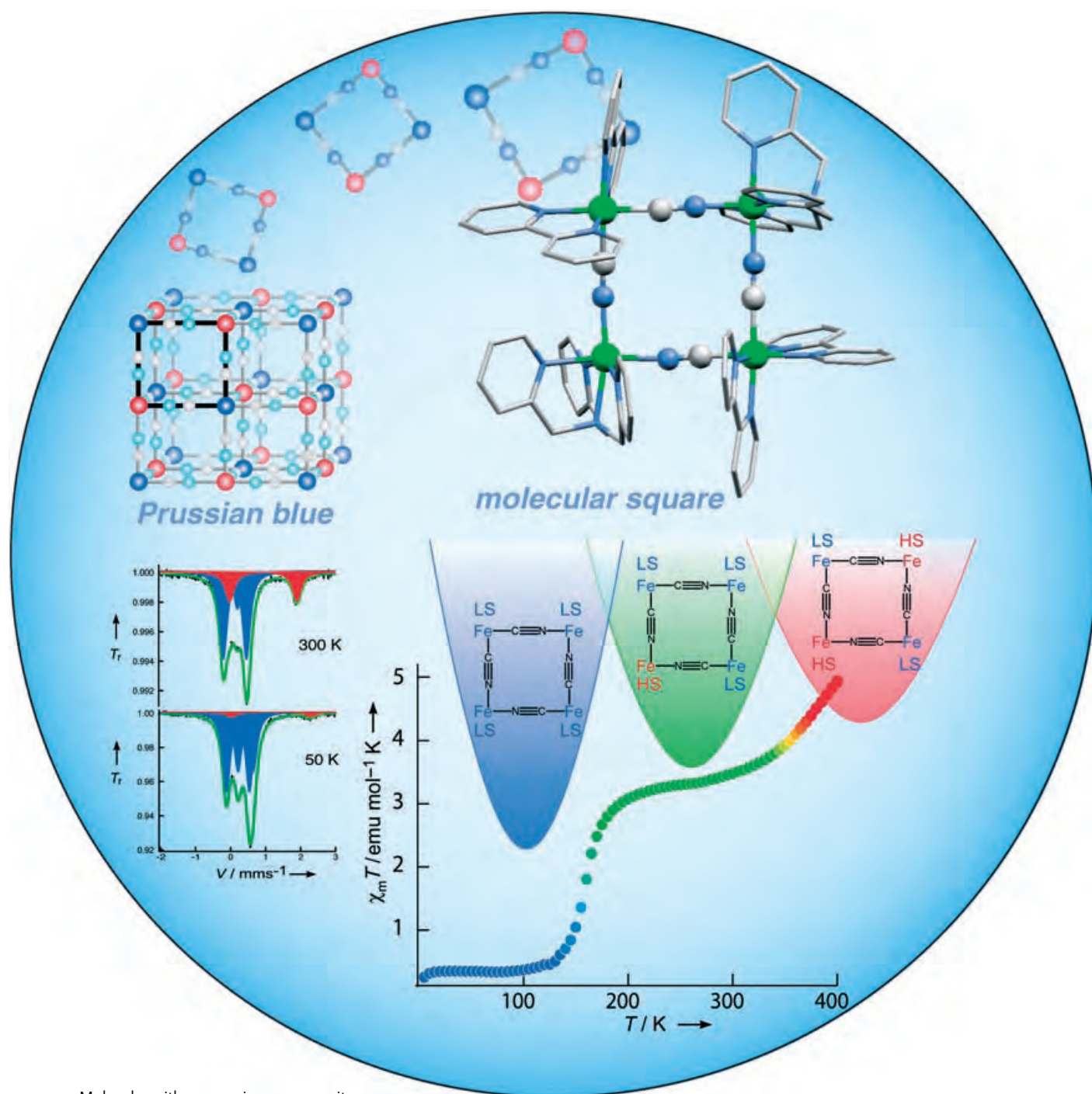
Revised: April 20, 2005

- [1] J. D. Horvath, A. J. Gellman, *Top. Catal.* **2003**, 25, 9.
- [2] a) O. Beeck, *Disc. Farad. Soc.* **1950**, 8, 118; b) Y. Y. Yeo, L. Vattuone, D. A. King, *J. Chem. Phys.* **1997**, 106, 392.
- [3] H. S. Taylor, *Proc. R. Soc. London A* **1925**, 108, 105.
- [4] J. M. Thomas, *Adv. Catal.* **1969**, 19, 293.
- [5] a) G. A. Somorjai, *Introduction to Surface Chemistry and Catalysis*, Wiley, New York, **1994**; b) S. Dahl, A. Logadottir, R. C. Egeberg, J. H. Larsen, I. Chorkendorff, E. Tornqvist, J. K. Nørskov, *Phys. Rev. Lett.* **1999**, 83, 1814.
- [6] E. J. Arlman, P. Cossee, *J. Catal.* **1964**, 3, 99.
- [7] R. Imbihl, G. Ertl, *Chem. Rev.* **1995**, 95, 697.
- [8] G. Ertl, H. J. Freund, *Phys. Today* **1999**, 52, 32.
- [9] V. P. Zhdanov, B. Kasemo, *Phys. Chem. Chem. Phys.* **2004**, 6, 4347.
- [10] H. Schubert, U. Tegtmeier, D. Herein, X. Bao, M. Muhler, R. Schlögl, *Catal. Lett.* **1995**, 33, 305.
- [11] a) C. T. Campbell, *Science* **2004**, 306, 234; b) M. S. Chen, D. W. Goodman, *Science* **2004**, 306, 252.
- [12] J. M. Thomas, *Angew. Chem.* **1988**, 100, 1735; *Angew. Chem. Int. Ed. Engl.* **1988**, 27, 1673.
- [13] J. M. Thomas, *Angew. Chem.* **1999**, 111, 3800; *Angew. Chem. Int. Ed.* **1999**, 38, 3589.
- [14] B. M. Weckhuysen in *In Situ Spectroscopy of Catalysts* (Ed.: B. M. Weckhuysen), American Scientific, New York, **2004**, p. 1.
- [15] a) F. J. Feher, D. A. Newman, J. F. Walzer, *J. Am. Chem. Soc.* **1989**, 111, 1741; b) H. C. L. Abbenhuis, S. Krijnen, R. A. van Santen, *Chem. Commun.* **1997**, 331.
- [16] R. Murugavel, A. Voigt, M. G. Walawalkar, H. W. Roesky, *Chem. Rev.* **1996**, 96, 2205.
- [17] J. M. Thomas, G. Sankar, M. C. Klunduk, M. P. Attfield, T. Maschmeyer, B. F. G. Johnson, R. G. Bell, *J. Phys. Chem. B* **1999**, 103, 8809.
- [18] see J. M. Basset, A. Choplin, *J. Mol. Catal.* **1983**, 21, 95.
- [19] a) D. G. H. Ballard, *Adv. Catal.* **1973**, 23, 263; b) J. P. Candlin, H. Thomas, *Adv. Chem. Ser.* **1974**, 132, 212.
- [20] C. Coperet, M. Chabanas, R. P. Saint-Arroman, J. M. Basset, *Angew. Chem.* **2003**, 115, 164; *Angew. Chem. Int. Ed.* **2003**, 42, 156.
- [21] C. T. Kresge, M. E. Leonowicz, W. J. Roth, J. C. Vartuli, J. S. Beck, *Nature* **1992**, 359, 710.
- [22] S. Inagaki, Y. Fukushima, K. Kuroda, *J. Chem. Soc. Chem. Commun.* **1993**, 680.
- [23] A. Corma, M. T. Navarro, J. P. Pariente, *J. Chem. Soc. Chem. Commun.* **1994**, 147.
- [24] G. Sankar, F. Rey, J. M. Thomas, G. N. Greaves, A. Corma, B. R. Dobson, A. J. Dent, *J. Chem. Soc. Chem. Commun.* **1994**, 2279.
- [25] J. M. Thomas, *Nature* **1994**, 368, 289.
- [26] P. T. Tanev, M. Chibwe, T. J. Pinnavaia, *Nature* **1994**, 368, 321.
- [27] a) T. Maschmeyer, F. Rey, G. Sankar, J. M. Thomas, *Nature* **1995**, 378, 159; b) P. E. Sinclair, G. Sankar, C. R. A. Catlow, J. M. Thomas, T. Maschmeyer, *J. Phys. Chem. B* **1997**, 101, 4232.
- [28] J. W. Couves, J. M. Thomas, D. Waller, R. H. Jones, A. J. Dent, G. E. Derbyshire, G. N. Greaves, *Nature* **1991**, 354, 465.
- [29] R. A. Sheldon, *J. Mol. Catal.* **1983**, 20, 1.
- [30] I. J. Shannon, T. Maschmeyer, R. D. Oldroyd, G. Sankar, J. M. Thomas, H. Pernot, J. P. Balikdjian, M. Che, *J. Chem. Soc. Faraday Trans.* **1998**, 94, 1495.
- [31] a) J. M. Thomas, R. Raja, *Stud. Surf. Sci. Catal.* **2004**, 148, 163; b) A. Sakthivel, J. Zhao, F. E. Kühn, *Catal. Lett.* **2005**, 102, 115.
- [32] J. Jarupatrakorn, J. D. Tilley, *J. Am. Chem. Soc.* **2002**, 124, 8380.
- [33] K. L. Fajdala, T. D. Tilley, *J. Catal.* **2003**, 216, 265.
- [34] a) C. Pak, A. T. Bell, T. D. Tilley, *J. Catal.* **2002**, 206, 49; b) I. J. Drake, K. L. Fajdala, A. T. Bell, T. D. Tilley, *J. Catal.* **2005**, 230, 14.
- [35] A. T. Bell, *Science* **2003**, 299, 1688.
- [36] S. Abbet, A. Sanchez, U. Heiz, W. D. Schneider, A. M. Ferrari, G. Pacchioni, N. Rösch, *J. Am. Chem. Soc.* **2000**, 122, 3453.
- [37] S. Abbet, U. Heiz, H. Hakkinen, U. Landman, *Phys. Rev. Lett.* **2001**, 86, 5950.
- [38] H. Ahn, C. P. Nicholas, T. J. Marks, *Organometallics* **2002**, 21, 1788.
- [39] H. Ahn, T. J. Marks, *J. Am. Chem. Soc.* **2002**, 124, 7103.
- [40] C. P. Nicholas, H. S. Ahn, T. J. Marks, *J. Am. Chem. Soc.* **2003**, 125, 4325.
- [41] M. W. McKittrick, C. W. Jones, *J. Am. Chem. Soc.* **2004**, 126, 3052.
- [42] C. Bianchini, D. G. Burnaby, J. Evans, P. Frediani, A. Meli, W. Oberhauser, R. Psaro, L. Sordelli, F. Vizza, *J. Am. Chem. Soc.* **1999**, 121, 5961.
- [43] J. Rouzaud, M. D. Jones, R. Raja, B. F. G. Johnson, J. M. Thomas, M. J. Duer, *Helv. Chim. Acta* **2003**, 86, 1753.

- [44] R. Raja, J. M. Thomas, M. D. Jones, B. F. G. Johnson, D. E. W. Vaughan, *J. Am. Chem. Soc.* **2003**, *125*, 14982.
- [45] J. M. Thomas, R. Raja, *J. Organomet. Chem.* **2004**, *689*, 4110.
- [46] F. M. de Rege, D. K. Morita, K. C. Ott, W. Tumas, R. D. Broene, *Chem. Commun.* **2000**, 1797.
- [47] W. Z. Zhou, J. M. Thomas, D. S. Shephard, B. F. G. Johnson, D. Ozkaya, T. Maschmeyer, R. G. Bell, Q. F. Ge, *Science* **1998**, *280*, 705.
- [48] R. Raja, G. Sankar, S. Hermans, D. S. Shephard, S. Bromley, J. M. Thomas, B. F. G. Johnson, *Chem. Commun.* **1999**, 1571.
- [49] a) J. M. Thomas, B. F. G. Johnson, R. Raja, G. Sankar, P. A. Midgley, *Acc. Chem. Res.* **2003**, *36*, 20; b) If too high a surface density of tethered active sites is introduced within a mesopore, the active sites themselves become so close to one another that they are no longer isolated. Under these circumstances it is no longer valid to describe such prepared catalysts as “single site.” When, however, the length of the tether is sufficiently long that the pendant active site becomes close to the (opposite) wall of the pore, a new phenomenon occurs as described in the ensuing text.
- [50] J. M. Thomas, R. Raja, G. Sankar, B. F. G. Johnson, D. W. Lewis, *Chem. Eur. J.* **2001**, *7*, 2973.
- [51] J. M. Thomas, P. A. Midgley, *Chem. Commun.* **2004**, 1253.
- [52] J. M. Thomas, P. A. Midgley, T. J. V. Yates, J. S. Barnard, R. Raja, I. Arslan, M. Weyland, *Angew. Chem.* **2004**, *116*, 6913; *Angew. Chem. Int. Ed.* **2004**, *43*, 6745.
- [53] R. D. Adams, B. Captain, L. Zhu, *J. Am. Chem. Soc.* **2004**, *126*, 3042.
- [54] R. D. Adams, B. Captain, *J. Organomet. Chem.* **2004**, *689*, 4521.
- [55] H. Brunner in *Applied Homogeneous Catalysis with Organometallic Compounds, Vol. 1* (Eds.: B. Cornils, W. A. Hermann), Wiley-VCH, Weinheim, **1996**, p. 206.
- [56] G. J. Hutchings, J. M. Thomas, D. J. Willock, *Top. Catal.* **2003**, *25*, 1.
- [57] M. D. Jones, R. Raja, J. M. Thomas, B. F. G. Johnson, D. W. Lewis, J. Rouzaud, K. D. M. Harris, *Angew. Chem.* **2003**, *115*, 4462; *Angew. Chem. Int. Ed.* **2003**, *42*, 4326.
- [58] G. J. Hutchings, *Chem. Commun.* **1999**, 301.
- [59] B. M. L. Dooos, W. A. Geurts, P. A. Jacobs, *Catal. Lett.* **2004**, *97*, 125.
- [60] B. F. G. Johnson, S. A. Raynor, D. S. Shephard, T. Mashmeyer, J. M. Thomas, G. Sankar, S. Bromley, R. Oldroyd, L. Gladden, M. D. Mantle, *Chem. Commun.* **1999**, 1167.
- [61] S. A. Raynor, J. M. Thomas, R. Raja, B. F. G. Johnson, R. G. Bell, M. D. Mantle, *Chem. Commun.* **2000**, 1925.
- [62] *Fine Chemicals Through Heterogeneous Catalysis* (Eds.: R. A. Sheldon, H. van Bekkum), Wiley-VCH, Weinheim, **2001**.
- [63] N. Herron, *Inorg. Chem.* **1986**, *25*, 4714.
- [64] R. Raja, P. Ratnasamy, *Appl. Catal. A* **1997**, *158*, L7.
- [65] R. Raja, C. R. Jacob, P. Ratnasamy, *Catal. Today* **1999**, *49*, 171.
- [66] S. Ray, S. Vasudevan, *Inorg. Chem.* **2003**, *42*, 1711.
- [67] A. Zsigmond, F. Notheisz, G. Csornyik, J. E. Backvall, *Top. Catal.* **2002**, *19*, 119.
- [68] R. F. Parton, R. A. Uytterhoeven, P. A. Jacobs in *Heterogeneous Catalysis and Fine Chemicals* (Ed.: M. Guisnet), Elsevier, Amsterdam, **1995**, p. 395.
- [69] P. P. Knops-Gerrits, D. Devos, F. Thibault-Starzyk, P. A. Jacobs, *Nature* **1994**, *369*, 543.
- [70] a) D. E. de Vos, J. L. Meinershagen, T. Bein, *Angew. Chem.* **1996**, *108*, 2355; *Angew. Chem. Int. Ed. Engl.* **1996**, *35*, 2211; b) V. Trevisan, M. Signoretto, S. Colonna, V. Pironti, G. Strukul, *Angew. Chem.* **2004**, *116*, 4189; *Angew. Chem. Int. Ed.* **2004**, *43*, 4097.
- [71] D. J. Parrillo, C. Lee, R. J. Gorte, *Appl. Catal. A* **1994**, *110*, 67.
- [72] J. M. Thomas, G. N. Greaves, G. Sankar, P. A. Wright, J. S. Chen, A. J. Dent, L. Marchese, *Angew. Chem.* **1994**, *106*, 1922; *Angew. Chem. Int. Ed. Engl.* **1994**, *33*, 1871.
- [73] a) P. A. Barrett, R. H. Jones, J. M. Thomas, G. Sankar, I. J. Shannon, C. R. A. Catlow, *Chem. Commun.* **1996**, 2001; b) J. S. Chen, J. M. Thomas, *J. Chem. Soc. Chem. Commun.* **1994**, 603.
- [74] R. Raja, J. M. Thomas, *Chem. Commun.* **1998**, 1841.
- [75] J. M. Thomas, R. Raja, G. Sankar, R. G. Bell, *Nature* **1999**, *398*, 227.
- [76] B. Notari, *Adv. Catal.* **1996**, *41*, 253.
- [77] G. Panov, *Appl. Catal. A* **1995**, *123*, N14.
- [78] N. C. Gianneschi, P. A. Bertin, S. T. Nguyen, C. A. Mirkin, L. N. Zakharov, A. L. Rheingold, *J. Am. Chem. Soc.* **2003**, *125*, 10508.
- [79] R. Raja, G. Sankar, J. M. Thomas, *J. Am. Chem. Soc.* **2001**, *123*, 8153.
- [80] W. Buijs, R. Raja, J. M. Thomas, H. Wolters, *Catal. Lett.* **2003**, *91*, 253.
- [81] S. Feast, M. Rafiq, H. Siddiqui, R. P. K. Wells, D. J. Willock, F. King, C. H. Rochester, D. Bethell, P. C. B. Page, G. J. Hutchings, *J. Catal.* **1997**, *167*, 533.
- [82] C. Langham, P. Piaggio, D. Bethell, D. F. Lee, P. McMorn, P. C. B. Page, D. J. Willock, C. Sly, F. E. Hancock, F. King, G. J. Hutchings, *Chem. Commun.* **1998**, 1601.
- [83] W. O. Haag, R. M. Lago, P. B. Weisz, *Nature* **1984**, *309*, 589.
- [84] P. A. Wright, J. M. Thomas, A. K. Cheetham, A. K. Nowak, *Nature* **1985**, *318*, 611.
- [85] E. G. Derouane, D. J. van der Veken, *Appl. Catal.* **1988**, *45*, L15.
- [86] J. M. Thomas, *Angew. Chem.* **1994**, *106*, 963; *Angew. Chem. Int. Ed. Engl.* **1994**, *33*, 913.
- [87] R. A. van Santen, *Catal. Tech.* **1998**, *2*, 161.
- [88] R. Raja, P. Ratnasamy, *J. Mol. Cat. A* **1995**, *100*, 93.
- [89] S. O. Lee, G. Sankar, S. J. Kitchin, M. Dugal, J. M. Thomas, K. D. M. Harris, *Catal. Lett.* **2001**, *73*, 91.
- [90] S. O. Lee, S. J. Kitchin, K. D. M. Harris, G. Sankar, M. Dugal, J. M. Thomas, *J. Phys. Chem. B* **2002**, *106*, 1322.
- [91] *Introduction to Zeolite Science and Practice* (Eds.: H. van Bekkum, E. M. Flanigan, J. C. Jansen), Elsevier, Amsterdam, **1991**, and references therein.
- [92] A. K. Cheetham, G. Ferey, T. Loiseau, *Angew. Chem.* **1999**, *111*, 3466; *Angew. Chem. Int. Ed.* **1999**, *38*, 3269.
- [93] J. M. Thomas, G. A. Somorjai, *Top. Catal.* **1999**, *8*, U1.
- [94] a) J. M. Thomas, G. N. Greaves, *Science* **1994**, *265*, 1675; b) J. M. Thomas, *Chem. Eur. J.* **1997**, *3*, 1557.
- [95] a) R. Raja, P. Ratnasamy, *Stud. Surf. Sci. Catal.* **1996**, *101*, 181; b) see also M. Eswaramoorthy, S. Neeraj, C. N. R. Rao, *Chem. Commun.* **1998**, 615.
- [96] R. Raja, P. Ratnasamy, *Stud. Surf. Sci. Catal.* **1997**, *105*, 1037.
- [97] R. Raja, P. Ratnasamy, *J. Catal.* **1997**, *170*, 244.
- [98] J. M. Thomas, R. Raja, *Chem. Rec.* **2001**, *1*, 448.
- [99] N. Herron, C. A. Tolman, *J. Am. Chem. Soc.* **1987**, *109*, 2837.
- [100] J. M. Thomas, R. Raja, *Chem. Commun.* **2001**, 675.
- [101] R. Raja, G. Sankar, J. M. Thomas, *Angew. Chem.* **2000**, *112*, 2403; *Angew. Chem. Int. Ed.* **2000**, *39*, 2313.
- [102] J. M. Thomas, R. Raja, G. Sankar, R. G. Bell, D. W. Lewis, *Pure Appl. Chem.* **2001**, *73*, 1087.
- [103] J. M. Thomas, R. Raja, G. Sankar, B. F. G. Johnson, D. W. Lewis, *Chem. Eur. J.* **2001**, *7*, 2973.
- [104] K. Sato, M. Aoki, R. Noyori, *Science* **1998**, *281*, 1646.
- [105] S. O. Lee, R. Raja, K. D. M. Harris, J. M. Thomas, B. F. G. Johnson, G. Sankar, *Angew. Chem.* **2003**, *115*, 1558; *Angew. Chem. Int. Ed.* **2003**, *42*, 1520.
- [106] Biocatalytic conversion of starch yields *cis,cis* muconic acid. Our test experiments^[106b] for convenience employed the more readily (commercially) available *trans,trans* variant. a) K. M. Draths, J. W. Frost, *J. Am. Chem. Soc.* **1994**, *116*, 399; b) J. M. Thomas, R. Raja, B. F. G. Johnson, T. J. O'Connell, G. Sankar, T. Khimyak, *Chem. Commun.* **2003**, 1126; See also “Editor's Choice”, *Science*, **2003**, *300*, 867.

- [107] L. J. Burcham, L. E. Briand, I. E. Wachs, *Langmuir* **2001**, *17*, 6164.
- [108] R. Noyori, M. Aoki, K. Sato, *Chem. Commun.* **2003**, 1977.
- [109] I. J. Shannnon, T. Maschmeyer, R. D. Oldroyd, G. Sankar, J. M. Thomas, H. Pernot, J. P. Balikdjian, M. Che, *J. Chem. Soc. Faraday Trans.* **1998**, *94*, 1495.
- [110] R. Murugavel, H. W. Roesky, *Angew. Chem.* **1997**, *109*, 491; *Angew. Chem. Int. Ed. Engl.* **1997**, *36*, 477.
- [111] M. Guidotti, N. Ravasio, R. Psaro, E. Gianotti, L. Marchese, S. Coluccia, *Green Chem.* **2003**, *5*, 421.
- [112] N. Ravasio, F. Zaccheria, M. Guidotti, R. Psaro, *Top. Catal.* **2004**, *27*, 157.
- [113] D. H. Olson, W. M. Meier, *Atlas of Zeolite Structures*, Elsevier, Amsterdam, **2003**.
- [114] a) P. Ratnasamy, D. Srinivas, H. Knözinger, *Adv. Catal.* **2004**, *48*, 1; b) J. M. Thomas, K. I. Zamaraev, *Angew. Chem.* **1994**, *106*, 316; *Angew. Chem. Int. Ed. Engl.* **1994**, *33*, 308.
- [115] It is recognized that, so far as TS-1 is concerned, this catalyst works best in selective oxidation when H₂O₂ is the oxidant. On the other hand, the Ti/SiO₂ catalysts for epoxidation studied by us, Ravasio et al., and others functions best with an alkylhydroperoxide as oxidant. a) J. M. Thomas, C. R. A. Catlow, G. Sankar, *Chem. Commun.* **2002**, 2921; b) C. R. A. Catlow, S. A. French, A. A. Sokol, J. M. Thomas, *Phil. Trans. Roy. Soc. A* **2005**, *363*, 765.
- [116] M. Fujiwara, H. Wessel, P. Hyung-Suh, H. W. Roesky, *Tetrahedron* **2002**, *58*, 239.
- [117] J. M. Thomas, G. Sankar, M. C. Klunduk, M. P. Attfield, T. Maschmeyer, B. F. G. Johnson, R. G. Bell, *J. Phys. Chem. B* **1999**, *103*, 8809.
- [118] R. Raja, J. M. Thomas, *Proceedings of the 13th International Congress on Catalysis*, Paris, **2004**, P5, 103.
- [119] a) R. Raja, J. M. Thomas, G. Sankar, *Chem. Commun.* **1999**, 525; b) see also G. Strukul, *Angew. Chem.* **1998**, *110*, 1256; *Angew. Chem. Int. Ed.* **1998**, *37*, 1198.
- [120] H. Oevering, R. Raja, H. Wolters, W. Buijs, J. M. Thomas, *Process for the production of an oxime from a ketone or aldehyde*, European Patent Filing No. EP 03078997, 2003.
- [121] G. G. Hlatky, *Chem. Rev.* **2000**, *100*, 1347.
- [122] *Chiral Catalyst Immobilization and Recycling* (Eds.: D. E. de Vos, I. F. J. Vankelecom, P. A. Jacobs), Wiley-VCH, Weinheim, **2000**.
- [123] P. McMorn, G. J. Hutchings, *Chem. Soc. Rev.* **2004**, *33*, 108.
- [124] C. Bianchini, P. Barbaro, V. Dal Santo, R. Gobetto, A. Meli, W. Oberhauser, R. Psaro, F. Vizza, *Adv. Synth. Catal.* **2001**, *343*, 41, and references therein.
- [125] a) M. J. Sabater, A. Corma, A. Domenech, V. Fornes, H. Garcia, *Chem. Commun.* **1997**, 1285; b) A. Corma, H. Garcia, *Chem. Rev.* **2002**, *102*, 3837; c) A. Corma, H. Garcia, *Chem. Rev.* **2003**, *103*, 4307.
- [126] S. Xiang, Y. L. Zhang, Q. Xin, C. Li, *Angew. Chem.* **2002**, *114*, 849; *Angew. Chem. Int. Ed.* **2002**, *41*, 821.
- [127] a) B. M. L. Dioso, W. A. Geurts, P. A. Jacobs, *Catal. Lett.* **2004**, *97*, 125; b) C. Simons, U. Hanefeld, I. W. C. E. Arends, A. J. Minnaard, T. Maschmeyer, R. A. Sheldon, *Chem. Commun.* **2004**, 2830; c) M. van den Berg, A. J. Minnaard, E. P. Schudde, J. van Esch, A. H. M. de Vries, J. G. de Vries, B. L. Feringa, *J. Am. Chem. Soc.* **2000**, *122*, 11539.
- [128] a) R. Raja, J. M. Thomas, M. D. Jones, B. F. G. Johnson, *Process for reducing ketocarboxylic esters*, German Patent Filing No. DE 10305946, **2003**; b) R. Raja, J. M. Thomas, M. D. Jones, B. F. G. Johnson, *Process for preparing enantiomerically enriched α - β -hydroxycarboxylic esters*, German Patent Filing No. DE 10305943, **2003**.
- [129] R. Raja, J. M. Thomas, M. D. Jones, B. F. G. Johnson, *Process for asymmetrically hydrogenating ketocarboxylic esters*, US Patent Filing No. US 10326915, **2004**.
- [130] R. Raja, J. M. Thomas, M. D. Jones, B. F. G. Johnson, *Verfahren zur asymmetrischen Hydrierung von Ketocarbonsäureestern*, European Patent Filing No. EP 4001904, **2004**.
- [131] J. M. Thomas, *Sci. Am.* **1992**, *266*, 112.
- [132] a) W. Hölderich, *New Frontiers in Catalysis*, Elsevier, Amsterdam, **1992**, p. 145; b) A. Corma, *Chem. Rev.* **1997**, *97*, 2373; c) K. Hedden, J. Weitkamp, *Chem. Ing. Tech.* **1983**, *55*, 907; d) P. B. Weisz, *Pure Appl. Chem.* **1980**, *52*, 99.
- [133] R. A. van Santen, P. W. N. M. van Leeuwen, J. A. Moulijn, B. A. Avenill, *Catalysis: An Integrated Approach*, 2nd ed., Netherlands Institute of Catalysis Research, Eindhoven, **2000**.
- [134] J. M. Thomas, W. J. Thomas, *Heterogeneous Catalysis: Principles and Practice*, Wiley-VCH, Weinheim, **1997**, Chap. 8.
- [135] I. Chorkendorff, J. W. Niemantsverdriet, *Concepts in Modern Catalysis and Kinetics*, Wiley-VCH, **2003**, p. 365.
- [136] C. S. John, D. M. Clark, I. E. Maxwell in *Perspectives in Catalysis* (Eds.: J. M. Thomas, K. I. Zamaraev), Blackwell, Oxford, **1992**, p. 387.
- [137] Smith et al.^[138] showed that nitration of halogenobenzene using the H⁺ form of zeolite beta (Si:Al ratio 25:1) as a catalyst and a combination of liquid N₂O₄ and gaseous O₂ as the nitrating agents lead to high yields and significant *para* selectivity (e.g. 85:15 *para:ortho*).
- [138] K. Smith, S. Almeer, S. J. Black, *Chem. Commun.* **2000**, 1571.
- [139] M. Nowotny, T. Maschmeyer, B. F. G. Johnson, P. Lahuerta, J. M. Thomas, J. E. Davies, *Angew. Chem.* **2001**, *113*, 981; *Angew. Chem. Int. Ed.* **2001**, *40*, 955.
- [140] C. Copéret, F. Lefebvre, J. M. Basset in *Handbook of Metathesis, Vol. 1* (Ed.: R. H. Grubbs), Wiley-VCH, Weinheim, **2003**, p. 190.
- [141] L. Lefort, M. Chabanas, O. Maury, D. Meunier, C. Copéret, J. Thivolle-Cazat, J. M. Basset, *J. Organomet. Chem.* **2000**, *594*, 96.
- [142] M. W. McKittrick, C. W. Jones, *Chem. Mater.* **2003**, *15*, 1132.
- [143] S. Bordiga, G. Ricchiardi, G. Spoto, D. Scarano, L. Carnelli, A. Zecchina, C. O. Areán, *J. Chem. Soc. Faraday Trans.* **1993**, *89*, 1843.
- [144] C. K. Chiang, C. R. Fisher, Y. W. Park, A. J. Heeger, H. Shirakawa, E. J. Louis, S. C. Gau, A. G. MacDiarmid, *Phys. Rev. Lett.* **1977**, *39*, 1098.
- [145] K. Yamaguchi, K. Mori, T. Mizugaki, K. Ebitani, K. Kaneda, *J. Am. Chem. Soc.* **2000**, *122*, 7144.
- [146] F. T. Edelmann, S. Gießmann, A. Fischer, *J. Organomet. Chem.* **2001**, *620*, 80.
- [147] S. T. Bromley, G. Sankar, C. R. A. Catlow, T. Maschmeyer, B. F. G. Johnson, J. M. Thomas, *Chem. Phys. Lett.* **2001**, *340*, 524.
- [148] J. M. Thomas, R. Raja, *Proc. Natl. Acad. Sci.* **2005**, in press.

Communications



Molecules with many spin-crossover sites could be used as multistep molecular switches. The CN-bridged molecular square $[\text{Fe}^{\text{II}}_4(\mu\text{-CN})_4(\text{bpy})_4(\text{tpa})_4](\text{PF}_6)_4$ (bpy = 2,2'-bipyridine; tpa = tris(2-pyridylmethyl)amine), a Prussian blue analogue, undergoes thermally induced, two-step spin conversion. For more information, see the Communication by H. Oshio and co-workers on the following pages.

DOI: 10.1002/anie.200502216

Two-Step Spin Conversion in a Cyanide-Bridged Ferrous Square**

Masayuki Nihei, Mayumi Ui, Mizuho Yokota,
Lingqin Han, Atsushi Maeda, Hideo Kishida,
Hiroshi Okamoto, and Hiroki Oshio*

An important route to the development of switches for advanced molecular devices involves changes in magnetic properties at the molecular level.^[1] Spin crossover in transition-metal complexes, in which spin-state conversions occur as a result of heat, pressure, or light irradiation, is a key phenomenon for designing molecular switches.^[2] Because cyanide-bridged complexes are relatively easy to synthesize and have rich magnetic properties, they have become the focus of this area of research. Prussian blue, which is a ferromagnet with a Curie temperature (T_C) of 5.6 K,^[3] and some heterometal analogues that are high- T_C magnets with an ordering temperature up to 372 K are examples of well-known cyanide-bridged metal complexes.^[4] Metal ions in cyanometalates typically adopt a low-spin configuration. However, introduction of ligands with weak ligand-field strengths and combinations of heterometal ions afford interesting magnetic properties such as spin crossover,^[5] photoinduced magnetism,^[6] and superparamagnetism.^[7] Furthermore, molecules with more than one spin-crossover site can be used as multistep molecular switches. Recently, some thermally induced, two-step spin-crossover complexes were reported.^[8] However, the number of such systems is still small.^[9] We have studied cyanide-bridged molecular squares, $[\text{Fe}_2\text{M}_2(\mu\text{-CN})_4(\text{bpy})_8]^{n+}$ (M = late first-row transition-metal ion; bpy = 2,2'-bipyridine), in which cyanide ions bridge four metal ions to form the macrocyclic tetranuclear core.^[10] We found that by replacing bpy with tris(2-pyridylmethyl)amine (tpa), the ligand-field strength on the Fe^{II} centers is weakened and the resulting ferrous square, $[\text{Fe}^{\text{II}}_4(\mu\text{-CN})_4(\text{bpy})_4(\text{tpa})_2](\text{PF}_6)_4$ (**1**-(PF_6)₄), showed two-step spin conversion.

The reaction of $[\text{Fe}(\text{CN})_2(\text{bpy})_2] \cdot 3\text{H}_2\text{O}$ ^[11] with $\text{FeCl}_2 \cdot 4\text{H}_2\text{O}$, tpa ,^[12] and NH_4PF_6 in methanol afforded the tetranuclear complex **1**(PF_6)₄.^[13] X-ray crystal structure analyses were performed at 100, 200, and 300 K, and the molecular structure of **1**⁴⁺ at 200 K is shown in Figure 1.

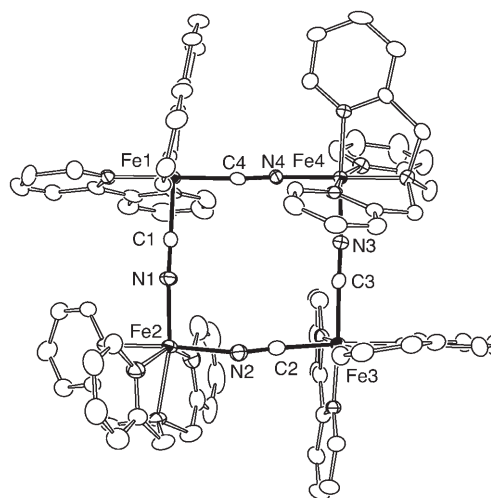


Figure 1. ORTEP diagram of **1**⁴⁺ at 200 K. Average coordination bond lengths [Å] about Fe^{II} ions at 100 K: Fe1 1.958, Fe2 1.976, Fe3 1.958, Fe4 1.963; at 200 K: Fe1 1.954, Fe2 2.154, Fe3 1.955, Fe4 1.965; and at 300 K: Fe1 1.954, Fe2 2.165, Fe3 1.959, Fe4 1.968.

The tetranuclear macrocycle **1**⁴⁺ is composed of four cyanide-bridged Fe^{II} ions, and the overall geometry is almost square. In the square, two $\{\text{Fe}(\text{bpy})_2\}^{2+}$ centers and two $\{\text{Fe}(\text{tpa})\}^{2+}$ centers are alternately bridged by four CN^- groups with the carbon atoms coordinated to the Fe^{II} ions in $\{\text{Fe}(\text{bpy})_2\}^{2+}$. The Fe^{II} ions have octahedral coordination geometry, and four of the coordination sites are occupied by nitrogen atoms from one tpa or two bpy ligands. The two remaining *cis* positions are coordinated by either carbon or nitrogen atoms from the cyanide groups. The carbon and nitrogen atoms of the cyanide ligands act as π acceptors and σ donors, respectively, and because the cyanide carbon atom has a stronger ligand-field strength,^[14] the $\text{Fe}^{\text{II}}\text{-C}(\text{cyanide})$ bond distances become shorter than the $\text{Fe}^{\text{II}}\text{-N}(\text{cyanide})$ distances. The average $\text{Fe}-\text{C}(\text{cyanide})$ bond length in the $\{\text{Fe}(\text{bpy})_2\}^{2+}$ units is 1.916 Å, and the average $\text{Fe}-\text{N}(\text{cyanide})$ bond length in the $\{\text{Fe}(\text{tpa})\}^{2+}$ units is 1.950 Å. Because the coordination bond lengths about Fe^{II} ions differ between the low-spin (LS) and high-spin (HS) states ($\Delta d = 0.2\text{--}0.3$ Å), the average bond lengths are related to the spin state of the Fe^{II} ions. At 100 K, the average coordination bond lengths involving the Fe^{II} ions are between 1.958 and 1.976 Å in both $\{\text{Fe}(\text{bpy})_2\}^{2+}$ and $\{\text{Fe}(\text{tpa})\}^{2+}$, and these values are characteristic of LS Fe^{II} ions. At 200 and 300 K, three of the Fe^{II} centers (Fe1, Fe3, and Fe4) stay in the LS state with average Fe^{II} bond lengths the same as the values at 100 K. One of the Fe^{II} ions (Fe2) in the $\{\text{Fe}(\text{tpa})\}^{2+}$ moieties forms longer bonds to the ligands ($d_{\text{Fe2-N}} = 2.154\text{--}2.165$ Å), characteristic of a HS Fe^{II} ion.

Magnetic susceptibility measurements for **1**-(PF_6)₄ were carried out in the temperature range of 5–400 K, and a $\chi_m T$

[*] Dr. M. Nihei, M. Ui, M. Yokota, L. Han, Prof. H. Oshio
Graduate School of Pure and Applied Sciences
University of Tsukuba
Tennodai 1-1-1, Tsukuba, Ibaraki 305-8571 (Japan)
Fax: (+81) 29-853-4238
E-mail: oshio@chem.tsukuba.ac.jp
Dr. A. Maeda, Dr. H. Kishida, Prof. H. Okamoto
Department of Advanced Materials Science
Graduate School of Frontier Science
The University of Tokyo
Kashiwa, Chiba 277-8651 (Japan)

[**] This work was supported by a Grant-in-Aid for Scientific Research from the Ministry of Education, Science, Sports, and Culture, Japan, and by the COE and TARA projects at the University of Tsukuba.

Supporting information for this article is available on the WWW under <http://www.angewandte.org> or from the author.

versus temperature plot is shown in Figure 2. X-ray crystal structure analyses suggest that four Fe^{II} ions in the square are in a LS state below 100 K. The $\chi_{\text{m}}T$ values below 100 K were constant ($0.3 \text{ emu mol}^{-1} \text{ K}$), and the nonzero $\chi_{\text{m}}T$ values are

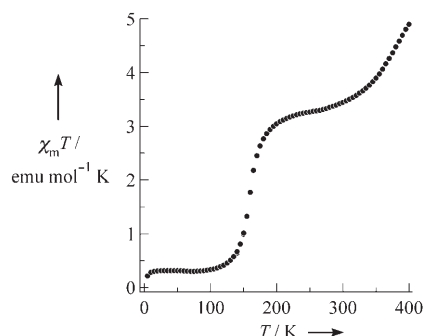


Figure 2. $\chi_{\text{m}}T$ versus T plot for $1\text{-(PF}_6)_4$.

due to a paramagnetic impurity corresponding to 2.5 % of the HS Fe^{II} ($S=2$) species. As the temperature was raised to 200 K, the $\chi_{\text{m}}T$ values increased and reached a plateau value at $3.2 \text{ emu mol}^{-1} \text{ K}$, which is close to the value ($3.0 \text{ emu mol}^{-1} \text{ K}$) expected for a free HS Fe^{II} ion. The plateau has a width of approximately 100 K and is centered at about 240 K. Upon increasing the temperature, another spin conversion occurred. However, the $\chi_{\text{m}}T$ values did not reach the plateau value ($6.0 \text{ emu mol}^{-1} \text{ K}$) expected for two uncorrelated HS Fe^{II} ions, even at 400 K. The $\chi_{\text{m}}T$ value at 400 K is $4.9 \text{ emu mol}^{-1} \text{ K}$, which corresponds to 57 % of the Fe_4 ion being in the HS state. The magnetic susceptibility measurements clearly show the occurrence of a two-step spin conversion in $1\text{-(PF}_6)_4$. Notably, no hysteresis was observed in temperature-dependence measurements of the $\chi_{\text{m}}T$ values.

Reflectance spectra for a single crystal of $1\text{-(PF}_6)_4$ were measured on the (001) plane at 100 and 300 K with unpolarized light (Figure 3). The spectrum at 100 K consists of one sharp (2.13 eV) and two broad (2.3 and 2.6 eV) bands, and a new peak at 1.47 eV appeared with a decrease in the broad bands at 300 K. Absorption data for component molecules were used to assign the reflectance spectra. The LS Fe^{II} ion in $[\text{Fe}(\text{CN})_2(\text{bpy})_2]$ showed a d–d band at 570 nm ($=2.17 \text{ eV}$),^[15] whereas d–d bands for the LS and HS Fe^{II} ions in $[\text{Fe}(\text{tpa})(\text{L})_2]^{2+}$ ($\text{L} = \text{CH}_3\text{CN}, \text{CH}_3\text{OH}$) were observed at 516 ($=2.40 \text{ eV}$) and 914 nm ($=1.34 \text{ eV}$), respectively.^[16] MLCT bands for the LS Fe^{II} species appeared in the high-energy region above 3.3 eV.^[15,16] The sharp (2.13 eV) and broad (2.3 and 2.6 eV) bands in the reflectance spectrum at 100 K were, therefore, assigned to d–d transitions for the LS iron(II) ions in $[\text{Fe}(\text{bpy})_2]^{2+}$ and $[\text{Fe}(\text{tpa})]^{2+}$ moieties, respectively, and the new band (1.47 eV $=838 \text{ nm}$) at 300 K is due to d–d transitions for HS Fe^{II} species in the $[\text{Fe}(\text{tpa})]^{2+}$ moiety. The observed changes in the reflectance spectra are in accord with the magnetic and Mössbauer data.

Selected ^{57}Fe Mössbauer spectra of $1\text{-(PF}_6)_4$ are shown in Figure 4. The Mössbauer spectrum at 50 K is dominated by two LS doublets (four lines in blue), whose Mössbauer parameters (LS1: $\delta=0.21$ and $\Delta E_{\text{Q}}=0.66 \text{ mm s}^{-1}$; LS2: $\delta=0.43$ and $\Delta E_{\text{Q}}=0.43 \text{ mm s}^{-1}$) are characteristic of LS Fe^{II}

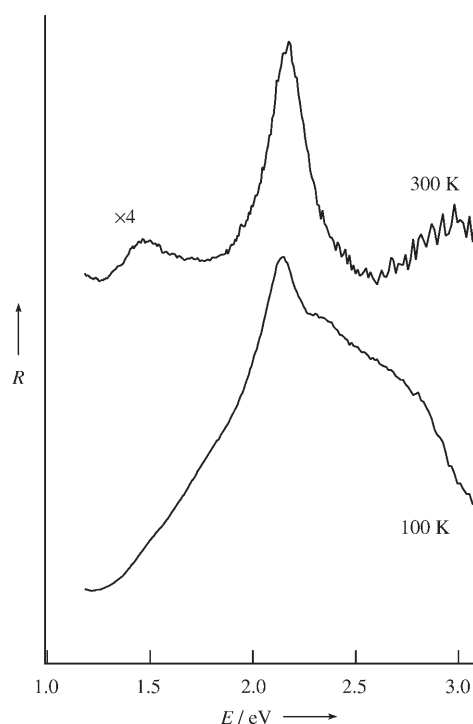


Figure 3. Reflectance spectra of $1\text{-(PF}_6)_4$ at 100 and 300 K. R = reflectivity, E = photon energy.

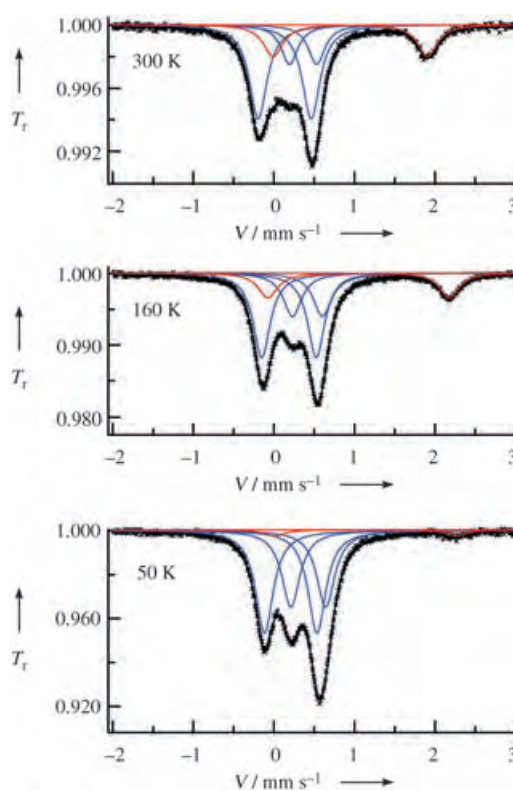


Figure 4. Selected ^{57}Fe Mössbauer spectra of $1\text{-(PF}_6)_4$. Velocity (V) is relative to iron metal. Low-spin pairs in blue and high-spin pair in red. T_r = relative transmission.

species. An additional small doublet (two lines in red, $\delta = 1.13$ and $\Delta E_Q = 2.26 \text{ mms}^{-1}$) corresponds to a HS Fe^{2+} species, which is a paramagnetic impurity. The bpy ligand is a strong π acid, and the cyanide carbon atoms act as π acceptors. Furthermore, the LS Fe^{II} ions (Fe1 and Fe3) in the $\{\text{Fe}(\text{CN})_2(\text{bpy})_2\}$ centers have smaller isomer shifts than the Fe2 and Fe4 ions in $\{\text{Fe}(\text{NC})_2(\text{tpa})\}$ centers. Therefore, the LS1 and LS2 doublets were assigned to the Fe1/Fe3 and Fe2/Fe4 pairs, respectively. The peak-area ratio of the LS1, LS2, and HS doublets is 0.52:0.44:0.04 at 50 K, even though X-ray crystal structure analysis at 100 K showed that all Fe^{II} ions are in LS states. The deviation of the area ratio for LS1 and LS2 is caused by the different Lamb–Mössbauer factors for each LS species.

As the temperature was increased, the LS2 doublet lost intensity, and the HS doublet gained intensity. The ratios of the peak areas for LS1, LS2, and HS doublets became 0.53:0.29:0.18 and 0.56:0.22:0.21 at 160 and 300 K, respectively, meaning that either Fe2 or Fe4 is in a HS state at 300 K. The Mössbauer measurements and X-ray crystallographic analyses suggest the occurrence of a complete spin conversion on the Fe2 ion at 300 K. In summary, $\mathbf{1}(\text{PF}_6)_4$ exhibits a two-step spin conversion with the first step occurring on the Fe2 ion at $T_{\text{sc}} = 160 \text{ K}$ (T_{sc} = spin-conversion temperature) and the second step starting to occur on Fe4 at 300 K. Light-induced excited-spin-state trapping (LIESST) experiments are currently underway to explore the possibility of two-step spin conversion by irradiation.

Experimental Section

All procedures were carried out under a nitrogen atmosphere. $\text{FeCl}_2 \cdot 4\text{H}_2\text{O}$ (36 mg, 0.18 mmol) in methanol (6.5 mL) was added to a solution of $[\text{Fe}(\text{CN})_2(\text{bpy})_2] \cdot 3\text{H}_2\text{O}$ (86 mg, 0.18 mmol) in methanol (13.5 mL), followed by the addition of tpa (52 mg, 0.18 mmol). A methanolic solution (20 mL) of NH_4PF_6 (118 mg, 0.72 mmol) was added to the dark red solution by diffusion in an H tube to afford dark-red tablets of $\mathbf{1}(\text{PF}_6)_4$. Elemental analysis (%) calcd for $\text{C}_{80}\text{H}_{68}\text{N}_{20}\text{F}_{24}\text{Fe}_4\text{P}_4$: C 45.48, H 3.24, N 13.26; found: C 45.36, H 3.08, N 13.20.

Received: June 24, 2005

Keywords: cyanides · iron · magnetic properties · Mössbauer spectroscopy · spin crossover

- 701; h) O. Sato, T. Iyoda, A. Fujishima, K. Hashimoto, *Science* **1996**, 271, 49; i) W. R. Entley, G. S. Girolami, *Inorg. Chem.* **1994**, 33, 5165; j) J. Larionova, R. Clérac, J. Sanchiz, O. Kahn, S. Golhen, L. Ouahab, *J. Am. Chem. Soc.* **1998**, 120, 13088.
- [5] a) C. P. Berlinguette, A. Dragulescu-Andrasi, A. Sieber, J. R. Galan-Mascarós, H.-U. Güdel, C. Achim, K. R. Dunbar, *J. Am. Chem. Soc.* **2004**, 126, 6222; b) R. Herchel, R. Boča, M. Gembicky, J. Kožíšek, F. Renz, *Inorg. Chem.* **2004**, 43, 4103.
- [6] J. M. Herrera, V. Marvaud, M. Verdager, J. Marrot, M. Kalisz, C. Mathonière, *Angew. Chem.* **2004**, 116, 5584; *Angew. Chem. Int. Ed.* **2004**, 43, 5468.
- [7] a) J. J. Sokol, A. G. Hee, J. R. Long, *J. Am. Chem. Soc.* **2002**, 124, 7656; b) C. P. Berlinguette, D. Vaughn, C. Cañada-Vilalta, J. R. Galán-Mascarós, K. R. Dunbar, *Angew. Chem.* **2003**, 115, 1561; *Angew. Chem. Int. Ed.* **2003**, 42, 1523; c) S. Wang, J.-L. Zuo, H.-C. Zhou, H. J. Choi, Y. Ke, J. R. Long, X.-Z. You, *Angew. Chem.* **2004**, 116, 6066; *Angew. Chem. Int. Ed.* **2004**, 43, 5940; d) M. Ferbinteanu, H. Miyasaka, W. Wernsdorfer, K. Nakata, K. Sugiura, M. Yamashita, C. Coulon, R. Clerac, *J. Am. Chem. Soc.* **2005**, 127, 3090.
- [8] a) V. Ksenofontov, A. B. Gaspar, V. Niel, S. Reiman, J. A. Real, P. Gülich, *Chem. Eur. J.* **2004**, 10, 1291; b) J. A. Real, H. Bolvin, A. Bousseksou, A. Dworkin, O. Kahn, F. Varret, J. Zarembowitch, *J. Am. Chem. Soc.* **1992**, 114, 4650; c) A. J. Simaan, M.-L. Boillot, E. Livière, A. Boussac, J.-J. Girerd, *Angew. Chem.* **2000**, 112, 202; *Angew. Chem. Int. Ed.* **2000**, 39, 196.
- [9] a) E. Breuning, M. Ruben, J.-M. Lehn, F. Renz, Y. Garcia, V. Ksenofontov, P. Gülich, E. Wegelius, K. Rissanen, *Angew. Chem.* **2000**, 112, 2563; *Angew. Chem. Int. Ed.* **2000**, 39, 2504; b) S. G. Telfer, B. Bocquet, A. F. Williams, *Inorg. Chem.* **2001**, 40, 4818; c) J.-F. Letard, J. A. Real, N. Moliner, A. B. Gaspar, L. Capes, O. Cadot, O. Kahn, *J. Am. Chem. Soc.* **1999**, 121, 10630.
- [10] a) H. Oshio, H. Onodera, O. Tamada, H. Mizutani, T. Hikichi, T. Ito, *Chem. Eur. J.* **2000**, 6, 2523; b) H. Oshio, M. Yamamoto, T. Ito, *Inorg. Chem.* **2002**, 41, 5817; c) H. Oshio, H. Onodera, T. Ito, *Chem. Eur. J.* **2003**, 9, 3946; d) H. Oshio, T. Ito, *Inorg. Chem.* **2004**, 43, 178.
- [11] A. A. Schilt, *Inorg. Synth.* **1970**, Vol. XII, 249.
- [12] K. D. Karlin, J. C. Hayes, S. Juen, J. P. Hutchinson, J. Zubieta, *Inorg. Chem.* **1982**, 21, 4106.
- [13] Crystal data for **1** at 100 K: $\text{C}_{80}\text{H}_{68}\text{N}_{20}\text{F}_{24}\text{Fe}_4\text{P}_4$, dark red tablet ($0.2 \times 0.2 \times 0.2 \text{ mm}^3$), $M_r = 2112.82$, $\lambda(\text{MoK}\alpha) = 0.71073 \text{ \AA}$, triclinic $P\bar{1}$, $a = 14.426(2)$, $b = 15.042(2)$, $c = 22.272(3) \text{ \AA}$, $\alpha = 77.270(3)^\circ$, $\beta = 83.486(3)^\circ$, $\gamma = 64.112(3)^\circ$, $V = 4240(1) \text{ \AA}^3$, $Z = 2$, $\rho_{\text{calcd}} = 1.655 \text{ Mg m}^{-3}$, 20179 reflections collected, 12124 independent reflections ($R_{\text{int}} = 0.0435$), final refinement with 1189 parameters converged with agreement factors $R1 = 0.0531$, $wR2 = 0.1279$ using 1189 reflections with $I > 2\sigma$. Crystal data at 200 K: triclinic $P\bar{1}$, $a = 14.470(2)$, $b = 15.165(2)$, $c = 22.536(3) \text{ \AA}$, $\alpha = 77.326(2)^\circ$, $\beta = 83.317(2)^\circ$, $\gamma = 63.709(2)^\circ$, $V = 4324.7(9) \text{ \AA}^3$, $Z = 2$, $\rho_{\text{calcd}} = 1.622 \text{ Mg m}^{-3}$, 20649 reflections collected, 12371 independent reflections ($R_{\text{int}} = 0.0479$), final $R1 = 0.0600$, $wR2 = 0.1445$ using 1189 reflections with $I > 2\sigma$. Crystal data at 300 K: triclinic $P\bar{1}$, $a = 14.561(3)$, $b = 15.297(3)$, $c = 22.661(4) \text{ \AA}$, $\alpha = 77.391(4)^\circ$, $\beta = 83.209(4)^\circ$, $\gamma = 63.602(4)^\circ$, $V = 4411(2) \text{ \AA}^3$, $Z = 2$, $\rho_{\text{calcd}} = 1.591 \text{ Mg m}^{-3}$, 20765 reflections collected, 12553 independent reflections ($R_{\text{int}} = 0.0588$), final $R1 = 0.0689$, $wR2 = 0.1612$ using 1189 reflections with $I > 2\sigma$. CCDC 274454 (**1** at 100 K), 274455 (**1** at 200 K), and 274456 (**1** at 300 K) contain the supplementary crystallographic data for this paper. These data can be obtained free of charge from the Cambridge Crystallographic Data Centre via www.ccdc.cam.ac.uk/data_request/cif.
- [14] H. Vahrenkamp, A. Geiß, G. N. Richardson, *J. Chem. Soc. Dalton Trans.* **1997**, 3643.
- [15] J. R. Winkler, N. Sutin, *Inorg. Chem.* **1987**, 26, 220.
- [16] A. Diebold, K. S. Hagen, *Inorg. Chem.* **1998**, 37, 215.

DOI: 10.1002/anie.200502185

A Three-Dimensional Metal–Organic Framework with an Unprecedented Octahedral Building Unit**

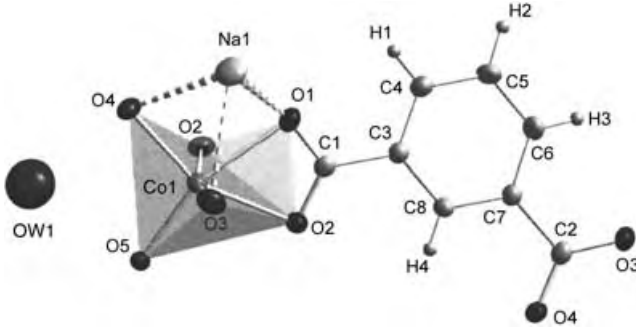
Carine Livage,* Nathalie Guillou, Julienne Chaigneau, Pierre Rabu, Marc Drillon, and Gérard Férey

Among the numerous works devoted to porous hybrid solids, those on structures built up from a chosen inorganic unit reticulated with rigid organic linkers are very topical. The major goal is to control the “design” of the architectures to obtain materials with required properties.^[1–5] Interesting architectures have been obtained with tetrameric ZnO₄ units,^[6] cuboid zinc silicate cores,^[7] and triangular oxo-centered building units with vanadium,^[8] zinc,^[4] and iron.^[9] Recently, a crystalline metal–organic framework (MOF), MIL-100, with a giant cell and a large sorption capacity (3100 m² g^{−1}) was constructed from this type of triangular unit containing chromium and trimesate ions.^[10]

Depending on their architecture, compounds based on polynuclear metallic units offer potential for catalysis, gas storage, or separation. In the search for inorganic “seeds” to grow original 3D networks, we describe here a new hexacobalt octahedral building block.^[11,12] This type of metal cage could also be useful for magnetic materials with potential applications as molecular magnets.^[13,14] The synthetic challenge in this area is to increase and control the degree of nuclearity of the inorganic “clusters” that are responsible for the physical properties. Oligomerization is induced by heating either in solution or in the solid state.^[15–17] The title compound, Na₃[Co₆O(OH)(C₈H₄O₄)₆]·H₂O (MIL-104), was synthesized by a classical solvothermal reaction. The hexamers are formed in situ by self-assembly and linked into an original three-dimensional network by the isophthalate dianions.

The structure of MIL-104 is generated by a cobalt atom and a carboxylate on general positions and a sodium ion, water molecule, and oxo-hydroxo oxygen on symmetry elements (Table 1). The metal is octahedrally coordinated to five oxygen atoms of four isophthalate ligands and a μ₃-O ion.

Table 1: Selected bond lengths [Å] and angles [°] as well as the atom-labeling scheme for Na₃[Co₆O(OH)(C₈H₄O₄)₆]·H₂O (MIL-104) with displacement ellipsoids drawn at the 50% probability level.^[a]



Co1–O5	1.9465(6)	Co1–O2	2.171(2)
Co1–O4	2.033(2)	Co1–O1	2.192(2)
Co1–O3 ^A	2.129(2)	Co1–O2 ^B	2.258(2)
Na1–O1	2.256(2)	Na1–O4	2.523(2)
Na1–O3 ^A	2.592(2)		
O5–Co1–O4	105.32(7)	O4–Co1–O1	95.79(6)
O5–Co1–O3 ^A	100.81(7)	O4–Co1–O3 ^A	86.83(7)
O5–Co1–O2	98.41(8)	O4–Co1–O2	155.28(7)
O5–Co1–O1	158.58(8)	O3 ^A –Co1–O2	95.51(7)
O5–Co1–O2 ^B	91.17(6)	O3 ^A –Co1–O1	83.63(6)
O2–Co1–O1	60.20(6)		

[a] Symmetry code: A: $-x+y-1, -x+1, z$; B: $x-y+1, x+1, -z$.

The geometry is highly distorted, with a narrow O–Co–O angle (60.20(6)°) *trans* to a large one (105.32(7)°), and a short O–O distance (2.188(2) Å) opposite to a long one (3.165(2) Å). This peculiar geometry is always encountered when a carboxylate group binds the metal center in a chelating fashion (Figure 1).^[18] The “bite” of the rigid group (ca. 2.1–2.2 Å) is too short for a regular octahedral symmetry. Six octahedra are associated to form a polynuclear “cluster”. This

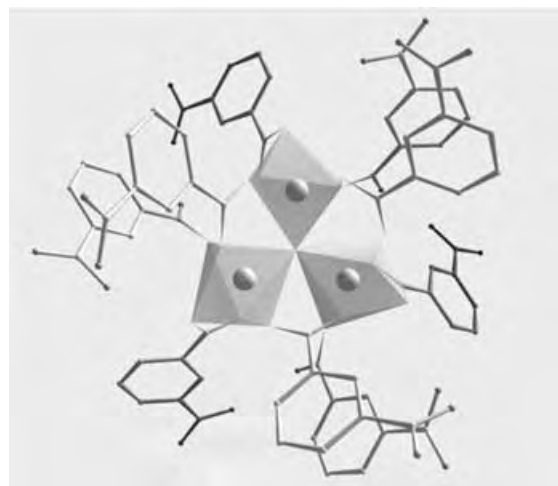


Figure 1. View of the octahedral triangular unit connected by nine isophthalate ions showing the cobalt environment. The 1,3-benzenedicarboxylate ligands adopt two modes of bonding, namely bridging and chelating. The cobalt octahedron presents an important distortion that is attributed to the chelating connection of the organic molecule.

[*] Dr. C. Livage, Dr. N. Guillou, J. Chaigneau, Prof. G. Férey
Institut Lavoisier, UMR-CNRS 8637
Université de Versailles Saint-Quentin-en-Yvelines
45 avenue des Etats-Unis, 78035 Versailles Cedex (France)
Fax: (+33) 1-3925-4358
E-mail: livage@chimie.uvsq.fr

Dr. P. Rabu, Dr. M. Drillon
Institut de physique et de Chimie des Matériaux de Strasbourg
UMR-CNRS 7504
23 rue du Loess, 67037 Strasbourg (France)

[**] The authors are indebted to Dr. Jérôme Marrot at the Institut Lavoisier for X-ray data collection.

Supporting information for this article is available on the WWW under <http://www.angewandte.org> or from the author.

hexameric core is located on an inversion threefold axis and may be easily viewed as the association of two trimers (Figure 2). Each triangle, on a threefold axis, is composed of octahedra sharing a central μ_3 -oxygen ($\text{Co}-\mu_3\text{-O}-\text{Co}$ $116.33(5)^\circ$). At variance to what is usually observed for oxo-centered trimers, the metal atoms are not coplanar with the central oxygen.^[8,9] The cobalt “cluster” constructed by the connection through the vertices (six $\mu_2\text{-O}$) of two trimers forms an unusual $\{\text{Co}_6(\mu_3\text{-O})_2(\mu_2\text{-O})_6(\mu_1\text{-O})_{18}\}$ super-octahedron (Figure 2).^[19,20] Bond valence calculations give a value of 1.5 for the $\mu_3\text{-O}$ atom.^[21] This value, as well as the neutrality of the compound, leads to the statistical half occupancy of the μ_3 site by oxo and hydroxo anions. To the best of our knowledge, this unusual hexanuclear unit has never been observed either in the solid state or in coordination chemistry. This structure can be described as a classical MOF organization, with each hexamer joined by twelve bridging isophthalate ions to six neighboring units, with each metal unit serving as the octahedral node of a



Figure 2. Schematic representation of the $\{\text{Co}_6(\mu_3\text{-O})_2(\mu_2\text{-O})_6(\mu_1\text{-O})_{18}\}$ unit showing its octahedral geometry.

cuboid net (Figure 3a). The connection between two “clusters” is ensured by two nearly parallel bridging isophthalates with weak π – π interactions. In this description, the sodium ions occupy small cavities left free by the hexamers’ packing. The alkali-metal cation has a distorted octahedral geometry formed by oxygen atoms of six carboxylate groups, with O–Na–O angles ranging from $68.02(2)^\circ$ to $132.8(1)^\circ$ and bond lengths ranging from $2.256(2)$ to $2.592(2)$ Å. Taking into account the sodium polyhedron, MIL-104 can also be considered as a 3D inorganic framework with sodium octahedra linking the hexameric units through face-sharing in a pseudo-cubic net (Figure 3b). In fact, each cobalt polyhedron is linked to a sodium ion to form a larger “super octahedron” around the hexamer. The topology here is the same as that found for ReO_3 , with $\{\text{Na}_6\text{Co}_6\text{O}_{26}\}$ units as giant octahedra (Figure 3c). Thus MIL-104 provides a new example of scale chemistry.^[22]

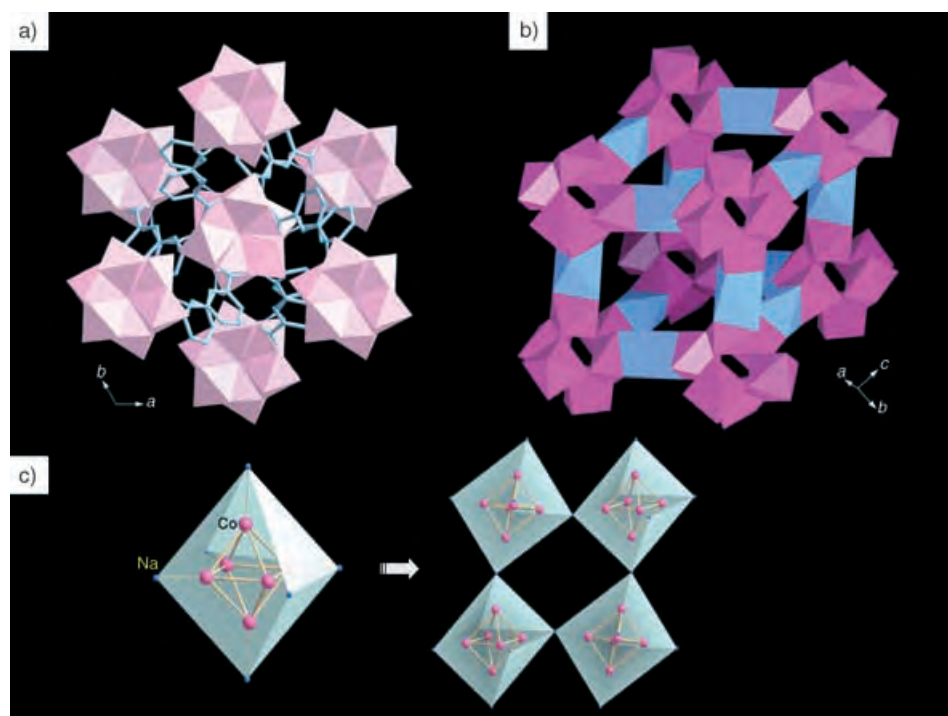


Figure 3. a) Projection of the structure showing one hexameric unit connecting six crystallographically equivalent “clusters” that lie at the corners of an octahedron. Each unit serves as a 6-connecting node of an infinite 3D network. b) View of the inorganic pseudo-cubic network including the sodium cation octahedra. c) Schematic representation of the $\{\text{Na}_6\text{Co}_6\text{O}_{26}\}$ “super octahedron” highlighting the relationship between the inorganic network and the ReO_3 structure.

The temperature variation of the magnetic susceptibility measured in a 500 Oe field is shown in Figure 4.^[23] Paramagnetic behavior is observed down to 50 K. A “plateau” is then observed in the χ versus T curve at $0.12 \text{ cm}^3 \text{ mol}^{-1}$ in the range 30–14 K, followed by an increase up to $1.98 \text{ cm}^3 \text{ mol}^{-1}$ at 1.8 K. The fit of the χ^{-1} versus T curve in the high temperature region gives a Weiss temperature, θ , of -118.5 K and a Curie constant of 2.92 K cm^3 per cobalt atom, which agrees well with that expected for high-spin Co^{II} in an octahedral site.^[24] The negative sign of θ and the decrease of χT , which tends to zero at 1.8 K, point to the existence of antiferromagnetic exchange interactions. Spin–orbit coupling most certainly also contrib-

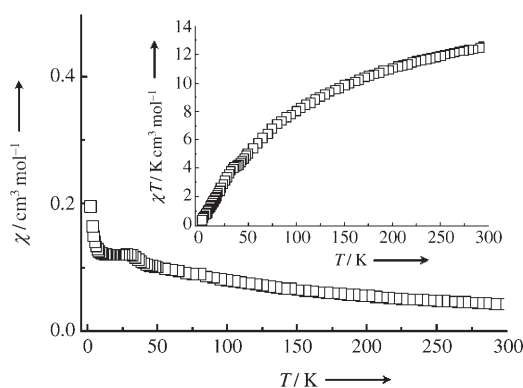


Figure 4. Temperature dependence of the magnetic susceptibility of compound MIL-104 recorded in a field of 550 Oe. The inset shows the corresponding variation of the χT product.

utes to this decay.^[24–26] The hexamers are interconnected by large isophthalate bridges and are quite well isolated. Thus, the magnetic behavior is interpreted as being due to antiferromagnetic intrahexamer coupling. Moreover, the presence of a “plateau” in the susceptibility and of a Curie-like tail at low temperature indicate the existence of a residual moment, which might be due to the stabilization of an uncompensated moment by a frustration effect in the triangular cobalt motifs.^[26]

In summary, a cobalt isophthalate constructed from a unique $\{\text{Co}_6\text{O}_{26}\}$ cage with octahedral geometry has been prepared. The novelty of the hexanuclear unit illustrates the influence of rigid organic partners upon metal oxide condensation. The great challenge in building-block chemistry is to establish reliable synthetic routes to stabilize desired inorganic motifs.^[9,27] Complex inorganic units frequently appear as isolated compounds, and the relationship between “clusters” and synthetic conditions is often unpredictable.^[28] For the formation of the title hexamer the crucial point seems to be the distortion of the trimer, which is characterized by an asymmetric linkage of the carboxylate groups: three bridging ones on one side and six nonbridging (intratrimer) ones on the opposite side (Figure 1). Therefore, no steric obstruction limits the condensation increment. On the contrary, with symmetrical triangles (three bridging groups on both side), the association of two trimers through vertices is topologically impossible. However, although it is understandable that chelating carboxylic groups help to induce the formation of the hexamer, the link between synthetic conditions and this type of coordination is far from being understood.^[18]

Experimental Section

Preparation of $\text{Na}_3[\text{Co}_6\text{O}(\text{OH})(\text{C}_8\text{H}_4\text{O}_4)_6]\cdot\text{H}_2\text{O}$ (MIL-104):^[29] The reactions were carried out in a Teflon-lined autoclave at 180 °C for three days under autogenous pressure. The reaction mixture contained $\text{CoSO}_4\cdot7\text{H}_2\text{O}$ (1.16×10^{-3} mol), isophthalic acid ($\text{HO}_2\text{C}(\text{C}_6\text{H}_4)\text{CO}_2\text{H}$; 1.73×10^{-3} mol), NaOH (3.46×10^{-3} mol), and H_2O /ethanol (25/75 v/v, 7.5 mL) in a ratio of 1:1.5:3:90. After the mixture was cooled (pH 6), the resulting violet crystals were washed with distilled water. IR (KBr pellet): $\tilde{\nu}=3580$ (w) and 3445 cm^{-1} (s) (oxygen–hydrogen stretch of the water molecules and hydroxy group); 1613 (s), 1559 (s), 1539 (s), 1485 (s), 1457 (s), and 1395 cm^{-1} (s) (symmetric and asymmetric stretching bands of the deprotonated carboxylic functions). Elemental analysis calcd (%) C 39.5, H 1.8, Co 24.3, Na 4.7; found: C 37.8, H 1.8, Co 22.5, Na 5.6. A single crystal was selected for structure determination by X-ray diffraction. Calculated density: 1.973 g cm^{-3} ; measured: $1.961(2)\text{ g cm}^{-3}$. The thermal behavior of $\text{Na}_3[\text{Co}_6\text{O}(\text{OH})(\text{C}_8\text{H}_4\text{O}_4)_6]\cdot\text{H}_2\text{O}$ was studied by thermogravimetric analysis under nitrogen. It decomposes through two major processes, namely the loss of water molecules and the combustion of the organic moiety. The first loss appears at around 80 °C with the loss of the free water molecules (theoretical loss: 1.2%; observed loss: 1.6%). The structure of MIL-104 is preserved upon dehydration, as proved by X-ray thermodiffraction in air, up to 250 °C, which shows only tiny variations of the peak intensities. It reabsorbs water molecules upon cooling. The second weight loss occurs between 450 and 550 °C and is characteristic of the combustion of the organic moiety (theoretical weight loss: 59.0%; observed loss: 58.5%).

A violet crystal ($1.08\times0.34\times0.30\text{ mm}^3$) was glued to a glass fiber. Intensity data were collected at room temperature with a Siemens SMART diffractometer equipped with a CCD two-dimensional

detector ($\lambda(\text{MoK}\alpha_1)=0.71073\text{ \AA}$).^[30] The structure was solved and refined by full-matrix least-squares techniques, based on F^2 , using the SHELX-TL software package.^[31] Cobalt, sodium, and oxygen atoms were located by direct methods, and all remaining atoms, including hydrogen atoms, were found by successive difference Fourier maps. All atoms were refined anisotropically, except for hydrogen atoms. The refinement converged to $R_1=0.0339$ and $wR_2=0.0916$ for 2177 unique reflections and 146 parameters.^[32]

The Supporting Information contains the atomic coordinates, the atom-labelling scheme, the TGA graph, the X-ray thermodiffraction study, and the magnetization versus field cycle.

Received: June 22, 2005

Published online: September 15, 2005

Keywords: carboxylate ligands · cobalt · metal–organic frameworks · solvothermal synthesis · supramolecular chemistry

- [1] G. Férey, *Chem. Mater.* **2001**, *13*, 3084–3098.
- [2] B. Moulton, J. Lu, R. Hajndl, S. Hariharan, M. J. Zaworotko, *Angew. Chem.* **2002**, *114*, 2945–2948; *Angew. Chem. Int. Ed.* **2002**, *41*, 2821–2824.
- [3] N. L. Rosi, J. Kim, M. Eddaoudi, B. Chen, M. O’Keeffe, O. M. Yaghi, *J. Am. Chem. Soc.* **2005**, *127*, 1504–1518.
- [4] J. S. Seo, D. Whang, H. Lee, S. I. Jun, J. Oh, Y. J. Jeon, K. Kim, *Nature* **2000**, *404*, 982–986.
- [5] G. Férey, C. Mellot-Draznieks, C. Serre, F. Millange, *Acc. Chem. Res.* **2005**, *38*, 217–225.
- [6] O. M. Yaghi, M. O’Keeffe, N. W. Ockwig, H. K. Chae, M. Eddaoudi, J. Kim, *Nature* **2003**, *423*, 705–714.
- [7] S. Y. Yang, L. S. Long, Y. B. Jiang, R. B. Huang, L. S. Zheng, *Chem. Mater.* **2002**, *14*, 3229–3231.
- [8] K. Barthelet, D. Riou, G. Férey, *Chem. Commun.* **2002**, 1492–1493.
- [9] C. Serre, F. Millange, S. Surblé, G. Férey, *Angew. Chem.* **2004**, *116*, 6445–6449; *Angew. Chem. Int. Ed.* **2004**, *43*, 6285–6289.
- [10] G. Férey, C. Serre, C. Mellot-Draznieks, F. Millange, S. Surblé, J. Dutour, I. Margiolaki, *Angew. Chem.* **2004**, *116*, 6456–6461; *Angew. Chem. Int. Ed.* **2004**, *43*, 6296–6301.
- [11] D. S. Kim, P. M. Forster, R. Le Toquin, A. K. Cheetham, *Chem. Commun.* **2002**, 2148–2149.
- [12] H. Kumagai, M. Ohba, H. Okawa, Y. Oka, K. Inoue, S. Kawata, M. Kurmoo, *Polyhedron* **2003**, *22*, 1917–1920.
- [13] R. Sessoli, D. Gatteschi, H.-L. Tsai, D. N. Hendrickson, A. R. Schake, S. Wang, J. B. Vincent, G. Christou, K. Folting, *J. Am. Chem. Soc.* **1993**, *115*, 1804–1816.
- [14] E. K. Brechin, R. A. Coxall, A. Parkin, S. Parsons, P. A. Tasker, R. E. P. Winpenny, *Angew. Chem.* **2001**, *113*, 2772–2775; *Angew. Chem. Int. Ed.* **2001**, *40*, 2700–2703.
- [15] C. Livage, C. Egger, G. Férey, *Chem. Mater.* **2001**, *13*, 410–414.
- [16] P. M. Forster, A. R. Burbank, A. K. Cheetham, C. Livage, G. Férey, *Chem. Commun.* **2004**, *10*, 368–369.
- [17] R. A. Coxall, A. Parkin, S. Parsons, A. A. Smith, G. A. Timco, R. E. P. Winpenny, *J. Solid State Chem.* **2001**, *159*, 321–327.
- [18] C. Livage, N. Guillou, J. Marrot, G. Férey, *Chem. Mater.* **2001**, *13*, 4387–4392.
- [19] J.-P. Jolivet, *Metal Oxide Chemistry and Synthesis*, Wiley, Chichester, **2000**.
- [20] G. Aromí, P. Christian, M. Helliwell, A. A. Smith, R. E. P. Winpenny, A. S. Batsanov, A. Parkin, S. Parsons, G. A. Timco, *Chem. Eur. J.* **2003**, *9*, 5142–5161.
- [21] N. E. Brese, M. O’Keeffe, *Acta Crystallogr. Sect. B* **1991**, *47*, 192–197.
- [22] G. Férey, *J. Solid State Chem.* **2000**, *152*, 37–48.
- [23] The magnetic properties of the compound were investigated on powder samples with a Quantum Design MPMS-XL SQUID

magnetometer. All the magnetic data were corrected for the diamagnetism of the sample and of the holder.

- [24] R. L. Carlin, *Magnetochemistry*, Springer, Berlin, **1986**.
- [25] F. E. Mabbs, D. J. Machin, *Magnetism and Transition Metal Complexes*, Chapman and Hall, London, **1973**.
- [26] E. Coronado, M. Drillon, P. R. Nugteren, L. J. De Jongh, D. Beltran, *J. Am. Chem. Soc.* **1988**, *110*, 3907–3913.
- [27] a) S. Kitagawa, M. Kondo, *Bull. Chem. Soc. Jpn.* **1998**, *71*, 1739–1753; b) S. Noro, S. Kitagawa, M. Kondo, K. Seki, *Angew. Chem.* **2000**, *112*, 2161–2164; *Angew. Chem. Int. Ed.* **2000**, *39*, 2081–2084.
- [28] N. Guillou, C. Livage, W. van Beek, M. Noguès, G. Férey, *Angew. Chem.* **2003**, *115*, 667–671; *Angew. Chem. Int. Ed.* **2003**, *42*, 643–647.
- [29] FT-IR spectra were recorded on a Nicolet Magna-IR 550 spectrometer. Thermogravimetric analyses were performed with a TA-Instruments TGA-2050 apparatus (oxygen flow 60 mL min⁻¹, 5 °C min⁻¹). Density experiments were performed with a Micromeritics multipycnometer operating under He flow. All the reagents were purchased from Aldrich Chemicals and used as supplied.
- [30] Crystallographic data: C₄₈H₂₇Co₆Na₃O₂₇, trigonal, space group $R\bar{3}c$, $a = 14.100(1)$, $c = 42.727(5)$ Å, $V = 7356(1)$ Å³, $Z = 6$, $\rho_{\text{calcd}} = 1.973$ g cm⁻³. Intensity data were collected in 1271 frames with ω scans (width of 0.30° and exposure time 30 s per frame). Data reduction was performed with the SAINT software and absorption corrections with SADABS (G. M. Sheldrick, SADABS: Program for Scaling and Correction of Area Detector Data, University of Göttingen, Göttingen, Germany, **1997**). $\mu(\text{MoK}\alpha) = 2.109$ mm⁻¹, $F(000) = 4347$, $2\theta_{\text{max}} = 59.9^\circ$; 7477 reflections collected of which 2177 unique ($R_{\text{int}} = 0.0244$). Final R indices (2177 observed reflections, $I > 2\sigma(I)$): $R_1 = 0.0339$, $wR_2 = 0.0916$. Highest residual electron density 0.55 e Å⁻³.
- [31] G. M. Sheldrick, SHELXS97 and SHELXL97: Software package for Crystal Structure Determination, University of Göttingen, Germany, **1997**.
- [32] CCDC-273335 contains the supplementary crystallographic data for this paper. These data can be obtained free of charge from the Cambridge Crystallographic Data Centre via www.ccdc.cam.ac.uk/data_request/cif.

DOI: 10.1002/anie.200502128

Fabrication of Random Assemblies of Metal Nanobands: A General Method***Michael E. Hyde, Trevor J. Davies, and
Richard G. Compton**

Nanoscale electrodes have several advantages over their macroscopic counterparts: they are well suited to applications that require high sweep rates, low internal-resistance (iR) drops, and low capacitance.^[1] A significant disadvantage of such electrodes is, however, that they generate extremely small currents. One useful compromise is to use a band electrode, in which the electrode is small enough in one dimension to give rise to nonlinear diffusion, while its size in the other dimension is increased to maximize the current output. Band electrodes are particularly favored when attempts are made to achieve very low analytical detection limits: the part of the residual current associated with the double-layer charging is lowered in proportion to the surface area of the electrode, while the Faradaic current is not.^[2]

Nanoband electrodes are usually fabricated by using one of two general methods. The simpler of these approaches is to generate an insulator-metal-insulator sandwich and then expose one of the edges by polishing or cutting the material. If vacuum-evaporated films are used, extremely narrow bands (potentially down to approximately 1 nm) may be created. However, the technique suffers from some difficulties: the band width is defined by the thickness of the deposited film, which may be difficult to determine accurately. In addition, polishing of such small electrodes is likely to cause significant variations in its final shape, surface area, and so forth. There may be significant doubts about the real surface area of the band even when no polishing step is used.^[3] This method is best suited to the creation of single bands.

The other commonly used method involves the use of lithography. In this case, there are two possibilities: First, a metal film may be evaporated on to a substrate, photoresist is applied and patterned lithographically, the unprotected metal is etched, and finally the remaining photoresist is removed.^[4] Second, a "lift-off" technique may be employed, in which the photoresist is applied directly to the substrate and patterned.

[*] M. E. Hyde, T. J. Davies, Prof. R. G. Compton
Physical and Theoretical Chemistry Laboratory
Oxford University
South Parks Road, Oxford OX1 3QZ (UK)
Fax: (+44) 1865-275-410
E-mail: richard.compton@chemistry.ox.ac.uk

[**] The authors thank the EPSRC for studentships for T.J.D. and M.E.H. We further thank Roger Bowler for his expertise in the preparation of the highly ordered pyrolytic-graphite (HOPG) electrode housing, Robert M. J. Jacobs for his help with the metal deposition, and Andrew J. Wain for his assistance with the sodium sulfite experiments. T.J.D. thanks Lincoln College and the Lord Crewe's Society for a scholarship (2004–2005) and Abi Smith for all her support.

The metal film is then applied on top, and when the remaining photoresist is removed, the corresponding metal film is also removed, thus leaving only the metal attached directly to the substrate.^[4] These methods are highly reproducible and allow precise control of the electrode geometry. Recently, band widths and gap widths down to 30 nm have been achieved by using a lift-off procedure combined with high-resolution electron-beam lithography.^[5] Lithographic methods, however, require specialized equipment and are relatively complex to implement.

A related approach to the modification of surfaces with conductive bands has been explored by Penner and co-workers,^[6–8] who have shown that metal nanowires may be obtained by selective electrodeposition of conducting metal oxides onto the step edges present at highly ordered pyrolytic-graphite (HOPG) surfaces, followed by reduction with hydrogen. (Although the direct deposition of metals onto the step edges is possible and conceptually simpler, the resulting wires are usually of poorer quality for various reasons.^[6]) This effect results from the specialized structure of HOPG, which consists of atomically flat basal-plane graphite terraces separated by defects that expose relatively thin (335 pm or multiples thereof) bands of edge-plane graphite. Given the correct deposition potential, these edges are strongly favored because of their much greater electrochemical activity.^[9–11]

We have recently extended this methodology in a three-step electrochemical process to generate nanotrenches by using the following procedure:^[9] MoO₂ nanowires are deposited on HOPG in a manner similar to that described by Penner and co-workers. A reducing potential is then applied to a solution of 4-nitrobenzenediazonium ions, thus leading to the deposition of a polymeric film on the electrode which has a thickness on the order of 10 nm. (Although the molybdenum oxide deposited under these conditions is in fact a mixture of MoO₂ and MoO₃, it is usually described as MoO₂.^[6–9] Herein, we follow this convention to avoid confusion.) Finally, the MoO₂ is dissolved in hydrochloric acid; as with the lithographic “lift-off” procedure, any polymer above the MoO₂ wires is removed at the same time. The result is that the HOPG electrode is covered entirely by an impermeable film except for the step edges, which are uncovered. Herein, we extend this method further through the presentation of a simple, general, and mostly solution-phase method for the generation of assemblies of metal nanobands by using the original MoO₂ nanowires as a template.

The process for the fabrication of these nanoband assemblies is illustrated conceptually in Figure 1. MoO₂ nanowires were electrodeposited onto the freshly cleaved HOPG surface (Figure 1 a) using a solution of 1.1 mM sodium molybdate, 1M sodium chloride, and 1M ammonium hydroxide adjusted to pH 8.5 with sodium hydroxide. The mean thickness of the nanowires has been shown to be dependent on the deposition time, thus allowing wires with controlled diameters to be prepared (see below). In the present case, deposition was performed at –1.0 V (versus the saturated calomel electrode (SCE)) for 130 seconds (Figure 1 b). An atomic force microscopy (AFM) image of the resulting

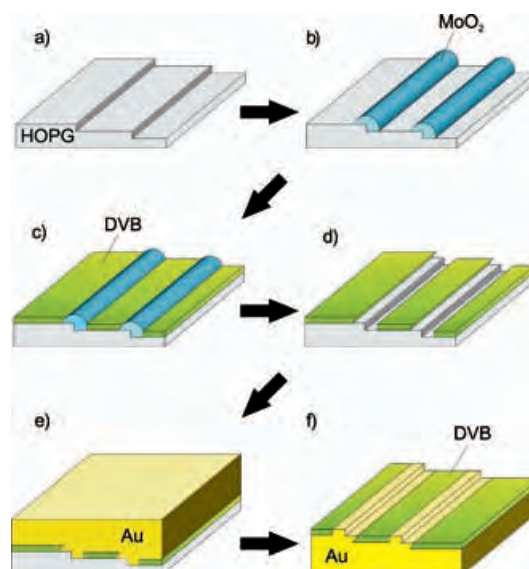


Figure 1. Schematic diagram showing the six stages involved in metal-nanoband fabrication: a) freshly cleaved HOPG; b) after deposition of the MoO₂ nanowires; c) after deposition of the DVB (divinylbenzene) polymer film; d) after removal of the MoO₂ nanowires; e) after evaporation of a gold layer onto the surface; and f) after cleavage of the gold layer from the HOPG substrate.

nanowires is shown in Figure 2 a. To test the homogeneity of the nanowire coverage, AFM images were collected at several separated points on the electrode; this image (and those presented below) was found to be representative of the whole electrode.

The second step was to cover the remaining exposed carbon again with a layer of polymer. However, a solution of 50 mM divinylbenzene (DVB) and 0.1M tetrabutylammonium perchlorate in acetonitrile was used instead of the solution of 4-nitrobenzenediazonium. DVB has been shown to readily polymerize under oxidation conditions,^[12] and we found that

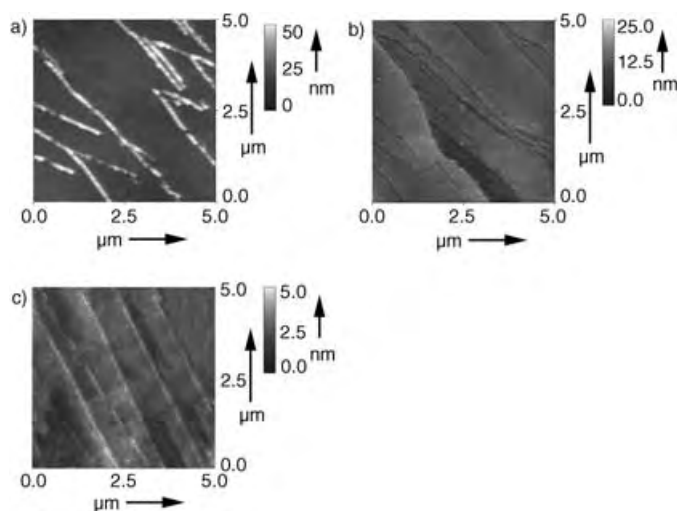


Figure 2. AFM images showing steps in nanoband fabrication: a) MoO₂ nanowires (corresponding to Figure 1 b); b) nanotrenches (corresponding to Figure 1 d); and c) completed gold nanobands (corresponding to Figure 1 f).

application of +1.6 V for 30 s reproducibly generated an even, relatively insulating film (see below), with a thickness of approximately 5–10 nm (Figure 1 c).

The nanowires were removed and nanotrenches created by immersion of the HOPG electrode in a stirred solution of 1 M hydrochloric acid for 300 s (Figure 1 d). An AFM image of these nanotrenches is shown in Figure 2 b. The texture of the DVB film is clearly visible when compared with the background HOPG in Figure 1 a, and the nanotrenches have a mean depth of approximately 6 nm. It should be noted that the fact that the MoO₂ deposits can be removed in this way implies that the film is somewhat porous, thus allowing the solution of HCl to penetrate. However, the surface is effectively blocked in an electrochemical sense: cyclic voltammetry (CV) in a solution of 1.0 mM [Ru(NH₃)₆]³⁺/1 M KCl after DVB-film deposition shows a tiny signal (in proportion to the results obtained from a bare HOPG electrode or metal nanobands). This residual current presumably arises from the slightly porous nature of the film, but is negligible relative to the contribution from the completed nanoband array. The effect of a polymer blocking HOPG electrodes has been previously discussed in greater detail.^[9]

The electrode was removed from the acid, rinsed, and dried. A 200-nm-thick layer of gold was then evaporated on top of the nanotrenches under the conditions described in the Experimental Section, and a supporting stub was attached to the gold layer using a cyanoacrylate adhesive (Figure 1 e). The HOPG was finally cleaved as close to the gold layer as possible using a knife. The original HOPG block is regenerated, and any thin layer of HOPG that remains on top of the gold layer may be removed with adhesive tape, thus leaving what was originally the underside of the gold layer exposed. We found that the DVB layer adheres preferentially to the gold surface (rather than the HOPG block) and leaves the structure illustrated in Figure 1 f, which has exposed gold nanobands surrounded by an insulating layer of polymer. (AFM analysis of the HOPG surface separated from the gold layer showed no sign of nanotrenches, thus confirming that the polymerized DVB deposit adheres to the gold surface.) An AFM image of these bands is shown in Figure 2 c. Note that the decreasing height scale in Figure 2 a–c shows that the nanobands are somewhat difficult to resolve because of the very small height difference between the DVB layer and the exposed gold surface. This small height difference might be predicted from Figure 1 f, as the edges of the bands should in theory be flush with the top of the DVB layer.

To study the nanobands in more detail, a representative band was chosen and examined at a scan range of approximately 800 nm. An AFM image of this band is shown in Figure 3 a, along with a section analysis of a line perpendicular to the nanoband axis in Figure 3 c. Some important features are apparent: the width of the nanoband is around 180 nm, the maximum height of the nanoband above the polymer layer is approximately 700 pm, and the band has a characteristic “m” shape. The depth of the central “v” is approximately 300 pm, suggesting that this shape is related to that of the original HOPG step edge. The shape of the band may in fact be beneficial in terms of the electrochemical behavior of the electrode, as most of the current flow at a nanoband electrode

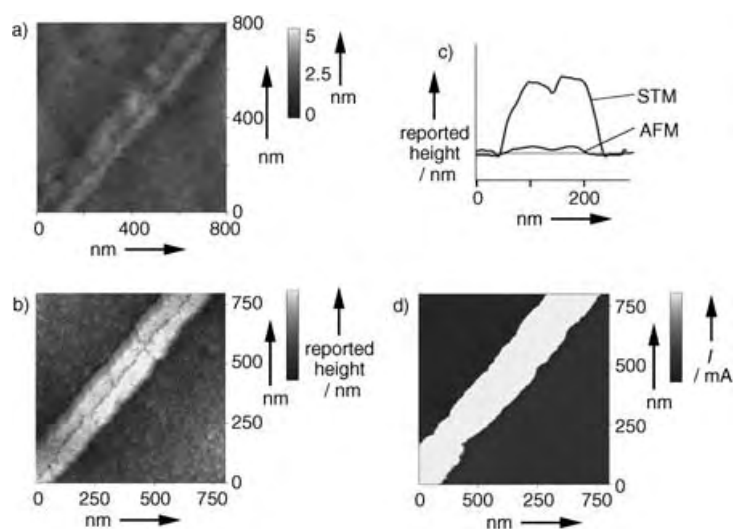


Figure 3. A single gold nanoband shown at a scan range of approximately 800 nm. a) AFM image (height). b) Constant-current STM image (height). c) Section analyses perpendicular to the band axis from the AFM (a) and constant-current STM (b) images; note that the actual height of the band is approximately 0.8 nm (estimated by using AFM). d) Constant-height STM image (current).

occurs near the edges. Therefore, a partial reinforcement of the metal thickness at the band edges may decrease the ohmic drop of the nanoband precisely where this drop is required. Next, the sample was analyzed by using scanning tunnel microscopy (STM). Initially, the scan-feedback parameters were increased as much as possible (“constant-current” mode). On typical surfaces (in which the conductivity is uniform), this procedure gives the most accurate reproduction of the real surface. However, we found that in the current case although the texture of the background and the band itself are well resolved, the height of the band is significantly over-reported (Figure 3 c). In addition, the STM current appears as in Figure 3 d when the feedback parameters are minimized (“constant-height” mode). Together these observations are direct evidence of the presence and relatively much lower conductivity of the DVB film. In constant-height mode, the bias is set high enough for electrons to tunnel through the DVB film. When the tip reaches a nanoband, the much higher conductivity of the gold surface causes the tip to over-compensate, thus moving a large distance away to maintain the same current. For this reason, the absolute heights recorded in the constant-current STM mode should be considered unreliable and have been omitted from the relevant figures. In constant-height mode, the tip remains at a fixed height (irrespective of any surface features) and the tunneling current is recorded. We would clearly expect the gold areas to pass a much greater current at a given bias potential, which is exactly as observed.

In principle, the method described above for the generation of nanobands should be effective for any material that can be evaporated onto the nanotrenches. To test this hypothesis, the procedure was repeated exactly as described above except silver was used instead of gold in the evaporation step. It was found that the resulting nanobands were

impossible to resolve by AFM because of the small height of the bands relative to the roughness of the surface. Again, however, the bands are clearly visible when constant-current STM is used. STM images at two scan ranges are shown in Figure 4. Again, the “m” shape is visible, and the bands shown

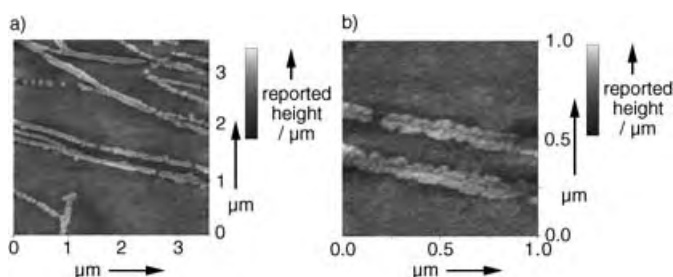


Figure 4. Constant-current STM images of silver nanobands at various scan ranges: a) $3 \times 3 \mu\text{m}^2$ and b) $1 \times 1 \mu\text{m}^2$.

in Figure 4b have a width of approximately 150 nm, which is consistent with the results for the gold nanobands (given that some variation in nanowire/nanotrench width over the whole electrode is always observed).

As stated above, it should also be possible to control the mean nanoband width by adjusting the length of time for which MoO_2 is deposited, which was tested by repeating the above procedure. However, this time MoO_2 was deposited at -1.0 V for 30 s (see Figure 5a). Finer nanowires were produced with a mean diameter of approximately 80–90 nm, nanotrenches were produced as usual from these wires, and copper was evaporated onto the surface to a depth of 200 nm. After cleavage, again no nanobands could be distinguished by using AFM, but STM clearly revealed their presence (Figure 5b,c). As expected, the bands are narrower than in the two previous cases: the magnified image in Figure 5c shows a typical band with a width of 100 nm.

The nanoband arrays produced by using this method were analyzed voltammetrically. An important parameter for any

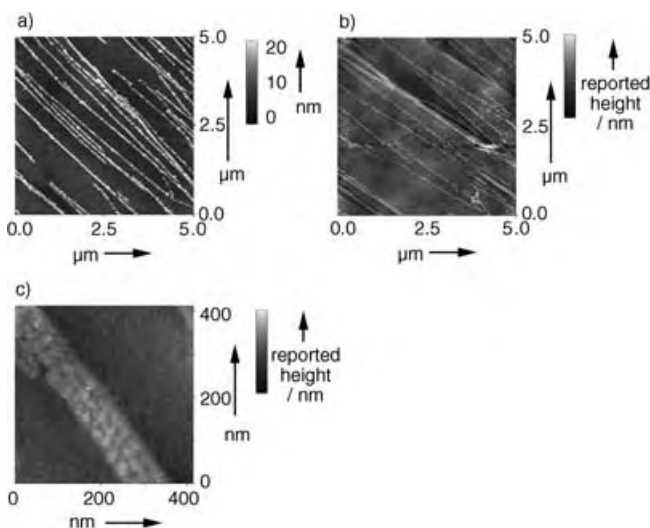


Figure 5. a) AFM image of MoO_2 nanowires after deposition for 30 s. b), c) Constant-current STM images of copper nanobands prepared using the nanowires in (a).

type of electrode array is the global coverage Θ as defined by Equation (1):

$$\Theta = \frac{A_{\text{ins}}}{A_{\text{array}}} \quad (1)$$

A_{ins} is the area of insulating material and A_{array} is the total surface area of the array. It follows that the area of electrode material is given by $A_{\text{array}}(1-\Theta)$. Now consider the case in which we perform cyclic voltammetry at an electrode of material i in a simple one-electron redox couple given by Equation (2):



A and B are the oxidized and reduced species, respectively, k° is the electron-transfer rate constant, and α is the symmetry coefficient for the heterogeneous reaction to give B. The observed response is dependent on a number of system parameters, such as the diffusion coefficient D , the area of the electrode A_{elec} , and k° . For the purpose of this argument, we label the whole response as $[I-E(k^\circ)]$. Now consider the case in which we have a nanoband array of material i and global coverage Θ in the same redox couple and $A_{\text{array}} = A_{\text{elec}}$. Previous investigations have shown that if the spacing between the individual bands is considerably smaller than the diffusion-layer thickness δ , the CV response will be given by $[I-E\{k^\circ(1-\Theta)\}]$.^[10,13] That is, the $I-E$ response of the array will be equal to that of a naked electrode of the same area in the same redox couple but with an electron-transfer rate constant of $k^\circ(1-\Theta)$.

Figure 6a illustrates a cyclic voltammogram recorded with the gold nanoband array in Figure 2c immersed in a solution of 1.0 mM $[\text{Ru}(\text{NH}_3)_6]^{3+}/1 \text{ M KCl}$, in which the scan rate was 1 V s^{-1} . Overlaid as a dashed curve is the corresponding response for a gold electrode of the same surface area, that is, $A_{\text{elec}} = A_{\text{array}}$ (in this case the gold electrode was prepared by gold plating a metal slab and was used in the same electrode housing as the array). It is necessary to estimate the proportion of the array surface which is exposed gold to compare these curves meaningfully. To this end, ten STM images, each with a scan range of $5 \mu\text{m}$, were collected from randomly selected points on the electrode surface. A custom-written Matlab program was then used to analyze the images by using the following method: the bands appear significantly higher on the surface than the DVB background so the band surface and DVB surface can be differentiated simply by setting an appropriate height threshold and counting the total number of data points above and below this threshold for all the images. In this way, the proportional area of exposed gold was found to be approximately 10%. Although the polymer coverage of the nanoband array was approximately 90%, an $I-E$ response almost equal in magnitude to that of the “naked” gold electrode was observed.

In addition, the peak-to-peak separation for the array was larger than that for the naked electrode. This observation is in complete agreement with the theory discussed above. At 1 V s^{-1} , the diffusion-layer thickness at the peak potential of the forward scan will be approximately $15 \mu\text{m}$.^[14] It can be seen from Figure 2c that the spacing between the bands is less

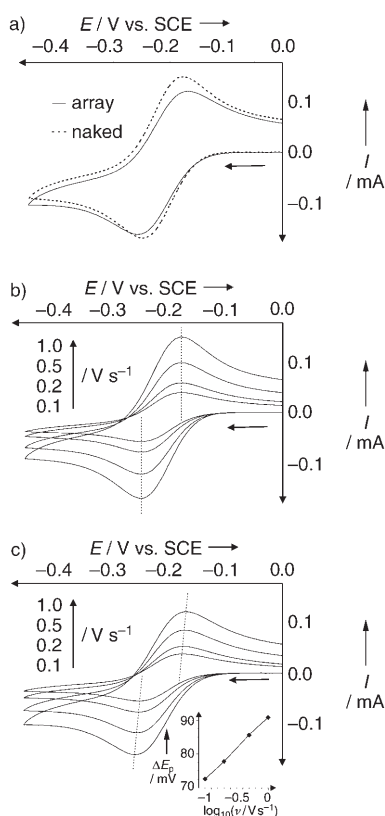


Figure 6. a) Cyclic voltammogram taken at 1 V s^{-1} in a solution of $1.0 \text{ mM } [\text{Ru}(\text{NH}_3)_6]^{3+}/1 \text{ M KCl}$ at the gold nanoband array in Figure 2c (solid) and a gold electrode of the same surface area (dashed). b), c) Cyclic voltammograms taken at varying scan rates in a solution of $1.0 \text{ mM } [\text{Ru}(\text{NH}_3)_6]^{3+}/1 \text{ M KCl}$ at the gold electrode (b) and the gold nanoband array (c).

than $1 \mu\text{m}$; therefore, the observed response obtained in Figure 6 is as expected. The fact that the nanoband array with a coverage Θ of approximately 0.9 gives a response almost equal in magnitude to that of the naked electrode indicates that the mass transport to the nanobands must be considerably faster than to the naked electrode. A potential application of this response is illustrated in Figure 6b,c, which shows cyclic voltammograms recorded at various scan rates at the naked gold electrode and the gold nanoband array in the same solution used for the cyclic voltammogram shown in Figure 6a. The $[\text{Ru}(\text{NH}_3)_6]^{3+}/[\text{Ru}(\text{NH}_3)_6]^{2+}$ redox reaction has an electron-transfer rate constant of approximately 0.5 cm s^{-1} at the gold electrodes, thus making it electrochemically reversible at the scan rates employed in Figure 6b.^[15,16] Hence, the same peak-to-peak separation ΔE_p ($\approx 60 \text{ mV}$) in Figure 6b was observed at all scan rates. In this situation, only thermodynamic data for the redox reaction can be deduced and much higher scan rates would be needed (or smaller electrodes) to deduce reliable kinetic data.^[15,16] However, the nanoband array effectively reduces k^0 to $(1-\Theta)k^0$, such that the redox reaction now appears to be quasireversible at the scan rates employed, as shown in Figure 6c, in which ΔE_p increases with scan rate. Thus, well-characterized nanoband arrays could have fundamental applications (namely, alternative methods to investigate fast electron-transfer reactions)

in addition to their use in electroanalysis. Also, as well as scanning probe microscopy (SPM) image analysis, a nanoband array could be characterized by using a redox couple of known k^0 (for example, determined through a previous microdisk experiment). Subsequent analysis of the nanoband cyclic voltammograms would yield k_{eff}^0 , in which $(1-\Theta) = k_{\text{eff}}^0/k^0$.

In conclusion, we have demonstrated a method for the generation of large assemblies of metal nanobands (the size of which was only limited by the HOPG block employed). The method has been shown to be effective for the generation of gold, silver, and copper nanobands and may work with any material that can be evaporated onto the electrode surface to form a stable 200-nm-thick layer. Control of the mean nanoband width has also been demonstrated: we have created bands with widths between approximately 90 and 180 nm by varying the deposition time of MoO_2 . In principle, the method can be readily extended to produce narrower bands simply by decreasing the deposition time further. However, in practice we found this approach somewhat problematic as shorter deposition times tended to produce “patchier” and less-continuous nanowires. Conversely, wider nanobands can be produced by increasing the deposition time. Although not considered in the present study, it should also be possible to vary the nanoband density. The band density is a function of the density of the step edges on the HOPG surface; it could, therefore, be decreased by employing a higher grade of HOPG or increased by using a lower grade.^[17] The method for the preparation of a fresh HOPG surface can also effect the edge-step density; for example, McDermott and McCreery found that cleavage of an HOPG surface with a sharp blade results in far less edge steps than the adhesive cleaving technique employed herein.^[18]

Experimental Section

All reagents were of the highest grade that was commercially available and were used as received without any further purification. These were sodium molybdate (Aldrich; 98 + %), potassium chloride (Reidel-de-Haen; $\geq 99.5\%$), sodium chloride (BDH; AnalaR), ammonium chloride (BDH, GPR), sodium hydroxide (Acros; $\geq 98\%$), hexaammineruthenium(III) chloride (Aldrich; 98 %), sulfuric acid (BDH; AnalaR, sp. gr. 1.84), sodium sulfide (Aldrich; 98 + %), tetrabutylammonium perchlorate (Fluka; puriss electrochemical grade), and DVB (Aldrich; 80 %, mixture of isomers). All aqueous solutions were prepared with deionized water with a resistivity of not less than 18.2 MW cm (Vivendi water systems, UK). Solutions of DVB were prepared with acetonitrile (Fischer Scientific; anhydrous synthesis grade). The temperature was $294 \pm 2 \text{ K}$ for all experiments.

The metal layers were prepared on the HOPG surface by metal-vapor deposition in a BOC Edwards Auto 306 vacuum coater with a Cryo-pumping system (with a base pressure of $2 \times 10^{-7} \text{ mbar}$). The metals were evaporated from an alumina-coated molybdenum boat (R. D. Mathis, Long Beach, CA, USA) with a 3.2-V 300-A power supply. The current was controlled so that the rate of deposition on the sample was maintained at about 1 nm s^{-1} and monitored with a quartz-crystal microbalance (FTM5 thickness monitor, BOC Edwards), which was mounted adjacent to the sample, both of which were 120 mm from the evaporation source. During the evaporation, the sample was rotated at about 5 rpm around a circle radius of 50 mm centered directly above the source with the pressure maintained below $1 \times 10^{-6} \text{ mbar}$. The evaporation was stopped once the film had reached the required thickness, and the system was

allowed to cool to room temperature before venting and removing the sample. Gold and silver were obtained from Alfa (99.99%), and copper was obtained from Goodfellow (99.999%).

Voltammetric measurements were carried out with a μ -Autolab type II potentiostat (ECO-Chemie, The Netherlands). All electrochemical experiments were conducted by using a three-electrode configuration, in which the substrate for the working electrode was basal-plane HOPG. The HOPG was purchased in the form of a $10 \times 10 \times 2 \text{ mm}^3$ block from SPI Supplies (PA, USA; type SPI-2). The HOPG experiments were conducted by using the HOPG housing, as previously described, which resulted in an exposed electrode area of 0.32 cm^2 .^[19] The HOPG surfaces were prepared by cleavage with adhesive tape before each experiment. At all times, the counter electrode was a bright platinum wire with a surface area much larger than that of the working electrode. A saturated calomel electrode (Radiometer, Copenhagen, Denmark) was employed as the reference.

All the SPM experiments employed a Multimode SPM (Digital Instruments, now a division of Veeco). A model "J" scanner was used, with a lateral range of $125 \times 125 \mu\text{m}$ and a vertical range of $5 \mu\text{m}$. All the AFM experiments were performed in the tapping mode, with standard silicon probes (Nascatec GMBH part NST-NCHF). STM experiments used Pt/Ir tips (Veeco part PT) at a bias of $+200 \text{ mV}$ in all experiments. All SPM experiments were performed in air.

Received: June 19, 2005

Published online: September 20, 2005

Keywords: electrochemistry · nanostructures · scanning probe microscopy · surface chemistry

- [1] M. Samuelsson, M. Armgarth, C. Nylander, *Anal. Chem.* **1991**, 63, 931.
- [2] J. Wang, X. Rongrong, T. Baomin, J. Wang, C. L. Renschler, C. A. White, *Anal. Chim. Acta* **1994**, 293, 43.
- [3] S. L. Caston, R. L. McCarley, *J. Electroanal. Chem.* **2002**, 529, 124.
- [4] R. W. Dyson, *Specialty Polymers*, Chapman and Hall, New York, **1987**.
- [5] K. Ueno, M. Hayashida, J.-Y. Ye, H. Misawa, *Electrochem. Commun.* **2005**, 7, 161.
- [6] E. C. Walter, M. P. Zach, F. Favier, B. J. Murray, K. Inazu, J. C. Hemminger, R. M. Penner, *ChemPhysChem* **2003**, 4, 131.
- [7] M. P. Zach, K. Inazu, K. H. Ng, J. C. Hemminger, R. M. Penner, *Chem. Mater.* **2002**, 14, 3206.
- [8] M. P. Zach, K. H. Ng, R. M. Penner, *Science* **2000**, 290, 2120.
- [9] T. J. Davies, M. E. Hyde, R. G. Compton, *Angew. Chem.* **2005**, 117, 5251; *Angew. Chem. Int. Ed.* **2005**, 44, 5121.
- [10] T. J. Davies, R. R. Moore, C. E. Banks, R. G. Compton, *J. Electroanal. Chem.* **2004**, 574, 123.
- [11] C. E. Banks, T. J. Davies, G. G. Wildgoose, R. G. Compton, *Chem. Commun.* **2005**, 829.
- [12] H. O. Finklea, R. S. Vithanage, *J. Electroanal. Chem.* **1984**, 161, 283.
- [13] C. Amatore, J. M. Saveant, D. Tessier, *J. Electroanal. Chem.* **1983**, 147, 39.
- [14] T. J. Davies, E. R. Lowe, S. J. Wilkins, R. G. Compton, *ChemPhysChem* **2005**, 6, 1340.
- [15] H. Matsuda, Y. Ayabe, *Z. Elektrochem. Angew. Phys. Chem.* **1955**, 59, 494.
- [16] H. Matsuda, Y. Ayabe, *Z. Elektrochem. Angew. Phys. Chem.* **1955**, 59, 1059.
- [17] <https://secure.2spi.com/catalog/new/hopgsub.shtml>.
- [18] M. T. McDermott, R. L. McCreery, *Langmuir* **1994**, 10, 4307.
- [19] R. Bowler, T. J. Davies, M. E. Hyde, R. G. Compton, *Anal. Chem.* **2005**, 77, 1916.

DOI: 10.1002/anie.200502505

**Linking Rings through Diamines and Clusters:
Exploring Synthetic Methods for Making
Magnetic Quantum Gates****

Marco Affronte,* Ian Casson, Marco Evangelisti,
Andrea Candini, Stefano Carretta,
Christopher A. Muryn, Simon J. Teat,
Grigore A. Timco,* Wolfgang Wernsdorfer, and
Richard E. P. Winpenny*

Those of us interested in polymetallic complexes still strive to control the structures formed, as this is vital if we are ever to exploit their properties. One of the more interesting approaches is to use “templates” to control either the size of clusters^[1] or even their shape.^[2] Beyond that challenge lies another: how do we assemble cage complexes into materials in a controlled manner? Further motivation to answer this latter question has arisen from theoretical studies,^[3,4] which propose that $S = 1/2$ clusters could be used as quantum bits (qubits) in quantum information processing (QIP). Herein, we describe our initial experiments in which we link $S = 1/2$ wheels to each other. Linking two molecules with $S = 1/2$ will allow the study of conditioned dynamics of the magnetization of each molecule and thus let us examine the possibility of implementing quantum gates within molecular clusters.

Previously we reported the first heterometallic octanuclear rings, $[\{\text{NH}_2\text{R}_2\}\{\text{Cr}_7\text{MF}_8(\text{O}_2\text{CCMe}_3)_{16}\}]$ ($\text{R} = \text{alkyl}$ side chains; $\text{M} = \text{Ni}^{\text{II}}$, Co^{II} , Fe^{II} , Mn^{II} , or Cd^{II}).^[5] For QIP, single-qubit operations require an $S = 1/2$ ground state. Among the heterometallic $\{\text{Cr}_7\text{M}\}$ rings, this condition is met for $\text{M} = \text{Ni}^{\text{II}}$, which therefore represents an appealing candidate.^[6] How-

[*] Prof. M. Affronte, Dr. M. Evangelisti, A. Candini

I.N.F.M.-S³ National Research Center

41100 Modena (Italy)

Fax: (+39) 059-374-794

E-mail: affronte@unimore.it

I. Casson, Dr. C. A. Muryn, Dr. G. A. Timco, Prof. R. E. P. Winpenny

Department of Chemistry

The University of Manchester

Oxford Road, Manchester, M13 9PL (UK)

Fax: (+44) 161-275-4616

E-mail: grigore.timco@manchester.ac.uk

richard.winpenny@manchester.ac.uk

Dr. S. Carretta

I.N.F.M. and Department of Physics

Università di Parma

43100, Parma (Italy)

Dr. S. J. Teat

Diamond Light Source Ltd.

Chilton, Didcot, Oxfordshire, OX11 0DE (UK)

Dr. W. Wernsdorfer

Laboratoire Louis Néel—CNRS, BP 166

25 Avenue des Martyrs, 38042 GRENOBLE Cedex 9 (France)

[**] This work was supported by the EPSRC (UK), the EC-RTN

“QueMolNa” (contract no. MRTN-CT-2003-504880), and INTAS.

ever, the efficient implementation of a quantum computer requires the creation of a two-qubit quantum gate as pointed out by Loss and co-workers^[3,4] and Troiani et al.^[7] For such a purpose, it is necessary to have dimers of coupled $\{\text{Cr}_7\text{Ni}\}$ rings. As the ring is templated about protonated amine cations, a straightforward method is to use a diamine with a carbon chain of sufficient length so that a $\{\text{Cr}_7\text{Ni}\}$ ring can be attached at either end. In initial experiments we found that 1,8-diaminooctane (1,8-dao) and 1,9-diaminononane (1,9-dan) are suitable, while slightly more complex diamines such as 1,3-di(piperidine)propane (1,3-dpp) also produce a pair of linked clusters. Longer diamines are also suitable, such as 1,12-diaminododecane (1,12-dad), but the resulting crystal structures are significantly disordered. The linked clusters, $[\{1,8\text{-daoH}_2\}\{\text{Cr}_7\text{NiF}_8(\text{O}_2\text{CCMe}_3)_{16}\}_2]$ (**1**), $[\{1,9\text{-danH}_2\}\{\text{Cr}_7\text{NiF}_8(\text{O}_2\text{CCMe}_3)_{16}\}_2]$ (**2**), and $[\{1,3\text{-dppH}_2\}\{\text{Cr}_7\text{NiF}_8(\text{O}_2\text{CCMe}_3)_{16}\}_2]$ (**3**) were structurally characterized (Figure 1).^[8] The Ni^{II} ions in these compounds may be replaced with other metal dications.

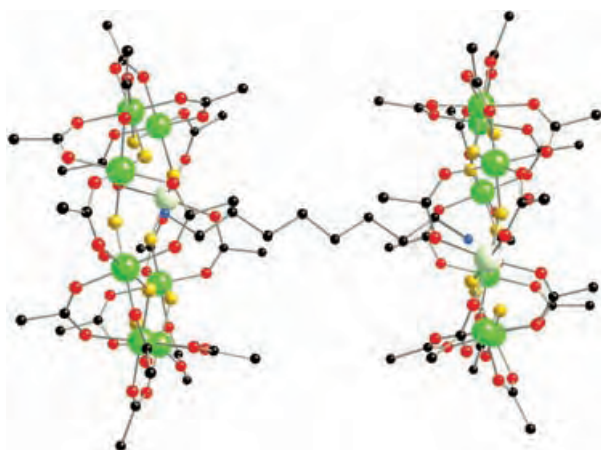


Figure 1. Crystal structure of **1** (hydrogen atoms and methyl groups of pivalate groups on rings have been omitted for clarity; Cr green, Ni light green, F yellow, O red, N blue, C black). Selected bond-length ranges: M–F 1.891–1.964, M–O 1.872–2.016 Å. Average estimated standard deviation (av esd): 0.012 Å.

The structure of the heterometallic octanuclear $\{\text{Cr}_7\text{M}\}$ rings is a regular octagon of metal ions with each side bridged by one fluoride and two carboxylate ions, as reported previously.^[5] Although it is not possible to distinguish between Ni^{II} and Cr^{III} sites in a single ring, elemental analysis confirmed the formulation given. The protonated amine head groups hydrogen bond to the fluoride ions within the ring.

We wished to include switchable links between the rings. To this end, we synthesized $[\{\text{EtNH}_2\text{CH}_2\text{py}\}\{\text{Cr}_7\text{NiF}_8(\text{O}_2\text{CCMe}_3)_{16}\}]$ (**4**; py = pyridine)^[8] knowing that the ring will

encapsulate the secondary ammonium group to leave the pyridine moiety free to bind to further metal sites. To illustrate the potential of such an approach, we treated **4** with the dinuclear metal complexes, $[\text{Cu}_2(\text{O}_2\text{CCMe}_3)_4(\text{HO}_2\text{CCMe}_3)_2]$ and $[\text{M}_2(\text{H}_2\text{O})(\text{O}_2\text{CCMe}_3)_4(\text{HO}_2\text{CCMe}_3)_4]$ ($\text{M} = \text{Ni}$ or Co). This gave the structures $[\{\text{M}_2(\text{O}_2\text{CCMe}_3)_4\}\{\{\text{EtNH}_2\text{CH}_2\text{py}\}\{\text{Cr}_7\text{NiF}_8(\text{O}_2\text{CCMe}_3)_{16}\}_2\}]$ (**5**: $\text{M} = \text{Cu}$; **6**: $\text{M} = \text{Ni}$; **7**: $\text{M} = \text{Co}$),^[8] as depicted in Figure 2.

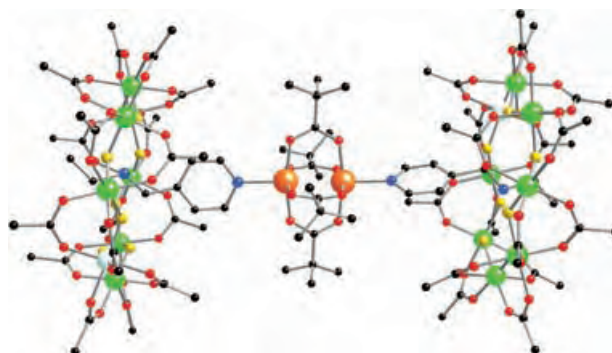


Figure 2. Crystal structure of **5** (see Figure 1 legend for color scheme; Cu orange). Selected bond-length ranges: M–F 1.909–1.967, M–O 1.914–1.997, Cu–O 1.953–1.960 Å. Av esd: 0.008 Å.

The pyridine group from **4** binds to the axial sites of the metal dimer. The $\text{M}\cdots\text{M}$ distance is fairly similar, at 2.63 Å in **5** and 2.61 Å in **6**. The $\text{Cu}\cdots\text{Cu}$ distance is similar to that reported for a previously reported copper dimer bridged by pivalate.^[10] In related Ni dimers,^[11] the $\text{Ni}\cdots\text{Ni}$ distance depends on the terminal ligands: approximately 2.60 Å for pyridine and longer (ca. 2.72 Å) for lutidines. Complex **4** therefore appears to be similar to pyridine in its donating properties. While these dimers are not switchable, we believe that we can prepare equivalent supramolecules in which M is a 4d or 5d metal and where we could vary the interaction between the $[\text{Cr}_7\text{MF}_8(\text{O}_2\text{CCMe}_3)_{16}]$ complexes by redox chemistry or photoexcitation of the multiply bonded dimer.^[12]

Magnetic and specific heat studies of **1–3** and **5–7** were performed. The ac susceptibility was measured over the temperature range 2–100 K (Figure 3a). Each linked ring

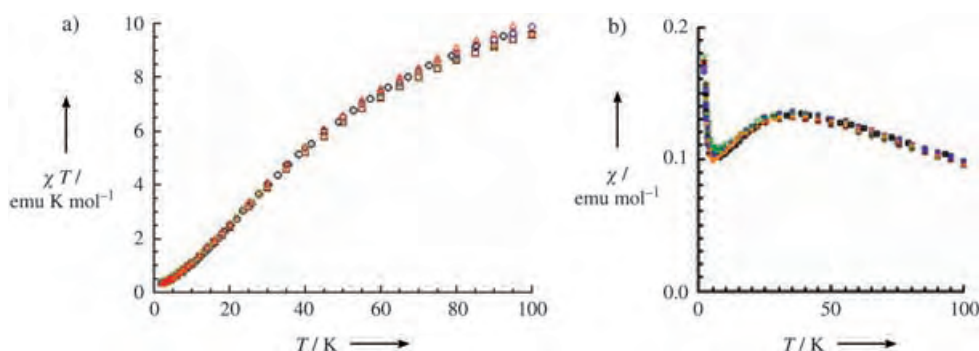


Figure 3. a) The χT product of $\{\text{Cr}_7\text{Ni}\}$ rings (black \circ) and the molecular dimers **1** (brown \square), **2** (blue \circ), **3** (red \triangle), **5** (green \times), and **6** (yellow $+$); for **5** and **6**, χ was normalized to half a mole) over the temperature range 2–100 K. Note that χT values saturate to the Curie value expected for an $S = 1/2$ system for all of the derivatives. b) Temperature dependence of the ac susceptibility χ (the susceptibility of dimer **7** is reported in the Supporting Information).

shows essentially the same χT versus T behavior for this temperature range, and after normalization to half a mole the $\chi T(T)$ curves overlap that of a single $\{\text{Cr}_7\text{Ni}\}$ ring. The anomalies in the χ versus T plot (Figure 3b) are related to the pattern of the lowest lying states in a single $\{\text{Cr}_7\text{Ni}\}$ ring^[5,6] that comprises an $S=1/2$ ground state and an $S=3/2$ first excited multiplet. The field dependencies of the magnetization as collected at $T=0.4$ K for each linked ring almost overlap one another, and as only the ground state is significantly populated at this temperature no deviation from the Brillouin curve calculated for $S=1/2$ is observed (see Supporting Information).

The temperature dependencies of the specific heat c , normalized to the gas constant R , were recorded over the temperature range 0.4–10 K. Figure 4 shows that after normalization to half a mole for the dimers the data overlap one

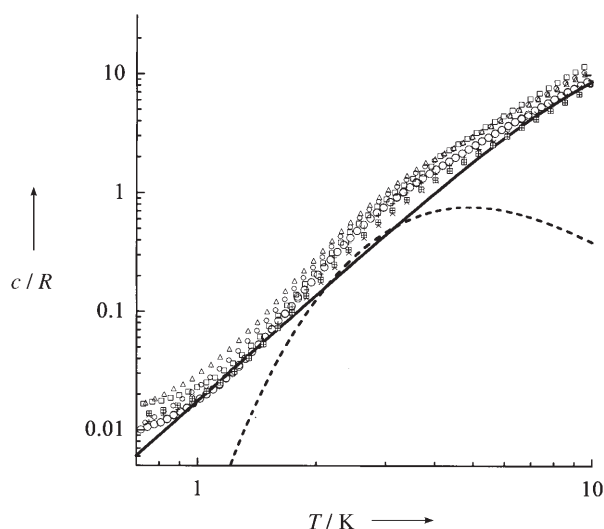


Figure 4. Specific heat c , normalized to the gas constant R , of $\{\text{Cr}_7\text{Ni}\}$ rings (\circ) and of the molecular dimers **1** (\square), **2** (\circ), **3** (\triangle), **5** (\times), **6** ($+$), and **7** (square with cross); for **5–7**, c was normalized to half a mole for comparison with $\{\text{Cr}_7\text{Ni}\}$ rings measured as a function of temperature at zero field. Continuous (—) and dotted (----) lines represent the estimated lattice and magnetic contribution, respectively.

another and with those of $\{\text{Cr}_7\text{Ni}\}$. The hump in the $c(T)$ curves at 3–5 K confirms the Schottky anomaly related to the main energy gap, approximately 9 cm^{-1} , between the ground state $S=1/2$ doublet and the $S=3/2$ quartet. As a magnetic field is applied, these multiplets are split and the Schottky anomaly evolves for all derivatives similarly to that observed for the $\{\text{Cr}_7\text{Ni}\}$ ring (Figure 5). This behavior is well-accounted for by the spin Hamiltonian of a single wheel [Eq. (1)].

$$H = \sum_i J S_i \cdot S_{i+1} + \sum_i d_i [S_{z,i}^2 - S_i(S_i + 1)/3] + \sum_{i < j} S_i \cdot D_{ij} \cdot S_j + \mu_B \sum_i g_i S_i \cdot B \quad (1)$$

The first term corresponds to the dominant antiferromagnetic Heisenberg exchange between nearest-neighboring

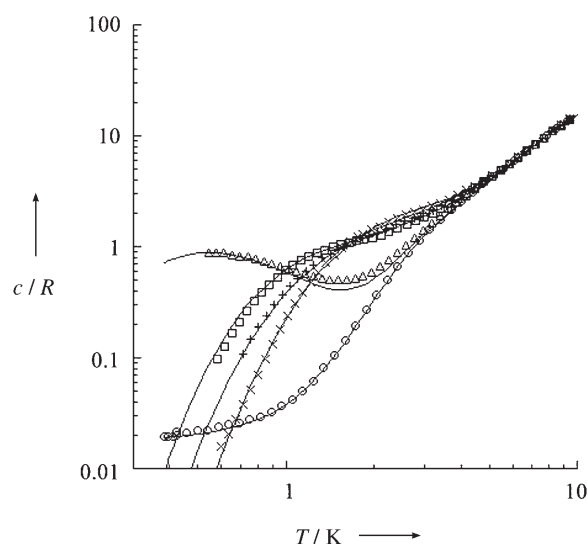


Figure 5. Specific heat c , normalized to the gas constant R , of **7** measured as a function of temperature at different magnetic fields: zero field (\circ); 1 T (\triangle); 3 T (\square); 5 T (\times); 7 T ($+$). It is evident that the evolution of the Schottky anomaly is essentially due to the Zeeman effect on the lowest lying levels with $S=1/2$ and $S=3/2$ of the single $\{\text{Cr}_7\text{Ni}\}$ wheels. Lines are fitting curves obtained by diagonalizing the spin Hamiltonian of single $\{\text{Cr}_7\text{Ni}\}$ wheels, as described in the text.

spins; the second and third anisotropic terms account for the coupling due to the crystal field and for the intracluster dipole–dipole interaction, respectively; the fourth term accounts for the Zeeman coupling to the external field. The microscopic parameters can be determined by fitting the magnetic-field-dependent specific heat data, and within the experimental accuracy for all derivatives the best set of parameters was $J_{\text{Cr-Cr}} = 1.46\text{ meV}$, $J_{\text{Cr-Ni}} = 1.69\text{ meV}$, $d_{\text{Cr}} = -0.03\text{ meV}$, $d_{\text{Ni}} = -0.35\text{ meV}$, $g_{\text{Cr}} = 1.98$, and $g_{\text{Ni}} = 2.2 \pm 0.2$. The addition of a coupling term between two wheels does not improve the quality of the fit for $T > 0.4$ K.

These results show that for all these linked complexes, the pattern of the lowest lying states of a single wheel is very close to that of the isolated $\{\text{Cr}_7\text{Ni}\}$ ring. We estimate an upper limit for a possible coupling interaction between two wheels to be less than about 0.1 cm^{-1} . To check this, we examined the magnetization of microcrystallites of **5** between 40 mK and 400 mK by using a micro-SQUID array and found no evidence for an interaction between the $\{\text{Cr}_7\text{Ni}\}$ rings even at this temperature (see Supporting Information).

At one level, the lack of a sizeable magnetic coupling may seem disappointing, however this work demonstrates that $[\text{Cr}_7\text{MF}_8(\text{O}_2\text{CCMe}_3)_{16}]$ complexes are relatively stable and that they can be attached to one another by different linkers. At another level, implementation of quantum computing will require one state where the single qubits in the gate do not communicate. These results show that the rings can be brought into close proximity without changing magnetic behavior due to through-space exchange. In the future we hope to switch on the interaction by using photo- or redox chemistry.

Experimental Section

All reagents were used as received from Aldrich. $[\text{Cu}_2(\text{O}_2\text{CCMe}_3)_4(\text{HO}_2\text{CCMe}_3)_2]^{[13]}$ and $[\text{M}_2(\text{H}_2\text{O})(\text{O}_2\text{CCMe}_3)_4(\text{HO}_2\text{CCMe}_3)_4]^{[14,15]}$ were prepared according to published methods.

1: $\text{Me}_3\text{CCO}_2\text{H}$ (20.0 g, 195 mmol), $\text{H}_2\text{N}(\text{CH}_2)_8\text{NH}_2$ (0.16 g, 1.11 mmol), and $\text{CrF}_3 \cdot 4\text{H}_2\text{O}$ (3.0 g, 16 mmol) were heated at 140°C with stirring in a teflon flask for 0.5 h, then $2\text{NiCO}_3 \cdot 3\text{Ni}(\text{OH})_2 \cdot 4\text{H}_2\text{O}$ (0.35 g, 0.6 mmol) was added. After 1 h the temperature of the reaction was increased to 160°C for 8 h. The flask was cooled to room temperature, then acetone (35 mL) was added while stirring. The green microcrystalline product was collected by filtration, washed with a large quantity of acetone, dried in air, and then dissolved in hexane (100 mL). The solution was filtered, and the filtrate was evaporated to dryness. The product was recrystallized twice from toluene. Yield: 1.9 g (35%; all yields based on Cr unless otherwise stated). Elemental analysis (%) calcd for $\text{C}_{168}\text{H}_{310}\text{Cr}_{14}\text{F}_{16}\text{N}_2\text{Ni}_2\text{O}_{64}$: Cr 16.06, Ni 2.59, C 44.53, H 6.90, N 0.62; found: Cr 16.62, Ni 2.51, C 45.48, H 7.06, N 0.50.

Compounds **2–4** were obtained by similar procedures to that for **1**, except that 1,8-diaminooctane was replaced with the amines listed below and the period of heating at 160°C and the crystallization solvents were also varied.

2: 1,9-diaminononane; heated at 160°C for 9 h; extracted and crystallized from 1:2 hexane/ethyl acetate. Yield: 1.5 g (28%). Elemental analysis (%) calcd for $\text{C}_{169}\text{H}_{312}\text{Cr}_{14}\text{F}_{16}\text{N}_2\text{Ni}_2\text{O}_{64}$: Cr 16.01, Ni 2.58, C 44.65, H 6.92, N 0.62, F 6.69; found: Cr 15.81, Ni 2.64, C 44.37, H 6.96, N 0.54, F 6.68.

3: 1,3-bis(4-piperidinyl)propane monohydrate; heated at 160°C for 11 h; extracted and crystallized from 5:1 pentane/acetone. Yield: 1.0 g (18%). Elemental analysis (%) calcd for $\text{C}_{173}\text{H}_{316}\text{Cr}_{14}\text{F}_{16}\text{N}_2\text{Ni}_2\text{O}_{64}$: Cr 15.83, Ni 2.55, C 45.19, H 6.93, N 0.61; found: Cr 15.47, Ni 2.54, C 44.81, H 6.90, N 0.54.

4: $\text{Me}_3\text{CCO}_2\text{H}$ (20.0 g, 196 mmol), 4-(ethylaminomethyl)pyridine (0.32 g, 2.4 mmol), $\text{CrF}_3 \cdot 4\text{H}_2\text{O}$ (3.0 g, 17 mmol), and $2\text{NiCO}_3 \cdot 3\text{Ni}(\text{OH})_2 \cdot 4\text{H}_2\text{O}$ (0.3 g, 0.5 mmol) were heated while stirring at 140°C for 2.0 h and then at 160°C for 24 h. The teflon flask was cooled to room temperature, then acetone (35 mL) was added, and the mixture was stirred for 3 h. The precipitated product was collected by filtration and washed with acetone (3×15 mL). The solid was dissolved in pentane (40 mL), the solution was filtered, then the filtrate was diluted with acetone (60 mL). Evaporation of this solution at room temperature produced green crystals. Yield: 2.3 g (42%). Elemental analysis (%) calcd for $\text{C}_{88}\text{H}_{157}\text{Cr}_7\text{F}_8\text{N}_2\text{NiO}_{32}$: Cr 15.62, Ni 2.52, C 45.37, H 6.79, N 1.20; found: Cr 15.58, Ni 2.65, C 45.33, H 6.84, N 1.18. Crystals suitable for X-ray studies were obtained by recrystallization from THF/MeCN.

5: $[\text{Cu}_2(\text{O}_2\text{CCMe}_3)_4(\text{HO}_2\text{CCMe}_3)_2]^{[12]}$ (0.077 g, 0.105 mmol) was added to a solution of **4** (0.5 g, 0.2 mmol) in toluene (7 mL), and the mixture was stirred until the copper complex dissolved. Green microcrystalline product began to form during this time and was collected after 2 days, washed with toluene and acetone, and dried in air. Yield: 0.44 g (81.0% based on Cu). Elemental analysis (%) calcd for $\text{C}_{196}\text{H}_{350}\text{Cr}_{14}\text{F}_{16}\text{N}_4\text{Ni}_2\text{Cu}_2\text{O}_{72}$: Cr 14.02, Ni 2.26, Cu 2.45, C 45.35, H 6.80, N 1.08; found: Cr 13.91, Ni 2.23, Cu 2.29, C 45.77, H 6.86, N 0.97. Crystals suitable for X-ray studies were obtained by slow evaporation of a solution of **5** in THF/toluene at room temperature.

6: $[\text{Ni}_2(\text{H}_2\text{O})(\text{O}_2\text{CCMe}_3)_4(\text{HO}_2\text{CCMe}_3)_4]^{[14]}$ (0.1 g, 0.1 mmol) was added to a solution of **4** (0.5 g, 0.2 mmol) in Et_2O (7 mL) and briefly stirred. The solution was filtered and diluted with toluene (ca. 5 mL). Green crystals (including some that were suitable for X-ray studies) were formed by slow concentration of this solution at room temperature over 2 days. Crystals were washed with toluene and dried in air. Yield: 0.4 g (71% based on Ni). Elemental analysis (%) calcd for $\text{C}_{196}\text{H}_{350}\text{Cr}_{14}\text{F}_{16}\text{N}_4\text{Ni}_4\text{O}_{72}$: Cr 14.05, Ni 4.53, C 45.43, H 6.81, N 1.08; found: Cr 13.77, Ni 4.45, C 45.55, H 6.90, N 1.03.

7: All manipulations were carried out under a N_2 atmosphere. $[\text{Co}_2(\text{H}_2\text{O})(\text{O}_2\text{CCMe}_3)_4(\text{HO}_2\text{CCMe}_3)_4]^{[14]}$ (0.1 g, 0.1 mmol) was dis-

solved in Et_2O (5 mL), and the solution was added to a solution of **4** (0.5 g, 0.2 mmol) in toluene (10 mL). Green crystals (including some that were suitable for X-ray studies) were formed by slow concentration of this solution at room temperature over 2 days. Crystals were collected by filtration, washed with toluene, and dried under N_2 . Yield: 0.31 g (57% based on Co). Elemental analysis (%) calcd for $\text{C}_{196}\text{H}_{350}\text{Co}_2\text{Cr}_{14}\text{F}_{16}\text{N}_4\text{Ni}_2\text{O}_{72}$: Cr 14.05, Co 2.27, Ni 2.27, C 45.43, H 6.81, N 1.08; found: Cr 13.88, Co 2.29, Ni 2.21, C 45.09, H 6.71, N 0.99.

Magnetic and thermal measurements: The magnetic properties and the heat capacity of polycrystalline samples of **1–3** and **5–7** were investigated using a Quantum Design PPMS-7T system provided with an ac susceptometer and a microcalorimeter, respectively. Home-made Hall magnetometer and micro-SQUIDS were used for magnetization measurements below 1 K.

Received: July 18, 2005

Published online: September 13, 2005

Keywords: cage compounds · chromium · heterometallic complexes · quantum computing · supramolecular chemistry

- [1] R. W. Saalfrank, I. Bernt, E. Uller, F. Hampel, *Angew. Chem.* **1997**, 109, 2596–2599; *Angew. Chem. Int. Ed. Engl.* **1997**, 36, 2482–2485.
- [2] R. M. Yeh, A. V. Davis, K. N. Raymond, *Comp. Coord. Chem. II* **2004**, 7, 327.
- [3] F. Meier, J. Levy, D. Loss, *Phys. Rev. Lett.* **2003**, 90, 047901.
- [4] F. Meier, J. Levy, D. Loss, *Phys. Rev. B* **2003**, 68, 134417.
- [5] F. K. Larsen, E. J. L. McInnes, H. El Mkami, J. Overgaard, S. Piligkos, G. Rajaraman, E. Rentschler, A. A. Smith, G. M. Smith, V. Boote, M. Jennings, G. A. Timco, R. E. P. Winpenny, *Angew. Chem.* **2003**, 115, 105–109; *Angew. Chem. Int. Ed.* **2003**, 42, 101–105.
- [6] F. Troiani, A. Ghirri, M. Affronte, P. Santini, S. Carretta, G. Amoretti, S. Piligkos, G. A. Timco, R. E. P. Winpenny, *Phys. Rev. Lett.* **2005**, 94, 207208–207211.
- [7] F. Troiani, M. Affronte, P. Santini, S. Carretta, G. Amoretti, *Phys. Rev. Lett.* **2005**, 94, 190501–190504.
- [8] Crystal data for **1**: $\text{C}_{182}\text{H}_{328}\text{Cr}_{14}\text{F}_{16}\text{N}_2\text{Ni}_2\text{O}_{66}$; $M_r = 4749.88 \text{ g mol}^{-1}$; green plate, monoclinic, space group $P2_1/c$, $a = 25.247(3)$, $b = 16.668(2)$, $c = 31.313(4)$ Å, $\beta = 111.042(11)^\circ$, $V = 12298(3) \text{ Å}^3$, $Z = 2$, $T = 100(2) \text{ K}$, $\rho = 1.283 \text{ g cm}^{-3}$, $F(000) = 4996$, $\mu(\text{MoK}\alpha) = 0.822 \text{ mm}^{-1}$. Crystal data for **2**: $\text{C}_{169}\text{H}_{314}\text{Cr}_{14}\text{F}_{16}\text{N}_2\text{Ni}_2\text{O}_{66}$; $M_r = 4579.64 \text{ g mol}^{-1}$, green prism, orthorhombic, space group $P2_12_12_1$, $a = 19.9276(10)$, $b = 25.4432(10)$, $c = 52.423(2)$ Å, $V = 26580(2) \text{ Å}^3$, $Z = 4$, $T = 100(2) \text{ K}$, $\rho = 1.144 \text{ g cm}^{-3}$, $F(000) = 9624$, $\mu(\text{MoK}\alpha) = 0.759 \text{ mm}^{-1}$. Crystal data for **3**: $\text{C}_{179}\text{H}_{316}\text{Cr}_{14}\text{F}_{16}\text{N}_2\text{Ni}_2\text{O}_{66}$; $M_r = 4570.72 \text{ g mol}^{-1}$; green prism, orthorhombic, space group $P2_12_12_1$, $a = 19.5184(13)$, $b = 25.5867(15)$, $c = 52.214(4)$ Å, $V = 26076(3) \text{ Å}^3$, $Z = 4$, $T = 100(2) \text{ K}$, $\rho = 1.164 \text{ g cm}^{-3}$, $F(000) = 9352$, $\mu(\text{MoK}\alpha) = 0.774 \text{ mm}^{-1}$. Crystal data for **4**: $\text{C}_{88}\text{H}_{157}\text{Cr}_7\text{F}_8\text{N}_2\text{NiO}_{32}$; $M_r = 2329.87 \text{ g mol}^{-1}$; green prism, orthorhombic, space group $P2_12_12_1$, $a = 23.8811(9)$, $b = 31.6801(13)$, $c = 18.1427(7)$ Å, $V = 13726.0(9) \text{ Å}^3$, $Z = 4$, $T = 100(2) \text{ K}$, $\rho = 1.127 \text{ g cm}^{-3}$, $F(000) = 4892$, $\mu(\text{MoK}\alpha) = 0.735 \text{ mm}^{-1}$. Crystal data for **5**: $\text{C}_{196}\text{H}_{350}\text{Cr}_{14}\text{Cu}_2\text{F}_{16}\text{N}_4\text{Ni}_2\text{O}_{72}$; $M_r = 5191.30 \text{ g mol}^{-1}$; green prism, monoclinic, space group $I2/a$, $a = 31.2663(15)$, $b = 17.4002(7)$, $c = 52.952(2)$ Å, $\beta = 101.873(4)^\circ$, $V = 28182(2) \text{ Å}^3$, $Z = 4$, $T = 100(2) \text{ K}$, $\rho = 1.223 \text{ g cm}^{-3}$, $F(000) = 10896$, $\mu(\text{MoK}\alpha) = 0.870 \text{ mm}^{-1}$. Crystal data for **6**: $\text{C}_{196}\text{H}_{350}\text{Cr}_{14}\text{F}_{16}\text{N}_4\text{Ni}_4\text{O}_{72}$; $M_r = 5181.64 \text{ g mol}^{-1}$; green prism, orthorhombic, space group $Pna2_1$, $a = 31.1780(15)$, $b = 17.4191(11)$, $c = 51.967(3)$ Å, $V = 28223(3) \text{ Å}^3$, $Z = 4$, $T = 100(2) \text{ K}$, $\rho = 1.219 \text{ g cm}^{-3}$, $F(000) = 10888$, $\mu(\text{MoK}\alpha) = 0.852 \text{ mm}^{-1}$. Complex **7** is isostructural to **5** with cell parameters

$a = 30.8649(33)$, $b = 17.3439(19)$, $c = 52.5855(57)$ Å, $\beta = 101.734(9)^\circ$; the structure was not refined. Data were collected on Bruker SMART CCD diffractometer ($\text{MoK}\alpha$, $\lambda = 0.71073$ Å). In all cases the selected crystals were mounted on the tip of a glass pin using Paratone-N oil and placed in the cold flow produced with an Oxford Cryocooling device. Complete hemispheres of data were collected using ω scans (0.3° , 30 seconds/frame). Integrated intensities were obtained with SAINT+^[9] and they were corrected for absorption using SADABS.^[9] Structure solution and refinement were performed with the SHELX package.^[9] The structures were solved by direct methods and completed by iterative cycles of ΔF syntheses and full-matrix least-squares refinement against F^2 to give: for **1**, using 794 parameters and 1491 restraints, $wR_2 = 0.4206$ (9618 unique reflections), $R_1 = 0.1572$ (6122 reflections with $I > 2\sigma(I)$); for **2**, using 1557 parameters and 8038 restraints, $wR_2 = 0.2888$ (16004 unique reflections), $R_1 = 0.1033$ (12655 reflections with $I > 2\sigma(I)$); for **3**, using 1757 parameters and 799 restraints, $wR_2 = 0.2317$ (20443 unique reflections), $R_1 = 0.0880$ (12520 reflections with $I > 2\sigma(I)$); for **4**, using 1594 parameters and 5111 restraints, $wR_2 = 0.2933$ (24202 unique reflections), $R_1 = 0.0957$ (18997 reflections with $I > 2\sigma(I)$); for **5**, using 1470 parameters and 2210 restraints, $wR_2 = 0.2814$ (14738 unique reflections), $R_1 = 0.0898$ (8692 reflections with $I > 2\sigma(I)$); for **6**, using 1292 parameters and 6095 restraints, $wR_2 = 0.2736$ (12046 unique reflections), $R_1 = 0.1040$ (8302 reflections with $I > 2\sigma(I)$). CCDC 278508–278513 contain the supplementary crystallographic data for this paper. These data can be obtained free of charge from the Cambridge Crystallographic Data Centre via www.ccdc.cam.ac.uk/data_request/cif.

- [9] *SHELX-PC Package*, Bruker Analytical X-ray Systems, Madison, WI, **1998**.
- [10] M. A. Golubnichaya, S. E. Nefedov, I. B. Baranovskii, I. A. Olshnitskaya, O. G. Ellert, V. M. Novotortsev, L. T. Eremenko, D. A. Nesterenko, *Zh. Neorg. Khim.* **1996**, *41*, 2029–2043.
- [11] I. L. Eremenko, S. E. Nefedov, A. A. Sidorov, M. A. Golubnichaya, P. V. Danilov, V. N. Ikorskii, Y. G. Shvedenkov, V. M. Novotortsev, I. I. Moiseev, *Inorg. Chem.* **1999**, *38*, 3764–3773.
- [12] F. A. Cotton, R. A. Walton, *Multiple Bonds Between Metal Atoms*, 2nd ed., Clarendon Press, Oxford, **1993**.
- [13] E. G. Il'ina, N. A. Santalova, K. M. Dunaeva, *Zh. Neorg. Khim.* **1991**, *36*, 2301–2305.
- [14] G. Chaboussant, R. Basler, H.-U. Güdel, S. Ochsenein, A. Parkin, S. Parsons, G. Rajaraman, A. Sieber, A. A. Smith, G. A. Timco, R. E. P. Winpenny, *Dalton Trans.* **2004**, 2758–2765.
- [15] G. Aromi, A. S. Batsanov, P. Christian, M. Helliwell, A. Parkin, S. Parsons, A. A. Smith, G. A. Timco, R. E. P. Winpenny, *Chem. Eur. J.* **2003**, *9*, 5142–5161.

DOI: 10.1002/anie.200502004

Control of the Coil-to-Globule Transition and Ultrahigh Mechanical Properties of PNIPA in Nanocomposite Hydrogels***Kazutoshi Haraguchi* and Huan-Jun Li*

The coil-to-globule transition of polymer chains caused by external stimuli, such as temperature, pH, pressure, solute, or solvent, is one of the most interesting properties in polymer science, and a polymer that undergoes this transition is referred to as a stimuli-responsive polymer. For example, poly(*N*-isopropylacrylamide) (PNIPA) is the most typical stimuli-responsive polymer and exhibits a well-defined coil-to-globule transition in aqueous media at its lower critical solution temperature (LCST $\approx 32^\circ\text{C}$).^[1] To utilize the coil-to-globule transition effectively, PNIPA is mainly used in the form of polymeric hydrogels, which consist of three-dimensional polymer networks highly swollen with large quantities of water. As PNIPA hydrogels can exhibit many characteristic changes in their properties owing to the coil-to-globule transition, such as swelling/deswelling, absorption/desorption, transparency (transparent/opaque), and surface hydrophilicity (hydrophilic/hydrophobic),^[2–5] they have increased importance as advanced soft materials, such as smart gels (e.g. photoresponsive gels),^[6] enzyme carriers,^[7] colloid crystals,^[8] separation devices,^[9] drug-delivery systems (e.g. glucose-responsive insulin-releasing gels),^[10] and biocompatible materials in tissue engineering (e.g. cell-cultivation substrates, scaffolds).^[11] So far, it has been desired to control the stimuli-sensitivity of PNIPA hydrogels over a wide range. However, substantial control of the coil-to-globule transition of PNIPA has not been reported.

In previous studies, the inherent mechanical weakness of polymeric, including PNIPA, hydrogels was an unavoidable problem and there were constant efforts to overcome this.^[12] Recently, we proposed a new type of hydrogel, nanocomposite hydrogels (NC gels), which consist of poly(*N*-alkylacrylamides) and inorganic clay.^[13] As a result of their unique organic–inorganic network structure, which consists of exfoliated clay platelets uniformly dispersed in an aqueous medium with a number of flexible polymer chains linking them together, NC gels simultaneously solved all of the problems concerning the optical, mechanical, and swelling/deswelling properties associated with conventional, chemi-

[*] Dr. K. Haraguchi, Dr. H.-J. Li
Material Chemistry Laboratory
Kawamura Institute of Chemical Research
631 Sakado, Sakura, Chiba 285-0078 (Japan)
Fax: (+81) 43-498-2182
E-mail: hara@kicr.or.jp

[**] This work was partially supported by the Ministry of Education, Science, Sports, and Culture, Japan (Grant-in-Aid 16550181).
PNIPA = poly(*N*-isopropylacrylamide).

cally cross-linked PNIPA hydrogels (OR gels).^[14–17] NC gels are anticipated to be promising hydrogels with possibly the most extensive control over both mechanical properties and stimuli-sensitivity. By using NC gels, reversible force generation as a result of the coil-to-globule transition of PNIPA chains was observed for the first time in response to alternating the temperature across the LCST.^[18] Additionally, NC gels exhibit many interesting functions such as the formation of unique porous morphologies with a three-layered structure in the freeze-dried state,^[19] characteristic sliding frictional behavior with remarkable changes in the coefficient of friction at the surface of the NC gel,^[20] and biocompatibility (including implantation, antithrombogenicity, etc.).^[21] Herein, we report the first observation of total control over the coil-to-globule transition of PNIPA chains by inorganic (clay) nanoparticles and the achievement of strikingly ultrahigh mechanical properties such as the strength, elongation, and fracture energies of NC gels.

Synthetic hectorite ($[\text{Mg}_{5.34}\text{Li}_{0.66}\text{Si}_8\text{O}_{20}(\text{OH})_4]\text{Na}_{0.66}$; layer size $\approx 30 \text{ nm} \times 1 \text{ nm}$, cation-exchange capacity: 104 meq/100 g) was used as the inorganic clay after washing and freeze-drying. Sample codes for NC gels (NC c) are defined by the concentration of clay (c_{clay}) on a molar basis in their as-prepared states: for example, NC5 gel indicates 5×10^{-2} moles of clay (38.1 g) in 1 L of H_2O . Here, c_{clay} was varied over a wide range from 1×10^{-2} mole (NC1) to 20×10^{-2} mole (NC20), while the concentration of the monomer, NIPA, was fixed at 1 mol L^{-1} in H_2O . The synthetic procedure for formation of the NC gels is almost the same as that reported previously,^[17] except for the mixing process used to prepare the reaction solution. In the present study, mixing by combined rotation and revolution was used to overcome difficulties in forming uniform dispersions of clay, initiator, and catalyst at high contents of clay. Thus, throughout the range of c_{clay} used, uniform dispersion was achieved by controlling the mixing conditions, including the temperature ($1\text{--}35^\circ\text{C}$). Next, free-radical polymerization in situ was performed at 20°C for 20 h. As yields for polymerization were almost 100% for all NC gels, the composition of the NC gel was virtually the same as that of the corresponding initial solution.

The resulting NC gels were all uniform and mostly transparent regardless of the concentration of clay (Figure 1a), although conventional OR gels became totally opaque when the concentration of organic cross-linker (N,N' -methylenebis(acrylamide); BIS) exceeded 5 mol% relative to NIPA (Figure 1b). All NC gels were mechanically very tough, although they differed greatly in softness depending on the content of clay. Figure 1a shows a soft NC5 hydrogel which was readily deformed on compression, while the NC20 gel could hardly be deformed by hand. Here, the deformation of NC5 gel was almost totally reversible, and all NC gels including NC5 and NC20 gels did not break during the compression tests. Figure 2a shows tensile stress versus strain curves for NC5, NC10, NC15, NC18, and NC20 gels. It is seen that both the initial modulus of elasticity (E_i) and the tensile strength (σ) increase monotonically with increasing values of c_{clay} . NC20 gel exhibits a tensile strength of nearly 1000 kPa, an E_i value of 400 kPa, and approximately 1000%

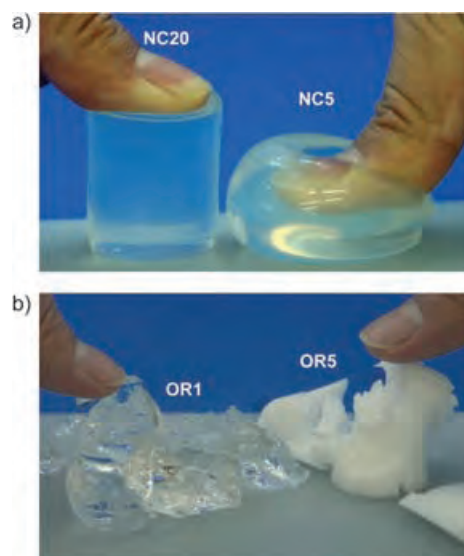


Figure 1. a) NC5 and NC20 gels with high transparencies exhibit differing degrees of softness. Both NC gels did not rupture under repeated compressions by hand. b) OR gels with different transparencies, transparent OR1 and opaque OR5, are both very brittle under compression.

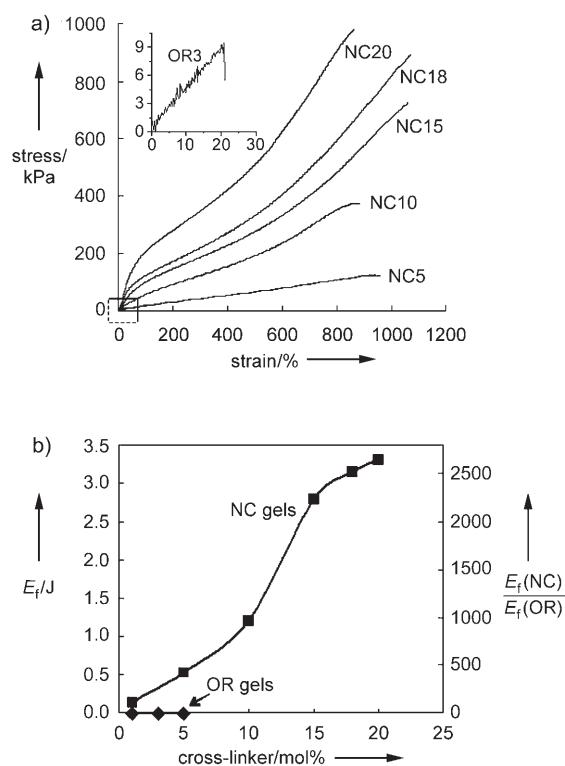


Figure 2. a) Tensile stress versus strain curves for NC gels with different contents of clay (NC5–NC20). The inset shows a magnified view of the dotted box at the origin, with the curve for OR3 gel. b) Fracture energies (E_f) for the gels and ratios of E_f for NC/OR gels as functions of the amount of cross-linker.

elongation at break—these are the highest tensile properties by far ever reported for polymeric hydrogels and are comparable to those of pristine styrene–butadiene rubber.^[22]

If the high water content (ca. 80–90 wt %) of NC gels is taken into account, this is quite a striking result. Also, in most solid polymers, whether they are linear or cross-linked, it is a common feature that the fracture strain ϵ_f decreases inversely in proportion to E_i .^[23] However, in the case of NC gels, ϵ_f was maintained at a high value (ca. 1000 %) despite large increases in the initial modulus of elasticity, E_i . Contrary to this, as shown in Figure 1b (under compression) and Figure 2a (under elongation), OR gels show a very brittle mechanical nature and the brittleness changes little with a varying content of cross-linker. Note that OR gels have the same composition (water and PNIPA) as NC gels except for the difference in cross-linker. The fracture energy for each NC and OR gel was calculated from the areas under the stress–strain curves. The fracture energies (E_f) of NC gels and their dependence on c_{clay} are shown in Figure 2b relative to those of OR gels. The fracture energies of OR gels are almost the same, regardless of the content of BIS cross-linker (the average value for OR1, OR3, and OR5 gels is used in Figure 2b). It is also striking that the fracture energy of NC20 gel could be as much as 2650-times higher than that of the OR gel. All these advantageous results may be ascribed to the unique organic–inorganic network structure^[13–15] of NC gels in which the density of cross-links was controlled without sacrificing the large extensional capability of its constituent polymer chains.

We previously reported that NC gels show a distinct change in transparency across the LCST as a result of the coil-to-globule transition.^[13,14] In the present study, we found that decreases in transparency at the LCST varied dramatically with the concentration of clay, as shown in Figure 3a; that is, the loss in transparency gradually decreased as c_{clay} increased until, finally, at c_{clay} values greater than $15 \times 10^{-2} \text{ mol L}^{-1}$, there was no loss in transparency and gels remained transparent regardless of the temperature. Figure 3b shows NC5 and NC15 gels that exhibit different transparency behaviors at ambient temperature (upper, 20 °C) and in hot water (lower, 50 °C). The NC15 gel did not change its transparency but retained a high transmittance regardless of the surrounding temperature. In contrast, NC5 gel showed an abrupt change, as previously reported, between transparent and opaque by alternating the temperature across the LCST. The results shown in Figure 3a,b indicate that the thermal molecular motion of PNIPA chains was completely restricted in NC gels with c_{clay} greater than $15 \times 10^{-2} \text{ mol L}^{-1}$, and, consequently, the thermosensitivity was totally depressed in NC gels with such high concentrations of clay. The molecular restriction of PNIPA chains in NC gels was attributed to restriction by exfoliated clay platelets incorporated in NC gels. As the clay platelets (hectorite) are strongly hydrophilic, the conformational change from coil (hydrophilic) to globular (hydrophobic) form may be hindered in PNIPA chains attached to clay surfaces or lying close to them. This is the first observation of complete control over the coil-to-globule transition of PNIPA chains by inorganic nanoparticles. Note that through interactions with clay platelets, the thermal molecular motions (associated with the transition between random-coil and globular forms) of PNIPA chains towards the globular form are hindered despite the increasing temper-

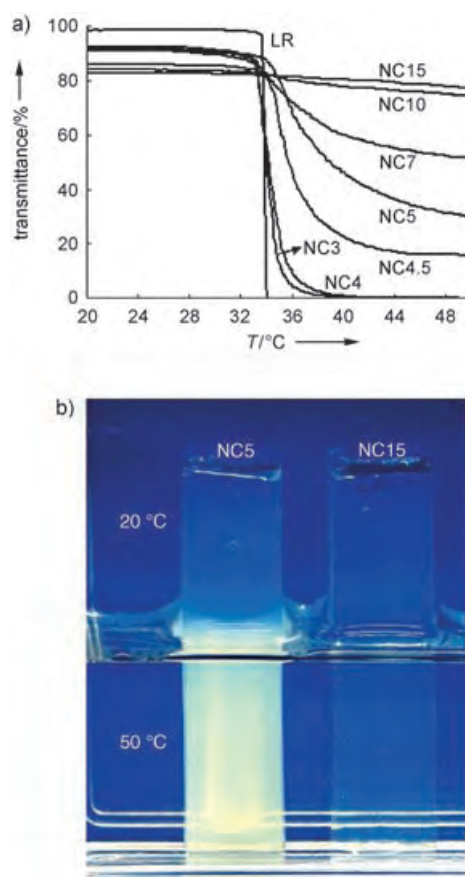


Figure 3. a) Temperature dependence of the optical transmittance for a linear polymer (LR) and NC gels with different c_{clay} . b) Transparency of NC5 and NC15 gels below (in air: upper) and above the LCST (in water: lower). The observed change in transparency for NC5 gel was not observed for NC15 gel (its transparency was maintained upon heating).

ature. At the same time, PNIPA chains adopt random conformations amongst the clay platelets so that large reversible deformations are possible on applying external stresses as shown in Figure 2a.

Concerning the swelling in water, all NC gels swell to equilibrium at 20 °C ($< \text{LCST}$) and their swelling markedly decreases with increasing concentrations of clay. These results clearly indicate that clay platelets act as an effective cross-linking agent in NC gels over the whole range of c_{clay} . At temperatures above the LCST, we previously found that NC gels exhibit very rapid deswelling (volume contraction) compared with OR gels; for example, an NC1 gel took less than 10 minutes to reach equilibrium, although an OR1 gel took more than 1 month.^[14] This result was attributed to the rapid dehydration of flexible PNIPA chains, including grafts, in organic–inorganic networks of NC gels. For NC gels with high concentrations of clay, as the conformational change of PNIPA chains was substantially restricted as described above, it is expected that the deswelling behavior may also be depressed. As shown in Figure 4a, deswelling was decreased markedly with increasing c_{clay} values, and for NC gels with c_{clay} values greater than that for NC12 no contraction of volume

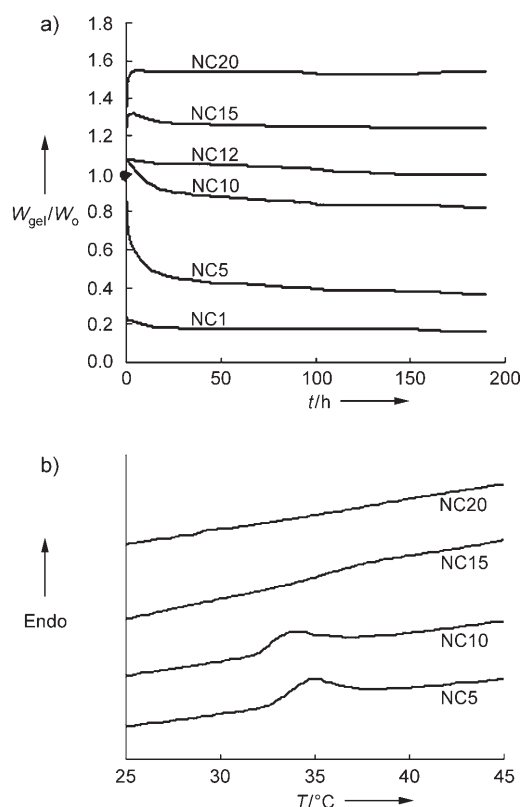


Figure 4. a) Deswelling kinetics (at 50 °C) for NC gels with different c_{clay} values. W_0 is the weight of each initial (as-prepared) gel; W_{gel} is the weight of the swollen hydrogel. b) Heats for the coil-to-globule transition measured by DSC for NC gels with different contents of clay. The transition peak disappeared for NC gels with a concentration of clay greater than that for NC15.

was observed. Instead, NC gels simply swelled, even at 50 °C (> LCST). Here, PNIPA behaves like a hydrophilic polymer without exhibiting a thermosensitive transition. Thus, the volume changes (due to either swelling or deswelling) of NC gels can be controlled greatly by altering c_{clay} over a wide range. From the variations in both swelling and deswelling, it is expected that certain NC gels with high concentrations of clay will maintain a stable volume in water regardless of the temperature.

All the results herein, particularly the superior mechanical properties and good transparencies, indicate that the unique organic–inorganic network structure is retained even for NC gels with high concentrations of clay. However, from the results of suppressed thermosensitivities of transparency and swelling/deswelling it was concluded that PNIPA chains are subject to steric hindrance by clay platelets and that finally the coil-to-globule transition is prohibited at sufficiently high c_{clay} values. This conclusion was confirmed by differential scanning calorimetric (DSC) measurements for NC gels with various concentrations of clay (Figure 4b). The heat change associated with the coil-to-globule transition in the gel state decreased with increasing c_{clay} and disappeared at c_{clay} values greater than that for NC15. Also, from measurements on dried NC gels it was found that the change in heat capacity at the glass transition temperature (≈ 142 °C) decreased with

increasing c_{clay} values, and by analogy with the coil-to-globule transition in the gel state the glass transition in the dried state due to the micro Brownian motion of PNIPA disappeared at c_{clay} values greater than that for NC15. These phenomena are specific to NC gels and are totally different from those of OR gels, which become opaque at high contents of BIS as a result of the formation of inhomogeneous networks.

In conclusion, we have presented the extraordinarily high strength and high fracture energy of polymeric hydrogels (NC gels) as well as complete control over the coil-to-globule transition in PNIPA chains, in terms of transparency and swelling/deswelling, by inorganic clay nanoparticles. In comparison with conventional rubbers (e.g. styrene–butadiene rubber) that consist of 100% organic polymers, NC gels comprise mostly water (80–90 wt %) and are also essentially nonflammable without the need for any harmful halogen or phosphorus additives. Thus, NC gels can be referred to as truly environmentally friendly soft materials, from both production and disposal viewpoints. By recognizing the control over mechanical and functional properties as reported here, NC gels may lead to new horizons in the fields of advanced research and technologies.

Experimental Section

Synthesis of NC gels with high clay contents: The inorganic clay “Laponite XLG” (Rockwood Ltd., UK) and NIPA monomer were used after purification. The synthetic procedure for NC gels with low concentrations of clay ($c_{\text{clay}} \leq 5 \times 10^{-2} \text{ mol L}^{-1}$) is the same as that reported previously.^[17] For NC gels with high concentrations of clay ($c_{\text{clay}} \geq 10 \times 10^{-2} \text{ mol L}^{-1}$), the experimental procedure differed in the preparation of the initial reaction solution: For example, for NC20 gel only a part of the clay was used at first and a transparent aqueous solution consisting of water (19 mL), NIPA (2.26 g), and inorganic clay (0.76 g) was prepared by normal magnetic stirring. Next, the remainder of clay (2.29 g) was added to the aqueous solution while stirring at 1 °C and subsequently heating to 35 °C and then cooling again to 1 °C, to avoid flocculation and to accelerate dispersion. Then, to achieve the exfoliation of clay and the good dispersion of all components, the solution was further mixed at 1–5 °C for 30 minutes by utilizing two combinations of rotation and revolution (800/2000 rpm and 60/2200 rpm). The mixtures were subsequently mixed for further periods of 1 minute each after the addition of initiator and catalyst. The amount of clay was varied from 0.152 g to 3.05 g. The concentration of monomer (NIPA) was fixed at 1 mol L^{-1} in H_2O , and the molar ratios of monomer, initiator (potassium persulfate), and catalyst (N,N,N',N' -tetramethylethylenediamine) were fixed at 100:0.426:0.735, respectively. Then, free-radical polymerization in situ was allowed to proceed in a water bath at 20 °C for 20 h. Throughout all experiments, oxygen was excluded from the system. Meanwhile, OR1 and OR5 gels were prepared using NIPA (2.26 g, 1 mol L^{-1} in H_2O) and the organic cross-linker N,N' -methylenebis-(acrylamide) (BIS; 0.028 g, 1 mol%, or 0.140 g, 5 mol%, respectively) instead of clay.

Measurements: Swelling and deswelling experiments were performed by immersing as-prepared gels (initial size: 5.5 mm diameter \times 30 mm long) in a large excess of water for approximately 200 h at 20 and 50 °C, respectively, and changing the water several times. Swelling and deswelling ratios are represented as the ratios of weights of the swollen hydrogel (W_{gel}) to the corresponding dried gel (W_{dry}). Tensile mechanical measurements were performed on as-prepared NC and OR gels of the same size (5.5 mm diameter \times 70 mm long) using a Shimadzu Autograph AGS-H under the following conditions: 25 °C; gauge length: 30 mm; cross-head speed: 100 mm min^{-1} . The initial

cross section (23.75 mm^2) and loads detected between elongations of 10 % and 50 % were used to calculate the tensile strengths (σ) and the initial modulus of elasticity (E_i). Thermogravimetric analyses were conducted using a TG/DTA 220 (Seiko Denshi Ind. Inc.) instrument, by heating samples from 30°C to 1000°C at a heating rate of 10°Cmin^{-1} in an air flow. DSC measurements were performed using a Perkin–Elmer DSC-7 apparatus in a nitrogen atmosphere for NC gels and milled dried gels, with heating from -50 to 60°C and from 30 to 250°C , respectively, at a heating rate of 10°Cmin^{-1} .

Received: June 10, 2005

Published online: September 13, 2005

Keywords: gels · mechanical properties · nanostructures · organic–inorganic hybrid composites · phase transitions

- [1] a) M. Heskins, J. E. Guillet, *J. Macromol. Sci. Part A* **1968**, *2*, 1441–1455; b) G. Graziano, *Int. J. Biol. Macromol.* **2000**, *27*, 89–97; c) P. Kujawa, F. M. Winnik, *Macromolecules* **2001**, *34*, 4130–4135.
- [2] Y. H. Bae, T. Okano, S. W. Kim, *J. Polym. Sci. Part B* **1990**, *28*, 923–936.
- [3] Y. Hirokawa, T. Tanaka, *J. Chem. Phys.* **1984**, *81*, 6379–6380.
- [4] E. S. Matuo, T. Tanaka, *J. Chem. Phys.* **1988**, *89*, 1695–1703.
- [5] F. Afroze, E. Nies, H. Berghmans, *J. Mol. Struct.* **2000**, *554*, 54–68.
- [6] R. Akashi, H. Tsutusi, A. Komura, *Adv. Mater.* **2002**, *14*, 1808–1811.
- [7] a) P. S. Stayton, T. Shimoboji, C. Long, A. Chilkoti, G. Chen, J. M. Harris, A. S. Hoffman, *Nature* **1995**, *378*, 472–474; b) S. Takeuchi, I. Omodaka, *Makromol. Chem.* **1993**, *194*, 1991–1999.
- [8] T. Hellweg, C. D. Dewhurst, E. Bruckner, K. Kratz, W. Eimer, *Colloid Polym. Sci.* **2000**, *278*, 972–978.
- [9] a) S. Champ, W. Xue, M. B. Huglin, *Macromol. Chem. Phys.* **2000**, *201*, 931–940; b) W. Cai, E. C. Anderson, R. B. Gupta, *Ind. Eng. Chem. Res.* **2001**, *40*, 2283–2288.
- [10] a) K. Kataoka, H. Miyazaki, M. Bunya, T. Okano, Y. Sakurai, *J. Am. Chem. Soc.* **1998**, *120*, 12694–12695; b) A. Matsumoto, R. Yoshida, K. Kataoka, *Biomacromolecules* **2004**, *5*, 1038–1045.
- [11] a) T. Okano, N. Yamada, H. Sakai, Y. Sakurai, *J. Biomed. Mater. Res.* **1993**, *27*, 1243–1251; b) R. A. Stile, W. R. Burghardt, K. E. Healy, *Macromolecules* **1999**, *32*, 7370–7379; c) M. Yamato, T. Okano, *Mater. Today* **2004**, *7*, 42–47.
- [12] a) Y. Okumura, K. Ito, *Adv. Mater.* **2001**, *13*, 485–487; b) J. P. Gong, Y. Katsuyama, T. Kurokawa, Y. Osada, *Adv. Mater.* **2003**, *15*, 1155–1158.
- [13] K. Haraguchi, T. Takehisa, *Adv. Mater.* **2002**, *14*, 1120–1124.
- [14] K. Haraguchi, T. Takehisa, S. Fan, *Macromolecules* **2002**, *35*, 10162–10171.
- [15] K. Haraguchi, R. Farnworth, A. Ohbayashi, T. Takehisa, *Macromolecules* **2003**, *36*, 5732–5741.
- [16] M. Shibayama, J. Suda, T. Karino, S. Okabe, T. Takehisa, K. Haraguchi, *Macromolecules* **2004**, *37*, 9606–9612.
- [17] K. Haraguchi, H. J. Li, K. Matsuda, T. Takehisa, E. Elliott, *Macromolecules* **2005**, *38*, 3482–3490.
- [18] K. Haraguchi, S. Taniguchi, T. Takehisa, *ChemPhysChem* **2005**, *6*, 238–241.
- [19] K. Haraguchi, K. Matsuda, *Chem. Mater.* **2005**, *17*, 931–934.
- [20] K. Haraguchi, T. Takada, *Macromol. Chem. Phys.* **2005**, *206*, 1530–1540.
- [21] K. Haraguchi, T. Takehisa, *Proceedings of IMECE2005* (Orlando, FL), **2005**, IMECE2005-80533.
- [22] E. L. Bedia, Y. Kasai, Y. Ikeda, S. Kohjiya, *J. Appl. Polym. Sci.* **2005**, *95*, 68–73.
- [23] L. E. Nielsen, *Mechanical Properties of Polymers and Composites*, Vol. 2, Marcel Dekker, New York, **1974**, pp. 257–340.

DOI: 10.1002/anie.200501920

Synthetic Macrocyclic Peptidomimetics as Tunable pH Probes for the Fluorescence Imaging of Acidic Organelles in Live Cells***Francisco Galindo,* M. Isabel Burguete, Laura Vigara, Santiago V. Luis,* Nurul Kabir, Jelena Gavrilovic, and David A. Russell**

Synthetic fluorescent probes have found widespread applications in cell biology for the intracellular measurement of several species, from the zinc(II) cation^[1] and citrate anion^[2] to singlet oxygen^[3] and nitric oxide.^[4] In recent years, several reviews have appeared that deal with synthetic fluorescent chemosensors.^[5,6] Protons are one of the most important targets among the intracellular species of interest, as it is well-known that pH plays a central role in many cellular events.^[7] In general terms, two broad ranges of pH values are found in cells. Consequently, two types of synthetic probes have been developed,^[8] namely, probes for cytosol that work at a pH of about 6.8–7.4, and probes for the so-called acidic organelles (for example, lysosomes) that function over the pH range of about 4.5–6.0. It is possible to find a large array of commercial probes for the former pH range; however, this is not the case for acidic organelles. Many reports have appeared that connect some cellular dysfunction with abnormal pH values in acidic organelles. For instance, defective pH regulation of acidic compartments has been observed in human breast cancer cells.^[9] Another illustrative example is the finding of elevated lysosomal pH in neural ceroid lipofuscinoses, a common inherited neurodegenerative disorder that affects

[*] Dr. F. Galindo, Dr. M. I. Burguete, L. Vigara, Prof. Dr. S. V. Luis
Departamento de Química Inorgánica y Orgánica
Universitat Jaume I
Avda. Sos Baynat, s/n, 12071 Castellón (Spain)
Fax: (+34) 964-72-8214
E-mail: francisco.galindo@qio.uji.es
luiss@qio.uji.es

Dr. N. Kabir, Prof. Dr. D. A. Russell
School of Chemical Sciences and Pharmacy
University of East Anglia
Norwich, Norfolk NR4 7TJ (UK)
Fax: (+44) 1603-593-012
E-mail: d.russell@uea.ac.uk

Dr. N. Kabir, Prof. Dr. J. Gavrilovic
School of Biological Sciences
University of East Anglia
Norwich, Norfolk NR4 7TJ (UK)

[**] This work was supported by the Spanish Ministerio de Ciencia y Tecnología (Project BQU-2003-0915-C03-02), Fundació Caixa Castelló-Bancaixa and Universitat Jaume I (Project 041007.25/1 to F.G.), and The Wellcome Trust (Showcase award to D.A.R. and J.G.). F.G. thanks the Spanish MEC for financial support (Ramón y Cajal Program).

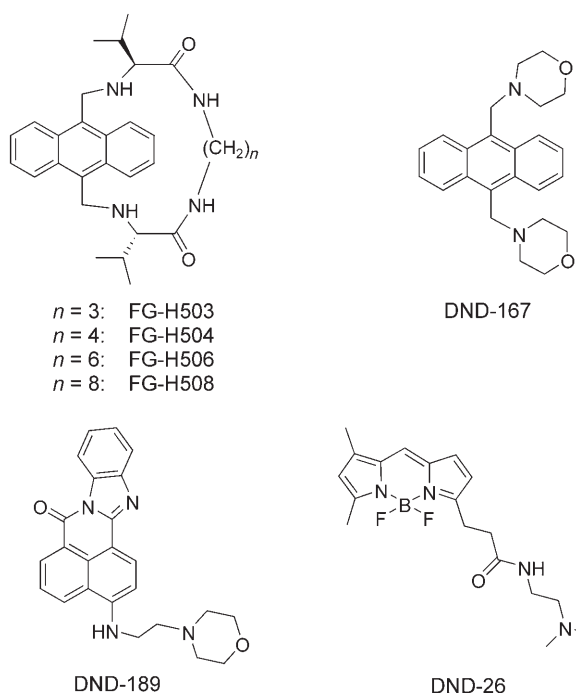


Supporting information for this article is available on the WWW under <http://www.angewandte.org> or from the author.

children.^[10] It would, therefore, be extremely desirable to have access to a broad variety of “acidic” probes to study these and other conditions. Unfortunately, as a consequence of the current unavailability of probes for the acidic pH range, there is a research bottleneck as regards progress in some areas of cell biology or medicine. Additionally, in the light of the above discussion, a further fundamental criterion emerges for the design of new probes. This criterion is the possibility of chemical control of the pH reporter probe under extracellular conditions, that is, the potential for precise control (and prediction) of the pK_a value of the probe by adjusting the appropriate elements in the molecular architecture.

Herein, we present a new family of fluorescent macrocyclic probes (FG-H series)^[11] that consist of a 9,10-anthracene subunit linked by a C_2 -symmetric peptidomimetic chain (Scheme 1). The probes differ only in the size of the chain

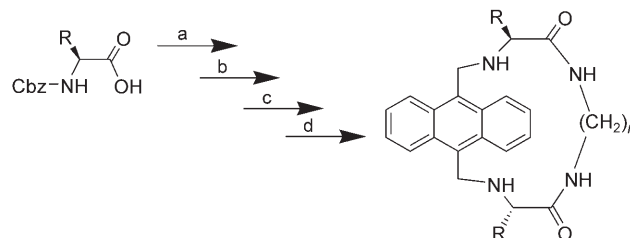
cycles in moderate to high yields without the need for high-dilution conditions. In the case of the FG-H series shown in Scheme 1, two units of L-valine were selected because of their reported ability to induce the formation of β sheets.^[14] However, it should be possible to introduce virtually any α -amino acid with an appropriate protecting group into the general synthetic procedure (Scheme 2) to obtain a new



Scheme 1. Structures of the fluorescent probes studied.

($n = 3, 4, 6, 8$), but this structural variation produces a smooth shift in the pK_a values, which is an essential feature that enables a range of pH “windows”. The synthesis of the FG-H family members is facile, and the compounds exhibit good photostability and present excellent cellular uptake without the need for derivatization to improve crossing of the cellular membrane. Moreover, the series extends the range of pH utility by about 0.5 pH units (toward a lower pH) over that of currently available probes.

Compounds FG-H503, FG-H504, FG-H506, and FG-H508 were synthesized according to a procedure developed for the preparation of peptidomimetic macrocycles in high yields.^[12,13] It has been previously demonstrated that the β -turn conformation adopted by the synthetic intermediates (arising from the presence of two α -amino acids as building blocks) allows the synthesis of the peptidomimetic macro-



Scheme 2. a) Acid activation; b) coupling with 1, n -diaminoalkane; c) deprotection; d) ring-closing with 9,10-bis(bromomethyl)anthracene. Cbz = carbobenzyloxy.

family of peptidomimetics with different properties as pH probes. The 9,10-dimethylantracene moiety was chosen as a fluorophore as it is known to be photostable and also to allow comparison with the widely used pH probe for acidic organelles, LysoSensor Blue DND-167 (Scheme 1). DND-167, which was originally studied by de Silva et al.,^[15] is also an anthracene derivative that shares with the compounds in the FG-H series the presence of two amine groups decoupled electronically from the fluorophore by both methylene spacers. However, in the case of DND-167, there is the possibility that more flexible configurations could be adopted. For comparison a second commercial probe, LysoSensor Green DND-189, which has a different photochemical nature, was also selected. LysoTracker Green DND-26 (see Scheme 1)^[16] was also used for fluorescence imaging experiments in vivo. This latter compound was employed to certify the acidic nature of the organelles, as it is known to accumulate in lysosomes. (Note, however, that LysoTracker Green DND-26 is not a pH “reporter”, as its fluorescence emission does not vary with changing pH.^[8a])

Standard fluorescence pH titrations were performed for all the compounds in Scheme 1 in buffered aqueous media (containing 0.2 % DMSO from the initial stock solution) at a probe concentration of 2 μ M, with measurement at pH intervals narrow enough to allow a precise determination of the apparent pK_a value. Figure 1 shows the absorption spectrum of FG-H503 (Figure 1 a) along with the fluorescence emission spectra at different pH values (Figure 1 b–g). The fluorescence changes in systems composed of fluorophore– CH_2 –amine moieties, such as the FG-H series, can be rationalized according to the photoinduced electron-transfer (PET) scheme developed by the research groups of de Silva and Czarnik.^[6] Under basic conditions the amino groups are not protonated, and hence the PET process takes place (if thermodynamically allowed by the Rehm–Weller formalism^[17]) which leads to fluorescence quenching. In acidic media the electron pair in each amine is protonated, thus preventing

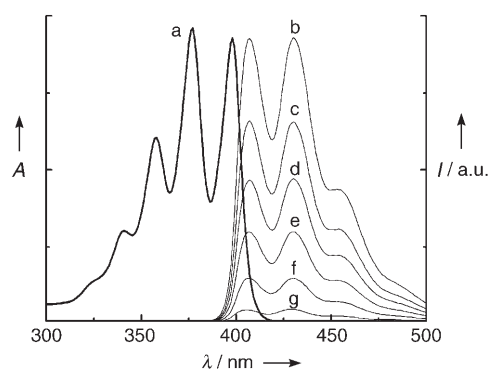


Figure 1. FG-H503 (2 μM) in aqueous solution (0.2% DMSO). a) Normalized absorption spectrum at pH 1.02, and fluorescence spectra ($\lambda_{\text{ex}} = 377$ nm) at b) pH 2.55, c) 4.70, d) 5.10, e) 5.41, f) 5.83, and g) 6.90.

PET from occurring, and hence emission from the fluorophore takes place.

In the case of the FG-H series, a minimal variation in the chemical structure of the probe causes an appreciable change in the titration curve (see Figure 2 for some of the titration

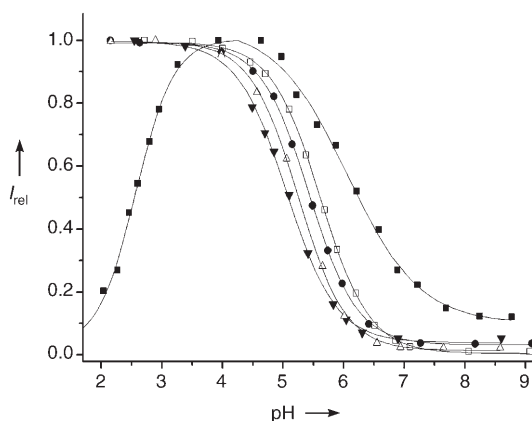


Figure 2. Fluorescence versus pH titration curves for the probes under study. Data are normalized at the maximum emission (I_{rel}). Probe concentration: 2 μM in aqueous solution (0.2% DMSO); excitation wavelengths as indicated in Table 1. FG-H503 (▲), FG-H504 (△), FG-H508 (●), DND-167 (□), DND-189 (■).

curves; complete spectra and titration results can be found in the Supporting Information).^[18,19] The pK_{a} values are derived from the nonlinear curve-fitting of the data and are shown in Table 1 along with the excitation and emission wavelengths.

It can be seen in Figure 2 that the DND-189 probe exhibits a fluorescence intensity versus pH profile that is not the same as the other profiles, which reflects its different chemical nature with respect to the anthracene framework. Additionally, a sharp decrease in the fluorescence intensity is measured with DND-189 at acidic pH values.

To examine the useful pH range for each probe, the pH interval for which the tested compound changes from 20 to 80% of its maximum fluorescence was determined (Figure 3; the maximum is measured at pH 2 for the FG-H series and

Table 1: Spectral characteristics and pK_{a} values of the studied systems.

Entry	Compound ^[a]	λ_{ex} [nm]	λ_{em} [nm]	pK_{a}
1	FG-H503	377	430	5.06 ± 0.02
2	FG-H504	377	430	5.24 ± 0.02
3	FG-H506	377	430	5.41 ± 0.01
4	FG-H508	377	430	5.43 ± 0.01
5	DND-167	374	427	5.61 ± 0.01
6	DND-189	443	505	6.06 ± 0.06
7	FG-H503 + Cu^{II}	377	430	5.02 ± 0.02
8	DND-167 + Cu^{II}	374	427	5.57 ± 0.01
9	DND-189 + Cu^{II}	443	505	6.01 ± 0.03
10	FG-H503 + Zn^{II}	377	430	4.95 ± 0.03
11	DND-167 + Zn^{II}	374	427	5.52 ± 0.01
12	DND-189 + Zn^{II}	443	505	5.70 ± 0.03

[a] Probe concentration: 2 μM in aqueous solution (0.2% DMSO); metal concentration: 200 μM .

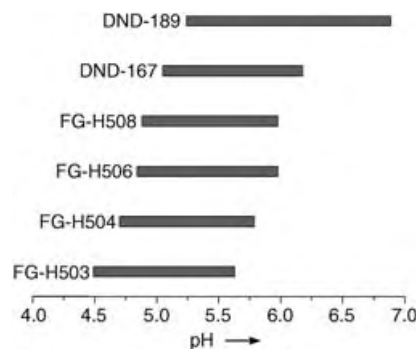


Figure 3. Schematic representation of the pH intervals where the fluorescence emission of each probe experiences a change between 20 and 80% of its maximum intensity. Probe concentration: 2 μM in aqueous solution (0.2% DMSO); excitation and emission wavelengths as indicated in Table 1.

DND-167, and at pH 4 for DND-189). Thus, it can be seen that the peptidomimetic macrocycles are complementary to the DND probes, as they extend the pH range of measurement toward the acidic side.

On account of the complexity of the intracellular environment, an additional examination of the probes was performed to determine whether other ions were potential interferents. For example, it is well-known that amines can bind many metal cations in solution.^[6] In fact, many chemosensors for metal ions use the ability of amines to coordinate the vacant orbitals of such analytes. Among them, zinc(II) and copper(II) are the types of species likely to be targeted by free amines in solution. Consequently, control experiments with FG-H503, DND-167, and DND-189 in the presence of an excess of Zn^{II} and Cu^{II} ions were performed to assess such possible coordination. As can be seen in Table 1, the effect of such metals on the peptidomimetic macrocycle is negligible, particularly when considering that the concentrations used for the experiment were significantly higher than those present in the intracellular environment.

FG-H503 was investigated as a fluorescent probe in cultured cells and was compared to DND-189. The probe

DND-167 did not produce images with sufficient resolution; therefore, the additional probe LysoTracker Green DND-26^[16] was also used which is known to be retained specifically in acidic organelles. Two series of experiments were performed: Raw 264.7, a mouse macrophage cell line, was loaded with FG-H503 and with either DND-189 or DND-26. As shown in Figure 4b,g, FG-H503 exhibited a vesicular distri-

Experimental Section

Synthesis of the peptidomimetic macrocycles: The appropriate 1,*n*-diaminoalkane was reacted with *N*-protected (Cbz) L-valine through the formation of an *N*-hydroxysuccinimide ester.^[12] Yields of these intermediate peptidomimetic compounds were about 70%. The cyclization step was performed by treating 9,10-bis-bromomethylanthracene with the diamine formed by *N*-deprotection of the intermediates with HBr/AcOH (deprotection yields over 90%). The products of the cyclization step (at reflux in acetonitrile as the solvent, and anhydrous K₂CO₃ as the base) were purified by column chromatography to afford the final products in about 30% yield (see Supporting Information for chemical characterization).

Fluorescence measurements: The probes were dissolved in dimethyl sulfoxide (DMSO) to obtain 1 mM stock solutions, and then aliquots were diluted to 2 μ M with water containing a mixture of several buffers to facilitate titrations between pH 9 and 2 (40 mM of each sodium salt: acetate, phosphate, borate, and carbonate). All the measurements were performed in the presence of 100 mM NaCl to

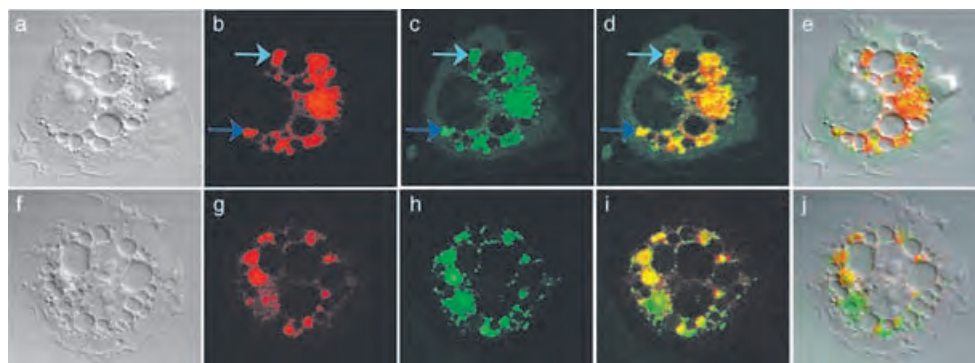


Figure 4. Distribution and co-localization of FG-H503 with lysosomal probes DND-189 (a–e) and DND-26 (f–j) in Raw 264.7 cells. Differential interference contrast (DIC; a, f) and fluorescence images of FG-H503 (b, g) and DND-189 (c) or DND-26 (h) were collected with a confocal laser scanning microscope in the DIC, DAPI, and FITC modes. d, i) Merged images of red and green channels; e, j) composite images of red, green, and DIC channels. DND-189 (a–e) and DND-26 (f–j) are from a different set of experiments.

bution. The probe predominantly co-localized with both DND-189 and DND-26, which indicates that the probe is taken up by the cells and that it localizes within acidic organelles. Note that the different excitation and emission wavelengths of FG-H503, as compared to those of the commercial probes, allow simultaneous visualization of both probes (FG-H503 and either DND-189 or DND-26) from the same intracellular compartment. Interestingly, the fluorescence intensity of FG-H503 appears to match that of DND-189: areas of low and high fluorescence (light and dark blue arrows, respectively, in Figure 4b–d) of the probe match those of DND-189, which indicates that the FG-H probe can distinguish between different pH values in the cell in a manner similar to the commercial probe. Analogous results are obtained from the joint use of FG-H503 and DND-26. Composite images of the fluorescence and differential interference contrast (Figure 4e, j) confirm that FG-H503 is located within acidic compartments of this macrophage cell line.

In summary, a new family of fluorescent macrocyclic peptidomimetic compounds has been synthesized, and their abilities as pH probes have been tested both in solution and in live cells with positive results. The synthetic modular scheme is an excellent approach for the development of new tailor-made probes with targeted pH “windows” ideal for measurement of the changing acidic environment of intracellular organelles. Current efforts involve the expansion of the FG-H family with other α -amino acids, spacers, and fluorophores, and determination of the extent by which the peptidomimetic nature of the new probes favors their performance in biological media.

maintain a constant ionic strength. Slight variations in the pH of the solutions were achieved by adding the minimum volumes (typically 10 μ L added to 10 mL) of 0.1–1.0 M NaOH or 0.1–1.0 M HCl, in such a way that dilution effects were negligible. Fluorescence spectra were recorded (Spex Fluorolog Max-2) with excitation at the wavelengths indicated in Table 1. Plots of the fluorescence intensity versus pH were fitted by using a nonlinear curve-fitting technique (Microcal Origin 6.0). All the measurements were carried out at ambient temperature and in air-equilibrated solutions. Copper(II) and zinc(II) were added as the chloride and nitrate salts, respectively (200 μ M).

Confocal fluorescence imaging: Raw 264.7, a mouse macrophage cell line, was cultured on 42-mm-diameter round glass coverslips in Dulbecco's modified Eagle's medium (MEM) containing fetal bovine serum (10%), L-glutamine (2 mg mL^{−1}), and antibiotics (penicillin/streptomycin). The cells were stimulated with interferon- γ (IFN- γ) and lipopolysaccharide (LPS) for 16 h, loaded with the dyes for 15 min in serum-free media, and then mounted on a stage at 37°C after changing to phenol-red-free L15 medium containing the above supplements. The cells were observed with a confocal laser scanning microscope (Carl Zeiss, LSM 510 meta) with 350- and 488-nm laser excitation for the 4,6-diamidino-2-phenylindole (DAPI) and fluorescein isothiocyanate (FITC) channels, respectively. An appropriate emission band was selected for the two fluorescent channels. A 63 \times , 1.4-NA objective was used to ensure high-resolution images. DIC images were collected simultaneously with transmitted light by excitation at 488 nm. Sequential rather than simultaneous acquisition was used to avoid bleed-through between the two fluorescent channels. Images were processed, and double- and composite-merged images were made with Adobe Photoshop.

Received: June 2, 2005

Published online: September 15, 2005

Keywords: biosensors · fluorescent probes · macrocycles · peptidomimetics · protonation

- [1] T. Hirano, K. Kikuchi, Y. Urano, T. Higuchi, T. Nagano, *Angew. Chem.* **2000**, *112*, 1094–1096; *Angew. Chem. Int. Ed.* **2000**, *39*, 1052–1054.
- [2] Z. H. Lin, M. Wu, M. Schaferling, O. S. Wolfbeis, *Angew. Chem.* **2004**, *116*, 1767–1770; *Angew. Chem. Int. Ed.* **2004**, *43*, 1735–1738.
- [3] N. Umezawa, K. Tanaka, Y. Urano, K. Kikuchi, T. Higuchi, T. Nagano, *Angew. Chem.* **1999**, *111*, 3076–3079; *Angew. Chem. Int. Ed.* **1999**, *38*, 2899–2901.
- [4] H. Kojima, Y. Urano, K. Kikuchi, T. Higuchi, Y. Hirata, T. Nagano, *Angew. Chem.* **1999**, *111*, 3419–3422; *Angew. Chem. Int. Ed.* **1999**, *38*, 3209–3212.
- [5] a) P. D. Beer, P. A. Gale, *Angew. Chem.* **2001**, *113*, 502–532; *Angew. Chem. Int. Ed.* **2001**, *40*, 486–516; b) R. Martínez-Máñez, F. Sancenón, *Chem. Rev.* **2003**, *103*, 4419–4476.
- [6] a) A. P. de Silva, H. Q. N. Gunaratne, T. Gunnlaugsson, A. J. M. Huxley, C. P. McCoy, J. T. Rademacher, T. E. Rice, *Chem. Rev.* **1997**, *97*, 1515–1566; b) A. W. Czarnik, *Acc. Chem. Res.* **1994**, *27*, 302–308; c) *Fluorescent Chemosensors for Ion and Molecule Recognition*, ACS Symp. Ser. **1993**, 538.
- [7] a) H. Izumi, T. Torigoe, H. Ishiguchi, H. Uramoto, Y. Yoshida, M. Tanabe, T. Ise, T. Murakami, T. Yoshida, M. Nomoto, K. Kohno, *Cancer Treat. Rev.* **2003**, *29*, 541–549; b) M. Chesler, *Physiol. Rev.* **2003**, *83*, 1183–1221; c) M. M. Wu, J. Llopis, S. Adams, J. M. McCaffery, M. S. Kulomaa, T. E. Machen, H.-P. H. Moore, R. Y. Tsien, *Chem. Biol.* **2000**, *7*, 197–209; d) A. M. Paradiso, R. Y. Tsien, T. E. Machen, *Nature* **1987**, *325*, 447–450.
- [8] a) R. P. Haugland, *Handbook of Fluorescent Probes and Research Products*, 9th ed., Molecular Probes, Eugene, OR, **2002**; b) Z. J. Diwu, C.-S. Chen, C. Zhang, D. H. Klaubert, R. P. Haugland, *Chem. Biol.* **1999**, *6*, 411–418; c) J. Liu, Z. J. Diwu, W.-Y. Leung, *Bioorg. Med. Chem. Lett.* **2001**, *11*, 2903–2905; d) H.-J. Lin, P. Herman, J. S. Kang, J. R. Lakowicz, *Anal. Biochem.* **2001**, *294*, 118–125; e) J. Liu, Z. Diwu, D. H. Klaubert, *Bioorg. Med. Chem. Lett.* **1997**, *7*, 3069–3072.
- [9] M. Schindler, S. Grabski, E. Hoff, S. M. Simon, *Biochemistry* **1996**, *35*, 2811–2817.
- [10] J. M. Holopainen, J. Saarikoski, P. K. J. Kinnunen, I. Jarvela, *Eur. J. Biochem.* **2001**, *268*, 5851–5856.
- [11] Patent pending. Application number GB 0509245.7
- [12] J. Becerril, M. Bolte, M. I. Burguete, F. Galindo, E. García-España, S. V. Luis, J. F. Miravet, *J. Am. Chem. Soc.* **2003**, *125*, 6677–6686.
- [13] a) F. Galindo, M. I. Burguete, S. V. Luis, *Chem. Phys.* **2004**, *302*, 287–294; b) F. Galindo, J. Becerril, M. I. Burguete, S. V. Luis, L. Vigara, *Tetrahedron Lett.* **2004**, *45*, 1659–1662; c) B. Escuder, J. Becerril, M. I. Burguete, F. Galindo, R. Gavara, J. F. Miravet, S. V. Luis, G. Peris, *Chem. Eur. J.* **2004**, *10*, 3879–3890.
- [14] J. S. Nowick, S. Insaf, *J. Am. Chem. Soc.* **1997**, *119*, 10903–10908.
- [15] a) A. P. de Silva, R. A. D. D. Rupasinghe, *J. Chem. Soc. Chem. Commun.* **1985**, 1669–1670; b) R. A. Bissell, E. Calle, A. P. de Silva, S. A. de Silva, H. Q. N. Gunaratne, J.-L. Habib-Jiwan, S. L. A. Peiris, R. A. D. D. Rupasinghe, T. K. S. D. Samarasinghe, K. R. A. S. Sandanayake, J.-P. Soumillion, *J. Chem. Soc. Perkin Trans. 2* **1992**, 1559–1564.
- [16] LysoSensor and LysoTracker probes are available from Molecular Probes, Eugene, OR, USA.
- [17] D. Rehm, A. Weller, *Isr. J. Chem.* **1970**, *8*, 259–271.
- [18] Such a different protonation behavior must occur for a combination of reasons. To partially explain the phenomenon, the observation made years ago for related systems (ref. [15b]) is relevant: The protonation of the second amine in a 9,10-

bis(aminomethyl)anthracene derivative is negatively influenced by the first protonated amine, as a result of the repulsion existing between its ammonium group and the second incoming proton. In this way, larger macrocycles like those presented here would protonate the second amine (and hence lead to restoration of the fluorescence) at a lower concentration of protons (higher pK_a) than the smaller macrocycles, as the former macrocycles would accommodate the second positive charge more easily than the latter. However, other contributions should not be disregarded, in particular solvation effects in protonated species. A more extensive study of a larger family of peptidomimetic molecules is in progress.

- [19] For a recent and comprehensive study of the effect of variations of the chemical structure on the photophysical properties of pH probes useful in vivo, see: C. J. Fahrni, L. Yang, D. G. VanDerveer, *J. Am. Chem. Soc.* **2003**, *125*, 3799–3812.

Host–Guest Systems

DOI: 10.1002/anie.200501867

Dielectric Properties of Porous Molecular Crystals That Contain Polar Molecules

Heng-Bo Cui, Kazuyuki Takahashi, Yoshinori Okano, Hayao Kobayashi, Zheming Wang, and Akiko Kobayashi*

Molecular materials with porous coordination frameworks have recently drawn considerable interest because of attractive properties arising from the synergy of the host lattice and the guest molecules. These properties include guest-switched spin-crossover transitions,^[1] gas sorption,^[2] molecular storage,^[3] and magnetic solvent sensing.^[4] However, to our knowledge, reports on the dielectric properties of porous molecular materials are rare, although the ferroelectric properties of molecular materials have been studied.^[5] As large charges can be induced in the highly polarizable materials upon application of a relatively low electric field, it may be useful to construct novel electronic devices such as

[*] Dr. H.-B. Cui, Dr. K. Takahashi, Dr. Y. Okano, Prof. H. Kobayashi
Institute for Molecular Science
and CREST, Japan Science and Technology Corporation
Okazaki 444-8585 (Japan)
Fax: (+81) 564-54-2254
E-mail: hayao@ims.ac.jp

Prof. Z. Wang
College of Chemistry and Molecular Engineering
Peking University
Beijing 100871 (China)

Prof. A. Kobayashi
Research Centre for Spectrochemistry
Graduate School of Science
The University of Tokyo
Hongo, Bunkyo-ku, Tokyo 113-0033 (Japan)

ferroelectric field-effect transistors.^[6] Except for ferroelectric (or antiferroelectric) materials, heavy-metal compounds such as PbCl_2 ($\epsilon_r = 33.5$ at 20°C), PbO ($\epsilon_r = 25.9$ at 20°C), and TlBr ($\epsilon_r = 30.3$ at 25°C) are typical materials with large dielectric constants, ϵ_r . It would be desirable to develop highly polarizable materials without pernicious heavy metal atoms, in particular, molecular materials with dielectric properties that switch between high and low dielectric states.

As most molecules do not have positional freedom in the crystalline state, the dielectric constants of molecular crystals are usually very small and almost independent of temperature. On the other hand, there exist polar molecules with fairly large polarizabilities in the liquid state. Considering that the guest molecules in the porous materials will have a large degree of positional freedom, molecular solids with large dielectric constants could be designed by the suitable combination of porous molecular materials and polar guest molecules. If the positions of the guest molecules are fixed at low temperature, the material will transform into a low dielectric system, thus allowing the desired variability between high and low dielectric states.

Water and methanol are typical solvents with high polarizabilities. The dielectric constants ϵ_r of H_2O , CH_3OH , and C_6H_6 measured down to 4.2 K are shown in Figure 1. In

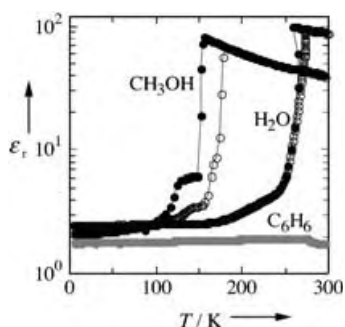


Figure 1. a) Plot of the dielectric constants ϵ_r of H_2O and CH_3OH as a function of temperature. The closed and open circles correspond to ϵ_r values of the cooling and heating processes, respectively. The dielectric constant of C_6H_6 is also presented for comparison.

contrast to nonpolar benzene, which displays a very small and constant dielectric constant, the ϵ_r value of liquid H_2O was as high as 10^2 just above the freezing point and then dropped very sharply. At low temperature, H_2O became a nonpolarizable material like benzene ($\epsilon_r \approx 2$ at 5 K). Similar behavior was observed for CH_3OH .

We then measured the dielectric constants for $[\text{Mn}_3(\text{HCOO})_6]$ and $[\text{Mn}_3(\text{HCOO})_6](\text{H}_2\text{O})(\text{CH}_3\text{OH})$ in the temperature range 4.2–300 K. As reported before, $[\text{Mn}_3(\text{HCOO})_6](\text{guest})$ (guest = vacant; H_2O and CH_3OH ; acetic acid; *N,N*-dimethylformamide, furan; or benzene and iodine) is a porous ferrimagnet ($T_c = 5\text{--}10\text{ K}$).^[7] Most guest molecules were removed below 100°C and the open framework was thermally stable up to about 260°C . The number of guest molecules was determined by elemental and thermogravimetric (TGA) analyses.^[8] We reexamined the TGA results and confirmed a 10% weight loss around 100°C , which

exactly corresponds to the weight percent of guest molecules in $[\text{Mn}_3(\text{HCOO})_6](\text{H}_2\text{O})(\text{CH}_3\text{OH})$. The dielectric constants of $[\text{Mn}_3(\text{HCOO})_6]$ and $[\text{Mn}_3(\text{HCOO})_6](\text{H}_2\text{O})(\text{CH}_3\text{OH})$ were measured for electric fields applied approximately parallel to the *a*, *b*, and *c* directions ($E = 1\text{ V}$, 10 kHz; Figure 2).

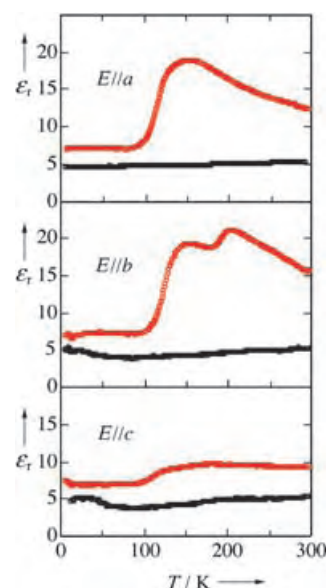


Figure 2. Plot of the dielectric constants ϵ_r of $[\text{Mn}_3(\text{HCOO})_6](\text{H}_2\text{O})(\text{CH}_3\text{OH})$ as a function of temperature (red) upon application of an electric field approximately parallel to the *a* ($E//a$), *b* ($E//b$), and *c* directions ($E//c$). The dielectric constants of $[\text{Mn}_3(\text{HCOO})_6]$ without guest molecules are also presented (black).

The porous crystal $[\text{Mn}_3(\text{HCOO})_6]$ without guest molecules showed a small dielectric constant that was basically independent of temperature. The difference between the maximum and minimum ϵ_r values in the temperature range 4.2–300 K was less than one for $E//a$, and about two for $E//b$ and $E//c$. Although relatively large changes were observed for $E//b$ and $E//c$, accurate measurements were difficult for these directions due to problems in cutting suitable rectangular parallelepipeds from small single crystals. The ϵ_r values of the guest-containing system $[\text{Mn}_3(\text{HCOO})_6](\text{H}_2\text{O})(\text{CH}_3\text{OH})$ increased with lowering temperature to a maximum of $\epsilon_r \approx 20$ around 150 K for $E//a$, and then decreased sharply to $\epsilon_r = 7$. This sharp decrease resembles the large drop of ϵ_r associated with liquid↔solid phase transitions of H_2O and CH_3OH shown in Figure 1. Thus, the guest molecules seem to be free to some extent at high temperature and then almost fixed at low temperature, as indicated by the large decrease in ϵ_r ; the movement of guest molecules is frozen fairly collectively around 120 K.

As expected, by insertion of polar molecules the porous molecular crystal could be changed into a novel system with high-temperature polarizable and low-temperature nonpolarizable states. Unlike the temperature dependencies of ϵ_r for H_2O and CH_3OH , no distinct hysteresis was observed. However, if it is considered that the guest molecules in the one-dimensional channel can contact with only a few other

guest molecules arranged along the channel (parallel to the b direction; see Figure 3), the sharp drop in ϵ_r is surprising.

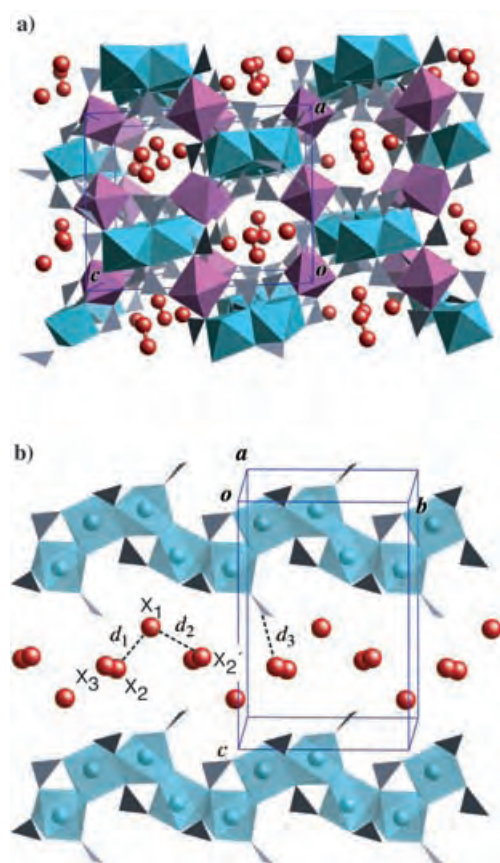


Figure 3. a) Perspective view of the crystal structure of $[\text{Mn}_3(\text{HCOO})_6]$. The edge-sharing MnO_6 octahedrons (pale blue) form an infinite chain along the b axis, which are connected by apex-sharing MnO_6 octahedrons (purple) to produce the channel structure along b . The red spheres in the channel are non-hydrogen atoms (C, O) of water and methanol molecules. The gray triangles are HCOO ligands. b) The array of the edge-sharing MnO_6 octahedrons and the arrangement of water and methanol molecules along the b axis (at 155 K). The positions of the non-hydrogen atoms of the guest molecules (X_1 , X_2 , and X_3) were obtained from the structure refinements based on the main peaks in the difference Fourier maps. The distance (d) from X_2 to X_3 is about 1.5 Å, and the distances from X_1 to X_2 and X_2 to X_3 are about 3.2 (d_1) and 3.5 Å (d_2) at 155 K, suggesting the alternating arrangement of water (X_1 or O) and methanol (X_2 , X_3) molecules along the b axis. The short contact of 3.2 Å (d_3) between the O atom of ligand HCOO and X_1 is consistent with the expected compact molecular packing along the c axis.

The temperature dependence of ϵ_r for $E//b$ showed two characteristic peaks around 200 K and 150 K followed by a sharp drop around 120 K; the latter peak seems to correspond to that observed for $E//a$ (Figure 2). For $E//c$, ϵ_r exhibited only small changes. The difference between the maximum and minimum values of ϵ_r was only about three. If we take into account the difficulty associated with accurate shaping of the crystal, the small changes in ϵ_r for $E//c$ around 120 K is insignificant. For $E//c$, there seems to be only a negligible contribution from the guest molecules. As the dielectric

properties of a liquid cannot be anisotropic, the anisotropic behavior of the dielectric properties of $[\text{Mn}_3(\text{HCOO})_6](\text{H}_2\text{O})-(\text{CH}_3\text{OH})$ cannot be explained by a simple liquid model of the guest molecules.

Similar measurements were made for $[\text{Mn}_3(\text{HCOO})_6](\text{CH}_3\text{OH})$ and $[\text{Mn}_3(\text{HCOO})_6](\text{C}_2\text{H}_5\text{OH})$ (Figure 4).^[9] As CH_3OH (Figure 1) and $[\text{Mn}_3(\text{HCOO})_6](\text{CH}_3\text{OH})$ display a

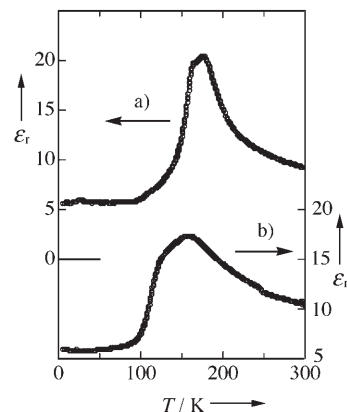


Figure 4. Plot of the dielectric constants of a) $[\text{Mn}_3(\text{HCOO})_6](\text{C}_2\text{H}_5\text{OH})$ and b) $[\text{Mn}_3(\text{HCOO})_6](\text{CH}_3\text{OH})$ for $E//a$ as a function of temperature. The dielectric constants of both systems exhibited negligible temperature dependencies for $E//b$ and $E//c$.

prominent peak around 150 K, the peak at 150 K for $[\text{Mn}_3(\text{HCOO})_6](\text{H}_2\text{O})(\text{CH}_3\text{OH})$ (Figure 2) might be related to a change in the polarizability of the CH_3OH molecules. It seems surprising that CH_3OH molecules in very different environments exhibit dielectric anomalies around the temperature of the bulk liquid \leftrightarrow solid transition. As H_2O shows a peak around 250 K (Figure 1), this solvent may be responsible for the peak observed at 200 K for $E//b$ (Figure 2). As shown in Figures 2 and 4, the polarizabilities of $[\text{Mn}_3(\text{HCOO})_6](\text{H}_2\text{O})-(\text{CH}_3\text{OH})$, $[\text{Mn}_3(\text{HCOO})_6](\text{CH}_3\text{OH})$, and $[\text{Mn}_3(\text{HCOO})_6](\text{C}_2\text{H}_5\text{OH})$ display a characteristic peak for $E//a$. Thus, guest molecules in $[\text{Mn}_3(\text{HCOO})_6]$ seem to have a considerable amount of freedom along the a direction at high temperature. However, for $E//b$, only $[\text{Mn}_3(\text{HCOO})_6](\text{H}_2\text{O})(\text{CH}_3\text{OH})$ gave the characteristic temperature dependence of ϵ_r . $[\text{Mn}_3(\text{HCOO})_6](\text{CH}_3\text{OH})$ and $[\text{Mn}_3(\text{HCOO})_6](\text{C}_2\text{H}_5\text{OH})$ showed small and featureless behaviors upon application of an electric field parallel to this direction. For $E//c$, every system demonstrated characterless dielectric behavior similar to that of $[\text{Mn}_3(\text{HCOO})_6]$.

To obtain information on the thermal motion of guest molecules in the low and high polarizability states, we reexamined the crystal structures at 90, 155, and 230 K,^[10] and calculated the channel spaces of $[\text{Mn}_3(\text{HCOO})_6](\text{H}_2\text{O})-(\text{CH}_3\text{OH})$. The unit cell volume (V_{cell}), the volume of the space occupied by the atoms of the host lattice (V_{host} , determined from the van der Waals radii), and the channel space ($V_{\text{por}} = V_{\text{cell}} - V_{\text{host}}$) were calculated to be $V_{\text{cell}} = 1769$, $V_{\text{host}} = 893$, and $V_{\text{por}} = 876 \text{ Å}^3$ at 230 K (for all calculations, similar values were obtained at 90 and 155 K).^[11] That is, about half of the volume of the unit cell is vacant. As the “van

der Waals volumes" (the volume occupied by the atoms based on the van der Waals radii) of CH₃OH and H₂O are 35.0 and 17.5 Å³, respectively, V_{guest} is 210 Å³ ($= (35.0 + 17.5) \times 4$) for the unit cell containing four CH₃OH and four H₂O molecules. Therefore, the guest molecules occupy only 24% of the vacant space (V_{por}) and have a large degree of positional freedom in the channel.

We first imagined the possibility of a "1D liquidlike state" for the guest molecules along the channel at high temperature, but the results of the dielectric measurements suggest that the packing of the guest molecules in the channel tends to be loose along the *a* direction (and not the *b* direction). Due to the heavy disorder of the guest molecules, it was very difficult to determine accurately their atomic positions, although the reliability factor of the structure refinement could be reduced significantly by including solvent molecules. The difference Fourier syntheses based on the host lattice atoms gave similar peak distributions at 230, 155, and 90 K. The peaks become relatively large at lower temperatures. The carbon and oxygen atoms of the CH₃OH molecules could not be located uniquely. However, the distribution of the large peaks suggested that the water and methanol molecules are arranged alternately along the channel (parallel to *b*; Figure 3b). The structure refinements gave extremely large temperature factors for the guest molecules (the average B_{eq} value of the non-hydrogen atoms was about 15 at 155 K); the temperature factors reflect not only the large thermal motion but also the broad distribution of the guest molecules in the channel. Examination of the distribution of the main peaks in the difference Fourier maps and the results of the subsequent structure refinements did not provide information on the distribution of the guest molecules. As for the roughly refined positions of the non-hydrogen atoms, there are no contacts shorter than 3.3 Å between guest molecules and the host lattice. The positions of the non-hydrogen atoms X₁, X₂, and X₃ (Figure 3) showed only slight changes between 230 and 155 K. However, the positions of X₂ and X₃ changed significantly between 155 and 90 K, suggesting an alteration in the molecular orientation of CH₃OH. Thus, the change in the orientation polarization due to the CH₃OH molecules is expected below 155 K, which is consistent with the assumption that the peak at 150 K is related to the change of polarizability of the CH₃OH molecules. It is suggested that the non-hydrogen atoms of the guest molecules are arranged along the *b* axis with very short contacts (3.2, 3.5 Å at 155 K; broken lines in Figure 3b). Therefore, the guest molecules do not appear to be as free along this direction. It is possible that the peak at 200 K for $E//b$ (Figure 2b) is related to the formation of weak O(methanol)⋯O(water) hydrogen bonds. However, due to the absence of information on the hydrogen atoms, clear structural evidence for the expected role of H₂O in the appearance of a peak at 200 K for $E//b$ was not obtainable. As seen from Figures 3a and b, the distribution of the guest molecules is fairly compact along the *c* direction (transverse direction of the channel). In contrast, the guest molecule seems to have a large open space along the *a* direction. These structural features then cause the anisotropic dielectric behavior of [Mn₃(HCOO)₆](H₂O)(CH₃OH).

Although the desired dielectric properties could be realized by the combination of porous molecular crystals and polar guest molecules, these properties do not originate from the simple 1D liquidlike behavior of the guest molecules. It is nonetheless interesting that molecules confined in the narrow 1D channel show sharp "transition-like behavior", because systems with strong a 1D nature generally do not exhibit this phase transition. As shown in Figure 4, [Mn₃(HCOO)₆](C₂H₅OH) demonstrates a surprisingly steep increase in the dielectric constant around 175 K. Such a strong temperature dependence of ϵ_r was quite unexpected. This behavior indicates the possibility of a collective freezing of guest molecules, which will be studied in the future. Other than porous molecular crystals with 1D channel structures, there are many interesting capsule-type molecular complexes.^[12] Can guest molecules confined in zero-dimensional nanocapsules exhibit characteristic dielectric behaviors? The dielectric properties of such cluster complexes that contain water molecules will be examined in the near future.

Experimental Section

The samples were synthesized according to a reported method.^[7] Freshly distilled water, methanol, ethanol, and benzene were used. The guest-containing crystals were obtained by soaking [Mn₃(HCOO)₆] crystals in these solvents. The temperature dependencies of the dielectric constants of H₂O, CH₃OH, C₆H₆, and [Mn₃(HCOO)₆](guest) (guest = vacant, CH₃OH, H₂O, CH₃OH, C₂H₅OH) were measured in the temperature range 4.2–300 K with an LCR meter (Precision Component Analyzer 6440B of Wayne Kerr Electronics). The liquid samples were measured by using a small cylindrical platinum cell with a cell volume of about 0.25 cm³ (the liquid samples were frozen at low temperatures). The single-crystal measurements were made with crystals cut into rectangular parallelepipeds (ca. 2.2 × 1.5 × 0.5 mm³). Silver conduction paste painted on the crystal surfaces was used as the electrodes. A 10-kHz electric field of 0.1 V (for the liquid sample) or 1 V (for the single crystal) was applied. Owing to the difficulties in shaping the small crystal, the accuracy of the dielectric constant obtained was not so high (especially for $E//b$ and $E//c$ because of the small size of the crystal along the *a* direction). However, the temperature dependencies were determined fairly precisely.

Received: May 30, 2005

Published online: September 15, 2005

Keywords: dielectric properties · host–guest systems · hybrid materials · inclusion compounds · porous materials

- [1] G. J. Halder, C. J. Kepert, B. Moubaraki, K. S. Murray, J. D. Cashion, *Science* **2002**, 298, 1762–1765.
- [2] a) M. Kondo, T. Okubo, A. Asami, S. Noro, T. Yoshitomi, S. Kitagawa, T. Ishii, H. Matsuzaka, K. Seki, *Angew. Chem.* **1999**, 11, 190–193; *Angew. Chem. Int. Ed.* **1999**, 38, 140–143; b) R. Kitaura, S. Kitagawa, Y. Kubota, T. C. Kobayashi, K. Kindo, Y. Mita, A. Matsuo, M. Kobayashi, H. C. Chang, T. C. Ozawa, M. Suzuki, M. Sakata, M. Takata, *Science* **2002**, 298, 2358–2361.
- [3] a) M. Eddaoudi, J. Kim, N. Rosi, D. Vodak, J. Watcher, M. O'Keefe, O. M. Yaghi, *Science* **2002**, 295, 469–472; b) N. L. Rosi, J. Eckert, M. Eddaoudi, D. T. Vodak, J. Kim, M. O'Keefe, O. M. Yaghi, *Science* **2003**, 300, 1127–1129; c) P. Sozzani, S. Bracco, A. Comotti, L. Ferretti, R. Simonutti, *Angew.*

- Chem.* **2005**, *117*, 1850–1854; *Angew. Chem. Int. Ed.* **2005**, *44*, 1816–1820.
- [4] D. Maspoch, D. Ruiz-Molina, K. Wurst, N. Domingo, M. Cavallini, F. Biscarini, J. Tejada, C. Rovira, J. Veciana, *Nat. Mater.* **2003**, *2*, 190–195.
- [5] a) S. Horiuchi, Y. Okimoto, R. Kumai, Y. Tokura, *Science* **2003**, *299*, 229–232; b) S. Horiuchi, F. Ishii, R. Kumai, Y. Okimoto, H. Tachibana, N. Nagaosa, Y. Tokura, *Nat. Mater.* **2005**, *4*, 163–166.
- [6] R. C. G. Naber, C. Tanase, P. W. M. Blom, G. H. Gelink, A. W. Marsman, F. J. Touwslager, S. Setayesh, D. M. Leeuw, *Nat. Mater.* **2005**, *4*, 243–248.
- [7] a) Z.-M. Wang, B. Zhang, H. Fujiwara, H. Kobayashi, M. Kurmoo, *Chem. Commun.* **2004**, 416–417; b) Z.-M. Wang, B. Zhang, T. Otsuka, K. Inoue, H. Kobayashi, M. Kurmoo, *Dalton Trans.* **2004**, *15*, 2209–2216; c) Z.-M. Wang, B. Zhang, M. Kurmoo, H. Fujiwara, T. Otsuka, H. Kobayashi, *Inorg. Chem.* **2005**, *44*, 1230–1237.
- [8] As reported in the supplementary data of reference [7a], the composition of $[\text{Mn}(\text{HCOO})_3](\text{H}_2\text{O})(\text{CH}_3\text{OH})$ was determined by elemental analysis and TGA measurements. We reexamined the TGA and confirmed the previous results. The chemical compositions of $[\text{Mn}_3(\text{HCOO})_6](\text{CH}_3\text{OH})_x$ and $[\text{Mn}_3(\text{HCOO})_6](\text{C}_2\text{H}_5\text{OH})_y$ were also determined by elemental analyses and TGA experiments. Although the content of CH_3OH could be larger than 1.0, these experiments indicated that both x and y were approximately equal to 1.0.
- [9] As the crystals of $[\text{Mn}_3(\text{HCOO})_6]$ were destroyed upon placement in water, the susceptibility of $[\text{Mn}_3(\text{HCOO})_6](\text{H}_2\text{O})_x$ could not be examined.
- [10] Although the details of the structural data of $[\text{Mn}_3(\text{HCOO})_6](\text{H}_2\text{O})(\text{CH}_3\text{OH})$ were reported in reference [7], we reexamined the crystal structures at 230, 155, and 90 K. We previously reported that the crystal has the space group $P2_1/c$, with $\beta \approx 127^\circ$. However, here we adopted the space group $P2_1/n$ in order for β to be approximately 90° so that it was easier to adjust the direction of the electric field E to each crystal axis: $[\text{Mn}_3(\text{HCOO})_6](\text{H}_2\text{O})(\text{CH}_3\text{OH})$, monoclinic, $P2_1/n$, $a = 11.683(1) \text{ \AA}$, $b = 10.166(1)$, $c = 14.904(2)$, $\beta = 91.674(3)^\circ$, $V = 1769 \text{ \AA}^3$, $Z = 4$, $R = 0.030$, $R_w = 0.033$ at 230 K ($R = 0.032$, $R_w = 0.036$ at 155 K and $R = 0.039$, $R_w = 0.047$ at 90 K).
- [11] Pauling's van der Waals radii were used.
- [12] For example, see: A. Lützen, *Angew. Chem.* **2005**, *117*, 1022–1025; *Angew. Chem. Int. Ed.* **2005**, *44*, 1000–1002.

DOI: 10.1002/anie.200500558

Quantitative Spatial Mapping of Mixing in Microfluidic Systems***Steven W. Magennis, Emmelyn M. Graham, and Anita C. Jones**

Microfluidics promises to revolutionize chemical analysis,^[1,2] synthesis,^[3–5] and biotechnology^[6] by combining processes such as mixing, separation, reaction, and detection in a single device. These systems function as “labs-on-a-chip”,^[7] creating a technology that is low-cost, high-throughput, miniaturized, and automated. Their decreased size imparts microfluidics with many benefits, but miniaturization results in a fundamental change in flow characteristics. Turbulent flow predominates at the macroscale, whereas fluids flow in a laminar fashion at the microscale, without the random mixing that is characteristic of turbulence.^[8] These laminar flow conditions mean that multiple fluid streams tend to flow in parallel through microchannels, mixing only by diffusion across their interfaces.^[9] Whereas laminar flow behavior has been exploited to good effect in microanalytical systems, many emerging applications of microfluidic devices require rapid and efficient mixing.

Miniaturizing the mixing process has been identified as a major hurdle in the performance and development of microfluidic devices.^[10] In labs-on-a-chip, the purpose of mixing is generally to bring together solute species from two (or more) flows. In the laminar flow regime, mixing occurs slowly by diffusion of solute (and solvent) molecules across the flow boundary. For rapid mixing, laminar flow must be disrupted to give chaotic mixing, in which there is bulk transfer of fluid (solvent carrying solute) between the flows.

Micromixers can be either passive (static) or active devices. Passive micromixing strategies frequently rely on diffusion-controlled mixing, with multilamination or flow-splitting techniques to minimize the mixing equilibration time.^[11] To increase the mixing rate beyond that limited by diffusion, passive mixers that induce lateral transport of fluid between streams have been devised.^[12,13] Active micromixers use miniature stirrers or external fields to chaotically

[*] Dr. S. W. Magennis, E. M. Graham, Dr. A. C. Jones
Collaborative Optical Spectroscopy, Micromanipulation and
Imaging Centre (COSMIC)
and the School of Chemistry
The University of Edinburgh
King's Buildings, Edinburgh EH9 3JZ (UK)
Fax: (+44) 131-650-4743
E-mail: a.c.jones@ed.ac.uk

[**] This work was supported by the EPSRC Insight Faraday Partnership, SHEFC and Lab 901 Ltd. We thank Andy Garrie for fabricating the flow cell, and Dave Towers and Ken Macnamara for helpful discussions.



Supporting information for this article is available on the WWW under <http://www.angewandte.org> or from the author.

intersperse fluid flows. In spite of the increasing attention paid to the mixing problem, devices are still designed by trial-and-error methods.^[14] It is therefore essential that techniques that permit the visualization of fluid composition with high quantitative and spatial resolution are found. This will allow testing of prototype devices and will provide essential experimental data to guide the development of theoretical models and to validate computational simulations. Computational fluid dynamics models have proven useful in preliminary mixer designs, but a rigorous understanding of the fundamental principles of microfluidics would lead to the development of better models for complex mixing devices.^[15]

The most common methods for visualizing flow and mixing efficiency are fluorescence intensity imaging^[9,10,13,16] and transmitted light microscopy with colored dyes, pH indicators, and colored reaction products.^[8,15,17] These techniques are relatively cheap, easy to set up, and, in the case of fluorescence imaging, provide excellent contrast. Unfortunately, the ability of these intensity-based techniques to provide a quantitative picture of fluid composition in microfluidic systems is severely limited by their sensitivity to variations in the optical path, instability of the light source, scattering, uncertainty in the dye concentration, and photobleaching effects.^[18]

Herein, we describe a superior approach to the imaging of microfluidic systems by using fluorescence lifetime imaging microscopy (FLIM). This technique involves spatially resolving the fluorescence lifetime of a fluorescent dye, rather than the intensity. It overcomes all of the aforementioned problems of intensity-based methods, because the lifetime is independent of the number of fluorescing molecules. To date, the use of FLIM has been restricted to the imaging of biological systems.^[19–21] Herein, we demonstrate that FLIM enables spatially resolved quantitation of fluid mixing in microfluidic devices.

Solutions of the fluorescent dye 1,8-anilinonaphthalene sulfonate (ANS) in pure methanol and a water/methanol mixture (1:1 molar ratio, which corresponds to water at 30.8% v/v) were pumped into a microchannel flow cell to meet head-on at a T-junction, as illustrated in Figure 1a. The flow channels had a depth of 200 μm and a width of 400 μm . The flow rates were varied from 10–75 $\mu\text{L min}^{-1}$. These dimensions and flow rates correspond to Reynolds numbers of less than 10 so that the fluids are in the laminar flow regime.^[17]

Fluorescence lifetime images were obtained by using wide-field illumination of the microfluidic cell with an ultrafast pulsed laser. A gated intensified CCD camera was used to collect the resultant fluorescence within a short time window after a defined delay following the laser pulse. A series of images was acquired by varying the delay time between the detection window and the laser pulse, thereby sampling the entire fluorescence decay of the ANS probe (Figure 1b); the data from each pixel was then fitted to a single exponential decay. ANS was chosen as the dye because its fluorescence lifetime is extremely sensitive to the composition of water/methanol mixtures, showing a near-linear variation from 250 ps in pure water to 6 ns in pure methanol.^[22] The calibration curve in Figure 1c, which correlates

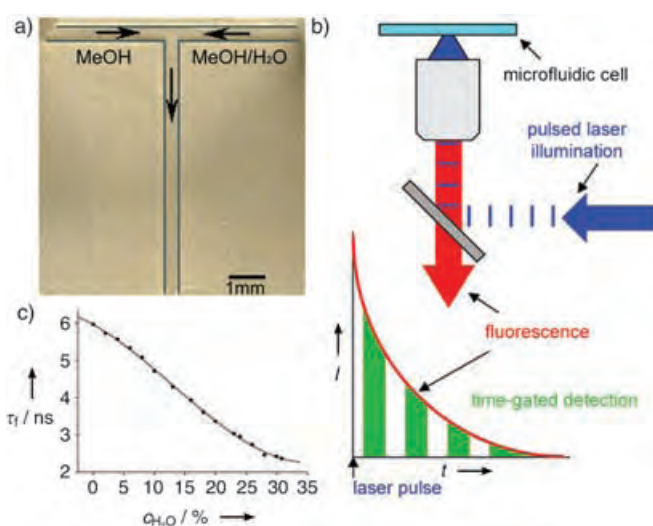


Figure 1. a) Photograph of the microfluidic flow cell, in which arrows indicate the direction of flow; the channel edges have been highlighted for clarity. b) Schematic of fluorescence lifetime imaging microscopy (FLIM). c) Calibration curve showing ANS fluorescence lifetime (τ_f) as a function of the methanol/water ratio in the solution. The following equation gave a good fit to the data: $\gamma = 5.97258 - (0.09267x) - (0.00382x^2) + (9.82168 \times 10^{-5}x^3)$, in which γ is the lifetime in ns and x is the concentration of water (% v/v) in the water/methanol mixture. The concentration of ANS was 1 mM. Lifetimes were measured by TCSPC. The decays and fitted data are given in the Supporting Information.

the fluorescence decay rate of ANS with the percentage of water in solution, was determined by time-correlated single-photon counting (TCSPC, Supporting Information). ANS displays a single exponential decay at all water/methanol ratios, making it an ideal and unambiguous probe of solvent composition.

The effectiveness of the time-resolved technique is demonstrated in Figure 2, which compares intensity and lifetime images for two regions of the flow cell during a typical experiment. The intensity and FLIM images, which are displayed with the same pseudocolor scale, are noticeably different. The intensity images (Figure 2a) show large, irregular variations in intensity across the field of view, with the regions of highest intensity located near the input of the solution of ANS in methanol. The FLIM images give a clear and unambiguous picture of the liquid composition (Figure 2b). These images show smooth transitions from long to short lifetime (left to right), across a clearly defined mixing region. By using the calibration curve in Figure 1c, the solution composition at each point in the FLIM image can be directly determined. In principle, there should be a clear correlation between the intensity images and the lifetime images; the longer the fluorescence lifetime, the higher the quantum yield and hence the higher the fluorescence intensity (given that the ANS concentration is constant). In practice, however, no such correlation is apparent, and it is clear that the intensity-based images are strongly distorted by variation of the illuminating field, the collection efficiency, and the other variables mentioned above. The microfluidic flow cell

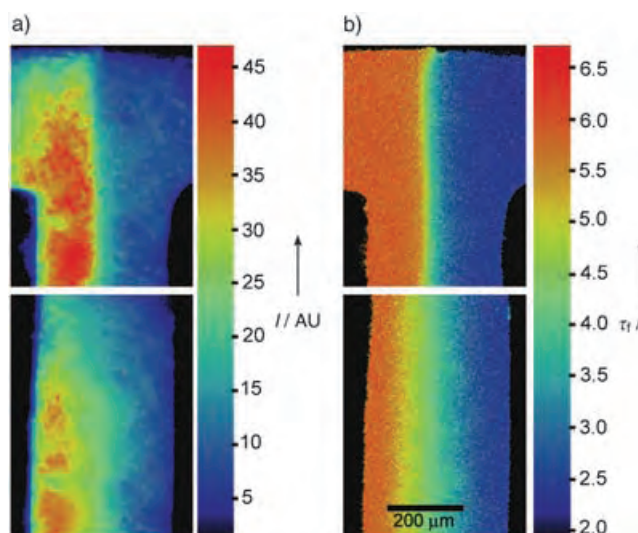


Figure 2. Comparison of a) fluorescence intensity images with b) FLIM images for the mixing of solutions of ANS in pure methanol and ANS in a water/methanol mixture (30:70 v/v) by using the arrangement shown in Figure 1a. The concentration of ANS in both input solutions was 1 mM, and the flow rate was 50 $\mu\text{L min}^{-1}$. For FLIM, the gate width was 600 ps, and 46 images were recorded at intervals of 500 ps. Every image represents the average of five separate exposures, each with an integration time of 0.1 s and a readout time of 50 ms to give a total acquisition time of about 35 s. The lifetimes of ANS in pure methanol and the equimolar water/methanol solution at the input to the flow cell are the same as those measured by the TCSPC method. The intensity image was constructed by summing the lifetime images, which allows a direct comparison between the time-resolved and intensity-based methods. By using the calibration curve in Figure 1c, the composition of the fluid can be read directly from the FLIM map.

used in this study is of a simple design, and it is likely that intensity-based imaging will be even more prone to optical artifacts in complex devices. FLIM, on the other hand, faithfully reports the fluid composition, as the lifetime is governed solely by the solvent environment of the ANS probe, and is immune to other undesirable effects.

The FLIM technique has been used to monitor mixing as a function of flow rate and flow distance (Figure 3). The compositional variation observed in Figure 3 is indicative of two fluids under laminar flow, as expected. One striking feature of the resultant images is how little mixing occurs in the region where the two input streams meet. Despite being forced together, there is no sign of turbulent mixing. The input streams are well-behaved, with no fluctuations in the position of the boundary between them (Supporting Information). Instead, the two streams stay completely separate, except for a narrow mixing region that results from diffusion. The overall trend is for the mixing region to broaden as the flow rate decreases and as the fluids move further downstream, as expected for diffusion-controlled mixing. For the highest flow rate (75 $\mu\text{L min}^{-1}$), regions that are identical in composition to the input streams persist, even after traveling 1 cm

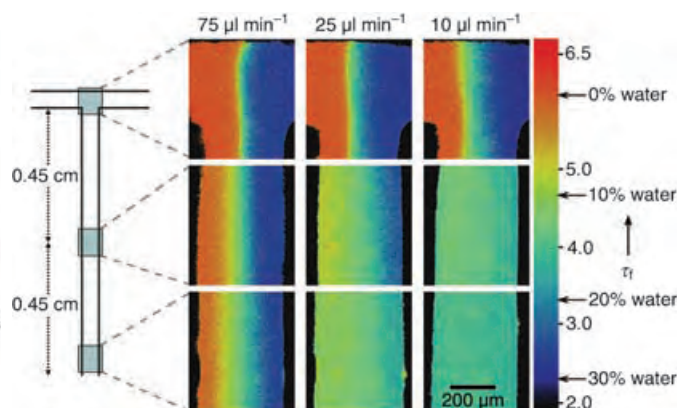


Figure 3. FLIM images for the mixing of solutions of ANS in pure methanol and ANS in a water/methanol mixture (30:70 v/v), showing the spatial dependence of fluorescence lifetime (τ_f) on the flow rate and the position within the flow cell. Images were acquired at three positions in the flow cell and for three flow rates, as indicated. Other experimental parameters are as described for Figure 2b.

down the channel. In contrast, the two fluids have completely mixed at this distance downstream at the lowest flow rate (10 $\mu\text{L min}^{-1}$).

FLIM allows mixing to be monitored with high spatial resolution (Figure 4a,b); it is possible to accurately measure small changes in the fluid composition in sub-picoliter interrogation volumes. The technique is sensitive enough to reliably detect a change in the volume fraction of approximately 2% (Figure 4c); this is equivalent to a lifetime change of about 250 ps, which is a measurement limit set by the

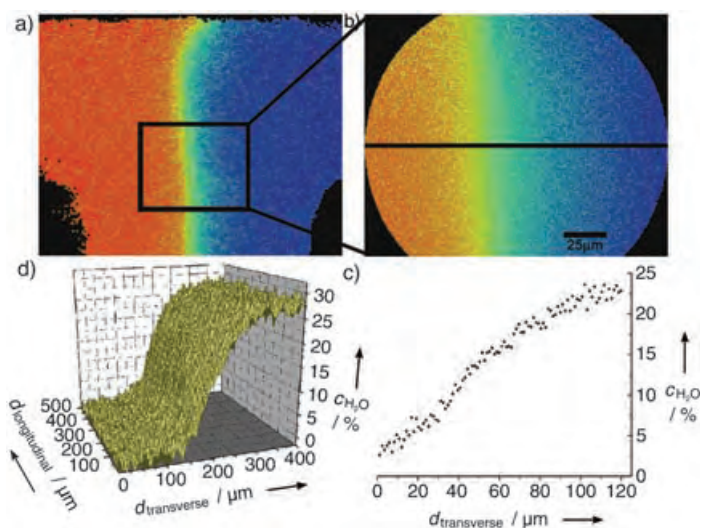


Figure 4. Quantitation of mixing by using FLIM: a) FLIM image of the mixing of methanol and water/methanol with a 20x objective. The arrangement shown in Figure 1a was used, and the flow rate was 75 $\mu\text{L min}^{-1}$. b) Expanded image of the same mixing region from a 100x objective. c) Composition profile along the cross section indicated in Figure 4b. d) Representation of the fluorescence lifetime data in Figure 4a as a composition surface; composition values were calculated with the calibration curve in Figure 1c.

temporal width of the detection windows. The compositional resolution could be improved by increasing the time-resolution of fluorescence detection, using photon counting methods. This method is equally applicable to diffusion-controlled mixing (the fluorescence lifetime responds to the net diffusion of water molecules across the flow boundary) and mixing by mass transport of fluid. Therefore, it is generally applicable to the evaluation of all types of micro-mixers. The quantitative spatial profiles of fluid composition that can be generated by FLIM (Figure 4c,d) will be particularly valuable for supporting and guiding theoretical models of fluid flow in microfluidic systems.

The present results demonstrate that wide-field FLIM can directly measure the 2D mixing of fluids in microfluidic systems with a level of quantitation that is not available from other methods. It has been shown that intensity-based techniques such as confocal microscopy^[13] and optical coherence tomography^[23] can provide 3D imaging of microfluidic flows. This is important for cases in which the variations in fluid composition are aligned with the optical axis, as these cannot be resolved by intensity-based wide-field methods.^[23] Our wide-field FLIM technique would, however, detect nonuniform mixing along the optical axis, that is, the depth axis of the microchannel, as the superposition of a number of layers of varying composition along this axis would result in the observation of a multiexponential fluorescence decay, rather than the single exponential decay characteristic of uniform mixing throughout the depth of field. The FLIM approach can be extended to full 3D imaging with confocal or multiphoton excitation without loss of the attendant benefits of time-resolved detection that have been established herein. In this version of the technique, the tightly focused excitation laser beam is raster-scanned across the sample, and the fluorescence decay is acquired point-by-point, using TCSPC. The use of multiphoton excitation would also enhance imaging penetration through strongly absorbing or scattering fluids and structures.

The mixed solvent system reported herein, in conjunction with the ANS probe, was devised purely as a measurement tool for the generic study of micromixing, and was not intended to relate to any specific applications of lab-on-a-chip systems. Our approach is, however, generally applicable to any solvent system, as long as there is a change in molecular environment upon mixing that results in variation in the fluorescence lifetime of an appropriate probe. For example, the mixing of aqueous solutions could be studied by using streams of different pH that incorporate a pH-sensitive dye, such as a seminaaphthorhodafluor (SNARF) probe. Alternatively, streams containing different concentrations of a collisional quencher, such as iodide, could be used. In view of the flexibility of this approach, we anticipate that FLIM will become an essential tool in the design, modeling, and evaluation of microfluidic systems.

Experimental Section

All measurements were made with the ammonium salt of ANS (Fluka, used as received). The methanol and water used in this study

were HPLC grade (Fisher Scientific) and were used as received. Solutions of ANS (≈ 1 mM) were stored in the dark, and the lifetime of ANS fluorescence at room temperature was used as a routine check of sample purity after storage. No emission could be detected from the solvents under the instrumental conditions employed. Time-resolved fluorescence spectroscopy was performed by using the technique of TCSPC as described previously.^[22]

The microfluidic cell was fabricated from Perspex with the T-shaped channel milled out to a depth of 0.2 mm using an end mill of diameter 0.4 mm (Drill Service Ltd.). The three inlet/outlet holes were drilled 1.6 mm in diameter and fitted with polypropylene tubing. The cell was sealed by gluing (Norland Optical Adhesive No. 61) a cover-glass over the channels, and was attached to syringes with silicone tubing. The flow of fluids from the syringes was controlled by a syringe pump (Univentor 802, Univentor Ltd.).

For FLIM, frequency-doubled light from a mode-locked Ti sapphire laser ($\lambda = 400$ nm, repetition rate = 4.75 MHz) was expanded, collimated, and directed into a Nikon TE300 inverted microscope operating in an epifluorescence configuration. This excitation light was reflected from a dichroic filter (DM430, Nikon) and focused onto the microfluidic flow cell with either $20\times$ (PA, NA = 0.75, Nikon) or $100\times$ (Ph3, NA = 1.3, oil immersion, Nikon) objectives. The laser power incident on the flow cell was typically ≈ 100 μ W. The resultant fluorescence was collected through the same objective, passed through a barrier filter (515–555 nm, Nikon) and imaged onto a Picostar HR-12QE gated intensified CCD camera system (LaVision GMBH, Berlin). The excitation beam was split, and one portion was used to trigger a fast photodiode. The photodiode output was passed through a constant fraction discriminator (CF4000, Ortec), and used as the trigger signal for the Picostar system. The experiments described herein were recorded with a gate width of 600 ps, which was measured by detecting laser light reflected from a mirror (the minimum gate width for this camera is 200 ps). The intensifier gate was delayed relative to the laser trigger signal by using a DEL150 picosecond delay module (Becker and Hickl). The 12-bit CCD camera is a progressive scan interline sensor ($1370(\text{H}) \times 1040(\text{V})$ pixels; pixel size = 6.45×6.45 μm^2). Images were the average of five separate exposures, were recorded in steps of 500 ps over a range of 23 ns, and employed 4×4 hardware binning. The integration time for each image was 100 ms, with a readout time of 50 ms to give a total acquisition time of approximately 35 s. The excitation intensity was adjusted to give a peak intensity of 3000–4000 counts in the brightest image, which corresponds to the start of the fluorescence decay. The background signal of ≈ 50 counts was subtracted from each image. DaVis 6.2 software running the Picostar DaVis module was used to control the Picostar system and delay card, and to analyze the data. The peak of the fluorescence intensity was found in the fourth image of the image series. To ensure that the instrument response did not interfere with the fitting, the first five images were not used for analysis. The sixth image (which was 1 ns after the peak) and subsequent images were analyzed to allow a decay curve to be constructed for each pixel. Pixels with low counts in the first analyzed image (typically 700 counts) were removed at this stage. Each of these curves was then fitted to a single exponential decay. A lifetime map was produced by assigning a color on a 16-bit pseudocolor scale to each of the fitted lifetimes, and these were displayed over a range of 2.0–6.8 ns.

Received: February 15, 2005

Revised: June 24, 2005

Published online: September 21, 2005

Keywords: fluorescence · imaging · microfluidics · microreactors · mixing

- [1] T. Vilkner, D. Janasek, A. Manz, *Anal. Chem.* **2004**, 76, 3373.
- [2] A. Hibara, M. Nonaka, M. Tokeshi, T. Kitamori, *J. Am. Chem. Soc.* **2003**, 125, 14954.
- [3] S. Xu, Z. Nie, M. Seo, P. Lewis, E. Kumacheva, H. A. Stone, P. Garstecki, D. B. Weibel, I. Gitlin, G. M. Whitesides, *Angew. Chem.* **2005**, 117, 734; *Angew. Chem. Int. Ed.* **2005**, 44, 724.
- [4] H. Song, J. D. Tice, R. F. Ismagilov, *Angew. Chem.* **2003**, 115, 792; *Angew. Chem. Int. Ed.* **2003**, 42, 768.
- [5] P. D. I. Fletcher, S. J. Haswell, E. Pombo-Villar, B. H. Warrington, P. Watts, S. Y. F. Wong, X. Zhang, *Tetrahedron* **2002**, 58, 4735.
- [6] M. U. Kopp, A. J. de Mello, A. Manz, *Science* **1998**, 280, 1046.
- [7] D. R. Reyes, D. Iossifidis, P.-A. Auroux, A. Manz, *Anal. Chem.* **2002**, 74, 2623.
- [8] B. Zhao, J. S. Moore, D. J. Beebe, *Science* **2001**, 291, 1023.
- [9] B. H. Weigl, P. Yager, *Science* **1999**, 283, 346.
- [10] H. Chen, J.-C. Meiners, *Appl. Phys. Lett.* **2004**, 84, 2193.
- [11] L. E. Locascio, *Anal. Bioanal. Chem.* **2004**, 379, 325.
- [12] T. J. Johnson, D. Ross, L. E. Locascio, *Anal. Chem.* **2002**, 74, 45.
- [13] A. D. Stroock, S. K. W. Dertinger, A. Ajdari, I. Mezja, H. A. Stone, G. M. Whitesides, *Science* **2002**, 295, 647.
- [14] J. M. Ottino, S. Wiggins, *Science* **2004**, 305, 485.
- [15] F. Schönfeld, V. Hessel, C. Hofmann, *Lab Chip* **2004**, 4, 65.
- [16] M. S. Munson, P. Yager, *Anal. Chim. Acta* **2004**, 507, 63.
- [17] P. J. A. Kenis, R. F. Ismagilov, G. M. Whitesides, *Science* **1999**, 285, 83.
- [18] R. M. Clegg, O. Holub, C. Gohlke, *Methods Enzymol.* **2003**, 360, 509.
- [19] F. G. Haj, P. J. Verveer, A. Squire, B. G. Neel, P. I. H. Bastiaens, *Science* **2002**, 295, 1708.
- [20] T. W. J. Gadella Jr., T. M. Jovin, *J. Cell Biol.* **1995**, 129, 1543.
- [21] J. R. Lakowicz, H. Szmajdzinski, K. Nowaczyk, M. L. Johnson, *Proc. Natl. Acad. Sci. USA* **1992**, 89, 1271.
- [22] L. Dougan, J. Crain, H. Vass, S. W. Magennis, *J. Fluoresc.* **2004**, 14, 91.
- [23] C. Xi, D. L. Marks, D. S. Parikh, L. Raskin, S. A. Boppart, *Proc. Natl. Acad. Sci. USA* **2004**, 101, 7516.

DOI: 10.1002/anie.200501331

The Internal Structure of Helical Pores Self-Assembled from Dendritic Dipeptides is Stereochemically Programmed and Allosterically Regulated**

Virgil Percec,* Andrés E. Dulcey, Mihai Peterca, Monica Ilies, Janine Ladislaw, Brad M. Rosen, Ulrica Edlund, and Paul A. Heiney

Pore-forming proteins, peptides, and their remodeled structures perform diverse biological and biologically inspired functions. These include the formation of viral helical coats^[1a] and transmembrane channels,^[1b,c] mediation of protein folding,^[1d] reversible encapsulation,^[1e] stochastic sensing,^[1f] as well as pathogenic^[1g] and antibacterial^[1h] activity. Synthetic strategies to obtain porous or tubular supramolecular assemblies have been elaborated.^[2] However, only several synthetic supramolecular pore structures are stable in solution and in solid state.^[3] Recently, we reported a class of amphiphilic dendritic dipeptides (amphiphilic dendrons functionalized at their apex with a dipeptide) that self-assemble both in solution and in bulk into supramolecular helical pores.^[4a] A *trans* conformation of the dendron is required to mediate self-assembly and to provide a new hydrogen-bonding mechanism of a parallel and partially interdigitated array of dipeptides. This conformation is selected by a solvophobic solvent^[4a] or in solid state by the microsegregation of the aliphatic and aromatic parts of the dendron. It has also been suggested that the stereochemistry of the peptide determines the sense of the helical pore.^[4]

Herein, we report that the structure of the helical porous structure self-assembled from dendritic dipeptides is programmed by the stereochemistry encoded in the dipeptide. A combination of solution and solid-state analysis techniques together with molecular modeling has been used to provide the sequential pathway to this self-assembly process that

[*] Prof. V. Percec, A. E. Dulcey, Dr. M. Ilies, J. Ladislaw, B. M. Rosen, Dr. U. Edlund

Roy & Diana Vagelos Laboratories, Department of Chemistry
Laboratory for Research on the Structure of Matter
University of Pennsylvania
Philadelphia, PA 19104-6323 (USA)
Fax: (+1) 215-573-7888
E-mail: percec@sas.upenn.edu

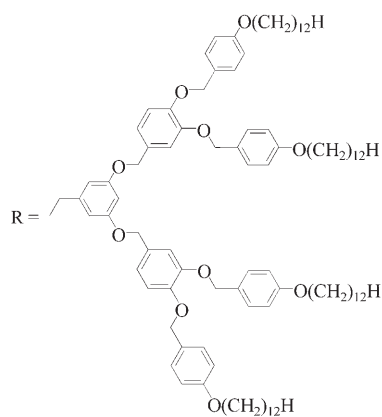
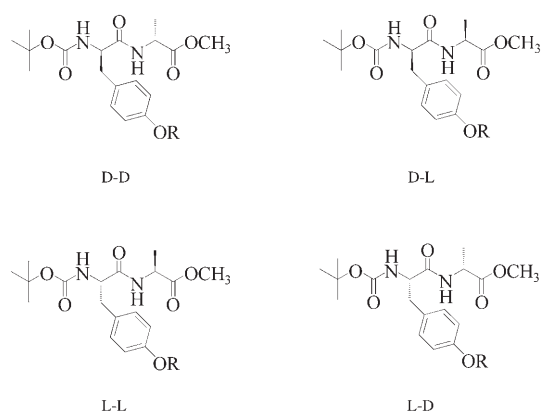
M. Peterca, Prof. P. A. Heiney
Department of Physics and Astronomy
Laboratory for Research on the Structure of Matter
University of Pennsylvania
Philadelphia, PA 19104-6396 (USA)

[**] Financial support by the National Science Foundation (DMR-9996288 and DMR-0102459) and the Office of Naval Research is gratefully acknowledged.



Supporting information for this article is available on the WWW under <http://www.angewandte.org> or from the author.

seems to operate by allosteric^[5] control. The dendritic dipeptide used in these investigations is (4-3,4-3,5)12G₂-CH₂-X, in which X = Boc-L-Tyr-L-Ala-OMe, Boc-D-Tyr-D-Ala-OMe, Boc-L-Tyr-D-Ala-OMe and Boc-D-Tyr-L-Ala-OMe, and Boc = *tert*-butoxycarbonyl.



In a previous communication,^[4a] we reported the self-assembly of an L-L dendritic dipeptide in solvophobic solvents^[2f,6a,6b] such as cyclohexane and deuterated cyclohexane by a combination of ¹H NMR spectroscopy, UV/Vis and circular dichroism (CD) techniques. Small- and wide-angle X-ray diffraction (XRD) experiments were carried out on powder and oriented fibers obtained from the porous structures assembled from L-L, D-D, L-D, D-L, and from the racemic dendritic dipeptides. The pore diameter (d_{pore}) was computed for all samples from XRD data^[4a,b] at temperatures between 71 and 75.4°C in their 2D hexagonal columnar liquid-crystal phase. XRD experiments on oriented fibers concluded that the amphiphilic dendron mediates the self-assembly into a helical structure, the helical sense of which is endowed by the stereochemistry of the Tyr residue. This mechanism is related to other examples in which a stereocenter determines the twist sense of racemic helical structures,^[6a-e] as suggested by the groundbreaking work of Green et al.^[6c] However, the assembly of our system differs from published examples in

which a stereocenter induces helicity in an achiral tubular assembly^[2g] and in other supramolecular structures.^[6f] It is also the dipeptide part of the dendron apex that directs the self-assembly into porous^[4a] rather than closed supramolecular columnar structures.^[7] However, the role of the stereochemistry of Ala, the potential cooperativity between the stereochemistry of Ala and Tyr, the structure of the dendron in the supramolecular assembly, and the stability of the porous structure at various temperatures are important mechanistic questions that were not previously addressed.^[4a]

The CD data of L-L, D-D, L-D, and D-L dendritic dipeptides obtained at different temperatures during their self-assembly in cyclohexane are compared in Figure 1. In all cases, only the weak positive or negative Cotton effect associated with the molecular solution of a dendritic dipeptide^[4a] is observed above 30°C (inset in Figure 1). Below 30°C the dendritic dipeptides self-assemble into helical porous columns, and their CD data are associated with the aromatic part of the helical supramolecular dendrimer as demonstrated by wide-angle XRD on oriented fibers^[4a] (Figure 2), and by CD and

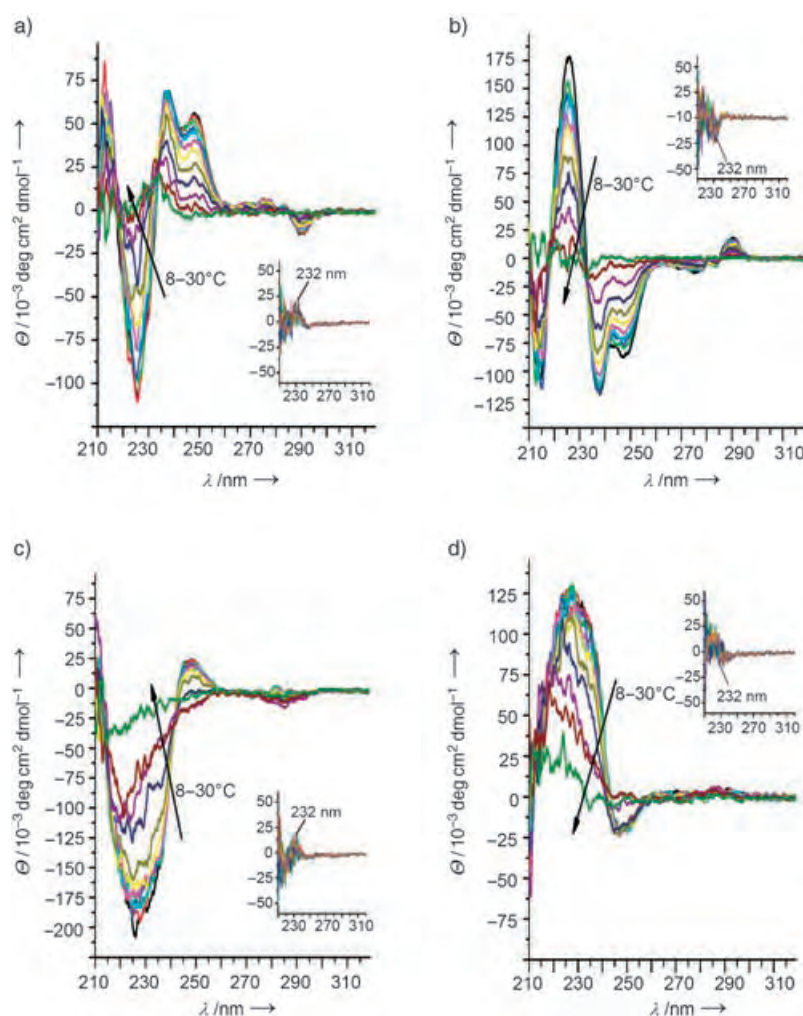


Figure 1. CD spectra (1.6×10^{-4} M in cyclohexane) of a) (4-3,4-3,5)12G₂-CH₂-Boc-L-Tyr-L-Ala-OMe; b) (4-3,4-3,5)12G₂-CH₂-Boc-D-Tyr-D-Ala-OMe; c) (4-3,4-3,5)12G₂-CH₂-Boc-L-Tyr-D-Ala-OMe; d) (4-3,4-3,5)12G₂-CH₂-Boc-D-Tyr-L-Ala-OMe. The arrows indicate temperature increases. Insets: 30–60°C.

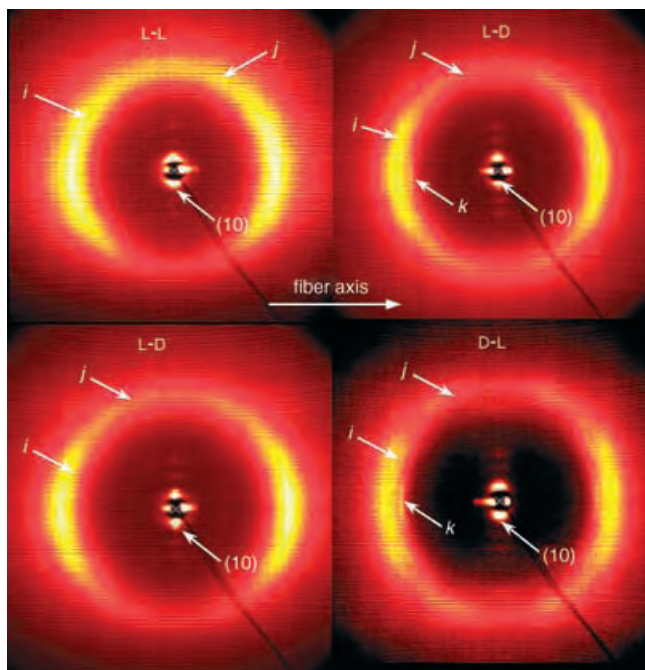


Figure 2. X-ray diffraction patterns of aligned fibers collected at 23 °C from the dendritic dipeptides L-L, D-D, L-D, and D-L. *i* = short-range helical feature of dendron at ≈ 4.5 Å, *j* = dendron tilt $\approx 60^\circ$, *k* = 5-Å registry along the column axis feature.

UV/Vis spectra of model dendrons with and without dipeptide stereocenters (Supporting Information). The CD data of L-L with D-D, and of L-D with D-L dendritic dipeptide assemblies show respective mirror-image Cotton effects. However, the CD results of L-L and D-D are different from those of L-D and D-L. This structural difference observed by CD is supported by the XRD patterns obtained from aligned samples (Figure 2). The XRD of L-L is similar with that of D-D while that of L-D to that of D-L derived porous structures. The *k* diffraction of L-D and D-L is sharper than that of L-L and D-D. In L-L and D-D, *k* is most likely overlapped with the *i* diffraction (Figure 2).

The difference between the CD of the L-L/D-D pair and those of the L-D/D-L pair indicates that the stereochemistry of Ala also plays an important role in the programming of the supramolecular pore structure. These different CD data are generated by various modes of intramolecular and intermolecular dendron arrangements in the helical porous structure that are induced by dipeptide stereochemistry.

To quantify the role of the stereochemistry of Tyr and Ala we used both small- and wide-angle XRD to investigate the structure of the supramolecular pore. The temperature-dependence of the column (d_{col}) and pore (d_{pore}) diameters^[4a,b] is shown in Figure 3 for all combinations of dipeptide stereochemistry (XRD data provided in the Supporting Information). Regardless of the dipeptide stereochemistry, the supramolecular assemblies exhibit a glass transition (T_g) at 57 to 60 °C, followed by the 2D columnar hexagonal phase that becomes an isotropic liquid at 94 °C for L-D and D-L, and at 96 °C for L-L and D-D.^[4a] Within experimental error, both

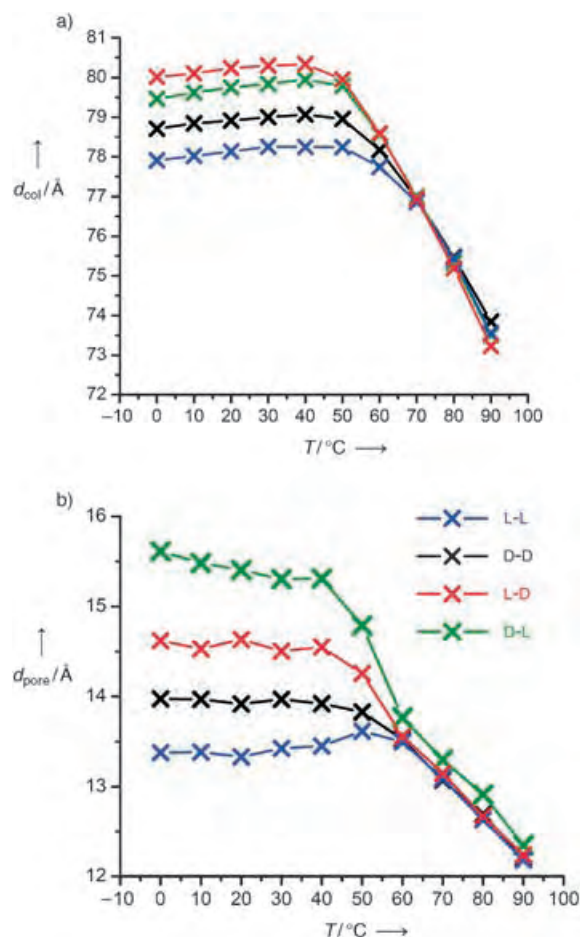


Figure 3. Influence of dipeptide stereochemistry and temperature on a) column diameter and b) pore diameter.

d_{col} and d_{pore} are temperature-dependent above T_g and temperature-independent below T_g (Supporting Information). There are two messages provided in Figure 3. The large slopes of d_{col} and d_{pore} temperature-dependence above T_g and below the isotropic state introduce large errors in the estimation of the role of stereochemistry on pore structure in this temperature range. However, the constant values of d_{pore} and d_{col} below T_g provide access to a quantitative structure analysis in the temperature range of interest for practical applications. As can be observed in Figure 3b, the stereochemistry of the dipeptide influences d_{pore} . Within the experimental error of the XRD method^[4a,b] and of the enantiomeric purity of the Tyr and Ala used (Supporting Information), d_{col} and d_{pore} of L-L are equal to D-D and the respective values for L-D are equal to D-L. A combination of small- and wide-angle XRD results, molecular modeling, and simulation experiments together with density data^[4a] was used to create the structure of the porous columns below T_g . Figure 4 indicates that the helical sense of each column is determined by the stereochemistry of Tyr. The cross-section of the porous columns is illustrated in Figure 5. These cross-sections show that within experimental error, the internal structure obtained from L-L is identical to that obtained from

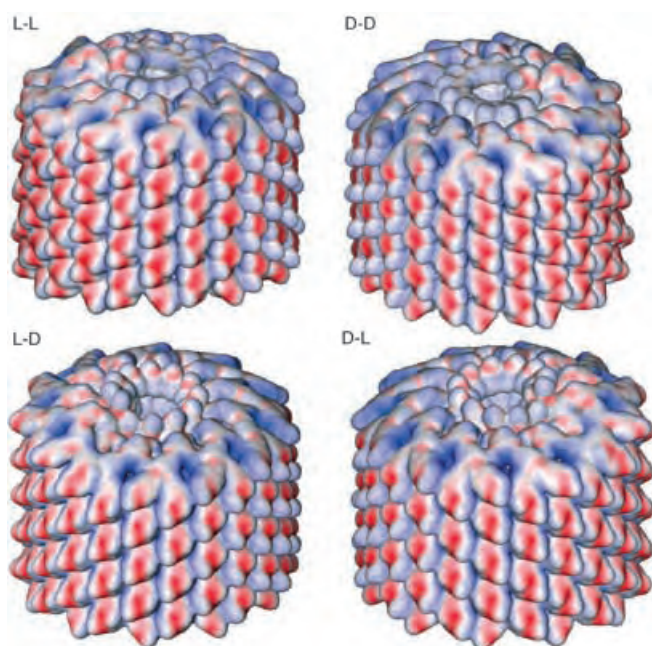


Figure 4. Molecular models of the helical porous columns constructed from XRD, molecular modeling, and density data showing the influence of dipeptide stereochemistry on the helical sense of the column. For simplicity, the alkoxy groups of the dendrons were replaced with methoxy groups.

the D-D dendritic dipeptide, whereas that of L-D is similar to D-L. In all cases, the internal structure of the pore is hydrophobic.

The mechanism responsible for the construction of the pore can be envisioned by inspecting the dendritic dipeptide conformations from the supramolecular structures presented in Figure 4 and 5. Fragments of these dendritic dipeptide conformations containing only the benzyl ether dendritic unit attached to Tyr are compared in Figure 6 (the complete dendritic dipeptide conformations are in the Supporting Information). In all stereoisomers, the hydroxyphenyl group of Tyr is in an *anti* conformation with respect to the Boc group, whereas the dendron is *syn*. The orientation of the tetrahedral carbon atom of the Tyr stereocenter determines the dendron sense and therefore the handedness of the helix. To create a larger pore size with the stereochemistry of L-Tyr-D-Ala and D-Tyr-L-Ala, the methyl group of Ala must be located in the inner part of the pore, whereas in the case of L-Tyr-L-Ala and D-Tyr-D-Ala the methyl ester group of Ala is in the inner part of the pore. This model suggests that the stereochemistry of the dipeptide influences the conformation of the dendron, which in turn determines the conformation of the Ala part of the dipeptide. This cooperative process^[4a] resembles a primitive allosteric control mechanism.^[5]

The cooperativity between the stereochemistry of Tyr and Ala seems to be required to switch the overall conformation of the dendritic dipeptide and therefore, to determine the internal hydrophobic structure of the pore below T_g . The parallel and partially interdigitated arrangement of peptides in the pore^[4a] facilitates the formation of the hydrogen-bonding network structure shown in Figure 7. This structure

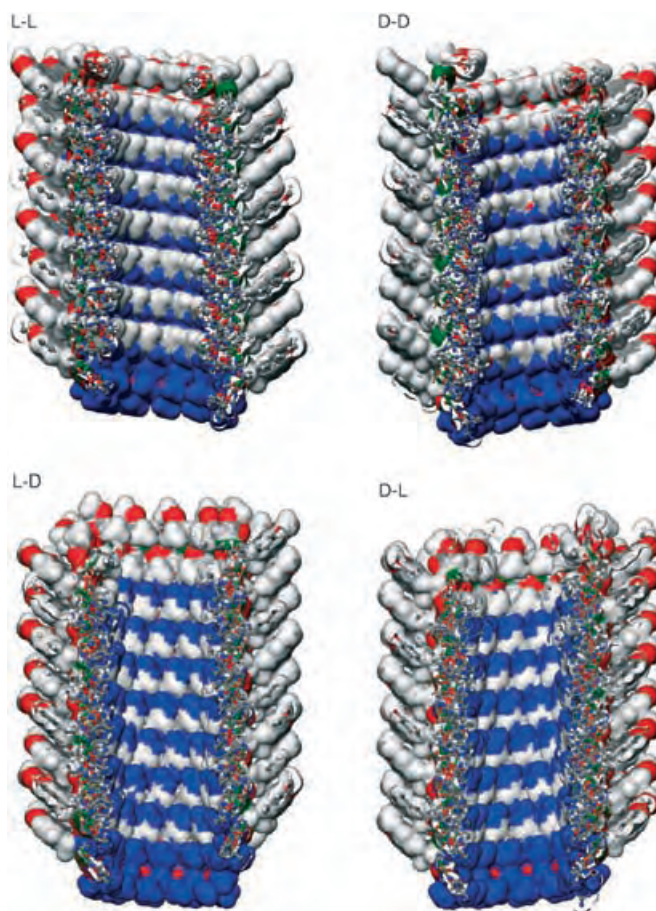


Figure 5. Influence of dipeptide stereochemistry on the cross-section structure of the hydrophobic pore and d_{pore} below T_g : L-L, $d_{\text{pore}} = 13.4 \pm 1.2$ Å; D-D, $d_{\text{pore}} = 14.0 \pm 1.2$ Å; L-D, $d_{\text{pore}} = 14.6 \pm 1.4$ Å; D-L, $d_{\text{pore}} = 15.6 \pm 1.4$ Å (white = methyl groups of Ala, blue = methyl groups of Boc, red = oxygen atoms, green = N-H of dipeptides, gray = other carbon atoms). These structures were obtained as cross-sections of the columns from Figure 4. For simplicity, the dendrons are not shown.

can be divided in two main types of hydrogen-bonding networks. The first is the bonding network inside one layer indicated by $j-k$ or $l-m$. This is the most important for the stability and order of the supramolecular assembly. These directional in-layer hydrogen bonds are responsible for the translation along the column axis from one unit to the proximal neighbors. This translation step is controlled both by the dipeptide and by the dendron size. The in-layer network is independent on dipeptide stereochemistry and creates a $j-k-j-k...$ or $l-m-l-m-l-m...$ helical pattern (Supporting Information). The second hydrogen-bonding network is programmed by dipeptide stereochemistry containing the hydrogen bonds between n^{th} to $n \pm 12^{\text{th}}$ units. For L-Tyr-L-Ala and D-Tyr-D-Ala, the oxygen atoms of Ala do not participate in any hydrogen bond, whereas for L-Tyr-D-Ala and D-Tyr-L-Ala, the Ala oxygen atoms create the second cross-layer network of hydrogen bonds.

L-Tyr-L-Ala and D-Tyr-D-Ala supramolecular structures have a smaller pore size than L-Tyr-D-Ala and D-Tyr-L-Ala, which indicates that the Ala stereochemistry affects the pore

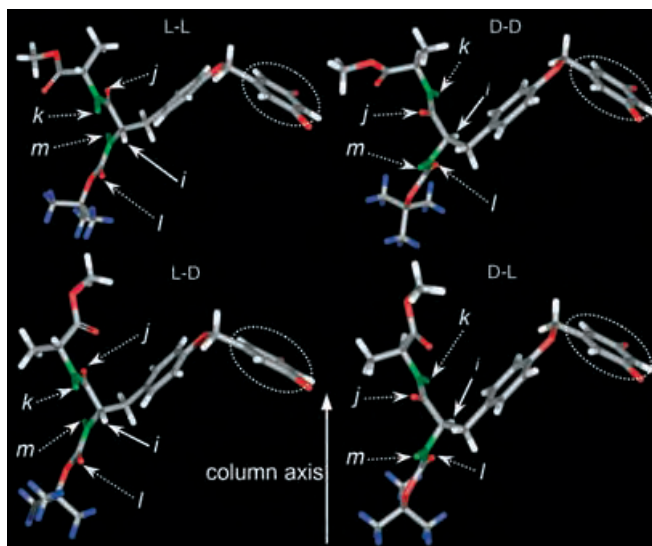


Figure 6. Influence of dipeptide stereochemistry on dipeptide conformation in the assembled supramolecular porous columns from Figure 4: *i* indicates that orientation of the L-Tyr or D-Tyr tetrahedral stereocenter determines the rotation sense, whereas the strong directional in-layer hydrogen-bonding networks *j-k-j-k-j-k...* or *l-m-l-m-l-m...* require a translation along the column axis in the supramolecular assembly. The proposed mechanism explains the cause of the helical supramolecular columnar assembly in which the stereochemistry of Tyr determines the helical sense. For simplicity, only the first benzyl ether of the dendron is shown (dotted circle).

size. At the same time, there is a slightly larger distance between layers for the latter two (see the 5-Å registry feature in Figure 2). These two results are reflected in dipeptide conformation (Figure 7), with the Ala upper region oriented perpendicular to the column axis for the L-Tyr-L-Ala or D-Tyr-D-Ala, and parallel to the column axis for L-Tyr-D-Ala or D-Tyr-L-Ala. The supramolecular helical hydrogen-bonded structure between *k-j* and *l-m* is shown in Supporting Information together with the inner and outer regions of the pore (the other cross-layer hydrogen bonds have been omitted for simplicity).

In conclusion, we report herein the first synthetic example of a helical porous supramolecular structure self-assembled from a hybrid dendritic dipeptide in which the internal structure is programmed by the stereochemistry of the dipeptide. The amphiphilic dendron is responsible for the assembly of the dipeptide into a parallel and partially interdigitated porous structure.^[4a] The stereochemistry of Tyr selects the sense of the helical porous structure. However, the stereochemistry of the entire dipeptide determines the overall arrangement of the dendron in the supramolecular structure, which in turn determines the conformation of the dipeptide and the structure and diameter of the pore in a cooperative process. This supramolecular porous structure is stable over a broad range of temperatures, has a constant d_{pore} below T_g and represents the first example of a supramolecular dendronized tubular polymer^[7,8] exhibiting a 3D structure^[9] that is stereochemically programmed. Allosteric regulation^[5] seems to be operating in this process. This self-assembly

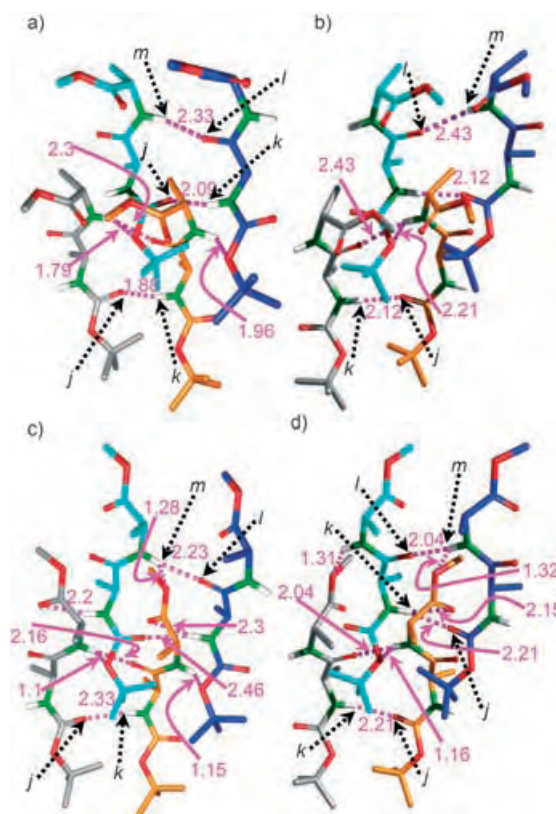


Figure 7. Hydrogen-bonding network determined by a combination of ^1H NMR spectroscopy, XRD analysis, and molecular modeling^[4a] for a) L-L, b) D-D, c) L-D, and d) D-L dendritic dipeptides during the formation of the supramolecular pore structure (all distances in Å). The strongest in-layer directional hydrogen bonds are labeled by the same convention as in Figure 6 (*j-k* and *l-m*). The column axis is vertical; for simplicity only the N-bound hydrogen atoms are shown (white).

concept expands the synthetic capabilities of dendrimers and dendrons.^[10]

Received: April 16, 2005

Revised: June 1, 2005

Published online: September 13, 2005

Keywords: dendrimers · helical structures · liquid crystals · peptides · self-assembly

- [1] a) A. Klug, *Angew. Chem.* **1983**, 95, 579–596; *Angew. Chem. Int. Ed. Engl.* **1983**, 22, 565–636; b) R. MacKinnon, *Angew. Chem.* **2004**, 116, 4363–4376; *Angew. Chem. Int. Ed.* **2004**, 43, 4265–4277; c) P. Agre, *Angew. Chem.* **2004**, 116, 4377–4390; *Angew. Chem. Int. Ed.* **2004**, 43, 4278–4290; d) K. Braig, Z. Otwinowski, R. Hegde, D. C. Boisvert, A. Joachimiak, A. L. Horwich, P. B. Sigler, *Nature* **1994**, 371, 578–586; e) D. Ishii, K. Kinbara, Y. Ishida, N. Ishii, M. Okochi, M. Yohda, T. Aida, *Nature* **2003**, 423, 628–632; f) H. Bayley, P. S. Cremer, *Nature* **2001**, 413, 226–230; g) E. Gouaux, *J. Struct. Biol.* **1998**, 121, 110–122; h) S. Fernandez-Lopez, H.-S. Kim, E. C. Choi, M. Delgado, J. R. Granja, A. Khasanov, K. Kraehenbuehl, G. Long, D. A. Weinberger, K. M. Wilcoxon, M. R. Ghadiri, *Nature* **2001**, 412, 452–455.
- [2] a) U. F. Kragten, M. F. M. Raks, R. J. M. Nolte, *J. Chem. Soc. Chem. Commun.* **1985**, 1275–1276; b) M. J. Pregel, L. Juillien, J.-

- M. Lehn, *Angew. Chem.* **1992**, *104*, 1695–1697; *Angew. Chem. Int. Ed. Engl.* **1992**, *31*, 1637–1640; c) G. W. Gokel, R. Ferdani, J. Liu, R. Pajewski, H. Shabany, R. Utrecht, *Chem. Eur. J.* **2001**, *7*, 33–39; d) D. T. Bong, T. D. Clark, J. R. Granja, M. R. Ghadiri, *Angew. Chem.* **2001**, *113*, 1016–1041; *Angew. Chem. Int. Ed.* **2001**, *40*, 988–1011; e) S. Rosselli, A.-D. Ramminger, T. Wagner, B. Silier, S. Wiegand, W. Häussler, G. Lieser, V. Scheumann, S. Höger, *Angew. Chem.* **2001**, *113*, 3233–3237; *Angew. Chem. Int. Ed.* **2001**, *40*, 3137–3141; f) D. J. Hill, M. J. Mio, R. B. Prince, T. S. Hughes, J. S. Moore, *Chem. Rev.* **2001**, *101*, 3893–4011; g) H. Fenniri, B.-L. Deng, A. E. Ribbe, *J. Am. Chem. Soc.* **2002**, *124*, 11064–11072; h) Y. Kim, M. F. Mayer, S. C. Zimmerman, *Angew. Chem.* **2003**, *115*, 1153–1158; *Angew. Chem. Int. Ed.* **2003**, *42*, 1121–1126; i) S. Hecht, A. Khan, *Angew. Chem.* **2003**, *115*, 6203–6206; *Angew. Chem. Int. Ed.* **2003**, *42*, 6021–6024; j) N. Sakai, J. Mareda, S. Matile, *Acc. Chem. Res.* **2005**, *38*, 79–87.
- [3] a) M. R. Ghadiri, R. J. Granja, R. A. Milligan, D. E. McRee, N. Khazanovich, *Nature* **1993**, *366*, 324–327; b) A. Petitjean, L. A. Cuccia, J.-M. Lehn, H. Nierengarten, M. Schmutz, *Angew. Chem.* **2002**, *114*, 1243–1246; *Angew. Chem. Int. Ed.* **2002**, *41*, 1195–1198; c) M. Ohkita, J.-M. Lehn, G. Baum, D. Fenske, *Chem. Eur. J.* **1999**, *5*, 3471–3481; d) J.-L. Schmitt, A.-M. Stadler, N. Kyritsakas, J.-M. Lehn, *Helv. Chim. Acta* **2003**, *86*, 1598–1624; e) J.-L. Schmitt, J.-M. Lehn, *Helv. Chim. Acta* **2003**, *86*, 3417–3426.
- [4] a) V. Percec, A. E. Dulcey, V. S. K. Balagurusamy, Y. Miura, J. Smidrkal, M. Peterca, S. Nummelin, U. Edlund, S. D. Hudson, P. A. Heiney, H. Duan, S. N. Maganov, S. A. Vinogradov, *Nature* **2004**, *430*, 764–768; b) D. C. Turner, S. M. Gruner, *Biochemistry* **1992**, *31*, 1340–1355.
- [5] a) J. Monod, J.-P. Changeux, F. Jacob, *J. Mol. Biol.* **1963**, *6*, 306–329; b) M. Perutz, *Mechanisms of Cooperativity and Allosteric Regulation in Proteins*, Cambridge University Press, Cambridge, UK, **1990**; c) P. R. Evans, *Curr. Opin. Struct. Biol.* **1991**, *1*, 773–779.
- [6] a) J. C. Nelson, J. G. Saven, J. S. Moore, P. G. Wolynes, *Science* **1997**, *277*, 1793–1796; b) R. B. Prince, L. Brunsveld, E. W. Meijer, J. S. Moore, *Angew. Chem.* **2000**, *112*, 234–236; *Angew. Chem. Int. Ed.* **2000**, *39*, 228–230; c) A. E. Rowan, R. J. M. Nolte, *Angew. Chem.* **1998**, *110*, 65–71; *Angew. Chem. Int. Ed.* **1998**, *37*, 63–68; d) J. J. L. M. Cornelissen, A. E. Rowan, R. J. M. Nolte, N. A. J. M. Sommerdijk, *Chem. Rev.* **2001**, *101*, 4039–4070; e) M. M. Green, J.-W. Park, T. Sato, A. Teramoto, S. Lifson, R. L. B. Selinger, J. V. Selinger, *Angew. Chem.* **1999**, *111*, 3328–3345; *Angew. Chem. Int. Ed.* **1999**, *38*, 3138–3154; f) J.-H. Fuhrhop, J. Köning, *Membranes in Molecular Assemblies. The Synkinetic Approach*, Cambridge University Press, Cambridge, UK, **1994**.
- [7] a) S. D. Hudson, H.-T. Jung, V. Percec, W.-D. Cho, G. Johansson, G. Ungar, V. S. K. Balagurusamy, *Science* **1997**, *278*, 449–452; b) V. Percec, C.-H. Ahn, G. Ungar, D. J. P. Yeardley, M. Möller, S. S. Sheiko, *Nature* **1998**, *391*, 161–164; c) V. Percec, M. Glodde, T. K. Bera, Y. Miura, I. Shiyankovskaya, K. D. Singer, V. S. K. Balagurusamy, P. A. Heiney, I. Schnell, A. Rapp, H.-W. Spiess, S. D. Hudson, H. Duan, *Nature* **2002**, *419*, 384–387.
- [8] a) J.-M. Lehn, *Polym. Int.* **2002**, *51*, 825–839; b) J. S. Moore, *Curr. Opin. Colloid Interface Sci.* **1999**, *4*, 108–116; c) L. Brunsveld, B. J. B. Folmer, E. W. Meijer, R. P. Sijbesma, *Chem. Rev.* **2001**, *101*, 4071–4097.
- [9] S. Hecht, *Mater. Today* **2005**, *8*, 48–55.
- [10] a) T. Emrick, J. M. J. Fréchet, *Curr. Opin. Colloid Interface Sci.* **1999**, *4*, 15–23; b) D. A. Tomalia, *Mater. Today* **2005**, *8*, 34–46.

DOI: 10.1002/anie.200501548

Straightforward Access to a Structurally Diverse Set of Oxacyclic Scaffolds through a Four-Component Reaction**

Oscar Jiménez, Guillermo de la Rosa, and Rodolfo Lavilla*

Multicomponent reactions (MCRs) constitute an important group of transformations that combine many elements of an ideal synthesis, such as operational simplicity, atom economy, bond-forming efficiency, the access to molecular complexity from simple starting materials, and so on. The modular character of this approach is extremely suitable for drug discovery, and therefore it is widely used for the fast generation of bioactive compounds.^[1] Recently, the concept of chemical genomics has sparked the development of diversity-oriented synthesis (DOS)^[2] to reach the structural flexibility needed in the small-molecule range, thus demanding new and versatile synthetic methodology. We report herein new processes leading to diversely functionalized oxacycles (privileged structures including carbohydrate-related compounds)^[3] based on an MCR that allows access to a variety of scaffolds using commercially available reagents.

The Povarov reaction (the condensation of an aniline, an aldehyde, and an activated olefin), has been useful in the formation of tetrahydroquinoline adducts, including aza- and oxacyclic fused derivatives.^[4] Previous reports^[5] suggested that the formal [4+2] cycloaddition was nonconcerted and, consequently, opened the possibility to trap the final oxocarbenium intermediate with an external nucleophile (terminator), thus leading to a four-component reaction.^[6] Herein, we describe a Lewis acid catalyzed four-component reaction of an amine, an aldehyde, a cyclic enol ether, and an alcohol, which acts as the terminator of the process^[7] (Scheme 1).

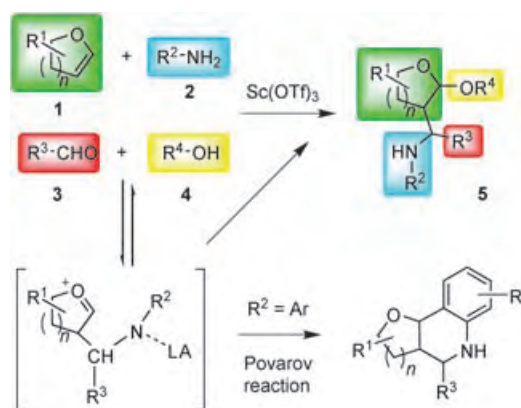
The first experiment was carried out using equimolar amounts of 3,4-dihydro-2H-pyran (**1a**), 3-nitroaniline (**2a**),

[*] Dr. R. Lavilla
Laboratory of Organic Chemistry
Faculty of Pharmacy
University of Barcelona
Avda Joan XXIII sn, 08028 Barcelona (Spain)
Fax: (+34) 93-403-7114
E-mail: rlavilla@pcb.ub.es
Dr. O. Jiménez, G. de la Rosa, Dr. R. Lavilla
Barcelona Science Park
University of Barcelona
Josep Samitier 1–5, 08028 Barcelona (Spain)

[**] This work was supported by DGICYT (Spain, project BQU 2003-00089) and Almirall-Prodesfarma (Barcelona). We also thank Inés Carranco, Prof. F. Albericio, Dr. Miriam Royo, and Marc Vendrell for their assistance with syntheses and analyses.

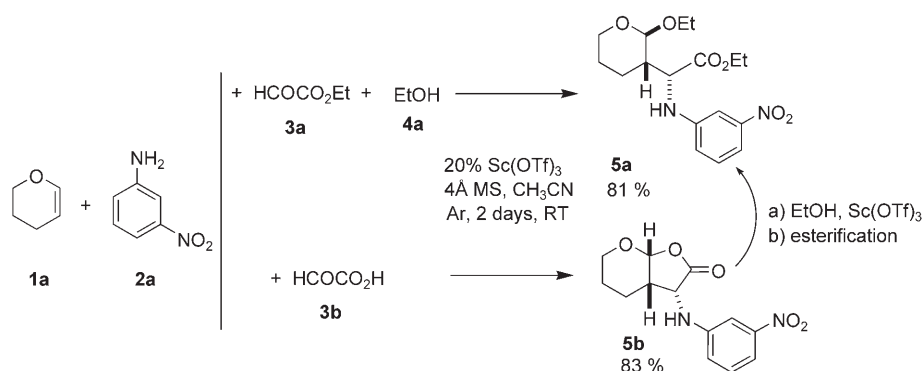


Supporting information for this article is available on the WWW under <http://www.angewandte.org> or from the author.



Scheme 1. General four-component reaction and proposed mechanism. LA = Lewis acid.

ethyl glyoxylate (**3a**),^[8] and an excess of ethanol (**4a**). Under $\text{Sc}(\text{OTf})_3$ catalysis,^[9] the reaction was successful, and the desired product **5a** (81 %) was obtained as a mixture of two isomers in a ratio of 70:30.^[10] Similarly, by using glyoxylic acid (**3b**) we obtained the compound **5b** in high yield (83 %, isomer ratio 70:30). Purification of this mixture afforded the major component and allowed the stereochemical elucidation of the process^[11] by conversion of **5b** into the major isomer of **5a** with EtOH and $\text{Sc}(\text{OTf})_3$ and subsequent esterification using Mukaiyama's reagent.^[12] As expected, the approach of the imine to the enol ether was similar in both cases whereas the trapping of the oxocarbenium ion took place with opposite stereoselectivity (Scheme 2).



Scheme 2. Three- and four-component reactions leading to **5a** and **5b**. MS = molecular sieves.

All the components were systematically varied in order to investigate the scope of the reaction, starting with the amine **2** (Table 1). The process seemed to be general to anilines with electron-donating or electron-withdrawing groups, as well as alkyl amines. Therefore, there is no need for deactivated anilines to avoid the formal [4+2] cycloaddition (see Scheme 1). Under these conditions, the reaction progresses through a four-component reaction pathway to yield the corresponding adduct with no evidence of the Povarov compound. *n*-Butylamine (entry 2) was less reactive and the reaction required heating (40 °C for 48 h). The diastereoselectivity in these series seems to depend on the amine used,

Table 1: Range of amines **2**.

Entry	2	Yield [%]	5	Isomer ratio ^[a]
1		81		5c 2.3:1
2	<i>n</i> BuNH ₂	55		5d 2.3:1
3		82		5e 2.3:1
4		93		5f 9:1

[a] Determined by ¹H NMR spectroscopic or HPLC methods; see Reference [11].

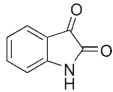
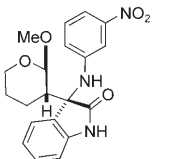
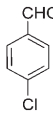
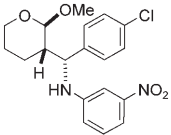
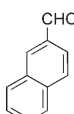
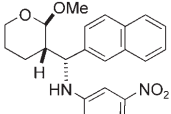

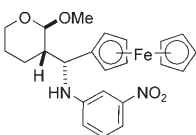
ranging from 2.3:1 with anilines and linear amines (entries 1–3) to 9:1 with more bulky amines (entry 4).

The range of carbonyl compounds was also investigated (Table 2). Besides glyoxylic acid and ethyl glyoxylate, aromatic aldehydes showed convenient reactivity and isatin and 2-ferrocenecarboxaldehyde also yielded the expected adducts.^[13]

The range of alcohols (terminators) was studied next (Table 3). Primary alcohols such as MeOH, EtOH (Table 1, entries 1–4), and *n*BuOH (Table 3, entry 1) worked very well. Even secondary and long-chain primary alcohols yielded the desired products (entries 2 and 3), although in low yields. The use of water was more problematic, probably because of the reduced stability of the hemiacetal **5n**. Interestingly, ethanethiol could be efficiently used to afford adduct **5o** (entry 5). As expected, the alcohols do not play a significant role in the stereocontrol of the reaction. We have preliminarily explored the possibility of using quenchers with higher structural and biological relevance, such as terpenes (entry 6) and carbohydrate derivatives.^[14] Other oxygen-based species with reduced nucleophilicity (AcOH, CF₃CH₂OH, *p*-nitrophenol) did not afford the expected four-component reaction adducts. With these species, the process furnished the Povarov compound (e.g. **6a**) in a regio- and stereoselective manner (Figure 1).

The study of the fourth component (the cyclic enol ether) opened the possibility to further increase the molecular diversity as well as to better control the stereochemical outcome of the reaction (Table 4).

Table 2: Set of carbonyl derivatives **3**.

Entry	3	Yield [%]	5	Isomer ratio ^[a]
1		55		4:1
2		42		2.5:1
3		88		2:1
4		40		2.5:1

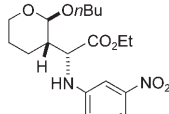
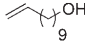
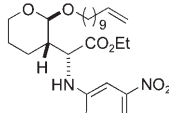
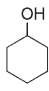
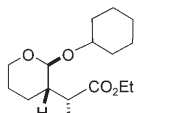
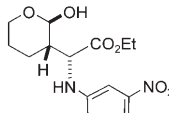
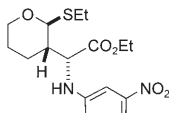
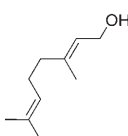
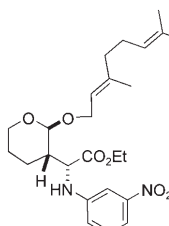
[a] See Reference [11].

A hydroxymethyl substituent at position 2 of the dihydropyran ring (**1c**) efficiently traps the oxocarbenium intermediate to yield adduct **5q** (entry 1), a compound which is structurally related to the sexual attractant insect pheromone brevicomin.^[15] An acetoxymethyl at position 6 did not exert relevant stereodirecting effects on the MCR, and mixtures of stereoisomers were isolated as shown in entry 2. In sharp contrast, glycals bearing a substituent at position 4 displayed excellent facial stereoselectivity and enabled access to enantiopure compounds. For instance, compound **5s** (36%) was obtained from tri-*O*-acetyl-D-galactal in a process carried out at 40 °C during 14 days.^[16] Extension of this methodology to the D-glucal derivative afforded **5t** (20%). Microwave irradiation efficiently promoted faster and cleaner reactions, and **5s** and **5t** were obtained in 71% and 45% yield, respectively, in only 2 minutes (entries 3 and 4). Remarkably, we did not observe Ferrier-type or ring-opening transformations, which are common in acid-promoted reactions involving glycals and other enol ethers.^[17] Additionally, the Povarov reaction proceeds with improved stereoselectivity to yield compound **6b** as a single stereoisomer (Figure 1).^[18]

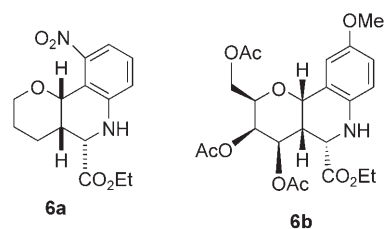
Tailored enol ethers also worked in this MCR. For example, substrates **1g** and **1h**, respectively prepared by Heck^[19] and hetero-Diels–Alder reactions,^[20] afforded the desired adducts stereoselectively with diastereomeric ratios of 4:1 for **5u** (the minor isomer is the epimer at the *p*-methoxyphenyl center) and 2.5:1 for **5v**^[11] (Scheme 3).

One interesting application of this methodology is the ready access to new α -amino acid derivatives that bear an oxacycle substituent. This was done in just one additional step by hydrogenolysis of the benzhydryl derivative **5f** to afford the corresponding α -amino ester **7a** (78%). Interestingly, the oxidation of the *p*-methoxyaniline derivative **5e** with CAN

Table 3: Set of terminators **4**.

Entry	4	Yield [%]	5 ^[a]
1	<i>n</i> BuOH	83	
2		10	
3		15	
4	H ₂ O	35	
5	EtSH	83	
6		62	

[a] The isomer ratio in all cases was around 2.5:1; see Reference [11].


Figure 1. Povarov-type compounds **6a** and **6b**.

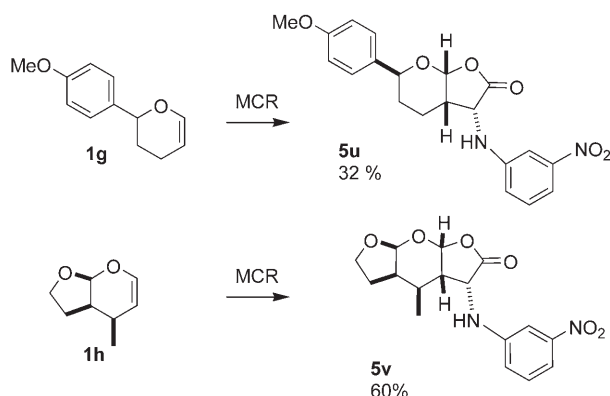
afforded the quinoline **8a** (55%). An improved protocol (71%) for this transformation involved treatment of **5e** with TFA in open atmosphere (O₂ as the oxidant). Analogously, oxidative treatment of **6b** produced the quinoline derivative **8b** (58%) bearing a stereodefined polyoxygenated chain at position 3 (Scheme 4).

The structural flexibility of this protocol is remarkable and allows the formation of four different scaffolds (Scheme 5) by applying post-condensation reactions to the MCR. Thus, it is possible to obtain compounds such as **5e** by a four-component reaction, **6c** by the Povarov three-compo-

Table 4: Range of cyclic enol ethers.

Entry	1	Yield [%]	5	Isomer ratio ^[a]
1		46		2.5:1
2		77		1.5:1 ^[b]
3		71 ^[c]		99:1
4		45 ^[c]		99:1

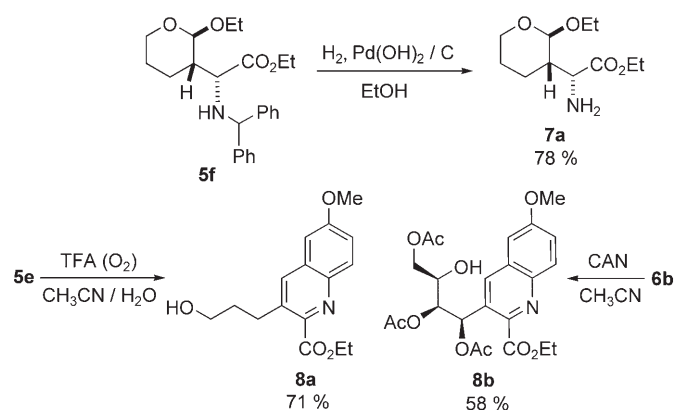
[a] See Reference [11]. [b] The minor isomer is the epimer at the acetoxymethyl center. [c] Microwave-promoted reaction.



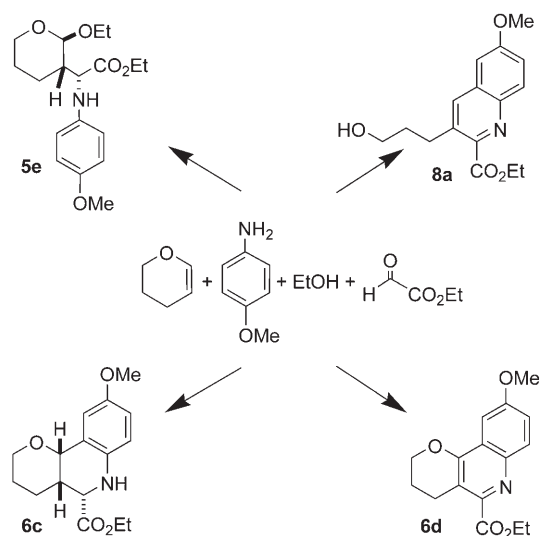
Scheme 3. Multicomponent reactions (MCRs) with preformed enol ethers.

ment reaction, **8a** by treatment of either **5e** or **6c** with acid, and **6d** by oxidation of **6c** with DDQ.^[21]

In conclusion, we have developed a four-component reaction based on the nucleophilic interference of the Povarov reaction. The process is general and allows a broad range of variations in every component. The stereoselectivity of the reaction strongly depends on the substrates and ranges from low to moderate to excellent. Good stereocontrol is observed when sterically demanding amines and enol ethers are used.^[22] The modular character of this approach, the simplicity and availability of most building blocks used, and the remarkable level of structural diversity attained make this



Scheme 4. Preparation of α -amino ester **7a** and quinolines **8a** and **8b**. TFA=trifluoroacetic acid; CAN=cerium ammonium nitrate.



Scheme 5. MCR-derived scaffolds.

process attractive for combinatorial, target-oriented, and diversity-oriented synthesis.^[23]

Received: May 6, 2005

Revised: July 7, 2005

Published online: September 15, 2005

Keywords: glycosides · Lewis acids · multicomponent reactions · oxygen heterocycles · synthetic methods

- [1] For an overview of MCRs, see: a) *Multicomponent Reactions* (Eds.: J. Zhu, H. Bienaymé), Wiley-VCH, Weinheim, **2005**. For recent reviews, see: b) D. J. Ramón, M. Yus, *Angew. Chem.* **2005**, *117*, 1628; *Angew. Chem. Int. Ed.* **2005**, *44*, 1602; c) C. Simon, T. Constantieux, J. Rodriguez, *Eur. J. Org. Chem.* **2004**, 4957; d) R. V. A. Orru, M. de Greef, *Synthesis* **2003**, *10*, 1471; e) J. Zhu, *Eur. J. Org. Chem.* **2003**, 1133; f) H. Bienaymé, C. Hulme, G. Oddon, P. Schmitt, *Chem. Eur. J.* **2000**, *6*, 3321; g) A. Dömling, I. Ugi, *Angew. Chem.* **2000**, *112*, 3300; *Angew. Chem. Int. Ed.* **2000**, *39*, 3168.
- [2] M. D. Burke, S. L. Schreiber, *Angew. Chem.* **2004**, *116*, 48; *Angew. Chem. Int. Ed.* **2004**, *43*, 46.

- [3] a) F. Schweizer, *Angew. Chem.* **2002**, *114*, 240; *Angew. Chem. Int. Ed.* **2002**, *41*, 230; b) S. A. W. Gruner, E. Locardi, E. Lohof, H. Kessler, *Chem. Rev.* **2002**, *102*, 491.
- [4] a) L. S. Povarov, *Russ. Chem. Rev.* **1967**, *36*, 656; b) K. A. Jorgensen, *Angew. Chem.* **2000**, *112*, 3702; *Angew. Chem. Int. Ed.* **2000**, *39*, 3558; c) S. Kobayashi, R. Akiyama, H. Kitagawa, *J. Comb. Chem.* **2001**, *3*, 196; d) I. Carranco, J. L. Díaz, O. Jiménez, M. Vendrell, F. Albericio, M. Royo, R. Lavilla, *J. Comb. Chem.* **2005**, *7*, 33, and references therein.
- [5] a) V. Lucchini, M. Prato, G. Scorrano, M. Stivanello, G. Valle, *J. Chem. Soc. Perkin Trans. 2* **1992**, 259; b) S. Hermitage, D. A. Jay, A. Whiting, *Tetrahedron Lett.* **2002**, *43*, 9633; c) R. Lavilla, M. C. Bernabeu, I. Carranco, J. L. Díaz, *Org. Lett.* **2003**, *5*, 717; d) S. Kobayashi, R. Matsubara, Y. Nakamura, H. Kitagawa, M. Sugiura, *J. Am. Chem. Soc.* **2003**, *125*, 2507.
- [6] Very recently, multistep syntheses of similar compounds have been described; see: a) A. K. Ghosh, C.-X. Xu, S. S. Kulkarni, D. Wink, *Org. Lett.* **2005**, *7*, 7; b) T. Sommermann, B. G. Kim, K. Peters, E.-M. Peters, T. Linker, *Chem. Commun.* **2004**, 22, 2624; c) P. R. Sridhar, K. C. Ashalu, S. Chandrasekaran, *Org. Lett.* **2004**, *6*, 1777.
- [7] Only two compounds of this type have been described in the literature as by-products in low-yielding Povarov-type reactions; see: a) R. Baudelle, P. Melnyk, B. Déprez, A. Tartar, *Tetrahedron* **1998**, *54*, 4125; and b) Ref. [5a].
- [8] W. J. N. Meester, J. H. van Maarseveen, H. E. Schoemaker, H. Hiemstra, F. P. J. T. Rutjes, *Eur. J. Org. Chem.* **2003**, 2519.
- [9] S. Kobayashi in *Lewis Acids in Organic Synthesis*, Vol. 2 (Ed.: H. Yamamoto), Wiley-VCH, Weinheim, **2000**, p. 883.
- [10] For related processes, see: a) A. K. Ghosh, R. Kawahama, D. Wink, *Tetrahedron Lett.* **2000**, *41*, 8425; b) A. K. Ghosh, R. Kawahama, *Tetrahedron Lett.* **1999**, *40*, 4751.
- [11] The minor isomer in these series is the epimer at the *N*-substituted stereogenic center.
- [12] T. Mukaiyama, *Angew. Chem.* **1979**, *91*, 798; *Angew. Chem. Int. Ed. Engl.* **1979**, *18*, 707.
- [13] Aldehydes with α -hydrogen atoms were not included in this study.
- [14] In these series, protected (isopropylidene) D-ribonolactone and D-galactose derivatives were efficiently used as terminators, and the corresponding adducts were obtained with good conversions as mixtures of diastereomers.
- [15] For brevicomin-related derivatives, see: V. I. Tyvorskii, D. A. Astashko, O. G. Kulinkovich, *Tetrahedron* **2004**, *60*, 1473.
- [16] Experiments run at higher temperatures resulted in very complex mixtures.
- [17] For recent results, see: a) J. S. Yadav, B. V. S. Reddy, K. V. Rao, K. S. Raj, A. R. Prasad, S. K. Kumar, A. C. Kunwar, P. Jayaparakash, B. Jagannath, *Angew. Chem.* **2003**, *115*, 5356; *Angew. Chem. Int. Ed.* **2003**, *42*, 5198; b) S. K. Das, K. A. Reddy, J. Roy, *Synlett* **2003**, *11*, 1607; c) R. A. Batey, D. A. Powell, A. Acton, A. J. Lough, *Tetrahedron Lett.* **2001**, *42*, 7935; d) J. Zhang, C.-J. Li, *J. Org. Chem.* **2002**, *67*, 3969.
- [18] To our knowledge, this is the first example of Povarov-type reaction with glycals.
- [19] I. Arai, G. D. Daves, Jr., *J. Org. Chem.* **1979**, *44*, 21.
- [20] R. I. Longley, W. S. Emerson, *J. Am. Chem. Soc.* **1950**, *72*, 3079.
- [21] E. Borrione, M. Prato, G. Scorrano, M. Stivanello, V. Lucchini, *J. Heterocycl. Chem.* **1988**, *25*, 1831.
- [22] Studies directed toward the improvement of the stereoselectivity of the process are underway; we are currently evaluating the role of additives and ligands in these reactions.
- [23] *Note added in proof*: Dihydrofurans react in this MCR following similar trends to dihydropyrans; for examples, see the Supporting Information.

DOI: 10.1002/anie.200501603

Enhanced Metabolic Stability and Protein-Binding Properties of Artificial α Helices Derived from a Hydrogen-Bond Surrogate: Application to Bcl-xL**

Deyun Wang, Wei Liao, and Paramjit S. Arora*

*Dedicated to Professor Peter B. Dervan
on the occasion of his 60th birthday*

The α helix plays a fundamental role in imparting specificity to protein–protein and protein–nucleic acid interactions. Molecules that can predictably and selectively disrupt these interactions would be invaluable as tools in molecular biology and, potentially, as leads in drug discovery.^[1] We recently described a new strategy for the synthesis of artificial α helices in which one main-chain i to $i+4$ hydrogen bond in the target α helix is replaced with a carbon–carbon bond derived from a ring-closing metathesis reaction (Figure 1).^[2] A key feature of this hydrogen-bond surrogate (HBS) approach is that the internal placement of the cross-link affords short helices with minimal perturbations to their molecular recognition surfaces. This method differs significantly from the commonly employed side-chain cross-linking method for helix stabilization. A limitation of the latter approach is that side-chain functionality must be sacrificed to nucleate stable helical conformations. The modified side chains are unavailable for molecular recognition; moreover, the resulting tether blocks at least one face of the putative helix. The HBS approach uniquely allows the synthesis of artificial helices with all side chains available for molecular recognition, and does not place any steric encumbrances on the helix surface. We believe that our artificial α helices have the potential to target protein receptors and regulate protein–protein interactions more successfully than helices with cross-linked side chains.

Our initial studies demonstrated that the HBS approach affords highly stable α helices from alanine-rich peptide sequences. Herein, we show that this metathesis-based

[*] D. Wang, W. Liao, Prof. P. S. Arora
Department of Chemistry, New York University
New York, NY 10003 (USA)
Fax: (+1) 212-260-7905
E-mail: arora@nyu.edu

[**] We thank Prof. Neville Kallenbach for insightful comments. P.S.A. is grateful for financial support from the NIH (GM073943), the American Chemical Society Petroleum Research Fund, Research Corporation (Cottrell Scholar Award), and the New York State Office of Science, Technology, and Academic Research (James D. Watson investigator). We thank the National Science Foundation for equipment grants for the NMR spectrometer (MRI-0116222) and the capillary LC–ion-trap mass spectrometer (CHE-0234863).



Supporting information for this article is available on the WWW under <http://www.angewandte.org> or from the author.

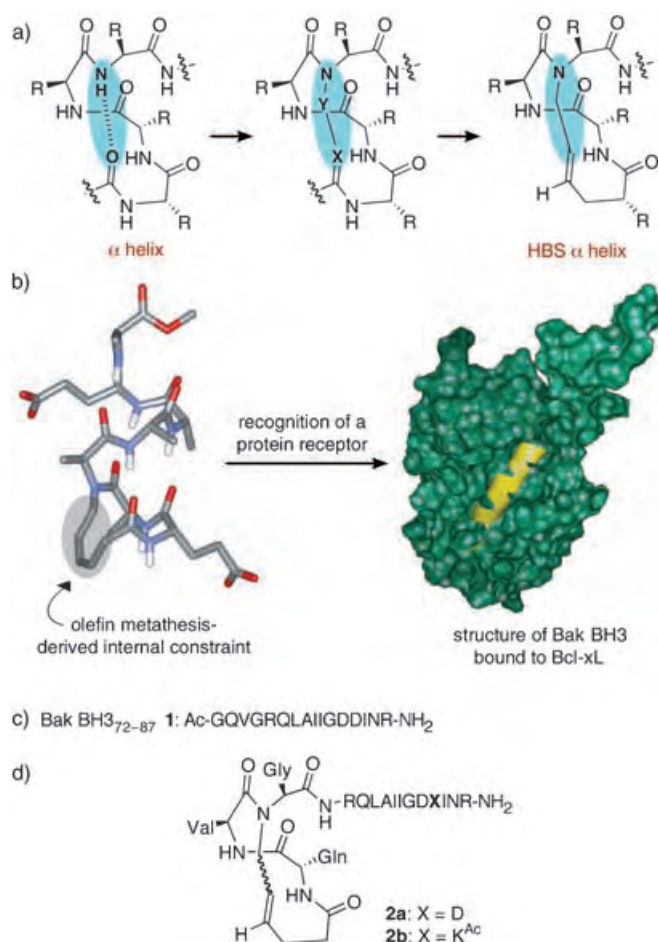


Figure 1. a) Formation of hydrogen-bond surrogate (HBS) derived α helices by replacement of a main-chain hydrogen bond with a carbon-carbon bond. b) HBS α helix and recognition of Bcl-xL (green) with Bak BH3 α helix (yellow); PDB code: 1BXL. c) Sequence of the unconstrained Bak BH3 peptide **1**. d) Structures of HBS Bak α helices **2a** and **2b**.

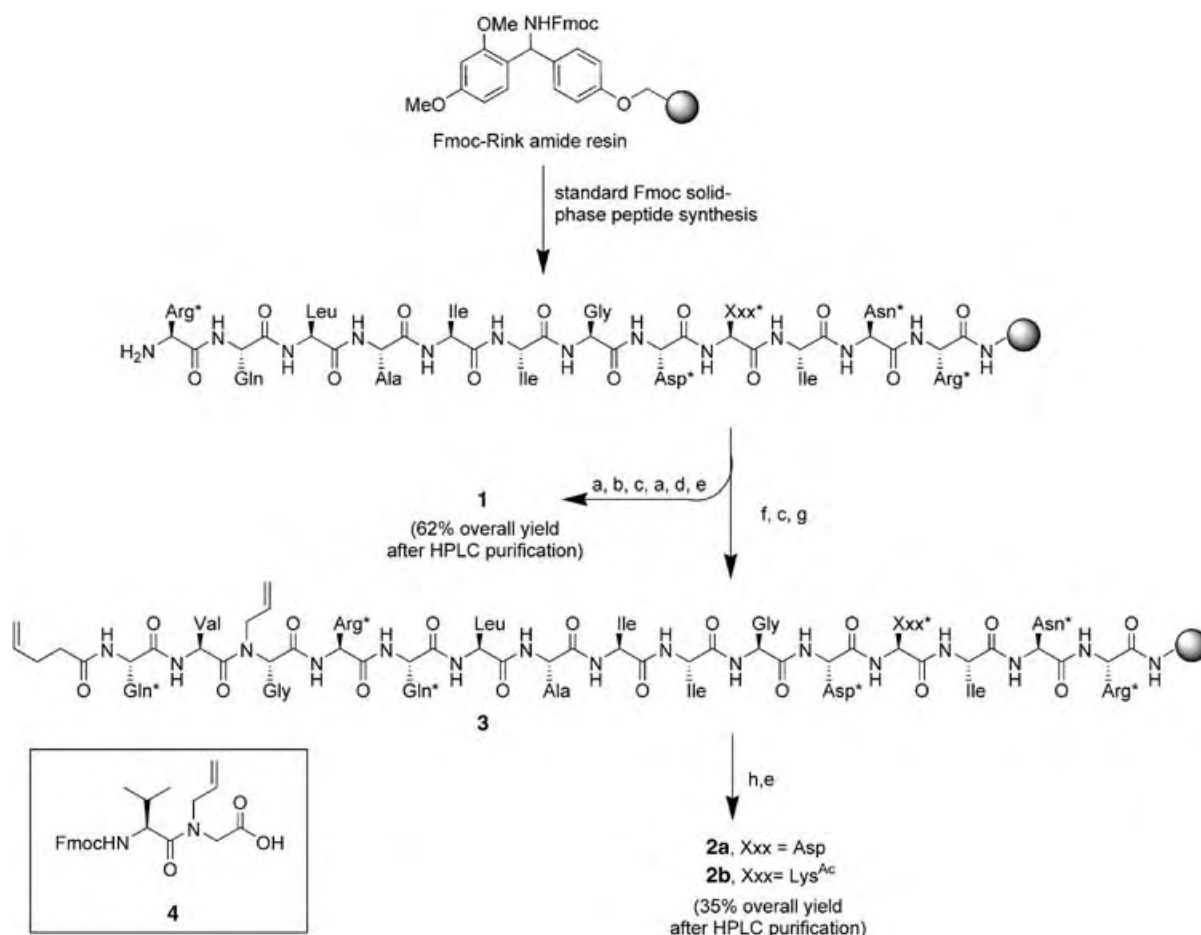
method can effectively stabilize α -helical conformations in biologically relevant sequences, that the resulting molecules resist proteolytic degradation as compared with the unconstrained analogues, and that the HBS helices can bind a protein target with high affinity. For these proof-of-principle protein-binding studies with our artificial helices, we chose to target the extensively studied α helix binding protein, Bcl-xL.^[3] Bcl-xL is an antiapoptotic protein that regulates cell death by binding the α -helical BH3 domain of a family of proapoptotic proteins (including Bak, Bad, Bid, and Bax).^[4–6] NMR spectroscopic studies by Fesik and co-workers have shown that the 16-mer peptide **1** derived from the Bak BH3 domain adopts an α -helical conformation upon binding to Bcl-xL (Figure 1b).^[3] Circular dichroism (CD) studies demonstrated that this peptide is unstructured under physiological conditions in the absence of the protein partner and only slightly helical in trifluoroethanol (TFE), a helix-promoting solvent.^[7]

Several methods that afford stabilized α helices or helix mimetics have already been used to target Bcl-xL, thus

allowing us to directly compare the performance of our internally constrained artificial α helices.^[8–10] Significantly, Huang and co-workers recently reported that Bak BH3 α helices stabilized by a lactam-based side-chain cross-linking strategy were unable to bind Bcl-xL.^[11] The authors speculated that the lack of binding might be a result of steric clashes between the cross-link and the narrow binding pocket of Bcl-xL. However, Verdine and co-workers found that side-chain-bridged α helices corresponding to the BH3 domain of a different proapoptotic protein, Bid, can target Bcl-xL and suppress the growth of leukemia cells in mice.^[1] Judicious placement of the side-chain constraints requires prior knowledge of the protein-ligand complex; otherwise, multiple randomly constrained helices must be prepared and tested. Nevertheless, their report highlights the potential of constrained α helices as tools for the control of protein-protein interactions in vivo. Taken together, these two protein-binding studies from the Huang and Verdine research groups illustrate potential problems with the side-chain bridging strategy. The fundamental advantage of the HBS approach over this strategy for stabilizing helices is that the helix surfaces are not encumbered by the constraining element. The HBS approach should therefore greatly simplify the helix design process. The key question we ask herein is whether the HBS-derived Bak α helix can bind Bcl-xL when the side-chain-constrained (lactam bridge) Bak helix is unable to target this same protein receptor.

The artificial Bak BH3 α helix **2a** was synthesized on Rink amide resin by the ring-closing metathesis reaction shown in Scheme 1.^[12] HBS α helices can be synthesized from commercially available amino acids or simple amino acid derivatives and do not require preparation of enantiomerically pure amino acid analogues. In the present case, standard solid-phase peptide synthesis using appropriate Fmoc-modified amino acids, dipeptide **4**, and pentenoic acid afforded the fully protected resin-bound bis-olefin peptide **3**, which was subjected to the Hoveyda-Grubbs ring-closing metathesis catalyst to afford the peptide macrocycles. The metathesized peptide was cleaved from the resin with trifluoroacetic acid to give the constrained peptide **2a** as a mixture of the *cis*- and *trans*-alkene isomers. We were unable to separate these isomers by HPLC.

The helical conformation of constrained peptide **2a** was investigated by CD. CD studies on **2a** and the control peptide **1** were performed in TFE/phosphate-buffered saline (PBS, 1:4) to obtain a quantitative measure of their helical content (Figure 2). The CD results of the artificial α helix **2a** display double minima at 206 and 222 nm and a maximum at 189 nm, consistent with those observed for canonical α helices. The HBS α helix **2a** is roughly 46% helical as measured by Yang's method (Supporting Information).^[13] In agreement with previous studies,^[7] we found that the unconstrained Bak peptide **1** is only weakly helical ($\approx 20\%$). We hypothesized that the GDD tripeptide residue (residues 82–84 in the Bak BH3 domain) in the middle of the Bak peptide sequence may limit the propagation of the helix and lower the overall helical content of **2a**, as glycine is known to be a potent "helix breaker", and aspartic acid has been implicated as a helix stop signal.^[14–16] Fesik and co-workers have previously shown that



Scheme 1. Solid-phase synthesis of HBS α helices **2a** and **2b**: a) 1. Fmoc Gly-OH (3.2 equiv), HBTU (2.88 equiv), *i*Pr₂NEt, NMP; 2. piperidine, NMP; b) 1. Fmoc Val-OH (3.2 equiv), HBTU (2.88 equiv), *i*Pr₂NEt, NMP; 2. piperidine, NMP; c) 1. Fmoc Gln*-OH (3.2 equiv), HBTU (2.88 equiv), *i*Pr₂NEt, NMP; 2. piperidine, NMP; d) acetic anhydride, *i*Pr₂NEt, DMF; e) CF₃CO₂H/H₂O/triisopropylsilane (95:2.5:2.5), 1.5 h; f) 1. **4** (3.2 equiv), HBTU (2.88 equiv), *i*Pr₂NEt, NMP; 2. piperidine, NMP; g) pentenoic acid (3.2 equiv), HBTU (2.88 equiv), *i*Pr₂NEt, NMP; h) Hoveyda-Grubbs catalyst (20 mol%), dichloroethane, 50 °C, 24 h. Arg*: Pbf-protected Arg; Asn*: trityl-protected Asn; Asp*: *tert*-butyl-protected Asp; Gln*: trityl-protected Gln; Xxx*: Asp* or Lys^{Ac}. Fmoc = 9-fluorenylmethoxycarbonyl; HBTU = O-(benzotriazol-1-yl)-N,N,N',N'-tetramethyluronium hexafluorophosphate; NMP = *N*-methyl pyrrolidinone; Pbf = 2,2,4,6,7-pentamethylidihydrobenzofuran-5-sulfonyl.

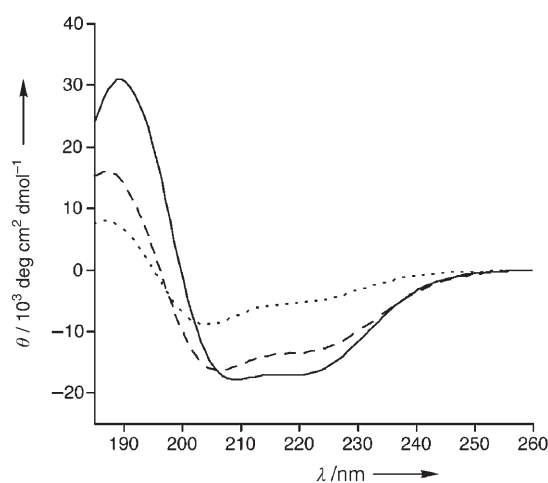


Figure 2. Circular dichroism data of peptides Bak BH3 **1** (-----), HBS helix **2a** (----), and HBS helix **2b** (—) in TFE/PBS (1:4).

the residues Gly82 and Asp83 cannot be substituted with alanine without sacrificing binding affinity for the protein; however, Asp84 may be replaced without any deleterious effects.^[3] To test the effect of replacing Asp84 on the helicity of Bak peptide, we prepared HBS α helix **2b** in which Asp84 is substituted with a side-chain-acetylated lysine (Lys^{Ac}) (Figure 1). We made this particular substitution because the Bak BH3 peptide with a capped lysine residue was previously shown to bind Bcl-xL with high affinity.^[17] We were gratified to find that this single substitution provided a significant boost in α helicity (Figure 2). HBS helix **2b** is roughly 65 % helical: an increase in helicity of 140 % over that of **2a**. As expected, this substitution provided a similar increase in helicity for the unconstrained Bak BH3 (Supporting Information). Importantly, this set of experiments shows that the HBS approach can successfully stabilize α -helical conformations in biologically relevant sequences.

The binding affinities of the unconstrained Bak peptide **1** and artificial Bak α helices **2a** and **2b** for Bcl-xL were assessed by using a previously described fluorescence polar-

ization assay with a fluorescein-labeled 16-mer Bak peptide (fl-Bak, **5**; see Supporting Information). The affinity of fl-Bak for Bcl-xL was determined to be 264 ± 18 nM, which is in agreement with the previously reported values. Competitive inhibition of the fl-Bak–Bcl-xL complex by the Bak peptides (**1**, **2a**, and **2b**) is detected by a decrease in fluorescence polarization as the immobilized probe dissociates from the protein. Regression analysis^[18] provided a K_d value of 154 ± 23 nM for the unconstrained Bak peptide **1**, within range of the previously reported values (Figure 3). Under the same

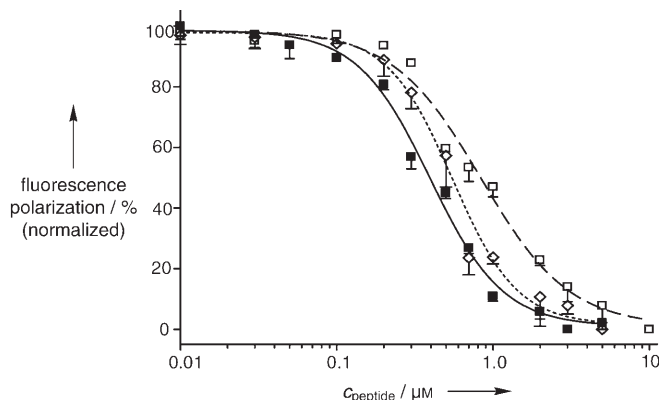


Figure 3. Fluorescence polarization studies indicate that HBS α helices **2a** and **2b** target Bcl-xL with high affinity. The K_d value for each peptide was determined by competitive inhibition of fluorescein-labeled Bak peptide (15 nM) and Bcl-xL (500 nM) complex. Bak BH3 **1** ($K_d = 154 \pm 23$ nM, ---- \diamond ----), HBS helix **2a** ($K_d = 325 \pm 51$ nM, ---- \square ----), and HBS helix **2b** ($K_d = 69 \pm 16$ nM, —■—).

assay conditions, HBS helices **2a** and **2b** bound Bcl-xL with K_d values of 325 ± 51 and 69 ± 16 nM, respectively. These binding results point to a potential transition-state problem involved in forcing a preformed helix into this pocket, as the unconstrained Bak BH3 peptide **1** targets this protein with twofold higher affinity than the constrained peptide **2a**. Nevertheless, the data validate our helix design principle as we find that our internally constrained Bak α helices do indeed access this deep hydrophobic cleft, whereas Bak α helices prepared by the side-chain-bridging method show no affinity for the same target. Moreover, we show that a very high-affinity binder, **2b**, for the Bcl-xL can be developed by increasing the helicity of the constrained peptide through rational substitutions. On the basis of these preliminary results, we are now preparing a second generation of HBS Bak α helices designed to be more helical and to bind Bcl-xL with higher affinity than **2b**. It remains to be determined if these HBS α helices show selectivity for Bcl-xL over other closely related members of the Bcl-2 family (and over other helix-binding proteins).^[8,19,20]

Proteolytic cleavage is one of the principal reasons limiting the in vivo efficacy of peptides as reagents. Proteases are known to bind their substrates in linear or beta-strand conformations,^[21] and peptides locked into helical conformations have been shown to resist proteolytic degradation.^[22,23] Accordingly, we determined the proteolytic stability of HBS Bak helices **2a** and **2b** relative to Bak peptide **1** in the presence of trypsin, which is expected to cleave the peptide at

the arginine residue (Arg76) positioned two residues away from the macrocycle in helices **2a** and **2b**. We questioned how this residue that lies outside the constraint, yet is close enough to be in a highly helical conformation, responds to the protease. Comparison of the initial velocities of cleavage by trypsin indicated that the HBS α helix **2a** is proteolyzed roughly 30-fold slower than the unconstrained Bak peptide analogue **1** (Figure 4). As expected, an increase in the helicity of the constrained peptide results in a further decrease in the initial velocity of cleavage by trypsin. Thus, the HBS helix **2b** is roughly twofold more stable than **2a** and 60-fold more stable than **1** against proteolysis by trypsin. The proteolytic

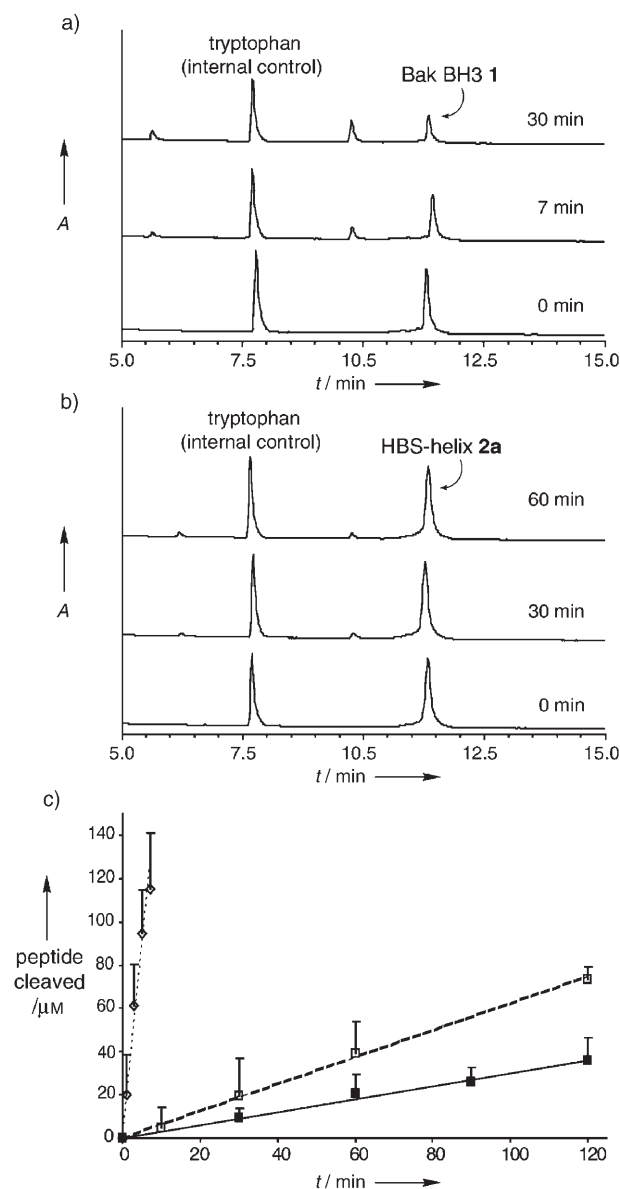


Figure 4. Metabolic stability of HBS α helices. HPLC assay shows rapid proteolysis of a) the unconstrained peptide **1** in the presence of trypsin, whereas b) the HBS α helix **2a** degrades at a much slower rate. Tryptophan (500 μ M) was used as an internal control for the HPLC studies. c) Comparison of the initial velocities for the proteolysis of Bak BH3 **1** ($k = 18.0$ μ M min⁻¹, ---- \diamond ----), HBS helix **2a** ($k = 0.60$ μ M min⁻¹, ---- \square ----), and HBS helix **2b** ($k = 0.30$ μ M min⁻¹, —■—).

stability observed for **2a** and **2b** is similar to that reported for a side-chain cross-linked α helix.^[22]

In summary, we have demonstrated that artificial α helices prepared by the replacement of a hydrogen bond between the i and $i + 4$ residues at the N terminus of a short peptide with a carbon–carbon bond can stabilize biologically relevant peptides in helical conformations. These HBS α helices can bind their expected protein receptor with high affinity and resist trypsin-mediated proteolysis. The results are an important step in our efforts to develop rationally designed modulators of protein–protein interactions. These molecules encompass larger surface areas than those displayed by typical small molecules, and may ultimately prove to be more effective in targeting large protein interfaces.

Received: May 10, 2005

Published online: September 19, 2005

Keywords: helical structures · hydrogen bonds · molecular recognition · peptidomimetics · protein–protein interactions

- [1] L. D. Walensky, A. L. Kung, I. Escher, T. J. Malia, S. Barbuto, R. D. Wright, G. Wagner, G. L. Verdine, S. J. Korsmeyer, *Science* **2004**, *305*, 1466–1470.
- [2] R. N. Chapman, G. Dimartino, P. S. Arora, *J. Am. Chem. Soc.* **2004**, *126*, 12252–12253.
- [3] M. Sattler, H. Liang, D. Nettlesheim, R. P. Meadows, J. E. Harlan, M. Eberstadt, H. S. Yoon, S. B. Shuker, B. S. Chang, A. J. Minn, C. B. Thompson, S. W. Fesik, *Science* **1997**, *275*, 983–986.
- [4] S. Cory, D. C. Huang, J. M. Adams, *Oncogene* **2003**, *22*, 8590–8607.
- [5] A. Letai, M. C. Bassik, L. D. Walensky, M. D. Sorcinelli, S. Weiler, S. J. Korsmeyer, *Cancer Cell* **2002**, *2*, 183–192.
- [6] S. E. Rutledge, J. W. Chin, A. Schepartz, *Curr. Opin. Chem. Biol.* **2002**, *6*, 479–485.
- [7] A. M. Petros, D. G. Nettlesheim, Y. Wang, E. T. Olejniczak, R. P. Meadows, J. Mack, K. Swift, E. D. Matayoshi, H. Zhang, C. B. Thompson, S. W. Fesik, *Protein Sci.* **2000**, *9*, 2528–2534.
- [8] J. W. Chin, A. Schepartz, *Angew. Chem.* **2001**, *113*, 3922–3925; *Angew. Chem. Int. Ed.* **2001**, *40*, 3806–3809.
- [9] A. Degterev, A. Lugovskoy, M. Cardone, B. Mulley, G. Wagner, T. Mitchison, J. Yuan, *Nat. Cell Biol.* **2001**, *3*, 173–182.
- [10] O. Kutzki, H. S. Park, J. T. Ernst, B. P. Orner, H. Yin, A. D. Hamilton, *J. Am. Chem. Soc.* **2002**, *124*, 11838–11839.
- [11] B. Yang, D. Liu, Z. Huang, *Bioorg. Med. Chem. Lett.* **2004**, *14*, 1403–1406.
- [12] G. Dimartino, D. Wang, R. N. Chapman, P. S. Arora, *Org. Lett.* **2005**, *7*, 2389–2392.
- [13] Y. H. Chen, J. T. Yang, H. M. Martinez, *Biochemistry* **1972**, *11*, 4120–4131.
- [14] A. Chakrabartty, T. Kortemme, R. L. Baldwin, *Protein Sci.* **1994**, *3*, 843–852.
- [15] J. W. Nelson, N. R. Kallenbach, *Biochemistry* **1989**, *28*, 5256–5261.
- [16] K. T. O'Neil, W. F. DeGrado, *Science* **1990**, *250*, 646–651.
- [17] H. Zhang, P. Nimmer, S. H. Rosenberg, S. C. Ng, M. Joseph, *Anal. Biochem.* **2002**, *307*, 70–75.
- [18] M. H. Roehrl, J. Y. Wang, G. Wagner, *Biochemistry* **2004**, *43*, 16056–16066.
- [19] A. C. Gemperli, S. E. Rutledge, A. Maranda, A. Schepartz, *J. Am. Chem. Soc.* **2005**, *127*, 1596–1597.
- [20] H. Yin, G. I. Lee, H. S. Park, G. A. Payne, J. M. Rodriguez, S. M. Sebt, A. D. Hamilton, *Angew. Chem.* **2005**, *117*, 2764–2767; *Angew. Chem. Int. Ed.* **2005**, *44*, 2704–2707.
- [21] J. D. Tyndall, T. Nall, D. P. Fairlie, *Chem. Rev.* **2005**, *105*, 973–999.
- [22] C. E. Schafmeister, J. Po, G. L. Verdine, *J. Am. Chem. Soc.* **2000**, *122*, 5891–5892.
- [23] N. E. Shepherd, H. N. Hoang, G. Abbenante, D. P. Fairlie, *J. Am. Chem. Soc.* **2005**, *127*, 2974–2983.

Biomaterials

DOI: 10.1002/anie.200501944

Saccharide–Peptide Hybrid Copolymers as Biomaterials***Mark Metzke, Naphtali O'Connor, Soumen Maiti, Edward Nelson, and Zhibin Guan**

Biomaterials are important for many biomedical applications such as implants and prosthetics, pharmaceutical formulations, drug and gene-delivery agents, DNA and protein microarrays, and tissue engineering.^[1] Synthetic polymers remain the most versatile class of biomaterials because of the ease in controlling their compositions, structures, and properties.^[2,3] There is currently a great demand for novel polymeric biomaterials with tailored structures and more-defined functions. Ideally, desired biomaterials can be chemically synthesized in a ground-up approach to exhibit precisely the needed chemical, biological, and engineering properties for the targeted medical application.

An important strategy for designing new biomaterials is to construct synthetic polymers from natural building blocks. The premise is to combine the advantages of both bio- and synthetic polymers, thereby gaining the biocompatibility and biodegradability of natural materials and the versatility of synthetic structural design. Examples of biomaterials made

[*] M. Metzke, N. O'Connor, Dr. S. Maiti, Prof. Dr. Z. Guan
Department of Chemistry
University of California
Irvine, CA 92697-2025 (USA)
Fax: (+1) 949-824-2210
E-mail: zguan@uci.edu
Prof. Dr. E. Nelson
School of Medicine
University of California
Irvine, CA 92697 (USA)

[**] We thank the Arnold and Mabel Beckman Foundation and the University of California at Irvine (UCI) for partial financial support. We thank Professor Ken Longmuir and Sherry Haynes for generous help with cell culturing and gene transfection studies, Professor Gregory Weiss and Sara Avrantinis for assistance in DNA electrophoresis study, and Jane Z. Bai and Derek Weisel for the AFM study.



Supporting information for this article is available on the WWW under <http://www.angewandte.org> or from the author.

from natural building blocks include poly(lactic acid),^[4] poly(glycolic acid),^[5] poly(anhydride)s,^[6] poly(amino acid)s,^[7] pseudo-poly(amino acid)s,^[8] carbohydrate-derived polyesters,^[9] and artificial proteins.^[10] Whereas these polymers generally exhibit good biocompatibility, and some are used in important clinical applications, their structural diversity and functional properties are relatively limited, warranting further development of more versatile biomaterials.

Herein we describe a new class of biomaterials derived from natural saccharide and amino acid building blocks (Figure 1). Our design is based on the following consider-

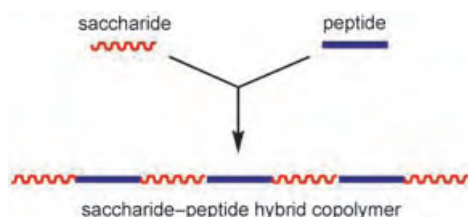


Figure 1. Formation of the saccharide-peptide hybrid copolymer.

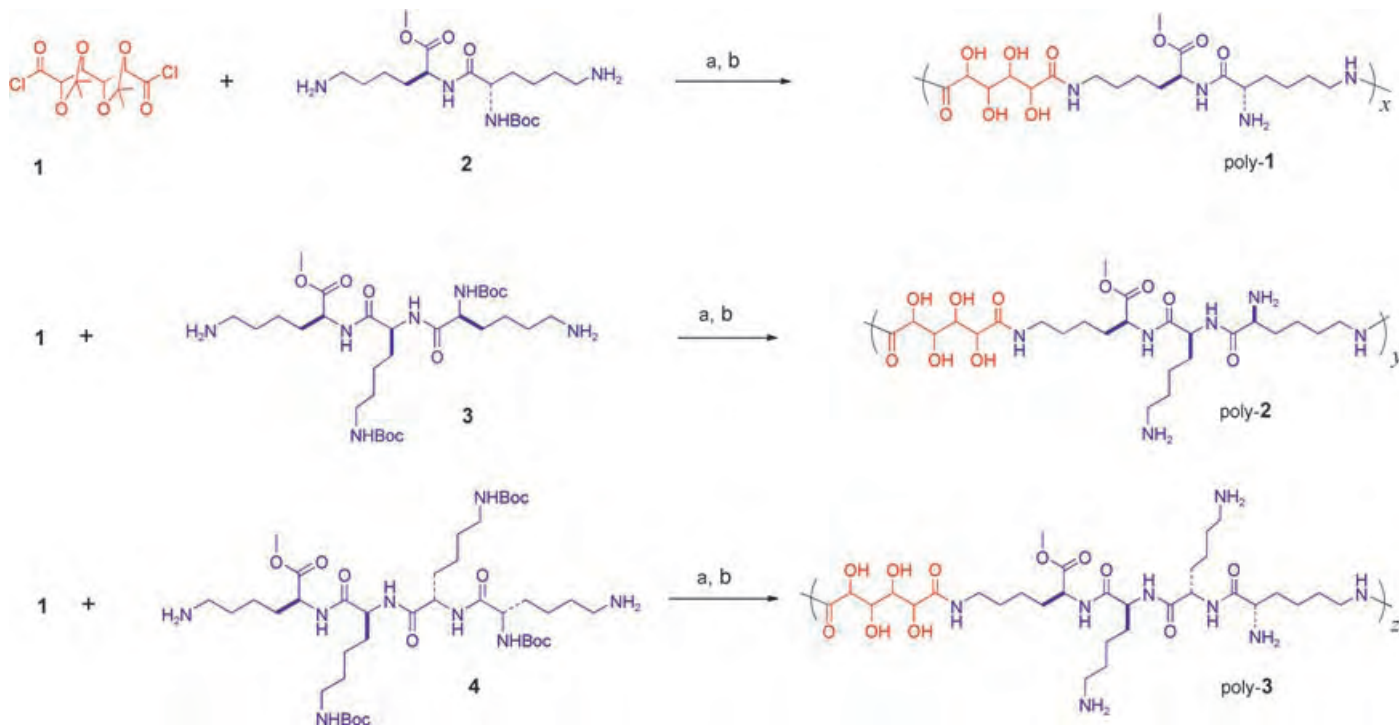
ations; 1) saccharides and amino acids are abundant and readily available natural monomers, 2) these natural building blocks are likely to yield polymers with inherent biocompatibility that then degrade into natural, nontoxic, and biosorbable species, 3) their rich functionalities allow convenient modification/tailoring of materials for desired applications, and 4) the modular synthesis offers advantages in combining structural precision with design flexibility.

The combination of various modules gives rise to numerous polymers suitable for combinatorial screening of the

chemical, biological, and mechanical properties of these polymers. Although much effort has been devoted to making oligomeric glycopeptides that can mimic the structure and function of natural glycoproteins,^[11,12] little has been reported on the synthesis of high-molecular-weight saccharide-peptide polymers.^[13,14] In our novel design, both the saccharide and peptide building blocks are incorporated into the main chain of the polymer. Herein we report our general design concept, synthesis, and the initial testing of a new class of biomaterials. We also discuss our studies of these saccharide-peptide hybrid copolymers in one specific biomedical application, gene delivery.

We chose oligosines and a galactose-derived monomer **1** for copolymerization. Three hybrid polymers (poly-**1**, poly-**2**, and poly-**3**) were synthesized by interfacial polymerization with various peptide monomers **2–4** (Scheme 1). ¹H and ¹³C NMR spectroscopic analyses were used to confirm the structure of each polymer. The number-averaged molecular weights (M_n) of the three prepolymers for poly-**1**, poly-**2**, and poly-**3** were measured by gel-permeation chromatography with polystyrene calibration standards to be 15 000, 9085, and 13 200 g mol⁻¹ respectively. Global cleavage of the acetonide and *tert*-butoxycarbonyl (Boc) protecting groups afforded the final carbohydrate-peptide hybrid copolymers, poly-**1**, poly-**2**, and poly-**3** (details of the synthesis and characterization can be found in the Supporting Information).

After the successful synthesis of the hybrid copolymers, we investigated their general properties as biomaterials including the biodegradability, cytotoxicity, and immunological properties. Enzymatic-degradation studies with serine proteases (subtilisin A and trypsin) showed that the polymers are indeed biodegradable. MALDI-TOF mass spectra were measured periodically to monitor qualitatively the decrease



Scheme 1. Synthesis of galactaro-oligosine hybrid copolymers (poly-**1**, poly-**2**, poly-**3**). a) Interfacial polymerization, H₂O/CCl₄; b) 30% trifluoroacetic acid in THF/water.

in the molecular weight of the polymer over time. The resultant profile indicated that the polymers were nearly completely degraded after 5–7 days of exposure to an enzyme (see Supporting Information).

The cytotoxicity of the polymers was then assayed at various concentrations by means of a standard MTT (3-(4,5-dimethylthiazol-2-yl)-2,5-diphenyl tetrazolium bromide) test. The hybrid copolymers exhibited minimal cytotoxicity to Cos 7 cells at a range of concentrations (Figure 2). Poly-L-lysine (PLL) with $M_n = 8500 \text{ g mol}^{-1}$ was used as a control

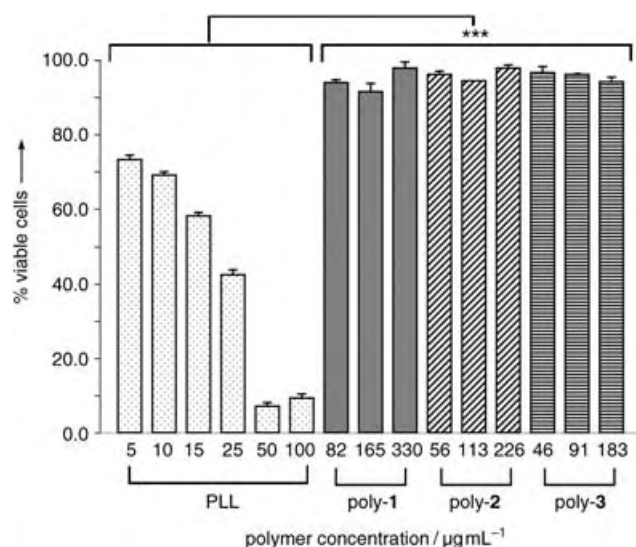


Figure 2. Cytotoxicity data acquired through MTT testing at various polymer concentrations with PLL as the control. Comparison was made with cationic amino groups at equivalent molar concentrations, consistent with those used in gene transfection studies. Standard deviations are shown with error bars ($n = 4$). The symbol *** indicates statistical significance at levels of $p < 0.001$ for the experimental polymers versus each concentration of PLL (indicated by brackets). The p values were obtained by using Student–Newman–Keuls multiple comparisons testing.

because our polymers are derived partially from L-lysine and are of comparable molecular weight, which affects both cytotoxicity and transfection levels.^[15] Comparisons between the polymers and the control were made at equivalent molar concentrations of cationic amino groups (the same as those used in later gene-transfection studies). The contrast is striking: whereas the PLL homopolymer exhibits high cytotoxicity at relatively low concentrations (5–100 $\mu\text{g mL}^{-1}$), our hybrid copolymers show lower cytotoxicity even at higher concentrations (82–330 $\mu\text{g mL}^{-1}$ for poly-1; 56–226 $\mu\text{g mL}^{-1}$ for poly-2; and 46–183 $\mu\text{g mL}^{-1}$ for poly-3). The placement of saccharide spacers on the main chain of the polymers lowered their cytotoxicity to levels approaching the blank controls in the absence of polymer. Although the exact mechanism for this decrease in toxicity remains to be investigated, we believe that the breakage of the cationic polypeptide into short segments with saccharide spacers lowers continuous charge density while the hydrophilic saccharide fragments shield the surface charge of the polyplexes. Both effects are hypothesized to alleviate disruptive coulombic interactions of the polyplexes with the cell

membrane. Other studies have shown that the introduction of carbohydrate units into other polymers also results in a lower cytotoxicity.^[16]

As our carbohydrate–peptide copolymers are new compounds, it is important to test whether they generate immune responses in vivo. As a representative example, the immunogenicity of poly-3 was evaluated by ELISA with Fisher 344 rats as models. Based on a standard protocol, 100 μg of poly-3 was administered in the first, third, and sixth weeks by either subcutaneous (SC) injections in the footpad or by intravenous (IV) injections into tail veins. The animals underwent a phlebotomy 21 days after each administration of the polymer. The serum for ELISA testing was obtained at three-week intervals. If a positive immunogenic response is elicited by the polymer, then antibodies generated in the rat serum would bind to the polymer-coated wells. An anti-rat immunoglobulin (IgG) conjugated HRP (horseradish peroxidase) then binds to the adsorbed polymer antibodies, catalyzing oxidation of a substrate that can be detected by UV/Vis spectrometry (see Supporting Information for experimental details). Figure 3 summarizes the ELISA data, which show no evidence of antibody response. All rats were healthy (no weight loss, normal activity, good hygiene/quality fur), which suggests that there is no adverse immune response or toxicity.

After the assays to test their biodegradability, cytotoxicity, and immunogenicity, the hybrid copolymers were evaluated for a specific biomedical application. Synthetic cationic

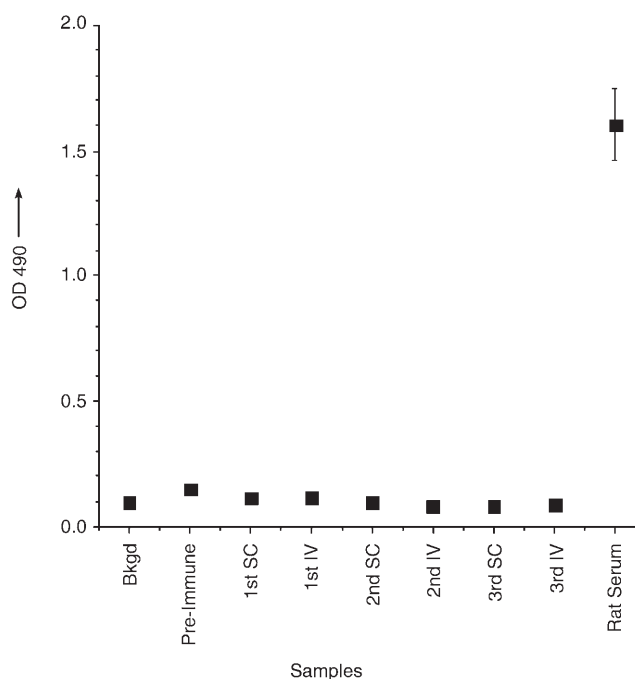


Figure 3. Anti-polymer ELISA data, which include the results for background (Bkgd), pre-immune serum, subcutaneous (SC), intravenous (IV), and normal rat serum (positive control: the wells were coated with rat serum enriched in antibodies, hence resulting in an expected positive signal). The y axis is the optical density (OD) at $\lambda = 490 \text{ nm}$ for the oxidation product of ELISA substrate, tetramethylbenzidine (TMB), which represents the level of immunogenic response of the polymer. The first, second, and third sera were taken at the third, sixth, and ninth week, respectively ($n = 3$). All experimental details are included in the Supporting Information.

polymers are currently being actively pursued as gene delivery vectors because they can neutralize and condense DNA into particles capable of undergoing endocytosis.^[17] A critical issue in developing effective synthetic polymeric vectors is that competent gene carriers, such as PLL and polyethyleneimine (PEI), are often cytotoxic.^[17,18] As our hybrid copolymers carry cationic charges at physiological pH values, and have minimal cytotoxicity, they were evaluated as vectors for gene delivery. Electrophoretic mobility-shift assays (EMSAs) indicated that poly-1, poly-2, and poly-3 efficiently complex pSV- β -gal plasmid DNA under physiological conditions. For poly-1 and poly-3, an N/P (ammonium positive charge on polymer/phosphate negative charge on DNA) ratio of 1.5 completely retarded the DNA; for poly-2 this ratio was 2 (see Supporting Information). The difference in DNA/polymer binding efficiency is presumably due to the difference in the molecular weight of the polymer as poly-2 has a slightly shorter chain length than poly-1 and poly-3. Complex formation occurs largely because of entropic gains owing to the liberation of smaller counterions along the macromolecular chains.^[19] Thus, as the chain is shortened (as for poly-2), there is less entropic gain during DNA complexation, which results in slightly weaker binding. The physical characteristics of the polymer/DNA complexes were then investigated by using AFM. Each polymer condensed DNA into spherical nanoparticles with typical diameters of 50–200 nm (Supporting Information), which is within the normal size range for cellular internalization.^[20]

The transfection efficiency of the three hybrid polymers was tested and compared with PLL by using a luciferase-assay kit under serum-free conditions. As PLL and poly-1, poly-2, and poly-3 have only primary amines and lack other amino residues to afford proton sponge effects, chloroquin (which is known to disrupt the membrane of the endosome) was used in all gene-transfection studies to enhance the endosomal release after entrance into the cell. Figure 4 summarizes the gene-transfection efficiency (normalized to the total cellular protein). Poly-2 and poly-3 showed a significantly higher transfection ability than PLL at similar N/P ratios. This is due primarily to the high toxicity of PLL at those concentrations. The lower transfection efficiency of poly-1 compared to poly-2 or poly-3 is presumably due to lower local charge density on poly-1 and the varied nature of the amino groups on the polymer chain. Poly-2 and poly-3 have both α -amino and more-flexible ε -amino functionalities, whereas poly-1 has only α -amine groups. It has been reported that very subtle changes in polymer structure can result in significant changes in gene-transfection efficiency.^[16a] Further structure-property correlation will be investigated in the future, which will provide information for structural optimization to improve the transfection efficiency.

In summary, we have described our concept for the design of saccharide-peptide hybrid copolymers as a new class of biomaterials. As examples, galactaro-dilysine (poly-1), trilysine (poly-2), and tetralysine (poly-3) hybrid copolymers were synthesized through interfacial polymerization of a galactose-derived monomer and corresponding L-lysine-derived peptide monomers. Enzymatic degradation, MTT tests, and immunological assays show that the hybrid copoly-

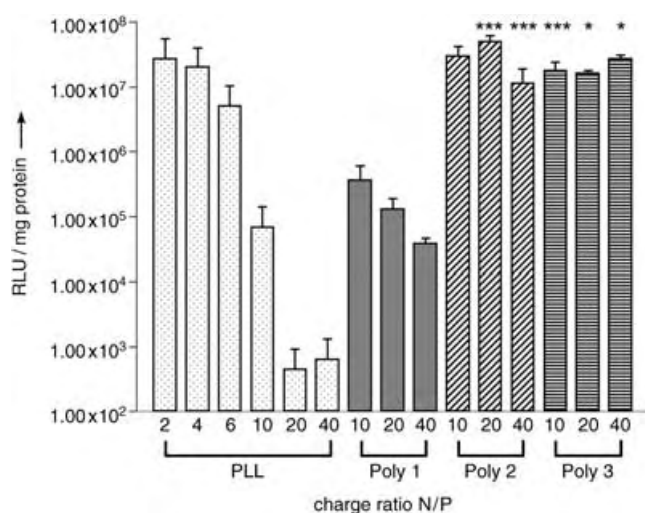


Figure 4. Luciferase gene-transfection data for the hybrid copolymers with PLL as control. Standard deviations are shown by the error bars ($n=3$). Relative light units (RLU) were normalized by using the total cellular protein in each well. The symbols * and *** indicate statistical significance at levels of $p < 0.05$ and $p < 0.001$, respectively, for the experimental polymers and PLL at corresponding N/P ratios. The p values were obtained by using Student–Newman–Keuls multiple comparisons testing.

mers are biodegradable, nontoxic, and nonimmunogenic. The hybrid copolymers were tested as vectors for possible application in gene delivery. EMSA, AFM, and luciferase-transfection studies demonstrate that the hybrid copolymers can efficiently compact plasmid DNA into soluble nanoparticles and be used as safe gene carriers. Given the natural abundance and functional diversity of saccharides and amino acids, their biodegradability, low cytotoxicity, and nonimmunogenicity, a diverse family of saccharide-peptide hybrid polymers are currently under development in our laboratory for various biomedical applications including gene/drug delivery and tissue engineering.

Received: June 6, 2005

Revised: July 21, 2005

Published online: September 15, 2005

Keywords: biomaterials · gene technology · polymers · peptides · saccharides

- [1] *Biomaterials Science: An Introduction to Materials in Medicine* (Eds.: B. D. Ratner, A. S. Hoffman, F. J. Schoen, J. E. Lemons), Elsevier, London, England, **1996**.
- [2] *Polymeric Biomaterials*, 2nd ed. (Ed.: S. Dumitriu), Marcel Dekker, Inc., New York, USA, **2002**.
- [3] R. Langer, D. A. Tirrell, *Nature* **2004**, 428, 487.
- [4] M. Vert, J. Mauduit, S. Li, *Biomaterials* **1994**, 15, 1209.
- [5] J. Mauduit, M. Vert, *S.T.P. Pharma Sci.* **1993**, 3, 197.
- [6] A. J. Domb, O. Elmalak, V. R. Shastri, Z. Ta-Shma, D. M. Masters, I. Ringel, D. Teomim, R. Langer, *Drug Targeting Delivery* **1997**, 7, 135.
- [7] F. Rypacek, M. Dvorak, I. Stefkó, L. Machova, V. Skarda, D. Kubies, *ACS Symp. Ser.* **2001**, 786, 258.
- [8] J. Kohn, *Drugs Pharm. Sci.* **1990**, 45, 195.

- [9] M. Metzke, J. Z. Bai, Z. Guan, *J. Am. Chem. Soc.* **2003**, *125*, 7760.
- [10] J. G. Tirrell, D. A. Tirrell, M. J. Fournier, T. L. Mason, *Protein-Based Mater.* **1997**, 61.
- [11] H. Herzner, T. Reipen, M. Schultz, H. Kunz, *Chem. Rev.* **2000**, *100*, 4495.
- [12] S. A. W. Gruner, E. Locardi, E. Lohof, H. Kessler, *Chem. Rev.* **2002**, *102*, 491.
- [13] K. Aoi, K. Tsutsumiuchi, M. Okada, *Macromolecules* **1994**, *27*, 875.
- [14] K. Aoi, K. Tsutsumiuchi, E. Aoki, M. Okada, *Macromolecules* **1996**, *29*, 4456.
- [15] A. Zelikin, D. Putman, P. Shastri, R. Langer, V. Izumrudov, *Bioconjugate Chem.* **2002**, *13*, 548.
- [16] a) S. J. Hwang, N. C. Bellocq, M. E. Davis, *Bioconjugate Chem.* **2001**, *12*, 280; b) Y. Liu, L. Wenning, M. Lynch, T. M. Reineke, *J. Am. Chem. Soc.* **2004**, *126*, 7422.
- [17] S. C. De Smedt, J. Demeester, W. E. Hennink, *Pharm. Res.* **2000**, *17*, 113.
- [18] W. Zauner, M. Ogris, E. Wagner, *Adv. Drug Delivery Rev.* **1998**, *30*, 97.
- [19] Z. Kakizawa, K. Kataoka, *Adv. Drug Delivery Rev.* **2002**, *54*, 203.
- [20] T. Friedmann, *Sci. Am.* **1997**, *276*, 96.

Natural Product Synthesis

DOI: 10.1002/anie.200502119

A Diels–Alder Macrocyclization Enables an Efficient Asymmetric Synthesis of the Antibacterial Natural Product Abyssomicin C**

Christoph W. Zapf, Bryce A. Harrison, Carmen Drahl, and Erik J. Sorensen*

In memory of Murray Goodman

In their pioneering report on the diene synthesis, or the Diels–Alder reaction, Otto Diels and Kurt Alder recognized the profound impact that this pericyclic reaction would have in

the syntheses of “complex compounds related to or identical with natural products” and speculated that this process may also be involved in the biosyntheses of natural products.^[1] As the premier method for the construction of functionalized and stereochemically complex six-membered-ring systems,^[2] the Diels–Alder reaction is the foundation of some of the most important achievements in chemical synthesis, and the question concerning its relevance in biosynthesis is the subject of much active research.^[3] There is a wealth of natural products that could conceivably arise from biosyntheses that feature the Diels–Alder reaction.^[4] We reasoned that much of the architectural complexity of the polycyclic marine natural product abyssomicin C (**1**) could arise from a Diels–Alder macrocyclization step and were intrigued by the possibility that such a transformation may also occur in the biogenesis of this natural product.

Süssmuth and co-workers recently described the isolation of abyssomicin C and two related compounds from a sediment sample collected 289 m beneath the surface of the Sea of Japan.^[5] These natural products are produced by the rare actinomycete *Verrucosisspora* and possess complex polyketide-like structures that were elucidated through extensive NMR spectroscopic studies and an X-ray crystallographic analysis. Abyssomicin C is unique within this new class of marine natural product in its ability to inhibit Gram-positive bacteria, including pathogenic methicillin-resistant and vancomycin-resistant *Staphylococcus aureus* strains.^[5,6] Although its biomolecular target in bacteria is not yet known, abyssomicin C blocks the conversion of chorismate to *para*-aminobenzoic acid (*p*ABA) and is thus an early-stage inhibitor of the biosynthesis of tetrahydrofolate (Scheme 1).

Inhibitors of the biosynthesis of *p*ABA are highly attractive as potential antibacterial drugs because *p*ABA is produced in many microorganisms but not in humans. As the first bacterial metabolite that inhibits the biosynthesis of *p*ABA, abyssomicin C is an attractive lead structure for the development of new inhibitors of pathogenic bacteria and a compelling objective for research in chemical synthesis.^[7] Herein, we describe a remarkably diastereoselective Diels–Alder macrocyclization in the context of a convergent asymmetric synthesis of (–)-abyssomicin C (**1**). Our preferred design reduced the complexity of the target structure to three fragments and called for two carbonyl addition reactions to achieve key bond formations (Scheme 2).

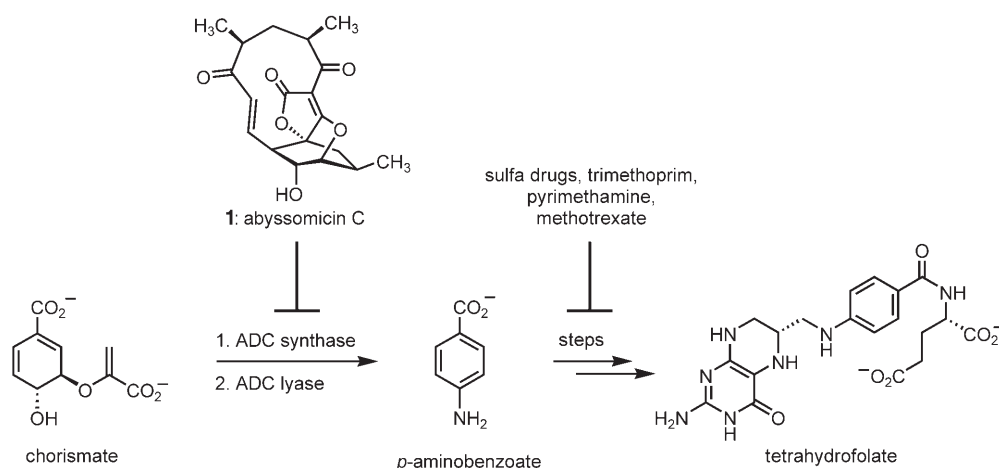
In this scenario, an intermolecular aldol reaction between the hypothetical ketone enolate **2** and commercially available *trans,trans*-2,4-hexadienal (**3**) would be followed by the addition of a lithiated tetronate **4** to an aldehyde carbonyl group. A simple adjustment of the oxidation state would then furnish the needed γ -methylene- β -tetronate derivative **5** for the crucial intramolecular Diels–Alder step.^[8] Some impressive large-ring formations that were achieved by the Diels–Alder method^[9] bolstered our confidence in the idea that **5** might cycloisomerize to tricycle **6**. If successful, this transformation would establish a substantial portion of the architecture of abyssomicin C and afford a valuable cyclohexenyl double bond for a late-stage epoxidation reaction. Provided that such an oxidation reaction could be achieved in a site- and diastereoselective fashion, we hoped to form the

[*] Dr. C. W. Zapf, Dr. B. A. Harrison, C. Drahl, Prof. Dr. E. J. Sorensen
Department of Chemistry
Princeton University
Princeton, NJ 08544-1009 (USA)
Fax: (+1) 609-258-1980
E-mail: ejs@princeton.edu

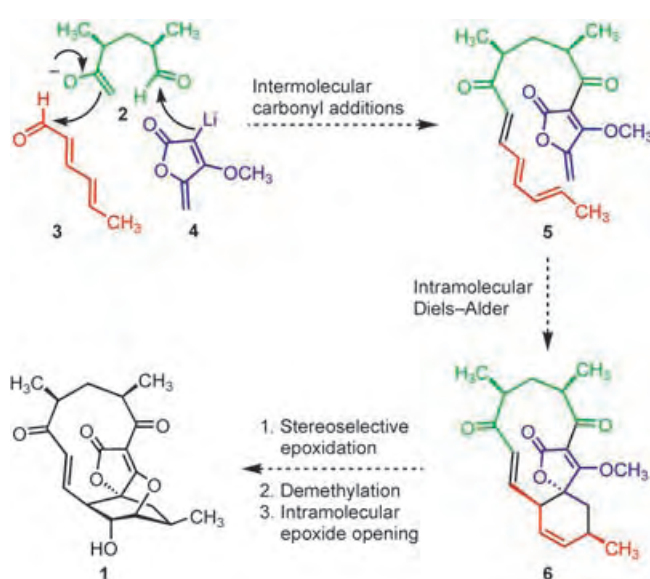
[**] This work was supported by Princeton University, a Bristol-Myers Squibb unrestricted research grant in synthetic organic chemistry (E.J.S.), the National Institute of General Medical Sciences (GM065483), Merck Research Laboratories (E.J.S.), a NRSA fellowship (1 F32 GM070235) from the National Institutes of Health (USA; B.A.H.), and a National Science Foundation (USA) Predoctoral Fellowship (C.D.). We thank Prof. Robert Pascal, Jr. for the conformational analysis of compound **5** and Dr. István Pelczar for assistance with the NMR spectroscopic analysis.



Supporting information for this article is available on the WWW under <http://www.angewandte.org> or from the author.



Scheme 1. The marine natural product abyssomicin C (**1**) inhibits the conversion of chorismate into *para*-aminobenzoic acid (*p*ABA). ADC = aminodeoxychorismate.^[6]



Scheme 2. Design for a synthesis of abyssomicin C which features a Diels–Alder macrocyclization.

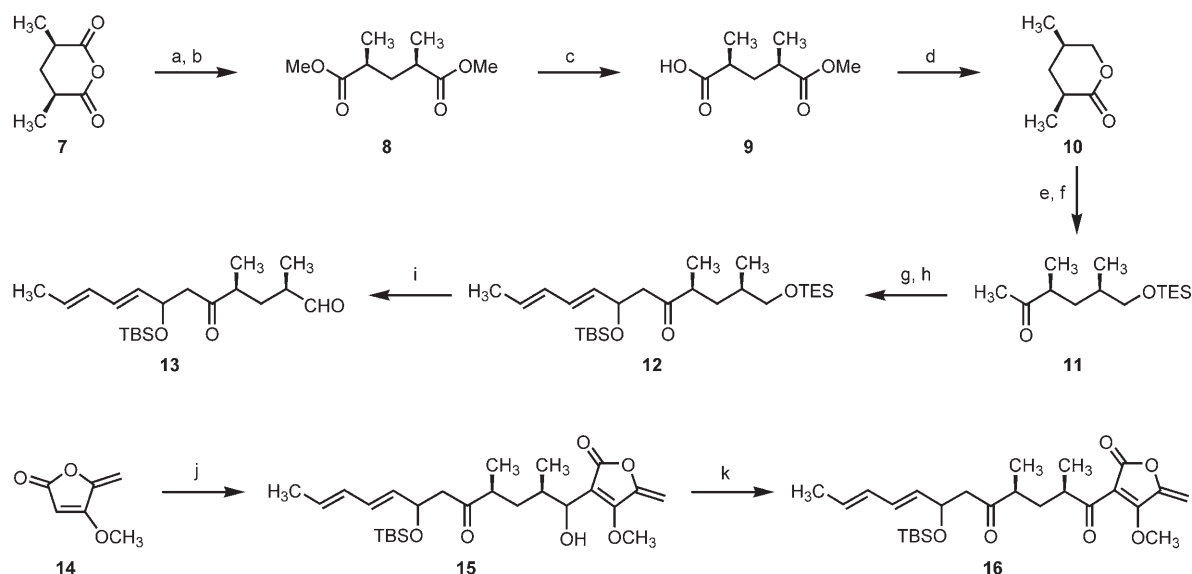
rigid oxabicyclo[2.2.2]octane substructure of **1** by a *trans*-diaxial opening of the epoxide by a tetrone acid function that would be exposed by demethylation. The successful execution of this general plan is described below.

Because of the symmetrical nature of the hypothetical species **2**, *meso*-2,4-dimethylglutaric anhydride (**7**) was considered to be an ideal starting material for our synthesis (Scheme 3). This substance was prepared on a 100-gram scale by a combination of the procedures developed by Paquette and Boulet^[10] and Lautens and co-workers^[11] and was subsequently advanced to the known prochiral dimethyl ester **8** in the straightforward fashion shown. The enzymatic desymmetrization procedure of Lautens and co-workers, which had previously been applied to the acyclic *meso*-diester **8**,^[11] provided a smooth high-yielding route to the optically active monocarboxylic acid **9**. A chemoselective reduction of the ester function with lithium borohydride was followed by

an acid-catalyzed lactonization to **10**, a known substance^[12] that was judged to have an optical purity of 93 % *ee* by HPLC analysis. The action of methyllithium on lactone **10** gave the corresponding lactol, after which a simple alcohol silylation step caused ring-opening and afforded methyl ketone **11**.

Our aim was to utilize **11** in an intermolecular aldol addition reaction with **3**. The commercially obtained dienal **3** is admixed with as much as 10 mol % of the 4-*cis* geometrical isomer, so we opted to produce this compound from all-*trans* 2,4-hexadien-1-ol through a Swern oxidation.^[13] Aldehyde **3**, prepared in this manner, was taken forward into the key aldol step in crude form. Under the reaction conditions shown, **3** joined efficiently with the kinetic lithium enolate derived from **11**, thus resulting in the formation of a 1:1 mixture of secondary alcohol epimers. A straightforward alcohol silylation step then gave a diastereoisomeric mixture of silyl ethers, shown as **12**. Our intent was to unveil the sensitive triene array of the targeted Diels–Alder substrate immediately before (or perhaps during) the key cycloaddition event through a simple β elimination. Therefore, the production of epimers in the aldol construction of **12** was ultimately inconsequential.

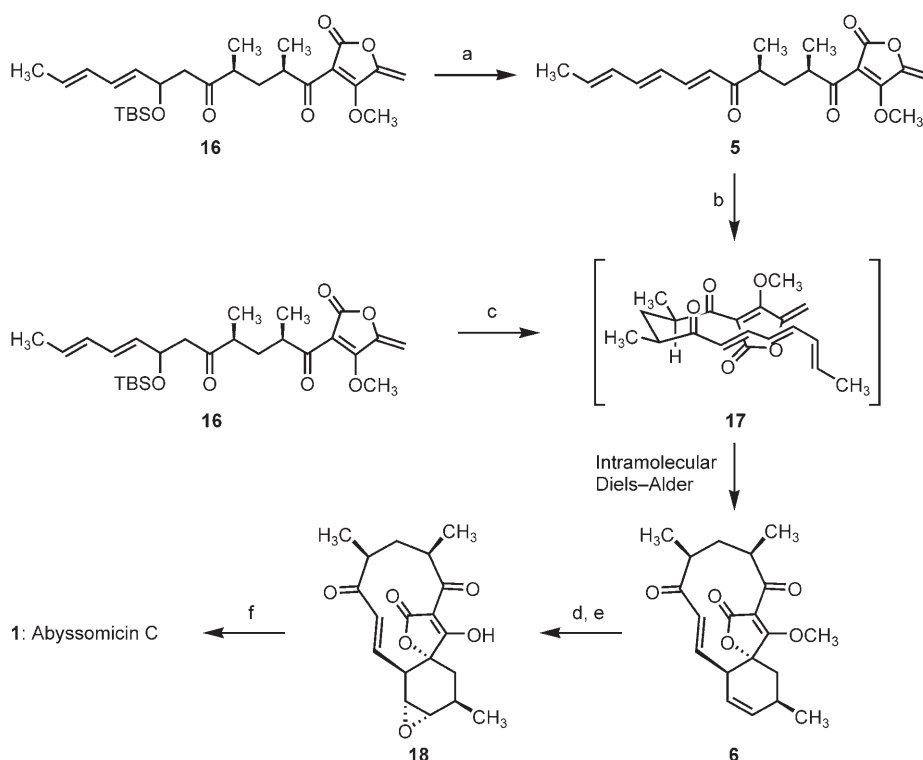
It was pleasing to discover that the triethylsilyl ether in **12** could be directly transformed to keto aldehyde **13** by a Swern oxidation.^[14] Our expectation that this electrophilic compound would react chemoselectively with organolithium reagent **4**, the conjugate base derived from the known methyl tetronate **14**,^[15] was justified by the construction of intermediate **15** under the conditions shown. This reaction, which established a key carbon–carbon bond and afforded material that contains all of the carbon atoms of abyssomicin C, can be performed on gram scales, although its yield is typically modest and variable (e.g., 35–55 %).^[16] This aldehyde addition process also yielded a mixture of alcohol diastereoisomers that could be resolved by chromatography on silica gel. However, it was our custom to convert this mixture of four diastereoisomers into two through an alcohol oxidation with the Dess–Martin periodinane reagent.^[17] This oxidation proceeded efficiently and yielded the desired acyl tetronate **16**.



Scheme 3. a) MeOH, reflux, 24 h; b) MeOH, H₂SO₄ (cat.), benzene, reflux, 18 h (87%, 2 steps); c) α -chymotrypsin, phosphate buffer pH 7.8, 23 °C, 4 days (96%); d) LiBH₄ (2 equiv), THF, 50 °C, 5 h; then HCl, H₂O, 23 °C, 15 h (60%, 93% ee); e) MeLi (1.3 equiv), THF, –78 °C, 1.5 h; f) TESCl (1.1 equiv), imidazole (2 equiv), DMF, 0 °C, 1.5 h (79%, 2 steps); g) LDA, THF, –78 °C, 2.5 h; then *trans,trans*-2,4-hexadienal (1.1 equiv), 1.5 h (94%, d.r. = 1:1); h) TBSOTf (1 equiv), 2,6-lutidine (2 equiv), CH₂Cl₂, 0 °C, 0.5 h (85%); i) (COCl)₂ (5 equiv), DMSO (10 equiv), Et₃N (10 equiv), CH₂Cl₂, –40 → –78 °C, 5 h (60–70%); j) LDA, toluene, –78 °C, 6 min; then aldehyde **13**, 1.5 h (35–55%, d.r. = 1:1); k) DMP (1.5 equiv), CH₂Cl₂, 0 → 23 °C, 1.5 h (84%). TES = triethylsilyl, TBS = *tert*-butyldimethylsilyl, Tf = trifluoromethanesulfonyl, DMF = *N,N*-dimethylformamide, DMSO = dimethyl sulfoxide, LDA = lithium diisopropylamide, DMP = Dess–Martin periodinane.

The decision to utilize a β -*tert*-butyldimethylsilyloxy keto function as a progenitor to the required trienone array proved to be well founded. Preliminary observations indicated that trienone **5** is a rather unstable substance. Fortunately, we could generate this compound upon exposure of a solution of intermediate **16** in dichloromethane to 5 mol% of the Lewis acid scandium(III) triflate (Scheme 4). Much to our delight, the crude trienone **5** underwent a remarkably efficient and highly diastereoselective cycloisomerization to tricycle **6** when heated to 100 °C in toluene. To avoid handling the sensitive trienone **5**, we searched for reaction conditions that would permit the β -elimination/Diels–Alder sequence to be conducted in a one-pot process. We hoped to find a Lewis acid catalyst that would effect the required elimination of *tert*-butyldimethylsilylanol on heating and that this event would trigger the desired Diels–Alder cyclization of the intermediate trienone **5** to **6**. Among the metal triflates that were examined, lanthanum(III) triflate was capable of inducing the direct conversion of **16** into tricycle **6** under the conditions shown. This transformation was also highly diastereoselective; **6** formed cleanly, and we did not observe any other regioisomeric or diastereoisomeric cycloadducts. In an effort to gain some insight

into this interesting and fortunate selectivity, we located the transition states for all of the possible intramolecular Diels–



Scheme 4. a) Sc(OTf)₃ (5 mol%), CH₂Cl₂, 0 °C, 40 min (65%); b) toluene, 100 °C, 4 h (79%); c) [La(OTf)₃] (10 mol%), toluene, 100 °C, 4 h (50%); d) DMDO (1 equiv), acetone, 0 → 23 °C, 18 h (67%); e) LiCl (10 equiv), DMSO, 50 °C, 2 h (quant.); f) *p*-TsOH (1.2 equiv), LiCl (5 equiv), CH₃CN, 50 °C, 2 h (50%). DMDO = dimethyldioxirane, *p*-TsOH = *para*-toluenesulfonic acid monohydrate.

Alder reactions at the HF/3-21G level of theory.^[18] The lowest-energy transition-state conformation clearly resembled **17**, and the next lowest transition-state conformation was 5.7 kcal mol⁻¹ higher in energy. This analysis predicts that **5** should cycloisomerize through conformer **17**, an asynchronous transition state that has an *anti* relationship between the two carbonyl groups that are part of the acyl tetronate moiety.

From the vantage of **6**, only three seemingly straightforward transformations were needed to reach the target structure. Fortunately, dimethyldioxirane was well suited to the oxidation of the newly formed cyclohexenyl double bond.^[19] This site- and diastereoselective oxidation produced the desired epoxide and was followed by a quantitative nucleophilic demethylation of the acyl methyl tetronate substructure. This two-step reaction sequence afforded **18**, a compound that appeared to be an ideal precursor to abyssomicin C (**1**). Because of its carboxylic acid like nature, the hydroxy group in **18** is a weak nucleophile. Compound **18** is essentially impervious to basic reagents; all efforts to achieve base-induced heterocyclizations to abyssomicin C were unsuccessful. After much experimentation, we found that warming a solution of **18**, *para*-toluenesulfonic acid monohydrate, and lithium chloride in acetonitrile to 50°C for 2 h resulted in the formation of abyssomicin C (**1**) and a regioisomeric substance that we named “iso-abyssomicin C”. Under these conditions, the ratio of these two compounds is 1:1, but they are readily separated by chromatography on silica gel. Optical rotation studies of our sample of synthetic abyssomicin C (**1**) showed an $[\alpha]_D^{20}$ value of -40 ($c = 0.1$, MeOH), and spectroscopic studies (¹H and ¹³C NMR, UV, and IR) resulted in data that matched those reported by Süssmuth and co-workers.^[5]

In summary, a concise enantioselective synthesis of (–)-abyssomicin C was achieved in 15 steps from the known *meso*-2,4-glutaric anhydride (**7**) by a reaction sequence that features a highly diastereoselective Diels–Alder macrocyclization. We can procure significant amounts of the natural product by this route, which should facilitate an investigation of the intriguing biological properties of abyssomicin C. It was proposed that the rigid oxabicyclo[2.2.2]octane substructure of abyssomicin C (**1**) may serve as a structural surrogate for the conformation of chorismate in solution and that its electrophilic enone system may inactivate one of the enzymes involved in the biosynthesis of *p*ABA in bacteria (Scheme 1) through covalent alkylation.^[5] By adapting the chemistry described herein, we anticipate that it will be possible to synthesize affinity-tagged variants of abyssomicin C for studies of its potential chemical reactivity and binding properties in human-tissue proteomes.^[20,21] This information would be part of a comprehensive analysis of the potential of abyssomicin C as an antibacterial drug candidate. Further studies of this fascinating early-stage inhibitor of the biosynthesis of tetrahydrofolate in bacteria are clearly warranted.

Received: June 17, 2005

Published online: September 15, 2005

Keywords: desymmetrization · Diels–Alder reaction · enzymes · natural products

- [1] O. Diels, K. Alder, *Justus Liebigs Ann. Chem.* **1928**, 460, 98–122.
- [2] For selected reviews and discussions of intermolecular and intramolecular Diels–Alder reactions, see: a) W. Oppolzer, *Comprehensive Organic Synthesis*, Vol. 5 (Eds.: B. M. Trost, I. Fleming), Pergamon, New York, **1991**, pp. 315–399; b) W. R. Roush, *Comprehensive Organic Synthesis*, Vol. 5 (Eds.: B. M. Trost, I. Fleming), Pergamon, New York, **1991**, pp. 513–550; c) ACS Monograph 180: G. Desimoni, G. Tacconi, A. Barco, G. P. Pollini, *Natural Products Synthesis Through Pericyclic Reactions*, American Chemical Society, Washington, DC, **1983**; d) E. J. Corey, *Angew. Chem.* **2002**, 114, 1724–1741; *Angew. Chem. Int. Ed.* **2002**, 41, 1650–1667; e) K. C. Nicolaou, S. A. Snyder, T. Montagnon, G. Vassilikogiannakis, *Angew. Chem.* **2002**, 114, 1742–1773; *Angew. Chem. Int. Ed.* **2002**, 41, 1668–1698.
- [3] a) H. Oikawa, K. Katayama, Y. Suzuki, A. Ichihara, *J. Chem. Soc. Chem. Commun.* **1995**, 1321–1322; b) S. Laschat, *Angew. Chem.* **1996**, 108, 313–315; *Angew. Chem. Int. Ed. Engl.* **1996**, 35, 289–291; c) K. Auclair, A. Sutherland, J. Kennedy, D. J. Witter, J. P. Van den Heever, C. R. Hutchinson, J. C. Vederas, *J. Am. Chem. Soc.* **2000**, 122, 11519–11520; d) T. Ose, K. Watanabe, T. Mie, M. Honma, H. Watanabe, M. Yao, H. Oikawa, I. Tanaka, *Nature* **2003**, 422, 185–189; e) T. Ose, K. Watanabe, M. Yao, M. Honma, H. Oikawa, I. Tanaka, *Acta Crystallogr. Sect. D* **2004**, 60, 1187–1197; f) C. R. W. Guimarães, M. Udier-Blagovic, W. L. Jorgensen, *J. Am. Chem. Soc.* **2005**, 127, 3577–3588.
- [4] E. M. Stocking, R. M. Williams, *Angew. Chem.* **2003**, 115, 3186–3223; *Angew. Chem. Int. Ed.* **2003**, 42, 3078–3115.
- [5] B. Bister, D. Bischoff, M. Ströbele, J. Riedlinger, A. Reicke, F. Wolter, A. T. Bull, H. Zähler, H.-P. Fiedler, R. D. Süssmuth, *Angew. Chem.* **2004**, 116, 2628–2630; *Angew. Chem. Int. Ed.* **2004**, 43, 2574–2576.
- [6] J. Riedlinger, A. Reicke, H. Zähler, B. Krismer, A. T. Bull, L. A. Maldonado, A. C. Ward, M. Goodfellow, B. Bister, D. Bischoff, R. D. Süssmuth, H.-P. Fiedler, *J. Antibiot.* **2004**, 57, 271–279.
- [7] a) J.-P. Rath, M. Eipert, S. Kinast, M. E. Maier, *Synlett* **2005**, 314–318; b) J.-P. Rath, S. Kinast, M. E. Maier, *Org. Lett.* **2005**, 7, 3089–3092.
- [8] a) K. Takeda, M. Sato, E. Yoshii, *Tetrahedron Lett.* **1986**, 27, 3903–3906; b) J. Uenishi, R. Kawahama, O. Yonemitsu, *J. Org. Chem.* **1997**, 62, 1691–1701.
- [9] a) E. J. Corey, M. Petrzilka, *Tetrahedron Lett.* **1975**, 16, 2537–2540; b) G. Stork, E. Nakamura, *J. Am. Chem. Soc.* **1983**, 105, 5510–5512; c) H. Dyke, P. G. Steel, E. J. Thomas, *J. Chem. Soc. Perkin Trans. 1* **1989**, 525–528; d) K. Takeda, Y. Igarashi, K. Okazaki, E. Yoshii, K. Yamaguchi, *J. Org. Chem.* **1990**, 55, 3431–3434; e) J. A. McCauley, K. Nagasawa, P. A. Lander, S. G. Mischke, M. A. Semones, Y. Kishi, *J. Am. Chem. Soc.* **1998**, 120, 7647–7648.
- [10] L. A. Paquette, S. L. Boulet, *Synthesis* **2002**, 888–894.
- [11] M. Lautens, J. T. Colucci, S. Hiebert, N. D. Smith, G. Bouchain, *Org. Lett.* **2002**, 4, 1879–1882.
- [12] R. Ozegowski, A. Kunath, H. Schick, *Tetrahedron: Asymmetry* **1993**, 4, 695–698.
- [13] A. J. Mancuso, D. Swern, *Synthesis* **1981**, 165–185.
- [14] For general review articles on the deprotection of silyl ethers, see: a) J. Muzart, *Synthesis* **1993**, 11–27; b) T. D. Nelson, R. D. Crouch, *Synthesis* **1996**, 1031–1069; for applications of the removal of TES under Swern conditions, see: c) G. A. Tolstikov, M. S. Miftakhov, M. E. Adler, N. G. Komissarov, O. M. Kuznetsov, N. S. Vostrikov, *Synthesis* **1989**, 940–942; d) G. C. Hirst, T. O. Johnson, Jr., L. E. Overman, *J. Am. Chem. Soc.* **1993**, 115, 2992–2993; e) G. H. Posner, K. Crawford, M.-L. Siu-Caldera, G. S. Reddy, S. F. Sarabia, D. Feldman, E. van Etten, C. Mathieu, L. Gennaro, P. Vourros, S. Peleg, P. M. Dolan, T. W. Kensler, J.

- Med. Chem.* **2000**, *43*, 3581–3586; f) A. Rodriguez, M. Nomen, B. W. Spur, J. J. Godfroid, T. H. Lee, *Tetrahedron* **2001**, *57*, 25–37; g) G. Rassu, L. Auzzas, L. Pinna, V. Zambrano, F. Zanardi, L. Battistini, E. Gaetani, C. Curti, G. Casiraghi, *J. Org. Chem.* **2003**, *68*, 5881–5885.
- [15] K. Takeda, S. Yano, M. Sato, E. Yoshii, *J. Org. Chem.* **1987**, *52*, 4135–4137.
- [16] Ketone addition products were not observed in this step.
- [17] a) D. B. Dess, J. C. Martin, *J. Org. Chem.* **1983**, *48*, 4155–4156; b) D. B. Dess, J. C. Martin, *J. Am. Chem. Soc.* **1991**, *113*, 7277–7287.
- [18] These conformational analyses were performed by Professor Robert Pascal, Jr., Princeton University; see the Supporting Information for the Cartesian coordinates and calculated energies for the transition states.
- [19] Excess dimethyldioxirane caused epoxidation of the enone double bond.
- [20] G. C. Adam, C. D. Vanderwal, E. J. Sorensen, B. F. Cravatt, *Angew. Chem.* **2003**, *115*, 5638–5642; *Angew. Chem. Int. Ed.* **2003**, *42*, 5480–5484.
- [21] C. Drahl, B. F. Cravatt, E. J. Sorensen, *Angew. Chem.* *117*, 5936–5958; *Angew. Chem. Int. Ed.* **2005**, *44*, 5788–5809.

Metal–Metal Bonds

DOI: 10.1002/anie.200500138

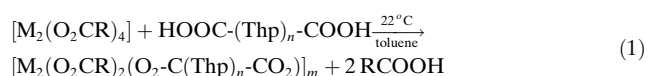
Oligothiophenes Incorporating Metal–Metal Quadruple Bonds**

Malcolm H. Chisholm,* Arthur J. Epstein,*
Judith C. Gallucci, Florian Feil, and Wesley Pirkle

There is considerable interest at this time in inorganic–organic hybrid materials, and metal-containing polymers constitute an important section within this general field. The work of Manners and co-workers^[1] with metallocene-derived polymers, Friend, Raithby, and co-workers^[2] with metallated polyynes and poly(phenylvinylene)s, Wolf and co-workers^[3] with metallated polythiophenes, and Thompson, Forrest, and co-workers^[4] with iridium and platinum complex doped conjugated polymers, represent four prime areas of recent research interest. The majority of efforts thus far have focused

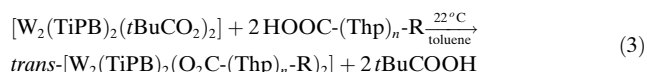
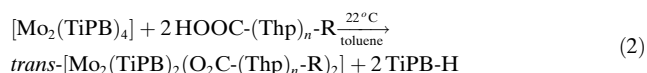
on the use of the Group 8 metals (the metals of the iron, cobalt, and nickel triads), in which the metal ions are d⁶ or d⁸. We are interested in incorporating metal–metal quadruple bonds with a $\sigma^2\pi^4\delta^2$ configuration into organic conjugated polymers because the dinuclear center is redox-active and its ease of oxidation can be tuned over a considerable range by the selection of the metal (M = Cr, Mo, W) and the ancillary ligands,^[5] even to the point that the M₂ center is more easily oxidized than cesium.^[6] The M₂ center may also be brought into conjugation with the π system of the organic polymer through the agency of a carboxylate link.^[7] The carboxylate π system couples with both the π system of the polymer backbone and the M₂ δ orbitals. We recently illustrated this by the preparation of some discrete model complexes of the type [M₂(O₂CR)₄], in which R = mono-, bi-, and terthienyl (α,α') groups.^[8]

Herein, we describe our synthesis of oligomeric/polymeric thienyl-based materials incorporating metal–metal quadruple bonds. The general reaction is shown in Equation (1),



although, as noted below, there are important restrictions (Thp = thiophene = 2,5-C₄H₂S). Full experimental details are given in the Supporting Information.

To prepare soluble oligomers/polymers of the desired empirical formula, we found it necessary to introduce chain-branching alkyl substituents on both the spectator carboxylate and the thienyl dicarboxylate. Thus far, we have enjoyed most success with 2,4,6-triisopropylbenzoate (2,4,6-*i*Pr₃C₆H₂CO₂ = TiPB) as the ancillary ligand. This group has the added advantage that the *trans*-disubstituted product appears to be the preferred thermodynamic product. This is also evident from the preparations of the discrete compounds for molybdenum [Eq. (2)] and for tungsten [Eq. (3)]. For



molybdenum, we used the corresponding homoleptic carboxylate [Mo₂(TiPB)₄]^[9] and for tungsten, the mixed compound [W₂(TiPB)₂(*t*BuCO₂)₂] as starting materials. Even with the use of only 1 equivalent of the thienyl carboxylic acid, the bis,bis-substituted product [M₂(TiPB)_{4-*x*}(O₂C-(Thp)_{*n*}-R)_{*x*}] (Thp = 2,4-C₄H₂S; *n* = 1,2; R = H; *n* = 3; R = Me) is formed in preference to other combinations.

Only one isomer is observed in solution for these M₂ complexes and, as is shown in Figure 1, steric factors favor the *trans* substitution about the M₂ paddle-wheel core. The twisting of the phenyl rings out of the plane of their attendant carboxylate groups removes M₂(δ)-to-C₆(π) conjugation. In the UV/Vis spectrum, the M₂(δ)-to-(aryl carboxylate) transition is very weak in comparison with the M₂(δ)-to-(thienyl carboxylate) transition. As is shown in Figure 2, the M₂(δ)-to-thienyl(π^*) transition moves to lower energy as *n* increases

[*] Prof. Dr. M. H. Chisholm, J. C. Gallucci, Dr. F. Feil
Department of Chemistry, The Ohio State University
Columbus, Ohio 43210 (USA)
Fax: (+1) 614-292-0368
E-mail: chisholm@chemistry.ohio-state.edu

Prof. Dr. A. J. Epstein, W. Pirkle
Department of Physics, The Ohio State University
Columbus, OH 43210 (USA)

[**] We thank the National Science Foundation for financial support, Dr. Kari Green-Church for recording MALDI mass spectra, and Prof. Claudia Turro, Dr. Ramkrishna Ramnauth, and Dr. Yao Liu for measuring the emission spectra.

Supporting information for this article is available on the WWW under <http://www.angewandte.org> or from the author.

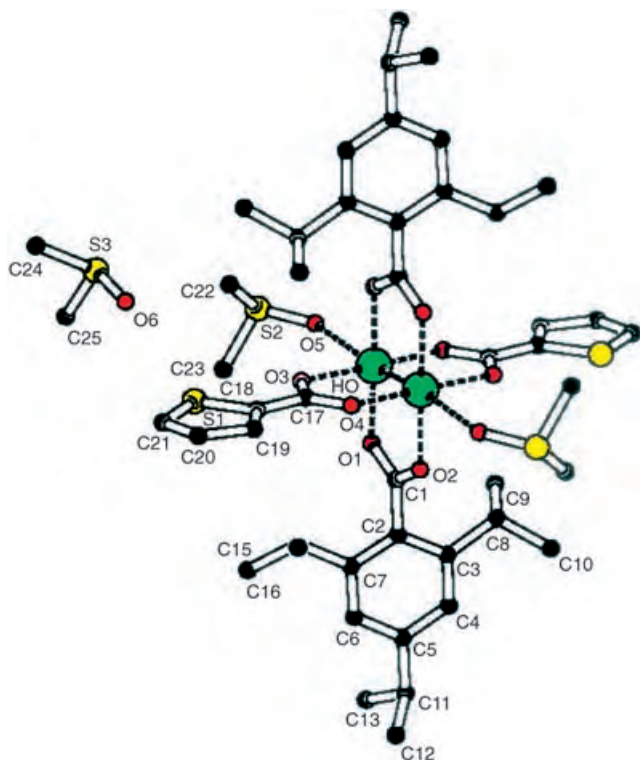
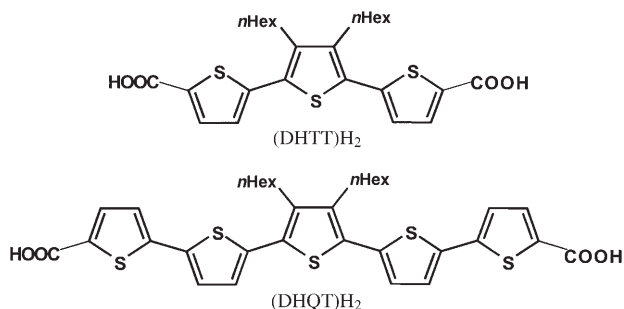


Figure 1. Molecular structure of the centrosymmetric $[\text{Mo}_2(\text{TiPB})_2(\text{O}_2\text{C-Thp-H})_2]$ molecule found in the solid state with two axially coordinating DMSO molecules and one noncoordinating DMSO molecule. The Mo–Mo, Mo–O(TiPB carboxylate), and Mo–O(thiophene carboxylate) interatomic distances are 2.113, 2.111 (Å), and 2.110 Å (Å), respectively. The dihedral angle between the thienyl ring and its carboxylate group is 0.35° (°).

from 1 to 2 to 3 and is markedly red-shifted and more intense on going from $M = \text{Mo}$ to W . The latter is a result of the higher orbital energy of the W_2 d electrons and the greater degree of $\text{W}_2(\delta)$ -to-thienyl(π^*) overlap.

In reactions of Equation (1), we employed the *n*-hexyl-substituted thienyl dicarboxylic acids $(\text{DHTT})\text{H}_2$ (3',4'-dihexyl-2,2':5',2''-terthiophene-5,5''-dicarboxylic acid)^[10] and $(\text{DHQT})\text{H}_2$ (3'',4''-dihexyl-2,2':5',2''':5'',2''':5''',2''''-quinque-thiophene-5,5''''-dicarboxylic acid)^[11] shown below. Furthermore, an excess of $[\text{Mo}_2(\text{TiPB})_4]$ or $[\text{W}_2(\text{TiPB})_4]$ was used to ensure the total conversion of the dicarboxylic acids. The polymeric materials $[\text{M}_2(\text{TiPB})_2(\text{O}_2\text{C-Thp})_n\text{-CO}_2]$ are formed as flocculent precipitates that are difficult to filter. They are best isolated by centrifugation followed by repeated washings, first with toluene and then hexanes, to remove the



acid TiPB-H and any unreacted monomeric M_2 tetracarboxylates. The resulting dried red ($M = \text{Mo}$) or bluish-green ($M = \text{W}$) powders are somewhat soluble in THF and swell to form gels by absorbing approximately 20 times their mass of THF. The ^1H NMR spectra of the samples in $[\text{D}_8]\text{THF}$ only show evidence for one type of TiPB and $\text{O}_2\text{C-Thp-CO}_2$ groups. However, the MALDI-MS data show molecular ions that correspond to $[\text{M}_2(\text{TiPB})_2(\text{O}_2\text{C-Thp})_n\text{-CO}_2]_2^+$ loops, $[\text{M}_2(\text{TiPB})_2(\text{O}_2\text{C-Thp})_n\text{-CO}_2]_3^+$ triangles, and even higher oligomers. These can only arise from a *cis*-substitution pattern at the M_2^{4+} center. We propose that this substitution pattern is less common than that of *trans* substitution, but that it is this property, together with some *trans* substitution at the Mo_2^{4+} center, that facilitates the gel-forming capability of the entangled chains. The system can be described as a dynamic equilibrium of chains, cycles, and cross-linked oligomers/polymers^[12] as a result of facile carboxylate-exchange reactions, which are well-documented to be catalyzed by both acid and base (H^+ , carboxylate).^[13] A reasonable estimate of the molecular weight is over 10 000 Daltons, or more than 10 repeating units.

The electronic absorption spectra of these oligomers closely resemble those of the model compounds (Figure 2) in that they have well-defined, although broad, absorptions assignable to $\text{M}_2(\delta)$ -to-thienyl(bridge)(π^*) and thienyl(π)-to-thienyl(π^*) (bridge-to-bridge) transitions. The emission spectra show only the thienyl(π^*)-to- $\text{M}_2(\delta)$ transition, as shown in

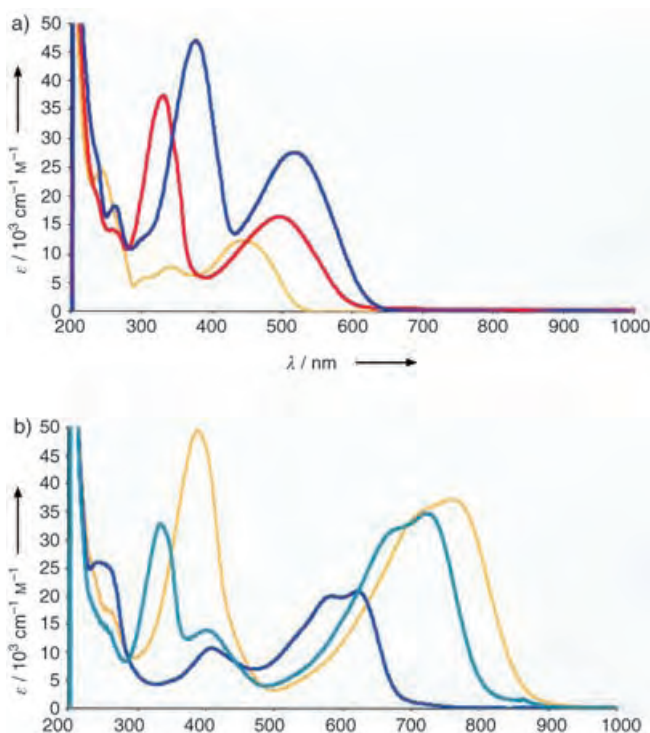


Figure 2. a) Electronic absorption spectra of $[\text{Mo}_2(\text{TiPB})_2(\text{O}_2\text{C-Thp-H})_2]$ (yellow), $[\text{Mo}_2(\text{TiPB})_2(\text{O}_2\text{C-Thp})_2\text{-H})_2]$ (red), and $[\text{Mo}_2(\text{TiPB})_2(\text{O}_2\text{C-Thp})_3\text{-Me})_2]$ (blue) in THF at room temperature. b) Electronic absorption spectra of $[\text{W}_2(\text{TiPB})_2(\text{O}_2\text{C-Thp-H})_2]$ (blue), $[\text{W}_2(\text{TiPB})_2(\text{O}_2\text{C-Thp})_2\text{-H})_2]$ (green), and $[\text{W}_2(\text{TiPB})_2(\text{O}_2\text{C-Thp})_3\text{-Me})_2]$ (yellow) in THF at room temperature.

Figure 3 for the terthienyl-bridged polymer. These photophysical properties can be described in terms of the Jablonski diagram shown in Figure 4.

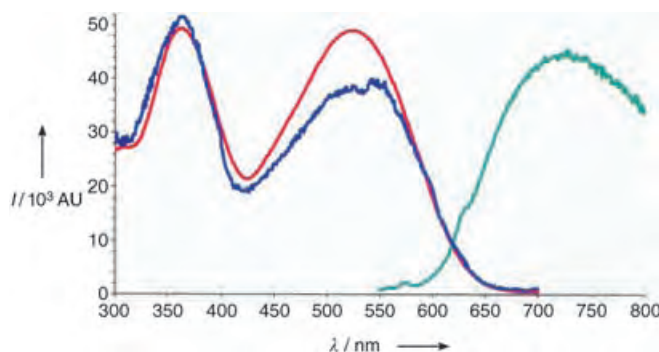


Figure 3. Absorption spectrum (red) of “ $\text{Mo}_2(\text{TiPB})_2(\text{DHTT})$ ” in THF at room temperature, and photoluminescence spectrum (green) with excitation at 531 nm. Higher-energy excitation (360 nm) results in a similar spectral profile. The excitation spectrum is shown in blue.

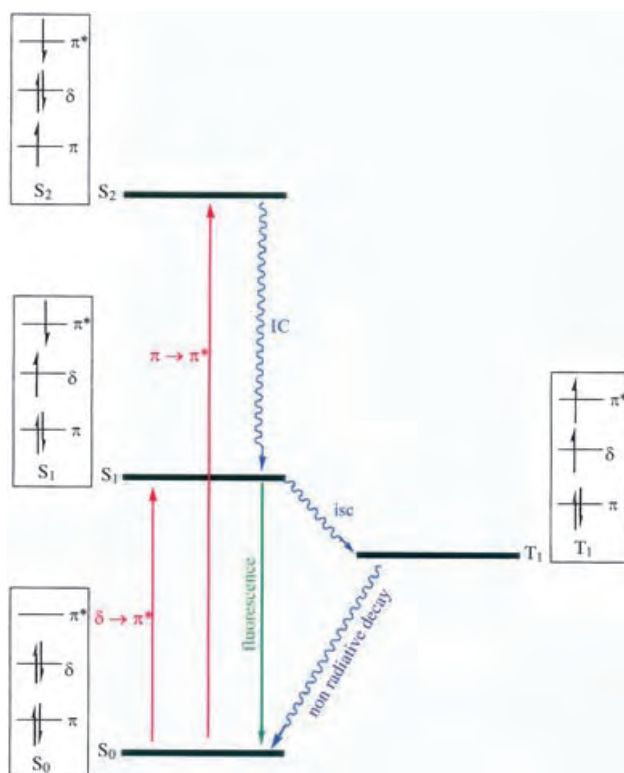


Figure 4. Proposed Jablonski scheme of the absorptions and emission of $[\text{M}_2(\text{TiPB})_2(\text{O}_2\text{C}(\text{Thp})_n\text{CO}_2)]$ oligomers. Absorptions to S_1 and S_2 are observed; emission occurs from S_1 while a nonemissive T_1 state is also observed. IC = internal conversion; ISC = intersystem crossing.

The gels dry to form thin films, and THF solutions can be used to deposit thin films of these metallated oligomers by spin-coating in a dry-box under argon. Deposition on an indium–tin oxide (ITO)-coated glass plate followed by vapor deposition of aluminum or calcium was carried out to make conductivity measurements. As shown in Figure 5, the thin

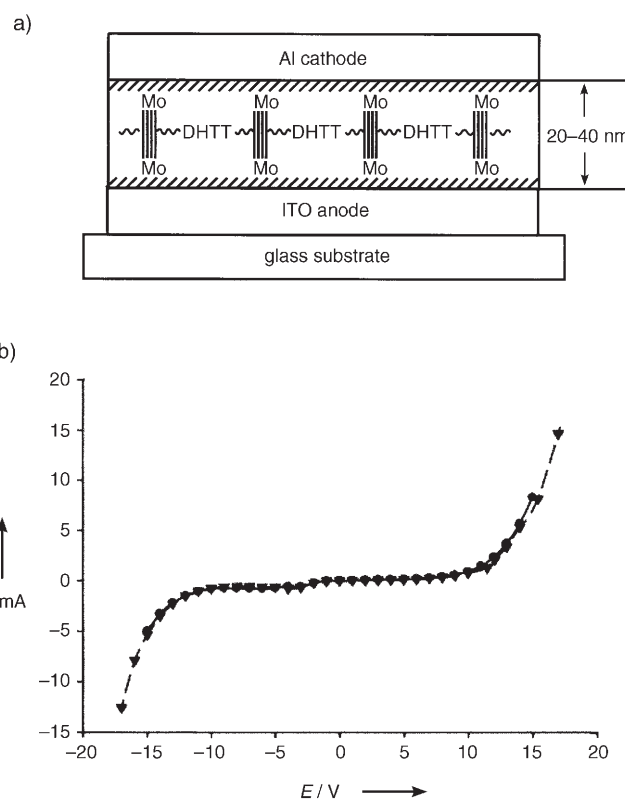


Figure 5. a) Structure of an Al-“ $\text{Mo}_2(\text{TiPB})_2(\text{DHTT})$ ”-ITO device; b) current as a function of voltage for the same device (●: IV curve from 14 to -14 V; ▼: IV curve from 16 to -16 V).

films of the molybdenum terthienyl-bridged material display diode properties, with current being drawn nearly equally in both the forward and reverse bias, reminiscent of interface-controlled symmetrically configured ac-light-emitting (SCALE) devices.^[14] Whereas the terthienylmolybdenum-containing films do not show electroluminescence with aluminum, the pentathienyl analogue (derived from $(\text{DHQT})\text{H}_2$) does, and both the ter- and pentathienyl-derived thin films show electroluminescence when lower-work-function calcium was used as the cathode (Figure 6). The emission from these films is red-shifted relative to that of the parent

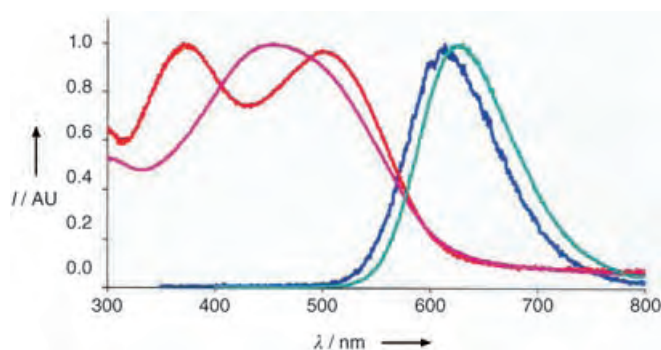


Figure 6. Absorption spectra of an “ $\text{Mo}_2(\text{TiPB})_2(\text{DHTT})$ ” thin film (red) and an “ $\text{Mo}_2(\text{TiPB})_2(\text{DHQT})$ ” thin film (purple), and electroemission of a Ca-“ $\text{Mo}_2(\text{TiPB})_2(\text{DHTT})$ ”-ITO device (blue) and a Ca-“ $\text{Mo}_2(\text{TiPB})_2(\text{DHQT})$ ”-ITO device (green).

acids (DHTT)H₂ and (DHQT)H₂.^[15] Furthermore, the electroluminescence spectra display an unusual blue shift relative to the photoluminescence spectra, which suggests the important role of charge trapping in these materials.

In conclusion, we believe that the preliminary findings reported herein indicate that polythiophenes incorporating metal–metal quadruple bonds should have interesting and tunable electronic properties. The M₂ δ electrons lie within the band-gap of the polymer, but are strongly coupled by M₂(δ)-to-CO₂(π) conjugation. We anticipate that the electroluminescence for tungsten can be moved into the near-IR region. Further work in this area is in progress.

Received: January 13, 2005

Revised: May 30, 2005

Published online: September 15, 2005

Keywords: electroluminescence · metal–metal interactions · molybdenum · sulfur heterocycles · tungsten

- [1] a) C. Paquet, P. W. Cyr, E. Kumacheva, I. Manners, *Chem. Mater.* **2004**, *16*, 5205; b) I. Manners, *Synthetic Metal-Containing Polymers*, Wiley, New York, **2002**.
- [2] a) M. S. Khan, M. R. A. Al-Mandhary, M. K. Al-Suti, F. R. Al-Battashi, S. Al-Saadi, B. Ahrens, J. K. Bjernemose, M. F. Mahon, P. R. Raithby, M. Younus, N. Chawdhury, A. Koehler, E. A. Marseglia, E. Tedesco, N. Feeder, S. J. Teat, *Dalton Trans.* **2004**, *15*, 2377; b) M. S. Khan, M. R. A. Al-Mandhary, M. K. Al-Suti, T. C. Corcoran, Y. Al-Mahrooqi, J. P. Attfield, N. Feeder, W. I. F. David, K. Shankland, R. H. Friend, A. Koehler, E. A. Marseglia, E. Tedesco, C. C. Tang, P. R. Raithby, J. C. Collings, K. P. Roscoe, A. S. Batsanov, L. M. Stimson, T. B. Marder, *New J. Chem.* **2003**, *27*, 140.
- [3] a) For organometallic and coordination clusters and polymers, see: C. Moorlag, O. Clot, Y. Zhu, M. O. Wolf, *Macromol. Symp.* **2004**, *209*, 133; b) C. Moorlag, O. Clot, M. O. Wolf, *Polym. Prepr. (Am. Chem. Soc. Div. Polym. Chem.)* **2004**, *45*, 437; c) T. L. Stott, M. O. Wolf, *Coord. Chem. Rev.* **2003**, *246*, 89.
- [4] a) X. Wang, M. R. Andersson, M. E. Thompson, O. Inganäs, *Thin Solid Films* **2004**, *468*, 226; b) C. Adachi, M. A. Baldo, S. R. Forrest, S. Lamansky, M. E. Thompson, *Appl. Phys. Lett.* **2001**, *78*, 1622; c) M. A. Baldo, S. Lamansky, P. E. Burrows, M. E. Thompson, S. R. Forrest, *Appl. Phys. Lett.* **1999**, *75*, 4.
- [5] F. A. Cotton, R. A. Walton, *Multiple Bonds Between Metal Atoms*, 2nd ed., Oxford University Press, Oxford, UK, **1994**.
- [6] F. A. Cotton, N. E. Gruhn, J. Gu, P. Huang, D. L. Lichtenberger, C. A. Murillo, L. D. Van Dorn, C. C. Wilkinson, *Science* **2002**, *298*, 1971.
- [7] M. H. Chisholm, *Dalton Trans.* **2003**, 3941.
- [8] M. J. Byrnes, M. H. Chisholm, R. J. H. Clark, J. C. Gallucci, C. M. Hadad, N. J. Patmore, *Inorg. Chem.* **2004**, *43*, 6334.
- [9] F. A. Cotton, L. M. Daniels, E. A. Hillard, C. A. Murillo, *Inorg. Chem.* **2001**, *40*, 1639.
- [10] M. Belletete, L. Mazerolle, N. Desrosiers, M. Leclerc, G. Durocher, *Macromolecules* **1995**, *28*, 8587.
- [11] A. Donat-Bouillud, L. Mazerolle, P. Gagnon, L. Goldenberg, M. C. Petty, M. Leclerc, *Chem. Mater.* **1997**, *9*, 2815.
- [12] a) S. J. Rowan, S. J. Cantrill, G. R. L. Cousins, J. K. M. Sanders, J. F. Stoddart, *Angew. Chem.* **2002**, *114*, 938; *Angew. Chem. Int. Ed.* **2002**, *41*, 898; Erratum: S. J. Rowan, S. J. Cantrill, G. R. L. Cousins, J. K. M. Sanders, J. F. Stoddart, *Angew. Chem.* **2002**, *114*, 1528; *Angew. Chem. Int. Ed.* **2002**, *41*, 1460; b) R. E. Furlan, S. Otto, J. K. M. Sanders, *Proc. Natl. Acad. Sci. USA* **2002**, *99*, 4801.
- [13] M. H. Chisholm, A. M. Macintosh, *J. Chem. Soc. Dalton Trans.* **1999**, 1205.
- [14] Y. Z. Wang, D. D. Gebler, L. B. Lin, J. W. Blatchford, S. W. Jessen, H. L. Wang, A. J. Epstein, *Appl. Phys. Lett.* **1996**, *68*, 894.
- [15] N. DiCesare, M. Belletete, A. Donat-Bouillud, M. Leclerc, G. Durocher, *J. Lumin.* **1999**, *81*, 111.

Magnetic Clusters

DOI: 10.1002/anie.200501881

Linking Centered Manganese Triangles into Larger Clusters: A {Mn₃₂} Truncated Cube**

*Richard T. W. Scott, Simon Parsons, Muralee Murugesu, Wolfgang Wernsdorfer, George Christou, and Euan K. Brechin**

Single-molecule magnets (SMMs) have many potential applications including high-density information storage, in which each bit of information is stored as the magnetization orientation of an individual molecule, and as qubits for quantum computation, in which the required arbitrary superposition of quantum states with opposite projections of spin can be produced by either quantum tunneling of the magnetization, intermolecular exchange, or multifrequency EPR pulses.^[1–4] The fundamental requirements for a molecule to behave as an SMM are a) a relatively large spin ground state (S) and b) a large and negative zero-field splitting (zfs) of that ground state (as measured by the zfs parameter D). The upper limit of the barrier to the reorientation of the magnetization is given by $S^2 |D|$ for integer spins and $(S^2 - 1/4) |D|$ for half-integer spins.

To make large molecular clusters, two successful, but somewhat opposing, synthetic strategies have generally been employed. The first is the use of rigid bridging ligands, for example, cyanide, that impose the geometry on the resultant cluster,^[5] and the second is the use of flexible ligands, for example, carboxylates, that impose little or no geometry.^[6] Both approaches have produced molecules with extremely

[*] R. T. W. Scott, Dr. S. Parsons, Dr. E. K. Brechin
School of Chemistry
The University of Edinburgh
West Mains Road, Edinburgh, EH93JJ (UK)
Fax: (+44) 131-650-4743
E-mail: ebrechin@staffmail.ed.ac.uk

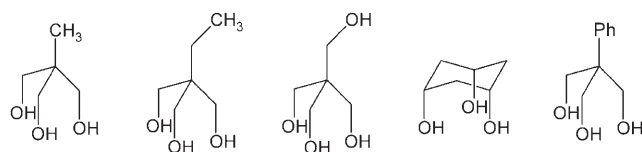
Dr. M. Murugesu, Prof. G. Christou
Department of Chemistry
University of Florida
Gainesville, Florida 32611-7200 (USA)

Dr. W. Wernsdorfer
Laboratoire Louis Néel-CNRS
38042 Grenoble, Cedex 9 (France)

[**] This work was supported by the EPSRC, The Leverhulme Trust, and the USA National Science Foundation.

large spin ground states: $S = 39/2$ for the former^[7] and $S \geq 23$ and $S = 51/2 \pm 1$ for the latter.^[8]

We have been exploring the reactivity of tripodal alcohol ligands (Scheme 1) in the synthesis of 3d transition metal



Scheme 1. The tripodal ligands (from left to right) 1,1,1-tris(hydroxymethyl)ethane (H₃thme), 1,1,1-tris(hydroxymethyl)propane (H₃tmp), pentaerythritol (H₄peol), *cis,cis*-1,3,5-cyclohexanetriol (H₃cht), and 1',1',1'-tris(hydroxymethyl)toluene (H₃thmt).

SMMs. The basic principle here is that paramagnetic metal ions linked together in triangular arrays may lead to molecules with large spin ground states. If these arrays consist of simple {M₃} equilateral triangles then the resultant competing exchange interactions or spin frustration may stabilize a nonzero spin ground state. If the arrays consist of {M₄} centered triangles or “metal stars”, in which the three peripheral ions are connected only to the central ion and not to each other, then the antiferromagnetic interaction between these ions may stabilize a large spin state. If these high-spin triangular units can then be linked together by using bridging ligands that promote ferromagnetic exchange then the resultant complexes could well be characterized by extremely large spin ground states.

The cation [Mn₃₂(thme)₁₆(bpy)₂₄(N₃)₁₂(OAc)₁₂]⁸⁺ (Figure 1; bpy = bipyridine) consists of eight such {M₄} centered triangles linked together to form a truncated cube. Each [Mn₄(thme)₂]⁴⁺ corner unit consists of a central Mn⁴⁺ ion and three peripheral Mn²⁺ ions. The Mn²⁺ ions are linked to the Mn⁴⁺ ion through the μ₂-oxygen arms of two thme³⁻ ligands, which sit directly above and below the [Mn^{IV}Mn^{II}]₃ plane. The coordination of the peripheral Mn²⁺ ions is completed by one chelating bpy ligand, one acetate group and one azide function. The CH₃CO₂⁻ and N₃⁻ ligands bridge the Mn²⁺ ions in neighboring corner units along each edge of the cube (Figure 2). The charge balance of the complex is completed by the presence of eleven ClO₄⁻ ions and one and a half [Mn(bpy)₃]²⁺ molecules, thus giving the complex the overall formula {Mn(bpy)₃}_{1.5}[Mn₃₂(thme)₁₆(bpy)₂₄(N₃)₁₂(OAc)₁₂](ClO₄)₁₁ (**1**). The oxidation states of the Mn ions were confirmed by BVS (bond-valence-sum) calculations and bond-length considerations.

To probe the magnetic properties of **1**, susceptibility measurements were performed on powdered crystalline samples in the ranges 1.8–300 K and 0–7 T, and on single crystals at temperatures down to 40 mK. Direct current (dc) susceptibility measurements were carried out in a 0.1-T dc field in the temperature range 1.8–300 K, with the sample restrained in eicosane to prevent torquing. The calculated ($g = 2$) contribution from the 1.5 [Mn(bpy)₃]²⁺ cations per [Mn₃₂] was subtracted from the measured data. The room temperature $\chi_M T$ value of approximately 78.8 cm³ K mol⁻¹

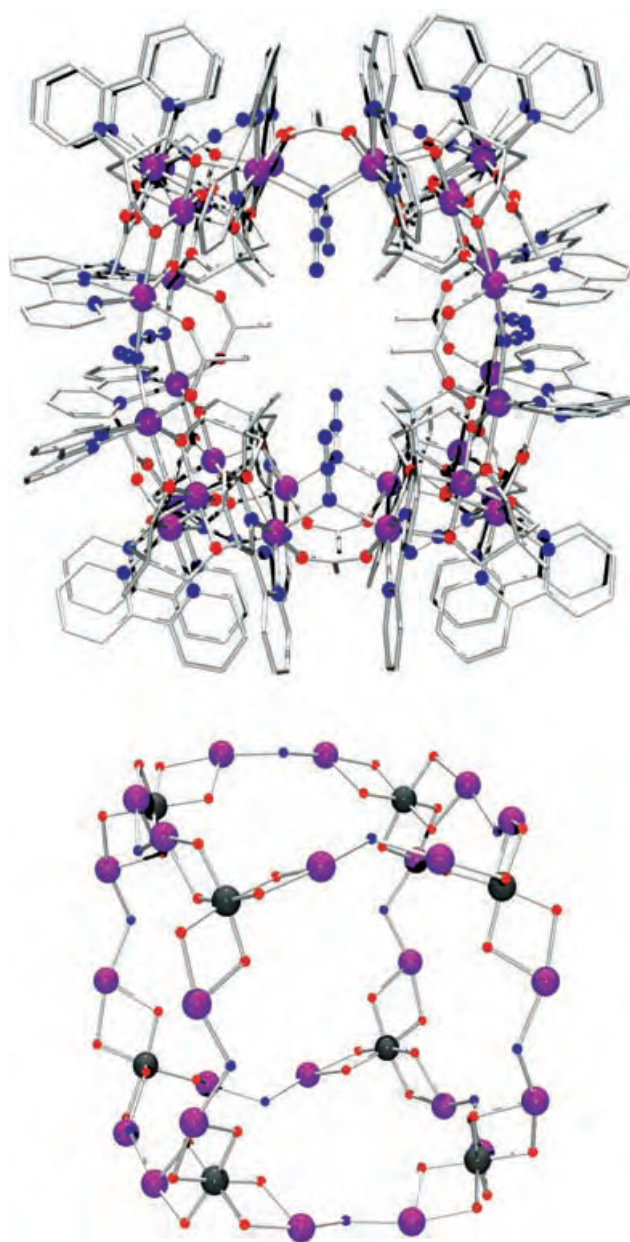


Figure 1. The structure of the [Mn₃₂]⁸⁺ cation (top) and its core (bottom). In the lower picture the eight corner Mn⁴⁺ ions of an ideal cube are highlighted in black.

slowly increases upon cooling to a maximum of approximately 86.2 cm³ K mol⁻¹ at 90 K, and then decreases rapidly to a value of approximately 37.8 cm³ K mol⁻¹ at 2 K. This behavior is indicative of dominant antiferromagnetic exchange between the metal centers with the value at 2 K in the region expected for an $S = 9$ ground state (spin-only ($g = 2$) value of 45 cm³ K mol⁻¹).

In alternating current (ac) susceptibility experiments, a weak field (typically 1–5 G) oscillating at a particular frequency (ν) is applied to a sample to probe the dynamics of the magnetization (magnetic-moment) relaxation. The ac susceptibility measurements, which avoid Zeeman and other effects of an applied dc field, are an excellent complementary

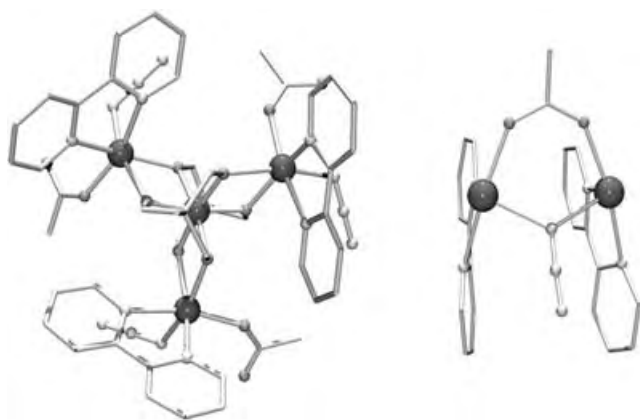


Figure 2. The building blocks of complex **1**: the $[\text{Mn}^{\text{IV}}\text{Mn}^{\text{II}}_3]$ “corner” unit (left) and the $[\text{Mn}^{\text{II}}]$ “edge” (right).

tool for the estimation of S as the presence of a temperature-independent (in-phase) χ_M'/T versus T signal would indicate a well-isolated ground state, whereas a sloping χ_M'/T vs T signal would indicate the population of a number of low-lying excited states.^[9] In-phase ac susceptibility measurements for complex **1** taken in the temperature range 1.8–10 K are shown in Figure 3. The steeply sloping lines observed show a rapid decrease in χ_M'/T with decreasing temperature and therefore suggest the population of many excited states with larger S values. This is a common feature in many Mn clusters that are either a) of high nuclearity and thus exhibit a large density of spin states or b) contain multiple Mn^{2+} ions that typically promote weak exchange. Extrapolation of the χ_M'/T signal from values above about 3 K (to avoid decreases due to effects such as intermolecular interactions at lower temperatures) to 0 K gives a value of 42–43 $\text{cm}^3\text{K mol}^{-1}$, which suggests a spin ground state of $S=9$ (or 10), consistent with the dc data.

Magnetization measurements also confirm the presence of many excited states. Studies on a single crystal of complex **1** at temperatures down to 40 mK and in fields of up to 1.4 T performed on a micro-SQUID setup show curves that do not reach saturation (Figure 3). At all temperatures studied, the magnetization continues to rise sharply with increasing field strength. This is as expected for field-induced stabilization of M_S levels of excited states with S values greater than that of the ground state; approach to and crossing of excited-state M_S levels with those of the ground state lead to increases in the measured magnetization. Thus, for example, the magnitude of the magnetization at 40 mK in an applied field of 1 T is suggestive of $S \geq 25$. Similarly, magnetization measurements (Figure 3) carried out on a powdered crystalline sample at temperatures below 10 K in fields of up to 7 T saturate at a value of $M/N\mu_B \approx 85$, a value consistent with the stabilization of an $S \geq 43$ spin state (with $g=2.0$). However, when smaller applied fields are used, the magnitude of $M/N\mu_B$ decreases and does not saturate. Again this is indicative of a field-induced stabilization of excited states with larger S values than that of the ground state.

If we were to assume the interaction between the central Mn^{4+} ion and the three peripheral Mn^{2+} ions within an

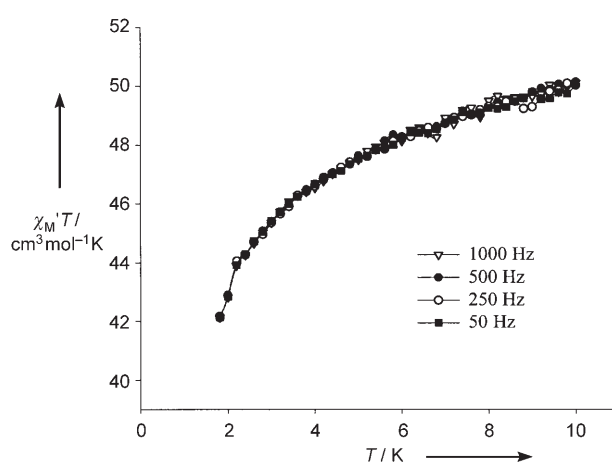
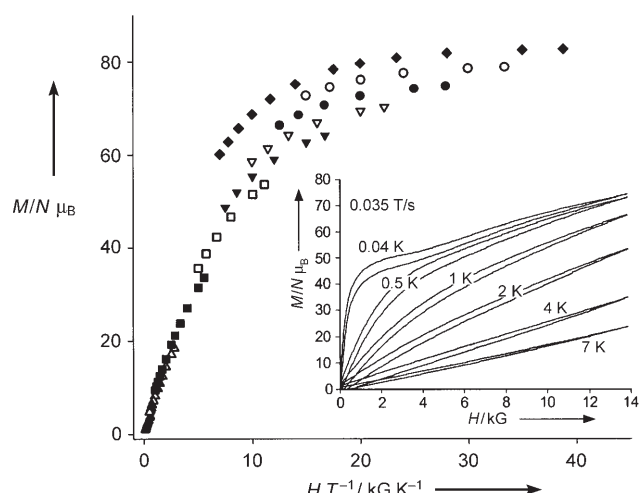


Figure 3. Top: Magnetization data for **1** plotted as reduced magnetization ($M/N\mu_B$) versus H/T in the temperature range 1.8–10 K and in fields of 0.1 T (\blacktriangle), 0.5 T (\triangle), 1 T (\blacksquare), 2 T (\square), 3 T (\blacktriangledown), 4 T (\triangledown), 5 T (\bullet), 6 T (\circ), and 7 T (\blacklozenge). Inset: Magnetization measurements performed on single crystals of complex **1** by using an array of micro-SQUIDs (SQUID = superconducting quantum interference device) at the indicated sweep rate and temperature range. Bottom: In-phase ac susceptibility (χ_M'/T) measurements of complex **1** measured below 10 K at the indicated frequencies.

isolated $[\text{Mn}^{\text{IV}}\text{Mn}^{\text{II}}_3]$ unit to be antiferromagnetic, then we would expect a spin ground state of $S=6$ for this unit. Between each of these corner units, the *syn, syn* $\mu\text{-CH}_3\text{CO}_2^-$ ligands are likely to promote antiferromagnetic exchange, but the end-on N_3^- ligands are likely to promote ferromagnetic exchange. If the antiferromagnetic interactions were to dominate, then we might expect to observe an overall spin ground state of $S=0$, but if the ferromagnetic interactions were to dominate then a ground state with $S=48$ could result. However, there are a total of 24 Mn^{2+} ions present in the $[\text{Mn}_{32}]^{8+}$ cation and these are known to promote weak exchange between the metal centers, the result of which is likely to be a large number of S states with comparable energies to the ground state. This “problem” is then further compounded by the fact the $[\text{Mn}^{\text{IV}}\text{Mn}^{\text{II}}_3]$ units are linked

together by two different ligands—one azide and one carboxylate—and this countercomplementarity will likely lead to an interaction that is either weakly ferro- or weakly antiferromagnetic, but in either case near 0 cm^{-1} . Weak intermolecular interactions—if comparable in magnitude to the intracluster exchange—will also complicate the analysis. Essentially all of the above means that an accurate quantitative analysis is impossible.

In conclusion, the use of the tripodal ligand H_3thme has again been shown to stabilize elaborate triangular arrays of Mn ions. In the studies described herein, these “high-spin” building blocks have self-assembled in the presence of end-on-bridging azide ligands to form a $\{\text{Mn}_{32}\}$ truncated cube. This is the second largest Mn cluster reported to date.^[10] Initial magnetic studies revealed that the complex has a spin ground state of $S = 9$ (or 10), but the presence of multiple Mn^{2+} ions, ligand countercomplementarity, and possible weak intermolecular interactions precludes a more accurate analysis. Application of strong magnetic fields effectively overcomes weak antiferromagnetic exchange, thus stabilizing spin states with larger values of S .

However, the combination of tripodal alcohol ligands and end-on bridging azides may be an excellent, yet simple, route to clusters with potentially extremely large spin ground states and promises many more exciting compounds.

Experimental Section

1: NaOAc (1 equiv) and NaN_3 (1 equiv) were added with stirring to a solution of $[\text{Mn}_2(\text{Hthme})_2(\text{bpy})_4](\text{ClO}_4)_2$ ^[11] (1 equiv) in MeCN. After 30 min the solution was filtered and layered with diethyl ether. Black crystals grew during one week. Elemental analysis (%): calcd for $\text{C}_{411}\text{H}_{465}\text{Cl}_{11}\text{Mn}_{33.5}\text{N}_{104}\text{O}_{128}$: C 44.31, H 4.21, N 13.08, Mn 16.52; found: C 44.62, H 3.93, N 12.94, Mn 16.73. Crystallographic details for **1**: $\text{C}_{412}\text{H}_{545.50}\text{Cl}_{11}\text{Mn}_{33.50}\text{N}_{104.50}\text{O}_{127.50}$, crystal size: $0.41 \times 0.38 \times 0.27\text{ mm}^3$, triclinic, $P\bar{1}$, $a = 25.9460(6)$, $b = 26.1225(6)$, $c = 40.5498(9)\text{ Å}$, $\alpha = 91.2630(10)$, $\beta = 93.3990(10)$, $\gamma = 97.4450(10)^\circ$, $V = 27191.7(11)\text{ Å}^3$, $T = 150(2)\text{ K}$, $Z = 2$, $\rho_{\text{calcd}} = 1.372\text{ g cm}^{-3}$, $\mu(\lambda = 0.71073\text{ Å}) = 1.574\text{ mm}^{-1}$, 364332 reflections collected, 78020 unique ($R_{\text{int}} = 0.0959$), $R1 = 0.1068$ and $wR2 = 0.2973$ using 55631 reflections with $I > 4\sigma(I)$. CCDC-273452 contains the supplementary crystallographic data for this paper. These data can be obtained free of charge from the Cambridge Crystallographic Data Centre via www.ccdc.cam.ac.uk/data_request/cif.

Received: May 31, 2005

Revised: July 5, 2005

Published online: September 21, 2005

Keywords: cluster compounds · magnetic properties · manganese · O ligands · tripodal ligands

- [5] a) V. Marvaud, C. Decroix, A. Scuiller, C. Guyard-Duhayon, J. Vaissermann, F. Gonnet, M. Verdaguer, *Chem. Eur. J.* **2003**, *9*, 1677–1691; b) H. J. Choi, J. J. Sokol, J. R. Long, *Inorg. Chem.* **2004**, *43*, 1606–1608; c) C. P. Berlinguette, D. Vaughn, C. Cañada-Vilalta, J. R. Galán-Mascarós, K. M. Dunbar, *Angew. Chem.* **2003**, *115*, 1561–1564; *Angew. Chem. Int. Ed.* **2003**, *42*, 1523–1526.
- [6] a) D. N. Hendrickson, G. Christou, H. Ishimoto, J. Yoo, E. K. Brechin, A. Yamaguchi, E. M. Rumberger, S. M. J. Aubin, Z. Sun, G. Aromí, *Polyhedron* **2001**, *20*, 1479–1488; b) C. J. Milios, C. P. Raptopoulou, A. Terzis, F. Lloret, R. Vicente, S. P. Perlepes, A. Escuer, *Angew. Chem.* **2004**, *116*, 212–214; *Angew. Chem. Int. Ed.* **2004**, *43*, 210–212; c) L. M. Wittick, K. S. Murray, B. Moubaraki, S. R. Batten, L. Spiccia, K. J. Berry, *Dalton Trans.* **2004**, 1003–1011; d) C. Cadiou, M. Murrie, C. Paulsen, V. Villar, W. Wernsdorfer, R. E. P. Winpenny, *Chem. Commun.* **2001**, 2666–2667.
- [7] Z. J. Zhong, H. Seino, Y. Mizobe, M. Hidai, A. Fujishima, S. Ohkoshi, K. Hashimoto, *J. Am. Chem. Soc.* **2000**, *122*, 2952–2953.
- [8] a) M. Murugesu, M. Habrych, W. Wernsdorfer, K. A. Abboud, G. Christou, *J. Am. Chem. Soc.* **2004**, *126*, 4766–4767; b) D. M. Low, L. F. Jones, A. Bell, E. K. Brechin, T. Mallah, E. Riviere, S. J. Teat, E. J. L. McInnes, *Angew. Chem.* **2003**, *115*, 3911–3914; *Angew. Chem. Int. Ed.* **2003**, *42*, 3781; c) G. Rajaraman, J. Cano, E. K. Brechin, E. J. L. McInnes, *Chem. Commun.* **2004**, 1476–1477.
- [9] a) M. Soler, W. Wernsdorfer, K. Folting, M. Pink, G. Christou, *J. Am. Chem. Soc.* **2004**, *126*, 2156–2165; b) E. C. Sañudo, W. Wernsdorfer, K. A. Abboud, G. Christou, *Inorg. Chem.* **2004**, *43*, 4137–4144; c) E. K. Brechin, E. C. Sañudo, W. Wernsdorfer, C. Boskovic, J. Yoo, D. N. Hendrickson, A. Yamaguchi, H. Ishimoto, T. E. Concolino, A. L. Rheingold, G. Christou, *Inorg. Chem.* **2005**, *44*, 502–511.
- [10] A. J. Tasiopoulos, A. Vinslava, W. Wernsdorfer, K. A. Abboud, G. Christou, *Angew. Chem.* **2004**, *116*, 2091–2095; *Angew. Chem. Int. Ed.* **2004**, *43*, 2117–2121.
- [11] G. Rajaraman, E. C. Sañudo, M. Helliwell, S. Piligkos, W. Wernsdorfer, G. Christou, E. K. Brechin, *Polyhedron* **2005**, in press (doi:10.1016/j.poly.2005.03.046).

- [1] R. Sessoli, D. Gatteschi, D. N. Hendrickson, G. Christou, *MRS Bull.* **2000**, *25*, 66–71.
- [2] J. Tejada, E. M. Chudnovsky, E. del Barco, J. M. Hernandez, T. P. Spiller, *Nanotechnology* **2001**, *12*, 181–186.
- [3] a) W. Wernsdorfer, N. Aliaga-Acalde, D. N. Hendrickson, G. Christou, *Nature* **2002**, *416*, 406–409; b) S. Hill, R. S. Edwards, N. Aliaga-Acalde, G. Christou, *Science* **2003**, *302*, 1015–1018.
- [4] M. N. Leuenberger, D. Loss, *Nature* **2001**, *410*, 789–793.

DOI: 10.1002/anie.200502020

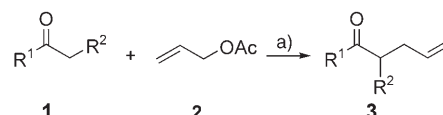
Highly Enantioselective Pd-Catalyzed Allylic Alkylations of Acyclic Ketones**

Xiao-Xia Yan, Chun-Gen Liang, Yan Zhang, Wei Hong, Bo-Xun Cao, Li-Xin Dai, and Xue-Long Hou*

Since the first example of Pd-catalyzed asymmetric allylic alkylation (AAA) was reported by Trost and Strege,^[1] great achievements in this area of chemistry have been made. Today, AAA is not only a well-studied transition-metal-catalyzed asymmetric reaction but also one of the most important asymmetric carbon–carbon bond-forming reactions.^[2] As a diversity of bond types can be formed and many chiral elements can be installed at the nucleophile, the electrophile, or both, transition-metal-catalyzed AAAs have become a powerful tool in organic synthesis.^[2c] Although a variety of substrates and reagents are suitable in AAA reactions, the use of carbon nucleophiles is mainly limited to the stabilized “soft” carbanions such as β -keto ester and malonate derivatives.^[2] Simple ketone enolates are an important class of nucleophiles, but AAA had been ineffective with these nucleophiles because they are nonstabilized and hard. The breakthrough came in 1999, when Trost and Schroeder obtained high enantioselectivity in Pd-catalyzed AAAs with tetralone and cyclohexanone derivatives by using a “chiral pocket” ligand.^[3] Since then, several examples were reported and excellent enantioselectivities were obtained.^[4,5] Cyclic ketones have been used as substrates in these reactions. Recently, Braun et al. reported the Pd-catalyzed allylic alkylation of 1,3-diphenylallyl acetate with high diastereoselectivity by using mesityl ethyl ketone.^[4c] However, the reaction was not asymmetric. Thus, an asymmetric version of Pd-catalyzed AAAs with acyclic ketones remains a challenge. Recently, we designed some ferrocene-derived

chiral P,N ligands and employed them successfully in Pd-catalyzed AAAs.^[5,6] High regio- and enantioselectivities were provided by using monosubstituted allyl derivatives as substrates and by using cyclic ketones as nucleophiles. For Pd-catalyzed AAAs with acyclic ketones to be enantioselective, we have modified the ligands. Herein, we report our preliminary results in the synthesis of a novel chiral ligand and its application to a Pd-catalyzed asymmetric allylic reaction that uses acyclic ketones as nucleophiles.

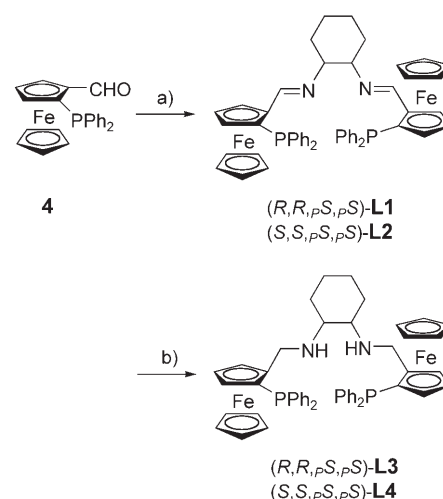
Initially, we examined the reaction of 1-phenyl-propan-1-one (**1a**) with allyl acetate (**2**) in the presence of $[\text{Pd}(\text{C}_3\text{H}_5\text{Cl})_2]$ and a variety of ligands,^[6a] but we obtained no encouraging results (Scheme 1). All reactions gave almost no



Scheme 1. a) $[\text{Pd}(\text{C}_3\text{H}_5\text{Cl})_2]$ (2.5 mol %), ligand (5 mol %), lithium 1,1,3,3-hexamethyldisilazane (LiHMDS), THF, 0 °C.

desired product **3a** under these conditions. According to the reports by Trost et al.^[3,4a] as well as our own previous work,^[5] chiral pocket ligands have emerged as ligands of choice for the highly enantioselective allylic alkylation of simple cyclic ketone enolates. Thus the modified chiral pocket imine and amine derivatives **L1–L4**^[8] were synthesized from ferrocene **4**^[7] (Scheme 2).

In the presence of **L3**, the reaction of **1a** with **2** gave the allyl product **3a** in 69 % yield and with 31 % *ee*, whereas in the presence of **L4**, the reaction gave **3a** in 23 % yield and with 2.5 % *ee*. The lower yield and enantioselectivity is attributed to the mismatched chiralities in **L4**.^[9] A further increase in the enantioselectivity (from 31 % to 48 % *ee*) was observed when **L1** was used in place of **L3**. The choice of base is important: the use of sodium hydride or potassium *tert*-butoxide in conjunction with ligand **L1** led to very low yields. The use of a



Scheme 2. Synthesis of ligands **L1–L4**. Reagents and conditions: a) (S,S)- or (R,R)-cyclohexane-1,2-diamine, *p*-TsOH, 4-Å MS, toluene; b) NaBH_4 , EtOH.

[*] X.-X. Yan, Dr. C.-G. Liang, Y. Zhang, B.-X. Cao, Prof. L.-X. Dai, Prof. Dr. X.-L. Hou
State Key Laboratory of Organometallic Chemistry
Shanghai Institute of Organic Chemistry
Chinese Academy of Sciences
354 Fenglin Road, Shanghai 200032 (P.R. China)
Fax: (+86) 21-5492-5100
E-mail: xlhou@mail.sioc.ac.cn

W. Hong, Prof. Dr. X.-L. Hou
Shanghai–Hong Kong Joint Laboratory in Chemical Synthesis
Shanghai Institute of Organic Chemistry
Chinese Academy of Sciences
354 Fenglin Road, Shanghai 200032 (P.R. China)

[**] Financially supported by the Major Basic Research Development Program (Grant G 200077506), National Nature Science Foundation of China, Chinese Academy of Sciences, Shanghai Committee of Science and Technology, and the Croucher Foundation of Hong Kong.

Supporting information for this article is available on the WWW under <http://www.angewandte.org> or from the author.

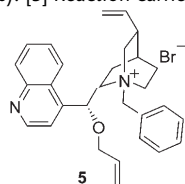
bulkier base such as LiHMDS led to a slight increase in both yield (77%) and enantioselectivity (57% *ee*), and the use of lithium tetramethylpiperidine gave the product in 48% yield with 56% *ee*. The metal ion of the base has a great effect on the yield and enantioselectivity of the reaction. For example, the reaction with LiHMDS gave the product in 77% yield and with 57% *ee*, but the corresponding reactions with NaHMDS and KHMDS provided products with 2% *ee* and 9% *ee*, respectively, although the yields were higher. A study of the effect of solvent on the reaction showed that among the solvents tested (Et₂O, 1,4-dioxane, 1,2-dimethoxyethane, toluene), THF gave the best results.

On the basis of these results, we envisioned that the lithium enolate derived from an α -alkoxy-substituted ketone would provide a general approach to the control of enantioselectivity in the AAA of acyclic ketones due to the propensity of this ketone to form the *Z*-chelated enolate. Our results demonstrate that the alkoxy group exhibits a remarkable effect on the level of enantioselectivity. When 1-phenyl-3-methoxypropan-1-one (**1b**) was used with LiHMDS as base, the enantioselectivity significantly increased to 68% *ee* and the yield was 72%. Takemoto and co-workers as well as Wang reported that chiral ammonium salts have a dramatic effect on the enantioselectivity of Pd-catalyzed AAA reactions.^[10] In our case, the ammonium salts, both chiral and achiral, also showed an ability to improve the enantioselectivity of the reaction (see Table 1). We inferred that this

Table 1: The effect of additives on the reaction.^[a]

Entry	Additives	Yield [%]	<i>ee</i> [%]
1	Bu ₄ NBr	48	75
2	Hex ₄ NBr	62	75
3	5	60	74
4	ZnCl ₂	66	83
5	CuClO ₄	70	89
6	AgOTf	84	87
7	Ag ₂ O	89	73
8	AgBr	96	89
9	AgBr	98 ^[b]	93 ^[b]

[a] Reactions performed at 0°C; [{Pd(C₃H₅)Cl}₂] (2.5 mol%); **L1** (5.0 mol%); additives (10 mol%); LiHMDS (120 mol%); **1b** (100 mol%); **2** (130 mol%). [b] Reaction carried out at –20°C.



increase in enantioselectivity in the presence of ammonium salts is caused to some extent by their Lewis acid character. Thus, several Lewis acids were tested (see Table 1).^[11]

Lewis acids have a greater effect on the reaction than ammonium salts. Among the Lewis acids tested, silver bromide gave the best result both in terms of enantioselectivity and yield. When the reaction proceeded at –20°C in the presence of a catalytic amount of AgBr, the product was obtained in 98% yield with 93% *ee*. The effect of the amount

of catalyst on the reaction was also studied. Reducing the catalyst amount to 1 mol% gave rise to a slight decrease in both yield (93%) and enantioselectivity (90% *ee*). When the amount of catalyst was decreased to 0.5 mol%, the reaction still proceeded smoothly to give the product in 83% yield with 90% *ee*. Under these optimized conditions, a variety of acyclic ketones were tested (see Scheme 1) and the results are given in Table 2.

Table 2: Pd-catalyzed AAA of acyclic ketones **1**.^[a]

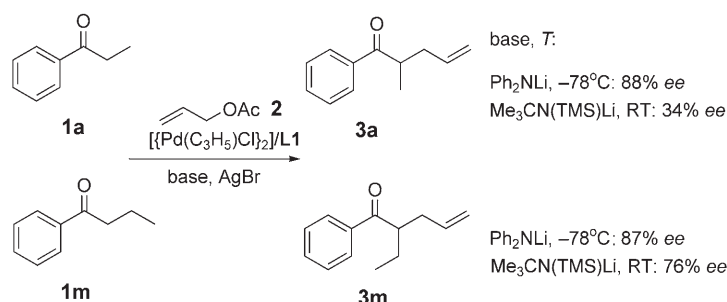
Entry		Substrate 1		Product 3	
		R ¹	R ²	Yield [%] ^[b]	<i>ee</i> [%] ^[c]
1	a	Ph	Me	93	77
2	b	Ph	OMe	98	93
3	c	Ph	OEt	88	92
4	d	Ph	O <i>i</i> Pr	95	79
5	e	<i>p</i> -MeOC ₆ H ₄	OMe	83	94
6	f	<i>p</i> -ClC ₆ H ₄	OMe	91	91
7	g	Ph	Ph	89	73
8	h	<i>c</i> Hex	OMe	76	87
9	i	2-furyl	Me	50	80
10	j	Ph	OAc	50	86
11	k	Ph	O <i>Ph</i>	89	71
12	l	Ph	SO ₂ Ph	83	0

[a] All reactions were performed at –20°C; [{Pd(C₃H₅)Cl}₂] (2 mol%); **L1** (4 mol%); **1** (100 mol%); LiHMDS (120 mol%); **2** (130 mol%); AgBr (10 mol%). [b] Yield of isolated product. [c] Determined by chiral HPLC.

All acyclic nonstabilized hard ketones gave products in good to excellent yields and enantioselectivities. However, the stabilized soft ketone **1l** gave a racemic product (entry 12, Table 2). The nature of the alkoxy substituent has a great effect on the enantioselectivity. Substrates **1b** and **1c** with less sterically hindered MeO and EtO groups gave the corresponding allylated products with *ee* values of 93% and 92%, respectively (entries 2 and 3, Table 2). However, the substrates with the bulky *i*PrO, **1d**, and PhO, **1k**, furnished products with *ee* values of 79% and 71%, respectively, although the yields were good to excellent (entries 4 and 11, Table 2). It was unexpected that the reactivity of ketone **1j** with the ester substituent would be so low, although the enantioselectivity was good (50% yield and 86% *ee*; entry 10, Table 2). The electronic property of the substituent on the phenyl ring of the substrate has little effect on the reaction. Thus, the methoxy-substituted aryl ketone **1e** and the chloro-substituted aryl ketone **1f** gave allylated products with 94% and 91% *ee*, respectively. Importantly, the aliphatic cyclohexyl methoxymethyl ketone (**1h**) afforded the corresponding product in 76% yield with 87% *ee* (entry 8, Table 2). The heteroaryl-substituted simple ketone **1i** gave rise to the corresponding product in 50% yield with 80% *ee*.

Under different conditions, *Z* or *E* forms of an enolate are favored,^[12] which may influence the enantioselectivity of the alkylation. Xie et al. reported that the *Z* form of an enolate was formed exclusively by using Ph₂NLi at –78°C, while *Z* and *E* forms of an enolate were provided in a ratio of 48:52 with Me₃CN(TMS)Li (TMS = trimethylsilyl) as base at room temperature.^[12] In the reactions reported here, we found that different forms of an enolate dramatically affected the

enantioselectivity of a reaction. In the presence of Ph_2NLi at -78°C , the reaction of ketone **1a** gave the product **3a** with 88% *ee*. Even phenyl propyl ketone (**1m**) gave the product **3m** with 87% *ee*, but only enantioselectivities of 34% and 76% *ee* were obtained with $\text{Me}_3\text{CN}(\text{TMS})\text{Li}$ (Scheme 3).



Scheme 3. The reactions of **1a** and **1m** to form **3a** and **3m**, respectively.

These results may explain why substrates with an alkoxy group at the α -position of the carbonyl group led to products with high enantioselectivities. The presence of AgBr did not influence the ratio of *Z* and *E* isomers of an enolate: the reaction of **1a** with **2** in the presence of NaHMDS and AgBr gave **3a** with 9% *ee*.

In conclusion, we have synthesized a novel chiral imino ferrocene ligand and used this ligand to carry out highly enantioselective Pd-catalyzed allylic alkylations of simple acyclic ketones. The dramatic effect of AgBr as well as the dependency of the enantioselectivity on the different forms of the enolate have been demonstrated. Further investigations on the role of AgBr and the applications of the ligand **L1** in other types of acyclic ketones are in progress.

Received: June 11, 2005

Published online: September 20, 2005

Keywords: alkylation · enantioselectivity · enolates · ketones · palladium

- [6] a) L.-X. Dai, T. Tu, S.-L. You, W.-P. Deng, X.-L. Hou, *Acc. Chem. Res.* **2003**, *36*, 659–667; b) S.-L. You, X.-Z. Zhu, Y.-M. Luo, X.-L. Hou, L.-X. Dai, *J. Am. Chem. Soc.* **2001**, *123*, 7471–7472; c) X.-L. Hou, N. Sun, *Org. Lett.* **2004**, *6*, 4399–4401. (Corrections: X.-L. Hou, N. Sun, *Org. Lett.* **2005**, *7*, 1435.)
- [7] O. Riant, O. Samuel, T. Flessner, S. Taudien, H. B. Kagan, *J. Org. Chem.* **1997**, *62*, 6733–6745.
- [8] J.-X. Gao, X.-D. Yi, P.-P. Xu, C.-L. Tang, H.-L. Wan, T. Ikariya, *J. Organomet. Chem.* **1999**, *592*, 290–295.
- [9] a) K. Muñiz, C. Bolm, *Chem. Eur. J.* **2000**, *6*, 2309–2316; b) S.-L. You, X.-L. Hou, L.-X. Dai, Y. H. Yu, W. Xia, *J. Org. Chem.* **2002**, *67*, 4684–4695.
- [10] a) M. Nakoji, T. Kanayama, T. Okino, Y. Takemoto, *J. Org. Chem.* **2002**, *67*, 7418–7423; b) Y. Wang, Ph.D. Thesis, Shanghai Institute of Organic Chemistry, Chinese Academy of Sciences, **2002**.
- [11] Other metal salts, including $\text{Sc}(\text{OTf})_3$, AgNO_3 , AgClO_4 , AgBF_4 , AgPF_6 , AgCl , AgOAc , and AgSbF_6 , were also tested. All of them gave the product in 68–97% yield with enantioselectivities of 76–87% *ee*.
- [12] For example: a) L. Xie, K. Vanlandeghem, K. M. Isenberger, C. Bernier, *J. Org. Chem.* **2003**, *68*, 641–643; b) L. Xie, K. M. Isenberger, G. Held, L. M. Dahl, *J. Org. Chem.* **1997**, *62*, 7516–7519.

- [1] B. M. Trost, P. E. Strege, *J. Am. Chem. Soc.* **1977**, *99*, 1649–1651.
- [2] For some reviews, see: a) B. M. Trost, D. L. Van Vranken, *Chem. Rev.* **1996**, *96*, 395–422; b) A. Pfaltz, M. Lautens in *Comprehensive Asymmetric Catalysis, Vol. II* (Eds.: E. N. Jacobsen, A. Pfaltz, H. Yamamoto), Berlin, Springer, **1999**, pp. 833–884; c) B. M. Trost, M. L. Crawley, *Chem. Rev.* **2003**, *103*, 2921–2944; d) T. Graening, H.-G. Schmalz, *Angew. Chem.* **2003**, *115*, 2684–2688; *Angew. Chem. Int. Ed.* **2003**, *42*, 2580–2584.
- [3] B. M. Trost, G. M. Schroeder, *J. Am. Chem. Soc.* **1999**, *121*, 6759–6760.
- [4] a) B. M. Trost, G. M. Schroeder, J. Kristensen, *Angew. Chem.* **2002**, *114*, 3642–3645; *Angew. Chem. Int. Ed.* **2002**, *41*, 3492–3945; b) B. M. Trost, G. M. Schroeder, *Chem. Eur. J.* **2005**, *11*, 174–184; c) M. Braun, F. Laicher, T. Meier, *Angew. Chem.* **2000**, *112*, 3637–3640; *Angew. Chem. Int. Ed.* **2000**, *39*, 3494–3497; d) B. M. Trost, J. Xu, *J. Am. Chem. Soc.* **2005**, *127*, 2846–2847; e) D. C. Behenna, B. M. Stoltz, *J. Am. Chem. Soc.* **2004**, *126*, 15044–15045.
- [5] a) S.-L. You, X.-L. Hou, L.-X. Dai, X.-Z. Zhu, *Org. Lett.* **2001**, *3*, 149–151; b) S.-L. You, X.-Z. Zhu, X.-L. Hou, L.-X. Dai, *Acta Chim. Sin.* **2001**, *59*, 1667–1674.

Domino Pericyclic Processes

DOI: 10.1002/anie.200501737

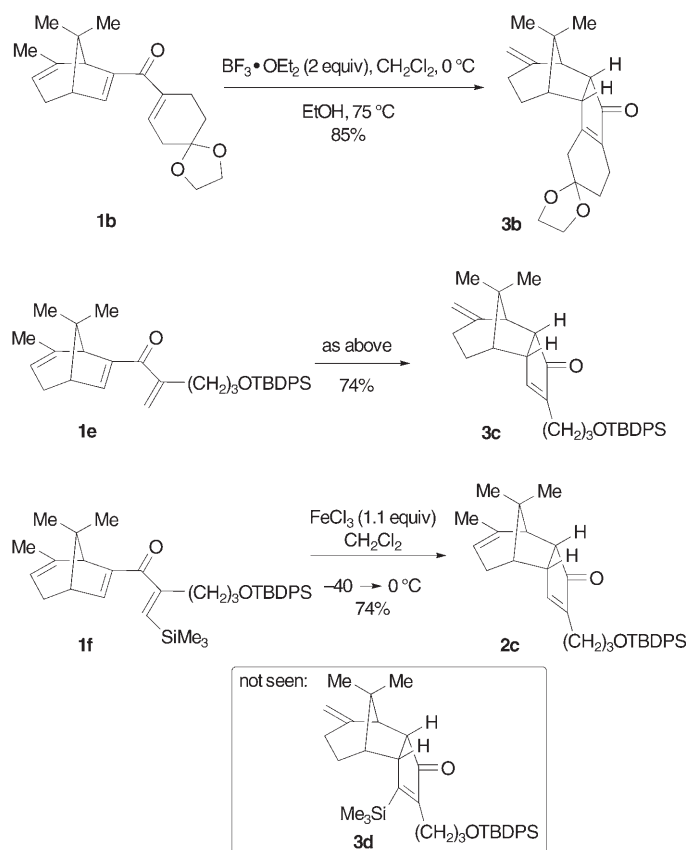
Unexpected Participation of an Unconjugated Olefin during Nazarov Cyclization of Bridged Bicyclic Dienones**

*Sören Giese, Robert D. Mazzola, Jr., Clare M. Amann, Atta M. Arif, and F. G. West**

The Nazarov reaction is a well-established method for the generation of new cyclopentenone rings from simple dienone precursors.^[1] This reaction has enjoyed considerable recent attention with regard to its use in tandem or domino processes,^[2] as well as in approaches for controlling the absolute configuration of the stereocenters generated during or after the electrocyclization process.^[3] We have recently

[*] Prof. Dr. F. G. West
 Department of Chemistry
 University of Alberta
 W5-67 Gunning-Lemieux Chemistry Centre
 Edmonton, Alberta T6G 2G2 (Canada)
 Fax: (+1) 780-492-8231
 E-mail: frederick.west@ualberta.ca
 Dr. S. Giese, Dr. R. D. Mazzola, Jr., Dr. C. M. Amann, Dr. A. M. Arif,
 Prof. Dr. F. G. West
 Department of Chemistry
 University of Utah
 315 S. 1400 East, Room 2020
 Salt Lake City, UT 84112-0850 (USA)

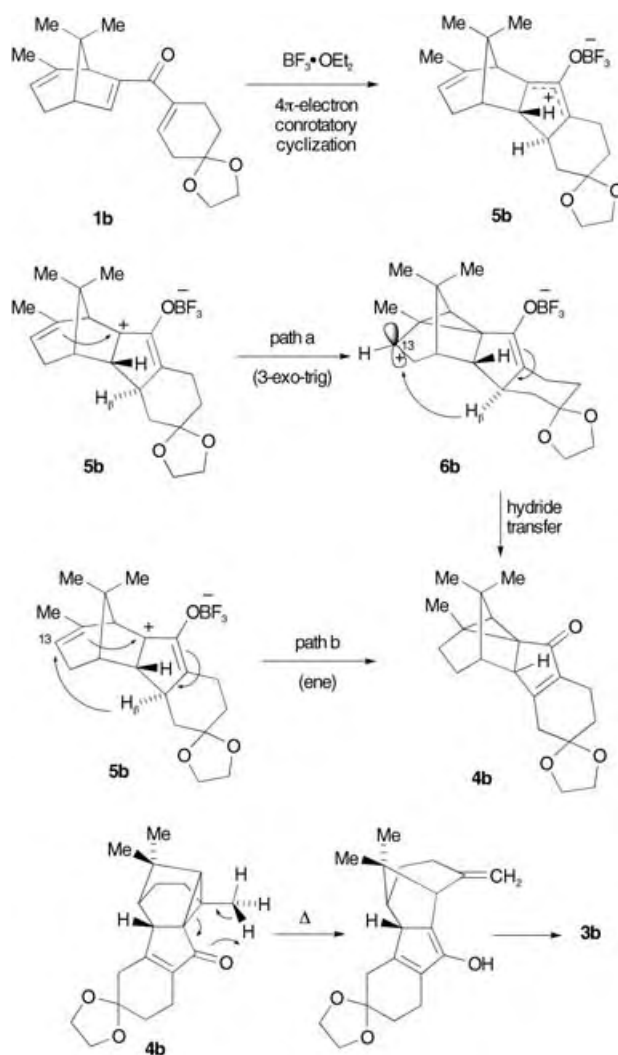
[**] We thank NIGMS and NSF (CHE 0078974) for support of this work.



Scheme 4. Direct conversion of **1b** and **1e** into **3b** and **3c**, and formation of **2c** by the silyl-directed Nazarov cyclization of **1f**.

comparison, reaction of **1f** under standard silyl-directed Nazarov cyclization conditions was performed. In this case, authentic **2c** was produced in good yield and, interestingly, none of the silyl-containing product **3d**, analogous to **3a**, was isolated.

Formation of **4b** presumably involves an initial Nazarov electrocyclozation to give the 2-oxocyclopentenyl cation **5b** (Scheme 5). Conversion into the cyclopropyl ketone could involve a homoallyl/cyclopropylcarbinyl rearrangement to give **6b** (path a), with subsequent intramolecular hydride transfer of H_β to the secondary cyclopropylcarbinyl center.^[8] Alternatively, direct conversion of **5b** into **4b** is possible through a concerted ene-like rearrangement (path b).^[9] In either mechanism, delivery of H_β should be facile because of its proximity to C13, which results from the complete selectivity of the Nazarov electrocyclozation in which the new cyclopentenyl ring is appended in an *endo* disposition. This stereoselectivity is in accord with that seen in the silyl-directed Nazarov reactions of **1a**^[4] and **1f**. The thermal conversion of **4b** into **3b** most likely occurs by the precedented homo-1,5-hydrogen shift or "enolene" rearrangement of alkyl-substituted cyclopropyl ketones,^[10] followed by enol \rightarrow keto tautomerization; notably, this thermal conversion typically occurs at much higher temperatures. The ease with which **4b** undergoes rearrangement is likely to be a result of the additional ring strain that resides in its polycyclic skeleton, as compared with simpler cyclopropyl ketones. Given the



Scheme 5. Proposed mechanisms for the formation of **4b** and **3b**.

exclusive formation of **3c**, dienone **1e** is presumed to follow an analogous mechanistic pathway.

In summary, a new class of novel and mechanistically fascinating "interrupted" Nazarov reactions has been observed. In these systems, a nonconjugated alkene held near the dienone nucleus undergoes intramolecular trapping of the Nazarov 2-oxocyclopentenyl intermediate to yield a strained polycyclic cyclopropyl ketone intermediate. This process may occur by stepwise cation–olefin cyclization/hydride transfer or by a direct ene-like mechanism. Involvement of the alkene is possible because of the high diastereoselectivity of the initial conrotatory electrocyclozation. The resulting cyclopropyl ketones undergo thermal opening to provide the anomalous products **3**. In systems that lack a low-energy desilylative termination option, this transformation occurs in high yield, thus providing convenient access to elaborate polycyclic products of potential use in the construction of naturally occurring taxane natural products and their structural analogues. Further studies along these lines will be reported in due course.

Experimental Section

4b: Trienone **1b** (912 mg, 2.90 mmol) was dissolved in CH_2Cl_2 (290 mL) in a 500-mL round-bottom flask under N_2 and cooled to 0°C . $\text{BF}_3\cdot\text{OEt}_2$ (0.71 mL, 5.8 mmol) was added by syringe, and the resulting yellow reaction mixture was stirred at 0°C for 10 min. Water (100 mL) was added, the phases were separated, and the aqueous layer was extracted with CH_2Cl_2 (100 mL). The combined organic layers were dried (MgSO_4) and concentrated to furnish a solid residue, which was purified by flash chromatography (silica gel, gradient increasing from 15→20→25→30→35% EtOAc in hexanes) to provide **4b** as a tan solid (775 mg, 85%). M.p.: $98\text{--}101^\circ\text{C}$; $R_f = 0.31$ (20% acetone/hexanes); IR (thin film): $\tilde{\nu} = 1690\text{ cm}^{-1}$; ^1H NMR (500 MHz, CDCl_3): $\delta = 4.02\text{--}3.99$ (m, 4H), 3.34 (brs, 1H), 2.66 (dd, $J = 18.6, 1.9$ Hz, 1H), 2.54 (dd, $J = 18.8, 1.8$ Hz, 1H), 2.42–2.29 (m, 2H), 1.98 (s, 1H), 1.81 (dd, $J = 6.5, 6.5$ Hz, 1H), 1.78 (ddd, $J = 14.8, 11.9, 4.6$ Hz, 1H), 1.66–1.59 (m, 2H), 1.53 (ddd, $J = 14.9, 12.0, 4.4$ Hz, 1H), 1.45 (ddd, $J = 8.3, 2.9, 2.9$ Hz, 1H), 1.40–1.33 (m, 1H), 1.13 (s, 3H), 1.05 ppm (s, 3H), 0.90 (s, 3H); ^{13}C NMR (125 MHz, CDCl_3): $\delta = 197.7, 163.7, 142.6, 108.4, 64.9, 64.8, 50.3, 49.8, 45.4, 45.1, 38.4, 37.8, 33.2, 30.9, 26.9, 23.6, 21.4$ (2 overlapping C nuclei), 19.7, 18.6 ppm; elemental analysis (%) calcd for $\text{C}_{20}\text{H}_{26}\text{O}_3$: C 76.40, H 8.33; found: C 76.47, H 8.37.

3b: Trienone **1b** was treated with $\text{BF}_3\cdot\text{OEt}_2$ as described above (on the same scale). The solid residue obtained after aqueous work up was dissolved under N_2 in absolute EtOH (70 mL), and the resulting solution was heated to 75°C for 3 h. The reaction mixture was cooled and carefully concentrated under reduced pressure to leave a solid residue, which was purified by flash chromatography (silica gel, gradient increasing from 10→15→20→25→30→35% EtOAc in hexanes) to furnish **3b** as a white solid (775 mg, 85%). M.p.: $119\text{--}120^\circ\text{C}$; $R_f = 0.24$ (20% acetone/hexanes); IR (thin film): $\tilde{\nu} = 1695, 1646\text{ cm}^{-1}$; ^1H NMR (500 MHz, CDCl_3): $\delta = 4.66$ (dd, $J = 2.3, 2.3$ Hz, 1H), 4.64 (dd, $J = 2.1, 2.1$ Hz, 1H), 4.01–4.00 (m, 4H), 3.40–3.37 (m, 1H), 3.21 (dd, $J = 7.6, 7.6$ Hz, 1H), 2.64 (d, $J = 18.1$ Hz, 1H), 2.53 (d, $J = 7.9$ Hz, 1H), 2.51 (s, 1H), 2.37–2.30 (m, 1H), 2.28–2.21 (m, 1H), 2.03–1.96 (m, 1H), 1.85–1.68 (m, 5H), 1.46–1.39 (m, 1H), 1.09 (s, 3H), 0.93 ppm (s, 3H); ^{13}C NMR (125 MHz, CDCl_3): $\delta = 207.8, 168.5, 147.1, 140.0, 110.2, 108.5, 64.9, 64.8, 54.4, 54.0, 50.0, 48.1, 43.3, 38.9, 30.8, 26.9, 26.7, 23.6, 23.2, 19.2$ ppm; elemental analysis (%) calcd for $\text{C}_{20}\text{H}_{26}\text{O}_3$: C 76.40, H 8.33; found: C 76.11, H 8.35.

Received: May 20, 2005

Published online: September 19, 2005

Keywords: alkenes · carbocations · cyclization · cyclopropanes · diastereoselectivity

- [5] S. Ceccarelli, U. Piarulli, C. Gennari, *J. Org. Chem.* **2000**, *65*, 6254–6256; R. D. Mazzola, Jr., S. Giese, C. L. Benson, F. G. West, *J. Org. Chem.* **2004**, *69*, 220–223.
- [6] T. K. Jones, S. E. Denmark, *Helv. Chim. Acta* **1983**, *66*, 2377–2396.
- [7] Crystal data for **3b**: $\text{C}_{20}\text{H}_{26}\text{O}_3$, $M_r = 314.41$, prismatic crystal ($0.44 \times 0.42 \times 0.39\text{ mm}^3$), triclinic, space group $P\bar{1}$, $a = 7.333(1)$, $b = 10.578(1)$, $c = 11.255(2)\text{ \AA}$, $\alpha = 98.038(10)$, $\beta = 93.278(10)$, $\gamma = 96.230(10)^\circ$, $V = 857.0(2)\text{ \AA}^3$, $Z = 2$, $\rho_{\text{calcd}} = 1.218\text{ g cm}^{-3}$, $F(000) = 340.0$, $T = 293(2)\text{ K}$, $\text{MoK}\alpha$ radiation ($\lambda = 0.71073\text{ \AA}$, $\mu = 0.08\text{ mm}^{-1}$), data collected with a Nonius CAD4 diffractometer; of 2945 measured reflections ($2\theta: 3.22\text{--}52.72^\circ$, $\theta: 2\theta$ scan), a psican absorption correction was applied with min./max. transmission factors of 0.965/0.969; structure solved by SIR97, refined by using SHELXL97; final agreement factors were $R1 = 0.0458$ (2330 observed reflections, $F^2 > 4\sigma(F^2)$) and $wR2 = 0.1134$; data/restraints/parameters 2945/0/295; GOF = 1.045. CCDC-272581 contains the supplementary crystallographic data for this paper. These data can be obtained free of charge from the Cambridge Crystallographic Data Centre via www.ccdc.cam.ac.uk/data_request/cif.
- [8] We have previously observed such transannular hydride-transfer processes in intermediates that result from cation–olefin cyclization of the Nazarov intermediate; see: C. C. Browder, F. G. West, *Synlett* **1999**, 1363–1366.
- [9] For previous observations of ene-like processes that involve 2-oxidoallyl cations generated under reductive and photochemical conditions, respectively, see: R. Noyori, F. Shimizu, Y. Hayakawa, *Tetrahedron Lett.* **1978**, 2091–2094; A. R. Matlin, P. M. Lahti, D. Appella, A. Straumanis, S. C. Lin, H. R. Patel, K. Jin, K. P. Schreiber, J. Pauls, P. Raulerson, *J. Am. Chem. Soc.* **1999**, *121*, 2164–2173.
- [10] G. Ohloff, *Tetrahedron Lett.* **1965**, 3795–3800; R. M. Roberts, R. G. Landolt, R. N. Greene, E. W. Heyer, *J. Am. Chem. Soc.* **1967**, *89*, 1404–1411; X. Creary, F. Hudock, M. Keller, J. F. Kerwin, Jr., J. P. Dinnocenzo, *J. Org. Chem.* **1977**, *42*, 409–414; P. G. Khazanie, E. Lee-Ruff, *Can. J. Chem.* **1978**, *56*, 808–813; H. J. M. Gijzen, J. B. P. A. Wijnberg, A. de Groot, *Tetrahedron* **1994**, *50*, 4745–4754; K. C. W. Chong, J. R. Scheffer, *J. Am. Chem. Soc.* **2003**, *125*, 4040–4041.

- [1] Review: K. L. Habermas, S. E. Denmark, T. K. Jones, *Org. React. (N.Y.)* **1994**, *45*, 1–158.
- [2] V. Nair, S. Bindu, V. Sreekumar, A. Chiaroni, *Org. Lett.* **2002**, *4*, 2821–2823; Y. Wang, B. D. Schill, A. M. Arif, F. G. West, *Org. Lett.* **2003**, *5*, 2747–2750; C. C. Browder, F. P. Marmsäter, F. G. West, *Can. J. Chem.* **2004**, *82*, 375–385; A. Yungai, F. G. West, *Tetrahedron Lett.* **2004**, *45*, 5445–5448.
- [3] L. N. Pridgen, K. Huang, S. Shilcrat, A. Tickner-Eldridge, C. DeBrosse, R. C. Haltiwanger, *Synlett* **1999**, 1612–1614; D. J. Kerr, C. Metje, B. L. Flynn, *Chem. Commun.* **2003**, 1380–1381; C. Bee, E. Leclerc, M. A. Tius, *Org. Lett.* **2003**, *5*, 4927–4930; G. Liang, S. N. Gradl, D. Trauner, *Org. Lett.* **2003**, *5*, 4931–4934; V. K. Aggarwal, A. J. Belfield, *Org. Lett.* **2003**, *5*, 5075–5078; C. Prandi, A. Ferrali, A. Guarna, P. Venturello, E. G. Occhiato, *J. Org. Chem.* **2004**, *69*, 7705–7709; G. Liang, D. Trauner, *J. Am. Chem. Soc.* **2004**, *126*, 9544–9545.
- [4] R. D. Mazzola, Jr., T. D. White, H. R. Vollmer-Snarr, F. G. West, *Org. Lett.* **2005**, *7*, 2799–2801.

DOI: 10.1002/anie.200501663

Synthesis of Nanowire and Mesoporous Low-Temperature LiCoO₂ by a Post-Templating Reaction**

Feng Jiao, Kuthanapillil Mani Shaju, and Peter G. Bruce*

The synthesis of transition-metal oxides with controlled nanostructures, such as mesoporous solids, nanotubes, or nanowires, is an important task because such nanostructuring may have a profound influence on the properties of these materials.^[1–3] This includes nanostructured materials for energy conversion and storage.^[4] Soft templating routes have been used to synthesize mesoporous transition-metal compounds, for example, Nb₂O₅, TiO₂, MnO_x, and Fe₂O₃; however, the materials often have poorly crystallized walls and are thermally unstable, which limits their applications.^[3,5]

The introduction of hard templating methods represents a significant step forward in the synthesis of mesoporous solids.^[6,7] Solution-based precursors of the desired phase may be loaded within the pores of a mesoporous silica, and, after firing, the hard silica template may be removed to yield a mesoporous compound with highly crystalline walls and good thermal stability. Such nanocasting approaches have been used to form several transition-metal oxides, for example, Cr₂O₃, Fe₂O₃, MnO_x, CeO₂, Co₃O₄, and WO₃.^[8–11] The nanocasting method is, however, limited to the use of precursors that do not react with the hard template and to compounds that may be prepared within the temperature range over which the silica template is stable. The former problem renders it difficult to synthesize mesoporous oxides that contain alkali metals. However, the synthesis of nanostructured oxides containing lithium is essential if such materials are to be used as positive electrodes in rechargeable lithium batteries, as the positive electrode is the only source of Li in the cells (the negative electrode is graphite). Mesoporous materials are attractive for electrodes because the controlled and regular porosity permits intimate flooding of the electrolyte within the particles. Hard-templated materials permit the formation of crystalline walls, which can be important in promoting Li intercalation.

Herein, we describe the synthesis of nanowire and mesoporous low-temperature LiCoO₂ (LT-LiCoO₂), a Li

intercalation compound, by the hard template route. The synthesis involves, first, preparation of mesoporous or nanowire Co₃O₄, then, after template removal, reaction of Co₃O₄ with a lithium source whilst retaining the nanostructured morphology. Hence, the lithium-containing compounds may be prepared by avoiding reaction between the lithium precursor and the silica template, which would occur if the compounds were prepared directly. The formation of large (≈100 nm) nanowire arrays of high-temperature LiCoO₂ within an anodic aluminum oxide membrane has been reported, however, the template was only partially removed.^[12]

Two mesoporous silica compounds, SBA-15 and KIT-6, were used as hard templates.^[7,13] The former contains parallel cylindrical pores arranged with hexagonal symmetry (space group *P6mm*). The latter has a three-dimensional cubic arrangement of pores (space group *Ia3d*). Such pore structures yield nanowire and mesoporous morphologies, respectively. The hard templates were impregnated with a solution of cobalt nitrate in ethanol, calcined at 300 °C, impregnated again to maximize pore filling, and heated at 500 °C, then the silica templates were removed with aqueous HF. Analysis by energy dispersive X-ray spectroscopy (EDX) and inductively coupled plasma demonstrated that all the silica had been removed. Flame emission and atomic absorption spectrometry confirmed that the Li-to-Co mole ratios for nanowire and mesoporous LT-LiCoO₂ samples were 0.95:1.

The nanowire structure of Co₃O₄ arising from SBA-15 is shown in Figure 1 A and B. SBA-15 comprises short bridges between the cylindrical pores and these serve to organize the wires into parallel bundles.^[9] Co₃O₄ formed from KIT-6 has a cubic nanostructure replicating the pore structure of the template (Figure 1 C and D). Mesoporous Co₃O₄, with *Ia3d* symmetry, was prepared for the first time very recently.^[11] It

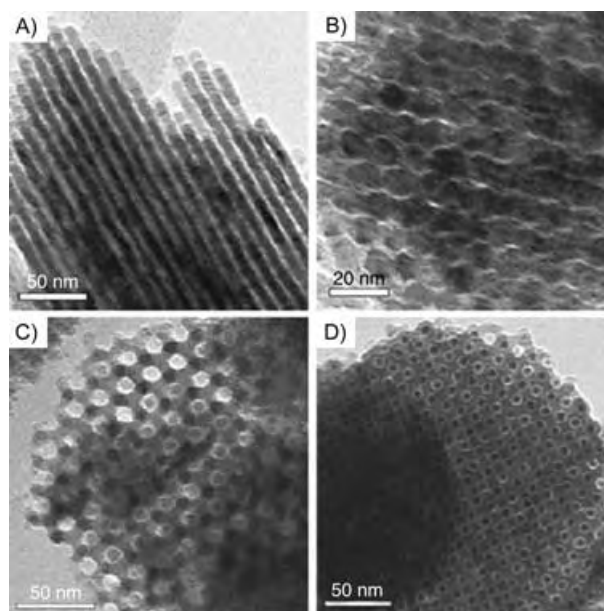


Figure 1. TEM images of Co₃O₄ nanowires A) perpendicular and B) parallel to the wire axis. TEM images of mesoporous Co₃O₄ along the C) [111] and D) [100] directions.

[*] F. Jiao, Dr. K. M. Shaju, Prof. P. G. Bruce
School of Chemistry
University of St. Andrews
The Purdie Building, North Haugh, St Andrews KY169ST (UK)
Fax: (+44) 1334-463808
E-mail: p.g.bruce@st-and.ac.uk

[**] P.G.B. is indebted to the EPSRC, the EU, and The Royal Society for financial support.

Supporting information for this article is available on the WWW under <http://www.angewandte.org> or from the author.

was found necessary to functionalize the pores by attaching vinyl groups to provide superior coordination of Co ions and hence high loadings. As demonstrated here, this is not essential.^[10]

Nanowire and mesoporous LT-LiCoO₂ samples were prepared by reacting the respective nanostructured Co₃O₄ materials with LiOH at 400 °C for 1 h. LiCoO₂ synthesized at around 800 °C exhibits a layered α -NaFeO₂ structure, whereas synthesis at lower temperatures yields LT-LiCoO₂ composed predominantly of a spinel structure that contains additional lithium, Li₂Co₂O₄.^[14,15] LT-LiCoO₂ was anticipated from the temperature at which the synthesis was performed, and this was verified by wide-angle powder X-ray diffraction (PXRD, Figure 2A). Although the diffraction data for high-temper-

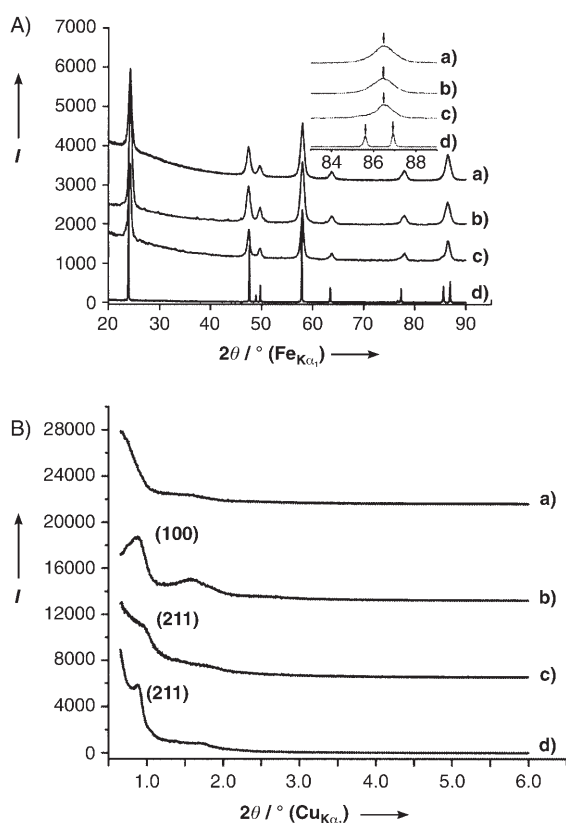


Figure 2. A) Wide-angle PXRD patterns: a) LT-LiCoO₂ nanowires; b) mesoporous LT-LiCoO₂; c) bulk LT-LiCoO₂; d) high-temperature LiCoO₂. The inset shows the expanded scale from 83–89°. B) Low-angle PXRD patterns: a) LT-LiCoO₂ nanowires; b) Co₃O₄ nanowires; c) mesoporous LT-LiCoO₂; d) mesoporous Co₃O₄.

ature and low-temperature materials are similar, it is evident, especially on examining the insets in Figure 2A, that the material synthesized here is LT-LiCoO₂. The use of temperatures that are sufficiently high to promote the formation of HT-LiCoO₂ resulted in a loss of the nanostructure.

The nanowire morphology of LT-LiCoO₂ prepared from SBA-15 is shown in Figure 3A–C. This morphology dominates throughout the material. Although the wires are continuous, close inspection of high-resolution transmission electron microscopy (HR-TEM) data (Figure 3C) indicate

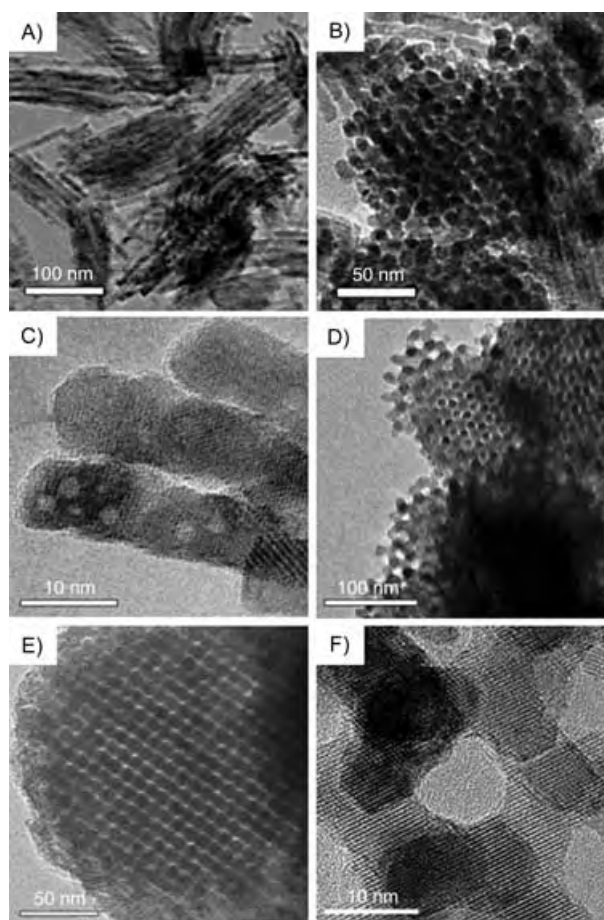


Figure 3. TEM images of LT-LiCoO₂ nanowires A) perpendicular and B) parallel to the wire axis, and C) high-resolution image of LT-LiCoO₂ nanowires. TEM images of mesoporous LT-LiCoO₂ along the E) [111] and F) [531] directions, and G) high-resolution image of mesoporous LT-LiCoO₂.

that they are composed of domains that are not structurally coherent. This is different from the single-crystal-like nature of the Co₃O₄ nanowires. However, importantly, the nanowire morphology of the Co₃O₄ material has been maintained. By TEM analysis, the diameter of LT-LiCoO₂ wires is measured as approximately 10 nm, only slightly larger than the value of 9.5 nm for Co₃O₄. Turning to mesoporous LT-LiCoO₂ formed from KIT-6, TEM data for this material are shown in Figure 3D–F. It is clear that the cubic mesoporous morphology of Co₃O₄ is maintained; the morphology extends throughout the sample. The wall thickness of mesoporous LT-LiCoO₂ observed in the [111] direction is estimated from the TEM data (Figure 3F) to be approximately 8.0 nm, which is consistent with that for Co₃O₄ (7.8 nm). In contrast to nanowire LT-LiCoO₂, it is interesting that mesoporous LT-LiCoO₂ maintains a single-crystal-like structure; the HR-TEM image (Figure 3F) indicates that the lattice fringes for LT-LiCoO₂ run in the same direction throughout the particle. Further studies will be required to understand the mechanism by which the single-crystal structure is maintained during reaction with LiOH.

A comparison of Figures 1 and 3 reveals that the LT-LiCoO₂ nanowires are less ordered than the corresponding Co₃O₄ nanowires. The loss of order between the wires in LT-LiCoO₂ may be a result of the breaking up of narrow bridges on reaction with LiOH. Despite this, a lattice parameter a_0 of 108 Å may be estimated for the hexagonal (*P6mm*) mesostructure. This is in reasonable agreement with the value of 117 Å calculated from the low-angle PXRD pattern of the Co₃O₄ nanowires. The low-angle PXRD pattern of nanowire LT-LiCoO₂ (Figure 2B, line a) does not show a well-defined peak in the range 0.6–1.0 degrees because the nanowire bundles are insufficiently well ordered (Figure 3A). In the case of LT-LiCoO₂ formed from KIT-6, a lattice parameter, a_0 of 226 Å may be extracted for the cubic structure from the TEM data. This value is similar to the lattice parameter of 235 Å calculated from the first peak in the low-angle PXRD pattern of mesoporous LT-LiCoO₂ (Figure 2B, line c). This value is a little smaller than the parameter a_0 for mesoporous Co₃O₄ (241 Å) calculated from Figure 2B, line d, and is due to pore shrinkage accompanying the solid-state reaction.

N₂ adsorption/desorption isotherms (Figure 4A, B) for both forms of nanostructured LT-LiCoO₂ show type IV

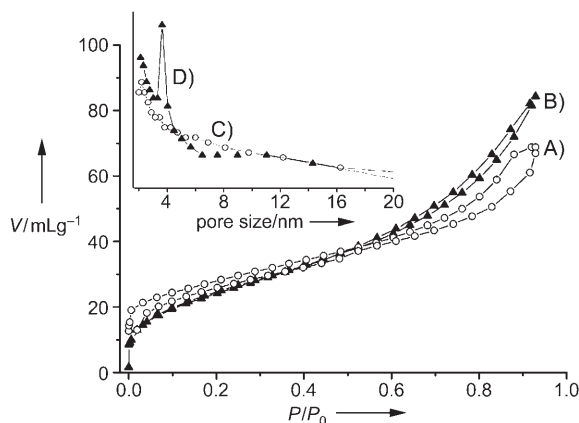


Figure 4. Nitrogen adsorption/desorption isotherms for A) nanowire and B) mesoporous LT-LiCoO₂. The inset shows the pore size distributions for C) nanowire and D) mesoporous LT-LiCoO₂.

isotherms with an H₁ hysteresis loop, which confirms the mesoporosity. The specific surface areas of nanowire and mesoporous LT-LiCoO₂ estimated from the Brunauer–Emmett–Teller (BET) method are 70 m²g⁻¹ and 92 m²g⁻¹, respectively. In the case of the LT-LiCoO₂ nanowires, the size of the pores between the wires exhibits a wide distribution (Figure 4C), indicating a disordered pore structure, which is consistent with the absence of a low-angle PXRD peak (Figure 2B, line a) and with the TEM images (Figure 3A, B); the more-ordered Co₃O₄ nanowires show a narrow distribution around 3.8 nm (see Supporting Information). In the case of mesoporous LT-LiCoO₂, the pore size distribution (Figure 4D) is narrow with a peak at 3.67 nm, which is close to the value for mesoporous Co₃O₄ (3.8 nm; see Supporting Information).

The present communication concentrates on the synthesis of LT-LiCoO₂ with different nanoarchitectures. The electro-

chemical behavior of these Li intercalation materials and their comparison with normal LT-LiCoO₂ will be described in a subsequent paper; however, some preliminary data are presented here. The surface area of the normal LT-LiCoO₂, prepared by a solid-state reaction between CoCO₃ and Li₂CO₃ at 400 °C, was 42 m²g⁻¹. The cells were first charged to remove lithium from the electrodes. Figure 5 reports the

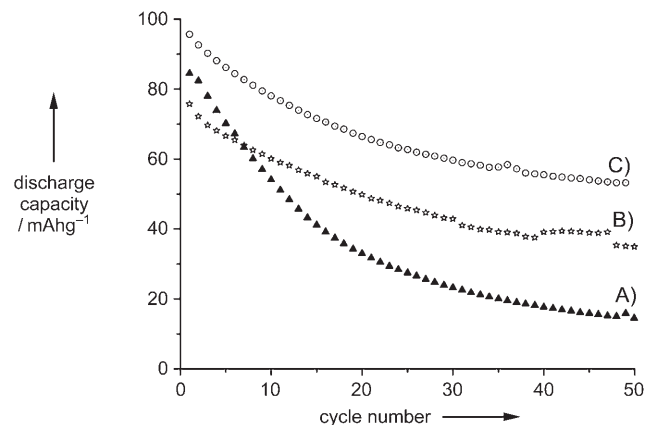


Figure 5. Discharge capacities for A) normal (▲), B) nanowire (*), and C) mesoporous (○) forms of LT-LiCoO₂.

discharge capacity for the first and subsequent cycles, for which cycling was carried out at a constant rate of 30 mA g⁻¹ between potential limits of 3.0 V and 4.2 V. The first discharge capacity for mesoporous LT-LiCoO₂ is some 20 mA h g⁻¹ higher than that for the equivalent nanowire material. The initial discharge capacity of normal LT-LiCoO₂ lies between the two nanostructured materials. The fade of discharge capacity on cycling is the same for both nanostructured forms of LT-LiCoO₂, however, the fade is markedly less than that of normal LT-LiCoO₂. The capacity of the nanostructured materials decreases by around 45% after 50 cycles whereas this decrease is 75% for normal LT-LiCoO₂.

In conclusion, it has been shown that lithium-containing nanostructured materials may be prepared by a hard templating route, by first forming the transition-metal oxide and then treating this with a lithium source, with preservation of the nanostructure. Both one-dimensional nanowire LT-LiCoO₂ (based on SBA-15) and three-dimensional mesoporous LT-LiCoO₂ (based on KIT-6) have been synthesized with highly crystalline structures. Preliminary electrochemical data demonstrate that the nanostructured materials exhibit superior capacity retention on cycling compared with normal LT-LiCoO₂.

Experimental Section

The preparation of the mesoporous silicas, SBA-15 and KIT-6, has been described previously.^[7,10,13] A typical synthesis of nanostructured LT-LiCoO₂ was as follows: Co(NO₃)₂·6H₂O (98%, Aldrich; 1 g) was dissolved in ethanol (20 mL) then mesoporous silica (2 g) was added. After stirring at room temperature until all the solution had been absorbed, the sample was heated slowly to 300 °C and calcined at that temperature for 3 h. The impregnation procedure was repeated, and the sample was then calcined at 500 °C for 3 h. The resulting sample

was treated twice with a 10% solution of HF in water to remove the silica template, then washed with water and ethanol several times, and then dried at 60 °C. 0.2 g of the as-prepared nanostructured Co_3O_4 was mixed with excess $\text{LiOH}\cdot\text{H}_2\text{O}$ (0.6 g) in ethanol (20 mL). The solvent was removed by stirring overnight at room temperature, and the mixture was calcined at 400 °C for 1 h. The final product was washed with water and ethanol several times to remove the unreacted lithium salt and then dried at 60 °C for 2 h. The materials were characterized by TEM (Jeol JEM-2011), PXRD (Stoe STADI/P diffractometer operating in transmission mode with $\text{Fe}_{\text{K}\alpha 1}$ radiation, $\lambda = 1.936 \text{ \AA}$), low-angle XRD (Rigaku/MSD, D/max-rB with $\text{Cu}_{\text{K}\alpha 1}$ radiation, $\lambda = 1.541 \text{ \AA}$), and N_2 adsorption (Hiden IGA porosimeter).

Electrochemical cells were constructed by mixing the active material, Kynar 2801 (a copolymer based on polyvinylidene fluoride), and Super P carbon in the weight ratio 80:10:10. The mixture was cast onto Al foil from THF using a Doctor-Blade technique. After evaporation of the solvent at 45 °C, the electrodes were assembled into cells with a Li electrode and LP 30 electrolyte (Merck; 1M LiPF_6 in 1:1 v/v EC:DMC, EC = ethylene carbonate, DMC = dimethyl carbonate). The cells were constructed and handled in an Ar-filled MBraun glovebox. Electrochemical measurements were carried out using a Biologic MacPile II system.

Received: May 13, 2005

Published online: September 13, 2005

Keywords: intercalations · lithium · mesoporous materials · template synthesis · transition metals

- [1] a) M. Antonietti, G. A. Ozin, *Chem. Eur. J.* **2004**, *10*, 29; b) J. T. Hu, T. W. Odom, C. M. Lieber, *Acc. Chem. Res.* **1999**, *32*, 435; c) C. N. R. Rao, M. Nath, *Dalton Trans.* **2003**, *1*; d) M. Remskar, *Adv. Mater.* **2004**, *16*, 1497; e) F. Schuth, *Angew. Chem.* **2003**, *115*, 3730; *Angew. Chem. Int. Ed.* **2003**, *42*, 3604; f) R. Tenne, *Angew. Chem.* **2003**, *115*, 5280; *Angew. Chem. Int. Ed.* **2003**, *42*, 5124.
- [2] a) A. Taguchi, F. Schuth, *Microporous Mesoporous Mater.* **2005**, *77*, 1; b) C. C. Wang, J. Y. Ying, *Chem. Mater.* **1999**, *11*, 3113; c) D. M. Antonelli, *Adv. Mater.* **1999**, *11*, 487.
- [3] F. Jiao, P. G. Bruce, *Angew. Chem.* **2004**, *116*, 6084; *Angew. Chem. Int. Ed.* **2004**, *43*, 5958.
- [4] A. S. Aricò, P. G. Bruce, B. Scrosati, J.-M. Tarascon, W. van Schalkwijk, *Nat. Mater.* **2005**, *4*, 366.
- [5] a) D. M. Antonelli, J. Y. Ying, *Angew. Chem.* **1995**, *107*, 2202; *Angew. Chem. Int. Ed. Engl.* **1995**, *34*, 2014; b) Z. R. Tian, W. Tong, J. Y. Wang, N. G. Duan, V. V. Krishnan, S. L. Suib, *Science* **1997**, *276*, 926; c) P. D. Yang, D. Y. Zhao, D. I. Margolese, B. F. Chmelka, G. D. Stucky, *Nature* **1998**, *396*, 152.
- [6] a) H. F. Yang, D. Y. Zhao, *J. Mater. Chem.* **2005**, *15*, 1217; b) J. Lee, S. Han, T. Hyeon, *J. Mater. Chem.* **2004**, *14*, 478.
- [7] F. Kleitz, S. H. Choi, R. Ryoo, *Chem. Commun.* **2003**, 2136.
- [8] a) S. C. Laha, R. Ryoo, *Chem. Commun.* **2003**, 2138; b) B. Z. Tian, X. Y. Liu, H. F. Yang, S. H. Xie, C. Z. Yu, B. Tu, D. Y. Zhao, *Adv. Mater.* **2003**, *15*, 1370; c) E. L. Crepaldi, G. Soler-Illia, D. Grosso, F. Cagnol, F. Ribot, C. Sanchez, *J. Am. Chem. Soc.* **2003**, *125*, 9770; d) F. Jiao, B. Yue, K. K. Zhu, D. Y. Zhao, H. Y. He, *Chem. Lett.* **2003**, *32*, 770; e) W. C. Li, A. H. Lu, C. Weidenthaler, F. Schuth, *Chem. Mater.* **2004**, *16*, 5676; f) V. Escax, M. Imperor-Clerc, D. Bazin, A. Davidson, *C. R. Chim.* **2005**, *8*, 663.
- [9] K. K. Zhu, B. Yue, W. Z. Zhou, H. Y. He, *Chem. Commun.* **2003**, 98.
- [10] B. Z. Tian, X. Y. Liu, L. A. Solovyov, Z. Liu, H. F. Yang, Z. D. Zhang, S. H. Xie, F. Q. Zhang, B. Tu, C. Z. Yu, O. Terasaki, D. Y. Zhao, *J. Am. Chem. Soc.* **2004**, *126*, 865.
- [11] Y. Q. Wang, C. M. Yang, W. Schmidt, B. Spliethoff, E. Bill, F. Schuth, *Adv. Mater.* **2005**, *17*, 53.
- [12] Y. K. Zhou, C. M. Shen, H. L. Li, *Solid State Ionics* **2002**, *146*, 81.
- [13] D. Y. Zhao, J. L. Feng, Q. S. Huo, N. Melosh, G. H. Fredrickson, B. F. Chmelka, G. D. Stucky, *Science* **1998**, *279*, 548.
- [14] a) K. Mizushima, P. C. Jones, P. J. Wiseman, J. B. Goodenough, *Mater. Res. Bull.* **1980**, *15*, 783; b) L. A. Depicciotto, M. M. Thackeray, W. I. F. David, P. G. Bruce, J. B. Goodenough, *Mater. Res. Bull.* **1984**, *19*, 1497; c) R. J. Gummow, M. M. Thackeray, W. I. F. David, S. Hull, *Mater. Res. Bull.* **1992**, *27*, 327; d) R. J. Gummow, D. C. Liles, M. M. Thackeray, *Mater. Res. Bull.* **1993**, *28*, 235.
- [15] Y. Shao-Horn, S. A. Hackney, A. J. Kahaian, M. M. Thackeray, *J. Solid State Chem.* **2002**, *168*, 60.

Aromaticity

DOI: 10.1002/anie.200501632

The Aromaticity of the Stannole Dianion**

Masaichi Saito,* Ryuta Haga, Michikazu Yoshioka,
Kazuya Ishimura, and Shigeru Nagase

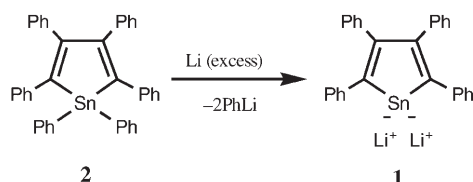
In the last decade, much attention has been focused on the anions and dianions of siloles^[1] and germoles,^[1f,2] which are heavier congeners of the cyclopentadienyl anion.^[3] The degree of aromaticity of silolyl anions depends on the substituent,^[1b,f] while the germolyl anions do not show aromaticity because the negative charge is localized on the germanium atom.^[1f,2a,2c] In contrast, the negative charges in the dianions of siloles and germoles are significantly delocalized in the C₄M (M = Si, Ge) ring and they were concluded to be aromatic.^[1d–f,2b,2d,2e,4] The aromatic delocalization in these dianions was evidenced by NMR studies, calculations, and X-ray crystal structural analyses, which showed no alternation of the C–C bonds within the ring. In contrast to the well-investigated mono- and dianions of siloles and germoles, neither mono- nor dianions of stannoles had been reported before we undertook a study of such species a few years ago.

[*] Assoc. Prof. Dr. M. Saito, R. Haga, Prof. Dr. M. Yoshioka
Department of Chemistry, Faculty of Science
Saitama University
Shimo-okubo, Saitama City, Saitama 338-8570 (Japan)
Fax: (+81) 48-858-3700
E-mail: masaichi@chem.saitama-u.ac.jp
Dr. K. Ishimura, Prof. Dr. S. Nagase
Department of Theoretical Molecular Science
Institute for Molecular Science
Myodaiji, Okazaki, Aichi 444-8585 (Japan)

[**] This work was partially supported by Grants-in-Aid for Young Scientists (B) No. 17750032 (M.S.) and the Nanotechnology Support Project from the Ministry of Education, Culture, Sports, Science, and Technology of Japan. M.S. acknowledges a research grant from Toray Science Foundation. R.H. thanks the Research Fellowships of the Japan Society for the Promotion of Science for Young Scientists.

In the course of our studies on the synthesis of tin-containing aromatic compounds,^[5] mono- and dianions of stannoles were revealed as fascinating synthetic targets because these species are potential intermediates for the synthesis of tin-containing aromatic compounds. Recently, we reported the synthesis of compound **1** by the reduction of bi(1,1'-pentaphenylstannole)^[6] or hexaphenylstannole with the concomitant formation of phenyllithium.^[7] The dianion in **1** was characterized by ¹H, ¹³C, and ¹¹⁹Sn NMR spectroscopy and chemical trapping with methyl iodide. However, the formation of phenyllithium prevented the isolation of **1** in a pure form as well as the estimation of its aromaticity by using ⁷Li chemical shifts^[4b,8] because of the intermolecular exchange of lithium cations. Herein, we report the isolation of compound **1** and the crystallographic and theoretical studies of its aromaticity.

The reduction of hexaphenylstannole **2**^[9] with excess lithium in ether at room temperature gave **1** and phenyllithium. Refluxing the reaction mixture for 14 h completely decomposed phenyllithium,^[10] and **1** was obtained as deep-red crystals in 98% yield (Scheme 1).



Scheme 1. Synthesis of stannole dianion **1** by the reduction of hexaphenylstannole **2**.

The structure of **1** was determined by X-ray analysis. As shown in Figure 1, two lithium atoms lie above and below the stannole ring. Each lithium atom is coordinated to the stannole ring in an η^5 fashion and is also coordinated to an ether molecule. Each unit molecule of **1** contains a benzene molecule in a unit cell. η^5 -Bonded lithium atoms were also found in the lithium salts of the dianions of tetraphenylger-

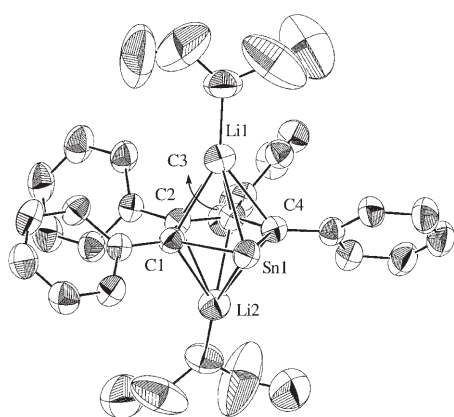


Figure 1. ORTEP drawing of **1** with thermal ellipsoid plots (40% probability for non-hydrogen atoms). All hydrogen atoms and a benzene molecule are omitted for clarity. Selected bond lengths [Å] and angles [°]: Sn1–C1 2.179(4), C1–C2 1.422(6), C2–C3 1.442(5), C3–C4 1.446(6), C4–Sn1 2.133(4), Sn1–Li1 2.758(8), Sn1–Li2 2.769(8); C1–Sn1–C4 77.43(15).

mole^[2d] and tetramethylsilole.^[1e,f] The C2–C3 bond significantly shortens to 1.442(5) Å from 1.511(6) Å in **2**.^[9b] On the contrary, the C1–C2 and C3–C4 bonds significantly lengthen to 1.422(6) and 1.446(6) Å, respectively, from 1.352 Å in **2**.^[9b] The stannole ring is almost planar and the C–C distances within the ring are nearly equal, ranging from 1.422(6) to 1.446(6) Å, which suggests a considerable aromatic character of dianion in **1**.

To aid in understanding the structure of **1**, the geometry of unsolvated **1** was optimized with the hybrid density functional theory at the B3LYP^[11] level by using Huzinaga's (433321/43321/421; DZP) basis set and a polarization d function ($\xi = 0.183$) for Sn^[12] and 6-31G(d) for C,^[13,14] H,^[15] and Li.^[14,16,17] Two different dilithio complexes were found to be minima (Figure 2). One of these (**1a**), which corresponds closely to

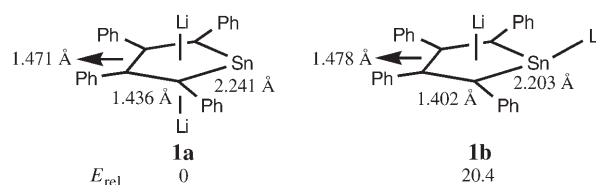
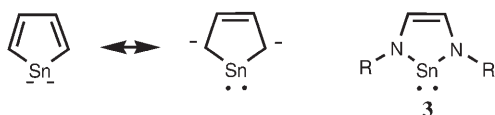


Figure 2. Geometry optimization and relative energies of **1a** and **b**.

the X-ray crystal structure, is of C_2 symmetry with both lithium atoms η^5 -coordinated to the aromatic ring. The other structure (**1b**) is of C_1 symmetry with one lithium atom bonded to the tin atom and the other bonded in an η^5 fashion to the ring. The structure **1a** was calculated to be more stable than **1b** by 20 kcal mol^{−1}. The calculated C–C distances within the ring of **1a** are nearly equal (1.436 and 1.471 Å), which suggests a considerable aromatic delocalization of the negative charges in **1a**. The calculated structure of **1a** is in good agreement with the X-ray crystal structure of **1** (Figure 1). According to the natural population analysis, the α carbon atoms are considerably negatively charged (−0.713) in **1a**. This finding suggests the large contribution of a resonance form with stannylene character, as indicated in dianions of siloles and germales, although the natural population analyses of these dianions were not reported. The β carbon atoms are also negatively charged (−0.273) in **1a**, whereas the α (−0.415) and β (−0.030) carbon atoms of **2** are less negatively charged than those of **1a**, which suggests a considerable delocalization of negative charges into the stannole ring.

The NMR spectroscopic analysis of **1** was also carried out. The ¹¹⁹Sn signal for **1** ($\delta = 163.3$) appeared at a lower field than that for **2** ($\delta = -88$ ppm in CDCl₃), which reflects the strong contribution of a resonance form with stannylene character in **1** consistent with the natural population analysis of **1a**. The central tin atom of the isolobal diaminostannylene **3** (Scheme 2) is known to resonate at about $\delta = 240$ ppm.^[18] However, the ¹³C NMR signal assignable to the α carbon atom in the five-membered ring ($\delta = 187$ ppm) was observed at a lower field than that for **2** ($\delta = 143$ ppm in CDCl₃). This result is contrary to the low-frequency resonance predicted by the natural population analysis and the major resonance contribution. The signal arising from the β carbon atom in the



Scheme 2. Mesomeric forms of diaminostannylene **3**.

five-membered ring appeared at a higher field than that for **2** ($\delta = 133$ vs. 155 ppm).

The observed values of **1** are in good agreement with the calculated values of $\delta = 207$ and 138 ppm, respectively (Table 1).^[19] The high-frequency resonance of the α carbon

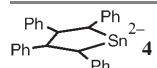
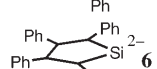
Table 1: Calculated and measured chemical shifts for **1**.

	C_α	C_β	Li
Calculated	206.69	138.15	−6.30
Experimental	187.68	133.46	−4.36

atom could be explained by the paramagnetic contribution of a tin–carbon bond.^[20] The ^7Li NMR signal attributable to **1** was observed at $\delta = -4.36$ ppm; the calculation predicted $\delta = -6.30$ ppm (Table 1). This appreciable low-frequency resonance is evidently caused by the strong shielding effect of the diatropic ring current resulting from the 6π -electron system, and hence the stannole dianion in **1** is concluded to have considerable aromatic character.^[4b,8]

The nucleus-independent chemical shift (NICS) value of $\delta = -5.96$ ppm^[19] calculated at 1.0 Å above the ring (non-weighted mean of the heavy-atom coordinate) of non-lithium-coordinated **4** also suggests that the stannole dianion in **1** should be aromatic (Table 2).^[21] The origin of the aromaticity

Table 2: NICS(1) calculation for **4–6**.

Compound	NICS(1)/ppm
 4	−5.96
 5	−6.26
 6	−6.30

of **1** could be reasonably interpreted in terms of the delocalization of negative charges of the tin out-of-plane p orbital into the LUMO of the butadiene moiety (Figure 3).^[22] However, the degree of aromaticity of **1** is smaller than those of the germanium and silicon analogues, judging from the NICS(1) values of non-lithium-coordinated dianions **4–6** (Table 2).

In summary, the lithium salt **1** of a stannole dianion was isolated and characterized by NMR and X-ray crystal structural studies, and the related calculations were carried out. The stannole dianion has a planar structure with almost equal C–C distances within the ring, and hence the negative

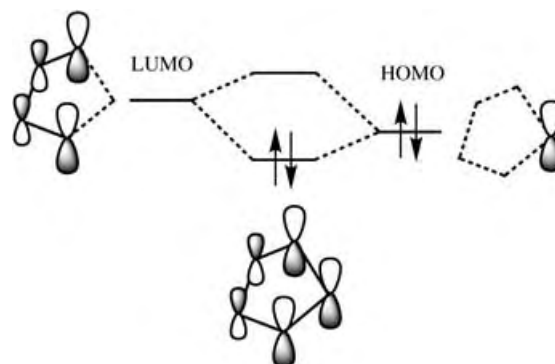


Figure 3. Orbital correlation between butadiene and tin dianion moieties.

charges considerably are delocalized in the ring. The strong low-frequency resonance arising from the diatropic ring current from the 6π -electron system was observed by ^7Li NMR spectroscopy. Compound **1** is concluded to be the first tin-containing carbocyclic aromatic compound.

Experimental Section

Synthesis of **1**: Ether (10 mL) was added to a mixture of **2** (971 mg, 1.54 mmol) and lithium (103 mg, 14.8 mmol), and the resulting suspension was refluxed for 17 h. Insoluble materials were removed by filtration, and the filtrate was concentrated in a glove box. The residue was washed with hexane to give **1** (741 mg, 98 %); ^1H NMR (400 MHz, $\text{Et}_2\text{O}/\text{C}_6\text{D}_6$): $\delta = 6.61$ – 6.68 (m, 4H), 6.75– 6.82 (m, 12H), 6.88– 6.93 ppm (m, 4H); ^{13}C NMR (101 MHz, $\text{Et}_2\text{O}/\text{C}_6\text{D}_6$): $\delta = 121.90$ (d), 124.09 (d), 127.17 (d), 127.21 (d), 128.43 (d), 132.64 (d), 133.46 (s, $J(\text{Sn}, \text{C}) = 29$ Hz), 144.18 (s, $J(\text{Sn}, \text{C}) = 14$ Hz), 150.57 (s, $J(\text{Sn}, \text{C}) = 34$ Hz), 187.68 ppm (s, $J(\text{Sn}, \text{C}) = 375$, 393 Hz); ^{119}Sn NMR (149 MHz, $\text{Et}_2\text{O}/\text{C}_6\text{D}_6$): $\delta = 163.3$ ppm; ^7Li NMR (156 MHz, $\text{Et}_2\text{O}/\text{C}_6\text{D}_6$): $\delta = -4.36$ ppm. An elemental analysis and the measurement of the melting point of **1** could not be carried out because of its extremely high reactivity toward water.

Crystal data for **1**: Crystals suitable for X-ray diffraction were obtained by slow evaporation of the solvent from a solution of **1** in ether performed in a glove box. The crystal was mounted in a glass capillary. Data for the X-ray crystallographic analysis were collected on Mac Science DIP3000 diffractometers with MoK_α radiation ($\lambda = 0.71073$ Å) at 298 K. The structure was solved by direct methods by using SIR^[23] and refined with full-matrix least-squares procedures on F^2 (SHELXL-97).^[24] The non-hydrogen atoms were refined anisotropically except for the disordered carbon atoms (see below), and all the hydrogen atoms were placed at calculated positions ($d(\text{C}-\text{H}) = 0.96$ Å). Disorder around one of the ether molecules was found. The occupancies of the disordered ether molecules were fixed as 0.50:0.50 and the corresponding hydrogen atoms were not placed. Formula $\text{C}_{36}\text{H}_{35}\text{Li}_2\text{O}_2\text{Sn}$, C_6H_6 , $M_r = 710.34$, crystal dimension $0.40 \times 0.40 \times 0.20$ mm³, triclinic, space group $P\bar{1}$, $Z = 2$, $a = 10.8280(6)$, $b = 13.3290(7)$, $c = 15.2920(10)$ Å, $\alpha = 104.449(3)^\circ$, $\beta = 94.865(3)^\circ$, $\gamma = 113.249(3)^\circ$, $V = 1921.6(2)$ Å³, $\rho_{\text{calcd}} = 1.228$ g cm^{−3}, $R1 = 0.057$ ($I > 2\sigma(I)$), 5247 reflections, $wR2 = 0.169$ (for all reflections) for 6519 reflections and 423 parameters, GOF = 1.146. CCDC-271622 contains the supplementary crystallographic data for this paper. These data can be obtained free of charge from the Cambridge Crystallographic Data Centre via www.ccdc.cam.ac.uk/data_request/cif.

Received: May 12, 2005

Published online: September 12, 2005

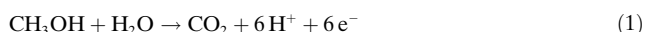
Keywords: anions · aromaticity · carbocycles · NMR spectroscopy · tin

- [1] a) W.-C. Joo, J.-H. Hong, S.-B. Choi, H.-E. Son, C. H. Kim, *J. Organomet. Chem.* **1990**, 391, 27; b) J.-H. Hong, P. Boudjouk, *J. Am. Chem. Soc.* **1993**, 115, 5883; c) J.-H. Hong, P. Boudjouk, S. Castellino, *Organometallics* **1994**, 13, 3387; d) U. Bankwitz, H. Sohn, D. R. Powell, R. West, *J. Organomet. Chem.* **1995**, 499, C7; e) R. West, H. Sohn, U. Bankwitz, J. Calabrese, Y. Apeloig, T. Mueller, *J. Am. Chem. Soc.* **1995**, 117, 11608; f) W. P. Freeman, T. D. Tilley, G. P. A. Yap, A. L. Rheingold, *Angew. Chem.* **1996**, 108, 960; *Angew. Chem. Int. Ed. Engl.* **1996**, 35, 882; g) W. P. Freeman, T. D. Tilley, L. M. Liable-Sands, A. L. Rheingold, *J. Am. Chem. Soc.* **1996**, 118, 10457.
- [2] a) P. Dufour, J. Dubac, M. Dartiguenave, Y. Dartiguenave, *Organometallics* **1990**, 9, 3001; b) J.-H. Hong, P. Boudjouk, *Bull. Soc. Chim. Fr.* **1995**, 132, 495; c) W. P. Freeman, T. D. Tilley, F. P. Arnold, A. L. Rheingold, P. K. Gantzel, *Angew. Chem.* **1995**, 107, 2029; *Angew. Chem. Int. Ed. Engl.* **1995**, 34, 1887; d) R. West, H. Sohn, D. R. Powell, T. Müller, Y. Apeloig, *Angew. Chem.* **1996**, 108, 1095; *Angew. Chem. Int. Ed. Engl.* **1996**, 35, 1002; e) S.-B. Choi, P. Boudjouk, J.-H. Hong, *Organometallics* **1999**, 18, 2919.
- [3] For examples of reviews, see: a) E. Colomer, R. J. P. Corriu, M. Lheureux, *Chem. Rev.* **1990**, 90, 265; b) J. Dubac, C. Guérin, P. Meunier in *The Chemistry of Organic Silicon Compounds* (Eds.: Z. Rappoport, Y. Apeloig), Wiley, Chichester, **1998**, p. 1961; c) M. Saito, M. Yoshioka, *Coord. Chem. Rev.* **2005**, 249, 765.
- [4] a) B. Goldfuss, P. von R. Schleyer, F. Hampel, *Organometallics* **1996**, 15, 1755; b) B. Goldfuss, P. von R. Schleyer, *Organometallics* **1997**, 16, 1543.
- [5] a) M. Saito, M. Nitta, M. Yoshioka, *Organometallics* **2001**, 20, 749; b) M. Saito, N. Henzan, M. Nitta, M. Yoshioka, *Eur. J. Inorg. Chem.* **2004**, 7437.
- [6] M. Saito, R. Haga, M. Yoshioka, *Chem. Commun.* **2002**, 1002.
- [7] M. Saito, R. Haga, M. Yoshioka, *Chem. Lett.* **2003**, 912.
- [8] The high-field $^6\text{Li}/^7\text{Li}$ chemical shift is diagnostic of aromatic ring currents. For examples, see: a) R. H. Cox, H. W. Terry, Jr., L. W. Harrison, *J. Am. Chem. Soc.* **1971**, 93, 3297; b) R. H. Cox, H. W. Terry, Jr., *J. Magn. Reson.* **1974**, 14, 317; c) L. A. Paquette, W. Bauer, M. R. Sivik, M. Bühl, M. Feigel, P. von R. Schleyer, *J. Am. Chem. Soc.* **1990**, 112, 8776; d) A. Sekiguchi, Y. Sugai, K. Ebata, C. Kabuto, H. Sakurai, *J. Am. Chem. Soc.* **1993**, 115, 1144.
- [9] a) W. Z. Rhee, J. J. Zuckerman, *J. Am. Chem. Soc.* **1975**, 97, 2291; b) J. Ferman, J. P. Kakareka, W. T. Klooster, J. L. Mullin, J. Quattrucci, J. S. Ricci, H. J. Tracy, W. J. Vining, S. Wallace, *Inorg. Chem.* **1999**, 38, 2464.
- [10] A new singlet was observed in the ^1H NMR spectrum in ether/ C_6D_6 at $\delta = 5.23$ ppm. In a separate experiment, a solution of phenyllithium was refluxed in ether/ C_6D_6 for 14 h. The ^1H NMR spectrum of the resulting mixture showed a singlet at $\delta = 5.23$ ppm with the complete disappearance of the signals for phenyllithium. The ^{13}C NMR spectrum showed signals at $\delta = 122.79$ and 128.53 ppm, the latter being assignable to benzene. The signals at $\delta = 5.23$ ppm in the ^1H NMR spectrum and $\delta = 122.79$ ppm in the ^{13}C NMR spectrum probably arise from ethylene.
- [11] a) A. D. Becke, *J. Chem. Phys.* **1993**, 98, 5648; b) C. Lee, W. Yang, R. G. Parr, *Phys. Rev. B* **1988**, 37, 785.
- [12] S. Huzinaga, J. Andzelm, M. Klobukowski, E. Radzio-Andzelm, Y. Sakai, H. Tatewaki, *Gaussian Basis Sets for Molecular Calculations*, Elsevier, Amsterdam, **1984**.
- [13] W. J. Hehre, R. Ditchfield, J. A. Pople, *J. Chem. Phys.* **1972**, 56, 2257.
- [14] P. C. Hariharan, J. A. Pople, *Theor. Chim. Acta* **1973**, 28, 213.
- [15] R. Ditchfield, W. J. Hehre, J. A. Pople, *J. Chem. Phys.* **1971**, 54, 724.
- [16] J. D. Dill, J. A. Pople, *J. Chem. Phys.* **1975**, 62, 2921.
- [17] All calculations were performed with Gaussian 98, Revision A.11.1, M. J. Frisch, G. W. Trucks, H. B. Schlegel, G. E. Scuseria, M. A. Robb, J. R. Cheeseman, V. G. Zakrzewski, J. A. Montgomery, Jr., R. E. Stratmann, J. C. Burant, S. Dapprich, J. M. Millam, A. D. Daniels, K. N. Kudin, M. C. Strain, O. Farkas, J. Tomasi, V. Barone, M. Cossi, R. Cammi, B. Mennucci, C. Pomelli, C. Adamo, S. Clifford, J. Ochterski, G. A. Petersson, P. Y. Ayala, Q. Cui, K. Morokuma, P. Salvador, J. J. Dannenberg, D. K. Malick, A. D. Rabuck, K. Raghavachari, J. B. Foresman, J. Cioslowski, J. V. Ortiz, A. G. Baboul, B. B. Stefanov, G. Liu, A. Liashenko, P. Piskorz, I. Komaromi, R. Gomperts, R. L. Martin, D. J. Fox, T. Keith, M. A. Al-Laham, C. Y. Peng, A. Nanayakkara, M. Challacombe, P. M. W. Gill, B. Johnson, W. Chen, M. W. Wong, J. L. Andres, C. Gonzalez, M. Head-Gordon, E. S. Replogle, J. A. Pople, Gaussian, Inc., Pittsburgh, PA, **2001**.
- [18] T. Gans-Eichler, D. Gudat, M. Nieger, *Angew. Chem.* **2002**, 114, 1966; *Angew. Chem. Int. Ed.* **2002**, 41, 1888.
- [19] The calculations were carried out at GIAO-B3LYP/(433311/433111/421) with two polarization d functions ($\xi = 0.253, 0.078$; TZDP) for Sn,^[12] GIAO-B3LYP/(433111/43111/211) with two polarization d functions ($\xi = 0.382, 0.108$; TZDP) for Ge,^[12] GIAO-B3LYP/(53111/5111) with two polarization d functions ($\xi = 0.424, 0.118$; TZDP) for Si,^[12] and 6-31G(d) for C and H. The geometry optimization for **3**, **4**, and **5** was carried out at B3LYP/DZP for Sn,^[12] Ge,^[12] and Si^[12] and at 6-31G(d) for C and H.
- [20] The strong high-frequency resonance of the α carbon atoms was predicted by calculations in reference [4b].
- [21] NICS values are effective probes for dia- and paratropic ring currents associated with aromaticity and antiaromaticity, respectively, see: P. von R. Schleyer, C. Maerker, A. Dransfeld, H. Jiao, N. J. R. van Eikema Hommes, *J. Am. Chem. Soc.* **1996**, 118, 6317.
- [22] The contribution of the resonance form with allyl anion character is small because the bond order of the Sn–C $_{\alpha}$ bond of $\text{C}_4\text{H}_4\text{Sn}^{2-}$ is calculated to be 1.171, which is nearly the same as that of $\text{C}_4\text{H}_4\text{SnH}_2$ (0.986).
- [23] A. Altomare, G. Cascarano, C. Giacovazzo, A. Guagliardi, *J. Appl. Crystallogr.* **1993**, 26, 343.
- [24] G. M. Sheldrick, *SHELXL-97*, Program for Crystal Structure Refinement, Universität Göttingen, Göttingen, Germany, **1997**.

Tungsten Carbide Microspheres as a Noble-Metal-Economic Electrocatalyst for Methanol Oxidation**

Raman Ganesan and Jae Sung Lee*

Among various fuel cells, the direct methanol fuel cell (DMFC) is suited for portable devices or transportation applications owing to its high energy density at low operating temperatures and the ease of handling a liquid fuel.^[1] However, the DMFC has some critical technical drawbacks including the slow oxidation kinetics of methanol relative to hydrogen in the polymer-electrolyte membrane fuel cell (PEMFC). The reaction occurring at the anode of the DMFC is the oxidation of methanol in the presence of water to produce CO₂, electrons, and protons [Eq. (1)].



Currently the most promising anode materials for the DMFC are Pt–Ru bimetallic catalysts dispersed on carbon. This catalyst is favored because of its high activity for methanol oxidation and for water activation, which is critical for the removal of strongly adsorbed CO formed during the decomposition of methanol. However, it still requires high loadings of these expensive noble metals, which makes the cost of DMFC prohibitively high. Further, this catalyst system is susceptible to CO poisoning.^[2] Thus, in recent years there has been considerable interest in replacing noble metals in DMFC electrodes.^[3]

Tungsten carbides have been studied extensively because of their interesting chemical and physical properties.^[4] The carbides of Groups 4–6 (Ti–Cr groups) show catalytic properties similar to those of platinum group metals.^[5,6] There have been several attempts to utilize tungsten carbide as an electrocatalyst because of its platinum-like catalytic behavior, its stability in acid solutions at anodic potentials, and its resistance to CO poisoning.^[7] But when used for an anodic material under DMFC conditions, tungsten carbide alone showed low electrocatalytic activity although it showed resistance to CO poisoning.^[8] Recent surface-science studies have demonstrated that the activity of tungsten carbide film

or carbon-modified W(111) or W(110) single-crystal surfaces could be promoted by adding submonolayer coverages of platinum.^[9] Herein we report for the first time the synthesis of W₂C microspheres with high surface areas and chemisorption capacity. The material when combined with platinum showed very high activity for the electrooxidation of methanol exceeding that of a commercial Pt–Ru catalyst with a higher metal loading. Thus Pt/W₂C microspheres could be a promising alternative anodic material for DMFC replacing ruthenium entirely and saving substantial amount of platinum from the current Pt–Ru electrodes. In addition, inorganic spheres have tailored properties, low densities, higher surface areas, and unique optical and surface properties, which are desired for applications as catalysts, sensors, and fillers.^[10]

We synthesized W₂C microspheres by heating mixtures of resorcinol–formaldehyde polymer (a carbon precursor) and ammonium metatungstate salt (AMT) (a tungsten precursor). In a typical synthesis, a mixture containing AMT, resorcinol, formaldehyde, and water was mixed in a molar ratio of 8.1 × 10^{−4}:1.1 × 10^{−2}:2.2 × 10^{−2}:1.1 and heated under reflux at 367 K for 24 h. The resulting gel was dried at room temperature then heated at 1173 K for 1 h in an argon flow and 2 h in a hydrogen flow (100 mL min^{−1}). The H₂ treatment was to remove the free carbon deposited on the W₂C surface.^[11] The carbon microsphere was prepared in the same way without AMT salt.

The typical X-ray diffraction (XRD) pattern of the resulting W₂C microspheres is shown in Figure 1. The

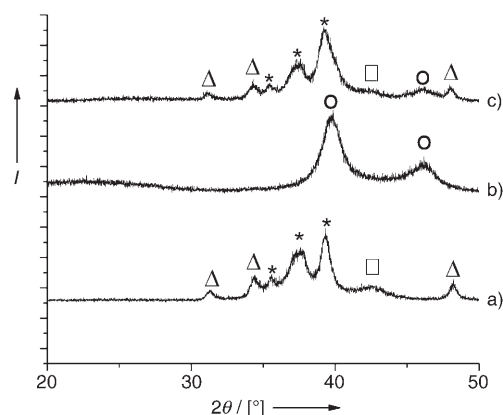


Figure 1. XRD patterns of a) W₂C microsphere, b) Pt–Ru/C microsphere, and c) Pt/W₂C microsphere. * W₂C, Δ WC, □ WC_{1−x}, ○ Pt.

reflections of the microsphere correspond to W₂C (hexagonal-close packed (hcp)) as the major phase and to WC (hcp) and WC_{1−x} (face-centered cubic (fcc)) as minor phases. The formation of tungsten–carbide phases depends on heating rate, temperature, and especially, the amount of carbon present in the sample.^[11–13] To study this phase variation, the amount of AMT was varied from 4.1 × 10^{−4} mol to 16 × 10^{−4} mol in the polymer while keeping all others factors constant. A phase transition was observed from W₂C (with minor amount of WC_{1−x}) to pure WC (no other phases were present) as the amount of AMT increased. But at higher amounts of AMT, the surface area decreased and the spherical structure

[*] Dr. R. Ganesan, Prof. J. S. Lee
Department of Chemical Engineering
Pohang University of Science and Technology
San 31 Hyoja-Dong, Pohang, 790-784 (Republic of Korea)
Fax: (+82) 542-795-528
E-mail: jlee@postech.ac.kr

[**] This work has been supported by National Research Laboratory program, National R&D Project for Nano Science and Technology, Bioplus Ltd and Hydrogen R&D Center.

Supporting information for this article is available on the WWW under <http://www.angewandte.org> or from the author.

collapsed into bulk particles. The optimized molar ratio for the spherical structure with a high surface area was the composition specified above. Under these optimized conditions, we observed W_2C as the major phase with WC_{1-x} and WC as minor phases. There were no XRD peaks corresponding to tungsten trioxide, metallic tungsten, and carbon materials. Tungsten trioxide should be present as an amorphous phase because we observed the phase by X-ray photoelectron spectroscopy (XPS). The XRD pattern of carbon microspheres prepared without the tungsten salt AMT indicated an amorphous nature and showed no peaks.

The BET surface area of the W_2C microspheres was about $176\text{ m}^2\text{ g}^{-1}$ (compared to $635\text{ m}^2\text{ g}^{-1}$ for carbon microspheres). The CO uptake was calculated from temperature-programmed desorption (TPD) (see Supporting Information) by referring the area under the CO mass signal (28) to the known quantity of CO used. The CO uptake value ($956\text{ }\mu\text{mol g}^{-1}$) indicates that the number of CO molecules taken up corresponds to 18.7% of the total number of tungsten atoms in the sample. To our knowledge, these surface area and CO uptake values are the highest reported for tungsten carbide.^[12,13] Carbon microspheres prepared without the tungsten salt AMT, and the commercial WC (Alfa-JM) did not chemisorb CO molecules. XPS of the W_{4f} doublet ($4f_{5/2}$ and $4f_{7/2}$) showed peaks at 31.6 eV and 32.5 eV, arising from the presence of tungsten carbide (see Supporting Information).^[14] Peaks observed at higher binding energies indicate that a part of the tungsten is present as an oxide, which probably arises from surface oxidation of W_2C in air after preparation.^[15]

The microscopic images of carbon and W_2C microspheres are shown in Figure 2. Both microspheres showed uniform morphology with diameters of 2–4 μm . The carbon microspheres appear to act as a template for the formation of W_2C microspheres. The W_2C microspheres were also observed under a high-resolution transmission electron microscope (HRTEM). As shown in Figure 2c, the microsphere appears to be a collection of W_2C nanoparticles wrapped with a carbon-rich skin. The surface was fairly rough (Figure 2d). The microspheres must be porous to give the high BET surface area of $176\text{ m}^2\text{ g}^{-1}$. Furthermore, application of the Debye–Scherrer equation to the XRD peaks shown in Figure 1 gives a W_2C crystal size of approximately 12 nm. Energy dispersive X-ray spectroscopy (EDX) analysis of the W_2C microspheres showed that the surface was composed of tungsten, carbon, and oxygen and gave a composition of $WCO_{0.06}$ (see Supporting Information). There is a 100% excess of carbon over the stoichiometry of the observed main phase of W_2C . Thus, it appears that the microsphere is a composite material made of W_2C particles and carbon.

Platinum particles were supported on these W_2C and Pt–Ru particles on carbon microspheres by the conventional borohydride reduction method.^[16] The HRTEM images (Figure 2e,f) show that the platinum particles are finely dispersed on W_2C microspheres but Ru–Pt alloy particles form large aggregates on carbon microspheres. The average platinum particle size is around 6 nm on W_2C , which is in good agreement with the value calculated from XRD (Figure 1) using the Debye–Scherrer equation (6 nm for 7.5 wt % Pt on

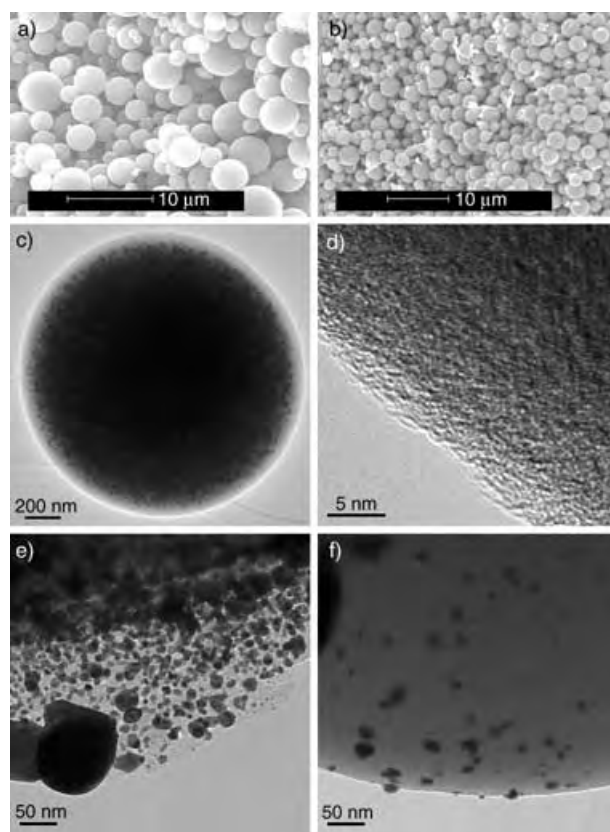


Figure 2. a) SEM image of carbon microspheres, b) SEM image of W_2C microspheres, c) HRTEM image of a W_2C microsphere, d) HRTEM image of the surface of a W_2C microsphere, e) HRTEM image of a Pt–Ru/carbon microsphere, f) HRTEM image of a Pt(7.5wt%)/ W_2C microsphere.

W_2C , 14 nm for 15 wt % Pt on W_2C , and 14 nm for 20 wt % Pt–Ru on carbon microspheres).

By using hydrogen adsorption–desorption methods in conjunction with cyclic voltammetry the electrochemical surface area (ESA) of platinum supported on various catalysts was measured. As shown in Table 1, the ESA of platinum supported on W_2C is several-times higher than those of Pt–Ru supported on carbon microspheres and commercial (E-Teck) 20% Pt–Ru(1:1 atomic ratio)/Vulcan XC-72R carbon. This result indicates that the platinum particles were better dispersed on the W_2C spheres than on the other

Table 1: Electrocatalytic activity of various catalysts for methanol oxidation.

Catalyst	ESA ^[a] [$\text{m}^2\text{ g}^{-1}$ Pt]	Specific activity ^[b]	Mass activity ^[c]
W_2C	0.0	0.0	0.0
7.5 wt % Pt/ W_2C	327	156	728
15 wt % Pt/ W_2C	189	224	560
11 wt % Pt–9 wt % Ru/Carbon microsphere	58	87	280
13 wt % Pt–7 wt % Ru/VulcanXC-72R ^[d]	71	114	307

[a] Electrochemical surface area. [b] At 0.75 V [mA cm^{-2}]. [c] At 0.75 V [mA mg^{-1} Pt]. [d] Commercial E-Teck catalyst

supports. This dispersion is reflected in the electrochemical activity towards the oxidation of methanol (Table 1 and Figure S4 in Supporting Information). The W_2C microspheres alone without platinum showed no activity. In contrast, both 7.5 wt % and 15 wt % Pt supported on W_2C microspheres show higher current density (taken at 0.75 V, after the cycle was stabilized) than Pt–Ru supported on carbon microspheres and a commercial 20 % Pt–Ru E-Teck catalyst. The mass activity of platinum (mA mg^{-1} of Pt taken at 0.75 V) supported on W_2C microspheres (7.5 wt % Pt) is higher by factors of 2.6 and 2.4 than those of Pt–Ru/carbon microspheres and the commercial E-Teck catalyst, respectively (that is, a lower amount of platinum is required to generate the same current. The mass activity of Pt/ W_2C was greater for the lower platinum-loading electrocatalyst (7.5 wt % Pt versus 15 wt % Pt). These results clearly show that platinum dispersed on W_2C microspheres provides much better utilization of platinum than in the Pt–Ru/carbon catalysts and that ruthenium could be entirely replaced.

There are several reasons why Pt/ W_2C -microsphere catalyst performs better than the commercial catalyst even with the smaller platinum loadings and in the absence of ruthenium. The first is the ability of W_2C to stabilize the high dispersion of platinum relative to carbon supports as discussed above. Second, in the presence of platinum, W_2C is active in the electrochemical methanol oxidation and water decomposition as discussed by Chen and co-workers.^[9] The formation of hydroxy groups from water activation is essential for the removal of metal-poisoning CO from the surface. This conversion is the main role played by ruthenium in conventional Pt–Ru catalysts and this role can be played by W_2C . Finally, W_2C shows high CO resistance. The CO desorption temperature for pure platinum is 460 K.^[17] It decreases to 420 K (Figure S1 in Supporting Information), when the platinum is supported on W_2C . This feature would decrease the poisoning of the catalyst surface by CO and increase the activity for electrooxidation of methanol.

The stability of the Pt/ W_2C -microsphere catalyst was tested by repeating electrochemical reaction cycles in a 1 M H_2SO_4 /1 M CH_3OH solution. As shown in Figure 3, the specific activity as represented by the area of cyclovoltammogram

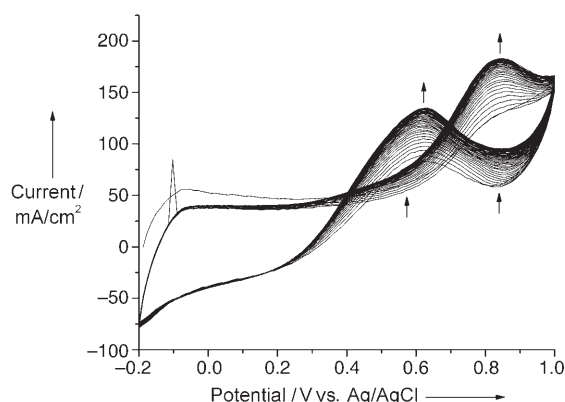


Figure 3. Cyclic voltammogram of 7.5 % Pt/ W_2C -microsphere in a 1 M H_2SO_4 /1 M CH_3OH solution at a scan rate of 50 mV s^{-1} at 298 K, arrows indicate changes with increasing numbers of scans.

increased initially, but stabilized after around 30 cycles. We believe that surface oxygen species formed on the catalyst are removed during this transient period. Once a steady state is established, there was no sign of deactivation during 100 consecutive reaction cycles.

In summary we have for the first time synthesized and characterized W_2C microspheres by a polymer method. A new ruthenium-free electrocatalyst composed of platinum supported on these microspheres shows higher activity for electrochemical oxidation of methanol than a commercial Pt–Ru/C catalyst by a factor of 2.4 (per mass of Pt). This activity could be further increased with optimization of the platinum-loading technique to deposit platinum particles smaller than 6 nm. Since the catalyst is also stable in electrochemical environment, it could become a noble-metal-economic electrocatalyst for DMFC and has the potential to replace current Pt–Ru catalysts.

Experimental Section

Before TPD experiments, the catalysts were activated at 473 K in hydrogen for 1 h. After cooling to room temperature the CO chemisorption was carried out at room temperature for 1 h. Finally CO was desorbed by heating from room temperature to 573 K in He flow.

The working electrodes for the electrochemical measurements were fabricated by dispersing the platinum supported catalysts in 1 mL of distilled water and 5 wt % Nafion (10 μL). The dispersion was ultrasonicated for 15 min. A known amount of suspension was added on to the glassy carbon and the solvent was slowly evaporated. 5 wt % Nafion (10 μL) was added onto the coatings and the solvent was slowly evaporated. Pt foil and Ag/AgCl/3 M NaCl were used as counter and reference electrodes, respectively. A solution of 1 M H_2SO_4 /1 M CH_3OH was used for electrochemical studies using Princeton Applied Research (PAR) voltammetry.

Received: April 12, 2005

Revised: May 18, 2005

Published online: August 11, 2005

Keywords: carbides · fuel cells · heterogeneous catalysis · platinum · tungsten

- [1] M. Winter, R. J. Brodd, *Chem. Rev.* **2004**, *104*, 4245.
- [2] H. Zhang, Y. Wang, E. R. Fachini, C. R. Cabrera, *Electrochem. Solid-State Lett.* **1999**, *2*, 437.
- [3] a) H. C. Yu, K. Z. Fung, Tz. C. Guo, W. L. Chang, *Electrochim. Acta* **2004**, *50*, 807; b) V. Raghuvier, B. Viswanathan, *Fuel* **2002**, *81*, 17; c) V. Raghuvier, K. R. Thampi, J. M. Bonard, N. Xanthopoulos, H. J. Mathieu, B. Viswanathan, *Solid State Ionics* **2001**, *140*, 263.
- [4] a) J. S. Lee, S. Locatelli, S. T. Oyama, M. Boudart, *J. Catal.* **1990**, *125*, 157; b) J. S. Lee, S. T. Oyama, M. Boudart, *J. Catal.* **1987**, *106*, 125; c) R. B. Levy, M. Boudart, *Science* **1973**, *181*, 547.
- [5] a) M. A. Merino, F. C. Marin, J. L. G. Fierro, C. M. Castilla, *J. Catal.* **2003**, *192*, 363; b) J. S. Lee, M. Boudart, *Catal. Lett.* **1993**, *20*, 97; c) S. Li, J. S. Lee, *J. Catal.* **1998**, *173*, 134; d) S. Li, J. S. Lee, *J. Catal.* **1998**, *178*, 119; e) J. S. Lee, M. Boudart, *Catal. Lett.* **1991**, *8*, 107; f) J. S. Lee, L. Volpe, F. H. Ribeiro, M. Boudart, *J. Catal.* **1988**, *112*, 44; g) J. S. Lee, M. Boudart, *Appl. Catal.* **1985**, *19*, 207.
- [6] a) M. J. Ledoux, C. P. Huu, J. Guille, H. Dunlop, *J. Catal.* **1992**, *134*, 383; b) M. J. Ledoux, C. P. Huu, *Catal. Today* **1992**, *15*, 263; c) C. P. Huu, M. J. Ledoux, J. Guille, *J. Catal.* **1993**, *143*, 249;

- d) M. J. Ledoux, P. D. Gallo, C. P. Huu, A. P. E. York, *Catal. Today* **1996**, 27, 145; e) M. J. Ledoux, C. P. Huu, R. R. Chianelli, *Curr. Opin. Solid State Mater. Sci.* **1996**, 1, 96; f) F. Eunier, P. Delporte, B. Heinrich, C. Bouchy, C. Crouzet, C. P. Huu, P. Panissod, J. J. Lerou, L. P. Mills, M. J. Ledoux, *J. Catal.* **1997**, 169, 33; g) C. P. Huu, C. Bouchy, T. Dintzer, G. Ehret, C. Estournes, M. J. Ledoux, *Appl. Catal. A* **1999**, 180, 385; h) M. J. Ledoux, F. Meunier, B. Heinrich, C. P. Huu, M. E. Harlin, A. I. Krause, *Appl. Catal. A* **1999**, 181, 157; i) N. Keller, C. P. Huu, G. Ehret, V. Keller, M. J. Ledoux, *Carbon* **2003**, 41, 2131; j) D. Mordenti, D. Brodzki, G. Djega-Mariadassou, *J. Solid State Chem.* **1998**, 141, 114; k) S. H. Kim, G. Bugli, G. Djega-Mariadassou, *J. Solid State Chem.* **1999**, 142, 100; l) T. Becue, J. M. Manoli, C. Potvin, R. J. Davis, G. Djega-Mariadassou, *J. Catal.* **1999**, 186, 110; m) J. S. Choi, G. Bugli, G. Djega-Mariadassou, *J. Catal.* **2000**, 193, 238; n) A. Szymanska, M. S. Lewandowski, C. Sayag, G. Djega-Mariadassou, *J. Catal.* **2003**, 218, 24; o) J. Y. Piquemal, C. Potvin, J. M. Manoli, G. Djega-Mariadassou, *Catal. Lett.* **2004**, 92, 189; p) A. Otamba, G. Adamski, W. Piskorz, Z. Sojka, C. Sayag, G. Djega-Mariadassou, *J. Phys. Chem. B* **2004**, 108, 2885; q) F. H. Ribeiro, B. Dalla, A. Ralph M. Boudart, J. Baumgartner, E. Iglesia, *J. Catal.* **1991**, 130, 86; r) F. H. Ribeiro, M. Boudart, B. Dalla, A. Ralph, E. Iglesia, *J. Catal.* **1991**, 130, 498; s) E. Iglesia, J. E. Baumgartner, F. H. Ribeiro, M. Boudart, *J. Catal.* **1991**, 131, 523; t) E. Iglesia, F. Ribeiro, M. Boudart, J. E. Baumgartner, *Catal. Today* **1992**, 15, 307; u) E. Iglesia, F. H. Ribeiro, M. Boudart, J. E. Baumgartner, *Catal. Today* **1992**, 15, 455.
- [7] a) C. J. Barnett, G. T. Burstein, A. R. J. Kucernak, K. R. Williams, *Electrochim. Acta* **1997**, 42, 2381; b) S. Bodoardo, M. Maja, N. Penazzi, F. E. G. Henn, *Electrochim. Acta* **1997**, 42, 2603.
- [8] a) M. B. Zellner, J. G. Chen, *Catal. Today* **2005**, 99, 299; b) D. R. McIntyre, G. T. Burstein, A. Vossen, *J. Power Sources* **2002**, 107, 67.
- [9] H. H. Wu, J. G. Chen, *J. Vac. Sci. Technol. A* **2003**, 21, 148.
- [10] a) D. E. Bergbreiter, *Angew. Chem.* **1999**, 111, 3044; *Angew. Chem. Int. Ed.* **1999**, 38, 2870; b) X. M. Sun, Y. D. Li, *Angew. Chem.* **2004**, 116, 607; *Angew. Chem. Int. Ed.* **2004**, 43, 597; c) X. L. Li, T. J. Lu, X. M. Sun, Y. D. Li, *Inorg. Chem.* **2004**, 43, 5442.
- [11] F. H. Ribeiro, R. A. D. Betta, G. J. Guskey, M. Boudart, *Chem. Mater.* **1991**, 3, 805.
- [12] S. Ramanathan, S. T. Oyama, *J. Phys. Chem.* **1995**, 99, 16365.
- [13] L. Volpe, M. Boudart, *J. Solid State Chem.* **1985**, 59, 348.
- [14] A. Katrib, F. Hemming, L. Hilaire, P. Wehrer, G. Maire, *J. Electron Spectrosc. Relat. Phenom.* **1994**, 68, 589.
- [15] S. Wanner, L. Hilaire, P. Wehrer, J. P. Hindermann, G. Maire, *Appl. Catal. A* **2000**, 203, 55.
- [16] P. R. Van Rhennen, M. J. McKelvy, W. S. Glaunsingers, *J. Solid State Chem.* **1987**, 67, 151.
- [17] a) G. Ertl, M. Neuman, K. M. Streit, *Surf. Sci.* **1977**, 64, 393; b) A. Crossley, D. A. King, *Surf. Sci.* **1977**, 68, 528.

DOI: 10.1002/anie.200501446

Rapid Synthesis in Ionic Liquids of Room-Temperature-Conducting Solid Microsilica Spheres**

David S. Jacob, Augustine Joseph,
Somashekarappa P. Mallenahalli,
Sangaraju Shanmugam, Shirley Makhluף,
Jose Calderon-Moreno, Yuri Koltypin, and
Aharon Gedanken*

Herein, we report the rapid synthesis of monodispersed conducting solid microsilica spheres by hydrolyzing tetramethylorthosilicate (TMOS) and tetraethylorthosilicate (TEOS) in an ionic liquid, 1-butyl-3-methylimidazolium hexafluorophosphate, at room temperature. We also report the effect of varying experimental conditions such as the temperature and pH of the solutions on the synthesis and morphology of the silica spheres.

Metal oxide spheres have attracted much attention in fields such as optical materials and catalysts, as well as other nanotechnologies.^[1–5] The sol–gel method is one of the most useful means to prepare metal oxide spheres and small particles with high densities.^[6] Stöber et al. developed an excellent method to prepare monodispersed silica spheres from silicon alkoxides in alcoholic solutions.^[7] This process was extended to the preparation of various metal oxides such as Al₂O₃, TiO₂, and ZrO₂.^[8–10] While the original Stöber technique yields silica spheres with sizes in the range of 200–700 nm, a modified Stöber method yields larger spheres of 1–2 µm.^[11] However, it is difficult to prepare monodispersed silica spheres larger than 2 µm in alcoholic basic media at room temperature,^[7,11] while the synthesis of silica spheres in acidic media has been reported to produce spheres as well as irregularly shaped particles of 10–60 µm in size.^[12] Controlling the size, shape, monodispersity, and yield of the desired product has become a challenge for material chemists.

[*] D. S. Jacob, Dr. A. Joseph, Dr. S. P. Mallenahalli, Dr. S. Shanmugam, S. Makhluף, Prof. Y. Koltypin, Prof. A. Gedanken
Department of Chemistry and
Kanbar Laboratory for Nanomaterials
Bar-Ilan University Center for Advanced Materials and
Nanotechnology
Bar-Ilan University
Ramat-Gan, 52900 (Israel)
Fax: (+97) 235-351-250
E-mail: gedanken@mail.biu.ac.il
Prof. J. Calderon-Moreno
Universitat Politècnica de Catalunya
EPSC-PMTA-201
Av. Canal Olímpic s/n
Castelldefels, Barcelona 08860 (Spain)

[**] We thank Dr. Yakov Langsam for SEM analyses, Michael Riboch for AFM measurements, and Dr. Boris Markovsky for conductivity measurements.

Room-temperature ionic liquids (RTILs) have received much attention as solvents, and significant progress has been made in their applications to biphasic reactions, chemical synthesis, electrochemistry, catalysis, polymerization, biocatalysis, liquid–liquid separations, extractions, dissolution, biopolymer, molecular self-assembly, and interfacial synthesis.^[13,14] Recently, an ionic liquid was used as both a solvent and a template in the synthesis of zeolites.^[15] Supermicroporous lamellar and well-defined inverse opal microstructured silicas have been prepared in ionic liquids, which serve as templates.^[16,17] Hollow TiO₂ microspheres have been prepared in ionic liquids, and it was reported that their size was influenced by the rate of stirring and the reaction temperature.^[14] Elsewhere, mesoporous silica nanoparticles of various morphologies that contained an ionic liquid were used as a controlled-release delivery nanodevice to discharge antibacterial ionic liquids against *Escherichia coli* K12.^[18]

Moreover, owing to their diverse electrochemical properties, ionic liquids have been used as electrolytes for electrochemical devices such as lithium secondary batteries, electric double-layer capacitors, dye-sensitized solar cells, fuel cells, and actuators.^[19] Several important properties of ionic liquids make them attractive substitutes for volatile organic solvents.^[20] The properties of RTILs can be controlled over a wide range through variation of both the anion and cation as well as the chain lengths of the substituent groups. An increasing chain length in the cation alters the melting point of the ionic liquids and increases their viscosity and hydrophobicity.^[21] Varying the anion also affects the property of ionic liquids; for example, salts based on the tetrachloroaluminate(III) anion are extremely water sensitive, whereas those based on the hexafluorophosphate anion are neutral and extremely hydrophobic.^[22] Through careful consideration of the conducting properties and hydrophobicity of the ionic liquid, we chose 1-butyl-3-methylimidazolium hexafluorophosphate, BMI⁺PF₆[−], as the solvent for the preparation of the silica spheres.

The hydrolysis of TMOS and TEOS in a fixed amount of ionic liquid under different reaction conditions (temperature, pH) were studied. The products were characterized by small-angle X-ray diffraction (SAXRD), energy-dispersive X-ray (EDX) spectroscopy, mass spectrometry, and Raman spectroscopy. An in-depth morphological study of the silica spheres prepared under different conditions was carried out by scanning electron microscopy (SEM), and the solid-state nature of the silica spheres was confirmed from the microtomed cross-section of the sample by transmission electron microscopy (TEM).

SAXRD results revealed a lack of organization of the pores for the as-prepared silica spheres, whereas some extent of order could be observed in a sample that was calcined at 1000 °C. EDX spectroscopy showed the presence of phosphorus and chlorine from the encapsulation of the ionic liquid, BMI⁺PF₆[−], and aqueous HCl solution within the silica spheres in the as-prepared sample, whereas their absence was noted in the sample calcined at 1000 °C. Desorption chemical ionization mass spectrometry indicated the presence of 1-butyl-3-methylimidazole (BIM-H) in the sample, while the Raman spectrum of the as-prepared silica spheres revealed

C–H stretching and ring-stretching vibration bands that confirmed the presence of the entrapped ionic liquid as well as O–H stretching bands from water molecules. The entrapped ionic liquid remained intact in the silica spheres even after several washings with acetone. The D and G bands in the Raman spectrum indicate the carbon content of the sample annealed at about 1000 °C.

The size distribution of the microspheres was confirmed by SEM, which revealed diameters in the range of 50–85 µm. The surface area measured for the as-prepared sample was 3.17 m² g^{−1}, while that for the calcined sample ranged from 8–12 m² g^{−1}, which is much higher than reported values.^[12] The increase in surface area is a result of the evaporation or decomposition of the entrapped molecules of water and ionic liquid inside the silica spheres; upon removal of the entrapped species, empty pores are left behind. Thermogravimetric analysis of the silica spheres showed a weight loss of about 9.6 % at 150 °C due to the removal of water, whereas a weight loss of 17 % at 550 °C was attributed to the decomposition and removal of the entrapped ionic liquid, as confirmed by Raman spectroscopy.

The proposed mechanism for the formation of the different morphologies of the spheres is shown in Figure 1. As a

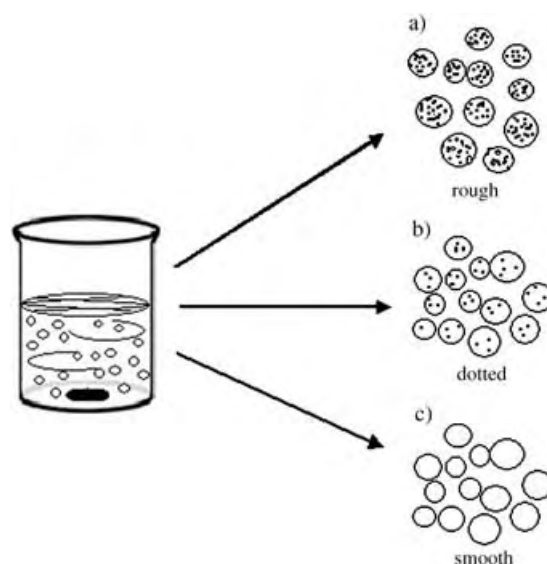


Figure 1. Schematic representation for the formation of different morphologies of silica spheres under different experimental conditions.

result of the hydrophobicity of the ionic liquid, micro-sized droplets of aqueous HCl solution are formed under vigorous stirring. Molecules of the silica precursor (TMOS, TEOS) enter these aqueous acidic microdroplets and are hydrolyzed, leading to the formation of microspheres. Aggregated and overgrown dimeric silica spheres also result from the above mechanism, as hydrolysis of the silica precursor takes place inside two attached microdroplets of water.

The formation of silica spheres with rough surfaces (Figure 1a) depends on the reaction time and the temperature. With a longer reaction time, microdroplets of water adhere to the fully grown silica spheres and the silica

precursor is hydrolyzed in those microdroplets to yield a rough surface, as depicted in Figure 2. Changes in the reaction time, the pH of the aqueous solution, the temperature, and the hydrophobicity of the ionic liquid (all under stirring) have

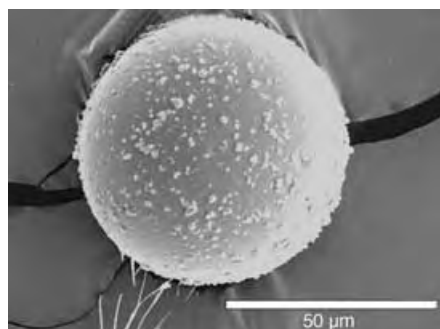


Figure 2. Silica spheres with rough surfaces as synthesized from TMOS at 50°C for 1 h in aqueous HCl solution (0.25 M).

an important effect on the preparation and the peripheral morphology of the silica microspheres. By decreasing the reaction time (Figure 1b,c), silica spheres with smoother surfaces were obtained as shown in Figures 3 and 4.

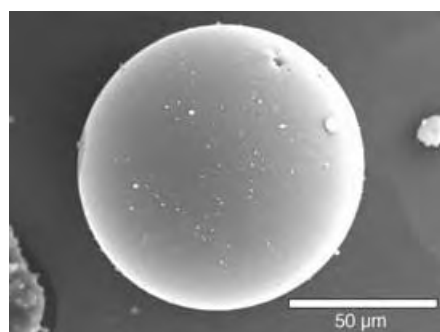


Figure 3. Silica spheres with a dotted morphology as synthesized from TMOS at 50°C for 1 h in aqueous HCl solution (0.1 M).

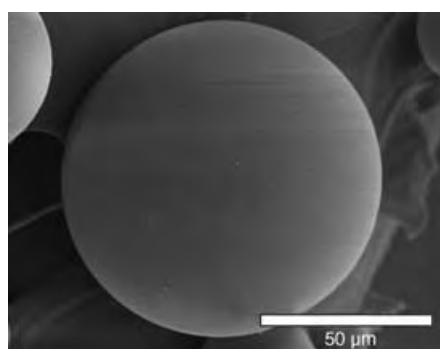


Figure 4. Silica spheres with smooth morphology as synthesized from TMOS at 50°C for 5 min in aqueous HCl solution (0.25 M).

It was observed that the pH of the acidic solutions as well as the temperature affect the rate of hydrolysis. Reactions were carried out at pH 1–2 (0.25–0.01 M HCl) at room temperature and at 50°C under vigorous stirring. Under similar reaction

conditions (room temperature, 0.1 M HCl, 30 minutes), a clear solution was observed for the TEOS precursor whereas silica spheres formed in the case of TMOS which suggests that the rate of hydrolysis of TMOS is faster than that of TEOS. This difference in rate was also confirmed upon hydrolysis of TMOS at room temperature with 0.01 M HCl for 30 minutes by which smooth silica spheres were obtained; under the same reaction conditions with TEOS, a clear solution was obtained. Thus, variation of the reaction conditions leads to the formation of different morphologies of silica.

To determine whether the silica spheres were hollow or solid we microtomed the products, and studied the cross-section of a sample (Figure 5). The TEM image shows a smooth outer layer and small particles arranged inside to form a solid microsilica sphere.

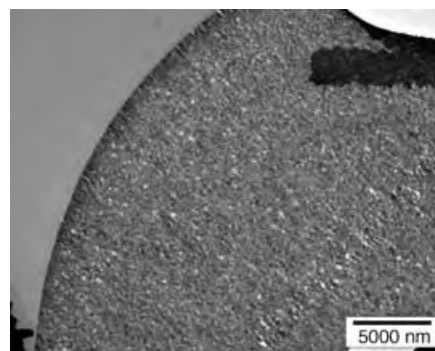


Figure 5. TEM image of the cross-section of single silica spheres.

Control hydrolysis reactions (1 h) in the absence of ionic liquids were also carried out to study the morphology of the hydrolyzed products of TMOS (0.5 mL) and TEOS (0.5 mL) with aqueous HCl solution (0.25 M) under vigorous stirring at room temperature as well as at 50°C. Clear solutions were observed for the reactions performed at room temperature, but silica gels were observed at 50°C, which suggests that the ionic liquid accelerates the rate of reaction at room temperature and plays an essential role in the formation of the spheres. A second control reaction (1 h) in the presence of the ionic liquid but in the absence of aqueous HCl solution was performed to study the morphology of the hydrolysis products of TMOS (0.5 mL) and TEOS (0.5 mL) under vigorous stirring at 50°C. In both cases, dustlike particles (1-micron particles as well as aggregates) were observed. These results demonstrate that in the presence of aqueous HCl solutions, the dustlike particles play a significant role by functioning as seeds for the formation of fully grown silica spheres. These dustlike silica particles tested positive for antibacterial activity (*E. coli*, Gram-negative). Reactions carried out for shorter periods of time and in the absence of aqueous HCl solution resulted in clear mixtures, which substantiate the roles of the acidic solution and the reaction time. The above findings demonstrate the necessity of the ionic liquid and the aqueous HCl solution under vigorous stirring in order to develop silica microspheres.

It is known that silica acts as an insulator and that the conducting properties of silica can be improved through doping with electrolytes.^[23] Interestingly, with our synthetic route to the silica microspheres, the entrapped molecules of the ionic liquid induce their conducting properties at room temperature.^[24] The bulk conductivity as determined by impedance measurements for pristine 1-butyl-3-methylimidazolium hexafluorophosphate $\text{BIM}^+\text{PF}_6^-$ is reported as $3.8 \times 10^{-2} \text{ Scm}^2 \text{ mol}^{-1}$.^[19] The conductivity of the silica spheres was also measured by the impedance method over the frequency range 5–50 kHz at room temperature and 60°C. The conductivities observed at 5 kHz at different time intervals are 7.87×10^{-6} , 8.50×10^{-6} (72 h), and $9.83 \times 10^{-6} \text{ Scm}^{-2}$ (144 h) at room temperature. The conductivity decreased after 192 h to $6.77 \times 10^{-6} \text{ Scm}^{-2}$. Thus, the presence of entrapped ionic liquid and water were needed to improve the conductive properties of our synthesized silica spheres. The observed increase in the conductivity with increasing time was due to adsorption of water molecules on the silica.^[25] The conductivity was found to increase with an increase in temperature, with values of 8.14×10^{-6} (194 h) and $9.76 \times 10^{-6} \text{ Scm}^{-2}$ (216 h) measured at 60°C. These results are interpreted as a result of the increased mobility of entrapped molecules of the ionic liquid.^[24]

The conductivity of the silica spheres will hopefully gain importance for their applicability in electrochemistry and sensors.^[26a–c] The conductivity is most probably due to a special oriented alignment of the molecules of ionic liquid along the surface. A detailed study of the conductivity of an individual silica sphere is in progress and will be reported soon. The current process for the synthesis of silica spheres in an ionic liquid has opened new directions and opportunities to explore their application in several fields, however more research has to be carried out to address the challenges that remain and to explore the importance of ionic liquids in other fields.

Experimental Section

In a typical synthesis, TMOS (0.5 mL, 0.516 g, 3.38 mmol; Aldrich Chemical Co, 99%) and $\text{BIM}^+\text{PF}_6^-$ (3 g, 0.01 mol; Aldrich Chemical Co., 96%; density = 1.37 g cm^{-3}) were stirred in a 15-mL teflon vessel for 1 min at room temperature to form a homogeneous transparent solution. Then, 0.01M aq. HCl (0.25 mL) was added under stirring. (Milli-Q water was used to prepare the acid solution and a 0.2- μm Whatman Anotop 25 filter was used for filtration). The reaction mixture was stirred vigorously at room temperature for 30 min and then quenched by the addition of acetone. The white spheres were separated by centrifuging at 9000 rpm for 10 min, and the product was washed with acetone several times to remove excess ionic liquid, then centrifuged at 9000 rpm for 10 min, and dried under vacuum for 24 h. The size of the silica spheres obtained ranged from 50 to 85 μm .

Received: April 27, 2005

Published online: September 13, 2005

Keywords: conducting materials · hydrolysis · ionic liquids · silica · synthesis design

- [1] W. Wang, B. H. Gu, L. y. Liang, W. A. Hamilton, *J. Phys. Chem. B* **2003**, *107*, 12113.
- [2] J. E. G. J. Wijnhoven, W. L. Vos, *Science* **1998**, *281*, 802.
- [3] P. Jiang, J. F. Bertone, V. L. Colvin, *Science* **2001**, *291*, 453.
- [4] O. D. Velev, E. W. Kaler, *Adv. Mater.* **2000**, *12*, 531.
- [5] Y. N. Xia, B. Gates, Z. Y. Li, *Adv. Mater.* **2001**, *13*, 409.
- [6] G. L. Messing, W. T. Minehan, *J. Ceram. Soc. Jpn.* **1991**, *99*, 1036.
- [7] W. Stöber, A. Fink, E. Bohn, *J. Colloid Interface Sci.* **1968**, *26*, 62.
- [8] T. Ogihara, H. Nakajima, T. Yanagawa, N. Ogata, K. Yoshida, N. Matsusita, *J. Am. Ceram. Soc.* **1991**, *74*, 2263.
- [9] a) J. H. Jean, T. A. Ring, *Langmuir* **1986**, *2*, 251; b) K. Chen, Y. Chen, *J. Sol-Gel Sci. Technol.* **2003**, *27*, 111.
- [10] T. Ogihara, N. Mizutani, M. Kato, *Ceram. Int.* **1987**, *13*, 35.
- [11] H. Nishimori, M. Tatsumisago, T. Minami, *J. Sol-Gel Sci. Technol.* **1997**, *9*, 25.
- [12] B. Karmakar, G. De, D. Ganguli, *J. Non-Cryst. Solids* **2000**, *272*, 119.
- [13] D. S. Jacob, V. Kahlenberg, K. Wurst, L. A. Solovyov, I. Felner, L. Shomon, H. Gottlieb, A. Gedanken, *Eur. J. Inorg. Chem.* **2005**, 522.
- [14] T. Nakashima, N. Kimizuka, *J. Am. Chem. Soc.* **2003**, *125*, 6386.
- [15] E. R. Cooper, C. D. Andrews, P. S. Wheatley, P. B. Webb, P. Wormald, R. Morris, *Nature* **2004**, *430*, 1012.
- [16] Y. Zhou, M. Antonietti, *Adv. Mater.* **2003**, *15*, 1452.
- [17] Y. Zhou, M. Antonietti, *Chem. Commun.* **2003**, 2564.
- [18] B. G. Trewyn, C. M. Whitman, V. S.-Y. Lin, *Nano Lett.* **2004**, *4*, 2139.
- [19] H. Tokuda, K. Hayamizu, K. Ishii, Md. A. B. H. Susan, M. Watanabe, *J. Phys. Chem. B* **2004**, *108*, 16593.
- [20] H. L. Ngo, K. LeCompte, L. Hargens, A. B. McEwen, *Thermochim. Acta* **2000**, *357*, 97.
- [21] J. D. Holbrey, K. R. Seddon, *J. Chem. Soc. Dalton Trans.* **1999**, 2133.
- [22] C. M. Gordon, J. D. Holbrey, A. R. Kennedy, K. R. Seddon, *J. Mater. Chem.* **1998**, *8*, 2627.
- [23] M. Tatsumisago, H. Honjo, Y. Sakai, T. Minami, *Solid State Ionics* **1994**, *74*, 105.
- [24] M. Morita, T. Shirai, N. Yoshimoto, M. Ishikawa, *J. Power Sources* **2005**, *139*, 351.
- [25] H. Li, M. Nogami, *Adv. Mater.* **2002**, *14*, 912.
- [26] a) Y. G. Lee, T. C. Chou, *Bio. Bioelect.* **2004**, *20*, 33; b) M. C. Buzzeo, C. Hardacre, R. G. Compton, *Anal. Chem.* **2004**, *76*, 4583; c) R. Wang, S. Hoyano, T. Ohsaka, *Chem. Lett.* **2004**, *33*, 6.

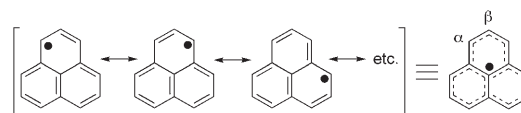
DOI: 10.1002/anie.200502303

Synthesis, Intermolecular Interaction, and Semiconductive Behavior of a Delocalized Singlet Biradical Hydrocarbon**

Takashi Kubo,* Akihiro Shimizu, Maki Sakamoto, Mikio Uruichi, Kyuya Yakushi, Masayoshi Nakano, Daisuke Shiomi, Kazunobu Sato, Takeji Takui, Yasushi Morita, and Kazuhiro Nakasuji*

Most Kekulé hydrocarbons, which are characterized by a closed-shell electron configuration, accommodate their π electrons only in bonding orbitals and consequently are quite stable. In general, such stable Kekulé compounds have wide HOMO–LUMO gaps, and their electronic structures in the ground state can be well described by a single electron configuration $^1\Phi_0$. In contrast, some Kekulé compounds, such as quinoid hydrocarbons, have a relatively small HOMO–LUMO gap, which leads to an admixture of a doubly excited configuration $^1\Phi_{H,H\rightarrow L,L}$ into the ground configuration $^1\Phi_0$ in the description of the ground state.^[1a] As a result of this configuration mixing, the repulsion between the two electrons is taken into consideration and the two electrons with antiparallel spins are permitted to correlate in separate spaces. This electron correlation diminishes the bond covalency and increases the biradical character of the system.

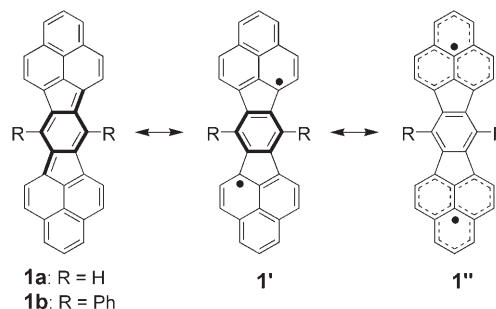
The quinoidal Kekulé hydrocarbons are highly reactive and easily dimerize or polymerize at normal temperature.^[2] Such behavior is strongly reminiscent of radical reactivity. Related interesting reactivity has been observed for pleiadene, which dimerizes readily even at 110 K through a two-step cycloaddition or a symmetry-forbidden $[4s+4s]$ concerted process.^[1] The latter process is predicted to be related to the $^1\Phi_{H,H\rightarrow L,L}$ configuration. The biradical-like reactivity implies strong intermolecular interactions in the ground state, which would be a most remarkable feature for singlet biradical compounds. However, great difficulties are encountered in estimating the intermolecular interaction due to the instability. Although kinetically stabilized singlet biradicals such as Chichibabin's hydrocarbon have been isolated and characterized, sterically crowded structures mask the effective intermolecular π – π interactions.^[3] To estimate the intermolecular interactions, thermodynamic stabilization of the singlet biradicals would be required instead of kinetic stabilization. One of the most effective means of thermodynamic stabilization is delocalization of unpaired electrons. Herein, we focus on phenalenyl radical as a highly spin-delocalized molecule (Scheme 1). The radical is known to be



Scheme 1. Spin delocalization of phenalenyl radical.

persistent, and many related compounds have been isolated.^[4] We report the synthesis and isolation of a singlet biradical utilizing the highly spin delocalizing property of the phenalenyl radical. Furthermore, we present the intermolecular interaction and solid-state properties of a delocalized singlet biradical.^[5]

For the purpose of estimating the intermolecular interaction, we focused on a closed-shell conjugated system that contains the phenalenyl radical structure.^[6] Hydrocarbon **1a** consists of *p*-quinodimethane and two phenalenyl moieties.^[7] The quinoid Kekulé compound **1a** would resonate well with biradical structure **1a'** as a result of gaining the aromatization energy of the central six-membered ring (Scheme 2). The unpaired electrons emerging on the terminal carbon atoms of the *p*-quinodimethane moiety can delocalize on the phenalenyl rings (structure **1a''**). This consideration of resonance



Scheme 2. Resonance structures of **1**.

[*] Dr. T. Kubo, A. Shimizu, M. Sakamoto, Prof. Dr. Y. Morita, Prof. Dr. K. Nakasuji
Department of Chemistry
Graduate School of Science
Osaka University
Machikaneyama 1-1, Toyonaka, Osaka 560-0043 (Japan)
Fax: (+81) 6-6850-5395
E-mail: kubo@chem.sci.osaka-u.ac.jp
nakasuji@chem.sci.osaka-u.ac.jp

Dr. M. Uruichi, Prof. Dr. K. Yakushi
Department of Applied Molecular Science
Institute for Molecular Science
Okazaki 444-8585 (Japan)

Prof. Dr. M. Nakano
Department of Materials Engineering Science
Graduate School of Engineering Science
Osaka University
Toyonaka, Osaka 560-8531 (Japan)

Prof. Dr. D. Shiomi, Prof. Dr. K. Sato, Prof. Dr. T. Takui
Departments of Chemistry and Materials Science
Graduate School of Science
Osaka City University
Sumiyoshi-ku, Osaka 558-8585 (Japan)

[**] This work was supported by a Grant-in-Aid for Scientific Research on Priority Areas (No. 17550034, and Area No. 769, Proposal No. 15087202) from the Ministry of Education, Culture, Sports, Science, and Technology (MEXT), Japan.



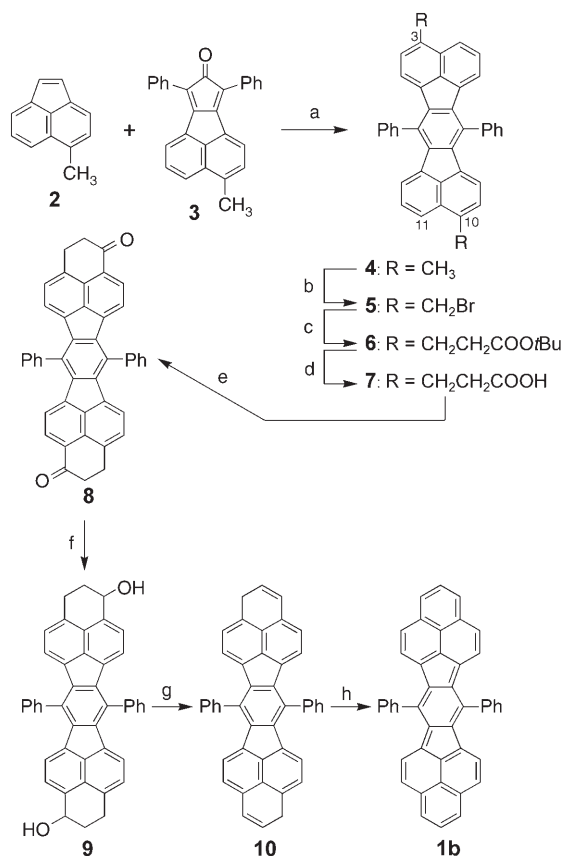
Supporting information for this article is available on the WWW under <http://www.angewandte.org> or from the author.

structures leads to the conclusion that **1a** would be a thermodynamically stabilized singlet biradical. Quantum chemical calculations on **1a** strongly support the biradical character. A CASSCF(2,2)/6-31G//RB3LYP/6-31G** calculation gave an admixture of 15% of the doubly excited configuration $^1\Phi_{H,H\rightarrow L,L}$ into the singlet ground state. A broken-symmetry UB3LYP/6-31G** calculation also gave a similar biradical character; the natural orbital occupation number (NOON)^[8] of the LUMO was 0.37, and the spin contamination $\langle S^2 \rangle = 0.65$ (see Supporting Information). Thus, the singlet biradical character of **1a** is estimated to be 30–37%.

The synthetic procedure for the diphenyl derivative **1b** is shown in Scheme 3. The key intermediates **4** were obtained as a mixture of 3,10- and 3,11-dimethyl isomers by Diels–Alder reaction between **2** and **3** followed by decarbonylation and dehydration with *p*-chloranil. Individual isomers were not isolated for further transformations because the two isomers can lead to a single compound **1b**. Bis(propionic acid) derivatives **7** were obtained in three steps. Intramolecular Friedel–Crafts cyclization of the acyl chloride of **7** with AlCl_3 gave diketone **8**, which was reduced and subsequently

dehydrated to afford dihydro compound **10**. Dehydrogenation of **10** with *p*-chloranil provided the target compound **1b** as dark green plates. Compound **1b** was found to be stable in the solid state at room temperature, even in air.

As mentioned above, a small HOMO–LUMO gap is an essential factor for a singlet biradical electronic structure. The small HOMO–LUMO gap of **1b** was confirmed by electrochemical and optical methods. The cyclic voltammogram of **1b** gave an irreversible oxidation wave ($E_{\text{pa}}^{\text{ox}} = +0.08$ V vs ferrocene/ferrocenyl couple (Fc/Fc^+)) and a quasi-reversible reduction wave ($E_{1/2}^{\text{red}} = -1.07$ V vs Fc/Fc^+), which led to an electrochemical energy gap (HOMO–LUMO gap) of approximately 1.1 eV. The electronic absorption spectrum of **1b** in CH_2Cl_2 showed an intense low-energy band at 746 nm ($\epsilon = 178000$, $f = 0.649$). An INDO/S configuration interaction (CI) calculation suggested that the low-energy band could be assigned to a symmetry-allowed B_{3u} HOMO–LUMO transition. These findings indicate an optical energy gap of 1.66 eV for **1b**. The small HOMO–LUMO gap is ascribable to the nonbonding character of the frontier orbitals, as shown in Figure 1. The frontier orbitals of **1a** retain the nonbonding



Scheme 3. Synthesis of **1b**. a) Xylene, reflux, 83%; b) NBS, benzoyl peroxide (cat.), benzene, reflux, 99%; c) CH_3COOtBu , LDA, THF, $-78 \rightarrow -30^\circ\text{C}$, 66%; d) *p*-toluenesulfonic acid (cat.), benzene, reflux, 98%; e) 1) $(\text{COCl})_2$, reflux; 2) AlCl_3 , CH_2Cl_2 , $-78 \rightarrow -30^\circ\text{C}$, 88%; f) NaBH_4 , $\text{EtOH} + \text{CH}_2\text{Cl}_2$, room temperature, 95%; g) *p*-toluenesulfonic acid (cat.), benzene, reflux, 89%; h) *p*-chloranil, benzene, reflux, 99%. NBS = *N*-bromosuccinimide, LDA = lithium diisopropylamide.

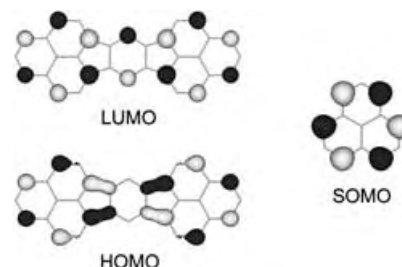


Figure 1. The HOMO and LUMO of **1a**, and the SOMO of the phenalenyl radical.

character of the singly occupied molecular orbital (SOMO) of the phenalenyl radical. The most important feature is a quite large spatial overlap between HOMO and LUMO. The large spatial overlap and small energy gap are responsible for the admixture of a doubly excited configuration into the ground state, that is, a singlet biradical character.^[9]

Recrystallization of **1b** from a solution in chlorobenzene gave relatively large single crystals ($1 \times 0.3 \times 0.2$ mm³), including chlorobenzene molecules of solvation, which were analyzed by X-ray diffraction. As shown in Figure 2, **1b** forms one-dimensional (1D) chains with a slipped stacking arrangement and an average π – π distance of 3.137 Å,^[10] which is substantially shorter than the van der Waals contact of carbon atoms (3.4 Å). The π – π overlap was found only on phenalenyl moieties in the same arrangement as that of the phenalenyl radical dimer.^[4a] The staggered stacking of the radical dimer maximizes the SOMO–SOMO interaction between radicals, and the overlap of SOMOs is one of the crucial attractive bonding interactions.^[11] The dominant attractive force for **1b** would originate from the bonding interaction between the unpaired electrons that appear in the singlet biradical canonical structure **1b'**, in addition to a general attractive dispersion force. In the valence bond description, the interaction of the two unpaired electrons could be repre-

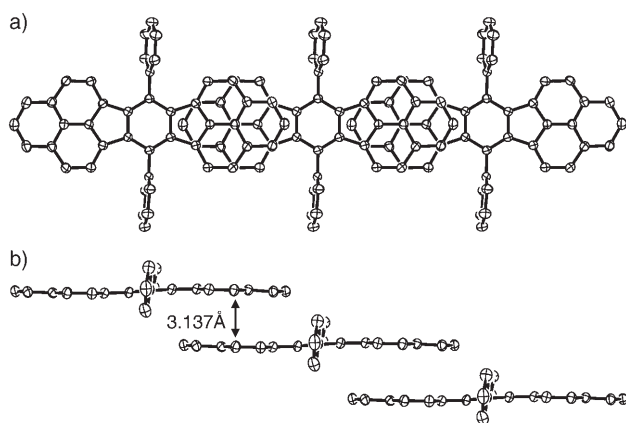
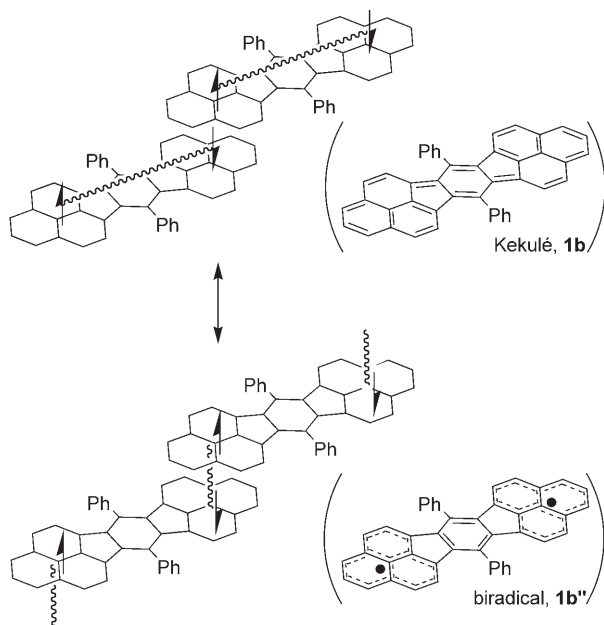


Figure 2. Crystal structure of **1b**. Hydrogen atoms and the solvated chlorobenzene molecule are omitted for clarity.

sented by the resonance between intra- and intermolecular interaction, as shown schematically in Scheme 4. Thus, a strong intermolecular covalent character is a characteristic



Scheme 4. Resonance structures of intra- and intermolecular interactions of two unpaired electrons in the 1D chain. Wavy lines denote electron–electron interactions. In parentheses: best descriptions of the electronic structure in each resonance state.

feature of singlet biradicals. A restricted Hartree–Fock (RHF) plus CI method is useful for understanding the intermolecular covalency. For simplicity, the following discussion focuses on a dimer of **1b**, which is the smallest unit of the 1D chain. As described above, **1b** has a biradicaloid ground state with 15% of the doubly excited configuration as a result of the configuration interaction between HOMO and LUMO. The interaction between the partially occupied HOMOs would lead to the partially occupied “HOMO” of the dimer (1.4e), as shown in Figure 3. The partial occupancy suppresses a four-electron repulsion generally arising from

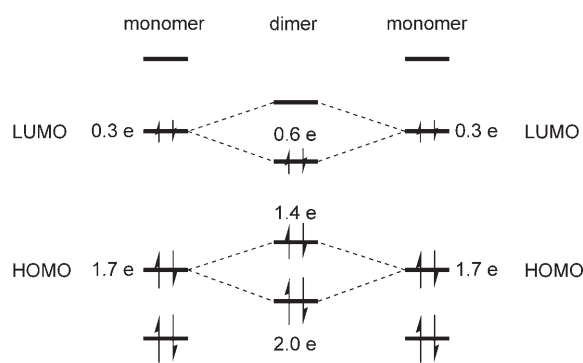


Figure 3. Schematic drawing of the molecular orbital interaction of dimeric **1a** through the doubly excited configuration ${}^1\Phi_{H,H\rightarrow L,L}$.

the interaction between fully occupied orbitals. The LUMO–LUMO interaction would also contribute to stabilization of the system, because a newly formed “LUMO” of the dimer, which is more strongly stabilized than the original LUMO, can accommodate 0.6 electrons.^[12] The presence of the well-stabilized intermolecular orbitals would indicate intermolecular covalency.

The electrical conductivity of a compressed pellet of doubly recrystallized **1b** was measured by a two-probe method. The room-temperature conductivity was $1.0 \times 10^{-5} \text{ S cm}^{-1}$ with an activation energy of 0.3 eV at 200–300 K (see Supporting Information). The conductivity of a single crystal along the stacking direction (*b* axis) was slightly larger ($5.0 \times 10^{-5} \text{ S cm}^{-1}$ at room temperature) than that of the powdered sample. To the best of our knowledge, **1b** shows the best single-component conductivity among structurally well-defined hydrocarbon molecules in a neutral state.^[13] To estimate the electronic structure in the solid state, we performed band-structure calculations using extended Hückel theory (EHT) on the crystal structure of **1b**.^[14] The dispersions of valence and conduction bands were found to be substantial (0.54 and 0.51 eV, respectively) along the π – π stacking direction (*Y*), whereas only slight dispersions were seen along *X* (Figure 4).^[15] The dispersion along *Z* (0,0,1/2) should be very small as a result of the presence of chlorobenzene of solvation and bulky phenyl groups of **1b**. Thus, the single crystal of **1b** has an ideal 1D electronic structure with large bandwidths in both HOMO and LUMO, which might lead to ambipolar field-effect transistor (FET) properties.^[16] The large bandwidths are ascribed to the short π – π distance (due to the singlet biradical electronic structure) and efficient HOMO–HOMO and LUMO–LUMO overlap (due to a π -overlap arrangement similar to the SOMO–SOMO overlap of the phenalenyl radical dimer).

Solid **1b** gave an extraordinary lower energy shift in the optical spectrum compared to the solution spectrum (Figure 5). The optical conductivity spectra were obtained by Kramers–Kronig transformation of the reflection spectra. Polarization of light along the stacking direction (*b* axis) on the (001) face gave an intense peak at 6804 cm^{-1} ($f = 1.9$), whereas no distinct conductivity was recognized below 13000 cm^{-1} along the *a* axis. The oscillator strength along the *b* axis is almost three times larger than that of the intense

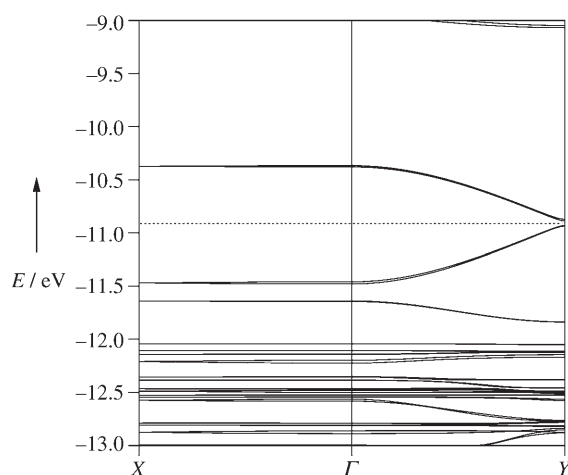


Figure 4. Band structure of **1b** near the Fermi level along X (1/2,0,0) and Y (0,1/2,0). The dotted line represents the Fermi level.

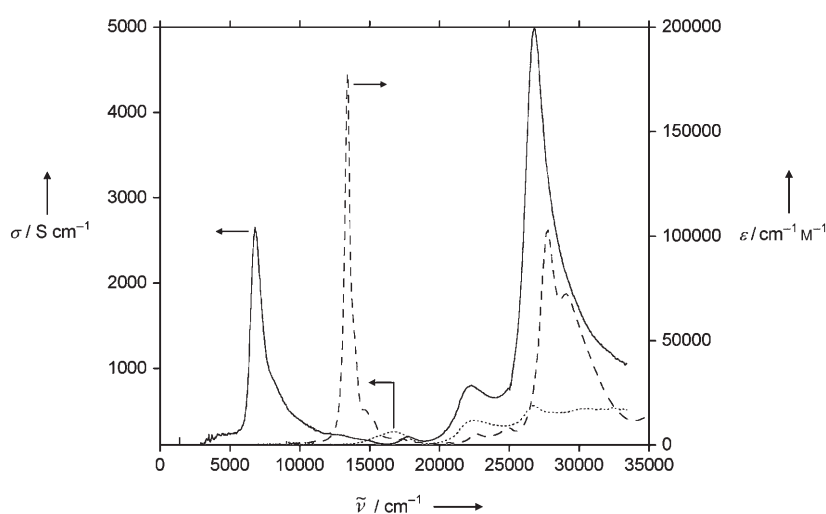


Figure 5. Optical spectra of **1b**. Absorption spectrum in CH_2Cl_2 (----) and optical conductivities obtained with light polarized along the *a* (.....) and *b* axes (—).

absorption at 746 nm (13400 cm^{-1}) in solution; that is, the intense band at 6804 cm^{-1} is derived from the lower energy shift of the HOMO–LUMO transition of the monomer due to the intermolecular interactions. The *J*-type stacking of the 1D chain of **1b** seems to imply that the traditional transition dipole–dipole interaction (exciton resonance) is responsible for the lower energy shift. At short intermolecular distances, however, an electron-exchange interaction (charge resonance, i.e., intermolecular HOMO–LUMO transition) becomes important for intermolecular interactions.^[17] Of course, the exchange mechanism requires adequate orbital overlap. The orbital overlap between the HOMO and LUMO of solid **1b** is almost identical to the SOMO–SOMO overlap of the phenalenyl radical dimer, and consequently a large overlap integral is expected. Thus, the origin of the lower energy shift should be the configuration interaction between the exciton resonance and the charge resonance states.

Finally, we describe thermal excitation to a triplet state of **1b**. The weak intramolecular coupling between two unpaired

electrons leads to a decreased singlet–triplet energy gap ($\Delta E_{\text{S-T}}$). The ^1H NMR spectrum of **1b** exhibited severe line broadening of ring protons except for those of phenyl groups at room temperature. On cooling, progressive line sharpening was observed (see Supporting Information). Similar results have been obtained for a tetra-*tert*-butyl derivative of **1a**, which had a $\Delta E_{\text{S-T}}$ value of 20.4 kJ mol^{-1} based on solid-state ESR measurements.^[18] Equilibrium with the thermally accessible triplet state would cause line broadening of the NMR signals for **1b**. Magnetic measurements on **1b** showed a gradual increase of χT values above 200 K (see Supporting Information). Using the Bleaney–Bowers equation^[19] in the singlet–triplet model gave an estimated $\Delta E_{\text{S-T}}$ value of 2200 K (18 kJ mol^{-1}), which is in good agreement with the result of the ESR measurement.

In conclusion, we have successfully isolated and characterized a biradicaloid hydrocarbon with moderate singlet biradical character. In contrast to most closed-shell compounds, the singlet biradical compound shows strong inter- and intramolecular interactions between two unpaired electrons. Such intermolecular covalency causes substantially close π – π contact, and consequently wide valence and conduction bands are established. Thus, phenalenyl-based singlet biradicals will open up a new avenue for highly delocalized 1D electronic structures.

Experimental Section

The detailed synthetic procedure for **1b** is described in the Supporting Information.

Crystal data for **1b**: $\text{C}_{56}\text{H}_{34}\text{Cl}_2$, $M_r = 777.73$, monoclinic, space group $P2_1/a$ (no. 14), $a = 16.382(14)$, $b = 9.869(8)$, $c = 24.09(2)\text{ Å}$, $\beta = 97.065(2)^\circ$, $V = 3865(5)\text{ Å}^3$, $Z = 4$, $\mu(\text{MoK}\alpha) = 0.209\text{ cm}^{-1}$, $\rho_{\text{calcd}} = 1.337\text{ g cm}^{-3}$, $R1(wR2) = 0.0691(0.1868)$ for 523 parameters and 6604 unique reflections with $I > 2\sigma(I)$, GOF = 1.135. Data were collected on Rigaku/MSC Mercury CCD diffractometer ($\text{MoK}\alpha$ radiation, $\lambda = 0.71069\text{ Å}$) at 200 K. The structure was solved by direct methods

and refined with full-matrix least-squares techniques (teXsan). CCDC 275077 contains the supplementary crystallographic data for this paper. These data can be obtained free of charge from the Cambridge Crystallographic Data Centre via www.ccdc.cam.ac.uk/data_request/cif.

Received: July 1, 2005

Published online: September 13, 2005

Keywords: charge transfer · conjugation · density functional calculations · radicals · semiconductors

- [1] a) J. Kolc, J. Michl, *J. Am. Chem. Soc.* **1973**, 95, 7391–7401; b) J. Kolc, J. Michl, *J. Am. Chem. Soc.* **1970**, 92, 4147–4148; c) J. Downing, V. Dvořák, J. Kolc, A. Manzara, J. Michl, *Chem. Phys. Lett.* **1972**, 17, 70–73.
- [2] M. S. Platz in *Diradicals* (Ed.: W. T. Borden), Wiley, New York, **1982**, pp. 195–258.

- [3] L. K. Montgomery, J. C. Huffman, E. A. Jurczak, M. P. Grendze, *J. Am. Chem. Soc.* **1986**, *108*, 6004–6011, and references therein.
- [4] Isolation and characterization of phenalenyl radicals: a) K. Goto, T. Kubo, K. Yamamoto, K. Nakasuji, K. Sato, D. Shiomi, T. Takui, M. Kubota, T. Kobayashi, K. Yakusi, J. Ouyang, *J. Am. Chem. Soc.* **1999**, *121*, 1619–1620; b) Y. Morita, T. Ohba, N. Haneda, S. Maki, J. Kawai, K. Hatanaka, K. Sato, D. Shiomi, T. Takui, K. Nakasuji, *J. Am. Chem. Soc.* **2000**, *122*, 4825–4826; c) P. A. Koutentis, Y. Chen, Y. Cao, T. P. Best, M. E. Itkis, L. Beer, R. T. Oakley, A. W. Cordes, C. P. Brock, R. C. Haddon, *J. Am. Chem. Soc.* **2001**, *123*, 3864–3871; d) Y. Morita, T. Aoki, K. Fukui, S. Nakazawa, K. Tamaki, S. Suzuki, A. Fuyuhiko, K. Yamamoto, K. Sato, D. Shiomi, A. Naito, T. Takui, K. Nakasuji, *Angew. Chem.* **2004**, *116*, 6503–6506; *Angew. Chem. Int. Ed.* **2002**, *41*, 1793–1796; e) S. Zheng, J. Lan, S. I. Khan, Y. Rubin, *J. Am. Chem. Soc.* **2003**, *125*, 5786–5791; for experimental and theoretical magnetic interaction of phenalenyl radical, see: f) K. Fukui, K. Sato, D. Shiomi, T. Takui, K. Itoh, K. Gotoh, T. Kubo, K. Yamamoto, K. Nakasuji, A. Naito, *Synth. Met.* **1999**, *103*, 2257–2258; g) K. Fukui, K. Sato, D. Shiomi, T. Takui, K. Itoh, T. Kubo, K. Gotoh, K. Yamamoto, K. Nakasuji, A. Naito, *Mol. Cryst. Liq. Cryst.* **1999**, *334*, 49–58; h) Y. Takano, T. Taniguchi, H. Isobe, T. Kubo, Y. Morita, K. Yamamoto, K. Nakasuji, T. Takui, K. Yamaguchi, *J. Am. Chem. Soc.* **2002**, *124*, 11122–11130; phenalenyl-based molecular conductors: i) X. Chi, M. E. Itkis, B. O. Patrick, T. M. Barclay, R. W. Reed, R. T. Oakley, A. W. Cordes, R. C. Haddon, *J. Am. Chem. Soc.* **1999**, *121*, 10395–10402; j) M. E. Itkis, X. Chi, A. W. Cordes, R. C. Haddon, *Science* **2002**, *296*, 1443–1445; k) S. K. Pal, M. E. Itkis, R. W. Reed, R. T. Oakley, A. W. Cordes, F. S. Tham, T. Siegrist, R. C. Haddon, *J. Am. Chem. Soc.* **2004**, *126*, 1478–1484.
- [5] Recent advances in singlet biradicals: a) D. R. McMasters, J. Wirz, *J. Am. Chem. Soc.* **2001**, *123*, 238–246; b) D. Scheschke-witz, H. Amii, H. Gornitzka, W. W. Schoeller, D. Bourissou, G. Bertrand, *Science* **2002**, *295*, 1880–1881; c) D. Herebian, K. E. Wieghardt, F. Neese, *J. Am. Chem. Soc.* **2003**, *125*, 10997–11005; d) D. Scheschke-witz, H. Amii, H. Gornitzka, W. W. Schoeller, D. Bourissou, G. Bertrand, *Angew. Chem.* **2004**, *116*, 595–597; *Angew. Chem. Int. Ed.* **2004**, *43*, 585–587; e) M. Bendikov, H. M. Duong, K. Starkey, K. N. Houk, E. A. Carter, F. Wudl, *J. Am. Chem. Soc.* **2004**, *126*, 7416–7417; f) M. Abe, W. Adam, W. T. Borden, M. Hattori, D. A. Hrovat, M. Nojima, K. Nozaki, J. Wirz, *J. Am. Chem. Soc.* **2004**, *126*, 574–582.
- [6] a) K. Nakasuji, T. Kubo, *Bull. Chem. Soc. Jpn.* **2004**, *77*, 1791–1801, and references therein; b) Short π – π contact due to a singlet biradical electronic structure: T. Kubo, M. Sakamoto, M. Akabane, Y. Fujiwara, K. Yamamoto, M. Akita, K. Inoue, T. Takui, K. Nakasuji, *Angew. Chem.* **2004**, *116*, 6636–6641; *Angew. Chem. Int. Ed.* **2004**, *43*, 6474–6479.
- [7] A referee suggests that the *s*-indacene core should also contribute to the biradical character of **1a** by application of a previously described theoretical consideration: J. R. Dias, *J. Chem. Inf. Comput. Sci.* **2003**, *43*, 1494–1501; we thank the referee for this valuable suggestion.
- [8] Y. Jung, M. Head-Gordon, *ChemPhysChem* **2003**, *4*, 522–525, and references therein.
- [9] C. R. Flynn, J. Michl, *J. Am. Chem. Soc.* **1974**, *96*, 3280–3288.
- [10] Short atom–atom distances: C4–C26 3.088(3), C14–C24 3.101(3), C6–C28 3.160(4), C12–C22 3.104(3), C8–C30 3.167(3), C10–C20 3.121(3), C16–C32 3.224(3) Å; atom-numbering schemes are shown in the Supporting Information.
- [11] D. Small, V. Zaitsev, Y. Jung, S. V. Rosokha, M. Head-Gordon, J. K. Kochi, *J. Am. Chem. Soc.* **2004**, *126*, 13850–13858.
- [12] The RB3LYP/6-31G** calculation on **1a** dimer produces HOMO–HOMO and LUMO–LUMO interactions instead of the HOMO–LUMO interaction which is generally formed in electron donor–acceptor charge-transfer complexes; see Supporting Information.
- [13] Hydrocarbon semiconductors: a) H. Inokuchi, N. Matsubara, Y. Maruyama, E. Clar, *Nature* **1965**, *205*, 64; b) Y. Maruyama, H. Inokuchi, Y. Harada, *Bull. Chem. Soc. Jpn.* **1963**, *36*, 1193–1198; c) I. Shiro-tani, H. Inokuchi, S. Minomura, *Bull. Chem. Soc. Jpn.* **1966**, *39*, 386–390; see also: M. Bendikov, F. Wudl, D. F. Perepichka, *Chem. Rev.* **2004**, *104*, 4891–4945.
- [14] The RHF calculation without CI cannot describe the accurate solid-state electronic structure of singlet biradicals; however, we could not obtain a solution maintaining the singlet biradical character using ab initio programs.
- [15] Extended Hückel molecular orbital (EHMO) calculation is known to underestimate HOMO–LUMO energy gaps of molecules, and consequently band structure calculations based on EHT tend to give band gaps smaller than experimental gaps of semiconductors or insulators. In the case of **1b**, the EHMO calculation afforded a HOMO–LUMO gap of 0.511 eV and a band gap of 0.047 eV, which were substantially smaller than the experimentally estimated values.
- [16] C. D. Dimitrakopoulos, P. R. L. Malenfant, *Adv. Mater.* **2004**, *16*, 99–117.
- [17] G. D. Scholes, K. P. Ghiggino, *J. Phys. Chem.* **1994**, *98*, 4580–4590.
- [18] K. Ohashi, T. Kubo, T. Masui, K. Yamamoto, K. Nakasuji, T. Takui, Y. Kai, I. Murata, *J. Am. Chem. Soc.* **1998**, *120*, 2018–2027.
- [19] B. Bleaney, K. D. Bowers, *Proc. R. Soc. London Ser. A* **1952**, *214*, 451–465.

Metallaboranes

DOI: 10.1002/anie.200502212

Borane Mimics of Classic Organometallic Compounds: $[(\text{Cp}^*\text{Ru})\text{B}_8\text{H}_{14}(\text{RuCp}^*)]^{0,+}$, Isoelectronic Analogues of Dinuclear Pentalene Complexes**

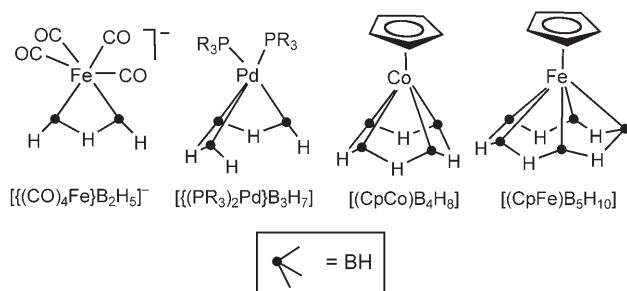
Sundargopal Ghosh, Bruce C. Noll, and Thomas P. Fehlner**

Like carbon, the element boron in combination with hydrogen displays rich catenation chemistry.^[1] In contrast to carbon, its structural chemistry must reflect a more complex electronic structure which is associated with having to satisfy the same number of valence functions as carbon with one less electron per atom.^[2] Hence, one fascinating aspect of metal-

[*] Dr. S. Ghosh, Dr. B. C. Noll, Prof. T. P. Fehlner
Department of Chemistry and Biochemistry
University of Notre Dame
Notre Dame, IN 46556 (USA)
Fax (+1) 574-631-6652
E-mail: sghosh@nd.edu
fehlner.1@nd.edu

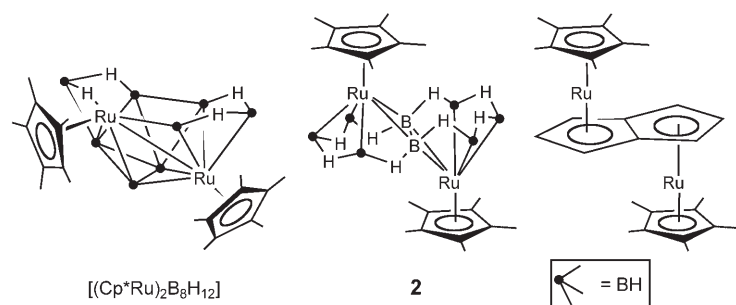
[**] This work was supported by the National Science Foundation (CHE-0304008), $\text{Cp}^* = \eta^5\text{-C}_5\text{Me}_5$.

laborane chemistry is that several classic organometallic complexes that defined fundamental structural and bonding paradigms for the field are mimicked by isoelectronic metallaborane analogues.^[3] In most cases, the geometric structures can be generated by simply replacing C with B plus B-H-B bridging hydrogen atoms and/or net charge to match the valence electron count. Thus, for analogues of polyhaptic π complexes^[4] there are: $[(\text{CO})_4\text{Fe}(\eta^2\text{-C}_2\text{H}_4)]$ versus $[(\text{CO})_4\text{Fe}]\text{B}_2\text{H}_5^-$,^[5] $[(\text{PR}_3)_3\text{ClPd}(\eta^3\text{-C}_3\text{H}_5)]$ versus $[(\text{PR}_3)_3\text{Pd}]\text{B}_3\text{H}_7$,^[6] $[(\eta^5\text{-C}_5\text{H}_5)\text{Co}(\eta^4\text{-C}_4\text{H}_4)]$ versus $[(\eta^5\text{-C}_5\text{H}_5)\text{Co}]\text{B}_4\text{H}_8$,^[7] and $[(\eta^5\text{-C}_5\text{H}_5)\text{Fe}(\eta^5\text{-C}_5\text{H}_5)]$ versus $[(\eta^5\text{-C}_5\text{H}_5)\text{Fe}]\text{B}_5\text{H}_{10}$ ^[8] (Scheme 1).



Scheme 1. A selection of metallaboranes with borane fragments that are analogous to π ligands in organometallic complexes. Cp = $\eta^5\text{-C}_5\text{H}_5$.

Related are polyhaptic organic ligands capable of binding two metal centers. In these complexes the metal-metal interactions are of significant interest particularly when mixed-valence organometallic complexes may be formed.^[9] In particular, the chemistry of dinuclear metal complexes of pentalene, C_8H_6 , (Scheme 2) has been developed extensively



Scheme 2. Schematic drawings of the structures of polyhedral $[(\text{Cp}^*\text{Ru})_2\text{B}_8\text{H}_{12}]$, pentalene analogue **2**, and $[\text{Cp}^*\text{Ru}(\text{pentalene})\text{RuCp}^*]$.

because the strength of the electronic coupling between the two metal centers can be larger than that found in cationic Werner complexes such as the Creutz-Taube ion.^[10–12] Herein, we present the synthesis and characterization of borane analogues of $[\text{Cp}^*\text{Ru}(\text{pentalene})\text{RuCp}^*]^{0,+}$ (Cp* = $\eta^5\text{-C}_5\text{Me}_5$) where the monocation is a mixed-valence complex.

Recently we have shown that the reaction of $[(\text{Cp}^*\text{Ru})_2\text{B}_3\text{H}_9]$ with $\text{BH}_3\cdot\text{THF}$ leads to metallaboranes containing six, eight, and ten boron atoms.^[13,14] The ten boron atom cluster has two colorless isomeric forms, one with an exo-cluster borane atom on a Ru_2B_9 cluster framework. This species was shown to be an intermediate on the path to

the second isomer which has a Ru_2B_{10} cluster framework. Given the importance of this isomer pair in defining the broad mechanistic outlines of the cluster-building process, we have investigated this system more extensively for the presence of additional colorless products that may be intermediates in the cluster-building process. This approach has led to the isolation of $[(1\text{-Cp}^*\text{Ru})\text{B}_5\text{H}_{10}]$ (**1**; in which the Cp^*Ru fragment occupies the 1-position of the BH cage) and $[(\text{Cp}^*\text{Ru})\text{B}_8\text{H}_{14}]$ (**2**). Metallaborane **2** converts into the isomer pair $[(\text{Cp}^*\text{Ru})_2\text{B}_{10}\text{H}_{16}]$ ^[14] on heating in the presence of $\text{BH}_3\cdot\text{THF}$ showing that it is indeed another intermediate in the cluster-building process.

Although separated initially from the other reaction products as a mixture, both **1** and **2** are insensitive to air and moisture and can be separated by careful thin-layer chromatography on the laboratory bench by using UV light for detection. Mass spectrometric data for **1** yield the composition $\text{C}_{10}\text{H}_{25}\text{RuB}_5$ which suggests a molecular formulation of $\text{Cp}^*\text{RuB}_5\text{H}_{10}$. In addition to 15 Cp* protons, the ^1H NMR spectrum of **1** shows one resonance at $\delta = 2.71$ ppm arising from five terminal hydrogen atoms and one resonance at $\delta = -4.05$ ppm for five bridging hydrogen atoms. In the ^{11}B NMR spectrum of **1**, the high symmetry is confirmed by the observation of a single doublet at $\delta = -0.6$ ppm which collapses to a sharp singlet upon proton decoupling. No suitable crystals for structure determination were obtained but, given the similarity of the spectroscopic data to those of $[(\text{CpFe})\text{B}_5\text{H}_{10}]$ (Scheme 1),^[8] **1** is proposed to be 1-ruthenahexaborane, a borane analogue of ruthenacene.

The mass spectroscopic data for **2** showed a molecular formula two mass units higher than that of red $[(\text{Cp}^*\text{Ru})_2\text{B}_8\text{H}_{12}]$, a compound which has structure based on a $\text{B}_{10}\text{H}_{14}$ skeleton which has undergone one diamond-square-diamond (dsd) rearrangement associated with its low formal skeletal electron pair (sep) count of 12 (Scheme 2).^[13] With 13 sep does **2** have the structure of $[(\text{Cp}^*\text{Ru})_2\text{B}_8\text{H}_{14}]$ but without the dsd rearrangement? In fact, the three resonances in the intensity ratio 2:2:4 found in the ^{11}B NMR spectrum would be consistent with such a structure if the metals occupied the 2,4-positions. However, the six terminal and eight B-H-B bridging hydrogen atoms suggested by the ^1H NMR spectrum are not consistent with this cluster shape and heating **2** in the absence of $\text{BH}_3\cdot\text{THF}$ did not produce $[(\text{Cp}^*\text{Ru})_2\text{B}_8\text{H}_{14}]$.

A solid-state structure determination of **2** (Scheme 2 and Figure 1)^[15] revealed an unexpected geometry. It could be viewed as two ruthenaborane cages of **1**, fused in a transoid fashion with two common boron atoms, to give a planar B_8 fragment, and eight B-H-B bridges on the eight available edges. It is, in fact, a structure analogous to those of isoelectronic dinuclear pentalene complexes $[\text{Cp}^*\text{M}(\text{C}_8\text{H}_6)\text{MCp}^*]$, M = Fe, Ru (Scheme 2).^[10,16] In **2** the ruthenium atoms are bonded symmetrically to the Cp* ligands (Ru-C 2.04 Å av) but the binding to the five-membered boron rings is not quite symmetric (Ru-B 2.15 Å av versus Ru-BH 2.10 Å av). This asymmetry is also found in structures of dinuclear pentalene complexes.^[10]

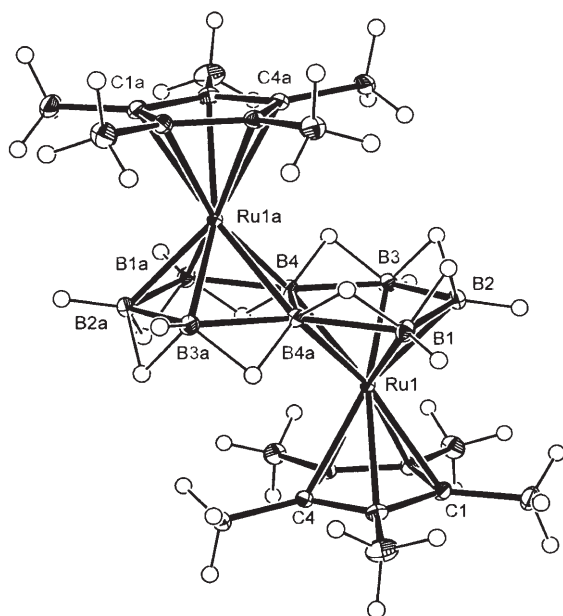
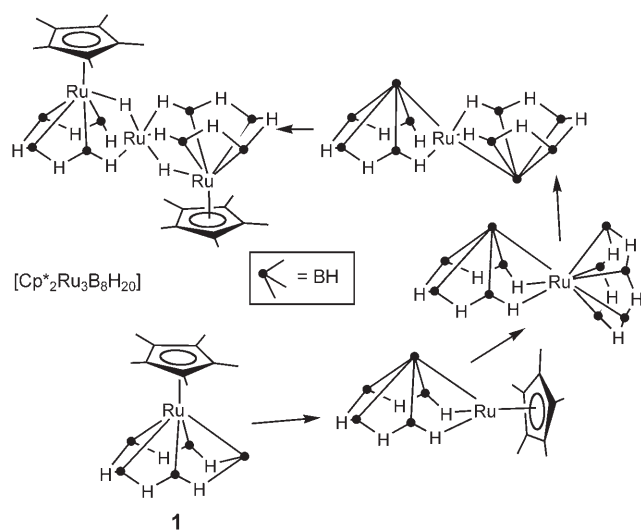


Figure 1. X-ray structure of **2**. Selected interatomic distances [Å] and angles [°]: Ru1-B1 2.1115(10), Ru1-B2 2.1076(10), Ru1-B3 2.1067(10), Ru1-B4 2.1491(9), B1-B2 1.8204(15), B2-B3 1.8233(15), B3-B4 1.8274(14), B1a-B4 1.8232(14), B1-B4a 1.8232(14), B4-B4a 1.8198(18); B2-Ru1-B1 51.12(4), B2-Ru1-B4 85.39(4), B3-Ru1-B4a 88.55(4), B2-B1-B4a 104.84(7), Ru1-B4-Ru1a 129.94(4), B3-B4-Ru1a 136.54(6), B4a-B4-B3 109.22(8), B1a-B4-B3 141.75(7).

There is another known ruthenaborane related to both **1** and **2**. It has the formula $\text{Cp}^*_2\text{Ru}_3\text{B}_8\text{H}_{20}$ and a structure corresponding to *commo*-[$\{1-(\text{Cp}^*\text{Ru})(\mu\text{-H})\text{B}_4\text{H}_9\}_2\text{Ru}$] as shown in Scheme 3.^[17] Viewed as a pair of fused pentagonal pyramidal clusters with one common atom, it is a structural variation on **2**. But a relationship to **1** follows from the retro isolobal synthesis shown in Scheme 3 based on the following connections: $\{\text{Cp}^*\text{Ru}\} + \text{H}$ is equivalent to BH ; $\{1-(\text{Cp}^*\text{Ru})\text{B}_5\text{H}_{10}\}$ is an analogue of ruthenacene; and $\{2-$



Scheme 3. A retro-isolobal analysis showing the relationship between ruthenacene analogue **1**, and the *commo*-cluster $[\text{Cp}^*_2\text{Ru}_3\text{B}_8\text{H}_{20}]$.

$(\text{Cp}^*\text{Ru})\text{B}_5\text{H}_{10}$ is an accessible isomer of $\{1-(\text{Cp}^*\text{Ru})\text{B}_5\text{H}_{10}\}$. Hence, although the production of the pentalene analogue **2** from a ruthenaborane cluster and its conversion into a larger ruthenaborane cluster may seem bizarre, the analysis in Scheme 3 is a reminder that forms analogous to organometallic complexes are just one structural guise available to chameleonic metallaboranes.

In addition to conceptual connections to pentalene dinuclear complexes, there are real chemical connections to **2**. In its cyclic voltammogram, $[\text{Cp}^*\text{Ru}(\text{C}_8\text{H}_6)\text{RuCp}^*]$ exhibits one reversible oxidation wave and an irreversible wave at 0.29 V higher potential.^[10] The irreversible behavior is attributed to the oxidation reaction of the Cp^* ligand and is analogous to the behavior of $[\text{Cp}^*_2\text{Ru}]$ on oxidation.^[18] Likewise **2** exhibits two successive one-electron oxidations separated by approximately 0.8 V. The first redox event $2^0/2^+$ is quasireversible, but the second oxidation $2^+/2^{2+}$ is not reversible as shown by the lack of a return wave. The larger ΔE observed for **2** compared to the pentalene analogue may result from a stronger interaction between the metal centers as well as more extensive delocalization in the mixed-valence 2^+ form.^[19] If so, the greater delocalization found for the borane analogue of $[\text{Cp}^*\text{Ru}(\text{C}_8\text{H}_6)\text{RuCp}^*]^+$ is consistent with a better match of frontier-orbital energies of the borane and ruthenium fragment energies than of the pentalene and ruthenium fragment energies.

The B_8H_{14} fragment of **2** is a true analogue of the $\eta^5\text{-}\eta^5$ -pentalene ligand. However, comparison with two related ruthenaboranes both containing eight boron atoms, $[(\text{Cp}^*\text{Ru})_2\text{B}_8\text{H}_{14}]$ and *commo*-[$\{1-(\text{Cp}^*\text{Ru})(\mu\text{-H})\text{B}_4\text{H}_9\}_2\text{Ru}$], reveals once more the versatility of the boron/hydrogen element combination in accommodating the electronic requirements of a set of metal fragments.

Experimental Section

1 and 2: $[(\text{Cp}^*\text{Ru})_2\text{B}_3\text{H}_9]$ (0.19 g, 0.369 mmol) in toluene (25 mL) was stirred with 10 equivalent of $\text{BH}_3\cdot\text{THF}$ (3.7 mL, 3.69 mmol) for 20 h at 100°C. The solvent was removed in vacuo; the residue was extracted in hexane/ CH_2Cl_2 , (2:8, v/v) and the filtrate was purified by chromatography on silicagel TLC plates. Elution with pure hexane yielded **1** (0.004 g, 4%) and **2** (0.05 g, 26%).

Selected data for **1**: MS (FAB) $\text{P}^+(\text{max})$ 293 (isotopic pattern for 1Ru and 5B atoms), exact mass; calcd for $[\text{C}_{10}\text{H}_{24}\text{B}_5\text{Ru}]^+$ fragment ion as weighted average of isotopomers lying within the instrument resolution 302.1465, obsd 302.1483. ^{11}B NMR (C_6D_6 , 22°C, 128 MHz): $\delta = -0.6$ ppm (d, $J_{\text{B-H}} = 151$ Hz, 5B); ^1H NMR (C_6D_6 , 22°C, 400 MHz): $\delta = 2.71$ (partially collapsed quartet (pcq), 5BH), 1.80 (s, 15H, Cp*), -4.05 ppm (br, 5B-H-B); IR (hexane): $\tilde{\nu} = 2502\text{w}$, 2428w cm^{-1} (B-H). Several attempts to grow X-ray quality crystals of **1** failed. All attempts generated very thin hair-like crystals that gave data sets with no viable solution.

Selected data for **2**: MS (FAB) $\text{P}^+(\text{max})$ 567 (isotopic pattern for 2Ru and 8B atoms), exact mass; calcd for $[\text{C}_{20}\text{H}_{36}\text{B}_8\text{Ru}_2]^+$ fragment ion as weighted average of isotopomers lying within the instrument resolution 569.1727, obsd 569.1702; ^{11}B NMR (C_6D_6 , 22°C, 128 MHz): $\delta = 11.2$ (d, $J_{\text{B-H}} = 147$ Hz, 2B), -0.7 (d, $J_{\text{B-H}} = 143$ Hz, 2B-Hr), -3.1 ppm (d, $J_{\text{B-H}} = 148$ Hz, 4B-Hr); ^1H NMR (C_6D_6 , 22°C, 400 MHz): $\delta = 3.03$ (pcq, 4BH), 2.41 (pcq, 2BH), 1.68 (s, 30H, 2Cp*), 0.02 (pcq, 4B-H-B); -4.44 ppm (pcq, 4B-H-B); IR (hexane): $\tilde{\nu} = 2508$ w, 2478w cm^{-1} (B-Hr); elemental analysis calcd (%) for $\text{C}_{20}\text{H}_{44}\text{B}_8\text{Ru}_2$, C 41.91, H 7.74; found: C 40.95, H 7.42.

The cyclic voltammetry of **2** was carried out in CH₂Cl₂/toluene (8.5:1.5 v/v) as scan rates of 50–100 mV s⁻¹ using a Pt working electrode, Pt plate counter electrode, and Pt wire pseudo reference electrode, and 0.1 M Bu₄NPF₆ as supporting electrolyte. Under these conditions the ferrocene/ferrocenium ion couple appears at 0.46 V. For a scan from -0.8 to 0.6 V at 50 mV s⁻¹, the 2⁰/2⁺ couple is found at 0.17 V ($E_{1/2}$ = 0.258, 0.085 V) and in a scan from -0.2 to 1.2 V at 50 mV s⁻¹, the difference in the half wave potentials for 2⁰ → 2⁺ and 2⁺ → 2²⁺ is 0.76 V.

Received: June 23, 2005

Published online: September 20, 2005

Keywords: boranes · metallaboranes · pentalenes · ruthenium

- [1] N. N. Greenwood, A. Earnshaw, *Chemistry of the Elements*, Pergamon, Oxford, **1984**.
- [2] W. N. Lipscomb, *Boron Hydrides*, Benjamin, New York, **1963**.
- [3] *Inorganometallic Chemistry* (Ed.: T. P. Fehlner), Plenum, New York, **1992**.
- [4] C. Elschenbroich, A. Salzer, *Organometallics*, VCH, New York, **1989**.
- [5] T. J. Coffy, G. Medford, J. Plotkin, G. J. Long, J. C. Huffman, S. G. Shore, *Organometallics* **1989**, 8, 2404.
- [6] L. J. Guggenberger, A. R. Kane, E. L. Muettterties, *J. Am. Chem. Soc.* **1972**, 94, 5665.
- [7] T. L. Venable, E. Sinn, R. N. Grimes, *J. Chem. Soc. Dalton Trans.* **1984**, 2275.
- [8] R. Weiss, R. N. Grimes, *J. Am. Chem. Soc.* **1977**, 99, 8087.
- [9] C. Le Vanda, D. O. Cowan, C. Leitch, K. Bechgaard, *J. Am. Chem. Soc.* **1974**, 96, 6788.
- [10] J. M. Manriquez, M. D. Ward, W. M. Reiff, J. C. Calabrese, N. L. Jones, P. J. Carroll, E. E. Brunel, J. S. Miller, *J. Am. Chem. Soc.* **1995**, 117, 6182.
- [11] M. T. Garland, J.-Y. Saillard, I. Chávez, B. Oëlckers, J. M. Manriquez, *J. Mol. Struct.* **1977**, 39, 199.
- [12] C. Creutz, H. Taube, *J. Am. Chem. Soc.* **1973**, 95, 1086.
- [13] S. Ghosh, A. M. Beatty, T. P. Fehlner, *Angew. Chem.*, **2003**, 115, 4826; *Angew. Chem. Int. Ed.* **2003**, 42, 4678.
- [14] S. Ghosh, B. C. Noll, T. P. Fehlner, *Angew. Chem.*, **2005**, 117, 2976; *Angew. Chem. Int. Ed.* **2005**, 44, 2916.
- [15] Crystal structure data for **2** (C₂₀H₄₄B₈Ru₂): Crystal size, 0.36 × 0.27 × 0.11 mm³, triclinic, space group: *P* $\bar{1}$. Unit cell dimensions, a = 8.6697(1), b = 10.9546(1), c = 14.3313(2) Å, α = 110.559(1), β = 95.017(1), γ = 94.021(1)°; Z = 2, ρ_{calcd} 1.508 Mg m⁻³. Final R indices [$I > 2\sigma(I)$] R_1 = 0.0175, wR_2 = 0.0426, R indices (all data) R_1 = 0.0208, wR_2 = 0.0460. Goodness-of-fit on F^2 1.130. Crystals were examined under light hydrocarbon oil. Cell parameters were determined using reflections harvested from three sets of 20 0.3° ω scans and refined using 9065 reflections with $I \geq 10\sigma(I)$ and $2.37^\circ \leq \theta \leq 36.44^\circ$ from the entire data collection. The asymmetric unit consists of two half-molecules; each is completed by inversion. All non-hydrogen atoms were refined with parameters for anisotropic thermal motion. CCDC-275048 (**2**) contains the supplementary crystallographic data for this paper. These data can be obtained free of charge from the Cambridge Crystallographic Data Centre via www.ccdc.cam.ac.uk/data_request/cif.
- [16] E. E. Bunel, L. Valle, N. L. Jones, P. J. Carroll, C. Barra, M. Gonzalez, N. Munoz, G. Visconti, A. Aizman, J. M. Manriquez, *J. Am. Chem. Soc.* **1988**, 110, 6596.
- [17] X. Lei, M. Shang, T. P. Fehlner, *Angew. Chem.* **1999**, 111, 2186; *Angew. Chem. Int. Ed.* **1999**, 38, 1986.
- [18] U. Kölle, J. Grub, *J. Organomet. Chem.* **1985**, 289, 133.
- [19] D. E. Richardson, H. Taube, *J. Am. Chem. Soc.* **1983**, 105, 40.

The Hierarchical Architecture of Nacre and Its Mimetic Material**

Yuya Oaki and Hiroaki Imai*

Biomaterials fascinate many researchers because of their seemingly well-designed morphologies and hierarchical structures, which provide versatile properties.^[1–4] The architecture emerging from self-organization under ambient conditions provides a sophisticated model for materials science. The design of nanostructured materials with tailored morphologies, such as particles, rods, wires, tubes, and sheets, has attracted much interest because of their potential as functional materials. Controlled assembly into a three-dimensional architecture is an important challenge in the broad application of these materials.

Living organisms make up hierarchically organized materials through self-organization from precursors in aqueous solution, and scientists have developed various biomimetic techniques to prepare and organize building blocks.^[5,6] It is believed that an exquisite association of organic and inorganic compounds is required for the construction of bioinorganic superstructures; therefore, understanding the roles of macromolecules in the biomineralization process is a significant challenge in biomimetic materials chemistry. Recent findings, for example, the discovery of calcitic microlenses in brittlestars,^[2] chiral morphologies with stereochemical recognition,^[3] and the handedness of a snail's shell,^[4] bring out hidden elaborate structures and properties of biomaterials.

The nacreous layer (mother-of-pearl) has attracted the interest of researchers in a broad range of chemistry disciplines,^[7–25] especially in terms of its detailed structure,^[10,13,14] defects in different scales,^[10] incorporated macromolecules,^[15,16] mechanical strength,^[17,18] formation mechanisms,^[19,20] and mimetics.^[21–25] The macroscopic assembly and orientation of aragonite plates, 200–600-nm thick, has been well investigated.^[7–11] Although the presence of nanoscopic surface roughness and nanograins was implied in microscopic units reported previously,^[13,14,18] morphology and orientation

[*] Y. Oaki, Prof. H. Imai
Department of Applied Chemistry
Faculty of Science and Technology
Keio University
3-14-1 Hiyoshi, Kohoku-ku, Yokohama, 223-8522 (Japan)
Fax: (+81) 45-566-1551
E-mail: hiroaki@aplc.keio.ac.jp

[**] This work was supported by a Grant-in-Aid for Scientific Research (No. 15560587) and the 21st Century COE program "KEIO Life Conjugated Chemistry" from the Ministry of Education, Culture, Sports, Science, and Technology, Japan. We thank Mikimoto Pearl Museum for kindly providing nacre samples. Y. O. is grateful for a JSPS research fellowship for young scientists.



Supporting information for this article is available on the WWW under <http://www.angewandte.org> or from the author.

of the subunits were not clearly demonstrated. The emergent function resulting from an aragonite–biopolymer nanohybrid has never been investigated. An understanding of the real hierarchically organized structure in biominerals is required to advance to the next stage of chemistry, biology, and materials science.

In this study, we show that the nacreous layer is a three-level hierarchical architecture associated with two forms of oriented assembly (Figure 1). Electron microscope analysis determined the morphology of the nanobuilding blocks and their oriented assembly into platy units. Storage, an additional nanoscopic function leading to the incorporation of versatile organic dye molecules, is attributed to the aragonite–biopolymer nanohybrid. Our results are beneficial to the understanding of the overall architecture in the nacreous layer from the nanoscopic to the macroscopic scale. In addition, we demonstrate herein that an organized architecture similar to a real nacreous layer emerged from potassium sulfate (K_2SO_4) in the presence of poly(acrylic acid) (PAA; Figure 2).

Although the formation of mother-of-pearl requires several macromolecules, the two roles of PAA make up the mimetic architecture through oriented assembly. The K_2SO_4 –PAA composite also generates nanostorage for the inclusion of organic dye molecules, as is the case with the nacreous layer. To gain a more comprehensive understanding of the superstructures, we show the detailed structures of two hierarchical architectures that have “nanostorage” properties and discuss the mutual growth process associated with the two respective roles of each polymer. The results imply that the manipulation of crystals and polymers could lead to a novel type of excellent inorganic–organic hybrid composites under ambient conditions.

We investigated the nacreous layer (Japanese pearl oyster: *Pinctada fucata* and its artificially induced pearl) by using field-emission scanning electron microscopy (FESEM), field-emission transmission electron microscopy (FETEM) with selected-area electron diffraction (SAED), and powder X-ray diffraction (XRD). In previous studies,^[13,14] special techniques were used for FESEM and FETEM. In this study, fractured samples were used for the investigation of the actual nanoscopic structures and morphologies.^[26]

As shown in Figure 1 a–h, mother-of-pearl has a hierarchical structure, with tiers 1–3 mediating the oriented assembly in two ways. As previously reported,^[7–12] the layered structure (tier 1, Figure 1a,d) consists of aragonite plates (tier 2, Figure 1b,e) that are about 1–5- μm wide and 200–700-nm thick. The magnified FESEM image (Figure 1b) clearly indicates the presence of smaller components in each aragonite plate. We took an FETEM image of such a nanobuilding block, which had the pseudohexagonal habit of aragonite (tier 3, Figure 1c,f). The appearance of the nanobuilding blocks was neither attributable to the sample preparation process nor to radiation damage arising from FETEM as preceding FESEM clearly showed the presence of nanobuilding blocks in a plate (see Supporting Information). The high-resolution image on the fringe of the nanobuilding block shows a lattice spacing of 0.423 nm, which corresponds to the (110) plane of aragonite (see Supporting Information). The lengths of the nanobuilding blocks were in the range of

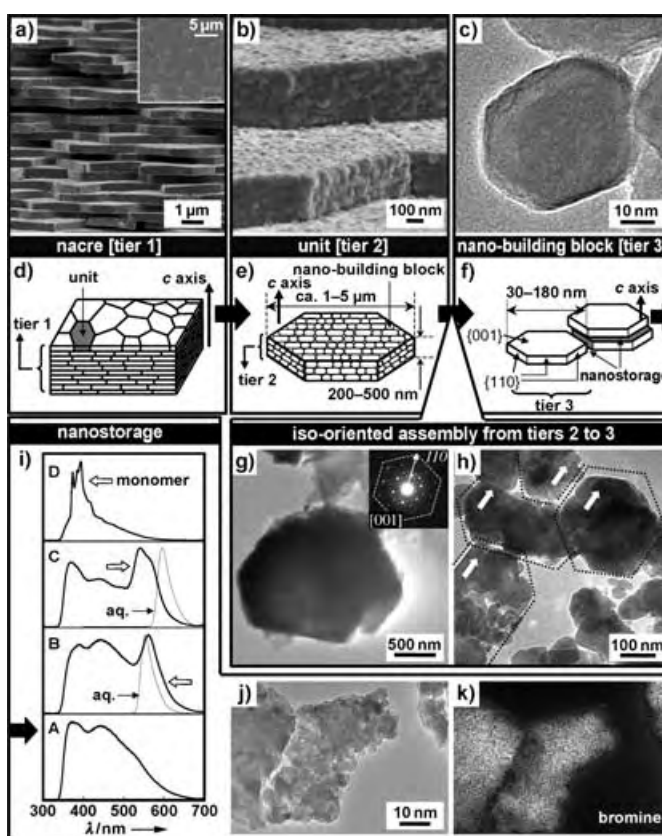


Figure 1. Hierarchically organized structure of the nacreous layer. a,b) FESEM and c) FETEM images of tiers 1–3; d–f) schematic representations of tiers 1–3; g, h) FETEM images with an SAED pattern indicating that the oriented assembly of the nanobuilding blocks make up a unit; i) photoluminescence spectra of comminuted powder of the nacreous layer (A) and with incorporation of EY (B), RB (C), and PY (D) with excitation at 290 nm; j, k) FETEM and corresponding EFTEM mapping image of the aragonite–biopolymer composite with the incorporation of EY. The bromine substituent in the EY molecule was mapped by using an energy-filtering technique.

20–180 nm, whereas the nanobuilding blocks in the mother-of-pearl shell of the oyster were smaller (see Supporting Information).

Oriented assembly mediated the formation of the hierarchical architecture. We consider the layered structure of mother-of-pearl (tier 1) to be an oriented assembly of the aragonite units (tier 2) along the *c* axis (Figure 1d), although the orientation of the *a* and *b* axes in a layer remains unclear. The mineral-bridges model of Schäffer et al. implies that the *a* and *b* axes should be perfectly oriented in all the layers in tier 1.^[19,20] However, DaiMasi and Sarikaya recently reported dark-field TEM images showing that the *a* and *b* axes were not perfectly aligned in all the layers.^[11] Our XRD analysis indicates that the layers are perpendicular to the *c* axis (Supporting Information). Consequently, the oriented assembly of the plates (tier 2) in the *c* axis make up the layered structure (tier 1). A single unit (tier 2) is also an oriented assembly of nanobuilding blocks (tier 3). The SAED pattern of the fragment of a unit is spotted, which indicates that the inside of a unit is a highly aligned assembly of nanobuilding blocks (Figure 1g). Aggregations of the nanobuilding blocks

that exhibit a hexagonal habit are commonly observed and are roughly arranged in the same direction (Figure 1 h). The peak broadening due to the crystallite-size effect is not recognizable in the XRD profiles of the powdered sample (Supporting Information). These results support the idea that the nanobuilding blocks (tier 3) generate a unit (tier 2) with oriented assembly. This concept has been implied in previous reports,^[13,14] but the presence of nanobuilding blocks and their assembly were unclear.

Powdered samples of the nacreous layer were immersed in ethanol solutions of organic dyes for one day. Anionic dyes, eosin Y (EY) and rhodamine B (RB), and a hydrophobic dye, pyrene (PY), were introduced into samples of the aragonite–biopolymer composite (see Supporting Information). The resulting powders were washed with acetone and dried at room temperature. Photoluminescence spectroscopy revealed an emission from each of the included dye molecules upon excitation with UV light (Figure 1 i, white arrows); these spectra show that the aragonite–biopolymer composite incorporated not only hydrophilic but also hydrophobic dyes, such as PY. The luminescence of the aragonite–biopolymer composite was blue, as previously reported (spectrum A, Figure 1 i).^[25] The aragonite–biopolymers with EY, RB, and PY incorporated gave strong orange, yellow, and blue luminescence, respectively (spectra B–D, Figure 1 i), which suggests that the EY molecules formed a J aggregate^[27] and the PY molecules were included as a monomer,^[28] whereas the inclusion of the RB molecules is unclear.

The incorporation of dye molecules suggests that an additional nanoscopic function resides in the aragonite–biopolymer composite. To investigate the dispersion and inclusion behavior of the EY molecules, we next performed FETEM with energy-filtered mapping (EFTEM) and electron energy-loss spectroscopy (EELS). The bromine substituents in the EY molecules were apparent in the EELS spectra (see Supporting Information) and EFTEM images (Figure 1 j,k). The images suggest that the EY molecules were homogeneously dispersed and incorporated into the aragonite–biopolymer composite on a nanoscopic scale. In the case of RB and PY, similar homogeneous incorporation leads to a strong emission. These results indicate that the aragonite–biopolymer composite behaves as a host for organic molecules. We have called this property “nanostorage”.

We found that a nacre-mimetic architecture with hierarchy and nanostorage was formed spontaneously from a precursor solution containing K_2SO_4 and PAA under ambient conditions (Figure 2). Herein, we clarify the structural analogy between the K_2SO_4 –PAA composite and natural mother-of-pearl. The layered morphology of the prepared material is composed of platy units (tier 1, Figure 2 a,d) that are about 0.5–1.0- μm thick (tier 2, Figure 2 b,e). The layered architecture (tier 1) is an oriented assembly of smaller units (tier 2) along the *b* axis (Figure 2 d,e); the top face of the layered structure and the unit were inferred to be the (010) face through XRD and SAED analyses. The *a* and *c* axes also align in the layered structure in tier 1, as was the case in our previous study.^[29] Further FETEM observation shows that nanobuilding blocks 20 nm in diameter (tier 3, Figure 2 c,f) made up a unit (tier 2, Figure 2 b,e). FESEM and FETEM

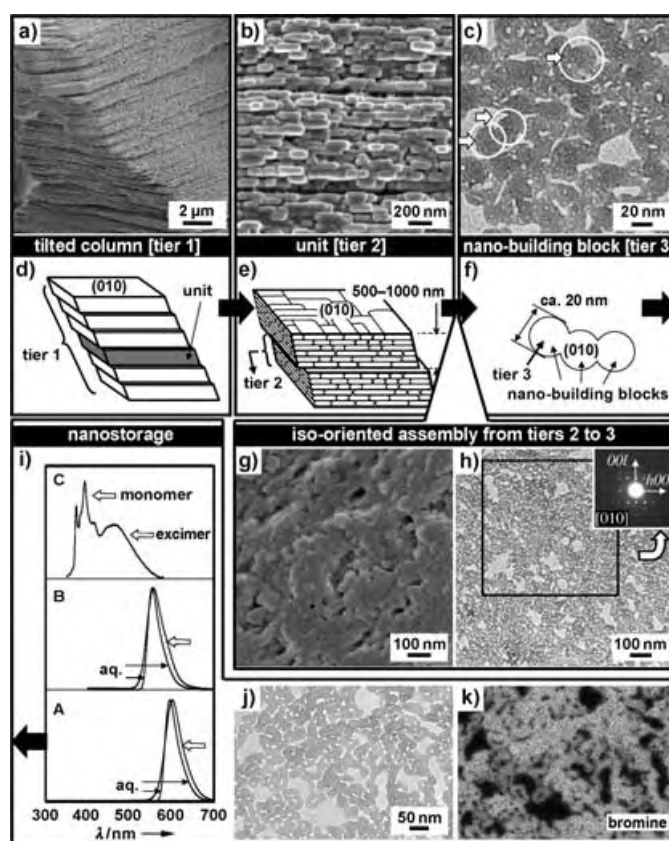


Figure 2. Hierarchically organized structure on a K_2SO_4 –PAA composite. a,b) FESEM and c) FETEM images of tiers 1–3; d–f) schematic representations of tiers 1–3; g,h) FESEM and EFTEM images with an SAED pattern indicating that the oriented assembly of the nanobuilding blocks make up a unit; i) photoluminescence spectra of the nacreous layer with the inclusion of RB (A), EY (B), and PY (C) with excitation at 290 nm; j,k) FETEM and corresponding EFTEM mapping image of the K_2SO_4 –PAA composite with the incorporation of EY, similar to those of the nacreous layer shown in Figure 1.

images show that the inside of a unit is an aggregate of nanobuilding blocks (Figure 2 g,h). The corresponding SAED pattern is spotted, which results from the oriented assembly of nanobuilding blocks (inset of Figure 2 h). Because peak broadening was not recognizable in the XRD profile of the powdered sample (Supporting Information), we concluded that the unit, like the nacreous layer, is an oriented assembly of nanobuilding blocks.

Dye molecules were homogeneously introduced by two methods. In the first method, EY and RB molecules were dissolved in the precursor solution and incorporated into a sample of the K_2SO_4 –PAA composite as the crystals grew. In the second method, the resultant K_2SO_4 –PAA composite was immersed in an ethanol solution of EY, RB, or PY. Photoluminescence spectra of samples with PY incorporated by the second method, EY incorporated by the first method, and RB also incorporated by the first method are given in Figure 2 i. On the basis of a comparison of these spectra with previously reported ones,^[27,30] we surmise that EY and RB molecules organize into a J aggregate within the K_2SO_4 –PAA compo-

sites (spectra A and B, Figure 2i). The incorporated PY molecules exhibit monomer and excimer emissions around 392 and 466 nm, respectively (spectrum C, Figure 2i).^[28] Results obtained by FETEM, EFTEM, and EELS also suggest the homogeneous incorporation of EY molecules on a nanoscopic scale (Figure 2j,k and Supporting Information). Therefore, we concluded that, as in the case of the nacreous layer, the K_2SO_4 -PAA composite has nanostorage properties.

The mutual growth process associated with the organic polymers lies in the hierarchical structures. Two types of polymers (types I and II) are required for the construction of these architectures (Figure 3a). Soluble and insoluble organic

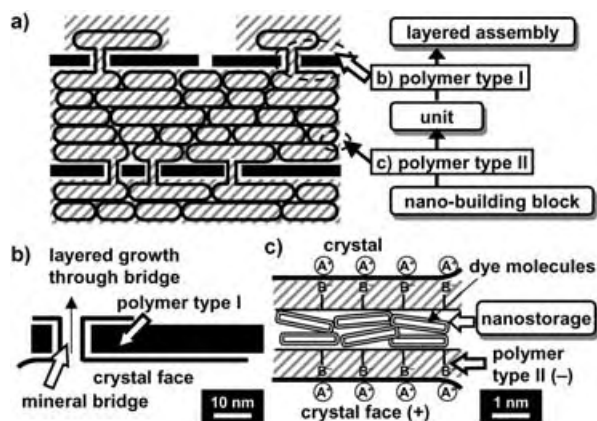


Figure 3. Schematic illustration of the mutual formation process for both the nacreous layer and the K_2SO_4 -PAA composite. a) Overview of the architectures associated with polymers I and II; b) the role of polymer I: growth inhibition and subsequent promotion through the formation of a mineral bridge by polymer II; c) the role of polymer II: the control of polymorphism, crystal size, and incorporation of organic molecules (nanostorage).

molecules that are incorporated into the nacreous layer play the two respective roles in the mineralization process.^[8–12,15,16] Since chitin and hydrophobic proteins (type I) form the layered sheets,^[19,20] a unit eventually forms that inhibits further growth. The next layer is induced by the formation of a mineral bridge through a small pore in the sheets (Figure 3b).^[19,20] The soluble acid proteins (type II) that consist of amino acids with carboxy and hydroxy groups strongly interact with carbonate crystals and produce miniaturized nanobuilding blocks, which have controlled polymorphism and orientation (Figure 3a,c). The nacre-mimetic K_2SO_4 -PAA architecture is similarly caused by the two respective roles of the PAA molecules.^[29] The strongly interacting PAA molecules (type II) form the nanobuilding blocks and direct the oriented assembly in tiers 2 and 3. The excess PAA molecules (type I) concurrently limit the diffusion of K^+ and SO_4^{2-} ions and inhibit further growth, so a platy unit is eventually formed (Figure 3b). However, growth is not perfectly inhibited by the PAA molecules. After the concentrations of K^+ and SO_4^{2-} ions recover around the surface of a platy unit, the next layer is mediated through the

formation of a mineral bridge. The mineral bridge can be seen in the magnified FESEM image.^[31]

In this way, the macroscopic periodic architecture is ascribed to the repetition of growth inhibition and subsequent restarting of the growth process. Switching between the two growth modes results in the generation of platy units and their layered assembly in tiers 1 and 2. An increase in the initial PAA concentration strongly affects the assembly of the units (tier 1),^[29] whereas the morphologies in the nanoscopic architectures in tiers 2 and 3 are not much influenced. These results support the two roles played by the PAA molecules in the mineralization process. Nanostorage for organic molecules is generated by electrostatic interactions between the crystals and type II polymer because the carbon main chains not related to any interaction with crystals provide an appropriate nanoscopic environment (Figure 3c). The emergence of a hierarchical architecture associated with the respective roles of polymers can be summarized as follows: type I polymer generates the miniaturized nanobuilding blocks, which strongly interact with the crystals, and subsequently mediates the oriented assembly in a platy unit. Since the consecutive growth is inhibited by type II polymer, a layered assembly is eventually produced through the formation of a mineral bridge. These two types of polymers are combined in the crystal-growth process of real mother-of-pearl and its mimetic material. Moreover, the hierarchy in a bioinorganic superstructure emerges from the two types of polymers that fulfill the respective roles in the mineralization process.

In summary, we have elucidated the hierarchical architecture in nacre and identified its ability to host organic molecules, which we have termed “nanostorage”. A nacre-mimetic architecture in terms of hierarchy, oriented assembly, and nanostorage has been generated through biomimetic crystallization of K_2SO_4 and PAA. This model case suggests that a hierarchy similar to that of nacre can be induced through an appropriate combination of inorganic crystals and organic polymers. The specific interaction of the two components generates the nanoscopic architecture, and the switching between the modes of growth leads to the formation of macroscopic structure. Furthermore, an improved understanding of real and mimetic biominerals holds promise for the further development of chemical, biological, and materials sciences.

Experimental Section

Nacreous layer: Samples of nacre comminuted by mortar were used without further washing. For the incorporation of organic dyes, nacreous powder (0.03 g) was immersed in an ethanolic solution of RB (0.2 mM), EY (0.2 mM), or PY (10 mM). The reaction mixture was subjected to ultrasound for 30 min, then left at 25 °C for 24 h. The resulting powder was isolated by centrifugation and washed with acetone.

K_2SO_4 -PAA composite: A stock solution (100 g dm⁻³) of K_2SO_4 (Kanto Chemical, 99.0%) was prepared with purified water (0.01 dm³) at room temperature. An aqueous solution of PAA (Aldrich Chemicals, 35 wt % aqueous solution, $M_w = 250000$) was added to the stock solution and the PAA concentration was adjusted to 10 g dm⁻³.^[29] After these materials had completely dissolved, the

sample bottle of the precursor solution was maintained at 25°C for several days without sealing. Crystal growth proceeded as water evaporated from the solution. The soluble dye molecules EY and RB were preliminarily dissolved in the stock solution and the concentration was adjusted to 0.2 mM. Introduction of PY was carried out by the same method as that described for the nacreous layer.

Characterization: The morphologies were observed by FESEM (FEI Sirion, operating at 2.0 kV) and FETEM (FEI Tecnai F20, equipped with an energy filter (Gatan Imaging Filter), operating at 200 kV). The samples for FESEM were coated by ultrathin osmium films (plasma osmium coater, HPC-1S, Vacuum Device). For FETEM, the powder samples were added in dehydrated ethanol or purified water and subjected to ultrasound for 30 min to ensure a good dispersion. The dispersion liquid was dropped on a copper grid. XRD was performed by using an X-ray powder diffractometer with $\text{Cu}_{\text{K}\alpha}$ radiation (XRD, Rigaku RAD-C, $2\theta/\theta$ scanning). The photoluminescence spectra were measured at room temperature by using a Shimadzu RF-5300PC spectrofluorophotometer with a xenon lamp (150 W) as the light source.

Received: January 28, 2005

Revised: June 26, 2005

Published online: September 15, 2005

Keywords: bioinorganic chemistry · biomimetic synthesis · crystal growth · organic–inorganic hybrid composites · self-assembly

- [1] a) S. Mann, *Biomimetic Mineralization*, Oxford University Press, Oxford, **2001**; b) S. Mann, *Angew. Chem.* **2000**, *112*, 3532–3548; *Angew. Chem. Int. Ed.* **2000**, *39*, 3392–3406; c) S. Weiner, L. Addadi, *J. Mater. Chem.* **1997**, *7*, 689–702; d) L. Addadi, S. Weiner, *Angew. Chem.* **1992**, *104*, 159–176; *Angew. Chem. Int. Ed. Engl.* **1992**, *31*, 153–169.
- [2] J. Aizenberg, A. Tkachenko, S. Weiner, L. Addadi, G. Hendler, *Nature* **2001**, *412*, 819–822.
- [3] a) R. M. Hazen, D. S. Sholl, *Nat. Mater.* **2003**, *2*, 367–374; b) L. Addadi, S. Weiner, *Nature* **2001**, *411*, 753–755, and references therein.
- [4] a) R. Ueshima, T. Asami, *Nature* **2003**, *425*, 679; b) Y. Shibasaki, M. Shimizu, R. Kuroda, *Curr. Biol.* **2004**, *14*, 1462–1467.
- [5] a) S. H. Yu, H. Cölfen, *J. Mater. Chem.* **2004**, *14*, 2124–2147; b) E. Dujardin, S. Mann, *Adv. Mater.* **2002**, *14*, 775–788; c) M. Antonietti, G. A. Ozin, *Chem. Eur. J.* **2004**, *10*, 28–41; d) H. Cölfen, S. Mann, *Angew. Chem.* **2003**, *115*, 2452–2468; *Angew. Chem. Int. Ed.* **2003**, *42*, 2350–2365, and references therein.
- [6] a) Y. Oaki, H. Imai, *J. Am. Chem. Soc.* **2004**, *126*, 9271–9275; b) H. Imai, Y. Oaki, *Angew. Chem.* **2004**, *116*, 1387–1392; *Angew. Chem. Int. Ed.* **2004**, *43*, 1363–1368; c) Y. Oaki, H. Imai, *Cryst. Growth Des.* **2003**, *3*, 711–716.
- [7] N. Watabe, *J. Ultrastruct. Res.* **1965**, *12*, 351.
- [8] T. Kato, A. Sugawara, N. Hosoda, *Adv. Mater.* **2002**, *14*, 869–877.
- [9] T. Kato, *Adv. Mater.* **2000**, *12*, 1543–1546.
- [10] M. Sarikaya, *Microsc. Res. Tech.* **1994**, *27*, 360–375.
- [11] E. DaiMasi, M. Sarikaya, *J. Mater. Res.* **2004**, *19*, 1471–1476.
- [12] P. Calvert, S. Mann, *J. Mater. Res.* **1988**, *3*, 3801–3815.
- [13] X. Li, W. C. Chang, Y. J. Chao, R. Wang, M. Chang, *Nano Lett.* **2004**, *4*, 613–617.
- [14] K. Takahashi, H. Yamamoto, A. Onoda, M. Doi, T. Inaba, M. Chiba, A. Kobayashi, T. Taguchi, T. Okamura, N. Ueyama, *Chem. Commun.* **2004**, 996–997.
- [15] B. A. Gotliv, L. Addadi, S. Weiner, *ChemBioChem* **2003**, *4*, 522–529.
- [16] Y. L. Kalisman, G. Falini, L. Addadi, S. Weiner, *J. Struct. Biol.* **2001**, *135*, 8–17.
- [17] A. P. Jackson, J. F. V. Vincent, R. M. Turner, *Proc. R. Soc. London Ser. B* **1988**, *234*, 415–440.
- [18] R. Z. Wang, Z. Suo, A. G. Evans, N. Yao, I. A. Aksay, *J. Mater. Res.* **2001**, *16*, 2485–2493.
- [19] L. Addadi, S. Weiner, *Nature* **1997**, *389*, 912–913.
- [20] T. E. Schäffer, C. Ionescu-Zanetti, R. Proksch, M. Fritz, D. A. Walters, N. Almqvist, C. M. Zaremba, A. M. Belcher, B. L. Smith, G. D. Stucky, D. E. Morse, P. K. Hansma, *Chem. Mater.* **1997**, *9*, 1731–1740.
- [21] N. Hosoda, A. Sugawara, T. Kato, *Macromolecules* **2003**, *36*, 6449–6452.
- [22] N. Hosoda, T. Kato, *Chem. Mater.* **2001**, *13*, 688–693.
- [23] A. Sugawara, T. Ishii, T. Kato, *Angew. Chem.* **2003**, *115*, 5457–5461; *Angew. Chem. Int. Ed.* **2003**, *42*, 5299–5303.
- [24] D. Volkmer, M. Harms, L. Gower, A. Ziegler, *Angew. Chem.* **2005**, *117*, 645–650; *Angew. Chem. Int. Ed.* **2005**, *44*, 639–644.
- [25] a) T. Miyoshi, Y. Matsuda, S. Akamatsu, *Jpn. J. Appl. Phys.* **1988**, *27*, 151–152; b) T. Miyoshi, Y. Matsuda, H. Komatsu, *Jpn. J. Appl. Phys.* **1987**, *26*, 578–581; c) T. Miyoshi, Y. Matsuda, H. Komatsu, *Jpn. J. Appl. Phys.* **1986**, *25*, 1606–1607.
- [26] We used the fractured and the powdered samples to avoid damaging and contaminating the sample during preparation for electron microscopy analysis; the special techniques, such as focused-ion-beam, ion-milling, and microtome were not used to avoid the artifacts.
- [27] a) E. Nicol, A. Moussa, J. L. Habib-Jiwan, A. M. Jonas, *J. Photochem. Photobiol. A* **2004**, *167*, 31–35; b) A. K. Dutta, C. Salesse, *Langmuir* **1997**, *13*, 5401–5408.
- [28] a) A. Thomas, S. Polarz, M. Antonietti, *J. Phys. Chem. B* **2003**, *107*, 5081–5087; b) T. Förster, *Angew. Chem.* **1969**, *81*, 364–374; *Angew. Chem. Int. Ed. Engl.* **1969**, *8*, 333–343.
- [29] Y. Oaki, H. Imai, *Langmuir* **2005**, *21*, 863–869.
- [30] F. del Monte, D. Levy, *J. Phys. Chem. B* **1998**, *102*, 8036–8041, and references therein.
- [31] The magnified FESEM images of the mineral bridge in K_2SO_4 -PAA are given in the Supporting Information.

Catalytic Enantioselective Friedel–Crafts Alkylation of Indoles with Nitroalkenes by Using a Simple Thiourea Organocatalyst**

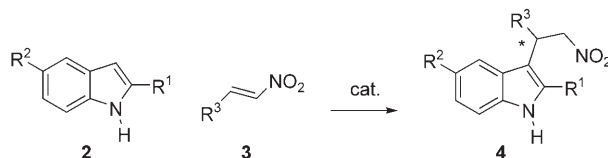
Raquel P. Herrera, Valentina Sgarzani, Luca Bernardi, and Alfredo Ricci*

The addition of aromatic substrates to electron-deficient alkenes, which in many respects may be considered a Friedel–Crafts type alkylation, is a key reaction in synthetic organic chemistry for the formation of new C–C bonds.^[1] Catalytic, enantioselective versions of this fundamental transformation have been reported,^[2] which use metal-based chiral complex catalysts^[3] or an imidazolidinone organocatalyst.^[4] Both catalysts are capable of activating α,β -unsaturated carbonyl compounds, through a Lewis acid/Lewis base interaction with the carbonyl moiety in the former case, or through the formation of an iminium ion intermediate in the latter case. In sharp contrast with these remarkable achievements in the enantioselective Friedel–Crafts alkylation of aromatic substrates with α,β -unsaturated carbonyl compounds, to the best of our knowledge there are no reports in which nitroalkenes are employed. Nevertheless nitroalkenes are very attractive Michael acceptors,^[5] since the nitro moiety is a strong electron-withdrawing group^[6] that can be readily transformed into a range of different functionalities.^[7]

The double hydrogen-bonding motif is becoming a powerful tool in organocatalysis for the activation of carbonyl groups and related compounds through weak hydrogen-bond interactions.^[8] Considering the various molecular scaffolds that have proved effective as bidentate hydrogen-bond donors, urea- and thiourea-derived catalysts are certainly amongst the most competent structures,^[9] and these are useful

for many enantioselective transformations.^[10] Accordingly, we have recently reported^[11] the Friedel–Crafts alkylation of aromatic and heteroaromatic compounds with nitroalkenes, which are activated by the bidentate hydrogen-bonding motif present in the bis[3,5-bis(trifluoromethyl)phenyl]thiourea first developed by Schreiner for the Diels–Alder reaction.^[9b,c]

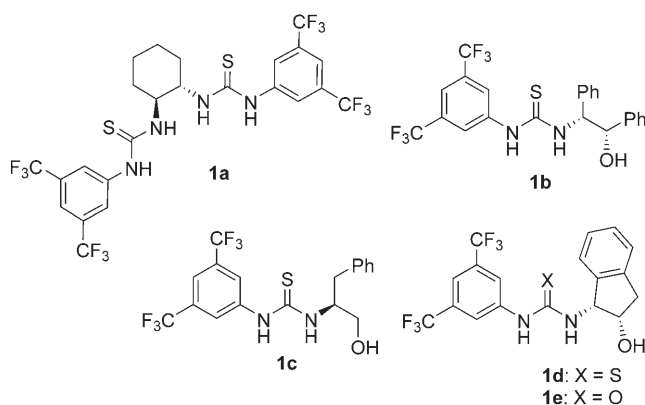
Herein we present our results on the use of simply obtainable thiourea organocatalysts for the first catalytic enantioselective Friedel–Crafts alkylation of indoles **2** with nitroalkenes **3** (Scheme 1). The indole skeleton is considered



Scheme 1. Addition of indole **2** to *trans*- β -nitrostyrene **3** to give access to optically active 2-indolyl-1-nitro derivatives **4**.

to be one of the “privileged” structures in pharmaceutical chemistry,^[4b,12] and the present method provides an easy and practical access to optically active 2-indolyl-1-nitro derivatives **4**. Taking into consideration the synthetic versatility of the nitro group, these compounds are useful intermediates for the synthesis of molecules of biological interest, such as tryptamines^[13] and 1,2,3,4-tetrahydro- β -carboline,^[14] containing the indole framework in their structures.

The addition of indole **2a** to *trans*- β -nitrostyrene **3a** was used as the test reaction to explore the feasibility of the enantioselective Friedel–Crafts alkylation of indoles with nitroalkenes catalyzed by chiral thiourea- and urea-based derivatives. Besides the known C₂-symmetric bis-thiourea **1a**,^[10c] we prepared and screened catalysts **1b–e**, which were easily obtained in one step and in nearly quantitative yields from the coupling reaction between 3,5-bis(trifluoromethyl)-phenyl isothiocyanate or isocyanate and the corresponding amino alcohols, both of which are commercially available. All



four thiourea-based organocatalysts **1a–d** were able to increase the reactivity of *trans*- β -nitrostyrene **3a** in the Friedel–Crafts alkylation reaction with indole **2a**, performed at room temperature in toluene (Table 1, entries 2–5), with

[*] V. Sgarzani, Dr. L. Bernardi, Prof. A. Ricci
Dipartimento di Chimica Organica “A. Mangini”
Università di Bologna
Viale Risorgimento 4, 40136, Bologna (Italy)
Fax: (+39) 051-209-3654
E-mail: ricci@ms.fci.unibo.it
Dr. R. P. Herrera^[†]
Dpto Química Orgánica
Universidad de Alicante
Apdo 99, 03080-Alicante (Spain)

[†] Current address:
Dipartimento di Chimica Organica “A. Mangini”
Università di Bologna
Viale Risorgimento 4, 40136, Bologna (Italy)

[**] We acknowledge financial support by the “Progetti FIRB”, by the National Project “Stereoselezione in Sintesi Organica Metodologie ed Applicazioni, 2003”, and by the EC-RTN project “Design, Analysis and Computation for Catalytic Organic Reactions”, contract HPRN-CT-2001-00172.

Supporting information for this article is available on the WWW under <http://www.angewandte.org> or from the author.

Table 1: Catalytic enantioselective Friedel–Crafts reaction of indole **2a** with *trans*- β -nitrostyrene **3a** in the presence of catalysts **1a–e** under different reaction conditions.^[a]

Entry	Catalyst	Solvent	<i>T</i> [°C]	<i>t</i> [h]	Conversion [%] ^[b]	<i>ee</i> [%] ^[c]
1	–	toluene	20	65	17	–
2	1a	toluene	20	64	40	7
3	1b	toluene	20	64	63	13
4	1c	toluene	20	45	41	13
5	1d	toluene	20	60	>95	35
6	1e	toluene	20	118	23	25
7	1d	THF	20	110	74	27
8	1d	CH ₂ Cl ₂	20	66	>95	48
9	1d	CH ₂ Cl ₂	–24	72	92	85

[a] Experimental conditions: to a solution of *trans*- β -nitrostyrene **3a** (0.1 mmol) and catalyst **1** (0.02 mmol) in a solvent (100 μ L), indole **2a** (0.15 mmol) was added. After the stated reaction time, the product was purified by preparative TLC. [b] Determined by ¹H NMR spectroscopy of the crude reaction mixture. [c] Determined by chiral stationary phase HPLC (See Supporting Information).

respect to the noncatalyzed reaction (Table 1, entry 1). However, only catalyst **1d**, obtained from 3,5-bis(trifluoromethyl)-phenyl isothiocyanate and (1*R*,2*S*)-*cis*-1-amino-2-indanol, showed a moderate yet promising asymmetric induction, as the product **4a** was produced in 35% *ee* (Table 1, entry 5). Catalyst **1d** was also the most active in terms of conversion, the reaction being complete in less than 60 h; as predicted,^[9c] the corresponding urea derivative **1e** gave much poorer conversion and lower enantioselectivity (Table 1, entry 6). We found that ethereal solvents such as THF had a negative influence on the activity of the catalyst **1d** (Table 1, entry 7), whereas the use of CH₂Cl₂ led to a slight improvement in the enantioselectivity, giving **4a** in 48% *ee* (Table 1, entry 8). Finally, we were pleased to find that cooling the reaction mixture to –24 °C had a remarkable positive effect on the enantioselectivity; the product **4a** was obtained in 85% *ee* while good levels of conversion were maintained (Table 1, entry 9).

We next explored the scope of this new enantioselective Friedel–Crafts alkylation of indoles with nitroalkenes, under the optimized reaction conditions (Table 2). We first tested a few indoles **2a–d** bearing different substituents in the reaction with *trans*- β -nitrostyrene **3a** catalyzed by **1d**.^[15] Whereas the reaction of indole **2a** afforded the corresponding product **4a** in good yield and optical purity (Table 2, entry 1), when performed at –24 °C, the Friedel–Crafts alkylation of electron-rich 2-methylindole **2b** and 5-methoxyindole **2c** proceeded at a reasonable reaction rate even at lower temper-

atures, furnishing the corresponding derivatives **4b** and **4c** in satisfactory yields and enantioselectivities at –45 °C (Table 2, entries 2 and 3). Unfortunately, an electron-withdrawing substituent such as chlorine in the 5-position of the indole ring in **2d** caused a considerable decrease in the yield of **4d**, though the enantioselectivity was only moderately lowered (Table 2, entry 4). The generality of the reaction was further demonstrated by variation of the nitroalkene partner. Nitroalkenes **3b** and **3c**, bearing heteroaromatic groups, reacted smoothly with indole **2a** affording the corresponding products **4e** and **4f** in good yields and moderate enantioselectivities (Table 2, entries 5 and 6). Finally we tested nitroalkenes bearing aliphatic side chains such as **3d** and **3e**, and both gave good results in terms of enantioselectivity as the expected 2-indolyl-1-nitro derivatives **4g** and **4h** were produced in 83% and 81% *ee*, respectively (Table 2, entries 7 and 8), although the yield of the reaction turned out to be rather poor in the case of the more hindered isopropyl-substituted nitroalkene **3e**.^[16]

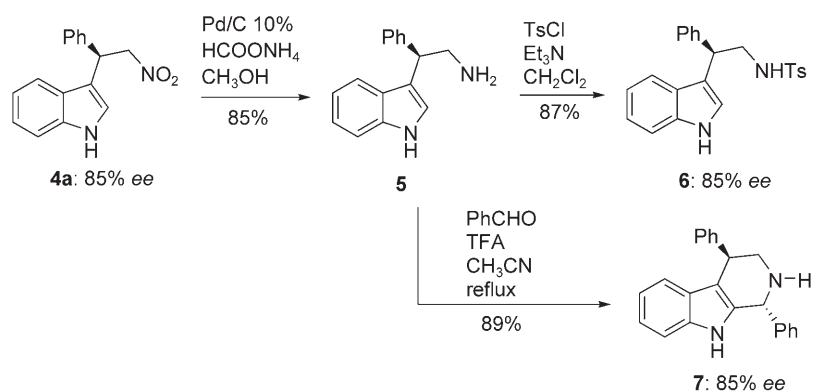
The high synthetic potential of the present asymmetric transformation was then demonstrated by the straightforward conversion of the optically active product **4a** into highly valuable compounds such as tryptamine **5** and 1,2,3,4-tetrahydro- β -carboline **7**. As shown in Scheme 2, reduction

Table 2: Friedel–Crafts alkylation of indoles **2a–d** with nitroalkenes **3a–d** catalyzed by thiourea **1d**.^[a]

Entry	Indole	R ¹	R ²	Nitroalkene	R ³	Product	Yield [%] ^[b]	<i>ee</i> [%] ^[c]
1	2a	H	H	3a	Ph	4a	78	85
2	2b	Me	H	3a	Ph	4b	82 ^[d]	74 ^[d]
3	2c	H	OMe	3a	Ph	4c	86 ^[d]	89 ^[d]
4	2d	H	Cl	3a	Ph	4d	35 ^[e]	71 ^[e]
5	2a	H	H	3b	2-furyl	4e	88	73
6	2a	H	H	3c	2-thienyl	4f	70	73
7	2a	H	H	3d	<i>n</i> -pentyl	4g	76	83
8	2a	H	H	3e	<i>i</i> Pr	4h	37 ^[f]	81 ^[f]

[a] Experimental conditions: Indole **2** (0.15 mmol) was added to a solution of nitroalkene **3** (0.1 mmol) and catalyst **1d** (0.02 mmol) in CH₂Cl₂ (100 μ L), cooled to –24 °C. After 72 h, the product was isolated by flash chromatography. [b] Yield of isolated product. [c] Determined by chiral stationary phase HPLC (see Supporting Information). [d] Reaction performed at –45 °C. [e] Reaction time: 142 h. [f] Reaction time: 96 h.

of the nitro group of **4a** proceeded under mild reaction conditions^[17] giving tryptamine **5**, which could be isolated in good yield as the corresponding sulfonamide derivative **6**. Alternatively, crude **5** could be directly subjected to Pictet–Spengler cyclization^[18] with benzaldehyde to furnish a previously unreported 1,4-diphenyl-substituted 1,2,3,4-tetrahydro- β -carboline as a 91:9 mixture of diastereoisomers. The highly prevailing 1,4-*trans* isomer **7** was isolated in good yield and in diastereomerically pure form after chromatography on silica gel (Scheme 2). All reactions occurred without any loss in the enantiomeric enrichment of the products, and the relative stereochemistry of **7** was tentatively assigned as 1,4-



Scheme 2. Conversion of the optically active product **4a** into valuable products such as tryptamine **5** and 1,2,3,4-tetrahydro- β -carboline **7**. Ts = toluene-4-sulfonyl, TFA = trifluoroacetic acid.

trans by means of NOE experiments. Furthermore, the formation of the sulfonamide derivative **6** allowed the assignment of the absolute configuration of the catalytic product **4a** as *2R*, from the comparison of its optical rotation and HPLC retention time with those of an authentic sample of *ent-6* (in 94% *ee*), which was synthesized by the ring-opening at the benzylic position of (2*S*)-2-phenyl-1-*p*-toluenesulfonyl aziridine^[19] with indole **2a** promoted by LiClO₄.^[20]

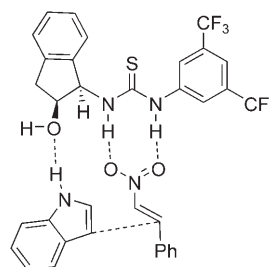
The ability of thiourea **1d** to promote the Friedel–Crafts additions of indoles **2** to nitroalkenes **3** may be interpreted on the basis of the reversible formation of a complex involving a double hydrogen bond between the thiourea hydrogen atoms and the two oxygen atoms of the nitroalkene. The recognition of the nitro group by urea moieties in solution as well as in the solid phase, leads to crystal structures that clearly present this type of interaction.^[21] To gain some insight into the substrate–catalyst interactions that lead to the observed stereoselectivity, we prepared catalyst **1f**, in which the hydroxy group was protected by a sterically hindering trimethylsilyl group, and thiourea **1g**, which lacks the alcoholic function. Surprisingly, both catalysts showed poor performances in the reaction between indole **2a** and *trans*- β -nitrostyrene **3a**, not only with regard to the enantioselectivity but also in terms of the catalyst activity (Scheme 3).

On these grounds, but considering also the poor asymmetric induction observed in the reaction of *N*-methyl indole,^[15] we envisioned that catalyst **1d** would act in a bifunctional fashion. Therefore, whereas the two thiourea

	Yield 4a	<i>ee</i>
1d : R = OH	78%	85%
1f : R = OSi(CH ₃) ₃	18%	39%
1g : R = H	15%	0%

Scheme 3. The hydroxy-protected catalyst **1f** and the thiourea **1g** lacking the alcoholic function and their performance in the Friedel–Crafts alkylation of **2a** with **3a** to give **4a**.

hydrogen atoms activate the nitroalkene, the free alcoholic function will interact with the indolic proton through a weak hydrogen bond, directing the attack of the incoming nucleophile on the *Si* face of the nitroolefin as depicted in Scheme 4.



Scheme 4. Possible bifunctional mode of action of the catalyst **1d**.

In conclusion, we have developed the first catalytic, enantioselective Friedel–Crafts alkylation of indoles **2** with nitroalkenes **3**, which provides optically active 2-indolyl-1-nitro derivatives **4** in fairly good yields and enantioselectivities. The reaction is efficiently catalyzed by the simple thiourea-based organocatalyst **1d**, which can be easily accessed in both enantiomeric forms from commercially available materials. The extremely simple operational procedure and the high synthetic versatility of the products render this new approach highly appealing for the synthesis of optically active target compounds such as tryptamines and 1,2,3,4-tetrahydro- β -carbolines.

Received: January 20, 2005

Revised: April 19, 2005

Published online: September 19, 2005

Keywords: asymmetric synthesis · electrophilic substitution · hydrogen bonds · indoles · organocatalysis

- a) “Friedel–Crafts Alkylation”: G. A. Olah, R. Krishnamurty, G. K. S. Prakash in *Comprehensive Organic Synthesis*, Vol. III (Eds.: B. M. Trost, I. Fleming), Pergamon, Oxford, 1st ed., **1991**, p. 293; b) R. M. Roberts, A. A. Khalaf, *Friedel–Crafts Alkylation Chemistry A Century of Discovery*, Marcel Dekker, New York, **1984**; c) G. A. Olah, *Friedel–Crafts and Related Reactions*, Vol. II, part 1, Wiley-Interscience, New York, **1964**.
- For reviews, see: a) K. A. Jørgensen, *Synthesis* **2003**, 1117; b) M. Bandini, A. Melloni, A. Umami-Ronchi, *Angew. Chem.* **2004**, *116*, 560; *Angew. Chem. Int. Ed.* **2004**, *43*, 550.
- See, for example: a) K. B. Jensen, J. Thorhauge, R. G. Hazell, K. A. Jørgensen, *Angew. Chem.* **2001**, *113*, 164; *Angew. Chem. Int. Ed.* **2001**, *40*, 160; b) J. Zhou, Y. Tang, *J. Am. Chem. Soc.* **2002**, *124*, 9030; c) M. Bandini, M. Fagioli, P. Melchiorre, A. Melloni, A. Umami-Ronchi, *Tetrahedron Lett.* **2003**, *44*, 5846; d) D. A. Evans, K. A. Scheidt, K. R. Fandrick, H. W. Lam, J. Wu, *J. Am. Chem. Soc.* **2003**, *125*, 10780.
- a) N. A. Paras, D. W. C. MacMillan, *J. Am. Chem. Soc.* **2001**, *123*, 4370; b) J. F. Austin, D. W. C. MacMillan, *J. Am. Chem. Soc.* **2002**, *124*, 1172; c) N. A. Paras, D. W. C. MacMillan, *J. Am. Chem. Soc.* **2002**, *124*, 7824.

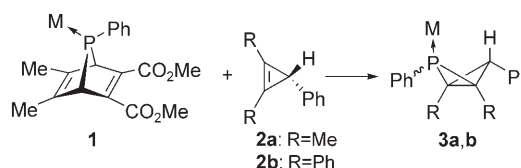
- [5] O. M. Berner, L. Tedeschi, D. Enders, *Eur. J. Org. Chem.* **2002**, 1877.
- [6] D. Seebach, E. W. Colvin, F. Lehr, T. Weller, *Chimia* **1979**, 33, 1.
- [7] N. Ono, *The Nitro Group in Organic Synthesis*, Wiley-VCH, New York, **2001**.
- [8] a) P. R. Schreiner, *Chem. Soc. Rev.* **2003**, 32, 289; b) P. M. Pihko, *Angew. Chem.* **2004**, 116, 2110; *Angew. Chem. Int. Ed.* **2004**, 43, 2062.
- [9] a) D. P. Curran, L. H. Kuo, *J. Org. Chem.* **1994**, 59, 3259; b) P. R. Schreiner, A. Wittkopp, *Org. Lett.* **2002**, 4, 1115; c) A. Wittkopp, P. R. Schreiner, *Chem. Eur. J.* **2003**, 9, 407; d) D. J. Maher, S. J. Connon, *Tetrahedron Lett.* **2004**, 45, 1301.
- [10] See, for example: a) M. S. Sigman, E. N. Jacobsen, *J. Am. Chem. Soc.* **1998**, 120, 4901; b) M. S. Taylor, E. N. Jacobsen, *J. Am. Chem. Soc.* **2004**, 126, 10558, and references therein; c) Y. Sohtome, A. Tanatani, Y. Hashimoto, K. Nagasawa, *Tetrahedron Lett.* **2004**, 45, 5589; d) T. Okino, Y. Hoashi, Y. Takemoto, *J. Am. Chem. Soc.* **2003**, 125, 12672; e) T. Okino, S. Nakamura, T. Furukawa, Y. Takemoto, *Org. Lett.* **2004**, 6, 625; f) T. Okino, Y. Hoashi, T. Furukawa, X. Xu, Y. Takemoto, *J. Am. Chem. Soc.* **2005**, 127, 119; g) A. Berkessel, F. Cleemann, S. Mukherjee, T. N. Müller, J. Lex, *Angew. Chem.* **2005**, 117, 817; *Angew. Chem. Int. Ed.* **2005**, 44, 807; h) T. P. Yoon, E. N. Jacobsen, *Angew. Chem.* **2005**, 117, 470; *Angew. Chem. Int. Ed.* **2005**, 44, 466.
- [11] a) G. Dessole, R. P. Herrera, A. Ricci, *Synlett* **2004**, 2374; for other examples of non-stereoselective Friedel–Crafts additions to nitroalkenes, see: b) W. E. Noland, P. J. Hartman, *J. Chem. Soc.* **1954**, 76, 3227; c) W. E. Noland, G. M. Christensen, G. L. Sauer, G. G. S. Dutton, *J. Chem. Soc.* **1955**, 77, 456; d) M. Bandini, P. Melchiorre, A. Melloni, A. Umani-Ronchi, *Synthesis* **2002**, 1110, and references therein.
- [12] For leading references see: A. Kleeman, J. Engel, B. Kutscher, D. Reichert, *Pharmaceutical Substances*, Thieme, New York, 4th ed., **2001**.
- [13] a) J. P. Yevic, F. D. Zocca, *Curr. Med. Chem.* **1997**, 4, 295; b) J. Arendt, S. Deacon, *Melatonin Chromobiol. Int.* **1997**, 14, 185.
- [14] H. J. Zhu, B. T. Zhao, G. Y. Zuo, C. U. Pittman, Jr., W. M. Ma, X. J. Hao, *Tetrahedron: Asymmetry* **2001**, 12, 2613.
- [15] An alkyl substituent on the indolic nitrogen atom is not tolerated in this catalytic enantioselective reaction, as the addition of *N*-methylindole to **3a** catalyzed by **1d** gave the product in good yield (75%) but in a nearly racemic form (6% *ee*) under the optimized reaction conditions.
- [16] The yield of the Friedel–Crafts alkylation of **2a** with **3e** could be considerably increased by simply performing the reaction at higher temperatures, and only a moderate loss of enantioselectivity in the product **4h** occurs (0°C, 76% yield, 72% *ee*).
- [17] a) S. Ram, R. E. Ehrenkauf, *Tetrahedron Lett.* **1984**, 25, 3415; b) J. O. Osby, B. Ganem, *Tetrahedron Lett.* **1985**, 26, 6413.
- [18] W. Jiang, X. Zhang, Z. Sui, *Org. Lett.* **2003**, 5, 43.
- [19] L. W. Bieber, M. C. F. de Araujo, *Molecules* **2002**, 7, 902.
- [20] J. S. Yadav, B. V. S. Reddy, G. Parimala, *J. Chem. Res.* **2003**, 78.
- [21] a) M. C. Etter, Z. Urbańczyk-Lipkowska, M. Zia-Ebrahimi, T. W. Panunto, *J. Am. Chem. Soc.* **1990**, 112, 8415; b) T. R. Kelly, M. H. Kim, *J. Am. Chem. Soc.* **1994**, 116, 7072.

Valence Isomerization of 2-Phosphabicyclo[1.1.0]butanes**

J. Chris Slootweg, Steffen Krill, Frans J. J. de Kanter, Marius Schakel, Andreas W. Ehlers, Martin Lutz, Anthony L. Spek, and Koop Lammertsma*

The unique electronic properties of the strained bicyclo[1.1.0]butanes^[1] are enhanced by the heteroatoms in the molecular frame. Illustrative is the bond-stretch isomerization of the P₂C₂ and P₂B₂ bicycles.^[2] However, very few systems are known with a single heteroatom,^[3] probably because of their high reactivity, which is only moderated when the heteroatom occupies a bridgehead position as in the 1-aza derivatives.^[4] The increased reactivity of the hetero systems is due to the valence isomerization to which the bicyclo[1.1.0]butanes are prone. We now report on the first 2-phospha derivatives.

The carbene-like phosphinidene Ph-P=W(CO)₅^[5] was generated in situ by cheletropic elimination from **1** at 110 °C in toluene and then allowed to react with cyclopropene **2a**^[6] (Scheme 1). This led to the desired W(CO)₅-complexed 2-phosphabicyclo[1.1.0]butanes *exo*-**3a** ($\delta^{31}\text{P} = -85.1$ ppm) and *endo*-**3a** ($\delta^{31}\text{P} = -36.7$ ppm)^[7] in a 10:9 ratio, which were isolated in 69% yield as colorless solids. The remarkably



Scheme 1. Synthesis of the 2-phosphabicyclo[1.1.0]butanes **3**.
M = W(CO)₅.

[*] J. C. Slootweg, Dr. F. J. J. de Kanter, Dr. M. Schakel, Dr. A. W. Ehlers, Prof. Dr. K. Lammertsma
Department of Organic and Inorganic Chemistry
Faculty of Sciences
Vrije Universiteit
De Boelelaan 1083, 1081 HV, Amsterdam (The Netherlands)
Fax: (+31) 20-598-7488
E-mail: lammert@chem.vu.nl
Dr. S. Krill, Prof. Dr. K. Lammertsma
Formerly associated with the Department of Chemistry
University of Alabama at Birmingham
Birmingham, AL 35294 (USA)
Dr. M. Lutz, Prof. Dr. A. L. Spek
Bijvoet Center for Biomolecular Research
Crystal and Structural Chemistry
Utrecht University
Padualaan 8, 3584 CH, Utrecht (The Netherlands)

[**] This work was supported by the Council for Chemical Sciences of the Netherlands Organization for Scientific Research (NWO/CW).



Supporting information for this article is available on the WWW under <http://www.angewandte.org> or from the author.

stable products were characterized by single-crystal X-ray analyses, which showed puckered geometries with P1–C1–C2–C3 folding angles of $-114.66(15)^\circ$ for *exo*-**3a** and $-120.65(14)^\circ$ for *endo*-**3a**, and transannular C1–C2 bonds of 1.516(3) and 1.550(3) Å, respectively (Figure 1). The flatter

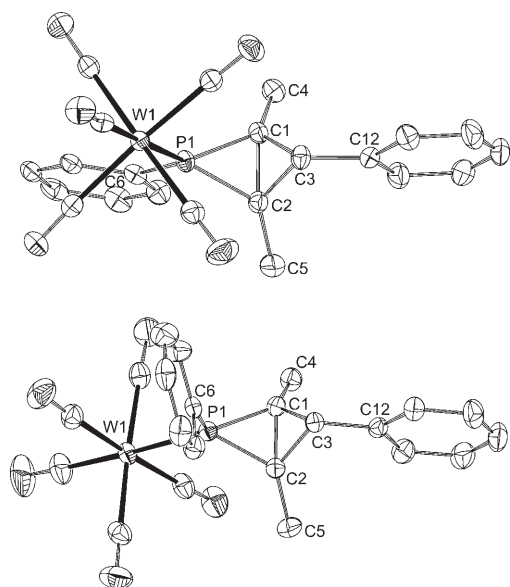
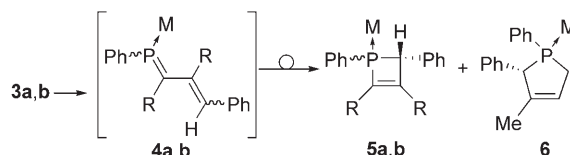


Figure 1. The displacement ellipsoid plot of *exo*-**3a** (top) and *endo*-**3a** (bottom) with ellipsoids drawn at the 50% probability level. Hydrogen atoms are omitted for clarity. Selected bond lengths [Å], angles [°], and torsion angles [°] for *exo*-**3a**: W1–P1 2.5013(6), P1–C1 1.808(2), P1–C2 1.811(2), P1–C6 1.820(2), C1–C2 1.516(3), C1–C3 1.515(3), C1–C4 1.500(3), C2–C3 1.512(3), C2–C5 1.505(3), C3–C12 1.488(3); C1–P1–C2 49.52(10), P1–C1–C2 65.35(12), P1–C1–C3 96.79(15), C2–C1–C3 59.83(15), C2–C1–C4 139.6(2), P1–C2–C1 65.13(12), P1–C2–C3 96.78(15), C1–C2–C3 60.06(15), C1–C2–C5 141.4(2), C1–C3–C2 60.11(15); P1–C1–C2–C3 $-114.66(15)$. *endo*-**3a**: W1–P1 2.4851(5), P1–C1 1.801(2), P1–C2 1.792(2), P1–C6 1.823(2), C1–C2 1.550(3), C1–C3 1.511(3), C1–C4 1.502(3), C2–C3 1.521(3), C2–C5 1.500(3), C3–C12 1.495(3); C1–P1–C2 51.11(9), P1–C1–C2 64.13(11), P1–C1–C3 100.05(14), C2–C1–C3 59.57(14), C2–C1–C4 135.80(19), P1–C2–C1 64.76(11), P1–C2–C3 100.08(13), C1–C2–C3 58.94(13), C1–C2–C5 136.7(2), C1–C3–C2 61.49(13); P1–C1–C2–C3 $-120.65(14)$.

endo structure with the longer C1–C2 bond is the least stable of the two and decomposes at about 130°C . At this temperature, the *exo* isomer undergoes valence isomerization to give 3-phosphacyclobutene complexes *cis*-**5a** ($\delta^{31}\text{P} = 46.3$ ppm) and *trans*-**5a** ($\delta^{31}\text{P} = 55.2$ ppm, $^2J(\text{H},\text{P}) = 9.5$ Hz)^[8] in a 4:1 ratio (35%) besides the phospholene complex **6** as the major product (41%, $\delta^{31}\text{P} = 37.9$ ppm; Scheme 2). Formation of the phospholene was confirmed by crystal structure analysis.



Scheme 2. Valence isomerization of **3** to form **5** and, for R = Me, **6**. M = W(CO)₅.

The BP86/6-31G* (LANL2DZ) calculations^[9] on models (labeled with an apostrophe (')), no C substituents) did not demonstrate a direct path from **3** to **5**,^[10] but instead the involvement of 1-phosphabutadiene **4** was established (see Scheme 2). Isomerization of *exo*-**3'** to give *trans*-**4'** proceeds by a concerted, asynchronous conrotatory ring opening ($\Delta E = -18.4$, $\Delta E^\ddagger = 32.8$ kcal mol⁻¹; Figure 2). With subsequent conrotatory electrocyclic ring closure, via the *gauche* form of **4'** ($\Delta E = 3.7$, $\Delta E^\ddagger = 7.9$ kcal mol⁻¹), the more stable phosphacyclobutene **5'** is formed ($\Delta E = -4.4$, $\Delta E^\ddagger = 19.2$ kcal mol⁻¹). This route implies that 1-phosphabutadiene **4** is a reaction intermediate. The small energy difference between **4'** and 3-phosphacyclobutene **5'** is reflected in Tran Huy and Mathey's^[11] use of derivatives of **5** as masked 1-phosphabutadienes.^[12] These results highlight that the stability order $\mathbf{3'} \ll \mathbf{4'} < \mathbf{5'}$ of the three valence isomers differs from the established values for the hydrocarbons ($\mathbf{3''} \ll \mathbf{5''} \ll \mathbf{4''}$).^[13]

To gain more insight into the formation of phospholene **6**, we resorted to the more gentle CuCl-catalyzed reaction of **1**^[5,14] with **2a** (55°C , 15 h; Scheme 3). This reaction gave, with the exception of **6**, the same products as the noncatalyzed

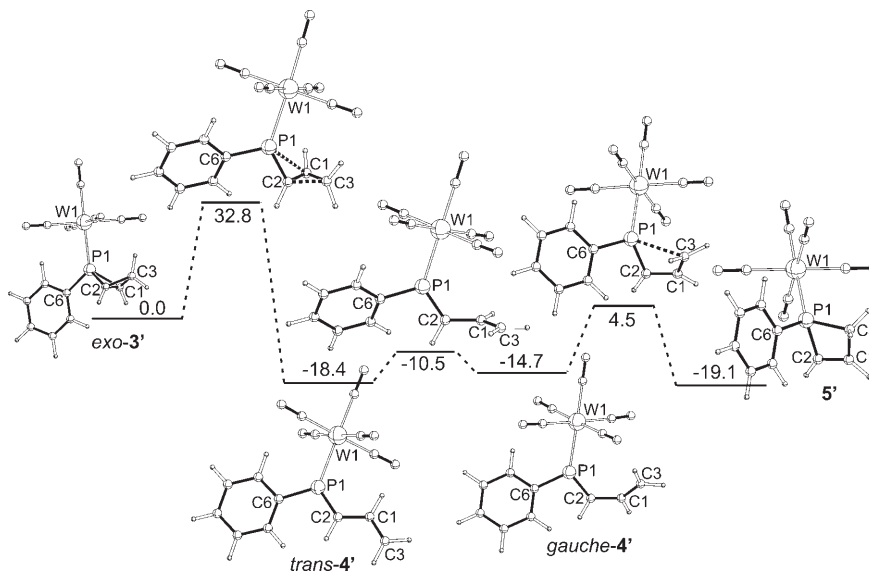
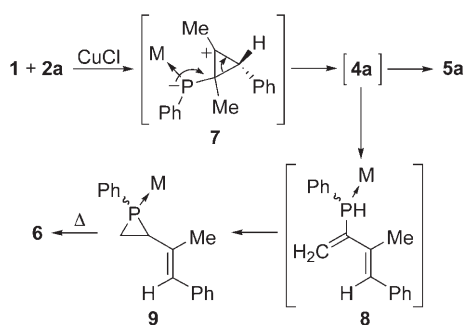


Figure 2. The relative BP86/6-31G* (LANL2DZ for W) energies (ZPE corrected, in kcal mol⁻¹) for the rearrangement of *exo*-**3'** into **5'**. Selected bond lengths [Å], angles [°], and torsion angles [°] of *exo*-**3'** (C_s): W1–P1 2.536, P1–C1 1.833, P1–C6 1.846, C1–C2 1.527, C1–C3 1.506; C1–P1–C2 49.2, C1–C3–C2 60.9, P1–C1–C2–C3 120.2; **TS***exo*-**3'**-*trans*-**4'**: W1–P1 2.541, P1–C1 2.709, P1–C2 1.801, P1–C6 1.820, C1–C2 1.474, C1–C3 1.446, C2–C3 1.595; *trans*-**4'** (C_s): W1–P1 2.515, P1–C2 1.703, P1–C6 1.830, C1–C2 1.441, C1–C3 1.359; **TS***trans*-**4'**-*gauche*-**4'**: P1–C2–C1–C3 95.2; *gauche*-**4'**: P1–C2–C1–C3 31.0; **TS***gauche*-**4'**-**5'**: W1–P1 2.568, P1–C2 1.774, P1–C3 2.558, C1–C2 1.391, C1–C3 1.419, P1–C2–C1–C3 26.4; **5'**: W1–P1 2.539, P1–C2 1.838, P1–C3 1.915, P1–C6 1.848, C1–C2 1.355, C1–C3 1.518.



Scheme 3. The CuCl-catalyzed formation of **5a** and **9**. M = W(CO)₅.

reaction, that is, *exo*- and *endo*-**3a** (4:1 ratio, 16%) and *cis*- and *trans*-**5a** (7:8 ratio, 30%). Additionally, the vinyl-phosphirane complexes *anti*-**9** ($\delta^{31}\text{P} = -157.1$ ppm) and *syn*-**9** ($\delta^{31}\text{P} = -150.2$ ppm) were also produced in a 3:1 ratio (6%). The vinyl-phosphiranes formed in this milder process (55°C vs. 110°C) corroborates the role of phosphabutadienes as reaction intermediates. Heating of isolated *anti*-**9** at 110°C effected epimerization of the phosphorus center to give the *syn*-**9** isomer, which underwent the established [1,3]-sigmatropic shift^[15] to phospholene complex **6**. The presumed reagent, the [PhP(Cl)W(CO)₅]-Cu-alkene complex,^[14] is more sensitive than PhP=W(CO)₅ to steric congestion in the 1,2-cycloaddition, which is reflected in the lower yield of the 2-phosphabicyclobutanes **3a**. The competitive reaction is, in our opinion, the formation of zwitterion **7**, for which there is computational support on related systems.^[16] Compound **7** can also rearrange to phosphabutadiene **4a** in analogy to the addition of dichlorocarbene to cyclopropenes.^[17] Ring closure then gives **5a**,^[8] while two known hydride shifts^[18] lead, via the secondary vinylphosphane complex **8**, to vinyl-phosphirane **9** (Scheme 3). The **4**→**9** process is exothermic by -1.8 kcal mol⁻¹ for the parent system (no phenyl substituent on the diene).^[9]

Valence isomerization is sensitive to the nature of the bridgehead substituents, and this also applies to **3**→**4**→**5**. Reaction of cyclopropene **2b**, which has phenyl instead of methyl substituents, with the phosphinidene precursor **1** at 110°C gave as sole products the 3-phosphacyclobutene complexes *cis*-**5b** ($\delta^{31}\text{P} = 43.8$ ppm, $^2J(\text{H},\text{P}) = 6.2$ Hz) and *trans*-**5b** ($\delta^{31}\text{P} = 53.4$ ppm, $^2J(\text{H},\text{P}) = 9.6$ Hz)^[8] (5:1 ratio, 95%); *cis*-**5b** was characterized by X-ray crystallography. Apparently, **3b** isomerizes faster than **3a**. In this case, phospholene **6** cannot be formed because the phenyl substituents render a hydride shift (to give **8**) impossible.

2-Phosphabicyclo[1.1.0]butanes *exo*-**3b** ($\delta^{31}\text{P} = -70.5$ ppm) and *endo*-**3b** ($\delta^{31}\text{P} = 3.8$ ppm)^[7] could be obtained (4:1 ratio, 33%) by the milder CuCl-catalyzed reaction (2 equiv of **1**, 55°C, 0.5 h). The X-ray crystal structure of the *exo* isomer revealed two different triclinic polymorphs with $Z=2$ and $Z=6$, respectively, and very similar molecular structures. Polymorph I shows a folding angle (113.27(10)°) and a transannular bond length (1.510(2) Å) that are similar to those of *exo*-**3a**. Heating of isolated **3b** (*exo* + *endo*, 4:1) in toluene at 50°C for 60 h gave the favored phosphacyclobutene *cis*-**5b**, indicating that

valence isomerization of the novel 2-phosphabicyclo[1.1.0]butanes is indeed directed by the bridgehead substituents (**3b** 50°C; **3a** 130°C). This behavior parallels that observed for the all-carbon analogue 2,2-dimethyl-bicyclo[1.1.0]butane, where the 1,3-diphenyl derivative isomerizes at 130°C and the 1,3-dimethyl derivative at temperatures above 280°C.^[19]

In conclusion, W(CO)₅-complexed 2-phosphabicyclo[1.1.0]butanes are remarkably stable compounds that valence-isomerize to 3-phosphacyclobutenes via 1-phosphabutadienes at elevated temperatures. In contrast to the hydrocarbon analogues, the diene can be trapped as a phospholene due to rearrangements that are specific for the phosphorus compounds.

Experimental Section

3a and **6**: Compounds **1**^[5] (591 mg, 0.90 mmol) and **2a**^[6] (156 mg, 1.08 mmol) were heated in toluene (3 mL) at reflux for 17 h. Removal of the solvents under vacuum and chromatography of the residue over silica with pentane/toluene (9:1) as eluent gave *endo*-**3a** (155 mg, 30%) and *exo*-**3a** (200 mg, 39%) as colorless solids as well as **6** (20 mg, 4%) as a pale yellow solid together with minor amounts of *cis*-**5a** (10 mg, 2%) and *trans*-**5a** (5 mg, 1%). *exo*-**3a**: m.p.: 115–116°C; $^{31}\text{P}\{^1\text{H}\}$ NMR (101.3 MHz, CDCl₃): $\delta = -85.1$ ($^1J(\text{P},\text{W}) = 263.7$ Hz). *endo*-**3a**: m.p.: 79–82°C; $^{31}\text{P}\{^1\text{H}\}$ NMR (101.3 MHz, CDCl₃): $\delta = -36.7$ ppm ($^1J(\text{P},\text{W}) = 260.3$ Hz); HRMS (EI, 70 eV): m/z (%): 576 (9) [M]⁺; calcd for C₂₂H₁₇O₅PW: 576.0323; found: 576.0325. **6**: m.p.: 107°C; $^{31}\text{P}\{^1\text{H}\}$ NMR (101.3 MHz, CDCl₃): $\delta = 37.9$ ppm ($^1J(\text{P},\text{W}) = 240.4$ Hz); HRMS (EI, 70 eV): m/z (%): 576 (30) [M]⁺; calcd for C₂₂H₁₇O₅PW: 576.0323; found: 576.0329.

3b: Compounds **2b** (122.6 mg, 0.46 mmol), **1** (598 mg, 0.91 mmol), and CuCl (10 mg, 0.1 mmol) in toluene (2 mL) were heated at 55°C for 30 min. The reaction was stopped at incomplete conversion to ensure maximum yield of **3b**. Removal of the solvents under vacuum and chromatography of the residue over silica with pentane/toluene (9:1) as eluent gave a 4:1 mixture of *exo*-**3b** and *endo*-**3b** (107 mg, 33%) as a pale yellow solid. *exo*-**3b**: m.p.: 124°C (decomp.); $^{31}\text{P}\{^1\text{H}\}$ NMR (101.3 MHz, CDCl₃): $\delta = -70.5$ ppm ($^1J(\text{P},\text{W}) = 262.0$ Hz); HRMS (EI, 70 eV): m/z (%): 700 (22) [M]⁺; calcd for C₃₂H₂₁O₅PW: 700.0636; found: 700.0634. *endo*-**3b**: $^{31}\text{P}\{^1\text{H}\}$ NMR (101.3 MHz, CDCl₃): $\delta = 3.8$ ppm ($^1J(\text{P},\text{W}) = 271.8$ Hz).

3a, **5a**, and **9**: Compounds **1** (1.24 g, 1.90 mmol), **2a** (410 mg, 2.84 mmol), and CuCl (10 mg, 0.1 mmol) in toluene (8 mL) were heated at 55°C for 15 h. Removal of the solvents under vacuum and chromatography of the residue (an insoluble black residue remains) over silica with pentane/toluene (9:1) as eluent gave *endo*-**3a** (40 mg, 4%), *cis*-**5a** (160 mg, 14%), *exo*-**3a**, and *trans*-**5a** in a 10:8 ratio (310 mg, 28%), and *syn*- and *anti*-**9** in a 3:1 ratio (65 mg, 6%) as colorless oils. *cis*-**5a**: $^{31}\text{P}\{^1\text{H}\}$ NMR (101.3 MHz, CDCl₃): $\delta = 46.3$ ppm ($^1J(\text{P},\text{W}) = 221.4$ Hz). Crystallization of the mixture of *exo*-**3a** and *trans*-**5a** from pentane at -80°C afforded the pale yellow crystals of *trans*-**5a**: M.p. 111°C; $^{31}\text{P}\{^1\text{H}\}$ NMR (101.3 MHz, CDCl₃): $\delta = 55.2$ ppm ($^1J(\text{P},\text{W}) = 237.5$ Hz); HRMS (EI, 70 eV): m/z (%): 576 (39) [M]⁺; calcd for C₂₂H₁₇O₅PW: 576.0323; found: 576.0318. *syn*-**9**: $^{31}\text{P}\{^1\text{H}\}$ NMR (101.3 MHz, CDCl₃): $\delta = -157.1$ ppm ($^1J(\text{P},\text{W}) = 255.2$ Hz); HRMS (EI, 70 eV): m/z (%): 576 (20) [M]⁺; calcd for C₂₂H₁₇O₅PW: 576.0323; found: 576.0318. *anti*-**9**: $^{31}\text{P}\{^1\text{H}\}$ NMR (101.3 MHz, CDCl₃): $\delta = -150.2$ ppm ($^1J(\text{P},\text{W}) = 263.3$ Hz).

5b: Compounds **1** (261 mg, 0.40 mmol), **2b** (118 mg, 0.44 mmol), and CuCl (10 mg, 0.1 mmol) in toluene (2 mL) were heated at 55°C for 38 h or, alternatively (without CuCl), at reflux for 16 h. Removal of the solvents under vacuum and chromatography of the residue over silica with pentane/toluene (4:1) as eluent gave *cis*-**5b** (215 mg, 77%) as a pale yellow solid together with a trace of *trans*-**5b** ($\approx 2\%$).

Removal of the solvents under vacuum and chromatography of the residue over silica with pentane/toluene (4:1) as eluent gave a 5:1 mixture of *cis*-**5b** and *trans*-**5b** (300 mg, 95%) as a pale yellow oil. Crystallization from pentane at -20°C afforded colourless crystals of *cis*-**5b**: m.p.: $117\text{--}118^{\circ}\text{C}$; $^{31}\text{P}\{^1\text{H}\}$ NMR (101.3 MHz, CDCl_3): $\delta = 43.8$ ppm ($^1\text{J}(\text{P,W}) = 230.9$ Hz); HRMS (EI, 70 eV): m/z (%): 700 (23) [$\text{M}]^+$; calcd for $\text{C}_{32}\text{H}_{21}\text{O}_5\text{PW}$: 700.0636; found: 700.06486. *trans*-**5b**: $^{31}\text{P}\{^1\text{H}\}$ NMR (101.3 MHz, CDCl_3): $\delta = 53.4$ ppm ($^1\text{J}(\text{P,W}) = 247.0$ Hz).

Crystal structure data (see Supporting Information): *exo*-**3a** ($\text{C}_{22}\text{H}_{17}\text{O}_5\text{PW}$): $P2_1/c$ (no. 14); $a = 6.8439(1)$, $b = 21.3415(2)$, $c = 14.4400(1)$ Å, $\beta = 95.2844(3)^{\circ}$, $V = 2100.13(4)$ Å 3 ; $Z = 4$; R [$I > 2\sigma(I)$]: $R1 = 0.0178$, $wR2 = 0.0406$. *endo*-**3a** ($\text{C}_{22}\text{H}_{17}\text{O}_5\text{PW}$): $P2_1/c$ (no. 14); $a = 8.2108(1)$, $b = 15.0945(1)$, $c = 17.8628(2)$ Å, $\beta = 99.0907(3)^{\circ}$, $V = 2186.07(4)$ Å 3 ; $Z = 4$; R [$I > 2\sigma(I)$]: $R1 = 0.0175$, $wR2 = 0.0403$. **6** ($\text{C}_{22}\text{H}_{17}\text{O}_5\text{PW}$): $C2/c$ (no. 15); $a = 37.996(3)$, $b = 8.9553(4)$, $c = 26.4314(15)$ Å, $\beta = 110.813(5)^{\circ}$, $V = 8406.9(9)$ Å 3 ; $Z = 16$; R [$I > 2\sigma(I)$]: $R1 = 0.0213$, $wR2 = 0.0462$. *cis*-**5b** ($\text{C}_{32}\text{H}_{21}\text{O}_5\text{PW}$): $P2_1/c$ (no. 14); $a = 10.9428(1)$, $b = 22.9359(2)$, $c = 15.0824(1)$ Å, $\beta = 133.2674(4)^{\circ}$, $V = 2756.40(4)$ Å 3 ; $Z = 4$; R [$I > 2\sigma(I)$]: $R1 = 0.0192$, $wR2 = 0.0474$. *exo*-**3b** (polymorph I, $\text{C}_{32}\text{H}_{21}\text{O}_5\text{PW}$): $P1$ (no. 2); $a = 10.4005(8)$, $b = 10.7789(8)$, $c = 14.4436(12)$ Å, $\alpha = 83.618(6)$, $\beta = 78.886(6)$, $\gamma = 61.670(5)^{\circ}$, $V = 1398.2(2)$ Å 3 ; $Z = 2$; R [$I > 2\sigma(I)$]: $R1 = 0.0163$, $wR2 = 0.0332$. *exo*-**3b** (polymorph II, $\text{C}_{32}\text{H}_{21}\text{O}_5\text{PW}$): $P1$ (no. 2); $a = 10.4176(8)$, $b = 17.1058(17)$, $c = 23.9196(19)$ Å, $\alpha = 96.436(6)$, $\beta = 92.693(7)$, $\gamma = 97.143(8)^{\circ}$, $V = 4194.7(6)$ Å 3 ; $Z = 6$; R [$I > 2\sigma(I)$]: $R1 = 0.0246$, $wR2 = 0.0444$. CCDC 275002–275007 contain the supplementary crystallographic data for this paper. These data can be obtained free of charge from the Cambridge Crystallographic Data Centre via www.ccdc.cam.ac.uk/data_request/cif.

Received: June 27, 2005

Published online: September 13, 2005

Keywords: bicyclic compounds · heterocycles · phosphorus · substituent effects · valence isomerization

- [1] *The Chemistry of the Cyclopropyl Group*, Part 2 (Ed.: Z. Rappoport), Wiley, Chichester, **1987**, chap. 19.
- [2] P_2C_2 : a) E. Niecke, A. Fuchs, M. Nieger, *Angew. Chem.* **1999**, *111*, 3213–3216; *Angew. Chem. Int. Ed.* **1999**, *38*, 3028–3031; P_2B_2 : b) D. Scheschkewitz, H. Amii, H. Gornitzka, W. W. Schoeller, D. Bourissou, G. Bertrand, *Angew. Chem.* **2004**, *116*, 595–597; *Angew. Chem. Int. Ed.* **2004**, *43*, 585–587; c) A. Rodriguez, R. A. Olsen, N. Ghaderi, D. Scheschkewitz, F. S. Tham, L. J. Mueller, G. Bertrand, *Angew. Chem.* **2004**, *116*, 4988–4991; *Angew. Chem. Int. Ed.* **2004**, *43*, 4880–4883.
- [3] Phosphorus: a) K. Blatter, W. Rösch, U.-J. Vogelbacher, J. Fink, M. Regitz, *Angew. Chem.* **1987**, *99*, 67–68; *Angew. Chem. Int. Ed. Engl.* **1987**, *26*, 85–86; b) M. Regitz, S. Haber, U. Hees, *Phosphorus Sulfur Silicon Relat. Elem.* **1990**, *51/52*, 324; silicon: K. Wakita, N. Tokitoh, R. Okazaki, N. Takagi, S. Nagase, *J. Am. Chem. Soc.* **2000**, *122*, 5648–5649.
- [4] R. Bartnik, A. P. Marchand, *Synlett* **1997**, 1029–1039.
- [5] a) K. Lammertsma, M. J. M. Vlaar, *Eur. J. Org. Chem.* **2002**, 1127–1138; b) F. Mathey, N. H. Tran Huy, A. Marinetti, *Helv. Chim. Acta* **2001**, *84*, 2938–2957.
- [6] I. N. Domnin, J. Kopf, S. Keyaniyan, A. de Meijere, *Tetrahedron* **1985**, *41*, 5377–5382.
- [7] *exo*- and *endo*-phosphabicyclo[1.1.0]butanes differ significantly in terms of the ^{31}P NMR chemical shift; see: a) C. Jones, J. A. Platts, A. F. Richards, *Chem. Commun.* **2001**, 663–664; b) M. White, L. Ricard, F. Mathey, *Organometallics* **2003**, *22*, 4825–4828; c) Ref. [2a].

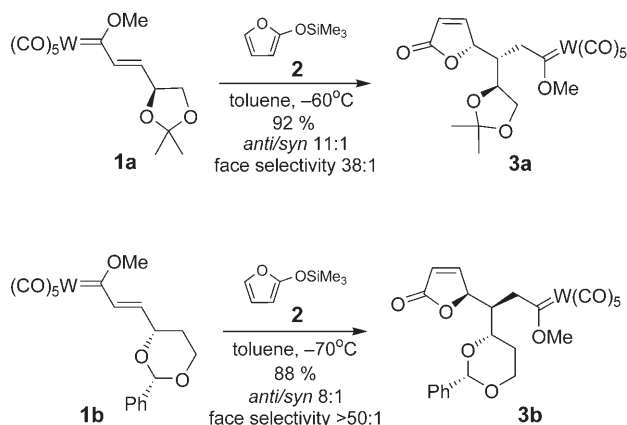
- [8] a) N. H. Tran Huy, L. Ricard, F. Mathey, *Organometallics* **1988**, *7*, 1791–1795; b) A. Marinetti, L. Ricard, F. Mathey, *Organometallics* **1990**, *9*, 788–793.
- [9] Intrinsic reaction coordinate (IRC) calculations were performed on the transition structures to ascertain the connection between reactant and product: Gaussian 98 (Revision A.11.4): M. J. Frisch, G. W. Trucks, H. B. Schlegel, G. E. Scuseria, M. A. Robb, J. R. Cheeseman, V. G. Zakrzewski, J. A. Montgomery, Jr., R. E. Stratmann, J. C. Burant, S. Dapprich, J. M. Millam, A. D. Daniels, K. N. Kudin, M. C. Strain, O. Farkas, J. Tomasi, V. Barone, M. Cossi, R. Cammi, B. Mennucci, C. Pomelli, C. Adamo, S. Clifford, J. Ochterski, G. A. Petersson, P. Y. Ayala, Q. Cui, K. Morokuma, N. Rega, P. Salvador, J. J. Dannenberg, D. K. Malick, A. D. Rabuck, K. Raghavachari, J. B. Foresman, J. Cioslowski, J. V. Ortiz, A. G. Baboul, B. B. Stefanov, G. Liu, A. Liashenko, P. Piskorz, I. Komaromi, R. Gomperts, R. L. Martin, D. J. Fox, T. Keith, M. A. Al-Laham, C. Y. Peng, A. Nanayakkara, M. Challacombe, P. M. W. Gill, B. Johnson, W. Chen, M. W. Wong, J. L. Andres, C. Gonzalez, M. Head-Gordon, E. S. Replogle, and J. A. Pople, Gaussian, Inc., Pittsburgh PA, **2002**; see also Supporting Information.
- [10] a) J. C. Slootweg, A. W. Ehlers, K. Lammertsma, *J. Mol. Model.* **2005**, *11*, in press; b) J. C. Slootweg, F. J. J. de Kanter, M. Schakel, A. W. Ehlers, B. Gehrhus, M. Lutz, A. M. Mills, A. L. Spek, K. Lammertsma, *Angew. Chem.* **2004**, *116*, 3556–3559; *Angew. Chem. Int. Ed.* **2004**, *43*, 3474–3477.
- [11] a) N. H. Tran Huy, F. Mathey, *Tetrahedron Lett.* **1988**, *29*, 3077–3078.
- [12] a) S. Ito, H. Jin, S. Kimura, M. Yoshifuji, *J. Org. Chem.* **2005**, *70*, 3537–3541; Stable 1-phosphabutadienes are also reported: b) B. A. Boyd, R. J. Thoma, W. H. Watson, R. H. Nellson, *Organometallics* **1988**, *7*, 572–574; c) R. Appel, F. Knoch, H. Kunze, *Chem. Ber./Recueil* **1984**, *117*, 3151–3159.
- [13] a) K. A. Nguyen, M. S. Gordon, *J. Am. Chem. Soc.* **1995**, *117*, 3835–3847; b) L. Deng, T. Ziegler, *J. Phys. Chem.* **1995**, *99*, 612–618; c) O. Wiest, K. N. Houk, K. A. Black, B. E. Thomas IV, *J. Am. Chem. Soc.* **1995**, *117*, 8594–8599.
- [14] K. Lammertsma, A. W. Ehlers, M. L. McKee, *J. Am. Chem. Soc.* **2003**, *125*, 14750–14759.
- [15] R. E. Buló, A. W. Ehlers, S. Grimme, K. Lammertsma, *J. Am. Chem. Soc.* **2002**, *124*, 13903–13910; and references therein.
- [16] a) J. C. Slootweg, M. Schakel, F. J. J. de Kanter, A. W. Ehlers, S. I. Kozhushkov, A. de Meijere, M. Lutz, A. L. Spek, K. Lammertsma, *J. Am. Chem. Soc.* **2004**, *126*, 3050–3051; b) R. E. Buló, A. W. Ehlers, F. J. J. de Kanter, M. Schakel, M. Lutz, A. L. Spek, K. Lammertsma, B. Wang, *Chem. Eur. J.* **2004**, *10*, 2732–2738.
- [17] J. Weber, U. H. Brinker, *Angew. Chem.* **1997**, *109*, 1689–1692; *Angew. Chem. Int. Ed. Engl.* **1997**, *36*, 1623–1626.
- [18] a) F. Mercier, C. Hugel-Le Goff, F. Mathey, *Tetrahedron Lett.* **1989**, *30*, 2397–2398; b) S. Haber, P. Le Floch, F. Mathey, *J. Chem. Soc. Chem. Commun.* **1992**, 1799–1800; c) S. Ito, S. Kimura, M. Yoshifuji, *Org. Lett.* **2003**, *5*, 1111–1114.
- [19] Phenyl: A. Padwa, T. Kumagai, M. Tohidi, *J. Org. Chem.* **1983**, *48*, 1834–1840; Methyl: W. R. Moore, K. G. Taylor, P. Müller, S. S. Hall, Z. L. F. Gaibel, *Tetrahedron Lett.* **1970**, 2365–2368.

Uncatalyzed Mukaiyama–Michael Reaction: Rapid Access to Simple and Complex Enantiopure γ -Butenolides**

José Barluenga,* Ana de Prado, Javier Santamaría, and Miguel Tomás

Access to enantiopure γ -butenolides currently represents a research area of great interest because of their presence as a subunit in many natural products and, particularly, in compounds with biological activity.^[1] Elaboration of the commercial 2-trimethylsilyloxyfuran (TMSOF) reagent by means of an asymmetric Mukaiyama–aldol reaction has been, thus far, the most efficient method for the formation of substituted chiral γ -butenolides.^[2] The Mukaiyama–Michael reaction is much less common and can be brought about through the use of either chiral metal catalysts and alkenoyl oxazolidinones^[3] or chiral organocatalysts and enals, as was elegantly demonstrated by MacMillan and co-workers.^[4] In looking for novel acceptor substrates, we focused on the suitability of enantiopure Fischer carbene complexes **1** as they are strongly electrophilic in nature,^[5,6] and are readily accessible by condensation of methylcarbene complexes and chiral aldehydes.^[7] Furthermore, the presence of both the acetal/ketal moiety and especially the metal carbene functionality in the Michael adduct permits further elaboration.^[8]

We found that enantiopure tungsten carbene complexes **1** are reactive toward 2-trimethylsilyloxyfuran at low temperatures (Scheme 1). Thus, the treatment of carbene **1a** with TMSOF in toluene (-60°C , 42 h) resulted in the formation of the carbene complex **3a** almost exclusively (92% yield). The high *anti/syn* ratio (11:1) and face selectivity (97:3 d.r.) is notable and allowed the isolation of pure **3a** in 81% yield after a single purification step by flash chromatography. Under similar reaction conditions (toluene, -70°C , 48 h), the conjugate addition of TMSOF to the carbene complex **1b** afforded the adduct **3b** with high selectivity (*anti/syn* = 8:1,



Scheme 1. Stereoselective Mukaiyama–Michael reaction of TMSOF (**2**) with carbene complexes **1**.

and $>98:2$ d.r.) and yield (88% yield; 76% of pure **3b** after chromatographic purification). Both chiral subunits are reactive and complement each other in terms of stereoselective induction as the configuration of the stereogenic centers created in **3a** and **3b** each subunit are opposite.^[9]

The stereoselectivity can be rationalized by assuming the model calculated for the [4+2] cycloaddition of the corresponding isolobal esters.^[10] Thus, the less hindered approach of TMSOF to the C=C bond of **1a** from the minimum energy conformation **A** would lead to the major isomer **3a**. In the same way, the adduct **3b** would arise by the attack of TMSOF at **1b** through the conformation **B** (Figure 1).^[11]

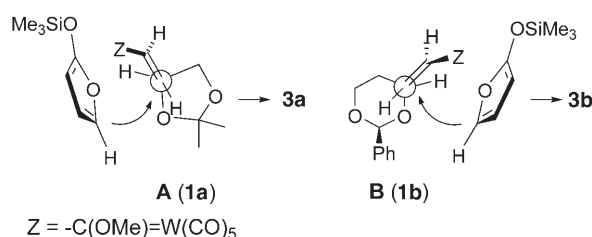


Figure 1. Proposed TMSOF–carbene complex approach.

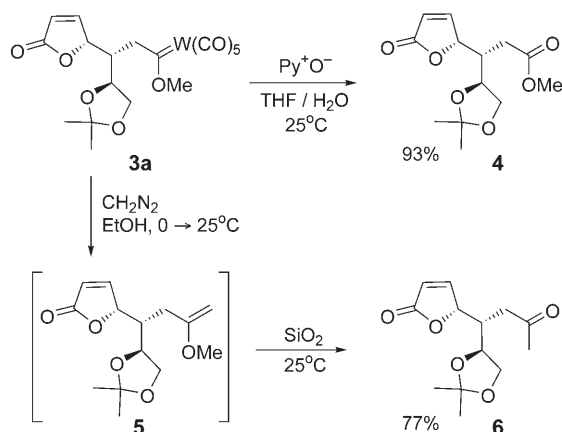
The potential of this facile approach to γ -butenolides can be stressed by taking advantage of the broad chemistry of the metal carbene functionality. First, oxidative removal of the metal from **3a** through the action of pyridinium oxide yielded the corresponding ester derivative **4** in 93% yield ($[\alpha]_{\text{D}}^{20} = +74.7$ ($c = 0.17$, CH_2Cl_2); Scheme 2). In turn, methylenation of **3a** with diazomethane afforded the enol ether **5**, which was transformed into the methyl ketone **6** in situ by hydrolysis over silica gel (77% yield from **3a**; $[\alpha]_{\text{D}}^{20} = +70.2$ ($c = 0.55$, CH_2Cl_2)). These simple processes constitute efficient alternatives to the unknown Mukaiyama–Michael addition of TMSOF to both esters and ketones (75% and 62% overall yields of **4** and **6**, respectively, from carbene **1a**).^[12,13]

The ease of synthesis of some complex enantiopure architectures containing the butenolide nucleus is exemplified in Scheme 3, which illustrates the transformation of **3a** into the fused lactone **8** (a process that formally involves an

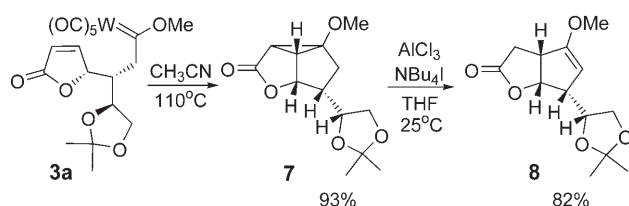
[*] Prof. Dr. J. Barluenga, A. de Prado, Dr. J. Santamaría, Prof. Dr. M. Tomás
Instituto Universitario de Química Organometálica “Enrique Moles”
Unidad Asociada al C.S.I.C., Universidad de Oviedo
33006 Oviedo (Spain)
Fax: (+34) 98-5103450
E-mail: barluenga@uniovi.es

[**] This research was partially supported by the Spain and Principado de Asturias Governments (BQU-2001–3853 and GE-EXP01–11). A.P. acknowledges the F.I.C.Y.T (Principado de Asturias) for a fellowship. We are also grateful to Dr. A. L. Suárez-Sobrino (Universidad de Oviedo) for his assistance in the X-ray crystallographic analysis and Dr. A. C. Valdés (Universidad de Oviedo) for ab initio calculations.

Supporting information for this article is available on the WWW under <http://www.angewandte.org> or from the author.



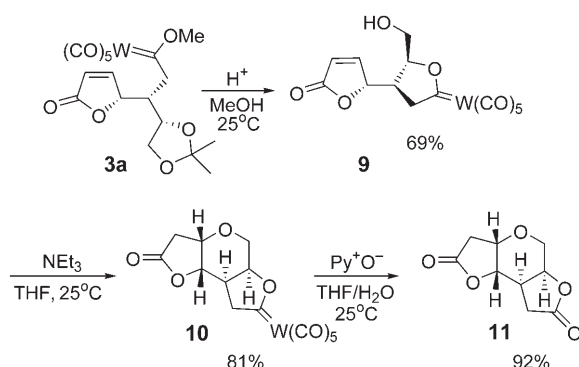
Scheme 2. Oxidation and methylenation of carbene complex **3a**.



Scheme 3. Transformation of complex **3a** into **7** and **8**: cyclopropanation and ring-opening reactions.

umpolung Michael addition reaction and therefore requires a metal catalyst). The intramolecular cyclopropanation of **3a** is carried out in acetonitrile (110°C, 5 h, sealed tube) to furnish **7** as the sole stereoisomer (93 % yield; $[\alpha]_D^{20} = -58.8$ ($c = 0.34$, CH_2Cl_2)). The subsequent Lewis acid promoted cyclopropane ring opening of **7** gave the *cis*-fused γ -lactone **8** (82 % yield; $[\alpha]_D^{20} = -21.5$ ($c = 0.55$, CH_2Cl_2)).

The ketal chiral subunit is also useful for the formation of further complex enantiopure molecules (Scheme 4). As a result of the advantageous location of the protected diol functionality of **3a**, it might be possible, among other transformations, to assemble both γ -lactone and tetrahydropyran cores which would therefore give access to linearly fused furan–pyran–furan structures.^[14] Simple deprotection of



Scheme 4. Diol deprotection of complex **3a**: Formation of bislactone **9** and enantiopure fused furan–pyran–furan compounds **10–11**. Py = pyridine.

the ketal functionality of **3a** with acid and subsequent intramolecular displacement of the methoxy group resulted in the regioselective formation of the cyclic metal carbene **9** (69 % yield). The carbene **9** was subsequently treated with base ($\text{Et}_3\text{N}/\text{CH}_2\text{Cl}_2$, 25°C) to yield the enantiopure metal complex **10** (81 % yield) through a diastereoselective intramolecular Michael-type addition.^[15,16] Notably, the metal carbene functionality does survive under acidic and basic conditions, thus allowing its reactivity to be exploited at any stage. The oxidative demetalation of **10** gave rise to the enantiopure bislactone **11** in 92 % yield ($[\alpha]_D^{20} = -94.2$ ($c = 0.48$, CH_2Cl_2)), which features, two γ -lactone rings as well as a highly functionalized central pyran ring with four stereogenic carbon centers.

In conclusion, we reported herein the first uncatalyzed, diastereoselective Mukaiyama–Michael addition reaction and showed efficient access to a number of enantiopure butenolide-based structures. This sequence is a successful combination of two major features: 1) Fischer alkenyl carbenes that incorporate a chiral fragment at the β -carbon—readily available from the chiral pool—undergo very rapid diastereoselective Mukaiyama–Michael reaction with TMSOF, 2) these adducts can be transformed into valuable enantiopure molecules owing to the diverse reactivity of the metal carbene function, as well as to the conventional functional group transformations of the protected diol. Moreover, the synthetic utility of this strategy could be enhanced as a number of chiral pool derived aldehydes could provide structurally diverse alkenyl carbene complexes.

Received: May 20, 2005

Published online: September 19, 2005

Keywords: asymmetric synthesis · carbenes · chirality · diastereoselectivity · lactones

- [1] Selected examples: a) Y. S. Rao, *Chem. Rev.* **1976**, 76, 625; b) R. Bloch, L. Gilbert, *J. Org. Chem.* **1987**, 52, 4603; c) K. Mori, *Tetrahedron* **1989**, 45, 3233; d) E. Fukusaki, S. Senda, Y. Nakazono, T. Omata, *Tetrahedron* **1991**, 47, 6223; e) A. D. Rodríguez, J. G. Shi, S. P. D. Huang *J. Org. Chem.* **1998**, 63, 4425.
- [2] a) G. Casiraghi, G. Rassu, *Synthesis* **1995**, 607; b) G. Casiraghi, F. Zanardi, G. Appendino, G. Rassu, *Chem. Rev.* **2000**, 100, 1929.
- [3] a) H. Kitajima, T. Katsuki, *Synlett* **1997**, 568; b) H. Kitajima, K. Ito, T. Katsuki, *Tetrahedron* **1997**, 53, 17015; c) H. Suga, T. Kitamura, A. Kakehi, T. Baba, *Chem. Commun.* **2004**, 1414.
- [4] P. Brown, N. C. Goodwin, D. W. C. MacMillan, *J. Am. Chem. Soc.* **2003**, 125, 1192.
- [5] For selected reviews on Fischer carbene complexes, see a) F. Zaragoza Dörwald, *Metal Carbenes in Organic Synthesis*; Wiley-VCH, New York, **1999**; b) J. W. Herndon, *Coord. Chem. Rev.* **2004**, 248, 3; c) A. de Meijere, H. Schirmer, M. Duetsch, *Angew. Chem.* **2000**, 112, 4124; *Angew. Chem. Int. Ed.* **2000**, 39, 3964; d) J. Barluenga, J. Santamaría, M. Tomás, *Chem. Rev.* **2004**, 104, 2259; for reviews on enantiopure Fischer carbene complexes, see: e) W. D. Wulff, *Organometallics* **1998**, 17, 3116; f) K. H. Dötz, P. Tomuschat, *Chem. Soc. Rev.* **1999**, 28, 187.
- [6] For a review on 1,2- and 1,4-addition of carbon nucleophiles to Fischer carbenes, see: a) J. Barluenga, J. Flórez, F. J. Fañanás, *J. Organomet. Chem.* **2001**, 624, 5, for Michael addition reactions of alkyl/aryl and enolate anions to alkenyl carbenes derived from

- enantiopure alcohols, see: b) J. Barluenga, J. M. Montserrat, J. Flórez, S. García-Granda, E. Martín, *Angew. Chem.* **1994**, *106*, 1451; *Angew. Chem. Int. Ed. Engl.* **1994**, *33*, 1392; c) J. Barluenga, J. M. Montserrat, J. Flórez, S. García-Granda, E. Martín, *Chem. Eur. J.* **1995**, *1*, 236; for Michael additions of enantiopure enolate anions to alkenyl carbenes: d) J. Barluenga, A. Diéguez, F. Rodríguez, J. Flórez, F. J. Fañanás, *J. Am. Chem. Soc.* **2002**, *124*, 9056.
- [7] Complexes **1a** and **1b** are easily prepared from (*R*)-2,3-*O*-isopropylidene-D-glyceraldehyde and (*S*)-2,4-*O*-benzylidene-3-deoxyerythrose, respectively: J. Barluenga, N. Panday, J. Santamaría, A. de Prado, M. Tomás, *ARKIVOC* **2003**, 576.
- [8] Alkenyl Fischer carbene complexes with a monosaccharide unit at the β -carbon atom have been synthesized, and their Diels–Alder and Michael reactions toward cyclopentadiene and cyclohexanone enolates tested: K. H. Dotz, C. Jakel, W. C. Haase, *J. Organomet. Chem.* **2001**, *617–618*, 119.
- [9] Both compounds **3a** and **3b** were crystallized from a hexane-CH₂Cl₂, and their structure was determined by X-ray crystallographic analysis.
- [10] a) J. Mulzer, M. Kappert, G. Huttner, I. Jibril, *Tetrahedron Lett.* **1985**, *26*, 1631; b) R. Casas, T. Parella, V. Branchadell, A. Oliva, R. M. Ortuno, A. Guingant, *Tetrahedron* **1992**, *48*, 2659.
- [11] In the case of carbene **1b**, a fixed conformation may result from π stacking between the phenyl and alkenyl moieties that would produce the same stereoisomer **3b** and therefore cannot be ruled out.
- [12] At room temperature, TMSOF does not add to the methyl enoate that is structurally analogous to metal carbene **1a**, even in the presence of BF₃·OMe₂.
- [13] For a recent example of enantioselective Mukaiyama–Michel addition of ketene silyl acetals to enones, see: X. Wang, S. Adachi, H. Iwai, H. Takatsuki, K. Fujita, M. Kubo, A. Oku, T. Harada *J. Org. Chem.* **2003**, *68*, 10046.
- [14] A SciFinder search reveals that such a substructure remains unknown.
- [15] For a review on the construction of the pyran ring by intramolecular Michael reactions, see: R. D. Little, M. R. Masjedizadeh, O. Wallquist, J. I. McLoughlin, *Org. React.* **1995**, *47*, 315.
- [16] The configuration of the new stereogenic center was determined by NMR COSY and NOESY experiments. Moreover, this stereochemical reaction pathway is in agreement with molecular modeling studies. The two possible cyclization approaches were analyzed with ab initio calculations by using the anionic Michael-type cyclization to the lactone **11** (replacing W(CO)₅ in **10** by O) as the model. At the MP2/6-31G*//HF/6-31G* level of theory, the transition state that gives rise to the isomer observed, is 17.4 kcal mol^{−1} more stable than the alternative transition state.

DOI: 10.1002/anie.200501671

Finding Adiabatically Bound Anions of Guanine through a Combinatorial Computational Approach***Maciej Harańczyk and Maciej Gutowski**

Anions of nucleic acid bases may be formed by trapping low-energy electrons produced in living cells by high-energy radiation. Recent experiments suggested that single- and double-strand breaks develop in DNA exposed to low-energy electrons.^[1] Furthermore, charged nucleobases play a critical role in electron and hole transfer in DNA.^[2–4] Anionic states of nucleic acid bases have been intensively studied both experimentally and theoretically. On the basis of calculations, guanine is believed to have the lowest electron affinity among the nucleobases.^[5–7] This is consistent with the results of electron spin resonance experiments on γ -irradiated DNA, in which the anion is divided between the pyrimidine but not the purine bases.^[8]

Gas-phase experiments on guanine are scarce because this nucleic acid base easily decomposes at elevated temperatures. Burrow and co-workers reported a vertical electron affinity of -0.49 eV for guanine and assigned it to a hydroxy (enol) tautomer.^[9] We have recently determined—at the coupled cluster level of theory with single, double, and perturbative triple excitations (CCSD(T))^[10]—a negative adiabatic electron affinity (AEA) of -0.49 eV for the canonical tautomer.^[11] In contrast to earlier experimental and computational predictions, we demonstrate here that guanine supports anionic tautomers that are adiabatically bound with respect to the neutral canonical tautomer by as much as 8 kcal mol⁻¹,^[12] as calculated at the CCSD(T) level of theory. These

[*] M. Harańczyk, Prof. M. Gutowski
Department of Chemistry
University of Gdańsk
80-952 Gdańsk (Poland)
and
Chemical Sciences Division
Pacific Northwest National Laboratory
Richland, Washington 99352 (USA)
Fax: (+1) 509-375-4381
E-mail: maciej.gutowski@pnl.gov

[**] This work was supported by the U.S. DOE Office of Biological and Environmental Research, Low Dose Radiation Research Program (M.G.), and the Polish State Committee for Scientific Research (KBN, grant 4 T09A 012 24 for M.H.). Computing resources were available through a Computational Grand Challenge Application grant from the Molecular Sciences Computing Facility in the Environmental Molecular Sciences Laboratory, the National Energy Research Scientific Computing Center (NERSC), and the Academic Computer Center in Gdańsk (TASK). PNNL is operated by Battelle for the U.S. DOE under contract DE-AC06-76RLO 1830.



Supporting information for this article is available on the WWW under <http://www.angewandte.org> or from the author. Supporting Information Available: Color versions of Figures 1 and 2.

tautomers do not result from proton transfer between the electronegative atoms N or O, which were studied in the past for the neutral and anionic species. Instead they result from enamine–imine transformations, that is, a proton is transferred between the N and C atoms. Some of these anionic tautomers do not require a proton transfer from the N9 position (see Figure 1). Thus, they might exist in DNA or RNA, in which N9 is connected to a sugar unit. The new anionic tautomers might affect the structure of DNA and RNA, and might initiate chemical transformations leading to lesions in nucleic acids.^[13,14]

The unexpected positive values of AEA for the new imine tautomers were initially counterintuitive, and their discovery was facilitated by two factors. First, we recently demonstrated that the most stable valence anions of pyrimidine bases, such as 1-methylcytosine^[13] and uracil,^[14] also result from enamine–imine transformations, though a biologically relevant adiabatically bound anion has not been identified so far. Second, a combinatorial computational approach was invoked in the current study to identify the most stable anionic tautomers, without a bias dictated by stereotypes developed from studies on neutral tautomers of nucleic acid bases, that is, a proton being transferred between N or O atoms.^[15]

The computational screening of the anionic tautomers of guanine was started from a buckled molecular framework of heavy atoms among which five hydrogen atoms were distributed. We imposed the following constraints: zero or one hydrogen atom on N1, C2, N3, C4, C5, C6, N7, and N9; one or two hydrogen atoms on N2 or C8; zero, one, or two hydrogen atoms on O4 (Figure 1). With these constraints we generated 499 initial structures including the *E* and *Z* tautomers as well as rotamers of imino and hydroxy groups. These structures were divided into three groups: 2N2 (amino tautomers), N2c, and N2t (imino tautomers with a hydrogen atom at N2 arranged *cis* or *trans* with respect to N1). Additionally, each group was divided into two subgroups C8 and 2C8, depending on the number of hydrogen atoms attached to C8. We use the notation G_{ab}^b , where “a” is the group and subgroup and “b” is a string of heavy atoms to which the remaining hydrogen atoms are connected. The anionic species bear a prefix a_{val} .

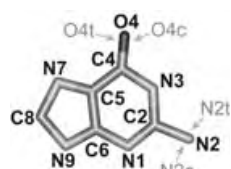


Figure 1. The heavy atoms of guanine; the *cis* and *trans* positions for N2 and O4 are shown.

We found that 2.81% of all screened structures are adiabatically stable at the B3LYP/6-31++G** level of theory, with the range of stability at 0.4–12.2 kcal mol^{−1}. For

further studies we selected the following: 1) the most stable valence anion $a_{val}G_{2N2,C8}^{C2,N3}$, which has no hydrogen atom attached to N9; 2) three valence anions that might be biologically relevant because a hydrogen atom is attached to N9 ($a_{val}G_{2N2,2C8}^{N3,N9}$, $a_{val}G_{N2c,2C8}^{N3,N9}$, and $a_{val}G_{N2t,2C8}^{N3,N9}$); and 3) the valence anions $a_{val}G_{2N2,C8}^{N3,N9}$ and $a_{val}G_{2N2,C8}^{N3,N7}$, which are based on the two most stable tautomers of neutral guanine (Figure 2).

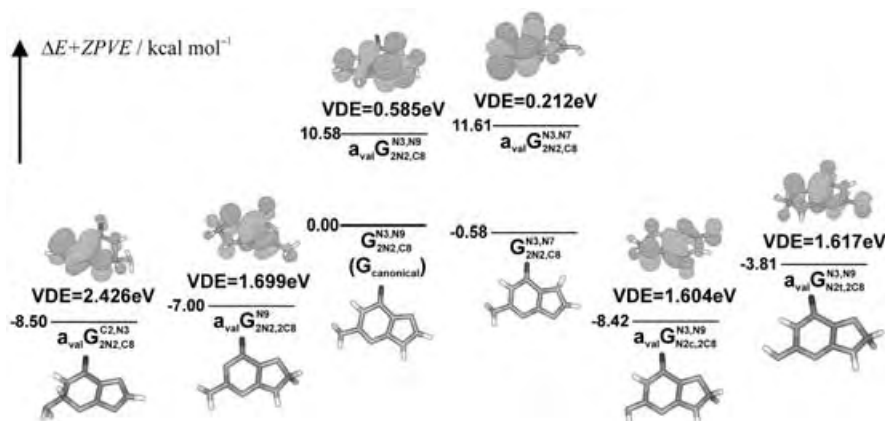


Figure 2. The relative electronic energies of the various tautomers studied, corrected for energies of zero-point vibrations ($\Delta E + ZPVE$), as well as the electron vertical detachment energies (VDEs). The adiabatically bound anions are on the left and right sides. In the middle, the two most stable tautomers of the neutral and their accompanying valence anions are shown.

These anionic structures were further optimized, and harmonic frequencies were calculated at the second-order Møller–Plesset level (MP2), and the final energies were then calculated at the CCSD(T) level. The aug-cc-pVDZ basis set^[16] was used in the MP2 and CCSD(T) calculations. The effects of hydration were included within the IEF-PCM method with the cavity built up using the United Atom model (UA0).^[17] The calculations were performed using Gaussian03^[18] NWChem,^[19] and Molpro software packages,^[20] and the molecular structures and orbitals were drawn with the Molden program.^[21]

We found that the four anionic tautomers that result from enamine–imine transformations were adiabatically bound with respect to both the neutral $G_{2N2,C8}^{N3,N9}$ canonical tautomer and the most stable neutral tautomer $G_{2N2,C8}^{N3,N7}$. These gas-phase results, presented in Figure 2, are based on the CCSD(T) electronic energies and MP2 geometries and harmonic vibrational frequencies. The most stable anion $a_{val}G_{2N2,C8}^{C2,N3}$ is bound with respect to $G_{2N2,C8}^{N3,N9}$ by 8.50 kcal mol^{−1}. This anion is characterized by a large vertical detachment energy (VDE) of 2.426 eV. Among the three anionic tautomers that have a hydrogen atom on N9, the anion $a_{val}G_{2N2,C8}^{N3,N9}$ is 8.42 kcal mol^{−1} more stable than $G_{2N2,C8}^{N3,N9}$. This value is much larger than our estimation of uncertainties of the AEAs determined at the CCSD(T)/aug-cc-pVDZ level, which is about 1 kcal mol^{−1}. The two other anions $a_{val}G_{2N2,2C8}^{N3,N9}$ and $a_{val}G_{N2t,2C8}^{N3,N9}$ are more stable than $G_{2N2,C8}^{N3,N9}$ by 7.00 and 3.81 kcal mol^{−1}, respectively. The values of VDE for the last three anionic tautomers are similar, about 1.6 eV, and still much larger than the VDE values of anions based on the most stable neutral tautomers. We predict that there are many anionic enamine–imine

tautomers that are adiabatically bound with respect to neutral guanine.

The effect of an aqueous environment on the stability of the new anionic tautomers was tested within the PCM model (Table 1). The new imine tautomers are again more stable

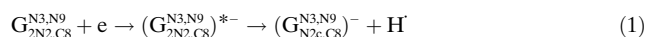
Table 1: Adiabatic electron affinities (AEAs) and electron vertical detachment energies (VDEs) for the tautomers of hydrated guanine characterized within the PCM model.

Tautomer	AEA [eV] ^[a]	VDE [eV] ^[b]
G ^{N3,N9} _{2N2,C8}	1.329	3.381
G ^{N3,N7} _{2N2,C8}	1.496	2.643
G ^{N9} _{2N2,2C8}	2.211	4.625
G ^{N3,N9} _{2N2,C8}	2.026	4.424
G ^{N3,N9} _{2N2,C8}	1.953	4.566
G ^{N2,C8} _{2N2,C8}	1.861	5.350

[a] $\epsilon = 78$. [b] $\epsilon = 78$ and 2 for the initial and final states, respectively.

than anions based on the two most stable tautomers of the neutral molecule. Additionally, the three imine tautomers with a hydrogen atom attached to N9 are more stable than $a_{\text{val}}G_{2N2,C8}^{N3,N9}$. Thus the tautomers with a hydrogen atom attached to N9 might dominate in aqueous solution. These tautomers might be susceptible to further transformations, and lesions in the DNA might develop. For instance, the $a_{\text{val}}G_{2N2,C8}^{N3,N9}$ and $a_{\text{val}}G_{2N2,C8}^{N3,N9}$ tautomers cannot maintain Watson–Crick-type hydrogen bonding with cytosine.

We suggest two formation pathways for the new anionic tautomers. First, they might be formed through intermolecular proton transfer, with acidic and basic sites interacting with $a_{\text{val}}G_{2N2,C8}^{N3,N9}$. Second, dissociative electron attachment^[22,23] to $G_{2N2,C8}^{N3,N9}$ [Eq. (1)]—where $(G_{2N2,C8}^{N3,N9})^{*-}$ denotes a scattering



state for an excess electron and $(G_{2N2,C8}^{N3,N9})^{-}$ denotes a deprotonated guanine in the ground electronic state—can be followed by attachment of a hydrogen atom to C8 [Eq. (2)].



We have found that this step is barrier-free.

In summary, guanine supports many adiabatically bound valence anions, which result from enamine–imine transformations of the most stable neutral tautomers. These stable anionic tautomers were found using combinatorial computational prescreening at the B3LYP level of theory followed by CCSD(T)/aug-cc-pVDZ calculations. The new anionic tautomers might be formed by dissociative electron attachment followed by attachment of a hydrogen atom to a carbon atom. These tautomers may affect the structure and properties of DNA and RNA exposed to low-energy electrons. Chemical transformations of DNA triggered by the new anionic tautomers will be explored in our future studies.

Received: May 15, 2005

Published online: September 15, 2005

Keywords: ab initio calculations · anions · combinatorial chemistry · guanine · nucleobases

- [1] B. Boudaiffa, P. Cloutier, D. Hunting, M. A. Huels, L. Sanche, *Science* **2000**, 287, 1658–1660.
- [2] a) Z. Cai, M. D. Sevilla, *J. Phys. Chem. B* **2000**, 104, 6942–6949; b) A. Messer, K. Carpenter, K. Forzley, J. Buchanan, S. Yang, Y. Razskazovskii, Z. Cai, M. D. Sevilla, *J. Phys. Chem. B* **2000**, 104, 1128–1136; c) Z. Cai, Z. Gu, M. D. Sevilla, *J. Phys. Chem. B* **2000**, 104, 10406–10411.
- [3] Y. A. Berlin, A. L. Burin, M. A. Ratner, *J. Am. Chem. Soc.* **2001**, 123, 260–268, and references therein.
- [4] M. Bixio, J. Jortner, *J. Phys. Chem. A* **2001**, 105, 10322–10328, and references therein.
- [5] X. Li, Z. Cai, M. D. Sevilla, *J. Phys. Chem. A* **2002**, 106, 1596–1603.
- [6] S. D. Wetmore, R. J. Boyd, L. A. Eriksson, *Chem. Phys. Lett.* **2000**, 322, 129–135.
- [7] S. S. Wesolowski, M. L. Leininger, P. N. Pentchev, H. F. Schaefer III, *J. Am. Chem. Soc.* **2001**, 123, 4023–4028.
- [8] M. D. Sevilla, D. Becker, M. Yan, S. R. Summerfield, *J. Phys. Chem.* **1991**, 95, 3409–3415.
- [9] K. Aflatoon, G. A. Gallup, P. D. Burrow, *J. Phys. Chem. A* **1998**, 102, 6205–6207.
- [10] P. R. Taylor in *Lecture Notes in Quantum Chemistry II* (Ed.: B. O. Roos), Springer, Berlin, **1994**.
- [11] M. Harańczyk, M. Gutowski, *J. Am. Chem. Soc.* **2005**, 127, 699–706.
- [12] 1 eV = 23.068 kcal mol^{−1}.
- [13] M. Harańczyk, J. Rak, M. Gutowski, *J. Phys. Chem. A*, in press.
- [14] R. Bachorz, J. Rak, M. Gutowski, *Phys. Chem. Chem. Phys.* **2005**, 7, 2116–2125.
- [15] P. Hobza, J. Sponer, *Chem. Rev.* **1999**, 99, 3247–3276.
- [16] R. A. Kendall, T. H. Dunning, Jr., R. J. Harrison, *J. Chem. Phys.* **1992**, 96, 6796–6806.
- [17] J. Tomasi, M. Perisco, *Chem. Rev.* **1994**, 94, 2027–2094.
- [18] Gaussian 03, Revision C.02, M. J. Frisch, G. W. Trucks, H. B. Schlegel, G. E. Scuseria, M. A. Robb, J. R. Cheeseman, J. A. Montgomery, Jr., T. Vreven, K. N. Kudin, J. C. Burant, J. M. Millam, S. S. Iyengar, J. Tomasi, V. Barone, B. Mennucci, M. Cossi, G. Scalmani, N. Rega, G. A. Petersson, H. Nakatsuji, M. Hada, M. Ehara, K. Toyota, R. Fukuda, J. Hasegawa, M. Ishida, T. Nakajima, Y. Honda, O. Kitao, H. Nakai, M. Klene, X. Li, J. E. Knox, H. P. Hratchian, J. B. Cross, V. Bakken, C. Adamo, J. Jaramillo, R. Gomperts, R. E. Stratmann, O. Yazyev, A. J. Austin, R. Cammi, C. Pomelli, J. W. Ochterski, P. Y. Ayala, K. Morokuma, G. A. Voth, P. Salvador, J. J. Dannenberg, V. G. Zakrzewski, S. Dapprich, A. D. Daniels, M. C. Strain, O. Farkas, D. K. Malick, A. D. Rabuck, K. Raghavachari, J. B. Foresman, J. V. Ortiz, Q. Cui, A. G. Baboul, S. Clifford, J. Cioslowski, B. B. Stefanov, G. Liu, A. Liashenko, P. Piskorz, I. Komaromi, R. L. Martin, D. J. Fox, T. Keith, M. A. Al-Laham, C. Y. Peng, A. Nanayakkara, M. Challacombe, P. M. W. Gill, B. Johnson, W. Chen, M. W. Wong, C. Gonzalez, J. A. Pople, Gaussian, Inc., Wallingford CT, **2004**.
- [19] NWChem, Version 4.6, E. Aprà, T. L. Windus, T. P. Straatsma, E. J. Bylaska, W. de Jong, S. Hirata, M. Valiev, M. Hackler, L. Pollack, K. Kowalski, R. Harrison, M. Dupuis, D. M. A. Smith, J. Nieplocha, V. Tipparaju, M. Krishnan, A. A. Auer, E. Brown, G. Cisneros, G. Fann, H. Früchtl, J. Garza, K. Hirao, R. Kendall, J. Nichols, K. Tsemekhman, K. Wolinski, J. Anchell, D. Bernholdt, P. Borowski, T. Clark, D. Clerc, H. Dachsel, M. Deegan, K. Dyall, D. Elwood, E. Glendening, M. Gutowski, A. Hess, J. Jaffe, B. Johnson, J. Ju, R. Kobayashi, R. Kutteh, Z. Lin, R. Littlefield, X. Long, B. Meng, T. Nakajima, S. Niu, M. Rosing, G. Sandrone, M. Stave, H. Taylor, G. Thomas, J. van Lenthe, A. Wong, Z.

Zhang, Pacific Northwest National Laboratory, Richland, Washington, **2004**.

- [20] MOLPRO, Version 2002.1, R. D. Amos, A. Bernhardsson, A. Berning, P. Celani, D. L. Cooper, M. J. O. Deegan, A. J. Dobbyn, F. Eckert, C. Hampel, G. Hetzer, P. J. Knowles, T. Korona, R. Lindh, A. W. Lloyd, S. J. McNicholas, F. R. Manby, W. Meyer, M. E. Mura, A. Nicklass, P. Palmieri, R. Pitzer, G. Rauhut, M. Schütz, U. Schumann, H. Stoll, A. J. Stone, R. Tarroni, T. Thorsteinsson, H.-J. Werner.
- [21] G. Schaftenaar, J. H. Noordik, *J. Comput.-Aided Mol. Des.* **2000**, *14*, 123–134.
- [22] H. Abdoul-Carime, S. Gohlke, E. Illenberger, *Phys. Rev. Lett.* **2004**, *92*, 168103.
- [23] S. Denifl, S. Ptasinska, M. Cingel, S. Matejcik, P. Scheier, T. D. Mark, *Chem. Phys. Lett.* **2003**, *377*, 74–80.

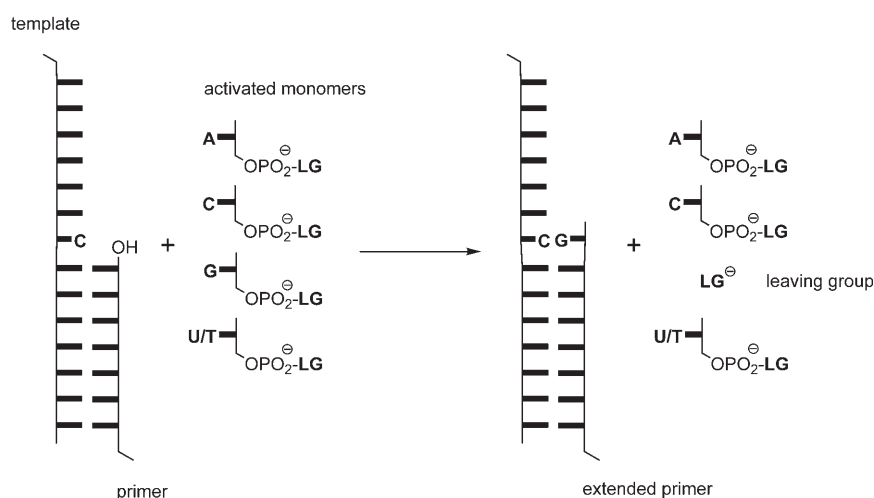
DNA Replication

DOI: 10.1002/anie.200501794

Chemical Primer Extension: Efficiently Determining Single Nucleotides in DNA**

Patrizia Hagenbuch, Eric Kervio, Annette Hochgesand, Ulrich Plutowski, and Clemens Richert*

The replication and transcription of genetic information requires the stepwise extension of DNA or RNA primers in sequence-specific, template-directed reactions (Scheme 1). Template-directed primer extension also underlies PCR,^[1] dideoxy sequencing,^[2] and attempts to recreate life from inanimate materials.^[3] Primer extension presents a formidable chemical challenge. Four different, richly functionalized monomers (the mononucleotides) have to be converted into good electrophiles that react in sequence-selective oligomerization reactions in aqueous solution without polymerizing or hydrolyzing rapidly. Nature employs pyrophosphates as leaving groups and



Scheme 1. Primer extension.

enzymes with proofreading capabilities (polymerases) to meet this challenge. Entirely chemical, non-enzymatic systems employing imidazolides as leaving groups show a certain level of spontaneous primer extension, but successful replication has remained elusive.^[3]

Known non-enzymatic replication reactions with monomers are slow. For ribonucleotides and 2-methylimidazolides as activated monomers, reaction times of days are required, even if the monomers are employed near their solubility limit (≥ 50 mM)^[4] under extreme salt conditions (up to 1M Mg²⁺).^[5] Weakly base pairing nucleotides (A or U/T as nucleobase) are incorporated more slowly than those that form stable base pairs (C or G as nucleobase).^[6] Even the ligation of oligonucleotides requires the templating of G and C residues.^[7] This makes non-enzymatic primer extension seemingly unattractive for practical applications, such as the genotyping of single-nucleotide polymorphisms (SNPs) by mass spectrometry.^[8] Herein we demonstrate how these reactions can be accelerated, so that the determination of nucleotides at selected sites of DNA within hours becomes feasible, starting from subpicomole quantities of analytes.

We first used 2-methylimidazolides^[9] (LG = MeIm) of 2'-deoxynucleosides **1a–t** as activated monomers **2a–t** (Scheme 2), which were treated with 3'-amino-terminal primers. Amines are known to react faster than alcohols with activated nucleotides,^[10,11] so that singly extended primers rather than the product mixtures typical for chemical replication reactions are formed. Assays were monitored by

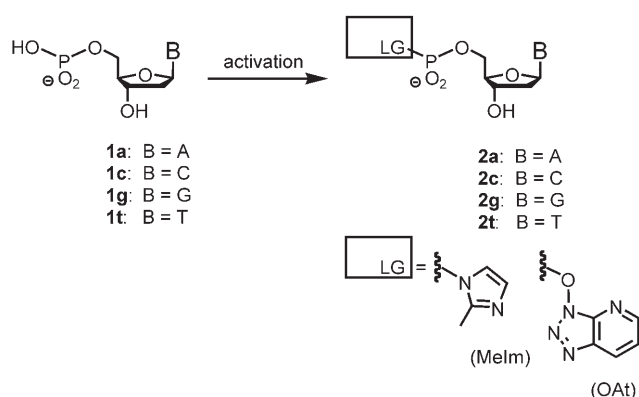
[*] Dr. P. Hagenbuch, Dr. E. Kervio, A. Hochgesand, U. Plutowski, Prof. C. Richert
Institut für Organische Chemie
Universität Karlsruhe (TH)
76131 Karlsruhe (Germany)
Fax: (+49) 721-608-4825
E-mail: cr@rrg.uka.de

[**] The authors thank Dr. J. Rojas Stütz for helpful discussions. This work was supported by the DFG (grant no. RI 1063/1-3) and the Fonds der Chemischen Industrie (project 164431).

Supporting information for this article is available on the WWW under <http://www.angewandte.org> or from the author.

quantitative MALDI-TOF mass spectrometry,^[12] thus allowing competitive reactions with all four activated nucleotides in the same solution and selective detection of products in mass spectra.^[13] Second-order rate constants were derived from fits to the kinetic data.^[13] We tested whether non-enzymatic primer extension was detectable with any of the four possible bases (A, C, G, T) at the templating position of 40-mer templates **4a–t** (Scheme 3).

Sequence-selective extension was observed for each of the four reactions (Table 1). Although this established that chemical primer extension was sufficiently selective to



Scheme 2. Activated monomers **2a–t**.

Table 1: Results from primer extension reactions with a mixture of the four 2-methylimidazolides **2a–t**/MeIm.^[a]

Primer/ template	k' [h ⁻¹ M ⁻¹] ^[b]	Product ratio (primer+C/T/A/G)
3/4a	46	3:84:5:8
3/4c	84	4:5:8:83
3/4g	38	84:5:10:1
3/4t	43	6:9:74:11

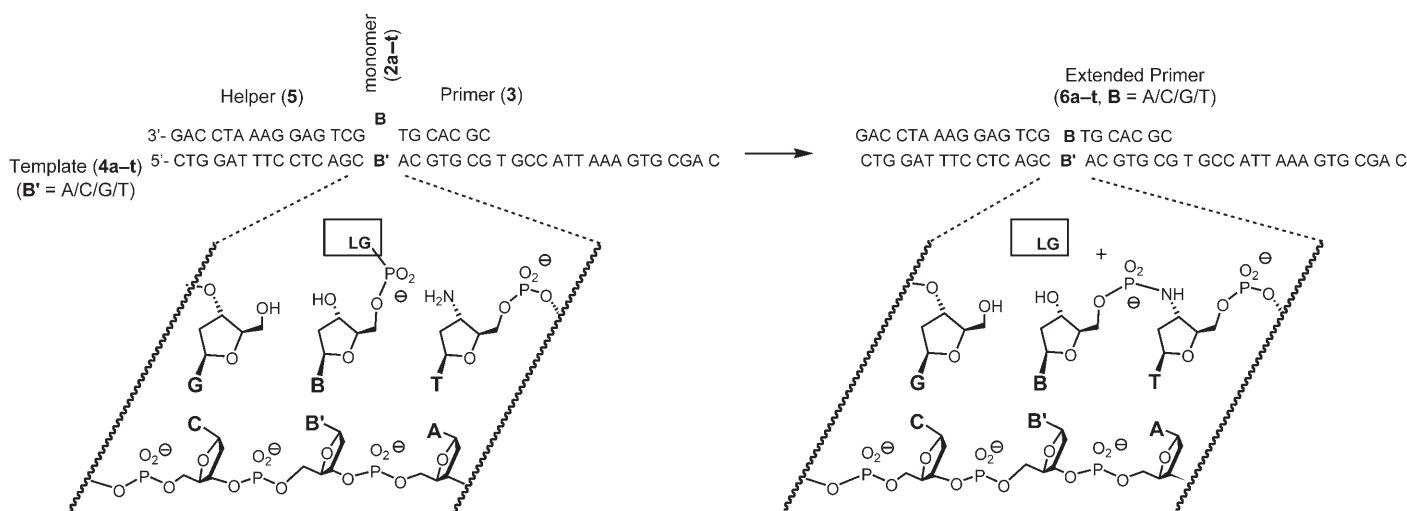
[a] **[2a–t]** = 19.3 mM; primer/template: 360 μM; pH 7.9; buffer: HEPES (200 mM), NaCl (400 mM), MgCl₂ (80 mM). [b] k' = second-order rate constant for the formation of desired product; oligonucleotide complexes treated as one reactant, activated nucleotide as the other.

identify a templating nucleotide in DNA, the assay was not attractive for genotyping or analyzing epigenomic methylation patterns,^[14,15] as it requires 1.8 nmol of template for a 5-μL assay, that is, more template than is available in typical clinical samples after PCR. We therefore decreased the concentration of template and primer tenfold and reduced the concentration of the activated monomers from 19.3 mM to 3.6 mM. Dilution favors hydrolysis of the activated nucleotides, an unavoidable competing reaction, and disfavors the

association of monomers and template. Under these conditions, even a strongly base pairing nucleotide at the templating position, when offered the matched monomer alone, gave a second-order rate constant that was almost an order of magnitude lower than that measured at higher concentration (compare Table 1, entry 3 with Table 2, entry 1). In the absence of competing reactions and/or changes in binding equilibria, second-order rate constants should, of course, be independent of concentration.

We then focused on identifying alternative leaving groups for the activated deoxynucleotides. Ferris and co-workers had previously shown that oligomerization of ribonucleotides on mineral surfaces can be accelerated through judicious choice of leaving groups,^[16] but template-directed reactions have proven to be a challenge to accelerate.^[17] With EDC^[18] alone, template **4a** gives non-sequence-selective extensions. Attempts to improve extension reactions through activation in situ with EDC in the presence of possible leaving groups or through addition of organic catalysts to methylimidazolides failed (see Supporting Information). Proflavine^[19] increased the conversion with **2c**-MeIm minimally from 16 to 21% after 4 h, and this effect was observed only at the highest concentration tested (0.67 mM).

Therefore, we focused on the activation of **1c** in organic solvents and the addition of the activated monomers to **3/4g** in aqueous buffer. The tetrazolide of **2c** gave a slight acceleration over **2c**-MeIm, but the only substantial acceleration was observed after activation with HATU^[20] and HOAt, reagents originally developed for peptide coupling. Optimized activation conditions gave an active ester in satisfactory yield after precipitation (see Supporting Information). Azabenzotriazolidine **2c**-OAt reacts four times faster than **2c**-MeIm with **3/4g** (Table 2) and does not undergo significant side reactions with the primer. Interestingly, an even more dramatic acceleration of primer extension is observed in an all-RNA system when switching from methylimidazolides to azabenzotriazolidines, even though the nucleophile is a hydroxy group in that case.^[21]



Scheme 3. Primer-extension system employed.

Table 2: Effect of activation of monomers, helper, and pH shift on the rate of non-enzymatic single-nucleotide-extension reactions.^[a]

Oligomers	Monomer(s)/ LG/reagent ^[b]	pH	k' [h ⁻¹ M ⁻¹] ^[c]	Product ratio (primer+C/T/A/G) ^[d]	$t_{1/2}$ primer [h]
noncompetitive reactions					
3/4g	2c/Melm	7.9	5	–	38.5
3/4g	2c/OAt	7.9	19	–	10.0
3/4g/5	2c/Melm	7.9	20	–	9.5
3/4g/5	2c/OAt	7.9	112	–	1.7
3/4g/5	2c/OAt ^[e]	7.9	205	–	0.9
3/4g/5	2c/OAt ^[e]	8.9	381	–	0.5
3/4g/5	2c/OAt ^[e]	9.5	393	–	0.5
competitive reactions					
3/4a/5	2a-t/OAt	8.9	94	4:64:14:18	2.0
3/4c/5	2a-t/OAt	8.9	259	1:1:5:93	0.7
3/4g/5	2a-t/OAt	8.9	212	86:1:8:5	0.9
3/4t/5	2a-t/OAt	8.9	217	1:1:89:9	0.9
competitive reactions, one-pot activation/extension					
3/4a/5	2a-t/OAt/EDC	8.9	81	4:75:18:3	2.4
3/4c/5	2a-t/OAt/EDC	8.9	177	1:3:1:95	1.1
3/4g/5	2a-t/OAt/EDC	8.9	230	97:1:1:1	0.8
3/4t/5	2a-t/OAt/EDC	8.9	134	1:1:97:1	1.4
competitive one-pot assays with dT-boosted monomer mixture					
3/4a/5	2a-t/OAt/EDC	8.9	47	2:90:5:3	0.8
3/4c/5	2a-t/OAt/EDC	8.9	146	1:1:1:97	1.3
3/4g/5	2a-t/OAt/EDC	8.9	217	97:1:1:1	0.9
3/4t/5	2a-t/OAt/EDC	8.9	117	1:1:97:1	1.6

[a] Template and primer: 36 μ M; activated **2**: 3.6 mM; aqueous solution; buffer: HEPES (200 mM), NaCl (400 mM), MgCl₂ (80 mM). [b] LG=leaving group; Melm=2-methylimidazole; OAt=oxyazabenzotriazole, EDC=excess carbodiimide from one-pot activation/extension assay. [c] k' =second-order rate constant; oligonucleotide complexes treated as one reactant, activated nucleotide as the other. [d] Perfectly matched primer-extension products are highlighted in boldface. [e] Activated monomer purified by HPLC.

Next, we studied whether an additional or helper oligonucleotide **5** that binds immediately downstream from the templating base would create a tighter binding site for the incoming monomer (Scheme 3). The rate was accelerated several fold for both **2c**-Melm and **2c**-OAt (Table 2). For azabenzotriazole-activated **2c**-OAt, the rate enhancement over the helper-free reaction with **2c**-Melm is 22-fold. A further twofold acceleration resulted from purification of the azabenzotriazole **2c**-OAt by HPLC prior to use in our assay, an effort invested only for the kinetic study. The azabenzotriazole-driven primer-extension reaction benefits further from elevated pH values. At pH 9.5, the acceleration of the helper-assisted reaction over that of the unassisted reaction with **2c**-Melm is 79-fold (Table 2). A pH value of 8.9 gives a similar effect, but lowers the risk of losing sequence selectivity through deprotonation of dT and dG.

We then established HATU/HOAt activation for monomers **1a**, **1g**, and **1t** (CH₃CN was required as solvent for **1t** as cleaner activations were observed when starting from slurries). Hydrolysis of OAt esters, despite their reactivity towards amino and ribo primers,^[21] is sufficiently slow. An exploratory study of the hydrolysis of **2t**-OAt in the assay buffer in D₂O by NMR spectroscopy shows a half-life of 16.2 h (see Supporting Information). Mixtures of all four OAt

esters employed in competitive reactions give rapid primer extension and acceptable sequence selectivities for all four templates **4a–t** (Table 2).

To make the chemical primer extension reactions more attractive for biomedical applications, we investigated one-pot activation/primer-extension protocols. When solutions of **1a–t** (0.4 M) were treated with EDC (5 equiv)^[16] and HOAt (3 equiv) at pH 5, the solution contained >90% of OAt esters after 2 h, as determined by ³¹P NMR. Dilution and adjustment of the pH value to 8.9 followed by addition of DNA strands led to reactions similar to those with HATU-activated OAt esters (Table 2), at least in the presence of **5**. Because the excess of activation reagents allows reactivation of nucleotides, the kinetics of these reactions are more complex, but the one-pot procedure makes assays easier to perform by personnel not trained as synthetic chemists.

The lower reactivity and selectivity of the reaction templated by adenine was then addressed. We increased the concentration of **2t**-OAt fivefold to compensate for the

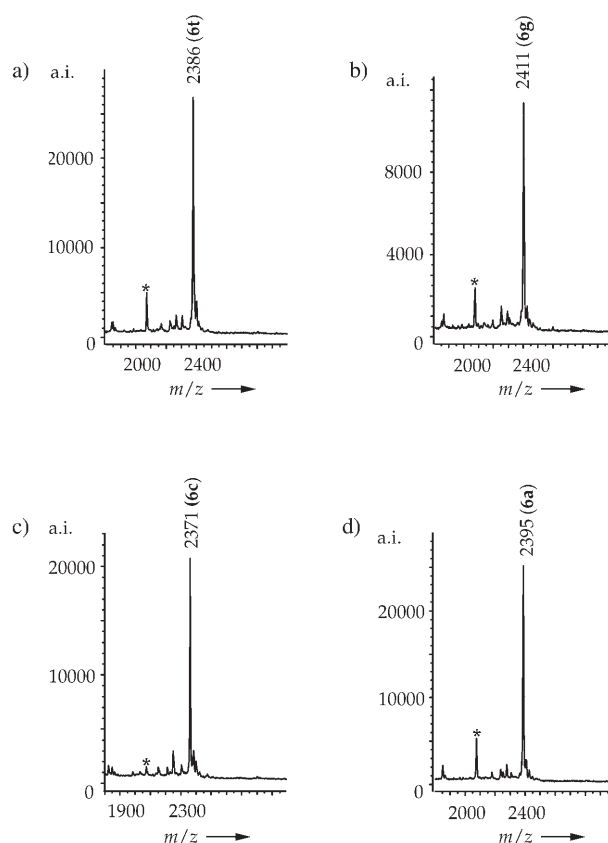


Figure 1. MALDI-TOF mass spectra from competitive primer extension reactions with 3/4a–t/5 and a dT-boosted mixture of 2a–t/OAt at pH 8.9, 8 h. a) Template **4a**, b) template **4c**, c) template **4g**, d) template **4t**. The asterisk denotes the peak for unconverted primer.

lower target affinity. The dT-boosted mixture gives sequence-selective reactions for all four templates **4a–t** in which the correctly extended primer constitutes $\geq 90\%$ of the elongation products. Furthermore, the half-life of the reactions is ≤ 1.6 h and within a factor of 2 for all four reactions (Table 2). More-refined reactivity-adjusted mixtures may make the rate differences even smaller. Representative MALDI spectra and kinetics are shown in Figures 1 and 2.

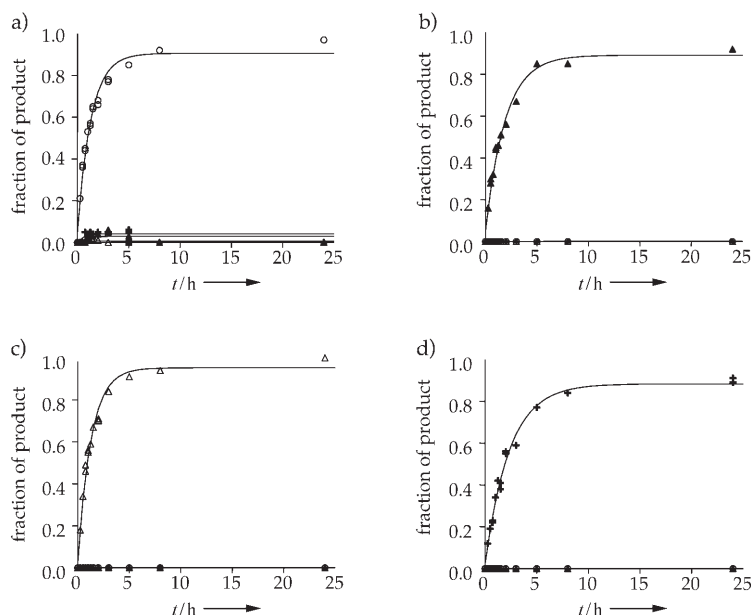


Figure 2. Kinetics of competitive primer-extension reactions with **3/4a–t/5** and dT-boosted mixture of **2a–t/OAt** at pH 8.9. a) Template **4a**, b) template **4c**, c) template **4g**, d) template **4t**. Δ **6c**, \circ **6t**, $+$ **6a**, \blacktriangle **6g**.

Finally, we performed exploratory primer extension reactions with the microarray system shown schematically in Figure 3. It consists of capture oligonucleotide **7**, immobilized on spots of flame-smoothed gold surfaces background-passivated by oligo(ethylene glycol ether) self-assembled monolayers.^[22] The spots were exposed to solutions containing one of two different DNA 60-mers **8** or **9** (which contain either nucleotide A (**8**) or G (**9**) at the site of primer extension), primer **10**, and helper **11**. After hybridization, template-directed reactions were induced that employed EDC-activated mononucleotides (3.6 mM each) in the extension buffer at pH 8.9 and 8°C. After 160 min, the surface was washed, treated with MALDI matrix solution, and subjected to mass-spectrometric analysis. Figure 4 shows spectra obtained in assays starting from solutions containing templates **8** or **9** (500 fmol). Even at 50 fmoles, an SNP call could be made for the A-template (see Supporting Information).

Our optimized activation of nucleotides is a one-step process employing commercial reagents. No significant non-nucleoside extensions of primers have been detected. Given the rate accelerations observed, practical applications of chemical-primer extension, such as SNP genotyping^[23] can be envisioned. Chemical-primer extension on a chip does not require purification after the elongation step and avoids sample transfer, as all steps are performed on the same

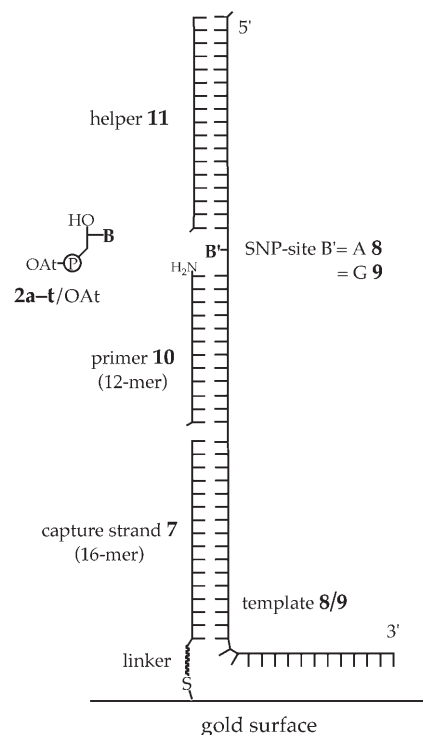


Figure 3. System for determining single-nucleotide identity on DNA microarrays for on-chip MALDI-TOF mass spectrometry.^[22] DNA strands used: **7** (capture strand): 5'-taaaagataccatcaa-3'; **8** (dA template): 5'-cagcgtgaaattagggtAgaacagaatgattgatggtatcttttaggaaccttaggtc-3'; **9** (dG template): 5'-cagcgtgaaattagggtGagaacagaatgattgatggtatcttttaggaaccttaggtc-3'; **10** (3'-amino-primer): 5'-tcattctgttct-3'; **11** (helper): 5'-accctaatttcacgctg-3'. Lower-case letters denote deoxynucleotides, SNP sites are highlighted as upper-case letters.

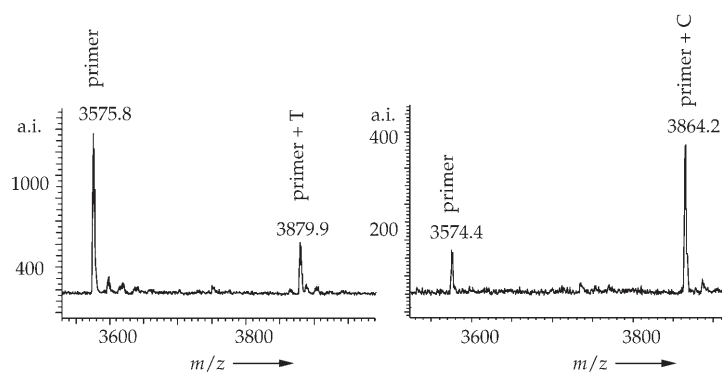


Figure 4. MALDI-TOF mass spectra from primer extensions performed with the system shown in Figure 3 and 60 mer templates **8/9** featuring the nucleotides A (left) or G (right) at the SNP site after 160 min. Spectra were obtained directly from the surface on which the primer-extension reaction had been performed. Surfaces had been incubated with 500 fmol of template **8** or **9**. See Supporting Information for further details.

surface. This should lower the cost of high-throughput assays. Heavily modified nucleotides, including those that form non-natural base pairs, may be incorporated into primers without the constraints imposed by active sites of polymerases. An extension of this work to assays with fluorophore-labeled monomers that allow optical detection on DNA microarrays

is being actively pursued in these laboratories. A fluorophore-labeled form of activated **1t** suitable for non-enzymatic primer extension reactions was recently described.^[24] Exploratory experiments with 3'-Cy3-labeled **2c**-OAt, and **3/4g/5** gave 42 % primer conversion after 1 h and 72 % conversion after 3.5 h,^[25] demonstrating the feasibility of fluorophore-based genotyping.

Received: May 24, 2005

Revised: July 1, 2005

Published online: September 21, 2005

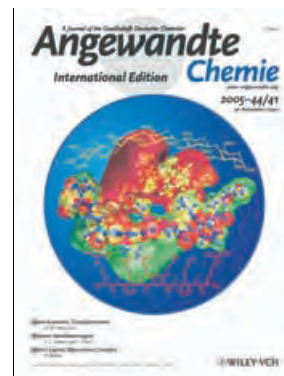
Keywords: DNA recognition · non-enzymatic replication · oligonucleotides · primer extension · single-nucleotide polymorphisms

-
- [1] K. B. Mullis, *Angew. Chem.* **1994**, *106*, 1271–1276; *Angew. Chem. Int. Ed. Engl.* **1994**, *33*, 1209–1213.
- [2] F. Sanger, S. Nicklen, A. R. Coulson, *Proc. Natl. Acad. Sci. USA* **1977**, *74*, 5463–5467.
- [3] L. E. Orgel, *Crit. Rev. Biochem. Mol. Biol.* **2004**, *39*, 99–123.
- [4] M. Hey, C. Hartel, M. W. Göbel, *Helv. Chim. Acta* **2003**, *86*, 844–854.
- [5] T. Wu, L. E. Orgel, *J. Am. Chem. Soc.* **1992**, *114*, 317–322.
- [6] T. Wu, L. E. Orgel, *J. Am. Chem. Soc.* **1992**, *114*, 7963–7969.
- [7] A. Luther, R. Brandsch, G. von Kiedrowski, *Nature* **1998**, *396*, 245–248.
- [8] J. Tost, I. G. Gut, *Mass Spectrom. Rev.* **2002**, *21*, 388–418.
- [9] T. Inoue, L. E. Orgel, *J. Am. Chem. Soc.* **1981**, *103*, 7666–7667.
- [10] L. E. Orgel, R. Lohrmann, *Acc. Chem. Res.* **1974**, *7*, 368–377.
- [11] A. Kanavarioti, M. W. Stronach, R. J. Ketner, T. B. Hurley, *J. Org. Chem.* **1995**, *60*, 632–637.
- [12] D. Sarracino, C. Richert, *Bioorg. Med. Chem. Lett.* **1996**, *6*, 2543–2548.
- [13] J. A. Rojas Stütz, C. Richert, *J. Am. Chem. Soc.* **2001**, *123*, 12718–12719.
- [14] C. Grunau, W. Hindermann, A. Rosenthal, *Hum. Mol. Genet.* **2000**, *9*, 2651–2663.
- [15] G. Egger, G. N. Liang, A. Aparicio, P. A. Jones, *Nature* **2004**, *429*, 457–463.
- [16] a) K. J. Prabahar, T. D. Cole, J. P. Ferris, *J. Am. Chem. Soc.* **1994**, *116*, 10914–10920; b) K. J. Prabahar, J. P. Ferris, *J. Am. Chem. Soc.* **1997**, *119*, 4330–4337; c) W. Huang, J. P. Ferris, *Chem. Commun.* **2003**, 1458–1459.
- [17] L. Rodriguez, L. E. Orgel, *J. Mol. Evol.* **1991**, *32*, 278–281.
- [18] J. Sulston, R. Lohrmann, L. E. Orgel, H. T. Miles, *Proc. Natl. Acad. Sci. USA* **1968**, *59*, 726–733.
- [19] S. S. Jain, F. A. Anet, C. J. Stahle, N. V. Hud, *Angew. Chem.* **2004**, *116*, 2038–2042; *Angew. Chem. Int. Ed.* **2004**, *43*, 2004–2008.
- [20] L. A. Carpino, *J. Am. Chem. Soc.* **1993**, *115*, 4397–4398.
- [21] S. R. Vogel, C. Deck, C. Richert, *Chem. Commun.* **2005**, DOI: 10.1039/B510775.
- [22] U. Plutowski, C. Richert, *Angew. Chem.* **2005**, *117*, 627–631; *Angew. Chem. Int. Ed.* **2005**, *44*, 621–625.
- [23] K. Tang, D.-J. Fu, D. Julien, A. Braun, C. R. Cantor, H. Köster, *Proc. Natl. Acad. Sci. USA* **1999**, *96*, 10016–10020.
- [24] N. Griesang, E. Kervio, C. Richert, *Synthesis* **2005**, 2327–2334.
- [25] N. Griesang, C. Richert, unpublished results.
-

Cover Picture

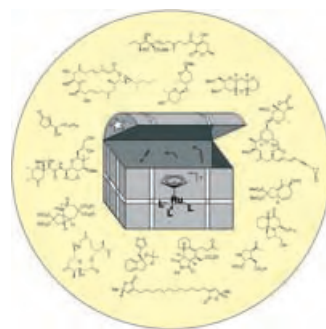
Sungwook Choi, Dylan J. Clements, Vojislava Pophristic, Ivaylo Ivanov, Satyavani Vemparala, Joel S. Bennett, Michael L. Klein, Jeffrey D. Winkler, and William F. DeGrado*

Small inhibitors for low-molecular-weight heparin, namely short aryl amide foldamers, were designed with the aid of molecular-dynamics calculations. The cover picture shows that the binding is primarily dominated by electrostatic interactions between a pentasaccharide sequence of heparin and the antagonist. In their Communication on page 6685 ff., W. F. DeGrado and co-workers show that heparin binds and modulates the biological properties of a number of proteins, including antithrombin II and factor Xa.



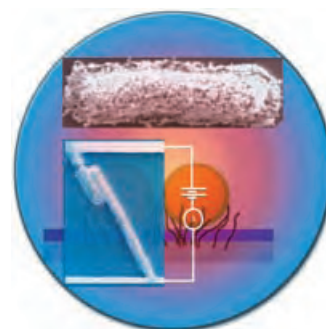
Ruthenium Catalysis

Ruthenium catalysts allow the rapid, highly selective, and atom-economic construction of complex molecules. In their Review on page 6630 ff., B. M. Trost and co-workers report how new reactions were developed through semirational design.



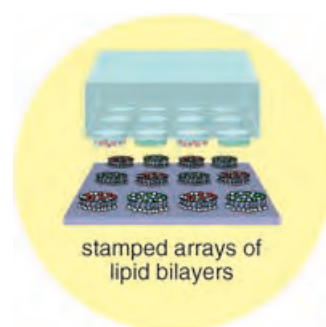
Bioelectronics

In their Communication on page 6668 ff., R. F. Saraf and V. Berry describe the dependence of the conductivity of lysine-coated gold nanoparticles assembled on *Bacillus cerius*, a Gram-Positive bacterium, on humidity.



Screening Techniques

A fast and straightforward approach to the preparation of functional membrane arrays with a variety of lipid compositions is described by M. Mayer and S. Majd in their Communication on page 6697 ff.





The following Communications have been judged by at least two referees to be “very important papers” and will be published online at www.angewandte.org soon:

C. Drago, L. Caggiano, R. F. W. Jackson*

Vanadium-Catalyzed Sulfur Oxidation/Kinetic-Resolution Process for the Synthesis of Enantiomerically Pure Alkyl Aryl Sulfoxides

Q. Qing, F. Chen, P. Li, W. Tang, Z. Wu, Z. Liu*

Finely Tuning the Metallic Nanogap Size with Electrodeposition Utilizing High-Frequency Impedance in Feedback

X. Rocquefelte,* S. E. Boulfelfel, M. B. Yahia, J. Bauer, J.-Y. Saillard,* and J.-F. Halet*

The Structural Preferences of Boron and Carbon within MB₂C₂ (M = Mg, Sc, Ca, Y, Ln) Phases: The “Coloring Problem” Revisited by DFT Calculations

G. C. Lloyd-Jones,* R. G. Margue, J. G. de Vries

Rate Enhancement by Ethylene in the Ru-Catalyzed Ring-Closing Metathesis of Enynes: Evidence for an “Ene-then-Yne” Pathway that Diverts through a Second Catalytic Cycle

S. Klaus, H. Neumann, A. Zapf, D. Strübing, S. Hübner, J. Almerna,* T. Riermeier, P. Groß, M. Sarich, W.-R. Krahnert, K. Rossen, M. Beller*

A General and Efficient Method for the Formylation of Aryl and Heteroaryl Bromides

N. Martín,* Á. Martín-Domenech, S. Filippone, M. Altable, L. Echegoyen,* C. M. Cardona

Retro-Cycloaddition Reactions of Pyrrolidinofullerenes

News

Organometallic Chemistry: P. Braunstein Elected _____ **6614**

Surface Chemistry: Science Academy Membership for J.-M. Basset _____ **6614**

Organic Chemistry: P. Metrangola Honored _____ **6614**

Books

Life Saving Drugs

John Mann

reviewed by O. Prien _____ **6615**

Fundamentals of Molecular Symmetry

Philip R. Bunker, Per Jensen

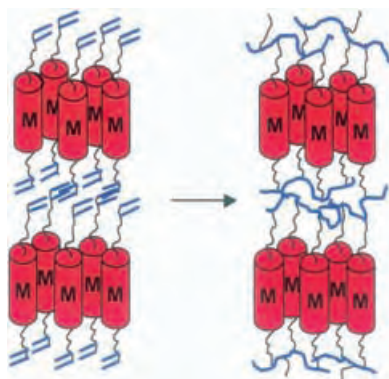
reviewed by H. Bettermann _____ **6616**

Highlights

Metallomesogenic Polymers

L. Oriol, J. L. Serrano* _____ **6618–6621**

Metal-Containing Nanostructured Materials through In Situ Polymerization of Reactive Metallomesogens



A challenging strategy for the design of metal-containing polymeric systems with a controlled nanostructure is the introduction of polymerizable groups that are both compatible with the mesomorphic order and reactive in the presence of metals. 1,3-Diene groups have recently been reported to offer such compatibility and reactivity, leading to efficient polymerization (see picture).

Asymmetric Catalysis

K. Muñoz* _____ **6622–6627**

Bifunctional Metal–Ligand Catalysis: Hydrogenations and New Reactions within the Metal–(Di)amine Scaffold

No metal–substrate interactions: A transition-metal complex of a primary amine can serve as an efficient bifunctional metal–ligand catalyst that functions without direct interaction of the metal and the substrate. The example shows the transition-state structure of the enantioselective reduction of acetophenone at the molecular surface of a ruthenium hydride complex bearing a diamine with one free NH₂ group (O red, Ru green, N blue).

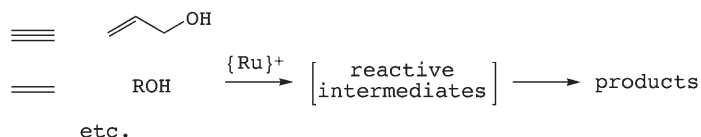


Reviews

Ruthenium Catalysis

B. M. Trost,* M. U. Frederiksen,
M. T. Rudd ——— 6630 – 6666

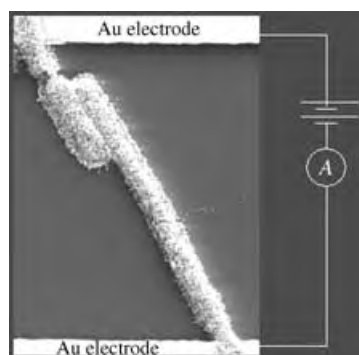
Ruthenium-Catalyzed Reactions—A
Treasure Trove of Atom-Economic
Transformations



Ru complexes emerged from obscurity to become accepted as ideal catalysts for diverse C–C bond-forming reactions beyond the more-well-known redox and metathesis processes. These reactions are highly selective and atom-economic pro-

cesses for the synthesis of complex molecules (see scheme). Mechanistic principles provide the basis for the semi-rational design of new reactions, notably for C–C coupling.

24-Carat bacteria: A bacteria/nanoparticle composite device is operated by applying a bias of 10 V across a bacterial bridge, which is coated with gold nanoparticles and spans two gold electrodes, and measuring the current (see image). A change in humidity from 0 to 20% causes swelling of the bacteria membrane which results in a 40-fold decrease of the current although the interparticle distance increases less than 0.2 nm.

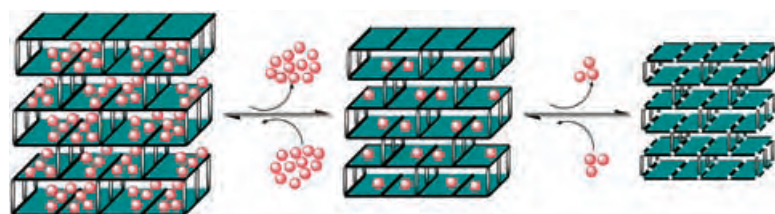


Communications

Nanodevices

V. Berry, R. F. Saraf* ——— 6668 – 6673

Self-Assembly of Nanoparticles on Live
Bacterium: An Avenue to Fabricate
Electronic Devices



Shrinkage factor: The ligand ppca (4-(pyridin-4-yl)pyridine-2-carboxylic acid) has enabled the synthesis of a new 3D framework material, $[\{[\text{Co}_2(\text{ppca})_2(\text{H}_2\text{O})-(\text{V}_4\text{O}_{12})_{0.5}]\cdot 3.62\text{H}_2\text{O}\}]_n$, which exhibits so-called “dynamic structural changes”.

Temperature changes lead to the reversible removal of guest molecules and/or ligands (e.g. H_2O) bound to the framework with a concomitant reversible structure change (see scheme).

Framework Materials

C.-L. Chen, A. M. Goforth, M. D. Smith,
C.-Y. Su, H.-C. zur Loye* — 6673 – 6677

$[\text{Co}_2(\text{ppca})_2(\text{H}_2\text{O})(\text{V}_4\text{O}_{12})_{0.5}]$: A Framework
Material Exhibiting Reversible Shrinkage
and Expansion through a Single-Crystal-
to-Single-Crystal Transformation Involving
a Change in the Cobalt Coordination
Environment

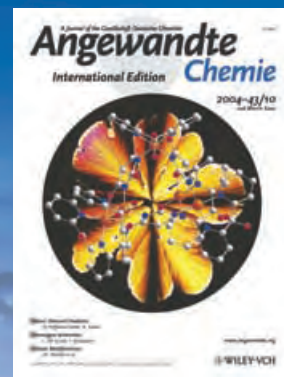
For the USA and Canada:

ANGEWANDTE CHEMIE International
Edition (ISSN 1433-7851) is published weekly
by Wiley-VCH PO Box 191161, D 69451 Wein-
heim, Germany. Air freight and mailing in the
USA by Publications Expediting Inc. 200

Meacham Ave., Elmont, NY 11003. Periodicals
postage paid at Jamaica NY 11431. US POST-
MASTER: send address changes to *Angewandte
Chemie*, Wiley-VCH, 111 River Street, Hoboken,
NJ 07030. Annual subscription price for insti-
tutions: US\$ 5685/5168 (valid for print and

electronic / print or electronic delivery); for
individuals who are personal members of a
national chemical society prices are available
on request. Postage and handling charges
included. All prices are subject to local VAT/
sales tax.

The best in chemistry – for more than a hundred years



A Journal of the Gesellschaft Deutscher Chemiker
Angewandte Chemie
International Edition

www.angewandte.org

1888: The beginning
of a success story

Constant Innovations

- 1962:** First issue of the International Edition
- 1976:** Graphical abstracts
- 1979:** Cover pictures
- 1988:** Centenary of Angewandte
- 1989:** Routine use of color
- 1991:** New section: Highlights
- 1992:** Computerized editorial tracking system
- 1995:** Internet service for readers
- 1998:** Regular press service; full-text online
- 2000:** New section: Essays; EarlyView: Communications available online ahead of the printed version
- 2001:** New section: Minireviews
- 2002:** Online submission of manuscripts
- 2003:** Weekly publication; new section: News; new layout
- 2004:** Backfiles (1962-1997); ManuscriptXpress: Online system for authors and referees



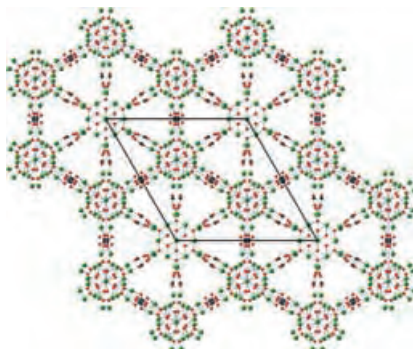
**Angewandte's
advisors...**

Richard R. Ernst
ETH Zürich

» I support **Angewandte Chemie** because it is a first rank international journal of European origin. More than many other renowned journals, it implements a pioneering spirit, being ready for innovating its form and contents. Its bilingual mode of appearance is another plus. I am looking forward to an equally prosperous future for **Angewandte Chemie**. «

Angewandte Chemie International Edition is
a journal of the German Chemical Society (GDCh)



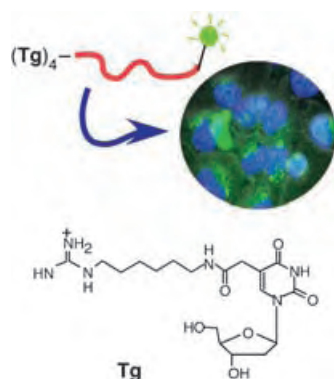


Iron aggregates are arranged into a close-packed structure through coordination bonds to give a material that displays a structural and magnetic hierarchy. The tripodal proligand nitrilotripropionic acid ($\text{H}_3\text{ntp} = \text{N}(\text{CH}_2\text{CH}_2\text{COOH})_3$) successfully traps $\{\text{Fe}_{13}\}$ aggregates, thus producing a lattice that displays three levels of organization (see picture of its 3D packing arrangement; Fe green; O red; N blue; C black; H white).

Hierarchical Structures

M. Murugesu, R. Clérac, W. Wernsdorfer, C. E. Anson, A. K. Powell* — **6678–6682**

Hierarchical Assembly of $\{\text{Fe}_{13}\}$ Oxygen-Bridged Clusters into a Close-Packed Superstructure



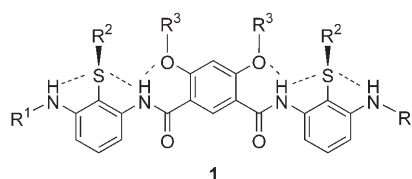
Quick on the uptake: A 20-mer DNA oligomer modified with 5-[(6-guanidiniohexylcarbamoyl)methyl]-2'-deoxyuridine (**Tg**) shows efficient cellular uptake (blue arrow) in HeLa cells without any other reagents. The fluorescence microscopy image reveals FAM-labeled DNA oligomer (green) and stained nuclei (blue). FAM = 6-carboxyfluorescein.

Nucleic Acids

T. Ohmichi, M. Kuwahara, N. Sasaki, M. Hasegawa, T. Nishikata, H. Sawai, N. Sugimoto* — **6682–6685**

Nucleic Acid with Guanidinium Modification Exhibits Efficient Cellular Uptake

Controlling blood loss: The synthesis of a series of arylamide oligomers **1**, which interact with heparin is described. The heparin–small molecule interaction inhibits the heparin's ability to activate antithrombin. These arylamide oligomers are the first example of low-molecular-weight antagonists that inhibit the anticoagulant function of heparin.



Protein Interactions

S. Choi, D. J. Clements, V. Pophristic, I. Ivanov, S. Vemparala, J. S. Bennett, M. L. Klein, J. D. Winkler, W. F. DeGrado* — **6685–6689**

The Design and Evaluation of Heparin-Binding Foldamers



Correlated bond rotations within biconcave molecules that comprise a semirigid C_3 -symmetric core and pendant *m*-terphenyl groups (see figure) assist mechanical coupling between the two vertices such that structural changes on one side of the molecule are effectively transmitted to the other side. Self-assembly of one such compound affords a nonporous solid from which entrapped guests can completely escape in the absence of channels that connect interstitial voids.

Host–Guest Systems

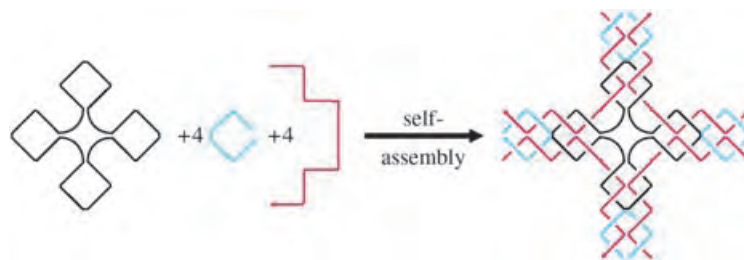
J. A. Riddle, J. C. Bollinger, D. Lee* — **6689–6693**

Escape from a Nonporous Solid: Mechanically Coupled Biconcave Molecules

DNA Nanostructures

Y. He, Y. Tian, Y. Chen, Z. Deng,
A. E. Ribbe, C. Mao* — 6694 – 6696

Sequence Symmetry as a Tool for
Designing DNA Nanostructures



Grand designs: DNA sequence symmetry is explored as a tool for designing DNA nanostructures. The resulting symmetric DNA motifs can self-assemble into two-

dimensional arrays as wide as 1 mm (see picture). The DNA arrays can be used as templates to fabricate nanostructures of other materials, such as gold.

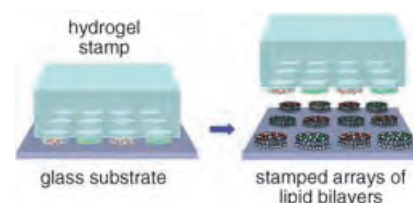


Lipid Bilayers

S. Majd, M. Mayer* — 6697 – 6700

Hydrogel Stamping of Arrays of
Supported Lipid Bilayers with Various
Lipid Compositions for the Screening of
Drug–Membrane and Protein–Membrane
Interactions

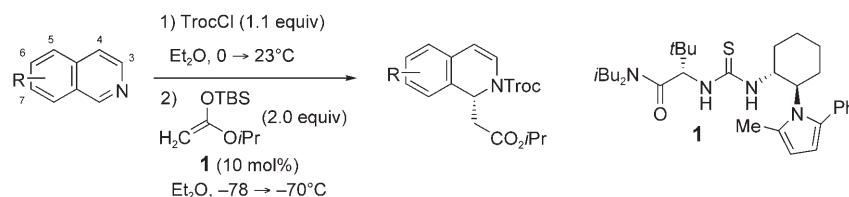
Stamping on fat: Agarose gel stamps were used to create ≥ 100 membrane arrays (see picture) by using only picomolar amounts of lipids. This constitutes a rapid and straightforward method for the fabrication of functional membrane arrays with a variety of lipid compositions which can be used for screening assays, for example, for drug–membrane interactions.



Asymmetric Catalysis

M. S. Taylor, N. Tokunaga,
E. N. Jacobsen* — 6700 – 6704

Enantioselective Thiourea-Catalyzed Acyl-
Mannich Reactions of Isoquinolines



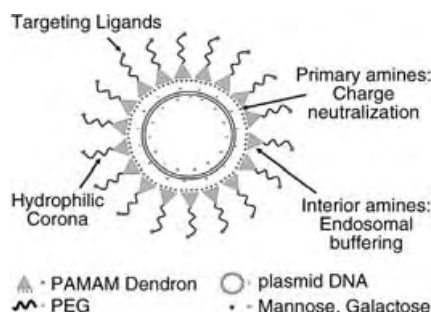
Inexpensive aromatic feedstocks are substrates for highly enantioselective acylative Mannich reactions catalyzed by a thiourea chiral hydrogen-bond donor **1**. This methodology provides access to useful 1-substituted dihydroisoquinolines

(see scheme; TrocCl = 2,2,2-trichloroethyl chloroformate, TBS = *tert*-butyldimethylsilyl), which serve as precursors to enantioenriched 1-substituted tetrahydroisoquinolines.

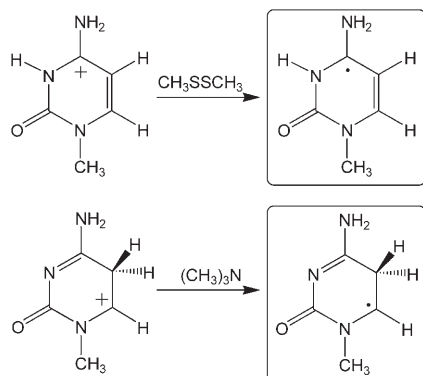
Gene Therapy

K. C. Wood, S. R. Little, R. Langer,*
P. T. Hammond* — 6704 – 6708

A Family of Hierarchically Self-Assembling
Linear-Dendritic Hybrid Polymers for
Highly Efficient Targeted Gene Delivery



Modular materials composed of concentric functional “shells” with independently tuneable properties are prepared from the self-assembly of DNA and linear-dendritic hybrid polymers (see scheme; PAMAM = poly(amidoamine), PEG = poly(ethylene glycol)). These ligand-targeted systems demonstrate serum stability, low toxicity, and transfection efficiencies that exceed those of the most efficient commercially available polymer poly-(ethylenimine).



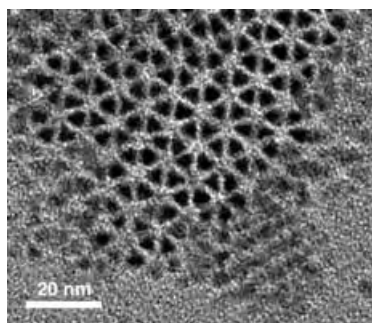
What a radical target! Two key hydrogen-atom adducts of 1-methylcytosine have been prepared by the targeted chemical generation of cytosine radicals. Femto-second collisional transfer of electrons to gas-phase tautomers of protonated 1-methylcytosine using molecular electron donors (dimethyl disulfide and trimethylamine) produces stable radical adducts with the hydrogen atoms positioned at N3 and C5 of the cytosine ring, respectively.

Nucleobases

C. Yao, M. L. Cuadrado-Peinado, M. Polášek, F. Tureček* — 6708–6711

Specific Generation of 1-Methylcytosine Radicals in the Gas Phase

With high quality and in high yield: The synthesis presented here affords CdSe and CdTe semiconductor nanocrystals without the need of a precursor injection. It allows the detailed control of the size and shape of the nanocrystals, as can be seen from the tetrahedral CdSe nanocrystals that have been prepared (TEM image). The method is suitable for industrial-scale preparations.

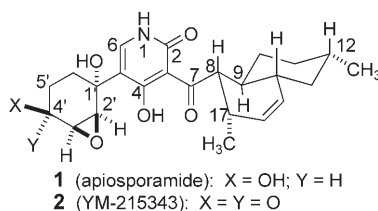


Semiconductors

Y. A. Yang, H. Wu, K. R. Williams, Y. C. Cao* — 6712–6715

Synthesis of CdSe and CdTe Nanocrystals without Precursor Injection

Antipodal relationship: A convergent synthetic pathway leading to 4-hydroxy-2-pyridinones was involved in the synthesis of apiosporamide (**1**) and YM-215343 (**2**). Both have an antipodal relationship to the natural metabolites, whose relative and absolute configurations have been established. Activated β -alanine enolate equivalents derived from β -lactams were the key to the synthesis.

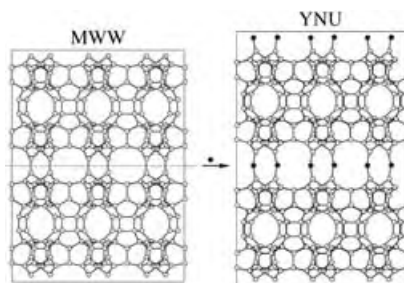


Assignment of Configuration

D. R. Williams,* D. C. Kammler, A. F. Donnell, W. R. F. Goundry — 6715–6718

Total Synthesis of (+)-Apiosporamide: Assignment of Relative and Absolute Configuration

Between the sheets: The structure of the titanasilicate Ti-YNU-1 reveals a much larger spacing along the c axis between the MWW sheets than its lamellar precursor and 3D Ti-MWW (see picture). Formation of twelve-membered rings would explain this cell expansion, which results in increased steric accessibility and may explain the higher catalytic activity of Ti-YNU-1 relative to other titanasilicates.



Zeolite Structures

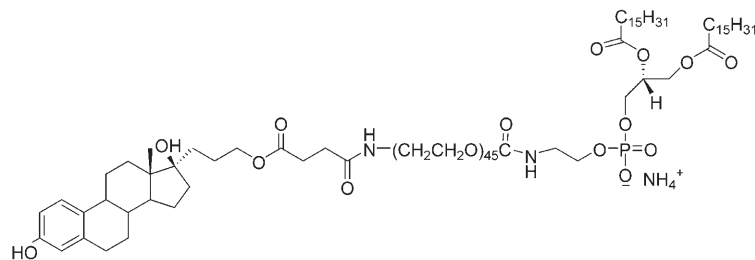
J. Ruan, P. Wu, B. Slater, O. Terasaki* — 6719–6723

Structure Elucidation of the Highly Active Titanasilicate Catalyst Ti-YNU-1

Anticancer Genes

B. S. Reddy, R. Banerjee* — 6723–6727

17 β -Estradiol-Associated Stealth-Liposomal Delivery of Anticancer Gene to Breast Cancer Cells



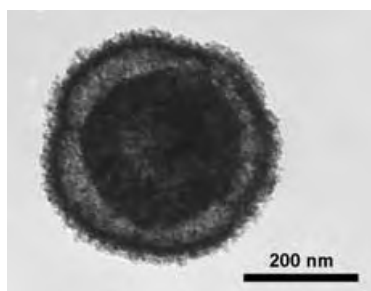
Killing by stealth: The highly specific mutual affinity of estrogen receptor and 17 β -estradiol (ES) allows apoptotic genes to be targeted at primary human breast adenocarcinoma cells through the use of

stealth liposomes. Cells are transfected with a cationic lipoplex containing a targeting lipid (see picture; DPPE = 1,2-dipalmitoyl-Sn-glycero-phosphatidylethanolamine, PEG = poly(ethylene glycol)).

Template Synthesis

M. Yang, J. Ma, C. Zhang, Z. Yang,*
Y. Lu* — 6727–6730

General Synthetic Route toward Functional Hollow Spheres with Double-Shelled Structures

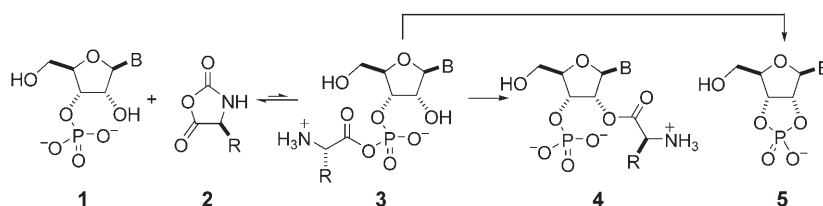


Double agent: Controlled sulfonation of polystyrene hollow spheres gives hydrophilic layers with sulfonic acid groups that allow the formation of a wide variety of functional composites. In this way, double-shelled hollow spheres have been prepared in one step by using such sulfonated polystyrene hollow spheres as templates (see TEM image of titania sphere).

Nucleotides

J.-P. Biron, A. L. Parkes, R. Pascal,*
J. D. Sutherland* — 6731–6734

Expeditious, Potentially Primordial, Aminoacylation of Nucleotides



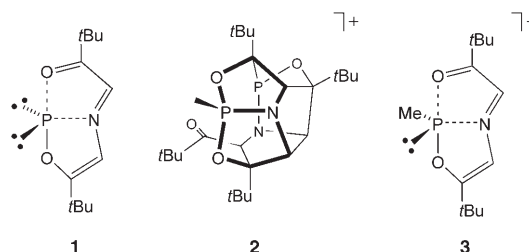
In the beginning: Mixed carboxylic phosphoric anhydrides **3**, formed from 3'-nucleotides **1** and amino acid *N*-carboxyanhydrides **2**, undergo competing rearrangement to 2'-aminoacyl esters **4** and cyclization to 2',3'-cyclic phosphates

5. The intramolecular aminoacyl transfer is faster than the cyclization despite the ease with which 2',3'-cyclic phosphates are formed through any other form of phosphate activation.

Phosphorus Cage Compounds

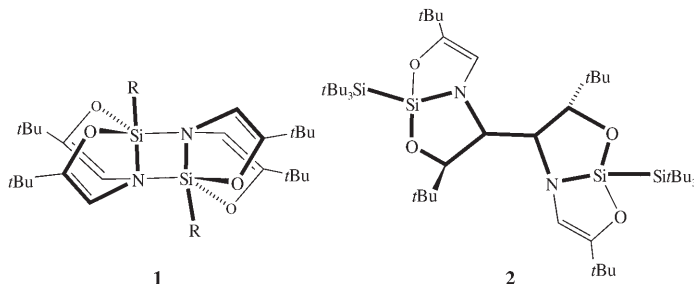
M. Driess,* N. Muresan, K. Merz,
M. Päch — 6734–6737

Formation of a Bowl-Shaped, Pentacyclic Phosponium Cage by Methylation of a Nucleophilic Phosphinidene



Domino-cyclization of two phosphinidene molecules: Methylation of the nucleophilic phosphinidene **1** with MeOTf (OTf = triflate) affords the unusual phosponium

cage **2**, which implies the formation of the novel phosphenium ion **3** as a reactive intermediate.



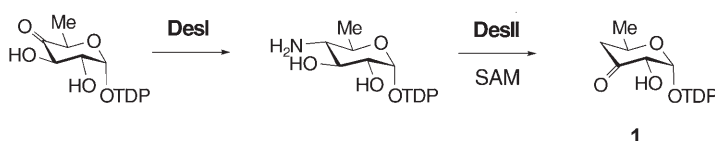
Coordination Chemistry of Silicon

M. Driess,* N. Muresan,
K. Merz ————— 6738–6741

A Novel Type of Pentacoordinate Silicon
Complexes and Unusual Ligand Coupling
by Intramolecular Electron Transfer

Even the electropositive element silicon initiates electron-transfer processes in amido-bis(enolate) complexes: This is shown by the reactions of halides RSiX_3 with $\text{HN}[\text{CH}_2\text{C}(\text{O})\text{tBu}]_2$ in the presence of

a base. While small substituents ($\text{R}=\text{H}$, Cl , Br , Ph) furnish the dinuclear pentacoordinate complexes **1**, the bulkier tBu_3Si group favors formation of the dinuclear tetracoordinate complex **2**.



The proteins **DesI** and **DesII** are proposed to catalyze a C4 deoxygenation reaction to give the key intermediate **1** in the biosynthesis of D-desosamine. Biochemical characterization of purified **DesII** showed

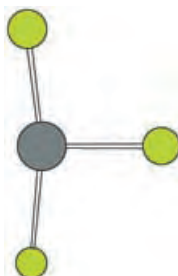
that it is a member of the S-adenosylmethionine (SAM) family of radical enzymes. The involvement of a SAM radical in the reaction with **DesII** identifies a new strategy for deoxygenation reactions of sugars.

Biosynthesis

P.-h. Szu, X. He, L. Zhao,
H.-w. Liu* ————— 6742–6746

Biosynthesis of TDP-D-Desosamine:
Identification of a Strategy for C4
Deoxygenation

Matrix-isolation IR, electronic-absorption, and Au L_3 -edge EXAFS (extended X-ray absorption fine structure) data have provided the first experimental evidence that the ground-state structure of AuCl_3 is not D_{3h} symmetric (trigonal-planar), but rather has a Jahn–Teller-distorted T-shaped geometry (see picture).

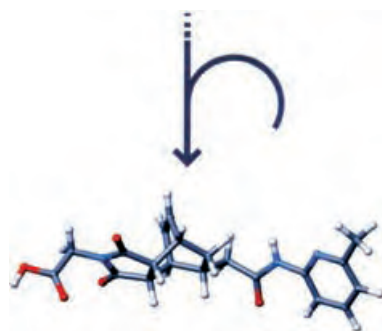


Matrix Isolation

I. J. Blackmore, A. J. Bridgeman, N. Harris,
M. A. Holdaway, J. F. Rooms,
E. L. Thompson,
N. A. Young* ————— 6746–6750

Experimental Evidence for a Jahn–Teller
Distortion in AuCl_3

Combining kinetic, structural, and computational studies on complex dynamic feedback systems may lead to the field of “systems chemistry”. The approach is exemplified by the analysis of a simple organic self-replicating system that has the potential to express both homochiral autocatalysis and heterochiral cross-catalysis (see picture).



Chirality

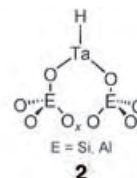
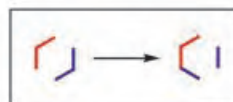
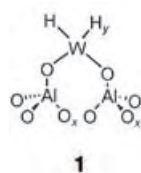
M. Kindermann, I. Stahl, M. Reimold,
W. M. Pankau,
G. von Kiedrowski* ————— 6750–6755

Systems Chemistry: Kinetic and
Computational Analysis of a Nearly
Exponential Organic Replicator

Alkane Metathesis

E. Le Roux, M. Taoufik,* C. Copéret,
A. de Mallmann, J. Thivolle-Cazat,
J.-M. Basset,* B. M. Maunders,
G. J. Sunley _____ **6755–6758**

Development of Tungsten-Based
Heterogeneous Alkane Metathesis
Catalysts Through a Structure–Activity
Relationship



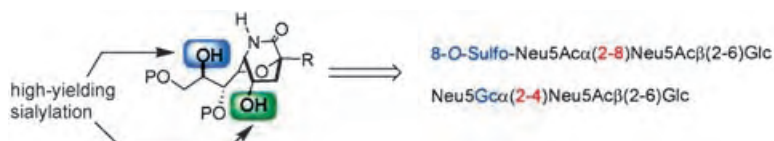
More active and selective catalysts of alkane metathesis (see scheme) that are based on well-defined tungsten carbyne and hydride complexes supported on alumina have been developed through a structure–activity relationship. The

improvement of activity on changing from Ta in **2** to W in **1** and the product selectivity show that olefin metathesis is probably the key process in C–C bond formation in the alkane metathesis reaction.

Sialylation

H. Ando,* Y. Koike, S. Koizumi, H. Ishida,
M. Kiso* _____ **6759–6763**

1,5-Lactamized Sialyl Acceptors for
Various Disialoside Syntheses: Novel
Method for the Synthesis of Glycan
Portions of Hp-s6 and HLG-2
Gangliosides



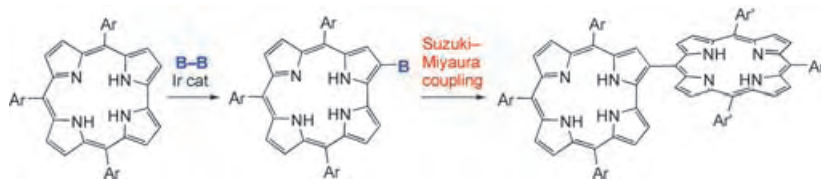
A dramatic enhancement of the reactivity of the C4- and C8-hydroxy groups of sialic acid has been demonstrated by 1,5-lactam bridging. Sialyl-α(2→4)sialoside and sialyl-α(2→8)sialoside were made avail-

able in high yields through direct sialylation (see scheme). Furthermore, the glycan parts of the new gangliosides Hp-s6 and HLG-2 were synthesized for the first time.

Corrole Derivatives

S. Hiroto, I. Hisaki, H. Shinokubo,*
A. Osuka* _____ **6763–6766**

Synthesis of Corrole Derivatives through
Regioselective Ir-Catalyzed Direct
Borylation



Showdown at the OK corrole: The direct borylation of corroles under iridium catalysis through C–H activation proceeds with perfect regioselectivity and excellent

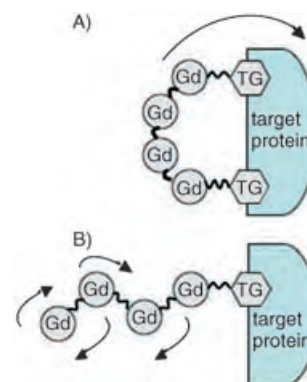
yields. 2-Borylated corroles allow an easy access (two steps) to directly linked corrole–porphyrin conjugates and other functionalized corroles (see scheme).

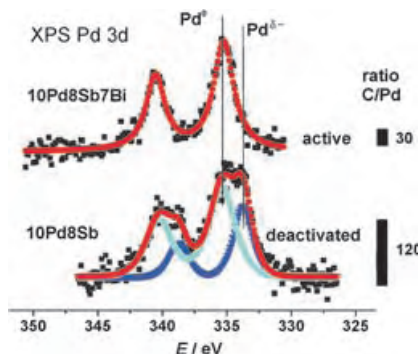
Protein Relaxivity

Z. Zhang, M. T. Greenfield, M. Spiller,
T. J. McMurry, R. B. Lauffer,
P. Caravan* _____ **6766–6769**

Multilocus Binding Increases the
Relaxivity of Protein-Bound MRI Contrast
Agents

Spinning around: The sensitivity of MRI contrast agents can be increased through multilocus binding. This restricts the internal motion and therefore increases the relaxivity of a bound protein multimer (see picture; A) relative to a single binding group (B), whose flexibility and internal motion limits the relaxivity gain. Protein-targeting groups (TG) can be used to anchor the multimer.



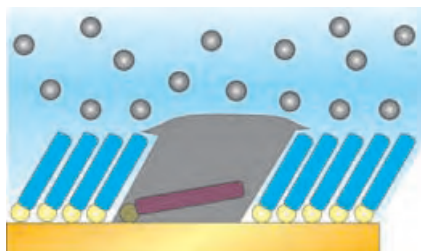


Addition of Bi prevents deactivation of Pd–Sb catalysts in the acetoxylation of toluene. The presence of Bi hinders the formation of an inactive Pd^{δ+} state and the blockage of the active Pd sites by carbon species from coke deposits (see the photoelectron spectrum). The modified catalyst displays extremely high selectivity for benzyl acetate (≥ 95 %) at higher toluene conversions.

Heterogeneous Catalysis

J. Radnik,* A. Benhmid, V. N. Kalevaru, M.-M. Pohl, A. Martin, B. Lücke, U. Dingerdisen ————— **6771–6774**

Deactivation of Pd Acetoxylation Catalysts: Direct Observations by XPS Investigations



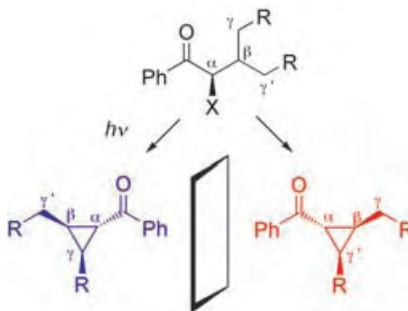
Reduction on the spot: Planarly adsorbed thiolated porphyrin molecules (purple) incorporated in an insulating alkanethiol monolayer (blue) function as nanoelectrodes for the local reduction of metals (gray). This approach was applied for the in situ synthesis of nanoparticles of a predetermined size.

Nanoparticle Deposition

T. Hirsch, M. Zharnikov, A. Shaporenko, J. Stahl, D. Weiss, O. S. Wolfbeis, V. M. Mirsky* ————— **6775–6778**

Size-Controlled Electrochemical Synthesis of Metal Nanoparticles on Monomolecular Templates

Influential neighbors: 1,2-Chirality transfer provides the basis for a novel asymmetric synthesis of cyclopropanes by irradiation of enantiomerically pure alkyl phenyl ketones bearing a leaving group X in the α position. The photochemically excited carbonyl group is able to distinguish between the diastereotopic positions γ and γ' in terms of a desymmetrization. In some cases the configuration is influenced by the temperature.



Asymmetric Synthesis

P. Wessig,* O. Mühling ————— **6778–6781**

1,2-Chirality Transfer in the Synthesis of Cyclopropanes

The issues for October 2005 appeared online on the following dates

Issue 37: September 14 • Issue 38: September 20 • Issue 39: September 30 • Issue 40: October 7

Sources

Product and Company Directory

You can start the entry for your company in “Sources” in any issue of *Angewandte Chemie*.

If you would like more information, please do not hesitate to contact us.

Wiley-VCH Verlag – Advertising Department

Tel.: 0 62 01 - 60 65 65

Fax: 0 62 01 - 60 65 50

E-Mail: MSchulz@wiley-vch.de

Service

Keywords ————— **6782**

Authors ————— **6783**

Angewandte's
Sister Journals ————— **6784–6785**

Preview ————— **6787**



P. Braunstein Elected

Pierre Braunstein (Université L. Pasteur, Strasbourg, France) was elected to the Deutsche Akademie der Naturforscher Leopoldina (Halle), Germany's oldest science academy (founded in 1652). He is also the first Frenchman

to be elected to the Council of the Royal Society of Chemistry in London, whose membership was recently reduced from 50 to a maximum of 18. The research in his group is devoted to polytopic phosphorus ligands, enolate complexes, heteronuclear complexes with silicon ligands, and molecular clusters. Recently, he reported in *Angewandte Chemie* on

hydrogen bonds in supramolecular metal carbonyl complexes and on oriented one-dimensional organometallic molecular wires with silver–palladium bonds. He also co-edited a multivolume handbook on metal clusters.^[1] Braunstein has been a corresponding member of the French Academy of Science since 1993 and was a recipient of the Grignard–Wittig Award of the French and German Chemical Societies (SFC and GDCh).

Braunstein studied chemistry at the Ecole Supérieure de Chimie in Mulhouse, France, and earned a PhD under the guidance of J. Dehand at the University of Strasbourg in 1971. As a postdoc, he worked with R. S. Nyholm at Imperial College (London). Having received a Doctorat d'Etat in Strasbourg in 1974, he joined E. O. Fischer's group at the Technische Universität München. He is currently a CNRS research director as well as director of

the Laboratoire de Chimie de Coordination at the Université L. Pasteur (Strasbourg, France).

J.-M. Basset Elected to the French Academy of Science

Jean-Marie Basset (Ecole Supérieure de Chimie Physique Electronique de Lyon, CPE) was elected member of the Académie des Sciences (Paris) and recently received his member's sword during a colloquium in Lyon. Basset's research group focuses on organometallic chemistry at interfaces. In *Chemistry – A European Journal*, he recently reported on the grafting of $[\text{Mn}(\text{CH}_2\text{tBu})_2(\text{tmeda})]$ (tmeda: *N,N,N',N'*-tetramethylethylenediamine) on silica and on structure–activity relationships of heterogeneous tungsten catalysts for alkane metathesis.^[2]

J.-M. Basset

Basset received his PhD under the guidance of M. Prettre at the Catalysis Research Institute in Lyon, France, in 1969. Subsequently, he worked as a postdoc in the research groups of W. Graydon (University of Toronto, Canada) and G. Wilkinson (Imperial College). When he returned to Lyon, he was appointed assistant professor at the Université C. Bernard, and, later, deputy director of the Catalysis Research Institute. In 1983, he founded the surface organometallic chemistry group at the CPE and has been its scientific director since 1994.

P. Metrangolo Receives Ciamician Medal

Pierangelo Metrangolo (Politecnico di Milano, Italy) was awarded the Società Italiana di Chimica's Giacomo Ciamician Medal, an award for young organic chemists. Metrangolo received his PhD in industrial chemistry in 2001 under the guidance of G. Resnati (University of Milan). In 2001, he was a guest professor at the Université Paul Sabatier in Toulouse, France. In 2002 he was appointed assistant professor and was promoted to

associate professor at the Politecnico di Milano in 2005. His research interests include supramolecular chemistry, in particular halogen bonding as a new principle of self-assembly, for which he was cited and that he presented in a Concept article in *Chemistry – A European Journal*. Recently, he reported on halogen bonds between nitrogen and bromine in infinite one-dimensional chains of dibromotetrafluorobenzene and bipyridyl derivatives.^[3] In addition, he works on fluorinated reagents for organic synthesis, such as the oxidation properties of perfluorinated heterocycles, and self-assembled thin films for nonlinear optics.



P. Metrangolo

- [1] a) P. Braunstein, J.-P. Taquet, O. Siri, R. Welter, *Angew. Chem.* **2004**, *116*, 6048; *Angew. Chem. Int. Ed.* **2004**, *43*, 5922, b) P. Braunstein, C. Frison, N. Oberbeckmann-Winter, X. Morise, A. Messaoudi, M. Bénard, M.-M. Rohmer, R. Welter, *Angew. Chem.* **2004**, *116*, 6426; *Angew. Chem. Int. Ed.* **2004**, *43*, 6120, c) *Metal Clusters in Chemistry*, (Eds.: P. Braunstein, L. A. Oro, P. R. Raithby), Wiley-VCH, Weinheim, **1999**.
- [2] a) V. Riollot, E. A. Quadrelli, C. Copéret, J.-M. Basset, R. A. Andersen, K. Köhler, R.-M. Böttcher, E. Herdtweck, *Chem. Eur. J.* September 15, **2005**, DOI: 10.1002/chem.200500401, b) E. Le Roux, M. Taoufik, C. Copéret, A. de Mallmann, J. Thivolle-Cazat, J.-M. Basset, B. M. Maunders, G. J. Sunley, *Angew. Chem.* September 19, **2005**, DOI: 10.1002/ange.200501382; *Angew. Chem. Int. Ed.* September 19, **2005**, DOI: 10.1002/anie.200501382.
- [3] a) P. Metrangolo, G. Resnati, *Chem. Eur. J.* **2001**, *7*, 2511, b) A. De Santis, A. Forni, R. Liantonio, P. Metrangolo, T. Pilati, G. Resnati, *Chem. Eur. J.* **2003**, *9*, 3974.

DOI: 10.1002/anie.200503365

Metal-Containing Nanostructured Materials through In Situ Polymerization of Reactive Metallomesogens

Luis Oriol and José Luis Serrano*

Keywords:

alkenes · liquid crystals · metallomesogens · polymerization · transition metals

Metallomesogens, or metal-containing liquid crystals, have been widely studied over recent years as a new type of mesomorphic material. Most of the work in this field has involved structural studies as the rich coordination chemistry of metals affords fascinating new geometries for the design of liquid crystals (LCs).^[1] Furthermore, the high level of interest in these materials also arises from the potential properties derived from the presence of metal ions within anisotropic phases. Metal ions can be redox active, photosensitive, display magnetic or catalytic properties, and may, in general, extend the properties of organic LCs, which are based on a small range of different atoms. Nevertheless, the stability and processability of metallomesogens is lower than that of similar organic compounds and this drawback has restricted the development of these materials.

One strategy to improve their processability with the aim of fabricating useful devices is the incorporation of metals into liquid-crystalline polymeric assemblies. Metallomesogenic polymers have been studied to a much lesser extent than low-molecular-weight metallomesogens, but such systems combine in a unique material the anisotropy of LCs, the new properties derived from the presence of the metal, and the favorable processing properties of poly-

mers. The design of metallomesogenic polymers generally employs similar approaches to those used for organic liquid-crystalline polymers.^[2] In addition, supramolecular polymeric structures can be envisaged by means of metal complexation to give rise to new functional and dynamic liquid-crystalline polymers.^[3] Accordingly, both lyotropic (temperature- and concentration-dependent phase transitions) and thermotropic (temperature-dependent phase transitions) metallomesogenic polymers have been reported with main-chain, side-chain, or cross-linked architectures.

Metallomesogenic polymers can be processed into films or other morphologies with controlled macroscopic orientation and a high metal content.^[4] Orientation is mainly achieved by means of mechanical forces, as polymers are difficult to orient by other techniques that are successful with low-molecular-weight liquid crystals. In this sense, an excellent method to fix the orientation of liquid-crystal phases into polymeric films is the bulk polymerization of reactive LCs.^[5] The polymerization of these materials in situ at the mesophase temperature converts the fragile structure of a self-organized molecular assembly into a polymeric material that displays good mechanical tractability and a structure that corresponds to the organization of the mesophase in which the polymerization takes place.^[6] In the design of these reactive mesogens, moieties that undergo radical polymerization (mainly acrylates or methacrylates) have generally been chosen because radical polymerization is more tolerant of organic functional groups than other polymerization techniques.

Furthermore, if the polymerization is photochemically initiated, the processing is decoupled from the temperature — a situation that allows prior macroscopic orientation of the liquid crystal into monodomains and subsequent irradiation to yield highly oriented polymeric nanostructured films that are useful, for example, as optical devices^[7] or low-dimensional ion conductors.^[8]

In Situ Polymerization of Lyotropic Metallomesogens

The advantageous processability of reactive LCs has also been applied to metallomesogens, mainly in lyotropic systems but also in some thermotropic ones. The templated polymerization of lyotropic mesomorphic materials gives rise to nanostructured materials that have been used as biomembrane models, drug-delivery systems, and templates for nanocomposites.^[9] A number of different lyotropic mesomorphic aggregates are known, but the inverted hexagonal (H_{II}) system has probably received most attention in the polymerization of lyotropic reactive metallomesogens. The specific interest in this system is due to the architecture of this H_{II} phase, which is highly reminiscent of zeolites or mesoporous sieves — materials that are investigated in different areas such as nanotechnology or catalysis. As a consequence, it is clear that the combination of tunable organic analogues and functional metal ions in the nanometric channels is a field of increasing interest.^[10]

Gin and co-workers have described several examples of reactive lyotropic metallomesogens for different applica-

[*] Dr. L. Oriol, Prof. Dr. J. L. Serrano
Polymer and Liquid Crystal Group
Departamento de Química Orgánica
Facultad de Ciencias-Instituto de Ciencia de
Materiales de Aragón
Pedro Cerbuna 12, Zaragoza 50009 (Spain)
Fax: (+34) 976-761-209
E-mail: joseluis@unizar.es

Nevertheless, the Zn^{II} and Mg^{II} complexes could be polymerized in a manner similar to that for the organic monomers, whose polymerization kinetics depend on the ordering effect of polymerizable groups, anisotropic mobility, and diffusion in a liquid-crystalline medium. Another remarkable result of this study was the observation of reduced mesomorphic properties of these monomers in comparison with the nonreactive complexes which was attributed to the steric and dipolar effects introduced by the acrylate groups.

Metal complexes of *N*-alkyl^[18] or *N*-aryl^[19] salicylaldiminates (Figure 4) have also been studied, and conclusions similar to those mentioned above were drawn. The Cu^{II} complexes did not polymerize, but the Zn^{II} (nonmesogenic) or Pd^{II} complexes could be polymerized in situ upon both thermal and photochemical initiation (note, polymerization was more efficient with the Zn^{II} complex). As an alternative, the photopolymerization of homologous reactive metallomesogens that contain vinyl ethers was also attempted by a cationic mechanism promoted by free-radical species. However, evidence for

polymerization was not found in these systems. Similar problems were encountered in the photopolymerization in situ of mesogenic acrylates based on dicarbonylrhodium(I) salicylaldiminate complexes, whereby the presence of the metal ions inhibited the polymerization of the acrylates.^[20]

1,3-Diene Tails as an Alternative in the Preparation of Reactive Metallomesogens

The drawbacks of thermotropic metallomesogens mentioned above, which are mainly based on acrylates, can be avoided by using different reactive groups. To this end, Attard and Templar proposed the preparation of oriented networks by irradiation with UV light of highly ordered crystalline fibers, processed from an unusual lamellar discotic phase of a Cu^{II} carboxylate that bears diacetylene groups in the linear carboxylate chains.^[21] The authors suggested this topochemical polymerization as an easy way to obtain macroscopically ordered single crystals of good optical quality with a view to using the materials in nonlinear optics.^[21] Nevertheless, this

polymerization took place in the crystalline phase.

As far as the polymerization of mesogens in situ is concerned, reactive 1,3-diene groups located at the end of an aliphatic terminal chain have proved to be an interesting alternative for the preparation of cross-linkable liquid-crystal monomers.^[22] This kind of monomer can be polymerized in situ by either using a conventional radical photochemical initiator or thermally. In the case of thermal initiation, 1,3-dienes have a tendency to undergo [4+2] cycloaddition with one another. Furthermore, the replacement of acrylate terminal groups by 1,3-dienes improves the mesomorphic properties of the reactive monomers because these tails more closely resemble the conventional terminal *n*-alkyl or *n*-alkoxy chains generally used in the design of low-molecular-weight LCs. Several series of thermotropic LCs that comprise a bent core^[23] or a polycatenar structure,^[24] as well as lyotropic monomers,^[25] have been described using this kind of polymerizable group.

Very recently, Gin and co-workers described the first examples of reactive metallomesogens that contain these kinds of groups as an alternative to acrylate-containing metallomesogens for the formation of anisotropic networks.^[26] The Pd^{II} and Ni^{II} metallomesogens shown in Figure 5 were synthesized, and the properties of diene- and acrylate-containing and nonreactive metallomesogens were compared. The comparison highlighted several advantages for the diene derivatives: First, reactive diene groups have a less marked destabilizing effect on the mesomorphic state than the acrylate groups do. Second, thermally induced cycloaddition of the diene monomers yielded metallopolymeric networks that re-

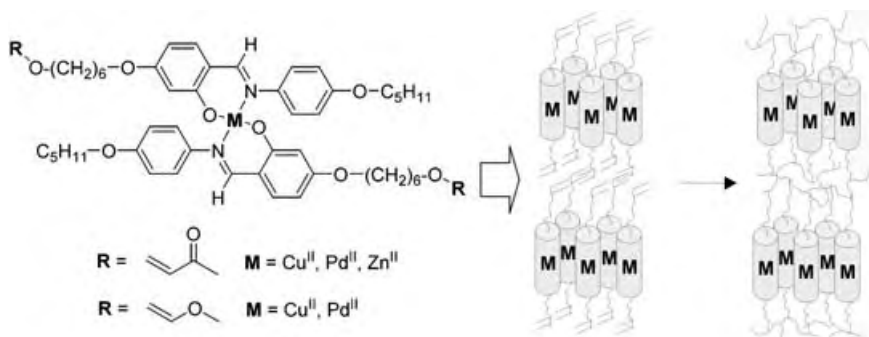


Figure 4. Examples of thermotropic reactive metallomesogens based on salicylaldiminates,^[19] and schematic representation of their polymerization in situ.

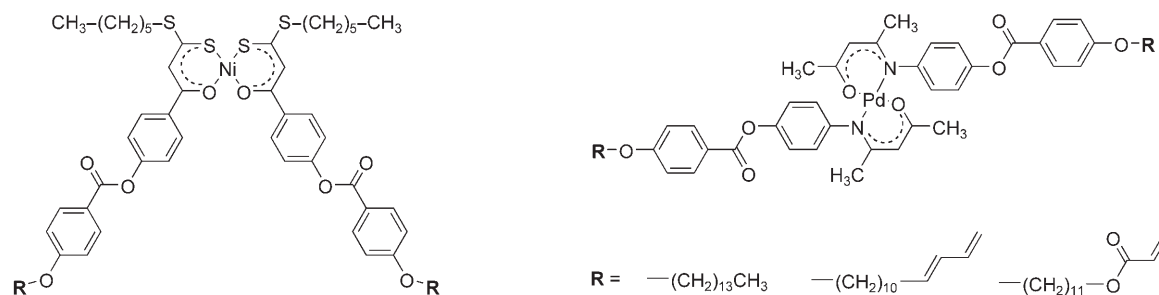


Figure 5. Structures of the reactive and nonreactive thermotropic metallomesogens described by Gin and co-workers.

tained the structure of the mesophase in which polymerization took place. In contrast, attempts to obtain a cross-linked anisotropic network from diene or acrylate derivatives by radical photopolymerization failed as a consequence of either the reduction of Pd^{II} ions or chain transfer to thioester ligands in the case of Ni^{II} metallomesogens. Consequently, diene groups seem to be more compatible with redox-active metal ions or functional groups than acrylates are in the design of metallomesogens.

In conclusion, the polymerization of reactive metallomesogens in situ opens up new possibilities for the processing of nanostructured metal-containing materials. Nevertheless, metals may have an adverse effect on the efficiency of the polymerization, especially in the free-radical polymerization of acrylates — the most widely studied polymerizable groups used to design both lyotropic and thermotropic reactive metallomesogens. Recent research has demonstrated that 1,3-dienes offer new possibilities relative to the acrylates: on the one hand, dienes have a higher compatibility with mesomorphic ordering than acrylates, and, on the other hand, they can react by an alternative mechanism to the free-radical route to undergo efficient polymerization and consequently avoid the inhibition or retardation introduced by metal ions and some organic groups.

Published online: September 27, 2005

- [1] a) *Metallomesogens: Synthesis and Applications* (Ed.: J. L. Serrano), VCH, Weinheim, **1996**; b) R. Giménez, D. P. Lidon, J. L. Serrano, *Curr. Opin. Solid State Mater. Sci.* **2002**, *6*, 527–535; c) R. W. Date, E. Fernández-Iglesias, K. E. Rowe, J. M. Elliott, D. W. Bruce, *Dalton Trans.* **2003**, 1914–1931; d) “Metallomesogens”: B. Donnio, D. Guillon, R. Deschenaux, D. Bruce in *Comprehensive Coordination Chemistry II*, Vol. 7 (Eds.: J. A. McCleverty, T. J. Meyer), Elsevier, Oxford, **2003**, pp. 357–627.
- [2] a) L. Oriol, J. L. Serrano, *Adv. Mater.* **1995**, *7*, 348–369; b) L. Oriol, M. Piñol, J. L. Serrano, *Prog. Polym. Sci.* **1997**, *22*, 873–911; c) M. H. Chisholm, *Acc. Chem. Res.* **2000**, *33*, 53–61.
- [3] For example, see: a) H. Plesnivý, T. Plesnivý, H. Ringsdorf, M. Seitz, *J. Mater. Chem.* **1998**, *8*, 343–351; b) J. M. Lehn, *Polym. Int.* **2002**, *51*, 825–839.
- [4] For example, see: a) A. A. Dembek, R. R. Burch, A. E. Feiring, *J. Am. Chem. Soc.* **1993**, *115*, 2087–2089; b) P. Cerrada, L. Oriol, M. Piñol, J. L. Serrano, *J. Am. Chem. Soc.* **1997**, *119*, 7581–7582.
- [5] For example, see: S. I. Stupp, S. Son, H. C. Lin, L. S. Li, *Science* **1993**, *259*, 59–63.
- [6] For example, see: a) S. M. Kelly, *J. Mater. Chem.* **1998**, *24*, 71–82 (calamitic LCs); b) C. D. Favre-Nicolin, J. Lub, P. van der Sluis, *Adv. Mater.* **1996**, *8*, 1005–1008 (discotic LCs); c) J. Barbera, N. Gimeno, L. Monreal, R. Piñol, M. B. Ros, J. L. Serrano, *J. Am. Chem. Soc.* **2004**, *126*, 7190–7197 (banana LCs).
- [7] For example, see: a) K. Robbie, D. J. Broer, M. J. Brett, *Nature* **1999**, *399*, 764–766; b) U. Theissen, S. J. Zilker, T. Pfeuffer, P. Strohriegel, *Adv. Mater.* **2000**, *12*, 1698–1700; c) R. Penterman, S. I. Klink, H. de Koning, G. Nisato, D. J. Broer, *Nature* **2002**, *417*, 55–58.
- [8] K. Kishimoto, M. Yoshio, T. Mukai, M. Yoshizawa, H. Ohno, T. Kato, *J. Am. Chem. Soc.* **2003**, *125*, 3196–3197.
- [9] a) A. Mueller, D. F. O'Brien, *Chem. Rev.* **2002**, *102*, 727–757; b) H. P. Hentze, E. W. Kaler, *Curr. Opin. Colloid Interface Sci.* **2003**, *8*, 164–178.
- [10] a) S. A. Miller, J. H. Ding, D. L. Gin, *Curr. Opin. Colloid Interface Sci.* **1999**, *4*, 338–347; b) D. L. Gin, D. H. Gray, R. C. Smith, *Synlett* **1999**, 1509–1522; c) D. L. Gin, W. Gu, B. A. Pindzola, W. J. Zhou, *Acc. Chem. Res.* **2001**, *34*, 973–980.
- [11] H. Deng, D. L. Gin, R. C. Smith, *J. Am. Chem. Soc.* **1998**, *120*, 3522–3523.
- [12] R. C. Smith, W. M. Fischer, D. L. Gin, *J. Am. Chem. Soc.* **1997**, *119*, 4092–4093.
- [13] J. H. Ding, D. L. Gin, *Chem. Mater.* **2000**, *12*, 22–24.
- [14] W. Gu, W. J. Zhou, D. L. Gin, *Chem. Mater.* **2001**, *13*, 1949–1951.
- [15] D. H. Gray, D. L. Gin, *Chem. Mater.* **1998**, *10*, 1827–1832.
- [16] J. F. van der Pol, E. Neeleman, J. C. van Miltenburg, J. W. Zwikker, R. J. M. Nolte, W. Drenth, *Macromolecules* **1990**, *23*, 155–162.
- [17] L. Marcot, P. Maldivi, J. C. Marchon, D. Guillon, M. Ibn-Elhaj, D. J. Broer, G. N. Mol, *Chem. Mater.* **1997**, *9*, 2051–2058.
- [18] U. Carusso, A. Nacca, A. Roviello, A. Sirigu, *New Polym. Mater.* **1995**, *4*, 309–322.
- [19] a) J. C. Galán, L. Oriol, M. Piñol, J. L. Serrano in *The Wiley Polymer Networks Group Review Series, Vol. 1* (Eds.: K. te Nijenhuis, W. J. Mijis), Wiley, Chichester, **1998**, pp. 421–430; b) M. Cano, L. Oriol, M. Piñol, J. L. Serrano, *Chem. Mater.* **1999**, *11*, 94–100.
- [20] L. Oriol, M. Piñol, S. Poelsma, J. L. Serrano, A. Viñuales, *J. Polym. Sci. Part A* **2000**, *38*, 4466–4477.
- [21] G. S. Attard, R. H. Templer, *J. Mater. Chem.* **1993**, *3*, 207–213.
- [22] B. P. Hoag, D. L. Gin, *Macromolecules* **2000**, *33*, 8549–8558.
- [23] A. C. Sentman, D. L. Gin, *Angew. Chem.* **2003**, *115*, 1859–1863; *Angew. Chem. Int. Ed.* **2003**, *42*, 1815–1819.
- [24] B. P. Hoag, D. L. Gin, *Liq. Cryst.* **2004**, *31*, 185–199.
- [25] B. A. Pindzola, B. P. Hoag, D. L. Gin, *J. Am. Chem. Soc.* **2001**, *123*, 4617–4618.
- [26] A. G. Martín, S. Harms, W. Weigand, D. L. Gin, *Adv. Mater.* **2005**, *17*, 602–606.

- [1] a) *Metallomesogens: Synthesis and Applications* (Ed.: J. L. Serrano), VCH, Weinheim, **1996**; b) R. Giménez, D. P. Lidon, J. L. Serrano, *Curr. Opin. Solid State Mater. Sci.* **2002**, *6*, 527–535; c) R. W. Date, E. Fernández-Iglesias,

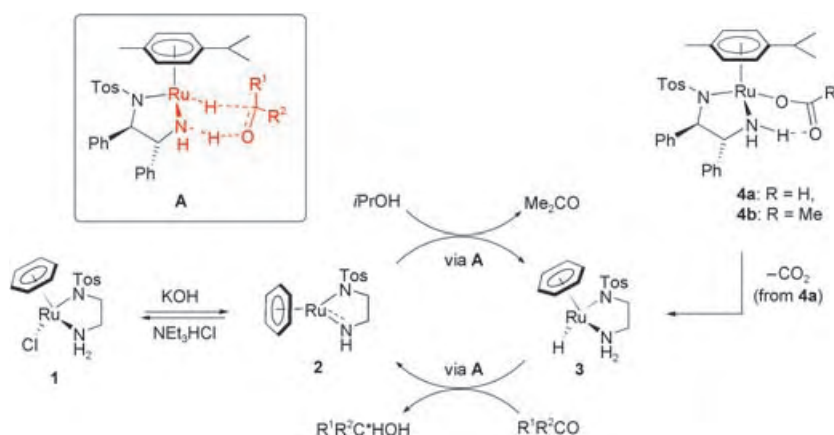
Bifunctional Metal–Ligand Catalysis: Hydrogenations and New Reactions within the Metal–(Di)amine Scaffold**

Kilian Muñiz*

Keywords:

diamines · homogeneous catalysis · hydrogenation · reduction · transition metals

The observation of the ligand-associated heterolytic splitting of H_2 dates back to pioneering work by Fryzuk et al. on organometallic amide complexes of rhodium and iridium.^[1] The general importance of the reversible storage of dihydrogen within a transition metal/ligand framework was later proposed by Crabtree but remained restricted to the stoichiometric formation of hydrides of iridium–amide complexes.^[2] Starting in 1995, Noyori disclosed novel ruthenium diamine complexes that enabled a conceptually new enantioselective hydrogenation process and thereby marked that start of the rational design of chiral catalysts with unprecedented activity in the reduction of prochiral ketones and imines.^[3] In principle, the basic task of the catalyst consists of the concerted transfer of dihydrogen within a hydride–ruthenium–diamine assembly. If the diamine or the remaining coordination sphere of the metal center bears defined stereochemical information, an enantio-



Scheme 1. Catalytic enantioselective transfer hydrogenation of ketones.

selective process is possible (e.g., structure **A**, Scheme 1).

For this purpose, two types of reactions were envisioned. Transfer hydrogenation of both ketones and imines used 2-propanol or formic acid/triethylamine as the hydrogen source.^[3a,c,d] The overall reaction pathway was determined in a seminal study in which all active metal complexes involved in the catalytic cycle were isolated.^[4] Typically the actual catalyst is generated in situ through interaction of base which causes elimination of HCl from precatalyst **1**. The resulting low-coordinate ruthenium–amide complex **2** interacts with 2-propanol (**A**, $R^1 = R^2 = \text{Me}$) and within a concerted process takes up hydride and proton to generate the hydride catalyst **3**. Reduction of the carbonyl is then accomplished via transition state **A** ($R^1 \neq R^2$) without metal–carbonyl interaction to yield the chiral alcohol or amine product and **2**. In principle, the

reaction turns endlessly at the Ru–NH surface of the two catalytically active species **2** and **3** (Scheme 1).

For transfer hydrogenation in formic acid/triethylamine azeotrope, the working mode of catalyst formation was addressed recently by Ikariya et al., who published an extensive investigation including the first structural elucidation of a transition-state analogue for this step.^[5] Reaction of the isolated ruthenium–amide complex **2**^[4] with formic acid at -40°C in THF generated the formate complex **4a** as a single diastereoisomer. This confirms once again that the formation of the actual hydride catalyst proceeds with complete stereoselectivity.^[4] As expected for an immediate catalyst precursor of high reactivity, **4a** was found to be rather unstable and no crystal structure could be obtained. Instead, the related acetate **4b** was characterized by X-ray structure analysis. The structure is in accordance

[*] Dr. K. Muñiz
Kekulé-Institut für Organische Chemie
und Biochemie
Rheinische Friedrich-Wilhelms-Universität
Gerhard-Domagk-Strasse 1
53121 Bonn (Germany)
Fax: (+49) 228-735-813
E-mail: kilian.muniz@uni-bonn.de

[**] This work was supported by the Fonds der Chemischen Industrie. Abbreviations within this article: S/C = ratio of substrate to catalyst, TON = total turnover number, binap = 2,2'-bis(diphenylphosphanyl)-1,1'-binaphthyl. For simplicity, in Schemes 1 and 3 the ligands 1,2-diphenylethylenediamine and η^6 -cymene are depicted as ethylenediamine and benzene, respectively.

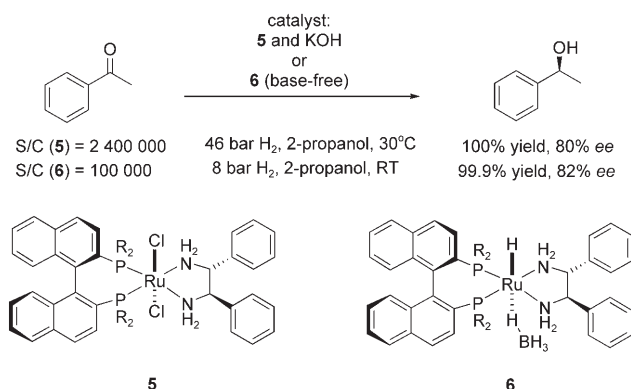
with the expected absolute configuration at the Ru atom, and the distance between the carbonyl group and the NH_2 entity is only 2.77 Å. Kinetic NMR studies on the decarboxylation of **4a** revealed a first-order rate dependence in substrate. Activation parameters of $\Delta H^\ddagger = 76 \text{ kJ mol}^{-1}$, $\Delta S^\ddagger = -38 \text{ J mol}^{-1} \text{ K}^{-1}$, and $\Delta G^\ddagger = 87 \text{ kJ mol}^{-1}$ were obtained, and the negative entropy value suggests that the active hydride catalyst **3** is formed from **4a** by an intramolecular process. Within this context, a remarkable study on the transfer hydrogenation of aromatic ketones in water was reported recently, which suggested a dramatic pH dependence of both catalyst performance and regeneration mode.^[6]

recently led to an efficient catalyst class for the enantioselective hydrogenation of *tert*-alkyl ketones.^[7c,d]

These extremely efficient catalysts have stimulated ongoing mechanistic investigations.^[8] The exact working mode of the uniquely enantioselective catalyst derived from **5** was uncovered by Noyori et al. in 2003.^[9a] The structurally defined hydride–borohydride–ruthenium precursor **6**^[9b] was found to initiate catalysis even without addition of base and therefore served as the molecular basis for the unambiguous determination of the underlying kinetics and the influence of solvent, base, and hydrogen pressure on the overall reaction profile. Two cycles turned out to be of importance. Borohydride dissociation

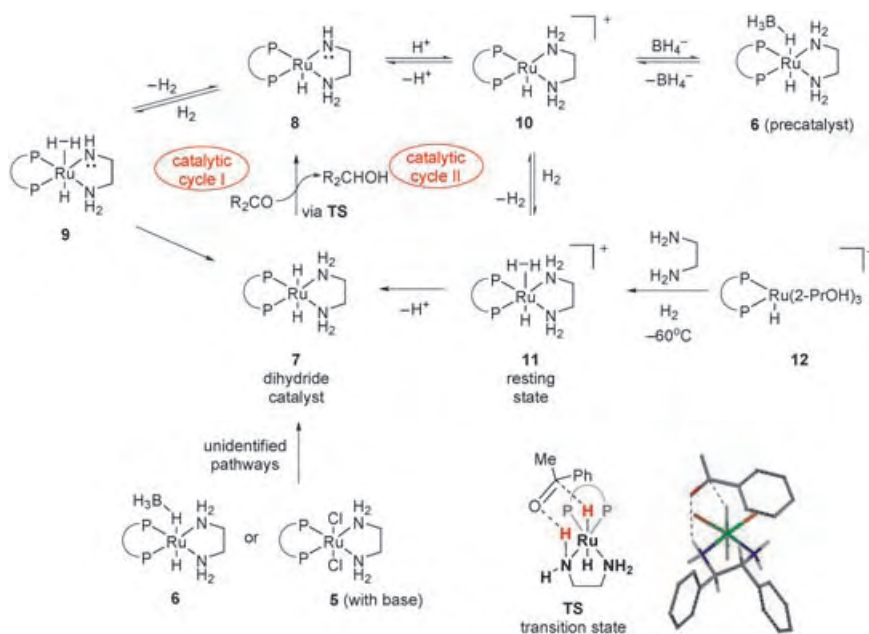
from **6** gives the cationic complex **10** (Scheme 3). In protic solvents such as 2-propanol this intermediate originates from protonation of the basic imido function in neutral **8**. Complex **10** then accommodates dihydrogen to yield the cationic dihydrogen complex **11**, which represents the resting state of the catalyst and is the immediate catalyst precursor. Dihydride catalyst **7** is formed from **11** by loss of a proton (Scheme 3, cycle II).

In an elegant experiment Bergens et al. showed that **11** can be generated directly from the cationic binap–Ru–hydride complex **12** (with tetrafluoroborate as the counterion) by addition of the diamine ligand under 1 atmosphere of hydrogen.^[10] The general structure of **11** was determined by NMR spectroscopy as was the absence of deuterium scrambling between the η^2 -bound dihydrogen and the hydride ligand. However, when generated this way **11** is not an active catalyst precursor in the absence of base. This shows that 2-propanol itself is not sufficiently basic to deprotonate the dihydrogen ligand in **11** and that the nature of the formal counterion is of high importance. For reactions in aprotic solvents, **6** generates the dihydride catalyst **7**, which reduces the ketone substrate to give amide complex **8**. This complex splits dihydro-



Scheme 2. Enantioselective hydrogenation of ketones. R = phenyl, 4-tolyl, xyllyl.

In contrast to transfer hydrogenation, the direct enantioselective hydrogenation of ketones requires the use of ternary ruthenium complexes made up of a bisphosphine, a diamine, and a ruthenium(II) center, which are usually provided as preformed dichlorides such as **5** (Scheme 2). In view of catalyst efficiency, these compounds are unparalleled. Peak turnover rates reach 62 per second, while enantioselectivities of up to 99% ee can generally be obtained.^[3b,c] Since the ternary composition allows for selective replacement of the individual ligands, the catalyst can be fine-tuned.^[3b] For example, a binap–Ru^{II} complex with a 1,4-diamine ligand acts as a precatalyst for the enantioselective hydrogenation of tetralones,^[7a,b] a substrate class which proves problematic for the conventional 1,2-diamine-chelated catalysts such as **5**. Application of pyridinyl amines has



Scheme 3. Catalytic cycles for ketone hydrogenation and the transition-state structure.

gen in a heterolytic manner ($\rightarrow 9$) to regenerate catalyst **7** (Scheme 3, cycle I).

Thus, the mechanistic scenario for the occurrence of peak turnover frequencies in bifunctional metal–ligand hydrogenation is based on a well-balanced overall neutral environment with only a local appearance of acidic and basic species as provided by **6**. Complexes **6** and **12** are the only direct catalyst precursors isolated to date, since the exact formation of **7** either from **6** under nonprotic conditions or from the dichloride **5** or related monohydrides through base interaction remains to be determined. Significant contributions by Morris et al. include the isolation of various ruthenium dihydrides related to **7**, hydride chlorides, and amide complexes which all show the expected catalytic activity in ketone and imine hydrogenation.^[11] An extensive comparative study on some dihydrides from monophosphine complexes aimed to clarify the preferential geometrical arrangement of these catalysts.^[12] In the predominant catalysts the two hydrides were found to adopt a *trans* arrangement, a result that in agreement with the suggested geometry for **7**.^[9a]

The enantiofacial differentiation of the substrate is accomplished kinetically on the molecular surface of the chirally modified RuH_2 catalyst. The final hydrogen transfer proceeds through a six-membered transition state and involves simultaneous transfer of a proton from an amino moiety of the chiral diamine ligand to the carbonyl oxygen atom and hydride transfer from ruthenium to the carbonyl group. A molecular model of the active *trans*- RuH_2 species from the hydrogenation is depicted in Scheme 3; it shows how the hydride and the amine proton ($\text{H}-\text{Ru}-\text{N}-\text{H}_{\text{ax}}$) are involved in the transition state. The prerequisite diamine ligand plays a dual role: it contributes to the chiral environment of the catalyst and takes part actively in hydrogen transfer.

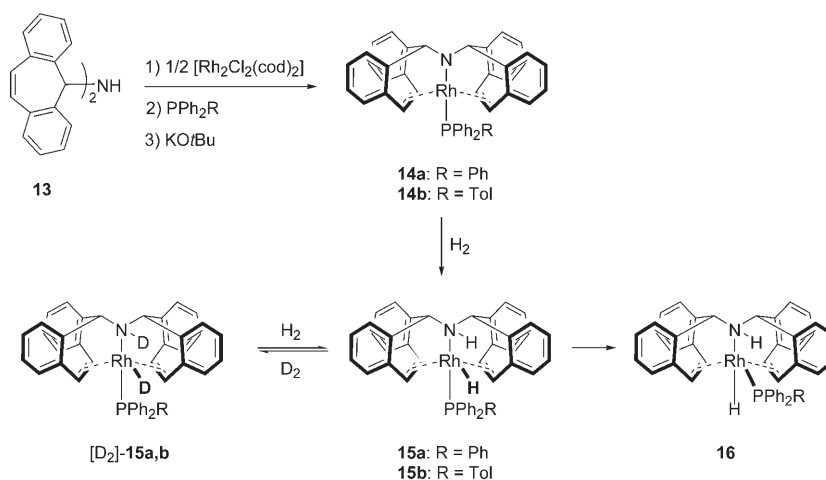
Although the two catalytic systems with hydride and dihydride catalysts (**3** and **7**, respectively) apparently share the mode of hydrogen transfer, they differ from each other in catalyst regeneration. The decisive step of the hydrogen transfer from the polarized donor molecules 2-propanol or formic acid consists of a

concerted addition across the polar Ru–amide bond. The ionic character of the hydrogen-transfer reagent is necessary, since direct activation of Ru–amide **2** with hydrogen requires a pressure of 80 bar.^[4] In contrast, cationic ruthenium complexes such as **10** can activate dihydrogen heterolytically by η^2 coordination. The subsequent deprotonation of this dihydrogen ligand is rapid and results in the high productivity of the overall reaction, that is, the kinetic preference of cycle II over cycle I.

In what represents a significant structural alternative in this area of hydrogenation catalysts, Grützmacher et al. introduced a novel rhodium–amide system for the heterolytic activation of hydrogen activation.^[13] Starting from the bistropyridenylamine **13**, a two-step sequence led to the formation of a defined rhodium complex in which the bistropyridenylamine acts as a tridentate ligand. The amino hydrogen displays the expected acidity ($\text{p}K_{\text{a,DMSO}} = 15\text{--}20$) and can be removed upon addition of base (Scheme 4). The resulting rhodium–

splitting at -78°C under 1 atm of hydrogen and are transformed into the corresponding rhodium hydrides **15a,b**. Compound **15b** was again characterized by X-ray structure analysis, and its structure was very similar to that of **14b**. This result indicates that the accommodation of hydrogen in this system is readily reversible; this was confirmed by the observation of selective and reversible deuterium incorporation under D_2 .

The structure and reactivity of the resulting rhodium hydrides thus match that required for bifunctional metal–ligand hydrogenation catalysts. Comparative DFT calculations confirm a high preference for the heterolytic dihydrogen cleavage, which yields the amino rhodium hydride by an exothermic pathway ($\Delta H_{\text{R}} = -67 \text{ kJ mol}^{-1}$), while the conventional homolytic splitting to yield a rhodium dihydride would proceed by an endothermic pathway ($\Delta H_{\text{R}} = 71 \text{ kJ mol}^{-1}$) and via an higher energy transition state ($\Delta H^\ddagger = 61 \text{ kJ mol}^{-1}$ for heterolytic vs $\Delta H^\ddagger = 75 \text{ kJ mol}^{-1}$ for homolytic cleavage). Under 100 bar of

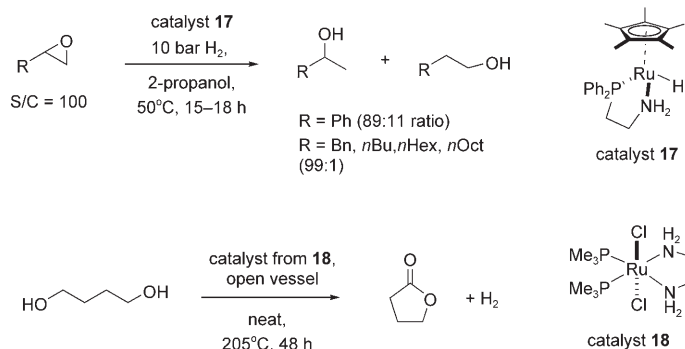


Scheme 4. A structurally novel rhodium amide complex for the heterolytic cleavage of dihydrogen. cod = cyclooctadiene.

amide complexes **14a,b** are sufficiently stable. Complex **14b** was characterized by its solid-state structure, which revealed a Rh–N bond length of 2.0 Å. In addition, the observed sawhorse structure of the four-coordinate **14b** is unique among this type of complexes and appears to be a geometrical prerequisite for dihydrogen splitting. Compounds **14a,b** readily induce heterolytic H_2

hydrogen, both the crystalline amide and the isolated hydride catalyze hydrogenation of ketones and imines with TONs of up to 650. No further additives are required; that is, the reaction proceeds under neutral conditions. Aside from the borohydride complexes of type **6**, this is a rare example of a base-free bifunctional metal–ligand hydrogenation catalyst.^[14]

Apart from their unmatched efficiency in the enantioselective hydrogenation and transfer hydrogenation of carbonyl compounds, bifunctional metal–ligand complexes have been employed recently for other processes as well. Sadler et al. described a structurally closely related cationic (η^6 -arene)-Ru(en) unit for the recognition of nucleoside and nucleotide binding sites.^[15] In the area of transition-metal catalysis, Ikariya et al. reported the catalytic hydrogenolysis of epoxides in 2-propanol in the presence of an aminophosphine ligand and a pentamethylcyclopentadienyl (Cp*) ruthenium precursor.^[16] The catalyst formed in situ was suggested to be the ruthenium hydride **17**, which at S/C = 100 gave yields from 79 to 99% and a 99:1 ratio in favor of the branched alcohol over the linear (Scheme 5).



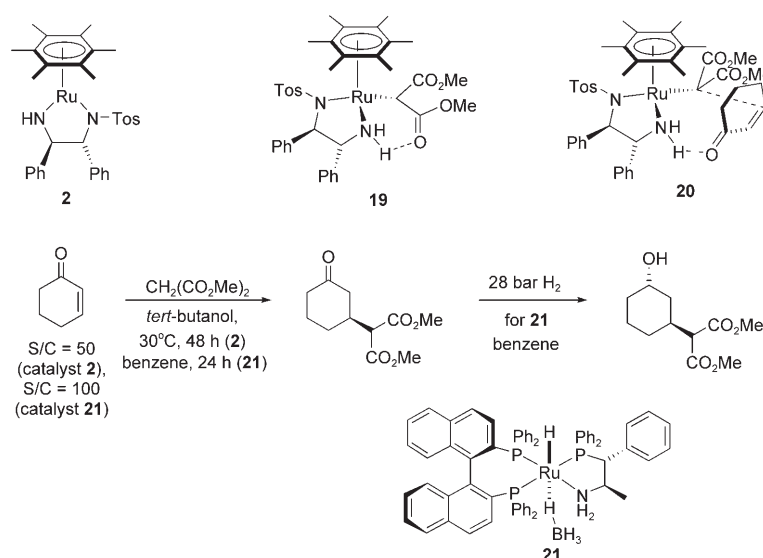
Scheme 5. Ruthenium catalysts for the hydrogenolysis of epoxides and for the conversion of diols to lactones.

Hartwig et al. employed catalysts of ternary composition for lactone formation from the dehydrogenative cyclization of 1,4-butanediol. Among various catalysts screened for this purpose, **18** performed best and converted the diol quantitatively. The reaction could be performed on a large scale; 22 g of diol was converted into the lactone in 100% yield with as little as 5.4 mg of catalyst, which corresponds to an overall TON of 17000.^[17]

The successful ruthenium diamine motif was used to develop an enantioselective Michael addition.^[18] Here, the addition of dimethyl malonate across prochiral cyclic enones such as cyclopentenone and cyclohexenone was catalyzed by **2** with selectivities of up to 99% *ee*.^[18a–c] The reaction is believed to

start from an α -metalated structure **19** and to proceed through a highly organized transition state **20** with hydrogen bonding toward the carbonyl oxygen and olefin-face selection through the imposing stereochemical environment of the catalyst surface (Scheme 6).

The identical transformation was accomplished by Morris et al. using ternary catalysts of the binap–ruthenium–aminophosphine composition.^[18d] Here, the borohydride complex **21** proved to be the most efficient catalyst precursor, leading to the Michael addition with 96% *ee* at S/C = 100. Since complexes derived from binap, ruthenium, and aminophosphines have proven to be versatile hydrogenation catalysts as well,^[19] **21** can be used for a domino catalysis.^[18d] Thus, when the Michael

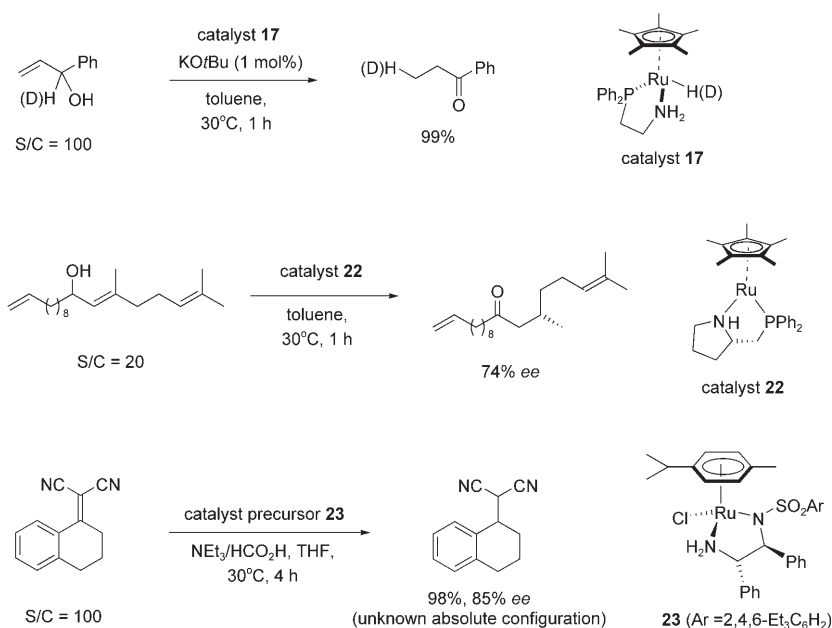


Scheme 6. Enantioselective Michael additions employing bifunctional ligand–metal catalysts.

addition was complete, application of 28 bar of hydrogen pressure led to concomitant reduction of the ketone to the corresponding alcohol with 30:1 selectivity in favor of the *trans*-configured cyclohexanol. An identical sequence with slightly lower selectivities (90% *ee* for the Michael addition and 10:1 selectivity at 99% yield) was observed for related ruthenium complexes based on binol-derived bisphosphinites.^[18e]

A ruthenium–amine moiety proved successful for the isomerization of allylic alcohols to ketones.^[20] Again, the established Cp* ruthenium catalyst **17** from epoxide hydrogenolysis was employed and was generated in situ with KO^{*t*}Bu. Various allylic alcohols could be isomerized to give the corresponding ketones (Scheme 7).

Isotopic labeling provided the first information about the mechanism. Apparently the reaction is initiated by alcohol dehydration to give the unsaturated ketone together with a ruthenium hydride or deuteride. Regioselective conjugate addition of this complex furnishes the simple ketone product with the observed deuterium incorporation in the 3-position. This observation matches the chemoselectivity observed in related Michael addition processes (Scheme 6). The fact that the reaction proceeds with complete chemoselectivity for substrates containing further C=C bonds led to the development of an enantioselective allylic isomerization



Scheme 7. Bifunctional metal–ligand catalysts for the isomerization of allylic alcohols and the reduction of polarized C=C bonds.

with a proline-derived ligand. At 5 mol% loading, catalyst **22** selectively converted the shown triene into the corresponding enantioenriched ketone, which within two subsequent steps gave the natural product (*S*)-muscone.

While the original Noyori transfer-hydrogenation catalyst displayed high chemoselectivity for the preferential reduction of C=O over C=C bonds, Deng et al. have now found that this preference can be reversed for strongly polarized olefinic substrates.^[21] In addition, application of the triethylamine/formic acid protocol led to an efficient saturation of the C=C bonds for a variety of unsaturated nitriles when a slightly modified diamine ligand was employed (precatalyst **23**). Enantiomeric excesses of up to 89% could be obtained, and experiments with deuterated formic acid suggest that the reaction involving the polarized amine–ruthenium hydride catalyst follows a conjugate reduction pathway related to the Michael additions from Scheme 6.

Bifunctional metal–ligand catalysis had originally been conceived as a synthetic methodology for the enantioselective hydrogenation of ketones and imines. The first transition metal employed, ruthenium, is still the most broadly applicable, but similar reactivity has been shown for other metals as well.


Certainly future interest in this area will focus on the elucidation of the few remaining mechanistic questions, for example, the exact mode of catalyst formation, and the development of structurally new systems such as the rhodium catalyst **15**. Apart from this, bifunctional metal–ligand catalysis may develop into a more general concept for enantioselective catalysis. In view of the first examples of enantioselective Michael additions and the isomerization of allylic alcohols, and considering the yet unexplored hydrometalation^[22] and the recent detection of highly reactive ruthenium and iridium alkoxides,^[23] one expects further exciting reactions to emerge in due course.

Published online: September 27, 2005

- [1] a) M. D. Fryzuk, P. A. MacNeil, *Organometallics* **1983**, 2, 355; b) M. D. Fryzuk, P. A. MacNeil, *Organometallics* **1983**, 2, 682; c) M. D. Fryzuk, P. A. MacNeil, S. J. Rettig, *J. Am. Chem. Soc.* **1987**, 109, 2803.
- [2] Reviews: a) R. H. Crabtree, P. E. M. Siegbahn, O. Eisenstein, A. L. Rheingold, T. F. Koetzle, *Acc. Chem. Res.* **1996**, 29, 348; b) M. J. Calhorda, *Chem. Commun.* **2000**, 801; c) R. H. Crabtree, O. Eisenstein, G. Sini, E. Peris, *J. Organomet. Chem.* **1998**, 567, 7; d) R. H. Crabtree, *Science* **1998**, 282, 2000.

- [3] Reviews: a) R. Noyori, *Angew. Chem.* **2002**, 114, 2108; *Angew. Chem. Int. Ed.* **2002**, 41, 2008; R. Noyori, *Adv. Synth. Catal.* **2003**, 345, 15; b) R. Noyori, T. Ohkuma, *Angew. Chem.* **2001**, 113, 40; *Angew. Chem. Int. Ed.* **2001**, 40, 40; c) R. Noyori, M. Yamakawa, S. Hashiguchi, *J. Org. Chem.* **2001**, 66, 7931; d) R. Noyori, S. Hashiguchi, *Acc. Chem. Res.* **1997**, 30, 97; e) R. Noyori, *Chem. Commun.* **2005**, 1807.
- [4] K.-J. Haack, S. Hashiguchi, A. Fujii, T. Ikariya, R. Noyori, *Angew. Chem.* **1997**, 109, 297; *Angew. Chem. Int. Ed. Engl.* **1997**, 36, 285.
- [5] T. Koike, T. Ikariya, *Adv. Synth. Catal.* **2004**, 346, 37.
- [6] X. Wu, X. Li, F. King, J. Xiao, *Angew. Chem.* **2005**, 117, 3473; *Angew. Chem. Int. Ed.* **2005**, 44, 3407.
- [7] a) T. Ohkuma, T. Hattori, H. Ooka, T. Inoue, R. Noyori, *Org. Lett.* **2004**, 6, 2681; b) For a related 1,4-diamine ligand, see: G. A. Grasa, A. Zanotti-Gerosa, J. A. Medlock, W. P. Hems, *Org. Lett.* **2005**, 7, 1449; c) T. Ohkuma, C. A. Sandoval, R. Srinivasan, Q. Lin, Y. Wei, K. Muñiz, R. Noyori, *J. Am. Chem. Soc.* **2005**, 127, 8288; d) For an earlier report on the conventional hydrogenation of alkyl ketones, see: Q. Jiang, Y. Jiang, D. Xiao, P. Cao, X. Zhang, *Angew. Chem.* **1998**, 110, 1203–1207; *Angew. Chem. Int. Ed.* **1998**, 37, 1100.
- [8] S. E. Clapham, A. Hadzovic, R. H. Morris, *Coord. Chem. Rev.* **2004**, 248, 2201. This excellent review provides a complete overview of all mechanistic aspects and related chemistry of ruthenium hydrides.
- [9] a) C. Sandoval, T. Ohkuma, K. Muñiz, R. Noyori, *J. Am. Chem. Soc.* **2003**, 125, 13490; b) T. Ohkuma, M. Koizumi, K. Muñiz, G. Hilt, C. Kabuto, R. Noyori, *J. Am. Chem. Soc.* **2002**, 124, 6508.
- [10] R. J. Hamilton, C. G. Leong, G. Bigam, M. Miskolzie, S. H. Bergens, *J. Am. Chem. Soc.* **2005**, 127, 4152.
- [11] a) K. Abdur-Rashid, J. A. Lough, R. H. Morris, *Organometallics* **2001**, 20, 1047; b) K. Abdur-Rashid, A. J. Lough, R. H. Morris, *Organometallics* **2000**, 19, 2655; c) K. Abdur-Rashid, M. Faatz, J. A. Lough, R. H. Morris, *J. Am. Chem. Soc.* **2001**, 123, 7473; d) K. Abdur-Rashid, S. E. Clapham, A. Hadzovic, J. N. Harvey, J. A. Lough, R. H. Morris, *J. Am. Chem. Soc.* **2002**, 124, 15104; e) V. Rautenstrauch, X. Hoang-Cong, R. Churlaud, K. Abdur-Rashid, R. H. Morris, *Chem. Eur. J.* **2003**, 9, 4954.
- [12] R. Abbel, K. Abdur-Rashid, M. Faatz, A. Hadzovic, A. J. Lough, R. H. Morris, *J. Am. Chem. Soc.* **2005**, 127, 1870.
- [13] P. Maire, T. Büttner, F. Breher, P. Le Floch, H. Grützmaier, *Angew. Chem.*

- 2005, 117, 6477–6481; *Angew. Chem. Int. Ed.* **2005**, 44, 6318–6323.
- [14] a) For other base-free hydrogenation catalysts see ref. [18e] and b) L. Dahlenburg, R. Götz, *Eur. J. Inorg. Chem.* **2004**, 888.
- [15] a) H. Chen, J. A. Parkinson, R. E. Morris, P. J. Sadler, *J. Am. Chem. Soc.* **2003**, 125, 173; b) H. Chen, J. A. Parkinson, S. Parsons, R. A. Coxall, R. O. Gould, P. J. Sadler, *J. Am. Chem. Soc.* **2004**, 126, 3064.
- [16] M. Ito, M. Hirakawa, A. Osaku, T. Ikariya, *Organometallics* **2003**, 22, 4190.
- [17] J. Zhao, J. F. Hartwig, *Organometallics* **2005**, 24, 2441.
- [18] a) M. Watanabe, K. Murata, T. Ikariya, *J. Am. Chem. Soc.* **2003**, 125, 7508; b) T. Ikariya, H. Wang, M. Watanabe, K. Murata, *J. Organomet. Chem.* **2003**, 689, 1377; c) H. Wang, M. Watanabe, T. Ikariya, *Tetrahedron Lett.* **2005**, 46, 963; d) R. Guo, R. H. Morris, D. Song, *J. Am. Chem. Soc.* **2005**, 127, 516; e) R. Guo, C. Elpelt, X. Chen, D. Song, R. H. Morris, *Org. Lett.* **2005**, 7, 1757.
- [19] K. Abdur-Rashid, R. Guo, A. J. Lough, R. H. Morris, D. Song, *Adv. Synth. Catal.* **2005**, 347, 571.
- [20] M. Ito, S. Kitahara, T. Ikariya, *J. Am. Chem. Soc.* **2005**, 127, 6172.
- [21] D. Xue, Y.-C. Chen, X. Cui, Q.-W. Wang, J. Zhu, J.-G. Deng, *J. Org. Chem.* **2005**, 70, 3584.
- [22] K. Matsumura, S. Hashiguchi, T. Ikariya, R. Noyori, *J. Am. Chem. Soc.* **1997**, 119, 8738.
- [23] T. Koike, T. Ikariya, *Organometallics* **2005**, 24, 724.


WILEY InterScience®
 DISCOVER SOMETHING GREAT
 Access some of the finest full text journals, reference works, books, and databases from around the globe. It's just what you need to make some important discoveries of your own.

ABOUT US
 VIEW DEMO
 CONTACT US
 HELP

Log in to your saved titles, articles, queries and alerts in My Profile.
 USER NAME: PASSWORD:
☐ Remember Me
[Register Now](#) | [Forgot My Password](#)

Manage your access easily with “MY PROFILE”

Simply register. Registration is fast and free to all internet users.



Easy Access

- Save Titles, Articles & Queries for quick access
- Set up roaming access to access content outside of your institutions network
- Get free online sample copies
- Get free online trial subscriptions
- View a complete list of your subscriptions and accessible products

Enhanced Tools

- Receive E-Mail Alerts when new content is available
- Purchase Article Select Tokens online
- Purchase individual articles online with Pay-Per-View

www.interscience.wiley.com

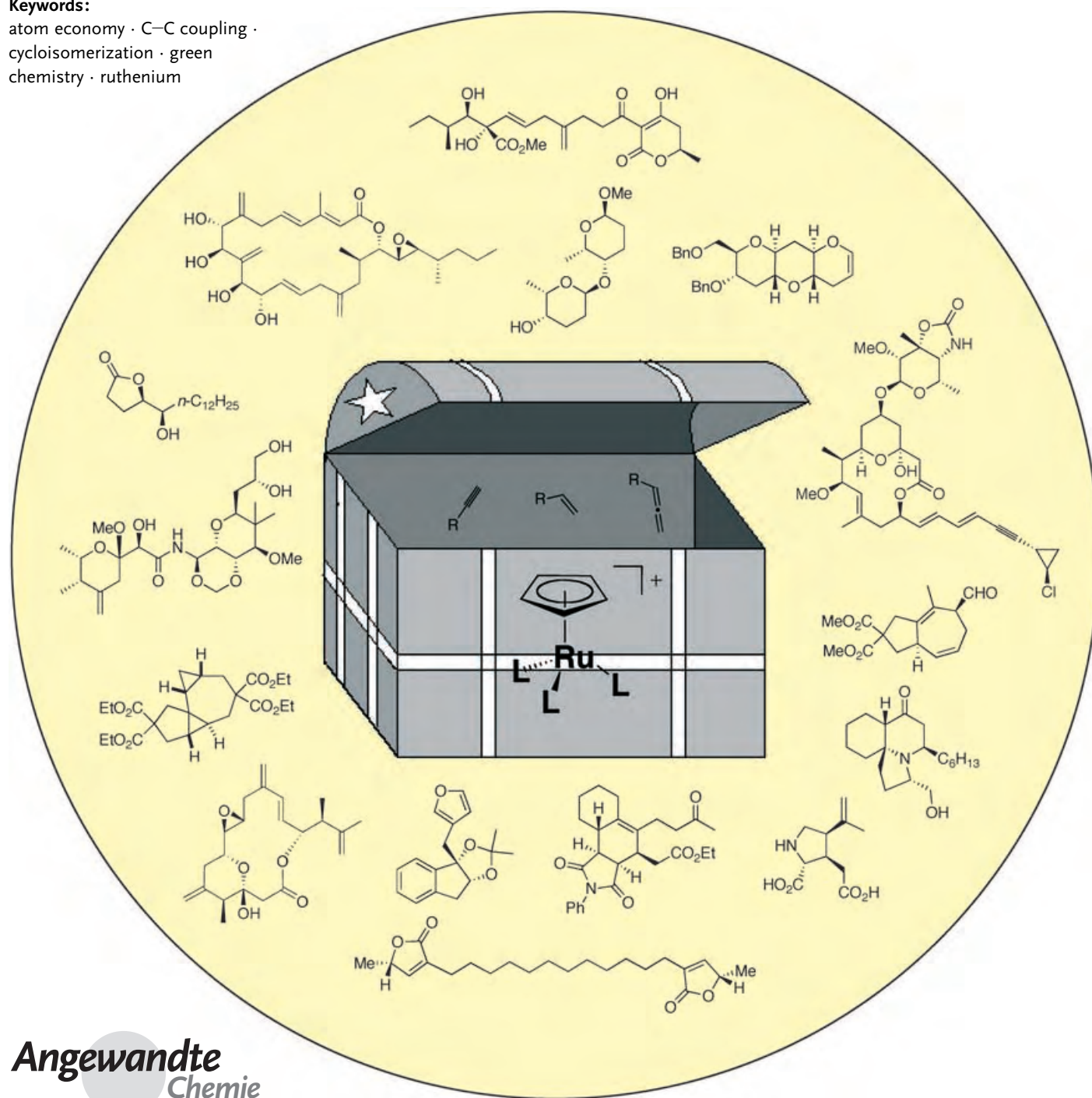

WILEY InterScience®
 DISCOVER SOMETHING GREAT

Ruthenium-Catalyzed Reactions—A Treasure Trove of Atom-Economic Transformations

Barry M. Trost,* Mathias U. Frederiksen, and Michael T. Rudd

Keywords:

atom economy · C–C coupling ·
cycloisomerization · green
chemistry · ruthenium



The demand for new chemicals spanning the fields of health care to materials science combined with the pressure to produce these substances in an environmentally benign fashion pose great challenges to the synthetic chemical community. The maximization of synthetic efficiency by the conversion of simple building blocks into complex targets remains a fundamental goal. In this context, ruthenium complexes catalyze a number of non-metathesis conversions and allow the rapid assembly of complex molecules with high selectivity and atom economy. These complexes often exhibit unusual reactivity. Careful consideration of the mechanistic underpinnings of the transformations can lead to the design of new reactions and the discovery of new reactivity.

From the Contents

1. Introduction	6631
2. Additions via Vinylidene Complexes	6632
3. Additions via Allenylidene Complexes	6637
4. Redox Isomerization	6639
5. The Ruthenium-Catalyzed Alkene–Alkyne Coupling Reaction	6640
6. The Allene–Alkene Addition via Ruthenacyclopentene Intermediates	6658
7. Ruthenium-Catalyzed [5+2] Cycloaddition	6661
8. Summary and Outlook	6663

1. Introduction

The synthetic chemical community has been put under increased pressure to produce, in an environmentally benign fashion, the myriad of substances required by society. Thus, green chemistry has emerged as a discipline that permeates all aspects of synthetic chemistry. A major goal of this endeavor must be to maximize the efficient use of raw materials and simultaneously to minimize waste. Thus, synthetic efficiency has to address not only selectivity (i.e. chemo-, regio-, diastereo-, and enantioselectivity) but also atom economy.^[1,2] That is, in chemical transformations of the general form $A + B \rightarrow C + D$, if the desired product is C, then the by-product D must be as small and innocuous as possible if no use for it can be found. In an ideal scenario D would vanish all together, and the general scheme would simplify to $A + B \rightarrow C$, with anything else needed only catalytically. In other words, the use of simple addition reactions must be emphasized if we are to make chemical manufacturing more efficient.

Several reactions of this type have been developed, with the Diels–Alder reaction perhaps representing the ideal reaction in that C–C bonds may be formed, not only with a high degree of chemo-, regio-, diastereo-, and enantioselectivity, but also atom economically. Few industrial processes make use of the exquisite power of the Diels–Alder transformation, even though it is an invaluable tool in the synthesis of complex molecules.^[3] Hydroformylation, on the other hand, is an atom economic reaction that enjoys widespread industrial use, but sees only limited use in typical research laboratories.^[4,5] Finally, catalytic hydrogenation represents an almost ideal reaction that is extensively used both industrially

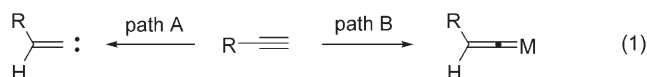
and academically. Unfortunately, few reactions in multistep synthetic sequences are simple addition reactions, and as a result few types of molecular transformations are possible in an atom-economic fashion. Expanding the synthetic toolbox to include more addition reactions will certainly change this picture. In this context transition-metal catalysts have occupied and continue to occupy a central role, both in improving existing processes and, more importantly, in discovering new ones. In this regard our research program directed at the development of non-metathesis ruthenium-catalyzed reactions has been a particularly fruitful avenue of investigation.

A comprehensive treatment of this area goes well beyond the scope of this Review.^[6] Rather, we illustrate that by approaching the development of reactions in a semirational way, one can discover, indeed invent, new reactions guided by the mechanistic underpinnings of these transformations. An understanding of the mechanisms of these reactions continues to provide the basis and impetus for the discovery of new reactions, even if the proposed hypothesis does not always turn out to be the actual mechanism! This Review is roughly divided into sections along the lines of the proposed operating mechanisms, with special care being taken to guide the reader through the reasoning behind the design of the reactions.

[*] Prof. B. M. Trost, Dr. M. U. Frederiksen, Dr. M. T. Rudd
Department of Chemistry
Stanford University
Stanford, CA 94305-5080
Fax: (+1) 650-725-0002
E-mail: bmtrost@stanford.edu

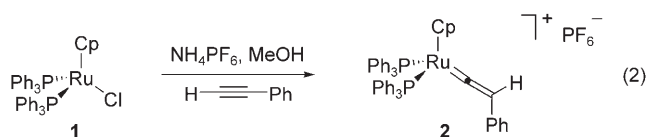
2. Additions via Vinylidene Complexes

A number of reactions have been reported in which alkynes were reported to be converted either thermally into carbenes,^[7,8] or in the presence of a metal into the corresponding metal complexed carbenes.^[9] There were, however, several issues with the generation of these carbenes. First, the thermal route [Eq. (1), path A], required extremely high



temperatures, which made the synthetic usefulness of this method doubtful. The formation of metal vinylidenes [Eq. (1), path B], on the other hand, proceeds under extremely mild conditions, but unfortunately these complexes were generally too stable to be synthetically useful.^[10–16]

The work disclosed by Bruce and co-workers in which various ruthenium vinylidene complexes (e.g. **2**) were reportedly synthesized from [CpRu(PPh₃)₂Cl] (**1**) [Eq. (2); Cp =



cyclopentadienyl),^[17–21] stimulated a search for how such complexes may function as reactive intermediates in a catalytic cycle. These complexes are remarkably stable towards nucleophiles, for example, complex **2** must be heated at reflux in methanol to obtain the addition product. Moreover, higher alcohols do not react with this complex at all.^[19]

To overcome the inherent low reactivity of **2** towards alcohols, the possibility of pre-coordinating the nucleophile may offer a viable option. In such a scenario the double bond of an allylic alcohol would coordinate to the metal, and hence deliver the hydroxy group in an intramolecular fashion (Scheme 1). Thus, the reaction of a coordinatively unsatu-



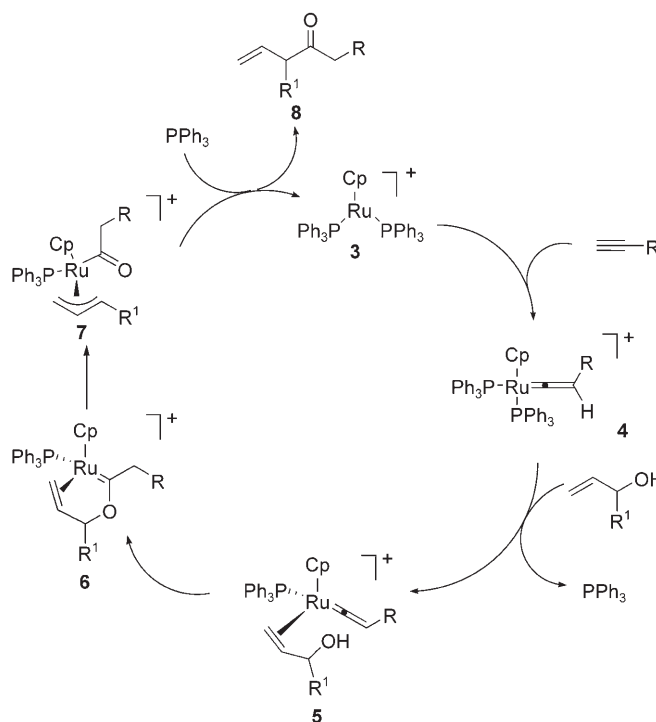
Barry M. Trost was born in Philadelphia, PA in 1941 and studied at the University of Pennsylvania (BA, 1962). He obtained his PhD in 1965 at MIT. He moved to the University of Wisconsin where he was made Professor in 1969 and subsequently Vilas Research Professor in 1982. He moved to Stanford University in 1987 and became Tamaki Professor of Humanities and Sciences in 1990. In addition to holding Visiting Professorships at several universities worldwide, he has been awarded numerous prizes. His interests span the entire field of organic synthesis, particularly in the development of novel methodology.



Michael T. Rudd was born in 1976 and studied chemistry at Purdue University. After obtaining his BS in 1999, he joined the research group of Professor Barry M. Trost at Stanford University, where he obtained his PhD in 2004. He is currently a medicinal chemist at Merck Research Laboratories in West Point, PA.



Mathias U. Frederiksen was born in 1975 in Luxemburg. He studied chemistry at Mount Allison University, Canada. After the completion of his undergraduate studies, he joined the research group of Professor Tony Barrett at Imperial College in London, UK, where he obtained his PhD in 2002. After postdoctoral studies in the group of Professor Barry M. Trost, he is now a medicinal chemist at the Novartis Institutes for Biomedical Research in Basel, Switzerland.

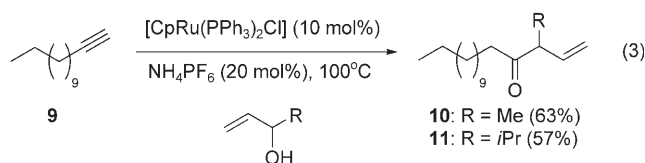


Scheme 1. Mechanistic rationale for the reconstitutive addition of alkynes and allylic alcohols.

rated Ru complex such as **3** with a terminal alkyne was expected to generate the corresponding vinylidene complex **4**. Ligand exchange would form the complex **5** in which the nucleophilic hydroxy group is proximal to the vinylidene carbon atom. Nucleophilic attack then generates ruthenadiene **6**, which may undergo sigmatropic rearrangement followed by reductive elimination to give the β,γ -unsaturated ketone **8** via allyl complex **7**.

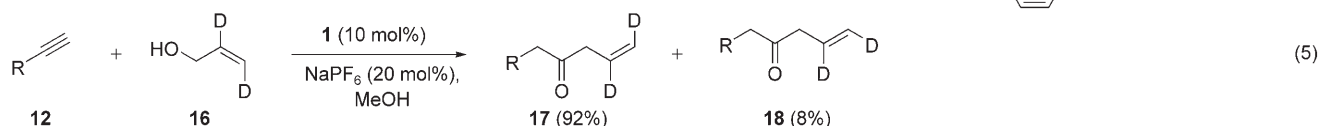
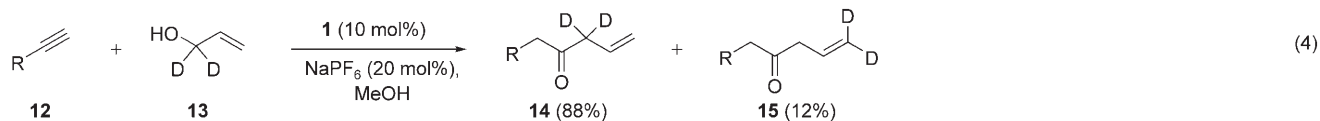
Initial studies in this program focused on the reaction between complex **1** and various terminal alkynes. These

revealed that in contrast to other aliphatic alcohols, various allylic alcohols reacted cleanly with terminal acetylenes in the presence of catalytic amounts of complex **1** and ammonium hexafluorophosphate to form the desired β,γ -unsaturated ketones in good yield [Eq. (3)].^[22] The reaction tolerates



branching at the allylic position, but not substituents on the double bond, presumably due to steric factors. Mechanistic studies lent strong support for the proposed mechanism.^[23] First, the coordination of the allylic alcohol is proposed to take place by ligand exchange with triphenylphosphane in the second step of the catalytic cycle. Several results support this rationale. For example, the rate of reaction between **9** and allyl alcohol is significantly retarded in the presence of excess triphenylphosphane (> 1 equiv/Ru). Moreover, the use of a bidentate ligand such as dppe (1,2-bis(diphenylphosphanyl)-ethane) instead of triphenylphosphane completely shuts down the reaction, presumably due to the reluctance of the dppe ligand to dissociate from the ruthenium center, which in turn precludes coordination of the olefin.

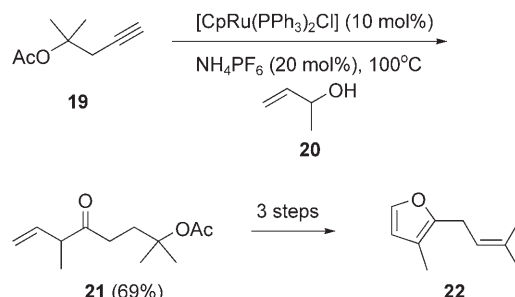
Labeling experiments cast light on other aspects of the proposed mechanism [Eq. (4) and Eq. (5)]. Treatment of 1-



ethynyl naphthalene (**12**) with deuterated allylic alcohol **13** led to addition products **14** and **15** ($\approx 7:1$). The carbon atom that bears the allylic hydroxy group preferentially formed the new C–C bond with the terminal alkyne carbon atom [Eq. (4)]. Similarly, treatment of **12** with *trans*-dideuterated allylic alcohol **16** gave the with a 11.5:1 ratio [Eq. (5)]. The retention of the geometry of the alkene demonstrates the intervention of a π -allyl species (e.g. **7**) in the catalytic cycle, in which isomerization is slower than reductive elimination. More-hindered allylic alcohols show complete scrambling of the olefin geometry, thus indicating that $\eta^3\text{-}\eta^1\text{-}\eta^3$ isomerization now competes with reductive elimination.

This reaction exhibits excellent chemoselectivity and allows the presence of acetals, esters, conjugated ketones,

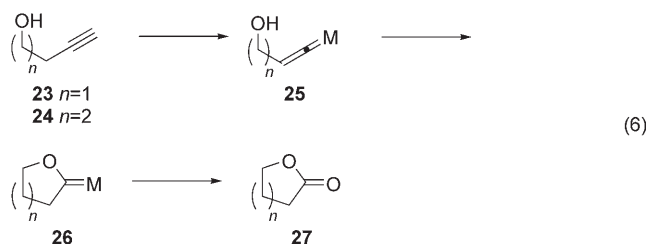
internal alkynes, as well as alcohols to be present in the acetylenic coupling partner.^[24] Moreover, it lends itself well to synthesis. For example rosefuran (**22**), the essence of rose oil, was synthesized in 23 % overall yield in a concise six-step sequence starting with acetylene **19** and allylic alcohol **20**. In this case, the Ru-catalyzed reaction generates the 1:1 adduct **21**, which is readily converted into the target furan **22** (Scheme 2).^[25]



Scheme 2. Reconstitutive condensation in the total synthesis of rosefuran (**22**).

Later, a second-generation catalyst system with $\text{In}(\text{OTf})_3$ as a halophilic cocatalyst allowed a decrease in the amounts of allylic alcohol required for complete conversion into a nearly equimolar ratio with respect to the alkyne coupling partner.^[24,26] The role of the cocatalyst is probably to remove chloride ion, thus generating a coordinatively more unsaturated Ru cation.

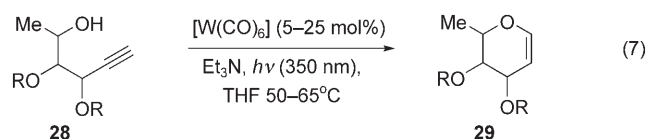
The potential susceptibility of vinylidene complexes towards nucleophilic attack by pre-coordinated nucleophiles prompted an examination of the possibility of intercepting such species by a tethered nucleophile [Eq. (6)]. In this



scenario a homopropargylic (**23**, $n = 1$) or higher alcohol (**24**, $n = 2$) was expected to attack the vinylidene complex **25** to form the oxacarbene species **26**. An oxygen heterocycle may then be released upon oxidative decomplexation, for example, in the form of a lactone **27**.

The synthesis of Fischer oxacarbene species such as **26** has been known since the early 1970s, and systems containing five-,^[27] six-,^[28] and seven-membered rings^[29] have been prepared. The development of preparatively useful methods that make use of the Fischer oxacarbene complexes has been hampered by the perceived difficulty of the decomplexation step.^[30] Many useful transition-metal-mediated methods for alkynol cycloisomerization have nevertheless been developed.^[31]

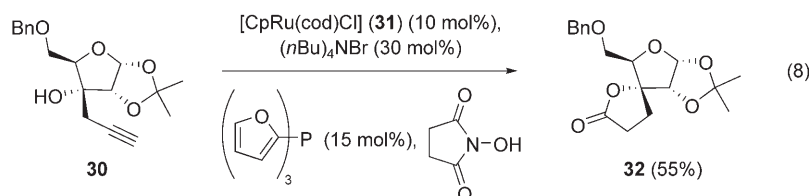
The logical extension of this work has been the development of viable catalytic methods for alkynyl cycloisomerization-type reactions. In this regard McDonald and co-workers developed elegant catalytic versions of their tungsten-mediated *endo* cycloisomerization, which provides access to structurally diverse dihydropyrans in a highly efficient manner [Eq. (7)].^[32–36] This methodology has been extensively



utilized in the synthesis of biologically significant glycosides.^[37–40]

The key to using the ability of Ru vinylidene complexes to be trapped by a homopropargylic alcohol is the design of a decomplexation pathway of Ru–oxacarbene complexes. One approach considers a subsequent oxidative decomplexation step, which would lead to γ -butyrolactones (see **27**, $n = 1$ [Eq. (6)]). Literature precedent indicated that the latter step had been effected by strong oxidants such as cerium ammonium nitrate^[41,42] and dimethyl dioxirane.^[43] The critical issue seemed to be the discovery of an oxidant that would be chemoselective and would maintain the catalytic cycle. The choice of oxidant (*N*-hydroxysuccinimide) and a small

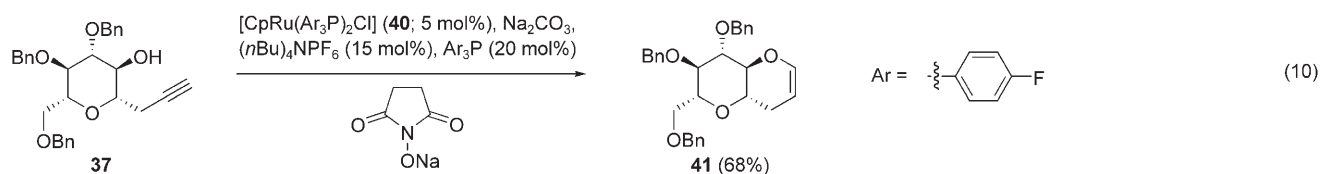
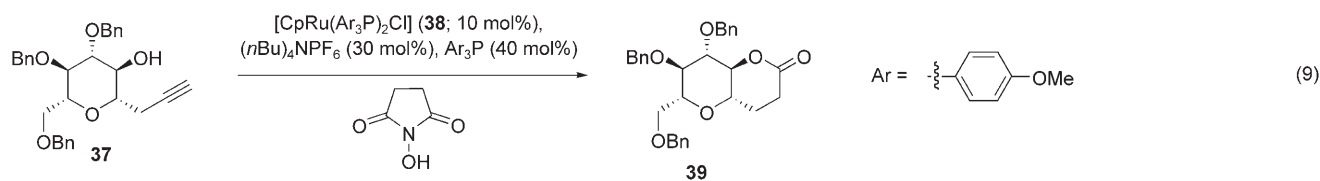
electron-poor phosphine (trifurylphosphane) was critical for achieving the catalytic reaction as shown in the transformation of substrate **30** into product **32** catalyzed by Ru complex **31** [Eq. (8)].^[44]

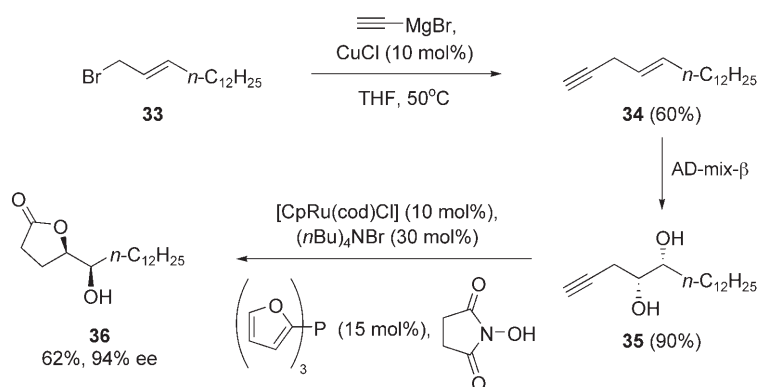


This methodology was applied in a short asymmetric synthesis of (–)-muricatacin, a natural product with antitumor properties (Scheme 3).^[45,46] The chemoselectivity of this oxidative cyclization of **35** for the formation of a five-preferentially to a six-membered ring is noteworthy.

This synthetic methodology can be extended to 5-hydroxy-1-alkynes. Initial forays in this direction met with limited success owing to significant competitive *exo* cyclization, rather than cyclization in the desired *endo* mode. Considerable experimentation revealed a most intriguing divergence. When a 5-hydroxy-1-alkyne (e.g. **37**) was exposed to catalytic [CpRu(Ar₃P)₂Cl] with electron-donating phosphine ligands (e.g. tris(*para*-methoxyphenyl)phosphane) the lactone **39** formed exclusively [Eq. (9)]. In contrast, the catalyst bearing electron-withdrawing phosphine ligands (e.g. tris(*para*-fluorophenyl)phosphane) led to clean conversion into the dihydropyran **41** [Eq. (10)].^[47] Slightly higher catalyst loadings are necessary to reach complete conversion in the former case.

This interesting dichotomy can be explained by considering the proposed mechanism (Scheme 4). The initial stages of the catalytic cycle are common for both pathways. Thus, vinylidene **43** is formed, and nucleophilic attack of the hydroxy group at the vinylidene carbon atom leads to the pivotal intermediate **44**. In the case of the cycloisomerization (Scheme 4, cycle A), the electron-deficient ligand favors ligand exchange to form anionic intermediate **45**, which upon protonation liberates the dihydropyran **46** and Ru-complex **47**. Simple ligand exchange liberates *N*-hydroxysuccinimide and regenerates the catalyst **42**. An electron-rich





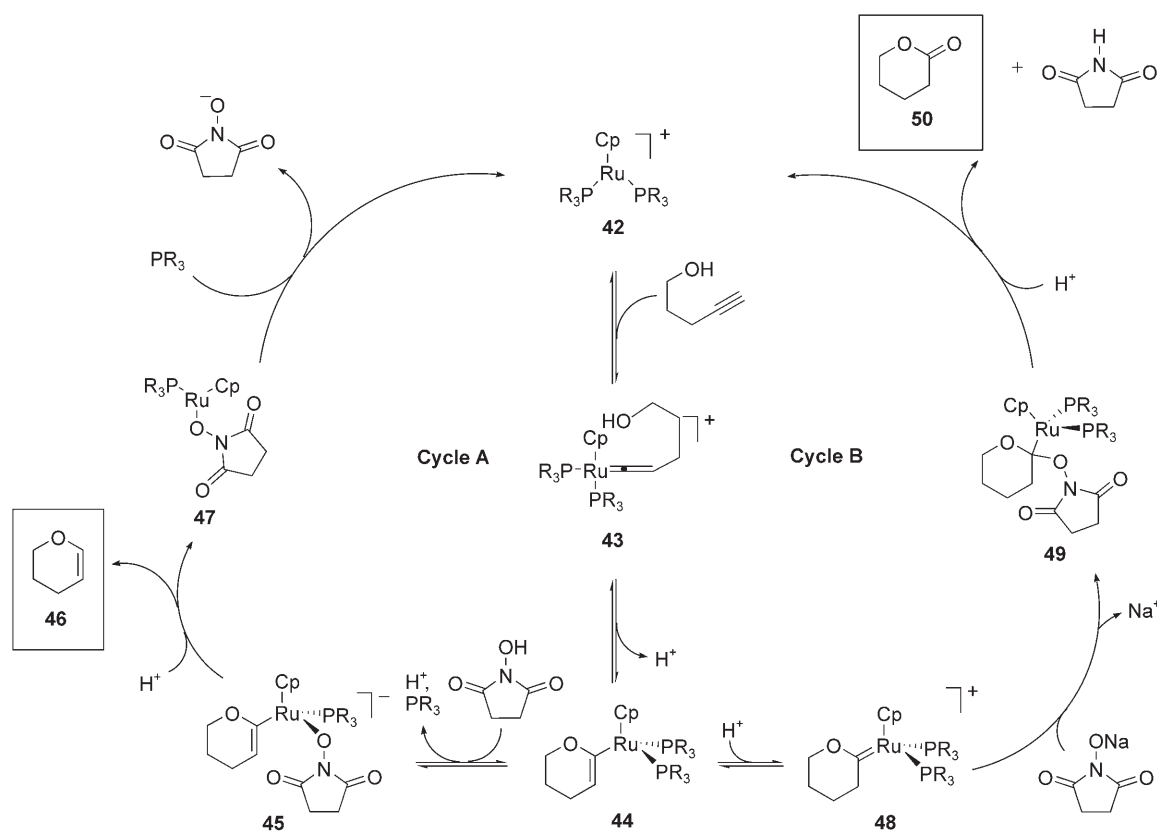
Scheme 3. Total synthesis of (–)-muricatacin (**36**) by Ru-catalyzed cycloisomerization/oxidation; cod = 1,5-cyclooctadiene.

phosphine is used in the oxidative cyclization (Scheme 4, cycle B), in which protonation of the ruthenadihydropyran **44** is preferred and affords the cationic complex **48**. Attack at the anomeric center by the nucleophilic oxidant gives complex **49**, followed by protonation to liberate the lactone **50** and regenerate the catalyst **42**. The formation of the dihydropyran is particularly interesting as some groups have reported the attempted formation of dihydropyrans from the ruthenium intermediates and noncoordinating bases.^[48] In the case at hand the choice of a coordinating base, specifically *N*-hydroxysuccinimide, is critical for turnover, as other bases failed entirely to give the dihydropyrans.^[49]

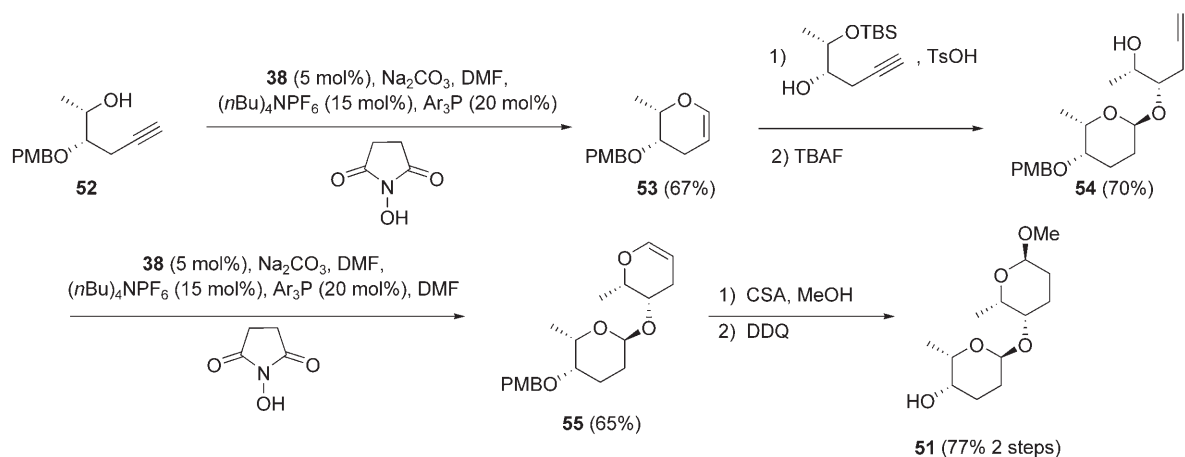
The divergent reaction lends itself well to synthetic applications. For example, iterative cycloisomerization, akin to the elegant application of tungsten-catalyzed cycloisomerization by McDonald and Wu,^[39] opened up an approach to narboline A (**51**), an antiviral bistetrahydropyran natural product isolated from *Streptomyces* (Scheme 5).^[50] Thus, alcohol **52** was converted into the dihydropyran **53** under the standard conditions. Stereoselective formation of the anomeric ether **54** preceded the second cycloisomerization, which afforded the glycal **55** in very good yield. Finally, acid-catalyzed addition of methanol followed by deprotection gave narboline A (**51**).

Likewise, the oxidative cyclization is also useful for the synthesis of natural products, for example, in the concise formal synthesis of the mosquito pheromone **56** (Scheme 6).^[51,52] In this case, oxidative cyclization of **57** under the standard conditions revealed the hydroxylactone **58** (64% yield), an intermediate in the synthesis by Kotsuki et al.^[53]

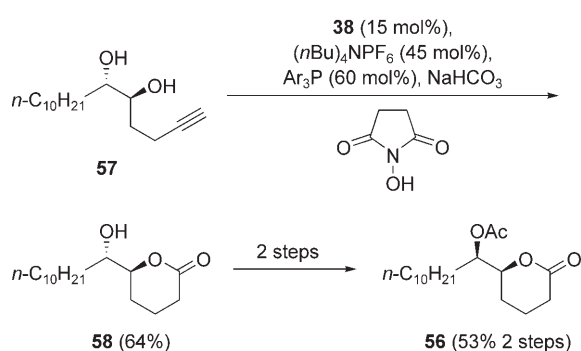
The marine ladder toxins represent a structurally fascinating class of natural products.^[54] With the efficient Ru-catalyzed cycloisomerization in hand, an iterative approach to the *trans*-fused tetrahydropyran ring systems found in the BCD ring fragment of yessotoxin,^[55] a polyether toxin implicated in diarrhetic shellfish poisoning, was envisaged (Scheme 7). Readily available alcohol **59** was subjected to the standard cycloisomerization conditions to afford glycal **60** in



Scheme 4. Postulated mechanism for the cycloisomerization (cycle A) and oxidative cyclization (cycle B).



Scheme 5. Iterative cycloisomerization in the total synthesis of narbosine A (**51**); PMB = *para*-methoxybenzyl; TBS = *tert*-butyldimethylsilyl; Ts = *para*-toluenesulfonyl; CSA = 10-camphorsulfonic acid; DDQ = 2,3-dichloro-5,6-dicyano-1,4-benzoquinone.

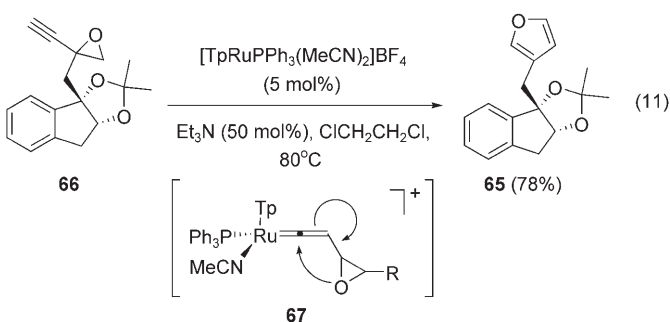


Scheme 6. Formal total synthesis of insect pheromone **56** by a Ru-catalyzed oxidative cyclization reaction.

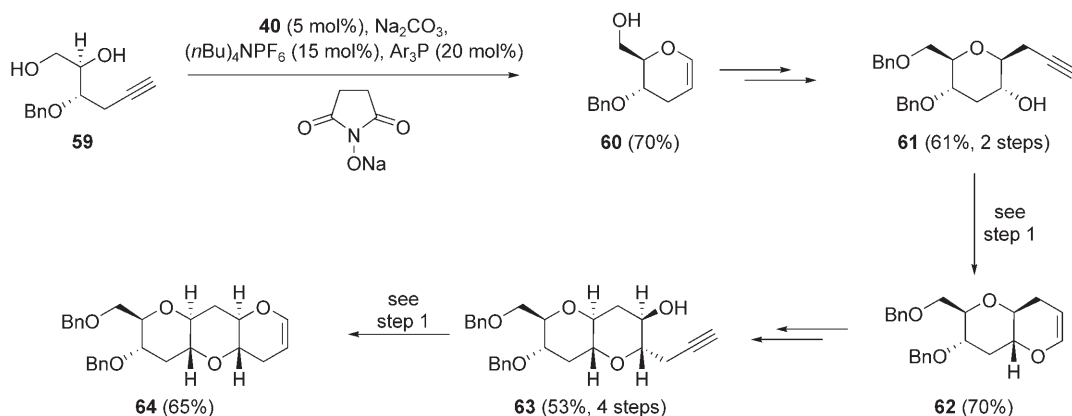
excellent yield. This was readily converted into the alkynyl alcohol **61** in two steps, thus setting the stage for a second cycloisomerization reaction, which proceeded uneventfully to give bicycle **62**. Straightforward manipulations again delivered the requisite 5-hydroxy-1-alkyne **63**. A third cycloisomerization then gave tricyclic glycal **64** in excellent yield.

Alternative methods for the interception of ruthenium vinylidene complexes by nucleophiles have also led to

catalytic cycles. For example, Liu and co-workers recently described an efficient Ru-catalyzed synthesis of functionalized furans (e.g. **65**) from propargylic epoxides (e.g. **66**) in very good yield [Eq. (11); Tp = tris(pyrazolyl)borate].^[56]

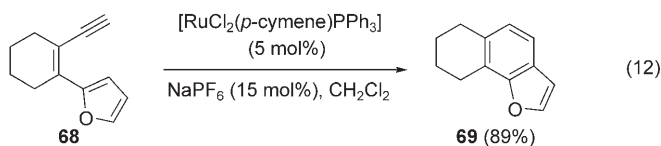


Ruthenium vinylidene **67** is proposed to be the key intermediate in this reaction, and evidence for this mechanism was supported by deuterium-labeling experiments. Similarly, carbon nucleophiles have also been used to trap ruthenium vinylidenes. Merlic and co-workers demonstrated that dienyl

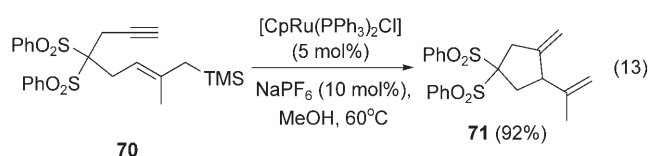


Scheme 7. Iterative Ru-catalyzed cycloisomerization in the synthesis of *trans*-fused tetrahydropyrans.

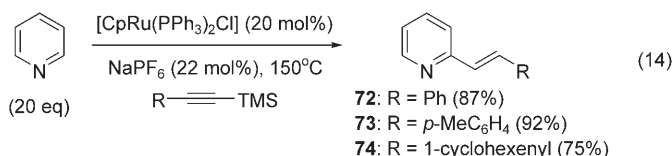
alkynes (e.g. **68**) could be cyclized to the corresponding furan (e.g. **69**) in high yield in the presence of $[\text{RuCl}_2(p\text{-cymene})\text{PPh}_3]$ and NaPF_6 [Eq. (12)].^[57]



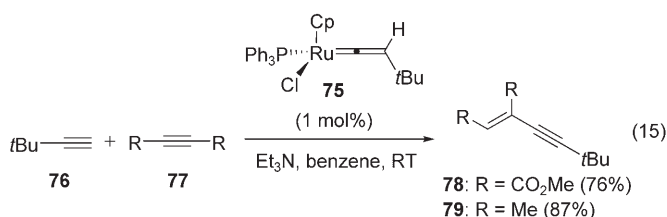
A ruthenium vinylidene species is also invoked as an intermediate in the cyclization of 1-alkyne-6-allyl silanes **70** to produce 1,4-dienes **71**. Echavarren demonstrated that enyne **70** cyclized smoothly to diene **71** in the presence of the $[\text{CpRu}(\text{PPh}_3)_2\text{Cl}]$ precatalyst and NaPF_6 . The silane is proposed to stabilize the positive charge that develops during ring closure [Eq. (13)].^[58] Ruthenium catalysis was also used



to mediate the alkenylation of pyridine to give 2-alkenyl pyridines **72–74** in high yield. The pyridine species is thought to undergo ligand exchange with one phosphine ligand, thereby placing the heterocycle proximal to the vinylidene moiety and thus enabling regioselective alkenylation [Eq. (14)]. Evidence for this mechanism was found by switching to a bidentate phosphine, dppe, which led to no alkenylation.^[59]



Ruthenium vinylidenes can also participate in carbemetalation reactions, and a number of these have emerged in the literature.^[60] A particularly interesting example was revealed by Yi and co-workers: vinylidene complex **75** was found to catalyze the cross-coupling of *tert*-butyl acetylene (**76**) with a variety of alkynes (e.g. **77**) to give the addition products (e.g. **78** and **79**) in excellent yield [Eq. (15)].^[61] Notably both



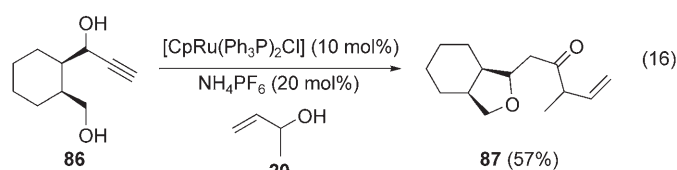
electron-poor and electron-rich alkynes functioned equally well in this cross-coupling reaction.

3. Additions via Allenylidene Complexes

Transition-metal–allenylidene complexes have attracted a great deal of attention in recent years owing to their interesting structural features as well the multitude of transformations they undergo.^[62,63] Most syntheses are based on the spontaneous dehydration of propargylic alcohols first reported by Selegue, or on variations thereof.^[64] Several stoichiometric metal–allenylidene complexes have been described, and their chemistry has been well documented.^[13] Their use in non-metathesis catalytic applications, however, are less developed.

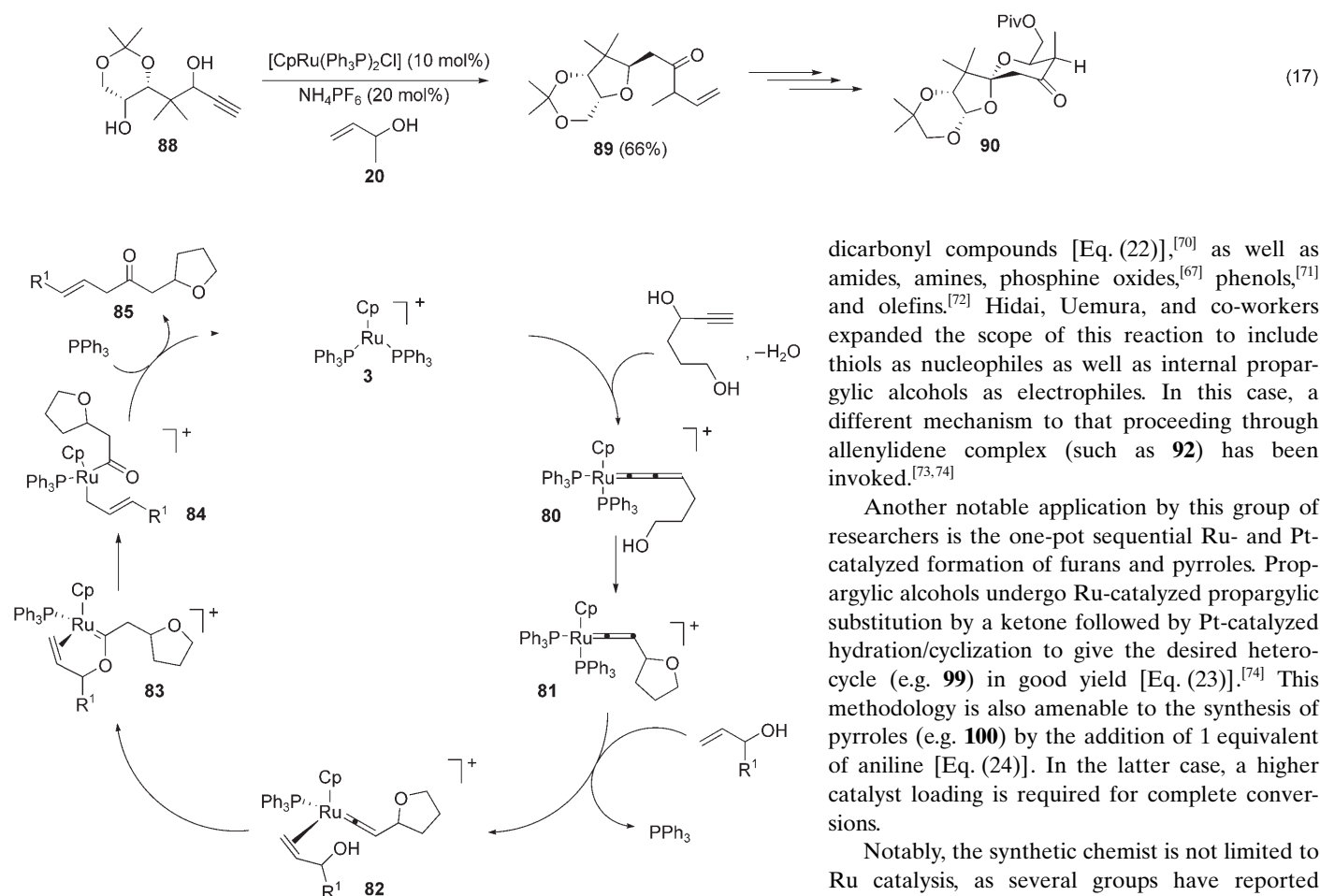
It was the potential for the activation of three carbon atoms that primarily evoked our interest in the use of Ru–allenylidene complexes in catalytic processes. At the outset, complexes had been utilized in stoichiometric amounts in several interesting settings, but no catalytic applications had been developed. The use of ruthenium–vinylidene complexes in the reconstitutive condensation (see Section 2) encouraged exploratory studies with allenylidene complexes. Specifically, the use of tethered nucleophiles could potentially trap the allenylidene complex, thereby generating a vinylidene complex that could undergo the standard reconstitutive addition process (Scheme 8). The allenylidene complex **80** is expected to form readily from Ru complex **3** and the propargylic alcohol. The tethered hydroxy group would lead to concomitant formation of the tetrahydrofuran **81** as well as the vinylidene complex, which would undergo a standard reconstitutive addition (via **82–85**) as described previously.

ω -Hydroxypropargylic alcohols participated well to form both five- and six-membered cyclized products in good yield when exposed to catalytic $[\text{CpRu}(\text{Ph}_3\text{P})_2\text{Cl}]$ and NH_4PF_6 [Eq. (16)]. For example, diol **86** cyclized smoothly to give



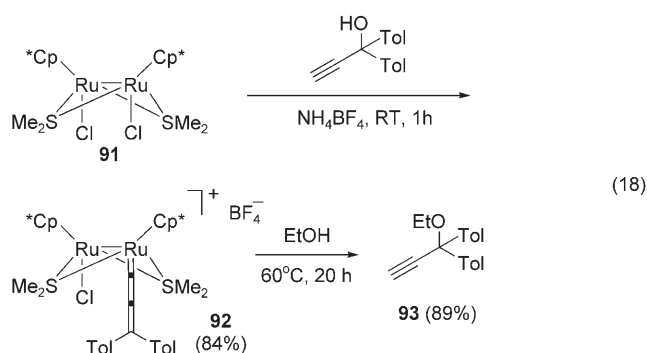
bicycle **87** in very good yield (57%).^[65] Similarly, the spiroketal subunit of calyculin A was accessed readily by subjecting propargylic alcohol **88** to the tandem cyclization–reconstitutive addition protocol [Eq. (17); Piv = pivaloyl]^[66] to give ketone **89**, a precursor for **90**.

More recently, Ru–allenylidene intermediates have been invoked in several fascinating reactions. For example, Hidai, Uemura, and co-workers have published extensively on the use of thiolate-bridged bimetallic ruthenium complex **91** in several Nicholas-type addition reactions to terminal propargylic alcohols.^[67] They isolated the allenylidene complex **92**



Scheme 8. Tandem cyclization/reconstitutive addition of propargyl alcohols with allyl alcohols.

in 84% yield by treating **91** with 1,1-ditolylpropargylic alcohol. Complex **92**, in turn, underwent substitution at the C₇ position when heated in ethanol to afford ether **93** in 89% [Eq. (18); Cp* = pentamethylcyclopentyl, Tol = tolyl].

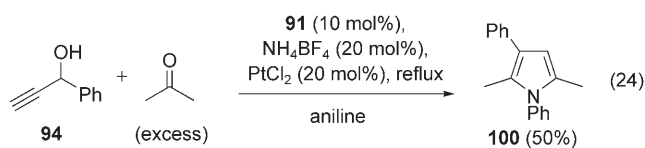
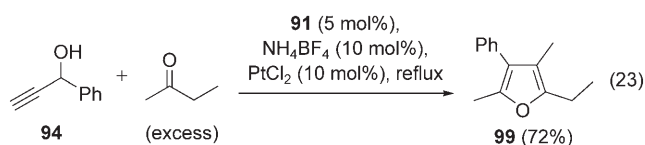


The precatalyst **91** was screened in a number of different propargylic substitution reactions and found to be a very efficient and general catalyst system for the addition of a number of nucleophiles, including alcohols [Eq. (19)], ketones [Eq. (20)],^[68] aromatic groups [Eq. (21)],^[69] 1,3-

dicarbonyl compounds [Eq. (22)],^[70] as well as amides, amines, phosphine oxides,^[67] phenols,^[71] and olefins.^[72] Hidai, Uemura, and co-workers expanded the scope of this reaction to include thiols as nucleophiles as well as internal propargylic alcohols as electrophiles. In this case, a different mechanism to that proceeding through allenylidene complex (such as **92**) has been invoked.^[73,74]

Another notable application by this group of researchers is the one-pot sequential Ru- and Pt-catalyzed formation of furans and pyrroles. Propargylic alcohols undergo Ru-catalyzed propargylic substitution by a ketone followed by Pt-catalyzed hydration/cyclization to give the desired heterocycle (e.g. **99**) in good yield [Eq. (23)].^[74] This methodology is also amenable to the synthesis of pyrroles (e.g. **100**) by the addition of 1 equivalent of aniline [Eq. (24)]. In the latter case, a higher catalyst loading is required for complete conversions.

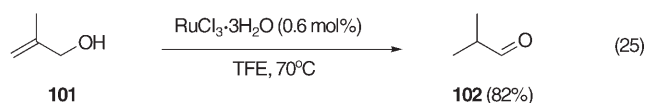
Notably, the synthetic chemist is not limited to Ru catalysis, as several groups have reported metal-catalyzed propargylic substitutions. For example, Mahrwald and co-workers developed a



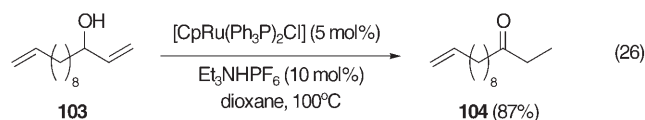
titanium-catalyzed propargylic substitution.^[75] Toste and co-workers described the rhenium-catalyzed addition of alcohols,^[76] allyl silanes,^[77] and electron-rich aryl groups^[78] to terminal and internal alkynes in excellent yields. Finally, Matsuda and co-workers reported the iridium-catalyzed alkylation of propargylic esters with enoxysilanes.^[79]

4. Redox Isomerization

The adjustments of oxidation levels are transformations of fundamental importance in organic synthesis. These processes often suffer from poor atom economy, as they frequently require multiple steps and stoichiometric amounts of reagents. Thus, much effort has been expended on developing more-atom-economical ways to effect this transformation. The transformation of unsaturated alcohols (e.g. allylic alcohols) into their corresponding ketones or aldehydes represents an attractive one-step alternative to traditional reduction–oxidation procedures. Many catalyst systems based on transition metals have been developed.^[80,81] Among these, Ru-catalysis has occupied a central role ever since early work by Strohmeier and Weigelt^[82] and later Pascal and Dedieu^[83] demonstrated the utility of $\text{RuCl}_3 \cdot 3\text{H}_2\text{O}$ as a catalyst for the isomerization of allylic alcohols (e.g. **101**) into the corresponding aldehydes (e.g. **102**) [Eq. (25); TFE = trifluoroethanol].

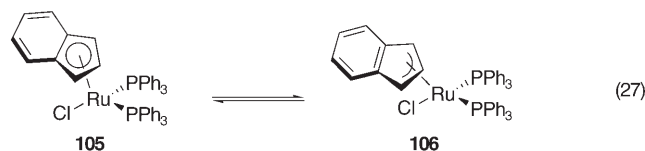


The studies on the reconstitutive addition reaction revealed that some allylic alcohols were isomerized to saturated ketones by certain Ru complexes. This interesting observation warranted further examination, especially as the complexes in question had exhibited high chemoselectivity, which might overcome the inherent problems of chemoselectivity usually observed in transition-metal-catalyzed isomerization reactions. Indeed, compounds that contain isolated olefins (such as **103**) [Eq. (26)] undergo clean isomerization to yield the corresponding ketones **104** in excellent yield simply by exposing the allylic alcohols to

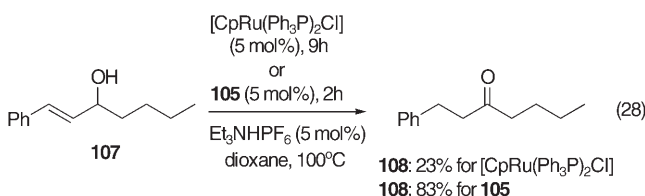


catalytic $[\text{CpRu}(\text{Ph}_3\text{P})_2\text{Cl}]$ (**1**) and triethylammonium hexafluorophosphate in hot dioxane; the isolated double bond is not affected.^[84] Chemoselectivity was also demonstrated by the compatibility with free alcohols, esters, carbonyl groups, alkynes, and terminal alkenes.

Cyclic substrates along with sterically encumbered allylic alcohols reacted sluggishly with the cyclopentadienyl complex. The lower rates were attributed to the slower coordination of a sterically demanding olefin to the catalyst as well as the to the requirement that a coordination site must be liberated for β -hydrogen elimination. The dissociation of a phosphine group to free such a coordination site would be disfavored in this case as phosphine–Ru bond is stronger than the olefin–Ru bond. A decrease in the hapticity of the cyclopentadienyl ligand from η^5 to η^3 would also achieve the same result [Eq. (27)]. Thus, changing to a ligand that would

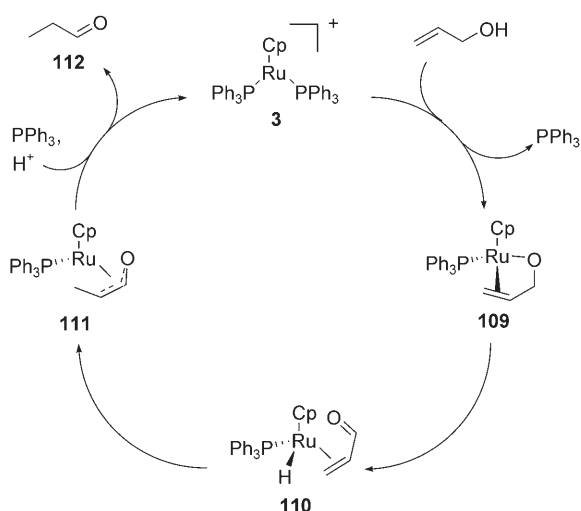


more readily undergo a switch of hapticity was expected to enhance the reactivity in the isomerization of more-difficult substrates.^[85] Indeed, the indenyl complex **105**^[86–88] proved to be much more reactive and afforded the isomerized product **108** in excellent yield in only 2 h [Eq. (28)]. However, the increased reactivity is offset by some loss in chemoselectivity.



Scheme 9 outlines the mechanism for the redox isomerization of allylic alcohols. Initial coordination of the olefin and the allylic hydroxy group would give rise to a complex such as **109**. Subsequent β -hydride elimination leads to the ruthenium hydride **110**. Migratory insertion gives the ruthenaenolate **111**, which is readily protonated to give the aldehyde **112** with regeneration of the catalyst **3**. Deuterium-labeling experiments support this mechanism.^[89]

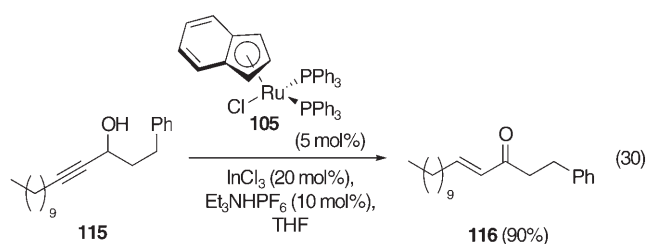
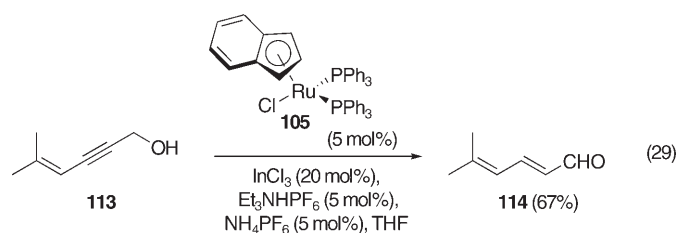
Ru complexes that give the critical 14-electron species **3** more readily would probably serve as more-reactive isomerization catalysts. Indeed, complexes that bear more-labile ligands (e.g. $[\text{RuCp}(\text{PR}_3)(\text{MeCN})_2][\text{PF}_6]$) have been examined and found to be more reactive; they allow the reaction to



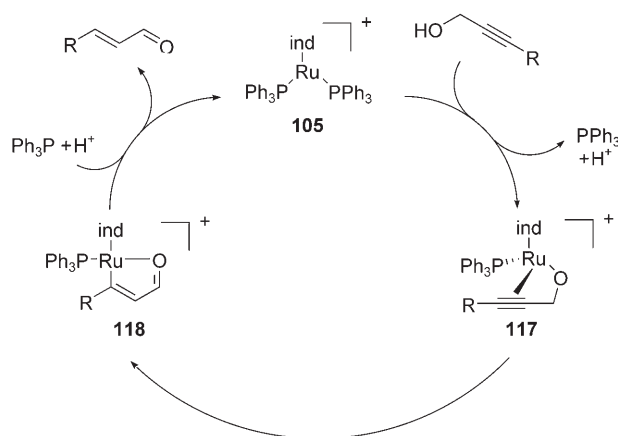
Scheme 9. Postulated mechanism for the redox isomerization of allylic alcohols.

be carried out at lower temperatures.^[90] Concomitant with increased reactivity, however, is lower chemoselectivity. Finally, other Ru complexes, including several Ru hydride species,^[80] tetrapropylammonium perruthenate (TPAP),^[91] and the Grubbs vinylidene-metathesis catalyst^[92] have been found to catalyze the redox isomerization of allylic alcohols effectively.

The Ru-catalyzed isomerization distinguishes itself from other isomerization reactions as it is not limited to allylic alcohols. In fact, propargylic alcohols function equally well in the redox isomerization to form α,β -unsaturated carbonyl compounds. This transformation is normally effected by the Meyer–Schuster rearrangement, in which a propargylic hydroxy group is transposed.^[93] Transition-metal-catalyzed isomerizations based on Pd,^[94–96] Rh,^[97] Ir,^[98] and Ru^[99] have been described. The latter employs tris(triphenylphosphine)-ruthenium dichloride precatalyst in combination with a trialkyl phosphine. This reaction did not show good reproducibility in our hands. Inspired by this and our success in the isomerization of allylic alcohols catalyzed by [CpRu(Ph₃P)₂Cl] and triethylammonium hexafluorophosphate, we applied this methodology to the isomerization of propargylic alcohols. In the event, the indenyl catalyst **105** effected the redox isomerization of propargylic alcohols (e.g. **113**), cocatalyzed by indium(III) chloride and sodium hexafluorophosphate. Enals **114** [Eq. (29)], and enones **116** [Eq. (30)] are readily available by using this methodology.^[100] The reaction is highly chemoselective and allows the presence of carbonyl, hydroxy, alkyne, and alkene groups.



The apparent analogy of the isomerization of propargylic alcohols into enones with that of allyl alcohols into saturated ketones is completely misleading. Mechanistic work indicates that an intramolecular 1,2-hydride migration is the critical step (Scheme 10) that gives rise to the presumed vinyl–



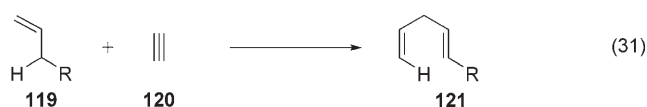
Scheme 10. Redox isomerization of propargylic alcohols.

ruthenium species **118** from **117**, in stark contrast to the mechanism of the redox isomerization of allyl alcohols. The exact role of the indium(III) salt is not entirely clear; most likely it functions as a halophile, and enables the formation of the coordinatively unsaturated ruthenium cation. The mechanistic proposal has been supported by deuterium-labeling experiments.^[100]

5. The Ruthenium-Catalyzed Alkene–Alkyne Coupling Reaction

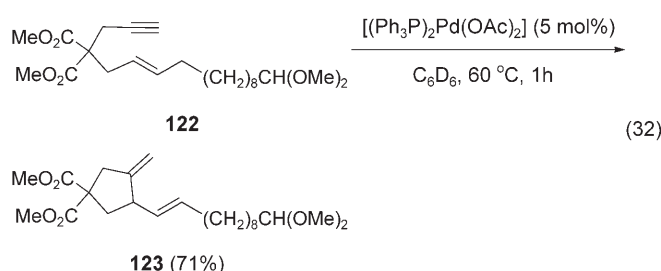
5.1. Background

The Alder–ene reaction^[101,102] is a prime example of an atom-economic reaction that only involves a simple addition of an alkene **119** with allylic protons to an enophile acceptor, which is typically another unsaturated compound such as an alkyne **120**, to give the corresponding 1,4-diene **121** [Eq. (31)].

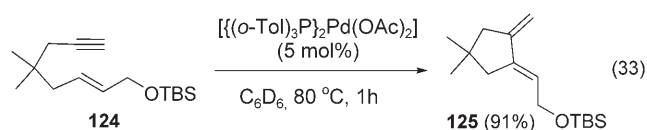


In a classical sense, this reaction is promoted by heat and is believed to take place through a supra-suprafacial *endo* or *exo* six-electron electrocycloization.^[103] Electron-withdrawing groups on the enophile accelerate the coupling, and strong Lewis acids accentuate this effect.^[104] Conversely, electron-rich alkenes can also greatly accelerate this reaction.^[105–107] Although the thermal ene reaction has found some use in synthesis,^[105,106] the generally harsh conditions required have limited its synthetic utility.

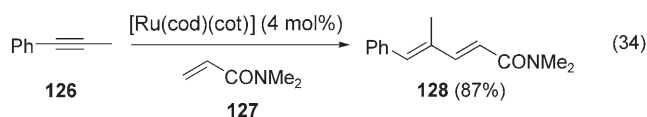
The expansion of the synthetic utility of this reaction requires the development of a catalyst that could selectively carry out this type of transformation. It has long been known that palladium can mediate^[108] and even catalyze^[109] sigma-tropic reactions, and similar ene-type reactions were known with dienes catalyzed by rhodium^[110–113] and palladium.^[114] A major advance arose from discovery of the palladium-catalyzed formal Alder-ene-type reaction of enynes [Eq. (32)],^[115,116] the alkene–alkyne addition.



For example, enyne **122** is readily cyclized to 1,4-diene **123** in 71 % yield in the presence of $[(\text{Ph}_3\text{P})_2\text{Pd}(\text{OAc})_2]$ (5 mol %). Previous to this work, several references to the oligomerization of alkynes and alkenes had appeared,^[117–119] along with one case of allyl halide–alkyne coupling, which results in a 1,4-diene.^[120] Related palladium-catalyzed alkene–alkyne coupling to yield 1,3-dienes have been noted,^[121] as well as ruthenium-catalyzed alkyne–diene coupling to yield 1,3-enynes.^[122] The mechanism of the palladium-catalyzed alkene–alkyne coupling reaction is clearly different from that of the thermal Alder-ene reaction, and thus selectivity can often be different.^[123] The conditions of the catalytic reaction are generally mild, and its utility has been demonstrated in synthesis.^[116] Palladium can be quite effective for the catalytic cycloisomerization of enynes, but, importantly, the intermolecular alkene–alkyne coupling reaction is not feasible under these conditions. Furthermore, 1,4- versus 1,3-diene formation is often substrate-controlled.^[124] For example, a 1,3-diene is generally the major product if an allylic oxygen functionality or a tertiary carbon atom is present at the allylic position [Eq. (33)]. Catalytic palladium rapidly converts enyne **124** into the diene **125** as a single geometrical



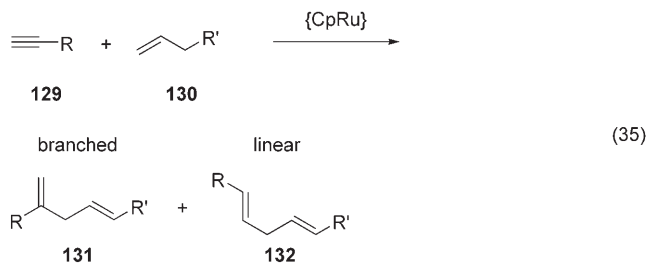
isomer in 91 % yield. In a related reaction, 1,3-dienes can also be obtained by using ruthenium catalysis in an intermolecular fashion from alkynes and α,β -unsaturated olefins [Eq. (34)].^[125]



Given the factors listed above, the development of a general catalytic system that carries out the inter- and intramolecular alkene–alkyne coupling reaction with control of olefin geometry and regiochemistry would constitute an important synthetic development.

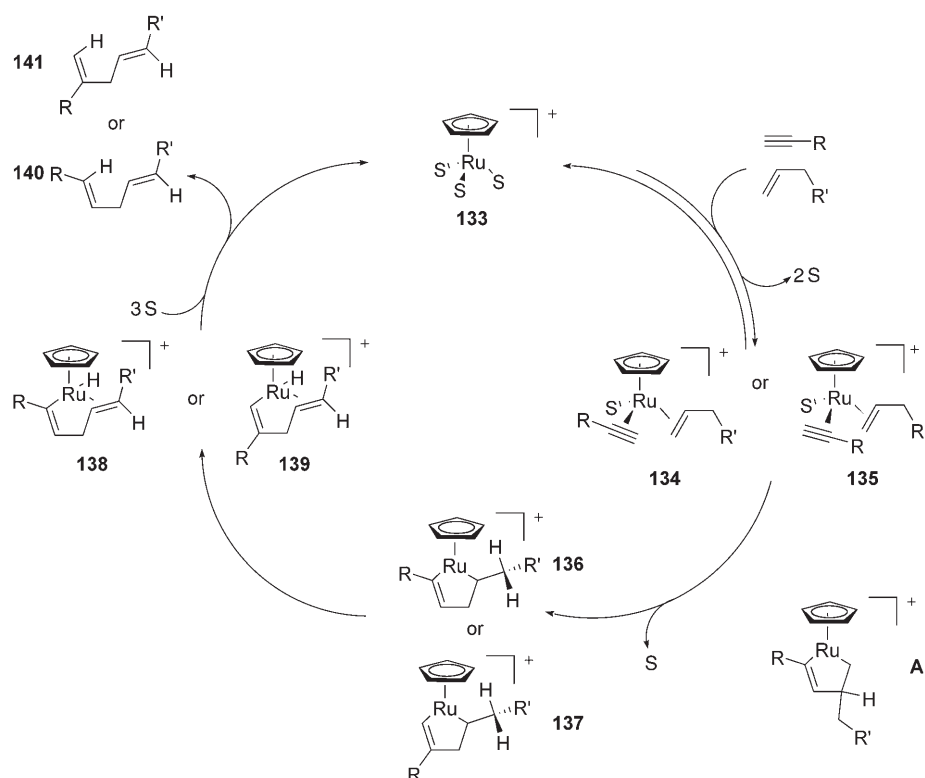
5.2. Intermolecular Alkene–Alkyne Coupling Reactions To Form 1,4-Dienes

Inspired by our successful development of the Ru-catalyzed reconstitutive addition reaction (see Section 2) in which a coordinatively unsaturated Ru complex derived from $[\text{CpRu}(\text{PPh}_3)_2\text{Cl}]$ catalyzes the addition of an alkyne and an allylic alcohol,^[22] we were interested to examine the effect of replacing the phosphine ligands with more-labile ligands, thereby generating a coordinatively more-unsaturated $\{\text{CpRu}\}$ cationic complex that can catalyze alkene–alkyne coupling reactions.^[126] This reaction could give rise to two regioisomeric products, a “branched” (**131**) and a “linear” 1,4-diene (**132**) [Eq. (35)].



Mechanistically, two scenarios may account for the addition reaction. First, an insertion of an alkyne into a π -allyl ruthenium hydride species generated through C–H activation could lead to the coupled products **131** and **132**. Alternatively, a mechanism that involves a ruthenacyclopentene intermediate, analogously to the well-known Pauson–Khand reaction^[127] and the [2+2] addition of strained olefins and alkynes,^[128] could be involved. Both mechanisms appear reasonable. Although the C–H activation mechanism was originally proposed,^[129] it has since been found that the ruthenacycle mechanism explains many key features of this reaction more accurately (Scheme 11).

As alkynes are better ligands than alkenes, coordination of two molecules of alkyne and formation of ruthenacyclopentadiene is both possible and likely. However, no product



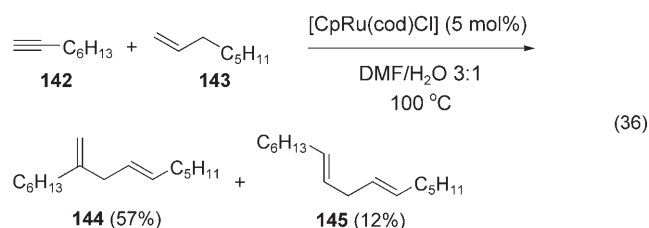
Scheme 11. Mechanistic rationale for the alkene–alkyne coupling reaction. L = solvent.

formation is seen through this pathway, presumably due to the reversible nature of the oxidative cyclization and the lack of productive pathways leading from the ruthenacyclopentadiene. Following coordination and cyclization to either of two ruthenium(IV) species, **136** and **137**, *syn* β-hydride elimination yields two different regioisomeric vinyl ruthenium species **138** and **139**, which undergo reductive elimination to yield the observed products **140** and **141** along with regeneration of the catalyst **133**. The coordination and subsequent cyclization of the alkyne can proceed in two distinct ways: 1) Coordination such that the R group on the alkyne is adjacent to ruthenium (i.e. **134**) leads to ruthenacyclopentene intermediate **136**, which thus results in “linear” product **140**. 2) Coordination and cyclization in the opposite regioisomeric sense (i.e. **135**) leads to “branched” product **141**. Presumably the olefin may coordinate in two different orientations, but the product derived from ruthenacyclopentene **A** is not observed. The principal reason for this is that the geometrical constraints of the endocyclic *syn* β-hydride elimination step are difficult to achieve in such a cyclic species.

To render this reaction truly synthetically useful, control of the two regioisomeric products is necessary. Indeed, when simple unfunctionalized monosubstituted alkenes and alkynes are subjected to a catalytic amount of [CpRu], the “branched” isomer is typically favored, with ratios ranging from 5:1 to 10:1.^[129] 1-Octyne (**142**) is coupled to 1-octene (**143**) to give “branched” 1,4-diene **144** selectively in a 5:1 ratio with “linear” 1,4-diene **145** [Eq. (36)]. Remarkably, no homocoupling products from either alkyne **142** or alkene **143** partner are isolated.

There are several factors that explain the observed isomeric products (i.e. **144** and **145**), of which the simplest is based on steric arguments (Scheme 12). Thus, in the path to branched products, steric interactions occur during the C–C bond-forming event, **146**, whereas in the pathway to linear products, steric interactions occur between the {CpRu}⁺ moiety and the R group on a monosubstituted alkyne in the intermediate **138** following β-hydride elimination, rather than in the transition state **147**. Thus, the kinetically formed ruthenacycle is **136**, whereas **137** can lead to the major product under thermodynamically controlled conditions (i.e. when β-hydride elimination is slow). The inherent selectivity for branched products with simple alkenes and alkynes can be explained by assuming that the ruthenacyclopentene formation is fast and reversible when both isomers **137** and **136** (Scheme 12) are accessible (as should be the case with simple alkenes and alkynes).

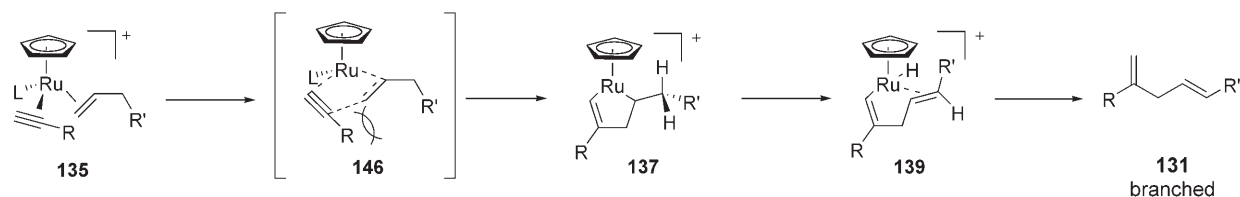
Transition state **146** contains significant steric interaction in the formation of the ruthenacyclopentene **137**. The product formation, however, is not determined until



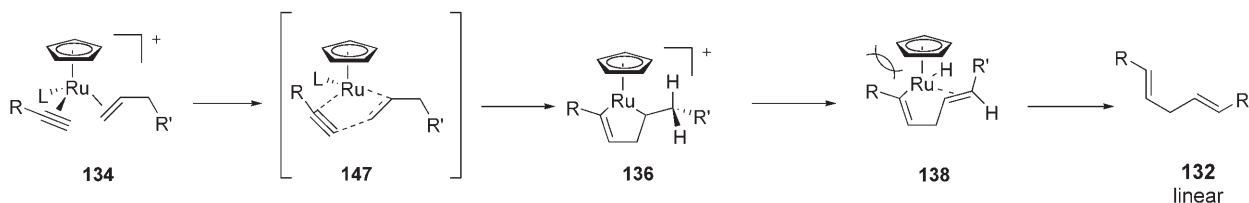
the β-hydride-elimination step, which is slower than the ruthenacyclopentene formation. As β-hydride elimination is disfavored in the path towards linear products owing to the accumulating steric strain resulting from β-elimination (i.e. **138**), the branched product is favored with simple unbranched alkenes and alkynes (Curtin–Hammett situation). However, this inherent selectivity can be modified through various pathways. Most simply, if the rate of β-hydride elimination is increased relative to ruthenacycle formation, then the kinetically formed ruthenacyclopentene **136** leads to the formation of predominantly “linear” products. Other factors that influence the inherent selectivity are discussed in this section.

The original catalyst discovered for this reaction was [CpRu(cod)Cl], which is a precatalyst for the presumed active species (CpRuL₂Cl or [CpRuL₃]Cl; L = solvent). The typical reaction conditions for this catalyst system involve the ruthenium catalyst (5 mol %) in a mixture of DMF (*N,N*-dimethylformamide) and water at 100 °C. Before any alkene–alkyne coupling takes place, cyclooctadiene reacts with one molecule of alkyne in an unusual ruthenium-catalyzed

thermodynamic path



kinetic path



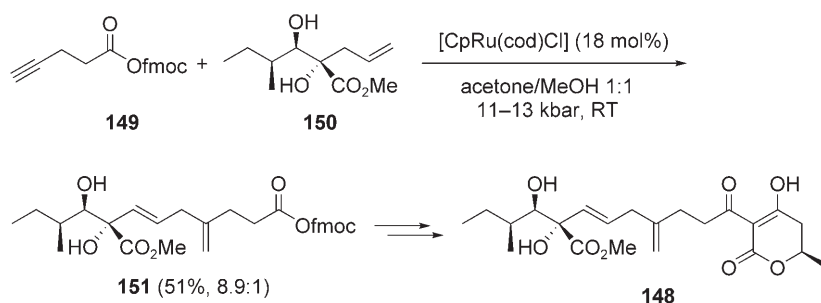
Scheme 12. Steric interactions in alkene–alkyne coupling.

[2+2+2] cycloaddition reaction.^[130] This reaction results in a coordinatively more-unsaturated and thus more reactive ruthenium catalyst. The second-generation catalyst $[\text{CpRu}(\text{CH}_3\text{CN})_3]\text{PF}_6$ ^[131,132] is generally much more active, and under typical conditions the reaction is carried out at room temperature in acetone or DMF. Presumably the enhanced reactivity is due to the greater coordinative unsaturation provided by the absence of a chloride ion in the precatalyst and the rate of ligand exchange of the bound acetonitrile molecules.

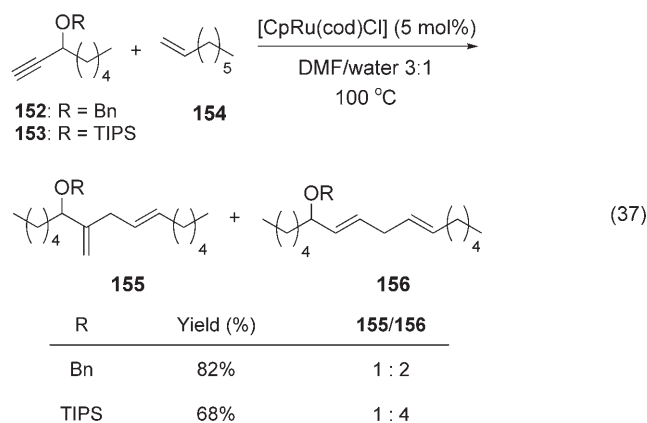
The power of this methodology to assemble complex building blocks rapidly from simple alkenes and alkynes was demonstrated in the formal synthesis of alternaric acid (**148**)^[133] (Scheme 13). In this example, the coupling of the unbranched alkyne **149** and the highly functionalized alkene **150** under standard conditions leads to predominantly branched product **151** (4.9:1 ratio). Interestingly, this ratio increased to 8.9:1 when the reaction was conducted under higher pressure.

The introduction of propargyl substituents leads to lower amounts of branched products. For example, propargylic oxygen substituents effectively reverse the observed regiochemistry such that linear products are favored. This result can be rationalized by assuming that both ruthenacyclopentanes must be readily accessible in order to produce branched products. If the rate of ruthenacyclopentene formation is retarded significantly owing to the presence of extreme steric interactions during C–C bond formation (i.e. **146**), then the β -hydride elimination is no longer the rate-limiting step, and the major product is determined by the kinetic ratio of ruthenacyclopentene intermediates **136** and **137**. An illustration of this effect is presented in Equation (37) (Bn = benzyl, TIPS = triisopropylsilyl) in the coupling of differentially protected alcohols **152** and **153** with alkene **154**.

In this case, changing the steric bulk of the propargylic protecting group from benzyl (i.e. **152**) to TIPS (i.e. **153**) alters the ratio of branched to linear products from 1:2 to 1:4. While the explanation for the propargylic oxygen effect could be

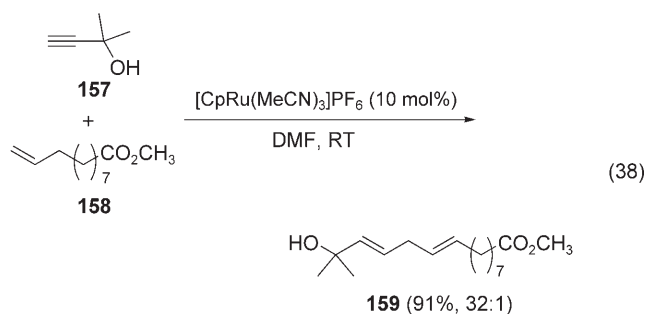


Scheme 13. Formal synthesis of alternaric acid (**148**). Fmoc = 9-fluorenylmethoxycarbonyl.

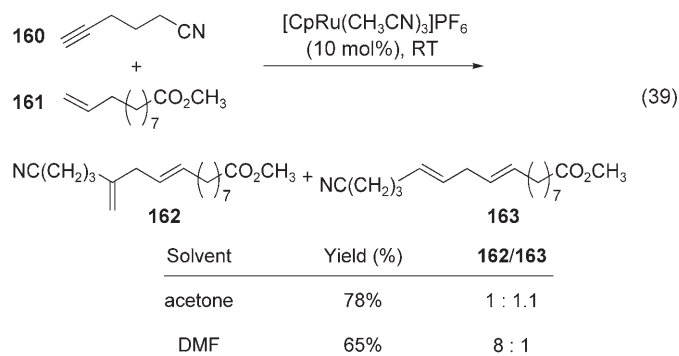


thought of as a coordination effect, the fact that a non-coordinating propargylic oxygen functionality (OTIPS) also promotes the formation of the linear product reinforces the notion of a primarily steric effect.^[129]

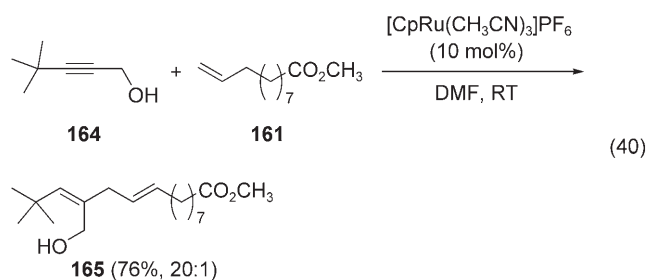
Nearly exclusive formation of the linear product is possible when a tetrasubstituted center is adjacent to the alkyne. For example, 2-methyl-3-butyn-2-ol (**157**) reacts with monosubstituted olefin **158** in the presence of the second-generation catalyst to give the linear product **159** in excellent yield (91 %) in a 32:1 ratio with respect to the corresponding branched isomer [Eq. (38)].^[134]



Not surprisingly, the choice of solvent also plays a major role in determining the product ratios. For example, DMF generally favors production of the branched isomer, whereas acetone tends to produce a large fraction of linear product. This disparate behavior is due to the greater ligating ability of DMF relative to acetone. First, this would make the effective size of the ruthenium center larger, thus enhancing the steric effect present in **138** (Scheme 12). Furthermore, a more fully ligated ruthenium center decreases the rate of β -hydride elimination, as the latter requires an open coordination site. Essentially, the use of DMF as solvent decreases the rate of β -hydride elimination to the extent that the thermodynamic pathway (Scheme 12) becomes the major route. This effect is further enhanced in the presence of the chloride-free catalyst $[\text{CpRu}(\text{CH}_3\text{CN})_3]\text{PF}_6$. For example, the reaction between 5-hexynenitrile (**160**) and alkene **161** in acetone with this catalyst leads to branched and linear products in a 1:1 ratio. However, switching the solvent to DMF resulted in a much improved ratio of 8:1 [Eq. (39)].^[132]

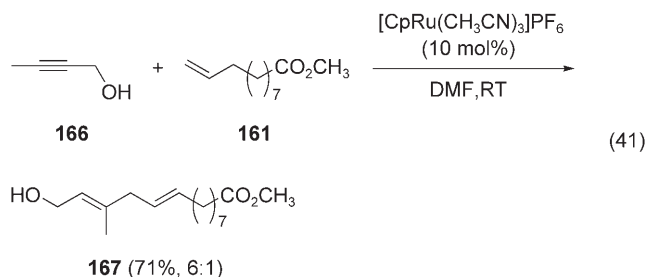


The possibility of using disubstituted alkynes would dramatically expand the power and scope of this method.^[135] The selectivity issue becomes even more complicated with unsymmetrical alkynes, as the regiodifferentiation with respect to the alkyne is greatly diminished. As was seen with monosubstituted alkynes, the selectivity is dominated by the presence of propargylic substituents. In the case at hand, the determining factor in product formation is not the propargylic alcohol moiety but rather the *tert*-butyl group of the alkyne **164**; the linear product **165** is formed almost exclusively [Eq. (40)].^[135] This example demonstrates that a *tert*-butyl group is a more powerful director than an unhindered propargylic alcohol.^[135] This is plausible due to the



greater steric bulk of the *tert*-butyl group and again reiterates that coordination is not a major factor in determining the regiochemistry.

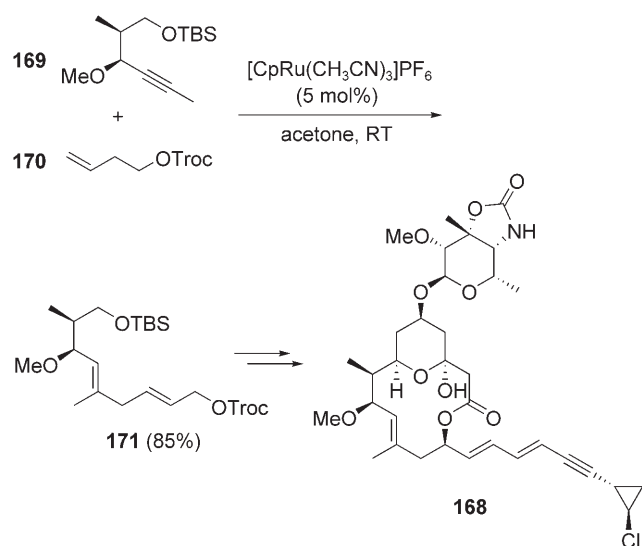
The propargylic alcohol may still be a significant directing group in simple disubstituted alkynes. For example, when but-2-yn-1-ol (**166**) is coupled to a monosubstituted olefin **161**, there is seemingly little steric difference between the two propargylic positions. Still the propargylic hydroxy group directs the C–C bond formation at the alkyne carbon atom distal to the hydroxy group and results in a 6:1 ratio in favor of the isomer **167** [Eq. (41)].



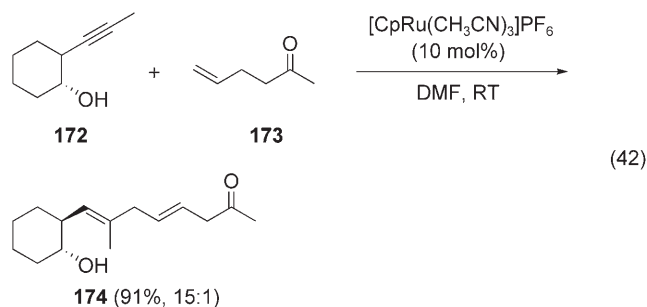
Clearly, the steric difference between a methyl group and a primary propargylic alcohol is minimal, and thus the selectivity arises from the differing electronic properties. The electron-withdrawing nature of the hydroxy group preferentially promotes the formation of linear products. This effect has been exploited successfully in a key step in the total synthesis of callipeltoside A (**168**) (Scheme 14).^[136,137] The functionalized propargylic ether **169** was treated with protected alcohol **170** to give the 1,4-diene **171** as a single regioisomer in 85% yield, as a result of carbon–carbon bond formation distal to the propargylic oxygen atom.

The carbon–carbon bond formation can also be directed to the distal carbon atom to a lesser degree by homopropargylic alcohols. The ratio for simple homopropargylic alcohols is generally approximately 4:1 in favor of linear products. If some steric bias is included (secondary or tertiary alcohol), then this selectivity can be raised to excellent levels [Eq. (42)].^[135] For example, cyclohexanol **172** gave almost exclusively linear product **174** when coupled to alkene **173**.

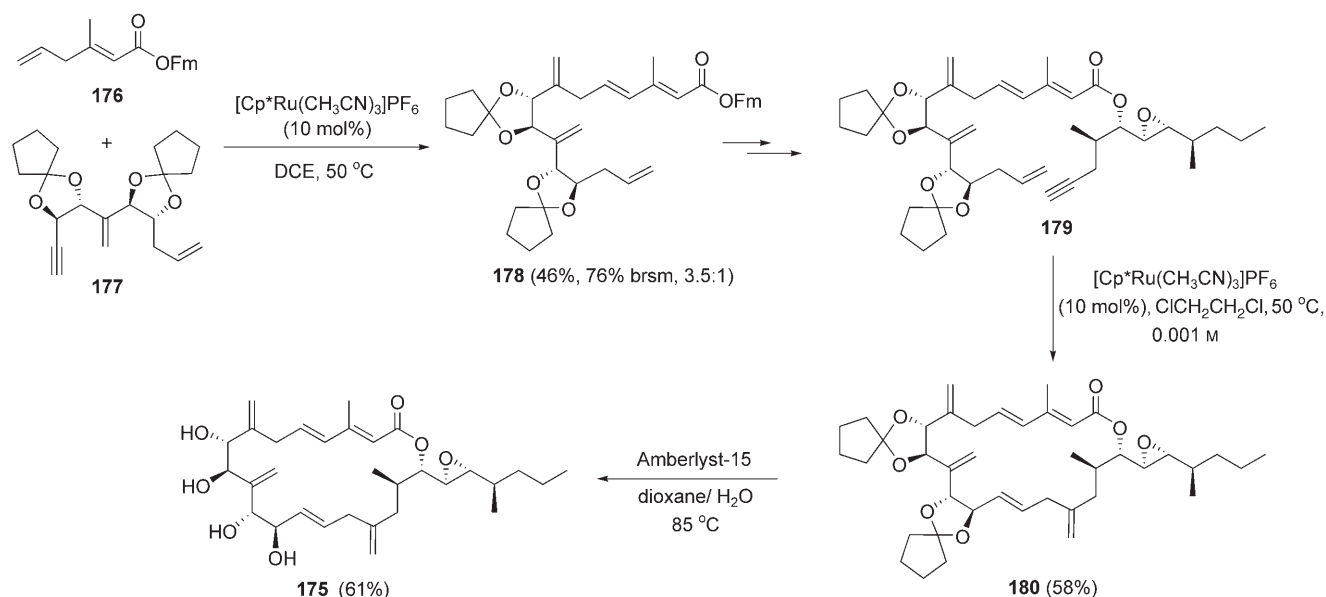
In general, the effect of simple steric and electronic factors can be summarized as follows: In the absence of propargylic substituents, branched isomers are favored. However, when propargylic substituents are present, then the steric demand at the forming C–C bond leads to larger



Scheme 14. Total synthesis of callipeltoside A (**168**). Troc = trichloroethoxycarbonyl.



proportions of linear products. When proximal polar functional groups are present on the alkyne, linear products are favored.

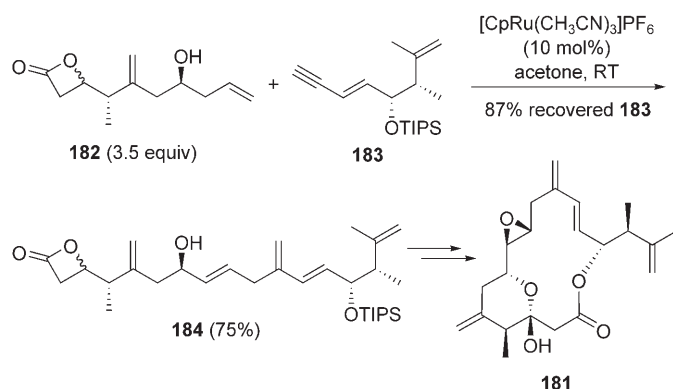


Scheme 15. Total synthesis of amphidinolide A (**175**). Fm = fluorenylmethyl; brsm = based on recovered starting material.

Yet another way that the selectivity rules can be modified is with a change to the more sterically demanding catalyst $[\text{Cp}^*\text{Ru}(\text{CH}_3\text{CN})_3]\text{PF}_6$, in which the cyclopentadienyl ligand has been replaced with the sterically encumbered pentamethylcyclopentadienyl (Cp^*) ligand. This was elegantly illustrated in the synthesis of the proposed structure of amphidinolide A (**175**).^[138,139] The target molecule was rapidly assembled through an intermolecular followed by an intramolecular alkene-alkyne coupling reaction (Scheme 15).^[140]

As one would anticipate from the above discussion, with either of the standard catalysts, the selectivity in the first alkene-alkyne coupling between **176** and **177** tends towards the linear product because of the propargylic oxygen substituent. The branched product **178** can be favored, however, if a bulky catalyst is used, which disfavors alkyne substituents near the ruthenium center (see **136**). The steric interaction of the $[\text{Cp}^*\text{Ru}]$ moiety is more severe in the potential intermediate **136**; thus the pathway towards branched products predominates. The $[\text{Cp}^*\text{Ru}(\text{CH}_3\text{CN})_3]\text{PF}_6$ catalyst resulted in a 3.5:1 ratio of branched to linear isomers (46% yield of isolated product, 76% based on recovered **178**). Although it is unclear that the same factors that govern intermolecular reaction would also be applicable to a macrocyclization, the second alkene-alkyne coupling reaction of **179** proceeds to favor the branched product **180** in 58% yield; this result was anticipated given that neither alkyne nor alkene partner has severe bulk or functionality that could readily coordinate. The efficiency of this macrocyclization is noteworthy, as it is significantly more effective than either Stille cross-coupling^[141] or olefin metathesis^[142] in the formation of the same ring system. More recently, the robust nature of the ruthenium-catalyzed alkene-alkyne coupling reaction as well as the extraordinary chemoselectivity was demonstrated in the determination of the correct structure of amphidinolide A.^[143] Nine different amphidinolide diastereomers were synthesized by using this chemistry, finally resulting in the identification of the natural isomer.

Another member of the amphidinolide family of natural products, namely apmhidinolide **P** (**181**), was recently synthesized by using an alkene–alkyne coupling reaction (Scheme 16). In the key step, monosubstituted olefin **182** was coupled with enyne **183** with complete selectivity for



Scheme 16. Synthesis of amphidinolide **P** (**181**).

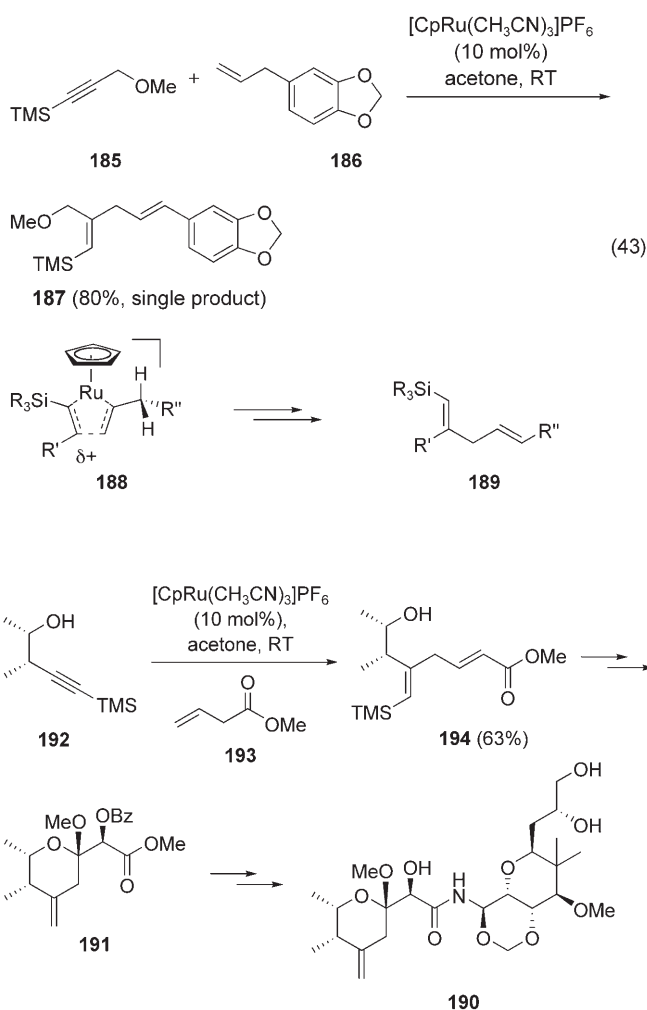
formation of the branched product **184**, which was isolated in 75% yield. Apparently, conjugation increases the rate of the equilibration of the ruthenacycles and thus results in a greater selectivity for the branched product. The synthesis of amphidinolide **P** (**181**) highlights several features of the Ru-catalyzed alkene–alkyne coupling: 1) the remarkable chemoselectivity of the Ru catalyst—four double bonds are present in the two partners, but only the monosubstituted alkene function reacts; 2) the sensitive β -lactone is also tolerated under the reaction conditions; 3) an enyne may participate in the coupling reaction.

The propargylic steric effects alluded to earlier can be utilized to an even greater extent through the use of alkynyl silanes. The bulky silyl group on the alkyne **185** acts in a similar fashion to the *tert*-butyl group, but the vinyl silane products have further synthetic utility owing to the variety of subsequent transformations possible, including cross-coupling,^[144] *ipso* substitution with halides,^[145] and oxidation.^[146] A wide variety of silyl groups can be used to give exclusively products resulting from carbon–carbon bond formation distal to the silyl group **187** [Eq. (43)].^[147] This effect can be thought of in purely steric terms, but an electronic factor could also be contributing: Silicon is well known to stabilize positive charge in the β position, and in this case one could visualize attack of the olefin at this partially positive alkyne terminus (i.e. **188**), which would lead to the branched regioisomer **189**.

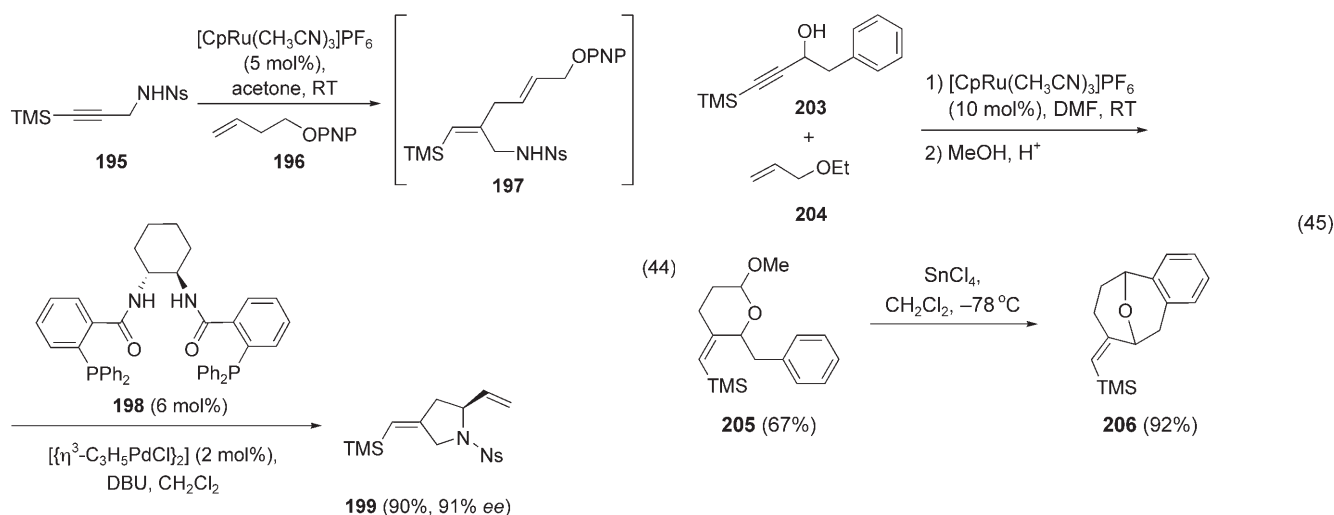
The ability of alkynyl silanes to give exclusively branched products opens up a wide range of potential synthetic applications, exemplified by the formal synthesis of (–)-mycalamide **A** (**190**) (Scheme 17).^[148] In the key step for the construction of the pyran moiety **191**, the functionalized alkyne **192** was coupled to β,γ -unsaturated alkene **193** to afford the 1,4-diene **194** in 63% yield as a single regioisomer. The coupling is noteworthy as the β,γ -unsaturation is isomerized into conjugation with the ester as a result of the reaction. In the case at hand, the trimethylsilyl group was

simply protodesilylated, thereby unmasking the delicate exo methylene functionality present in the target molecule **190**. However, the trimethylsilyl group served two important roles in this synthesis. First, the TMS group controlled the regioselectivity of the coupling reaction, and secondly it also stabilized the olefin in the desired exo position until this sensitive functionality could be revealed later in the synthesis.

The highly selective coupling reaction with alkynyl silanes may be combined with other metal-catalyzed processes, such as the palladium-catalyzed cyclization of nitrogen and oxygen nucleophiles onto π -allyl species. This tandem process could give access to a wide variety of heterocycles in an expeditious manner.^[145] For example, the *N*-protected alkynylsilane **195** is readily coupled to *para*-nitrophenyl-protected homoallyl alcohol **196** to give **197** as a single regioisomer [Eq. (44); Ns = 4-nitrophenylsulfonyl, PNP = 2,6-bis(diphenylphosphanyl)methyl)pyridine, DBU = 1,8-diazabicyclo[5.4.0]undec-7-ene]. The diene **197** may be added without isolation to an asymmetric palladium catalyst (derived from ligand **198** under basic conditions) to afford the pyrrolidine **199** in 90% yield with 91% *ee*. This process also gave access to six-membered nitrogen heterocycles as well as five- and six-membered oxygen heterocycles.^[145] In this case, the alkyne–

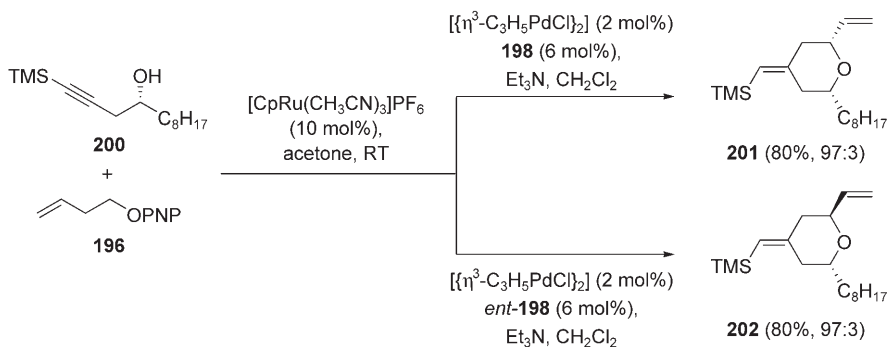


Scheme 17. Synthesis of (–)-mycalamide **A** (**190**).



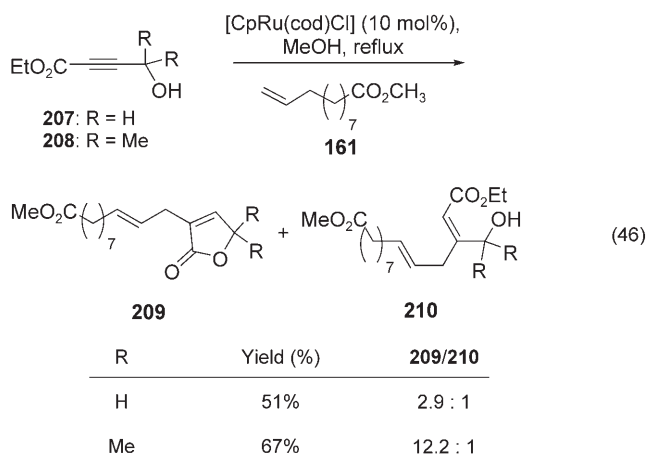
alkene coupling isomerizes the homoallyl ether **196** to the allylic ether **197**, thereby setting the stage for Pd-catalyzed π -allyl formation and subsequent trapping with the tethered nucleophile.

If a chiral homopropargylic alcohol (**200**, Scheme 18) is utilized as the coupling partner, either diastereomer **201** and **202** of the target heterocycles may be accessed, by simply switching the chirality of the ligand, **198** or *ent*-**198**, used in the second Pd-catalyzed step (Scheme 18). The ruthenium-catalyzed alkene–alkyne coupling reaction has also been coupled by means of Prins and Friedel–Crafts cyclizations to form various medium-sized rings in an expeditious fashion.^[149] For example, silylpropargyl alcohol **203** was coupled to allyl ether **204** with complete regioselectivity to yield acetal **205** in good yield. Subsequently, a Sn-mediated Friedel–Crafts-type cyclization gave tricycle **206** in excellent yield [Eq. (45)].



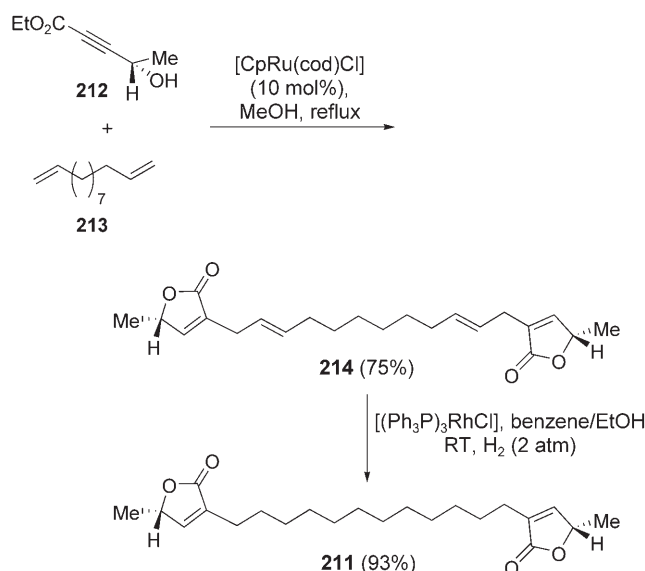
Scheme 18. Diastereoselective formation of heterocycles.

The convergence of steric and electronic effects observed with alkynyl silanes can also be seen when alkynoates are used in the alkene–alkyne coupling reaction. Normally, addition of these Michael acceptors occurs at the β -carbon atom. This is also true for Lewis acid catalyzed ene reactions. In contrast, the major products in the presence of a ruthenium catalyst result from addition to the α -carbon atom. Moreover, in the case of γ -hydroxybutynoates such as **207** or **208**, the product reacts further under the conditions of the reaction to give the unsaturated lactone **209** [Eq. (46)].^[150]



Both the ester and the hydroxy group contribute to the observed selectivity. The ester group potentially stabilizes a partial negative charge β to the ruthenium center in the initially formed ruthenacyclopentene **137** (Scheme 12). Whereas a simple unhindered substrate **207** leads to moderate levels of selectivity (2.9:1) in favor of addition α to the ester when coupled to olefin **161**, an increase in steric bulk at the propargylic position with two geminal methyl groups (i.e. **208**) results in excellent levels of selectivity (12.2:1).

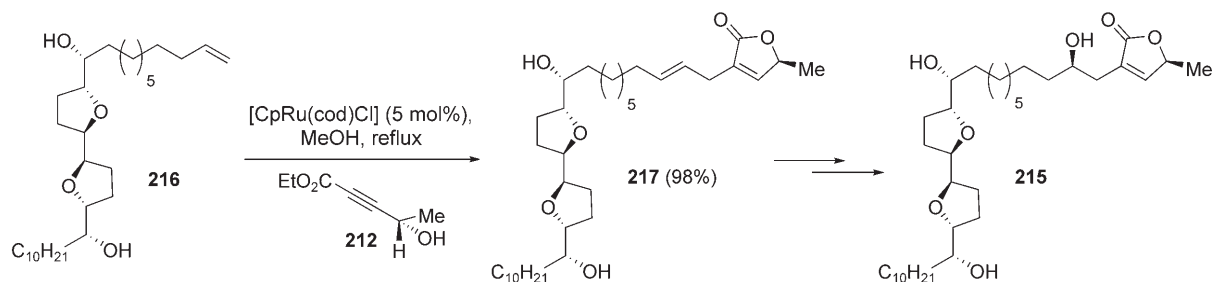
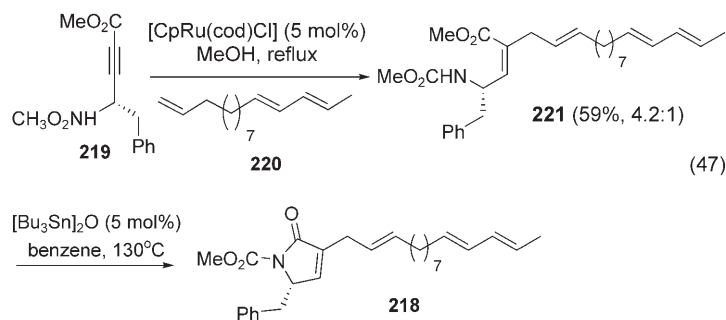
This strategy was used in the synthesis and assignment of configuration of (+)-ancepsenolide (**211**; Scheme 19).^[150,151] Its expedient assembly utilized a bidirectional coupling of propargylic alcohol **212** and diene **213** to afford the bislactone **214** in excellent yield. The latter, in turn, was transformed into the target molecule **211** by hydrogenation. A similar alkynoate–alkene coupling was also used in the synthesis of the squamocins, exemplified by squamocin E (**215**; Scheme 20).^[152,153] Alkene **216** was coupled with alkynoate **212** regioselectively to produce **217**, which was readily



Scheme 19. Total synthesis of (+)-ancepsenolide (**211**).

converted into the target molecule **215** in only four steps. Similarly, squamocin K was produced in a single step from **217** by simple hydrogenation of the disubstituted double bond. Another related butenolide natural product, (+)-solamin, was also synthesized by using this methodology.^[154]

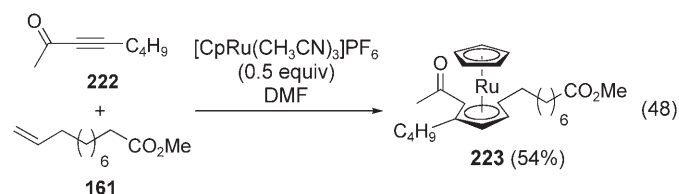
Pyrrolinones such as **218** [Eq. (47)] are also readily accessible in a two-step protocol by this method.^[155] In this case, propargylic amine **219** was coupled to triene **220**, which gave the unsaturated amine **221** in good yield. Lactamization of **221** upon treatment with a suitable Lewis acid gave lactam **218**. This example demonstrates the regioselectivity (4.2:1 ratio of $\alpha:\beta$ regioisomers) obtained with alkynoates, as well as



Scheme 20. Total synthesis of (+)-squamocin E (**215**).

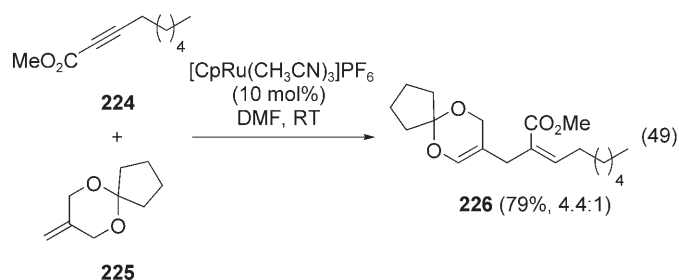
the remarkable chemoselectivity for monosubstituted olefins. No reaction was seen at the 1,3-diene portion of **220**, even though 1,3-dienes are generally more reactive than isolated olefins [Eq. (47)].

When the seemingly related α,β -unsaturated ynone **222** is used in this reaction, no 1,4-diene product is isolated. Interestingly, the half-open ruthenocene compound **223** is the only isolable product [Eq. (48)].^[156] It is unclear why there



is such a marked difference between alkynoates and alkynones. Not only is catalytic turnover not seen, but the regiochemistry of the coupling is reversed as well.

With the first-generation catalyst, disubstituted olefins are unreactive; however, the cationic catalyst $[\text{CpRu}(\text{CH}_3\text{CN})_3]\text{PF}_6$ enables these substrates to react well. In a similar fashion for the propargyl alcohols for which steric bulk at the propargylic position is key for high regioselectivity, the more sterically hindered 1,1-disubstituted alkenes lead predominately to linear products. The steric bulk that directs the reactivity towards the linear product in this case comes from the olefin partner and not from the alkyne [Eq. (49)].^[157]



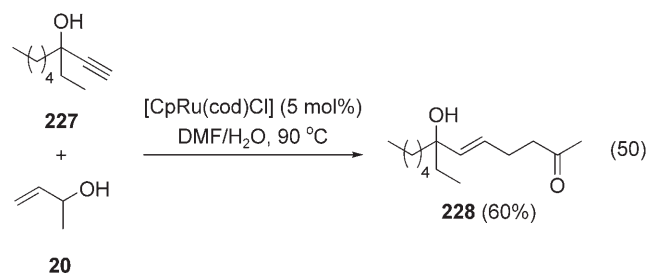
Unhindered alkynoate **224** is cleanly coupled with 1,1-disubstituted olefin **225** to furnish the 1,4-diene **226** in 79% yield as a mixture of regioisomers (4.4:1 ratio).

The 1,4-diene products of alkene-alkyne coupling reaction can also be obtained in related, but less-atom-economic reactions, for example, indium-mediated allyl halide addition

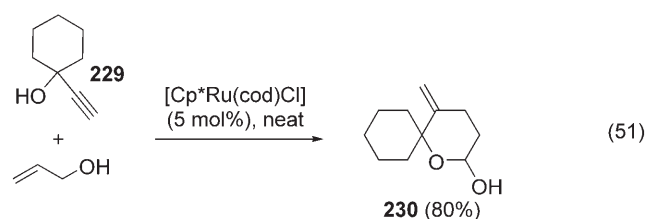
to alkynes,^[158–161] Lewis acid catalyzed addition of allyl silanes/stannanes,^[162–164] or palladium-catalyzed addition of allyl halides to alkynes.^[165]

5.3. Ruthenium-Catalyzed Alkene–Alkyne Coupling Reactions That Do Not Result in Simple 1,4-dienes

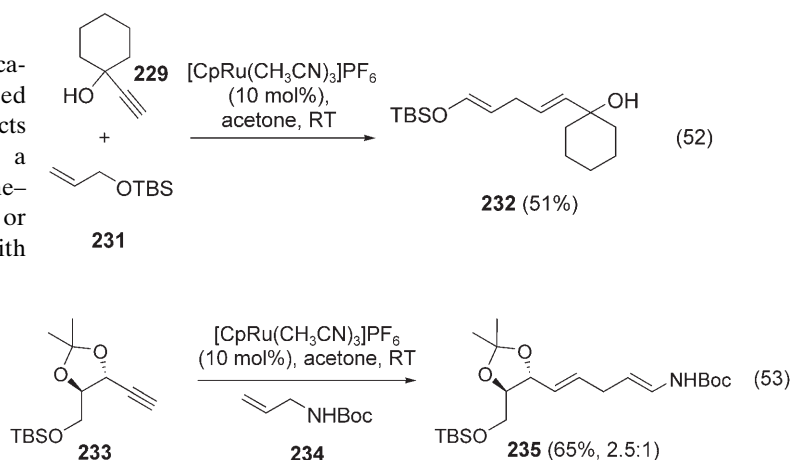
Besides all the above-mentioned reactions and applications, the principles of alkene–alkyne coupling can be applied to several more specialized systems that give rise to products other than 1,4-dienes. Exposure of allyl alcohols to a phosphine-free {CpRu} catalyst system results in an alkene–alkyne coupling reaction to give γ,δ -unsaturated ketones or aldehydes.^[126] When this coupling reaction is attempted with simple alkynes, mixtures of branched and linear products are obtained; however, the same principles discussed above can be used to tune the reaction to give largely a single product. An explanation for the increased production of linear isomer when allyl alcohols and ethers are used may lie in the weaker allylic C–H bond in these substrates which should increase the rate of β -hydride elimination, thus resulting in the formation of more linear/kinetic product (see Section 5.2). A combination of this effect with the tendency of tertiary propargylic alcohols **227** to promote linear product as well, leads to the generation of a single product **228** [Eq. (50)].^[126] In this case, both electronic and steric factors lead primarily to the linear product. Dixneuf and co-workers also developed such a reaction.^[166]



As detailed in Section 5.2, this inherent selectivity for linear product in the case of propargyl alcohols can be overcome with the more sterically bulky $[\text{Cp}^*\text{Ru}(\text{cod})\text{Cl}]$ catalyst.^[167] For example, the propargyl alcohol **229** can be coupled with excess allyl alcohol to yield tetrahydropyran **230** in excellent yield [Eq. (51)]. In contrast, when the less sterically encumbered $[\text{CpRu}(\text{MeCN})_3]\text{PF}_6$ catalyst system is utilized in combination with a silyl-protected allyl alcohol



231, exclusive formation of the linear silyl enol ether **232** is observed [Eq. (52)].^[168] This contrasting product distribution is quite remarkable. In a further extension of this principle, enamides can be constructed in an expeditious fashion from allyl amides [Eq. (53); Boc = *tert*-butoxycarbonyl].^[169] Func-

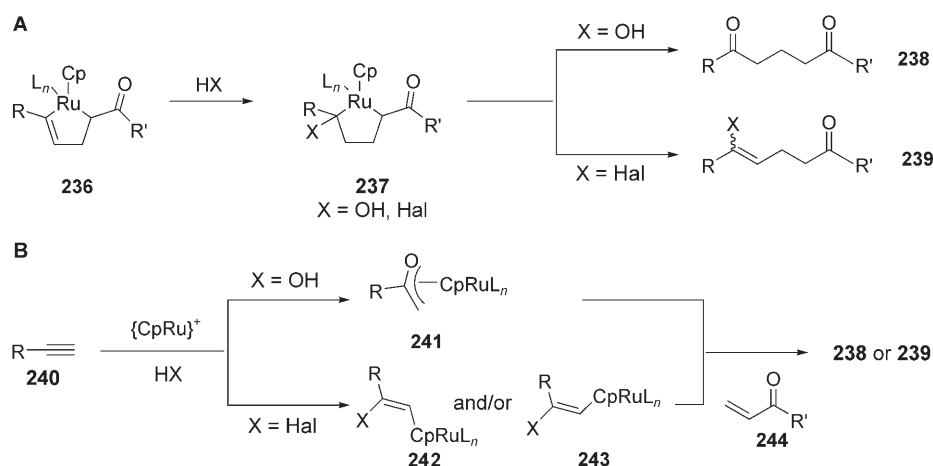


tionalized propargyl ether **233** reacts with Boc-protected allyl amine **234** to yield carbamate **235** in 65 % yield as a mixture of regioisomers (2.5:1). In the presence of the standard {CpRu} catalyst used in these cases, the propargylic heteroatom functions as the directing element for the generation of primarily linear products. The ratio is lower mainly because the alkyne substrate is a secondary propargylic ether.

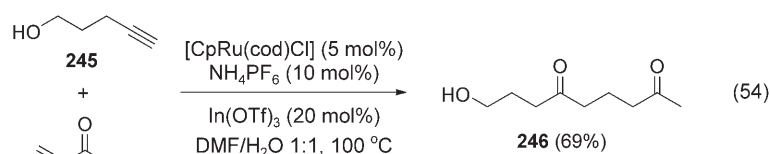
5.4. Multicomponent Alkene–alkyne Coupling Reactions

The indication that ruthenacyclopentenes are key intermediates in alkene–alkyne coupling reactions led to the investigation of whether nucleophiles could participate in addition reactions when no protons were available for β -hydride elimination. These reactions were designed to differ from the previously mentioned examples in that the proposed ruthenacyclopentene would be trapped by the addition of an external nucleophile (Scheme 21, path A) analogously to the alkyne/carboxylate addition chemistry to form vinyl esters developed by Dixneuf and co-workers.^[170] Either water or HX could attack the ruthenacyclopentene **236** formed from an alkyne and a vinyl ketone to give ruthenacyclopentane intermediate **237**; β -hydride elimination and reductive elimination would then give ketone **238** or vinyl halide **239** (Scheme 21, path A).

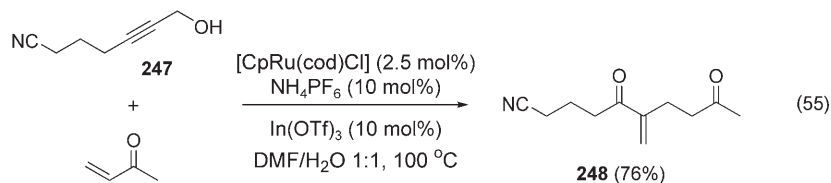
The same products could also be produced through a *cis* or *trans* Wacker-type addition to the alkyne **240**, either by water to produce intermediate **241** or by halides to give intermediates **242** or **243**. Subsequent 1,4-addition to an acceptor alkene (Scheme 21, path B) would then yield **238** or **239**. The first of these processes explored was a three-component addition of a vinyl ketone, an alkyne, and water to form 1,5-diketones [Eq. (54)].^[171] 4-Pentyn-1-ol (**245**) is coupled with methyl vinyl ketone (MVK) to yield 1,5-diketone **246** as the sole



Scheme 21. Mechanistic rationale for three-component coupling reactions.



identifiable product. This reaction works with a variety of terminal alkynes and vinyl ketones to serve as a versatile synthesis of 1,5-diketones. A related addition reaction with enones and propargylic alcohols (e.g. **247**) was developed to provide α,β -unsaturated 1,5-diketone products **248** [Eq. (55)].



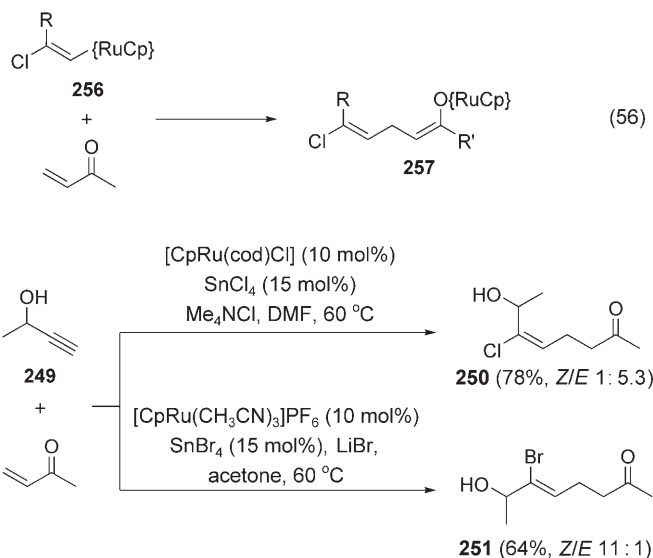
The absence of any branched product, which would be anticipated at least in minor amounts, may lead one to propose a tandem Wacker/Michael non-ruthenacycle mechanism.

During the course of the development of the intermolecular hydrative alkyne/alkene coupling, side products containing vinyl chlorides were isolated. It was postulated that these products arose from competitive addition of chloride, which originates from the precatalyst, to the alkyne. This observation was explored, and the process was optimized (Scheme 22).^[172,173] This reaction works well for a variety of mono- and disubstituted alkynes and monosubstituted vinyl ketones to give *E* vinyl chlorides and *Z* vinyl bromides in generally good yields. [CpRu(cod)Cl] was used as the catalyst for optimization of the chloride addition, but [CpRu(CH₃CN)₃]PF₆ can also be used and leads to similar yields and *E/Z* selectivities.

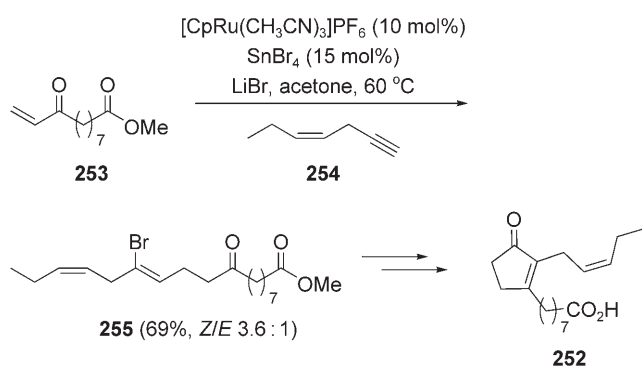
For the chloride addition reaction, the observed isomeric mixtures can be rationalized by assuming that both *cis*- and

trans-chlororuthenation are possible in a Wacker-type mechanism. A less-polar solvent such as acetone leads predominately to *Z* products—presumably due to the lower polarization of the Ru–Cl bond, thus leading to more internal attack and therefore the observed *Z* products. Even though the Ru–Cl bond is stronger than the Ru–Br bond,^[174] increased amounts of *Z* products during bromide addition can be explained by the weaker nucleophilicity of bromide relative to that of chloride in aprotic solvents.^[175] As a consequence, excellent *Z/E* ratios can be attained with bromide addition in acetone (Scheme 22).^[176] The potential utility of this methodology has been demonstrated in an expeditious synthesis of various cyclopentanoids, for example, that of tetrahydrodicranenone (**252**) from the vinyl ketone **253** and alkyne **254** via vinyl bromide **255** (Scheme 23).^[177,178]

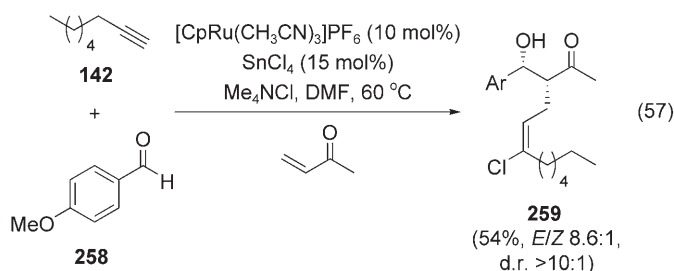
We were drawn towards the possibility of expanding the scope of the three-component coupling to include a fourth component. Indeed, if the proposed tandem Wacker/Michael mechanism (Scheme 21, path B) is at play, then the addition of a vinyl ketone to the vinyl ruthenium species **256** should lead to a ruthenium enolate **257** [Eq. (56)]. Support for this mechanism could be gained if the enolate could be trapped with any species other than a proton, for example, an aldehyde. In fact, when alkyne **142**, halide source (Me₄NCl), vinyl ketone, and aldehyde **158** were combined under the standard reaction conditions the corresponding keto alcohol **259** was obtained [Eq. (57)].^[179] The diastereoselectivity in the aldol addition step is generally quite high. The main limitation is that the inability to suppress completely the proton-quenched three-component coupling



Scheme 22. Vinyl halides through ruthenium-catalyzed three-component coupling.

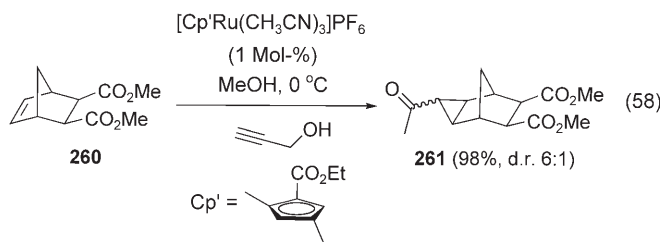


Scheme 23. Synthesis of tetrahydrodicranenone B (**252**).



leads to slightly lower yields. The resulting *syn* relationship following the aldol reaction indicates the preferential formation of the *Z* enolate.

More recently, it was shown that terminal alkynes can be added to vinyl ketones in a 1,4-fashion, thus showing the mechanistic diversity that can be obtained through the use of various ruthenium catalysts.^[180,181] Furthermore, recent work demonstrated that treatment of strained olefins (such as **260**) with propargyl alcohol in the presence of a ruthenium catalyst give the corresponding cyclopropanes **261** in excellent yield [Eq. (58)].^[182] The mechanism of this reaction is proposed to proceed via a ruthenacyclopentene, and diverges from the known [2+2]^[128] and [4+2] reactions^[130] because of the presence of the propargyl alcohol moiety.

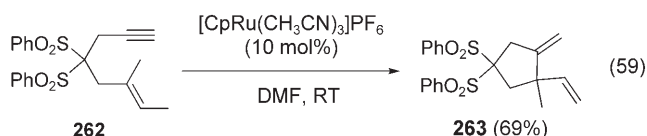


5.5. Cycloisomerization of Enynes To Form 1,4-Dienes

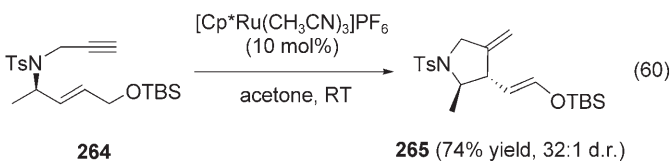
In a test of the synthetic versatility of the alkene–alkyne coupling reaction, the possibility of an intramolecular coupling reaction was also examined. Ruthenium has been shown to mediate a large variety of ring-closing reactions, including the widely used metathesis reactions,^[183–185] many of which

have been thoroughly reviewed.^[6] Furthermore, many metals have been shown to promote ene-type cyclizations or the related isomerizations to 1,3-dienes: palladium,^[115] rhodium,^[186,187] iridium,^[188] titanium,^[189] and other ruthenium systems.^[190,191]

In fact, the ruthenium catalyzed alkene–alkyne coupling reactions to form 1,4-dienes can be applied very successfully in an intramolecular sense,^[192] and a wide range of substrates function extremely well, including trisubstituted olefins **262** as well as electron-poor alkynes, to give the corresponding cycloisomerized product **263** in good yield [Eq. (59)]. This

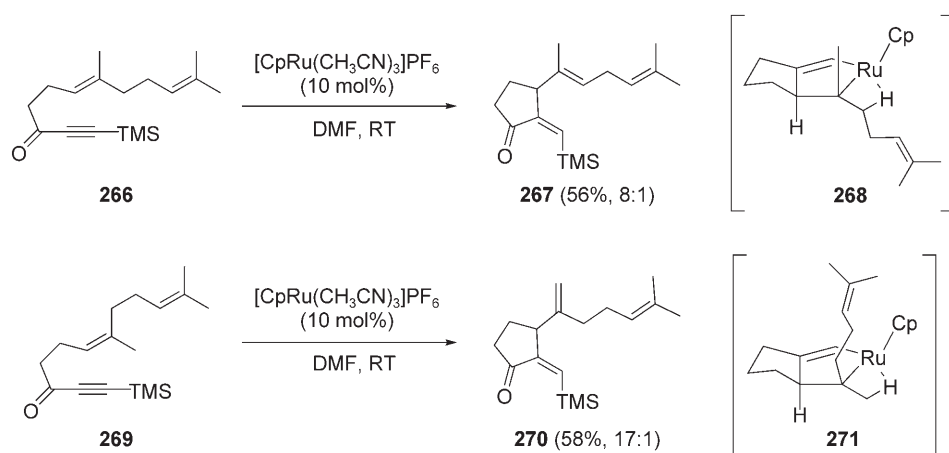


method is complementary to the palladium-catalyzed reaction as selectivities are often different, and 1,4-dienes are almost always obtained with the $\{\text{CpRu}\}$ catalysts. One of the biggest differences between the palladium- and the ruthenium-catalyzed systems is that allylic silyloxy functionality (i.e. **264**) leads to geometrically defined 1,4-dienol silyl ethers **265** [Eq. (60)],^[193] in a similar manner to the intermolecular version (see [Eq. (52)]).



When unsymmetrical trisubstituted olefins are used, two possible β -hydride abstractions are possible which lead to two different products. However, in this system, one pathway is preferred to a large degree based on the original geometry of the olefin. As illustrated in Scheme 24, *E*-olefin **266** undergoes cycloisomerization to 1,4-diene **267** in moderate yield and good selectivity for formation of the trisubstituted double bond.^[192] On the other hand, *Z* olefin **269** produces 1,1-disubstituted olefin **270** selectively.

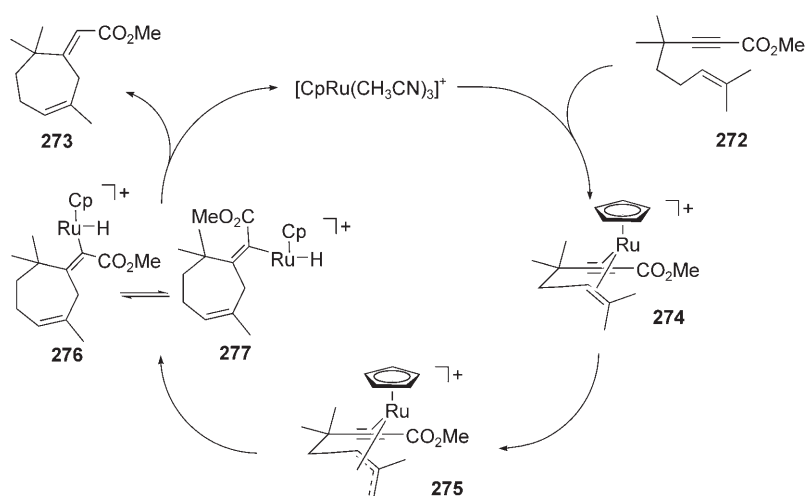
This selectivity can be explained through analysis of intermediates **268** and **271**. In both cases, the pseudoequatorial substituent, which is determined by the starting geometry of the olefin, has a β -hydrogen atom adjacent to the metal such that the required overlap is easily obtained. These results are in contrast to the thermal ene reaction in which the olefin geometry has little effect on the allylic proton abstracted.^[102] Generally, this cycloisomerization to 1,4-dienes is effective for the formation of five- and six-membered rings. Although the asymmetric version of the enyne cycloisomerization is not yet feasible with ruthenium catalysis, Zhang and co-workers have demonstrated that rhodium in combination with chiral phosphines can be quite effective for this task with a limited range of substrates.^[194,195] The groups of Trost,^[196] Ito,^[197] and



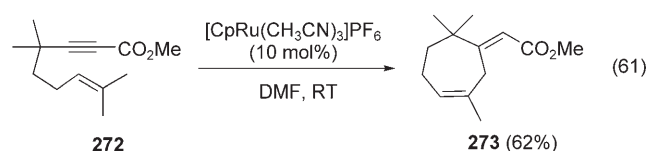
Scheme 24. Regioselectivity control in the cycloisomerization of enynes.

Mikami^[198–200] have also developed palladium-catalyzed systems for asymmetric enyne cycloisomerization.^[201]

When the Ru-catalyzed enyne cycloisomerization is attempted with alkynoate substrates **272** that contain a tetrasubstituted propargylic center, an alternate reaction takes place to yield a seven-membered ring **273** [Eq. (61)].^[202,203] In general, this reaction functions well for 1,6-enynoates with a *cis* methyl group and a tetrasubstituted propargylic carbon atom. 1,7-Enynoates give “normal” enyne cycloisomerization products (six-membered-ring 1,4-dienes), whereas 1,6-enynoates that lack a *cis* methyl group do not react well or result in “normal” five-membered-ring 1,4-dienes (if a *trans*-1,2-olefin is used).

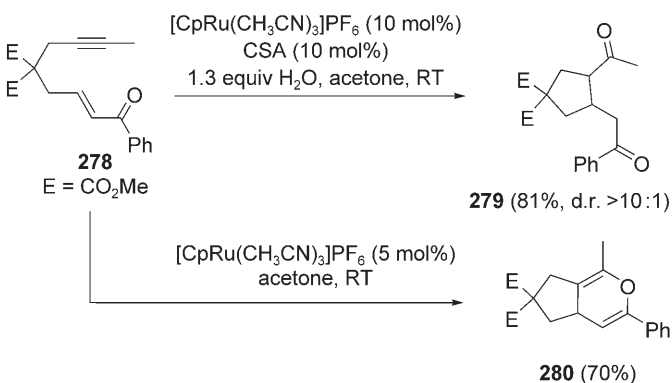


Scheme 25. Postulated mechanism for the formation of seven-membered rings.



tion just as in the intermolecular case to yield 1,5-diketone **279** in good yield. However, when the reaction is carried out under anhydrous conditions, [4+2] cycloaddition takes place to yield the pyran **280**. The production of the pyran products supports the ruthenacycle mechanism. The formation of ruthenacyclopentene **281** followed by isomerization to the

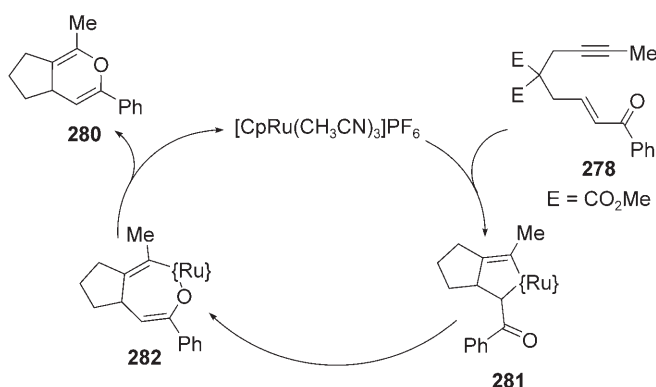
The proposed mechanism of this reaction involves π -allyl formation through C–H activation (Scheme 25). Enynoate **272** coordinates to the ruthenium catalyst to form intermediate **274**. Subsequent C–H activation of the *cis* allylic hydrogen atoms gives intermediate **275**, which can undergo conjugate addition to the alkynoate to produce intermediates **276** and **277** as an equilibrium mixture. To produce a *cis* double bond in the seven-membered-ring product, **275** must be present as the *anti* π -allyl species. The addition could also form a five-membered ring from the opposite end of the π -allyl system; however, this addition is only seen in the formation of six-membered rings. The product **273** is then released following β -hydride elimination from **276**. No product is seen from **277** owing to the severe allylic strain that would occur after β -hydride elimination. This mechanism is supported by deute-



Scheme 26. Hydrative cyclization and [4+2] cycloaddition of ynenones.

oxygen-bound enolate (**282**) and reductive elimination account for the observed product **280** (Scheme 27).

Such pyran products can sometimes also be isolated through intermolecular hydrative cyclization. This observation suggests that all the products result from this type of mechanism, with diketones simply arising by hydrolysis of the initially formed pyrans. However, a different mechanism cannot be excluded for reactions carried out under anhydrous conditions.

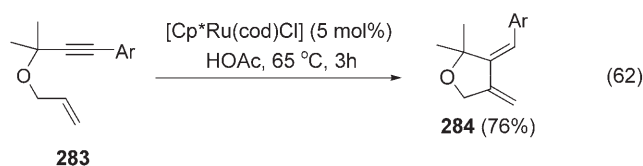


Scheme 27. Postulated mechanism for the [4+2] cycloaddition ynenones.

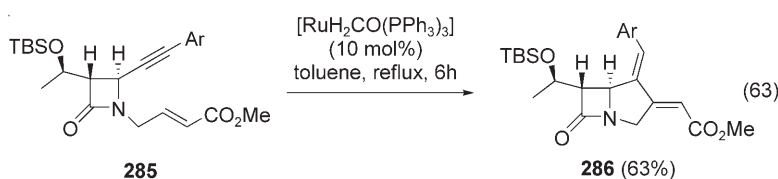
5.6. Related Ruthenium-Catalyzed Cycloisomerizations of Enynes

Ruthenium can also catalyze many other reactions of enynes through ruthenacyclopentene intermediates, and several comprehensive reviews are available.^[6,205] Some of the more recent applications are detailed in this section. If no β -hydride elimination pathway is available to an enyne, 1,3-dienes can be formed by utilizing ruthenium hydride catalysts,^[190,206] in analogy to palladium-catalyzed chemistry.^[116]

Monosubstituted enyne **283** [Eq. (62)] undergoes cycloisomerization to 1,3-diene **284** in the presence of [Cp*Ru-

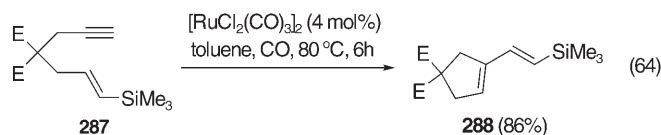


(cod)Cl] in acetic acid, whereas highly functionalized yne-noate **285** is cyclized to 1,3-diene **286** when treated with a ruthenium hydride catalyst [Eq. (63)]. Besides this modifica-

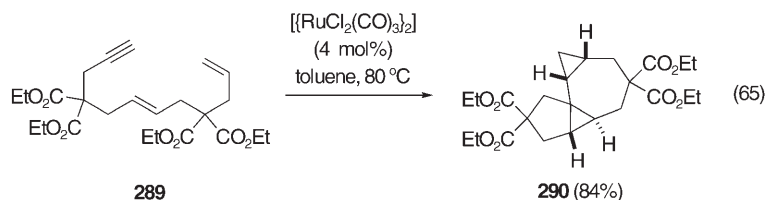


tion of the substrate and catalyst to control the direction of the reaction, different ruthenium catalysts can be used to alter the reaction pathway.

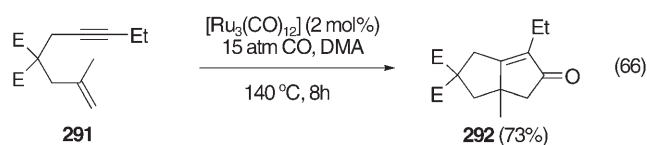
Under an atmosphere of CO and in the presence of a dimeric ruthenium carbonyl catalyst, an enyne (e.g. **287**) that bears a terminal alkyne and an appropriately substituted alkene undergoes an enyne-metathesis reaction to give rearranged 1,3-dienes **288** [Eq. (64)].^[207] The mechanism of



this reaction is unknown, but, analogously to the alkene-alkyne coupling reaction, is presumed to go through a ruthenacycle intermediate. In another related reaction, an appropriately substituted dienynone **289** can be transformed into a complex tetracyclic product **290**, which contains two cyclopropane units [Eq. (65)].^[208]



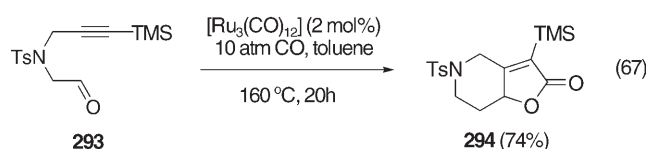
The proposed ruthenacyclopentane may be intercepted by small, coordinating molecules such as CO; in this case, the reaction is a ruthenium-catalyzed version of the venerable Pauson–Khand reaction [Eq. (66); *N,N*-dimethylacetamide]



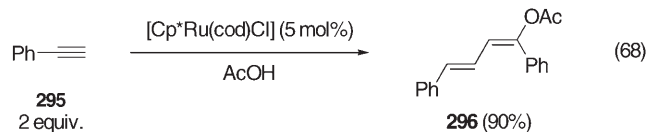
and affords a variety of ketones (e.g. **292**).^[209] Similarly, catalytic ruthenium complexes can also promote hetero-Pauson–Khand reactions in which a tethered aldehyde (e.g. **293**) acts as one unsaturated component to produce, after carbonylation, unsaturated lactones **294** [Eq. (67)].^[210]

5.7. Ruthenium-Catalyzed Alkyne–Alkyne and Diyne–Coupling Reactions

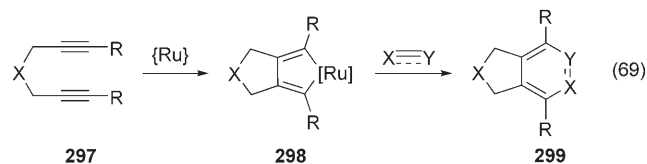
Whereas Section 5.6 dealt with the coupling of an alkene and an alkyne, Section 5.7 describes various ruthenium-catalyzed alkyne–alkyne coupling reactions. Ruthenacyclopentenes are



believed to be key intermediates in the former case, whereas the corresponding ruthenacyclopentadienes are frequently invoked in the latter processes. The simplest example of an alkyne–alkyne addition reaction is the metal-catalyzed dimerization of terminal alkynes **295** to produce enynes^[211–213] or 1,3-dienol esters **296** when carried out in the presence of a carboxylic acid (e.g. acetic acid) [Eq. (68)].^[214,215]

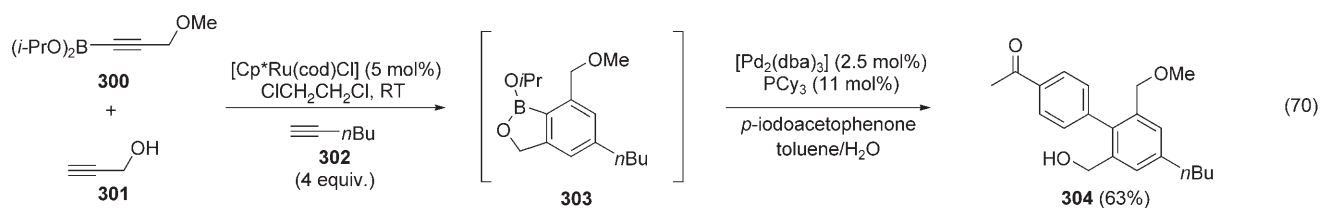


Two alkynes can also be coupled by the addition of a third unsaturated component through a [2+2+2] cycloaddition. Reactions of this type can be catalyzed by many different metals.^[216–219] The use of ruthenium in a wide range of intramolecular [2+2+2] cycloadditions is also well established. The mechanism proposed for these reactions involves the formation of a ruthenacyclopentadiene **298** from a diyne **297** [Eq. (69)], followed by cycloaddition or insertion of



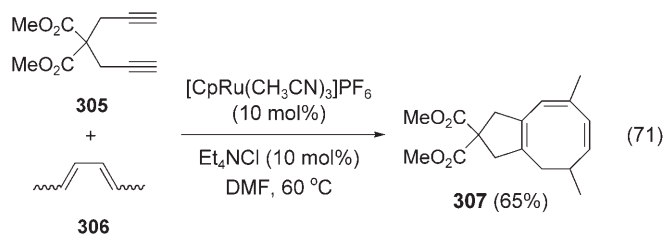
another unsaturated molecule to yield, after expulsion of ruthenium, cyclized products **299**.

When all three components are alkynes, benzenoid compounds are formed.^[220] A particularly intriguing application of this concept was recently described by Yamamoto and co-workers [Eq. (70); Cy = cyclohexyl, dba = *trans,trans*-dibenzylideneacetone].^[221] To achieve complete regioselectivity in the cycloaddition, a boronic acid **300** was used. It is thought that a boronate ester is initially formed in situ from **300** and **301**. The boronate tethered



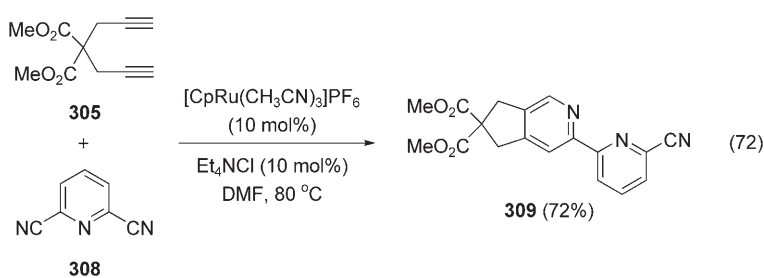
diyne then participates in a cycloaddition with 1-hexyne (**302**) to yield bicycle **303**, which was used directly in a Suzuki–Miyaura coupling with 4-iodoacetophenone to give **304** in 63% yield over two steps. In this example, the known^[222] *meta* selectivity of the {Cp*Ru} catalyst was used to yield **304** as a single regioisomer.

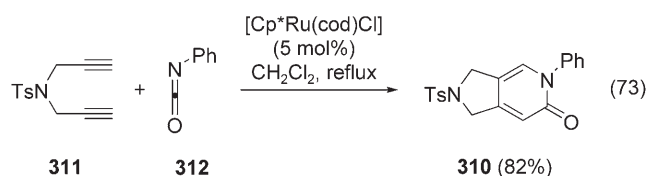
The ruthenacyclopentadiene can also be trapped with various other unsaturated molecules. If an olefin^[223] or a



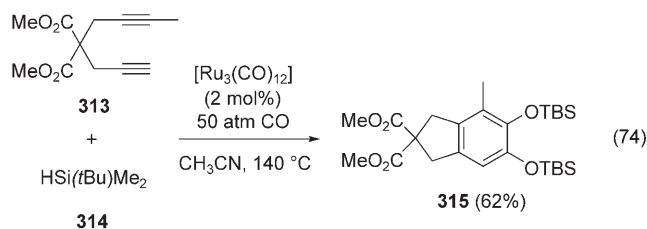
diene^[224] is substituted for the third alkyne moiety, cyclic dienes and trienes can be formed [Eq. (71)]. The use of diyne **305** and diene **306** is key to the isolation of cyclooctatriene **307** in good yields. Less-substituted 1,3-dienes give significant amounts of vinyl cyclohexadiene products as well. The mechanism of this reaction is proposed to involve insertion of one double bond of the diene into ruthenacyclopentadiene **298** [Eq. (69)], β -hydride elimination, reductive elimination, and conrotatory 8π -electrocyclization. A variety of heterocycles can also be accessed through this general concept. For example, activated nitriles **308** undergo cycloaddition with diyne **305** to yield substituted pyridines **309** [Eq. (72)].^[225–228]

Simple nitriles generally do not function well in this reaction, and require activation by an electron-withdrawing group or adjacent coordinating nitrile. It has been proposed that reactions with electron-deficient nitriles proceed via an azaruthenacyclopentadiene instead of the all-carbon analogue. Heterocumulenes also participate readily to produce pyridones **310** from diynes **311** and isocyanates **312** [Eq. (73)].^[229] 2*H*-Thiopyran-2-imines are formed from isothiocyanates,^[230] and dithiopyrones from carbon disulfide.^[230]



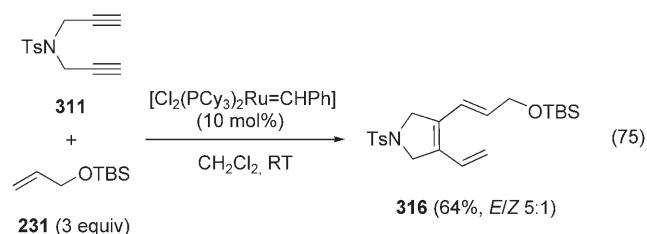


Other quite different ruthenium-catalyzed alkyne–alkyne cycloaddition reactions are also known. For example, a versatile synthesis of bicyclic catechol derivatives proceeds in the presence of a ruthenium carbonyl complex [Eq. (74)].^[231] In this transformation, two molecules of



carbon monoxide are incorporated to form catechol derivative **315**, reportedly through the formation of a hydrido ruthenium carbyne in situ. Along with the well-known alkene and enyne metathesis reactions, ruthenium complexes can also promote metathesis-type processes with diynes.

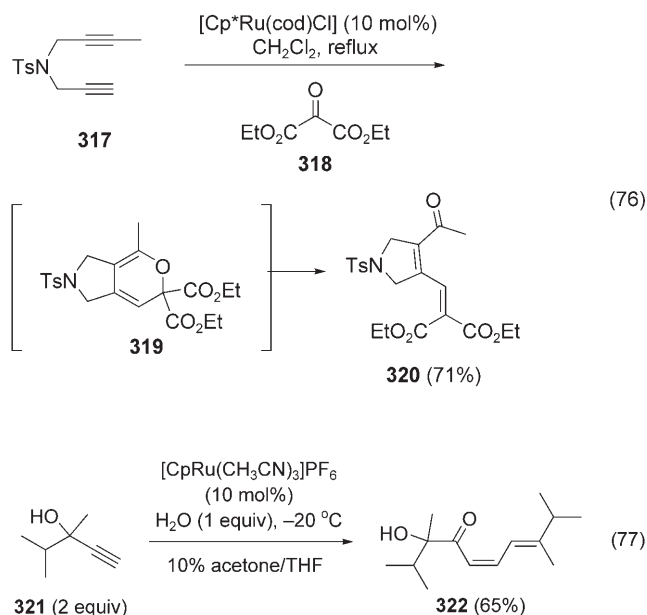
A recent example employs a tandem diyne cycloisomerization/cross-olefin metathesis to yield 1,3,5-trienes [Eq. (75)].^[232] Various diynes (e.g. **311**) and olefins (e.g. **231**)



may be utilized. The *E/Z* selectivity, however, is low unless the olefin bears a bulky group (e.g. TBSO).

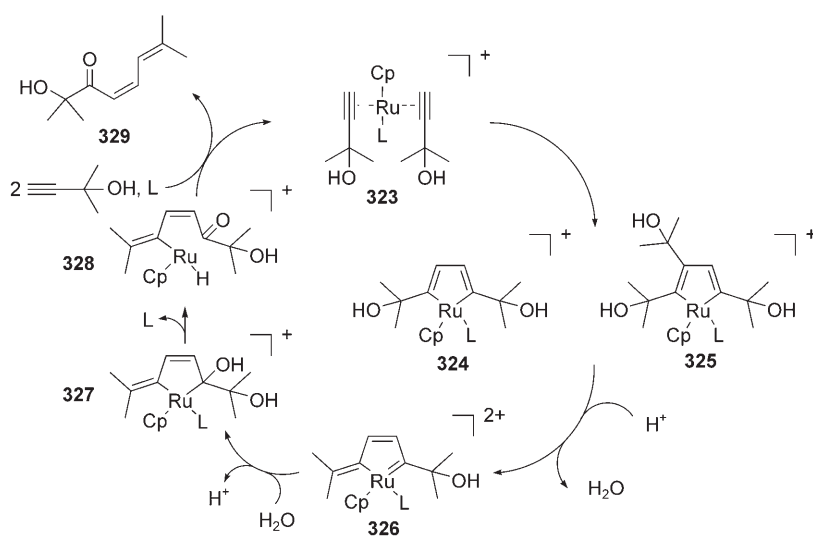
Activated carbonyl compounds participate in a cycloaddition-type reaction to form highly unsaturated carbonyl compounds [Eq. (76)].^[233] The unsymmetrical diyne **317** undergoes coupling with diethyl ketomalonate (**318**) to yield unsaturated ketone **320**. Although the mechanism is unknown, a cycloaddition is proposed that presumably would give 2*H*-pyran **319**; an electrocyclic opening would then yield the product **320**.

Analogously, a range of propargylic alcohols (e.g. **321**) dimerize in the presence of a {CpRu} catalyst to produce $\alpha,\beta,\gamma,\delta$ -unsaturated ketones **322** in good to excellent yields [Eq. (77)].^[234] The conditions of the reaction have been optimized to yield exclusively the



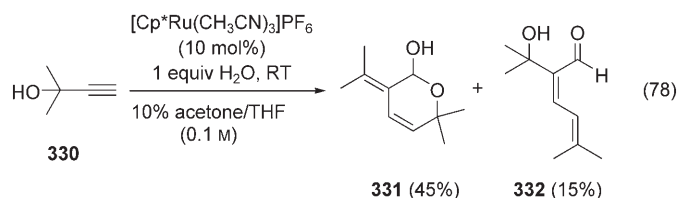
α,β -*Z* olefin isomer, as well as a single γ,δ geometrical isomer if there is branching in the alkyl substituent.

A mechanistic rationale for this unusual dimerization is represented in Scheme 28. Initial coordination of two alkyne molecules to the coordinatively unsaturated Ru catalyst forms the complex **323**. After cyclization to ruthenacyclopentadiene **324**, a molecule of water is expelled to give carbene intermediate **326**. Water then presumably adds again to the carbene carbon atom, thus resulting in an overall 1,4-shift of the hydroxy group to give intermediate **327**, which upon β -hydride elimination and reductive elimination releases product **329** (via vinyl ruthenium species **328**). The expulsion of a molecule of water is depicted as a simple elimination, but could also be viewed as a series of 1,2-shifts. The degree of reactivity of the propargyl alcohols in this reaction is linked to the leaving-group ability of the alcohol, with tertiary or

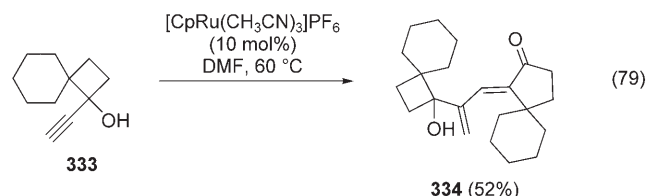


Scheme 28. Mechanistic rationale for the dimerization of propargyl alcohols.

secondary benzylic being the best. This mechanism is supported by the formation of the thermodynamically less stable *Z*-olefin isomer, as well as by the isolation, under different reaction conditions, of other products that should result from alternate ruthenacyclopentadiene isomer **325**. Additionally, a vinylidene-based mechanism is unlikely given the fact that internal alkynes also react, albeit with a lower efficiency. The more-electron-rich and sterically encumbered complex $[\text{Cp}^*\text{Ru}(\text{CH}_3\text{CN})_3]\text{PF}_6$ may also be used in this reaction to form unsaturated aldehyde hemiacetal products from ruthenacyclopentadiene **325** [Eq. (78)].



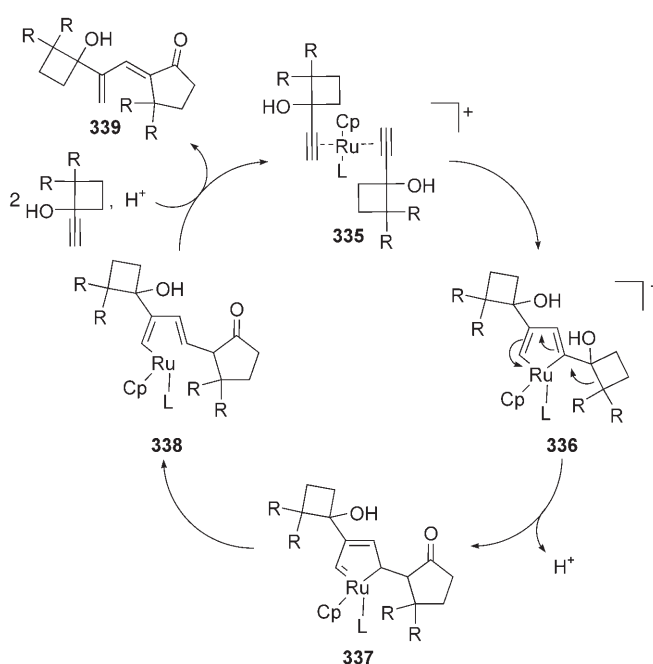
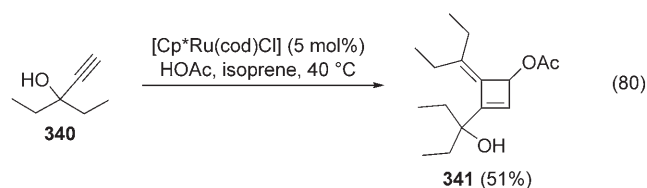
When this type of reaction is carried out in DMF with the 1-ethynylcyclobutanol **333**, then a different reaction manifold is accessed to produce the 1,3-diene **334** [Eq. (79)].^[235] The



mechanism of this ring expansion/dimerization is proposed to proceed via a ruthenacyclopentadiene similar to **325** (Scheme 25), but prior to elimination, a 1,2-alkyl shift occurs to expand the four-membered ring into a five-membered ring (Scheme 29).

The reason for this type of reaction occurring and not the previously mentioned elimination-type reaction (see [Eq. (77)]) is likely related to the change in solvent as well as the presence of the cyclobutane ring. Attempts to perform the same transformation with alkyne **330** in DMF led to a very sluggish reaction, which indicates that the elimination is disfavored in this solvent. Thus, with a slow elimination, the ring expansion can occur. Notably, higher temperatures are required for the ring expansion/dimerization to proceed.

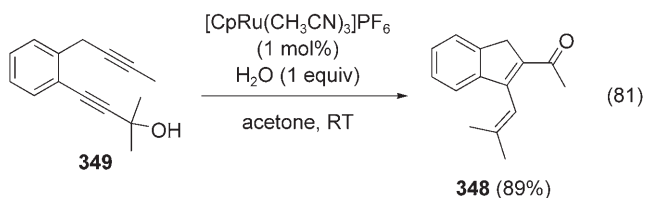
A completely different, but related, dimerization of similar tertiary propargylic alcohol substrates is possible in the presence of $[\text{CpRu}(\text{cod})\text{Cl}]$ catalyst in isoprene [Eq. (80)].^[236] Tertiary propargylic alcohols (e.g. **340**) dimerize



Scheme 29. Mechanistic rationale for the ring-expansion/dimerization of acetylenylcyclobutanol.

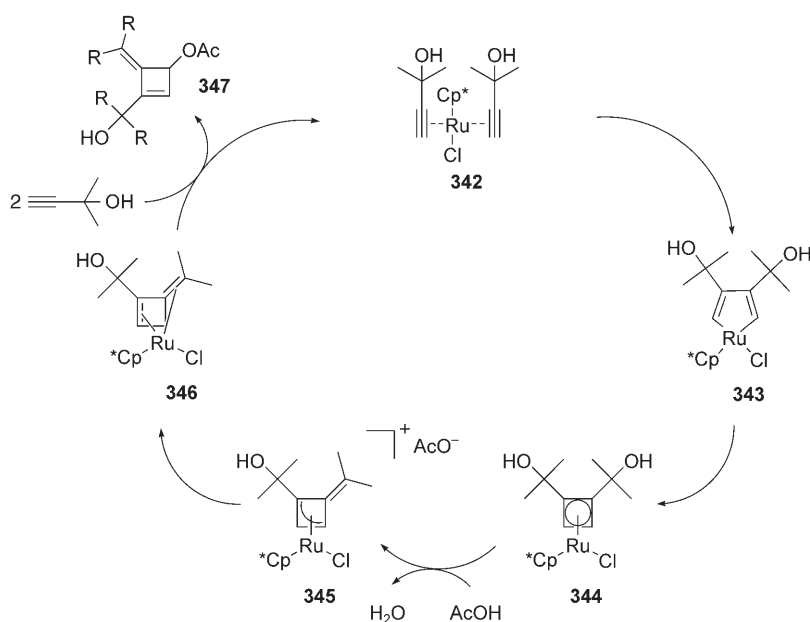
upon addition of a carboxylic acid to form alkylidene cyclobutenes (e.g. **341**) in moderate to good yields. The mechanism of this reaction is proposed to proceed through ruthenium cyclobutadiene complexes, one of which (**344**, Scheme 30) was isolated and characterized by X-ray crystallography. The reason for the observed difference in reactivity is likely to be related to the use of a $\{\text{Cp}^*\text{Ru}\}$ complex in combination with the very nonpolar solvent.

A similar dimerization of allenyl alcohols in the presence of the same ruthenium catalyst to produce 1,4-dienol esters was recently reported by Ihara and co-workers.^[237] Based on these mechanisms, we believed that only a single propargylic alcohol should be required for a reaction to take place, and a cross-coupling between an unfunctionalized alkyne and a propargylic alcohol should therefore be possible. Indeed, an intramolecular version works well to form a wide range of five- and six-membered rings [Eq. (81)].^[238] In this case, a

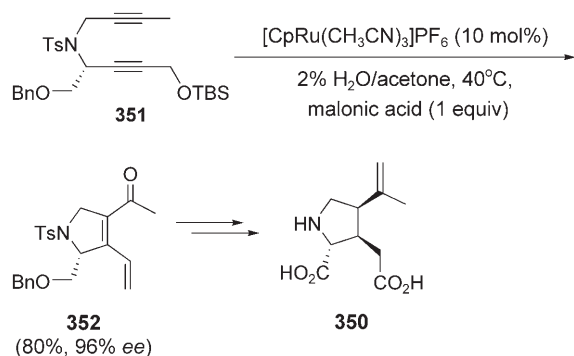


bicyclic product **348** is formed in very high yield in the presence of only 1 mol% of catalyst. In contrast to the intermolecular dimerization, even secondary and primary propargylic alcohols function well in this cycloisomerization reaction.

The utility of this method was demonstrated in the total synthesis of (+)- α -kainic acid (**350**; Scheme 31).^[239] In this



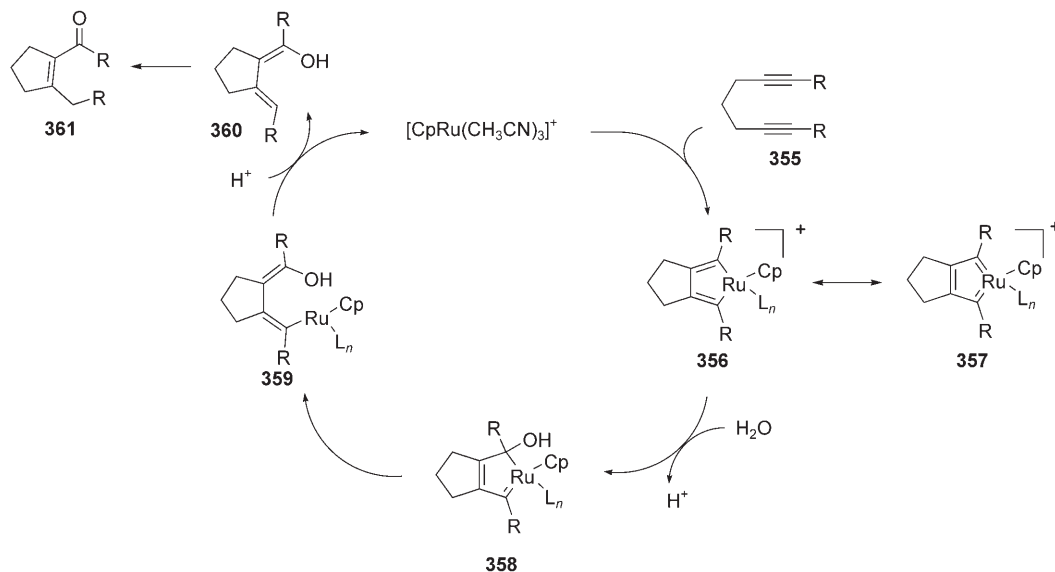
Scheme 30. Postulated mechanism for the dimerization of propargyl alcohols upon addition of carboxylic acids.



Scheme 31. Synthesis of (+)-α-kainic acid (**350**).

case, protected aminodiyne **351** underwent regioselective cycloisomerization to unsaturated ketone **352** in high yield and with no loss of enantiopurity at the propargylic center. This intermediate could be elaborated into the neuroexcitatory natural product (+)-α-kainic acid in several steps. The ability of the catalyst to cleave unhindered TBS ethers is exploited to cyclize the protected propargyl alcohol directly.

During the ruthenium-catalyzed reaction in the aforementioned synthesis of (+)-kainic acid (Scheme 31), we isolated a side product **354**,

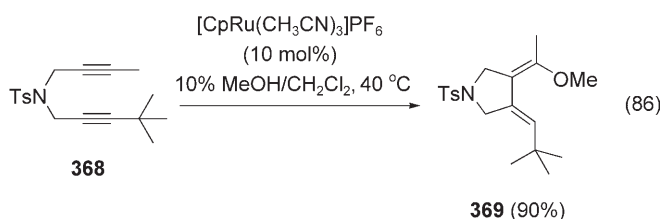
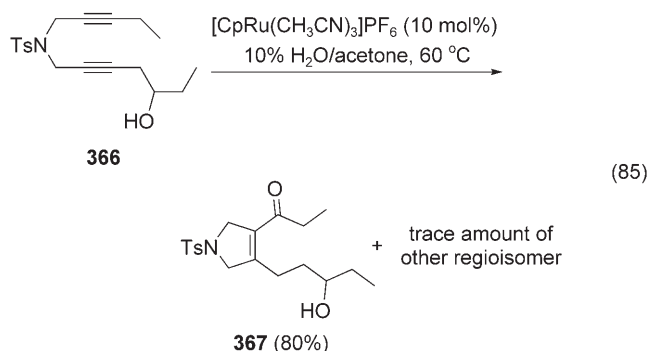
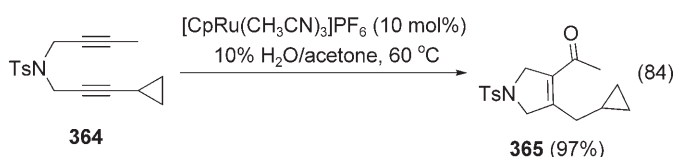
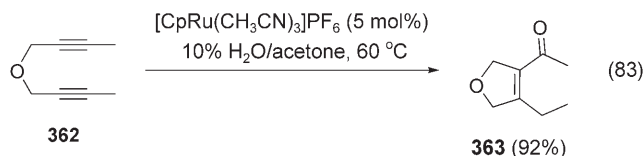
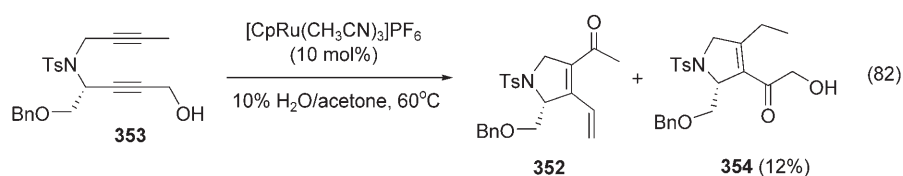


Scheme 32. Mechanistic rationale for the hydrative diyne cyclization.

which resulted from the addition of a molecule of water to the starting diyne **353** [Eq. (82)]. This result led us to believe that a hydrative diyne cyclization could be possible, thus enabling the transformation of diynes into enones. We envisioned a mechanism for the reaction based on the addition of water to a ruthenacyclopentadiene/ruthenacyclopentatriene intermediate in analogy to the mechanism proposed by Kirchner and co-workers^[240] and by Dixneuf and co-workers^[214,215] (Scheme 32).

Attack of a molecule of water on ruthenacyclopentadiene **356**, or its tautomer **357**, would give carbene **358**, which could, in turn, rearrange to vinyl ruthenium species **359**. Protonation would yield dienol **360**, which would readily tautomerize to the observed product **361**. This process works for a variety of diynes. For example, simple, symmetrical diynes **362** are converted into unsaturated ketones **363** in high yield and selectivity in the presence of only 5 mol% of catalyst [Eq. (83)].^[241]

This hydrative cyclization works well for the formation of a broad array of five- and six-membered ring enones and is tolerant of most functionalities, including epoxides. Even more dramatic is the chemoselective addition of water to unsymmetrical diynes (e.g. **364** and **366**) [Eq. (84) and Eq. (85)], almost exclusively at the least sterically hindered alkyne. Thus, regioselective addition is possible if the steric differentiation (i.e. the branch site) is α to the alkyne (e.g. **364**) [Eq. (85)]. Excellent selectivity (~20:1) is realized if the steric element is β to the alkyne (e.g. **366**) [Eq. (85)]; even a hydroxy group may act as a branch site. The fact that the methanol-addition product was isolated when water was replaced with methanol lends further support to the proposed mechanism [Eq. (86)].



Remarkably, effects other than steric differentiation may be utilized to direct attack of water to either alkyne function in the diyne. For example, in the case of diyne **370**, which contain an alkene function conjugated to one of the alkyne groups, water adds to the sterically most encumbered alkyne to give ketone **372** (Scheme 33). If, on the other hand, the olefin is replaced with a methyl group (e.g. **371**), water is added, as expected, to the sterically least hindered alkyne to afford ketone **373**. The potential utility of the chemoselective hydrative diyne was demonstrated in the total synthesis of several cylindricine alkaloid natural products, for example, cylindricine C (**376**; Scheme 33).^[242]

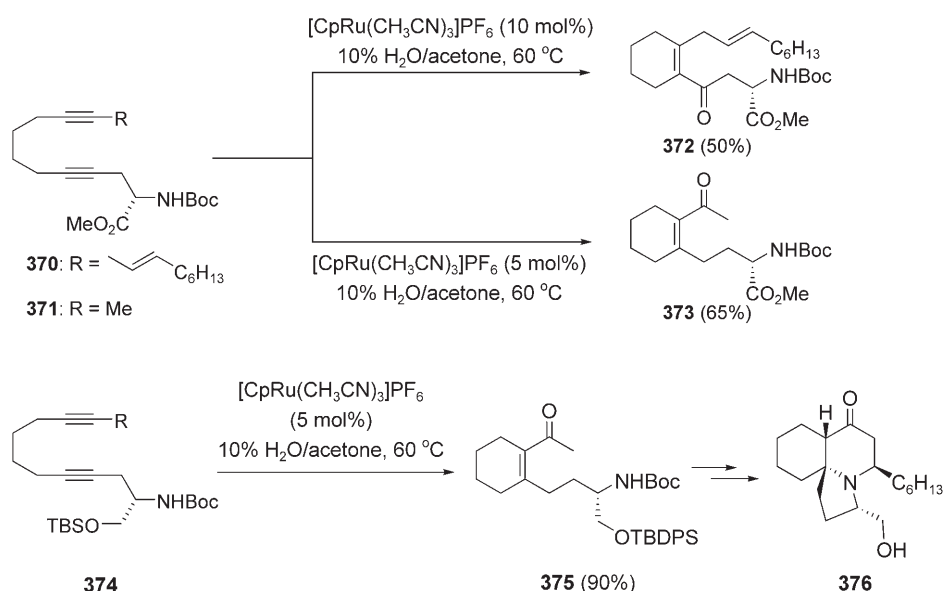
6. The Allene-Alkene Addition via Ruthenacyclopentene Intermediates

Allenes constitute important building blocks in organic synthesis.^[243] Recent developments have been extensively investigated in a wide array of transition-metal-catalyzed reactions of allenes in intra-^[244] or intermolecular fashion.^[245,246] In the latter case, several elegant Pd^{II} -catalyzed studies, in which allenes that contain several tethered nucleophiles were coupled with other unsaturated groups to give interesting heterocycles, were described by Ma and co-workers.^[247–250]

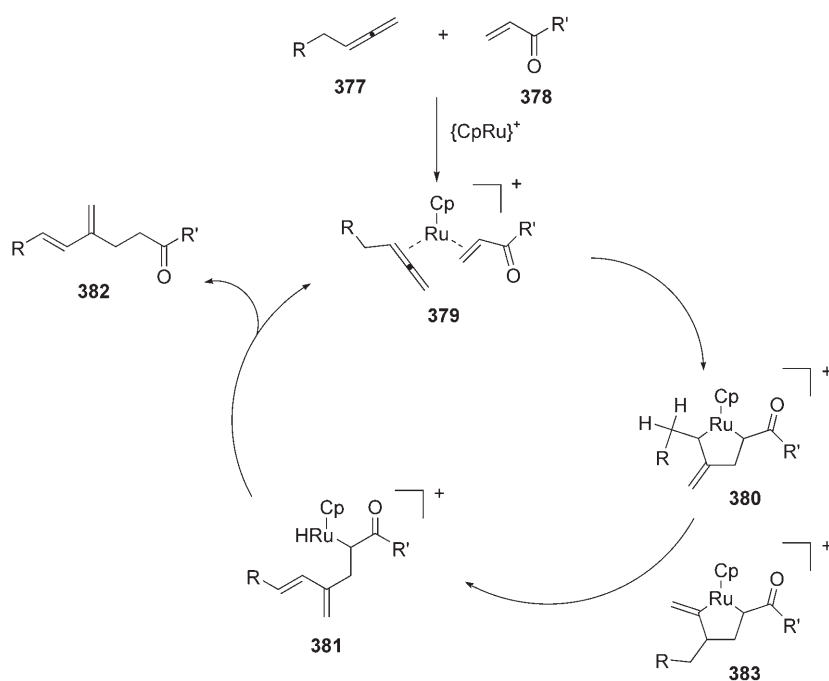
After our successful application of alkynes in the alkene-alkyne coupling reactions it was tempting to pose the question as to whether other sp -hybridized species, such as allenes, may enter into similar mechanistic manifolds under Ru catalysis. Such a coupling reaction would give rise to 1,3-dienes, an important structural motif in organic synthesis.^[251,252] The mechanistic proposal based on the alkene-alkyne reaction is detailed in Scheme 34. The active catalyst is envisioned to be the coordinatively unsaturated cationic ruthenium complex, which facilitates the coordination of the two reaction partners. Thus, initial bonding to the allenic $\text{C}(\text{sp})$ atom in **377** and the double bond of the enone **378** leads to the ruthenacyclopentane **380** via **379**. The stage is now set for β -hydride elimination, which generates a 1,3-diene **381**, with concomitant formation of a ruthenium hydride species. The steric constraints of the vinylic substituent and the exo methylene group would presumably favor the depicted conformation, which leads to the *E* isomer. Reductive elimination completes the catalytic cycle and regenerates the Ru^{II} catalyst. Importantly, a second ruthenacyclopentane **383** may emanate from the initial coordination (step 1), but only **380** is capable of further reaction. Thus the formation of **383** is probably reversible, which enables equilibration to **380** and leads to a productive reaction.

The initial studies examined the reaction between allene **384** and MVK in the presence of $[\text{CpRu}(\text{cod})\text{Cl}]$ (10 mol%) and hydrated cerium(III) chloride in DMF. MVK was chosen to avoid β -elimination. In any event, the reaction gave the desired 1,3-diene **385** in satisfactory yield (66%). We had discovered earlier that the activation of the $[\text{CpRu}(\text{cod})\text{Cl}]$ complex stemmed from a $[2+2+2]$ -type cycloaddition of cod and the alkyne substrate. We reasoned that the allene moiety might be a poorer activator of ruthenium, and added a catalytic amount of an alkyne “activator” **386**, which gratifyingly increased the yield of the desired product **385** to 81% (Scheme 35).^[253] The 1,3-dienes obtained in this manner are useful intermediates; for example, treatment with maleic anhydride and acidic methanol gave bicyclic lactone **387** with excellent chemo- and diastereoselectivity as well as atom economy.

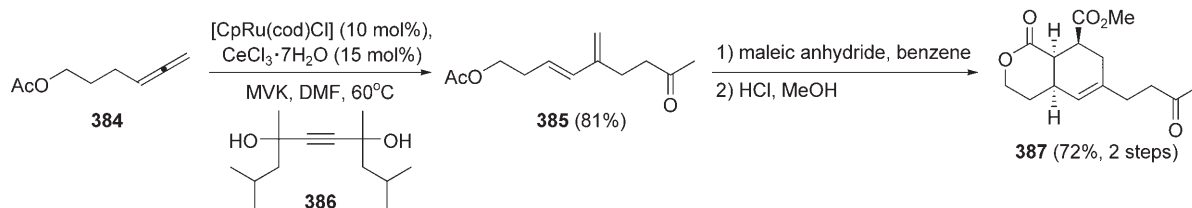
The reaction is not limited to monosubstituted allenes; in fact, polysubstituted systems may also be used in the two-component coupling. In these cases, regioselectivity issues may occur, but synthetically useful ratios are attained with suitable directing functionality, that is, either electronic or steric factors may control the regiochemical outcome of the



Scheme 33. Chemoselective hydrative diyne cyclization and application in the total synthesis of cyclindricine C (**376**).



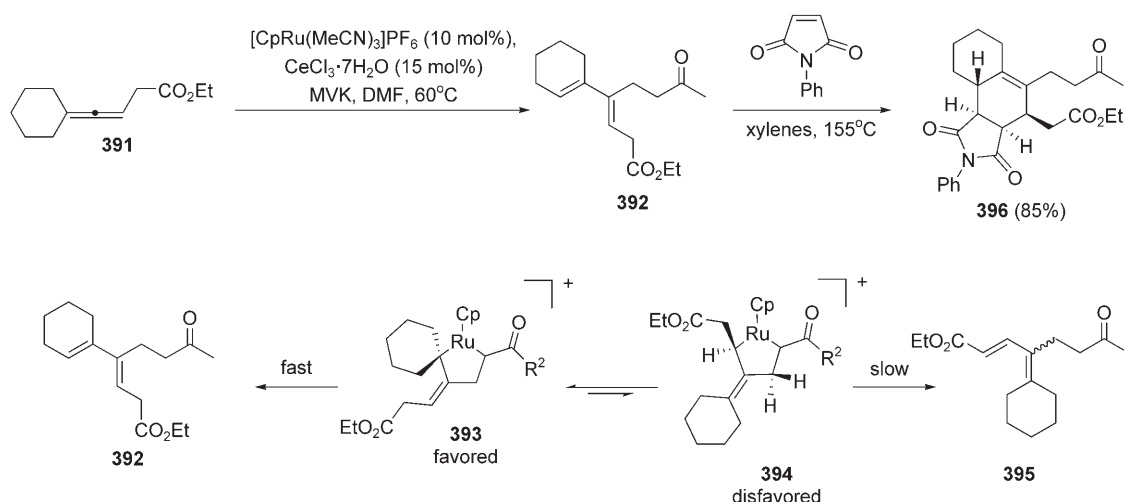
Scheme 34. Proposed mechanism for allene–alkene coupling.



Scheme 35. Ru-catalyzed two-component coupling of allenes with vinyl ketones.

reaction.^[254] The use of a 1,1-disubstituted allene, for example, raises the question of regioselectivity in the β -hydrogen elimination, which may be influenced by placing an “activating” functional group proximally to the hydrogen atom. When a 1,1-disubstituted allene such as **388** is exposed to MVK and the cationic catalyst system, only the depicted regioisomer **389** is obtained. In this case, β -hydride elimination of **390** is greatly aided by the conjugated ester functionality, thus leading to exclusive elimination of H_B over H_A . When this functionality is reduced to the corresponding alcohol, no selectivity is observed, leading to a 1:1 ratio of regioisomers [Eq. (87)].

Steric strain is a useful way to induce regiocontrol in trisubstituted allenes. For example, allene **391** undergoes smooth reaction to afford regioisomer **392** in a 8.3:1 ratio with the other regioisomer in 70% combined yield (Scheme 36). The origins of the regioselectivity become apparent when considering the possible ruthenacyclopentanes emerging in the mechanism of this reaction: Two metallacycles **393** and **394**, which are formed reversibly, can be envisioned. The fact that the apparently more hindered ruthenacyclopentane **393** leads to the observed major product should not be surprising seeing that the reaction is under Curtin–Hammett control. As β -hydride elimination, not ruthenacyclopentane formation, is the product-determining step, the formation of **392** should be favored as β -hydride elimination relieves strain in the spiro metallacycle **394**. The latter, on the other hand, develops considerable strain in the β -elimination step in which a tetrasubstituted exo double bond is formed. The synthetic utility of this substrate is evident when exposed to *N*-phenylmaleimide to generate the highly functionalized polycyclic system **396** in



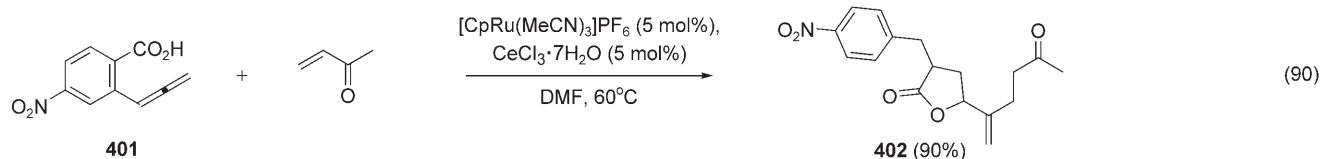
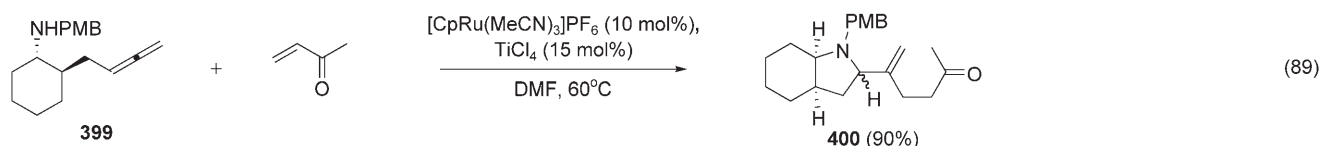
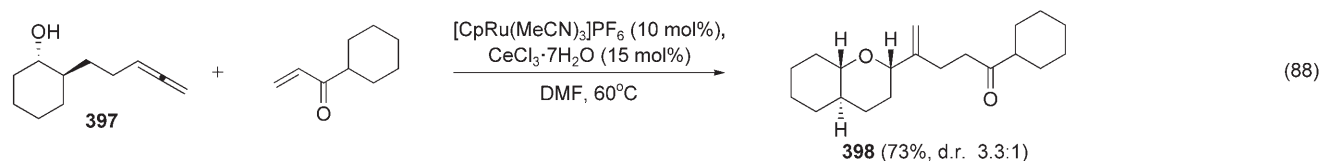
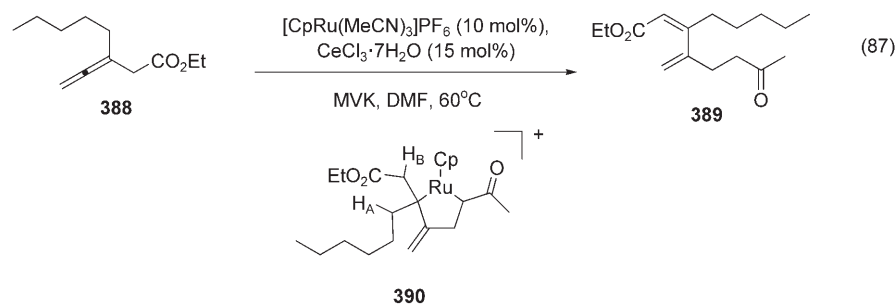
Scheme 36. Coupling of trisubstituted allenes with vinyl ketones.

excellent yield. The potential for this reaction to generate complexity rapidly should render it useful for diversity-oriented synthesis.^[255,256]

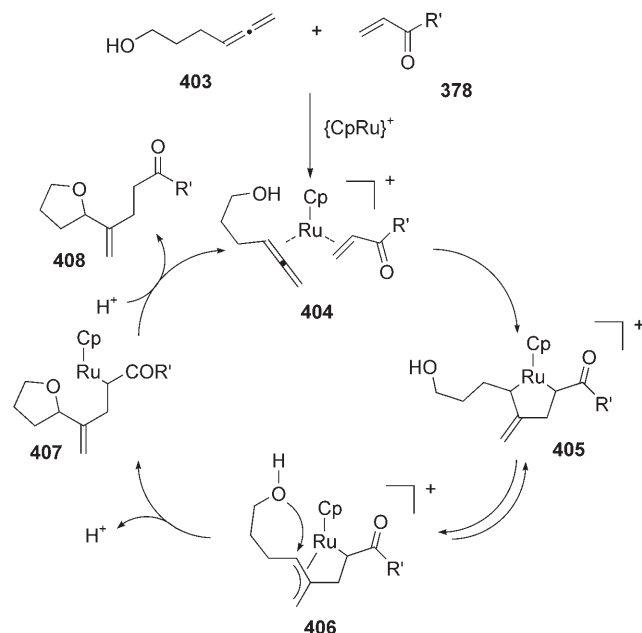
The postulated mechanism for the formation of 1,3-dienes from the two-component coupling between allenes and vinyl ketones suggests the intermediacy of a ruthenacyclopentane. This ruthenacycle undergoes β-hydride elimination on the route towards the 1,3-diene (Scheme 31, step 2). The suggested presence of the allyl ruthenium moiety enticed us to

question whether this could serve in chemical transformations typical of other allyl metal complexes. The known susceptibility of such complexes towards nucleophilic attack suggested that a suitably tethered nucleophile might trap the incipient Ru allyl species faster than it underwent the β-hydride elimination.^[257] At the time, relatively little was known about ruthenium-catalyzed allylic substitutions.^[258] The scant precedence, nevertheless, encouraged us to explore the feasibility of this reaction. We were pleased to discover

that tethered hydroxy groups and amines work well for the formation of bicyclic ethers (e.g. **398**) [Eq. (88)] and amines (e.g. **400**), respectively [Eq. (89)]. These reactions were run in the presence of the cationic catalyst and a Lewis acidic cocatalyst and enabled access to a wide range of five- and six-membered fused heterocycles with good diastereoselectivity. Carboxylates **401** are also competent nucleophiles in this reaction and generate structurally diverse lactones **402** in very good yields [Eq. (90)].^[259]



Our working hypothesis for the mechanism is detailed in Scheme 37. The ruthenacyclopentane **405** intermediate can exist in an equilibrium with the π -allyl species **406**. In the absence of the tethered nucleophile, the intermediate **405** undergoes β -hydride elimination to reveal the 1,3-diene as described earlier (see Scheme 34). In the presence of a

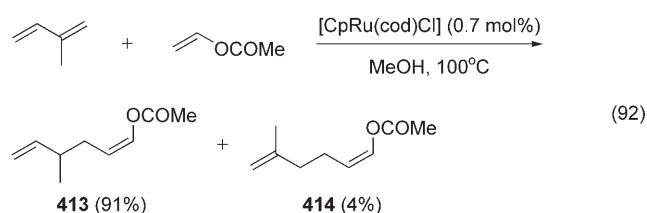
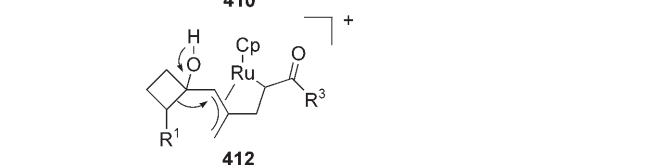
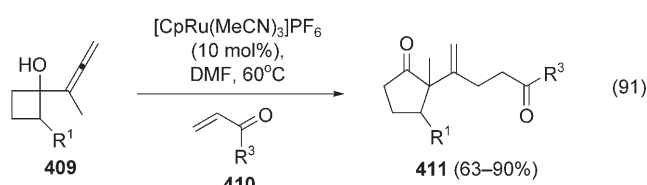


Scheme 37. Postulated mechanism for Ru-catalyzed alkylative cyclization.

tethered nucleophile, however, the π -allyl **406** is trapped, resulting in the ring-closed neutral species **407**. Subsequent protonation releases the cyclized product **408** and regenerates the coordinatively unsaturated complex. Thus, product formation is critically dependent on the relative rates of β -hydride elimination and nucleophilic attack. In accord with this hypothesis, the formation of small rings should be favored, whereas medium-sized rings should be disfavored owing to the slower rates of cyclization. Similarly, when β -hydride elimination is favored, for example, by conjugation of the resulting double bond to an ester, no nucleophilic trapping is observed.

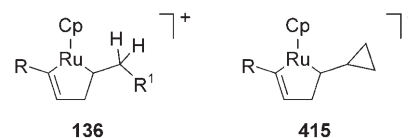
Ihara and co-workers reported an interesting alkylative ring expansion catalyzed by ruthenium that also intercepts the proposed π -allyl intermediate.^[260] In this reaction, allenecyclobutanes such as **409** undergo alkylation with an activated olefin **410**, which in turn expands presumably via **412** to form the α -substituted cyclopentanone **411** in good to excellent yield [Eq. (91)].

Fujiwhara et al. recently disclosed a related cross-dimerization.^[261] Although an allene is not involved as a coupling partner, it is nevertheless proposed to proceed via a ruthenacyclopentane intermediate. In the event, Fujiwhara et al. found that when isoprene and vinyl acetate was warmed in methanol in the presence of [CpRu(cod)Cl], the coupled products **413** and **414** were formed in 95% overall yield (96:4 ratio) [Eq. (92)].



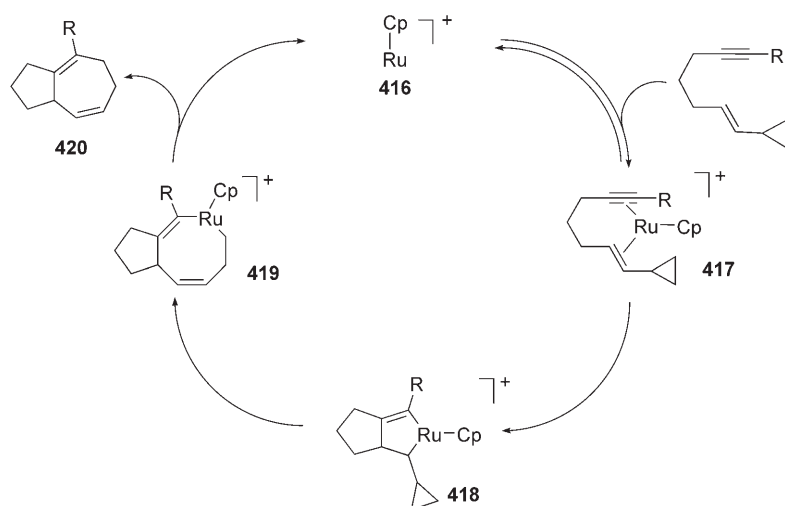
7. Ruthenium-Catalyzed [5+2] Cycloaddition

A common theme for many of the reactions described herein invokes various ruthenacycles (e.g. **136**) as intermediates in our working mechanisms, the fate of which has been β -



hydride elimination to give the desired products. Spurred by our desire to extend our understanding of these intermediates, we pondered the possibility of placing a small, strained ring proximal to the double bond (e.g. **415**), analogous to the highly successful rhodium-catalyzed system pioneered by Wender and co-workers.^[262–281] The key question in this mechanistic scenario would be whether the presence of a small, strained ring would lead to cleavage of the cyclopropyl moiety rather than to β -hydride elimination. If the latter could be suppressed, intermediates such as **415** should prove to be useful in higher-order cycloaddition reactions, and as such would provide an attractive alternative to the aforementioned Rh-catalyzed cycloadditions championed by Wender and co-workers.

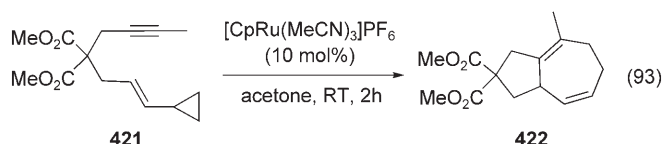
Thus, inspired by the mechanistic underpinnings of the Ru-catalyzed alkyne–alkene coupling reaction and the Rh-catalyzed [5+2] cycloaddition, we proposed the mechanism illustrated below (Scheme 38). Initial complexation (see **417**) of the cationic ruthenium complex **416** and the vinyl cyclopropane leads to the ruthenacyclopentene **418**. This cyclopropylcarbinyl intermediate was expected to undergo a cyclopropylcarbinyl-to-homoallyl rearrangement to **419**, driven by the release of ring strain. Competitive β -elimination is suppressed in **418**, as it would necessarily lead to a highly strained alkylidenecyclopropane species. Finally, reductive



Scheme 38. Proposed mechanism for Ru-catalyzed [5+2] cycloaddition.

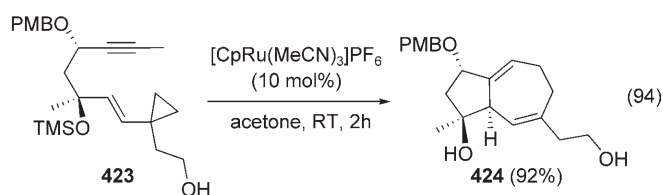
elimination would complete the catalytic cycle by formation of the cycloheptadiene **420** and regeneration of the Ru catalyst **416**.

Initial experiments in this program revealed that the Ru-catalyzed [5+2] cycloaddition proceeds with extraordinary efficiency. For example, catalyzed by $[\text{CpRu}(\text{MeCN})_3]\text{PF}_6$ (10 mol %) in acetone at ambient temperature, the cyclopropylenyne **421** underwent cyclization to give the hexahydroazulene **422** in excellent yield after only 2 h [Eq. (93)].^[282]



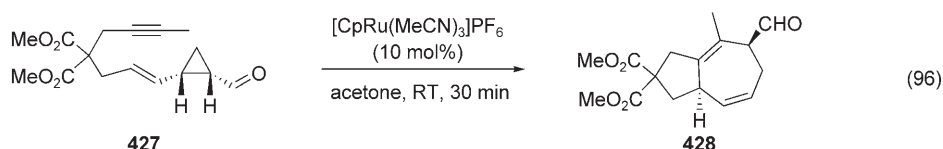
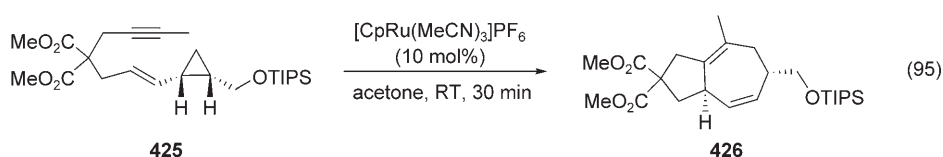
The investigation of substrates that contain more highly substituted backbones revealed that the 1,1-disubstituted cyclopropane **423** cyclized smoothly to give the corresponding bicycle **424** in excellent yield as a single diastereomer [Eq. (94)]. The reaction strongly favors the hydrogen atom at the newly formed bridgehead stereocenter to be *anti* with respect to the homoallylic hydroxy group.^[283] This apparently general trend is in agreement with the Stork–Houk–Jäger “inside-alkoxy” model.^[284–286]

The examination of substrates that contain 1,2-disubstituted cyclopropanes revealed several interesting trends. For



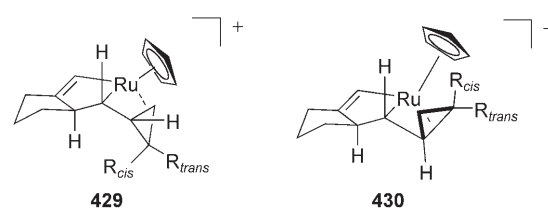
example, treatment of the 1,2-*cis*-disubstituted cyclopropane **425** with the Ru catalyst under standard conditions produced exclusively the diastereomer **426** [Eq. (95)]. Changing the group at C2 to an electron-withdrawing group (e.g. CHO; **427**) reveals a complete switch in regioselectivity [Eq. (96)] to give **428** as a single diastereomer.^[287]

These observations show that the regioselectivity of the reaction of *cis*-disubstituted cyclopropanes may be controlled by simply switching the electronic nature of the substituent at C2; electron-withdrawing substituents show a total preference for cleaving the more-substituted cyclopropyl bond. In the case of electron-neutral or -donating substituents a preference for the less-substituted cyclopropyl bond is observed. For 1,2-*trans*-disubstituted cyclopropanes poorer selectivities are generally observed. In these cases, the best strategy for obtaining regioselective cyclopropyl cleavage is to alter the steric



demands of the substituents at C2. Notably, the reaction is completely diastereoselective in all the aforementioned cases.

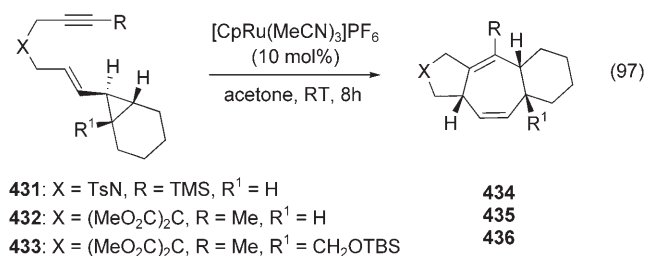
The observed regio- and diastereoselectivities provide circumstantial evidence for the proposed mechanism and act as a guiding principle for applications of this chemistry. Thus, when considering the possible ruthenacyclopentenes **429** and



430, it appears evident that the *cis* substituent is better accommodated in structure **429** than in **430**, in which severe steric interactions lead to exclusive cleavage of the least-hindered cyclopropane bond. In the case of electron-withdrawing groups, the steric effect is offset by the strong preference for the cleavage of the more-substituted (i.e. weakest) bond. In the case of *trans*-cyclopropanes, it is clear that the R_{trans} substituent is easily accommodated in both conformers.

The extraordinarily mild conditions of the Ru-catalyzed [5+2] cycloaddition, combined with the regio- and diaster-

eocontrol that can be readily invoked, render this methodology highly suitable for applications to the total synthesis of bioactive natural products that contain the polyhydroazulene motif concealed in more-complex architectures. Indeed, complex polycyclic frameworks have been accessed by fusing the cyclopropane to various carbocycles (e.g. **431–433**) to give the desired tricycles (e.g. **434–436**) in excellent yields; these ring systems are present in many bioactive natural products [Eq. (97)].^[288]



8. Summary and Outlook

Transition-metal catalysis provides a rich avenue of research opportunities that address key questions of selectivity and atom economy. In this regard, the extraordinary potential of Ru complexes to catalyze highly unusual and powerful transformations has added valuable processes to the synthetic toolbox. Yet one can only have a feeling that we have barely begun to scratch the surface of the immense possibilities afforded by Ru catalysis, particularly when considering the vast number of ruthenium complexes that may be synthesized combined with the incredible array of possible oxidation states possible for ruthenium. Indeed, only a handful of ruthenium species have been described herein, yet an impressive number of unusual and powerful transformations have been discovered. Thus, by careful design of novel catalysts combined with a semirational approach to reaction design, we should be able to tap into the virtually boundless opportunities for research provided by Ru catalysis in particular and transition metals in general. It is therefore with a great degree of confidence that we can assure that new reactions and processes will be discovered that address the goals of simultaneously decreasing the depletion of raw materials as well as the generation of waste, while satisfying the ever-expanding demand for sophisticated molecular targets.

The work emanating in our laboratories was derived from an exceptionally talented group of co-workers who are identified individually in the references. This work was supported by the National Science Foundation and the National Institutes of Health, General Medical Sciences Institute. M.U.F. thanks GlaxoSmithKline Research and Development for partial postdoctoral fellowship support.

Received: January 13, 2005

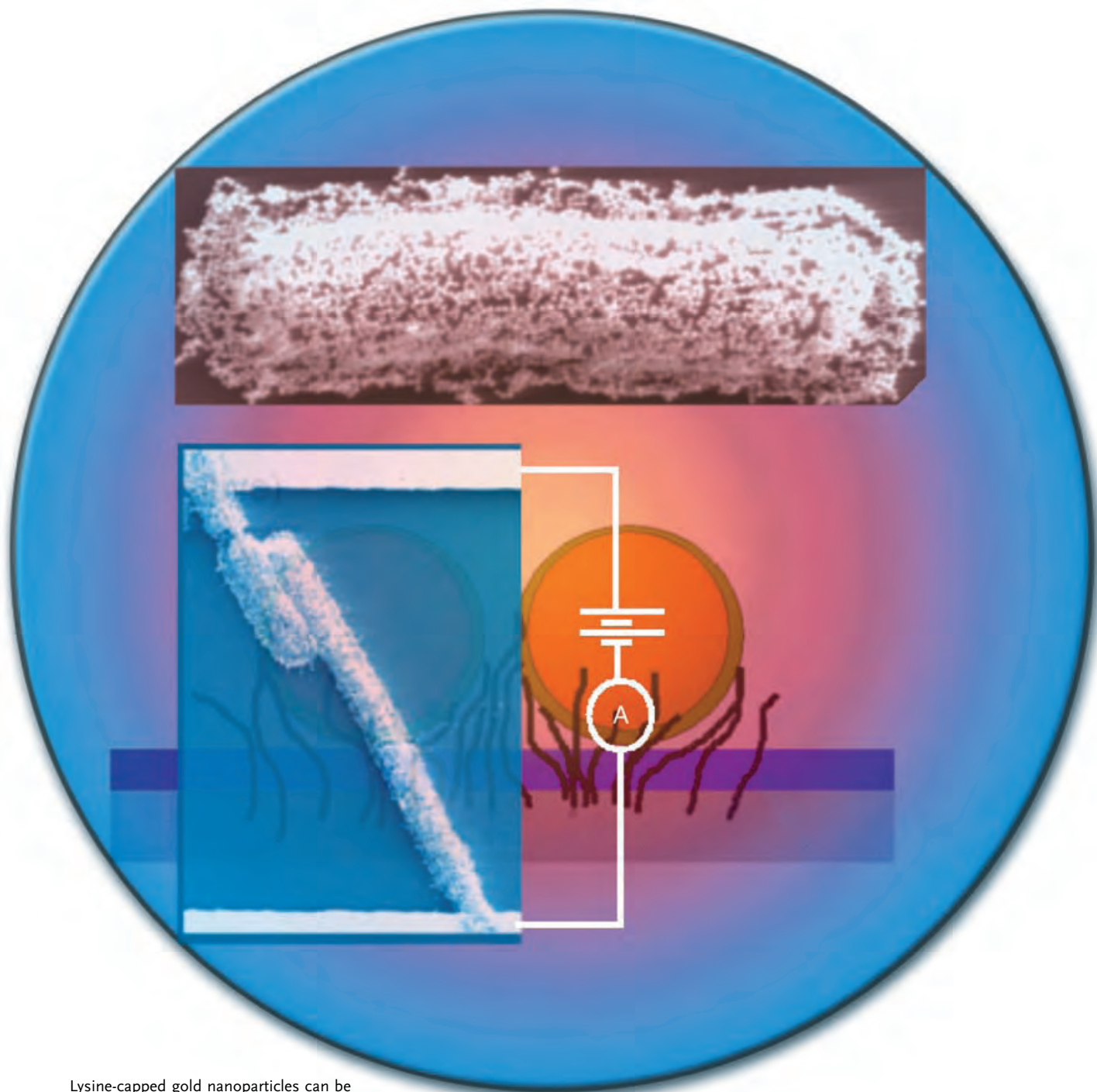
Published online: October 5, 2005

- [1] B. M. Trost, *Science* **1991**, 254, 1471.
- [2] B. M. Trost, *Angew. Chem.* **1995**, 107, 285; *Angew. Chem. Int. Ed. Engl.* **1995**, 34, 259.
- [3] K. C. Nicolaou, S. A. Snyder, T. Montagnon, G. Vassilikogiannakis, *Angew. Chem.* **2002**, 114, 1742; *Angew. Chem. Int. Ed.* **2002**, 41, 1668.
- [4] B. Breit, W. Seiche, *Synthesis* **2001**, 1.
- [5] B. Breit, *Acc. Chem. Res.* **2003**, 36, 264.
- [6] B. M. Trost, F. D. Toste, A. B. Pinkerton, *Chem. Rev.* **2001**, 101, 2067.
- [7] B. Solaja, J. Huguet, M. Karpf, A. S. Dreiding, *Tetrahedron* **1987**, 43, 4875.
- [8] J. Ackroyd, M. Karpf, A. S. Dreiding, *Helv. Chim. Acta* **1984**, 67, 1963.
- [9] W. A. Nugent, J. M. Mayer, *Metal-Ligand Multiple Bonds*, Wiley, New York, **1988**.
- [10] Y. Wakatsuki, Z. M. Hou, M. Tokunaga, *Chem. Rec.* **2003**, 3, 144.
- [11] C. Menendez, D. Morales, J. Perez, V. Riera, D. Miguel, *Organometallics* **2001**, 20, 2775.
- [12] Y. C. Lin, *J. Organomet. Chem.* **2001**, 617, 141.
- [13] V. Cadierno, M. P. Gamasa, J. Gimeno, *Eur. J. Inorg. Chem.* **2001**, 571.
- [14] B. Weyershausen, K. H. Dotz, *Eur. J. Inorg. Chem.* **1999**, 1057.
- [15] M. C. Puerta, P. Valerga, *Coord. Chem. Rev.* **1999**, 195, 977.
- [16] C. Bruneau, P. H. Dixneuf, *Acc. Chem. Res.* **1999**, 32, 311.
- [17] M. I. Bruce, R. C. Wallis, *J. Organomet. Chem.* **1978**, 161, C1.
- [18] M. I. Bruce, A. G. Swincer, R. C. Wallis, *J. Organomet. Chem.* **1979**, 171, C5.
- [19] M. I. Bruce, A. G. Swincer, *Aust. J. Chem.* **1980**, 33, 1471.
- [20] M. I. Bruce, R. C. Wallis, *Aust. J. Chem.* **1981**, 34, 209.
- [21] M. I. Bruce, F. S. Wong, B. W. Skelton, A. H. White, *J. Chem. Soc. Dalton Trans.* **1982**, 2203.
- [22] B. M. Trost, G. Dyker, R. J. Kulawiec, *J. Am. Chem. Soc.* **1990**, 112, 7809.
- [23] B. M. Trost, R. J. Kulawiec, *J. Am. Chem. Soc.* **1992**, 114, 5579.
- [24] B. M. Trost, R. J. Kulawiec, A. Hammes, *Tetrahedron Lett.* **1993**, 34, 587.
- [25] B. M. Trost, J. A. Flygare, *J. Org. Chem.* **1994**, 59, 1078.
- [26] B. M. Trost, M. Thommen, unpublished results.
- [27] M. H. Chisholm, H. C. Clark, *J. Am. Chem. Soc.* **1972**, 94, 1532.
- [28] M. I. Bruce, A. G. Swincer, B. J. Thomson, R. C. Wallis, *Aust. J. Chem.* **1980**, 33, 2605.
- [29] C. Bianchini, A. Marchi, N. Mantovani, L. Marvelli, D. Masi, M. Peruzzini, R. Rossi, *Eur. J. Inorg. Chem.* **1998**, 211.
- [30] G. Davies, J. P. McNally, A. J. Smallbridge, *Adv. Organomet. Chem.* **1990**, 30, 1.
- [31] F. E. McDonald, *Chem. Eur. J.* **1999**, 5, 3103.
- [32] S. J. Danishefsky, M. T. Bilodeau, *Angew. Chem.* **1996**, 108, 1482; *Angew. Chem. Int. Ed. Engl.* **1996**, 35, 1380.
- [33] P. H. Seeberger, M. T. Bilodeau, S. J. Danishefsky, *Aldrichimica Acta* **1997**, 30, 75.
- [34] F. E. McDonald, K. S. Reddy, Y. Diaz, *J. Am. Chem. Soc.* **2000**, 122, 4304.
- [35] F. E. McDonald, K. S. Reddy, *J. Organomet. Chem.* **2001**, 617, 444.
- [36] Y. H. Sheng, D. G. Musaev, K. S. Reddy, F. E. McDonald, K. Morokuma, *J. Am. Chem. Soc.* **2002**, 124, 4149.
- [37] M. H. Davidson, F. E. McDonald, *Org. Lett.* **2004**, 6, 1601.
- [38] W. W. Cutchins, F. E. McDonald, *Org. Lett.* **2002**, 4, 749.
- [39] F. E. McDonald, M. L. Wu, *Org. Lett.* **2002**, 4, 3979.
- [40] F. E. McDonald, K. S. Reddy, *Angew. Chem.* **2001**, 113, 3765; *Angew. Chem. Int. Ed.* **2001**, 40, 3653.
- [41] P. Quayle, S. Rahman, E. L. M. Ward, *Tetrahedron Lett.* **1994**, 35, 3801.
- [42] P. Quayle, S. Rahman, *Tetrahedron Lett.* **1995**, 36, 8087.

- [43] M. Gilbert, M. Ferrer, A.-M. Lluch, F. Sanchez-Baeza, A. Messegue, *J. Org. Chem.* **1999**, *64*, 1591.
- [44] B. M. Trost, Y. H. Rhee, *J. Am. Chem. Soc.* **1999**, *121*, 11680.
- [45] S. H. Yoon, H. S. Moon, S. K. Hwang, S. R. Choi, S. K. Kang, *Bioorg. Med. Chem.* **1998**, *6*, 1043.
- [46] M. J. Rieser, J. F. Kozlowski, K. V. Wood, J. L. Mclaughlin, *Tetrahedron Lett.* **1991**, *32*, 1137.
- [47] B. M. Trost, Y. H. Rhee, *J. Am. Chem. Soc.* **2002**, *124*, 2528.
- [48] J. L. Bowman, F. E. McDonald, *J. Org. Chem.* **1998**, *63*, 3680.
- [49] B. M. Trost, Y. H. Rhee, unpublished results.
- [50] T. Henkel, S. Breidingmack, A. Zeeck, S. Grabley, P. E. Hammann, K. Hutter, G. Till, R. Thiericke, J. Wink, *Liebigs Ann. Chem.* **1991**, 575.
- [51] G. Q. Lin, H. J. Xu, B. C. Wu, G. Z. Guo, W. S. Zhou, *Tetrahedron Lett.* **1985**, *26*, 1233.
- [52] K. Machiya, I. Ichimoto, M. Kirihata, H. Ueda, *Agric. Biol. Chem.* **1985**, *49*, 643.
- [53] H. Kotsuki, I. Kadota, M. Ochi, *J. Org. Chem.* **1990**, *55*, 4417.
- [54] T. Yasumoto, M. Murata, *Chem. Rev.* **1993**, *93*, 1897.
- [55] M. Murata, M. Kumagai, J. S. Lee, T. Yasumoto, *Tetrahedron Lett.* **1987**, *28*, 5869.
- [56] C.-Y. Lo, H. Guo, J.-J. Lian, F.-M. Shen, R.-S. Liu, *J. Org. Chem.* **2002**, *67*, 3930.
- [57] C. A. Merlic, M. E. Pauly, *J. Am. Chem. Soc.* **1996**, *118*, 11319.
- [58] C. Fernandez-Rivas, M. Mendez, A. M. Echavarren, *J. Am. Chem. Soc.* **2000**, *122*, 1221.
- [59] M. Murakami, S. Hori, *J. Am. Chem. Soc.* **2003**, *125*, 4720.
- [60] C. S. Yi, N. Liu, *Synlett* **1999**, 281.
- [61] C. S. Yi, N. Liu, *Organometallics* **1998**, *17*, 3158.
- [62] D. Touchard, P. H. Dixneuf, *Coord. Chem. Rev.* **1998**, *178–180*, 409.
- [63] M. I. Bruce, *Chem. Rev.* **1998**, *98*, 2797.
- [64] J. P. Selegue, *Organometallics* **1982**, *1*, 119.
- [65] B. M. Trost, J. A. Flygare, *J. Am. Chem. Soc.* **1992**, *114*, 5476.
- [66] B. M. Trost, J. A. Flygare, *Tetrahedron Lett.* **1994**, *35*, 4059.
- [67] Y. Nishibayashi, I. Wakiji, M. Hidai, *J. Am. Chem. Soc.* **2000**, *122*, 11019; Y. Nishibayashi, M. D. Milton, Y. Inada, M. Yoshikawa, I. Wakiji, M. Hidai, S. Uemura, *Chem. Eur. J.* **2005**, *11*, 1433.
- [68] Y. Nishibayashi, I. Wakiji, Y. Ishii, S. Uemura, M. Hidai, *J. Am. Chem. Soc.* **2001**, *123*, 3393.
- [69] Y. Nishibayashi, M. Yoshikawa, Y. Inada, M. Hidai, S. Uemura, *J. Am. Chem. Soc.* **2002**, *124*, 11846.
- [70] Y. Nishibayashi, M. Yoshikawa, Y. Inada, M. Hidai, S. Uemura, *J. Org. Chem.* **2004**, *69*, 3408.
- [71] Y. Nishibayashi, Y. Inada, M. Hidai, S. Uemura, *J. Am. Chem. Soc.* **2002**, *124*, 7900.
- [72] Y. Nishibayashi, Y. Inada, M. Hidai, S. Uemura, *J. Am. Chem. Soc.* **2003**, *125*, 6060.
- [73] Y. Inada, Y. Nishibayashi, M. Hidai, S. Uemura, *J. Am. Chem. Soc.* **2002**, *124*, 15172.
- [74] Y. Nishibayashi, Y. Inada, M. Yoshikawa, M. Hidai, S. Uemura, *Angew. Chem.* **2003**, *115*, 1533; *Angew. Chem. Int. Ed.* **2003**, *42*, 1495.
- [75] R. Mahrwald, S. Quint, S. Scholtis, *Tetrahedron* **2002**, *58*, 9847.
- [76] B. D. Sherry, A. T. Radosevich, F. D. Toste, *J. Am. Chem. Soc.* **2003**, *125*, 6076.
- [77] M. R. Luzung, F. D. Toste, *J. Am. Chem. Soc.* **2003**, *125*, 15760.
- [78] J. J. Kennedy-Smith, L. A. Young, F. D. Toste, *Org. Lett.* **2004**, *6*, 1325.
- [79] I. Matsuda, K. Komori, K. Itoh, *J. Am. Chem. Soc.* **2002**, *124*, 9072.
- [80] R. Uma, C. Crevisy, R. Gree, *Chem. Rev.* **2003**, *103*, 27.
- [81] R. C. Van Der Drift, E. Bouwman, E. Drent, *J. Organomet. Chem.* **2002**, *650*, 1.
- [82] W. Strohmeier, L. Weigelt, *J. Organomet. Chem.* **1975**, *86*, C17.
- [83] M. Dedieu, Y. Pascal, *J. Mol. Catal.* **1980**, *9*, 59.
- [84] B. M. Trost, R. J. Kulawiec, *Tetrahedron Lett.* **1991**, *32*, 3039.
- [85] B. M. Trost, R. J. Kulawiec, *J. Am. Chem. Soc.* **1993**, *115*, 2027.
- [86] L. Oro, M. A. Ciriano, M. Campo, C. Foces-Foces, F. H. Cano, *J. Organomet. Chem.* **1985**, *289*, 117.
- [87] T. B. Marder, D. C. Roe, D. Milstein, *Organometallics* **1988**, *7*, 1451.
- [88] C. P. Casey, J. M. O'Connor, *Organometallics* **1985**, *4*, 384.
- [89] B. M. Trost, R. J. Kulawiec, *J. Am. Chem. Soc.* **1993**, *115*, 2027.
- [90] C. Slugovc, E. Ruba, R. Schmid, K. Kirchner, *Organometallics* **1999**, *18*, 4230.
- [91] I. E. Markó, A. Gautier, M. Tsukazaki, A. Llobet, E. Plantalech-Mir, C. J. Urch, S. M. Brown, *Angew. Chem.* **1999**, *111*, 2126; *Angew. Chem. Int. Ed.* **1999**, *38*, 1960.
- [92] M. K. Gurjar, P. Yakambram, *Tetrahedron Lett.* **2001**, *42*, 3633.
- [93] S. Swaminathan, K. V. Narayanan, *Chem. Rev.* **1971**, *71*, 429.
- [94] D. Ma, X. Lu, *J. Organomet. Chem.* **1989**, *359*, 259.
- [95] K. Minn, *Synlett* **1991**, 115.
- [96] T. J. J. Mueller, M. Ansorge, D. Aktah, *Angew. Chem.* **2000**, *112*, 1323; *Angew. Chem. Int. Ed.* **2000**, *39*, 1253.
- [97] M. K. Eddine Saiah, R. Pellicciari, *Tetrahedron Lett.* **1995**, *36*, 4497.
- [98] D. W. Ma, X. Y. Lu, *Tetrahedron Lett.* **1989**, *30*, 2109.
- [99] D. Ma, X. Y. Lu, *J. Chem. Soc. Chem. Commun.* **1989**, 890.
- [100] B. M. Trost, R. C. Livingston, *J. Am. Chem. Soc.* **1995**, *117*, 9586.
- [101] H. M. R. Hoffman, *Angew. Chem.* **1969**, *81*, 597; *Angew. Chem. Int. Ed. Engl.* **1969**, *8*, 557.
- [102] D. F. Taber, *Intramolecular Diels–Alder and Alder Ene Reactions*, Springer, Berlin, **1984**.
- [103] W. Oppolzer, V. Snieckus, *Angew. Chem.* **1978**, *90*, 506; *Angew. Chem. Int. Ed. Engl.* **1978**, *17*, 476.
- [104] B. B. Snider, *Acc. Chem. Res.* **1980**, *13*, 426.
- [105] W. Oppolzer, H. F. Strauss, D. P. Simmons, *Tetrahedron Lett.* **1982**, *23*, 4673.
- [106] W. Oppolzer, K. Battig, *Tetrahedron Lett.* **1982**, *23*, 4669.
- [107] H. Felkin, J. D. Umpleby, *Tetrahedron Lett.* **1972**, *13*, 2285.
- [108] J. C. Trebella, J. R. Olechows, H. B. Jonassen, *J. Organomet. Chem.* **1966**, *6*, 412.
- [109] L. E. Overman, F. M. Knoll, *J. Am. Chem. Soc.* **1980**, *102*, 865.
- [110] A. Bright, J. K. Nicholson, J. Powell, B. L. Shaw, J. F. Malone, *J. Chem. Soc. D* **1971**, 712.
- [111] E. Schmitz, U. Heuck, D. Habisch, *J. Prakt. Chem.* **1976**, *318*, 471.
- [112] E. Schmitz, R. Urban, U. Heuck, G. Zimmermann, E. Grundemann, *J. Prakt. Chem.* **1976**, *318*, 185.
- [113] R. Grigg, T. R. B. Mitchell, A. Ramasubbu, *J. Chem. Soc. Chem. Commun.* **1980**, 27.
- [114] R. Grigg, T. R. B. Mitchell, A. Ramasubbu, *J. Chem. Soc. Chem. Commun.* **1979**, 669.
- [115] B. M. Trost, M. Lautens, *J. Am. Chem. Soc.* **1985**, *107*, 1781.
- [116] B. M. Trost, *Janssen Chim. Acta* **1991**, *9*, 3.
- [117] T. L. Cairns, V. A. Engelhardt, H. L. Jackson, G. H. Kalb, J. C. Sauer, *J. Am. Chem. Soc.* **1952**, *74*, 5636.
- [118] D. M. Singleton, *Tetrahedron Lett.* **1973**, *14*, 1245.
- [119] H. Suzuki, K. Itoh, Y. Ishii, K. Simon, J. A. Ibers, *J. Am. Chem. Soc.* **1976**, *98*, 8494.
- [120] K. Kaneda, T. Uchiyama, Y. Fujiwara, T. Imanaka, S. Teranishi, *J. Org. Chem.* **1979**, *44*, 55.
- [121] K. Kaneda, T. Uchiyama, H. Kobayashi, Y. Fujiwara, T. Imanaka, S. Teranishi, *Tetrahedron Lett.* **1977**, *18*, 2005.
- [122] T. Mitsudo, Y. Nakagawa, H. Watanabe, K. Watanabe, H. Misawa, Y. Watanabe, *J. Chem. Soc. Chem. Commun.* **1981**, 496.
- [123] B. M. Trost, M. Lautens, *Tetrahedron Lett.* **1985**, *26*, 4887.
- [124] B. M. Trost, J. Y. L. Chung, *J. Am. Chem. Soc.* **1985**, *107*, 4586.
- [125] T. Mitsudo, S. W. Zhang, M. Nagao, Y. Watanabe, *J. Chem. Soc. Chem. Commun.* **1991**, 598.

- [126] B. M. Trost, J. A. Martinez, R. J. Kulawiec, A. F. Indolese, *J. Am. Chem. Soc.* **1993**, *115*, 10402.
- [127] I. U. Khand, G. R. Knox, P. L. Pauson, W. E. Watts, M. I. Foreman, *J. Chem. Soc. Perkin Trans. 1* **1973**, 977.
- [128] T. Mitsudo, K. Kokuryo, T. Shinsugi, Y. Nakagawa, Y. Watanabe, Y. Takegami, *J. Org. Chem.* **1979**, *44*, 4492.
- [129] B. M. Trost, A. Indolese, *J. Am. Chem. Soc.* **1993**, *115*, 4361.
- [130] B. M. Trost, K. Imi, A. F. Indolese, *J. Am. Chem. Soc.* **1993**, *115*, 8831.
- [131] B. M. Trost, C. M. Older, *Organometallics* **2002**, *21*, 2544.
- [132] B. M. Trost, F. D. Toste, *Tetrahedron Lett.* **1999**, *40*, 7739.
- [133] B. M. Trost, G. D. Probst, A. Schoop, *J. Am. Chem. Soc.* **1998**, *120*, 9228.
- [134] B. M. Trost, A. B. Pinkerton, F. D. Toste, M. Sperrle, *J. Am. Chem. Soc.* **2001**, *123*, 12504.
- [135] B. M. Trost, H. C. Shen, A. B. Pinkerton, *Chem. Eur. J.* **2002**, *8*, 2341.
- [136] B. M. Trost, J. L. Gunzner, *J. Am. Chem. Soc.* **2001**, *123*, 9449.
- [137] B. M. Trost, J. L. Gunzner, O. Dirat, Y. H. Rhee, *J. Am. Chem. Soc.* **2002**, *124*, 10396.
- [138] J. Kobayashi, M. Ishibashi, H. J. Hirota, *J. Nat. Prod.* **1991**, *54*, 1435.
- [139] J. Kobayashi, M. Ishibashi, H. Nakamura, Y. Ohizumi, T. Yamasu, T. Sasaki, Y. Hirata, *Tetrahedron Lett.* **1986**, *27*, 5755.
- [140] B. M. Trost, J. D. Chisholm, S. T. Wroblewski, M. Jung, *J. Am. Chem. Soc.* **2002**, *124*, 12420.
- [141] H. W. Lam, G. Pattenden, *Angew. Chem.* **2002**, *114*, 4887; *Angew. Chem. Int. Ed.* **2002**, *41*, 508.
- [142] R. E. Maleczka, L. R. Terrell, F. Geng, J. S. Ward, *Org. Lett.* **2002**, *4*, 2841.
- [143] B. M. Trost, *Chem. Soc. Rev.* **1982**, *11*, 141.
- [144] B. M. Trost, M. R. Machacek, Z. T. Ball, *Org. Lett.* **2003**, *5*, 1895.
- [145] B. M. Trost, M. R. Machacek, *Angew. Chem.* **2002**, *114*, 4887; *Angew. Chem. Int. Ed.* **2002**, *41*, 4693.
- [146] K. Tamao, M. Kumada, K. Maeda, *Tetrahedron Lett.* **1984**, *25*, 321.
- [147] B. M. Trost, M. Machacek, M. J. Schnaderbeck, *Org. Lett.* **2000**, *2*, 1761.
- [148] B. M. Trost, H. Yang, G. D. Probst, *J. Am. Chem. Soc.* **2004**, *126*, 48.
- [149] F. Lopez, L. Castedo, J. L. Mascarenas, *J. Am. Chem. Soc.* **2002**, *124*, 4218.
- [150] B. M. Trost, T. J. J. Muller, *J. Am. Chem. Soc.* **1994**, *116*, 4985.
- [151] B. M. Trost, T. J. J. Muller, J. Martinez, *J. Am. Chem. Soc.* **1995**, *117*, 1888.
- [152] B. M. Trost, T. L. Calkins, C. G. Bochet, *Angew. Chem.* **1997**, *109*, 2749; *Angew. Chem. Int. Ed. Engl.* **1997**, *36*, 2632.
- [153] B. M. Trost, T. L. Calkins, *Tetrahedron Lett.* **1995**, *36*, 6021.
- [154] B. M. Trost, Z. P. Shi, *J. Am. Chem. Soc.* **1994**, *116*, 7459.
- [155] B. M. Trost, G. J. Roth, *Org. Lett.* **1999**, *1*, 67.
- [156] F. D. Toste, PhD thesis, Stanford University, Stanford, **2001**.
- [157] B. M. Trost, F. D. Toste, *Tetrahedron Lett.* **1999**, *40*, 7739.
- [158] B. C. Ranu, A. Majee, *Chem. Commun.* **1997**, 1225.
- [159] S. Araki, A. Imai, K. Shimizu, M. Yamada, A. Mori, Y. Butsugan, *J. Org. Chem.* **1995**, *60*, 1841.
- [160] M. M. Salter, S. Sardo-Inffiri, *Synlett* **2002**, 2068.
- [161] E. Klaps, W. Schmid, *J. Org. Chem.* **1999**, *64*, 7537.
- [162] N. Asao, J. X. Liu, T. Sudoh, Y. Yamamoto, *J. Org. Chem.* **1996**, *61*, 4568.
- [163] N. Asao, E. Yoshikawa, Y. Yamamoto, *J. Org. Chem.* **1996**, *61*, 4874.
- [164] N. Asao, Y. Matsukawa, Y. Yamamoto, *Chem. Commun.* **1996**, 1513.
- [165] A. N. Thadani, V. H. Rawal, *Org. Lett.* **2002**, *4*, 4317.
- [166] S. Derien, P. H. Dixneuf, *J. Chem. Soc. Chem. Commun.* **1994**, 2551.
- [167] S. Derien, L. Ropartz, J. Le Pailh, P. H. Dixneuf, *J. Org. Chem.* **1999**, *64*, 3524.
- [168] B. M. Trost, J. P. Surivet, F. D. Toste, *J. Am. Chem. Soc.* **2001**, *123*, 2897.
- [169] B. M. Trost, J. P. Surivet, *Angew. Chem.* **2001**, *113*, 1516; *Angew. Chem. Int. Ed.* **2001**, *40*, 1468.
- [170] H. Doucet, B. Martin-Vaca, C. Bruneau, P. H. Dixneuf, *J. Org. Chem.* **1995**, *60*, 7247.
- [171] B. M. Trost, M. Portnoy, H. Kurihara, *J. Am. Chem. Soc.* **1997**, *119*, 836.
- [172] B. M. Trost, A. B. Pinkerton, *J. Am. Chem. Soc.* **1999**, *121*, 1988.
- [173] B. M. Trost, A. B. Pinkerton, *J. Am. Chem. Soc.* **2002**, *124*, 7376.
- [174] L. Luo, C. Li, M. E. Cucullu, S. P. Nolan, *Organometallics* **1995**, *14*, 1333.
- [175] F. A. Carey, R. J. Sunberg, *Advanced Organic Chemistry, Part B, 3rd ed.*, Plenum, New York, **1990**.
- [176] B. M. Trost, A. B. Pinkerton, *Angew. Chem.* **2000**, *112*, 368; *Angew. Chem. Int. Ed.* **2000**, *39*, 360.
- [177] B. M. Trost, A. B. Pinkerton, *J. Org. Chem.* **2001**, *66*, 7714.
- [178] B. M. Trost, A. B. Pinkerton, *Org. Lett.* **2000**, *2*, 1601.
- [179] B. M. Trost, A. B. Pinkerton, *J. Am. Chem. Soc.* **2000**, *122*, 8081.
- [180] M. Picquet, C. Bruneau, P. H. Dixneuf, *Tetrahedron* **1999**, *55*, 3937.
- [181] S. Chang, Y. Na, E. Choi, S. Kim, *Org. Lett.* **2001**, *3*, 2089.
- [182] H. Kikuchi, M. Uno, S. Takahashi, *Chem. Lett.* **1997**, 1273.
- [183] R. H. Grubbs, S. Chang, *Tetrahedron* **1998**, *54*, 4413.
- [184] A. Furstner, *Alkene Metathesis on Organic Synthesis*, Springer, New York, **1998**.
- [185] S. T. Diver, A. J. Giessert, *Chem. Rev.* **2004**, *104*, 1317.
- [186] P. Cao, B. Wang, X. M. Zhang, *J. Am. Chem. Soc.* **2000**, *122*, 6490.
- [187] K. M. Brummond, H. F. Chen, P. Sill, L. F. You, *J. Am. Chem. Soc.* **2002**, *124*, 15186.
- [188] N. Chatani, H. Inoue, T. Morimoto, T. Muto, S. Murai, *J. Org. Chem.* **2001**, *66*, 4433.
- [189] S. J. Sturla, N. M. Kablaoui, S. L. Buchwald, *J. Am. Chem. Soc.* **1999**, *121*, 1976.
- [190] J. Le Pailh, D. C. Rodriguez, S. Derien, P. H. Dixneuf, *Synlett* **2000**, 95.
- [191] Y. Yamamoto, Y. Nakagai, N. Ohkoshi, K. Itoh, *J. Am. Chem. Soc.* **2001**, *123*, 6372.
- [192] B. M. Trost, F. D. Toste, *J. Am. Chem. Soc.* **2000**, *122*, 714.
- [193] B. M. Trost, J. P. Surivet, F. D. Toste, *J. Am. Chem. Soc.* **2004**, *126*, 15592.
- [194] A. W. Lei, M. S. He, S. L. Wu, X. M. Zhang, *Angew. Chem.* **2002**, *114*, 3607; *Angew. Chem. Int. Ed.* **2002**, *41*, 3457.
- [195] P. Cao, X. M. Zhang, *Angew. Chem.* **2000**, *112*, 4270; *Angew. Chem. Int. Ed.* **2000**, *39*, 4104.
- [196] B. M. Trost, B. A. Czeskis, *Tetrahedron Lett.* **1994**, *35*, 211.
- [197] A. Goeke, M. Sawamura, R. Kuwano, Y. Ito, *Angew. Chem.* **1996**, *108*, 686; *Angew. Chem. Int. Ed. Engl.* **1996**, *35*, 662.
- [198] M. Hatano, M. Terada, K. Mikami, *Angew. Chem.* **2001**, *113*, 255; *Angew. Chem. Int. Ed.* **2001**, *40*, 249.
- [199] M. Hatano, M. Yamanaka, K. Mikami, *Eur. J. Org. Chem.* **2003**, 2552.
- [200] M. Hatano, K. Mikami, *J. Am. Chem. Soc.* **2003**, *125*, 4704.
- [201] I. J. S. Fairlamb, *Angew. Chem.* **2004**, *116*, 255; *Angew. Chem. Int. Ed.* **2004**, *43*, 1048.
- [202] B. M. Trost, F. D. Toste, *J. Am. Chem. Soc.* **1999**, *121*, 9728.
- [203] B. M. Trost, F. D. Toste, *J. Am. Chem. Soc.* **2002**, *124*, 5025.
- [204] B. M. Trost, R. E. Brown, F. D. Toste, *J. Am. Chem. Soc.* **2000**, *122*, 5877.
- [205] T. Naota, H. Takaya, S. I. Murahashi, *Chem. Rev.* **1998**, *98*, 2599.
- [206] M. Mori, Y. Kozawa, M. Nishida, M. Kanamaru, K. Onozuka, N. Takimoto, *Org. Lett.* **2000**, *2*, 3245.
- [207] N. Chatani, T. Morimoto, T. Muto, S. Murai, *J. Am. Chem. Soc.* **1994**, *116*, 6049.

- [208] N. Chatani, K. Kataoka, S. Murai, N. Furukawa, Y. Seki, *J. Am. Chem. Soc.* **1998**, *120*, 9104.
- [209] T. Kondo, N. Suzuki, T. Okada, T. Mitsudo, *J. Am. Chem. Soc.* **1997**, *119*, 6187.
- [210] N. Chatani, T. Morimoto, Y. Fukumoto, S. Murai, *J. Am. Chem. Soc.* **1998**, *120*, 5335.
- [211] A. K. Dash, M. S. Eisen, *Org. Lett.* **2000**, *2*, 737.
- [212] T. Ohmura, S. Yorozyu, Y. Yamamoto, N. Miyaara, *Organometallics* **2000**, *19*, 365.
- [213] H. Schmitt, H. Singer, *J. Organomet. Chem.* **1978**, *153*, 165.
- [214] J. Le Pailh, S. Derien, P. H. Dixneuf, *Chem. Commun.* **1999**, 1437.
- [215] J. Le Pailh, F. Monnier, S. Derien, P. H. Dixneuf, E. Clot, O. Eisenstein, *J. Am. Chem. Soc.* **2003**, *125*, 11964.
- [216] D. B. Grotjahn, K. P. C. Vollhardt, *J. Am. Chem. Soc.* **1986**, *108*, 2091.
- [217] M. Lautens, W. Klute, W. Tam, *Chem. Rev.* **1996**, *96*, 49.
- [218] N. E. Schore, *Chem. Rev.* **1988**, *88*, 1081.
- [219] S. Saito, Y. Yamamoto, *Chem. Rev.* **2000**, *100*, 2901.
- [220] Y. Yamamoto, R. Ogawa, K. Itoh, *Chem. Commun.* **2000**, 549.
- [221] Y. Yamamoto, J. I. Ishii, H. Nishiyama, K. Itoh, *J. Am. Chem. Soc.* **2004**, *126*, 3712.
- [222] Y. Yamamoto, T. Arakawa, R. Ogawa, K. Itoh, *J. Am. Chem. Soc.* **2003**, *125*, 12143.
- [223] Y. Yamamoto, H. Kitahara, R. Ogawa, K. Itoh, *J. Org. Chem.* **1998**, *63*, 9610.
- [224] J. A. Varela, L. Castedo, C. Saa, *Org. Lett.* **2003**, *5*, 2841.
- [225] J. A. Varela, L. Castedo, C. Saa, *J. Org. Chem.* **2003**, *68*, 8595.
- [226] J. A. Varela, C. Saa, *Chem. Rev.* **2003**, *103*, 3787.
- [227] Y. Yamamoto, S. Okuda, K. Itoh, *Chem. Commun.* **2001**, 1102.
- [228] Y. Yamamoto, R. Ogawa, K. Itoh, *J. Am. Chem. Soc.* **2001**, *123*, 6189.
- [229] Y. Yamamoto, H. Takagishi, K. Itoh, *Org. Lett.* **2001**, *3*, 2117.
- [230] Y. Yamamoto, H. Takagishi, K. Itoh, *J. Am. Chem. Soc.* **2002**, *124*, 28.
- [231] N. Chatani, Y. Fukumoto, T. Ida, S. Murai, *J. Am. Chem. Soc.* **1993**, *115*, 11614.
- [232] R. Stragies, M. Schuster, S. Blechert, *Chem. Commun.* **1999**, 237.
- [233] Y. Yamamoto, H. Takagishi, K. Itoh, *J. Am. Chem. Soc.* **2002**, *124*, 6844.
- [234] B. M. Trost, M. T. Rudd, *J. Am. Chem. Soc.* **2001**, *123*, 8862.
- [235] M. Yoshida, K. Sugimoto, M. Ihara, *Arkivoc* **2003**, *8*, 35.
- [236] J. Le Pailh, S. Derien, C. Bruneau, B. Demerseman, L. Toupet, P. H. Dixneuf, *Angew. Chem.* **2001**, *113*, 2996; *Angew. Chem. Int. Ed.* **2001**, *40*, 2912.
- [237] M. Yoshida, T. Gotou, M. Ihara, *Tetrahedron Lett.* **2003**, *44*, 7151.
- [238] B. M. Trost, M. T. Rudd, *J. Am. Chem. Soc.* **2002**, *124*, 4178.
- [239] B. M. Trost, M. T. Rudd, *Org. Lett.* **2003**, *5*, 1467.
- [240] K. Mauthner, K. M. Soldouzi, K. Mereiter, R. Schmid, K. Kirchner, *Organometallics* **1999**, *18*, 4681.
- [241] B. M. Trost, M. T. Rudd, *J. Am. Chem. Soc.* **2003**, *125*, 11516.
- [242] B. M. Trost, M. T. Rudd, *Org. Lett.* **2003**, *5*, 4599.
- [243] H. F. Schuster, *Allenenes in Organic Synthesis*, Wiley, New York, **1984**.
- [244] T. Makino, K. Itoh, *J. Org. Chem.* **2004**, *69*, 395.
- [245] A. S. K. Hashmi, *Angew. Chem.* **2000**, *112*, 3737; *Angew. Chem. Int. Ed.* **2000**, *39*, 3590.
- [246] R. Zimmer, C. U. Dinesh, E. Nandan, F. A. Khan, *Chem. Rev.* **2000**, *100*, 3067.
- [247] S. Ma, Z. Yu, *Angew. Chem.* **2002**, *114*, 1853; *Angew. Chem. Int. Ed.* **2002**, *41*, 1775.
- [248] S. Ma, W. Gao, *J. Org. Chem.* **2002**, *67*, 6104.
- [249] S. Ma, W. Gao, *J. Org. Chem.* **2003**, *68*, 5943.
- [250] S. Ma, Z. Yu, *Chem. Eur. J.* **2004**, *10*, 2078.
- [251] W. Oppolzer in *Comprehensive Organic Synthesis*, Vol. 5 (Eds.: B. M. Trost, I. Fleming), Pergamon, Oxford, **1991**, p. 315.
- [252] W. R. Roush in *Comprehensive Organic Chemistry*, Vol. 5 (Eds.: B. M. Trost, I. Fleming), Pergamon, Oxford, **1991**, p. 513.
- [253] B. M. Trost, A. B. Pinkerton, *J. Am. Chem. Soc.* **1999**, *121*, 4068.
- [254] B. M. Trost, A. B. Pinkerton, M. Seidel, *J. Am. Chem. Soc.* **2001**, *123*, 12466.
- [255] S. L. Schreiber, *Science* **2000**, *287*, 1964.
- [256] S. L. Schreiber, *Chem. Eng. News* **2003**, *81*, 51.
- [257] R. W. Bates, V. Satcharoen, *Chem. Soc. Rev.* **2002**, *31*, 12.
- [258] S. K. Kang, D. Y. Kim, R. K. Hong, P. S. Ho, *Synth. Commun.* **1996**, *26*, 3225.
- [259] B. M. Trost, A. McClory, A. B. Pinkerton, unpublished results.
- [260] M. Yoshida, K. Sugimoto, M. Ihara, *Tetrahedron Lett.* **2001**, *42*, 3877.
- [261] M. Fujiwara, T. Nishikawa, Y. Hori, *Org. Lett.* **1999**, *1*, 1635.
- [262] P. A. Wender, J. A. Love, T. J. Williams, *Synlett* **2003**, 1295.
- [263] P. A. Wender, T. M. Pedersen, M. J. C. Scanio, *J. Am. Chem. Soc.* **2002**, *124*, 15154.
- [264] P. A. Wender, T. J. Williams, *Angew. Chem.* **2002**, *114*, 4732; *Angew. Chem. Int. Ed.* **2002**, *41*, 4550.
- [265] P. A. Wender, G. G. Gamber, R. D. Hubbard, L. Zhang, *J. Am. Chem. Soc.* **2002**, *124*, 2876.
- [266] P. A. Wender, G. G. Gamber, M. J. C. Scanio, *Angew. Chem.* **2001**, *113*, 4013; *Angew. Chem. Int. Ed.* **2001**, *40*, 3895.
- [267] P. A. Wender, F. C. Bi, M. A. Brodney, F. Gosselin, *Org. Lett.* **2001**, *3*, 2105.
- [268] P. A. Wender, C. M. Barzilay, A. J. Dyckman, *J. Am. Chem. Soc.* **2001**, *123*, 179.
- [269] P. A. Wender, A. G. Correa, Y. Sato, R. Sun, *J. Am. Chem. Soc.* **2000**, *122*, 7815.
- [270] P. A. Wender, L. Zhang, *Org. Lett.* **2000**, *2*, 2323.
- [271] P. A. Wender, A. J. Dyckman, C. O. Husfeld, M. J. C. Scanio, *Org. Lett.* **2000**, *2*, 1609.
- [272] P. A. Wender, A. J. Dyckman, *Org. Lett.* **1999**, *1*, 2089.
- [273] P. A. Wender, M. Fuji, C. O. Husfeld, J. A. Love, *Org. Lett.* **1999**, *1*, 137.
- [274] P. A. Wender, A. J. Dyckman, C. O. Husfeld, D. Kadereit, J. A. Love, H. Rieck, *J. Am. Chem. Soc.* **1999**, *121*, 10442.
- [275] P. A. Wender, F. Glorius, C. O. Husfeld, E. Langkopf, J. A. Love, *J. Am. Chem. Soc.* **1999**, *121*, 5348.
- [276] P. A. Wender, H. Rieck, M. Fuji, *J. Am. Chem. Soc.* **1998**, *120*, 10976.
- [277] P. A. Wender, D. Sperandio, *J. Org. Chem.* **1998**, *63*, 4164.
- [278] P. A. Wender, C. O. Husfeld, E. Langkopf, J. A. Love, N. Pleuss, *Tetrahedron* **1998**, *54*, 7203.
- [279] P. A. Wender, C. O. Husfeld, E. Langkopf, J. A. Love, *J. Am. Chem. Soc.* **1998**, *120*, 1940.
- [280] P. A. Wender, T. E. Smith, *Tetrahedron* **1998**, *54*, 1255.
- [281] P. A. Wender, H. Takahashi, B. Witulski, *J. Am. Chem. Soc.* **1995**, *117*, 4720.
- [282] B. M. Trost, F. D. Toste, H. Shen, *J. Am. Chem. Soc.* **2000**, *122*, 2379.
- [283] B. M. Trost, H. C. Shen, T. Schulz, C. Koradin, H. Schirok, *Org. Lett.* **2003**, *5*, 4149.
- [284] J. Haller, T. Strassner, K. N. Houk, *J. Am. Chem. Soc.* **1997**, *119*, 8031.
- [285] K. N. Houk, S. R. Moses, Y. D. Wu, N. G. Rondan, V. Jäger, R. Schohe, F. R. Fronczek, *J. Am. Chem. Soc.* **1984**, *106*, 3880.
- [286] G. Stork, M. Kahn, *Tetrahedron Lett.* **1983**, *24*, 3951.
- [287] B. M. Trost, H. C. Shen, *Org. Lett.* **2000**, *2*, 2523.
- [288] B. M. Trost, H. C. Shen, *Angew. Chem.* **2001**, *113*, 2375; *Angew. Chem. Int. Ed.* **2001**, *40*, 2313.



Lysine-capped gold nanoparticles can be electrostatically assembled on the surface of *Bacillus cerius*, a Gram-Positive bacterium. The conductivity of the “gold-plated” bacteria assembly immobilized between electrodes is a function of the humidity experienced by the nanoparticles. For more details on this bioelectronic device, see the Communication by R. F. Saraf and V. Berry on the following pages.

Self-Assembly of Nanoparticles on Live Bacterium: An Avenue to Fabricate Electronic Devices**

Vikas Berry and Ravi F. Saraf*

Recently, hybrid structures of microorganisms with inorganic nanoscale moieties have received great interest owing to their potential in fabricating electronic systems. The electronic properties of metal nanoparticles, as a result of the single-electron transport of current,^[1] make them ideal materials for nanodevices. Concomitantly, the nanostructure of microorganisms such as bacteria,^[2] viruses,^[3,4] and yeast^[5] are attractive scaffolds for the templating of metal nanoparticles through the interactions of the former with surface charges and the affinity of certain metals for specific biological molecules.^[2–7] However, the key challenges in building hybrid devices are 1) to pattern nanostructures without destroying the biological construct of the microorganism and 2) to achieve active integration of a biological response to the electrical transport in a nanoparticle device.

Herein, we present a simple method to build hybrid devices that use the biological response of a microorganism to control the electrical properties of the system. In our design, a monolayer of gold nanoparticles is deposited on the peptidoglycan membrane of a live Gram-positive bacterium. The hydrophilic peptidoglycan membrane is then actuated by humidity to modulate the width of the electron-tunneling barrier between the metal nanoparticles. A decrease in interparticle separation by less than 0.2 nm (decrease in humidity from 20 to $\approx 0\%$) causes more than a 40-fold increase in tunneling current. Vapor sensors based on the increase in resistance due to separation of Au nanoparticles have been reported in three-dimensional (3D) clusters of Au nanoparticle/organic composite films.^[8–10] In the present study, the coupling between the large expansion of an underlying hygroscopic bacterium membrane and the monolayer of Au particles is key to achieving a larger change in current, by an order of magnitude, relative to the above-mentioned 3D nanocomposite devices, for which the change in current results from the swelling of an interparticle organic

phase. The method shown herein could be used to pattern various nanoscale inorganic materials, whose optical, electrical, and magnetic properties could be biologically controlled, and thereby lead to an important advance in the present technology.

Electrically percolating clusters of metal nanoparticles, in contrast to their microparticle cousins, are fundamentally different in terms of electrical properties as a result of the nature of interparticle electron transport.^[1] On the nanoscale, the energy cost to insert a single electron in a nanoparticle is over 1–10 times greater than the thermal energy, and the flow of the interparticle current takes place through the transport of single electrons, as explicitly shown by transport studies on single nanoparticles,^[11,12] their 2D and 3D assemblies,^[13–16] and single-nanoparticle devices (such as single-electron transistors^[17,18]). The above studies demonstrate that a percolating cluster of metal nanoparticles is a viable unit to fabricate single-electron devices, whereby micron-scale clusters allow an easy-to-fabricate, robust interconnection network for the nanodevice system. Because metal nanoparticles such as gold are stabilized in solution by electrostatic repulsion, the formation of a percolating cluster on physical substrates requires either an organic cross-linker to bind the particles^[13,19] or a polyelectrolyte to shield the charge of the particles.^[16,20] For biological substrates, the highly selective deposition of nanoparticles relies on either highly specific binding (such as DNA hybridization^[21–23] or biotin–streptavidin interactions^[24]) or strong specific intermolecular interaction (such as electrostatic interactions^[25–27]).

Bacillus cereus, a Gram-positive bacterium, was deposited by using a previously described technique on a silicon substrate with a layer of 500 nm of thermally grown silica and gold electrode lines spaced 7 ± 0.2 microns apart and coated with poly(L-lysine) (average molecular weight 164 kDa).^[2] In a typical deposition process, the bacteria were cultured in nutrient broth (Difco) in a shake flask for approximately 14 h at 30 °C. The bacteria were subsequently filtered and centrifuged to extract similar sized cells that were around 4–6 μm in length and 0.8–1.0 μm in diameter. The bacteria were suspended again in sterile water and were deposited on the poly(L-lysine)-coated substrate. On the substrate, there are 20 sets of electrodes. The deposition time of the bacteria was approximately 10–15 min to form bridges spanning the Au electrodes. Usually, about 10 bridges were formed along the 10-mm-long Au electrode pair. The extracellular polymeric substances (EPS) on the bacteria (and around the bacterium) were removed by washing with 2N NaOH for 1 min. The bacteria-deposited chip was then immediately immersed in a solution of poly(L-lysine)-coated gold nanoparticles (of diameter $d = 30$ nm).^[2] Highly controlled deposition of nanoparticles was achieved by regulating the deposition time in the solution of gold nanoparticles (see Figure 1 a–e). As the Au nanoparticles and the substrate are both positively charged, the deposition is highly selective with formation of the monolayer only on the negatively charged bacteria surface. However, a simple negative surface charge is not sufficient to obtain electrically percolating deposition. Figure 1 f shows the result of deposition of Au nanoparticles on a negatively charged physical surface prepared by

[*] V. Berry, Prof. R. F. Saraf
Department of Chemical Engineering
University of Nebraska
Lincoln, NE 68588 (USA)
Fax: (+1) 402-472-6989
E-mail: rsaraf@unlnotes.unl.edu

[**] R.F.S. thanks the Optical Science and Engineering Research Center, Virginia Tech, and the ONR for financial support. We thank Dr. Inan at the University of Nebraska for his help in identifying the assay to determine the fate of the bacteria at various stages of the device fabrication. We thank Dr. Adenwalla at the University of Nebraska for allowing us access to a low-temperature I – V measurement system.

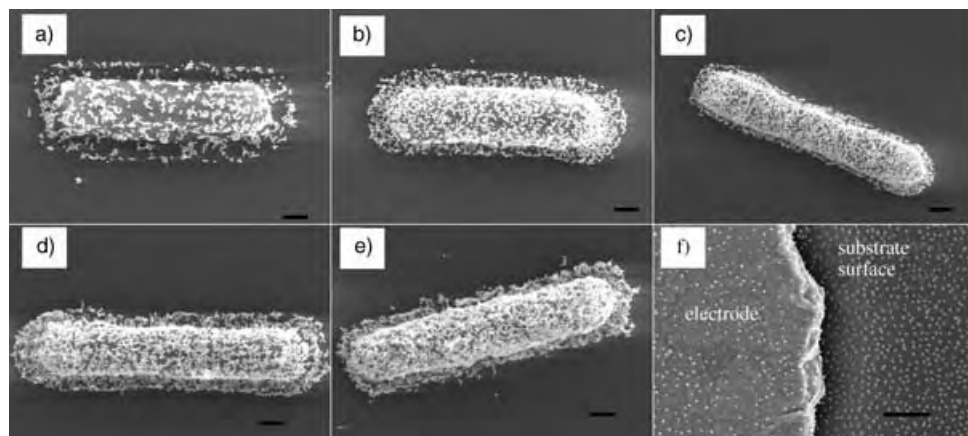


Figure 1. Scanning electron microscopy (SEM) images reveal the highly controlled and selective deposition on bacteria of poly(L-lysine)-coated 30-nm Au nanoparticles from a solution at pH 7 over a) 30 min, b) 1 h, c) 2 h, d) 4 h, and e) 8 h. f) Positively charged Au nanoparticles are deposited on a negatively charged PSS-coated lysine/SiO₂/Si substrate over 16 h. The Au nanoparticles percolate after deposition during 4 h on the bacteria, while no conduction is observed for the physical surface in (f). The small amount of multilayer formation with a long deposition time is due to contraction of the membrane through loss of water in the scanning electron microscope. Scale bar: 300 nm.

adsorbing a monolayer of poly(sulfonated styrene) (PSS; 70 kDa with < 90 % sulfonation) on the poly(L-lysine)-coated SiO₂/Si substrate. For maximal deposition, poly(L-lysine) and PSS were introduced at pH values of around 4 and 8.5, respectively, and 1 mM NaCl was added to the suspension of the nanoparticles at pH 7. However, the 2D packing density was found to be low and nonpercolating. X-ray reflectivity measurements showed that in the multilayer films of polyelectrolytes (in our case, PSS on poly(L-lysine)) the polymers are layered and their conformations are flat with no significant loops caused by multiple-point binding.^[28] As a result, the mobility of the polymer is highly restricted. On the other hand, the polyelectrolyte on the bacterium surface, that is, teichoic acid (-OCH₂CH(OCH₃)CH₂OPO₂-), is a flexible “brush” that is tethered to the peptidoglycan surface at one end which leaves the remainder of the chain in high thermal motion (i.e. high mobility). Furthermore, because the brush contour length is typically around 18 nm,^[29] it is reasonable to expect that the negatively charged teichoic acid molecule with its high mobility and chain flexibility may wrap over the positively charged Au nanoparticle up to a maximum possible subtended angle of 135° from the point of contact to minimize the free energy. A similar screening of charge by PSS would be difficult in the case of the PSS–poly(L-lysine) structure owing to restricted mobility. Specific attachment of a concanavalin–fluorescein isothiocyanate dye conjugate to teichoic acid^[30] followed by confocal microscopy confirmed the uniform distribution of the acid molecules on the bacterium. As no deposition of nanoparticles on the bacterium occurs subsequent to the neutralization of teichoic acid after attach-

ment with concanavalin, the role of the acid in high-density deposition is justified.

A standard assay of PI/SYTO 9 dye was used to confirm the fate of the bacteria.^[31] The green fluorescence in Figure 2 confirms that the bacteria survived the complete fabrication process of the device. As the integrity of the peptidoglycan surface membrane in which the teichoic acid molecular brush is imbedded is critical for the deposition of Au nanoparticles, the survival of the bacteria for the fabrication of the device is important: Any lysis of the bacteria (or release of EPS and/or internal bacterial fluids) will lead to ill-formed, nonfunctional devices.

The insets of Figure 3 show a typical bacterial bridge, coated with a monolayer of gold nanoparticles, con-



Figure 2. The standard PI/SYTO 9 assay in combination with confocal microscopy is used to probe the survival of the bacteria at various stages of the fabrication process: a) immediately after immobilization from the nutrient broth on the substrate; b) after deposition of the gold nanoparticles over 4 h; and c) after subjecting to 10⁻⁵ Torr vacuum for 2 h. The green and red fluorescence indicate that the bacteria are alive and dead, respectively.

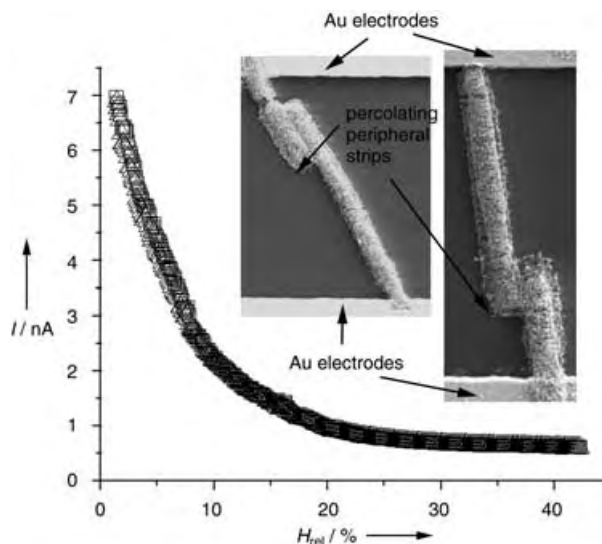


Figure 3. Typical device current (I , normalized per bridge) as a function of relative humidity (H_{rel}) for “up” (i.e. decreasing humidity; Δ) and “down” cycles (i.e. increasing humidity; \square) at a bias voltage of 10 V. The inset shows SEM images of two typical bacterial bridges which span the electrodes. The peripheral strip is a (percolating) monolayer of deposited gold nanoparticles.

nected to the gold electrodes. One bridge constitutes a device. All the currents reported subsequently were measured at 22°C and were normalized according to the number of bridges between the electrodes. Figure 3 depicts the normalized current, I , between the bridges as a function of the relative humidity, H_{rel} . The deposition of the Au nanoparticles was optimized for 4 h (see Figure 1) to obtain the largest change in current due to humidity. Figure 3 indicates that the device behavior is reversible and stable over a slow run, measured over approximately 40 min per cycle. Because of the complete reversibility of the device, it is unlikely that the water inside the bacteria plays any significant role. In contrast to most impedance-based microelectronic humidity probes,^[32] the resistance of this device decreases as humidity increases. The largest change in current, and hence the highest sensitivity, was observed for the low humidity region of $H_{\text{rel}} < 20\%$.

The simple model shown in Figure 4 explains the observation in Figure 3. As the humidity increases, the peptidoglycan membrane absorbs water. If it is assumed that there is no

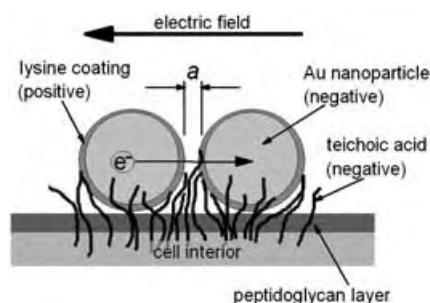


Figure 4. Schematic showing two poly(L-lysine)-coated Au nanoparticles clutched by negatively charged teichoic acid molecules. The distance between the surfaces of the Au nanoparticles is given by a . The electron transport from left to right takes place across a mixture of organics (lysine, teichoic acid) and air. The role of the electric-field-inducing electron transport is discussed in Figures 3 and 5.

excess volume of absorbed water, the volume fraction of water absorbed is fH_{rel} , in which f is Henry's constant. If it is also assumed that there is affine swelling of the peptidoglycan membrane, the linear extension of the membrane due to absorption is $(1-fH_{\text{rel}})^{-1/3}$. As the nanoparticles are fixed on the membrane, the interparticle separation is given by $a/a_0 = (1-fH_{\text{rel}})^{-1/3}$, where a_0 is the separation at $H_{\text{rel}} = 0$. Also, as electron tunneling is the primary transport mechanism, the current is given by the Fowler–Nordheim equation [Eq. (1)],^[33] where $K = (32\pi^2 m_e \varphi / h^2)^{0.5}$ (h is Planck's constant, m_e is the mass of an electron at rest, and φ is the barrier height at the nanoparticle/organic interface), R_B is the resistance to the leakage current from the peripheral as shown in Figure 3, R_0 is a normalization constant proportional to the resistance of the device at $H_{\text{rel}} = 0$, and V is the bias across the device (i.e. the bacteria bridge).

$$I = \left\{ \frac{V}{R_0} \exp \left[-\frac{K a_0}{\sqrt[3]{(1-f H_{\text{rel}})}} \right] + \frac{V}{R_B} \right\} \quad (1)$$

We assume that the peripheral strip that leads to finite R_B is due to deposition of proteinaceous substances secreted by the bacterium (probably for adhesion to the substrate). To study the effect of water absorption by poly(L-lysine) on the performance of the device after the fabrication of the device, we capped the amine groups of poly(L-lysine) with glutaraldehyde to decrease the water uptake by lysine. No significant change in the performance of the device was observed which indicates that the role of moisture absorption by poly(L-lysine) on the performance is negligible.

Figure 5a shows the fit of the experimental results to Equation (1) for the same device at different bias V . Each exposure to humidity lasted approximately 40 min, and the lapse between consecutive runs was about 1 h on average. Although Equation (1) requires four fitting parameters, the validity of the model is justified because they are reasonably constant over all the biasing voltages (see Figure 5b). The constant R_B implies ohmic behavior (independent of H_{rel}) for leakage current given by $I_B = V/R_B$. This is reasonable because on the peripheral region, the nanoparticles are not located on the peptidoglycan membrane but adsorbed onto proteinaceous corona of the bacteria that do not change significantly in the lateral dimension with humidity. As the contact resistance is not expected to be large^[2] and is a strong function of humidity, it is included in R_B . We also note that because the current through a bacteria bridge that lacks deposited gold nanoparticles is insignificant, ionic currents can be neglected.

Figure 5c shows the corrected current, $I - I_B$, which flows through the nanoparticle monolayer as a function of the change in the interparticle separation (estimated from f). Interestingly, for a humidity change from 20 to 0%, which corresponds to a calculated decrease of only 7% in the interparticle distance, the corrected current increases over 40-fold. As the corresponding increase in the total current I is only about sevenfold (see Figure 5a), a decrease in peripheral deposition will improve the device sensitivity significantly. The high sensitivity to subtle changes in the interparticle distance is attributed to transport by single-electron tunneling through the percolation network because the charging energy $e^2/(2\pi\epsilon\epsilon_0 d)$ (ϵ is the dielectric constant of the organic coating and is approximately 3; e is the electron charge) approximates to $1.5 k T$. Using the model parameters and a tunneling barrier of 5.1 eV (i.e. a is much larger than the thickness of the coating of poly(L-lysine) shown in Figure 4 at the metal–poly(L-lysine)/air/metal–poly(L-lysine) junction), the nanoparticle separation at 0% humidity was determined as about 2.3 nm, which implies an absolute change (for the 0–20% humidity range) of less than 0.2 nm. We note that the sensitivity is significantly lower for devices fabricated with deposition times of greater than 8 h and that ohmic I – V behavior is observed^[2] in contrast to the non-ohmic behavior observed for devices prepared with deposition times of 4 h (see Figure 5d). At the other extreme, for a deposition time of 2 h the interparticle distance in the contiguous clusters is too large for a significant tunneling current to be observed. Thus, a combination of the exponential dependence on a and that $a \approx 2.3$ nm explains the high sensitivity of the system. Furthermore, in contrast to the earlier reports on gold nanoparticle/

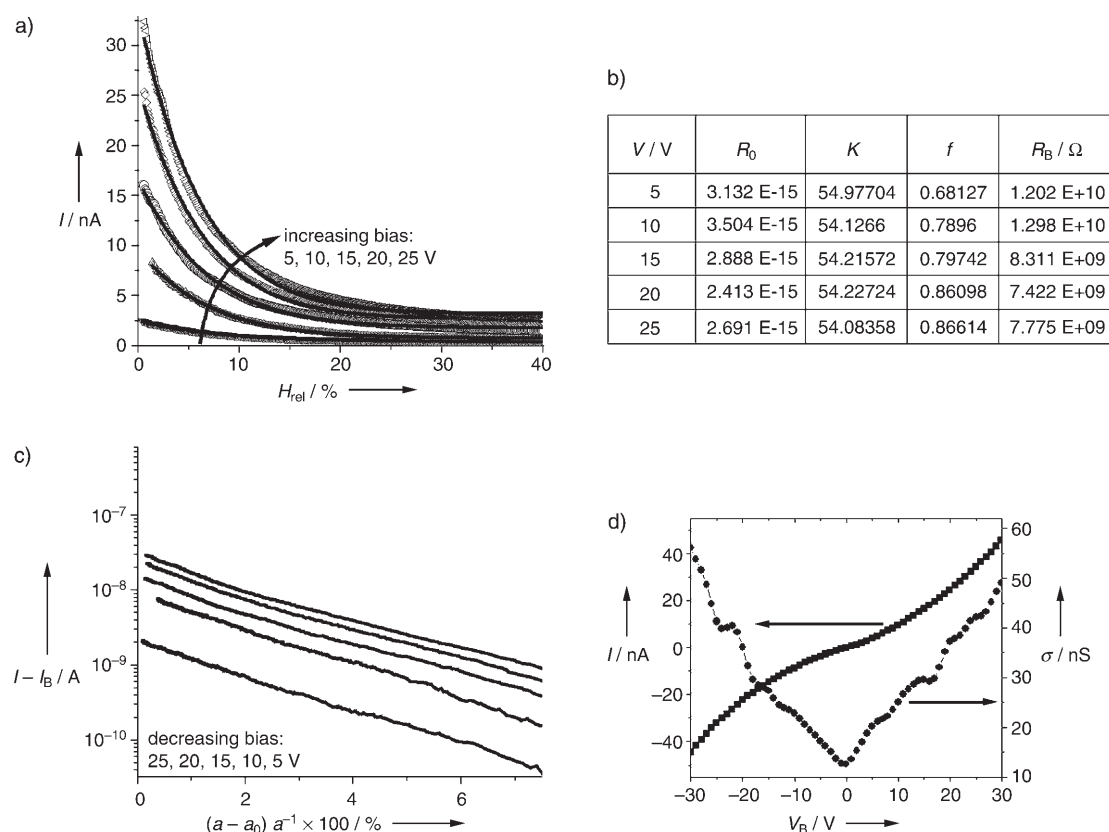


Figure 5. The validity of model and peptidoglycan actuation. a) A comparison of theoretical values (according to Equation (1); solid lines) and experimental observations (data points) for the current I as a function of the relative humidity (H_{rel}) at various bias voltages for the same device. b) The four fitting parameters, K , f , T_0 , and R_B . c) The corrected current, $I - I_B$ (after subtraction of the calculated leakage current, I_B) as a function of the calculated percentage change in the interparticle distance, a , due to humidity-induced dimensional changes in the peptidoglycan membrane. Consistent with the model given by [Eq. (1)], the straight line for all bias voltages in the semi log plot indicates an exponential dependence of a . d) The non-ohmic I - V characteristics and differential conductance σ of the device at 2% humidity. ■: current; ●: differential conductance.

organic composite thin-film sensors^[8–10] in which electron transport takes place by thermionic emission or activated tunneling, electron transport in our device takes place through tunneling because the activation energy for tunneling is approximately 1.7 meV (see Figure 6), which is much lower

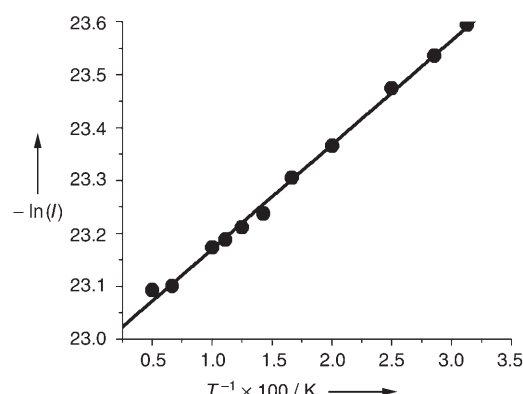


Figure 6. Temperature dependence of the device current at 0% humidity shown by a plot of the negative natural logarithm of the current I at an applied bias of 0.1 V. $I = 1.05 \times 10^{-10} \exp(-E_a/kT)$, with an activation energy $E_a = 1.71$ meV.

than the thermal energy of a free electron ($kT \approx 25$ meV) at room temperature.

In summary, we have illustrated an approach to fabricate an active hybrid bioelectronic device using physical nanomaterials and a live microorganism. The electrical properties of a monolayer of gold nanoparticles is controlled by actuating the peptidoglycan layer of the bacterium. An actuation of less than 8% in the peptidoglycan membrane, induced by a change in humidity from 20 to 0%, leads to more than a 40-fold increase in the tunneling current. These results open up an avenue to obtain active coupling between microorganisms and electrical, optical, and/or magnetic nanodevices. We believe that such hybrids will be the key to conceptually new electronic devices that can be integrated with microorganisms on flexible plasticlike substrates by using simple chemistry.

Received: May 18, 2005

Revised: July 27, 2005

Keywords: electrochemistry · gold · monolayers · nanostructures · self-assembly

- [1] B. Su, V. J. Goldman, J. E. Cunningham, *Science* **1992**, 255, 313–315.
- [2] V. Berry, S. Rangaswamy, R. F. Saraf, *Nano Lett.* **2004**, 4, 939–942.
- [3] E. Dujardin, C. Peet, G. Stubbs, J. N. Culver, S. Mann, *Nano Lett.* **2003**, 3, 413–417.
- [4] C. E. Fowler, W. Shenton, G. Stubbs, S. Mann, *Adv. Mater.* **2001**, 13, 1266–1269.
- [5] M. Kowshik, S. Ashtaputre, S. Kharrazi, W. Vogel, J. Urban, S. K. Kulkarni, K. M. Paknikar, *Nanotechnology* **2003**, 14, 95–100.
- [6] Z. Li, S. W. Chung, J. M. Nam, D. S. Ginger, C. A. Mirkin, *Angew. Chem.* **2003**, 115, 2408–2411; *Angew. Chem. Int. Ed.* **2003**, 42, 2306–2309.
- [7] N. L. Rosi, C. S. Thaxton, C. A. Mirkin, *Angew. Chem.* **2004**, 116, 5616–5619; *Angew. Chem. Int. Ed.* **2004**, 43, 5500–5503.
- [8] N. Krasteva, I. Besnard, B. Guse, R. E. Bauer, K. Mullen, A. Yasuda, T. Vossmeier, *Nano Lett.* **2002**, 2, 551–555.
- [9] H. Wohltjen, A. W. Snow, *Anal. Chem.* **1998**, 70, 2856–2859.
- [10] F. P. Zamborini, M. C. Leopold, J. F. Hicks, P. J. Kulesza, M. A. Malik, R. W. Murray, *J. Am. Chem. Soc.* **2002**, 124, 8958–8964.
- [11] M. F. Crommie, C. P. Lutz, D. M. Eigler, *Science* **1993**, 262, 218–220.
- [12] H. Ohnishi, Y. Kondo, K. Takayanagi, *Nature* **1998**, 395, 780–783.
- [13] R. P. Andres, J. D. Bielefeld, J. I. Henderson, D. B. Janes, V. R. Kolagunta, C. P. Kubiak, W. J. Mahoney, R. G. Osifchin, *Science* **1996**, 273, 1690–1693.
- [14] H. Imamura, J. Chiba, S. Mitani, K. Takanashi, S. Takahashi, S. Maekawa, H. Fujimori, *Phys. Rev. B* **2000**, 61, 46–49.
- [15] A. A. Middleton, N. S. Wingreen, *Phys. Rev. Lett.* **1993**, 71, 3198–3201.
- [16] P. E. Trudeau, A. Escorcia, A. A. Dhirani, *J. Chem. Phys.* **2003**, 119, 5267–5273.
- [17] T. Sato, H. Ahmed, D. Brown, B. F. G. Johnson, *J. Appl. Phys.* **1997**, 82, 696–701.
- [18] C. Thelander, M. H. Magnusson, K. Deppert, L. Samuelson, P. R. Poulsen, J. Nygard, J. Borggreen, *Appl. Phys. Lett.* **2001**, 79, 2106–2108.
- [19] M. Brust, D. Bethell, D. J. Schiffrin, C. J. Kiely, *Adv. Mater.* **1995**, 7, 795.
- [20] A. Rosidian, Y. J. Liu, R. O. Claus, *Adv. Mater.* **1998**, 10, 1087.
- [21] E. Braun, Y. Eichen, U. Sivan, G. Ben-Yoseph, *Nature* **1998**, 391, 775–778.
- [22] J. D. Le, Y. Pinto, N. C. Seeman, K. Musier-Forsyth, T. A. Taton, R. A. Kiehl, *Nano Lett.* **2004**, 4, 2343–2347.
- [23] Y. Maeda, H. Tabata, T. Kawai, *Appl. Phys. Lett.* **2001**, 79, 1181–1183.
- [24] H. Y. Li, S. H. Park, J. H. Reif, T. H. LaBean, H. Yan, *J. Am. Chem. Soc.* **2004**, 126, 418–419.
- [25] A. Kumar, M. Pattarkine, M. Bhadbhade, A. B. Mandale, K. N. Ganesh, S. S. Datar, C. V. Dharmadhikari, M. Sastry, *Adv. Mater.* **2001**, 13, 341–344.
- [26] H. Nakao, H. Shiigi, Y. Yamamoto, S. Tokonami, T. Nagaoka, S. Sugiyama, T. Ohtani, *Nano Lett.* **2003**, 3, 1391–1394.
- [27] M. G. Warner, J. E. Hutchison, *Nat. Mater.* **2003**, 2, 272–277.
- [28] G. Decher, *Science* **1997**, 277, 1232–1237.
- [29] W. Fischer, S. Markwitz, H. Labischinski, *Eur. J. Biochem.* **1997**, 244, 913–917.
- [30] R. J. Doyle, M. L. McDannel, J. R. Helman, U. N. Streips, *J. Bacteriol.* **1975**, 122, 152–158.
- [31] M. Virta, S. Lineri, P. Kankaanpää, M. Karp, K. Peltonen, J. Nuutila, E. M. Lilius, *Appl. Environ. Microbiol.* **1998**, 64, 515–519.
- [32] E. Traversa, *Sens. Actuators B* **1995**, 23, 135–156.
- [33] S. O. Kasap, *Principals of Electrical Engineering Materials and Devices*, McGraw-Hill, New York **1997**, pp. 284–287.

DOI: 10.1002/anie.200502309

[Co₂(ppca)₂(H₂O)(V₄O₁₂)_{0.5}]: A Framework Material Exhibiting Reversible Shrinkage and Expansion through a Single-Crystal-to-Single-Crystal Transformation Involving a Change in the Cobalt Coordination Environment**

Chun-Long Chen, Andrea M. Goforth, Mark D. Smith, Cheng-Yong Su, and Hans-Conrad zur Loye*

It is well known that many materials undergo structural phase transitions as a function of temperature, and that different atomic arrangements are stable in different temperature ranges. Although some of these phase transitions are irreversible, the original structure generally re-forms readily upon returning to the initial temperature. This process is fundamentally different from that observed for a small and rather unique category of organic–inorganic framework materials that exhibit so-called “dynamic structural changes”.^[1] In these materials, temperature changes lead to the reversible removal of guest molecules which is often accompanied by large atomic motion and significant changes in the framework structures.^[1b,c] Importantly, the original framework structure is not restored by a temperature change, but rather by the reabsorption of the guest molecules.^[2] As structural changes upon loss of guest-molecules are typically induced by heating of a porous three-dimensional framework, significant thermal stability, both in the presence and absence of guest molecules, is a necessity.

Dynamic structural changes induced by the removal/reabsorption of guest molecules are rare, and even less common are those structural changes that are caused by the removal/addition of ligands from the framework itself. Such changes in metal coordination environment can lead to changes in physical properties, for example, color, and could potentially lead to their use in sensing devices.^[1,2]

Herein, we describe the synthesis and structural characterization of a new, mixed-metal 3D porous coordination polymer: $[[[Co_2(ppca)_2(H_2O)(V_4O_{12})_{0.5}] \cdot 3.62 H_2O]_n]$ (1, ppca = 4-(pyridin-4-yl)pyridine-2-carboxylic acid; Scheme 1),

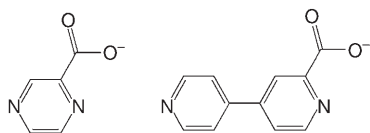
[*] C.-L. Chen, A. M. Goforth, Dr. M. D. Smith, Prof. Dr. H.-C. zur Loye
Department of Chemistry and Biochemistry
University of South Carolina
Columbia, SC 29208 (USA)
Fax: (+1) 803-777-8508
E-mail: zurloye@mail.chem.sc.edu

C.-L. Chen, Prof. Dr. C.-Y. Su
School of Chemistry and Chemical Engineering
Sun Yat-Sen University
Guangzhou 510275 (China)

[**] Financial support was provided by the National Science Foundation through Grant CHE:0314164 and by the NNSF of China (No. 20303027). ppca = 4-(pyridin-4-yl)pyridine-2-carboxylic acid.



Supporting information for this article is available on the WWW under <http://www.angewandte.org> or from the author.



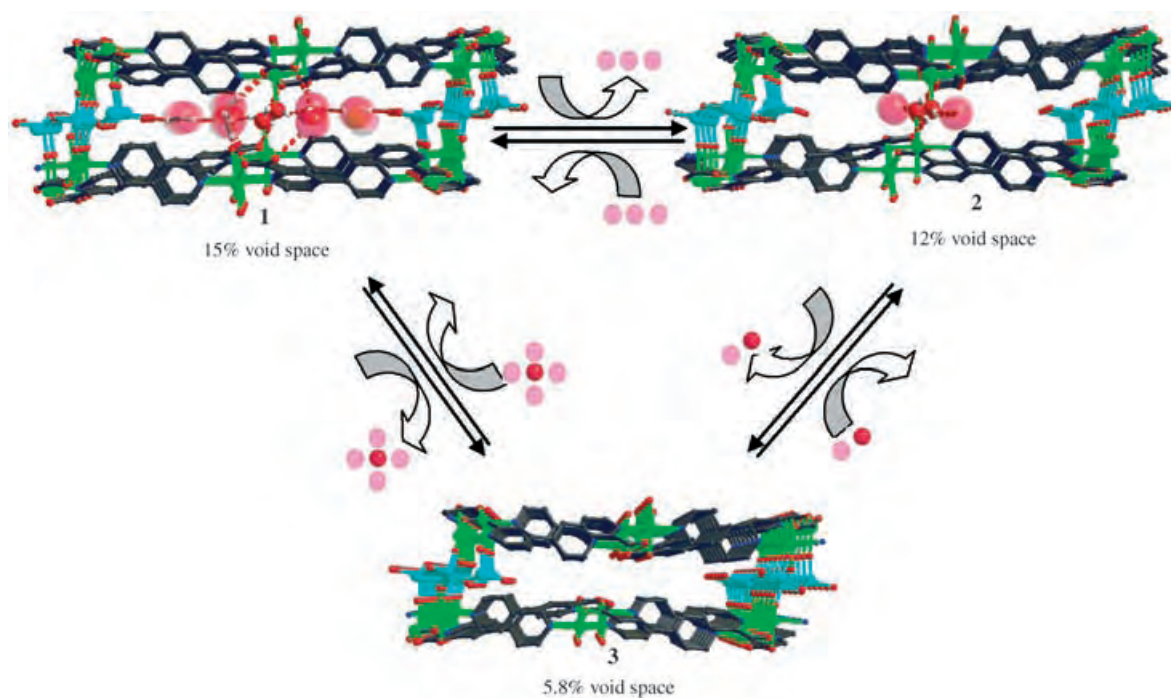
Scheme 1. Structure of 2-pyrazinecarboxylate (left) and the much longer 4-(pyridin-4-yl)pyridine-2-carboxylic acid (ppca) (right).

which undergoes two distinct, reversible single-crystal-to-single-crystal transformations (Scheme 2). The first involves a volume change owing to the reversible removal of guest solvent molecules from the pores of the framework, where shrinkage occurs upon dehydration and reexpansion occurs upon reintroduction of the guests. The second process involves an unusual change in the coordination number of the cobalt center, from 6 (octahedral) to 5 (trigonal bipyramidal), with a concomitant color change.

Our group has previously explored heterometallic coordination polymers with the pyrazinecarboxylate ligand,^[3] (Scheme 1) as the simultaneous presence of two different metals can give rise to increased structural diversity and, potentially, to unusual physical properties resulting from the synergistic interaction of two different metal centers.^[4] The pyrazinecarboxylate ligand and its substituted derivatives have proven to be extremely versatile for the construction of mixed-metal framework structures because of their ability to engage in several different coordination modes.^[3,5] In framework structures synthesized from pyrazinecarboxylate-based ligands, however, the cavity dimensions are limited by the length of the pyrazine ring. Consequently, to increase the cavity dimensions, we recently synthesized a new ligand, 4-(pyridin-4-yl)pyridine-2-carboxylic acid (Hppca) (Scheme 1),^[6] which is significantly longer than the pyrazine-

carboxylate ligand, but maintains the same number, type, and arrangement of Lewis basic sites. Molecular modeling showed that the terminal N–N separation is about 7.10 Å in Hppca in contrast to 2.75 Å in pyrazinecarboxylate-based ligands. This extension of pyrazinecarboxylate chemistry allows the synthesis of frameworks with larger cavities than those observed in the pyrazinecarboxylate-based framework structures. Consequently, we are exploring the use of this ligand in the preparation of new mixed-metal systems, and herein we report an interesting new framework structure in which cobalt atoms are linked into a 2D array by ppca and cross-linked into a 3D array by vanadium-oxo units. It is well known that vanadium oxide groups are often engaged in the cross-linking of structural components and that they can promote the formation of unique structural geometries.^[7] Whereas the coordination modes of the cobalt and the vanadium in this structure are fairly typical for these elements, surprising is the observation of dynamic structural changes that take place upon the thermal removal of both noncoordinated and coordinated water molecules, the process of which is highlighted herein.

The hydrothermal reaction of Hppca, $\text{Co}(\text{NO}_3)_2 \cdot 6\text{H}_2\text{O}$, and NH_4VO_3 in a 1:1:1 ratio at 160 °C for 48 h yielded small, red, block-shaped crystals of the title compound. Structural analysis of **1** by single-crystal X-ray diffraction revealed that the vanadium centers are part of 1D mixed-metal chains, in which $\{\text{V}_4\text{O}_{12}\}$ cyclic units bridge neighboring 2D Co/ppca metal–organic layers to form a 3D open framework. The structure contains two crystallographically independent cobalt atoms, Co1 and Co2, which are both found in pseudooctahedral coordination environments. Co1 is coordinated to two oxygen atoms from two different $\{\text{V}_4\text{O}_{12}\}$ units and to three different ppca ligands; Co2 is likewise coordi-



Scheme 2. The reversible single-crystal-to-single-crystal transformations between **1**, **2**, and **3**; noncoordinated and coordinated H_2O molecules are shown as large opaque and large solid, red spheres, respectively. Hydrogen bonds are indicated by dotted red lines.

nated to three different ppca ligands, but to only one oxygen from one $\{V_4O_{12}\}$ unit, leaving the sixth coordination site occupied by a water molecule (Figure 1).

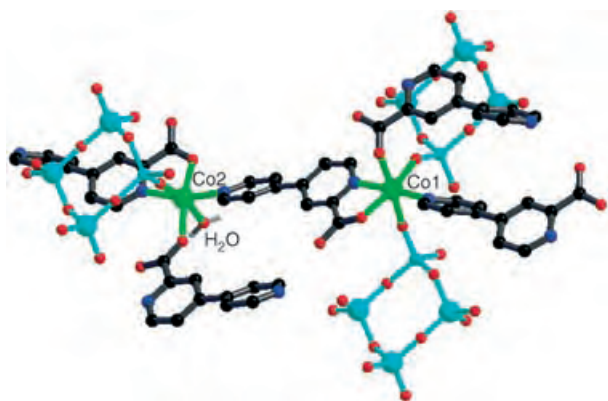


Figure 1. View of the coordination environments of the two crystallographically independent cobalt centers and the ligand coordination mode of **1**. Co: green; V: cyan; O: red; C: black; N: blue; H: white.

As shown in Figure 1, each ppca ligand is coordinated to one cobalt atom in a bidentate fashion through one carboxylate oxygen atom and the adjacent nitrogen atom of the ring. The second nitrogen atom of the ligand is coordinated to a second cobalt atom, and the remaining carboxylate oxygen atom further coordinates to a third cobalt atom in a monodentate fashion in the *syn,anti* carboxy mode. Thus, each ppca ligand functions in a μ_3 -bridging mode that leads to 2D layers with the composition $[\{Co_2(ppca)_2(H_2O)\}_\infty]$ (Figure 2a).

The VO_3^- anion of the ammonium vanadate reagent is the source of the tetrahedral vanadium in the present structure. Vanadium is found in complex **1** as $\{V_4O_{12}\}$ units, which bridge the 2D metal–organic layers described above, and in doing so, become an integral part of 1D inorganic $[\{Co_4(V_4O_{12})\}_\infty]$ chains (Figure 2b). When one considers the connectivity between the 2D metal–organic layers and the 1D mixed-metal chains, the overall structure is best described as a 3D porous organic–inorganic framework containing rectangular channels of approximate dimensions $5.2 \times 22.3 \text{ \AA}^2$ (atom-to-atom) running parallel to the *c* axis (Figure 3) and $5.6 \times 11.3 \text{ \AA}^2$ along the *a* axis (see Supporting Information). These channels constitute 15 % of the crystal volume^[8] and are much larger than those found in similar complexes constructed from the simple pyrazinecarboxylate ligand.^[6b,c] The channels are filled by guest water molecules that participate in a collective, well-ordered hydrogen-bonded network involving water molecules, carboxylate oxygen atoms, and the vanadium oxide units of the framework (see Supporting Information).

It is a well-known phenomenon that guest solvent molecules located in cavities or channels can often be removed from the framework structure without causing framework collapse and, furthermore, that they can sometimes also be reinserted. To explore this possibility, single crystals of the present cobalt–vanadium framework were heated to different temperatures. These crystals were then analyzed by single-crystal X-ray diffraction. Heating the single crystals to 150°C for 1 day yielded $[\{Co_2(ppca)_2(H_2O)\}_\infty]$

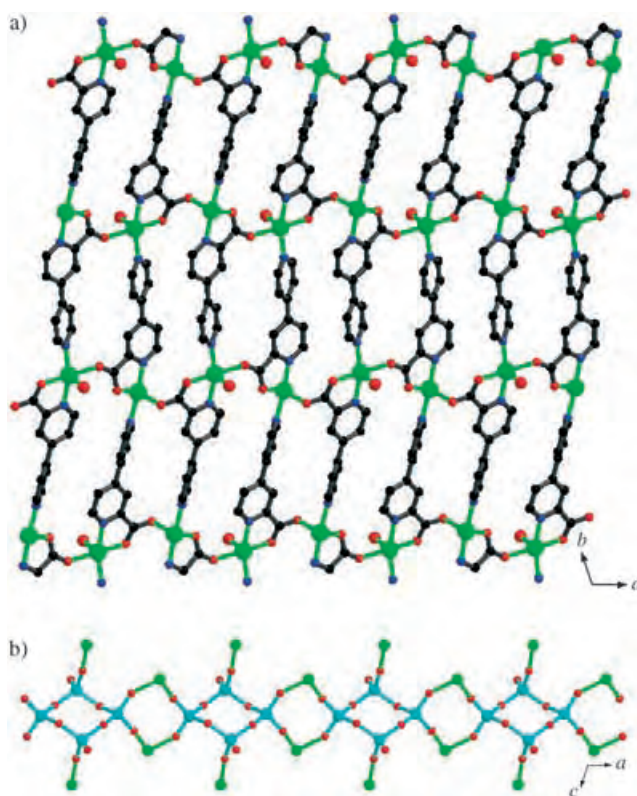


Figure 2. a) 2D metal–organic layer of composition $[\{Co_2(ppca)_2(H_2O)\}_\infty]$; b) 1D inorganic chains of composition $[\{Co_4(V_4O_{12})\}_\infty]$. Co: green; V: cyan; C: black; O: red.

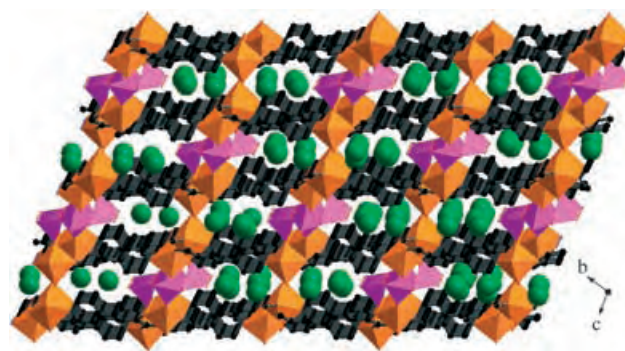


Figure 3. View of the 3D porous organic–inorganic framework with rectangular channels filled with guest water molecules. The guest water molecules are shown as large green spheres; Co octahedra: orange; V tetrahedra: pink.

$(V_4O_{12})_{0.5}] \cdot 0.55 H_2O)_n$ (**2**) (see Supporting Information). The structure determination of **2** revealed that the crystal system and space group remain the same as those of **1**, but that approximately three water molecules had been removed from the pores per formula unit. The remaining water molecules are located near Co2, where they form hydrogen bonds to the coordinated water ligand (see Supporting Information). These hydrogen bonds appear to impart the noncoordinated water molecules with enhanced thermal stability. The removal of the three water molecules of hydration is accompanied by a slight decrease in cell volume (from 1411 to 1336 \AA^3) and in

the volumes of the channels (from 15 to 12% of the total crystal volume).^[8]

Immersion of crystals of **2** in water results in complete rehydration and re-formation of the original structure, including the hydrogen-bonding network observed in the original structure of **1** (see Supporting Information). The unit-cell volume of the rehydrated framework material was determined to be 1409.5(1) Å³, and the channels again constitute 15% of the total crystal volume.^[8] The reintroduction of guest water molecules also occurs spontaneously when crystals of **2** are exposed to air; they take less than 1 week to become fully saturated, and the process demonstrates that the removal and reinsertion of the guest water molecules is completely reversible.

Next, to investigate the removal of all noncoordinated and coordinated water molecules, single crystals of **1** were heated to 300 °C for 2 h. The effects of heating were again analyzed by single-crystal X-ray diffraction. The structure determination of $[\{\text{Co}_2(\text{ppca})_2(\text{V}_4\text{O}_{12})_{0.5}\}_n]$ (**3**) confirmed the complete removal of the guest water molecules as well as the removal of the water molecule coordinated to Co2 (see Supporting

Information). Although the crystal system and space group remain unchanged, the 3D framework is significantly changed from that of **1** or **2** in that the Co2 center in **3** is now only five-coordinate and has changed from an octahedral (as in **1** or **2**) to a trigonal bipyramidal coordination environment (Figure 4). Accompanying this change in the cobalt coordination environment is a color change from red to brown (Figure 5). Whereas **3** remains almost isostructural with **1** or **2**, the 2D metal-organic layer in **3** has the composition $[\{\text{Co}_2(\text{ppca})_2\}_\infty]$, rather than $[\{\text{Co}_2(\text{ppca})_2(\text{H}_2\text{O})\}_\infty]$. More importantly, however, the unit-cell volume is decreased further and the channels only retain one-third of their original volume, now constituting only 5.8% of the total crystal volume.^[8]

Brief immersion of **3** into water or exposure to air for several days completely reverses the structural change, and the original material, **1**, including the coordinated water molecule, is reconstituted (see Supporting Information). Thus the rehydration process is accompanied by return of the original color (Figure 5). A crystallographic investigation determined that the structure of the reconstituted **3** is the same as that of **1** (see Supporting Information).

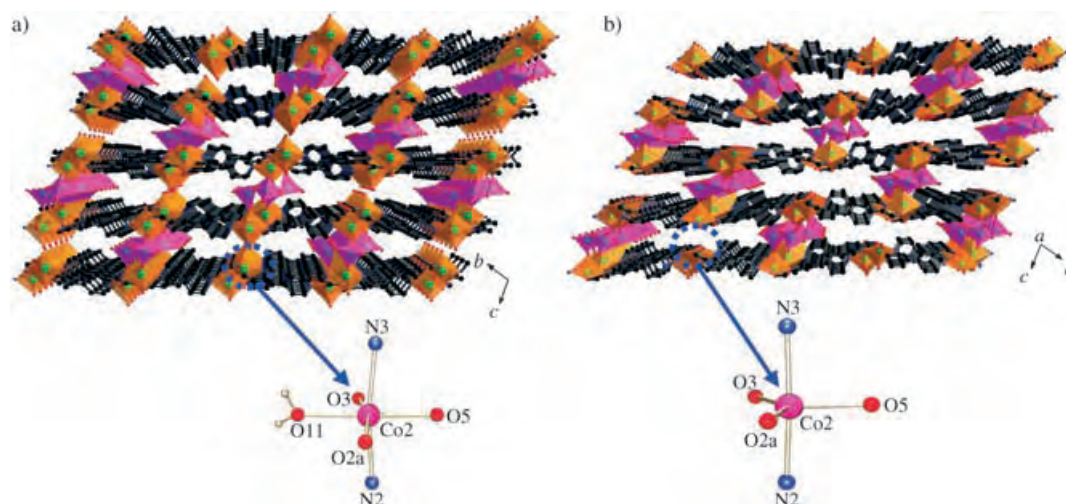


Figure 4. a) View of the $[\{\text{Co}_2(\text{ppca})_2(\text{H}_2\text{O})(\text{V}_4\text{O}_{12})_{0.5}\}_n]$ framework containing hydrated Co2 in an octahedral coordination environment; b) view of the dehydrated $[\{\text{Co}_2(\text{ppca})_2(\text{V}_4\text{O}_{12})_{0.5}\}_n]$ framework containing Co2 in a trigonal-bipyramidal coordination environment.

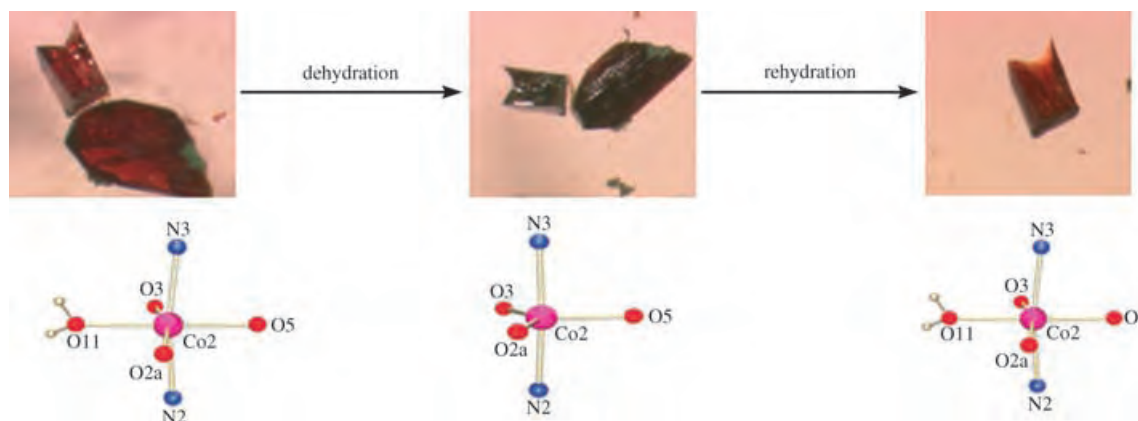


Figure 5. Pictorial representation of the dehydration and rehydration processes. The red crystal turns brown upon dehydration and change of the cobalt coordination environment from octahedral to trigonal bipyramidal. The crystal changes back to the original red color upon rehydration and returns to the original octahedral cobalt coordination environment.

A closer analysis of the structure of **3** suggests a possible cause for such a large decrease in volume upon complete dehydration. The removal of the coordinated water molecule from Co2 removes a quasi-pillaring between the channel walls (Figure 4), hence allowing a shear motion to bring the channel walls closer together. Thus, whereas the removal of the guest water molecules leads to a small decrease in volume, similar to what has been observed in other framework materials,^[9] it is the removal of the coordinated water molecules that initiates the more substantial channel “collapse”.

In summary, we have successfully synthesized a vanadium oxide bridged, mixed-metal 3D porous framework by using the new ligand ppca. The framework undergoes a dynamic structural change initiated by the removal of both non-coordinated and coordinated water molecules. The most significant structural change involves an unusual transformation of the local Co2 coordination environment, permitting unusual shrinkage and expansion in a single-crystal-to-single-crystal dehydration/rehydration process. Clearly, the existence of the five-coordinate cobalt center suggests a series of follow-up experiments to determine if the religation is possible with, for example, ammonia, rather than water. Such experiments will be performed in the near future.

Experimental Section

1: Hppca (0.2 mmol), Co(NO₃)₂·6H₂O (0.2 mmol), and NH₄VO₃ (0.2 mmol) were mixed in an aqueous solution (12 mL). The mixture was stirred at room temperature for about 1 h, and then placed in a 45-mL teflon-lined autoclave and heated at 160 °C for 2 days. Red crystals of **1** formed and were manually isolated, washed with water, and dried in air (9.4 mg, 12 %). The structural consistency and phase purity of the product was checked by comparison of the observed X-ray diffraction pattern with that calculated from the single-crystal structural data (see Supporting Information). Single-crystal X-ray crystallography was carried out on a Bruker SMART APEX CCD diffractometer system.^[10]

1: C₂₂H_{23.25}Co₂N₄O_{14.62}V₂, *M* = 797.42, triclinic, space group *P* $\bar{1}$, *a* = 9.7957(5), *b* = 11.3068(6), *c* = 14.1357(8) Å, α = 101.755(1), β = 104.449(1), γ = 104.087(1)°, *V* = 1411.0(1) Å³, *Z* = 2, ρ_{calcd} = 1.877 g cm⁻³, *T* = 150(1) K, *F*(000) = 800, $\mu(\text{MoK}\alpha)$ = 1.877 mm⁻¹, red block crystal, 16 047 reflections measured, 5759 unique (*R*_{int} = 0.0417), 432 parameters, *R*₁ = 0.0320 (*I* > 2σ(*I*)), *wR*₂ = 0.0743 (all data), *GOF* = 0.957.

2: C₂₂H_{17.10}Co₂N₄O_{11.55}V₂, *M* = 742.04, triclinic, space group *P* $\bar{1}$, *a* = 9.6788(8), *b* = 10.8844(9), *c* = 13.925(1) Å, α = 99.698(2), β = 106.605(2), γ = 101.615(2)°, *V* = 1336.5(2) Å³, *Z* = 2, ρ_{calcd} = 1.844 g cm⁻³, *T* = 150(1) K, *F*(000) = 739, $\mu(\text{MoK}\alpha)$ = 1.966 mm⁻¹, red block crystal, 11 562 reflections measured, 4269 unique (*R*_{int} = 0.0458), 386 parameters, *R*₁ = 0.0391 (*I* > 2σ(*I*)), *wR*₂ = 0.0927 (all data), *GOF* = 1.075.

1 (reconstituted from **2**): C₂₂H_{23.26}Co₂N₄O_{14.63}V₂, *M* = 797.53, triclinic, space group *P* $\bar{1}$, *a* = 9.7941(6), *b* = 11.2958(7), *c* = 14.1310(9) Å, α = 101.728(1), β = 104.447(1), γ = 104.054(1)°, *V* = 1409.5(1) Å³, *Z* = 2, ρ_{calcd} = 1.879 g cm⁻³, *T* = 150(1) K, *F*(000) = 801, $\mu(\text{MoK}\alpha)$ = 1.879 mm⁻¹, red block crystal, 13 392 reflections measured, 5009 unique (*R*_{int} = 0.0458), 432 parameters, *R*₁ = 0.0349 (*I* > 2σ(*I*)), *wR*₂ = 0.0821 (all data), *GOF* = 0.978.

3: C₂₂H₁₄Co₂N₄O₁₀V₂, *M* = 714.11, triclinic, space group *P* $\bar{1}$, *a* = 9.6775(9), *b* = 10.3376(9), *c* = 13.7956(13) Å, α = 76.531(2), β = 75.321(2), γ = 82.387(2)°, *V* = 1294.4(2) Å³, *Z* = 2, ρ_{calcd} = 1.832 g cm⁻³, *T* = 150(1) K, *F*(000) = 708, $\mu(\text{MoK}\alpha)$ = 2.022 mm⁻¹, brown block crystal, 12 073 reflections measured, 4140 unique

(*R*_{int} = 0.0639), 361 parameters, *R*₁ = 0.0429 (*I* > 2σ(*I*)), *wR*₂ = 0.0873 (all data), *GOF* = 1.021.

1 (reconstituted from **3**): C₂₂H_{22.66}Co₂N₄O_{14.33}V₂, *M* = 792.13, triclinic, space group *P* $\bar{1}$, *a* = 9.7987(8), *b* = 11.270(1), *c* = 14.200(1) Å, α = 101.799(2), β = 104.251(2), γ = 103.899(2)°, *V* = 1416.3(2) Å³, *Z* = 2, ρ_{calcd} = 1.857 g cm⁻³, *T* = 294(2) K, *F*(000) = 795, $\mu(\text{MoK}\alpha)$ = 1.868 mm⁻¹, red block crystal, 10 344 reflections measured, 4522 unique (*R*_{int} = 0.0481), 401 parameters, *R*₁ = 0.0363 (*I* > 2σ(*F*)), *wR*₂ = 0.0750 (all data), *GOF* = 0.966.

CCDC-275335 (**1**), -275336 (**2**), -275337 (**1** reconstituted from **2**), -275338 (**3**), and -275339 (**1** reconstituted from **3**) contain the supplementary crystallographic data for this paper. These data can be obtained free of charge from The Cambridge Crystallographic Data Centre via www.ccdc.cam.ac.uk/data_request/cif.

Received: July 1, 2005

Published online: September 21, 2005

Keywords: cobalt · dynamic structural changes · ligand design · microporous materials · vanadium

- [1] a) K. Takaoka, M. Kawano, M. Tominaga, M. Fujita, *Angew. Chem.* **2005**, *117*, 2189; *Angew. Chem. Int. Ed.* **2005**, *44*, 2151; b) the dehydration/rehydration and color change of a cobalt-containing open-framework structure that undergoes a rare single-crystal-to-single-crystal transformation was recently reported: K. Hanson, N. Calin, D. Bugaris, M. Scancella, S. C. Sevov, *J. Am. Chem. Soc.* **2004**, *126*, 10502; c) S. Kitagawa, K. Uemura, *Chem. Soc. Rev.* **2005**, *34*, 109; d) E. Y. Lee, S. Y. Jang, M. P. Suh, *J. Am. Chem. Soc.* **2005**, *127*, 6374.
- [2] a) D. N. Dybtsev, H. Chun, K. Kim, *Angew. Chem.* **2004**, *116*, 5143; *Angew. Chem. Int. Ed.* **2004**, *43*, 5033; b) B. Rather, M. J. Zaworotko, *Chem. Commun.* **2003**, 830; c) M.-H. Zeng, X.-L. Feng, X.-M. Chen, *Dalton Trans.* **2004**, 2217; d) G. J. Halder, C. J. Kepert, *J. Am. Chem. Soc.* **2005**, *127*, 7891.
- [3] a) D. M. Ciurtin, M. D. Smith, H.-C. zur Loye, *Chem. Commun.* **2002**, 74; b) Y.-B. Dong, M. D. Smith, H.-C. zur Loye, *Angew. Chem.* **2000**, *112*, 4441; *Angew. Chem. Int. Ed.* **2000**, *39*, 4271; c) D. M. Ciurtin, M. D. Smith, H.-C. zur Loye, *Dalton Trans.* **2003**, 1245.
- [4] a) I. Imaz, G. Bravic, J.-P. Sutter, *Chem. Commun.* **2005**, 993; b) R. Kitaura, G. Onoyama, H. Sakamoto, R. Matsuda, S.-I. Noro, S. Kitagawa, *Angew. Chem.* **2004**, *116*, 2738; *Angew. Chem. Int. Ed.* **2004**, *43*, 2684; c) T. E. Vos, J. S. Miller, *Angew. Chem.* **2005**, *117*, 2468; *Angew. Chem. Int. Ed.* **2005**, *44*, 2416.
- [5] a) L.-M. Zheng, T. Whitfield, X. Q. Wang, A. J. Jacobson, *Angew. Chem.* **2000**, *112*, 4702; *Angew. Chem. Int. Ed.* **2000**, *39*, 4528; b) J. H. Luo, B. Alexander, T. R. Wagner, P. A. Maggard, *Inorg. Chem.* **2004**, *43*, 5537; c) P. A. Maggard, B. B. Yan, J. H. Luo, *Angew. Chem.* **2005**, *117*, 2609; *Angew. Chem. Int. Ed.* **2005**, *44*, 2553.
- [6] C.-L. Chen, A. M. Goforth, M. D. Smith, C.-Y. Su, H.-C. zur Loye, unpublished results.
- [7] M. I. Khan, E. Yohannes, R. C. Nome, S. Ayesh, V. O. Golub, C. J. O'Connor, R. J. Doedens, *Chem. Mater.* **2004**, *16*, 5273, and references therein.
- [8] PLATON, A Multipurpose Crystallographic Tool, Utrecht University, Utrecht, The Netherlands, A. L. Spek, **1998**.
- [9] R. Matsuda, R. Kitaura, S. Kitagawa, Y. Kubota, T. C. Kobayashi, S. Horike, M. Takata, *J. Am. Chem. Soc.* **2004**, *126*, 14063, and references therein.
- [10] a) SMART Version 5.625, SAINT+ Version 6.22. Bruker Analytical X-ray Systems, Inc., Madison, Wisconsin, USA, **2001**; b) G. M. Sheldrick, SHELXTL Version 6.1; Bruker Analytical X-ray Systems, Inc., Madison, Wisconsin, USA, **2000**.

Hierarchical Assembly of {Fe₁₃} Oxygen-Bridged Clusters into a Close-Packed Superstructure**

Muralee Murugesu, Rodolphe Clérac, Wolfgang Wernsdorfer, Christopher E. Anson, and Annie K. Powell*

Dedicated to Professor Heinrich Vahrenkamp on the occasion of his 65th birthday

Hierarchical materials can be regarded as systems in which small units are incorporated into larger superstructures, thereby investing the resulting construct with a hierarchy of properties that operate on different scales. Such systems become of particular interest when nanometer scales are involved, as these represent a situation in which nanoparticles are organized into a specific array. The organization of nanoparticles is important in terms of creating devices but poses significant difficulties if the particles have to be physically arranged, for example, by using electron-beam lithography. Therefore, the idea of the combination of such particles along chemical principles is attractive as it leaves the chemical-bonding interactions to do the work. Herein, we describe the realization of this idea in a material obtained from aqueous solution and composed of a close-packed superstructure of connected iron(III) nanomagnets, which themselves display close-packed core architectures.

Our conceptual hierarchy begins at the atomic level with Fe^{III} ions in water in the form of the hexaaqua ion [Fe(H₂O)₆]³⁺. Under normal conditions, a variety of hydrolysis reactions would lead to the precipitation of an amorphous hydroxide, which would then age into well-defined mineral phases, such as the oxyhydroxide and goethite phases, and finally transform into the most thermodynamically stable oxide haematite.^[1] We have observed that supply of tripodal chelating ligands of the general form N(RCOOH)₂R' (in

which R' can be any organic residue) to such solutions can halt this process through the stabilization of captured intermediate phases composed of close-packed cores, which are portions of the brucite structure (exemplified by Mg(OH)₂) encased in a shell of the ligand units.^[2,3] It is worth looking at this hydrolysis process in more detail: The brucite structure is an AB₂ lattice composed of close-packed hydroxide (B) layers that are arranged as double strips and M^{II} ions (A) that sit in the octahedral holes between these strips so that each hydroxide unit bridges three metal ions (Figure 1). In the hydrolysis process, we can imagine the

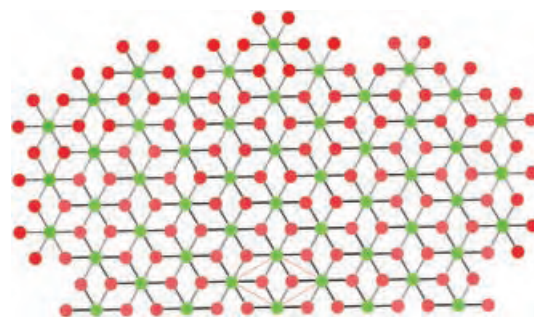


Figure 1. The AB₂ lattice as seen in the brucite Mg(OH)₂ structure. Green: metal atoms; red: oxygen atoms.

starting point (first generation) to be a hexaaqua metal ion which will link to six further metal ions (second generation) on production of the hexahydroxo metal ion, and the process will continue through production of the hydroxide ions and coordination to a further six metal centers (third generation), then twelve (fourth generation), and so on, as can be seen in Figure 1.

Aggregates that contain portions of such core structures have been structurally characterized for a variety of metal ions.^[2–15] Clearly, an infinite brucite structure is not possible for the examples of M^{III} ions on the basis of charge imbalance, which could be stabilized by the shell of ligands coordinated to the outermost metal ions of the hydroxide lattice in the observed aggregates. A further pertinent point is that removal of half the protons from the double strips of hydroxide moieties in brucite leads to a layer of the α -oxyhydroxide structure, which is exemplified for the Fe^{III} center by goethite, α -FeO(OH), itself the precursor to the most thermodynamically stable phase haematite. Thus, we can think of such aggregates as metastable intermediates that are trapped through the process of crystallization. These aggregates prove to be magnetically interesting for the Fe^{III} center because, although the overall coupling is antiferromagnetic, the pairwise interactions are unequal in magnitude over the whole molecule, thus leading to residual ground-state spins of up to 33/2 and a display of hysteresis of the magnetization.^[3,16–18] Thus, a secondary level of organization both in terms of the structure and properties of the compound is demonstrated. In the specific case we describe herein, the tripodal proligand nitrilotripropionic acid (H₃ntp = N(CH₂CH₂COOH)₃) has been used to successfully trap {Fe₁₃} aggregates (Figure 2), in which the production of the

[*] Dr. M. Murugesu, Dr. C. E. Anson, Prof. A. K. Powell
Institut für Anorganische Chemie der Universität Karlsruhe
Engesserstrasse Geb. 30.45
76128 Karlsruhe (Germany)
Fax: (+49) 721-608-8142
E-mail: powell@chemie.uni-karlsruhe.de

Dr. R. Clérac
Centre de Recherche Paul Pascal
CNRS-UPR 8641, 115 Avenue Dr. A. Schweitzer
33600 Pessac (France)

Dr. W. Wernsdorfer
Laboratoire Louis Néel, CNRS
25 Avenue Des Martyrs BP166
38042 Grenoble Cedex 9 (France)

[**] This work was supported by the DFG through the Schwerpunkt Programm SPP 1137 on "Molecular Magnetism", the Center for Functional Nanostructures (CFN), the Conseil Régional d'Aquitaine, Bordeaux I University, and the CNRS.

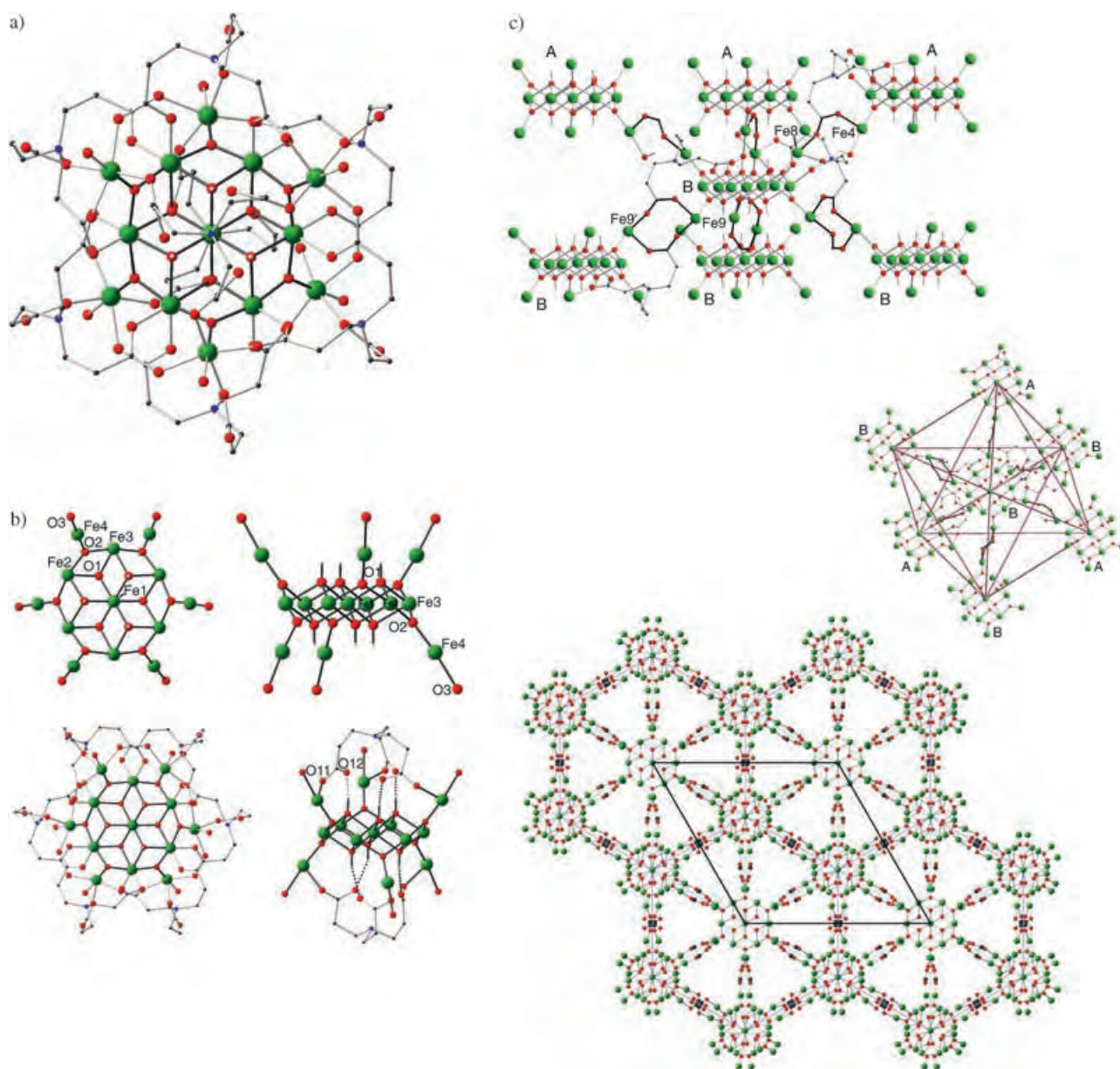


Figure 2. The structural features of the $\{\text{Fe}_{13}\}$ aggregate. a) One complete $[\text{Fe}_{13}(\mu_3\text{-OH})_6(\mu_3\text{-O})_6(\text{H}_2\text{O})_6(\text{Hntp})_8]^{5+}$ cluster. b) Top and side views of the $[\text{Fe}_{13}(\mu_3\text{-OH})_6(\mu_3\text{-O})_6(\text{H}_2\text{O})_6]^{21+}$ core in $[\text{Fe}_{13}(\mu_3\text{-OH})_6(\mu_3\text{-O})_6(\text{H}_2\text{O})_6(\text{Hntp})_8]^{5+}$ and the coordination of the Hntp^{2-} ligands to this core. c) The connections between the A- and B-type clusters; linkage of a B-type cluster with its six surrounding neighbors showing the octahedral arrangement of the clusters; and the 3D packing arrangement of the compound viewed down the c axis (most of the ligand atoms have been omitted for clarity). Fe green; O red; N blue; C black; H white.

brucite lattice has effectively been arrested at the third generation.

The iron–oxygen framework is shown in Figure 2b, which shows that the central core of the $[\text{Fe}_7(\text{OH})_6]^{15+}$ ion clearly corresponds to the first two generations of the brucite lattice and that the final six Fe^{III} centers of the third generation are connected to this core by six triply bridging oxide rather than hydroxide ions. These oxides provide an important structural element as they link three metal ions in a trigonal rather than pyramidal fashion. This coordination mode has the result that the final six iron centers are disposed above and below the core, thus alternating with the hydroxide units to give a “diabolo” arrangement, and means that the iron centers form

a trigonal-antiprismatic arrangement, which becomes important in the quaternary structure.

The proligand H_3ntp did not coordinate to the aggregate in the tripodal chelation mode as expected and as seen in the $\{\text{Cu}_{44}\}$ compound we recently reported^[19] because the central nitrogen atom carries a proton and, therefore, does not form bonds with the peripheral iron centers. This coordination mode has, however, been observed by us in some different Cu^{II} compounds.^[20] Consequently, the carboxylate groups are not constrained to form chelate rings, and so the carboxylate functionalities from six ligands display extensive bridging interactions around the periphery of the molecule. Two further ligands complete the encapsulation of the iron core by

capping above and below, with coordination to the peripheral iron centers from the carboxylate groups and hydrogen-bonding interactions between the non-coordinated carboxylate oxygen atoms and the hydroxide functionalities in the core. The proton on the central nitrogen atom of each ligand also forms hydrogen-bonding interactions with the carboxylate oxygen atoms in a trifurcated fashion. The resulting structure is nearly spherical, with a diameter of about 1.5 nm. The positive charge of 5+ on the aggregate (the ligand is dinegative in this zwitterionic form) is balanced in the crystal structure by nitrate counterions. In fact, there are two almost identical aggregates, $[\text{Fe}_{13}(\mu_3\text{-OH})_6(\mu_3\text{-O})_6(\text{Hntp})_8(\text{H}_2\text{O})_6]^{5+}$ (cluster **A**; $\text{Hntp} = \text{HN}(\text{CH}_2\text{CH}_2\text{COO})_3$) and $[\text{Fe}_{13}(\mu_3\text{-OH})_6(\mu_3\text{-O})_6(\text{Hntp})_8]^{5+}$ (cluster **B**), in a 1:2 ratio in the three-dimensional structure. The subtle difference between these clusters becomes clear when the structure is examined in detail: In the third level of organization, the **A**-type clusters are linked to the **B**-type clusters by a *syn-anti* carboxylate bridge from a ligand located on **A** which connects a peripheral Fe^{III} center in **A** to a peripheral Fe^{III} center in **B**. In addition, the **B**-type clusters are linked to each other through double *syn-anti* carboxylate bridges (Figure 2c).

The molecules are arranged in layers that correspond to an ABBABBABBA ordering. A closer examination of the packing reveals the consequences of the arrangement of the peripheral Fe^{III} centers in the trigonal antiprismatic geometry and the fourth level of organization. As a result of the links between the aggregates that arise from ligands coordinated to these iron centers, each aggregate is octahedrally surrounded by six further aggregates (Figure 2c); therefore, for a given **A** aggregate there are six **B** aggregates, whereas for a **B** aggregate there are three **A** and three further **B** aggregates that assume three facial positions of the octahedral "coordination" geometry in each case. The overall result for the organization of the aggregates can be visualized as the interpenetration of *pseudo*-cubic lattices, which is exemplified by the sodium chloride structure. The fact that this organization is actually an AB_2 structure complicates the description slightly, but if we refer back to the brucite structure shown in Figure 1, in which the green and red spheres now represent the **A** and **B** clusters, respectively, the hierarchical nature of this material becomes clear. The unit cell marked in Figure 1 corresponds to the unit cell for our compound (also marked in Figure 2c). In this way, nanoscale aggregates with cores of close-packed atoms with an AB_2 structure have been organized into a close-packed AB_2 superstructure. It is of particular note that within the cores of the aggregates we see Fe^{III} centers that occupy octahedral holes between two layers of close-packed hydroxide moieties and in the superstructure we have **A** clusters that occupy octahedral sites between two layers of **B** clusters.

The question now arises as to whether this hierarchical structure is reflected in the magnetic properties of the material. The plot of χT versus T decreases continuously over the whole temperature range studied from 16.5 emu K mol^{-1} at 300 K to 4.11 emu K mol^{-1} at 30 K (Figure 3). Below this temperature, the χT product decreases faster to reach 1.37 emu K mol^{-1} at 1.8 K. The χT value at room temperature is well below the expected value (56.9 emu K mol^{-1} , if $g = 2$)

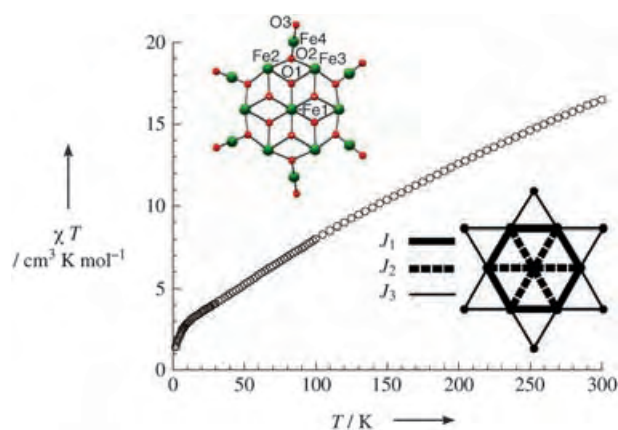


Figure 3. Temperature dependence of the χT product (per Fe^{III} aggregate) at 1000 Oe. Inset: Topology of the magnetic interactions in the iron aggregates.

for 13 high-spin Fe^{III} centers ($S = 5/2$), thus indicating strong antiferromagnetic interactions between the centers.

A simplified scheme of the magnetic-interaction topology based on the coordination modes between the Fe^{III} centers can be proposed (inset Figure 3) with three types of pathway: J_1 coupling through the $\mu_3\text{-O}$ and $\mu_3\text{-OH}$ double bridges, J_2 coupling through the $\mu_3\text{-OH}$ double bridges, and J_3 coupling through the single $\mu_3\text{-O}$ bridges. All of these exchange couplings are known to lead to antiferromagnetic interactions. Therefore, the topology and the symmetry of the $\{\text{Fe}_{13}\}$ aggregates (inset Figure 3) reveal the presence of a triangular assembly, with a competing set of antiferromagnetic interactions. Modeling the magnetic susceptibility is not possible as 1) there is no analytical model available for 13 coupled Fe^{III} centers in such a configuration and 2) numerical methods would require the diagonalization of too large a matrix. However, numerical density functional theory calculations on $[\text{Fe}_{19}(\text{methedi})_{10}(\mu_3\text{-OH})_6(\mu\text{-OH})_8(\mu_3\text{-O})_6(\text{H}_2\text{O})_{12}]\text{NO}_3$ ($\text{H}_3\text{methedi} = \text{N}(\text{CH}_2\text{COOH})_2(\text{CH}(\text{Me})\text{CH}_2\text{CH}_2\text{OH})$), a molecule with the same brucite-core structure as seen in the $\{\text{Fe}_{13}\}$ aggregate,^[21] were recently used to evaluate $\text{Fe}^{\text{III}}\text{-Fe}^{\text{III}}$ magnetic coupling through different types of oxygen bridges. Herein, we suggest that the J_3 coupling through the $\mu_3\text{-O}$ bridge will be the strongest and will occur at around -100 K and that the J_2 coupling should be almost half of the J_1 coupling (namely, around -10 K compared with -20 K). Therefore, a simple view of the ground state can be proposed based on this coupling scheme in which all the outermost spins are parallel to each other and antiparallel to the spins on their neighbors that make up the middle ring. Finally, the J_2 coupling results in the spin on the central Fe center being antiparallel to these neighboring spins and, thus, parallel to the outermost spins, which would result in a spin ground state for the $\{\text{Fe}_{13}\}$ aggregates of 5/2.

Low-temperature measurements give further insight into the ground state and the anisotropy of the $\{\text{Fe}_{13}\}$ units. The fact that the χT product does not go directly to zero at low temperature indicates that it is not a singlet ground state, as to be expected for an odd number of antiferromagnetically coupled spin carriers. The value reached at 30 K is 4.1 emu K

mol^{-1} , which is compatible with a ground state of $S = 5/2$. The further decrease of the χT product at lower temperature is probably because of the intercluster interactions mediated by the *syn-anti* carboxylate bridges, a zero-field-splitting contribution, or both of these. This interpretation is confirmed by the field dependence of the magnetization at 1.8 K (Figure 4a). Two regimes are observed: 1) at low field below 1 T,

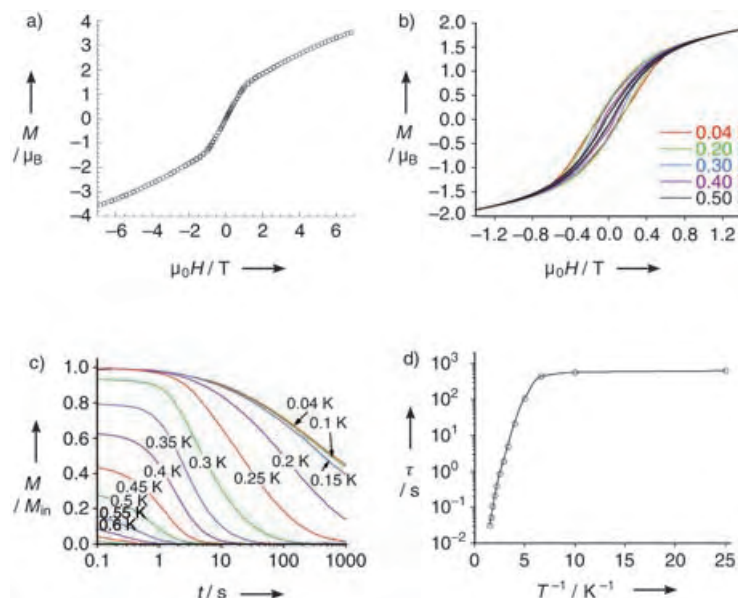


Figure 4. a) Bulk-field dependence of the magnetization (per Fe^{III} aggregate) at 1.83 K and b) field dependence of the magnetization on a single crystal from 0.04 to 0.5 K by the micro-SQUID technique with the magnetic field applied along the *c* axis. c) Relaxation of the magnetization below 0.7 K normalized to the initial magnetization at 0.04 K by the micro-SQUID technique with the magnetic field applied along the *c* axis. d) Plot of relaxation time τ versus $1/T$.

where the magnetization increases rapidly and linearly, and 2) above 1 T, where the increase is slower. Although saturation is not achieved at 7 T, the nonlinear behavior indicates that the saturation should be achievable at higher fields and have a value probably close to $5 \mu_B$, which is to be expected for a ground state of $S = 5/2$. The presence of these two regimes may be the result of the anisotropy and/or the interactions between the aggregates; therefore, micro-SQUID measurements were performed on a single crystal at temperatures lowered to 0.04 K for yet further insight into the magnetic behavior. This technique and rotation of the applied field around the single crystal shows that the measured magnetization becomes clearly uniaxially anisotropic below 2 K, thus implying a negative value of D . Furthermore, below 1 K and when the applied field does not coincide with the *c* direction, the curves for M versus H exhibit a characteristic S shape that is typical for antiferromagnetically coupled systems with an inflexion point at around 0.6 T at 40 mK. Therefore, these two simple observations demonstrate that both anisotropy and interaggregate interactions are relevant in the low-temperature regime. Hysteresis loops are observed below 1 K with the largest effect seen when the field coincides with the *c* axis, thus suggesting that this effect corresponds to the easy axis (Figure 4b). Although the loops do not show a large temper-

ature dependence, we can rule out the possibility that they result from a spin-glass behavior from the temperature dependence of the magnetization relaxation time. In a classical spin-glass system, the relaxation time follows what looks like an Arrhenius behavior but with nonphysical values for the energy barrier and the pre-exponential factor,^[22] which is, in fact, not the case, as seen in Figure 4d.

As the curves for M/M_{in} versus t (M/M_{in} is the magnetization normalized to its initial value at 0.04 K) obtained below 0.7 K have the same shape (Figure 4c), the data were scaled to a single master curve and the relaxation time τ was extracted by simply taking the time when M/M_{in} reaches the value $1/e$ (Figure 4d). The relaxation time for the high-temperature section of the plot of τ versus $1/T$ does not follow the simple Arrhenius behavior expected for single-molecule magnets (SMM) in the thermally activated regime. This nonexponential behavior is probably a result of the magnetic interactions between the $\{\text{Fe}_{13}\}$ aggregates and suggests that these units when isolated from each other would behave as SMMs. Below 0.1 K, saturation of τ is reached, thus indicating that the dominant process of relaxation becomes time independent. This feature is reminiscent of SMM behavior when quantum tunneling of the magnetization is the main pathway for the relaxation. In our case, the slow relaxation of the magnetization is induced necessarily not only by the spin ground state and the anisotropy of the $\{\text{Fe}_{13}\}$ aggregates but also by the significant three-dimensional antiferromagnetic coupling between them. This result illustrates the influence of the hierarchical structure of this compound and the role of the chemical and magnetic coupling between the $\{\text{Fe}_{13}\}$ aggregates that give rise to a hierarchy of magnetic properties.

Although further work needs to be carried out on the physics of this complicated system, it is clear that by physically connecting the spins of the aggregates with chemical bonds, cooperative interaction at low temperature has been enabled, thus giving rise to the exotic effects observed. Overall, we feel that this system is fascinating both in terms of the aesthetic appeal of the structural concepts and its potential to provide detailed insight into magnetic interactions between nanoscale particles.

Experimental Section

$[\{\text{Fe}_{13}(\mu_3\text{-OH})_6(\mu_3\text{-O})_6(\text{Hntp})_8(\text{H}_2\text{O})_6\}\{\text{Fe}_{13}(\mu_3\text{-OH})_6(\mu_3\text{-O})_6(\text{Hntp})_8\}] \cdot 15\text{NO}_3 \cdot 13\text{H}_2\text{O}$ (**1**): A solution of H_3ntp (0.058 g, 0.25 mmol) and ethylenediamine (0.017 mL, 0.25 mmol) in H_2O (5 mL) was added to a solution of $[\text{Fe}(\text{NO}_3)_3] \cdot 9\text{H}_2\text{O}$ (0.202 g, 0.5 mmol) in H_2O (5 mL) with stirring. Vapor diffusion of EtOH into the resulting brown solution gave red-brown diamond-shaped crystals after three weeks (17% yield). Elemental analysis (%) calcd for $\text{C}_{216}\text{H}_{444}\text{Fe}_{39}\text{N}_{39}\text{O}_{282}$: C 25.24, H 4.35, N 5.31; found: C 25.23, H 4.03, N 5.38.

Crystal structure data for **1**: $\text{C}_{216}\text{H}_{450}\text{Fe}_{39}\text{N}_{39}\text{O}_{244}$, $M_r = 9676.2$; trigonal, $P\bar{3}c1$, $a = 24.2756(12)$, $c = 35.4381(19)$ Å, $U = 18085.9(16)$ Å³, $Z = 4$, $T = 200$ K, $\rho_{\text{calcd}} = 1.777$ Mg m⁻³, $\mu = 1.647$ mm⁻¹; Stoe IPDS area detector diffractometer with graphite-monochromated $\text{MoK}\alpha$ radiation; 105 539 reflections measured, 13 313

unique, $R_{\text{int}} = 0.1290$, $2\theta_{\text{max}} = 56.3^\circ$, 99.8% completeness, $wR_2(\text{all data}) = 0.2134$, $R_1 = 0.0829$ using 8706 reflections with $I \geq 2\sigma(I)$, parameters/restraints 884/50, residual electron density $+0.86/-0.93$; semiempirical absorption correction by using XPRED in SHELXTL;^[22] structure solution by direct-methods and full-matrix least-squares refinement against F^2 (all data) by using SHELXTL;^[23] anisotropic refinement for all non-hydrogen atoms except for some minor disorder components, hydrogen atoms isotropic. CCDC-260817 contains the supplementary crystallographic data for this paper. These data can be obtained free of charge from the Cambridge Crystallographic Data Center via www.ccdc.cam.ac.uk/data_request/cif.

Magnetic susceptibility measurements on **1** were obtained on a finely ground polycrystalline sample (5.9 mg) using a Quantum Design SQUID magnetometer MPMS-XL. The dc measurements were collected from 1.8 to 300 K and from -70 to 70 kOe. Experimental data were also corrected for the sample holder and for the diamagnetic contribution calculated from Pascal constants.^[24] Field and time dependences of the magnetization on single crystals were measured with an array of micro-SQUIDs.^[25]

Received: January 19, 2005

Revised: June 14, 2005

Published online: September 27, 2005

Keywords: cluster compounds · coordination modes · hierarchical structures · iron · magnetic properties

- [18] M. Affronte, R. Sessoli, D. Gatteschi, W. Wernsdorfer, J. C. Lasjaunias, S. L. Heath, A. K. Powell, A. Fort, A. Rettori, *J. Phys. Chem. Solids* **2004**, 65, 745.
- [19] M. Murugesu, R. Clérac, C. E. Anson, A. K. Powell, *Inorg. Chem.* **2004**, 43, 7269.
- [20] M. Murugesu, R. Clérac, C. E. Anson, A. K. Powell, *J. Phys. Chem. Solids* **2004**, 65, 667.
- [21] E. Ruiz, A. Rodríguez-Fortea, J. Cano, S. Alvarez, *J. Phys. Chem. Solids* **2004**, 65, 799.
- [22] J. A. Mydosh, *Spin Glasses: An Experimental Introduction*, Taylor and Francis, London, **1993**.
- [23] G. M. Sheldrick, SHELXTL 5.1, Bruker AXS Inc., 6300 Enterprise Lane, Madison, WI 53719-1173, USA, **1997**.
- [24] E. A. Boudreaux, L. N. Mulay, *Theory and Applications of Molecular Paramagnetism*, Wiley, New York, **1976**.
- [25] W. Wernsdorfer, *Adv. Chem. Phys.* **2001**, 118, 99.

- [1] R. M. Cornell, U. Schwertmann, *The Iron Oxides*, VCH, Weinheim, **1996**.
- [2] S. L. Heath, A. K. Powell, *Angew. Chem.* **1992**, 104, 191; *Angew. Chem. Int. Ed. Engl.* **1992**, 31, 191.
- [3] J. C. Goodwin, R. Sessoli, D. Gatteschi, W. Wernsdorfer, A. K. Powell, S. L. Heath, *J. Chem. Soc. Dalton Trans.* **2000**, 1835.
- [4] M. A. Bolcar, S. M. J. Aubin, K. Folting, D. N. Hendrickson, G. Christou, *Chem. Commun.* **1997**, 1485.
- [5] M. Tesmer, B. Müller, H. Vahrenkamp, *Chem. Commun.* **1997**, 721.
- [6] G. L. Abbati, A. Cornia, A. C. Fabretti, A. Caneschi, D. Gatteschi, *Inorg. Chem.* **1998**, 37, 3759.
- [7] H. Oshio, N. Hoshino, T. Ito, M. Nakano, F. Renz, P. Güthlich, *Angew. Chem.* **2003**, 115, 233; *Angew. Chem. Int. Ed.* **2003**, 42, 223.
- [8] S. Boulmaaz, R. Papiernik, L. G. Hubertpfalzgraf, J. Vaissermann, J. C. Daran, *Polyhedron* **1992**, 11, 1331.
- [9] I. A. M. Pohl, L. G. Westin, M. Kritikos, *Chem. Eur. J.* **2001**, 7, 3438.
- [10] J. T. Brockman, J. C. Huffman, G. Christou, *Angew. Chem.* **2002**, 114, 2616; *Angew. Chem. Int. Ed.* **2002**, 41, 2506.
- [11] M. Murrie, H. Stoeckli-Evans, H. U. Güdel, *Angew. Chem.* **2001**, 113, 2011; *Angew. Chem. Int. Ed.* **2001**, 40, 1957.
- [12] E. K. Brechin, S. G. Harris, A. Harrison, S. Parsons, A. G. Whittaker, R. E. P. Winpenny, *Chem. Commun.* **1997**, 653.
- [13] J. C. Goodwin, S. J. Teat, S. L. Heath, *Angew. Chem.* **2004**, 116, 4129; *Angew. Chem. Int. Ed.* **2004**, 43, 4037.
- [14] S. L. Heath, P. A. Jordan, I. D. Johnson, G. R. Moore, A. K. Powell, M. Helliwell, *J. Inorg. Biochem.* **1995**, 59, 785.
- [15] W. Schmitt, E. Baissa, A. Mandel, C. E. Anson, A. K. Powell, *Angew. Chem.* **2001**, 113, 3689; *Angew. Chem. Int. Ed.* **2001**, 40, 3578.
- [16] A. K. Powell, S. L. Heath, D. Gatteschi, L. Pardi, R. Sessoli, G. Spina, F. Del Giallo, F. Pieralli, *J. Am. Chem. Soc.* **1995**, 117, 2491.
- [17] D. J. Price, F. Lioni, R. Ballou, P. T. Wood, A. K. Powell, *Philos. Trans. R. Soc. London Ser. A* **1999**, 357, 3099.

Nucleic Acids

DOI: 10.1002/anie.200500904

Nucleic Acid with Guanidinium Modification Exhibits Efficient Cellular Uptake**

*Tatsuo Ohmichi, Masayasu Kuwahara, Naoko Sasaki, Masatoshi Hasegawa, Takahito Nishikata, Hiroaki Sawai, and Naoki Sugimoto**

Both chemical and biological technologies have been used in the development of oligonucleotides as therapeutic agents. Antisense and antisense oligonucleotides, aptamers, and

[*] Prof. Dr. N. Sugimoto
Frontier Institute for Biomolecular Engineering Research (FIBER)
and Department of Chemistry
Faculty of Science and Engineering
Konan University
8-9-1 Okamoto, Higashinada-ku, Kobe 658-8501 (Japan)
Fax: (+81) 78-435-2766
E-mail: sugimoto@konan-u.ac.jp

Dr. T. Ohmichi
FIBER, Konan University
and I.S.T. Corporation
13-13-5 Ichiriyama, Otsu 520-2153 (Japan)

Prof. Dr. M. Kuwahara, M. Hasegawa, Prof. Dr. H. Sawai
Faculty of Engineering, Gunma University
1-5-1 Tenjin-cho, Kiryu, Gunma 376-8515 (Japan)

Prof. Dr. M. Kuwahara
PRESTO, Japan Science and Technology Agency (JST)
Gunma 376-8515 (Japan)

Dr. N. Sasaki
FIBER, Konan University (Japan)

Prof. Dr. T. Nishikata
FIBER and Department of Biology
Faculty of Science and Engineering, Konan University (Japan)

[**] This work was supported in part by Grants-in-Aid for Scientific Research and the "Academic Frontier" Project (2004–2009) from MEXT (Japan).



Supporting information for this article is available on the WWW under <http://www.angewandte.org> or from the author.

ribozymes (catalytic RNAs) are typically used for the regulation of gene expression.^[1–4] The recent discovery of RNA interference promises an efficient gene regulation method for both basic and therapeutic research.^[5–7] However, the cell membrane is a formidable barrier against the delivery of nucleic acids,^[8–10] and therefore effective implementation of oligonucleotide technology depends on the efficient transfection of oligonucleotides. Thus, the enhancement of oligonucleotide uptake for targeted delivery is still a topic of great interest.

Cationic peptides are efficient tools for the transfection of oligonucleotides and cationic liposomes,^[11,12] polycationic dendrimers,^[13] and polyethyleneimine,^[14,15] but if antisense oligonucleotide–cationic peptide conjugates are used in cellular delivery, the conjugates are often insoluble.^[16] Furthermore, the conjugation is still not chemically straightforward and needs improvement,^[17] and the peptide inhibits the function of the nucleic acid to which it is conjugated.^[18] In the development of oligonucleotide technology, direct chemical modification of DNA or RNA is one method of improving function or adding a novel function, because the oligonucleotide-based structure and synthesis allow easy conjugation to DNA and RNA molecules for biochemical and biophysical applications. For example, a base-pair-mimic nucleoside induces site-selective RNA cleavage,^[19] and the creation of modified DNA analogues with fluorescent aromatic compounds allows the rapid combinatorial screening and discovery of color-changing sensors of light exposure from a library.^[20] Therefore, a modified nucleic acid analogue with efficient cellular uptake would be a useful tool for biochemical applications.

Herein, we report the initial synthesis of 5-[(6-guanidino-hexylcarbamoyl)methyl]-2'-deoxyuridine (**Tg**), which has a guanidinium group at the C5 position of deoxyuridine (Figure 1 a). The guanidinium group is a side chain of arginine (Arg). Previous studies revealed that basic peptides such as

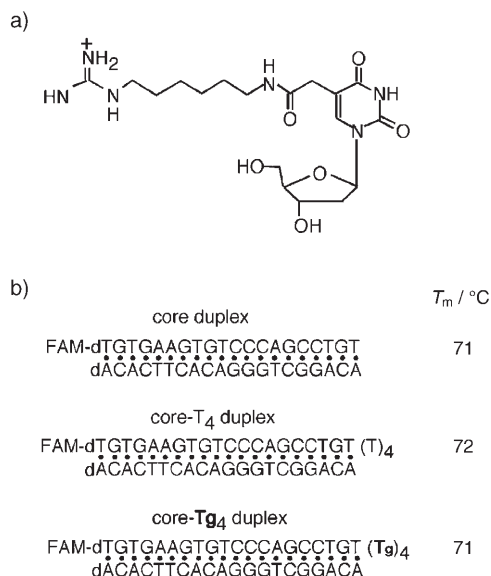


Figure 1. a) 5-[(6-Guanidino-hexylcarbamoyl)methyl]-2'-deoxyuridine (**Tg**); b) sequences and melting temperatures (T_m) of the core duplex, core-T₄ duplex, and core-Tg₄ duplex (3 μM each) in a buffer containing NaCl at 100 mM. FAM = 6-carboxyfluorescein.

human immunodeficiency virus type 1 (HIV-1) Tat-(48-60) have membrane permeability and carrier function for intracellular protein delivery.^[21] Moreover, many Arg-rich peptides such as HIV-1 Rev-(34-50) and octaarginine (Arg₈) can translocate efficiently through cell membranes.^[22,23] Therefore, it is expected that **Tg** is likely to perform as an excellent transmembrane carrier for oligonucleotides. Herein, the guanidinium-modified DNA clearly shows cellular uptake in HeLa cells without any reagents.

A 20-mer DNA oligomer labeled with 6-carboxyfluorescein (FAM) at the 5' end was prepared as the core strand: 5'-FAM-dTGTGAAGTGTCCCAGCCTGT. Then, four **Tg** moieties were added to the core at the 3' end by a primer-extension reaction. After optimization of the reaction conditions (Supporting Information), the primer-extension reaction was performed with DNA polymerase. The primer extension used in this study might be useful for further applications because its products are easily purified. Next, the effect of the modified DNA (core-Tg₄) on duplex stability was measured, because modified DNA base analogues often destabilize duplex formation. The melting temperatures (T_m) of the 20-mer core duplex (5'-FAM-dTGTGAAGTGTCCCAGCCTGT-3'/5'-ACAGGCTGGACACTTCACA-3'), a duplex in which the core strand has four dangling T nucleotides at the 3' end (core-T₄ duplex: 5'-FAM-dTGTGAAGTGTCCCAGCCTGT(T)₄-3'/5'-ACAGGCTGGACACTTCACA-3'), and a core duplex with **Tg₄ at the 3' end (core-Tg₄ duplex: 5'-FAM-dTGTGAAGTGTCCCAGCCTGT(**Tg**)₄-3'/5'-ACAGGCTGGACACTTCACA-3') were measured by UV/Vis spectroscopy in a buffer containing NaCl (100 mM), in close approximation to typical physiological conditions (Figure 1 b). The T_m values of the core, core-T₄, and core-Tg₄ duplexes (3 μM each) were 71, 72, and 71 $^\circ\text{C}$, respectively. The data indicate that **Tg₄ as a dangling end does not noticeably inhibit duplex stability; these data are in agreement with previously observed trends. The 3' dangling ends in B-form DNA are not energetically favored as a result of fewer geometric intrastrand stacking events.^[24]****

Next, the uptake of single-stranded core-Tg₄ by HeLa cells was studied with both fluorescence-activated cell sorting (FACS) and microscopy. In typical experiments, HeLa cells were cultured in Eagle's minimum essential medium containing single-stranded core-Tg₄ (4 μM) for 48 hours, washed with phosphate-buffered saline, and quantified by fluorescence measurement. The uptake of core-Tg₄ was monitored by FACS analysis of FAM (Supporting Information). After 48 hours, cells incubated with core-Tg₄ had higher fluorescence than a population of cells incubated in the absence of core-Tg₄. To confirm the role of the guanidinium group, we synthesized 5-[(6-amino-hexylcarbamoyl)methyl]-2'-deoxyuridine (**Ta**),^[25] which has a Lys side chain (Supporting Information); it is known that Arg peptides undergo cellular uptake more readily than Lys peptides.^[26,27] If the cellular uptake does not depend on the guanidinium group, then one would expect the cellular uptake efficiency of **Tg**- and **Ta**-modified DNA to be the same. Quantitation of FAM by FACS analysis showed that the uptake of core-Ta₄ was 1.8% of that of core-Tg₄, which suggests that the guanidinium group works efficiently as a carrier.

The microscopy images of HeLa cells cultured in the presence of 4 μM core-**Tg**₄ are shown in Figure 2. Figure 2a shows a fluorescence overlay image of phase contrast, core-**Tg**₄, and nuclei of living cells. The green and blue colors are a

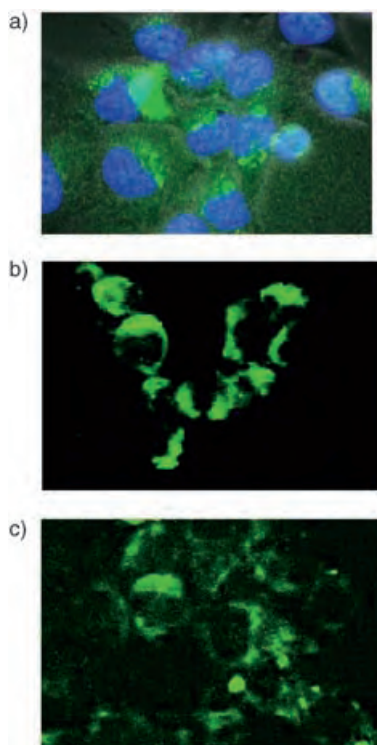


Figure 2. Microscopy images of HeLa cells cultured in the presence of core-**Tg**₄ (4 μM): a) fluorescence overlay image of DNA oligomer, nuclei, and phase contrast of living cells; b) confocal microscopy image of DNA oligomer of fixed cells; c) confocal microscopy image of DNA oligomer of living cells.

result of fluorescence of the FAM-labeled DNA oligomer and stained nuclei, respectively. As the cells incubated with the core (FAM-labeled DNA without **Tg**₄) did not exhibit this green color (Supporting Information), the images clearly show that the chemical modification induces the cellular uptake activity. Moreover, the green areas do not seem to overlap the blue, which suggests that the cellular localization of these compounds is in the cytoplasm. Confocal microscopy studies were carried out to determine whether the guanidinium-modified DNA is internalized or simply attached to the cell surface. Fixed cells are usually used for confocal microscopy to obtain clear images, but recent studies indicate that cell fixation leads to the artifactual redistribution of cationic peptides into the nucleus.^[28] Therefore, images of fixed cells and living cells were obtained (Figure 2b,c). Interestingly, these images showed that the distribution of the green color observed in the cytoplasm was similar to that observed with the fluorescence microscope. This suggests that the cellular localization of these compounds is mainly cytoplasmic. Recent studies on cationic peptides, such as the Tat peptide, support the notion that uptake occurs through an endocytosis pathway and that most cationic peptides reside in cytosol.^[29–32] Our result for modified DNA is consistent with this behavior

of cationic peptides. Although detailed future investigations are necessary, the intracellular redistribution of the modified DNA might occur through endocytosis.

Finally, the effect of modified DNA length on the cellular uptake efficiency was investigated (Figure 3). The amount of cellular uptake with core-**Tg**₃ was 70 % of that of core-**Tg**₄. Interestingly, the amount of cellular uptake with core-**Tg**₆ was

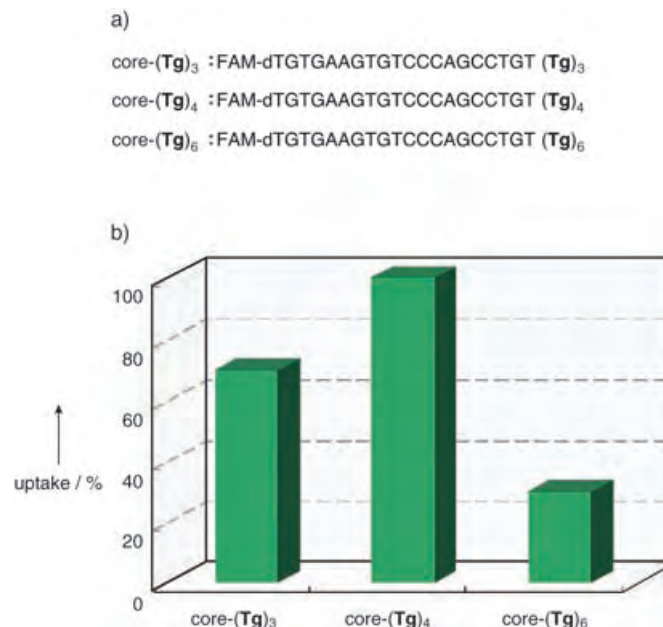


Figure 3. a) DNA sequence studied to investigate the effect of modified DNA length on cellular uptake. b) Uptake efficiency relative to core-**Tg**₄ quantified by FACS analysis of FAM.

only 30 % of that of core-**Tg**₄. Even at DNA concentrations that were twice as high (8 μM), the order of the amount of cellular uptake was still core-**Tg**₄ > core-**Tg**₃ > core-**Tg**₆. In the case of Arg peptides, the efficiency of cellular uptake decreased with increasing polypeptide length because of aggregation. The length range showing more efficient uptake was between eight and ten Arg residues.^[23] Our data are in agreement with an increase in length being unfavorable for cellular uptake. However, the most favorable length (four **Tg** nucleotides) is shorter than an eight- to ten-residue poly-Arg peptide. Although the reaction conditions of core-**Tg**₄ were not optimized, the degree of cellular uptake for core-**Tg**₄ at 8 μM with incubation for 48 hours was about 75 % that of the uptake for the core through a commercial liposome transfection agent (LipofectAMINE 2000 reagent (Invitrogen)) under optimized conditions. This indicates that the cellular uptake of core-**Tg**₄ is not so inefficient.

In summary, we have found that 5-[(6-guanidiniohexyl-carbamoyl)methyl]-2'-deoxyuridine (**Tg**) plays the important role of carrier for cellular uptake. In the case of the Arg-rich peptide, HeLa cells are a typical example of a cell type that is difficult for intracellular peptide delivery.^[23] Therefore, the cellular uptake of **Tg** in HeLa cells indicates that **Tg** could be applied as a carrier agent for a wide range of cell types. The activity of **Tg** as the carrier was observed not only for HeLa

cells but also for RAW 264.7 cells, which are known to allow uptake readily (Supporting Information).^[23] Interestingly, the optimal number of **Tg**-modified bases as a carrier for a 20-nucleotide DNA oligomer was only four. Oligonucleotide-based functional molecules allow easy conjugation to DNA and RNA for biochemical and biophysical applications. Thus, **Tg** could be used as a new tool in future applications for intracellular oligonucleotide delivery.

Received: March 11, 2005

Revised: May 24, 2005

Published online: September 19, 2005

Keywords: biotechnology · cellular uptake · nucleic acids · nucleosides · oligonucleotides

- [1] R. A. Stull, F. C. Szoka, *Pharm. Res.* **1995**, *12*, 465–483.
- [2] S. Agrawal, *Trends Biotechnol.* **1996**, *14*, 376–387.
- [3] W. Pawlak, J. Zolnieriek, T. Sarosiek, C. Szczylik, *Cancer Treat. Rev.* **2000**, *26*, 333–350.
- [4] J. D. Thompson, *Drug Discov. Today* **2002**, *7*, 912–917.
- [5] S. M. Elbashir, J. Harborth, W. Lendeckel, A. Yalcin, K. Weber, T. Tuschl, *Nature* **2001**, *411*, 494–498.
- [6] G. T. Hannon, *Nature* **2002**, *418*, 244–251.
- [7] J. Soutschek, A. Akinc, B. Bramlage, K. Charisse, R. Constien, M. Donoghue, S. Elbashir, A. Geick, P. Hadwiger, J. Harborth, M. John, V. Kesavan, G. Lavine, R. K. Pandey, T. Racie, K. G. Rajeev, I. Rohl, I. Toudjarska, G. Wang, S. Wuschko, D. Bumcrot, V. Kotliansky, S. Limmer, M. Manoharan, H. P. Vornlocher, *Nature* **2004**, *432*, 173–178.
- [8] J. Zabner, A. J. Fasbender, T. Moninger, K. A. Poellinger, M. J. Welsh, *J. Biol. Chem.* **1995**, *270*, 18997–19007.
- [9] F. LabatMoleur, A. M. Steffan, C. Brisson, H. Perron, O. Feugeas, P. Furstemberger, F. Oberling, E. Brambilla, J. P. Behr, *Gene Ther.* **1996**, *3*, 1010–1017.
- [10] D. Luo, W. M. Saltzman, *Nat. Biotechnol.* **2000**, *18*, 33–37.
- [11] S. Capaccioli, G. Dipasquale, E. Mini, T. Mazzei, A. Quattrone, *Biochem. Biophys. Res. Commun.* **1993**, *197*, 818–825.
- [12] J. G. Lewis, K. Y. Lin, A. Kothavale, W. M. Flanagan, M. D. Matteucci, R. B. DePrince, R. A. Mook, R. W. Hendren, R. W. Wagner, *Proc. Natl. Acad. Sci. USA* **1996**, *93*, 3176–3181.
- [13] H. Yoo, R. L. Juliano, *Nucleic Acids Res.* **2000**, *28*, 4225–4231.
- [14] O. Boussif, F. Lezoualch, M. A. Zanta, M. D. Mergny, D. Scherman, B. Demeneix, J. P. Behr, *Proc. Natl. Acad. Sci. USA* **1995**, *92*, 7297–7301.
- [15] M. Robaczewska, S. Guerret, J. S. Remy, I. Chemin, W. B. Offensperger, M. Chevallier, J. P. Behr, A. J. Podhajski, H. E. Blum, C. Trepo, *Hum. Gene Ther.* **2001**, *8*, 874–881.
- [16] C. E. Prater, P. S. Miller *Bioconjug. Chem.* **2004**, *15*, 498–507.
- [17] D. A. Stetsenko, M. J. Gait, *Methods Mol. Biol.* **2005**, *288*, 205–224.
- [18] C. H. Tung, S. Stein, *Bioconjug. Chem.* **2000**, *11*, 605–618.
- [19] S. Nakano, Y. Uotani, K. Uenishi, M. Fujii, N. Sugimoto, *J. Am. Chem. Soc.* **2005**, *127*, 518–519.
- [20] J. Gao, S. Watanabe, E. T. Kool, *J. Am. Chem. Soc.* **2004**, *126*, 12748–12749.
- [21] S. R. Schwarze, A. Ho, A. Vocero-Akbani, S. F. Dowdy, *Science* **1999**, *285*, 1569–1572.
- [22] M. Rojas, J. P. Donahue, Z. Tan, Y. Z. Lin, *Nat. Biotechnol.* **1998**, *16*, 370–375.
- [23] S. Futaki, T. Suzuki, W. Ohashi, T. Yagami, S. Tanaka, K. Ueda, Y. Sugiura, *J. Biol. Chem.* **2001**, *276*, 5836–5840.
- [24] T. Ohmichi, S. Nakano, D. Miyoshi, N. Sugimoto, *J. Am. Chem. Soc.* **2002**, *124*, 10367–10372.
- [25] H. Sawai, A. N. Ozaki, F. Satoh, T. Ohbayashi, M. M. Masud, H. Ozaki, *Chem. Commun.* **2001**, 2604–2605.
- [26] P. A. Wender, D. J. Mitchell, K. Pattabiraman, E. T. Pelkey, L. Steinman, J. B. Rothbard, *Proc. Natl. Acad. Sci. USA* **2000**, *97*, 13003–13008.
- [27] D. J. Mitchell, D. T. Kim, L. Steinman, C. G. Fathman, J. B. Rothbard, *J. Pept. Res.* **2000**, *56*, 318–325.
- [28] L. P. Richard, K. Melikov, E. Vives, C. Ramos, B. Verbeure, M. J. Gait, L. V. Chernomordik, B. Lebleu, *J. Biol. Chem.* **2003**, *278*, 585–590.
- [29] J. P. Richard, K. Melikov, H. Brooks, P. Prevot, B. Lebleu, L. V. Chernomordik, *J. Biol. Chem.* **2005**, *280*, 15300–15306.
- [30] I. Nakase, M. Niwa, T. Takeuchi, K. Sonomura, N. Kawabata, Y. Koike, M. Takehashi, S. Tanaka, K. Ueda, J. C. Simpson, A. T. Jones, Y. Sugiura, S. Futaki, *Mol. Ther.* **2004**, *10*, 1011–1022.
- [31] G. Drin, S. Cottin, E. Blanc, A. R. Rees, J. Temsamani, *J. Biol. Chem.* **2003**, *278*, 31192–31201.
- [32] A. Fittipaldi, A. Ferrari, M. Zoppe, C. Arcangeli, V. Pellegrini, F. Beltram, M. Giacca, *J. Biol. Chem.* **2003**, *278*, 34141–34149.

Protein Interactions

DOI: 10.1002/anie.200501279

The Design and Evaluation of Heparin-Binding Foldamers**

*Sungwook Choi, Dylan J. Clements,
Vojislava Pophristic, Ivaylo Ivanov,
Satyavani Vemparala, Joel S. Bennett, Michael L. Klein,
Jeffrey D. Winkler, and William F. DeGrado**

Foldamers, nonbiological oligomers with well-defined secondary or tertiary structures,^[1,2] provide novel templates for the design of biologically active molecules that compete for a

[*] S. Choi, Dr. I. Ivanov, Dr. S. Vemparala, Prof. Dr. M. L. Klein,
Prof. Dr. J. D. Winkler, Prof. Dr. W. F. DeGrado
Department of Chemistry, University of Pennsylvania
Philadelphia, PA 19104-6323 (USA)
Fax: (+1) 215-573-7229
E-mail: wdegrado@mail.med.upenn.edu

S. Choi, D. J. Clements, Prof. Dr. W. F. DeGrado
Department of Biochemistry and Biophysics
University of Pennsylvania
Philadelphia, PA 19104-6059 (USA)

Prof. Dr. V. Pophristic
Department of Chemistry and Biochemistry
University of the Sciences in Philadelphia
Philadelphia, PA 19104 (USA)

Prof. Dr. J. S. Bennett
Department of Medicine, Hematology and Oncology Division
University of Pennsylvania
Philadelphia, PA 19104 (USA)

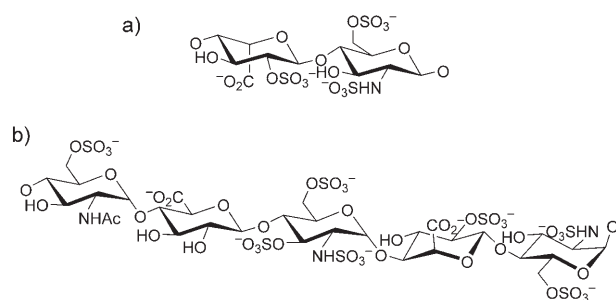
[**] We thank the National Institutes of Health (grant no. 65803),
PolyMedix, Inc., and Burroughs Wellcome Fund (fellowship to I.I.)
for financial support



Supporting information for this article is available on the WWW
under <http://www.angewandte.org> or from the author.

variety of protein–protein^[3] and protein–membrane interactions.^[4] Their semirigid structures and their adjustable lengths mean that they provide excellent starting points for the elaboration of protein mimics that might be difficult to design based on small-molecule scaffolds. Here we describe the design of aryl amide oligomers that compete for heparin–protein interactions. Heparin, a linear and highly sulfated polysaccharide, is a crucial component in a variety of biological processes mediated by specific heparin–protein interactions including blood coagulation, viral infection, and cell growth. Heparin has become a commonly used clinical anticoagulant to prevent and treat thrombotic diseases.^[5,6] However, bleeding complications including hemorrhage and heparin-induced thrombocytopenia (HIT), which is a common immune-mediated disorder, are major adverse effects associated with heparin therapy.^[7] Therefore, frequent coagulation monitoring may be necessary to minimize the risk of life-threatening hemorrhages resulting from an overdose, while at the same time maximizing the anticoagulant efficacy.

Low-molecular-weight (LMW) heparins, like unfractionated (UF) heparin, consist of repeating units of L-iduronic acid and D-glucosamine (Scheme 1 a). LMW heparins have



Scheme 1. a) The major repeating unit and b) the antithrombin III binding pentasaccharide of heparin.

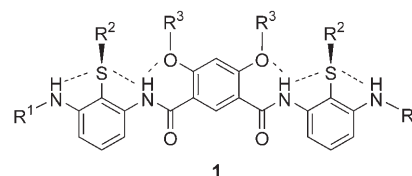
resolved some of the problems associated with UF-heparin use, in that they have a more predictable dose response, an improved bioavailability, and a longer half-life.^[8] Protamine is used extensively as a clinical heparin antidote to neutralize the anticoagulation function of heparin following cardiovascular surgery^[9] but it is not prescribed for use with LMW-heparin therapy. Protamine treatment can also cause several side effects mediated by nonimmunologic and immunoglobulin-mediated pathways.^[10] Thus, much safer and more effective agents for neutralizing the anticoagulant function of heparin are currently of great interest.

The interaction between heparin and antithrombin, a plasma serine proteinase inhibitor that is the major inhibitor of the coagulation cascade, facilitates a conformational change in antithrombin. This conformational change accelerates inhibition of coagulation factors such as thrombin and factor Xa.^[11,12] Through X-ray crystallographic analysis of the antithrombin–pentasaccharide complex^[13,14] and several studies of site-directed mutagenesis of antithrombin,^[15,16] it has been shown that the negatively charged pentasaccharide binds to the basic amino acids (lysine and arginine) of antithrombin.

Furthermore, by comparing various heparin-binding proteins, Cardin and Weintraub classified two consensus sequences responsible for binding, XBBXB and XBBBXXB, where B is a basic residue and X is any other amino acid. It was suggested that these sequence motifs fold along one face of an α helix or β sheet.^[17] Most heparin-binding sites have a bipolar structure, in which the basic amino acids are facing one side; neutral or lipophilic amino acids generally face the opposite side, regardless of the secondary structure.^[18]

A few medium-sized peptides such as protamine analogues,^[10,19] antithrombin-derived peptides,^[20] and polyarginine peptides,^[21] have been reported as potent heparin antidotes. Small-molecule inhibitors of heparin may alleviate complications associated with peptide-based heparin antidotes, such as proteolytic stability, distribution, and difficulty of scale-up. We have previously reported the synthesis of amphiphilic arylamide oligomers that mimic the biological properties of antimicrobial peptides and proteins.^[4] Herein, we expand this strategy towards the design of small molecules that strongly interact with highly sulfated heparin.

Our design is based on a 1,3-substituted arylamide oligomer with additional hydrogen-bonding substituents included to increase solubility and conformational rigidity and to provide appropriately spaced cationic groups to interact with heparin. The thioether and ether groups of the generic oligomer **1** provide internal hydrogen-bond acceptors, while simultaneously providing points of attachment for additional functional groups.



Initially, a molecular dynamics study on binding of one of the arylamide analogues (shown in Figure 1, compound **8c**) to heparin in aqueous solution was undertaken. Analysis of the obtained trajectory suggests that these compounds might interact strongly with the pentasaccharide sequence of heparin (PDB code: 1E03). Owing to the extensive charge complementarity between the inhibitor and the heparin analogue, the binding is dominated by electrostatic interactions. At early stages in the trajectory, the two guanidium cations of the terminal side chains (R^4 , Table 1) anchor compound **8c** to the pentasaccharide in a nearly parallel mode, by closely interacting with $\text{CH}_2\text{--OSO}_3^-$ groups of the two terminal pentasaccharide sugars (Figure 1 a). The other positively (NH_3^+) and negatively (COO^- , OSO_3^-) charged groups of compound **8c** and the pentasaccharide, respectively, are then aligned. The limited flexibility of the pentasaccharide (Figure 1 a) allows these groups to assume optimal positions, thereby maximizing the attractive interactions (Figure 1 b) and hydrogen bonding without incurring an overly large loss in conformational entropy, which might occur with more flexible small peptides. All the side chains of compound **8c** are involved in the binding, with the terminal ones playing an

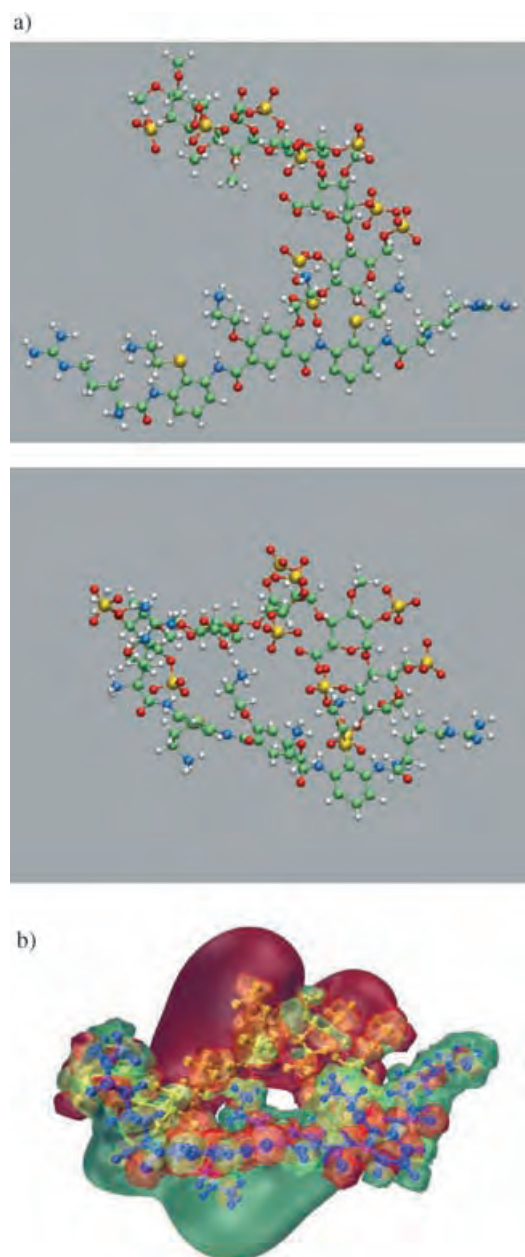


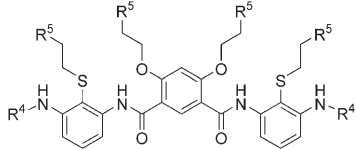
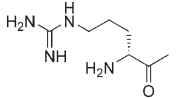
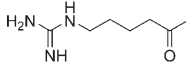
Figure 1. a) The initial (top) and final (after 7 ns, bottom) conformations of the aryl amide oligomer–pentasaccharide heparin system. In the initial stage of the simulation, the aryl amide backbone undergoes an internal twist, which facilitates the anchoring of the terminal aryl amide groups to pentasaccharide. Color code: S: yellow; C: cyan; N: blue; O: red. Water molecules and hydrogen atoms are not shown for clarity. b) The final aryl amide oligomer–pentasaccharide conformation, with electrostatic potential surfaces^[29] shown in red (aryl amide oligomer) and green (pentasaccharide).

additional role of initial anchoring and aligning. However, some of the pentasaccharide charged groups are pointing away from the complex, toward the solution.

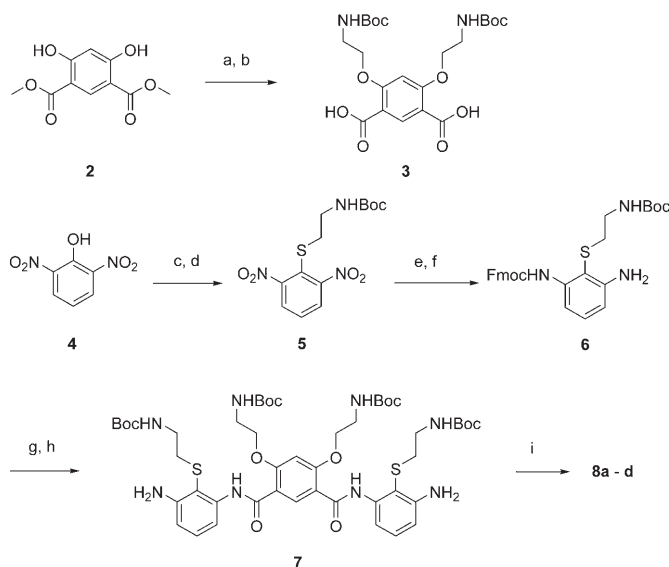
Based on these observations, we synthesized a series of aryl amide oligomers, as described in Scheme 2.

We examined the interaction between compounds **8a–d** and LMW heparin (Lovenox, M_w = 4500 Daltons) and UF heparin, respectively, both of which contain an antithrombin-

Table 1: Biological activity of small molecules **8a–d**.

					
Compound	R ⁴	R ⁵	IC ₅₀ [μM]	K _B [μM] ^[a]	HC ₅₀ [μM] ^[b]
8a	H	NH ₂	256	6.7	> 1540
8b	H	HN=C(NH) ₂	77.9	3.2	> 1363
8c		NH ₂	22.5	1.8	> 1087
8d		NH ₂	28.1	2.0	927

[a] The dissociation constant (K_B) was measured by Schild plot analysis by using the anti-Factor Xa assay. [b] The HC₅₀ value (measurement of hemolytic activity) was obtained by measuring 50% lysis of human erythrocytes.



Scheme 2. a) Boc-NH(CH₂)₂OH, DEAD, PPh₃, THF; b) 2 N LiOH, MeOH, THF; c) TsCl, DIEA, CH₂Cl₂; d) Boc-NH(CH₂)₂SH, DIEA, CH₂Cl₂; e) SnCl₂·2 H₂O, NaOAc·3 H₂O, EtOH, 78 °C; f) FmocCl, pyridine, THF, 0 °C; g) **2**, (COCl)₂, pyridine, DMF (cat.), THF, then **6**, Et₃N, DMAP, CH₂Cl₂; h) 20% PIP in DMF; i) for **8a**: 50% TFA in CH₂Cl₂; for **8b** and **8a**: *N,N'*-bis(*tert*-butoxycarbonyl)-1*H*-pyrazole-1-carboxamide, DIEA, MeCN/H₂O, then 50% TFA in CH₂Cl₂; for **8c** and **8d**: RCO₂H, POCl₃, pyridine, –15 °C, then 50% TFA in CH₂Cl₂. Boc = *tert*-butoxycarbonyl, DEAD = diethylazodicarboxylate, DIEA = *N,N*-diisopropylethylamine, DMAP = 4-dimethylaminopyridine, DMF = *N,N*-dimethylformamide, Fmoc = 9-fluorenylmethoxycarbonyl, PIP = piperidine, TFA = trifluoroacetic acid, THF = tetrahydrofuran, Ts = toluene-4-sulfonyl.

binding domain (pentasaccharide, Scheme 1 b). The ability of the compounds to compete with antithrombin for binding to Lovenox at physiological salt concentration (0.15 M NaCl) was assessed by a standard *anti*-factor Xa chromogenic assay (Figure 2).

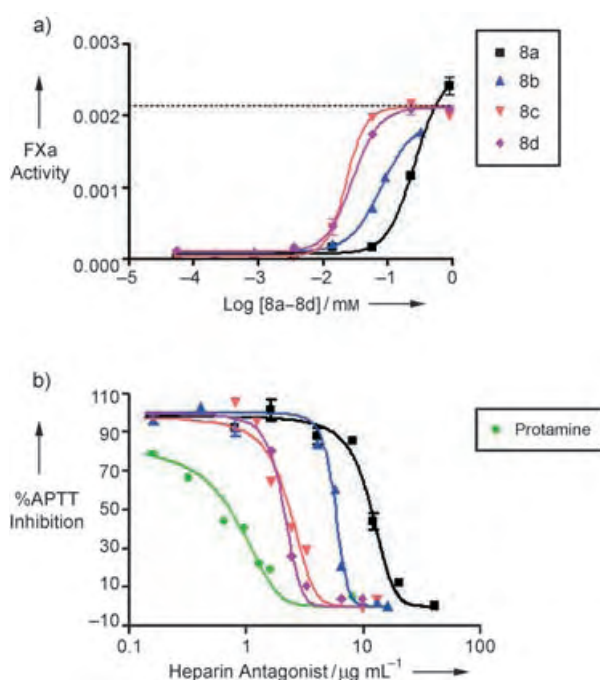


Figure 2. Dose-dependent neutralization of a) LMW heparin and b) UF heparin by compounds **8a–d**. a) Factor Xa assay. b) aPTT clotting assay in the presence of UF heparin ($2.42 \mu\text{g mL}^{-1}$).

Compound **8a** served as an initial lead compound to inhibit the function of Lovenox. Although it exhibited a low in vitro inhibition ($\text{IC}_{50} = 256 \mu\text{M}$, Table 1) against Lovenox, we were inspired to investigate the possible role of the basic side chain of the compound in its interaction with polysulfated heparin. The conversion of the side chains of **8a** to give the polyguanidinylated derivative **8b** resulted in a threefold increase in potency. This result is consistent with observations reported by Linhardt and co-workers. They suggested that arginine binds about 2.5 times more tightly than lysine to the sulfate groups of heparin due to distinct hydrogen bonding.^[22] Therefore, we reasoned that the increased activity of compound **8b** arose from differences in hydrogen bonding between ammonium or guanidinium cations and the sulfate groups of LMW heparin.

To obtain more potent heparin inhibitors, further chemical modification was necessary. The introduction of extra positively charged substituents at the terminal amines gave compounds **8c** and **8d**, which exhibited a greater than tenfold increase in potency compared to that of **8a**. Additionally, **8d** was found to have a similar in vitro efficacy to **8c**, in that both compounds provide significant improvement and have similar inhibition constants ($\text{IC}_{50} = 28.1$ and $22.5 \mu\text{M}$, respectively, Table 1). The introduction of additional positive charges enhanced the potency of the compounds, as expected from the molecular dynamics study.

To estimate the binding affinities of compounds **8a–d**, Schild plot analysis, which measures agonist dose–response curve shifts by a competitive antagonist, was used to evaluate their capacity to interact with LMW heparin. Table 1 lists the dissociation constants (K_B) of these four compounds. These compounds prevent the binding of heparin to antithrombin in

a dose-dependent manner. The Schild plot of inhibition for compounds **8a–d** establishes that they are competitive inhibitors for heparin–antithrombin formation with dissociation constants (K_B) of 6.7, 3.2, 1.8, and $2.0 \mu\text{M}$, respectively. These data also show that **8c** was the most potent inhibitor among compounds **8a–d**.

To further address the specificity and affinity of these foldamers in a stringent biological medium, we examined their abilities to inhibit clotting in human plasma by measuring the neutralization of UF heparin by **8a–d** and protamine in an activated partial thromboplastin time (aPTT) clotting assay. The study was conducted with UF heparin because conventional aPTT clotting assays are a relatively insensitive method for measuring the activity of LMW heparin. As shown in Figure 2b, **8a–d** and protamine efficiently reversed heparin-induced aPTT clotting. Also, similar patterns of neutralization of heparin by **8a–d** were observed, which were consistent with those from the factor Xa assay. The most active compounds **8c** and **8d** were only two- to threefold less potent than protamine (average $M_w = 5100$ Daltons), despite the fact that these are small molecules.

Finally, as an initial test of toxicity, we measured hemolytic activities of the compounds against human erythrocytes. None of these small molecules lysed human red cells at concentrations as high as $1000 \mu\text{M}$.

In summary, we have described the synthesis of a series of arylamide oligomers, which interact with LMW heparin and UF heparin. This interaction inhibits the ability of LMW heparin to activate antithrombin and, in this way, affects the biological function of LMW heparin. These arylamide oligomers are the first example of low-molecular-weight antagonists that inhibit the anticoagulant function of heparin.

Experimental Section

The synthesis of all compounds is described in the Supporting Information. The factor Xa assay in the presence of Lovenox and inhibitor was measured in a chromogenic assay by using reagents purchased from DiaPharma. In brief, the reagents were reconstituted in a 0.02 M tris(hydroxymethyl)aminomethane (Tris) buffer at pH 8.4. Antithrombin was prepared with 0.336 M NaCl for a physiological salt concentration (0.15 M) in the final reaction. Antithrombin (0.08 IU mL^{-1} ; $50 \mu\text{L}$) was mixed with Lovenox ($11.2 \mu\text{g mL}^{-1}$; $1 \mu\text{L}$). After the incubation for 5 min, different concentrations of inhibitor ($1 \mu\text{L}$) were added to each row of wells; the wells were then gently shaken and incubated for 20 min. Factor Xa (2.8 nkat mL^{-1} ; $50 \mu\text{L}$) was then added and the reaction mixture was shaken and incubated for an additional 10 min. Substrate (S-2765; $10 \mu\text{L}$) was added and the 96-well plate was then shaken and read every 30 s for 7 min at 405 nm on a ThermoLabsystems Multiskan Spectrum. In the assay for Schild plot analysis, we followed the same protocol as for the anti-factor Xa assay except the concentrations of Lovenox and inhibitors were varied.

aPTT activity was resolved by using a BBL Fibrometer (Becton Dickinson, San Jose, CA) and a commercial kit containing Citrex I Control Plasma and Cephalinex-Activated PTT Reagent (Bio/Data Corporation, Horsham, PA). In brief, heparin ($5 \mu\text{L}$) and antagonist ($5 \mu\text{L}$) were preincubated (37°C on a Fibrometer's heating block) for 10 s prior to addition of control plasma (0.1 mL) into the test cuvette. This mixture was allowed to incubate for 2 min at 37°C . Meanwhile, 25 mM CaCl_2 (0.2 mL) was set to preincubate in a separate cuvette. Cephalinex (0.1 mL) was pipetted into the test cuvette containing the

plasma and incubated for exactly 5 min. The preincubated CaCl_2 (0.1 mL) was added with simultaneously starting of the Fibrometer's timer. Once a clot formed, the timer stopped and the clotting time was recorded. Biochemicals not provided with the kit were heparin sodium salt from bovine intestinal mucosa (Sigma, H-0777, 150 Units mg^{-1}) and protamine sulfate from salmon (Sigma, p4020).

The details of the interaction between heparin and compound **8c** were investigated by using molecular dynamics simulations. A pentasaccharide heparin sequence (charge -11) was placed in a box ($55.69 \times 53.09 \times 60.04 \text{ \AA}$) with compound **8c** (+8 charges, Table 1) and three Na^+ ions to balance the charge. The system was solvated by TIP3P water,^[23] thereby resulting in a size of ≈ 17500 atoms. Parameters for compound **8c** were derived from the newly developed force field for aryl amide oligomers,^[24] to ensure proper description of the backbone conformational dynamics, in combination with semi-empirical (MOPAC) charges.^[25] Heparin parameters were developed partly by analogy with the existing Amber parameters,^[26] augmented by parameters for the SO_4^- groups,^[27] partly from semiempirical calculations.^[25] The system was equilibrated for 1 ns and the analysis was performed based on a subsequent 6 ns production run. The simulations were carried out by using the NAMD2 software^[28] with full electrostatics by use of the Particle Mesh Ewald method and a time step of 1.5 fs.

Received: April 12, 2005

Published online: August 11, 2005

Keywords: antithrombin · heparin · inhibitors · oligomers · protein interactions

- [1] D. J. Hill, M. J. Mio, R. B. Prince, T. S. Hughes, J. S. Moore, *Chem. Rev.* **2001**, 101, 3893.
- [2] S. H. Gellman, *Acc. Chem. Res.* **1998**, 31, 173.
- [3] J. A. Kritzer, M. E. Hodsdon, A. Schepartz, *J. Am. Chem. Soc.* **2005**, 127, 4118.
- [4] D. Liu, S. Choi, B. Chen, R. J. Doerksen, D. J. Clements, J. D. Winkler, M. L. Klein, W. F. DeGrado, *Angew. Chem.* **2004**, 116, 1178; *Angew. Chem. Int. Ed.* **2004**, 43, 1158.
- [5] I. Capila, R. J. Linhardt, *Angew. Chem.* **2002**, 114, 426; *Angew. Chem. Int. Ed.* **2002**, 41, 390.
- [6] R. Lever, C. P. Page, *Nat. Rev. Drug Discovery* **2002**, 1, 140.
- [7] T. E. Warkentin, M. N. Levine, J. Hirsh, P. Horsewood, R. S. Roberts, M. Gent, J. G. Kelton, *N. Engl. J. Med.* **1995**, 332, 1330.
- [8] J. I. Weitz, *N. Engl. J. Med.* **1997**, 337, 688.
- [9] G. R. Jones, R. Hashim, D. M. Power, *Biochim. Biophys. Acta* **1986**, 883, 69.
- [10] L.-C. Chang, J. F. Liang, H.-F. Lee, L. M. Lee, V. C. Yang, *AAPS Pharmsci.* **2001**, 3(2), article 18.
- [11] R. D. Rosenberg, P. S. Damus, *J. Biol. Chem.* **1973**, 248, 6490.
- [12] S. T. Olson, Y.-J. Chuang, *Trends Cardiovasc. Med.* **2002**, 12, 331.
- [13] L. Jin, J. P. Abrahams, R. Skinner, M. Petitou, R. N. Pike, R. W. Carrell, *Proc. Natl. Acad. Sci. USA* **1997**, 94, 14683.
- [14] D. J. D. Johnson, J. A. Huntington, *Biochemistry* **2003**, 42, 8712.
- [15] S. Schedin-Weiss, V. Arocas, S. C. Bock, S. T. Olson, I. Bjork, *Biochemistry* **2002**, 41, 12369.
- [16] S. Schedin-Weiss, U. R. Desai, S. C. Bock, S. T. Olson, I. Bjork, *Biochemistry* **2004**, 43, 675.
- [17] A. D. Cardin, H. J. Weintraub, *Arteriosclerosis* **1989**, 9, 21.
- [18] H. Margalit, N. Fischer, S. A. Ben-Sasson, *J. Biol. Chem.* **1993**, 268, 19228.
- [19] T. W. Wakefield, P. C. Andrews, S. K. Wroblewski, *J. Surg. Res.* **1996**, 63, 280.
- [20] S. Onoue, Y. Nemoto, S. Harada, T. Yajima, K. Kashimoto, *Life Sci.* **2003**, 73, 2793.
- [21] J. R. Fromm, R. E. Hileman, E. E. O. Caldwell, J. M. Weiler, R. J. Linhardt, *Arch. Biochem. Biophys.* **1997**, 343, 92.
- [22] J. R. Fromm, R. E. Hileman, E. E. O. Caldwell, J. M. Weiler, R. J. Linhardt, *Arch. Biochem. Biophys.* **1995**, 323, 279.
- [23] W. L. Jorgensen, J. Chandrasekhar, J. D. Madura, R. W. Impey, M. L. Klein, *J. Chem. Phys.* **1983**, 79, 926.
- [24] V. Pophristic, S. Vemparala, I. Ivanov, Z. Liu, M. L. Klein, W. F. DeGrado, *J. Phys. Chem. B*, unpublished results.
- [25] A. Jakalian, B. L. Bush, D. B. Jack, C. I. Bayly, *J. Comput. Chem.* **2000**, 21, 132.
- [26] D. A. Pearlman, D. A. Case, J. W. Caldwell, W. S. Ross, I. T. E. Cheatham, S. DeBolt, D. Ferguson, G. Seibel, P. Kollman, *Comput. Phys. Commun.* **1995**, 91, 1.
- [27] C. J. M. Huige, C. Altona, *J. Comput. Chem.* **1995**, 16, 56.
- [28] L. Kale, R. Skeel, M. Bhandarkar, R. Brunner, A. Gursoy, N. Krawetz, J. Phillips, A. Shinozaki, K. S. Varadarajan, *J. Comput. Phys.* **1999**, 151, 283.
- [29] N. A. Baker, D. Sept, S. Joseph, M. J. Holst, J. A. McCammon, *Proc. Natl. Acad. Sci. USA* **2001**, 98, 10037.

Host–Guest Systems

DOI: 10.1002/anie.200501888

Escape from a Nonporous Solid: Mechanically Coupled Biconcave Molecules**

Justin A. Riddle, John C. Bollinger, and Dongwhan Lee*

Molecular motions play a central role in many biologically important processes.^[1] The correlated movement of a finite number of symmetrically disposed building blocks in naturally occurring constructs can amplify a local distortion into a global structural change.^[2,3] This process is well illustrated by the unidirectional rotation of C_3 -symmetric transmembrane protein complexes^[4] and the pH-induced conformational changes of viral fusion proteins,^[5] which continue to inspire synthetic mimics of their structural as well as functional properties.^[6–9] Relaying mechanical signals to remote sites within such functional aggregates requires structurally rigid units, and the noncovalent interactions between these units can be maximized by positioning them in a symmetric fashion. In an effort to implement such an architectural motif in a small-molecule setting, we have devised a general synthetic

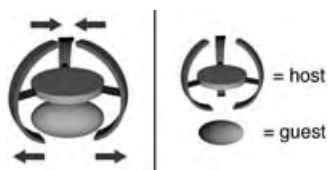
[*] J. A. Riddle, Dr. J. C. Bollinger, Prof. Dr. D. Lee
Department of Chemistry and Molecular Structure Center
Indiana University, Bloomington, IN 47405 (USA)
Fax: (+1) 812-855-8300
E-mail: dongwhan@indiana.edu

[**] This work was supported by Indiana University. We also acknowledge the donors of the American Chemical Society Petroleum Research Fund for their support of this research. J.A.R. gratefully acknowledges a GAANN Fellowship from the U.S. Department of Education.



Supporting information for this article, including the synthesis, characterization, and crystallographic data for compounds 4–6, is available on the WWW under <http://www.angewandte.org> or from the author.

route to a new class of C_3 -symmetric biconcave molecules. The solid-state structures of these molecules reveal effective mechanical communication between two vertices, by which structural changes on one side of the molecule are effectively transmitted to the other side (Scheme 1). Remarkably, the



Scheme 1. Schematic representation of conformational transmission by correlated opening and closing of the two concave sides of a molecule.

flexible solid-state structure of one such compound allows the complete release of clathrated guest molecules from a nonporous solid under ambient conditions. This dynamic crystal-to-crystal transformation has been confirmed by single-crystal X-ray crystallography.

We developed a convergent synthetic route in order to realize the mechanical coupling illustrated in Scheme 1. Our molecular design positions three *m*-terphenyl “wings” at the periphery of a C_3 -symmetric core. The six wing-tips of these elongated aromatic groups converge to define the two vertices of a biconcave molecule. As each pseudo- C_2 -symmetric terphenyl unit is disposed nearly perpendicular to the disc-shaped core, expansion of one cavity was expected to nicely correlate with contraction of the other (Scheme 1). Preliminary molecular modeling suggested that a triphenylene-type core **2** (Scheme 2) should be able to support three symmetrically disposed *m*-terphenyl fragments without severe steric constraints. As a structural surrogate of this planar polyaromatic platform, tris(salicylideneamine) **1**^[10,11]

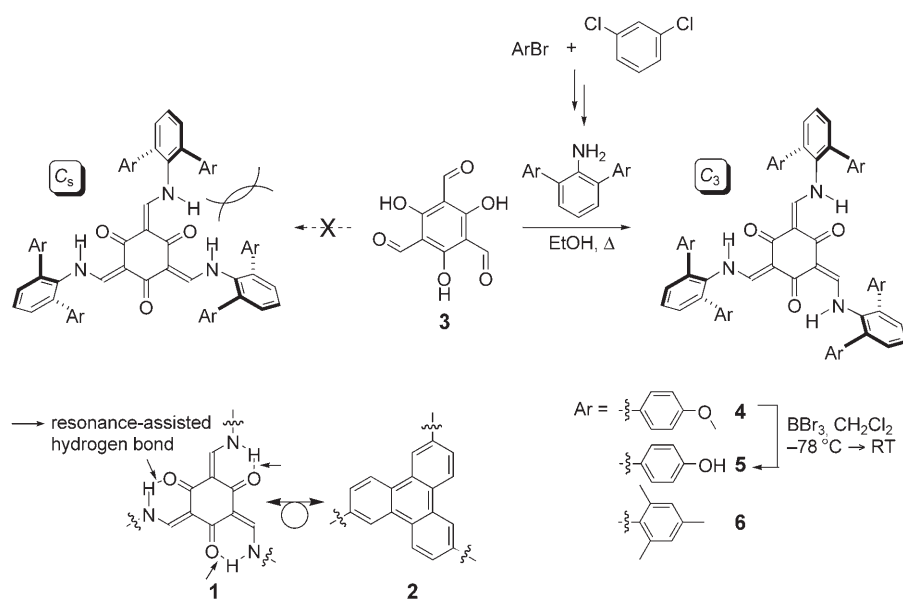
(Scheme 2) was chosen in our synthesis. In addition to assisting the facile construction of three-dimensional structures from modularly accessible building blocks, the semirigid six-membered rings afforded by the resonance-assisted hydrogen bonds (RAHBs)^[12] were expected to better accommodate the structural changes depicted in Scheme 1.

The reaction between 1,3,5-triformylphloroglucinol (**3**)^[10] and five equivalents of 2,6-di(*p*-methoxyphenyl)aniline^[13] in EtOH at reflux cleanly afforded the desired Schiff base product **4** in over 85 % yield (Scheme 2). The ^1H and ^1H - ^1H COSY NMR spectra of this compound in CD_2Cl_2 at 25 °C display a doublet ($\delta = 12.43$ ppm, 3H, =CNH) coupled ($J = 13$ Hz) to another doublet ($\delta = 7.53$ ppm, 3H, =CHN).^[14] Upon treatment with D_2O , the resonance at lower field completely disappears and the upper-field signal merges into a sharp singlet. This observation is consistent with the keto-enamine tautomer of the C_3 -symmetric tris(salicylideneamine) core rather than the enol-imine.^[10,11] The six methyl groups in **4** could be removed by treatment with BBr_3 at -78°C to furnish **5** in a yield of 70 %. A more sterically hindered homologue **6** could be obtained (65 % yield) by triple Schiff base condensation of **3** with 2,6-dimesitylaniline.^[13]

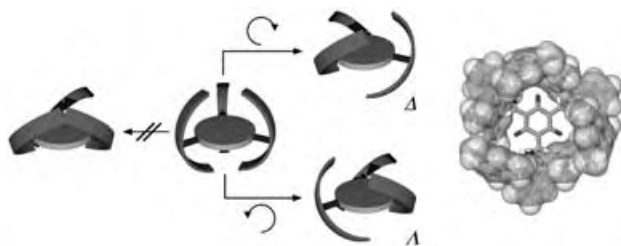
This high-yielding and operationally simple route afforded **4–6** in four to five steps from readily available materials without the need for chromatographic separation of synthetic intermediates. Notably, the selective formation of C_3 -symmetric **4–6** stands in stark contrast to the previous synthesis of less hindered tris(salicylideneamine) derivatives,^[15] in which mixtures of C_s and C_3 isomers were generally obtained (Scheme 2).^[10,11] By defining symmetric spaces above and below the molecular core, the *m*-terphenyl fragments apparently suppress the formation of the undesired C_s isomer. The reaction between **3** and 2-(4-hydroxyphenyl)aniline still furnished a mixture of C_s and C_3 isomers ($\approx 3:1$ ratio).

The nine aromatic rings in each of **4–6** are all connected by single C–C bonds rather than by direct ring fusion, thus allowing a balance between structural rigidity and flexibility. As shown in Scheme 3,^[16,17] the three *m*-terphenyl wings can undergo concerted tilting with respect to the threefold axis.^[18] Intramolecular steric considerations demand that this molecular motion proceeds in a merry-go-round fashion to establish a pair of C_3 -symmetric enantiomers, similar to the Δ and Λ isomers of an octahedral tris(chelate)–metal complex. The pseudo- Δ and pseudo- Λ enantiomers are present in equal amounts in solids **4–6**.

As part of this iris-like opening and closing motion, **5** displays conformational communication between two vertices in that the opening of one concave side closes the other side of the molecule (Figure 1).^[19] The pronounced asymmetry of the cavity topology is reflected by the distances between adjacent *m*-terphenyl wing-tips on each side



Scheme 2. Synthetic routes to C_3 -symmetric biconcave hosts **4–6**.



Scheme 3. Iris-like opening and closing motion: concerted tilting affords an enantiomeric pair of open conformers (right); reversing one rotation imposes steric constraints between adjacent *m*-terphenyl groups (left). Shown next to the schematic diagram is a capped-stick (core) and space-filling (mesityl groups) representation of the crystal structure of **6** (only the Δ isomer is shown).

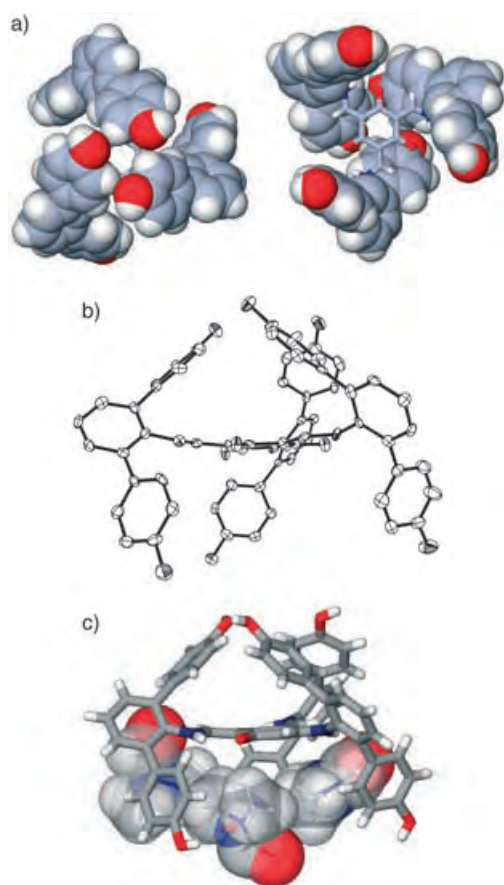


Figure 1. Crystal structure of **5**·6.5 DMF: a) space-filling and capped-stick representations viewed from the top (left) and bottom (right) of the molecule (DMF molecules are omitted); b) ORTEP diagram with thermal ellipsoids at the 50% probability level (hydrogen atoms and DMF guests have been omitted for clarity); c) three DMF molecules (in space-filling model) occupy the open concave side of **5** (capped-stick representation).

of the molecule: the “open” side $C_{para} \cdots C_{para}$ distances range from 10.470 to 10.988 Å (mean value: 10.697 Å), whereas the “closed” side distances range from 5.183 to 5.491 Å (mean value: 5.339 Å). In the solid state, three molecules of DMF (*N,N*-dimethylformamide) are located on one concave side of **5**. Although the detailed nature of this van der Waals host–

guest interaction is yet to be elucidated, this adaptive structural change convincingly demonstrates the conformational transmission proposed in Scheme 1.

The immediate functional relevance of structural semi-rigidity was highlighted by a single-crystal-to-single-crystal transformation of **4**, in which clathrated CHCl_3 molecules completely escape the crystal lattice without disrupting it. Compound **4** crystallizes in the trigonal system (space group $P31c$). Two chemically identical, but crystallographically unique, molecules **4a** and **4b** were identified in the lattice, each having a crystallographic threefold axis passing through the molecular core (Figure 2 a). In the solid state, facing pairs

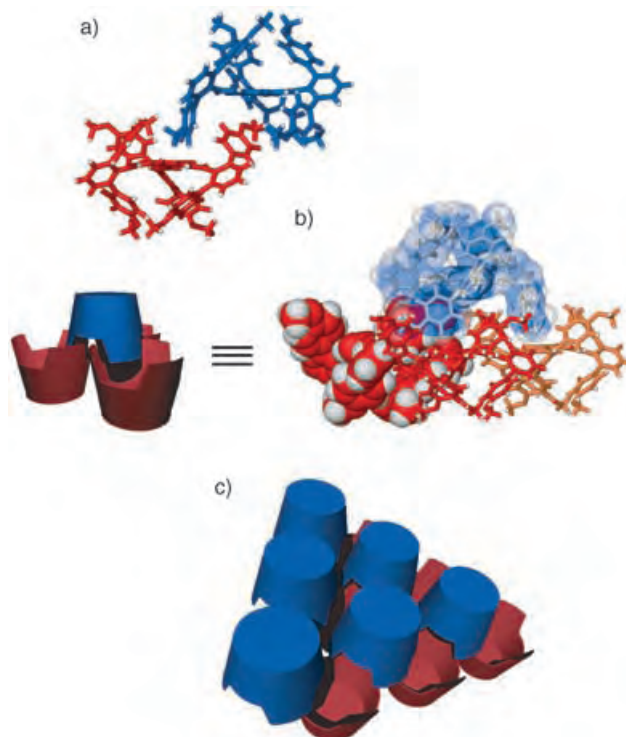


Figure 2. Molecular packing of **4a** (blue) and **4b** (red) in solvent-free solid **4**: a) capped-stick representation of two unique molecules interpenetrating each other; b) interaction between **4a** and a trigonal array of **4b**; c) schematic representation of a portion of the interdigitated bilayer comprising **4a** (six molecules, top) and **4b** (six molecules, bottom).

of **4a** and **4b** interpenetrate each other to open one side of the molecule and close up the other side. The *m*-terphenyl wings on the open side of **4a** function as a tripod when it docks with a triangular array of molecules of **4b** underneath (Figure 2 b). In turn, each molecule of **4b** is associated with three **4a** molecules stacked on top of it, thus defining repeating interdigitated bilayers of **4a**·**4b** perpendicular to the crystallographic *c* axis (Figure 2 c). The overall shape complementarity of the C_3 -symmetric **4** reinforces intermolecular van der Waals contacts and assists in efficient molecular packing. As a result, only 3.9% of the crystal volume is available to guests.

Evenly spaced interstitial spaces were identified within the two-dimensional closest packed layer of **4** (Figure 3). Each of these C_3 -symmetric crevices, with a volume of around

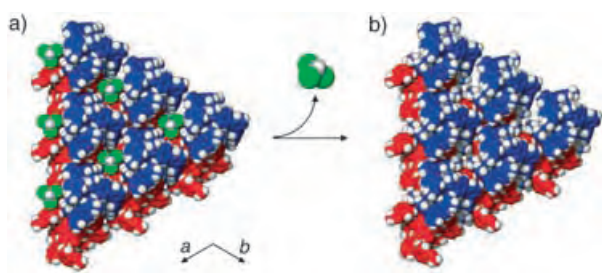


Figure 3. a) Crystal structure of a portion of $4 \cdot 1/2 \text{CHCl}_3$, shown as a space-filling representation of six **4a** molecules (blue) stacked on top of six **4b** molecules (red) viewed along the crystallographic c axis. Every interstitial void space is surrounded by a triangular array of **4a** and fully occupied by one molecule of CHCl_3 (green), which is disordered over two positions (not illustrated). b) Crystal structure of **4** redetermined after the complete release of CHCl_3 .

112 \AA^3 , is centered over a triangular array of **4a** and is fully occupied by one molecule of CHCl_3 when **4** is recrystallized from $\text{CHCl}_3/\text{Et}_2\text{O}$.^[20] After standing at room temperature for 10 weeks, the co-crystal of **4** and CHCl_3 perfectly retained its crystallinity despite the complete loss of CHCl_3 from the interstitial space. This was confirmed by a redetermination of the X-ray crystal structure of the same crystal, which also revealed a substantial ($\approx 4.3\%$) decrease in the volume of the

unit cell.^[21,22] Except for $\text{C}_{\text{aryl}}\text{--C}_{\text{aryl}}$ rotations involving three p -methoxyphenyl groups of **4a** close to CHCl_3 (Figure 4), no significant structural changes were observed before and after solvent loss. The rigid tris(salicylideneamine) cores perfectly fit each other with a maximum deviation of less than 0.05 \AA , and the aryl groups on the closed side of **4a** show a maximum deviation of 0.270 \AA . The structure of **4b** revealed deviations of less than 0.250 \AA for all atoms.^[14]

Unlike conventional microporous materials developed for the uptake and release of small-molecule substrates,^[23] no unobstructed channels could be found that connect individual cavities within **4** (Figure 4).^[24] Escape of CHCl_3 therefore requires a cooperative movement within the crystal lattice, which could provide a transient passage for CHCl_3 in its hopping between adjacent interstitial voids.^[25,26] We suggest that $\text{C}_{\text{aryl}}\text{--C}_{\text{aryl}}$ rotations of **4a** accompany this process because its overlaid X-ray crystal structures reveal a concerted movement of three m -terphenyl groups in response to the departure of adjacent CHCl_3 molecules.^[14] As shown in Figure 4, the contours of the accessible surface also exhibit drastic morphological changes following this motion.

We note that structural distortions might seem insignificant at the single-molecule level, but their collective effects could be amplified by interlocking arrangements within higher-order assemblies (Figure 2). Harnessing the flexibility of a loosely held aromatic-rich scaffold could be a viable approach to amplifying adaptive molecular motions. This is currently being investigated in our laboratory.

Received: May 31, 2005

Revised: June 26, 2005

Published online: September 19, 2005

Keywords: crystal engineering · host–guest systems · receptors · self-assembly · supramolecular chemistry

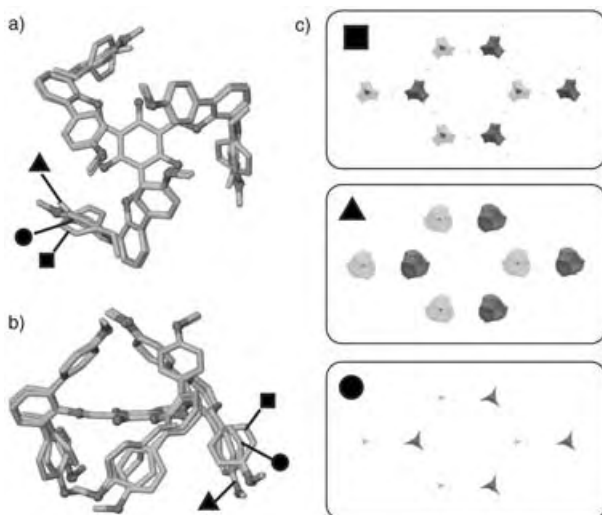


Figure 4. a) Overlaid structures of **4a** in capped-stick representations viewed along the crystallographic threefold axis. b) Perpendicular view. For each conformer, all three m -terphenyl groups are related by crystallographic C_3 symmetry. Structures \blacksquare and \blacktriangle , which are related by positional disorder of 0.13 and 0.87 site occupancy, respectively, were obtained before the release of CHCl_3 , whereas \bullet is from the desolvated crystal. c) Cavities in the crystal structures of **4** corresponding to different conformations \blacksquare , \blacktriangle , and \bullet viewed along the crystallographic c axis. The surface of the cavities was constructed by tracing the center of a van der Waals sphere of 4.5 \AA diameter as it rolls over the surface of **4** within a $2 \times 2 \times 1$ array of unit cells. Dark gray surfaces correspond to voids in the upper layer and light gray surfaces correspond to those in the lower layer when viewed along the crystallographic c axis. The van der Waals volume of CHCl_3 , calculated to be about 75 \AA^3 , corresponds to that of a spherical object with a diameter of about 5 \AA . Therefore, the actual space explored by the center of CHCl_3 should reside within the cavity surfaces depicted in this figure.

- [1] M. Schliwa, *Molecular Motors*, Wiley-VCH, Weinheim, **2003**.
- [2] D. S. Goodsell, A. J. Olson, *Annu. Rev. Biophys. Biomol. Struct.* **2000**, *29*, 105–153.
- [3] G. Krauss, *Biochemistry of Signal Transduction and Regulation*, 3rd ed., Wiley-VCH, Weinheim, **2003**.
- [4] a) V. Koronakis, A. Sharff, E. Koronakis, B. Luisi, C. Hughes, *Nature* **2000**, *405*, 914–919; b) C. Andersen, E. Koronakis, E. Bokma, J. Eswaran, D. Humphreys, C. Hughes, V. Koronakis, *Proc. Natl. Acad. Sci. USA* **2002**, *99*, 11103–11108; c) V. Koronakis, *FEBS Lett.* **2003**, *555*, 66–71.
- [5] J. J. Skehel, D. C. Wiley, *Cell* **1998**, *95*, 871–874.
- [6] V. Balzani, A. Credi, F. M. Raymo, J. F. Stoddart, *Angew. Chem.* **2000**, *112*, 3484–3530; *Angew. Chem. Int. Ed.* **2000**, *39*, 3348–3391.
- [7] V. Balzani, M. Venturi, A. Credi, *Molecular Devices and Machines: A Journey into the Nanoworld*, Wiley-VCH, Weinheim, **2003**.
- [8] R. Krauss, U. Koert, *Synlett* **2003**, 598–608.
- [9] J. Clayden, A. Lund, L. Vallverdú, M. Helliwell, *Nature* **2004**, *431*, 966–971.
- [10] J. H. Chong, M. Sauer, B. O. Patrick, M. J. MacLachlan, *Org. Lett.* **2003**, *5*, 3823–3826.
- [11] C. V. Yelamagad, A. S. Achalkumar, D. S. S. Rao, S. K. Prasad, *J. Am. Chem. Soc.* **2004**, *126*, 6506–6507.

- [12] P. Gilli, V. Bertolasi, V. Ferretti, G. Gilli, *J. Am. Chem. Soc.* **2000**, *122*, 10405–10417.
- [13] a) S. Sasaki, H. Hatsushiba, M. Yoshifuji, *Chem. Commun.* **1998**, 2221–2222; b) B. Twamley, C.-S. Hwang, N. J. Hardman, P. P. Power, *J. Organomet. Chem.* **2000**, *609*, 152–160; c) J. Gavenonis, T. D. Tilley, *J. Am. Chem. Soc.* **2002**, *124*, 8536–8537.
- [14] See Supporting Information.
- [15] The only crystallographically characterized analogue of **4–6** is the condensation product of **3** and *N*-(*tert*-butoxycarbonyl)-1,2-diaminobenzene.^[10] The ¹H NMR spectrum of this compound, however, indicates the presence of both *C_s* and *C₃* isomers.
- [16] CCDC 273250 (**4**), 273251 (**4**·0.5 CHCl₃), 273252 (**5**·6.5 DMF), and 273253 (**6**·C₅H₁₂) contain the supplementary crystallographic data for this paper. These data can be obtained free of charge from the Cambridge Crystallographic Data Centre via www.ccdc.cam.ac.uk/data_request/cif.
- [17] Crystallographic data for **6**·C₅H₁₂: 0.35 × 0.30 × 0.10 mm³, triclinic, space group *P* $\bar{1}$, *a* = 15.3889(12), *b* = 16.0641(12), *c* = 16.8427(13) Å, α = 98.072(2)°, β = 93.593(2)°, γ = 118.488(2)°, *V* = 3582.8(5) Å³, and ρ_{calcd} = 1.128 g cm⁻³ at 125 K. Data were collected by ω scans with MoK α radiation (λ = 0.71073 Å), and all available reflections to $2\theta_{\text{max}}$ = 50° were harvested (65417 reflections, 12610 unique) and corrected for Lorentz and polarization factors with Bruker SAINT 6.45 A. Reflections were subsequently corrected for absorption (empirical correction, μ = 0.067 mm⁻¹), interframe scaling, and other systematic errors with SADABS 2004/1 (combined transmission and other correction factors min./max. = 0.977/0.993). The structure was solved (direct methods) and refined (full-matrix least-squares against *F*²) with the Bruker SHELXTL package (version 6.12). All reflections were used in the refinement of 901 parameters, in which hydrogen atoms were refined with a riding model (*R_F*(observed data) = 0.0585, *R_F*²(all data) = 0.1818, maximum residual density = 0.539 e⁻ Å⁻³).
- [18] For correlated rotations in *n*-fold molecular rotors, see: a) S. Brydges, L. E. Harrington, M. J. McGlinchey, *Coord. Chem. Rev.* **2002**, *233–234*, 75–105; b) G. S. Kottas, L. I. Clarke, D. Horinek, J. Michl, *Chem. Rev.* **2005**, *105*, 1281–1376, and references therein.
- [19] Crystallographic data for **5**·6.5 DMF: Twinned crystal of 0.28 × 0.22 × 0.12 mm³, triclinic, space group *P* $\bar{1}$, *a* = 15.760(5), *b* = 16.863(5), *c* = 16.878(5) Å, α = 60.127(11)°, β = 82.659(11)°, γ = 84.258(10)°, *V* = 3854.1(19) Å³, and ρ_{calcd} = 1.260 g cm⁻³ at 122 K. Data were collected by ω scans with MoK α radiation (λ = 0.71073 Å), and all available reflections to $2\theta_{\text{max}}$ = 50° were harvested (50955 reflections, 20663 unique, including unique combinations of twin component contributions) and corrected for Lorentz and polarization factors with Bruker SAINT 6.45A. Reflections were subsequently corrected for absorption (empirical correction, μ = 0.088 mm⁻¹), interframe scaling, and other systematic errors with TWINABS 1.05 (combined transmission and other correction factors min./max. = 0.781/0.989). The structure was solved (direct methods) and refined (full-matrix least-squares against *F*²) with the Bruker SHELXTL package (version 6.12). All reflections were used in the refinement of 1059 parameters, in which hydrogen atoms were refined with a riding model. (*R_F*(observed data) = 0.0778, *R_F*²(all data) = 0.1930, maximum residual density = 0.480 e⁻ Å⁻³).
- [20] Crystallographic data for **4**·0.5 CHCl₃: 0.31 × 0.30 × 0.15 mm³, trigonal, space group *P*31c, *a* = 16.9447(14), *c* = 24.072(4) Å, *V* = 5985.7(12) Å³, and ρ_{calcd} = 1.256 g cm⁻³ at 123 K. Data were collected by ω scans with MoK α radiation (λ = 0.71073 Å), and all available reflections to $2\theta_{\text{max}}$ = 50° were harvested (104520 reflections, 7053 unique) and corrected for Lorentz and polarization factors with Bruker SAINT 6.45A. Reflections were subsequently corrected for absorption (empirical correction, μ = 0.082 mm⁻¹), interframe scaling, and other systematic errors with SADABS 2004/1 (combined transmission and other correction factors min./max. = 0.814/0.983). The structure was solved (direct methods) and refined (full-matrix least-squares against *F*²) with the Bruker SHELXTL package (version 6.12). All reflections were used in the refinement of 703 parameters, including full isotropic refinement of most hydrogen atoms but riding refinement for low-occupancy hydrogen atoms of one disordered group (*R_F*(observed data) = 0.0404, *R_F*²(all data) = 0.1100, maximum residual density = 0.276 e⁻ Å⁻³).
- [21] Crystallographic data for **4**: 0.31 × 0.30 × 0.15 mm³, trigonal, space group *P*31c, *a* = 16.7934(14), *c* = 23.463(2) Å, *V* = 5730.5(7) Å³, and ρ_{calcd} = 1.243 g cm⁻³ at 121 K. Data were collected by ω scans with MoK α radiation (λ = 0.71073 Å), and all available reflections to $2\theta_{\text{max}}$ = 50° were harvested (100574 reflections, 6742 unique) and corrected for Lorentz and polarization factors with Bruker SAINT 6.45A. Reflections were subsequently corrected for absorption (face-indexed correction, μ = 0.082 mm⁻¹, transmission min./max. = 0.978/0.991, Bruker XPREP 2005/1) and for interframe scaling and other systematic errors (SADABS 2004/1). The structure was solved (direct methods) and refined (full-matrix least-squares against *F*²) with the Bruker SHELXTL package (version 6.12). All reflections were used in the refinement of 639 parameters, including full isotropic refinement of all hydrogen atoms (*R_F*(observed data) = 0.0338, *R_F*²(all data) = 0.0868, maximum residual density = 0.369 e⁻ Å⁻³).
- [22] Diffraction data for a precise structural comparison were collected for the same crystal at essentially the same temperatures. See references [20] and [21].
- [23] For recent reviews, see: a) M. Eddaoudi, D. B. Moler, H. Li, B. Chen, T. M. Reineke, M. O'Keeffe, O. M. Yaghi, *Acc. Chem. Res.* **2001**, *34*, 319–330; b) B. Moulton, M. J. Zaworotko, *Chem. Rev.* **2001**, *101*, 1629–1658; c) O. M. Yaghi, M. O'Keeffe, N. W. Ockwig, H. K. Chae, M. Eddaoudi, J. Kim, *Nature* **2003**, *423*, 705–714; d) S. Kitagawa, R. Kitaura, S.-i. Noro, *Angew. Chem.* **2004**, *116*, 2388–2430; *Angew. Chem. Int. Ed.* **2004**, *43*, 2334–2375; e) *Acc. Chem. Res.* **2005**, *38*, 215–378 (special issue on molecular architecture).
- [24] For recent demonstrations of the uptake and release of small molecules by nonporous molecular structures, see: a) J. L. Atwood, L. J. Barbour, A. Jerga, *Science* **2002**, *296*, 2367–2369; b) G. D. Enright, K. A. Udachin, I. L. Moudrakovski, J. A. Ripmeester, *J. Am. Chem. Soc.* **2003**, *125*, 9896–9897; c) J. L. Atwood, L. J. Barbour, A. Jerga, *Angew. Chem.* **2004**, *116*, 3008–3010; *Angew. Chem. Int. Ed.* **2004**, *43*, 2948–2950; d) P. K. Thallapally, G. O. Lloyd, J. L. Atwood, L. J. Barbour, *Angew. Chem.* **2005**, *117*, 3916–3919; *Angew. Chem. Int. Ed.* **2005**, *44*, 3848–3851.
- [25] The rotation of *tert*-butyl groups has been proposed to assist release of entrapped gaseous molecules from a nonporous solid matrix of *p*-*tert*-butylcalix[4]arene: J. L. Atwood, L. J. Barbour, P. K. Thallapally, T. B. Wirsig, *Chem. Commun.* **2005**, 51–53.
- [26] For a highly synchronized phase transition that assists the transport of guest molecules in the absence of continuous channels, see: J. L. Atwood, L. J. Barbour, A. Jerga, B. L. Schottel, *Science* **2002**, *298*, 1000–1002.

Sequence Symmetry as a Tool for Designing DNA Nanostructures**

Yu He, Ye Tian, Yi Chen, Zhaoxiang Deng, Alexander E. Ribbe, and Chengde Mao*

DNA sequence symmetry brings at least three advantages to any given DNA structure: 1) minimization of the required sequence space and simplification of sequence design; 2) reduction of the number of different DNA strands; and 3) cancellation of some unpredictable distortions in DNA nanostructures, thus allowing DNA two-dimensional (2D) arrays to grow to large sizes. Herein, DNA sequence symmetry is introduced into the design of DNA nanostructures, to give DNA 2D arrays that reach a width of 1 mm.

DNA is an excellent system for studying self-assembly and constructing nanoscale patterns^[1,2] because of its extraordinary capability of molecular recognition, well-predictable double-helix structures, huge diversity of unique sequences, and various preexisting toolkits. It is generally believed that DNA sequence symmetry should be eliminated when designing a DNA motif. Each DNA segment has to be unique and can only base pair with its sole, complementary segment, which promotes the formation of designed structures. This rule has been established for 20 years^[3] and strictly followed in the field of DNA nanotechnology.^[1,4,5] The success of DNA nanotechnology proves the effectiveness of this rule. As DNA nanotechnology has matured, more knowledge and experience have accumulated. We would like to ask: can sequence symmetry provide any advantage? Herein, we will address this question and show a successful application of sequence symmetry.

We studied sequence symmetry with a cross motif (Figure 1)^[4d] in which nine different strands (1–9) associate with each other and fold into a nearly planar structure (Figure 1a). There is a pseudo-fourfold rotational symmetry of the DNA backbones, but no symmetry when taking the bases into account. If a true fourfold symmetry exists, strands 2–5 will be related to each other by the symmetry and be identical, strands 6–9 will be identical, and strand 1 will become a circular repetitive tetramer. The symmetric cross structure still consists of nine strands, but only three different sequences (Figure 1b). The unique DNA sequences are

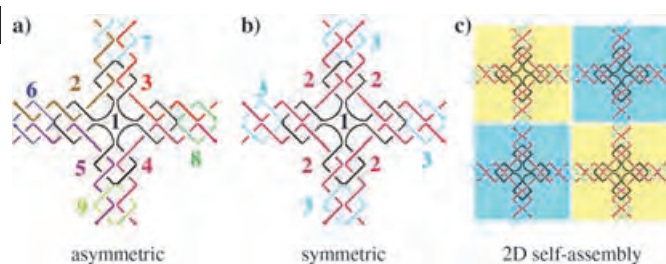


Figure 1. Introduction of sequence symmetry. a) An asymmetric cross motif consisting of nine unique strands. The arrows indicate the 3' ends of the DNA strands. b) A symmetric cross motif containing only three unique strands. c) Corrugated self-assembly in two dimensions. Any two neighboring units face in opposite directions; yellow and turquoise squares indicate units facing up and down, respectively. The dimensions of a unit cell of the 2D array are 4.5×4.5 turns.

reduced by four times as all four arms of the cross become identical to each other. Note that sequence symmetry is still avoided when designing each individual DNA strand. Symmetry is only applied to the construction of the cross motif out of the three different strands.

Sequence symmetry substantially influences the self-assembly behavior of the cross motif. The cross structures with sticky ends can be programmed to self-assemble into 2D arrays. Some unpredictable curvatures are associated with the cross motif, because of our limited understanding of branched DNA structures and oversimplification by the DNA duplex model. If the curvatures accumulate, small aggregates will be generated instead of large 2D arrays. A corrugation strategy has been used^[4d] to prevent curvature from accumulating during 2D assembly. Adjacent building blocks face up and down alternately in each growing direction, such that the curvatures cancel each other out (Figure 1c). This strategy has been proved to be effective.

However, each arm of the asymmetric cross motif has a different base composition and a curvature of different direction and extent. The corrugation strategy is not enough to cancel all curvatures. To further remove any curvature and promote growth of planar 2D arrays, new strategies are needed. The introduction of sequence symmetry is promising for this purpose. If a true fourfold symmetry exists, the four arms are symmetrically related and have exactly the same curvatures no matter what they are. When blocks of the symmetric cross assemble in two dimensions, all curvatures are cancelled, and large 2D arrays would be expected. In previous reports, DNA 2D arrays often showed anisotropic shapes,^[4] presumably resulting from unequal cohesion strengths between DNA blocks in different directions or from curvature accumulation, or both. Sequence symmetry will remove this problem. The block containing the symmetric cross has exactly the same pair of sticky ends in each direction. Thus, the cohesion strength between the blocks in any direction is exactly the same, which allows equal growth of the 2D arrays in each direction.

The strategy of sequence symmetry has been experimentally proved to be very successful. We followed previously reported experimental protocols (see the Supporting Information).^[4] First, the symmetric cross motif was characterized

[*] Y. He, Y. Tian, Y. Chen, Z. Deng, A. E. Ribbe, Prof. C. Mao
Department of Chemistry
Purdue University
West Lafayette, IN 47907 (USA)
Fax: (+1) 765-494-0239
E-mail: mao@purdue.edu

[**] This work was supported by NSF (EIA-0323452), DARPA/DSO (MDA 972-03-1-0020), and Purdue University (a start-up fund). The AFM study was carried out in the Purdue Laboratory for Chemical Nanotechnology (PLCN). We thank Ms. S. H. Lee for help with fluorescence imaging.

by native polyacrylamide gel electrophoresis (PAGE). The symmetric cross complex migrated as a single sharp band with an expected mobility in the gel (Figure 2, the second lane from the right), which indicates that the cross complex is

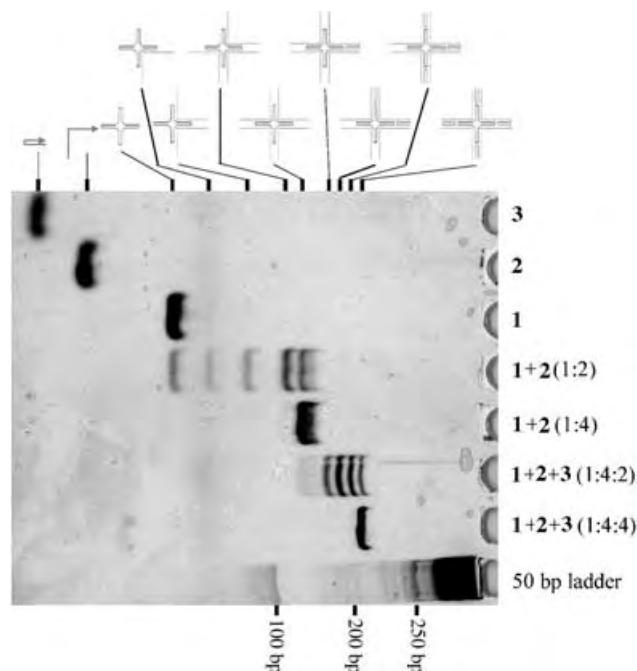


Figure 2. Native PAGE (6%) analysis of the symmetric cross motif. The DNA content of each lane is indicated at the top of the gel image and the identity of each band is indicated on the left. The molar ratios of the strands are given in parentheses. The lane on the far right (50 bp ladder) contains a series of DNA duplex size markers.

stable. Then we modified strand **3** to get complementary sticky ends, and used atomic force microscopy (AFM) to examine whether the cross motif could self-assemble into 2D arrays (Figure 1c and Figure 3). In previous reports^[4] and in our own studies,^[6] DNA 2D arrays with asymmetric motifs were normally less than 1 μm wide. In sharp contrast, DNA 2D arrays assembled from the symmetric motif are normally in a size range of 20 to 40 μm . The arrays are well-ordered, as judged by direct observation of the images and by Fourier-transform analysis. The observed repeating distance is (18.9 ± 0.3) nm, in good agreement with the value calculated from the

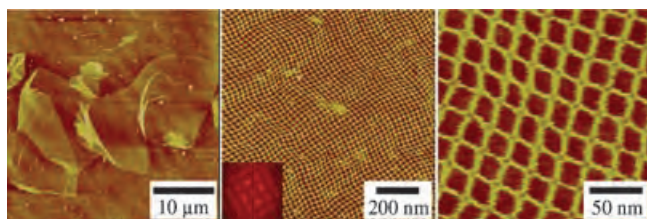


Figure 3. AFM analysis of DNA 2D arrays self-assembled from a symmetric cross motif. Image scanning areas decrease from left to right, thus showing the entire 2D array and the detailed structure. A Fourier-transform pattern (inset, center) shows the regularity of the DNA array.

model $((46 \times 0.33) + (2 \times 2)) = 19.2$ nm by assuming that the pitch of the DNA duplex is 0.33 nm per base pair and the diameter of a DNA duplex is 2 nm.

The DNA arrays were often larger than the AFM imaging fields. AFM imaging is well-suited to the study of nanoscale structures. Its drawbacks are that the imaging area is small (practically limited to less than 50 μm for our DNA samples), and that the imaging process is very slow, which prevented us from surveying the overall situation of the DNA samples. To overcome these limitations, we used fluorescence microscopy, which allows the imaging of arrays with areas up to the millimeter scale. This technique provides complementary information to that from the AFM images.

Figure 4 shows fluorescence images of DNA arrays stained with YOYO-1 immediately before imaging. Sample preparation for fluorescence imaging is much simpler than for

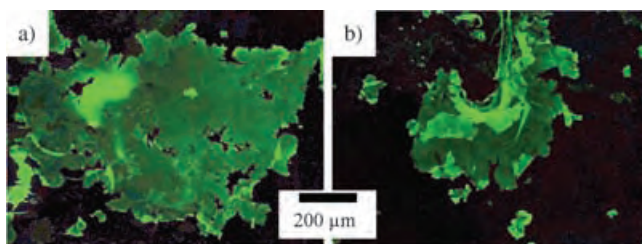


Figure 4. a) and b) Fluorescence images (taken from different areas within the same sample) of DNA 2D arrays self-assembled from the symmetric cross motif with a) the largest DNA array found with width 1 mm.

AFM imaging and avoids destroying the DNA arrays. DNA arrays can be easily found under a fluorescence microscope. The overall morphologies of the arrays are very similar to each other when observed by both fluorescence and AFM imaging. The largest array that we have found reaches a size of 1 mm width (Figure 4a), which is hundreds of times larger than previously reported DNA 2D arrays self-assembled from asymmetric motifs.^[4]

The DNA arrays can be used as templates to fabricate nanostructures of other materials. We have previously reported a strategy to transfer DNA nanostructures to gold structures by vapor deposition of gold against flat substrate-supported DNA structures.^[6] One major concern of this strategy is that the areas of the gold structures are too small to be useful for technological applications. With the new DNA arrays developed here, we can easily address this concern. The gold structures extend up to 40 μm^2 (Figure 5).

In conclusion, we have demonstrated that sequence symmetry is a powerful tool for designing DNA nanostructures. We are currently testing the symmetry strategy in various DNA nanostructures and hope to determine how general sequence symmetry can be applied. Sequence symmetry dramatically reduces the size of unique sequences and decreases the number of DNA strands. This reduction is important for the fabrication of complicated structures because they need large pools of unique sequences, which, in turn, dramatically increase the difficulty of sequence design. We believe that sequence symmetry will be appreci-

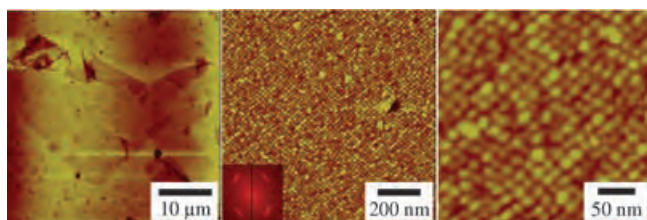


Figure 5. AFM imaging analysis of gold nanostructures replicated from DNA 2D arrays. Scanning areas decrease from left to right, thus showing the entire domain and the detailed structure. A Fourier-transform pattern (inset, center) shows the regularity of the metal structure.

ated as a new tool for the design in these complicated cases. Sequence symmetry is also a useful tool for fine-tuning the structures of DNA motifs, as in the example herein. It is a common concern for molecular self-assembly as to whether self-assembled 2D arrays can be grown to sizes large enough to satisfy the requirements of many technological applications. Herein, we have clearly demonstrated that large 2D arrays are feasible.

Experimental Section

Oligonucleotides: DNA sequences were designed by the computer program SEQUIN.^[3b] All oligonucleotides were purchased from IDT, Inc. and purified by 20% denaturing PAGE. Strand 1: 5'-AggCAC-CATCgTAggTTTTCTTgCCAggCACCATCg-TAggTTTCTTgCCAggCACCATCgTA ggTTTTCTTgCCAgg-CACCATCgTAggTTTTCTTgCC-3' (circularized); strand 2: 5'-ACTATgCAACCTgCCTggCAA gCCTACgATggACACgg-TAACg-3'; strand 3: 5'-CgTTACCGTgTggTTgCATAgT-3'; strand 3': 5'-CgCgCgTTACCGTgTggTTgCATAgT-3'.

Formation of DNA complexes and 2D arrays: Strands 1 (0.6 μM), 2 (2.4 μM), and 3 or 3' (2.4 μM) were combined in Tris/acetate/EDTA/Mg²⁺ (TAE-Mg²⁺) buffer, which consisted of Tris (40 mM, pH 8.0), acetic acid (20 mM), EDTA (2 mM), and Mg(CH₃COO)₂ (12.5 mM). Individual DNA complexes for native PAGE analysis were formed by cooling solutions of the mixture as follows: 95 K/1 min, 65 K/30 min, 50 K/30 min, 37 K/30 min, and 22 K/30 min. DNA 2D arrays were formed by slowly cooling the DNA solution from 95°C to room temperature over 48 h. For individual cross molecules, we used strands 1, 2, and 3; for 2D arrays, we used strands 1, 2, and 3'.

Denaturing PAGE: Gels contained 20% polyacrylamide (19:1 acrylamide/bisacrylamide) and 8.3M urea. The running buffer was Tris/borate/EDTA (TBE), which consisted of Tris buffer (89 mM, pH 8.0), boric acid (89 mM), and EDTA (2 mM). Electrophoresis runs were performed on a Hoefer SE 600 unit at 55°C and 600 V (constant voltage). After electrophoresis, the gels were stained with Stains-All dye (Sigma) and scanned.

Native PAGE: Gels contained 6% polyacrylamide (19:1 acrylamide/bisacrylamide), and electrophoresis runs were performed on an FB-VE10-1 electrophoresis unit (FisherBiotech) at 4°C and 100 V (constant voltage). The running buffer was TAE-Mg²⁺. After electrophoresis, the gels were stained with Stains-All dye (Sigma) and scanned.

Replication of DNA patterns: All the metal evaporations were carried out with a thermal evaporator (Turbo Vacuum Evaporator EFA). The evaporation speed was adjusted to 0.2 nm s⁻¹. After metal evaporation (to a thickness of about 20 nm), a drop of premixed epoxy adhesive was placed on the gold film and immediately covered by a glass slide. The epoxy was allowed to solidify completely

(normally left overnight), and the metal replicas were mechanically lifted off the mica surfaces.

AFM imaging: A drop of DNA sample solution (2 μL) was spotted onto a freshly cleaved mica surface and left there for 10 s to allow for strong adsorption. The sample drop was then washed off with Mg(CH₃COO)₂ solution (10 mM, 30 μL) and the surface was dried by compressed air. DNA samples and their metal replicas were imaged by tapping-mode AFM on a Nanoscope IIIa microscope (Digital Instruments) with NSC15 tips (silicon cantilever, Mikro-Masch). The tip-surface interaction was minimized by optimizing the scan set-point.

Fluorescence microscopy imaging: A drop of DNA sample solution (3 μL, in TAE-Mg²⁺ buffer) was spotted onto a clean glass slide and left for 5 min to allow DNA arrays to adsorb onto the glass surface. Then a YOYO-1 (Molecular Probes) solution (1.7 μM in TAE-Mg²⁺ buffer, 1 μL) was spotted onto the DNA sample, which was immediately protected with a coverslip and imaged with a fluorescence microscope.

Received: June 23, 2005

Revised: August 5, 2005

Published online: September 27, 2005

Keywords: DNA structures · gold · nanostructures · scanning probe microscopy · self-assembly

- [1] N. C. Seeman, *Nature* **2003**, *421*, 427–431.
- [2] a) A. P. Alivisatos, K. P. Johnsson, X. Peng, T. E. Wilson, C. J. Loweth, M. P. Bruchez, P. G. Schultz, *Nature* **1996**, *382*, 609–611; b) C. A. Mirkin, R. L. Letsinger, R. C. Mucic, J. J. Storhoff, *Nature* **1996**, *382*, 607–609; c) C. M. Niemeyer, T. Sano, C. L. Smith, C. R. Cantor, *Nucleic Acids Res.* **1994**, *22*, 5530–5539; d) E. Braun, Y. Eichen, U. Sivan, G. Ben-Yoseph, *Nature* **1998**, *391*, 775–778.
- [3] a) N. R. Kallenback, R.-I. Ma, N. C. Seeman, *Nature* **1983**, *305*, 829–831; b) N. C. Seeman, *J. Biomol. Struct. Dyn.* **1990**, *8*, 573–581.
- [4] a) E. Winfree, F. Liu, L. A. Wenzler, N. C. Seeman, *Nature* **1998**, *394*, 539–544; b) T. H. LaBean, H. Yan, J. Kopatsch, F. Liu, E. Winfree, J. H. Reif, N. C. Seeman, *J. Am. Chem. Soc.* **2000**, *122*, 1848–1860; c) C. Mao, W. Sun, N. C. Seeman, *J. Am. Chem. Soc.* **1999**, *121*, 5437–5443; d) H. Yan, S. H. Park, G. Finkelstein, J. H. Reif, T. H. LaBean, *Science* **2003**, *301*, 1882–1884; e) D. Liu, M. Wang, Z. Deng, R. Walulu, C. Mao, *J. Am. Chem. Soc.* **2004**, *126*, 2324–2325; f) B. Ding, R. Sha, N. C. Seeman, *J. Am. Chem. Soc.* **2004**, *126*, 10230–10231; g) P. W. K. Rothmund, N. Papadakis, E. Winfree, *PLoS Biol.* **2004**, *2*, 2041–2053; h) W. M. Shih, J. D. Quispe, G. F. Joyce, *Nature* **2004**, *427*, 618–621; i) J. Malo, J. C. Mitchell, C. Venien-Bryan, J. R. Harris, H. Wille, D. J. Sherratt, A. J. Turberfield, *Angew. Chem.* **2005**, *117*, 3117–3121; *Angew. Chem. Int. Ed.* **2005**, *44*, 3057–3061; j) F. Mathieu, S. Liao, J. Kopatsch, T. Wang, C. Mao, N. C. Seeman, *Nano Lett.* **2005**, *5*, 661–665; k) S. H. Park, R. Barish, H. Li, J. H. Reif, G. Finkelstein, H. Yan, T. H. LaBean, *Nano Lett.* **2005**, *5*, 693–696; l) A. Chworos, I. Severcan, A. Y. Koyfman, P. Weinkam, E. Oroudjev, H. G. Hansma, L. Jaeger, *Science* **2004**, *306*, 2068–2072.
- [5] N. Chelyapov, Y. Brun, M. Gopalkrishnan, D. Reishus, B. Shaw, L. Adleman, *J. Am. Chem. Soc.* **2004**, *126*, 13924–13925. This work reports the only exception to the rule. However, the motif did not self-assemble into extended, ordered 2D arrays.
- [6] Z. Deng, C. Mao, *Angew. Chem.* **2004**, *116*, 4160–4162; *Angew. Chem. Int. Ed.* **2004**, *43*, 4068–4070.

DOI: 10.1002/anie.200502189

Hydrogel Stamping of Arrays of Supported Lipid Bilayers with Various Lipid Compositions for the Screening of Drug–Membrane and Protein–Membrane Interactions**

Sheereen Majd and Michael Mayer*

Herein we describe a rapid, reproducible, and straightforward method to form copies of functional membrane arrays with various lipid compositions and the application of these arrays for the screening of drug–membrane and protein–membrane interactions. We employed topographically patterned agarose gels to stamp spatially addressable arrays of supported bilayers on glass and confirmed the fluidity of these membranes by fluorescence recovery experiments. We took advantage of the storage capability of hydrogels and demonstrated that inking posts on an agarose stamp, with extremely small volumes ($\leq 1 \mu\text{L}$) of a solution that contains liposomes, was sufficient to transfer at least 100 copies of a membrane array without the need for reinking. We used stamped membrane arrays for screening the interactions of a protein (annexin V) and an anti-inflammatory drug (nimesulide) with bilayers of various lipid compositions and discovered that the interaction of the prescription drug nimesulide with membranes depends on the membrane cholesterol content.

Interest in supported bilayers^[1–3] includes studies of the dynamic structure of membranes,^[4,5] their self-assembly,^[5] lipid–protein interactions,^[5] ligand–receptor interactions,^[5–8] development of membrane-based biosensors,^[5,9–15] and drug discovery.^[16] Furthermore, many pharmaceuticals are known to interact with biological membranes and, as such, assays for testing drug–membrane interactions are important for a better understanding of drug activity, targeting, and toxicity.^[17] To use supported bilayers efficiently for the study of the aforementioned processes, the membranes must be fluid^[1,16,18,19] and mechanically stable.^[19] Techniques that are currently employed to form arrays of supported membranes exploit a) the deposition of droplets of a liposome solution

onto surfaces,^[6,18] b) vesicle fusion from a bulk solution onto patterned substrates,^[20,21] c) delivery of liposomes by microfluidic channels,^[22,23] and d) microcontact printing with poly-(dimethylsiloxane) (PDMS).^[24]

An ideal fabrication method for the application of membrane arrays for screening protein–membrane or drug–membrane interactions would consist of the rapid creation of many functional copies of an array of different bilayers with minimal consumption of the amount of lipid. Among the existing methods, microcontact printing allows the creation of many spots of membranes in parallel. To prepare arrays with various compositions, however, posts of the stamp used for microcontact printing must be inked individually. Such an inking procedure can be time consuming and can introduce heterogeneity into the stamped arrays. It would therefore be advantageous if a biocompatible stamp, once inked, could store the inking solution and allow multiple transfers without the need for reinking.

Herein, we demonstrate that stamping with hydrogel stamps allows multiple stamping while using minute amounts of material. We fabricated stamps from agarose gel (4 %) with a pore size sufficiently large to allow the diffusion of macromolecules and small liposomes (the pore size of 2 % agarose gel is $\approx 470 \text{ nm}$ ^[25]). This capability makes it possible to store inking solution within the stamp while replenishing molecules at the surface and, thus, to perform multiple stamping of biomolecules.^[25] Recently, agarose stamps^[26,27] were applied to pattern arrays of proteins,^[28,29] bacteria,^[30] and mammalian cells.^[31] Herein we present the first attempt to use hydrogel stamps to create functional arrays of fluid lipid membranes.

To form arrays of lipid bilayers, we inked each post on the agarose stamp with a sub-microliter volume of liposome suspension. After the posts had absorbed the solution, we placed the inked stamp in contact with glass slides for 5–10 s (see Supporting Information for details and stamp dimensions). Immediately after removal of the stamp, we immersed the patterned substrates in either deionized water or PBS buffer solution. We hypothesize that during stamping, supported membranes form by diffusion of small liposomes (diameter 20–80 nm)^[32] through the pores of the agarose stamp and the subsequent spread of liposomes onto the regions in contact with the glass. As the agarose stamps used in this method consist mostly ($\geq 96 \%$ w/w) of water, we suggest that the mechanism of bilayer formation is similar to the mechanism of the established method of vesicle fusion from solution.^[16]

We examined the structure of the stamped lipid bilayer spots on the glass substrate by atomic force microscopy (AFM) experiments (see Supporting Information). The AFM results revealed a smooth surface of bilayer with scattered defects. The area of the defect sites was $\leq 23 \%$ of the total imaged bilayer area. Cross-section analysis of the defects revealed a thickness of $4.3 \pm 0.8 \text{ nm}$, which corresponds to the height of a single lipid bilayer.^[6]

To investigate the capability of agarose stamps to store small liposomes, we used a stamp that was inked once and stamped 100 times without intermediate reinking. This stamp was inked with a solution of liposomes composed of L- α -

[*] Prof. M. Mayer
Department of Biomedical Engineering
and Department of Chemical Engineering, University of Michigan
Engineering Research Building (ERB), Room 4107
2200 Bonisteel Blvd., Ann Arbor, MI 48109-2099 (USA)
Fax: (+1) 734-763-4371
E-mail: mimayer@umich.edu

S. Majd
Department of Biomedical Engineering
University of Michigan,
2200 Bonisteel Blvd., Ann Arbor, MI 48109-2099 (USA)

[**] We thank Jerry Yang, Irina Gitlin, and Adam Urbach for valuable discussions. We also thank Jessica Hessler and Almut Mecke for assistance with AFM.

Supporting information for this article is available on the WWW under <http://www.angewandte.org> or from the author.

phosphatidylcholine derived from chicken egg (egg PC) and 1,2-dipalmitoyl-*sn*-glycero-3-phosphoethanolamine-*N*-(lissamine-rhodamine B sulfonyl) (rh-PE; 1 % *w/w*). We found no significant loss in the fluorescence intensity of the spots over 100 stamping events (Figure 1a). Figures 1b and c show

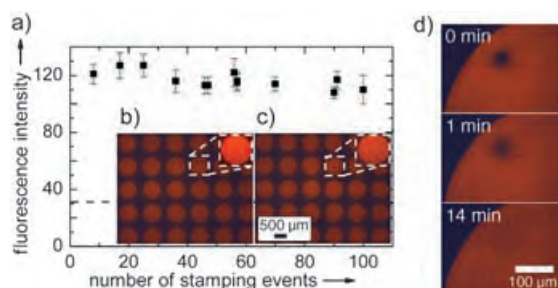


Figure 1. Fluorescence intensity after stamping of 100 arrays of membranes by using a hydrogel stamp (without intermediate inking), and test of bilayer fluidity. The bilayers composed of egg PC and rh-PE (1 % *w/w*) were stamped on glass slides. a) Mean fluorescence intensity of supported bilayers as a function of the number of stamping events. The error bars represent the standard deviation of the intensity of all spots in each array. The dashed line represents the mean fluorescence intensity of the background. b) Micrograph of spots of supported bilayers after the 6th and c) 100th stamping event. d) Fluorescence images from a FRAP experiment performed on the array from the last (100th) stamping event after photobleaching for 8 min.

fluorescent micrographs of membrane arrays on glass that were obtained after 6 and 100 stamping events, respectively. To test the fluidity of the stamped bilayers, we performed fluorescence recovery after photobleaching (FRAP) experiments (see Supporting Information for details). Figure 1d shows the recovery of a photobleached spot in a bilayer of the last (100th) array. Fluorescence recovery of the bilayers in this array was similar to that in the 6th array (difference in diffusion constant $\leq 5\%$) which therefore indicates that the quality of the stamped arrays remained constant over ≈ 100 stamping events. The fluorescence intensity in the photobleached spot recovered to $\approx 90\%$ of its original intensity, a value typical for supported membranes of high quality.^[6]

We used a stamp with 200- μm -diameter posts to explore the potential of this method for the production of membrane arrays with a high density. Figure 2a shows such a resultant array with a density of 600 membrane spots per cm^2 . If such a stamp were inked by using robotics, it should, in principle, be possible to stamp multiple copies of high-density arrays with various membrane compositions.^[29]

To demonstrate the ability of this method to create, in parallel, bilayers with different lipid compositions, we transferred arrays of supported membranes by using liposomes that contained 0–50 % negatively charged lipids and 0–50 % cholesterol. Remarkably, hydrogel stamping resulted in high-quality membrane arrays on glass substrates even when the bilayers contained 50 % negatively charged lipids (Figure 3a). Figure 2b shows an array of bilayers with two different fluorescently labeled lipids. These spots were transferred in parallel from the same stamp.

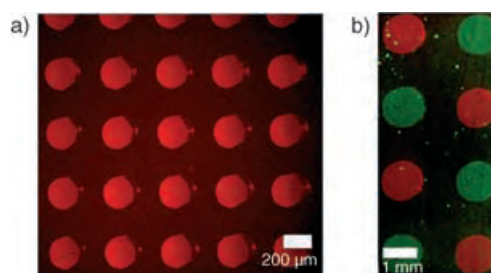


Figure 2. Stamped high-density array of supported bilayers and membrane arrays with various compositions. a) Fluorescent micrograph of a patterned array of bilayers composed of egg PC with rh-PE (1 % *w/w*) by using an agarose stamp with a post size of 200 μm . b) Fluorescent micrograph of an array of bilayers that contains egg PC and rh-PE (1 % *w/w*; red) and NBD-PE (3 % *w/w*; green).

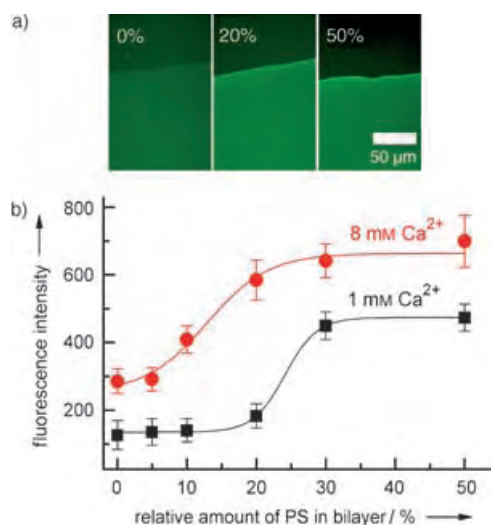


Figure 3. The protein annexin V binds to bilayers with different DOPS content. a) Micrographs of fluorescently labeled annexin V bound to bilayers that contain 0, 20, and 50 % (*w/w*) DOPS. b) Increase in fluorescence intensity due to the binding of annexin V to an array of bilayers with a gradient in DOPS. The binding of annexin V is calcium-dependent; these data were obtained in (■) 1 mM and (●) 8 mM Ca^{2+} . The error bars represent the standard deviations in fluorescence intensity.

To determine if liposomes with different lipid compositions are transferred differentially from the agarose stamp to the glass slide, we inked the posts of a stamp with mixtures of two different liposome populations (the first population was composed of egg PC (99 % *w/w*) and rh-PE (1 % *w/w*) and the second was composed of egg PC (50 % *w/w*) and 1, 2-dioleoyl-*sn*-glycero-3-[phospho-L-serine] (DOPS; 50 % *w/w*)). We used this stamp to create a membrane array and subsequently studied the compositions of the resultant bilayers (see Supporting Information for details). Epifluorescence microscopy images showed that the fluorescence of the transferred bilayers was proportional to the ratio of the two liposome populations in the inking solution. This result suggests that there is no significant preference in transfer between the neutral and negatively charged liposomes.

To explore the possible applications of membrane arrays with various compositions for the screening of protein–

membrane interactions, we formed arrays from egg PC with a gradient in the negatively charged lipid, DOPS, and measured the binding of annexin V to these bilayers. Annexin V is a calcium-dependent binding protein that interacts with negatively charged lipids.^[33] Figure 3a shows micrographs of the binding of fluorescently labeled annexin V to supported bilayers with three different concentrations of DOPS. Figure 3b illustrates that the binding of annexin V to supported membranes increases with an increasing concentration of both DOPS in the bilayer and calcium ions in solution. These results show that stamped arrays of supported membranes can be used effectively to quantify protein–membrane interactions.

Further to the investigation of protein–membrane binding, membrane arrays may be useful for screening drug–membrane interactions. These interactions can depend on the composition of the lipid membrane^[17] (e.g. the content of cholesterol) and can induce a change in the fluidity of the bilayer.^[34] The therapeutic and toxic effects of many drugs are affected by their interactions with lipid membranes.^[17,34] To demonstrate the influence of the lipid composition on drug–membrane interactions, we studied the fluidity changes that are introduced by the non-steroidal anti-inflammatory drug (NSAID), nimesulide, in bilayers with various cholesterol content. NSAIDs, (e.g. aspirin or ibuprofen) are the most-important drugs in the treatment of inflammation, pain, and fever.^[34]

Lucio et al. reported that nimesulide increases the fluidity of membranes composed of egg PC.^[34] In the studies described herein, we incubated stamped membrane arrays of egg PC with various cholesterol content in solutions that contain 0, 50, and 100 μM nimesulide for 2 h, and monitored the changes in fluidity by FRAP experiments.^{[35], [36]} Figure 4 shows the fluorescence recovery of bleached spots in the presence of nimesulide. In agreement with Lucio et al.,^[34] we found that nimesulide (50 μM) increased the fluidity in egg PC membranes. We discovered the same effect in bilayers with a moderate cholesterol content ($\leq 20\%$). Surprisingly, however, nimesulide had the opposite effect, namely a decrease in fluidity, on bilayers with a high cholesterol content ($\geq 50\%$). Furthermore, nimesulide decreased the fluidity of all the examined bilayers when it was added at a concentration of 100 μM (Figure 4c). The diffusion coefficients of fluorescently labeled lipids in these bilayers are summarized in Table 1.

Table 1: Diffusion coefficients, D of rh-PE in supported membranes composed of egg PC and rh-PE (1% w/w) with various cholesterol content in the presence of nimesulide.

Cholesterol content [%]	0 μM nimesulide	50 μM nimesulide	100 μM nimesulide
0	2.0×10^{-9}	2.7×10^{-9}	1.4×10^{-9}
20	1.8×10^{-9}	2.4×10^{-9}	1.2×10^{-9}
50	1.5×10^{-9}	0.7×10^{-9}	0.4×10^{-9}

[a] The errors of the diffusion coefficients are $\pm 7\%$ and were obtained through measurement of the differences between diffusion coefficients of fluorescently labeled lipids in bilayers made from the same lipid composition, but stamped on different days.

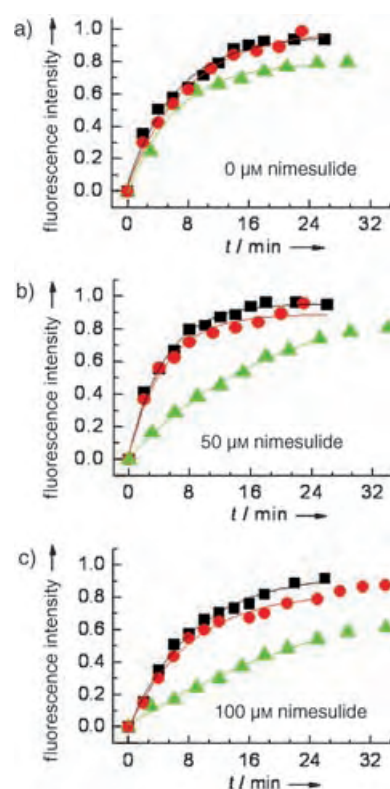


Figure 4. Influence of nimesulide on the fluidity of stamped lipid bilayers with various cholesterol content. Recovery curves of supported lipid bilayers of egg PC and rh-PE (1% w/w) which contain (■) 0% cholesterol, (●) 20% cholesterol, and (▲) 50% cholesterol in the presence of a) 0, b) 50, and c) 100 μM nimesulide.

In conclusion, we present a strikingly simple and reproducible method to obtain copies of functional membrane arrays from a range of lipids (including up to 50% negatively charged lipids). This method allows the fabrication of at least 100 copies of a bilayer array while using only picomolar amounts of lipids per spot—a characteristic that may be particularly beneficial for stamping precious membrane preparations that can often only be obtained in limited quantities, such as cellular membrane fragments. Binding assays with these arrays elucidated an unknown effect of cholesterol on the interaction of a prescription drug with bilayers, and as such, we expect liposome stamping to be useful for the rapidly growing interest in drug–membrane interactions,^[17,34] protein–membrane interactions,^[5] and arrays of membrane proteins.^[6]

Received: June 22, 2005

Published online: September 27, 2005

Keywords: hydrogel · lipids · membranes · micropatterning

[1] E. Sackmann, *Science* **1996**, 271, 43.

[2] H. M. McConnell, T. H. Watts, R. M. Weis, A. A. Brian, *Biochim. Biophys. Acta* **1986**, 864, 95.

[3] M. Tanaka, A. P. Wong, F. Rehfeldt, M. Tutus, S. Kaufmann, *J. Am. Chem. Soc.* **2004**, 126, 3257.

- [4] S. J. Johnson, T. M. Bayerl, D. C. McDermott, G. W. Adam, A. R. Rennie, R. K. Thomas, E. Sackmann, *Biophys. J.* **1991**, *59*, 289.
- [5] M. L. Wagner, L. K. Tamm, *Biophys. J.* **2000**, *79*, 1400.
- [6] Y. Fang, A. G. Frutos, J. Lahiri, *J. Am. Chem. Soc.* **2002**, *124*, 2394.
- [7] C. Bieri, O. P. Ernst, S. Heyse, K. P. Hofmann, H. Vogel, *Nat. Biotechnol.* **1999**, *17*, 1105.
- [8] S. Heyse, T. Stora, E. Schmid, J. H. Lakey, H. Vogel, *Biochim. Biophys. Acta* **1998**, *1376*, 319.
- [9] E. Sackmann, M. Tanaka, *Trends Biotechnol.* **2000**, *18*, 58.
- [10] P. Fromherz, W. Arden, *J. Am. Chem. Soc.* **1980**, *102*, 6211.
- [11] H. Kiefer, B. Klee, E. John, Y. D. Stierhof, F. Jahnig, *Biosens. Bioelectron.* **1991**, *6*, 233.
- [12] U. Radler, J. Mack, N. Persike, G. Jung, R. Tampe, *Biophys. J.* **2000**, *79*, 3144.
- [13] S. M. Schiller, R. Naumann, K. Lovejoy, H. Kunz, W. Knoll, *Angew. Chem.* **2003**, *115*, 219; *Angew. Chem. Int. Ed.* **2003**, *42*, 208.
- [14] K. Morigaki, T. Baumgart, A. Offenhäusser, W. Knoll, *Angew. Chem.* **2001**, *113*, 184; *Angew. Chem. Int. Ed.* **2001**, *40*, 172.
- [15] H. Bayley, P. S. Cremer, *Nature* **2001**, *413*, 226.
- [16] J. T. Groves, *Curr. Opin. Drug Discovery Dev.* **2002**, *5*, 606.
- [17] J. K. Seydel, M. Wiese, *Drug-membrane Interactions*, Wiley-VCH, Weinheim, **2002**.
- [18] P. S. Cremer, J. T. Groves, L. A. Kung, S. G. Boxer, *Langmuir* **1999**, *15*, 3893.
- [19] Y. Fang, A. G. Frutos, J. Lahiri, *ChemBioChem* **2002**, *3*, 987.
- [20] J. T. Groves, N. Ulman, S. G. Boxer, *Science* **1997**, *275*, 651.
- [21] L. A. Kung, J. T. Groves, N. Ulman, S. G. Boxer, *Adv. Mater.* **2000**, *12*, 731.
- [22] L. Kam, S. G. Boxer, *J. Am. Chem. Soc.* **2000**, *122*, 12901.
- [23] T. L. Yang, S. Y. Jung, H. B. Mao, P. S. Cremer, *Anal. Chem.* **2001**, *73*, 165.
- [24] J. S. Hovis, S. G. Boxer, *Langmuir* **2001**, *17*, 3400.
- [25] A. Pluen, P. A. Netti, R. K. Jain, D. A. Berk, *Biophys. J.* **1999**, *77*, 542.
- [26] M. Fialkowski, C. J. Campbell, I. T. Bensemann, B. A. Grzybowski, *Langmuir* **2004**, *20*, 3513.
- [27] B. A. Grzybowski, K. J. M. Bishop, C. J. Campbell, M. Fialkowski, S. K. Smoukov, *Soft Matter* **2005**, *1*, 114.
- [28] B. D. Martin, B. P. Gaber, C. H. Patterson, D. C. Turner, *Langmuir* **1998**, *14*, 3971.
- [29] M. Mayer, J. Yang, I. Gitlin, D. H. Gracias, G. M. Whitesides, *Proteomics* **2004**, *4*, 2366.
- [30] D. B. Weibel, A. Lee, M. Mayer, S. F. Brady, D. Bruzewicz, J. Yang, W. R. DiLuzio, J. Clardy, G. M. Whitesides, *Langmuir* **2005**, *21*, 6436.
- [31] M. M. Stevens, M. Mayer, D. G. Anderson, D. B. Weibel, G. M. Whitesides, R. Langer, *Biomaterials* **2005**, *26*, 7636.
- [32] M. A. Cooper, *J. Mol. Recognit.* **2004**, *17*, 286.
- [33] J. F. Tait, D. F. Gibson, C. Smith, *Anal. Biochem.* **2004**, *329*, 112.
- [34] M. Lucio, H. Ferreira, J. Lima, C. Matos, B. de Castro, S. Reis, *Phys. Chem. Chem. Phys.* **2004**, *6*, 1493.
- [35] R. Gilmanishin, C. E. Creutz, L. K. Tamm, *Biochemistry* **1994**, *33*, 8225.
- [36] C. Klein, T. Pillot, J. Chambaz, B. Drouet, *Res. Protoc.* **2003**, *11*, 46.

DOI: 10.1002/anie.200502277

Enantioselective Thiourea-Catalyzed Acyl-Mannich Reactions of Isoquinolines***Mark S. Taylor, Norihito Tokunaga, and
Eric N. Jacobsen**

Aromatic molecules represent an attractive class of feedstock compounds for organic synthesis because of their ready availability, their stability, and the wealth of classical and modern chemistry available for their preparation and manipulation. The development of enantioselective, catalytic methodologies that engage aromatic π systems as substrates offers particular promise for synthetic applications. Despite this potential, it is only recently that aromatic frameworks have been employed successfully as electrophiles^[1] or nucleophiles^[2] in asymmetric, catalytic reactions, and many important challenges in this area remain unmet. The addition of carbon-centered nucleophiles to nitrogen-containing heteroaromatic compounds is a particularly interesting problem, in light of the potential impact of such a methodology on alkaloid synthesis. Diastereoselective reactions controlled by chiral auxiliaries currently constitute the state-of-the-art methods for the majority of stereocontrolled transformations of this type.^[3] The elegant alkaloid syntheses of Comins et al. based on diastereoselective nucleophilic additions to chiral (4-methoxy)acetylpyridinium derivatives illustrate the utility of such approaches.^[4] Only one enantioselective, catalytic method for the addition of carbon-centered nucleophiles to aromatic nitrogen heterocycles has been developed to date: the aluminum-catalyzed acylcyanation of quinolines, isoquinolines, and pyridines (the Reissert reaction) developed by Shibasaki and co-workers.^[1a-d] Herein, we report the first example of an asymmetric, catalytic addition of enolate equivalents to heteroaromatic electrophiles. This acyl-Mannich reaction,^[5] catalyzed by a chiral thiourea derivative, provides access to useful enantioenriched dihydroisoquinoline building blocks.^[6]

N-Alkylations or *N*-acylations of nitrogen-containing heteroaromatic compounds give rise to highly electrophilic

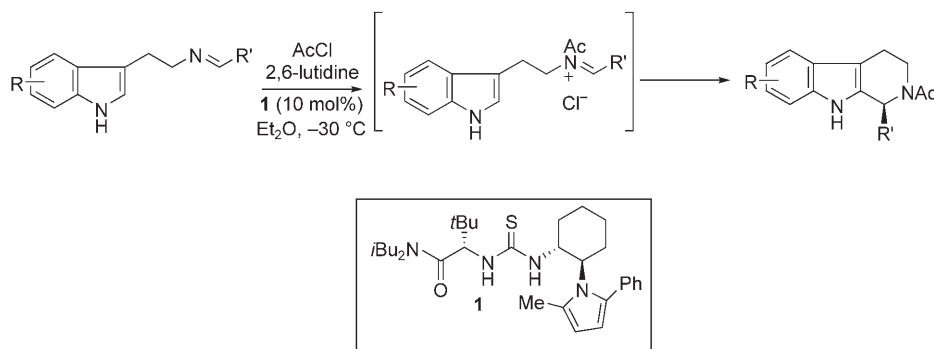
[*] M. S. Taylor, N. Tokunaga, Prof. Dr. E. N. Jacobsen
Department of Chemistry and Chemical Biology
Harvard University
Cambridge, MA 02138 (USA)
Fax: (+1) 617-496-1880
E-mail: jacobsen@chemistry.harvard.edu

[**] This work was supported by the NIH (GM-43214 and P50 GM069721). M.S.T. gratefully acknowledges Bristol-Myers-Squibb for a Graduate Fellowship and Harvard University for a John Parker Graduate Scholarship. N.T. thanks the Japan Society for the Promotion of Science for the award of a fellowship for graduate students. Dr. Richard Staples is acknowledged for the determination of the X-ray crystal structure of 1.



Supporting information for this article is available on the WWW under <http://www.angewandte.org> or from the author.

iminium or acyliminium ions that are susceptible to a variety of addition reactions. There are very few examples of the asymmetric catalysis of such additions,^[1a-e] a fact that may reflect, to some extent, the difficulty in the development of catalysts capable of the activation of such intermediates. In that context, we were highly encouraged by the discovery that chiral thiourea **1** catalyzes an enantioselective acylative variant of the Pictet–Spengler reaction (Scheme 1). The



Scheme 1. Enantioselective acyl-Pictet–Spengler reaction catalyzed by **1**.

possibility that **1** can activate a putative intermediate acyliminium ion towards enantioselective cyclization by hydrogen-bond donation^[7,8] prompted us to study its application to the reactions of acyliminium ions derived from nitrogen heterocycles.

In light of the prevalence of the 1-substituted tetrahydroisoquinoline motif in alkaloid architecture,^[9] we selected isoquinoline as a model substrate (Table 1). The enantioselectivity of acyl-Mannich-type reactions catalyzed by **1** was found to depend strongly on the nature and structure of the acylating agent and nucleophile. A screen of acylating agents was performed using the *O*-*tert*-butyldimethylsilyl (TBS) ketene acetal derived from methyl acetate as the nucleophile.^[10] Acetyl chloride, the optimal reagent for enantiose-

lective Pictet–Spengler reactions, furnished the acyl-Mannich product in poor enantiomeric excess (28 % *ee*; entry 1). More encouraging results were obtained using chloroformates (entries 2–5), with which tuning of the alkoxy substituent had a pronounced effect upon enantioselectivity. The dihydroisoquinoline product was obtained in a promising 82 % *ee* by using 2,2,2-trichloroethyl chloroformate (TrocCl). Further improvement upon this result was realized by variation of the

structure of the nucleophile (entries 5–7), with the best result provided by the silyl ketene acetal derived from isopropyl acetate. The acyl-Mannich reaction of isoquinoline proceeded in 80 % yield with 86 % *ee* under the optimized conditions.

Despite markedly different dependences of enantiomeric excess upon the structure of the acyl group, the acyl-Mannich and acyl-Pictet–Spengler reactions share several common features. Pronounced solvent effects were

observed in both cases, with diethyl ether affording the highest enantioselectivity. In addition, **1** is the optimal catalyst identified to date for both reactions.^[11] In particular, the *ee* values of both the acyl-Mannich and acyl-Pictet–Spengler reaction exhibit a dramatic dependence upon the substitution pattern of the pyrrole moiety (Table 2). The crystal structure of **1** may help to explain this behavior (Figure 1).^[12] The orientation of the 2-methyl-5-phenylpyrrole structural motif places the phenyl group in position to interact closely with any species that undergoes hydrogen-bonding interactions with the acidic thiourea protons (Figure 1).^[13] In the solid state, **1** exists as a dimeric structure through bifurcated hydrogen-

Table 1: Optimization of the acylating agent and nucleophile.

Entry	R	R'	Yield [%] ^[a]	<i>ee</i> [%] ^[b]
1	Me	Me	80	28
2	OBn	Me	60	41
3	OC(CH ₃) ₂ CCl ₃	Me	70	47
4	OCH ₂ (fluorenyl)	Me	75	64
5	OCH ₂ CCl ₃	Me	65	82
6	OCH ₂ CCl ₃	Bn	80	73
7	OCH ₂ CCl ₃	<i>i</i> Pr	80	86 ^[c]

[a] Yield of isolated product after column chromatography. [b] Enantiomeric excess determined by supercritical fluid chromatography (SFC) using commercially available chiral stationary-phase columns. [c] Reaction temperature was –70 °C.

Table 2: Dependence of reaction enantioselectivity on catalyst structure.

Entry	R	R'	Yield [%] ^[a]	<i>ee</i> [%] ^[b]
1	Me	Me	60	30
2	Ph	Ph	55	78
3	Me	Ph	55	85

[a] Yield of isolated product after column chromatography. [b] Enantiomeric excess determined by SFC using commercially available chiral stationary-phase columns.

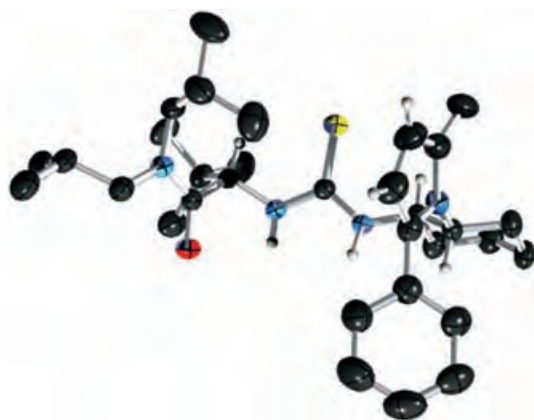


Figure 1. Solid-state structure of catalyst 1.

bonding interactions between the thiourea N–H protons and the amide carbonyl group.^[14]

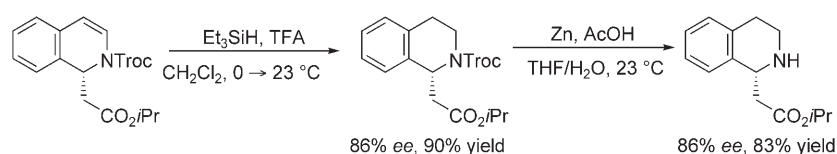
A number of substituted dihydroisoquinolines are accessible through this new methodology (Table 3) and serve as

Table 3: Acyl-Mannich reaction of substituted isoquinolines.

$ \begin{array}{c} \text{1) TrocCl (1.1 equiv)} \\ \text{Et}_2\text{O, 0} \rightarrow \text{23}^\circ\text{C} \\ \text{2) } \begin{array}{c} \text{OTBS} \\ \\ \text{H}_2\text{C} \\ \\ \text{O}^i\text{Pr} \end{array} \text{ (2.0 equiv)} \\ \text{1 (10 mol\%)} \\ \text{Et}_2\text{O, -78} \rightarrow \text{-70}^\circ\text{C} \end{array} \longrightarrow $			
Entry	R	Yield [%] ^[a]	ee [%] ^[b]
1	H	80	86
2	3-Me	75	92
3	4-Br	78	91
4	5-Br	77	87
5	5-OTBS	77	83
6	5-NO ₂	71	71
7	6-OSO ₂ CF ₃	67	83
8	7-OTBS	86	60

[a] Yield of isolated product after column chromatography. [b] Enantiomeric excess determined by SFC or HPLC using commercially available chiral stationary-phase columns.

precursors to enantioenriched 1-substituted tetrahydroisoquinolines: hydrogenation of the enamide moiety and reductive cleavage of the trichloroethyl carbamate group occur in good yield without detectable racemization (Scheme 2).^[15] Thus, this method represents a straightforward approach to the preparation of enantioenriched heterocycles with potential



Scheme 2. Synthesis of an enantioenriched tetrahydroisoquinoline. TFA = trifluoroacetic acid.

utility for alkaloid synthesis from stable, readily accessible aromatic starting materials. For certain applications, this methodology may prove complementary to the Pictet–Spengler reaction, both in terms of electronic requirements (both electron-rich and electron-poor products may be accessed) and regioselectivity (the substitution pattern of the product is determined only by the choice of the isoquinoline starting material). In addition, this study demonstrates that thiourea catalyst **1** mediates two distinct enantioselective transformations of *N*-acyliminium ions: intramolecular Friedel–Crafts reactions of acyliminium ions derived from acyclic, aliphatic imines (the acyl-Pictet–Spengler reaction) and intermolecular Mannich reactions of acyloisoquinolinium ions. Further extension of this mode of catalysis to encompass other reactions of *N*-acyliminium intermediates and investigation of the mechanism by which these electron-poor species are activated by a hydrogen-bond donor are the focus of future study.

Experimental Section

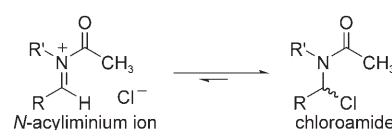
General procedure for acyl-Mannich reactions catalyzed by **1**: 1-Isopropoxycarbonylmethyl-1*H*-isoquinoline-2-carboxylic acid 2,2,2-trichloroethyl ester (Table 3, entry 1): Isoquinoline (61 μL , 0.50 mmol; 97% purity) was dissolved in diethyl ether (5.0 mL) in a flame-dried round-bottomed flask and cooled to 0 °C. 2,2,2-Trichloroethyl chloroformate (76 μL , 0.55 mmol, 1.1 equiv; 98% purity) was added dropwise by syringe, and the resulting white suspension was warmed to 23 °C, stirred for 30 min, and then cooled to –78 °C (dry ice/isopropanol bath). Catalyst **1** (26.9 mg, 0.050 mmol, 10 mol%) in diethyl ether (4.0 mL + 1.0 mL rinse volume) and then 1-(*tert*-butyldimethylsilyloxy)-1-isopropoxyethene (216 mg, 1.0 mmol, 2.0 equiv) were added. The reaction mixture was warmed to –70 °C (isopropanol bath equipped with immersion cooler) and stirred for 14 h. Cooling was stopped and the bath allowed to warm to 23 °C over 3 h. After the solvent was removed in vacuo, the residue was purified by chromatography on silica gel (0–5% ethyl acetate/hexanes), thus yielding a colorless oil (161 mg, 0.40 mmol, 80% yield). The enantiomeric excess was determined to be 86% by SFC using a commercial chiral stationary phase (Chiralpak OD-H, 5% methanol/CO₂, 5 mL min^{–1}, 50 °C, 285 nm; *t*_r(minor): 2.23 min, *t*_r(major): 2.66 min); α_{D}^{20} = –240° (*c* = 1.1 g 100 mL^{–1}, CH₂Cl₂); ¹H NMR (500 MHz, CDCl₃): the compound exists as a 1.7:1 mixture of carbamate rotamers; signals corresponding to the major rotamer: δ = 7.26–7.17 (3 H, m), 7.10 (1 H, d, *J* = 7.5 Hz), 6.90 (1 H, d, *J* = 7.5 Hz), 5.99 (1 H, d, *J* = 8.0 Hz), 5.84–5.82 (1 H, m), 4.97–4.88 (2 H, m), 4.78 (1 H, d, *J* = 12.0 Hz), 2.67–2.58 (2 H, m), 1.20 (3 H, d, *J* = 6.0 Hz), 1.16 ppm (3 H, d, *J* = 6.5 Hz); representative signals corresponding to the minor rotamer: δ = 6.90 (1 H, d, *J* = 7.5 Hz), 6.04 (1 H, d, *J* = 8.0 Hz), 4.82 (1 H, d, *J* = 11.5 Hz), 2.77 (1 H, dd, *J* = 14.0, 9.0 Hz), 1.11 ppm (3 H, d, *J* = 5.5 Hz); ¹³C NMR (100 MHz, CDCl₃), signals corresponding to both rotamers: δ = 169.6, 169.5, 151.6, 151.2, 131.4, 131.2, 129.9, 129.8, 128.6, 128.5, 127.7, 127.5, 126.7, 126.6, 125.5, 125.3, 124.5, 123.6, 110.7, 110.6, 95.2, 95.2, 75.7, 75.6, 68.4, 68.4, 53.3, 53.1, 40.8, 40.1, 22.0, 22.0, 21.9, 21.9 ppm; IR (neat): $\tilde{\nu}$ = 3063 (w), 2980 (m), 2936 (w), 1728 (s), 1651 (s), 1452 (m), 1262 (m), 1109 (m), 968 cm^{–1} (w); HRMS (ES): *m/z* calcd for [C₁₇H₁₈N₂O₄ + H]⁺: 406.0380; found: 406.0380.

Received: June 29, 2005

Published online: September 21, 2005

Keywords: asymmetric catalysis · heterocycles · hydrogen bonds · Mannich reaction · urea derivatives

- [1] Enantioselective, catalytic Reissert reactions: a) M. Takamura, K. Funabashi, M. Kanai, M. Shibasaki, *J. Am. Chem. Soc.* **2000**, *122*, 6327–6328; b) M. Takamura, K. Funabashi, M. Kanai, M. Shibasaki, *J. Am. Chem. Soc.* **2001**, *123*, 6801–6808; c) K. Funabashi, H. Ratni, M. Kanai, M. Shibasaki, *J. Am. Chem. Soc.* **2001**, *123*, 10784–10785; d) E. Ichikawa, M. Suzuki, K. Yabu, M. Albert, M. Kanai, M. Shibasaki, *J. Am. Chem. Soc.* **2004**, *126*, 11808–11809; enantioselective catalytic hydrogenation of *N*-iminopyridinium ylides: e) C. Y. Legault, A. B. Charette, *J. Am. Chem. Soc.* **2005**, *127*, 8966–8967; enantioselective hydrogenation of quinolines: f) W.-B. Wang, S.-M. Lu, P.-Y. Yang, X.-W. Han, Y.-G. Zhou, *J. Am. Chem. Soc.* **2003**, *125*, 10536–10537.
- [2] For a review of enantioselective catalytic Friedel–Crafts reactions, see: a) M. Bandini, A. Melloni, A. Umani-Ronchi, *Angew. Chem.* **2004**, *116*, 560–566; *Angew. Chem. Int. Ed.* **2004**, *43*, 550–556; for recent developments, see: b) M. S. Taylor, E. N. Jacobsen, *J. Am. Chem. Soc.* **2004**, *126*, 10558–10559; c) D. Uraguchi, K. Sorimachi, M. Terada, *J. Am. Chem. Soc.* **2004**, *126*, 11804–11805; d) C. Palomo, M. Oiarbida, B. G. Kardak, J. M. García, A. Linden, *J. Am. Chem. Soc.* **2005**, *127*, 4154–4155; e) D. A. Evans, K. R. Fandrick, H.-J. Song, *J. Am. Chem. Soc.* **2005**, *127*, 8942–8943; asymmetric, catalytic C–H activation: f) R. K. Thalji, J. A. Ellman, R. G. Bergman, *J. Am. Chem. Soc.* **2004**, *126*, 7192–7193.
- [3] a) D. L. Comins, M. M. Badawi, *Heterocycles* **1991**, *32*, 1869–1873; b) G. B. Richter-Addo, D. A. Knight, M. A. Dewey, A. M. Arif, J. A. Gladysz, *J. Am. Chem. Soc.* **1993**, *115*, 11863–11873; c) D. L. Comins, S. P. Joseph, R. R. Goehring, *J. Am. Chem. Soc.* **1994**, *116*, 4719–4728; d) D. Barbier, C. Marazano, C. Riche, B. C. Das, P. Potier, *J. Org. Chem.* **1998**, *63*, 1767–1772; e) K. T. Wanner, H. Beer, G. Höfner, M. Ludwig, *Eur. J. Org. Chem.* **1998**, 2019–2029; f) T. Itoh, K. Nagata, M. Miyazaki, A. Ohsawa, *Synlett* **1999**, 7, 1154–1156.
- [4] For representative examples, see reference [3c], references cited therein, and: a) D. L. Comins, X. Chen, L. A. Morgan, *J. Org. Chem.* **1997**, *62*, 7435–7438; b) D. L. Comins, D. H. LaMunyon, X. Chen, *J. Org. Chem.* **1997**, *62*, 8182–8187; c) J. T. Kuethe, D. L. Comins, *Org. Lett.* **2000**, *2*, 855–857.
- [5] a) T. Itoh, M. Miyazaki, K. Nagata, H. Hasegawa, A. Ohsawa, K. T. Nakamura, *Heterocycles* **1998**, *47*, 125–128; b) for a diastereoselective variant that employs a chiral acyl chloride, see reference [3f].
- [6] a) Examples of enantioselective additions of silyl ketene acetals to 6,7-dialkoxy-3,4-dihydroisoquinoline *N*-oxides have been reported: S.-I. Murahashi, Y. Imada, T. Kawakami, K. Harada, Y. Yonemushi, N. Tomita, *J. Am. Chem. Soc.* **2002**, *124*, 2888–2889; b) proline-catalyzed Mannich reactions of 3,4-dihydro- β -carboline have been reported: T. Itoh, M. Yokoya, K. Miyauchi, K. Nagata, A. Ohsawa, *Org. Lett.* **2003**, *5*, 4301–4304.
- [7] For enantioselective reactions catalyzed by chiral urea or thiourea compounds, see reference [2b] and: a) M. S. Sigman, E. N. Jacobsen, *J. Am. Chem. Soc.* **1998**, *120*, 4901–4902; b) P. Vachal, E. N. Jacobsen, *Org. Lett.* **2000**, *2*, 867–870; c) M. S. Sigman, P. Vachal, E. N. Jacobsen, *Angew. Chem.* **2000**, *112*, 1336–1338; *Angew. Chem. Int. Ed.* **2000**, *39*, 1279–1281; d) P. Vachal, E. N. Jacobsen, *J. Am. Chem. Soc.* **2002**, *124*, 10012–10014; e) A. G. Wenzel, E. N. Jacobsen, *J. Am. Chem. Soc.* **2002**, *124*, 12964–12965; f) A. G. Wenzel, M. P. Lalonde, E. N. Jacobsen, *Synlett* **2003**, *12*, 1919–1922; g) T. Okino, Y. Hoashi, Y. Takemoto, *J. Am. Chem. Soc.* **2003**, *125*, 12672–12673; h) G. D. Joly, E. N. Jacobsen, *J. Am. Chem. Soc.* **2004**, *126*, 4102–4103; i) T. Okino, S. Nakamura, T. Furukawa, Y. Takemoto, *Org. Lett.* **2004**, *6*, 625–627; j) Y. Sohtome, A. Tanatani, Y. Hashimoto, K. Nagasawa, *Tetrahedron Lett.* **2004**, *45*, 5589–5592; k) Y. Hoashi, T. Yabuta, Y. Takemoto, *Tetrahedron Lett.* **2004**, *45*, 9185–9188; l) T. Okino, Y. Hoashi, T. Furukawa, X. Xu, Y. Takemoto, *J. Am. Chem. Soc.* **2005**, *127*, 119–125; m) T. P. Yoon, E. N. Jacobsen, *Angew. Chem.* **2005**, *117*, 470–472; *Angew. Chem. Int. Ed.* **2005**, *44*, 466–468; n) A. Berkessel, F. Cleemann, S. Mukherjee, T. N. Müller, J. Lex, *Angew. Chem.* **2005**, *117*, 817–821; *Angew. Chem. Int. Ed.* **2005**, *44*, 807–811; o) A. Berkessel, S. Mukherjee, F. Cleemann, T. N. Müller, J. Lex, *Chem. Commun.* **2005**, 1898–1900; p) B.-J. Li, L. Jiang, M. Liu, Y.-C. Chen, L.-S. Ding, Y. Wu, *Synlett* **2005**, *4*, 603–606; q) D. E. Fuerst, E. N. Jacobsen, *J. Am. Chem. Soc.* **2005**, *127*, 8964–8965.
- [8] For representative examples of other classes of chiral hydrogen-bond-donor catalysts, see: a) E. J. Corey, M. J. Grogan, *Org. Lett.* **1999**, *1*, 157–160; b) Y. Huang, A. K. Unni, A. N. Thadani, V. H. Rawal, *Nature* **2003**, *424*, 146; c) B. M. Nugent, R. A. Yoder, J. N. Johnston, *J. Am. Chem. Soc.* **2004**, *126*, 3418–3419; d) N. T. McDougal, S. E. Schaus, *J. Am. Chem. Soc.* **2003**, *125*, 12094–12095; e) T. Akiyama, J. Itoh, K. Yokota, K. Fuchibe, *Angew. Chem.* **2004**, *116*, 1592–1594; *Angew. Chem. Int. Ed.* **2004**, *43*, 1566–1568.
- [9] a) K. W. Bentley, *Nat. Prod. Rep.* **2004**, *21*, 395–424, and references therein; b) for a review of methods for the preparation of enantioenriched tetrahydroisoquinolines, see: M. Chrzanoska, M. D. Rozwadowska, *Chem. Rev.* **2004**, *104*, 3341–3370.
- [10] A preliminary survey of ketone enolates did not yield satisfactory results; for example, 2-(trimethylsilyloxy)propene underwent addition to isoquinoline in the presence of TrocCl and **1** to yield the corresponding dihydroisoquinoline in 14 % *ee* (unoptimized).
- [11] A list of solvents and other catalysts tested may be found in the Supporting Information.
- [12] Slow evaporation of a solution of **1** in hexanes/diethyl ether yielded crystals suitable for X-ray analysis; crystal data for **1**: C₃₂H₅₀N₄O₈, *M_r* = 538.82, colorless prism, 0.20 × 0.18 × 0.14 mm, orthorhombic, *a* = 16.590(3), *b* = 17.202(3), *c* = 22.411(4) Å, *V* = 6396(2) Å³, *T* = 193(2) K, space group C22₂₁, *Z* = 8, ρ_{calc} = 1.119 g cm^{−3}, μ = 0.130 mm^{−1}; a total of 22451 reflections were measured, 7659 independent, final residuals were *R*1 = 0.0394 and *wR*2 = 0.0877 for 7659 observed reflections with *I* > 2 σ (*I*), 543 parameters, GOF = 0.960, maximum residual electron density 0.438 e Å^{−3}; data were collected on a Bruker SMART CCD (charge-coupled device) based diffractometer equipped with an Oxford Cryostream low-temperature apparatus; data were measured by using scans of 0.3° per frame for 45 s, such that a hemisphere was collected; a total of 1271 frames were collected with a maximum resolution of 0.76 Å; the first 50 frames were recollected at the end of data collection to monitor for decay; the structure was solved by the direct method (G. M. Sheldrick, SHELXL-97, Program for the Solution of Crystal Structures, University of Göttingen, Germany, 1997) followed by refinement by the least-squares method on *F*² (SHELXL-97); all non-hydrogen atoms were refined anisotropically; the positions of hydrogen atoms were found by difference Fourier methods and refined isotropically. CCD-275454 contains the supplementary crystallographic data for this paper. These data can be obtained free of charge from The Cambridge Crystallographic Data Centre via www.ccdc.cam.ac.uk/data_request/cif.
- [13] A neutral chloroamide structure, rather than an ion pair, may represent a more accurate depiction of the bonding interactions in *N*-acyliminium chlorides in nonpolar organic solvents (for an NMR spectroscopic study that supports this assertion, see: A. K. Bose, G. Spiegelman, M. S. Manhas, *Tetrahedron Lett.* **1971**, 3167–3170). Calculations that use the density-functional theory



(B3LYP/6-31G++(d,p)) predict substantial chloroamide character for *N*-acylisoquinolinium chloride (M. S. Taylor, E. N. Jacobsen, unpublished results), and the strong dependence of enantioselectivity upon solvent polarity observed in both acyl-Mannich and acyl-Pictet–Spengler reactions may be a reflection of the importance of the pairing of the *N*-acyliminium ions in these processes. These reactions are also subject to dramatic leaving-group effects upon reactivity and enantioselectivity, a phenomenon that seems difficult to reconcile with a fully ionized *N*-acyliminium ion as the reactive species. The possibility that **1** activates intermediate chloroamides toward substitution reactions by hydrogen-bonding interactions with the carbonyl group represents an intriguing, albeit speculative, mechanistic hypothesis that is consistent with these observations.

- [14] For a discussion of the crystallization and cocrystallization of urea compounds directed by bifurcated hydrogen-bond interactions, see: a) M. C. Etter, T. W. Panunto, *J. Am. Chem. Soc.* **1988**, *110*, 5896–5897; b) M. C. Etter, Z. Urbańczyk-Lipkowska, M. Zia-Ebrahimi, T. W. Panunto, *J. Am. Chem. Soc.* **1990**, *112*, 8415–8426; c) M. C. Etter, *Acc. Chem. Res.* **1990**, *23*, 120–126.
- [15] Transesterification of the resulting product permitted the absolute configuration to be assigned (see the Supporting Information for details).

Gene Therapy

DOI: 10.1002/anie.200502152

A Family of Hierarchically Self-Assembling Linear-Dendritic Hybrid Polymers for Highly Efficient Targeted Gene Delivery***Kris C. Wood, Steven R. Little, Robert Langer,* and Paula T. Hammond**

To fully realize the potential for new medical advances in the postgenomic era, safe and efficient delivery systems for nucleotide-based drugs must be developed.^[1] Ideally, such

[*] S. R. Little, Prof. R. Langer
Department of Chemical Engineering, Room E25-342
Massachusetts Institute of Technology
Cambridge, MA 02139 (USA)
Fax: (+1) 617-258-8827
E-mail: rlanger@mit.edu
K. C. Wood, Prof. P. T. Hammond
Department of Chemical Engineering, Room 66-546
Massachusetts Institute of Technology
Cambridge, MA 02139 (USA)
Fax: (+1) 617-258-5766
E-mail: hammond@mit.edu

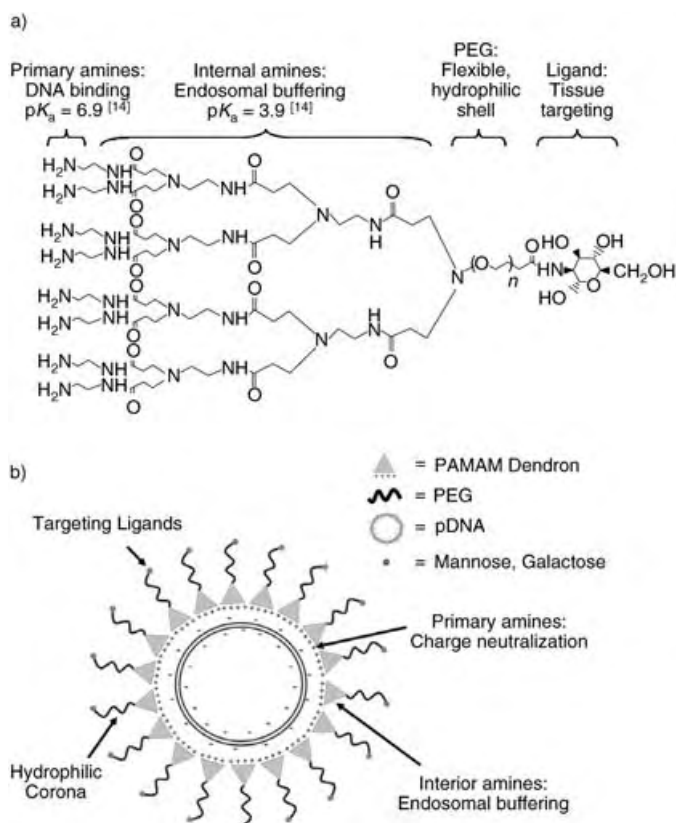
[**] This work was supported by the National Institutes of Health (EB 00244), the Division of Materials Research of the National Science Foundation (DMR 9903380), the Office of Naval Research, and the Mark Hyman, Jr. Professorship in Chemical Engineering at MIT. S.R.L. thanks the National Science Foundation for a graduate research fellowship. We thank Gregory Zugates and Kristoffer Stokes for helpful discussions and Ryan Bennett for assistance with the transmission electron microscopy.

Supporting information for this article is available on the WWW under <http://www.angewandte.org> or from the author.

systems will be nontoxic, nonimmunogenic, and made from versatile building blocks that allow optimal delivery to a range of cells or tissues of interest. Herein, for the first time, we present the design, synthesis, and evaluation of a unique family of hierarchically structured linear-dendritic hybrid polymers that self-assemble with DNA to form stable nanoparticles with a series of concentric, functional “shells” that display independently tuneable properties necessary for effective targeted delivery. The resultant ligand-functionalized systems demonstrate receptor-mediated delivery to targeted cells with robust serum stability, transfection efficiencies that exceed the most efficient commercially available polymer poly(ethylenimine) (PEI), and low toxicity at concentrations one to two orders of magnitude higher than those at which PEI is toxic. These systems may find potential utility as targeted in vivo gene delivery systems for DNA- or RNA-based therapies.

The success of gene-based therapies is dependent upon the ability to deliver genes that express key proteins when and where they are needed. As of yet, no such therapies have been approved for clinical use, primarily because of the lack of versatile, safe, and efficient gene delivery systems.^[2,3] A suite of electrical, mechanical, and modified viral delivery systems have been investigated with some success, but these systems suffer from significant drawbacks.^[4–7] Notably, modified viruses often elicit severe immunogenicity, are prone to insertional mutagenesis, and are refractory to repeated administrations. Chemical delivery systems, such as cationic linear polymers, dendrimers, or lipid-based reagents, while generally safer than their viral counterparts, typically lack the high efficiency or multiple functionalities required for in vivo administration. Moreover, even subtle synthetic modifications to these systems can dramatically influence existing biological properties.^[8–10] Herein, we present a new family of multifunctional gene delivery polymers based on dendritic poly(amidoamine) (PAMAM) and linear poly(ethylene glycol) (PEG) with a wide array of properties (namely, blood stability, cellular targeting, DNA binding, and endosomal buffering capacity) that can be independently tuned in a modular fashion to address each of the barriers to effective gene delivery. As a proof of concept, we demonstrate the ability to independently modulate targeting and expression levels by choice of the ligand and dendrimer species, respectively. Furthermore, these systems represent a platform on which additional functionalities may be added to impart properties such as vector unpackaging and nuclear targeting.^[11,12]

Linear-dendritic hybrid polymers were designed based on the hypothesis that these unique polymer architectures, which contain functionalities that are both chemically orthogonal and physically separate, could self-assemble with DNA to yield nanoparticles with an outer shell of targeting ligands accessible to cell-surface receptors, a flexible hydrophilic corona designed to prevent protein opsonization, plasma clearance, and nonspecific uptake, and an interior of amine groups to promote DNA binding and escape from endosomal vesicles into the cytoplasm^[13,14] (see Scheme 1 and the Supporting Information). Ligand-functionalized linear-dendritic polymers were synthesized as follows: Fmoc-PEG-NHS



Scheme 1. Rational design and hierarchical self-assembly of linear-dendritic polymers with plasmid DNA (pDNA). a) Molecular structure–function relationship in a mannose-PEG-PAMAM G3.0 system. b) Structure of linear-dendritic polyplexes show the relative positions of the functional elements (not to scale).

($M_n=3500$, $n=72$, polydispersity index (PDI)=1.01; Fmoc = 9-fluorenylmethoxycarbonyl, NHS = *N*-hydroxysuccinimide) was dissolved in 0.1M NaHCO₃ buffer (37.5 mg mL⁻¹) and adjusted to pH 8.5 with 1M NaOH. Amine-modified mannose and galactose ligands were dissolved separately in 0.1M NaHCO₃ buffer (30 mg mL⁻¹), adjusted to pH 8.5, and added to an aliquot of dissolved polymer in solution at a molar excess of 10:1 (24 h, 25 °C, under N₂). The polymers were recovered by filtration and lyophilization, dissolved in dimethylformamide (DMF; 100 mg mL⁻¹), and added dropwise to a solution of 20% piperidine in DMF to remove the Fmoc protecting group (30 min, 25 °C, under N₂). Following this step, the polymers were recovered by precipitation with diethyl ether and dried overnight under vacuum. The dendrimer synthesis proceeded by serial Michael addition and amidation steps by the addition of methyl acrylate and ethylene diamine, respectively, as described previously (see Supporting Information).^[15] In general, the ligand-functionalization and deprotection steps proceeded at 80–85%, and all the dendrimer synthetic steps proceeded with conversions of 90–100% (see Supporting Information). The physical properties of these polymers are listed in Table 1. The growth of the amide (3200–3400 cm⁻¹) and carbonyl (1600–1800 cm⁻¹) bands

Table 1: Theoretical molecular weights and number of amine end groups for ligand-functionalized PEG–PAMAM hybrid polymers.

Polymer	M_n (theoretical)	Number of amine end groups
ligand-PEG-PAMAM-G0.0	3344	1
ligand-PEG-PAMAM-G1.0	3572	2
ligand-PEG-PAMAM-G2.0	4028	4
ligand-PEG-PAMAM-G3.0	4940	8
ligand-PEG-PAMAM-G4.0	6764	16
ligand-PEG-PAMAM-G5.0	10 412	32
ligand-PEG-PAMAM-G6.0	17 708	64

during dendrimer synthesis can be seen qualitatively in Figure 1.

An array of techniques was used to probe the biophysical character of polymer/DNA complexes, or “polyplexes” (see Figure 2). Gel electrophoresis demonstrates binding and

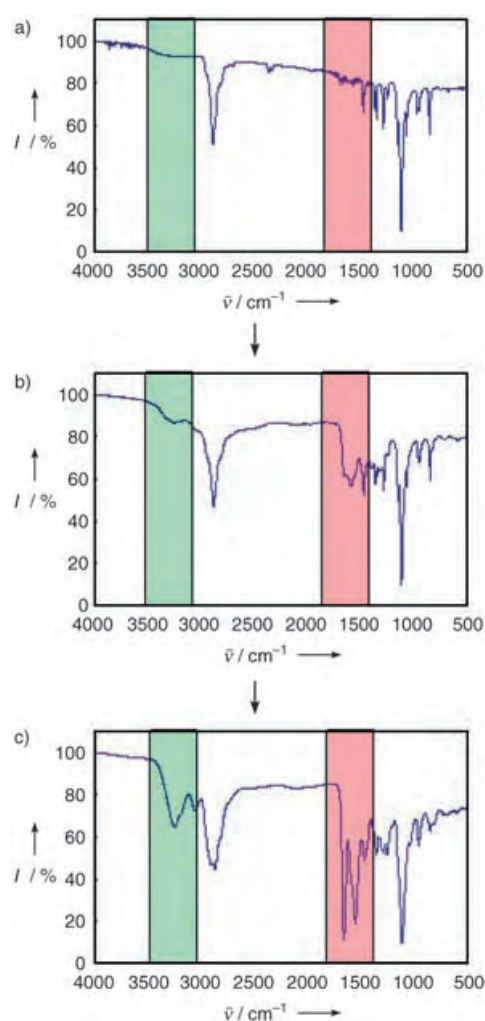


Figure 1. FTIR spectroscopic analysis demonstrates exponential dendron growth in sugar-PEG-PAMAM a) G0.0, b) G2.0, and c) G4.0 systems. Growth of the amide and carbonyl signals are highlighted in green and pink, respectively. (Conversion at the deprotection step was approximately 80%, and conversion at each branching step was 90–100%.) Complete NMR and FTIR spectroscopic analysis is given in the Supporting Information.

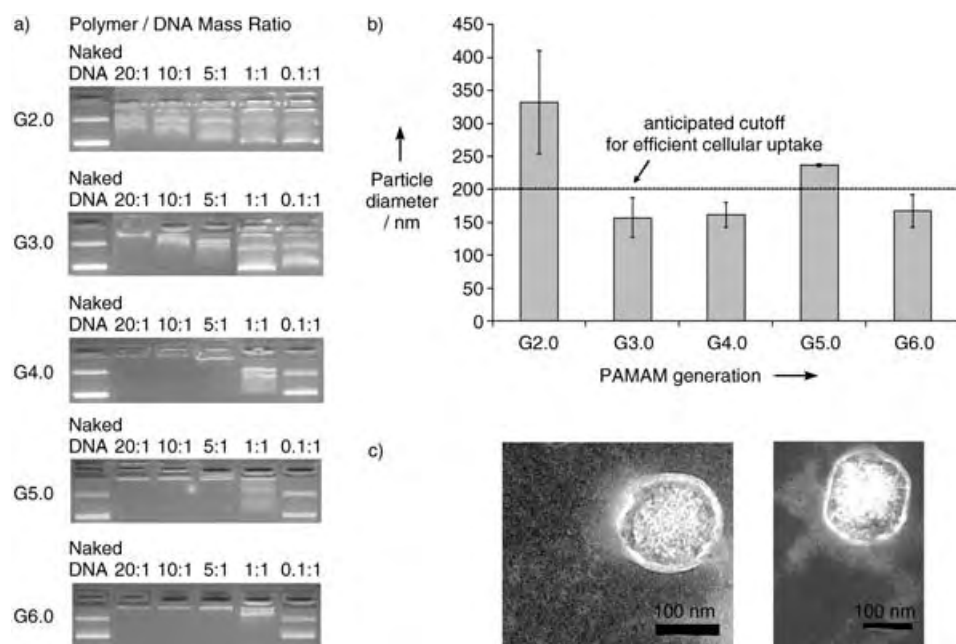


Figure 2. Biophysical characterization of linear-dendritic polyplexes. a) Electrophoresis on 1 % agarose gel demonstrates DNA binding at the indicated mass ratios. b) Particle diameter measured with dynamic light scattering (DLS). c) Transmission electron microscopy (TEM) images depict narrowly dispersed, roughly spherical particles.

charge neutralization of DNA by linear-dendritic polymers incubated at mass ratios of > 20:1, 10:1, 5:1, 1:1, and 1:1 for generations 2.0 (G2.0), 3.0 (G3.0), 4.0 (G4.0), 5.0 (G5.0), and 6.0 (G6.0), respectively (an acetate buffer of pH 5.1 was used in all cases to ensure complete protonation of the primary amines on the dendrimer periphery). The nature of this trend is consistent with intuition, as the exponentially increasing number of the amine functionalities with increasing dendrimer generation results in higher charge density with increasing dendrimer size. Dynamic light scattering (DLS) suggests that polyplexes of G3.0, G4.0, and G6.0 are around 150 nm in diameter on average, which is under the reported cut-off point of around 200 nm that is required for efficient cellular uptake (Figure 2b).^[16] G5.0 polyplexes form larger particles with DNA, a seemingly anomalous result that was nevertheless highly repeatable. The large size of G2.0 polyplexes reflects the fact that little DNA binding and charge neutralization occurred in these systems. In all cases, mass ratios in the range 0.1:1–200:1 were tested, and polyplex size was shown to be relatively insensitive to mass ratio above the point at which complexation occurs in each system, thus suggesting that in all cases the polyplexes consist of a single DNA plasmid and that excess polymers remain dispersed in solution. Thus, particle diameters given in Figure 2b represent average diameters for an evenly weighted range of mass ratios up to 200:1. Finally, transmission electron micrographs of G6.0 polyplexes show narrowly dispersed, roughly spherical complexes with an outer corona of approximately 6–8 nm, which is consistent with the expected size of PEG–PAMAM G6.0 (Figure 2c).^[17]

In all of the above cases, complexes were formed prior to assay by incubation of the dilute solutions of the plasmid-DNA-encoding firefly luciferase (6.2 kb, $2.05 \times 10^6 \text{ g mol}^{-1}$, 0.1 mg mL^{-1} , 25 mM acetate buffer, pH 5.1) with equal volumes of solutions that contain polymers (in 25 mM acetate buffer (pH 5.1) at appropriate concentrations to achieve the indicated mass ratios) for 20 min at room temperature.^[18]

To evaluate the ability of polyplexes to transfect target cells by receptor-mediated uptake, we transfected two cell types, P388D1 murine macrophages bearing a mannose receptor and HepG2 human hepatocytes bearing an asialoglycoprotein receptor (for galactosylated ligands).^[19–22] The transfections were performed in quadruplicate in a 96-well plate format. The polymers and DNA were combined for 20 min at mass ratios in the range 1:1–200:1 (polymer/DNA) in 25 mM acetate buffer, added to a serum-free or 10 % serum-containing medium, and incubated with cells for 4 h ($587 \text{ ng DNA well}^{-1}$), after which the polyplex-containing medium was removed and replaced with growth medium. The cells were assayed for expression of the luciferase reporter gene after 72 h.^[18] Figure 3a shows the

transfection of P388D1 macrophages bearing the mannose receptor. a) Transfection by linear-dendritic polyplexes with and without the mannose ligand and in the presence of soluble mannose (0.1 mg well^{-1}); * indicates $p < 0.04$, ** indicates $p < 0.002$ (two-tailed, unpaired Student's T-Test). Results normalized to an optimized formulation of PEI (2:1 PEI/DNA, serum free, no free mannose added). b) Serum stability is demonstrated through transfection in the presence of serum proteins. Results normalized to an optimized formulation of PEI (2:1 PEI/DNA, 10 % serum, no free mannose added). All results are given as an average \pm standard error.

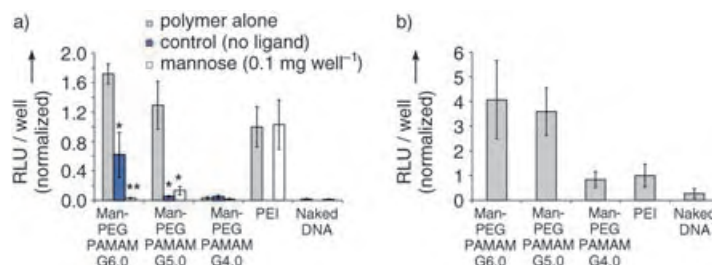


Figure 3. Transfection of P388D1 macrophages bearing the mannose receptor. a) Transfection by linear-dendritic polyplexes with and without the mannose ligand and in the presence of soluble mannose (0.1 mg well^{-1}); * indicates $p < 0.04$, ** indicates $p < 0.002$ (two-tailed, unpaired Student's T-Test). Results normalized to an optimized formulation of PEI (2:1 PEI/DNA, serum free, no free mannose added). b) Serum stability is demonstrated through transfection in the presence of serum proteins. Results normalized to an optimized formulation of PEI (2:1 PEI/DNA, 10 % serum, no free mannose added). All results are given as an average \pm standard error.

levels of luciferase-reporter-gene expression in macrophages (in the absence of serum) with optimized formulations of ligand-functionalized polyplexes, control polyplexes bearing no ligand, ligand-functionalized polyplexes in the presence of excess soluble ligand, and PEI. The G6.0 mannose-bearing polyplexes demonstrate transfection 1.6- to 1.8-fold higher than PEI, the most efficient commercially available polymer for in vitro transfections. The G5.0 polyplexes mediate

reporter expression levels approximately 1.3-fold higher than PEI, whereas the G4.0 polyplexes (as well as G3.0 and G2.0, data not shown) transfect at low levels comparable to naked DNA. The highest transfection levels were observed in polymer/DNA ratios under 50:1 in all systems (under 20:1 in G6.0), presumably because of the effects of toxicity at high concentrations. Polyplexes with no mannose ligand exhibited significantly lower transfection efficiencies, and competitive inhibition of mannose receptors by an excess of soluble ligand virtually silenced reporter-gene expression without affecting expression levels in the positive and negative controls (Figure 3a). These data further support the hypothesis of cellular internalization by means of specific receptor-mediated endocytosis. Finally, macrophages were transfected in the presence of a 10% serum-containing medium to probe the serum stability of pegylated polyplexes (Figure 3b). Fourfold transfection enhancements were observed relative to PEI, most likely because of the “stealth” effect imparted by PEG, which is known to lower particle agglomeration by attenuation of opsonization of serum proteins.^[23]

Transfection of HepG2 hepatocytes by linear-dendritic polyplexes bearing the galactose ligand is shown in Figure 4. In the absence of serum, optimized formulations of G6.0 and G4.0 ligand-functionalized polyplexes transfect significantly more efficiently ($p < 0.06$) than control polymers with no

yield enhanced targeting relative to the monomeric species.^[24,25]

To assess the cellular toxicity of linear-dendritic hybrid-polymer-based systems, a methylthiazolyldiphenyltetrazolium bromide (MTT) assay was performed to measure the relative viability of cells treated with various polymer/DNA mass ratios. Cells were seeded in clear 96-well plates and transfected exactly as previously described. A range of polymer/DNA mass ratios were studied that corresponded to concentrations equal to and above those at which the optimal transfection levels were observed. In P388D1 macrophages (Figure 5a), cells that we have found to be highly

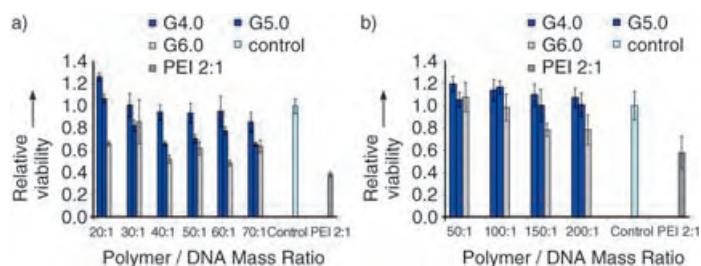


Figure 5. Relative viability of a) P388D1 macrophages and b) HepG2 hepatocytes 72 h after transfection at indicated polymer/DNA mass ratios (control cells untreated). All results are given as an average \pm standard error.

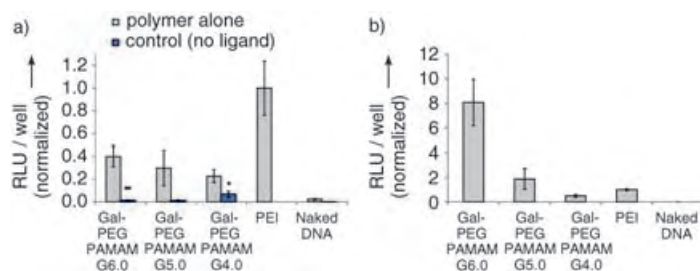


Figure 4. Transfection of HepG2 hepatocytes bearing the asialoglycoprotein receptor. a) Transfection by linear-dendritic polyplexes with and without the galactose ligand; * indicates $p < 0.06$; ** indicates $p < 0.03$ (two-tailed, unpaired Student's T-Test). Results normalized to PEI = 1.0 (serum free, no free galactose added). b) Serum stability is demonstrated through transfection in the presence of serum proteins. Results normalized to PEI = 1.0 (10% serum, no free galactose added). All results are given as an average \pm standard error.

ligand (Figure 4a). Moreover, G6.0-, G5.0-, and G4.0-targeted systems mediate transfection levels within one order of magnitude of PEI in the absence of serum and as much as eightfold more than PEI in the presence of serum (Figure 4a,b). Optimal polymer/DNA mass ratios were in the range 100:1–200:1 for all the systems studied. Taken together, these data suggest that the hepatocyte-targeted polyplexes are serum-stable and demonstrate enhanced transfection because of a cell-specific receptor-mediated process. Interestingly, expression levels were unaffected by the presence of an excess of soluble galactose, a finding that may arise from the multivalent nature of ligand binding to the asialoglycoprotein receptor; thus, it is suggested that multivalent ligand presentation through synthetic multimeric galactose ligands may

sensitive to environmental conditions in culture, no measurable toxicity was observed in the G4.0-based systems over the entire concentration range studied. More significant toxicity was observed at high mass ratios in G5.0 (60–80% viability relative to untreated controls) and the G6.0 systems (50–70%), though these toxicities were primarily observed at concentrations higher than those optimal for transfection. In HepG2 hepatocytes (Figure 5b), no measurable toxicity was observed in the G4.0 and G5.0 systems at polymer/DNA mass ratios up to 200:1; in G6.0, moderate toxicity became apparent at ratios of 150:1 and above. In all cases, linear-dendritic systems failed to display toxicity until concentrations reached one to two orders of magnitude greater than those at which PEI was toxic.

Herein, we have described the design, synthesis, and evaluation of a new family of linear-dendritic hybrid polymers for their ability to deliver DNA to two distinct mammalian cell lines. These hierarchically self-assembling polymers have functionalities that are physically and chemically distinct and can be independently modified. The modular nature of these systems makes them a platform from which further, serial modifications may be added to impart additional desired characteristics without any substantial alteration of the existing properties. As a proof of concept, we have demonstrated the condensation of DNA by linear-dendritic polymers into nanoparticle structures with small size and robust serum stability appropriate for systemic delivery. Moreover, through the presentation of an outer shell of targeting ligands, these particles can transfect cells bearing targeted surface receptors with low toxicities and efficiencies that exceed the best commercially available polymer PEI.

Taken together, our data suggest that this new family of materials may find use as safe and highly efficient in vivo delivery agents for DNA, siRNA, or other nucleotide-based therapeutics.

Received: June 21, 2005

Published online: September 20, 2005

Keywords: dendrimers · DNA · gene therapy · self-assembly

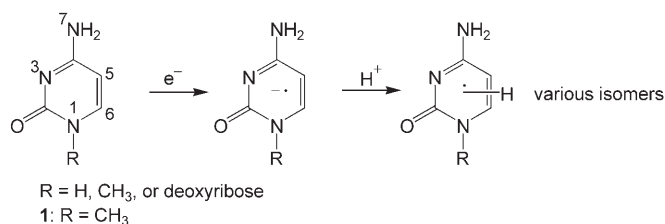
- [1] I. M. Verma, N. Somia, *Nature* **1997**, 389, 239.
- [2] I. M. Verma, M. D. Weitzman, *Annu. Rev. Biochem.* **2005**, 74, 711.
- [3] E. Wagner, *Pharm. Res.* **2004**, 21, 8.
- [4] E. Neumann, M. Schaefer-Ridder, Y. Wang, P. Hofschneider, *EMBO J.* **1982**, 1, 841.
- [5] S. Mehier-Humbert, R. H. Guy, *Adv. Drug Delivery Rev.* **2005**, 57, 733.
- [6] D. Luo, W. Saltzman, *Nat. Biotechnol.* **2000**, 18, 33.
- [7] D. J. Glover, H. J. Lipps, D. A. Jans, *Nat. Rev. Genet.* **2005**, 6, 299.
- [8] D. Luo, K. Haverstick, N. Belcheva, E. Han, W. M. Saltzman, *Macromolecules* **2002**, 35, 3456.
- [9] D. G. Anderson, A. Akinc, N. Hossain, R. Langer, *Mol. Ther.* **2005**, 11, 426.
- [10] D. G. Anderson, D. M. Lynn, R. Langer, *Angew. Chem.* **2003**, 115, 3261; *Angew. Chem. Int. Ed.* **2003**, 42, 3153.
- [11] F. M. Munkonge, D. A. Dean, E. Hillery, U. Griesenbach, E. W. Alton, *Adv. Drug Delivery Rev.* **2003**, 55, 749.
- [12] D. V. Schaffer, N. A. Fidelman, N. Dan, D. A. Lauffenburger, *Biotechnol. Bioeng.* **2000**, 67, 598.
- [13] N. D. Sonawane, F. C. Szoka, A. S. Verkman, *J. Biol. Chem.* **2003**, 278, 44826.
- [14] D. A. Tomalia, A. M. Naylor, W. A. Goddard, *Angew. Chem.* **1990**, 102, 119; *Angew. Chem. Int. Ed. Engl.* **1990**, 29, 138.
- [15] J. Iyer, K. Fleming, P. T. Hammond, *Macromolecules* **1998**, 31, 8757.
- [16] J. Rejman, V. Oberle, I. S. Zuhorn, D. Hoekstra, *Biochem. J.* **2004**, 377, 159.
- [17] D. A. Tomalia, *Prog. Polym. Sci.* **2005**, 30, 294.
- [18] The experimental methods are described in the Supporting Information.
- [19] S. S. Diebold, C. Plank, M. Cotten, E. Wagner, M. Zenke, In *Synthetic DNA Delivery Systems* (Eds.: D. Luo, W. M. Saltzman), Kluwer, New York, **2003**.
- [20] B. Hoflack, S. Kornfeld, *Proc. Natl. Acad. Sci. USA* **1985**, 82, 4428.
- [21] J. S. Remy, A. Kichler, V. Mordvinov, F. Schubert, J. P. Behr, *Proc. Natl. Acad. Sci. USA* **1995**, 92, 1744.
- [22] R. J. Stockert, *Physiol. Rev.* **1995**, 75, 591.
- [23] J. M. Harris, R. B. Chess, *Nat. Rev. Drug Discovery* **2003**, 2, 214.
- [24] D. T. Connolly, R. R. Townsend, K. Kawaguchi, W. R. Bell, Y. C. Lee, *J. Biol. Chem.* **1982**, 257, 939.
- [25] Y. C. Lee, R. T. Lee, *Acc. Chem. Res.* **1995**, 28, 321.

DOI: 10.1002/anie.200502363

Specific Generation of 1-Methylcytosine Radicals in the Gas Phase**

Chunxiang Yao, Maria L. Cuadrado-Peinado, Mirosław Polášek, and František Tureček*

Nucleobase-derived radicals are crucial transient intermediates in the radiation damage of nucleic acids (RNA and DNA). Among the recognized mechanisms of radiation damage, capture of a low-energy electron followed by protonation of the transient anion radical results in the formation of hydrogen-atom adducts that can undergo further degradation reactions.^[1] Radiation damage has been studied extensively by pulse radiolysis in solution and the solid state, in which characterization of the transient nucleobase radicals relied mainly on the detection of species with unpaired electrons by electron paramagnetic resonance (EPR) spectroscopy. In particular, cytosine and cytosine-containing nucleosides have been the subject of numerous studies that reported the formation of adducts with the hydrogen atom positioned at C5, C6, N3, and N7 in the solid state (Scheme 1).^[2] However, the identity of these radicals has



Scheme 1. Formation of cytosine radicals by the direct mechanism.

been subject to discussion, and the factors that affect their formation and kinetic and thermodynamic stability have not been established unequivocally by EPR in the complex mixtures produced by pulse radiolysis. EPR analysis can be further complicated by the formation of cation radicals upon

[*] C. Yao, M. L. Cuadrado-Peinado, Prof. Dr. F. Tureček
Department of Chemistry
University of Washington,
Bagley Hall, Box 351700
Seattle, WA 98195-1700 (USA)
Fax: (+1) 206-685-3478
E-mail: turecek@chem.washington.edu

Dr. M. Polášek
J. Heyrovsky Institute of Physical Chemistry
Dolejškova 3, 182 23 Praha 8 (Czech Republic)

[**] F.T. is supported by the National Science Foundation (grants CHE-0349595 for the practical experiments and CHE-0342956 for the computational studies). M.P. is supported by the Grant Agency of the Academy of Sciences of the Czech Republic (Grant No. IAA400400502).

radiolysis.^[2f,g] To our knowledge, the chemically specific generation of cytosine radicals has not been attempted.

In contrast to the condensed phase, the rarefied gas phase, which exists in the vacuum system of a mass spectrometer, offers an inert medium for the specific generation and investigation of highly reactive transient molecules, radicals, biradicals, and so forth.^[3] We report herein on the targeted generation of two key hydrogen-atom adducts of 1-methylcytosine (**1**), namely, 1-methyl-3,4-dihydrocytosine-4-yl (**2**) and 1-methyl-5,6-dihydrocytosine-6-yl (**3**; Scheme 2). 1-Methylcytosine was selected as a simple model system that

the reaction products that originate from the nucleobase radical.^[5]

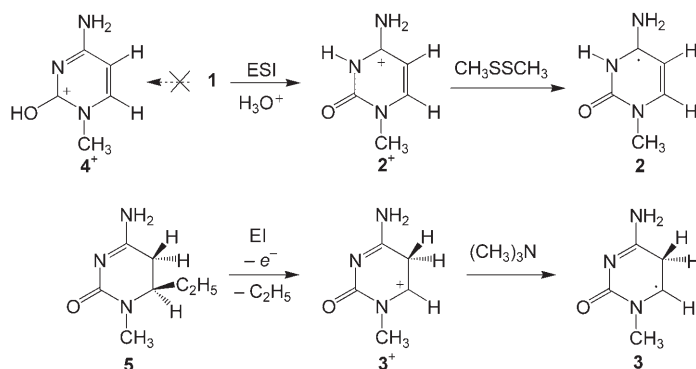
The synthetic route to **2** utilizes electrospray ionization (ESI) of **1** to generate the pertinent ion **2**⁺ and transfer it in the mass spectrometer. Compound **1** is the most stable tautomer in solution^[6] and is protonated exclusively at N3, thus specifically yielding **2**⁺.^[7] Our concurrent ab initio calculations^[8] have established that **2**⁺ is more stable (by 31–32 kJ mol^{−1}) than the tautomer protonated at O2 (**4**⁺), which is the second most stable in water and methanol. Tautomer **2**⁺ is also the most stable structure in gas-phase

clusters with water, thus strongly indicating that **2**⁺ is transferred from solution to the gas-phase by electrospray without isomerization. Unimolecular isomerization **2**⁺→**4**⁺ requires a high-energy barrier (153 kJ mol^{−1})^[8] that is inaccessible to thermalized ions formed by electrospray ionization.^[9]

Tautomer **3**⁺ is substantially less stable than **2**⁺ ($\Delta H_{g,0}(\mathbf{2}^+ \rightarrow \mathbf{3}^+) = 111 \text{ kJ mol}^{-1}$) and cannot be generated specifically by protonation of **1**.^[8] However, electron-ionization-induced α -cleavage dissociation of a stable precursor, 1-methyl-6-ethyl-5,6-dihydrocytosine (**5**),^[10] yields **3**⁺ as the most abundant ion in the mass spectrum and provides access to the generation of radical **3**.

Ions **2**⁺ and **3**⁺ were characterized by collisionally activated dissociation (CAD) mass spectra that showed characteristic differences in ion-dissociation patterns (Figure 1). Ion **2**⁺ dissociates by loss of NH₃ (m/z 109) and HO–C≡N (m/z 83), whereas **3**⁺ dissociates by loss of CH₂=C=NH (m/z 85) and HN=C=O (m/z 83). The identity of the fragments and the dissociation mechanisms have been established by deuterium labeling and ab initio calculations.^[8] The important outcome from the CAD spectra and theoretical calculations is that **2**⁺ and **3**⁺ are distinct stable isomers that reside in potential-energy minima and do not interconvert under our experimental conditions.

Collisional neutralization of **2**⁺ and **3**⁺ followed by reionization yielded NR mass spectra that showed peaks of survivor ions at m/z 126 for both **2** and **3** (Figure 2). These signals indicate that a fraction of the cytosine radicals **2** and **3** did not dissociate on the 5.7- μ s timescale of the measurement. Thus, **2** and **3** represent intrinsically stable neutral species in the gas phase. The NR mass spectra also show substantially different dissociations of **2** and **3**. In particular, **3** undergoes the facile loss of a hydrogen atom (m/z 125) and C₂H₄N (m/z 84) and the formation of C₂H₃N (m/z 41). The elimi-



Scheme 2. Generation of 1-methylcytosine radicals **2** and **3** by collisional electron transfer in the gas phase.

exists as a dominant tautomer and, thus, avoids the problems of gas-phase tautomerism that are present in the parent cytosine, which exists as a mixture of three major tautomers in the gas phase.^[4] Our approach relies on the specific generation of 1-methylcytosine cations that have the same bond connectivity as the target radicals. The cations are accelerated to a high velocity (105 000 m s^{−1}) and discharged by a glancing collision with a molecular electron donor (dimethyl disulfide or trimethylamine). The nascent radicals are formed with the structure of the precursor cation because of the extremely short duration of the electron transfer (10–12 fs). The radicals are observed for several microseconds, during which time dissociation may occur. The neutral precursors and their dissociation products are then nonselectively ionized, the resulting cations are separated by mass and detected by neutralization–reionization (NR) mass spectrometry. The spectra, thus, provide a more-or-less complete analysis of all

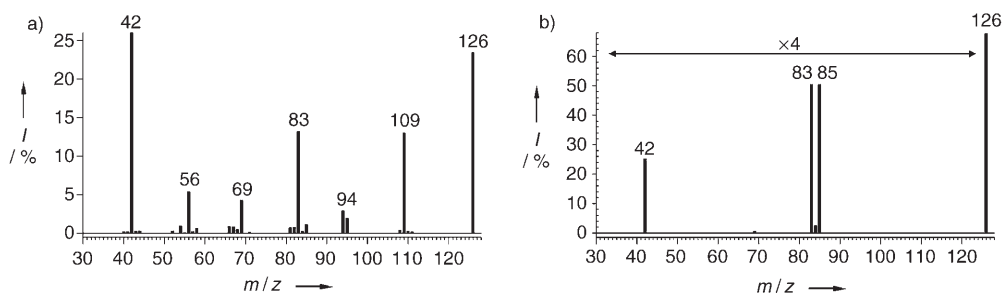


Figure 1. CAD mass spectra of a) **2**⁺ and b) **3**⁺ obtained at 5.5-eV center-of-mass collision energy in a radio-frequency-only quadrupole under multiple-collision conditions. The ion intensities are relative (%) to the total ion current.

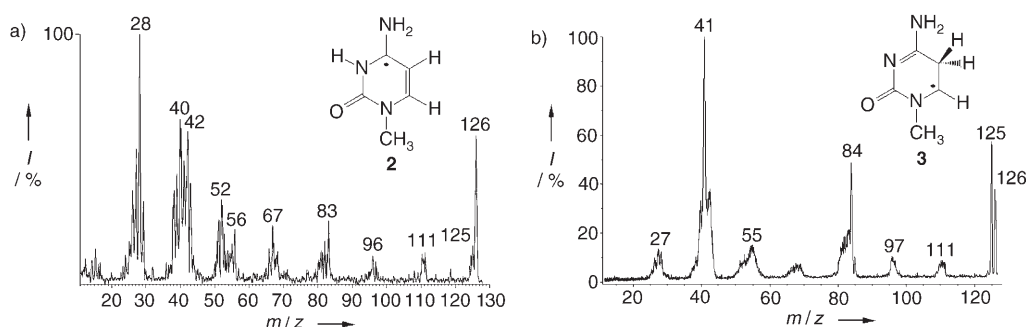
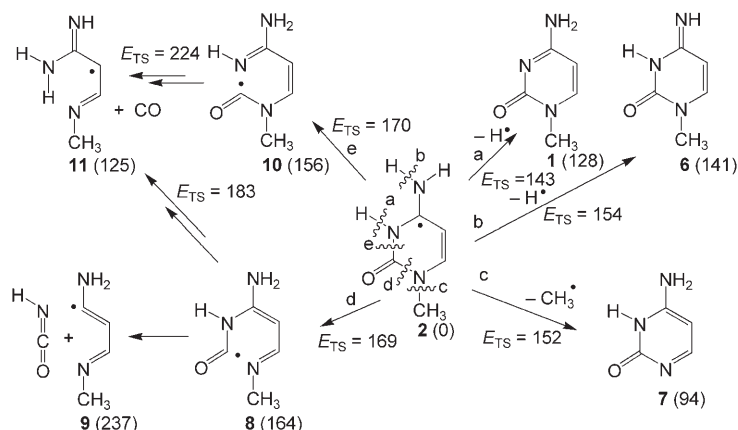


Figure 2. NR mass spectra. a) Neutralization of 2^+ with CH_3SSCH_3 and reionization with O_2 at 70% ion transmittance. b) Neutralization of 3^+ with $(\text{CH}_3)_3\text{N}$ and reionization with O_2 at 70% ion transmittance.

nation of $\text{C}_2\text{H}_4\text{N}$ may be because of the combined losses of $(\text{H} + \text{C}_2\text{H}_3\text{N})$ or $(\text{CH}_3 + \text{HCN})$, which would require a detailed mechanistic study to be distinguished. In contrast to **3**, **2** shows only minor loss of hydrogen atoms, no fragment ion at m/z 84, and a dominant CO fragment ion at m/z 28. The differences in the spectra confirm that **2** and **3** do not interconvert by unimolecular isomerizations. This deduction was further corroborated by dissociations of deuterium-labeled radicals $[3,7,7\text{-D}_3]\text{-2}$, $[6\text{-D}]\text{-3}$, and $[5,7\text{-D}_2]\text{-3}$, of which $[6\text{-D}]\text{-3}$ showed a specific loss of a hydrogen atom, thus indicating the absence of hydrogen/deuterium exchange at C5 and C6. A competitive loss of hydrogen and deuterium atoms from the methylene group at C5 was seen in $[5,7\text{-D}_2]\text{-3}$. These dissociations indicate that **1** forms as the stable product from the loss of a hydrogen atom from **3**. This conclusion is corroborated by the NR mass spectrum of 1^+ , which showed a dominant survivor ion at m/z 125 and so confirmed that **1** was stable when formed by collisional electron transfer in the gas phase.

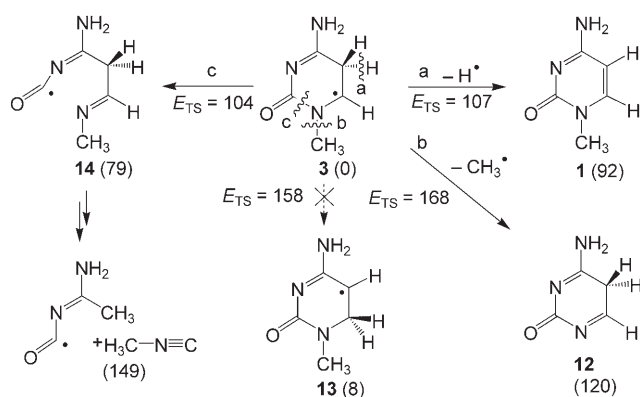
The relative stability and dissociation energetics of **2** and **3** were addressed by combined ab initio and density-functional theory calculations^[6] to provide insight into the dissociation mechanisms. Both **2** and **3** are found to reside in potential-energy minima; whereby, **2** is more stable than **3** by 36 kJ mol^{-1} . The minimum-energy reaction pathway of **2** is the dissociation of the N3–H bond (path a) to yield **1** (Scheme 3). Competitive dissociations may involve the loss of a hydrogen atom from the amino group at N7 (path b) to yield the imine–oxo tautomer **6**. We note that it has been postulated that **6** is formed by tautomerization of **1** in the gas phase at 463 K.^[11] Loss of the methyl group at N1 (path c) yields a cytosine tautomer **7**. The loss of the CH_3 group is seen to occur competitively with the loss of a hydrogen atom in the NR mass spectrum of **2** (Figure 2a). Ring opening by C2–N1 and C2–N3 bond dissociations (paths d and e) require somewhat higher transition-state (TS) energies ($169\text{--}170 \text{ kJ mol}^{-1}$) to form **8** and **10**, respectively, as transient intermediates in the loss of CO and HNCN (Scheme 3). However, the ring cleavage of **2** and subsequent dissociations require several steps with high TS energies or product threshold energies (e.g., **9** and **11**) and can be expected to be kinetically disfavored on the potential-energy surface of



Scheme 3. The relative energies in parentheses (kJ mol^{-1}) are from B3-PMP2/6-311++G(3df,2p) + ZPVE calculations. E_{TS} = transition-state energy.

the ground electronic state. The preponderance of small fragments of m/z 26–29 and 38–43 in the NR mass spectrum of **2** (Figure 2a) is probably because of a combination of dissociations that originate from the excited electronic states of $2^{[12]}$ and post-reionization dissociations of the primary dissociation products. The calculations further indicate that vertical electron transfer in 2^+ results in only a modest vibrational excitation in the ground electronic state of **2** by Franck–Condon effects ($E_{\text{exc}} = 39 \text{ kJ mol}^{-1}$), which is in keeping with the detection of a stable fraction of **2** in the spectrum.

The potential-energy surface for dissociations of **3** (Scheme 4) is substantially different from that of **2**. In particular, **3** shows a low-energy dissociation pathway for the loss of a hydrogen atom from the methylene group at C5 (path a), which is consistent with the prominent loss of a hydrogen atom in the NR mass spectrum (Figure 2b). The loss of the hydrogen atom competes with the loss of the CH_3 group (path b, **12**) and ring opening by cleavage of the weak C2–N1 bond (path c, **14**). The latter leads to expulsion of $\text{CH}_3\text{N}=\text{C}$, which appears as the intense peak at m/z 41 in the NR mass spectrum of **3**. The formation of another major fragment at m/z 84 (Figure 2b) maybe because of combined losses of $(\text{H} + \text{C}_2\text{H}_3\text{N})$ or $(\text{CH}_3 + \text{HCN})$, which are currently unresolved and will require further study for satisfactory elucidation. In contrast, a 1,2-hydrogen migration between C5



Scheme 4. The relative energies in parentheses (kJ mol⁻¹) are from B3-PMP2/6-311++G(3df,2p)+ZPVE calculations.

and C6 in **3** that yields isomer **13** requires a high-energy TS to be crossed. This energy barrier explains why **3** does not exchange H5 and H6 atoms prior to the loss of the methylene hydrogen atom at C5.

In conclusion, transient radicals that correspond to adducts with a hydrogen atom positioned at N3 and C5 of the cytosine ring have been specifically generated in the gas phase for the first time. The isomeric radicals **2** and **3** are found to be intrinsically stable, distinct species that show specific unimolecular dissociations by loss of a hydrogen atom or the CH₃ group and ring cleavage followed by expulsion of small molecules. It can be expected that substituents at N1 larger than a methyl group (for example, 2'-deoxyribose-1-yl) would increase the propensity for N1–C bond dissociation in cytidine radicals, as the proposed mechanisms for nucleobase loss from radiation damage to DNA suggest.^[1] Generation and computational studies of such nucleoside radical systems are underway.

Experimental Section

NR mass spectra were measured on a tandem-quadrupole mass spectrometer equipped with an electrospray ion source, as described previously.^[13] Precursor ions **2**⁺ were produced by the electrospray of 50–100 μM solutions of 1-methylcytosine in methanol/water (70:30), desolvated, cooled to ambient temperature, transferred to high vacuum, accelerated to 7200 eV, and discharged by collisions with dimethyl disulfide under predominantly (83%) single-collision conditions. Radical **2** and its dissociation products were nonselectively ionized after 5.7 μs by collisions with O₂, decelerated to 70–75 eV, and analyzed by mass. Another set of NR mass spectra of **3**⁺ was measured at 8-keV ion kinetic energy on a ZAB2-SEQ double-focusing mass spectrometer that was furnished with an additional collision cell in the first field-free region. The spectra were obtained by a linked scan of the magnet and electrostatic sectors. Ion **3**⁺ was generated in the ion source by 70-eV electron ionization of 1-methyl-6-ethyl-5,6-dihydro-cytosine. The details of the computational methods were described previously.^[6,14]

Received: July 7, 2005

Published online: September 27, 2005

Keywords: cytosine · mass spectrometry · potential-energy surfaces · radicals

- [1] a) C. von Sonntag in *Physical and Chemical Mechanisms in Molecular Radiation Biology* (Eds.: W. A. Glass, M. N. Varma), Plenum, New York, **1991**, pp. 287–321; b) *Free Radical Toxicology* (Ed.: K. B. Wallace), Taylor and Francis, Washington, DC, **1997**.
- [2] For representative studies of cytosine radicals see: a) E. Westhof, W. Flossmann, A. Müller, *Int. J. Radiat. Biol.* **1975**, *28*, 427–438; b) W. A. Bernhard, R. A. Farley, *Radiat. Res.* **1976**, *66*, 189–198; c) E. Sagstuen, E. O. Hole, W. H. Nelson, D. M. Close, *J. Phys. Chem.* **1992**, *96*, 8269–8276; d) P. M. Cullis, M. E. Malone, I. D. Podmore, M. C. R. Symons, *J. Phys. Chem.* **1995**, *99*, 9293–9298; e) E. O. Hole, W. H. Nelson, E. Sagstuen, D. M. Close, *Radiat. Res.* **1998**, *149*, 109–119; f) J. Barnes, W. A. Bernhard, K. R. Mercer, *Radiat. Res.* **1991**, *126*, 104–107; g) M. G. Debije, D. M. Close, W. A. Bernhard, *Radiat. Res.* **2002**, *157*, 235–242.
- [3] a) F. Tureček, *Org. Mass Spectrom.* **1992**, *27*, 1087–1097; b) F. Tureček, *J. Mass Spectrom.* **1998**, *33*, 779–795.
- [4] M. Szczesniak, K. Szczepaniak, J. S. Kwiatkowski, K. Kubulat, W. B. Person, *J. Am. Chem. Soc.* **1988**, *110*, 8319–8330.
- [5] For recent reviews of the techniques of NR mass spectrometry and its use for the generation of transient intermediates, see: a) C. Schalley, G. Hornung, D. Schröder, H. Schwarz, *Chem. Soc. Rev.* **1998**, *27*, 91–104; b) D. V. Zagorevskii, J. L. Holmes, *Mass Spectrom. Rev.* **1999**, *18*, 87–118; c) F. Tureček, *Top. Curr. Chem.* **2003**, *225*, 77–129.
- [6] F. Tureček, C. Yao, *J. Phys. Chem. A* **2003**, *107*, 9221–9231.
- [7] E. D. Becker, H. T. Miles, R. B. Bradley, *J. Am. Chem. Soc.* **1965**, *87*, 5575–5582.
- [8] C. Yao, M. Cuadrado-Peinado, M. Polášek, F. Tureček, *J. Mass Spectrom.* **2005**, in press.
- [9] L. Drahos, R. M. A. Heeren, C. Collette, E. De Pauw, K. Vekey, *J. Mass Spectrom.* **1999**, *34*, 1373–1379.
- [10] D. M. Brown, M. J. E. Hewlins, *J. Chem. Soc. C* **1968**, 2050–2055.
- [11] M. Szczesniak, J. Leszczynski, W. B. Person, *J. Am. Chem. Soc.* **1992**, *114*, 2731–2733.
- [12] For the role of excited electronic states in nucleobase radical dissociations, see: a) E. A. Syrtstad, S. Vivekananda, F. Tureček, *J. Phys. Chem. A* **2001**, *105*, 8339–8351; b) J. K. Wolken, F. Tureček, *J. Phys. Chem. A* **2001**, *105*, 8352–8360.
- [13] a) F. Tureček, M. Gu, S. A. Shaffer, *J. Am. Soc. Mass Spectrom.* **1992**, *3*, 493–501; b) J. L. Seymour, E. A. Syrtstad, C. C. Langley, F. Tureček, *Int. J. Mass Spectrom.* **2003**, *228*, 687–702.
- [14] Structures were fully optimized with B3LYP/6-31+G(d,p) and stationary points were confirmed by an appropriate number of imaginary frequencies; single-point energies were calculated with B3LYP and spin-projected MP2 by using the 6-311++G(3df,2p) basis set and combined as described previously.^[15]
- [15] F. Tureček, *J. Phys. Chem. A* **1998**, *102*, 4703–4713.

Synthesis of CdSe and CdTe Nanocrystals without Precursor Injection**

Yongan Andrew Yang, Huimeng Wu,
Kathryn R. Williams, and Y. Charles Cao*

With the growing interest in applications based on nanoscale materials^[1] comes a need for an industrial-scale synthesis of colloidal semiconductor nanocrystals with uniform size and shape and well-confined surface passivation. To date, the most successful and widely used nanocrystal synthesis relies on rapid precursor injection.^[2,3] However, it is difficult to scale up such a synthesis for making nanocrystals in large quantities (e.g., tens to hundreds of kilograms).^[4] Therefore, there is a need to develop nanocrystal synthesis without precursor injection.

Although many publications have described the synthesis of semiconductor nanocrystals without precursor injection,^[5] only a few of them have led to nanocrystals with very good monodispersity.^[5a-c] However, these nanocrystals exhibit optical properties inferior to those of nanocrystals produced by the injection method. They normally do not show as many multiple exciton absorption peaks, which are critical for nanocrystal applications in advanced optical and electronic devices. Recently, we reported a non-injection-based synthesis of CdS nanocrystals.^[4] The sample quality (i.e., size distribution and optical properties) is as good as that of the best CdS nanocrystals synthesized by using precursor injection. Nucleation initiators are important to the CdS synthesis, but unfortunately, such nucleation initiators are not readily available for making nanocrystals with other compositions. Herein, we report how to design a noninjection synthesis for making high-quality CdSe and CdTe nanocrystals without nucleation initiators.

The formation of high-quality nanocrystals is often favored at high temperatures (e.g., > 200 °C). This factor creates a major challenge for making monodispersed nanocrystals through a noninjection synthesis because such a synthesis involves a period of increasing temperature over a broad range (e.g., from room temperature to over 200 °C). If the reactivity of a precursor is too high, this broad change of temperature often leads to concurrent nucleation and growth

of nanocrystals in the synthesis, which results in products with poor monodispersity. However, if the precursors are too stable, a very small number of nuclei may form, which leads to uncontrollable particle growth. (Note that suitable nucleation initiators could lead to a synthesis of monodisperse nanocrystals in this case.) Therefore, when suitable nucleation initiators are not available, only precursors with suitable reactivity can result in monodisperse nanocrystals. In general, the ideal precursors should exhibit no (or very low) reactivity below the desired temperature for growth of the chosen nanocrystals, but they should also exhibit high reactivity when the temperature reaches the desired point.

To test this hypothesis, we first designed a noninjection synthesis for making CdSe nanocrystals. We chose 240 °C as the growth temperature, which was in accordance with the lesson learned from the injection-based synthesis of CdSe nanocrystals.^[2,3] At this growth temperature, pure cadmium myristate is a suitable cadmium precursor because it has a decomposition point at about 226 °C.^[6] Selenium powder can be an effective selenium precursor for two reasons: 1) it has a melting point at 221 °C;^[6] 2) it is insoluble in octadecene (ODE) at room temperature and becomes slightly soluble at temperatures over 190 °C. As selenium has low solubility in ODE, it is unreactive with cadmium myristate up to 200 °C. In a typical synthesis (see Experimental Section for detailed conditions), small particles (i.e., nuclei) suddenly appeared at 210 °C (Figures 1a and b). As the nanocrystals grew, the number of particles quickly increased to a maximum, and then during further growth it continued to decrease. Significantly, about 72 % of the particles formed in the initial stage disappeared after two hours of growth, while the size distribution of the nanocrystals continued to become more narrow throughout the synthesis (Figure 1c–e). Such size

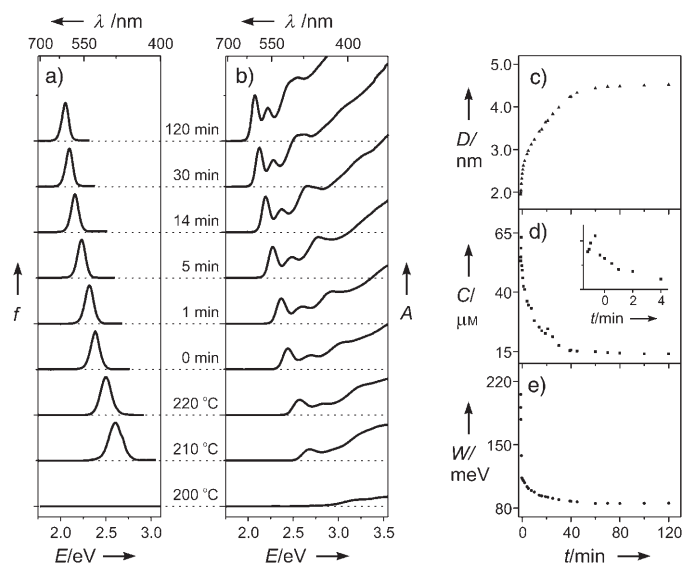


Figure 1. Temporal evolution of a) the fluorescence (*f*) spectrum, b) the absorption spectrum, c) the diameter (*D*) of the nanocrystals, d) (and inset) the concentration (*C*) of the nanocrystals, and e) full width at half-maximum (FWHM) of the fluorescence spectrum during the CdSe synthesis. The size and concentration of the nanocrystals were obtained according to a reported procedure.^[2b, 3b]

[*] Dr. Y. A. Yang, H. Wu, Dr. K. R. Williams, Prof. Y. C. Cao
Department of Chemistry
University of Florida
Gainesville, FL 32611 (USA)
Fax: (+1) 352-392-0588
E-mail: cao@chem.ufl.edu

[**] Y.C.C. acknowledges the University of Florida and the ACS Petroleum Research Fund for financial support. We thank Charles R. Martin and Willard W. Harrison for helpful discussions, and Kerry Siebin for technical assistance.

Supporting information for this article is available on the WWW under <http://www.angewandte.org> or from the author.

focusing is not likely to arise from diffusion-limited growth because this growth does not lead to a decreasing number of nanocrystals.^[2b] Additional investigation is required to understand the detailed mechanism involved in this phenomenon.

The addition of oleic acid during the synthesis is important to control the quality of the nanocrystals. Without oleic acid, the nanocrystals show absorption spectra with a tail of higher intensity at the low-energy end after their diameter reaches around 3.0 nm and with further growth, they show broad absorption spectra (Figure 2, dotted lines). Such spectral

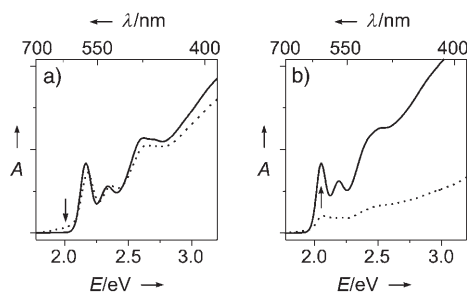


Figure 2. Absorption spectra of CdSe nanocrystals with (solid lines) and without (dotted lines) oleic acid a) after 16 min of growth and b) after 60 min of growth.

changes are normally attributed to broadening of the particle size distribution due to Ostwald ripening. However, in this synthesis we found that the phenomenon was caused by particle aggregation as it could be reversed by adding a small amount of oleic acid into the growth solution (Figure 2, solid lines). After this addition, nanocrystal growth turned out to be extremely stable. The size distribution of the nanocrystals further narrowed with particle growth (Figure 1), and the narrow size distribution was maintained for at least 16 h at the reaction temperature.

Without size sorting, typical CdSe nanocrystals from this synthesis show sizes with a standard deviation (σ) of less than 5% (see Figure 3d) and a quantum yield of photoluminescence (PL) of about 30 to 40%. Interestingly, these nanocrystals have a zinc-blende (ZB) structure but not a wurtzite (W) structure. Although these two crystal phases produce similar X-ray powder diffraction (XRD) results with nanocrystals, the XRD pattern of 4.0-nm particles shows unambiguous evidence that the particles have a ZB structure (Figure 3a): a) the valley between the (220) and (311) peaks is deep; b) the (400) peak is at 61.0° ; c) the (620) peak is at 106.2° . In the case of wurtzite crystals, there are no peaks in these positions.^[2a,4,6] This structural assignment is consistent with the high-resolution transmission electron microscopy (HRTEM) observation (JEOL-JEM 2010 operated at 200 kV): a square cross-fringe pattern represents an ordered distance of 0.22 nm, which corresponds to the lattice spacing of the (220) faces in ZB CdSe (Figure 3a, inset). Such a cross-fringe pattern does not exist in a wurtzite structure. Note that ZB CdSe nanocrystals have been made recently by an injection-based synthesis.^[7] However, this synthesis only led to high-quality nanocrystals in very small sizes, and these small nanocrystals show nearly identical XRD patterns to

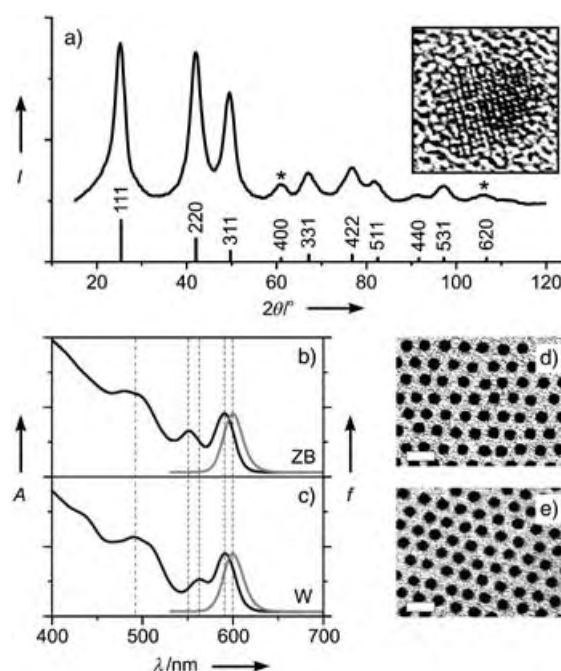


Figure 3. a) XRD pattern of 4.0-nm-diameter ZB CdSe nanocrystals. The standard diffraction peak positions and relative intensities of bulk ZB CdSe are indicated. The inset shows an HRTEM image (5 nm \times 5 nm) of the nanocrystal sample. b) Absorption (black) and emission (gray) spectra of the ZB CdSe sample. c) Absorption (black) and emission (gray) spectra of a wurtzite (W) CdSe nanocrystal sample made by chalcogen precursor injection according to a reported procedure.^[3a] d, e) TEM images of ZB (d) and W (e) CdSe nanocrystals. Scale bar: 10 nm.

those of small wurtzite nanocrystals made by Bawendi and co-workers.^[2a] In contrast, the noninjection method presented in this paper can also result in larger CdSe nanocrystals, which allow us to unambiguously identify ZB nanocrystals.

Indeed, zinc-blende and wurtzite CdSe nanocrystals can be easily distinguished by their optical properties (Figure 3b–e). For both cases, nanocrystals with an identical position of the absorption peak for the first exciton transition band are nearly identical in size. The Stokes shifts of the emission peaks are nearly identical and PL quantum yields of band-gap emissions are similar. However, the fine structures in their absorption spectra are different. The gap between the first ($1S_{3/2}1S_e$) and second ($2S_{3/2}1S_e$) exciton transition peaks for ZB particles is clearly wider than that for W particles. The peak positions for the exciton transitions with higher energies also vary for these two types of CdSe nanocrystals. These differences in the absorption spectra originate from the different electronic band structures at the center of the Brillouin zone for these two types of crystal phases.^[8]

To further demonstrate the power of noninjection synthesis, we synthesized nonspherical CdSe nanocrystals. In the case of a ZB structure, nonspherical particles are normally cubes, tetrahedral pyramids, or triangular prisms, and these particles have a higher surface energy than spherical particles.^[9] Therefore, making nonspherical particles requires growth conditions with a high chemical potential, which we

thought could be achieved by increasing the per-particle concentration of the precursors.^[6] To create such conditions, we chose a method to decrease the number of initial nuclei while leaving the precursor concentration unchanged. Because more reactive precursors can lead to fewer nuclei,^[4] we used tributylphosphine selenide (TBPSe) in place of selenium powder for making CdSe nanocrystals. Indeed, the number of nuclei at the initial stage in this synthesis decreased by 75 % as compared with the synthesis with selenium powder; after 30 min, tetrahedral particles with edge length of 5.0 nm and σ of 7 % were formed. The high uniformity of these nanocrystals allows the formation of ordered, triangular close-packed nanocrystal assemblies on TEM grids (Figure 4).

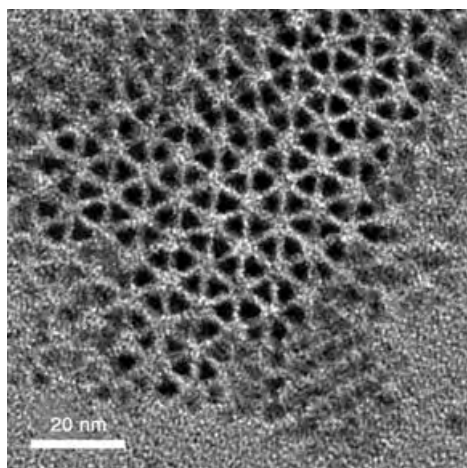


Figure 4. TEM image of tetrahedral CdSe nanocrystals.

Moreover, the principle for designing a noninjection synthesis can be applied to the synthesis of CdTe nanocrystals. The key point is to find suitable precursors. The reactivity of cadmium myristate with tellurium powder in ODE is too low, whereas with tributylphosphine telluride (TBPTe) it is too high. Neither case resulted in the formation of uniform nanocrystals. We then decreased the reactivity of the cadmium precursor by replacing cadmium myristate with cadmium octadecylphosphonate. The reaction between cadmium octadecylphosphonate and TBPTe just perfectly fits the need for growth of monodisperse CdTe nanocrystals. A typical synthesis led to CdTe nanocrystals with a size distribution of less than 5 %, which exhibit up to five exciton absorption bands (Figure 5). Such particle quality is at least comparable with that of the best particles made by the injection synthesis.^[3b]

In summary, we reported the synthesis of high-quality CdSe and CdTe nanocrystals without precursor injection. This noninjection synthesis allows detailed control of nanocrystal size and shape. In addition, because it exhibits easily controllable nanocrystal-growth kinetics, such a synthesis is very important for a large-scale industrial preparation of CdSe and CdTe nanocrystals in which the rates of heating and cooling of reaction solutions are limited.

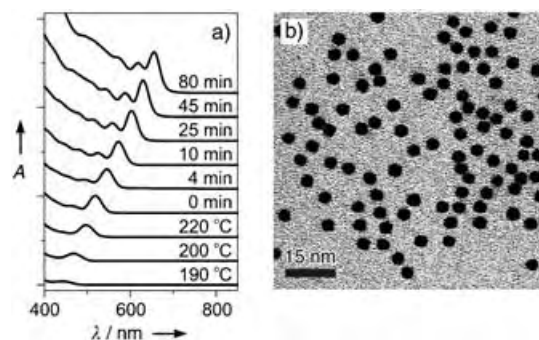


Figure 5. a) Temporal evolution of the absorption spectrum in CdTe nanocrystal synthesis. b) TEM image of CdTe nanocrystals with a first absorption peak at 625 nm.

Experimental Section

Cadmium myristate was prepared by an ex situ method: a solution of cadmium nitrate in methanol (0.05 M, 40 mL) was added to a solution of sodium myristate in methanol (0.025 M, 240 mL). The resulting white precipitate was washed twice with methanol and dried under vacuum overnight to remove all solvents. Note that the purity of cadmium myristate is important to the following CdSe nanocrystal syntheses.

Synthesis of spherical CdSe nanocrystals: selenium powder (0.05 mmol, 100 mesh from Aldrich) and cadmium myristate (0.1 mmol) were added into a three-neck flask with ODE (5.0 g). The mixture was degassed for 10 min under vacuum ($\approx 3 \times 10^{-2}$ Torr) at room temperature. Under a flow of Ar, the solution was stirred and heated to 240 °C at a rate of 25 K min⁻¹. Serial quantitative aliquots (50 μ L) were taken for kinetic studies,^[6] and the time was counted as zero when the temperature reached 240 °C. After the particle diameter had reached about 3.0 nm (i.e., the first absorption peak at 550 nm), a solution of oleic acid in ODE (0.05 M, 1.0 mL) was added dropwise into the reaction solution to stabilize the growth of the nanocrystals.

The synthesis of tetrahedral CdSe nanocrystals followed a similar protocol as above, but TBPSe was used instead of selenium powder (cadmium myristate: 0.1 mmol, and TBPSe in ODE: 0.05 mmol of TBPSe in a mixture of tributylphosphine and ODE, 0.012 g and 0.5 g, respectively^[2]).

In the synthesis of CdTe nanocrystals, cadmium octadecylphosphonate was made in situ: a mixture of CdO (0.1 mmol), octadecylphosphonic acid (0.22 mmol), and ODE (5.0 g) was heated to 300 °C to give a colorless solution. The solution was cooled to room temperature, and TBPTe (0.20 mmol in 0.19 g of tributylphosphine,^[2a]) was added. The mixture was degassed, then stirred and heated to 240 °C (25 K min⁻¹) under a flow of Ar. Note that adding oleic acid is not needed during the CdTe synthesis.

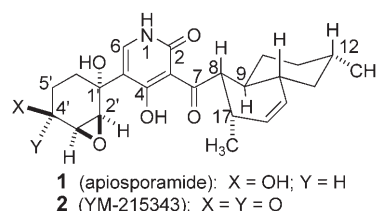
Received: June 29, 2005

Published online: September 27, 2005

Keywords: crystal growth · fluorescence spectroscopy · nanotechnology · self-assembly · semiconductors

- [1] a) A. P. Alivisatos, *Nat. Biotechnol.* **2004**, 22, 47; b) H. Weller, *Philos. Trans. R. Soc. London Ser. A* **2003**, 361, 229; c) M. Han, X. Gao, J. Z. Su, S. Nie, *Nat. Biotechnol.* **2001**, 19, 631; d) M. Kazes, D. Y. Lewis, Y. Ebenstein, T. Mokari, U. Banin, *Adv. Mater.* **2002**, 14, 317; e) L. Zhu, M. Zhu, J. K. Hurst, A. D. Q. Li, *J. Am. Chem. Soc.* **2005**, 127, 8968.

- [2] a) C. B. Murray, D. J. Norris, M. G. Bawendi, *J. Am. Chem. Soc.* **1993**, *115*, 8706; b) X. Peng, J. Wickham, A. P. Alivisatos, *J. Am. Chem. Soc.* **1998**, *120*, 5343.
- [3] a) L. Qu, X. Peng, *J. Am. Chem. Soc.* **2002**, *124*, 2049; b) W. W. Yu, L. Qi, W. Guo, X. Peng, *Chem. Mater.* **2003**, *15*, 2854; c) R. Xie, U. Kolb, J. Li, T. Basché, A. Mews, *J. Am. Chem. Soc.* **2005**, *127*, 7480.
- [4] Y. C. Cao, J. Wang, *J. Am. Chem. Soc.* **2004**, *126*, 14336.
- [5] a) S. L. Cumberland, K. M. Hanif, A. Javier, G. A. Khitrov, G. F. Strouse, S. M. Woessner, C. Yun, *Chem. Mater.* **2002**, *14*, 1576; b) N. Pradhan, S. Efrima, *J. Am. Chem. Soc.* **2003**, *125*, 2050; c) D. V. Talapin, S. Haubold, A. L. Rogach, A. Kornowski, M. Haase, H. Weller, *J. Phys. Chem. B* **2001**, *105*, 2260; d) Y. Wang, N. J. Herron, *J. Phys. Chem.* **1991**, *95*, 525.
- [6] See the Supporting Information.
- [7] M. B. Mohamed, D. Tonti, A. Al-Salman, A. Chemseddine, M. Chergui, *J. Phys. Chem. B* **2005**, *109*, 10533.
- [8] S. Ninomiya, S. Adachi, *J. Appl. Phys.* **1995**, *78*, 4681.
- [9] a) R. Jin, Y. C. Cao, E. Hao, G. S. Métraux, G. C. Schatz, C. A. Mirkin, *Nature* **2003**, *425*, 487; b) F. Kim, S. Connor, H. Song, T. Kuykendall, P. Yang, *Angew. Chem.* **2004**, *116*, 3759; *Angew. Chem. Int. Ed.* **2004**, *43*, 3673.



challenging. Although homonuclear and heteronuclear 2D NMR spectroscopic experiments permitted the assignment of the relative configuration of the decalin ring, the configuration of the epoxydiol system could not be determined unambiguously. The latter moiety was tentatively assumed to have an all-*syn* topology. Unfortunately, the stereochemical features of the *trans* decalin portion present an independent ^1H NMR spectroscopic system relative to the cyclohexanediol moiety owing to the planarity of the central pyridinone linkage. Lastly, the substitution pattern of the pyridinone ring was assumed by comparison with the ^{13}C NMR spectroscopic chemical shifts of **1** with ilicicolin H, which was previously described and confirmed by total synthesis as a 5-aryl-4-hydroxy-3-acyl-2-pyridone.^[3] Some examples of this family include militarinone A,^[4] oxysporidinone,^[5] fischerin,^[6] and funiculosin.^[7] Herein, we report a convergent total synthesis of (+)-apiosporamide (**1**) and its subsequent oxidation to yield YM-215343 (**2**). Our efforts have established the assignments of the relative and absolute configurations, which confirm the antipodal relationship of our synthetic materials with the naturally occurring metabolites.

To address the structural ambiguities of **1**, we chose to explore a convergent plan for stereocontrolled syntheses of the *trans*-decalin and the epoxydiol components. This strategy required appropriate functionalization of each subunit for the late stage formation of the central pyridone. Additionally, we sought to devise general, stereodivergent schemes that would permit the flexibility necessary to examine the substantial stereochemical issues previously outlined.

Studies of the cyclohexanediol portion of **1** began with the synthesis of nonracemic 4-hydroxy-2-cyclohexenones. The multigram preparation of **4** (Scheme 1) utilized (–)-quinic acid as a chiral-pool precursor through formation of the pure acetonide **3** as described by Danishefsky and co-workers.^[8] Consideration of the appropriate functionality for direct linkage with the decalin component as well as subsequent pyridone ring formation led us to examine the enolate condensation of *N*-(4-methoxybenzyloxy)azetidin-2-one (**5**) with **4**.

Techniques for the incorporation of intact β -lactams are rare.^[9] Although the ring strain of **5** incorporates the desired activation for coupling operations, the limited prospects for addition reactions with unsubstituted β -lactams suggest issues of incompatibility that arise from enolate instability, self-condensation, and acylation of alkoxide intermediates. Thus, we were gratified to find that the hydroxamic acid derivative **5** led to solutions of dependable enolates.^[10] The starting β -lactam **5** was readily obtained through procedures described by Reinhoudt and van Elburg.^[11] Complete deprotonation was initially recorded through reaction with LiHMDS for 2 h

Assignment of Configuration

DOI: 10.1002/anie.200502015

Total Synthesis of (+)-Apiosporamide: Assignment of Relative and Absolute Configuration**

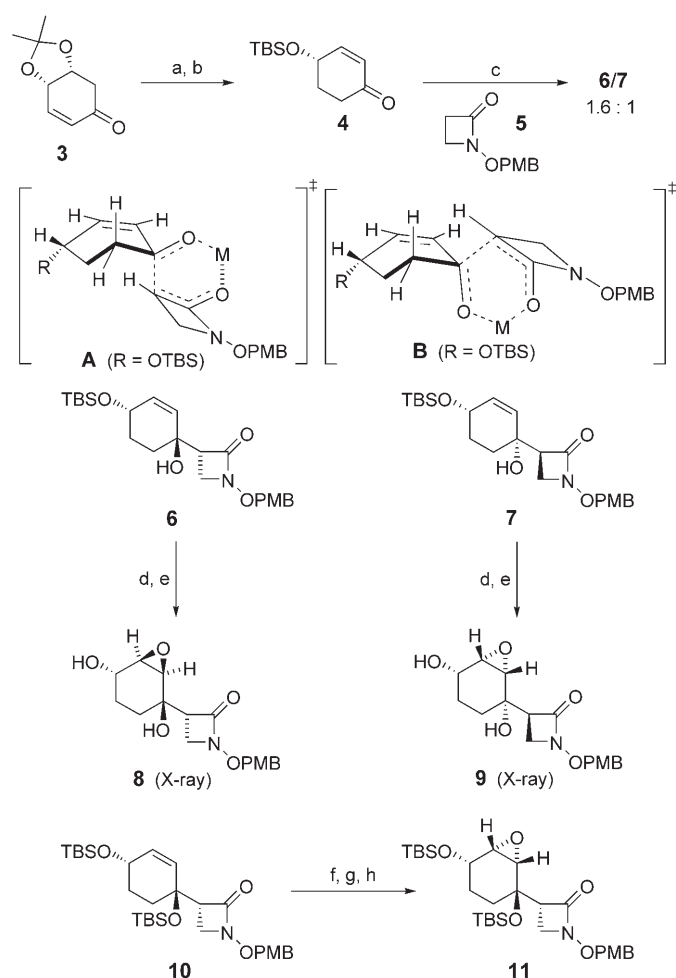
David R. Williams,* David C. Kammler,
Andrew F. Donnell, and William R. F. Goundry

Apiosporamide (**1**) was isolated from the fungus *Apiospora montagnei* Saccardo (Amphisphaeriaceae) in 1994 by Gloer and co-workers.^[1] This unique 4-hydroxy-2-pyridinone exhibits potent antifungal activity against the coprophilous fungus *Ascoibolus furfuraceus* and exhibits antibacterial activity against *Bacillus subtilis* and *Staphylococcus aureus*. Recently, the corresponding ketone YM-215343 (**2**) was identified and shown to demonstrate cytotoxicity against HeLa S3 cell cultures.^[2] Structural assignments of **1** (and **2**) have proven

[*] Prof. D. R. Williams, D. C. Kammler, A. F. Donnell,
Dr. W. R. F. Goundry
Department of Chemistry
Indiana University
800 East Kirkwood Avenue
Bloomington, IN 47405-7102 (USA)
Fax: (+1) 812-855-8300
E-mail: williamd@indiana.edu

[**] We thank the National Institutes of Health (National Institute of General Medical Sciences (GM41560)) for support of this research. We also thank Professor Gloer for providing a ^1H NMR spectrum of authentic **1**.

Supporting information for this article is available on the WWW under <http://www.angewandte.org> or from the author.

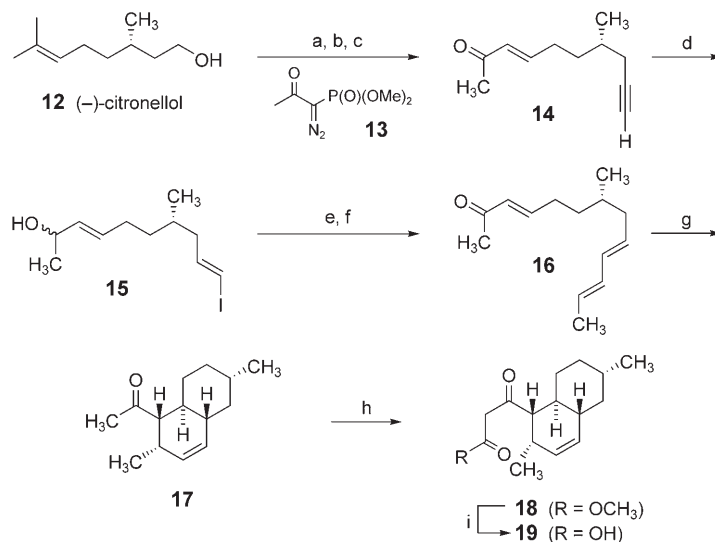


at -78°C . Although the enolate decomposed upon warming to -40°C , the addition of simple aldehydes at -78°C immediately led to the formation of addition adducts in 80–95% yields.^[12] In the case of cyclohexenone **4**, these experiments gave the two readily separated β -lactam diastereomers **6** and **7** (1.2:1) in high yields, (Scheme 1) without evidence of competing α deprotonation or conjugate addition. The stereochemical features of **6** and **7** are rationalized by arrangements **A** and **B** (Scheme 1), which illustrate nucleophilic addition to either face of the carbonyl group while minimizing nonbonded interactions with the α -methylene of the starting ketone. Coordination with the lithium cation is not essential as reactions in the presence of 12[crown]-4 produced similar product ratios. This conclusion was supported when the reactions were increased to multigram levels, as the

use of KHMDS afforded diastereomers **6** and **7** (1.6:1 d.r.) in 97% yield. Although modest improvements in stereocontrol were recorded,^[13] the overall efficiency, scale, and ease of separation for reactions with KHMDS proved most advantageous for these efforts.

The relative stereochemistry within the cyclohexane ring of **1** was investigated through the epoxidation of **6** and **7** with catalytic molybdenum hexacarbonyl and *tert*-butylhydroperoxide,^[14] to yield a single oxirane in each case. Coupling constants derived from ^1H NMR spectroscopic data for these materials failed to provide a clear basis for stereochemical assignments. However, mild hydrolysis of the TBS ethers gave the crystalline diols **8** and **9**, which were unambiguously assigned by X-ray diffraction studies.^[15] Internally directed reactions were confirmed, and led to the use of the secondary allylic alcohol derived from **10** for Henbest epoxidation and silyl protection to yield diastereomer **11**. Further studies to prepare sufficient quantities of the remaining fourth diastereomer that corresponds to the C' epimer of **11** encountered several problems. Comparisons of ^1H NMR spectroscopic data for various derivatives of **8**, **9**, and **11** with the reported ^1H NMR spectroscopic characteristics of apiosporamide were not feasible. The presence of the pyridone ring of **1** effectively inverts the relative positions of chemical shifts observed for the hydrogen atoms of the neighboring oxirane moiety. Thus, each β -lactam of Scheme 1 was independently advanced in the synthetic pathway.

The decalin portion of **1** was prepared through an intramolecular Diels–Alder reaction that began with (*S*)-citronellol (**12**; Scheme 2). Oxidation^[16] of **12** with TEMPO



and treatment with the Ohira–Bestmann reagent **13**^[17] provided a volatile alkyne. Selective oxidative cleavage of the trisubstituted olefin followed by treatment with $\text{H}_3\text{CC}(\text{O})\text{CH}_2\text{P}(\text{OMe})_2$ led to the conjugated enone in **14** (13:1 *E/Z*). The *syn* hydrozirconation of **14** followed by treatment with iodine yielded the *E* alkenyl iodide **15** with concomitant reduction of the ketone.^[18] Facile Negishi coupling^[19] with (*E*)-prop-1-enylzinc(II) bromide cleanly delivered a single diene diastereomer without the need for protection strategies to prevent the competing Heck reaction, and subsequent mild oxidation recovered the intact enone of **16**.

The Lewis acid mediated intramolecular Diels–Alder reaction of **16** proceeded in toluene at -78°C with subsequent warming to 22°C . Excellent stereoselectivity was observed, and the *trans* decalin **17** was assigned by ^1H NMR spectroscopy. Decalin **17** arises through an *exo* bridging arrangement with *endo* positioning of the ester function; a chairlike conformation of the tether is adopted with a pseudoequatorial disposition of the methyl substituent.^[20] The corresponding thermal cycloaddition (toluene, 180°C) occurred with poorer stereocontrol (d.r. 70:30). Deprotonation of **17** under kinetic conditions and C-acylation according to the Mander protocol^[21] gave pure β -ketoester **18**, which was then used to produce the labile carboxylic acid **19** prior to coupling studies.

The synthesis of **1** was pursued from **11** (Scheme 3). Although several pathways were examined, superior results involved the initial nucleophilic opening of **11** to give the *N*-alkoxyamine **20** for quantitative *N*-acylation with the carboxylic acid **19**. Subsequent acyl activation in the presence of DBU resulted in ring closure to form **21**. Reduction with

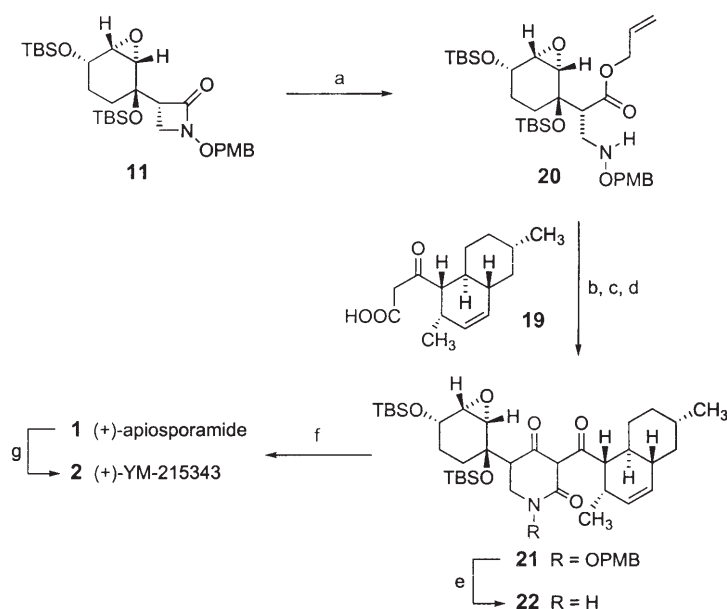
samarium diiodide yielded the dihydropyridone **22** with selective N–O bond cleavage. Subsequent oxidation with bromotrichloromethane, based upon our previous studies,^[22] gave the expected 4-hydroxy-2-pyridinone for final deprotection to afford (+)-apiosporamide (**1**). The spectral data of **1** proved to be identical to that reported for the naturally occurring **1**, but the optical rotation was opposite.^[1,23,24] Further confirmation was obtained by the Dess–Martin oxidation^[25] of synthetic **1** to yield the antipode of **2**, (+)-YM-215343, which was validated by comparison with published data for the natural product.^[2,26] Although the structural homology of pyridones **1** and **2** suggest evidence of a common biogenesis, we did not assume homochirality. However, the characterization of these natural products provides physical and spectral data that uniquely identify the synthetic **1** and **2** compared to other diastereomers of this series.

In conclusion, we have established the relative and absolute configuration of apiosporamide and have illustrated an efficient strategy for the synthesis of complex pyridinones. The use of unsubstituted β -lactams as β -alanine enolate equivalents has been demonstrated. Finally, the conversion of synthetic (+)-apiosporamide into (+)-YM-215343 has been described and has confirmed the antipodal relationship to the natural products.

Received: June 10, 2005

Published online: September 27, 2005

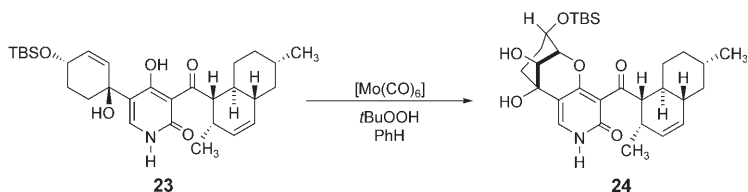
Keywords: lactams · antifungal agents · antitumor agents · heterocycles · total synthesis



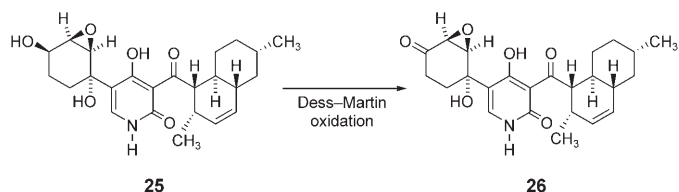
Scheme 3. Synthesis of apiosporamide (**1**). a) Allyl alcohol, *n*BuLi (1 equiv); then **11**; $-78^\circ\text{C} \rightarrow \text{RT}$; 80%; b) BOP, Et_3N , MeCN, RT, 99%; c) $[\text{Pd}(\text{PPh}_3)_4]$, pyrrolidine, CH_2Cl_2 , 85%; d) BOP, CH_2Cl_2 , DBU, -20°C , 56%; e) SmI_2 , THF, 98%; f) BrCCl_3 , TMG, 65%; then HF-pyr, THF, 75%; g) Dess–Martin periodinane, CH_2Cl_2 , 92%. BOP = benzotriazol-1-yloxy-tris(dimethylamino)phosphonium hexafluorophosphate, TMG = 1,1,3,3-tetramethylguanidine.

- [1] A. A. Alfatafta, J. B. Gloer, J. A. Scott, D. Malloch, *J. Nat. Prod.* **1994**, *57*, 1696.
- [2] M. Shibasaki, M. Taniguchi, T. Yokoi, K. Nagai, M. Watanabe, K. Suzuki, T. Yamamoto, *J. Antibiot.* **2004**, *57*, 379.
- [3] D. R. Williams, M. L. Bremmer, D. L. Brown, J. D'Antuono, *J. Org. Chem.* **1985**, *50*, 2807, and references therein.
- [4] K. Schmidt, W. Günther, S. Stoyanova, B. Schubert, Z. Li, M. Hamburger, *Org. Lett.* **2002**, *4*, 197.
- [5] J. Breinholt, S. Ludvigsen, B. R. Rassing, C. N. Rosendahl, S. E. Nielsen, C. E. Olsen, *J. Nat. Prod.* **1997**, *60*, 33.
- [6] H. Fujimoto, M. Ikeda, K. Yamamoto, M. Yamazaki, *J. Nat. Prod.* **1993**, *56*, 1268.
- [7] K. Ando, I. Matsuura, Y. Nawata, H. Endo, H. Sasaki, T. Okyotomi, T. Saehi, D. Tamura, *J. Antibiot.* **1978**, *31*, 533; Y. Nawata, I. Matsuura, K. Ando, Y. Iitaka, *Acta Crystallogr. Sect. C* **1990**, *46*, 515.
- [8] J. E. Audia, L. Biosvert, A. D. Patten, A. Villalobos, S. J. Danishefsky, *J. Org. Chem.* **1989**, *54*, 3738; see also: B. M. Trost, A. G. Romero, *J. Org. Chem.* **1986**, *51*, 2332; J. B. Everts, P. L. Fuchs, *Tetrahedron Lett.* **2001**, *42*, 3673.
- [9] For some examples of enolate formation for addition reactions of β -lactams, see: a) F. A. Bouffard, D. B. R. Johnston, B. G. Christensen, *J. Org. Chem.* **1980**, *45*, 1130; b) F. A. Bouffard, T. N. Salzmann, *Tetrahedron Lett.* **1985**, *26*, 6285, and references therein; c) I. Ojima, Y. Pei, *Tetrahedron Lett.* **1990**, *31*, 977; d) E. J. Thomas,

- A. C. Williams, *J. Chem. Soc. Perkin Trans. 1* **1995**, 351; e) B. J. Kim, Y. S. Park, P. Beak, *J. Org. Chem.* **1999**, 64, 1705.
- [10] For a review of *N*-alkoxy- β -lactams see: M. J. Miller, *Acc. Chem. Res.* **1986**, 19, 49.
- [11] P. A. van Elburg, D. N. Reinhoudt, *Heterocycles* **1987**, 26, 437.
- [12] D. R. Williams, A. F. Donnell, D. C. Kammler, *Heterocycles* **2004**, 62, 167.
- [13] Studies of sparteine with various chiral boron enolates, Ti-based complexes of (*R*)- and (*S*)-binol, and incorporation of non-racemic amines in β -lactams will be described in the full account.
- [14] K. B. Sharpless, R. C. Michaelson, *J. Am. Chem. Soc.* **1973**, 95, 6136.
- [15] a) Crystal data for **8**: colorless plate, $0.50 \times 0.24 \times 0.08$ mm³, C₁₇H₂₁N₁O₆, $M = 335.35$, orthorhombic, space group $P2_12_12_1$, $a = 5.6693(2)$, $b = 10.2239(3)$, $c = 28.4168(10)$ Å, $V = 1647.10(10)$ Å³, $T = 111(2)$ K, $Z = 4$, $\rho_{\text{calcd}} = 1.352$ Mg m⁻³, $\mu = 0.1026$ mm⁻¹, $2\theta_{\text{max}} = 60.02$, $\text{MoK}\alpha$ ($\lambda = 0.71073$). A total of 23 151 reflections were measured, of which 4801 were independent ($R_{\text{int}} = 0.032$). Final residuals were $R1 = 0.0382$ and $wR1 = 0.0406$ (for 4385 observed reflections with $I > 2\sigma(I)$, 301 parameters, 0 restraints) with GOF = 1.029, Flack parameter $-0.2(7)$, and largest residual peak 0.603 e Å⁻³ and hole -0.198 e Å⁻³; b) crystal data for **9**: colorless plate, $0.20 \times 0.18 \times 0.10$ mm³, C₁₇H₂₁NO₆, $M = 1099.67$, orthorhombic, space group $P2_12_12_1$, $a = 5.8978(2)$, $b = 7.5734(3)$, $c = 35.1598(13)$ Å, $V = 1570.46(10)$ Å³, $T = 112(2)$ K, $Z = 4$, $\rho_{\text{calcd}} = 0.108$ Mg m⁻³, $\mu = 0.108$ mm⁻¹, $2\theta_{\text{max}} = 60.06$, $\text{MoK}\alpha$ ($\lambda = 0.71073$). A total of 16 372 reflections were measured, of which 4597 were independent ($R_{\text{int}} = 0.031$). Final residuals were $R = 0.0502$ and $wR2 = 0.1108$ (for 4319 observed reflections with $I > 2\sigma(I)$, 247 parameters, 46 restraints) with GOF = 1.056, Flack parameter $-0.1(10)$, and largest residual peak 0.388 e Å⁻³ and hole -0.415 e Å⁻³. CCDC-274063 (**8**) and -274064 (**9**) contain the supplementary crystallographic data for this paper. These data can be obtained free of charge from the Cambridge Crystallographic Data Centre via www.ccdc.cam.ac.uk/data_request/cif.
- [16] A. De Mico, R. Margarita, L. Parlanti, A. Vescovi, G. Piancatelli, *J. Org. Chem.* **1997**, 62, 6974.
- [17] S. Müller, B. Liepold, G. J. Roth, H. J. Bestmann, *Synlett* **1996**, 521; see also: S. Ohira, *Synth. Commun.* **1989**, 19, 561.
- [18] For a review, see: P. Wipf, H. Jahn, *Tetrahedron* **1996**, 52, 12853.
- [19] For examples of related couplings, see: P. Knochel, R. D. Singer, *Chem. Rev.* **1993**, 93, 2117.
- [20] For a related intramolecular Diels–Alder reaction, see: D. J. Witter, J. C. Vederas, *J. Org. Chem.* **1996**, 61, 2613.
- [21] L. N. Mander, S. P. Sethi, *Tetrahedron Lett.* **1983**, 24, 5425.
- [22] D. R. Williams, P. D. Lowder, Y.-G. Gu, D. A. Brooks, *Tetrahedron Lett.* **1997**, 38, 331; for an example in total synthesis, see: D. R. Williams, R. A. Turske, *Org. Lett.* **2000**, 2, 3217.
- [23] Optical rotation data for naturally occurring apiosporamide was recorded as $[\alpha]_{\text{D}} = -97.4^\circ$ ($c = 0.0004$ MeOH). Characterization of synthetic **1**: $R_{\text{f}} = 0.12$ (19:1 CH₂Cl₂/MeOH); $[\alpha]_{\text{D}}^{24} = +108^\circ$ ($c = 0.40$, MeOH); IR (film): $\tilde{\nu} = 3248$ (br), 3072, 3006, 2953, 2925, 1656, 1652, 1602, 1544, 1455, 1214, 1063, 1021, 964 cm⁻¹; ¹H NMR (400 MHz, CD₃OD): $\delta = 7.45$ (s, 1H), 5.51 (m, 1H), 5.31 (d, $J = 9.8$, 1H), 4.30 (dd, $J = 11.2, 5.7$ Hz, 1H), 4.04 (ddd, $J = 5.9, 5.9, 3.1$ Hz, 1H), 3.53 (d, $J = 3.2$ Hz, 1H), 3.32 (dd, $J = 3.2, 3.1$ Hz, 1H), 2.73 (m, 1H), 2.11 (dd, $J = 13.0, 9.0$, 1H), 1.85 (dd, $J = 12.1, 2.5$ Hz, 1H), 1.78–1.70 (m, 2H), 1.70–1.56 (m, 3H), 1.52–1.37 (m, 2H), 1.30–1.20 (m, 1H), 0.94 (ddd, $J = 12.8, 12.1, 3.3$ Hz, 1H), 0.87–0.76 (m, 1H), 0.84 (d, $J = 6.5$ Hz, 3H), 0.74 (d, $J = 7.2$ Hz, 3H), 0.71 ppm (ddd, $J = 12.4, 12.4, 12.4$ Hz, 1H); ¹³C NMR (101 MHz, MeOH): $\delta = 211.7, 179.5, 164.2, 139.9, 132.7, 131.7, 116.7, 108.8, 70.6, 67.1, 60.5, 57.6, 54.3, 43.3, 43.2, 37.6, 36.7, 34.4, 32.5, 31.6, 31.0, 25.8, 23.0, 18.4$ ppm; HRMS: m/z calcd for C₂₄H₃₂NO₆ [$M + H$]⁺ 430.2224; found: 430.2225.
- [24] Due to the anticipated similarities of ¹H and ¹³C NMR spectroscopic data, and the discrepancy in the specific optical rotation in **1**, the route was adapted for independent preparation of three diastereomers with the *syn* relationship between the epoxide and tertiary alcohol (as in **8** and **9**). All of these isomers demonstrated great instability and underwent opening of the oxirane, as illustrated in the formation of **24** through directed oxidation of **23**. Interestingly, five-membered-ring products were not observed. Additional information will be provided in a full account.



- [25] D. B. Dess, J. C. Martin, *J. Am. Chem. Soc.* **1991**, 113, 7277.
- [26] Synthetic and natural **2** were identical in all respects, except for rotation. Optical rotation for natural YM-215343 was recorded as $[\alpha]_{\text{D}}^{25} = -44^\circ$ ($c = 0.10$ MeOH), and synthetic **2** was $[\alpha]_{\text{D}}^{24} = +47^\circ$ ($c = 0.225$ MeOH). Diastereoisomer **25** proved to be stable and spectroscopically similar to apiosporamide. However, oxidation gave ketone **26** which was clearly diastereomeric to **2**.



Structure Elucidation of the Highly Active Titanosilicate Catalyst Ti-YNU-1**

Juanfang Ruan, Peng Wu, Ben Slater, and Osamu Terasaki*

A major breakthrough in the field of zeolite catalysis was the development of MFI-type (a zeolite framework type of ZSM-5) titanosilicate (TS-1) as a liquid-phase oxidation catalyst.^[1] Nevertheless, TS-1 has a major disadvantage in that its medium-sized pores with 10-membered rings (10-MRs) restrict its application to molecules of relatively small size. To overcome this problem of TS-1, other titanosilicates with larger pores, such as Ti-Beta,^[2,3] Ti-MOR,^[4] Ti-ITQ-7,^[5] and Ti-MCM-41,^[6] have been prepared and have partially solved the problems of steric constraints encountered in the oxidation of bulky molecules. However, it seems that none of the above titanosilicates has sufficient intrinsic activity and stability, and this has stimulated researchers to prepare Ti-containing catalysts that are both highly stable and accessible to bulky substrates. In this context, MWW-type zeolite has a promising framework structure consisting of MWW sheets and contains two independent noninterconnected pore systems with 10-MR channels.^[7,8] Three-dimensional (3D) Ti-MWW was successfully prepared by hydrothermal synthesis,^[9] but on calcination of the layered MWW sheets, access to the supercages is seriously restricted by the openings of the 10-MR pores. Thus, in the case of aluminosilicate, a micro-mesoporous hybrid material MCM-36 was prepared by swelling the MWW sheets of the lamellar precursor with

organic surfactant followed by pillaring with a silica precursor.^[10] With similar objectives, ITQ-2 was synthesized by swelling the layers of the MWW lamellar precursor and then sonicating the product.^[11] Both MCM-36 and ITQ-2 have an extremely high surface area that is highly accessible to bulky molecules, but lack an ordered crystalline structure. From a steric point of view, it is desirable to retain the space between the MWW sheets after calcining the lamellar precursor. In the particular case of the titanosilicate, this not only makes the active sites within the supercages more accessible to bulky molecules, but also promotes activity in oxidation reactions with aqueous H₂O₂ as oxidant, as the silanol groups are less hydrophilic than in pillared and delaminated materials. This could open up new applications for titanosilicates in the synthesis of fine chemicals. Previously, a novel titanosilicate denoted Ti-YNU-1 was prepared from an MWW-type precursor.^[12] It has an expanded pore window between the crystalline MWW sheets and shows a far higher intrinsic catalytic activity than 3D Ti-MWW and large-pore Ti-Beta in the epoxidation of bulky alkenes with H₂O₂. Although Ti-YNU-1 was reported to contain MWW sheets, the nature and structure of the linkage between the sheets were not established. We have now investigated the structure of Ti-YNU-1 by focusing on the pore structure and space between the MWW sheets at the atomic scale by high-resolution transmission electron microscopy (HRTEM), powder X-ray diffraction (XRD), scanning electron microscopy (SEM), and NMR spectroscopy. From a combination of computer simulations and experimental observations, we suggest a likely structure of Ti-YNU-1.

The SEM images of the MWW lamellar precursor, 3D Ti-MWW, and Ti-YNU-1 samples are shown in Figure 1. All

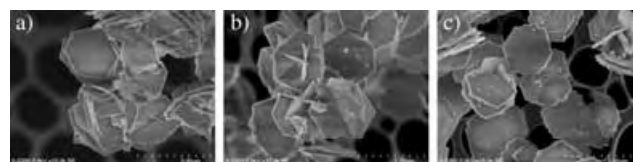


Figure 1. SEM images of a) lamellar precursor, b) 3D Ti-MWW, and c) Ti-YNU-1.

samples crystallized as thin platelets with hexagonal morphology, and the unit cell *c* axis lies perpendicular to the plate surface. The thin platelets of all samples were approximately 2 μm in width and 0.1 μm in thickness; no significant differences in morphology between the three samples can be discerned from the images, although some roughening of the crystal edges in the Ti-YNU-1 sample is evident.

The XRD pattern of the lamellar precursor shows reflections at large scattering angles that are much broader than those of 3D Ti-MWW and Ti-YNU-1 (Figure 2). This indicates that the lamellar precursor is composed of MWW sheets, and on acid treatment or calcination the sheets are fully connected to form 3D Ti-MWW or Ti-YNU-1. The powder XRD pattern of Ti-YNU-1 appears to be similar to those of the lamellar precursor and 3D Ti-MWW, but the principal difference is that the diffraction peaks associated

[*] J. Ruan, Prof. O. Terasaki
Structural Chemistry, Arrhenius Laboratory
Stockholm University
Stockholm, 10691 (Sweden)
Fax: (+46) 8-163-118
E-mail: terasaki@struc.su.se

Prof. P. Wu
Shanghai Key Laboratory of Green Chemistry and Chemical Processes
Department of Chemistry, East China Normal University
North Zhongshan Rd. 3663, Shanghai, 200062 (China)
Dr. B. Slater
Davy Faraday Research Laboratory
The Royal Institution of Great Britain
21 Albemarle Street, London W1S4BS (UK)

[**] O.T. thanks the Swedish Science Research Council (VR) and the Japan Science and Technology Cooperation (JST) for financial support. P.W. thanks the Program for New Century Excellent Talents in University (NCET), the NSFC (No. 20473027), and Prof. T. Tatsumi for his encouragement. B.S. thanks Prof. Julian D. Gale and Prof. Javier Junquera for basis and pseudopotential data for SIESTA, and the EPSRC for computing time on the HPC(x) UK national supercomputer facility.

Supporting information for this article is available on the WWW under <http://www.angewandte.org> or from the author.

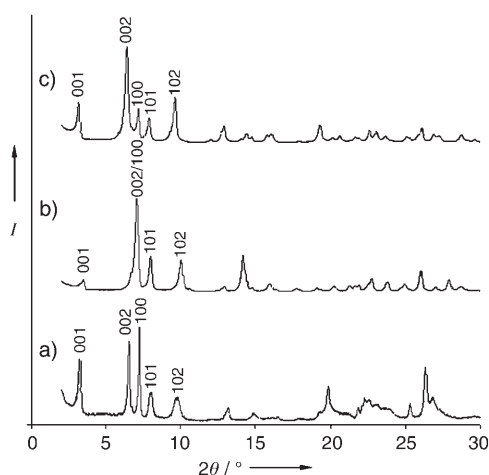


Figure 2. Powder XRD profiles of a) lamellar precursor, b) 3D Ti-MWW, and c) Ti-YNU-1.

with unit-cell distance c are all shifted to lower 2θ values in comparison to the lamellar precursor and 3D Ti-MWW. For example, the (001) peak of Ti-YNU-1 is found at 3.20° , (002) at 6.41° , and (101) at 7.85° , but for 3D Ti-MWW and the lamellar precursor, (001) is found at 3.52° and 3.29° , (002) at 7.04° and 6.56° , and (101) at 7.97° and 7.94° . In contrast, the diffraction peaks associated with unit-cell distance a remain almost constant: (100) is found at 7.16° , as opposed to 7.15° and 7.23° for 3D Ti-MWW and the lamellar precursor, respectively. These observations suggest that calcination and acid treatment do not affect the basic crystalline structure within the layers, but do influence the space between the MWW sheets. Table 1 lists the powder XRD data of the lamellar precursor, 3D Ti-MWW, and Ti-YNU-1. The unit-cell parameters were calculated to be $a=b=14.238\text{ \AA}$ and $c=27.571\text{ \AA}$ for Ti-YNU-1, $a=b=14.263\text{ \AA}$ and $c=25.098\text{ \AA}$ for 3D Ti-MWW, and $a=b=14.108\text{ \AA}$ and $c=26.926\text{ \AA}$ for the lamellar precursor. The parameter c of Ti-YNU-1 is enlarged by about 2.5 and 0.6 \AA relative to those of 3D Ti-MWW and the lamellar precursor, respectively. The structural expansion also led to an enlarged specific surface area and pore volume for Ti-YNU-1 ($654\text{ m}^2\text{ g}^{-1}$ and 0.20 mL g^{-1}) in comparison to 3D Ti-MWW ($548\text{ m}^2\text{ g}^{-1}$ and 0.16 mL g^{-1} ; see Supporting Information).

The [001] HRTEM images of the lamellar precursor, 3D Ti-MWW, and Ti-YNU-1 are shown in Figure 3 together with corresponding Fourier diffractograms (FDs). The image and

FD of Ti-YNU-1 show no significant differences from those of the lamellar precursor and 3D Ti-MWW, which clearly exhibit the characteristic hexagonal framework topology of MWW-type materials in this projection.^[7] It is apparent that postprocessing does not alter the structure within the MWW sheet, and there is no evidence for aperiodically or periodically repeating defects. As all three materials show the same projected images of the MWW sheet (and the same FDs), structural study of Ti-YNU-1 perpendicular to the MWW sheet, that is, along [100], is essential to find differences between the lamellar precursor, 3D Ti-MWW, and Ti-YNU-1.

The HRTEM images of the lamellar precursor, 3D Ti-MWW, and Ti-YNU-1 with [100] incidence and the corresponding FDs are shown in Figure 4. The image of the lamellar precursor was taken under overfocus conditions and indicates the presence of 3D order (Figure 4a). The image of

Table 1: Powder XRD data of lamellar precursor, 3D Ti-MWW, and Ti-YNU-1.

Lamellar precursor			3D Ti-MWW			Ti-YNU-1		
<i>hkl</i>	2θ [$^\circ$]	d_{hkl} [\AA]	<i>hkl</i>	2θ [$^\circ$]	d_{hkl} [\AA]	<i>hkl</i>	2θ [$^\circ$]	d_{hkl} [\AA]
001	3.29	26.926	001	3.52	25.089	001	3.20	27.571
002	6.56	13.463	002	7.04	12.544	002	6.41	13.786
100	7.23	12.218	100	7.15	12.352	100	7.16	12.331
101	7.94	11.126	101	7.97	11.082	101	7.85	11.257
102	9.77	9.047	102	10.04	8.801	102	9.62	9.191
003	9.85	8.975	003	10.57	8.363	003	9.62	9.191
103	12.23	7.233	103	12.77	6.925	103	12.00	7.369
111	12.96	6.824	111	12.89	6.860	111	12.83	6.893
004	13.14	6.731	004	14.11	6.272	004	12.83	6.893
112	14.16	6.248	112	14.27	6.200	112	13.99	6.326
200	14.49	6.109	200	14.33	6.176	200	14.35	6.166
201	14.86	5.957	201	14.76	5.997	201	14.71	6.017
104	15.01	5.896	104	15.83	5.593	104	14.71	6.017
202	15.92	5.563	202	15.98	5.541	202	15.73	5.628
113	15.97	5.546	113	16.32	5.426	113	15.73	5.628
005	16.45	5.385	005	17.66	5.018	005	16.06	5.514
203	17.55	5.050	203	17.84	4.968	203	17.30	5.120
105	17.99	4.928	210	18.99	4.669	105	19.03	4.661
210	19.20	4.618	105	19.08	4.649	210	19.03	4.661
211	19.49	4.551	211	19.32	4.590	211	19.30	4.596
204	19.61	4.524	204	20.16	4.401	204	19.30	4.596
006	19.77	4.488	212	20.28	4.375	006	19.30	4.595
212	20.31	4.368	006	21.23	4.181	212	20.09	4.415
115	20.73	4.280	300	21.57	4.117	115	20.35	4.360
106	21.07	4.212	115	21.64	4.104	106	20.61	4.306
213	21.62	4.106	213	21.78	4.076	213	21.36	4.157
300	21.81	4.073	301	21.86	4.063	300	21.60	4.111

Ti-YNU-1 in Figure 4c was taken under underfocus conditions and reveals that it has a structure similar to that 3D Ti-MWW (Figure 4b) but with a different c distance. Selected-area electron diffraction with the calibration of the camera length was conducted to show the different c distances of Ti-YNU-1 and 3D Ti-MWW (see Supporting Information). To confirm the above observations, HRTEM images for [100] incidence were simulated for both over- and underfocus conditions by the multislice method using the structural parameters of 3D MWW (see Supporting Information). By comparing these simulated images with the observed

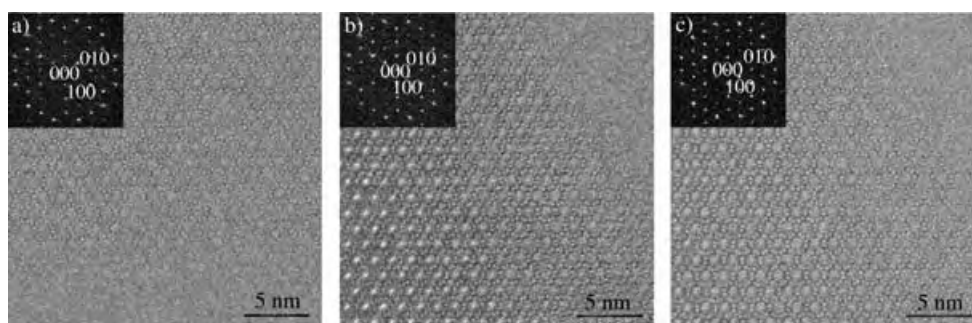


Figure 3. HRTEM images of a) lamellar precursor, b) 3D Ti-MWW, and c) Ti-YNU-1 taken with [001] incidence. Corresponding FDs are inset in each image.

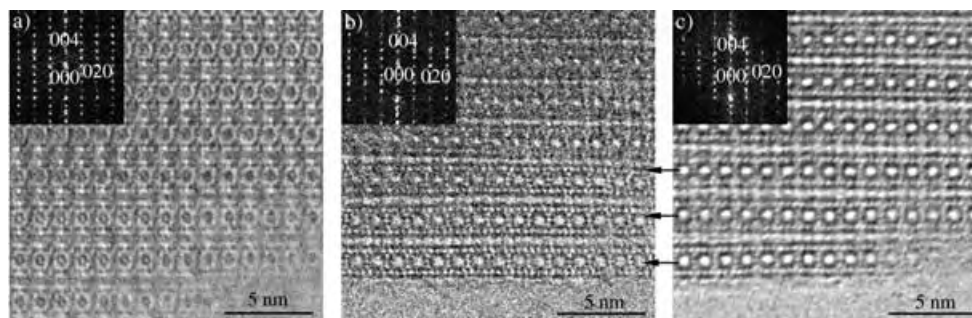


Figure 4. HRTEM images of a) lamellar precursor, b) 3D Ti-MWW, and c) Ti-YNU-1 taken with [100] incidence. Corresponding FDs are inset in each image.

HRTEM images of Figure 4, we conclude that Ti-YNU-1 has a 3D-connected framework structure of the MWW type, analogous to that of 3D Ti-MWW. On the other hand, the lamellar precursor also has a 3D ordered structure, which indicates that the structure-directing agent present in the interlayer region causes regular stacking along *c* at a well-defined distance.

To further probe the nature of the interlayer structure in Ti-YNU-1, ^{29}Si MAS (magic-angle spinning) NMR spectroscopy was performed. The spectrum of Ti-YNU-1 (Figure 5) showed a Q^2 band around 89 ppm which was absent for 3D Ti-MWW. This band implies the possible presence of $\text{Si}(\text{OH})_2$ (SiO_2)₂ or $\text{Si}(\text{OH})(\text{OTi})(\text{SiO}_2)$ ₂ linkages between the MWW sheets. Considering that Ti-YNU-1 has a lattice expansion of about 2.5 Å, as confirmed by XRD, wholly intact linkages

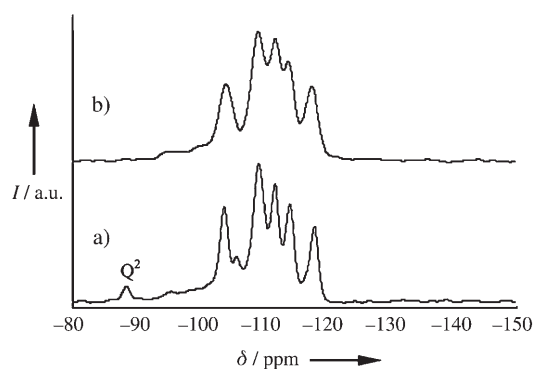


Figure 5. ^{29}Si MAS NMR spectra of a) Ti-YNU-1 and b) 3D Ti-MWW.

between MWW layers according to HRTEM observations, and the potential linking species indicated by NMR spectra, it is proposed that the Ti-YNU-1 structure is simply an expanded form of MWW in which a single T site acts as a pillar connecting the MWW layers (Figure 6).

Atomistic computer simulation techniques were used to model the proposed crystal structure. Initially, we used methods based on interatomic potentials, as described by, for example, Chiu et al.^[13] and Jentys and Catlow,^[14] to verify the bulk structure of pure Si-MWW, using the GULP code.^[15] The computed cell parameters of 14.187, 14.187, and 24.957 Å are within 0.5% of the measured values reported by Corma and co-workers.^[16]

To assess potential Ti-YNU-1 structures, we first constructed a model in which two additional T sites are introduced per unit cell, midway between the lamellar layers of MWW, to form layer spacing or $\text{Si}(\text{OH})_2$ “pillars”. This

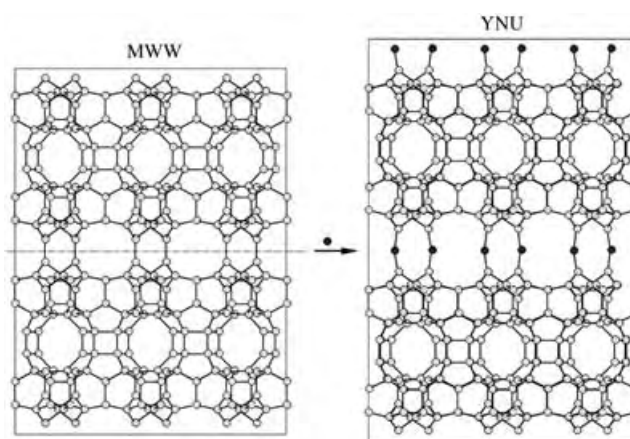


Figure 6. Schematic transformation of MWW to YNU.

structure was then relaxed by using the computational approach outlined above to give the structure shown in Figure 7a. Introduction of two additional T sites causes essentially no change in the *a* and *b* lattice parameters but an expansion in the *c* direction of 2.59 Å relative to pure Si-MWW. This increase closely agrees with the magnitude of the structural expansion inferred from XRD and TEM. Critically, the introduction of the additional T sites expands the

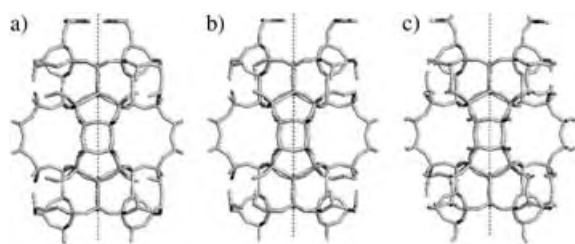


Figure 7. Three possible configurations for Si-YNu indicating the flexible nature of the 12-MR, viewed along [100].

interlayer ten-membered ring to form a twelve-membered ring, which affords increased transport rates and the potential to filter larger products than the 10-MR. Two other possible configurations were generated, one in which the T sites are placed as close together as possible and an “indented 12-MR” configuration (Figure 7b and c). The relative energies of the configurations shown in Figure 7a–c (0.079, 0.084, and 0.000 eV, respectively) are almost identical and are comparable to kT , and this suggests that at moderate temperature, because the $\text{Si}(\text{OH})_2$ group can freely rotate, all three of these configurational states will be occupied on a picosecond timescale. The breathing of the 12-MR will lead to electron scattering and hence weak contrast in the HRTEM image.

Finally, the substitution energetics for Ti in MWW was assessed by the interatomic potential approach. The span of Ti substitution energies measured relative to the most favorable site is 0.70 eV for the potentials reported by Jentys and Catlow.^[14] The spread of energies is substantially greater than that in silicalite, for which the range is about 0.22 eV, from which it can be inferred that the selectivity of Ti for particular lattice sites within MWW is rather high. As the typical Ti/Si ratio for MWW is about 1:240, it follows that the sixfold rim site shown in Figure 8, which is identified as the lowest energy site, may be selectively occupied. As the next most favorable site is 0.14 eV higher in energy than the rim site, the rim site is likely to be occupied first. In Figure 8, the location of the most (rim) and least (spiro) favorable sites (shown in white and black, respectively) are displayed. However, it is worth noting that the activation barrier for formation of MWW/YNu is likely to be comparable to the range of substitution energies,



Figure 8. A [001] view of Ti-YNu indicating favorable substitution at the “rim” site (white) and less favorable incorporation at the “spiro” site (black).

and hence ordering of Ti towards particular lattice sites may be relaxed due to kinetically favored pathways.

To assess the preferred location of framework Ti in Ti-YNu, the proposed Si-YNu structure was first relaxed using the local-orbital-based, periodic density functional code SIESTA.^[17] A titanium center was then introduced into the unit cell at the pillar site and at the most and least favorable sites in the MWW sheet, identified by the interatomic potential calculations, to give three distinct configurations that were relaxed at constant pressure. The relative stability of the three sites was rim > pillar > spiro, with relative energies of 0, +0.24, +0.27 eV, respectively, under anhydrous conditions. Although the pillar site appears not to be the most favorable framework site, the position of Ti within the YNU lattice will depend strongly on the water content^[18] in the lattice and on the susceptibility to Ti leaching from MWW lamellae under acid conditions. It is possible that under acid/reflux conditions, Ti would leach from the rim site and occupy the pillar site, where it could easily expand its coordination sphere to give a quasi-octahedral configuration. In the pillar site, Ti could easily physisorb one or more water molecules and thus enhance its stability within the lattice while retaining steric accessibility and a flexible coordination number for catalytic activity.

The simulated XRD pattern of the proposed Ti-YNu-1 structure compares well with measured data (see Supporting Information). The HRTEM images simulated for the new structure with 12-MRs match very favorably with the observed images (see Supporting Information). However the differences between the images of MWW 10-MRs and Ti-YNu-1 12-MRs are extremely slight, except for the marked increase in c . The weight of evidence suggests that Ti-YNu-1 has 12-MRs between the MWW sheets from the observed c period in the HRTEM image and the XRD data.

In conclusion, the structure of Ti-YNu-1, which is structurally related to MWW, was studied by TEM in combination with powder XRD, SEM, NMR spectroscopy, and computer simulations. We found that Ti-YNu-1 has a 3D-connected MWW-like framework with much larger spacing along the c axis between the MWW sheets than the lamellar precursor and 3D Ti-MWW. A newly formed 12-MR that is distinct from the 10-MR of the MWW structure would explain this cell expansion. The expanded pore window, which would result in a concomitant increase in steric accessibility, may explain the significant enhancement of catalytic activity measured relative to other titanosilicates. Additionally, simulation results suggest that Ti has high site selectivity relative to materials such as MFI,^[18] and we speculate that the Ti centers could occupy the pillar sites, which have a much higher steric accessibility than framework positions in MWW and, for example, TS-1. It is tempting to speculate that Ti in the pillar site of YNU will be conducive to temporary expansion of the Ti coordination sphere, which is thought to be crucial to epoxidation activity in, for example, TS-1.^[19] As the silicon or titanium ions that intercalate the sheets must originate from the framework by acid treatment, an intriguing possibility would be to adjust the postsynthesis procedure to include silicate monomers or larger oligomers, and thus to potentially design the pillar height and hence ring size. Such

an approach could lead to tailored zeolites with the capability to obtain extremely high selectivity.

Experimental Section

The lamellar precursor of the MWW titanasilicate was synthesized from highly siliceous MWW zeolite, tetrabutyl orthotitanate (TBOT), piperidine (PI), and deionized water following procedures reported elsewhere.^[12] Typically, PI (7.24 g) and TBOT (0.29 g) were dissolved in 22.5 g of deionized water, then a highly deboronated MWW (5 g) was added to the solution. The resultant mixture was rotated in an autoclave at 443 K for 5 days. The as-synthesized precursor (Si/Ti = 100, containing 15.4 wt % PI) was directly calcined at 823 K for 10 h to burn off PI and obtain the 3D MWW titanasilicate Ti-MWW (Si/Ti = 100). This was heated at reflux in 2 M HNO₃ solution and further calcined at 823 K for 10 h to obtain a novel titanasilicate, denoted Ti-NU-1 (Si/Ti = 240).

Powder X-ray diffraction (XRD) patterns were collected on a MAC Science MX-Labo diffractometer (CuK α radiation). The crystal size and morphology were monitored by SEM on a Hitachi S-5200 microscope. For TEM measurements, the sample was crushed in an agate mortar, dispersed in ethanol (95 vol %) by ultrasonication, and then dropped onto a carbon microgrid. HRTEM observations were carried out with a 300 kV TEM (JEOL-3010, C_s = 0.6 mm, resolution 1.7 Å). Images were recorded with a Kodak electron film SO-163 using low-electron-dose conditions. The HRTEM images were simulated by the multislice method using the MacTempas program as a function of crystal thickness and defocus values under the parameters of an accelerated voltage of 300 kV, C_s = 0.6 mm, and semiangle of beam convergence of 0.6 mrad. The ²⁹Si MAS NMR spectra were recorded on a JEOL ECA-400 multinuclear solid-state magnetic resonance spectrometer at 79.6 MHz at a spinning rate of 5 kHz and with a pulse interval of 15 s.

Received: June 4, 2005

Revised: July 14, 2005

Published online: September 19, 2005

Keywords: layered compounds · silicates · structure elucidation · titanates · zeolite analogues

- [16] M. A. Camblor, A. Corma, M. Díaz-Cabañas, C. Baerlocher, *J. Phys. Chem. B* **1998**, *102*, 44.
- [17] D. Sanchez-Portal, P. Ordejón, E. Canadell, *Struct. Bonding (Berlin)* **2004**, *113*, 103.
- [18] G. Ricchiardi, A. J. M. de Man, J. Sauer, *Phys. Chem. Chem. Phys.* **2000**, *2*, 2195.
- [19] M. Neurock, L. E. Manzer, *Chem. Commun.* **1996**, 1133.

- [1] G. Bellussi, M. S. Rigutto, *Stud. Surf. Sci. Catal.* **2001**, *137*, 911.
- [2] M. A. Camblor, A. Corma, A. Martínez, J. Pérez-Pariente, *J. Chem. Soc. Chem. Commun.* **1992**, 589.
- [3] T. Tatsumi, N. Jappari, *J. Phys. Chem. B* **1998**, *102*, 7126.
- [4] P. Wu, T. Komatsu, T. Yashima, *J. Phys. Chem.* **1996**, *100*, 10316.
- [5] M. Díaz-Cabañas, L. A. Villaescusa, M. A. Camblor, *Chem. Commun.* **2000**, 761.
- [6] A. Corma, *Chem. Rev.* **1997**, *97*, 2373.
- [7] M. E. Leonowicz, J. A. Lawton, S. L. Lawton, M. K. Rubin, *Science* **1994**, *264*, 1910.
- [8] G. G. Juttu, R. F. Lobo, *Microporous Mesoporous Mater.* **2000**, *40*, 9.
- [9] P. Wu, T. Tatsumi, T. Komatsu, T. Yashima, *J. Phys. Chem. B* **2001**, *105*, 2897.
- [10] W. J. Roth, C. T. Kresge, J. C. Vartuli, M. E. Leonowicz, A. S. Fung, S. B. McCullen, *Stud. Surf. Sci. Catal.* **1995**, *94*, 301.
- [11] A. Corma, V. Fornés, S. B. Pergher, Th. L. M. Maesen, J. G. Buglass, *Nature* **1998**, *396*, 353.
- [12] W. B. Fan, P. Wu, S. Namba, T. Tatsumi, *Angew. Chem.* **2004**, *116*, 238; *Angew. Chem. Int. Ed.* **2004**, *43*, 236.
- [13] M. E. Chiu, B. Slater, J. D. Gale, *Angew. Chem.* **2005**, *117*, 1239; *Angew. Chem. Int. Ed.* **2005**, *44*, 1213.
- [14] A. Jentys, C. R. A. Catlow, *Catal. Lett.* **1993**, *22*, 251.
- [15] J. D. Gale, A. L. Rohl, *Mol. Simul.* **2003**, *29*, 291.

Anticancer Genes

DOI: 10.1002/anie.200501793

17 β -Estradiol-Associated Stealth-Liposomal Delivery of Anticancer Gene to Breast Cancer Cells**
*Bathula S. Reddy and Rajkumar Banerjee**

Estrogen receptor (ER), a member of the nuclear hormone receptor superfamily, is classically known to express as intracellular steroid receptor. It shows up predominantly in estrogen-responsive organs, such as ovary, uterus, and mammary cells. ER possesses mainly genomic properties but nongenomic, steroidal functions are also known.^[1–5] Interestingly, classical ERs are implicated in several cancer phenotypes in the female population and are expressed in 60–80 % of breast cancer samples.^[6] These receptors are mostly confined to the primary stage of the tumor, and therefore endocrine-based therapy is generally used in the initial stages of neoplastic transformation.

β -Estradiol or estrogen is the endogenous ligand of ER. Estrogen-induced ER acts as a ligand-dependent transcription factor during its genomic activity, and regulates cell proliferation in cancer cells such as that observed in breast carcinoma, thereby becoming the principal target for breast cancer therapy. There are several ER antagonists, aromatase inhibitors, and selective estrogen receptor modulators (SERMs) that alone, or in combination, provide several clinical options for breast cancer therapy with limited efficacy.^[7–11]

Liposomes have long been utilized as viable options for targeting cancers.^[12–14] Poly(ethylene glycol)(PEG)-associ-

[*] B. S. Reddy, Dr. R. Banerjee
Division of Lipid Science & Technology
Indian Institute of Chemical Technology
Hyderabad 500 007 (India)
Fax: (+91) 40-2719-3370
E-mail: rkbanerjee@yahoo.com

[**] This is IICT communication no. 050509. B.S.R. thanks the University Grants Commission (UGC), Government of India, for a PhD fellowship. R.B. acknowledges financial assistance from the Department of Science & Technology (DST), Government of India, in the form of a “Fast Track Project Proposal for Young Scientists”.

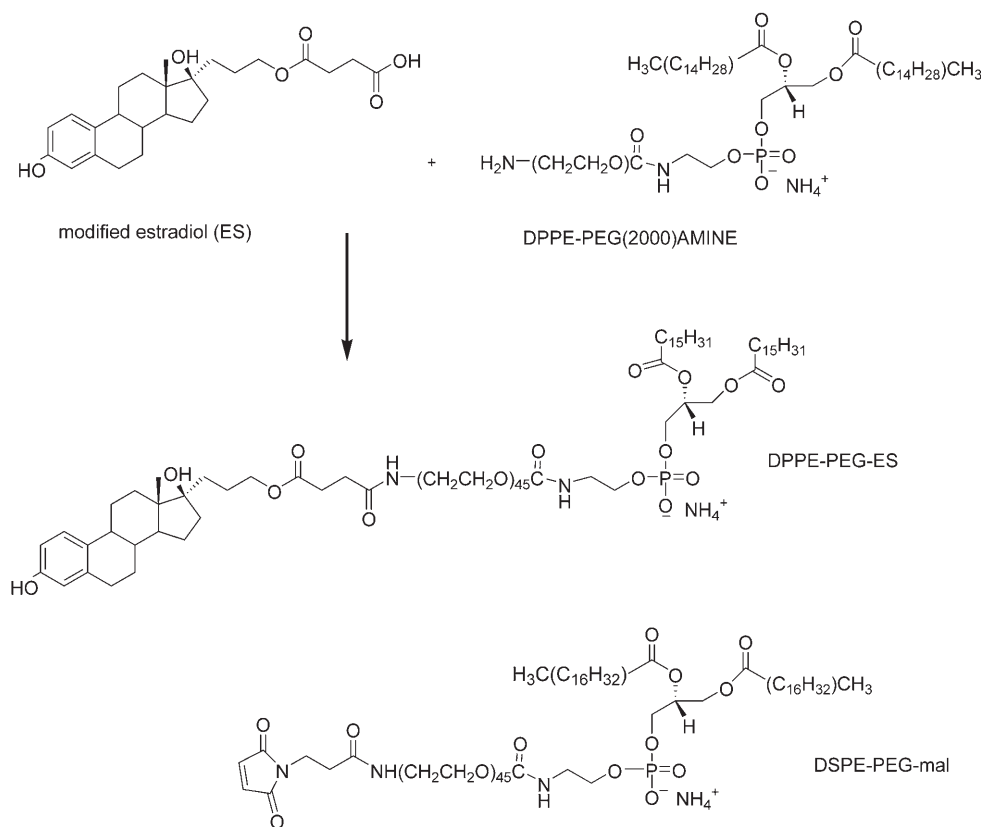


Supporting information for this article is available on the WWW under <http://www.angewandte.org> or from the author.

ated liposomes offer a stealth property to the payloads encapsulated in liposomal formulations with enhanced circulation half-lives.^[14–16] Recently, a PEG- and cyclic RGD-associated (RGD: Arg-Gly-Asp) polymeric micelle has been exploited to deliver encapsulated doxorubicin to integrin-expressing specific tumorigenic cell types.^[17] We have also shown that genetic payloads can be efficiently targeted to sigma-receptor-expressing breast cancer cells when haloperidol, a low-molecular-weight sigma-receptor-targeting drug, is covalently grafted to the headgroup region of a stealth cationic liposome.^[18] This finding prompted us to investigate whether estrogen, the natural ER ligand, associating with a gene-carrying stealth liposomal system can act as a targeting ligand for delivering genes to breast cancer cells implicated with ER. This option of targeting genes at breast or estrogen-responsive cancer cells is expected to eliminate the chemotherapeutic drug-induced toxicity to normal cells.

Recently, it was found that estrogen exhibits high affinity to GPR30, an orphan receptor ubiquitously present in most of the cell types. In association with estrogen, GPR30 executes several nongenomic functions.^[1,19] We envisaged that an estrogen-associated reporter-gene-carrying liposomal delivery system would uniquely target ER-expressing cells irrespective of existing GPR30.

With such a rationale in mind, we conjugated 17 β -estradiol (ES) to the distal end of a phospholipid with a PEG spacer in between. The conjugation was performed without potentially diminishing the estrogenic property of the ligand. 3-Hydroxy-protected estrone was subjected to a Grignard reaction by following a previously reported procedure^[20] to obtain the 17 α -allyl moiety. This moiety was converted to a primary alcohol which was reacted with succinic anhydride to obtain an estradiol-associated molecule with a carboxylic acid end group. After silyl deprotection, the carboxylic acid group was conveniently conjugated to the amine end group of the 1,2-dipalmitoyl-Sn-glycero-phosphatidylethanolamine (DPPE)-linked PEG moiety to obtain the targeting lipid DPPE-PEG-ES (Scheme 1). NMR peaks at $\delta = 6.6$ – 7.2 ppm ascertained the conjugation of the estrogen moiety in DPPE-PEG-ES (Figure 1 B), whereas no aromatic peaks were obtained in the PEG-suppressed NMR spectrum



Scheme 1. Representative synthesis and structure of the lipids. Modified ES, which is produced in five steps, is treated with DPPE-PEG-NH₂ to obtain the targeting lipid DPPE-PEG-ES. DSPE-PEG-mal is the control lipid (DSPE = distearoylphosphatidylethanolamine, mal = maleimide).

of DPPE-PEG-NH₂ (Figure 1 A). The MALDI mass spectrum of DPPE-PEG-ES showed an inverted U-shaped pattern with an increment of 44 mass units between molecular weights 2756 and 3410. In spite of the two PEG populations in the sample, the peak of the U-shaped spectral pattern was obtained at a molecular weight of 3018.8, which was about 132 (that is, about three CH₂CH₂O residues) less than the calculated molecular weight of the product of 3151.67 (comparable to the peak at 3151.7 in Figure 1 C). The calculated molecular weight was obtained by summing the molecular weights of the contributing estrogen fragment (413.3) and the starting material (DPPE-PEG-NH₂; 2739.37), and then subtracting one (the hydrogen lost from the lipid fragment upon conjugation). The mass spectrum of the starting material also revealed two different populations of PEG (the spectrum contains a molecular ion peak at 2739; see the Supporting Information).

This ligand-conjugated PEG-lipid was included at 5 mol % with respect to the known cationic lipid *N,N*-di-*n*-octadecyl-*N,N*-di-hydroxyethylammonium chloride (DODEAC)^[18] and the neutral colipid cholesterol (at 1:1 molar ratio), to form long-circulating and targeting cationic liposomes. We used 5 mol % DSPE-PEG-mal (Scheme 1) in association with a DODEAC/cholesterol (1:1) formulation as our control liposome. This nontargeting lipid was included in the study to show the effect of the estradiol moiety in targeting liposomes to ER-expressing MCF-7 cells.

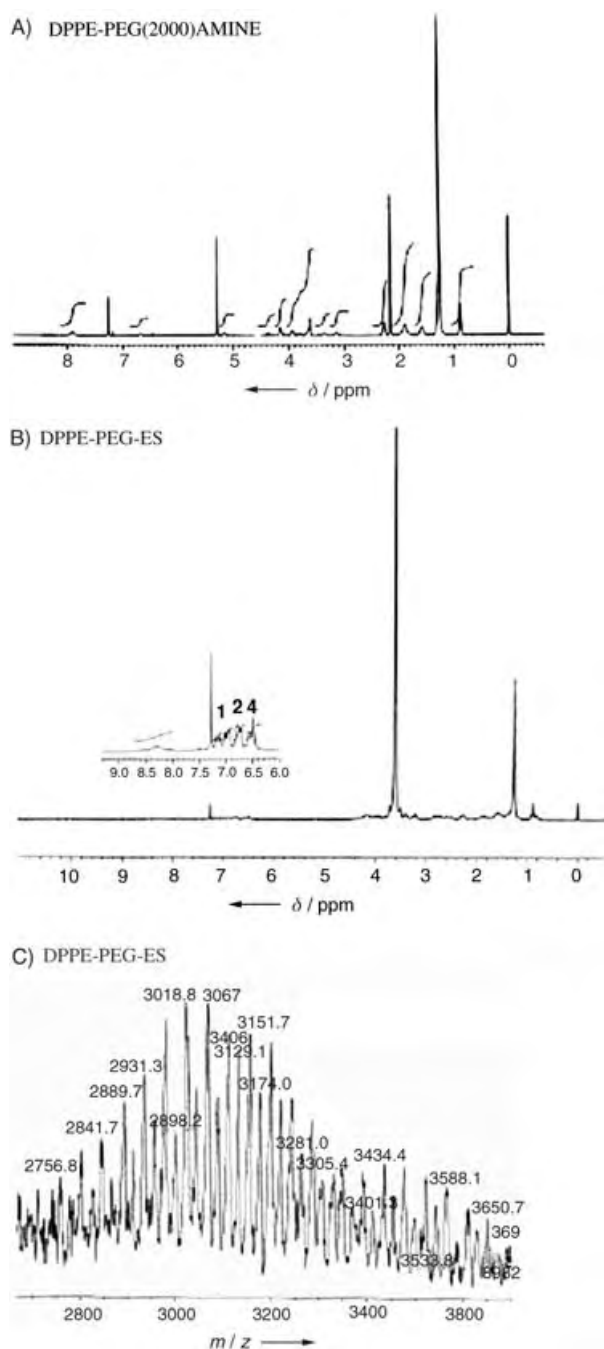


Figure 1. ¹H NMR spectra of A) the starting material, DPPE-PEG-NH₂, and B) the final product, DPPE-PEG-ES. The inset in (B) shows the aromatic proton signals from the lipid-associated estradiol. C) MALDI mass spectrum of DPPE-PEG-ES.

The DNA-binding characteristics of both the targeting and the nontargeting liposomes were confirmed by a simple gel retardation assay, and the DNase I sensitivity of the lipoplex-associated DNA was evaluated by a conventional DNase I protection experiment (see the Supporting Information). The sizes and surface charges of the lipoplexes under transfection conditions were also measured (see the Supporting Information). The targeting and nontargeting lipoplexes showed a comparable stability. Except for lipoplex sizes with

a charge ratio of 8:1, the surface charges and sizes of lipoplexes in the presence of serum were comparable.

We measured the β-gal gene expression in ER-expressing breast adenocarcinoma MCF-7 cells pretreated or untreated with 100 μM tamoxifen, an ER antagonist. Cells were transfected with cationic lipoplex containing either the targeting lipid DPPE-PEG-ES or the nontargeting lipid DSPE-PEG-mal. To mimic in vivo conditions, the transfection was carried out in the presence of a serum-containing medium. Figure 2

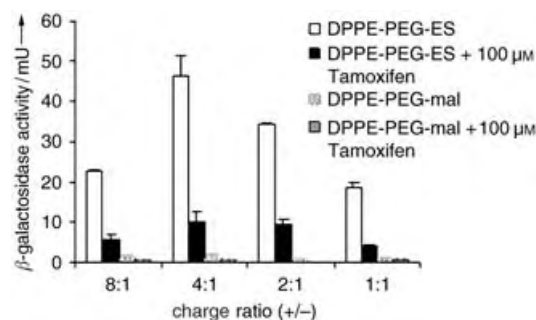


Figure 2. β-Gal gene expression in MCF-7 cells. MCF-7 cells, with or without pretreatment by tamoxifen (100 μM), were transfected with 0.3 μg of pCMV-β-gal DNA complexed in the estradiol-associated targeting cationic liposome (DPPE-PEG-ES) or in the nontargeting control cationic liposome (DSPE-PEG-mal). All cells were treated in the presence of 7% serum. Transgene expression is represented as β-galactosidase activity. The targeting and nontargeting lipoplexes were treated with the cells in cationic lipid/DNA charge ratios (+/-) of 8:1, 4:1, 2:1, and 1:1. The transgene expression obtained for each data point was acquired from triplicate treatments performed in a single day. The difference between the data obtained for DPPE-PEG-ES and DSPE-PEG-mal is statistically significant at all charge ratios (the probability of getting more extreme results than the observed value ($p < 0.0001$), whereas that for DPPE-PEG-ES and DPPE-PEG-ES + 100 μM tamoxifen is statistically significant at all charge ratios ($p < 0.0001$) except for a charge ratio of 4:1, when $p = 0.00029$).

shows that the cells treated with targeting lipoplex express significantly more reporter gene than cells treated with nontargeting lipoplex at all the charge ratios (20- to 100-fold). Moreover, the presence of tamoxifen significantly inhibits targeting-lipoplex-mediated gene expression at all the charge ratios. However, in the case of the nontargeting-lipoplex-mediated transfection, the presence of tamoxifen has almost no effect ($p > 0.1$). This result demonstrates the ability of the DPPE-PEG-ES containing targeting lipoplex to transfect MCF-7 cells in a target-specific manner. The number of ligands is higher at a charge ratio of 8:1, but the highest transfection was obtained at a ratio of 4:1. This is probably because the lipoplex size at a charge ratio of 8:1 is almost three times that at a charge ratio of 4:1 (see the Supporting Information), and also because the larger lipoplex size may not be favorable for efficient cellular uptake, particularly in this system. However, the size and surface charge of lipoplexes with other charge ratios are comparable. Therefore, in comparison to lipoplexes obtained at charge ratios of 2:1 or 1:1, the lipoplex obtained at a charge ratio of 4:1 tends to have a greater targeting ability as a result of the availability of more

ligands on the surface, and hence a higher transfection efficiency.

MDA-MB-231 is an advanced-stage breast cancer cell with drug-resistant properties. This cell does not possess ERs but expresses GPR30 protein^[19] and therefore it is a natural, ER-knockout cell line. This cell line was chosen for transfection with targeting lipoplex, and the extent of transgene expression was compared with that obtained from MCF-7 cells. Figure 3 shows that there was almost negligible β -gal

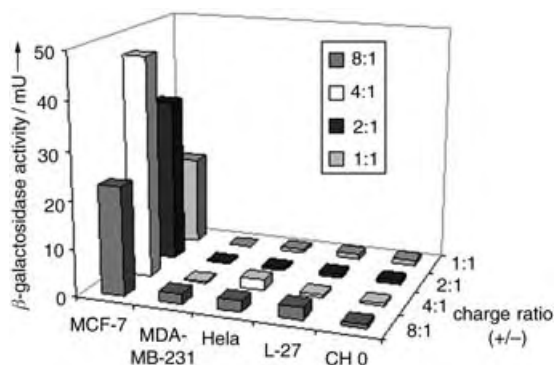


Figure 3. β -Gal transfection in various cell lines. MDA-MB-231 (ER-knockout cell), HeLa, CHO, and L-27 cells were transfected with targeting cationic lipoplex containing DPPE-PEG-ES and the results were compared with those for MCF-7 (ER-positive cell) for lipid/DNA charge ratios (+/–) of 8:1, 4:1, 2:1, and 1:1. The transgene expression obtained for each data point was acquired from triplicate experiments performed in a single day. The transgene expressions obtained in MCF-7 cells were all statistically significant ($p < 0.0001$) when compared to those obtained from other cell lines.

expression in MDA-MB-231 cells compared to that obtained in MCF-7 cells ($p < 0.0001$). This result shows that the targeting lipoplex can deliver and hence express genes only in cells possessing ER. GPR30 has a high affinity for estrogen,^[19] and perhaps upon interacting with targeting lipoplex it can deliver gene to the cytoplasm. However, the lipoplex is probably unable to mediate delivery of genes to the nucleus because of the absence of ER. It is not clear how ER mediates selective delivery of genes to the MCF-7 nucleus in association with or in the absence of a lipid shell. This interesting observation in itself warrants further investigation, especially in the light of the finding that PEG blocks the intracellular trafficking of DNA associated with the liposomal system.^[21]

Next, we evaluated the gene-targeting efficiencies of the DPPE-PEG-ES-associated lipoplex in three more cell lines not known to express ER, namely human cervical carcinoma (HeLa), Chinese hamster ovary (CHO), and murine sarcoma cells (L-27, which is genetically modified to overexpress integrin receptors), by using β -gal plasmid. The transgene expression from these cell lines was compared with that obtained from MCF-7 cells. Figure 3 shows that gene expression in HeLa, CHO, and L-27 cells is statistically insignificant in comparison to that obtained in MCF-7 cells. In general, the CHO and HeLa cell lines are highly transfectable with cationic lipids and the present targeting, stealth,

cationic transfection lipid/DNA complex mediates negligible transfection in these cells, probably because the gene targeting is inefficient in the absence of ER.

Finally, we tested the targeting delivery system and estimated the relative anticancer efficacies of the apoptosis-inducing p53 gene delivered to MCF-7 cells with both the targeting and nontargeting lipoplexes. Figure 4 shows that the

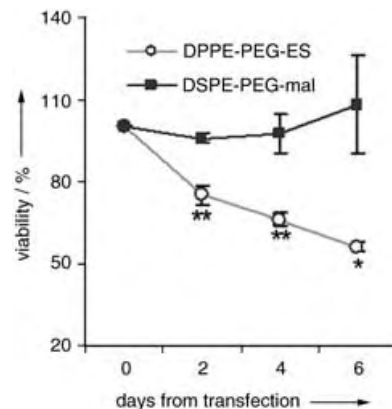


Figure 4. Anticancer-gene-mediated targeted killing of MCF-7 cells. The cells were treated with 0.3 μ g of pCMV-p53 DNA complexed with cationic liposomes containing targeting lipid, DPPE-PEG-ES (○), and nontargeting lipid, DSPE-PEG-mal (■), in a cationic lipid/DNA charge ratio (+/–) of 2:1. The treatment was similar to that described for the β -gal transfection experiments. The cells underwent MTT assay on days 2, 4, and 6 after transfection. The y axis shows the percentage viability, and each data point was acquired from triplicate treatments; $p < 0.005$ (**), $p = 0.007$ (*).

targeting lipoplex can indeed induce cell death, possibly through apoptosis, in a target-specific manner. From the second day onwards, the cell viability of the group treated with DPPE-PEG-ES-associated targeting lipoplex showed significant toxicity ($p < 0.005$ and $p = 0.007$), which persisted during the subsequent six days. Furthermore, we examined the stability of the targeting lipoplex at various serum concentrations. No perceptible change in the targeting efficiency, even at the biologically relevant *in vivo* serum concentration of 53%, was observed (see the Supporting Information). This result proves that the targeting gene delivery system will remain undeterred in its targeting efficiency *in vivo*.

In summary, our findings demonstrate a highly efficient, novel route for targeting anticancer genes at breast cancer cells through the use of 17 β -estradiol-associated stealth liposomes. The chemistry involved is simple and inexpensive. Evaluation of the *in vivo* potential of the technique for eradicating breast cancer is currently in progress.

Received: May 24, 2005

Revised: July 30, 2005

Published online: September 27, 2005

Keywords: antitumor agents · gene expression · hormones · liposomes · receptors

-
- [1] P. Thomas, Y. Pang, E. J. Filardo, J. Dong, *Endocrinology* **2005**, *146*, 624–632.
- [2] M. Razandi, A. Pedram, G. L. Greene, E. R. Levin, *Mol. Endocrinol.* **1999**, *13*, 307–319.
- [3] Z. Chen, I. S. Yuhanna, Z. Galcheva-Gargova, R. H. Karas, M. E. Mendelsohn, P. W. Shaul, *J. Clin. Invest.* **1999**, *103*, 401–406.
- [4] R. X. Song, R. A. McPherson, L. Adam, Y. Bao, M. Shupnik, R. Kumar, R. J. Santen, *Mol. Endocrinol.* **2002**, *16*, 116–127.
- [5] P. Monje, R. Boland, *Mol. Cell. Endocrinol.* **1999**, *147*, 75–84.
- [6] C. K. Osborne, *Breast Cancer Res. Treat.* **1998**, *51*, 227–238.
- [7] L. W. Wattenberg, *Cancer Res.* **1985**, *45*, 1–8.
- [8] A. Fugh-Berman, S. Epstein, *Lancet* **1992**, *340*, 1143–1145.
- [9] J. F. Robertson, *Cancer Treat. Rev.* **2004**, *30*, 695–706.
- [10] K. L. Jones, A. U. Buzdar, *Endocr. Relat. Cancer* **2004**, *11*, 391–406.
- [11] I. C. Henderson, *Semin. Oncol.* **2004**, *31*, 31–34.
- [12] A. Huang, L. Huang, S. J. Kennel, *J. Biol. Chem.* **1980**, 255, 8015–8018.
- [13] A. Huang, S. J. Kennel, L. Huang, *J. Biol. Chem.* **1983**, 258, 14034–14040.
- [14] K. Maruyama, S. J. Kennel, L. Huang, *Proc. Natl. Acad. Sci. USA* **1990**, *87*, 5744–5748.
- [15] A. L. Klibanov, K. Maruyama, V. P. Torchilin, L. Huang, *FEBS Lett.* **1990**, *268*, 235–237.
- [16] S. Zalipsky, E. Brandeis, M. S. Newman, M. C. Woodle, *FEBS Lett.* **1994**, *353*, 71–74.
- [17] N. Nasongkla, X. Shuai, H. Ai, B. D. Weinberg, J. Pink, D. A. Boothman, J. Gao, *Angew. Chem.* **2004**, *116*, 6483–6487; *Angew. Chem. Int. Ed.* **2004**, *43*, 6323–6327.
- [18] A. Mukherjee, T. K. Prasad, N. M. Rao, R. Banerjee, *J. Biol. Chem.* **2005**, *280*, 15619–15627.
- [19] C. M. Revankar, D. F. Cimino, L. A. Sklar, J. B. Arterburn, E. R. Prossnitz, *Science* **2005**, *307*, 1625–1630.
- [20] R. P. Boivin, V. Luu-The, R. Lachance, F. Labrie, D. Poirier, *J. Med. Chem.* **2000**, *43*, 4465–4478, and references cited therein.
- [21] M. Keller, R. P. Harbottle, E. Perouzel, M. Colin, I. Shah, A. Rahim, L. Vaysse, A. Bergau, S. Moritz, C. Brahimi-Horn, C. Coutelle, A. D. Miller, *ChemBioChem* **2003**, *4*, 286–298.
-

DOI: 10.1002/anie.200501556

General Synthetic Route toward Functional Hollow Spheres with Double-Shelled Structures***Mu Yang, Jin Ma, Chengliang Zhang,
Zhenzhong Yang,* and Yunfeng Lu**

Hollow spheres and capsules have stimulated great interest because of their potential applications in controlled delivery systems, artificial cells, lightweight fillers, catalysis, and as vessels for confined reactions.^[1] Hollow spheres, in particular those with complex core-shell structures, have increasingly attracted interest as a result of their superior properties.^[2] For example, a unique plasmon hybridization has been reported on hollow spheres with two concentric metallic nanoshells, thus providing a novel method of tuning resonance frequency by nanostructure engineering.^[2a] Polymeric hollow spheres with a movable gold nanoparticle core have also been obtained, which allow the optical sensing of chemicals diffused into the cavity.^[2b] In addition, polyelectrolyte capsules with a shell-in-shell structure exhibit an enhanced mechanical strength and preserved permeability.^[2d] To date, the synthesis of such complex structures is essentially based on a time-consuming layer-by-layer templating technique, in which layers of desired materials (for example, metals, polymers, and polyelectrolytes) and of sacrificial materials (such as silica) are alternately grown on preformed spheres (for example, silica and polystyrene particles).^[2,3]

Herein, we report a one-step approach to the synthesis of hollow spheres with a double-shelled complex structure by using commercial polymer hollow spheres as templates. As shown in Figure 1, a polystyrene hollow sphere containing a thin hydrophilic inner layer and transverse channels of poly(methyl methacrylate)-poly(methacrylic acid) (PMMA-PMA)^[2c] is treated with sulfuric acid, and sulfonation takes place in three locations: the exterior shell surface, the interior shell surface, and the transverse channels. This procedure

[*] M. Yang, J. Ma, C. Zhang, Prof. Z. Yang
State Key Laboratory of Polymer Physics and Chemistry
Institute of Chemistry, Chinese Academy of Sciences
Beijing 100080 (China)
Fax: (+86) 10-6255-9373
E-mail: yangzz@iccas.ac.cn
Prof. Y. Lu
Department of Chemical and Biomolecular Engineering
Tulane University
New Orleans, LA 70118 (USA)
Fax: (+1) 504-865-6744
E-mail: ylu@tulane.edu

[**] We thank the NSF of China (50573083, 50325313, 20128004, and 90206025), the Chinese Academy of Sciences, and the China Ministry of Science and Technology (KJCX2-SW-H07, 2004-01-09, and 2003CB615600) for financial support.



Supporting information for this article is available on the WWW under <http://www.angewandte.org> or from the author.

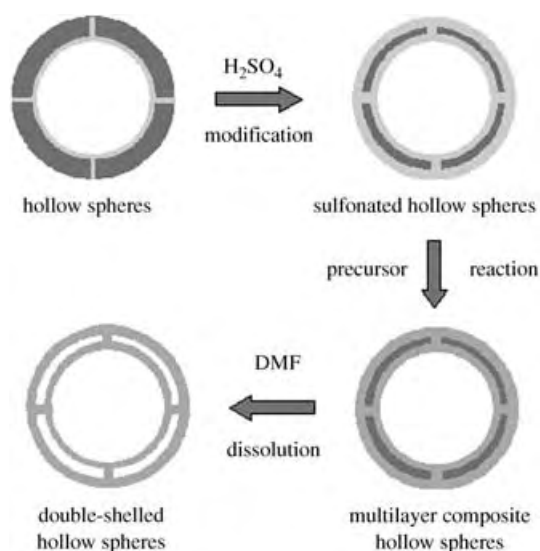


Figure 1. Schematic illustration of the formation of double-shelled hollow spheres.

creates a hollow sphere that contains a hydrophilic inner layer, outer layer, and channels of sulfonated polystyrene gel. Control of the shell thickness of the original polystyrene sphere and the degree of sulfonation allows precise control over the thickness of the hydrophilic sulfonated layers and of the unsulfonated polystyrene middle layer. The sulfonation process produces hydrophilic shells with sulfonic acid (SO_3^-H^+) groups that are capable of adsorption or of forming complexes with a large variety of functional components, such as metal ions, metal oxide precursors (for example, titania alkoxides), and basic organic precursors (for example, aniline).^[4] Preferential growth of desired materials (such as TiO_2)^[4c] within the hydrophilic sulfonated regions followed by removal of the middle polystyrene layer creates various functional composites with a double-shelled structure. This direct approach allows the fabrication of double-shelled functional-composite spheres with controllable shell thickness and shell separation distance.

Figure 2 shows scanning electron microscopy (SEM) and transmission electron microscopy (TEM) images of unsulfonated spheres, sulfonated spheres, and the resultant double-shelled titania spheres. The unsulfonated hollow spheres (Figure 2a) have an average diameter of 500 nm and a smooth, uniform shell of thickness 80 nm. Sulfonation at 40 °C for 0.5, 2, and 4 h results in sulfonated hollow-sphere templates denoted as S1, S2, and S3, respectively. Compared to the unsulfonated spheres, the S1 spheres (Figure 2b) show a significantly thickened shell (from 80 to 125 nm), a decreased cavity diameter (from 340 to 260 nm), and a slightly deformed spherical shape, which indicate the effective sulfonation and gel formation on both exterior and interior shell surfaces. The appearance of the sulfonic and sulfonyl peaks in the FTIR spectrum further confirms the sulfonation (see Supporting Information). Elemental analysis showed that the S1 spheres contain 2.5 wt % of sulfur atoms. An increase in the sulfonation time to 2 h (sample S2) increased the amount of sulfur to 6.1 wt % and resulted in a thinner

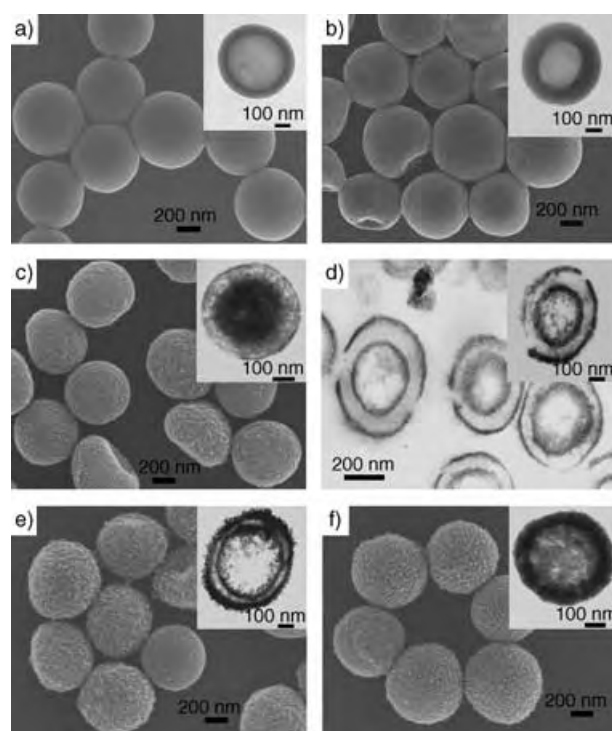


Figure 2. Morphologies of representative templates and titania hollow spheres. a) SEM and TEM (inset) images of unsulfonated polymer hollow-sphere templates. b) SEM and TEM (inset) images of the sulfonated S1 templates. c) SEM image of titania composite hollow spheres templated by S1; the inset shows a TEM image of the corresponding double-shelled titania hollow spheres after treatment with DMF. d) Cross-sectional TEM images of ultramicrotomed titania hollow spheres before and after (inset) treatment with DMF. e) SEM image of titania composite hollow spheres templated by S2; the inset shows a cross-sectional TEM image of the composite hollow spheres after treatment with DMF. f) SEM image of titania composite hollow spheres templated by S3; the inset shows a TEM image of the corresponding titania hollow spheres after treatment with DMF.

unsulfonated polystyrene middle layer, which indicates a higher degree of sulfonation. An excess degree of sulfonation may completely consume the entire polystyrene middle layer, and cause collapse of the structure upon drying. Indeed, the S3 spheres were easily deformed and lost their spherical contour after freeze-drying (see Supporting Information).

We have previously found that tetrabutyl titanate (TBT) can favorably undergo a sol–gel process within sulfonated polystyrene gel to form titania.^[4c] The same reactions can be applied to the sulfonated hollow spheres. Figure 2c and d shows the resultant titania spheres produced with S1 as the template. The spheres are approximately 500 nm in diameter (Figure 2c) with a similar morphology to that of the S1 template (Figure 2b). The removal of the polystyrene templates, which was confirmed by the weakening of the characteristic peaks of polystyrene in the FTIR spectrum, creates the double-shelled, concentric titania hollow spheres shown in the TEM image (Figure 2c, inset). The thickness of the shells is around 25 nm and the distance between the shells is around 75 nm, although the contour of the inner shell is somewhat unclearly defined (Figure 2d). The use of sulfonated templates with a higher degree of sulfonation results in

hollow titania spheres with an increased diameter and decreased shell-to-shell distance. For example, the S2-templated titania hollow spheres show an average diameter of 580 nm, a reduced shell-to-shell distance of approximately 30 nm, and a thicker shell of 50 nm (Figure 2 e). The use of the S3 template results in 630-nm single-shelled titania hollow spheres (Figure 2 f). These results demonstrate the efficiency of controlling the morphology of the double-shelled structure by simply tuning the degree of sulfonation. As a control experiment, titania spheres were prepared by using the unsulfonated hollow spheres as templates. Titania was formed only within the hydrophilic inner layer^[2e] and not on the exterior surface, which indicates the key role of sulfonation in the formation of such double-shelled structures.

The synthesized double-shelled titania hollow spheres are strong enough to survive calcination at 450 °C in air, which removes the polymer and generates titania crystalline phases. In contrast to the dissolution of polystyrene by *N,N*-dimethylformamide (DMF), calcination leads to a significant volume contraction. For example, the diameter of the S1-templated titania spheres contracts from 500 to 400 nm (see Figure 3 a and Supporting Information). The inner shell, in

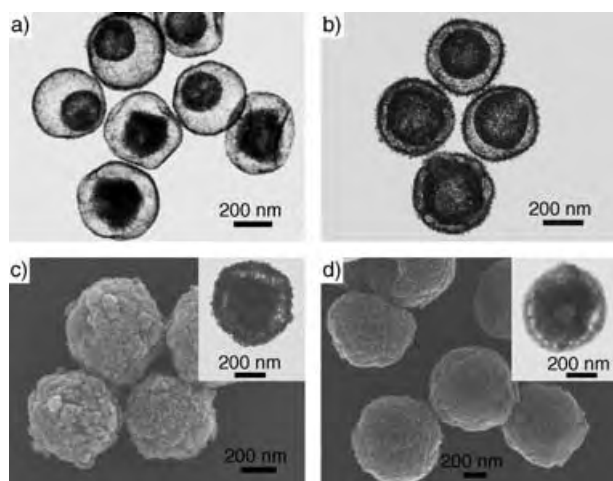


Figure 3. Morphologies of representative double-shelled crystalline metal oxides and conducting polymer hollow spheres. a, b) TEM images of titania hollow spheres templated by S1 and S2, respectively, followed by template removal by calcination at 450 °C in air to form anatase. c) SEM image of double-shelled Fe_3O_4 hollow spheres templated by S2. d) SEM image of double-shelled polyaniline hollow spheres templated by S2. The insets in (c) and (d) show TEM images of the spheres after treatment with DMF.

particular, contracts remarkably and becomes a movable inner hollow sphere. High-resolution TEM analysis indicates that the nanoparticles in both the shell layers have a crystalline order and form almost fully crystallized inorganic frameworks (see Supporting Information). Increasing the amount of titania in the composite helps to stabilize the double-shelled structure. For example, thermogravimetric analysis (TGA) shows that titania/S1 and titania/S2 composite spheres contain 24.3 and 37.1 wt % titania, respectively. As a result, the S2-templated titania spheres maintain the concentric double-shelled structure after calcination (Figure 3 b and

Supporting Information). X-ray diffraction (XRD) studies show that the calcined titania is composed of anatase (Figure 4 a). The average particle size calculated using Scherrer's formula is about 11.4 nm, consistent with the

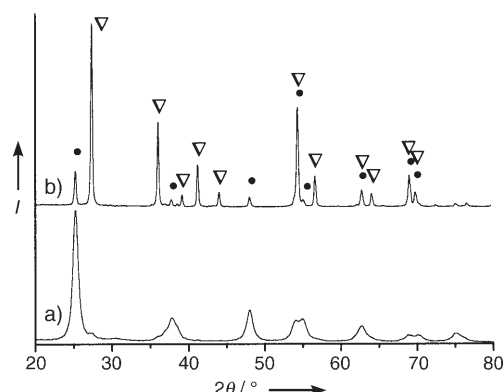


Figure 4. X-ray powder diffraction spectra of TiO_2 hollow spheres calcined at a) 450 and b) 600 °C for 2 h in air (rutile ∇ ; anatase \bullet).

TEM result. A higher calcination temperature (for example, 600 °C) results in a dominant rutile phase with a small amount of the anatase phase (see Figure 4 b and Supporting Information; the calculated average particle size is 32.0 nm) and also deterioration of the spherical structure (see Supporting Information).

The unique template structure combined with the complexation capability of the sulfonic acid groups within the sulfonated layers allows this synthesis approach to be generalized for the production of a large variety of double-shelled composite spheres. For example, double-shelled composite hollow spheres containing crystalline Fe_3O_4 nanoparticles can be fabricated, based on the complex of iron ions and sulfonic acid groups. Figure 3 c shows SEM and TEM (inset) images of the Fe_3O_4 nanoparticle composite spheres prepared with S2 as the template. The composite spheres contain 57 wt % of Fe_3O_4 nanoparticles of diameter 10–15 nm, as deduced from TGA and TEM studies. The positions and relative intensities of all the XRD diffraction peaks (see Supporting Information) are well-matched with those of magnetite (JCPDS card 19-0629). Thus, it can be concluded that magnetite dominates the nanoparticles. The crystallographic form was further verified by its color change from the dark brown of the as-prepared sample to red, which corresponds to maghemite, upon oxidation at 100 °C for 4 h. The average particle size calculated from the XRD data is 11.0 nm. Such crystalline nanoparticles show superparamagnetic behavior at room temperature (see Supporting Information). Similarly, by utilizing acid–base interactions, aniline monomer can favorably be adsorbed within the sulfonated layer. Subsequent polymerization leads to the formation of conductive double-shelled polyaniline composite spheres. Figure 3 d shows the SEM and TEM (inset) images of the polyaniline composite spheres prepared with S2 as the template; the spheres have a smooth surface with well-retained spherical contour. Compared with the easily deformed single-shelled polyaniline hollow spheres,^[4d] the

double-shelled structure effectively enhances the mechanical stability of the hollow spheres, which is similar to the previous reports of double-shelled polyelectrolyte capsules.^[2c,d] As revealed by the FTIR spectrum (see Supporting Information), the resultant polyaniline (36.8 wt % of the composite, estimated from elemental analysis) was doped in situ with the sulfonated polystyrene and formed the emeraldine salt,^[5] which resulted in an appreciable conductivity of $6 \times 10^{-3} \text{ Scm}^{-1}$. Studies aimed at a detailed understanding and possible applications of such functional spheres are in progress.

In conclusion, we have demonstrated a one-step method for the synthesis of double-shelled composite hollow spheres by using sulfonated hollow spheres as templates. Controlled sulfonation allows the synthesis of templates with tunable thickness of the sulfonated outer layer, sulfonated inner layer, and unsulfonated middle layer. The sulfonation process gives layers with sulfonic acid groups that allow the formation of a wide variety of functional composites. This research provides a novel and efficient approach to the synthesis of various double-shelled functional spheres for many important applications.

Experimental Section

Sulfonated hollow-sphere templates: Freeze-dried polymer hollow spheres^[2e] (Rhom & Haas Company) were immersed in concentrated sulfuric acid. Sulfonation at 40 °C for 0.5, 2, and 4 h resulted in the sulfonated hollow-sphere templates denoted as S1, S2, and S3, respectively. The sulfonated spheres were thoroughly rinsed with water and ethanol.

Titania hollow spheres: Freeze-dried sulfonated templates (0.1 g) were immersed in tetrabutyl titanate (TBT)/ethanol (1:1 v/v, 5 mL) for 24 h. After centrifugation and rinsing with ethanol, the resultant materials were transferred to a closed vessel containing ethanol (5 mL) at ambient temperature. Water (5 mL) was then added to the dispersion with stirring, and the sol–gel process was allowed to proceed for 4 h. Double-shelled titania hollow spheres were obtained after centrifugation, rinsing with ethanol, and template removal by dissolution in DMF or calcination at 450 °C for 2 h in air.

Magnetite hollow spheres: Freeze-dried S2 (0.1 g) was immersed in ammonium hydroxide (10 M, 5 mL) for 12 h before transfer to a solution containing water (10 mL). Aqueous ferrous chloride/ferric chloride (1:2 M, 0.6 mL) was then added dropwise with stirring under a nitrogen atmosphere.^[6] Magnetite hollow spheres were obtained after the polymer was dissolved with DMF and collected by a magnet (see Supporting Information). The collected spheres could be readily redispersed by ultrasonication.

Polyaniline hollow spheres: Freeze-dried S2 (0.1 g) was dispersed in water (10 mL) containing monomeric aniline (0.1 g) with stirring. After 2 h, aqueous ferric chloride (1 M, 0.5 mL) was added to initiate oxidative polymerization at room temperature for 24 h. Polyaniline hollow spheres were obtained after centrifugation and treatment with DMF to dissolve the polystyrene.

Characterization: The structure and morphology of the spheres were characterized by TEM (JEOL 100CX instrument operated at 100 kV) and SEM (Hitachi S-4300 instrument operated at an accelerating voltage of 15 kV). TEM samples were prepared by dispersing the spheres from dilute ethanol dispersions onto carbon-coated copper grids or by the ultramicrotomy technique. The ultramicrotomed samples were prepared by embedding the spheres in resin and ultramicrotomy to form 30–50-nm-thick slices with a Leica ultracut UCT ultramicrotome at room temperature. The SEM

samples were prepared by vacuum sputtering of Pt onto the dried samples at ambient temperature.

FTIR spectroscopy was performed using a Bruker Equinox 55 spectrometer with the samples pressed into KBr pellets. X-ray powder diffractometry (Rigaku D/max-2500) was used to characterize the crystalline phases of the materials. A Perkin-Elmer TGA 7 apparatus was used to determine the inorganic content of the composite spheres. Elemental analysis was carried out with a Flash EA-1112 apparatus. A vibrating-sample magnetometer (VSM JDM-13) was used to characterize the magnetic properties of the magnetite composite spheres. Conductivity measurements were performed on pieces of compressed dry powder by using a standard four-probe method at room temperature.^[4d]

Received: May 7, 2005

Revised: July 1, 2005

Published online: September 27, 2005

Keywords: nanostructures · polymers · sol–gel processes · template synthesis · titanium

- [1] a) F. Caruso, *Chem. Eur. J.* **2000**, *6*, 413; b) F. Caruso, *Adv. Mater.* **2001**, *13*, 11; c) F. Caruso, R. A. Caruso, H. Möhwald, *Science* **1998**, *282*, 1111; d) D. L. Wilcox, M. Berg, T. Bernat, D. Kelleman, J. K. Cochran, *Hollow and Solid Spheres and Microspheres: Science and Technology Associated with Their Fabrication and Application*, Vol. 372, Materials Research Society Proceedings, Pittsburgh, **1994**.
- [2] a) E. Pordan, C. Radloff, N. J. Halas, P. Nordlander, *Science* **2003**, *302*, 419; b) K. Kamata, Y. Lu, Y. N. Xia, *J. Am. Chem. Soc.* **2003**, *125*, 2384; c) Z. F. Dai, L. Dähne, H. Möhwald, B. Tiersch, *Angew. Chem.* **2002**, *114*, 4191; *Angew. Chem. Int. Ed.* **2002**, *41*, 4019; d) Z. F. Dai, H. Möhwald, B. Tiersch, L. Dähne, *Langmuir* **2002**, *18*, 9533; e) M. Yang, J. Ma, Z. W. Niu, H. F. Xu, Z. K. Meng, Y. F. Lu, Z. B. Hu, Z. Z. Yang, *Adv. Funct. Mater.* **2005**, *15*, 1523.
- [3] a) K. Zhang, X. H. Zhang, H. T. Chen, L. L. Zheng, J. H. Zhang, B. Yang, *Langmuir* **2004**, *20*, 11312; b) M. Kim, K. Sohn, H. B. Na, T. Hyeon, *Nano Lett.* **2002**, *2*, 1383; c) J. Y. Kim, S. B. Yoon, J.-S. Yu, *Chem. Commun.* **2003**, 790; d) A. G. Dong, N. Ren, W. L. Yang, Y. J. Wang, Y. H. Zhang, D. J. Wang, J. H. Hu, Z. Gao, Y. Tang, *Adv. Funct. Mater.* **2003**, *13*, 943.
- [4] a) R. F. Ziolo, E. P. Giannelis, B. A. Weinstein, M. P. O'Horo, B. N. Ganguly, V. Mehrotra, M. W. Russell, D. R. Huffman, *Science* **1992**, *257*, 219; b) M. Breulmann, S. A. Davis, S. Mann, H. P. Hentze, M. Antonietti, *Adv. Mater.* **2000**, *12*, 502; c) Z. Z. Yang, Z. W. Niu, Y. F. Lu, Z. B. Hu, C. C. Han, *Angew. Chem.* **2003**, *115*, 1987; *Angew. Chem. Int. Ed.* **2003**, *42*, 1943; d) Z. W. Niu, Z. Z. Yang, Z. B. Hu, Y. F. Lu, C. C. Han, *Adv. Funct. Mater.* **2003**, *13*, 949.
- [5] a) Z. X. Wei, M. X. Wan, *Adv. Mater.* **2002**, *14*, 1314; b) A. L. Briseno, S. Han, I. E. Rauda, F. M. Zhou, *Langmuir* **2004**, *20*, 219; c) S. A. Chen, H. T. Lee, *Macromolecules* **1995**, *28*, 2858.
- [6] a) Y. S. Kang, S. Risbud, J. F. Rabolt, P. Stroeve, *Chem. Mater.* **1996**, *8*, 2209; b) L. A. Harris, J. D. Goff, A. Y. Carmichael, J. S. Riffle, J. J. Harburn, J. G. St. Pierre, M. Saunders, *Chem. Mater.* **2003**, *15*, 1367.

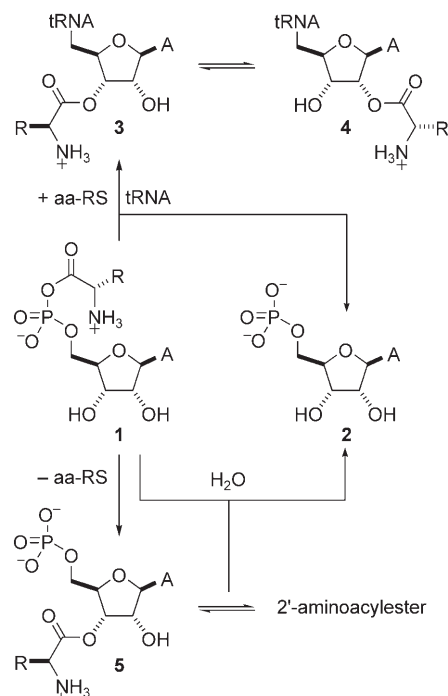
Expeditious, Potentially Primordial, Aminoacylation of Nucleotides**

Jean-Philippe Biron, Alastair L. Parkes, Robert Pascal,* and John D. Sutherland*

In contemporary biochemistry, enzymatically synthesized, activated aminoacyl-tRNA esters (aa-tRNA) serve as substrates for coded peptide synthesis by ribosomes,^[1] and a major goal is to understand the evolutionary path through which this process arose. As a first step towards this goal, we have been looking to find a prebiotically plausible means for the aminoacylation of ribonucleotide 2'-/3'-hydroxy groups. A number of simple, potentially prebiotic, activated amino acid derivatives have been reported, most notably *N*-carboxyanhydrides (NCAs).^[2] The case for NCAs in prebiotic evolution has recently been strengthened by the finding that they can be produced from amino acids through the action of the simple volcanic gas carbonyl sulfide.^[3]

We therefore decided to investigate the aminoacylation of nucleotides by NCAs. Initially we were concerned that the nucleobase amino groups of adenine and cytosine would prove more nucleophilic than the 2'-/3'-hydroxy groups; however, recent findings show that NCAs react with inorganic phosphate to give aminoacyl phosphates.^[4] This suggests that it might be possible to generate nucleotide aminoacyl esters by initial aminoacylation of the phosphate monoester, followed by intramolecular aminoacyl transfer. Nucleotide aminoacylation by way of intermediate carboxylic phosphoric anhydrides would be analogous to the chemistry of aminoacyl-tRNA synthetase (aa-RS) enzymes. These enzymes

generate 5'-aminoacyladenylates (5'-aa-AMP) **1** (A = adenine) through an initial nucleophilic attack of an amino acid carboxylate on ATP. The aa-RS then catalyzes the intermolecular aminoacyl transfer from **1** to the 2'/3'-terminus of a cognate tRNA to give adenosine-5'-monophosphate (5'-AMP) (**2**) and an equilibrating mixture of 3'- and 2'-aa-tRNAs **3** and **4** (Scheme 1).



Scheme 1. The biochemistry and chemistry of 5'-aa-AMP **1**: biochemically (upper), **1** is used by aa-RS enzymes for the aminoacylation of cognate tRNA. In the absence of enzymes (lower), **1** can undergo intramolecular aminoacyl transfer and hydrolysis reactions.

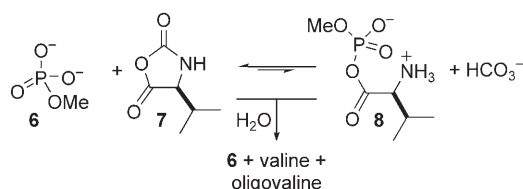
[*] J.-P. Biron, Dr. R. Pascal
Dynamique des Systèmes Biomoléculaires Complexes UMR 5073-CC 017
Département de Chimie, Université Montpellier 2
Place Eugène Bataillon, 34095 Montpellier (France)
Fax: (+33) 46-763-1046
E-mail: rpascal@univ-montp2.fr
Dr. A. L. Parkes, Prof. Dr. J. D. Sutherland
School of Chemistry, The University of Manchester
Oxford Road, Manchester M13 9PL (UK)
Fax: (+44) 161-275-4939
E-mail: john.sutherland@manchester.ac.uk

[**] This work was carried out within working group D27/001/02 of the EU COST action "Prebiotic Chemistry and Early Evolution", and was funded by COST and the Engineering and Physical Sciences Research Council. We thank Dr Jo Kirkpatrick (Oxford University) for the LC/ESI MS analysis and Jean-Pascal Gimeno for experimental assistance in the chemistry of the mixed anhydride **8**. We gratefully acknowledge Peter Strazewski (Université Claude Bernard, Lyon 1) for his helpful comments on the manuscript and Auguste Commeyras (Université Montpellier 2) for facilitating the initiation of this collaborative project.

Supporting information for this article is available on the WWW under <http://www.angewandte.org> or from the author.

When separated from the protective environment of an aa-RS, 5'-aa-AMPs are highly unstable and undergo hydrolysis and isomerization in aqueous solution.^[5,6] The isomerization involves a slow initial intramolecular aminoacyl transfer from the 5'-phosphate to the 3'-hydroxy group via an eight-membered transition state to give the 3'-aminoacyl ester **5**, followed by rapid equilibration of the latter with a 2'-aminoacyl ester. If it were possible to generate 5'-aa-AMP **1** from 5'-AMP **2** by reaction with an NCA, then this intramolecular transfer would hopefully result in the sought-after formation of aminoacyl esters.

We first investigated whether the aminoacylation of a simple model phosphate monoester with an NCA was possible. We chose methyl phosphate **6** as the model phosphate monoester and the valyl derivative **7** to allow comparison with the previous work on inorganic phosphate^[4] and because **7** can be easily prepared and stored (Scheme 2).^[7] In a general sense, the reaction of a phosphate monoester with any electrophile is faster at pH values above 7 when the phosphate is in its dianionic state, (pK_a for the monoanionic state $\approx 6-7$ (Supporting Information)); however, NCA hydrolysis/polymerization is also favored at high pH values.

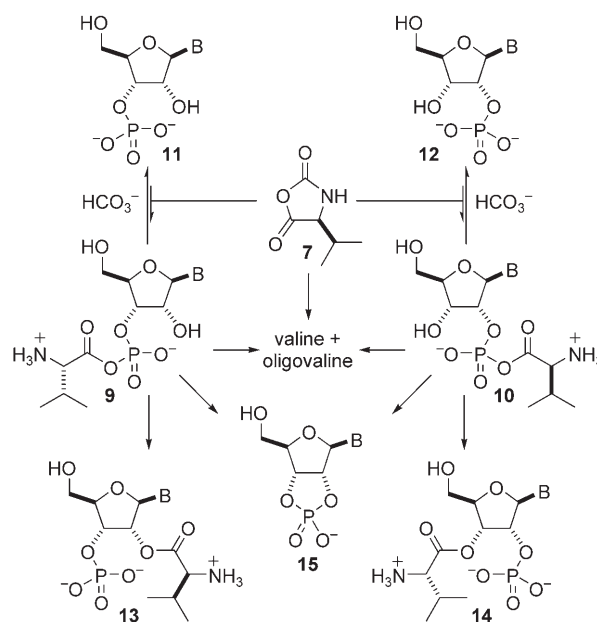


Scheme 2. Aminoacylation of model phosphate monoester by Val-NCA **7**.

To slow such degradative reactions while still allowing reaction of the NCA with the phosphate group of **6**, we conducted our experiments under very slightly acidic conditions. In this case, although **6** was predominantly mono-anionic, some of the reactive dianionic form still existed. Using ^1H NMR spectroscopy for analysis, we observed a low-level conversion of **6** and **7** into L-valyl methyl phosphate **8** (not isolated, according to ^1H NMR integration $\approx 23\%$ based on **7**, see Supporting Information). The conversion was only transient, however, and **8** was gradually converted back into the starting methyl phosphate **6** along with valine and oligovaline.

These observations imply that the reaction of **6** and **7** to give **8** is an equilibrium that is rapidly established and lies in favor of **6** and **7**. The equilibrium is eventually dissipated through the hydrolysis of **7** and **8** to valine, and the subsequent reaction of the valine with further **7** and **8** giving oligovaline. The existence of the proposed equilibrium was proven when we found that **8**, as prepared by conventional synthesis, was almost completely converted into **6** and **7** in the presence of bicarbonate. Once again, hydrolysis/polymerization of the activated valine derivatives subsequently yielded the free amino acid and oligomers.

We next turned our attention to the reaction of nucleotides with Val-NCA **7**. 5'-AMP **2** showed similar behavior to methyl phosphate **6**, and we observed an equilibrium production of 5'-Val-AMP **1** ($R = i\text{Pr}$). However, the equilibrium was dissipated by NCA hydrolysis/polymerisation before the rearrangement of **1** into **5** occurred (see Supporting Information).^[5,8] We next studied the reaction of other regioisomeric nucleotides with Val-NCA **7**. We recognized that if a nucleoside 3'/2'-valyl phosphate **9/10** could be transiently formed from the corresponding 3'/2'-nucleotide **11/12** and **7**, then intramolecular aminoacyl transfer to the 2'/3'-OH group, via a seven-membered transition state^[9] might now be faster than hydrolysis/polymerization of the NCA or the intermediate mixed anhydrides (Scheme 3). We reasoned, therefore, that even an unfavorable equilibrium situation might lead to subsequent intramolecular aminoacyl transfer, and that this transfer should then displace the equilibrium according to Le Chatelier's principle. There was a major concern with the 3'/2'-nucleotides, however, as we foresaw cyclization of the intermediate 3'/2'-aminoacyl phosphates **9/10** to give the 2',3'-cyclic phosphate **15** as a likely competing reaction (Scheme 3). Indeed, 2'/3'-phosphates can be cyclized with great ease, to 2',3'-cyclic phosphates via five-membered transition states, by almost any form of phosphate activation.^[10]



Scheme 3. Aminoacylation/cyclization of 3'- and 2'-nucleotides by Val-NCA **7**.

Undeterred by this concern, we initially studied the reaction of cytidine-3'-monophosphate (3'-CMP) **11** (base (B) = cytosine (C)) with Val-NCA **7**, again under very slightly acidic conditions. After 55 min, no new signals consistent with **9** (B = C) were observed in the ^1H NMR spectrum. However, new signals were observed which were tentatively assigned to the aminoacyl-transfer product **13** (B = C) (Figure 1 a)). In

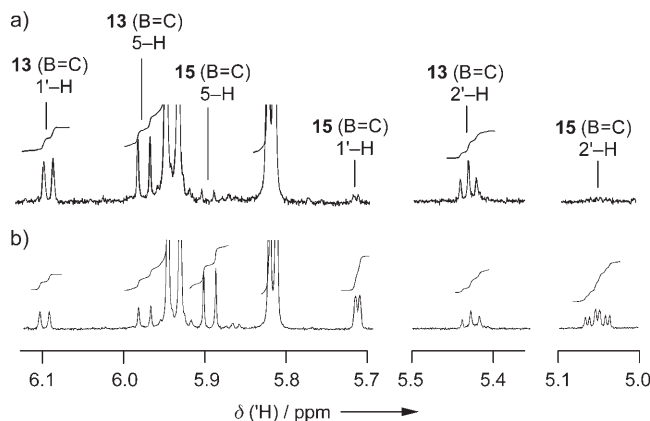


Figure 1. ^1H NMR spectra (500 MHz, D_2O) of the products of the reaction of 3'-CMP **11** (B = C) with Val-NCA **7**. a) Spectrum acquired after 1 h. b) Spectrum acquired after spiking the sample with authentic **15** (B = C) (0.5 mg).

particular, a diagnostic triplet between $\delta = 5.4$ and 5.5 ppm was shown by COSY analysis to correspond to 2'-H of the new species, and the downfield shift of this signal was consistent with a 2'-ester. Although **13** was not isolated,^[11] integration of the ^1H NMR spectrum of the reaction mixture suggested that it had been formed in $\approx 9\%$ overall yield (Table 1).

Table 1: Yields of the products observed in the reactions of 3'/2'-nucleotides **11/12** with Val-NCA **7**.

Nucleotide	t [min]	Starting material [%]	Valyl ester (13 or 14) [%]	Divalyl ester [%]	15 [%]
11 (B = C)	55	90.6	(13) 8.7	trace	0.7
11 (B = A)	30	82.2	(13) 13.8	3.9	trace
	90	79.5	(13) 13.4	5.6	1.5
12 (B = C)	45	94.9	(14) 3.0	0	2.1
12 (B = A)	90	99.0	(14) 0.5	0	0.5

As our experiment was initiated at a pD value close to the pK_a of the monoanionic form of **11**, the yield of **13**, based upon the reactive dianionic form of **11**, is probably considerably higher. This suggests that isomerization of the intermediate **9** into **13** is highly efficient relative to the fast backwards reaction of **9** with CO₂. After further time had passed (> 1 h), ¹H NMR spectroscopic analysis suggested that **13** underwent very slow reversion to **11**, presumably by a combination of hydrolysis and nucleophilic attack by the amino group of valine and valyl derivatives, including **13**. The minor signals in the ¹H NMR spectrum (accompanying the signals of **13**) in the reaction of **11** and **7** were shown, by spiking the reaction with an authentic sample, to be due to the 2',3'-cyclic phosphate **15** (B = C) (Figure 1 b)). However, this anticipated by-product was formed in much lower amounts (**13/15** > 10:1), and we have not been able to prove the structure of the second minor product definitively, but MS and HMBC data strongly suggest that it is the 2'-divalyl analogue of **13**.

We next investigated the effect of the nucleobase on this remarkable conversion and examined the reaction of 3'-AMP **11** (B = A) with Val-NCA **7**. Again, we could not detect the intermediate aminoacyl phosphate **9** (B = A) but observed the aminoacyl-transfer product **13** (B = A) in a maximal overall yield of ≈ 14% after 30 min (Table 1). In this experiment the putative 2'-divalyl analogue of **13** was also formed in a greater quantity and, after 90 min, had accumulated to the level of ≈ 6%. On the basis of the amount of the reactive dianionic starting material, the combined synthesis efficiency of **13** (B = A) and the divalyl analogue is again, probably considerably higher. Close examination of the ¹H NMR spectra revealed the presence of the 2',3'-cyclic phosphate **15** (B = A) in low yield (**13/15** > 8:1). It thus appeared that the nucleobase had a relatively small effect on the aminoacylation of 3'-nucleotides with Val-NCA, and as such, we switched our attention to the isomeric 2'-nucleotides with the expectation of equally efficient aminoacylation.

Through the use of the same conditions employed for the 3'-isomer, we found that cytidine-2'-monophosphate (2'-CMP) **12** (B = C), in the presence of Val-NCA **7**, gave the 3'-ester **14** (B = C) in only ≈ 3% yield after 45 min (Table 1). Not only was the aminoacyl-transfer product formed in low yield, but it was accompanied by a comparable (≈ 2%) amount of the 2',3'-cyclic phosphate **15** (B = C) (**14/15** < 2:1). The lower yield of the ester product and the higher yield of **15** suggest that aminoacyl transfer from **10** is less efficient than it is from the 3'-phosphoryl isomer **9**. This conclusion was

supported by experiments with 2'-AMP **12** (B = A) and Val-NCA **7** in which we found that both the 3'-ester **14** (B = A) and the cyclic phosphate **15** (B = A) were formed in only trace amounts. This marked contrast in aminoacylation behavior between 3'- and 2'-nucleotides was not anticipated. It now seems likely that the efficiency of the aminoacylation reaction depends on the pK_a value of the phosphate and 2'/3'-OH groups, and possibly on conformational effects such as the furanose ring pucker. The pK_a value of the phosphate presumably influences the efficiency of the intramolecular aminoacyl-transfer step through a correlation with the leaving-group ability. Although the absolute pK_a values reported in the literature for the individual nucleotides differ (Supporting Information),^[12–14] there is a consensus that the 3'-phosphates are more acidic than the 2'-phosphates by approximately 0.2 pK_a units and this is consistent with the more efficient conversion of **11** into **13**. Within the 3'-phosphate series, the greater yield of **13** (B = A) relative to **13** (B = C) is possibly related to the fact that aden-9-yl is a better stabilizer for the 2'-oxyanion than any other aglycons.^[15]

The results described herein indicate that uncoded aminoacylation of 3'-nucleotides by NCAs is a prebiotically plausible reaction. The chemical mechanism of this process suggests that it should also be possible for 3'-phosphoryl oligoribonucleotides to undergo aminoacylation by NCAs in the same way, but with potential assistance by the ribonucleic acid chain through stereocomplementary binding. It is therefore possible that ribozymes, capable of coded aminoacylation by NCAs might have evolved and could have been key intermediates in the emergence of translation.^[16] The use of 5'-aa-AMPs as intermediates in coded aminoacylation of RNA is most likely a later evolutionary development.

Received: May 10, 2005

Revised: June 27, 2005

Published online: September 27, 2005

Keywords: amino acids · cyclization · N-carboxyanhydrides · ribonucleotides · RNA

- [1] P. Schimmel, *Annu. Rev. Biochem.* **1987**, 56, 125.
- [2] K. Wen, L. E. Orgel, *Origins Life Evol. Biosphere* **2001**, 31, 241.
- [3] L. Leman, L. Orgel, M. R. Ghadiri, *Science* **2004**, 306, 283.
- [4] J.-P. Biron, R. Pascal, *J. Am. Chem. Soc.* **2004**, 126, 9198.
- [5] N. S. M. D. Wickramasinghe, M. P. Staves, J. C. Lacey, *Biochemistry* **1991**, 30, 2768.
- [6] N. S. M. D. Wickramasinghe, J. C. Lacey, *Origins Life Evol. Biosphere* **1992**, 22, 361.
- [7] In preliminary work, we found that other NCAs (e.g. Ile-NCA) behave in a manner similar to **7** and we are now extending the study to NCAs that are most conveniently generated in situ in water (e.g. Gly-NCA).
- [8] J. C. Lacey, N. Senaratne, D. W. Mullins, *Origins Life* **1984**, 15, 45.
- [9] D. H. Rammner, Y. Lapidot, H. G. Khorana, *J. Am. Chem. Soc.* **1963**, 85, 1989.
- [10] L. E. Orgel, R. Lohrmann, *Acc. Chem. Res.* **1974**, 7, 368.
- [11] Our early attempts to isolate **13** were thwarted by its instability in the presence of (oligo)valine at the pH value of the reaction and over the time period required for HPLC. The successful characterization of **13** by LC-MS (see the Supporting Informa-

tion) involved an acidic mobile phase, and we are now attempting preparative separations under similar conditions.

- [12] D. D. Perrin, *Dissociation Constants of Organic Bases in Aqueous Solution*, Butterworths, London, **1965**.
- [13] S. C. Gupta, N. B. Islam, D. L. Whalen, H. Yagi, D. M. Jerina, *J. Org. Chem.* **1987**, 52, 3812.
- [14] L. F. Cavalieri, *J. Am. Chem. Soc.* **1953**, 75, 5268.
- [15] I. Velikyan, S. Acharya, A. Trifonova, A. Földesi, J. Chattopadhyaya, *J. Am. Chem. Soc.* **2001**, 123, 2893.
- [16] V. Borsenberger, M. A. Crowe, J. Lehbauer, J. Raftery, M. Helliwell, K. Bhutia, T. Cox, J. D. Sutherland, *Chem. Biodiversity* **2004**, 1, 203.

Phosphorus Cage Compounds

DOI: 10.1002/anie.200501990

Formation of a Bowl-Shaped, Pentacyclic Phosphonium Cage by Methylation of a Nucleophilic Phosphinidene

Matthias Driess,* Nicoleta Muresan, Klaus Merz, and Michael Päch

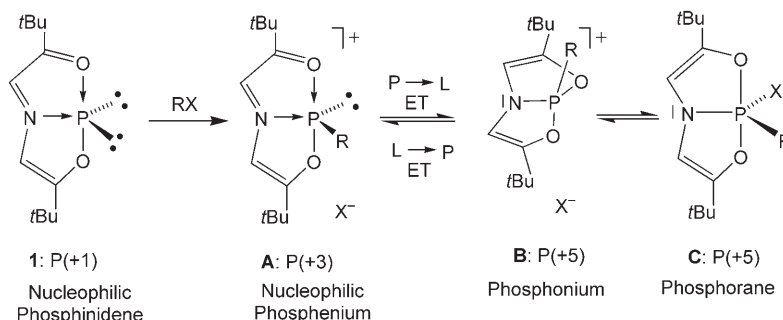
Dedicated to Professor Gottfried Huttner on the occasion of his 68th birthday

Phosphinidenes, that is, carbene-analogous compounds of monovalent phosphorus (phosphanylidenes, $R-P$) represent a simple class of valuable electrophilic building blocks in organophosphorus chemistry, which are usually highly reactive transients and therefore difficult to isolate.^[1]

However, one simple chemical trick that aids the preparation of a room-temperature stable phosphinidene is the intra- or intermolecular addition of a donor group D to the initially electron-deficient phosphorus atom ($D \rightarrow PR$); this affords an electron-rich (nucleophilic) phosphinidene, having eight or more valence electrons at the phosphorus center. Several types of donor-stabilized phosphinidenes have already been isolated and used as versatile precursors for the preparation of “free” phosphinidenes such as phospho-Wittig reagents ($R_3P=PR'$)^[2] and related phosphinidene metal complexes ($L_nM=PR$).^[3] The intramolecular donor-stabilization of a

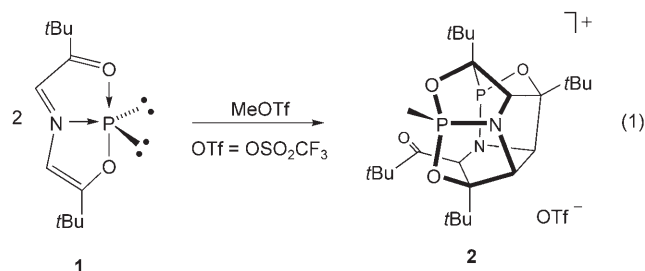
$P(+1)$ atom is also the reason for the intriguing stability of the nucleophilic phosphinidene **1** (Scheme 1), which has a planar, T-shaped three-coordinate phosphorus atom with 10 valence electrons (10-P-3 system).^[4] Although **1** is a promising versatile building block for the synthesis of novel electronically tunable organophosphorus ligands, its reactivity has only been sparingly investigated.^[5] The relatively high nucleophilicity at the P atom prompted us to investigate whether alkylation of phosphorus with classical alkylation reagents RX (R = alkyl; X = anionic leaving group) leads to a nucleophilic phosphonium salt **A**, phosphonium species **B**, or neutral phosphorane **C** as possible valence isomers, depending on the electronic nature and steric demand of R and X , respectively (Scheme 1).

Here we report the surprising formation of the unusual phosphonium cage cation in **2**, which results from a domino cyclization of two molecules of **1** in the presence of methyl trifluoromethylsulfonate (MeOTf). When a solution of MeOTf in CH_2Cl_2 was added to a solution of **1** in CH_2Cl_2 in the molar ratio of 1:1 at 20 °C, a rapid reaction occurs (^{31}P NMR monitoring), affording the unexpected phosphoni-



Scheme 1. The possible valence isomers **A**, **B**, and **C** formed by alkylation of **1** with RX (R = alkyl, X = anionic leaving group; ET = electron transfer).

um salt **2** [Eq. (1)]. The latter is insoluble in hydrocarbon solvents and other nonpolar solvents and can be isolated in



the form of a colorless solid in 35 % yield. The yield can be increased up to 78 % by changing the molar ratio of the starting materials MeOTf and **1** to 1:2. Interestingly, compound **2** results also exclusively even if a solution of **1** in CH_2Cl_2 is slowly added to a very large molar excess or even by using neat MeOTf at room temperature or below (−10 °C).

The composition and constitution of **2** was established by EI-FAB and ESI (electrospray ionization) mass spectrometry

[*] Prof. Dr. M. Driess, Dr. N. Muresan, Dr. M. Päch
Institute of Chemistry: Metalorganics and Inorganic Materials
Technical University of Berlin
Strasse des 17. Juni 135, Sekr. C2, 10623 Berlin (Germany)
Fax: (+49) 303-142-2168
E-mail: matthias.driess@tu-berlin.de
Dr. K. Merz
Fakultät für Chemie der Ruhr-Universität Bochum
Universitätsstrasse 150, 44801 Bochum (Germany)

(m/z 497), correct combustion analyses (C,H,N,P), and NMR spectroscopy (^1H , ^{13}C , ^{31}P). The ^{31}P NMR spectrum of **2** in CD_2Cl_2 shows two multiplets at $\delta = 107.4$ and 112.8 ppm without scalar ^{31}P – ^{31}P coupling. Since the connectivity of **2** was difficult to interpret based exclusively on the NMR spectra, its structure was unequivocally established by a single-crystal X-ray diffraction analysis (Figure 1).^[6] The latter revealed that **2** is an ion pair that consists of a bowl-shaped phosphonium cage with a λ^3 -pyramidal and a λ^4 -tetrahedral coordinate phosphorus atom, and a “non-coordinating” triflate anion.

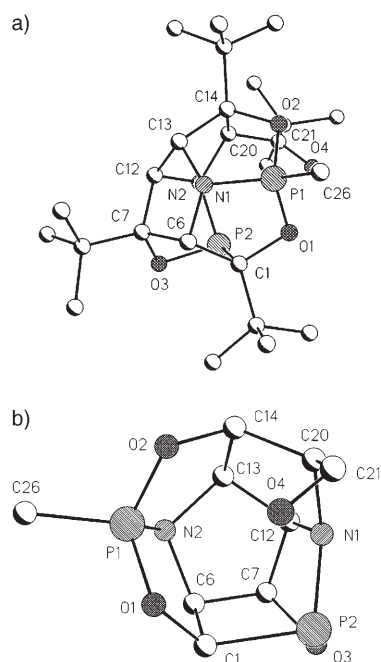
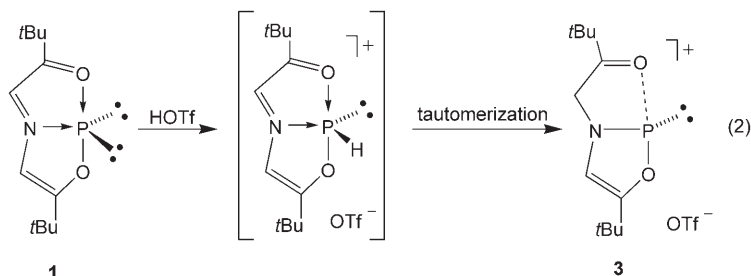


Figure 1. a) Molecular structure of the cation in **2**; b) core of the cage in **2**, including the terminal methyl carbon atom (C26) at the phosphonium P atom; hydrogen atoms are omitted for clarity. Selected distances [pm] and angles [°]: P1–O1 155.3(4), P1–O2 156.1(4), P1–N2 164.0(5), P1–C26 175.8(6), P2–O3 165.1(5), P2–N1 171.7(5), P2–C1 191.2(5), O2–P1–O1 117.0(2), O2–P1–C26 106.8(3), N2–P1–C26 121.8(3), O3–P2–N1 89.5(2), C20–N1–C12 106.6(4), C20–N1–P2 132.4(4), C12–N1–P2 111.1(3), C13–N2–C6 110.6(4), C13–N2–P1 108.6(3), C6–N2–P1 108.7(3).

The pentacyclic cation consists of a $\text{C}_7\text{O}_3\text{N}_2\text{P}_2$ skeleton with “globular-fused” five-membered rings. The core of the cation can be simply described as a cycloadduct of two molecules of **1**. The P–O and P–N distances are shorter than those in **1** but similar to the values for related phosphane–P–O and –P–N systems^[7] and corresponding phosphonium–P–O^[8] and –P–N systems,^[9] respectively. The terminal P1–C26 distance of the phosphonium–P atom (175.8(6) pm) is significantly shorter than the other P–C distances within the cation core and in other phosphonium cations with P–CH₃ bonds.^[10] This is probably due to the relatively high positive partial charge at the phosphorus center and the resulting σ -bond polarity of the P1–C26 bond. Because of the steric congestion around the N1 atom, it adopts an almost trigonal-planar configuration (sum of bond angles $\Sigma = 350.2^\circ$); this is in

contrast to the coordination geometry around the N2 atom which displays a less distorted pyramidal configuration ($\Sigma = 328^\circ$). The structural parameters have been consistently reproduced by density functional theory (DFT) calculations^[11] on the model cation **2'**, in which the *t*Bu groups were replaced by Me groups: The values for the distances and angles differ by less than 3 pm and 2° , respectively. The formation of **2** is in strong contrast to the result of the related protonation of **1** with HOTf, which, surprisingly, leads to the nucleophilic phosphonium ion in **3** as the sole product [Eq. (2)].^[12] Since the molecular structure of the cation in **3**



was hitherto unknown, we carried out a single-crystal X-ray diffraction analysis (Figure 2).^[6] The phosphonium cation consists of a planar, five-membered C_2NOP ring, which has close structural and electronic similarities to other related cyclic phosphonium ions.^[13]

The P1–N1 distance of 165.1(3) pm is slightly longer than that in the acyclic phosphonium ion $[\text{P}(\text{NiPr}_2)_2]^+$ (161.3(4) pm)^[14] but similar to the values in related cyclic phosphonium ions.^[13] The relatively long P–O distances of 282

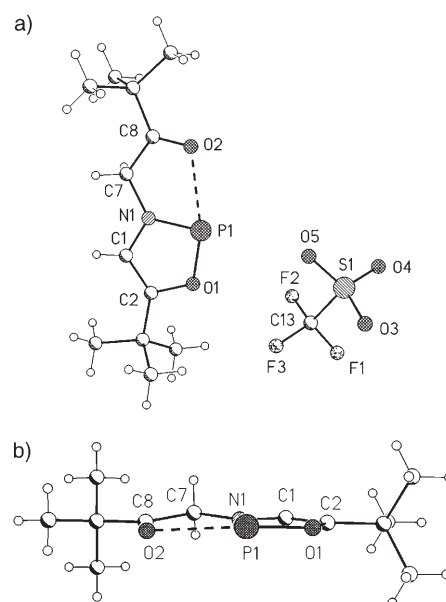
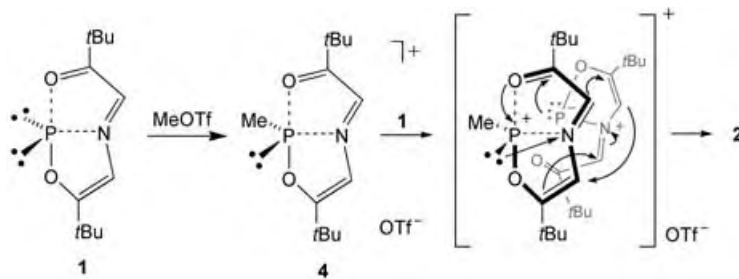


Figure 2. a) Molecular structure of **3**; b) side view of the cation in **3**. Selected distances [pm] and angles [°]: P1–O1 163.1(3), P1–N1 165.1(3), O1–C2 137.7(4), N1–C1 139.2(5), N1–C7 146.5(4), O2–C8 122.4(4), C7–C8 149.0(5), C1–C2 134.3(5), P1–O2 250.1(1), O1–P1–N1 90.65(1), O1–P1–O2 165.2(2), C2–O1–P1 115.0(2), C1–N1–C1 118.9(3), C1–N1–P1 112.4(2), C7–N1–P1 128.6(2).

and 285 pm of two oxygen atoms of neighboring OTf groups reflect the very weak donor–acceptor interactions between the phosphorus atom and the counterion. Thus, it is peculiar that the low-coordinate P atom is only weakly stabilized by intramolecular coordination of the carbonyl oxygen atom as indicated by the relatively long O2–P1 distance of 250.1(1) pm. Surprisingly, the carbonyl oxygen atom approaches the P atom in the ONP plane and not perpendicular to it, as usually observed for other donor adducts of phosphonium ions.^[13] This is confirmed by DFT calculations of the respective model compound **3C**, which show that instead of the vacant p_z orbital at the phosphorus center, the P1–O1 σ^* orbital serves as the acceptor orbital.^[11] The respective geometry optimizations of the corresponding isomers **3A–3C** clearly confirm the preference for **3C** by 10.6 (**3A**) and 37.5 kcal mol^{−1} (**3B**) (Figure 3). The nature of the phosphorus atoms in **3A** and **3B** should be quite different: While **3A** possesses a P(+3) atom with a lone pair of electrons and the atom is coordinated by a monobasic, tridentate ketoimino-enolate, **3B** has a P(+5) atom of the “classical” phosphonium type,

coordinated by a tribasic, tridentate bis(enolate)amido ligand. How can one explain the formation of the cation in **2**? Apparently, the reaction implies a remarkable domino-cycloaddition reaction between the hitherto unknown P-methylated cationic species **4** and **1**, which involves the formation of one new P–C and three additional C–C bonds. However, the structural analogue of **3c**, that is, the donor-stabilized phosphonium ion **4c** (see Figure 3), can be excluded as the key intermediate for the formation of **2**. Since no intermediate could be observed, we performed DFT calculations^[11] of the respective model systems **4A**, **4B**, and **4C**



Scheme 2. Proposed domino-cyclization for the formation of **2**.

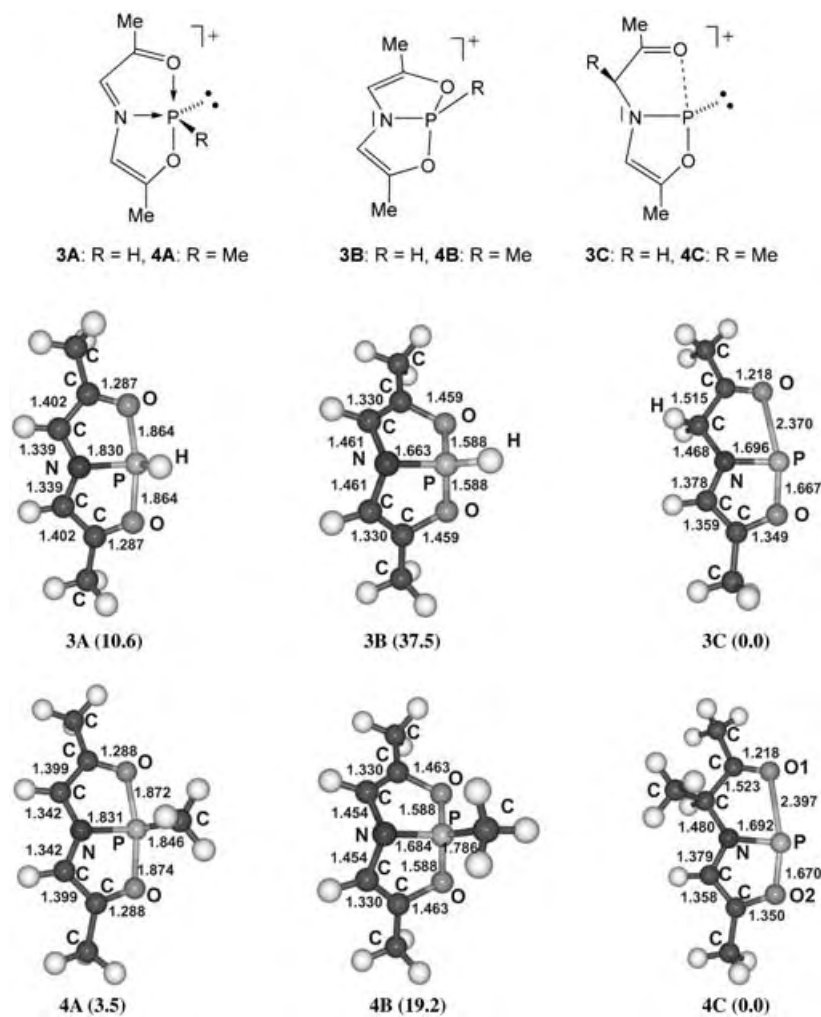


Figure 3. B3LYP/6-311+G(d)-optimized structures of **3A–3C** and **4A–4C**.^[11] Relative energies in parentheses [kcal mol^{−1}]; distances in Å.

(Me groups instead of *t*Bu groups in **4**) to learn whether the phosphonium cation **4A** or the symmetric phosphonium valence isomer **4B** is the preferred initial product of the oxidative addition of a methyl cation. Interestingly, the geometry optimizations revealed that even in the series **4A–4C**, the O→P stabilized phosphonium analogue **4C** (O→P distance 237.0 pm) is slightly favored over **4A** by 3.5 kcal mol^{−1} but is 19.2 kcal mol^{−1} lower in energy than **4B** (ΔE (**4B–4A**) = 15.7 kcal mol^{−1}). DFT calculations of the possible experimental systems **4** (A-type and C-type with *t*Bu groups) at a lower level of theory (BLYP/6-31G*) revealed that the A-type is now slightly favored over the C-type by about 2 kcal mol^{−1} due to steric hindrance.^[11] Accordingly, the formation of the unexpected phosphonium cage cation in **2** as the sole “self-trapping” product during the methylation of **1** clearly suggests the preferred population of the **4A**-type compound as the reactive intermediate. Since the latter phosphonium cation possesses a highly electrophilic backbone, it gets easily attacked by the electron-rich phosphinidene **1**, which initiates the tandem-cyclization (Scheme 2).

Further investigations in the presence of other competing trapping reagents are currently underway to explore the use of the strong electrophilic phosphonium transient **4** as a novel building block for other polycyclic phosphonium ions.

Experimental Section

2: MeOTf (0.432 g, 2.65 mmol) was added to a stirring solution of **1** (1.27 g, 5.31 mmol) in dichloromethane (50 mL). The resulting clear solution was stirred at room

temperature and then concentrated to 10 mL. The desired product was precipitated by addition of diethyl ether (10 mL), filtered, and dried under vacuo to yield a white solid (1.32 g; 78 %). Slow diffusion of diethyl ether in a solution of **2** in dichloromethane afforded crystals suitable for an X-ray structure analysis. M.p.: 205–207 °C (decomp); ^1H NMR (CD_2Cl_2): δ = 1.27 (s, 9H; *t*Bu), 1.32 (s, 9H; *t*Bu), 1.35 (s, 9H; *t*Bu), 1.49 (s, 9H; *t*BuCO), 2.62 (d, $^3J(^1\text{H}, ^{31}\text{P})$ = 17.3 Hz, 3H; MeP), 3.62–3.65 (m, 2H; HC-N), 4.92 ppm (d, $^3J(^1\text{H}, ^{31}\text{P})$ = 17.0 Hz, 1H; HC-N); $^{31}\text{P}\{^1\text{H}\}$ NMR (CD_2Cl_2): δ = 107.4 (s), 112.8 ppm (s); EI-FAB: m/z (%): 497 ($[M-\text{OTf}]^+$, 5), 57 (*t*Bu $^+$, 100); ESI-MS (CH_2Cl_2): m/z : 497 ($[M-\text{OTf}]^+$, 100); elemental analysis (%) calcd. for $\text{C}_{26}\text{H}_{46}\text{F}_3\text{N}_2\text{O}_7\text{P}_2\text{S}$ (649.67): C 48.06, H 7.13, N 2.15, P 9.54; found: C 47.65, H 7.15, N 2.08, P 9.33.

3: The compound was prepared as reported by Arduengo et al. and the NMR data (^1H , ^{31}P) of the sample were identical with the reported values.^[12]

Received: June 8, 2005

Published online: September 21, 2005

Keywords: cage compounds · cyclization · phosphonium ions · phosphonium ions · phosphorus

- [1] a) Review: “Phosphorus compounds with coordination number 1”: F. Mathey in *Multiple Bonds and Low Coordination in Phosphorus Chemistry* (Eds.: M. Regitz, O. Scherer), Thieme, Stuttgart, **1990**, pp. 33–47; b) K. Lammertsma, *Top. Curr. Chem.* **2003**, 229, 95–119; c) X. Li, S. I. Weissman, T.-S. Lin, P. P. Gaspar, A. H. Cowley, A. I. Smirnov, *J. Am. Chem. Soc.* **1994**, 116, 7899–7900; d) G. Bucher, M. L. G. Borst, A. W. Ehlers, K. Lammertsma, S. Ceola, M. Huber, D. Grote, W. Sander, *Angew. Chem.* **2005**, 117, 3353–3356; *Angew. Chem. Int. Ed. Engl.* **2005**, 44, 3289–3293.
- [2] a) S. Bauer, A. Marinetti, F. Mathey, *Heteroat. Chem.* **1991**, 2, 277–281; b) review: S. Shah, J. D. Protasiewicz, *Coord. Chem. Rev.* **2000**, 210, 181–201; c) S. Shah, M. C. Simpson, R. C. Smith, J. D. Protasiewicz, *J. Am. Chem. Soc.* **2001**, 123, 6925–6926; d) E. Matern, J. Olkowska-Oetzel, J. Pikies, G. Fritz, *Z. Anorg. Allg. Chem.* **2001**, 627, 1767–1770.
- [3] a) Review: F. Mathey, *Angew. Chem.* **1987**, 99, 285; *Angew. Chem. Int. Ed. Engl.* **1987**, 26, 275; b) review: A. H. Cowley, A. R. Barron, *Acc. Chem. Res.* **1988**, 21, 81; c) see also [1a]; d) G. Huttner, H. Lang, *Binuclear Phosphinidene Compounds in Multiple Bonds and Low Coordination in Phosphorus Chemistry* (Eds.: M. Regitz, O. J. Scherer), Thieme, Stuttgart, **1990**, pp. 48–57; e) C. C. Cummins, R. R. Schrock, W. M. Davis, *Angew. Chem.* **1993**, 105, 758–761; *Angew. Chem. Int. Ed. Engl.* **1993**, 32, 756–759; f) F. Mathey, A. Marinetti, S. Bauer, P. Le Floch, *Pure Appl. Chem.* **1991**, 63, 855–858; g) A. T. Termaten, T. Nijbacker, A. W. Ehlers, M. Schakel, M. Lutz; A. L. Spek, M. L. McKee, K. Lammertsma, *Chem. Eur. J.* **2004**, 10, 4063–4072.
- [4] Reviews: a) A. J. Arduengo, C. A. Steward, *Chem. Rev.* **1994**, 94, 1215, and references therein; b) V. I. Minkin, R. M. Minyaev, *Chem. Rev.* **2001**, 101, 1247.
- [5] Review: A. J. Arduengo, D. A. Dixon, “Electron Rich Bonding at Low Coordination Main Group Element Centers” in *Heteroatom Chemistry* (Ed.: E. Block), Wiley-VCH, New York, **1990**, p. 47, and references therein.
- [6] Crystal structure analysis: A crystal of **2** and **3** were each mounted on a glass capillary in perfluorinated oil and measured in a cold gas flow. The intensity data were measured with a Bruker axis area detector (MoK_α radiation), λ = 0.71073 Å, ω scan) at -60°C . **2** ($\text{C}_{28}\text{H}_{47}\text{Cl}_4\text{F}_3\text{N}_2\text{O}_7\text{P}_2\text{S}$): triclinic, $P\bar{1}$, a = 12.49(2), b = 13.22(2), c = 14.99(2) Å, α = 100.05(5), β = 102.58(7), γ = 114.80(8)°, V = 2092(6) Å³, Z = 2, μ = 0.462 mm⁻¹. A total of 8652 reflections were collected ($2\theta_{\text{max}}$ = 50°), 6694 independent, 3828 observed ($F_o > 4\sigma(F_o)$), 424 parameters; $R1$ = 0.0722, $wR2$ (all data) = 0.1977. **3** ($\text{C}_{13}\text{H}_{21}\text{F}_3\text{NO}_5\text{PS}$): monoclinic, $P2_1/n$, a = 6.612(3), b = 22.88(1), c = 12.710(6) Å, β = 102.163(8)°, V = 1879(1) Å³, Z = 4, μ = 0.307 mm⁻¹. A total of 9002 reflections were collected ($2\theta_{\text{max}}$ = 50°), 3288 independent, 1901 observed ($F_o > 4\sigma(F_o)$), 217 parameters; $R1$ = 0.0573, $wR2$ (all data) = 0.1604. Structure solutions by direct methods (SHELXS 97), refinement against F^2 with all measured reflections (SHELXTL 97). The positions of the H atoms were calculated and considered isotropically according to a riding model. CCDC 274136 (**2**) and 274167 (**3**) contain the supplementary crystallographic data for this paper. These data can be obtained free of charge from the Cambridge Crystallographic Data Centre via www.ccdc.cam.ac.uk/data_request/cif.
- [7] C. Bonninque, D. Houalla, R. Wolf, *J. Chem. Soc. Perkin Trans. 1* **1983**, 773.
- [8] a) M. Dzyk, Dissertation Universität Dortmund, **2000**; b) A. Chandrasekaran, R. O. Day, R. Holmes, *Inorg. Chem.* **2000**, 39, 5683–5689; c) D. Schomburg, *J. Am. Chem. Soc.* **1980**, 102, 1055.
- [9] a) M. B. Hursthouse, N. P. C. Walker, *J. Chem. Soc. Dalton Trans.* **1985**, 1043; b) H. Vogt, A. Fischer, P. G. Jones, *Z. Naturforsch. B* **1996**, 51, 865; c) A. Schmidpeter, K. Polborn, *Heteroat. Chem.* **1997**, 8, 347.
- [10] a) N. Leyser, K. Schmidt, H.-H. Brintzinger, *Organometallics* **1998**, 17, 2155; b) R. W. Alder, C. Ganter, M. Gil, R. Gleiter, C. J. Harris, S. E. Harris, H. Lange, A. G. Orpen, P. N. Taylor, *J. Chem. Soc. Perkin Trans. 1* **1998**, 1643–1655; c) R. J. Staples, T. Carlson, S. Wang, J. P. Fackler, *Acta. Crystallogr. Sect. C* **1995**, 51, 498.
- [11] Gaussian 98 (Revision A.7), M. J. Frisch, G. W. Trucks, H. B. Schlegel, G. E. Scuseria, M. A. Robb, J. R. Cheeseman, V. G. Zakrzewski, J. A. Montgomery, R. E. Stratmann, J. C. Burant, S. Dapprich, J. M. Millam, A. D. Daniels, K. N. Kudin, M. C. Strain, O. Farkas, J. Tomasi, V. Barone, M. Cossi, R. Cammi, B. Mennucci, C. Pomelli, C. Adamo, S. Clifford, J. Ochterski, G. A. Petersson, P. Y. Ayala, Q. Cui, K. Morokuma, D. K. Malick, A. D. Rabuck, K. Raghavachari, J. B. Foresman, J. Cioslowski, J. V. Ortiz, B. B. Stefanov, G. Liu, A. Liashenko, P. Piskorz, I. Komaromi, R. Gomperts, R. L. Martin, D. J. Fox, T. Keith, M. A. Al-Laham, C. Y. Peng, A. Nanayakkara, C. Gonzalez, M. Challacombe, P. M. W. Gill, B. G. Johnson, W. Chen, M. W. Wong, J. L. Andres, M. Head-Gordon, E. S. Replogle, J. A. Pople, Gaussian, Inc., Pittsburgh, PA, **1998**; Geometry and energy optimizations were performed by using the B3LYP/6-311+G(d) level of theory. Additionally, energy minimizations at the B3LYP/CC-PVTZ level of theory revealed identical geometries for the respective compounds. According to the frequency calculations of the respective compounds, the optimized structures represent minima (no imaginary frequencies).
- [12] A. J. Arduengo, A. C. Steward, F. Davidson, D. A. Nixon, J. Y. Becker, S. A. Culley, M. B. Minzen, *J. Am. Chem. Soc.* **1987**, 109, 627.
- [13] a) M. K. Denk, S. Gupta, A. J. Lough, *Eur. J. Inorg. Chem.* **1999**, 41; b) C. J. Carmalt, V. Lomeli, B. G. McBurnett, A. H. Cowley, *Chem. Commun.* **1997**, 2095; c) V. A. Jones, S. Sriprang, M. Thornton-Pett, T. P. Kee, *J. Organomet. Chem.* **1998**, 567, 199; d) J.-P. Bezombes, F. Carre, C. Chuit, R. J. P. Corriu, A. Mehdi, C. Reye, *J. Organomet. Chem.* **1997**, 535, 81–90; e) F. Carre, C. Chuit, R. J. P. Corriu, A. Mehdi, C. Reye, *J. Organomet. Chem.* **1997**, 529, 59–68; f) D. Gudat, *Eur. J. Inorg. Chem.* **1998**, 1087–1094; g) D. Gudat, A. Haghverdi, H. Hupfer, M. Nieger, *Chem. Eur. J.* **2000**, 6, 3414–3425; h) M. B. Abrams, B. L. Scott, R. T. Baker, *Organometallics* **2000**, 19, 4944–4956.
- [14] A. H. Cowley, M. C. Cushner, J. S. Szobota, *J. Am. Chem. Soc.* **1978**, 100, 7784.

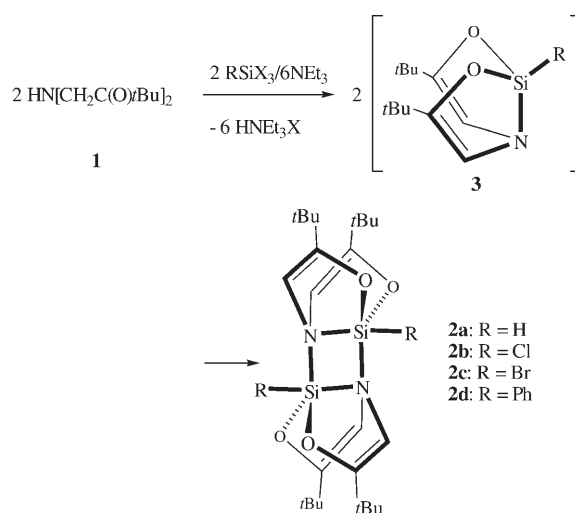
A Novel Type of Pentacoordinate Silicon Complexes and Unusual Ligand Coupling by Intramolecular Electron Transfer

Matthias Driess,* Nicoleta Muresan, and Klaus Merz

Dedicated to Professor Herbert Schumann
on the occasion of his 70th birthday

There are only a few reports on intramolecular electron-transfer (ET) reactions in coordination compounds of the main-group elements.^[1] Some years ago, Arduengo et al. reported on the intriguing coordination properties of the electron-rich trianionic amido-bis(enolate) ligand $[N\{CH=C(tBu)O\}_2]^{3-}$ (generated in situ from $HN[CH_2C(O)tBu]_2$ (**1**) and a base),^[2] which can serve both as a tridentate NO_2 ligand and intramolecular two-electron reducing agent toward heavier Group 15 elements (P, As, Sb, Bi) owing to ligand-to-element ET.^[3,4] Thus, reaction of PCl_3 with **1** in the presence of a base furnishes solely the corresponding nucleophilic phosphinidene with a planar λ^3 , T-shape-coordinated phosphorus atom with 10 valence electrons. Recently, we have shown that trilitiated **1** is a remarkable redox ligand even towards metal dihalides of the Group 14 elements Ge, Sn, and Pb, leading to novel nucleophilic carbene homologues.^[5] The fascinating coordination properties of **1** prompted us to explore whether the ligand is also capable of ET to a tetracoordinate Si^{4+} center. Here we describe the unexpected coordination behavior of **1** toward halosilanes, which affords two different types of unprecedented silicon complexes. Reaction of SiX_4 ($X = Cl, Br$) or $RSiCl_3$ ($R = H, Ph$) with **1** in the presence of NEt_3 as an auxiliary base furnishes deeply colored solutions from which the dimeric bis($N \rightarrow Si$) donor complexes **2a–d** can be isolated as the sole products (Scheme 1) in high yields. As expected, there is no reaction or color change if the halosilanes are added to solutions of **1** without the presence of a base. The final products **2a–d** are air-stable, moisture-sensitive, colorless solids that are well soluble in common aprotic organic solvents.

The composition and constitution of **2a–d** was confirmed by EI mass spectrometry, combustion analyses, and multinuclear NMR spectroscopy. The high-field ^{29}Si NMR chem-



Scheme 1. Synthesis of **2a–d** via the hypothetical monomers **3a–d**.

ical shifts in solution and in the solid state are diagnostic for λ^5 -coordinate silicon, and the similarity of respective solid state and solution values proves that the dimeric structure is retained in solution (see Table 1).^[6]

Table 1: ^{29}Si NMR chemical shift values for **2a–d**; CP-MAS solid-state values in parentheses.

Complex	2a	2b	2c	2d
δ [ppm]	−81.8 ^[a] (−87)	−85.9 (−93)	−106.7 (−112)	−38.3 (−45)

[a] $J_{Si,H} = 276.6$ Hz.

The shielding of the ^{29}Si nucleus is influenced by the nature of the substituents, thus the least shielding in the case of the phenyl-substituted complex **2d** is in accordance with values for related pentacoordinate silicon complexes with $N \rightarrow Si$ donor bonds (e.g., intramolecular amine $\rightarrow Si(Ph)$ donor-acceptor adducts).^[7] Remarkably, there was no indication for a dissociation up to 100 °C in toluene solutions, as shown by variable-temperature ^{29}Si NMR experiments. The dimeric structure of **2c** was additionally confirmed by a single-crystal X-ray diffraction analysis.^[8] Compound **2c** crystallizes in the triclinic space group $P\bar{1}$, and the molecular structure consists of a planar four-membered Si_2N_2 ring as the central structural motif (Figure 1). The latter results from a head-to-tail dimerization through $N \rightarrow Si$ donor-acceptor bonds of two hypothetical monomeric amido-bis(enolate) silicon bromide units. This leads to a slightly distorted trigonal-bipyramidal coordination of silicon with the Br1 and N1 atoms in axial and the O1, O2, and N1A atoms in equatorial positions. The axial Si1–N1 distance is about 20 pm longer than the equatorial Si1–N1A value (180.4(14) pm) but similar to $N \rightarrow Si$ distances observed in related Si_2N_2 dimers and silatranes.^[9] The Si1–O1 distance (166.2(13) pm) is slightly longer than the Si1–O2 value (163.8(13) pm) but similar to Si–O distances observed for hypercoordinate silicon in silatranes with a N_2O_3 coordination.^[9] Both the

[*] Prof. Dr. M. Driess, Dr. N. Muresan
Institute of Chemistry: Metalorganics and Inorganic Materials
Technical University Berlin
Strasse des 17. Juni 135, Sekr. C2, 10623 Berlin (Germany)
Fax: (+49) 30-314-22168
E-mail: matthias.driess@tu-berlin.de
Dr. K. Merz
Lehrstuhl für Anorganische Chemie I
Fakultät für Chemie
Ruhr-Universität Bochum
Universitätsstrasse 150, 44801 Bochum (Germany)

Si–O single and the endocyclic C6–C7 and C11–C14 double-bond lengths of the ligand skeleton confirm that each silicon atom in **2c** is coordinated by a trianionic amido-bis(enolate) chelate ligand.

Since similarly substituted amido-di-alkoxyhalosilanes such as $\text{XSi}(\text{OR})_2(\text{NR}')_2$ ($\text{X} = \text{Cl}$, $\text{R} = \text{Me}$, $\text{R}' = \text{alkyl}$, SiMe_3)^[10] are reluctant to dimerize, the formation of the thermally resistant dimers **2a–d** is amazing. To understand the facile dimerization of the hypothetical monomers **3** (see Scheme 1), we performed DFT calculations (B3LYP/6-311G** level of theory)^[11] of the three possible monomeric valence isomers **3A–3C**. The resulting energy profile for **3A–3C** is depicted in Figure 2. The calculations revealed that the amido-bis(enolate)-chloro silicon complex **3A**, which has a puckered, bicyclic $\text{C}_4\text{O}_2\text{NSi}$ skeleton, is most favored, whereas the silylene-like species **3C**, which implies a two-electron transfer from the ligand to silicon, is disfavored by $34.4 \text{ kcal mol}^{-1}$ and the least stable one. This is in marked contrast to the Ge and Sn analogues, which clearly prefer the formation of nucleophilic germynes and stannynes,^[4,5] reflecting that Si^{4+} is more electropositive than Ge^{4+} and Sn^{4+} . Interestingly, the optimized structure of **3B** with a planar-tetra-coordinate silicon atom represents the transition state (one imaginary frequency) for the ring inversion of **3A**, being only $12.3 \text{ kcal mol}^{-1}$ higher in energy (Figure 2). The latter process is reminiscent of related theoretical results on the hypothetical bis(*o*-catecholate)silicon complex with a much higher inversion barrier of $32.9 \text{ kcal mol}^{-1}$.^[12] In accordance to previous predictions,^[12] the significant lowering of the barrier in **3** indicates that the tridentate amido-bis(enolate) chelate is a more efficient π -donor- σ -acceptor than the

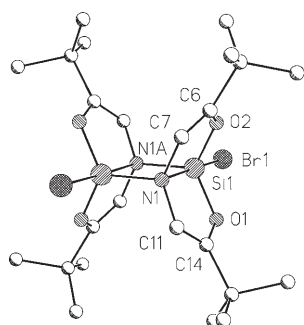


Figure 1. Molecular structure of **2c**; hydrogen atoms are omitted for clarity. Selected distances [pm] and angles [°]: Si1–Br1 227.5(6), Si1–O1 166.2(13), Si1–O2 163.8(13), Si1–N1 200.6(13), Si1–N1A 180.4(14), O1–C14 139(2), O2–C6 143(2), C7–N1 146(2), C11–N1 145(2), C6–C7 129(2), C11–C14 131(2); O1–Si1–O2 124.1(6), O2–Si1–N1A 115.8(6), O1–Si1–N1 85.1(6), N1–Si1–N1A 79.4(6), Br1–Si1–N1 177.4(4).

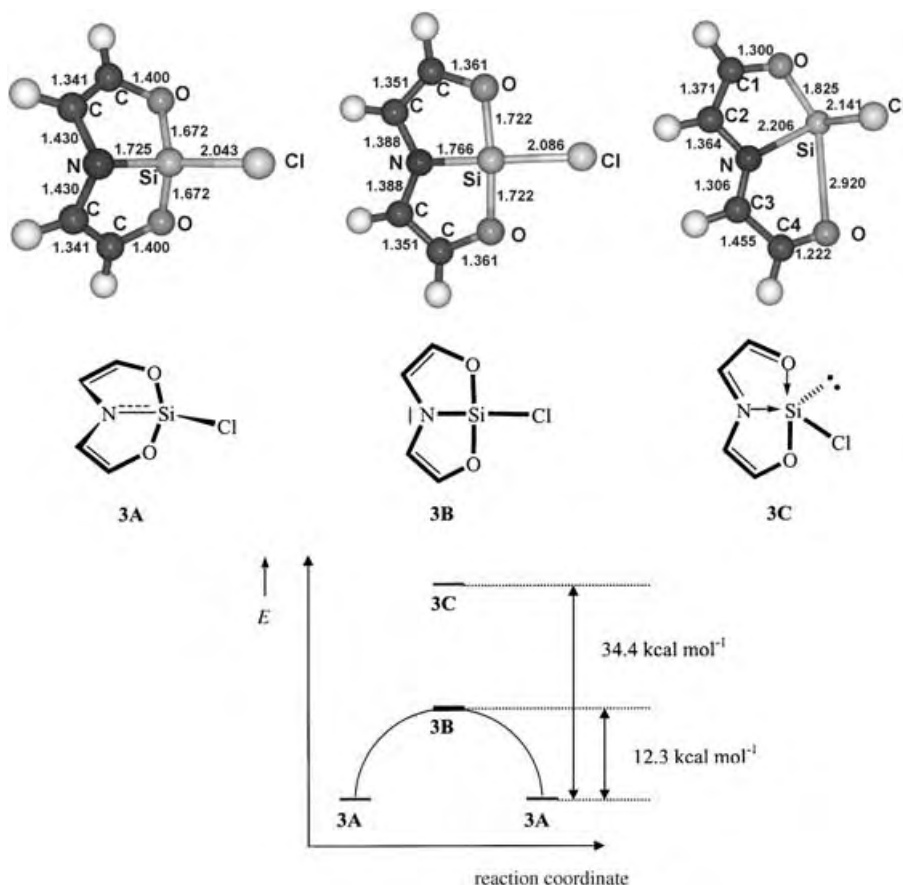


Figure 2. Top: DFT-(B3LYP/6-311G**)-optimized structures of **3A–3C**; distances are given in Å. Bottom: Energy profile for the isomerization of **3A** to **3B** and **3C**. The valence isomer **3B** is the transition state (one imaginary frequency) for ring-inversion of **3A**.

bidentate *o*-catecholate ligand. What is the driving force for the facile dimerization of **3A**? According to the calculation of the natural atomic charges in **3A**, the Si and the N atoms bear partial charges (Si +2.14, N –0.88) in accordance with the presence of a masked (ylide-like) Si–N π bond, reminiscent of iminosilane adducts with λ^4 -coordinate silicon and λ^3 -coordinate nitrogen atoms.^[13]

In fact, the HOMO exhibits an unsymmetrical π -charge distribution around the nitrogen and silicon atom and two symmetrical C–C π bonds (Figure 3). The calculated energy of the head-to-tail Si=N dimerization of **3A** to the corresponding dimer **2a** is $-21 \text{ kcal mol}^{-1}$, and the geometrical

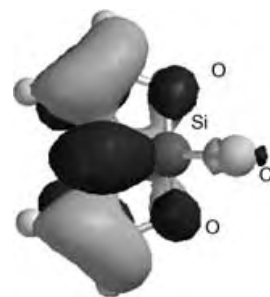
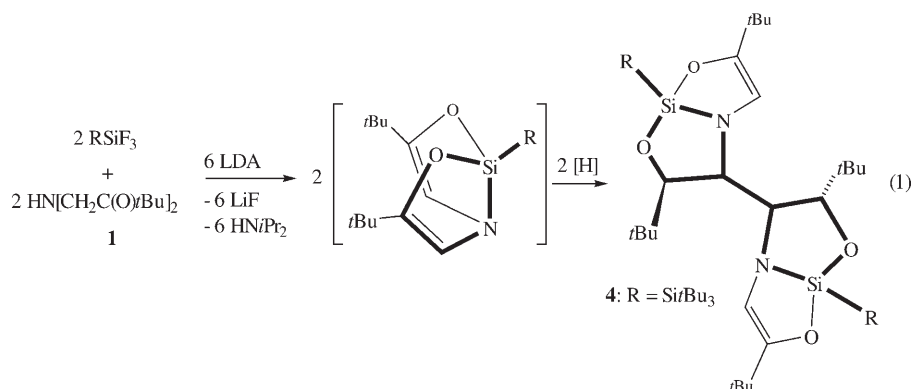


Figure 3. HOMO of **3A** with an ylidic Si–N π bond.

parameters of the latter are in good agreement with the respective experimental data of **2c**. Thus, the remarkably exothermic process prevents the observation of the monomeric units in **2a–d**. To protect the Si=N moiety against dimerization, we used the highly substituted trifluoro(silyl)silane $t\text{Bu}_3\text{SiSiF}_3$ as starting material.^[14] The latter readily reacts with trilitiated **1** in THF at -78°C but leads to the unusual dimer **4** in the form of pale yellow crystals in moderate yield (29%) as the only isolable product [Eq. (1); LDA = lithium diisopropylamide].



The composition and constitution of **4** was confirmed by NMR spectroscopy, EI mass spectrometry, and an X-ray diffraction analysis (Figure 4).^[8] The latter reveals that **4** crystallizes as a racemic mixture in the triclinic space group $P\bar{1}$.

In contrast to the dimeric complexes **2a–d**, the dinuclear compound **4** possesses only tetracoordinate silicon atoms. Its formation involves a remarkably mild C–C bond coupling of two amido-bis(enolate) frameworks of **1** and the concomitant

hydrogenation of the C8 and C8A atoms, presumably by a radical mechanism in which THF functions as the hydrogen source, to afford a hexa-basic bis[amido(enolate)-alkoxide] ligand capable of coordination of two formal $t\text{Bu}_3\text{Si}-\text{Si}^{3+}$ fragments. The observed distances and angles (Figure 4) are in the range expected for tetravalent silicon compounds (e.g., amido-alkoxysilanes).^[10] In summary, the deprotonated (anionic) ligand **1** shows remarkable coordination and electron-donor ability even towards tetravalent silicon, leading to the new types of silicon complexes **2** and **4**. Further investigations aimed at isolating the initial colored intermediates during the conversion of the halosilanes with deprotonated **1** and at synthesizing a stable monomeric silicon complex **3** are underway.

Experimental Section

General procedure for the synthesis of 2a–2d: To a mixture of **1** (2 g, 9.38 mmol) and the equimolar amount of the corresponding halosilane (HSiCl_3 for **2a**, SiCl_4 for **2b**, SiBr_4 for **2c**, and PhSiCl_3 for **2d**) in dried, Ar-saturated THF (50 mL) at -78°C was added dropwise three molar equivalents of triethylamine. The reaction mixture was allowed to warm up to room temperature (6 h) and was then stirred for an additional 2 h. All volatiles

were removed in vacuo and the solid residue was extracted with hexane ($3 \times 10\text{ mL}$). After filtration, the solvent was evaporated off and the residue was recrystallized from CH_2Cl_2 to afford a microcrystalline sample of **2a** (0.73 g, 1.52 mmol; 33%); m.p.: $127\text{--}129^\circ\text{C}$; ^1H NMR (CDCl_3): $\delta = 1.18$ (s, 36H; $t\text{Bu}$), 4.22 (brs, 2H; SiH), 5.67 ppm (brs, 4H; NCH); $^{13}\text{C}\{^1\text{H}\}$ NMR (CDCl_3): $\delta = 27.56$ (s, CH_3), 34.87 (s, $\text{C}(\text{CH}_3)_3$), 106.01 (s, CN), 164.17 ppm (s, CO); ^{29}Si NMR (CDCl_3): $\delta = -81.8$ ppm (d, $J_{\text{Si,H}} = 276.56\text{ Hz}$); EI-MS: m/z (%): 478 ($[M]^+$, 20), 463 ($[M-\text{Me}]^+$, 10), 239 ($[M/2]^+$, 15), 224 ($[M/2-\text{Me}]^+$, 20), 209 ($[M/2-2\text{Me}]^+$, 20), 57 ($t\text{Bu}^+$, 100); correct elemental analyses (C,H,N,Si).

2b: (2.5 g, 4.69 mmol; 100%); m.p.: $120\text{--}122^\circ\text{C}$; ^1H NMR (CDCl_3): $\delta = 1.12$ (s, 36H; $t\text{Bu}$), 5.55 ppm (s, 4H; NCH); $^{13}\text{C}\{^1\text{H}\}$ NMR (CDCl_3): $\delta = 27.19$ (s, CH_3), 33.84 (s, $\text{C}(\text{CH}_3)_3$), 107.63 (s, CN), 163.83 ppm (s, CO); ^{29}Si NMR (CDCl_3): $\delta = -85.9$ ppm (s); EI-MS: m/z (%): 546 ($[M]^+$, 90), 431 ($[M-\text{Me}]^+$, 20), 511 ($[M-\text{Cl}]^+$, 10), 273 ($[M/2]^+$, 95), 258 ($[M/2-\text{Me}]^+$, 100), 243 ($[M/2-2\text{Me}]^+$, 20); correct elemental analyses (C,H,N,Si).

2c: (2.5 g, 3.94 mmol; 84%); m.p.: $131\text{--}133^\circ\text{C}$ (decomp); ^1H NMR (CDCl_3): $\delta = 1.07$ (s, 36H; $t\text{Bu}$), 5.48 ppm (s, 4H; NCH); $^{13}\text{C}\{^1\text{H}\}$ NMR (CDCl_3): $\delta = 27.38$ (s, CH_3), 34.47 (s, $\text{C}(\text{CH}_3)_3$), 107.63 (s, CN), 163.81 ppm (s, CO); ^{29}Si NMR (CDCl_3): $\delta = -107.6$ ppm (s); EI-MS: m/z (%): 636 ($[M]^+$, 100), 621 ($[M-\text{Me}]^+$, 20), 557 ($[M-\text{Br}]^+$, 17), 318 ($[M/2]^+$, 87), 302 ($[M/2-\text{Me}]^+$, 78), 289 ($[M/2-2\text{Me}]^+$, 18); correct elemental analyses (C,H,N,Si).

2d: (1.56 g, 2.73 mmol, 58%); m.p.: $117\text{--}119^\circ\text{C}$ (decomp); ^1H NMR (CDCl_3): $\delta = 1.17$ (s, 36H; $t\text{Bu}$), 5.55 (s, 4H; NCH), 7.3–7.9 ppm (m, 10H; Ph); $^{13}\text{C}\{^1\text{H}\}$ NMR (CDCl_3): $\delta = 28.73$ (s, CH_3), 34.97 (s, $\text{C}(\text{CH}_3)_3$), 112.39 (s, CN), 127.9 (s, Ph), 129.8 (s, Ph), 135.8 (s, Ph), 149.7 ppm (s, CO); ^{29}Si NMR (CDCl_3): $\delta = -38.3$ (s); EI-MS: m/z (%): 630 ($[M]^+$, 30), 615 ($[M-\text{Me}]^+$, 10), 315 ($[M/2]^+$, 35), 300 ($[M/2-\text{Me}]^+$, 30), 57 ($t\text{Bu}^+$, 100); correct elemental analyses (C,H,N,Si).

4: A solution of BuLi in hexane (Aldrich, 0.76 g, 12 mmol) at -78°C was added to a stirred solution of diisopropylamine (1.21 g, 12 mmol) in THF (10 mL). The solution was allowed to warm up to room temperature and stirred for 0.5 h. To this freshly prepared solution of LDA, a solution of **1** (0.8 g, 3.75 mmol) in THF (10 mL)

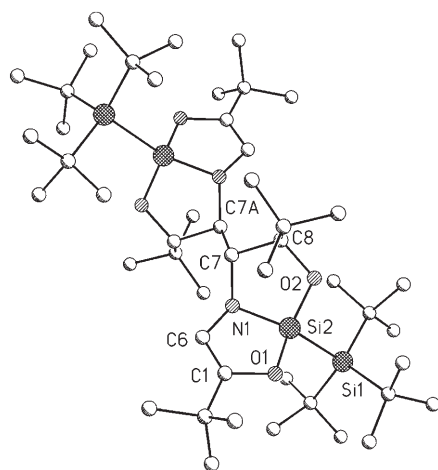


Figure 4. Molecular structure of **4**; hydrogen atoms are omitted for clarity. Selected distances [pm] and angles $^\circ$: Si1–Si2 236.8(10), Si2–O1 168.6(5), Si2–O2 164.7(6), Si2–N1 174.9(8), C1–O1 139.8(6), C8–O2 144.7(8), C6–N1 144.6(5), C1–C6 132.2(6), C7–C8 156.3(7), C7–C7A 154.7(6); O1–Si2–O2 122.3(2), O1–Si2–N1 94.2(3), O1–Si2–Si1 104.1(3), N1–Si2–Si1 136.8(2), C1–O1–Si2 110.6(3), C6–N1–C7 115.8(3), C1–C6–N1 115.8(3).

was added dropwise at -20°C over 10 min, affording a deep red solution of lithated **1**. The reaction mixture was warmed up to room temperature and stirred overnight. Subsequently, all volatile components were removed in vacuo and the red solid was redissolved in THF. To this solution was added a solution of $(t\text{Bu})_3\text{SiSiF}_3$ (1.06 g, 3.75 mmol) THF (in 10 mL) and the reaction mixture was stirred overnight. The solvent was removed under vacuo and the pale yellow solid was taken up in CH_2Cl_2 (30 mL). The filtrate, a slightly yellow solution, afforded (at -30°C) pale yellow crystals suitable for X-ray diffraction analysis (0.48 g, 0.54 mmol, 29%); ^1H NMR (CDCl_3): δ = 0.88 (s, 54H; $t\text{BuSi}$), 1.22 (s, 18H; $t\text{Bu}$), 1.14 (s, 18H; $t\text{Bu}$), 1.34 (m, 2H; HCN), 1.39 (m, 2H; HCO), 5.21 (s, 2H; NCH); EI-MS: m/z (%): 877 ($[\text{M}]^+$, 40), 862 ($[\text{M}-\text{Me}]^+$, 30), 438 ($[\text{M}/2]^+$, 15), 57 ($[\text{tBu}]^+$, 100); correct elemental analyses (C,H,N,Si).

Received: June 9, 2005

Published online: September 27, 2005

Keywords: charge transfer · diketoamine ligands · electron transfer · hypervalent compounds · silicon

- [1] a) J.-M. Barbe, C. Ratti, P. Richard, C. Lecomte, R. Gerardin, R. Guillard, *Inorg. Chem.* **1990**, *29*, 4126; b) D. A. Atwood, V. O. Atwood, A. H. Cowley, *Inorg. Chem.* **1992**, *31*, 3871; c) D. A. Atwood, V. O. Atwood, A. H. Cowley, H. R. Gobran, *Inorg. Chem.* **1992**, *31*, 6471; d) P. Riviere, A. Castel, J. Satge, D. Guyot, *J. Organomet. Chem.* **1986**, *315*, 157; e) G. M. Barnard, M. A. Brown, H. E. Mabrouk, B. R. McGarvey, D. G. Tuck, *Inorg. Chim. Acta* **2003**, *349*, 142; f) M. Riviere-Baudet, M. Dahrough, H. Gornitzka, *J. Organomet. Chem.* **2000**, *651*, 44; g) P. Chaudhuri, M. Hess, K. Hildenbrand, E. Bill, T. Weyhermüller, K. Wieghardt, *Inorg. Chem.* **1999**, *38*, 2781, and references therein; h) B. R. McGarvey, A. Ozarowski, Z. Tian, D. G. Tuck, *Can. J. Chem.* **1995**, *73*, 1213.
- [2] D. J. Cram, F. A. Abd Elhafez, *J. Am. Chem. Soc.* **1952**, *74*, 5828.
- [3] A. Culley, A. J. Arduengo, *J. Am. Chem. Soc.* **1984**, *106*, 1164.
- [4] Reviews: a) A. J. Arduengo, C. A. Steward, *Chem. Rev.* **1994**, *94*, 1215; b) V. I. Minkin, R. M. Minyaev, *Chem. Rev.* **2001**, *101*, 1247; c) "Electron Rich Bonding at Low Coordination Main Group Element Centers", A. J. Arduengo, D. A. Dixon in *Heteroatom Chemistry* (Ed.: E. Block), VCH, New York, **1990**, p. 47, and references therein.
- [5] M. Driess, N. Dona, K. Merz, *Chem. Eur. J.* **2004**, *10*, 5971.
- [6] a) K. Tamao, M. Asahara, A. Kawachi, A. Toshimitsu, *J. Organomet. Chem.* **2002**, *643–644*, 479; b) B. J. Helmer, R. West, R. J. P. Corriu, M. Poitier, G. Royo, A. de Saxcé, *J. Organomet. Chem.* **1983**, *251*, 285; c) "NMR Spectroscopy of Organosilicon Compounds", E. A. Williams in *The Chemistry of Organic Silicon Compounds, Vol. 1* (Ed.: Z. Rappoport), Wiley, Chichester **1989**, chap. 8, p. 511; d) F. Carré, G. Cerveau, C. Chuit, R. J. P. Corriu, N. K. Nayyar, C. Reyé, *Organometallics* **1990**, *9*, 1989; e) K. Tamao, M. Asahara, T. Saeki, A. Toshimitsu, *Chem. Lett.* **1999**, 35.
- [7] Review: "Hypervalent silicon compounds", D. Kost, I. Kalikhman in *The Chemistry of Organic Silicon Compounds, Vol. 2, Part 2* (Eds.: Z. Rappoport, Y. Apeloig), Wiley, Chichester **1998**, p. 1380.
- [8] Crystal structure analyses of **2c** and **4**: A crystal of **2c** and **4** were each mounted on a glass capillary in perfluorinated oil and measured in a cold gas flow. The intensity data were measured with a Bruker axs area detector (MoK_α radiation), $\lambda = 0.71073 \text{ \AA}$, ω scan at -60°C . **2c**: ($\text{C}_{24}\text{H}_{40}\text{Br}_2\text{N}_2\text{O}_4\text{Si}_2$): triclinic, $P\bar{1}$, $a = 11.47(2)$, $b = 11.80(2)$, $c = 11.95(2) \text{ \AA}$, $\alpha = 74.76(4)$, $\beta = 89.66(7)$, $\gamma = 76.31(4)^{\circ}$, $V = 1514(4) \text{ \AA}^3$, $Z = 2$, $\mu = 2.786 \text{ mm}^{-1}$. A total of 6817 reflections were collected ($2\theta_{\text{max}} = 50^{\circ}$), 3907 independent, 2921 observed ($F_o > 4\sigma(F_o)$), 307 parameters; $R1 = 0.0792$, $wR2$ (all data) = 0.2273. **4**: ($\text{C}_{48}\text{H}_{96}\text{N}_2\text{O}_4\text{Si}_4$): triclinic, $P\bar{1}$, $a = 8.68(3)$, $b = 10.72(3)$, $c = 15.87(7) \text{ \AA}$, $\alpha = 106.6(2)$, $\beta = 94.4(3)$, $\gamma = 99.1(1)^{\circ}$, $V = 1386(9) \text{ \AA}^3$, $Z = 1$, $\mu = 0.146 \text{ mm}^{-1}$. A total of 4872 reflections were collected ($2\theta_{\text{max}} = 50^{\circ}$), 3652 independent, 3029 observed ($F_o > 4\sigma(F_o)$), 262 parameters; $R1 = 0.0525$, $wR2$ (all data) = 0.1554. Structure solution by direct methods (SHELXS 97), refinement against F^2 with all measured reflections (SHELXTL 97). The positions of the H atoms were calculated and considered isotropically according to a riding model. CCDC 274140(**2c**) and 274141 (**4**) contain the supplementary crystallographic data for this paper. These data can be obtained free of charge from the Cambridge Crystallographic Data Centre via www.ccdc.cam.ac.uk/data_request/cif.
- [9] a) S. P. Narula, R. Shankar, M. Kumar, R. K. Chadha, C. Janaik, *Inorg. Chem.* **1997**, *36*, 1268; b) Y. Wan, J. G. Verkade, *Organometallics* **1996**, *15*, 5769; c) see also reference [7]; d) review: "Silatranes and their tricyclic analogs", V. Pestunovich, S. Kirpichenko, M. Voronkov in *The Chemistry of Organic Silicon Compounds, Vol. 2, Part 2* (Eds.: Z. Rappoport, Y. Apeloig), Wiley, Chichester **1998**, p. 1447.
- [10] a) U. Wannagat, H. Bürger, P. Geymayer, G. Torper, *Monatsh. Chem.* **1964**, *95*, 39; b) U. Wannagat, W. Veigl, H. Bürger, *Monatsh. Chem.* **1965**, *96*, 593; c) U. Wannagat, H. Bürger, *Z. Anorg. Allg. Chem.* **1964**, *629*, 309; d) J. Grobe, H. Schröder, N. Auner, *Z. Naturforsch. B* **1990**, *45*, 785; e) W. Uhlig, C. Tretner, *J. Organomet. Chem.* **1994**, *467*, 31.
- [11] Gaussian98 (Revision A.3), M. J. Frisch, G. W. Trucks, H. B. Schlegel, G. E. Scuseria, M. A. Robb, J. R. Cheeseman, V. G. Zakrzewski, J. A. Montgomery, R. E. Stratmann, J. C. Burant, S. Dapprich, J. M. Millam, A. D. Daniels, K. N. Kudin, M. C. Strain, O. Farkas, J. Tomasi, V. Barone, M. Cossi, R. Cammi, B. Mennucci, C. Pomelli, C. Adamo, S. Clifford, J. Ochterski, G. A. Petersson, P. Y. Ayala, Q. Cui, K. Morokuma, D. K. Malick, A. D. Rabuck, K. Raghavachari, J. B. Foresman, J. Cioslowski, J. V. Ortiz, B. B. Stefanov, G. Liu, A. Liashenko, P. Piskorz, I. Komaromi, R. Gomperts, R. L. Martin, D. J. Fox, T. Keith, M. A. Al-Laham, C. Y. Peng, A. Nanayakkara, C. Gonzalez, M. Challacombe, P. M. W. Gill, B. G. Johnson, W. Chen, M. W. Wong, J. L. Andres, M. Head-Gordon, E. S. Replogle, J. A. Pople, Gaussian, Inc., Pittsburgh, PA, **1998**; geometry and energy optimizations were performed by using the B3LYP/6-311 + G(d) level of theory. With exception of **3b'**, the frequency calculations of the respective compounds revealed that the optimized structures represent minima at the hyperenergy surface (no imaginary frequencies).
- [12] a) E.-U. Würthwein, P. von R. Schleyer, *Angew. Chem.* **1979**, *91*, 588; *Angew. Chem. Int. Ed. Engl.* **1979**, *18*, 553; b) H. Meyer, G. Nagorsen, *Angew. Chem.* **1979**, *91*, 587; *Angew. Chem. Int. Ed. Engl.* **1979**, *18*, 552.
- [13] Review: I. Hemme, U. Klingebiel, *Adv. Organomet. Chem.* **1996**, *39*, 159.
- [14] N. Wiberg, W. Niedermayer, H. Nöth, J. Knizek, W. Ponikwar, K. Polborn, *Z. Naturforsch. B* **2000**, *55*, 389.

DOI: 10.1002/anie.200501998

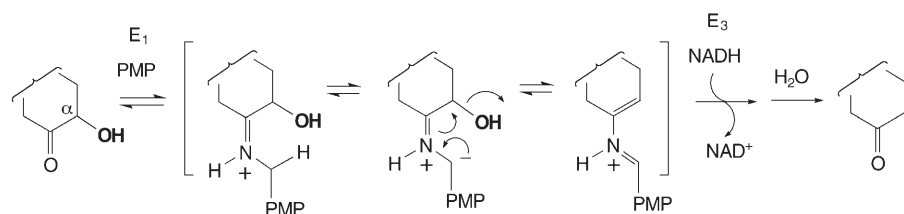
Biosynthesis of TDP-D-Desosamine: Identification of a Strategy for C4 Deoxygenation**

Ping-hui Szu, Xuemei He, Lishan Zhao, and Hung-wen Liu*

Dedicated to Professor Koji Nakanishi on the occasion of his 80th birthday

D-Desosamine (**1**), a 3-(dimethylamino)-3,4,6-trideoxyhexose found in a number of macrolide antibiotics including methymycin and pikromycin produced by *Streptomyces venezuelae*, plays an essential role in conferring biological activities to its parent aglycones.^[1] Although numerous strategies for the biological C–O bond scission have been elucidated, little is known about the mechanism of deoxygenation at the C4 position in the formation of desosamine.^[2] Insight into the mechanism of this key transformation is essential to fully establish the sequence of reactions in the desosamine pathway.

Past studies of the biosynthesis of various deoxyhexoses showed that the deoxygenation mechanism correlates with the position of the scissile C–O bond, either α or β to an activating group such as a keto group.^[3] For example, a stepwise dehydration–reduction sequence catalyzed by a pyridoxamine 5'-phosphate (PMP)-dependent [2Fe-2S]-containing enzyme, E₁,^[4] and an iron–sulfur flavoprotein reductase, E₃,^[5] is the prototypical mechanism for α -deoxygenation of a ketosugar substrate (Scheme 1).^[6] Hence, deoxygenation



Scheme 1. A prototypical mechanism for α -deoxygenation of a ketosugar substrate. E₁ and E₃ are iron- and sulfur-containing enzymes. PMP = pyridoxamine 5'-phosphate; NAD(H) = (reduced) nicotinamide adenine dinucleotide.

[*] P.-h. Szu, X. He, L. Zhao, Prof. Dr. H.-w. Liu
Division of Medicinal Chemistry
College of Pharmacy and
Department of Chemistry and Biochemistry
University of Texas
Austin, TX 78712 (USA)
Fax: (+1) 512-471-2746
E-mail: h.w.liu@mail.utexas.edu

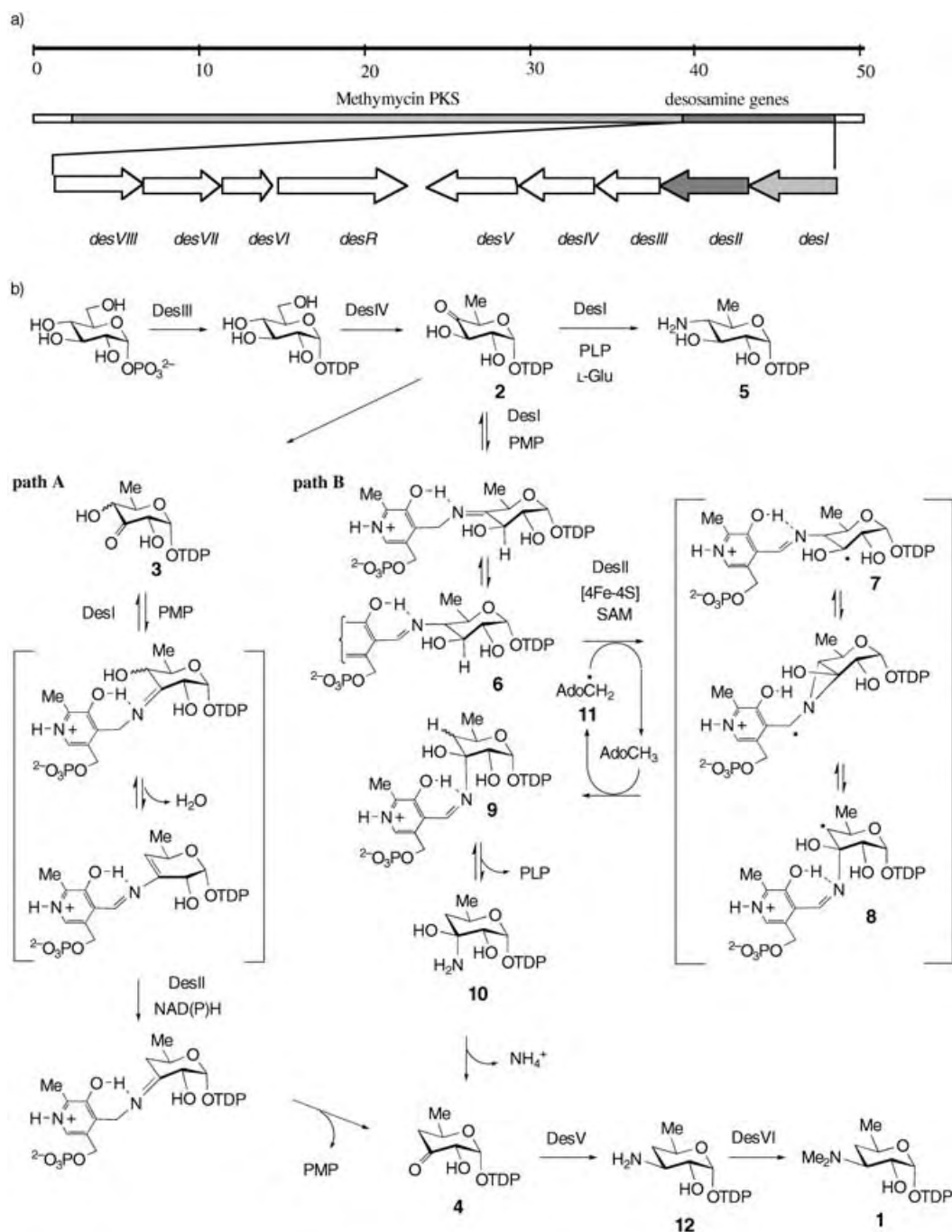
[**] The authors gratefully acknowledge financial support provided by the National Institutes of Health (GM 35906 and 54346). H.-w.L. also thanks the National Institute of General Medical Sciences for a MERIT Award. We are particularly grateful to Professor Duilio Arigoni for his comments on the deoxygenation mechanism. TDP = thymidine diphosphate.

at C4 in the biosynthesis of D-desosamine could follow the α -deoxygenation path similar to that catalyzed by E₁ and E₃ starting from 3-keto-6-deoxyhexose (**3**) to give 3-keto-4,6-dideoxyhexose (**4**, Scheme 2, path A). This possibility is supported by the fact that the translated sequences of two genes, *desI* and *desII*, which are assigned to encode proteins involved in the C4 deoxygenation in the desosamine biosynthetic gene cluster,^[7] are highly similar to B₆-dependent enzymes and those containing an iron–sulfur center, respectively.

However, recent characterization of the purified DesI protein showed that it catalyzes the C4 transamination of **2** to generate TDP-4-amino-4,6-dideoxy-D-glucose (**5**; TDP = thymidine diphosphate) in the presence of pyridoxal 5'-phosphate (PLP) and L-glutamate.^[8] Further sequence analysis revealed that DesII, which contains a [4Fe-4S] consensus motif (CXXXCXXC), belongs to the recently identified S-adenosylmethionine (SAM) superfamily of radical enzymes.^[9] These two observations prompted a revision of the proposed biosynthetic pathway for TDP-D-desosamine. As depicted in Scheme 2 (path B), the DesI/DesII reaction may be initiated by the incorporation of a nitrogen-containing functional group from PMP at C4 (such as **6**), followed by a radical-induced 1,2-nitrogen shift (**6** → **7** → **8** → **9**) to yield an aminol intermediate (such as **10**). Subsequent elimination of an ammonium ion would afford the predicted product **4**. The regeneration of PMP may be facilitated by the transamination activity of DesI in the presence of L-glutamate.

The key mechanistic components of this reaction are reminiscent of those used in the reaction catalyzed by lysine 2,3-aminomutase (LAM), which is a [4Fe-4S]-containing enzyme that requires PLP and SAM for activity.^[10] Catalysis by LAM is triggered by the abstraction of a hydrogen atom from the lysine-PLP adduct by the 5'-deoxyadenosyl radical (**11**; AdoCH₂[•]), which is formed by the reductive cleavage of SAM through involvement of the reduced [4Fe-4S] center.^[11] A similar abstraction of a hydrogen atom, induced by the 5'-deoxyadenosyl radical, from **6** at C3 to give **7** may also be the key event of the C4 deoxygenation reaction. To test this hypothesis, we purified and studied the catalytic properties of DesII. Herein, we report the biochemical characterization of DesII and the mechanistic implications for the overall C4 deoxygenation reaction.

The *desII* gene was amplified from the genomic DNA of *S. venezuelae*^[7b] by the polymerase chain reaction and cloned into the pET24b(+) vector at the *NdeI* and *XhoI* restriction sites.^[12] The DesII protein with a His₆ tag at the C terminus was purified to near-homogeneity by using a Ni-NTA column followed by elution from a MonoQ column attached to an FPLC system.^[13] A molecular mass of 48.4 kDa for DesII as estimated by gel filtration chromatography suggests that DesII, which has a calculated molecular mass of 54.265 kDa (including the His₆ tag), is a monomer in solution. Although purified DesII exhibits a broad absorption band between 400 and 500 nm ($\epsilon_{420} = 4000 \text{ M}^{-1} \text{ cm}^{-1}$), which is indicative of an iron–sulfur center,^[14] titration showed the presence of only



Scheme 2. a) Organization of the D-desosamine biosynthetic gene cluster. Scale indicates the length of DNA (kb). b) Possible mechanisms of deoxygenation at the C4 position in the biosynthesis of D-desosamine. TDP=thymidine diphosphate; L-Glu=L-glutamate; NAD(P)H=reduced nicotinamide adenine dinucleotide (phosphate).

0.6 equivalents of iron^[15] and 0.5 equivalents of sulfur^[16] per DesII monomer. Hence, most of the iron–sulfur cluster was depleted and/or decomposed during purification under aerobic conditions. Anaerobic reconstitution, carried out in the presence of a sixfold molar excess of Na₂S and Fe(NH₄)₂(SO₄)₂ in 100 mM Tris-HCl buffer, at pH 8 containing 5 mM dithiothreitol (DTT) at 18 °C,^[17] led to holo-DesII, which contains nearly 4 equivalents of iron and 3.9 equivalents of sulfur atoms per subunit, with a broad absorption band at

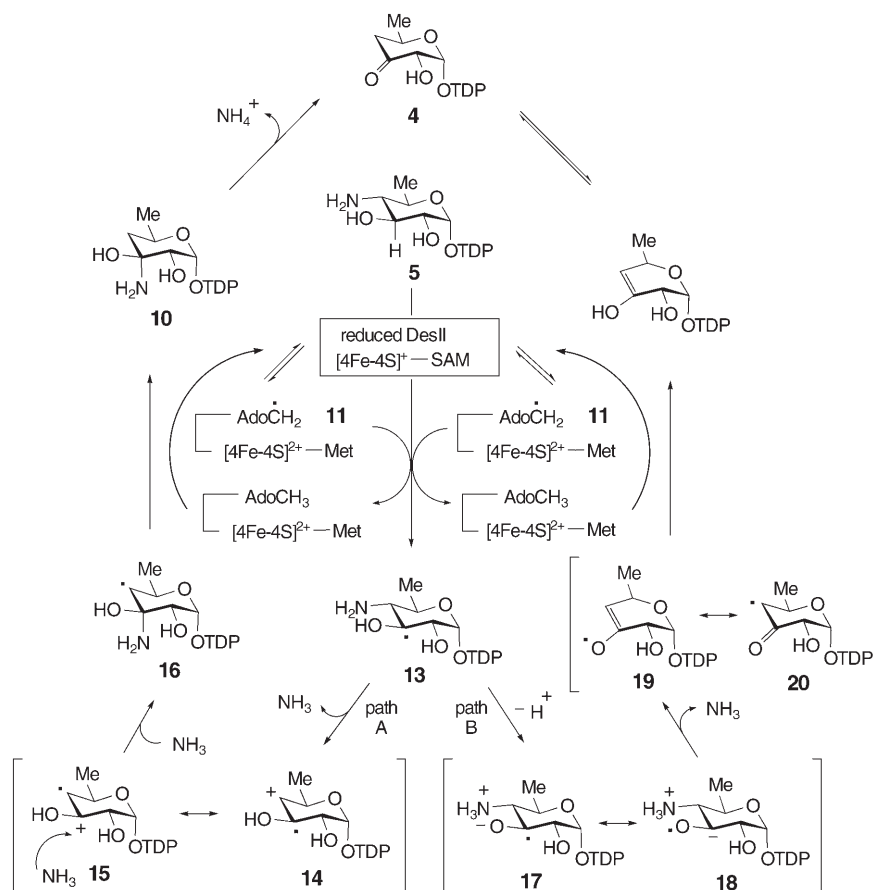
420 nm ($\epsilon_{420} = 9200 \text{ M}^{-1} \text{ cm}^{-1}$). Both features are characteristic of a [4Fe-4S]²⁺ cluster.^[14]

To test the proposed mechanism of C4 deoxygenation, the purified and reconstituted DesII was treated with sodium dithionite anaerobically to reduce the [4Fe-4S]²⁺ cluster to the [4Fe-4S]⁺ state.^[18] The reduced DesII was then incubated with DesI and 2^[8] in the presence of SAM, PMP (or PLP), and L-glutamate under anaerobic conditions.^[19] HPLC analysis of the reaction mixture using a Dionex anion-exchange column

(4 × 250 mm)^[20] revealed a new product with a retention time of 28.2 minutes which was not detected when dithionite or SAM was omitted from the incubation mixture. This new product was identified as **4** on the basis of its retention time, which was identical to that of a standard,^[21] as well as high-resolution FAB-MS data (calcd for $[M-H]^-$: 529.0625, found: 529.0621). These results clearly demonstrate that SAM and the reduced $[4Fe-4S]^+$ cluster are required for DesII activity and they establish, for the first time, an essential role for DesII in the C4 deoxygenation reaction. The fact that the addition of DesV (in the presence of PLP and L-glutamate) to the above incubation mixture^[22] led to the isolation of **12** as the final product^[23] provided further evidence for the formation of **4** as a result of reaction with DesI/DesII.

To our surprise, when the reduced DesII was incubated by itself under anaerobic conditions with SAM and **5**, which was generated separately using DesI and **2** in the presence of PLP and L-glutamate,^[8] compound **4** was again detected as the sole TDP-sugar product.^[24] This finding, obtained in the absence of DesI, strongly suggests that the actual substrate of DesII is **5** and that the conversion of **2** into **4** proceeds in two steps, in which DesI catalyzes the C4 transamination of **2** to **5** and DesII carries out the C4 deamination of **5** to give **4**. The failure to establish the formation of a DesI–DesII complex in vivo by the yeast two-hybrid assay^[25] is consistent with the observation that DesI and DesII function independently. Taken together, these results clearly demonstrate that DesII is a SAM-dependent deaminase, not a deoxygenase as previously surmised.

To account for these results, two possible mechanisms for the DesII-catalyzed reaction can be envisioned. As depicted in Scheme 3, generation of the 5'-deoxyadenosyl radical (**11**) is expected to be the first part of the reaction facilitated by the reduced $[4Fe-4S]^+$ center as found in other SAM-radical-dependent enzymes.^[26] The actual chemical conversion may be triggered by abstraction of a hydrogen atom at C3 of **5** by **11** to give **13**. The mechanism for the subsequent transformation is less obvious, but may parallel the reaction catalyzed by the coenzyme B₁₂ dependent ethanolamine ammonia lyase, which converts ethanolamine into ammonia and acetaldehyde.^[27] As shown in Scheme 3 (path A), the key step may be a radical-induced deamination followed by the readdition of ammonia to the resulting cation radical intermediate (**14/15**), which is effectively a 1,2-amino shift (**13**→**14/15**→**16**→**10**), to form an aminol radical **16**.^[28] Reclaiming a hydrogen atom from 5'-deoxyadenosine results



Scheme 3. Possible mechanisms of deoxygenation at C4 in the biosynthesis of D-desosamine. Generation of 5'-deoxyadenosyl radical (**11**) is expected to be the first part of the reaction. Met = methionine.

in the formation of **10** and the regeneration of **11**, or more likely the reduced $[4Fe-4S]^+$ -SAM complex.^[29] Elimination of an ammonium ion from **10** would afford the desired product **4**. The reaction may also involve deprotonation of the 3-hydroxy group of **13** to yield a ketyl radical anion **17**,^[30] whose resonance form **18** facilitates the β-elimination of the 4-amino group (Scheme 3, path B). The reaction catalyzed by (R)-2-hydroxyacyl-CoA dehydratase^[31] in the fermentation of α-amino acids by anaerobic bacteria provides a precedent. The key step of the latter reaction involves ketyl radical anion induced C_β–O cleavage to expel a hydroxy group. Experiments to distinguish these mechanistic proposals are in progress.

In summary, the data reported herein show that DesII is a SAM-dependent $[4Fe-4S]$ -containing enzyme and is directly responsible for the production of a key intermediate **4** in the biosynthesis of desosamine. In contrast to our previous proposal that DesI/DesII function as a pair to catalyze the α-deoxygenation of a 3-ketosugar substrate **3**, the C4 deoxygenation step is now established to proceed in two stages via an amino sugar intermediate **5**. These results are significant for two reasons: DesII has been identified as a unique deaminase, and the entire desosamine pathway has now been characterized (**2**→**5**→**4**→**12**→**1**). Although the mechanism of DesII catalysis remains elusive, utilization of 5'-

deoxyadenosyl radical (**11**) derived from SAM to abstract a hydrogen atom from **5** is believed to be an integral part of the reaction of DesII. Evidently, the mode of C4 deoxygenation by DesI/DesII is distinctly different from that of the E₁/E₃ paradigm. Currently, only a handful of SAM–radical enzymes have been characterized and all are involved in unusual biotransformations.^[32] The fact that DesII is responsible for a radical-induced deamination further illustrates the catalytic versatility of this class of enzymes. Its participation with a transaminase (DesI) in an overall deoxygenation reaction underscores Nature's ingenuity in devising strategies for C–O bond scission.

Received: June 10, 2005

Revised: August 2, 2005

Published online: September 27, 2005

Keywords: amino sugars · biosynthesis · deoxygenation · desosamine · radicals

- [1] a) J. S. Thorson, T. J. Hosted, Jr., J. Jiang, J. B. Biggins, J. Ahlert, *Curr. Org. Chem.* **2001**, 5, 139–167; b) V. Kren, L. Martinkova, *Curr. Med. Chem.* **2001**, 8, 1303–1328.
- [2] a) D. A. Johnson, H.-w. Liu in *The Biology–Chemistry Interface: A Tribute to Koji Nakanishi* (Eds.: R. Cooper, J. D. Snyder), Marcel Dekker, New York, **1999**, pp. 351–396; b) D. A. Johnson, H.-w. Liu in *Comprehensive Natural Products Chemistry*, Vol. 3 (Eds.: D. Barton, K. Nakanishi, O. Meth-Cohn), Elsevier, Amsterdam, **1999**, pp. 311–365; c) X. He, H.-w. Liu, *Annu. Rev. Biochem.* **2002**, 71, 701–754.
- [3] X. He, H.-w. Liu, *Curr. Opin. Chem. Biol.* **2002**, 6, 590–597.
- [4] a) J. S. Thorson, H.-w. Liu, *J. Am. Chem. Soc.* **1993**, 115, 7539–7540; b) Y. Lei, O. Ploux, H.-w. Liu, *Biochemistry* **1995**, 34, 4643–4654.
- [5] V. P. Miller, J. S. Thorson, S. F. Lo, O. Ploux, H.-w. Liu, *Biochemistry* **1993**, 32, 11934–11942.
- [6] a) D. A. Johnson, G. T. Gassner, V. Bandarian, F. J. Ruzicka, D. P. Ballou, G. H. Reed, H.-w. Liu, *Biochemistry* **1996**, 35, 15846–15856; b) C.-w. T. Chang, D. A. Johnson, V. Bandarian, H. Zhou, R. LoBrutto, G. H. Reed, H.-w. Liu, *J. Am. Chem. Soc.* **2000**, 122, 4239–4240.
- [7] a) L. Zhao, D. H. Sherman, H.-w. Liu, *J. Am. Chem. Soc.* **1998**, 120, 9374–9375; b) Y. Xue, L. Zhao, H.-w. Liu, D. H. Sherman, *Proc. Natl. Acad. Sci. USA* **1998**, 95, 12111–12116.
- [8] L. Zhao, S. Borisova, S.-M. Yeung, H.-w. Liu, *J. Am. Chem. Soc.* **2001**, 123, 7909–7910.
- [9] H. J. Sofia, G. Chen, B. G. Hetzler, J. F. Reyes-Spindola, N. E. Miller, *Nucleic Acids Res.* **2001**, 29, 1097–1106.
- [10] a) P. A. Frey, G. H. Reed, *Arch. Biochem. Biophys.* **2000**, 382, 6–14; b) P. A. Frey, *Annu. Rev. Biochem.* **2001**, 70, 121–148.
- [11] D. Chen, C. Walsby, B. M. Hoffman, P. A. Frey, *J. Am. Chem. Soc.* **2003**, 125, 11788–11789.
- [12] Two primers were designed to amplify the *desII* gene by the polymerase chain reaction (PCR). The start primer, 5'-CGCG-CATATGACCGCCCCGCGCTTTCC-3', contained an *NdeI* restriction site (in bold), and the stop primer, 5'-GCGCCTCGAGGCGCAGGAAGCC-3', contained a *XhoI* restriction site (in bold). Amplification was carried out by using an initial incubation step at 95°C for 3 min, followed by 30 cycles comprising incubation at 95°C for 30 s, 60°C for 30 s, and 72°C for 90 s. The PCR product was purified and ligated into the *NdeI*/*XhoI* sites of the vector pET24b(+). The resulting plasmid was used to transform *E. coli* BL21(DE3).
- [13] The elution profile began with a linear gradient of 0 to 50% of buffer B (buffer A with 0.5 M NaCl) in buffer A (20 mM Tris-HCl, pH 7.5) for 25 min, followed by a gradient of 50–70% of buffer B in buffer A for 2 min. The flow rate was 3 mL min⁻¹ and the detector was set at 280 nm. The DesII protein eluted at 55% buffer B.
- [14] a) S. Ollagnier, E. Mulliez, J. Gaillard, R. Eliasson, M. Fontecave, P. Reichard, *J. Biol. Chem.* **1996**, 271, 9410–9416; b) R. Külzer, T. Pils, R. Kappl, J. Hüttermann, J. Knappe, *J. Biol. Chem.* **1998**, 273, 4897–4903; c) N. B. Ugulava, B. R. Gibney, J. T. Jarrett, *Biochemistry* **2000**, 39, 5206–5214.
- [15] For titration of iron, see: W. W. Fish, *Methods Enzymol.* **1988**, 158, 357–364.
- [16] For determination of sulfur, see: H. Beinert, *Anal. Biochem.* **1983**, 131, 373–383.
- [17] Protein-bound iron was removed by incubating the as-isolated DesII in 100 mM Tris-HCl buffer (pH 8), containing 100 mM EDTA and 2 mM sodium dithionite, for 1 h at 25°C. The apo-protein was loaded and eluted through a Sephadex G-25 column with the above Tris-HCl buffer and concentrated to 10 mg mL⁻¹ by an Amicon concentrator with a YM10 membrane. This apo-DesII was incubated with a sixfold molar excess of Na₂S and Fe(NH₄)₂(SO₄)₂ in 1 mL of 100 mM Tris-HCl buffer (pH 8) containing 5 mM DTT for 3 h at 18°C. A deaerated solution of EDTA (2 mM) was then added, and the incubation was continued for another 30 min. The reconstituted DesII was eluted through a Sephadex G-25 column as described above, and the green-gray protein fractions were pooled and concentrated to approximately 10 mg mL⁻¹ by an Amicon concentrator with a YM10 membrane. All of the above operations were performed in an anaerobic chamber.
- [18] Reduction of the [4Fe-4S] center of reconstituted DesII (0.19 mM) was achieved by using sodium dithionite (sixfold molar excess) prepared in 100 mM Tris-HCl buffer (pH 8) over 40 min. Reduction was conducted in an anaerobic chamber and monitored by the decrease of the absorbance at 420 nm.
- [19] The activity assay was carried out anaerobically by mixing **2** (0.6 mM), L-glutamate (0.5 mM), pyridoxal 5'-phosphate (PLP; 0.14 mM), DesI (0.026 mM), reduced DesII (0.1 mM), and SAM (0.1 mM) in 100 mM Tris-HCl buffer (pH 8) in the presence of DTT (2 mM). The final volume was 1 mL. The reaction mixture was incubated at 25°C for 3 h, and the reaction was quenched by filtering through an Amicon ultrafiltration cell equipped with a YM10 membrane to remove the enzymes. The reaction progress was monitored by HPLC.
- [20] A linear gradient from 20 to 35% of eluent B (1 M ammonium acetate, pH 7.0) in eluent A (H₂O) over 30 min gave a satisfactory separation. The flow rate was 0.6 mL min⁻¹ and the detector was set at λ = 267 nm. The retention time for the substrate **2** is 13.8 min and that for DesII product **4** is 28.2 min, which is identical to that of the synthesized standard.^[21]
- [21] Compound **4** was prepared by incubating synthetic **12**^[23] with purified DesV in the presence of PLP and α-ketoglutarate.
- [22] To the reaction mixture prepared under conditions described in reference [19] (after 3 h incubation) were added L-glutamate (10 mM), PLP (0.8 mM), and DesV enzyme (0.1 mM). The resulting mixture was incubated at 25°C for 30 min, and then passed through an Amicon ultrafiltration cell equipped with a YM10 membrane to remove the enzymes. The formation of the DesV product **12** was detected by HPLC;^[20] the retention time of 3.7 min is identical to that of the synthesized standard.^[23]
- [23] C.-w. T. Chang, L. Zhao, H. Yamase, H.-w. Liu, *Angew. Chem.* **2000**, 112, 2244–2247; *Angew. Chem. Int. Ed.* **2000**, 39, 2160–2163.
- [24] Typically, 1 mL of assay solution contained substrate **5** (0.5 mM), reduced DesII (0.1 mM), and SAM (0.1 mM) in 100 mM Tris-HCl buffer (pH 8) with 2 mM DTT. The assay mixture was incubated

anaerobically at 25°C for 1 h, and then the reaction was quenched by removing the enzymes by ultrafiltration through a YM10 membrane (Amicon). The reaction progress was monitored by HPLC as described above.^[20]

- [25] A. Osman, *Methods Mol. Biol.* **2004**, 270, 403–422.
- [26] P. A. Frey, O. Th. Magnusson, *Chem. Rev.* **2003**, 103, 2129–2148.
- [27] a) R. LoBrutto, V. Bandarian, O. Th. Magnusson, X. Chen, V. L. Schramm, G. H. Reed, *Biochemistry* **2001**, 40, 9–14; b) G. M. Sandala, D. M. Smith, L. Radom, *J. Am. Chem. Soc.* **2005**, 127, 8856–8864.
- [28] This 1,2-migration may be a stepwise transfer (**13**→**14/15**→**16**) or a direct transfer (**13**→**16**).
- [29] As reclaiming a hydrogen atom from AdoCH₃ by **16** (or **19/20** in path B) is energetically unfavorable, stabilization of the resulting 5'-deoxyadenosyl radical (**11**) by reforming the [4Fe-4S]⁺-SAM complex may provide the driving force to complete the catalytic cycle. A similar argument which invokes reversible cleavage of SAM by the [4Fe-4S] center has been proposed for the lysine 2,3-aminomutase reaction (D. Chen, C. Walsby, B. M. Hoffman, P. A. Frey, *J. Am. Chem. Soc.* **2003**, 125, 11788–11789).
- [30] The pK_a value of the hydroxy group in a ketyl radical can be lower by approximately 5 units than that of the corresponding alcohol: E. Hayon, M. Simic, *Acc. Chem. Res.* **1974**, 7, 114–121. Such a deprotonation in **13** to give **17** could be an intramolecular process.
- [31] a) W. Buckel, *FEBS Lett.* **1996**, 389, 20–24; b) W. Buckel, B. T. Golding, *FEMS Microbiol. Rev.* **1999**, 22, 523–541; c) W. Buckel, *Appl. Microbiol. Biotechnol.* **2001**, 57, 263–273; d) J. Kim, M. Hetzel, C. D. Boiangiu, W. Buckel, *FEMS Microbiol. Rev.* **2004**, 28, 455–468.
- [32] Examples include lysine 2,3-aminomutase, spore photoproduct lyase, biotin synthase, lipoate synthase, anaerobic coproporphyrinogen III oxidase, formylglycine synthase, pyruvate formate-lyase activase, anaerobic ribonucleotide reductase activase, benzylsuccinate synthase activase, and glycerol dehydratase activase (E. N. G. Marsh, A. Patwardhan, M. S. Huhta, *Bioorg. Chem.* **2004**, 32, 326–340).

DOI: 10.1002/anie.200502503

Experimental Evidence for a Jahn–Teller Distortion in AuCl₃**

*Ian J. Blackmore, Adam J. Bridgeman, Neil Harris,
Mark A. Holdaway, John F. Rooms,
Emma L. Thompson, and Nigel A. Young**

Gold halides have generated considerable interest amongst both computational and experimental chemists because of their intriguing bonding and structures.^[1–4] Advances in gas-phase (mass-spectrometry) experiments^[5] and the theoretical importance of relativistic effects in gold chemistry^[6] have recently been reviewed. The common oxidation states for gold are Au^{III} and Au^I, with Au^{II} being comparatively rare. The Au^I monohalides display large structural relativistic effects, and the very short Au...Au distances in their dimers (caused by the so-called “aurophilic attraction”) are regarded as classic examples of metallophilic interactions.^[6] All of the monohalides have been characterized experimentally.^[1,5,7] Monomeric Au^{II} is a rare oxidation state, although multi-nuclear complexes are more common,^[8] and some examples such as solid-state AuCl₂ are mixed valent.^[9] Perhaps the most significant Au^{II} complexes are those containing Au–Xe bonds, such as [AuXe₄][Sb₂F₁₁]₂.^[10] Schröder et al. have recently identified AuCl₂ (as neutral, anionic, and cationic species) in sophisticated mass-spectrometric experiments.^[11] The *D*_{3h} trigonal-planar structure of the d⁸ Au^{III} halides are Jahn–Teller distorted to T-, Y-, and L-shaped geometries. This distortion was highlighted computationally by Schwerdtfeger et al. in 1992,^[12] and recently elaborated by Hargittai and co-workers^[1–3] as well as by Schwerdtfeger and co-workers.^[4] Both the stability of the gold trihalides and the Jahn–Teller stabilization energy decrease from the fluoride through to the iodide. The T-shaped structure is the minimum of the Jahn–Teller surface for AuF₃, AuCl₃, and AuBr₃, and is the global minimum of the ground state for the first two. The Y-shaped geometry is a transition state between the T-shaped geometries. For AuI₃, the Y-shaped structure lies at lower energy than the T-shaped structure, but for both AuBr₃ and AuI₃ the potential-energy surface is very flat, and the energy gain arising from a Jahn–Teller distortion is small. Schulz and Hargittai^[1] suggest that AuF₃ and AuCl₃ are static Jahn–Teller

[*] I. J. Blackmore, Dr. A. J. Bridgeman, Dr. N. Harris, M. A. Holdaway, Dr. J. F. Rooms, Dr. E. L. Thompson, Dr. N. A. Young
Department of Chemistry
The University of Hull
Kingston upon Hull, HU6 7RX (UK)
Fax: (+44) 1482-466-410
E-mail: n.a.young@hull.ac.uk

[**] This work was supported by the Engineering and Physical Sciences Research Council UK (EPSRC-GR/T09651) and the University of Hull.



Supporting information for this article is available on the WWW under <http://www.angewandte.org> or from the author.

systems, whereas AuBr_3 and AuI_3 are dynamic Jahn–Teller systems. Of the monomeric Au^{III} halides, experimental data is only available for AuF_3 , with the T-shaped structure being confirmed by electron diffraction studies.^[13] AuI_3 has been reported to be stabilized in a cuprate lattice,^[14] but more recent calculations^[15] and experiments^[16] suggest that the gold is present as Au^{I} and not Au^{III} , therefore the D_{3h} structure is unsurprising. The solid-state structures of both Au_2Cl_6 and Au_2Br_6 consist of discrete D_{2h} -symmetric halogen-bridged dimers^[12] which become the principal gold-containing vapor species. Vaporization is accompanied by extensive decomposition, and in the recent electron-diffraction study, only approximately 6% of the vapor was Au_2Cl_6 (the remainder being Cl_2), and it was noted that it was not possible to obtain any data for monomeric AuCl_3 .^[2] Therefore, the authors proposed that the only way forward was to use detailed computational methods.

We have previously used matrix isolation in combination with IR, UV/Vis and extended X-ray absorption fine structure (EXAFS) spectroscopy to synthesize and characterize monomeric noble-metal chlorides such as PtCl and PtCl_2 .^[17] For the platinum chlorides, hollow-cathode sputtering with chlorine-doped argon was used to generate the atomic Pt, and although this approach was used for AuCl_3 , thermal evaporation and laser ablation were also employed.

Figure 1a shows the electronic absorption spectrum of Au_2Cl_6 in an argon matrix, and is in good agreement with the vapor-phase spectrum.^[18] The intense bands at 40590 and

46060 cm^{-1} were assigned to bridging- and terminal-ligand-to-metal charge-transfer transitions, respectively.^[18] The weaker features at 22300 and 32890 cm^{-1} were assigned to d-d transitions.^[18] Figure 1b shows the spectrum obtained when thermally evaporated gold atoms were matrix isolated in 1% Cl_2/Ar . The sharp peaks at 39050, 43670, and 44085 cm^{-1} are due to atomic gold.^[19] The broad feature at approximately 30500 cm^{-1} and the tail into the UV region are both due to Cl_2 . In addition to these, a weaker band at about 16000 cm^{-1} with vibrational fine structure was observed. The spectra obtained when thermally evaporated gold atoms were trapped in a 5% Cl_2/Ar matrix were very similar, except that there was less unreacted gold, and the fine structure on the band at 16000 cm^{-1} was less well resolved. A similar spectrum was obtained when gold was sputtered with Cl_2/Ar mixtures, and the band at 16000 cm^{-1} was also present when HCl was used as the chlorine source in the sputtering experiments. Figure 1c shows the spectrum obtained when thermally evaporated gold atoms were condensed in a 1% Cl_2/Ar mixture that had passed through a microwave discharge just prior to deposition. This process had the effect of increasing the yield of the feature at 16000 cm^{-1} relative to similar experiments with no discharge, as well as reducing the amount of residual Cl_2 present, although there is a substantial amount of unreacted gold. These observations indicate that the band at 16000 cm^{-1} only appears when chlorine atoms or molecules are present, and that there are no high energy features associated with the band at 16000 cm^{-1} that are obscured by the UV tail arising from the presence of Cl_2 (Figure 1b). As the feature at 16000 cm^{-1} was only present in spectra which contained both gold and chlorine and is independent of the source of both gold atoms and chlorine, it can readily be assigned to an AuCl_x species. An expansion of the vibrational fine structure on this band is shown in Figure 1d, and the separation of about 310 cm^{-1} between the sharpest peaks on the low energy side is consistent with a symmetric Au–Cl stretching mode in an excited state. The observation of only one band implies the presence of one AuCl_x species. As this band is much lower in energy than both the charge-transfer and d-d bands in Au_2Cl_6 , it is most likely to be a d-d transition, with any charge-transfer bands beyond the effective upper spectral limit of about 50000 cm^{-1} .

IR spectroscopy of the Au–Cl stretching modes ($\nu_{\text{Au-Cl}}$) in combination with the natural isotopic abundances of Cl (^{35}Cl , 75.5%; ^{37}Cl , 24.5%) is a very powerful method of identifying molecular shape. For AuCl , a simple 3:1 isotope pattern is expected. For AuCl_2 , a 9:6:1 pattern would be observed, and if the separation of the outermost components could be identified accurately, the bond angle could be determined. The presence of threefold rotation axes in both D_{3h} - and C_{3v} -symmetric AuCl_3 would result in nonbinomial isotope patterns for the degenerate modes. One IR-active E' $\nu_{\text{Au-Cl}}$ band with a 81:9:27:11 pattern is expected for D_{3h} -symmetric AuCl_3 , whereas C_{3v} -symmetric AuCl_3 would have two IR-active $\nu_{\text{Au-Cl}}$ bands, an E mode with a 81:9:27:11 isotope pattern, and an A_1 mode with a 27:27:9:1 pattern. Calculations^[1,2] for T-shaped AuCl_3 predict three IR-active $\nu_{\text{Au-Cl}}$ modes ($2A_1 + B_2$), but the two A_1 modes have very low intensity so that only the B_2 mode is expected to be observed.

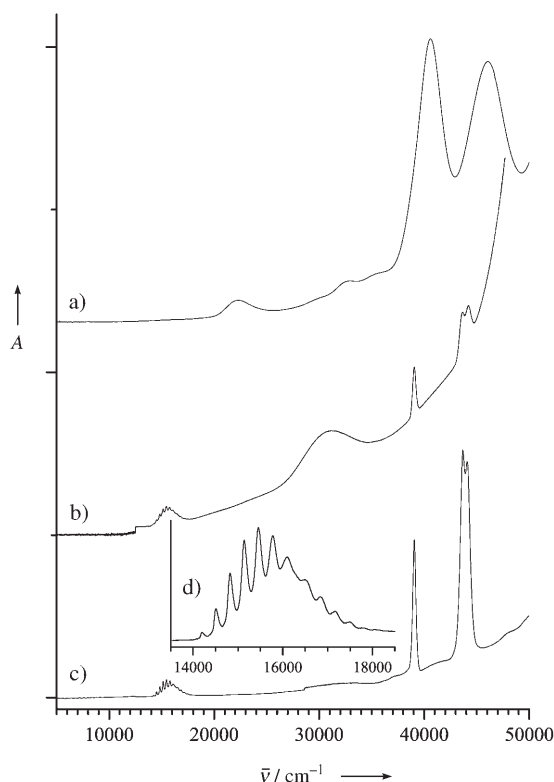


Figure 1. Matrix-isolation electronic absorption spectra of a) Au_2Cl_6 in Ar, b) thermally evaporated gold atoms in 1% Cl_2/Ar , c) thermally evaporated gold atoms mixed with 1% Cl_2/Ar passed through microwave discharge, d) expansion of (c).

Our calculations indicate that the B_2 mode will display a 9:6:1 chlorine isotope pattern, and the two very low intensity A_1 modes will yield a complex isotope pattern derived from 9:6:1 and 3:1 isotope patterns, but which is dependent on their separation. The Y-shaped transition state is also calculated^[1,2] to have three IR-active $\nu_{\text{Au-Cl}}$ modes ($2A_1 + B_2$) with similar frequency, intensity (intense A_1 , very weak $A_1 + B_2$), and isotope patterns to the T-shaped geometry.

The argon-matrix IR spectrum of Au_2Cl_6 is shown in Figure 2a. This spectrum is in very good agreement with the

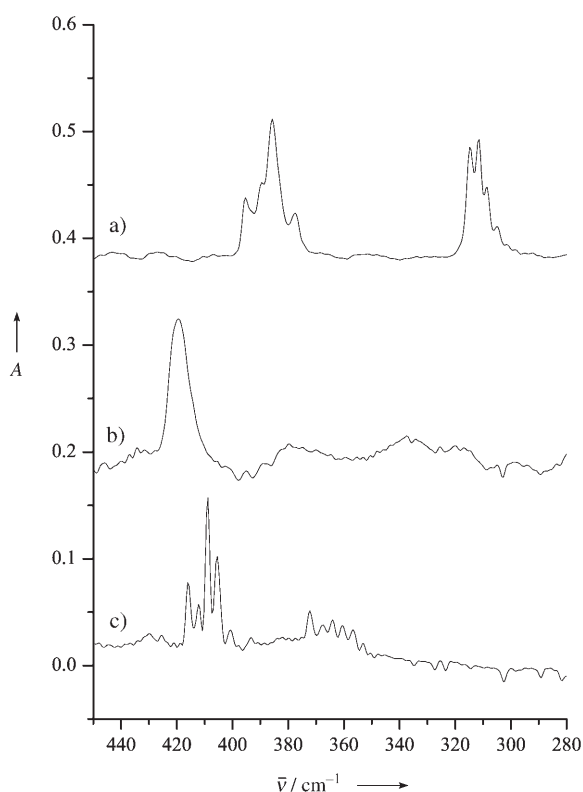


Figure 2. Matrix-isolation IR spectra of a) Au_2Cl_6 in Ar, b) gold atoms sputtered with 5% Cl_2/Ar , c) thermally evaporated gold atoms in 100% Cl_2 .

previous data from both the solid state and the gas phase,^[20] and complex chlorine isotopic structure is observed in both bands. The feature at approximately 386 cm^{-1} arises from terminal $\nu_{\text{Au-Cl}}$ asymmetric stretching modes ($\nu_{12}(\text{B}_{2u})$ and $\nu_{16}(\text{B}_{3u})$), and the bridging $\nu_{\text{Au-Cl}}$ asymmetric stretching modes are at about 312 cm^{-1} ($\nu_{13}(\text{B}_{2u})$ and $\nu_{17}(\text{B}_{3u})$). Figure 2b displays the spectrum of the matrix-isolated products from a gold foil sputtered with 5% Cl_2/Ar . The only significant $\nu_{\text{Au-Cl}}$ band is at approximately 420 cm^{-1} , and it is clear that there is no evidence for the formation of Au_2Cl_6 under these conditions. Although this band shows signs of asymmetry, it did not display isotopic chlorine features at higher spectral resolution, probably because of the considerable Cl_2 concentration in the matrix. Although sputtering, thermal evaporation, and laser ablation were all used with lower Cl_2/Ar concentrations, the spectral quality was not sufficient to

provide convincing evidence of the geometry of the gold-containing species. Pure Cl_2 matrices were then used, and thermally evaporated gold atoms were condensed at 50 K and then cooled to about 12 K. The resulting spectrum is shown in Figure 2c. The most intense band at approximately 410 cm^{-1} clearly displays a 9:6:1 isotopic pattern with a splitting that is consistent with a vibrational mode involving two chlorine atoms attached to a heavy element. There is also evidence for a second 9:6:1 pattern with a similar peak separation a few wavenumbers higher. The most reasonable interpretation of this is that there are two 9:6:1 patterns in close proximity that are derived from the same vibrational mode, which is subject to matrix-site effects in the pure Cl_2 matrix. This band is in a very similar position to that obtained for argon matrices with sputtering, laser ablation, and thermal evaporation, thus indicating that it arises from the same species in all cases, which also gives rise to the band at 16000 cm^{-1} in the electronic absorption spectra. In addition to the relatively intense bands around 410 cm^{-1} , there is a complex multiplet at $375\text{--}350\text{ cm}^{-1}$. Although TaCl_5 is known to have spectral features in this region,^[21] no such bands were observed when a bare tantalum filament was heated during the deposition of a pure Cl_2 matrix. Therefore, this multiplet is also assigned to an AuCl_x species.

The presence of 9:6:1 isotope patterns in the bands at 410 cm^{-1} rules out AuCl , but they could be assigned to either AuCl_2 or AuCl_3 . Au^{II} is commonly considered to be a rare oxidation state, especially for monomeric compounds.^[8] Solid-state AuCl_2 is known to be mixed valent^[9] and AuCl_2 has only been detected in the vapor phase by using sophisticated mass spectrometric experiments starting with mass-selected AuCl_2^- .^[11] Stace and co-workers have reported that Au^{II} can be stabilized in the gas phase by σ -donor, π -acceptor ligands, especially if the ligands have a large dipole moment and high ionization energy,^[22] but this is not the case for chloride. It would be expected that pure Cl_2 matrices would yield stable gold chloride with the highest oxidation state. From all of the various experimental conditions used for the electronic absorption spectra, only one band at 16000 cm^{-1} was associated with both gold and chlorine, and whereas the presence of Cl atoms increased its intensity, no other bands were observed. The presence of weak features in the region between 375 and 350 cm^{-1} is compatible with AuCl_3 , but not with AuCl_2 . Despite reporting an extensive set of calculations on monomeric, dimeric, and anionic gold halides, Hargittai and co-workers^[1,2] did not appear to consider AuCl_2 . Schröder et al. have carried out some DFT calculations that indicate that AuCl_2 would be stable to disproportionation in the idealized gas phase, but not in the solid state.^[11] Our DFT calculations^[23] indicate that although the $\Delta_f H$ values for $\text{AuCl}_{2(\text{g})}$ and $\text{AuCl}_{3(\text{g})}$ from gold atoms and Cl_2 are very similar (-271 and -273 kJ mol^{-1} , respectively), the enthalpy of atomization to gold and chlorine atoms is much larger for AuCl_3 than for AuCl_2 (672 and 537 kJ mol^{-1} , respectively). The previous MP2 and B3LYP calculations^[2] indicate that the IR-active $\nu_{\text{Au-Cl}}$ mode of “T-shaped” AuCl_3 should be about 20 cm^{-1} higher than the terminal $\nu_{\text{Au-Cl}}$ modes in Au_2Cl_6 , with the most intense $\nu_{\text{Au-Cl}}$ mode of the Y-shaped transition state being a few wavenumbers less than that of the T-shaped $\nu_{\text{Au-Cl}}$

mode. The $\nu_{\text{Au-Cl}}$ mode of AuCl is calculated^[2] to be just above midway in terms of energy between the terminal and bridging $\nu_{\text{Au-Cl}}$ modes in Au_2Cl_6 , although our DFT calculations incorporating the high-level relativistic effects within ADF (Amsterdam Density Functional package) indicate that the value should be closer to that of the terminal $\nu_{\text{Au-Cl}}$ mode in Au_2Cl_6 . Our calculations on AuCl_2 indicate that its IR-active $\nu_{\text{Au-Cl}}$ mode should be higher than that of AuCl_3 by about 17 cm^{-1} .

Therefore, on the basis of both experimental and computational considerations, the most reasonable assignment of the bands at about 420 cm^{-1} in the IR spectrum is to AuCl_3 . The 9:6:1 chlorine isotope pattern demonstrates that it does not have D_{3h} (or C_{3v}) symmetry but adopts a Jahn–Teller-distorted geometry, which on the basis of the calculations^[2] is most likely to be T shaped. These calculations also indicate that the two A_1 modes in the T-shaped AuCl_3 species will be separated by about 10 cm^{-1} and be about 30 cm^{-1} lower than the B_2 mode, but will have very low (effectively zero) intensity. The two low-intensity A_1 and B_2 modes in the Y-shaped geometry are also calculated to be separated by 10 cm^{-1} , and about $30\text{--}40\text{ cm}^{-1}$ lower than the intense A_1 mode. The complex multiplet at $375\text{--}350\text{ cm}^{-1}$ clearly falls into this region, but the intensity is incompatible with the calculations.^[2] It is possible that the Cl_2 matrix exerts sufficient perturbation so that these modes gain some intensity. The isotope pattern is very sensitive to the separation of the two modes, and as a site effect was observed on the intense $\nu_{\text{Au-Cl}}$ mode, it is likely that this multiplet is also subject to site effects.

The Au L_3 -edge EXAFS and FT for the matrix products of gold sputtered with 5% Cl_2/Ar are shown in Figure 3. Sputtering was chosen as it gives the best dilution of metal atoms in the matrix, thus avoiding the problems of aggregation.^[17] The FT contains one peak that fits^[24] to a single Au–Cl bond length with no evidence for two different bond lengths, thus ruling out the presence of Au_2Cl_6 . The Au–Cl bond length of $2.22(2)\text{ \AA}$ is 0.06 \AA shorter than that observed for $[\text{AuCl}_4]^-$ with the same analysis protocols. Previous B3LYP and MP2 calculations^[2] indicate that the T-shaped ground state of AuCl_3 will have Au–Cl bond lengths shorter by about 0.07 \AA than $[\text{AuCl}_4]^-$, and our ADF calculations indicate that the Au–Cl bond length in AuCl_2 will be approximately 0.04 \AA shorter than that of AuCl_3 . The chlorine occupation number refined to a value of about 1.7, or an AuCl_3 fraction of about 57%. Whereas this could indicate a lower-coordination species, the presence of bands corresponding to unreacted gold in all of the electronic absorption spectra, the IR evidence for AuCl_3 , as well as the Au–Cl bond lengths, indicate it is much more likely to be caused by the presence of both AuCl_3 and Au in the matrix. Although the small peak at around 4.4 \AA in the FT might be due to multiple scattering pathways through the central Au atom, indicative of a linear or very near linear ($>160^\circ$) AuCl_2 unit,^[25] its intensity is too low to make any firm conclusions, and this is also where Au...Ar interactions would be expected.

In conclusion a combination of matrix-isolation electronic absorption, IR, and Au L_3 -edge EXAFS has provided the first experimental data for AuCl_3 and shown conclusively that it

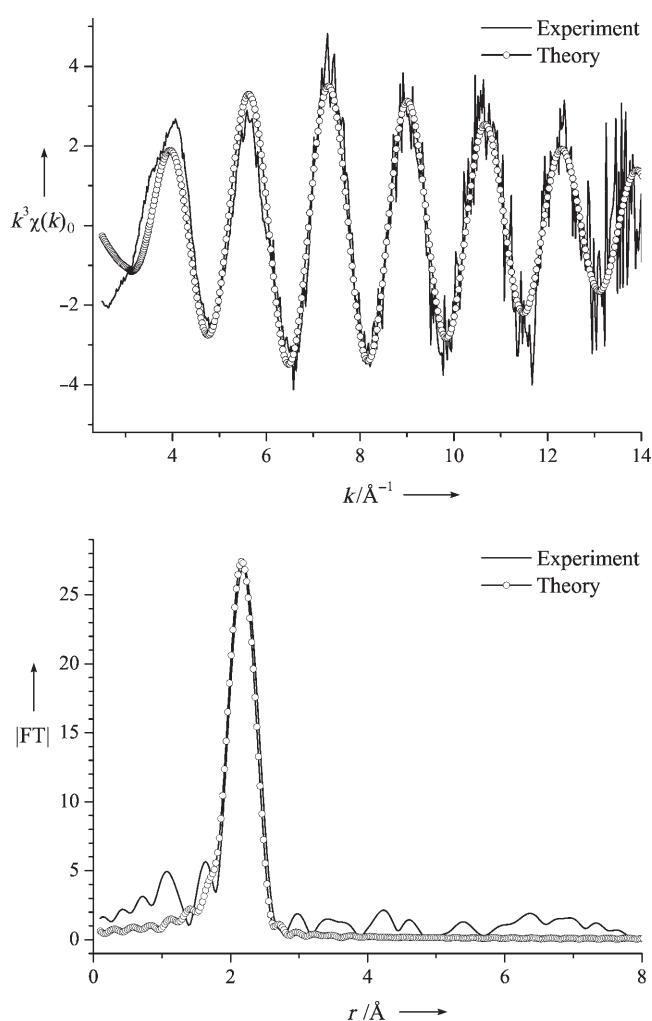


Figure 3. Au L_3 -edge EXAFS (top) and FT (bottom) of the matrix-isolated products of gold atoms sputtered with 5% Cl_2/Ar .

does not have D_{3h} symmetry in the matrix, but rather a Jahn–Teller-distorted geometry. The experimental data is consistent with a calculated ground state having a T-shaped geometry.

Experimental Section

The general features of our matrix-isolation experimental methodology have been described previously.^[17] The gold atoms were sputtered from a gold-foil hollow cathode, thermally evaporated from gold wire wound onto a tungsten filament, or laser ablated (Xe–Cl excimer laser) from a gold target disc. The Cl_2/Ar mixtures were prepared by using standard manometric procedures. The Au L_3 -edge EXAFS spectra were collected on station 9.2 of the Daresbury Laboratory SRS (2 GeV, 150–250 mA) using a Si220 monochromator detuned by 50% to reduce harmonic contamination. The fluorescence data were collected with a Canberra 13-element solid-state detector. The spectra were averaged, calibrated (using the first maximum in the first derivative of gold foil at 11919 eV), and background subtracted (quadratic pre-edge, 6th-order polynomial post-edge) by using PAXAS.^[26] The data were modeled with EXCURV98.^[27] The DFT calculations at 0 K with zero-point energy

and basis-set supposition-error corrections used ADF BP86/TZP with ZORA.^[28]

Received: July 18, 2005

Published online: September 27, 2005

Keywords: density functional calculations · EXAFS spectroscopy · gold · Jahn–Teller distortion · matrix isolation

- [1] A. Schulz, M. Hargittai, *Chem. Eur. J.* **2001**, 7, 3657.
- [2] M. Hargittai, A. Schulz, B. Réffy, M. Kolonits, *J. Am. Chem. Soc.* **2001**, 123, 1449.
- [3] B. Réffy, M. Kolonits, A. Schulz, T. M. Klapötke, M. Hargittai, *J. Am. Chem. Soc.* **2000**, 122, 3127.
- [4] T. Soehnel, R. Brown, L. Kloo, P. Schwerdtfeger, *Chem. Eur. J.* **2001**, 7, 3167.
- [5] H. Schwarz, *Angew. Chem.* **2003**, 115, 4580; *Angew. Chem. Int. Ed.* **2003**, 42, 4442.
- [6] P. Pykkö, *Angew. Chem.* **2004**, 116, 4512; *Angew. Chem. Int. Ed.* **2004**, 43, 4412.
- [7] D. Schröder, J. Hrusák, I. C. Tornieporth-Oetting, T. M. Klapötke, H. Schwarz, *Angew. Chem.* **1994**, 106, 223; *Angew. Chem. Int. Ed. Engl.* **1994**, 33, 212.
- [8] A. Laguna, M. Laguna, *Coord. Chem. Rev.* **1999**, 195, 837.
- [9] D. B. Dell'Amico, F. Calderazzo, F. Marchetti, *J. Chem. Soc. Dalton Trans.* **1976**, 1829; D. B. Dell'Amico, F. Calderazzo, F. Marchetti, S. Merlino, G. Perego, *J. Chem. Soc. Chem. Commun.* **1977**, 31.
- [10] S. Seidel, K. Seppelt, *Science* **2000**, 290, 117; T. Drews, S. Seidel, K. Seppelt, *Angew. Chem.* **2002**, 114, 470; *Angew. Chem. Int. Ed.* **2002**, 41, 454; K. Seppelt, *Z. Anorg. Allg. Chem.* **2003**, 629, 2427.
- [11] D. Schröder, R. Brown, P. Schwerdtfeger, X. B. Wang, X. Yang, L. S. Wang, H. Schwarz, *Angew. Chem.* **2003**, 115, 323; *Angew. Chem. Int. Ed.* **2003**, 42, 311.
- [12] P. Schwerdtfeger, P. D. W. Boyd, S. Brienne, A. K. Burrell, *Inorg. Chem.* **1992**, 31, 3411.
- [13] B. Réffy, M. Kolonits, A. Schulz, T. M. Klapötke, M. Hargittai, *J. Am. Chem. Soc.* **2001**, 123, 1545.
- [14] J. H. Choy, Y. I. Kim, S. J. Hwang, P. V. Huong, *J. Phys. Chem. B* **2000**, 104, 7273.
- [15] M. L. Munzarova, R. Hoffmann, *J. Am. Chem. Soc.* **2002**, 124, 5542.
- [16] J. H. Choy, Y. I. Kim, *J. Phys. Chem. B* **2003**, 107, 3348.
- [17] A. J. Bridgeman, G. Cavigliasso, N. Harris, N. A. Young, *Chem. Phys. Lett.* **2002**, 351, 319.
- [18] D. S. Rustad, N. W. Gregory, *Polyhedron* **1991**, 10, 633; L. Nalbandian, S. Boghosian, G. N. Papatheodorou, *Inorg. Chem.* **1992**, 31, 1769.
- [19] D. M. Gruen, S. L. Gaudioso, R. L. McBeth, J. L. Lerner, *J. Chem. Phys.* **1974**, 60, 89; D. M. Gruen, J. K. Bates, *Inorg. Chem.* **1977**, 16, 2450.
- [20] L. Nalbandian, G. N. Papatheodorou, *Vib. Spectrosc.* **1992**, 4, 25.
- [21] R. K. Bellingham, J. T. Graham, P. J. Jones, J. R. Kirby, W. Levason, J. S. Ogden, A. K. Brisdon, E. G. Hope, *J. Chem. Soc. Dalton Trans.* **1991**, 3387.
- [22] N. R. Walker, R. R. Wright, P. E. Barran, J. N. Murrell, A. J. Stace, *J. Am. Chem. Soc.* **2001**, 123, 4223; N. R. Walker, R. R. Wright, P. E. Barran, A. J. Stace, *Organometallics* **1999**, 18, 3569.
- [23] The $\Delta_f H$ values for $\text{AuCl}_{(g)}$, $\text{AuCl}_{2(g)}$, and $\text{AuCl}_{3(g)}$ from $\text{Au}_{(g)}$ and $\text{Cl}_{2(g)}$ are -147 , -271 , and -273 kJ mol^{-1} , respectively. The $\Delta_{\text{atm}} H$ values for $\text{AuCl}_{(g)}$, $\text{AuCl}_{2(g)}$, and $\text{AuCl}_{3(g)}$ are $+280$, $+537$, and $+672 \text{ kJ mol}^{-1}$, respectively.
- [24] Refined Au $L_{3\text{-edge}}$ EXAFS parameters. AuCl_3 ($r_{\text{Au-Cl}}$, $2.224(5) \text{ \AA}$; $2\sigma^2$, $0.007(1)$; E_0 , $-8.1(12)$, R , 41.1%). $\text{H}[\text{AuCl}_4]\cdot 3\text{H}_2\text{O}$ ($r_{\text{Au-Cl}}$, $2.282(2) \text{ \AA}$; $2\sigma^2$, $0.006(1)$; E_0 , $-11.7(4)$, R , 19%). The literature $r_{\text{Au-Cl}}$ values for $\text{H}[\text{AuCl}_4]\cdot 4\text{H}_2\text{O}$ are 2.283 and 2.286 \AA (J. M. Williams, S. W. Peterson, *J. Am. Chem. Soc.* **1969**, 91, 776).
- [25] A. van der Gaauw, O. M. Wilkin, N. A. Young, *J. Chem. Soc. Dalton Trans.* **1999**, 2405.
- [26] N. Binsted, *PAXAS, Program for the analysis of X-ray absorption spectra*, University of Southampton, UK, **1988**.
- [27] N. Binsted, *EXCURV98, CCLRC Daresbury Laboratory Computer Program*, CCLRC, Daresbury Laboratory, UK, **1998**.
- [28] C. Fonseca Guerra, J. G. Snijders, G. te Velde, E. J. Baerends, *Theor. Chem. Acc.* **1998**, 99, 391; G. te Velde, F. M. Bickelhaupt, E. J. Baerends, C. Fonseca Guerra, S. J. A. van Gisbergen, J. G. Snijders, T. Ziegler, *J. Comput. Chem.* **2001**, 22, 931; *ADF2002.02*, SCM, Theoretical Chemistry, Vrije Universiteit, Amsterdam, **2002**.

Chirality

DOI: 10.1002/anie.200501527

Systems Chemistry: Kinetic and Computational Analysis of a Nearly Exponential Organic Replicator***Maik Kindermann, Insa Stahl, Malte Reimold, Wolf Matthias Pankau, and Günter von Kiedrowski**

In 1997, Wang and Sutherland reported a case of self-replication in a Diels–Alder reaction.^[1] This system is remarkable for at least two reasons: it constituted the first example of nearly exponential growth and it had the potential to exhibit two kinds of self-replication, homochiral autocatalysis and heterochiral cross-catalysis, because a chiral diene was employed. Unfortunately, the authors could not complete a stereochemical analysis of their system. We report herein mechanistic and stereochemical studies of variants of the Wang–Sutherland replicator. We show that only one of four potential diastereomers is formed within our detection limits and that this diastereomer is involved in both autocatalytic and cross-catalytic channels. A computational study suggests that the system can be classified as an example of a nearby

[*] Dr. M. Kindermann,^[†] I. Stahl,^[†] M. Reimold, Dr. W. M. Pankau, Prof. Dr. G. von Kiedrowski
Lehrstuhl für Organische Chemie I
Ruhr-Universität Bochum
Universitätsstrasse 150, 44780 Bochum (Germany)
Fax: (+49) 234-32-14355
E-mail: kiedro@rub.de

[†] These authors contributed equally to this work.

[**] This work was supported by Deutsche Forschungsgemeinschaft (SFB 452), COST-D27, and the European integrated project PACE (IST-FET complex systems). We thank Dr. K. Merz for performing the X-ray analysis of **6b** and Dr. A. Tamulis (University of Vilnius) for a current recomputation of the approximated transition states.



Supporting information for this article is available on the WWW under <http://www.angewandte.org> or from the author.

strong-exponential replicator according to our minimal replicator theory.^[2]

Self-replication of chiral information has recently received considerable interest from its relevance to the question of the breaking of chiral symmetry on the early earth^[3]. An impressive implementation of Frank's model^[4] now exists in the reaction of Soai et al., whose kinetic analysis has recently revealed important insight.^[5] Further examples of self-replication with prochiral precursors were successfully designed for cycloaddition reactions.^[6] Self-replication experiments with peptides as chiral building blocks constituted the first example of homochiral autocatalysis in the sense that templating requires the same helicity, as in the case of template precursors.^[7] The general predictability of homochiral autocatalysis versus heterochiral cross-catalysis is, however, far less pronounced for molecules without a predefined secondary structure (Figure 1).

We therefore became interested in the re-evaluation of the Wang–Sutherland system with respect to its stereochemical features.^[1] Our approach is guided by our curiosity as to whether a combination of kinetic, computational, and theoretical methods could lead to a better understanding of structurally simple but dynamically complex systems. The

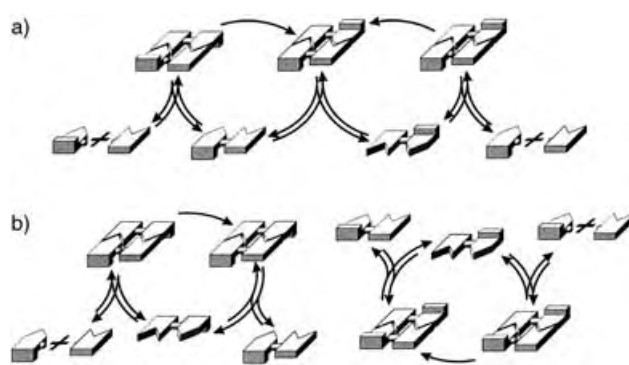


Figure 1. Principle of a) heterochiral cross-catalysis and b) homochiral autocatalysis.

components and principle reactions of the Wang–Sutherland system are shown in Figure 2a.

We thought that the replacement of the heterocyclic recognition units by amidopyridines and carboxylic acids, independently used by the research groups of Hamilton^[8] and Philp,^[6] could also expand the solubility range in the Wang–Sutherland system. Our components and reaction products as

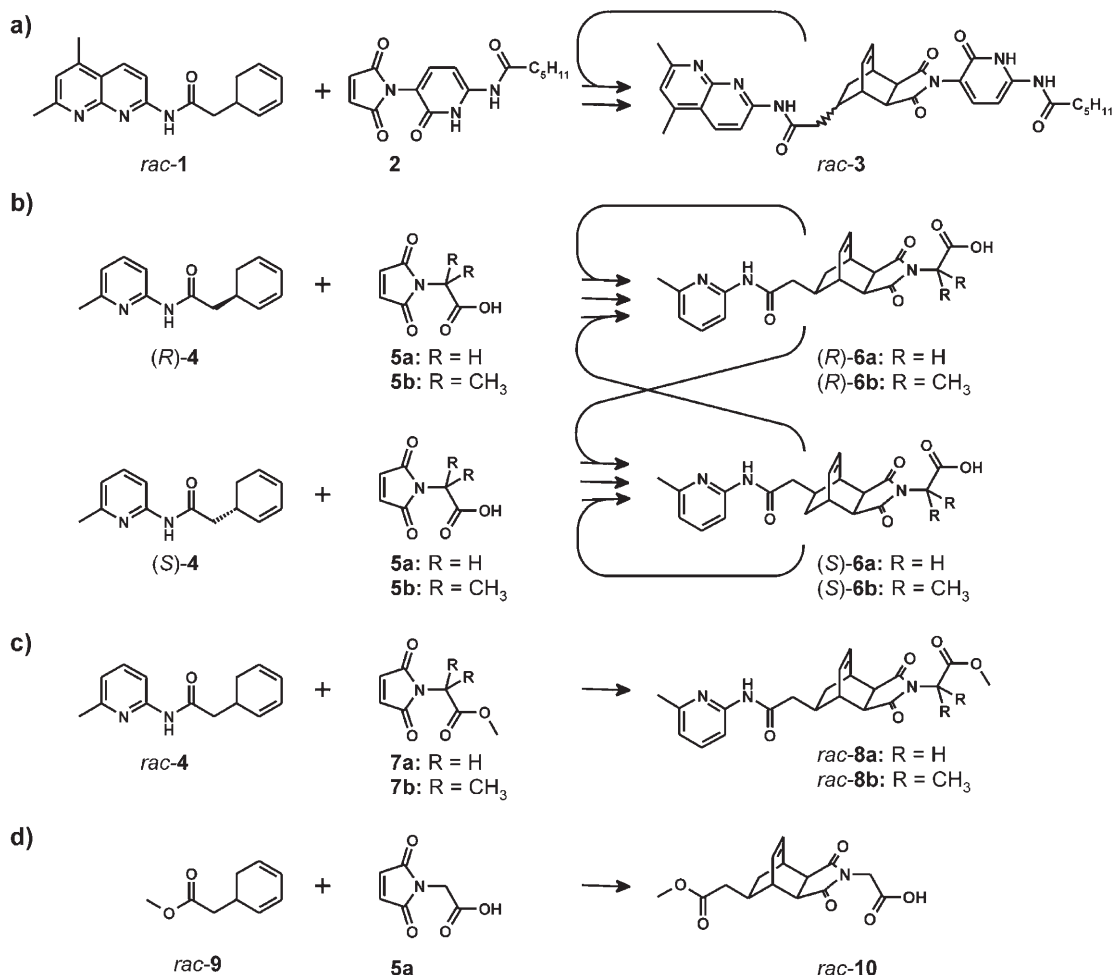


Figure 2. Reaction schemes; each arrow indicates a distinguishable reaction channel. a) Self-replicating Diels–Alder reaction as described by Wang and Sutherland.^[1] b) Our self-replicating system taking into account both enantiomeric forms. c), d) Control reactions with compounds without recognition properties.

well as model components without recognition properties are depicted in Figure 2 b–d.

We synthesized diene **4** in racemic form and as separate enantiomers from the corresponding 2,4-cyclohexadienylacetic acids^[9] (Supporting Information). The reactions were monitored by ¹H NMR spectroscopy and evaluated by using our SimFit program.^[10] A stack plot of the ¹H NMR spectrum of the reaction of *rac*-**4** with **5a** to give *rac*-**6a** is depicted in Figure 3, which shows the olefinic protons of *rac*-**6a**.

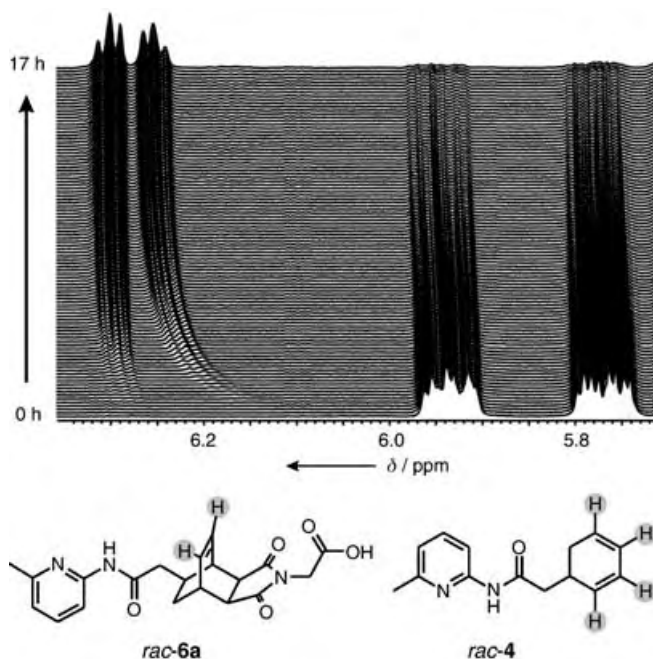


Figure 3. Stack plot of ¹H NMR spectra of the reaction of *rac*-**4** with **5a** to give *rac*-**6a** (CDCl₃, 600 MHz, 293 K).

Three phenomena are directly observable: an induction period, an autocatalytic increase of integrals, and a concomitant change of chemical shifts for the development of the product signal. The latter caused by the transition of free templates at low concentrations to template complexes and duplexes at higher product concentrations. Minimal modeling according to $A + B + pC \rightarrow (1 + p)C$ for the autocatalytic channel and $A + B \rightarrow C$ for the non-autocatalytic channel, both for the building blocks **5a** and **5b** as B, leads to the profiles of theoretical concentration over time shown in Figure 4 and yields the kinetic parameters given in Table 1. From this data it is evident that our variants are reasonable approximations of the Wang–Sutherland system, of which the autocatalytic reaction order p over similar conversion was 0.8.^[1]

Wang and Sutherland assumed an *endo* product but were not sure whether one or two diastereomers that differ in the configuration of the stereocenter carrying the recognition site at the [2.2.2]bicyclo-octene scaffold are formed. We were able to crystallize a single racemic diastereomer of the reaction product, *rac*-**6b**, the X-ray crystallographic structure is shown in Figure 5.^[11]

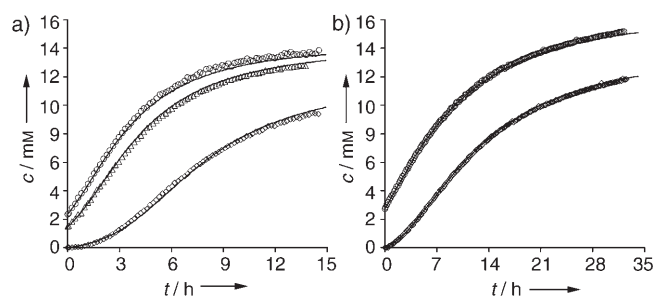


Figure 4. Profiles of concentration over time for the reaction of a) *rac*-**4** and **5a** (CDCl₃, 293 K, 15 mM) with template *rac*-**6a** initially added at 0 (□), 10 (△), and 15% (○); b) *rac*-**4** and **5b** (CDCl₃, 313 K, 15 mM) with template *rac*-**6b** initially added at 0 (□) and 17% (○). Continuous lines represent theoretical curves.

Table 1: Results of the analysis of the reactions of *rac*-**4** and **5a/5b** based on the value of p .

R	p	k_a [M ^{-(p+1)} s ⁻¹]	k_b [M ⁻¹ s ⁻¹]	RMS [%]	T [K]
H	0.89	$(4.48 \pm 0.01) \times 10^{-1}$	$(2.10 \pm 0.02) \times 10^{-4}$	2.21 ^[a]	293
CH ₃	0.9	$(6.32 \pm 0.13) \times 10^{-2}$	$(4.43 \pm 0.23) \times 10^{-4}$	1.09 ^[b]	313

[a] Based on experiments with added template initially at 0, 10, and 15%.

[b] Based on experiments with added template initially at 0 and 17%.

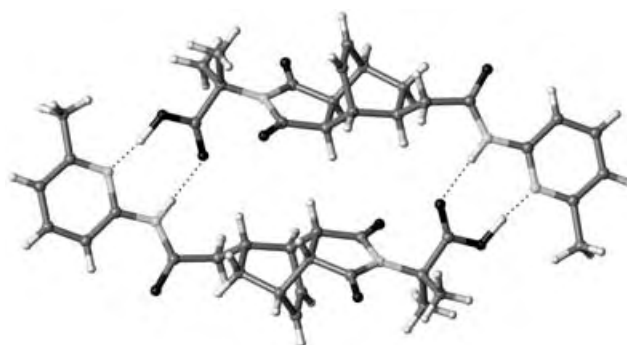


Figure 5. X-ray crystallographic structure of *rac*-**6b**.

There is no indication for another diastereomer above the detection limits of NMR spectroscopy. Transition-state modeling of simplified model reactions at the B3LYP/6-31G* level of calculation confirmed that the diastereomer with NN orientation is expected (Supporting Information).^[12] An interesting detail from these studies is the presence of weak bifurcating hydrogen bonds, which stabilize the transition state of the model reaction between 5'-methyl-1,3-cyclohexadiene and *N*-carboxymethylmaleimide, but these are absent in the product. Weak bifurcating hydrogen bonds were also found to stabilize the transition state of the noncatalytic template-formation reaction in the NNN conformation.^[12] As expected, model reactions with the building blocks **7a** and **9** that are without recognition properties revealed no autocatalysis, but allowed us to determine the second-order rate constants: (*rac*-**4** + **7a** → *rac*-**8a**, $T = 293$ K, $k = 4.49 \times 10^{-5} \text{ M}^{-1} \text{ s}^{-1}$; **9** + **5a** → **10**, $T = 293$ K, $k = 5.83 \times 10^{-5} \text{ M}^{-1} \text{ s}^{-1}$).

We studied the individual reactions involving diene (*R*)-**4** and (*S*)-**4** in the presence of the template (*R*)-**6a** at 10%.

From Figure 6 it is clear that the effect of the template is similar in both cases, which indicates the presence of autocatalytic and cross-catalytic reaction channels. This finding could be confirmed by kinetic modeling and fitting both

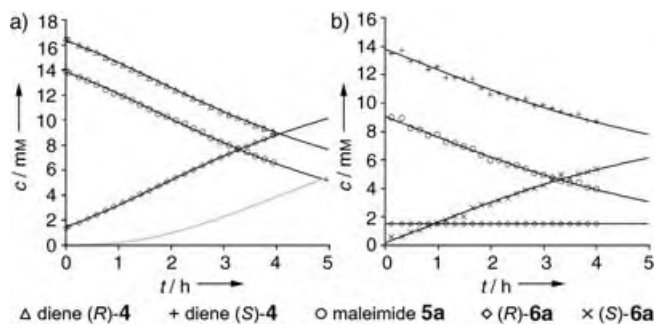


Figure 6. Profiles of concentration over time for the reaction of maleimide **5a** with: a) diene (*R*)-**4** to give (*R*)-**6a** (the gray line demonstrates product formation without any template added initially); b) diene (*S*)-**4** to give (*S*)-**6a**, both with 10% of template (*R*)-**6a** added initially (CDCl_3 , 293 K, 15 mm). The first four hours of the reaction time were analyzed.

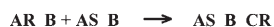
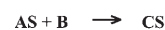
data sets simultaneously to the model shown in Figure 7. The ratio of the association constants of the template duplexes ($K_{2\text{ hetero}}/K_{2\text{ homo}} \approx 2$) suggests that homochiral and heterochiral duplexes are nearly equally populated.

The limited structural and dynamic complexity of our replication system led us to the question of whether computational chemistry could help to explain the kinetic data on the base of an energy profile. We took the following approach: a conformational search of the noncomplexed template at the MMFF94 level followed by further refinement at the B3LYP/6-31G* level led to two conformational families, NNN and NNX,^[12] which differed in the orientation of the carboxy group relative to the C–C double bond.

Formation of template duplexes requires the units of recognition to be in a specific orientation, coaligned in the same direction. Considering that each of these template conformations can exist in both enantiomeric forms, we systematically constructed the six possible duplexes by manual docking and energy refinement at MMFF94, PM3, and B3LYP/6-31G* levels, successively. As expected, duplexes arising from inner-family combinations were found to be centrosymmetric in the heterochiral case and to have rotational symmetry in the homochiral case. The lowest-energy duplex has the conformation that was found in the crystal structure of **6b**. Transition states were derived from a transition-state search of the model reaction between *N*-methylmaleimide and 5-methyl-1,3-cyclohexadiene; all atoms, except those of the methyl groups, were frozen and the skeleton of frozen atoms were inserted into the respective position of the corresponding duplex. Geometry optimization of the nonfrozen atoms was carried out at the B3LYP/6-31G* level. The termolecular complexes were derived from the transition states by relaxation after unfreezing. Figure 8 shows the result of our computational study. For the case of the nontemplated reactions, we were able to find the true transition states. These are greater than 6 kcal mol^{−1} below

Background reactions

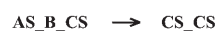
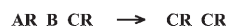
$$k_{\text{fix}} = 5.83 \times 10^{-5} \text{ M}^{-1} \text{ s}^{-1}$$



Template-directed reactions

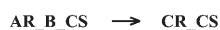
auto-catalysis

$$k_{\text{auto}} = 3.77 \times 10^{-3} \text{ s}^{-1}$$



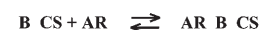
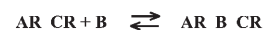
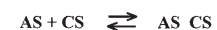
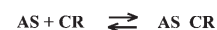
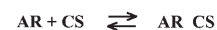
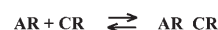
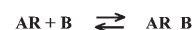
cross-catalysis

$$k_{\text{cross}} = 4.87 \times 10^{-3} \text{ s}^{-1}$$



Single amidopyridine-carboxylate equilibria

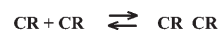
$$K_1 = 1.38 \times 10^2 \text{ M}^{-1}$$



Template-duplex equilibria

homochiral

$$K_{2\text{ homo}} = 4.80 \times 10^4 \text{ M}^{-1}$$



heterochiral

$$K_{2\text{ hetero}} = 8.05 \times 10^4 \text{ M}^{-1}$$

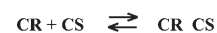


Figure 7. Full model that considers the complexes participating in the reaction (CDCl_3 , 293 K, 15 mm), which results from a distinction between the diene enantiomers (A = diene **4**, B = maleimide **5a**, C = template **6a**). RMS = 1.44 %.

the approximated counterparts in Figure 8. We observed that the energy difference between the respective conformations is similar to their counterparts in the approximated transition states with frozen atoms. Therefore, we trust the approximated transition states.

The largest energy differences between autocatalytic and cross-catalytic pathways were found at the level of transition states and template duplexes. Interestingly, transition-state stabilization by weak bifurcating hydrogen bonds (approximately $-1.5 \text{ kcal mol}^{-1}$) leads to the lowest-energy conformations only in the autocatalytic cases. For the cross-catalytic cases the effect is counterbalanced by repulsive and/or dihedral distortion, which leads to a less optimal geometry at the recognition sites. The cross-catalytic pathway shows the lowest enthalpy of activation. There is always a clear enthalpic preference of termolecular complexes over the respective template duplexes. Further work on the temper-

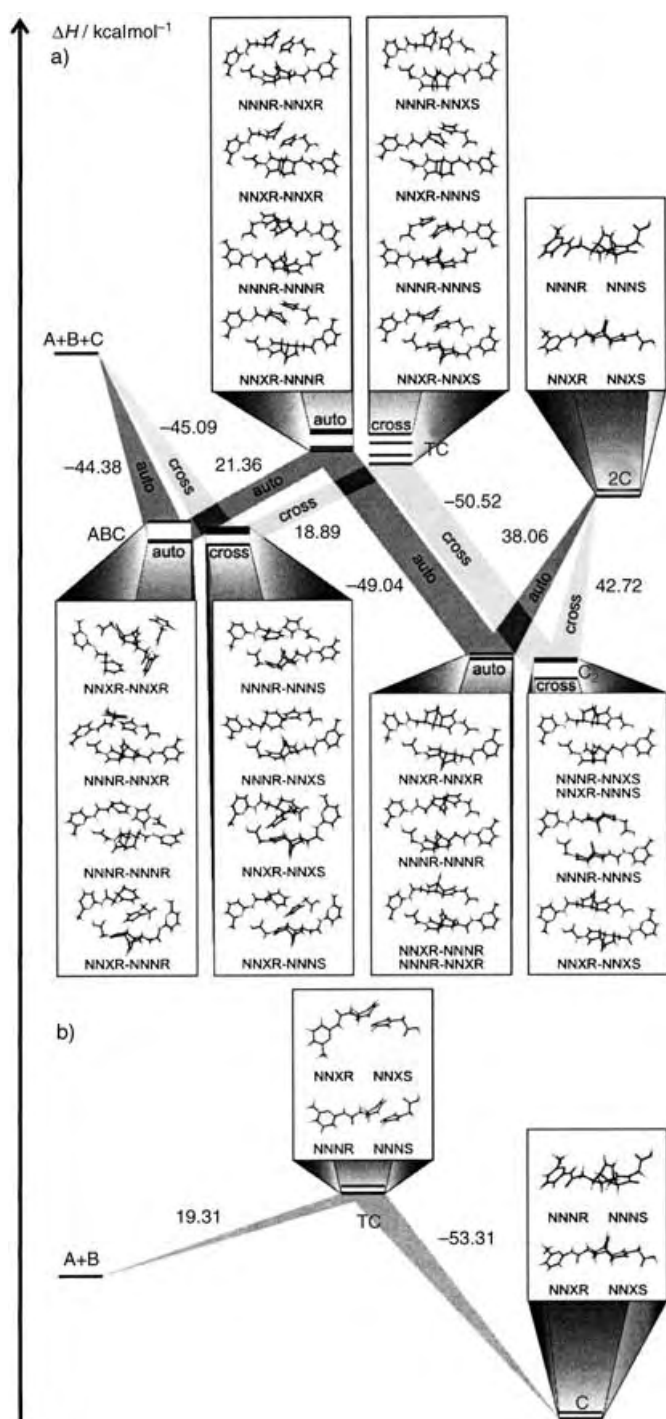


Figure 8. Energy profiles correlated to the corresponding structures (B3LYP/6-31G*) of the reaction of 4 and 5a through the a) autocatalytic and b) nontemplate-directed pathways.

ature dependence of rates and equilibria in a slightly modified self-replicating system has revealed evidence that the above enthalpic preference is not overcompensated by the respective entropy differences.^[13]

In summary, our re-evaluation of the Wang–Sutherland replicator with simplified variants reveals that the exponential dynamics arise from conformational constraints. Whereas the termolecular complexes offer enough freedom for an

optimal docking of the reactants with the template, template duplexes are conformationally restricted in their finding of an optimal orientation of the recognition units. A similar rationale was reported to explain the nearly exponential growth of a peptide replicator.^[14] Our replicator theory predicts that for systems with a negligible background channel, the question of parabolic versus exponential growth is solely answerable by the stabilities of the ground-state and not the transition-state complexes involved.^[2] Further cases are needed to prove that exponential growth can be literally designed by taking into account the conformational control of ground states. If this recipe can be generalized, it could open a door to a field that may be termed “systems chemistry”, namely, the design of prespecified dynamic behavior.

Received: May 4, 2005

Revised: July 5, 2005

Published online: September 27, 2005

Keywords: chirality · computer chemistry · molecular modeling · supramolecular chemistry · template synthesis

- [1] B. Wang, I. O. Sutherland, *Chem. Commun.* **1997**, 1495–1496.
- [2] G. von Kiedrowski, *Bioorg. Chem. Front.* **1993**, 3, 113–146.
- [3] I. Weissbuch, L. Leiserowitz, M. Lahar, *Top. Curr. Chem.* **2005**, in press.
- [4] F. C. Frank, *Biochim. Biophys. Acta* **1953**, 11, 459–463.
- [5] a) K. Soai, T. Shibata, H. Morioka, K. Choji, *Nature* **1995**, 378, 767–768; b) D. G. Blackmond, *Proc. Natl. Acad. Sci. USA* **2004**, 101, 5732–5736.
- [6] a) V. C. Allen, D. Philp, N. Spencer, *Org. Lett.* **2001**, 3, 777–780; b) R. J. Pearson, E. Kassianidis, A. M. Z. Slavin, D. Philp, *Org. Biomol. Chem.* **2004**, 2, 3434–3441.
- [7] A. Saghatelian, Y. Yokobayashi, K. Soltani, M. R. Ghadiri, *Nature* **2001**, 409, 797–801.
- [8] F. Garcia-Tellado, S. Goswami, S. K. Chang, S. J. Geib, A. D. Hamilton, *J. Am. Chem. Soc.* **1990**, 112, 7393–7394.
- [9] Synthesis of *rac*-2,4-cyclohexadienylacetic acid: a) C. Jonasson, M. Roenn, J.-E. Baeckvall, *J. Org. Chem.* **2000**, 65, 2122–2126; (*R*)-2,4-cyclohexadienylacetic acid: b) M. Asaoka, K. Kobayashi, H. Takei, *Bull. Chem. Soc. Jpn.* **1994**, 67, 1141–1146; (*S*)-2,4-cyclohexadienylacetic acid: c) J. E. Baeckvall, R. Gatti, H. E. Schink, *Synthesis* **1993**, 343–348, 642.
- [10] For other SimFit applications, see: a) D. Sievers, G. von Kiedrowski, *Nature* **1994**, 369, 221–224; b) D. Sievers, G. von Kiedrowski, *Chem. Eur. J.* **1998**, 4, 629–641; c) H. Schöneborn, J. Bülle, G. von Kiedrowski, *ChemBioChem*, **2001**, 2, 922–927; d) K. Severin, D. H. Lee, A. J. Kennan, M. R. Ghadiri, *Nature* **1997**, 389, 706–709; e) S. Yao, I. Gosh, R. Zutshi, J. Chmielewski, *Angew. Chem.* **1998**, 110, 489–492; *Angew. Chem. Int. Ed. Engl.* **1998**, 37, 478–481; f) see Pearson et al.^[6b]
- [11] Crystallographic data for *rac*-6b: crystal size = 0.2 × 0.2 × 0.3 mm³; crystal system = monoclinic; space group = *P*2₁/*n*; unit cell dimensions: *a* = 5.8973(17), *b* = 26.318(8), *c* = 18.881(5) Å, β = 91.693(6)°, *V* = 2929.1(15) Å³, ρ_{calcd} = 0.931 g cm⁻³; $2\theta_{\text{max}}$ = 45°; $\lambda_{\text{MoK}\alpha}$ = 0.71073 Å; *T* = 213(2) K; reflections collected = 10714, unique reflections = 3803, for 2983 reflections observed (*I* > 2σ(*I*)); The structure was solved by direct methods and refined by full-matrix least squares by using SHELXTL-97; 271 parameters; the non-H atoms were refined anisotropically, H atoms were included but not refined; final *R* indices: *R*₁ = 0.0670, *wR*₂ = 0.1893; *R* indices (all data): *R*₁ = 0.0785, *wR*₂ = 0.1998; goodness-of-fit on $|F^2|$ = 1.079; max-

imum positive and negative peaks in ΔF map were $\rho_{\max} = 0.348 \text{ e } \text{\AA}^{-3}$ and $\rho_{\min} = -0.292 \text{ e } \text{\AA}^{-3}$. CCDC 269658 contains the supplementary crystallographic data for this paper. These data can be obtained free of charge from the Cambridge Crystallographic Data Centre via www.ccdc.cam.ac.uk/data_request/cif.

- [12] We use a four-letter notation to describe the configuration and conformation of template molecules. The first letter is either N or X to indicate an *endo* or *exo* Diels–Alder product, respectively. The latter distinction is based on the relative orientation of the C=C double bond to the maleimide ring. We employed the C=C double bond also as a reference to describe the relative orientation of the 5-pyridinylaminocarbonylmethyl substituent (second letter) and of the carboxymethyl substituent (third letter). *R/S* (fourth letter) is determined by the absolute configuration of the precursor diene.
- [13] I. Stahl, *Analysis and classification of minimal self-replicating systems based on Diels–Alder ligation chemistry*, PhD thesis, Ruhr-Universität Bochum, **2005**: <http://www-brs.ub.ruhr-uni-bochum.de/netahtml/HSS/Diss/StahlInsa/>.
- [14] R. Issac, J. Chmielewski, *J. Am. Chem. Soc.* **2002**, *124*, 6808–6809.

Alkane Metathesis

DOI: 10.1002/anie.200501382

Development of Tungsten-Based Heterogeneous Alkane Metathesis Catalysts Through a Structure–Activity Relationship**

Erwan Le Roux, Mostafa Taoufik,* Christophe Copéret, Aimery de Mallmann, Jean Thivolle-Cazat, Jean-Marie Basset,* Barry M. Maunders, and Glenn J. Sunley

The transformation of lower alkanes into higher homologues is still a great challenge in chemistry.^[1–3] A highly electrophilic

tantalum hydride supported on silica, $[(\equiv\text{SiO})_2\text{TaH}]$, catalytically transforms a given alkane into its higher and lower homologues—an alkane metathesis reaction.^[4,5] This reaction involves selective cleavage and formation of carbon–carbon bonds; for example, propane metathesis selectively gives ethane (45–50 %) and butanes (30–35 %) along with methane and minor amounts of higher alkanes. Moreover, it is possible to catalyze the reverse reaction, which allows methane to be incorporated into higher alkanes.^[6] Similarly, the cross-metathesis of ethane and toluene is also catalyzed by $[(\equiv\text{SiO})_2\text{TaH}]$.^[7] With $[(\equiv\text{SiO})\text{Ta}(\equiv\text{CH}t\text{Bu})(\text{CH}_2t\text{Bu})_2]$ as a catalyst precursor,^[8] the ratio of cross-metathesis products and the selectivity in higher alkanes led us to propose that the key step in alkane metathesis involves metallocarbenes and metallacyclobutane intermediates as is the case with olefin metathesis.^[9,10]

This discovery led us to investigate the use of Group 6 metals, particularly W, which play a central role in olefin metathesis.^[11] By using surface organometallic chemistry (SOMC), the goal of which is to enter directly into the catalytic cycle via reaction intermediates,^[12] several attempts have been directed at generating well-defined tungsten carbene complexes on oxide surfaces by grafting $[\text{W}(\equiv\text{CrBu})(\text{X})_3]$ ($\text{X} = \text{Cl}, \text{OtBu}, \text{CH}_2t\text{Bu}$). It was proposed that metallocarbenes were formed on the basis of their activity in olefin metathesis.^[13–15] In fact, we have recently shown that the reaction of $[\text{W}(\equiv\text{CrBu})(\text{CH}_2t\text{Bu})_3]$ (**1**) with partially dehydroxylated silica (PDS) at 700 °C generates the corresponding supported metallocarbyne $[(\equiv\text{SiO})\text{W}(\equiv\text{CrBu})(\text{CH}_2t\text{Bu})_2]_{\text{PDS}}$ (**2**) instead of a metallocarbene.^[16] Although highly active in olefin metathesis and highly electrophilic (formal 12-electron species),^[13–15] this complex and the corresponding hydride displayed little to no activity in alkane metathesis.^[4,5] Therefore, we decided to generate more electrophilic centers by preparing the corresponding W alkyl and hydride on partially dehydroxylated alumina (PDA).^[17–23] Herein, we report the grafting and characterization of **1** on alumina, the preparation of the corresponding hydride, and their respective activity in alkane metathesis.

Grafting of **1** was performed typically by heating a mixture containing an excess of **1** (0.40 mmol per gram of alumina) and $\text{Al}_2\text{O}_{3-(500)}$ at 66 °C to provide solid **1**– Al_2O_3 . Excess molecular complex was removed by washing the solid with pentane (3 cycles), and the final solid was dried under vacuum. A yellow solid was obtained, which was fully characterized by IR and NMR spectroscopy as well as elemental and chemical analysis. During grafting, 0.9 equivalents of 2,2-dimethylpropane/W was formed, and the W loading of the resulting solid was 3.8–4.7 wt % (0.20–0.26 mmol W g^{-1}). The reaction with surface hydroxy groups was only partial, as revealed by IR spectroscopy (presence of residual hydroxy groups; see Figure 1b). Carbon elemental analysis data (3.6–4.6 wt %) corresponded to 14.3–14.8 C/W, and the reaction of the solid with excess H_2 at 150 °C for 15 h gave a mixture of CH_4 (13.7–14.7 CH_4/W) and C_2H_6 (0.3–0.4 $\text{C}_2\text{H}_6/\text{W}$), corresponding to 14.3–15.5 C/W. Both results are consistent with about 2.9 ± 0.15 neopentyl-like ligands per W atom for **1**– Al_2O_3 . Therefore, the surface complex has the following average structure: $[(\text{Al}_5\text{O})\text{W}(\equiv\text{CrBu})(\text{CH}_2t\text{Bu})_2]$ (**2**,

[*] Dr. E. Le Roux, Dr. M. Taoufik, Dr. C. Copéret, Dr. A. de Mallmann, Dr. J. Thivolle-Cazat, Prof. Dr. J.-M. Basset
Laboratory of Surface Organometallic Chemistry, UMR 9986
Ecole Supérieure de Chimie Physique Electronique de Lyon
43 Bd du 11 Novembre 1918, 69616 Villeurbanne Cedex (France)
Fax: (+33) 4-7243-1795
E-mail: taoufik@cpe.fr
basset@cpe.fr

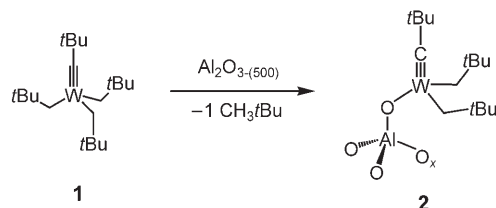
Dr. B. M. Maunders
BP Chemicals Ltd.
Chertsey Road
Sunbury-On-Thames, Middlesex, TW1 67LN (UK)

Dr. G. J. Sunley
BP Chemicals Ltd.
Hull Research and Technology Centre
Saltend, Hull, HU1 28DS (UK)

[**] This work was supported by BP Chemicals, the CNRS, and the ESCPE Lyon.

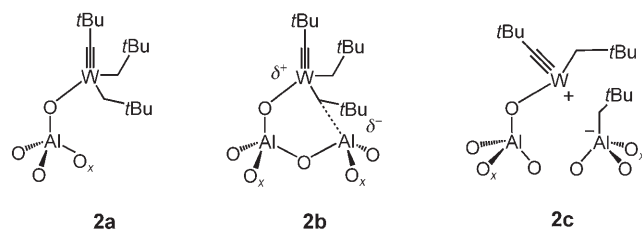
Supporting information for this article is available on the WWW under <http://www.angewandte.org> or from the author.

Scheme 1). The solid-state magic-angle spinning (MAS) ^1H NMR spectrum exhibits only one broad signal at $\delta = 1.0$ ppm, whereas the solid-state cross-polarization (CP)/MAS ^{13}C NMR spectrum of the ^{13}C -enriched complex,



Scheme 1. Grafting of molecular complex **1** on $\text{Al}_2\text{O}_3\text{-(500)}$ to give **2**.

selectively labeled on the carbon atom bonded to the metal, displays the following features (Supporting Information): a broad and weak signal at $\delta = 318$ ppm, a broad intense signal at $\delta = 85$ ppm with a shoulder at $\delta = 103$ ppm, several signals around $\delta = 52$ ppm, and a signal at $\delta = 32$ ppm with a shoulder at $\delta = 29$ ppm. The signal at $\delta = 318$ ppm is consistent with a neopentylidyne ligand.^[16] The two broad signals at $\delta = 85$ and 103 ppm are attributed to different types of methylene carbon atoms (CH_2tBu), probably associated with the heterogeneity of alumina and possibly with the presence of neutral and cationic W surface complexes.^[22,23] The signals at $\delta = 52$ and 32 ppm, already observed on silica materials, have been assigned respectively to the quaternary carbon atoms of the neopentylidyne group and to the methyl groups of the various *t*Bu groups.^[16] The shoulder at $\delta = 29$ ppm, not observed on other supports, may correspond to the presence of small amounts of $[(\text{Al}-\text{CH}_2\text{tBu})^-]$ fragments. This species would result from the reaction of a neopentyl group with an adjacent Lewis acidic Al site, as already proposed.^[22,23] The data are therefore consistent with an average structure formulated as $[(\text{Al}_5\text{O})\text{W}(\equiv\text{CtBu})(\text{CH}_2\text{tBu})_2]_{\text{PDA}}$, which corresponds to a mixture of a neutral complex **2a** as the probable major species ($\delta = 85\text{--}95$ ppm), along with the possible minor cationic or partially cationic surface complexes **2b** and **2c** ($\delta = 95\text{--}110$ ppm).^[17–23] Whereas the neutral complex **2a** arises from the reaction of **1** with the hydroxy groups of alumina, the partially and fully cationic surface complexes **2b** and **2c** would have been formed by the interaction/reaction of **2a** with a neighboring Lewis acidic site; the latter complex is consistent with the formation of a small amount of $[(\text{Al}_5-\text{CH}_2\text{tBu})^-]$ (as revealed by a



shoulder at $\delta = 29$ ppm in the ^{13}C NMR spectrum).^[22,23] The structure was further confirmed by extended X-ray absorption fine structure (EXAFS) data (Table 1 and Supporting Information), and is consistent with the following coordina-

Table 1: EXAFS parameters for solid **2** (R factor $\rho = 10\%$).

Neighboring atom of W (bold)	Number of atoms	Distance [Å]	Debye–Waller factor [Å]
$\equiv\text{CMe}_3$	1.1	1.773	0.0411
OAl_5	1.1	1.862	0.0623
CH_2tBu	2.1	2.110	0.0724
CH_2CMe_3	2.0	3.314	0.0882
$\equiv\text{CMe}_3$	1.0	3.323	0.0917

tion sphere around W: 1) about one carbon (1.773 Å) and one oxygen (1.862 Å) atom, the distances of which are consistent with a carbynic carbon atom^[24–28] and σ -bonded OAl_5 , respectively;^[25] 2) two carbon atom neighbors at a greater distance (2.110 Å) assigned to two neopentyl ligands;^[28,29] 3) two carbon atoms at 3.314 Å, assigned to the two quaternary carbon atoms of the neopentyl ligands; and 4) a carbon atom at 3.323 Å, corresponding to the quaternary carbon atoms of the neopentylidyne ligand.

The preparation of the corresponding hydride was then investigated. Heating of **2** under H_2 for 15 h at 150°C caused the pale yellow solid to turn brown. Monitoring by IR spectroscopy (Figure 1) shows the disappearance of 95 % of

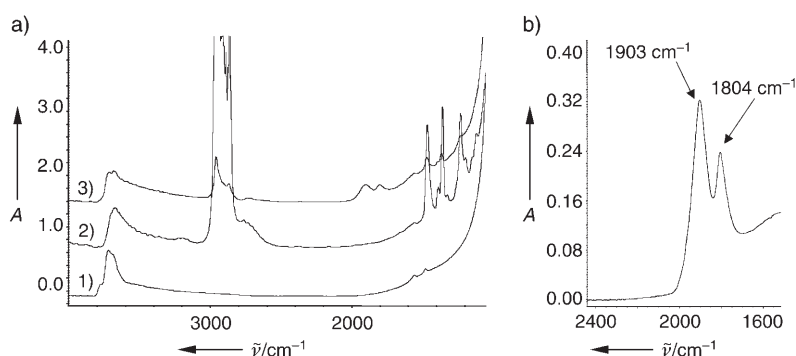
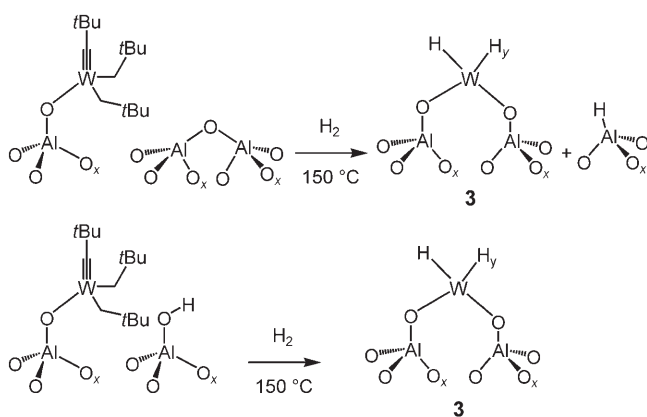


Figure 1. a) Monitoring the reaction of $[\text{W}(\equiv\text{CtBu})(\text{CH}_2\text{tBu})_3]$ and $\text{Al}_2\text{O}_3\text{-(500)}$ (100 mg) by IR spectroscopy; 1) $\text{Al}_2\text{O}_3\text{-(500)}$, 2) $[\text{W}(\equiv\text{CtBu})(\text{CH}_2\text{tBu})_3]/\text{Al}_2\text{O}_3\text{-(500)}$, 3) after treatment under H_2 at 150°C for 15 h. b) Spectrum (1) subtracted from spectrum (3).

the bands associated with $\nu(\text{C}-\text{H})$ and $\delta(\text{C}-\text{H})$, as well as consumption of some residual AlOH , while two large bands appear at 1903 and 1804 cm^{-1} . The latter are readily exchanged under D_2 to generate the corresponding W–D bands at 1388 and 1293 cm^{-1} . After this D_2 treatment, a weak band at 1930 cm^{-1} remains unexchanged and is assigned to $\nu(\text{Al}-\text{H})$.^[30] Solid-state NMR and ESR spectroscopy on this alumina-supported tungsten hydride **3** provided no further information.^[31] Moreover, no particles were detected in the transmission electron microscopy (TEM) image, in contrast to what is observed on silica, which shows that the migration of W atoms (sintering) is prevented on alumina. These data are

therefore consistent with the presence of isolated W atoms grafted to the surface through covalent $\text{Al}_3\text{O}-\text{W}$ bonds. The formation of the final species probably involves the reaction of WH with adjacent $\text{Al}-\text{O}-\text{Al}$ bridges or AlOH species (Scheme 2). The former generates AlH , as observed in the



Scheme 2. Proposed structure of **3** on $\text{Al}_2\text{O}_3-(500)$ ($x=1-3$; $y=1-3$).

formation of other hydrides,^[32–35] and the latter is consistent with partial consumption of AlOH . As the formation of WH species is accompanied by the formation of AlH and the consumption of AlOH , we propose this WH species to be the bis-aluminoxyl tungsten hydride **3**, but further work will be necessary to propose a definitive structure.

The activity of species **2** and **3** is noteworthy. In contrast to the W complex supported on silica, **2** is active in the metathesis of propane under our standard conditions (Supporting Information). The initial rate is 1.8 molpropane $\text{mol}_\text{W}^{-1}\text{h}^{-1}$, which is slightly lower than that of $[(\text{SiO})\text{Ta}(\text{=CHtBu})(\text{CH}_2\text{tBu})_2]$ (3.0 molpropane $\text{mol}_\text{Ta}^{-1}\text{h}^{-1}$, turnover number (TON)=35 molpropane $\text{mol}_\text{Ta}^{-1}$ at 120 h), but the TONs after 120 h are similar, which indicates that deactivation of this catalyst is slower (Table 2).^[9] Under similar conditions, the initial rate (8–9 molpropane $\text{mol}_\text{W}^{-1}\text{h}^{-1}$) and the TON (120 molpropane mol_W^{-1}) after 120 h for tungsten hydride **3** are higher than those obtained with the best Ta-based catalysts. For example, the initial rate and TON at 120 h

for $[(\text{SiO})_2\text{TaH}]$ are 3–4 molpropane $\text{mol}_\text{Ta}^{-1}\text{h}^{-1}$ and 60 molpropane $\text{mol}_\text{Ta}^{-1}$ under the same experimental conditions. To understand the origin of this beneficial effect, alumina-supported tantalum hydride **4** was prepared (Supporting Information). However, its activity is similar to that of $[(\text{SiO})_2\text{TaH}]$ (for **4**: initial rate = 2.5 molpropane $\text{mol}_\text{Ta}^{-1}\text{h}^{-1}$ and TON = 60 molpropane $\text{mol}_\text{Ta}^{-1}$). Thus, W is indeed the key to the improved activity in alkane metathesis.

The product selectivities are also noteworthy (Table 2). As observed for Ta, linear alkanes are favored over branched alkanes, and the selectivities for higher homologues are as follows: $\text{C}_{n+1} > \text{C}_{n+2} \gg \text{C}_{n+3}$. These selectivities are fully consistent with the model proposed earlier (Scheme 3),^[9,10] which



Scheme 3. Model for product selectivities in alkane metathesis. $\text{R}^1 = \text{tBu}$, $\text{R}^2 = \text{H}$; $\text{R}^1 = \text{Et}$, $\text{R}^2 = \text{H}$; $\text{R}^1 = \text{Me}$, $\text{R}^2 = \text{Me}$.

is based on olefin metathesis intermediates and predicts that the favored pathway for the formation of higher homologues involves a 1,3-disubstituted metallacyclobutane rather than a 1,2-disubstituted one, as proposed in olefin metathesis.^[36] The higher selectivity of linear over branched compounds is also consistent with this model, as the latter would involve the less-reactive disubstituted carbenes. The major difference between the Ta and the W catalysts is that the selectivity for methane is less than 3% (after 120 h) for the W-based catalysts **2** and **3**, whereas it is about 10% for the corresponding Ta-supported catalysts, which is consistent with the greater hydrogenolysis capability of Ta.

In conclusion, we have shown that organo- and hydrido-tungsten surface complexes (**2** and **3**, respectively) supported on alumina catalyze the metathesis of propane. Tungsten hydride **3** has an overall turnover number of 120 mol propane mol_W^{-1} , which is much higher than that of the best known Ta system, that is, tantalum hydrides supported on silica or alumina. This significant improvement in activity probably reflects the difference between the intrinsic properties of W and those of Ta. Interestingly, in olefin metathesis, the same trend is observed (W-based are much better than Ta-based homogeneous catalysts because of the instability of tantalacyclobutanes).^[28,37] These data corroborate what we observed and proposed earlier: alkane meta-

Table 2: Propane metathesis: comparison of the activity (TON) and the product selectivities of tungsten and tantalum perhydrocarbyl species on oxide and their corresponding hydrides after 120 h of reaction in a batch reactor (see Supporting Information).

Precatalysts	TON ^[a]	Product selectivity [%] ^[b]				
		Methane	Ethane	Butanes ^[c]	Pentanes ^[d]	Hexanes ^[e]
$[(\text{SiO})\text{Ta}(\text{=CHtBu})(\text{CH}_2\text{tBu})_2]$	35 (5.8)	12.8	47.7	22.8/10.4	3.5/2.5	0.9
$[(\text{SiO})_2\text{TaH}]$	60 (6.1)	10.0	46.0	30.6/6.0	4.8/2.2	0.4
$[(\text{SiO})\text{W}(\text{=CtBu})(\text{CH}_2\text{tBu})_2]$	0 (0)	—	—	—	—	—
$[\text{WH}/\text{SiO}_2]$	8 (1.2)	5.7	56.0	29.0/2.8	5.1/1.4	n.d. ^[f]
$[(\text{Al}_3\text{O})\text{W}(\text{=CtBu})(\text{CH}_2\text{tBu})_2]$ (2)	28 (3.2)	2.7	65.4	20.7/2.9	5.3/1.5	1.5
$[\text{WH}/\text{Al}_2\text{O}_3]$ (3)	121 (18)	2.4	57.3	28.9/3.7	5.0/1.3	1.4
$[\text{TaH}/\text{Al}_2\text{O}_3]$ (4)	60 (8.2)	9.5	47.6	32.6/3.8	5.0/1.1	0.4

[a] TON (turnover number) is expressed in moles of propane transformed per mole of metal (Ta, W). The values in parentheses are conversions after 120 h. [b] The selectivities are defined as the amount of product *i* over the total amount of products; they do not significantly change with time and conversion. [c] C_4/iC_4 . [d] C_5/iC_5 . [e] Selectivity for the sum of all C_6 isomers. [f] Not determined.

thesis proceeds via carbene and metallacyclobutane intermediates.^[9,10,38]

Experimental Section

Representative procedure for grafting **1** on Al₂O₃: An excess of **1** (311 mg, 0.66 mmol, 1.1 equiv) and Al₂O₃-(500) (1.8 g) were stirred at 66 °C for 4 h. All volatile compounds were condensed into another reactor (of known volume) to quantify 2,2-dimethylpropane evolved during grafting. GC analysis indicated the formation of 0.21 ± 0.05 mmol of 2,2-dimethylpropane (0.9 ± 0.1 CH₃/Bu/W). Pentane (10 mL) was introduced into the reactor by distillation, and the solid was washed three times. After evaporation of the solvent, the resulting light brown powder was dried under vacuum to yield **2**.

Preparation of **3**: Solid **2** was heated at 150 °C in the presence of a large excess of anhydrous H₂ (77 kPa). After 15 h, the gaseous products were quantified by GC, and the resulting solids were obtained after evacuating the gas phase for 15 min.

General procedure for propane metathesis: In a glove box, the solid was introduced into a batch reactor (of known volume). After evacuation of Ar, dry propane was added, and the reaction mixture was heated at 150 °C. To monitor the reaction, aliquots were expanded in a small volume, brought to atmospheric pressure, and analyzed by GC (see Supporting Information for experimental details).

Received: April 21, 2005

Revised: June 15, 2005

Published online: September 19, 2005

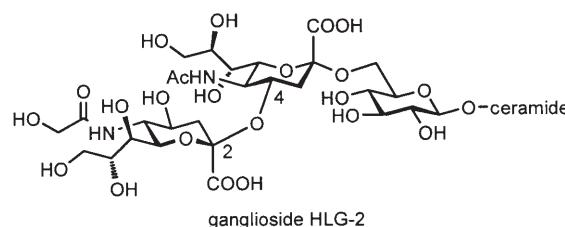
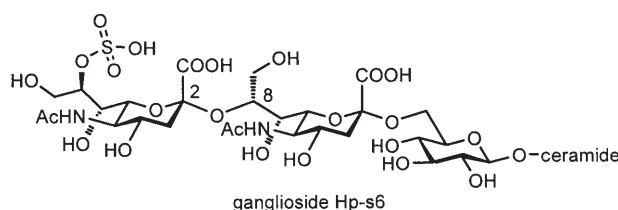
Keywords: alkanes · carbyne ligands · hydride ligands · metathesis · tungsten

- [1] R. H. Crabtree, *Chem. Rev.* **1985**, 85, 245.
- [2] A. E. Shilov, G. B. Shul'pin, *Chem. Rev.* **1997**, 97, 2879.
- [3] R. H. Crabtree, *J. Chem. Soc. Dalton Trans.* **2001**, 2437.
- [4] V. Vidal, A. Theolier, J. Thivolle-Cazat, J.-M. Basset, *Science* **1997**, 276, 99.
- [5] O. Maury, L. Lefort, V. Vidal, J. Thivolle-Cazat, J.-M. Basset, *Angew. Chem.* **1999**, 111, 2121; *Angew. Chem. Int. Ed.* **1999**, 38, 1952.
- [6] D. Soulivong, C. Copéret, J. Thivolle-Cazat, J.-M. Basset, B. M. Maunders, R. B. A. Pardy, G. J. Sunley, *Angew. Chem.* **2004**, 116, 5480; *Angew. Chem. Int. Ed.* **2004**, 43, 5366.
- [7] M. Taoufik, E. Schwab, M. Schultz, D. Vanoppen, M. Walter, J. Thivolle-Cazat, J.-M. Basset, *Chem. Commun.* **2004**, 1434.
- [8] C. Copéret, O. Maury, J. Thivolle-Cazat, J.-M. Basset, *Angew. Chem.* **2001**, 113, 2393; *Angew. Chem. Int. Ed.* **2001**, 40, 2331.
- [9] E. Le Roux, M. Chabanas, A. Baudouin, A. de Mallmann, C. Copéret, E. A. Quadrelli, J. Thivolle-Cazat, J.-M. Basset, W. Lukens, A. Lesage, L. Emsley, G. J. Sunley, *J. Am. Chem. Soc.* **2004**, 126, 13391.
- [10] J. M. Basset, C. Copéret, L. Lefort, B. M. Maunders, O. Maury, E. Le Roux, G. Saggio, S. Soignier, D. Soulivong, G. J. Sunley, M. Taoufik, J. Thivolle-Cazat, *J. Am. Chem. Soc.* **2005**, 127, 8604.
- [11] K. J. Ivin, I. C. Mol, *Olefin Metathesis and Metathesis Polymerization*, 2nd ed., Academic Press, San Diego, **1996**.
- [12] C. Copéret, M. Chabanas, R. Petroff Saint-Arroman, J.-M. Basset, *Angew. Chem.* **2003**, 115, 164; *Angew. Chem. Int. Ed.* **2003**, 42, 156.
- [13] K. Weiss, G. Löbel, *Angew. Chem.* **1989**, 101, 75; *Angew. Chem. Int. Ed. Engl.* **1989**, 28, 62.
- [14] R. Buffon, M. Leconte, A. Choplin, J. M. Basset, *J. Chem. Soc. Chem. Commun.* **1993**, 361.
- [15] R. Buffon, M. Leconte, A. Choplin, J.-M. Basset, *J. Chem. Soc. Dalton Trans.* **1994**, 1723.
- [16] E. Le Roux, M. Chabanas, M. Taoufik, D. Alcor, A. Baudouin, C. Copéret, C. J. Thivolle, J.-M. Basset, A. Lesage, L. Emsley, *Organometallics*, **2005**, 24, 4274.
- [17] K. H. Dahmen, D. Hedden, R. L. Burwell, Jr., T. J. Marks, *Langmuir* **1988**, 4, 1212.
- [18] W. C. Finch, R. D. Gillespie, D. Hedden, T. J. Marks, *J. Am. Chem. Soc.* **1990**, 112, 6221.
- [19] M. S. Eisen, T. J. Marks, *J. Am. Chem. Soc.* **1992**, 114, 10358.
- [20] T. J. Marks, *Acc. Chem. Res.* **1992**, 25, 57.
- [21] M. S. Eisen, T. J. Marks, *J. Mol. Cat.* **1994**, 86, 23.
- [22] M. Jezequel, V. Dufaud, M. J. Ruiz-Garcia, F. Carrillo-Hermosilla, U. Neugebauer, G. P. Niccolai, F. Lefebvre, F. Bayard, J. Corker, S. Fiddy, J. Evans, J.-P. Broyer, J. Malinge, J.-M. Basset, *J. Am. Chem. Soc.* **2001**, 123, 3520.
- [23] H. Ahn, T. J. Marks, *J. Am. Chem. Soc.* **2002**, 124, 7103.
- [24] S. M. Rocklage, R. R. Schrock, M. R. Churchill, H. J. Wasserman, *Organometallics* **1982**, 1, 1332.
- [25] M. H. Chisholm, D. M. Hoffman, J. C. Huffman, *Inorg. Chem.* **1983**, 22, 2903.
- [26] M. R. Churchill, J. W. Ziller, J. H. Freudenberger, R. R. Schrock, *Organometallics* **1984**, 3, 1554.
- [27] R. R. Schrock, *Acc. Chem. Res.* **1986**, 19, 342.
- [28] R. R. Schrock, *Chem. Rev.* **2002**, 102, 145.
- [29] L. P. H. Lopez, R. R. Schrock, *J. Am. Chem. Soc.* **2004**, 126, 9526.
- [30] S. Liu, U. Fooker, C. M. Burba, M. A. Eastman, R. J. Wehm-schulte, *Chem. Mater.* **2003**, 15, 2803.
- [31] No characteristic WH signal in the solid-state ¹H NMR spectrum could be detected, possibly because of broadening due to the presence of ²⁷Al, a quadrupolar nucleus, or H exchange in **3**.
- [32] J. Corker, F. Lefebvre, C. Lecuyer, V. Dufaud, F. Quignard, A. Choplin, J. Evans, J.-M. Basset, *Science* **1996**, 271, 966.
- [33] F. Rataboul, A. Baudouin, C. Thieuleux, L. Veyre, C. Copéret, J. Thivolle-Cazat, J.-M. Basset, A. Lesage, L. Emsley, *J. Am. Chem. Soc.* **2004**, 126, 12541.
- [34] V. Vidal, A. Theolier, J. Thivolle-Cazat, J.-M. Basset, J. Corker, *J. Am. Chem. Soc.* **1996**, 118, 4595.
- [35] C. Rosier, G. P. Niccolai, J.-M. Basset, *J. Am. Chem. Soc.* **1997**, 119, 12408.
- [36] J. L. Bilhou, J. M. Basset, R. Mutin, W. F. Graydon, *J. Am. Chem. Soc.* **1977**, 99, 4083.
- [37] K. C. Wallace, A. H. Liu, J. C. Dewan, R. R. Schrock, *J. Am. Chem. Soc.* **1988**, 110, 4964.
- [38] J. L. Herisson, Y. Chauvin, *Makromol. Chem.* **1971**, 141, 161.

1,5-Lactamized Sialyl Acceptors for Various Disialoside Syntheses: Novel Method for the Synthesis of Glycan Portions of Hp-s6 and HLG-2 Gangliosides**

Hiromune Ando,* Yusuke Koike, Sachiko Koizumi, Hideharu Ishida, and Makoto Kiso*

The ongoing studies on oligosaccharide synthesis have resulted in the development of precise synthetic methods by which a large portion of the complex natural oligosaccharides can be duplicated.^[1] Although the synthesis of the sequence Neu5Ac α (2 \rightarrow 8)Neu5Ac (α (2 \rightarrow 8)disialic acid; Neu5Ac = *N*-acetylneuraminic acid) has been a major difficulty, the emergence of several exquisite methods^[2] that employ indirect coupling by using a C3-functionalized *N*-acetyl sialyl donor and direct coupling by using an *N*-trifluoroacetyl (TFAc)-protected sialic acid donor with the help of the nitrile solvent effect have paved the way for the successful synthesis of α (2 \rightarrow 8)disialic acid containing oligosaccharides, such as those with GD3^[2c] and GQ1b^[3] glycan portions. However, it is obvious that the synthesis of new congeners of disialic acid, such as 8-*O*-sulfo-Neu5Ac α (2 \rightarrow 8)Neu5Ac in ganglioside Hp-s6^[4] and Neu5Gc α (2 \rightarrow 4)Neu5Ac in ganglioside HLG-2^[5] (Scheme 1), is still difficult because of the diverse modifications possible at the functionality level. On the basis of the predicted biological functions of the disialic acid congener containing oligosaccharides relevant to functions such as neural network formation and fertilization, the establishment of an expedient synthetic method that includes the entire disialic acid family seems essential not only for the progress of glycochemistry but also for studying in detail the molecular



Scheme 1. Structures of novel disialyl gangliosides Hp-s6 and HLG-2.

basis underlying the biological functions of these compounds. In this study, we report a novel synthetic method for the synthesis of disialic acid congener containing glycans that uses highly reactive lactamized sialyl acceptors and an *N*-2,2,2-trichloroethoxycarbonyl (Troc)-protected sialyl donor.

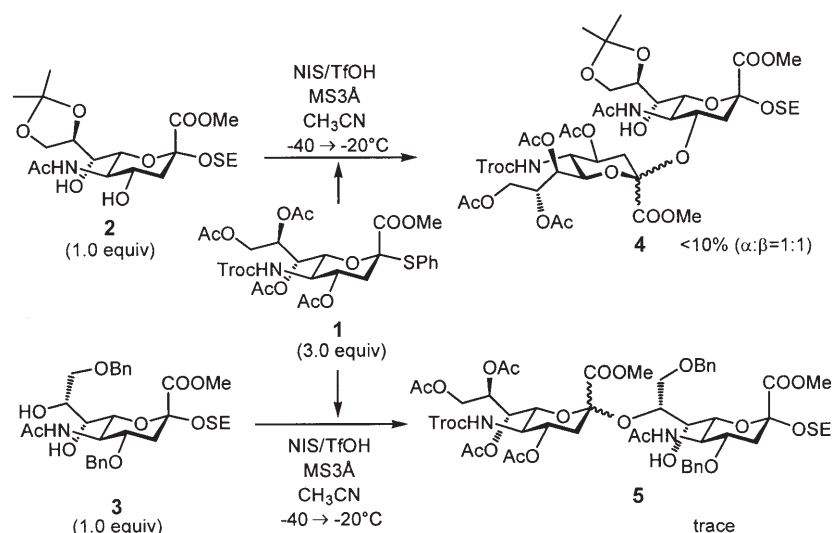
Recently, we reported an *N*-Troc-protected sialyl donor (*N*-Troc donor **1**) that shows elevated reactivity and a high degree of accessibility for various sialic acid congeners such as *N*-glycolylneuraminic acid (Neu5Gc), 8-*O*-sulfo-Neu5Ac, and 1,5-lactam-Neu.^[6] Initially, we anticipated that use of the *N*-Troc donor would enable the design of HLG-2 and Hp-s6 glycan sequences in an expedient manner. However, as depicted in Scheme 2, the results of the condensations with 4-OH and 8-OH sialyl acceptors, **2** and **3**, respectively, did not meet expectations with regard to yields and stereoselectivity. Even in the case of **2**, which showed the relatively higher reactivity, α -disialyl glycoside was obtained in less than 5%. We hypothesized that the poor results were mainly due to unfavorable hydrogen bonding with the amide moiety at C5, as proposed previously by Tsvetkov and Schmidt.^[7] This hypothesis was the basis of the idea that the conformational transformation from the ²C₅ chair form to the fixed boat form with the 1,5-lactam bridge would result in increased reactivity of both the C4- and C8-hydroxy groups.^[8]

To form the 1,5-lactam bridge in the sialoside, the previously reported *N*-TFAc-sialic acid derivative **6**^[9] was used as the key precursor (Scheme 3). After the coupling reaction of **6** and tribenzylated glucosyl acceptor **7**, the resulting sialyl- α (2 \rightarrow 6)Glc disaccharide, **8**, was subjected to 1,5-lactamization. First, we attempted a carbodiimide-mediated intramolecular amide formation after the complete deacylation and saponification of **8**, but this reaction yielded a complex mixture. The optimum yield was obtained when **8** was treated with methanolic sodium methoxide in the presence of Drierite under reflux to provide the 1,5-lactam-sialyl glucoside **9** in 85% yield; through regioselective benzylation of the C9-hydroxy group of **9** with benzoyl chloride and pyridine, under kinetic control, triol acceptor **10** was produced. For the synthesis of the 8-hydroxy-1,5-lactam

[*] Dr. H. Ando
Division of Instrumental Analysis
Life Science Research Center
Gifu University
1-1 Yanagido, Gifu-shi, Gifu 501-1193 (Japan)
Fax: (+81) 58-293-2617
E-mail: hando@cc.gifu-u.ac.jp
Y. Koike, S. Koizumi, Dr. H. Ishida, Dr. M. Kiso
Department of Applied Bioorganic Chemistry
Faculty of Applied Biological Sciences
Gifu University
1-1 Yanagido, Gifu-shi, Gifu 501-1193 (Japan)
Fax: (+81) 58-293-2918
E-mail: kiso@cc.gifu-u.ac.jp

[**] Synthetic Studies on Sialoglycoconjugates, Part 139. This work was financially supported by CREST of JST (M.K.), MEXT of Japan (Grant-in-Aid for Scientific Research; no. 16780083 to H.A., no. 16580086 to H.I., and no. 17101007 to M.K.), and the Mitsubishi Chemical Corporation Fund (H.A.). We thank Ms. Kiyoko Ito for technical assistance. For Part 138, see: M. Yamaguchi, H. Ishida, A. Kanamori, R. Kannagi, M. Kiso, *Glycoconjugate J.* **2005**, *22*, 83–96.

Supporting information for this article is available on the WWW under <http://www.angewandte.org> or from the author.

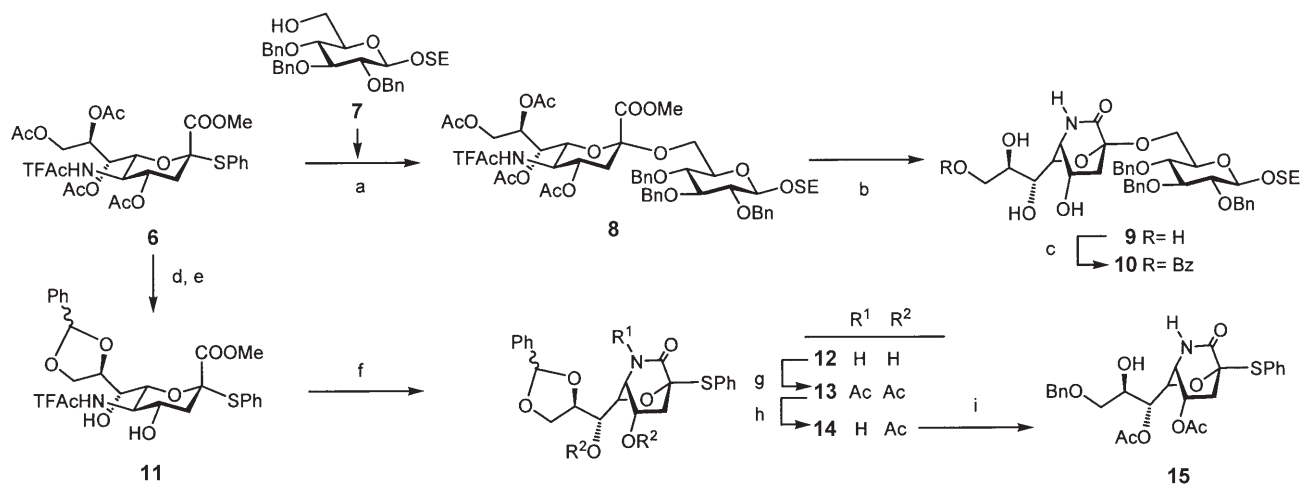


Scheme 2. Unsuccessful sialylation to 4-OH and 8-OH sialyl acceptors. Bn = benzyl, MS = molecular sieves, NIS = *N*-iodosuccinimide, SE = 2-(trimethylsilyl)ethyl, TfOH = tri-fluoromethanesulfonic acid.

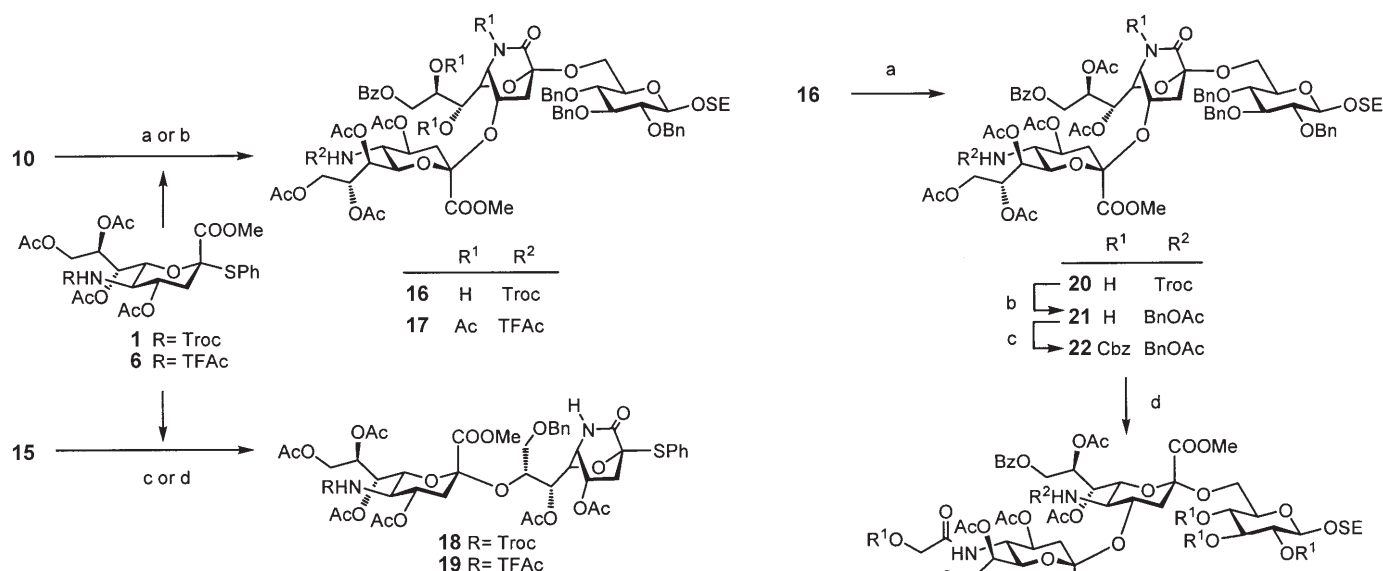
mized sialyl acceptor, 8,9-*O*-benzylidenation was required prior to the lactamization because 8,9-*O*-acetalization of the lactamized derivative was unsuccessful. Thus, compound **6** was de-*O*-acetylated and this was followed by the conventional 8,9-*O*-benzylidenation with benzaldehyde dimethyl acetal and camphorsulfonic acid to produce **11**, which was then subjected to the one-pot 1,5-lactam formation mentioned earlier to yield bicyclo-sialoside **12** in 89 % yield. Next, **12** was completely acetylated with Ac₂O in the presence of pyridine and the product was successively de-*N*-acetylated with hydrazinium acetate in a chemoselective manner to produce compound **14**. Finally, reductive ring opening of the benzylidene acetal moiety, influenced by BH₃·NMe₃ and AlCl₃ in THF,^[10] produced the 8-OH lactam acceptor **15**.

Next, we carried out the glycosylation of the lactam acceptors **10** and **15** with *N*-Troc- and *N*-TFAC-sialyl donors to evaluate their properties as glycosyl acceptors (Scheme 4). First, the triol acceptor **10** was treated with *N*-Troc donor **1** in the presence of NIS, TfOH, and a molecular sieve in EtCN^[11] at –40 °C to provide the Neuα(2→4)Neuα-(2→6)Glc sequence **17**, along with the corresponding β isomer. The anomeric configuration of the new ketosidic linkage was determined on the basis of previous reports^[12] by measuring the long-range ³*J*_{C1,H3ax} coupling constants. For compound **17** this coupling constant was 5.4 Hz, whereas for the β isomer it was less than 1.0 Hz, a fact indicating that the anomeric configuration of **17** was α. Similarly, the coupling reaction with the *N*-TFAC donor **6** and the complete acetylation that followed yielded the corresponding Neuα(2→4)Neuα(2→6)Glc sequence **17** in 41 % yield, along with the β isomer (10 %) and the Neu(2→8)[[Neu(2→4)]Neuα](2→6)Glc sequences as an anomeric mixture (8 %).

Next, we attempted to fashion the purest form of Neuα(2→8)Neu sequence (Scheme 4). As initially expected, the glycosylation reactions of the lactam acceptor **15** with *N*-Troc and *N*-TFAC donors (**1** and **6**) yielded the corresponding Neuα(2→8)Neu sequences. Thus, *N*-Troc donor **1** and *N*-TFAC donor **6** were incorporated, in the presence of NIS, TfOH, and a molecular sieve in EtCN, at –80 °C to yield α(2→8)disialosides **18** and **19** in 49 and 71 % yield, respectively; no corresponding β form was generated in either event. To the best of our knowledge, the yield of addition to the C8-hydroxy group of sialic acid (71 %) during the sialylation process was the highest value obtained by direct coupling methods^[2] In keeping with the results of the previous experiments, the anomeric configuration of the new linkages was determined to be α from ³*J*_{C1,H3ax} coupling constants that



Scheme 3. a) **7**, NIS, TfOH, CH₃CN/CH₂Cl₂, MS (3 Å), –30 °C, 5 min, 74 %; b) NaOMe, MeOH, Drierite, reflux, 44 h, 85 %; c) BzCl, py/CH₂Cl₂, –40 °C, 90 min, 79 %; d) NaOMe, MeOH, room temperature, 29 h; e) PhC(OMe)₂, CSA, DMF, 40 °C, 2 h, 88 % (2 steps); f) NaOMe, MeOH, Drierite, reflux, 5 d, 89 %; g) Ac₂O, py, DMAP, room temperature, 3 h; h) NH₂NH₂·AcOH, THF, room temperature, 80 min, 94 % (2 steps); i) BH₃·NMe₃, AlCl₃, THF, MS (4 Å), 0 °C → RT, 6 h, 74 %. Bz = benzoyl, CSA = (±)-10-camphorsulfonic acid, DMF = *N,N*-dimethylformamide, DMAP = 4-dimethylaminopyridine, py = pyridine, THF = tetrahydrofuran.



Scheme 4. a) **1** (2.0 equiv), NIS (3.0 equiv), TfOH (0.3 equiv), EtCN, MS (3 Å), -40°C , 6 h, 84% (α/β 66:18); b) **1**, **6** (2.0 equiv), NIS, TfOH, EtCN, MS (3 Å), -40°C , 6 h; 2. Ac_2O , py, DMAP, 40°C , 17 h, 51%; c) **1** (3.0 equiv), NIS, TfOH, EtCN, MS (3 Å), -80°C , 5 h, 49% (α only); d) **6** (3.0 equiv), NIS, TfOH, EtCN, MS (3 Å), -80°C , 3 h, 71% (α only).

ranged from 6.7 to 6.9 Hz. Furthermore, the phenylsulfenyl group at the bridgehead anomeric center of acceptor **15** remained unaffected during the coupling reactions. This result confirmed our initial hypothesis, based on Bredt's rule, suggesting the basis of a novel method for the complete deactivation of a sialyl donor.

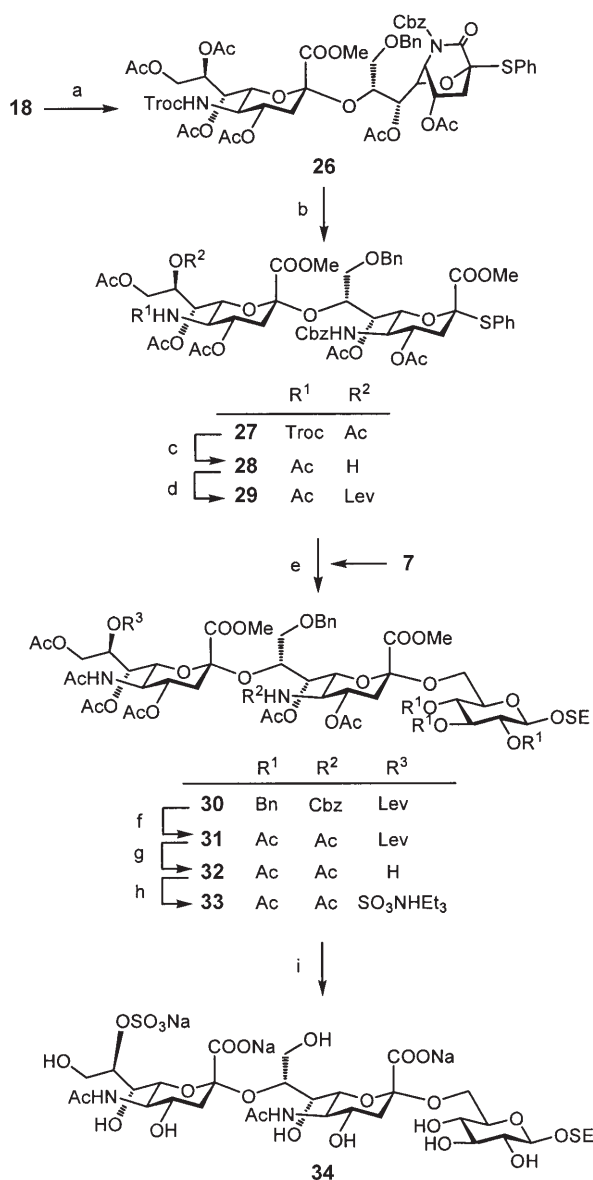
On the basis of the results obtained with regard to the performance of 1,5-lactamized sialic acid acceptors **10** and **15** in the sialylation reactions, we focused on the synthesis of the glycan portions of HLG-2 and Hp-s6 gangliosides of **16** and **18**, respectively, in order to demonstrate the practical efficacy of the synergic strategy for synthesizing variant disialosides from the 1,5-lactam-sialyl acceptor and *N*-Troc-sialyl donor.

In the initial stages of the synthesis of the HLG-2 glycan portion (Scheme 5), the trisaccharide **16** was *O*-acetylated to provide **20**, to which the *N*-glycolyl moiety was introduced by our reported method,^[6] thereby providing **21** in a relatively high yield (66% from **16**). Next, we attempted to recover the $^2\text{C}_5$ conformation of the inner sialic acid unit. The following reaction sequences supplied HLG-2 glycan frame **23** in a high yield: *N*-benzyloxycarbonylation, basic hydrolysis, and ensuing methylation of the carboxy group. Debenzylation and acetylation to replaced the Cbz group of **23** by the acetyl group and full deprotection of the product **24** yielded the HLG-2 glycan structure **25**.

In the case of the Hp-s6 glycan frame, the "locked-up" phenylsulfenyl group at the bridgehead carbon atom of **18** was converted into an active state in the initial stages (Scheme 6). To be precise, the reaction sequences mentioned earlier yielded $^2\text{C}_5$ conformer **27** in 62% overall yield. For the purpose of 8-*O*-sulfonylation in the final stages of the synthesis, **27** was further transformed into the 8-hydroxy derivative **28** by our regioselective acetyl-transfer method,^[6] and the C8 hydroxy group was capped with a levulinoyl group

Scheme 5. a) Ac_2O , py, room temperature, 10 h, 89%; b) 1. Zn, AcOH, room temperature, 2 h; 2. BnOAcCl, THF, room temperature, 1 h, 74% (2 steps); c) Cbz₂O, DMAP, py, 40°C , 26 h, 95%; d) 1. Et_3N , $\text{H}_2\text{O}/\text{CH}_3\text{CN}$, room temperature, 2 d; 2. MeI, K_2CO_3 , DMF, room temperature, 30 min, 74% (2 steps); e) 1. H_2 , 10% Pd(OH)₂/C, NH_3 , EtOH, room temperature, 2 h; 2. AcCl, room temperature, 1 h, 68% (2 steps); f) 1. H_2 , 10% Pd(OH)₂/C, EtOH; 2. Ac_2O , py, room temperature, 54% (2 steps). Cbz = benzyloxycarbonyl.

to produce high yields (89%) of the suitably protected disialic acid donor **29** in two steps. Compound **29** was then treated with glucosyl acceptor **7**, influenced by the NIS/TfOH activator system in EtCN at $-80 \rightarrow -60^{\circ}\text{C}$, to provide Neu α -(2 \rightarrow 8)Neu α -(2 \rightarrow 6)Glc sequence **30** in 66% yield, predominantly in the α configuration. Next, replacement of the Cbz and benzyl groups of trisaccharide **30** by the acetyl group, followed by chemoselective deblocking of the levulinoyl group with hydrazinium acetate^[13] and sulfonylation with SO_3 -pyridine resulted in the formation of a completely protected Hp-s6 glycan frame, **33**.^[14] The ^1H NMR signal for the C8 proton of the outer sialic acid appeared in compound **33** at lower magnetic field ($\delta = 4.92$ ppm) than in compound **32** ($\delta = 4.22$ ppm), and the heteronuclear multiple-bond coherence (HMBC) spectrum of compound **33** contained cross-coupling signals between carbonyl carbon atoms of acetyl groups at C7 and C9, and H7 ($\delta = 5.40$ ppm) and H9



Scheme 6. a) CbzOSu, DMAP, py, room temperature, 42 h, 79%; b) 1. Et₃N, H₂O/CH₃CN, 40 °C, 45 h; 2. MeI, K₂CO₃, DMF, room temperature, 3 h, 79% (2 steps); c) Zn, AcOH, THF, room temperature, 28 h, 94%; d) LevOH, DCC, DMAP, CH₂Cl₂, room temperature, 2 h, 95%; e) 7, NIS, TFOH, EtCN, MS (3 Å), –80 → –60 °C, 4 d, 66%; f) 1. H₂, 10% Pd(OH)₂/C, NH₃, EtOH, room temperature, 1 h; 2. Ac₂O, py, room temperature, 30 min; 3. H₂, 10% Pd(OH)₂/C, EtOH, 40 °C, 3 h; 4. Ac₂O, py, room temperature, 12 h, 86% (4 steps); g) NH₂NH₂·AcOH, EtOH, room temperature, 6 h, 90%; h) SO₃·py, py, room temperature, 7 h, 65%. Lev = levulinoyl = 4-oxopentanoyl, Su = succinimidyl, DCC = N,N'-dicyclohexyl carbodiimide.

(δ = 4.19 ppm). Thereby, the installation of the sulfonyl group on the C8-hydroxy group was determined.

In conclusion, we have discovered that 1,5-lactam bridging in sialic acid endows high reactivity to the C4- and C8-hydroxy groups, thereby leading to the supply of α (2→4)- and α (2→8)disialic acid sequences in high yields. Furthermore, the practical efficacy of the synergic synthetic approach toward diverse disialic acid containing oligosaccharides,

based on the *N*-Troc donor and the lactamized acceptors as the main units, has been demonstrated by the novel method for the synthesis of the HLG-2 and Hp-s6 glycan chains. On the basis of these results, we are now investigating the synthesis of α (2→8)-linked oligosialic acids.

Received: May 11, 2005

Revised: July 13, 2005

Published online: September 27, 2005

Keywords: gangliosides · glycosylation · lactams · sialic acids

- Selected reviews: a) H. Herzner, T. Reipen, M. Schultz, H. Kuntz, *Chem. Rev.* **2000**, *100*, 4495–4537; b) K. C. Nicolaou, H. J. Mitchell, *Angew. Chem.* **2001**, *113*, 1624–1672; *Angew. Chem. Int. Ed.* **2001**, *40*, 1576–1624; selected papers on oligosaccharide synthesis: c) H. Yoshizaki, N. Fukuda, K. Sato, M. Oikawa, K. Fukase, Y. Suda, S. Kusumoto, *Angew. Chem.* **2001**, *113*, 1523–1528; *Angew. Chem. Int. Ed.* **2001**, *40*, 1475–1480; d) I. Matsuo, M. Wada, S. Manabe, Y. Yamaguchi, K. Ohtake, K. Kato, Y. Ito, *J. Am. Chem. Soc.* **2003**, *125*, 3402–3403; e) K. Hori, N. Sawada, H. Ando, H. Ishida, M. Kiso, *Eur. J. Org. Chem.* **2003**, 3752–3760; f) P. Wang, Y.-J. Kim, M. Navarro-Villalobos, B. D. Rohde, D. Gin, *J. Am. Chem. Soc.* **2005**, *127*, 3256–3257.
- a) Review: G.-J. Boons, A. V. Demchenko, *Chem. Rev.* **2000**, *100*, 4539–4565; leading articles on sialyl- α (2→8)sialoside synthesis: b) K. Okamoto, T. Kondo, T. Goto, *Tetrahedron Lett.* **1986**, *27*, 5229–5232; c) Y. Ito, M. Numata, M. Sugimoto, T. Ogawa, *J. Am. Chem. Soc.* **1989**, *111*, 8508–8510; d) J. C. Castro-Palmino, Y. E. Tsvetkov, R. R. Schmidt, *J. Am. Chem. Soc.* **1998**, *120*, 5434–5440; e) A. V. Demchenko, G.-J. Boons, *Chem. Eur. J.* **1999**, *5*, 1278–1283; f) C. De Meo, A. V. Demchenko, G.-J. Boons, *J. Org. Chem.* **2001**, *66*, 5490–5497.
- Y. Ito, S. Numata, S. Shibayama, T. Ogawa, *J. Org. Chem.* **1992**, *57*, 1821–1831.
- T. Ijuin, K. Kitajima, Y. Song, S. Kitazume, S. Inoue, S. T. Haslam, H. R. Morris, A. Dell, Y. Inoue, *Glycoconjugate J.* **1996**, *13*, 401–413.
- K. Yamada, R. Matsubara, M. Kaneko, T. Miyamoto, R. Higuchi, *Chem. Pharm. Bull.* **2001**, *49*, 447–452.
- H. Ando, Y. Koike, H. Ishida, M. Kiso, *Tetrahedron Lett.* **2003**, *44*, 6883–6886.
- Y. E. Tsvetkov, R. R. Schmidt, *Tetrahedron Lett.* **1994**, *35*, 8583–8586.
- Schmidt's group first disclosed the idea of conformational change of the sialyl acceptor to enhance the reactivity of the C8-hydroxy group. They exploited the 1,7-lactonated sialyl acceptor for 8-*O*-sialylation but obtained mainly β -disialoside. See reference [7].
- S. Komba, C. Glalustian, H. Ishida, T. Feizi, R. Kannagi, M. Kiso, *Angew. Chem.* **1999**, *111*, 1203–1206; *Angew. Chem. Int. Ed.* **1999**, *38*, 1131–1133.
- M. Ek, P. J. Garegg, H. Hultberg, S. Oscarson, *J. Carbohydr. Chem.* **1983**, *2*, 305–311.
- a) T. Murase, H. Ishida, M. Kiso, A. Hasegawa, *Carbohydr. Res.* **1988**, *184*, c1–c4; b) A. Hasegawa, T. Nagahama, H. Ohki, K. Hotta, H. Ishida, M. Kiso, *J. Carbohydr. Chem.* **1991**, *10*, 493–498.
- a) H. Hori, T. Nakajima, Y. Nishida, H. Ohnishi, H. Meguro, *Tetrahedron Lett.* **1988**, *29*, 6317–6320; b) J. Haverlamp, T. Spoormaker, L. Dorland, J. F. G. Vliegthart, R. Shauer, *J. Am. Chem. Soc.* **1979**, *101*, 4851–4853; c) S. Prytulla, J. Lauterwein, M. Klessinger, J. Thiem, *Carbohydr. Res.* **1991**, *215*, 345–349.

- [13] J. H. van Boom, P. M. J. Burgers, *Tetrahedron Lett.* **1976**, 4875–4878.
- [14] Furuhata's group first reported the 8-*O*-sulfonylation of neuraminic acid. They also confirmed that no migration or cleavage of the sulfonyl group at the C8-hydroxy group had occurred during the full deacylation and saponification process: M. Tanaka, T. Kai, X.-L. Sun, H. Takayanagi, K. Furuhata, *Chem. Pharm. Bull.* **1995**, 43, 2095–2098.

Corrole Derivatives

DOI: 10.1002/anie.200502335

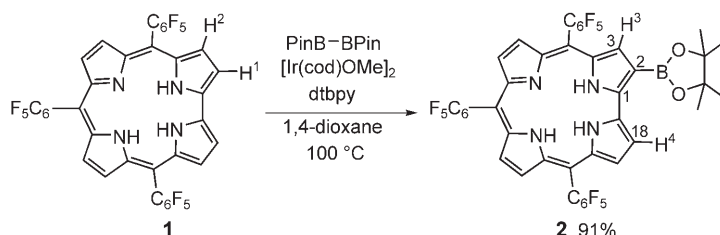
Synthesis of Corrole Derivatives through Regioselective Ir-Catalyzed Direct Borylation**

Satoru Hiroto, Ichiro Hisaki, Hiroshi Shinokubo,* and Atsuhiko Osuka*

Corroles are 18- π -aromatic tetrapyrrolic macrocycles that contain a direct pyrrole–pyrrole linkage, that exhibit interesting optical properties and unique metal-coordination chemistry, and serve as excellent ligands for oxidation catalysis.^[1] Although covalently linked multiporphyrinic molecules have received much attention from the viewpoint of the development of novel functional materials and molecular devices,^[2] the synthesis of molecular assemblies based on corroles has remained rather limited owing to the lack of effective synthetic strategies for their regioselective modification.^[3] Thus, considerable efforts have been made to develop selective methods that allow the effective functionalization of corroles. However, electrophilic substitution of corroles can occur at the C3 position, and multisubstitution products are sometimes formed.^[4] To the best of our knowledge, the selective derivatization of corroles at the C2 position has not been reported. Very recently, we reported the highly regioselective direct borylation of porphyrins at the β position under iridium catalysis.^[5,6] Herein, we disclose the successful application of this strategy to 5,10,15-triarylcor-

roles which enables easy functionalization of the corrole structure at the 2-position with perfect regioselectivity. Owing to the rich chemistry of organoboranes, this strategy offers a powerful tool for the construction of corrole-based molecular assemblies.

A solution of 5,10,15-tris(pentafluorophenyl)corrole (**1**)^[7] in dioxane was heated at 100 °C for 24 h with bis(pinacolato)diborane (1.1 equiv) in the presence of a catalytic amount of [Ir(cod)OMe]₂ (1.5 mol %) and 4,4'-di-*tert*-butyl-2,2'-bipyridyl (dtbpy; 3.0 mol %) according to the Miyaura–Hartwig–Smith protocol (Scheme 1).^[5,6b] Purification by preparative GPC–HPLC afforded the monoborylated corrole **2** in 91 %



Scheme 1. Iridium-catalyzed direct borylation of corrole **1**. PinB–BPin = bis(pinacolato)diborane; cod = cycloocta-1,8-diene.

yield. Introduction of the boryl group was confirmed by the presence of the parent-ion peak at m/z 921.1529 (calcd for (C₄₃H₂₁BF₁₅N₄O₂)⁺: 921.1531 ([*M*–H]⁺)) by high-resolution electrospray-ionization time-of-flight mass spectrometry (HRMS). Even with the use of excess diborane reagent for a prolonged period, bisborylated corrole could not be obtained. The ¹H NMR spectrum of the product revealed its unsymmetrical nature. One singlet and one doublet peak, which can be assigned to hydrogen atoms H³ and H⁴, respectively, were shifted downfield as a result of the neighboring effect of the boryl group which indicates that the boryl group is introduced at the 2-position. This reaction proceeded with perfect regioselectivity, and none of the other isomers were detected.

The structure of the 2-boryl-substituted corrole **2** was unambiguously confirmed by X-ray diffraction analysis (Figure 1).^[8] The most sterically accessible hydrogen atom H¹ in **1** is replaced by boron. The dioxaborolane rings in **2** are only slightly tilted (27.8°) relative to the corrole core, thereby probably maintaining electronic interaction between the vacant orbital of boron and the π orbital of the core. In this conformation, the bulky tetramethyldioxaborolane moiety hampers the access of a second molecule of the reactive metal complex, hence preventing the second borylation at another pyrrolic site (18-position). While electronic factors generally dominate the regioselectivity at the 3-position in the electrophilic substitution of corroles,^[4c–e] the regioselectivity in the present protocol is likely to be determined by steric reasons: the peripheral aromatic groups block borylation at sites other than the 2- and 18-positions. This selectivity is consistent with our observations with previous borylation reactions of porphyrins under iridium catalysis.

Figure 2 shows the UV/Vis absorption and emission spectra of **1** and **2**. The Soret bands as well as the Q bands

[*] S. Hiroto, Dr. I. Hisaki, Prof. Dr. H. Shinokubo, Prof. Dr. A. Osuka
Department of Chemistry
Graduate School of Science
Kyoto University
Sakyo-ku, Kyoto 606-8502 (Japan)
and
PRESTO & CREST
Japan Science and Technology Agency (JST)
Fax: (+81) 75-753-3970
E-mail: hshino@kuchem.kyoto-u.ac.jp
osuka@kuchem.kyoto-u.ac.jp

[**] This work was partly supported by a Grant-in-Aid for Scientific Research from the Ministry of Education, Culture, Sports, Science, and Technology, Japan. I.H. acknowledges the Research Fellowships of the JSPS for Young Scientists.

Supporting information for this article is available on the WWW under <http://www.angewandte.org> or from the author.

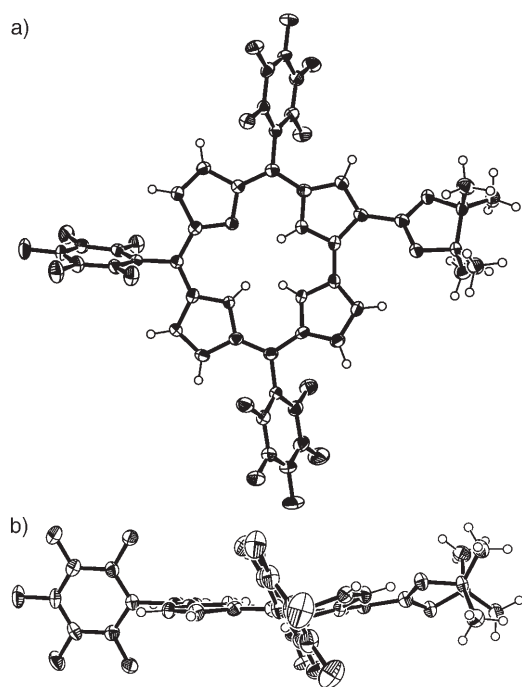
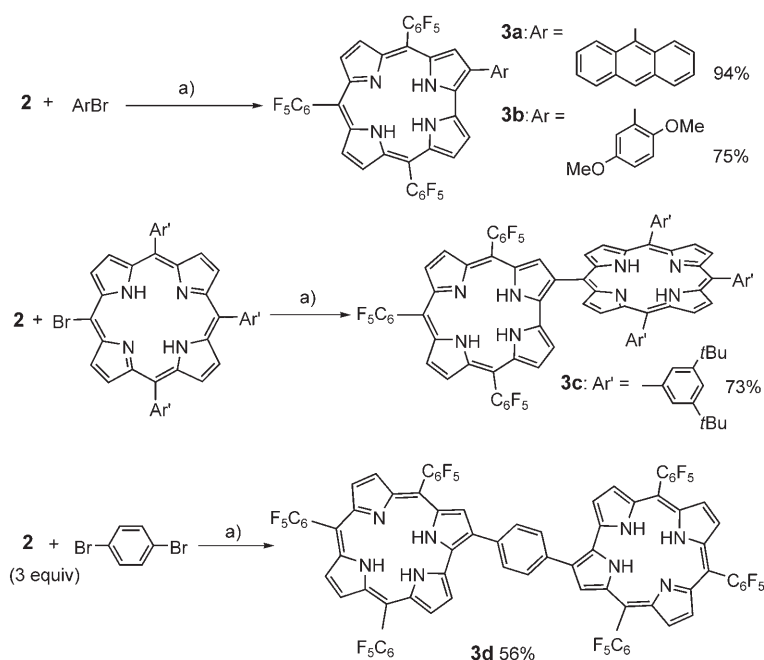


Figure 1. X-ray crystal structure of **2**: a) top view and b) side view.



Scheme 2. Syntheses of 2-functionalized corroles by Suzuki–Miyaura coupling reactions. a) [(Pd(dba)₂), PPh₃, Cs₂CO₃, CsF, toluene/DMF/H₂O. DMF = *N,N*-dimethylformamide; dba = dibenzylideneacetone.

of **2** are slightly red-shifted relative to those of **1**. Interestingly, introduction of the boryl group resulted in an increase in the fluorescence intensity.

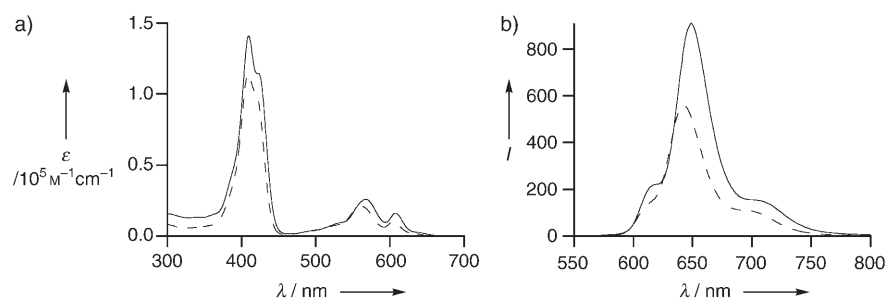
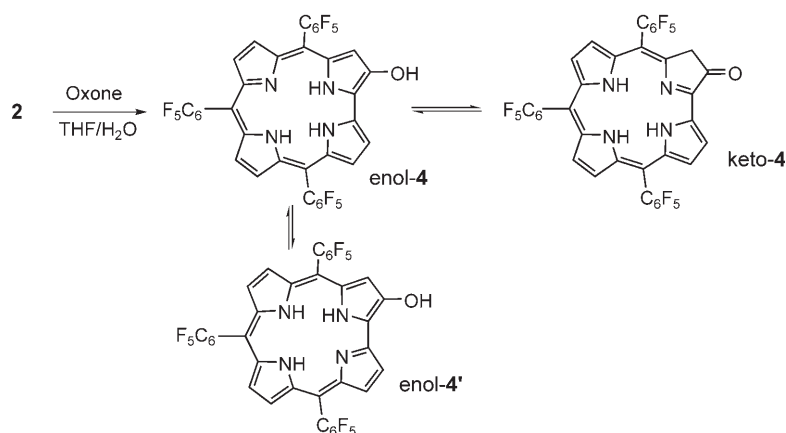


Figure 2. a) UV/Vis absorption spectra and b) emission spectra of **1** (----) and **2** (—) in CH₂Cl₂.

Organoboron compounds are the most useful substrates for the formation of carbon–carbon bonds by the Suzuki–Miyaura cross-coupling reaction. Indeed, the reaction of **2** with bromoanthracene or bromodimethoxybenzene afforded the desired coupling products **3a** and **3b** in excellent yields (Scheme 2). We also report the synthesis of a directly linked corrole–porphyrin hybrid **3c** through the coupling of **2** with *meso*-bromoporphyrin. In contrast to the recent developments in directly linked porphyrin arrays,^[9,10] there has been no previous report on directly linked corrole–porphyrin molecules. Corrole–porphyrin **3c** may be used to ligate two metal ions in different valence

states (M²⁺ and M³⁺). Additionally, the 1,4-phenylene-bridged dimer **3d** was also very easily obtained by the Suzuki–Miyaura coupling of **2** with 1,4-dibromobenzene. The present procedure provides the desired compounds in excellent yields in only two steps—borylation and cross-coupling—from the original corroles.

The oxidation of organoboranes is a versatile tool for the synthesis of alcohols and phenols. Thus, we attempted the synthesis of 2-hydroxycorroles by oxidation of **2** with oxone according to Smith's procedure (Scheme 3),^[11] and oxidation product **4** was obtained in 62 % yield. HRMS revealed a parent-ion peak for **4** at *m/z* 811.0629 (calcd for (C₃₇H₁₀F₁₅N₄O): 811.0621 ([M–H][–]). The ¹H NMR spectrum



Scheme 3. Synthesis of 2-hydroxycorrole and its tautomerization.

of the product in CDCl_3 revealed that the keto form, keto-**4**, had been isolated, with the presence of a peak at $\delta = 4.75$ ppm for the two methylene hydrogen atoms (H^a) at the α position of the ketone group. Additionally, signals for the carbonyl and sp^3 -hybridized carbon atoms were detected at $\delta = 197.9$ and 45.6 ppm, respectively, in the ^{13}C NMR spectrum of the product in CDCl_3 . To the best of our knowledge, this is the first reported isolation of the keto form of a dihydrocorrole.^[12]

In contrast, the enol form enol-**4** was predominant in solution in $[\text{D}_6]\text{DMSO}$, and the hydroxy proton was detected at $\delta = 11.8$ ppm (Figure 3).^[13] While the keto form is exclusively observed in solution in CDCl_3 and CD_2Cl_2 , both keto and enol structures were detected in varying ratios in $[\text{D}_8]\text{THF}$, CD_3CN , $[\text{D}_6]\text{acetone}$, and CD_3OD . Interestingly, the inner NH protons appear as sharp signals at $\delta = -0.44$, -3.05 , and -4.84 ppm for the keto form (in CDCl_3 , while the corresponding signals were very broad at $\delta \approx -0.59$, -1.02 , and -3.51 ppm for the enol form (in $[\text{D}_6]\text{DMSO}$). This observation is consistent with the presence of fixed NH protons in the keto form keto-**4** versus fast NH tautomerism on the NMR timescale between enol forms **4** and **4'** (Scheme 3), as observed for regular corroles.^[14] In the enol form, a signal at $\delta = 7.82$ ppm, which was assigned as H^b on the basis of H–H COSY experiments, appeared at higher field than the other β -pyrrolic signals. This shift is

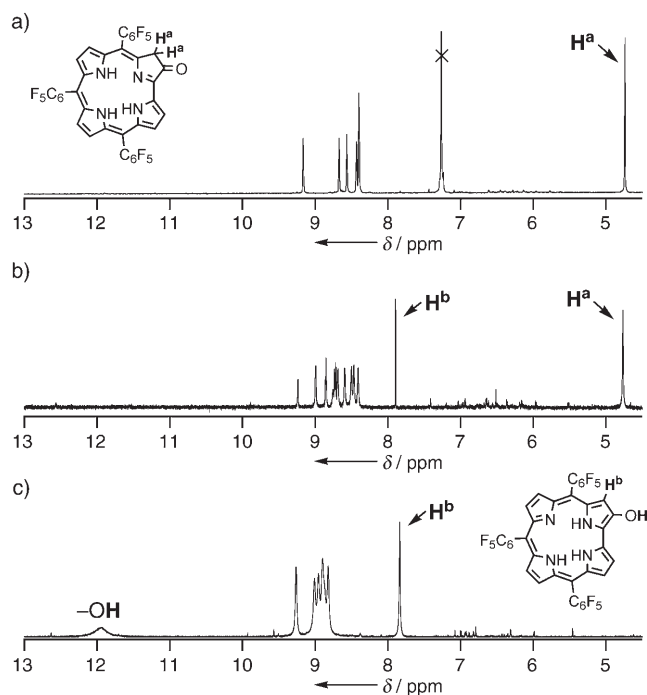


Figure 3. ^1H NMR spectra of **4**: a) keto-**4** in CDCl_3 , b) keto and enol forms in CD_3CN , and c) enol-**4** in $[\text{D}_6]\text{DMSO}$ (dimethyl sulfoxide).

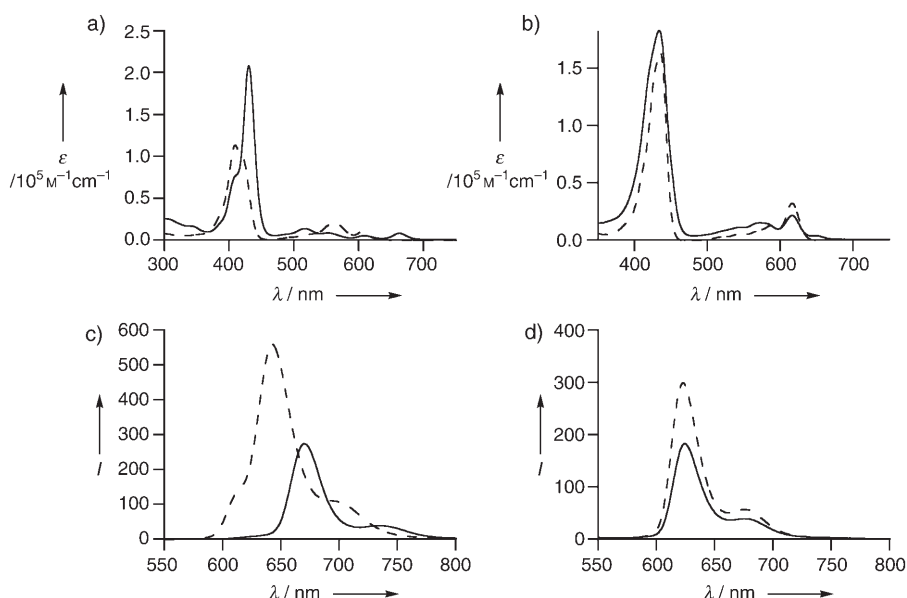


Figure 4. UV/Vis absorption spectra of a) keto-**4** (—) and **1** (----) in CH_2Cl_2 , and b) enol-**4** (—) and **1** (----) in DMSO. Emission spectra of c) keto-**4** (—) and **1** (----) in CH_2Cl_2 , and d) enol-**4** (—) and **1** (----), intensity scaled down by 1/10 in DMSO.

caused by the electron-donating nature of the neighboring hydroxy substituent. Interestingly, the signal for H^b gradually decreased upon the addition of D_2O while that for the hydroxy proton disappeared. This result supports the presence of exchange between the OH proton and hydrogen atom H^b through tautomerization.

The UV/Vis and emission spectra of **4** showed a strong dependence on the solvent, reflecting the structural difference between the keto and enol forms (Figure 4). The absorption spectrum of **4** in DMSO is quite similar in shape to that of the original corrole **1** in the same solvent (Figure 4b). In contrast, four Q bands were observed in CH_2Cl_2 , probably as a result of the dihydrocorrole structure of the keto form, and the same holds for the red shift of the Soret band (Figure 4a). The enol form emits enol-**4** at the same wavelength as **1**, with a similarly shaped but less-intense spectrum in DMSO (Figure 4d), while the spectrum of the keto form keto-**4** in CH_2Cl_2 was significantly red-shifted relative to that of **1** in the same solvent (Figure 4c). The effect of the hydroxy group in the enol form upon the fluorescence intensity is not clear at this stage.

In conclusion, we have demonstrated the highly regioselective synthesis of a 2-borylated corrole, which is a useful platform for the functionalization of corroles and the construction of molecular assemblies based on corroles. The utility of the present protocol has been demonstrated by the first syntheses of the directly linked corrole–porphyrin hybrid **3c** and the 2-hydroxy-substituted corrole **4**. Further studies involving borylated porphyrins and corroles are currently underway in our laboratory.

Received: July 5, 2005

Published online: September 19, 2005

Keywords: boron · corroles · cross-coupling · iridium · porphyrinoids

- [1] For excellent reviews on corroles, see: a) (synthesis) D. T. Gryko, *Eur. J. Org. Chem.* **2002**, 1735; b) (oxidation catalysis) Z. Gross, H. B. Gray, *Adv. Synth. Catal.* **2004**, 346, 165; c) (electronic properties) A. Ghosh, E. Steene, *J. Inorg. Biochem.* **2002**, 91, 423.
- [2] a) D. Gust, T. A. Moore, A. L. Moore, *Acc. Chem. Res.* **2001**, 34, 40; b) M. R. Wasielewski, *Chem. Rev.* **1992**, 92, 435; c) M. G. H. Vicente, L. Jaquinod, K. M. Smith, *Chem. Commun.* **1999**, 1771; d) H. L. Anderson, *Chem. Commun.* **1999**, 2323; e) D. Holten, D. F. Bocian, J. S. Lindsey, *Acc. Chem. Res.* **2002**, 35, 57; f) D. Kim, A. Osuka, *Acc. Chem. Res.* **2004**, 37, 735; g) J.-H. Chou, M. E. Kosal, N. H. Nalwa, S. A. Rakow, K. S. Suslick in *The Porphyrin Handbook*, Vol. 6 (Eds.: K. M. Kadish, K. M. Smith, R. Guilard), Academic Press, New York, **1999**, p. 43.
- [3] a) K. M. Kadish, Z. Ou, J. Shao, C. P. Gros, J.-M. Barbe, F. Jérôme, F. Bolze, F. Burdet, R. Guilard, *Inorg. Chem.* **2002**, 41, 3990; b) R. Guilard, F. Jérôme, J.-M. Barbe, C. P. Gros, Z. Ou, J. Shao, J. Fischer, R. Weiss, K. M. Kadish, *Inorg. Chem.* **2000**, 39, 4856; c) R. Paolesse, R. K. Pandey, T. P. Forsyth, L. Jaquinod, K. R. Gerzevske, D. J. Nurco, M. O. Senge, S. Licoccia, T. Boschi, K. M. Smith, *J. Am. Chem. Soc.* **1996**, 118, 3869.
- [4] a) R. Paolesse, S. Nardis, F. Sagone, R. G. Khoury, *J. Org. Chem.* **2001**, 66, 550; b) G. Golubkov, J. Bendix, H. B. Gray, A. Mahammed, I. Goldberg, A. J. DiBilio, Z. Gross, *Angew. Chem.* **2001**, 113, 2190; *Angew. Chem. Int. Ed.* **2001**, 40, 2132; c) A. Mahammed, I. Goldberg, Z. Gross, *Org. Lett.* **2001**, 3, 3443; d) I. Saltsman, A. Mahammed, I. Goldberg, E. Tkachenko, M. Botoshansky, Z. Gross, *J. Am. Chem. Soc.* **2002**, 124, 7411; e) R. Paolesse, S. Nardis, M. Venanzi, M. Mastroianni, M. Russo, F. R. Fronczek, M. G. H. Vicente, *Chem. Eur. J.* **2003**, 9, 1192.
- [5] H. Hata, H. Shinokubo, A. Osuka, *J. Am. Chem. Soc.* **2005**, 127, 8264.
- [6] For Ir-catalyzed direct borylations of aromatic compounds, see: T. Ishiyama, N. Miyaara, *J. Organomet. Chem.* **2003**, 680, 3; a) J.-Y. Cho, M. K. Tse, D. Holmes, R. E. Maleczka, Jr., M. R. Smith III, *Science* **2002**, 295, 305, and references therein; b) T. Ishiyama, J. Takagi, K. Ishida, N. Miyaara, N. R. Anastasi, J. F. Hartwig, *J. Am. Chem. Soc.* **2002**, 124, 390, and references therein.
- [7] a) D. T. Gryko, B. Koszarna, *Org. Biomol. Chem.* **2003**, 1, 350; b) Z. Gross, N. Galili, I. Saltsman, *Angew. Chem.* **1999**, 111, 1530; *Angew. Chem. Int. Ed.* **1999**, 38, 1427; c) J. P. Collman, R. A. Decreau, *Tetrahedron Lett.* **2003**, 44, 1207.
- [8] Crystal data for **2**: C₄₃H₂₂BF₁₅N₄O₂, *M*_w = 922.46, monoclinic *P*2₁/*n* (No. 14), *a* = 18.12(7), *b* = 10.95(5), *c* = 19.39(10) Å, β = 93.74(13)°, *V* = 3838(3) Å³, *T* = 123 K, ρ_{calcd} = 1.596 g cm⁻³, *Z* = 4. For 30529 reflections measured; *R* = 0.096, *wR* (all data) = 0.1616, GOF = 1.099 [*I* > 2σ(*I*)]. CCDC-276228 contains the supplementary crystallographic data for this paper. These data can be obtained free of charge from the Cambridge Crystallographic Data Centre via www.ccdc.cam.ac.uk/data_request/cif.
- [9] a) K. Susumu, T. Shimidzu, K. Tanaka, H. Segawa, *Tetrahedron Lett.* **1996**, 37, 8399; b) M. O. Senge, X. Feng, *Tetrahedron Lett.* **1999**, 40, 4165; c) R. G. Khoury, L. Jaquinod, K. M. Smith, *Chem. Commun.* **1997**, 1057; d) A. Osuka, H. Shimidzu, *Angew. Chem.* **1997**, 109, 93; *Angew. Chem. Int. Ed. Engl.* **1997**, 36, 135; e) N. Aratani, A. Osuka, Y. H. Kim, D. H. Jeong, D. Kim, *Angew. Chem.* **2000**, 112, 1517; *Angew. Chem. Int. Ed.* **2000**, 39, 1458.
- [10] A cobalt complex of a directly linked dicorrole has been synthesized; see: A. Mahammed, I. Giladi, I. Goldberg, Z. Gross, *Chem. Eur. J.* **2001**, 7, 4259.
- [11] R. E. Maleczka, Jr., F. Shi, D. Holmes, M. R. Smith III, *J. Am. Chem. Soc.* **2003**, 125, 7792.
- [12] For the isolation of other types of dihydrocorroles, see: A. Mahammed, Z. Gross, *J. Inorg. Biochem.* **2002**, 898, 305.
- [13] For the tautomerization of 2-hydroxyporphyrins, see: M. J. Crossley, M. M. Harding, S. Sternhell, *J. Org. Chem.* **1988**, 53, 1132.
- [14] a) T. Ding, J. D. Harvey, C. J. Ziegler, *J. Porphyrins Phthalocyanines* **2005**, 9, 22; b) Y. S. Balazs, I. Saltsman, A. Mahammed, E. Tkachenko, G. Golubkov, J. Levine, Z. Gross, *Magn. Reson. Chem.* **2004**, 42, 624.

Protein Relaxivity

DOI: 10.1002/anie.200502245

Multilocus Binding Increases the Relaxivity of Protein-Bound MRI Contrast Agents

Zhaoda Zhang, Matthew T. Greenfield, Marga Spiller, Thomas J. McMurry, Randall B. Lauffer, and Peter Caravan*

*Dedicated to Professor Iwao Ojima
on the occasion of his 60th birthday*

The utility of clinical magnetic resonance imaging (MRI) has been greatly expanded by the use of contrast agents—gadolinium complexes that serve to increase the longitudinal nuclear relaxation rate ($1/T_1$) of water protons. Commercial contrast agents are only effective at high concentrations (>0.1 mM) and, as a result, there has been considerable effort to increase their sensitivity. One approach is to increase the number of gadolinium ions in the molecule by making polymeric or dendrimeric contrast agents.^[1] A second approach is to optimize the parameters that influence relaxation enhancement, such as rotational diffusion and water exchange.^[2]

An effective mechanism for increasing relaxivity ($r_1 = (\Delta 1/T_1)/[\text{Gd}]$) is the receptor-induced magnetization-enhancement (RIME) effect.^[3] An example is the GdDTPA derivative MS-325, which targets serum albumin. When MS-325 binds to albumin, the rotational correlation time (τ_R) increases from that of a small molecule to that of the protein,

[*] Dr. Z. Zhang, M. T. Greenfield, Dr. T. J. McMurry, Dr. R. B. Lauffer, Dr. P. Caravan
EPIX Pharmaceuticals, Inc.
67 Rogers Street, Cambridge, MA 02142 (USA)
Fax: (+1) 617-250-6127
E-mail: pcaravan@epixpharma.com
M. Spiller
Department of Radiology
New York Medical College
Valhalla, NY 10595 (USA)



Supporting information (synthesis of **1**, **2**, and **3**) for this article is available on the WWW under <http://www.angewandte.org> or from the author.

and the relaxivity increases ninefold to $51 \text{ mM}^{-1} \text{ s}^{-1}$ (37°C , 20 MHz).^[4] This is shown schematically in Figure 1a and b. Despite this increased relaxivity, there is still a drive to increase relaxivity further to allow imaging of lower concentration targets. One approach for increased molecular relaxivity would be to combine the RIME effect with a multimeric gadolinium agent (Figure 1c). However, polymeric contrast agents such as GdDTPA-monoamide tethered to polylysine^[5–8] or dextran^[9,10] have much lower relaxivities ($r_1 < 13 \text{ mM}^{-1} \text{ s}^{-1}$ per ion at 37°C) than one might expect based on their molecular weight because of internal motion along the polymer.^[11] Furthermore, targeting multimeric contrast agents to a specific protein may also result in lower relaxivity than expected because of internal flexibility within the multimer.

It was hypothesized that a large RIME effect could be maintained if the multimer exhibited a certain rigidity when bound to the protein target. One approach would be to prepare a rigid multimer^[12] by limiting the degrees of rotational freedom along the chain and then attaching a targeting vector to the multimer. A second approach in which a second targeting vector is used to anchor the terminus of the chain (multilocus binding) is outlined in Figure 1d. The second vector can be designed to bind nonspecifically to a hydrophobic patch on the target. In the absence of a target, there is rotational flexibility and low relaxivity; however, upon binding of the protein with both binding groups, the bound complex becomes more rigid and the relaxivity increases. In the absence of the second targeting group, the relaxivity of the bound species is lower because of internal flexibility. It is possible that the second targeting group could target a second protein which would also induce rigidity and enhance relaxivity.

To test this hypothesis, three tetrameric GdDTPA-based compounds were prepared (Figure 2) containing zero, one, or

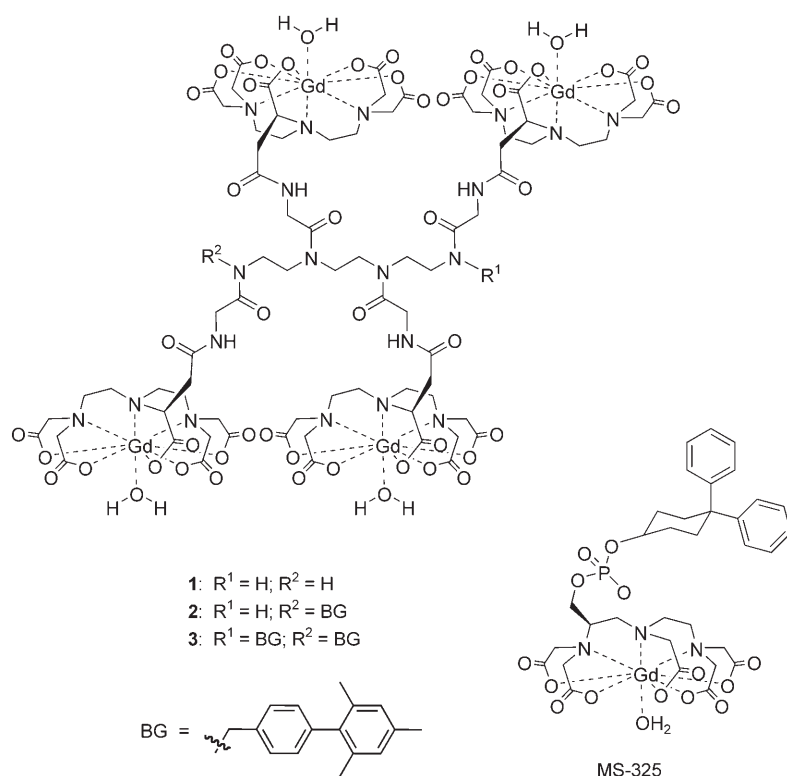


Figure 2. Compounds described in this study: GdDTPA tetramer containing zero (1), one (2), or two (3) HSA-binding groups (BG), and benchmark GdDTPA monomer MS-325.

two protein-binding moieties. The DTPA moiety^[13] shown in Figure 2 was used instead of the monoamide, because the GdDTPA complex has a more favorable water-exchange rate and the thermodynamically stable GdDTPA core is already present in several clinically approved contrast agents.^[14] Human serum albumin (HSA) was chosen as the protein target for proof of principle and MS-325 (Figure 2) was used as a benchmark compound. Although MS-325 does not contain the same biphenyl albumin-binding group, it exhibits both high relaxivity and albumin binding and represents the state of the art.

The binding of each compound 1–3 (0.1 mM) to HSA ($4.5\% \text{ w/v} = 0.67 \text{ mM}$) was assessed by ultrafiltration^[4] through a 5-kDa -molecular-weight cut-off membrane at 37°C and at $\text{pH } 7.4$; the gadolinium concentration in both the initial solution (total) and the filtrate was measured by inductively coupled plasma mass spectrometry (ICP-MS). Not surprisingly, compound 3 (with two binding groups) exhibits the highest affinity for HSA (Table 1). The relaxivities of 1–3 (0.1 mM) were measured at 20 MHz , $\text{pH } 7.4$, 37°C in phosphate-buffered saline (PBS), in the presence or absence of HSA (0.67 mM). As a result of their increased molecular size, the relaxivities per Gd of the tetramers in buffer solution are higher than that of MS-325. When the measurement is made in an excess of HSA, the observed relaxivities follow the order $3 > 2 > 1$. To determine if this is simply a result of increasing albumin affinity, the relaxivity of the bound fraction can also be calculated ($r_1^{\text{bd}} = \{r_1^{\text{obs}} - f_{\text{free}} r_1^{\text{free}}\} / f^{\text{bd}}$). Table 1 shows that compound 3 has the highest albumin-

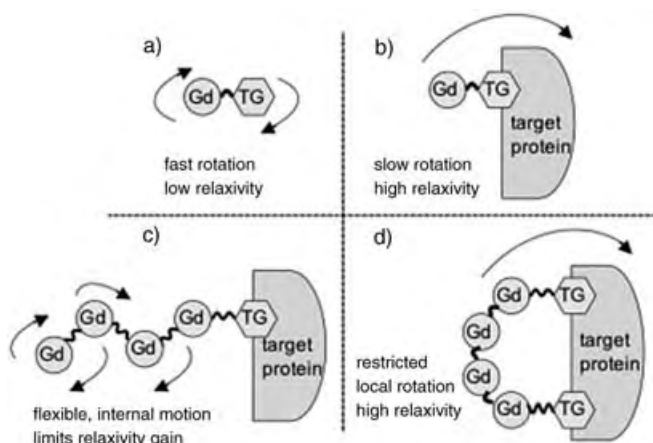


Figure 1. Strategies for increasing relaxivity: a) Discrete Gd chelate and targeting moiety, for example, the fast tumbling of MS-325 limits the relaxivity. b) Binding to the target slows tumbling, and relaxivity is increased. c) Gd chelate multimer with targeting; relaxivity may be limited by the fast internal motion. d) Gd chelate multimer with multi-locus binding rigidifies the bound complex and increases the relaxivity.

Table 1: Binding of MS-325, **1**, **2**, and **3**.^[a]

Compound	Number of Gd	% bound	r_1^{obs} (PBS)	r_1^{obs} + HSA	r_1^{bd} (HSA)
MS-325	1	88	5.8 (5.8)	46 (46)	50.8 (50.8)
1	4	30	11.3 (45.2)	15.0 (60)	23.9 (95.6)
2	4	78	10.1 (40.4)	26.2 (104.8)	30.8 (123.2)
3	4	94	10.3 (41.2)	39.1 (156.4)	41.3 (165.2)

[a] Percentage of 0.1 mM compound bound to 0.67 mM HSA, observed per Gd relaxivities ($\text{mM}^{-1} \text{s}^{-1}$) at 20 MHz in the absence and presence of 0.67 mM HSA, and calculated albumin-bound relaxivities. Numbers in parentheses refer to relaxivity per molecule; all measurements were performed at pH 7.4, 37°C, with 0.1 mM compound in PBS.

bound relaxivity of the three multimeric chelates. Although the GdDTPA moieties of **3** have a somewhat flexible linkage to the albumin-binding groups, the relaxivity per Gd of **3** in HSA approaches that of the more compact and rigid MS-325/HSA. On a per molecule basis, the relaxivity of **3** is clearly the highest.

To demonstrate that this result is indeed a rotational phenomenon, nuclear magnetic relaxation dispersion (NMRD) profiles were recorded for each of the three compounds, both with and without excess HSA at 35°C. Figure 3 shows the relaxivity profiles for each compound

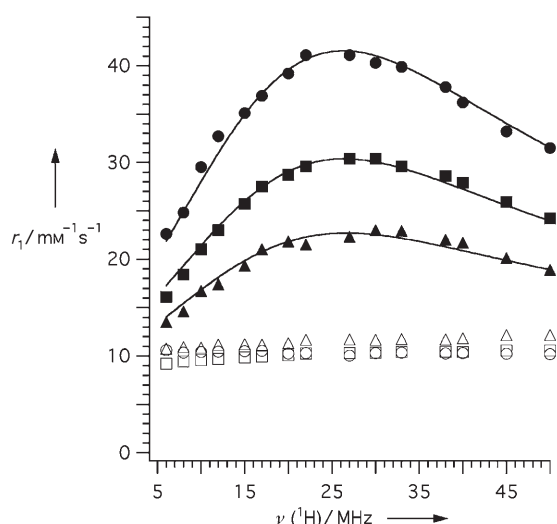


Figure 3. ^1H NMRD relaxivities expressed per Gd (35°C, pH 7.4) of **1** (triangles), **2** (squares), and **3** (circles) (0.1 mM) in PBS only (open symbols) or bound to 4.5% HSA (filled symbols).

when bound to albumin (solid symbols, r_1^{bd}) or in buffer solution only (open symbols). The NMRD of the three compounds in buffer solution are similar and rather featureless, with an estimated rotational correlation time of about 0.3 ns. In the presence of excess albumin, however, the relaxivities of all three compounds are increased. Notably, the appearance of a high-field peak at about 25 MHz is typical of a slow-motion fraction.

The relaxivity in buffer solution and the HSA-binding data were used to calculate the bound relaxivity NMRD profiles. The high-field region is shown in Figure 3. Despite

the complexity of the system (multiple chelates, complex rotational motion), it is informative to model these curves and this was performed in an approach previously described for the high-field part of the NMRD curve.^[15] The NMRD of a $q=0$ triethylenetetraamine hexaacetic acid (TTTHA) derivative reported earlier^[4] was used to estimate the second- and outer-sphere contributions to relaxivity. The water residency time at 35°C was fixed for all three compounds at 100 ns based on an analogy with other substituted GdDTPA compounds.^[4,14] As the chelate part of the molecule is the same for all three compounds, it was assumed that the water-exchange rate would also be the same. The Gd—H(water) distance was fixed at 3.1 Å.^[16] The three bound relaxivity NMRD data sets were fit simultaneously, the two parameters for electronic relaxation (Δ^2 , τ_v) were treated as global parameters (owing to the identical chelating portions), and the rotational parameters were treated locally.

These data were fit in two ways: first, an isotropic model of rotation was employed to analyze these data. This model did not fit well—the peak shape was not well reproduced—and the fitted curve gave a much flatter peak that underestimated the relaxivity maximum and overestimated the relaxivity at higher fields. The correlation times from the fitting are in the 1-ns range and do not reflect the physical reality of an albumin tethered complex. The second method was a Lipari–Szabo model-free approach that has been described previously.^[15] Equation (1) describes the dipolar

$$\frac{1}{T_{1M}} = \frac{C}{r_{\text{GdH}}^6} \left(\frac{3F\tau_{\text{cg}}}{1 + \omega_H^2\tau_{\text{cg}}^2} + \frac{3(1-F)\tau_{\text{cl}}}{1 + \omega_H^2\tau_{\text{cl}}^2} \right);$$

$$\frac{1}{\tau_{\text{cg}}} = \frac{1}{\tau_g} + \frac{1}{T_{1e}} + \frac{1}{\tau_m}; \quad \frac{1}{\tau_{\text{cl}}} = \frac{1}{\tau_{\text{cg}}} + \frac{1}{\tau_l}$$
(1)

relaxation of the coordinated water. In this case, the spectral density function has two terms that are related by a factor F (sometimes called an order parameter and denoted S^2), which describes the degree of spatial restriction. If the motion of the Gd chelate is independent of the protein, then $F=0$; if the chelate is completely immobilized on the protein, then $F=1$. There are two correlation times, τ_{cg} and τ_{cl} , which contain contributions from global (τ_g) and local (τ_l) rotational correlation times, as well as from the electronic relaxation time T_{1e} .

A global correlation time based on fluorescence anisotropy decay was fixed at 41 ns,^[17] whereas the local correlation time for each compound was allowed to vary along with its order parameter. In this case, the peak shape is much better reproduced, and the resultant fitted parameters are given in Table 2. As may be expected, the order parameter F increases from compound **1** to **2** to **3** as the number of binding groups

Table 2: Fitted NMRD parameters for compounds **1**, **2**, and **3**.^[a]

τ_v [ps]	Δ^2 [10^{18}s^{-2}]	1 F	1 τ_l [ns]	2 F	2 τ_l [ns]	3 F	3 τ_l [ns]
13	7.1	0.05	0.68	0.09	0.92	0.16	1.40
(1)	(0.2)	(0.01)	(0.03)	(0.01)	(0.03)	(0.02)	(0.04)

[a] Global (HSA) rotational correlation time fixed at 41 ns. Numbers in parentheses represent one standard deviation.

increase. The local correlation time also increases in the order $1 < 2 < 3$, which suggests that compound **3** is the most rigid when bound to albumin. Although the order parameters are relatively low, it was noted that they correlated with the global correlation time—arbitrarily chosen shorter global correlation times also gave good fits, but the order parameter was increased. Although the Lipari–Szabo approach models the data well, motion within this system is complex and care should be taken in comparing these rotational parameters with other unrelated systems.

There have been gains reported in increasing the relaxivity of single gadolinium complexes through the optimization of water exchange, hydration number, etc. Multilocus binding may prove to be a useful technique for maintaining this high relaxivity when these complexes are incorporated into targeted multimeric MRI contrast agents.

Experimental Section

The compounds **1**, **2**, and **3** were synthesized in an analogous fashion (see Supporting Information for full details). 4-Mesitylbenzoic acid was coupled to zero, one, or two of the primary amine groups of triethylenetetraamine. After reduction of the amide, the resultant tetraamine was coupled to four protected DTPA moieties. Deprotection, chelation, and purification by HPLC yielded the complexes shown in Figure 2. All Gd concentrations were determined by ICP-MS (Agilent 7500). NMRD profiles were recorded on a Koenig-Brown field-cycling relaxometer.

Received: June 26, 2005

Published online: September 20, 2005

Keywords: gadolinium · imaging agents · MRI · NMR spectroscopy · relaxivity

- [1] H. Kobayashi, M. W. Brechbiel, *Curr. Pharm. Biotechnol.* **2004**, *5*, 539.
- [2] M. P. Lowe, *Aust. J. Chem.* **2002**, *55*, 551.
- [3] R. B. Lauffer, *Magn. Reson. Med.* **1991**, *22*, 339.
- [4] P. Caravan, N. J. Cloutier, M. T. Greenfield, S. A. McDermid, S. U. Dunham, J. W. Bulte, J. C. Amedio, Jr., R. J. Looby, R. M. Supkowski, W. D. Horrocks, Jr., T. J. McMurphy, R. B. Lauffer, *J. Am. Chem. Soc.* **2002**, *124*, 3152.
- [5] P. F. Sieving, A. D. Watson, S. M. Rocklage, *Bioconjugate Chem.* **1990**, *1*, 65.
- [6] M. Spanoghe, D. Lanens, R. Dommissie, A. van der Linden, F. Alder Weireldt, *Magn. Reson. Imaging* **1992**, *10*, 913.
- [7] G. Schuhmann-Giampieri, H. Schmitt-Willich, T. Frenzel, W. R. Press, H. J. Weinmann, *Invest. Radiol.* **1991**, *26*, 969.
- [8] A. A. Bogdanov, R. Weissleder, H. W. Frank, A. V. Bogdanova, N. Nossif, B. K. Schaffer, E. Tsai, M. I. Papisov, T. J. Brady, *Radiology* **1993**, *187*, 701.
- [9] R. Rebizak, M. Schaefer, E. Dellacherie, *Bioconjugate Chem.* **1998**, *9*, 94.
- [10] C. Casali, M. Janier, E. Canet, J. F. Obadia, S. Benderbous, C. Carot, D. Revel, *Acta Radiol.* **1998**, *5*, S214.
- [11] E. Toth, I. van Uffelen, L. Helm, A. E. Merbach, D. Ladd, K. Briley-Saebo, K. E. Kellar, *Magn. Reson. Chem.* **1998**, *36*, S125.
- [12] R. S. Ranganathan, M. E. Fernandez, S. I. Kang, A. D. Nunn, P. C. Ratsep, K. M. R. Pillai, X. Zhang, M. F. Tweedle, *Invest. Radiol.* **1998**, *33*, 779.
- [13] J. C. Amedio, Jr., G. Van Wagenen, Jr., G. Zavlin, A. Gyorkos, S. A. Peterson, *Synth. Commun.* **2000**, *30*, 3755.
- [14] P. Caravan, J. J. Ellison, T. J. McMurphy, R. B. Lauffer, *Chem. Rev.* **1999**, *99*, 2293.
- [15] J. S. Troughton, M. T. Greenfield, J. M. Greenwood, S. Dumas, A. J. Wiethoff, J. Wang, M. Spiller, T. J. McMurphy, P. Caravan, *Inorg. Chem.* **2004**, *43*, 6313.
- [16] P. Caravan, A. V. Astashkin, A. M. Raitsimring, *Inorg. Chem.* **2003**, *42*, 3972.
- [17] J. D. Dattelbaum, O. O. Abugo, J. R. Lakowicz, *Bioconjugate Chem.* **2000**, *11*, 533.

**Deactivation of Pd Acetoxylation Catalysts:
Direct Observations by XPS Investigations****

Jörg Radnik,* Abdulhadi Benhmidi,
Venkata Narayana Kalevaru, Marga-Martina Pohl,
Andreas Martin, Bernhard Lücke, and
Uwe Dingerdissen

Catalyst deactivation is a problem of great concern in industrial catalytic processes. Hence, prevention of catalyst deactivation poses substantial challenges in the design and operation of large-scale catalytic processes. The usual way to overcome the deactivation problem is to modify the catalyst composition by using different promoters. Although various promoters have been used for different oxidation reactions,^[1–4] their precise role is not known. Unfortunately, most of the interpretations on the role of promoters are rather hypothetical probably owing to the lack of information about the exact surface structure. Among the known promoters, bismuth has very attractive properties as a promoting element in numerous heterogeneous oxidation catalysts, particularly in association with noble metals.^[1–6] However, the origin of the promoting role of Bi is still a matter of discussion.

Acetoxylation is an industrially important reaction for producing esters in a single step. Benzyl acetate (BA), the desired product from acetoxylation of toluene, is widely used in the food, perfumery, and chemical industries. Most of the work reported so far on the acetoxylation of toluene is confined to liquid-phase and batch reactors.^[7–9] Vapor-phase processes were previously not successful in terms of obtaining higher yields of BA with acceptable time-on-stream stability of the catalysts.^[10,11] However, the recently developed Pd–Sb/TiO₂ catalysts^[12–13] displayed remarkably higher conversion of toluene (> 90 %) and yields of BA (> 75 %) with a space–time yield of up to 700 g kg^{−1} h^{−1}. To our knowledge, this is the best result reported so far under gas-phase conditions. However, these catalysts are observed to undergo deactivation readily after several hours of operation as a result of coke deposits, which obviously hampers their application on a commercial scale.

Considering the limited lifetime of these catalysts, we have directed our research efforts to develop stable and novel

Pd compounds that have improved catalyst lifetime as well as the higher activity and selectivity of the earlier catalysts. To achieve this objective, we modified the composition of the Pd–Sb/TiO₂ catalysts by adding promoters such as Bi, Cu, and Sn.^[14–15] Among these promoters, the Bi modification improved both the catalyst life as well as the selectivity for desired product (BA). However, the precise role of Bi remained unclear. In the present study we examine the catalyst deactivation phenomenon of Pd–Sb/TiO₂ catalysts and the role of Bi in improving catalyst lifetime and selectivity.

In the earlier investigations on Pd–Sb/TiO₂ catalysts^[13] we clearly detected differences between the fresh and used catalysts. The used catalysts displayed drastic increase in Pd particle size, coke deposition, loss of both Pd and Sb at the surface etc. In view of this, a TiO₂-supported catalyst with 10 wt % Pd and 8 wt % Sb was then chosen as a model catalyst (designated as 10Pd8Sb) and subjected to reaction conditions for a wide range of reaction times. We could thus obtain useful information on the changes that occur during the course of the reaction.

In a similar way, in the present study we chose a sample containing 10 wt % Pd, 8 wt % Sb, and 7 wt % Bi as a model catalyst (designated as 10Pd8Sb7Bi). We subjected it to reaction conditions for a range of reaction times and analyzed the sample by X-ray diffraction (XRD), transmission electron microscopy (TEM), and X-ray photoelectron spectroscopy (XPS). This catalyst was selected because it lies in the middle of the series (i.e. between high and low Pd loading) and displays good performance (55 % toluene conversion, 95 % selectivity for BA). We intended to discover the changes that take place during the course of reaction, which in turn can give hints to understand the cause of deactivation. The reaction times in these long-term tests were 1, 2, and 4 days.

Interesting effects of the addition of Bi are 1) high selectivity for BA (≥ 95 %) and 2) improved catalyst lifetime. Figure 1a and b compare the time-on-stream catalytic performance of 10Pd8Sb/TiO₂ in the presence and absence of Bi. It is obvious from Figure 1a that the catalyst displays a very low initial activity (toluene conversion: 3 %), which increases until ca. 11 h (> 68 %), remains stable for few more hours, and then decreases with extended reaction times (ca. 30 % after 34 h). The yield of BA and benzaldehyde (BAL) as a by-product also changes in a similar way. The increase in toluene conversion with time can be attributed to an increase in Pd particle size, while the decrease in catalytic activity can be attributed to the increase in coke deposition with time on stream.^[13] TEM studies showed that the size of Pd particles increases to a critical size with time (i.e. during the course of the reaction) and then remains more or less constant even though the catalytic activity decreases. Both the most active and completely deactivated catalysts contained the Pd particles of similar size, indicating that the particle growth during reaction has no effect on deactivation. The only difference between these samples is the considerable amount of coke deposition in the deactivated catalysts, which is the primary cause of catalyst deactivation. Nevertheless, the deactivated samples can be regenerated in air and reused with consistent performance.

[*] Dr. J. Radnik,^[†] A. Benhmidi, Dr. V. N. Kalevaru, Dr. M.-M. Pohl, Dr. A. Martin, Prof. Dr. B. Lücke, Dr. U. Dingerdissen
Institut für Angewandte Chemie Berlin-Adlershof e.V.
Richard-Willstätter-Strasse 12, 12489 Berlin (Germany)

[†] A member of the EU-funded “Coordination Action of Nanostructured Catalytic Oxide Research and Development in Europe” (CONCORDE).

[**] We thank Dr. M. Schneider for his help in characterizing these catalysts and for valuable discussions. XPS = X-ray photoelectron spectroscopy.

Supporting information for this article is available on the WWW under <http://www.angewandte.org> or from the author.

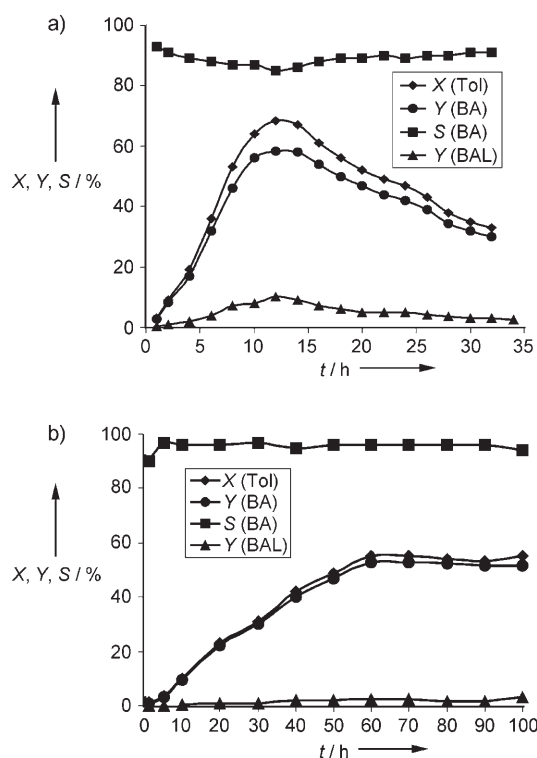


Figure 1. Comparison of the conversion (X), yield (Y), and selectivity (S) of 10Pd8Sb catalysts versus time on stream: a) without Bi; b) with Bi. Molar ratio of toluene/acetic acid/oxygen(air)/argon = 1:4:3(15):16, $T = 210^{\circ}\text{C}$, gas hourly space velocity (STP) = 2688 h^{-1} , $\tau = 1.34\text{ s}$.

In contrast, the Bi-modified catalyst (Figure 1b) exhibits low initial activity (1 %), attains a steady state (maximum activity: $\approx 55\%$ toluene conversion) after about 55 h, and then displays quite stable performance with almost constant conversion and product selectivity up to 100 h on stream in contrast to the non-Bi-containing Pd–Sb catalyst. However, this phenomenon has no effect on the selectivity for BA, which remains more or less constant (95 %) throughout. In other words, selectivity is independent of conversion regardless of the presence of Bi in the catalyst. This result reflects the fact that BA is quite stable and does not undergo any subsequent reactions.

No clues were found from XRD for the formation of any kind of crystalline intermetallic phases between Pd and Bi, which are, however, known from literature.^[3,11] XRD results show the presence of Pd and PdO phases only in the catalysts tested for 1 day and 2 days. However, after a reaction time of 4 days the PdO disappeared. This result is in good agreement with XPS results (see Figure 4).

Electron micrographs of 10Pd8Sb7Bi catalyst recorded after different reaction times are shown in Figure 2. In the fresh catalysts Bi exhibits a sheetlike morphology and is located far from the TiO_2 support (Figure 2a, left). On the other hand, the Pd particles show a spherical morphology and are clearly present on TiO_2 surface. The size of Pd particles ranges from 1 to 2 nm. In other words, Pd and Bi display different morphologies (no free Sb particles can be seen by TEM). Furthermore, the presence of Bi leads to very fine Pd particles (1–2 nm) in these solids compared to those in the

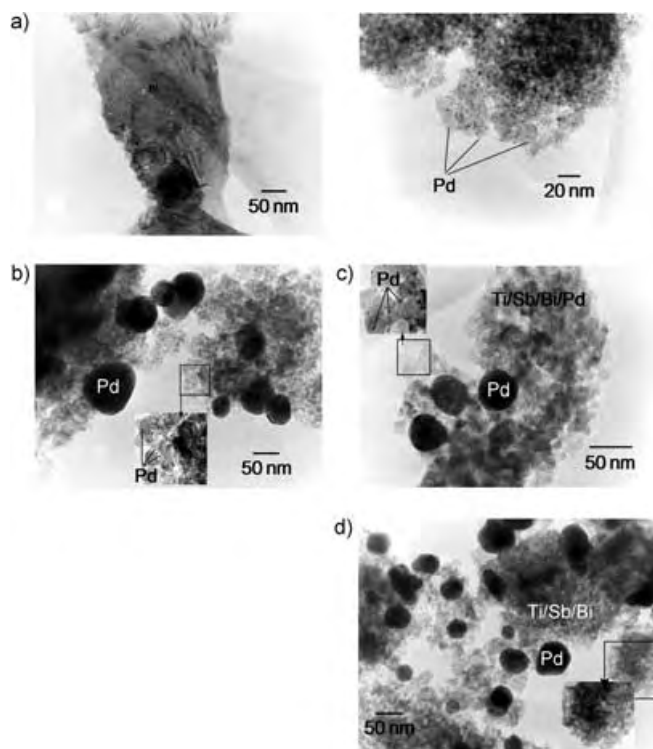


Figure 2. Electron micrographs of 10Pd8Sb7Bi catalysts: a) fresh sample showing Bi-containing sheets (left) and Pd (right); b) after 1 day; c) after 2 days; d) after 4 days.

non-Bi-containing Pd–Sb catalysts (1–10 nm). The catalyst tested for 1 day (Figure 2b) contains a mixture of both smaller (below 5 nm) and bigger Pd particles (even up to 45 nm). Interestingly, Bi moves closer to the TiO_2 support as the reaction proceeds. This movement is most pronounced during the first 24 h on stream and thereafter no such significant movement is observed.

These results are well supported by XPS. In the catalyst tested for 2 days (Figure 2c), one can still find a mixture of both smaller and bigger particles. Particles up to 70 nm can be found, while the smaller ones are mostly $< 5\text{ nm}$. With regards to the catalyst tested for 4 days (Figure 2d), the smaller Pd particles have almost disappeared and bigger ones up to 100 nm can be seen. This observation supports the view that the size of the Pd particles increases progressively with time under the influence of reactant feed mixture in the same way as the activity of the catalysts. The growth of Pd particles appears to be essential for obtaining better catalyst performance. Pd particles up to 100 nm form in Pd–Sb solids after only 11 h on stream, whereas for the Bi-modified catalysts particles of this size are obtained after 4 days. This result suggests that the growth of Pd particles is a slow process in the presence of Bi. In addition, larger Pd particles often contain some traces of Sb. The deactivated 10Pd8Sb catalyst sample and the stable 10Pd8Sb7Bi catalyst (after 4-day tests) contain large Pd particles of more or less the same size. This indicates that the growth of Pd particles during the course of the reaction has no effect on catalyst deactivation and is in fact favorable for better performance.

Figure 3 depicts the variation of surface Pd/Ti, Sb/Ti, and Bi/Ti ratios in the 10Pd8Sb7Bi catalyst with time on stream. The amounts of Pd, Sb, and Bi in the near-surface region decrease mainly during the first 24 h on stream and then

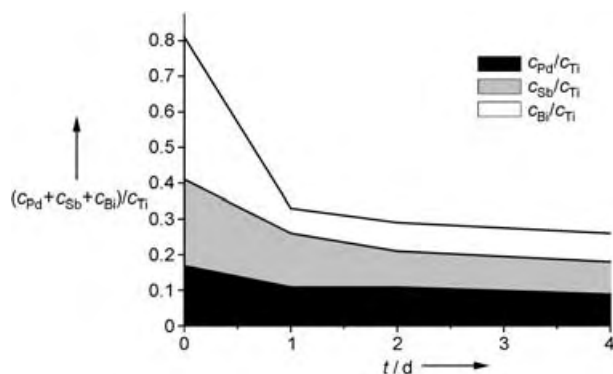


Figure 3. Change in the surface concentrations c in the 10Pd8Sb7Bi catalyst with time on stream.

remain more or less constant throughout the 4-day test. Interestingly, the decrease in the Bi/Ti ratio (from 0.4 to 0.08) is much more pronounced than the decrease of the Pd/Ti ratio (from 0.17 to 0.1) and that of the Sb/Ti ratio (from 0.24 to 0.1). TEM examination of this particular 10Pd8Sb7Bi catalyst (Figure 2) also support these observations: During the first day of testing the sheetlike morphology of Bi vanishes and Bi moves closer to the TiO_2 support. This movement of Bi is assumed to be the more probable reason for such significant decrease in the Bi/Ti ratio.

To check the influence of Bi on the surface composition and the electronic states of the surface components, the results of XPS investigations on Bi-modified samples were compared with those of recently published results on 10Pd8Sb catalysts.^[13] Normalized XP spectra of the Pd 3d state of fresh and used 10Pd8Sb catalysts with and without Bi are shown in Figure 4. The variation of surface Pd/Ti ratios and the presence of different surface Pd species in the presence and absence of Bi at different stages of reaction are also compared in this figure. Bi-containing catalysts (10Pd8Sb7Bi) exhibit only two states, either metallic (Pd^0), or oxidized (PdO_x), or both, at different stages of the reaction (i.e. after 1, 2, and 4 days). It is not possible to distinguish between bi-, tetra-, and hexavalent Pd, because the reference data available ranges from 336 to 338 eV for all these oxidation states. XRD experiments indicate the existence of a PdO phase, in other words, bivalent Pd, but other oxidation states at the surface of the particles cannot be excluded. In contrast, Bi-free catalysts (10Pd8Sb) exhibited three states: metallic (Pd^0), oxidized (PdO_x), and a $\text{Pd}^{\delta-}$ state, in which the electron binding energy of the Pd electron is lower than that of metallic Pd (335.1 eV). The formation of this third state is correlated with a strong interaction between the carbon deposits and surface Pd. The most striking feature here is that in the 10Pd8Sb7Bi sample even after 4 days of testing the $\text{Pd}^{\delta-}$ species is not observed. In contrast, the deactivated 10Pd8Sb sample contains up to 35 % $\text{Pd}^{\delta-}$ on its surface, indicating the adverse effect of the $\text{Pd}^{\delta-}$

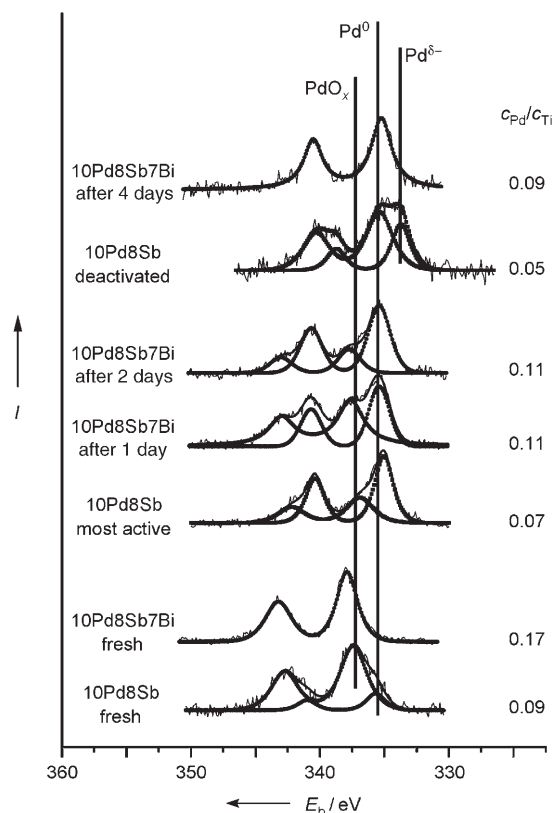


Figure 4. Normalized XP spectra of the Pd 3d state for fresh and used 10Pd8Sb catalysts with and without Bi (after Shirley background subtraction).

species on the life of the catalyst. The addition of Bi apparently prevents the formation of such undesired $\text{Pd}^{\delta-}$ species and thereby improves the lifetime of the catalysts.

Another interesting observation is that even after 1 and 2 days of use, oxidized Pd species could still be found in the Bi-modified samples whereas in the Bi-free catalysts the PdO phase disappeared after only 20 h of operation. This result suggests that PdO_x species are more stable in presence of Bi (Figure 4). Nevertheless, after 4 days of reaction the oxidized Pd is completely reduced to metallic Pd, which indicates that the presence of Bi slows the reduction of Pd. XRD studies also show an improved stability of PdO phase in the presence of Bi. However, no significant changes in the electronic states of the other components, Bi and Sb, were observed.

Another notable difference is the surface Pd/Ti ratio of the catalyst. (Figure 4). Bi-containing catalysts exhibit significantly higher Pd/Ti ratios than the Bi-free catalysts. Both systems further show a decrease in the Pd/Ti ratios during the course of the reaction. However, Bi-containing catalysts showed a large decrease in the Pd/Ti ratio (from 0.17 to 0.11) only during the first 24 h on stream (see also Figure 3). This change might be a result of catalyst restructuring as reflected by the movement of Bi closer to TiO_2 during this time. Once the restructuring has occurred, the amount of surface Pd remains more or less constant without any significant loss and hence the catalyst has a longer lifetime. In contrast, Bi-free catalysts display a continuous and significant decrease in the

Pd/Ti ratios of over 40% (from 0.09 (fresh) to 0.05 (deactivated); Figure 4). This ultimately leads to the deactivation of the catalyst, and this finding undeniably supports the proposition of the stronger interaction of surface Pd with the deposited coke.

The experimental observations such as 1) the absence of the $\text{Pd}^{\delta-}$ state and 2) the higher Pd/Ti ratios for the Bi-containing catalyst even after longer test times (100 h) undeniably indicate a weaker interaction between carbon atoms from deposited coke and the surface Pd atoms. To check this hypothesis, the C/Pd ratios were also estimated for both 10Pd8Sb and 10Pd8Sb7Bi samples (Figure 5). If we

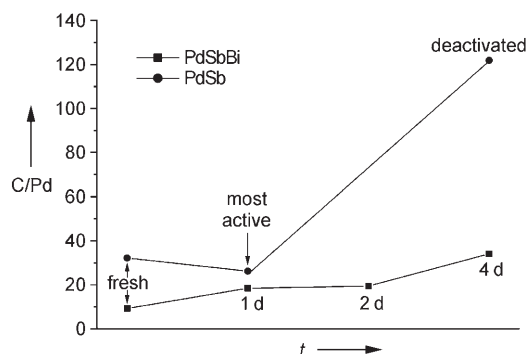


Figure 5. Changes in the C/Pd ratio of the near-surface region of the 10Pd8Sb7Bi catalyst and the Bi-free catalyst 10Pd8Sb catalyst after 1, 2, and 4 days.

compare the C/Pd ratios between the most active (after ca. 10 h) and deactivated (after ca. 20 h) 10Pd8Sb catalyst, an abrupt increase (from ca. 30 to 122) was found, which might be due to stronger interaction between C and Pd. This strong interaction not only leads to the high carbon amount but also modifies the electronic state of Pd, as evidenced from the appearance of the $\text{Pd}^{\delta-}$ state and the formation of a carbide-like or similar such structures cannot be ruled out. However, in XRD experiments we could not find any such crystalline Pd-C phases in any of these catalysts. In contrast, the presence of Bi weakened the interaction between the deposited coke and the surface Pd atoms, and hence low C/Pd ratios in the range of about 10 to 34 are found even after 100 h on stream. All these findings clearly show that the prevention of such unwanted $\text{Pd}^{\delta-}$ species results in a remarkable enhancement of catalyst life.

Mechanistically, catalyst deactivation results the formation of $\text{Pd}^{\delta-}$ species by the interaction between the carbon atoms from deposited coke and surface Pd species. Our results show that this interaction between Pd and C can be significantly reduced by the addition of Bi, as evidenced by the low C/Pd ratios in Bi-modified catalysts compared to those of Bi-free catalysts.

In this first report on catalyst deactivation phenomenon in the gas-phase synthesis of benzyl acetate from toluene we have identified the role of Bi in preventing catalyst deactivation and in enhancing the selectivity. The results indicate room for further improvements in the preparation and development of suitable catalysts with novel compositions

for the acetoxylation of various alkyl aromatics and hetero-aromatics in the near future.

Experimental Section

The Pd-Sb-Bi/TiO₂ catalysts were prepared by impregnation in two steps. In the initial step, first SbCl₃ then BiCl₃ were deposited on an anatase carrier in an aqueous HCl solution with subsequent removal of excess solvent. The solid was dried and then calcined at 400 °C (3 h, air). In the second step, the above solid was impregnated with PdCl₂ in the desired amounts followed by drying (120 °C, 16 h). The detailed procedures for catalyst preparation,^[16] screening of the catalysts, and product analysis have been described elsewhere.^[13] The XPS measurements were conducted at a VG ESCALAB220iXL with Al_{Kα} radiation. The TEM analyses were carried out with a Philips CM20 (twin) at 200 kV with EDAX PV9900 (energy dispersive X-ray spectroscopy (EDX)).

Received: May 13, 2005

Revised: July 5, 2005

Published online: September 27, 2005

Keywords: acetoxylation · bismuth · gas-phase reactions · heterogeneous catalysis · palladium

- [1] M. Besson, F. Lahmer, P. Gallezot, P. Fuertes, G. Fleche, *J. Catal.* **1995**, *152*, 116.
- [2] F. Alardin, B. Delmon, P. Ruiz, M. Devillers, *Catal. Today* **2000**, *61*, 255.
- [3] M. Wenkin, P. Ruiz, B. Delmon, M. Devillers, *J. Mol. Catal. A* **2002**, *180*, 141.
- [4] T. Mallat, Z. Bodnar, A. Baiker, O. Greis, H. Strübig, A. Rellier, *J. Catal.* **1993**, *142*, 237.
- [5] T. Mallat, A. Baiker, *Catal. Today* **1994**, *19*, 247.
- [6] H. Kimura, A. Kimura, I. Kokubo, T. Wakisaka, Y. Strübig, A. Mitsuda, *Appl. Catal. A* **1993**, *95*, 143.
- [7] E. Benazzi, H. Mimoun, C. J. Cameron, *J. Catal.* **1993**, *140*, 311.
- [8] S. K. Tanielyan, R. Augustine, *J. Mol. Catal.* **1994**, *87*, 311.
- [9] T. Miyake, A. Hattori, M. Hanaya, S. Tokumura, H. Hamaji, T. Okada, *Top. Catal.* **2000**, *13*, 243.
- [10] L. Ebersson, L. Jönsson, *Acta Chem. Scand. B* **1974**, *28*, 597.
- [11] T. Komatsu, K. Inaba, T. Uezono, A. Onda, T. Yashima, *Appl. Catal. A* **2003**, *251*, 315.
- [12] A. Benhmid, K. V. Narayana, A. Martin, B. Lücke, *Chem. Commun.* **2004**, 2118.
- [13] A. Benhmid, K. V. Narayana, A. Martin, B. Lücke, S. Bischoff, M.-M. Pohl, J. Radnik, M. Schneider, *J. Catal.* **2005**, *230*, 420.
- [14] A. Benhmid, K. V. Narayana, A. Martin, B. Lücke, M.-M. Pohl, *Chem. Commun.* **2004**, 2416.
- [15] A. Benhmid, K. V. Narayana, A. Martin, B. Lücke, M.-M. Pohl, *Chem. Lett.* **2004**, *33*, 1238.
- [16] A. Benhmid, K. V. Narayana, A. Martin, B. Lücke, S. Bischoff (Institute for Applied Chemistry Berlin-Adlershof e.V.), P241303DE-WT, **2004**.

Size-Controlled Electrochemical Synthesis of Metal Nanoparticles on Monomolecular Templates**

Thomas Hirsch, Michael Zharnikov,
Andrey Shaporenko, Joachim Stahl, Dieter Weiss,
Otto S. Wolfbeis, and Vladimir M. Mirsky*

The introduction of in situ synthesis on the surface of solid substrates has resulted in tremendous progress in different fields of science and technology. Immobilized metallic nanoparticles are of particular interest. Their applications include electrocatalysis, data storage systems, new electronic devices, electrochemical chemo- and biosensors, and refractometric and fluorescent sensors based on plasmon effects.^[1–4] The strategies for the preparation of these systems are mostly based on the deposition of presynthesized nanoparticles with^[5] or without^[6,7] further treatment. So far the particles have been deposited mostly by the electrospray technique^[8] or by adsorption,^[6,9] and only a few techniques based on the in situ synthesis of nanoparticle have been tested. Such a synthesis is possible by electroless deposition or by electroplating. The electroless deposition of nanoparticles was used for the deposition of gold, silver, nickel, palladium, copper, and cobalt nanoparticles onto different substrates.^[1,2,10,11] Deposition by electroplating was used for formation of bulk phases of nanocrystalline metals by the reduction of corresponding salts in ionic liquids.^[12,13] Formation of metallic nanoparticles by electrochemical reduction on the tip of a scanning tunneling microscope (STM) followed by transfer to planar metal electrodes was reported^[14,15] and then reproduced by other groups.^[16] Here, we describe an alternative approach for the preparation of metallic nanoparticles on electrode surfaces that does not require STM. Our approach

is based on the reduction of metals on nanoelectrodes formed by the recently developed spreader-bar technique.^[17]

We tested the approach for the deposition of platinum and copper nanoparticles but do not see any principal limitations for its extension to other conductive or semiconductive materials such as metals, electrochemically synthesized polymers, and nanocomposites. The size of the nanoparticles can be controlled by the value of the reduction charge. In the present work the nanoparticles are between 20 and 1000 nm, but smaller particles are most likely possible.

The spreader-bar technique^[17] is based on the coadsorption of two types of molecules: long-chain matrix molecules and large rigid planar molecules (templates or molecular spreader-bars). This results in the fabrication of heterogeneous monomolecular film in which the spreader-bar moieties are imbedded in the matrix. In contrast to two-dimensional molecular imprinting, the structures formed by this technique are permanently stable, because the spreader-bar molecules remain in the monolayer. This approach was successfully applied to generate stable artificial receptors for different purines and pyrimidines.^[18] Also, the formation of enantioselective receptors was reported.^[19] In the present work, the spreader-bar approach was used to design a nanostructured self-assembled monolayer (SAM) consisting of insulating matrix (long-chain alkylthiols) with incorporated conductive “islands” (large, planarly adsorbed molecules). Then, metals were deposited onto the heterogeneous film by reduction. Since the density of the electrical current through the spreader-bar molecules was much higher than through the insulating alkylthiol environment, metallic nanoparticles formed.

The monolayer was formed on the gold substrate by coadsorption of 1-dodecanethiol (C12) and a thiolated derivative of tetraphenylporphyrin (TMPP, Figure 1), a large planar rigid molecule with an extended π -electron system. The ratio of C12 to TMPP in the solution was varied. The deposition time was 72 h, which is far beyond the kinetic limit for surface–solution exchange of thiolated compounds on a gold surface.^[20] Therefore one can expect a quasi-equilibrium ratio of the template and matrix molecules in the film.

The structure and the composition of the mixed C12/TMPP monolayers were analyzed by near-edge X-ray absorption fine-structure (NEXAFS) spectroscopy, X-ray photoemission spectroscopy (XPS), and X-ray absorption spectromicroscopy (XAM). The XPS and NEXAFS data (Figure 2a and Figure 3) indicate that the amount of TMPP in the mixed film can be precisely adjusted by the composition of the solution. The monolayer formed from the C12/TMPP (1:10000) solution contains only TMPP moieties, that from the 1:1000 solution is mostly TMPP with only a few percent of C12, that from the 1:100 solution contains a minor amount of TMPP, and that from the 1:10 solution consists exclusively of C12 moieties. According to the NEXAFS difference curves (Figure 2b), the TMPP molecules in both the one-component and the mixed films have an in-plane (strongly inclined) orientation. XAM data (not shown) demonstrate that these molecules are incorporated individually into the C12 matrix and do not form clusters.

[*] Dipl.-Chem. T. Hirsch, Prof. Dr. O. S. Wolfbeis, Dr. V. M. Mirsky
Institute of Analytical Chemistry
Chemo- and Biosensors
93040 Regensburg (Germany)
Fax: (+49) 941-943-4064
E-mail: vladimir@mirsky.de

J. Stahl, Prof. D. Weiss
Institute of Experimental and Applied Physics
University of Regensburg
93040 Regensburg (Germany)

Dr. M. Zharnikov, Dr. A. Shaporenko
Institute of Applied Physical Chemistry
University of Heidelberg
69120 Heidelberg (Germany)

[**] We thank M. Grunze for support of this work and the BESSY II and ALS staff for help during the synchrotron experiments. This research was supported by the Volkswagenstiftung and the BMBF (05KS4VHA/4).

Supporting information for this article is available on the WWW under <http://www.angewandte.org> or from the author.

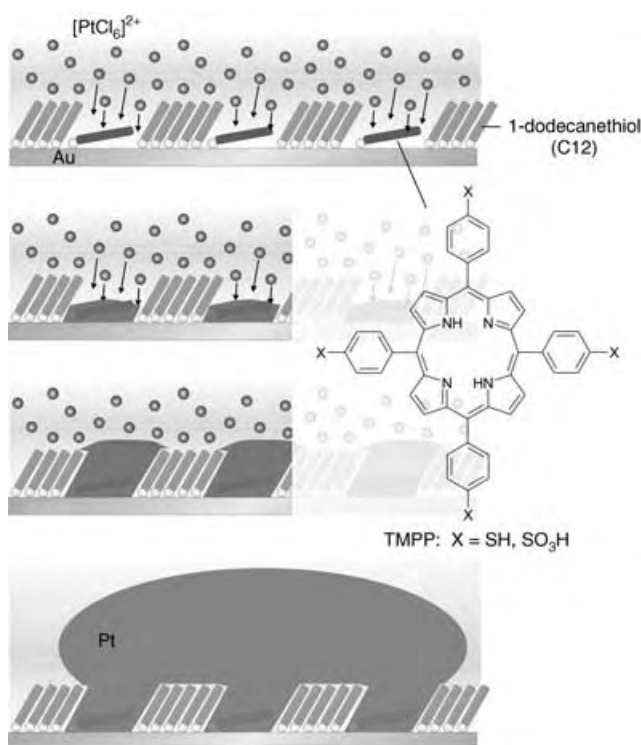


Figure 1. Electrochemical preparation of platinum nanoparticles on a template SAM made up of dodecanethiol (C12) and TMPP.

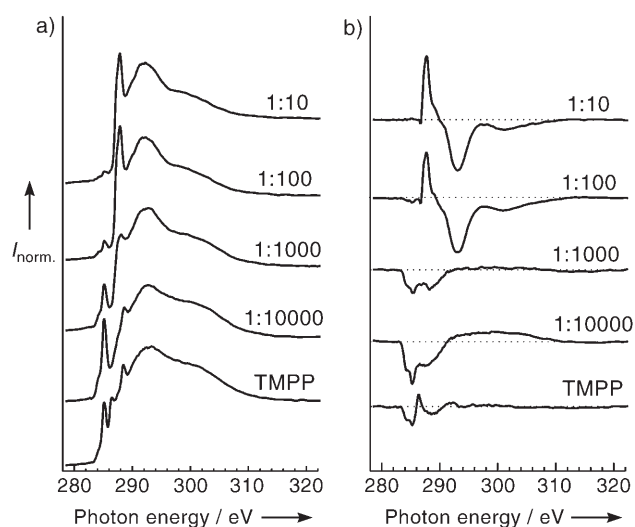


Figure 2. a) NEXAFS spectra (carbon K-edge, $\theta = 55^\circ$) of SAMs formed from one-component and mixed solutions of TMPP and C12. b) Corresponding difference spectra for X-ray incidence angles of $\theta = 90^\circ$ and 20° . A continuous variation of the spectra and difference curves with the solution composition (C12/TMPP) is observed, which indicates the formation of a mixed monolayer of variable composition. The π_1^* resonance at 285.1 eV (TMPP) and R^* resonance at 287.7 eV (C12) are characteristic for these two molecules in the TMPP/C12 film. The one-component TMPP film contains contamination as, for example, evidenced by the $\pi(\text{C}=\text{O})$ resonance at 288.5 eV.

A similar large planar molecule but without thiol anchor groups (Al-PC) was also tested as a spreader-bar. Because of the 12 conjugated aromatic rings in this molecule and the

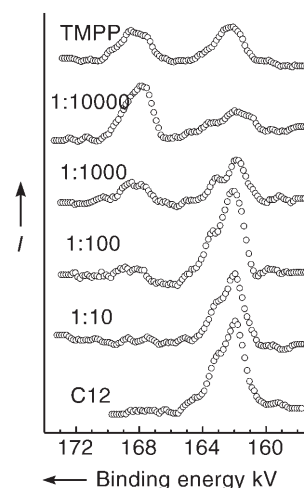


Figure 3. XPS spectra (sulfur 2p orbital, $h\nu = 400 \text{ eV}$) of SAMs formed from one-component and mixed solutions of TMPP and C12. In the film formed from pure TMPP, two doublets arising from the thiols (a binding energy of 162.0 eV for $\text{S } 2p_{3/2}$) and sulfones (a binding energy of 168.5 eV for $\text{S } 2p_{3/2}$) are observed. The occurrence of the thiol-related doublet implies the chemical anchoring of the TMPP species to the substrate. Because C12 films do not contain sulfones (see the bottom spectrum), the sulfone-related peak can be considered as a fingerprint of TMPP and used to monitor the composition of the TMPP/C12 films.

presumed strong π interaction with the metal substrate, we hoped that it would adsorb in a planar fashion even without gold–thiolate binding. In fact, the immersion of a gold substrate in a one-component Al-PC solution led to a highly oriented film consisting of two to three molecular layers. However, when a two-component Al-PC/C12 solution was used, even with a 100-fold excess of Al-PC, the Al-PC molecules were completely expelled by the C12 species and a one-component C12 SAM formed. This result demonstrates that even large planar molecules with extended π -electron systems but without anchor groups do not form mixed monolayers with alkanethiols on deposition under quasi-equilibrium conditions.

The designed architecture and stability of the C12/TMPP nanostructures were exploited for the selective reduction of platinum into the nanopores formed by the spreader-bar TMPP molecules. Metal nanoparticles were visualized by electron microscopy. Depending on the reduction charge, the size of the nanoparticles could be varied between 20 and 1000 nm (Figure 4): an increase in the reduction charge led to an increase in the mean size of the particles and a decrease in their surface concentration. Presumably, an increase of the reduction charge results in the fusion of smaller particles due to secondary nucleation. This is confirmed by the increased roughness of the particle surface (Figure 4).

The total area of the formed platinum nanoelectrodes was estimated by underpotential deposition of copper; the respective charge density was $920 \mu\text{C cm}^{-2}$. If one takes into account the usual surface scaling factor of $420 \mu\text{C cm}^{-2}$, the surface area is about 220 % of the geometrical electrode area. Such a high increase in the surface area can be obtained only for nanoparticles having high surface roughness. Similar

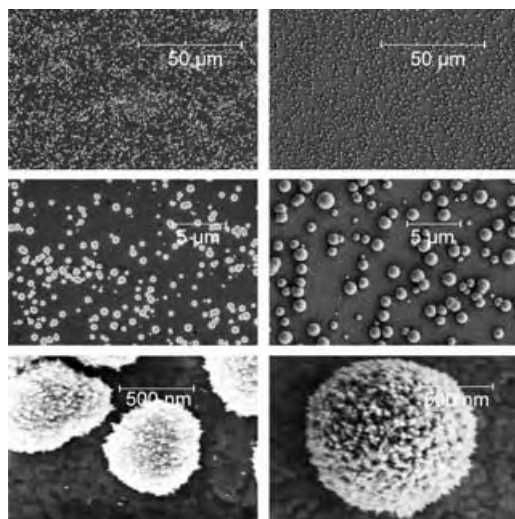


Figure 4. SEM images of platinum particles formed electrochemically on gold electrodes coated by the nanostructured TMPP/C12 monolayer. The deposition charge was 41 C cm^{-2} (left) and 160 C cm^{-2} (right). The observed differences in contrast are caused by different detectors and accelerating voltages.

experiments were performed with gold electrodes coated with a pure matrix monolayer (C12). Platinum deposition on such electrodes resulted in widely spaced large metallic islands. For example, the particles generated on C12-coated electrodes by the deposition charge similar to the system presented in the right panels of Figure 4 were as large as $10 \mu\text{m}$. We assume that these particles were formed at borders of gold microcrystals or on other defects in the monolayer.

We have described a new nanoelectrochemical approach for the in situ synthesis of metallic nanoparticles. To our knowledge this is the first application of spreader-bar-stabilized nanostructured monomolecular films as templates for electrochemical synthesis. This new bottom-up technology does not require expensive instrumentation and can be easily transferred to industrial applications. Possible application fields include the development of novel (electro)catalysts, (bio)fuel cells, chemo- and biosensors, and nanoelectronic devices. Preliminary experiments have confirmed the high electrocatalytic activity of platinum nanoparticles formed on the spreader-bar-structured electrode in the electrochemical oxidation of ascorbic acid.

Experimental Section

1-Dodecanethiol (C12, Sigma-Aldrich) was used without further purification. TMPP (Porphyrin Systems) was fabricated from a precursor, 5,10,15,20-tetrakis(4-sulfonatophenyl)porphyrin. The sulfonate groups of the latter compound were chemically reduced to thiol groups by triphenylphosphine and iodine;^[21] XPS detected two thiol groups per TMPP molecule. The substrates were fabricated by evaporation of gold (200 nm) on Si(100) wafers precoated with a Ti/Pd adhesion layer (5 nm). The SAMs were prepared at room temperature by immersing the substrates for 72 h in an ethanol (Baker) solution of C12 and TMPP. The TMPP concentration in the solution was varied from $15 \mu\text{mol L}^{-1}$ to 15 mmol L^{-1} while that of C12 was maintained at $1.5 \mu\text{mol L}^{-1}$.

The SAMs were characterized by XPS, NEXAFS spectroscopy, and XAM (room temperature, UHV conditions). The XPS and NEXAFS measurements were carried out at the HE-SGM beamline of the synchrotron storage ring BESSY II in Berlin, Germany. The energy resolution was $\approx 0.40 \text{ eV}$, and the binding energy scale was referenced to the $\text{Au } 4f_{7/2}$ peak at 84.0 eV . The NEXAFS spectra were collected at the carbon K-edge in the partial electron yield mode with a retarding voltage of -150 V . Linearly polarized synchrotron light was used. The X-ray incidence angle was varied to monitor the orientational order within the TMPP/C12 films. The original NEXAFS spectra were normalized to the incident photon flux. The energy scale was referenced to the π_1^* resonance of highly oriented pyrolytic graphite at 285.38 eV . The spectromicroscopic characterization of the SAMs was performed at a microscopy branch (7.3.1.1) of the beamline 7.3.1 at the Advanced Light Source in Berkeley, USA, using an X-ray photoelectron emission microscope, which was operated in the total electron yield acquisition mode and provided a spatial resolution of typically $50\text{--}100 \text{ nm}$.

C12/TMPP SAMs for the metal deposition were fabricated at a TMPP concentration of 1.5 mmol L^{-1} . Electrodeposition of platinum on these templates was performed at a constant potential of -25 mV vs SCE from $2.5 \text{ mmol L}^{-1} \text{ H}_2[\text{PtCl}_6]$ in $50 \text{ mmol L}^{-1} \text{ KCl}$. Electrochemical measurements were conducted with AutoLab-PG-stat-12 Electrochemical Workplace (EcoChemie, The Netherlands). SEM measurements were conducted with a LEO SUPRA35 scanning electron microscopy. Other experimental details are described elsewhere.^[17–19, 22–26]

Received: March 11, 2005

Revised: June 30, 2005

Published online: September 27, 2005

Keywords: imprinting · monolayers · nanoparticles · nanotechnology

- [1] G. Schmid, B. Corain, *Eur. J. Inorg. Chem.* **2003**, 3081–3098.
- [2] U. Erb, K. T. Aust, G. Palumbo in *Nanostructured Materials. Processing, Properties and Potential Applications* (Ed.: C. C. Koch), Noyes, New York, **2002**, pp. 179–222.
- [3] *Handbook of Nanoscience, Engineering, and Technology* (Eds.: W. A. Goddard III, D. W. Brenner, S. E. Lyshevski, G. J. Iafrate), CRC, Boca Raton, **2002**.
- [4] P. Mulvaney in *Nanoscale Materials in Chemistry* (Ed.: K. J. Klabunde), Wiley, New York, **2001**, pp. 121–168.
- [5] D.-Q. Yang, M. Meunier, E. Sacher, *J. Appl. Phys.* **2004**, *9*, 5023–5026.
- [6] J. J. Kakkassery, J.-P. Abid, M. Carrara, D. J. Fermín, *Faraday Discuss.* **2004**, *125*, 157–169.
- [7] Y. Jin, Y. Shen, S. Dong, *J. Phys. Chem. B* **2004**, *108*, 8142–8147.
- [8] F. Schults, S. Franzka, G. Schmid, *Adv. Funct. Mater.* **2002**, *12*, 532–536.
- [9] C.-J. Zhong, M. M. Maye, *Adv. Mater.* **2001**, *13*, 1507–1511.
- [10] G. Martara, L. Prati, C. Manfredotti, S. Biella, M. Rossi, S. Coluccia, *J. Phys. Chem. B* **2003**, *107*, 5453–5459.
- [11] U.-W. Grummt, M. Geissler, T. Drechsler, H. Fuchs, R. Staub, *Angew. Chem.* **1998**, *110*, 3480–3482; *Angew. Chem. Int. Ed.* **1998**, *37*, 3286–3289.
- [12] F. Endres, M. Bukowski, R. Hempelmann, H. Natter, *Angew. Chem.* **2003**, *115*, 3550–3552; *Angew. Chem. Int. Ed.* **2003**, *42*, 3428–3430.
- [13] J. A. Switzer in *Electrochemistry of Nanomaterials*, (Ed.: G. Hodes), Wiley-VCH, Weinheim, **2001**, pp. 67–101.
- [14] D. M. Kolb, R. Ullmann, T. Will, *Science* **1997**, *275*, 1097–1099.
- [15] D. M. Kolb, R. Ullmann, J. Ziegler, *Electrochim. Acta* **1998**, *43*, 2751–2760.

- [16] J. Meier, K. A. Friedrich, U. Stimming, *Faraday Discuss.* **2002**, *121*, 365–372.
- [17] V. M. Mirsky, T. Hirsch, S. A. Piletsky, O. S. Wolfbeis, *Angew. Chem.* **1999**, *111*, 1179–1181; *Angew. Chem. Int. Ed.* **1999**, *38*, 1108–1110.
- [18] T. Hirsch, H. Kettenberger, O. S. Wolfbeis, V. M. Mirsky, *Chem. Commun.* **2003**, *3*, 432–433.
- [19] M. I. Prodromidis, T. Hirsch, V. M. Mirsky, O. S. Wolfbeis, *Electroanalysis* **2003**, *15*, 1795–1798.
- [20] J. B. Schlenoff, M. Li, H. Ly, *J. Am. Chem. Soc.* **1995**, *117*, 12528–12536.
- [21] T. Oae, *Bull. Chem. Soc. Jpn.* **1984**, *57*, 232–237.
- [22] J. Stöhr, *NEXAFS Spectroscopy*, Springer, Berlin, **1992** (Springer Series in Surface Science 25).
- [23] J. F. Moulder, W. E. Stickle, P. E. Sobol, K. D. Bomben, *Handbook of X-ray Photo-electron Spectroscopy* (Ed.: J. Chastian), Perkin-Elmer, Eden Prairie, MN, **1992**.
- [24] P. E. Batson, *Phys. Rev. B* **1993**, *48*, 2608.
- [25] M. Zharnikov, M. Grunze, *J. Phys. Condens. Matter* **2001**, *13*, 11333–11365.
- [26] M. Zharnikov, Y. Ouchi, M. Hasegawa, A. Scholl, *J. Phys. Chem. B* **2004**, *108*, 859–863.

Asymmetric Synthesis

DOI: 10.1002/anie.200501481

1,2-Chirality Transfer in the Synthesis of Cyclopropanes**

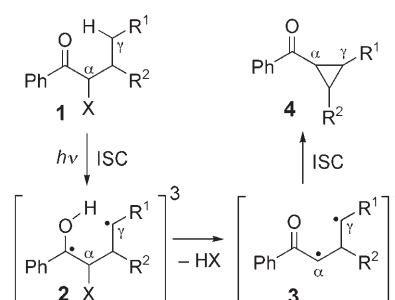
Pablo Wessig* and Olaf Mühling

In the last few years organic photochemistry has made remarkable progress in the area of asymmetric synthesis.^[1] A range of new strategies has been developed that drastically enhance the diastereo- and enantioselectivity of certain photochemical processes. Here we report on an entirely novel concept concerning the synthesis of enantiomerically enriched cyclopropanes based on a photochemically induced intramolecular 1,2-chirality transfer.

During chirality transfer a prochiral moiety incorporates the chiral information of a chiral moiety, which simultane-

ously loses this information. A distinguishing feature in the intramolecular transfer of central chirality is the distance between the source and the target of the chiral information. While relatively many examples of 1,3-chirality transfer exist,^[2] which are mainly based on the transfer of chirality along an allylic system, there are only a few examples of 1,2-chirality transfer.^[3]

Some time ago we developed the concept of spin-center shift,^[4,5] which provides a completely new access to cyclopropanes. In contrast to the classical Norrish–Yang reaction,^[6] phenyl ketones **1** with a suitable leaving group X in α position are used. At the stage of 1,4-diradicals **2** this results in a shift of the radical center from the carbonyl C atom to the adjacent C atom as a result of HX elimination. The resulting 1,3-diradicals **3** cyclize with often complete diastereoselectivity and good to very good yields to give cyclopropanes **4** (Scheme 1).^[4]



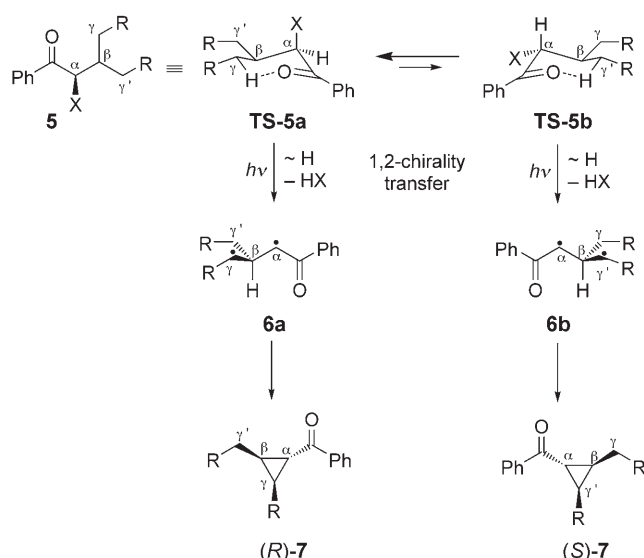
Scheme 1. The principle of spin-center shift in the synthesis of cyclopropanes.^[4] ISC = intersystem crossing.

By extensive quantum chemical calculations we could elucidate details of the mechanism and found that the leaving group X already has a significant impact on the first reaction step, the photochemical H-shift (**1**→**2**, Scheme 1).^[4] Owing to hyperconjugation between the σ^* orbital of the C–X bond and the π system of the excited carbonyl group, X prefers a pseudoaxial arrangement with respect to the approximately chairlike six-membered transition state.^[4b] If we consider enantiomerically pure ketones of type **5** with two identical substituents in β position, we can formulate two different transition states for the γ -H abstraction (**TS-5a** and **TS-5b**), which differ in the arrangement of the leaving group X (axial or equatorial, Scheme 2). Based on the quantum chemical calculations,^[4b] **TS-5a** with X in the axial position should be favored over **TS-5b**. In **TS-5a** the γ -methylene group is attacked, whereas in **TS-5b** the attack takes place at the γ' -methylene group, which means that the carbonyl oxygen atom must distinguish between the two diastereotopic methylene groups. During the photochemically induced H-transfer and the following elimination of HX, the enantiomeric diradicals **6a** and **6b** are formed, and the chiral information of the α -C atom has been transferred to the adjacent prochiral β -C atom (1,2-chirality transfer). Consequently, after the cyclization the enantiomeric cyclopropyl ketones (*R*)-**7** and (*S*)-**7** are obtained, whereby the formation of (*R*)-**7** should be favored over (*S*)-**7**. Thus, during such a process desymmetrization relative to the methylene groups (γ and γ') takes place.

[*] Dr. P. Wessig, O. Mühling
Institut für Chemie
Humboldt-Universität zu Berlin
Brook-Taylor-Strasse 2, 12489 Berlin (Germany)
Fax: (+49) 30-2093-7450
E-mail: pablo.wessig@chemie.hu-berlin.de

[**] This work was supported by the Deutsche Forschungsgemeinschaft. We thank Dr. Hans-Hermann Drews, Bruker Optics (Ettlingen), for measuring the VCD spectra and for valuable discussions about VCD spectroscopy. We also thank Priv.-Doz. Dr. Detlef Heller, Leibnitz-Institut für Organische Katalyse (IfOK) (University Rostock), for helpful advice about the temperature dependency of selectivities.

Supporting information for this article is available on the WWW under <http://www.angewandte.org> or from the author.



Scheme 2. The concept of 1,2-chirality transfer in ketones **5** (simplified representation). The configuration designations are relative to C- β .

The concept shown in Scheme 2 should in principle be applicable to all ketones of type **5** carrying two identical substituents in β position. It can be expected that bridging between the substituents R, in other words, a conformational constraint in flexibility, creates the best situation for an efficient 1,2-chirality transfer. Therefore, for our investigations we chose systems in which the atoms β , γ , and γ' (Scheme 2) are part of a saturated six-membered ring.

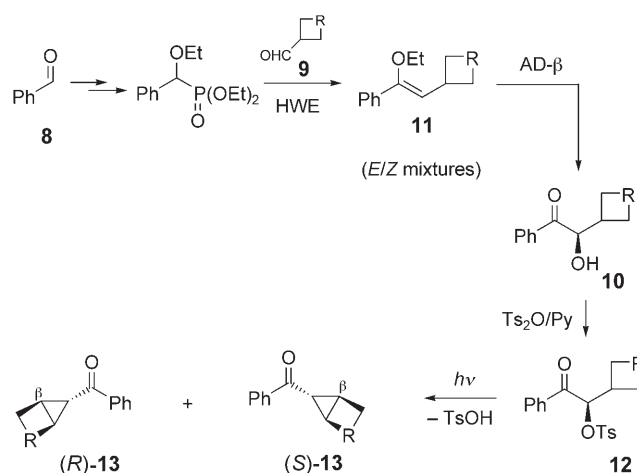
To verify the concept shown in Scheme 2 we first of all needed an efficient method for the synthesis of enantiomerically pure ketones of type **5**. As sulfonates were found to be suitable leaving groups,^[4] the retrosynthetic analysis of **5** led to α -hydroxy ketones. Various methods for the synthesis of enantiomerically pure α -hydroxy ketones are known, whereby oxidative methods starting from the ketones or their enol ethers are the most common.^[7] Based on the results of Sharpless et al.^[8] and Kirschning et al.,^[9] we developed a very efficient sequence for the synthesis of enantiomerically pure α -hydroxy ketones. The sequence starts with aldehydes **8** and **9**, which provide the enantiomerically pure α -hydroxy ketones **10** in only a few very efficient steps. The key step in this synthetic sequence is a Horner–Wadsworth–Emmons olefination (HWE), which is followed by an asymmetric dihydroxylation (AD) of enol ethers **11**. It should be pointed out that this very reliable method delivers α -hydroxy ketones **10** in high enantiomeric excesses and generally unaffected by R (Table 1). Furthermore the configuration of the product can be determined by the choice of the ligand during the AD (AD-mix- α or AD-mix- β).^[10] Tosylation of **10** with tosyl anhydride finally yields ketones **12**.

Irradiation of the ketones **12** delivers the cyclopropyl ketones **13** in good yields and in part with considerable enantiomeric excess (Scheme 3, Table 1). It should be pointed out that the stereoselectivity obtained in the formation of **13** exclusively reflects the efficiency of the 1,2-chirality transfer, whereas the asymmetric induction of the chiral center in the β position of diradicals **6** on the two newly formed chiral centers

Table 1: Results of irradiation of **12 a–d** to give **13 a–d**.^[a]

Reactant (<i>ee</i> [%]) ^[b]	R	Yield [%]	<i>ee</i> [%] ^[b]	CT ^[c]	Config. ^[d]
12a (91)	-CH ₂ -O-CH ₂ -	74	28	31	S
12b (99)	-CH ₂ -N(Ts)-CH ₂ -	78	38	38	S
12c (93)	-CH ₂ -N(Boc)-CH ₂ - ^[e]	69	23	25	R ^[f]
12d (95)	-CH ₂ -CH(<i>t</i> Bu)-CH ₂ - ^[g]	79	52	55	R

[a] Irradiation in dichloromethane at 25 °C; for experimental details see ref. [4b]. [b] The enantiomeric excess (*ee*) was determined by HPLC (Chiralpak-AD-H, Chiralcel-OD). [c] Chirality transfer (CT) according to ref. [2e]: CT = [*ee*(**13**)/*ee*(**12**)] 100. [d] Configuration of the main enantiomer at 25 °C, assigned by VCD spectroscopy. [e] Boc = *tert*-butoxycarbonyl. [f] Conclusive assignment by VCD spectroscopy was not possible. [g] The *t*Bu substituent is *trans* with respect to C- β .



Scheme 3. Synthesis and photochemical cyclization of ketones **12**. The configuration designations are relative to C- β . Py = pyridine, Ts = *para*-toluenesulfonyl.

leads to the formation of the *exo* products **13** with complete selectivity (Scheme 2).^[4]

To verify the postulated stereochemical course depicted in Scheme 2 it was necessary to determine the absolute configuration of compounds **13**. Particularly predestined for conformationally rigid molecules of type **13** is vibrational circular dichroism (VCD).^[11] By this method, which is based on the comparison of experimental and calculated VCD spectra, we succeeded in unambiguously determining the absolute configuration of **13 a,b,d**.^[12]

Since lowering the reaction temperature, also in photochemical reactions, often leads to an increase in stereoselectivity, we examined the temperature dependence of the stereoselectivity. In Figure 1 the relevant Eyring plots ($\ln([(\text{R})\text{-13a}]/[(\text{S})\text{-13a}]) = f(T^{-1})$) are shown for irradiation in dichloromethane and methanol.

Surprisingly, we found in both solvents increasing stereoselectivity with increasing temperature and decreasing stereoselectivity with decreasing temperature, starting from room temperature. This behaviour, which has already been observed in other thermal and photochemical reactions,^[13–15] seems to be contrainuitive at first but can be explained easily. The preferred formation of one enantiomer during an

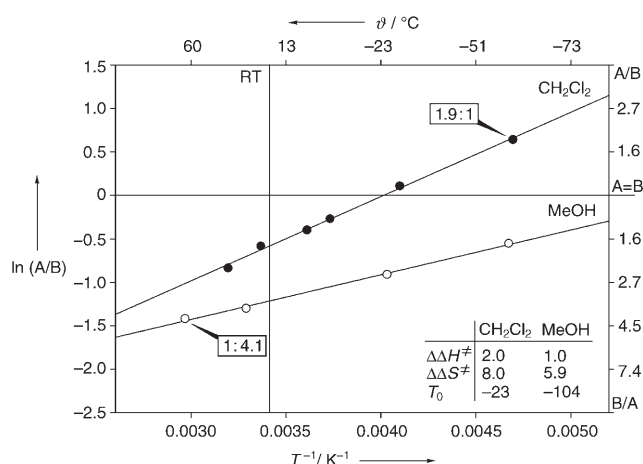


Figure 1. Eyring plots for the irradiation of **12a**. A = (*R*)-**13a**, B = (*S*)-**13a**. Inset: $\Delta\Delta H^\ddagger$ values in kcal mol⁻¹, $\Delta\Delta S^\ddagger$ values in cal mol⁻¹ K⁻¹, $T_0 = \Delta\Delta H^\ddagger / \Delta\Delta S^\ddagger$ in °C.

unimolecular reaction like **12** → **13** is based on a difference in the free enthalpy of activation $\Delta\Delta G^\ddagger$, which in turn is the sum of an enthalpic and an entropic term ($\Delta\Delta G^\ddagger = \Delta\Delta H^\ddagger - T\Delta\Delta S^\ddagger$, Gibbs–Helmholtz equation). Thus, the stereoselectivity of such a reaction is always a function of temperature if the entropies of activation of the two channels of selectivity are different. A special situation occurs if the differences of the enthalpies of activation $\Delta\Delta H^\ddagger$ and the entropies of activation $\Delta\Delta S^\ddagger$ have the same sign. In this case a temperature $T_0 = \Delta\Delta H^\ddagger / \Delta\Delta S^\ddagger$ exists, at which the selectivity is inverted.

We observed exactly this behavior when we irradiated compound **12a** (Figure 1). For the reaction in dichloromethane as well as in methanol, $\Delta\Delta H^\ddagger$ and $\Delta\Delta S^\ddagger$ have the same sign, so that in both cases a temperature T_0 can be calculated, at which **13a** is formed as a racemic mixture and below which the formation of the other enantiomer is favored ((*R*)-**13a**, Scheme 3). While for methanol this temperature lies at an experimentally impractical region (−104 °C), for dichloromethane it is −23 °C. The selectivity for the formation of **13** at room temperature is determined by the entropies of activation, which compensate the enthalpic influence. Only below T_0 do the differences in the enthalpies of activation determine the selectivity.^[16]

In summary, we have described a novel concept for a 1,2-chirality transfer. The mechanistic basis is the preferred colinear arrangement of a leaving group and the π system of a photochemically excited carbonyl group, which can be explained by stereoelectronic effects.^[4b] We were able to demonstrate this concept by means of the photochemical cyclization of four ketones **12a–d** to the bicyclic compounds **13a–d**. The configuration of the preferred enantiomer at room temperature has been determined easily for the photolytic products **13a,b,d** by a combination of quantum chemical calculations and VCD spectroscopy. Because both the differences of the entropies of activation and the enthalpies of activation are positive, the stereoselectivity increases at temperatures above T_0 . On the other hand, at temperatures below T_0 the ratio of the enantiomers is inverted, and

selectivity increases with decreasing temperature in favor of the other enantiomer. This behavior can be explained by the compensation of entropic and enthalpic influences. At low temperatures, the *R*-configured reactants **5** always lead to the products with *R* configuration at C- β , which is consistent with our prediction (see Scheme 2).

Received: April 29, 2005

Revised: July 1, 2005

Published online: September 19, 2005

Keywords: asymmetric synthesis · chirality transfer · cyclization · photochemistry · vibrational circular dichroism

- [1] Selected reviews and books concerning asymmetric photochemistry: a) Memory effect of chirality: H. Zhao, D. C. Hsu, P. R. Carlier, *Synthesis* **2005**, 1–16; b) “Chiral photochemistry”: *Molecular and Supramolecular Photochemistry, Vol. 11* (Eds.: Y. Inoue, V. Ramamurthy), Dekker, New York, **2004**; c) Asymmetric photochemistry and photochirogenesis: A. G. Griesbeck, U. J. Meierhenrich, *Angew. Chem.* **2002**, *114*, 3279–3286; *Angew. Chem. Int. Ed.* **2002**, *41*, 3147–3154; d) “Oxetane formation: stereocontrol”: A. G. Griesbeck, S. Bondock in *Organic Photochemistry and Photobiology*, 2nd ed. (Eds.: W. M. Horspool, F. Lenci), CRC, Boca Raton, FL, **2003**, pp. 59/1–59/19; e) “Enantioselective photocycloaddition reactions in solution”: B. Grosch, T. Bach in *Organic Photochemistry and Photobiology*, 2nd ed. (Eds.: W. M. Horspool, F. Lenci), CRC, Boca Raton, FL, **2003**, pp. 61/1–61/14; f) “Induced diastereoselectivity in photodecarboxylation reactions”: K. Pitchumani, D. Madhavan in *Organic Photochemistry and Photobiology*, 2nd ed. (Eds.: W. M. Horspool, F. Lenci), CRC, Boca Raton, FL, **2003**, pp. 65/1–65/14; g) Stereoselective intermolecular [2+2] photocycloadditions: T. Bach, *Synthesis* **1998**, 683–703; h) Y. Inoue, *Chem. Rev.* **1992**, *92*, 741–770; i) H. Rau, *Chem. Rev.* **1983**, *83*, 535–547.
- [2] a) “Chirality transfer via sigmatropic rearrangements”: R. K. Hill in *Asymmetric Synthesis, Vol. 3* (Ed.: J. D. Morrison), Academic Press, San Diego, **1984**, pp. 503–572; b) [3,3] Sigmatropic rearrangements: U. Nubbemeyer, *Synthesis* **2003**, 961–1008; c) [3,3] Sigmatropic rearrangements: H. Frauenrath in *Methods Of Organic Chemistry (Houben Weyl), Vol. E21*, Thieme, Stuttgart, **1995**, pp. 3301–3756; d) [2,3] Sigmatropic rearrangements: J. Kallmerten in *Methods Of Organic Chemistry (Houben Weyl), Vol. E21*, Thieme, Stuttgart, **1995**, pp. 3757–3809; e) Wittig rearrangement: T. Nakai, K. Mikami in *Organic Reactions, Vol. 46*, Wiley, New York, **1994**, pp. 105–209; f) Copper-mediated allylic substitution: B. Breit, P. Demel, C. Studte, *Angew. Chem.* **2004**, *116*, 3874–3877; *Angew. Chem. Int. Ed.* **2004**, *43*, 3786–3789, and references therein.
- [3] A search for the keyword “1,2-chirality transfer” provided only two references: a) W. Smadja, S. Czernecki, G. Ville, C. Georgoulis, *Organometallics* **1987**, *6*, 166–169; b) P. Compain, J. Goré, J.-M. Vattelè, *Tetrahedron* **1996**, *52*, 6647–6664.
- [4] a) P. Wessig, O. Mühling, *Angew. Chem.* **2001**, *113*, 1099–1101; *Angew. Chem. Int. Ed.* **2001**, *40*, 1064–1065; b) P. Wessig, O. Mühling, *Helv. Chim. Acta* **2003**, *86*, 865–893.
- [5] a) P. Wessig, J. Schwarz, U. Lindemann, M. C. Holthausen, *Synthesis* **2001**, 1258–1262; b) P. Wessig, C. Glombitza, G. Müller, J. Teubner, *J. Org. Chem.* **2004**, *69*, 7582–7591; c) P. Wessig, G. Müller, A. Kühn, R. Herre, H. Blumenthal, S. Troelenberg, *Synthesis* **2005**, 1445–1454.
- [6] a) R. G. W. Norrish, M. E. S. Appleyard, *J. Chem. Soc.* **1934**, 874; b) N. C. Yang, D.-D. H. Yang, *J. Am. Chem. Soc.* **1958**, *80*, 2913; c) P. J. Wagner, *Acc. Chem. Res.* **1971**, *4*, 168; d) P. J. Wagner,

- Top. Curr. Chem.* **1976**, 66, 1; e) P. J. Wagner, *Acc. Chem. Res.* **1989**, 22, 83; f) "Regioselective photochemical synthesis of carbo- and heterocyclic compounds: The Norrish–Yang reaction": P. Wessig in *Organic Photochemistry and Photobiology*, 2nd ed. (Eds.: W. M. Horspool, F. Lenci), CRC, Boca Raton, FL, **2003**, pp. 57/1–57/20; g) P. J. Wagner in *Molecular and Supramolecular Photochemistry, Vol. 12* (Eds.: A. G. Griesbeck, J. Mattay), Dekker, New York, **2005**, pp. 11–39; h) P. Wessig, O. Mühling in *Molecular and Supramolecular Photochemistry, Vol. 12* (Eds.: A. G. Griesbeck, J. Mattay), Dekker, New York, **2005**, pp. 41–87.
- [7] a) Comprehensive review about the α -hydroxylation of enolates and silyl enol ethers: B.-C. Chen, P. Zhou, F. A. Davis, E. Ciganek in *Organic Reactions, Vol. 62*, Wiley, New York, **2003**, pp. 1–356, and references therein; b) Short review concerning the preparation of α -hydroxy carbonyl compounds by organocatalytic α -aminoxylation: P. Merino, T. Tejero, *Angew. Chem.* **2004**, 116, 3055–3058; *Angew. Chem. Int. Ed.* **2004**, 43, 2995–2997.
- [8] a) T. Hashiyama, K. Morikawa, K. B. Sharpless, *J. Org. Chem.* **1992**, 57, 5067–5068; b) K. Morikawa, J. Park, P. G. Andersson, T. Hashiyama, K. B. Sharpless, *J. Am. Chem. Soc.* **1993**, 115, 8463–8464.
- [9] a) A. Kirschning, G. Dräger, A. Jung, *Angew. Chem.* **1997**, 109, 253–255; *Angew. Chem. Int. Ed. Engl.* **1997**, 36, 253–255; b) H. Monenschein, G. Dräger, A. Jung, A. Kirschning, *Chem. Eur. J.* **1999**, 5, 2270–2280.
- [10] AD-mix- β and AD-mix- α : 1.4 g AD-mix (for 1 mmol substrate) contain 0.980 g $K_3[Fe(CN)_6]$, 0.410 g K_2CO_3 , 0.0078 g (1 mol %) $(DHQD)_2$ -Phal (AD-mix- β) or $(DHQ)_2$ -Phal (AD-mix- α) and $K_2[OsO_2(OH)_4]$ (0.2 mol %); see also ref. [8].
- [11] a) H.-H. Drews, *Nachr. Chem.* **2003**, 51, 999–1000; b) T. B. Freedman, X. Cao, R. K. Dukor, L. A. Nafie, *Chirality* **2003**, 15, 743–758, and references therein.
- [12] See the Supporting Information.
- [13] Photochemically induced reactions with a selectivity reversal at T_0 ($\ln(A/B) = 0$): a) Y. Inoue, H. Ikeda, M. Kaneda, T. Sumimura, S. R. L. Everitt, T. Wada, *J. Am. Chem. Soc.* **2000**, 122, 406–407, and references therein; b) S. Kohmoto, H. Masu, C. Tatsuno, K. Kishikawa, M. Yamamoto, K. Yamaguchi, *J. Chem. Soc. Perkin Trans. 1* **2000**, 4464–4468; c) O. Benali, M. A. Miranda, R. Tormos, S. Gil, *J. Org. Chem.* **2002**, 67, 7915–7918; d) W. Adam, V. R. Stegmann, *J. Am. Chem. Soc.* **2002**, 124, 3600–3607, and references therein; e) N. Hoffmann, H. Buschmann, G. Raabe, H.-D. Scharf, *Tetrahedron* **1994**, 50, 11167–11186; f) M. Abe, T. Kawakami, S. Ohata, K. Nozaki, M. Nojima, *J. Am. Chem. Soc.* **2004**, 126, 2838–2856; g) X.-M. Hei, Q.-H. Song, X.-B. Li, W.-J. Tang, H.-B. Wang, Q.-X. Guo, *J. Org. Chem.* **2005**, 70, 2522–2527.
- [14] Thermal reactions with a selectivity reversal at T_0 : a) K. Harada, T. Yoshida, *J. Chem. Soc. Chem. Commun.* **1970**, 1071; b) I. Tóth, I. Guo, B. E. Hanson, *Organometallics* **1993**, 12, 848–852; c) J. Otera, K. Sakamoto, T. Tsukamoto, A. Orita, *Tetrahedron Lett.* **1998**, 39, 3201–3204; d) G. Cainelli, P. Galletti, D. Giacomini, P. Orioli, *Angew. Chem.* **2000**, 112, 533–537; *Angew. Chem. Int. Ed.* **2000**, 39, 523–527, and references therein; e) N. Guiseppe, I. Santos, J. Collin, *Tetrahedron Lett.* **2000**, 41, 639–642.
- [15] Reactions without selectivity reversal in the investigated temperature region, but with an entropy-controlled increase of selectivity with increasing temperature: a) T. Bach, K. Jödicke, K. Kather, R. Fröhlich, *J. Am. Chem. Soc.* **1997**, 119, 2437–2445; b) M. Lombardo, S. Fabbroni, C. Trombini, *J. Org. Chem.* **2001**, 66, 1264–1268.
- [16] Publications dealing with the influence of reaction parameters (temperature, solvent, etc.) on the selectivity as well as with the compensation of entropic and enthalpic factors: a) isoinversion principle: H. Buschmann, H.-D. Scharf, N. Hoffmann, P. Esser, *Angew. Chem.* **1991**, 103, 480–518; *Angew. Chem. Int. Ed. Engl.* **1991**, 30, 477–515, and references therein; b) isoselectivity relationship: B. Giese, *Acc. Chem. Res.* **1984**, 17, 438–442; c) G. Cainelli, D. Giacomini, P. Galletti, *Chem. Commun.* **1999**, 567–572; d) Y. Inoue, T. Wada, S. Asaoka, H. Sato, J.-P. Pete, *Chem. Commun.* **2000**, 251–259; e) L. Liu, Q.-X. Guo, *Chem. Rev.* **2001**, 101, 673–695.

Cover Picture

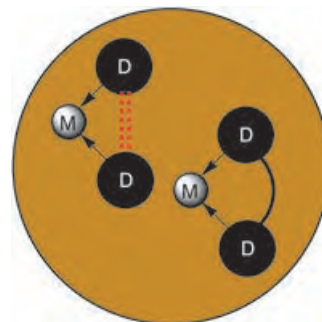
Kit T. Rodolfa, Andreas Bruckbauer, Dejian Zhou, Yuri E. Korchev, and David Klenerman*

The persistence of Edgar Degas is illustrated in the formation of highly complex, graded, 'two-color' images on the submicron scale. Two species can be delivered independently from a single pipette through the use of scanning ion-conductance distance control. The cover picture shows biological molecules being delivered in air through a liquid meniscus at the tip of a double-barreled nanopipette (Salvador Dali, not to scale, is shown painting the Degas Dancers with a nanopipette) as described by D. Klenerman et al. in their Communication on page 6854 ff.



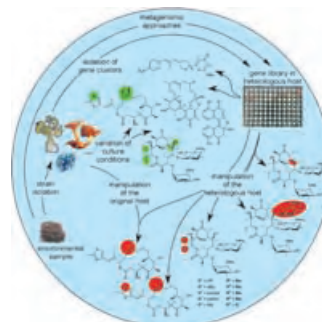
Combinatorial Catalysis

In many reactions catalysts with bidentate ligands yield the best results. In his Minireview on p. 6816 ff., B. Breit describes how these chelates can be emulated by two monodentate ligands held together by attractive interactions.



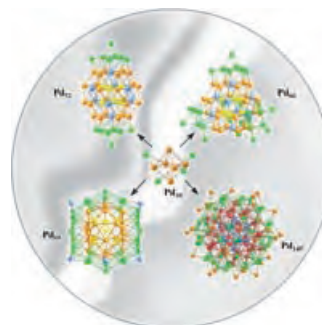
Natural Product Discovery

How are leads for drug development identified? In their Review on page 6828 ff., H. B. Bode and R. Müller describe the identification and manipulation of biosynthetic pathways towards new natural products and derivatives potentially suitable for this task.



Cluster Compounds

In their Communication on page 6848 ff., L. F. Dahl, E. G. Mednikov, and co-workers describe the synthesis and structural characterization of two new large palladium-carbonyl-triethylphosphine clusters that contain Pd₅₂ and Pd₆₆ cores.





The following Communications have been judged by at least two referees to be “very important papers” and will be published online at www.angewandte.org soon:

C. Drago, L. Caggiano, R. F. W. Jackson*

Vanadium-Catalyzed Sulfur Oxidation/Kinetic-Resolution Process for the Synthesis of Enantiomerically Pure Alkyl Aryl Sulfoxides

Q. Qing, F. Chen, P. Li, W. Tang, Z. Wu, Z. Liu*

Finely Tuning the Metallic Nanogap Size with Electrodeposition Utilizing High-Frequency Impedance in Feedback

X. Rocquefelte,* S. E. Boulfelfel, M. B. Yahia, J. Bauer, J.-Y. Saillard,* and J.-F. Halet*

The Structural Preferences of Boron and Carbon within MB₂C₂ (M = Mg, Sc, Ca, Y, Ln) Phases: The “Coloring Problem” Revisited by DFT Calculations

G. C. Lloyd-Jones,* R. G. Margue, J. G. de Vries

Rate Enhancement by Ethylene in the Ru-Catalyzed Ring-Closing Metathesis of Enynes: Evidence for an “Ene-then-Yne” Pathway That Diverts through a Second Catalytic Cycle

S. Klaus, H. Neumann, A. Zapf, D. Strübing, S. Hübner, J. Almerna,* T. Riermeier, P. Groß, M. Sarich, W.-R. Krahnert, K. Rossen, M. Beller*

A General and Efficient Method for the Formylation of Aryl and Heteroaryl Bromides

N. Martín,* Á. Martín-Domenech, S. Filippone, M. Altable, L. Echegoyen,* C. M. Cardona

Retrocycloaddition Reactions of Pyrrolidinofullerenes

Meeting Reviews

The Diverse World of Silicon Chemistry

G. Kickelbick _____ 6804

Books

Metallocenes in Regio- and Stereoselective Synthesis

Tamotsu Takahashi

reviewed by T. Nishimura _____ 6807

Integrated Chemical Processes

Kai Sundmacher, Achim Kienle, Andreas Seidel-Morgenstern

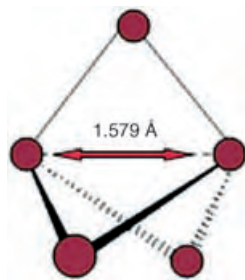
reviewed by B. Cornils _____ 6807

Highlights

Chemical Bonding

P. Coppens* _____ 6810–6811

Charge Densities Come of Age

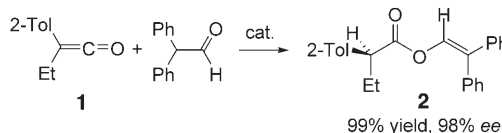


To be or not to be (a bond, that is)? Recent progress in X-ray charge-density analysis is discussed with emphasis on the characterization of unusual bonding situations, such as the recently reported C–C “bonding” interaction in a [1.1.1]propellane (see structure).

Asymmetric Catalysis

T. T. Tidwell* _____ 6812–6814

Catalytic Asymmetric Esterification of Ketenes



Ketene esterification after 100 years: In the latest advance in the esterification of ketenes, Schaefer and Fu described the catalytic asymmetric conversion of 2-

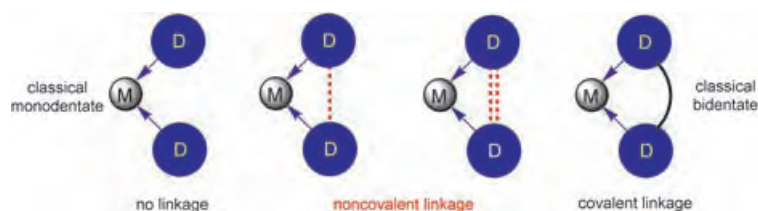
tolyl(ethyl)ketene (**1**) and diphenylacetaldehyde to give the enol ester **2** in 99% yield and 98% *ee* (see scheme).

Minireviews

Combinatorial Catalysis

B. Breit* — 6816–6825

Supramolecular Approaches to Generate Libraries of Chelating Bidentate Ligands for Homogeneous Catalysis



Ligands scoot together: Noncovalent attractive interactions between ligands in the coordination sphere of a metal center lead to a situation typical for complexes with classical bidentate ligands (see pic-

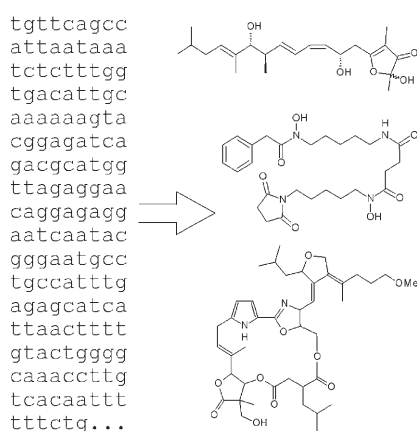
ture). In tests with catalyzed reactions these self-assembled systems gave results comparable to those obtained with complexes having classical bidentate ligands.

Reviews

Metabolic Pathway Mining

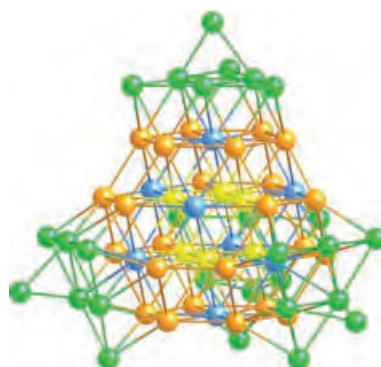
H. B. Bode, R. Müller* — 6828–6846

The Impact of Bacterial Genomics on Natural Product Research



Increasing genomic information together with new tools in molecular microbiology have led to powerful and rational applications in natural product research (see picture). Today, it is possible to produce novel and altered secondary metabolites with biological activity.

Room for one more? The structures of nanosized Pd_{52} and Pd_{66} clusters that are based upon a common Pd_{38} vertex-truncated ν -octahedral kernel have been determined. The 45 CO ligands in the Pd_{66} cluster (see core structure), $[\text{Pd}_{66}(\text{CO})_{45}(\text{PEt}_3)_{16}]$, are described in terms of one extra and 44 normal ligands, two of which undergo rearrangement to accommodate the 45th CO ligand without causing any substantial changes to the architecture of the metal core.



Communications

Palladium Clusters

E. G. Mednikov,* S. A. Ivanov,
I. V. Slovokhotova,
L. F. Dahl* — 6848–6854

Nanosized $[\text{Pd}_{52}(\text{CO})_{36}(\text{PEt}_3)_{14}]$ and $[\text{Pd}_{66}(\text{CO})_{45}(\text{PEt}_3)_{16}]$ Clusters Based on a Hypothetical Pd_{38} Vertex-Truncated ν_3 Octahedron

For the USA and Canada:

ANGEWANDTE CHEMIE International Edition (ISSN 1433-7851) is published weekly by Wiley-VCH PO Box 191161, D 69451 Weinheim, Germany. Air freight and mailing in the USA by Publications Expediting Inc. 200

Meacham Ave., Elmont, NY 11003. Periodicals postage paid at Jamaica NY 11431. US POSTMASTER: send address changes to *Angewandte Chemie*, Wiley-VCH, 111 River Street, Hoboken, NJ 07030. Annual subscription price for institutions: US\$ 5685/5168 (valid for print and

electronic / print or electronic delivery); for individuals who are personal members of a national chemical society prices are available on request. Postage and handling charges included. All prices are subject to local VAT/sales tax.

The best in chemistry – for more than a hundred years



A Journal of the Gesellschaft Deutscher Chemiker
Angewandte
International Edition **Chemie**

www.angewandte.org

1888: The beginning
of a success story

Constant Innovations

- 1962:** First issue of the International Edition
- 1976:** Graphical abstracts
- 1979:** Cover pictures
- 1988:** Centenary of Angewandte
- 1989:** Routine use of color
- 1991:** New section: Highlights
- 1992:** Computerized editorial tracking system
- 1995:** Internet service for readers
- 1998:** Regular press service; full-text online
- 2000:** New section: Essays; EarlyView: Communications available online ahead of the printed version
- 2001:** New section: Minireviews
- 2002:** Online submission of manuscripts
- 2003:** Weekly publication; new section: News; new layout
- 2004:** Backfiles (1962-1997); ManuscriptXpress: Online system for authors and referees



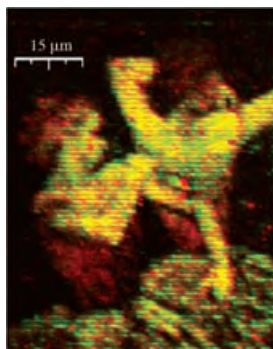
Angewandte's advisors...

Horst Kessler
Institut für Organische
und Biochemie, Technische
Universität München

» If you want to be recognized send your best papers to **Angewandte Chemie**. The journal is scientifically of top quality; the layout makes the articles easy to read and contributes to the overall impact. An important step forward was the coverage in Medline making the life sciences community aware of the journal's content. Now the field of bioorganic chemistry is also becoming stronger in **Angewandte Chemie**. «

Angewandte Chemie International Edition is
a journal of the German Chemical Society (GDCh)



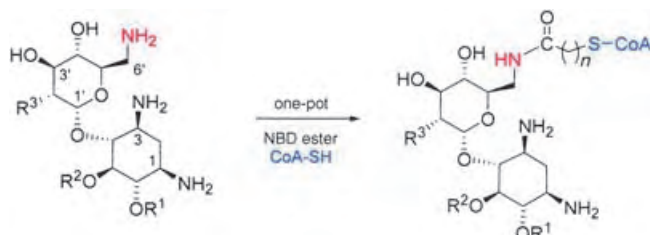


Pretty as a picture: The printing of highly complex graded images with two different species (see picture) has been developed through the use of double-barreled pipettes. This method of submicron deposition of biomolecules eliminates registry problems that are inherent to other deposition techniques.

Lithography

K. T. Rodolfa, A. Bruckbauer, D. Zhou, Y. E. Korchhev, D. Klenerman* — 6854 – 6859

Two-Component Graded Deposition of Biomolecules with a Double-Barreled Nanopipette



Complex nanomolar inhibitors in one pot: Aminoglycoside–coenzyme A derivatives were prepared through an efficient regioselective 6'-N modification of aminoglycosides (see scheme). These bisubstrates

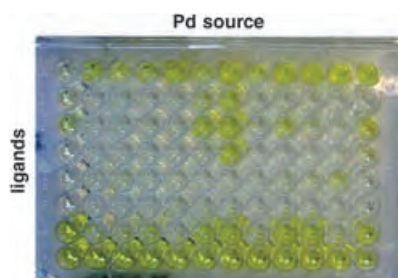
show tight-binding competitive inhibition of aminoglycoside 6'-N-acetyltransferase, an enzyme involved in antibiotic resistance.

Aminoglycosides

F. Gao, X. Yan, O. M. Baettig, A. M. Berghuis, K. Auclair* — 6859 – 6862

Regio- and Chemoselective 6'-N-Derivatization of Aminoglycosides: Bisubstrate Inhibitors as Probes To Study Aminoglycoside 6'-N-Acetyltransferases

Catalyst sandwich: An efficient and sensitive high-throughput-screening method that uses sandwich immunoassays was developed and applied to the Sonogashira reaction. This new method is amenable to coupling reactions and allows the screening of more than 1000 catalyst samples per day.

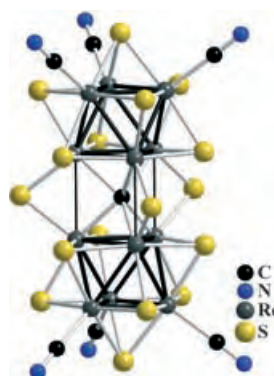


Immunoassays

P. Vicennati, N. Bense, A. Wagner, C. Cr  minon, F. Taran* — 6863 – 6866

Sandwich Immunoassay as a High-Throughput Screening Method for Cross-Coupling Reactions

Cyanide clusters $[\text{Re}_{12}\text{CS}_{17}(\text{CN})_6]^{n-}$ ($n = 8$ or 6), which may be used to form polymeric material, have been prepared by treating ReS_2 with molten KCN at 750°C . The cluster unit comprises two $\{\text{Re}_6\}$ octahedra connected by three $\mu_2\text{-S}$ bridges and one interstitial $\mu_6\text{-C}$ atom (see picture).



Cluster Compounds

Y. V. Mironov, N. G. Naumov, S. G. Kozlova, S.-J. Kim,* V. E. Fedorov* — 6867 – 6871

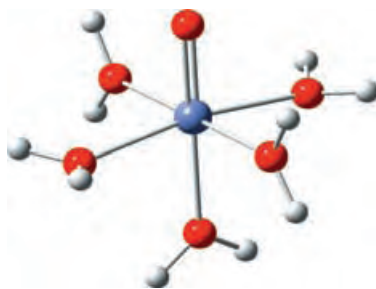
$[\text{Re}_{12}\text{CS}_{17}(\text{CN})_6]^{n-}$ ($n = 6, 8$): A Sulfido–Cyanide Rhenium Cluster with an Interstitial Carbon Atom



Redox Chemistry

O. Pestovsky, S. Stoian, E. L. Bominaar,
X. Shan, E. Münck,* L. Que, Jr.,*
A. Bakac* _____ **6871 – 6874**

Aqueous $\text{Fe}^{\text{IV}}=\text{O}$: Spectroscopic
Identification and Oxo-Group Exchange



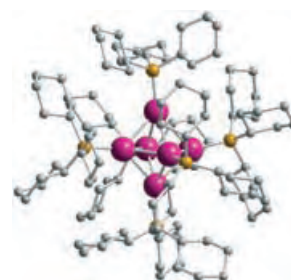
A combination of techniques (Mössbauer and X-ray absorption spectroscopy, H_2^{18}O exchange experiments, and DFT calculations) has shown that the reaction of $[\text{Fe}(\text{H}_2\text{O})_6]^{2+}$ with ozone generates $[(\text{H}_2\text{O})_5\text{Fe}^{\text{IV}}=\text{O}]^{2+}$ (see calculated structure). The oxidation of selected substrates with $[(\text{H}_2\text{O})_5\text{Fe}^{\text{IV}}=\text{O}]^{2+}$ yields unique products that are different from those generated in the Fenton reaction or derived from HO^\bullet radicals.

Cluster Chemistry

S. K. Brayshaw, M. J. Ingleson, J. C. Green,
P. R. Raithby, G. Kociok-Köhn,
J. S. McIndoe, A. S. Weller* **6875 – 6878**

Holding onto Lots of Hydrogen:
A 12-Hydride Rhodium Cluster That
Reversibly Adds Two Molecules of H_2

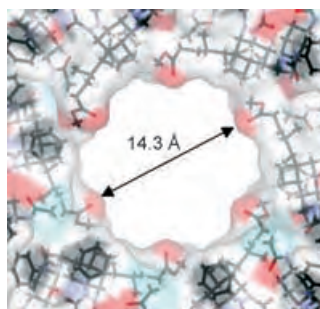
H Box: The clusters $[\text{Rh}_6(\text{PR}_3)_6\text{H}_{12}][\text{BAR}_4]_2$ ($\text{R} = \text{cyclohexyl}$, $i\text{Pr}$; see scheme, pink Rh, orange P) reversibly take up two molecules of H_2 under ambient conditions (1 atm H_2 , 298 K) to give discrete octahedral clusters surrounded by 16 hydride ligands.



Crystal Engineering

A. L. Sisson, V. del Amo Sanchez,
G. Magro, A. M. E. Griffin, S. Shah,
J. P. H. Charmant,
A. P. Davis* _____ **6878 – 6881**

Spiraling Steroids: Organic Crystals with
Asymmetric Nanometer-Scale Channels

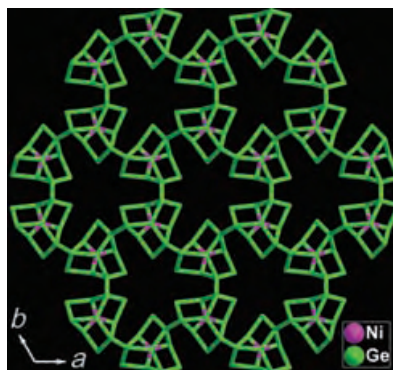


Crystals with broad robust channels are rare, especially if self-assembled without the aid of metal ions. Three such crystals were prepared based on a common steroid motif. The channels formed are chiral, directional, aligned, and wide enough ($> 1 \text{ nm}$) to accept a variety of guests (see picture; red: oxygen, blue: nitrogen, green: fluorine).

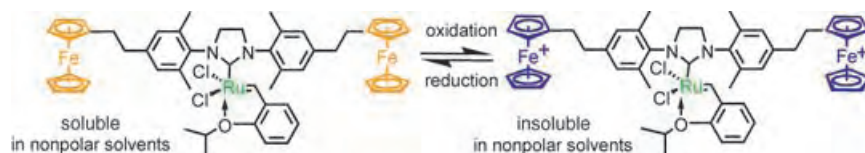
Microporous Germanates

Z.-E. Lin, J. Zhang, J.-T. Zhao, S.-T. Zheng,
C.-Y. Pan, G.-M. Wang,
G.-Y. Yang* _____ **6881 – 6884**

A Germanate Framework Containing
24-Ring Channels, Ni–Ge Bonds, and
Chiral $[\text{Ni}@\text{Ge}_{14}\text{O}_{24}(\text{OH})_3]$ Cluster Motifs
Transferred from Chiral Metal Complexes



Microporous: Chiral metal complexes as templates under solvothermal conditions resulted in two novel germanates $\text{Ni}@\text{Ge}_{14}\text{O}_{24}(\text{OH})_3 \cdot 2\text{Ni}(\text{L})_3$ ($\text{L} = \text{ethylene-diamine}$, $1,2\text{-diaminopropane}$). The chiral $\text{Ni}@\text{Ge}_{14}\text{O}_{24}(\text{OH})_3$ cluster motifs have an unprecedented trigonal-bipyramidal $\text{Ni}@\text{Ge}_5$ core with Ni–Ge bonds and are linked to each other to form a 3D germanate framework containing 24-ring channels (see picture).



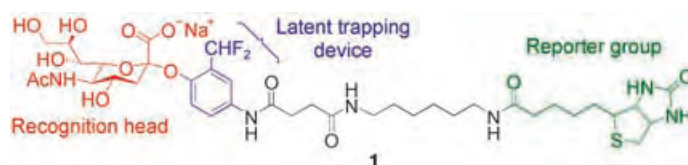
A homogeneous catalytic complex is tagged with two ferrocenyl groups to control its solubility properties by reversible switching between its neutral and dicationic states (see scheme). This approach is carried out on an olefin-

metathesis catalyst and is shown to effectively switch its catalytic activity on and off; furthermore, efficient separation of the catalyst from the reaction products and subsequent recycling of the catalyst is possible.

Homogeneous Catalysis

M. Süßner, H. Plenio* — 6885 – 6888

Redox-Switchable Phase Tags for Recycling of Homogeneous Catalysts



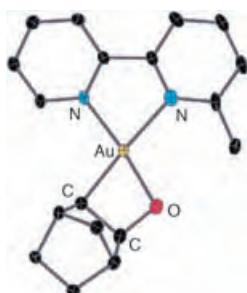
Getting a grip on the flu: A mechanism-based probe, **1**, for neuraminidase was developed. It is capable of forming a biotinylated adduct with neuraminidase (NA) from *Arthrobacter ureafaciens*. It also

displays an inhibitory effect on a number of NA activities. ELISA experiments successfully demonstrated that influenza viruses can be selectively captured with this probe.

Activity Probes

C.-P. Lu, C.-T. Ren, Y.-N. Lai, S.-H. Wu,*
W.-M. Wang, J.-Y. Chen,
L.-C. Lo* — 6888 – 6892

Design of a Mechanism-Based Probe for Neuraminidase To Capture Influenza Viruses



An auroxetane, obtained from the reaction of norbornene with a gold(III) oxo complex, has been isolated and fully characterized (see structure). Action of the olefin leads to elimination of the epoxide from the auroxetane.

Gold Chemistry

M. A. Cinellu,* G. Minghetti, F. Cocco,
S. Stoccoro, A. Zucca,
M. Manassero — 6892 – 6895

Reactions of Gold(III) Oxo Complexes with Cyclic Alkenes



The isolation and intramolecular cyclization of (S)-(1-alkynyl)isothiuronium and (S)-(1-alkynyl)thiobenzimidonium salts suggest the mechanism for the one-pot synthesis of 2,4-disubstituted thiazoles

(see scheme; Ms = methanesulfonyl): Michael addition of sulfur nucleophiles to hypervalent iodanes followed by the 1,2-rearrangement of sulfonyl groups in the resulting alkylidene carbenes.

Hypervalent Iodine

K. Miyamoto, Y. Nishi,
M. Ochiai* — 6896 – 6899

Thiazole Synthesis by Cyclocondensation of 1-Alkynyl(phenyl)- λ^3 -iodanes with Thioureas and Thioamides

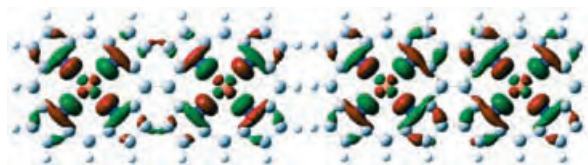
Metal Porphyrins

T. Ikeue, K. Furukawa, H. Hata, N. Aratani,
H. Shinokubo, T. Kato,*
A. Osuka* ————— 6899 – 6901

The Importance of a β – β Bond for Long-Range Antiferromagnetic Coupling in Directly Linked Copper(II) and Silver(II) Diporphyrins

Interaction over a distance: Long-range antiferromagnetic interactions between distant copper(II) and silver(II) ions are observed only for triply and singly linked diporphyrins with at least one β – β bond, which underscores the critical importance

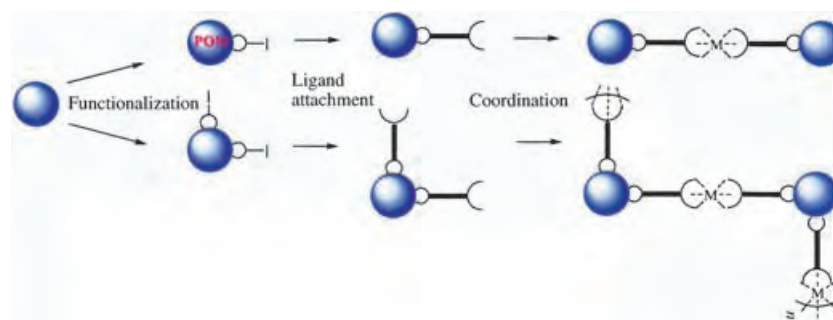
of this direct bond for antiferromagnetic coupling. These results can be qualitatively accounted for in terms of the spin distribution of copper(II) and silver(II) porphyrins (see picture).



Organic–Inorganic Hybrids

J. Kang, B. Xu, Z. Peng,* X. Zhu, Y. Wei,
D. R. Powell ————— 6902 – 6905

Molecular and Polymeric Hybrids Based on Covalently Linked Polyoxometalates and Transition-Metal Complexes



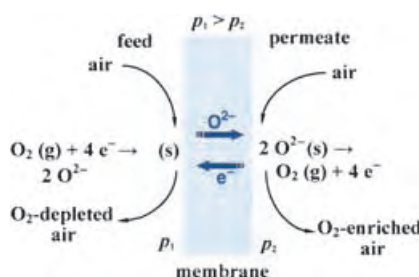
A rational building-block approach was employed to construct organometallic/polyoxometalate (POM) hybrids in which POM clusters and transition-metal complexes are linked by a π -conjugated bridge. The synthetic strategy for mole-

cular and polymeric hybrids—POM functionalization with iodo-bearing groups, attachment of a terpyridine-type ligand, and metal coordination—is shown schematically in the picture.

Membranes

H. Wang,* S. Werth, T. Schiestel,
J. Caro ————— 6906 – 6909

Perovskite Hollow-Fiber Membranes for the Production of Oxygen-Enriched Air

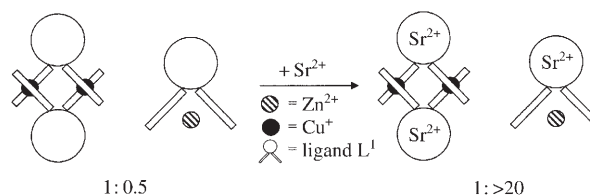


Mixed-ion and electron-conducting perovskite membranes are used to produce oxygen-enriched air (see picture). These membranes are thermally and mechanically stable at high temperatures ($> 875^\circ\text{C}$) over a long period of time, thus making them suitable for industrial processes. Oxygen concentrations of the enriched air typically reach 30–50 vol%.

Helicate Ligands

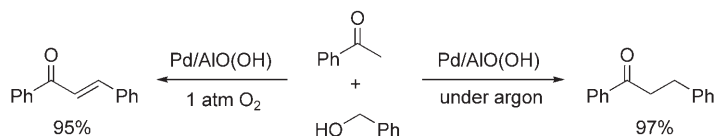
C. J. Baylies, T. Riis-Johannessen,
L. P. Harding, J. C. Jeffery, R. Moon,
C. R. Rice,* M. Whitehead — 6909 – 6912

Allosteric-Controlled Metal Specificity of a Ditopic Ligand



To twist or not to twist? A ditopic ligand, L^1 , that contains a potentially tetradentate pyridyl–thiazole ligand chain and a “external” crown ether unit is presented. Reaction of L^1 with Cu^+ or Zn^{2+} ions results in the formation of a dinuclear

double helicate $[\text{Cu}_2(\text{L}^1)_2]^{2+}$ or a mononuclear $[\text{ZnL}^1]^{2+}$ species. This ditopic system changes its preference for Cu^+ or Zn^{2+} ions on the inclusion of s-block-metal ions at the crown ether binding site (e.g., Sr^{2+} ions as shown in the scheme).



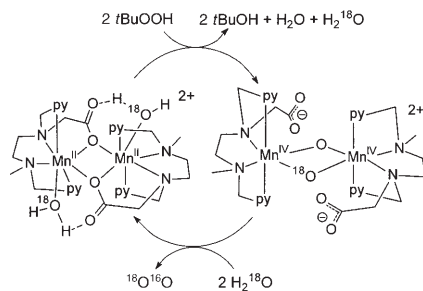
An air-stable, heterogeneous, and recyclable catalyst composed of palladium nanoparticles entrapped in aluminum hydroxide was applied to a highly selective α alkylation. A wide range of aliphatic and

aromatic ketones and primary alcohols were coupled to prepare enones in an O_2 atmosphere and ketones in an argon atmosphere (see scheme).

Synthetic Methods

M. S. Kwon, N. Kim, S. H. Seo, I. S. Park, R. K. Cheedra, J. Park* — 6913–6915

Recyclable Palladium Catalyst for Highly Selective α Alkylation of Ketones with Alcohols



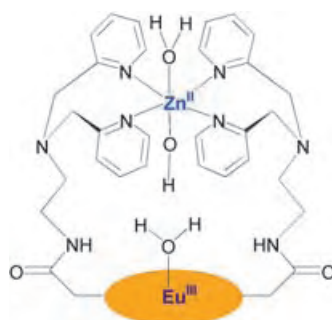
A highly specific and catalytic oxidation of water occurs when using a dinuclear Mn complex of a mononegative carboxylate-containing pentadentate ligand (see scheme). Isotope-labeling experiments coupled with membrane inlet mass spectrometry show that one oxygen atom in the evolved O_2 molecule is derived from water and the other from the oxidant.

Biomimetic Complexes

A. K. Poulsen, A. Rompel, C. J. McKenzie* — 6916–6920

Water Oxidation Catalyzed by a Dinuclear Mn Complex: A Functional Model for the Oxygen-Evolving Center of Photosystem II

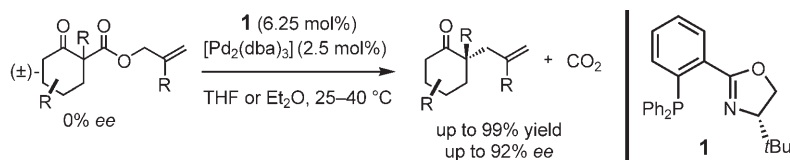
A europium complex capable of selectively binding zinc (see picture) has been developed as a new paramagnetic chemical exchange saturation transfer (PARACEST) imaging agent for use in magnetic resonance imaging (MRI). A hydroxide group on the bound Zn ion increases the rate of water exchange on the Eu ion.



Magnetic Resonance Imaging

R. Trokowski, J. Ren, F. K. Kálmán, A. D. Sherry* — 6920–6923

Selective Sensing of Zinc Ions with a PARACEST Contrast Agent



Stereochemical alchemy! Racemic allyl β -ketoesters allow the regiocontrolled formation of enolates, where the same catalyst is intimately involved in both the stereoablative (C–C bond-breaking) and

stereoselective (C–C bond-forming) steps. This mechanistic and practical insight led to the formation of multiple quaternary carbon stereocenters in a single cascade reaction (see scheme).

Asymmetric Catalysis

J. T. Mohr, D. C. Behenna, A. M. Harned, B. M. Stoltz* — 6924–6927

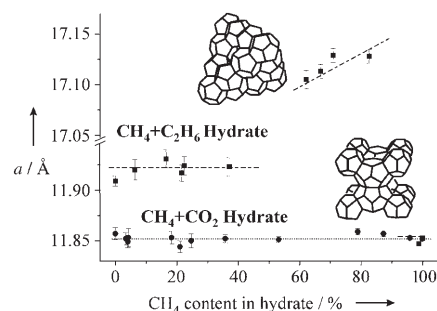
Deracemization of Quaternary Stereocenters by Pd-Catalyzed Enantioconvergent Decarboxylative Allylation of Racemic β -Ketoesters

Clathrate Hydrates

S. Takeya,* T. Uchida, Y. Kamata,
J. Nagao, M. Kida, H. Minami,
H. Sakagami, A. Hachikubo, N. Takahashi,
H. Shoji,* O. Khlystov, M. Grachev,
V. Soloviev ————— **6928–6931**

Lattice Expansion of Clathrate Hydrates of
Methane Mixtures and Natural Gas

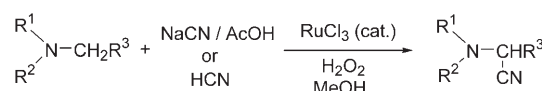
Structural transition from type I to type II is accompanied by a large increase in lattice constant a in $\text{CH}_4 + \text{C}_2\text{H}_6$ clathrate hydrates (see picture). In contrast, the lattice constants of $\text{CH}_4 + \text{CO}_2$ clathrate hydrates are independent of composition. Data for a natural gas hydrate from the sediments of Lake Baikal are also consistent with these trends.



Oxidative Cyanations

S.-I. Murahashi,* N. Komiya,
H. Terai ————— **6931–6933**

Ruthenium-Catalyzed Oxidative Cyanation
of Tertiary Amines with Hydrogen
Peroxide and Sodium Cyanide



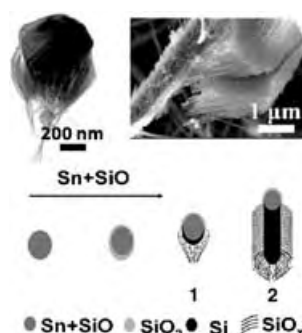
Versatile intermediates for the synthesis of *N*-aryl- α -amino acids and *N,N*-disubstituted 1,2-diamines can now be synthesized with high efficiency by the ruthenium-catalyzed oxidative cyanation of ter-

tiary amines. The use of hydrogen peroxide as an oxidant in the presence of NaCN/AcOH or HCN provides the corresponding α -aminonitriles (see reaction).

Hierarchical Nanostructures

H. Wang, X.-H. Zhang,* X.-M. Meng,
S.-M. Zhou, S.-K. Wu, W.-S. Shi,
S.-T. Lee* ————— **6934–6937**

Bulk Preparation of Si–SiO_x Hierarchical
Structures: High-Density Radially
Oriented Amorphous Silica Nanowires on
a Single-Crystal Silicon Nanocore

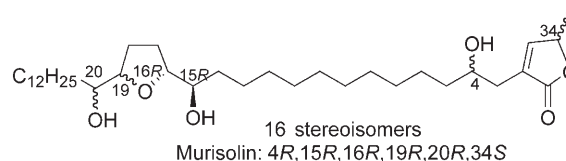


Promising building blocks: High-density radially-oriented amorphous silica nanowires standing on a single-crystal Si nanocore were synthesized by simple thermal evaporation of silicon with tin as catalyst. The growth process (see schematic picture) appears to involve concurrent vapor–liquid–solid and oxide-assisted growth mechanisms. Scanning electron micrographs corresponding to **1** and **2** are also shown.

Synthetic Methods

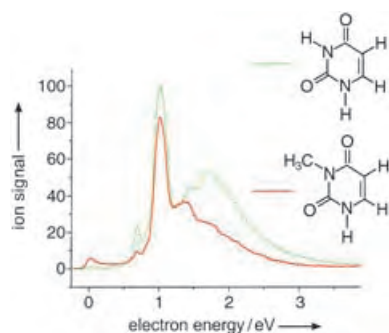
C. S. Wilcox,* V. Gudipati, H. Lu,
S. Turkyilmaz, D. P. Curran* ————— **6938–6940**

Solution-Phase Mixture Synthesis with
Double-Separation Tagging: Double
Demixing of a Single Mixture Provides a
Stereoisomer Library of 16 Individual
Murisolin



Two tags are better than one: Sixteen individual stereoisomers of murisolin (see scheme) are synthesized together and isolated in pure form with the aid of a double-separation tagging procedure. A

strategy for solution-phase stereoisomer synthesis based on double-separation tagging and double demixing is implemented with fluoroalkyl and oligoethylene glycol (OEG, $(\text{OCH}_2\text{CH}_2)_n\text{OCH}_3$) tags.



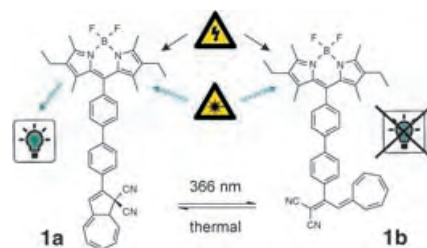
When excess charge is deposited on thymine and uracil by resonant attachment of low-energy electrons (0–3 eV), H atoms are cleaved exclusively from the N positions. This bond selectivity can be made site selective (N1 vs. N3 position) by properly tuning the electron energy. This conclusion was drawn from experiments with methylated thymine and uracil (see picture) in crossed beam experiments.

Gas-Phase Reactions

S. Ptasinska, S. Denifl, P. Scheier, E. Illenberger,* T. D. Märk — 6941 – 6943

Bond- and Site-Selective Loss of H Atoms from Nucleobases by Very-Low-Energy Electrons (< 3 eV)

Optical control of the photo- and electrochemiluminescence of a brightly fluorescent reporter group is possible by switching between the photochromic units of dyads **1a** and **1b**. Irradiation, that is, writing in information, with UV light converts the highly luminescent dihydroazulene **1a** into the weakly emissive vinylheptafulvene **1b**. Readout of the system can be performed by either electrochemically generated or photogenerated luminescence.

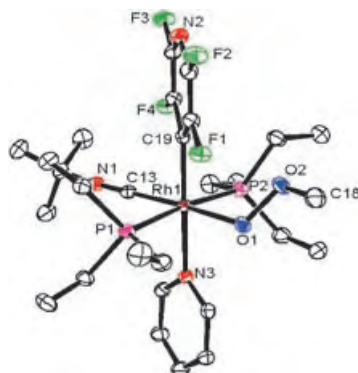


Optical Switches

C. Trieflinger, H. Röhr, K. Rurack,* J. Daub* — 6943 – 6947

Multiple Switching and Photogated Electrochemiluminescence Expressed by a Dihydroazulene/Boron Dipyrromethene Dyad

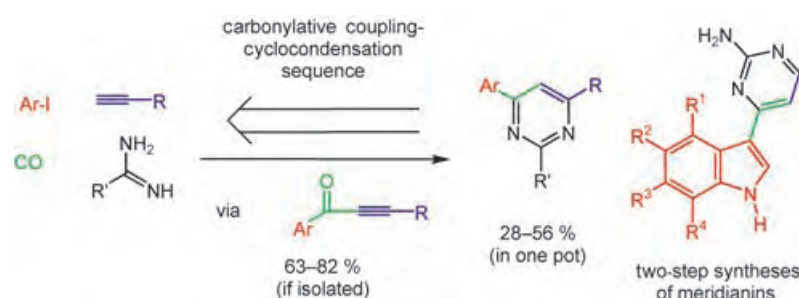
Out of thin air, a rhodium complex converts molecular oxygen into hydrogen peroxide, bis(trimethylsilyl) peroxide, and methyl hydroperoxide. Intermediate η^1 -hydroperoxy and η^1 -silylperoxy, and η^1 -methylperoxy complexes have been isolated. Another η^1 -methylperoxy (see picture) and an η^1 -hydroperoxy complex have been characterized by X-ray crystallography.



Peroxo Complexes

M. Ahijado, T. Braun,* D. Noveski, N. Kocher, B. Neumann, D. Stalke, H.-G. Stammler — 6947 – 6951

Rhodium-Mediated Formation of Peroxides from Dioxygen: Isolation of Hydroperoxy, Silylperoxy, and Methylperoxy Intermediates



In one go: (Hetero)aryl iodides, alkynes, carbon monoxide, and amidines can be assembled in a consecutive four-component reaction to give pyrimidines by a sequence of carbonylative alkylation

and cyclocondensation. Carbonylative alkylation also is the key step in the two-step syntheses of meridianins and meridianin derivatives.

Multicomponent Reactions

A. S. Karpov, E. Merkul, F. Rominger, T. J. J. Müller* — 6951 – 6956

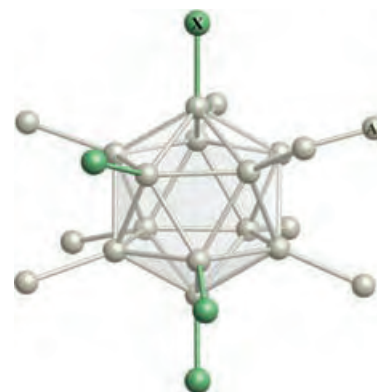
Concise Syntheses of Meridianins by Carbonylative Alkynylation and a Four-Component Pyrimidine Synthesis

Aluminum Clusters

J. Vollet, R. Burgert,
H. Schnöckel* _____ **6956 – 6960**

$\text{Al}_{20}\text{Cp}_8^*\text{X}_{10}$ ($\text{X} = \text{Cl}, \text{Br}$): Snapshots of the Formation of Metalloid Clusters from Polyhedral Al_nX_m Molecules?

Polyhedral Al halides: Four halogen atoms directly coordinated to an Al_{12} icosahedron in two structurally characterized Al_{20} clusters indicate the mechanism of formation of $\text{Al}_{22}\text{X}_{20}$ subhalides. No Al atom is located in the center of the icosahedron in either of these icosahedral compounds!



Sources

Product and Company Directory

You can start the entry for your company in "Sources" in any issue of *Angewandte Chemie*.

If you would like more information, please do not hesitate to contact us.

Wiley-VCH Verlag – Advertising Department

Tel.: 0 62 01 - 60 65 65

Fax: 0 62 01 - 60 65 50

E-Mail: MSchulz@wiley-vch.de

Service

Keywords _____ **6962**

Authors _____ **6963**

Angewandte's Sister Journals _____ **6964**

Preview _____ **6965**



Fast, Individual, Popular...
REPRINTS
Available to order anytime!
Contact Carmen Leitner (e-mail: cleitner@wiley-vch.de)



The Diverse World of Silicon Chemistry**

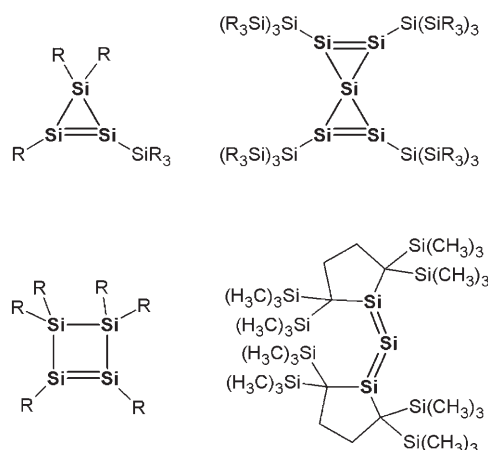
Guido KICKELBICK*

Besides carbon, the only other element that reveals a similarly rich chemistry is silicon, spanning classical main-group to organometallic to materials chemistry, biochemistry and biotechnology, as well as theoretical chemistry. Although both elements have many properties in common, silicon often reveals a remarkably different reactivity compared to carbon. The extraordinary properties of silicon and the large variety of products that can be prepared given its similarity to carbon make it not only a prominent element in academic research but also in industry, where its value has been recognized, for example, in polymers and as a semiconductor material.

The particular reactivity of silicon and its highly innovative chemistry are also reflected by the fact that a conference series celebrated its 40 year tradition, namely, the 14th International Symposium on Organosilicon Chemistry. Hundreds of scientists gathered in Würzburg (Germany) to discuss ground-breaking news in the field of silicon chemistry. For the first time, this meeting was held in conjunction with the European Organosilicon Days. The exceptional characteristic of this meeting series was the close contact between scientists from both academia and

industry as well as the variety of research from both areas, as evident from the composition of the lecture program which covered all of the above-mentioned aspects of silicon chemistry. The scientific program included more than 150 talks and over 220 posters.

Silicon chemistry still is mainly driven by the interest to compare the similarities and differences in its reactivity relative to that of carbon. A major challenge is the synthesis of Si–Si multiple bonds. A pioneer in this area is Mitsuo Kira (Tohoku University, Sendai, Japan), who presented an overview of the latest developments in the field of dialkylsilylenes and Si=Si double-bonded compounds, such as spiropentasiladiene and trisilaallene (Scheme 1). Kira and co-workers suc-



Scheme 1. Some extraordinary Si compounds produced by Kira's group.^[1]

ceeded in isolating stable disilene in the form of the silicon analogues of cyclopropene and cyclobutene.^[1] Further highlights from Kira's laboratory were the first stable compound with a formal sp²-hybridized silicon atom, cross-conjugated Si=C compounds, and 1,3-disilabicyclo[1,1,0]butane as the first isomer with an inverted bridged Si–Si bond. In honor of his pioneering work in this field, Kira was awarded the 2005 Wacker Silicon Award in Würzburg.

Research in the field of silicon-containing polymers is currently fuelled by an interest in controlling their composition and morphology as well as the patterning of materials by using macromolecules. Ian Manners (University of

Toronto, Canada) revealed the many possible applications of polyferrocenylsilanes. These metal-containing polymers that are produced by ring-opening polymerization reveal a controllable structure, which facilitates the control over their self-organization. The resultant supramolecular metal-containing structures can be used, for example, as magnetic materials. Application of UV photolithography allows the use of polyferrocenylsilanes for the patterning of thin films, which can be additionally metalated by binding cobalt carbonyl compounds.^[2,3] Catalytic cross-dehydrocoupling reactions of silanols and silanes represent a route to novel siloxane-based polymers. Yusuke Kawakami (Japan Advanced Institute of Science and Technology, Nomi, Japan) and co-workers have used tris(pentafluorophenyl)borane as an effective catalyst for the synthesis of such polymers.^[4] Patterning of silicon-based materials is regularly carried out by applying the self-organization of amphiphilic macromolecules. Ulrich Wiesner (Cornell University, Ithaca, USA) and his team make use of the organization of amphiphilic block copolymers in complex three-dimensional structures as templates to perform chemistry in the formed domains. By application of this method, it is possible to produce three-dimensional silica-based structures as well as SiCN- and SiC-based systems, which can be viewed as the reproduction of the previously formed structures.^[5,6]

Nicola Hüsing (University of Ulm, Germany) demonstrated new possibilities of the structuring of sol–gel-based materials using tetrakis(2-hydroxyethyl)silane as precursor, which releases glycol instead of an alcohol during hydrolysis and condensation.^[7] The use of a drying process, which leads to a more-hydrophobic surface, helps to produce highly porous monoliths.^[8] Besides pure oxidic materials, organically modified silsesquioxanes have become an important topic of research in recent years. Speculations that were often reasons for scientific discussion about the structure of ladder-type silsesquioxanes produced by the sol–gel process of

[*] Dr. G. Kickelbick
Vienna University of Technology
Institute of Materials Chemistry
Getreidemarkt 9-165
A1060 Vienna (Austria)
E-mail: kickelgu@mail.zserv.tuwien.ac.at

[**] 14th International Symposium on Organosilicon Chemistry (ISOS XIV) in conjunction with the 3rd European Organosilicon Day in Würzburg (Germany), 31st July to 5th August, 2005.

trialkoxysilanes were seen in a new light by Masumui Unno (Gunma University, Kiryu, Japan) and co-workers. They succeeded in the synthesis of oligomeric silsesquioxanes with control over the stereochemistry.^[9] Besides ladder-type structures, cage-type silsesquioxane are used as precursors for nanocomposites in materials chemistry. For example, Gion Calzaferri (University of Bern, Switzerland) and his co-workers have used $R-H_7Si_8O_{12}$ to close channels of dye-carrying zeolites and created new photonic devices by this technique.^[10] The corners of cage-like silsesquioxanes and spherosilicates can be functionalized through various methods by organic groups. Such molecular building blocks are used by Richard Laine (University of Michigan, Ann Arbor, USA) and his group to form three-dimensional nanocomposites.^[11]

The controlled formation of nanoparticles is also an important topic in the field of silicon chemistry. Application of novel types of surfactant molecules that contain a citrate head group allowed Michael Brook (McMaster University, Hamilton, Canada) and co-workers to prepare and stabilize silver nanoparticles. Self-organization of the derived systems leads to chains and ellipsoidal rings, as well as structures of higher complexity, such as multilayer bands (Figure 1). Solvent-based methods to produce silicon nanoparticles and functionalize their surfaces in situ were presented by Susan Kauzlarich (University of California, Davis, USA).^[12,13] The particles thus obtained show a photoluminescence that is stable over long periods of time.

Graham Showell (Paradigm Therapeutics Ltd., Cambridge, GB) impressively convinced the audience that organosilicon-based medicinal chemistry can lead to the development of novel drugs. Often this development is based on the selection of proven compounds and the formation of derivatives that contain silicon atoms or silicon-containing groups. Sila substitution (C–Si exchange) in well-known drugs—the formation of so-called bioisosters—is one possibility to search for novel compounds that reveal advantageous biological properties, such as improved pharmacodynamic profiles. Furthermore, this approach can be used to get

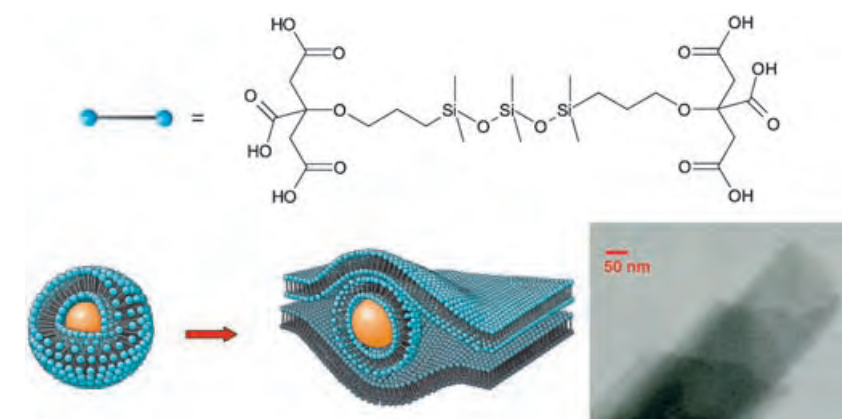


Figure 1. Novel surfactant molecules for the production of silver nanoparticles and their supramolecular arrangements, as presented by Brook.

around existing patents and help to minimize costs in pharmaceutical research. Some fundamental differences in the reactivity of silicon compared to that of carbon can also lead to changes in the biological properties of the silicon-containing analogues, and the advantageous differences are exploited in the design of novel pharmaceuticals.^[14]

Iain MacKinnon (Dow Corning Ltd., Barry, GB) presented to the predominantly academic audience the many industrial applications of functionalized polysiloxanes. He showed industrial solutions for the large-scale production of *N*-functionalized polysiloxanes, which are used in everyday products such as shampoos, shoe polish, or conditioners. The introduction of organic functional groups to avoid the yellowing of the *N*-functionalized polysiloxanes was one of the many examples discussed.

The functionalization of silicon surfaces is an important aspect in many

applications as well as being of fundamental chemical interest. Jillian Buriak (University of Alberta, Edmonton, Canada) revealed a selection of chemical reactions at surfaces that differ fundamentally from the molecular chemistry of silicon compounds. One of the methods her group has used is electrografting, which has allowed the covalent attachment of alkynes to H-terminated silicon surfaces by conducting-probe atomic force microscopy (CP-AFM). This method allowed the production of structures with dimensions of less than 30 nm (Figure 2).^[15]

Manfred Sumper (University of Regensburg, Germany) introduced the audience to the world of biomineralization, where silicates and the biochemistry of silicon play an important role. The complex and sometimes spectacular shapes of diatoms are an interesting display of Nature. Analysis of the silicate cell walls reveal that they are formed by composites that contain zwitterionic proteins (silaffines) and long-

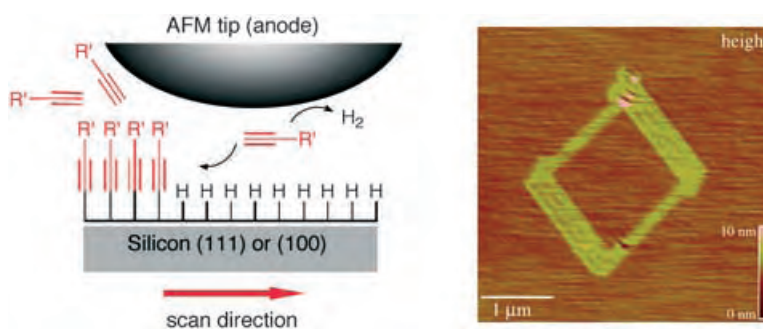


Figure 2. Application of CP-AFM makes it possible to connect molecules covalently on modified silicon surfaces and to form patterns. Adapted from Reference [15].

chain polyamines together with the inorganic phase. Quaternized ammonium groups seem to play a particular role in these systems.^[16] The complex mechanisms of their patterning can be explained by the self-organization processes of polyamines, which act as templates.

ISOS XIV showed how exciting and full of innovation the research into a single element can be, and we look forward again to see how this field develops until the next meeting.

- [1] M. Kira, *J. Organomet. Chem.* **2004**, 689, 4475.
- [2] A. Y. Cheng, S. B. Clendenning, G. Yang, Z.-H. Lu, C. M. Yip, I. Manners, *Chem. Commun.* **2004**, 780..

- [3] W. Y. Chan, S. B. Clendenning, A. Berenbaum, A. J. Lough, S. Aouba, H. E. Ruda, I. Manners, *J. Am. Chem. Soc.* **2005**, 127, 1765..
- [4] D. Zhou, Y. Kawakami, *Macromolecules* **2005**, 38, 6902.
- [5] A. C. Finnefrock, R. Ulrich, A. Du Chesne, C. C. Honeker, K. Schumacher, K. K. Unger, S. M. Gruner, U. Wiesner, *Angew. Chem.* **2001**, 113, 1247; *Angew. Chem. Int. Ed.* **2001**, 40, 1208.
- [6] M. Kamperman, C. B. W. Garcia, P. Du, H. Ow, U. Wiesner, *J. Am. Chem. Soc.* **2004**, 126, 14708.
- [7] D. Brandhuber, V. Torma, C. Raab, H. Peterlik, A. Kulak, N. Hüsing, *Chem. Mater.* **2005**, 17, 4262.
- [8] D. Brandhuber, H. Peterlik, N. Hüsing, *J. Mater. Chem.* **2005**, 15, 3896.
- [9] M. Unno, Y. Kawaguchi, Y. Kishimoto, H. Matsumoto, *J. Am. Chem. Soc.* **2005**, 127, 2256.

- [10] G. Calzaferri, S. Huber, H. Maas, C. Minkowski, *Angew. Chem.* **2003**, 115, 3860; *Angew. Chem. Int. Ed.* **2003**, 42, 3732.
- [11] R. M. Laine, *J. Mater. Chem.* **2005**, 15, 3725.
- [12] R. K. Baldwin, K. A. Pettigrew, E. Ratai, M. P. Augustine, S. M. Kauzlarich, *Chem. Commun.* **2002**, 1822.
- [13] J. Zou, R. K. Baldwin, K. A. Pettigrew, S. M. Kauzlarich, *Nano Lett.* **2004**, 4, 1181.
- [14] G. A. Showell, J. S. Mills, *Drug Discov. Today* **2003**, 8, 551.
- [15] P. T. Hurley, A. E. Ribbe, J. M. Buriak, *J. Am. Chem. Soc.* **2003**, 125, 11334.
- [16] S. Wenzl, R. Deutzmann, R. Hett, E. Hochmuth, M. Sumper, *Angew. Chem.* **2004**, 116, 6059; *Angew. Chem. Int. Ed.* **2004**, 43, 5933.

DOI: 10.1002/anie.200503350


WILEY InterScience®
 DISCOVER SOMETHING GREAT
 Access some of the finest full text journals, reference works, books, and databases from around the globe. It's just what you need to make some important discoveries of your own.



Manage your access easily with "MY PROFILE"

Simply register. Registration is fast and free to all internet users.

Easy Access

- Save Titles, Articles & Queries for quick access
- Set up roaming access to access content outside of your institutions network
- Get free online sample copies
- Get free online trial subscriptions
- View a complete list of your subscriptions and accessible products

Enhanced Tools

- Receive E-Mail Alerts when new content is available
- Purchase Article Select Tokens online
- Purchase individual articles online with Pay-Per-View


WILEY InterScience®
 DISCOVER SOMETHING GREAT
www.interscience.wiley.com

Charge Densities Come of Age

Philip Coppens*

Keywords:

charge-density analysis · chemical bonding · electron density · X-ray diffraction

In 1915, just three years after the discovery of X-ray diffraction by Von Laue, Peter Debye noted that “*the scattering from light atoms should get more attention, since along this way it should be possible to determine the arrangement of electrons in crystals*”.^[1] Debye’s statement preceded the development of quantum mechanics and Born’s definition of electron probability distribution, but correctly assumed that the electron distribution was an observable that had become accessible. Interestingly, it took the better part of a century for this vision to be realized and for X-ray charge-density analysis to become a true analytical technique that was capable of providing quantitative insight into controversial issues and sufficiently rapid to be applicable to a series of related problems. In 1990 we wrote, “At present, charge-density analysis is far from a routine technique”, pointing out the need for time-consuming collection of large data sets and the limitations in accuracy of the experimental measurements.^[2] These limitations have now to a large extent been overcome as a result of the development of more-intense X-ray sources, sensitive area detectors that allow rapid (and redundant) data collection, much improved cryogenic techniques, and last, but not least, the dramatic increase in computing power. As a result, not only has the accuracy improved but the analysis can be fast and precise, as demonstrated by Koritsanszky et al. in 1998 with the determination of accurate

experimental electronic properties of DL-proline monohydrate within 1 day.^[3] It illustrates the disappearance of time limitations, making the time required for experimental charge-density analysis comparable with that for theoretical calculations. Of course, the experiment yields the charge density for the molecule in the solid state rather than the isolated molecule or complex, thus incorporating in the case of molecular crystals the small but subtle effects of the molecular environment. It must also be kept in mind that the charge distribution and not the wave function is accessible, a crucial distinction, though recently wave functions derived from experiment have been obtained by constraining Hartree–Fock variational calculations to fit the experimental structure factor amplitudes.^[4] However, the theory of “atoms in molecules”, as pioneered by Richard Bader, which provides a quantitative link between the total electron density and the all-important physical properties of a molecule, bypasses the wave function in the analysis.^[5] Topological analysis of the total density has been exploited to obtain net atomic moments, including charges, and to infer the nature of chemical bonding directly from the electron-density distribution. The chemical bond analysis derives much of its power from the characteristics of the topological bond path between atoms, including the density (ρ) at the bond critical point (BCP) and the Laplacian of the electron density at the BCP and in other regions around the atoms. At the BCP, ρ is a minimum along the bond path but is a maximum along the perpendicular directions.

The results recently reported by Luger and co-workers on the bonding in a [1,1,1]propellane with its inverted

carbon atoms^[6] are a culmination of a series of careful studies of charge density on strained hydrocarbons^[7] and other small molecules^[8] from Luger’s laboratory. The work on the propellane addresses the important issue of the nature of this relatively short ($< 1.6 \text{ \AA}$) C–C interaction, which has been the subject of earlier theoretical^[9] and experimental^[10] studies. The analysis showed the presence of a bond path between the two inverted carbon atoms with a significant electron density at the BCP, corresponding to a bond order of 0.71, as derived with Bader’s empirical relationship, in very good agreement with theory. The agreement is less close for the value of the Laplacian ($\nabla^2\rho(r_{\text{BCP}})$) at the BCP, which is much more positive according to the experiment, and indicates a closed-shell rather than a shared interaction. To assess this discrepancy, it must be realized that the experimental Laplacian, being a second derivative, is quite sensitive to the functions used in both the experimental and theoretical analyses. To obtain precise experimental information on a second-derivative function such as the Laplacian, very high order X-ray data would be needed. These are weak or even absent as the X-ray scattering falls off with scattering angle as a result of interference and the effects of thermal motion. The experimental Laplacian may therefore be rather dependent on the functions used in the fitting of the experimental observations.^[11] Similarly, the theoretical Laplacian may vary with the nature of the basis set and its completeness. In this context it is relevant that the X-ray refinement on which the static density is based is performed with Slater-type functions, while Gaussian functions are used in the theoretical computation with which comparison is made. So the dis-

[*] Prof. P. Coppens
Department of Chemistry
State University of New York at Buffalo
Buffalo, New York, 14260-3000 (USA)
Fax: (+1) 716-645-6948
E-mail: coppens@buffalo.edu

agreement between the experimental and theoretical Laplacians in the bridgehead bonds may be less surprising than appears at first glance.

The results from Luger and co-workers may be compared with another unusual C–C interaction. Topological analysis of the experimental electron density of *syn*-1,6:8,13-biscarbonyl-[14]annulene (Figure 1),^[12] derived from high-resolution data at 19 K, shows a bond path between the two bridgehead carbon atoms across the central ring, as

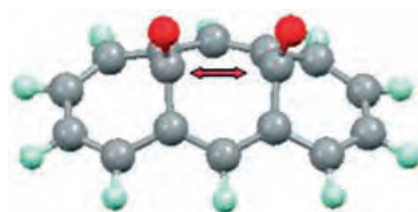


Figure 1. The *syn*-1,6:8,13-biscarbonyl-[14]annulene molecule.^[12] The bridgehead carbon atoms between which a bond path was found are indicated by the arrow.

indicated by the arrow in Figure 1, even though the C···C distance is much longer than that for the bridgehead bond in the [1.1.1]propellane (2.593 Å versus 1.579 Å). Also, $\rho(r_{\text{BCP}})$ is much smaller for the annulene (0.116(3) versus 1.31(3) e Å⁻³), whereas the Laplacian $\nabla^2\rho(r_{\text{BCP}})$ has a value of 1.53(1) e Å⁻⁵ for the annulene at the BCP compared to $\nabla^2\rho(r_{\text{BCP}}) = 10.3(1)$ e Å⁻⁵ for the [1.1.1]propellane. In the annulene, no BCPs were found along other transannular lines although the distances are shorter (by about 0.1 Å) than the distance between the bridgehead atoms. Such results demonstrate the need for additional criteria for judging the nature of atomic interactions. Several such criteria have been applied in particular to bonds involving heavier atoms, for which the radial shape of the atomic Laplacian makes this function less useful in characterizing the bonding interaction.^[13] In the classification proposed initially by Cremer and Kraka,^[14] and extensively applied in later work,^[15] covalent interactions are characterized

by local excess of the negative potential-energy density $V(r)$, over the positive kinetic-energy density $G(r)$. Thus the total energy density, $H(r) = G(r) + V(r)$, will be negative at the BCP for covalent bonds. A second, most useful measure is the electron-localization function (ELF),^[16] which provides information on the pairing of electrons in the bonding region. This function can be obtained approximately from the experimental density^[17] by the use of a functional proposed by Kirshnitz.^[18] As the functional is approximate, the experimental ELF is often referred to as the “approximate ELF” (AELF). The AELF contains a number of undesirable artifacts, but its features are in broad agreement with the ELF.^[19] A third function that has been successfully used in the analysis of M–M bonding (M = metal) but can only be obtained from the pair density distribution is the delocalization index $\delta(A,B)$ of Bader and Stephens,^[20] which corresponds to the number of electron pairs delocalized between atoms A and B. In a combined experimental/theoretical analysis of the M–M bonding in $[\text{FeCo}(\text{CO})_8]^-$, Macchi et al. compared the various criteria upon the (hypothetical) fluxional rearrangement of the CO coordination from terminal to bridging.^[21] For the Fe–Co bond, $\delta(\text{Fe},\text{Co})$ varies smoothly along the fluxional rearrangement path, even though the topological bond path disappears somewhere along the transition from the terminal to the ligand-supported conformation, which suggests the shortcomings of a sole reliance on the bond path criterion. When the M–M BCP is present, the energy density is small but nevertheless negative.

Clearly, although much progress has been made in recent years, the characterization of the chemical bond is not a closed subject. Experimental studies of unusual bonds, as presented in the recent report by Luger and co-workers, demonstrate how new light can be shed on longstanding issues in chemical bonding.

Published online: September 27, 2005

- [1] P. Debye, *Ann. Phys.* **1915**, 46, 809–823.
- [2] P. Coppens, D. Feil, *NATO ASI Ser. Ser. B* **1991**, 250, 7–22.
- [3] T. Koritsanzsky, R. Flaig, D. Zobel, H.-G. Krane, W. Morgenroth, P. Luger, *Science* **1998**, 279, 356–358.
- [4] D. J. Grimwood, I. Bytheway, D. Jayatilaka, *J. Comput. Chem.* **2003**, 24, 470–483; I. Bytheway, D. J. Grimwood, B. N. Figgis, G. S. Chandler, D. Jayatilaka, *Acta Crystallogr. Sect. A* **2002**, 58, 244–251; D. J. Grimwood, D. Jayatilaka, *Acta Crystallogr. Sect. A* **2001**, 57, 87–100; D. Jayatilaka, D. J. Grimwood, *Acta Crystallogr. Sect. A* **2001**, 57, 76–86.
- [5] R. F. W. Bader, *Atoms in Molecules: A Quantum Theory*, Clarendon, Oxford, **1990**.
- [6] M. Messerschmidt, S. Scheins, L. Grubert, M. Pätz, G. Szeimies, C. Paulmann, P. Luger, *Angew. Chem.* **2005**, 117, 3993–3997; *Angew. Chem. Int. Ed.* **2005**, 44, 3925–3928.
- [7] For example, see: T. Koritsanzsky, J. Buschmann, P. Luger, *J. Phys. Chem.* **1996**, 100, 10547–10553.
- [8] For example, see: P. Luger, M. Messerschmidt, S. Scheins, A. Wagner, *Acta Crystallogr. Sect. A* **2004**, 60, 390–396.
- [9] K. B. Wiberg, R. F. W. Bader, C. D. H. Lau, *J. Am. Chem. Soc.* **1987**, 109, 985–1001.
- [10] M. D. Levin, P. Kaszynski, J. Michl, *Chem. Rev.* **2000**, 100, 169–234, and Table 2 on p. 176 therein.
- [11] P. Coppens, *X-ray Charge Densities and Chemical Bonding*, Oxford University Press, New York, **1997**.
- [12] R. Destro, F. Merati, *Acta Crystallogr. Sect. B* **1995**, 51, 559–570.
- [13] P. Macchi, D. M. Proserpio, A. Sironi, *J. Am. Chem. Soc.* **1998**, 120, 13429–13435.
- [14] D. Cremer, E. Kraka, *Angew. Chem.* **1984**, 96, 612–614; *Angew. Chem. Int. Ed. Engl.* **1984**, 23, 627–628.
- [15] For example, see: G. Frenking, N. Fröhlich, *Chem. Rev.* **2000**, 100, 717–774.
- [16] A. D. Becke, K. E. Edgecombe, *J. Chem. Phys.* **1990**, 92, 5397.
- [17] V. Tsirelson, A. Stash, *Chem. Phys. Lett.* **2002**, 351, 142–148.
- [18] D. A. Kirshnitz, *Sov. Phys. JETP* **1957**, 5, 64.
- [19] D. Jayatilaka, D. Grimwood, *Acta Crystallogr. Sect. A* **2004**, 60, 111–119.
- [20] R. F. W. Bader, M. E. Stephens, *J. Am. Chem. Soc.* **1975**, 97, 7391–7399.
- [21] P. Macchi, L. Garlaschelli, A. Sironi, *J. Am. Chem. Soc.* **2002**, 124, 14173–14184.

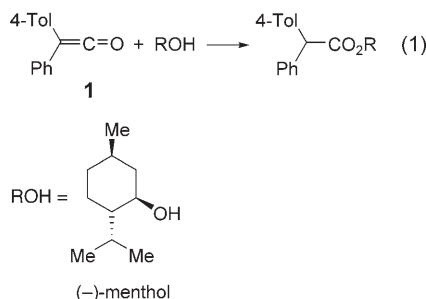
Catalytic Asymmetric Esterification of Ketenes**

Thomas T. Tidwell*

Keywords:

asymmetric catalysis · enol esters · homogeneous catalysis · ketenes

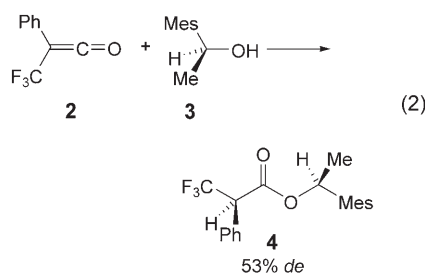
Ester formation by addition of alcohols to ketenes was discovered 100 years ago, when Hermann Staudinger prepared diphenylketene as the first isolated member of this versatile and reactive family, and by reaction with ethanol formed the ethyl ester of diphenylacetic acid.^[1a] As soon as unsymmetrical disubstituted ketenes were prepared it became apparent that esterification of these ketenes by alcohols generates a new chiral center, and by 1919 an attempt was made by Weiss to achieve asymmetric synthesis in this reaction, by the addition of the optically active alcohol (–)-menthol to phenyl(4-tolyl)-ketene (**1**) [Eq. (1)].^[1b] This report at-



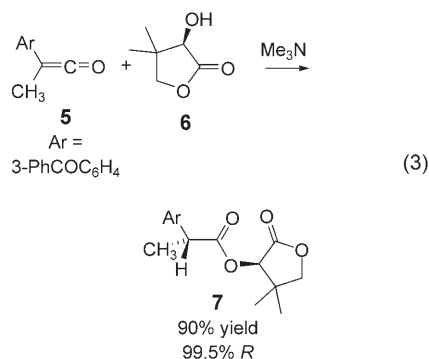
tracted considerable attention at the time and was initially accepted, but upon reexamination it was agreed there was no selectivity in the formation of the new stereocenter.^[1c–e] This was an un-

suitable substrate and an improbable outcome, as the only difference between the two aryl groups is the 4-methyl substituent in one aryl ring, which would have an imperceptible effect on proton transfer forming the new chiral center. However, the goal of achieving stereoselectivity in ketene esterification has been a major challenge for synthetic chemistry ever since, especially in view of the prominent bioactivity of many 2-arylalkanoic acids that are potentially available by this reaction.

The search for stereoselectivity using this methodology received new impetus with a prominent report of the reaction of phenyl(trifluoromethyl)-ketene (**2**) with several chiral alcohols including **3** (Mes = 2,4,6-trimethylphenyl) which formed **4** with significant 53 % stereoselectivity, and showed the way to reach the goal envisaged by Weiss [Eq. (2)].^[2]

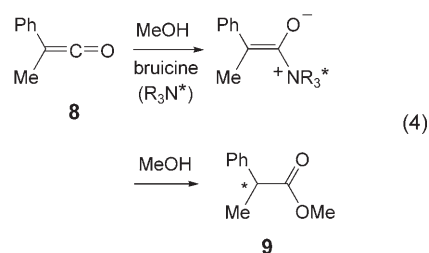


This path for asymmetric synthesis by ketene esterification using chiral alcohols was pursued at the Merck laboratories, where the addition of the chiral alcohol (*R*)-pantolactone (**6**) to ketene **5** was found to give 2-arylpropionate **7** with 99.5 % diastereoselectivity [Eq. (3)].^[3a] The origins of the selectivity in this reaction have been elucidated by computational means using (*S*) methyl lactate as a model.^[3b] Many variations



on this reaction have been reported, including the use of a polymer-bound analogue of pantolactone.^[3]

The use of chiral catalysts to induce stereoselectivity in ketene esterification offers an attractive alternative to the use of stoichiometric chiral alcohols to achieve this result, and a major achievement in this quest came in 1960 when the brucine-catalyzed stereoselective addition of methanol to phenyl(methyl)ketene (**8**) forming the ester **9** was reported by Pracejus [Eq. (4)].^[4a]

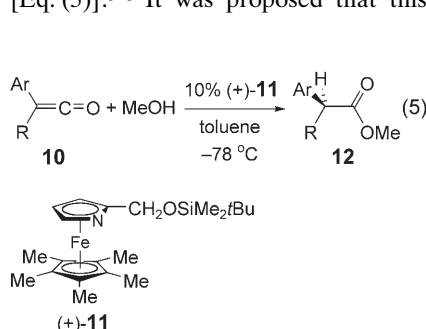


The selectivity was temperature dependent, ranging from 25 % *ee* for the *S* ester at –110 °C to 10 % *ee* for the *R* ester at 80 °C.^[4a] This was improved to 76 % *ee* for the *S* ester when benzoylquinine was used at –110 °C.^[4b,c] This discovery invited further improvements in the enantioselectivity using new catalysts,^[4d–f] but it was a long wait before this was to take place.

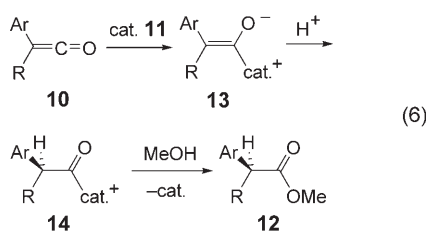
[*] Prof. T. T. Tidwell
Department of Chemistry
University of Toronto
Toronto, ON M5S 3H6 (Canada)
Fax: (+1) 416-978-3585
E-mail: ttidwell@chem.utoronto.ca

[**] Financial support by the Natural Sciences and Engineering Research Council of Canada is gratefully acknowledged

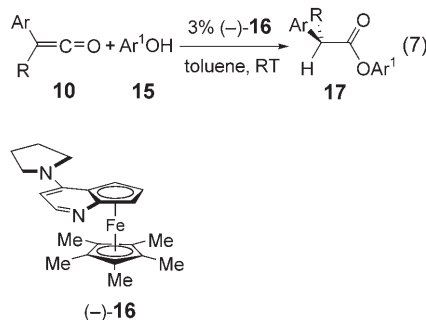
Then in 1999 Fu and co-workers introduced a designed catalyst to supplement the use of cinchona alkaloids for the catalytic asymmetric synthesis of esters from ketenes. They reported that addition of methanol to aryl(alkyl)-ketenes **10** catalyzed by the azaferrocene catalyst **11** in the presence of 2,6-di(*tert*-butyl)pyridinium triflate gave up to 80% *ee* in the formation of esters **12** [Eq. (5)].^[5a] It was proposed that this



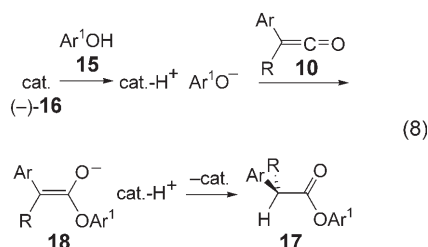
reaction took place by a catalytic cycle with nucleophilic attack of the catalyst on the ketene forming the enolate **13**, which was protonated by the pyridinium triflate to form **14** stereoselectively, and then methanol displaced the catalyst to give the ester **12** [Eq. (6)].^[5a]



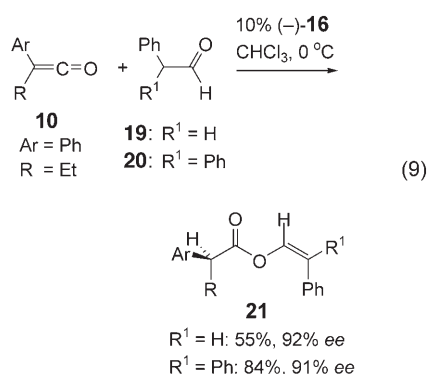
This procedure was further improved for the esterification of ketenes **10** by phenols **15** using the second-generation catalyst **16**. Aryl esters **17** were obtained with a selectivity of 35–91% *ee*, and the highest *ee* value was achieved with 2-*tert*-butylphenol [Eq. (7)].^[5b] Reactions of a variety of



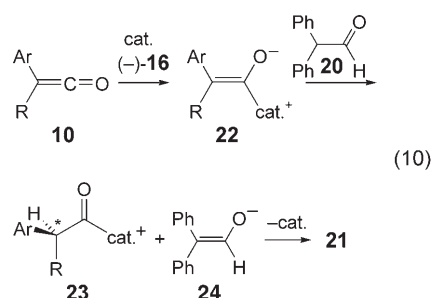
ketenes with this phenol gave *ee* values of 79–94% and yields of 66–97%. The mechanism proposed for this process is different than that for the addition of methanol and involves deprotonation of the phenol, followed by phenoxide attack on the ketene forming enolate **18**, and proton transfer from the resulting ion pair forming **17** [Eq. (8)].^[5b]



In a novel and unexpected extension of the search for catalyzed stereoselective esterification of ketenes, Schaefer and Fu have now discovered that alkyl(aryl)ketenes **10** react with the readily enolizable aldehydes **19** and **20** with catalysis by (–)-**16** to give stereoselective formation of enol esters **21** [Eq. (9)].^[5c] The reaction of phenyl-



(ethyl)ketene and diphenylacetaldehyde resulted in the formation of **21** in 84% yield and 91% *ee*. For other ke-



tenes the reaction was even more successful; the reaction of 2-tolyl(ethyl)ketene gave 99% yield and 98% *ee* (Table 1).^[5c]

Two possible mechanisms were proposed for this reaction, namely, initial addition of the catalyst to the ketene giving **22**, which stereoselectively abstracts a proton from the aldehyde giving **23**, which combines with the aldehyde enolate **24** [Eq. (10)]. Alternatively, addition of **24** to the ketene gives **25**, which is converted to **21** by stereoselective proton transfer by the protonated catalyst [Eq. (11)].^[5c]

The use of diphenylacetaldehyde (**20**) is a shrewd choice for this reaction, as it exists in the enol form ($\text{p}K_a = 9.4$) to the extent of 10% in aqueous solution at 25°C .^[6] Interestingly this is the same $\text{p}K_a$ as for phenol and suggests that the mechanism of Equation (11), which resembles that of Equation (8) found for phenols, may be preferred.

There is precedent for the O-acylation of ketone enolates by ketenes,^[7a-c]

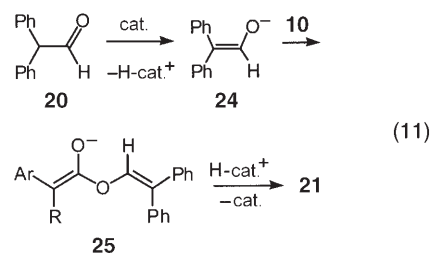
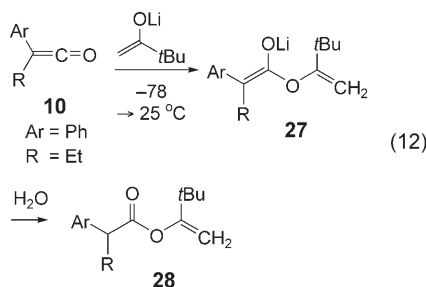


Table 1: Stereoselective formation of vinyl esters from ketenes **10** and diphenylacetaldehyde (**20**) [Eq. (9)].^[5c]

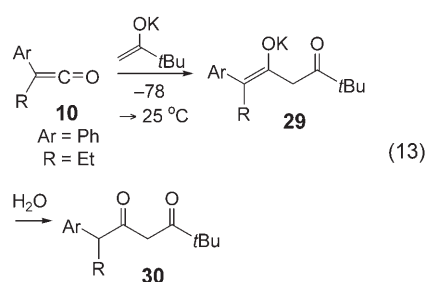
10				21			
Ar	R	Yield [%]	<i>ee</i> [%]	Ar	R	Yield [%]	<i>ee</i> [%]
Ph	Me	74	78	Ph	<i>t</i> Bu	96	88
Ph	Et	84	91	2-Tol	Et	99	98
Ph	<i>i</i> Bu	81	77	2-MeOC ₆ H ₄	Me	95	97
Ph	<i>i</i> Pr	95	98	4-MeOC ₆ H ₄	Et	89	92
Ph	<i>c</i> Pent	99	97	4-ClC ₆ H ₄	Et	96	88

including the involvement of ester enolates in the polymerization of dimethylketene.^[7a] Also the reaction of phenyl(ethyl)ketene with lithium pinacolate at -78°C followed by warming to 25°C and protonation with water gave the enol ester **28** in 57% yield, evidently through the intermediacy of the enolate **27** [Eq. (12)].^[7c] When the potassium



enolate was reacted similarly, the diketone **30** from acylation on carbon was the observed product, indicating the intermediacy of the enolate **29** [Eq. (13)].^[7c] Rearrangement of the initially formed enolates was also shown to occur.^[7c] Catalyst **16** is reported not to promote rearrangement of the enol esters **21** formed in Equation (9) to 1,3-dicarbonyl compounds.^[5c]

The unique features of the work by Schaefer and Fu suggest myriad possible extensions of their work. The enol esters derived from this reaction undergo fac-



ile hydrolysis to give chiral carboxylic acids, but this is wasteful of the interesting enol ester functionality contained in the molecule. Possibly stereoselective addition to the carbon-carbon double bond of the esters generating useful new functionality could be achieved. Other easily enolized carbonyl functions such as 1,3-dicarbonyl compounds or fluorinated ketones may be susceptible to this methodology. Further progress in this area can be expected.

Published online: September 14, 2005

- [1] a) H. Staudinger, *Ber. Dtsch. Chem. Ges.* **1905**, 38, 1735–1739; b) R. Weiss, *Monatsh. Chem.* **1919**, 40, 391–402; c) A. McKenzie, E. W. Christie, *J. Chem. Soc.* **1934**, 1070–1075; d) J. D. Morrison, H. S. Mosher, *Asymmetric Organic Reactions*, Prentice Hall, New York, **1971**, pp. 276–281, 295, 322, 326; e) For a historical summary of the beginnings of ketene chemistry see T. T. Tidwell, *Angew.*

Chem. **2005**, 117, 5926–5933; *Angew. Chem. Int. Ed.* **2005**, 44, 5778–5785.

- [2] E. Anders, E. Ruch, I. Ugi, *Angew. Chem.* **1973**, 85, 16–20; *Angew. Chem. Int. Ed. Engl.* **1973**, 12, 25–29.
- [3] a) R. D. Larsen, E. G. Corley, P. Davis, P. J. Reider, E. J. J. Grabowski, *J. Am. Chem. Soc.* **1989**, 111, 7650–7651; b) C. E. Cannizzaro, K. N. Houk, *J. Am. Chem. Soc.* **2004**, 126, 10992–11008; c) R. Akkari, M. Calmes, N. Mai, M. Rolland, J. Martinez, *J. Org. Chem.* **2001**, 66, 5859–5865.
- [4] a) H. Pracejus, *Justus Liebigs Ann. Chem.* **1960**, 634, 9–22; b) H. Pracejus, G. Kohl, *Justus Liebigs Ann. Chem.* **1969**, 722, 1–11; c) H. Pracejus, *Fortsch. Chem. Forsch.* **1967**, 8, 493–553; d) H. Buschmann, H.-D. Scharf, N. Hoffmann, P. Esser, *Angew. Chem.* **1991**, 103, 480–518; *Angew. Chem. Int. Ed. Engl.* **1991**, 30, 477–515; e) C. Fehr, *Angew. Chem.* **1996**, 108, 2726–2748; *Angew. Chem. Int. Ed. Engl.* **1996**, 35, 2566–2587; f) R. K. Orr, M. A. Calter, *Tetrahedron* **2003**, 59, 3545–3565.
- [5] a) B. L. Hodous, J. C. Ruble, G. C. Fu, *J. Am. Chem. Soc.* **1999**, 121, 2637–2638; b) S. L. Wiskur, G. C. Fu, *J. Am. Chem. Soc.* **2005**, 127, 6176–6177; c) C. Schaefer, G. C. Fu, *Angew. Chem.* **2005**, 117, 4682–4684; *Angew. Chem. Int. Ed.* **2005**, 44, 4606–4684.
- [6] Y. Chiang, A. J. Kresge, E. T. Krogh, *J. Am. Chem. Soc.* **1987**, 109, 2600–2607;
- [7] a) K. Yoshida, Y. Yamashita, *Tetrahedron Lett.* **1966**, 7, 693–696; b) H. O. House, R. A. Auerbach, M. Gall, N. P. Peet, *J. Org. Chem.* **1973**, 38, 514–522; c) L. Gong, R. Leung-Toung, T. T. Tidwell, *J. Org. Chem.* **1990**, 55, 3634–3639.

Supramolecular Approaches to Generate Libraries of Chelating Bidentate Ligands for Homogeneous Catalysis

Bernhard Breit*

Keywords:

homogeneous catalysis · chelating ligands · combinatorial chemistry · selectivity · self-assembly

The process of catalyst discovery and development relying on combinatorial methods has suffered so far from the difficult access to structurally diverse and large libraries of ligands, in particular the structurally more complex class of bidentate ligands. A completely new approach to streamline the difficult ligand synthesis process is to use structurally less complex monodentate ligands that self-assemble in the coordination sphere of a metal center through noncovalent attractive ligand–ligand interactions to generate bidentate, chelating ligands. When complementary attractive ligand–ligand interactions are employed, it is even possible to generate libraries of defined chelate–ligand catalysts by simply mixing two different monomeric ligands. This Minireview summarizes the first approaches and results in this new field of combinatorial homogeneous catalysis.

1. Introduction

The evolution of modern homogeneous catalysis is driven by the quest for higher efficiency and selectivity. While enzymes are highly substrate specific, their scope is limited. Synthetic catalysts are of particular interest because of their potential for a broader range of substrates. However, in both fields no general catalyst giving optimal results for all kinds of substrates is available. Hence, to achieve the desired selectivity for a catalytic reaction of interest, the catalyst must be optimized and adjusted to the particular problem. Especially in the field of metal-complex catalysis, the choice of the right ligand, which shapes the microenvironment at the catalytically active metal center, is crucial.

However, despite significant progress in the field of theoretical and computational chemistry, there is still no rational way to model from scratch the best ligand for a given reaction and selectivity problem. So far, finding the optimal ligand is an unpredictable high-risk endeavor, which is driven to a large extent by various combinations of intuition,

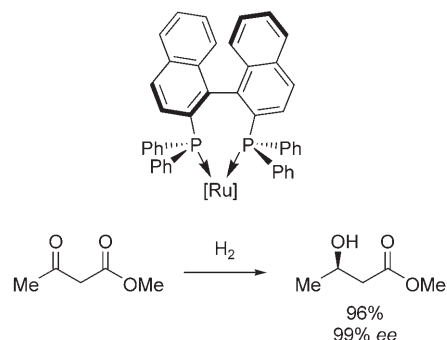
experience, hard labor, and in many cases serendipity. This is a long-standing problem and has, at least for asymmetric catalysis, a simple physicochemical origin. In 1983 Knowles noted:^[1] “Since achieving 95 % ee only involves energy differences of about 2 kcal, which is no more than the barrier encountered in a simple rotation of ethane, it is unlikely that before the fact one can predict what kind of ligand structures will be effective.”

Inspired by developments in the pharmaceutical industry to accelerate lead discovery and optimization, scientists have adapted methods of combinatorial chemistry to homogeneous (and heterogeneous) catalysis to speed up catalyst discovery and optimization.^[2] Many elegant solutions for high-throughput screening of catalyst libraries are available today which facilitate the testing of large catalyst libraries for optimal activity and selectivity.^[3] However, the full potential of the combinatorial approach for catalyst discovery has not been reached so far owing to the difficulty of accessing large and structurally diverse ligand libraries. This problem is particularly acute for the important class of bidentate ligands. Although monodentate ligands have gained increasing importance recently, a considerable number of catalytic reactions require a bidentate ligand for maximum selectivity. A prominent example for enantioselectivity control is the reduction of β -keto esters with ruthenium(II)–binap catalysts (Scheme 1 a).^[4] Another example is the control of regioselectivity for the industrially important rhodium-catalyzed hydroformylation of terminal alkenes, which requires tailor-made

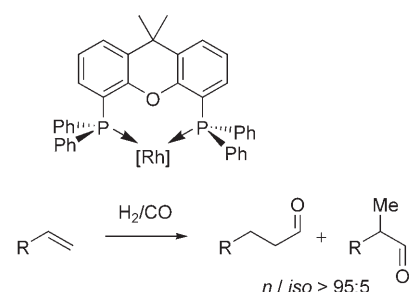
[*] Prof. Dr. B. Breit
Institut für Organische Chemie und Biochemie
Albert-Ludwigs-Universität Freiburg
Albertstrasse 21, 79104 Freiburg (Germany)
Fax: (+49) 761-203-8715
E-mail: bernhard.breit@organik.chemie.uni-freiburg.de

bidentate ligands.^[5] Among the few ligands known to achieve efficient regiocontrol is the xantphos system (Scheme 1 b).

a) Enantioselectivity: binap



b) Regioselectivity: xantphos



Scheme 1. Control of enantio- and regioselectivity with selected metal catalysts with bidentate ligands.

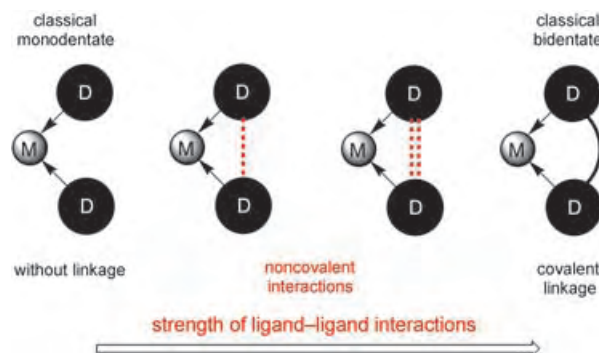
The problem in constructing ligand libraries is closely related to the number of synthetic steps required to synthesize a bidentate ligand. These steps are in many cases nontrivial synthetic operations that render the ligand synthesis unsuited for automation. A particular challenge is the synthesis of nonsymmetric bidentate ligands equipped with two different donor sites.^[6,7]



Bernhard Breit obtained his doctorate in 1993 under the direction of Prof. M. Regitz at the University of Kaiserslautern. After postdoctoral training with Prof. B. M. Trost at Stanford University, he worked in Marburg with Prof. R. W. Hoffmann to obtain his habilitation. In 1998/99 he was a Visiting Professor at Harvard University, and subsequently he was Professor of Organic Chemistry at the University of Heidelberg. Since April 2001 he has held a chair in Organic Chemistry at the University of Freiburg. His awards include the Steinhof award, the Heinz-Maier-Leibnitz award (DFG), the "Dozenten Award" of the Fonds der Chemischen Industrie, the Alfred Krupp award, and the Novartis European Young Investigator Award. His research interests focus on catalysis and organic synthesis.

2. Emulation of Chelation through Self-Assembly of Monodentate Ligands

Recently, attempts have been made to simplify access to bidentate ligands by a conceptually new approach: The basic idea is to use structurally less complex monodentate ligands, which imitate the situation of a bidentate ligand at the catalytically active metal center through a noncovalent connection between the two binding sites (Scheme 2). Nature provides a range of noncovalent interactions such as van der Waals interactions, π stacking, cation– π interactions, charge-transfer interactions, electrostatic interactions, hydrogen bonding, and coordinative interactions.^[8] Thus, on going from a metal complex having two truly monodentate ligands with no attractive interaction between them, to a metal complex with a bidentate ligand having two covalently connected binding sites, there is a continuum of arrangements consisting of two donor ligands and a metal center that emulate chelation through noncovalent attractive ligand–ligand interactions. A differentiation within this continuum may be made according to the strength and nature of the attractive ligand–ligand interaction (Scheme 2).^[8]



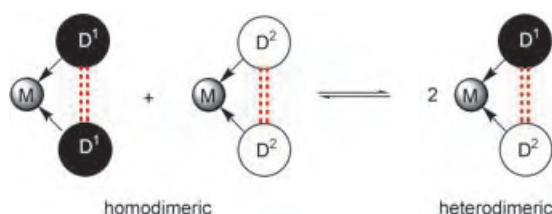
Scheme 2. Continuum of attractive ligand–ligand interactions in an MD_2 complex.

Beyond the benefit of a simplified ligand synthesis, the true potential of this approach now lies in the inherent possibility for the generation of combinatorial ligand libraries through simple ligand mixing. Thus, provided that two ligands are bound to one catalytically active metal center, one could obtain from a set of n different monodentate donor ligands a library of $(n^2 + n)/2$ ML^xL^y catalysts (Table 1).

If, however, the interaction between the two ligands bound to one metal center is *noncomplementary*, mixing the two different ligands will result in a mixture of the two homodimeric and the heterodimeric ligand metal complexes

Table 1: Ligand library generated by mixing n monodentate ligands L^x and L^y .

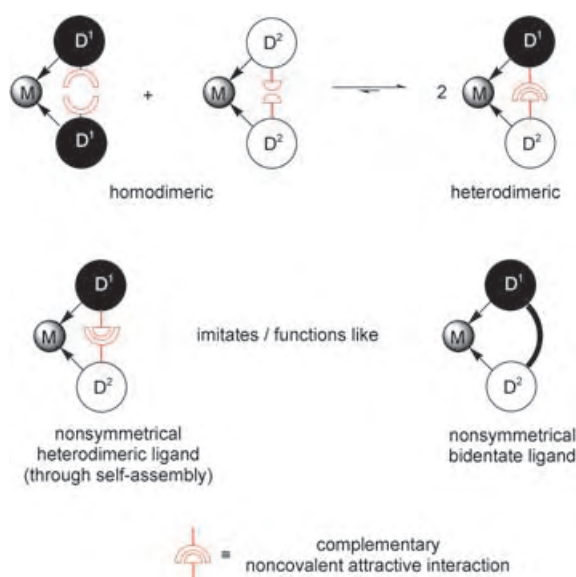
Ligand	L^1	L^2	...	L^n
L^1	L^1L^1			
L^2	L^1L^2	L^2L^2		
...	
L^n	L^1L^n	L^2L^n	...	L^nL^n



Scheme 3. Catalyst mixtures from mixing of two different ligands D^1 and D^2 and a metal source; noncomplementary D^1 - D^2 interactions are represented by dotted red lines.

almost irrespective of the nature and strength of the attractive ligand–ligand interaction (Scheme 3). In this scenario three potential catalysts are present simultaneously. Only in cases when the heterocombination is more reactive and at the same time more selective than the homodimer is optimization towards a better catalyst possible.

To facilitate the evaluation of structure–activity relations and optimization strategies, it would be desirable to have a situation in which ligand mixing generates the heterodimeric ligand metal complex exclusively. Thus, shifting the equilibrium to the desired heterodimeric species completely would require two different sets of monodentate ligands with *complementary* binding sites in order to generate attractive ligand–ligand interactions (Scheme 4).



Scheme 4. Defined heterodimeric catalysts from mixing and self-assembly of monodentate ligands with complementary binding sites in the presence of a metal source.

Hence, a heterodimeric ligand system formed by complementary self-assembly could imitate a classical nonsymmetrical ligand system (Scheme 4). Furthermore, mixing m ligands of set D^1 with n ligands of set D^2 in the presence of a metal species would generate a library of $m \times n$ defined heterodimeric bidentate ligand metal complexes (Table 2).

It is the aim of this review to summarize the first accomplishments in this new field of combinatorial catalysis

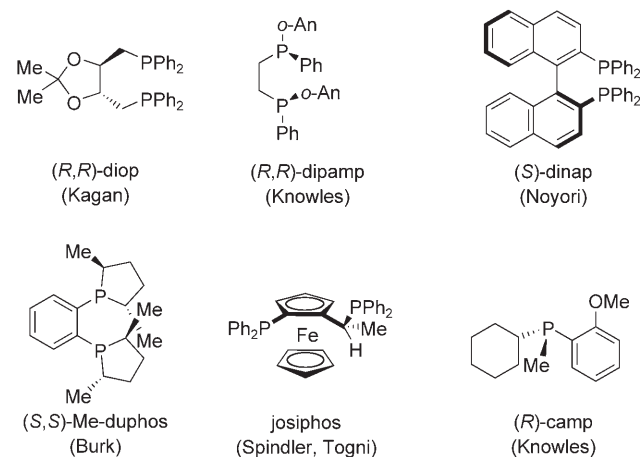
Table 2: Ligand library of $m \times n$ different and defined heterodimeric ligands generated through mixing two sets of monodentate ligands with complementary binding sites.

Ligand	m_1	m_2	...	m_i
n_1	$m_1 n_1$	$m_2 n_1$...	$m_i n_1$
n_2	$m_1 n_2$	$m_2 n_2$...	$m_i n_2$
...
n_j	$m_1 n_j$	$m_2 n_j$...	$m_i n_j$

with homogeneous metal complexes employing ligand libraries obtained through self-assembly.

3. Weak Ligand–Ligand Interactions: van der Waals, π Stacking, Dipole–Dipole Interactions

For almost three decades the field of homogeneous catalytic asymmetric hydrogenation has been dominated by chelating ligand systems such as diop,^[9] dipamp,^[10] binap,^[11] dufhos,^[12] and josiphos,^[13] which have been shown to furnish excellent asymmetric induction for a number of substrates.



Already in 1972 Knowles and co-workers reported on a rhodium catalyst modified with the monodentate phosphine camp to yield enantioselectivities up to 90% for the hydrogenation of precursors of *N*-acetyl phenylalanine.^[14] However, it was not before 2000 when the dominance of bidentate ligands was questioned independently by the research groups of Orpen and Pringle,^[15] Reetz,^[16] Feringa, Minnaard, and de Vries.^[17] Chiral monodentate phosphinites, phosphates, and phosphoramidites showed excellent levels of enantioselectivity for the asymmetric rhodium-catalyzed hydrogenation of a number of substrates. A quadrant model was proposed based on an X-ray structure platinum(II) complex with a binol-derived phosphonite ligand (Figure 1).^[15,16]

Interestingly, the two monodentate phosphorus ligands are *cis* coordinated at the platinum center, which is supposed to be a sterically less favorable arrangement than the alternative *trans* orientation. Hence, one may speculate that the preferred formation of the *cis* complex results from weak attractive ligand–ligand interactions based on van der Waals

interactions, π stacking, and/or dipole–dipole interactions of the P–O bond dipoles. As a consequence of the *cis* coordination mode, a conformational “locking” of the two monodentate ligands is achieved, thus mimicking the conformational properties of a bidentate ligand (Figure 1).

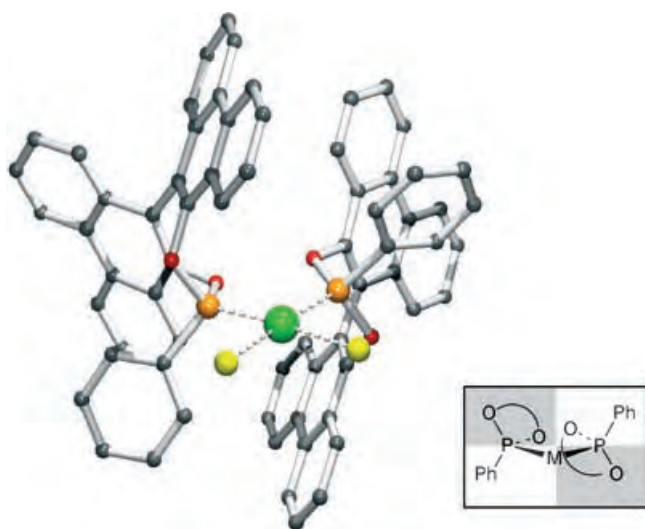


Figure 1. X-ray crystal structure of a *cis*-bisphosphonite platinum(II) complex and the proposed quadrant model. Pt green, Cl yellow, P orange, O red, C gray.

The full potential of this arrangement of two monodentate ligands mimicking a bidentate ligand was recognized and used soon afterwards by Reetz et al.^[19] Thus, high structural diversity is achieved by mixing two different monodentate ligands in the presence of a metal salt. In this scenario an equilibrium mixture of three different catalysts is formed, the two homocombinations ML^xL^x and ML^yL^y as well as the heterocombination ML^xL^y . Thus, if ML^xL^y is more reactive and more enantioselective, one could expect an increased reaction rate and higher enantioselectivity. In fact, ligand mixtures of phosphonites **1** and phosphites **2** furnished catalysts that operated with higher enantioselectivities than those of the corresponding homocombinations. A few selected results for the asymmetric hydrogenation of *N*-acylenamines are given in Table 3.^[19–21]

The same principle but with achiral ligands was applied recently to control regioselectivity in the rhodium-catalyzed hydroformylation of a methacrylate derivative (Table 4).^[22] Thus, a library of mixtures of 14 monodentate P-donor ligands was screened. While the homocombinations (Table 4, entries 1–4) gave only moderate regioselectivity, interestingly the best results were obtained with ligand mixtures. Among the many combinations tested, optimal regioselectivity in favor of the branched aldehyde **4** was achieved by combining triphenylphosphane (**6**) and the phosphinine **19** (Table 4, entry 5). The phosphabenzene **19** was introduced recently as an efficient modifying ligand for the rhodium-catalyzed hydroformylation of higher substituted alkenes.^[23]

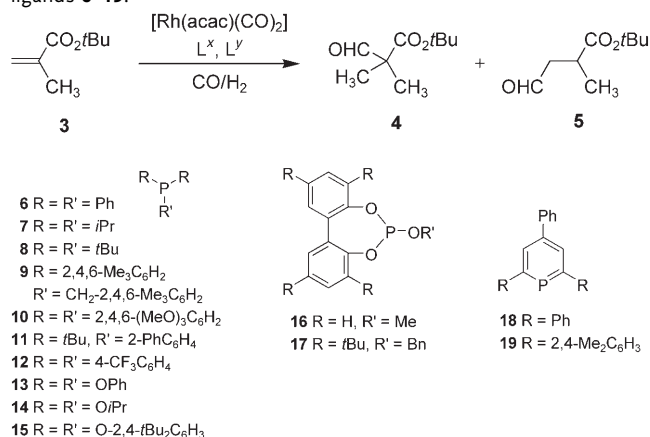
Almost simultaneously Feringa, Minnaard, et al. probed the same concept for mixtures of monodentate phosphor-

Table 3: Hydrogenation of *N*-acylenamines with mixtures of binol-derived phosphonites.^[a]

Entry	Ligand combination	Ar	Ligand		ee [%]
			Phosphonite	Phosphite	
			 1a R = Me 1b R = <i>t</i> Bu 1c R = Et	2a R = OMe 2b R = OBn	
1	(<i>R</i>)- 1a	Ph			75.6 (S)
2	(<i>R</i>)- 1b	Ph			13.2 (S)
3	(<i>R</i>)- 2a	Ph			76.0 ^[b]
4	(<i>R</i>)- 2b	Ph			90.4 ^[b]
5	(<i>R</i>)- 1a /(<i>R</i>)- 1b	Ph			96.1 (S)
6	(<i>R</i>)- 1a /(<i>R</i>)- 1b	2-naphthyl			97.0 (S)
7	(<i>R</i>)- 1b /(<i>R</i>)- 2a	Ph			95.0 ^[b]
8	(<i>R</i>)- 1b /(<i>R</i>)- 2b	Ph			97.4 ^[b]

[a] Rh/substrate = 1:250, 1.5 bar H₂, CH₂Cl₂, 22 h. [b] Configuration not reported.

Table 4: Regioselective hydroformylation of *tert*-butyl methacrylate (**3**) with rhodium catalysts derived from mixtures of monodentate P-donor ligands **6–19**.^[a]



[a] Rh/L^x/L^y/Substrate = 1:1.2:1.2:200, 60 bar CO/H₂ (1:1), CH₂Cl₂, 50 °C, 22 h. [b] Alkene hydrogenation.

amidites in the course of asymmetric hydrogenation^[24] and for rhodium-catalyzed conjugate addition of phenylboronic acid to enones.^[25] Although in the latter case the enantioselectivities are still moderate (< 77 %), again, ligand mixtures provided the best results (Table 5, entry 5).

Interestingly, in ³¹P NMR investigations of the catalyst mixtures, preferred formation of the heterodimeric catalyst

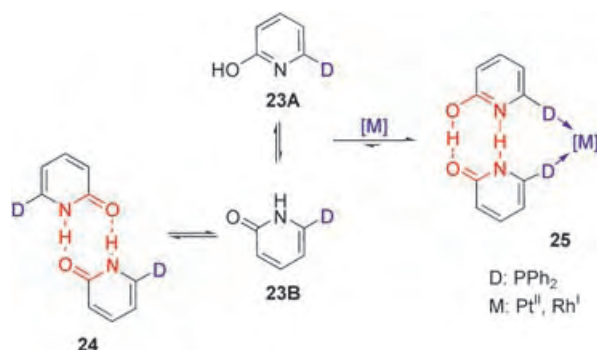
Table 5: Enantioselective conjugate addition of phenylboronic acid to cyclohexenone with rhodium catalysts derived from phosphoramidites **20–23**.

Entry	Ligand combination	Conv. [%]	ee [%]
1	20/20	26	33
2	21/21	22	≈ 27
3	22/22	18	≈ 16
4	20/21	93	75
5	20/22	40	77
6	21/22	16	≈ 60

was observed (up to 91 %).^[25] These significant deviations from the statistical 50:25:25 mixture, expected for the equilibrium mixture of the heterodimeric and the two homodimeric catalyst, have been explained by the complementary size and shape of the ligands. An additional explanation may invoke stronger attractive ligand–ligand interactions in the heterodimeric catalyst based on dipole–dipole, van der Waals, and π -stacking interactions. However, the complete shift of this equilibrium in favor of the exclusive formation of the heterodimeric catalyst could not be achieved so far.

4. Attractive Ligand–Ligand Interactions through Hydrogen Bonding

Recently, the in situ generation of bidentate ligands based on self-assembly through hydrogen bonding of monodentate ligands in the coordination sphere of a metal center was described.^[26] As a platform for hydrogen bonding, the



Scheme 5: Self-assembly of the 2-pyridone/2-hydroxypyridine system **23** through hydrogen bonding to generate complexes **25** for homogeneous catalysis.

tautomer system 2-pyridone (**23B**)/2-hydroxypyridine (**23A**) was employed. The parent system ($D=H$) is known to dimerize in aprotic solvents to form predominantly the symmetrical pyridone dimer **24** (Scheme 5).^[27,28] However, if D were a donor atom capable of binding to a metal center (e.g. PPh_2), the equilibrium could be shifted towards the mixed hydroxypyridine/pyridone dimer **25**.^[29] This intermediate may be stabilized by the chelation effect exhibited through coordinative binding to the metal center (Scheme 5).

In fact the reaction of 2 equiv of 6-diphenylphosphanyl-2-pyridone (6-DPPon, **23**, $D=PPh_2$) with $[PtCl_2(cod)]$ (cod = cycloocta-1,5-diene) furnished quantitatively *cis*- $[PtCl_2(23)_2]$, which showed the expected hydrogen-bonding network both in solution and in the solid state (Figure 2).^[26]

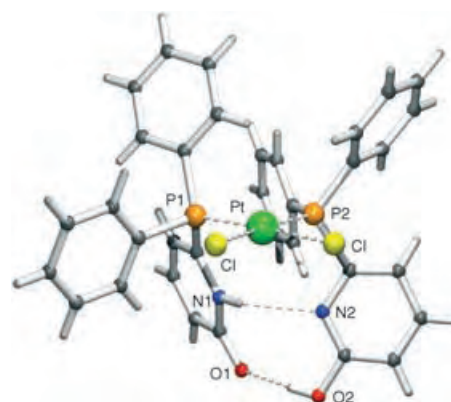


Figure 2: X-ray crystal structure of *cis*- $[PtCl_2(23)_2]$.

Table 6: Comparison of the regioselective hydroformylation of functionalized terminal alkenes with the Rh/**23** catalyst and with the standard industrial catalyst Rh/ PPh_3 .^[a]

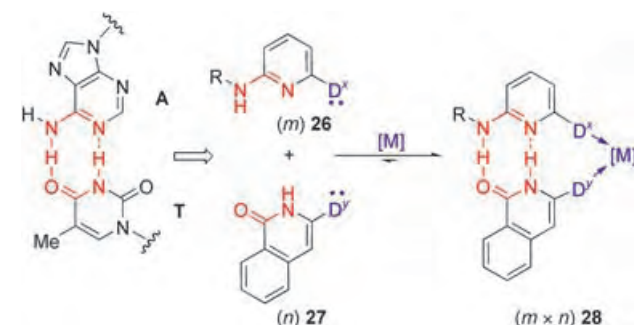
Entry	Substrate	<i>n</i> / <i>iso</i>	
		$L = \mathbf{23}$	$L = PPh_3$
1	Br-CH ₂ -(CH ₂) ₄ -CH=CH ₂	97:3	72:28
2	AcO-CH ₂ -(CH ₂) ₄ -CH=CH ₂	96:4	71:29
3	MeO ₂ C-CH ₂ -(CH ₂) ₄ -CH=CH ₂	97:3	74:26
4	Me-C(=O)-CH ₂ -(CH ₂) ₄ -CH=CH ₂	94:6	71:29
5	PhHN-C(=O)-O-CH ₂ -(CH ₂) ₄ -CH=CH ₂	96:4	69:31
6	Ph-OH-C(=O)-CH ₂ -(CH ₂) ₄ -CH=CH ₂	95:5	70:30
7	HO-CH ₂ -(CH ₂) ₄ -CH=CH ₂	95:5	89:11
8	HO-CH ₂ -(CH ₂) ₅ -CH=CH ₂	96:4	77:23
9	HO-CH ₂ -(CH ₂) ₆ -CH=CH ₂	83:17	77:23
10	HO-CH ₂ -(CH ₂) ₇ -CH=CH ₂	81:19	–

[a] Reaction conditions: $Rh/L/alkene = 1:20:1000$, $c_0(alkene) = 0.698$ M, toluene, 10 bar CO/H_2 (1:1), 70 °C. Complete conversion was reached in every case after 20 h. [b] MeOH as solvent. [c] Addition of 0.5 equiv AcOH with respect to substrate.

A rhodium catalyst derived from the ligand **23** displayed the typical behavior of a bidentate ligand in the hydroformylation of terminal alkenes.^[26] Thus, excellent regioselectivity in favor of the linear aldehyde was noted for hydroformylation of a range of functionalized terminal alkenes (Table 6). Among them, even those with functional groups capable of hydrogen bonding were tolerated (Table 6, entries 5–8). However, the hydrogen-bonding network in the ligands and thus the chelating binding mode can be disrupted by employing either temperatures above 110 °C or protic solvents such as methanol and acetic acid; low regioselectivity results (Table 6, entries 9 and 10).^[26]

Since the two tautomers—the hydroxypyridine **23A** and the pyridone **23B**—equilibrate rapidly, mixing two pyridone ligands with different donor sites would result in mixtures of the heterodimeric and homodimeric catalysts (cf. Scheme 3). If, however, one wanted to generate the heterodimeric catalyst exclusively, for example, to study structure–activity and structure–selectivity relations, then the pyridone self-assembly platform is unsuitable. The heterodimeric structure would require the self-assembly of two complementary species through hydrogen bonding—a principle employed by nature in DNA base pairing. Thus an A–T base-pair model relying on the aminopyridine **26**/isoquinolone **27** platform was selected to serve for specific heterodimeric ligand assembly (Scheme 6).^[30]

When phosphine ligands based on this platform were mixed in the presence of a Pt^{II} salt, the heterodimeric complex *cis*-[PtCl₂(**28**)] formed exclusively. An X-ray structure of *cis*-[PtCl₂(**28aa**)] (D^x = D^y = PPh₂) shows the expected hydrogen-bonding network reminiscent of the Watson–Crick base



Scheme 6. An A–T base-pair model (highlighted in red) as a complementary platform for the specific self-assembly of heterodimeric bidentate ligands.

Table 7: Rh-catalyzed hydroformylation of 1-octene with a 4 × 4 ligand matrix of bidentate ligands self-assembled from aminopyridines (**26a–d**) and isoquinolones (**27a–d**).^[a]

$$n\text{Hex} \text{CH=CH}_2 \xrightarrow[\text{toluene, 80 } ^\circ\text{C}]{\text{cat. Rh / L(26)-L(27), H}_2/\text{CO (1:1) 10 bar}} n\text{Hex} \text{CH}_2\text{CH}_2\text{CHO} + n\text{Hex} \text{CH(CH}_3\text{)CHO}$$

n
iso

	27a	27b	27c	27d
	2425 h ⁻¹ ^[b] 94:6 ^[c]	1040 h ⁻¹ 94:6	2732 h ⁻¹ 96:4	2559 h ⁻¹ 95:5
	2033 h ⁻¹ 93:7	1058 h ⁻¹ 92:8	1281 h ⁻¹ 96:4	1772 h ⁻¹ 94:6
	3537 h ⁻¹ 94:6	1842 h ⁻¹ 93:7	1808 h ⁻¹ 96:4	2287 h ⁻¹ 94:6
	7439 h ⁻¹ 96:4	2695 h ⁻¹ 95:5	7465 h ⁻¹ 94:6	8643 h ⁻¹ 96:4

[a] Reaction conditions: [Rh(acac)(CO)₂], Rh/**26**/**27**/1-octene = 1:10:10:7500, 10 bar CO/H₂(1:1), toluene, c_0 (1-octene) = 2.91 M, 5 h. Catalyst preformation: 5 bar CO/H₂(1:1), 30 min, RT → 80 °C. [b] Turnover frequency TOF = (mol aldehyde) (mol catalyst)⁻¹ t⁻¹ at 20–30% conversion. [c] Regioselectivity: ratio of linear to branched product (*n*/*iso*).

pairing of A and T in DNA (Figure 3). NMR studies provided support that a similar structural situation occurs in solution, too. On this platform the first 4 × 4 self-assembled ligand

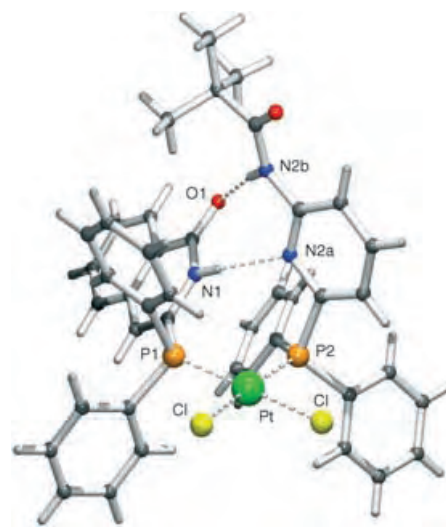
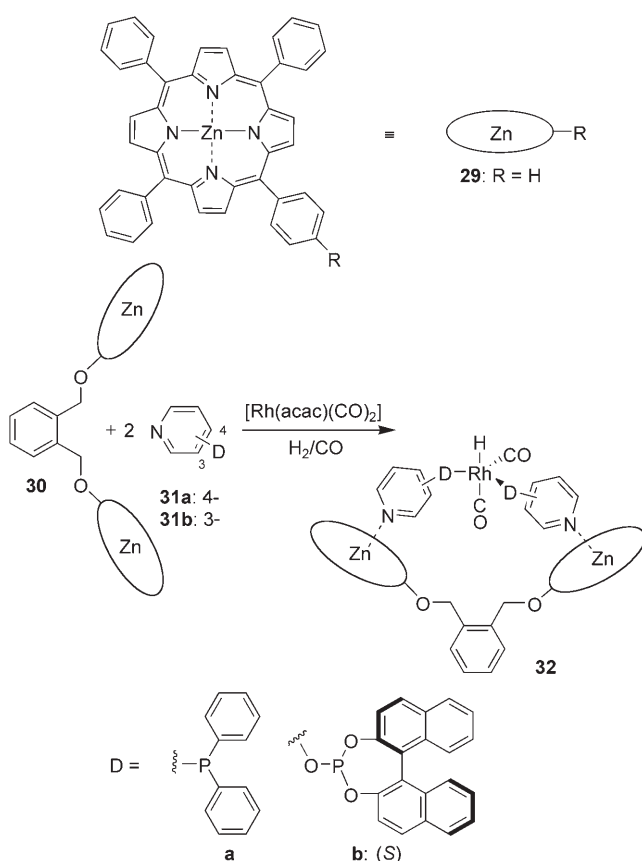


Figure 3. X-ray crystal structure of *cis*-[PtCl₂(**28aa**)] (D^x = D^y = PPh₂).

library based on hydrogen bonding was generated and explored for regioselective hydroformylation of terminal alkenes. In this study a catalyst was identified that operated with outstanding activity and regioselectivity (Table 7).^[30]

5. Attractive Ligand–Ligand Interactions through Coordinative Bonding

Zinc(II) porphyrins form stable complexes with nitrogen donors.^[31] This bonding motif was used recently by the group of Reek and van Leeuwen for the supramolecular construction of bidentate ligands (Scheme 7).^[32] To distinguish a



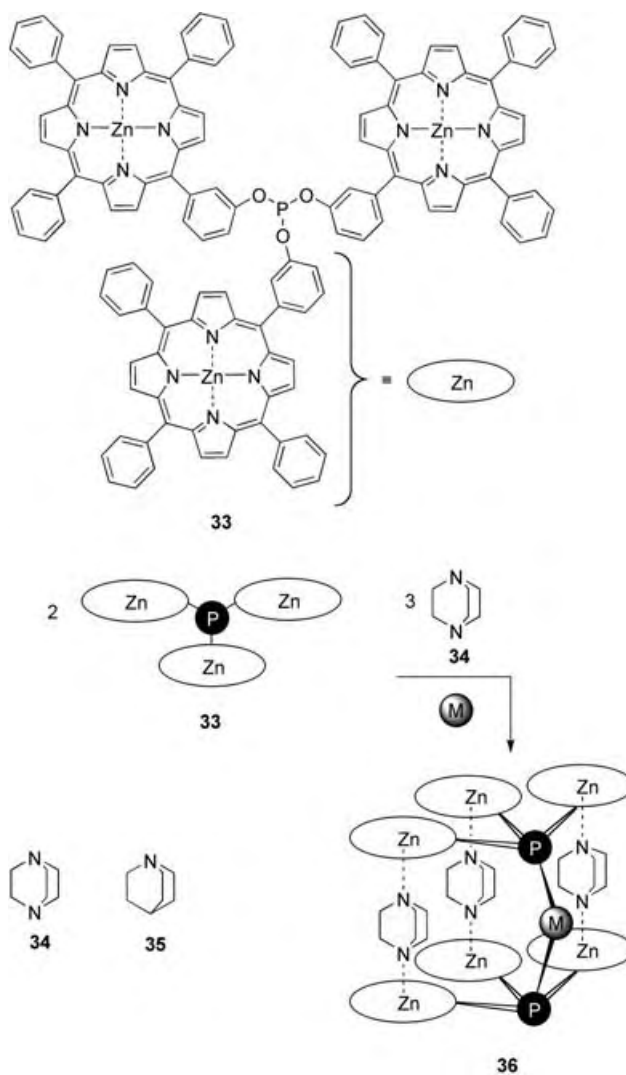
Scheme 7. Self-assembly of bidentate (and monodentate) ligands through coordination of a zinc(II) porphyrin complex to pyridyl-functionalized P donors.

bidentate from a monodentate binding mode, the hydroformylation of terminal alkenes was chosen as a test reaction (Table 8). Thus, the monodentate P-donor ligands alone or mixed with the monomeric zinc template **29** generated hydroformylation catalysts that displayed, as expected for monodentate donor ligands, low regioselectivity in the hydroformylation of 1-octene (Table 8, entries 1, 2, 4, and 6). Conversely, the combination of the dimeric zinc(II) porphyrin template **30** with two equivalents of the 3-pyridyl-functionalized phosphite donor **31b** led to good regioselectivity in favor of *n*-nonanal, which is the typical behavior expected for

Table 8: Rhodium-catalyzed hydroformylation of 1-octene with catalysts **32**.^[a]

Entry	Ligand combination ^[b]	T [°C]	Conv. [%]	TOF ^[c] [h ⁻¹]	2-Octene [%]	<i>n</i> -Nonanal [%]
1	31a	80	93	2250	1.8	71.7
2	29/31a	80	89	2100	1.8	71.5
3	30/2-31a	80	33	727	0.5	74.5
4	29/31a	25	6.2	7.4	0.1	74.1
5	30/2-31a	25	4.7	5.6	0.1	76.5
6	29/31b	25	1.1	1.3	0.0	83.3
7	30/2-31b	25	0.8	0.9	0.0	94.3

[a] $c([Rh(acac)(CO)_2]) = 0.084$ mM in toluene, 20 bar CO/H₂ (1:1), 1-octene/Rh = 5200. [b] $c(\mathbf{31a}$ or $\mathbf{31b}) = 2.1$ mM; $c(\mathbf{29}$ or $\mathbf{30}) = 1.1$ mM; $\mathbf{31a}$ (or $\mathbf{31b})/\mathbf{29}$ (or $\mathbf{30})/\text{Rh} = 25:13:1$. [c] Turnover frequency TOF = (mol aldehyde) (mol Rh)⁻¹ t⁻¹.



Scheme 8. Multicomponent assembly of zinc(II) porphyrin units for the construction of bidentate ligands.

a bidentate ligand. Unfortunately, the catalyst activity was low (Table 8, entry 7).^[32]

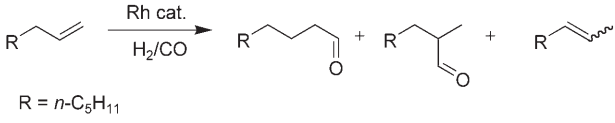
Switching the roles of the zinc porphyrin template and N-donor adapter provides an alternative mode for the supramolecular construction of bidentate ligands (Scheme 8).^[33] Thus, mixing two equivalents of the threefold zinc(II) porphyrin substituted phosphite **33** with 1,4-diazabicyclo[2.2.2]octane (dabco, **34**) in the presence of a rhodium(I) salt formed the chelating metal complex **36** (Scheme 8). Again, the hydroformylation of 1-octene served as a test case (Table 9). Thus, when the phosphite ligand **33** was used with or without the monoamine donor **35**, low regioselectivities were noted (Table 9, entries 1 and 2). Conversely, addition of diamine **34** provided a catalyst that operated with reduced activity but significantly increased regioselectivity (Table 9, entries 3 and 4). These properties can be ascribed to the bidentate coordination of the ligand to the catalytically active metal center.^[33]

Similarly, a set of zinc(II) porphyrin functionalized phosphites (**46–51**) and eight monodentate phosphorus donor ligands equipped with N-donor functions (**38–45**) were used to generate a library of 48 chelating ligands (Scheme 9).^[34]

This library of bidentate ligand assemblies plus the catalysts derived from the monodentate ligands alone were tested by application to the asymmetric allylic alkylation of 1,3-diphenylallyl acetate (Table 10). The best heterodimer combinations gave up to 60 % *ee* of either the *R* or *S* product depending on the absolute configuration of the ligand employed (Table 10, entries 2 and 6). Unexpectedly, optimal enantioselectivities (96–97 % *ee*) were observed for the monodentate zinc(II)porphyrin substituted phosphite ligands **48** and **49** (Table 10, entries 1 and 5).^[34]

An alternative complementary binding motif relying on coordinative interactions for the assembly of heterodimeric

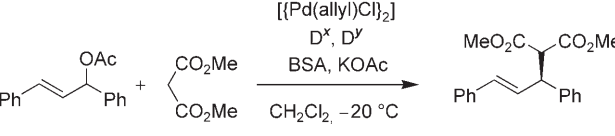
Table 9: Hydroformylation of 1-octene with catalysts **36**.^[a,b]



Entry	Ligand	Template	<i>T</i> [°C]	TOF ^[c] [h ⁻¹]	<i>n</i> / <i>iso</i> ^[d]	2-Octene [%]
1	33	—	80	2000	2.5	10.6
2	33	35	80	3400	1.9	16.1
3	33	34	80	1100	15.1	11.9
4	33	34	30	25	22.8	10.3

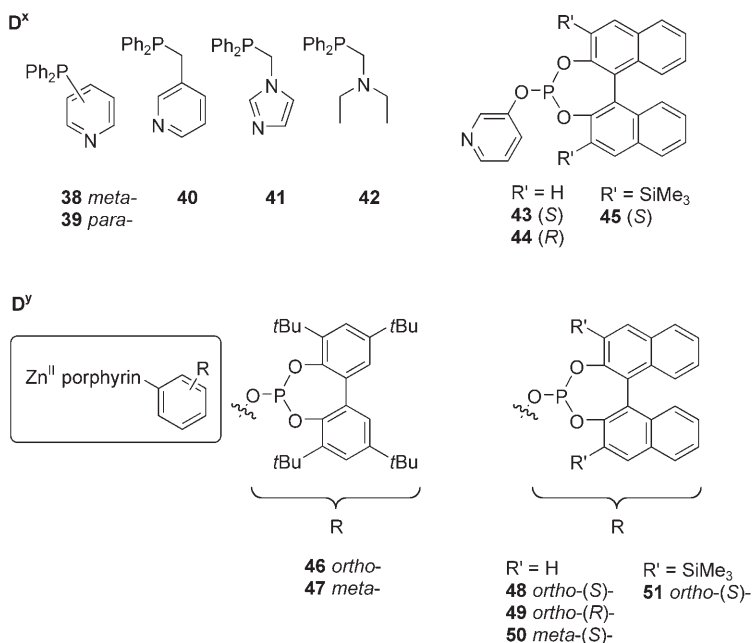
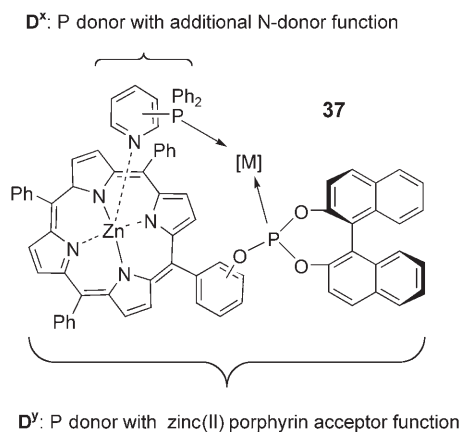
[a] $c(\text{[Rh(acac)(CO)}_2\text{]}) = 0.084 \text{ mM}$ in toluene, 20 bar CO/H₂ (1:1), 1-octene/Rh = 5160. [b] $c(\textbf{33}) = 2.1 \text{ mM}$; $c(\textbf{34}) = 3.1 \text{ mM}$; $c(\textbf{35}) = 6.3 \text{ mM}$; **33**/**34**/Rh = 25:36.9:1; **33**/**35**/Rh = 25:75:1. [c] TOF (turnover frequency) = (mol aldehyde) (mol Rh)⁻¹ t⁻¹. [d] Product ratio *n*/*iso* aldehyde.

Table 10: Pd-catalyzed allylic substitution with catalysts of type **37**.^[a]



Entry	Ligand	Conv. [%]	<i>ee</i> [%]
1	48	56	97 (<i>S</i>)
2	48-38	100	60 (<i>R</i>)
3	48-39	100	0
4	48-40	100	44 (<i>S</i>)
5	49	54	96 (<i>R</i>)
6	49-38	100	60 (<i>S</i>)
7	50	73	42 (<i>S</i>)
8	50-38	40	70 (<i>S</i>)

[a] $c(\text{[Pd(allyl)Cl]}_2) = 0.1 \text{ mM}$ in CH₂Cl₂, $c(\text{D}^*) = c(\text{D}^*) = 0.6 \text{ mM}$; Pd/D^{*}/D^y = 1:6:6.



Scheme 9. A library of heterodimeric bidentate ligands generated by self-assembly and based on the complementary binding of zinc(II) porphyrin acceptors and nitrogen donors.

chelating ligand systems was reported by Tacacs et al. (Scheme 10).^[35] Thus, a bimetallic complex **52** is used in which M_c represents the catalytically active metal center and M_s functions as a structure-determining element. More

influence on the ligand topography around the palladium center.

6. Conclusion and Outlook

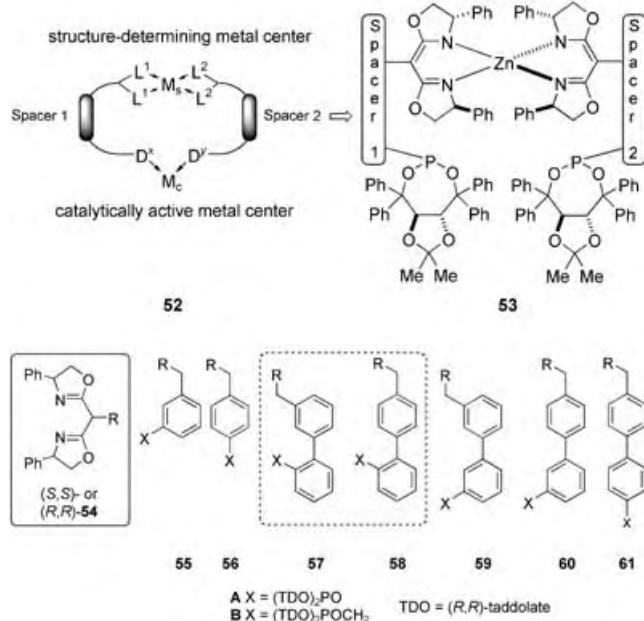
The quest in homogeneous transition-metal catalysis for the ultimate ligand to provide a catalyst with optimal activity and selectivity is a difficult task despite recent progress in rational ligand design. This is why combinatorial methods have gained increased importance in ligand design and discovery recently. However, the limiting step so far has been the generation of structurally meaningful and diverse ligand libraries, which has been particularly difficult for the structurally more demanding class of bidentate ligands.

This review summarizes recent reports, in which the synthesis of chelating ligands has been simplified significantly and which rely on a new concept to emulate chelating ligands. The basic idea is to use two structurally less complex monodentate ligands, which are held together through non-covalent attractive interactions and imitate a bidentate ligand at the catalytically active metal center. There is a continuum of attractive ligand–ligand interactions, which span a range from weak van der Waals, π stacking, charge-transfer, and dipole–dipole interactions to hydrogen bonding and even stronger coordinative interactions.^[37] Irrespective of the strength of the interaction, the specific formation of heterodimeric ligands requires two different sets of monodentate ligands with complementary binding sites. This concept was applied for the generation of the first bidentate ligand libraries based on self-assembly either through hydrogen bonding or coordinative interactions and has resulted in the identification of excellent catalysts for regioselective hydroformylation and asymmetric allylic alkylation.

This new field merges the principles of supramolecular chemistry, coordination chemistry, and catalysis for the generation of chelation-emulating ligand libraries for homogeneous metal catalysts. The proof of principle has been achieved, and the concept can now be used to develop larger ligand libraries to identify new tailor-made ligands for homogeneous catalysis in organic synthesis.

Received: May 24, 2005

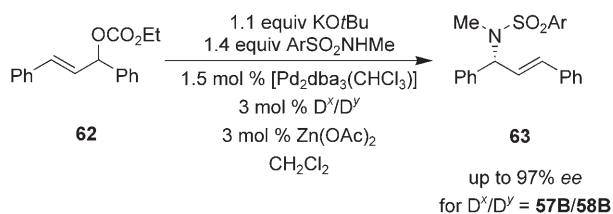
Published online: October 11, 2005



Scheme 10. Heterodimeric taddol–phosphite ligands based on a heterochiral metal complex template.

precisely, this structural element enforces an attractive ligand–ligand interaction through formation of zinc(II) complexes **53** with two chiral bisoxazoline ligands. Each of the bisoxazoline units **54** is connected through a spacer to a chiral phosphite donor (ligands **55–61A** and **B** based on (R,R) -taddol). Since the heterochiral zinc complex **53** is significantly more stable than the alternative homochiral complex, the selective formation of heterodimeric chelating ligands based on this template is possible.^[35,36]

A library of 50 combinations of heterodimers from subunits **55–61A** and **B** was screened in the palladium-catalyzed asymmetric allylic amination of racemic carbonate **62** to give allylic sulfonamide **63** (Scheme 11). 50 Ligand combinations were tested, and the enantioselectivities ranged from 20 up to 97% *ee*, although the chiral diphosphite ligands differed in the structure of the ligand backbone only. Thus, seemingly subtle changes in the ligand backbone have a major



Scheme 11. Allylic amination of racemic carbonate **62** with palladium catalysts of type **52**.

- [1] W. S. Knowles, *Acc. Chem. Res.* **1983**, *16*, 106–112.
- [2] C. Gennari, U. Piarulli, *Chem. Rev.* **2003**, *103*, 3071–3100.
- [3] For a review see: M. T. Reetz, *Angew. Chem.* **2001**, *113*, 292–310; *Angew. Chem. Int. Ed.* **2001**, *40*, 284–310.
- [4] “Asymmetric Hydrogenation”: T. Ohkuma, M. Kitamura, R. Noyori in *Catalytic Asymmetric Synthesis* (Ed.: I. Ojima), Wiley-VCH, New York, **2000**, chap. 1, pp. 1–110. For recent promising results employing monodentate ligands see: K. Junge, B. Hagemann, S. Enthaler, G. Oehme, M. Michalik, A. Monsees, T. Riermeier, U. Dingerdissen, M. Beller, *Angew. Chem.* **2004**, *116*, 5176–5179; *Angew. Chem. Int. Ed.* **2004**, *43*, 5066–5096.
- [5] a) “Bidentate Ligands”: P. W. N. M. van Leeuwen, C. P. Casey, G. T. Whiteker in *Rhodium Catalyzed Hydroformylation* (Eds.: P. W. N. M. van Leeuwen, C. Claver), Kluwer, Dordrecht, **2000**, chap. 4, pp. 76–105; b) B. Breit, W. Seiche, *Synthesis* **2001**, 1–36.

- [6] For reviews on the construction of libraries of classical bidentate ligands, see ref. [3] and O. Lavastre, F. Bonnette, L. Gallard, *Curr. Opin. Chem. Biol.* **2004**, *8*, 311–318.
- [7] For an alternative combinatorial approach employing catalytically active metal centers bearing two bidentate ligands, see: K. Ding, H. Du, Y. Yuan, J. Long, *Chem. Eur. J.* **2004**, *10*, 2872–2884.
- [8] H.-J. Schneider, A. K. Yatsimirsky, *Principles and Methods in Supramolecular Chemistry*, Wiley-VCH, New York, **2000**.
- [9] T. P. Dang, H. B. Kagan, *J. Chem. Soc. D* **1971**, 481.
- [10] B. D. Vineyard, W. S. Knowles, M. J. Sabacky, G. L. Bachmann, D. J. Weinkauff, *J. Am. Chem. Soc.* **1977**, *99*, 5946–5952.
- [11] A. Miyashita, A. Yasuda, H. Takaya, K. Toriumi, T. Ito, T. Souchi, R. Noyori, *J. Am. Chem. Soc.* **1980**, *102*, 7932–7934.
- [12] M. J. Burk, *J. Am. Chem. Soc.* **1991**, *113*, 8518–8519.
- [13] H.-U. Blaser, W. Brieden, B. Pugin, F. Spindler, M. Studer, A. Togni, *Top. Catal.* **2002**, *19*, 3–16.
- [14] W. S. Knowles, M. J. Sabacky, B. D. Vineyard, *J. Chem. Soc. Chem. Commun.* **1972**, 10–11.
- [15] C. Claver, E. Fernandez, A. Gillon, K. Heslop, D. J. Hyett, A. Martorell, A. G. Orpen, P. G. Pringle, *Chem. Commun.* **2000**, 961–962.
- [16] M. T. Reetz, T. Sell, *Tetrahedron Lett.* **2000**, *41*, 6333–6336; M. T. Reetz, G. Mehler, *Angew. Chem.* **2000**, *112*, 4047–4049; *Angew. Chem. Int. Ed.* **2000**, *39*, 3889–3890.
- [17] M. v. d. Berg, A. J. Minnaard, E. P. Schudde, J. v. Esch, A. H. M. de Vries, J. G. de Vries, B. L. Feringa, *J. Am. Chem. Soc.* **2000**, *122*, 11539–11540.
- [18] For a review see: I. V. Komarov, A. Börner, *Angew. Chem.* **2001**, *113*, 1237–1240; *Angew. Chem. Int. Ed.* **2001**, *40*, 1197–1200.
- [19] a) M. T. Reetz, T. Sell, A. Meiswinkel, G. Mehler, *Angew. Chem.* **2003**, *115*, 814–817; *Angew. Chem. Int. Ed.* **2003**, *42*, 790–793; b) M. T. Reetz, *Chim. Oggi* **2003**, *21*, 5–8.
- [20] a) M. T. Reetz, G. Mehler, *Tetrahedron Lett.* **2003**, *44*, 4593–4596; b) M. T. Reetz, X. Li, *Tetrahedron* **2004**, *60*, 9709–9714.
- [21] M. T. Reetz, X. Li, *Angew. Chem.* **2005**, *117*, 3019–3021; *Angew. Chem. Int. Ed.* **2005**, *44*, 2959–2962.
- [22] M. T. Reetz, X. Li, *Angew. Chem.* **2005**, *117*, 3022–3024; *Angew. Chem. Int. Ed.* **2005**, *44*, 2962–2964.
- [23] a) B. Breit, R. Winde, T. Mackewitz, R. Paciello, K. Harms, *Chem. Eur. J.* **2001**, *7*, 3106–3121; b) B. Breit, R. Winde, K. Harms, *J. Chem. Soc. Perkin Trans. 1* **1997**, 2681–2682; c) B. Breit, *Chem. Commun.* **1996**, 2071–2072.
- [24] a) D. Pena, A. J. Minnaard, J. A. F. Boogers, A. H. M. de Vries, J. G. de Vries, B. L. Feringa, *Org. Biomol. Chem.* **2003**, *1*, 1087–1089; b) D. Pena, A. J. Minnaard, A. H. M. de Vries, J. G. de Vries, B. L. Feringa, *Org. Lett.* **2003**, *5*, 475–478; c) D. Pena, A. J. Minnaard, J. G. de Vries, B. L. Feringa, *J. Am. Chem. Soc.* **2002**, *124*, 14552–14553.
- [25] A. Duursma, R. Hoen, J. Schuppan, R. Hulst, A. J. Minnaard, B. L. Feringa, *Org. Lett.* **2003**, *5*, 3111–3113.
- [26] B. Breit, W. Seiche, *J. Am. Chem. Soc.* **2003**, *125*, 6608–6609.
- [27] P. Beak, *Acc. Chem. Res.* **1977**, *10*, 186–192.
- [28] P.-T. Chou, C.-Y. Wie, F.-T. Hung, *J. Phys. Chem. B* **1997**, *101*, 9119–9126.
- [29] M. Meuwly, A. Müller, S. Leutwyler, *Phys. Chem. Chem. Phys.* **2003**, *5*, 2663–2672.
- [30] B. Breit, W. Seiche, *Angew. Chem.* **2005**, *117*, 1666–1669; *Angew. Chem. Int. Ed.* **2005**, *44*, 1640–1643.
- [31] Other supramolecular catalysts based on porphyrin assemblies: C. J. Walter, H. L. Anderson, J. K. M. Sanders, *J. Chem. Soc. Chem. Commun.* **1993**, 458–460; L. G. Mackay, R. S. Wylie, J. K. M. Sanders, *J. Am. Chem. Soc.* **1994**, *116*, 3141–3142; M. L. Merlau, M. del Pilar Mejia, S. T. Nguyen, J. T. Hupp, *Angew. Chem.* **2001**, *113*, 4369–4372; *Angew. Chem. Int. Ed.* **2001**, *40*, 4239–4242; J. A. A. W. Elemans, E. J. A. Bijsterveld, A. E. Rowan, R. J. M. Nolte, *Chem. Commun.* **2000**, 2443–2444.
- [32] V. F. Slagt, P. W. N. M. van Leeuwen, J. N. H. Reek, *Chem. Commun.* **2003**, 2474–2475.
- [33] V. F. Slagt, P. W. N. M. van Leeuwen, J. N. H. Reek, *Angew. Chem.* **2003**, *115*, 5777–5781; *Angew. Chem. Int. Ed.* **2003**, *42*, 5619–5623.
- [34] V. F. Slagt, P. C. J. Kamer, P. W. N. M. van Leeuwen, H. N. J. Reek, *J. Am. Chem. Soc.* **2004**, *126*, 4056–4057.
- [35] J. M. Takacs, D. S. Reddy, S. A. Moteki, D. Wu, H. Palencia, *J. Am. Chem. Soc.* **2004**, *126*, 4494–4495.
- [36] J. M. Takacs, P. M. Hrvatin, J. M. Atkins, D. S. Reddy, J. L. Clark, *New J. Chem.* **2005**, *29*, 263–265.
- [37] For alternative approaches using noncovalent interactions for emulating chelating ligands which have not been used in catalysis yet, see: a) V. W.-W. Yam, X.-X. Lu, C.-C. Ko, *Angew. Chem.* **2003**, *115*, 3507–3510; *Angew. Chem. Int. Ed.* **2003**, *42*, 3385–3388; b) X.-X. Lu, H.-S. Tang, C.-C. Ko, J. K.-Y. Wong, N. Zhu, V. W.-W. Yam, *Chem. Commun.* **2005**, 1572–1574.

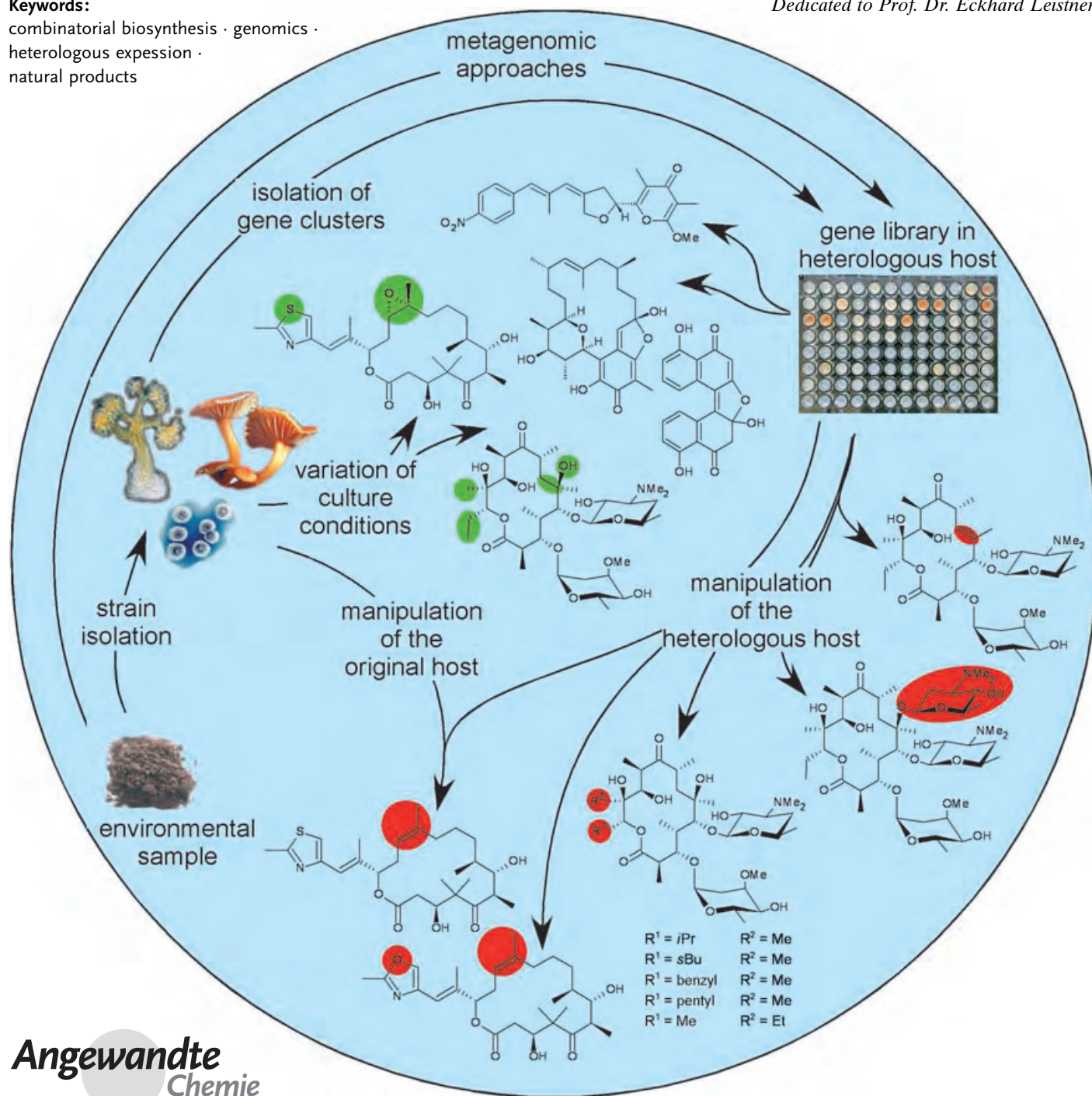
The Impact of Bacterial Genomics on Natural Product Research

Helge B. Bode and Rolf Müller*

Keywords:

combinatorial biosynthesis · genomics · heterologous expression · natural products

Dedicated to Prof. Dr. Eckhard Leistner



“There’s life in the old dog yet!” This adage also holds true for natural product research. After the era of natural products was declared to be over, because of the introduction of combinatorial synthesis techniques, natural product research has taken a surprising turn back towards a major field of pharmaceutical research. Current challenges, such as emerging multidrug-resistant bacteria, might be overcome by developments which combine genomic knowledge with applied biology and chemistry to identify, produce, and alter the structure of new lead compounds. Significant biological activity is reported much less frequently for synthetic compounds, a fact reflected in the large proportion of natural products and their derivatives in clinical use. This Review describes the impact of microbial genomics on natural products research, in particularly the search for new lead structures and their optimization. The limitations of this research are also discussed, thus allowing a look into future developments.

1. Introduction

Without medically applied natural products^[4] human life would be less comfortable and definitely much shorter: More than 75 % of all antibacterial and approximately 50 % of all anticancer compounds currently in clinical use are either natural products themselves or derivatives thereof.^[1] Clinically useful antibacterial natural products are often the drugs of last resort for the treatment of multidrug-resistant and, without treatment, often deadly microorganisms. However, resistance against new antibiotics, including those representing our last line of defence, is emerging. Even with the adoption of antibiotics with novel mechanisms of action, we do not have to ask the question *if* resistance will develop but only *when* it will occur. This situation is mainly a consequence of the enormous speed at which microorganisms exchange and mutate their genes. The more often antibiotics are used, the more rapidly resistance is spread.^[2] It is predictable that the winner in this game will always be the microbe, simply because of its huge numbers, short generation times, and mutation rates. Nevertheless, pharmaceutical research must try to fight back to maintain the status quo. However, to find a promising new natural product for the treatment of any kind of disease is an expensive and difficult challenge,^[3,4] which has led major pharmaceutical companies to rely solely on synthetic chemicals.^[5,6]

The reason for this can be seen in several disadvantages that natural products appear to have compared to synthetic chemicals: 1) The isolation and characterization is often laborious and, therefore; 2) it is not possible to obtain as many natural products as synthetic chemicals in the same time; 3) by definition there is a biological source involved in the production of any natural product, which requires experienced handling plus specialized and expensive equipment.

However, these disadvantages are more than balanced by the positive aspects of natural products, and some of the arguments against them can in fact be turned into strong

From the Contents

1. Introduction	6829
2. Approaches to Explore the Genetic Potential	6833
3. Be Prepared! Natural Product Research in the Postgenomic Era	6843

advantages: 1) Natural products occupy a complementary region of chemical space compared with synthetic compounds as discussed extensively in recent reviews.^[7–12] These

differences range from simple features such as elemental composition and molecular weight to specific structural elements such as ring size and type, and overall complexity and stereochemistry in general. 2) Natural products have evolved in a biological context and the percentage of biologically active natural products is much higher than that of synthetic compounds (although not all of them have an identified biological activity).^[13] These two findings result in a new trend of “natural productlike” synthetic strategies: new lead compounds can be identified from natural product scaffolds or by creating analogues to natural products.^[14–16] These approaches have also led to a cooperation between natural product research and combinatorial chemistry, the latter of which was earlier thought to completely replace the need for novel natural products. In general, it is now accepted that both disciplines support, fertilize, and rely on one another.^[10,17] 3) The biological source of the compound is often renewable and thus opens up the possibility to scale-up production. This is especially true if the producing organism is easy to cultivate, and is a major reason why bacteria and fungi are the dominant source of the natural products in clinical use. Furthermore, because of our increased understanding of genetics and the principles of biological regulation the production of these compounds can be optimized (see Section 2.5). The biosynthesis of the compounds themselves can also be manipulated to yield new derivatives with possibly superior qualities (see Section 2.6). Possible ways to obtain

[*] Jr. Prof. Dr. H. B. Bode, Prof. Dr. R. Müller
Institut für Pharmazeutische Biotechnologie
Universität des Saarlandes
Postfach 151150, 66041 Saarbrücken (Germany)
Fax: (+49) 681-3025473
E-mail: rom@mx.uni-saarland.de

Supporting information for this article is available on the WWW under <http://www.angewandte.org> or from the author.

[†] The expressions natural product and secondary metabolite are used interchangeably throughout this Review.

these goals for pharmacologically relevant natural products are the focus of this Review and will be described in later sections. Most of the work cited was performed with polyketides and nonribosomally biosynthesized peptides. Since these natural products are derived from enzymatic systems called polyketide synthases (PKSs) and nonribosomal peptide synthetases (NRPSs), these enzymes and the resulting secondary metabolites are introduced briefly (Scheme 1). It should be noted that many bacterial natural products are derived from other pathways, such as the isoprenoid or shikimate pathways.^[18–20]

Bacterial PKSs (type I) are multifunctional enzymes that are organized into modules, each of which harbors a set of distinct, non-iteratively acting activities responsible for several biosynthetic steps during the catalysis of one cycle of the polyketide chain elongation.^[21] Type I PKSs are involved in the biosynthesis of macrolides, polyethers, and polyenes. Type II PKSs are multienzyme complexes that carry a single set of iteratively acting proteins and are involved in the biosynthesis of aromatic and often polycyclic polyketides.^[22,23] Type III PKSs, also known as chalcone synthase like PKSs, are homodimeric enzymes which iteratively act as condensing enzymes, as exemplified by the formation of flaviolin.^[23] NRPSs are similar to the type I PKSs in that they are multifunctional enzymes that are organized into modules with sets of non-iteratively acting activities for the incorporation and processing of one amino acid per module.^[24,25]

1.1. Increase in Sequence Information

Since the publication of the first complete microbial genome sequence of *Haemophilus influenzae* in 1995,^[31] more than 250 fully sequenced genomes have been reported (Figure 1) and more than 600 prokaryotes and 460 eukaryotes are currently being sequenced.^[32] Although there was a clear focus on pathogenic bacteria in the early days of genome sequencing, biotechnology is catching up rapidly: currently 47% of all bacterial-sequencing projects deal with organisms having industrial applications, including secondary metabolism (52% of the projects remain focused on pathogens and about 1% involve the sequence of exotic organisms).^[32] The value of the exponentially growing sequence information is

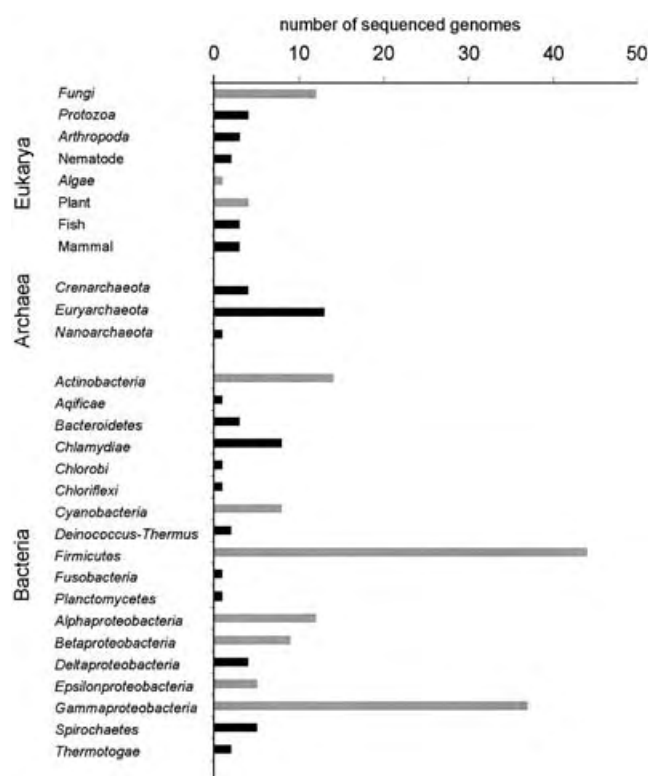


Figure 1. Currently finished genomes ordered according to their intermediate taxonomic rank. Classes and orders that harbor experimentally verified secondary metabolite producing members are shown in gray.

immeasurable because bioinformatic methods, along with large-scale approaches such as transcriptomics and proteomics, are only just beginning to reveal insights into numerous important research topics such as virulence genes, host–pathogen interactions, new molecular targets, and novel ways to produce secondary metabolites. Sequence data from multiple isolates or different strains of a single pathogen are accumulating. This type of information has proven invaluable for providing new insights into the genetic variability present in a particular species as well as facilitating correlations between genotype and phenotype.^[33]

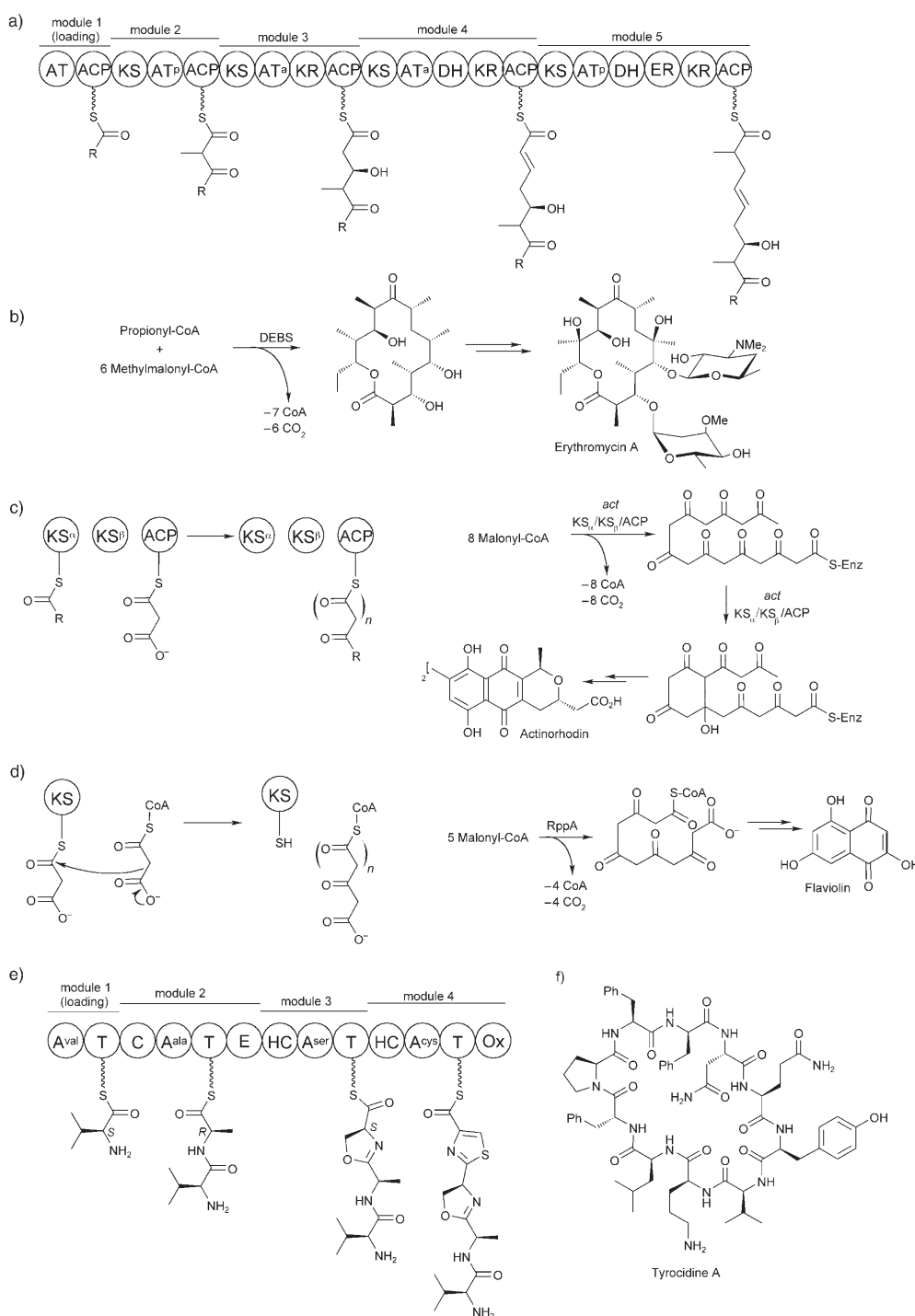
Unexpectedly, genome sequencing of known producers of secondary metabolites (*Streptomyces* sp.^[34,35] and *Arabidop-*



Helge B. Bode was born in 1973 and studied chemistry and biology in Göttingen and Stockholm. After his Diploma and PhD (2000) studies in natural product chemistry with Prof. A. Zeeck, he received a Diploma in molecular microbiology with Prof. G. Braus in 2001. After postdoctoral research with R. Müller in Braunschweig and Prof. D. Kaiser in Stanford, he was appointed Junior professor for Natural Product Biotechnology at Saarland University in April 2004. His research focuses on the elucidation of the biochemical basis of the complex life cycle of myxobacteria.



Rolf Müller studied pharmacy at Bonn University and received his PhD with Prof. E. Leistner in 1994. He worked for two years as a research fellow of the DFG with Prof. H. Floss in Seattle, and then studied myxobacteria at the German Research Centre for Biotechnology (GBF) for his Habilitation (TU Braunschweig, 2001). In 2003 he received the BioFuture prize of the BMBF and in the same year was appointed head of the Department of Pharmaceutical Biotechnology at Saarland University. His recent work focuses on the biotechnological exploitation of myxobacterial genome projects and the heterologous expression and modification of complex megasynthetases in pseudomonads and fast-growing myxobacteria.



Scheme 1. Mechanisms and structures of bacterial PKSs and NRPSs. a) Generalized example of a type I PKS consisting of non-iteratively acting domains; acyltransferase (AT), acyl carrier protein (ACP), ketosynthase (KS), ketoreductase (KR), dehydratase (DH), enoylreductase (ER); a and p indicate the specificity of the AT domain for malonyl-CoA or methylmalonyl-CoA.^[21] b) Biosynthesis of erythromycin A is a well-studied example of the action of a type I PKS; 6-deoxyerythronolide B synthase (DEBS). c) Type II PKS consisting of iteratively acting subunits as exemplified for actinorhodin biosynthesis; chain length factor (KS_α).^[21, 26] d) Type III PKS consisting of an iteratively acting enzyme as exemplified by flaviolin biosynthesis.^[23, 27] e) Generalized example of NRPS biosynthesis; adenylation (A), peptidyl carrier protein (T), condensation (C), epimerization (E), heterocyclization (HC), oxidation (Ox).^[28, 29] f) Formation of tyrocidine A is a well-documented example for NRPS biosynthesis.^[29, 30]

sis^[36]) revealed the capacity to synthesize many more secondary metabolites than were actually known from these organisms. Even more surprising, many organisms that were not known as secondary metabolite producers, harbor the typical genes and often huge biosynthesis gene clusters for the production of several hypothetical or unidentified natural products. A possible explanation for this might be that only a few taxa (plants, fungi, and some bacterial taxa) have been investigated with respect to secondary metabolism. Almost all bacteria, fungi, and plants sequenced to date show at least some biosynthesis genes typical for secondary metabolite production, thus indicating the old evolutionary origin of these genes.

1.2. Plants—Potential and Problems

Plants have the greatest potential to produce any type of natural product. This situation is exemplified by the enormous variety of low-molecular-weight compounds present in most plant materials.^[37] The complexity of plant metabolomes is far beyond those from other organisms. However, the organization of the genes in a typical plant genome makes research dealing with plant secondary metabolism a major challenge: 1) The genes for the production of secondary metabolites are not found in one genomic region (that is, as a biosynthetic gene cluster, such as those usually present in bacteria or fungi) but scattered throughout the entire genome. Therefore, the

identification of a complete biosynthetic pathway in plants is extremely tedious and time-consuming. 2) The exon/intron structure of the genes leads to a number of problems. Therefore, it is necessary to work with cDNA which is generated from enriched mRNA pools to identify the genes of interest.

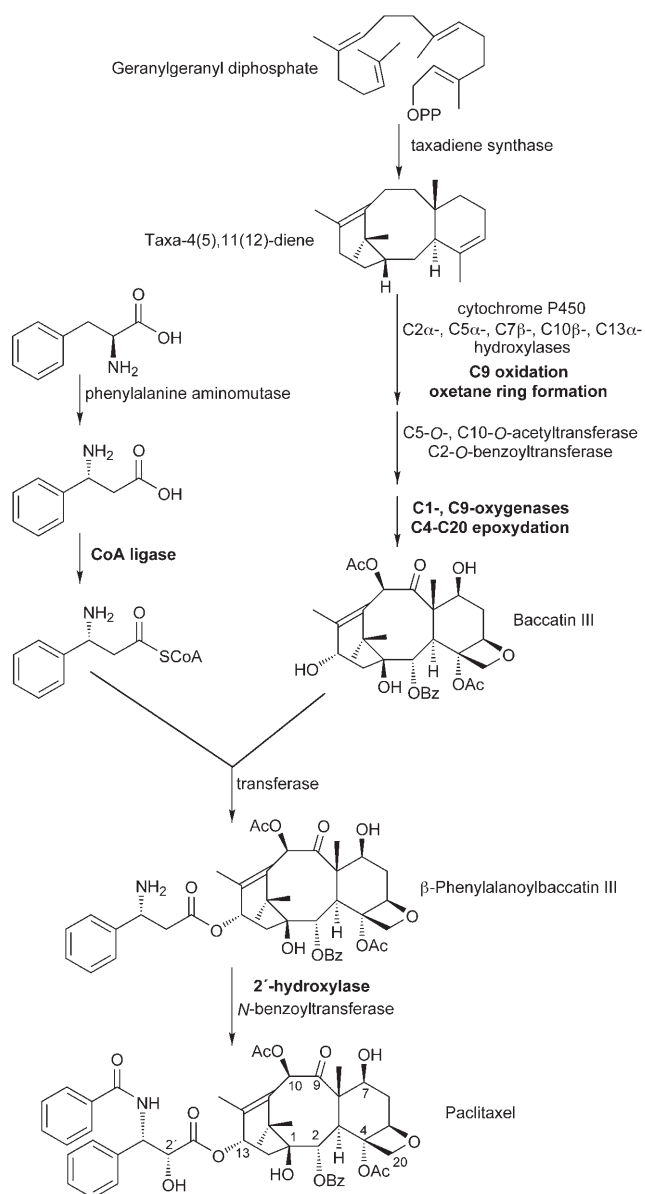
A good example of these challenges is the potent anticancer agent paclitaxel (taxol), which was isolated from the bark of the pacific yew as a pure compound in 1971. This source is environmentally unfriendly and gave rise to serious supply issues, and today it is produced by a semisynthetic approach starting from 10-deacetylbaccatin III, which can be isolated from yew tree needles (and thus a renewable source) in large quantities.^[38] The broad use of paclitaxel in breast cancer treatment has triggered several efforts to produce this valuable compound more efficiently, either in plant cell cultures^[39] or alternatively in fast-growing bacterial hosts after heterologous expression of the required biosynthetic machinery. Unfortunately, the complex biosynthesis of taxol requires approximately 19 biosynthetic steps, which explains that despite groundbreaking efforts, especially by the Croteau research group, several genes for the biosynthesis are still unknown (Scheme 2).^[40–43] Interestingly, endophytic fungi have been isolated from various yew trees that produce paclitaxel. Despite their small production titers, these fungi open up the possibility to study paclitaxel biosynthesis in comparison to the plant system and lead to potential biotechnological processes.^[39]

1.3. Fungi—The Promised Land?

Fungi have been a major source of natural products used in food processing and medicine as well as for religious rituals since the very early days of human culture. The modern era of fungal natural product research started with the well-known story of a contaminated agar plate in Alexander Fleming's laboratory in 1928, which eventually led to the clinical use of penicillin to treat bacterial infections.^[44] Since then, fungi have been an impressive source of biologically active lead structures for pharmaceutical development, including the immunosuppressant cyclosporin^[45] and the cholesterol-lowering agent lovastatin.^[46]

Fungal genomics started with the availability of the complete sequence of the model yeast *Saccharomyces cerevisiae* in 1997.^[47] Since then genome sequences of additional model strains used to study fungal molecular biology and/or fermentative biotechnology have been reported (*Schizosaccharomyces pombe* (2002),^[48] *Neurospora crassa* (2003),^[49] *Phanerochaete chrysosporium* (2004),^[50] *Yarrowia lipolytica* (2004), and *Kluyveromyces lactis* (2004)^[51]).

The first complete sequence of a fungus that produced secondary metabolites was the white-rot fungus *Phanerochaete chrysosporium* in 2004.^[50] More than 50 genes involved in secondary metabolite biosynthesis including several genes encoding PKS and NRPS have been identified in the 30 Mbp genome. It is noteworthy that the biosynthesis of polyketides often involves post-PKS assembly steps, including the action of cytochrome P450 like enzymes, and an impressive number



Scheme 2. Biosynthesis of paclitaxel (taxol). Enzymatic activities encoded by genes that have not been cloned yet are shown in bold.^[40–43]

of corresponding genes (more than 100) have been identified in this genome. Fortunately, most genes for secondary metabolite biosynthesis in *P. chrysosporium* and in fungi in general are clustered on the chromosome so that the identification and study of complete secondary metabolite biosynthetic pathways is much easier than in plants.

Currently 113 fungal genome projects are in progress worldwide.^[32] The majority of these involve classical secondary metabolite producers (for example, *Penicillium chrysogenum* and 13 different *Aspergillus* sp.) or plant pathogenic strains which are also known for the production of natural products (for example, *Fusarium* sp., *Botrytis* sp., and *Magnaporthe* sp.). These projects will undoubtedly add valuable insights into fungal secondary metabolite biosynthesis, which is currently little studied relative to related bacterial systems.

One foreseeable problem with fungal systems is the lack of genetic methods for the manipulation of many strains and the fact that in some cases the biosynthetic genes are not clustered on the chromosome. Nevertheless, there is enormous potential in fungal systems, and most of the advantages discussed below with respect to bacteria also apply for fungi.

1.4. Bacteria—The Bigger the Better?

Research focussing on bacteria and in particular on bacterial secondary metabolism has a number of advantages in comparison to plants and fungi: 1) Genes for the biosynthesis of the desired compounds are mostly clustered; 2) the coding density of bacterial genomes is high and thus sequence costs can be reduced; 3) no introns are present, thus enabling expression methods starting directly from chromosomal DNA; 4) the compact genetic composition allows the fast identification of bacterial gene clusters and their transfer into different expression hosts; and 5) fermentation processes can be developed, thus enabling large-scale production (which is also true for fungi).

Many more bacteria have been sequenced than eukaryotes because of their relatively small genome sizes. Early sequencing efforts focused mostly on pathogenic bacteria, while 47% of all current bacterial sequencing projects deal with biotechnologically relevant strains. Up to now only a few species have been sequenced that were known in advance to be secondary metabolite producers. However, the sequencing of these strains revealed a plethora of biosynthetic gene clusters for the production of additional unknown secondary metabolites (Figure 2). The best studied examples are *Strepto-*

myces coelicolor and *S. avermitilis*, which were known to produce 4 and 3 secondary metabolites, respectively, but actually possess 20 and 25 clusters for secondary metabolite biosynthesis, respectively.^[34,35] A detailed post-genomic examination of the production profile of *S. coelicolor* has already led to the isolation of two additional compounds, the existence of which had been postulated after genome annotation.^[52,53]

Statistical analysis of all bacterial genomes sequenced to date revealed that there is a positive correlation between the genome size and the number of genes involved in the biosynthesis of secondary metabolites.^[54] Large genomes found in most producers of secondary metabolites might be a consequence of the complex ecological niches they occupy—requiring adaptation to several microenvironments and/or competition between species. Further ecologically relevant species need to be sequenced to learn more about this dependency.^[55] However, two questions arise from the tremendous discrepancy between isolated compounds and genomic potential: How can we identify and obtain the hypothetical products that have not yet been isolated? How can we use the enormous genetic potential in the most efficient way? We will try to address these questions in the following sections by using selected examples from the recent literature.

2. Approaches to Explore the Genetic Potential

2.1. Random, but Simple and Successful

The easiest way to obtain more secondary metabolites from a single strain bearing the genetic potential to produce several compounds is to vary the culture conditions. The rationale behind this approach is that the production of secondary metabolites might be a specific response of the producing organisms to a changing environment.^[13] For example, soil bacteria living in the rhizosphere have to compete with fungi for nutrients. Thus, the production of antifungal compounds would be advantageous in such an environment. In contrast, the artificial media composition, cultivation conditions, and high cell densities used under laboratory conditions might cause regulatory cascades in the cells thus enabling the production of some compounds but disabling the production of others that might be produced under different and perhaps more “natural” conditions. Since our knowledge of any ecological network is very poor, random approaches which vary the easily accessible cultivation parameters are chosen (media composition, aeration, addition of chemicals, etc.) to trigger the expression of latent biosynthetic genes. This approach might influence directly or indirectly the transcription, translation, and enzyme activity/specificity in the whole organism (Figure 3). Very similar techniques have been used widely for the optimization of the production of a desired compound, and their use in screening for novel natural products has led to some impressive examples of microbial chemical diversity. These methods are regularly used today by pharmaceutical and biotech companies.^[15]

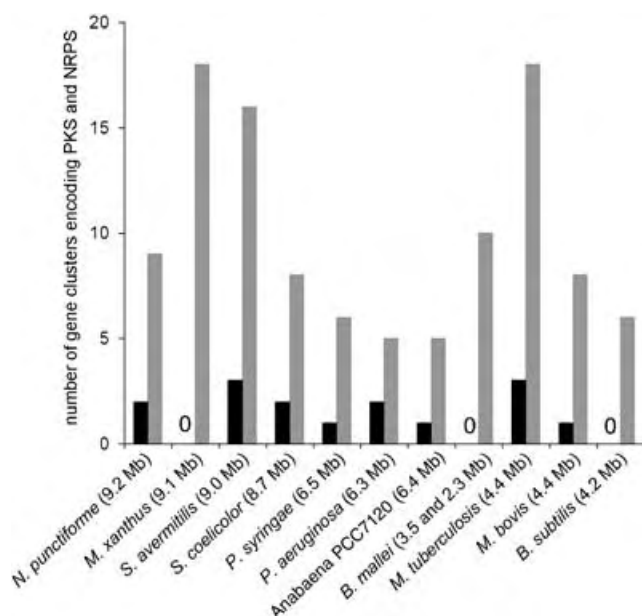


Figure 2. Selected fully sequenced prokaryotic secondary metabolite producers with numbers of isolated polyketides and nonribosomal peptides at the time of the genome sequence (black bars). Identified gene clusters encoding PKS and NRPS in the genome are shown as gray bars.^[32] The data was taken from the original publications or generated by BLAST searches of KS, KR, TE, ACP, T, and A domains.

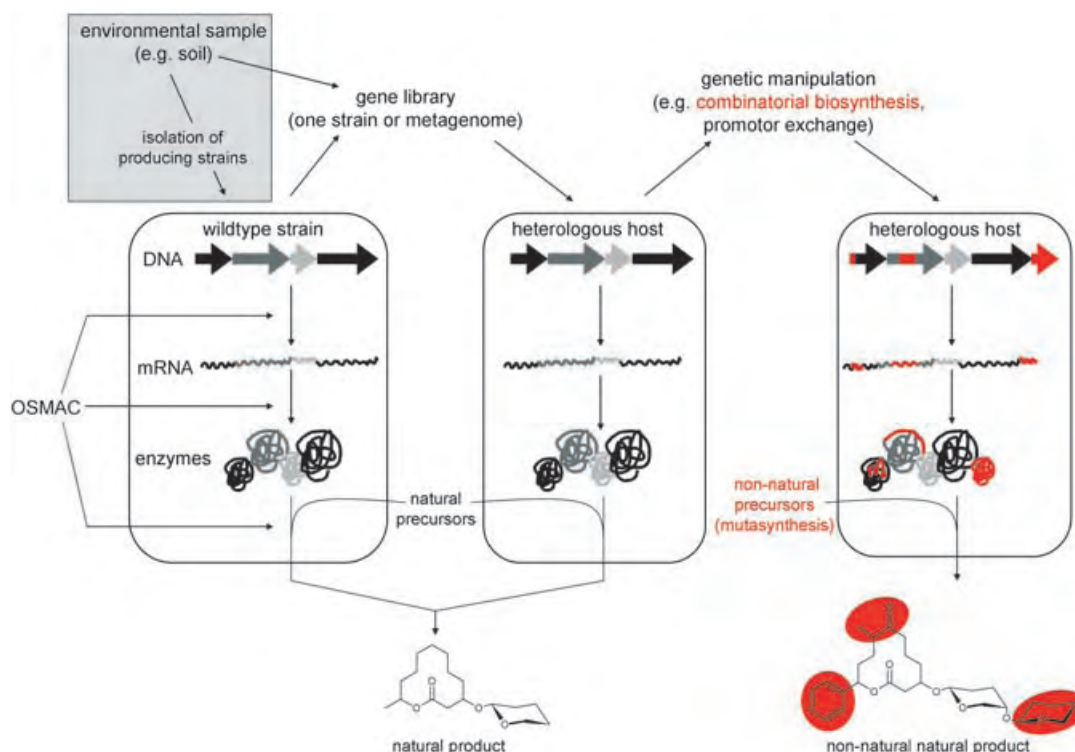


Figure 3. Possible ways to influence the production of secondary metabolites. Isolation of new producing strains and metagenome approaches prior to methods dealing with secondary metabolites are shown in gray. Genetic modifications and/or addition of genes leading to modified compounds are shown in red.

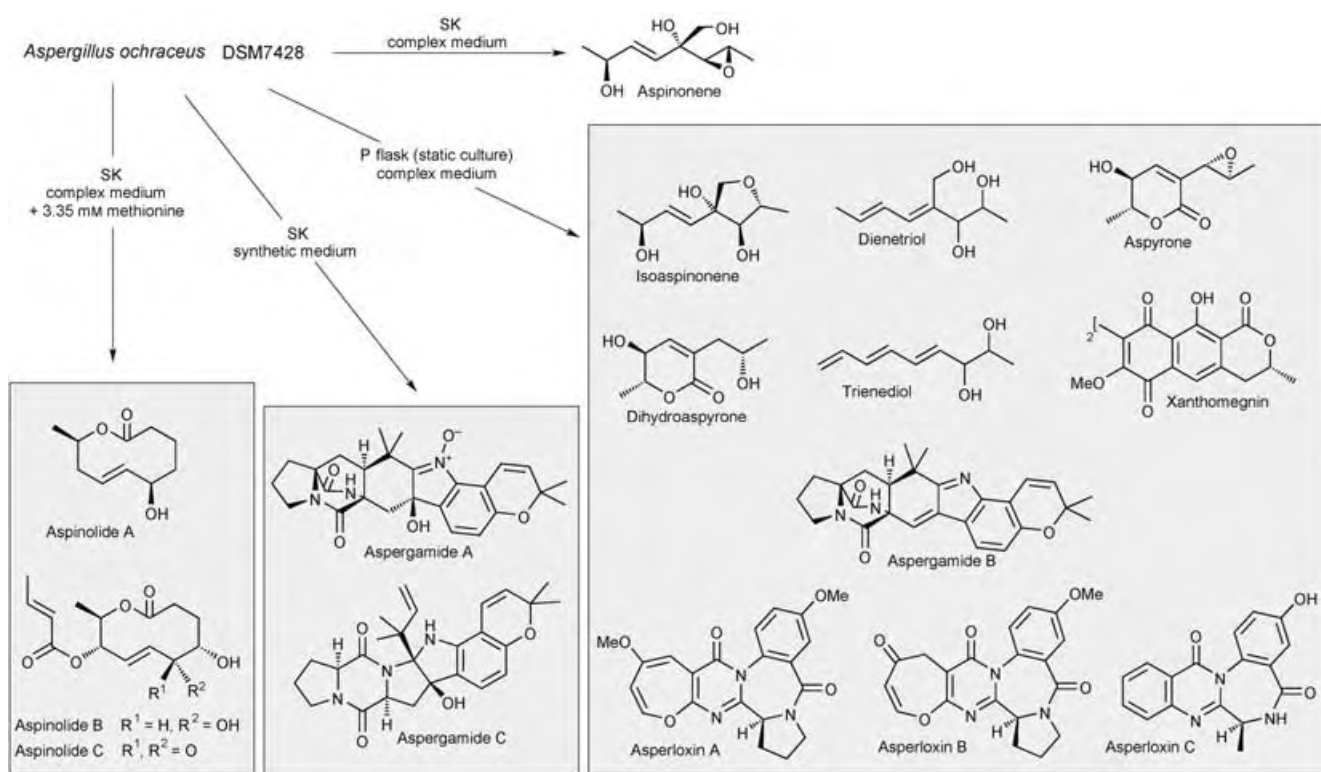
After the cultivation of the aspinonene producer *Aspergillus ochraceus* DSM7428 in different media and cultivation vessels (resulting in different aeration rates), 15 additional secondary metabolites belonging to unrelated structural and biosynthetic families were isolated. Of particular note was the static cultivation for several days which led to a completely different metabolite profile (Scheme 3).^[56,57] Similar results were also obtained with another fungus which produced up to 2.6 g L^{-1} of a reduced precursor of the main metabolite (120 mg L^{-1} in shaking culture) under similar conditions.^[58] Since variation of the growth conditions very often results in the production of several compounds by a single organism, this approach was termed “one strain—many compounds” (OSMAC).^[56] Recently, the addition of organic solvents and signaling compounds to growth media was even used to increase the chemical diversity of selected strains.^[59,60]

2.2. Possible Ways to Use the Endless Resources

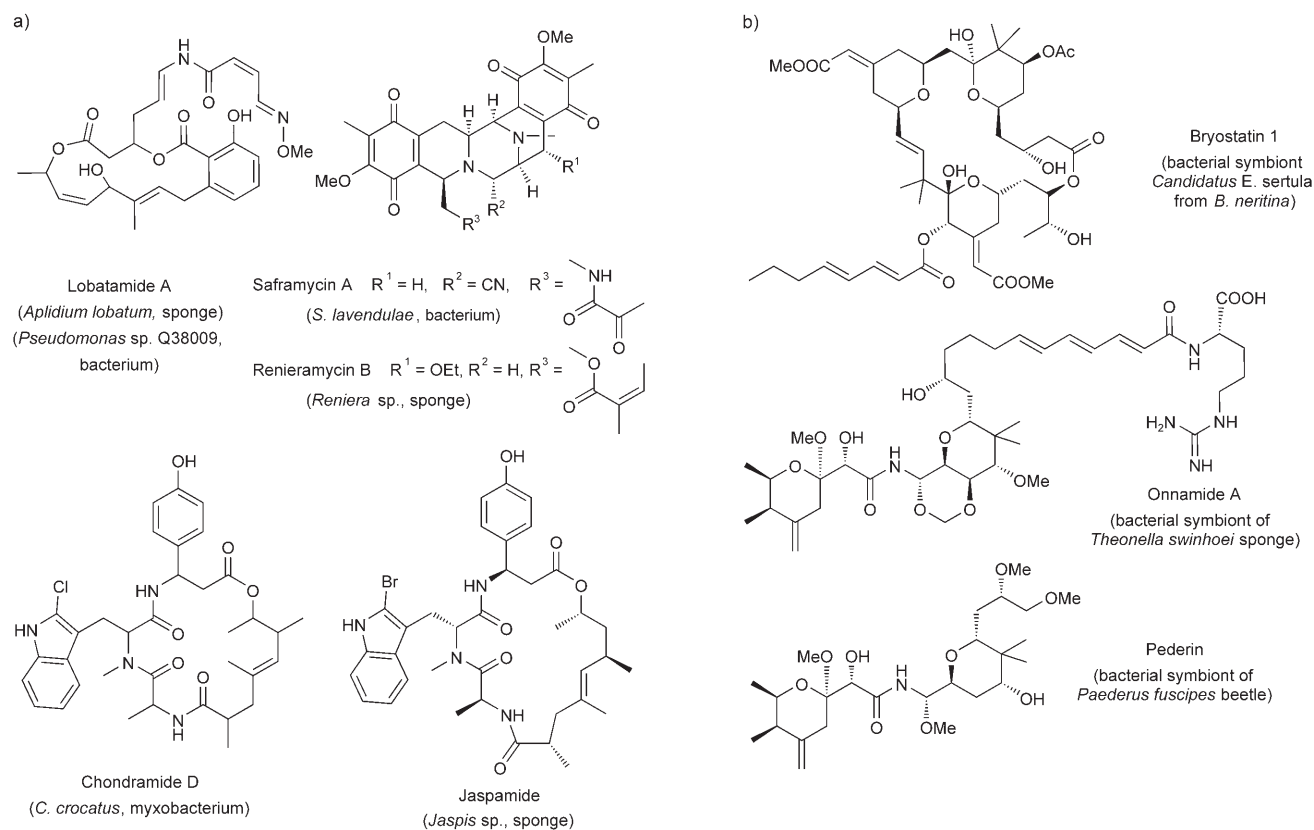
The microbial world cultured in the laboratory represents less than one percent of the microbial diversity in different natural environments.^[61] The biosynthetic potential of this unexplored resource is nearly endless and raises the question: Why do we only work with this limited number of bacteria? The answer to this is that these “lab” strains behave well in artificial conditions and can be cultivated easily. Microorganisms currently in use grow fast in pure culture and reach high cell densities. However, fast growth is not advantageous when

nutrients are not available. Too much food might even kill cells if they require a specialized diet. In nature, poor nutrient conditions represent the rule and not the exception, and areas completely devoid of nutrients occur.

New techniques are currently being developed to cultivate and enrich formerly “not-yet-culturable” organisms.^[62–65] The work required is very laborious and time-consuming. Therefore, additional techniques have been developed that circumvent the cultivation of organisms but still enable the exploration of chemical diversity. DNA libraries from environmental samples are generated bearing the genetic information of all organisms present at a specific location at the sampling time.^[66–68] After sequencing such so called “metagenomes”, the genetic information of single organisms can still be assembled and analyzed by using established bioinformatic tools, as was most impressively shown recently for the microbial community of the Sargasso Sea.^[69] Furthermore, the DNA libraries generated in this way can be transferred into suitable host organisms that can then be tested for the production of the desired compounds and enzymes (see also Section 2.5). This methodology is especially important for those potent biologically active compounds which have been isolated from organisms not amenable to large-scale cultivation (for example, bryozoae, sponges, and molluscs).^[70] Intriguingly, structural similarities exist between several marine natural products of unknown origin and compounds isolated from soil bacteria (Scheme 4). On the basis of genetic evidence, it is now generally accepted that several of the “marine” natural products from higher organisms are in fact



Scheme 3. Secondary metabolites isolated from *Aspergillus ochraceus* DSM7428 after variation of the cultivation parameters; Shaking culture (SK).^[56]



Scheme 4. Examples of structurally related natural products isolated from bacteria and marine organisms (a)^[73–77] and of natural products produced by uncultivated bacterial symbionts of higher organisms (b).^[71, 72, 78, 79]

marine microbial products (for example, onnamide^[71] and bryostatin^[72]). Therefore, the isolation of the corresponding biosynthetic gene clusters and their heterologous production should become possible in the future, thus enabling the large-scale production of the corresponding natural products (see also Section 2.5).

2.3. Screening of Genomic DNA Leads to the Production of Novel Secondary Metabolites

The enormous amount of sequence data becoming available from all types of microbial sources has led to an increase in bioinformatic approaches to find novel secondary metabolites. Although this methodology is limited to the interpretation of biosynthetic genes typical for secondary metabolism, many novel secondary metabolic gene clusters can be found because they are frequently related to PKS and/or NRPS pathways. Farnet and co-workers sequenced numerous biosynthetic gene clusters that were identified by their similarity to known genes by using a genome scanning approach. These researches have significantly increased the small number of known enediyne antibiotic producing strains^[80] by growing the strains identified by genome scanning under different growth conditions and subsequent product analysis. Therefore, this approach resembles a combination of DNA sequencing with the OSMAC methodology described above (see Section 2.1).

In addition to the complete sequencing of novel biosynthetic gene clusters, small fragments of these genomic regions can be used to identify novel metabolites if the host strain can be genetically manipulated. Numerous strategies for the amplification of fragments from PKS and/or NRPS genes by using degenerate PCR have been described and non-sequenced genomic libraries can be probed and screened for the presence of PKS and/or NRPS gene fragments in single or multiple biosynthetic gene clusters. Once the genomic regions involved in natural product biosynthesis have been identified, the fragments can be used for gene inactivation studies and the resulting mutants and their wild-type strains can be compared for their production profile. At least three novel compounds were found in *Stigmatella aurantiaca*^[81] by using this approach (myxochelin,^[82] myxochromid,^[83] and aurafuron^[84]; see Figure 4).

It could be argued that these compounds could have been found in the strain by an intense variation of the culture conditions. However, the application of genetic knowledge has tremendously increased the chances of identifying novel compounds whose production is dependent on the corresponding genes. In the case of metabolites produced at low levels, it is difficult to define whether the “novel compounds” are indeed such or just components of the medium. The latter can be ruled out if production is dependent on an identified gene locus.

While many research groups focus on identifying and then sequencing novel biosynthetic pathways, bioinformaticians preferentially use the numerous new microbial genome sequences to predict new pathways by in silico methods. On the basis of PKS and NRPS enzymology logic,^[21,28,85] even

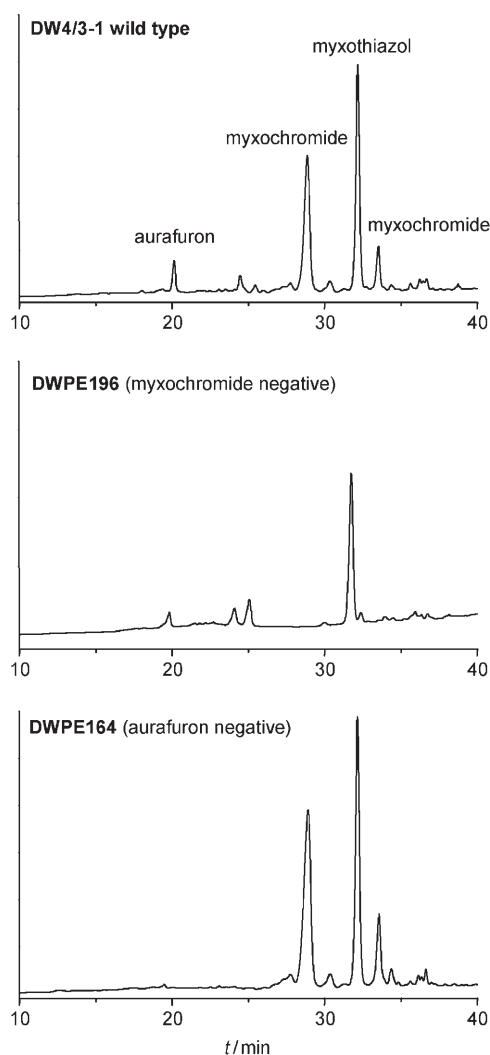


Figure 4. HPLC traces with UV detection (200–400 nm) showing the correlation of biosynthesis gene clusters and the corresponding natural products in *S. aurantiaca* DW4/3-1 by comparison of wild types and mutants.^[81]

structures of unknown compounds can theoretically be predicted depending on bioinformatic gene cluster analyses.^[86–89] A biosynthetic gene cluster of unknown function was identified from *S. aurantiaca* that was predicted to be involved in iron chelator biosynthesis and was indeed found subsequently to be responsible for myxochelin formation in this strain.^[82,90] Bacillibactin was found in *Bacillus subtilis* on the basis of genome analysis,^[91] and coelichelin has been predicted to be an iron chelator from *S. coelicolor*.^[92] The latter compound was indeed found three years later.^[53] Although this bioinformatics methodology for predicting structures seems very attractive and convincing at first, to date there are only very few examples for the subsequent identification of these “theoretical compounds”. This situation is presumably a consequence of the limitations discussed below.

All predictions were based on the nonribosomal code and/or in silico analyses of the corresponding biosynthetic PKS and NRPS gene clusters. It turns out that there are numerous exceptions to the commonly accepted “rules” for polyketide

and nonribosomal peptide biosynthesis.^[93,94] One of these rules is the biosynthetic logic of “colinearity”, which means that a correlation exists between the number and type of modules and the number and type of extender units incorporated by the megasynthetase. Nevertheless, module skipping^[95] as well as iterative use of modules have been described in PKS systems. Prediction of substrates (for example, malonyl-CoA and methylmalonyl-CoA) is difficult, and modules or domains can be inactive or “missing”.^[94,96] Similarly, NRPS domains have been found to be inactive^[83,97] and the nonribosomal code, although exceptionally useful in many cases, turns out to be not applicable in certain examples.^[98,99] To make the situation even more complicated, nonclustering of bacterial biosynthetic genes also occurs, which would make a structure prediction impossible.^[99–101]

In general, if biosynthetic systems closely related to those already described in the literature are found, predictions of similar structures using bioinformatics seems feasible. For more complicated cases, predictions will be very difficult using existing tools alone. For example, neither the mupirocin^[102] nor the disorazol biosynthetic genes^[103] could have been used to predict the structure of the compounds produced. A combined approach involving more experimental biochemistry coupled to advanced bioinformatics should improve the situation dramatically in the future.

2.4. Activation of “Silent” Biosynthetic Gene Clusters

As a viable alternative to the OSMAC and the genome scanning approaches^[80] described above, the insertion of inducible promoters into the chromosome capable of driving the expression of so far uncharacterized “silent” biosynthetic gene clusters seems practicable. Although a random activation approach of gene expression has been described,^[104] we are not aware of any proof of principle for this technology in natural product producing microorganisms. Therefore, this idea awaits practical exploitation, although problems with biosynthetic gene clusters requiring the insertion of numerous promoter regions for gene activation have to be expected.

Alternatively, influencing pleiotropic or direct regulatory mechanisms within the host cell should enable the artificial expression of uncharacterized genes and might lead to the (over)production of natural products. Whereas negative regulators might be inactivated, positive regulators can be overproduced. A recent example describes the partial activation of a silent angucycline-type gene cluster from a streptomycete.^[105] A putative repressor gene was inactivated which resulted in the production of angucycline metabolites. The ferric uptake regulator (Fur) controls numerous regulatory genes, such as *pvdS* in *Pseudomonas aeruginosa*, which encodes an alternative sigma factor. A hierarchical cascade of direct and indirect iron regulation has been analyzed by transcriptome analysis in response to iron.^[106] Strong iron regulation was observed for previously identified genes involved in biosynthesis or uptake of the siderophores pyoverdine and pyochelin. Iron-controlled regulatory genes include seven alternative sigma factors and five other transcriptional regulators.

Additionally, xenobiotics and pheromones can influence the expression of biosynthetic pathways.^[107] Although the role of *S*-adenosyl methionine (SAM) in antibiotic production is far from understood, a correlation between actinorhodin production and the level of SAM in the cell has been reported.^[108,109] Another example of defined chemicals that exhibit secondary metabolite regulatory functions in streptomycetes are the γ -butyrolactones.^[110] Davies and co-workers have shown convincingly that even antibiotics themselves, when present at subinhibitory concentrations, influence the expression of numerous genes.^[111] Secondary metabolites might very well be involved in the regulation of their own biosynthesis or of the biosynthesis of similar or totally unrelated compounds in different microorganisms and thus might be used to induce the production of additional compounds. Recently, Uchiyama et al.^[112] have shown in an elegant approach that novel metagenomic catabolic gene clusters can be identified. They measured the expression of a metagenome reporter gene library after induction with a variety of chemicals. Next, they used a fluorescence-activated cell-sorting system (FACS) to identify clones in which expression was induced, and then characterized the activated gene's product(s). One can envisage cloning fragments of “silent” biosynthetic gene clusters in a similar approach and finding low-molecular-weight inducers that enable the expression of secondary metabolite genes. Once inducers of the respective promoters are identified, they could be used to trigger expression of the silent genes in the natural host. However, since the size of many biosynthetic gene clusters makes complete cloning difficult, this approach does not seem feasible for complete heterologous expression of a whole gene cluster (see Section 2.5).

The study of the regulatory mechanisms underlying secondary metabolism is still tedious and time-consuming for examples where genomic sequences are not available. This situation is changing rapidly because of a variety of ongoing functional genome projects of natural product producers (for example, *S. coelicolor*, *S. avermitilis*, *B. subtilis*, and *Sorangium cellulosum*). The availability of genomic information sets the stage to study complex regulatory mechanisms by using transcriptomic and proteomic tools. Moreover, the genome sequence from one species enables the identification of regulatory and metabolic proteins required for the biosynthesis of the desired compound from closely related strains.^[113]

2.5. Heterologous Expression of Biosynthetic Gene Clusters

Numerous PKS and NRPS biosynthetic gene clusters have been cloned over the past decade, and the increasing biochemical knowledge from studies dealing with the corresponding enzymes has led to the emergence of combinatorial biosynthesis technologies that aim at generating novel compounds through genetic manipulation.^[114,115] In principle, the availability of the genetic information makes heterologous expression possible in improved production hosts. This technology can also be used to express biosynthetic pathways

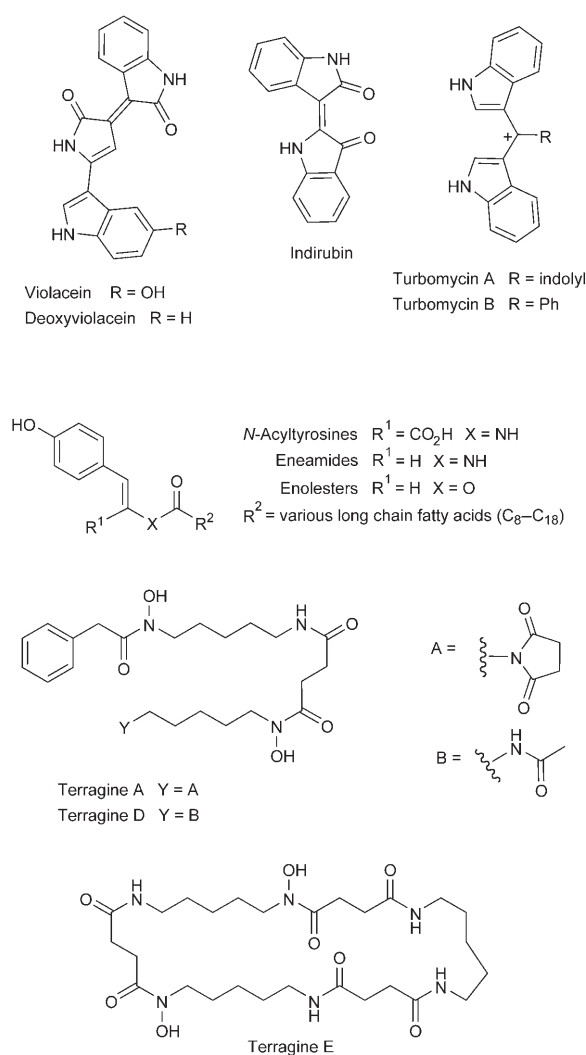
from currently not-yet-culturable microorganisms (see Section 2.2).

Genetic manipulation is straightforward in some model strains (for example, *S. coelicolor* and *B. subtilis*), but the genetic tools are insufficient or not developed for many microbial producers of natural products. A number of them are slow-growing or currently not-yet-culturable and thus not suited for genetic modification of biosynthetic pathways (for example, myxobacteria, cyanobacteria, and presumed bacterial symbionts as producers of “marine natural products”; see Section 2.2).

These circumstances and the rapidly increasing number of microbial genome sequences have led to a considerable demand in heterologous expression techniques for complete secondary metabolite pathways in natural product research and drug discovery. It is a viable alternative to the improvement of the strain and the fermentation process as well as to the genetic modification of the native producer strain.^[116]

A number of strategies for the heterologous expression of secondary metabolite pathways have been described, which range from the targeted expression of specific natural products to the expression of large unknown DNA fragments (also termed the expression of the metagenome; see Section 2.2).^[117] Bacterial artificial chromosome (BAC) shuttle vectors were used for constructing environmental libraries, followed by expression in multiple expression hosts (for example, pseudomonads, streptomycetes, and *Escherichia coli*).^[67,118] However, only products from relatively small biosynthetic gene clusters have been produced with this method to date, and the producing heterologous host has mostly been from the same genus as the natural producer (Scheme 5).^[118]

Similarly, there are a number of reports on the heterologous production of biosynthetic pathways from bacteria in closely related genera. As an example, Marahiel and co-workers have expressed and engineered the bacitracin biosynthetic pathway from *Bacillus licheniformis* in *B. subtilis* which produces almost twice as much of bacitracin as the natural producer.^[125] Salas and co-workers have recently generated more than 30 derivatives of the antitumor compound indolocarbazole in yields comparable to those from the original producer after heterologous expression of varying combinations of biosynthetic genes in *Streptomyces albus*.^[126] Most of the examples in the literature relate to small type II PKS systems,^[127–132] whereas the heterologous expression of large type I PKS and/or NRPS gene clusters has been achieved by coexpression from several plasmids, each harboring parts of the biosynthetic pathway.^[133,134] Expression of the epothilone biosynthetic gene cluster from *Sorangium cellulosum* in *Myxococcus xanthus*^[135] is another example. The methodology employed relied on several rounds of cloning and heterologous host modification because no autonomously replicating units are known for myxobacteria. Whereas the yields in this case were only 1% of that produced in *S. cellulosum*, optimization of the medium resulted in a respectable increase in epothilone titer up to the level of the original natural producer.^[136] Nevertheless, it has to be considered that the original strain has in the meantime been significantly improved for production by classical methods,



Scheme 5. Low-molecular-weight compounds produced from fragments of different metagenomes.^[119–124]

similarly to the soraphen-producing strain *S. cellulosum* Soce26.^[137]

Only within the last few years has it been shown that the production of complex natural products in unrelated bacteria is feasible. In these elegant studies a genetically engineered *E. coli* host was used to produce the aglycone precursor of erythromycin.^[116] Subsequently, precursors of ansamycin macrolactam were produced in *E. coli* after expression of part of the biosynthetic operon.^[138] Epothilone as well as soraphen derived from myxobacteria that belong to the genus *Sorangium* have been produced in streptomycetes, although in very low yields.^[139,140] Despite increasing experience with the various hosts, the product yields have typically been much lower than those in the original producer. This might be a consequence of weaknesses in the natural promoter, problems with expression levels of correctly folded proteins,^[141] difficulties with the essential posttranslational activation of carrier proteins,^[142] differences in mRNA stability, or precursor supply, to name just a few possible drawbacks of the technique. Numerous ongoing studies in many laboratories are addressing these questions in various ways, including the

application of novel genetic engineering systems and the use of a variety of heterologous hosts.

In all of the studies mentioned above, classical and time-consuming cloning procedures were employed, and the expression of large secondary metabolite clusters was only achieved by coexpression from several genetic units. Recently, the application of recombinogenic engineering^[143] in *E. coli* for cloning and manipulating large natural product assembly lines has been used successfully by several research groups. This technique is particularly suitable for large DNA molecules such as BACs and cosmids, as it does not rely on classical cloning procedures. After overexpression of proteins facilitating efficient homologous recombination (Red/ET) in *E. coli*, PKS and NRPS pathways can be altered and redesigned based on short homology arms.

Researchers at Cubist have applied this methodology to engineer the daptomycin biosynthetic pathway from *Streptomyces roseosporus* in *E. coli* on a BAC; they then expressed it in a daptomycin-negative mutant of *S. roseosporus* to produce novel and active lipopeptides.^[144] In this example, a closely related (here in fact the same) expression host was used, which is feasible and sensible when well-developed hosts are available. As this prerequisite has not been achieved in many areas of research, efficient heterologous expression of biosynthetic gene clusters from microbial producers is still a challenging task, especially for the slow-growing or not-yet-culturable sources. In a recent example, Red/ET recombination^[143] has also been used to rebuild the complete assembly line from the myxobacterial myxochromid PKS/NRPS hybrid gene cluster in one genetic unit and to introduce the elements required for conjugation, stable integration, and regulated expression in the heterologous host *Pseudomonas putida*.^[97]

One of the important advantages of this method is that the whole secondary metabolite pathway is located on one construct, which can be accurately manipulated in *E. coli* and transferred into the heterologous host strain. Surprisingly, the fermentation time is reduced threefold when producing myxochromide S in *P. putida* while the product yield is fivefold higher relative to that of the natural producer *S. aurantiaca*. *P. putida* is able to produce all the required activated precursors for myxochromide S biosynthesis (acetyl-CoA, malonyl-CoA, and propionyl-CoA) and expresses a broad spectrum phosphopantetheinyl transferase which is necessary for activation of the carrier protein.^[145] As genetic manipulation in *P. putida* is straightforward, it should be possible to engineer the strain to produce further precursors that are essential for the biosynthesis of other secondary metabolites (for example, unusual extension units and amino acids) from various sources. Therefore, this strategy, which combines the power of advanced DNA engineering and mutagenesis in *E. coli* with the utility of pseudomonads as the heterologous host, provides a new alternative for the analysis and mutagenesis of known and unknown secondary metabolite pathways.

Another alternative approach focuses on artificial DNA synthesis of complete biosynthetic gene clusters. This approach depends on the ability to synthesize long, accurate DNA sequences efficiently. The idea was validated by building a synthetic PKS gene cluster whose functionality

was demonstrated by its ability to produce the megaenzyme and its polyketide product in *Escherichia coli* by synthesizing approximately 5-kb segments of DNA, followed by their assembly into longer sequences by conventional cloning methods.^[146]

It should be pointed out that it is unlikely that there will be a single solution to the immense variety of heterologous expression problems in the future. Closely related and well-established production hosts which can be manipulated genetically may be regarded as first-choice organisms. However, since these are often unavailable, as many production hosts as possible should be further developed to provide a battery of possible expression technologies, the strength and weaknesses of which will become evident in the future.

2.6. Combinatorial Biosynthesis

2.6.1. Genetic Engineering of the Natural Host

The modularity and versatility of PKS and NRPS as well as challenges and opportunities in combinatorial biosynthesis have been discussed in excellent reviews.^[24, 147–153] To illustrate our growing knowledge related to the genetic engineering and the production of novel compounds with altered structures, we refer here to some studies that have been published in recent years. Further examples of combinatorial biosynthesis approaches are presented in Section 2.5 (heterologous expression techniques).

The Leadlay and Staunton research groups have extended their pioneering work in PKS research by engineering starter unit specificity in the erythromycin-producing PKS in vivo.^[154] They were even able to show in the same biosynthetic system that a longer polyketide chain can be generated after insertion of an extra module into the PKS.^[155] The same research group was also able to produce ivermectin-like drugs after domain exchange in the avermectin PKS of *S. avermitilis* although in a reduced overall yield.^[156] In yet another example they employed the loading domain of the soraphen PKS, which was speculated to load benzoyl-CoA onto the megasynthase from *S. cellulorum*.^[157] To prove this hypothesis, this domain was used to make a DEBS1-TE hybrid (fusing the thioesterase domain of DEBS3 to DEBS1 and exchanging the erythromycin-loading module against the soraphen loading module), which resulted in the production of 5-phenyltriketide lactone with a yield of approximately 1 % of the regular DEBS1-TE triketide.^[158] Subsequent studies showed that additional phenyl-substituted polyketides could also be made.^[159]

Researchers at Kosan Biosciences and Stanford University have performed equally impressive work in PKS engineering.^[160, 161] They were able to reengineer the genes that encode the erythromycin formation to produce the antiparasitic agent megalomicin in *Saccharopolyspora erythraea* in better yields than could be obtained from the natural producer.^[162] They also performed studies to understand the substrate specificity of PKS modules by generating hybrid multimodular synthases.^[163] Katz and co-workers produced a new epothilone derivative in good yields by engineering the epothilone megasynthetase (albeit not in the natural pro-

ducer, see above).^[164] The combinatorial biosynthesis of pikromycin-related macrolides in *Streptomyces venezuelae* has also been studied^[165] and led to the generation of multiple bioactive macrolides by hybrid modular PKSs in this streptomycete.^[166]

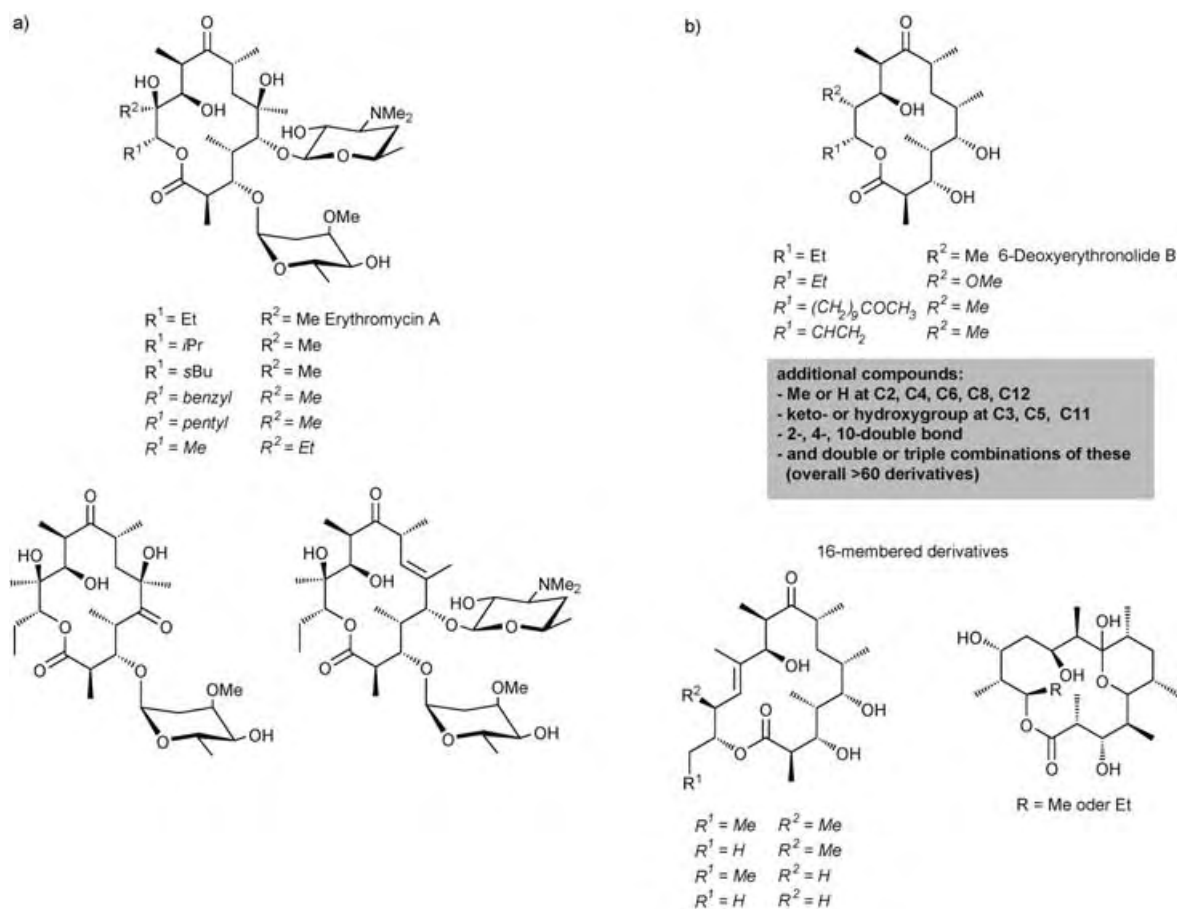
Combinatorial biosynthesis using type II PKSs is the focus of several research groups.^[114,115,131,167] Chromomycin analogues differing in the methylation, acylation, and glycosylation pattern were recently made by manipulating the respective post-PKS genes.^[168,169] Other examples of the engineering of biosynthetic pathways using such post-PKS enzymes are derived from the characterization of glycosyl transferases, which can be employed to generate novel structures in vivo and in vitro (see Section 2.6.2).^[170,171] It can be expected that genomic information from natural product producers will provide increasing knowledge about nature's secondary metabolite assembly tool box which can be applied in various ways to rational pathway engineering.

All the examples reported in this section have resulted in the production of new compounds, however, there may be many more examples that did not work at all and will presumably never appear in the literature. A failed example of pathway engineering is related to various manipulations of the myxothiazol megasynthetase in *S. aurantiaca*. Although relatively simple genetic manipulations were performed, neither intermediates nor expected derivatives of the biosyn-

thetic pathway could be observed, no matter what part of the biosynthetic gene cluster was manipulated (Scheme 6).^[172]

2.6.2. In Vitro Studies Using Biosynthetic Enzymes

Biosynthetic genes identified in the search for new secondary metabolic gene loci are widely used for the expression of catalytic modules and domains for in vitro studies with purified enzymes. These recombinant proteins were initially employed to decipher the biochemistry of biosynthetic pathways^[28,173,174] and in vitro reconstitutions of complex natural product biosyntheses were reported.^[90,175,176] In vitro combinatorial biosynthesis techniques have mostly relied on genetic engineering and mutation in *E. coli* because this technique is much faster than the engineering of most, or probably all, typical secondary metabolite producers. Consequently, most functional biochemical and also combinatorial studies have been performed with proteins that could be actively expressed in *E. coli*. Pioneering work by the Marahiel and Walsh research groups has shown that recombinant NRPS and PKS proteins can be engineered to produce novel and altered products.^[30,174,177] The feasibility of combinatorial biosynthesis to make commercially useful compounds has been shown by creating a recombinant NRPS capable of synthesizing in vitro α -L-aspartyl-L-phenylalanine, the precursor of the artificial sweetener aspartame.^[178] New inter-



Scheme 6. Selected variations of erythromycin (a) and its aglycone 6-deoxyerythronolide B (b) obtained by combinatorial biosynthesis and mutasynthesis (italics). Overall, more than 100 derivatives have been generated by using combinatorial biosynthesis and mutasynthesis.

mediates of epothilone^[179] and rifamycin^[180,181] biosynthesis, but with alternative starter units, were made using purified proteins from the respective gene clusters. In another study, the modification of the acyl carrier protein with alternative starter units enabled the biosynthesis of novel polyketides with 16 (instead of 14) carbon atoms by employing the minimal actinorhodin type II PKS.^[182] An alternative way to generate chemical diversity using purified bacterial biosynthetic proteins is exemplified by recent in vitro studies using the iterative and relatively small type III PKSs. These “plant-like PKSs” were first described by the Horinouchi research group.^[27,183] It was realized that these enzymes are commonly found in bacteria^[23,184–186] and that they are versatile systems for generating novel products.^[187–190] Up to 14 compounds of different structural types (pyrones and phenoles varying in side-chains length) have been produced in vitro by using RppA (type III PKS involved in red-brown pigment production) to elongate five different starting units with malonyl-CoA.^[187] Type III PKS are also involved in the formation of precursors of glycopeptides by NRPS; such enzymes from the balhimycin and the vancomycin biosynthetic gene clusters were identified as synthases of 3,5-dihydroxyphenylacetic acid, which serves as a precursor for the unusual amino acid 3,5-dihydroxyphenylglycine^[191,192] that is part of the glycopeptide backbone.

Recently, proteins or excised catalytic domains from natural product biosynthetic pathways have also been used in chemoenzymatic syntheses. PKSs and NRPSs responsible for the production of macrocyclic compounds often employ their C-terminal thioesterase (TE) domain to catalyze enzymatic cyclization of a linear precursor.^[193] Walsh and co-workers showed that excised TE domains retain their autonomous ability to catalyze the macrocyclization of linear peptide thioesters with native peptide sequences. Additionally, they can cyclize peptide analogues with alterations in the peptide sequence and peptide/polyketide-like hybrids with longer chain lengths.^[194] Thus, these macrocyclization catalysts raise the prospect of using TE catalysis for the generation of macrocyclic peptide libraries.^[195] Isolated TEs can also catalyze the cyclization of linear peptides immobilized on a solid-phase support, which offers the possibility to merge natural product biosynthesis with combinatorial solid-phase chemistry.^[196] In an extension of this approach, even glycosylated glycopeptides could be cyclized in good yields.^[197]

Glycosyltransferases are frequently found as tailoring enzymes associated with products derived from PKS and NRPS. They play a key role in the decoration of natural product core structures with sugar moieties that are often essential for biological activity. The corresponding proteins utilize activated sugars and can be altered genetically to accept and glycosylate a variety of substrates. Thorson and co-workers pioneered this approach and called it “glycorandomization” (Scheme 7).^[198,199] Progress in the understanding of deoxyhexose and aminosugar biosynthesis will facilitate the future use of new sugars or those which are difficult to prepare chemically.^[200,201]

In general, it can be expected that any type of tailoring enzyme capable of decorating the product of a megasynthe-

tase (for example, glycosyl transferases, methyl transferases, hydrolases, P450-dependent enzymes, or prenylating enzymes) can be used for similar in vitro studies in the future. As genome sequencing efforts reveal more and more of the genetic basis of microbial biochemical diversity, the corresponding biosynthetic genes await exploitation in combinatorial approaches.

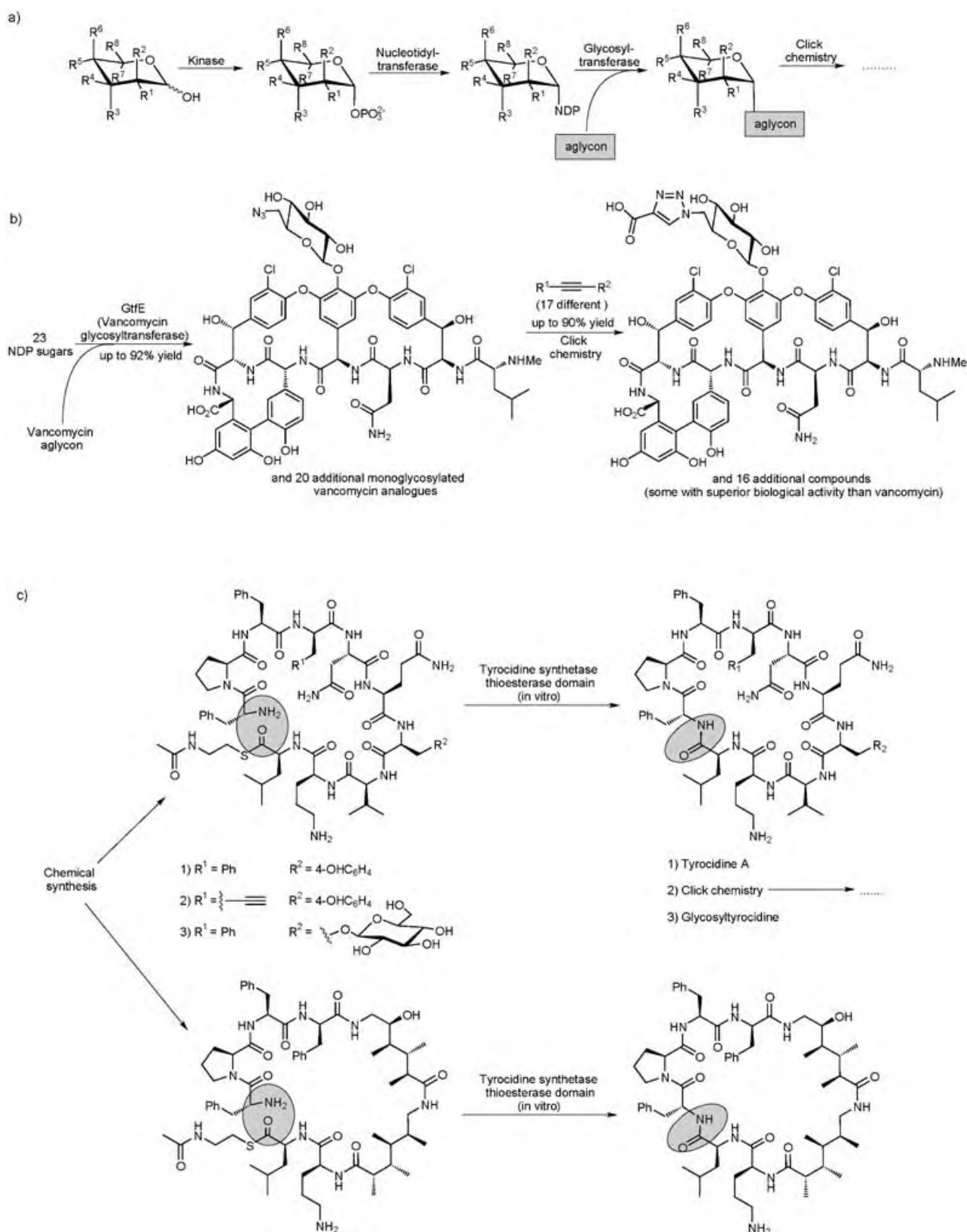
2.7. Mutasynthesis

The extraordinary possibilities of the combination of genomic techniques with “old-fashioned” mutasynthesis^[204] has been excellently reviewed.^[205,206] We will thus only provide some recent examples which best exemplify the potential of this approach.

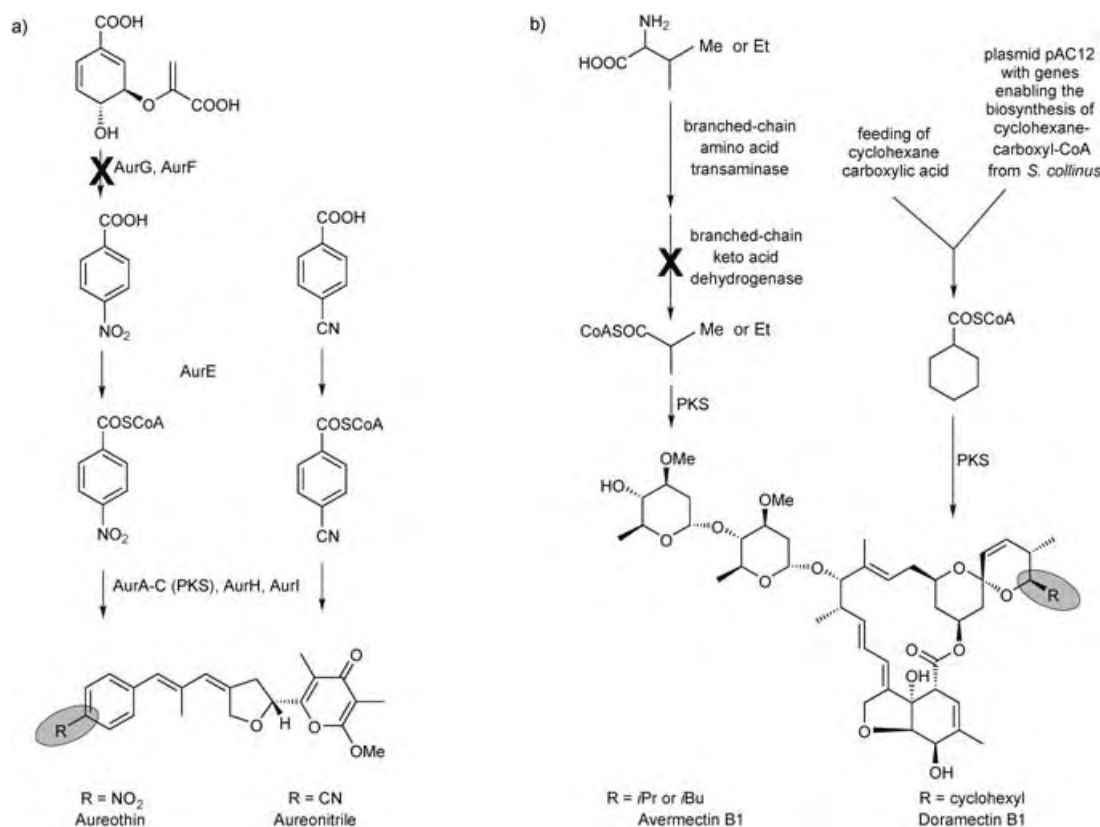
Biosynthesis of synthetic precursors has been used extensively in polyketide and nonribosomal peptide producing organisms using precursors that are activated as *N*-acetyl cysteamine (NAC) thioesters which mimic the carrier-protein-bound biosynthetic intermediates.^[207–212] In mutasynthesis approaches, the efficiency of the incorporation of an intermediate which is fed to a culture can be significantly increased if the biosynthesis of the natural precursor is blocked by mutagenesis. Hertweck and co-workers generated the novel cytostatic compound aureonitrile using *p*-cyano-benzoyl-SNAC as an unnatural starter unit of the aureothin biosynthesis in a mutant unable to produce the natural primer *p*-nitrobenzoyl-CoA.^[213] The authors showed that the addition of *p*-cyanobenzoate is sufficient for the production of aureonitrile, presumably because the endogenous *p*-nitrobenzoate CoA ligase can activate both precursors (Scheme 8).

The biosynthesis and the mode of attachment of a wide range of PKS starter units in bacteria are covered in a recent review by Moore and Hertweck.^[215] A prominent example of the practical application of a combined mutasynthesis/combinatorial biosynthesis approach is the production of the unnatural natural compound doramectin, a derivative of the anthelmintic type I polyketide avermectin that differs in the starting unit.^[216]

Avermectin biosynthesis is usually primed with thioesters of activated short branched-chain carboxylic acids which are derived from the degradation of branched-chain amino acids. Once this degradation pathway is inactivated, avermectin production is stalled. However, the lack of precursors can be overcome by the addition of cyclohexylcarboxylic acid (or other related precursors), which leads to the production of doramectin, a broad-spectrum antiparasitic compound with activity superior to avermectin. After a pathway involved in the biosynthesis of cyclohexylcarboxyl-CoA has been identified in *Streptomyces collinus*,^[217] Reynolds and co-workers transferred these genes into the *S. avermitilis* mutant impaired in the production of the natural starter unit. This approach led to the direct production of doramectin in excellent yields that were comparable to those found after the exogenous addition of cyclohexylcarboxylic acid to the *S. avermitilis* mutant.^[214] The experiment represents metabolic engineering rather than mutasynthesis, because no precursor or intermediate is added to the fermentation broth.



Scheme 7. In vitro derivatization and synthesis of natural products. a) General outline of the glycorandomization approach.^[198] b) Glycorandomization applied to vancomycin.^[202] c) Generation of tyrocidine analogues by using a combination of chemical synthesis and thioesterase-catalyzed cyclization.^[194,197,203]



Scheme 8. Generation of aureonitrile by mutasynthesis (a) and doramectin by metabolic engineering (b).^[213,214]

Combinations of mutational and chemoenzymatic approaches have been exploited to generate new rapamycins^[218] and aminocoumarins.^[219, 220] Novel glycopeptides were made using the biosynthetic potential of halogenases.^[221]

The potential of mutasynthesis can be evaluated prior to in vivo experiments in studies employing recombinant biosynthetic enzymes, in an analogous way to the work described in Section 2.6.2. Walsh and co-workers could show in vitro that the first modules of the epothilone synthetase can utilize alternative starter units and substrates to generate novel intermediates.^[179,222] It will be interesting to see whether these experiments will lead to the large-scale production of novel epothilones in vivo as well.

As can be deduced from the examples given above, there often appears to be no clear borderline between the types of approaches described. Several commonly used phrases such as “combinatorial biosynthesis” and “mutasynthesis” are not well defined and might be summarized as different forms of “metabolic (or biosynthetic) engineering” techniques. The strengths of the experimental ideas lie in the application of combined techniques for the particular problem to be solved.

3. Be Prepared! Natural Product Research in the Postgenomic Era

The impact of increasing genomic information as well as biosynthetic and regulatory studies that decipher the molec-

ular basis of natural product formation have been described in this Review, and technologies exploiting this knowledge for the generation of new natural products with biological activity have been summarized. These techniques have already led to the production of several novel compounds. The prerequisite of rational pathway engineering is a comprehensive understanding of complex natural product biosynthesis at the molecular level, but since this has not been achieved in many cases, numerous manipulations of biosynthetic pathways are ineffective or lead to low production yields; thus, further in depth biochemical studies are needed. Furthermore, exponentially increasing sequencing information, novel cultivation techniques, metagenomic approaches, and progress in heterologous expression and molecular biology in general are expected to give natural products research a promising future. The rapid progress in all areas of metabolic/biosynthetic engineering offers opportunities to alter and/or derivatize auspicious natural product leads in vivo and in vitro. Considering the structural complexity of natural products, this approach might well become a cornerstone of pharmaceutical lead development in the future.

Research in the authors laboratory was supported by the DFG and the BMBF. The authors would like to acknowledge Mark Zabriskie, Barrie Wilkinson, Christian Hertweck, and an unknown reviewer for providing helpful comments.

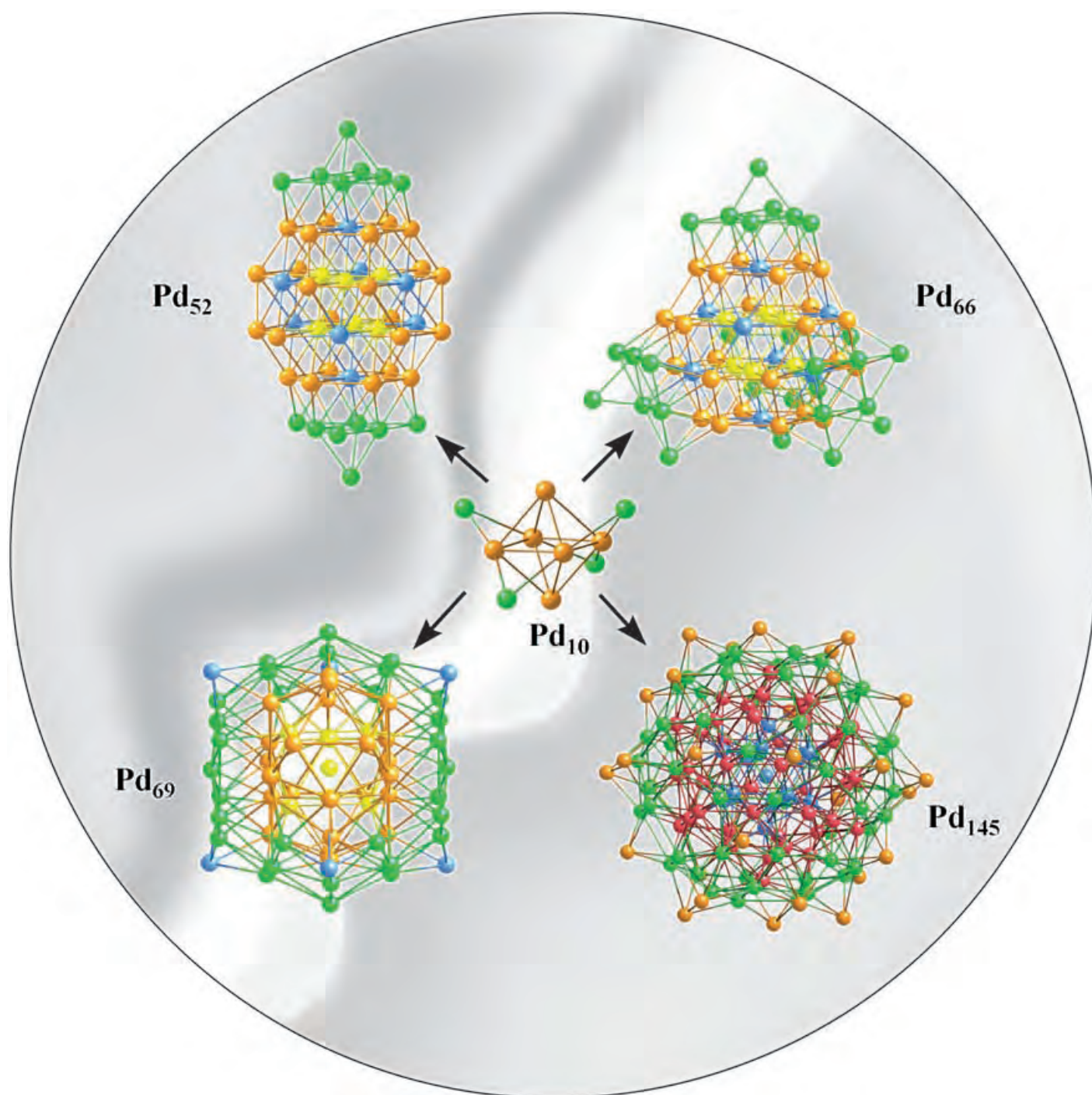
Received: March 25, 2005

- [1] D. Newman, G. Cragg, K. Snader, *J. Nat. Prod.* **2003**, 66, 1022.
- [2] G. D. Wright, *Chem. Biol.* **2000**, 7, R127.
- [3] R. P. Wenzel, *N. Engl. J. Med.* **2004**, 351, 523.
- [4] C. J. Thomson, E. Power, H. Ruebsamen-Waigmann, H. Labischinski, *Curr. Opin. Microbiol.* **2004**, 7, 445.
- [5] R. Nelson, *Lancet* **2003**, 362, 1726.
- [6] T. Clarke, *Nature* **2003**, 425, 225.
- [7] T. Henkel, R. M. Brunne, H. Müller, F. Reichel, *Angew. Chem.* **1999**, 111, 688; *Angew. Chem. Int. Ed.* **1999**, 38, 643.
- [8] M. L. Lee, G. Schneider, *J. Comb. Chem.* **2001**, 3, 284.
- [9] M. Feher, J. M. Schmidt, *J. Chem. Inf. Comput. Sci.* **2003**, 43, 218.
- [10] J. Y. Ortholand, A. Ganesan, *Curr. Opin. Chem. Biol.* **2004**, 8, 271.
- [11] C. M. Dobson, *Nature* **2004**, 432, 824.
- [12] C. Lipinski, A. Hopkins, *Nature* **2004**, 432, 855.
- [13] R. D. Firn, C. G. Jones, *Nat. Prod. Rep.* **2003**, 20, 382.
- [14] J. Niggemann, K. Michaelis, R. Frank, N. Zander, G. Höfle, *J. Chem. Soc. Perkin Trans. 1* **2002**, 2490.
- [15] U. Abel, C. Koch, M. Speitling, F. G. Hansske, *Curr. Opin. Chem. Biol.* **2002**, 6, 453.
- [16] A. M. Boldi, *Curr. Opin. Chem. Biol.* **2004**, 8, 281.
- [17] A. Ganesan, *Curr. Opin. Biotechnol.* **2004**, 15, 584.
- [18] A. R. Knaggs, *Nat. Prod. Rep.* **2003**, 20, 119.
- [19] A. R. Knaggs, *Nat. Prod. Rep.* **2001**, 18, 334.
- [20] P. M. Dewick, *Nat. Prod. Rep.* **2002**, 19, 181.
- [21] J. Staunton, K. J. Weissman, *Nat. Prod. Rep.* **2001**, 18, 380.
- [22] B. Shen, *Top. Curr. Chem.* **2000**, 209, 1.
- [23] M. B. Austin, J. P. Noel, *Nat. Prod. Rep.* **2003**, 20, 79.
- [24] C. T. Walsh, *Science* **2004**, 303, 1805.
- [25] D. Cane, C. Walsh, *Chem. Biol.* **1999**, 6, R319.
- [26] B. Shen in *Topics in Current Chemistry*, Vol. 209 (Eds.: A. de Meijere, K. Houk, H. Kessler, J.-M. Lehn, S. V. Ley, S. L. Schreiber, J. Thiem), Springer, Berlin, **2000**, p. 1.
- [27] N. Funai, Y. Ohnishi, I. Fujii, M. Shibuya, Y. Ebizuka, S. Horinouchi, *Nature* **1999**, 400, 897.
- [28] D. Schwarzer, R. Finking, M. A. Marahiel, *Nat. Prod. Rep.* **2003**, 20, 275.
- [29] H. D. Mootz, M. A. Marahiel, *J. Bacteriol.* **1997**, 179, 6843.
- [30] H. D. Mootz, D. Schwarzer, M. A. Marahiel, *Proc. Natl. Acad. Sci. USA* **2000**, 97, 5848.
- [31] R. D. Fleischmann et al., *Science* **1995**, 269, 496.
- [32] www.genomesonline.org and www.tigr.org.
- [33] W. C. Nierman, C. M. Fraser, *Trends Microbiol.* **2004**, 12, 62.
- [34] H. Ikeda, J. Ishikawa, A. Hanamoto, M. Shinose, H. Kikuchi, T. Shiba, Y. Sakaki, M. Hattori, S. Omura, *Nat. Biotechnol.* **2003**, 21, 526.
- [35] S. D. Bentley et al., *Nature* **2002**, 417, 141.
- [36] C. R. Buell et al., *Proc. Natl. Acad. Sci. USA* **2003**, 100, 10181.
- [37] R. Croteau, T. Kutchan, N. Lewis in *Biochemistry and Molecular Biology of Plants* (Eds.: B. Buchanan, W. Gruissem, R. Joneas), American Society of Plant Biologists, Rockville, MD, **2000**, p. 1250.
- [38] S. Jennewein, R. Croteau, *Appl. Microbiol. Biotechnol.* **2001**, 57, 13.
- [39] E. Leistner, *Pharm. Unserer Zeit* **2005**, 34, 98.
- [40] S. Jennewein, M. R. Wildung, M. Chau, K. Walker, R. Croteau, *Proc. Natl. Acad. Sci. USA* **2004**, 101, 9149.
- [41] M. Chau, S. Jennewein, K. Walker, R. Croteau, *Chem. Biol.* **2004**, 11, 663.
- [42] K. Walker, R. Croteau, *Proc. Natl. Acad. Sci. USA* **2000**, 97, 13591.
- [43] K. D. Walker, K. Klettke, T. Akiyama, R. Croteau, *J. Biol. Chem.* **2004**, 279, 53947.
- [44] P. I. Lerner, *N. Engl. J. Med.* **2004**, 351, 524.
- [45] G. Testa, G. B. Klintmalm, *Clin. Liver Dis.* **1997**, 1, 417.
- [46] J. A. Tobert, *Nat. Rev. Drug Discovery* **2003**, 2, 517.
- [47] A. Goffeau et al., *Nature* **1997**, 387, 5.
- [48] V. Wood et al., *Nature* **2002**, 415, 871.
- [49] J. E. Galagan et al., *Nature* **2003**, 422, 859.
- [50] D. Martinez et al., *Nat. Biotechnol.* **2004**, 22, 695.
- [51] B. Dujon et al., *Nature* **2004**, 430, 35.
- [52] F. Barona-Gomez, U. Wong, A. E. Giannakopoulos, P. J. Derrick, G. L. Challis, *J. Am. Chem. Soc.* **2004**, 126, 16282.
- [53] S. Lautru, R. J. Deeth, L. M. Bailey, G. L. Challis, *Nature Biotechnol.* **2005**, 1, 265.
- [54] K. T. Konstantinidis, J. M. Tiedje, *Proc. Natl. Acad. Sci. USA* **2004**, 101, 3160.
- [55] A. T. Bull, A. C. Ward, M. Goodfellow, *Microbiol. Mol. Biol. Rev.* **2000**, 64, 573.
- [56] H. B. Bode, B. Bethe, R. Höfs, A. Zeeck, *ChemBioChem* **2002**, 3, 619.
- [57] J. Fuchser, A. Zeeck, *Liebigs Ann./Recl.* **1997**, 87.
- [58] H. B. Bode, M. Walker, A. Zeeck, *Eur. J. Org. Chem.* **2000**, 3185.
- [59] G. Chen, G. Y. Wang, X. Li, B. Waters, J. Davies, *J. Antibiot.* **2000**, 53, 1145.
- [60] K. Ueda, S. Kawai, H. Ogawa, A. Kiyama, T. Kubota, H. Kawanobe, T. Beppu, *J. Antibiot.* **2000**, 53, 979.
- [61] N. R. Pace, *Science* **1997**, 276, 734.
- [62] M. Keller, K. Zengler, *Nat. Rev. Microbiol.* **2004**, 2, 141.
- [63] K. Zengler, G. Toledo, M. Rappe, J. Elkins, E. J. Mathur, J. M. Short, M. Keller, *Proc. Natl. Acad. Sci. USA* **2002**, 99, 15681.
- [64] T. Kaeberlein, K. Lewis, S. S. Epstein, *Science* **2002**, 296, 1127.
- [65] K. E. Davis, S. J. Joseph, P. H. Janssen, *Appl. Environ. Microbiol.* **2005**, 71, 826.
- [66] W. R. Streit, R. A. Schmitz, *Curr. Opin. Microbiol.* **2004**, 7, 492.
- [67] R. Daniel, *Curr. Opin. Biotechnol.* **2004**, 15, 199.
- [68] W. R. Streit, R. Daniel, K. E. Jaeger, *Curr. Opin. Biotechnol.* **2004**, 15, 285.
- [69] J. C. Venter et al., *Science* **2004**, 304, 66.
- [70] D. J. Newman, G. M. Cragg, *J. Nat. Prod.* **2004**, 67, 1216.
- [71] J. Piel, D. Hui, G. Wen, D. Butzke, M. Platzer, N. Fusetani, S. Matsunaga, *Proc. Natl. Acad. Sci. USA* **2004**, 101, 16222.
- [72] M. Hildebrand, L. E. Waggoner, H. Liu, S. Sudek, S. Allen, C. Anderson, D. H. Sherman, M. Haygood, *Chem. Biol.* **2004**, 11, 1543.
- [73] T. Arai, K. Takahashi, A. Kubo, S. Nakahara, S. Sato, K. Aiba, C. Tamura, *Tetrahedron Lett.* **1979**, 20, 2355.
- [74] H. Y. He, D. J. Faulkner, *J. Org. Chem.* **1989**, 54, 5822.
- [75] T. M. Zabriskie, J. A. Klocke, C. M. Ireland, A. H. Marcus, T. F. Molinski, D. J. Faulkner, C. Xu, J. Clardy, *J. Am. Chem. Soc.* **1986**, 108, 3123.
- [76] B. Kunze, R. Jansen, F. Sasse, G. Höfle, H. Reichenbach, *J. Antibiot.* **1995**, 48, 1262.
- [77] K. Suzumura, I. Takahashi, H. Matsumoto, K. Nagai, B. Setiawan, R. M. Rantiatmodjo, K. Suzuki, N. Nagano, *Tetrahedron Lett.* **1997**, 38, 7573.
- [78] S. K. Davidson, S. W. Allen, G. E. Lim, C. M. Anderson, M. G. Haygood, *Appl. Environ. Microbiol.* **2001**, 67, 4531.
- [79] J. Piel, *Proc. Natl. Acad. Sci. USA* **2002**, 99, 14002.
- [80] E. Zazopoulos et al., *Nat. Biotechnol.* **2003**, 21, 187.
- [81] B. Silakowski, B. Kunze, R. Müller, *Gene* **2001**, 275, 233.
- [82] B. Silakowski, B. Kunze, G. Nordsiek, H. Blöcker, G. Höfle, R. Müller, *Eur. J. Biochem.* **2000**, 267, 6476.
- [83] S. C. Wenzel, B. Kunze, G. Höfle, B. Silakowski, M. Scharfe, H. Blöcker, R. Müller, *ChemBioChem* **2005**, 6, 375.
- [84] B. Kunze, H. Reichenbach, R. Müller, G. Höfle, *J. Antibiot.* **2005**, 58, 244.
- [85] C. T. Walsh in *Antibiotics: Actions, Origins, Resistance*, ASM, Washington, DC, **2003**, p. 175.
- [86] G. Yadav, R. S. Gokhale, D. Mohanty, *J. Mol. Biol.* **2003**, 328, 335.

- [87] G. Yadav, R. S. Gokhale, D. Mohanty, *Nucleic Acids Res.* **2003**, *31*, 3654.
- [88] G. L. Challis, J. Ravel, C. A. Townsend, *Chem. Biol.* **2000**, *7*, 211.
- [89] T. Stachelhaus, H. D. Mootz, M. A. Marahiel, *Chem. Biol.* **1999**, *6*, 493.
- [90] N. Gaitatzis, B. Kunze, R. Müller, *Proc. Natl. Acad. Sci. USA* **2001**, *98*, 11 136.
- [91] J. J. May, T. M. Wendrich, M. A. Marahiel, *J. Biol. Chem.* **2001**, *276*, 7209.
- [92] G. L. Challis, J. Ravel, *FEMS Microbiol. Lett.* **2000**, *187*, 111.
- [93] B. Shen, *Curr. Opin. Chem. Biol.* **2003**, *7*, 285.
- [94] R. Müller, *Chem. Biol.* **2004**, *11*, 4.
- [95] I. Thomas, C. J. Martin, C. J. Wilkinson, J. Staunton, P. F. Leadlay, *Chem. Biol.* **2002**, *9*, 781.
- [96] S. J. Moss, C. J. Martin, B. Wilkinson, *Nat. Prod. Rep.* **2004**, *21*, 575.
- [97] S. C. Wenzel, F. Gross, Y. Zhang, J. Fu, F. A. Stewart, R. Müller, *Chem. Biol.* **2005**, *12*, 349.
- [98] D. Tillett, E. Dittmann, M. Erhard, H. von Döhren, T. Börner, B. A. Neilan, *Chem. Biol.* **2000**, *7*, 753.
- [99] A. Sandmann, F. Sasse, R. Müller, *Chem. Biol.* **2004**, *11*, 1071.
- [100] T. W. Yu et al., *Proc. Natl. Acad. Sci. USA* **2002**, *99*, 7968.
- [101] J. Piel, G. P. Wen, M. Platzer, D. Q. Hui, *ChemBioChem* **2004**, *5*, 93.
- [102] A. K. El-Sayed, J. Hotherhall, S. M. Cooper, E. Stephens, T. J. Simpson, C. M. Thomas, *Chem. Biol.* **2003**, *10*, 419.
- [103] M. Kopp, H. Irschik, S. Pradella, R. Müller, *ChemBioChem* **2005**, 1277.
- [104] J. J. Harrington et al., *Nat. Biotechnol.* **2001**, *19*, 440.
- [105] M. Metsä-Ketela, K. Ylihönö, P. Mantsala, *J. Antibiot.* **2004**, *57*, 502.
- [106] U. A. Ochsner, P. J. Wilderman, A. I. Vasil, M. L. Vasil, *Mol. Microbiol.* **2002**, *45*, 1277.
- [107] Y. Ohnishi, *Nippon Nogei Kagaku Kaishi* **2003**, *77*, 852.
- [108] S. Okamoto, A. Lezhava, T. Hosaka, Y. Okamoto-Hosoya, K. Ochi, *J. Bacteriol.* **2003**, *185*, 601.
- [109] D. J. Kim, J. H. Huh, Y. Y. Yang, C. M. Kang, I. H. Lee, C. G. Hyun, S. K. Hong, J. W. Suh, *J. Bacteriol.* **2003**, *185*, 592.
- [110] E. Takano, R. Chakraborty, T. Nihira, Y. Yamada, M. J. Bibb, *Mol. Microbiol.* **2001**, *41*, 1015.
- [111] E. B. Goh, G. Yim, W. Tsui, J. McClure, M. G. Surette, J. Davies, *Proc. Natl. Acad. Sci. USA* **2002**, *99*, 17025.
- [112] T. Uchiyama, T. Abe, T. Ikemura, K. Watanabe, *Nat. Biotechnol.* **2005**, *23*, 88.
- [113] A. M. Lum, J. Huang, C. R. Hutchinson, C. M. Kao, *Metab. Eng.* **2004**, *6*, 186.
- [114] C. Hutchinson in *Drug Discovery from Nature* (Eds.: S. Grabley, R. Thiericke), Springer, Berlin, **1999**, p. 233.
- [115] C. Mendez, J. A. Salas, *Comb. Chem. High Throughput Screening* **2003**, *6*, 513.
- [116] B. A. Pfeifer, S. J. Admiraal, H. Gramajo, D. E. Cane, C. Khosla, *Science* **2001**, *291*, 1790.
- [117] J. Handelsman, M. R. Rondon, S. F. Brady, J. Clardy, R. M. Goodman, *Chem. Biol.* **1998**, *5*, R245.
- [118] A. Martinez, S. J. Kolvek, C. L. T. Yip, J. Hopke, K. A. Brown, I. A. MacNeil, M. S. Osburne, *Appl. Environ. Microbiol.* **2004**, *70*, 2452.
- [119] D. E. Gillespie, S. F. Brady, A. D. Bettermann, N. P. Cianciotto, M. R. Liles, M. R. Rondon, J. Clardy, R. M. Goodman, J. Handelsman, *Appl. Environ. Microbiol.* **2002**, *68*, 4301.
- [120] S. F. Brady, C. J. Chao, J. Clardy, *J. Am. Chem. Soc.* **2002**, *124*, 9968.
- [121] S. F. Brady, C. J. Chao, J. Handelsman, J. Clardy, *Org. Lett.* **2001**, *3*, 1981.
- [122] S. F. Brady, J. Clardy, *J. Am. Chem. Soc.* **2000**, *122*, 12903.
- [123] G. Y. Wang et al., *Org. Lett.* **2000**, *2*, 2401.
- [124] M. S. Osburne, T. H. Grossman, P. R. August, I. A. MacNeil, *ASM News* **2000**, *66*, 411.
- [125] K. Eppelmann, S. Doekel, M. A. Marahiel, *J. Biol. Chem.* **2001**, *276*, 34824.
- [126] C. Sanchez, L. Zhu, A. F. Brana, A. P. Salas, J. Rohr, C. Mendez, J. A. Salas, *Proc. Natl. Acad. Sci. USA* **2005**, *102*, 461.
- [127] A. Bechthold, J. K. Sohng, T. M. Smith, X. Chu, H. G. Floss, *Mol. Gen. Genet.* **1995**, *248*, 610.
- [128] C. Y. Kim, H. J. Park, E. S. Kim, *J. Microbiol. Biotechnol.* **2003**, *13*, 819.
- [129] S. T. Hong, J. R. Carney, S. J. Gould, *J. Bacteriol.* **1997**, *179*, 470.
- [130] U. von Mülert, A. Luzhetskyy, C. Hofmann, A. Mayer, A. Bechthold, *FEMS Microbiol. Lett.* **2004**, *230*, 91.
- [131] K. Ichinose, M. Ozawa, K. Itou, K. Kunieda, Y. Ebizuka, *Microbiology (Reading, U.K.)* **2003**, *149*, 1633.
- [132] J. A. Kalaitzis, B. S. Moore, *J. Nat. Prod.* **2004**, *67*, 1419.
- [133] C. M. Kao, L. Katz, C. Khosla, *Science* **1994**, *265*, 509.
- [134] C. Hertweck, *ChemBioChem* **2000**, *1*, 103.
- [135] B. Julien, S. Shah, *Antimicrob. Agents Chemother.* **2002**, *46*, 2772.
- [136] J. Lau, S. Frykman, R. Regentin, S. Ou, H. Tsuruta, P. Licari, *Biotechnol. Bioeng.* **2002**, *78*, 280.
- [137] K. Gerth, S. Pradella, O. Perlova, S. Beyer, R. Müller, *J. Biotechnol.* **2003**, *106*, 233.
- [138] K. Watanabe, M. A. Rude, C. T. Walsh, C. Khosla, *Proc. Natl. Acad. Sci. USA* **2003**, *100*, 9774.
- [139] L. Tang, S. Shah, L. Chung, J. Carney, L. Katz, C. Khosla, B. Julien, *Science* **2000**, *287*, 640.
- [140] R. Zirkle, J. M. Ligon, I. Molnar, *Microbiology (Reading, U.K.)* **2004**, *150*, 2761.
- [141] S. Murli, M. Piagentini, R. McDaniel, C. R. Hutchinson, *Biochemistry* **2004**, *43*, 15884.
- [142] C. T. Walsh, A. M. Gehring, P. H. Weinreb, L. E. Quadri, R. S. Flugel, *Curr. Opin. Chem. Biol.* **1997**, *1*, 309.
- [143] J. Muylers, Y. Zhang, G. Testa, A. Stewart, *Nucleic Acids Res.* **1999**, *27*, 1555.
- [144] D. Ritz et al. in *BMP Conference*, Society for Industrial Microbiology, San Diego, **2004**, p. 38.
- [145] F. Gross, D. Gottschalk, R. Müller, *Appl. Microbiol. Biotechnol.* **2005**, *68*, 66.
- [146] S. J. Kodumal, K. G. Patel, R. Reid, H. G. Menzella, M. Welch, D. V. Santi, *Proc. Natl. Acad. Sci. USA* **2004**, *101*, 15573.
- [147] C. T. Walsh, *ChemBioChem* **2002**, *3*, 125.
- [148] F. Del Vecchio, H. Petkovic, S. G. Kendrew, L. Low, B. Wilkinson, R. Lill, J. Cortes, B. A. Rudd, J. Staunton, P. F. Leadlay, *J. Ind. Microbiol. Biotechnol.* **2003**, *30*, 489.
- [149] J. Staunton, B. Wilkinson, *Curr. Opin. Chem. Biol.* **2001**, *5*, 159.
- [150] C. Khosla, P. B. Harbury, *Nature* **2001**, *409*, 247.
- [151] C. R. Hutchinson, *Proc. Natl. Acad. Sci. USA* **2003**, *100*, 3010.
- [152] H. G. Floss, *J. Ind. Microbiol. Biotechnol.* **2001**, *27*, 183.
- [153] S. Pelzer, A. Vente, A. Bechthold, *Curr. Opin. Drug Discovery Dev.* **2005**, *8*, 228.
- [154] P. F. Long et al., *Mol. Microbiol.* **2002**, *43*, 1215.
- [155] C. Ruyter et al., *Chem. Biol.* **2001**, *8*, 475.
- [156] S. Gaisser et al., *Org. Biomol. Chem.* **2003**, *1*, 2840.
- [157] J. Ligon, S. Hill, J. Beck, R. Zirkle, I. Molnar, J. Zawodny, S. Money, T. Schupp, *Gene* **2002**, *285*, 257.
- [158] C. J. Wilkinson, E. J. Frost, J. Staunton, P. F. Leadlay, *Chem. Biol.* **2001**, *8*, 1197.
- [159] J. Garcia-Bernardo, L. Xiang, H. Hong, B. S. Moore, P. F. Leadlay, *ChemBioChem* **2004**, *5*, 1129.
- [160] R. McDaniel, A. Thamchaipenet, C. Gustafsson, H. Fu, M. Betlach, G. Ashley, *Proc. Natl. Acad. Sci. USA* **1999**, *96*, 1846.
- [161] Q. Xue, G. Ashley, C. R. Hutchinson, D. V. Santi, *Proc. Natl. Acad. Sci. USA* **1999**, *96*, 11 740.
- [162] Y. Volchegursky, Z. Hu, L. Katz, R. McDaniel, *Mol. Microbiol.* **2000**, *37*, 752.

- [163] K. Watanabe, C. C. C. Wang, C. N. Boddy, D. E. Cane, C. Khosla, *J. Biol. Chem.* **2003**, 278, 42020.
- [164] R. L. Arslanian, L. Tang, S. Blough, W. Ma, R. G. Qiu, L. Katz, J. R. Carney, *J. Nat. Prod.* **2002**, 65, 1061.
- [165] Y. Q. Xue, D. H. Sherman, *Metab. Eng.* **2001**, 3, 15.
- [166] Y. J. Yoon, B. J. Beck, B. S. Kim, H.-Y. Kang, K. A. Reynolds, D. H. Sherman, *Chem. Biol.* **2003**, 10, 9, 203.
- [167] K. Ichinose, D. J. Bedford, D. Tornus, A. Bechthold, M. J. Bibb, W. P. Revill, H. G. Floss, D. A. Hopwood, *Chem. Biol.* **1998**, 5, 647.
- [168] N. Menendez, E. A. M. Nur, A. F. Brana, J. Rohr, J. A. Salas, C. Mendez, *Mol. Microbiol.* **2004**, 53, 903.
- [169] N. Menendez, M. Nur-e-Alam, A. F. Brana, J. Rohr, J. A. Salas, C. Mendez, *Chem. Biol.* **2004**, 11, 21.
- [170] D. Hoffmeister, B. Wilkinson, G. Foster, P. J. Sidebottom, K. Ichinose, A. Bechthold, *Chem. Biol.* **2002**, 9, 287.
- [171] C. Dürr, D. Hoffmeister, S. E. Wohler, K. Ichinose, M. Weber, U. von Mulert, J. S. Thorson, A. Bechthold, *Angew. Chem.* **2004**, 116, 3022; *Angew. Chem. Int. Ed.* **2004**, 43, 2962.
- [172] S. Weinig, T. Mahmud, R. Müller, *Chem. Biol.* **2003**, 10, 953.
- [173] T. Weber, M. A. Marahiel, *Structure (Cambridge, MA, U.S.)* **2001**, 9, R3.
- [174] S. A. Sieber, M. A. Marahiel, *J. Bacteriol.* **2003**, 185, 7036.
- [175] A. M. Gehring, I. Mori, C. T. Walsh, *Biochemistry* **1998**, 37, 2648.
- [176] T. Keating, G. Marshall, C. Walsh, *Biochemistry* **2000**, 39, 1522.
- [177] H. D. Mootz, D. Schwarzer, M. A. Marahiel, *ChemBioChem* **2002**, 3, 490.
- [178] T. Duerfahrt, S. Doekel, T. Sonke, P. Quaedflieg, M. A. Marahiel, *Eur. J. Biochem.* **2003**, 270, 4555.
- [179] S. E. O'Connor, C. T. Walsh, F. Liu, *Angew. Chem.* **2003**, 115, 4047; *Angew. Chem. Int. Ed.* **2003**, 42, 3917.
- [180] S. J. Admiraal, C. Khosla, C. T. Walsh, *Biochemistry* **2002**, 41, 5313.
- [181] S. J. Admiraal, C. Khosla, C. T. Walsh, *J. Am. Chem. Soc.* **2003**, 125, 13664.
- [182] T. P. Nicholson, C. Winfield, J. Westcott, J. Crosby, T. J. Simpson, R. J. Cox, *Chem. Commun.* **2003**, 686.
- [183] K. Ueda, K. M. Kim, T. Beppu, S. Horinouchi, *J. Antibiot.* **1995**, 48, 638.
- [184] H. B. Bode, R. Müller, *Plant Physiol.* **2003**, 132, 1153.
- [185] B. S. Moore et al., *J. Nat. Prod.* **2002**, 65, 1956.
- [186] B. S. Moore, J. N. Hopke, *ChemBioChem* **2001**, 2, 35.
- [187] N. Funa, Y. Ohnishi, Y. Ebizuka, S. Horinouchi, *J. Biol. Chem.* **2002**, 277, 4628.
- [188] N. Funa, Y. Ohnishi, Y. Ebizuka, S. Horinouchi, *Biochem. J.* **2002**, 367, 781.
- [189] P. Saxena, G. Yadav, D. Mohanty, R. S. Gokhale, *J. Biol. Chem.* **2003**, 278, 44780.
- [190] J. C. Jeong, A. Srinivasan, S. Gruschow, H. Bach, D. H. Sherman, J. S. Dordick, *J. Am. Chem. Soc.* **2005**, 127, 64.
- [191] T. Li, O. Choroba, H. Hong, D. Williams, J. Spencer, *Chem. Commun.* **2001**, 20, 2156.
- [192] V. Pfeifer, G. J. Nicholson, J. Ries, J. Recktenwald, A. B. Schefer, R. M. Shawky, J. Schröder, W. Wohlleben, S. Pelzer, *J. Biol. Chem.* **2001**, 276, 38370.
- [193] J. W. Trauger, R. M. Kohli, H. D. Mootz, M. A. Marahiel, C. T. Walsh, *Nature* **2000**, 407, 215.
- [194] R. M. Kohli, M. D. Burke, J. Tao, C. T. Walsh, *J. Am. Chem. Soc.* **2003**, 125, 7160.
- [195] R. M. Kohli, J. Takagi, C. T. Walsh, *Proc. Natl. Acad. Sci. USA* **2002**, 99, 1247.
- [196] R. M. Kohli, C. T. Walsh, M. D. Burkart, *Nature* **2002**, 418, 658.
- [197] H. Lin, D. A. Thayer, C. H. Wong, C. T. Walsh, *Chem. Biol.* **2004**, 11, 1635.
- [198] J. S. Thorson, W. A. Barton, D. Hoffmeister, C. Albermann, D. B. Nikolov, *ChemBioChem* **2004**, 5, 16.
- [199] J. Yang, L. Liu, J. S. Thorson, *ChemBioChem* **2004**, 5, 992.
- [200] X. M. He, H. W. Liu, *Annu. Rev. Biochem.* **2002**, 71, 701.
- [201] X. He, H. W. Liu, *Curr. Opin. Chem. Biol.* **2002**, 6, 590.
- [202] X. Fu, C. Albermann, J. Jiang, J. Liao, C. Zhang, J. S. Thorson, *Nat. Biotechnol.* **2003**, 21, 1467.
- [203] H. Lin, C. T. Walsh, *J. Am. Chem. Soc.* **2004**, 126, 13998.
- [204] K. L. Rinehart, *Pure Appl. Chem.* **1977**, 49, 1361.
- [205] W. Wohlleben, S. Pelzer, *Chem. Biol.* **2002**, 9, 1163.
- [206] S. Weist, R. D. Sussmuth, *Appl. Microbiol. Biotechnol.* **2005**, 68, 141.
- [207] K. Kinoshita, B. A. Pfeifer, C. Khosla, D. E. Cane, *Bioorg. Med. Chem. Lett.* **2003**, 13, 3701.
- [208] K. Kinoshita, C. Khosla, D. E. Cane, *Helv. Chim. Acta* **2003**, 86, 3889.
- [209] K. J. Weissman et al., *Chem. Biol.* **1998**, 5, 743.
- [210] D. E. Ehmman, J. W. Trauger, T. Stachelhaus, C. T. Walsh, *Chem. Biol.* **2000**, 7, 765.
- [211] D. E. Cane, F. Kudo, K. Kinoshita, C. Khosla, *Chem. Biol.* **2002**, 9, 131.
- [212] J. Staunton, A. C. Sutkowski, *J. Chem. Soc. Chem. Commun.* **1991**, 1110.
- [213] M. Ziehl, J. He, H.-M. Dahse, C. Hertweck, *Angew. Chem.* **2005**, 117, 1226; *Angew. Chem. Int. Ed.* **2005**, 44, 1202.
- [214] T. A. Cropp, D. J. Wilson, K. A. Reynolds, *Nat. Biotechnol.* **2000**, 18, 980.
- [215] B. S. Moore, C. Hertweck, *Nat. Prod. Rep.* **2002**, 19, 70.
- [216] C. J. Dutton, S. P. Gibson, A. C. Goudie, K. S. Holdom, M. S. Pacey, J. C. Ruddock, J. D. Bu'Lock, M. K. Richards, *J. Antibiot.* **1991**, 44, 357.
- [217] S. Chen, D. von Bamberg, V. Hale, M. Brauer, B. Hardt, R. Müller, H. G. Floss, K. A. Reynolds, E. Leistner, *Eur. J. Biochem.* **1999**, 261, 98.
- [218] L. E. Khaw, G. A. Bohm, S. Metcalfe, J. Staunton, P. F. Leadlay, *J. Bacteriol.* **1998**, 180, 809.
- [219] H. Xu, L. Heide, S. M. Li, *Chem. Biol.* **2004**, 11, 655.
- [220] U. Galm, M. A. Dessoy, J. Schmidt, L. A. Wessjohann, L. Heide, *Chem. Biol.* **2004**, 11, 173.
- [221] B. Bister et al., *ChemBioChem* **2003**, 4, 658.
- [222] T. L. Schneider, C. T. Walsh, S. E. O'Connor, *J. Am. Chem. Soc.* **2002**, 124, 11272.

Communications



Two new additions to the family of large palladium–carbonyl–triethylphosphine clusters, with Pd_{52} and Pd_{66} cores, have been prepared from the common parent precursor $[\text{Pd}_{10}(\text{CO})_{12}(\text{PEt}_3)_6]$. For a detailed discussion on the geometrical variety of such nanosized homometallic clusters, see the Communication by E. G. Mednikov, L. F. Dahl, and co-workers on the following pages.

Nanosized $[\text{Pd}_{52}(\text{CO})_{36}(\text{PET}_3)_{14}]$ and $[\text{Pd}_{66}(\text{CO})_{45}(\text{PET}_3)_{16}]$ Clusters Based on a Hypothetical Pd_{38} Vertex-Truncated ν_3 Octahedron**

Evgueni G. Mednikov,* Sergei A. Ivanov,
Irina V. Slovokhotova, and Lawrence F. Dahl*

Dedicated to Professor Giuliano Longoni

Palladium is a unique transition metal in that it forms an exceptionally versatile family of high-nuclearity palladium carbonyl phosphine clusters (i.e., with cores of at least 10 metal atoms with direct metal–metal bonding) that display a truly remarkable diversity of geometries about the metal cores.^[1a–h] Fifteen distinctly different geometries have been identified crystallographically for Pd_n cores with $n = 10$,^[2a–c] 12,^[2d,e] 16,^[2f,g] 23 (two different metal cores have been observed),^[2h–j] 29,^[2e] 30,^[2k] 34,^[1a,2l] 35,^[2g] 38,^[2m] 39,^[2g] 54,^[2k] 59,^[2g,n] 69,^[2o] and 145.^[2p] All but two of these highly condensed palladium clusters have close-packed frameworks that contain metal fragments whose structural units may be described as ccp (cubic close-packed), mixed ccp/hcp (hexagonal close-packed) stacking layers (which include layer sequences corresponding to capped octahedra, centered cuboctahedra, or centered anti-cuboctahedra), and as icosahedra. One exception is the Pd_{38} cluster, which has a highly irregular geometry about the metal core;^[1a,2m] the other exception is one of the Pd_{23} clusters, which has a highly distorted body-centered-cubic metal framework.^[2j] Close-packed structural units of the Pd_n cores also include “twinned interpenetrating” centered cuboctahedral and icosahedral geometries as well as one mixed, face-fused icosahedral/octahedral Pd_{59} architecture, which consists of two centered icosahedra that *trans*-cap a biocuboctahedron.^[2g,n] The largest known crystallographically determined discrete metal cluster, Pd_{145} , contains a capped

three-shell 145-atom metal core, whose geometry closely conforms to I_h icosahedral symmetry.^[2p]

A most impressive stereochemical aspect of this extraordinary family of $[\text{Pd}_n(\text{CO})_x\text{L}_y]$ clusters, where L denotes phosphine ligands, is that practically all of the above-mentioned members of the Pd_n series have been prepared with the same phosphine ligand, $\text{L} = \text{PET}_3$, which is sterically non-bulky and also a good σ donor. The exceptions reported to date are the Pd_{12} cluster, which was isolated only with PnBu_3 ^[2d] and PPh_3 ,^[2e] and the Pd_{35} ,^[2g] Pd_{39} ,^[2g] and Pd_{59} ^[2g,n] clusters, which were obtained only with sterically smaller PMe_3 ligands. Furthermore, all of the triethylphosphine-containing $[\text{Pd}_n(\text{CO})_x\text{L}_y]$ ($\text{L} = \text{PET}_3$) clusters may be obtained from reactions with the same tetracapped octahedral Pd_{10} precursor, $[\text{Pd}_{10}(\text{CO})_{12}(\text{PET}_3)_6]$,^[2b,c] through different kinetically controlled synthetic pathways to give relatively thermodynamically stable products in most cases. For the majority of the Pd_n clusters, reasonably good yields (at least 30 %) were ultimately obtained by optimization of the reaction conditions and in particular cases by the structure-to-synthesis approach from different synthetic routes.

Herein, we report the synthesis of two new extraordinary members to the series of palladium carbonyl phosphine clusters, namely, $[\text{Pd}_{52}(\text{CO})_{36}(\text{PET}_3)_{14}]$ (**1**) and $[\text{Pd}_{66}(\text{CO})_{45}(\text{PET}_3)_{16}]$ (**2**), from the precursor $[\text{Pd}_{10}(\text{CO})_{12}(\text{PET}_3)_6]$ (**3**). Cluster **1** was prepared as an extremely minor product (< 5 % yield) from the reaction of **3** with $[\text{Pd}_2(\text{dba})_3]$ (dba = dibenzylideneacetone) at 50 °C.^[3] Subsequent attempts to increase the yield of **1** were unsuccessful; in the best cases, reactions usually (but not always) afforded **1** as a minor product in powder samples. Initial attempts to prepare the Pd_{66} cluster **2** were carried out by Mednikov and Kanteeva from the reproducible deligation of **3** with $\text{CF}_3\text{CO}_2\text{H}/\text{Me}_3\text{NO}$ under optimized ratios of **3**/ $\text{CF}_3\text{CO}_2\text{H}$ and **3**/ Me_3NO at 1:120 and 1:16, respectively (42 % yield; note that the product obtained by this procedure is labeled as **2'** (see below)).^[2i] However, at that time attempts to characterize the product by X-ray diffraction were unsuccessful. Crystals of this unknown cluster **2'** were again isolated from the above-stated reaction,^[4] and new efforts were undertaken to determine both its atomic arrangement and stoichiometry. However, we experienced great difficulty in obtaining the entire crystal structure. Complete X-ray data sets (two with synchrotron radiation) were collected from at least 10 monoclinic crystals (different preparations): despite poor refinements, solutions of the structure from several data sets confirmed the $[\text{Pd}_{66}\text{P}_{16}]$ architecture of **2'** but did not provide any information concerning the number and coordination modes of the carbonyl ligands. Major problems included unusually high diffuse-scattering background and merohedral twinning (i.e., due to a monoclinic unit cell with $\beta \approx 90^\circ$), which was taken into account in least-squares refinements. Nevertheless, the entire crystal structure was eventually established from monoclinic crystals (with a larger angle $\beta = 90.9^\circ$) that were obtained from a different preparative route, through the reaction of **3** with $[\text{Pd}(\text{MeCN})_4](\text{BF}_4)_2$,^[5] to give **2**. Although the IR spectra of **2** and **2'** are virtually identical and their crystallographic unit-cell parameters are analogous, it should be noted that the Pd_{66} cluster **2'** obtained from the reaction of

[*] Dr. E. G. Mednikov, Dr. S. A. Ivanov, Prof. L. F. Dahl
Department of Chemistry
University of Wisconsin–Madison
Madison, WI 53706 (USA)
Fax: (+1) 608-262-6143
E-mail: mednikov@chem.wisc.edu
dahl@chem.wisc.edu

I. V. Slovokhotova
Zelinsky Institute of Organic Chemistry
Russian Academy of Sciences
Moscow (Russia)

[**] This research was supported by the National Science Foundation. Color figures were prepared with Crystal Maker, Interactive Crystallography Software [David C. Palmer, Begbroke Park, Bldg 5, Sandy Lake, Yarnnton OX5 1PF (UK)]. The authors are grateful to Dr. Ilia Guzei (UW–Madison) and Prof. Yuri Slovokhotov (Nesmeyanov Institute of Organoelement Compounds, RAS, Moscow) for crystallographic advice.

3 with $\text{CF}_3\text{CO}_2\text{H}$ and Me_3NO may possibly contain a different number of carbonyl ligands to that found in **2**.^[6]

The molecular structures^[7] of **1** and **2** are based upon a common hypothetical Pd_{38} kernel that can be formally derived by vertex-truncating of a likewise unknown $\nu_3 \text{Pd}_{44}$ octahedron, where ν_n refers to $n+1$ equally spaced atoms (namely, four) along each of the 12 octahedral edges. This cubic O_h -symmetric Pd_{38} kernel contains six {100} square Pd_4 faces and eight {111} centered hexagonal Pd_7 faces, and has six interior (encapsulated) metal atoms that are located at the vertices of a regular octahedron.

The Pd_{52} core in **1** (Figure 1) formally arises from the remaining 14 Pd atoms, which form two monocapped $\nu_2 \text{Pd}_7$ triangles that sequentially condense on centrosymmetrically opposite, *trans*-oriented {111} centered hexagonal Pd_7 faces^[8] of the Pd_{38} kernel. This *trans* attachment of the two Pd_7 triangles to the Pd_{38} kernel lowers the symmetry of the resulting Pd_{52} core, which has crystallographically imposed C_{3i} ($\bar{3}$) symmetry, from pseudo- O_h to pseudo- D_{3d} ($\bar{3}2/m$). The Pd_{52} core contains eight interior Pd atoms that conform to a *trans*-bicapped octahedron.

The Pd_{66} core in **2** is formally constructed by the sequential condensation of the same monocapped $\nu_2 \text{Pd}_7$ triangles on four non-adjacent (tetrahedral) {111} centered hexagonal Pd_7 faces of the Pd_{38} kernel (Figure 2). The crucial stage is the condensation of the second triangular Pd_7 fragment which must occur on any of three tetrahedrally oriented {111} faces of the Pd_{38} core. As a result, further condensation of the remaining two $\nu_2 \text{Pd}_7$ triangles can sterically occur only on the remaining two tetrahedral centered hexagonal Pd_7 faces to thereby complete the Pd_{66} core of **2**. Because the probability of the condensation of the second $\nu_2 \text{Pd}_7$ triangle on one of the tetrahedrally oriented centered hexagonal faces of the Pd_{38} kernel is three-times greater than that on the opposite face, this formal construction of the Pd_{66} core is significantly favored over that of the Pd_{52} core. Hence, it is not surprising that this building-block scheme is consistent with the good synthetic reproducibility of the Pd_{66} cluster as well as with its preparation from different procedures. In contrast, the Pd_{52}

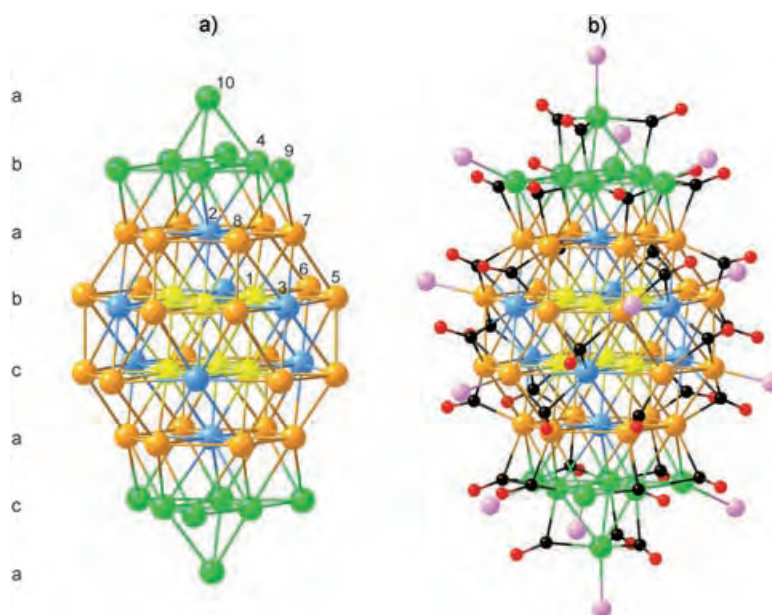


Figure 1. a) Crystallographic C_{3i} and pseudo- D_{3d} geometry of the nanosized Pd_{52} core in $[\text{Pd}_{52}(\text{CO})_{36}(\text{PEt}_3)_{14}]$ (**1**). Symmetry-independent Pd atoms are numbered. The maximum diameter of the metal core is 1.58 nm parallel and 0.84 nm perpendicular to the principal threefold axis that passes through Pd(10), Pd(2) and the crystallographic inversion centre; the latter is situated between the two middle 12-atom Pd layers. b) Molecular structure of **1** displaying the arrangement of 14 PEt_3 ligands (P pink; ethyl substituents not shown) and 36 bridging carbonyl ligands (O red, C black) about the Pd_{52} core. Two crystallographically independent carbonyl ligands are each disordered between two sites with occupancy factors of 0.54/0.46 and 0.76/0.24; only their main orientations are shown.

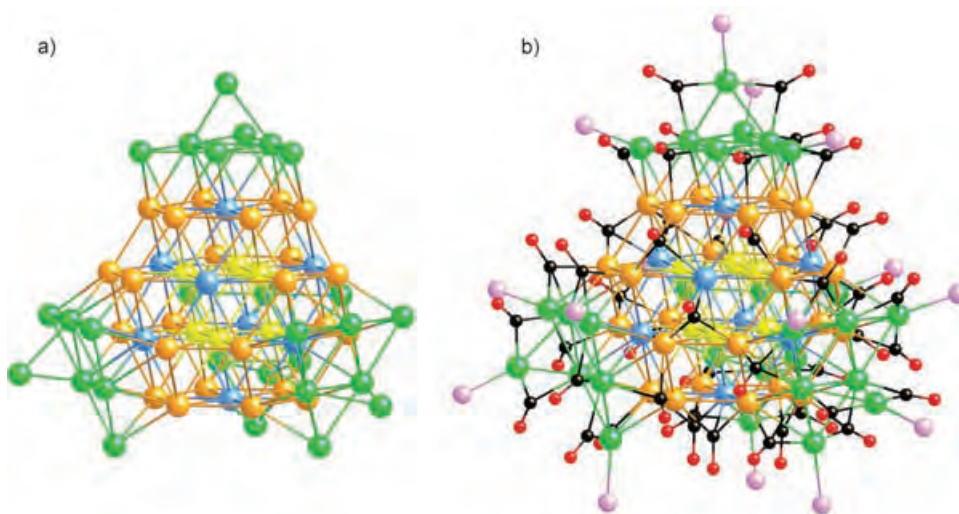


Figure 2. a) Geometry of the nanosized Pd_{66} core in $[\text{Pd}_{66}(\text{CO})_{45}(\text{PEt}_3)_{16}]$ (**2**). The maximum diameter of the metal core of this spherically shaped Pd_{66} cluster is approximately 1.14 nm along each of the four tetrahedral body-diagonal {111} directions. b) Molecular structure of **2** exhibiting the arrangement of 16 PEt_3 ligands (P pink; ethyl substituents not shown) and 45 bridging carbonyl ligands (O red, C black) about the Pd_{66} core. Four carbonyl ligands are each disordered between two sites with occupancy factors of approximately 0.5/0.5 in each case; only one of the two orientations is shown.

cluster **1** is difficult to isolate. A close examination of the particular orientations of the four monocapped Pd_7 triangles relative to the Pd_{38} kernel in **2** reveals that the Pd_{66} core has

approximately C_{3v} symmetry instead of the expected T_d symmetry. However, the 10 interior (encapsulated) atoms ideally conform to a tetracapped T_d Pd_{10} octahedron, which alternatively may be viewed as a ν_2 Pd_{10} tetrahedron with three equally spaced Pd atoms along each of the six tetrahedral edges.

The resulting metal arrangements of the entire Pd_{52} core along the threefold axis in **1** and of each of the four $\{Pd_{38}Pd_7\}$ fragments with the common Pd_{38} kernel along the $\langle 111 \rangle$ directions in **2** may be considered as mixed ccp/hcp layer-stacking structures. Figure 1 shows that the eight layers in **1** adopt an ababcba stacking sequence. In **2**, which has pseudo- C_{3v} symmetry, the alternation of the stacked layers (Figure 2) depends on the $\langle 111 \rangle$ direction: namely, the layer-stacking sequence along the proper C_3 axis is ababca, whereas along each of the other three symmetry-equivalent $\langle 111 \rangle$ directions the sequence is ababca. Similar four-, five-, and six-layer stacking sequences involving mixed ccp/hcp metal arrangements have been observed in other large carbonyl clusters, including $[Rh_{22}(CO)_{37}]^{4-}$ (abcb),^[9a] $[Pd_{13}Ni_{13}(CO)_{34}]^{4-}$ (abac),^[9b] $[Pd_{16}Ni_{16}(CO)_{40}]^{4-}$ (abcbca),^[9c] $[Ni_{32}Pt_{24}(CO)_{56}]^{6-}$ (ababcb sequence along its threefold axis),^[9d] and neutral $[Pd_{54}(CO)_{40}(PET_3)_{14}]$ (abaca).^[2k]

Overall mean Pd–Pd distances of 2.80 Å (range: 2.70–2.95 Å) and 2.81 Å (range: 2.66–3.00 Å) in **1** and **2**, respectively, are typical for palladium carbonyl phosphine clusters, as exemplified by the overall mean Pd–Pd distance of 2.81 Å previously reported for the ccp Pd_{30} and ccp/hcp Pd_{54} clusters.^[2k] The significantly shorter mean Pd–Pd distances of 2.74 Å in the interior (encapsulated) bicapped Pd_8 octahedron in **1** and 2.77 Å in the interior (encapsulated) tetracapped Pd_{10} octahedron (ν_2 tetrahedron) in **2**, which are essentially identical to the Pd–Pd distance of 2.75 Å in ccp Pd metal,^[10] are consistent with the interior Pd_n atoms presumably having metallic character.

In **1**, four PET_3 ligands are attached to each of the two monocapped ν_2 Pd_7 triangles, with one to the capped Pd atom and the other three to the corner atoms of the Pd_6 triangles. The six other PET_3 ligands are coordinated to the six $\bar{3}$ (S_6)-equivalent Pd(6) atoms (see Figure 1) in the middle two Pd_{12} layers. In **2**, the 16 PET_3 ligands are equally distributed among the four monocapped ν_2 Pd_7 triangles in coordination modes that are analogous to those found in **1**.

The 36 CO groups in **1** were all located without any difficulties. They comprise 12 doubly bridging μ_2 -CO groups and 24 triply bridging μ_3 -CO groups (Figure 1), and under crystallographically $\bar{3}$ (S_6) site symmetry, they may be divided into the following three distinct groups: 1) Six μ_2 -CO groups (one independent), with three of these connecting each of the two monocapped μ_3 -Pd atoms to the three inner Pd atoms of the triangular Pd_6 layer.^[11] 2) Twelve μ_3 -CO groups (two independent), with six of these connecting each of the two monocapped ν_2 Pd_7 triangles to a centered hexagonal Pd_7 face of the Pd_{38} kernel. This carbonyl arrangement may be readily visualized as six edge-bridging CO groups that span the six Pd–Pd pairs in each Pd_6 triangle being formally converted into face-capped μ_3 -CO groups by each becoming attached to one of the six hexagonal Pd atoms of the centered hexagonal face. 3) Twelve μ_3 -CO groups (two independent) and six μ_2 -CO

groups (one independent) joined to the six “open” symmetry-related centered hexagonal faces of the Pd_{38} kernel. These consist of two μ_3 -CO groups, which connect the centered Pd atom of a given Pd_7 face with four of the Pd atoms in the hexagon, and one μ_2 -CO group that links the remaining two Pd atoms. These bridging carbonyl ligands in **1** are consistent with the observation of only one strong broad CO band in the solid-state IR spectrum at 1856 cm^{-1} with a shoulder at 1875 cm^{-1} .

In sharp contrast, the ultimate location of all 45 independent carbonyl ligands in the Pd_{66} cluster **2** (Figure 2) proved to be difficult and time-consuming. Nevertheless, a careful examination of their composite steric dispositions provides complete reassurance for the presence of 45 CO groups in **2**. Particularly intriguing is that normally 44 CO groups would be predicted from general symmetry considerations, thus the 45th CO group in **2** constitutes an unexpected extra one.^[12] It is most convenient to initially describe the carbonyl arrangement of the 44 normal CO groups in **2** and then consider the observed major steric deformations of two CO groups that allow for the addition of the extra 45th CO ligand. In this analysis the carbonyl ligands in **2** are likewise separated into the same three groups: 1) Eight μ_2 -CO groups, of which two edge-bridge each of the four monocapped μ_2 -Pd atoms that are coordinated to only two of the three inner triangular Pd atoms within the four ν_2 Pd_7 triangles. 2) Twenty-four μ_3 -CO groups with six face-capped ones connecting each of the four monocapped ν_2 Pd_7 triangles to a centered hexagonal Pd_7 face of the Pd_{38} kernel, as described above in **2**. 3) Six μ_3 -CO groups and three μ_2 -CO groups attached (as found in **1**) to three of the four “open” centered hexagonal Pd_7 faces of the Pd_{38} kernel; the fourth “open” face has three μ_3 -CO ligands instead of one μ_2 -CO and two μ_3 -CO groups. This above description accounts for 44 of the 45 CO units found in **2**. To provide sufficient space for the addition of the extra (45th) μ_3 -CO ligand, the one-bond-connectivity of each of two adjacent normally disposed μ_3 -CO groups that connect one monocapped ν_2 Pd_7 triangle to its centered hexagonal Pd_7 face is broken, such that these two adjacent μ_3 -CO groups are then transformed into μ_2 -CO units that are highly bent above the ν_2 Pd_6 triangle (away from the centered hexagonal Pd_7 face) to increase intraligand contact distances and thereby minimize steric repulsions. This extensive localized deformation thus allows the extra μ_3 -CO unit to face-cap the resulting Pd_3 triangle, which is composed of the two adjacent Pd atoms of the centered hexagonal Pd_7 face and the central atom of the ν_2 Pd_6 triangle that is also linked to the two highly bent μ_2 -CO groups. These bridging CO coordinations give rise to only one broad strong CO band at 1884 cm^{-1} in the solid-state IR spectrum of **2**.^[11–13]

This comparative analysis of the carbonyl ligands in **1** and **2** discloses two important stereochemical features that originated from the observed $\{111\}$ face-condensations of the hypothetical Pd_{38} vertex-truncated ν_3 -octahedral kernel: 1) in **1**, each triply bridging monocapped Pd atom connected to the three inner Pd atoms of the Pd_6 triangle contains *three* edge-bridged μ_2 -CO groups, whereas in **2** each of the four doubly bridging monocapped Pd atoms connected to two of the three inner Pd atoms of the Pd_6 triangle contains *two*

edge-bridged μ_2 -CO ligands; 2) the observed localized carbonyl rearrangement in **2** which sterically allows the presence of the extra (45th) CO ligand suggests that the geometry of the nanosized Pd_{66} core with 44 normal CO groups may potentially accommodate up to four additional carbonyl ligands without any substantial changes in the architecture of the metal core.^[6] In fact, a current investigation has indicated the formation of another Pd_{66} cluster with 47 CO groups (three extra) from the reaction of **3** with dicobalt octocarbonyl.^[13]

The possibility of variable numbers of carbonyl ligands for close-packed nanosized $[\text{Pd}_n(\text{CO})_x(\text{PR}_3)_y]$ clusters without the need for significant geometrical changes in the common $\{\text{Pd}_n(\text{PR}_3)_y\}$ fragments was recently observed for the cuboctahedral $[\text{Pd}_{23}(\text{CO})_x(\text{PET}_3)_{10}]$ clusters with $x = 20, 21, 22$.^[6] The arrangements of their composite carbonyl groups revealed that the formal addition of an extra CO ligand produces considerable localized displacements of certain neighboring CO ligands (with concomitant changes in their coordination modes) in order to increase intraligand contacts and thereby minimize steric effects. The geometric effects of the expanded carbonyl ligation in the Pd_{66} cluster also have special relevance to the well-known Muetterties cluster–science analogy^[14] that chemisorbed CO molecules are not static but undergo both dissociative processes and nondissociative migratory processes about the metal surface as a function of the CO pressure.

Of particular relevance to our hypothesized modular construction of **1** and **2** from the hypothetical Pd_{38} vertex-truncated ν_3 octahedron is that the congeneric Pt_{38} core of the classic Chini $[\text{Pt}_{38}(\text{CO})_{44}]^{2-}$ dianion displays this same O_h geometry.^[15] More-recent comprehensive synthetic, stereochemical, spectroscopic, and electrochemical studies by Longoni, Zanello, and co-workers^[16,17] have revealed the only other known cluster with a 38-atom metal core that displays the truncated ν_3 octahedral geometry; namely, the ordered $[\text{H}_2\text{Ni}_{24}\text{Pt}_{14}(\text{CO})_{44}]^{4-}$ cluster for which the 24 Ni atoms occupy the 24 equivalent square corner sites and the 14 Pt atoms occupy the six vertices of the encapsulated octahedron and the centers of the eight hexagonal faces.^[9d,16,18] They also prepared and characterized heterometallic 44-atom ν_3 octahedral clusters that contain a ccp 38-atom truncated ν_3 octahedral $\text{M}_{38-x}\text{M}'_x$ kernel with six additional Ni atoms capping the six {100} square faces. These include $[\text{H}_{6-n}\text{Ni}_{38}\text{Pt}_6(\text{CO})_{48}]^{n-}$ ($n = 4-6$)^[17a,b] and $[\text{Ni}_{35}\text{Pt}_9(\text{CO})_{48}]^{6-}$,^[17c] both with an encapsulated Pt_6 octahedron, and $[\text{Ni}_{36}\text{Pd}_8(\text{CO})_{48}]^{6-}$ ^[17c] with an encapsulated Pd_6 octahedron and with the other two Pd atoms occupying two of the eight centered sites of the crystal-disordered 10-atom ν_3 octahedral faces.

The salient structural feature of **1** and **2** is that their hypothesized formation from the Pd_{38} truncated ν_3 octahedron occurs through six-atom condensations of monocapped Pd_7 triangles on {111} octahedral faces instead of one-atom metal condensations on six {100} square faces, as found in the $[\text{Ni}_{38}\text{Pt}_6]$,^[17a,b] $[\text{Ni}_{35}\text{Pt}_9]$,^[17c] and $[\text{Ni}_{36}\text{Pd}_8]$ ^[17c] clusters. The resulting condensation pattern of 44 metal atoms comprises eight “open” triangular ν_3 $[\text{Ni}_{10-x}\text{M}'_x]$ faces, which are only occupied by ligands. Stereochemical analysis of the known

$[\text{Pd}_n(\text{CO})_x\text{L}_y]$ clusters reveals that, in general, Pd_n cores do not form such relatively large triangular 10-atom “open” faces, but they prefer instead to undergo face condensations.

In general, the formation of different kinds of large ligated close-packed metal clusters critically depends upon the subtle interplay of cohesive energies, electronegativities, and relative sizes of the metal atoms, the electronic and steric properties of the ligands, and, of course, the reaction conditions. The dissimilar growth processes presented above in the formal construction of the Pd_{52} and Pd_{66} clusters **1** and **2**, respectively, versus that of the 44-atom Ni–Pt and Ni–Pd carbonyl clusters from their nonisolated precursors with the same 38-atom vertex-truncated ν_3 octahedral geometry may be largely attributed to the markedly weaker metal–metal and metal–carbonyl interactions in palladium carbonyl/triethylphosphine clusters compared to those in nickel and platinum carbonyl clusters.

Received: July 1, 2005

Keywords: carbonyl ligands · cluster compounds · palladium · phosphane ligands · X-ray diffraction

- [1] For reviews, see: a) O. A. Belyakova, Yu. L. Slovokhotov, *Russ. Chem. Bull. (Engl. Transl.)* **2003**, 52, 2299; b) D. Collini, C. Femoni, M. C. Iapalucci, G. Longoni, P. Zanello in *Perspectives in Organometallic Chemistry* (Eds.: C. G. Screttas, B. R. Steele), Special Publication No. 287, Royal Society of Chemistry, **2003**, 183; c) T. A. Stromnova, I. I. Moiseev, *Usp. Khim.* **1998**, 67, 542. [*Russ. Chem. Rev. (Engl. Transl.)* **1998**, 67, 485]; d) A. D. Burrows, D. M. P. Mingos, *Transition Met. Chem.* **1993**, 18, 129; e) R. B. King, *Gazz. Chim. Ital.* **1992**, 122, 383; f) N. K. Eremenko, S. P. Gubin, *Pure Appl. Chem.* **1990**, 62, 1179; g) K. C. C. Kharas, L. F. Dahl, *Adv. Chem. Phys.* **1988**, 70 (Part 2), 1; h) N. K. Eremenko, E. G. Mednikov, S. S. Kurasov, *Usp. Khim.* **1985**, 54, 671. [*Russ. Chem. Rev. (Engl. Transl.)* **1985**, 54, 394].
- [2] a) E. G. Mednikov, N. K. Eremenko, V. A. Mikhailov, S. P. Gubin, Yu. L. Slovokhotov, Yu. T. Struchkov, *J. Chem. Soc. Chem. Commun.* **1981**, 989; b) E. G. Mednikov, N. K. Eremenko, Yu. L. Slovokhotov, Yu. T. Struchkov, S. P. Gubin, *J. Organomet. Chem.* **1983**, 258, 247; c) D. M. P. Mingos, C. M. Hill, *Croat. Chem. Acta* **1995**, 67, 745; d) E. G. Mednikov, Yu. T. Struchkov, Yu. L. Slovokhotov, *J. Organomet. Chem.* **1998**, 566, 15; e) M. Kawano, J. W. Bacon, C. F. Campana, B. E. Winger, J. D. Dudeck, S. A. Sirchio, S. L. Scruggs, U. Geiser, L. F. Dahl, *Inorg. Chem.* **2001**, 40, 2554; f) E. G. Mednikov, Yu. L. Slovokhotov, Yu. T. Struchkov, *Metalloorg. Khim.* **1991**, 4, 123. [*Organomet. Chem. USSR (Engl. Transl.)* **1991**, 4, 65]; g) N. T. Tran, M. Kawano, L. F. Dahl, *J. Chem. Soc. Dalton Trans.* **2001**, 2731; h) E. G. Mednikov, N. K. Eremenko, Yu. L. Slovokhotov, Yu. T. Struchkov, *J. Organomet. Chem.* **1986**, 301, C35; i) E. G. Mednikov, J. Wittayakun, L. F. Dahl, *J. Cluster Sci.* **2005**, 16, in press; j) E. G. Mednikov, N. K. Eremenko, Yu. L. Slovokhotov, Yu. T. Struchkov, *Zh. Vses. Khim. O-va. im. D. I. Mendeleeva* **1987**, 32, 101; k) E. G. Mednikov, S. A. Ivanov, L. F. Dahl, *Angew. Chem.* **2003**, 115, 337; *Angew. Chem. Int. Ed.* **2003**, 42, 323; l) E. G. Mednikov, N. I. Kanteeva, *Izv. Akad. Nauk Ser. Khim.* **1995**, 167. [*Russ. Chem. Bull. (Engl. Transl.)* **1995**, 44, 163]; m) E. G. Mednikov, N. K. Eremenko, Yu. L. Slovokhotov, Yu. T. Struchkov, *J. Chem. Soc. Chem. Commun.* **1987**, 218; n) N. T. Tran, M. Kawano, D. R. Powell, L. F. Dahl, *J. Am. Chem. Soc.* **1998**, 120, 10986; o) N. T. Tran, L. F. Dahl, *Angew. Chem.*

- 2003, 115, 3657; *Angew. Chem. Int. Ed.* **2003**, 42, 3533; p) N. T. Tran, D. R. Powell, L. F. Dahl, *Angew. Chem.* **2000**, 112, 4287; *Angew. Chem. Int. Ed.* **2000**, 39, 4121.
- [3] a) A mixture of $[\text{Pd}_{10}(\text{CO})_{12}(\text{PET}_3)_6]$ (**3**)^[3b] (0.200 g, 0.095 mmol) and $[\text{Pd}_2(\text{dba})_3]$ (0.304 g, 0.332 mmol) in Me_2CO (7 mL) and $i\text{Pr}_2\text{O}$ (2 mL) was stirred for 4.5 h under N_2 at 50°C . The resulting brown solution was filtered from the black precipitate of $[\text{Pd}_{34}(\text{CO})_{24}(\text{PET}_3)_{12}]$ (**4**) and left under H_2O vapor. Black block crystals of **1** were isolated and washed with MeOH (estimated yield < 5 %); IR (nujol): $\tilde{\nu} = 1875$ (sh), 1856 cm^{-1} (s). The black precipitate of **4** (0.182 g, 67 % yield based on combined content of palladium in **3** and $[\text{Pd}_2(\text{dba})_3]$, or 114 % based on **3**) was identified by its IR spectrum (nujol): $\tilde{\nu} = 1892$ (s), 1867 (s), 1837 (s), 1810 cm^{-1} (s–m).^[21] The yield of **4** calculated on the basis of **3** unambiguously indicates its formation from both **3** and $[\text{Pd}_2(\text{dba})_3]$. A crystal of **1** of dimensions $0.30 \times 0.20 \times 0.20\text{ mm}^3$ was used for the determination of the crystal structure; b) E. G. Mednikov, N. K. Eremanko, *Izv. Akad. Nauk SSSR Ser. Khim.* **1982**, 2540. [*Bull. Acad. Sc. USSR Div. Chem. Sc. (Engl. Transl.)* **1982**, 31, 2240].
- [4] In a typical experiment $[\text{Pd}_{10}(\text{CO})_{12}(\text{PET}_3)_6]$ (**3**; 0.150 g, 0.071 mmol) and $\text{Me}_3\text{NO} \cdot 2\text{H}_2\text{O}$ (0.127 g, 1.143 mmol) were dissolved in a mixture of Me_2CO (7.5 mL), THF, $i\text{Pr}_2\text{O}$ or Et_2O (2.5 mL), and $\text{CF}_3\text{CO}_2\text{H}$ (0.66 mL, 8.57 mmol) in a 100-mL flask with 4–6 min of ultrasonication or heating ($\approx 35^\circ\text{C}$) under Ar. After ten days, black plate arrow-end crystals of **2'** were isolated by decanting the mother liquors and washed with acetone (50–55 mg, 45–50 %). Elemental analysis (Zelinsky Institute of Organic Chemistry): calcd (%) for $\text{Pd}_{66}(\text{CO})_{46}(\text{PET}_3)_{16}$: C 16.72, H 2.37, P 4.86, Pd 68.84; found: C 16.38, H 2.30, P 4.89, Pd 69.28; IR (nujol): $\tilde{\nu} = 1883$ – 1881 cm^{-1} (s br). Crystals obtained from this procedure were monoclinic with a β angle close to 90° ; for example, $a = 20.417(5)$, $b = 35.711(9)$, $c = 30.877(11)\text{ \AA}$, $\beta = 90.04(2)^\circ$, $V = 22512(12)\text{ \AA}^3$; or $a = 20.48(1)$, $b = 35.48(4)$, $c = 30.55(2)\text{ \AA}$, $\beta = 90.10(5)^\circ$, $V = 22194(49)\text{ \AA}^3$, etc. Solution of the structural data from their X-ray data sets could not be refined but did disclose the $\{\text{Pd}_{66}\text{P}_{16}\}$ fragment of **2'**.
- [5] $[\text{Pd}_{10}(\text{CO})_{12}(\text{PET}_3)_6]$ (**3**; 0.150 g, 0.071 mmol) and $[\text{Pd}(\text{MeCN})_4](\text{BF}_4)_2$ (0.063 g, 0.142 mmol) were dissolved in a mixture of THF (10 mL) and Me_2CO (5 mL) under N_2 . On the next day, the solvent was evaporated and the black residue was extracted with MeCN. Crystallization in the presence of vapor from a 1:1 mixture of $i\text{Pr}_2\text{O}$ /hexane gave black needlelike crystals of **2** (15 mg; 13 %). IR (nujol): $\tilde{\nu} = 1884\text{ cm}^{-1}$ (s br) with shoulders at 1916 and 1867 cm^{-1} . A crystal of dimensions $0.61 \times 0.28 \times 0.18\text{ mm}^3$ was used for the determination of the X-ray crystal structure.
- [6] On a related note, a recent systematic preparative/structural investigation^[21] has provided compelling geometrical evidence for a previously unknown stereochemical example involving close-packed, nanosized cuboctahedral-based $[\text{Pd}_{23}(\text{CO})_x(\text{PET}_3)_{10}]$ clusters that comprise structurally analogous $\{\text{Pd}_{23}(\text{PET}_3)_{10}\}$ fragments with variable numbers of carbonyl ligands ($x = 20, 21, 22$). This observed expanded capacity of CO coordination on the same centered Pd_{23} polyhedron from the thermodynamically stable structure with 20 CO ligands to the kinetic products with additional CO ligands ($x = 21, 22$) without notable changes in the geometry of the common $\{\text{Pd}_{23}(\text{PET}_3)_{10}\}$ fragment was attributed to the nanosized (≈ 0.8 – 0.9 nm) architecture of the metal core.
- [7] a) **1**: trigonal; $R\bar{3}$; $a = b = 17.303(2)$, $c = 51.067(13)\text{ \AA}$, $\alpha = \beta = 90^\circ$, $\gamma = 120^\circ$, $V = 13240(4)\text{ \AA}^3$; $Z = 3$, $\rho_{\text{calcd}} = 3.083\text{ Mg m}^{-3}$. $\text{MoK}\alpha$ data collected at $173(2)\text{ K}$ with Bruker SMART CCD-1000 area-detector diffractometer by 0.3ω scans over a 2θ range from 2.40 to 46.62° ; empirical absorption correction (SADABS) applied; $\mu(\text{MoK}\alpha) = 5.328\text{ mm}^{-1}$; max/min transmission, $0.416/0.298$. Full-matrix least-squares refinement (SHELXTL)^[7c] (300 parameters; 27 restraints) on 4253 independent reflections converged at $\omega R_2(F^2) = 0.176$ with $R_1(F) = 0.071$ for $I > 2\sigma(I)$; GOF (on F^2) = 1.03; max/min residual electron density $8.87/-5.10\text{ e \AA}^{-3}$. All non-hydrogen atoms were refined anisotropically, except for those of disordered carbonyl groups and disordered ethyl substituents; b) **2**: monoclinic; $P2_1/n$; $a = 20.717(2)$, $b = 35.756(4)$, $c = 30.623(4)\text{ \AA}$, $\beta = 90.904(1)^\circ$, $V = 22682(5)\text{ \AA}^3$; $Z = 4$, $\rho_{\text{calcd}} = 2.979\text{ Mg m}^{-3}$. $\text{MoK}\alpha$ data collected at $100(2)\text{ K}$ with Bruker SMART CCD-1000 area-detector diffractometer by 0.3ω scans over a 2θ range from 1.76 to 46.36° ; empirical absorption correction (SADABS) applied; $\mu(\text{MoK}\alpha) = 5.247\text{ mm}^{-1}$; max/min transmission, $0.452/0.142$. Full-matrix least-squares refinement (SHELXTL)^[7c] (1540 parameters; 236 restraints) on 31516 independent reflections converged at $\omega R_2(F^2) = 0.278$ with $R_1(F) = 0.108$ for $I > 2\sigma(I)$; GOF (on F^2) = 0.894; max/min residual electron density $3.48/-2.41\text{ e \AA}^{-3}$. Palladium and phosphorus atoms were refined anisotropically. CCDC 276453 (**1**) and 276454 (**2**) contain the supplementary crystallographic data for this paper. These data can be obtained free of charge from the Cambridge Crystallographic Data Centre via www.ccdc.cam.ac.uk/data_request/cif; c) G. M. Sheldrick: SHELXTL version 6.10 Program Library, Bruker Analytical X-Ray Systems, Madison, WI, **2000**.
- [8] a) Similar formal condensations of monocapped ν_2 Pd_7 triangles to centered metal hexagons are encountered in Pd_{30} ^[2k] and Pd_{23} ^[2h,j] clusters. The condensation of four noncapped ν_2 Ni_6 triangles on four centered hexagonal faces of a ccp Ag_{16} metal core was observed in the pseudo- T_d $[\text{Ag}_{16}\text{Ni}_{24}(\text{CO})_{40}]^{4-}$ cluster^[8b]; b) J. Zhang, L. F. Dahl, *J. Chem. Soc. Dalton Trans.* **2002**, 1269.
- [9] a) S. Martinengo, G. Ciani, and A. Sironi, *J. Am. Chem. Soc.* **1980**, 102, 7565; b) N. T. Tran, M. Kawano, D. R. Powell, L. F. Dahl, *J. Chem. Soc. Dalton Trans.* **2000**, 4138; c) C. Femoni, M. C. Iapalucci, G. Longoni, P. H. Svensson, J. Wolowska, *Angew. Chem.* **2000**, 112, 1702; *Angew. Chem. Int. Ed.* **2000**, 39, 1635; d) C. Femoni, M. C. Iapalucci, G. Longoni, P. H. Svensson, *J. Chem. Soc. Chem. Commun.* **2004**, 2274.
- [10] J. Donohue, *The Structures of the Elements*, Wiley, New York, **1974**, p. 216.
- [11] An anisotropic pancake-shaped displacement ellipsoid observed for the crystallographically independent monocapped $\text{Pd}(10)$ atom, which lies on the crystallographic C_3 axis of **1** (Figure 1), is attributed to it being randomly disordered among three sites toward each of the three equivalent inner $\text{Pd}(4)$ atoms in the Pd_6 triangle. Nevertheless, we consider its site displacements from the threefold axis to be relatively small such that $\text{Pd}(10)$ still undergoes μ_3 coordination with three threefold-related edge-bridging carbonyl ligands that span the three $\text{Pd}(10)$ – $\text{Pd}(4)$ edges. This premise is based upon the least-squares refinement, which indicates that the carbon and oxygen atoms of the crystallographically independent doubly bridging carbonyl group that connects $\text{Pd}(10)$ to the inner Pd_3 triangle have whole-weighted occupancy factors.
- [12] a) The $[\text{Cu}_x\text{Ni}_{35-x}(\text{CO})_{40}]^{5-}$ cluster ($x = 3$ or 5)^[12b] provides another striking example of a nanosized close-packed metal-core carbonyl cluster that contains an extra carbonyl ligand. The presence of the extra CO moiety on one of three otherwise symmetry-equivalent sides of the metal core results in a markedly different arrangement on the side of the extra CO to the similar arrangements of CO groups on the other two sides. Its inclusion lowers the symmetry of the 35-atom triangular stacking-layer sequence from pseudo- D_{3h} to C_s symmetry (i.e., a pseudo-vertical mirror plane); b) P. D. Mlynec, M. Kawano, M. A. Kozee, L. F. Dahl, *J. Cluster Sci.* **2001**, 12, 313.
- [13] E. G. Mednikov, L. F. Dahl, unpublished results.
- [14] a) E. L. Muettterties, T. N. Rhodin, E. Band, C. F. Brucker, W. R. Pretzer, *Chem. Rev.* **1979**, 79, 91, and references therein;

- b) C. M. Friend, R. M. Gavin, E. L. Muetterties, M.-C. Tsai, *J. Am. Chem. Soc.* **1980**, *102*, 1717; c) E. Shustorovich, R. G. Baetzold, E. L. Muetterties, *J. Phys. Chem.* **1983**, *87*, 1100; d) G. Pacchioni, J. Koutecky, *J. Phys. Chem.* **1987**, *91*, 2658; e) R. Hoffmann, *Rev. Mod. Phys.* **1988**, *60*, 601; f) J. E. Adams, *J. Chem. Phys.* **1990**, *92*, 1849; g) B. C. Gates, *Angew. Chem.* **1993**, *105*, 240; *Angew. Chem. Int. Ed. Engl.* **1993**, *32*, 228.
- [15] a) P. Chini, *J. Organomet. Chem.* **1980**, *200*, 37; b) A. Ceriotti, N. Masciocchi, P. Macchi, G. Longoni, *Angew. Chem.* **1999**, *111*, 3724; *Angew. Chem. Int. Ed.* **1999**, *38*, 3941, and references therein; c) J. D. Roth, G. J. Lewis, L. K. Safford, X. Jiang, L. F. Dahl, M. J. Weaver, *J. Am. Chem. Soc.* **1992**, *114*, 6159.
- [16] C. Femoni, M. C. Iapalucci, G. Longoni, P. H. Svensson, *Chem. Commun.* **2001**, 1776.
- [17] a) A. Ceriotti, F. Demartin, G. Longoni, M. Manassero, M. Marchionna, G. Piva, M. Sansoni, *Angew. Chem.* **1985**, *97*, 708; *Angew. Chem. Int. Ed. Engl.* **1985**, *24*, 697; b) F. F. de Biani, C. Femoni, M. C. Iapalucci, G. Longoni, P. Zanello, A. Ceriotti, *Inorg. Chem.* **1999**, *38*, 3721; c) C. Femoni, M. C. Iapalucci, G. Longoni, P. H. Svensson, P. Zanello, F. F. de Biani, *Chem. Eur. J.* **2004**, *10*, 2318.
- [18] This current formulation for the Ni–Pt cluster is based on ref. [9d] (see footnote 2 therein), which states that “circumstantial evidence suggests the presence of two hydride atoms in the cluster originally formulated as $[\text{Ni}_{24}\text{Pt}_{14}(\text{CO})_{44}]^{4-}$.”^[16]

DOI: 10.1002/anie.200502338

Two-Component Graded Deposition of Biomolecules with a Double-Barreled Nanopipette***Kit T. Rodolfa, Andreas Bruckbauer, Dejian Zhou, Yuri E. Korchev, and David Klenerman**

There is currently great interest in depositing submicron features of biological molecules on surfaces for miniaturized assays^[1–6] and to assemble new structures from biological building blocks.^[7] Several methods that have been used to produce these features are based on scanning probe microscopy (SPM) and use either the tip of an atomic force

microscope (AFM) or a nanopipette. Dip-pen lithography operates in air and uses an AFM tip to write features of sizes less than 100 nm.^[1,5,8–14] Fountain pen lithography has been developed by using apertured AFM tips to produce sub-100-nm features^[14] or nanopipettes^[6] to produce features of around 300 nm. In both cases, the fountain pen lithography operates in air.

Nanopipettes have also been used for deposition in a buffer solution by using a method based on scanning ion-conductance microscopy (SICM).^[15] In this case, voltage-driven deposition gives fine control for delivery at the single-molecule level; however, diffusion of molecules in solution and over the surface broadens the feature size when compared with deposition in air and results in features no smaller than 800 nm.^[16–18] The nanopipette, however, has the advantage that it eliminates the need for conditioning of the tip (as is required by dip-pen nanolithography (DPN) for deposition) and provides a large reservoir of molecules. Registry is a common problem with all of these methods and makes it difficult to deposit a different type of molecule on top of or at a defined position relative to another feature. This is, however, a key requirement for the production of complex patterns on surfaces and the assembly of structures made from biological molecules. Currently, this difficulty has been addressed with DPN, by using nanofabricated surfaces with defined topographic features to give registry,^[10] or through the use of a ‘multiple-pen’ array.^[11] In our own two-component work, we have addressed this problem by using nanopipettes with fluorescent imaging to provide registry.^[17] All of these solutions, however, require the use of a second tip to deposit an additional species.

Herein we present a methodology that eliminates the registry problem for the deposition of two different species on a surface. This is accomplished with a new form of scanning probe microscopy that we developed based on a double-barreled pipette. In this case, two species are independently delivered from each of the pipette barrels of a single tip. Furthermore, fine voltage-driven control of the deposition of two types of biomolecules can be achieved, in the absence of a bath, by creating a potential between the two barrels of the pipette. Operation in air provides smaller feature sizes than deposition in liquid as lateral diffusion is avoided. These advantages allow complex ‘two-color’ graded patterns to be written with biomolecules.

Double-barreled pipettes are fabricated from glass capillaries (diameter of 1.5 mm, with a septum down the center) by using a pipette puller (Sutter Instruments, Model P-2000). These pipette tips were imaged with scanning electron microscopy (SEM), and the barrels maintained their D-shape throughout pulling (see Figure 1 inset). The heights of the individual barrel openings (when oriented as shown in the Figure 1 inset) ranged from 140 to 185 nm and widths from 100 to 125 nm. As depicted in Figure 1, both barrels are filled with electrolyte solution and a potential (V) is created between the Ag/AgCl electrodes that are placed in the two barrels. When the pipette is held above a surface, a liquid droplet forms automatically at the tip (Figure 1 A). This allows the electrolyte to flow between the barrels and hence provides an ion current (I_{DC}) for control over the surface

[*] K. T. Rodolfa, Dr. A. Bruckbauer, Dr. D. Zhou, Dr. D. Klenerman
Department of Chemistry
University of Cambridge
Lensfield Road, Cambridge CB21EW (UK)
Fax: (+44) 1223-336-362
E-mail: dk10012@cam.ac.uk

Dr. Y. E. Korchev
Division of Medicine
Imperial College London
Hammersmith Hospital Campus
Du Cane Road, London W120NN (UK)

[**] This work was funded by the BBSRC, and the Winston Churchill Foundation provided a studentship to K.T.R.

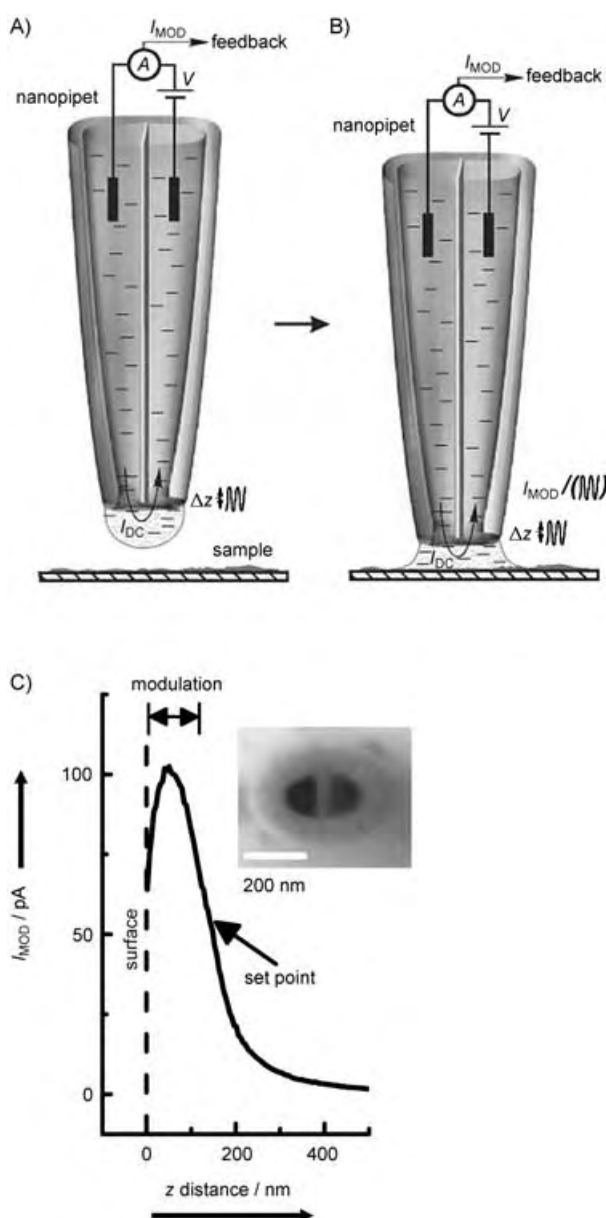


Figure 1. Schematic representation of the apparatus. A) A voltage (V) applied between Ag/AgCl electrodes in the two barrels of a glass-fabricated nanopipette creates an ion current (I_{DC}) through a droplet which forms at the tip. B) When the tip is brought into contact with a surface, modulation in the z direction creates a modulated ion current (I_{MOD}), which provides the feedback signal for control. C) Experimental approach curve for the double-barreled pipette obtained over a PDMS surface. Notice the steep dependence of I_{MOD} on the distance between the tip and the surface. The inset shows an SEM image of a gold-coated pipette tip.

without the need to insert the sample into a bath of conducting solution. As the pipette approaches the surface, a meniscus is formed between the tip and surface (Figure 1 B). I_{DC} is diminished as the tip moves closer to the surface.

To provide more robust distance control, the tip was modulated in the z direction (usually with an amplitude of ± 50 nm), and a modulated ion current (I_{MOD}) was detected with a lock-in amplifier (Model SR 830, Stanford Research

Systems).^[19] Generally, these pipettes are controlled at 75–125 nm above the sample, as determined by approach curves to the surface. Figure 1 C shows the steep dependence of the modulated ion current on the distance between the tip and the surface. The graph reaches a maximum when the tip just touches the surface at the peak of its modulation. Feedback control of the tip–surface distance is obtained by using a piezoelectric translation stage that adjusts the z position of the sample to maintain a constant value of I_{MOD} (indicated on the graph with ‘Set Point’; usually around 50 pA, which corresponds to a tip–surface distance of 100 nm).

To test the feedback control of this system, a sample surface fabricated from polydimethylsiloxane (PDMS) and consisting of ridges of 2 μm in width and 1.2 μm in height was imaged with the double-barreled pipette and tapping-mode AFM in air.^[20] Figure 2 shows the correspondence between the images obtained with the two techniques. Notably, the pipette cannot track up steep slopes or tight grooves quite as well as the AFM, and as such the ridges appear wider at their bases. This is understood to be a result of the differences in the size and geometry of the tips and has also been observed with single-barreled pipettes.^[21] Nonetheless, the agreement in feature heights and spacing is good; in particular, the pipette successfully characterized the smaller peaks in the grooves. These results indicate that double-barreled pipettes can be reliably controlled over a surface while operating in air and allows not only topographical scanning but also deposition of biomolecules.

A droplet must form at the tip of the pipette to produce an ion current, and as such it is not clear whether a significant residue of the solution is left behind as the tip moves across the surface, or whether the surface tension causes the solution to dewet as the tip moves away. To investigate this, a fluorescent dye (alexa 488) was added to both barrels and excited with 488-nm laser light while the pipette was scanned across a glass surface. No fluorescent trail was observed (with a highly sensitive CCD camera) as the tip moved across the glass, which indicates that dewetting was occurring. To deposit materials on a surface, therefore, we must functionalize the surface to interact with the molecules to be deposited. To achieve this, the glass surface was coated with a positively charged polymer, polyethyleneimine (PEI), and both barrels were loaded with alexa 488-labeled rabbit immunoglobulin G (IgG), which is known to adhere to positively charged surfaces.^[22] It was observed that the IgG migrated, due to electroosmotic flow, away from the positive electrode and towards the negative one^[17] so that the protein was only seen to come out of one barrel at any time. Alteration in the direction of the applied voltage, however, would switch the barrel in which the protein was seen to exit (Figure 3 A). As expected, the IgG delivered from the pipette adhered to the PEI-modified glass surface and left fluorescent IgG molecules deposited on the surface as the pipette was moved across it.

As the double-barreled pipette operates in air, we expected a finer feature size than that obtained with single-barreled pipettes operating in solution. In solution, molecules will spread through three-dimensional diffusion to the surface or two-dimensional diffusion on the surface and thus broaden the feature size.^[17] Previously, in solution we measured a spot

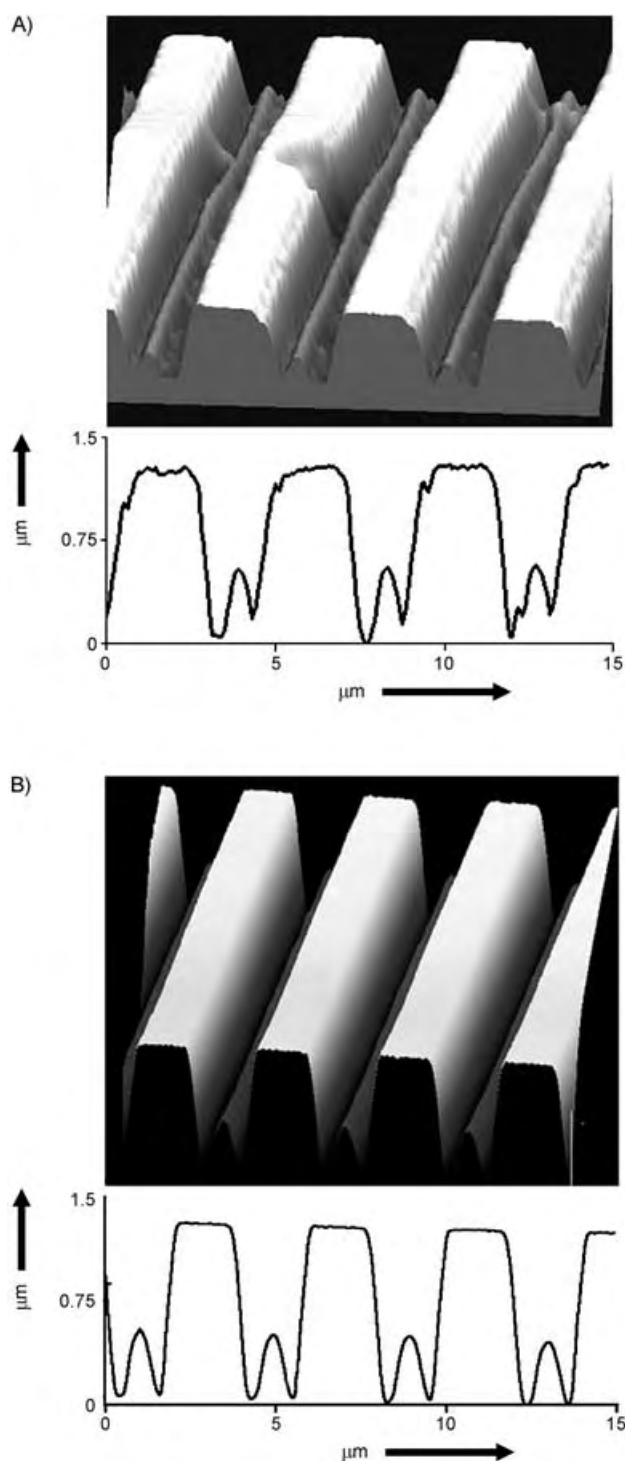


Figure 2. A) 3D image and cross-section of a PDMS stamp that was scanned in air with a double-barreled nanopipette. The image shown is a representation of 10 scans. The defect in the image is a physical defect in the stamp (control was maintained throughout taking this data). B) 3D Image and cross-section of the same stamp obtained with tapping-mode AFM in air.

size (full width at half-maximum, FWHM) of $1.3 \mu\text{m}$ with single-barreled pipettes and IgG ($830 \pm 80 \text{ nm}$ for biotinylated DNA on a streptavidin-coated glass surface).^[16] In these experiments, performed in air, the feature size deposited on

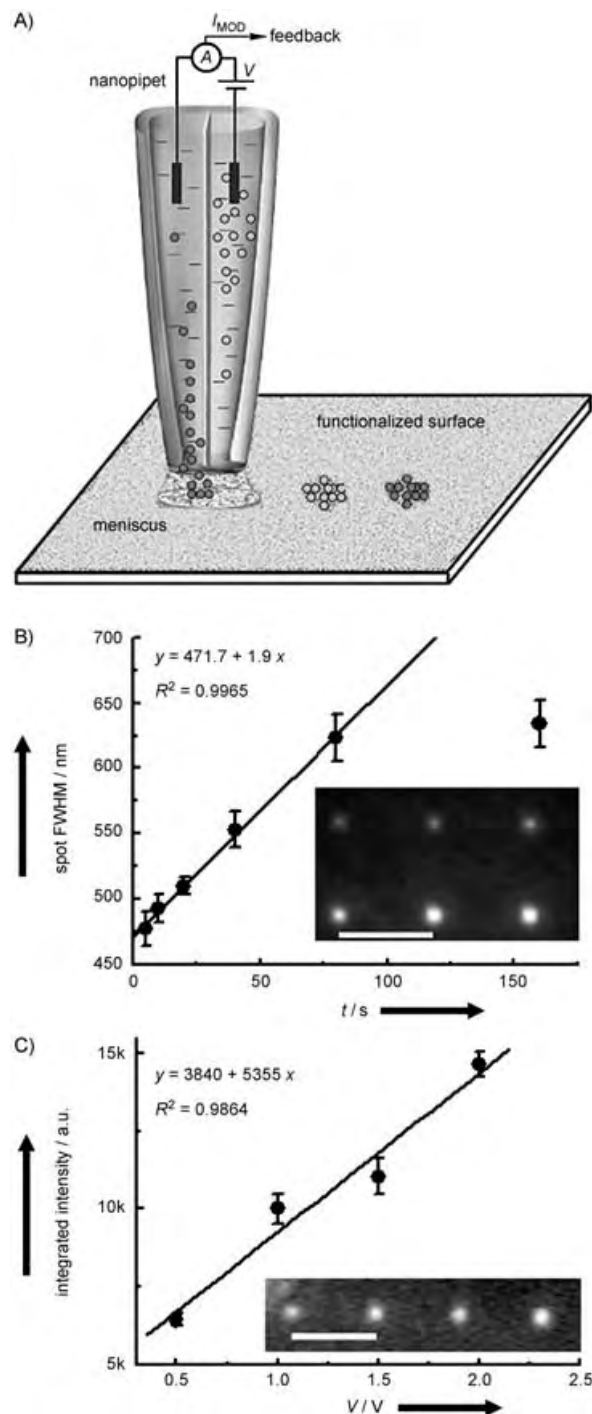


Figure 3. A) Principle of double-barreled pipette deposition. The two barrels of the nanopipette are filled with different fluorophore-labeled antibodies for deposition onto a PEI-coated glass surface. The voltage between the two barrels produces the distance–feedback control current and controls the molecular delivery. Note that antibodies are delivered only from one barrel at a time as they flow to the negative electrode. (B) & (C) show fluorescence images of alexa 488-labeled IgG spotted onto a PEI-coated glass surface. B) Spots at deposition times of 5, 10, 20, 40, 80, and 160 s and 2.0-V tip potential (inset) and linear fit to fwhm diameters of the spots. C) Spots deposited at 0.5-, 1.0-, 1.5-, and 2.0-V tip potentials for 10 s (inset) and linear fit to integrated intensities of the spots. Scale bars in both images are $5 \mu\text{m}$. The error bars represent the error in Gaussian fits. Data are representative for an individual pipette; however, fit parameters can vary between pipettes.

the surface was found to depend on both the applied voltage and the deposition time. Dots spotted at a fixed voltage of 2.0 V on the surface with dwell times of 5, 10, 20, 40, 80, and 160 s are shown in the inset in Figure 3B. Gaussian fits of the profiles of these spots yielded detected feature sizes that ranged from 440 to 630 nm and were linearly distributed with the deposition time ($R^2 = 0.9965$, from 5 to 80 s) as shown in Figure 3B.^[23]

A major advantage of the SICM-based writing method is the possibility for voltage control of the amount of material that is delivered. Voltage control of IgG delivery was tested through the application of 2.0, 1.5, 1.0, and 0.5 V across the two barrels with a deposition time of 10 s at each spot on the glass surface. At voltages lower than 500 mV, the ion current was too low to maintain control of the pipette and resulted in the pipette crashing into the surface. The inset in Figure 3C shows the fluorescent image from these dots. The integrated intensities of the Gaussian fits of the spot profiles were distributed linearly ($R^2 = 0.9864$, Figure 3C) with the applied voltage and shows that the amount of material being deposited can be controlled by variation of the voltage applied. The data shown in Figure 3B and 3C are representative of individual pipettes; the parameters were obtained by linear fits to these data and can vary between pipettes.^[24]

The feature sizes observed here are significantly smaller than those previously obtained with single-barreled pipettes. This is because molecules deposited by a double-barreled pipette operating in air reach the surface through a small liquid meniscus and cannot diffuse laterally beyond its boundary while still in transit. With increased deposition time, the material has a greater opportunity to diffuse throughout the volume of the meniscus and reach the surface. However, as seen in the 160-s point in Figure 3B, the amount of material being deposited and the resultant feature size reaches a natural plateau as the material fills out the limited volume of the meniscus and saturates the surface of its footprint. At constant deposition time, increased voltage is understood to affect feature size by simply speeding up the rate at which molecules are driven towards the surface by electroosmotic flow.

More-complex features can be achieved by using biotinylated, fluorescently labeled DNA deposited onto a streptavidin-coated glass surface. Although we found that DNA gave comparable feature sizes to that of IgG (25 dots with a 5-s deposition time yielded an average spot size of 510 ± 40 nm, individual spot sizes ranged from 350 to 600 nm (data not shown)),^[25] graded deposition was far more reliable with the DNA/streptavidin system. For instance, Figure 4A shows an example of a grayscale square of alexa 647-labeled DNA that was produced by writing several concentric squares of different sizes. Although graded depositions have been produced with a complex technique based on microfluidics,^[26] to our knowledge the only previous report of this ability with an SPM method is our work with single-barreled pipettes.^[16,17]

Furthermore, because double-barreled writing opens up the possibility for deposition of two separate species from the same tip, we explored this advantage by using DNA. The DNA was observed to migrate towards the positive electrode, only coming out of one barrel at a time, therefore allowing

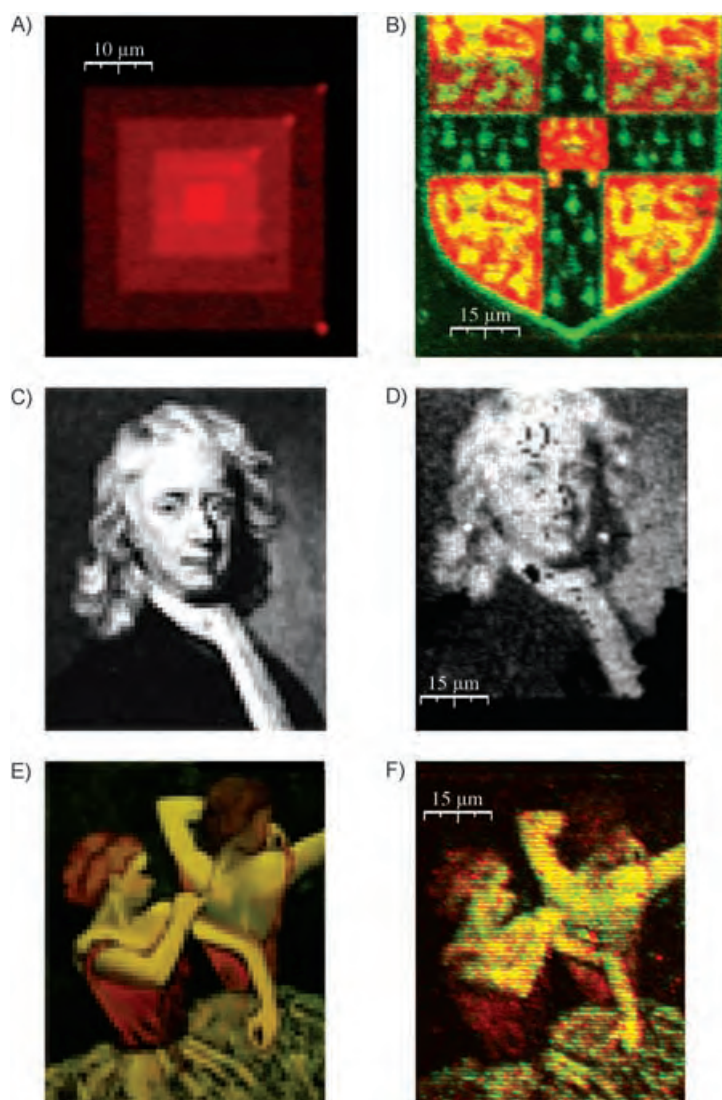


Figure 4. Fluorescence images of DNA deposited onto a streptavidin-coated glass surface. A) Gray-scale deposition of alexa 647-labeled DNA that was created by printing several squares on top of each other. B) Two DNA species, one labeled with alexa 647 and the other with rhodamine green were used to print a two-color image of the University of Cambridge crest. C) An image of Sir Isaac Newton downsized with Adobe Photoshop to 75×62 pixels. D) Double-barreled pipette-printed reproduction of the image shown in (C). The image was written with alexa 647-labeled DNA with 1- μm pixels (printed area is $75 \times 62 \mu\text{m}^2$). This image took 27 min to produce. E) An image of the painting "Degas Dancers" by Gina Candelori, downsized with Photoshop to 75×61 pixels and the blue channel removed. F) Double-barreled pipette-printed reproduction of the image in (E) with green and red channels written consecutively in rhodamine green and alexa 647-labeled DNA with 1- μm pixels (printed area is $75 \times 61 \mu\text{m}^2$). This image took 35 min to produce.

different DNA species to be driven from each barrel by a change in the sign of the applied voltage. Two different (noncomplementary) sequences of biotinylated DNA, one labeled with the fluorophore alexa 647 and the other with Rhodamine green, were loaded into the barrels and then delivered onto a streptavidin-coated glass surface. Figure 4B shows an example of two-color writing. In this case, the outline of the crest and lions were first drawn in green (Rhodamine green labeled DNA) and the red regions

(alexa 647-labeled DNA) then filled in after switching the sign of the tip potential. The yellow regions were produced where data from the two channels overlapped. The final image was created by measurement of the fluorescence on each channel individually (cross talk between the channels was measured as $<1\%$), scaling the data on a linear grayscale, and by using the two resulting images as 'red' and 'green' channels of an image in Photoshop (ver. 6.0.1, Adobe Systems Inc.) which overlays the two channels (with the third, the 'blue' channel, left blank). As Figure 4 indicates, it is easy to use this system to deliver different species to the same point on a surface. Registry problems are minimized because the tip location is always controlled by the x and y closed-loop piezos that can then be used to return the pipette to a given location after the voltage has been switched. This provides a significant advantage over our previous work with two-color deposition in which the switching of species was only possible by manually switching the pipettes and carefully placing the new tip in the same location.^[17]

The many advantages of the double-barreled writing can be combined with lithography software to produce highly complex grayscale and two-color patterning of surfaces. The original and DNA-on-streptavidin reproduction of an image of Sir Isaac Newton are shown in Figure 4C and D, respectively (see the Experimental Section for details). Although several regions of pixels are missing in the image (particularly in the lower right-hand corner), the general fidelity to the original is quite high and the image is clearly recognizable. The missing pixels are likely due to nonuniform coating of streptavidin on the surface, which results in bare patches where the DNA cannot adsorb. The Degas Dancers, shown in Figure 4F, represents another example of a complex pattern written with biomolecules on the submicron scale (presented in the same way as Figure 4B). The images in Figure 4 demonstrate that the double-barreled pipette can produce complex graded patterns of biomolecules on the submicron scale.

The methods described herein significantly improve upon previously published nanopipette methods. We have shown that double-barreled pipettes, when operated in air, can be used for both topographical imaging and reliable deposition of DNA and protein onto modified surfaces. Through the minimization of lateral diffusion, we observed smaller feature sizes in these deposition experiments than could be obtained with a single-barreled pipette operating in solution. Furthermore, the creation of a potential between the two barrels of the pipette presents the opportunity to fill the barrels with different materials and write in two 'colors' by simply switching the direction of the voltage to change the color of the 'ink'. As noted above, this is particularly beneficial because such in situ switching minimizes the registry errors inherent in attempting to bring a new tip to the same place on the surface. Naturally, many of the advantages described herein could be expanded to systems with more than two barrels—pullers currently exist that are capable of creating tips with as many as seven barrels.^[27] Such systems could use separate electrodes for control and delivery which would allow several species to be delivered simultaneously. The potential to deposit a larger number of species with the same

pipette also greatly increases the complexity of patterns that can be produced. Furthermore, the possible application to nanoscale biological assays and combinatorial chemistry would allow advancement in bionanotechnology.

Experimental Section

The apparatus consists of an inverted fluorescence microscope in which nanopipettes can be mounted and controlled over the sample stage by using closed-loop piezos.^[17] The PDMS stamp for topographical imaging was prepared by replicating a standard photolithography patterned photoresist master with sylgard 184 prepolymer (Dow Corning) through a literature procedure.^[20] Surfaces for the IgG writing experiments were prepared by immersing a glass coverslip in an aqueous solution of polythyleneimine (PEI, 2.2 mg mL^{-1}) for approximately 15 min and then washing with deionized water. alexa 488-labeled rabbit IgG and streptavidin-coated glass surfaces were prepared as described previously.^[16,17] Fluorophore-labeled DNA was purchased from MWG Biotech AG (Ebersberg, Germany) and the following sequences were used: biotin-5'-AGT CAA GCC ATT GTA GTC CCG CAA CAC ACT CGA GA-3'-alexa 647 and 5'-CTA TGC AGC CAT TGT AGT CC-3'-rhodamine green. IgG or DNA solutions were prepared in phosphate buffer solution (10 mM phosphate, 150 mM NaCl, 2 mM NaN_3 , pH 7.2) and routinely delivered from the pipette by using a tip bias of 1 to 2 V.

The images shown in Figure 4C–F were prepared as follows. The original image (not shown) was reduced with Adobe Photoshop to 75 pixels in height and 61 pixels in width, Microcal Origin 7.0 was then used to convert the resulting bitmap into an 8-bit integer ASCII matrix. The relative intensity of each pixel was then scaled to a dwell time between 0 and 1 s over individual pixels. The ASCII data was converted into a lithography file for RHK Lithoedit (RHK Technologies; MI, USA) by using the 'find and replace' function in Microsoft Word to produce the code for 1- μm step sizes between pixels. For the image of Degas Dancers in Figure 4F the blue channel of the original (not shown) was removed with Adobe Photoshop. The red and green channels were processed separately as described above to produce two sets of lithography code that could be run individually to draw first one channel, then the other.

Received: July 5, 2005

Keywords: DNA · nanotechnology · nanowriting · proteins · scanning probe microscopy

- [1] K. B. Lee, J. H. Lim, C. A. Mirkin, *J. Am. Chem. Soc.* **2003**, *125*, 5588.
- [2] D. J. Lockhart, E. A. Winzler, *Nature* **2000**, *405*, 827.
- [3] D. S. Wilson, S. Nock, *Angew. Chem.* **2003**, *115*, 510; *Angew. Chem. Int. Ed.* **2003**, *42*, 494.
- [4] G. MacBeath, S. L. Schreiber, *Science* **2000**, *289*, 1760.
- [5] R. D. Piner, J. Zhu, F. Xu, S. H. Hong, C. A. Mirkin, *Science* **1999**, *283*, 661.
- [6] H. Taha, R. S. Marks, L. A. Gheber, I. Rouso, J. Newman, C. Sukenik, A. Lewis, *Appl. Phys. Lett.* **2003**, *83*, 1041.
- [7] N. C. Seeman, *Nature* **2003**, *421*, 427.
- [8] L. M. Demers, S. J. Park, T. A. Taton, Z. Li, C. A. Mirkin, *Angew. Chem.* **2001**, *113*, 3161; *Angew. Chem. Int. Ed.* **2001**, *40*, 3071.
- [9] D. S. Ginger, H. Zhang, C. A. Mirkin, *Angew. Chem.* **2004**, *116*, 30; *Angew. Chem. Int. Ed.* **2004**, *43*, 30.
- [10] S. H. Hong, J. Zhu, C. A. Mirkin, *Science* **1999**, *286*, 523.
- [11] S. H. Hong, C. A. Mirkin, *Science* **2000**, *288*, 1808.
- [12] G. Agarwal, R. R. Naik, M. O. Stone, *J. Am. Chem. Soc.* **2003**, *125*, 7408.

- [13] G. Agarwal, L. A. Sowards, R. R. Naik, M. O. Stone, *J. Am. Chem. Soc.* **2003**, *125*, 580.
- [14] K. H. Kim, N. Moldovan, H. D. Espinosa, *Small* **2005**, *1*, 632.
- [15] P. K. Hansma, B. Drake, O. Marti, S. A. C. Gould, C. B. Prater, *Science* **1989**, *243*, 641.
- [16] A. Bruckbauer, L. M. Ying, A. M. Rothery, D. J. Zhou, A. I. Shevchuk, C. Abell, Y. E. Korchev, D. Klenerman, *J. Am. Chem. Soc.* **2002**, *124*, 8810.
- [17] A. Bruckbauer, D. J. Zhou, L. M. Ying, Y. E. Korchev, C. Abell, D. Klenerman, *J. Am. Chem. Soc.* **2003**, *125*, 9834.
- [18] L. M. Ying, A. Bruckbauer, A. M. Rothery, Y. E. Korchev, D. Klenerman, *Anal. Chem.* **2002**, *74*, 1380.
- [19] A. I. Shevchuk, J. Gorelik, S. E. Harding, M. J. Lab, D. Klenerman, Y. E. Korchev, *Biophys. J.* **2001**, *81*, 1759.
- [20] D. Zhou, A. Bruckbauer, L. M. Ying, C. Abell, D. Klenerman, *Nano Lett.* **2003**, *3*, 1517.
- [21] Y. E. Korchev, C. L. Bashford, M. Milovanovic, I. Vodyanoy, M. J. Lab, *Biophys. J.* **1997**, *73*, 653.
- [22] D. J. Zhou, X. Z. Wang, L. Birch, T. Rayment, C. Abell, *Langmuir* **2003**, *19*, 10557.
- [23] The 80- and 160-s dots did not differ significantly in either width or integrated intensity. This indicates that the surface saturation occurs at a deposition time of approximately 80 s (the linear fit mentioned herein was performed with the 160-s data point masked).
- [24] Spot sizes have been observed to vary by as much as 50% between tips. For instance, deposition of IgG at 2.0 V for 10 s yields spot sizes in the range of 500–750 nm depending on the pipette.
- [25] Feature sizes reported herein are true spot sizes, deconvoluted with an optical resolution of 350 nm.
- [26] X. Y. Jiang, Q. B. Xu, S. K. W. Dertinger, A. D. Stroock, T. M. Fu, G. M. Whitesides, *Anal. Chem.* **2005**, *77*, 2338.
- [27] Glass capillaries and pipette pullers for producing tips with up to seven barrels are available from a number of manufacturers: *World Precision Instruments Catalog*, **2004**, 98 and 193.

DOI: 10.1002/anie.200501399

Regio- and Chemoselective 6'-N-Derivatization of Aminoglycosides: Bisubstrate Inhibitors as Probes To Study Aminoglycoside 6'-N-Acetyltransferases**

Feng Gao, Xuxu Yan, Oliver M. Baettig,
Albert M. Berghuis, and Karine Auclair*

Aminoglycosides are among the most commonly used broad-spectrum antibiotics.^[1] The biological activity relies on their high affinity for the major groove of bacterial 16S rRNA,^[2] thereby impeding protein synthesis. A number of aminoglycosides also display antiviral activity owing to specific interactions with viral RNA.^[3] The rapid emergence of aminoglycoside resistance in the treatment of infections, however, is a serious threat.^[4] In clinical isolates of aminoglycoside-resistant strains, the most frequently observed cause of resistance is the expression of *N*-acetyltransferases.^[5] For example, aminoglycoside 6'-*N*-acetyltransferase type II (AAC(6')-II) is chromosomally encoded in *Enterococcus faecium*, which is one of the leading causes of hospital-acquired infections.^[6] Studies by Wright and co-workers suggest that catalysis by AAC(6')-II occurs through an ordered bi-bi mechanism in which acetyl coenzyme A (Ac-CoA) must bind the enzyme before the aminoglycoside.^[5,7] Next, attack of the aminoglycoside 6'-NH₂ at the thioester of Ac-CoA is believed to generate a tetrahedral intermediate that collapses to yield an 6'-*N*-acetylaminoglycoside and CoA. Although crystal structures have been reported for complexes of AAC(6')-II with either Ac-CoA or CoA, crystallization experiments of enzyme-aminoglycoside complexes have not been successful.^[8] It was envisaged that either 6'-*N*-(S-CoA)aminoglycoside derivatives or bisubstrates (Scheme 1) would facilitate the study of this important class of enzymes. Bisubstrate analogues have exhibited inhibition of serotonin

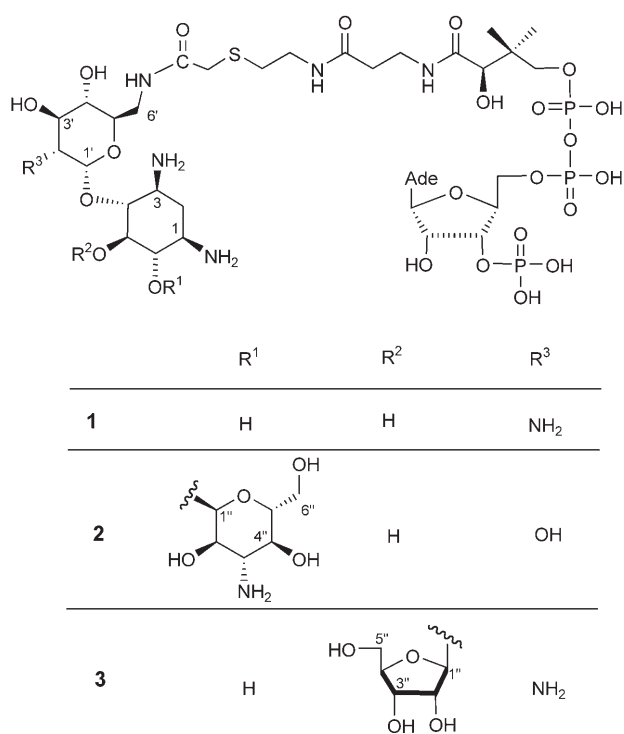
[*] F. Gao, X. Yan, Prof. K. Auclair
Department of Chemistry, McGill University
801 Sherbrooke Street West, Montréal, Québec, H3A2K6 (Canada)
Fax: (+1) 514-398-3797
E-mail: karine.auclair@mcgill.ca

O. M. Baettig, Prof. A. M. Berghuis
Department of Biochemistry, McGill University
801 Sherbrooke Street West, Montréal, Québec, H3A2K6 (Canada)

[**] This work was supported by the National Science and Engineering Research Council of Canada (NSERC), by the Canadian Institute of Health Research (CIHR), and by the Cancer Research Center (CRC). F.G., X.Y., and O.M.B. were supported by scholarship awards from the Chemical Biology Strategic Training Initiative of CIHR. The authors are grateful to G. D. Wright at McMaster University for sharing his AAC(6')-II expression plasmid.



Supporting information (including experimental procedures, characterization data, some NMR spectra and HPLC traces) for this article is available on the WWW under <http://www.angewandte.org> or from the author.



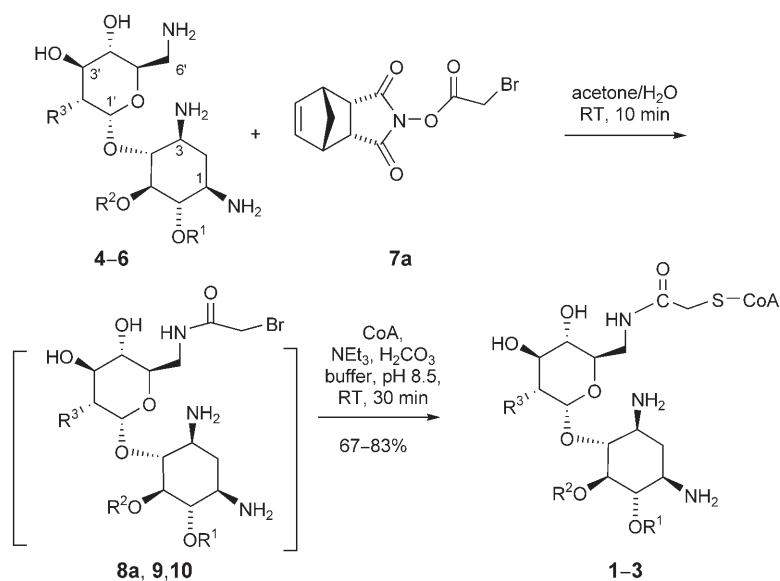
Scheme 1. Target aminoglycoside–CoA bisubstrates **1–3**. Ade = adenine.

acetyltransferase,^[9] GCN5 histone acetyltransferase,^[10] and carnitine acetyltransferases.^[11] 3-*N*-(2-*S*-CoA-acetyl)gentamicin C_{1a}, the only aminoglycoside–CoA derivative reported so far, was prepared enzymatically by using AAC(3)-I (3 mg) to yield the desired product (0.89 mg),^[12] which was subsequently found to inhibit AAC(3)-I with high affinity. To date, however, there are no reports of chemical syntheses of CoA-aminoglycoside derivatives. Naturally occurring aminoglycosides are complex molecules, and their regioselective modification remains challenging. Currently, the use of judicious functional-protection chemistry is common; however, the overall yields are low.^[13] Herein we report an efficient procedure for the regioselective derivatization of unprotected aminoglycosides at the 6'-NH₂ position. This strategy was shown to proceed with high chemoselectivity towards the assembly of CoA-aminoglycoside derivatives **1–3** and **11a–c** (Scheme 2 and Scheme 3). Activity assays of these bisubstrates reveal novel nanomolar tight-binding competitive inhibition of AAC(6')-Ii.

The target bisubstrates **1–3** were designed based on the proposed tetrahedral intermediate that results from the attack of the aminoglycoside 6'-NH₂ on the thioester carbonyl of Ac-CoA in the active site of the enzyme.^[5] As the crystal structures of AAC(6')-Ii^[8] did not reveal a potential oxyanion hole, it was envisaged that a bisubstrate containing an amide-based linker could mimic the intermediate. The targets were

built from neamine (**4**), kanamycin A (**5**), and ribostamycin (**6**), which are examples of nonsubstituted, 4,6-substituted, and 4,5-substituted aminoglycosides, respectively, and are AAC(6')-Ii substrates. The key step in the synthesis of **1–3** from **4–6** is the preparation of the bromide intermediates **8a**, **9**, and **10**, respectively (Scheme 2). The trifluoroacetic acid (TFA) salt of intermediate **8a** has been synthesized previously by using orthogonal protection/deprotection schemes, we envisaged the use of *N*-(2-bromoacetyl)oxy-5-norbornene-*endo*-2,3-dicarboximide (bromoacetyl-NBD ester, **7a**) to transfer regioselectively a bromoacetyl group to the 6'-NH₂ of the aminoglycosides. The Boc-NBD ester has been reported to effect regioselective Boc protection of aminoglycosides;^[15] however, NBD esters have not been employed for direct aminoglycoside derivatization.

Remarkably, simply mixing the free base neamine and reagent **7a** in either acetone/H₂O or acetonitrile/H₂O (1:1) at room temperature and in a vial open to the air for a few minutes (monitored by ESI MS) was sufficient to complete the reaction. In contrast, extended reaction times yielded complicated mixtures, possibly arising from the nucleophilic attacks of amino groups at the newly formed bromide. The desired *N*-6'-bromoacetylneamine (**8a**) was isolated in good yield (70 %) by quenching of the reaction mixture with TFA



Scheme 2. Synthesis of the bisubstrate analogues **1–3**; see Scheme 1 for R¹, R², R³; **4**: neamine; **5**: kanamycin A; **6**: ribostamycin; intermediates **9** and **10** were not isolated.

after 10 min and subsequent purification by reversed-phase HPLC. To avoid the isolation step and potential decomposition, a one-pot synthesis of **1** from **4** and CoA through **8a**, was evaluated. Bisubstrate **1** was obtained in excellent yield (83 %) after purification by HPLC (the crude sample was more than 85 % pure (Figure 1 a)). The reaction proceeded equally well with the aminoglycosides **5** and **6** (72 and 67 %, respectively). In spite of their significant structural differences, kinetic studies revealed that **1–3** showed nanomolar

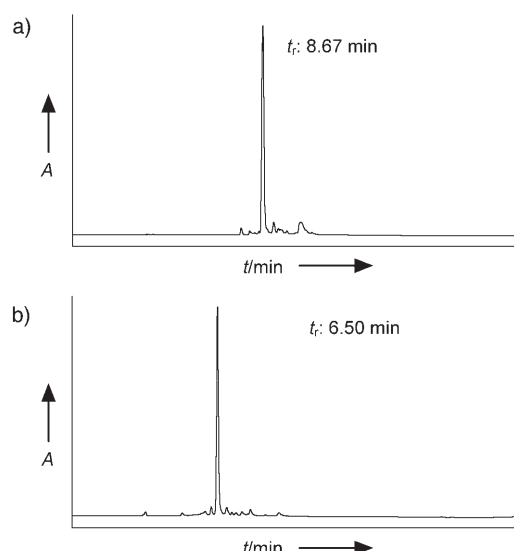


Figure 1. HPLC chromatograms for the purification of bisubstrate analogues: a) **1** and b) **11a**.

tight-binding competitive inhibition of AAC(6′)-Ii (Table 1). This observation is consistent with the fact that AAC(6′)-Ii has a broad substrate specificity.^[5]

Table 1: The AAC(6′)-Ii-inhibition constants (K_i) for the bisubstrates.

Inhibitor	K_i [nM]	Inhibitor	K_i [nM]
1	76 ± 25	11a	43 ± 23
2	111 ± 28	11b	161 ± 98
3	119 ± 14	11c	7990 ± 2663

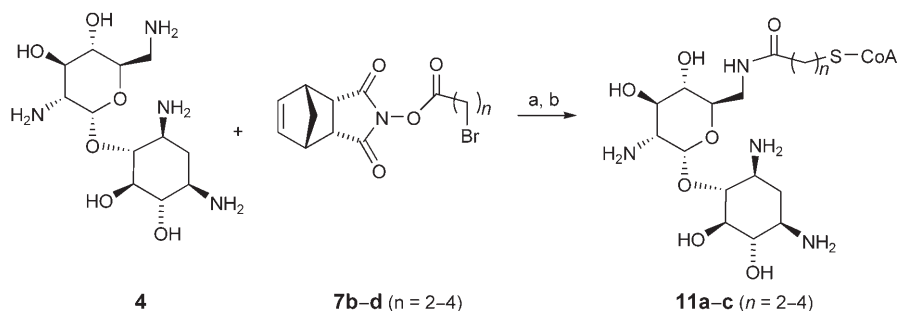
The size and geometry of linkers in serotonin-CoA bisubstrates have been reported to show important effects on the inhibition of serotonin *N*-acetyltransferase.^[9,16] A similar effect was expected for AAC(6′)-Ii and was investigated by using bisubstrates **1** and **11a–c** (Scheme 3). Unfortunately, the procedure described herein for the synthesis of bisubstrates **1–3** was not easily applicable to the preparation of **11a–c**. The major products observed when synthesis of **11a** was attempted were: an ammonium bromide (likely from the addition of triethylamine to 6′-*N*-(3-bromo-*n*-

propanoyl)neamine); 6′-*N*-acryloyl neamine (the elimination product); and a propanoyl-conjugated neamine dimer (either through S_N2 substitution at the bromide by a second neamine function or by Michael addition of a second neamine group to 6′-*N*-acryloyl neamine). Similar products resulted during the initial efforts to prepare **11b** and **11c**. A difference in the reactivities of these longer linkers was expected.^[17] Indeed, the 3-bromo-*n*-propanoyl, 4-bromo-*n*-butyryl, and 5-bromovaleryl neamine derivatives (**8b–d**, from the reaction of neamine with **7b–d**) are much less electrophilic than **8a**. Moreover, triethylamine may be too nucleophilic and used in too large an amount, which may favor *N* alkylation over *S* alkylation. As most reported chemoselective *S*/*N*-alkylation procedures^[17] are not compatible with our reagents, we reasoned that a less-nucleophilic base at a lower concentration may favor *S* alkylation. Model studies were performed by using *N*-acetylcysteine as a mimic of CoA, and an array of bases were screened, including KHCO_3 , NaHCO_3 , diisopropylethylamine (DIPEA), 1,4-diazabicyclo[2.2.2]octane (DABCO), 1,8-diazabicyclo[5.4.0]undec-7-ene (DBU), and 4-dimethylaminopyridine (DMAP). Excellent yields resulted when DIPEA (20 equiv) was used and the mixture was ultrasonicated (5 min). When applied to CoA, these conditions allowed the preparation of **11a**, **11b**, and **11c** in moderate to excellent yields (91, 52, and 93 %, respectively). The HPLC trace of crude **11a** is shown in Figure 1 b.

AAC(6′)-Ii-inhibition assays showed that **11a** is the most potent bisubstrate inhibitor of this series. Remarkably, the enzyme binds **11a** ≈ 200 -fold tighter than its natural substrate Ac-CoA ($K_m = 9.6 \mu\text{M}$). A further increase in the length of the linker, however, rapidly leads to a decrease in activity (Table 1). To demonstrate the usefulness of these inhibitors as structural and mechanistic probes, they were studied by X-ray crystallographic analysis. Although previous crystallization experiments of AAC(6′)-Ii-aminoglycoside complexes had not been successful,^[8b,c] bisubstrates **1–3** and **11a–c** crystallized well with the enzyme, providing X-ray diffraction data to $\approx 2.0\text{-\AA}$ resolution. Preliminary analysis of the diffraction data for the complex with bisubstrate **11a** (Figure 2) suggests that the conformation of the aminoglycoside bound to AAC(6′)-Ii is very different from that reported for AAC(6′)-Iy,^[18] even though both enzymes catalyze the same reaction. Detailed structural and mechanistic analysis of these structures will be reported elsewhere.

After the success of this methodology in the preparation

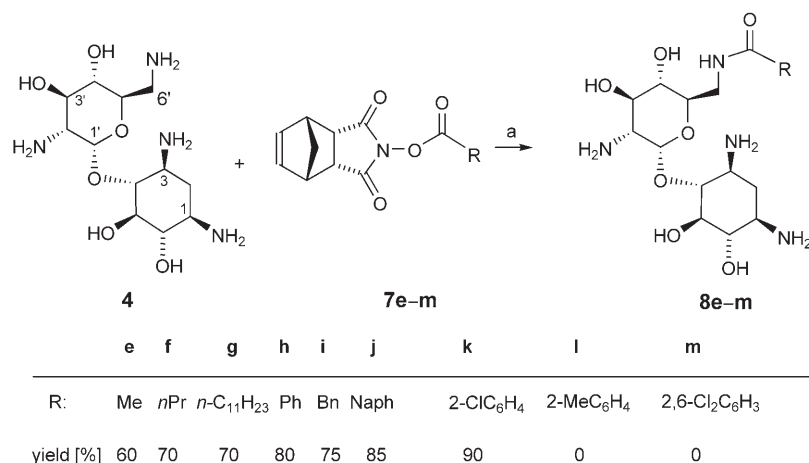
of CoA-aminoglycoside bisubstrates, its general applicability to acylation was investigated (Scheme 4). Most of the acyl groups tested were transferred regioselectively to neamine with excellent yields. NBD esters of highly hindered acyl groups such as 2-methylbenzoyl and 2,6-dichlorobenzoyl, however, did not react at all. The regioselectivity of the transfer to kanamycin A, ribostamycin, and neomycin was tested with benzoyl-NBD and showed excellent selectivity for *N*-6′-acylation.



Scheme 3. Reagents and conditions: a) acetone/ H_2O (1:1), room temperature, 10 min; b) CoA, DIPEA (20 equiv), sonicate 5 min; then room temperature, 1 h; **11a**: 91 %; **11b**: 52 %; **11c**: 93 %.



Figure 2. Crystallographically determined structure of the *E. faecium* AAC(6')-II dimer (blue and red) when complexed to the bisubstrate inhibitor **11a** (stick representation, C: light blue, N: dark blue, O: red, P: gray, S: orange).



Scheme 4. Regioselective *N*-6'-acylation of neamine. a) acetone/H₂O (1:1), room temperature, 30 min. Bn = benzyl, Naph = naphthyl

In conclusion, we have described a highly efficient synthetic strategy for the regioselective acylation of aminoglycosides at the 6'-NH₂ group. This process was successfully applied to the one-pot synthesis of 6'-*N*-(*S*-CoA)aminoglycoside analogues. Most of these bisubstrates were nanomolar tight-binding competitive inhibitors of AAC(6')-II, an important enzyme leading to antibiotic resistance. The high potency of these bisubstrate inhibitors and the crystal structure of enzyme-bound **11a** suggest that they may be good mimics of one of the enzymatic reaction intermediates.^[5] The bisubstrates reported here have allowed crystallization of AAC(6')-II with aminoglycoside derivatives. The resulting structures should provide valuable guidance in further studies of this enzyme and other members of this family.

Keywords: acetyltransferases · aminoglycosides · antibiotics · coenzyme A · inhibitors

- [1] a) G. D. Wright, A. M. Berghuis, S. Mobashery, *Resolving the Antibiotic Paradox* (Ed.: B. P. Rosen, S. Mobashery), Kluwer Academic/Plenum, New York, **1998**, pp. 27–69; b) A. Coates, Y.-M. Hu, R. Bax, C. Page, *Nat. Rev. Drug Discovery* **2002**, *1*, 895–910; c) S. B. Vakulenko, S. Mobashery, *Clin. Microbiol. Rev.* **2003**, *16*, 430–450.
- [2] a) M. I. Recht, S. Douthwaite, J. D. Puglisi, *EMBO J.* **1996**, *18*, 3133–3138; b) D. Fourmy, M. I. Recht, S. C. Blanchard, J. D. Puglisi, *Science* **1997**, *274*, 1367–1375; c) D. Fourmy, M. I. Recht, J. D. Puglisi, *J. Mol. Biol.* **1998**, *277*, 347–362.
- [3] a) J. Gallego, G. Varani, *Acc. Chem. Res.* **2001**, *34*, 836–843; b) T. Hermann, *Angew. Chem.* **2000**, *112*, 1962–1979; *Angew. Chem. Int. Ed.* **2000**, *39*, 1890–1905.
- [4] C. Walsh, *Nature* **2000**, *406*, 775–781.
- [5] G. D. Wright, P. Ladak, *Antimicrob. Agents Chemother.* **1997**, *41*, 956–960.
- [6] B. E. Murray, *Clin. Microbiol. Rev.* **1990**, *3*, 46–65.
- [7] a) K.-A. Draker, G. D. Wright, *Biochemistry* **2004**, *43*, 446–454; b) K.-A. Draker, D. B. Northrop, G. D. Wright, *Biochemistry* **2003**, *42*, 6565–6574.
- [8] a) L. E. Wybenga-Groot, K.-A. Draker, G. D. Wright, A. M. Berghuis, *Structure* **1999**, *7*, 497–507; b) D. L. Burk, N. Ghuman, L. E. Wybenga-Groot, A. M. Berghuis, *Protein Sci.* **2003**, *12*, 426–437; c) D. L. Burk, B. Xiang, C. Breitbach, A. M. Berghuis, *Acta Crystallogr. Sect. D*, **2005**, *61*, 1273–1279.
- [9] C. M. Kim, P. A. Cole, *J. Med. Chem.* **2001**, *44*, 2479–2485.
- [10] a) A. N. Poux, M. Cebat, C. M. Kim, P. A. Cole, R. Marmorstein, *Proc. Natl. Acad. Sci. USA* **2002**, *99*, 14065–14070; b) V. Sagar, W.-P. Zheng, P. Thompson, P. A. Cole, *Bioorg. Med. Chem.* **2004**, *12*, 3383–3390.
- [11] J. F. A. Chase, P. K. Tubbs, *Biochem. J.* **1969**, *111*, 225.
- [12] J. W. Williams, D. B. Northrop, *J. Antibiot.* **1979**, *32*, 1147–1154.
- [13] a) J. Roestamadji, I. Grapsas, S. Mobashery, *J. Am. Chem. Soc.* **1995**, *117*, 80–84; b) J. Haddad, L. P. Kotra, B. Llano-Sotelo, C.-K. Kim, E. F. Azucena, Jr., M.-Z. Liu, S. B. Vakulenko, C. S. Chow, S. Mobashery, *J. Am. Chem. Soc.* **2002**, *124*, 3229–3237; c) J. Roestamadji, S. Mobashery, *Bioorg. Med. Chem. Lett.* **1998**, *8*, 3483–3488.
- [14] J. Roestamadji, S. Mobashery, *Bioorg. Med. Chem. Lett.* **1998**, *8*, 3483–3488.
- [15] I. Grapsas, Y. J. Mobashery, *J. Org. Chem.* **1994**, *59*, 1918–1922.
- [16] a) E. M. Khalil, J. De Angelis, M. Ishii, P. A. Cole, *Proc. Natl. Acad. Sci. USA* **1999**, *96*, 12418; b) E. Wolf, J. De Angelis, E. M. Khalil, P. A. Cole, S. K. Burley, *J. Mol. Biol.* **2002**, *317*, 215.
- [17] a) I. K. Moiseev, N. V. Makarova, M. N. Zemtsova, *Russ. J. Org. Chem.* **2003**, *39*, 1685–1701; b) D. A. Perry, F. M. Uckun, *Tetrahedron Lett.* **2001**, *42*, 1859–1861; c) C.-C. Yang, C. K. Marlowe, R. Kania, *J. Am. Chem. Soc.* **1991**, *113*, 3177–3178.
- [18] M. W. Vetting, S. Magnet, E. Nieves, S. L. Roderick, J. S. Blanchard, *Chem. Biol.* **2004**, *11*, 565–573.

Received: April 22, 2005

Revised: July 25, 2005

Published online: October 5, 2005

Sandwich Immunoassay as a High-Throughput Screening Method for Cross-Coupling Reactions**

Paola Vicennati, Nicolas Bense, Alain Wagner, Christophe Créminon, and Frédéric Taran*

Combinatorial and parallel methods have become an important focus of research in catalysis. In particular, techniques that allow the simultaneous screening of numerous catalyst candidates have gained particular attention as they may accelerate the identification and optimization of active catalysts. To fully realize the potential of combinatorial approaches for catalyst discovery, general and powerful high-throughput screening (HTS) is therefore essential.^[1] In this context, several techniques, including IR thermography,^[2] capillary electrophoresis,^[3] mass spectrometry,^[4] image analysis,^[5] and chemosensing^[6] have been developed. The use of chromogenic^[7] and fluorogenic^[8] substrates is also a very popular approach for monitoring chemical transformations.

We recently demonstrated that, aside from spectroscopic or chemosensor-based methods, techniques that exploit the specific-binding properties of antibodies might be valuable tools for the high-throughput screening of enantioselective catalysts.^[9] Herein, we report a new versatile enzyme immunoassay (EIA) format that is suitable for the fast screening of coupling reaction.

One of the most convenient methods to screen reactions that involve bond formation is fluorescence resonance energy transfer (FRET).^[10] Although this method has many advantages, false positives caused by intermolecular quenching from the catalytic system may occur.^[11]

As our aim was to provide a more-general analytical tool, we chose to adapt sandwich immunoassays, a well-known diagnostic technique for antigen detection, for the high-throughput screening of cross-coupling reactions. Typically, sandwich immunoassays require two specific monoclonal antibodies (mAbs), one that ensures the capture of the

antigen onto a solid phase and the second that acts as a detector. Both antibodies can simultaneously bind the antigen through the recognition of two distinct epitopes. The principle of this assay might easily be extended to catalyst discovery through the use of substrates that are conveniently tagged with haptens. If hapten moieties (tags) are linked to the chemical functional groups **A** and **B**, which react through covalent-bond formation in the presence of a catalyst, the double-tagged product **A–B** is formed. This product should then be detected through a direct sandwich immunoassay with the help of two specific antitag antibodies (Figure 1).

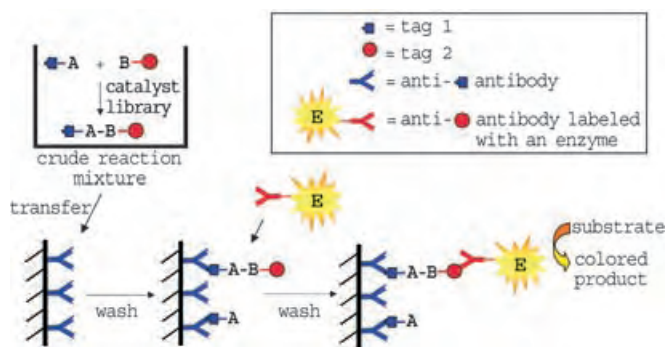


Figure 1. Schematic depiction of the HTS procedure by using a sandwich immunoassay.

In the first step, the crude chemical mixture is added to a microtitre plate that was previously coated with an antitag 1 antibody. The wells are washed with phosphate buffer (10mM, containing 0.05 % tween 20) to remove reactant **B** and any unbound material. The second antibody (antitag 2), labeled with an enzyme is then added. The concentration of the product **A–B** can now be determined from the absorbance signal, which is related to the activity of the solid-phase-bound enzyme. Thus, the yields of a reaction that involves any kind of covalent bond formation can be easily determined by using an inexpensive and automated absorbance plate reader.

To illustrate the efficiency of this concept, we applied this method to the screening of palladium-based catalysts for the Sonogashira reaction, which was chosen as the model coupling reaction. The alkyne and aryl iodide partners were tagged with imidazole-based (tag 1)^[12] and guaiacol-based (tag 2)) haptens, respectively, to form **1** and **2**. Specific monoclonal antibodies had been produced previously in our laboratories for these haptens.^[13] The feasibility of this assay depends on the possibility of the product **3** being bound by the two antibodies. Although routinely used for protein or virus detection, sandwich immunoassays for small molecules are less developed^[14] because of a common misconception that very small haptens, such as compound **3**, are not large enough to be simultaneously bound by two antibodies. To the best of our knowledge, the smallest molecule previously detected by sandwich immunoassay is angiotensin II, an octapeptide with a molecular weight of 1048 Da.^[15]

As several antibodies raised against tags 1 and 2 were available, we investigated a variety of combinations of antibodies (see Supporting Information). The couple,

[*] Dr. P. Vicennati, Dr. F. Taran
Service de Marquage Moléculaire et de Chimie Bio-Organique
DSV/DBJC CEA Saclay, 91191 Gif sur Yvette Cedex (France)
Fax: (+33) 1-6908-7991
E-mail: frederic.taran@cea.fr

Dr. C. Créminon
Service de Pharmacologie et d'Immunologie
DRM/DSV CEA Saclay, 91191 Gif-sur-Yvette Cedex (France)

Dr. N. Bense, Dr. A. Wagner
Novalyst Discovery
23 rue du Loess–BP 20, 67037 Strasbourg (France)

[**] Financial support from the European community (IBAAC project) is gratefully acknowledged. The authors also thank D. Buisson and S. Gabillet for assistance with the HPLC and product synthesis.

Supporting information for this article is available on the WWW under <http://www.angewandte.org> or from the author.

mAb 203 (antitag 1) and mAb 46 (antitag 2), provided the best specific signal and demonstrated an efficient simultaneous binding of product **3** (Figure 2). The wells of a microtitre plate were directly coated with mAb 203, and

The Sonogashira reaction, one of the most widely used carbon–carbon bond-forming reactions, usually proceeds in the presence of a homogeneous palladium catalyst and Cu^I salts.^[16] We were interested to evaluate the cross-coupling capabilities of heterogeneous palla-

dium catalysts with the aid of the EIA described above. Although the low cost, ease of handling, and high recovery are previously established advantages of heterogeneous catalysts, their use in the Sonogashira reaction is not well documented.^[17]

The catalyst library was prepared through the combination of a set of four homogeneous and eight solid-supported palladium sources as well as eight cocatalysts (copper, silver, or gold sources). These 96 catalytic reactions were run in a parallel manner, quenched by the addition of trifluoroacetic acid (TFA), diluted to the appropriate concentration with phosphate buffer, and assayed directly by a sandwich immunoassay (see Experimental Section). The results are shown in Figure 3.

The screening results indicate that under our reaction conditions, the activity of heterogeneous catalysts was similar to or greater than that of homogeneous catalysts. This was confirmed by HPLC analysis and subsequently reproduced on a larger scale. Among the tested catalytic systems, Pd/C combined with CuI or CuBr·Me₂S gave the best yields. We therefore carried out 192 more catalytic reactions in the presence of these two heterogeneous systems. The ligands, base, and solvents were varied to optimize the reaction conditions, the results of which are summarized in Figure 4. These experiments highlight the crucial role of all the tested reaction parameters. PPh₃/TMG in acetonitrile was found to be the most efficient system for both the palladium sources, and **3** was obtained in yields greater than 80%. The reactions were reproduced on the mmol scale without any significant decrease in yield.

To validate our technique, we compared the results of sandwich EIAs with those from HPLC analysis for 68 representative samples from the crude catalyzed reaction mixtures. A good correlation was obtained for EIA and HPLC analysis (Figure 5), with a linear regression that follows the equation $EIA = 1.04 HPLC + 0.88$ ($r^2 = 0.94$, $n = 68$), for the yield determination. The precision of the measurement was evaluated to be $\pm 3\%$.

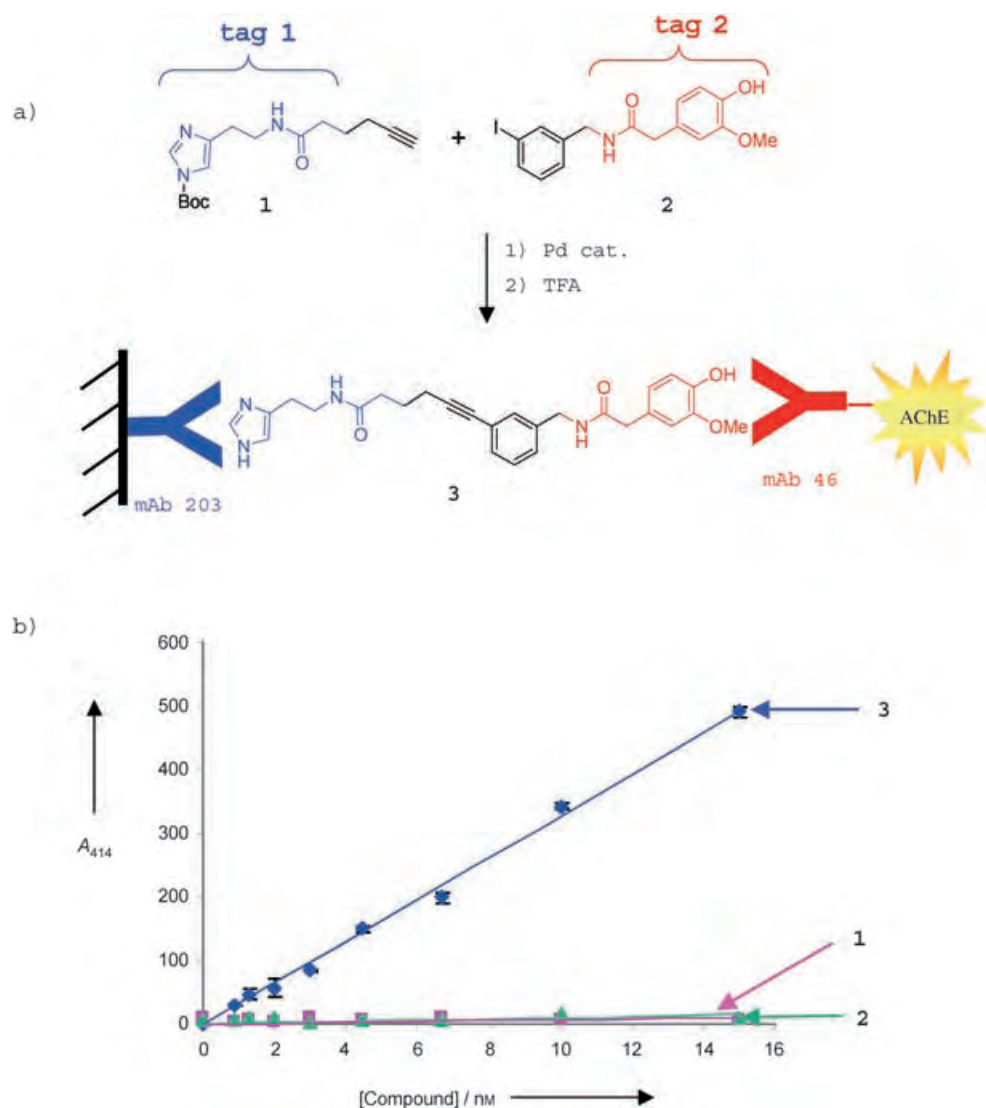


Figure 2. Schematic depiction of the HTS procedure by using sandwich immunoassay. a) the target reaction; b) the standard curves that were obtained with product **3** and reagents **1** and **2**. Boc = *tert*-butoxycarbonyl.

mAb 46 was conjugated to acetylcholinesterase (AChE). Through the use of a conventional sandwich immunoassay protocol and the Ellman reagent (colorimetric enzymatic substrate), product **3** was detected in a dose-dependent manner (Figure 2). This assay could detect **3** at concentrations as low as 10 nm (detection limits: ≈ 0.5 nm) and no signal was detected for reagents **1** and **2**. The high sensitivity and selectivity of this sandwich assay allowed us to cover a large array of reaction conditions without interference from the substrates, solvent, or catalysts. Thus the yields of the coupled products could be determined without the need for any workup of the reactions.

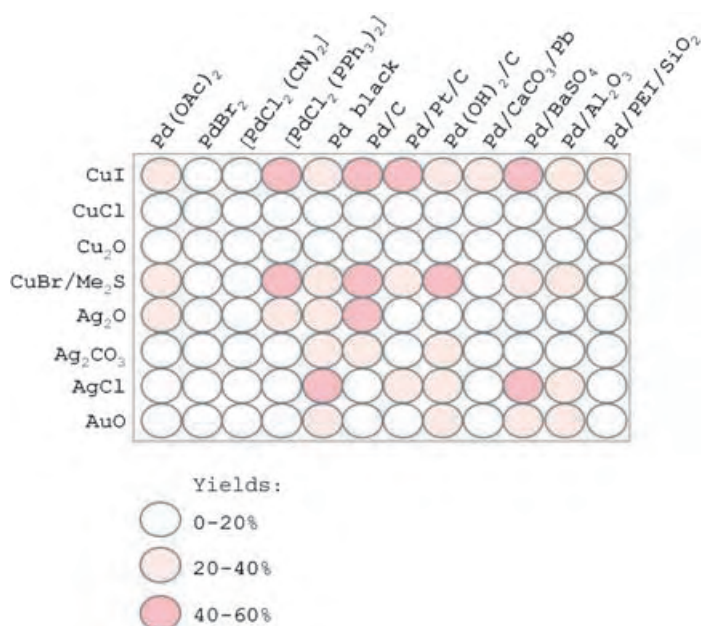


Figure 3. Sandwich immunoassay screening of the catalyst library for the formation of product **3** from reagents **1** and **2**. Catalyses were carried out in DMF/H₂O (95:5) in the presence of 3% of Pd and cocatalyst (10% (w/w)) at 80 °C for 20 h. PEI = polyethylenimine.

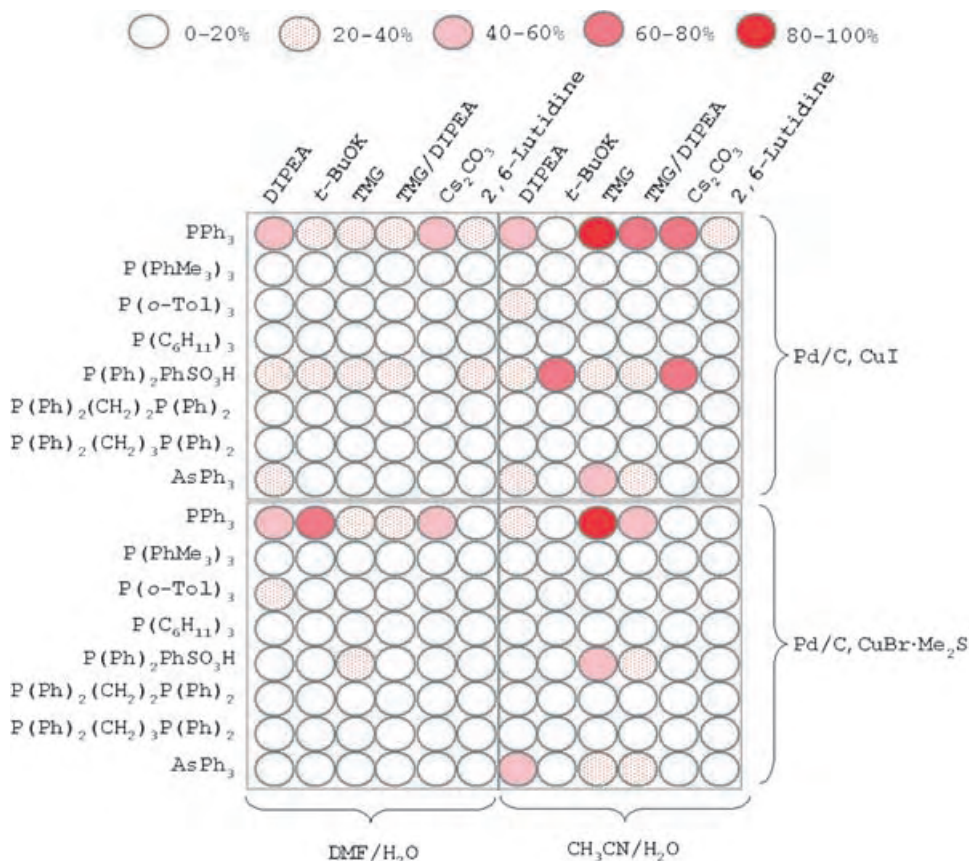


Figure 4. Sandwich immunoassay screening of the catalyst library for the formation of product **3** from reagents **1** and **2**. Catalyses were carried out in DMF/H₂O or CH₃CN/H₂O (95:5) in the presence of Pd source (3%) and cocatalyst (10% (w/w)) at 80 °C for 20 h. TMG = methyl-1-thio-β-D-galactopyranoside, DIPEA = diisopropylethylamine.

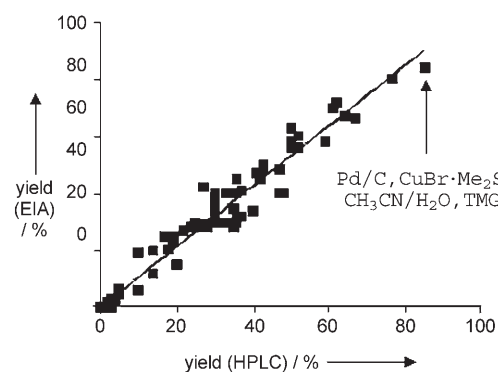


Figure 5. Graphical representation of the correlation between the yields determined by HPLC and EIA.

The most efficient catalytic system (Pd/C, CuBr·Me₂S, TMG, CH₃CN/H₂O) was finally and successfully applied to nontagged substrates. Good to high yields were attained for a variety of alkynes and aryl halides by using the optimized catalytic system (see Supporting Information).

In conclusion, we have demonstrated the usefulness of sandwich immunoassays as a highly efficient method of screening catalysts for cross-coupling reactions. We

believe that antibody-based immunoassays remain one of the most desirable noninvasive methods for accurate, sensitive, and routine analysis. Although the assay presented herein is restricted to conditions and catalysts that are at least partially compatible with tag structures, we expect that its versatility and efficiency will be of great help in the discovery of catalysts and reactions. Improvement of the presented method would require the production of antibodies directed against chemically inert tags. Furthermore, the high sensitivity of this type of immunoassay allows the exploration of reactions that occur under very dilute conditions (up to 100 nM for the reaction described herein), an advantage that is of great importance in the search for new reactions compatible with bioconjugation.^[18]

Experimental Section

Typical procedure: Pure base (1.5 equiv; 6.6 μL in the case of DIPEA), ligand (0.15 equiv; 19 μL

from a 0.2 M stock solution in DMF), and alkyne **1** (1.2 equiv; 36 μ L from a 0.84 M stock solution in DMF), supported Pd source (3 mg of 10%), cocatalyst source (1 mg), and a mixture of DMF/H₂O (95:5; 1 mL) were added to a 24-vial Miniblock reactor (solution phase synthesizer) that contained aryl iodide **2** (10 mg, 25.2 μ M). After two cycles of purging with argon, the reaction mixture was stirred for 20 h at 80 °C.

The crude mixtures were then quenched by TFA (100 μ L), diluted in EIA buffer (phosphate buffer (0.1 M) and BSA (1 mg mL⁻¹), pH 7.4) in a ratio 1:2 \times 10⁶. The diluted solutions (100 μ L) were transferred to the wells of a microtitre plate that were previously coated with mAb 203 (antitag 1; direct adsorption to the polystyrene support). After 3 h of incubation at room temperature, the plates were washed with phosphate buffer (10 mM, containing 0.05% tween 20, pH 7.4) and the antitag 2 (mAb 46)–AChE conjugate (100 μ L) was added. The AChE–mAb conjugate was prepared and stored as previously described.^[19] After 12 h of immunological incubation at 4 °C, the plates were washed, and Ellman reagent was added. The resultant absorbance (related to the solid-phase-bound AChE activity) was measured at 414 nm. The immunological reagents (antibody for the capture step and enzyme conjugate antibody) were used in excess. All measurements for the standards and samples were made in duplicate.

Received: May 12, 2005

Revised: August 10, 2005

Published online: October 7, 2005

Keywords: antibodies · C–C coupling · heterogeneous catalysis · high-throughput screening · immunoassays

- [1] a) M. T. Reetz, *Angew. Chem.* **2002**, *114*, 1391–1394; *Angew. Chem. Int. Ed.* **2002**, *41*, 1335–1338; b) J. G. de Vries, A. H. M. de Vries, *Eur. J. Org. Chem.* **2003**, 799–811.
- [2] a) S. J. Taylor, J. P. Morken, *Science* **1998**, *280*, 267–270; b) M. T. Reetz, M. H. Becker, K. M. Kühling, A. Holtzwarth, *Angew. Chem.* **1998**, *110*, 2792–2795; *Angew. Chem. Int. Ed.* **1998**, *37*, 2647–2650.
- [3] a) M. T. Reetz, K. M. Kühling, A. D. Deege, H. Hinrichs, D. Belder, *Angew. Chem.* **2000**, *112*, 4049–4052; *Angew. Chem. Int. Ed.* **2000**, *39*, 3891–3893; b) Y. Zhang, X. Gong, H. Zhang, R. C. Larock, E. S. Yeung, *J. Comb. Chem.* **2000**, *2*, 450–452.
- [4] a) M. T. Reetz, M. H. Becker, H. W. Klein, D. Stöckigt, *Angew. Chem.* **1999**, *111*, 1872–1875; *Angew. Chem. Int. Ed.* **1999**, *38*, 1758–1761; b) J. Guo, J. Wu, G. Siuzdak, M. G. Finn, *Angew. Chem.* **1999**, *111*, 1868–1871; *Angew. Chem. Int. Ed.* **1999**, *38*, 1755–1758; c) J. W. Szewczyk, R. L. Zuckerman, R. G. Bergman, J. A. Ellman, *Angew. Chem.* **2001**, *113*, 222–225; *Angew. Chem. Int. Ed.* **2001**, *40*, 216–219; d) C. Market, A. Pfaltz, *Angew. Chem.* **2004**, *116*, 2552–2554; *Angew. Chem. Int. Ed.* **2004**, *43*, 2498–2500.
- [5] S. Garbacia, R. Touzani, O. Lavastre, *J. Comb. Chem.* **2004**, *6*, 297–300.
- [6] a) G. T. Copeland, S. J. Miller, *J. Am. Chem. Soc.* **1999**, *121*, 4306–4307; b) A. C. Cooper, L. H. McAlexander, D.-H. Lee, M. T. Torres, R. H. Crabtree, *J. Am. Chem. Soc.* **1998**, *120*, 9971–9972.
- [7] a) O. Löber, M. Kawatsura, J. Hartwig, *J. Am. Chem. Soc.* **2001**, *123*, 4366–4367; b) O. Lavastre, J. P. Morken, *Angew. Chem.* **1999**, *111*, 3357–3359; *Angew. Chem. Int. Ed.* **1999**, *38*, 3163–3165; c) V. P. W. Böhm, W. A. Herrmann, *Eur. J. Org. Chem.* **2002**, 3679–3681.
- [8] a) F. Badalassi, D. Wahler, G. Klein, P. Crotti, J.-L. Reymond, *Angew. Chem.* **2000**, *112*, 4233–4236; *Angew. Chem. Int. Ed.* **2000**, *39*, 4067–4070; b) K. H. Shaughnessy, P. Kim, J. F. Hartwig, *J. Am. Chem. Soc.* **1999**, *121*, 2123–2132; c) F. Tanaka, R. Thayumanavan, C. F. Barbas III, *J. Am. Chem. Soc.* **2003**, *125*, 8523–8528.
- [9] F. Taran, C. Gauchet, B. Mohar, S. Meunier, A. Valleix, P. Y. Renard, C. Créminon, J. Grassi, A. Wagner, C. Mioskowski, *Angew. Chem.* **2002**, *114*, 132–135; *Angew. Chem. Int. Ed.* **2002**, *41*, 124–127.
- [10] a) S. R. Stauffer, N. A. Beare, J. P. Stambuli, J. F. Hartwig, *J. Am. Chem. Soc.* **2001**, *123*, 4641–4642; b) J. P. Stambuli, S. R. Stauffer, K. H. Shaughnessy, J. F. Hartwig, *J. Am. Chem. Soc.* **2001**, *123*, 2677–2678; c) S. R. Stauffer, J. F. Hartwig, *J. Am. Chem. Soc.* **2003**, *125*, 6977–6985.
- [11] W. G. Lewis, F. G. Magallon, V. V. Fokin, M. G. Finn, *J. Am. Chem. Soc.* **2004**, *126*, 9152–9153.
- [12] For compatibility reasons, the imidazole portion of tag 1 was protected as a *tert*-butyl carbamate; quantitative deprotection with TFA was performed after the catalysis step.
- [13] F. Taran, Y. Frobert, C. Créminon, J. Grassi, D. Olichon, C. Mioskowski, P. Pradelles, *Clin. Chem.* **1997**, *43*, 363–368.
- [14] a) A. Esahak, S. Judhajit, D. Tarun, *J. Immunol. Methods* **1992**, *147*, 173–179; b) H. Oguri, M. Hiramata, T. Tsumuraya, I. Fujii, M. Maruyama, H. Uehara, Y. Nagumo, *J. Am. Chem. Soc.* **2003**, *125*, 7608–7612.
- [15] J. Grassi, C. Créminon, Y. Frobert, E. Etienne, E. Ezan, H. Volland, P. Pradelles, *Clin. Chem.* **1996**, *42*, 1532–1536.
- [16] E.-i. Negishi, L. Anastasia, *Chem. Rev.* **2002**, *102*, 1979–2017.
- [17] a) Z. Novak, A. Szabo, J. Répasi, A. Kotschy, *J. Org. Chem.* **2003**, *68*, 3327–3329; b) Y. Mori, M. Seki, *J. Org. Chem.* **2003**, *68*, 1571–1574; c) R. G. Heidenreich, K. Köhler, J. G. E. Krauter, J. Pietsch, *Synlett* **2002**, 1118–1122; d) M. A. De la Rosa, E. Velarde, A. Guzman, *Synth. Commun.* **1990**, *20*, 2059–2064; e) F. Quignard, S. Larbot, S. Goutodier, A. Choplin, *J. Chem. Soc. Dalton Trans.* **2002**, 1147–1152.
- [18] a) Q. Wang, T. R. Chan, R. Hilgraf, V. V. Fokin, K. B. Sharpless, M. G. Finn, *J. Am. Chem. Soc.* **2003**, *125*, 3192–3193; b) M. Köhn, R. Breinbauer, *Angew. Chem.* **2004**, *116*, 3168–3178; *Angew. Chem. Int. Ed.* **2004**, *43*, 3106–3116; c) R. Breinbauer, M. Köhn, *ChemBioChem* **2003**, *4*, 1147–1149; d) E. Saxon, C. R. Bertozzi, *Science* **2000**, *287*, 2007–2010.
- [19] a) P. Pradelles, C. Antoine, J. P. Lellouche, J. Maclouf, *Methods Enzymol.* **1990**, *187*, 82–89; b) P. Pradelles, J. Grassi, J. Maclouf, *Anal. Chem.* **1985**, *57*, 1170–1173.

DOI: 10.1002/anie.200501911

$[\text{Re}_{12}\text{CS}_{17}(\text{CN})_6]^{n-}$ ($n = 6, 8$): A Sulfido–Cyanide Rhenium Cluster with an Interstitial Carbon Atom**

Yuri V. Mironov, Nikolai G. Naumov,
Svetlana G. Kozlova, Sung-Jin Kim,* and
Vladimir E. Fedorov*

The first compound with an octahedral sulfido–cyanide rhenium cluster, $\text{KCs}_3[\text{Re}_6\text{S}_8(\text{CN})_6]$, was synthesized ten years ago.^[1] Since then, the chemistry of chalcocyanide cluster complexes $[\text{Re}_6\text{Q}_8(\text{CN})_6]^{n-}$ ($\text{Q} = \text{S}, \text{Se}, \text{Te}$; $n = 3, 4$) has developed intensively.^[2–6] A remarkable feature of the $[\text{Re}_6\text{Q}_8(\text{CN})_6]^{n-}$ complexes is their ability to coordinate the transition-metal and post-transition-metal atoms through ambidentate CN^- ligands. Such coordination leads to the formation of cyanide-bridged polymeric structures with various dimensionalities and architectures. Many complex compounds containing similar octahedral chalcocyanide clusters have now been synthesized and their crystal structures and properties studied in detail.^[7]

The general approach for the synthesis of rhenium octahedral chalcocyanide complexes is to treat polymeric solids containing $\{\text{Re}_6\text{Q}_8\}$ cluster cores with molten KCN or NaCN. A similar method was applied to the synthesis of $[\text{Re}_6\text{Te}_8(\text{CN})_6]^{4-}$ from $[\text{Re}_6\text{Te}_{15}]^{[3,8]}$ and $[\text{Re}_6\text{Q}_8(\text{CN})_6]^{4-}$ ($\text{Q} = \text{S}, \text{Se}$) by using $[\text{Re}_6\text{Q}_8\text{Br}_2]^{[2]}$ as precursors.

A few years ago,^[9] it was found that ReS_2 and ReSe_2 react with molten KCN to form octahedral rhenium-cluster chalcocyanides with bridging S and Se_2 ligands in polymeric layered $\text{K}_4[\{\text{Re}_6\text{S}_8\}(\text{CN})_4\text{S}_{4/2}]$ and chainlike $\text{K}_4[\{\text{Re}_6\text{Se}_8\}(\text{CN})_4(\text{Se}_{2/2})_2]$ structures. Our further systematic study of phase formation in similar systems has culminated in the discovery of a unique rhenium sulfido–cyanide compound,

$\text{K}_8[\text{Re}_{12}\text{CS}_{17}(\text{CN})_6]$ (**1**), which contains a C-centered $\{\text{Re}_{12}\}$ cluster unit.

The diamagnetic compound **1** was prepared by treating ReS_2 with molten KCN with a mass ratio ReS_2/KCN of 1:2.^[10] Single crystals suitable for a structural study were found in the reaction mixture and the single crystal structure of **1** has been solved by X-ray diffraction.^[11] The cluster unit of **1** (Figure 1 a) consists of two $\{\text{Re}_6\}$ octahedra bonded by three μ_2 -S

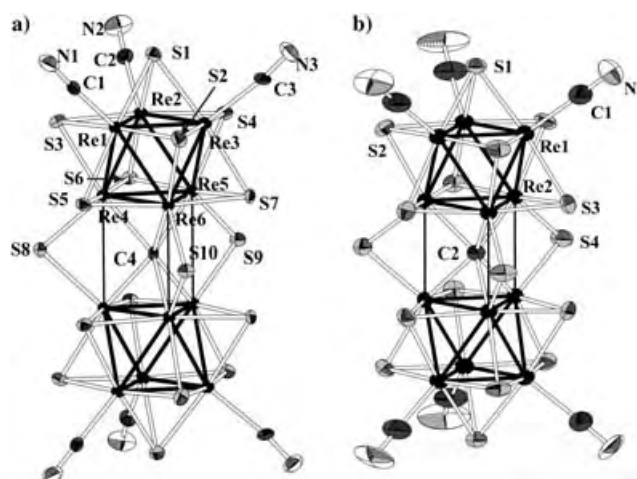


Figure 1. a) Structure of the $[\text{Re}_6(\mu_6\text{-C})\text{S}_{17}(\text{CN})_6]^{8-}$ ion in **1**. b) Structure of $[\text{Re}_6(\mu_6\text{-C})\text{S}_{17}(\text{CN})_6]^{6-}$ anion in **3**. For average bond lengths and angles, see Table 1. (Displacement ellipsoids are drawn at the 50% probability level.)

bridges and one common μ_6 -C atom. Each $\{\text{Re}_6\}$ cluster is capped by seven μ_3 -S atoms and additionally by the centered μ_6 -C ligand; thus, a typical octahedral cluster core analogous to $\{\text{Re}_6\text{Q}_8\}$ (i.e., $\{\text{Re}_6\text{S}_7\text{C}\}$) is formed. Through such bonding and coordination, we recognize trigonal μ_6 -C-centered prisms, $\{\text{Re}_6\text{C}\}$, in which the triangle faces belong to two adjacent $\{\text{Re}_6\}$ octahedra. Six outward Re atoms (three from each $\{\text{Re}_6\}$ cluster unit) are coordinated by CN ligands.

The Re–Re interatomic distances in the $\{\text{Re}_6\text{S}_7\text{C}\}$ fragments are comparable with those of $\{\text{Re}_6\text{S}_8\}$ cluster cores; their mean values are 2.595 Å for $\text{Re}^{\text{outer}}\text{--Re}^{\text{outer}}$, 2.591 Å for $\text{Re}^{\text{inner}}\text{--Re}^{\text{inner}}$, and 2.622 Å for $\text{Re}^{\text{outer}}\text{--Re}^{\text{inner}}$ (see Table 1). These values are within the range for Re–Re single bonds observed in octahedral rhenium clusters (in $[\text{Re}_6\text{Q}_8(\text{CN})_6]^{4-}$ mean Re–Re distances are 2.599, 2.633, and 2.684 Å for $\text{Q} = \text{S}, \text{Se}$, and Te , respectively^[7a]).

In the trigonal-prismatic $\{\text{Re}_6\text{C}\}$ units, the long Re...Re separations are 3.1576(17), 3.1722(17), and 3.1740(17) Å. Re–(μ_3 -S) bond lengths range from 2.401(6) to 2.445(6) Å. These separations are comparable with those found in other $\text{Re}_6\text{S}_8\text{L}_6$ cluster units, for example $[\text{Re}_6\text{S}_8(\text{CN})_6]^{4-}$ ^[4] and $[\text{Re}_6\text{S}_8\text{Br}_6]^{4-}$,^[12] and polymeric $\text{K}_4[\{\text{Re}_6\text{S}_8\}(\text{CN})_4\text{S}_{4/2}]$ and $\text{Li}_4[\{\text{Re}_6\text{S}_8\}\text{S}_{6/2}]$.^[13] The mean Re–(μ_2 -S) bond length of **1**, 2.425 Å is close to Re–S bond lengths found in numerous Bronger phases.^[14] Re–(μ_6 -C) bond lengths in the trigonal prism, $\{\text{Re}_6\text{C}\}$, range from 2.16(2) to 2.21(2) Å.

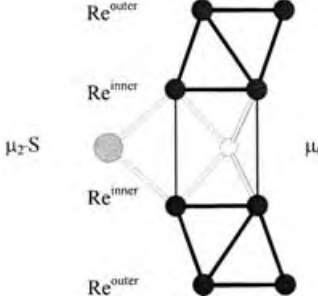
Dissolution of **1** in water resulted in fast oxidation of the $[\text{Re}_{12}\text{CS}_{17}(\text{CN})_6]^{8-}$ ion and formation of the $[\text{Re}_{12}\text{S}_{17}(\text{CN})_6]^{6-}$

[*] Prof. S.-J. Kim
Department of Chemistry
Ewha Womans University
Seoul 120-750 (Korea)
Fax: (+82) 2-3277-2384
E-mail: sjkim@ewha.ac.kr

Dr. Y. V. Mironov, Dr. N. G. Naumov, Dr. S. G. Kozlova,
Prof. V. E. Fedorov
Nikolaev Institute of Inorganic Chemistry
Siberian Branch of the Russian Academy of Sciences
3, Acad. Lavrentiev pr., 630090 Novosibirsk (Russia)
Fax: (+7) 3833-309489
E-mail: yuri@che.nsk.su

[**] This work was supported by the Russian Foundation for Basic Research (grants 05-03-08090 and 05-03-32123), the International Cooperation Research Program of the Ministry of Science & Technology of Korea (grant M60403000099-04A0100-02310), and the Division of Chemistry and Sciences on Materials of RAS (project No. 15 of Program 4.1). The authors are grateful to the Boreskov Institute of Catalysis SB RAS for an opportunity to use the ADF program.

Table 1: Experimental and calculated interatomic distances [Å] and angles [°] in the clusters $[\text{Re}_{12}(\mu_6\text{-C})\text{S}_{17}(\text{CN})_6]^{n-}$.



	Experimental			Calculated		
	$n=8$	$n=6$	$\Delta^{\text{[a]}}$	$n=8$	$n=6$	$\Delta^{\text{[a]}}$
$\text{Re}^{\text{outer}}-\text{Re}^{\text{outer}}$	2.595	2.600	+0.005	2.687	2.664	-0.023
$\text{Re}^{\text{inner}}-\text{Re}^{\text{inner}}$	2.591	2.692	+0.101	2.641	2.739	+0.098
$\text{Re}^{\text{inner}}-\text{Re}^{\text{outer}}$	2.622	2.630	+0.008	2.700	2.688	-0.012
$\text{Re}^{\text{inner}}-\text{Re}^{\text{inner}}$	3.168	2.901	-0.267	3.290	2.976	-0.314
(in prism)						
$\text{Re}^{\text{inner}}-\mu_6\text{-C}$	2.179	2.126	-0.053	2.243	2.171	-0.072
$\text{Re}^{\text{inner}}-\mu_2\text{-S}$	2.425	2.378	-0.047	2.452	2.392	-0.060
$\text{Re}^{\text{inner}}-\mu_2\text{-S}-\text{Re}^{\text{inner}}$	81.6	75.2	-6.4	84.30	76.94	-7.36

[a] Difference between values for anions with $n=8$ and $n=6$.

ion, which was isolated as a diamagnetic potassium or cesium salt— $\text{K}_6[\text{Re}_{12}\text{CS}_{17}(\text{CN})_6] \cdot 20\text{H}_2\text{O}$ (**2**) or $\text{Cs}_6[\text{Re}_{12}\text{CS}_{17}(\text{CN})_6]$ (**3**); single crystals of **2** and **3** were obtained by recrystallization of **1** from aqueous solutions.

Crystal structures of **2** and **3** contain the $[\text{Re}_{12}\text{CS}_{17}(\text{CN})_6]^{6-}$ cluster unit (Figure 1b). The removal of two electrons from the $[\text{Re}_{12}\text{CS}_{17}(\text{CN})_6]^{8-}$ ion leads to remarkable changes in the interatomic distances of the cluster, and at the same time, the interatomic distances in the trigonal prism, $\{\text{Re}_6\text{C}\}$, are most sensitive to these redox transformations. For example, in the $[\text{Re}_{12}\text{CS}_{17}(\text{CN})_6]^{8-}$ ion, the $\text{Re}\cdots\text{Re}$ distances are 3.168 Å while in the oxidized complex, $[\text{Re}_{12}\text{CS}_{17}(\text{CN})_6]^{6-}$, they are shortened to 2.902 Å. The mean bond lengths in these anions are presented in Table 1. These changes in interatomic distances are in a good agreement with DFT calculations for $[\text{Re}_{12}\text{CS}_{17}(\text{CN})_6]^{8-}$ and $[\text{Re}_{12}\text{CS}_{17}(\text{CN})_6]^{6-}$ ions with idealized D_{3h} symmetry.

The most surprising feature in these compounds is the presence of a carbon atom inside the cluster unit of the product. Its origin may be explained by the partial decomposition of KCN. If that is the case, a nitrogen atom might also be found in the cluster unit. However, X-ray diffraction studies did not identify the μ_6 interstitial atom. Therefore we studied by NMR spectroscopy solids enriched with ^{13}C and ^{15}N isotopes. Several samples of **2** were synthesized from K^{13}CN and K^{15}N starting materials. The ^{13}C NMR spectrum of **2** (Figure 2) displays two signals at $\delta = 127$ and 435 ppm with relative intensities close to 6:1. The signal at $\delta = 127$ ppm corresponds to coordinated CN ligands whereas the signal at $\delta = 435$ ppm may be attributed to the interstitial carbon atom.^[15]

The potassium salt of **2** readily dissolves in water and methanol, which allowed us to study its properties by solution-chemistry methods. The ESI mass spectrum (positive

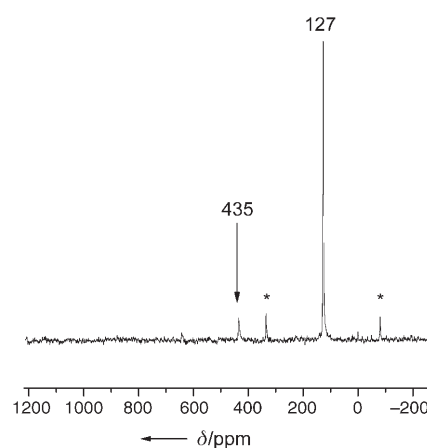


Figure 2. ^{13}C MAS NMR spectrum of **2**. Satellite signals are marked by asterisks.

mode) of a solution of **2** in a mixture of water and acetonitrile is shown in Figure 3. The most intense peak corresponds to the dicationic $\{\text{K}_8\text{Re}_{12}\text{CS}_{17}(\text{CN})_6\}^{2+}$ ($m/z = 1630.35$, 100 %).

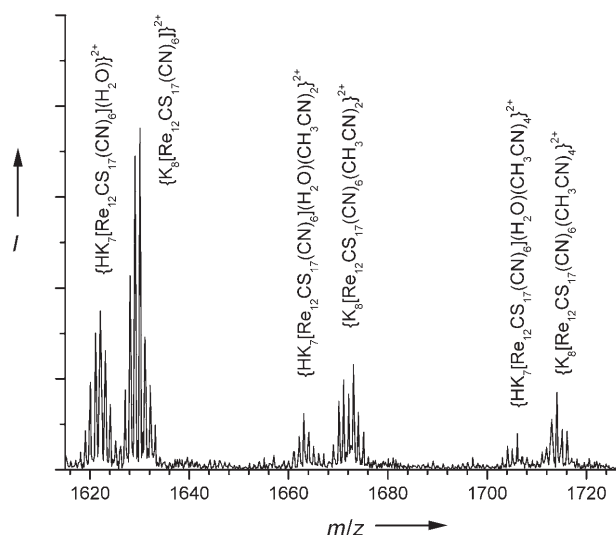


Figure 3. ESI mass spectrum of **2** in a $\text{H}_2\text{O}/\text{CH}_3\text{CN}$ solution.

The spectrum contains also two sets of less intense peaks: one set can be attributed to adducts with acetonitrile, $\{\text{K}_8\text{Re}_{12}\text{CS}_{17}(\text{CN})_6(\text{CH}_3\text{CN})_n\}^{2+}$, $n=2$ ($m/z = 1671.38$, 35 %), $n=4$ ($m/z = 1712.40$, 24 %), $n=6$ ($m/z = 1753.40$, 17 %); the other set belongs to a protonated species, $\{(\text{H}_3\text{O})\text{K}_7\text{Re}_{12}\text{CS}_{17}(\text{CN})_6(\text{CH}_3\text{CN})_n\}^{2+}$.

Cyclic voltammograms for aqueous solutions of **2** show two quasi-reversible waves: the $[\text{Re}_{12}\text{CS}_{17}(\text{CN})_6]^{6-}$ ion exhibits one reduction wave with the $[\text{Re}_{12}\text{CS}_{17}(\text{CN})_6]^{6-}/^{8-}$ couple centered at $E_{1/2} = -0.56$ V ($\Delta E = 200$ mV). The negative value of this potential is consistent with the fact that $\text{K}_8[\text{Re}_{12}\text{CS}_{17}(\text{CN})_6]$ is not stable in aqueous solution but rapidly converts into the $[\text{Re}_{12}\text{CS}_{17}(\text{CN})_6]^{6-}$ ion. The voltammogram for a solution of $[\text{Re}_{12}\text{CS}_{17}(\text{CN})_6]^{6-}$ has one oxidation wave at $E_{1/2} = 0.70$ V ($\Delta E = 100$ mV). This wave corresponds to further oxidation of the $[\text{Re}_{12}\text{CS}_{17}(\text{CN})_6]^{6-}$ ion, which was

confirmed by chemical oxidation with bromine. Isolation and characterization of this oxidized anion is in progress.

Density functional theory (DFT) calculations^[16] performed on the complexes $[\text{Re}_{12}\text{CS}_{17}(\text{CN})_6]^{6-}$ and $[\text{Re}_{12}\text{CS}_{17}(\text{CN})_6]^{8-}$ gave bond energies of -309.2 and -285.1 eV, respectively. For the $[\text{Re}_{12}\text{CS}_{17}(\text{CN})_6]^{6-}$ complex, the $13a_2'$ highest occupied molecular orbital (HOMO) consists predominantly of S and 3p orbitals ($\approx 80\%$) with a small contribution from the Re 5d orbitals. There is no contribution from the $\mu_6\text{-C}$ states (Figure 4). The HOMO orbital of

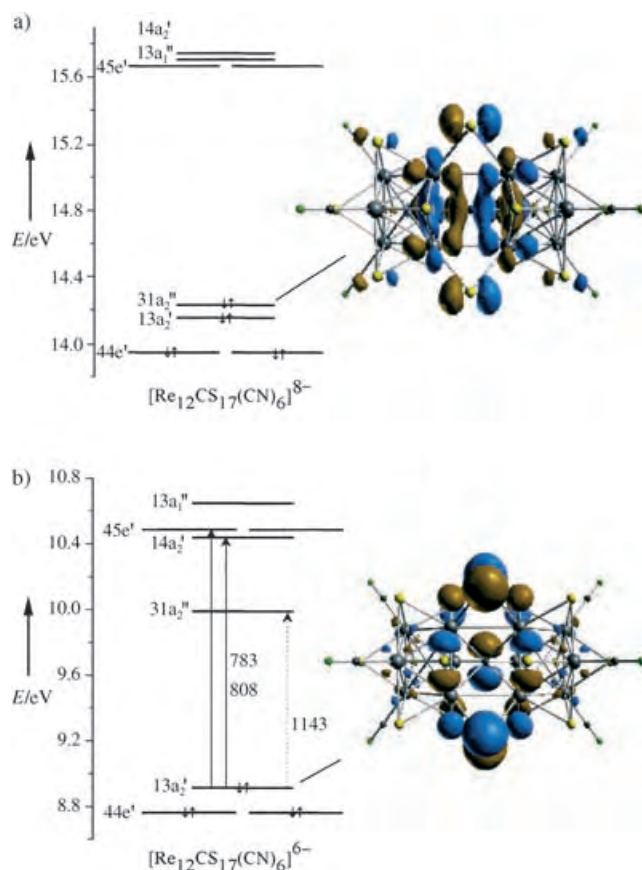


Figure 4. Calculated energy level diagrams and HOMO orbitals: a) $[\text{Re}_{12}\text{CS}_{17}(\text{CN})_6]^{8-}$: The $31a_2''$ MO is shown perpendicular to the C_3 axis. Calculated charges: Re^{inner} (+0.083), Re^{outer} (+0.054), $\mu_6\text{-C}$ (-0.209). b) $[\text{Re}_{12}\text{CS}_{17}(\text{CN})_6]^{6-}$: The $13a_2'$ MO is shown perpendicular to the C_3 axis. Arrows represent the forbidden (dotted) and allowed (solid) electronic transitions. Calculated charges: Re^{inner} (+0.090), Re^{outer} (+0.049), $\mu_6\text{-C}$ (-0.212).

$[\text{Re}_{12}\text{CS}_{17}(\text{CN})_6]^{8-}$ ($31a_2''$) consists of mainly Re 5d orbitals, the $\mu_6\text{-C}$ $2p_z$ orbital, and $\mu_2\text{-S}$ $3p_z$ orbitals. In prismatic $\{\text{Re}_6\text{C}\}$, short Re–Re and Re–($\mu_6\text{-C}$) contacts have bonding character while long Re...Re contacts along edges of the prism are strongly antibonding. Thus the removal of two electrons from the HOMO of complex **1** results in significant changes in the interatomic distances of cluster anions, mainly within the $\{\text{Re}_6\text{C}\}$ prism (Table 1). Removal of electrons elongates the $\text{Re}^{\text{inner}}\text{--Re}^{\text{inner}}$ bond and contracts the long prismatic Re...Re contacts and the Re–($\mu_6\text{-C}$) bond due to the strong antibond-

ing nature of Re...Re interaction. The calculated HOMO–LUMO gap is 1.08 eV for the $[\text{Re}_{12}\text{CS}_{17}(\text{CN})_6]^{6-}$ ion and 1.44 eV for the $[\text{Re}_{12}\text{CS}_{17}(\text{CN})_6]^{8-}$ ion. One interesting feature of the cluster is the position of $31a_2''$ orbital, which strongly depends on the charge of anion (Figure 4) and correlates with the length of the Re...Re interactions.

The absorption bands in the visible region of the electronic spectrum of $[\text{Re}_{12}\text{CS}_{17}(\text{CN})_6]^{6-}$ are in good agreement with the calculated electronic structure. According to symmetry rules for D_{3h} symmetry, the electron–dipole transitions from occupied $13a_2'$ to the next unoccupied $14a_2'$ and $45e'$ levels are allowed. Energies of calculated transitions (Figure 4) are close to the observed absorption band at 740 nm; very weak absorption at 1150 nm may be attributed to the forbidden $13a_2' \rightarrow 31a_2''$ transition.

A simple valence electron count shows that in the $[\text{Re}_{12}\text{CS}_{17}(\text{CN})_6]^{8-}$ ion the rhenium atoms have a charge of +3.^[17] Accordingly, the $[\text{Re}_{12}\text{CS}_{17}(\text{CN})_6]^{6-}$ ion contains slightly oxidized rhenium atoms ($\text{Re}^{3.17+}$), which correlate with charges of rhenium atoms calculated by DFT.

Vibrational spectra of the complexes display CN valence stretch vibrations and group vibrations associated with the $\{\text{Re}_{12}\text{CS}_{17}\}$ cluster core. The bands at $403\text{--}406\text{ cm}^{-1}$ may be attributed to ReS stretching. The decrease of anion charge leads to increase of CN stretching vibrations (from $\tilde{\nu} = 2114$ for **1** to 2120 cm^{-1} for **3**). This change is less than that for the $[\text{Re}_6\text{S}_8(\text{CN})_6]^{4-/3-}$ octahedral ions for which the difference is about 18 cm^{-1} ($\nu(\text{CN})$: $\tilde{\nu} = 2119\text{ cm}^{-1}$ for $[\text{Re}_6\text{S}_8(\text{CN})_6]^{4-}$ with 24 electrons per $\{\text{Re}_6\}$ cluster and 2137 cm^{-1} for $[\text{Re}_6\text{S}_8(\text{CN})_6]^{3-}$ with 23 electrons per $\{\text{Re}_6\}$ cluster).^[4,7b] The group of lines in the range $640\text{ to }950\text{ cm}^{-1}$ may be assigned to “breathing” vibrations of the $\{\text{Re}_{12}\text{C}\}$ cluster core.

Several dodecanuclear cluster chalcogenide complexes of Co, Mo, W, and Re were described earlier.^[18–22] However, the bonding in all of these clusters is different from that in the clusters described above: two octahedral $\{\text{M}_6\text{Q}_8\}$ units are bridged by a $\{\text{M}_2\text{Q}_2\}$ rhomblike Chevrel phase. The formation of atom-centered trigonal prisms has been found in some related anions with interstitial atoms— $[\text{W}_6(\mu_6\text{-Q})\text{Cl}_{18}]^{n-}$ ($\text{Q} = \text{C}$, $n = 0\text{--}3$; $\text{Q} = \text{N}$, $n = 1\text{--}3$),^[23] $[\text{Nb}_6(\mu_6\text{-S})\text{Br}_{17}]^{3-}$ ^[24]—and in polymeric chalcogenides of niobium $[\text{Nb}_6(\mu_6\text{-S})\text{I}_9]^{25}$ and molybdenum $[\text{Mo}_6(\mu_6\text{-Se})\text{I}_6\text{Se}]^{26}$. There are many other clusters, for example carbonyl compounds, with interstitial atoms around which atom-centered trigonal prisms are formed.

In summary, we have synthesized novel cluster complexes with a unique structure that may represent a new family of $\{\text{Re}_{12}\}$ clusters. The presence of terminal cyano ligands favors the use of these anions as building blocks for the formation of cyano-bridged polymeric materials such as those of the $[\text{Re}_6\text{Q}_8(\text{CN})_6]^{4-}$ family.^[7] Ions larger than $[\text{Re}_6\text{S}_8(\text{CN})_6]^{4-}$, such as $[\text{Re}_{12}\text{CS}_{17}(\text{CN})_6]^{n-}$ ions, may give polymers with larger voids and high porosity.

Experimental Section

ReS_2 was prepared from Re and S in an evacuated quartz tube at 650°C . Commercially available reagent-grade KCN was used. UV/Vis spectra were recorded on Shimadzu 3101PS spectrometer. IR spectra

in KBr pellets were recorded on a Bruker Scimifair FTS 2000 spectrometer in the range 4000–375 cm⁻¹. Electrospray mass-spectrometric measurements were performed in the positive-ion mode on a Q-ToF Ultima Global mass spectrometer.

1: ReS₂ (1 g, 0.004 mol) and KCN (2 g, 0.03 mol) were heated in an evacuated quartz tube at 750 °C for 48 h. After the reaction mixture had cooled, single crystals suitable for X-ray analysis were selected. The product was washed with dry methanol to remove excess KCN. A suspension of unconverted ReS₂ was removed by decantation with methanol. Yield: 0.65 g (60%). IR (KBr): $\tilde{\nu}$ = 383 (w), 403, 417 (sh), 619 (w), 641, 720 (w), 755 (w), 912 (w), 2114 cm⁻¹.

2: As for **1**, ReS₂ (1 g, 0.004 mol) and KCN (2 g, 0.03 mol) were heated in an evacuated quartz tube at 750 °C for 48 h. The reaction mixture was then dissolved in water (50 ml) and filtered. The filtrate was heated under reduced pressure until the volume was about 5 mL and the resulting solution was allowed to cool. The hexagonal plate crystals that formed were isolated by filtration and dried in air. Yield: 0.76 g (80%). UV/Vis: $\lambda(\epsilon)$ = 330 (9100), 360 (6500), 445 (2240 sh), 505 (1400), 605 (310 sh), 735 (175), 1150 nm (\approx 10 L mol⁻¹ cm⁻¹). IR (KBr): $\tilde{\nu}$ = 406, 639, 719 (w), 757 (w), 882, 2116 cm⁻¹.

3: Compound **3** was obtained by precipitation: CsCl (1 g, 0.006 mol) was added to an aqueous solution of **2**, obtained as above, to give **3** in quantitative yield. Single crystals were grown by diffusion of methanol into a dilute aqueous solution of **3**. IR (KBr): $\tilde{\nu}$ = 382 (w), 405, 643, 721 (w), 764 (w), 939, 2120 cm⁻¹.

Received: June 2, 2005

Published online: October 5, 2005

Keywords: cluster compounds · cyanides · density functional calculations · electronic structure · rhenium

- [1] a) Y. V. Mironov, A. V. Virovets, V. E. Fedorov, N. V. Podbereskaya, O. V. Shishkin, Y. T. Struchkov, *Polyhedron* **1995**, *14*, 3171–3173; b) A. Slougui, Y. V. Mironov, A. Perrin, V. E. Fedorov, *Croat. Chem. Acta* **1995**, *68*, 885–890.
- [2] N. G. Naumov, A. V. Virovets, N. V. Podbereskaya, V. E. Fedorov, *J. Struct. Chem. (Engl. Transl.)* **1997**, *38*, 857–862.
- [3] Y. V. Mironov, J. A. Cody, T. E. Albrecht-Schmitt, J. A. Ibers, *J. Am. Chem. Soc.* **1997**, *119*, 493–498.
- [4] N. G. Naumov, E. V. Ostanina, A. V. Virovets, M. Schmidtman, A. Müller, V. E. Fedorov, *Russ. Chem. Bull.* **2002**, *51*, 866–871.
- [5] a) T. Yoshimura, S. Ishizaka, Y. Sasaki, H. B. Kim, N. Kitamura, N. G. Naumov, M. N. Sokolov, V. E. Fedorov, *Chem. Lett.* **1999**, 1121–1122; b) S. A. Baudron, A. Deluzet, K. Boubekeur, P. Batail, *Chem. Commun.* **2002**, 2124–2125.
- [6] L. G. Beauvais, M. P. Shores, J. R. Long, *Chem. Mater.* **1998**, *10*, 3783–3786.
- [7] a) N. G. Naumov, A. V. Virovets, M. N. Sokolov, S. B. Artemkina, V. E. Fedorov, *Angew. Chem.* **1998**, *110*, 2043–2045; *Angew. Chem. Int. Ed.* **1998**, *37*, 1943–1945; b) N. G. Naumov, A. V. Virovets, V. E. Fedorov, *J. Struct. Chem. (Engl. Transl.)* **2000**, *41*, 499–520; c) N. G. Naumov, D. V. Soldatov, J. A. Ripmeester, S. B. Artemkina, V. E. Fedorov, *Chem. Commun.* **2001**, 571–572; d) Y. V. Mironov, N. G. Naumov, K. A. Brylev, O. A. Efremova, V. E. Fedorov, K. Hegetschweiler, *Angew. Chem.* **2004**, *116*, 1317–1321; *Angew. Chem. Int. Ed.* **2004**, *43*, 1297–1300; e) L. G. Beauvais, M. P. Shores, J. R. Long, *J. Am. Chem. Soc.* **2000**, *122*, 2763–2772; f) M. V. Bennett, L. G. Beauvais, M. P. Shores, J. R. Long, *J. Am. Chem. Soc.* **2001**, *123*, 8022–8032; g) Y. Kim, S. M. Park, W. Nam, S. J. Kim, *Chem. Commun.* **2001**, 1470–1471; h) Y. Kim, S. Kim, S. J. Kim, M. K. Lee, M. Kim, H. Lee, C. S. Chin, *Chem. Commun.* **2004**, 1692–1693.
- [8] H. Imoto, N. G. Naumov, A. V. Virovets, T. Saito, V. E. Fedorov, *J. Struct. Chem. (Engl. Transl.)* **1998**, *39*, 720–727.
- [9] Y. V. Mironov, V. E. Fedorov, C. C. McLauchlan, J. A. Ibers, *Inorg. Chem.* **2000**, *39*, 1809–1811.
- [10] The reaction of ReS₂ with KCN has been studied in the temperature range from 650 to 800 °C by using different ReS₂/KCN ratios. We found that for mass ratios of ReS₂/KCN from 1:2 to 1:20 the main product of the reaction was K₈[Re₁₂CS₁₇(CN)₆]. To understand the conditions that yield [Re₁₂CS₁₇(CN)₆]⁸⁻, K₂Cs₃[Re₆S₈(CN)₆] was used as the starting material. It was found that [Re₆S₈(CN)₆]⁴⁻ transforms into [Re₁₂CS₁₇(CN)₆]⁸⁻ if the temperature rises to between 700 and 800 °C. Furthermore, the reaction of [Re₆S₈Br₂] with KCN at high temperature also gave the [Re₁₂CS₁₇(CN)₆]⁸⁻ cluster, whereas below 650 °C [Re₆S₈(CN)₆]⁴⁻ formed. These data indicate that [Re₁₂CS₁₇(CN)₆]⁸⁻ cluster is thermodynamically stable within the 650 to 800 °C range.
- [11] X-ray structural analyses: Bruker SMART CCD diffractometer with area detector, graphite monochromator, MoK α radiation (λ = 0.71073 Å), SHELX-97 program^[27] for structure solution (direct methods) and refinement (full-matrix least-squares on F^2). **1:** C₇K₈N₆Re₁₂S₁₇ (M_r = 3260.35), crystal size 0.14 × 0.13 × 0.03 mm, monoclinic, space group $P2_1/m$, a = 9.1806(11), b = 29.210(2), c = 9.2006(8) Å, β = 119.777(1)°, V = 2141.5(4) Å³, Z = 2, ρ_{calcd} = 5.056 g cm⁻³, μ = 35.381 mm⁻¹, $2.55 < \theta < 28.21^\circ$, T = 293(2) K, face-indexed absorption correction (transmission coefficient: 0.0831, 0.4598). Reflections: 13011 collected, 4890 unique (R_{int} = 0.0512), 3756 observed ($I > 2\sigma(I)$). There were 239 parameters refined with R = 0.0619 ($I > 2\sigma(I)$), wR_2 = 0.1693 (all data), GOF = 1.107, residual electron density: +4.889/−4.827 e Å⁻³. **2:** C₇H₄₀K₆N₆O₂₀Re₁₂S₁₇ (M_r = 3542.47), crystal size 0.12 × 0.12 × 0.03 mm, hexagonal, space group $P6_3/mmc$, a = 10.8843(8), c = 27.840(4) Å, V = 2856.3(5) Å³, Z = 2, ρ_{calcd} = 4.119 g cm⁻³, μ = 26.427 mm⁻¹, $2.16 < \theta < 28.24^\circ$, T = 293(2) K, face-indexed absorption correction (transmission coefficient: 0.1436, 0.5044). Reflections: 16972 collected, 1383 unique (R_{int} = 0.0384), 1236 observed ($I > 2\sigma(I)$), 82 parameters refined with R = 0.0263 ($I > 2\sigma(I)$), wR_2 = 0.0589 (all data), GOF = 1.107, residual electron density: +1.643/−2.408 e Å⁻³. **3:** C₇Cs₆N₆Re₁₂S₁₇ (M_r = 3746.34), crystal size 0.09 × 0.09 × 0.01 mm, hexagonal, space group $P\bar{6}2m$, a = 9.7270(15), c = 14.629(3) Å, V = 1198.7(4) Å³, Z = 1, ρ_{calcd} = 5.190 g cm⁻³, μ = 35.407 mm⁻¹, $2.42 < \theta < 28.18^\circ$, T = 293(2) K, face-indexed absorption correction (transmission coefficient: 0.1428, 0.6760). Reflections: 7284 collected, 1105 unique (R_{int} = 0.0672), 913 observed ($I > 2\sigma(I)$), 59 parameters refined with R = 0.0340 ($I > 2\sigma(I)$), wR_2 = 0.0915 (all data), GOF = 1.046, residual electron density: +2.391/−1.234 e Å⁻³. Further details on the crystal structure investigation may be obtained from the Fachinformationszentrum Karlsruhe, 76344 Eggenstein-Leopoldshafen, Germany (fax: (+49) 7247-808-666; e-mail: crysdata@fiz-karlsruhe.de), on quoting the depository numbers CSD-415476–415478.
- [12] S. S. Yarovoi, S. F. Solodovnikov, Y. V. Mironov, V. E. Fedorov, *J. Struct. Chem. (Engl. Transl.)* **2003**, *44*, 318–321.
- [13] W. Bronger, H. J. Miessen, P. Müller, R. Neugröschel, *J. Less-Common Met.* **1985**, *105*, 303–310.
- [14] W. Bronger, *Metal Clusters in Chemistry, Vol. 3*, (Eds.: P. Braunstein, L. A. Oro, P. R. Raithby), Wiley-VCH, Weinheim, **1999**, pp. 1591–1611.
- [15] To determine isotropic chemical shifts of carbons the ¹³C magic-angle spinning (MAS) NMR measurements were made by using a BRUKER Bio-Spin Avance 400 MHz solid-state NMR spectrometer. The spinning rate was 20 kHz, the $\pi/2$ pulse duration was 5 s, the relaxation delay was 10 s. About 200 free induction decays were accumulated at room temperature. TMS was used as a reference. The ¹⁵N NMR spectrum contained one sharp signal at 311 ppm (relative to NH₃), which corresponds to coordinated cyano ligands. No signal attributable to an interstitial nitrogen atom was found. The diamagnetic properties of

compounds **1–3** indicated the presence of an interstitial atom with an even number of electrons.

- [16] a) Amsterdam Density Functional (ADF) program, Release 2003.02, Vrije Universiteit, Amsterdam, The Netherlands, **2002**; b) G. Te-Velde, F. M. Bickelhaupt, E. J. Baerends, C. Fonseca Guerra, S. J. A. Van-Gisbergen, J. G. Snijders, T. Ziegler, *J. Comput. Chem.* **2001**, 22, 931.
- [17] It is interesting to note that in rhenium cluster chemistry there are several types of cluster in which the rhenium atoms have a +III oxidation state; besides $[\text{Re}_{12}\text{CS}_{17}(\text{CN})_6]^{8-}$, there are three well-known cluster complexes, namely, dinuclear $[\text{Re}_2\text{X}_8]^{2-}$ with quadruple Re–Re bond, trigonal $[\text{Re}_3\text{X}_{12}]^{3-}$ with double Re–Re bonds, and octahedral $[\text{Re}_6\text{Q}_8\text{X}_6]^{4-}$ with single Re–Re bonds (X = halide ions).
- [18] F. Cecconi, C. A. Ghilardi, S. Midollini, A. Orlandini, *Inorg. Chim. Acta* **1993**, 214, 13–15.
- [19] S. Kamiguchi, H. Imoto, T. Saito, *Chem. Lett.* **1996**, 555–556.
- [20] S. Amari, H. Imoto, T. Saito, *Chem. Lett.* **1997**, 967–968.
- [21] Z. P. Zheng, R. H. Holm, *Inorg. Chem.* **1997**, 36, 5173–5178.
- [22] Z. P. Zheng, J. R. Long, R. H. Holm, *J. Am. Chem. Soc.* **1997**, 119, 2163–2171.
- [23] a) Y. Q. Zheng, H. G. von Schnering, J. H. Chang, Y. Grin, G. Engelhardt, G. Heckmann, *Z. Anorg. Allg. Chem.* **2003**, 629, 1256–1264; b) E. J. Welch, N. R. M. Crawford, R. G. Bergman, J. R. Long, *J. Am. Chem. Soc.* **2003**, 125, 11464–11465; c) E. J. Welch, C. L. Yu, N. R. M. Crawford, J. R. Long, *Angew. Chem.* **2005**, 117, 2605–2609; *Angew. Chem. Int. Ed.* **2005**, 44, 2549–2553.
- [24] H. Womelsdorf, H. J. Meyer, *Angew. Chem.* **1994**, 106, 2022–2023; *Angew. Chem. Int. Ed. Engl.* **1994**, 33, 1943–1944.
- [25] H. J. Meyer, J. D. Corbett, *Inorg. Chem.* **1991**, 30, 963–967.
- [26] C. Perrin, M. Sergent, *J. Chem. Res.* **1983**, 38–39.
- [27] a) G. M. Sheldrick, *SHELXL-97, Program for Crystal Structure Refinement*, University of Göttingen, Germany, **1997**; b) G. M. Sheldrick, *SHELXS-97, Program for Crystal Structure Solution*, University of Göttingen, Germany, **1997**.

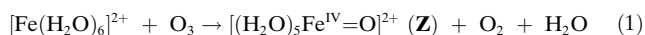
DOI: 10.1002/anie.200502686

Aqueous $\text{Fe}^{\text{IV}}=\text{O}$: Spectroscopic Identification and Oxo-Group Exchange**

Oleg Pestovsky, Sebastian Stoian, Emile L. Bominaar, Xiaopeng Shan, Eckard Münck,* Lawrence Que, Jr.,* and Andreja Bakac*

An aqua oxoiron(IV) species is believed to play important roles in environmental and catalytic chemistry, and has been proposed by some researchers as an alternative to HO^\bullet as the Fenton oxidant, that is, the intermediate produced in the reaction between $\text{Fe}_{\text{aq}}^{2+}$ and H_2O_2 in aqueous solution.^[1–8] The existence of a ferryl intermediate, most probably $[(\text{H}_2\text{O})_5\text{Fe}^{\text{IV}}=\text{O}]^{2+}$, has not been established independently in acidic and neutral solutions. Such a complex is, however, believed to be generated in the $[\text{Fe}(\text{H}_2\text{O})_6]^{2+}$ /ozone reaction,^[9–11] which simultaneously yields one equivalent of O_2 ,^[10] a fact that rules out the description of the intermediate as an ozonide complex. The ozone-generated transient species decays exponentially ($\tau \approx 10$ s in acidic aqueous solution),^[10,11] bears a 2+ charge,^[11] and oxidizes organic and inorganic substrates.^[11,12] All of these findings support the formulation of $[(\text{H}_2\text{O})_5\text{Fe}^{\text{IV}}=\text{O}]^{2+}$, but the decisive spectroscopic data have not been available until now.

The species of interest, which we call **Z**, was generated at pH 1 in aqueous solution from $[\text{Fe}(\text{H}_2\text{O})_6]^{2+}$ and O_3 ^[10,11] [Eq. (1)]



The sample preparation for Mössbauer spectroscopy and other experimental details are described in the Supporting Information. In addition to **Z**, the samples also contained up

[*] S. Stoian, Prof. Dr. E. L. Bominaar, Prof. Dr. E. Münck

Department of Chemistry
Carnegie Mellon University
Pittsburgh, PA 12513 (USA)
Fax: (+1) 412-268-1061
E-mail: emunck@cmu.edu

Dr. X. Shan, Prof. Dr. L. Que, Jr.
Department of Chemistry and Center for Metals in Biocatalysis
University of Minnesota
Minneapolis, MN 55455 (USA)
Fax: (+1) 612-624-7029
E-mail: que@chem.umn.edu

Dr. O. Pestovsky, Prof. Dr. A. Bakac
Ames Laboratory
Iowa State University
Ames, IA 50011 (USA)
Fax: (+1) 515-294-5233
E-mail: bakac@ameslab.gov

[**] Supported under DOE Contract No. W-7405-ENG-82 (A.B.) and NIH grants EB001475 (E.M.) and GM-38767 (L.Q.)



Supporting information for this article is available on the WWW under <http://www.angewandte.org> or from the author.

to 50 % $[\text{Fe}(\text{H}_2\text{O})_6]^{3+}$, produced mainly by the decomposition of **Z** during sample preparation and handling (see Supporting Information).

Figure 1 shows the Mössbauer spectra recorded at 4.2 K in magnetic fields applied parallel to the observed γ -radiation.

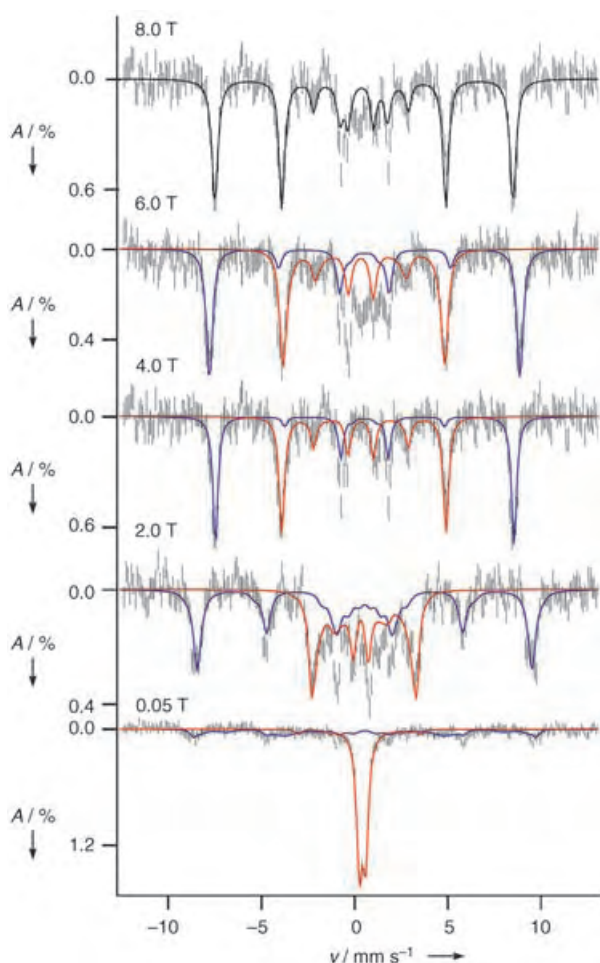


Figure 1. Mössbauer spectra of a sample at 4.2 K containing 250 μM **Z**, prepared by the rapid freeze-quench technique (see Supporting Information). The solid lines (red for **Z**, representing ca. 50% of total Fe) are simulations based on Equation (2). The contribution from $[\text{Fe}(\text{H}_2\text{O})_6]^{3+}$ is shown in blue. We found the following parameters for **Z**: $D = 9.7(7) \text{ cm}^{-1}$, $A_x/g_n\beta_n = A_y/g_n\beta_n = -20.3(3) \text{ T}$, $\Delta E_Q = -0.33(3) \text{ mm s}^{-1}$, $\delta = 0.38(2) \text{ mm s}^{-1}$. For the 8.0-T spectrum, the theoretical curves for **Z** and $[\text{Fe}(\text{H}_2\text{O})_6]^{3+}$ were added (black).

The spectra shown have contributions from two species: a paramagnetic complex (**Z**) with integer electron spin and a high-spin ferric species with parameters identical to those reported for $[\text{Fe}(\text{H}_2\text{O})_6]^{3+}$.^[13] The most prominent feature in the 0.05-T spectrum is a doublet with quadrupole splitting of $\Delta E_Q = 0.33(3) \text{ mm s}^{-1}$ and isomer shift of $\delta = 0.38(2) \text{ mm s}^{-1}$, relative to Fe metal at 298 K. This doublet represents the reactive species **Z** and, as expected, was absent in a sample that was allowed to age for several minutes at room temperature before freezing. The solid lines drawn through the data are spectral simulations (red for **Z**, blue for $[\text{Fe}(\text{H}_2\text{O})_6]^{3+}$)

based on the spin Hamiltonian H , where H_Q describes the quadrupole interactions [Eq. (2)].

$$H = D[(S_z^2 - S(S+1)/3) + E(S_x^2 - S_y^2) + 2\beta\mathbf{S} \cdot \mathbf{B} + SA \cdot \mathbf{I} - g_n\beta_n \mathbf{B} \cdot \mathbf{I} + H_Q] \quad (2)$$

The spectra of **Z** in the presence of applied fields exhibit paramagnetic hyperfine structure. The internal magnetic field, $\mathbf{B}_{\text{int}} = -\langle \mathbf{S} \rangle \cdot \mathbf{A} / g_n\beta_n$, is negative (namely, opposed to the applied field \mathbf{B}), and increases with increasing applied field \mathbf{B} . The outermost absorption lines of the spectrum of **Z** are remarkably sharp, thus showing that \mathbf{B}_{int} is axial, and implying that $E \approx 0$ and $A_x \approx A_y$ in Equation (2). The Mössbauer spectra measured at 12 K (see Supporting Information) show that the fluctuation of the electronic spin of **Z** is slow. In the slow-fluctuation limit, the 0.05-T Mössbauer spectrum of a mononuclear ferric complex (a Kramers system) must exhibit (in the same way as $[\text{Fe}(\text{H}_2\text{O})_6]^{3+}$ in Figure 1) paramagnetic hyperfine structure, whereas non-Kramers systems (such as Fe^{IV} complexes) usually exhibit quadrupole doublets. Our data thus imply that **Z** has integer spin, and suggest that it is (formally) an Fe^{IV} -oxo complex. The theoretical curves (red) for **Z** are spectral simulations generated for $S = 2$ by using the parameters quoted in the caption to Figure 1. The Mössbauer spectra show that **Z** is a pure species and rule out an equilibrium mixture of two forms, such as $\{\text{Fe}^{\text{IV}}=\text{O}\}^{2+}/\{\text{Fe}^{\text{IV}}(\text{OH})_2\}^{2+}$. The paramagnetic states of Fe^{IV} have spins of either $S = 2$ or $S = 1$. The latter spin can be ruled out because Equation (2) would yield $A_x = A_y \approx -38 \text{ T}$, which is substantially larger than the largest A values reported for any Fe^{IV} -oxo complex (-25 T).^[14,15] The parameters obtained for **Z** are similar to those for the $S = 2$ $\{\text{Fe}^{\text{IV}}=\text{O}\}$ intermediate of *E. coli* taurine: α -ketoglutarate dioxygenase (TauD);^[16] $D = 10.5 \text{ cm}^{-1}$, $A_x/g_n\beta_n = A_y/g_n\beta_n = -18.0 \text{ T}$, $\Delta E_Q = -0.88 \text{ mm s}^{-1}$, $\delta = 0.31 \text{ mm s}^{-1}$. Most plausibly, **Z** is formulated as $[(\text{H}_2\text{O})_5\text{Fe}^{\text{IV}}=\text{O}]^{2+}$.

X-ray absorption spectroscopy was carried out on two samples for which Mössbauer spectroscopy established **Z**/ $[\text{Fe}(\text{H}_2\text{O})_6]^{3+}$ ratios of 50/50 and 58/42. Figure 2 shows the

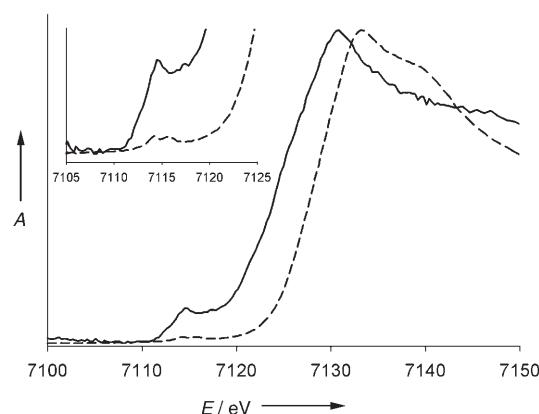


Figure 2. Normalized XANES spectra (Fe K-edge) of **Z** (solid line) and $[\text{Fe}(\text{H}_2\text{O})_6]^{3+}$ (dashed line). The spectrum of **Z** was obtained by subtraction of 50% of the spectrum of $[\text{Fe}(\text{H}_2\text{O})_6]^{3+}$ from the spectrum of the 1:1 **Z**/ $[\text{Fe}(\text{H}_2\text{O})_6]^{3+}$ sample. The inset shows a magnification of the $1s \rightarrow 3d$ region.

X-ray absorption near-edge structures (XANES) of $[\text{Fe}(\text{H}_2\text{O})_6]^{3+}$ (dashed line) and **Z** (solid line). The edge energy for $[\text{Fe}(\text{H}_2\text{O})_6]^{3+}$ was found to be 7129 eV. In contrast, Fe^{III} complexes with N/O coordination have edges around 7123 eV.^[17] On the basis of density functional theory (DFT) calculations (see Supporting Information) we attribute the higher-energy edge of $[\text{Fe}(\text{H}_2\text{O})_6]^{3+}$ to its high ionic character.^[13] Notably, the edge energy of **Z**, at 7126 eV, is midway between that for $[\text{Fe}(\text{H}_2\text{O})_6]^{3+}$ and the range reported for non-heme $[\text{Fe}^{\text{IV}}=\text{O}]$ complexes (7123 eV for the high-spin intermediate of the enzyme TauD,^[18] and 7124–7125 eV for the synthetic non-heme low-spin complexes^[15,17]). The reduction in the edge energy of **Z** relative to that of $[\text{Fe}(\text{H}_2\text{O})_6]^{3+}$ arises from the strong covalent bonding interaction with the terminal oxo group^[19] (see Supporting Information).

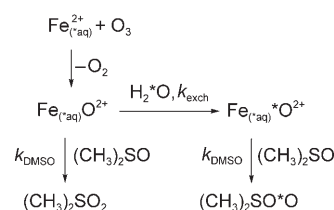
Another notable feature in the XANES spectrum of **Z** is its pronounced $1s \rightarrow 3d$ transition (Figure 2). The intensity of this feature reflects the deviation of the metal center from centrosymmetric geometry; the intensity generally increases upon conversion from octahedral into tetrahedral geometry^[20] or upon the introduction of an oxo ligand into a six-coordinate complex.^[15,17] The pre-edge feature of $[\text{Fe}(\text{H}_2\text{O})_6]^{3+}$ has a measured area of eight units, which is typical of nearly centrosymmetric, six-coordinate complexes. For the spectrum of **Z** we found an area of 60–70 units, which is the highest area yet for an iron center. This value is distinctly larger than those observed for known six-coordinate oxoiron(IV) species (25 to 38 units)^[15,17] and suggests an oxoiron(IV) center with substantial deviation from centrosymmetric geometry.

DFT calculations were performed on **Z** as an $[(\text{H}_2\text{O})_5\text{Fe}^{\text{IV}}=\text{O}]^{2+}$ species (see Supporting Information). The results can be summarized as follows: 1) Geometry optimization (Figure 3) yields an $\text{Fe}=\text{O}$ bond length of 1.62 Å, which is similar to the $\text{Fe}=\text{O}$ bond lengths in other non-heme oxoiron(IV) complexes^[14]. 2) DFT calculations yield a ground state with $S=2$, which is in agreement with the Mössbauer analysis. 3) The hyperfine parameters are equal to those obtained from the Mössbauer spectra. 4) The zero-field splitting of the $S=2$ ground state is correctly predicted on

the basis of electronic excitation energies involving an $(S=1)/(S=2)$ spin-mixing mechanism similar to that functioning in the $S=1$ complex $[\text{Fe}^{\text{IV}}(\text{O})(\text{tmc})(\text{MeCN})]^{2+}$ ($\text{tmc}=1,4,8,11$ -tetramethyl-1,4,8,11-tetraazacyclotetradecane). 5) The experimental values for δ , ΔE_{O} , and the contact contribution to the A-tensor A_c are different for $[\text{Fe}^{\text{IV}}(\text{O})(\text{tmc})(\text{MeCN})]^{2+}$ and **Z** in ways that the theory predicts if the equatorial sites in tmc are replaced by aqua ligands (see Supporting Information), that is, $\delta(\text{tmc}) < \delta(\text{Z})$, $\Delta E_{\text{O}}(\text{tmc}) > 0 > \Delta E_{\text{O}}(\text{Z})$, and $|A_c(\text{tmc})| < |A_c(\text{Z})|$. 6) DFT analysis of the K-edge energy supports the $[(\text{H}_2\text{O})_5\text{Fe}^{\text{IV}}=\text{O}]^{2+}$ formulation for **Z**.

The reaction between $[(\text{H}_2\text{O})_5\text{Fe}^{\text{IV}}=\text{O}]^{2+}$ (0.10 mM) and an excess (6–470 mM) of $(\text{CH}_3)_2\text{SO}$ or $(\text{CH}_3)(p\text{-tolyl})\text{SO}$ in 0.10 M aqueous HClO_4 produced the corresponding sulfone and regenerated $[\text{Fe}(\text{H}_2\text{O})_6]^{2+}$ quantitatively. The combination of this oxygen-atom-transfer step and the $\text{O}_3/[\text{Fe}(\text{H}_2\text{O})_6]^{2+}$ reaction constitutes a catalytic cycle for the oxidation of $(\text{CH}_3)_2\text{SO}$ by ozone.

The catalytic oxidation was carried out in H_2^{18}O (97% ^{18}O enrichment, pH 1) and utilized 0.4–7 mM $[\text{Fe}(\text{H}_2^{18}\text{O})_6]^{2+}$ as catalyst under continuous bubbling with $^{16}\text{O}_3$ until approximately 30% of the $(\text{CH}_3)_2\text{S}^{16}\text{O}$ (initial concentration 0.1 M) was oxidized. The direct oxidation of $(\text{CH}_3)_2\text{SO}$ by O_3 under these conditions contributes $\leq 1\%$ to the overall process. The products, identified and quantified by GC-MS, were $(\text{CH}_3)_2\text{S}^{16}\text{O}_2$ (88%) and $(\text{CH}_3)_2\text{S}^{16}\text{O}^{18}\text{O}$ (12%), irrespective of the concentration of $[\text{Fe}(\text{H}_2\text{O})_6]^{2+}$. With a substrate concentration of 0.010 M, the proportion of $(\text{CH}_3)_2\text{S}^{16}\text{O}^{18}\text{O}$ increased to 48%, which is as expected if the intermediate $[(\text{H}_2\text{O})_5\text{Fe}^{\text{IV}}=\text{O}]^{2+}$ undergoes both reaction with the substrate and oxygen exchange with water (Scheme 1). The data at the



Scheme 1.



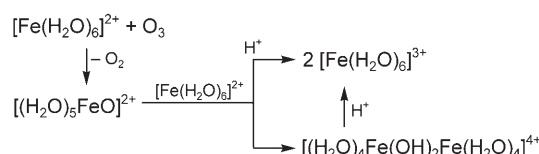
Figure 3. Proposed structure for **Z**, $[(\text{H}_2\text{O})_5\text{Fe}^{\text{IV}}=\text{O}]^{2+}$, calculated with the B3LYP functional and the 6-311G basis set with C_{2v} symmetry.

two concentrations of $(\text{CH}_3)_2\text{SO}$ were fitted to an equation for competition kinetics (see Supporting Information) and provided an estimate for the rate constant for oxygen exchange as $k_{\text{exch}} \approx 10^3 \text{ s}^{-1}$.

The nearly quantitative yield of $(\text{CH}_3)_2\text{S}^{16}\text{O}_2$ at high concentrations of $(\text{CH}_3)_2\text{SO}$ confirms the presence of one unique oxygen atom in the reactive form of the catalyst, which is most consistent with the $[(\text{H}_2\text{O})_n\text{Fe}^{\text{IV}}=\text{O}]^{2+}$ formulation. Other possible formulations, such as $[(\text{H}_2\text{O})_m\text{Fe}^{\text{IV}}(\text{OH})_2]^{2+}$, in which at least one of the two hydroxo groups would have to be derived from the ^{18}O -labeled water, would permit the incorporation of at most 50% ^{16}O into the product sulfone, and is thus ruled out by our observations. These conclusions are in accord with the Mössbauer data, which show that only one major Fe^{IV} species is present in our samples.

With the identification of **Z** as $[(\text{H}_2\text{O})_5\text{Fe}^{\text{IV}}=\text{O}]^{2+}$, the question of its participation in Fenton chemistry was addressed by studying the kinetic patterns and products for three substrates, namely $[\text{Fe}(\text{H}_2\text{O})_6]^{2+}$, $(\text{CH}_3)_2\text{SO}$, and (CH_3) -(*p*-tolyl)SO, in the Fenton reaction and in the reaction with $[(\text{H}_2\text{O})_5\text{Fe}^{\text{IV}}=\text{O}]^{2+}$ under identical and carefully selected conditions.

Stopped-flow mixing of O_3 (0.25 mM) and a large excess of $[\text{Fe}(\text{H}_2\text{O})_6]^{2+}$ (0.10 M) in HClO_4 (0.090 M) produced, within the mixing time ($k = 4.3 \times 10^4 \text{ M}^{-1} \text{ s}^{-1}$),^[11] a mixture of $[\text{Fe}(\text{H}_2\text{O})_6]^{3+}$ (84 % of total Fe^{III}) and the hydrolytic dimer, $[(\text{H}_2\text{O})_4\text{Fe}(\mu\text{-OH})_2\text{Fe}(\text{H}_2\text{O})_4]^{4+}$ (16 %), followed by hydrolysis of the dimer^[21] to $[\text{Fe}(\text{H}_2\text{O})_6]^{3+}$ with $k = 0.76 \text{ s}^{-1}$ ^[11] (Scheme 2).



Scheme 2.

In an otherwise identical experiment with H_2O_2 in place of O_3 , no dimer was produced, thus ruling out $[(\text{H}_2\text{O})_5\text{Fe}^{\text{IV}}=\text{O}]^{2+}$ as a reactive intermediate in the Fenton reaction (see Supporting Information).

The sole products of the oxidation of $(\text{CH}_3)_2\text{SO}$ and $(\text{CH}_3)(p\text{-tolyl})\text{SO}$ by $[(\text{H}_2\text{O})_5\text{Fe}^{\text{IV}}=\text{O}]^{2+}$ in both acidic and neutral solutions were the corresponding sulfones (see Supporting Information). The Fenton reaction with $(\text{CH}_3)_2\text{SO}$ under air-free conditions yielded mostly ethane, methylsulfinic acid, and small amounts of methane and dimethyl sulfone, that is, products known to be derived from OH radicals.^[22,23] The yields of all the products decreased in the presence of O_2 , and no sulfone was detected.

In summary, we have generated $[(\text{H}_2\text{O})_5\text{Fe}^{\text{IV}}=\text{O}]^{2+}$, characterized it spectroscopically, theoretically, and chemically, and developed criteria that made it possible to distinguish between hydroxyl radicals and aqueous ferryl-oxo species. These criteria have allowed us to settle a long-standing debate and unambiguously rule out $[(\text{H}_2\text{O})_5\text{Fe}^{\text{IV}}=\text{O}]^{2+}$ as a crucial Fenton intermediate in acidic and neutral aqueous solutions.^[24]

Received: July 30, 2005

Published online: October 5, 2005

Keywords: Fenton reaction · iron · Mössbauer spectroscopy · oxygen · X-ray absorption spectroscopy

- [6] C. Walling, *Acc. Chem. Res.* **1998**, *31*, 155.
- [7] C. Walling, *Acc. Chem. Res.* **1975**, *8*, 125.
- [8] F. Buda, B. Ensing, M. C. M. Gribnau, E. J. Baerends, *Chem. Eur. J.* **2003**, *9*, 3436.
- [9] T. J. Conocchioli, E. J. Hamilton, Jr., N. Sutin, *J. Am. Chem. Soc.* **1965**, *87*, 926.
- [10] T. Logager, J. Holcman, K. Sehested, T. Pedersen, *Inorg. Chem.* **1992**, *31*, 3523.
- [11] O. Pestovsky, A. Bakac, *J. Am. Chem. Soc.* **2004**, *126*, 13757.
- [12] F. Jacobsen, J. Holcman, K. Sehested, *Int. J. Chem. Kinet.* **1998**, *30*, 215.
- [13] J. E. Knudsen, *J. Phys. Chem. Solids* **1980**, *41*, 545.
- [14] J.-U. Rohde, J.-H. In, M. H. Lim, W. W. Brennessel, M. R. Bukowski, A. Stubna, E. Münck, W. Nam, L. Que, Jr., *Science* **2003**, *299*, 1037.
- [15] M. H. Lim, J.-U. Rohde, A. Stubna, M. R. Bukowski, M. Costas, R. Y. N. Ho, E. Münck, W. Nam, L. Que, Jr., *Proc. Natl. Acad. Sci. USA* **2003**, *100*, 3665.
- [16] C. Krebs, J. C. Price, J. Baldwin, L. Saleh, M. T. Green, J. M. Bollinger, Jr., *Inorg. Chem.* **2005**, *44*, 742.
- [17] J.-U. Rohde, S. Torelli, X. Shan, M. H. Lim, E. J. Klinker, J. Kaizer, K. Chen, W. Nam, L. Que, Jr., *J. Am. Chem. Soc.* **2004**, *126*, 16750.
- [18] P. J. Riggs-Gelasco, J. C. Price, R. B. Guyer, J. H. Brehm, E. W. Barr, J. M. Bollinger, Jr., C. Krebs, *J. Am. Chem. Soc.* **2004**, *126*, 8108.
- [19] A. Decker, E. I. Solomon, *Angew. Chem.* **2005**, *44*, 2292; *Angew. Chem. Int. Ed.* **2005**, *44*, 2252.
- [20] T. E. Westre, P. Kennepohl, J. G. DeWitt, B. Hedman, K. O. Hodgson, E. I. Solomon, *J. Am. Chem. Soc.* **1997**, *119*, 6297.
- [21] B. A. Sommer, D. W. Margerum, *Inorg. Chem.* **1970**, *9*, 2517.
- [22] B. C. Gilbert, R. O. C. Norman, R. C. Sealy, *J. Chem. Soc. Perkin Trans. 2* **1975**, *303*.
- [23] M. K. Eberhardt, R. Colina, *J. Org. Chem.* **1988**, *53*.
- [24] Our data, however, do not address the question of whether {Fe^{IV}=O} species are formed in the reaction of iron(II) salts with H₂O₂ in acetonitrile, as first discussed in the seminal papers: J. T. Groves, M. Van Der Puy, *J. Am. Chem. Soc.* **1974**, *96*, 5274; J. T. Groves, G. A. McCluskey, *J. Am. Chem. Soc.* **1976**, *98*, 859.

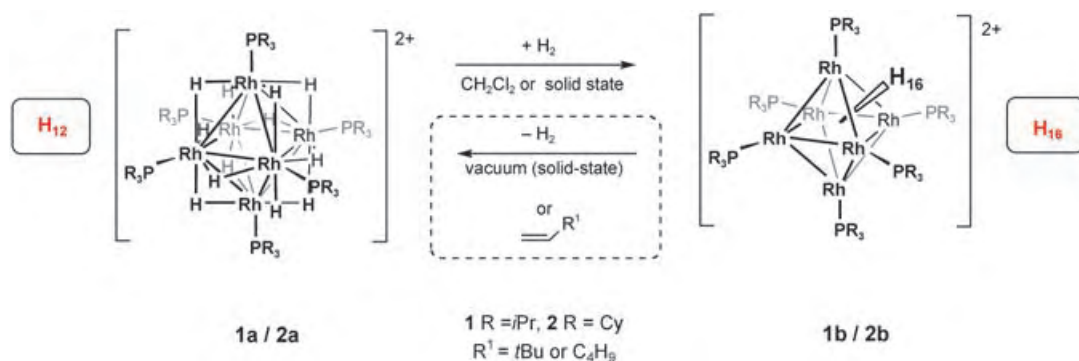
Holding onto Lots of Hydrogen: A 12-Hydride Rhodium Cluster That Reversibly Adds Two Molecules of H₂**

Simon K. Brayshaw, Michael J. Ingleson,
Jennifer C. Green, Paul R. Raithby, Gabriele Kociok-
Köhn, J. Scott McIndoe, and Andrew S. Weller*

The boundary between catalysis by nanocluster and molecular materials is an area of science that is attracting considerable attention.^[1] Much of this interest has centered on the role that such species play in hydrogenation reactions (especially arene hydrogenation), and in particular the nature of the actual species in catalysis (nanocluster versus molecular cluster).^[2] Given the inherent difficulty in characterizing nanocluster species at atomic resolution, well-defined molecular clusters that can be considered as models for hydrogen attachment to a metal surface are key to understanding the chemistry of these species. Despite this, molecular cluster species that reversibly take up dihydrogen,^[3,4] or have a hydrogen content that approaches that expected for a metal surface covered in chemisorbed H₂, are rare.^[5,6] We have previously described the complex [Rh₆(PiPr₃)₆(μ-H)₁₂]²⁺ (**1a**)—a cluster complex that not only has an unexpected geometry and cluster electron count (76 cluster valence electrons (cve), 10 lower than expected for an octahedral late-transition-metal cluster) but

also a rather high hydrogen content.^[7] We now report that this complex, and its PCy₃ (Cy = cyclohexyl) analogue, reversibly add two molecules of H₂ to give discrete clusters with exceptionally high hydride counts: [Rh₆(PR₃)₆H₁₆][BAR^F₄]₂ (R = Cy, *i*Pr; Ar^F = 3,5-(CF₃)₂C₆H₃; Scheme 1).

The tricyclohexylphosphine analogue of **1a**, [Rh₆(PCy₃)₆H₁₂][BAR^F₄]₂ (**2a**), is prepared in a similar manner to **1a** in modest (≈ 30 %) yield by gentle heating of [(PCy₃)₂Rh-(η²-H₂)₂H₂][BAR^F₄]₂^[8] in fluorobenzene. Cluster **2a** was characterized by NMR spectroscopy and ESI mass spectrometry, both of which unambiguously identify the cluster as having



Scheme 1.

12-hydride ligands. Addition of dihydrogen (≈ 1 atm) to **1a** or **2a** in solution (CH₂Cl₂) results in the immediate formation of the sixteen-hydride cluster complexes [Rh₆(PR₃)₆H₁₆][BAR^F₄]₂ (**1b**, R = *i*Pr and **2b**, R = Cy) in quantitative yield—in which two molecules of H₂ have been added to the octahedral cluster. Hydrogen uptake also occurs in the crystalline form but at a much slower rate (hours). The ESI MS of CH₂Cl₂ solutions were unambiguous in the characterization of **1b** and **2b** (Figure 1 for **2a/2b** pair), and clearly demonstrate the quantitative formation of a dicationic 16-hydride species: with “flagpole” spectra observed showing excellent matches to the calculated isotope distribution patterns.

The ¹H NMR spectra of both **1b** and **2b** confirm the hydride count from the ESI MS experiments. These spectra show upfield signals that integrate to a total of 16H relative to the alkyl phosphine protons. In the room-temperature ¹H NMR spectrum, two hydride signals are consistently (for five independently synthesized samples) observed in the ratio 15:1. Figure 2 shows the spectrum for the **1a/1b** pair. This 15:1 ratio suggests a structure in which fifteen hydrides are mutually exchanging on the NMR timescale and one is not. A plausible structure that accounts for this observation is one that invokes an interstitial hydride^[9,10] with 15 hydride ligands decorating the outside of the Rh₆ octahedron. On cooling the NMR sample to 200 K the hydride resonances in **1b** and **2b** become broader and resolve into many separate signals with an overall integral lower than 16H. The broad line width of some these signals indicate that any fluxional processes occurring are not completely frozen out at low temperature. T₁ measurements at 200 K indicate that all the observed

[*] Dr. S. K. Brayshaw, Dr. M. J. Ingleson, Prof. P. R. Raithby,
Dr. G. Kociok-Köhn, Dr. A. S. Weller
Department of Chemistry
University of Bath
Bath, BA2 7AY (UK)
Fax: (+44) 1225-386-231
E-mail: a.s.weller@bath.ac.uk

Prof. J. C. Green
Inorganic Chemistry Laboratory
South Parks Road, Oxford OX1 3QR (UK)

Professor J. S. McIndoe
Department of Chemistry
University of Victoria
PO Box 3065, Victoria, BC V8W 3V6 (Canada)

[**] We thank the EPSRC, under grant GR/T10169, and the Royal Society for support. Professor Paul Dyson and Dr Gabor Laurenczy (EPFL) are thanked for acquiring the high pressure NMR data.

Supporting information for this article is available on the WWW under <http://www.angewandte.org> or from the author.

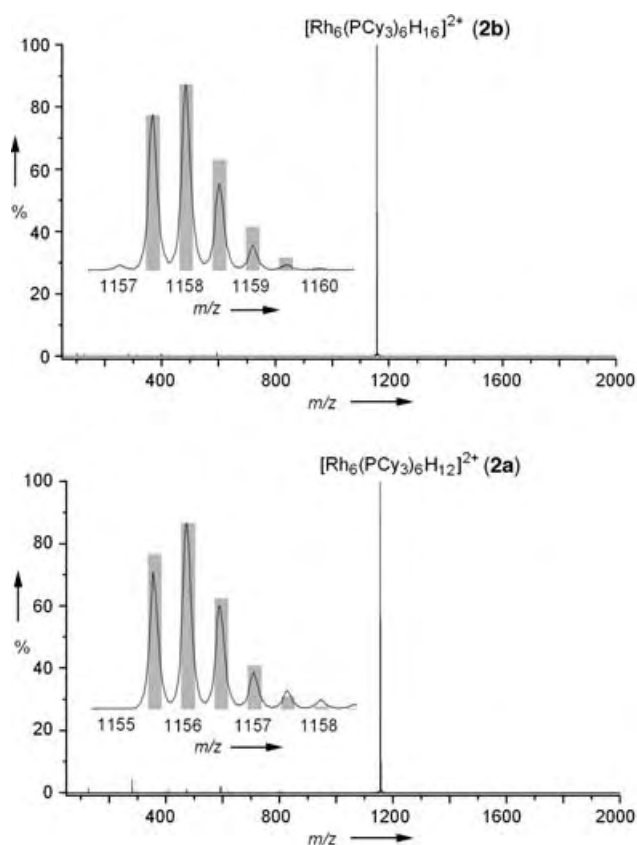


Figure 1. ESI mass spectra of **2a** and **2b**. Insets show observed isotopomer pattern overlaid with the calculated pattern (gray bars).

signals are best assigned to hydride ligands ($T_1 > 230$ ms). At higher temperatures (323 K) the 15:1 pattern is still observed, while heating further results in decomposition.

Preliminary density functional theory (DFT) calculations on model compounds $[\text{Rh}_6(\text{PH}_3)_6\text{H}_{16}]^{2+}$ and $[\text{Rh}_6(\text{PH}_3)_6\text{H}_{12}]^{2+}$ support the interstitial hydride assignment, indicating that a cluster with 15 hydride ligands on the surface and one interstitial is significantly more stable than one with 16 hydrides on the surface. Calculations also reveal the electronic reasons underlying the uptake of two molecules of H_2 .

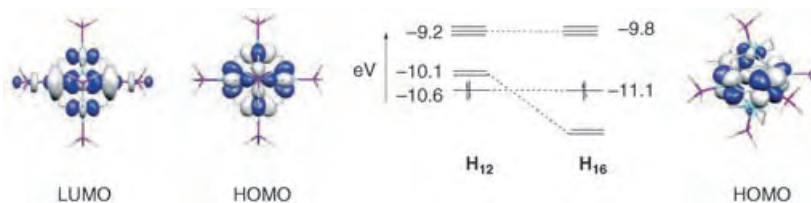


Figure 3. DFT calculated correlation diagram for $[\text{Rh}_6(\text{PH}_3)_6\text{H}_{12}]^{2+}$ and $[\text{Rh}_6(\text{PH}_3)_6\text{H}_{16}]^{2+}$.

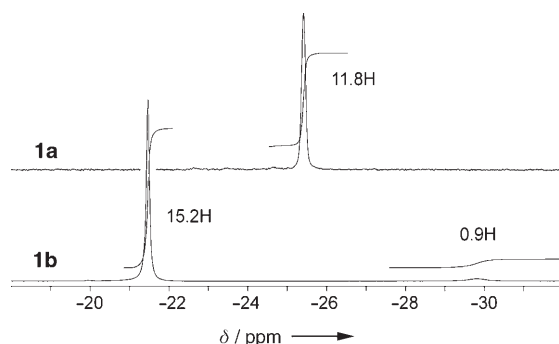


Figure 2. Upfield ^1H NMR spectra of **1a** and **1b**. See Supporting Information for the corresponding spectra for **2a** and **2b**.

Similar to recently reported $[\text{Pt}_3\text{Re}_2(\text{CO})_6(\text{PtBu}_3)_3]^{[6]}$ which takes up three molecules of H_2 and has five low-lying unoccupied molecular orbitals, the 12-hydride octahedral clusters reported herein have a small HOMO–LUMO gap (0.50 eV) and a degenerate pair of LUMO orbitals available for the uptake of four electrons (that is, two molecules of H_2 ; Figure 3). The resulting 16-hydride species (80 cve) has a larger HOMO–LUMO gap (1.3 eV) and thus would be expected to take up additional H_2 less readily. This result is confirmed experimentally; under higher pressures (100 bar H_2) **1b** is the only hydride species observed in solution.

Despite repeated and extended attempts using a variety of counterions and solvents, suitable single crystals of **1b** were not forthcoming. However, crystals of **2b** were eventually obtained by using the $[1\text{-H-closo-CB}_{11}\text{Me}_{11}]^-$ counterion and the structural refinement showed that the $[\text{Rh}_6(\text{PCy}_3)_6]^{2+}$ octahedral cluster core is retained (Figure 4a) in this high-hydride species, although it is somewhat distorted showing a wide range of Rh–Rh bond lengths (2.720(1)–3.132(1) Å). A similar span of bond lengths is observed in the DFT calculated structure of $[\text{Rh}_6(\text{PH}_3)_6\text{H}_{16}]^{2+}$. The Rh–Rh bonds in $[\text{Rh}_6(\text{PH}_3)_6\text{H}_{12}]^{2+}$ show a much narrower distribution, suggesting that the observed distortion is due (in part) to the distribution of the hydride ligands in the high-hydride species. Unfortunately, the hydride ligands could not be located reliably, a common problem in cluster chemistry given the low scattering factor associated with hydrogen and the fact that the hydrides are very often distributed asymmetrically in the solid-state leading to partial occupancy of sites. This situation is taken to the extreme with the 16 hydride ligands around the octahedral core in **1b** and **2b**.

The 16-hydride complexes **1b** and **2b** are stable under an argon atmosphere, but under vacuum both **1b** and **2b** lose two molecules of H_2 to quantitatively regenerate **1a** and **2a**. This

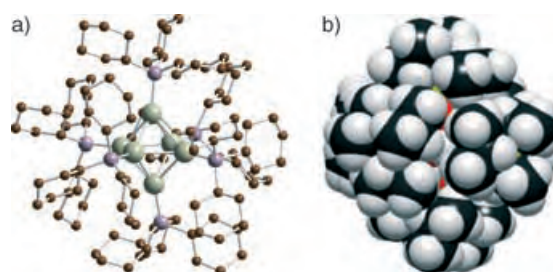


Figure 4. Molecular structure of the dicationic portion of **2b** (a; green Rh, purple P, brown C) and space-filling diagram of **2b** (b; black C, gray H, yellow P, red Rh).

process occurs both in solution and in the crystalline state, and is reversible; pressurizing with H_2 quantitatively (NMR spectroscopy, ESI MS) regenerates the H_{16} species. For **1b** H_2 loss is facile (hours), however for **2b** the process is longer (days) and this may be related to the increased steric shielding the cluster core receives from the cyclohexyl groups compared to the isopropyl groups (Figure 4b). Loss of two hydrogen molecules is also affected by addition of hydrogen acceptors such as *tert*-butylethene (tbe) or 1-hexene, as monitored by NMR spectroscopy and ESI MS (Figure 5). Interestingly, even with a large excess of alkene (>100 -fold) **1a** and **2a** remain—showing that these clusters holds onto the remaining twelve hydrides very strongly.

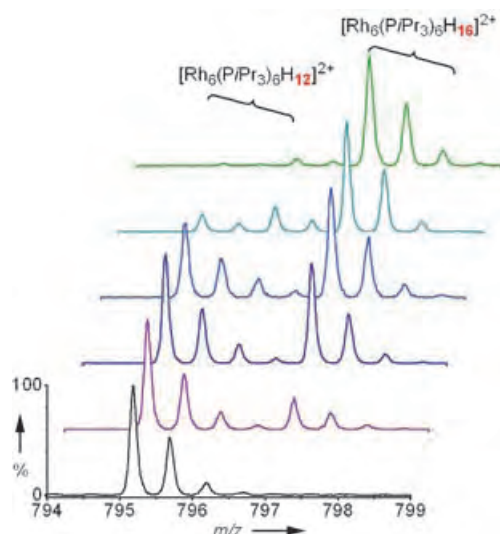


Figure 5. Stacked plot of ESI MS of **1b** on addition of the hydrogen acceptor tbe (≈ 100 -fold excess) in CH_2Cl_2 solution. The uppermost spectrum is 5 min after addition of tbe and the bottom after 24 h.

Although there are a significant number of cluster species known with a high hydride count (that is ≥ 5 hydride ligands)^[5,6,11] and some are formed by addition of H_2 to very unsaturated cluster species,^[6] only one has been shown to reversibly release H_2 , $[Pt_4H_7(PtBu_3)_4][BF_4]$,^[4] affording a cluster with one hydride. The species reported herein are thus unique in that H_2 uptake and loss is facile and the “low”-hydride species that result still have an exceptionally high number of hydride ligands. They thus have relevance for the modeling of surfaces that are catalytically active for hydrogenation reactions as well as hydrogen-spillover processes that result in supported catalysts showing enhanced activities.^[12] The cluster pairs **1a/1b** and **2a/2b**^[14] could also potentially serve as models for chemically reversible hydrogen-storage materials, albeit with a low ($\approx 0.25\%$ based on the Rh_6 dication) reversible hydrogen-storage capacity.

Experimental Section

Crystallographic data: Crystals were grown from CH_2Cl_2 /pentane under a H_2 atmosphere. Intensity data were collected at 150 K on a Nonius Kappa CCD diffractometer, using graphite monochromated

MoK_α radiation ($\lambda = 0.71073 \text{ \AA}$). Structure solution and refinement was achieved using the WinGX-1.64 package.^[13] $C_{132}H_{264}B_{22}P_6Rh_6 \cdot CH_2Cl_2$, $M_r = 2997.46$, $Pna2_1$, $a = 17.6720(2) \text{ \AA}$, $b = 28.0280(3) \text{ \AA}$, $c = 31.0780(5) \text{ \AA}$, $V = 15393.3(3) \text{ \AA}^3$, $Z = 4$, $\mu = 0.769 \text{ mm}^{-1}$, unique reflections = 27469 ($R(\text{int}) = 0.0614$), $R_1 = 0.0565$, $wR_2 = 0.0943$ ($I > 2\sigma(I)$). Up to 11 hydrogen atoms could be found in bridging positions around the Rh_6 core. However, they could not be refined reliably and were not considered in the final stages of the refinement. CCDC-275849 (**2b**) contains the supplementary crystallographic data for this paper. These data can be obtained free of charge from the Cambridge Crystallographic Data Centre via www.ccdc.cam.ac.uk/data_request/cif.

1b: 1H NMR (400 MHz, CD_2Cl_2): $\delta = 7.71$ (m, 16H, BAR^F_4), 7.55 (m, 8H, BAR^F_4), 2.27 (m, 18H, PCH), 1.24 (dd, $J = 15.4 \text{ Hz}$, $J = 7.1 \text{ Hz}$, 108H, CH_3), -21.46 (s, full width at half maximum height (fwhm) = 40 Hz, 15H, Rh-H), -29.81 ppm (br s, fwhm = 200 Hz, 1H, Rh-H). $^{31}P\{^1H\}$ NMR (162 MHz, CD_2Cl_2): $\delta = 109.2$ ppm (d, $J(\text{RhP})$ 140 Hz). ESI MS calcd for $[P_6Rh_6C_{54}H_{142}]^{2+}$ 797.2; found: 797.3.

2a: 1H NMR (400 MHz, CD_2Cl_2): $\delta = 7.71$ (m, 16H, BAR^F_4), 7.55 (m, 8H, BAR^F_4), 0.8–2.5 (m, 198H, PCy_3), -27.20 (br s, fwhm = 230 Hz, 9H, Rh-H), -28.9 ppm (br s, fwhm = 330 Hz, 3H, Rh-H). $^{31}P\{^1H\}$ NMR (162 MHz, CD_2Cl_2): $\delta = 91.9$ ppm (d, $J(\text{RhP})$ 102 Hz). ESI MS calcd for $[P_6Rh_6C_{108}H_{210}]^{2+}$ 1155.5; found: 1155.7.

2b: 1H NMR: $\delta = 7.71$ (m, 16H, BAR^F_4), 7.55 (m, 8H, BAR^F_4), 1.0–2.4 (m, 198H, PCy_3), -21.59 (br s, fwhm = 390 Hz, 15H, Rh-H), -28.37 ppm (br s, fwhm = 210 Hz, 1H, Rh-H). $^{31}P\{^1H\}$ NMR: $\delta = 107.4$ (br s, fwhm = 1100 Hz, 2P), 89.0 ppm (br s, fwhm = 900 Hz, 4P). ESI MS calc for $[P_6Rh_6C_{108}H_{214}]^{2+}$ 1157.5, obs. 1157.8.

Received: June 24, 2005

Published online: October 5, 2005

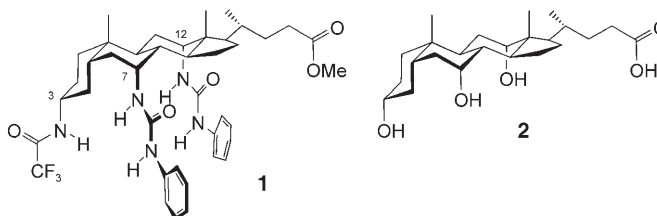
Keywords: cluster compounds · hydride ligands · hydrogen storage · NMR spectroscopy · structure elucidation

- [1] a) J. M. Thomas, B. F. G. Johnson, R. Raja, G. Sankar, P. A. Midgley, *Acc. Chem. Res.* **2003**, 36, 20; b) P. Braunstein, L. A. Oro, P. R. Raithby, *Metal Clusters in Chemistry*, Wiley-VCH, New York, **1999**; c) F. Dumestre, B. Chaudret, C. Amiens, P. Renaud, P. Fejes, *Science* **2004**, 303, 821.
- [2] a) C. M. Hagen, L. Vieille-Petit, G. Laurenczy, G. Süss-Fink, R. G. Finke, *Organometallics* **2005**, 24, 1819; b) C. M. Hagen, J. A. Widegren, P. M. Maitlis, R. G. Finke, *J. Am. Chem. Soc.* **2005**, 127, 4423; c) P. J. Dyson, *Dalton Trans.* **2003**, 2964.
- [3] a) L. J. Farrugia, M. Green, D. R. Hankey, A. G. Orpen, F. G. A. Stone, *J. Chem. Soc. Chem. Commun.* **1983**, 310; b) A. M. Arif, T. A. Bright, R. A. Jones, C. M. Nunn, *J. Am. Chem. Soc.* **1988**, 110, 6894; c) F. J. Safarowic, D. J. Bierdeman, J. B. Keister, *J. Am. Chem. Soc.* **1996**, 118, 11805; d) M. A. Aubart, B. D. Chandler, R. A. T. Gould, D. A. Krogstad, M. F. J. Schoondergang, L. H. Pignolet, *Inorg. Chem.* **1994**, 33, 3724.
- [4] R. J. Goodfellow, E. M. Hamon, J. A. K. Howard, J. L. Spencer, D. G. Turner, *J. Chem. Soc. Chem. Commun.* **1984**, 1604.
- [5] For example: a) D. Gregson, J. A. K. Howard, M. Murray, J. L. Spencer, *J. Chem. Soc. Chem. Commun.* **1981**, 716; b) L. F. Rhodes, J. C. Huffman, K. G. Caulton, *J. Am. Chem. Soc.* **1983**, 105, 5137; c) J. M. Bemis, L. F. Dahl, *J. Am. Chem. Soc.* **1997**, 119, 4545; d) G. Süss-Fink, L. Plasseraud, A. Maisse-Francois, H. Stoeckli-Evans, H. Berke, T. Fox, R. Gautier, J. Y. Saillard, *J. Organomet. Chem.* **2000**, 609, 196; e) H. Suzuki, T. Kakigano, K. Tada, M. Igarashi, K. Matsubara, A. Inagaki, M. Oshima, T. Takao, *Bull. Chem. Soc. Jpn.* **2005**, 78, 67; f) J. P. Lau, W. T. Wong, *Dalton Trans.* **2005**, 2579; g) R. D. Adams, M. P. Pompeo, W. Wu, *Inorg. Chem.* **1991**, 30, 2425.
- [6] R. D. Adams, B. Captain, *Angew. Chem.* **2005**, 117, 2587; *Angew. Chem. Int. Ed.* **2005**, 44, 2531; see also P. J. Dyson, J. S. McIndoe,

- Angew. Chem.* **2005**, *117*, 5918; *Angew. Chem. Int. Ed.* **2005**, *44*, 5772.
- [7] M. J. Ingleson, M. F. Mahon, P. R. Raithby, A. S. Weller, *J. Am. Chem. Soc.* **2004**, *126*, 4784; see also: P. J. Dyson, J. S. McIndoe, *Angew. Chem.* **2004**, *116*, 6152; *Angew. Chem. Int. Ed.* **2005**, *43*, 6028.
- [8] M. J. Ingleson, S. K. Brayshaw, M. F. Mahon, G. D. Ruggiero, A. S. Weller, *Inorg. Chem.* **2005**, *44*, 3162.
- [9] a) D. W. Hart, R. G. Teller, C. Y. Wei, R. Bau, G. Longoni, S. Campanella, P. Chini, T. F. Koetzle, *J. Am. Chem. Soc.* **1981**, *103*, 1458; b) P. F. Jackson, B. F. G. Johnson, J. Lewis, P. R. Raithby, M. McPartlin, W. J. H. Nelson, K. D. Rouse, J. Allibon, S. A. Mason, *J. Chem. Soc. Chem. Commun.* **1980**, 295.
- [10] Resonance signals for interstitial hydrides can span a wide chemical shift range in ^1H NMR spectra: T. Eguchi, B. T. Heaton, *J. Chem. Soc. Dalton Trans.* **1999**, 3523.
- [11] a) L. F. Chen, F. A. Cotton, W. T. Klooster, T. F. Koetzle, *J. Am. Chem. Soc.* **1997**, *119*, 12175; b) M. H. Chisholm, K. Folting, K. S. Kramer, W. E. Streib, *J. Am. Chem. Soc.* **1997**, *119*, 5528.
- [12] H. R. Gao, R. J. Angelici, *J. Am. Chem. Soc.* **1997**, *119*, 6937.
- [13] WinGX-1.64: L. J. Farrugia, *J. Appl. Crystallogr.* **1999**, *32*, 837.
- [14] Note added in proof, August 31, 2005: The solid-state structure of **2a** has been determined and shows it to be an essentially regular octahedron, in line with the DFT calculated structure (Rh–Rh bond lengths span the range 2.719–2.755 Å).

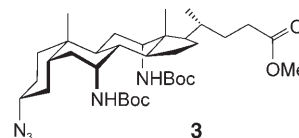
(MOF)^[1c-g] materials. However, purely organic structures with such dimensions are rare, especially if macrocyclic molecules are excluded.^[2] We now report a new class of nanoporous organic crystals with chiral, unidirectional channels, tunable to diameters in excess of 14 Å.

This discovery arose from our program on steroid-based anion receptors.^[3] The “cholapod” **1** belongs to a series of compounds derived from cholic acid **2**, in which hydrogen-



bond donor units are deployed on the bile acid scaffold. The urea groups at C7 and C12 are constrained by the axial orientation of the C–N bond, such that the NH groups point towards each other. The amide moiety at C3 can also point inwards, thus cooperating in hydrogen-bond donation to anionic guests. Molecules from this family are powerful anion receptors,^[4] and also act as anion carriers across bilayer membranes.^[5]

Cholapod **1** was prepared from **2** via intermediate **3**^[6] (see the Supporting Information; Boc = *tert*-butoxycarbonyl).



Crystallization from methyl acetate, which contained small amounts of water, gave needles up to 5 mm long and approximately 0.2 mm wide. The crystal structure was solved in the *P*6₁ space group.^[7] The individual molecules were found to bind one molecule of water (see Figure 1 a). The trifluoroacetamide unit rotates such that the carbonyl group points inwards acting as an hydrogen-bond acceptor, whereas the urea groups act as hydrogen-bond donors to the oxygen atom from the water molecule. The hydrated steroids form columns parallel to the crystallographic *c* axis, reinforced by hydrogen-bonding interactions between the free O–H group of a water molecule contained in one complex and a carbonyl oxygen atom of a urea group in the next (Figure 1 b). The columns then pack in a hexagonal array to give channels centered on the *c* axis, defined by a right-handed spiral of steroids (Figure 1 c).^[8] The internal surfaces possess an average diameter of 16.4 Å, with a minimum value of 14.3 Å (Figure 1 d).^[7] The surfaces are formed mainly from hydrophobic CH and CF units, but also feature the carbonyl oxygen atoms from the ester groups. Around 30 % of the crystal volume is accessible to guests. The channels are filled with delocalized electron density, consistent with disordered solvent molecules. Face indexing of a single crystal showed

Crystal Engineering

DOI: 10.1002/anie.200502330

Spiraling Steroids: Organic Crystals with Asymmetric Nanometer-Scale Channels**

Adam L. Sisson, Vicente del Amo Sanchez, Germinal Magro, Alex M. E. Griffin, Shilen Shah, Jonathan P. H. Charmant, and Anthony P. Davis*

Crystalline microporous (or nanoporous) solids are widely sought and studied.^[1] Such materials provide challenges for crystal engineering and find applications in catalysis, separation techniques, gas storage, sensors, lasers, and so forth. Robust structures with large voids are especially interesting, as they are able to accommodate the widest range of guests. Channels that measure ≥ 1 nm in diameter are fairly common in inorganic^[1a-c] and, especially, metal–organic-framework

[*] A. L. Sisson, V. del Amo Sanchez, Dr. G. Magro, A. M. E. Griffin, S. Shah, Dr. J. P. H. Charmant, Prof. A. P. Davis
School of Chemistry
University of Bristol, Cantock's Close
Bristol BS8 1TS (UK)
Fax: (+44) 117-929-8611
E-mail: anthony.davis@bristol.ac.uk

[**] Financial support was provided by the EPSRC (GR/R04584/01) and BBSRC (BBS/B/11044). Mass spectra were provided by the EPSRC National MS Service Center at the University of Swansea.

Supporting information for this article is available on the WWW under <http://www.angewandte.org> or from the author.

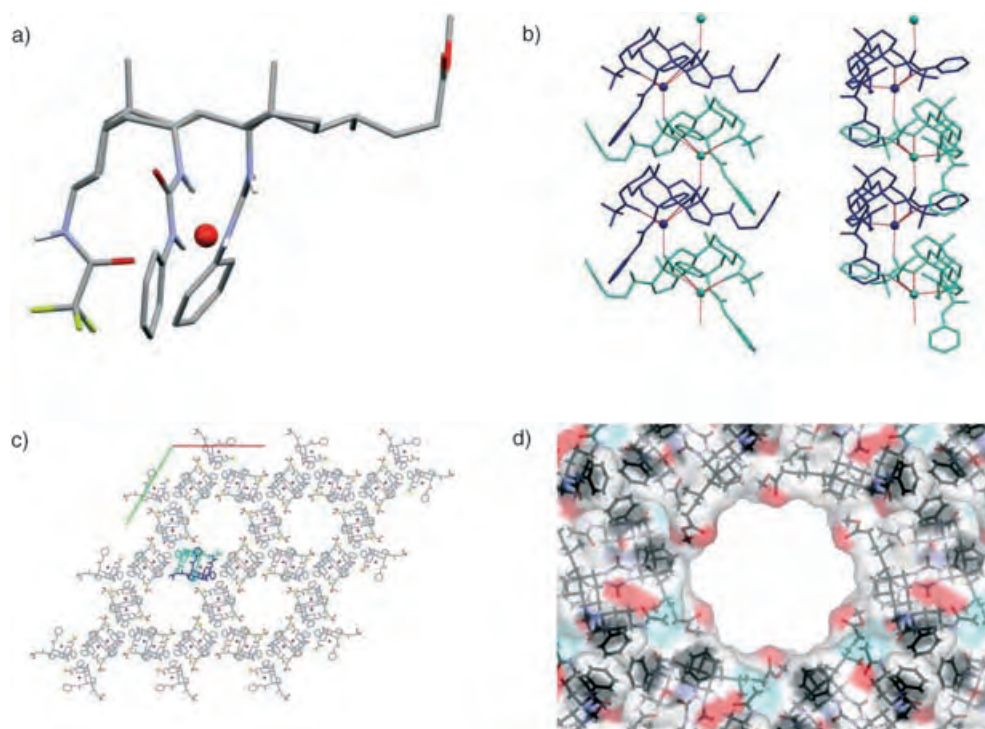


Figure 1. Representations of the crystal structure of **1**: a) A single molecule of **1** with the bound water molecule (red sphere; hydrogen atoms bound to carbon have been removed for clarity). b) Columns of **1**·H₂O parallel to the channel axis shown from two perspectives (the steroid molecules are shown in green and blue and the hydrogen-bonding interactions in red). c) The packing of columns to give channels, viewed along the channel axis (steroid molecules in one column are highlighted in green and blue). d) Interior surface of a channel, calculated by using a 1.4-Å probe; the surface is color coded according to the underlying atoms (red: oxygen, blue: nitrogen, green: fluorine).

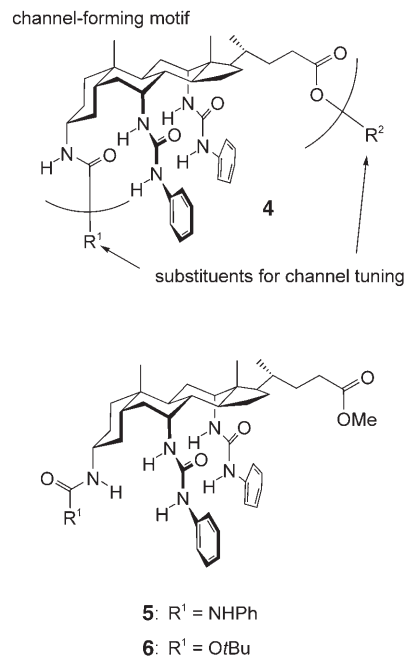
that, as expected, the channel axis coincided with the long axis of the needles.

The contents of the channels were investigated by ¹H NMR spectroscopic analysis. Crystals of **1** were removed from the solvent, air-dried,^[9] and dissolved in deuterated acetone (99.96 atom % D) under anhydrous conditions.^[7] Integration of the NMR spectrum implied a composition of **1**·0.75 MeOAc·3.5 H₂O.^[10] Even allowing for the single H₂O molecule bound to each molecule of **1**, this result implies that water is concentrated in the channels and explains our observation that small amounts of water aid crystallization. The solvent was lost and the crystals became opaque on vacuum drying;^[11] however, X-ray powder diffraction showed that the channel structure was maintained.^[7] Solvent exchange was also demonstrated. Samples removed from MeOAc were washed with diethyl ether or toluene, air-dried,^[9] and analyzed by ¹H NMR spectroscopy. In both cases, the MeOAc had disappeared and the replacement solvent was present (approximately 0.5 equiv). Vacuum-dried samples suspended in toluene also absorbed the solvent. When these toluene-solvated crystals were washed briefly (approximately 30 s) with CH₂Cl₂, the toluene was retained. Thus, solvent exchange is slow, which is consistent with absorption into the nanoporous framework.

The structure of **1** is notable in several respects. First, the channels are among the largest observed for purely organic systems. Second, they are persistent and accessible, as shown

above. Inclusion complexes of bile acid derivatives are well known and well studied,^[12] but the formation of such large, physically robust pores is unprecedented. The crystals are chiral and also lack any regular axis of symmetry, so the pores are aligned in one direction. Finally, the interactions which govern the packing do not seem to involve the terminal CF₃ and methyl ester groups, both of which point into the channels. This suggests a generalizable motif **4**, with potential for tuning. These interactions suggest the generalized motif of **4**, which can be potentially used to tune channel width and properties by variation of the R¹ and R² groups.

Considering this last point, we examined other steroids of type **4** from our anion-receptor program. Compounds **5**^[13] and **6**^[7]



crystallized as needles and were subjected to X-ray crystallographic studies. Both **5** and **6** formed nanoporous structures in which the disposition of the steroid nuclei was almost identical to that in **1**. However, the variation of the R¹

group induced significant changes. In the case of **5**, the bulky NHP group protrudes into the channel and, more importantly, displaces the OMe unit from the channel wall. The ester group rotates to create a more irregular, narrower pore with an average diameter of 15.7 Å (minimum diameter = 11.6 Å; Figure 2).^[7] In the case of **6**, the *Or*Bu group seems to

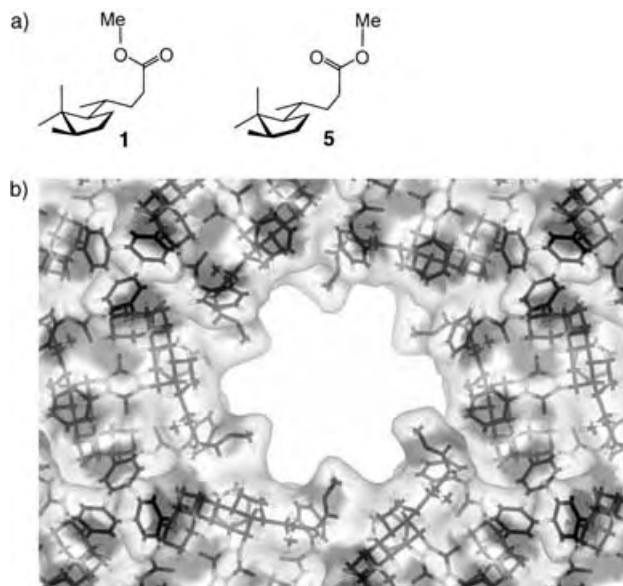


Figure 2. a) Orientation of the methyl ester groups in **1** and **5**. b) Interior surface of **5**. In contrast to **1** (see Figure 1d) the OMe groups are directed inwards, thus creating protrusions in the channel wall.

create an intermediate situation, in which the ester groups are randomly distributed between the two orientations. If an alternating arrangement is assumed, the average and minimum diameters are 16.4 and 12.3 Å, respectively.^[7] The crystal structures of **1**, **5**, and **6** are compared in Figure 3, which highlights the position of the terminal R^1 groups at the channel surfaces.

To conclude, we have found a new steroid-based motif which generates robust, asymmetric, and nanoporous structures of unusual dimensions. The channels are codirected^[14] and large enough to accommodate a wide variety of organic molecules, including, for example, dyes or substrates for catalysis. We will investigate such possibilities in future investigations, with a view to the development of novel functional organic materials.

Received: July 4, 2005

Published online: October 7, 2005

Keywords: chirality · crystal engineering · inclusion compounds · microporous materials · steroids

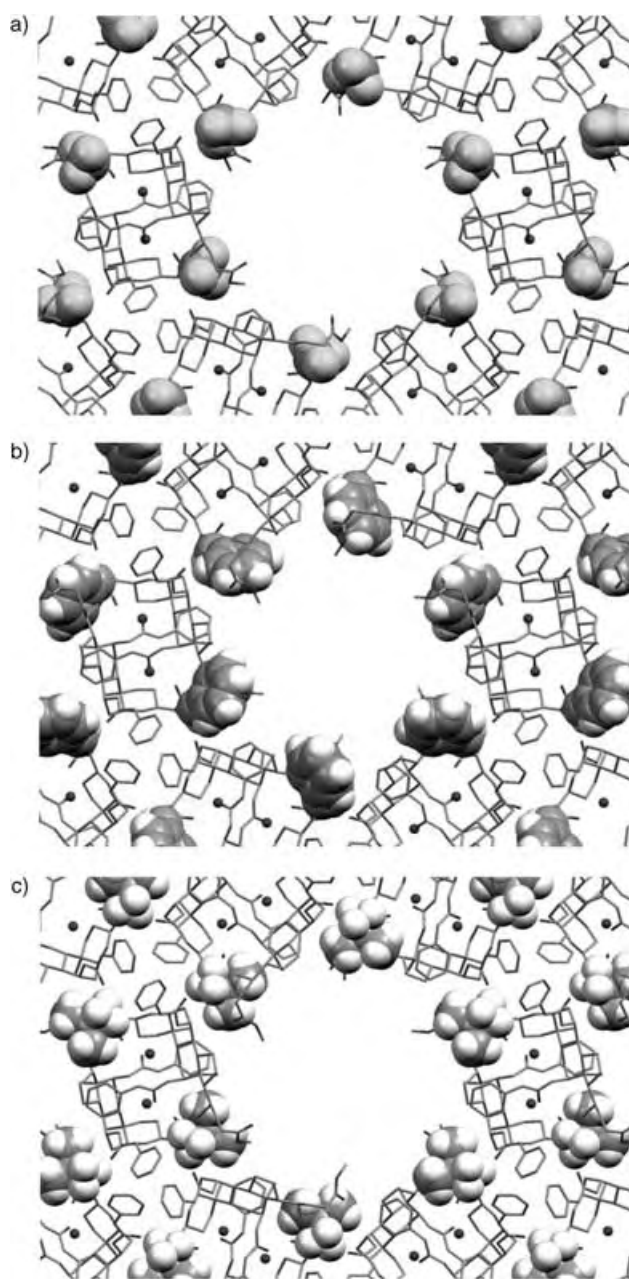


Figure 3. Structures of **1**, **5**, and **6** viewed down the channel axis, with terminal R^1 groups (see 4) represented in the space-filling mode. a) Trifluoroacetamide **1** ($R^1 = CF_3$), b) trisurea **5** ($R^1 = NHP$), c) carbamate **6** ($R^1 = OrBu$).

M. J. Rosseinsky, *Acc. Chem. Res.* **2005**, 38, 273; e) S. Kitagawa, R. Kitaura, S. Noro, *Angew. Chem.* **2004**, 116, 2388; *Angew. Chem. Int. Ed.* **2004**, 43, 2334; f) C. N. R. Rao, S. Natarajan, R. Vaidhyanathan, *Angew. Chem.* **2004**, 116, 1490; *Angew. Chem. Int. Ed.* **2004**, 43, 1466; g) O. M. Yaghi, M. O'Keeffe, N. W. Ockwig, H. K. Chae, M. Eddaoudi, J. Kim, *Nature* **2003**, 423, 705; h) K. T. Holman, A. M. Pivovarov, J. A. Swift, M. D. Ward, *Acc. Chem. Res.* **2001**, 34, 107; i) A. Nangia, *Curr. Opin. Solid State Mater. Sci.* **2001**, 5, 115.

[2] For a survey of channel-forming macrocycles, see: D. T. Bong, T. D. Clark, J. R. Granja, M. R. Ghadiri, *Angew. Chem.* **2001**, 113, 1016; *Angew. Chem. Int. Ed.* **2001**, 40, 988; for recent examples of organic crystals with self-assembled channels (with

[1] a) *Host-guest Systems Based on Nanoporous Crystals* (Eds.: F. Laeri, F. Schuth, U. Simon, M. Wark), Wiley-VCH, Weinheim, **2003**; b) M. E. Davis, *Nature* **2002**, 417, 813; c) G. Férey, C. Mellot-Draznieks, C. Serre, F. Millange, *Acc. Chem. Res.* **2005**, 38, 217; d) D. Bradshaw, J. B. Claridge, E. J. Cussen, T. J. Prior,

- internal diameters given if available), see: D. V. Soldatov, I. L. Moudrakovski, J. A. Ripmeester, *Angew. Chem.* **2004**, *116*, 6468; *Angew. Chem. Int. Ed.* **2004**, *43*, 6308 (5.1 and 4.9 Å); H. Mansikkamaki, M. Nissinen, K. Rissanen, *Angew. Chem.* **2004**, *116*, 1263; *Angew. Chem. Int. Ed.* **2004**, *43*, 1243 (5 Å); P. S. Sidhu, K. A. Udachin, J. A. Ripmeester, *Chem. Commun.* **2004**, 1358; D. MasPOCH, N. Domingo, D. Ruiz-Molina, K. Wurst, G. Vaughan, J. Tejada, C. Rovira, J. Veciana, *Angew. Chem.* **2004**, *116*, 1864; *Angew. Chem. Int. Ed.* **2004**, *43*, 1828 (5.2 Å); P. Brunet, E. Demers, T. Maris, G. D. Enright, J. D. Wuest, *Angew. Chem.* **2003**, *115*, 5461; *Angew. Chem. Int. Ed.* **2003**, *42*, 5303 (7.8–11.4 Å); H. Carrasco, C. Foces-Foces, C. Perez, M. L. Rodriguez, J. D. Martin, *J. Am. Chem. Soc.* **2001**, *123*, 11970 (5.7–9.4 Å); N. Malek, T. Maris, M.-E. Perron, J. D. Wuest, *Angew. Chem.* **2005**, *117*, 4089; *Angew. Chem. Int. Ed.* **2005**, *44*, 4021 (15.1 Å).
- [3] A. P. Davis, J.-B. Joos, *Coord. Chem. Rev.* **2003**, *240*, 143.
- [4] A. J. Ayling, M. N. Pérez-Payán, A. P. Davis, *J. Am. Chem. Soc.* **2001**, *123*, 12716.
- [5] A. V. Koulov, T. N. Lambert, R. Shukla, M. Jain, J. M. Boon, B. D. Smith, H. Y. Li, D. N. Sheppard, J. B. Joos, J. P. Clare, A. P. Davis, *Angew. Chem.* **2003**, *115*, 5081; *Angew. Chem. Int. Ed.* **2003**, *42*, 4931; B. A. McNally, A. V. Koulov, B. D. Smith, J.-B. Joos, A. P. Davis, *Chem. Commun.* **2005**, 1087.
- [6] V. del Amo, L. Siracusa, T. Markidis, B. Baragaña, K. M. Bhattarai, M. Galobardes, G. Naredo, M. N. Pérez-Payán, A. P. Davis, *Org. Biomol. Chem.* **2004**, *2*, 3320.
- [7] For further details, see the Supporting Information.
- [8] E. A. Meyer, R. K. Castellano, F. Diederich, *Angew. Chem.* **2003**, *115*, 1244; *Angew. Chem. Int. Ed.* **2003**, *42*, 1210.
- [9] Air was allowed to pass, for 10 minutes, through the crystals with a Hirsch or Buchner funnel.
- [10] This formula implies that approximately half of the volume in the NMR sample that was accessible to the guest species was occupied by solvent molecules; the remainder was presumably replaced by air during the drying process.
- [11] The crystals were evacuated by using an oil pump for 24 hours.
- [12] For a leading reference, see: M. Miyata, K. Sada, N. Yoshitani, in *Encyclopedia of Supramolecular Chemistry* (Eds.: J. L. Atwood, J. W. Steed), Marcel Dekker, New York, **2004**, p. 441.
- [13] V. del Amo, K. M. Bhattarai, M. Nissinen, K. Rissanen, M. N. Pérez-Payán, A. P. Davis, *Synlett* **2005**, *2*, 1319.
- [14] This term is used to imply that the channels are both directional (namely, asymmetric with respect to direction of view along the c axis) and aligned (pointing in the same direction).

DOI: 10.1002/anie.200502432

A Germanate Framework Containing 24-Ring Channels, Ni–Ge Bonds, and Chiral [Ni@Ge₁₄O₂₄(OH)₃] Cluster Motifs Transferred from Chiral Metal Complexes**

Zhi-En Lin, Jie Zhang, Jing-Tai Zhao,
Shou-Tian Zheng, Chun-Yang Pan,
Guo-Ming Wang, and Guo-Yu Yang*

Microporous materials have been extensively studied due to their widespread applications in ion exchange, separation, and catalysis.^[1] Since the discovery of the first aluminum phosphates (AlPOs) VPI-5 with 18-membered rings (18-MR) in 1988, some porous materials with larger rings, such as JDF-20 (20-MR), cloverite (20-MR), VSB-1 (24-MR), ND-1 (24-MR), VSB-5 (24-MR), NTHU-1 (24-MR), FDU-4 (24-MR), ASU-16 (24-MR), and SU-12 (24-MR), have been made.^[2] Recently, the replacement of framework O²⁻ with S²⁻ (Se²⁻, Te²⁻) anions has resulted in a new class of porous materials with giant cavities and channels.^[3] In general, the cations and anions of the above frameworks are linked to each other by T-X-T linkage modes, while framework containing T-M-T linkages are unexplored so far (where T and M are cations, and X anions).

Chiral metal complex (CMC) templates have shown great advantages in the synthesis of unusual open-framework materials, because the CMCs not only have unique spatial configurations, various charges, different flexibilities, and hydrogen-bonding sites, but can also induce a chiral environment in the host framework.^[4] Metal phosphates templated by an optically pure CMC or a racemic mixture of CMCs have been reported for AlPOs,^[4a,5] GaPOs,^[6] ZnPOs,^[4b,c,7] and BPO.^[8] Lately, the synthesis of open-framework germanates has made great progress,^[2b-i] but to our knowledge little attention has been paid to the possibility of using CMCs as

[*] Z.-E. Lin, Prof. Dr. J. Zhang, S.-T. Zheng, C.-Y. Pan, G.-M. Wang, Prof. Dr. G.-Y. Yang
State Key Laboratory of Structural Chemistry
Fujian Institute of Research on the Structure of Matter
Chinese Academy of Sciences
Fuzhou, Fujian 350002 (P. R. China)
Fax: (+ 86) 591-8371-0051
E-mail: ygy@fjirsm.ac.cn

Prof. Dr. J.-T. Zhao
State Key Lab of High Performance Ceramics and Superfine Microstructure
Shanghai Institute of Ceramics
Chinese Academy of Sciences
Shanghai 200050 (P. R. China)

[**] This work was supported by the NNSF of China (Nos. 20473093 and 20271050), the Talents Program of Chinese Academy of Sciences, and the NSF of Fujian Province (Nos. E0510030 and E0210029).



Supporting information for this article is available on the WWW under <http://www.angewandte.org> or from the author.

templates in the synthesis of germanates.^[9] To introduce CMCs into germanates and understand their role in determining the frameworks, we focused on the synthesis of germanates templated by CMCs and obtained the chainlike germanate [Ge₇O₁₃(OH)₂F₃]^{3−}·2[Ni(dien)₂]²⁺ (dien = diethylene triamine).^[9d] As a continuation of this work, by using a racemic mixture of a [NiCl₂(L)₃] complex [L = ethylenediamine (en), 1,2-diaminopropane (enMe)] as template, we have made two novel germanate frameworks Ni@Ge₁₄O₂₄(OH)₃·2Ni(L)₃ (L = en/enMe, denoted FJ-1a/FJ-1b), in which chiral [Ni@Ge₁₄O₂₄(OH)₃]^{4−} (Ni@Ge₁₄) clusters (Figure 1a,b) containing Ni–Ge bonds are connected to each other to form a three-dimensional (3D) framework with 24-ring windows (Figure 1c,d). FJ-1 is the first example of porous materials having T-M-T linkages (where T-M-T = Ge–Ni–Ge).

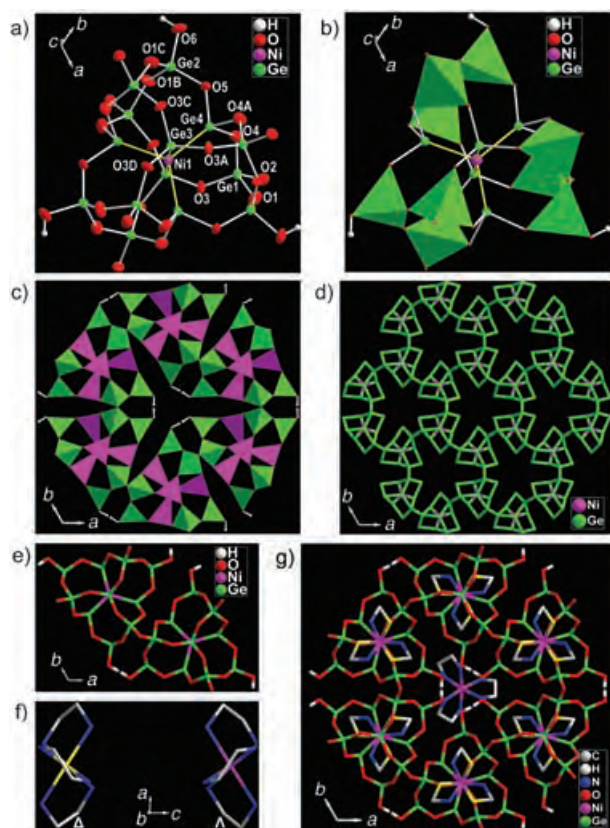


Figure 1. a) View of the coordination environments of the Ni and Ge atoms in the Ni@Ge₁₄ cluster (50% thermal ellipsoids). Selected bond lengths [Å] and angles [°]: Ni1–Ge3 2.251(2), Ni1–Ge4 2.317(2); Ge3–Ni1–Ge3A 180, Ge3–Ni1–Ge4 90, Ge4–Ni1–Ge4A 120. b) Polyhedral and ball-and-stick view of the Ni@Ge₁₄ unit. GeO₄, green. c) View of the 24-ring channel constructed from three pairs of enantiomers of adjacent Ni@Ge₁₄ motifs in FJ-1a. d) Topological framework of FJ-1a showing the 24-ring channels and the Ni@Ge₁₄ motif. e) View of one pair of enantiomers for adjacent Ni@Ge₁₄ motifs with Δ and Λ configurations in the *ab* plane in FJ-1a. f) The chiral octahedral [Ni₂(en)₃]²⁺ complexes with Δ and Λ configurations arranged along the *c* axis (Δ, Ni2 yellow; Λ, Ni2 purple). g) View of the orderly separation of chiral [Ni₂(en)₃]²⁺ complexes in the center of the 24-ring channel and achiral trigonal prismatic [Ni₃(en)₃]²⁺ complexes occluded between the same chiral structural motifs along the *c* axis (N2 blue, N2' yellow). The H atoms of C and N atoms are omitted for clarity.

Yellow hexagonal crystals of FJ-1a/FJ-1b (see the Supporting Information) were obtained by the solvothermal reaction of [NiCl₂(L)₃]·2H₂O and GeO₂ in mixed solvents of ethylene glycol and L at 170 °C. X-ray crystal analysis revealed that FJ-1a and FJ-1b are isostructural and crystallize in the high-symmetry hexagonal space group *P*6₂c. Therefore, only the structure of FJ-1a is described in detail. The Ni@Ge₁₄ unit consists of one Ni⁺ and five Ge²⁺ ions reduced from Ni²⁺ and Ge⁴⁺ by amine under solvothermal conditions, nine Ge⁴⁺ ions, and three H and 27 O atoms (Figures 1a and Supporting Information). The Ni1 atom is located in the center of the Ni@Ge₁₄ unit and is bonded to five Ge²⁺ (three Ge4 and two Ge3) atoms to yield a trigonal-bipyramidal {Ni@Ge₅} core (Figures 1a,b and Supporting Information). The Ni⁺–Ge²⁺ distances vary in the range 2.251(2)–2.317(2) Å, which is close to the sum of covalent radii for these elements and similar to the Ni⁰–Ge²⁺ bonds (2.206–2.291 Å) in nickel germylene complexes,^[10] but considerably shorter than a normal Ge–Ge bond or twice the covalent radius of Ge (2.44 Å).^[11] Thus, it is reasonable to identify the central atom of Ni@Ge₁₄ as Ni. The Ge:Ni ratio obtained from electron probe microanalysis agrees with this assignment. Of the fourteen Ge atoms, five Ge3/Ge4 atoms around Ni1 are tetrahedrally coordinated by one μ₅-Ni1 and three O atoms (Ge–O 1.803(9)–1.849(7) Å). The 4s electron lone pair of Ge²⁺ permits five Ge²⁺ atoms to function as novel ligands to the Ni1 atom with unusual Ge–Ni–Ge linkages. The remaining nine Ge1/Ge2 atoms are typical Ge⁴⁺ ions and are bonded to four O atoms; the Ge–O distances (1.722(10)–1.766(7) Å) and O–Ge–O angles (99.3(4)–115.3(6)°) are in agreement with those of four-connected germanates.^[12] Assuming the valences of nine Ge1/Ge2, five Ge3/Ge4, one Ni1, two Ni2/Ge3, twenty-seven O, and three H to be +4, +2, +1, +2, −2, and +1, respectively, in Ni@Ge₁₄O₂₄(OH)₃·2Ni(L)₃, the framework stoichiometry of [Ni@Ge₁₄O₂₄(OH)₃]^{4−} creates a net framework charge of −4, which can just be balanced by two [Ni(L)₃]²⁺ complex cations, that is, the low-valent Ni⁺ and Ge²⁺ ions indeed exist in the {Ni@Ge₅} core, as is further confirmed by magnetic and luminescence measurements (see below). In FJ-1a, three GeO₄ tetrahedra are linked together by sharing vertices to form a trimer (Ge₃O₁₀). Three trimers are linked alternately to three Ge(4)O₃Ni tetrahedra around the Ni1 atom in the *ab* plane to form a NiGe₁₂O₂₄(OH)₃ cluster that is further capped by two Ge3 atoms above and below the *ab* plane to form a novel Ni@Ge₁₄ unit (Figure 1b). Each Ni@Ge₁₄ building block is bridged to six others through O2 atoms to yield a 3D open framework with 24-ring channels (Figures 1c,d and Supporting Information) with dimensions of about 8.3 × 13.6 Å (see Supporting Information), which intersect with two 12-ring channels running along the *a* and *b* axes (see Supporting Information). The construction of 24-ring channels can also be understood as shape-controlled synthesis templated by octahedral [Ni₂(en)₃]²⁺ complex. The propellane-like shape of the 24-ring channel around the [Ni₂(en)₃]²⁺ templates is delimited by eighteen GeO₄ and six GeO₃Ni tetrahedra (Figures 1c,d and Supporting Information), which matches the shape of the [Ni₂(en)₃]²⁺ complex and is unique and different from that of known porous materials templated by amines.^[2]

Interestingly, there are two types of chiral Ni@Ge_{14} motifs and two types of $[\text{Ni}(\text{en})_3]^{2+}$ complexes (Figure 1 e,g) in FJ-1a. The $[\text{Ni}_2(\text{en})_3]^{2+}$ template located in the center of the 24-ring is chiral (Figures 1 g and Supporting Information). The enantiomers of $[\text{Ni}_2(\text{en})_3]^{2+}$ complexes are alternately arranged as Δ and Λ configurations in the 24-ring channels along the c axis (Figures 1 f and Supporting Information), and further interact with chiral Ni@Ge_{14} motifs through H-bonding interactions ($\text{N1}\cdots\text{O6}$, 3.072(16) Å). The Δ - $[\text{Ni}_2(\text{en})_3]^{2+}$ complex forms hydrogen bonds to six adjacent Ni@Ge_{14} motifs with both Δ and Λ configuration, or vice versa (see Supporting Information), while the $[\text{Ni}_3(\text{en})_3]^{2+}$ cations residing in the 12-ring channels (see Supporting Information) are achiral and separated by Ni@Ge_{14} motifs along the c axis. Adjacent $[\text{Ni}_3(\text{en})_3]^{2+}$ complexes in the ab plane exhibit different orientations (Figures 1 g and Supporting Information). The $[\text{Ni}_3(\text{en})_3]^{2+}$ complex also interacts with the Ni@Ge_{14} motifs through hydrogen-bonding interactions ($\text{N2}\cdots\text{O3}$ 3.142(18) and $\text{N2}\cdots\text{O3/O4}$ 3.144(9)–3.167(20) Å, see Supporting Information).

The chiral $[\text{Ni}_2(\text{en})_3]^{2+}$ complexes with regular octahedral and achiral $[\text{Ni}_3(\text{en})_3]^{2+}$ complex with rare trigonal-prismatic geometry in FJ-1a respectively have D_3 and D_{3h} symmetry (see Supporting Information), and the chiral Ni@Ge_{14} motif has C_3 symmetry (Figure 1 a and Supporting Information). It appears that the symmetry of the Ni@Ge_{14} motif is a good match with those of the chiral and achiral metal complex templates (Figures 1 g and Supporting Information). This suggests that the complex template can impose its individual symmetry constraint on the structural motifs,^[4] which have a subgroup of point-group symmetry of the complex template.^[4c] In addition, the configuration of the chiral Ni@Ge_{14} motif is also matched with that of the chiral $[\text{Ni}_2(\text{en})_3]^{2+}$ complex template (see Supporting Information). Furthermore, the orderly separation of chiral $[\text{Ni}_2(\text{en})_3]^{2+}$ and achiral $[\text{Ni}_3(\text{en})_3]^{2+}$ complexes in FJ-1a (Figures 1 g and Supporting Information) indicates that the host framework has molecular-recognition capability and stereospecificity for guest templates. From insight into the structure of FJ-1a and other metal phosphates templated by CMCs,^[4–7] it is found that the CMCs are responsible for the formation of the chiral motif/framework in the crystallization process and can impart their chirality and symmetry to an inorganic motif/framework, as well as leading to the existence of stereospecificity and molecular recognition between the inorganic host and CMC guest, while the achiral metal complex only transfers its symmetry to the inorganic motif. It is believed that the hydrogen bonding between the complex template and the host is the origin of the above phenomena.^[4–7]

Variable-temperature magnetic measurements on FJ-1a showed that the product of molar magnetic susceptibility and temperature $\chi_M T$ remains nearly constant down to 50 K and then rapidly decreases on further cooling (see Supporting Information). The magnetic data can be fitted well to the Curie–Weiss law with $\theta = -1.21$ K, which indicates weak antiferromagnetic coupling between metal centers. This is consistent with isolated Ni^{2+} centers and a long distance (10.71 Å) between Ni^{2+} centers in adjacent Ni@Ge_{14} units. The high-temperature value of $\chi_M T$ is $1.74 \text{ cm}^3 \text{ K mol}^{-1}$, much

smaller than that calculated for two Ni^{2+} ($S=1$, d^8 configuration) and one Ni^{+} ions ($S=1/2$, d^9 configuration) without magnetic interaction ($2.375 \text{ cm}^3 \text{ K mol}^{-1}$, $g=2$). This suggests that one Ni^{2+} ion should be in the nonmagnetic state, which might originate from the structural disorder of the trigonal-prismatic coordination of the Ni_3^{2+} ion. The experimental value of $1.74 \text{ cm}^3 \text{ K mol}^{-1}$ is in good agreement with the spin-only value expected for one Ni^{2+} and one Ni^{+} ions with an average g value of 2.25 that is within the generally observed range for Ni^{2+} and Ni^{+} ions.^[13,14] In view of the regular octahedral geometry around the Ni_2^{2+} ion, the zero-field splitting effect on the Ni^{2+} ion should be very small,^[15] and the sharp decrease in $\chi_M T$ at low temperature could be attributed to a weak antiferromagnetic interaction between Ni^{+} ions.^[16]

FJ-1a exhibits blue luminescence in the solid state at room temperature. On excitation at 200 nm, the luminescence of FJ-1a has two strong emission bands at 482 and 523 nm and one shoulder at 458 nm (see Supporting Information) that differ from those of reported open-framework phosphates and germanates, which usually show a single emission peak,^[17] that is, a more complex mechanism is involved in FJ-1a. Unlike crystalline porous materials incorporating organic dyes or doped with metal activators,^[18] the luminescence of phosphates and germanates is generally attributed to the presence of lattice defects.^[17] For FJ-1a, apart from lattice defects, low-valent Ge^{2+} with s^2 configuration and $\text{Ge}^{2+}(4s) \rightarrow \text{Ni}^{+}(3d)$ metal–metal charge transfer in the Ni@Ge_{14} cluster should also make contributions to the luminescence.^[19,20]

In summary, we have successfully made two novel germanate open frameworks with 24-MRs by using a metal complex as template under solvothermal conditions. The key points of the synthetic procedures have been well established. These are rare examples of metal–metal bonds in porous materials, and the presence of Ge–Ni–Ge linkages makes them different from other open-framework materials that only contain T–X–T linkages. This study may open up possibilities for the synthesis of novel frameworks with T–M–T linkages. FJ-1 exhibits stereospecificity and chiral molecular recognition between guest CMC and inorganic structural motif. The chirality and symmetry of the guest CMC template can induce that of the inorganic motif/framework. In addition, the symmetry of the achiral guest was transferred to the inorganic motif. These phenomena originate from hydrogen bonding between the guest and the inorganic motif/framework.

Experimental Section

Synthesis of FJ-1a/FJ-1b: GeO_2 (0.152 g) was dissolved in a mixture of water (0.5 mL), ethylene glycol (1.3 mL), and en/enMe (0.4 mL), followed by $[\text{Ni}(\text{L})_3\text{Cl}_2] \cdot 2\text{H}_2\text{O}$ ($\text{L} = \text{en/enMe}$, 0.171 g). The clear solution was heated at 170°C for 7 d in a Teflon-lined steel autoclave and then cooled to room temperature. Later, complex $[\text{Ni}(\text{L})_3\text{Cl}_2] \cdot 2\text{H}_2\text{O}$ was replaced by $\text{NiCl}_2 \cdot 2\text{H}_2\text{O}$ (0.170 g) and en/enMe (1.0 mL), and FJ-1a/FJ-1b was also obtained as a pure phase. The single yellow crystals with hexagonal shape were recovered by filtration, washed by distilled water and ethanol, and air-dried without further separation (17%/15% yield based on Ge for FJ-1a/FJ-1b). Elemental analysis (%) calcd for $\text{C}_{12}\text{N}_{12}\text{H}_{51}\text{Ge}_{14}\text{Ni}_3\text{O}_{27}$ (FJ-1a): C 7.25, H 2.59, N 8.46; found: C 7.34, H 2.39, N 8.26; calcd for

C₁₈N₁₂H₆₃Ge₁₄Ni₃O₂₇ (FJ-1b): C 10.43, H 3.06, N 8.11; found: C 10.15, H 2.87, N, 7.92.

Electron-probe microanalysis (EPMA) was performed on a Shimadzu electron microprobe EPMA-8705QH₂ to analyze Ge and Ni contents. Different points were selected, both from different areas of the same crystal and from different crystals. The Ge:Ni ratio obtained by EPMA are in agreement with the formula of FJ-1a obtained from the structure refinement (obsd Ge:Ni = 1:0.208, calcd Ge:Ni = 1:0.214).

Crystal data for FJ-1a: Ni@Ge₁₄O₂₄(OH)₃·2Ni(en)₃, *M*_r = 1988.04, hexagonal, space group *P*6₂*c*, *a* = 13.5567(4), *c* = 14.6138(5) Å, *V* = 2325.96(13) Å³, *Z* = 2, *ρ* = 2.839 g cm⁻³, *μ* = 10.173 cm⁻¹, *F*(000) = 1910, GOF = 1.171. *θ*_{max} = 25.01°. A total of 5454 reflections (1417 independent, *R*_{int} = 0.0418) were measured at 293 K. Final agreement indices were *R*₁ (*wR*₂) = 0.0405 (0.0829) for 120 parameters and 1288 reflections [*I* > 2σ(*I*)].

Crystal data for FJ-1b: Ni@Ge₁₄O₂₄(OH)₃·2Ni(enMe)₃, *M*_r = 2072.19, hexagonal, space group *P*6₂*c*, *a* = 13.6681(8), *c* = 14.5642(7) Å, *V* = 2356.3(2) Å³, *Z* = 2, *ρ* = 2.921 g cm⁻³, *μ* = 10.049 cm⁻¹, *F*(000) = 2006, GOF = 1.047. *θ*_{max} = 27.53°. A total of 9190 reflections (1861 independent, *R*_{int} = 0.1042) were measured at 293 K. Final agreement indices were *R*₁ (*wR*₂) = 0.0741 (0.1684) for 103 parameters and 1422 reflections [*I* > 2σ(*I*)].

Data were collected on a Siemens SMART CCD diffractometer with graphite-monochromated MoK_α radiation (*λ* = 0.71073 Å) at room temperature. All absorption corrections were performed with the SADABS program. The structure was solved by direct methods and refined by full-matrix least-squares methods on *F*² using the SHELXTL97 program package. All non-hydrogen atoms (except N1, N2, N2', C1, C2, C3, C4 in FJ-1b) were refined anisotropically. The unique N atoms coordinated to Ni3 in FJ-1a and FJ-1b occupy two split positions (N2, N2') and have occupancies of 0.5. The C2 and C4 (methyl group of enMe) atoms of FJ-1b have occupancies of 0.5. The positions of H atoms (except those on C2 in FJ-1a and N1, N2, N2', C1, C3 in FJ-1b) were placed geometrically and refined in a riding model. CCDC-277021/280327 (FJ-1a/FJ-1b) contain the supplementary crystallographic data for this paper. These data can be obtained free of charge from the Cambridge Crystallographic Data Centre via www.ccdc.cam.ac.uk/data_request/cif.

Received: July 12, 2005

Published online: October 5, 2005

Keywords: germanium · microporous materials · nickel · solvothermal synthesis · template synthesis

- [1] a) A. K. Cheetham, G. Férey, T. Loiseau, *Angew. Chem.* **1999**, *111*, 3466; *Angew. Chem. Int. Ed.* **1999**, *38*, 3268; b) M. E. Davis, *Nature* **2002**, *417*, 813.
- [2] a) M. E. Davis, C. Saldarriaga, C. Montes, J. M. Garces, C. Crowder, *Nature* **1988**, *331*, 698; b) Q. Hu, R. Xu, S. Li, Z. Ma, J. M. Thomas, R. H. Jones, A. M. Chippindale, *J. Chem. Soc. Chem. Commun.* **1992**, 875; c) M. Esterman, L. B. McCusker, C. Baerlocher, A. Merrouche, H. Kessler, *Nature* **1991**, *352*, 320; d) N. Guillou, Q. Gao, M. Nogués, R. E. Morris, M. Hervieu, G. Férey, A. K. Cheetham, *C. R. Acad. Sci. Paris Ser. II* **1999**, *2*, 387; e) G.-Y. Yang, S. C. Sevov, *J. Am. Chem. Soc.* **1999**, *121*, 8389; f) N. Guillou, Q. Gao, P. M. Forster, J.-S. Chang, M. Nogués, S.-E. Park, G. Férey, A. K. Cheetham, *Angew. Chem.* **2001**, *113*, 2913; *Angew. Chem. Int. Ed.* **2001**, *40*, 2831; g) C.-H. Lin, S.-L. Wang, K.-H. Lii, *J. Am. Chem. Soc.* **2001**, *123*, 4649; h) Y. Zhou, H. Zhu, Z. Chen, M. Chen, Y. Xu, H. Zhang, D. Zhao, *Angew. Chem.* **2001**, *113*, 2224; *Angew. Chem. Int. Ed.* **2001**, *40*, 2166; i) J. Plévert, T. M. Gentz, A. Laine, H. Li, V. G. Young, O. M. Yaghi, M. O'Keeffe, *J. Am. Chem. Soc.* **2001**, *123*, 12706; j) L. Tang, M. S. Dadachov, X. Zou, *Chem. Mater.* **2005**, *17*, 2530; k) J. Zhu, X. Bu, P. Feng, G. D. Stucky, *J. Am. Chem. Soc.* **2002**, *124*, 11563.
- [3] a) H. Li, A. Laine, M. O'Keeffe, O. M. Yaghi, *Science* **1999**, *283*, 1145; b) N. Zheng, X. Bu, B. Wang, P. Feng, *Science* **2002**, *298*, 2366; c) N. Zheng, X. Bu, P. Feng, *Nature* **2003**, *426*, 428; d) X. Bu, N. Zheng, P. Feng, *Chem. Eur. J.* **2004**, *10*, 3356.
- [4] a) K. Morgan, G. Gainsford, N. Milestone, *J. Chem. Soc. Chem. Commun.* **1995**, 425; b) Y. Wang, J. Yu, M. Guo, R. Xu, *Angew. Chem.* **2003**, *115*, 4223; *Angew. Chem. Int. Ed.* **2003**, *42*, 4089, and references therein; c) Y. Wang, J. Yu, Y. Li, Z. Shi, R. Xu, *Chem. Eur. J.* **2003**, *9*, 5048, and references therein.
- [5] a) D. J. Williams, J. S. Kruger, A. F. McLeroy, A. P. Wilkinson, *Chem. Mater.* **1999**, *11*, 2241, and references therein; b) K. Morgan, G. Gainsford, N. Milestone, *Chem. Commun.* **1997**, 61.
- [6] a) Y. Wang, J. Yu, Y. Li, Z. Shi, R. Xu, *J. Solid State Chem.* **2003**, *170*, 176, and references therein; b) S. M. Stalder, A. P. Wilkinson, *Chem. Mater.* **1997**, *9*, 2168.
- [7] J. Yu, Y. Wang, Z. Shi, R. Xu, *Chem. Mater.* **2001**, *13*, 2972.
- [8] G.-Y. Yang, S. C. Sevov, *Inorg. Chem.* **2001**, *40*, 2214.
- [9] a) C. Cascales, E. Gutierrez-Puebla, M. Iglesias, M. A. Monge, C. Ruiz-Valero, *Angew. Chem.* **1999**, *111*, 2592; *Angew. Chem. Int. Ed.* **1999**, *38*, 2436; b) X. Bu, P. Feng, G. D. Stucky, *Chem. Mater.* **2000**, *12*, 1811; c) N. N. Julius, A. Choudhury, C. N. R. Rao, *J. Solid State Chem.* **2003**, *170*, 124; d) H.-X. Zhang, J. Zhang, S.-T. Zheng, G.-Y. Yang, *Inorg. Chem.* **2003**, *42*, 6595; e) Z.-E. Lin, J. Zhang, S.-T. Zheng, G.-Y. Yang, *Micropor. Mesopor. Mater.* **2004**, *74*, 205.
- [10] a) M. Grenz, E. Hahn, W.-W. du Mont, J. Pickardt, *Angew. Chem.* **1984**, *96*, 69; *Angew. Chem. Int. Ed. Engl.* **1984**, *23*, 61; b) W. A. Herrmann, M. Denk, J. Behm, W. Scherer, F.-R. Klingan, H. Bock, B. Solouki, M. Wagner, *Angew. Chem.* **1992**, *104*, 1489; *Angew. Chem. Int. Ed. Engl.* **1992**, *31*, 1485; c) K. E. Litz, J. E. Bender IV, J. W. Kampf, M. M. Banaszak Holl, *Angew. Chem.* **1997**, *109*, 516; *Angew. Chem. Int. Ed. Engl.* **1997**, *36*, 496; d) P. Bazinet, G. P. A. Yap, D. S. Richeson, *J. Am. Chem. Soc.* **2001**, *123*, 11162; e) J. E. Bender IV, A. J. Shusterman, M. M. Banaszak Holl, J. W. Kampf, *Organometallics* **1999**, *18*, 1547.
- [11] a) G. Wulfsberg in *Inorganic Chemistry*, University Science Books, Sausalito, **2000**, p. 32; b) L. Pauling, *The Nature of the Chemical Bond*, 3rd ed., Cornell University Press, Ithaca, **1960**, p. 410; c) A. F. Wells, *Structural Inorganic Chemistry*, 5th ed., Oxford University Press, Oxford, **1984**, p. 1279.
- [12] a) H. Li, O. M. Yaghi, *J. Am. Chem. Soc.* **1998**, *120*, 10569; b) M. S. Dadachov, X. Zou, *Microporous Mesoporous Mater.* **2000**, *41*, 183; c) C. Cascales, E. Gutiérrez-Puebla, M. Iglesias, M. A. Monge, C. Ruiz-Valero, N. Snejko, *Chem. Commun.* **2000**, 2145.
- [13] R. L. Carlin, *Magnetochemistry*, Springer, Berlin, **1986**, chap. 4.
- [14] a) M. Hartmann, L. Kevan, *Chem. Rev.* **1999**, *99*, 635; b) A. M. Prakash, T. Wasowicz, L. Kevan, *J. Phys. Chem.* **1996**, *100*, 15947.
- [15] C. Ruiz-Pérez, P. A. Lorenzo Luis, F. Lloret, M. Julve, *Inorg. Chim. Acta* **2002**, *336*, 131.
- [16] K.-Y. Choi, H. Ryu, Y.-M. Lim, N.-D. Sung, U.-S. Shin, M. Suh, *Inorg. Chem. Commun.* **2003**, *6*, 412.
- [17] P. Feng, *Chem. Commun.* **2001**, 1668; and references therein.
- [18] a) P. Behrens, G. D. Stucky in *Comprehensive Supramolecular Chemistry*, Vol. 7 (Eds.: G. Albert, T. Bein), Elsevier, New York, **1996**, p. 721; b) I. Braum, G. Ihlein, F. Laeri, J. U. Nockel, G. Schulz-Ekloff, F. Schüth, U. Vietze, O. Weiss, D. Wöhrle, *Appl. Phys. B* **2000**, *70*, 335.
- [19] A. Ranfagni, M. Mugni, M. Viliani, M. P. Fontana, *Adv. Phys.* **1983**, *32*, 823.
- [20] G. Blasse, *Prog. Solid Bonding* **1999**, *42*, 1.

Redox-Switchable Phase Tags for Recycling of Homogeneous Catalysts**

Marcus Süßner and Herbert Plenio*

Dedicated to Professor H. W. Roesky
on the occasion of his 70th birthday

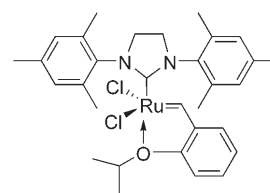
A fundamental problem of homogeneous catalysis is the difficulties associated with the recovery of the molecular catalyst after product formation, thus leading to loss of the catalyst and contamination of the reaction products with heavy-metal impurities.^[1,2] This problem is aggravated by the fact that increasingly sophisticated complexes with tailor-made ligands result in high-value catalysts. Consequently, numerous concepts have been tested to overcome the imminent problem of catalyst/product separation,^[3,4] such as soluble polymeric catalysts,^[5,6] biphasic solvent systems which involve various solvent combinations (namely, organic/organic,^[7] fluoruous/organic,^[8] ionic liquids/supercritical fluids,^[9] aqueous/organic^[10,11]), nanofiltration,^[12,13] incarcerated nanoparticles,^[14,15] interphase catalysts,^[16] supported liquid films,^[17] and immobilization of molecular catalysts on organic^[18] or inorganic supports.^[19]

Clearly, these approaches rely on manipulation of the solubility properties;^[20] most often, distinct solubility properties are imposed by so-called phase tags, such as sulfonate groups (in triphenyl phosphorothionates),^[21] fluoruous ponytails,^[8] or polar and nonpolar soluble polymers.^[22,23]

Such solubility-determining groups are referred to as phase tags and are an important tool in separation strategies.^[24] Despite the success of this approach, certain disadvantages of this concept are apparent. Clearly, two solvents are required in biphasic systems, one to hold the product and the other for the tagged catalyst complex. Both solvents need to be compatible with the catalytic reaction, their mutual solubility should be low, the leaching of the catalyst into the product-containing solvent has to be minimized, and the partition coefficient of the reactants/products needs to be in a suitable range. Alternatively, the tagged catalyst can be precipitated from the reaction solvent by addition of another solvent after the catalytic transformation. However, very large amounts of this second solvent are typically needed to effect the quantitative precipitation of the tagged catalyst.

To avoid these problems, we propose herein a strategy for the separation of homogeneous catalysts from the products of the reaction based on a new class of solubility-determining groups, which we term redox-switchable phase tags. In contrast to other phase tags, the solubility properties of redox-switchable phase tags can be altered through the employment of tag-centered reactions, thus resulting in drastic changes in the polarity of the respective solubility-determining group. In this manner, it should be possible to exert perfect control over the solubility behavior of catalysts^[25] by using a single solvent. We decided to utilize tag-centered redox reactions which mutate neutral (lipophilic) tags into charged (lipophobic) tags and back. One significant advantage of such an approach is that drastic changes in the solubility behavior can be effected with only very small amounts of switching reagent, which is stoichiometric with respect to the catalytic amounts of catalyst complex present in a reaction mixture.

To illustrate this principle, we chose a ruthenium-based catalyst of the Grubbs–Hoveyda type for olefin metathesis as numerous recycling concepts have been tested on these high-value catalysts because of their effectiveness.^[26–32] Prior to the synthesis of a modified olefin-metathesis catalyst of the Grubbs–Hoveyda type with redox-switchable tags, a suitable redox-active group needed to be found. We chose a ferrocene (Fc) unit because such metallocenes are well-behaved outer-sphere redox reagents that display a high degree of reversibility. Furthermore, the redox potential of the ferrocene unit can be varied readily over a large potential range through the attachment of different substituents on the cyclopentadienyl rings,^[33] which is clearly a very important property as the redox potential of the redox tag must be fine-tuned to avoid electron-transfer reactions that involve the catalytically active metal center. The Fe^{II}/Fe^{III} redox couple of the ferrocene unit should differ by between 236 mV (ratio of Fe/Ru oxidation = 100:1) and 354 mV (1000:1) from that of the olefin-metathesis catalyst to be useful. Thus, the Ru^{II}/Ru^{III} redox potential of the Grubbs–Hoveyda catalyst was first established by cyclic



Grubbs–Hoveyda catalyst

voltammetry (CV). The CV waves are well behaved, that is, they are fully reversible and the redox potential was +0.85 V in CH₂Cl₂ (Figure 1). As the redox potential of ferrocene itself is +0.46 V under the same conditions, we conclude that any ferrocene compound with electron-donating substituents can undergo independent Fe^{II}/Fe^{III} redox reactions that do not interfere with the catalytically active Ru^{II} center.

The synthesis of a ferrocenyl-tagged olefin-metathesis catalyst is shown in Scheme 1. We chose a monoalkylated ferrocene as the redox tag, as its redox potential fulfils the

[*] Dipl.-Ing. M. Süßner, Prof. Dr. H. Plenio
Anorganische Chemie im Zintl-Institut des FB Chemie
TU Darmstadt, Petersenstrasse 18
64287 Darmstadt (Germany)
Fax: (+49) 6151-16-6040
E-mail: plenio@tu-darmstadt.de

[**] This work was supported by the TU Darmstadt and the DFG. We thank Dr. A. Köllhofer for assistance with the electrochemical experiments.

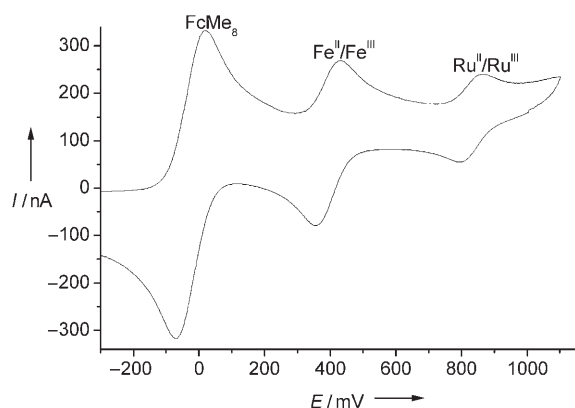
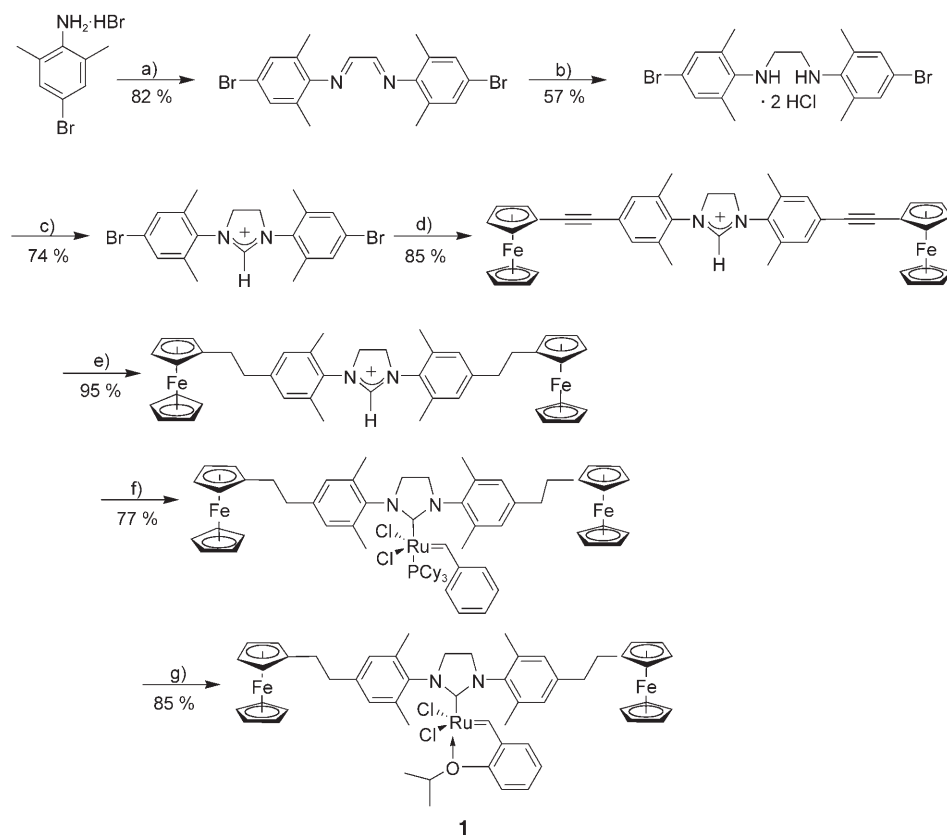


Figure 1. Cyclic voltammogram of the diferrocenyl-tagged Grubbs-Hoveyda-type catalyst **1**. $\Delta E_{1/2}$ ($\text{Fe}^{\text{II}}/\text{Fe}^{\text{III}}$) = +0.410 V (70 mV), $\Delta E_{1/2}$ ($\text{Ru}^{\text{II}}/\text{Ru}^{\text{III}}$) = +0.847 V (60 mV) referenced versus FcMe_8 (−0.010 V) in CH_2Cl_2 .



Scheme 1. Synthesis of the ferrocenyl-tagged olefin-metathesis catalyst **1** of the Grubbs-Hoveyda type: a) NEt_3 , EtOH, HCOOH , 24 h; b) 1. LiAlH_4 , THF; 2. HCl ; c) $\text{HC}(\text{OEt})_3$, 130 °C, 24 h; d) FcCCH , Na_2PdCl_4 , CuI , $\text{Ad}_2\text{PBn-HBr}$, DMSO, HNiPr_2 , 80 °C, 24 h; e) Pd/C 5 bar H_2 , 5 h, RT; f) KOtBu , Grubbs I catalyst, toluene, THF; g) 2-isopropoxystyrene, CuCl , CH_2Cl_2 , 40 °C, 1 h. Cy = cyclohexyl, Ad = adamantyl, DMSO = dimethyl sulfoxide.

criteria defined above. 4-Bromo-2,6-dimethylaniline was treated with glyoxal to give the respective 1,2-diimine in 75 % yield, which was reduced to the corresponding 1,2-diamine in 80 % yield using LiAlH_4 . Ring-closure with $\text{HC}(\text{OEt})_3$ yielded the respective imidazolium salt in 75 % yield. For the introduction of the redox tag, the aryl bromide

functionalities of this salt underwent Sonogashira coupling to ferrocenyl acetylene, thus giving the coupled product in 85 % yield. It should be noted that the reaction conditions for the Sonogashira coupling are critical: First, the imidazolium chloride displays solubility only in a few polar solvents, and second, the number of suitable bases is rather limited because the competing deprotonation of the imidazolium ring must be suppressed as the corresponding N-heterocyclic carbene appears to inhibit the Pd catalyst.

Next, the acetylene linker was reduced with H_2 over Pd/C to the $-\text{C}_2\text{H}_4-$ bridge in almost quantitative yield. The reason for this transformation is threefold: 1) an alkyl substituent attached to the ferrocene unit is electron donating rather than electron withdrawing, which consequently leads to an increase in the difference in the redox potential between the $\text{Fe}^{\text{II}}/\text{Fe}^{\text{III}}$ and $\text{Ru}^{\text{II}}/\text{Ru}^{\text{III}}$ redox couple; 2) the hydrogenation of the acetylene linker electronically decouples the redox-active ferrocene group from the catalytically active center to avoid any undesired influence of the ferrocene cation on the catalytically active center after oxidation; 3) the absence of a triple bond avoids potential problems in olefin metathesis.

Finally, the imidazolium cation is deprotonated with KOtBu and treated with the Grubbs I catalyst; subsequently, the remaining PCy_3 ligand and the benzylidene in the resulting complex are substituted with 2-isopropoxystyrene to yield the desired redox-tagged Grubbs-Hoveyda-type catalyst **1**.

The catalytic properties of **1** are demonstrated in the ring-closing metathesis (RCM) reaction of *N*-tosyldiallylamine (Figure 2). The unperturbed reaction (●) proceeds to completion exactly as expected for such catalysts. In a second run (■), a solution of two equivalents of oxidation reagent ($[\text{FcCOCH}_3][\text{CF}_3\text{SO}_3]$ as a 10 % solution in 0.1 mL of CH_2Cl_2 ($\Delta E = +0.73$ V)) with respect to the catalyst was added after exactly 60 minutes. The two ferrocenyl tags were oxidized virtually instantaneously, and the resulting dication **1**²⁺ precipitates from the solution of toluene within a few seconds. The precipitated catalyst does not display significant catalytic activity, as can be seen in the plot of conversion versus time (Figure 2, ■). The product of the catalytic reaction can be readily separated from the pre-

cipitated catalyst by filtration, which is preferably done after completion of the reaction. The catalyst can be reactivated (namely, redissolved) at any time by addition of two equivalents of a reducing agent (1,1',2,2',3,3',4,4'-octamethylferrocene (FcMe_8)), which was carried out after 135 minutes in our experiment. It can be seen that the catalytic activity is

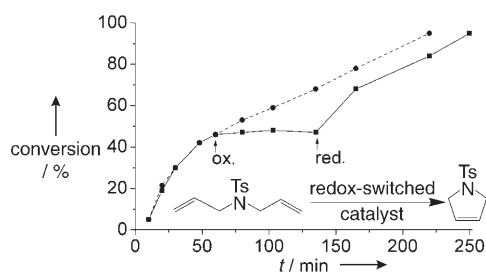


Figure 2. Switching of the olefin-metathesis catalyst **1** in toluene, monitored by GC: unperturbed RCM (●), off/on switched RCM (■). Ox. and red. denote the respective oxidation and reduction of the redox tag with $[\text{FcCOCH}_3][\text{CF}_3\text{SO}_3]$ and FcMe_8 . Ts = *p*-toluenesulfonyl.^[35]

immediately restored to its initial value and the reaction proceeds to completion (not shown in Figures 2 and 3).^[34]

Following this procedure, the catalyst can also be switched off and on^[36,37] several times after completion of the RCM reaction, thus allowing multiple recycling of the catalyst. We tested redox-switching of the phase tag for three consecutive reaction cycles composed of 1) olefin metathesis, 2) oxidation with an acetyl ferrocene cation, 3) precipitation and separation, and 4) reduction and redissolution of the catalyst, and we observed quantitative yields for all the reaction steps. We probed the identity of the recycled catalyst after a single oxidation/reduction sequence $\mathbf{1} \rightarrow \mathbf{1}^{2+} \rightarrow \mathbf{1}$ and identified the initial Grubbs–Hoveyda-type catalyst **1** by ^1H NMR spectroscopy.

Furthermore, it is also possible to adjust the rate of the catalytic transformation as desired by reversible precipitation of a limited amount of the catalyst after addition of substoichiometric amounts of the oxidation reagent. Although the curve denoted by ■ in Figure 3 displays a single off/on switching event, the double-switched RCM reaction in the curve denoted by ● shows an off/on switching event during the first 30 minutes and a partial-off event after 50 minutes, with a full restoration of catalytic activity after 75 minutes.

Instead of monitoring the switching events by gas-chromatographic or NMR spectroscopic analysis, the removal of the catalyst from the solution can be followed readily by

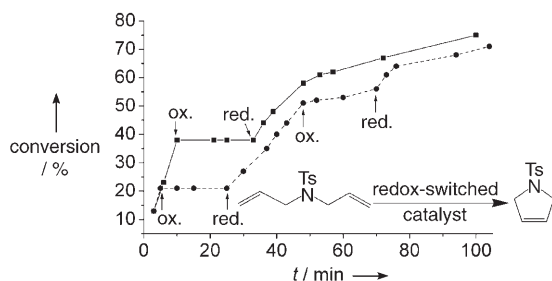


Figure 3. Switching of the olefin-metathesis catalyst **1** in C_6D_6 , monitored by ^1H NMR spectroscopy: single-switch RCM (■), off/on/partially-off/on switched RCM (●). Ox. = oxidation and red. = reduction for the redox tag with $[\text{FcCOCH}_3][\text{CF}_3\text{SO}_3]$ and FcMe_8 , respectively. Two equivalents of the oxidant were added to switch off the catalyst and one equivalent to partially switch off the catalyst.

monitoring the UV/Vis spectrum of the reaction mixture; catalyst **1** is characterized by a strong Ru-centered absorption band at 375 nm, the intensity of which reflects the concentration of the catalyst in solution.

As an alternative to chemical redox switching, which requires stoichiometric amounts of redox reagent (only with respect to the catalyst), electrochemical triggering of the tag switching only requires an applied current. Ideally, the catalyst is electrodeposited on the surface of an electrode on oxidation and is redissolved on application of a reductive potential. In this manner, the transfer of the loaded electrode from a solution containing the product into a solution containing fresh reactants allows efficient reuse of the catalyst. For the coulometric deposition of a redox-tagged catalyst, solvents are needed that display a reasonable conductivity after addition of supporting electrolytes. Consequently, electrolysis in toluene is not possible as the currents observed are far too small to effect electrolysis within a reasonable time frame, and so slightly more polar solvents are required. We tested a number of solvents of intermediate polarity and were able to quantitatively oxidize **1** electrochemically. However, the minute concentrations of catalytically active dication used for the RCM reactions are soluble in solvents of intermediate polarity (e.g., CH_2Cl_2). Therefore, the synthesis of new catalysts with multiple redox tags is required to solve these problems.^[38]

In conclusion, we have demonstrated that redox-switchable phase tags, whose solubility properties are controlled by redox reagents or electrochemical redox processes, can be used to effectively switch the catalytic activity of an olefin-metathesis catalyst of the Grubbs–Hoveyda type on and off. More importantly, this approach allows the efficient separation of such catalysts from the products of a catalytic reaction at any time during the reaction and after its completion. We expect the principle of redox-switchable phase tags to become a general concept for control over solubility properties and, consequently, the recyclability of a wide variety of homogeneous catalysts. We are currently working towards the application of this principle several to other types of homogeneous catalytic processes, such as enantioselective hydrogenation and various Pd-mediated cross-coupling reactions.

Received: June 22, 2005

Publication delayed at author's request.

Keywords: carbenes · cyclic voltammetry · homogeneous catalysis · olefin metathesis · phase tags

- [1] C. E. Garrett, K. Prasad, *Adv. Synth. Catal.* **2004**, 346, 889.
- [2] K. Königsberger, G.-P. Chen, R. R. Wu, M. J. Girgis, K. Prasad, O. Repic, T. J. Blacklock, *Org. Process Res. Dev.* **2003**, 7, 733.
- [3] J. A. Gladysz, *Chem. Rev.* **2002**, 102, 3215.
- [4] D. J. Cole-Hamilton, *Science* **2003**, 299, 1702.
- [5] D. E. Bergbreiter, *Chem. Rev.* **2002**, 102, 3345.
- [6] M. an der Heiden, H. Plenio, *Chem. Eur. J.* **2004**, 10, 1789.
- [7] A. Köllhofer, H. Plenio, *Chem. Eur. J.* **2003**, 9, 1416.
- [8] M. Wende, J. A. Gladysz, *J. Am. Chem. Soc.* **2003**, 125, 5861.

- [9] P. B. Webb, M. F. Sellin, T. E. Kunene, S. Williamson, A. M. Z. Slawin, D. J. Cole-Hamilton, *J. Am. Chem. Soc.* **2003**, *125*, 15577.
- [10] D. E. Bergbreiter, P. L. Osburn, T. Smith, C. Li, J. D. Frels, *J. Am. Chem. Soc.* **2003**, *125*, 6254.
- [11] *Aqueous-Phase Organometallic Chemistry*, (Eds.: B. Cornils, W. Herrmann), Wiley-VCH, Weinheim, **1998**.
- [12] A. Datta, K. Ebert, H. Plenio, *Organometallics* **2003**, *22*, 4685.
- [13] H. P. Dijkstra, G. P. M. vanKlink, G. vanKoten, *Acc. Chem. Res.* **2002**, *35*, 798.
- [14] R. W. J. Scott, O. M. Wilson, S.-K. Oh, E. A. Kenik, R. M. Crooks, *J. Am. Chem. Soc.* **2004**, *126*, 15583.
- [15] K. Okamoto, R. Akiyama, H. Yoshida, T. Yoshida, S. Kobayashi, *J. Am. Chem. Soc.* **2005**, *127*, 2125.
- [16] F. Gelman, J. Blum, D. Avnir, *J. Am. Chem. Soc.* **2002**, *124*, 14460.
- [17] C. P. Mehnert, R. A. Cook, N. C. Dispenziere, M. Afeworki, *J. Am. Chem. Soc.* **2002**, *124*, 12932.
- [18] C. A. McNamara, M. J. Dixon, M. Bradley, *Chem. Rev.* **2002**, *102*, 3275.
- [19] J. Sommer, Y. Yang, D. Rambow, J. Blümel, *Inorg. Chem.* **2004**, *43*, 7561.
- [20] V. K. Dioumaev, R. M. Bullock, *Nature* **2003**, *424*, 530.
- [21] C. W. Kohlpaintner, R. W. Fischer, B. Cornils, *Appl. Catal. A* **2001**, *221*, 219.
- [22] A. Datta, H. Plenio, *Chem. Commun.* **2003**, 1504.
- [23] J. Hillerich, H. Plenio, *Chem. Commun.* **2003**, 3024.
- [24] D. P. Curran, *Angew. Chem.* **1998**, *110*, 1230; *Angew. Chem. Int. Ed.* **1998**, *37*, 1174 (Erratum: D. P. Curran, *Angew. Chem.* **1998**, *110*, 2569; *Angew. Chem. Int. Ed.* **1998**, *37*, 2292).
- [25] M. E. Honigfort, W. J. Brittain, T. Bosanac, C. S. Wilcox, *Macromolecules* **2002**, *35*, 4849.
- [26] K. Grela, M. Tryznowski, M. Bieniek, *Tetrahedron Lett.* **2002**, *43*, 9055.
- [27] J. J. V. Veldhuizen, S. B. Garber, J. S. Kingsbury, A. H. Hoveyda, *J. Am. Chem. Soc.* **2002**, *124*, 4954.
- [28] L. Jafarpour, M.-P. Heck, C. Baylon, H. M. Lee, C. Mioskowski, S. P. Nolan, *Organometallics* **2002**, *21*, 671.
- [29] Q. Yao, Y. Zhang, *Angew. Chem.* **2003**, *115*, 3517; *Angew. Chem. Int. Ed.* **2003**, *42*, 3395.
- [30] S. B. Garber, J. S. Kingsbury, B. L. Gray, A. H. Hoveyda, *J. Am. Chem. Soc.* **2000**, *122*, 8168.
- [31] M. R. Buchmeiser, *New J. Chem.* **2004**, *28*, 549.
- [32] S. J. Connon, A. M. Dunne, S. Blechert, *Angew. Chem.* **2002**, *114*, 3989; *Angew. Chem.* **2002**, *41*, 3835.
- [33] N. G. Connelly, W. E. Geiger, *Chem. Rev.* **1996**, *96*, 877.
- [34] Dynamic phase-tag switching of **1**: Diallyltosylamide (25 mg, 0.1 mmol) was added to a solution of **1** (0.8 mg, 1 mol %) in toluene (10 mL), and the reaction mixture was warmed to 35 °C. After 3 h, the solution was cooled to room temperature with subsequent addition of [FcCOCH₃][BF₄] (2 equiv) in CH₂Cl₂ (200 mL; *c* = 0.01 mol L⁻¹) to oxidize/precipitate **1**²⁺. The solution was filtered over cotton wool, and the volatiles were evaporated to obtain the crude product. The cotton wool was rinsed with CH₂Cl₂ (0.5 mL) to dissolve **1**²⁺, which was subsequently treated with a solution of FcMe₈ (2.1 equiv) in toluene (300 mL; *c* = 7.0·10⁻³ mol L⁻¹) to regenerate **1**. After addition of fresh toluene (10 mL) and diallyltosylamide (25 mg, 0.1 mmol), a new reaction cycle was started. The whole procedure was repeated three times, and quantitative product formation was observed after each cycle. The switching on/off of catalyst **1** during the reaction was carried out by addition of solutions of [FcCOCH₃][BF₄] (**1**→**1**²⁺ = off) and FcMe₈ (**1**²⁺→**1** = on) as oxidizing and reducing agents, respectively. Spectroscopic data of **1**: ¹H NMR (500 MHz, C₆D₆): δ = 1.37 (d, 6H, *J* = 6.0 Hz, (CH₃)₂CHOAr), 2.61 (bs, 12H, *ortho*-CH₃), 2.73 (m, 4H, CH₂), 2.86 (m, 4H, CH₂), 3.47 (s, 4H, NCH₂CH₂N), 4.03 ("t", 4H, *J* = 1.8 Hz, FcH), 4.09 (s, 10H, FcH), 4.12 ("t", 4H, *J* = 1.8 Hz, FcH), 4.52 (sept, 1H, *J* = 6.2 Hz, (CH₃)₂CHOAr), 6.35 (d, 1H, *J* = 8.3 Hz, sp² CH), 6.73 (t, 1H, *J* = 7.4 Hz, sp² CH), 7.05 (s, 4H, *meta*-CH), 7.10 (m, 1H, sp² CH), 7.20 (dd, 1H, *J* = 7.6, 1.6 Hz, sp² CH), 16.74 ppm (s, 1H, RuCHAR); ¹³C NMR (125.75 MHz, C₆D₆): δ = 19.5, 20.2, 29.5, 36.6, 50.0, 66.4, 67.1, 67.6, 73.7, 87.5, 111.9, 120.7, 121.1, 123.2, 127.7, 142.0, 144.5, 151.3, 211.6, 293.5 ppm.
- [35] The rates of the catalytic reactions depicted in Figures 2 and 3 are different as the concentration of the catalyst and substrates were individually adjusted to suit the sensitivity of GC-FID (Figure 2) and ¹H NMR spectroscopic detection (Figure 3).
- [36] E. Katz, R. Baron, I. Willner, *J. Am. Chem. Soc.* **2005**, *127*, 4060.
- [37] L. Kovbasyuk, R. Krämer, *Chem. Rev.* **2004**, *104*, 3161.
- [38] D. Schoeps, H. Plenio, unpublished results.

Activity Probes

DOI: 10.1002/anie.200501738

Design of a Mechanism-Based Probe for Neuraminidase To Capture Influenza Viruses**

Chun-Ping Lu, Chien-Tai Ren, Yi-Ning Lai, Shih-Hsiung Wu, Wei-Man Wang, Jean-Yin Chen, and Lee-Chiang Lo**

Influenza viruses, which cause upper respiratory tract problems in humans, have long been a major threat to public health.^[1] It is estimated that 10–20 % of the general popula-

[*] C.-P. Lu,^[+] [§] Dr. C.-T. Ren,[§] Y.-N. Lai, Prof. S.-H. Wu^[+] ^[++]

Institute of Biological Chemistry, Academia Sinica
Taipei 115 (Taiwan)

Fax: (+ 886) 2-2653-9142

E-mail: shwu@gate.sinica.edu.tw

W.-M. Wang, J.-Y. Chen, Prof. L.-C. Lo

Department of Chemistry, National Taiwan University
Taipei 106 (Taiwan)

Fax: (+ 886) 2-2362-1979

E-mail: lclo@ntu.edu.tw

[+] Institute of Biochemical Sciences, National Taiwan University
Taipei 106, (Taiwan)

[++] Genomics Research Center, Academia Sinica
Taipei 115 (Taiwan)

[§] These authors contributed equally to this work.

[**] Influenza A virus (A/WSN/33) was a gift from Dr. Shin-Ru Shih, Chang Gung University, Taiwan) and polyclonal anti-FluA antibody was a gift from Dr. Hour-Young Chen (Center for Disease Control Taiwan). Japanese encephalitis virus (JEV, Taiwanese strain, RP-9) and the mouse monoclonal antibody specific for this virus were kindly provided by Dr. Yi-Ling Lin (IBMS Academia Sinica). Zanamivir was a gift from GlaxoWellcome Research and Development Ltd. (Stevenage, UK) and from Prof. Ching-Shih Chen (The Ohio State University, OH). We thank Prof. Yulin Lam for proof-reading the manuscript. This work was supported by the National Science Council (Grant nos. NSC92-2113M-001-023 to S.-H.W. and NSC93-3112-B-002-001 to L.-C.L.).



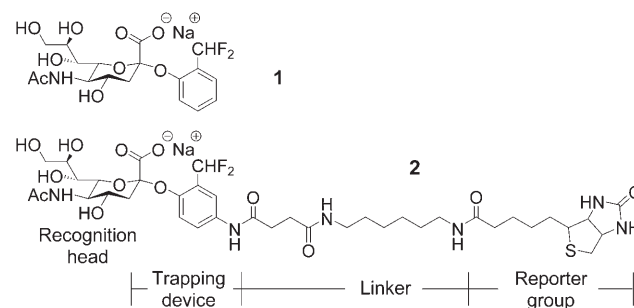
Supporting information for this article is available on the WWW under <http://www.angewandte.org> or from the author.

tion are affected in seasonal epidemics. Some devastating outbreaks recorded in history even claimed millions of lives worldwide.^[2] Influenza viruses are typically spherical with a diameter of about 100 nm.^[3] The pathogenic properties of the viruses have been extensively investigated.^[4] Significant advances in therapeutic treatments and in the detection of the viruses have been made in recent years as a result of this information. Among the limited number of proteins that are encoded by the viral RNA segments, two surface glycoproteins, namely, hemagglutinin (HA) and neuraminidase (NA), have often been the focus of research. These two surface glycoproteins play important roles in the infection process; HA is responsible for the binding of viruses to the host cells, whereas NA is involved in the budding process.^[5] Although the surface antigens of the viruses mutate frequently to avert attacks from the immune system of the hosts, the critical catalytic activity of NA has to be maintained for successful infection and propagation. This special feature makes it an excellent candidate for research.^[6]

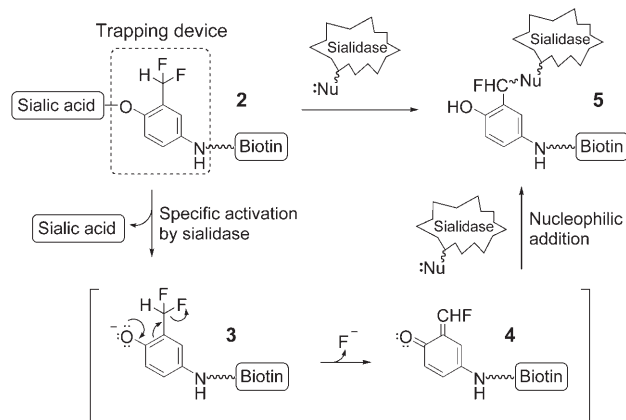
NA (sialidase, *N*-acetylneuraminosyl glycohydrolase, EC 3.2.1.18) is an *exo*-glycosidase that hydrolyzes the linkage of sialic acid residues, which are mostly found as terminal constituents of glycoconjugates. X-ray crystallographic information about the active site of NA has revealed important residues involved in the recognition and binding of sialic acid.^[7] This has assisted in the development of several reversible inhibitors of NA, such as zanamivir and oseltamivir, which have been approved for the treatment of influenza.^[8] Recently, McKimm-Breschkin et al. have demonstrated that ligands derived from biotin-conjugated zanamivir were able to bind influenza virion on microtiter plates; this could in turn serve as a basis for a diagnostic method.^[9] Besides influenza viruses, many NA-containing microorganisms are pathogenic and it has been proposed that this enzyme plays an important role in the pathogenicity of these infections.^[10] We therefore envision that the development of activity probes that selectively form a covalent linkage with NA would be of great value, as demonstrated by the application for capturing the virus particles in this report.

Chemical probes that are able to form covalent linkages with hydrolase subfamilies have proven to be a powerful tool in modern proteomics studies.^[11] We have previously developed activity probes for hydrolases such as phosphatases and β -glucosidase.^[12] The concept for the design of these activity probes originated from suicide substrates, or mechanism-based inhibitors, of enzymes.^[13] This approach is unique as the probes themselves are also the substrates of the corresponding hydrolases. The probes can be selectively activated once the recognition head is cleaved by the targeting hydrolase, thereby leading to covalent modifications of the hydrolase.^[14] More importantly and closely related to this report, the mechanism-based approach has been successfully applied in the screening and selection of biocatalysts from phage-displayed libraries, such as in the selection of mutant β -lactamases and in the search for catalytic antibodies with β -galactosidase activity.^[15] Earlier studies have shown that compound **1** was a mechanism-based inhibitor of *Clostridium perfringens* NA.^[16] We thus developed probe **2** as a mechanism-based probe for NA. Probe **2** carries four structural units

in its design; a sialic acid recognition head, which is connected to an *ortho*-difluoromethylphenyl latent trapping device, a linker, and a biotin reporter group. The biotin reporter group

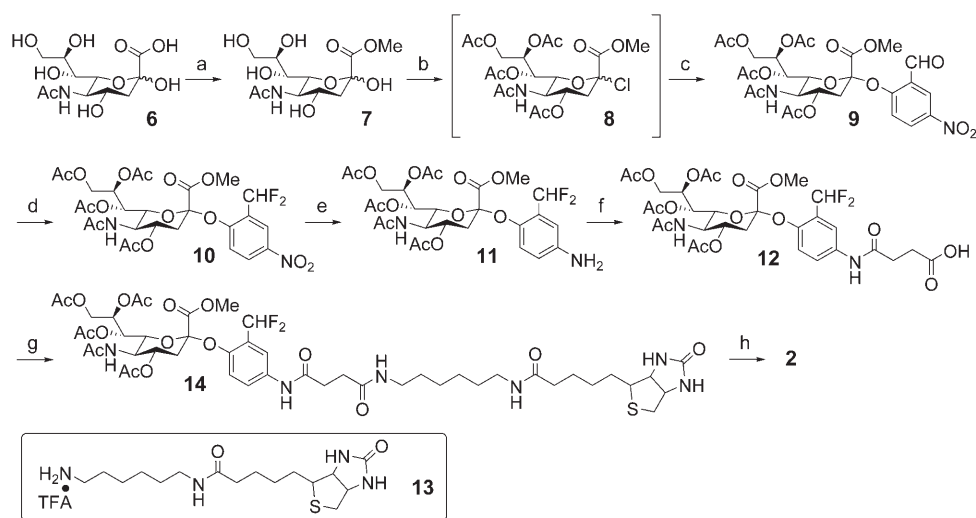


serves two functions. On one hand, it is used to visualize the labeled NA after Western blotting with streptavidin-conjugated peroxidase chemiluminescence. On the other hand, it could be used to attach the probe to the microtiter plates through avidin–biotin interactions during the virus-capturing study. When the designated glycosidic bond is cleaved by NA, the released intermediate **3** would undergo 1,4-elimination with removal of a fluoride ion to generate a reactive quinone methide, **4**. The highly reactive quinone methide intermediate **4** would alkylate nearby nucleophiles of the enzyme, thereby resulting in biotinylated adduct **5** (Scheme 1). Since the viral surface is spiked with NA, covalent attachment through NA would then lead to the capture of virus particles.



Scheme 1. Mechanism for selective activation and alkylation of neuraminidase with probe **2**.

The synthesis of probe **2** begins with a commercially available *N*-acetylneuraminic acid **6** (Scheme 2). All the synthetic procedures were combinations of efforts from previous publications.^[17] In brief, fully protected glycosyl chloride **8** was prepared and used directly for coupling with 2-hydroxy-5-nitrobenzaldehyde in a $\text{CHCl}_3/\text{H}_2\text{O}$ biphasic system by using tetrabutylammonium bromide as the phase-transfer catalyst to give compound **9**. The formyl group of compound **9** could be converted into the difluoromethyl moiety of the trapping device by the DAST reagent. The structure of the difluoromethylphenyl group in compound **10**



Scheme 2. Synthesis of probe **2** for neuraminidase. Conditions: a) MeOH, IR-120 (H⁺) resin, 92%; b) AcCl, AcOH; c) 2-hydroxy-5-nitrobenzaldehyde, Cs₂CO₃, Bu₄NBr, H₂O/CHCl₃, 67% for two steps; d) DAST, CH₂Cl₂, 47%; e) H₂, 5% Pd/C, MeOH, 95%; f) succinic anhydride, TEA, CH₂Cl₂, 94%; g) EDCI, HOBT, 13, DIEA, DMF, 75%; h) Na₂CO₃, MeOH; aqueous Na₂CO₃, 52%. TFA = trifluoroacetic acid; TEA = triethylamine; EDCI = 3-(3-dimethylaminopropyl)-1-ethylcarbodiimide; HOBT = 1-hydroxy-1H-benzotriazole; DIEA = N,N-diisopropylethylamine; DMF = N,N-dimethylformamide; DAST = (diethylamino)sulfur trifluoride.

was supported by its ¹H NMR spectroscopic data which showed a triplet at $\delta = 6.86$ ppm with a coupling constant of $^2J_{\text{H,F}} = 54.9$ Hz, a typical value for H–F coupling. A triplet at $\delta = 109.9$ ppm ($^1J_{\text{C,F}} = 237.2$ Hz) in the ¹³C NMR spectrum of **10** further confirmed the presence of the CHF₂ moiety. The nitro group of compound **10** was then reduced by catalytic hydrogenation to give amine **11**. Attachment of the linker and biotin reporter group yielded the fully protected probe **14**. Final deprotection under alkaline conditions offered the desired probe **2** after LH-20 purification.

Probe **2** was first tested for its ability to biotinylate NA obtained from *Arthrobacter ureafaciens*. *Arthrobacter ureafaciens* neuraminidase (0.8 U, Sigma) was incubated in the presence or absence of probe **2** (200 μM) at 4 °C in 100 mM ammonium acetate buffer (10 μL). Bovine serum albumin (BSA) was used as a negative control. Labeled samples were applied to a 10% polyacrylamide gel, which was then subjected to sodium dodecylsulfate (SDS) PAGE. After electrophoresis, the proteins were transferred from the gel onto a polyvinylidene fluoride (PVDF) membrane. The PVDF membrane was blocked, washed, and developed by using the enhanced chemiluminescence (ECL). Western blotting protocols as recommended by the supplier (Amersham Biosciences). The result of the Western blot analysis only shows biotinylated proteins (Figure 1). In this experiment, three biotinylated bands corresponding to isoenzymes at 88, 66, and 52 KDa were observed for NA (Lane 1).^[18] Probe **2** had no effect on BSA, as

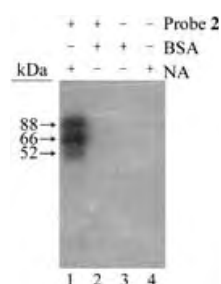


Figure 1. Western blot analysis of probe **2** labeling the *Arthrobacter ureafaciens* neuraminidase.

Probe **2** had no effect on BSA, as

shown by the lack of labeled bands (Lane 2). In the absence of the probe, neither NA nor BSA was biotinylated (Lanes 3 and 4). This result firmly supports the alkylation process described in Scheme 1. The actual labeling site was not further determined in this study, because a number of biological applications utilizing the same latent trapping device have already established the covalent-bond-forming feature.^[15,19] Moreover, Lee and co-workers recently used this activity-probe approach to characterize the catalytic domain of β -galactosidases from *Xanthomonas manihotis*, *Escherichia coli*, and *Bacillus circulans*, with the identification of mainly single modifications on Arg, Glu, and Glu residues, respectively.^[20]

We also compared the inhibitory effect of probe **2** and zanamivir on the activity of NA from influenza A virus (A/WSN/33, H1N1), as well as from *Arthrobacter ureafaciens* (AU), *Clostridium perfringens* (CP), and *Vibrio cholerae* (VC; Figure 2). Both compounds were tested at 3.3 mM in the NA inhibition assays with 2'-(4-methylumbelliferyl)- α -D-N-acetyl-

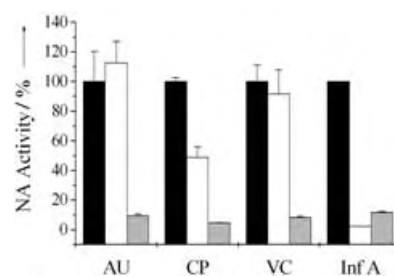


Figure 2. Inhibition study of NA activities from *A. ureafaciens* (AU), *C. perfringens* (CP), *V. cholerae* (VC), and influenza A virus (Inf A) with probe **2** (gray), zanamivir (white), and the control (black). Virus, suspended in 32.5 mM β -morpholinoethanesulfonic acid buffer (pH 6.5) was incubated with either probe **2** or zanamivir (3.3 mM) at room temperature for 45 min and then incubated with MUNANA at 37 °C for 30 min. The residual NA activity is expressed as the percentage of activity relative to that obtained in the absence of reagent. Assays for AU, CP, and VC were similarly carried out, except in 80 mM acetate buffer (pH 5.0).

neuraminic acid (MUNANA, Sigma) as the substrate.^[21] All samples were measured in duplicate and fluorometric determinations were performed with a fluorometer (ThermoLab systems, Sweden). The excitation wavelength was 355 nm and the emission wavelength was 460 nm. Probe **2** inhibited all four NA activities (H1N1, AU, CP, VC) with IC₅₀ values of 1.7, 0.68, 0.08, and 0.53 mM, respectively. These results indicate that probe **2** interferes with the activity of NA isolated from various sources at the active site, regardless of the variations the enzymes might have. On the other hand,

zanamivir effectively inhibited viral NA activity with an IC_{50} value of 2–3 nM, but it displayed weak inhibitory effects on the three bacterial NA activities, a result suggesting that the original strong binding interactions could be greatly compromised by possible variations in the active site. It must be emphasized that although one of the targets in this study, the influenza virus, is the same as one in the study of McKimm-Breschkin et al.,^[9] the concept and approach of the current strategy offers a versatile alternative for future applications. The labeling event in this study was a result of an activation step forming the reactive quinone methide and did not rely on the strong noncovalent binding which is a critical requirement in the previous approach, a fact which makes the current approach a more general one in targeting NA activities. It is especially worth noting that the advantage of the current approach becomes more prominent with the advent of zanamivir-resistant viruses.^[22]

Having established the efficacy of probe **2** to biotinylate NA and thus influenza virus A virions, we next studied the capturing performance by utilizing the covalent-bond-forming feature. The tests were carried out by a modified ELISA method as described previously.^[9] Briefly, a streptavidin-coated 96-well ELISA plate (NUNC Immobilizer) was saturated with probe **2**. BSA–biotin conjugate provided a negative control. After 1 hour of incubation, the plate was blocked with 0.1 % BSA/phosphate-buffered saline (PBS) for 1 hour and washed with PBS. Serial twofold dilutions of influenza A virus (A/WSN/33) were added and incubated for 1 hour at room temperature. After another wash, the captured viruses were detected by treatment with a polyclonal anti-FluA antibody, followed by a goat anti-rabbit IgG horseradish peroxidase (HRP) conjugate and a NeA-Blue tetramethylbenzidine substrate (TMB, Clinical Science Products, Inc.). The results indicated that probe **2** bound to the microplate wells could successfully capture influenza virus A and the intensity of the responding signal was proportional to the number of virus particles present (Figure 3). The wells loaded with BSA–biotin conjugate gave a negative response. The possibility of any noncovalent bindings could be ruled out by the modest IC_{50} value (1.7 nM) on the viral NA. More importantly, when the same procedure was applied to a mixture of influenza virus and a non-NA-containing Japanese encephalitis virus, only influenza virus was selectively cap-

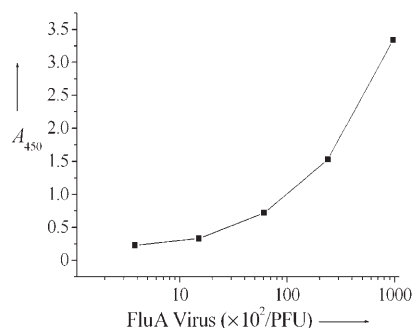


Figure 3. ELISA-based detection of influenza A (A/WSN/33) captured with probe **2** bound to streptavidin-coated microplate wells and detected with an anti-FluA antibody–HRP conjugate. PFU stands for plaque-forming unit.

tured and detected on the plate, a result strongly supporting the theory that the capture of virus particles was both probe and NA dependent. This conclusion was further supported by the experiment during which probe **2** failed to biotinylate influenza viruses that were preincubated with zanamivir, which effectively blocked the active site of NA on the viral surface. The results represent the first example of the use of a covalent-bond-forming mechanism for the capture of influenza virus particles. In addition, such covalent interactions between captured virus particles and the probe are known to be tolerant to harsh conditions,^[15] thus making this methodology amenable for further manipulations.

In summary, we have designed and synthesized a mechanism-based activity probe **2** for neuraminidase, which uses a latent quinone methide as the trapping device and forms a biotinylated adduct with *Arthrobacter ureafaciens* neuraminidase in a model study. By taking advantage of the essential role played by the NA activity in the life cycle of the influenza virus, we evaluated the interaction between probe **2** and the virus. The covalent-labeling event led to diminished NA activities. Furthermore, it serves as the basis for capturing influenza virus particles on microplate wells. This novel approach of capturing the influenza virus, which provides a stronger interaction between virus and the stationary phase, will certainly offer opportunities for developing new applications, such as rapid screening of antibodies against this group of viruses, and the development of sensitive and rapid diagnostic methods.

Received: December 15, 2004

Revised: May 20, 2005

Published online: October 7, 2005

Keywords: activity probes · hydrolases · influenza viruses · mechanism-based labeling · sialic acids

- [1] C. Liu, M. C. Eichelberger, R. W. Compans, G. M. Air, *J. Virol.* **1995**, *69*, 1099; K. Subbarao, A. Klimov, J. Katz, H. Regnery, W. Lim, H. Hall, M. Perdue, D. Swayne, C. Bender, J. Huang, M. Hemphill, T. Rowe, M. Shaw, X. Xu, K. Fukuda, N. Cox, *Science* **1998**, *279*, 393.
- [2] J. S. Oxford, *Rev. Med. Virol.* **2000**, *10*, 119; N. J. Cox, K. Subbarao, *Annu. Rev. Med.* **2000**, *51*, 407.
- [3] R. G. Webster, W. J. Beam, O. T. Gorman, T. M. Chambers, Y. Kawaoka, *Microbiol. Rev.* **1992**, *56*, 152.
- [4] C. M. Carr, P. S. Kim, *Science* **1994**, *266*, 234; M. Tashiro, R. Rott, *Semin. Virol.* **1996**, *7*, 237; D. A. Steinhauer, *Virology* **1999**, *258*, 1; G. R. Whittaker, *Exp. Rev. Mol. Med.* 8 February **2001**, can be found under <http://www-ermm.cbcu.cam.ac.uk/01002447h.htm>; T. M. Tumpey, A. Garcia-Sastre, J. K. Taubenberger, P. Palese, D. E. Swayne, C. F. Basler, *Proc. Natl. Acad. Sci. USA* **2004**, *101*, 3166.
- [5] J. J. Skehel, D. C. Wiley, *Annu. Rev. Biochem.* **2000**, *69*, 531.
- [6] G. Taylor, *Curr. Opin. Struct. Biol.* **1996**, *6*, 830.
- [7] J. N. Varghese, P. M. Colman, *J. Mol. Biol.* **1991**, *221*, 473; J. N. Varghese, J. L. McKimm-Breschkin, J. B. Caldwell, A. A. Kortt, P. M. Colman, *Proteins Struct. Funct. Genet.* **1992**, *14*, 327.
- [8] M. von Itzstein, W.-Y. Wu, G. B. Kok, M. S. Pegg, J. C. Dyason, B. Jin, T. V. Phan, M. L. Smythe, H. F. White, S. W. Oliver, P. M. Colman, J. N. Varghese, D. M. Ryan, J. M. Woods, R. C. Bethell,

- V. J. Hotham, J. M. Cameron, C. R. Penn, *Nature* **1993**, 363, 418; S. M. Cheer, A. J. Wagstaff, *Drugs* **2002**, 62, 71.
- [9] J. L. McKimm-Breschkin, P. M. Colman, B. Jin, G. Y. Krippner, M. McDonald, P. A. Reece, S. P. Tucker, L. Waddington, K. G. Watson, W.-Y. Wu, *Angew. Chem.* **2003**, 115, 3226; *Angew. Chem. Int. Ed.* **2003**, 42, 3118.
- [10] R. Schauer, *Trends Biochem. Sci.* **1985**, 10, 357; A. P. Corfield, *Glycobiology* **1992**, 2, 509; H. B. Tang, E. Dimango, R. Bryan, M. Gambello, B. H. Iglewski, J. B. Glodberg, A. Prince, *Infect. Immun.* **1996**, 64, 37.
- [11] B. F. Cravatt, E. J. Sorensen, *Curr. Opin. Chem. Biol.* **2000**, 4, 663; D. A. Campbell, A. K. Szardenings, *Curr. Opin. Chem. Biol.* **2003**, 7, 296; D. A. Jeffery, M. Bogyo, *Curr. Opin. Biotechnol.* **2003**, 14, 87; A. E. Speers, B. F. Cravatt, *ChemBioChem* **2004**, 5, 41.
- [12] L.-C. Lo, H.-Y. Wang, Z.-J. Wang, *J. Chin. Chem. Soc.* **1999**, 46, 715; L.-C. Lo, T.-L. Pang, C.-H. Kuo, Y.-L. Chiang, H.-Y. Wang, J.-J. Lin, *J. Proteome Res.* **2002**, 1, 35; C.-S. Tsai, Y.-K. Li, L.-C. Lo, *Org. Lett.* **2002**, 4, 3607.
- [13] M. Wakselman, *Nouv. J. Chim.* **1983**, 7, 439; R. B. Silverman, *Mechanism-Based Enzyme Inactivation: Chemistry and Enzymology*, Vols. 1 and 2, CRC, Boca Raton, FL, **1988**.
- [14] L.-C. Lo, C.-H. L. Lo, K. D. Janda, D. B. Kassel, F. M. Raushel, *Bioorg. Med. Chem. Lett.* **1996**, 6, 2117.
- [15] P. Soumillion, L. Jespers, M. Bouchet, J. Marchand-Brynaert, G. Winter, J. Fastrez, *J. Mol. Biol.* **1994**, 237, 415; K. D. Janda, L.-C. Lo, C.-H. L. Lo, M.-M. Sim, R. Wang, C.-H. Wong, R. A. Lerner, *Science* **1997**, 275, 945.
- [16] P.-A. Driguez, B. Barrere, B. Chantegrel, C. Deshayes, A. Doutheau, G. Quash, *Bioorg. Med. Chem. Lett.* **1992**, 2, 1361.
- [17] R. Kuhn, P. Lutz, P. L. MacDonald, *Chem. Ber.* **1966**, 99, 611; P. Meindl, H. Tuppy, *Monatsh. Chem.* **1965**, 96, 802; F. Baumberger, A. Vasella, *Helv. Chim. Acta* **1986**, 69, 1927; S. Halazy, V. Berges, A. Ehrhard, C. Danzin, *Bioorg. Chem.* **1990**, 19, 330; G. Sabatino, M. Chinol, G. Paganelli, S. Papi, M. Chelli, G. Leone, A. M. Papini, A. De Luca, M. Ginanneschi, *J. Med. Chem.* **2003**, 46, 3170.
- [18] M. Iwamori, Y. Ohta, Y. Uchida, Y. Tsukada, *Glycoconjugate J.* **1997**, 14, 67.
- [19] M. Ichikawa, Y. Ichikawa, *Bioorg. Med. Chem. Lett.* **2001**, 11, 1769; J. R. Betley, S. Cesaro-Tadic, A. Mekhalfia, J. H. Rickard, H. Denham, L. J. Partridge, A. Plueckthun, G. M. Blackburn, *Angew. Chem.* **2002**, 114, 801; *Angew. Chem. Int. Ed.* **2002**, 41, 775; Q. Zhu, X. Huang, G. Y. J. Chen, S. Q. Yao, *Tetrahedron Lett.* **2003**, 44, 2669.
- [20] M. Kurogochi, S. Nishimura, Y. C. Lee, *J. Biol. Chem.* **2004**, 279, 44704.
- [21] M. Potier, L. Mameli, M. Belishle, L. Dallaire, S. B. Melancom, *Anal. Biochem.* **1979**, 94, 287.
- [22] L. V. Gubareva, *Virus Res.* **2004**, 103, 199.

DOI: 10.1002/anie.200501754

Reactions of Gold(III) Oxo Complexes with Cyclic Alkenes***Maria A. Cinellu,* Giovanni Minghetti, Fabio Cocco, Sergio Stoccoro, Antonio Zucca, and Mario Manassero*

As pointed out in a recent review, metal-mediated olefin oxidation is still a subject of great interest.^[1] Various classes of mechanisms have been envisaged for different metal systems. Among these, that involving metallaoxetanes (1-metalla-2-oxacyclobutanes) as a key intermediate in the oxygen-transfer reaction has been recently corroborated by experimental evidence.^[2] While an oxametallacycle has been identified as the crucial surface intermediate in the ethylene epoxidation on Ag,^[3] a platinaoxetane, obtained from the reaction of a platinum(II) oxo complex with norbornene, has been structurally characterized.^[4] The same oxo complex has been found to stoichiometrically oxidize ethylene to acetaldehyde, thus providing a rare example of alkene oxidation by isolated late-transition-metal oxo complexes.^[5] Metallaoxetanes have also been obtained from the reaction of iridium(III) and rhodium(III) alkene complexes with molecular oxygen or hydrogen peroxide.^[6]

Gold oxo species are likely to be involved in oxidations catalyzed by gold supported on metal oxides,^[7] as, for example, in the direct epoxidation of propene with molecular oxygen.^[7d,8] As soluble oxo complexes are valuable models for species involved in heterogeneous catalytic oxidation systems, we studied the reactions of a series of gold(III) oxo complexes^[9] with olefins.^[10] The model reaction of $[\text{Au}_2(\text{bipy}^R)_2(\mu\text{-O})_2](\text{PF}_6)_2$ ($\text{bipy}^R = 6\text{-R-}2,2'\text{-bipyridine}$; see Scheme 1 for R) with styrene yielded novel cationic gold(III) alkene complexes $[\text{Au}(\text{bipy}^R)(\eta^2\text{-CH}_2=\text{CHPh})](\text{PF}_6)$ and oxygenated styrene derivatives.^[11,12] After these encouraging results, we searched

[*] Prof. M. A. Cinellu, Prof. G. Minghetti, F. Cocco, Dr. S. Stoccoro, Dr. A. Zucca
Dipartimento di Chimica
Università di Sassari
via Vienna 2, 07100 Sassari (Italy)
Fax: (+39) 079-229-559
E-mail: cinellu@uniss.it
Prof. M. Manassero
Dipartimento di Chimica Strutturale e Stereochimica Inorganica
Università di Milano
Centro CNR
via Venezian 21, 20133 Milano (Italy)

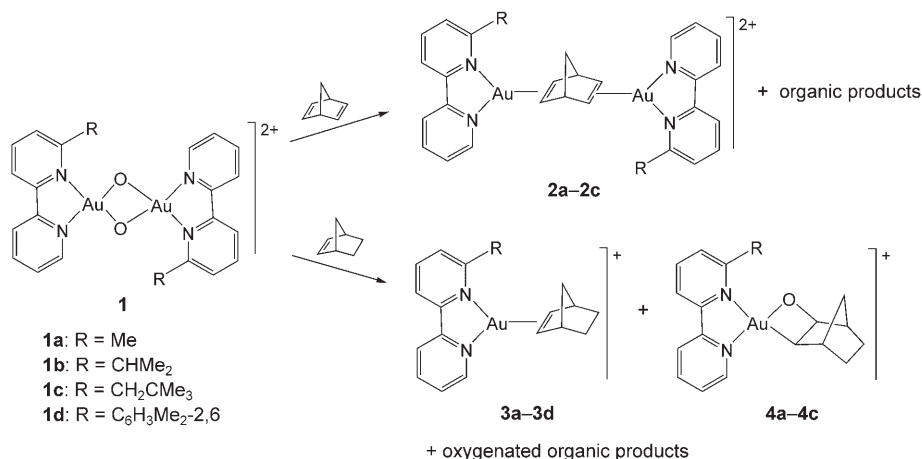
[**] Support from the University of Sassari (60%) is gratefully acknowledged. We thank Mrs. E. Azara (ICB, CNR, Sassari) and Dr. A. Furesi (PMP, USSL, Sassari) for performing GC-MS and LC-MS analyses. Thanks are also due to Dr. G. A. Chelucci (Dipartimento di Chimica, Università di Sassari) for support in the organic syntheses and simulation of NMR spectra.



Supporting information for this article is available on the WWW under <http://www.angewandte.org> or from the author.

for the supposed oxametallacyclic intermediate.^[13] A growing number of papers have appeared on the homogeneous gold-catalyzed addition of oxygen nucleophiles to C–C multiple bonds of alkynes or alkenes.^[14] Active gold–alkyne (gold–alkene) and cyclic organogold species, which have been suggested as key intermediates in the C–O bond formation,^[14f,i–n,q] have never been isolated.

Herein we describe the reaction of $[\text{Au}_2(\text{bipy}^R)_2(\mu\text{-O})_2](\text{PF}_6)_2$ [**1**-(PF_6)₂; R = Me (**1a**), CHMe₂ (**1b**), CH₂CMe₃ (**1c**), C₆H₃Me_{2-2,6} (**1d**)] with the strained cyclic alkenes norbornene (nb) and 2,5-norbornadiene (nbd) to give alkene complexes and unprecedented metallaoxetanes (Scheme 1).^[15] A dinuclear complex $[\text{Au}_2(\text{bipy}^R)_2(\mu\text{-}\eta^2, \eta^2\text{-nbd})](\text{PF}_6)_2$ [**2**-(PF_6)₂; R = Me (**2a**), CHMe₂ (**2b**), CH₂CMe₃ (**2c**)] with a bridging nbd ligand is the main product of the reaction as shown by NMR spectra and other analytical data; signals attributable to trace amounts of a second species are sometimes observed in the ¹H NMR spectra.



Scheme 1. Oxo complexes **1**-(PF_6)₂ (only the *trans* isomer is depicted; **1a** and **1b** are mixtures of the *cis* and *trans* isomer) and products of the reaction with 2,5-norbornadiene, **2**-(PF_6)₂, and with norbornene, **3**- PF_6 and **4**- PF_6 .

nb)](PF_6)₂ [**2**-(PF_6)₂; R = Me (**2a**), CHMe₂ (**2b**), CH₂CMe₃ (**2c**)] with a bridging nbd ligand is the main product of the reaction as shown by NMR spectra and other analytical data; signals attributable to trace amounts of a second species are sometimes observed in the ¹H NMR spectra.

In the case of the nb derivatives, the ¹H NMR spectra indicate the presence of two species, the ratio of which depends on the preparative conditions and the nature of the substituent of the bipyridine ligand. The main product is the alkene complex $[\text{Au}(\text{bipy}^R)(\text{nb})](\text{PF}_6)$ [**3**- PF_6 ; R = Me (**3a**), CHMe₂ (**3b**), CH₂CMe₃ (**3c**), C₆H₃Me_{2-2,6} (**3d**)]. When signals from the minor species, **4**, are not observed in the ¹H NMR spectrum, as in the case of the 6-(2,6-xylyl)-2,2'-bipyridine derivative, **4** is detected in the mass spectrum in which, besides the molecular ion, M^+ , corresponding to the nb complex (**3d**), a peak of low to medium intensity is found at $[M+16]^+$. Under comparable preparative conditions, significant amounts of the latter species are obtained from **1a**-(PF_6)₂.^[15] To separate the two species, different methods were employed in the case of the 6-methyl-2,2'-bipyridine (bipy^{Me}) derivatives **3a**- PF_6 and **4a**- PF_6 . Crystals of **3a**- PF_6 and **4a**- PF_6 , obtained by slow diffusion of diethyl ether into an acetonitrile solution of the mixture, were separated and subjected to X-ray diffraction analyses. Although full refinement of the structure of **3a**- PF_6 has not been accomplished,

the main feature of the coordination geometry has been established.^[16] The second species, **4a**- PF_6 , proved to be the auroxetane, $[\text{Au}(\text{bipy}^{\text{Me}})(\kappa^2\text{-O,C-2-oxynorbornyl})](\text{PF}_6)$.^[17]

The structure consists of the packing of **4a** cations and PF_6 anions in the molar ratio of 1:1 with normal van der Waals contacts. The molecular structure of **4a** is shown in Figure 1. The gold atom has a square-planar coordination environment with a slight square-pyramidal distortion; maximum deviations from the best plane are +0.024(8) and –0.027(1) Å for O and Au atoms, respectively. Carbon atom C13 lies in the metal coordination plane, and the oxametallacycle is strictly planar, as reported for other late-transition-metal metallaoxetanes.^[18] The Au–O bond length of 1.967(7) Å is very similar to the Au–O bond lengths of 1.971(4) and 1.960(6) Å found in $[\text{Au}(\text{bipy})(\text{OME})_2](\text{PF}_6)$,^[19] and the Au–C12 separation of 2.055(8) Å is comparable with the Au–C bond length of 2.028(7) Å found in $[\text{Au}\{\text{N}_2\text{C}_{10}\text{H}_7(\text{CMe}_2\text{CH}_2)_6\}\text{Cl}]^+$ (**5**), in which $\text{N}_2\text{C}_{10}\text{H}_7(\text{CMe}_2\text{CH}_2)_6$ is a cyclometalated 6-*tert*-butyl-2,2'-bipyridine ligand.^[20] The Au–N1 and Au–N2 bonds (2.026(6) and 2.183(6) Å, respectively) can be compared with corresponding interactions in **5** (1.976(5) and 2.151(5) Å, respectively).

As the isolation of oxametallacycles is unprecedented in the chemistry of gold, we tried to synthesize **4a**- PF_6 in better yields in order to study its reactivity.^[21] In

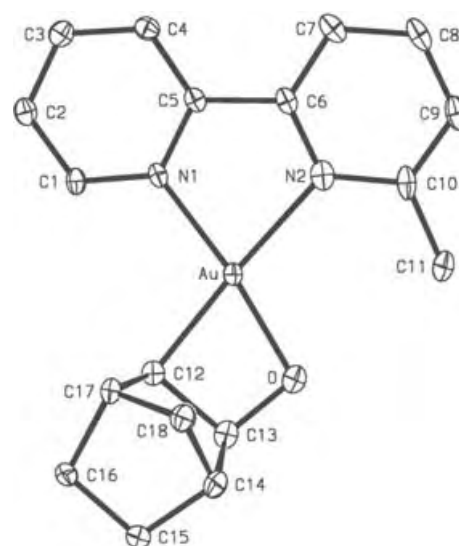


Figure 1. Molecular structure (ORTEP) of cation **4a**. Ellipsoids are drawn at the 30% probability level. Principal bond lengths [Å] and angles [°]: Au–N1 2.026(6), Au–N2 2.183(6), Au–O 1.967(7), Au–C12 2.055(8), C12–C13 1.550(14), C13–O 1.433(12); N1–Au–N2 78.2(3), N1–Au–C12 103.9(3), N1–Au–O 172.9(3), N2–Au–O 108.2(3), N2–Au–C12 177.7(3), C12–Au–O 69.6(3), Au–C12–C13 91.2(5), C12–C13–O 100.7(7), C13–O–Au 98.5(6).

reactions using different ratios of nb to **1a**-(PF₆)₂ and at different concentrations of **1a**-(PF₆)₂, in both CH₃CN and in CH₃CN/H₂O, we established a general trend.^[22] During the reaction of *trans*-[**1c**-(PF₆)₂] (the most soluble complex) with nb in CD₃CN, we observed by ¹H NMR spectroscopy that the ratio of **3** to **4** remains unchanged. Signals for **3c**-PF₆ and **4c**-PF₆ were detected after about 40 h (**3c**-PF₆/**4c**-PF₆ = 2:1); a resonance at δ = 9.58 ppm (d, *J*_{H-H} = 1.9 Hz), which is typical of an aldehyde proton, appeared at the same time. Isolation of the organic fraction obtained from the same reaction in MeCN identified *exo*-2,3-epoxynorbornane (**6**)^[23] as the main product accompanied by at least three aldehydes, **7**, **8**, and **9**.^[24] The main aldehyde species was cyclopentane-1,3-dicarbaldehyde (**7**, *M*⁺ 126)^[25], the others were likely to be 3-methylene-cyclopentane carbaldehyde (**8**, *M*⁺ 110)^[26] and 3-methyl-2-cyclopentene carbaldehyde (**9**, *M*⁺ 110). The epoxide and the dialdehyde were also the main products of the same reaction in MeCN in the presence of a small amount of water (3 %). When a larger amount was added (≥ 10 %), a 6:1 mixture of *cis-endo*-2,3-norbornanediol (**10**) and *trans*-2,3-norbornanediol (**11**) is obtained. GC-MS and LC-MS analyses showed peaks of *M*⁺ = 128, which correspond to C₇H₁₂O₂.

Formation of the epoxide in solution and direct loss of a C₇H₁₀O fragment from the molecular ion of [Au(bipy^{Me})(C₇H₁₀O)]⁺ in the gas phase—shown by the FAB mass spectrum of **4a**—point to the oxauracycle **4** being the origin of both the oxygenated products and the olefin complex **3**. Accordingly, the olefin complex **3a**-PF₆, 2,3-epoxynorbornane (**6**), and small amounts of aldehydes **8** and **9** were slowly formed when a MeCN solution of **4a**-PF₆ was treated with excess nb.^[27] To the best of our knowledge, elimination of an epoxide from an isolated oxametallacycle has never been previously observed.^[1,2b] Aldehydes or ketones are formed by isolated Rh^{III} and Ir^{III} 2-metalla-oxetanes.^[6e,f,28] Plausible reaction pathways for the formation of the oxauracycle, **4**, and the alkene complex, **3**, are given in Scheme 2.

Attempts to obtain **4a** by reaction of **3a** with O₂^[6a] or H₂O₂^[6b-d] in neutral MeCN solution were unsuccessful: partial decomposition of the alkene complex was observed in both cases.

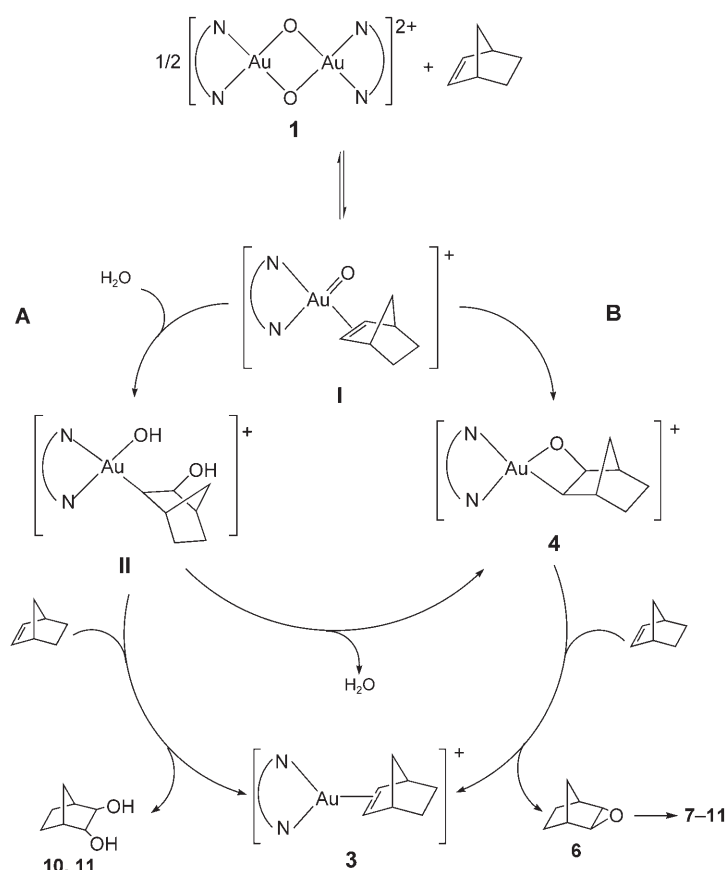
Complexes **4a–4c** are the first isolated oxauracyclobutanes. Their formation by the reaction of gold oxo complexes with alkenes may lead to a better understanding of the oxidation of olefins mediated by late-transition-metal complexes. Moreover, both the gold(II) alkene complex and the oxauracycle provide evidence for intermediates in the gold-catalyzed addition of oxygen nucleophiles to alkenes and alkynes.

Received: May 20, 2005

Revised: July 28, 2005

Published online: October 5, 2005

Keywords: alkene ligands · gold · oxidation · oxo ligands



Scheme 2. Proposed reaction pathways for the formation of **3**, **4**, and oxygenated organic products **6–11**: A) in MeCN/H₂O and B) in MeCN. **I** and **II** are supposed intermediates.

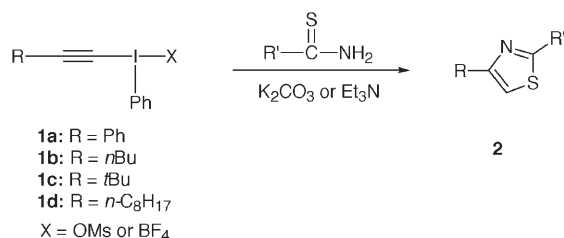
- [1] B. de Bruin, P. H. M. Budzelaar, A. W. Gal, *Angew. Chem.* **2004**, *116*, 4236–4251; *Angew. Chem. Int. Ed.* **2004**, *43*, 4142–4156.
- [2] a) K. B. Sharpless, A. Y. Teranishi, J.-E. Bäckvall, *J. Am. Chem. Soc.* **1977**, *99*, 3120–3128; b) K. A. Jørgensen, B. Schiøtt, *Chem. Rev.* **1990**, *90*, 1483–1506.
- [3] S. Linic, H. Piao, K. Adib, M. A. Barteau, *Angew. Chem.* **2004**, *116*, 2978–2981; *Angew. Chem. Int. Ed.* **2004**, *43*, 2918–2921.
- [4] E. Szuromi, H. Shan, P. R. Sharp, *J. Am. Chem. Soc.* **2003**, *125*, 10522–10523.
- [5] T. Hosokawa, M. Takano, S.-I. Murahashi, *J. Am. Chem. Soc.* **1996**, *118*, 3990–3991.
- [6] a) V. W. Day, W. G. Klemperer, S. P. Lockledge, D. J. Main, *J. Am. Chem. Soc.* **1990**, *112*, 2031–2033; b) B. de Bruin, M. J. Boerakker, J. J. M. Donners, B. E. C. Christiaans, P. P. J. Schlebos, R. de Gelder, J. M. M. Smits, A. L. Spek, *Angew. Chem.* **1997**, *109*, 2153–2157; *Angew. Chem. Int. Ed. Engl.* **1997**, *36*, 2064–2067; c) B. de Bruin, J. A. Brands, J. J. M. Donners, M. P. J. Donners, R. de Gelder, J. M. M. Smits, A. W. Gal, A. L. Spek, *Chem. Eur. J.* **1999**, *5*, 2921–2936; d) T. C. Flood, M. Imura, J. M. Perotti, A. L. Rheingold, T. E. Concolino, *Chem. Commun.* **2000**, 1681–1682; e) B. de Bruin, M. J. Boerakker, J. A. W. Verhagen, R. de Gelder, A. W. Gal, *Chem. Eur. J.* **2000**, *6*, 298–312; f) B. de Bruin, J. A. W. Verhagen, C. H. J. Schouten, A. W. Gal, D. Feichtinger, D. A. Plattner, *Chem. Eur. J.* **2001**, *7*, 416–422.
- [7] a) M. Haruta, *Gold Bull.* **2004**, *37*, 27–36; b) G. C. Bond, D. T. Thompson, *Gold Bull.* **2000**, *33*, 41–50; c) H. H. Kung, M. C.

- Kung, C. K. Costello, *J. Catal.* **2003**, *216*, 425–432; d) J. R. Monnier, *Appl. Catal. A* **2001**, *221*, 73–91.
- [8] A. K. Sinha, S. Seelan, S. Tsubota, M. Haruta, *Angew. Chem.* **2004**, *116*, 1572–1574; *Angew. Chem. Int. Ed.* **2004**, *43*, 1546–1548.
- [9] M. A. Cinellu, G. Minghetti, M. V. Pinna, S. Stoccoro, A. Zucca, M. Manassero, M. Sansoni, *J. Chem. Soc. Dalton Trans.* **1998**, 1735–1741.
- [10] D. Rais, Dissertation, Università di Sassari, **1998**.
- [11] M. A. Cinellu, G. Minghetti, S. Stoccoro, A. Zucca, M. Manassero, *Chem. Commun.* **2004**, 1618–1619.
- [12] Analogous alkene complexes are likewise obtained with other 1-alkenes, whereas no reaction occurs with linear internal alkenes; a small amount of an oxygenated gold species is also detected by ^1H NMR spectroscopy and FAB-MS of the α -methylstyrene derivative. Oxygenated organic products were characterized. Styrene derivatives: phenylacetaldehyde (main product) and benzaldehyde, reaction in MeCN; phenylacetaldehyde dimethyl acetal, reaction in MeCN/MeOH; styrene glycol, reaction in MeCN/ H_2O . α -Methylstyrene derivatives: acetophenone, reaction in MeCN; 2-phenyl-1,2-propanediol, reaction in MeCN/ H_2O ; this diol converts almost completely into methylbenzylketone after a prolonged reaction time.
- [13] Part of this work was presented in oral form: M. A. Cinellu, F. Cocco, G. Minghetti, S. Stoccoro, A. Zucca, M. Manassero, *III EuChem Conference on Nitrogen Ligands in Organometallic Chemistry and Homogeneous Catalysis*, Camerino, Italy, September 8–12, **2004**, O3.
- [14] For selected reviews on homogeneous catalysis by gold, see: a) A. Hoffmann-Röder, N. Krause, *Org. Biomol. Chem.* **2005**, *3*, 387–391; b) A. S. K. Hashmi, *Gold Bull.* **2004**, *37*, 51–65; c) A. S. K. Hashmi, *Gold Bull.* **2003**, *36*, 3–9; d) G. Dyker, *Angew. Chem.* **2000**, *112*, 4407–4409; *Angew. Chem. Int. Ed.* **2000**, *39*, 4237–4239; selected examples of alkyne transformations: e) Y. Fukuda, K. Utimoto, *J. Org. Chem.* **1991**, *56*, 3729–3731; f) J. H. Teles, S. Brode, M. Chabanas, *Angew. Chem.* **1998**, *110*, 1475–1478; *Angew. Chem. Int. Ed.* **1998**, *37*, 1415–1418; g) A. S. K. Hashmi, T. M. Frost, J. W. Bats, *Org. Lett.* **2001**, *3*, 3769–3771; h) E. Mizushima, K. Saro, T. Hayashi, M. Tanaka, *Angew. Chem.* **2002**, *114*, 4745–4747; *Angew. Chem. Int. Ed.* **2002**, *41*, 4563–4565; i) R. Casado, M. Contel, M. Laguna, P. Romero, S. Sanz, *J. Am. Chem. Soc.* **2003**, *125*, 11925–11935; j) T. Yao, X. Zhang, R. C. Larock, *J. Am. Chem. Soc.* **2004**, *126*, 11164–11165; k) A. S. K. Hashmi, J. P. Weyrauch, W. Frey, J. W. Bats, *Org. Lett.* **2004**, *6*, 4391–4394; l) V. Mamane, T. Gress, H. Krause, A. Fürstner, *J. Am. Chem. Soc.* **2004**, *126*, 8654–8655; m) A. S. K. Hashmi, P. Sinha, *Adv. Synth. Catal.* **2004**, *346*, 432–438; n) A. S. K. Hashmi, M. Rudolf, J. P. Weyrauch, M. Wölfe, W. Frey, J. W. Bats, *Angew. Chem.* **2005**, *117*, 2858–2861; *Angew. Chem. Int. Ed.* **2005**, *44*, 2798–2801; selected examples of alkene transformations: o) A. S. K. Hashmi, L. Schwarz, J.-H. Choi, T. M. Frost, *Angew. Chem.* **2000**, *112*, 2382–2385; *Angew. Chem. Int. Ed.* **2000**, *39*, 2285–2288; p) S. Kobayashi, K. Kakumoto, M. Sugiura, *Org. Lett.* **2002**, *4*, 1319–1322; q) C.-G. Yang, C. He, *J. Am. Chem. Soc.* **2005**, *127*, 6966–6967.
- [15] For full experimental data on the synthesis, spectroscopy, and elemental analysis of complexes **2a–2c**, **3a–3d**, **4a–4c** and for spectroscopic characterization of organic compounds **6–11** see Supporting Information.
- [16] Crystal data for **3a**-PF₆: $\text{C}_{18}\text{H}_{20}\text{AuF}_6\text{N}_2\text{P}$, $M_r = 606.30 \text{ g mol}^{-1}$, orthorhombic, space group $Pna2_1$ (no. 33), $a = 16.480(4)$, $b = 16.662(3)$, $c = 6.911(2) \text{ Å}$, $V = 1897.7(7) \text{ Å}^3$.
- [17] Crystal data for **4a**-PF₆: $\text{C}_{18}\text{H}_{20}\text{AuF}_6\text{N}_2\text{OP}$, $M_r = 622.30 \text{ g mol}^{-1}$, triclinic, space group $P\bar{1}$ (no. 2), $a = 6.466(1)$, $b = 8.822(1)$, $c = 17.548(1) \text{ Å}$, $\alpha = 103.45(1)$, $\beta = 90.38(1)$, $\gamma = 100.97(1)^\circ$, $V = 954.4(2) \text{ Å}^3$, $Z = 2$, $\rho_{\text{calcd}} = 2.165 \text{ g cm}^{-3}$, $T = 150 \text{ K}$, $\mu(\text{MoK}\alpha) = 78.4 \text{ cm}^{-1}$, $F(000) = 596$. Reflections measured 19839, independent 5795 with $R_{\text{int}} = 0.043$. Final R_2 (F^2 , all reflections) = 0.113, $wR_2 = 0.165$, conventional $R_1 = 0.052$ for 262 variables. Bruker SMART CCD area detector, MoK α radiation ($\lambda = 0.71073 \text{ Å}$), ω -scan mode, $\theta_{\text{min}} = 3^\circ$, $\theta_{\text{max}} = 26^\circ$. Structure solved by direct methods and refined by full-matrix least squares. The program used to refine the structure was Personal SDP. CCDC-272640 contains the supplementary crystallographic data for this paper. These data can be obtained free of charge from the Cambridge Crystallographic Data Centre via www.ccdc.cam.ac.uk/data_request/cif.
- [18] A. A. Zlota, F. Frolow, D. Milstein, *J. Am. Chem. Soc.* **1990**, *112*, 6411–6413; M. J. Calhorda, A. M. Galvão, C. Ünaleroğlu, A. A. Zlota, F. Frolow, D. Milstein, *Organometallics* **1993**, *12*, 3316–3325; and references therein.
- [19] M. A. Cinellu, G. Minghetti, M. V. Pinna, S. Stoccoro, A. Zucca, M. Manassero, *J. Chem. Soc. Dalton Trans.* **2000**, 1261–1265.
- [20] M. A. Cinellu, G. Minghetti, S. Stoccoro, A. Zucca, M. Manassero, M. Sansoni, *J. Chem. Soc. Dalton Trans.* **1996**, 4217–4225.
- [21] **4a**-PF₆ was isolated in low yield after elaborate workup of the mixture. **4a**-BPh₄ which conversely can be obtained in fairly good yields, is not stable enough in solution for carrying out a reactivity study.^[15]
- [22] General trend: 1) high **1a**-(PF₆)₂ conversions (high **3a** + **4a** yields) require a long reaction time (at least 15 days) a temperature of 10–15 °C and high nb/**1a** ratio (20:1–30:1) both in MeCN and in MeCN/ H_2O . 2) Under the same preparative conditions the overall yield (**3a** + **4a**) is only slightly higher in MeCN/ H_2O ; nevertheless, the **3a**/**4a** ratios are remarkably different: 6.5:1 (averaged) in MeCN and 1.5:1 in MeCN/ H_2O . 3) Under the same nb/**1a** ratio and time conditions higher **4a** yields are obtained from concentrated solutions; the overall yield (**3a** + **4a**) was slightly lower than that from dilute solutions.
- [23] Signals of the epoxide could not be detected in the spectrum of the reaction mixture (CD_3CN) as they overlapped with those of **1c**, **3c**, and **4c**.
- [24] ^1H NMR spectra were recorded soon after workup of the reaction mixture. Aldehyde signals (CDCl_3): **7**: 9.64 (d, 2.0 Hz; 2H); **8** or **9**: 9.63 (d, 2.4 Hz; 1H); **9** or **8**: 9.62 ppm (d, 2.4 Hz; 1H). Intensities: **7** \geq (**8** + **9**); **7** \leq **6** (molar ratio based on CHH-7 of the epoxide at $\delta = 0.70 \text{ ppm}$).
- [25] ^1H NMR and GC-MS spectra were compared to those of an authentic sample prepared according to: S. Göksu, R. Altundas, Y. Sütbeyaz, *Synth. Commun.* **2000**, *30*, 1615–1621.
- [26] Oxidation of nb with N_2O to give 3-methylenecyclopentane carbaldehyde (and norbornanone) has recently been reported: E. V. Starokon, K. A. Dubkov, D. E. Babushkin, V. N. Parmon, G. I. Panov, *Adv. Synth. Catal.* **2004**, *346*, 268–274. In default of ^1H NMR data for these aldehydes, the experimental spectra have been compared to the simulated ones obtained by ChemDraw 9.0 (CambridgeSoft).
- [27] Complex **3a** and **6** also form upon addition of nb and a catalytic amount (5%) of $\text{HBF}_4 \cdot \text{Et}_2\text{O}$ to **4a**; in this case small amounts of diols **10** and **11** are formed.
- [28] D. Milstein, J. C. Calabrese, *J. Am. Chem. Soc.* **1982**, *104*, 3773–3774.

Thiazole Synthesis by Cyclocondensation of 1-Alkynyl(phenyl)- λ^3 -iodanes with Thioureas and Thioamides**

Kazunori Miyamoto, Yoshio Nishi, and Masahito Ochiai*

In 1996, Wipf and Venkatraman reported an efficient method for the synthesis of thiazoles, which involved the cyclocondensation of hypervalent 1-alkynyl(phenyl)- λ^3 -iodanes with thioureas or thioamides.^[1] For instance, the reaction of phenylethynyl(phenyl)(mesylato)- λ^3 -iodane (**1a**) (X = OMs, Ms = methanesulfonyl) with thiourea in methanol in the presence of triethylamine at 0 °C directly afforded 2-amino-4-phenylthiazole (**2**; R = Ph, R' = NH₂) in a good yield (Scheme 1). 1-Hexynyl- λ^3 -iodane **1b** (X = OMs) also pro-



Scheme 1. Synthesis of thiazoles.

duced the thiazole **2** (R = *n*Bu, R' = NH₂ or Ph) by reaction with thiourea or thio benzamide. This direct method for the synthesis of thiazoles based on the cyclocondensation of 1-alkynyl- λ^3 -iodanes was applied to the synthesis of 2-mercaptothiazoles and selenazoles.^[2]

The one-step thiazole synthesis developed by Wipf and Venkatraman is a very useful reaction, as many biologically active natural products contain thiazole moieties.^[3] They proposed a reaction mechanism that involves a unique [3,3]-sigmatropic rearrangement of an initially formed 1-alkynyl(iminothio)- λ^3 -iodane **3** through ligand exchange on the hypervalent iodine. Reductive elimination of the resulting vinylodonium ylide **4** generates an α -thioamido alkylidene carbene **5**, which undergoes an intramolecular cyclization to yield 2,4-disubstituted thiazole **2** (Scheme 2, pathway A).^[4]

The more common Michael addition pathway with the initial formation of an isomeric vinylodonium ylide **6** was discarded, and it was proposed that this Michael addition pathway would provide thiazoles **8** with an inverse C4,C5-substitution pattern through successive reductive elimination of iodobenzene and intramolecular 1,5 N–H insertion of the alkylidene carbene **7** (pathway B).^[1]

It occurred to us that a third mechanism (pathway C) that involved the Michael addition of thio nucleophiles followed by a 1,2-rearrangement of the iminothio group in the alkylidene carbene **7**, instead of the intramolecular 1,5 N–H insertion, thus yielding the alkynyl sulfide **9**, seems to be a more attractive alternative. Further intramolecular cyclization of **9** probably provides **2** selectively. In fact, the 1,2-rearrangement of sulfonyl groups in alkylidene carbenes is known to be a facile and very rapid process because of the excellent migratory aptitude of sulfonyl groups.^[5] Furthermore, it has been shown that soft sulfur nucleophiles, such as thiolates,^[6] thiosulfonates,^[7] phosphorodithioates,^[8] thiocyanates,^[9] and sulfates,^[10] preferentially undergo Michael additions towards 1-alkynyl(phenyl)- λ^3 -iodanes. We report herein some evidence that **9** is a reactive intermediate in the cyclocondensation of hypervalent 1-alkynyl(phenyl)- λ^3 -iodanes with thioureas or thioamides and that the thiazole synthesis probably proceeds through pathway C.

The cyclocondensations of 1-alkynyl(phenyl)- λ^3 -iodanes with thioureas or thioamides that yield **2** were carried out in the presence of a base, such as potassium carbonate or triethylamine.^[1] The reaction course, however, dramatically changed without a base being present. Thus, when the reaction of phenylethynyl- λ^3 -iodane **1a** (X = OMs) with thiourea (1 equiv) was carried out in dichloromethane at –78 → 10 °C under nitrogen in the absence of triethylamine, no formation of **2** (R = Ph, R' = NH₂) was observed; instead, a hitherto unknown *S*-(phenylethynyl)isothiuronium mesylate **9**-MsOH (R = Ph, R' = NH₂) was isolated in 82 % yield after repeated decantation with hexane.^[11] The IR spectrum of this salt showed the characteristic peak of the triple bond at 2180 cm^{–1}, as well as the strong absorption of the iminium group at 1683 and 1662 cm^{–1}, whereas the ¹³C NMR spectra revealed two peaks of acetylenic carbon atoms at δ = 65.8 and 106.6 ppm.

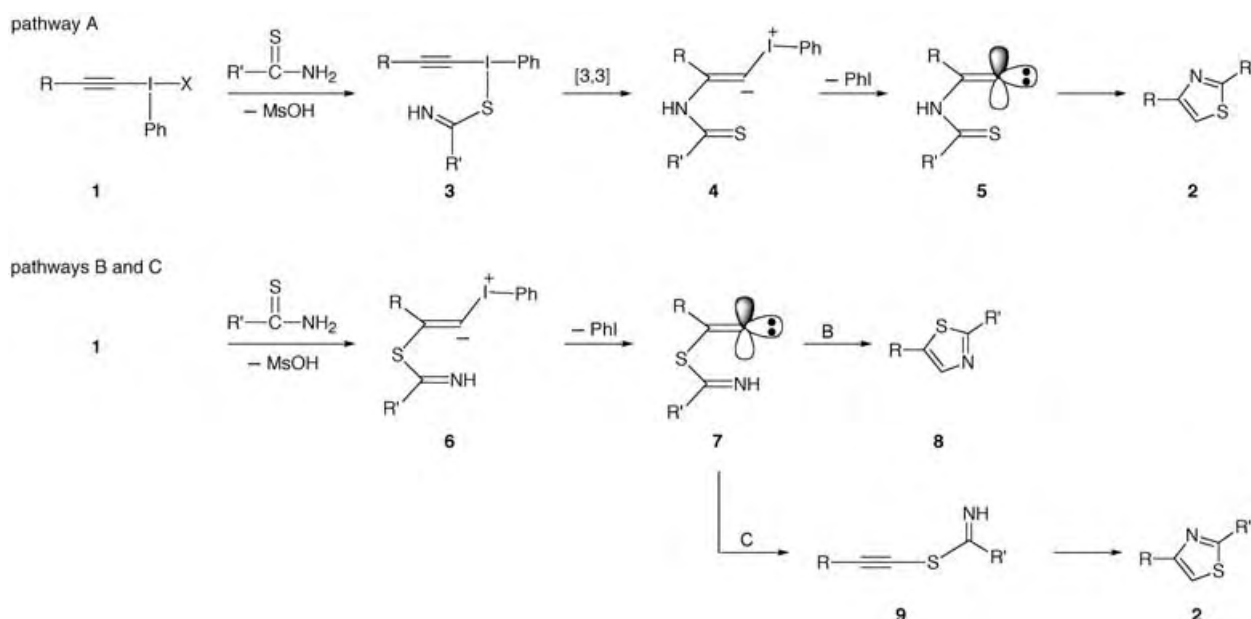
Single crystals of **9**-MsOH for X-ray structural analysis were grown from a mixture of methanol/dichloromethane/hexane.^[12] Figure 1a illustrates a planar *S*-(1-alkynyl)isothiuronium structure with the sum of the C(9)-centered bond angles $\Sigma^\circ\text{C}(9) = 359.97^\circ$. Interestingly, the phenyl and the isothiuronium groups lie almost on the same plane, with a dihedral angle of 8.19(3)°.

It should be noted that exposure of *S*-(phenylethynyl)isothiuronium mesylate (**9**-MsOH) to an aqueous saturated solution of NaHCO₃ at room temperature produced a moderate yield (51 %) of 2-amino-4-phenylthiazole (**2**) through an intramolecular 5-endo digonal cyclization. The same type of intramolecular cyclization in substituted *S*-alkynylisothiuronium salts has been reported.^[11,13] These results suggest that methanesulfonic acid generated from λ^3 -iodane **1a** (X = OMs) during the reaction with thiourea (Scheme 2) probably inhibits the intramolecular cyclization of **9** (R = Ph, R' = NH₂) under our conditions by formation of

[*] K. Miyamoto, Dr. Y. Nishi, Prof. M. Ochiai
 Faculty of Pharmaceutical Sciences
 University of Tokushima
 1-78 Shomachi, Tokushima 770-8505 (Japan)
 Fax: (+81) 88-633-9504
 E-mail: mochiai@ph.tokushima-u.ac.jp

[**] We gratefully acknowledge the Ministry of Education, Culture, Sports, Science, and Technology of Japan for financial support in the form of a grant.

Supporting information for this article is available on the WWW under <http://www.angewandte.org> or from the author.



Scheme 2. Possible reaction mechanisms.

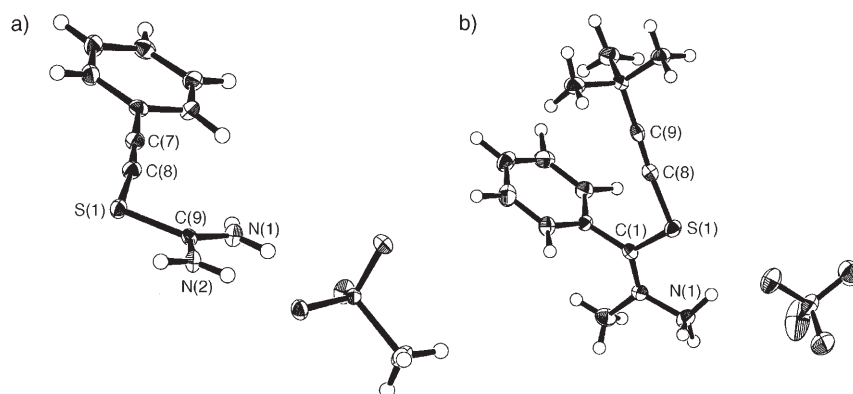


Figure 1. ORTEP drawing of a) isothiuronium salt **9**-MsOH ($R = \text{Ph}$, $R' = \text{NH}_2$) and b) thiobenzimidonium salt **10**. Selected interatomic distances [Å] and angles [°]: **9**-MsOH: C(7)-C(8) 1.193(1), S(1)-C(8) 1.6888(8), S(1)-C(9) 1.7695(7), C(8)-S(1)-C(9) 102.19(4); **10**: C(8)-C(9) 1.187(2), S(1)-C(8) 1.691(2), S(1)-C(1) 1.752(1), C(8)-S(1)-C(1) 101.69(7).

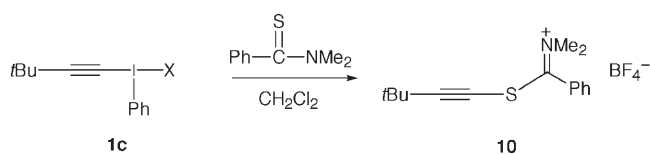
the **9**-MsOH. Treatment with a base regenerates the free sulfide **9** which undergoes spontaneous cyclization at room temperature. The isolation and cyclization of **9**-MsOH clearly indicate that this alkynyl sulfide **9** is probably a reactive intermediate in the one-step 2-aminothiazole synthesis in the presence of a base, which is compatible with the alkylidene carbene pathway C.

Comparable results were obtained from the reaction with thioamides. Reaction of 1-decynyl(tetrafluoroborate)- λ^3 -iodane (**1d**)^[14] ($X = \text{BF}_4$) with thiobenzamide in dichloromethane at $-78^\circ\text{C} \rightarrow$ room temperature afforded a 69:31 mixture of *S*-(1-decynyl)thiobenzimidonium tetrafluoroborate (**9**-HBF₄; $R = n\text{-C}_8\text{H}_{17}$, $R' = \text{Ph}$) and 4-octyl-2-phenylthiazolium tetrafluoroborate (**2**-HBF₄; $R = n\text{-C}_8\text{H}_{17}$, $R' = \text{Ph}$) quantitatively (as shown by ¹H NMR spectroscopic analysis of a crude reaction mixture). The thioimidonium salt **9**-HBF₄ is highly labile and tends to undergo intramolecular cyclization; thus, even the attempted purification of the crude

product by decantation with hexane/diethyl ether at room temperature resulted in partial cyclization, and the ratio of **9**-HBF₄/**2**-HBF₄ was reversed to 31:69 (91 % yield). Treatment with a base ($\text{Na}_2\text{CO}_3/\text{H}_2\text{O}$) accelerates the cyclization and gave 4-octyl-2-phenylthiazole (**2**)^[15] in 93 % yield. Reaction of 1-hexynyl- λ^3 -iodane **1b** ($X = \text{BF}_4$) with thiobenzamide also afforded a 94:6 mixture of labile *S*-(1-hexynyl)thiobenzimidonium tetrafluoroborate **9**-HBF₄ and 4-butyl-2-phenylthiazolium tetrafluoroborate **2**-HBF₄ (for each $R = n\text{Bu}$, $R' = \text{Ph}$), which on treatment with a solution of 5 % aqueous Na_2CO_3 produced 4-butyl-2-phenylthiazole (**2**)^[1] in a high yield (87 %).

Isolation and full characterization of the labile *S*-(1-alkynyl)thiobenzimidonium salts were achieved by reaction of the more-sterically demanding 3,3-dimethyl-1-butynyl- λ^3 -iodane **1c** ($X = \text{BF}_4$) with thiobenzamide, followed by acidification of the reaction mixture with HBF₄·Me₂O (1 equiv). This procedure makes the quantitative isolation of *S*-(3,3-dimethyl-1-butynyl)thiobenzimidonium tetrafluoroborate (**9**-HBF₄) as pale-yellow needles possible. Treatment with a base ($\text{Na}_2\text{CO}_3/\text{H}_2\text{O}$) afforded 4-*tert*-butyl-2-phenylthiazole (**2**)^[16] in 96 % yield.

N,N-Dimethylthiobenzamide seems to be an attractive nucleophile in the reaction, because the resulting *N,N*-dimethylthiobenzimidonium salts cannot undergo the intramolecular 5-endo digonal cyclization. In fact, *S*-(3,3-dimethyl-1-butynyl)thiobenzimidonium salt **10** was isolated as stable colorless plates by the reaction of *N,N*-dimethylthiobenzamide with 3,3-dimethyl-1-butynyl- λ^3 -iodane **1c** ($X = \text{BF}_4$) in 98 % yield (Scheme 3). The structure of the

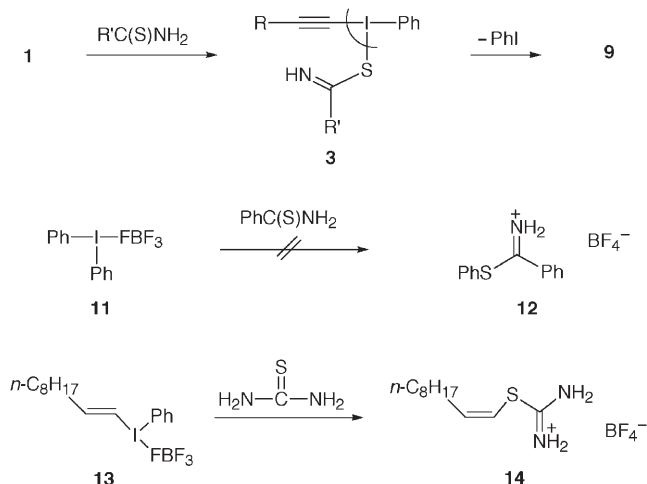


Scheme 3. Synthesis of (S)-(3,3-dimethyl-1-butynyl)thiobenzimidonium salt **10**.

salt **10** was firmly established by solid-state structure analysis (Figure 1b).^[12]

All of these results indicate that the one-step thiazole synthesis using 1-alkynyl(phenyl)- λ^3 -iodanes **1** developed by Wipf and Venkatraman involves the intermediate formation of the alkynyl sulfides **9** (and/or their salts), probably produced through the Michael addition of thioureas or thioamides and 1,2-shift in the alkylidene carbenes **7**. This Michael addition has been well established as the most common reaction pathway for 1-alkynyl- λ^3 -iodanes with soft nucleophiles.^[17,18]

An alternative mechanism that leads to the formation of **9** involves a tandem ligand exchange and ligand-coupling process at the iodine(III) center (Scheme 4). This tandem



Scheme 4. A mechanism that involves tandem ligand exchange and ligand-coupling reactions.

process does not, however, seem to take place, as the attempted reaction of diphenyl- λ^3 -iodane **11** with thiobenzamide did not show any evidence of the formation of the ligand-coupling product **12** and **11** was recovered (95%). Further evidence against the ligand-coupling mechanism was reported recently:^[19] that is, the reaction of (*E*)-1-decenyl(phenyl)- λ^3 -iodane **13** with thiourea resulted in unusual vinylic S_N2 displacement that yields the inverted (*Z*)-(S)-vinylisothiuronium salt **14** stereoselectively in a good yield (Scheme 4). In this reaction, no formation of the ligand-coupling product, the (*E*)-(S)-vinylisothiuronium salt, was detected.

In conclusion, the isolation and the intramolecular cyclization of (S)-(1-alkynyl)isothiuronium and (S)-(1-alkynyl)thiobenzimidonium salts indicate that these species are probably involved in the cyclocondensation of hypervalent 1-

alkynyl(phenyl)- λ^3 -iodanes with thioureas or thioamides yielding thiazoles.

Received: July 13, 2005

Published online: October 5, 2005

Keywords: azoles · carbenes · iodanes · Michael addition · sulfur

- [1] P. Wipf, S. Venkatraman, *J. Org. Chem.* **1996**, *61*, 8004.
- [2] a) Z.-C. Chen, P.-F. Zhang, *Synthesis* **2001**, 358; b) Z.-C. Chen, P.-F. Zhang, *J. Heterocycl. Chem.* **2001**, *38*, 503.
- [3] a) P. Brookes, A. T. Fuller, J. Walker, *J. Chem. Soc.* **1957**, 689; b) K. Shin-ya, K. Wierzb, K. Matsuo, T. Ohtani, Y. Yamada, K. Furihata, Y. Hayakawa, H. Seto, *J. Am. Chem. Soc.* **2001**, *123*, 1262; c) L. J. Perez, D. J. Faulkner, *J. Nat. Prod.* **2003**, *66*, 247; d) P. Wipf, *Chem. Rev.* **1995**, *95*, 2115; e) Z. Jin, *Nat. Prod. Rep.* **2005**, *22*, 196.
- [4] This [3,3]-sigmatropic rearrangement mechanism was also reported along with the synthesis of 2-mercaptothiazoles and selenazoles.^[2]
- [5] M. Ochiai, Y. Takaoka, Y. Nagao, *J. Am. Chem. Soc.* **1988**, *110*, 6565.
- [6] P. J. Stang, V. V. Zhdankin, *J. Am. Chem. Soc.* **1991**, *113*, 4571.
- [7] B. L. Williamson, P. Murch, D. R. Fischer, P. J. Stang, *Synlett* **1993**, 858.
- [8] Z.-D. Liu, Z.-C. Chen, *J. Org. Chem.* **1993**, *58*, 1924.
- [9] a) T. Kitamura, R. Furuki, L. Zheng, T. Fujimoto, H. Taniguchi, *Chem. Lett.* **1992**, 2241; b) D. R. Fischer, B. L. Williamson, P. J. Stang, *Synlett* **1992**, 535.
- [10] a) M. Ochiai, M. Kunishima, S. Tani, Y. Nagao, *J. Am. Chem. Soc.* **1991**, *113*, 3135; b) R. R. Tykwinski, J. A. Whiteford, P. J. Stang, *J. Chem. Soc. Chem. Commun.* **1993**, 1800; c) B. L. Williamson, R. R. Tykwinski, P. J. Stang, *J. Am. Chem. Soc.* **1994**, *116*, 93; d) T. Kosaka, T. Bando, K. Shishido, *Chem. Commun.* **1997**, 1167; e) K. S. Feldman, M. L. Wroblewski, *Org. Lett.* **2000**, *2*, 2603; f) K. S. Feldman, J. C. Saunders, *J. Am. Chem. Soc.* **2002**, *124*, 9060.
- [11] (S)-(Ethylthioethynyl)isothiuronium chloride was prepared from ethylthiochloroacetylene by reaction with thiourea in 44% yield; see: S. G. Dyachkova, N. K. Gusarova, E. A. Nikitina, L. I. Larina, L. M. Sinegovskaya, A. V. Abramov, B. A. Trofimov, *Russ. J. Gen. Chem.* **2001**, *71*, 1721.
- [12] Crystal data for **9**-MsOH ($R = Ph$, $R' = NH_2$): $C_{10}H_{12}N_2O_3S_2$, colorless block, dimensions $0.50 \times 0.50 \times 0.30$ mm³, orthorhombic, $P2_12_12_1$ (No. 19), $a = 6.271(1)$, $b = 12.077(2)$, $c = 16.638(3)$ Å, $V = 1260.0(4)$ Å³, $Z = 4$, $\rho_{calcd} = 1.436$ g cm⁻³. Data collected on a Rigaku RAXIS-RAPID imaging plate diffractometer with $Mo_{K\alpha}$ radiation ($\lambda = 0.71075$ Å) at $T = 93$ K, $2\theta_{max} = 54.9^\circ$, 12160 reflections measured, of which 12112 unique ($R_{int} = 0.017$), $\mu = 4.20$ cm⁻¹. $R = 0.026$, $R_w = 0.025$. For **10**: $C_{15}H_{20}BF_4NS$, colorless block, dimensions $0.30 \times 0.30 \times 0.20$ mm³, monoclinic, $P2_1/c$ (No. 14), $a = 11.756(5)$, $b = 23.188(8)$, $c = 12.865(5)$ Å, $\beta = 105.24(3)^\circ$, $V = 3383(2)$ Å³, $Z = 8$, $\rho_{calcd} = 1.308$ g cm⁻³. $Mo_{K\alpha}$ radiation ($\lambda = 0.71075$ Å) at $T = 93$ K, $2\theta_{max} = 54.8^\circ$, 31313 reflections measured, of which 30889 unique ($R_{int} = 0.076$), $\mu = 2.24$ cm⁻¹. $R = 0.122$, $R_w = 0.145$. CCDC-269174 (**9**-MsOH) and -269175 (**10**) contain the supplementary crystallographic data for this paper. These data can be obtained free of charge from the Cambridge Crystallographic Data Centre via www.ccdc.cam.ac.uk/data_request/cif.
- [13] T. N. Komarova, A. S. Nakhmanovich, T. E. Glotova, V. N. Elokhina, A. L. Albanov, V. A. Lopyrev, *Russ. Chem. Bull.* **1997**, *46*, 195.
- [14] M. Ochiai, M. Kunishima, K. Sumi, Y. Nagao, E. Fujita, M. Arimoto, H. Yamaguchi, *Tetrahedron Lett.* **1985**, *26*, 4501.
- [15] M. Ochiai, Y. Nishi, S. Hashimoto, Y. Tsuchimoto, D.-W. Chen, *J. Org. Chem.* **2003**, *68*, 7887.

- [16] G. Vernin, S. Treppendahl, J. Metzger, *Helv. Chim. Acta* **1977**, *60*, 284.
- [17] Reviews: a) M. Ochiai in *Topics in Current Chemistry*, Vol. 224 (Ed.: T. Wirth), Springer, Berlin, **2003**, p. 5; b) P. J. Stang, *J. Org. Chem.* **2003**, *68*, 2997; c) V. V. Zhdankin, P. J. Stang, *Tetrahedron* **1998**, *54*, 10927; d) G. F. Koser in *The Chemistry of Halides, Pseudo-halides, and Azides, Supplement D2* (Eds.: S. Patai, Z. Rappoport), Wiley, New York, **1995**, p. 1173; e) A. Varvoglis, *The Organic Chemistry of Polycoordinated Iodine*, VCH, Weinheim, **1992**.
- [18] However, hard nucleophiles, such as 2-lithiofuran and 2-lithiothiophene, attack the positively charged iodine of 1-alkynyl- λ^3 -iodanes; see: A. J. Margida, G. F. Koser, *J. Org. Chem.* **1984**, *49*, 4703.
- [19] M. Ochiai, S. Yamamoto, T. Suefuji, D.-W. Chen, *Org. Lett.* **2001**, *3*, 2753.

Metal Porphyrins

DOI: 10.1002/anie.200501943

The Importance of a β - β Bond for Long-Range Antiferromagnetic Coupling in Directly Linked Copper(II) and Silver(II) Diporphyrins**

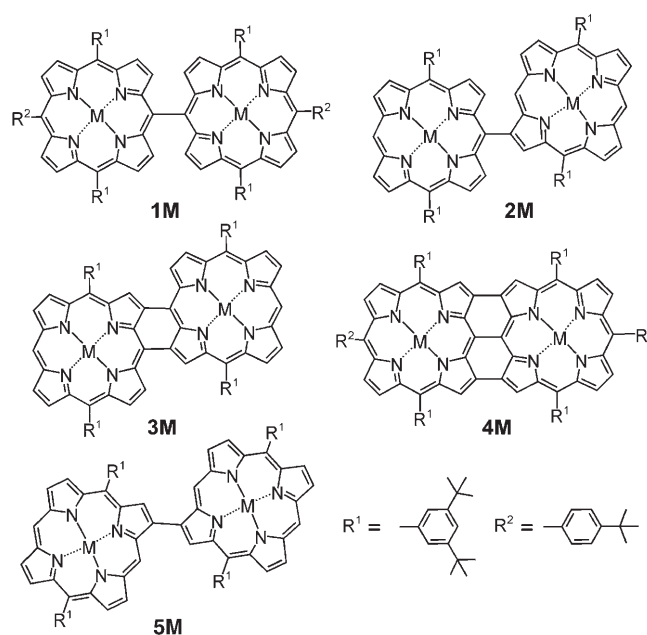
Takahisa Ikeue, Ko Furukawa, Hiroshi Hata,
Naoki Aratani, Hiroshi Shinokubo, Tatsuhisa Kato,*
and Atsuhiko Osuka*

Magnetic exchange coupling between distant metal centers is a major topic in the field of magnetochemistry.^[1] Although a

great number of covalently linked oligomacrocycles (e.g. porphyrins or phthalocyanines) have so far been prepared, only a few such molecules have been tested for the exploitation of long-range magnetic coupling.^[2,3] One difficulty in the use of these metalated macrocycles for magnetic coupling may be exemplified by the work of Eaton et al., in which a $-J$ value of only about 0.5 cm^{-1} was detected for a face-to-face coplanar bis- Cu^{II} diporphyrin with a short center-to-center distance of around 4.1 \AA .^[2a] However, suitably arranged intervening bridges may help magnetic communication between distant metal centers.^[3]

In recent years, we have explored a series of directly linked diporphyrins, including the *meso-meso* singly linked diporphyrin **1**,^[4a] the *meso*- β singly linked diporphyrin **2**,^[4b,e] the *meso*- β , β -*meso* doubly linked diporphyrin **3**,^[4c,e] and the *meso-meso*, β - β , β - β triply linked diporphyrin **4**.^[4d,e,f] Because of their direct covalent linkages, these diporphyrins exhibit a large electronic interaction, which increases in the order $2 < 1 \ll 3 \ll 4$, as judged from the absorption spectra.^[4] In these diporphyrins, two metal centers that are connected by various σ -bond networks are kept strictly apart due to the center-to-center distances of 8.34, 8.91, 8.60, and 8.42 \AA for **1**, **2**, **3**, and **4**, respectively.^[5] Herein we report antiferromagnetic coupling in bis- Cu^{II} and bis- Ag^{II} complexes of **1-4**. It is known that the unpaired spin of both Cu^{II} and Ag^{II} porphyrins is localized in the $d_{x^2-y^2}$ orbital, which leads to a situation where the unpaired electrons can be delocalized into the porphyrinic π -electronic network only through a σ -bond pathway.^[6] In this context, the diporphyrins **1-4** constitute a nice set for systematic studies on the dependence of antiferromagnetic interactions on a direct linkage.

The free-base diporphyrins **1-4** were prepared by the reported methods^[4] and metalated with $\text{Cu}(\text{OAc})_2$ and AgOAc to afford **1Cu-4Cu** and **1Ag-4Ag**, respectively (Scheme 1). The effective magnetic moments (χT) at 300 K



Scheme 1. Directly linked porphyrins **1M-5M**. M: Cu^{II} , Ag^{II} .

[*] Prof. Dr. T. Kato
Department of Chemistry
Graduate School of Science
Josai University
Sakado 350-0295 (Japan)
Fax: (+81) 49-271-7985
E-mail: rik@mail.josai.ac.jp

Dr. T. Ikeue, H. Hata, Dr. N. Aratani, Prof. Dr. H. Shinokubo,
Prof. Dr. A. Osuka
Department of Chemistry
Graduate School of Science
Kyoto University
and

Core Research for Evolutional Science and Technology (CREST)
Japan Science and Technology Agency
Sakyo-ku, Kyoto 606-8502 (Japan)
Fax: (+81) 75-753-3970
E-mail: osuka@kuchem.kyoto-u.ac.jp

Dr. K. Furukawa
Institute for Molecular Science
Myodaiji, Okazaki 444-8585 (Japan)

[**] This work was partly supported by Grants-in-Aid from the Ministry of Education, Culture, Sports, Science, and Technology, Japan (no. 15350022 and 21st Century COE on Kyoto University Alliance for Chemistry) and by the International Innovation Center of Kyoto University.



Supporting information for this article is available on the WWW under <http://www.angewandte.org> or from the author.

were determined to be 0.82–0.87 emu K mol^{-1} for **1Cu**–**4Cu**, thus indicating the presence of two magnetically uncoupled spin doublets (Figure 1a; see also Supporting Information (SI)). Variable-temperature magnetic susceptibility measurements revealed that the χT values of **1Cu**, **2Cu**, and **3Cu** are nearly temperature-independent in the range 2–300 K, with essentially constant values of about 0.8 emu K mol^{-1} .

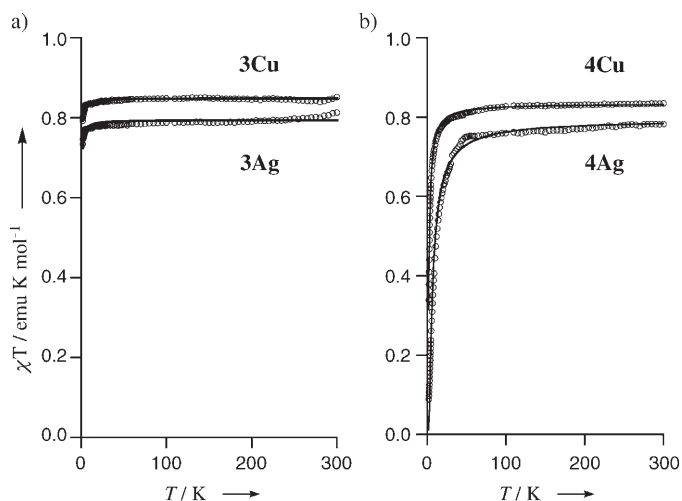


Figure 1. Variable-temperature magnetic susceptibility measurements in the range 2–300 K: a) **3Cu** and **3Ag**, b) **4Cu** and **4Ag**. The solid lines represent the fitting curves based on the Bleaney–Bowers equation.

The mean g values in the EPR spectra of **1Cu**, **2Cu**, and **3Cu** in frozen toluene at 4.0 K were 2.08, 2.13, and 2.13 (see SI), respectively, which were reproduced as a simple sum of an isolated Cu^{II} porphyrin. In contrast, the χT value of **4Cu** was found to drop sharply at temperatures below 20 K and to reach a value of 0.34 emu K mol^{-1} at 2.0 K (Figure 1b). This temperature dependence is indicative of Curie law behavior with a weak antiferromagnetic coupling between the two copper(II) ions. A least-squares fit with the Bleaney–Bowers equation gave a $-J$ value of 1.43 cm^{-1} for **4Cu**. In line with the χT measurement, the EPR spectrum of **4Cu** at the mean g value of 2.11 could not be reproduced as a sum of isolated Cu^{II} porphyrins but as two magnetically interacting Cu^{II} porphyrins. This means that the spectrum of **4Cu** is due to the thermally populated $S = 1$ triplet state above the $S = 0$ ground state.

The magnetic properties of **1Ag**–**4Ag** were also examined. In the range 2–300 K, the χT values of **1Ag**–**3Ag** are temperature independent (ca. 0.8 emu K mol^{-1} ; Figure 1a), thus indicating the presence of two magnetically uncoupled spin doublets, while the χT values of **4Ag** exhibit a sharp drop below 20 K, reaching a value of 0.09 emu K mol^{-1} at 2.0 K (see SI and Figure 1b). The mean g values in the EPR spectra of **1Ag**–**4Ag** in frozen toluene are 2.06, 2.07, 2.06, and 2.06, respectively. The spectra of **1Ag**–**3Ag** were reproduced as a simple sum of isolated Ag^{II} porphyrins, whereas that of **4Ag** could be reproduced as two magnetically interacting Ag^{II}

porphyrins, similarly to the case of **4Cu** (see SI). The least-squares fit with the Bleaney–Bowers equation gave a $-J$ value of 3.64 cm^{-1} for **4Ag** (Figure 1b).

The marked differences observed between the magnetic coupling behaviors of **4M** and **1M**–**3M** led us to consider the importance of a β – β bond for effective long-range magnetic coupling, since such a linkage only exists in **4M**. We thus prepared a new β – β singly linked diporphyrin **5M** from a β -borylated porphyrin precursor.^[7] Both bis-metalated complexes **5Cu** and **5Ag** exhibit long center-to-center distances of around 9.63 Å and the lowest excitonic coupling in the absorption spectra in the series. Nevertheless, as shown in Figure 2, both the χT values of **5Cu** and **5Ag** exhibit

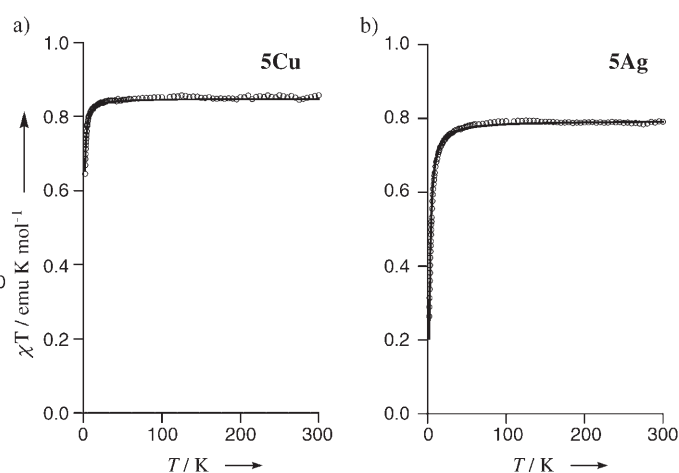


Figure 2. Variable-temperature magnetic susceptibility measurements in the range 2–300 K: a) **5Cu** and b) **5Ag**. The solid lines represent the fitting curves based on the Bleaney–Bowers equation.

temperature-dependent behavior at low temperature, reaching values of 0.65 and 0.24 emu K mol^{-1} at 2.0 K, respectively. The least-squares fit of the χT values with the Bleaney–Bowers equation provided $-J$ values of 0.55 and 1.73 cm^{-1} , respectively. These results clearly indicate the critical role of a direct β – β bond in the long-range antiferromagnetic coupling.

Although excited triplet states are present in **4Cu**, **4Ag**, **5Cu**, and **5Ag**, no EPR signal was observed at the half field. This can be accounted for in terms of a small fine-structure interaction $|D|$ in the triplet states (see SI) of these diporphyrins.^[8] The $|D|$ value should become smaller with increasing spin–spin distance. Actually, a simple estimation of $|D|$ for **4M** and **5M** led to a prediction that the “forbidden transition” at the half field is hardly observed in these cases (see SI); this seems to be a general feature of diporphyrins with a large center-to-center distance.

The critical importance of a direct β – β bond can be explained in terms of the spin densities of Cu^{II} and Ag^{II} porphyrin monomers, as calculated by the DFT method at the B3LYP level. The 6-31G* basis set was employed except for Cu and Ag, for which a basis set consisting of the Stuttgart effective core potential was used. In both cases, the calculations confirmed that the unpaired electron in the $d_{x^2-y^2}$

orbital develops only at the β position and not at the *meso* position (see SI), thus highlighting the importance of a direct β – β bond. In fact, the calculated singly occupied MOs (SOMOs; Figure 3) of a model compound for **4Cu**, in which

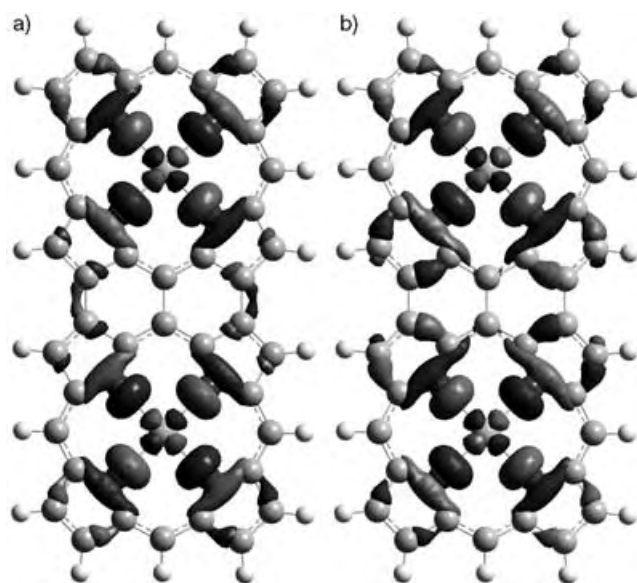


Figure 3. Two calculated SOMOs of a model for **4Cu** in the $S=1$ state.

all *meso* substituents were replaced with hydrogen, indicate that the spin orbital of the copper porphyrin interacts only through the β – β bond in the $S=1$ state (Figure 3a). In addition, the DFT calculations support our interpretation of the EPR measurements, namely that the $S=0$ ground state lies below the $S=1$ state.

The antiferromagnetic couplings are larger in the Ag^{II} complexes than in their Cu^{II} counterparts. Since the spin distribution patterns are similar due to the spin location in the $d_{x^2-y^2}$ orbital, the observed difference may be attributed to different spin densities. The spin density distribution via the σ -contact contribution can be estimated by a ^2H NMR method. Typically, the ^2H NMR spectrum of $\text{Cu}^{\text{II}}(\text{tpp})$ exhibits the pyrrole β - ^2H signal at around $\delta=41$ ppm as a broad signal,^[9] while the signals of $\text{Ag}^{\text{II}}(\text{tpp})$ are too broad to be detected, thus indicating that the σ -contact contribution is larger for Ag^{II} porphyrin than Cu^{II} porphyrin. The fact that **5Ag** lies roughly on the long-range limit predicted by the Coffman–Buettner equation^[10] suggests that the direct β – β bond allows an effective σ -bond pathway for long-range antiferromagnetic coupling between distal paramagnetic metal ions in porphyrins (see SI).

In conclusion, we have shown that antiferromagnetic coupling is only effective for **4Cu**, **4Ag**, **5Cu**, and **5Ag**, thus underlining the crucial importance of a direct β – β bond. However, even in the extensively π -conjugated diporphyrins **4Cu** and **4Ag**, the long-range antiferromagnetic interaction is considered to propagate via a β – β σ -bond pathway. These results will be quite useful for further molecular design of magnetically coupled molecules. The exploration of higher

Cu^{II} and Ag^{II} porphyrin arrays is an attractive subject that is actively being pursued in our laboratory.

Received: June 6, 2005

Published online: October 7, 2005

Keywords: copper · magnetochemistry · metal–metal interactions · porphyrinoids · silver

- [1] O. Kahn, *Molecular Magnetism*, VCH, New York, **1993**.
- [2] a) S. S. Eaton, G. R. Eaton, C. K. Chang, *J. Am. Chem. Soc.* **1985**, *107*, 3177; b) J. Wojacynski, L. Latos-Grażyński, P. J. Chmielewski, P. V. Calcar, A. L. Balch, *Inorg. Chem.* **1999**, *38*, 3040; c) M. Zhao, C. Zhong, C. Stern, A. G. M. Barrett, B. M. Hoffman, *Inorg. Chem.* **2004**, *43*, 3377.
- [3] Some directly linked oligoporphyrins have been used for spin alignment of π radicals; see: a) H. Segawa, D. Machida, Y. Senshu, J. Nakazaki, K. Hirakawa, F. Wu, *Chem. Commun.* **2002**, 3032; b) H. Segawa, Y. Senshu, J. Nakazaki, K. Susumu, *J. Am. Chem. Soc.* **2004**, *126*, 1354.
- [4] a) A. Osuka, H. Shimidzu, *Angew. Chem.* **1997**, *109*, 93; *Angew. Chem. Int. Ed. Engl.* **1997**, *36*, 135; b) T. Ogawa, Y. Nishimoto, N. Yoshida, N. Ono, A. Osuka, *Angew. Chem.* **1999**, *111*, 140; *Angew. Chem. Int. Ed.* **1999**, *38*, 176; c) A. Tsuda, A. Nakano, H. Furuta, H. Yamochi, A. Osuka, *Angew. Chem.* **2000**, *112*, 572; *Angew. Chem. Int. Ed.* **2000**, *39*, 558; d) A. Tsuda, H. Furuta, A. Osuka, *Angew. Chem.* **2000**, *112*, 2649; *Angew. Chem. Int. Ed.* **2000**, *39*, 2549; e) A. Tsuda, H. Furuta, A. Osuka, *J. Am. Chem. Soc.* **2001**, *123*, 10304; f) A. Tsuda, A. Osuka, *Science* **2001**, *293*, 79.
- [5] The center-to-center distances were estimated from the X-ray crystal structures of the related diporphyrins given in reference [4e].
- [6] G. N. La Mar, F. A. Walker in *The Porphyrins*, Vol. IVB (Ed.: D. Dolphin), Academic Press, New York, **1979**, p. 57.
- [7] H. Hata, H. Shinokubo, A. Osuka, *J. Am. Chem. Soc.* **2005**, *127*, 8264.
- [8] A. Bencini, D. Gatteschi, *EPR of Exchange Coupled Systems*, Springer, Berlin, **1989**.
- [9] G. M. Godziela, H. M. Goff, *J. Am. Chem. Soc.* **1986**, *108*, 2237.
- [10] R. E. Coffman, G. R. Buettner, *J. Phys. Chem.* **1979**, *83*, 2387.

Molecular and Polymeric Hybrids Based on Covalently Linked Polyoxometalates and Transition-Metal Complexes**

Jeonghee Kang, Bubin Xu, Zhonghua Peng,*
Xiaodong Zhu, Yongge Wei, and Douglas R. Powell

We report a rational synthetic approach to novel molecular and polymeric hybrids containing polyoxometalate (POM) clusters and transition-metal complexes covalently linked by an organic π -conjugated bridge. There continues to be extensive interest in hybrids containing both POMs and organometallic components.^[1–3] The motivation lies not only in chemists' steady desire to bring different structural units together but also in the prospect of generating new functional and multifunctional materials,^[4] although the overwhelming interest in organometallic/POM hybrids has so far been focused to their catalytic activity.^[1,5] A significant number of organometallic/POM hybrids have already been reported, most of which anchor the organometallic component by either the surface oxygen atoms of POM clusters or active metal centers incorporated within the POM cluster.^[1–5] The commonly adopted synthetic approach relies on a self-assembly process in which attachment of the organometallic component and assembly of the POM cluster occur simultaneously.^[1–5] Although various other preparation methods have been reported,^[6] one which allows rational design and predetermination of structure and properties remains elusive.

One fascinating aspect of POM clusters is their structural diversity, not only in the cluster frame itself but also in the ways of derivatizing them.^[1] Among the many types of organically functionalized POMs, organoimido derivatives are particularly interesting.^[7] Aside from remarkable stability of the imido metal–nitrogen linkage, which makes further structural modification on the cluster-anchored organic

component possible,^[8] delocalization of organic π electrons on the POM cluster may lead to a new class of electronic hybrid materials.^[9] Indeed, we have recently shown that organoimido derivatives with remote functionality can be used as building blocks to construct hybrid dumbbells,^[10] charge-transfer hybrids,^[11] and polymer hybrids^[12] which have been demonstrated to be photovoltaic materials. Here we report that the building block approach can be extended to the preparation of organometallic POMs with predetermined structures. In particular, we describe the synthesis and optical properties of the first molecular and polymeric hybrids (**3** and **6** in Schemes 1 and 2, respectively) in which POM clusters and transition-metal complexes are linked by an organic π -conjugated bridge. Such hybrids were designed to take advantage of the metal-to-ligand charge-transfer (MLCT) transitions of transition-metal complexes,^[13] the electron-accepting properties of POM clusters, and the charge-transport properties of π -conjugated systems, to realize systems with efficient photoinduced charge separation.

Schemes 1 and 2 show the structures and syntheses of molecular hybrid **3** and polymeric hybrid **6**, respectively. Polyoxometalate clusters functionalized with one or two iodo functional groups (**1** and **4**, respectively) were prepared according to previously reported procedures.^[14,15] Pd-catalyzed coupling of 4'-ethynyl-2,2',6',2''-terpyridine with **1** and **4** yielded terpyridine-functionalized clusters **2** and **5**, respectively. The crystal structure of hybrid **2** was communicated previously.^[16] Hybrid **5** was characterized by ¹H NMR spectroscopy (see Experimental Section), electrospray ionization mass spectrometry (ESI-MS), and X-ray single-crystal diffraction.

The mass spectrum of **5** shows isotopic clusters centered at m/z 853.05 (100), 1707.73 (9), and 1953.09 (3 %). These signals can be assigned to the cluster anion M^{2-} ($M = [Mo_6O_{17}N_8C_{58}H_{32}]$, calcd m/z : 854.36), $M^{2-} + H^+$ (calcd m/z : 1709.72), and $M^{2-} + Bu_4N^+$ (calcd m/z : 1952.17), respectively, consistent with its structure.

Hybrid **5** crystallizes in the triclinic space group $P\bar{1}$ ^[17] with two formula units per asymmetric unit of the cell. The anions of the two formula units adopt rather different configurations (Figure 1). Most notable are the different dihedral angles between one terpyridine system (2-3-4) and the adjacent phenyl ring (ring 1). In configuration a, the dihedral angle between rings 1 and 2 is only 19.7°, while the corresponding two rings are nearly perpendicular to each other in configuration b.

Coordination of hybrids **2** and **5** with Fe^{2+} was carried out in acetonitrile or dimethyl sulfoxide (DMSO) at room temperature. ¹H NMR titration (see Supporting Information (SI) for details) indicates that the terpyridine ligand in **2** almost completely coordinates with Fe^{2+} to form Fe^{2+} bis(terpyridine) complex when 0.5 equiv of Fe^{2+} (vs **2**) is added. Further addition of Fe^{2+} does not result in the dissociation of the bis(terpyridine) complex; this indicates a high kinetic barrier and thus kinetic inertness of $[Fe(tpy)_2]^{2+}$ complexes.^[18] Hybrid **3**, however, has a net –2 charge. Excess Fe^{2+} can replace Bu_4N^+ and form ion pairs with **3**. Indeed, when an excess of $FeCl_2$ (10 equiv) was added to a solution of **2** in acetonitrile, a green precipitate immediately formed,

[*] J. Kang, Dr. B. Xu, Prof. Z. Peng, Dr. X. Zhu

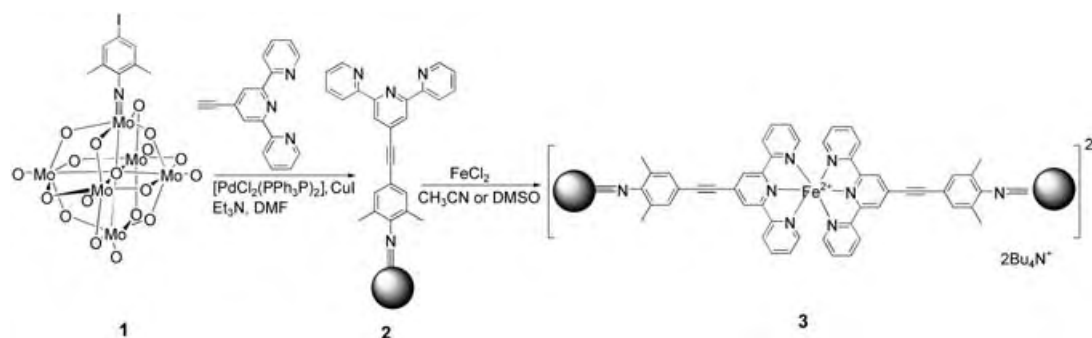
Department of Chemistry
University of Missouri-Kansas City
Kansas City, MO 64110 (USA)
Fax: (+1) 816-235-5502
E-mail: pengz@umkc.edu

Dr. Y. Wei
Department of Chemistry
Tsinghua University
Beijing, 100080 (China)

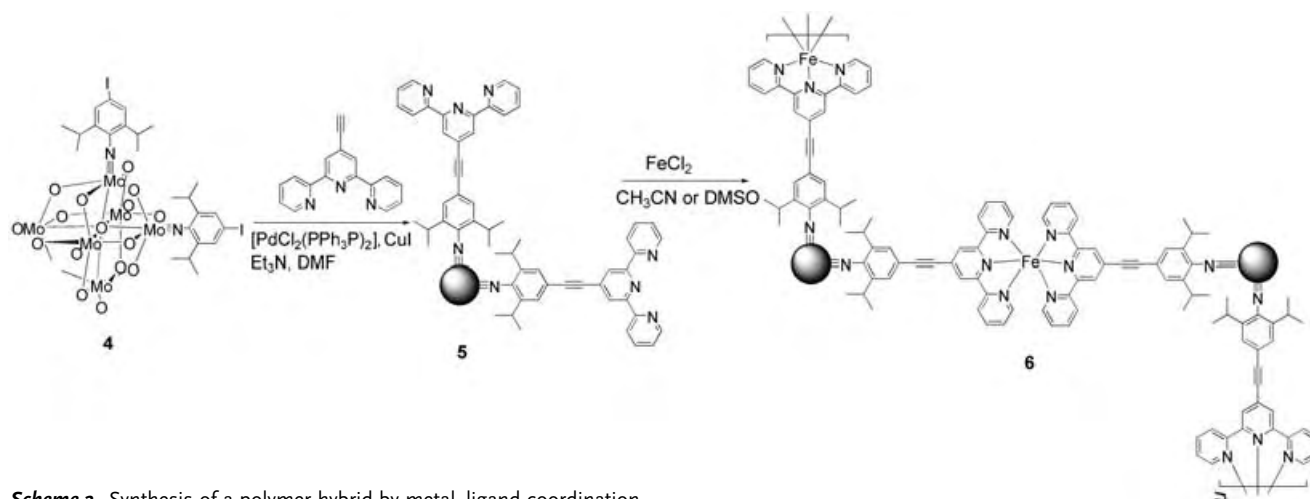
Dr. D. R. Powell
Department of Chemistry
University of Kansas
Lawrence, KS 66045 (USA)

[**] This work is supported by National Science Foundation (DMR 0134032) and the Office of Naval Research. We thank Dr. Nathan D. Leigh for the ESI-MS measurements on hybrid **5**.

Supporting information for this article is available on the WWW under <http://www.angewandte.org> or from the author.



Scheme 1. Synthesis of a molecular hybrid containing POM clusters and a transition-metal complex linked by a conducting bridge.



Scheme 2. Synthesis of a polymer hybrid by metal-ligand coordination.

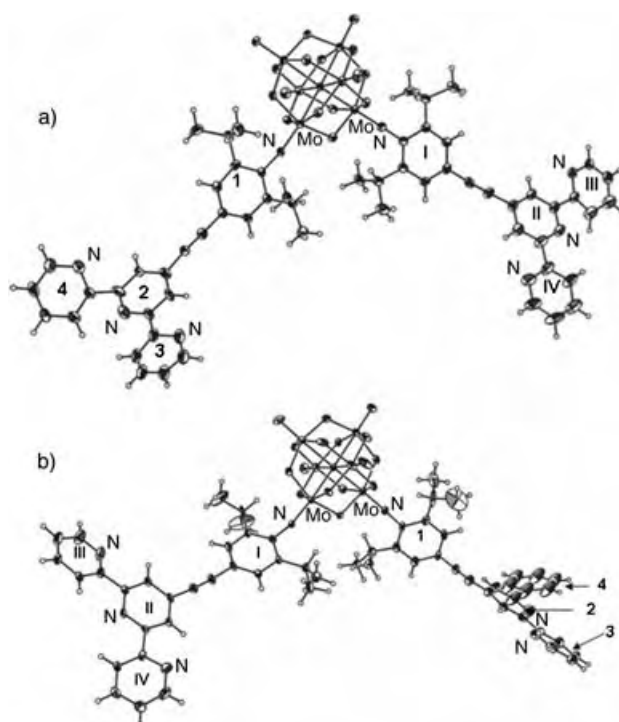


Figure 1. ORTEP representation for the two anion configurations in hybrid 5. Selected dihedral angles [°]: I–II, 25.1 (a), 25.6 (b); II–III, 18.8 (a), 17.2 (b); II–IV, 6.7 (a), 16.8 (b); 1–2, 19.7 (a), 81.6 (b); 2–3, 3.8 (a), 6.4 (b); 2–4, 35.2 (a), 33.6 (b).

whose ^1H NMR spectrum shows no proton signals of Bu_4N^+ (see the Supporting Information). A UV/Vis titration experiment (see the Supporting Information) also points to the formation of 3-Fe^{2+} ion pairs when an excess of Fe^{2+} is added. These results indicate that, to form **3** with Bu_4N^+ as the counterion, the appropriate ratio of $\text{Fe}^{2+}/\mathbf{2}$ is 1:2.

Hybrid **3** with the Bu_4N^+ counterion is soluble in dimethyl formamide (DMF) and DMSO. Its structure was confirmed by ^1H NMR and ESI-MS measurements. As shown in Figure 2, both hybrids **2** and **3** show nearly identical signals in the region of chemical shifts between 0 and 4 ppm, where protons in the Bu_4N^+ counterion (labeled a, b, c, d) and the benzyl methyl protons (proton 8) appear. The cluster-bound aryl protons (proton 7) also exhibit similar chemical shifts. Protons in the terpyridine ligands, however, show drastic changes in chemical shifts after Fe^{2+} –terpyridine coordination. By comparison with the ^1H NMR spectrum of Fe^{2+} –bis(terpyridine) model complex **7**, one can clearly identify the similarity in the aromatic region between **3** and **7**, assign all signals accordingly, and thus unambiguously confirm Fe^{2+} –terpyridine complexation. The lack of signals corresponding to free terpyridine ligands in the ^1H NMR spectrum of **3** indicates rather complete coordination. The integration ratio of signals associated with the hybrid anion versus those corresponding to the counterion also offers useful structural information. For example, the integration ratios of signal 3' over b are 1:7.76 for **2** and 1:3.82 for **3**, that is, one Fe^{2+} ion

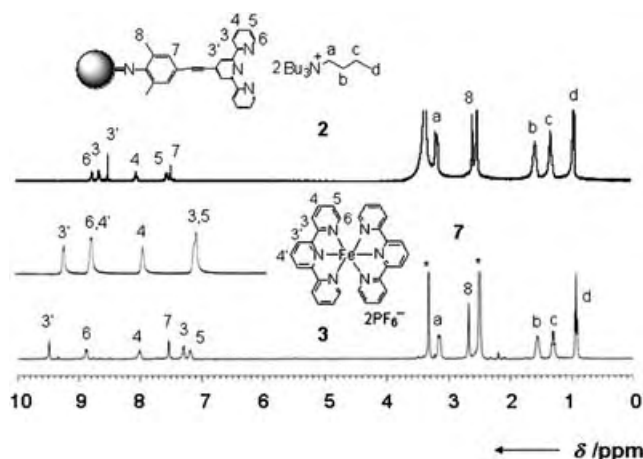


Figure 2. ^1H NMR spectra of **2** and **3**. The middle spectrum is the ^1H NMR spectrum of **7**. All spectra were recorded in $[\text{D}_6]\text{DMSO}$.

indeed binds to two terpyridyl ligands (the theoretical ratios of $3'$ over b for **2** and **3** are 1:8 and 1:4, respectively).

The structure of **3** is also confirmed by ESI-MS measurements. The ESI mass spectrum of hybrid **3** shows two major isotopic clusters centered at m/z 1265 and 1239.2. The first signal can be assigned to the cluster anion M^{2-} of **3** ($\text{M}^{2-} = [\text{Mo}_{12}\text{O}_{36}\text{N}_8\text{C}_{50}\text{H}_{36}\text{Fe}]^{2-}$, calcd m/z : 1266.0), while the second is attributed to hybrid **2** ($[\text{2}]^{2-} + \text{H}^+$, $[\text{Mo}_6\text{O}_{18}\text{N}_4\text{C}_{25}\text{H}_{19}]^-$, calcd m/z : 1239.1). The relative intensity of these two signals depends strongly on probe potential. Under relatively high probe potential (15 V), the signal corresponding to free hybrid ligand **2** dominates (1239.2, 100%; 1265, 55%), while under low probe potential (8 V), the relative intensity of the two signals reverses (1239.2, 38 %; 1265, 100 %); hence, the appearance of signals corresponding to noncoordinated hybrid **2** is due to in-source decomposition of **3**. Great efforts were made to grow single crystals of **3**, but all attempts so far were unsuccessful.

Unlike **3**, coordinated hybrid **6** exhibits poor solubility in common organic solvents. When the coordination of **5** with FeCl_2 is carried out in acetonitrile, the coordinated product precipitates immediately as a green solid, and the overlying clear solution becomes colorless. ^1H NMR measurements on the clear solution show no signals for aromatic proton but only for tetrabutylammonium counterion, indicating that all starting hybrid **5** has reacted and precipitated. Hybrid **6** does show slight solubility in DMSO, however. When the coordination process of hybrid **5** with FeCl_2 was carried out in $[\text{D}_6]\text{DMSO}$, a green precipitate was again produced. The color of the solution, however, remained green. After mixing with FeCl_2 for only 20 min, the ^1H NMR spectrum of the solution (see the Supporting Information) shows that the signals corresponding to free terpyridine ligands have completely disappeared, that is, all terpyridine ligands have coordinated with Fe^{2+} . The peaks in the aromatic region show chemical shifts nearly identical to those of hybrid **3**, further confirming the formation of iron(II)-bis(terpyridine) complexes. The overwhelming counterion signals in the solution indicate that, as coordinated hybrid **6** precipitates from solution, the tetrabutylammonium counterion remains.

Indeed, the ^1H NMR spectrum of **6** (the green precipitate), obtained after days of data collection due to its poor solubility, shows no signals attributable to the counterion, while signals consistent with iron(II)-bis(terpyridine) complex can be identified. Note that the lack of free terpyridyl ligands in **6** may also indicate the formation of cyclic oligomers.

The electronic properties of hybrids **3** and **6** were studied by UV/Vis absorption measurements. As shown in Figure 3,

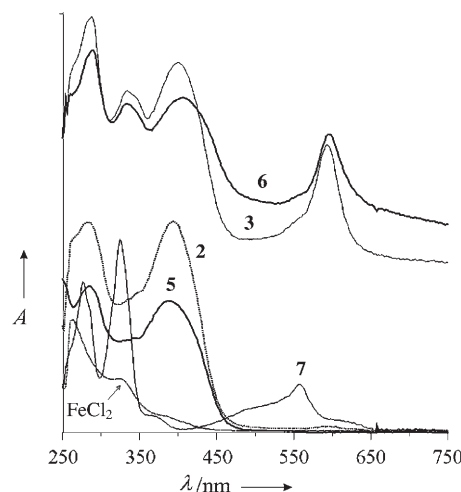


Figure 3. UV/Vis absorption spectra of hybrids **2**, **3**, **5**, **6**, and model Fe^{2+} -bis(terpyridine) complex **7** in DMSO.

terpyridine-anchored clusters **2** and **5** both show a maximum absorption at 392 nm, which is assigned to the ligand-to-metal charge-transfer (LMCT) transition associated with Mo–N π bonding. After coordination with Fe^{2+} , the resulting hybrids **3** and **6** show two new absorption bands, one at 595 nm and the other at 333 nm. The first band is attributed to MLCT, while the second is due to the ligand-centered (LC) transition, both associated with the Fe^{2+} -bis(terpyridine) complex. These assignments are confirmed by the UV/Vis absorption spectrum of model complex **7**, which shows two similar absorption bands. The MLCT bands of **3** and **6** are red-shifted by nearly 40 nm compared to that of **7**. The electron-withdrawing nature of the $\text{Mo}\equiv\text{N}$ bond lowers the π^* orbital of the ligand and thus decreases the MLCT band gap and results in its bathochromic shift.^[19] The more extended π conjugation of the ligands in **3** and **6** than in **7** also contributes to the red shift.^[20]

The electrochemical behavior of hybrids **3** and **6** was studied by cyclic voltammetry. Figure 4 shows the cyclic voltammogram of **6**, measured on its polymer film, together with those of **3**, model complex **7**, and hybrid **2**, measured in DMSO solutions. In the range -2.0 – 1.5 V (vs Ag/Ag^+), **7** shows one metal-localized ($\text{Fe}^{2+}/\text{Fe}^{3+}$) reversible oxidation wave at 0.805 V ($\Delta E = 0.11$ V) and two ligand-localized reversible reduction waves at -1.47 V ($\Delta E = 0.10$ V) and -1.62 V ($\Delta E = 0.10$ V).^[21] In the same potential range, hybrid **2** exhibits no oxidation process. Besides one semireversible reduction process at -1.60 V, which can be attributed to the reduction of the terpyridine ligand, a reversible reduction wave at a much lower potential of -0.80 V ($\Delta E = 0.17$ V) is

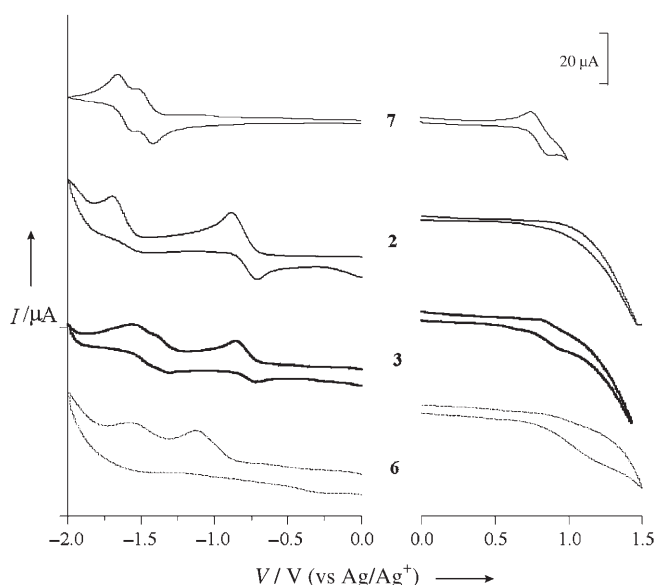


Figure 4. Cyclic voltammograms of **2**, **3**, and **7**.

observed. This reduction process is associated with the POM cluster.^[7] Under the same conditions and in the same potential range, hybrid **3** shows redox waves of both **2** and **7**. The observation of the $\text{Fe}^{2+/3+}$ oxidation wave, the POM-associated reduction wave, and the two ligand-centered reduction waves once again confirms the structure of **3**. For **6**, the $\text{Fe}^{2+/3+}$ oxidation wave is still noticeable, and the reduction peak at -1.12 V is consistent with diimido derivatives of POMs.^[7,12]

In conclusion, we have successfully prepared the first hybrid in which a POM cluster and transition-metal complexes are linked through an extended π -conjugated bridge. A coordinated POM-containing hybrid polymer is also demonstrated. The hybrids exhibit low-lying MLCT transitions associated with the transition-metal complexes and LMCT transitions located at the cluster/organic $\text{Mo}=\text{N}$ junction. This rational building-block approach may be extended to the preparation of hybrids with other metal ions, particularly those coordinating with terpyridine ligands at room temperature with large binding constants.

Experimental Section

See the Supporting Information for detailed synthetic procedures of hybrids **3**, **5**, and **6**, their ^1H NMR spectra, ^1H NMR titration and UV/Vis titration of the coordination process of **2** with FeCl_2 , and ESI-MS data of **5** and **3**.

Received: June 2, 2005

Published online: October 5, 2005

Keywords: C–C coupling · iron · molybdenum · organic–inorganic hybrids · polyoxometalates

- [2] a) D. Hagraman, C. Zubieta, D. J. Rose, J. Zubieta, R. C. Haushalter, *Angew. Chem.* **1998**, *109*, 904; *Angew. Chem. Int. Ed.* **1998**, *36*, 873; b) V. Shivaiah, M. Nagaraju, S. K. Das, *Inorg. Chem.* **2003**, *42*, 6604; c) X. B. Cui, J. Q. Xu, H. Meng, S. T. Zheng, G. Y. Yang, *Inorg. Chem.* **2004**, *43*, 8005.
- [3] a) R. S. Rarig, Jr., L. Bewley, V. Golub, C. J. O’Conner, J. Zubieta, *Inorg. Chem. Commun.* **2003**, *6*, 539; b) A. Dolbecq, P. Mialane, L. Lisnard, J. Marrot, F. Sécheresse, *Chem. Eur. J.* **2003**, *9*, 2914; c) C. D. Wu, C. Z. Lu, H. H. Zhuang, J. S. Huang, *J. Am. Chem. Soc.* **2002**, *124*, 3836.
- [4] a) S. I. Stupp, P. V. Braun, *Science* **1997**, *277*, 1242; b) O. M. Yaghi, H. Li, C. Davis, D. Richardson, T. L. Groy, *Acc. Chem. Res.* **1998**, *31*, 474.
- [5] a) Y. Lin, R. G. Finke, *J. Am. Chem. Soc.* **1994**, *116*, 8335; b) K. Takahashi, M. Yamaguchi, T. Shido, T. Ohtani, K. Isobe, M. Ishigawa, *J. Chem. Soc. Chem. Commun.* **1995**, 1301; c) R. Neumann, M. Dahan, *Nature* **1997**, 388, 353.
- [6] I. Bar-Nahum, H. Cohen, R. Neumann, *Inorg. Chem.* **2003**, *42*, 3677.
- [7] J. B. Strong, G. P. A. Yap, R. Ostrander, L. M. Liable-Sands, A. L. Rheingold, R. Thouvenot, P. Gouzerh, E. A. Maatta, *J. Am. Chem. Soc.* **2000**, *122*, 639.
- [8] a) A. R. Moore, H. Kwen, A. B. Beatty, E. A. Maatta, *Chem. Commun.* **2000**, 1793; b) B. Xu, Y. Wei, C. L. Barnes, Z. Peng, *Angew. Chem.* **2001**, *113*, 2353; *Angew. Chem. Int. Ed.* **2001**, *40*, 2290.
- [9] J. L. Stark, V. G. Young, Jr., E. A. Maatta, *Angew. Chem.* **1995**, *107*, 2751; *Angew. Chem. Int. Ed. Engl.* **1995**, *34*, 2547.
- [10] M. Lu, Y. Wei, B. Xu, C. F.-C. Cheung, Z. Peng, D. Powell, *Angew. Chem.* **2002**, *114*, 1636; *Angew. Chem. Int. Ed.* **2002**, *41*, 1566.
- [11] J. Kang, J. Nelson, M. Lu, B. Xie, Z. Peng, D. R. Powell, *Inorg. Chem.* **2004**, *43*, 6408.
- [12] M. Lu, B. Xie, J. Kang, F. Chen, Y. Yang, Z. Peng, *Chem. Mater.* **2005**, *17*, 402.
- [13] a) A. Juris, V. Balzani, F. Barigelli, S. Campagna, P. Belser, A. von Zelewsky, *Coord. Chem. Rev.* **1988**, *84*, 85; b) S. Baitalik, X. Wang, R. H. Schmehl, *J. Am. Chem. Soc.* **2004**, *126*, 16304.
- [14] Y. Wei, B. Xu, C. L. Barnes, Z. Peng, *J. Am. Chem. Soc.* **2001**, *123*, 4083.
- [15] L. Xu, M. Lu, B. Xu, Y. Wei, Z. Peng, D. R. Powell, *Angew. Chem.* **2002**, *114*, 4303; *Angew. Chem. Int. Ed.* **2002**, *41*, 4129.
- [16] a) B. Xu, Z. Peng, Y. Wei, D. R. Powell, *Chem. Commun.* **2003**, 2562; b) Z. Peng, *Angew. Chem.* **2004**, *116*, 948; *Angew. Chem. Int. Ed.* **2004**, *43*, 930.
- [17] Crystal data for **5**: $2(\text{C}_{16}\text{H}_{36}\text{N})^+(\text{C}_{58}\text{H}_{52}\text{Mo}_6\text{N}_8\text{O}_{17})^{2-}(\text{CH}_2\text{Cl}_2)$, $M_r = 2278.56$, triclinic, $P\bar{1}$, $a = 16.296(3)$, $b = 19.855(4)$, $c = 30.823(6)$ Å, $\alpha = 90.452(4)$, $\beta = 93.885(4)$, $\gamma = 90.316(4)^\circ$, $V = 9950(3)$ Å³, $Z = 4$, $Z' = 2$, $\rho_{\text{calcd}} = 1.521$ g cm⁻³, $T = 100(2)$ K, $R1 = 0.0711$, and $wR2 = 0.1973$. GOF (F^2) = 1.049. CCDC-272303 contains the supplementary crystallographic data for this paper. These data can be obtained free of charge from the Cambridge Crystallographic Data Centre via www.ccdc.cam.ac.uk/data_request/cif.
- [18] a) S. Schmatloch, A. M. J. van den Berg, A. S. Alexeev, H. Hofmeier, U. S. Schubert, *Macromolecules* **2003**, *36*, 9943; b) R. Dobrawa, M. Lysetska, P. Ballester, M. Grüne, F. Würthner, *Macromolecules* **2005**, *38*, 1315.
- [19] E. C. Constable, A. M. W. Cargill Thompson, *J. Chem. Soc. Dalton Trans.* **1994**, 1409.
- [20] S. Bernhard, J. I. Goldsmith, K. Takada, H. D. Aruña, *Inorg. Chem.* **2003**, *42*, 4389.
- [21] S. Bernhardt, K. Takada, D. J. Díaz, H. D. Aruña, H. Mürner, *J. Am. Chem. Soc.* **2001**, *123*, 10265.

[1] a) P. Gouzerh, A. Proust, *Chem. Rev.* **1998**, *98*, 77, and references therein; b) P. Gouzerh, R. Villanneau, R. Delmont, A. Proust, *Chem. Eur. J.* **2000**, *6*, 1184.

DOI: 10.1002/anie.200501914

Perovskite Hollow-Fiber Membranes for the Production of Oxygen-Enriched Air**

Haihui Wang,* Steffen Werth, Thomas Schiestel, and Jürgen Caro

Oxygen-enriched air with 30–50 vol % O₂ is used in a number of industrial processes, for example, in the synthesis of ammonia, the Claus process, and the regeneration of the catalyst for the fluid-catalytic-cracking (FCC) process.^[1,2] Another application of O₂-enriched air is the most efficient use of methane in high-temperature furnaces or cement kilns.^[2] There are different methods for producing O₂-enriched air, mainly by mixing air with pure O₂ obtained from a cryogenic technique or pressure swing adsorption (PSA). However, these techniques require high capital investment and operational costs. Depending on the O₂ concentration and the amount of the O₂-enriched air needed, membrane technology can be competitive. As organic polymeric hollow-fiber membranes have a separation factor between 2 and 6, a single-stage membrane permeation gives an O₂ concentration typically of the order of 30–50 vol % under a pressure difference of about 10 bar.^[3] Although higher O₂ concentration and permeability can be achieved by increasing the feed flow rate, by reducing the membrane thickness, or by increasing the pressure difference, these actions increase the separation costs. Furthermore, the organic polymeric membrane cannot be used for the recovery of heat from exhaust gas in high-temperature processes.

Herein we propose a new technique to produce O₂-enriched air by using a mixed-ion and electron-conducting (MIEC) perovskite membrane. The basic idea is shown in Figure 1. At elevated temperatures, under a slight difference in air pressure (1–2 bar) O₂ can be transported through a MIEC perovskite membrane in the form of oxygen ions from

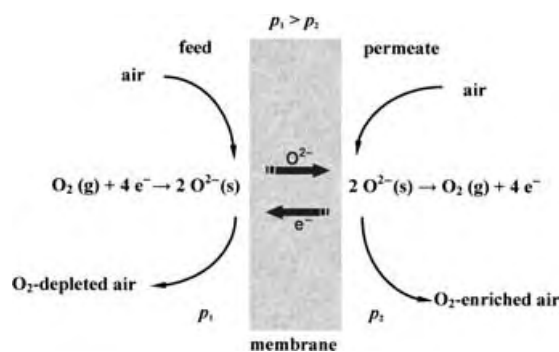


Figure 1. O₂ enrichment with perovskite mixed-conducting membranes.

the side of high air pressure to the side of low air pressure. Simultaneously, electrons are transported in the opposite direction to maintain electric neutrality. The permeated O₂ increases the O₂ concentration to typically 30–50 vol % in the sweep air that forms the O₂-enriched air on the low-pressure side. Therefore, the perovskite membrane combines the in situ O₂ supply with permeated O₂ and air in one unit thus simplifying the process of O₂ enrichment and reducing the operational and capital costs.

The obvious advantage of using perovskite membranes is their 100 % selectivity for O₂. Usually, polymeric membranes also transport noble or inert gases such as Ar or CO₂, which can be disadvantageous depending on the process. Synthesis gas for ammonia production, for example, is prepared at a pressure level of about 30 bar and afterwards compressed to a pressure of typically 170–190 bar. Any inert gases contained within the synthesis gas are also compressed to a higher pressure and fed into the synthesis loop. This in turn increases the energy expenditure for compression, the necessary loop volume, and the purge flow used to get rid of the inert components in the synthesis loop.

Moreover, compared with hollow-fiber membranes made from organic polymers, the perovskite hollow-fiber membrane requires a lower pressure difference (1–2 bar) across the membrane and can work at elevated temperatures, thus allowing high-temperature heat exchange. O₂-enriched air is used mostly in high-temperature oxidation processes such as in the generation of synthesis gas for ammonia production in which O₂-enriched air is used to run a secondary reformer typically operated at 1000 to 1100 °C. Therefore, in this process the temperature required to operate the perovskite hollow fiber is already available and can be used by heat exchange. Furthermore, the heat used for the O₂ enrichment is not consumed, for example, in an endothermic reaction and can be regained by heat exchange with the product streams that leave the O₂-permeation-membrane module. A similar setup may also apply to other applications for O₂ enrichment with perovskite membranes, for example, the temperature increase of firing systems in power plants or industrial furnaces.

The perovskite of composition BaCo_xFe_yZr_zO_{3-δ} (BCFZ; $x+y+z=1.0$) is a novel O₂-permeable membrane with high O₂ permeation fluxes and excellent thermal and mechanical stability.^[4,5] BCFZ was used in a hollow-fiber configuration as

[*] Dr. H. Wang, Prof. Dr. J. Caro
Institut für Physikalische Chemie und Elektrochemie
Universität Hannover
Callinstrasse 3–3A, 30167 Hannover (Germany)
Fax: (+49) 511-762-19121
E-mail: haihui.wang@pci.uni-hannover.de

Dr. S. Werth
Uhde GmbH
Friedrich-Uhde-Strasse 15, 44141 Dortmund (Germany)

Dr. T. Schiestel
Fraunhofer-Institut für Grenzflächen- und Bioverfahrenstechnik
(IGB)
Nobelstrasse 12, 70569 Stuttgart (Germany)

[**] H. Wang greatly thanks the financial support from the Alexander von Humboldt Foundation. The authors gratefully acknowledge the financial support of the BMBF for project 03C0343A under the auspices of ConNeCat.

Supporting information for this article is available on the WWW under <http://www.angewandte.org> or from the author.

the membrane, which showed an O_2 permeation flux of $6.5 \text{ cm}^3 \text{ min}^{-1} \text{ cm}^{-2}$ at 875°C .^[6] This flux is higher than those of $\text{Ba}_{0.5}\text{Sr}_{0.5}\text{Co}_{0.8}\text{Fe}_{0.2}\text{O}_{3-\delta}$ (BSCF)^[7] and $\text{La}_{1-x}\text{Sr}_x\text{Co}_{1-y}\text{Fe}_y\text{O}_{3-\delta}$ (LSCF)^[8] hollow-fiber membranes under similar conditions with a nonreactive sweep gas. The preparation and characterization of the hollow-fiber membrane was recently reported.^[6]

The performance of perovskite membranes for O_2 enrichment can be characterized by the O_2 permeation rate, the production rate of O_2 -enriched air, and the O_2 concentration on the permeate side. The force that drives O_2 transport through perovskite membranes is the gradient of the chemical potential, that is, the difference between the O_2 partial pressures across the perovskite membranes. Instead of separating O_2 by using inert sweep gases, it is possible to obtain O_2 -enriched air by using air as the sweep gas and applying a difference in air pressure as the driving force as shown in Figure 2. When the difference in air pressure

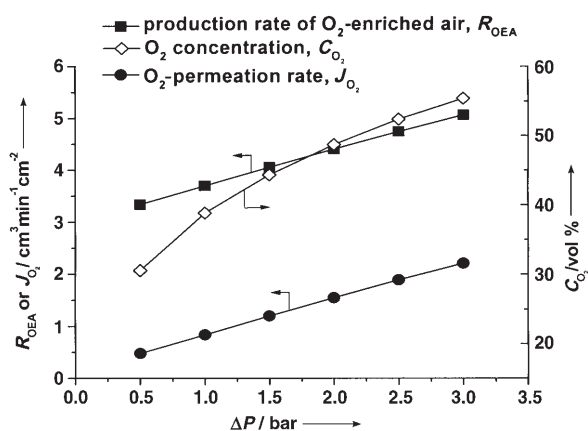


Figure 2. Influence of the pressure difference on the production of O_2 -enriched air. Air flow rate: feed side = $100 \text{ cm}^3 \text{ min}^{-1}$; permeate side = $10 \text{ cm}^3 \text{ min}^{-1}$, membrane surface area = 3.50 cm^2 , $T = 950^\circ\text{C}$.

increases from 0.5 to 3.0 bar, the O_2 concentration on the permeate side almost doubles from 30 to 55 vol %, and the O_2 permeation rates rise from 0.5 to $2.2 \text{ cm}^3 \text{ min}^{-1} \text{ cm}^{-2}$. Accordingly, the production rate of O_2 -enriched air increases from 3.3 to $5.0 \text{ cm}^3 \text{ min}^{-1} \text{ cm}^{-2}$. Silicone rubber—the polymeric membrane used most often commercially—with a thickness of $25 \mu\text{m}$ shows an O_2 permeation flux of about $0.11 \text{ cm}^3 \text{ min}^{-1} \text{ cm}^{-2} \text{ bar}^{-1}$ with an O_2 concentration of 35 vol % under a pressure difference of 9.0 bar.^[9] However, the perovskite hollow-fiber membrane with a thickness of around $180 \mu\text{m}$ can give an O_2 concentration higher than 38 vol % with a production rate of $3.7 \text{ cm}^3 \text{ min}^{-1} \text{ cm}^{-2}$ by applying only a pressure difference of 1.0 bar.

Figure 3 shows the influence of the temperature on O_2 enrichment under a fixed pressure difference of 1.5 bar. As expected, the O_2 permeation rate increases with rising temperature, which leads to an increase in both the production rate of the O_2 -enriched air and the O_2 concentration in the effluent air. Figure 4 shows how the rate of air flow on the permeate side affects the production of O_2 -enriched air at a constant pressure difference of 1.5 bar at 875°C . It was previously found that the O_2 permeation flux increases with

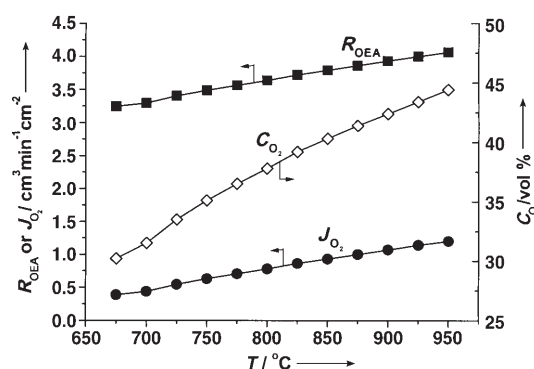


Figure 3. Influence of the temperature on the production of O_2 -enriched air. Air flow rates: Feed side = $100 \text{ cm}^3 \text{ min}^{-1}$; permeate side = $10 \text{ cm}^3 \text{ min}^{-1}$, membrane surface area = 3.50 cm^2 , pressure difference = 1.5 bar.

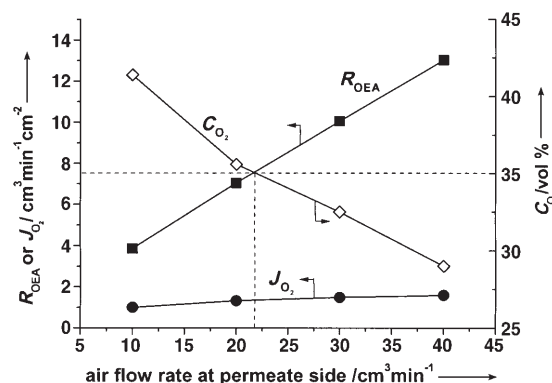


Figure 4. Influence of the air flow rate at the permeate side on the production of O_2 -enriched air. Air flow rate: feed side = $100 \text{ cm}^3 \text{ min}^{-1}$; permeate side = $10\text{--}40 \text{ cm}^3 \text{ min}^{-1}$, membrane surface area = 3.50 cm^2 , $T = 875^\circ\text{C}$, pressure difference = 1.5 bar.

raising the rate of He flow when He was fed to the permeate side as the sweep gas.^[10] The reason for this increase is that the partial pressure of O_2 on the permeate side decreases with an increase in He flow.^[10] As shown in Figure 4, the O_2 concentration decreases sharply when the air flow on the permeate side increases. This decrease leads to an increase in the rate of O_2 permeation when the air flow on the permeate side rises. Accordingly, the rate of production of O_2 -enriched air increases. An air flow of about $22 \text{ cm}^3 \text{ min}^{-1}$ on the permeate side gives a good compromise between the O_2 concentration ($\approx 35 \text{ vol} \%$) and the rate of production of O_2 -enriched air ($7.5 \text{ cm}^3 \text{ min}^{-1} \text{ cm}^{-2}$).

Teraoka et al.^[11,12] first reported O_2 permeability through perovskite membranes based on $\text{La}_{1-x}\text{A}_x\text{Co}_{1-y}\text{Fe}_y\text{O}_{3-\delta}$. Since then, there have been numerous reports on perovskite membranes.^[13–17] An attractive goal is the integration of perovskite membranes and the partial oxidation of methane (POM) to synthesis gas into a single reactor. Although a lot of effort has been made to apply perovskite membranes to an industrial POM process,^[18,19] so far there are no plants using this methodology. The formidable problem for this technology lies in the poor stability of the perovskite membranes at elevated temperatures under a reducing atmosphere (e.g., a

mixture of hydrogen and carbon monoxide).^[20] A further problem is the poor operational safety of such systems. In the event of a membrane leak, air, methane, and synthesis gas would mix at 800°C, thus causing serious trouble if not handled properly. However, these stability and operational-safety problems are avoided in the above-proposed O₂-enrichment process because both sides of the perovskite membranes are exposed to an oxidizing atmosphere (air).

As expected, the perovskite membranes exhibit excellent stability (Figure 5). A perovskite membrane operated steadily

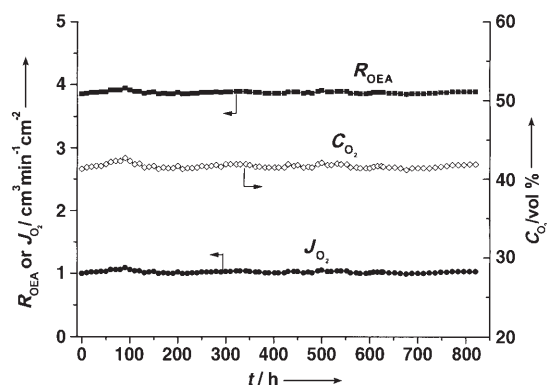


Figure 5. Long-term stability of perovskite hollow fibers for the production of O₂-enriched air. Air flow rate: feed side = 100 cm³ min⁻¹; permeate side = 10 cm³ min⁻¹, membrane surface area = 3.50 cm², pressure difference = 1.5 bar, *T* = 875 °C.

for more than 800 h at 875 °C under a constant pressure difference of 1.5 bar. During this operation, the O₂ concentration in the O₂-enriched air reached around 42 vol% with an O₂ permeation rate of about 1.0 cm³ min⁻¹ cm⁻² and an O₂-enriched air production rate of about 4.0 cm³ min⁻¹ cm⁻². It should be pointed out that although we had to stop the test, the perovskite membrane was still working after 800 h. XRD and element maps obtained from scanning electron microscopy–energy-dispersive X-ray spectra (SEM–EDX) of the spent hollow-fiber membrane show no structural change and no significant element segregation (see Supporting Information).

In summary, the results presented here demonstrate the possibility of applying perovskite membranes to high-temperature O₂ enrichment. The O₂ concentration reached around 35 vol% with a production rate of 7.5 cm³ min⁻¹ cm⁻² of O₂-enriched air at 875 °C under a pressure difference of 1.5 bar. The O₂ concentration and the rate of production can be adjusted by controlling the temperature, air pressure difference, and gas flow rates. It is important to note that hollow-fiber membranes can give very high values of the membrane area per unit volume (up to 5.000 m² per m³ of permeator; based on the densest packing of fibers with outer diameters of 0.75 mm). Economic goals such as a price of well below 1000 € per m² of membrane area can be also met by using this perovskite membrane. We estimate that 700 tons of O₂-enriched air (35 vol%) can be produced per day in a permeator volume of about 1 m³. The long-term stability found in our experiments indicates that perovskite mem-

branes have the potential to replace the current O₂-enrichment systems for high-temperature applications because they can integrate O₂ separation and mixing in one application.

Experimental Section

BCFZ was obtained by simple hydrolysis of Ba, Co, Fe, and Zr nitrates in a solution of ammonium hydroxide. It was then mixed with a solution of polysulfone in *N*-methylpyrrolidone and ball-milled for 16 h. The resulting slurry was spun through a spinneret and the green BCFZ perovskite fiber, thus obtained, was cut into 0.5-m pieces before being sintered above 1200 °C. On sintering, the length shrank to 0.33 m and the outer diameter went from around 1.75 mm to around 0.90 mm.

O₂-enrichment experiments were carried out in a high-temperature permeator (Figure 6). The two ends of the hollow-fiber

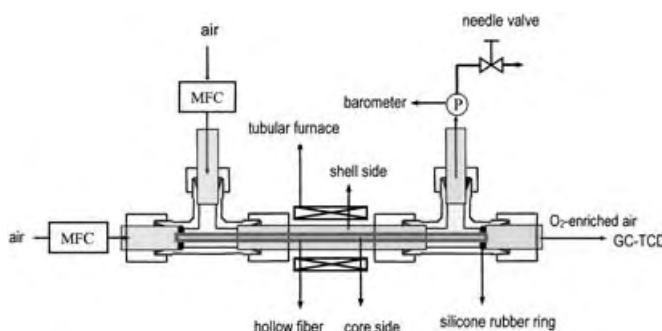


Figure 6. Scheme of the permeator for the O₂ enrichment at high temperatures.

membrane were sealed by two silicone rubber rings. Preheated air (100 cm³ min⁻¹) was fed into the shell side and different air pressures were obtained by adjusting the needle valve on the air outlet. The air pressures on the shell side were between 1.5 and 4.0 bar. Preheated air (10–40 cm³ min⁻¹) was fed to the core side and the air pressure was fixed at 1.0 bar. Due to the difference in air pressure between the shell side and the core side, the O₂ on the shell side permeates through the hollow-fiber membrane to the core side and mixes with air to form O₂-enriched air. The rate of O₂ permeation, *J*_{O₂} (cm³ min⁻¹ cm⁻²), can be calculated with Equation (1) in which *F*_{air,inlet} (cm³ min⁻¹) is the rate

$$J_{O_2} = \frac{F_{\text{air,inlet}} (C_{O_2} - 20.9)}{S(100 - C_{O_2})} \quad (1)$$

of air flow at the inlet of the core side; *C*_{O₂} (vol%) is the O₂ concentration at the outlet of the core side, which can be determined by GC; *S* (cm²) is the effective membrane surface area of the hollow fiber for O₂ permeation.

The O₂-enriched air production rate, *R*_{OEA} (cm³ min⁻¹ cm⁻²), is defined in Equation (2) in which *F*_{outlet} (cm³ min⁻¹) is the flow rate at

$$R_{\text{OEA}} = \frac{F_{\text{outlet}}}{S} \quad (2)$$

the outlet of the core side, which can be measured by soap film meter.

Received: June 2, 2005

Published online: October 5, 2005

Keywords: ceramics · electron transport · membranes · oxygen

- [1] D. P. Bhasin, M. S. Liebeison, G. J. Chapman, *Hydrocarbon Process.* **1983**, 62, 85.
- [2] "Membrane Technology in the Chemical Industry: Further Directions": R. Baker in *Membrane Technology in the Chemical Industry, Part II* (Eds.: S. P. Nunes, K.-V. Peinemann), Wiley-VCH, Weinheim, **2001**, p. 280.
- [3] "Economics of Gas Separation Membrane Processes": R. Spillman in *Membrane Science and Technology, Vol. 2* (Eds.: R. D. Noble, S. A. Stern), Elsevier, New York, **1996**, p. 269.
- [4] J. H. Tong, W. S. Yang, B. C. Zhu, R. Cai, *J. Membr. Sci.* **2002**, 203, 175.
- [5] J. H. Tong, W. S. Yang, R. Cai, B. C. Zhu, L. W. Lin, *Catal. Lett.* **2002**, 78, 129.
- [6] T. Schiestel, M. Kilgus, S. Peter, K. J. Caspary, H. H. Wang, J. Caro, *J. Membr. Sci.* **2005**, 258, 1.
- [7] S. M. Liu, G. R. Gavalas, *J. Membr. Sci.* **2005**, 246, 103.
- [8] X. Y. Tan, Y. T. Liu, K. Li, *AIChE J.* **2005**, 51, 1991.
- [9] S. L. Matson, W. J. Ward, S. G. Kimura, W. R. Browall, *J. Membr. Sci.* **1986**, 29, 79.
- [10] H. H. Wang, R. Wang, D. Liang, W. S. Yang, *J. Membr. Sci.* **2004**, 243, 405.
- [11] Y. Teraoka, H. M. Zhang, S. Furukawa, N. Yamazoe, *Chem. Lett.* **1985**, 11, 1743.
- [12] Y. Teraoka, T. Nobunaga, N. Yamazoe, *Chem. Lett.* **1988**, 3, 503.
- [13] A. C. V. Veen, M. Rebeilleau, D. Farrusseng, C. Mirodatos, *Chem. Commun.* **2003**, 1, 32.
- [14] J. P. Ramirez, B. Vigeland, *Angew. Chem.* **2005**, 44, 1136; *Angew. Chem. Int. Ed.* **2005**, 44, 1112.
- [15] R. Merkle, J. Maier, H. J. M. Bouwmeester, *Angew. Chem.* **2004**, 43, 5179; *Angew. Chem. Int. Ed.* **2004**, 43, 5069.
- [16] J. E. Ten Elshof, H. J. M. Bouwmeester, H. Verweij, *Solid State Ionics* **1996**, 89, 81.
- [17] Z. P. Shao, W. S. Yang, Y. Cong, H. Dong, J. H. Tong, G. X. Xiong, *J. Membr. Sci.* **2000**, 172, 177.
- [18] M. Schroeder, *Phys. Chem. Chem. Phys.* **2005**, 7, 166.
- [19] H. H. Wang, C. Tablet, A. Feldhoff, J. Caro, *Adv. Mater.* **2005**, 17, 1785.
- [20] C. Chen, S. J. Feng, S. Ran, D. C. Zhu, W. Liu, H. J. M. Bouwmeester, *Angew. Chem.* **2003**, 115, 5354; *Angew. Chem. Int. Ed.* **2003**, 42, 5196.

DOI: 10.1002/anie.200502571

Allosteric-Controlled Metal Specificity of a Ditopic Ligand**

Christian J. Baylies, T. Riis-Johannessen,
Lindsay P. Harding, John. C. Jeffery, Ryan Moon,
Craig R. Rice,* and Martina Whitehead

There are numerous examples in the field of metallocsupramolecular chemistry that demonstrate that careful design of ligands can produce species that are selective to certain metal ions.^[1] For example, Lehn et al. demonstrated that a mixture of two ligands that contain three bipyridine units and are linked either by aliphatic or ether units form only homonuclear and homoleptic trinuclear double and triple helicates upon reaction with Cu⁺ and Ni²⁺ ions, respectively.^[2] Another approach to enhance metal specificity is to introduce discrete binding domains within a ligand strand such that each domain is specific to a particular metal ion.^[3] However, when using the latter strategies, the information contained within the ligand system, that is, its “programming”, is finalized at the synthetic stage and cannot be altered thereafter. Herein, we describe a ditopic ligand L¹, whose selectivity for different transition-metal ions can effectively be “reprogrammed” by the addition of the larger s-block-metal ions to the crown ether moiety. This approach is related to the allosteric effect demonstrated by Rebek et al., in which the ability of a crown ether to coordinate Group 1 metal ions is influenced by coordination of a remote bipyridine coordination domain.^[4] In this case, however, the reverse occurs as coordination of the crown ether unit controls the ability of a remote nitrogen-donor unit to act as either a tetradentate or bisbidentate domain. Other reprogrammable systems have been shown to control the formation of helicates^[5] and modulate their pitch length.^[6]

The reaction of L¹ (Scheme 1) with an equimolar amount of [Cu(MeCN)₄]PF₆ in MeCN gave a dark-red solution, and ESI-mass-spectrometric analysis showed the formation of a dinuclear double helicate with an ion at *m/z* 1497 consistent with {[Cu₂(L¹)₂](PF₆)⁺}. In addition, the crown ether moiety

[*] Dr. C. J. Baylies, Dr. L. P. Harding, R. Moon, Dr. C. R. Rice, M. Whitehead

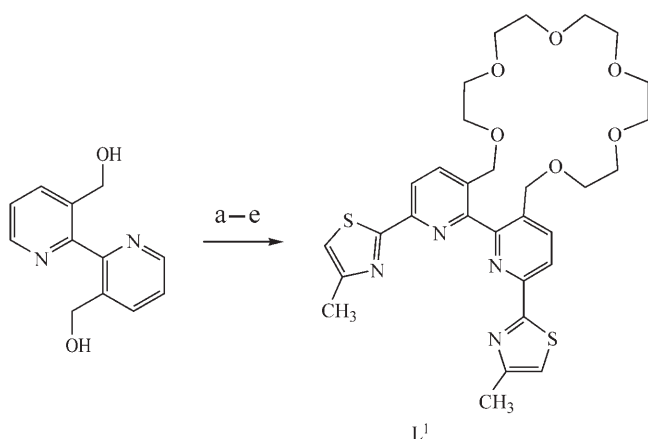
Department of Chemical and Biological Sciences
University of Huddersfield
Huddersfield HD1 3DH (UK)
Fax: (+44) 148-447-2182
E-mail: c.r.rice@hud.ac.uk

T. Riis-Johannessen, Dr. J. C. Jeffery
School of Chemistry
University of Bristol
Cantocks Close, Bristol BS8 1TS (UK)

[**] We thank the EPSRC and the University of Huddersfield for financial support.



Supporting information for this article is available on the WWW under <http://www.angewandte.org> or from the author.



Scheme 1. Conditions: a) penta(ethylene glycol) di-*para*-toluenesulfonate, DMF, NaH (60/45 %); b) *m*CPBA, CH₂Cl₂ (70 %); c) TMSCN, PhCOCl, CH₂Cl₂ (83 %); d) H₂S, Et₃N, EtOH (90 %); e) chloroacetone, EtOH (76 %). DMF = dimethylformamide, *m*CPBA = *meta*-chloroperoxybenzoic acid, TMSCN = trimethylsilyl cyanide.

can coordinate barium ions as the reaction of this copper-containing helicate with excess Ba(ClO₄)₂ gives rise to ions in the ESI mass spectrum of *m/z* 1788 and 2124, which correspond to [Cu₂(L¹)₂Ba](ClO₄)₃⁺ and [Cu₂(L¹)₂Ba₂](ClO₄)₅⁺, respectively. The formation of the complex [Cu₂(L¹)₂Ba₂·(H₂O)](ClO₄)₆·2 MeCN·0.5 Et₂O has been established by a single-crystal X-ray diffraction study (Figure 1).^[7] In the solid

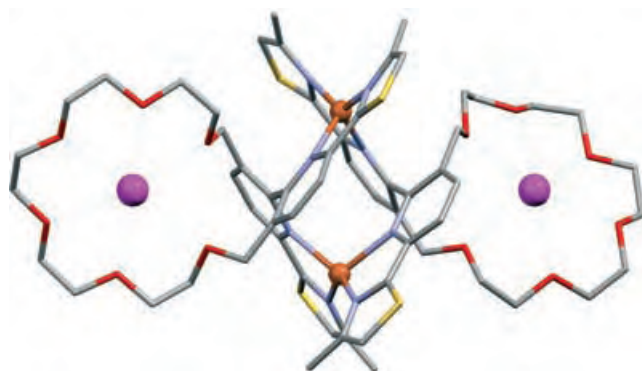


Figure 1. Crystal structure of the complex cation in [Cu₂(L¹)₂Ba₂](ClO₄)₆·2 MeCN·0.5 Et₂O.

state, the ligand splits into two bisbidentate binding domains with two Cu^I ions coordinated by two bridging ligands in a double helicate arrangement with an average interdomain torsion angle of 108.9° (N–C–C–N). Each of the Cu^I centers has a distorted-tetrahedral geometry formed by coordination of one bidentate pyridyl–thiazole nitrogen-donor unit from each ligand (Cu–N: 1.985(7)–2.158(8) Å). Furthermore, both of the crown ether units coordinate to barium ions (O–Ba_(crown ether): 2.760(8)–2.978(12) Å), with the longest bonds arising from coordination of the “benzylic” oxygen atoms (Ba–O_(methylene): 2.791(9)–2.978(12) Å).

The ¹H NMR spectrum of [Cu₂(L¹)₂]²⁺ in CD₃CN shows three aromatic signals for the pyridyl–thiazole moiety, con-

sistent with a highly symmetrical double helicate complex in which all four of the thiazole–pyridyl fragments are chemically equivalent (Figure 2a). The two doublets ascribed to the pyridyl protons show a characteristic upfield shift that arises

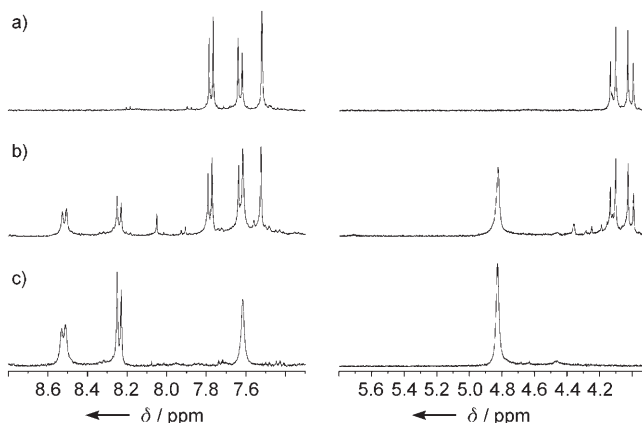


Figure 2. Selected regions of the ¹H NMR spectra (CD₃CN) of a) [Cu₂(L¹)₂]²⁺, b) L¹ + Cu⁺ + Zn²⁺, and c) [Zn(L¹)]²⁺.

because these protons are shielded by the aromatic-ring currents of a thiazole moiety in the adjacent ligand strand. In addition, the diastereotopic “benzylic” –CH₂O– protons give rise to two comparatively upfield doublets. The addition of barium ions affords a similar ¹H NMR spectrum, in which the “benzylic” –CH₂O– protons show a characteristic downfield shift because of the coordination of the electronegative Ba²⁺ ions in the crown ether cavities (Figure 3a).

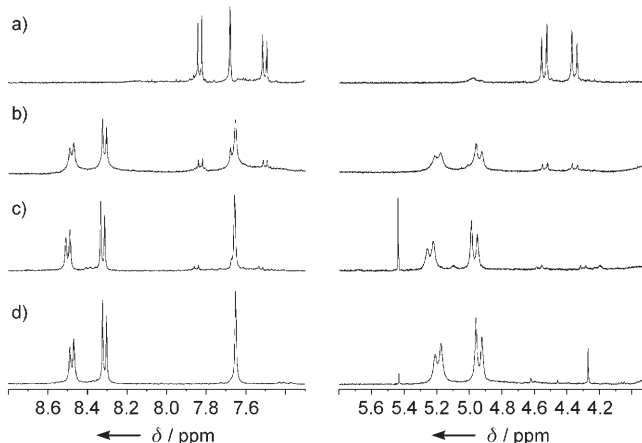


Figure 3. Selected regions of the ¹H NMR spectra (CD₃CN) of a) [Cu₂(L¹)₂]²⁺ + excess Ba²⁺ ions, b) L¹ + Cu⁺ + Zn²⁺ + excess Ba²⁺ ions, c) L¹ + Cu⁺ + Zn²⁺ + excess Sr²⁺ ions, and d) [Zn(L¹)]²⁺ + excess Ba²⁺ ions.

Reaction of L¹ with an equimolar amount of [Zn(H₂O)₆](ClO₄)₂ in MeCN gave a pale-yellow solution, and ESI-MS analysis showed an ion of *m/z* 776 consistent with the formation of the mononuclear [Zn(L¹)](ClO₄)⁺ complex. The ¹H NMR spectrum of [Zn(L¹)]²⁺ in CD₃CN (Figure 2c) shows more deshielded pyridyl proton resonances than the Cu

helicate $[\text{Cu}_2(\text{L}^1)_2]^{2+}$, thus reflecting an absence of the aromatic shielding caused by interstrand π stacking of the ligands in the latter complex. In addition, the “benzylic” $-\text{CH}_2\text{O}-$ protons appear as a broad singlet, which indicates that rapid conformational movement about the bipyridyl backbone occurs on the NMR timescale, thus rendering these methylene protons chemically equivalent. Upon addition of $\text{Ba}(\text{ClO}_4)_2$ to $[\text{Zn}(\text{L}^1)]^{2+}$, an ion of m/z 1112 that corresponds to $[\{\text{Zn}(\text{L}^1)\text{Ba}\}(\text{ClO}_4)_3]^+$ is observed in the ESI mass spectrum, thus indicating that a Ba^{2+} ion is again coordinated in the host cavity of the crown ether. Consistent with this observation, the ^1H NMR spectrum in CD_3CN shows small but significant changes as the “benzylic” $-\text{CH}_2\text{O}-$ protons resolve into two doublets on addition of Ba^{2+} ions (Figure 3d). This change could be ascribed to the restricted conformational mobility induced by coordination of a Ba^{2+} ion into the crown host cavity. Treatment of $[\text{Zn}(\text{L}^1)]^{2+}$ with excess $\text{Ba}(\text{ClO}_4)_2$ followed by crystallization afforded the complex $[\text{Zn}(\text{L}^1)\text{Ba}(\text{H}_2\text{O})_2](\text{ClO}_4)_4 \cdot \text{MeCN} \cdot 0.5 \text{Et}_2\text{O} \cdot 0.75 \text{H}_2\text{O}$, the structure of which has been established by single-crystal X-ray diffraction studies.^[8] In the solid state, the ligand coordinates to the equatorial plane of the Zn^{2+} center through all four nitrogen-donors, and two water molecules occupy the axial positions (Figure 4). The ligand is almost

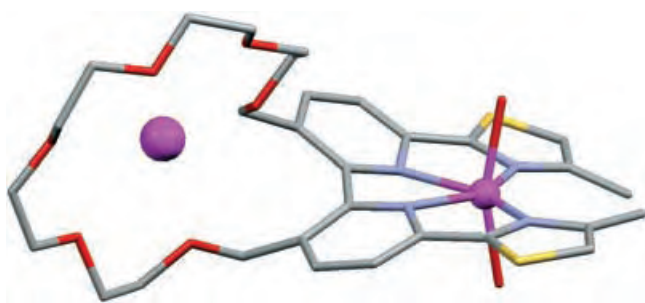


Figure 4. Crystal structure of the complex cation in $[\text{Zn}(\text{L}^1)\text{Ba}(\text{H}_2\text{O})_2](\text{ClO}_4)_4 \cdot \text{MeCN} \cdot 0.5 \text{Et}_2\text{O} \cdot 0.75 \text{H}_2\text{O}$.

planar and exhibits only a shallow helical twist about the metal center, which is caused by unfavorable steric interactions between the methylene substituents on the central bipyridine core ($\text{N}-\text{C}-\text{C}-\text{N}$ dihedral angle is approximately 31.0°). The arrangement of equatorial nitrogen-donors and axial water ligands generates a distorted-tetragonal geometry about the Zn^{2+} center ($\text{Zn}-\text{N}$: 2.178(5)–2.237(6) Å; $\text{Zn}-\text{O}$: 2.060(5) and 2.095(5) Å) similar to the geometry observed by Baxter et al. for the Zn^{II} complex of the analogous crown-free ligand.^[9] The $\text{Ba}-\text{O}$ separations are distributed over a narrower range than for $[\text{Cu}_2(\text{L}^1)_2\text{Ba}_2]^{6+}$ ($\text{Ba}-\text{O}$ in $[\text{Zn}(\text{L}^1)\text{Ba}]^{4+}$: 2.803(4)–2.893(4) Å), which is consistent with the barium ion being located more centrally within the crown ether in $[\text{Zn}(\text{L}^1)\text{Ba}]^{4+}$ (compare with, the range 2.736–2.875 Å for the $\text{Ba}-\text{O}$ separations observed in the barium complex of [18]crown-6).^[10]

As the ligand can partition into either tetradentate or bisbidentate binding domains, we decided to investigate its specificity towards different metal ions. The reaction of ligand L^1 with $[\text{Cu}(\text{MeCN})_4]\text{PF}_6$ and $[\text{Zn}(\text{CF}_3\text{SO}_3)_2]$ (in the ratio

1:1:1) in CD_3CN gave an orange solution whose ^1H NMR spectrum showed six aromatic-proton environments that correspond to two different L^1 -containing complexes. Comparison of the ^1H NMR spectrum of the mixed system with that of the individual $[\text{Cu}_2(\text{L}^1)_2]^{2+}$ and $[\text{Zn}(\text{L}^1)(\text{H}_2\text{O})_2]^{2+}$ complexes showed that both these species were present in the ratio 1.5:1 (Figure 2b). This observation is also supported by the ESI mass spectrum, in which ions are present for both copper- and zinc-containing species. Upon the addition of $\text{Ba}(\text{ClO}_4)_2$, the color of the solution became paler and the ^1H NMR spectrum revealed new signals for the barium-containing species $[\text{Cu}_2(\text{L}^1)_2\text{Ba}_2]^{6+}$ and $[\text{Zn}(\text{L}^1)\text{Ba}]^{4+}$ in a 1:10 ratio, respectively (Figure 3b). Analysis by ESI MS showed that ions are present for the mononuclear zinc complex $[\{\text{Zn}(\text{L}^1)\text{Ba}\}(\text{ClO}_4)_3]^+$, whereas ions that correspond to any copper-containing complexes were virtually nonexistent. Interestingly, the addition of excess $\text{Sr}(\text{ClO}_4)_2$ to a stoichiometric mixture of L^1 , $[\text{Cu}(\text{MeCN})_4]\text{PF}_6$, and $[\text{Zn}(\text{CF}_3\text{SO}_3)_2]$ resulted in virtually total conversion into the zinc-containing species ($[\text{Cu}_2(\text{L}^1)_2\text{Sr}_2]^{6+}/[\text{Zn}(\text{L}^1)\text{Sr}]^{4+}$, 1: > 20; Figure 3c).

Thus, upon addition of excess Zn^{2+} and Cu^+ ions, the ligand can act as either a tetradentate or bisbidentate donor unit to generate a mixture of the Cu^{I} helicate and Zn^{II} mononuclear species. However, upon addition of barium or strontium ions, the ligand is effectively reprogrammed to act as a tetradentate donor which is specific to Zn^{2+} ions.

As with similar systems,^[5,6] such control over the ligand coordination domains may be attributed to one or two effects. Firstly, an electrostatic effect is plausible given that the copper helicate will form a $6+$ ion $[\text{Cu}_2(\text{L}^1)_2\text{M}_2]^{6+}$ in the presence of excess Ba^{2+} or Sr^{2+} ions, whereas the zinc complex $[\text{Zn}(\text{L}^1)\text{M}]^{4+}$ carries an overall charge of only $4+$. Thus, electrostatic destabilization of the highly charged helicate with respect to the mononuclear Zn^{2+} species results in the formation of the lesser charged species. However, the change in specificity could also be attributed to an allosteric effect, whereby coordination of a guest s-block ion to the crown ether unit is mechanically coupled to the bipyridine interannular bond in such a way as to impede the necessary partitioning required for helicate formation. Although the crystal structure of $[\text{Cu}_2(\text{L}^1)_2\text{Ba}_2(\text{H}_2\text{O})](\text{ClO}_4)_6 \cdot 2 \text{MeCN} \cdot 0.5 \text{Et}_2\text{O}$ clearly demonstrates that barium ions can coordinate to the crown ether region when the ligand is acting as a bisbidentate donor, careful comparison of the solid-state structures of the barium-containing helicate species $[\text{Cu}_2(\text{L}^1)_2\text{Ba}_2]^{6+}$ and monozinc(II) species $[\text{Zn}(\text{L}^1)\text{Ba}]^{4+}$ reveals that separations between the barium ions and the methylene oxygen atoms are marginally shorter for the latter (mean $\text{Ba}-\text{O}_{(\text{methylene})}$ distances in $[\text{Cu}_2(\text{L}^1)_2\text{Ba}_2]^{6+}$: 2.895(2) Å; $[\text{Zn}(\text{L}^1)\text{Ba}]^{4+}$: 2.863(9) Å). Tentative extrapolation from these observations could imply that when acting as a tetradentate donor (compare with, bisbidentate), there is an effective contraction of the crown ether unit which serves to optimize the Ba^{2+} /etherate interactions. If sufficient, the difference in the binding energies between the barium/crown ether associations in the respective helicate and monomer (ligand) conformers could also account for the observed shift in equilibrium from the dicopper(I) helicate to the zinc(II) monomer. The apparent “mutual dependence” of effective

crown ether size and remote binding events has been previously suggested for related ditopic systems^[4] and is further supported by the observed increase in metal specificity when a smaller Sr^{2+} ion is employed (compare with, Ba^{2+} ions); therefore, the latter suggests that the Sr^{2+} ion is more sensitive to the difference in the effective size of the helicate and the monomer host cavities than the Ba^{2+} ion. Barium/strontium ion inclusion into the crown ether host of L^1 , thus, appears to influence the conformational preferences of the nitrogen-donor domains, such that the preferred coordination mode is tetradentate in the presence of a guest ion.

Other s-block-metal ions also exert measurable effects: the addition of Li^+ and Na^+ ions result in the formation of equal amounts of copper and zinc complexes, whereas the zinc complex is again favored ($[\text{Cu}_2(\text{L}^1)_2\text{K}_2]^{6+}/[\text{Zn}(\text{L}^1)\text{K}]^{4+}$, 1:4) upon addition of K^+ ions. Comparison of the effects of the addition of Ba^{2+} versus K^+ ions shows that, although both significantly alter the equilibrium composition and favor the formation of the zinc-containing species, the change in monomer/helicate ratio is more apparent for Ba^{2+} ions. In view of the fact that both ions have similar ionic radii, the stronger influence of Ba^{2+} ions must reflect the difference in ionic charge, thus highlighting the importance of both electrostatic and allosteric factors in the modification of ligand specificity.

In conclusion, we have shown that a ditopic system can change its preference for different transition-metal ions upon addition of a range of s-block-metal ions at a remote site.

Received: July 22, 2005

Published online: October 5, 2005

Keywords: allostereism · copper · helicates · metal specificity · zinc

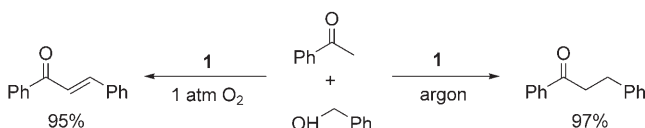
- [1] J.-M. Lehn, *Supramolecular Chemistry*, VCH, Weinheim, **1995**; M. Albrecht, *Chem. Rev.* **2001**, *101*, 3547; M. Albrecht, *Chem. Soc. Rev.* **1998**, *27*, 281; C. Piguet, G. Bernardinelli, G. Hopfgartner, *Chem. Rev.* **1997**, *97*, 2005; "Polynuclear Transition Metal Helicates": E. C. Constable in *Comprehensive Supramolecular Chemistry*, Vol. 9 (Ed.: J.-P. Sauvage), Elsevier, Oxford, **1996**, p. 213.
- [2] R. Krämer, J.-M. Lehn, A. Marquis-Rigault, *Proc. Natl. Acad. Sci. USA* **1993**, *90*, 5394.
- [3] E. C. Constable, A. J. Edwards, P. R. Raithby, D. R. Smith, J. V. Walker, L. Whall, *Chem. Commun.* **1996**, 2551; C. Piguet, J.-C. G. Bünzli, G. Bernardinelli, G. Hopfgartner, S. Petoud, O. Schaad, *J. Am. Chem. Soc.* **1996**, *118*, 6681; C. Edder, C. Piguet, J.-C. G. Bünzli, G. Hopfgartner, *Chem. Eur. J.* **2001**, *7*, 3014.
- [4] J. Rebek, Jr., J. E. Trend, R. V. Wattley, S. J. Chachravorti, *J. Am. Chem. Soc.* **1979**, *101*, 4333; J. Rebeck, Jr., R. V. Wattley, *J. Am. Chem. Soc.* **1980**, *102*, 4853; J. Rebeck, Jr., *Acc. Chem. Res.* **1984**, *17*, 258; for examples of artificial allosteric systems, see: T. Nabeshima, *Coord. Chem. Rev.* **1996**, *148*, 151; S. Shinkai, M. Ikeda, A. Sugasaki, M. Takeuchi, *Acc. Chem. Res.* **2001**, *34*, 494; Y. Kobuke, Y. Satoh, *J. Am. Chem. Soc.* **1992**, *114*, 789; P. D. Beer, A. S. Rothin, *J. Chem. Soc. Chem. Commun.* **1988**, 52; S. K. Dutta, D. Gan, M. W. Perkovic, *Eur. J. Inorg. Chem.* **2003**, 2812; S. A. McFarland, N. S. Finney, *Chem. Commun.* **2003**, 388; T. Nabeshima, Y. Yoshihira, T. Saiki, S. Akin, E. Horn, *J. Am. Chem. Soc.* **2003**, *125*, 28.
- [5] C. J. Baylies, L. P. Harding, J. C. Jeffery, T. Riis-Johannessen, C. R. Rice, *Angew. Chem.* **2004**, *116*, 4615; *Angew. Chem. Int. Ed.* **2004**, *43*, 4515.
- [6] C. J. Baylies, J. C. Jeffery, T. A. Miller, R. Moon, T. Riis-Johannessen, C. R. Rice, *Chem. Commun.* **2005**, 4158.
- [7] Single-crystal X-ray diffraction data were collected on a Bruker APEX-CCD area detector diffractometer under a stream of cold nitrogen. Crystal data for $[\text{Cu}_2(\text{L}^1)_2\text{Ba}_2(\text{H}_2\text{O})](\text{ClO}_4)_6 \cdot 2\text{MeCN} \cdot 0.5\text{Et}_2\text{O}$: $M_r = 2361.14$, triclinic, $P\bar{1}$, $a = 13.54(5)$, $b = 18.91(7)$, $c = 21.35(8)$ Å, $\alpha = 65.91(7)$, $\beta = 72.42(7)$, $\gamma = 85.18(7)^\circ$, $V = 4754(31)$ Å³, $Z = 2$, $\rho_c = 1.650$ Mg m⁻³, $F(000) = 2374$, $\mu(\text{MoK}\alpha) = 1.602$ mm⁻¹, $T = 100$ K. A total of 54400 reflections were measured in the range $1.09 \leq \theta \leq 27.54^\circ$ (hkl range indices $-17 \leq h \leq 17$, $-24 \leq k \leq 24$, $-27 \leq l \leq 27$), 21383 independent reflections ($R_{\text{int}} = 0.0386$). The structure was refined on F^2 to $R_w = 0.1603$ $R = 0.0582$ (16371 reflections with $I > 2\sigma(I)$) and GOF = 0.785 on F^2 for 1121 refined parameters, largest difference peak and hole 2.087 and -2.552 e Å⁻³. As with many supramolecular crystal structures, all of those described herein contain regions of disorder associated with diffuse-lattice solvent species (acetonitrile/non-coordinating perchlorate counterions) and the conformationally flexible crown ether fragments. Accordingly, geometric restraints and/or constraints were employed (in several cases throughout all stages of refinement) in attempt to model disorder where appropriate. Where such attempts failed to account for persistent peaks in the electron density map, a diffuse solvent correction was applied by using the SQUEEZE routine in PLATON. A full description of the refinement details is given in the Supporting Information.
- [8] Single-crystal X-ray diffraction data were collected on a Bruker SMART-CCD area detector diffractometer under a stream of cold nitrogen. Crystal data for $[\text{Zn}(\text{L}^1)(\text{H}_2\text{O})_2\text{Ba}](\text{ClO}_4)_4 \cdot \text{MeCN} \cdot 0.5\text{Et}_2\text{O} \cdot 0.75\text{H}_2\text{O}$: $M_r = 1340.66$, monoclinic, $P2_1/c$, $a = 18.431(1)$, $b = 17.981(1)$, $c = 17.614(1)$ Å, $\beta = 101.4330(10)^\circ$, $V = 5721.5(6)$ Å³, $Z = 4$, $\rho_c = 1.56$ Mg m⁻³, $F(000) = 2705$, $\mu(\text{MoK}\alpha) = 1.442$ mm⁻¹, $T = 173$ K. A total of 59644 reflections were measured in the range $1.13 \leq \theta \leq 27.54^\circ$ (hkl range indices $-23 \leq h \leq 23$, $-23 \leq k \leq 23$, $-22 \leq l \leq 22$), 13134 independent reflections ($R_{\text{int}} = 0.0858$). The structure was refined on F^2 to $R_w = 0.1888$ $R = 0.0702$ (7506 reflections with $I > 2\sigma(I)$) and GOF = 1.007 on F^2 for 667 refined parameters, largest difference peak and hole 1.347 and -1.045 e Å⁻³. CCDC-278717 and -278718 contain the supplementary crystallographic data for this paper. These data can be obtained free of charge from the Cambridge Crystallographic Data Center via www.ccdc.cam.ac.uk/data_request/cif.
- [9] P. N. W. Baxter, J. A. Connor, W. B. Schweizer, J. D. Wallis, *J. Chem. Soc. Dalton Trans.* **1992**, 3015.
- [10] L. Archer, M. J. Hampton-Smith, E. Duester, *Polyhedron* **1998**, *17*, 713; Y. Yi Wei, B. Tinant, J.-P. DeClercq, M. Van Meerssche, J. Dale, *Acta Crystallogr. Sect. C* **1998**, *44*, 77; S. A. Ivanov, N. P. Kuzmina, A. B. Liyukhin, *Russ. J. Inorg. Chem.* **1998**, *43*, 1469.

DOI: 10.1002/anie.200502422

Recyclable Palladium Catalyst for Highly Selective α Alkylation of Ketones with Alcohols**

Min Serk Kwon, Namdu Kim, Seong Hyeok Seo,
In Soo Park, Ravi Kumar Cheedra, and Jaiwook Park*

Carbon–carbon bond-forming reactions are fundamental in organic synthesis. The α alkylation of enolates derived from ketones with electrophiles such as alkyl halides is the conventional method to form C–C bonds.^[1] The metal-catalyzed α alkylation of ketones with alcohols is attracting much attention because of its critical advantage over the conventional α -alkylation method, which suffers from problems with waste salts. Recently, several groups have reported the use of homogeneous catalysts for the α alkylation of ketones with alcohols.^[2] However, these catalytic systems often suffer from low yield, low product selectivity, and/or the need for additives and strong bases. As a related C–C coupling reaction, Kaneda and co-workers developed an α alkylation of nitriles with primary alcohols using a Ru-grafted hydrotalcite as the catalyst.^[3] Herein, we report a heterogeneous and recyclable palladium catalyst, which does not require ligands or additives, for the α alkylation of ketones with primary alcohols. Furthermore, our catalyst is active in the presence of oxygen and can produce enones selectively under 1 atm O₂, whereas ketones are the major product under argon (Scheme 1).



Scheme 1. Palladium-catalyzed coupling of acetophenone and benzyl alcohol.

Recently, we reported a heterogeneous palladium catalyst, Pd/AlO(OH) (**1**), that is composed of palladium nanoparticles entrapped in aluminum hydroxide^[4] and is highly active for both alkene hydrogenation and aerobic alcohol oxidation. We envisioned that **1** would be applicable to the

α alkylation of ketones with primary alcohols as it is able to produce aldehydes from primary alcohols and hydrogenate intermediate enones formed from the coupling of aldehydes and ketones in the presence of a base.^[2d] In fact, 1,3-diphenylpropan-1-one was obtained in 97% yield in the reaction of acetophenone with 1.2 equivalents of benzyl alcohol in the presence of **1** (0.2 mol% of Pd) and K₃PO₄ (3 equiv) for 8 h at 80°C under argon. Notably, the same reaction under 1 atm O₂ produced chalcone in 95% yield after 20 h.

The reaction conditions were optimized for the alkylation of acetophenone with benzyl alcohol through variation of the base, temperature, and solvent. Among the bases tested, K₃PO₄ was found to be the best. Strong bases such as KOH, NaOH, and CaH₂ dissolved the aluminum hydroxide matrix, whereas the alkylation product was not detected in reactions with weak bases, such as K₂HPO₄, K₂CO₃, Na₂CO₃, and triethylamine. The reaction rate was affected by the amount of K₃PO₄,^[5] thus, three equivalents were needed to complete the reaction within 8 h at 80°C. The temperature was also an important factor for the reaction rate: as the temperature was raised to 110°C, the alkylation was completed in 2.5 h. Studies on the effect of the solvent revealed that toluene is more effective than trifluorotoluene, *n*-heptane, 1,4-dioxane, or water.

The high efficiency of **1** for the coupling of acetophenone and benzyl alcohol relative to commercially available catalysts and the α -alkylation catalysts reported previously was shown clearly (Table 1). Low selectivities (< 71%) and yields (< 55%) of 1,3-diphenylpropan-1-one (**2**) were observed for the reactions with commercially available heterogeneous palladium catalysts (entries 2–4). The reaction with [RuCl₂(PPh₃)₃] requires the addition of 1-dodecene to increase the selectivity.^[2c] The production of 1,3-diphenylpropan-1-one increases as the amount of benzyl alcohol is increased for the reactions with [RuCl₂(PPh₃)₃] and [Ru(dmsol)₄]Cl₂ (dmsol = dimethyl sulfoxide),^[2f] and phosphine ligands were needed with [IrCl(cod)]₂ (cod = cyclooctadiene).^[2e] The ruthenium-grafted hydrotalcite is a notable catalyst for α alkylation in the absence of a base, although a long reaction time at high temperature is required.^[3]

The main advantage of **1**, besides its selectivity, is its recyclability—it can be recovered by filtration or decantation (Table 2). To the best of our knowledge, **1** is the first recyclable catalyst for the α alkylation of ketones with alcohols.^[9] When the recovered catalyst was used without any treatment, the reaction rate decreased considerably (entry 2), whereas the addition of K₃PO₄ lead to resumption of the rate. Therefore, for each successive use, one equivalent of K₃PO₄ relative to acetophenone was added. Catalyst **1** retained its activity even during its sixth use, as **2** was prepared in 96% yield after 20 h.

With suitable reaction conditions established, a series of ketones and alcohols were employed to investigate the scope of the reaction (Table 3). Our catalytic system was effective for a wide combination of ketones and alcohols that produced the corresponding α -alkylated products under anaerobic conditions. It was also effective for the selective production of *trans* enones under 1 atm O₂, although the reaction rates

[*] M. S. Kwon, N. Kim, S. H. Seo, I. S. Park, R. K. Cheedra, Prof. J. Park
Center for Integrated Molecular Systems
Department of Chemistry
Division of Molecular and Life Sciences
Pohang University of Science and Technology (POSTECH)
San 31 Hyoja Dong, Pohang 790-784 (Korea)
Fax: (+82) 54-279-3399
E-mail: pjw@postech.ac.kr

[**] This work was supported by the SRC/ERC program of MOST/
KOSEF (R11-2000-070-05003-0).

Supporting information for this article is available on the WWW
under <http://www.angewandte.org> or from the author.

Table 1: Catalytic activity comparison.^[a]

Entry	Catalyst	Metal [mol %]	Base (equiv)	T [°C]	t [h]	Conv. [%] ^[b]	Product yield [%] ^[c]		
							2	3	4
1	1	0.2	K ₃ PO ₄ (3)	80	8	>99	97	2	0
2	5% Pd/C ^[d]	0.2	K ₃ PO ₄ (3)	80	8	78	55	4	10
3	5% Pd/Al ₂ O ₃ ^[d]	0.2	K ₃ PO ₄ (3)	80	8	47	21	2	17
4	5% Pd/BaCO ₃ ^[d]	0.2	K ₃ PO ₄ (3)	80	8	30	11	0	12
5	[RuCl ₂ (PPh ₃) ₃]	2.0	KOH (1)	80	20	84	82	2	[e]
6	[Ru(dmsO) ₄]Cl ₂	2.0	KOH (1)	80	[e]	[e]	72	[f]	[e]
7	[{Ir(cod)Cl} ₂]	1.0	KOH (0.1)	100	4	[e]	86	10	[e]
8	Ru/HT	0.75	none	180	20	85	85	[e]	[e]

[a] A solution of acetophenone (1.0 mmol) and benzyl alcohol (1.2 mmol) in toluene (2 mL) was heated under argon. [b] Conversion of acetophenone. [c] Determined by GC. [d] Commercially available catalysts. [e] No report. HT=hydrotalcite.

Table 2: Recycling **1** for the coupling of acetophenone and benzyl alcohol.^[a,b]

Use	T [°C]	t [h]	Yield [%] ^[c]
1	80	8	97
2	80	8	30 ^[d]
3	80	8	97
4	80	8	92
5	80	8	87
6	80	20	96

[a] A solution of acetophenone (1.0 mmol) and benzyl alcohol (1.2 mmol) in toluene (2 mL) was heated at 80°C in the presence of **1** (0.2 mol % of Pd) under argon. [b] K₃PO₄ (1 equiv) was added for the reuse of **1**. [c] Determined by GC. [d] Without the addition of K₃PO₄.

Table 3: α Alkylation of ketones with primary alcohols.^[a]

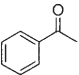
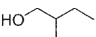
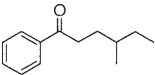
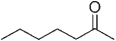
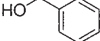
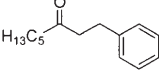
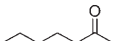
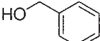
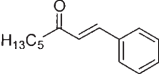
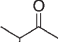
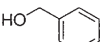
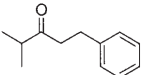
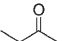
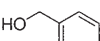
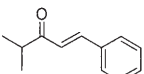
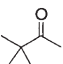
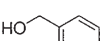
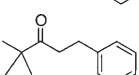
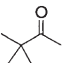
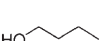
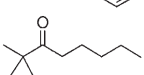
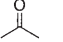
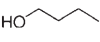
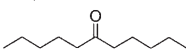
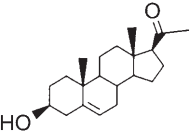
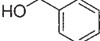
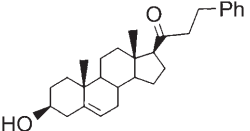
Entry	Ketone	Alcohol	t [h]	Product	Yield [%] ^[b]
1			2.5		97(92) ^[c]
2			2.5		96
3			2.5		96
4			2.5		98(90) ^[c]
5			20 ^[d]		87(80) ^[c]
6			3		87 ^[e]
7			3		97
8			12 ^[f]		95(88) ^[c]

were relatively slow (entries 5, 11, and 13). The alkylation of 4'-(trifluoromethyl)acetophenone was somewhat less selective, as the expected ketone was obtained in 87% yield along with the corresponding alcohol in 6% yield (entry 6).^[6] Indanone was alkylated successfully at the α-methylene position (entry 7). Acetophenone was also alkylated by aliphatic alcohols in high yield (entries 8 and 9). Furthermore, aliphatic ketones were alkylated by an aliphatic alcohol as well as by aromatic alcohols in high yields and with high selectivities (entries 10–15). Alkylation occurred almost exclusively at the methyl positions, and the coupling of acetone with 1-butanol produced undecan-6-one in 92% yield (entry 16). The reactions of aliphatic primary alcohols were slower than those of

aryl methanol derivatives. In particular, the coupling between an aliphatic ketone and an aliphatic alcohol required a reaction time about eight times longer than for the coupling between aryl methyl ketones and aryl methanol derivatives (entry 15). A noticeable example is the coupling of 5-pregnen-3β-ol-20-one with benzyl alcohol,^[7] as the secondary hydroxy group and the C=C bond are compatible with the coupling conditions (entry 17). Furthermore, the epimerization at C17 was negligible.^[8]

In summary, we have demonstrated a highly efficient α alkylation of ketones with primary alcohols by the use of a recyclable palladium catalyst that is easily prepared from readily available reagents. We are currently investigating

Table 3: (Continued)

Entry	Ketone	Alcohol	t [h]	Product	Yield [%] ^[b]
9			14 ^[f]		95
10			3		97(90) ^[c]
11			20 ^[d]		85 ^[c]
12			3		97
13			20 ^[d]		82 ^[c]
14			3		98(94) ^[c]
15			20		94
16			48 ^[f]		92
17			5		84 ^[c]

[a] A solution of ketone (1.0 mmol) and alcohol (1.2 mmol) in toluene (2 mL) was heated in the presence of **1** (0.2 mol % of Pd) and K₃PO₄ (3 mmol) at 110°C under argon. [b] Determined by GC. [c] Yield of isolated product. [d] Under 1 atm O₂. [e] 3-Phenyl-1-(4-trifluoromethyl)phenylpropanol was formed in 6% yield. [f] Excess 1-butanol (4 mmol) was used.

other one-pot multicatalytic reactions based on the versatile activity of the palladium catalyst.

Experimental Section

Coupling of acetophenone and benzyl alcohol: Acetophenone (120 mg, 1.00 mmol), benzyl alcohol (130 mg, 1.20 mmol), **1** (24 mg, 0.2 mol % of Pd), K₃PO₄ (636 mg, 3.00 mmol), and toluene (2 mL) were placed in a 20-mL flask under argon at 80°C for 8 h. The catalyst was separated by filtration, and the filtrate was purified by column chromatography (ethyl acetate/hexane 1:9) to give 1,3-diphenylpropan-1-one (193 mg) in 92% yield.^[10]

Received: July 12, 2005

Published online: October 5, 2005

Keywords: alkylation · aluminum · C–C coupling · heterogeneous catalysis · palladium

2001, 66, 9020–9022; c) C. S. Cho, B. T. Kim, T.-J. Kim, S. C. Shim, *Tetrahedron Lett.* **2002**, 43, 7987–7989; d) C. S. Cho, B. T. Kim, H.-S. Kim, T.-J. Kim, S. C. Shim, *Organometallics* **2003**, 22, 3609–3610; e) K. Taguchi, H. Nakagawa, T. Hirabayashi, S. Sakaguchi, Y. Ishii, *J. Am. Chem. Soc.* **2004**, 126, 72–73; f) R. Martínez, G.-J. Brand, D.-J. Ramón, M. Yus, *Tetrahedron Lett.* **2005**, 46, 3683–3686.

[3] K. Motokura, D. Nishimura, K. Mori, T. Mizugaki, K. Ebitani, K. Kaneda, *J. Am. Chem. Soc.* **2004**, 126, 5662–5663.

[4] M. S. Kwon, N. Kim, C. M. Park, J. S. Lee, K. Y. Kang, J. Park, *Org. Lett.* **2005**, 7, 1077–1079.

[5] The coupling reaction was completed in 16 h (10 h) when one equivalent (2 equiv) of K₃PO₄ was used.

[6] The major product is the corresponding alcohol when [Ru(dmsol)₄]Cl₂ is used as the catalyst; see ref. [2f].

[7] Pregnenolone is a main precursor of steroid hormones: K. Tsutsui, H. Sakamoto, K. Ukena, *J. Steroid Biochem. Mol. Biol.* **2003**, 85, 311–321.

[8] According to ¹H NMR spectroscopic analysis, no diastereomer of the major coupling product was formed in significant yield.

[9] Palladium was not detected in the filtrate with inductively coupled plasma (ICP) analysis.

[10] The NMR spectroscopic data for the coupling products shown in Table 3 and the experimental procedures for the preparation of **1**, *E*-1,3-diphenyl-2-propen-1-one, and 21-benzylpregnenolone are contained in the Supporting Information.

[1] a) D. Caine in *Comprehensive Organic Synthesis*, Vol. 3 (Eds.: B. M. Trost, I. Fleming), Pergamon, Oxford, **1991**, pp. 1–63; b) S. Carrettin, J. Guzman, A. Corma, *Angew. Chem.* **2005**, 117, 2282–2285; *Angew. Chem. Int. Ed.* **2005**, 44, 2242–2245; c) *Modern Carbonyl Chemistry* (Ed.: J. Otera), Wiley-VCH, Weinheim, **2000**.

[2] a) C. S. Cho, B. T. Kim, M. J. Lee, T.-J. Kim, S. C. Shim, *Angew. Chem.* **2001**, 113, 984–986; *Angew. Chem. Int. Ed.* **2001**, 40, 958–960; b) C. S. Cho, B. T. Kim, T.-J. Kim, S. C. Shim, *J. Org. Chem.*

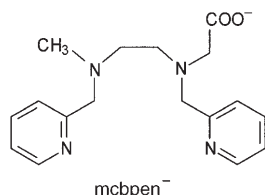
DOI: 10.1002/anie.200502114

Water Oxidation Catalyzed by a Dinuclear Mn Complex: A Functional Model for the Oxygen-Evolving Center of Photosystem II**

Allan K. Poulsen, Annette Rompel, and
Christine J. McKenzie*

Multinuclear manganese complexes have played an important role in the search for structural analogues of the active site of the oxygen-evolving complex (OEC) of photosystem II.^[1] However, the discovery of a functional biomimetic manganese complex that catalyzes the oxidation of water to dioxygen remains a challenge with enormous scientific implications. Reported here is the discovery that a dimanganese complex of the ligand *N*-methyl-*N'*-carboxymethyl-*N,N'*-bis(2-pyridylmethyl)ethane-1,2-diamine (mcbpen[−]) catalyzes the oxidation of water by *tert*-butylhydrogenperoxide (TBHP) or cerium nitrate to dioxygen. Furthermore, we have directly measured the evolved O₂ concentration in solution by using the relatively new method of membrane inlet mass spectrometry (MIMS). The isotopomer distribution is quantified with this method and shows that the reaction is highly specific: One oxygen atom in the evolved dioxygen comes from water, and the other is derived from the oxidant.

It did not escape our attention that a series of dinuclear manganese complexes of the new pentadentate ligand mcbpen[−],^[2] for which we have identified complexes with the



oxidation states Mn^{II}/Mn^{II}, Mn^{III}/Mn^{III}, Mn^{III}/Mn^{IV}, and Mn^{IV}/Mn^{IV}, is highly relevant as a model system for the OEC. Two molecules of water are coordinated in the stable, crystallo-

graphically characterized [Mn^{II}₂(mcbpen)₂(H₂O)₂](ClO₄)₂ (**1**-(ClO₄)₂). The X-ray crystal structure of **1**-(ClO₄)₂ shows two seven-coordinate Mn^{II} atoms with the carboxylate arms of mcbpen bridging the metal centers through one of the oxygen atoms to give a Mn⋯Mn separation of 4.0914(9) Å in the dinuclear structure. Manganese complexes of mcbpen[−] with a formal metal oxidation state higher than Mn^{II} are unstable, but have sufficiently long lifetimes in solution for spectroscopic (ESR and UV/Vis), spectrometric (ESIMS), and electrochemical characterization.^[2] A plausible precursor for dioxygen, two oxides in a Mn₂O₂ rhombus, is present in an unstable Mn^{IV}/Mn^{IV} complex [Mn^{IV}₂(O)₂(mcbpen)₂]²⁺, which has been identified in solutions of **1**-(ClO₄)₂ treated with TBHP in acetonitrile. The present work arose from our efforts to delineate the decomposition pathway of [Mn^{IV}₂(O)₂(mcbpen)₂]²⁺: Does this occur through release of O₂? In this scenario, [Mn^{II}₂(mcbpen)₂(H₂O)₂]²⁺ can be considered a low-valent complex with a substrate (H₂O) coordinated, and [Mn^{IV}₂(O)₂(mcbpen)₂]²⁺ the appropriate higher formal oxidation state species with the product precursors coordinated. As such, the mcbpen[−] dinuclear system is unique in manganese chemistry and pertinent to modeling the OEC.

We have now used both a Clark electrode and MIMS^[3–6] to prove that O₂ is evolved from aqueous solutions containing **1**-(ClO₄)₂ and two separate chemical oxidants. The complex catalyzes the oxidation of water. When **1**-(ClO₄)₂ is mixed with 5–100 equivalents of TBHP in water, the initially pale solutions turn dark brown and bubbles are observed with the higher amounts of TBHP. The solutions generally bleach within 24 h and **1**-(ClO₄)₂ can be reisolated. Figure 1 shows the profiles of the O₂ evolution in the reaction of an aqueous solution of **1**-(ClO₄)₂ treated with periodic additions of TBHP (20 equivalents). The evolution of O₂ ceases approximately 25 min after each addition, and essentially the same amount of O₂ is repeatedly produced on each addition. The pH value of the system was 4.75 and did not change during the experiment. Control experiments in which an aqueous solution of manganese(II) perchlorate at the same pH value is used produces no O₂ on addition of 20 or more equivalents of TBHP. The shape of the traces in the MIMS experiments indicates evolution of O₂ rather than a surge, for example, from its introduction by the syringe.^[7] The fact that there is little decay in the response to each TBHP addition implies convincingly that the system is turning over.^[8] To date, evolution of 10–20 equivalents of O₂ has been recorded with no detectable catalyst decomposition or inhibition.

A strength of the MIMS technique is that ¹⁸O labeling experiments can be carried out to investigate the source of the O atoms in the evolved O₂. The ¹⁸O¹⁶O isotopomer is produced exclusively when ¹⁸O-labeled water (min. 95 % ¹⁸O) is used. No significant levels of ¹⁶O₂ and ¹⁸O₂ are detected. Thus, one oxygen atom in the O₂ evolved in the **1**-(ClO₄)₂ catalyzed oxidation of water by TBHP is derived from water. The reaction was carried out in pure water, and the measuring cell was purged with Ar, so the only other source of oxygen atoms was the oxidant, TBHP.^[9] In these experiments, the concentration of one substrate, water, is in large excess (172-fold) of the other substrate TBHP. It is not realistic to change these ratios such that the reaction stoichiometry might

[*] A. K. Poulsen, Dr. A. Rompel, Dr. C. J. McKenzie
Departments of Chemistry, and
Biochemistry and Molecular Biology
University of Southern Denmark
Main Campus: Odense University
Campusvej 55, 5230 Odense M (Denmark)
Fax: (+45) 6615-8780
E-mail: chk@chem.sdu.dk

[**] This work was supported by Danish Technical and Natural Science Research Council.



Supporting information (ESI mass spectra of reaction solutions containing TBHP and (NH₄)₂[Ce(NO₃)₆] in water, labeled water, and acetonitrile; further MIMS traces) for this article is available on the WWW under <http://www.angewandte.org> or from the author.

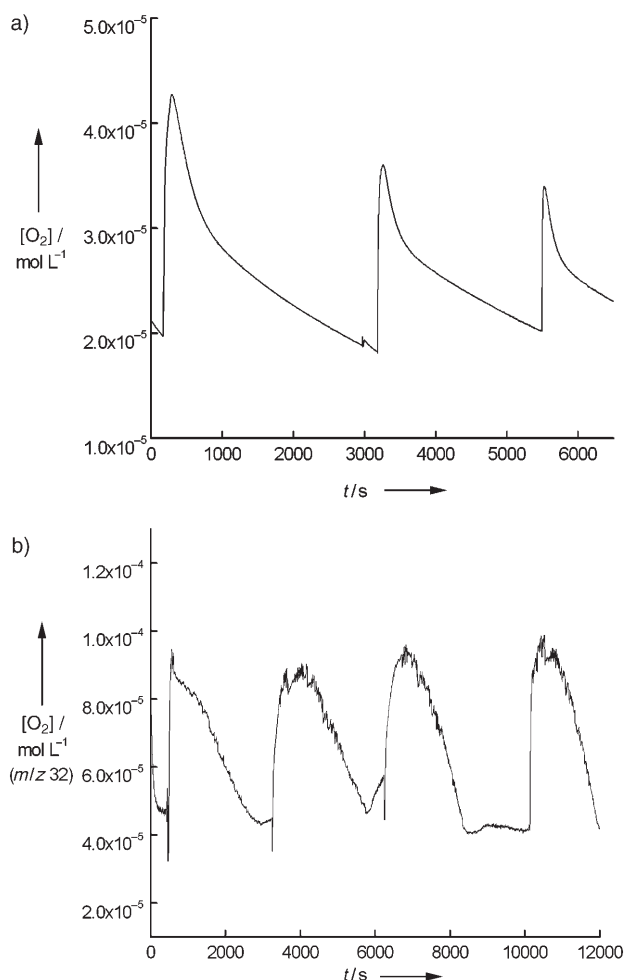
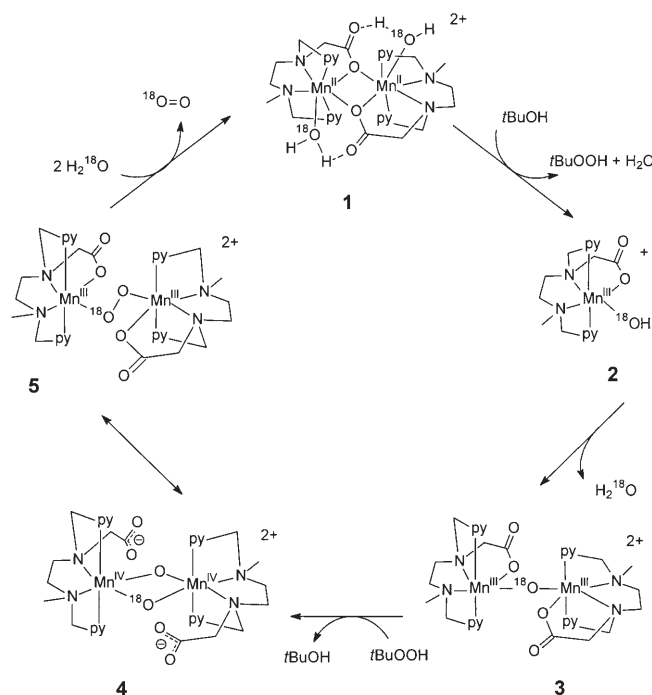


Figure 1. Measurement of O_2 concentration in an Ar-purged aqueous solution of $1-(ClO_4)_2$ with TBHP additions followed over time. a) Evolution measured by using a Clark electrode with injections of TBHP ($2.7 \mu\text{L}$, 1 M) at $t=0$, 50, and 90 min to $1-(ClO_4)_2$ (0.2 mM , $3.2 \times 10^{-7} \text{ mol}$) b) Evolution of $^{16}O_2$ measured by means of MIMS with injections of TBHP ($10 \mu\text{L}$, 0.323 M , $3.2 \times 10^{-6} \text{ mol}$) at $t=8$, 54, 104, and 169 min to $1-(ClO_4)_2$ (0.5 mM , $1.67 \times 10^{-7} \text{ mol}$). $^{18}O^{16}O$ (m/z 34) and $^{18}O_2$ (m/z 36) concentrations were followed but are not present in detectable amounts. The first, second, third, and fourth additions of TBHP generate 2.52×10^{-7} , 2.9×10^{-7} , 2.58×10^{-7} , and $2.62 \times 10^{-7} \text{ mol}$ of $^{16}O_2$ respectively (total: $1.062 \times 10^{-6} \text{ mol } ^{16}O_2$). Note: The relative concentrations of TBHP and $1-(ClO_4)_2$ in the two experiments are different, therefore, the measurement scales of the two experiments cannot be directly compared.

be experimentally verified because increasing the oxidant concentration will give an unreliable measurement, as MIMS, similar to an O_2 electrode, detects only the oxygen dissolved in the liquid and not the oxygen expelled as bubbles. Thus, with water as the solvent we were limited to using the concentrations of the TBHP and $1-(ClO_4)_2$ shown in Figure 1 in the quantitative experiments. It is likely that greater yields are achievable.

On the basis of our earlier characterization of the transient mononuclear and dinuclear Mn^{III} and dinuclear Mn^{IV} complexes of $mcbpen^-$ generated by oxidation of $1-(ClO_4)_2$ with TBHP in acetonitrile and water (see Supporting

Information and ref. [2]), we propose the speculative reaction mechanism outlined in Scheme 1. Oxidation of $1-(ClO_4)_2$ with TBHP cleaves the bridging carboxylate-O ligands of $1^{[10]}$ and produces the transient mononuclear hydroxide $[Mn^{III}(mcbpen)OH]^+$ (**2**). ESIMS studies of the reaction in both



Scheme 1. A speculative mechanism for water oxidation by $t\text{BuOOH}$ catalyzed by $1-(ClO_4)_2$.

D_2O and $H_2^{18}O$ clearly show that the oxygen atom in **2** is derived from water and not the oxidant, as the major ion generated is $[Mn^{III}(mcbpen)OD]^+$ (m/z 386.5) and $[Mn^{III}(mcbpen)^{18}OH]^+$ (m/z 387.3) in D_2O and $H_2^{18}O$, respectively. The next step in the catalytic cycle is dimerization and dehydration of **2** to give $[Mn^{III}_2(mcbpen)_2(O)]^{2+}$ (**3**). The dehydration in aqueous solution of manganese(III) and iron(III) complexes containing terminal hydroxides to give dinuclear mono-oxide bridged complexes is well documented. We have shown that reaction of $1-(ClO_4)_2$ with TBHP in water and acetonitrile produces the very short lived **3** as verified by ESIMS and UV/Vis spectroscopy.^[2] A facile oxidation of **3** on the basis of the known instability of such species to oxidation is expected, and differs from the first oxidation step, in that the TBHP may in this case act as an oxygen atom donor to give the dimeric $[Mn^{IV}_2(O)_2(mcbpen)_2]^{2+}$ (**4**). It is likely that during the **3**→**4** reaction step the carboxylate arms are concomitantly displaced to accommodate the two μ -oxo ligands. Thus, an arrangement similar to other, known bis(μ -oxo)-dimanganese complexes of linear N_4 bispicen-based^[11] ligands ($Mn \cdots Mn = 2.7 \text{ \AA}$)^[12–14] is achieved. The anticipated facile oxidation of **3** (oxidase activity) can be invoked to explain the slightly different curve shape in the first evolution step (the front of the peak shows a spike, which indicates an initial rapid reduction in O_2 concentration). This spike might

be caused by an initial trace amount of O₂ in the solution which oxidizes **3** in the first cycle.

Spontaneous collapse of **4** followed by release of dioxygen and coordination of two molecules of water will result in reformation of **1** in aqueous solution. We imagine that the carboxylate arms of mcbpen[−] are not innocent in the O₂-elimination reaction; by swinging in and re-coordinating the manganese atoms, as depicted in the resonance structures **4** and **5** (Scheme 1), the formation of a bond between the two oxide bridges might be favored as a Mn–O(Mn) bond at each Mn atom is displaced. Similar resonance in copper bis(μ-oxo)/μ-peroxo systems has been proposed.^[15,16] Oxygen release from the μ-peroxo-Mn^{III}₂ complex **5** to give a Mn^{II}₂ species would then ensue. A notable feature of this mechanism is the involvement of the coordinatively flexible carboxylate arm of the mcbpen[−] ligand: Bridging, terminal, and noncoordinated modes support the various dinuclear and mononuclear structures proposed, and the oxidation states deduced experimentally, in a chemically logical fashion. This is analogous to the so-called “carboxylate shift” proposed to be important in the mechanisms of several non-heme iron enzymes. Of course any mechanistic proposal is speculative; however, we have spectroscopic evidence for all the species in Scheme 1 except **5**. Furthermore, the species are all chemically reasonable, comprising water/hydroxo/oxo ligands on metal centers of the appropriate oxidation state.

The overall reaction for the mechanism proposed in Scheme 1 including an ¹⁸O label is described by Equation (1).^[17]



Equation (1) simplifies to Equation (2):



The attempt to establish the source of the O atoms in the evolved O₂ is clearly problematic where a terminal oxidant containing an O atom is used. We therefore tested (NH₄)₂[Ce(NO₃)₆] as the oxidant. This Ce^{IV} source has been used in the studies of the oxidation of [(bpy)₂(H₂O)RuORu(H₂O)-(bpy)₂]⁴⁺ (bpy = 2,2′-bipyridine) by Meyer and co-workers^[18,19] and recently in the report by Yagi and Narita that [Mn₂O₂(terpy)₂(H₂O)₂](NO₃)₃·6H₂O (terpy = 2,2′:6′,2′′-terpyridine) adsorbed onto kaolin clay produces O₂ from water.^[20] When (NH₄)₂[Ce(NO₃)₆] was used as the oxidant, the evolution of O₂ from water catalyzed by 1-(ClO₄)₂ was again detected, however, in lower yields than in the TBHP reaction. The pH value of the reaction mixture with (NH₄)₂[Ce(NO₃)₆] drops rapidly to 1 and this is most likely the cause of the lower yields—at low pH values, the formation of high-valent oxo-bridged Mn species is not favored. Furthermore, ligand decooordination caused by competing protonation is suggested by the ESI mass spectra of reaction mixtures containing (NH₄)₂[Ce(NO₃)₆] which show the presence of the free ligand mcbpenH₂⁺ at *m/z* 315.4 in addition to [Mn₂-(mcbpen)₂]²⁺ at 368.3 and [Mn^{III}(mcbpen)NO₃]⁺ at 430.2 (see Supporting Information). Figure 2 follows the concentration of the ¹⁸O¹⁶O isotopomer with time in experiments with

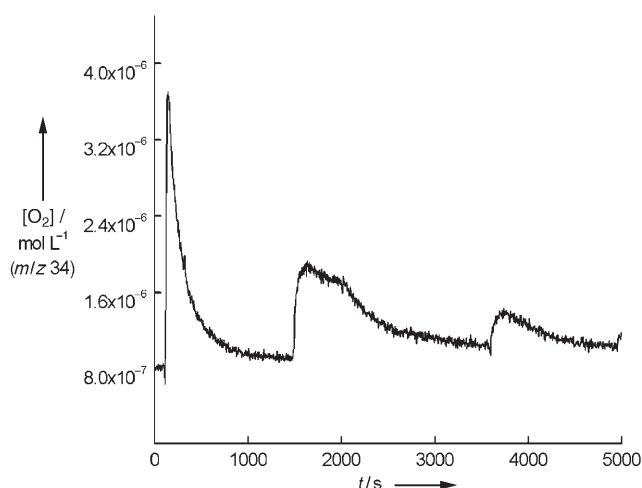
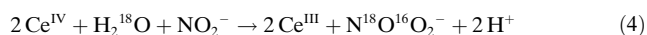
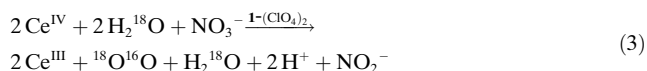


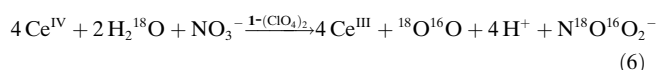
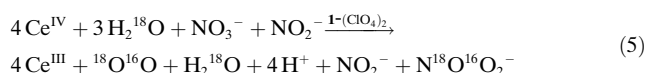
Figure 2. Trace of ¹⁸O¹⁶O evolution over time from a solution containing 1-(ClO₄)₂ (2 mM, 7.1 × 10^{−7} mol) in 95 % H₂¹⁸O after injections of (NH₄)₂[Ce(NO₃)₆] (20 μL, 0.6 M) in 95 % H₂¹⁸O at *t* = 2, 25, and 60 min. Total amounts of evolved oxygen are much lower, and the decrease in productivity with each addition of oxidant is evident from the comparison of the curve shape to that of Figure 1 b. The evolution of ¹⁶O₂ (*m/z* 32) and ¹⁸O₂ (*m/z* 36) was under detectable limits.

(NH₄)₂[Ce(NO₃)₆]. Again, and initially surprisingly, the ¹⁸O¹⁶O isotopomer is produced exclusively in the ¹⁸O labeling experiments with (NH₄)₂[Ce(NO₃)₆].

As the reaction is carried out in 95 % H₂¹⁸O water, the only source of one ¹⁶O atom is the nitrate^[21] anion in the Ce^{IV} salt. Thus, the exclusive production of ¹⁸O¹⁶O in the reactions with Ce^{IV} as the oxidant can be only explained by the involvement of nitrate as an O-atom donor.^[22] Thus, we propose that the water oxidation is coupled with both Ce^{IV} and nitrate reduction as shown in Equation (3). Inspection of the redox potentials of Ce^{IV} reduction and nitrite oxidation indicates any nitrite produced would be rapidly reoxidized to nitrate in the presence of excess Ce^{IV} [Eq. (4)].



By combining Equations (3) and (4), the overall reaction for the 1-(ClO₄)₂ catalyzed oxidation of water, including labels, by (NH₄)₂[Ce(NO₃)₆] is that in Equation (5), which can be simplified to Equation (6).



Aqueous solutions of [Mn₂O₂(terpy)₂(H₂O)₂](NO₃)₃·6H₂O, (**6**) have been shown to evolve dioxygen (without turnover) in the presence of aqueous sodium hypochlorite^[23] and oxone.^[24] In the presence of high concen-

trations of oxone ($\text{KHS}^{16}\text{O}_5$) (100:1 oxone:6) negligible amounts of labeled dioxygen were formed in the presence of H_2^{18}O , thus suggesting that oxone was the likely source of the O atoms in the O_2 produced under these conditions. However, by lowering the ratio of the oxone:6 to 20:1, labeled dioxygen was detected, with the highest yielding mixtures containing doubly-labeled $^{18}\text{O}_2$ ($12\% \pm 6\%$), mixed-labeled $^{18}\text{O}^{16}\text{O}$ ($39\% \pm 15\%$), and $^{16}\text{O}_2$ ($49\% \pm 19\%$).^[24] Solutions of 6 in these reactions decompose rapidly to give permanganate. These results are in contrast to those we report for the Mn/mcbpen[−] system. In neither of the oxidation reactions with TBHP or Ce^{IV} as oxidant and $1\text{-(ClO}_4)_2$ as catalyst was permanganate produced as a decomposition product of the catalyst; the reaction is highly specific as only one isotopomer is produced, and there is turnover.

Notably, mcbpen[−] is mononegative and provides one carboxylate donor for each Mn ion, which is analogous to the protein donors for all the Mn atoms of the 3+1 OEC cluster.^[25] The flexible carboxylate donor means that dinuclear manganese complexes of mcbpen[−] show the potential to change between 6 and 7 coordination as needed, depending on the Mn oxidation state and the presence of exogenous ligands. The Mn...Mn separations may vary between 4.0914(9) Å ($\text{Mn}^{\text{II}}/\text{Mn}^{\text{II}}$) and 2.7 Å ($\text{Mn}^{\text{IV}}/\text{Mn}^{\text{IV}}$). These features are a significant advance in ligand design for an OEC model and may in fact be crucial to the functionality of this system. The dinuclear complexes in the proposed catalytic cycle (Scheme 1) are all plausible intermediates and have structural precedents with either mcbpen[−] itself or related ligand systems. The highly specific and catalytic oxidation of water catalyzed by $1\text{-(ClO}_4)_2$ is a noteworthy advance in the mimicry of the activity of the OEC.

Experimental Section

All solutions were prepared using doubly deionized water. H_2^{18}O (95 atom %) was purchased from ISOTEC (Sigma Aldrich). All other chemicals were purchased from Aldrich and used without further purification. Solutions of *tert*-butylhydrogenperoxide (TBHP) in decane (6M) or water (1M and 0.32M) were used. $1\text{-(ClO}_4)_2$ was synthesized as reported previously.^[2] **Caution!** Perchlorate salts of metal complexes with organic ligands are potentially explosive!

Electrospray Ionization Mass spectra were obtained using a Finnigan TSQ 700 triple-quadrupole instrument equipped with a Finnigan API source in nanoelectrospray mode. The oxygen concentration was measured with an MI-730 oxygen electrode from Micro-electrodes Inc., USA and by means of membrane inlet mass spectrometry (MIMS). In the MIMS experiment, the sample cell had a volume of 500 μL and was made of stainless steel. The solution was stirred with an impeller connected through a stirring shaft to an electric motor operating at 400 rpm. The sample cell was mounted on a vacuum flange, and the only separation between the liquid in the sample cell and the vacuum chamber of a single-quadrupole mass spectrometer (Balzers QMG 420) was a 51- μm thick silicone membrane (SIL-TEC Sheeting, Technical products Inc., USA). The inlet was thermostatically controlled at 30°C. The concentration of O_2 was determined by using the calibration method described by Degn and Lauritsen.^[26]

Received: June 17, 2005

Revised: August 18, 2005

Published online: October 5, 2005

Keywords: bioinorganic chemistry · manganese · N,O ligands · oxidation · photosynthesis

- [1] S. Mukhopadhyay, S. K. Mandal, S. Bhaduri, W. H. Armstrong, *Chem. Rev.* **2004**, *104*, 3981–4026.
- [2] C. Baffert, M.-N. Collomb, A. Deronzier, S. Kjergaard-Knudsen, J.-M. Latour, K. H. Lund, C. J. McKenzie, M. Mortensen, L. P. Nielsen, N. Thorup, *Dalton Trans.* **2003**, 1765–1772.
- [3] R. C. Johnson, R. G. Cooks, T. M. Allen, M. E. Cisper, P. H. Hemberger, *Mass Spectrom. Rev.* **2000**, *19*, 1–37.
- [4] F. R. Lauritsen, and T. Kotiaho, *Anal. Chem.* **1996**, *68*, 237–264.
- [5] A. K. Poulsen, F. R. Lauritsen, L. F. Olsen, *FEMS Microbiol. Lett.* **2004**, *236*, 261–266.
- [6] MIMS is a method that allows the analysis of volatile compounds in liquid media. The only separation between the polar media and the mass spectrometer is a thin polymer film. Volatile and hydrophobic compounds dissolve in the membrane, diffuse through it, and evaporate into the ion source of the mass spectrometer, where they are ionized and analyzed according to their mass-to-charge ratios. The method is highly suited for measuring gases and organic compounds in aqueous media, and enables measurements in the low-ppm range. The response time is only a few seconds, and the method has been used for studies of complex chemical reactions^[26] and for online measurements in microbial media.^[5] We have attempted to assess the electron-impact mass spectrometry (EIMS) methods used in the analysis of ^{18}O -labelling experiments in references [20, 23, 24]. Unfortunately, insufficient detail was provided (in supplementary information) to describe the experimental protocols. Thus, we assume that the gas in the head space over the reactions was analyzed. This method is fundamentally different to MIMS and is not quantitative.
- [7] A deliberate injection of O_2 into the system does not invoke this response, rather the surge is recorded, and this immediately decays exponentially.
- [8] We are currently designing a new cell so that a continuous supply of TBHP can be added in order to attain a steady state of catalytic activity. Visual inspection of the reactions indicates that the concentrations used in the MIMS experiments are not optimal and the system potentially produces much greater amounts of product.
- [9] We have not found determinations of O-exchange between water and *t*BuOOH in the literature. However, the specific production of one isotopomer observed in our work is indirect evidence that any exchange of this nature is not kinetically relevant. If there was significant exchange then a distribution of isotopes, $^{16}\text{O}_2$, $^{18}\text{O}^{16}\text{O}$, and $^{18}\text{O}_2$, would be observed. Furthermore we have monitored the reaction solution at m/z 92, which corresponds to singly ^{18}O -labeled TBHP. No trace was detected (and we do see unlabeled TBHP at m/z 90). Therefore competing homolytic cleavage of the O–O bond in TBHP and consequent radical Haber–Weiss chemistry can be eliminated in mechanistic considerations. Furthermore oxidation is observed with the Ce^{IV} oxidant.
- [10] The complex is dimeric in solution as well as in the solid state as evidenced by solution ESR spectroscopy.^[2]
- [11] bispicen = *N,N'*-bis(2-methylpyridyl)ethane-1,2-diamine.
- [12] M. A. Collins, D. J. Hodgson, K. Michelsen, D. K. Towle, *Chem. Commun.* **1987**, 1659–1660.
- [13] J. Glerup, P. A. Goodson, A. Hazell, R. Hazell, D. J. Hodgson, C. J. McKenzie, K. Michelsen, U. Rychlewska, H. Toftlund, *Inorg. Chem.* **1994**, *33*, 4105–4111.
- [14] P. A. Goodson, J. Glerup, D. J. Hodgson, K. Michelsen, E. Pedersen, *Inorg. Chem.* **1990**, *29*, 503–508.

- [15] J. A. Halfen, S. Mahapatra, E. C. Wilkinson, S. Kaderli, V. G. Young, Jr., L. Que, Jr., A. D. Zuberbühler, W. B. Tolman, *Science* **1996**, 271, 1397–1400.
- [16] L. Que, W. B. Tolman, *Angew. Chem.* **2002**, 114, 1160–1137; *Angew. Chem. Int. Ed.* **2002**, 41, 1114–1137 Erratum: L. Que, W. B. Tolman, *Angew. Chem.* **2002**, 114, 1900; *Angew. Chem. Int. Ed.* **2002**, 41, 1821.
- [17] The reaction is not a catalase-like reaction. If this were the case, both O atoms would be derived from the oxidant.
- [18] S. W. Gersten, G. J. Samuels, T. J. Meyer, *J. Am. Chem. Soc.* **1982**, 104, 4029–4030.
- [19] J. A. Gilbert, D. S. Eggleston, W. R. Murphy, D. A. Geselowitz, S. W. Gersten, D. J. Hodgson, T. J. Meyer, *J. Am. Chem. Soc.* **1985**, 107, 3855–3864.
- [20] N. Yagi, K. Narita, *J. Am. Chem. Soc.* **2004**, 126, 8084–8085.
- [21] The nitrate complex $(\text{NH}_4)_2[\text{Ce}(\text{NO}_3)_6]$ is that normally used as a source of Ce^{IV} in oxidation reactions. However, participation by the nitrate ion is not normally considered.
- [22] As mentioned in the text, the nitrate-containing $[\text{Mn}^{\text{III}}(\text{mcbpen})\text{NO}_3]^+$ is in fact observed in the ESI mass spectra of the reaction solutions. This fact cannot be regarded as evidence for Mn activation for nitrate reduction. However, it does suggest a higher concentration of $[\text{Mn}^{\text{III}}(\text{mcbpen})\text{NO}_3]^+$ than the iso-electronic $[\text{Mn}^{\text{III}}(\text{mcbpen})\text{OH}]^+$, which is seen in the TBHP reactions. An attempt to verify the possible involvement of nitrate in the water oxidation was made by adding a 100-fold excess of sodium nitrate to the reaction. This resulted in complete inhibition of the reaction. This observation is not surprising if nitrate is capable of substituting the water ligands of **1-2** (ClO_4)₂ and consequently inhibiting the reaction. We have also attempted to detect the $\text{N}^{18}\text{O}^{16}\text{O}_2^-$ isotopomer by negative-ion ESIMS. Unfortunately, in the presence of such large excess of the unlabeled nitrate, this experiment was beyond the resolution capabilities of our instrument.
- [23] J. Limburg, J. S. Vrettos, L. M. Liable-Sands, A. L. Rheingold, R. H. Crabtree, G. W. Brudvig, *Science* **1999**, 283, 1524–1527.
- [24] J. Limburg, J. S. Vrettos, H. Chen, J. C. de Paula, R. H. Crabtree, G. W. Brudvig, *J. Am. Chem. Soc.* **2001**, 123, 423–430.
- [25] K. N. Ferreira, T. M. Iverson, K. Maghlaoui, J. Barber, S. Iwata, *Science* **2004**, 303, 1831–1838.
- [26] H. Degn, F. R. Lauritsen, *J. Phys. Chem.* **1989**, 93, 2781–2783.

DOI: 10.1002/anie.200502173

Selective Sensing of Zinc Ions with a PARACEST Contrast Agent***Robert Trokowski, Jimin Ren, Ferenc Krisztián Kálmán, and A. Dean Sherry**

Divalent zinc, the second most abundant transition-metal ion in seawater and in humans, is an essential integral component of numerous functional proteins involved in a wide range of physiological systems.^[1–4] Zinc ions also bind to many membrane receptors, transporters, and channels, and modulate their activity.^[5] Therefore, it is not surprising that zinc deficiency affects many organs, including the digestive, immune, and neuronal systems.^[4,6,7] Free Zn^{II} ions are released from loosely bound metal–protein complexes found in selected cell types and cell organelles in brain and other tissues.^[8] Various indirect evidence indicates that the concentration of free Zn^{II} ions ranges from 10^{-12} to 10^{-5} M in undifferentiated mammalian cells to approximately 0.3 mM in hippocampal-nerve synaptic vesicles.^[9,10] Understanding the importance and control of the release of Zn^{II} ions in living cells will require suitable detection and imaging reagents.^[11–13]

In the past two decades, magnetic resonance imaging (MRI) has grown into one of the most powerful techniques in diagnostic medicine and biomedical research. One of the first designs for sensing Zn^{II} ions by MRI was based on a Gd^{III} complex that showed an approximately 30 % decrease in water relaxivity in the presence of Zn^{II} ions.^[14] The ligand in this complex was prepared by treating diethylenetriamine-pentaacetic acid (dtpa) bisanhydride with *N,N*-bis(2-pyridylmethyl)ethylenediamine to form a ligand having both a Gd^{III} site and a Zn^{II} site, which is presumably formed by the four pyridine donors situated above the water molecule bound to the Gd^{III} ion. On the basis of recent success at creating imaging agents that respond to changes in water-exchange

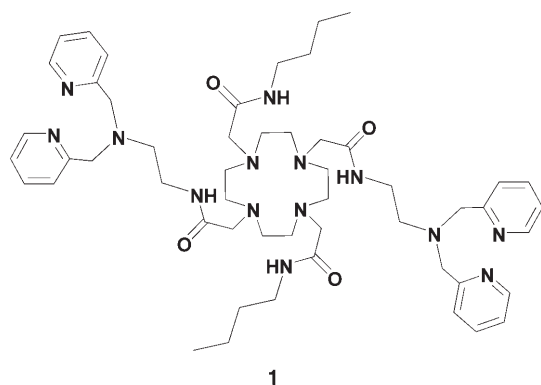
[*] Dr. R. Trokowski, F. K. Kálmán, Prof. A. D. Sherry
Department of Chemistry
The University of Texas at Dallas
P.O. Box 830688, Richardson, TX 75080 (USA)
Fax: (+1) 972-883-2925
E-mail: sherry@utdallas.edu
Dr. J. Ren, Prof. A. D. Sherry
The Rogers Magnetic Resonance Center
Department of Radiology
University of Texas
Southwestern Medical Center
5801 Forest Road, Dallas, TX 75235 (USA)

[**] This work was supported in part by grants from the Robert A. Welch Foundation (AT-584), the National Institutes of Health (CA-84697), the Division of Research Resources, the National Institutes of Health (RR-02584), and the Texas Advanced Technology Program. PARACEST = paramagnetic chemical exchange saturation transfer.



Supporting information for this article is available on the WWW under <http://www.angewandte.org> or from the author.

rates rather than relaxation rates, we decided to test the hypothesis that a chemical exchange saturation transfer (CEST) agent may be advantageous for measuring the levels of free Zn^{II} ions in tissues.^[15–18] Here, we report a first-generation paramagnetic CEST agent, [Eu(dotampy)] (dotampy = 1,7-bis(*N,N*-bis(2-pyridylmethyl)aminoethylcarbamoylmethyl)-4,10-bis(butylcarbamoylmethyl)-1,4,7,10-tetraazacyclododecane, **1**), as a novel sensor for Zn^{II} ions.



The CEST profile of [Eu(dotampy)] is typical of a system exhibiting intermediate to slow water exchange between a Eu^{III} -bound water species with a resonance at $\delta = 50$ ppm and that of bulk water at $\delta = 0$ ppm (Figure 1). Somewhat surprisingly, addition of Zn^{II} ions to this complex in buffered solution at pH 7.1 resulted in broadening of the resonances of both the Eu^{III} -bound water molecule ($\delta = 50$ ppm) and the bulk water ($\delta = 0$ ppm), suggestive of more rapid water exchange. As a result, the most dramatic changes that are observed in the CEST spectrum upon addition of Zn^{II} ions occur in the region between these two exchanging water signals (15–30 ppm). This effect was even more dramatic when Zn^{II} ions were added to [Eu(dotampy)] at pH 8.0 (Figure 1). In this case, water (or proton) exchange is so fast that the entire CEST signal at $\delta = 50$ ppm disappeared upon addition of Zn^{II} ions. The sensitivity of CEST to base catalysis was not anticipated for this system nor was the origin of this effect immediately apparent. One possibility is that if a Zn^{II} ion forms a mononuclear complex by coordinating the four pyridine donors, such binding could introduce “strain” around the Eu^{III} coordination complex and perhaps alter the geometry of [Eu(dotampy)] from a square-antiprism (SAP) structure with intermediate-to-slow water exchange to a twisted-square-antiprism (TSAP) structure with faster water exchange. A high-resolution ^1H NMR spectrum of [Eu(dotampy)] shows a single, highly shifted resonance near $\delta = 25$ ppm that is characteristic of the four axial macrocyclic protons in a SAP coordination geometry (Figure 2) and no indication of even a small population of a TSAP coordination isomer.^[19–22] Addition of Zn^{II} ions to [Eu(dotampy)] resulted in a slight shift of this resonance to low field and a broadening into three or more nearly resolved signals. This result indicates that [Eu(dotampy)] is less symmetric in the presence of Zn^{II} ions but, again, no new resonances were present in the region between $\delta = 12$ and 15 ppm, as would be anticipated if

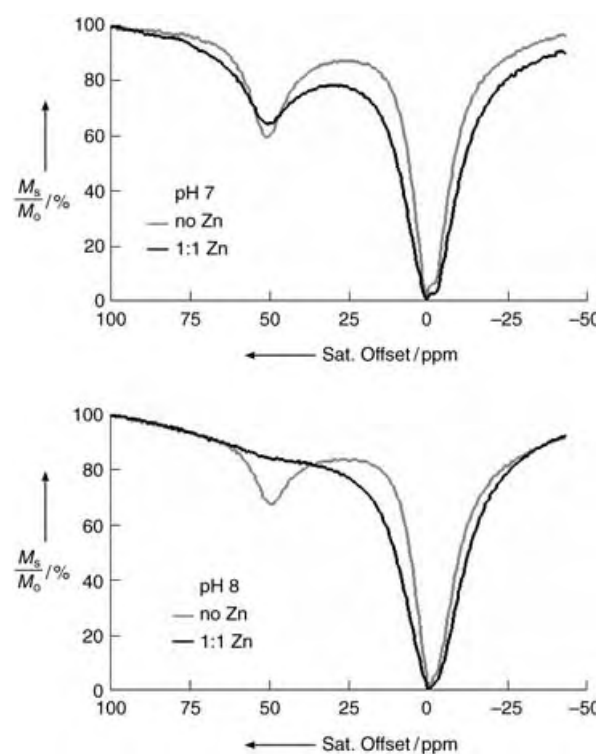


Figure 1. Top: Z-spectra of 20 mM [Eu(dotampy)] in the absence (gray line) and in the presence (black line) of 20 mM Zn^{II} ions in 1,4-piperazinebis(ethanesulfonic acid) (PIPES) buffer (100 mM; pH 7.1) at 25 °C. Bottom: Z-spectra of 20 mM [Eu(dotampy)] in the absence (gray line) and in the presence (black line) of 20 mM Zn^{II} ions in 2,4,6-tris[(dimethylamino)methyl]phenol (DMP) buffer (100 mM; pH 8.0) at 25 °C. The CEST profiles were collected by using a 2-s frequency-selective hard pulse ($B_1 = 1000$ Hz) followed by a non-frequency-selective 60° read-out hard pulse. M_s = bulk-water magnetization when a presaturation pulse is applied; M_0 = equilibrium magnetization without presaturation.

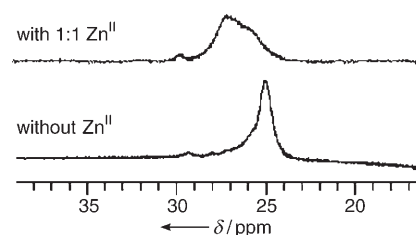
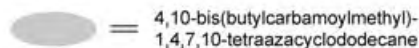


Figure 2. Low-field portion of a ^1H NMR spectrum (400 MHz, 25 °C) of 100 mM [Eu(dotampy)] in the absence (upper) and in the presence (lower) of 100 mM of Zn^{II} ions at pH 6.95.

there had been a change in structure from SAP to TSAP.^[23] Thus, the enhanced water-exchange characteristics of the [Eu(dotampy)]– Zn^{II} adduct cannot be traced to a switch in the coordination geometry of the complex.

A second possible reason why water (or proton) exchange is faster in the [Eu(dotampy)]– Zn^{II} adduct is that the Zn^{II} ion may itself have a coordinated water molecule that is partially deprotonated at these pH values, thereby positioning a $\text{Zn}^{\text{II}}\text{OH}$ species near the Eu^{III} -bound water molecule (a hypothetical model is illustrated in Scheme 1). Such a species



Scheme 1. Hypothetical structures of [Eu(dotampy)] in the presence and absence of Zn^{II} ions.

could act to catalyze prototropic exchange between the Eu^{III} -bound water molecule and the bulk solvent. Other ligand systems containing two *N,N*-bis(2-pyridylmethyl)amine (dpa) units frequently form dinuclear complexes with Zn^{II} ions, in which each dpa arm provides three nitrogen donors and the fourth coordination site is occupied by a bridging hydroxide ion.^[24–27] However, all of our data on this system (potentiometry, spectroscopy, and CEST titrations, see below) show that a mononuclear species is formed between $[\text{Eu}(\text{dotampy})]$ and Zn^{II} ions under all experimental conditions examined. Molecular modeling studies of the $[\text{Eu}(\text{dotampy})]\text{--Zn}^{\text{II}}$ adduct suggest that the positions of the tertiary amines on each side-arm are constrained by the size of bridging $\{\text{Eu}(\text{dotam})\}$ moiety and are therefore not likely to be coordinated to the Zn^{II} ion. This would leave only the four pyridyl nitrogen atoms and perhaps one or two water molecules available to form a complex with the Zn^{II} ions. Attempts to isolate crystals of $[\text{Eu}(\text{dotampy})]\text{--Zn}^{\text{II}}$ suitable for X-ray crystallographic analysis to confirm the structure illustrated in Scheme 1 have been unsuccessful.

Potentiometric titrations of [Eu(dotampy)] were performed in the absence and presence of Zn^{II} ions to examine whether either a Eu^{III}- or Zn^{II}-coordinated water molecule can be titrated over the pH range employed in the CEST studies (see Supporting Information). In the absence of Zn^{II} ions, [Eu(dotampy)] displays three stepwise protonation constants ($\log K_a = 3.60 \pm 0.03$, 5.75 ± 0.03 , 11.29 ± 0.02) over the usual pH range covered by potentiometry. The $\log K_a$ values of 3.60 and 5.75 are consistent with protonations

occurring at the two tertiary nitrogen atoms on the side-arms whereas the $\log K_a$ value of 11.29 likely corresponds to deprotonation of the Eu^{III} -bound water molecule.^[28] A fit of the titration data collected in the presence of a stoichiometric amount of Zn^{II} ions gave a stability constant of $\log K_{\text{st}} = 7.59 \pm 0.02$ for the $[\text{Eu}(\text{dotampy})]\text{-Zn}^{\text{II}}$ adduct. The potentiometric data also provided evidence for formation of a $\text{Zn}^{\text{II}}\text{OH}$ species above approximately pH 6 which could act as a catalyst for the exchange of protons between the Eu^{III} -bound water molecule and the bulk solvent. A similar mechanism has been proposed for proton catalysis by the appended phosphonate groups in $[\text{Gd}(\text{dota-4amp})]$ (dota-4amp-1,4,7,10-tetrakis(*N*-methylphosphate)-1,4,7,10-tetraazacyclododecane).^[29] Spectrophotometric titrations of $[\text{Eu}(\text{dotampy})]$ at pH 7.1 confirmed this potentiometric binding model. The absorbance between 225 and 285 nm changed linearly with an increase in the Zn^{II} concentration up to a $[\text{Eu}(\text{dotampy})]/\text{Zn}^{\text{II}}$ mole ratio of 1:1, with isosbestic points at 248, 267, and 272 nm, but then remained unchanged with further increases in Zn^{II} concentration. A Job plot of these binding data provided further evidence for the formation of a 1:1 complex (see Supporting Information). Finally, additional support is given by the Z-spectra collected after incremental additions of Zn^{II} ions at pH 7 (Figure 3); the CEST effect was

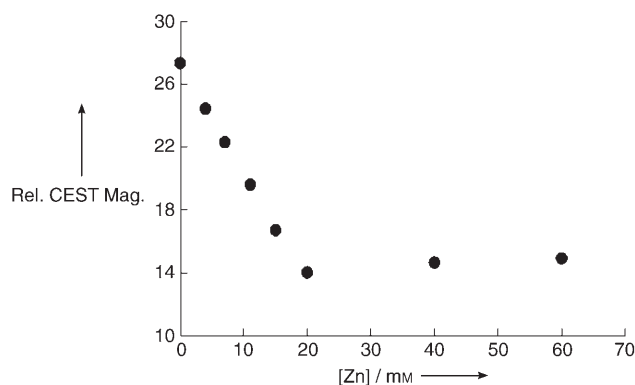


Figure 3. A plot of relative CEST magnitude versus Zn^{II} concentration for 20 mM [Eu(dotampy)] in PIPES buffer (100 mM; pH 7).

quenched linearly with addition of up to one equivalent of Zn^{II} ions, but then relatively small changes were observed upon further increases in the Zn^{II} concentration. This observation demonstrates that a 1:1 complex is formed both at 20 mM (the concentrations used to collect the CEST spectra) and 0.1–2.0 mM (the concentrations used in the potentiometric and UV/Vis experiments).

To demonstrate that Zn^{II} binding can be sensed in a CEST imaging experiment, a phantom consisting of four plastic tubes (i.d. 4 mm), each containing 20 mm [Eu(dotampy)] and different amounts of Zn^{II} ions, was prepared. Images were acquired after applying a selective Gaussian-shaped presaturation pulse at $\delta = 50$ ppm followed by a spin-echo gradient imaging sequence. A second image was collected after presaturation at $\delta = 25$ ppm and CEST images were generated by pixel-by-pixel subtraction of the two SE images. The image intensities (Figure 4) show a clear gradation that

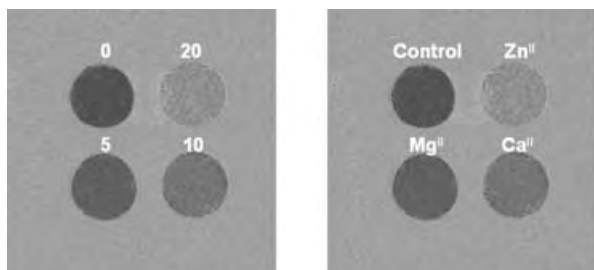


Figure 4. Left: CEST images of phantoms containing 20 mM [Eu(dotampy)] and either 0, 5, 10, 20 mM Zn^{II} ions. Right: CEST images of phantoms containing 20 mM [Eu(dotampy)] plus stoichiometric amounts of Zn^{II} , Mg^{II} or Ca^{II} ions. PIPES (100 mM) was used to buffer the solution at pH 7.1. A 1 s (left image) or 0.5 s (right image) frequency-selective Gaussian shaped pulse ($B_1 = 1000$ Hz) was used to presaturate the sample prior to applying spin-echo (SE) imaging pulses. The CEST images represent the intensity difference between the SE images for saturation at $\delta = 50$ ppm and $\delta = 25$ ppm from the bulk water. Other imaging parameters included: TR/TE 1300 ms/13 ms, thickness 2 mm, FOV 30×30 mm, data matrix 128×128 , 4 dummy scans, each image was the average of 2 scans. TR = repetition time; TE = echo time; FOV = field of view.

parallels the Zn^{II} concentrations in each sample. To test for selectivity, CEST images were also collected by replacement of Zn^{II} ions with either Mg^{II} or Ca^{II} ions. Those ions could not be detected by CEST imaging.

Finally, one needs to consider the practical use of this system for imaging of Zn^{II} ions in a real biological system. From the CEST results illustrated above, one can estimate that a minimum of approximately 2 mM agent would be needed to satisfy the sensitivity limits for detection of Zn^{II} ions by MRI. Given that the CEST MRI signal would only detect changes in total Zn^{II} concentration covering the range from 0.4 to 1.6 mM (as set by the sensitivity limits of MRI) and that $\log K_{\text{st}} = 7.59 \pm 0.02$ for the [Eu(dotampy)]– Zn^{II} system, one can then estimate that the effective sensitivity range for this sensor in detecting changes in concentration of “free” Zn^{II} ions varies from 5 nM to $0.12 \mu\text{M}$ —a reasonable concentration range for levels of free Zn^{II} ions in tissues. Of course, the practicality of this detection method remains to be proven, but the idea—detection of the catalysis of proton exchange by a nearby coordinated hydroxide group, as demonstrated in the current Zn^{II} system—serves as an attractive model for the design other responsive PARACEST imaging agents.

Received: June 21, 2005

Revised: August 5, 2005

Published online: October 5, 2005

Keywords: imaging agents · lanthanides · proton exchange · saturation transfer · zinc

- [7] A. S. Prasad, *Nutrition* **1995**, *11*, 93.
- [8] C. Frederickson, *Sci. STKE* **2003**, *182*, pe18.
- [9] T. Budde, A. Minta, J. A. White, A. R. Kay, *Neuroscience* **1997**, *79*, 347.
- [10] C. E. Outten, T. V. O'Halloran, *Science* **2001**, *292*, 2488.
- [11] Y. Wu, X. Peng, B. Guo, J. Fan, Z. Zhang, J. Wang, A. Cui, Y. Gao, *Org. Biomol. Chem.* **2005**, *3*, 1387.
- [12] C. C. Woodroffe, A. C. Won, S. J. Lippard, *Inorg. Chem.* **2005**, *44*, 3112.
- [13] N. C. Lim, H. C. Freake, C. Bruckner, *Chem. Eur. J.* **2004**, *11*, 38.
- [14] K. Hanaoka, K. Kikuchi, Y. Urano, T. Nagano, *J. Chem. Soc. Perkin Trans. 2* **2001**, 1840.
- [15] K. M. Ward, A. H. Aletras, R. S. Balaban, *J. Magn. Reson.* **2000**, *143*, 79.
- [16] S. Aime, D. Delli Castelli, F. Fedeli, E. Terreno, *J. Am. Chem. Soc.* **2002**, *124*, 9364.
- [17] S. Aime, C. Carrera, D. D. Castelli, S. G. Crich, E. Terreno, *Angew. Chem.* **2005**, *117*, 1847; *Angew. Chem. Int. Ed.* **2005**, *44*, 1813.
- [18] S. R. Zhang, R. Trokowski, A. D. Sherry, *J. Am. Chem. Soc.* **2003**, *125*, 15288.
- [19] F. A. Dunand, S. Aime, A. E. Merbach, *J. Am. Chem. Soc.* **2000**, *122*, 1506.
- [20] S. Aime, A. Barge, M. Botta, A. S. De Sousa, D. Parker, *Angew. Chem.* **1998**, *110*, 2819; *Angew. Chem. Int. Ed.* **1998**, *37*, 2673.
- [21] D. M. Corsi, L. Vander Elst, R. N. Muller, H. van Bekkum, J. A. Peters, *Chem. Eur. J.* **2001**, *7*, 1383.
- [22] U. Cosentino, A. Villa, D. Pitea, G. Moro, V. Barone, A. Maiocchi, *J. Am. Chem. Soc.* **2002**, *124*, 4901.
- [23] M. Woods, Z. Kovacs, S. R. Zhang, A. D. Sherry, *Angew. Chem.* **2003**, *115*, 6069; *Angew. Chem. Int. Ed.* **2003**, *42*, 5889.
- [24] M. Yashiro, A. Ishikubo, M. Komiyama, *J. Chem. Soc. Chem. Commun.* **1995**, 1793.
- [25] M. Taki, H. Hattori, T. Osako, S. Nagatomo, M. Shiro, T. Kitagawa, S. Itoh, *Inorg. Chim. Acta* **2004**, *357*, 3369.
- [26] D. H. Lee, J. H. Im, S. U. Son, Y. K. Chung, J. I. Hong, *J. Am. Chem. Soc.* **2003**, *125*, 7752.
- [27] M. Yashiro, H. Kaneiwa, K. Onaka, M. Komiyama, *Dalton Trans.* **2004**, 605.
- [28] M. Woods, G. E. Kiefer, S. Bott, A. Castillo-Muzquiz, C. Eshelbrenner, L. Michaudet, K. McMillan, S. D. K. Mudigunda, D. Grin, G. Tircso, S. R. Zhang, P. Zhao, A. D. Sherry, *J. Am. Chem. Soc.* **2004**, *126*, 9248.
- [29] N. Raghunand, C. Howison, A. D. Sherry, S. R. Zhang, R. J. Gillies, *Magn. Reson. Med.* **2003**, *49*, 249.

- [1] G. Parkin, *Chem. Rev.* **2004**, *104*, 699.
- [2] J. E. Coleman, *Curr. Opin. Chem. Biol.* **1998**, *2*, 222.
- [3] B. Sandstrom, *Analyst* **1995**, *120*, 913.
- [4] B. L. Vallee, K. H. Falchuk, *Physiol. Rev.* **1993**, *73*, 79.
- [5] E. P. Huang, *Proc. Natl. Acad. Sci. USA* **1997**, *94*, 13386.
- [6] R. A. Wapnir, *J. Nutr.* **2000**, *130*, 1388S.

DOI: 10.1002/anie.200502018

Deracemization of Quaternary Stereocenters by Pd-Catalyzed Enantioconvergent Decarboxylative Allylation of Racemic β -Ketoesters**

Justin T. Mohr, Douglas C. Behenna,
Andrew M. Harned, and Brian M. Stoltz*

Enantioconvergent catalysis is a powerful synthetic method that converts a racemic stereogenic substrate into an enantiomerically enriched product with a theoretical yield of 100% in a single operation.^[1] Conceptually, a catalytic system for such a reaction must achieve a stereomutation^[2] or stereoablation^[3,4] of the substrate (or an intermediate), followed by an enantioselective conversion into product (Figure 1, compare pathways I

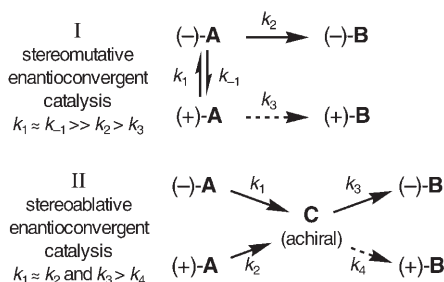
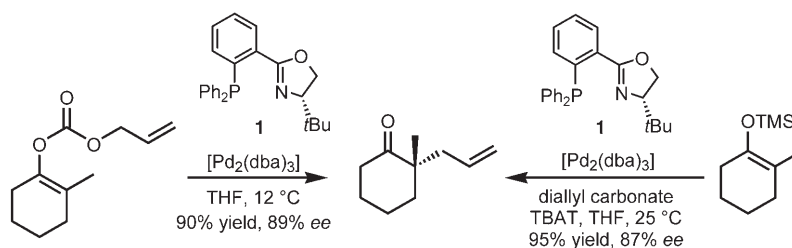


Figure 1. Stereomutative versus stereoablative enantioconvergent catalysis.

and II). A number of catalytic processes of this type have been developed, including chemical, enzymatic, and chemo-enzymatic strategies.^[1,2,4] Racemic compounds that contain quaternary carbon centers are typically unsuitable substrates for enantioconvergent catalysis because of the difficulty associated with C–C bond cleavage in the stereomutative or

stereoablative process.^[5,6] Herein, we describe the first catalytic system for the deracemization of quaternary carbon stereocenters. Our enantioconvergent method converts racemic α -substituted 2-carboxyallylcyclohexanones into highly enantioenriched cycloalkanones that bear quaternary stereocenters through catalytic asymmetric decarboxylative allylation.

We recently reported the first catalytic asymmetric allylation methods for the synthesis of 2-alkyl-2-allylcycloalkanones (Scheme 1).^[7] These reactions, based on racemic



Scheme 1. Enantioselective Tsuji allylations. dba = dibenzylideneacetone; TBAT = tetrabutylammonium difluorotriphenylsilicate; TMS = trimethylsilyl.

transformations reported in the early 1980s by Tsuji,^[8] use enol carbonates and silyl enol ethers along with various allyl carbonates and a Pd⁰ catalyst supported by a chiral phosphino-oxazoline ligand (e.g., **1**).^[9–11]

To demonstrate the utility of this methodology, we have started to employ these allylations as the key enantioselective reaction in multistep syntheses. In one such project, we required the substituted cyclohexenone **6** (Scheme 2). Unfortunately, the preparation of the allylation precursor **4** (R = CO₂allyl or SiMe₃) was hampered by nonselective enolization of **3** to form inseparable mixtures of **4** and **5**, which resulted in significant amounts of **7** after allylation.

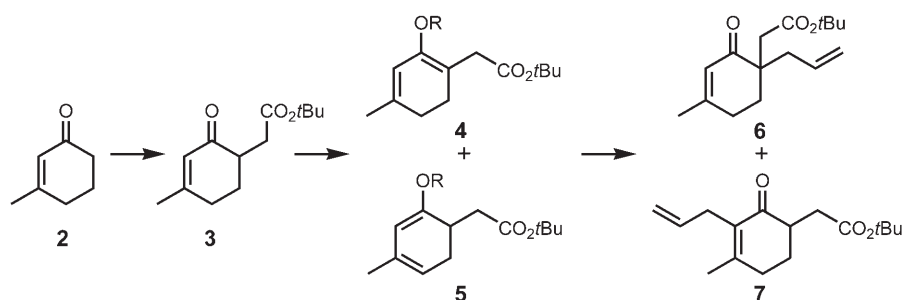
Prompted by the need for better position control in these synthetic sequences, we sought mechanistically guided alternatives to the reactions depicted in Scheme 1. To this end, we synthesized dideuterated carbonate **8** and trideuterated carbonate **9**. When **8** was subjected to our standard conditions for allylation, the deuterium label was almost evenly scrambled between the termini of the allyl fragment in the product (Scheme 3a).^[12] In a separate crossover experiment, the reaction of equimolar amounts of carbonates **8** and **9** was performed under our standard allylation conditions. As expected, NMR spectroscopic analysis of the product showed deuterium scrambling between the allyl termini, but interestingly, mass spectrometric analysis of the product showed an almost perfect statistical distribution of enolate and allyl fragment pairs with four possible masses (Scheme 3b).^[12] Thus, all six possible products were formed in the reaction including those derived from crossover reactions. Although the specific details associated with the enantiodiscrimination remain unclear, we hypothesized that a discrete achiral ketone enolate (namely, **10**) must exist in solution for some period to explain our observations.^[13]

We took this mechanistic insight into account, and so reasoned that the putative prochiral enolate needed for the

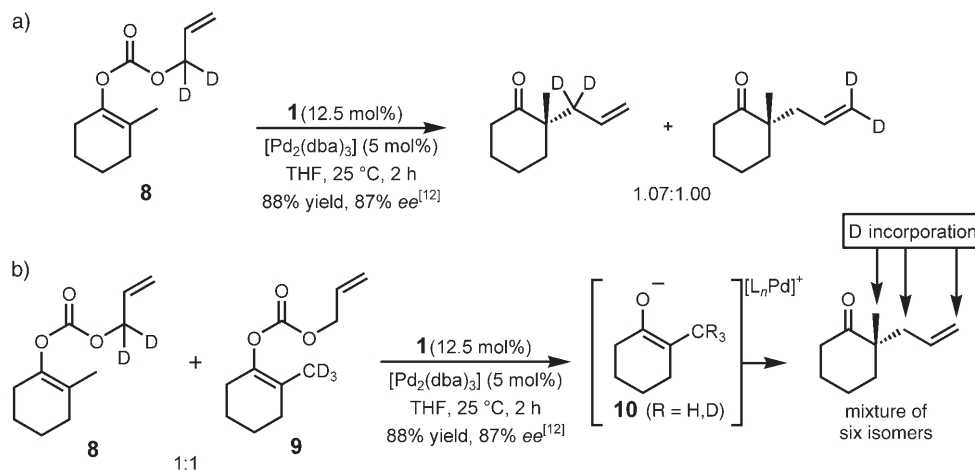
[*] J. T. Mohr, D. C. Behenna, Dr. A. M. Harned, Prof. B. M. Stoltz
The Arnold and Mabel Beckman Laboratories of Chemical Synthesis
Division of Chemistry and Chemical Engineering
California Institute of Technology
1200 E. California Boulevard
MC 164-30, Pasadena, CA 91125 (USA)
Fax: (+1) 626-564-9297
E-mail: stoltz@caltech.edu

[**] The authors wish to thank the Fannie and John Hertz Foundation (predoctoral fellowship to D.C.B.), the NIH (postdoctoral fellowship to A.M.H.), Research Corporation, the Camille and Henry Dreyfus Foundation, Merck, Pfizer, and Lilly for financial support, and Prof. D. A. Dougherty for helpful discussions.

Supporting information for this article is available on the WWW under <http://www.angewandte.org> or from the author.



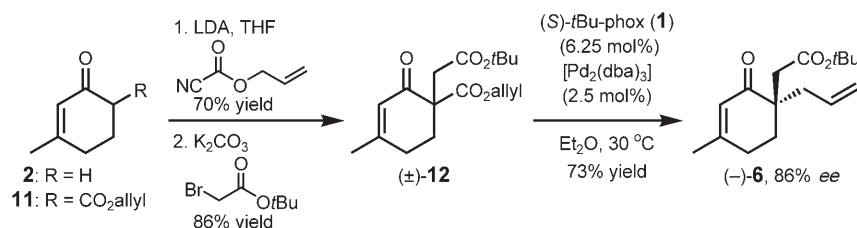
Scheme 2. Nonselective enol formation. R = anion.



Scheme 3. a) Deuterium-labeling experiment with enol carbonate **8**. b) Crossover experiment with deuterium-labeled enol carbonates **8** and **9**.

synthesis of **6** (namely, **4**; R = anion) could be derived through decarboxylation of a racemic β -ketoester precursor, such as (\pm) -**12** (Scheme 4).^[14] Moreover, this route would solve the enolization problem outlined above because the position-

In addition to changes at the α position, variation of the cyclic and allylic portions of the quaternary β -ketoester is tolerated (Table 2). Examples in which the cyclohexane ring has been substituted (entries 1–4), unsaturated (entry 5),



Scheme 4. β -Ketoester synthesis and enantioconvergent decarboxylative allylation. LDA = lithium diisopropylamide.

selective α -alkylation of ketoester **11** would be facile. We prepared β -ketoester (\pm) -**12** by acylation and alkylation of enone **2** to test the reaction (Scheme 4).^[15] To our delight, treatment of (\pm) -**12** with the complex derived from $[\text{Pd}_2(\text{dba})_3]$ and (S) -*t*Bu-phox ligand **1** in Et_2O exclusively produced allyl ketone $(-)$ -**6** in 73% yield and with 86% *ee*. Importantly, β -ketoester **12** remained racemic throughout the course of the reaction, thus indicating that significant kinetic resolution of the starting material had not occurred. This

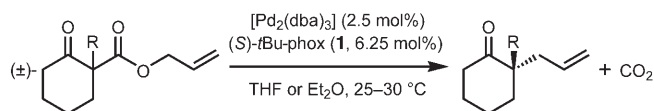
appended (entry 6), or enlarged (entry 7) proceed to products in high yield and enantioselectivity. Finally, substrates with internal allylic substitution (entries 8 and 9) and a racemic heterocycle (entry 10) also afford products in excellent yield and enantioselectivity.

With a general procedure for enantioconvergent decarboxylative allylation in hand and given our interest in tandem reactions and catalysis,^[16] we designed a substrate that could undergo a double allylation cascade to afford a product that possesses two all-carbon quaternary stereocenters. Thus, we prepared (\pm) -**13**, a substrate that contains a reactive enol carbonate and a latent β -ketoester moiety (Scheme 5).^[12] Treatment of (\pm) -**13** under our catalytic asymmetric conditions provided the double alkylation product in 76% yield as a 4:1 mixture of C_2 /*meso* diastereomers.^[17] Gratifyingly, the major diaster-

information, coupled with the product yield of over 50% and high enantiomeric excess, clearly demonstrates the enantioconvergent nature of the system (Figure 1, pathway II).

With the enantioconvergent decarboxylative allylation of (\pm) -**12** established, we investigated the scope of this unusual asymmetric transformation. In general, the system is highly tolerant to an array of functionalities and substitution patterns (Tables 1 and 2). A variety of α -substituted 2-carboxyallylcyclohexanones can be converted into products with high enantiopurity in excellent yields under the conditions for decarboxylative allylation (Table 1). The presence of enolizable functional groups (entries 4 and 5) and β -heteroatom substitution (entry 9) is of particular note. Furthermore, the 2-fluoro derivative (entry 10) allows for the high-yielding synthesis of stereodefined tertiary fluorides.

Table 1: Catalytic enantioconvergent decarboxylative allylation of α -substituted 2-carboxyallylcyclohexanones.



Entry	R	Solvent	T [°C]	t [h]	Yield [%] ^[a]	ee [%] ^[b]
1	CH ₃	THF	25	7.5	85	88
2	CH ₃	Et ₂ O	25	4.75	89	88
3	prenyl	Et ₂ O	30	6	97	91
4	CH ₂ CH ₂ CN	Et ₂ O	25	6.5	97	88
5 ^[c]	CH ₂ CH ₂ CO ₂ Et	Et ₂ O	25	6	96	90
6	CH ₂ C ₆ H ₅	THF	25	0.5	99	85
7	CH ₂ (4-CH ₃ OC ₆ H ₄)	THF	25	10	80	86
8	CH ₂ (4-CF ₃ C ₆ H ₄)	THF	25	0.5	99	82
9 ^[c]	CH ₂ OTBDPS	THF	25	5	86	81
10	F	Et ₂ O	30	3.5	80	91

[a] Yield of isolated product from reaction of 1.0 mmol substrate at 0.033 M in solvent, unless otherwise noted. [b] Determined by chiral GC or HPLC.^[12]

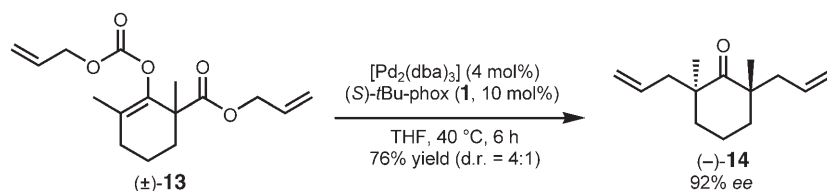
[c] Conditions: 4 mol % [Pd₂(dba)₃], 10 mol % (S)-tBu-phox (1), 0.021 M. phox = phosphinooxazoline; TBDPS = *tert*-butyldiphenylsilyl.

Table 2: Enantioconvergent decarboxylative allylation of β -ketoesters.

Entry	Substrate	Product	T [°C]	t [h]	Yield [%] ^[a]	ee [%] ^[b]
1			25	1.5	94	85
2 ^[c]			25	24	94	86
3			30	9	89	90
4			25	5	90	85
5 ^[d,e]			30	4	77	90
6 ^[d]			25	10	97	92
7			25	9.5	83	87
8 ^[d]			35	6.5	87	92
9 ^[d,e]			35	2.5	87	91
10			25	2.5	91	92

[a] Yield of isolated product from reaction of 1.0 mmol substrate, 2.5 mol % [Pd₂(dba)₃], and 6.25 mol % (S)-tBu-phox (1) at 0.033 M in THF, unless otherwise noted. [b] Determined by chiral GC or HPLC.^[12] [c] Conditions: 25 mmol substrate, 1.5 mol % [Pd₂(dba)₃], and 3.75 mol % (S)-tBu-phox (1).

[d] Performed in Et₂O. [e] Conditions: 4 mol % [Pd₂(dba)₃] and 10 mol % (S)-tBu-phox (1) at 0.021 M. Bn = benzyl.



Scheme 5. Enantioselective allylation cascade generating two quaternary carbon stereocenters.

omer (–)-**14** was obtained with 92% *ee* and bears two quaternary stereocenters set by a single catalytic asymmetric transformation.

In conclusion, we have developed the first example of a catalytic enantioconvergent synthesis of quaternary stereocenters from racemates with quaternary stereocenters. The decarboxylative allylation reaction described herein is an example of an enantioconvergent process in which the same catalyst is intimately involved in both the stereoablative (C–C bond-breaking) and stereoselective (C–C bond-forming) steps. The availability of racemic β -ketoesters of the type employed in this study greatly increases the practical value of these Pd-catalyzed allylations for the enantioselective synthesis of cyclic ketones with one or more quaternary stereocenters. The utility of this methodology for enantioselective synthesis of complex targets is currently under investigation.

Received: June 11, 2005

Published online: October 5, 2005

Keywords: allylation · asymmetric catalysis · enolates · palladium

Angew. Chem. **2005**, *117*, 2299–2301;
Angew. Chem. Int. Ed. **2005**, *44*, 2259–2261.

- [7] D. C. Behenna, B. M. Stoltz, *J. Am. Chem. Soc.* **2004**, *126*, 15044–15045.
- [8] a) J. Tsuji, I. Minami, *Acc. Chem. Res.* **1987**, *20*, 140–145; b) J. Tsuji, *Proc. Jpn. Acad. Ser. B* **2004**, *80*, 349–358.
- [9] a) G. Helmchen, A. Pfaltz, *Acc. Chem. Res.* **2000**, *33*, 336–345; b) J. M. J. Williams, *Synlett* **1996**, 705–710, and references therein.
- [10] Subsequent to our initial report, a similar transformation using a bisphosphine ligand was reported, see: B. M. Trost, J. Xu, *J. Am. Chem. Soc.* **2005**, *127*, 2846–2847.
- [11] An elegant alternative catalytic asymmetric alkylation of cyclic ketones for the synthesis of quaternary stereocenters has been recently described, see: A. G. Doyle, E. N. Jacobsen, *J. Am. Chem. Soc.* **2005**, *127*, 62–63.
- [12] See Supporting Information for details.
- [13] This hypothesis has been experimentally supported for non-enantioselective systems, see: a) J. Tsuji, T. Yamada, I. Minami, M. Yuhara, M. Nisar, I. Shimizu, *J. Org. Chem.* **1987**, *52*, 2988–2995; b) J.-F. Detalle, A. Riahi, V. Steinmetz, F. Hénin, J. Muzart, *J. Org. Chem.* **2004**, *69*, 6528–6532.
- [14] For an excellent review on metal-catalyzed decarboxylation, see: J. A. Tunge, E. C. Burger, *Eur. J. Org. Chem.* **2005**, *9*, 1715–1726.
- [15] a) L. N. Mander, S. P. Sethi, *Tetrahedron Lett.* **1983**, *24*, 5425–5428; b) D. M. X. Donnelly, J.-P. Finet, B. A. Rattigan, *J. Chem. Soc. Perkin Trans. 1* **1993**, 1729–1735.
- [16] a) J. A. May, B. M. Stoltz, *J. Am. Chem. Soc.* **2002**, *124*, 12426–12427; b) R. Sarpong, J. T. Su, B. M. Stoltz, *J. Am. Chem. Soc.* **2003**, *125*, 13624–13625.
- [17] When PPh_3 was used as the ligand for the conversion of (±)-**13** into (±)-**14** and the *meso* isomer of **14** (not shown), a diastereomeric ratio of 70:30 was observed.

- [1] For reviews, see: a) R. Noyori, M. Tokunaga, M. Kitamura, *Bull. Chem. Soc. Jpn.* **1995**, *68*, 36–56; b) H. Stecher, K. Faber, *Synthesis* **1997**, 1–16; c) F. F. Huerta, A. B. E. Minidis, J.-E. Bäckvall, *Chem. Soc. Rev.* **2001**, *30*, 321–331; d) H. Pellissier, *Tetrahedron* **2003**, *59*, 8291–8327.
- [2] For representative stereomutative examples, see: a) Ref. [1]; b) A. Pfaltz, M. Lautens in *Comprehensive Asymmetric Catalysis, Vol. 2* (Eds: E. N. Jacobsen, A. Pfaltz, H. Yamamoto), Springer, New York, **1999**, pp. 833–884; c) B. M. Trost, R. C. Bunt, R. C. Lemoine, T. L. Calkins, *J. Am. Chem. Soc.* **2000**, *122*, 5968–5976.
- [3] The term stereoablation describes the conversion of a chiral molecule to an achiral molecule (e.g., Figure 1, pathway II, (±)-**A**→**C**). Ablation from the Oxford English Dictionary meaning “the action or process of carrying away or removing; removal”.
- [4] For representative stereoablative examples, see: a) T. Hamada, A. Chieffi, J. Åhman, S. L. Buchwald, *J. Am. Chem. Soc.* **2002**, *124*, 1261–1268; b) N. Mase, F. Tanaka, C. F. Barbas III, *Angew. Chem.* **2004**, *116*, 2474–2477; *Angew. Chem. Int. Ed.* **2004**, *43*, 2420–2423; c) C. Fischer, G. C. Fu, *J. Am. Chem. Soc.* **2005**, *127*, 4594–4595; d) D. Magdziak, G. Lalic, H. M. Lee, K. C. Fortner, A. D. Aloise, M. D. Shair, *J. Am. Chem. Soc.* **2005**, *127*, 7284–7285.
- [5] To the best of our knowledge, there are no examples of the catalytic asymmetric synthesis of quaternary carbon stereocenters from racemates with quaternary stereocenters.
- [6] A diastereoselective example of such a process has been recently reported, see: K. Xu, G. Lalic, S. M. Sheehan, M. D. Shair,

DOI: 10.1002/anie.200501845

Lattice Expansion of Clathrate Hydrates of Methane Mixtures and Natural Gas**

Satoshi Takeya,* Tsutomu Uchida, Yasushi Kamata, Jiro Nagao, Masato Kida, Hirotsugu Minami, Hirotohi Sakagami, Akihiro Hachikubo, Nobuo Takahashi, Hitoshi Shoji,* Oleg Khlystov, Mikhail Grachev, and Valery Soloviev

Clathrate hydrates are inclusion compounds consisting of a hydrogen-bonded crystal of water molecules with cages that contain a guest molecule. The crystal structures of types I, II, and H are well known,^[1] and two other types of clathrate hydrate have recently been reported.^[2] Guest–host interactions play a crucial role in the crystal structure, and thus clathrate hydrates are thermodynamically stable only when guest molecules are engaged in the host cages. The relation between structural type of clathrate hydrate and guest molecule is categorized according to the size of the guest molecule.^[3] However, the use of these categories is not clear when applied to mixed hydrates; for example, a structural transition in methane (CH₄) + ethane (C₂H₆) mixed-gas hydrates from type I to II was observed, even though pure CH₄ and C₂H₆ each form type I.^[4,5] There is not much

difference between the molecular size of CO₂ (ca. 5.1 Å) and C₂H₆ (ca. 5.5 Å) with respect to the cavities of the hydrate cages, but their effect on hydrate structure may be completely different. Additionally, recent studies have shown that even pure CH₄ and pure CO₂ form type I and type II hydrates in coexistence. It has been shown that the correlation of guest size and formed structure type is not straightforward for pure systems, too.^[6]

The structural transitions of mixed-gas clathrates are interesting not only from a fundamental point of view but also from the practical viewpoint of natural gas resources and technology.^[7] For instance, natural gas clathrate hydrates in oceanic sediments and permafrost, also called natural gas hydrate, are recognized as an alternative natural fuel resource because they contain significant amounts of natural gases. The main gas in the hydrates is CH₄, but they also contain CO₂, C₂H₆, and small amounts of other gases. In addition, CH₄ + CO₂ mixed-gas hydrates have been studied as a medium to remove CO₂ from air; in particular, natural gas hydrates can be converted to CO₂ hydrate, and thus a fuel is obtained and an unwanted combustion byproduct is removed.^[8]

We present here our measurements of the lattice expansion of CH₄ + CO₂ and CH₄ + C₂H₆ hydrates as a function of mixed-gas composition. This is important because lattice expansion plays a crucial role in thermodynamic modeling of hydrate systems.^[5,9] Data for natural gas hydrate from the sediments of Lake Baikal are also reported to examine the effect of small amounts of other gases and the kinetic effect under natural conditions on their crystal structures.

X-ray diffraction (XRD) patterns of CH₄ + CO₂ hydrate identified it as type I, which is composed of two 12-hedra and six 14-hedra with space group *Pm3n* (Figure 1). The crystal structure of CH₄ + C₂H₆ hydrate changed from type I to type II with increasing C₂H₆ content in the mixed-gas hydrate, in agreement with previous studies.^[4,5] (The type II structure (Figure 1) is composed of sixteen 12-hedra and eight 16-hedra with space group *Fd3m*.) Since the type I and type II hydrates have cubic structures, only one unit-cell parameter—the lattice constant *a*—need be determined.

The lattice constants are plotted in Figure 2. The lattice constant of CH₄ + CO₂ hydrate is roughly independent of gas composition, and this suggests that changes in the occupancy of CH₄ or CO₂ in the cages of the mixed-gas hydrate do not affect the lattice size of type I hydrate. In the case of CH₄ + C₂H₆ hydrate, a large increase in the lattice constant occurs at approximately 60 to 80 % CH₄ content, which corresponds to the structural transition from type I to type II. In the region of high CH₄ content in CH₄ + C₂H₆ hydrate, from approximately 80 to 100 %, the lattice constants of type I hydrate are almost the same as that of pure CH₄ hydrate. In the region of low CH₄ content in CH₄ + C₂H₆ hydrate, from approximately 0 to 40 %, the lattice constants of type I hydrate are same as that of pure C₂H₆ hydrate and are approximately 0.07 Å larger than that of the high-CH₄ region. The deviation of the lattice constant of type I CH₄ + C₂H₆ hydrate corresponds to 0.6 % of the value for a pure CH₄ hydrate crystal. This deviation may not seem large, but it corresponds to a pressure difference of several hundred megapascals, in accordance with the bulk modulus of CH₄ hydrate.^[13]

[*] Dr. S. Takeya
Research Institute of Instrumentation Frontier (RIIF)
National Institute of Advanced Industrial Science and Technology (AIST)
Central 5, Higashi 1-1-1, Tsukuba 305-8565 (Japan)
Fax: (+81) 29-861-4506
E-mail: s.takeya@aist.go.jp

M. Kida, Dr. H. Minami, Dr. H. Sakagami, Dr. A. Hachikubo,
Prof. N. Takahashi, Prof. H. Shoji
Kitami Institute of Technology
165 Koencho, Kitami 090-8507 (Japan)
Fax: (+81) 157-26-9534
E-mail: shojihts@mail.kitami-it.ac.jp

Dr. T. Uchida
Department of Applied Physics
Hokkaido University
N13W8 Sapporo 060-8628 (Japan)

Dr. Y. Kamata, Dr. J. Nagao
Methane Hydrate Research Laboratory, AIST
2-17 Tukisamu Higashi Toyohira-ku, Sapporo 062-8517 (Japan)

Dr. O. Khlystov, Dr. M. Grachev
Russian Academy of Sciences Siberian Branch Limnological
Institute
3 Ulan-Batorskaya, Irkutsk 664033 (Russia)

Dr. V. Soloviev
All-Russia Research Institute for Geology and Mineral Resources of
the Ocean
Saint Petersburg 190121 (Russia)

[**] S.T. thanks H. Fujihisa, Y. Gotoh, and K. Honda of AIST for their valuable comments and discussions, and H. Narita of AIST for his support in experiments.

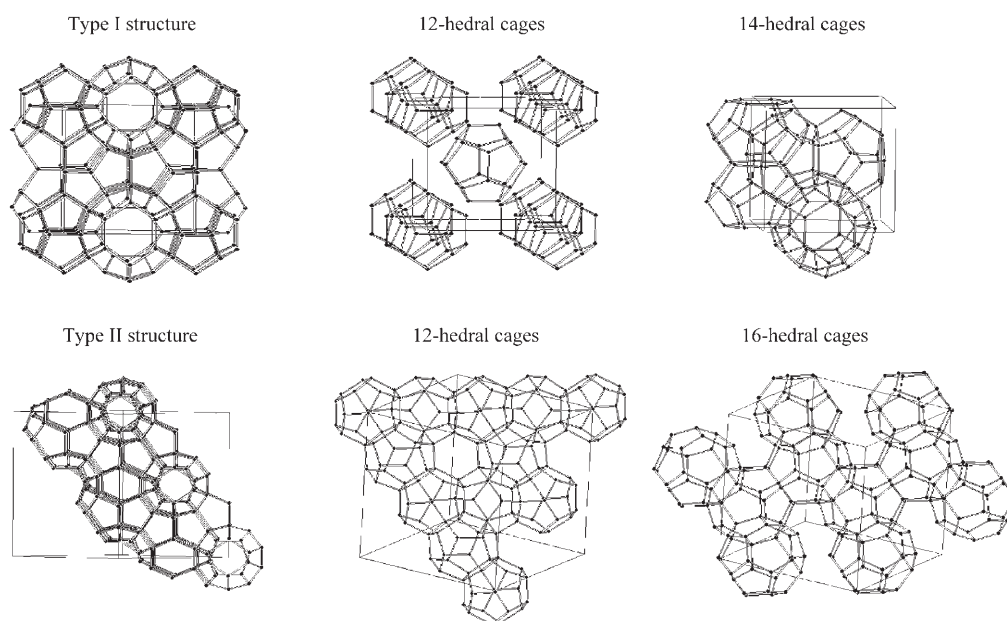


Figure 1. Ball-and-stick representations of the host lattices of types I and II clathrate hydrates. Only oxygen atoms are drawn and solid lines indicate the unit cell of each structure. Middle and right figures show only the small and large cages, respectively, of each structure.

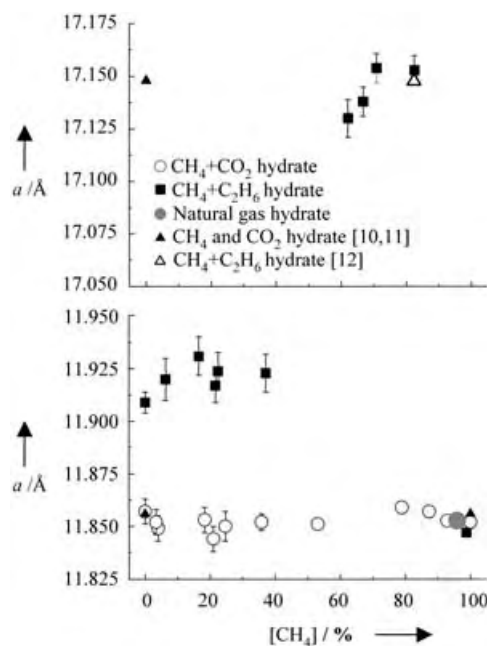


Figure 2. Variation of lattice constants of clathrate hydrates at 113 K as a function of CH_4 gas content in the hydrates. Lattice constants of $\text{CH}_4 + \text{CO}_2$ hydrate, $\text{CH}_4 + \text{C}_2\text{H}_6$ hydrate, and natural gas hydrate are from this study. Lattice constants of CO_2 hydrate ($\text{CO}_2 + \text{D}_2\text{O}$), deuterated methane hydrate ($\text{CD}_4 + \text{D}_2\text{O}$), and $\text{CH}_4 + \text{C}_2\text{H}_6$ hydrate ($\text{CH}_4/\text{C}_2\text{H}_6$ 82:18; $\text{CH}_4 + \text{C}_2\text{H}_6 + \text{D}_2\text{O}$) were determined at different temperatures and converted to values at 113 K.

The results also suggest that a change in the occupancy of CH_4 or C_2H_6 in the cages of the mixed-gas hydrate does not affect the lattice size of type I hydrate. On the other hand, the lattice constant of type II hydrate seems to increase as the CH_4 occupancy in the $\text{CH}_4 + \text{C}_2\text{H}_6$ hydrate increases. This difference between type I and type II hydrates implies a

major difference in guest–host or guest–guest interactions due to their different crystal structures. Differences in the properties of CO_2 and C_2H_6 molecules in the hydrate are also suggested. For example, the 12-hedral small cage has a large (ca. 71 %) CO_2 occupancy but a small (ca. 5 %) C_2H_6 occupation in pure CO_2 and C_2H_6 hydrate, respectively.^[10,14] Also, different locations of disordered CO_2 and C_2H_6 molecules in 12-hedral and 14-hedral cages in pure CO_2 hydrate and C_2H_6 hydrate have been shown by assuming that each molecule rotates about the cage symmetry axis at a constant angle to the equatorial plane.^[10,14] There may be several factors that affect the change of lattice constants of mixed gas hydrates.

We also analyzed the crystal structure of natural gas hydrate from the sediments of Lake Baikal (Figure 3). Using gas chromatography, we found that the gas content of the natural gas hydrate was 95.9 % CH_4 , 4.1 % CO_2 , and less than 500 ppm of C_2H_6 and C_3H_8 . The XRD profile showed that the crystal structure of the natural gas hydrate in the sediment sample was type I (Figure 4). Also, the ^{13}C NMR spectrum of

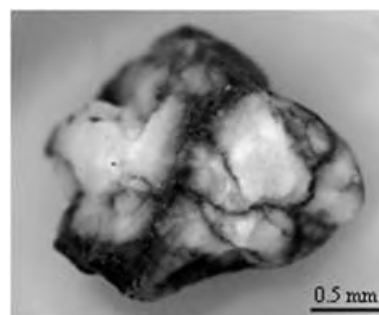


Figure 3. Hydrate-bearing sample from the sediment of Lake Baikal. The white regions are a mixture of natural gas hydrate and ice, and the black regions are sediment.

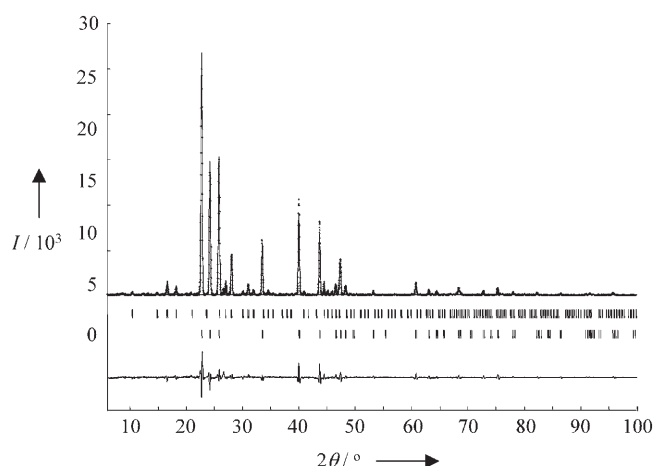


Figure 4. X-ray diffraction profiles of a sample from the sediment of Lake Baikal at 113 K. The dot marks are the observed intensities, and the solid line was calculated from the best-fit model of the Rietveld refinements. The upper tick marks represent the calculated peak positions for the type I gas hydrate, and the lower tick marks those for hexagonal ice. The bottom curve is the difference between the observed and calculated intensities. The sample was 18% hydrate and 82% hexagonal ice by mass, whereby some of the ice came from trapped lake water that froze during cooling.

the natural gas hydrate showed that CH_4 is encaged in the gas hydrate with a large-cage occupancy of 0.94 and a small-cage occupancy of 0.99. CO_2 , C_2H_6 , and C_3H_8 were not detected by ^{13}C NMR spectroscopy. We used this ^{13}C NMR data in the Rietveld refinement of the XRD profile.^[15] Thus, the lattice constant of the natural gas hydrate was estimated to be 11.8527(6) Å, and its density was calculated to be 0.948 g cm⁻³ at 113 K. The lattice constant of the natural gas hydrate is consistent with those of the artificially formed mixed-gas hydrates (see Figure 2), even though the differences in cage occupancies between artificial and natural gas hydrates is suggested experimentally to be due to differences in their formation conditions.^[16] This also shows that the small amounts of C_2H_6 and C_3H_8 did not influence the structural transition or the lattice expansion. This result suggests that the knowledge of artificial clathrate hydrate structures can be applied to natural gas hydrates.

In the present study, the effect of guest molecules on the lattice constant of mixed-gas hydrates was measured for the first time. The dependence of lattice expansion on gas occupancies differs for different guest molecules. For instance, lattice expansion of $\text{CH}_4 + \text{C}_2\text{H}_6$ hydrate depends on the composition of the guest molecules, whereas no lattice expansion of $\text{CH}_4 + \text{CO}_2$ hydrate was observed. Even a small deviation of the lattice constant corresponds to a large pressure difference at constant temperature, and thus crystal structure data should be considered in detail for optimal thermodynamic modeling. However, the guest molecules are difficult to locate because of their rotational disorder and nonstoichiometry due to their random occupancy in each cage, even though the clathrate hydrate lattice may be well defined. Therefore, further analysis of the guest molecules in the hydrate cages will be required for a better understanding of mixed-gas hydrates.

Experimental Section

Mixed-gas hydrate samples were synthesized by our previously reported method.^[5] Sediment samples containing natural gas hydrate were recovered by gravity coring at gas-vent fields in Lake Baikal in June 2002.^[17] The samples are from the lake bottom at a water depth of 1393 m, and the site had latitude 51°55.203' N and longitude 105°38.080' E. After the cores were brought up, the gas hydrate-containing samples were immediately stored at about 100 K in an atmosphere of nitrogen gas to prevent hydrate dissociation.

For the XRD measurements, finely powdered hydrate samples were put in a quartz glass capillary cell (Hilgenberg; 2.0 mm, 0.01 mm thick) and then mounted on the goniometer of the XRD apparatus. The XRD measurements were performed with $\text{Cu}_{\text{K}\alpha}$ radiation (50 kV, 200 mA; Rigaku model Rint-2000) at 113 K and atmospheric pressure. Lattice constants were determined at 113 K by using a two-phase Rietveld refinement method with RIETAN-2000.^[18] For this analysis, the lattice constant of hexagonal ice was fixed at 4.4793 Å for the *a* axis and 7.3216 Å for the *c* axis.^[19]

For the natural gas hydrate sample, ^{13}C NMR spectroscopy was used to determine the composition of the encaged gas molecules in the cages. Powdered samples of natural gas hydrate were put in a tube-shaped zirconium sampler that was then placed in the NMR probe (100 MHz; JEOL model JNM-AL400 FT). CP-MAS ^{13}C NMR spectra were recorded at 183 K on an NM-AL40/BU spectrometer at a frequency of 100 MHz. Chemical shifts were then determined by assuming that the polydimethylsilane (PDMS) peak was at 0 ppm.

Received: May 27, 2005

Published online: October 5, 2005

Keywords: alkanes · clathrates · host–guest systems · hydrates · inclusion compounds

- [1] a) H. R. Müller, M. von Stackelberg, *Naturwissenschaften* **1952**, 39, 20; b) M. von Stackelberg, H. R. Müller, *Naturwissenschaften* **1951**, 38, 456; c) J. A. Ripmeester, J. S. Tse, C. I. Ratcliffe, B. M. Powell, *Nature* **1987**, 325, 135.
- [2] a) K. A. Udachin, J. A. Ripmeester, *Nature* **1999**, 397, 420; b) K. A. Udachin, C. I. Ratcliffe, J. A. Ripmeester, *Angew. Chem.* **2001**, 113, 1343; *Angew. Chem. Int. Ed.* **2001**, 40, 1303.
- [3] E. D. Sloan, Jr., *Clathrate Hydrate of Natural Gases*, 2nd ed., Marcel Dekker, New York, **1998**.
- [4] a) S. Subramanian, R. A. Kini, S. F. Dec, E. D. Sloan, Jr., *Chem. Eng. Sci.* **2000**, 55, 1981; b) S. Subramanian, A. L. Ballard, R. A. Kini, S. F. Dec, E. D. Sloan, Jr., *Chem. Eng. Sci.* **2000**, 55, 5763; c) S. Takeya, Y. Kamata, T. Uchida, J. Nagao, T. Ebinuma, H. Narita, *Can. J. Phys.* **2003**, 81, 479.
- [5] T. Uchida, S. Takeya, Y. Kamata, I. Y. Ikeda, J. Nagao, T. Ebinuma, H. Narita, O. Zatssepina, B. A. Buffett, *J. Phys. Chem. B* **2002**, 106, 12426.
- [6] a) D. K. Staykova, W. F. Kuhs, A. N. Salamatin, T. Hansen, *J. Phys. Chem. B* **2003**, 107, 10299; b) J. M. Schicks, J. A. Ripmeester, *Angew. Chem.* **2004**, 116, 3372; *Angew. Chem. Int. Ed.* **2004**, 43, 3310.
- [7] E. D. Sloan, Jr., *Nature* **2003**, 426, 353.
- [8] a) Yu.-T. Seo, H. Lee, *J. Phys. Chem. B* **2001**, 105, 10084; b) H. Lee, Y. Seo, Yu.-T. Seo, I. L. Moudrakovski, J. A. Ripmeester, *Angew. Chem.* **2003**, 115, 5202; *Angew. Chem. Int. Ed.* **2003**, 42, 5048.
- [9] a) L. A. Ballard, E. D. Sloan, Jr., *Chem. Eng. Sci.* **2000**, 55, 5773; b) Y. Koyama, H. Tanaka, K. Koga, *J. Chem. Phys.* **2005**, 122, 074503.
- [10] K. A. Udachin, C. I. Ratcliffe, J. A. Ripmeester, *J. Phys. Chem. B* **2001**, 105, 4200.

- [11] C. Gutt, B. Asmussen, W. Press, M. R. Johnson, Y. P. Handa, J. S. Tse, *J. Chem. Phys.* **2000**, *113*, 4713.
- [12] C. J. Rawn, A. J. Rondinone, B. C. Chakoumakos, S. L. Marshall, L. A. Stern, S. Circone, S. H. Kirby, C. Y. Jones, B. H. Toby, Y. Ishii, *Proc. 4th Int. Conf. Gas Hydrate*, Yokohama, **2002**, p. 595.
- [13] H. Hirai, T. Kondo, M. Hasegawa, T. Yagi, Y. Yamamoto, T. Komai, K. Nagashima, M. Sakashita, H. Fujihisa, K. Aoki, *J. Phys. Chem. B* **2000**, *104*, 1429.
- [14] K. A. Udachin, C. I. Ratcliffe, J. A. Ripmeester, *J. Supramol. Chem.* **2002**, *2*, 405.
- [15] H. M. Rietveld, *J. Appl. Crystallogr.* **1969**, *2*, 65.
- [16] Z. Huo, K. Hester, D. Sloan, Jr., *AIChE J.* **2003**, *49*, 1300.
- [17] J. Klerkx, T. I. Zemskaya, T. V. Matveeva, O. M. Khlystov, B. B. Namsaraev, O. P. Dagurova, L. P. Golobokova, S. S. Vorob'eva, T. P. Pogodaeva, N. G. Granin, G. V. Kalmychkov, V. A. Ponomarchuk, H. Shoji, L. L. Mazurenko, V. V. Kaulio, V. A. Solov'ev, M. A. Grachev, *Dokl. Earth Sci.* **2003**, *393A*, 1342.
- [18] F. Izumi, T. Ikeda, *Mater. Sci. Forum* **2000**, *321–324*, 198.
- [19] K. Röttger, A. Endriss, J. Ihringer, S. Doyle, W. F. Kuhs, *Acta Crystallogr. Sect. B* **1994**, *50*, 644.

by two methods, that is, with low-valent transition metals by oxidative addition^[2,5] or with metal–oxo species.^[2,3]

Although various compounds can be used for the oxidation of amines, hydrogen peroxide is the oxidant that satisfies recent environmental and sustainable demands, because water is the sole by-product. Therefore, catalytic oxidation of substrates such as alkenes, alcohols, amines, sulfides, and alkanes with H₂O₂ has been explored extensively.^[6,7] However, there are few examples for the introduction of an external functional group to substrates upon H₂O₂ oxidation.^[7,8] We report here that a carbon–carbon bond forms at the α position (with respect to the nitrogen atom) of tertiary amines under the H₂O₂ oxidation conditions. Thus, the ruthenium-catalyzed oxidative cyanation of tertiary amines with H₂O₂ in the presence of sodium cyanide or hydrogen cyanide gives the corresponding α -aminonitriles with high efficiency [Eq. (1)]. The reaction is, to the best of our knowledge, the first example of direct C–H activation and C–C bond formation under H₂O₂ oxidation conditions.

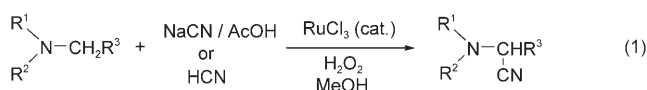
Oxidative Cyanations

DOI: 10.1002/anie.200501496

Ruthenium-Catalyzed Oxidative Cyanation of Tertiary Amines with Hydrogen Peroxide and Sodium Cyanide**

Shun-Ichi Murahashi,* Naruyoshi Komiya, and Hiroyuki Terai

There has been much interest in the development of clean and environmentally benign methods for the transformation of amines into the corresponding α -functionalized compounds. These compounds have proven to be versatile intermediates and have been widely used in the construction of biologically active nitrogen compounds such as alkaloids.^[1] Direct introduction of a substituent at the α position of tertiary amines is performed in two steps: α -C–H activation to produce iminium ion intermediates and subsequent reaction with nucleophiles.^[2–4] The initial C–H activation has been achieved



The catalytic activity for the oxidative cyanation of *N,N*-dimethylaniline with H₂O₂ in the presence of sodium cyanide was examined. RuCl₃ was found to be the most effective catalyst. [RuCl₂(PPh₃)₃] and Pr₄N[RuO₄] show moderate catalytic activity, while K₄[Ru(CN)₆] retards the reaction. Methanol is the most effective solvent, although ethanol, ethyl acetate, and acetonitrile can also be used. The addition of acetic acid is necessary for the reaction with sodium cyanide, as otherwise no reaction takes place.

As shown in Table 1, various tertiary amines can be efficiently converted into the corresponding α -aminonitriles^[9] with H₂O₂ in the presence of sodium cyanide. Reaction of substituted *N,N*-dimethylanilines bearing both electron-donating and electron-withdrawing substituents gave the corresponding cyanated products (entries 1–3). In the presence of other alkyl groups, the *N*-methyl group reacts predominantly. For example, the reaction of *N*-methyl-*N*-ethylaniline gave *N*-cyanomethyl-*N*-ethylaniline (**8**) along with a small amount of *N*-(1-cyanoethyl)-*N*-methylaniline (**9**; entry 4). The reaction can also be applied efficiently to cyclic amines: Piperidine, pyrrolidine, and tetrahydroisoquinoline derivatives can be converted into the corresponding α -cyanoamines (entries 5–8). In terms of the substrate, oxidative cyanation with H₂O₂ is more versatile than with molecular oxygen;^[10] for example, molecular oxygen cannot be used for reactions with piperidine and pyrrolidine derivatives. The ruthenium-catalyzed oxidative cyanation of *N*-(4-methoxyphenyl)pyrrolidine (**14**) with H₂O₂ gave the corresponding α -cyanated amine **15** in 80 % yield (entry 7), while the same reaction with molecular oxygen provided the product in only 23 % yield.

To gain insight into the reaction mechanism, the relative reaction rates for the oxidative cyanation of four *para*-substituted *N,N*-dimethylanilines (*p*-XC₆H₄NMe₂; X = MeO,

[*] Prof. Dr. S.-I. Murahashi,^[†] Dr. N. Komiya, H. Terai
Department of Chemistry
Graduate School of Engineering Science
Osaka University
1–3 Machikaneyama, Toyonaka, Osaka 560-8531 (Japan)
E-mail: murahashi@high.ous.ac.jp

[†] Present address: Department of Applied Chemistry
Faculty of Engineering
Okayama University of Science
1–1 Ridaicho, Okayama, Okayama 700-0005 (Japan)
Fax: (+81) 86-256-9513

[**] This work was supported by a Grant-in-Aid for Scientific Research from the Ministry of Education, Culture, Sports, Science, and Technology, Japan.

Supporting information for this article is available on the WWW under <http://www.angewandte.org> or from the author.

Table 1: Results of the ruthenium-catalyzed oxidative cyanation of tertiary amines with hydrogen peroxide and NaCN [see Eq. (1)].^[a]

Entry	Substrate	t [h]	Product	Yield [%] ^[b]
1		2		90 (80) ^[c]
2		1.5		81
3		3		67
4 ^[d]		1.5		63
5		2		69 ^[e]
6 ^[f]		1.5		73 ^[e]
7 ^[e]		1.5		80 ^[e]
8		1.5		83 ^[e]

[a] The reaction was carried out as follows: A 30% aqueous solution of H₂O₂ (2.5 mmol) was added dropwise over a period of 1 h to a mixture of amine (1.0 mmol), RuCl₃ (0.05 mmol), NaCN (1.2 mmol), and CH₃CO₂H (6 mmol) in MeOH (1.2 mL). The reaction mixture was then stirred for the given amount of time. [b] Determined by GLC using an internal standard. [c] Yield of the isolated product. [d] A small amount of **9** was also formed. [e] Determined by ¹H NMR spectroscopy. [f] 1.5 mmol of H₂O₂ was used. [g] 1.0 mmol of H₂O₂ was used.

Me, H, Br) with H₂O₂ in the presence of sodium cyanide were determined by ¹H NMR spectroscopy of the resulting cyanated products. The rate data correlate well ($R^2 = 0.998$) with the Hammett linear free energy relationship with use of σ values (Figure 1).

The ρ value was determined to be -3.61 , indicating a cationic intermediate at the rate-determining step. The intramolecular deuterium isotope effect for the ruthenium-cata-

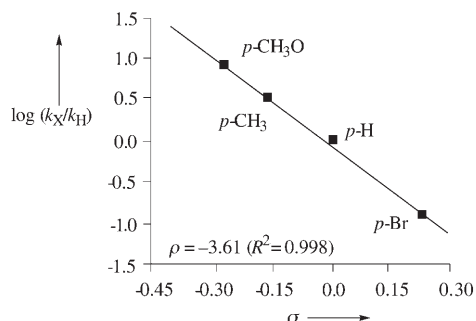
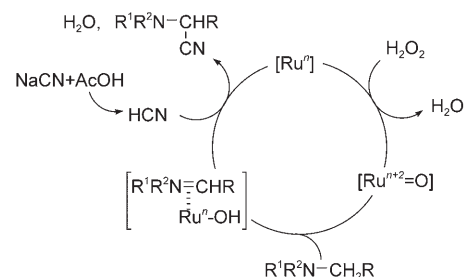


Figure 1. Hammett plot for the RuCl₃-catalyzed oxidative cyanation of the *para*-substituted *N,N*-dimethylanilines *p*-XC₆H₄NMe₂ (X = MeO, Me, H, Br) with H₂O₂ in the presence of NaCN.

lyzed oxidative cyanation of *N*-methyl-*N*-(trideuteriomethyl)aniline was found to be 4.1 by ¹H NMR spectroscopy. Similarly, the intermolecular deuterium isotope effect for the oxidative cyanation of an equimolar mixture of *N,N*-dimethylaniline and *N,N*-bis(trideuteriomethyl)aniline was determined to be 3.7. These intra- and intermolecular isotope effects are larger than those observed for *N*-demethylation with cytochrome P450 (1.6–3.1,^[11] and 1.0–1.1^[12]), suggesting that cleavage of the C–H bond proceeds via an intermediate bearing more ionic character. Under consideration of these data, the present reaction can be rationalized by assuming the cytochrome P450 type mechanism, as shown in Scheme 1. The

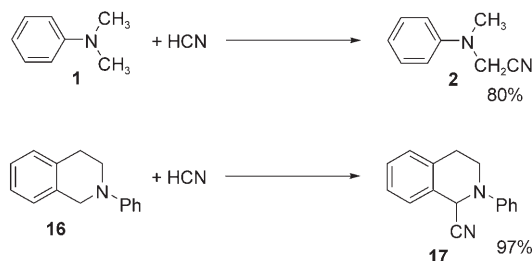


Scheme 1. The proposed reaction mechanism for the ruthenium-catalyzed oxidative cyanation of tertiary amines with H₂O₂.

low-valent ruthenium species [Ruⁿ] undergoes reaction with H₂O₂ to give the oxo-ruthenium species [Ruⁿ⁺²=O], which produces an iminium ion intermediate by electron transfer and subsequent hydrogen transfer. Nucleophilic attack by hydrogen cyanide on the iminium ion intermediate provides the corresponding α -cyanated products, water, and the [Ruⁿ] species to complete the catalytic cycle.

The participation of hydrogen cyanide, which is formed from sodium cyanide and acetic acid under the reaction conditions,^[13] was confirmed by the following reactions: The ruthenium-catalyzed oxidation of *N,N*-dimethylaniline with H₂O₂ in the presence of hydrogen cyanide in methanol gave the corresponding α -aminonitrile **2** in 80% yield (Scheme 2). The analogous reaction with *N*-phenyltetrahydroisoquinoline provided the α -cyanated tetrahydroisoquinoline **17** in 97% yield.

The oxidative cyanation of tertiary amines provides a convenient method for synthesizing various compounds,



Scheme 2. The ruthenium-catalyzed oxidative cyanation of tertiary amines with H₂O₂ in the presence of HCN. Reaction conditions: RuCl₃ (5 mol%), H₂O₂ (1.5 equiv), MeOH, RT, 24 h (**1**→**2**) or 4 h (**16**→**17**).

including *N*-aryl- α -amino acids^[14,15] and *N,N*-disubstituted 1,2-diamines. Upon hydrolysis, 2-cyano-*N*-(4'-methoxyphenyl)pyrrolidine (**15**) can be converted into *N*-(4'-methoxyphenyl)proline (**18**) in 69% yield, while the reduction of **15** with LiAlH₄ provides 2-aminoethyl-*N*-(4'-methoxyphenyl)pyrrolidine (**19**) in 99% yield. Quinoline skeletons can also be constructed from tertiary arylamines by iminium ion cyclization. Typically, the TiCl₄-promoted reaction of α -aminonitrile **2**, derived from oxidative cyanation of **1** with allyltrimethylsilane in CH₂Cl₂ at -78°C, gave 1-methyl-4-trimethylsilylmethyl-1,2,3,4-tetrahydroquinoline (**20**) in 75% yield.

In conclusion, we have demonstrated the novel ruthenium-catalyzed oxidative cyanation of tertiary amines with hydrogen peroxide. The reaction proceeds with high efficiency to give the corresponding α -cyanated amines, and thus provides a useful method for the synthesis of various nitrogen compounds from tertiary amines. Research is currently underway to elucidate the mechanism and to apply the principle to other catalytic systems.

Received: April 30, 2005

Revised: July 28, 2005

Published online: September 29, 2005

Keywords: amines · cyanides · hydrogen peroxide · oxidation · ruthenium

- [1] a) S.-I. Murahashi, N. Komiya, *Ruthenium in Organic Synthesis* (Ed.: S.-I. Murahashi), Wiley-VCH, Weinheim, **2004**, pp. 53–93; b) S.-I. Murahashi, Y. Imada, *Transition Metals for Organic Synthesis, Vol. 2* (Eds. M. Beller, C. Bolm), Wiley-VCH, Weinheim, **1998**, pp. 373–383; c) *Cytochrome P450, Structure, Mechanism and Biochemistry*, 2nd ed. (Ed.: P. R. Ortiz de Montellano), Plenum, New York, **1995**; d) C. Geoffrey, *Introduction to Alkaloids*, Wiley, New York, **1981**.
- [2] S.-I. Murahashi, *Angew. Chem.* **1995**, *107*, 2670; *Angew. Chem. Int. Ed. Engl.* **1995**, *34*, 2443.
- [3] S.-I. Murahashi, T. Naota, K. Yonemura, *J. Am. Chem. Soc.* **1988**, *110*, 8256.
- [4] a) S.-I. Murahashi, T. Naota, T. Kuwabara, T. Saito, H. Kumobayashi, S. Akutagawa, *J. Am. Chem. Soc.* **1990**, *112*, 7820; b) S.-I. Murahashi, T. Saito, T. Naota, H. Kumobayashi, S. Akutagawa, *Tetrahedron Lett.* **1991**, *32*, 5991.
- [5] a) S.-I. Murahashi, T. Hirano, T. Yano, *J. Am. Chem. Soc.* **1978**, *100*, 348; b) S.-I. Murahashi, T. Watanabe, *J. Am. Chem. Soc.* **1979**, *101*, 7429.
- [6] a) G. Strukul, *Catalytic Oxidations with Hydrogen Peroxide as Oxidant*, Kluwer, Dordrecht **1992**; b) C. W. Jones, *Application of Hydrogen Peroxide and Derivatives*, Royal Society of Chemistry, Cambridge **1999**; c) I. W. C. E. Arends, R. A. Sheldon, M. Wallau, U. Schuchardt, *Angew. Chem.* **1997**, *109*, 1190; *Angew. Chem. Int. Ed. Engl.* **1997**, *36*, 1144; d) C. C. Romano, F. E. Kühn, W. A. Herrmann, *Chem. Rev.* **1997**, *97*, 3197; e) I. W. C. E. Arends, R. A. Sheldon, *Top. Catal.* **2002**, *19*, 133; f) B. S. Lane, K. Burgess, *Chem. Rev.* **2003**, *103*, 2457; g) R. Noyori, M. Aoki, K. Sato, *Chem. Commun.* **2003**, 1977.
- [7] Oxidation of alkenes: a) K. Sato, M. Aoki, R. Noyori, *Science* **1998**, *281*, 1646; b) K. Kamata, K. Yonehara, Y. Sumida, K. Yamaguchi, S. Hikichi, N. Mizuno, *Science* **2003**, *300*, 964; c) Y. Ishii, K. Yamawaki, T. Ura, H. Yamada, T. Yoshida, M. Ogawa, *J. Org. Chem.* **1988**, *53*, 3587; d) R. Neumann, M. Gara, *J. Am. Chem. Soc.* **1995**, *117*, 5066; e) D. E. De Vos, J. L. Meinershagen, T. Bein, *Angew. Chem.* **1996**, *108*, 2355; *Angew. Chem. Int. Ed. Engl.* **1996**, *35*, 2211; f) P. Battioni, J. P. Renaud, J. F. Bartoli, M. Reina-Arfiles, M. Fort, D. Mansuy, *J. Am. Chem. Soc.* **1988**, *110*, 8462; g) V. Venturello, E. Alneri, M. Ricci, *J. Org. Chem.* **1983**, *48*, 3831; oxidation of alcohols: h) K. Sato, M. Aoki, J. Takagi, R. Noyori, *J. Am. Chem. Soc.* **1997**, *119*, 12386; i) G. Barak, J. Dakka, Y. Sasson, *J. Org. Chem.* **1988**, *53*, 3553; j) S. E. Jacobson, D. A. Muccigrosso, F. Mares, *J. Org. Chem.* **1979**, *44*, 921; k) O. Bortoline, V. Cobnte, F. D. Furia, G. Modena, *J. Org. Chem.* **1986**, *51*, 2661; l) R. Zennaro, F. Pinna, G. Strukul, H. Arzoumanian, *J. Mol. Catal.* **1991**, *70*, 269; m) C. Venturello, M. Gambaro, *J. Org. Chem.* **1991**, *56*, 5924; n) A. C. Dangel, W. P. Griffith, B. C. Parkin, *J. Chem. Soc. Dalton Trans.* **1993**, 2683; oxidation of secondary amines: o) H. Mitsui, S. Zenki, T. Shiota, S.-I. Murahashi, *J. Chem. Soc. Chem. Commun.* **1984**, 874; p) S.-I. Murahashi, H. Mitsui, T. Shiota, T. Tsuda, S. Watanabe, *J. Org. Chem.* **1990**, *55*, 1736; q) S.-I. Murahashi, T. Shiota, *Tetrahedron Lett.* **1987**, *28*, 2383; r) S.-I. Murahashi, T. Naota, N. Miyaguchi, T. Nakato, *Tetrahedron Lett.* **1992**, *33*, 6991; oxidation of alkanes: s) D. H. R. Barton, D. Doller, *Acc. Chem. Res.* **1992**, *25* 504; t) A. Sobkowiak, H.-C. Tung, D. T. Sawyer, *Progress in Organic Chemistry, Vol. 40* (Ed. S. J. Lippard), Wiley, New York, **1992**, pp. 291–352; u) A. S. Goldstein, R. H. Beer, R. S. Drago, *J. Am. Chem. Soc.* **1994**, *116*, 2424; v) N. Mizuno, C. Nozaki, I. Kiyoto, M. Misono, *J. Am. Chem. Soc.* **1998**, *120*, 9267.
- [8] For the copper-catalyzed alkylation of tertiary amines with *t*BuOOH, see Z. Li, C.-J. Li, *J. Am. Chem. Soc.* **2004**, *126*, 11810.
- [9] D. Enders, J. P. Shilvock, *Chem. Soc. Rev.* **2000**, *29*, 359.
- [10] a) S.-I. Murahashi, N. Komiya, H. Terai, T. Nakae, *J. Am. Chem. Soc.* **2003**, *125*, 15312; b) M. North, *Angew. Chem.* **2004**, *116*, 4218; *Angew. Chem. Int. Ed.* **2004**, *43*, 4126.
- [11] a) T. Shono, T. Toda, N. Oshino, *J. Am. Chem. Soc.* **1982**, *104*, 2639; b) G. T. Miwa, W. A. Garland, B. J. Hodshon, A. Y. H. Lu, D. B. Northrop, *J. Biol. Chem.* **1980**, *255*, 6049; c) G. T. Miwa, J. S. Walsh, G. L. Kedderis, P. F. Hollenberg, *J. Biol. Chem.* **1983**, *258*, 14445.
- [12] a) J. A. Thompson, J. L. Holtzman, *Drug Metab. Dispos.* **1974**, *2*, 577; b) D. C. Heimbrook, R. I. Murray, K. D. Egeberg, S. G. Sligar, M. W. Nee, T. C. Bruice, *J. Am. Chem. Soc.* **1984**, *106*, 1514.
- [13] C. F. H. Allen, R. K. Kimball, *Org. Synth. Coll. Vol. II* **1943**, p. 498.
- [14] a) N. Tanaka, T. Tamai, H. Mukaiyama, A. Hirabayashi, H. Muranaka, S. Akahane, H. Miyata, M. Akahane, *J. Med. Chem.* **2001**, *44*, 1436; b) R. E. Webb, A. D. Johnston, *J. Dent. Res.* **1991**, *70*, 211.
- [15] G. C. Barrett, *Chemistry and Biochemistry of the Amino Acids* (Ed.: G. C. Barrett), Chapman and Hall, London, **1985**, pp. 246–296.

DOI: 10.1002/anie.200501960

Bulk Preparation of Si–SiO_x Hierarchical Structures: High-Density Radially Oriented Amorphous Silica Nanowires on a Single-Crystal Silicon Nanocore**

Hui Wang, Xiaohong Zhang,* Xiangmin Meng, Shaomin Zhou, Shikang Wu, Wensheng Shi, and Shuitong Lee*

Assembling functional photoelectric nanodevices is of current interest in nanoscience and nanotechnology due to their potential applications in microelectronics and information science.^[1] Generally, fabrication routes to a functional nanodevice can be classified into two types: the “top-down” approach and the “bottom-up” approach. The latter refers to assembly or scale up of nanoscale building blocks into functional devices, in which the dimensions of the functional domain can be controlled through the size of the building blocks. Various methods, such as self-assembly and Langmuir–Blodgett (LB) techniques, have been used for fabrication^[2] with various degree of success, however, the small size of the nanoscale building blocks makes the fabrication process always costly and complex. Hierarchical nanostructures that have both the properties of nanoscale materials and ease of manipulation may facilitate assembly processes and provide an attractive alternative for bottom-up fabrication. They can be prepared directly by growing nanoscale structures of materials with different dimensions (nanoscale to microscale).^[3] In addition, the core and branches of a hierarchical structure can be composed of different chemical elements, making them suitable for assembly into a nanodevice with multiple functions. A few homogeneous and

heterogeneous hierarchically structured materials^[3] have been fabricated. It is envisaged that these large hierarchical nanostructures could find applications in a variety of fields such as optoelectronics, sensors, and field emission.

Silicon and its oxides have long been of great interest for applications in microelectronic devices, and silicon-on-insulator (SOI) devices are playing an important role in the modern semiconductor industry. Recently, an SiO_x–Si hierarchical nanostructure described as “silicon nanowires standing on silica microwires” was fabricated.^[4] However, oriented hierarchical nanostructures which are more amenable for device fabrication have yet to be reported. Herein, we report the synthesis of a highly ordered Si–SiO_x columnlike hierarchical nanostructure which consists of high-density, radially oriented amorphous silica nanowires standing on a single-crystal Si nanocore. Unlike the previous hierarchical nanostructures, which were assumed to form by the two-step growth mechanism,^[3] the growth of the present Si–SiO_x hierarchical nanostructure appears to occur by two concurrent processes: the vapor–liquid–solid (VLS) mechanism and the oxide-assisted growth (OAG) process. Interestingly, this novel structure emits UV light at 378 nm on excitation by a femtosecond laser at 300 nm.

Si/SiO_x strands were synthesized in a high-temperature tube furnace with tin as catalyst. The general morphology of the deposition product is shown in Figure 1 a–c, which reveals

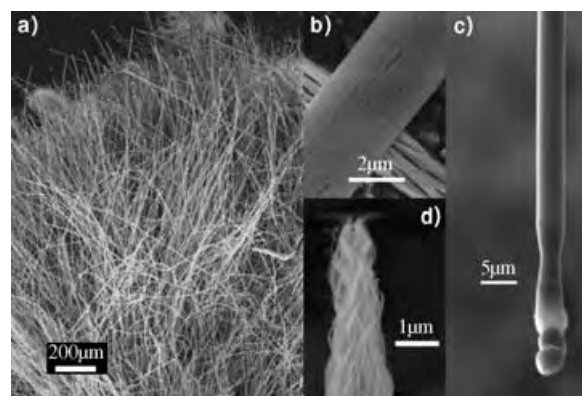


Figure 1. SEM images of as-synthesized Si–SiO_x hierarchical nanostructure.

that large-scale wirelike microscaled structures are aligned on the substrate, and that the microstructures are long, straight, and smooth strands. The products have diameters of hundreds of nanometers to several micrometers and lengths up to several millimeters (with an aspect ratio exceeding 1.6×10^3). The cross-sectional SEM images (Figure 2 a and b) show that the strands have a columnlike, radially aligned hierarchical structure. Energy dispersive X-ray (EDX) spectroscopy (Figure 2 c and d) confirms the stoichiometric elemental composition of silicon for the core and SiO_x ($x = 1.5\text{--}2$) for the branches of the strand. The SEM images further reveal that the strands have two different tip morphologies: one has a corn-shaped taper (Figure 1 d) and the other a spherical particle at the tip (Figure 1 c; EDX confirms the tip is made of Sn, as will be discussed below). It can also be observed that

[*] H. Wang, Prof. X.-H. Zhang, Prof. X.-M. Meng, Dr. S.-M. Zhou, Prof. S.-K. Wu, Prof. W.-S. Shi
Nano-organic Photoelectric Laboratory
Technical Institute of Physics and Chemistry
Chinese Academy of Sciences
Beijing 100101 (China)
Fax: (+86) 10-6487-9375
E-mail: xhzhang@mail.ipc.ac.cn

Prof. S.-T. Lee
Center of Super-Diamond and Advanced Films (COSDAF) and
Department of Physics and Materials Science
City University of Hong Kong
Hong Kong SAR (China)
Fax: (+852) 2784-4696
E-mail: apannale@cityu.edu.hk

H. Wang
Graduate School of Chinese Academy of Sciences
Beijing, 100101 (China)

[**] We thank the Chinese Academy of Sciences and the CAS-Croucher Funding Scheme for Joint Laboratories of the Croucher Foundation for financial support. The work in Hong Kong was supported by the Research Grants Council of Hong Kong SAR, China via a central allocation project (No. CityU 3/04C).

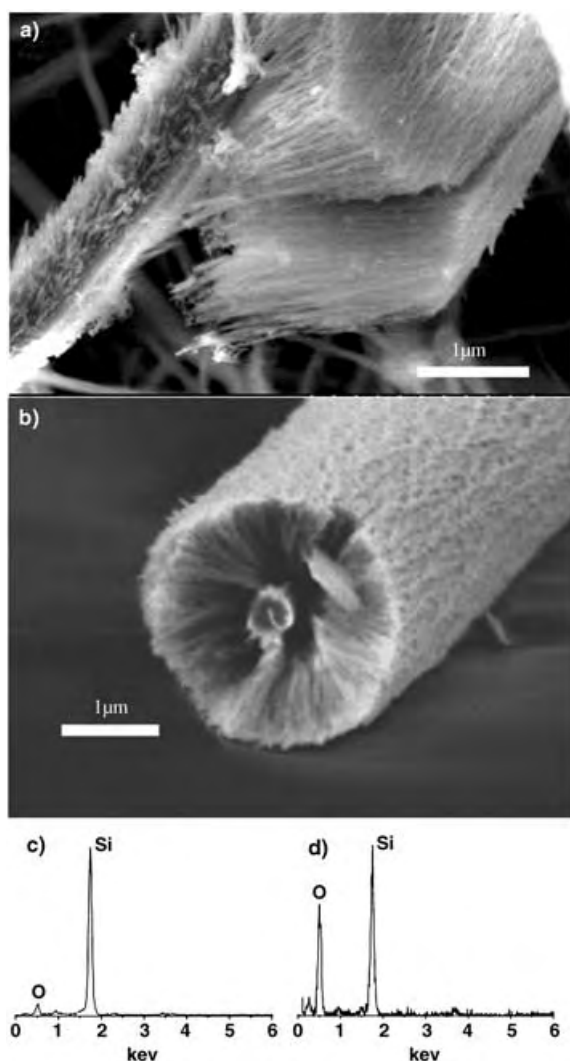


Figure 2. Cross-sectional SEM image of the Si-SiO_x hierarchical structure or strand (a and b) and the corresponding EDX spectra of the core (c) and shell (d) of the strand.

the SiO_x on the strand has fleecy surfaces (Figure 1d) and grows towards the tapered end where the strand diameter is less than 1 μm. When the diameter is more than 2 μm, the strand looks like a compact whisker or column, and the SiO_x nanowires stand vertically on the strand core (whiskerlike or columnlike; see Figures 1 and 2).

The structure of the strand was further studied by TEM (Figure 3). The sharp selected-area electron diffraction (SAED) spots (Figure 3a, upper inset) obtained from the center of the strand demonstrates that the solid Si core has a single-crystal structure, whereas the diffuse SAED pattern obtained from the edge of the strand (Figure 3a, lower inset) reveals that the radially oriented SiO_x nanowires standing on the core are an amorphous phase. According to statistical data from the TEM images, the Si core has an average diameter of 230 nm, and the SiO_x nanowires in the shell have a uniform diameter of 10–20 nm and a length of hundreds of nanometers to several micrometers (with an aspect ratio of about 1000).

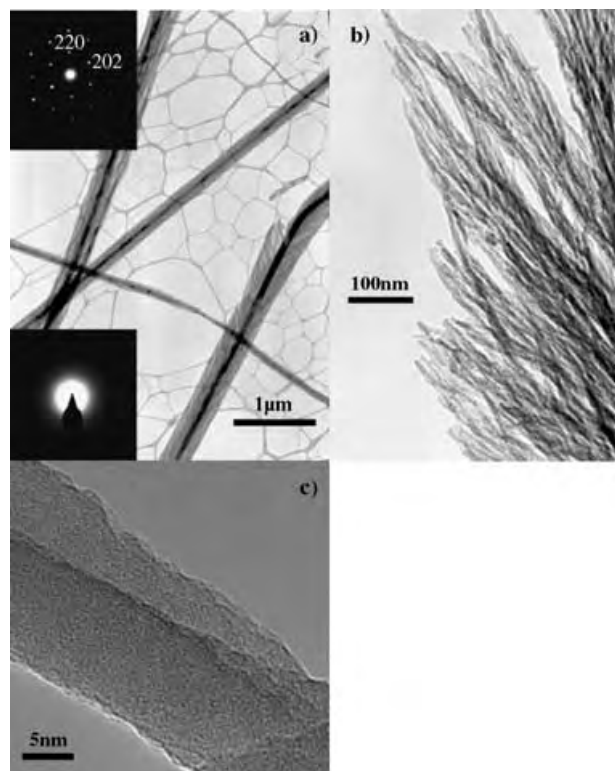


Figure 3. TEM images of the Si-SiO_x hierarchical nanostructure. a) TEM image of the strands and corresponding selected-area electron diffraction pattern of the core (upper inset) and the shell (lower inset). b) TEM image of the aligned SiO_x nanowires, detached from the shell of the cable by sonication. c) High-resolution TEM image of the amorphous SiO_x nanowire showing its featureless structure.

An X-ray diffraction spectrum of the as-synthesized hierarchical structure is shown in Figure 4, which reveals that the sample is dominated by the cubic silicon phase. The spectrum also shows reflections due to the body-centered crystalline structure of Sn. These results are in good agreement with those of SAED and EDX.

To elucidate the growth mechanism of the hierarchical structure, the tip regions of the strands were examined in detail. Figure 5 shows a TEM image of a single strand

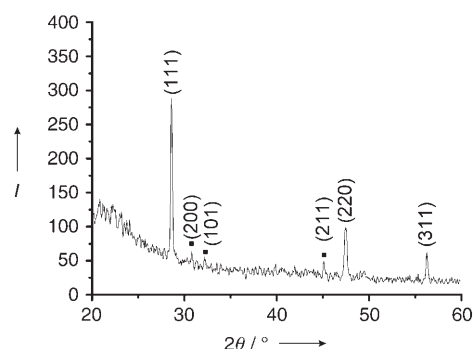


Figure 4. XRD spectrum of the Si-SiO_x hierarchical nanostructure. The peaks marked by ■ belong to the body-centered crystalline structure of Sn, and the rest to crystalline Si. The weak, broad peak at 21° is due to amorphous SiO_x.

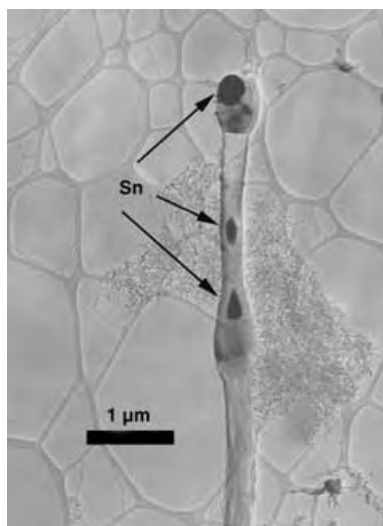


Figure 5. TEM image of the Si-SiO_x hierarchical nanostructure or strand with a spherical Sn particle at the tip and Sn inside the strand.

segment, in which a spherical particle at the tip can be clearly observed. The chemical composition at several different positions was analyzed by EDX. The spherical particle at the tip of the strand is an Sn particle surrounded by Si. The Sn particle is considered to act as a catalyst for nanowire growth, because the corresponding eutectic Si-Sn alloy can form at low temperature (232 °C). The presence of a spherical metallic particle at the tip is usually considered to be a signature of the VLS mechanism.^[5] The growth direction of the single-crystal Si core is (111), as determined by SAED, and is in good agreement with the VLS growth process.^[5] The part of the nanotube partially filled with Sn between the spherical particle at the tip and the main product is due to the temperature change at the end of the preparation, as was previously observed.^[5] Pan et al. also found that gallium catalyst could be wrapped inside Si in the synthesis of silicon oxide nanowire sandwich structures,^[6] in which they attributed the growth of amorphous silicon oxide nanowires outside the Si core to oxidation of silicon. We suggest that the silicon oxide wires standing on the silicon core in the present case may also grow by the same oxidation process.

We now discuss why the SiO_x nanostructure forms in a wirelike form instead of an agglomeration pattern. Previous models for explaining this phenomenon^[6–11] suggested that Si reacts with oxygen to form SiO_x particles, which then serve as nucleation sites to initiate the growth of SiO_x nanowires. However, we suggest that the OAG process proposed by Lee et al.^[12–14] may be more suitable to account for the formation of SiO_x nanowires in the present work. In contrast to the conventional VLS mechanism, the OAG process relies on an oxide or a redox reaction instead of a catalytic metal or metal compound to assist the formation of nanowires. We propose that the Si nuclei formed at the Si droplet surface covered by the SiO₂ layer are similar to the nanoparticles, which then were oxidized to SiO_x dots by reacting with the SiO₂ outside. Meanwhile, new Si extruded from the alloy would nucleate at the end of the nanoparticles. This recurrence or cycling process would maintain the continual growth of the amor-

phous SiO_x nanowire. Meanwhile, the Si core would continue its growth along the axial direction, guided by the Sn catalyst and following the VLS mechanism, and only the surface nuclei could be formed when the core remained in the liquid state. Concurrent with core growth, the end of the SiO_x nanowires grown from the surface nuclei would grow in the forward direction together. Consequently, the SiO_x nanowires would form at an angle with respect to the growth direction of the core, just as was discussed above. According to the above analysis, we propose the following process for the formation of the Si-SiO_x hierarchical structure, as shown schematically in Figure 6:

- 1) Thermal evaporation: vaporization of Sn and SiO powder to form Sn and SiO vapors.
- 2) Vapor deposition: deposition and formation of SiO-containing Sn liquid droplets in the low-temperature area (Figure 6a).
- 3) Separation: disproportionation of SiO into SiO₂ + Si and subsequent phase separation of Si and SiO₂, whereby SiO₂ wraps the alloy droplet (Si and Sn; Figure 6b).
- 4) Growth: precipitation and segregation of Si crystal from liquid Sn due to supersaturation of Si in the Sn + Si droplet (Figure 6c). Then the SiO₂ species on the surface react with Si nuclei or residual oxygen to form SiO_x nanowires. At the same time the central Si core would continue to grow by the VLS mechanism. The two concurrent processes would make the product grow in axial and lateral directions, and finally form an Si-SiO_x hierarchical structure (Figure 6d).

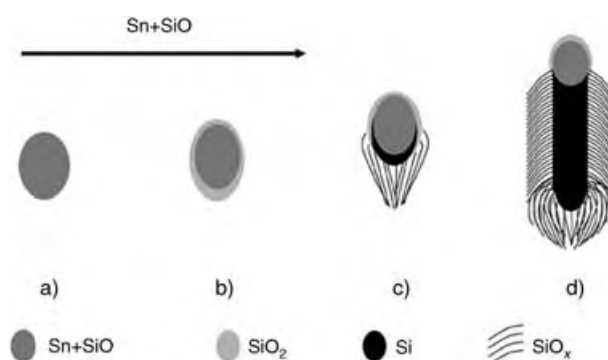


Figure 6. Proposed growth model for the Si-SiO_x hierarchical structure. a) Sn and SiO vapors from the evaporation area (1320 °C) condense and form a liquid alloy droplet in the growing area (750–850 °C). b) More SiO vapor is absorbed into the droplet and disproportionates into Si and SiO₂, which are then phase-separated (at 800 °C, the concentration of Si in the Si/Sn alloy is about 1 %). c) Si nucleates and oxide grows into a SiO_x nanowire. d) Single-crystal Si core grows with assistance of the Sn catalyst, and SiO_x nanowires grow concurrently.

Figure 7 shows the room-temperature photoluminescence (PL) spectrum of the as-synthesized Si-SiO_x hierarchical structures on excitation by a femtosecond laser at 300 nm. The spectrum is dominated by only one narrow UV emission peak centered at 378 nm with a half-peak width of 6 nm. This PL spectrum is radically different from that of nonhierarchical amorphous SiO₂ nanostructures, which usually show

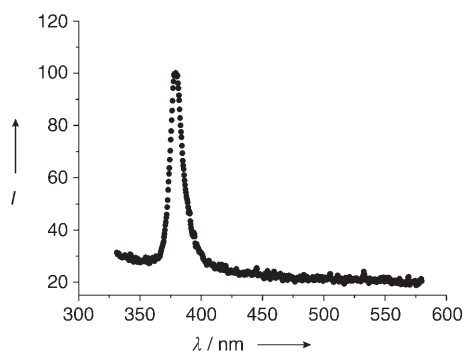


Figure 7. Photoluminescence spectrum of the Si-SiO_x hierarchical nanostructure ($\lambda_{\text{ex}} = 300$ nm).

multipeak blue or green emissions.^[6,15] The nature of the UV PL peak is not clear, although several luminescence bands with peak energies ranging from 743 to 328 nm have been observed in various types of silica by Nishikawa et al.^[16] On the other hand, the present emission centered at 378 nm may also be attributable to oxygen vacancies.^[16]

In conclusion, a novel hierarchical nanostructure consisting of high-density amorphous silica nanowires radially standing on a single-crystal silicon core were grown on a substrate in bulk (grams) quantity by a simple thermal evaporation process. The nanostructure shows a single sharp PL peak at 378 nm. The micro-sized hierarchically ordered nanostructures of Si and its luminescent oxide could serve as potential building blocks for ready assembly into various functional devices. Indeed, the Si-SiO_x hierarchical nanostructure has been shown to be an outstanding template for chemical and biosensors^[18] due to its large surface-to-volume ratio. The present facile growth process is expected to be readily extendable to fabricate similar functional hierarchical nanostructures of other semiconductors and oxides.

Experimental Section

The Si-SiO_x strands were synthesized in a high-temperature tube furnace, as described previously.^[9] An Al₂O₃ boat with a mixture of 3.00 g SiO (Aldrich, 325 mesh, 99.9%) and 0.50 g Sn was put in the center of an alumina tube and then mounted in the furnace. The system was pumped to 5×10^{-2} mbar and then heated to 1320 °C at 40 °C min⁻¹, then a mixture of argon (95%) and hydrogen (5%) at 350 mbar was kept flowing at a rate of 10 sccm. After growth for about 7 h, the furnace was cooled to room temperature at 40 °C min⁻¹. A dark yellow product (ca. 0.5 g) was obtained on the silicon wafer and the inside wall of the alumina tube in the 750–850 °C zone at the downstream end; the amount of product can be increased by lengthening the reaction time. The product was checked by SEM (Philips XL 30 FEG) and XRD (Siemens D500). Some of the sample was dispersed in ethanol and a drop of the dispersion was put on a carbon-coated copper TEM sample grid for examination by TEM (Philips, CM20, operated at 200 kV). To record the room-temperature photoluminescence spectrum, the sample was fixed between two crystal plates, and a 3941C-M1BB/Spitfire FF-1K/OPA-800CF-0.5 femtosecond laser (300 nm) was used as excitation source.

Received: June 7, 2005

Revised: August 5, 2005

Published online: October 7, 2005

Keywords: crystal growth · luminescence · materials science · nanostructures · silicon

- [1] a) A. M. Fennimore, T. D. Yuzvinsky, W.-Q. Han, M. S. Fuhrer, J. Cumings, A. Zettl, *Nature* **2003**, *424*, 408; b) Z. Zhong, D. Wang, Y. Cui, M. W. Bockrath, C. M. Lieber, *Science* **2003**, *302*, 1377; c) D. D. Ma, C. S. Lee, F. C. K. Au, S. Y. Tong, S. T. Lee, *Science* **2003**, *299*, 1874.
- [2] a) P. Yang, *Nature* **2003**, *425*, 243; b) D. Whang, S. Jin, Y. Wu, C. M. Lieber, *Nano Lett.* **2003**, *3*, 1255; c) A. Tao, F. Kim, C. Hess, J. Goldberger, R. He, Y. Sun, Y. Xia, P. Yang, *Nano Lett.* **2003**, *3*, 1229; d) Y. C. Zhu, Y. Bando, D. Feng Xue, D. Golberg, *Adv. Mater.* **2004**, *16*, 831.
- [3] a) J. Q. Hu, Q. Li, X. M. Meng, C. S. Lee, S. T. Lee, *Chem. Mater.* **2003**, *15*, 305; b) J. Y. Lao, J. G. Wen, Z. F. Ren, *Nano Lett.* **2002**, *2*, 1287; c) Z. L. Wang, Z. W. Pan, *Adv. Mater.* **2002**, *14*, 1029; d) Y. Q. Zhu, W. K. Hsu, W. Z. Zhou, M. Terrones, H. W. Kroto, D. R. M. Walton, *Chem. Phys. Lett.* **2001**, *347*, 337; e) M. H. Huang, S. Mao, H. Feick, H. Yan, Y. Wu, H. Kind, E. Weber, R. Russo, P. Yang, *Science* **2001**, *292*, 1897; f) X. M. Meng, J. Q. Hu, Y. Jiang, C. S. Lee, S. T. Lee, *Appl. Phys. Lett.* **2003**, *83*, 2241; g) K. C. Kam, F. L. Deepak, A. K. Cheetham, C. N. R. Rao, *Chem. Phys. Lett.* **2004**, *397*, 329.
- [4] C. Ye, L. Zhang, X. Fang, Y. Wang, P. Yan, J. Zhao, *Adv. Mater.* **2004**, *16*, 1019.
- [5] a) Y. F. Zhang, Y. H. Tang, N. Wang, D. P. Yu, C. S. Lee, I. Bello, S. T. Lee, *Appl. Phys. Lett.* **1998**, *72*, 1835; b) R. S. Wagner, W. C. Ellis, *Appl. Phys. Lett.* **1964**, *4*, 89; c) Z. W. Pan, Z. R. Dai, C. Ma, Z. L. Wang, *J. Am. Chem. Soc.* **2002**, *124*, 1817.
- [6] Z. W. Pan, S. Dai, D. B. Beach, D. H. Lowndes, *Appl. Phys. Lett.* **2003**, *83*, 3159.
- [7] Z. W. Pan, S. Dai, D. B. Beach, D. H. Lowndes, *Nano Lett.* **2003**, *3*, 1279.
- [8] B. Zheng, Y. Wu, P. Yang, J. Liu, *Adv. Mater.* **2002**, *14*, 122.
- [9] X. H. Sun, C. P. Li, W. K. Wong, N. B. Wong, C. S. Lee, S. T. Lee, B. K. Teo, *J. Am. Chem. Soc.* **2002**, *124*, 14464.
- [10] J. Q. Hu, X. M. Meng, Y. Jiang, C. S. Lee, S. T. Lee, *Adv. Mater.* **2003**, *15*, 70.
- [11] C. Wu, W. Qin, G. Qin, D. Zhao, J. Zhang, W. Xu, H. Lin, *Chem. Phys. Lett.* **2003**, *378*, 368.
- [12] S. T. Lee, Y. F. Zhang, N. Wang, Y. H. Tang, I. Bello, C. S. Lee, *J. Mater. Res.* **1999**, *14*, 4503.
- [13] N. Wang, Y. H. Tang, Y. F. Zhang, C. S. Lee, S. T. Lee, *Phys. Rev. B* **1998**, *58*, R16024.
- [14] R. Q. Zhang, Y. Lifshitz, S. T. Lee, *Adv. Mater.* **2003**, *15*, 635.
- [15] a) J. Q. Hu, Y. Jiang, X. M. Meng, C. S. Lee, S. T. Lee, *Chem. Phys. Lett.* **2003**, *367*, 339; b) D. P. Yu, Q. L. Hang, Y. Ding, H. Z. Zhang, Z. G. Bai, J. J. Wang, Y. H. Zou, W. Qian, G. C. Xiong, S. Q. Feng, *Appl. Phys. Lett.* **1998**, *73*, 3076; c) J. Jang, H. Yoon, *Adv. Mater.* **2004**, *16*, 799.
- [16] H. Nishikawa, T. Shiroiyama, R. Nakamura, Y. Ohki, *Phys. Rev. B* **1992**, *45*, 586.
- [17] a) S. Y. Ma, *Surf. Interface Anal.* **2001**, *31*, 890; b) J. H. Stathis, M. A. Kastner, *Phys. Rev. B* **1987**, *35*, 2972.
- [18] M. W. Shao et al., unpublished results.

DOI: 10.1002/anie.200501989

Solution-Phase Mixture Synthesis with Double-Separation Tagging: Double Demixing of a Single Mixture Provides a Stereoisomer Library of 16 Individual Murisolins**

Craig S. Wilcox,* Venugopal Gudipati, Hejun Lu, Serhan Turkyilmaz, and Dennis P. Curran*

Most small organic molecules are synthesized individually, but there is a compelling reason to synthesize molecules as mixtures—the effort conserved in a synthesis is directly proportional to the number of compounds that are mixed. “Split/mix” methods conduct reactions on mixtures of beads yet provide individual products at the end.^[1] Recently, a general concept for solution-phase mixture synthesis^[2] by separation tagging has been introduced^[3] and put into practice with homologous fluororous tags.^[4] Chemical reactions are conducted on tagged mixtures and the final reactions mixtures are demixed (sorted) in an orchestrated fashion by a tag-complementary separation technique. Finally, detagging provides the individual pure target products.

Generally, the availability of n tags in a single tagging strategy allows n compounds to be tagged (Figure 1, top). We

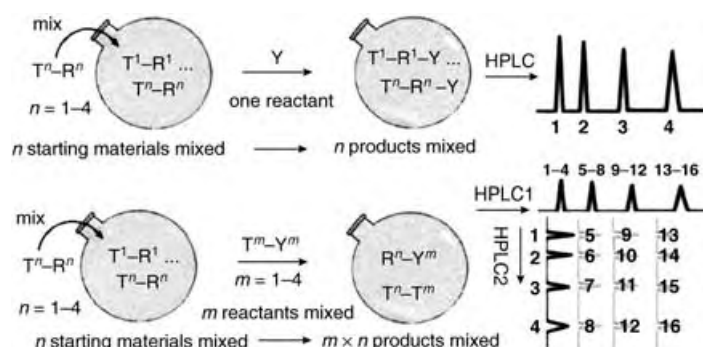


Figure 1. Single (top) and double (bottom) separation tagging.

define a tag “class” as a set of tags that all share a similarly useful response to a given separation process. The addition of m new tags to a given class of n tags increases the maximum possible size of a mixture to $n + m$.

Wilcox and Turkyilmaz recently introduced a new class of oligoethylene glycol (OEG; $(\text{OCH}_2\text{CH}_2)_n\text{OCH}_3$) tags. These were designed for solution-phase mixture synthesis, and a polarity-based demixing process was implemented.^[5] The availability of two different classes of tags opens up the possibility for double-tagging strategies. The tagging of n precursors with a first class of tag and m precursors with a complementary second class of tag provides $n + m$ precursors. However, reaction of these two mixtures provides a new mixture of $n \times m$ products, each of which has a unique pair of tags (Figure 1, bottom). Isolation of the final products is achieved by double demixing with a separate demixing process that targets each tag class. We report herein the first example of double tagging with tandem separation. The ability to leverage available tags is shown by the preparation of 16 stereoisomers of the natural product murisolin in a single reaction flask with only eight tags, four fluororous tags and four OEG tags.

A crucial question in any multiple-tagging exercise is tag orthogonality; when combined in a single molecule, will the fluororous tags and OEG tags enable a separation as well as each does alone. To address this question, a mixture of 16 doubly tagged analogues of vanillic acid (4-hydroxy-3-methoxybenzoic acid) M-1^[6] was created wherein each compound had one of four OEG tags on the phenolic hydroxy group ($n = 1-4$) and one of four homologous fluororous tags on the carboxylate group ($\text{R}^F = \text{C}_2\text{F}_5, \text{C}_4\text{F}_9, \text{C}_6\text{F}_{13}, \text{and } \text{C}_8\text{F}_{17}$). The resulting 16 compounds (4×4) are unique and differ by the combination of the OEG and fluororous tags.

The 16-compound mixture was demixed into its individual components according to the tags by using a series of two demixings, one targeted to each class of tag. TLC analysis of the reaction mixture on silica gel showed only four spots (Figure 2a). The mixture was separated by flash chromatography (pentane/EtOAc gradient) into four fractions based on the properties of the OEG tags. The least polar fraction contained all four molecules **1** that bear the OEG1 tag ($n = 1$) and the four different fluororous tags. The successive fractions each contained four molecules with the OEG2, OEG3, and OEG4 tags. Each of these four fractions was further demixed by fluororous HPLC chromatography on a FluoroFlash PF-C8 column.^[7] As expected, the products from this chromatographic procedure were eluted in the order of the fluororous tag from C_2F_5 up to C_8F_{17} , thus providing all 16 individual vanillic esters **1**.

We observed that the order of the demixings can also be reversed, with the fluororous demixing being conducted before the OEG demixings. Figure 2b shows an HPLC trace of the 16-compound mixture M-1 on a FluoroFlash PF-C8 column. The compounds emerge as four groups of four peaks. The larger separations correspond to the fluororous tags, with the four compounds bearing the C_2F_5 tag eluting well before the four compounds bearing the C_4F_9 tag, and so forth. The smaller separations within the groups of peaks correspond to OEG-tagged compounds, from the more polar $n = 4$ tag to the less polar $n = 1$ tag. The mixture was separated by semi-preparative fluororous HPLC. In this case, only four fractions that correspond to the four different groups of fluororous-tagged compounds were collected. Each of these fractions,

[*] Prof. Dr. C. S. Wilcox, V. Gudipati, H. Lu, S. Turkyilmaz, Prof. Dr. D. P. Curran
Department of Chemistry
University of Pittsburgh
Pittsburgh, PA, 15260 (USA)
Fax: (+1) 412-624-9861
E-mail: daylite@pitt.edu
curran@pitt.edu

[**] We thank the US National Institutes of Health for funding this work.

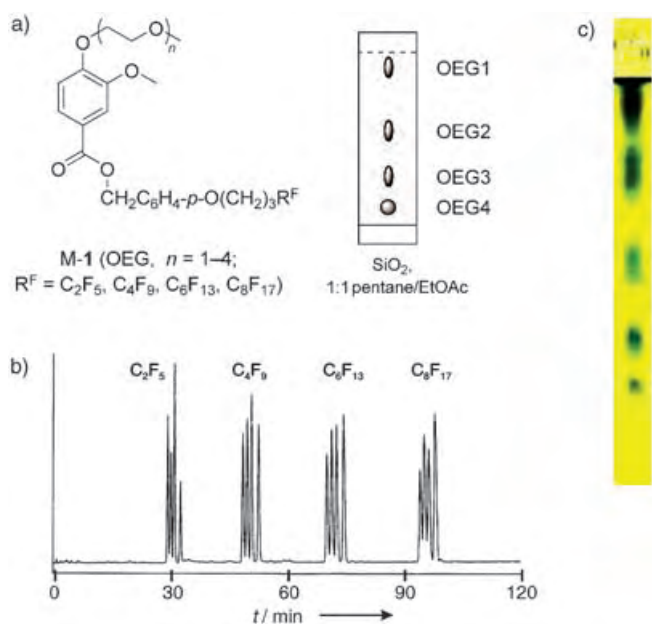


Figure 2. Demixing of 16 fluorine/OEG-tagged vanillic acid esters **M-1** and murisolin quasi-diastereomers **4**. a) TLC plate of the demixing of **M-1** on silica gel based on the OEG tags (pentane/EtOAc, 1:1). b) HPLC trace of the demixing of **M-1** on a FluoroFlash PF-C8 column based on the fluorine tags ($\text{CH}_3\text{CN}/\text{H}_2\text{O}$, 40:60 to 90:10). c) Photograph of a developed TLC plate of the mixture of 16 murisolin quasi-isomers **4** (silica gel; EtOAc/hexanes, 80:20); a small spot at the origin lies below the four spots that elute as groups of four fluorine-tagged compounds in order of increasing polarity for OEG $n=1-4$.

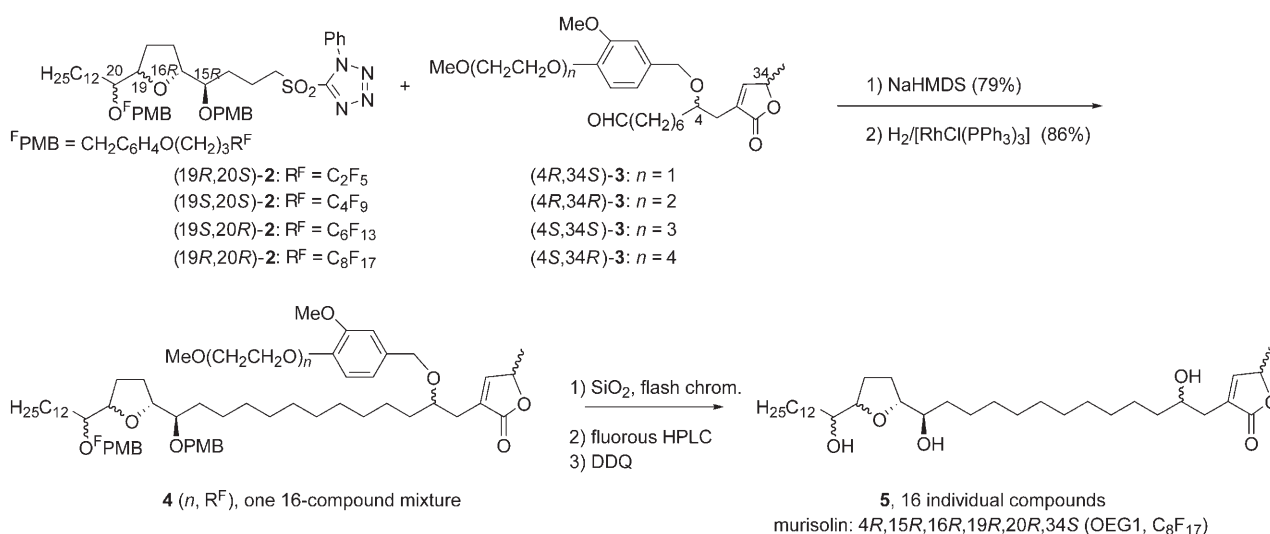
which contain four molecules with one fluorine tag and all four OEG tags, were then separated by simple flash column chromatography to provide the same 16 individual products.

These proof-of-concept experiments are remarkable. It is well known that the addition of CF_2 groups decreases the polarity of molecules,^[8] yet this effect is completely overwhelmed on silica gel by the presence of the OEG tag. Conversely, the large polarity effects of the OEG tags are

largely masked on the fluorine column, and the fluorine content rules. This complementarity suggests that fluorine tags and OEG tags are compatible partners in double-tagging strategies. To verify this hypothesis, we proceeded to synthesize 16 stereoisomers of the acetogenin murisolin in a single reaction flask. The pathway follows the recently completed fluorine mixture synthesis in which 16 stereoisomers were prepared in groups of four with the aid of four fluorine tags.^[4e]

We planned to use a Kocienski–Julia reaction^[9] to couple a mixture of four diastereomers of the dihydroxy THF subunit **M-2** with another mixture of four diastereomers of the hydroxybutenolide subunit **3** to give a doubly tagged 16-component mixture, in which the tag pairs encode the configurations and enable double demixing (Scheme 1). The tetrazolysulfonyl component **2** was synthesized as four stereoisomers coded with a fluorine PMB ($^{\text{F}}\text{PMB}$) tag by using methods described recently.^[4e] These stereoisomers all had the $15R,16R$ configuration, and all four possible isomers at C19 and C20 were present. In the first multistep OEG mixture synthesis, the aldehyde component **3** of the coupling was prepared as all four possible stereoisomers at C4,34 coded with the OEG-modified dimethoxybenzyl group (hereafter called an OEG tag).

The Kocienski–Julia coupling of the four-compound fluorine-tagged mixture **M-2** and the four-compound OEG-tagged mixture **M-3** provided a 16-compound mixture, which was directly hydrogenated to saturate the new alkene. This sequence provided mixture **M-4** composed of 16 doubly tagged murisolin. A photograph of the TLC analysis of the mixture on silica gel shows the anticipated demixing into four spots (Figure 2c).^[10] Flash column chromatography^[11] sorted this mixture into four fractions based on the OEG tag from OEG1 (least polar) to OEG4 (most polar). Each of these four-compound mixtures was then demixed on a semipreparative FluoroFlash PF-C8 HPLC column^[11] to provide all 16 individual tagged stereoisomers **4**. All pairs of peaks in the fluorine demixings were separated by 6 minutes or more, so quasi-isomer cross-contamination was not a problem. Even



Scheme 1. Preparation of the doubly tagged 16-component mixture and subsequent demixing. PMB = *para*-methoxybenzyl ($\text{CH}_2\text{C}_6\text{H}_4\text{OCH}_3$); HMDS = hexamethyldisilazide; DDQ = 2,3-dichloro-5,6-dicyano-1,4-benzoquinone; chrom. = chromatography.

though the tagged compounds **4** are now quasi-diastereomers,^[10,12] the double demixing in Scheme 1 proceeded analogously to the model demixing of **1** in Figure 2.

Simultaneous removal of the PMB protecting group, the fluorine tag, and the OEG tag was effected by DDQ oxidation. The 16 stereoisomers of **5** were purified by semi-preparative HPLC to provide the target isomers on a scale of 1–3 mg.

The stereoisomer library was designed with four control compounds (the OEG1-tagged compounds with 4*R*,34*S* configuration), and these compounds were shown to be identical to authentic samples by spectroscopic and chiral HPLC analysis.^[4e] The resulting data proved that the double demixing worked as expected and allowed the configurations of the remaining 12 new compounds to be assigned solely on the basis of their tag pairings and the associated demixing order. This identification was crucial because the ¹H and ¹³C NMR spectra of many of the compounds in the library are identical with other members of this or the prior library. In our previous 16-compound library, we observed only six different ¹H and ¹³C NMR spectra, and we predicted that six more sets of spectra were possible.^[13] This prediction was confirmed by observation of the other six spectra. Accordingly, none of the 32 possible diastereomers of murisolin is spectroscopically unique under standard NMR spectroscopic conditions.

Through combination of the known fluorine synthesis^[4e] and the new double-tagging synthetic technique, we have prepared 28 of the 64 possible stereoisomers of murisolin. Although all the compounds were prepared from mixtures of intermediates, each isomer has been isolated in pure form and characterized by the usual spectroscopic and chromatographic means, including optical-rotation studies.

The ability to prepare 16 stereoisomers of a natural product as complex as murisolin in a single solution-phase synthesis (without splits) demonstrates the potential of these new mixture methods. Central to the potential of this technique is the newly introduced method of double tagging.

Received: June 8, 2005

Published online: October 5, 2005

Keywords: asymmetric synthesis · mixture synthesis · natural products · separation · tags

- [1] a) A. Furka, L. K. Hamaker, M. L. Peterson in *Combinatorial Chemistry*, Vol. 233 (Ed.: H. Fenniri), Oxford University Press, New York, **2000**, pp. 1–31; b) K. S. Lam, M. Lebl, V. Krchnak, *Chem. Rev.* **1997**, 97, 411–448.
- [2] For solution-phase synthesis of mixture libraries without separation tagging, see: a) R. A. Houghten, C. Pinilla, J. R. Appel, S. E. Blondelle, C. T. Dooley, J. Eichler, A. Nefzi, J. M. Ostresh, *J. Med. Chem.* **1999**, 42, 3743–3778; b) H. Y. An, P. D. Cook, *Chem. Rev.* **2000**, 100, 3311–3340.
- [3] a) First paper: Z. Y. Luo, Q. S. Zhang, Y. Oderaotoshi, D. P. Curran, *Science* **2001**, 291, 1766–1769; b) Short review: W. Zhang, *ARKIVOC* **2004**, 101–109.
- [4] a) D. P. Curran in *The Handbook of Fluorous Chemistry*, J. Gladysz, I. Horváth, D. P. Curran, Wiley-VCH, Weinheim, **2004**, pp. 128–155; b) S. Dandapani, M. Jeske, D. P. Curran, *Proc. Natl. Acad. Sci. USA* **2004**, 101, 12008–12012; c) W. Zhang, *Tetrahedron* **2003**, 59, 4475–4489; d) W. Zhang, Z. Y. Luo, C. H.-T. Chen, D. P. Curran, *J. Am. Chem. Soc.* **2002**, 124, 10443–10450; e) Q. S. Zhang, H. J. Lu, C. Richard, D. P. Curran, *J. Am. Chem. Soc.* **2004**, 126, 36–37.
- [5] C. S. Wilcox, S. Turkyilmaz, *Tetrahedron Lett.* **2005**, 46, 1827–1829.
- [6] The prefix “M” denotes a tagged mixture of compounds.
- [7] The columns and fluorine-tagging reagents were purchased from Fluorous Technologies, Inc. (<http://www.fluorous.com>); D.P.C. holds an equity interest in this company.
- [8] a) P. C. Sadek, P. W. Carr, *J. Chromat.* **1984**, 288, 25–41; b) D. P. Curran in *The Handbook of Fluorous Chemistry* (Eds.: J. A. Gladysz, D. P. Curran, I. T. Horváth), Wiley-VCH, Weinheim, **2004**, pp. 101–127.
- [9] P. R. Blakemore, *J. Chem. Soc. Perkin Trans. 1* **2002**, 2563–2585.
- [10] On close inspection, each of the four main spots appears to be a composite of two almost overlapping spots, which are presumably the pairs of quasi-diastereomers with the same OEG tag.
- [11] Conditions for preparative demixings: a) flash column chromatography with a step gradient (25, 50, 65, and 80% EtOAc/hexanes) to elute each successive OEG-tagged fraction; b) fluorine HPLC separation of each of the four OEG-tagged demixed fractions with a 20 × 250 mm² PF-C8 column, linear gradient of 85% CH₃CN/H₂O to 100% CH₃CN over 25 min (typical retention times: C₂F₅ 8 min; C₄F₉ 14 min; C₆F₁₃ 20 min; C₈F₁₇ 28 min).
- [12] Q. Zhang, D. P. Curran, *Chem. Eur. J.* **2005**, 11, 4866–4880.
- [13] *Syn* and *anti* isomers at C₄,34 have slightly different spectra; the compounds are also differentiated by the ratio of *syn/anti* isomers at C₁₅,16 and C₁₉,20 and the ratio of *cis/trans* isomers at C₁₆,19.

Bond- and Site-Selective Loss of H Atoms from Nucleobases by Very-Low-Energy Electrons (< 3 eV)**

Sylwia Ptasinska, Stephan Denifl, Paul Scheier, Eugen Illenberger,* and Tilmann D. Märk

Excess charge deposited on gas-phase thymine (T) and uracil (U) by resonant attachment of low-energy (0–3 eV) electrons induces the loss of hydrogen, which exclusively takes place from the N positions. This bond selectivity can be made site selective by properly adjusting the electron energy. While electrons at 1 eV result in loss of hydrogen from N1, the reaction can be switched to loss of hydrogen from N3 by tuning the electron energy to 1.8 eV. We find that any energy (and charge) transfer is completely blocked when the N–H bond is replaced by N–CH₃. The present results have significant consequences for the exploration of the initial molecular processes leading to DNA damage, specifically in relation to recent observations of strand breaks in plasmid DNA induced by very low energy (0–4 eV) electrons.^[1]

Recent gas-phase experiments on the isolated nucleobases (NBs) thymine (T), cytosine (C), adenine (A), guanine (G), and uracil (U) have demonstrated that they all effectively capture low-energy electrons in the range below 3 eV.^[2–6] The generated transient negative ion (TNI) subsequently decomposes by the loss of a neutral hydrogen atom. The overall dissociative electron attachment (DEA) reaction can be expressed as Equation (1), in which NB^{−#} is the TNI of the



corresponding nucleobase and (NB–H)[−] is the closed-shell anion formed by the ejection of a neutral hydrogen radical whereby the excess charge remains on the nucleobase. The reaction is effective already at energies below the threshold for electronic excitation (at subexcitation energies) and driven by the appreciable electron affinity of the (NB–H) radicals, which is in the range between 3 and 4 eV, dependent

on the site from which the hydrogen atom is ejected^[2,6] (see below). Experiments with partly deuterated thymine^[5] demonstrated that hydrogen abstraction occurs exclusively from the N sites, although H loss from the C sites is energetically accessible within that energy range. In the present contribution we demonstrate by means of methylated thymine and uracil that by properly adjusting the electron energy, the loss of hydrogen can be made even site selective with respect to the N1 and N3 positions. In light of strong efforts to induce cleavage of particular bonds by coherent laser control using tailored ultrafast pulses^[7] the present result is very remarkable.

In addition to these basic aspects, our findings have direct implications for the molecular description of radiation damage in biological systems, more specifically, for DNA in living cells. It is well accepted that the main biological effect is usually not produced by the primary interaction of the high-energy quanta with the complex molecular network within a living cell, but rather by the action of the secondary species generated along the ionization track.^[8] The interaction of these secondary species (ions, electrons, radicals) with DNA and its surrounding can cause mutagenic, genotoxic, and other potentially lethal DNA lesions such as single-strand breaks (SSBs) and double-strand breaks (DSBs).

Electrons are by far the most abundant of these secondary species and have an initial energy distribution extending to about 20 eV.^[9,10] For the understanding of the effects of radiation in cells, it is therefore essential to investigate the action induced by these electrons on the vital cellular components such as water and DNA. In experiments directly exposing plasmid DNA on a surface to an electron beam of variable and well-defined energy, Boudaiffa et al.^[11] showed that electrons below the ionization threshold can produce SSBs and DSBs. The same research group showed very recently that in plasmid DNA SSBs are produced at energies as low as the nominal zero-energy threshold of the electron beam and that the yield as a function of the energy exhibits a sharp peak at 0.8 ± 0.3 eV and a broader feature centered at 2.2 eV.^[1]

On the other hand, the explicit molecular mechanism how low energy electrons damage DNA is yet unknown. Here we study in detail the processes that are initiated in isolated thymine (T) and uracil (U) by additional experiments on the compounds methylated at one of the N positions. These results have direct implications for the initial steps towards strand breaks in DNA.

The present investigations were performed in a crossed electron/molecule beams device previously described in detail.^[12] The electron beam is formed in a hemispherical electron monochromator, operated at an energy resolution between 60 and 110 meV and an electron current of 5–8 nA. The molecular beam emanates from a source consisting of a temperature-regulated oven and a capillary. Evaporation at 385–400 K results in an effusive beam of intact molecules. Negative ions formed in the collision zone are extracted by a weak electric field toward the entrance of the quadrupole mass spectrometer and are detected by a single-pulse counting technique. The intensity of a particular mass-selected negative ion is then recorded as a function of the electron

[*] Prof. Dr. E. Illenberger
Institut für Chemie – Physikalische und Theoretische Chemie
Freie Universität Berlin
Takustrasse 3, 14195 Berlin (Germany)
Fax: (+49) 30-838-55378
E-mail: iln@chemie.fu-berlin.de

S. Ptasinska, S. Denifl, P. Scheier, Prof. Dr. T. D. Märk^[†]
Institute for Ion Physics and Center for Molecular Biosciences
Universität Innsbruck
Technikerstrasse 25, 6020 Innsbruck (Austria)

[†] Also Adjunct Professor at Department of Experimental Physics
Comenius University, 84248 Bratislava (Slovakia).

[**] Financial support from the FWF (Vienna), the EU commission (Brussels) through the EPIC Network, and the DFG (Bonn) is gratefully acknowledged.

energy. The electron energy scale is calibrated using the well-known Cl^-/CCl_4 signal near 0 eV. Methylated thymine and uracil were purchased from Sigma-Aldrich at a stated purity of 98 %.

Figure 1 shows the loss of a neutral hydrogen atom from thymine methylated at the N1 position (m1T) compared to

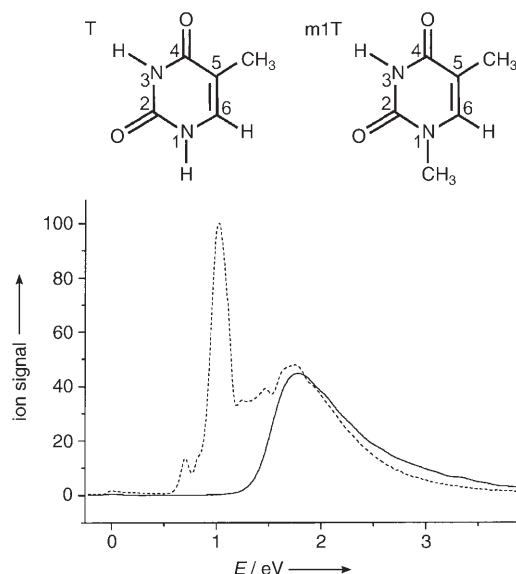


Figure 1. Plot of the ion yield of the fragment ion $(M-H)^-$ (loss of a hydrogen atom) from thymine methylated at the N1 position (m1T, —) with that of thymine (T, ----). E = electron energy.

the yield from (non-methylated) thymine (T), in both cases by measuring the yields of the corresponding anions $(M-H)^-$ [Eq. (1)]. For a detailed interpretation of these results we have to recall a previous study on thymine deuterated at the C positions^[5] which demonstrated that hydrogen loss at sub-excitation energies occurs exclusively at the N positions. Figure 1 directly shows that in m1T hydrogen loss is completely suppressed below 1.4 eV, and we consequently assign the smooth feature peaking at 1.8 eV to H loss from the N3 position. H loss is hence not only exclusively restricted to the N–H bonds, it can further be made site selective by tuning the electron energy.

Accordingly, uracil methylated at the N3 position (m3U) shows a nearly complementary behavior (Figure 2); in other words, hydrogen loss primarily occurs within the sharp feature at 1.0 eV, which we consequently assign to H loss from the N1 site. It should be noted that the relative shape of the ion yields due to H loss in T and U are virtually identical (as is also apparent from the spectra for T and U in Figure 1 and Figure 2, respectively). While in m3U some intensity on the $(M-H)^-$ signal (N1–H loss) remains above 1.4 eV, that in m1T (N3–H loss) below 1.4 eV is completely suppressed. This complete site selectivity for N1–H loss is a result of the corresponding energy threshold, which we shall briefly consider.

The threshold E_0 for the DEA reaction [Eq. (1)] is given by Equation (2), in which D is the corresponding bond

$$E_0 = D - EA(M-H) \quad (2)$$

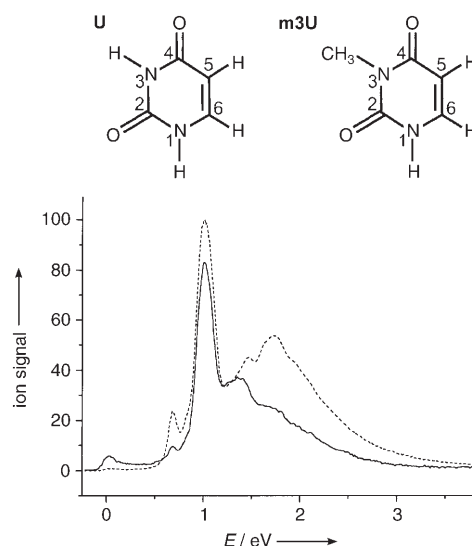


Figure 2. Plot of the ion yield of the fragment ion $(M-H)^-$ (loss of a hydrogen atom) from uracil methylated at the N3 position (m3U, —) with that of uracil (U, ----). E = electron energy.

dissociation energy $((N-H)/(C-H))$ and $EA(M-H)$ is the electron affinity of the radical formed by the loss of H from the particular site. E_0 refers to the energy threshold of the reaction at 0 K. The experimental threshold energy (the appearance energy of $(M-H)^-$) can be different from E_0 as a result of two main effects: 1) the transient negative ion is formed by means of a Franck–Condon transition, which can be viewed as the activation energy for the DEA reaction with the tendency that the fragment ion is observed above E_0 ; and 2) the internal energy of the target molecule tends to lower the appearance energy.

Since there are no experimental numbers available for the different C–H and N–H bond dissociation energies in the nucleobases, we refer to recent high-level ab initio studies on T and U. With the G2MP2 method the following data were calculated for thymine:^[6] $D(N1-H) = 4.4$ eV/ $EA(T-H) = 3.5$ eV; $D(N3-H) = 5.8$ eV/ $EA(T-H) = 4.5$ eV; $D(CH_2-H) = 4.5$ eV/ $EA(T-H) = 2.9$ eV; $D(C6-H) = 4.9$ eV/ $EA(T-H) = 2.7$ eV. From that the following energetic thresholds are obtained: $E_0(N1-H) = 0.9$ eV, $E_0(N3-H) = 1.3$ eV, $E_0(CH_2-H) = 1.6$ eV, and $E_0(C6-H) = 2.2$ eV.

In U the corresponding numbers are (also calculated with the G2MP2 method^[2]): $D(N1-H) = 4.4$ eV/ $EA(U-H) = 3.6$ eV; $D(N3-H) = 5.4$ eV/ $EA(U-H) = 4.0$ eV; $D(C5-H) = 5.2$ eV/ $EA(U-H) = 2.5$ eV; $D(C6-H) = 5.0$ eV/ $EA(U-H) = 2.8$ eV leading to the following energy thresholds: $E_0(N1-H) = 0.8$ eV, $E_0(N3-H) = 1.4$ eV, $E_0(C5-H) = 2.7$ eV, and $E_0(C6-H) = 2.2$ eV.

On this basis, we arrive at the following conclusions:

- Although H loss from the C sites is energetically accessible above 1.6 eV it is not observed within the entire resonant feature extending to more than 3 eV.
- At energies below 1.4 eV the loss of H occurs exclusively from the N1 position, since the competing channel (loss from N3) is energetically only accessible above 1.4 eV.
- At energies above 1.4 eV hydrogen loss takes place from both the N1 and N3 positions.

The fact that H loss from N1 occurs preferentially at low energy (1 eV) with respect to the range above 1.4 eV may be due to the different mechanisms contributing to reaction (1). Owing to the large dipole moment of uracil (≈ 4.5 D), it was recently proposed that a dipole-bound (DB) state could act as a doorway state for DEA.^[13] Supported by ab initio calculations, the sharp peak at 1 eV was assigned as a dipole-bound vibrational Feshbach resonance (exciting three quanta of the N1-H stretch mode), which couples to the repulsive σ^* (N1-H) valence state. The underlying broader feature would then be due to the π_2^* shape resonance,^[14] which can lead to DEA through vibronic mixing of the π states with the repulsive σ^* anion states. The overall DEA reaction is then more effective via the initial DB state in comparison to the initial π^* shape resonance leading to the dominant peak at 1 eV.

The fact that the loss of CH_3 is not observed when N1-H is replaced by N1- CH_3 has significant consequences for the molecular description of strand breaks by low-energy electrons. In a recent theoretical study^[15] (modeling a section of DNA containing cytosine, the sugar ring, and the (neutralized) phosphate group), a low-lying anionic curve was predicted which connects the initial π^* anion state of the base to a σ^* state in the backbone. An electron captured by a DNA base may thereby be transferred to the backbone, which may lead to rupture of the C-O bond between the phosphate and the sugar. In DNA the N1 position is coupled to the sugar moiety, and according to the present findings transfer of charge and energy via the N1-C bond will not take place. This is also strongly supported by very recent gas-phase experiments^[16] on thymidine (representing thymine coupled to a sugar moiety) which definitely exclude the transfer of electrons initially localized on thymine to the sugar moiety.

We therefore conclude that the direct migration of the excess charge from the π^* anions of the nucleobases to the DNA backbone can be excluded as a mechanism leading to strand breaks. Instead electrons near 2 eV induce H loss at N3, which, in a biological environment, may initiate further reactions eventually leading to strand breaks. In addition, experiments on isolated deoxyribose show effective low-energy DEA processes.^[17] If these DEA reactions are preserved for deoxyribose coupled within the DNA network, such processes will be of considerable importance for strand breaks.

Received: June 13, 2005

Published online: October 5, 2005

Keywords: anions · dissociative electron attachment · DNA damage · gas-phase reactions · nucleobases

- [6] S. Denifl, S. Ptasinska, M. Probst, J. Hrusak, P. Scheier, T. D. Märk, *J. Phys. Chem. A* **2004**, *108*, 6562.
- [7] C. Daniel, J. Full, L. Gonzales, C. Lupulescu, J. Manz, A. Merli, S. Vajda, L. Woeste, *Science* **2003**, *299*, 536.
- [8] C. von Sonntag, *The Chemical Basis for Radiobiology*, Taylor and Francis, London, **1987**.
- [9] J. F. Ward in *Advances in Radiobiology* 5 (Eds.: J. T. Lett, H. Adler), Academic Press, New York, **1977**, pp. 181–239.
- [10] J. A. La Verne, S. M. Pimblott, *Radiat. Res.* **1995**, *141*, 208.
- [11] B. Boudaiffa, P. Cloutier, D. Hunting, M. A. Huels, L. Sanche, *Science* **2000**, *287*, 1658.
- [12] D. Muigg, G. Denifl, A. Stamatovic, T. D. Märk, *Chem. Phys.* **1998**, *239*, 409.
- [13] A. M. Scheer, K. Aflatooni, G. A. Gallup, P. D. Burrow, *Phys. Rev. Lett.* **2004**, *92*, 068102.
- [14] K. Aflatooni, G. A. Gallup, P. D. Burrow, *J. Phys. Chem. A* **1998**, *102*, 6205.
- [15] J. Berdys, I. Anusiewicz, O. Skurski, J. Simons, *J. Am. Chem. Soc.* **2004**, *126*, 6441.
- [16] S. Ptasinska, S. Denifl, P. Scheier, E. Illenberger, T. D. Märk, unpublished results.
- [17] S. Ptasinska, S. Denifl, P. Scheier, T. D. Märk, *J. Chem. Phys.* **2004**, *120*, 8505.

[1] F. Martin, P. D. Burrow, Z. Cai, P. Cloutier, D. Hunting, L. Sanche, *Phys. Rev. Lett.* **2004**, *93*, 068101.

[2] G. Hanel, S. Denifl, P. Scheier, M. Probst, B. Farizon, M. Farizon, E. Illenberger, T. D. Märk, *Phys. Rev. Lett.* **2003**, *90*, 188104.

[3] S. Denifl, S. Ptasinska, M. Cingel, S. Matejcik, P. Scheier, T. D. Märk, *Chem. Phys. Lett.* **2003**, *377*, 74.

[4] R. Abouaf, J. Pommier, H. Dunet, *Int. J. Mass Spectrom.* **2003**, *226*, 397.

[5] S. Gohlke, H. Abdoul-Carime, E. Illenberger, *Phys. Rev. Lett.* **2004**, *92*, 168103.

Optical Switches

DOI: 10.1002/anie.200501573

**Multiple Switching and Photogated
Electrochemiluminescence Expressed by a
Dihydroazulene/Boron Dipyrromethene Dyad****

Christian Trieflinger, Holger Röhr, Knut Rurack, and
Jörg Daub**

Optical signal generation, control, and transduction are key processes in natural and technological systems that essentially rely on fast and efficient processing of information.^[1]

[*] Dr. C. Trieflinger, Prof. J. Daub
Institut für Organische Chemie
Universität Regensburg
Universitätsstrasse 31, 93053 Regensburg (Germany)
Fax: (+49) 941-943-4984
E-mail: joerg.daub@chemie.uni-regensburg.de
Dipl.-Phys. H. Röhr, Dr. K. Rurack
Div. I.3
Bundesanstalt für Materialforschung und -prüfung (BAM)
Richard-Willstätter-Strasse 11, 12489 Berlin (Germany)
Fax: (+49) 30-8104-5005
E-mail: knut.rurack@bam.de
Dipl.-Phys. H. Röhr
Associated with: Fachbereich Biologie, Chemie, Pharmazie
Freie Universität Berlin

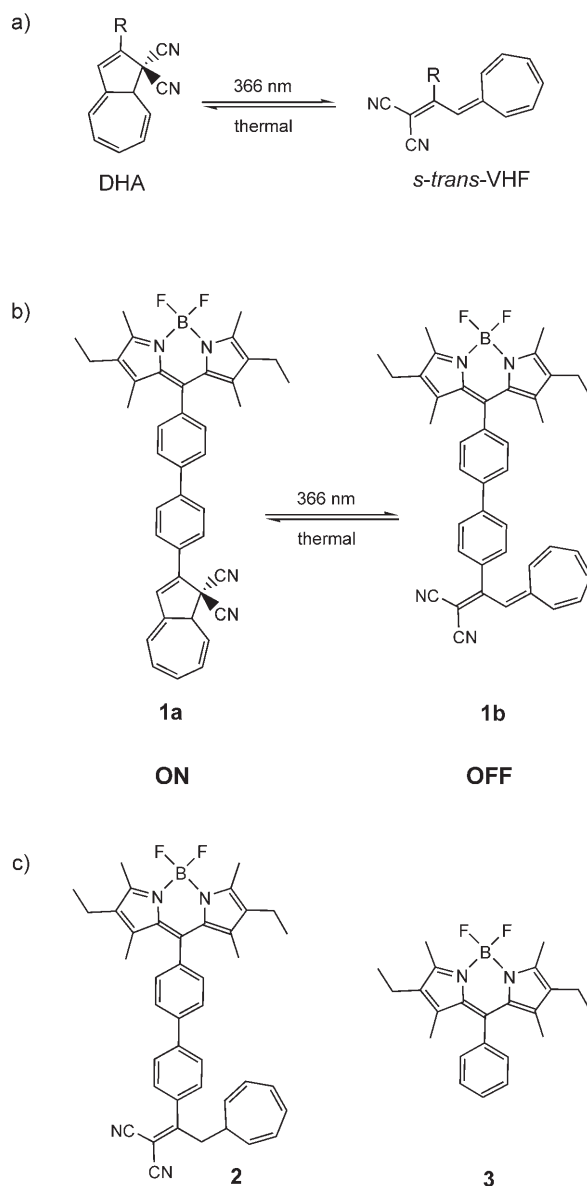
[**] This research was supported by the German Research Foundation (DFG), the German National Academic Foundation (C.T.), and BAM's PhD program (H.R.). This work is part of the Graduate College "Sensory Photoreceptors in Natural and Artificial Systems" supported by the DFG (GRK 640, University of Regensburg).

Prominent examples in nature are the vision process, phototropism, photomorphogenesis, and circadian rhythms where the response to light is realized by a variety of enzymatic photoreceptors, including rhodopsins, phototropins, phytochromes, cryptochromes, and BLUF domains.^[2] All of these photoreceptors rely on a functional chromophore as the photoactive element, which initiates a highly sophisticated signaling cascade with, for example, an electron transfer or a photochromic reaction as the primary step after light absorption.

In studying these biological systems chemists have recognized the superiority of signal processing by light in terms of velocity and efficiency, and they have strived to use light-driven and -controlled processes in artificial chromophoric ensembles at the molecular level for technological purposes such as molecular electronics and photonics, and artificial photosynthesis. Especially photochromic compounds have gained strong popularity here, for instance, in high-density optical data storage and multimode photoswitching.^[3] Using light as a trigger medium and as a tool for readout, the latter typically by fluorescence, offers the advantages of the non-destructive control and processing of information. However, up to now, only a few systems that show photochromically modulated luminescence have been realized, and the efficiency of the modulation and the overall brightness of the systems is often rather poor.^[4] Furthermore, to our knowledge, a photochromic ensemble in which the switching states are photocontrolled but the luminescence readout signal can be sampled by either optical or electrochemical excitation, i.e., by photo- or electrochemiluminescence (ECL), has not yet been reported. The latter feature would be a key link between OLEDs (organic light-emitting diodes) and conventional optical-gate technologies.

We realized our aim of a bright photochromic luminescent switch that can be either photo- or electrochemically excited by combining the photochromic system dihydroazulene/vinylheptafulvene (DHA/VHF; Scheme 1 a) with the boron dipyrromethene (BDP) fluorophore in dyad **1** (Scheme 1 b; for synthetic details see the Supporting Information). The DHA/VHF system shows UV/Vis photochromism that is particularly suitable for our present purposes and has been employed successfully in various molecular switches.^[5] The photochromic conversion of the alternant π system DHA into the non-alternant VHF occurs by means of a 10-electron rearrangement of the carbon framework, which strongly influences the electronic properties of the substituents attached to the photochromic system.^[6] The BDP chromophore provides favorable signaling features, as BDPs show green emission of high brightness and are also fluorophores that display photogenerated as well as electrochemically generated luminescence.^[7] Furthermore, the spectral and redox properties of both subunits complement each other well for the intended performance.

UV/Vis-spectrophotometric measurements of **1a** in chloroform clearly reveal the independence of both subchromophores, with main bands centered at 376 nm for the DHA and 527 nm for the BDP moiety (Table 1, Figure 1). The substantial difference between the lowest energy absorptions of DHA and BDP guarantees exclusive excitation of the



Scheme 1. The photochromic system dihydroazulene/vinylheptafulvene DHA/VHF (a) is combined with the fluorophore boron dipyrromethene (BDP) to give dyads **1a** and **1b** (b). The nonswitchable derivative **2** and the model fluorophore **3** (c) were used in control experiments.

Table 1: Absorption (in CHCl_3) and redox data (in MeCN) of **1a** and **1b** (E in mV vs. Fc^+/Fc).

	λ_{abs} [nm] ([lg(ϵ)]/[lg($\text{M}^{-1}\text{cm}^{-1}$)])	$E_{1/2}^{\text{red}}$ [mV]	$E_{\text{p}}^{\text{red}}$ [mV]	$E_{1/2}^{\text{ox}}$ [mV]	E_{p}^{ox} [mV]
1a	527 (4.86), 376 (4.60)	−1615	−1920	615	1025
1b	527 (4.90), 495 (4.69)	−1610	−1325	630	760

readout module, the BDP fluorophore, without initiating the “write-in process”, the photoreaction of DHA. Cyclic voltammetry supports these findings. The reversible reduction ($E_{1/2} = -1615$ mV vs. Fc^+/Fc) and oxidation ($E_{1/2} = +615$ mV vs. Fc^+/Fc) of BDP and the irreversible reduction ($E_{\text{p}} = -1920$ mV vs. Fc^+/Fc) and oxidation of DHA ($E_{\text{p}} =$

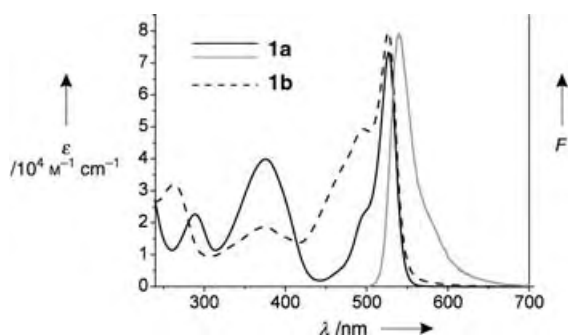


Figure 1. Absorption and emission spectra of **1a** and absorption spectrum of **1b** in CH_2Cl_2 ($c = 5 \times 10^{-6} \text{ M}$).

+1025 mV vs. Fc^+/Fc) are centered in the expected potential regions thus indicating electronically decoupled ground states.^[5d,7b] After excitation of **1a** in dichloromethane at $\lambda > 500 \text{ nm}$, the typical BDP emission with a maximum at 540 nm, a fluorescence quantum yield of 0.67, and a single exponential decay time of 4.06 ns is observed (Figure 2). Changing the

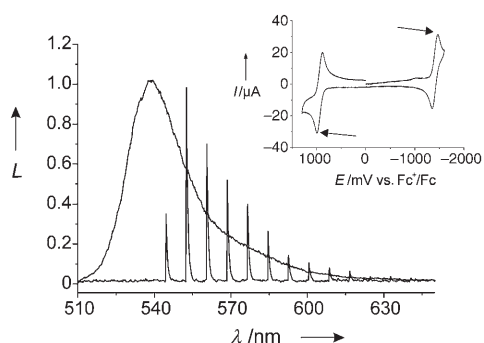


Figure 2. Emission spectrum of **1a** ($c = 1 \times 10^{-6} \text{ M}$) in CH_2Cl_2 . Discrete signals: ECL spectrum of **1a** ($c = 1 \times 10^{-3} \text{ M}$) in acetonitrile/0.2 M Bu_4NPF_6 . Applied potentials are marked in the cyclic voltammogram in the inset.^[8]

polarity of the solvent does not alter the spectroscopic properties significantly (Table 2). Furthermore, as the potential separation of BDP reduction and oxidation ($\Delta E_{\text{ox-red}} \approx 2.30 \text{ mV}$) is also sufficient to populate the excited state of the BDP in **1a** electrochemically, the dyad shows electro-

Table 2: Fluorescence properties of **1a**, **1b**, and **2**.

	Solvent	$\Phi_f^{[a]}$	$\tau_f [\text{ns}]^{[b]}$
1a	$\text{MeCN}^{[c]}$	0.62	3.96
	$\text{CH}_2\text{Cl}_2^{[d]}$	0.67	4.06
	$\text{Et}_2\text{O}^{[e]}$	0.66	3.87
1b	$\text{MeCN}^{[c]}$	0.01	0.03
	$\text{CH}_2\text{Cl}_2^{[d]}$	0.01	0.02
	$\text{Et}_2\text{O}^{[e]}$	0.01	0.03
2	$\text{MeCN}^{[c]}$	0.16	0.88
	$\text{CH}_2\text{Cl}_2^{[d]}$	0.27	1.72
	$\text{Et}_2\text{O}^{[e]}$	0.67	4.13

[a] Relative to fluorescein 27 in 0.1 N NaOH (0.90 ± 0.03),^[14] $\pm 5\%$ (**1a**, **2**) $\pm 15\%$ (**1b**). [b] At 298 K, $\pm 0.003 \text{ ns}$. [c] $\lambda_{\text{abs}}/\lambda_{\text{em}} = 523/536 \text{ nm}$. [d] $\lambda_{\text{abs}}/\lambda_{\text{em}} = 526/540 \text{ nm}$. [e] $\lambda_{\text{abs}}/\lambda_{\text{em}} = 524/536 \text{ nm}$.

chemiluminescence (ECL) (Figure 2, discrete signals).^[8] The strong fluorescence emission and electrochemically generated luminescence let us thus define **1a** as the ON state of the system.

Irradiation of **1a** at 366 nm induces the uniform photo-conversion to **1b**, which is apparent from the isosbestic points, the decrease of the band at 376 nm, and the appearance of a new band at 476 nm in the absorption spectrum (Figure 1). The BDP absorption remains virtually unaffected, stressing the fact that both modules of dyad **1b** are also decoupled in the ground state. Again, cyclic voltammetry provides support: the BDP reduction ($E_{1/2} = -1610 \text{ mV}$ vs. Fc^+/Fc) and oxidation ($E_{1/2} = +630 \text{ mV}$ vs. Fc^+/Fc) are negligibly shifted relative to values for **1a**. Moreover, the typical irreversible reduction ($E_p = -1325 \text{ mV}$ vs. Fc^+/Fc) and oxidation ($E_p = +760 \text{ mV}$ vs. Fc^+/Fc) of the VHF unit of **1b** are found at far lower potentials than those of DHA in **1a**.^[3c,5d] Photoconversion of **1a** to **1b** occurs with a quantum yield of ca. 0.01. This is quite low in comparison to other DHA/VHF systems and can be attributed to an overlap of the oscillator-weak $S_2 \leftarrow S_0$ transition localized on BDP^[7e] and the intense $S_1 \leftarrow S_0$ transition of DHA. Furthermore, analysis of the fluorescence excitation spectra revealed that despite the very weak fluorescence of DHA at room temperature ($\Phi_f \approx 10^{-4}$),^[6a] energy transfer from DHA to BDP might play an additional, competitive role here. The OFF state **1b** is thermally reconverted to **1a** with $t_{1/2} = 350 \text{ min}$ at room temperature.

In contrast to **1a**, **1b** shows a strongly reduced, typical green BDP emission upon excitation at $\lambda > 500 \text{ nm}$.^[9] Φ_f drops remarkably from 0.67 to 0.013 (Figure 3) and the fluorescence

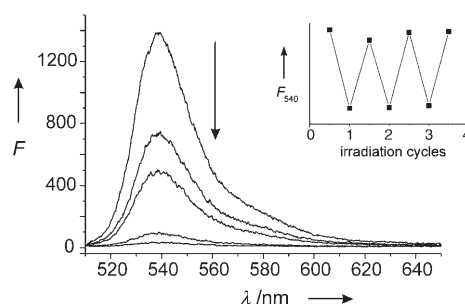


Figure 3. Change of the emission intensity during the photoreaction of **1a** ($c = 1 \times 10^{-6} \text{ M}$ in CH_2Cl_2) to **1b** with excitation of the BDP at 505 nm. Inset: Reversibility of the switch as shown by several cycles of irradiation and back-reaction.

lifetime is shorter (Table 2). The quenching mechanism can be rationalized in terms of intramolecular fluorescence resonance energy transfer (FRET). The broad absorption spectrum of the VHF fragment, which stretches well beyond 550 nm,^[6] and the narrow emission band of the BDP unit, centered between 530 and 540 nm, show considerable overlap. Analysis of the FRET process and its features yields a spectral overlap integral $J = 2.6 \times 10^{14} \text{ M}^{-1} \text{ cm}^{-1}$ and an effective interaction radius $R_0 = 39 \text{ \AA}$.^[10] Assuming that no other processes contribute significantly to the deactivation of the excited state of the BDP, we calculate the donor–acceptor distance of the FRET partners to be 15.1 \AA ,^[11] which

corresponds within $\pm 0.2 \text{ \AA}$ to the distance between the BDP core and the center of the VHF unit as obtained for the ground-state geometry optimized by semiempirical AM1 calculations. Moreover, the absence of solvatokinetic behavior of **1b**, that is, that the quenching process is not significantly accelerated upon increasing the polarity of the solvent, led us to assume that photoinduced electron transfer (PET) plays a negligible role here. Control experiments with **2**, where the DHA/VHF moiety has been replaced with a nonswitchable dihydro-VHF group that isolates the *p*-dicyanovinylbiphenyl from the cycloheptatrienyl fragment (Scheme 1c), support these findings. The spectral characteristics of the BDP fluorophore in **2** are very similar to those of **1a/1b** (Table 2). Furthermore, the fluorescence of **2** in nonpolar solvents is as bright as that of **1a**. Upon increasing solvent polarity, a slight quenching of the BDP emission in **2** is observed. The latter is apparently connected to the moderate PET activity of the *para*-cyanovinylbiphenyl group,^[12] emphasizing the fact that the entire VHF unit is mandatory for the performance of **1b**. As expected, after the photoreaction to **1b**, the latter remains ECL-silent, and **1b** thus represents the OFF state of the system.

In conclusion, we have presented a photochromic pair of BDP-DHA/VHF dyads as a versatile all-optically controllable switch, for which irradiation with near-UV light serves as the input and luminescence at 540 nm as the output. Furthermore, the readout signal of the ON state **1a** can be generated by conventional photoexcitation as well as electrochemically; in other words, the system shows photogated electrochemiluminescence. Light-induced conversion of **1a** to **1b** is accompanied by a 50-fold decrease of luminescence, defining the system as a true ON/OFF photoswitch. We have demonstrated here that the outstanding photo- and electrochemical properties of both modules, DHA/VHF and BDP, can be combined synergistically for highly interesting all-optical photochromic molecular switches. The ECL findings also indicate potential applications in gated organic light-emitting diodes (OLEDs).^[13]

Received: May 9, 2005

Published online: October 10, 2005

Keywords: boron dipyrromethene · electrochemiluminescence · fluorescence · molecular switches · photochromism

- [1] a) M. A. van der Horst, K. J. Hellingwerf, *Acc. Chem. Res.* **2004**, *37*, 13–20; b) F. M. Raymo, *Adv. Mater.* **2002**, *14*, 401–414; c) J.-M. Lehn, *Proc. Natl. Acad. Sci. USA* **2002**, *99*, 4763–4768; d) A. P. de Silva, N. D. McClenaghan, *Chem. Eur. J.* **2004**, *10*, 574–586.
- [2] a) R. R. Rando, *Chem. Rev.* **2001**, *101*, 1881–1896; b) W. R. Briggs, E. Huala, *Annu. Rev. Cell Dev. Biol.* **1999**, *15*, 33–62; c) A. R. Cashmore, J. A. Jarillo, Y. L. Wu, D. M. Liu, *Science* **1999**, *284*, 760–765; d) Y. Han, S. Braatsch, L. Osterloh, G. Klug, *Proc. Natl. Acad. Sci. USA* **2004**, *101*, 12306–12311.
- [3] a) M. Irie, *Chem. Rev.* **2000**, *100*, 1683; b) J.-M. Lehn, *Supramolecular Chemistry*, VCH, Weinheim, **1995**, pp. 124–138; c) J. Daub, J. Salbeck, T. Knöchel, C. Fischer, H. Kunkely, K. M. Rapp, *Angew. Chem.* **1989**, *101*, 1541–1542; *Angew. Chem. Int. Ed. Engl.* **1989**, *28*, 1494–1496.

- [4] a) G. M. Tsivgoulis, J.-M. Lehn, *Angew. Chem.* **1995**, *107*, 1188–1191; *Angew. Chem. Int. Ed. Engl.* **1995**, *34*, 1119–1122; b) N. P. M. Huck, B. L. Feringa, *J. Chem. Soc. Chem. Commun.* **1995**, 1095–1096; c) H. Spreitzer, J. Daub, *Liebigs Ann.* **1995**, 1637–1641; d) J. Daub, M. Beck, A. Knorr, H. Spreitzer, *Pure Appl. Chem.* **1996**, *68*, 1399–1404; e) T. Inada, S. Uchida, Y. Yokoyama, *Chem. Lett.* **1997**, 321–322; f) A. Fernandez-Acebes, J.-M. Lehn, *Adv. Mater.* **1998**, *10*, 1519–1522; g) S. Tsuchiya, *J. Am. Chem. Soc.* **1999**, *121*, 48–53; h) J. M. Endtner, F. Effenberger, A. Hartschuh, H. Port, *J. Am. Chem. Soc.* **2000**, *122*, 3037–3046; i) T. B. Norsten, N. R. Branda, *J. Am. Chem. Soc.* **2001**, *123*, 1784–1785; j) V. W.-W. Yam, C.-C. Ko, N. Zhu, *J. Am. Chem. Soc.* **2004**, *126*, 12734–12735.
- [5] a) H. Spreitzer, J. Daub, *Chem. Eur. J.* **1996**, *2*, 1150–1158; b) J. Achatz, C. Fischer, J. Salbeck, J. Daub, *J. Chem. Soc. Chem. Commun.* **1991**, 504–507; c) L. Gobbi, P. Seiler, F. Diederich, V. Gramlich, *Helv. Chim. Acta* **2000**, *83*, 1711–1723; d) T. Mrozek, J. Daub, A. Ajayaghosh in *Molecular Switches* (Ed.: B. L. Feringa), Wiley-VCH, Weinheim, **2001**, pp. 63–106; e) J. Daub, C. Trieflinger, O. Kushnir, R. Prochazka, *Mol. Cryst. Liq. Cryst.* **2005**, *430*, 115–122.
- [6] a) H. Görner, C. Fischer, S. Gierisch, J. Daub, *J. Phys. Chem.* **1993**, *97*, 4110–4117; b) J. Ern, M. Petermann, T. Mrozek, J. Daub, K. Kuldová, C. Kryschi, *Chem. Phys.* **2000**, *259*, 331–337; c) V. De Waele, U. Schmidhammer, T. Mrozek, J. Daub, E. Riedle, *J. Am. Chem. Soc.* **2002**, *124*, 2438–2439.
- [7] a) J. Karolin, L. B.-A. Johansson, L. Strandberg, T. Ny, *J. Am. Chem. Soc.* **1994**, *116*, 7801–7806; b) M. Kollmannsberger, T. Gareis, S. Heinl, J. Breu, J. Daub, *Angew. Chem.* **1997**, *109*, 1391–1393; *Angew. Chem. Int. Ed. Engl.* **1997**, *36*, 1333–1335; c) J. Daub, K. Kelnhofer, T. Gareis, A. Knorr, M. Kollmannsberger, Y.-H. Tak, H. Bässler, *Polym. Prepr. Am. Chem. Soc. Div. Polym. Chem.* **1997**, *38*, 339–340; d) R. Y. Lai, A. J. Bard, *J. Phys. Chem. B* **2003**, *107*, 5036–5042; e) P. Toebe, H. Zhang, C. Trieflinger, J. Daub, M. Glasbeek, *Chem. Phys. Lett.* **2003**, *368*, 66–75.
- [8] The ECL measurements were carried out with an unstirred solution ($c = 1 \times 10^{-3} \text{ M}$; supporting electrolyte: 0.1 M Bu₄NPF₆) in an electrochemical cell: Stefan Hien, PhD Thesis, University of Regensburg, **1995**. The potential was switched with alternation between the oxidation and reduction potentials (see inset of Figure 2, electrochemical switching frequency 1 s^{-1} , scan rate of the spectrometer: 240 nm min^{-1}). The spectrum consisting of discrete signals is the result of the relatively slow switching frequency. The bathochromic shift of ca. 20 nm between the fluorescence and the ECL spectrum is well known and can be attributed to reabsorption effects as a result of the higher dye concentration used in the ECL experiment and the different dielectric properties of the supporting electrolyte.
- [9] VHF was reported to be entirely nonfluorescent, see ref. [6a].
- [10] For a description of the analysis of FRET processes, see P. Wu, L. Brand, *Anal. Biochem.* **1994**, *218*, 1–13. The following equations apply: $k_{\text{FRET}} = (1/\tau_{\text{D}})(R_0/r)^6$ with r being the distance between the FRET partners and τ_{D} the lifetime of the unperturbed donor **3** (5.15 ns in CH₂Cl₂). $R_0^6 = 8.875 \times 10^{-5} (\kappa^2 \Phi_{\text{D}} J/n^4)$ mit $J = \int F_{\text{D}}(\lambda) \epsilon_{\text{A}}(\lambda) \lambda^4 d\lambda$, where J is the overlap integral between the fluorescence of the donor (i.e. **3** in CH₂Cl₂) and the absorption of the acceptor, obtained after deconvolution of the absorption spectrum of **1b**, $\kappa^2 = 2/3$ is a geometry factor for random orientation of the two subunits, Φ_{D} is the fluorescence quantum yield of the unperturbed donor (here, for model **3**: $\Phi_{\text{D}} = 0.95$ in CH₂Cl₂), and n is the refractive index of the solvent.
- [11] If no other deactivation processes are present, k_{FRET} can be also expressed as $k_{\text{FRET}} = (1/\tau_{\text{DA}}) - (1/\tau_{\text{D}})$ with τ_{DA} being the fluorescence lifetime of the FRET ensemble. By combining the equations in refs.[10] and [11] one may calculate a value for r .

- [12] J. Aihara, K. Araya, K. Chiba, Y. Matsunaga, *Adv. Mol. Relax. Interact. Processes* **1980**, 18, 199–210.
- [13] K. Kelnhofer, A. Knorr, Y.-H. Tak, H. Bässler, J. Daub, *Acta Polym.* **1997**, 48, 188–192.
- [14] J. Olmsted III, *J. Phys. Chem.* **1979**, 83, 2581–2584.

Peroxo Complexes

DOI: 10.1002/anie.200501615

Rhodium-Mediated Formation of Peroxides from Dioxygen: Isolation of Hydroperoxo, Silylperoxo, and Methylperoxo Intermediates**

Marcel Ahijado, Thomas Braun,* Daniel Noveski, Nikolaus Kocher, Beate Neumann, Dietmar Stalke, and Hans-Georg Stammer

Peroxo and hydroperoxo transition-metal complexes have been suggested to play a key role as intermediates in several oxygenation processes with molecular oxygen, including reactions mediated by cytochrome P450, the catalytic oxidation of olefins, and the generation of peroxides.^[1,2] A hydroperoxo ligand can also be found in oxyhemerythrin which is produced when dioxygen is bound at the nonheme oxygen carrier hemerythrin.^[3] The oxygen atoms of η^2 -bound peroxo ligands at electron-rich transition metals are usually nucleophilic.^[4] This is reflected in the formation of hydrogen peroxide or trityl peroxide from η^2 -peroxo complexes and the corresponding electrophilic sources (trityl = triphenylmethyl).^[4–6] Hydroperoxo and alkylperoxo complexes are thought to be intermediates in these reactions, but there is extremely little precedent on their identification.^[4,7] The conversion of coordinated oxygen into an OOR ligand (R = alkyl, H) can be considered to be one of the key steps in these transformations, but even model reactions for the formation of oxygen-derived hydroperoxo and alkylperoxo species are very sparse.^[2a,4,7–9] Stahl et al. showed that protonation of palladium η^2 -peroxo species, bearing N-heterocyclic carbene ligands, with acetic acid leads to η^1 -hydroperoxo compounds, which can be further protonated to give hydrogen peroxide.^[7]

The presence of the η^1 -hydroperoxo complex and of its ^{18}O -labeled isotopologue has been confirmed by comparison of the mass spectrometric data with simulated spectra. Otsuka et al. reported that the reaction of $[\text{Pt}(\text{O}_2)(\text{PR}_3)_2]$ (R = Ph, Cy) with BrCPh_3 leads to the tritylperoxo complexes $[\text{PtBr}(\text{OOCPh}_3)(\text{PR}_3)_2]$.^[4] These complexes can be converted into $\text{Ph}_3\text{COOCPh}_3$ and are presumably stabilized kinetically by the steric bulk of the trityl group. Moro-oka et al. found that a rhodium η^2 -peroxo complex can be protonated with pyrazole.^[9] The hydroperoxo species obtained is stabilized by a hydrogen bond between a pyrazole ligand and the β -oxygen in the hydroperoxo ligand. No further reactivity of this compound has been reported.

In this communication we report on the sequential conversion of molecular oxygen into hydrogen peroxide as well as into silyl and methyl peroxides via η^1 -hydroperoxo, η^1 -silylperoxo, and η^1 -methylperoxo complexes. Not only the isolation of the intermediate species bearing an OOSiMe_3 or OOMe ligand is unprecedented, but also η^1 -silylperoxo and η^1 -methylperoxo complexes have for the first time been unambiguously characterized by IR spectroscopy and X-ray crystallography. The stabilizing effect of a tetrafluoropyridyl ligand bound at rhodium^[10] presumably allows the isolation of the intermediates.

Exposure of a hexane solution of the tetrafluoropyridyl complex **1**^[10] to air or oxygen slowly leads to the generation of the dioxygen compound **2a** within hours (Scheme 1). Similarly, treatment of **1** with $^{18}\text{O}_2$ gives the peroxo complex $\text{trans}[\text{Rh}(^{18}\text{O}_2)(4\text{-C}_5\text{F}_4\text{N})(\text{CNtBu})(\text{PEt}_3)_2]$ (**2b**). Note that Selke et al. reported the formation of the complex $\text{trans}[\text{Rh}(\text{SC}_6\text{F}_5)(\text{O}_2)(\text{CO})(\text{PPh}_3)_2]$, which is unstable at room temperature, using singlet oxygen.^[11] In contrast, the formation of **2a** and **2b** is spin-forbidden and requires a triplet–singlet surface crossing on the reaction coordinate.^[12] The ^{19}F NMR spectrum of **2a** displays four signals for the tetrafluoropyridyl ligand indicating hindered rotation (Table 1).^[10] The rhodium–phosphorus coupling constant of 87 Hz in the ^{31}P NMR spectrum suggests the formation of a rhodium(III) complex. In the IR spectrum of **2a** an absorption band at 852 cm^{-1} can be detected. The band shifts to 805 cm^{-1} for the ^{18}O -labeled isotopologue **2b** and can be assigned unequivocally to the O–O stretching vibration of the η^2 -peroxo ligand.^[9,13] The difference $\Delta\tilde{\nu} = 47\text{ cm}^{-1}$ is fully consistent with a simple model for a diatomic harmonic oscillator.^[14]

Figure 1 shows the molecular structure of **2a** determined by X-ray crystallography.^[15] The molecule exhibits a distorted octahedral structure, if the oxygen is treated as a bidentate ligand. Alternatively if the dioxygen is treated as occupying a single coordination site, the structure is approximately trigonal-bipyramidal with two phosphine ligands occupying the axial sites. The O–O distance of $1.452(3)\text{ \AA}$ is similar to the corresponding bond length found in $\text{cis}[\text{Rh}(\text{CF}_3)(\text{O}_2)(\text{CNXy})_2(\text{PPh}_3)]$ ($1.438(3)\text{ \AA}$; $\text{Xy} = 2,6\text{-Me}_2\text{C}_6\text{H}_3$) and is also in the same range as these observed in other rhodium η^2 -peroxo complexes.^[16] Treatment of complex **2a** with a solution of HCl in Et_2O affords the dichloro compound **4** and H_2O_2 (Scheme 1). Low-temperature NMR experiments at 213 K reveal the formation of **3** as the initial product. A broad signal in the ^1H NMR spectrum at $\delta = 7.35\text{ ppm}$ can be attributed to

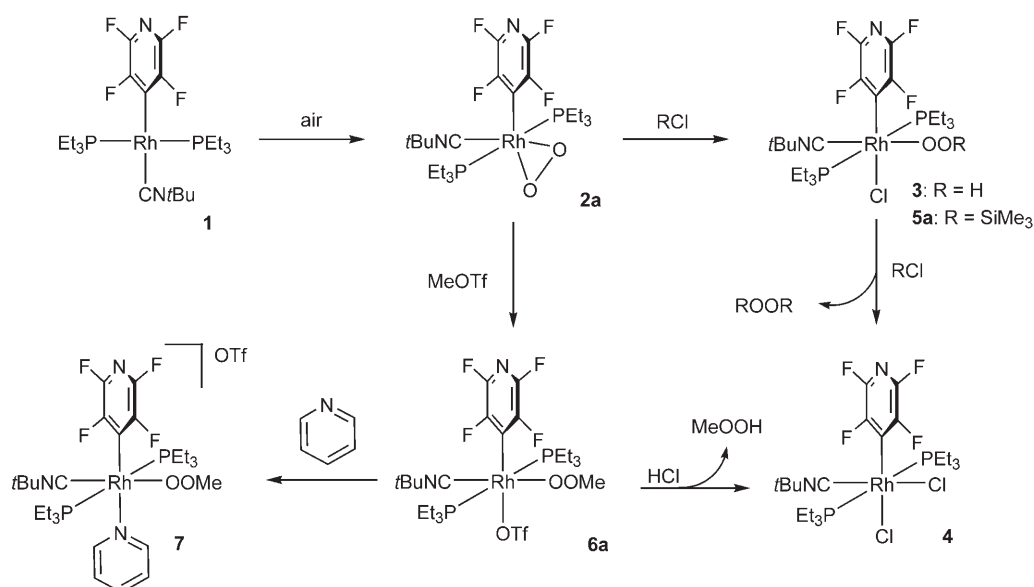
[*] M. Ahijado, Dr. T. Braun, D. Noveski, B. Neumann, Dr. H.-G. Stammer

Fakultät für Chemie, Universität Bielefeld
Postfach 100131, 33501 Bielefeld (Germany)
Fax: (+49) 521-106-6026
E-mail: thomas.braun@uni-bielefeld.de

Dr. N. Kocher, Prof. Dr. D. Stalke
Institut für Anorganische Chemie der Universität Göttingen
Tammannstrasse 4, 37077 Göttingen (Germany)

[**] This research was supported by the Deutsche Forschungsgemeinschaft. We also thank Prof. P. Jutzi for his support.

Supporting information for this article is available on the WWW under <http://www.angewandte.org> or from the author.



Scheme 1. The synthesis and reactivity of rhodium peroxo compounds. **2b**, **5b**, and **6b** are ^{18}O isotopologues of **2a**, **5a**, and **6a**, respectively.

Table 1: Selected NMR spectroscopic data.^[a]

2a: ^{19}F NMR (C_6D_6): $\delta = -98.1$ (m, 1 F), -98.6 (m, 1 F), -107.6 (m, 1 F), -117.3 ppm (m, 1 F); ^{31}P NMR (C_6D_6): $\delta = 24.6$ ppm (d, $J_{\text{P,Rh}} = 87$ Hz).

3:^[b] ^1H NMR ($[\text{D}_8]\text{toluene}$): $\delta = 7.35$ ppm (br. s, OOH); ^{19}F NMR ($[\text{D}_8]\text{toluene}$): $\delta = -96.1$ (m, 1 F), -97.8 (m, 1 F), -115.3 (m, 1 F), -120.4 ppm (m, 1 F); ^{31}P NMR ($[\text{D}_8]\text{toluene}$): $\delta = 17.8$ ppm (d, $J_{\text{P,Rh}} = 87$ Hz).

4: ^{19}F NMR ($[\text{D}_8]\text{toluene}$): $\delta = -95.3$ (m, 1 F), -97.6 (m, 1 F), -110.3 (m, 1 F), -112.3 ppm (m, 1 F); ^{31}P NMR ($[\text{D}_8]\text{toluene}$): $\delta = 15.3$ ppm (dd, $J_{\text{P,Rh}} = 80$, $J_{\text{P,F}} = 4$ Hz).

5a: ^{19}F NMR ($[\text{D}_8]\text{toluene}$): $\delta = -97.8$ (m, 1 F), -99.3 (m, 1 F), -114.2 (m, 1 F), -118.1 ppm (m, 1 F); ^{31}P NMR ($[\text{D}_8]\text{toluene}$): $\delta = 18.7$ ppm (d, $J_{\text{P,Rh}} = 87$ Hz); ^{29}Si NMR (119.2 MHz, $[\text{D}_8]\text{toluene}$): $\delta = 26.5$ ppm (s).

6a: ^1H NMR ($[\text{D}_8]\text{toluene}$): $\delta = 3.64$ ppm (s, 3 H, OOCH_3); ^{19}F NMR ($[\text{D}_8]\text{toluene}$): $\delta = -77.5$ (s, 3 F, CF_3), -95.9 (m, 1 F, CF), -97.9 (m, 1 F, CF), -115.2 (m, 1 F, CF), -120.0 ppm (m, 1 F, CF); ^{31}P NMR ($[\text{D}_8]\text{toluene}$): $\delta = 20.4$ ppm (dd, $J_{\text{P,Rh}} = 86$, $J_{\text{P,F}} = 4$ Hz).

7: ^1H NMR ($[\text{D}_8]\text{THF}$): $\delta = 3.69$ ppm (s, 3 H, OOCH_3); ^{19}F NMR ($[\text{D}_8]\text{THF}$): $\delta = -75.7$ (s, 3 F, CF_3), -94.7 (m, 1 F, CF), -96.0 (m, 1 F, CF), -110.1 (m, 1 F, CF), -116.0 ppm (m, 1 F, CF); ^{31}P NMR ($[\text{D}_8]\text{THF}$): $\delta = 12.8$ ppm (d, $J_{\text{P,Rh}} = 85$ Hz).

[a] Recorded at 300 K; Measurement frequencies: ^1H NMR 500 MHz, ^{19}F NMR 470.4 MHz, ^{31}P NMR 202.4 MHz. [b] Recorded at 213 K.

the hydroperoxo ligand. When **2a** is treated with DCl instead of HCl the resonance is not present. At 273 K complex **3** reacts with more HCl to give H_2O_2 and **4**. However, even when no further HCl is present, the slow generation of **2a** and **4** is observed. This indicates that the formation of **3** from **2a** and HCl is reversible. The latter can react with more **3** to yield **4** and H_2O_2 .

Compound **3** is unstable above 273 K, even in the solid state. However, crystals of **3** suitable for X-ray crystallog-

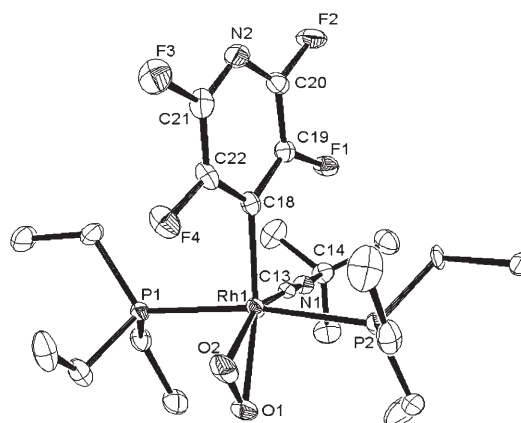


Figure 1. Molecular structure of **2a** in the crystal (ORTEF plot, ellipsoids at the 50% probability level). Selected distances [Å] and angles [°]: Rh1–O1 2.0332(16), Rh1–O2 2.0147(16), O1–O2 1.452(3); O1–Rh1–O2 42.05(7), C13–Rh1–O2 144.08(8), C18–Rh1–O2 110.63(8).

raphy were obtained from a THF/hexane solution at 193 K.^[15] The molecular structure depicted in Figure 2 reveals that the η^1 -bound hydroperoxo ligand is located in the *trans* position to the isocyanide ligand. Intermolecular hydrogen bonding of the hydroperoxo ligands also gives strong evidence for the presence of the OOH group. These interactions result in the formation of dimers with an intermolecular oxygen–oxygen separation of 2.680 Å (Figure S1, Supporting Information). The intramolecular oxygen–oxygen distance of 1.488(3) Å is greater than that found in complex **2a** but close to the value found for H_2O_2 (1.461(3) Å).^[17] So far, only very few transition-metal complexes with an η^1 -OOH ligand have been structurally characterized, for example, the rhodium compounds $[(\eta^5\text{-C}_5\text{Me}_5)\text{Ir}(\mu\text{-pz})_3\text{Rh}(\text{OOH})(\text{dppe})][\text{BF}_4]$ and $[\text{Tp}^{\text{Pr}}\text{Rh}(\text{OOH})(\text{pz})(\text{pzH})]$ (pzH = pyrazole, dppe = 1,2-bis-(diphenylphosphanyl)ethane, Tp^{Pr} = hydrotris(3,5-diisopropylpyrazolyl)borato).^[9,18]

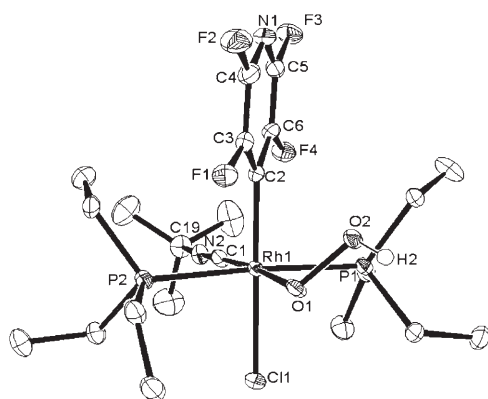


Figure 2. Molecular structure of **3** in the crystal (ORTEP plot, ellipsoids at the 50% probability level). Selected distances [Å] and angles [°]: Rh1–O1 2.025(2), O1–O2 1.488(3); Rh1–O1–O2 110.31(17).

The reactions of **2a** and **2b** with Me_3SiCl at 213 K furnished the silylperoxo complexes **5a** and **5b**, respectively (Scheme 1). After warming up to 273 K the slow generation of **4** and bis(trimethylsilyl) peroxide was observed. The latter was identified by comparison of the NMR data with those of an authentic sample. Compound **5a** was characterized by NMR and IR (Table 1). Convincing evidence for the presence of a OOSiMe_3 unit is given by an absorption band at 901 cm^{-1} (Figure 3).^[19] The signal shifts to 884 cm^{-1} for the isotopo-

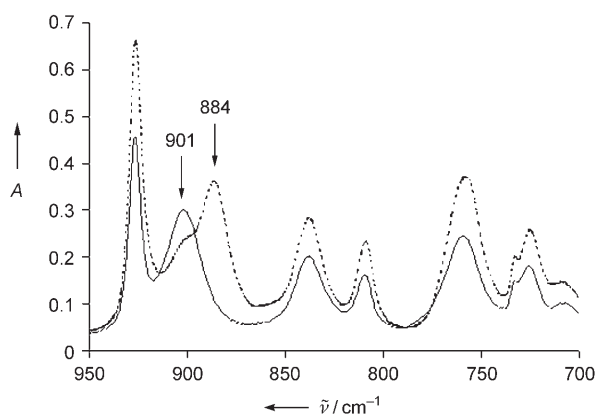


Figure 3. Part of the IR spectra of **5a** (—) and **5b** (----).

logue **5b**. For the configuration at rhodium in **5a** and **5b**, we assign a *trans* arrangement of the isocyanide and the silylperoxo ligand, as it was found for **3**. To our knowledge, complexes **5a** and **5b** are the first transition-metal silylperoxo compounds that have been characterized.^[20]

Treatment of a toluene solution of **2a** and **2b** with MeOTf yields the methylperoxo compounds **6a** and **6b**, respectively. A weak absorption band at 1004 cm^{-1} in the IR spectrum of **6b** can be assigned tentatively to the $^{18}\text{O}^{18}\text{OMe}$ unit. The high frequency might be attributed to a mixing of the O–O stretch and a bending vibration. The corresponding absorption band

in **6a** seems to be covered by a very strong broad band, which can be attributed to the triflate ligand at 1025 cm^{-1} .

The proposed structure of **6a** is further supported by its reactivity. Thus **6a** reacts smoothly with pyridine to give the cationic methylperoxo complex **7**. The structure of **7** was determined by X-ray crystallography.^[15] A view of the geometry of the cation is depicted in Figure 4. As was found

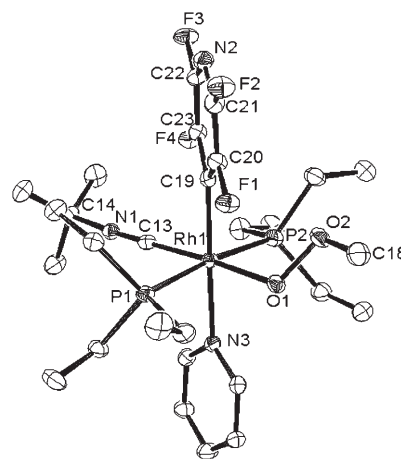


Figure 4. Structure of the cation in **7** in the crystal (ORTEP plot, ellipsoids at the 50% probability level). Selected distances [Å] and angles [°]: Rh1–O1 2.0196(14), O1–O2 1.479(2), O2–C18 1.412(3); Rh1–O1–O2 111.55(10), O1–O2–C18 104.32(16).

for the hydroperoxo group in **3**, the methylperoxo ligand is located in the *trans* position to the isocyanide. We assume a comparable configuration at rhodium for **6a**. The oxygen–oxygen distance of $1.479(2)\text{ Å}$ is similar to the O–O bond length in **3**. We note that Moro-oka et al. recently reported the crystal structure of a palladium complex with a $\{\text{PdOO}i\text{Bu}\}$ unit.^[18e] The structural data of two platinum compounds with $\text{OO}i\text{Pr}$ and $\text{OO}i\text{Bu}$ ligands were published earlier.^[21] Although there are indications for the existence of transition-metal methylperoxo complexes mainly based on UV and NMR data, to our knowledge in none of these compounds has the OOMe moiety been identified by IR data or X-ray crystallography.^[22]

Complex **6a** can also act as a source for organic peroxides. Thus, treatment of a solution of the triflate compound **6** with an excess HCl leads to complex **4** and the peroxide MeOOH , which was identified by comparison of its ^1H and ^{13}C NMR data with those of an authentic sample. The conversion is quantitative according to the NMR data. We assume that the reaction proceeds via the triflate complex *trans*- $[\text{Rh}(\text{Cl})(\text{OTf})(4\text{-C}_5\text{F}_4\text{N})(\text{CN}i\text{Bu})(\text{PET}_3)_2]$, which is readily converted into the dichloro compound **4**.

In conclusion, a η^1 -hydroperoxo complex and for the first time η^1 -silylperoxo and η^1 -methylperoxo species have been characterized unambiguously by IR spectroscopy or X-ray crystallography. The compounds are generated quantitatively according to the NMR data and have been isolated as intermediates in the rhodium-mediated formation of peroxides from molecular oxygen. The selective synthesis of **3**, **5a**,

and **6a** discloses a route for the controlled preparation of alkyl hydroperoxides and possibly dialkyl peroxides or alkylsilyl peroxides. We believe that the stabilizing effect of the tetrafluoropyridyl ligand with its π -acceptor properties might be the main reason for the stability of the rhodium complexes bearing an η^1 -bound peroxy unit.^[10] This stability also makes it possible to control the reactivity of the peroxy species and accounts for the selectivity of the reactions. It is intriguing that despite the presence of the phosphines and the anionic carbon ligand the reactions proceed smoothly. Neither the phosphines nor the metal-bound tetrafluoropyridyl ligand are oxygenated.

Received: May 11, 2005

Revised: July 5, 2005

Published online: October 6, 2005

Keywords: fluorinated ligands · oxygenation · peroxides · peroxy complexes · rhodium

- [1] a) R. A. Sheldon, J. K. Kochi, *Metal-Catalyzed Oxidations of Organic Compounds*, Academic Press, New York, **1981**; b) B. Meunier, S. P. de Visser, S. Shaik, *Chem. Rev.* **2004**, *104*, 3947–3980; c) M. Sono, M. P. Roach, E. D. Colther, J. H. Dawson, *Chem. Rev.* **1996**, *96*, 2841–2887; d) C. Limberg, *Angew. Chem.* **2003**, *115*, 6112–6136; *Angew. Chem. Int. Ed.* **2003**, *42*, 5932–5954; e) J.-M. Brégeault, *Dalton Trans.* **2003**, 3289–3302; f) A. L. Feig, S. J. Lippard, *Chem. Rev.* **1994**, *94*, 759–805; g) M. R. Bukowski, H. L. Halfen, T. A. van den Berg, J. A. Halfen, L. Que, Jr., *Angew. Chem.* **2005**, *117*, 590–593; *Angew. Chem. Int. Ed.* **2005**, *44*, 584–587.
- [2] Examples: a) M. Krom, T. P. J. Peters, R. G. E. Coumans, T. J. J. Sciarone, T. V. J. Hoogboom, S. I. ter Beek, P. J. P. Schlebos, J. M. M. Smits, R. de Gelder, A. W. Gal, *Eur. J. Inorg. Chem.* **2003**, 1072–1087; b) H. Mimoun in *The Chemistry of Peroxides* (Ed.: S. Patai), Wiley, Chichester **1985**, pp. 463–482; c) C. W. Dudley, G. Read, P. J. C. Walker, *J. Chem. Soc. Dalton Trans.* **1974**, 1926–1931; d) T. Nishimura, N. Kakiuchi, T. Onoue, K. Ohe, S. Uemura, *J. Chem. Soc. Perkin Trans. 1* **2000**, 1915–1918; e) F. Igersheim, H. Mimoun, *Nouv. J. Chim.* **1980**, *4*, 711–713; f) G. Read, *J. Mol. Cat.* **1988**, *44*, 15–33.
- [3] a) I. M. Klotz, D. M. Kurtz, *Acc. Chem. Res.* **1984**, *17*, 16–22; b) A. K. Shiemke, T. M. Loehr, J. Sanders-Loehr, *J. Am. Chem. Soc.* **1984**, *106*, 4951–4956; c) R. E. Stenkamp, *Chem. Rev.* **1994**, *94*, 715–726.
- [4] Y. Tatsuno, S. Otsuka, *J. Am. Chem. Soc.* **1981**, *103*, 5832–5839.
- [5] H. F. Haarman, F. R. Bregman, P. W. N. M. van Leeuwen, K. Vrieze, *Organometallics* **1997**, *16*, 979–985.
- [6] a) S. Bhaduri, L. Casella, R. Ugo, P. R. Raithby, C. Zuccaro, M. B. Hursthouse, *J. Chem. Soc. Dalton Trans.* **1979**, 1624–1629; b) S. Muto, Y. Kamiya, *Bull. Chem. Soc. Jpn.* **1976**, *49*, 2587–2589; c) S. Muto, K. Tasaka, Y. Kamiya, *Bull. Chem. Soc. Jpn.* **1977**, *50*, 2493–2494; d) S. Otsuka, A. Nakamura, Y. Tatsuno, M. Miki, *J. Am. Chem. Soc.* **1972**, *94*, 3761–3767; e) S. S. Stahl, J. L. Thorman, R. C. Nelson, M. A. Kozee, *J. Am. Chem. Soc.* **2001**, *123*, 7188–7189; f) S. S. Stahl, *Angew. Chem.* **2004**, *116*, 3480–3501; *Angew. Chem. Int. Ed.* **2004**, *43*, 3400–3420; g) B. A. Steinhoff, I. A. Guzei, S. S. Stahl, *J. Am. Chem. Soc.* **2004**, *126*, 11268–11278; h) D. R. Jensen, M. J. Schultz, J. A. Mueller, M. S. Sigman, *Angew. Chem.* **2003**, *115*, 3940–3843; *Angew. Chem. Int. Ed.* **2003**, *42*, 3810–3813.
- [7] M. M. Konnick, I. A. Guzei, S. S. Stahl, *J. Am. Chem. Soc.* **2004**, *126*, 10212–10213.
- [8] a) A. Morvillo, M. Bressan, *J. Organomet. Chem.* **1987**, *332*, 337–343; b) H. Suzuki, S. Matsuura, Y. Moro-oka, T. Ikawa, *J. Organomet. Chem.* **1985**, *286*, 247–258.
- [9] a) Y. Takahashi, M. Hashimoto, S. Hikichi, M. Akita, Y. Moro-oka, *Angew. Chem.* **1999**, *111*, 3259–3262; *Angew. Chem. Int. Ed.* **1999**, *38*, 3074–3077.
- [10] D. Noveski, T. Braun, B. Neumann, A. Stammeler, H.-G. Stammeler, *Dalton Trans.* **2004**, 4106–4119.
- [11] D. G. Ho, R. Ismail, N. Franco, R. Gao, E. P. Leverich, I. Tsyba, N. N. Ho, R. Bau, M. Selke, *Chem. Commun.* **2002**, 570–571.
- [12] C. R. Landis, C. M. Morales, S. S. Stahl, *J. Am. Chem. Soc.* **2004**, *126*, 16302–16303.
- [13] A. Nakamura, Y. Tatsuno, S. Otsuka, *Inorg. Chem.* **1972**, *11*, 2058–2064.
- [14] S. Pinchas, I. Laulicht, *Infrared Spectra of Labeled Compounds*, Academic Press, New York **1971**, p. 238.
- [15] Data for the X-ray structure analyses: **2a**: C₂₂H₃₀F₄N₂O₂P₂Rh, *M* = 604.40, crystal dimensions 0.24 × 0.20 × 0.09 mm³; monoclinic; *C*2/*c*; *a* = 19.080(1), *b* = 10.283(1), *c* = 28.402(2) Å, β = 99.86(1)°, *Z* = 8, *V* = 5490.2(3) Å³, ρ_{calcd} = 1.462 g cm⁻³; $2\theta_{\text{max}}$ = 55°; MoK α radiation (λ = 0.71073 Å), *T* = 100(2) K, 51638 reflections collected, 6294 were unique (*R*_{int} = 0.0448); Nonius KappaCCD diffractometer; multiscan absorption correction (min./max. transmission 0.8337/0.9326), μ = 0.787 mm⁻¹. The structure was solved by direct methods and refined with full matrix least square methods on *F*² (SHELX-97).^[23] Final *R*₁, *wR*₂ values on all data: 0.0564, 0.0680; *R*₁, *wR*₂ values for 4675 reflections with *I*₀ > 2σ(*I*₀): 0.0305, 0.0590; residual electron density +0.953/–0.536 e Å⁻³; disorder of one triethylphosphane ligand on two positions (89:11). **3·3 THF**: C₃₄H₆₄ClF₄N₂O₅P₂Rh, *M* = 857.17, crystal dimensions 0.40 × 0.20 × 0.05 mm³; monoclinic; *P*2₁/*c*; *a* = 11.7262(8), *b* = 15.3427(11), *c* = 22.9453(17) Å, β = 101.6470(10)°, *Z* = 4, *V* = 4043.1(5) Å³, ρ_{calcd} = 1.408 g cm⁻³; $2\theta_{\text{max}}$ = 52.08°; MoK α radiation (λ = 0.71073 Å), *T* = 100(2) K, 30127 reflections collected, 8265 were unique (*R*_{int} = 0.0420); Bruker Smart-Apex diffractometer equipped with a low-temperature device;^[24] empirical absorption correction with SADABS 2.05 (min./max. transmission 0.7466/0.9800),^[25] μ = 0.626 mm⁻¹. The structure was solved by direct methods and refined with full matrix least square methods on *F*².^[23] Hydrogen atoms were placed at calculated positions and refined using a riding model. Final *R*₁, *wR*₂ values on all data: 0.0642, 0.1191; *R*₁, *wR*₂ values for 7278 reflections with *I*₀ > 2σ(*I*₀): 0.0554, 0.1155; residual electron density +1.694/–1.182 e Å⁻³. **7**: C₂₉H₄₇F₇N₃O₅P₂RhS, *M* = 847.61, crystal dimensions 0.23 × 0.17 × 0.06 mm³; monoclinic; *P*2₁/*n*; *a* = 11.28100(10), *b* = 19.9970(2), *c* = 16.1900(2) Å, β = 94.3620(8)°, *Z* = 4, *V* = 3641.66(7) Å³, ρ_{calcd} = 1.546 g cm⁻³; $2\theta_{\text{max}}$ = 55°; MoK α radiation (λ = 0.71073 Å), *T* = 100(2) K, 66078 reflections collected, 8333 were unique (*R*_{int} = 0.059); Nonius KappaCCD diffractometer; multiscan absorption correction (min./max. transmission 0.8573/0.9597), μ = 0.691 mm⁻¹. The structure was solved by direct methods and refined with full matrix least square methods on *F*² (SHELX-97).^[23] Final *R*₁, *wR*₂ values on all data: 0.0435, 0.0747; *R*₁, *wR*₂ values for 6844 reflections with *I*₀ > 2σ(*I*₀): 0.0310, 0.0696; residual electron density +0.980/–0.582 e Å⁻³. CCDC-265303, -271512, and -265304 contain the supplementary crystallographic data for this paper. These data can be obtained free of charge from the Cambridge Crystallographic Data Centre via www.ccdc.cam.ac.uk/data_request/cif.
- [16] a) J. Vicente, J. Gil-Rubio, J. Guerrero-Leal, D. Bautista, *Organometallics* **2004**, *23*, 4871–4881; b) K. Osakada, K. Hataya, T. Yamamoto, *Inorg. Chem.* **1993**, *32*, 2360–2365; c) M. J. Bennett, P. B. Donaldson, *Inorg. Chem.* **1977**, *16*, 1581–1589; d) V. Circu, M. A. Fernandes, L. Carlton, *Polyhedron* **2002**, *21*, 1775–1778.

- [17] J.-M. Savariault, M. S. Lehmann, *J. Am. Chem. Soc.* **1980**, *102*, 1298–1303.
- [18] a) V. V. Rostovtsev, L. M. Henling, J. A. Labinger, J. E. Bercaw, *Inorg. Chem.* **2002**, *41*, 3608–3619; b) I. A. Guzei, A. Bakac, *Inorg. Chem.* **2001**, *40*, 2390–2393; c) D. D. Wick, K. I. Goldberg, *J. Am. Chem. Soc.* **1999**, *121*, 11900–11901; d) D. Carmona, M. P. Lamata, J. Ferrer, J. Modrego, M. Perales, F. J. Lahoz, R. Atencio, L. A. Oro, *J. Chem. Soc. Chem. Commun.* **1994**, 575–576; e) T. Miyaji, M. Kujime, S. Hikichi, Y. Moro-oka, M. Akita, *Inorg. Chem.* **2002**, *41*, 5286–5295.
- [19] Y. L. Fan, R. G. Shaw, *J. Org. Chem.* **1973**, *38*, 2410–2412.
- [20] The existence of the platinum silylperoxo complexes *cis*-[PtCl-(OOSiR₃)(PPh₃)₂] (R = Me, Ph) at low temperature has been suggested, but their assignment was based on ³¹P NMR data only: H. Kurosawa, T. Achiha, H. Kajimaru, I. Ikeda, *Inorg. Chim. Acta* **1991**, *190*, 271–277.
- [21] a) G. Strukul, R. A. Michelin, J. D. Orbell, L. Randaccio, *Inorg. Chem.* **1983**, *22*, 3706–3713; b) G. Ferguson, P. K. Monaghan, M. Parvez, R. J. Puddephatt, *Organometallics* **1985**, *4*, 1669–1674.
- [22] a) R. D. Arasasingham, A. L. Balch, L. Latos-Grazynski, *J. Am. Chem. Soc.* **1987**, *109*, 5846–5847; b) T. Szymanska-Buzar, J. Paál-Lukács, P. Sándor, I. P. Hajdu, D. Gál, *J. Organomet. Chem.* **1987**, *321*, 249–255; c) C. Giannotti, C. Fontaine, B. Septe, *J. Organomet. Chem.* **1974**, *71*, 107–124; d) A. Sauer, H. Cohen, D. Meyerstein, *Inorg. Chem.* **1988**, *27*, 4578–4581; e) a Mg compound bearing a methylperoxo ligand has been described: R. Han, G. Parkin, *J. Am. Chem. Soc.* **1990**, *112*, 3662–3663.
- [23] a) SHELXTL-PLUS, Siemens Analytical X-Ray Instruments Inc., Madison, WI, USA **1990**; b) G. M. Sheldrick, SHELX-97, Program for Crystal Structure Refinement, University of Göttingen **1997**; c) G. Cascarano, A. Altomare, C. Giacovazzo, A. Guagliardi, A. G. G. Moliterni, D. Sigli, M. C. Burla, G. Polidori, M. Camalli, *Acta Crystallogr. Sect. A* **1996**, *52*, C-79.
- [24] a) T. Kottke, D. Stalke, *J. Appl. Crystallogr.* **1993**, *26*, 615; b) T. Kottke, R. J. Lagow, D. Stalke, *J. Appl. Crystallogr.* **1996**, *29*, 465; c) D. Stalke, *Chem. Soc. Rev.* **1998**, *27*, 171.
- [25] G. M. Sheldrick, SADABS 2.05, Program for Area Detector Absorption Correction, University of Göttingen **2002**.

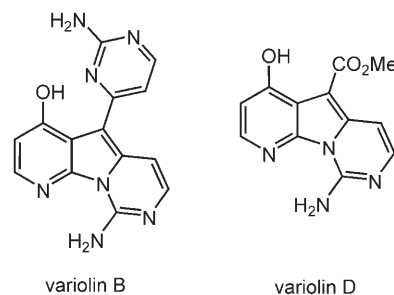
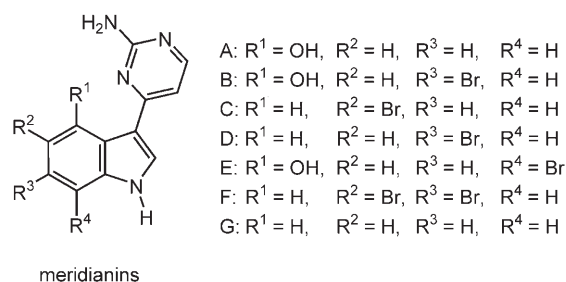
DOI: 10.1002/anie.200501703

Concise Syntheses of Meridianins by Carbonylative Alkynylation and a Four-Component Pyrimidine Synthesis**

Alexei S. Karpov, Eugen Merkul, Frank Rominger, and Thomas J. J. Müller*

Dedicated to Professor Franz Effenberger on the occasion of his 75th birthday

Pyrimidines constitute an important class of heterocycles,^[1] and many of the 2,4-substituted pyrimidines have been recognized to be pharmaceutically highly active.^[2] Particular attention has focused on meridianins A–G (indole alkaloids with a 2-aminopyrimidyl substituent which were recently isolated from the *Aplidium meridianum*, an ascidian collected in the South Atlantic; Scheme 1),^[3] since they inhibit numerous protein kinases in a low micromolar range.^[4] They are



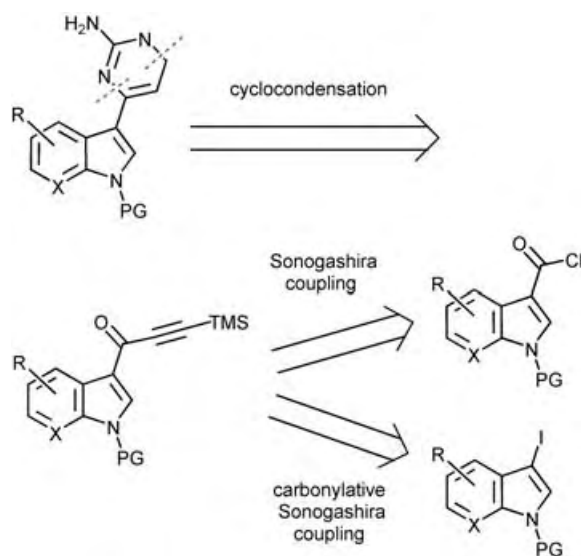
Scheme 1. Meridianins and selected variolin alkaloids.

[*] Dr. A. S. Karpov, E. Merkul, Dr. F. Rominger, Prof. Dr. T. J. J. Müller
Organisch-Chemisches Institut
Ruprecht-Karls-Universität Heidelberg
Im Neuenheimer Feld 270, 69120 Heidelberg (Germany)
Fax: (+49) 6221-54-6579
E-mail: Thomas_J.J.Mueller@urz.uni-heidelberg.de

[**] This work was supported by the Deutsche Forschungsgemeinschaft (Graduiertenkolleg 850), by the Fonds der Chemischen Industrie, and by the Dr.-Otto-Röhm Gedächtnisstiftung. We thank Dr. Dieter Dorsch, Merck KGaA, Darmstadt, for providing screening data of the meridianins and derivatives in kinase inhibition assays, BASF AG for the generous donation of chemicals, and Michaela Schmitt for experimental assistance.

related structurally to the variolins, alkaloids isolated from the Antarctic sponge *Kirkpatrickia variolosa*^[5] which display antitumor and antiviral activity. Among these alkaloids, variolin B is the most biologically active compound. It shows the inhibition of the growth of the P388 tumor cell line and is also active against *Herpes simplex* and the polio virus. In contrast, variolin D is completely inactive, emphasizing the importance of the 2-aminopyrimidine substituent for the biological activity.

Three approaches to meridianins and variolins are currently known. While the first two routes apply Stille^[6,7] or Suzuki couplings^[8] of suitable indole stannanes or boronates and halopyrimidine derivatives, the third more classical approach is based upon a Bredereck synthesis of the 2-aminopyrimidine moiety via β -enaminones.^[9,10] Just recently, we have developed a straightforward consecutive one-pot three-component access to pyrimidines by means of a modified Sonogashira coupling of acid chlorides with terminal alkynes and the subsequent transformation of alkynone intermediates with amidinium salts.^[11] Therefore, our diversity-oriented methodological approach to meridianin and variolin alkaloids suggests the use of trimethylsilylynes (TMS-ynones) as versatile synthetic equivalents of β -ketoaldehydes for the construction of the 2-aminopyrimidine ring (Scheme 2). Here, we report on the development of carbon-



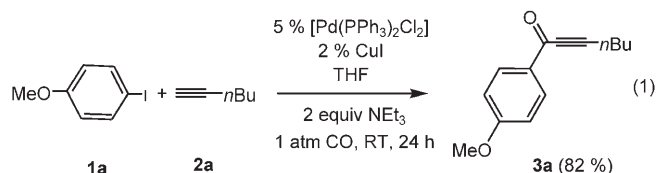
Scheme 2. Retrosynthetic analysis of meridianins and variolins.

ylative alkynylation to give TMS-alkynones, its application to concise two-step syntheses of meridianins starting from 3-iodoindole derivatives, first kinase inhibition tests of meridianins, and a new one-pot four-component syntheses of pyrimidines.

Our initial route was based upon our established approach to TMS-alkynones^[11] starting from acid chlorides. But we soon found that all attempts to prepare the required N-protected indolyl acid chlorides by standard Friedel–Crafts acylation^[12] were less promising. Only the phenylsulfonyl group could withstand these drastic, extremely acidic conditions; however, it was not really compatible for the

subsequent coupling-cyclocondensation sequence. We therefore readjusted our retrosynthetic analysis and decided to conceptually switch to a highly convergent carbonylative coupling-cyclocondensation approach. A literature survey on carbonylative alkynylation revealed that either high pressures of carbon monoxide^[13] are necessary, or for reactions under normal pressure a twofold excess of relatively precious aryl iodides is required.^[14] Recently, Mori reported a practical approach to ynones by carbonylative coupling using 2 equiv of aqueous ammonia as a base.^[15] However, our experience in the preparation of TMS-ynones by Sonogashira coupling suggested that we switch the base from ammonia to triethylamine in slight excess for the carbonylative Sonogashira coupling.

Upon reaction of *para*-anisyl iodide (**1a**) and 1-hexyne (**2a**) in THF at room temperature under 1 atm of carbon monoxide (a CO-filled balloon attached to the reaction vessel) and in the presence of 2 equiv of triethylamine and catalytic amounts of $[\text{Pd}(\text{PPh}_3)_2\text{Cl}_2]$ and CuI the alkynone **3a** was obtained in 82 % yield [Eq. (1)].



For carbonylative alkynylations with indoles *tert*-butoxycarbonyl(Boc)-protected 3-iodoindole derivatives **4** were identified to be the substrates of choice. Four representative indoles were prepared in a two-step sequence of iodination (79–99 % yield) and subsequent Boc protection of the indole nitrogen (72–86 % yield).^[16,17] However, the Pd catalyst system had to be optimized for sufficient conversion of the iodoindoles **4** into the desired TMS-alkynones **5** [Eq. (2), Table 1].

The structures of the TMS-alkynones **5** were unambiguously supported by spectroscopic (¹H, ¹³C and DEPT, COSY, HETCOR, and HMBC NMR experiments, IR, UV/Vis, mass spectrometry) and combustion analyses, and in addition by an X-ray structure analysis compound of **5d** (Figure 1).^[18,19]

The standard catalyst system (5 % $[\text{Pd}(\text{PPh}_3)_2\text{Cl}_2]$) appeared to be most efficient only for the pyrrolopyridine **4d** (entry 7), whereas in all other cases a mixture of 0.05 equiv of $[\text{Pd}(\text{PPh}_3)_2\text{Cl}_2]$ and 0.01 equiv of $[\text{Pd}(\text{dppf})\text{Cl}_2]$ accelerated the catalysis. However, when $[\text{Pd}(\text{dppf})\text{Cl}_2]$ alone was applied the catalyst, the desired alkynone became the minor product and the formation of the TMS-ethynylindole dominated (entry 4). To date, the mechanistic influence of this peculiar catalyst cocktail on the selectivity of the carbonylative alkynylation is not clear. Apparently the electronic nature of the iodo substrates in conjunction with the Pd catalyst precursor plays a key role and will be the subject of thorough investigations. As a consequence of different rates in oxidative addition and from a methodological point of view, the presence of bromo substituents (entries 3 and 5) does not interfere with the regioselective carbonylative alkynylation at the carbon–iodine bond. Most critical, however, was the

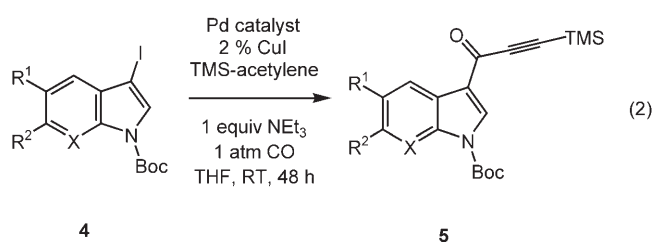


Table 1: Optimization of catalyst combinations for the carbonylative alkylation of iodoindole derivatives.^[a]

Entry	4	Catalyst system	5	Yield [%] ^[b]
1	R ¹ = R ² = H, X = CH (4a)	5% [Pd(PPh ₃) ₂ Cl ₂]		50
2	4a	5% [Pd(PPh ₃) ₂ Cl ₂], 1% [Pd(dppf)Cl ₂]	5a	68
3	R ¹ = Br, R ² = H, X = CH (4b)	5% [Pd(PPh ₃) ₂ Cl ₂], 1% [Pd(dppf)Cl ₂]		68
4	4b	5% [Pd(dppf)Cl ₂]	5b	25 ^[c]
5	R ¹ = H, R ² = Br, X = CH (4c)	5% [Pd(PPh ₃) ₂ Cl ₂], 1% [Pd(dppf)Cl ₂]		64
6	R ¹ = R ² = H, X = N (4d)	5% [Pd(PPh ₃) ₂ Cl ₂], 1% [Pd(dppf)Cl ₂]		39
7	4d	5% [Pd(PPh ₃) ₂ Cl ₂]	5d	63

[a] Reaction conditions: 3-iodoindole **4** (1.0 equiv), TMS-acetylene (1.5 equiv; 0.1 M in THF), triethylamine (1 equiv), CuI (0.02 equiv), and the Pd catalyst were stirred at room temperature for 48 h. [b] Yields refer to yields of compounds **5** isolated after flash chromatography on silica gel to be $\geq 95\%$ pure as determined by NMR spectroscopy and elemental analysis and/or HRMS. [c] 56% of the alkylation product.

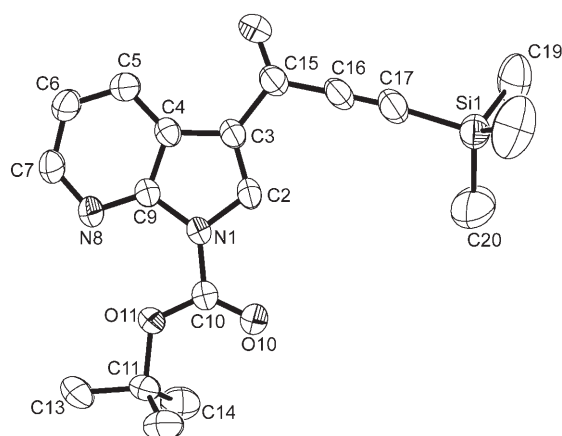


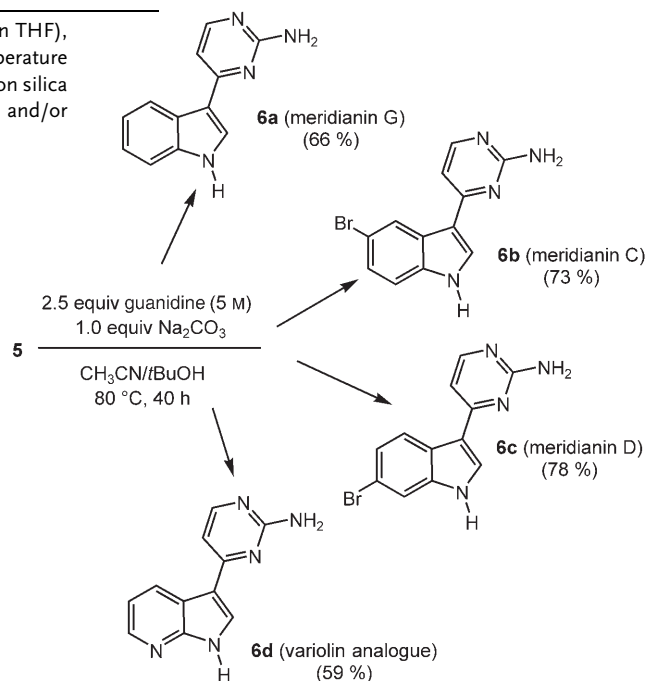
Figure 1. X-ray crystal structure of **5d**; thermal ellipsoids at 50% probability. Selected bond lengths [Å]: C10–N1 1.421, N1–C2 1.379, C2–C3 1.353, C3–C15 1.462, C15–C16 1.460, C16–C17 1.203, C17–Si1 1.849.

application of only one equivalent of triethylamine as an HI-scavenging base.

With this three-component carbonylative alkylation in hand, we set out to conclude the meridianin syntheses. First attempts to conduct the meridianin syntheses in a consecutive one-pot fashion failed, in particular, since the choice of the ideal solvent system for the concluding cyclocondensation step interferes with the carbonylative coupling step. There-

fore, a separation of carbonylative coupling and cyclocondensation seemed to be reasonable. The TMS-alkynones **5** were treated with a 5 M aqueous solution of guanidine (2.5 equiv) and Na₂CO₃ (1 equiv) at 80 °C in a 1:1 mixture of *t*BuOH/CH₃CN, and the desired natural products **6** were isolated in 59–78% yield (Scheme 3). Most surprisingly, the pyrimidine formation occurs with the concomitant cleavage of both TMS and Boc groups. Interestingly, the use of CH₃CN/MeOH as a solvent mixture led to the predominant formation of a double Michael addition product of methanol.

This new two-step synthesis of meridianins and related variolins is not only apparently very general but also extremely concise. If one considers that the iodoindole derivatives can be prepared in another two steps from indole derivatives, the overall yield of the four steps



Scheme 3. Cyclocondensation of TMS-alkynones **5** to give meridianins and meridianin derivatives **6**.

starting from the indoles lies between 25 and 41 %. A striking advantage over the β -enaminone pathway^[9,10] is that substituents other than H can be introduced readily at position 6 of the pyrimidine ring by choosing substituted alkynes. Furthermore, the extremely mild conditions of TMS-alkynone formation are highly compatible with polar functional groups. Polar substituents represent a significant drawback if stannane and boronate intermediates are required.^[6–8]

The structures of the meridianins **6a–c** and variolin analogue **6d** were unambiguously supported by their ¹H and ¹³C NMR spectra, which are in full agreement with published data.^[8,10]

Since we were aware of the biological activity of the natural-meridianines, we subjected the synthetic samples of compounds **6** to a screening assay with protein kinases,^[20] which play a key role in the “metabolic syndrome” (hSGK1) and in oncogenesis. All four compounds inhibit these tested kinases at low micromolar and even nanomolar levels (Table 2).

Encouraged by the successful total syntheses of meridianines, we attempted the methodological advance to the one-pot four-component syntheses of pyrimidines by a carbonylative coupling–cyclocondensation sequence. Reaction of (hetero)aryl iodides **1** and terminal alkynes **2** in THF at room temperature under 1 atm of carbon monoxide (a CO-filled balloon attached to the reaction vessel) and in the presence of 2 equiv of triethylamine and catalytic amounts of [Pd(PPh₃)₂Cl₂] and CuI for 48 h followed by addition of the amidinium salts **7** in the presence of 2.5 equiv of sodium carbonate in acetonitrile/water gave the 2,4,6-trisubstituted pyrimidines **8** moderate to good yield [Eq. (3), Table 3].

The structures of the pyrimidines **8** were unambiguously sup-

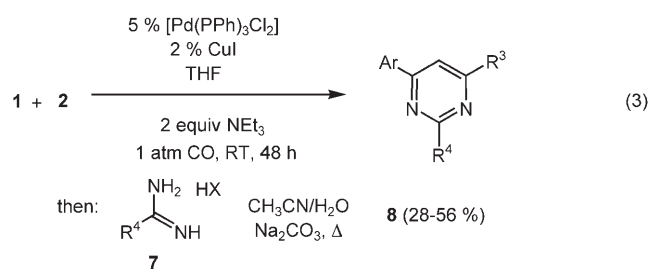


Table 3: One-pot four-component carbonylative coupling–cyclocondensation synthesis of 2,4,6-trisubstituted pyrimidines **8** from aryl iodides **1**, alkynes **2**, and amidinium salts **7**^[a] (see Equations (1) and (3)).

Entry	1	2	7	8	Yield [%] ^[b]
1	1a: Ar = <i>p</i> -MeOC ₆ H ₄	2a: R ³ = <i>n</i> Bu	7a: ^[c] R ⁴ = 2-thienyl	8a	51
2	1b: Ar = 2-thienyl	2b: R ³ = Ph	7b: ^[c] R ⁴ = Me	8b	56
3	1c: Ar = <i>p</i> -MeC ₆ H ₄	2a	7c: ^[d] R ⁴ = HN-2-CH ₃ -5-O ₂ NC ₆ H ₃	8c	29
4	1d: Ar = <i>p</i> -MeO ₂ CC ₆ H ₄	2b	7b: ^[c]	8d	43
5	1e: Ar = <i>p</i> -NCC ₆ H ₄	2a	7a: ^[c]	8e	28 ^[e]

[a] Reaction conditions: A mixture of **1** (1.0 mmol), **2** (1.2 mmol), [Pd(PPh₃)₂Cl₂] (0.05 mmol), CuI (0.02 mmol), and NEt₃ (2.0 mmol) (in THF (5 mL)) was stirred at room temperature for 48 h. Then **7** (1.2 equiv), Na₂CO₃ (2.5 equiv), water (0.5 mL), and CH₃CN (5 mL) were added, and the reaction mixture was heated at reflux for 12–24 h. [b] Yields refer to yields of compounds **8** isolated after flash chromatography on silica gel and crystallization to be $\geq 95\%$ pure as determined by NMR spectroscopy and elemental analysis. [c] Used as a hydrochloride. [d] Used as a nitrate. [e] Only 0.01 mmol of [Pd(PPh₃)₂Cl₂] without CuI was used as a catalyst; the reaction mixture was stirred for five days on the first step.

Table 2: IC₅₀ values [μ M] of meridianins **6a–c** and the variolin analogue **6d**.

Protein kinase	6a	6b	6c	6d
hSGK1	>10	2.0	4.5	2.4
Tie-2	>1	0.75	1.6	1.0
VEGFR2/KDR	>1	>1	>1	>1
PDGF-receptor β -kinase	>10	>10	>10	>10
Meck-EE kinase	>10	2.3	8.7	>10
IGF1-receptor tyrosine kinase	>10	>10	>10	>10

ported by spectroscopic (¹H, ¹³C and DEPT NMR experiments, IR, UV/Vis, mass spectrometry) and combustion analyses. It is noteworthy that this sequence proceeds efficiently only for neutral or electron-rich aryl iodides **1** (entries 1 and 2). When electron-deficient aryl iodides were examined, a 1:2 mixture of carbonylative and non-carbonylative products was isolated. On the other hand, attempts to replace the aryl iodides with aryl bromides to increase the selectivity led to the complete loss of reactivity, and only

starting material was recovered. Finally, after considerable experimentation, we found that stirring the electron-deficient aryl iodide **1e** for 5 days with only 1 mol % of [Pd(PPh₃)₂Cl₂] and in the absence of CuI predominantly led to the formation of carbonylative alkynylation product, which was subjected to the cyclocondensation, providing the desired pyrimidine in 28 % yield (entry 5).

Although this pyrimidine synthesis based upon consecutive carbonylative alkynylation and cyclocondensation is lower yielding than the synthesis starting from acid chlorides,^[11] it still can be considered as a complementary approach when acid-sensitive functionality cannot be tolerated.

In conclusion, we have developed concise syntheses of naturally occurring meridianins and derivatives based upon carbonylative alkynylation and subsequent cyclocondensation. Meridianins were found to inhibit “metabolic syndrome” and oncologically relevant protein kinases at low micromolar and even nanomolar levels. Furthermore, we have developed a novel one-pot four-component synthesis of 2,4,6-trisubstituted pyrimidines based upon a consecutive carbonylative coupling–cyclocondensation sequence. Studies addressing the methodological scope of this synthesis and syntheses of other unknown analogs of meridianins and variolins as well as thorough studies of the structure–activity relationship are currently underway.

Experimental Section

5b: In a Schlenk flask [Pd(PPh₃)₂Cl₂] (35 mg, 0.05 mmol), [Pd(dppf)Cl₂·CH₂Cl₂] (8 mg, 0.01 mmol), CuI (4 mg, 0.02 mmol), Boc-protected iodo indole **4b** (422 mg, 1.00 mmol), and THF (5 mL) were placed under nitrogen. Carbon monoxide was bubbled through the solution for 5 min, and then TMS-acetylene (0.21 mL, 1.50 mmol) and triethylamine (0.14 mL, 1.00 mmol) were added successively. The reaction mixture became dark red and was stirred at room temperature for 48 h under 1 atm of carbon monoxide (balloon filled with CO). The reaction mixture was then diluted with brine (20 mL) and extracted with dichloromethane (5 × 20 mL). The combined organic layers were dried with sodium sulfate, concentrated to dryness, and subjected to column chromatography on silica gel (hexane/ethyl acetate, 12:1) to give **5b** (287 mg; 68 %) as colorless crystals. M.p. 157–159 °C. ¹H NMR (300 MHz, CDCl₃): δ = 0.32 (s, 9H), 1.70 (s, 9H), 7.47 (dd, *J* = 8.8 Hz, 1.8 Hz, 1H), 8.00 (d, *J* = 8.8 Hz, 1H), 8.36 (s, 1H), 8.48 ppm (d, *J* = 1.8 Hz, 1H); ¹³C NMR (75 MHz, CDCl₃): δ = −0.7 (CH₃), 28.0 (CH₃), 86.1 (C_{quat.}), 97.0 (C_{quat.}), 101.3 (C_{quat.}), 116.5 (CH), 118.4 (C_{quat.}), 120.8 (C_{quat.}), 125.0 (CH), 128.1 (C_{quat.}), 128.9 (CH), 134.6 (C_{quat.}), 136.4 (CH), 148.4 (C_{quat.}), 171.5 ppm (C_{quat.}); EI-MS (70 eV): *m/z* (%): 421 [M]⁺, ⁸¹Br, (7); 419 [M]⁺, ⁷⁹Br, (5); 365 [M−C₄H₉]⁺, ⁸¹Br, (58); 363 [M−C₄H₉]⁺, ⁷⁹Br, (49); 321 [M−C₄H₉−CO₂−H]⁺, ⁸¹Br, (100); 319 [M−C₄H₉−CO₂−H]⁺, ⁷⁹Br, (84); 306 (23); 304 (19); 57 [C₄H₉]⁺ (99); elemental analysis calcd (%) for C₁₉H₂₂BrNO₃Si (420.4): C 54.29, H 5.28, N 3.33, Br 19.01; found: C 54.00, H 5.33, N 3.37, Br 19.27.

6b: To a solution of **5b** (185 mg, 0.44 mmol) in acetonitrile (1.5 mL) was added in succession sodium carbonate (47 mg, 0.44 mmol), *tert*-butyl alcohol (1.5 mL), and a 5 M aqueous solution of guanidine (0.22 mL, 1.1 mmol; prepared by dissolving guanidine hydrochloride (9.55 g, 0.10 mol) in water (20 mL) and neutralizing with sodium hydroxide (4.10 g, 0.10 mol). The reaction mixture was stirred at 80 °C for 38 h. After conversion to the meridianin was complete (TLC), brine was added and the mixture was extracted with dichloromethane (3 × 20 mL). The combined organic layers were dried with sodium sulfate, and after evaporation of the solvents in

vacuo the residue was chromatographed on deactivated silica gel (ethanol/ammonia 9:1) with ethyl acetate/ethanol (9:1) to give **6b** (93 mg; 73 %) as a light yellow solid (recrystallized from pentane). M.p. 238–240 °C (103–106 °C).^[10] ¹H NMR ([D₆]DMSO, 300 MHz): δ = 6.52 (br, 2H, NH₂), 7.00 (d, *J* = 5.1 Hz, 1H, H-5'), 7.29 (dd, *J* = 1.8, 8.5 Hz, 1H, H-6), 7.41 (d, *J* = 8.8 Hz, 1H, H-7), 8.10 (d, *J* = 5.1 Hz, 1H, H-6'), 8.26 (br, 1H, H-2), 8.76 (d, *J* = 1.8 Hz, 1H, H-4), 11.87 ppm (brs, 1H, NH); ¹³C NMR ([D₆]DMSO, 75 MHz): δ = 105.3 (CH), 113.3 (C_{quat.}), 113.4 (C_{quat.}), 113.8 (CH), 124.5 (CH), 124.6 (CH), 127.1 (C_{quat.}), 129.6 (CH), 135.8 (C_{quat.}), 157.2 (CH), 162.3 (C_{quat.}), 163.6 ppm (C_{quat.}); elemental analysis calcd (%) for C₁₂H₉BrN₄ (289.1): C 49.85, H 3.14, N 19.38; found: C 50.10, H 3.24, N 18.87.

8a: In a Schlenk flask [Pd(PPh₃)₂Cl₂] (35 mg, 0.05 mmol), CuI (4 mg, 0.02 mmol), *para*-iodoanisole (**1a**; 234 mg, 1.00 mmol), and THF (5 mL) were placed under nitrogen. Carbon monoxide was bubbled through the solution for 5 min, and then hexyne **2a** (0.14 mL, 1.20 mmol) and triethylamine (0.28 mL, 2.00 mmol) were added successively. The reaction mixture became dark red and was stirred at room temperature for 48 h under 1 atm of carbon monoxide (balloon filled with CO). Then the suspension was treated with Na₂CO₃ (265 mg, 2.50 mmol), amidinium salt **7a** (195 mg, 1.20 mmol), water (0.5 mL), and CH₃CN (5 mL), and the reaction mixture was heated at reflux for 24 h. After cooling to room temperature, the reaction mixture was diluted with brine (20 mL) and extracted with dichloromethane (5 × 20 mL). The combined organic layers were dried with sodium sulfate, concentrated to dryness, and subjected to column chromatography on silica gel (hexane/ethyl acetate, 6:1) to give **8a** (166 mg; 51 %) as a light yellow solid. M.p. 84–86 °C. ¹H NMR (CDCl₃, 300 MHz): δ = 0.97 (t, *J* = 7.4 Hz, 3H), 1.38–1.56 (m, 2H), 1.74–1.85 (m, 2H), 2.80 (t, *J* = 7.9 Hz, 2H), 3.87 (s, 3H), 7.01 (d, *J* = 8.9 Hz, 2H), 7.14 (dd, *J* = 5.0 Hz, 3.7 Hz, 1H), 7.29 (s, 1H), 7.45 (dd, *J* = 5.0 Hz, 1.1 Hz, 1H), 8.08 (dd, *J* = 3.7 Hz, 1.1 Hz, 1H), 8.14 ppm (d, *J* = 8.9 Hz, 2H); ¹³C NMR (CDCl₃, 75 MHz): δ = 13.9 (CH₃), 22.5 (CH₂), 30.9 (CH₂), 37.8 (CH₂), 55.4 (CH₃), 111.6 (CH), 114.1 (CH), 128.0 (CH), 128.5 (CH), 128.7 (CH), 129.2 (CH), 129.5 (C_{quat.}), 144.4 (C_{quat.}), 161.0 (C_{quat.}), 161.8 (C_{quat.}), 163.1 (C_{quat.}), 171.4 ppm (C_{quat.}); EI-MS (70 eV): *m/z* (%): 324 [M]⁺ (2); 309 [M−CH₃]⁺ (4); 295 [M−C₂H₅]⁺ (7); 282 [M−C₃H₆]⁺ (100); elemental analysis calcd (%) for C₁₉H₂₀N₂OS (324.3): C 70.34, H 6.21, N 8.63, S 9.88; found: C 69.95, H 6.17, N 8.59, S 9.86.

Received: May 18, 2005

Published online: October 5, 2005

Keywords: C–C coupling · carbonylation · heterocycles · multicomponent reactions · natural products

- [1] For reviews, see, for example, a) “The Pyrimidines”: D. J. Brown in *The Chemistry of Heterocyclic Compounds*, Vol. 16 (Ed.: A. Weissberger), Wiley-Interscience, New York, **1970**; b) “Fused Pyrimidines, Part II, The Purines”: J. H. Lister in *The Chemistry of Heterocyclic Compounds*, Vol. 24 (Eds.: A. Weissberger, E. C. Taylor), Wiley-Interscience, New York, **1971**; c) M. G. Hoffmann in *Houben-Weyl, Methoden der Organischen Chemie*, Vol. E9 (Ed.: E. Schaumann), Thieme, Stuttgart, **1996**; d) D. T. Hurst in *An Introduction to the Chemistry and Biochemistry of Pyrimidines, Purines and Pteridines*, Wiley, Chichester, **1980**; e) J. T. Bojarski, J. L. Mokrosz, H. J. Bartón, M. H. Paluchowska, *Adv. Heterocycl. Chem.* **1985**, 38, 229; f) D. J. Brown in *Comprehensive Heterocyclic Chemistry*, Vol. 3 (Eds.: A. R. Katritzky, C. W. Rees), Pergamon, Oxford, **1984**, chap. 2.13.
- [2] For the significance of 2,4-disubstituted pyrimidines as tyrosine kinase inhibitors see, for example, a) P. Traxler, G. Bold, E. Buchdunger, G. Caravatti, P. Furet, P. Manley, T. O'Reilly, J. Wood, J. Zimmermann, *Med. Res. Rev.* **2001**, 21, 499; b) J.

- Zimmermann, E. Buchdunger, H. Mett, T. Meyer, N. B. Lydon, *Bioorg. Med. Chem. Lett.* **1997**, 7, 187.
- [3] L. H. Franco, E. Joffé, L. Puricelli, M. Tatian, A. M. Seldes, J. A. Palermo, *J. Nat. Prod.* **1998**, 61, 1130.
- [4] M. L. Gompel, M. Leost, E. B. D. K. Joffe, L. Puricelli, L. H. Franco, J. Palermo, L. Meijer, *Bioorg. Med. Chem. Lett.* **2004**, 14, 1703.
- [5] a) N. B. Perry, L. Ettouati, M. Litaudon, J. W. Blunt, M. H. G. Munro, S. Parkin, H. Hope, *Tetrahedron* **1994**, 50, 3987; b) G. Trimurtulu, D. J. Faulkner, N. B. Perry, L. Ettouati, M. Litaudon, J. W. Blunt, M. H. G. Munro, G. B. Jameson, *Tetrahedron* **1994**, 50, 3993.
- [6] D. Fernández, A. Ahaidar, G. Danelón, P. Cironi, M. Marfil, O. Pérez, C. Cuevas, F. Albericio, J. A. Joule, M. Álvarez, *Monatsh. Chem.* **2004**, 135, 615.
- [7] a) M. Álvarez, D. Fernández, J. A. Joule, *Tetrahedron Lett.* **2001**, 42, 315; b) A. Ahaidar, D. Fernández, G. Danelón, C. Cuevas, I. Manzanaraes, F. Albericio, J. A. Joule, M. Álvarez, *J. Org. Chem.* **2003**, 68, 10020.
- [8] B. Jiang, C. Yang, *Heterocycles* **2000**, 53, 1489.
- [9] a) P. M. Fresneda, P. Molina, S. Delgado, J. A. Bleda, *Tetrahedron Lett.* **2000**, 41, 4777; b) P. Molina, P. M. Fresneda, S. Delgado, J. A. Bleda, *Tetrahedron Lett.* **2002**, 43, 1005; c) P. Molina, P. M. Fresneda, S. Delgado, *J. Org. Chem.* **2003**, 68, 489.
- [10] P. M. Fresneda, P. Molina, J. A. Bleda, *Tetrahedron* **2001**, 57, 2355.
- [11] a) A. S. Karpov, T. J. J. Müller, *Org. Lett.* **2003**, 5, 3451; b) A. S. Karpov, T. J. J. Müller, *Synthesis* **2003**, 2815.
- [12] D. M. Ketcha, G. W. Gribble, *J. Org. Chem.* **1985**, 50, 5451.
- [13] a) T. Kobayashi, M. Tanaka, *J. Chem. Soc. Chem. Commun.* **1981**, 333; b) K. Okuro, M. Furuune, M. Enna, M. Miura, M. Nomura, *J. Org. Chem.* **1993**, 58, 4716; c) L. Delude, A. M. Masdeu, H. Alper, *Synthesis* **1994**, 1149; d) B. C. Bishop, K. M. J. Brands, A. D. Gibb, D. J. Kennedy, *Synthesis* **2004**, 43.
- [14] A. Arcadi, S. Cacchi, F. Marinelli, P. Pace, G. Sanzi, *Synlett* **1995**, 823.
- [15] M. S. M. Ahmed, A. Mori, *Org. Lett.* **2003**, 5, 3057.
- [16] B. Witulski, N. Buschmann, U. Bergsträsser, *Tetrahedron* **2000**, 56, 8473.
- [17] 3-Iodoindoles were obtained in almost quantitative yields as beige solids still containing traces of DMF and can be stored without decomposition at 0 °C under nitrogen. However, it is advisable to convert them directly to the more stable *N*-Boc-protected 3-iodoindoles **4**, which were isolated as colorless solids by column chromatography on neutral aluminium oxide (column chromatography on silica gel leads to red color and accelerates the decomposition).
- [18] Colorless crystal (polyhedron), dimensions 0.40 × 0.30 × 0.24 mm³, triclinic, *P*1, *Z* = 2, *a* = 9.8618(5), *b* = 10.0262(5), *c* = 11.1585(6) Å, α = 107.5620(10), β = 103.5130(10), γ = 103.2620(10)°, *V* = 967.76(9) Å³, ρ = 1.175 g cm⁻³, *T* = 200(2) K, θ_{max} = 26.39°, MoK α radiation, λ = 0.71073 Å, 0.3° θ scans with CCD area detector, covering a whole sphere in reciprocal space, 9354 reflections measured, 3954 unique (*R*_{int} = 0.0282), 2889 observed (*I* > 2σ(*I*)), intensities were corrected for Lorentz and polarization effects, an empirical absorption correction was applied using SADABS (program SADABS V2.03 for absorption correction, G. M. Sheldrick, Bruker Analytical X-ray-Division, Madison, Wisconsin, **2001**) based on the Laue symmetry of the reciprocal space, μ = 0.14 mm⁻¹, *T*_{min} = 0.95, *T*_{max} = 0.97, structure solved by direct methods and refined against *F*² with a full-matrix least-squares algorithm using the SHELXTL-PLUS (5.10) software package (software package SHELXTL V5.10 for structure solution and refinement, G. M. Sheldrick, Bruker Analytical X-ray-Division, Madison, Wisconsin, **1997**), 223 parameters refined, hydrogen atoms were treated using appropriate riding models, goodness of fit 1.05 for observed reflections, final residual values *R*1(*F*) = 0.045, *wR*(*F*²) = 0.110 for observed reflections, residual electron density −0.30 to 0.27 e Å⁻³.
- [19] CCDC-278205 (**5d**) contains the supplementary crystallographic data for this paper. These data can be obtained free of charge from the Cambridge Crystallographic Data Centre via www.ccdc.cam.ac.uk/data_request/cif.
- [20] The kinase inhibition assays were carried out in collaboration with Merck KGaA as described in S. P. Davies, H. Reddy, M. Caivano, P. Cohen, *Biochem. J.* **2000**, 351, 95.

Aluminum Clusters

DOI: 10.1002/anie.200500671

Al₂₀Cp₈*X₁₀ (X = Cl, Br): Snapshots of the Formation of Metalloid Clusters from Polyhedral Al_nX_m Molecules?**Jean Vollet, Ralf Burgert, and Hansgeorg Schnöckel***Dedicated to Professor Peter Paetzold
on the occasion of his 70th birthday*

Two subgroups of Al-metal clusters with a predominant number of metal–metal bonds are known:^[1] “naked” metal-atom clusters, which are produced from solid metal by laser ablation techniques, and metalloid clusters, which are formed in solution starting with Al^I species and, for example, subsequent reduction.^[2,3] Here we present Al₂₀Cp₈*Br₁₀ (**1**) and Al₂₀Cp₈*Cl₁₀ (**2**) (Cp* = pentamethylcyclopentadienyl), two compounds of molecular, partially substituted subhalides belonging to the second group, which at first glance seem related to the species Al₁₃I_x[−]^[4] and Al₁₄I_x[−]^[5] (x = 1–12), which were generated in mass-spectrometric experiments. In both sets of compounds the halogen atoms form direct bonds to the Al atoms of the icosahedral Al₁₂ cluster core. However, quantum-chemical calculations for “naked” anionic clusters, for example, the Al₁₃I_x[−] anion mentioned above, indicate that an additional Al atom is located in the center.

The structures of **1** and **2** are furthermore closely related to those of the recently characterized Al₂₂X₂₀ compounds (X = Cl, Br), for example, Al₂₂Br₂₀ (**3**)^[6] because their cluster

[*] Dr. J. Vollet, R. Burgert, Prof. Dr. H. Schnöckel
Institut für Anorganische Chemie
Universität Karlsruhe (TH)
Engesserstrasse, Geb. 30.45, 76128 Karlsruhe (Germany)
Fax: (+49) 721-608-4854
E-mail: Hansgeorg.Schnoeckel@chemie.uni-karlsruhe.de

[**] We thank the Deutsche Forschungsgemeinschaft, the Center for Functional Nanostructures (CFN), and the Fonds der Chemischen Industrie for financial support.



Supporting information for this article is available on the WWW under <http://www.angewandte.org> or from the author.

centers contain icosahedral Al_{12} moieties without an additional Al atom. On the basis of the structural characterization of **1** and **2** the attempt will be made in the following a) to understand the formation of the $\text{Al}_{22}\text{X}_{20}$ species, as such intermediates are potential building blocks for a conceivable metastable non-metallic β -modification of aluminium;^[7] and b) to identify similarities and differences of the Al_{20} clusters (**1** and **2**) and the Al_n clusters and their reaction products (e.g. with I_2), which were studied spectroscopically by Castleman et al.^[5]

When freshly sublimed $[\{\text{AlCp}^*\}_4]^{[8]}$ and freshly isolated $[\{\text{AlBr}_2\text{NEt}_3\}_4]$ (**4**)^[9] were heated in heptane, the pale yellow suspension slowly turned orange, an initially beige precipitate turned brown, and finally Al metal precipitated. From this reaction mixture an orange heptane extract was obtained, from which orange crystals of **1** precipitated. Yellow crystals of $[\{\text{AlBr}_2\text{NEt}_3\}_2]$ (**5**) and colorless crystals of $[\text{AlBr}_3\text{NEt}_3]$ (**6**) were also obtained (see the Supporting Information).^[10]

The chloride analogue **2** of **1** is formed by adding MgCp_2^* to a solution of “ $\text{AlCl}\cdot\text{Et}_2\text{O}$ ”, in which the proportion of ether has been reduced by several evacuation steps (see the Experimental Section). By means of evacuation, we thought that an ether-stabilized chloride analogous to **4** should be generated in situ, but this has not yet been isolated.

Crystal structure analysis for **1** and **2** proves^[10] that both compounds have an almost regular icosahedron in the center with an average Al–Al distance of 268.5 pm (Figure 1). Structurally the central Al_{12} icosahedron consists of four Al^{I} atoms, which are coordinated terminally by a halogen atom, and eight Al^{II} atoms, which are coordinated exclusively to an exohedral Al atom. Each of the eight exohedral Al atoms bears a Cp^* ligand. While two ligand-bearing Al atoms are additionally terminally coordinated by halogen atoms, two pairs of the remaining six exohedral Al atoms are singly bridged and one pair is doubly bridged by halogen atoms. In summary, the Al_{12} icosahedron is surrounded by four halogen atoms, six $\text{Al}^{\text{II}}\text{BrCp}^*$ units, and two $\text{Al}^{\text{I}}\text{Cp}^*$ moieties. So in principle 26 skeletal electrons are available for the central Al_{12} icosahedron ($4 \times 2 e^-$ for bromine-bearing Al atoms + $6 \times 2 e^-$ for $\text{Al}^{\text{II}}\text{BrCp}^*$ -bearing Al atoms + and $2 \times 3 e^-$ for $\text{Al}^{\text{I}}\text{Cp}^*$ -coordinated Al atoms). In accordance with Wade's Rules^[11] this results in the bonding situation of a *closo* cluster. All relevant structural information for **1** and **2** is contained in Table 1 and in the Tables in the Supporting Information. The distances and bonding relationships in the Al_{12} icosahedron are in accordance with those of the $\text{Al}_{12}\text{R}_{12}^{2-}$ anion (268.6 pm, $\text{R} = i\text{Bu}$)^[12] and the $\text{Al}_{22}\text{X}_{20}$ species (270.1 pm).^[6,7] Furthermore the experimentally determined distances listed in Table 1 agree well with those calculated.^[13]

The observed ^{27}Al NMR spectra of **1** and **2** in solution each show only two signals, although in theory at least six different signals are expected (see the Supporting Information). The observed signals for **1** are in good agreement with calculated values,^[13] and those for **2** show the expected shift to

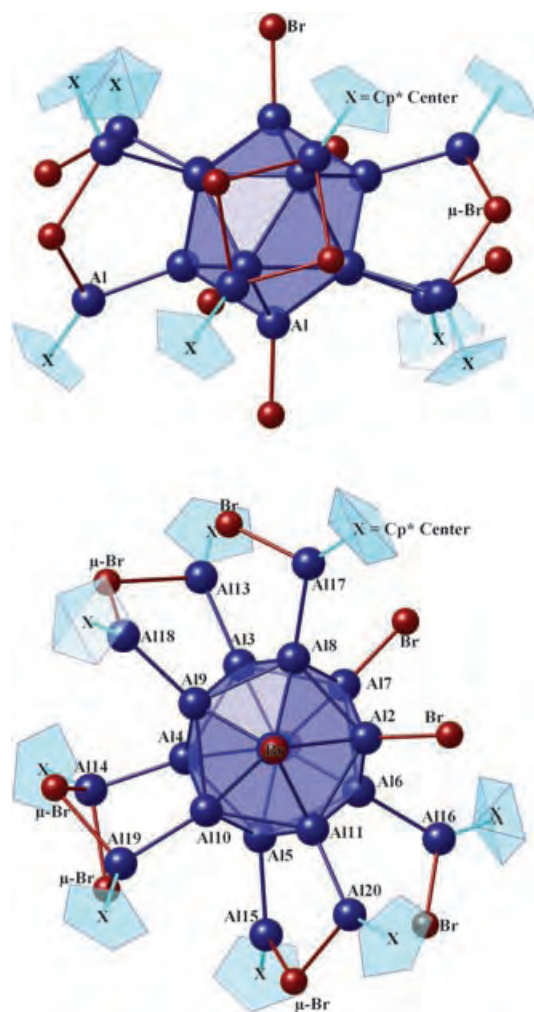


Figure 1. Side and top view of **1**. Cp^* groups are represented in simplified form for clarity.

Table 1: Average distances (min./max.) [pm] in **1** and **2**.

Distances ^[a]	1 (X = Br)	2 (X = Cl)	Calcd 2 ^[b]
$\text{Al}_{\text{ico}}-\text{Al}_{\text{ico}}$	268.43 (264.1/272.9)	268.47 (264.1/272.9)	270.43 (265.5/276.4)
$\text{Al}_{\text{ico}}-\text{Al}_{\text{Cp}^*}$	253.89 (250.1/256.8)	253.29 (250.0/255.7)	256.34 (253.5/258.2)
$\text{Al}_{\text{ico}}-\text{X}_{\text{term.}}$	231.13 (230.6/231.4)	218.63 (218.1/219.9)	220.20 (219.8/220.6)
$\text{Al}_{\text{Cp}^*}-\text{X}_{\text{bridg.}}$	265.53 (256.1/275.9)	244.55 (237.4/252.3)	250.48 (246.7/253.2)
$\text{Al}_{\text{Cp}^*}-\text{X}_{\text{term.}}$	242.05 (240.7/243.4)	223.05 (221.7/224.4)	227.40 (227.4/227.4)
$\text{Al}_{\text{Cp}^*}-\text{Cp}_{\text{cen}}$	191.28 (188.8/197.1)	191.28 (188.2/195.1)	194.98 (192.9/200.4)
$\text{Al}_{\text{Cp}^*}-\text{C}_{\text{CS}}$	226.10 (213.4/243.8)	225.74 (213.1/241.7)	230.24 (217.0/248.2)

[a] Al_{ico} : Al atom of the icosahedral moiety; Al_{Cp^*} : exohedral Al atom; $\text{X}_{\text{term.}}$: terminally coordinated halogen atom; $\text{X}_{\text{bridg.}}$: μ -bridging halogen atom; Cp_{cen} : Cp-disk centroid; C_{CS} : Cp-ring carbon atom.

[b] Calculated with DFT methods, see ref. [13].

lower frequencies (compared to **1**; see the Supporting Information).

The recently reported formation of $\text{Al}_{22}\text{X}_{20}$ species^[6,7] (e.g. **3**) has been described generally as the phenomenon of internal disproportionation: starting from metastable AlX solutions, 22 AlX molecules provide the twelve Al^{I} atoms of the icosahedral center and the ten peripheral AlX_2 units of this cluster species (Figure 2). In the compounds **1** and **2** the

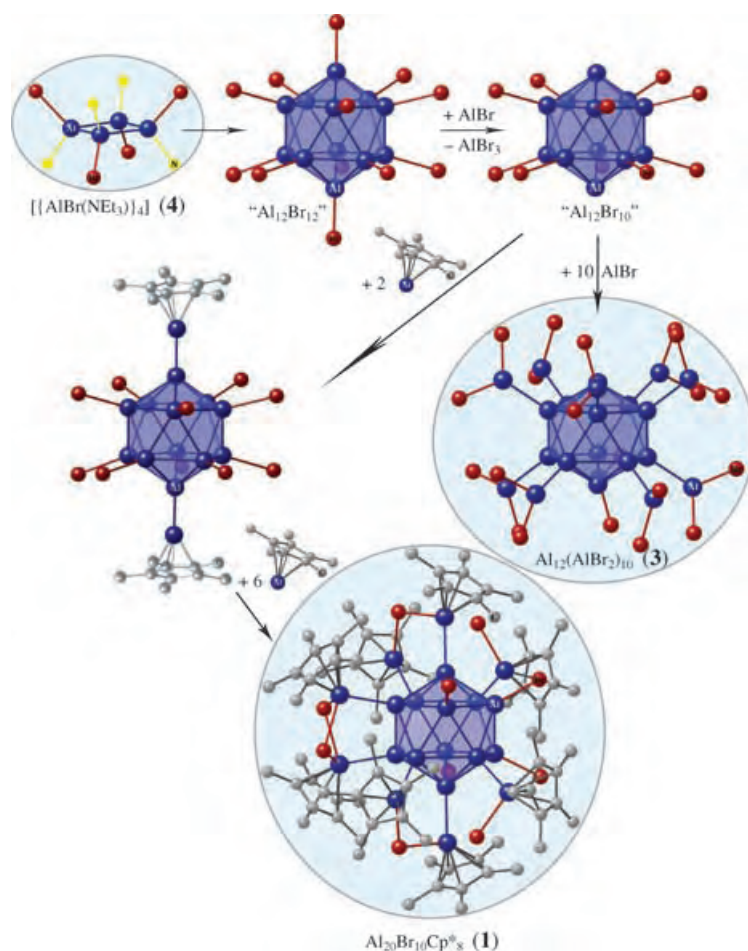


Figure 2. Mechanism of the formation of **1** and the subhalide **3** starting with compound **4** based on experimental findings and quantum-chemical calculations. These three compounds (colored background) were structurally characterized; all other species were calculated.

first halogen atoms coordinated directly to an Al_{12} icosahedron are observed. The synthesis of **1** furthermore succeeds only^[14] if one starts with the distinct halide $[\text{AlBr}(\text{NEt}_3)]_4$ (**4**).^[9] Therefore we propose the mechanism of formation for the compounds **3** and **1** (and **2**) represented in Figure 1, in which the dehalogenation of **4** to give **1** could occur also as a result of an excess of AlCp^* .^[15] The isolation of **1** and **2** makes the intermediacy of an $\text{Al}_{12}\text{Br}_{12}$ species (in the disproportionation of AlX) seem feasible;^[16] the $\text{Al}_{12}\text{Br}_{12}$ species could react to give $\text{Al}_{22}\text{Br}_{20}$, **3**, or compound **1**, depending on the reaction conditions (Figure 2).

Apart from the relevance of **1** and **2** to the understanding of the formation of an $\text{Al}_{22}\text{X}_{20}$ species, our results are of broader significance: They again indicate that the assumption that there are at least two different ways to reach the bulk phase of aluminium, which we presented earlier,^[6,7,17] is correct. The first pathway (a) leads via Al-centered clusters to metallic Al. A second reaction channel (b) leads via Al_n clusters with an icosahedral Al_{12} center (without a central Al atom as in, for example, **3**) towards a hypothetical novel, non-metallic modification of Al (β -Al).

With regards to pathway (a): All metalloid Al clusters with stabilizing $\text{N}(\text{SiMe}_3)_2$ ligands which are formed eventually in the disproportionation of AlX ($3\text{AlX} \rightarrow 2\text{Al} + \text{AlX}_3$) on the way to the metal^[2,3,18] are part of this class.^[2] Moreover the “naked” Al_n clusters observed in mass-spectrometric studies^[4,5] should be mentioned here, of which the icosahedral Al_{13}^- cluster with a central Al atom is especially frequent. The formation of the latter clusters,^[19] which basically can be considered as evaporation products of the bulk phase, happens in the opposite direction of the formation of metalloid clusters. Nevertheless, along both directions Al-centered species are obviously preferred.^[20]

With regards to pathway (b): The possibility of the formation of a metastable, non-metallic β -Al modification (equivalent to the α -boron structure) based on a $\text{Al}_{22}\text{X}_{20}$ species (e.g. **3**) with a noncentered icosahedral Al_{12} core has been discussed and made plausible by quantum-chemical calculations.^[21] If we partly insert sterically demanding groups such as AlCp^* into the Al–Br bonds of the hypothetical halide intermediate “ $\text{Al}_{12}\text{Br}_{12}$ ” presented in Figure 2, compound **1** is formed. Very similar conditions result in the formation of the $\text{Al}_{50}\text{Cp}^*_{12}$ cluster with its noncentered Al_8 core and its shell of twelve Cp^* units, which inhibits further reaction towards elemental aluminium.^[22] This metalloid Al_{50} cluster with its singular structure as well as the compounds **1** and **2** discussed here can be regarded as “molecular dead-ends”, that is, snapshots of the complex reaction events of metastable AlX species on their way towards elemental aluminium via a hypothetical β -modification which is made possible only by ligand stabilization.

For the first time the degree of complexity of such reaction pathways becomes rudimentally evident through the isolation of the intermediates **1** and **2** as well as mass-spectrometric investigations. These initial results hint at the challenges to be overcome in synthesis, spectroscopy, and theory to thoroughly understand these reaction mechanisms.

Experimental Section

1: Freshly sublimed $[\text{AlCp}^*]_4$ (0.7 g, 1.1 mmol) was mixed with $[\text{AlBr}(\text{NEt}_3)]_4$ (1.34 g, 1.6 mmol) in 50 mL of *n*-heptane. The initially pale yellow suspension was stirred for 12 h, and then a beige precipitate formed. After heating for 3 h at 60 °C the precipitate turned brown, and an Al mirror formed on the inner surface of the reaction vessel. The reaction suspension was cooled and filtered, and an orange heptane extract was obtained. At –30 °C rod-shaped orange crystals of **1** (150 mg, 0.057 mmol) grew overnight. Additionally yellow needle-shaped crystals of $[\text{AlBr}_2(\text{NEt}_3)]_2$ **3** and colorless crystals of **4** could be isolated. ¹H NMR (250 MHz, C_6D_6): δ = 1.72 ppm (s, 120H); ¹³C NMR (63 MHz, C_6D_6): δ = 11.7 (Me_5C_5) and 115.1 ppm (Me_5C_5); ²⁷Al NMR (78 MHz, C_7D_8): δ = –14 and –55 ppm.

2: A solution of “ $\text{AlCl} \cdot \text{Et}_2\text{O}$ ” in toluene (43 mL, 0.38 M, 25 vol % Et_2O , $\omega(\text{AlCl})$ = 92 %, 15 mmol) was concentrated continuously in vacuo between –50 and –40 °C for 8 h. MgCp^*_2 (4.42 g, 15 mmol) was dissolved in toluene and cooled to –78 °C. The “ $\text{AlCl} \cdot \text{Et}_2\text{O}$ ” solution in toluene with a reduced ether component was added dropwise to the second solution at –78 °C with stirring. The crimson reaction mixture was warmed to –30 °C and stirred for 3 h. Afterwards all volatile components were removed, and the residue was washed with a small amount of *n*-pentane to give the crude $[\text{AlCp}^*]_4$ product (1.8 g).

Tiny red crystals grew from the red pentane extract, and by careful, continuous concentration of the pentane solution crystals of **2** suitable for structural analysis could be isolated (90 mg, 0.044 mmol). ^1H NMR (300 MHz, C_6D_6): δ = 1.90 ppm (s, 120H, calc. 1.90 ppm); ^{13}C NMR (63 MHz, C_6D_6): δ = 15.1 (Me_5C_5 , calc. 14.6), 117.5 ppm (Me_5C_5 , calc. 118.0); ^{27}Al NMR (78 MHz, C_6D_6): δ = 88, 37, and –27 ppm.

Received: February 22, 2005

Revised: June 6, 2005

Published online: October 10, 2005

Keywords: aluminum · cluster compounds · halogens · metallocenes · structure elucidation

- [1] F. A. Cotton, *Q. Rev. Chem. Soc.* **1966**, 20, 397.
- [2] A. Schnepf, H. Schnöckel, *Angew. Chem.* **2002**, 114, 3683; *Angew. Chem. Int. Ed.* **2002**, 41, 3532.
- [3] H. Schnöckel, A. Schnepf, *Adv. Organomet. Chem.* **2001**, 47, 235.
- [4] D. E. Bergeron, P. J. Roach, A. W. Castleman Jr., N. O. Jones, S. N. Khanna, *Science* **2005**, 307, 231.
- [5] D. E. Bergeron, A. W. Castleman, T. Morisato, S. N. Khanna, *Science* **2004**, 304, 84.
- [6] C. Klemp, R. Köppe, E. Weckert, H. Schnöckel, *Angew. Chem.* **1999**, 111, 1851; *Angew. Chem. Int. Ed.* **1999**, 38, 1740.
- [7] C. Klemp, M. Bruns, J. Gauss, U. Häussermann, G. Stöber, L. van Wuelen, M. Jansen, H. Schnöckel, *J. Am. Chem. Soc.* **2001**, 123, 9099.
- [8] C. Dohmeier, C. Robl, M. Tacke, H. Schnöckel, *Angew. Chem.* **1991**, 103, 594; *Angew. Chem. Int. Ed. Engl.* **1991**, 30, 564.
- [9] M. Mocker, C. Robl, H. Schnöckel, *Angew. Chem.* **1994**, 106, 1860; *Angew. Chem. Int. Ed. Engl.* **1994**, 33, 862.
- [10] Crystal structure data of **1** ($[\text{Al}_{20}\text{Cp}_8^*\text{Br}_{10} \cdot 2n\text{-C}_7\text{H}_{16}]$): $Z = 2$, $M_w = 2620.86 \text{ g mol}^{-1}$, crystal dimensions: $0.65 \times 0.5 \times 0.2 \text{ mm}^3$, triclinic, space group $P\bar{1}$, $a = 18.9019(6)$, $b = 13.0056(4)$, $c = 24.6656(8) \text{ Å}$, $\alpha = 80.523(3)^\circ$, $\beta = 84.549(2)^\circ$, $\gamma = 90.231(2)^\circ$, $V = 5952.6(3) \text{ Å}^3$, $\rho_{\text{calc}} = 1.462 \text{ g cm}^{-3}$, $F(000) = 2652$, $T = 150(2) \text{ K}$, $\mu(\text{MoK}\alpha) = 3.553 \text{ mm}^{-1}$, 35320 reflections, 15611 independent ($R_{\text{int}} = 0.0368$), refinement on F^2 ($2\theta_{\text{max}} = 46.24^\circ$), 14556 independent (2σ), 1597 parameters, 0 restraints, $R_1(I > 2\sigma(I)) = 0.0343$, wR_2 (all data) = 0.0933, GooF (F^2) = 1.045, $\rho(\text{min/max}) = -0.559/0.835 \text{ e Å}^{-3}$; unit cell determination: 63356 reflections; Lorentz, polarization, and numerical absorption correction: $T_{\text{min}}/T_{\text{max}} = 0.1316/0.4191$; **2** ($[\text{Al}_{20}\text{Cp}_8^*\text{Cl}_{10} \cdot n\text{-C}_5\text{H}_{12}]$): $Z = 4$, $M_w = 2048.01 \text{ g mol}^{-1}$, crystal dimensions: $0.2 \times 0.15 \times 0.1 \text{ mm}^3$, monoclinic, space group $P2(1)/c$, $a = 12.9034(7)$, $b = 26.7258(11)$, $c = 31.431(3) \text{ Å}$, $\beta = 95.129(6)^\circ$, $V = 10795.8(12) \text{ Å}^3$, $\rho_{\text{calc}} = 1.260 \text{ g cm}^{-3}$, $F(000) = 4288$, $T = 150(2) \text{ K}$, $\mu(\text{MoK}\alpha) = 0.460 \text{ mm}^{-1}$, 25241 reflections, 13269 independent ($R_{\text{int}} = 0.0928$), refinement on F^2 ($2\theta_{\text{max}} = 44.58^\circ$), 6331 independent (2σ), 1045 parameters, 0 restraints, $R_1(I > 2\sigma(I)) = 0.0546$, wR_2 (all data) = 0.1309, GooF (F^2) = 0.834, $\rho(\text{min/max}) = -0.282/0.366 \text{ e Å}^{-3}$; unit cell determination: 10839 reflections; Lorentz, polarization, and numerical absorption correction: $T_{\text{min}}/T_{\text{max}} = 0.7954/0.9623$; **5** ($[\text{AlBr}_2\text{-NEt}_3]_2$): $Z = 8$, $M_w = 575.98 \text{ g mol}^{-1}$, crystal dimensions: $0.6 \times 0.6 \times 0.2 \text{ mm}^3$, orthorhombic, space group $Pna2(1)$, $a = 14.8678(9)$, $b = 20.6342(12)$, $c = 14.4841(11) \text{ Å}$, $V = 4443.5(5) \text{ Å}^3$, $\rho_{\text{calc}} = 1.772 \text{ g cm}^{-3}$, $F(000) = 2256$, $T = 199(2) \text{ K}$, $\mu(\text{MoK}\alpha) = 7.319 \text{ mm}^{-1}$, 30477 reflections, 8594 independent ($R_{\text{int}} = 0.0675$), refinement on F^2 ($2\theta_{\text{max}} = 51.88^\circ$), 7271 independent (2σ), 362 parameters, 1 restraint, $R_1(I > 2\sigma(I)) = 0.0378$, wR_2 (all data) = 0.0913, GooF (F^2) = 0.967, $\rho(\text{min/max}) = -0.542/1.156 \text{ e Å}^{-3}$; unit cell determination: 8000 reflections; Lorentz, polarization, and numerical absorption correction: $T_{\text{min}}/T_{\text{max}} = 0.0423/0.2916$; **6** ($[\text{AlBr}_3\text{-NEt}_3]$): $Z = 2$, $M_w = 367.90 \text{ g mol}^{-1}$, crystal dimensions: $0.4 \times 0.3 \times 0.2 \text{ mm}^3$, monoclinic, space group $P2(1)$, $a = 7.2921(11)$, $b = 11.8660(16)$, $c = 7.9135(12) \text{ Å}$, $\beta = 117.907(11)^\circ$, $V = 605.11(15) \text{ Å}^3$, $\rho_{\text{calc}} = 2.019 \text{ g cm}^{-3}$, $F(000) = 352$, $T = 293(2) \text{ K}$, $\mu(\text{MoK}\alpha) = 10.024 \text{ mm}^{-1}$, 2706 reflections, 2112 independent ($R_{\text{int}} = 0.0669$), refinement on F^2 ($2\theta_{\text{max}} = 52.14^\circ$), 2004 independent (2σ), 101 parameters, 1 restraint, $R_1(I > 2\sigma(I)) = 0.0513$, wR_2 (all data) = 0.1346, GooF (F^2) = 1.050, $\rho(\text{min/max}) = -0.719/0.695 \text{ e Å}^{-3}$; unit cell determination: spherical absorption correction. Diffractometer: $\lambda = 0.7103 \text{ Å}$, Stoe-IPDS-2-area detector (IPDS), two-circle goniometer; Software: SHELXS-97, SHELXL-97, Stoe-IPDS software; structural refinement with direct methods, H atoms calculated. CCDC-263377 (**1**), CCDC-263378 (**2**), CCDC-263375 (**5**), and CCDC-263376 (**6**) contain the supplementary crystallographic data for this paper. These data can be obtained free of charge from the Cambridge Crystallographic Data Centre via www.ccdc.cam.ac.uk/data_request/cif.
- [11] K. Wade, *J. Chem. Soc. Chem. Commun.* **1971**, 792; K. Wade, *Adv. Inorg. Radiochem.* **1976**, 18, 1.
- [12] K. W. Klinkhammer, W. Uhl, J. Wagner, W. Hiller, *Angew. Chem.* **1991**, 103, 182; *Angew. Chem. Int. Ed. Engl.* **1991**, 30, 179.
- [13] The ab initio calculations for compound **2** were carried out with the TURBOMOLE program package: O. Treutler, R. Ahlrichs, *J. Chem. Phys.* **1995**, 102, 346. The geometry was optimized with the RI-DFT module: a) K. Eichkorn, O. Treutler, H. Öhm, M. Häser, R. Ahlrichs, *Chem. Phys. Lett.* **1995**, 242, 652; b) K. Eichkorn, F. Weigend, O. Treutler, R. Ahlrichs, *Theor. Chim. Acta* **1997**, 97, 119. The BP86 functional with SVP basis sets was used for all chemical elements: c) A. D. Becke, *Phys. Rev. A* **1998**, 38, 3098; d) J. P. Perdew, *Phys. Rev. B* **1996**, 33, 8822. Calculations of NMR shifts were carried out with the MPSHIFT module with the GIAO method on the SCF level, using SCF molecular orbitals with the molecular geometry obtained by DFT methods: e) G. Schreckenbach, T. Ziegler, *J. Phys. Chem.* **1995**, 99, 606; f) M. Häser, R. Ahlrichs, H. P. Baron, P. Weiss, H. Horn, *Theor. Chim. Acta* **1992**, 83, 455.
- [14] The synthesis also succeeded when the donor component of the AlCl solution was reduced at low temperatures in vacuo; see the Experimental Section.
- [15] This type of dehalogenation has been described for the formation of $\text{SiAl}_4\text{Cp}_6^*$ from halogenated precursors: A. Purath, C. Dohmeier, A. Ecker, R. Köppe, H. Krautscheid, H. Schnöckel, R. Ahlrichs, C. Stoermer, J. Friedrich, P. Jutzi, *J. Am. Chem. Soc.* **2000**, 122, 6955.
- [16] Here connections to boron chemistry with its $\text{B}_{12}\text{X}_{12}$ cages and the groundbreaking work of W. Uhl on the $\text{Al}_{12}\text{R}_{12}$ dianion ($\text{R} = \text{isobutyl}$, see ref. [12]) become apparent.
- [17] H. Schnöckel, C. Klemp in *Inorganic Chemistry Highlights* (Eds.: G. Meyer, D. Naumann, L. Wesemann), Wiley-VCH, Weinheim, **2002**, p. 245.
- [18] For example, $\text{Al}_{77}(\text{N}(\text{SiMe}_3)_2)_{20}^{2-}$: A. Ecker, E. Weckert, H. Schnöckel, *Nature* **1997**, 387, 379.
- [19] The energy difference between the more stable icosahedral Al_{13} cluster and the cuboctahedral Al_{13} cluster is only about 55 kJ mol^{-1} according to quantum-chemical calculations. Thus it can be expected that different conditions, for example, in solution or in the gas phase could yield cuboctahedral as well as icosahedral Al_{13} species: R. Ahlrichs, S. D. Elliott, *Phys. Chem. Chem. Phys.* **1999**, 1, 13.
- [20] This statement can, for example, be supported by the structures of both the Al_{14}I anion, which was detected by mass spectrometry and calculated using quantum-chemical methods (see ref. [5]), and of the metalloid cluster $[\text{Al}_{14}\text{I}_6\text{R}_6]^{2-}$ ($\text{R} = \text{N}[\text{SiMe}_3]_2$), because both structures with their centered arrangement of Al atoms show similarities to the bulk phase (see the Supporting Information). $[\text{Al}_{14}\text{I}_6\text{R}_6]^{2-}$: H. Köhnlein, G. Stöber, E. Baum, E.

Möllhausen, U. Huniar, H. Schnöckel, *Angew. Chem.* **2000**, *112*, 828; *Angew. Chem. Int. Ed.* **2000**, *39*, 799.

- [21] a) After the isolation of a $\text{Ga}_{24}\text{X}_{22}$ halide, a hypothetical new gallium modification was recently proposed in a similar thought experiment using quantum-chemical calculations: T. Duan, E. Baum, R. Burgert, H. Schnöckel, *Angew. Chem.* **2004**, *116*, 3252; *Angew. Chem. Int. Ed.* **2004**, *43*, 3190; b) U. Häussermann, S. I. Simak, R. Ahuja, B. Johansson, *Phys. Rev. Lett.* **2003**, *90*, 065701.

- [22] J. Vollet, J. R. Hartig, H. Schnöckel, *Angew. Chem.* **2004**, *116*, 3248; *Angew. Chem. Int. Ed.* **2004**, *43*, 3186.

Quality counts...

The best of chemistry every week



Wiley-VCH

P.O. Box 10 11 61
69451 Weinheim
Germany

Phone +49 (0) 6201-606-400

Fax +49 (0) 6201-606-184

e-mail: angewandte@wiley-vch.de

www.angewandte.org

Angewandte Chemie International
Edition is a journal of the GDCh,
the German Chemical Society

GDCh



WILEY-VCH